



Hastecs : Hybrid aircraft : research on thermal and electric components and systems

Xavier Roboam, Sarah Touhami, Najoua Erroui, Amal Zeaiter, Flavio Accorinti, Philippe Collin, Matthieu Pettes-Duler

► To cite this version:

Xavier Roboam, Sarah Touhami, Najoua Erroui, Amal Zeaiter, Flavio Accorinti, et al.. Hastecs : Hybrid aircraft : research on thermal and electric components and systems. 2021. hal-03407214

HAL Id: hal-03407214

<https://ut3-toulouseinp.hal.science/hal-03407214>

Submitted on 28 Oct 2021

HAL is a multi-disciplinary open access archive for the deposit and dissemination of scientific research documents, whether they are published or not. The documents may come from teaching and research institutions in France or abroad, or from public or private research centers.

L'archive ouverte pluridisciplinaire **HAL**, est destinée au dépôt et à la diffusion de documents scientifiques de niveau recherche, publiés ou non, émanant des établissements d'enseignement et de recherche français ou étrangers, des laboratoires publics ou privés.



Distributed under a Creative Commons Attribution - NonCommercial 4.0 International License

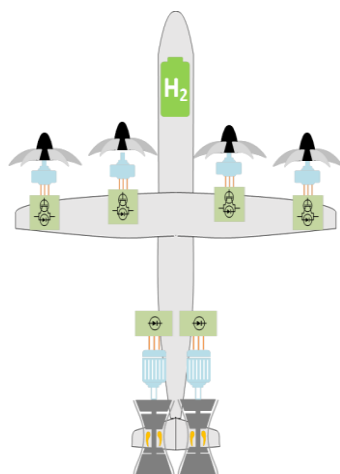


Université
de Toulouse

The Book



HASTECS: Hybrid Aircraft: reSearch on Thermal and Electric Components and Systems



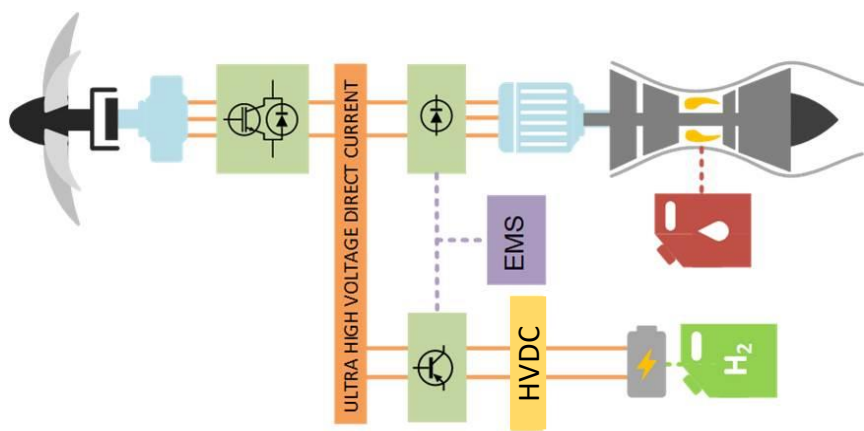
This project has received funding from the [European Union's Horizon 2020 (cleansky 2 JTI) research and innovation programme, 2014-2024] under grant agreement No 715483

November 2021

THE HASTECS BOOK



HASTECS: Hybrid Aircraft: reSearch on Thermal and Electric Components and Systems



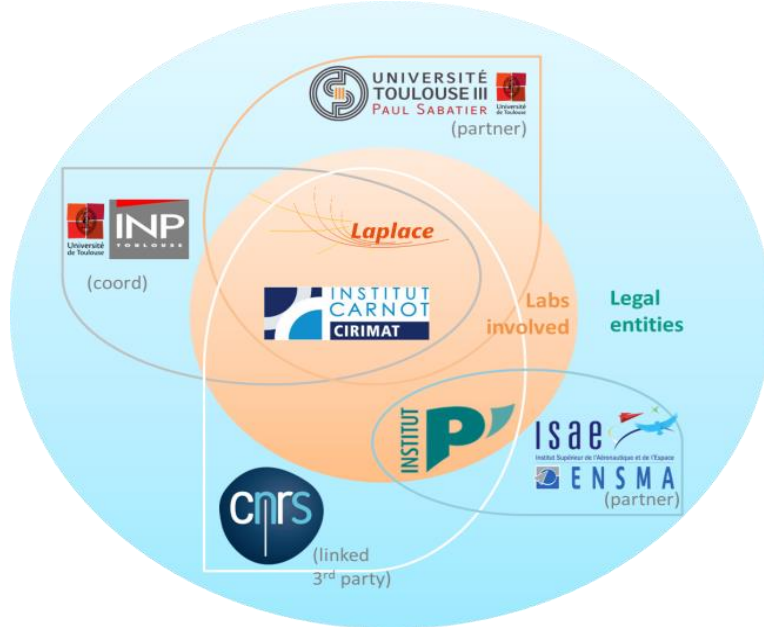
motors
cooling
power
discharges
partial
hybrid
design
electrical
propulsion
powertrain
electronics



This project has received funding from the [European Union's Horizon 2020 (Cleansky 2 JTI) research and innovation programme, 2014-2024] under grant agreement No 715483

November 2021

THE HASTECS BOOK



The research consortium

LAPLACE Lab, Université de Toulouse:

M. Banda (Post Doc), J. P. Cambronne, P. Collin (Phd Student), S. Dutour, N. Erroui (Phd Student), G. Gateau, Y. Lefevre, J.F. Llibre, D. Malec, M. Miscevic, M. Pettes-Duler (Phd Student), X. Roboam, N. Roux, B. Sareni, M. Tognan (Post Doc), S. Touhami (Phd Student), C. Turpin

Pprime institute, ISAE-ENSMA Poitiers:

F. Accorinti (Phd Student), V. Ayel, Y. Bertin, M. Fenot, E. Videcoq, A. Zeaiter (Phd Student)

CIRIMAT Lab, Université de Toulouse:

P. Simon

Coordinator (contact person) : xavier.roboam@laplace.univ-tlse.fr



This project has received funding from the [European Union's Horizon 2020 (Cleansky 2 JTI) research and innovation programme, 2014-2024] under grant agreement No 715483

November 2021

Contents of HASTECS Book

Content of the book	P4
Foreword	P5
Thesis 1: "Analytical Sizing Models to Assess the Performances of High Specific Power Electric Motors for Hybrid Aircraft", Sarah Touhami, Thesis of Toulouse INP defended , Sept 2020	16
Thesis 2: High power conversion chain for hybrid aircraft propulsion, Najoua Erroui, Thesis of Toulouse INP defended , Nov 2019	P157
Thesis 3: Thermal modelling and cooling of electric motors. Application to the propulsion of hybrid aircraft , Amal Zeaiter Thesis of ENSMA Poitiers defended , Oct 2020	P311
Thesis 4: Flavio Accorinti, "Two-Phase Power Electronics Cooling Solution Design in Air Context Answering to the Objectives of the Hybrid Aircraft 2035", Thesis of ENSMA Poitiers defended June 2020.	P551
Thesis 5: Philippe Collin, "Design taking into account the partial discharges phenomena of the Electrical Insulation System of high power electrical motors for hybrid electric propulsion for future aircrafts.	P884
Post Doc 1: Mallys E. Banda, Partial discharge (DP) prevention within power converter busbars dedicated to hybrid aircraft propulsion, LAPLACE-UPS2019	P1086
Post Doc 2: Malik Tognan, "Preliminary delivery Battery & Fuel Cell metamodels; HASTECS "M6.1 Technical report", LAPLACE-Toulouse INP, March 2019.	P1086
Thesis 6: Matthieu Pettes Duler, "integrated optimal design of the propulsive system for a regional hybrid electric aircraft	P1157



**Project title: Hybrid Aircraft,
academic reSearch on Thermal and Electrical Components and Systems**

Project Number: [715483]

Project Acronym: [HASTECS]

Foreword

1. Context of the HASTECS project
2. Objectives and main results
3. HASTECS references

The Airbus Vision: "written by our topic leader, September 2021"

"Through recent communications, it has been announced that AIRBUS is willing to prepare the future aeronautical landscape in order to cope with the new and future regulations in terms of decarbonization. In this frame, a huge effort of roadmapping in order to set the right performance targets of the technological bricks is mandatory. Moreover, the interdependence between systems pushes in the direction of an overall optimization of the propulsive electrical chain. It allows to maximize the performance, not directly at sub-system level but at architecture level, in order to take in consideration several physical fields such as electrical but also cooling, mechanical; under constraints of integration, safety etc... For this reason, the collaboration with the academic Hastecs project has been highly valuable for AIRBUS. Each work-package, which covers the development of a key technological brick seen as enablers for the future aircraft development, has performed a tremendous amount of work to deliver valuable analysis and sizing tools for each brick. Each of these tools has been internally used to better understand the technology and understand the limits which have to be considered for the future aircraft. Finally, the model integration platform developed by the work-package 6 allows one to better understand the way to proceed to optimize a propulsive electrical powertrain."

1 Context of the HASTECS project

1.1 Which context for hybrid electric architecture towards future "greener aircrafts" ?

In 2019, transportation was the fastest growing sector, contributing to environmental degradation. Finding sustainable solutions that pollute less is a key element in solving this problem, particularly for the aviation sector, which accounts for around 2-3% of global CO₂ emissions. With the advent of Covid-19, air traffic seems to have come to a fairly permanent halt, but this pandemic reinforces the need to move towards a "cleaner sky" and respect for the environment, which is the objective of the Clean Sky2 program (H2020 EU), the context in which the HASTECS project has been launched in September 2016.

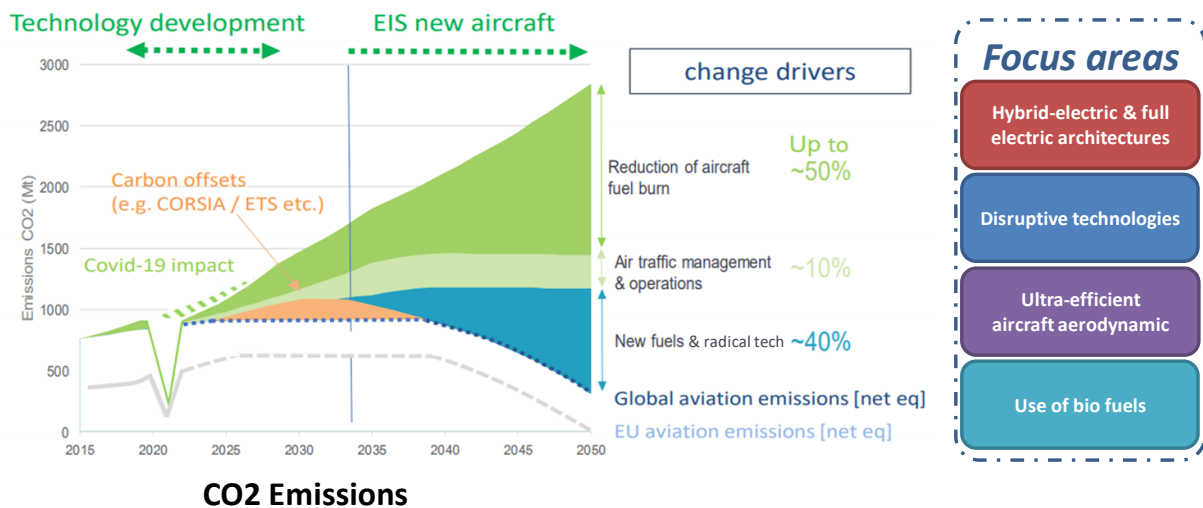


Figure 1: environmental challenges and main drivers

Reduced/Zero emission propulsion system:

- Much less noise,
- More precision and dynamics in the control,
- Less maintenance,
- Safer architectures (Distributed electric propulsion),
- Increased efficiency leading to reduced fuel consumption,
- Appearance of new vertical take-off and landing architectures,



Figure 2: main objectives for the current project of hybrid electric and electric aircrafts

The Figure 2 emphasizes that several issues have to be addressed for numerous innovative aircraft concepts also existing or to be designed from more electric (hybrid electric) to full electric architectures.

1.2 The HASTECS project

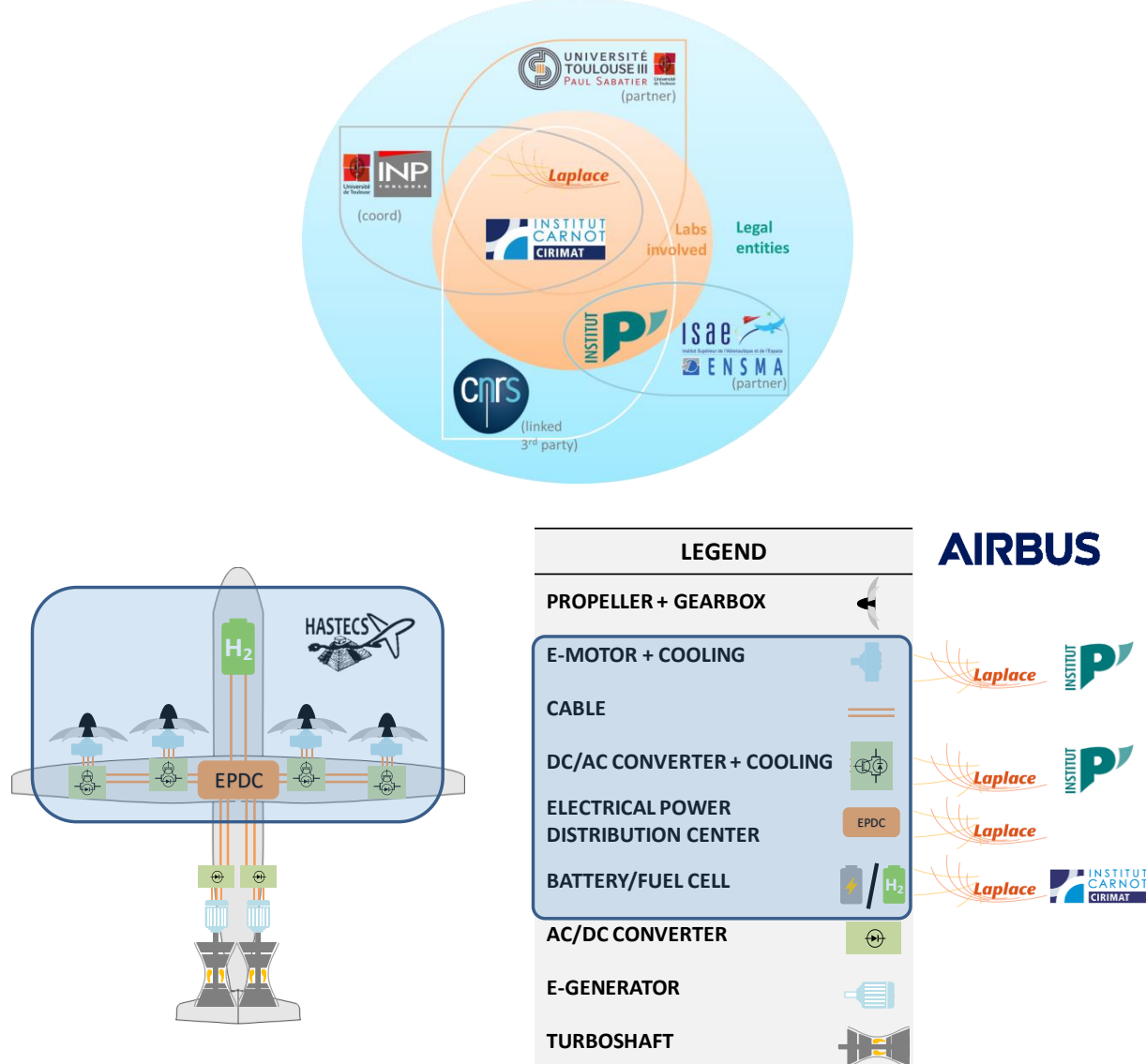


Figure 3: HASTECS scope and partnership

In that context, the HASTECS scope has been focused on the electromechanical powertrain dedicated to a series hybrid architecture of a regional aircraft: 70 pax, short range: 500-600nm with a propulsion power beyond 5MW. Airbus was at the origin of the call for proposal in cooperation with the Cleansky II JU and has leaded the project driving the research consortium with requirements and design choices: among them, the choice of a series hybrid architecture involving the most ambitious technological breakthrough towards high power high voltage powertrain with 100% of electric propulsion. Main requirements with the propulsion power mission was also originally assessed by Airbus.

The project was coordinated by Toulouse INP with the structure illustrated on the figure 3 emphasizing the involvement of three French research labs:

4. The LAPLACE lab (<http://www.laplace.univ-tlse.fr/>) in the “université de Toulouse”, involving 5 different and complementary research teams in the framework of energy conversion;
5. The Pprime institute (<https://pprime.fr/>) in ISAE-ENSMA of Poitiers, was involved on thermal management;

- The Cirimat lab (<https://cirimat.cnrs.fr/>) in the “université de Toulouse” with an expertise on high energy density batteries.

2 Objectives and main results

2.1 The HASTECS targets and objectives

As implicitly said in its acronym, the main objective of HASTECS (for Hybrid Aircraft Academic reSearch on Thermal and Electrical Components and Systems) was to couple thermal and electrical studies within the hybrid electric propulsion chain of a regional aircraft, by integrating the environmental constraints (in particular partial discharges) specific to the aviation sector.

Thus, the main challenges were related to:

- High specific power electric motors: towards and beyond 10kW/kg for 2035 !
- Highly integrated power electronics: towards and beyond 25kW/kg for 2035 !
- High efficient motor and power electronic cooling solutions: the thermal challenge!
- Facing partial discharges in electric motors and power electronics for ultra HVDC bus
- Future trends of new technologies for batteries and fuel cells
- System integration of the overall hybrid power chain

The aim was to identify the most promising technologies and breakthroughs and to develop the tools that will significantly increase the compactness and efficiency of the electrical processes within the hybrid propulsion chain. In our case, only series hybrid electric architecture was studied in this project, as it leads to a high dimensioning power maximizing the technological constraints on the chain.

The technological targets originally set in HASTECS, considered under two horizons (2025 then 2035), were the following:

	2025 target	2035 target
Electric motor + cooling system		
Specific power	5 kW/kg	10 kW/kg
Cruise efficiency	96%	98.5%
Maximal design point efficiency	94.5%	97%
Power electronics + cooling system		
Specific power	15 kW/kg	25 kW/kg
Cruise efficiency	98%	99.5%
Maximal design point efficiency	96.5%	99%

7 main technical objectives were proposed in the Description of Work. It can be concluded that, after closing the HASTECS project, the main results are roughly on line with those objectives:

Objective 1: to develop a “target setting tool” that helps to assess electric machine design for hybrid electric propulsion. The main goal is to analyse which phenomena actually limit the specific power of electrical machines and to propose technological and structural (geometry) innovations;

*Objective 2: to propose and analyse original **machine cooling solutions** aiming at fitting the challenging dissipation threshold*

Performance indicator (common for Objective 1 and 2): electric machine design including cooling with a 10kW/kg specific power in 2035, also called “2035 target”.

Objective 3: to develop sizing trends of static converters for a hybrid electric propulsion system. To define two or three levels of DC bus standards for which every component will be designed; the first at a "moderated voltage" (~700V); the second (and potentially third) at few kVs (<7kV)

Objective 4: to provide cooling and heat exchanger system solutions for power electronic converters
Performance indicator (common with Objective 3): *power converters including cooling with a 25kW/kg specific power in 2035*

Objective 5: to take into account the partial discharges phenomenon and to assess impacts in the design of the power electronics and electric machines of the Hybrid Electric Propulsion System

Performance indicator:

- a) *For power electronics in fuselage, zero partial discharge operation will be targeted*
- b) *For electric insulation of stator windings, partial discharges are unavoidable in non-pressurized zones; being impossible to define a quantitative indicator (lifetime, reliability) a reference design will be set and comparative analysis for machine reliability will be proposed*

Objective 6: to develop simplified models for the most promising technologies of auxiliary sources (Lithium Ion batteries, fuel cells) for 2035

Performance indicator: *assessments of specific power (kW/kg) and specific energy (kWh/kWh) targets.*

Objective 7: to integrate technological bricks (machines, power electronics, cables, storage components, cooling system) and new concepts proposed in other WPs, by taking account of external advances (other CS2 projects,...), then to optimize the overall hybrid chain integrating its power management strategy.

Performance indicator: *significant decrease of fuel burn (this indicator will be assessed on Airbus FPO tools; it means that the developed meta-models will be integrated in Airbus tools for global performance assessments)*

2.2 Main results on HASTECS

2.2.1. A real technological and scientific success

On Friday April 23, 2021, the last of the 6 doctoral thesis was defended, with also two post-doctorates associated, thus bringing a very fine finish to a scientific adventure particularly rich in results and scientific exchanges.

It should be noted from the outset that all of the project's expectations have been fulfilled. In particular, the targets in terms of specific power (power - mass ratio) and energy efficiency were even exceeded, which "would contribute to the weight loss and efficiency of a future aircraft"!: HASTECS is therefore a real technological and scientific success, punctuated by an abundant scientific production (~34 publications in conferences and scientific journals: see section 3) with the teams and research institutes of the consortium, bringing successful interdisciplinary research.



Figure 4: 6 doctoral students for 6 Work Packages: "very collaborative work for an integrated project"

2.2.2 High performance electric motors

The design of electric motors carried out by the GREM3 team of LAPLACE leads to high specific powers, exceeding 11kW/kg by integrating the cooling system, with high efficiencies, greater than 97%. This design has been obtained thanks to high performance permanent magnet synchronous motor with Halbach structure. The optimization under constraints of current densities, magnetic fields and the increase in rotation speeds are key drivers to which has been added the use of special windings (compact rectangular Litz wires) and high performance ultra-thin magnetic sheets to limit high frequency copper losses and iron losses: this is what makes it possible to obtain excellent efficiencies exceeding 97%. But optimising the electromechanical conversion is nothing without an equally powerful cooling system. This is the case of the concepts proposed by l'institut P' which combine glycol water cooling for the stator and the rotor, to which it was necessary to couple an internal cooling, directly within stator slots, to achieve such specific powers.

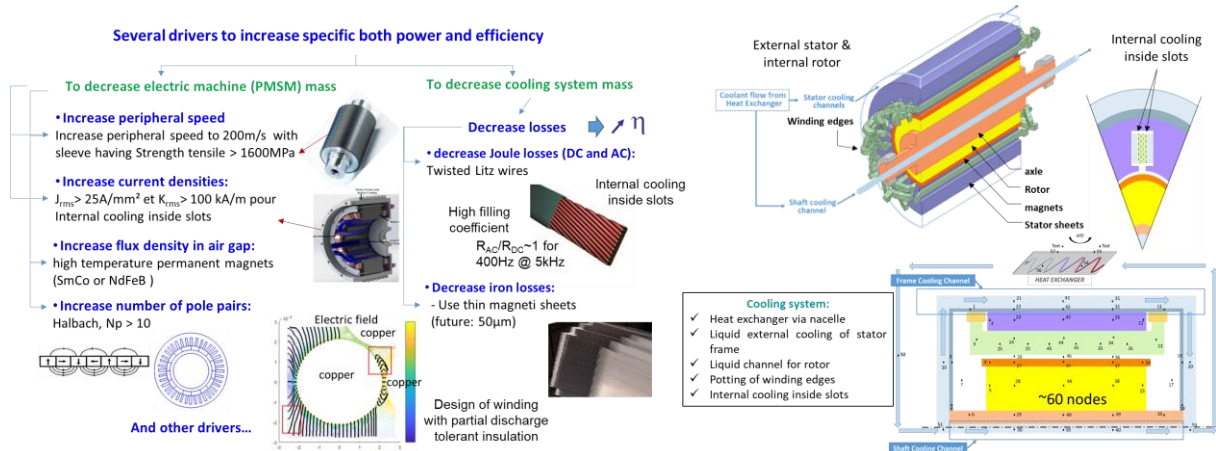


Figure 5: Electric motor: left - high density magnet synchronous machine design levers; right: internal and external engine cooling

2.2.3. Optimisation of power electronics and high voltage network

In order to efficiently convert the power between the electric distribution (high voltage DC bus) and the electric motors, solutions have been proposed by the “Convertisseur Statique” team at LAPLACE to optimise the integration of power electronics. The joint use of a high voltage bus (close to 2kV), with its optimised mechanical structure (bus bar), the best electronic components (7th generation IGBTs) and modulation strategies also optimised for various multilevel conversion structures has proven to be particularly effective in terms of compactness and efficiency (yield of the order of 99%). As with the machine, optimising the power electronics is nothing without a very high performance cooling system. This is the case with the concepts studied by the l'institut P' and the GREPHE team at LAPLACE, which proposed ultra-efficient two-phase capillary pumped cooling systems: the device is capable of extracting 4.5kW of heat losses for 1 kg of cooling system, allowing the complete power conversion system to greatly exceed 30kW/kg, well beyond the targets set!

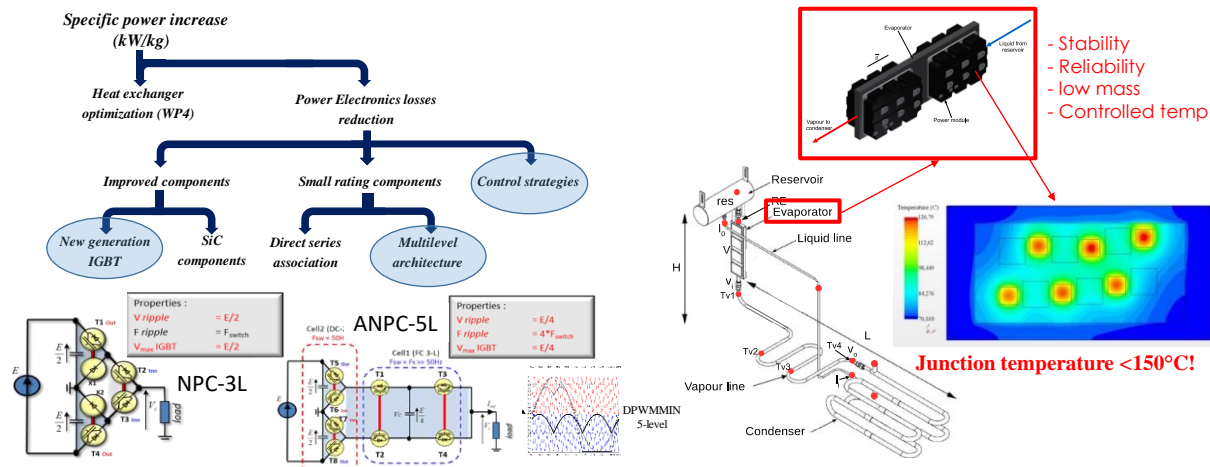


Figure 6: Power electronics: left - multi-cellular structures; right: two-phase cooling by CPLIP (capillary pumped loop for integrated power)

2.2.4. Fuel cells 2 times more compact in specific energy than the best "energy batteries" by 2030.

A study carried out jointly by CIRIMAT and LAPLACE (GENESYS group) also concerned the auxiliary electrical sources hybridized with thermal sources (gas turbine): the conclusions show that, for this case of application to series hybrid regional aircraft, fuel cells with cryogenic hydrogen storage (stored at 20°K in liquid form) are almost twice as compact in specific energy (Wh/kg) than the best “energy batteries” by 2030.

A promising device !

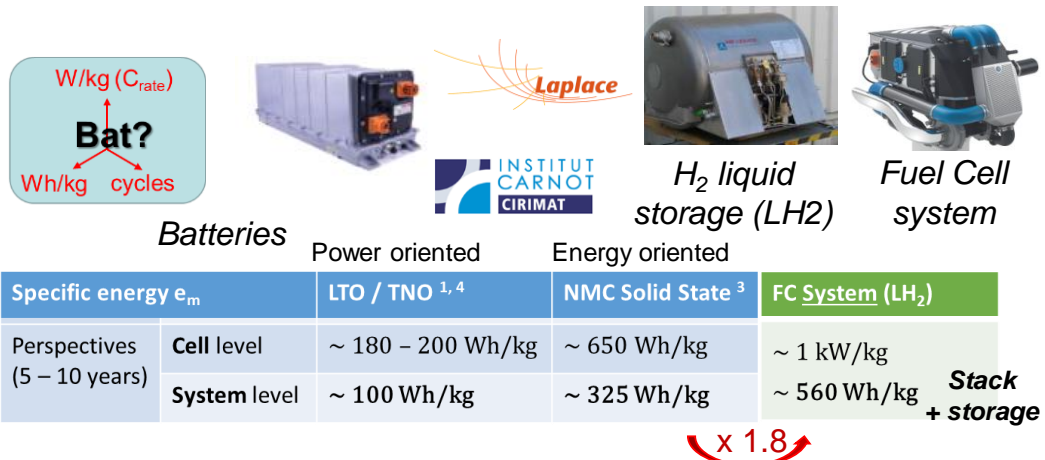


Figure 7: Auxiliary electrical sources

2.2.5. Optimized system integration: an improved compromise between on-board weight and kerosene consumption

Finally, one of the major expectations of the HASTECS project was the definition of the voltage level of the electric distribution (HVDC bus) which constitutes a significant coupling factor on the mass of the main components (electrical machine, power electronics, wiring, etc.) by integrating environmental constraints specific to aeronautics. In this context, an in-depth study on the impact of partial discharges in the electrical machines insulators and power electronics was carried out by the MDCE team of LAPLACE. In the end, the best system compromise on the choice of this voltage is between 1300 and 2000V. This result could not be obtained without the overall optimisation of the propulsion chain carried out by the GENESYS team at LAPLACE: all the technological choices and scientific concepts were integrated through surrogate models making it possible to offer a global vision on the complete propulsion chain, from sources to propellers.

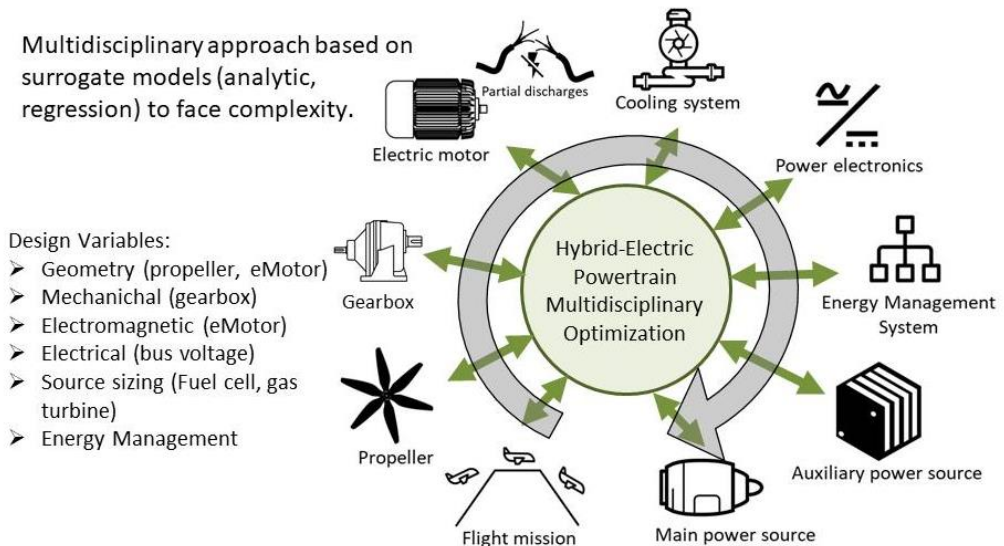


Figure 8: Optimal design of the complete hybrid electric propulsion chain

Ultimately, these optimized integration results lead to an improved compromise between on board mass and kerosene consumption compared to the targets initially set for the project.

3 HASTECS references

3.2 Thesis and post-doctoral reports

Thesis 1: S. Touhami, "Analytical Sizing Models to Assess the Performances of High Specific Power Electric Motors for Hybrid Aircraft," PhD Thesis, Institut National Polytechnique de Toulouse (Toulouse INP), 2020. <https://oatao.univ-toulouse.fr/28218/>

Thesis 2: N. Erroui, "Chaine de conversion forte puissance pour la propulsion aéronautique hybride," PhD Thesis, Institut National Polytechnique de Toulouse (Toulouse INP), 2019. https://oatao.univ-toulouse.fr/25529/1/Erroui_najoua.pdf

Thesis 3: A. Zeaiter, "Thermal modeling and cooling of electric motors application to the propulsion of hybrid aircraft," PhD Thesis, Ecole Nationale Supérieure de Mécanique et d'Aérotechnique (ENSMA), 2020. <https://tel.archives-ouvertes.fr/tel-03158868/document>

Thesis 4: F. Accorinti, "Two-phase power electronics cooling solution design in air context answer to the objectives of the hybrid aircraft 2035.," PhD Thesis, Ecole Nationale Supérieure de Mécanique et d'Aérotechnique (ENSMA), 2020. <https://tel.archives-ouvertes.fr/tel-02993195/document>

Thesis 5: P. Collin "Design, taking into account the partial discharges phenomena, of the electrical insulation system (eis) of high power electrical motors for hybrid electric propulsion of future regional aircrafts," PhD Thesis, Institut National Polytechnique de Toulouse (Toulouse INP), 2020. <http://thesesups.ups-tlse.fr/4730/1/2020TOU30116.pdf>

Thesis 6 M. Pettes Duler, "Integrated optimal design of a hybrid-electric aircraft powertrain," PhD Thesis, Institut National Polytechnique de Toulouse (Toulouse INP), 2021. https://oatao.univ-toulouse.fr/28350/1/Pettes_Duler_Matthieu.pdf

Post Doc 1: M. Tognan, Battery & Fuel Cell state of the art & metamodels; 'HASTECS Technical report, 2019.

Post Doc 2: M E Banda, D Malec and JP Cambronne, "Partial discharge (DP) prevention within power converter busbars dedicated to hybrid aircraft propulsion, HasteCS technical report, 2018.

3.3 HASTECS publications:

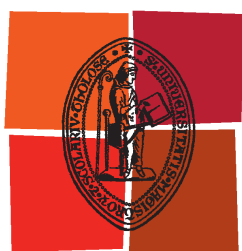
More than 40 references with 9 published in journals and 25 in conferences

Title	Authors	Published in	Repository Link
Lumped Parameter Thermal Model of Permanent Magnet Synchronous Machines	Touhami, Sarah; Bertin, Yves; Lefèvre, Yvan; Libre, Jean-François; Henaux, Carole; Fenot, Matthieu	Electrimacs 2017 conference, Toulouse, France. pp. 1-6.	https://hal.archives-ouvertes.fr/hal-01649396
Pré-dimensionnement de convertisseur de très forte puissance pour une application à la propulsion aéronautique hybride	Erroui, Najoua; Gateau, Guillaume; Roux, Nicolas	JCGE Conference, France, 2017	http://oatao.univ-toulouse.fr/19276/
Continuous-caliber semiconductor components	Najoua Erroui, Guillaume Gateau, Nicolas Roux	2018 IEEE International Conference on Industrial Technology (ICIT)	http://oatao.univ-toulouse.fr/20155/1/Erroui_20155.pdf

Thermal Sensitivity Analysis of a High Power Density Electric Motor for Aeronautical Application	Amal Zeaiter, Matthieu Fenot	2018 IEEE International Conference on Electrical Systems for Aircraft, Railway, Ship Propulsion and Road Vehicles & International Transportation Electrification Conference (ESARS-ITEC)	https://hal.archives-ouvertes.fr/hal-02086508/document
Numerical Approach to Determining Windings' Thermal Conductivity	Amal Zeaiter, Matthieu Fenot, Didier Saury	2018 XIII International Conference on Electrical Machines (ICEM)	https://hal.archives-ouvertes.fr/hal-02086510/document
Tool to Design the Primary Electrical Insulation System of Low Voltage Rotating Machines Fed by Inverters	Collin Philippe, Malec David, Lefevre Yvan	2018 IEEE Electrical Insulation Conference (EIC)	https://hal.archives-ouvertes.fr/hal-02185431
Simulation of Space Charge Impact on Partial Discharge Inception Voltage in Power Busbars Dedicated to Future Hybrid Aircrafts	Mallys Elliazar Banda, David Malec, Jean-Pascal Cambronne	Scientific research journal: Circuits and Systems, November 2018	https://hal.archives-ouvertes.fr/hal-02182458
Partial discharge risk under space charges generation and transport effects	M. E. Banda, D. Malec, Jean-Pascal Cambronne	Comsol International Conference, Lausanne 2018.	https://hal.archives-ouvertes.fr/hal-02182467
Joint Design of Halbach Segmented Array and Distributed Stator Winding	S. Touhami, Y. Lefevre, J. F. Llibre	2018 XIII International Conference on Electrical Machines (ICEM)	https://hal.archives-ouvertes.fr/hal-01885526v1
Performance assessment tool based on loadability concepts	Yvan Lefevre, Sami El-Aabid, Jean-François Llibre, Carole Henaux, Sarah Touhami	International Journal of Applied Electromagnetics and Mechanics	https://hal.archives-ouvertes.fr/hal-02326544v1
Design of Electric Machine Taking Into Account the Partial Discharges Phenomena for Future Hybrid Propelled Aircrafts	Collin, Philippe; Touhami, Sarah; Malec, David; Lefèvre, Yvan; Llibre, Jean-François	Proceedings of More Electric Aircraft - MEA 2019	https://hal.archives-ouvertes.fr/hal-02279651
Steady-state analysis of a Capillary Pumped Loop for Terrestrial Application with methanol and ethanol as working fluids	Flavio Accorinti, Vincent Ayel, Yves Bertin	International Journal of Thermal Sciences, Volume 137, March 2019, Pages 571-583	https://hal.archives-ouvertes.fr/hal-02284906
Outil d'aide au design du système d'isolation primaire de machines tournantes basse tension alimentées par onduleur	Collin, Philippe and Malec, David and Lefèvre, Yvan	SFE 2018 : 11ème conférence de la Société Française d'Electrostatique, 29 August 2018 - 31 August 2018 (Grenoble, France)	https://oatao.univ-toulouse.fr/23397/
Analyse de sensibilité d'un système de propulsion hybride électrique pour des futurs aéronefs	Matthieu Pettes-Duler, Bruno Sareni, Xavier Roboam	JCGE Conference, Ile Oleron, France, 2019	https://hal.archives-ouvertes.fr/hal-02489965
Integrated design process and sensitivity analysis of a hybrid electric propulsion system for future aircraft	Plettes-Duler M; Roboam x, Sareni B	Electrimacs conference Salerno, Italy, May 2019. Springer, Lecture Notes in Electrical Engineering, ISSN: 1876-1100, Electrimacs Conf selected papers, Volume 604, Edited by Springer, April 2020	https://hal.archives-ouvertes.fr/hal-02489890
Sensitivity analysis of a hybrid-electric aircraft powertrain based on Sobol indices	Matthieu Pettes-Duler, Xavier Roboam, Bruno Sareni, Sarah Touhami, Yvan Lefèvre, et al.	AEC (Aerospace Europe Conference), conference, Bordeaux, February 2020.	https://hal.archives-ouvertes.fr/hal-02538619
High-efficiency cooling system for highly integrated power electronics for hybrid propulsion aircraft	Flavio Accorinti, Najoua Erroui, Vincent Ayel, Guillaume Gateau, Yves Bertin, Nicolas Roux, Sébastien Dutour, Marc Miscevic	2019 IEEE 28th International Symposium on Industrial Electronics (ISIE)	https://hal.archives-ouvertes.fr/hal-02417709/document
Original optimization Procedures of Halbach Permanent Magnet Segmented Array	Sarah Touhami, Yvan Lefevre, Jean-François Llibre	2019 19th International Symposium on Electromagnetic Fields in Mechatronics, Electrical	https://hal.archives-ouvertes.fr/hal-02544431v1

		and Electronic Engineering (ISEF)	
Electro thermal models and design approach for high specific power electric motor for hybrid aircraft	Sarah Touhami, Amal Zeaiter, Matthieu Fénot, Yvan Lefèvre, Jean-François Libre, Etienne Videcoq	Aerospace Europe Conference, Feb 2020, Bordeaux, France	https://hal.archives-ouvertes.fr/hal-02570637v1
About the relevance of using Paschen's criterion for partial discharges inception voltage (PDIV) estimation when designing the electrical insulation system of inverter fed motors	Philippe Collin, David Malec, Yvan Lefèvre	2019 IEEE Electrical Insulation Conference (EIC)	https://hal.archives-ouvertes.fr/hal-02568005/document
A general model to compute the electric flux lines in the slots of electric machines for the evaluation of partial discharge risk.	P Collin, D Malec, Y Lefèvre	COMPUMAG conference, June 2019, Paris, France	https://hal.archives-ouvertes.fr/hal-02330891/document
Tool to predict and avoid Partial Discharges in stator slot of rotating motors fed by inverter.	Philippe Collin, David Malec, Yvan Lefèvre	AEROSPACE EUROPE CONFERENCE, Feb 2020, Bordeaux, France	https://hal.archives-ouvertes.fr/hal-02568019/document
Full wave modulation applied to 3-level FC and NPC inverters	Najoua Erroui, Guillaume Gateau, Nicolas Roux	2019 IEEE International Conference on Industrial Technology (ICIT)	https://oatao.univ-toulouse.fr/24285/
Determination of electric motor losses and critical temperatures through an inverse approach	Amal Zeaiter, Etienne Videcoq, Matthieu Fénot,	Electrical Engineering, Springer Verlag,	https://hal.archives-ouvertes.fr/hal-03281064
Experimental and Numerical Analysis of Start-up of a Capillary Pumped Loop	Flavio Accorinti, Nicolas Blet, Vincent Ayel, Sébastien Dutour, Yves Bertin	International Heat Pipe Conference	https://asmedigitalcollection.asme.org/heattransfer/article/141/9/091813/955228/Experimental-and-Numerical-Analysis-of-Start-Up-of
Thermal management & advanced cooling technologies of power electronics converters for hybrid aircraft applications	V. Ayel, F. Accorinti, S. Dutour, Y. Bertin	invited paper in MEA (More Electric Aircraft Conference), Bordeaux 2021	https://hal.archives-ouvertes.fr/hal-03353052
"HASTECS": a typical MDO process for future greener Hybrid Electric Aircrafts	Xavier Roboam	invited paper in MEA (More Electric Aircraft Conference), Bordeaux 2021	https://hal-univ-tlse3.archives-ouvertes.fr/hal-03351918
A General Method to Compute the Electric Flux Lines between Two Magnet Wires in Close Contact and Its Application for the Evaluation of Partial Discharge Risks in the Slots of Electric Machines Embedded in Future Transportation Systems	Philippe Collin, David Malec, Yvan Lefèvre	Advances in Aerospace Science and Technology	https://www.scirp.org/journal/paperinfoformation.aspx?paperid=107607
Multidisciplinary Design Optimization of the actuation system of a hybrid electric aircraft powertrain	Matthieu Pettes-Duler, Xavier Roboam, Bruno Sareni, Yvan Lefèvre, Jean-François Libre, Matthieu Fénot	MDPI Journal, May 2021, 10, 1297, Special Issue "High-Performance Electric Drives for Transport Applications".	https://hal.archives-ouvertes.fr/hal-03274378
Analytical Sizing Models to Assess the Performances of High Specific Power Electric Motors for Hybrid Aircraft	Sarah Touhami		https://oatao.univ-toulouse.fr/28218/1/Touhami_Sarah.pdf
Power electronics cooling solution design in air context answering to the objectives of the hybrid aircraft.	Flavio Accorinti		https://tel.archives-ouvertes.fr/tel-02993195
Deux modèles dans une situation de physique : le cas de l'optique : difficultés des étudiants, points de vue des enseignants et propositions pour structurer des séquences d'enseignement	Philippe Colin		https://hal.archives-ouvertes.fr/LAPLACE_GREM3/tel-03124398
Thermal Modeling and Cooling of Electric Motors : Application to the Propulsion of Hybrid Aircraft	Amal Zeaiter	Amal Zeaiter 1 Etienne Videcoq 1 Matthieu Fénot 1	https://tel.archives-ouvertes.fr/tel-03158868
Thèse : High power conversion chain for hybrid aircraft propulsion	Najoua Erroui		https://oatao.univ-toulouse.fr/25529/1/Erroui_najoua.pdf

			f
'Conception intégrée du système propulsif d'un avion régional hybride électrique	M. Pettes Duler, X. Roboam, B. Sareni	REE (Revue d'Energie Electrique) N°5 2020	
Conception intégrée par optimisation de chaines de propulsion : de l'hybride à l'électrique	XAVIER ROBOAM, BRUNO SARENI, MATTHIEU PETTES-DULER	La Revue 3EI, Vol 105, Juillet 2021	https://hal.archives-ouvertes.fr/hal-03351918
A General Method to Compute the Electric Flux Lines between Two Magnet Wires in Close Contact and Its Application for the Evaluation of Partial Discharge Risks in the Slots of Electric Machines Embedded in Future Transportation Systems	Philippe Collin, David Malec, Yvan Lefevre	Advances in Aerospace Science and Technology, 2021, 6, 24-42, Vol.6 No.1, March 2021	
Effects of splitting and twisting conductors on the AC Joule losses	Sarah Touhami , Yvan Lefèvre , Jean-François Libre ,	CEFC 2020 - Nov 2020	https://hal.archives-ouvertes.fr/hal-03113631
Pré-dimensionnement d'un Moteur Electrique de Très Forte Puissance Spécifique pour Avion Hybride	Sarah Touhami, Yvan Lefèvre, Jean-François Libre	REE (Revue d'Energie Electrique) N°5 2020	



Université
de Toulouse

THÈSE

En vue de l'obtention du

DOCTORAT DE L'UNIVERSITÉ DE TOULOUSE

Délivré par :

Institut National Polytechnique de Toulouse (Toulouse INP)

Discipline ou spécialité :

Génie Electrique

Présentée et soutenue par :

Mme SARAH TOUHAMI

le mardi 15 septembre 2020

Titre :

Analytical Sizing Models to Assess the Performances of High Specific
Power Electric Motors for Hybrid Aircraft

Ecole doctorale :

Génie Electrique, Electronique, Télécommunications (GEET)

Unité de recherche :

Laboratoire Plasma et Conversion d'Energie (LAPLACE)

Directeur(s) de Thèse :

M. YVAN LEFEVRE

M. JEAN-FRANCOIS LLIBRE

Rapporteurs :

M. ABDELMOUNAIM TOUNZI, UNIVERSITE LILLE 1

M. JEAN-FREDERIC CHARPENTIER, ECOLE NAVALE

Membre(s) du jury :

M. NOUREDDINE TAKORABET, INP LORRAINE, Président

M. JEAN-FRANCOIS LLIBRE, UNIVERSITE TOULOUSE 2, Membre

Mme NATHALIE RAVEU, TOULOUSE INP, Membre

M. YVAN LEFEVRE, TOULOUSE INP, Membre

Acknowledgment

The presented works have been carried out in Grem3 "Electrodynamic research group" at LAPLACE Laboratory "Laboratory on Plasma and Conversion of Energy", National Polytechnic Institute of Toulouse, between December 2016 and July 2020 in the framework of the European research project "HASTCES" of Clean Sky 2 European research program.

First of all, I would like to express my grateful to my supervisors, M. Yvan Lefevre, CNRS research fellow and M. Jean François Llibre, Associate Professor for their guidance and knowledge and constructive criticism throughout the journey that was this thesis. I would also like to express my deepest thanks for their kindness, patience, help and encouragement.

I would like to thank the examiners Professor Abdelmounaïm Tounzi and HDR Assistant Professor Jean-Frédéric Charpentier, for having read and evaluated this thesis. I would like to express my gratitude to Professor Noureddine Takorabet for chairing the jury of this thesis. I am also thankful to Professor Nathalie RAVEU for reading and examining my thesis. I am very thankful to M. M. Matthieu Fénot, Xavier Roboam and M. Jean-François Allias for accepting to participate as guests of this jury.

I would like to thanks Associate Professors Ms. Carole Henaux and M. François Pigache, for giving me the teaching opportunity. I would like also thanks Clement Nadal Associate Professor, Youness Rtimi and Linda Serairi to share with me these teaching classes.

I would like also to express my special thankful to M. Dominique Harribey, Research Engineer CNRS for his huge kindness and for his sharing with me his technical knowledge. I am also grateful others Grem3 permanent members: Professor Frédéric Messine, Professor Jean-François Rouchon and Associate Professor Thomas Huguet for their kindness, their help and their good environment inside the research group Grem3.

I am very grateful to the IT Managers M. Jacques Benaioun and M. Patrick Ferre for their great helping with big smile every time when I have a IT problem. I am also very grateful to the laboratory secretary staff Ms. Valerie Schwartz, Ms. Carine Alibert, Ms. Catherine Moll Mozella, Ms. Ariane Arnaud and Ms. Jessica Toscano for their administrative help of my thesis management.

I would now like to specially thank Thao Le Luong to for sharing with me the desk, its friendship, its support and its delicious Vietnamese food that she sometimes cooked specially for me.

I would like to specially thank Amal Zeaiter, PhD student at P'prim laboratory for its thesis interactions, its friendship and its huge support. I am grateful also to Phillippe Collin for its helps and its well thesis interactions. I would like also express my grateful to others HASTCES project colleagues Najoua Erroui, Matthieu Pettes-Duler, Flavio Accorinti for their all constructive discussions.

I thank Maxime Bonnet and Theo Capri for their thesis contributions and for their constructive discussions. I thank also all PhD students: André Mrad, Jessica Neumann, Carvalho Costa Mateus.

Finally, I would like to express my deeping thankful to my lovely parents Omar and Rachida, my sister Yasmine and my brothers chiefly my younger brother Mustapha for their all patience and their always support me, hoping that they are proud of me.

**Thank you all.
Sarah Touhami**

Abstract

After the industrial and the environmental successes of hybridization railways transport, the hybridization of aviation transport is acquiring more and more consideration. In this context, the European Union in partnership with the aerospace manufacturers, has launched in 2014 a largest research program Clean Sky 2 aiming to reduce aircraft fuel consumptions and noise levels. Clean Sky 2 research program includes several projects among of them: Academic reSearch on Thermal & Electric Components & Systems "HASTECS project" which aims to identify and to develop the most promising technologies for decreasing the weight and increasing efficiency of hybrid propulsion chain. "HASTECS project" is organized around six Work Packages (WPs) dedicated to the components of hybrid propulsion chain, for instance, the WP1 is dedicated to electric motors and the WP3 is dedicated to their cooling systems.

Indeed, the estimated reduction fuel consumptions for a short range flight would be 3.5% if the specific power of electric machines and power converters with their cooling systems is respectively increased to 5kW/kg and 15kW/kg for 2025, and also increased to 10kW/kg and 25kW/kg for 2035.

The targets are significantly higher than those of today. Specific power planned of the industrial electric machines and power converters is higher than the currently one. However, these specific powers present some limitations which depend on the involved material properties and by environment conditions such as: thermal limitations and partial discharges risk.

For reaching targeted specific powers for instance in electric machines, the mechanical, electrical and the magnetic loads linked to the materials and cooling technologies must be increased. However, considering the limitations and the environment constraints, choice of loads should be adequate. Therefore, it is important to develop models and tools allowing assessing the actual and the future technologies which allow achieving the HASTECS targets.

The present thesis focuses to the development of models and tools for satisfying the HASTECS targets about the electric machines and their cooling systems. There are several different electric machine topologies, namely: radial flux machines, axial flux machines, permanent magnet synchronous machines, wound rotor synchronous machines, asynchronous machines, etc. Performing for each electric machine topology a model for identifying the most promising technologies is a very complex and laborious task. Nevertheless, an analytical model of non-salient sine wave electric machines associated to load ability concepts characterizes a quite lot of electric machine topologies. Based on it, a Target Setting Tool is developed for assessing electric motor technologies considering limits and constraints while without specifying the electric motor topology. Therefore, very few input data are required to make quick trade-offs on electric motor performances as specific power and efficiency whereas Target Setting is based on huge assumptions. For assessing cooling system weight, sizing specified structure of electric motor is unavoidable. Moreover, studies of others work packages are strongly linked to the electric motor structure. Surface Mounted Permanent Magnet Synchronous Motor topology is one of electric motor topology which satisfies the analytical model of Target Setting Tool. A sizing tool called "SM-PMSM" has been carried out based on Surface Mounted Permanent Magnet topology helpful for others packages for providing more details and for checking the Target Setting Tool validity.

Two sizing of electric motors with their cooling systems were carried out using Target Setting Tool, SM-PMSM and others tools performed by WP3 to identify the required technologies for the term medium (2025) and long (2035) term HASTECS targets. The sizing using these tools was checked by finite element analysis.

Keywords— Hybrid Aircraft Propulsion, HASTECS Project, Clean sky 2 European Research Program, High Specific Power, Electric Motors, Cooling Systems, Technological Levels, Load concepts, High Speed, Thermal Constraints, Mechanical Constraints, Target Setting Tool, Sizing Tool, Analytical Model, Finite Element Analysis.

Résumé

Après les succès industriels et environnementaux de l'hybridation du transport ferroviaire, l'hybridation du transport aérien est de plus en plus envisagée. Dans ce contexte, l'Union européenne, en partenariat avec les constructeurs aéronautiques, a lancé en 2014 un vaste programme de recherche, Clean Sky 2, visant à réduire la consommation de carburant et le niveau sonore des avions. Le programme de recherche Clean Sky 2 comprend plusieurs projets parmi lesquels : Academic reSearch on Thermal & Electric Components & Systems "HASTECS project" qui vise à identifier et à développer les technologies les plus prometteuses pour réduire le poids et augmenter l'efficacité de la chaîne de propulsion hybride. Le "projet HASTECS" est organisé autour de six lot de travail (noté par WPs) dédiés aux différents composants de la chaîne de propulsion hybride, par exemple, le WP1 est dédié aux moteurs électriques et le WP3 à leurs systèmes de refroidissement. En effet, la réduction estimée des consommations de carburant pour un vol à courte distance serait de 3,5% si la puissance spécifique des machines électriques et des convertisseurs de puissance avec leurs systèmes de refroidissement est respectivement portée à 5kW/kg et 15kW/kg pour 2025, et également portée à 10kW/kg et 25kW/kg pour 2035. Les objectifs sont nettement plus élevés que ceux d'aujourd'hui. La puissance spécifique prévue des machines électriques industrielles et des convertisseurs de puissance est supérieure à celle d'aujourd'hui. Toutefois, ces puissances spécifiques présentent certaines limites qui dépendent des propriétés des matériaux concernés et des conditions environnementales, telles que les limitations thermiques et le risque de décharges partielles. Pour atteindre les puissances spécifiques visées, par exemple dans les machines électriques, les charges mécaniques, électriques et magnétiques liées aux matériaux et aux technologies de refroidissement doivent être augmentées. Toutefois, compte tenu des limitations et des contraintes environnementales, le choix des charges doit être adéquat. Par conséquent, il est important de développer des modèles et des outils permettant d'évaluer les technologies actuelles et futures qui permettent d'atteindre les objectifs d'HASTECS. La présente thèse se concentre sur le développement de modèles et d'outils permettant de satisfaire les objectifs d'HASTECS concernant les machines électriques et leurs systèmes de refroidissement. Il existe plusieurs topologies différentes de machines électriques, à savoir : les machines à flux radial, les machines à flux axial, les machines synchrones à aimants permanents, les machines synchrones à rotor bobiné, les machines asynchrones, etc. Réaliser pour chaque topologie de machine électrique un modèle permettant d'identifier les technologies les plus prometteuses est une tâche très complexe et laborieuse. Néanmoins, un modèle analytique de machines électriques sinusoïdales à pôles lisses basé sur le concept de charges peut satisfaire un grand nombre de topologies de machines électriques. Sur cette base, un outil "Target Setting Tool TST" est développé pour évaluer les technologies de moteurs électriques en tenant compte des limites et des contraintes sans spécifier la topologie des moteurs électriques. Par conséquent, très peu de données d'entrées sont nécessaires pour faire des compromis rapides sur les performances des moteurs électriques comme la puissance spécifique et l'efficacité, alors que l'atteinte d'objectifs ciblés nécessitent d'établir de nombreuses hypothèses. Pour évaluer le poids du système de refroidissement, le dimensionnement de la structure spécifique du moteur électrique est inévitable. De plus, les études des autres lots de travail sont fortement liées à la structure du moteur électrique. La topologie du moteur synchrone à aimants permanents montés en surface est une topologie de moteur électrique qui satisfait le modèle analytique de Target Setting Tool. Un outil de dimensionnement appelé "SM-PMSM" a été réalisé sur la base de la topologie des aimants permanents montés en surface, utile pour les autres lots ainsi pour vérifier la validité du TST. Deux dimensionnements de moteurs électriques avec leurs systèmes de refroidissement ont été effectués à l'aide du Target Setting Tool, SM-PMSM et d'autres outils réalisés par le WP3 pour identifier les technologies requises pour les cibles HASTECS à moyen (2025) et long (2035) termes. Le dimensionnement à l'aide de ces outils a été vérifié par analyse par éléments finis.

Mots-clés —Avion à Propulsion Hybride, Projet HASTECS, Programme de Recherche Européen Clean Sky2, Haute Puissance Spécifique, Moteurs Electriques, Systèmes de Refroidissement, Niveaux Technologiques, Concepts de Charge, Haute Vitesse, Contraintes Thermiques, Contraintes Mécaniques, Target Setting Tool, Outil de Dimensionnement, Model Analytique, Analyse par Eléments Finis.

Contents

Acknowledgment	ii
Abstract	iii
Résumé	iv
Contents	v
List of Figures	vii
List of Tables	xi
General introduction	xiv
Chapter I: State of the art	1
Introduction.....	2
I.1 Specifications, problematic, goals and solutions.....	2
I.2 Actual specific power of electric machines.....	5
I.2.1 Electric motor topologies.....	5
I.2.2 Magnetic Materials.....	5
I.2.3 Winding and insulations.....	10
I.2.4 Further improvement in terms of materials and technological solutions.....	14
I.2.5 Bearings.....	15
I.2.6 Sleeves.....	17
I.2.7 Cooling technologies.....	17
I.2.8 Conventional industrial motors.....	24
I.3 Limitations of specific power.....	25
I.3.1 Mechanical limits.....	25
I.3.2 Electromagnetic limits.....	26
I.3.3 Thermal limits.....	27
Conclusion.....	28
References.....	29
Chapter II: Target Setting Tool	33
Introduction.....	34
II. 1 Load concepts in electrical machines.....	34
II. 2 Sizing model of electric motors.....	35
II.2.1. Electromagnetic torque, fundamental waves and tangential stress.....	35
II.2.2. Magnetic flux balance.....	36
II.2.3. Electric current balance.....	39
II.2.4. Power balance.....	40
II.2.5. Main sizes of electric motor.....	40
II.2.6. Electric motor weight.....	42
II.2.7. Specific power and torque.....	44
II. 3 Loss assessment models.....	44
II.3.1. Analytical model of Joule losses.....	44
II.3.2. Analytical model of iron losses.....	44
II.3.3. Semi-empirical models of mechanical losses.....	45
II. 4 Thermal constraint.....	48
II. 5 Mechanical constraint.....	48
II. 6 Inputs and outputs of Target Setting Tool.....	49
Conclusion.....	51
Appendices.....	52
References.....	54
Chapter III: Surface Mounted Permanent Magnet Synchronous Motor Tool	56
Introduction	57
III. 1 Motivation to surface mounted permanent magnet synchronous motor topology.....	57
III. 2 Assumption and study domain.....	58
III. 3 Analytical model of surface mounted permanent magnet synchronous motor.....	58
III.3.1 Rotor configuration.....	58
III.3.1.1 Analytical 2D magnetic field model.....	58

III.3.1.2 Permanent magnet thickness calculation.....	61
III.3.1.3 Halbach permanent magnet design.....	64
III.3.2 Stator configuration.....	67
III.3.2.1 Conductor distribution function.....	67
III.3.2.2 Surface current density function.....	68
III.3.2.3 winding coefficient.....	69
III.4 Stator and rotor additional sizes.....	69
III.4.1 Additional stator sizes.....	69
III.4.2 Additional rotor sizes.....	69
III.5 Electric parameters of surface mounted permanent magnet synchronous motor.....	70
III.5.1 Noload magnetic flux.....	70
III.5.2 Electromotive force.....	71
III.5.3 Resistance, self and mutual inductances.....	71
III.5.4 Electromagnetic torque.....	72
III.6 Inputs and outputs of SM-PMSM Tool.....	72
Conclusion.....	74
Appendices.....	75
References.....	79
Chapter IV: Sizing of Electric Motors for Medium and Long Term Targets	80
Introduction.....	81
IV.1 Specifications and choice of sizing point.....	81
IV.2 Sizing procedure.....	81
IV.3 Sizing electric motor for medium term target 2025.....	83
IV.3.1 Issues, limitations and strategy to achieve target 2025.....	83
IV.3.2 Choice of technological levels.....	83
IV.3.3 Assessment of electric motor technologies: Target Setting Tool.....	84
IV.3.4 Sizing electric motor: Surface Mounted Permanent Magnet Synchronous Motor...	85
IV.3.5 Validation with Finite Element Analysis.....	86
IV.3.5.1 Slotless model.....	87
IV.3.5.2 Slotted model.....	90
IV.3.6 Thermal behaviour and cooling system design.....	96
IV.4 Sizing electric motor for long term target 2035.....	99
IV.4.1 Issues, limitations and strategy to achieve.....	99
IV.4.2 Choice of technological levels.....	100
IV.4.3 Assessment of electric motor technologies.....	100
IV.4.4 Sizing electric motor: Surface Mounted Permanent Magnet Synchronous Motor...	101
IV.4.5 Validation with Finite Element Analysis.....	102
IV.4.5.1 Slotless model.....	102
IV.4.5.2 Slotted model.....	105
IV.4.6 Thermal behaviour and cooling system design.....	110
Conclusion.....	113
Appendices.....	115
References.....	120
General conclusion and perspectives	122
List of publications	125

List of Figures

Figure I. 1. HASTECS Project research organization.....	2
Figure I. 2. Baseline Architecture: Serial hybrid electric architecture.....	3
Figure I. 3. (a) Power profile at shaft level vs flying time, (b) rotational profile per unit vs flying time.....	4
Figure I. 4. WP1 interaction with others WPs.....	4
Figure I. 5. Synchronous motors: (a) Surface mounted permanent magnet, (b) buried magnet; Induction motors: (c) wound rotor (b), squirrel cage, (e) solid rotor.....	5
Figure I. 6. Hysteresis curves of soft and hard magnetic materials.....	6
Figure I. 7. Maximum energy product (BH) _{max}	7
Figure I. 8. Development of energy densities.....	7
Figure I. 9. Typical demagnetization curves of Alnico and Ferrite in comparison to rare earth materials.....	7
Figure I. 10. NdFeB and SmCo permanent magnets of Arnold magnetic technologies: (a) remanence, (b) max magnetic energy.....	8
Figure I. 11. Comparison between NdFeB (N42UH) and SmCO (Recoma33E): (a) Characteristics at 20°C, (b) Characteristics at 100°C and 150°C.....	8
Figure I. 12. B(H) curve of Non-Grain- Oriented sheets having 0.35mm and 0.5mm thicknesses, (b) Specific iron losses at 400Hz of Non-Grain-Oriented and Thin Non-Oriented.....	9
Figure I. 13. Iron Cobalt alloy having 0.35mm: B(H) curve (b) Specific Iron losses at 400Hz.....	10
Figure I. 14. Comparison between Silicon-Iron and Cobalt-Iron alloys.....	10
Figure I. 15. Conductor types used in winding of electrical machines.....	10
Figure I. 16. Multi-stranded random wound: (a) inside slot, (b) end-winding.....	11
Figure I. 17. Hairpin winding: (a) Hairpin single conductor, (b) inside slot, (c) Toyota Prius MY17, (d) Chevrolet Bolt EV.....	11
Figure I. 18. Rectangular Litz wire (Vendor data single-layer polyimide)	11
Figure I. 19. Roebel bar.....	12
Figure I. 20. Winding configurations: (a) distributed winding, (b) concentrated overlapping winding, (c) concentrated non-overlapping winding.....	13
Figure I. 21. Insulation system in electrical motors.....	13
Figure I. 22. (a) IEEE Standard tests of insulation classes, (b) Insulation and thermal classes.....	14
Figure I. 23. Technological solution for reducing losses: (a) Vacuumschmelze lamination (Vacstack):50µm., (b) Specific iron losses, (c) segmentation in permanent magnets up to 0.5mm (Arnold Magnets)	14
Figure I. 24. Comparison of High temperature NdFeB with New high temperature GBD NdFeB: (a) Remanent flux density vs max. operating temperature, (b) Magnetic energy vs max. operating temperature (Arnold Magnets)	15
Figure I. 25. Ultra-thin and high temperature ceramic wire.....	15
Figure I. 26. Magnetic bearing.....	16
Figure I. 27. SKF Radial bearings types (a) Deep groove ball bearing, (b) Angular contact ball bearing, (c) Cylindrical roller bearing, (d) Spherical roller bearing (e) Toroidal roller bearings.....	16
Figure I. 28. SKF bearings: (a) Limiting speed vs inner radius of bearing, (b) Limiting speed vs static load	16
Figure I. 29. (a) Hybrid Bearings, comparison between classic deep groove ball bearings: (b) limiting speed vs inner radius, (c) limiting speed vs static load.....	17
Figure I. 30. Sleeves: (a) Titanium, (b) Inconel, (c) Carbon Fiber, (d) Glass Fiber.....	17
Figure I. 31. (a) Cooling jacket in housing, configurations: (b) spiral, (c) U-shaped (one duct), (d) U-shaped (bifurcated), (e) axial.....	17
Figure I. 31. (a) Cooling jacket in housing configurations: (b) spiral, (c) U-shaped (one duct), (d) U-shaped (bifurcated), (a) axial.....	19
Figure I. 32. Cooling channels inside stator core: (a) stator structure, (b) cooling channels.....	19
Figure I. 33. Direct winding heat exchanger placed between winding, (b) machine prototype.....	20
Figure I. 34. Indirect slot cooling: (a) cooling concept of slot with flat wires, (b) cooling in single tooth, (c) assembly electric machine with indirect slot cooling.....	20
Figure I. 35. (a) Stranded and transposed winding conductors with coolant ducts, (b) Prototype of the stator with its coils	21
Figure I.36. Laminated winding with electric conductive strips and air channel cooling, (b) zoom in prototype laminated winding, (c) machine prototype.....	21
Figure I. 37. laminated winding with oil channel cooling	21
Figure I. 38. (a) oil jet cooling system for end-winding, (b) experimental two jet impingement methods ...	22

Figure I. 39. Oil spray cooling on the stator and rotor distributed end-winding	22
Figure I. 40. Potting materials for end-windings cooling	22
Figure I. 41. Axial rotor ducts: forced air convection cooling method	23
Figure I. 42. Cooling channel in shaft	23
Figure I. 43. Heat transfer principle in heat pipe	23
Figure I. 44. Heat pipe cooling methods proposed in electric machines: (a) housing, (b) slots and stator core, (c) shaft	23
Figure I. 45. Conventional electric motors used in railway traction: (a) specific power vs power, (b) specific power vs max. speed	24
Figure I. 46. Rotor topologies of electric motors used in HEV	25
Figure I. 47. High Specific Power Electric Motor in Hybrid Electric Vehicle: (a)specific power vs Power, (b) specific power vs max. speed	25
Figure I. 48. (a) Static limit (centrifugal forces), (b) Dynamic limit (vibrations and elastic distortion)	26
Figure I. 49. Temperature-life characteristics for Class H (180°C) insulation systems	26
Figure II. 1. stator bore of a radial flux electric machine.....	36
Figure II. 2. (a)Two-pole sinewave distributed winding, (b) two-pole sinewave airgap flux density.....	36
Figure II. 3. tangential stress applied to the rotor surface.....	36
Figure II. 4. magnetic flux path in radial electric motor.....	36
Figure II. 5. study domain of magnetic flux per pole.....	38
Figure II. 6.slot and conductor cross section showing the slot filling and elliptical and circular cross section of conductor.....	39
Figure II. 7. twisting of conductors.....	39
Figure II. 8. main sizes of an electric motor.....	41
Figure II. 9. end-winding sizes.....	42
Figure II.10. (a) Frame sizes, (b) ratio function of housing diameter to external stator radius.....	42
Figure II.11. equivalent rotor density vs number of pole pairs.....	43
Figure II.12. specified iron losses using Bertotti model.....	45
Figure II.13. specified iron losses using proposed model.....	45
Figure II.14. windage losses in electrical motors (a) airgap, (b) rotor ends.....	46
Figure II.15. axial and radial loads applied on rotor.....	47
Figure II.16. losses taken to the bore stator surface.....	48
Figure II.17. Graphic user interface of Target Setting Tool "TST"	50
Figure II.18. specific iron losses using new model: (a) Iron cobalt alloy (Vacoflux 50)-0.35mm (b) Silicon Iron alloy (M330-35A)-0.35mm, (c) Silicon Iron alloy (NO20)-0.20mm, (d) Silicon Iron alloy (NO10)-0.10mm.....	52
Figure II.19. Mechanical constraint at low rotational speed $V_{pmax} < 100m/s$:(a) $\lambda = 0.1$, (b) $\lambda = 0.4$, (c) $\lambda = 1$	53
Figure II.20. Mechanical constraint at high rotational speed $V_{pmax} \geq 100m/s$: (a) $\lambda=0.1$, (b) $\lambda=0.4$, (c) $\lambda=1$	53
Figure III. 1. Permanent Magnet Synchronous Motors:(a) Surface Mounted Halbach Permanent Magnet, (b)Bread Loaf Permanent Magnet, (c)Buried Permanent Magnet, (d) Interior Permanent Magnet, (e)Interior Folded Permanent Magnet.....	57
Figure III. 2. Study domain for general 2D analytical field model	58
Figure III.3. Permanent Magnet Polarizations: (a) Radial polarization, (b) Tangential polarization, (c) Parallel polarization.....	61
Figure III. 4. Ideal Halbach Permanent Magnet in 2 pole pairs: (a) internal field Halbach, (b) external field Halbach.....	61
Figure III. 5. Discretized ideal Halbach PM: (a) radial component of polarization, (b) tangential component of polarization, (c) segmented Halbach PM.....	64
Figure III.6. (a) Resulting airgap flux density of discretized Halbach PM, (b) harmonic analysis of resulting airgap flux density.....	65
Figure III.7. (a) Unit radial polarization with its resulting elementary airgap flux density, (b) Unit tangential polarization with its resulting elementary airgap flux density.....	65
Figure III. 8. Optimization procedure: LSM inside the SQPM.....	66
Figure III. 9. Comparison of optimized and direct design Parallel Polarization of segmented Halbach PM....	66
Figure III.10. Elementary coil with full pitch: (a) winding function, (b) distributed winding function.....	67
Figure III.11. Full pitch distributed winding "several coils per poles and per phases": (a) winding function, (b) distributed winding function.....	67
Figure III.12. Full pitch distributed winding "several coils per poles and per phases with several layers": (a) winding function, (b) distributed winding function.....	68

Figure III.13. Approximated end winding geometry.....	70
Figure III.14. Magnetic flux lines established by the sinewave distributed winding.....	72
Figure III.15. Inputs and outputs of SM-PMSM Tool.....	73
Figure III.16. Elementary full pitch winding: distribution conductor and magnetomotive force functions....	76
Figure III.17 Distributed winding: distribution conductor and magnetomotive force functions.....	77
Figure III.18 Distributed winding with several layers: distribution conductor and magnetomotive force functions.....	78
Figure IV. 1. (a) Power profile at shaft level vs flying time with chosen sizing point, (b) Rotational speed profile per unit vs flying time with sizing point.....	81
Figure IV. 2. Sizing procedure of high specific electric motor with its cooling system.....	82
Figure IV. 3. Interaction sizing electric motor work package with others WPs.....	83
Figure IV. 4. Twisted strands.....	84
Figure IV. 5. Slotless model electric motor of medium term target 2025: (a) Slotless model structure on one pole, (b) boundary conditions applied on one pole structure.....	87
Figure IV. 6. (a) Halbach array 7 segment PMs, (b) Airgap flux density.....	87
Figure IV. 7. Slotless model: (a) No-load magnetic flux, (b) Back electromotive force.....	88
Figure IV. 8. Slotless model: (a) Airgap flux density, (b) harmonic analysis.....	88
Figure IV. 9. Slotless model: (a) Self-inductance, (b) Mutual inductance, (c) cyclic inductance.....	89
Figure IV. 10. Slotless model: (a) Surface current density and airgap flux density waves, (b) The electromagnetic torque.....	89
Figure IV. 11. Slotted model electric motor of medium term target 2025: (a) Slotted model structure on one pole, (b) boundary conditions applied on one pole structure.....	90
Figure IV. 12. Airgap flux density at no-load: (a) slotless and slotted models, (b) harmonic analysis.....	91
Figure IV. 13. Slotted model at no-load: (a) Magnetic paths, (b) tooth flux density, (c) stator yoke flux density.....	91
Figure IV. 14. Slotted model: (a) No-load magnetic flux, (b) Back electromotive force.....	92
Figure IV. 15. Noload simulation: cogging torque.....	92
Figure IV. 16. Slotted model at no-load simulation: (a) Magnetic flux density distribution, (b) Flux line distribution.....	92
Figure IV. 17. Slotted model at load: (a) airgap flux density, (b) harmonic analysis.....	93
Figure IV. 18. Slotted model at load: (a) tooth flux density, (b) stator yoke flux density.....	93
Figure IV. 19. Slotted model: (a) Self-inductance, (b)Mutual inductance, (c) cyclic inductance.....	94
Figure IV. 20. Slotted model at load simulation: (a) Magnetic flux density distribution, (b) Flux line distribution.....	94
Figure IV. 21. Slotted model: The electromagnetic torque.....	95
Figure IV. 22. Slotted model: Iron losses.....	95
Figure IV. 23. Nacelle architecture: electric motor with its cooling circuit.....	96
Figure IV. 24. Medium term target 2025: Electric motor with its cooling channels.....	97
Figure IV. 25. Medium term target 2025: Losses profiles and equivalent current density product function of time flying.....	97
Figure IV. 26. Medium term target 2025: (a) Axial and ortho-radial section of SM-PMSM including its cooling system with Lumped Parameter Thermal Model LPTM nodes location, and axial and motor-end connections, (b) Temperature evolution during flying mission in the sized electric motor [Zea_18] [Tou_20]	99
Figure IV. 27. Slotless model electric motor of long term target 2035: (a) Slotless model structure on one pole, (b) boundary conditions applied on one pole structure.....	102
Figure IV. 28. Electric motor of long term target 2035 (a) Halbach array 7 segment PMs, (b) Airgap flux density.....	103
Figure IV. 29. Slotless model: (a) No-load magnetic flux, (b) Back electromotive force.....	103
Figure IV. 30. Slotless model: (a) Airgap flux density, (b) harmonic analysis of airgap flux density given by Finite Element Analysis.....	104
Figure IV. 31. Slotless model: (a) Self-inductance, (b) Mutual inductance, (c) Cyclic inductance.....	104
Figure IV. 32. Slotless model: (a) Surface current density and airgap flux density waves, (b)The electromagnetic torque.....	105
Figure IV. 33. Slotted model electric motor of long term target 2035: (a) Slotted model structure on one pole, (b) boundary conditions applied on one pole structure.....	105
Figure IV. 34. Airgap flux density at noload: (a) slotless and slotted models, (b) harmonic analysis.....	106
Figure IV. 35. Slotted model at no-load: (a) tooth flux density, (b) stator yoke flux density.....	106
Figure IV. 36. Slotted model: (a) Noload magnetic flux, (b) Back electromotive force.....	106
Figure IV. 37. No-load simulation: cogging torque.....	107

Figure IV. 38. Slotted model at noload simulation: (a)Magnetic flux density distribution, (b) Flux line distribution.....	107
Figure IV. 39. Slotted model at load: (a) airgap flux density, (b) harmonic analysis.....	107
Figure IV. 40. Slotted model at load: (a) tooth flux density, (b) stator yoke flux density.....	108
Figure IV. 41. Slotted model at load simulation: (a)Magnetic flux density distribution, (b) Flux line distribution.....	108
Figure IV. 42. Slotted model: (a) Self-inductance, (b)Mutual inductance, (c) Cyclic inductance.....	109
Figure IV. 43. Slotted model: The electromagnetic torque.....	109
Figure IV. 44. Slotted model: Iron losses.....	109
Figure IV. 45. Long term target 2035: Losses profiles and equivalent current density product function of time flying.....	110
Figure IV. 46. Long term target 2035: axial and radial sections of electric motor and its cooling channels.....	111
Figure IV. 47. Long term target 2035: (a) Axial and ortho-radial section of SM-PMSM including its cooling system with Lumped Parameter Thermal Model LPTM nodes location, and axial and motor-end connections, (b) Temperature evolution during flying mission in the sized electric motor.....	112
Figure IV. 48. B(H) characteristic of iron cobalt magnetic sheet: Vacoflux 48-0.35mm.....	115
Figure IV. 49. Demagnetization curves of Samarium Cobalt ($\text{Sm}_2\text{Co}_{17}$): "Recoma 33E.....	115
Figure IV. 50. Rectangular compacted litz-wire type 8 [NewCat].....	116
Figure IV. 51. Arrangement of rectangular compacted Litz wires type 8 [NewCat]	117
Figure IV. 52. Rectangular compacted Litz wires type 8: (a) 3D view, (b) YZ view.....	118
Figure IV. 53. Circular and elliptical cross sections: (3D) view, YZ view.....	118
Figure IV. 54. Torque-speed characteristic of SM-PMSM.....	119

List of Tables

Table I. 1. Flight phases times.....	4
Table I. 2. Performance comparison between surfaces mounted PMs and interior PMs.....	5
Table I. 3. Performance comparison between synchronous motors and induction motors.....	5
Table I. 4. Some properties of rare earth magnets.....	8
Table I. 5. Properties of Non-Grain- Oriented SiFe alloy.....	9
Table I. 6. Properties of Iron Cobalt alloy Vacuumschmelze material.....	10
Table I. 7. Fill factor of rectangular Litz-wire conductor "Vendor catalogue"	11
Table I. 8. Fill factor of industrial electric machines with different conductor types.....	12
Table I. 9. Comparison of advantages and drawback of concentrated and distributed winding.....	12
Table I. 10. Intrinsic features of insulators.....	14
Table I. 11. Bearing performance characteristics.....	16
Table I. 12. Properties of retaining sleeve materials used in surface mounted permanent magnet synchronous machines.....	17
Table I. 13. Typical values of heat transfer coefficient of some coolants.....	18
Table I. 14. Summary of forced cooling methods.....	19
Table I. 15. Industrial electric motors of HEV use housing jacket.....	19
Table I. 16. Heat transfer coefficients and achieved current densities according to slot cooling methods.....	21
Table I. 17. Electrical and thermal properties of potting materials.....	22
Table I. 18. Typical values of thermal conductivity of constructional parts of electric machine.....	27
Table II. 1. Allowed flux densities for various standard induction and synchronous electrical machines.....	34
Table II. 2. Allowed RMS values of current and linear current " j_{rms} and A_{rms} " densities for various standard induction and synchronous electrical machines and according to cooling method.....	34
Table II. 3. Allowed tangential stress values for various standard induction and synchronous electrical machines and according to cooling method.....	34
Table II. 4. Friction coefficient according to the bearing types used mainly to withstand the radial loads.....	47
Table II. 5. Target Setting Tool inputs/outputs list.....	49
Table IV. 1. Magnetic, electric and thermal loads of Non-salient pole synchronous machines.....	84
Table IV. 2 Range values of electric, magnetic and thermal loads for medium term target 2025.....	84
Table IV. 3.Target Setting Tool inputs/outputs for medium term target 2025.....	85
Table IV. 4. SM-PMSM Tool Inputs for medium term target 2025.....	86
Table IV. 5. SM-PMSM Tool Outputs for medium term target 2025.....	86
Table IV. 6. Electric motor of medium term target 2025: Structure of 7 segment Halbach PMs.....	87
Table IV. 7. Electric motor of medium term target 2025: summary comparison of performances between analytical tools and finite element analysis.....	96
Table IV. 8.Characteristics of Ethylene Water-Glycol 50/50 [Ton_14]	96
Table IV. 9. Medium term target 2025: Cooling system characteristics given by WP3.....	98
Table IV. 10. Technological choices performed for medium term target 2025.....	99
Table IV. 11. Range values of electric, magnetic and thermal loads for long term target 2035.....	100
Table IV. 12. Target Setting Tool inputs/outputs for long term target 2035.....	101
Table IV. 13. SM-PMSM Tool Inputs for long term target 2035.....	101
Table IV. 14. SM-PMSM Tool Outputs for long term target 2035.....	101
Table IV. 15. Electric motor of long term target 2035: seven segment Halbach PMs.....	102
Table IV. 16. Electric motor of long term target 2035: summary comparison of performances between analytical tools and finite element analysis.....	110
Table IV. 17. Long term target 2035: Cooling system characteristics given by WP3.....	112
Table IV. 18. Bertotti model of iron loss for Vacoflux 48-0.35mm: equation (II-66)	115
Table IV. 19. New formulation of iron loss for Vacoflux 48-0.35mm: equation (II-67)	115
Table IV. 20. Magnetic properties of Samarium Cobalt (Sm_2Co_{17}): "Recoma 33E".....	115
Table IV. 21. Physical properties of Samarium Cobalt (Sm_2Co_{17}):"Recoma 33E.....	116
Table IV. 22. Rectangular compacted litz wire type 8 [NewCat].....	116
Table IV. 23. Copper whole AWG12 of Essex Magnet Wire Catalogue [EssCat].....	116

Glossary

- \mathbf{B} magnetic induction
- \mathbf{H} magnetic field intensity
- \mathbf{J} magnetic polarization
- μ_0 the magnetic vacuum permeability
- μ_r relative magnetic permeability
- μ_{pm} PM permeability
- B_r remanence
- H_c coercive field
- T temperature
- B_{r20° remanence at 20°C
- H_{c20° coercivity at 20°C
- α_B temperature coefficient of the remanence
- α_H temperature coefficient of the coercivity
- P_j joule losses
- P_f iron losses
- P_{edd} eddy current losses
- $P_{friction}$ friction losses
- $P_{windage}$ windage losses
- Ω rotational speed
- R_s resistance
- H_g magnetic field strength
- f synchronous frequency
- $R_{thermal}$ thermal resistance
- e thickness
- S surface
- λ_{th} thermal conductivity
- j_{rms} root mean square (RMS) of current density
- A_{rms} RMS of linear current density
- A_m amplitude of linear current density
- BH_{max} maximum energy product
- σ tangential stress
- T_{em} electromagnetic torque
- S_b inner stator surface
- K surface current density
- B_{rs} flux density resulting from the rotor source
- B_{ss} flux density resulting from the stator source
- B_{tot} amplitude of the total flux density in airgap
- p number of pole pairs
- θ angular position
- t time
- z axial direction
- λ shape coefficient
- B_m max. value the airgap flux density
- B_{rms} RMS of the airgap flux density
- K_m max. value the surface current density
- K_{rms} RMS of the surface current density
- q number of phase
- m number of slots per pole and per phase
- B_{ry} rotor flux density
- B_{sy} stator yoke flux density
- B_{st} stator tooth flux density
- R stator bore radius
- R_{out} external stator radius
- R_{fr} external frame radius
- L_m active length
- l_{ht} half-turn length
- L axial motor length
- e_g airgap thickness
- x_e airgap ratio
- h_s slot height
- l_s slot width
- l_t tooth width
- h_y stator yoke thickness
- R_r external rotor radius
- R_{sh} shaft radius
- e_{pm} permanent magnet thickness
- r_{tooth} ratio between l_t to R
- τ_r ratio between R_{fr} and R_{out}
- ρ_{fr} frame density
- ρ_{inst} insulation density
- ρ_c copper density
- ρ_{rot} rotor density
- ρ_{air} air density
- $W_{stat-wind}$ stator winding weight
- $W_{stat-core}$ stator core weight
- W_{stat} stator weight
- W_{rot} rotor weight
- W_{mot} motor weight
- S_p specific power
- S_T specific torque
- k_{tb} end-winding coefficient
- η efficiency
- k_h hysteresis loss coefficient
- k_e eddy loss coefficient
- k_e excess loss coefficient
- ρ_{cu20° copper resistivity at 20°C
- α_{th} temperature coefficient resistance
- ρ_{cu} copper resistivity
- T_{win} winding temperature
- α_{dis} electric angular displacement
- k_{fill} fill factor
- k_w winding coefficient
- h_{ry} rotor yoke thickness
- L_s self-inductance per phase
- M mutual inductance per phase
- L_{cs} cyclic inductance per phase
- Φ_{vm} max no-load magnetic flux
- E_i back-electromotive force per phase
- A magnetic vector potential
- P_{em} electromagnetic power
- P_{mech} mechanical power
- P_{ele} electric power

- S_{sy} stator yoke surface
- S_{slot} stator slot surface
- S_{tooth} tooth surface
- S_{cond} conductor cross section
- $S_{tot-cond}$ total cross section of conductors in one slot
- S_{rot} rotor surface
- ϕ_p magnetic flux per pole
- ϕ_{sy} stator yoke magnetic flux
- ϕ_{st} magnetic flux in stator teeth
- Aj_{eq} equivalent current density product
- l_c conductor length
- n_w number of wires
- l_w wire length
- **lay length** lay length
- W_c conductor width
- th_c conductor thickness
- S_w circular cross section of wire
- $S_{elliptical}$ elliptical cross section of wire
- $k_{fillcond}$ copper filling of conductor
- a_{ij} iron loss coefficient
- ω electrical pulse
- pr air pressure

- $P_{mech-loss}$ mechanical losses
- $P_{rot-loss}$ rotor windage losses
- P equivalent dynamic bearing load
- C_f friction coefficient in bearings
- C_{fa} friction coefficient in airgap
- C_{fr} friction coefficient in rotor ends
- R_{ea} Reynolds number of flow in airgap
- R_{erot} Reynolds number of flow in rotor ends
- N_{sin} sinewave distributed conductors
- N_{tsin} max number of turns
- E Young's modulus

- N_t number of stator teeth
- N_s number of slots
- N_c total number of conductors
- N_{cs} total number of conductors per slot
- n_l number of layers
- n_b number of segments
- I current
- I_m amplitude of current
- I_{rms} RMS value of the current
- Ψ_g airgap linkage flux
- N_{ts} number of turns per phase connected in series
- C conductor distribution function
- N winding distribution function
- N_e elementary coil function
- C_e elementary coil function
- MMF magnetomotive force function
- τ short pitch factor
- s skewing factor
- k_d distribution winding coefficient
- k_{pi} pitch coefficient
- k_s skewing coefficient
- k_{sc} coefficient taking into account elliptical cross-section
- k_{lc} coefficient taking into account twisting
- β_e angle between circular and elliptical cross sections
- β angular width
- α angular centre of permanent magnet
- γ orientation angle
- χ opening slot angle
- γ angular step between two neighbouring coils
- ξ angular step between two layers
- V_p peripheral speed
- σ_m mechanical stress
- v Poisson's ratio

General introduction

Nowadays, protecting environment becomes an unavoidable requirement especially in the transport sector. Electrification of rail transport has led to weight decreasing, fuel consumption decreasing and hence to CO₂ emission decreasing. In aeronautics, transition to electric power was initiated by the electrification of non-propulsive systems (e.g. in Airbus A380 and Boeing B787 aircrafts) with the aim of extending it to possible hybrid or electric propulsion systems. In the context of doing that, several research projects and programs have been launched, among of them the "Clean Sky 2 program". The last one is a largest European research programme developing innovative, cutting-edge technology aimed for reducing of 20% CO₂ emissions and noise levels for the Horizon 2020.

Hybrid aircraft research on thermal and electrical components and systems "HASTECS" project is part of Clean Sky 2 research program. It aims to study the hybridization regional aircraft propulsion systems by means of developing tools and models for reducing weights and increasing efficiencies. "HASTECS" project includes six work packages. Each work package is dedicated to the following topics: electric motors, power converters, electric motors and power converters cooling systems, partial discharges and integration systems.

Works presented in this thesis are included in the first work package dedicated to the development of tools allowing satisfying the HASTECS specifications and targets concerning the electric motors. Two targets are set in the HASTECS consortium: increasing specific power of electric motors including their cooling systems to reach 5kW/kg for 2025 and to reach 10kW/kg for 2035 despite of particularly severe environmental constraints (thermal, partial discharges, etc.). So far, these targets are higher than the achieved specific powers of industrial electric motors including their cooling systems. Typically, for increasing specific power of electric motors, electric, magnetic and mechanical loads linked to the materials and design technologies should be increased and improved. However, these improvements often lead to higher losses that need to be extract and evacuate in the small areas which is hence challenging. Indeed, decreasing weight of electric motor may lead to an increasing weight of its cooling system. This thesis will respond to the following problematic: according to the actual and future technological levels can we reach the targets respectively in 2025 and in 2035.

The thesis manuscript is organized around four chapters:

The first chapter presents an overall description of industrial context: specifications, problematics and goals for framing the thesis works. This chapter presents a state art of the actual industrial electric motors to situate the achieved specific power and to identify the involved technologies, namely: material technologies, construction technologies and cooling methods. They are overviewed in terms of topologies, weights and loads to identify the main limitations for increasing specific power. Issues and limitations are discussed in details. Future technological improvements for increasing specific power are also evoked although they are still under research.

A Target Setting Tool "TST" is carried out in Chapter II, for assessing the electric motor and cooling technologies presented in Chapter I. Based on the model of ideal sinewave non-salient electric motors and the loadability concepts, main sizes, weights and performances of electric motor are determined without specifying the structure. Thermal and mechanical constraint are the first limitations for increasing specific power. Thermal constraint is developed according to a particular electric load which depends on the cooling technology. Mechanical constraint is also developed according to rotor properties and to mechanical load. These constraints are introduced in Target Setting Tool in order to not exceed the limits in the electric motor assessment. The main purpose of TST is then to make from few data and huge assumptions quick trade-offs on the specific power and the efficiency for identifying the promising technologies. Nevertheless, TST outputs are not enough for the others Work Packages.

Chapter III deals with a sizing tool based on the analytical model of Surface Mounted Permanent Magnet Synchronous Motor "SM-PMSM" and based on the TST outputs. Motivations for choosing such topology are firstly outlined and discussed. 2D analytical model is dealt for sizing the rotor components as permanent magnets, rotor yoke and shaft. Additional stator sizes are derived from a chosen winding configuration. Through established conductor distribution functions, intrinsic electric parameters and performances are deduced. The intrinsic electric parameters are necessary for sizing power converters and their cooling systems. As the structure is specified, losses are updated for assessing the thermal constraint and for sizing the cooling systems of electric motors.

The fourth and last chapter focuses to the sizing of electric motors and their cooling systems for the medium and long term targets. Also, it aims to identify on the one hand the most actual promising and future technologies for achieving medium and long term targets using "TST" and "SM-PMSM" and on the other hand it aims to validate these tools using finite element analysis that are based on some assumptions especially the TST. According to the HASTECS flying profile, choice of sizing point is firstly discussed. To size both electric motors and their cooling system, a procedure is proposed. The last one includes the developed assessment tool "TST", sizing tool "SM-PMSM" and other sizing cooling system tools carried out by WP3. Sizing electric motor and its cooling system for 2025 HASTECS target begins with an analysis of issues, limitations and used strategy for achieving this target. Afterward, choice of technological levels is overviewed to carry out the assessment electric motor technologies with TST. After the assessment step, electric motor is sized using "SM-PMSM" and its cooling system is sized using tools developed by WP3. Validation of sizing of electric motor is carried out with Finite Element Analysis. Following the same approach, for long term target 2035 sizing electric motor including its cooling system is presented in this chapter. Finally, an emphasis is paid on the differences between the electric motor targeted for medium term target 2025 with the one targeted for long term target 2035 in order to identify achieved thermal limit for each target.

Eventually, several conclusions are presented and some perspectives are proposed.

Chapter I: State of the art

Contents

Introduction	2
I.1 Specifications, problematic, goals and solutions.....	2
I.2 Actual specific power of electric machines.....	5
I.2.1 Electric motor topologies.....	5
I.2.2 Magnetic Materials.....	5
I.2.3 Winding and insulations.....	10
I.2.4 Further improvement in terms of materials and technological solutions.....	14
I.2.5 Bearings.....	15
I.2.6 Sleeves.....	17
I.2.7 Cooling technologies.....	17
I.2.8 Conventional industrial motors.....	24
I.3 Limitations of specific power.....	25
I.3.1 Mechanical limits.....	25
I.3.2 Electromagnetic limits.....	26
I.3.3 Thermal limits.....	27
Conclusion.....	28
References.....	29

Introduction

This chapter provides an overall description of industrial context with a state of the art of electric motor technologies. Specifications, problematic, goals and solutions will be firstly detailed. Afterward a wide panorama of actual high specific power electric motors will be studied. It will include employed materials, cooling technologies and conventional industrial motors. Future technological improvements will be also highlighted. Finally, issues and limitations of increasing specific power electric motor will be discussed.

I.1 Specifications, problematic, goals and solutions

- Project Framework: "Cleansky 2 Program: HASTECS Project"

CleanSky2 is a big European research program in aeronautical innovation which aims to reduce noise and CO₂ emissions of regional aircraft. This research program includes several research projects, among them there is Hybrid Aircraft academic reSearch on Thermal and Electrical Components and Systems "HASTECS" project [Hor_20]. It consists in identifying the most promising technologies allowing increasing the specific power and efficiency of hybrid propulsion chain. Furthermore, HASTECS project aims also to identify the technological breakthroughs via the development of tools to meet these goals. HASTECS project involves "LAPLACE" laboratory, "Pprime" institute for power conversion systems associated with research center "CIRIMAT" for power supply, as shown in Figure I. 1. The HASTECS Work Packages (WPs) are organized into 6 WPs. The 1st WP is dedicated to the electric motor. The 2nd WP is dedicated to the power converter. These two WPs are leads by LAPLACE laboratory with its three research groups: Grem3, CS and GENESYS. While, the 3rd and 4th WP including the cooling systems of electric motor and power converter respectively are led by Pprime laboratory. The 5th and 6th WP carry on the partial discharge study in electric systems and the optimization study of propulsion chain, respectively. These latter are also leads by LAPLACE laboratory with its research groups: MDCE, Grem3 and GENESYS.



Figure I. 1. HASTECS Project research organization [Wor_18]

- General aircraft configuration

The electrical aircraft architecture is a serial architecture powered by some electrical generators mechanically linked (with or without gearbox) to the gas turbines shafts. Another electrical energy is supplied by batteries or fuel cells cf. Figure II. 2. This architecture is chosen as baseline architecture for assessment studies of HASTECS project. It has been taken also for "E-FanX" demonstrator [Air_19] and for hybrid electric aircraft "DA36 E-Star 2".

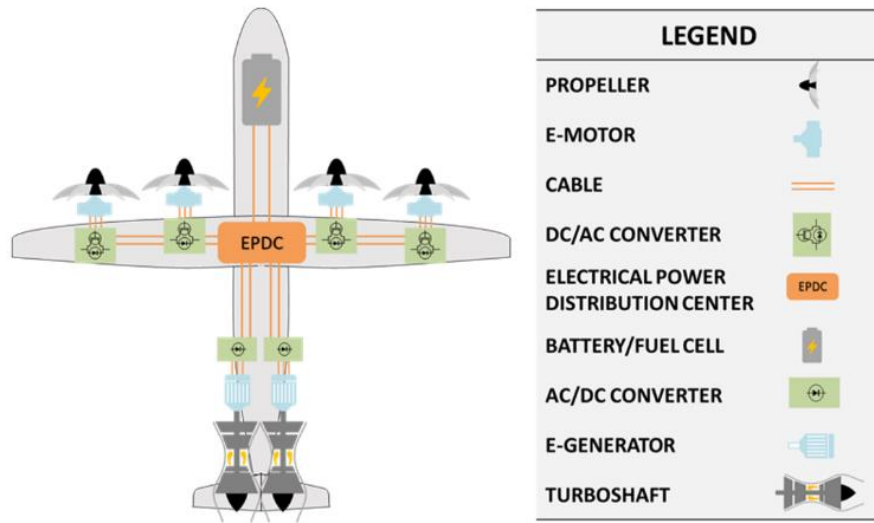


Figure I. 2. Baseline Architecture: Serial hybrid electric architecture [Wor_18] [All_17]

- *Specifications and targets*

According to Airbus specification [All_18], the electric motor should be ensuring a mechanical power 0.018 Per Unit¹ (PU) with a rotational speed per unit of 30% at shaft level during flying phases of taxi-in and taxi-out. In the take-off flying phase, the electric motor should be ensuring a mechanical power of 1PU with 100% of rotational speed. In the climb phase, the mechanical power decreases from 0.92PU to 0.746PU with the rotational speed comprised between 95% to 75%. During the cruise phase, mechanical power and rotational speed should be constant and equal respectively to 0.489PU and 70% as illustrated in Figure I. 3. In the descent phase, the mechanical power and the rotational speed of the electric motor is reduced to 0.02PU and 40%. In the approach and the landing phases, the mechanical power and the rotational speed are increased to 0.393PU and 82% due to go-around. Table I. 1 details each time flying phase.

HASTECS project fixes medium and long term targets to be achieved for electric motors including their cooling systems and for power converters with their cooling systems. Medium term target of 2025 is to achieve:

- Specific power 5kW/kg for electric motor with its cooling system
- Efficiency of electric motor at cruise point must be greater than 96%
- Efficiency of electric motor at design point greater than 94.5%
- Specific power 15kW/kg for power converter with its cooling system
- Efficiency of power converter at optimization point must be greater than 98%
- Efficiency of power converter at max power must be greater than 96.5%, without any allowed partial discharge in electric motor and power converter.

Long term target of 2035 is to achieve:

- Specific power 10kW/kg for electric motor with its cooling system
- Efficiency at cruise point greater than 98.5%
- Efficiency at design point greater than 97%
- Specific power 25kW/kg for power converter with its cooling system
- Efficiency of power converter at optimization point must be greater than 98%
- Efficiency of power converter at max power must be greater than 96.5%, with allowed partial discharge in electric motor and power converter [All_18].

Doubling specific power of electric machines and power converters from the 1st target to the 2nd target leads to weight reduction of 1.8 tons. It then allows a reduction of 3.5% fuel consummation and therefore a reduction of CO₂ emissions [Dis_18].

¹ For confidentiality reason, exact power value will not be provided, however, the maximum power is MW range

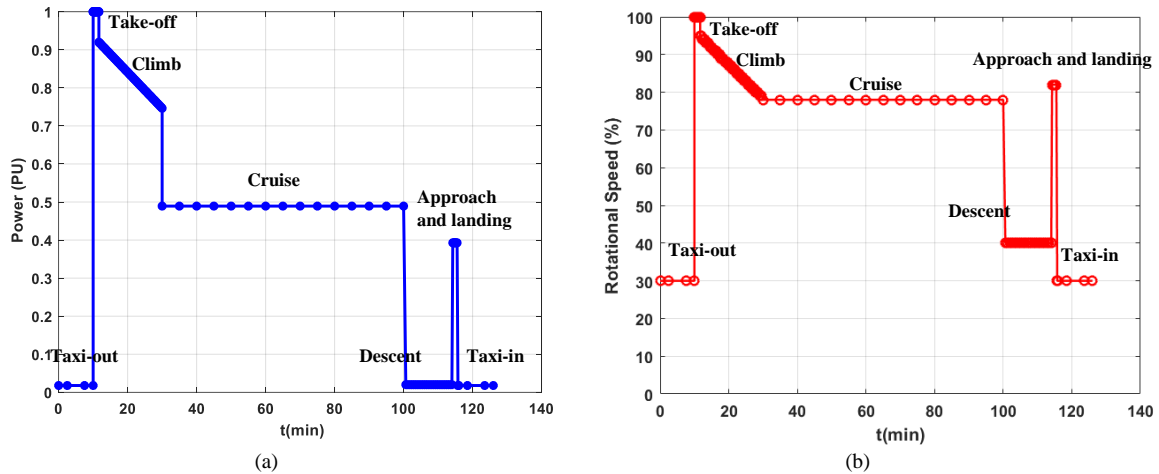


Figure I. 3. (a) Power profile at shaft level vs flying time, (b) Rotational speed profile per unit vs flying time [All_18]

Table I. 1. Flight phases times [All_18]

Phases	Taxi out and in	Take-off	Climb	Cruise	Descent	Approach and Landing	Total flying time
Time(min)	10	1.66	18.33	70	14	2	126 min
Speed (%)	30	100	95 to 79	78	40	82	
Power (PU)	0.018	1	0.92 to 0.746	0.489	0.02	0.393	

This thesis interests only on tasks WP1 (electric motor). However, WP1 interacts directly with 2nd, 3rd, 5th and 6th WP (cf. Figure I. 4). With WP2 the interaction allows to fix the DC bus voltage from the given electric parameters of the electric motor. While, with WP3 the interaction allows to design cooling system of the electric motor from its losses and geometric sizes. Finally, WP5 interacts with WP1 in order to determine the insulation system required to avoid the partial discharge for the medium term target and to minimize partial discharge for the long term target. Once the sizing of electric motor is done, WP1 gives to WP6 the electrical models of the motor for overall optimizations of the hybrid propulsion system. Therefore, this thesis aims to fulfill the HASTECS expectations for the electric motor.

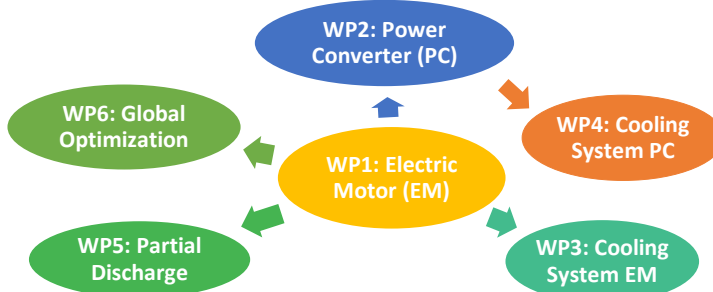


Figure I. 4. WP1 interaction with other WPs

- Thesis problematic

Specific power and efficiency of electric machines highly depend on available magnetic loading, electric loading and rotating speed, which are constrained by thermal and mechanical limitations of involved materials. Increasing both specific power and efficiency are a particular challenge. Indeed, increasing loads increases specific power on one side and decreases the efficiency on the other hand. Moreover, the electric machines for aircraft application should be high robustness and high reliability.

- Goals and solutions

This thesis aims to satisfy both the HASTECS specifications in terms of targets and the interaction requirements between all WPs. Develop assessment tools is the solution for these two expectations. Assessment tools allow making quick loads trade-off to achieve high specific power and efficiency in order to identify the existing and the future technologies the most promising. In addition, they allow identifying the physical and technological limits to overcome in the future. Assessment tools allow also to provide more information to other WPs and help to carry out global optimization for hybrid aircraft chain and local optimization for electric machine.

I.2 Actual specific power of electric machines

In order to develop assessment tools for electric machines, it is necessary to establish a detailed state of art of existing electric machines and their technologies. The focus will be on common topologies of electric motors, materials and cooling technologies. According to the power range required (some kW to some MW), only electric motors devoted to railway traction and hybrid electric vehicles will be overviewed to evaluate their actual specific power.

I.2.1 Electric motor topologies

Since AC power converter advances, alternative current rotating machines as synchronous and induction motors are the most used topologies in industrial applications.

- Synchronous motors are mostly built with permanent magnets in the rotor. Permanent Magnets (PMs) can be mounted on core rotor surface or positioned inside it, in order to develop a salience, as illustrated in Figure I. 5.a and b. A performance comparison between surface mounted and interior PMs is summarized in Table I. 2. It is possible to encounter wound synchronous motor without PMs; then the rotor can be salient or no salient depending on the shape of the pole shoe.
- Induction motors are built with short circuited rotor performed either squirrel cage or wound rotor or even solid rotor with or without slits as presented in Figure I. 5. c, d and e. In contrast to synchronous motors, induction motors are all no salient. Table I. 3 summarizes a brief performance comparison between synchronous and induction motors.

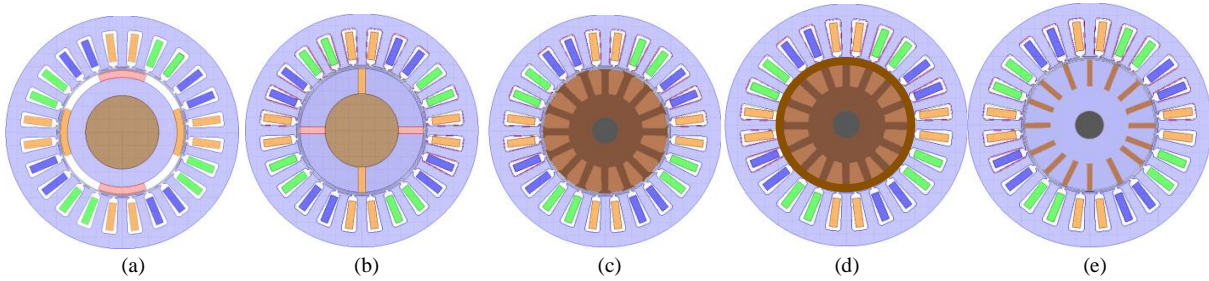


Figure I. 5. Synchronous motors: (a) Surface mounted permanent magnet, (b) Buried Magnet; Induction motors: (c) Wound Rotor (d) Squirrel cage, (e) Solid rotor

Table I. 2. Performance comparison between surfaces mounted PMs and interior PMs [Gie_10]

Surface Mounted PMs	Interior PMs
<ul style="list-style-type: none"> - Air-gap flux density lower than remanence flux density of PM - Lower armature reaction flux - Eddy current losses in PM - Low flux-weakening capability - No salient torque 	<ul style="list-style-type: none"> - Air-gap flux density greater than remanence flux density of PM - Higher armature reaction flux which require high performance power converter - No eddy current losses in PM - Operating with wide flux-weakening is possible - Salient torque

Table I. 3. Performance comparison between synchronous motors and induction motors [Gie_10]

Synchronous motors	Induction motors
<ul style="list-style-type: none"> - Low rotor losses - High efficiency - Low inductance due to high magnetic air-gap thus requiring additional inductance for power converter 	<ul style="list-style-type: none"> - High rotor losses due to induced currents thereby significant cooling effort can be required - Low efficiency - High inductance due to small magnetic air-gap, therefore reduced power converter weight

I.2.2 Magnetic Materials

The performances of electrical machines are strongly related to the magnetic materials used. The evolution of these materials contributes to the improvement of the performance of electrical machines. Two magnetic material categories are distinguished:

- Soft magnetic materials which present magnetic properties in the presence of an external excitation,
- Hard magnetic materials which have magnetic properties even in the absence of external excitation.

These two materials have a magnetic hysteresis curve depending both on their intrinsic characteristics and the magnetic excitation in which they are submitted. In fact, placed on a magnetic field H which varies alternately,

the induction B of the magnetic material presents a hysteresis curve. Figure I. 6 illustrates typical hysteresis cycles of soft and hard materials. B_r is the residual induction (remanence) corresponding to $(H=0)$ and H_c is the coercive field defined as the field value when $(B=0)$. From a certain value of H , the induction B is saturated and corresponds to B_s . In hard materials, the remanence B_r and the coercivity H_c are higher than soft ones as shown in Figure I. 6.

The general relationship between the magnetic induction B , and the magnetic field intensity H can be expressed as:

$$B = \mu_0 \mu_r H + J \quad (\text{I. 1})$$

where J is the magnetic polarization, μ_0 is the magnetic vacuum permeability, μ_r is the relative magnetic permeability.

Permanent magnets are sensitive to the temperature. Their remanence B_r and coercive field H_c vary with temperature as following equation:

$$\begin{cases} B_r = B_{r20^\circ} \left(1 + \frac{\alpha_B}{100} (T - 20^\circ)\right) \\ H_c = H_{c20^\circ} \left(1 + \frac{\alpha_H}{100} (T - 20^\circ)\right) \end{cases} \quad (\text{I. 2})$$

where T is the PM temperature of the permanent magnet, B_{r20° and H_{c20° are the remanence and the coercivity at 20°C and $\alpha_B < 0$ and $\alpha_H < 0$ are temperature coefficients in $[\%/\text{ }^\circ\text{C}]$.

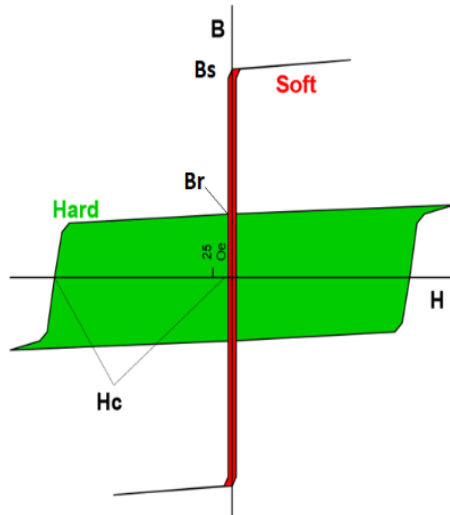


Figure I. 6. Hysteresis curves of soft and hard magnetic materials [Con_04]

- *Hard magnetic materials: Permanent Magnets (PMs)*

Alnico, Ferrites and Rare-earth materials are the three types of PMs commonly used in electric machines. Ferrites include Barium Ferrite and Strontium Ferrites. Rare-earth materials include Samarium-Cobalt (SmCo) and Neodymium-Iron-Boron (NdFeB). The operating point of the PM is located in the 2nd quadrant of the hysteresis loop. Figure I. 7 Presents the demagnetization curves and the magnetic energy of PM per volume unit. During the last few years, rare-earth materials have known huge magnetic energy improvement compared to Alnico and Ferrites (cf. Figure I. 8). In the following, we focused only on the rare earth PMs in terms of features given that Alnico materials have the lowest coercive field and are easy to demagnetize, and, Ferrite materials have the lowest remanence as shown in Figure I. 9.

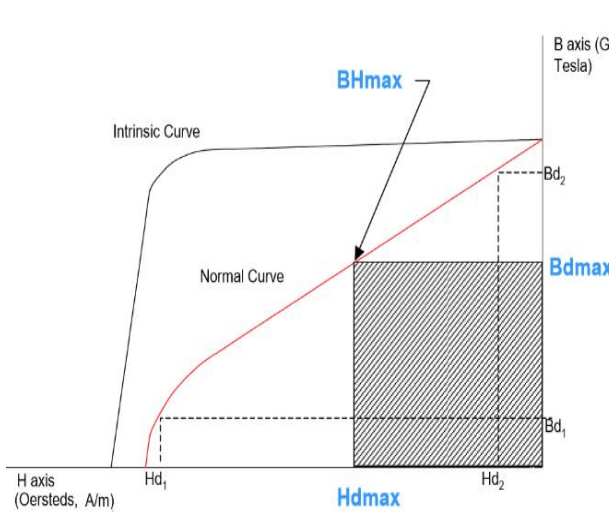


Figure I. 7. Maximum energy product (BH)_{max} [Con_04]

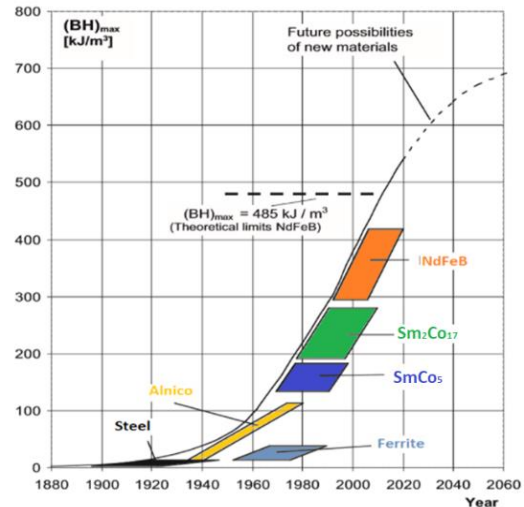


Figure I. 8. Development of energy densities [Vac_14]

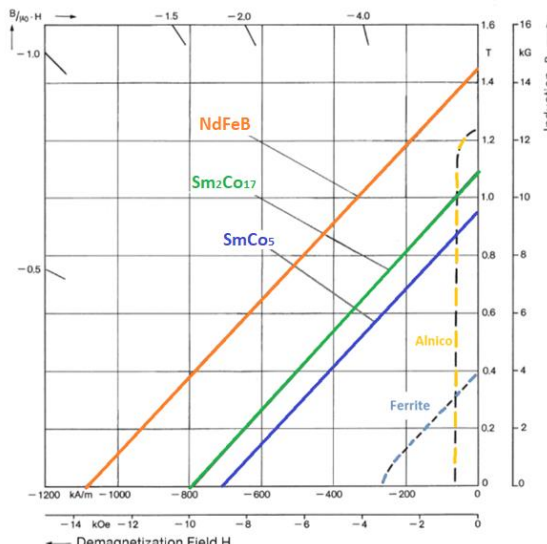


Figure I. 9. Typical demagnetization curves of Alnico and Ferrite in comparison to rare earth materials[Vac_14]
→ Samarium-Cobalt (SmCo)

Samarium-Cobalt magnets are the first generation of rare earth magnets. We distinguish two families: Sm_2Co_{17} and $SmCo_5$. Sm_2Co_{17} has the highest magnetic performance at high temperature unlike to $SmCo_5$. The latter has the best corrosion resistance of all rare earth magnets. $SmCo$ are characterized by linear demagnetization curve, low temperature coefficients and by:

- remanence between 0.87-1.19T,
- coercivity between 1800-2400kA/m,
- maximum energy product between 143-265 $kJ.m^{-3}$,
- Maximum operating temperature 250-350°C as shown in Figure I.10.

→ Neodymium-Iron-Boron (NdFeB)

Neodymium-Iron-Boron magnets are the second generation of rare earth magnets. They are characterized by linear demagnetization curve, higher temperature coefficients compared to $SmCo$, and by:

- remanence between 1.05-1.49T,
- coercivity between 876-2706kA/m,
- maximum energy product between 227-430 $kJ.m^{-3}$,
- Maximum operating temperature 80-220°C.

Although NdFeB magnets are lightweight (cf Table I. 4), have better magnet properties and less eddy losses than those of $SmCo$. NdFeB are very sensitive to the high temperature. Polarization decreases dramatically with quick demagnetization of NdFeB compared to $SmCo$ as illustrated in Figure I. 11. Moreover, from thermal

conductivity point of view, SmCo is better than NdFeB. It is also important to specify the mechanical properties of the PMs used in the rotor. Table I. 4 summarizes the mechanical properties of rare-earth PMs. Rare earth materials encounter degradation coming from corrosion, heat or mechanical impact. Therefore, their magnetic properties will degrade over time. In this way, NdFeB have relatively a low resistance to oxidation and corrosion without layer. They are usually covered by a surface protection, made of nickel for instance.

Table I. 4. Some properties of rare earth magnets [Arnold Cata]

	Density (kg/m ³)	electric resistance ($\mu\Omega \cdot \text{cm}$)	Thermal conductivity (W.m ⁻¹ .K ⁻¹)	Tensile strength (MPa)	Modulus of elasticity (GPa)	Hardness Vickers
SmCo ₅	8400	55	11	120	140	600
Sm ₂ Co ₁₇	8300	90	10	120	140	600
NdFeB	7600	180	7.6	285	-	620

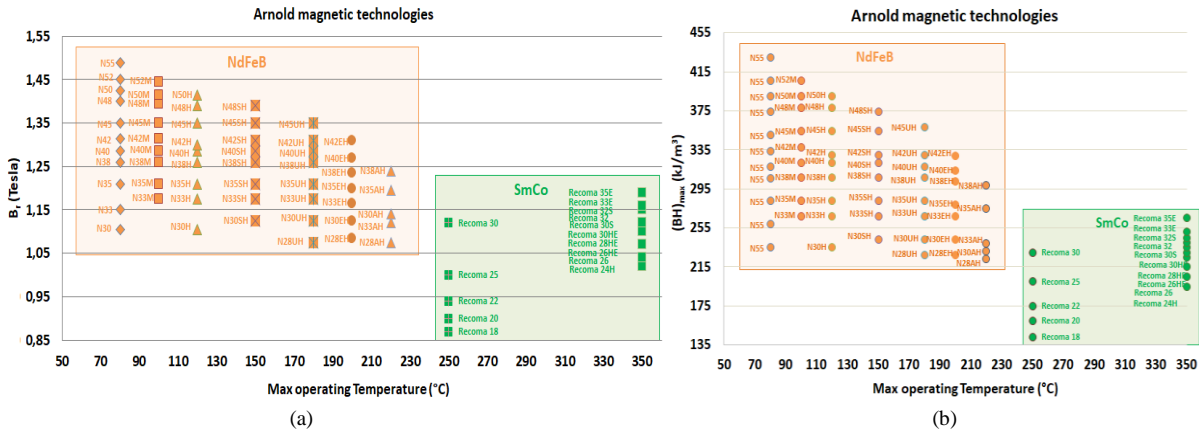


Figure I. 10. NdFeB and SmCo permanent magnets of Arnold magnetic technologies: (a) remanence, (b) max magnetic energy [Arnold Cata]

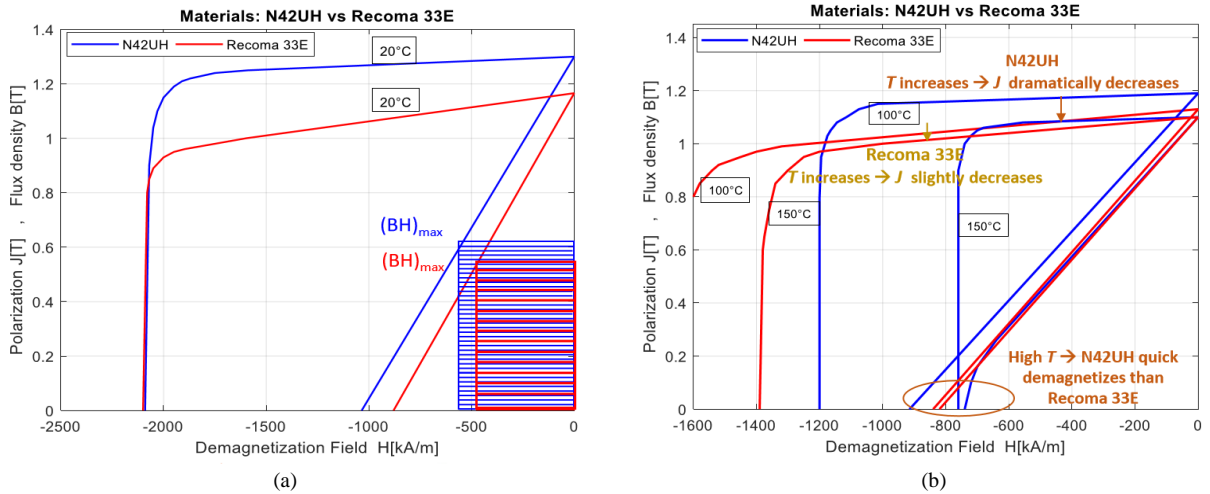


Figure I. 11. Comparison between NdFeB (N42UH) and SmCO (Recoma33E): (a) Characteristics at 20°C, (b) Characteristics at 100°C and 150°C [Arnold Cata]

- Electrical sheet

Electrical machines are submitted in most cases to alternating fields. To limit losses in high frequency due to eddy currents, magnetic alloys are generally used as thin sheets. There are three kind of alloys: Nickel Iron alloy (NiFe), Iron Silicon alloy (SiFe) and Cobalt Iron alloy (CoFe).

- Nickel Iron alloy (NiFe)

Nickel Iron alloy is based on nickel addition rates varying from 36% to 80%. The Nickel Iron alloy has very low magnetic coercivity, which leads to a superior relative permeability. The NiFe sheets have a thickness between 0.1-0.5mm. NiFe is characterized by high density 8200kg/m³ with low flux density $B_s=1.3-1.5$ T and $H_c=3-5$ kA/m. Typically, Nickel Iron sheets are used for high speed very low power electric motors.

- Silicon Iron alloy (SiFe)

In SiFe alloy, silicon makes iron mechanically harder; however, it decreases the saturation of flux density. We distinguish two types of SiFe sheets: Grain-Oriented and Non-Grain-Oriented sheets. The first one is

characterized by fixed magnetic flux orientation usually used in transformers, while Non-Grain-Oriented has multiple directions used in electrical machines. Non-Grain-Oriented SiFe alloys are often composed of iron with 1-3% of silicon, 1% of aluminum, 0.5% of manganese. Commonly, these sheets have flux density of 1.64T at 2.5kA/m as shown in Figure I. 12.a. Their typical thickness is between 0.35mm to 1mm. There are also non-grain-oriented sheets with thickness below 0.3mm manufactured for reducing losses (Figure I. 12.b). These sheets are called "Thin Non Oriented (NO)". They are composed of iron with 3% silicon content, 0.4% aluminum. The flux density of these laminations reaches 1.6T at 1.8kA/m. Table I. 5 presents all properties of some examples of these laminations.

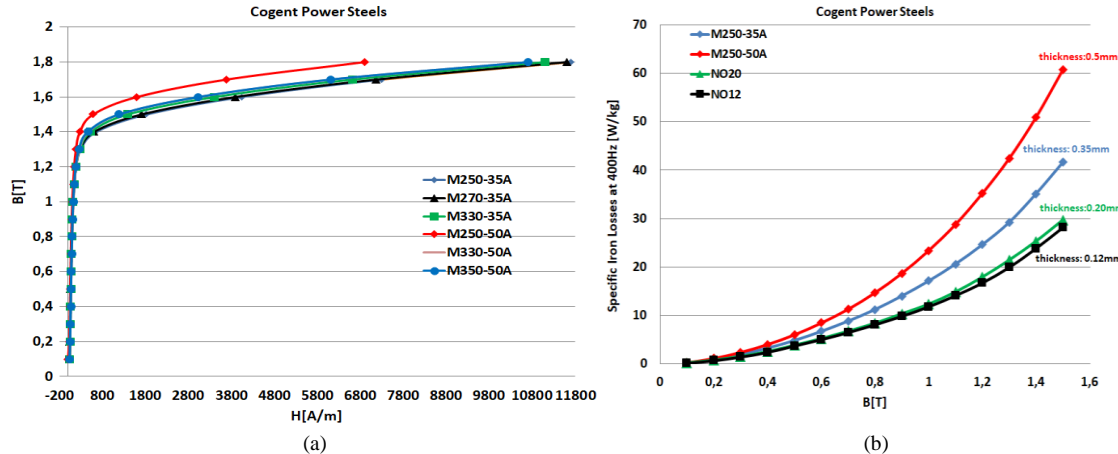


Figure I. 12. B(H) curve of Non-Grain- Oriented sheets having 0.35mm and 0.5mm thicknesses, (b) Specific iron losses at 400Hz of Non-Grain-Oriented and Thin Non-Oriented [CogCat]

Table I. 5. Properties of Non-Grain- Oriented SiFe alloy [CogCat]

Name	Magnetic properties			Physical properties			Mechanical properties		
	Saturation induction [T]	Loss at (50Hz&1.5T) [W/kg]	Coercivity field [A/m]	Density [kg/m ³]	Electrical resistivity [μΩm]	Thermal conductivity [W.m ⁻¹ .K ⁻¹]	Yield strength [MPa]	Tensile strength [MPa]	Modulus elasticity [GPa]
M235-35A	1.7	35	2.35	7600	0.59	36	460	580	185
M250-35A	1.76	40	2.50	7600	0.55	35	455	575	200
M250-50A	1.7	30	2.50	7600	0.59	36	475	590	175
M270-35A	1.77	40	2.70	7600	0.52	36	450	565	200
M310-50A	1.79	40	3.10	7650	0.55	36	385	500	185
M330-35A	1.77	40	3.30	7650	0.42	36	315	455	210
M350-50A	1.78	45	3.50	7650	0.42	36	320	460	200
M330-50A	1.77	40	3.30	7650	0.42	36	310	465	200
M400-50A	1.79	50	4.00	7700	0.42	36	325	465	200
M800-65A	1.85	100	8.00	7800	0.25	36	300	405	210

→ Cobalt iron alloy CoFe:

Cobalt iron alloys offer the most magnetic attractive features compared to FeSi alloys. In addition, their heat resistance makes them the suitable product for applications in severe environmental stress such as aerospace application. Typical CoFe laminations used in electrical machine have typical composition of 49% Cobalt, 49% Iron and 2% Vanadium. Typical thickness sheet is between 0.2 mm to 0.5mm. Prosperities of some CoFe alloys are summarized in Table I. 6. Cobalt Iron alloys has highest flux saturation level and lowest specific iron losses compared to Thin Non- Oriented. However, Cobalt Iron alloys remain heavyweight compared to SiFe alloys (cf. Figure. I. 13 and Figure I. 14). Therefore, to choose the suitable material, a trade-off between specific iron losses, induction and density should be carried out.

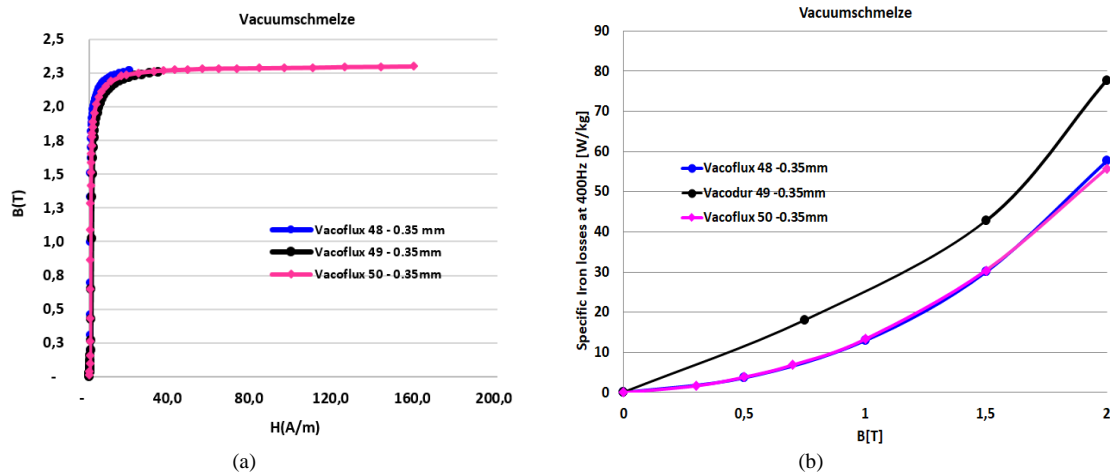


Figure I. 13. Iron Cobalt alloy having 0.35mm: (a) B(H) curve (b) Specific Iron losses at 400Hz [CogCat]
Table I. 6. Properties of Iron Cobalt alloy Vacuumschmelze materials [VacCat]

Name	Magnetic properties			Physical properties			Mechanical properties		
	Saturation induction [T]	Loss at (50Hz & 1.5T) [W/kg]	Coercivity field [A/m]	Density [kg/m ³]	Electrical resistivity [$\mu\Omega\text{m}$]	Thermal conductivity [W.m ⁻¹ .K ⁻¹]	Yield strength [MPa]	Tensile strength [MPa]	Modulus elasticity [GPa]
Vacoflux 48	2.35	1.5	35	8120	0.42	30	190	220	200
Vacodur 49	2.35	1.6	50	8120	0.42	32	210	400	200
Vacoflux 50	2.35	1.6	50	8120	0.42	30	250	550	210

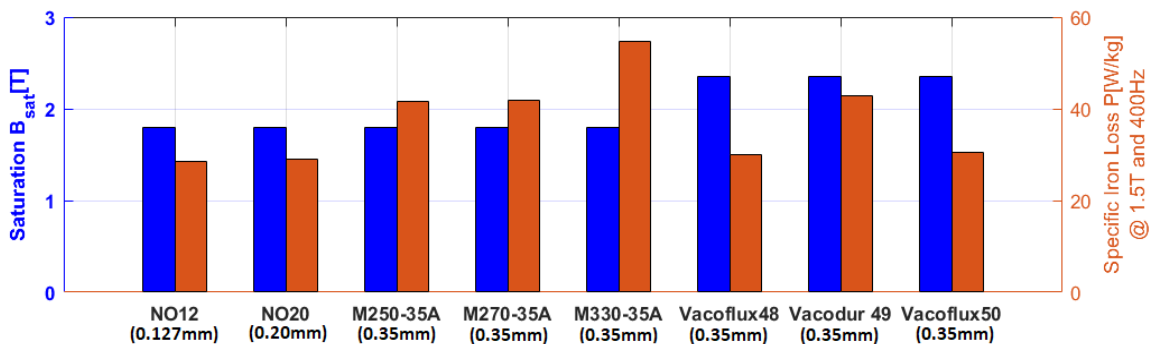


Figure I. 14. Comparison between Silicon-Iron and Cobalt-Iron alloys

I.2.3 Winding and insulations

- Conductors

Several conductor technologies are used in winding of electrical machines as summarized in Figure I. 15. The choice of the conductor type can be related to considerations regarding the filling factor, the losses at high frequency, the supply voltage...etc. In the following each conductor is detailed.

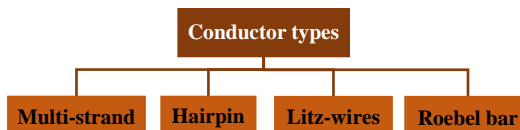


Figure I. 15. Conductor types used in winding of electrical machines

→ Multi-stranded conductors

Circular strand is a classical conductor type used in low and medium power electrical machines. Figure I. 16 illustrates an example of stranded random wound used in winding of HEV [Hen_14]. Usually, winding using this type of conductor has the lowest manufacture cost. However due to its circular shape, with a random wound the fill factor can be around 40-45% [Rey_16].



Figure I. 16. Multi-stranded random wound: (a) inside slot, (b) end-winding [Hen_14]

→ Hairpin conductors

Hairpin or "Hair-pin" conductors are another type of conductors used in the winding of HEV electric motors as illustrated in Figure I. 17 [Bur_17] [Liu_19]. Hairpin conductors are often enamelled copper rectangular cross-sections, which can reach higher copper filling unlike to previous conductors [Bia_18] [Gla_20] [Bur_17] [Rog_18] [Mil_19]. They are assembled at the one end by welding which allows reducing end-winding length (cf. Figure I. 16. b). Furthermore, using these conductors allow ensuring high mechanical stiffness and overload capacity due to high thermal conductivity of winding. However, Hairpin conductors are not suitable for high speed operation due to the increase in electrical losses due to skin and proximity effects [Dub_18]. The latter can be moderately decreased by using transposition as presented in [Bia_18] [Ber_18] or by using flat shape of hairpin which results in a loss of profit in the filling factor.

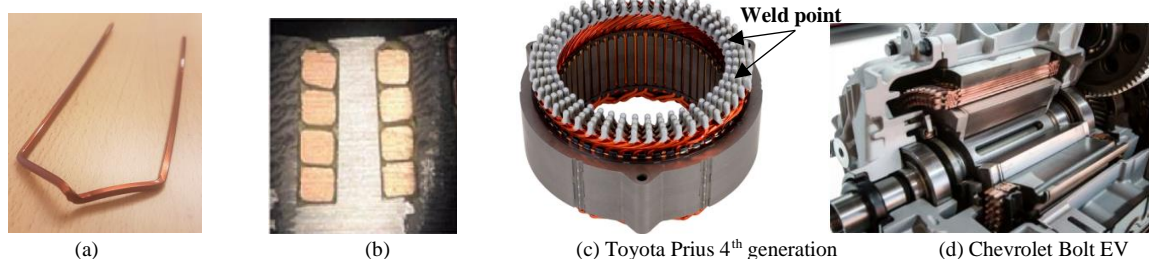


Figure I. 17. Hairpin winding: (a) Hairpin single conductor [Deu_19], (b) inside slot, (c) Toyota Prius MY17 [Bur_17], (d) Chevrolet Bolt EV [Liu_19]

→ Litz wire conductors

Litz-wire conductors are an alternative solution to hairpin conductors for high speed electric motors as it is used in [Yoo_16] [Mar_17]. Litz-wire conductor consists of several enamelled copper wires assembled in parallel under round or rectangular shapes. Its wires are twisted as illustrated in Figure I. 18 in order to reduce or even to remove losses due to skin and proximity effects. Several Litz-wire constructions are proposed by manufacturers according to the sizes and recommended operating frequency ranges. These manufacturers ensure that Joule losses due to skin and proximity effects are hugely lower. Although Litz-wire conductor seems advantageous in high operating frequency, it is less attractive due to its low own fill factor. Table I. 7 gives the fill factor of rectangle Litz-wires used in high speed electric motor [Yoo_16].

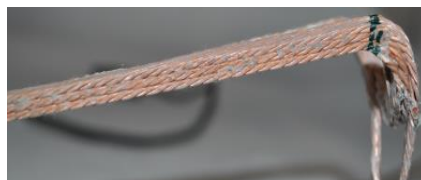


Figure I. 18. Rectangular Litz wire (Vendor data single-layer polyimide) [Yoo_16] [Mar_17]

Table I. 7. Fill factor of rectangular Litz-wire conductor "Vendor catalogue" [Mar_17]

AWG	30	32	34	36	38	40
Fill factor (%)	50.1	50.7	50.1	48.6	52.5	47.3

→ Roebel bar

Roebel bars are classical conductors used in very high power-high voltage electrical machines. They consisting of a large number of individual braided rectangular transposed strands as presented in Figure I. 19. Roebel bars ensure high fill factor in slots.

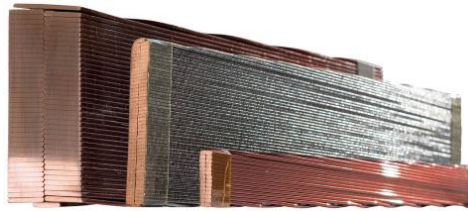


Figure I. 19. Roebel bar [Ast_cat]

Table I. 8 summarizes the fill factor for different conductors used in industrial electric machines.

Table I. 8. Fill factor of industrial electric machines with different conductor types

Conductor types	Muti-stranded conductors	Hairpin conductors	Litz-wire conductors
Electrical Machines EM Reference	BMW i3 [Bur_16][Mer_14]	Prius 4 th generation [Bur_17]	Illinoi University [Yoo_16]
Fill factor (%)	0.45	0.65	<0.5

- Winding configurations: "Concentrated and distributed windings"

Two winding configurations are employed in slotted electrical machines: distributed winding and concentrated winding. Traditionally, distributed and concentrated windings can be referred by number of slots per pole and per phase N_{spp} . Distributed winding is characterized by $N_{spp} > 1$, while when $N_{spp} \leq 1$, winding is concentrated overlapping for $N_{spp}=1$ and concentrated non-overlapping for $N_{spp} < 1$. Figure. I. 20 illustrates these configurations. Distributed and concentrated windings present advantages and drawbacks summarized in Table. I. 9. To choose winding configuration, the trade-off study between weight and performances is required.

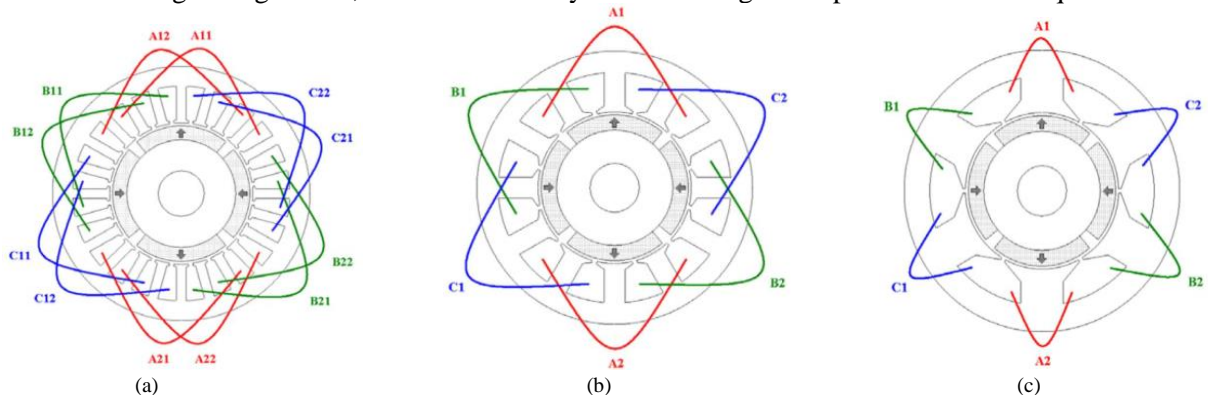


Figure I. 20. Winding configurations: (a) distributed winding, (b) concentrated overlapping winding, (c) concentrated non-overlapping winding [Ref_10]

Table I. 9. Comparison of advantages and drawback of concentrated and distributed winding [Sar_17] [Ref_10]

Winding configuration	Concentrated winding	Distributed winding
Advantages	<ul style="list-style-type: none"> → less end-winding length → less weight winding → high slot fill factor → improved fault tolerance capability due to small mutual inductance → high self-inductance → easy implementation of inner cooling 	<ul style="list-style-type: none"> → high fundamental electromagnetic torque → lower iron losses due to poor harmonic content → lower eddy current losses in PM → lower mechanical vibration risk in winding
Drawbacks	<ul style="list-style-type: none"> → high eddy current losses in PM → high iron losses due to high harmonic content → high mechanical vibration risk in winding → lower fundamental electromagnetic torque due wealthy harmonic content 	<ul style="list-style-type: none"> → high end-winding length → more weight winding → lower slot fill factor → lower self-inductance

- Insulation materials

Electrical machines use several insulation components as shown in Figure I. 21. Their material choices are very critical considering that electrical and thermal constraints are very harsh. The main insulation types are:

- Slot liner, slot separator
- Conductor or wire insulation

- Wedge
- Phase to phase insulation in slot and in end-winding
- Impregnating varnish and resin
- Insulation of the connection leads and the terminals.

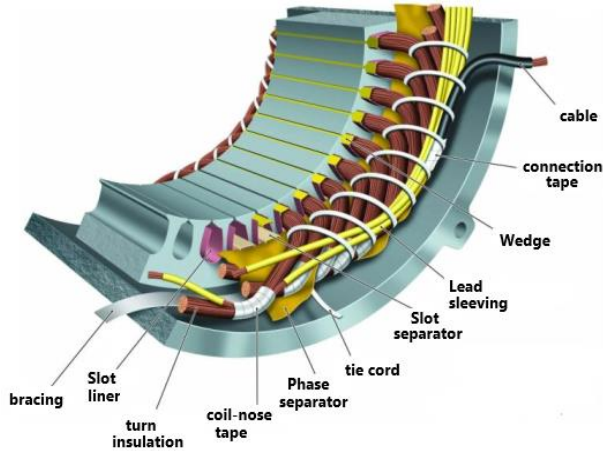


Figure I. 21. Insulation system in electrical motors [Cha_08]

Slot liner prevents conductors to be in contact with the electric sheets. Slot separator and phase insulation provide a high-voltage barrier between conductors, with good formability and mechanical strength. Most of insulation materials used for slot liner, slot separator, phase to phase insulations are made with organic paper, organic fibre, inorganic mica, organic laminated clothes and laminated papers. There are also laminated combinations of materials such as rag paper and organic polyester Film. Wedge is placed over the winding in each slot to close the slot and keep the wires compact and guard against vibration. Typically, wedges are made of paper, canvas and fibber Glass impregnated with a thermosetting resin such as silicone, and organic epoxy. Moreover, insulation comprises also impregnating with varnish and resin. They are used as protection and improve insulation life and reliability. Each insulation material has a characteristic temperature above which it should not operate. Several standard test procedures have been developed to rate the capability of the insulation to resist deterioration at high temperature. Among them there is IEEE standards. The characteristic temperature of IEEE standards is defined from nominal life of 20000 hours as presented in Figure. I. 22.a. Therefore, the following characteristic temperatures can be distinguished: 105°C, 130°C, 155°C and 180°C. Each characteristic temperature describes insulation and thermal class as:

- 105°C → Class "A"
- 130°C → Class "B"
- 155°C → Class "F"
- 180°C → Class "H"

Insulation and thermal classes are divided into maximum ambient temperature, allowable heating and thermal reserve, cf. Figure I. 22.b. Within technological thermal advances of insulation materials, other classes have been added: 200°C, 220°C and 240°C thermal classes. Usually, electric motors are sized to ensure that insulation does not operate above the maximum temperature capability. Furthermore, other characteristics linked to dielectric and mechanical strengths have to be taken into account. Dielectric strength of insulation materials defines the maximum voltage required to produce Partial Discharge (PD) leading progressive deterioration. Partial discharge usually takes place on the air bubbles located near to or inside the insulation material and under electric field higher than the dielectric strength. Moreover, under low pressure environment, PDs can be more prevalent. For high voltage strength, mixing organic insulation materials with inorganic material such as Mica is needed. Mica tolerates PDs during nominal operating of electric machines. Table I. 10 summarizes the intrinsic features of insulation materials.

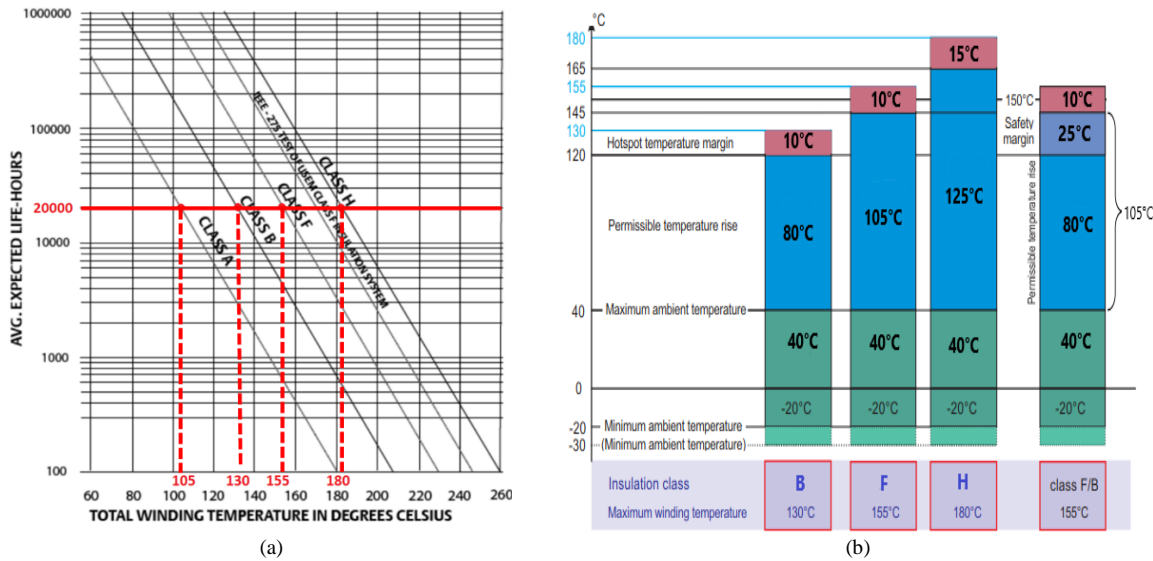


Figure I. 22. (a) IEEE Standard tests of insulation classes, (b) Insulation and thermal classes

Table I. 10. Intrinsic features of insulators [Pyrh_08]

Insulator (with trade names)	Density [kg/m ³]	Dielectric strength [kV/mm]	Tensile strength [N/mm ²]	Elasticity modulus [N/mm ²]	Operating temperature [°C]	Thermal conductivity [W.m ⁻¹ .K ⁻¹]
Polyester PTEP film (Mylar, Melinex, Hostaphan)	1380	150	140-160	3900	130	0.29
Polyimide film(Kapton)	1420	280	180	3000	220	0.12
Polysulphone PS film (Flacron, PES)	1370	175	90	2500	180	-
Polyamide(Teflon)	2150	260	13-27	500	180	0.20
Mica folium (silicone binder)	2883	20 to 200	30-50	-	180	0.5-0.6
Epoxy resin	1299	30	-	-	155	0.64
Glass Fiber	2560	18	1000-2000	70000	180	0.99
Cotton Fiber	1520		250-500	5000	105	0.07-0.14

I.2.4 Further improvements in terms of materials and technological solutions

Several technological solutions and material improvements are proposed in order to reduce their weaknesses and losses.

- Technological solution for reducing losses

Some technological solutions are under study to reduce main losses in electrical machines. Among these solutions, we can cite electrical steel sheets up to 50µm to reduce iron losses at high frequency (cf. Figure I. 23.b) and axial, radial and circumferential segmentations of permanent magnets up to 0.5mm in order to reduce eddy current losses.

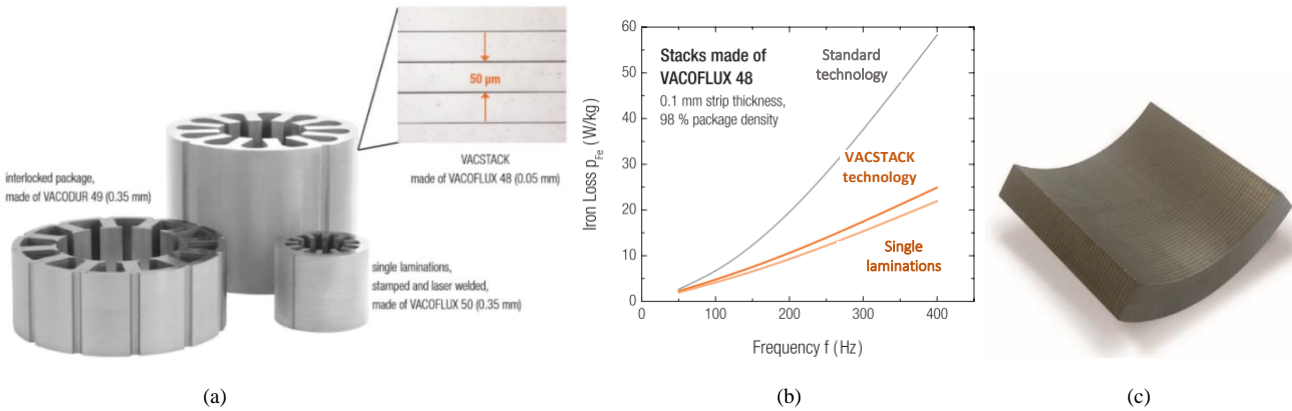


Figure I. 23. Technological solution for reducing losses: (a) Vacuumschmelze lamination (Vacstack):50µm, (b) Specific iron losses, (c) segmentation in permanent magnets up to 0.5mm (Arnold Magnets)

- High temperature NdFeB magnets

In 2018, Arnold magnetic technologies manufacturer proposed new NdFeB magnets called “Grain Boundary Diffused Neodymium Iron Boron *GBD Neo*” suitable for high operating temperature with high magnetic energy [ArnoldsCata]. GBD Neo is made with reducing Dysprosium (Dy) and Terbium (Tb) contents. Figure I. 24 compares the traditional NdFeB magnets with the new generation of NdFeB.

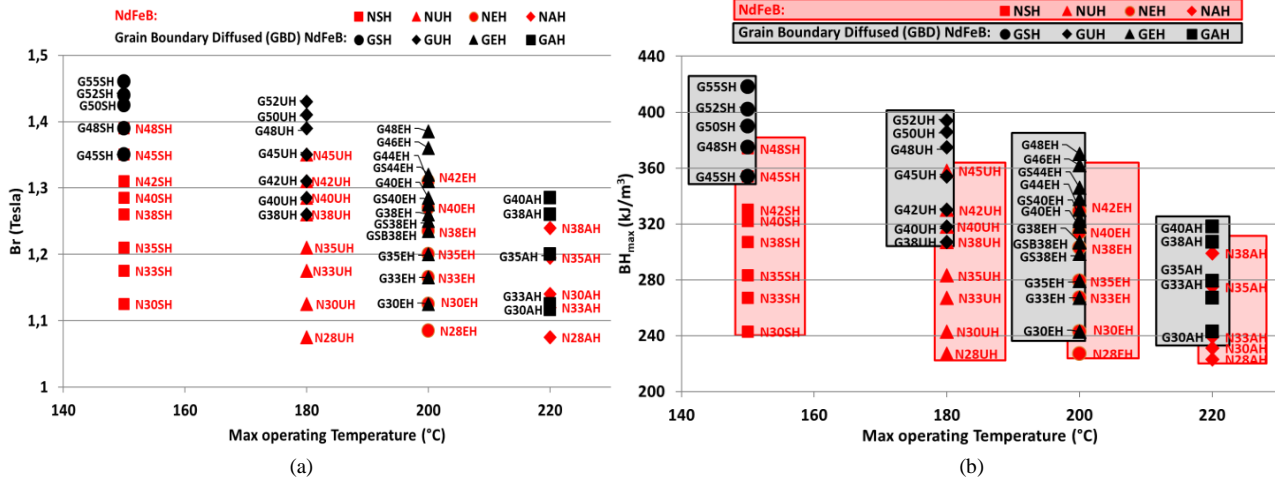


Figure I. 24. Comparison of High temperature NdFeB with New high temperature GBD NdFeB: (a) Remanent flux density vs max. operating temperature, (b) Magnetic energy vs max. operating temperature (Arnold Magnets) [ArnoldsCata]

- Wires for very high temperature

New wires with very thin ceramic insulation are proposed to improve the thermal resistance and the dielectric strength [CerCat]. These wires are made of 73% copper and 27% nickel. Their insulation thickness is between 5 to 20µm as shown in Figure I. 25. Using ceramic as insulation offers advantage of operating at high temperature up to +500°C, however ceramic insulator has very low dielectric strength. Its breakdown voltage is 150V AC. Therefore, ceramic insulator is attractive for electric motors with allowed partial discharges (case of long term target). Otherwise, ceramic insulator is less attractive (case of medium term target). It is also important to note that ceramic is mechanically sensitive to vibrations.



Figure I. 25. Ultra-thin and high temperature ceramic wire [CerCat]

I.2.5 Bearings

Bearings in electrical machines are used to eliminate friction, to carry loads, to locate and align the shaft axially [Mal_06] [TimPr]. There are two types of bearings: magnetic bearings and mechanical bearings. Magnetic bearings support loads using magnetic levitation as illustrated in Figure I. 26. They do not require lubrication and maintenance since there is no contact. Due to requirement of control device, electric supply and sensors for magnetic levitation operating, magnetic bearings are heavy and not compact unlike mechanical bearings. Mechanical bearings can be classified into: thrust bearings and radial bearings. Thrust bearings accommodate loads that are predominantly in the direction of shaft. In this thesis thrust bearings are not considered. Radial bearings accommodate loads that are perpendicular to the shaft. The commonly radial bearings used in electrical machines are:

- *Deep groove ball bearings*: rings of deep groove ball bearings are made with steel as illustrated in Figure I. 27.a. They are suitable for high speeds and small radial and axial loads as illustrated in Table I. 8.
- *Angular contact ball bearings*: have inner and outer ring raceways that are displaced relative to each other in the direction of the bearing axis (cf. Figure I. 27. b). Usually they are suitable for high combined loading. In addition, as deep groove ball bearings, angular contact ball bearings are used for high speed.

- *Cylindrical roller bearings*: rollers are cylindrical as shown in Figure I. 27. c. The shape of rollers allows bearings to handle high radial loads. Cylindrical roller bearings are also suitable to high speed.
- *Spherical roller bearings*: have two rows of spherical rollers. A common sphere outer ring raceway and two inner ring raceways inclined (see Figure I. 27d). This type of bearings can handle very heavy radial and lower axial loads at low speed.
- *Toroidal roller bearings*: have one row of long, slightly barrel-shaped symmetrical rollers and torus-shaped raceway profiles as presented in Figure I. 27e. They are designed to accommodate high radial loads and for high speed as noted in Table I. 11. Figure I. 28 shows limit speeds function of inner diameter and handle static loads of bearings manufactured by SKF.

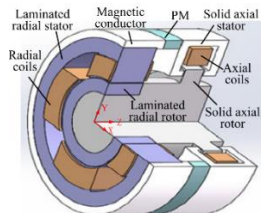


Figure I. 26. Magnetic bearings [Le_16]

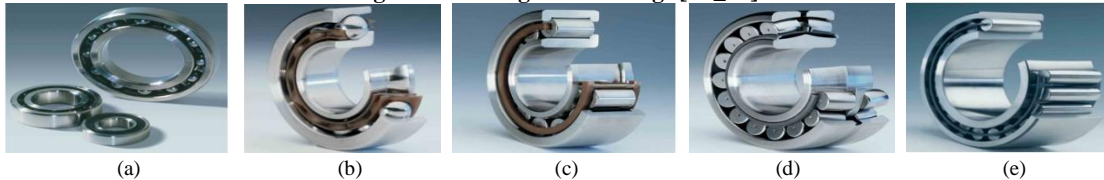


Figure I. 27. SKF Radial bearings types (a) Deep groove ball bearing, (b) Angular contact ball bearing, (c) Cylindrical roller bearing, (d) Spherical roller bearing (e) Toroidal roller bearings [SKFCat]

Table I. 11. Bearing performance characteristics [Mal_06] [TimPr]

Bearing type	Speed capability	Radial loading	Axial loading	Combined loading
Deep groove ball bearing	5	3	3	3
Angular contact ball bearing	5	3	4	4
Cylindrical roller bearing	5	5	2	2
Spherical roller bearing	3	5	2	3
Toroidal roller bearing	4	5	1	2

Notation is scaled from 1 (being poor) to 5 (being excellent)

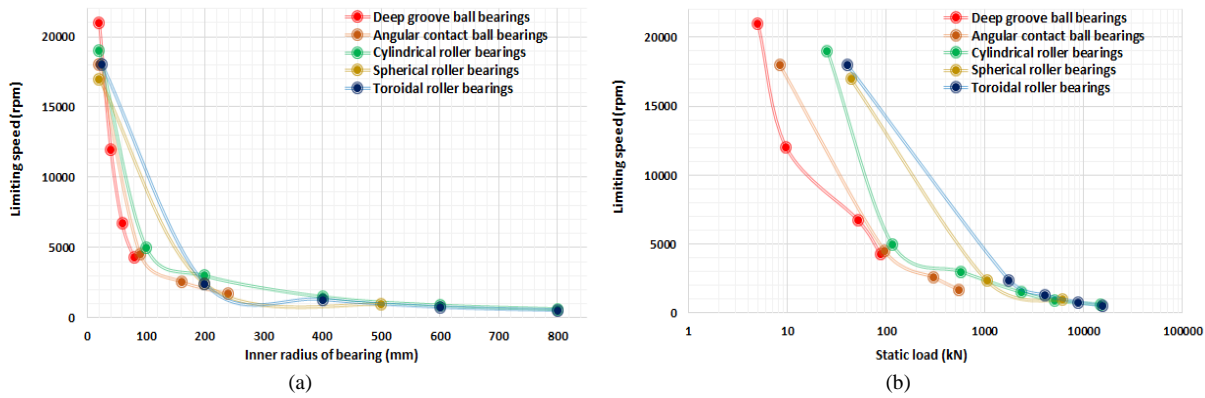


Figure I. 28. SKF bearings: (a) Limiting speed vs inner radius of bearing, (b) Limiting speed vs static load [SKFCat]

- Further radial bearing type: "Hybrid bearings"

Hybrid bearings have rolling element made with ceramic as shown in Figure I. 29. They are characterized by lower density of rolling element about 60% than other types of bearings with the same sizes. The reduced lower density and inertia offer a higher speed capability.

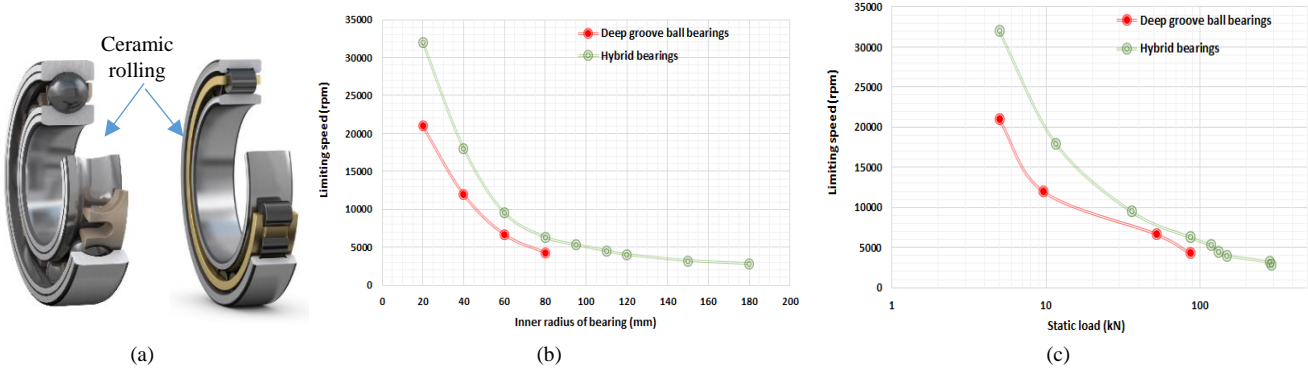


Figure I. 29. (a) Hybrid Bearings, comparison between classic deep groove ball bearings: (b) limiting speed vs inner radius, (c) limiting speed vs static load [SKFCat]

I.2.6 Sleeves

In high speed electric machines, permanent magnets are usually retained by sleeves for magnets mounted on the surface or by electrical sheets for buried magnets. Two groups of sleeves can be distinguished:

- Non-magnetic metallic sleeves: made with Titanium or Inconel,
- Non-metallic wound sleeves: made with Carbon Fiber or Glass Fiber as shown in Figure I. 30.

Due to their high permissible stress, non-metallic wound sleeves ensure high permitted peripheral speed up to 320m/s compared to non-magnetic metallic sleeves (cf. Table I. 12). Moreover, non-metallic wound sleeves are lighter weight than the non-magnetic metallic sleeves and have lower eddy current losses for Carbon Fiber and none losses for Glass Fiber. However, for high temperature environment higher than 180°C only non-magnetic metallic sleeves are suitable. Trade-off between mechanical, thermal and electrical properties should be done to choose sleeves for surface mounted permanent magnets electrical machines.

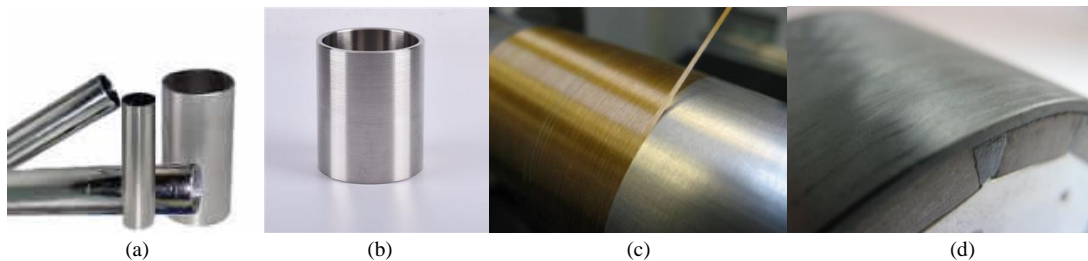


Figure I. 30. Sleeves: (a) Titanium, (b) Inconel, (c) Carbon Fiber, (d) Glass Fiber [ArnoldCata]

Table I. 12. Properties of retaining sleeve materials used in surface mounted permanent magnet synchronous machines
[Zha_15] [Gie_10] [Fan_15]

Sleeve materials		Non-magnetic metallic sleeve		Non-metallic wound sleeve	
		Titanium	Inconel	Carbon Fiber	
Properties	Unite			Radial	Tangential
Density	[kg.m ⁻³]	7850	4400	1620	
Elastic modulus	[GPa]	206	205	140	8.8
Poisson ratio	-	0.31	0.28	0.28	0.015
Maximum permissible stress	[MPa]	-	1100	1400	-100
Thermal conductivity	[W.m ⁻¹ .K ⁻¹]	16	7.5	0.71	
Electric conductivity	[S.m ⁻¹]	6.1×10^5	8×10^5	3×10^4	
Eddy current losses	-	high	high	low	
Maximum peripheral speed	[m/s]	240		320	
Maximum temperature	[°C]	290		180	

I.2.7 Cooling technologies

Cooling for electric machines is mandatory for remove heat and for decrease temperature within electric machine. In addition, cooling electric machines allow preserving the life of bearings and insulation system, to prevent the demagnetization of permanent magnets and to prevent excessive heating of the surroundings.

Typically, in industrial and commercial electric machines, heat transfer is: natural, forced or combination between natural and forced heat transfer modes.

In low power electric machines, heat is removed:

- by natural convection on the external surface of fins for closed configuration,

- by natural convection on all surfaces of opened configuration,
- by conduction on all solid area,
- by radiation to ambient environment.

In medium and high power electric machines, heat is removed:

- by conduction on all solid area,
- by forced convection of liquid coolant,
- by forced convection of air due to rotor rotation.

Natural and forced heat transfer modes can be distinguished by heat transfer coefficient " h_{cv} ". Table I. 13 shows some typical values of heat transfer coefficient of some common coolants and depending on cooling modes. Forced heat transfer mode is characterized by high heat transfer coefficient up to $7000\text{W.m}^{-2}\text{K}^{-1}$ while natural mode is characterized by low heat transfer coefficient.

There are several classical forced cooling methods used electric machines. They can be classified according to their location and to their cooling approach as given in Table I. 14.

Table I. 13. Typical values of heat transfer coefficient of some coolants [Wei_14]

Coolant	Heat transfer coefficient h_{cv} [$\text{W.m}^{-2}\text{K}^{-1}$]	
	Natural convection	Force convection
Air	5 to 20	20 to 200
Water	30 to 300	300 to 7000
Engine Oil	100 to 300	400 to 2000

Table I. 14. Summary of forced cooling methods

Location	Cooling approach	Cooling technology	Used coolant
Housing	Indirect cooling method	Housing jacket	Oil, Water, Ethylene Glycol Water 50/50
Stator core	Direct cooling method	Cooling channels	Water, oil, air
Slot	Direct cooling method	<ul style="list-style-type: none"> • Cooling channels • Inner coolant ducts 	<ul style="list-style-type: none"> • Air, oil • Water, Polyalphaolefin Oil (PAO)
	Indirect cooling method	<ul style="list-style-type: none"> • Direct heat exchanger • Cooling channels 	<ul style="list-style-type: none"> • Water • Ethylene Glycol Water 50/50
End-winding	Indirect cooling method	<ul style="list-style-type: none"> • Liquid jet impingement • Spray cooling • Potting materials 	<ul style="list-style-type: none"> • Oil • potting materials
Rotor core	Direct cooling method	Axial ducts	Air
Shaft	Direct cooling method	Cooling channels	Water, oil

• Housing cooling

Housing jacket is an indirect cooling method. It is used for improving the heat transfer from the active part of the stator to the housing through conduction by contact between the housing and the stator and by convection in the coolant ducts, cf. Figure I. 31. There are many housing jacket topologies: spiral housing jacket, U-shaped with one duct, U-shaped with bifurcations, axial housing jacket as shown in Figure I. 31. Due to its practical manufacturing, U-shaped with one duct topology is the most used in industrial motors, especially, electric motor of hybrid electric vehicles as given in Table I. 15.

Effectiveness and limitations: housing jacket is an efficient cooling method for stator active parts; however, it is not efficient to dissipate heat from end winding and rotor. Moreover, its heat transfer capacity strongly depends on the cooling surface [Satru_17].

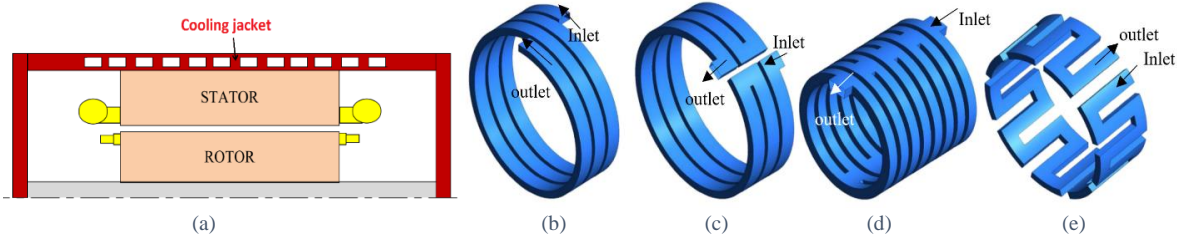


Figure I. 31. (a) Cooling jacket in housing, configurations: (b) spiral, (c) U-shaped (one duct), (d) U-shaped (bifurcated), (e) axial [Satru_2017]

Table I. 15. Industrial electric motors of HEV use housing jacket

HEV electric motor	Peak power [kW]	Specific power [kW/kg]	Coolant of housing jacket
Toyota Prius 2010	60	1.6	Oil
Sonata 2011	30	1.1	Oil
Nissan Leaf 2012	80	1.4	Ethylene Glycol Water 50/50
SRM 2015 Newcastle University	80	1.5	water

- **Stator core cooling**

Core stator can be directly cooled by channels as shown in Figure I. 32. Integrate cooling channels inside stator core allows to decrease the temperature winding more efficiently than housing jacket. However, high saturation magnetic flux can be achieved around cooling channels which leads to an increasing of iron losses and a decreasing in electromagnetic torque. For this purpose, cooling channels should be having small sizes. As previous cooling method, stator core cooling method is not enough efficient to dissipate heat of end-windings.

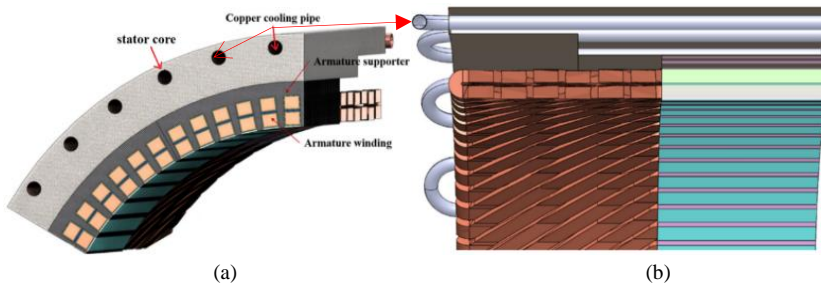


Figure I. 32. cooling channels inside stator core: (a) stator structure (b) cooling channels [Kim_17]

- **Slot cooling**

Several cooling methods used in slot are proposed given that losses in winding are the most difficult losses to remove due to the low thermal conductivity of insulation materials. We distinguish two cooling methods:

- indirect cooling methods: include all cooling techniques which are based on cooling applied between conductors,
- direct cooling methods: include all cooling techniques which are based on cooling inside conductors.

Indirect cooling method: "Direct Heat Exchanger":

Direct heat exchanger is an indirect cooling method. It is made up of several axial flow channels placed between slot winding as illustrated in Figure I. 33. These flow channels are connected through nonconductive bulkhead where the inlet and the outlet of fluid are located. Each flow channel is made of two copper plates using microfeature mesochannel technology to enhance the heat transfer coefficient. These copper plates are covered by insulation layer to separate them from conductors of winding. The fluid coolant is pumped by external pump [Sem_14].

Effectiveness and limitations: according to experimental tests carried out, direct heat exchanger cooling method is an efficient method by considering that the achieved current density was 24.7A/mm² for F (155°C) winding class [Sem_14]. Direct heat exchanger is straightforward to apply to the concentrated winding. However, the direct heat exchanger could be challenging to apply to a distributed winding due to significant end-winding length.

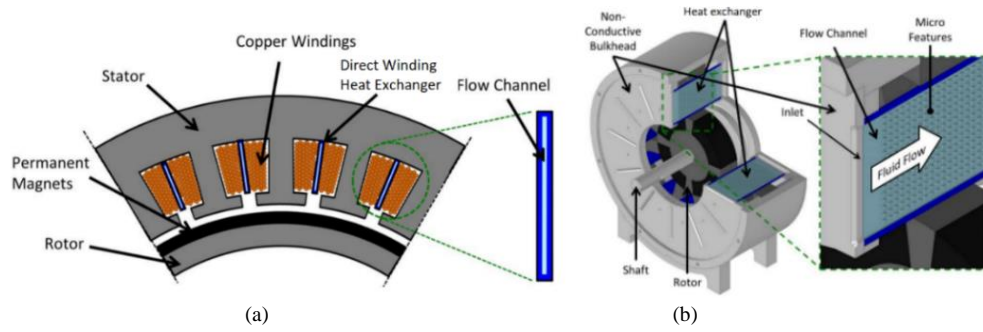


Figure I. 33. (a) Direct winding heat exchanger placed between winding, (b) machine prototype [Sem_14]

Indirect cooling method: "Cooling channels"

Cooling channels inside slot is another indirect cooling method applied on concentrated winding as illustrated in Figure I.34. The gaps resulting by chosen flat wires are used to insert parallel connected cooling channels in the bottom and in the middle as proposed in [Sch_15]. These channels are made of copper surrounded by a polyamide film which circulates inside the Ethylene Glycol Water 50/50.

Effectiveness and limitations: as previous cooling method, this technology is efficient when considering the high achieved current density (i.e. 20A/mm^2 according to [Sch_15]). However, it remains challenging to implement in distributed winding.

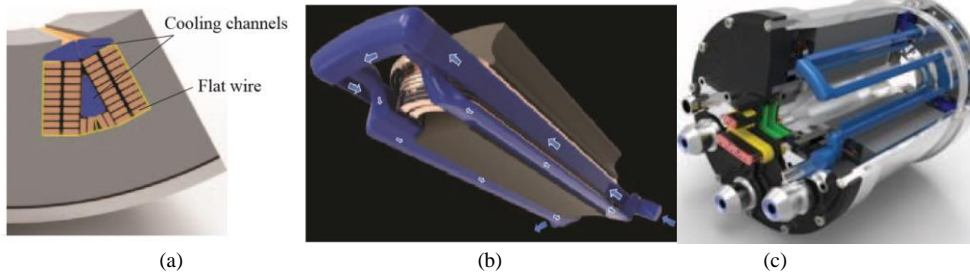


Figure I. 34. Indirect slot cooling: (a) cooling concept of slot with flat wires, (b) cooling in single tooth (c) assembly electric machine with indirect slot cooling [Sch_15]

Direct cooling methods:

Otherwise, for indirect cooling methods, the flow of coolant is directly integrated inside each conductor. Several direct cooling methods are proposed depending on the conductor types and structures:

- Litz wire winding with inner coolant ducts,
- Laminated winding with air and oil channels.

Inner coolant ducts for Litz-wire winding: are chosen by Lindh *et al* [Lin_16] to achieve high current density of axial electric motor winding. Figure I. 35 shows the conductor with its coolant conduit. 14A/mm^2 is achieved in steady state using this cooling technology.

Air and oil cooling channels for laminated winding: are proposed by [Rei_14] [Tig_16]. Coolant passes between laminations as illustrated in Figures I. 36 and 37. With an air flow rate of 600L/min , the achieved current density is 22.5A.mm^{-2} with H (180°) thermal class [Rei_14], whereas for an oil flow rate of 2L/min , the achieved current density is 50A.mm^{-2} [Tig_16].

Effectiveness and limitations: integration of coolant directly inside conductor has the advantage to reduce significantly the thermal resistance between conductor and coolant which improves cooling efficiency. However, this cooling method is more sensitive to damage risks compared to indirect cooling methods.

The heat transfer coefficients of indirect and direct cooling methods are summarized in Table I. 16.

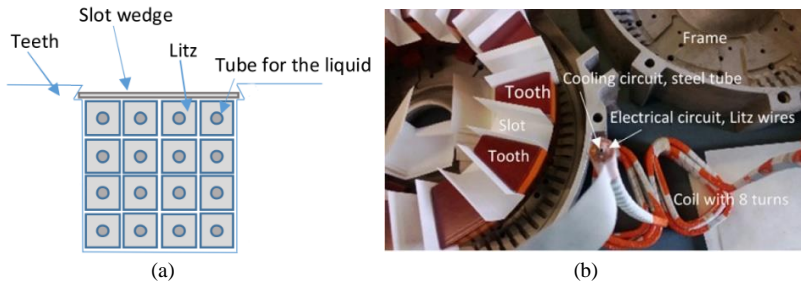


Figure I. 35. (a) Stranded and transposed winding conductors with coolant ducts, (b) Prototype of the stator with its coils [Lin_16]

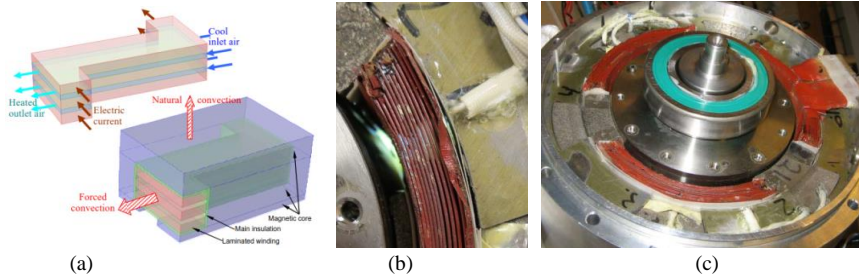


Figure I. 36. Laminated winding with electric conductive strips and air channel cooling, (b) zoom in prototype laminated winding, (c) machine prototype [Rei_14]

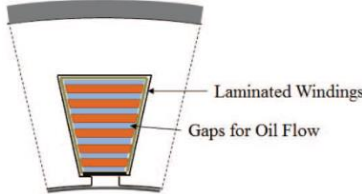


Figure I. 37. laminated winding with oil channel cooling [Tig_16]

Table I. 16. Heat transfer coefficients and achieved current densities according to slot cooling methods

Cooling methods		Current density (steady state)	Thermal class	Heat transfer coefficient (W.m ⁻² .K ⁻¹)	Reference
slot	Indirect cooling	24.7A.mm ⁻²	F (155°C)	5000 to 10000	[Sem_14]
	Cooling channel	20A.mm ⁻²	-	6000	[Sch_15]
	Direct cooling	14A.mm ⁻²	-	-	[Lin_16]
	Laminated winding	22.5A.mm ⁻²	H(180°C)	325 to 400	[Rei_14]

• End-winding cooling

Usually due to rotor rotation, end windings are naturally cooled by forced convection. Its efficiency requires important end-winding surface. To improve cooling of end-winding other methods are applied. We distinguish two cooling methods for end-windings using oil: Impingement of liquid jets or sprays and another cooling method using potting materials.

Oil jet impingements: as flat jet nozzle injections and dripping jets have been studied by [Dav_15]. Figure I. 38 illustrates oil jet impingements applied in end-winding. Oil jet impingement cooling method requires high flow rate for improving the heat dissipation in end-windings.

Oil sprays: in contrast to oil jet impingement, oil spray cooling method requires only low flow rate with high pressure [Lud_17]. Figure I. 39 shows examples of oil spray applied on distributed and hairpin end-windings.

Effectiveness and limitations: according to [Dav_15] the dissipation heat in end-winding using oil jet impingements cooling method can be multiplied by a factor of 2.5 to 5. In addition, through experimentally tests of oil sprays on stator and rotor end-winding performed by [Lud_17], high current densities are achieved: 18A/mm² for stator and 17A/mm² for rotor. As the coolant is in direct contact with the winding, damage risks limit the use of oil jet impingements and oil sprays cooling methods.

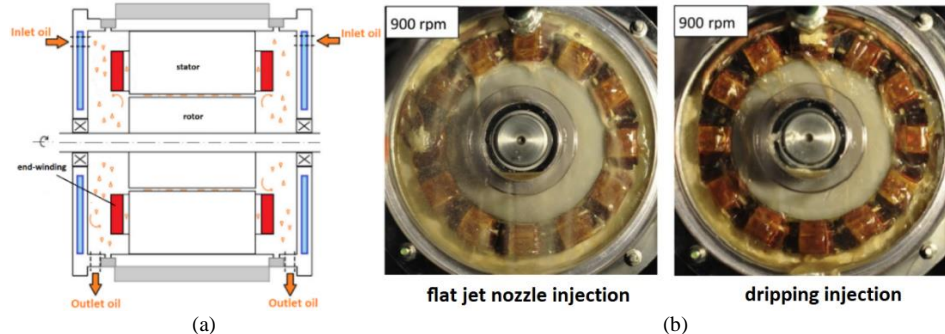


Figure I. 38. (a) oil jet cooling system for end-winding, (b) experimental two jet impingement methods [Dav_15]

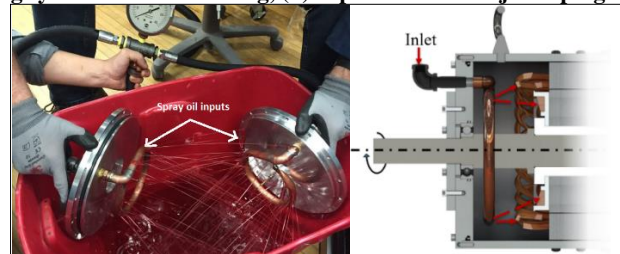


Figure I. 39. Oil spray cooling on the stator and rotor distributed end-winding [Lud_17]

Potting materials: consist of creating a conductive thermal path between end-windings and the housing, by using materials with a thermal conductivity higher than the thermal conductivity of the air, as it is illustrated in Figure I. 40. Table I. 17 summarizes some examples of potting materials applied in end-windings. Often, potting material cooling method requires a combination with water jacket in order to improve heat dissipation.

Effectiveness and limitations: a decreasing of 7°C and 6°C can be reached in end-winding according to [Pol_14]. However, potting material cooling method is less efficient than the previous two end-winding cooling methods.

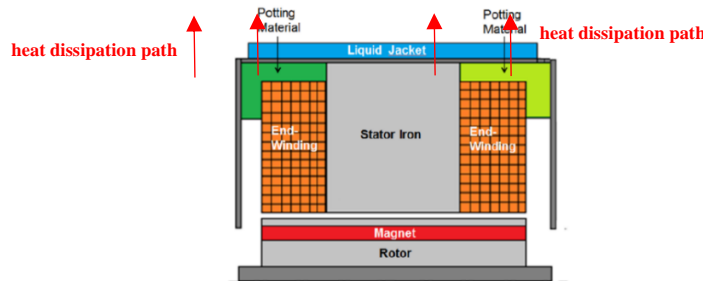


Figure I. 40. Potting materials for end-windings cooling [Pol_14]
Table I. 17. Electrical and thermal properties of potting materials [Pol_14]

Potting Materials	Thermal conductivity [W.m ⁻¹ .K ⁻¹]	Heat capacity [J.kg ⁻¹ .K ⁻¹]	Density [kg.m ⁻³]	Limit temperature [C°]	Dielectric strength [kV/m]	Electric resistivity [Ω.m]
Ceramacast 675N	100	740	3260	1200	1.2×10^4	10×10^{11}
Epoxy 2315	58	1000	1800	185	1.9×10^4	10×10^{14}
Alumina Filled Epoxy	20-25	-	-	-	-	10×10^{15}
AIN Filled Epoxy	3.8	-	2470	143	-	10×10^{16}
Silicone	2.0	-	1960	250	-	10×10^{16}

• Rotor core cooling

Often rotor cores are cooled by axial ducts as shown in Figure I. 41. An axial air flow passes through rotor ducts. Its flow rate increases within rotational speed increasing as it is experimentally demonstrated in [Ch_15]. Therefore, axial rotor ducts cooling method is efficient only for high rotational speed. Dipping rotor core to implement axial ducts allows to decrease the rotor weight and then to increase specific power of electric machine. However, the dipping should be carefully studied in sizing rotor phase in order to not decrease electromagnetic performances due to the increase in saturation of the flux density in the rotor core.

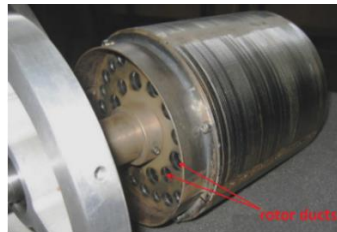


Figure I. 41. Axial rotor ducts: forced air convection cooling method [Ch_15]

- **Shaft cooling**

Liquid cooling method is the most involved in shaft. Figure I. 42 illustrates the proposed liquid coolant channel implemented in hollow shaft. A stationary cooling channel is implemented inside the shaft with a cross-section small enough to leave a gap between the shaft and the cooling channel. The liquid coolant enters through a stationary channel and exits through the gap between the shaft and the stationary cooling channel. Due to the shaft rotation, the cooling channel should be well maintained to avoid any vibration between the cooling channel and the shaft. Moreover, the shaft hollowing should be well studied due to mechanical stresses applied on the shaft, therefore manufacture this cooling method remains complicated.

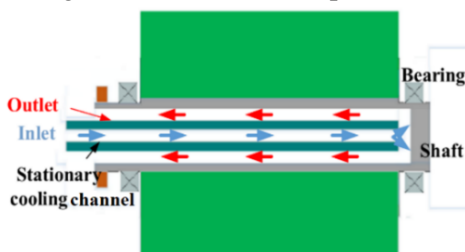


Figure I. 42. Cooling channel in shaft [Gia_17]

- **Further cooling methods "change phase cooling method: Heat pipes"**

Another cooling methods of electrical machines based on change phase principle are currently being developed. The phase change principle consists on a self-transportation of coolant from vapour phase located near the hot source to liquid phase near the cold source. In fact, the coolant is driven by an inner wick which does not require any external pumping as illustrated in Figure I. 43. This cooling method is widely used in electronic devices and it is known as "heat pipes". In the presence of temperature gradient, heat pipes can operate passively. In otherwise, heat pipes operate actively thanks an external condenser. In literature several structures using heat pipes actively operated are proposed:

- on the external surface of housing [Put_17],
- inside slots and stator core [Has_12],
- inside the shaft (Tesla motor patent [Tes_13]) as presented in Figure I. 44.

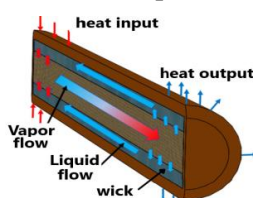


Figure I. 43. Heat transfer principle in heat pipe

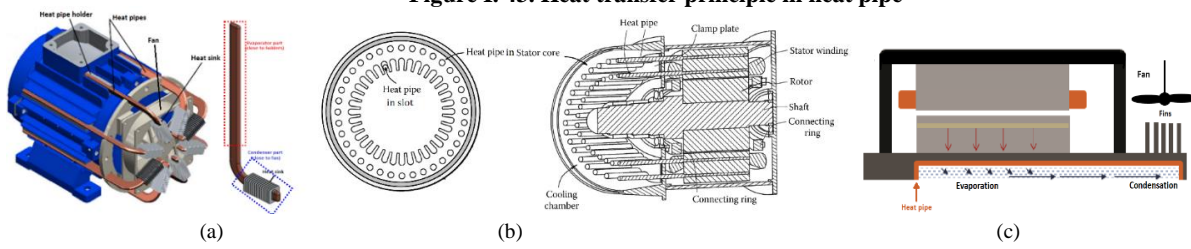


Figure I. 44. Heat pipe cooling methods proposed in electric machines: (a) housing [Put_17], (b) slots and stator core [Has_12], (c) shaft [Tes_13]

I.2.8 Conventional industrial motors

- Electric motors for railway traction application

In industrial applications with power range between 300kW-3MW such as railway tractions, three conventional electric motor topologies are involved:

- Wound Rotor Synchronous Machines (WRSM)
- Permanent Magnet Synchronous Machines (PMSM)
- Induction Machines (IM)

These topologies are most used due to:

- The high starting torque and high power factor of WRSM,
- The high efficiency and compactness of PMSM,
- The high robustness and low cost manufacturing and maintenance of IM.

In railway traction, the achieved specific power of WRSM and IM is less than 1kW/kg and equal to 1kW/kg for PMSM as shown in Figure I. 45.

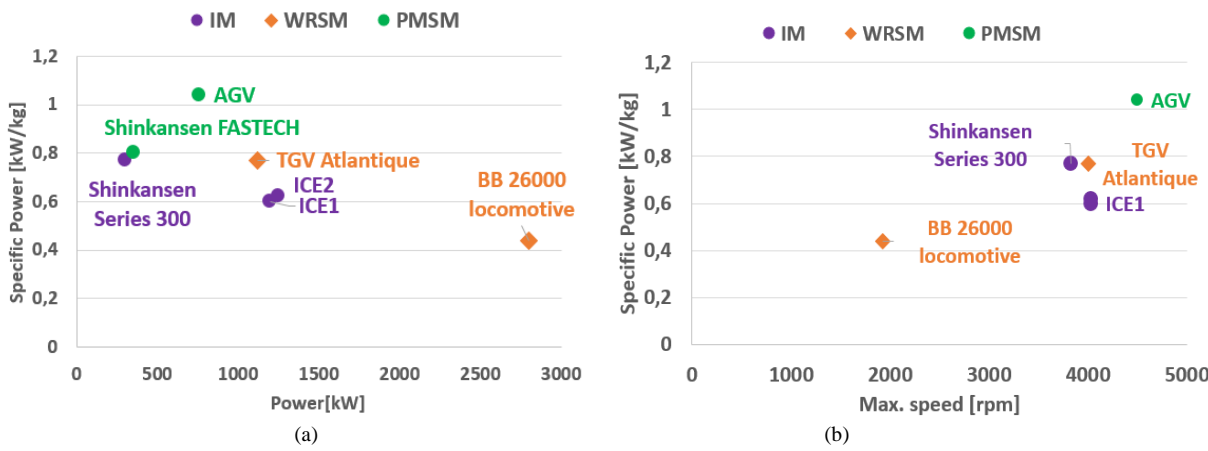


Figure I. 45. Conventional electric motors used in railway traction: (a) specific power vs power, (b) specific power vs max. speed [Aab_14]

- Electric motors of Hybrid Electric Vehicle application

In Hybrid Electric Vehicles (HEV), the electrical machines have been designed to reach high-specific power and high performances. Several topologies of electrical machines have been proposed as interior permanent magnet synchronous machine IPM, surface mounted permanent magnet synchronous machine PMSM, solid induction machine IM and hybrid permanent magnet synchronous machine HSM. IPM having a V shape is the most used topology in HEV (power range ≤ 200 kW) due to their advantages [Sar_17]. HEV using IPMs are: 2004 Prius, 2006 Accord, 2007 Camry, 2008LS600h and 2012 Leaf. IPM ensures high airgap flux density (greater than PM remanent flux density B_r) with no losses in PM. In addition, due to the reluctance torque generated by PM saliency, IPM can be designed with reduced electric loads compared to PMSM. Figure I. 46 illustrates the different rotor structures. Moreover, IPMs are suitable for high rotating speed up to 14000rpm (rotor magnetic sheet ensures mechanically holding, therefore no sleeve is used). However, the armature reaction flux of IPM is high, consequently high performances are required for power converter unlike to PMSM. The highest specific power density achieve with IPMs is 2.5kW/kg for a maximum rotating speed of 10230rpm and for a mechanical power of 110kW as shown in Figure I. 47. HSM is a special IPM designed for generating an high torque. BMWi3 used this topology to improve the efficiency of classic IPMs over the operating range. The achieved specific power of HSM is 1.9kW/kg for a maximum rotating speed of 11400rpm and for a mechanical power of 125kW. The surface Mounted PMSM is used in Sonata 2011 HEV. The achieved specific power is 1.1kW/kg for 6000rpm and 30kW. Tesla S60 has selected solid rotor induction topology for its electric motor (cf. Figure I. 47). Solid rotor ensures a highest mechanical strength for high speed electric machine, which allows to improve specific power [Bin_14]. IM of Tesla S60 has a power of 225kW with a rotation speed of 14800rpm. Its achieved specific power is 4.3kW/kg. The latter value is the highest specific power for electric motor of HEV [Hend_14].



Figure I. 46. Rotor topologies of electric motors used in HEV [Hend_14] [Sar_17] [Sta_17]

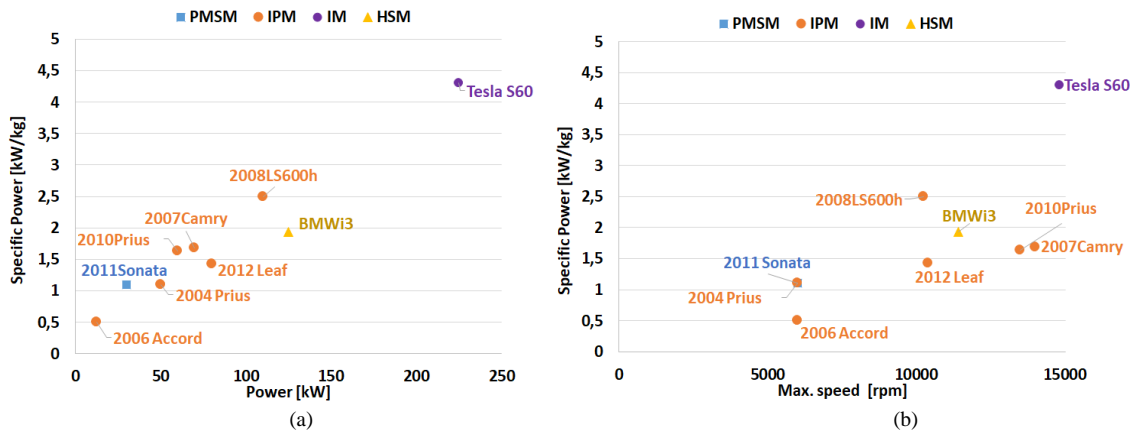


Figure I. 47. High Specific Power Electric Motor in Hybrid Electric Vehicle: (a) specific power vs Power, (b) specific power vs max. speed [Hend_14] [Sar_17] [Sta_17]

I.3 Limitations of specific power

Several aspects limit the increase of the specific power of electric motors; we can cite three main limits:

- Mechanical limits,
- Electromagnetic limits,
- Thermal limits.

I.3.1 Mechanical limits

Rotational speed of electric machines is limited by static and dynamic limits:

- Static limit is linked to the centrifugal forces,
- Dynamic limit is linked to the vibrations of rotor-bearings.

Under high speed rotation, centrifugal forces applied on rotor components become very significant and two vibration types can be arising. Centrifugal forces have ability to radially push out the rotor components as permanent magnet and winding as presented in Figure I. 48.a. While vibrations generate instability operating due to self-excited vibrations and elastic distortion due to resonant vibrations as presented in Figure I. 48.b. Self-excited vibrations arise after a certain threshold speed that is correlate with intrinsic properties of system. Above these vibrations, the rotor cannot operate. Resonant vibrations occur when the speed of the rotor coincides with one of the resonant frequencies as explained in [Sin_12] [Bor_10].

Furthermore, for high speed rotation, mechanical losses as windage losses are significant due to their nonlinearly increasing with rotational speed. Therefore, these losses induced additional heating on all rotor components causing then an irreversible demagnetised risk in permanent magnets. In chapter 2, the mechanical limits will be detailed.

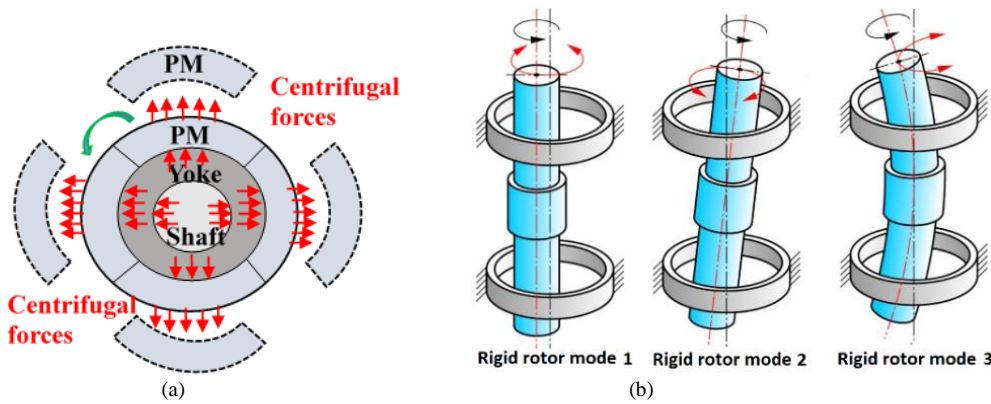


Figure I. 48. (a) Static limit (centrifugal forces), (b) Dynamic limit (vibrations and elastic distortion) [Can_14]

I.3.2 Electromagnetic limits

- Power Converter-Electric Motor limit:

Limits coming from connection "Power Converter-Electric Motor" are not insignificant. Usually, power converters with Pulse Width Modulation "PWM" control are used to limit the electric motor harmonics and their corresponding losses. However, high electric motor frequency may become problematic for power converter with PWM control due to its maximum allowed switch frequency (20kHz to 50kHz). Full Wave Control "FWC" may be an alternative to this problem of the power converter. However, using FWC for power converter can cause significant thermal issues for electric motor due to the FWC high harmonic contents [Dri_05].

- Dielectric insulation limit:

Another electric limit comes from high induced voltage due to high operating speed or from voltage rise generated by power converter. Therefore, insulation winding undergoes huge electric stress. The latter leads to recurrent partial discharge risks that create in turn degradation on insulation surface, an increasing of temperature and accelerate ageing. According to [Bra_92], time life of insulation winding decreases by half for every increasing of 10°C over their thermal class as shown in Figure I. 49.

To avoid partial discharge risks, insulation winding is often enhanced by using additional insulation systems. Nevertheless, as insulation materials are bad thermal conductors, extraction of heat from winding becomes a huge challenge for cooling. On other side, enhancing insulation of electric machines prevents the increase of the specific power.

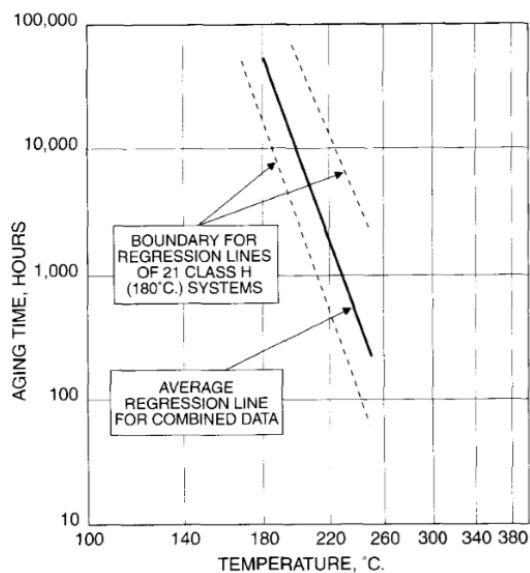


Figure I. 49. Temperature-life characteristics for Class H (180°C) insulation systems [Bra_92]

- Magnetic limit:

As highlighted previously, main magnetic limit is linked to hard materials due to irreversible demagnetization risk. The last one is due to the temperature sensitive of hard materials. Indeed, magnetic limits are strongly linked to thermal limits as discussed in the following section.

I.3.3 Thermal limits

Maximum temperatures sustained by insulation and hard magnetic materials define the main thermal limits in electric machines. Commonly, rising of temperature is caused by the heat sources due to electromagnetic and mechanical losses, including:

- joule losses in conductors $P_j \propto R_s(\rho(T), \Omega)j^2$,
- iron losses in electrical sheets $P_f \propto k \Omega^\alpha B^\beta$,
- eddy current losses in hard magnetic materials $P_{edd} \propto \rho(T) \Omega^2 B^2$,
- friction losses in bearings $P_{friction} \propto \Omega$,
- windage losses in all rotating surfaces $P_{windage} \propto \Omega^\gamma$.

Where: Ω is the rotational speed, k , α and β are the coefficients of iron losses, R_s is the resistance function of resistivity ρ and temperature T .

In fact, increasing technological levels for instance the rotation speed, the flux density level in hard and soft materials improve the specific power. But in the same time, losses increase. In this case, extraction and evacuation of the latter may be a serious issue due to the low thermal conductivity of the construction parts of the electric machine, with the exception of the conductors (cf Table I.18). Moreover, evacuation through small areas makes it more complicated from thermal standpoint as expressed thermal resistance:

$$R_{thermal} = \frac{e}{\lambda_{th}S} \quad (\text{I. 3})$$

where λ_{th} is the thermal conductivity, S is the surface and e is the thickness.

On the other hand, rising temperature may be dangerous when significant changes in material properties for instance in hard magnetic materials. Therefore, performance of electric machine can be easily affected.

Table I. 18. Typical values of thermal conductivity of constructional parts of electric machine

Construction parts of electrical machine	Thermal conductivity range [W.m ⁻¹ .K ⁻¹]
Insulation materials	0.15 to 1
Hard magnetic materials	7 to 11
Electrical sheet materials	10 to 46
Conductors: "copper"	380

Conclusion

Hybrid Aircraft academic reSearch on Thermal and Electrical Components and System "HASTECS" project is one of the **Clean Sky 2** program projects which aims to reduce noise and CO₂ emissions. Thereupon, increasing specific power of each hybrid propulsion components is the main HASTECS goal: electric motors, power converters, cooling systems...etc. This thesis focuses on the increasing specific power and efficiency of electric motors including their cooling systems for reaching:

- Specific power of 5kW/kg, efficiency greater than 94.5% at sizing point and greater than 96% at cruise point for 2025 HASTECS target.
- Specific power of 10kW/kg, efficiency greater than 97% at sizing point and greater than 98.5% at cruise point for 2035 HASTECS target.

Specific power and efficiency usually depend on several technological levels which are often limited. Within this context, it is being essential to identify all technologies currently employed in electrical motors and as well as the future technologies. These technologies are conventionally involved to materials used in electrical machines.

The chapter gives a state of the art of the electric machines to situate the actual specific power and identify the involved technologies. We have broadly compared the different synchronous and asynchronous motors topologies. It is difficult to select one topology and to discard the others considering that the selected topology is usually suitable for only one or two given performances as it has been attested by the established benchmarked of the industrial electric motors employed in transportation applications.

Besides, we have studied and compared in terms of weights, loads and limits:

- The different technologies linked to the materials such as magnetic, the insulating and the sleeve materials,
- The different technologies linked to the construction such as conductors, the winding configurations and the bearings,
- The technologies linked to the cooling methods.

As well as for electric motor topologies, it is difficult to identify and select the promising technologies allowing achieving high specific power. For instance, NdFeB permanent magnets seem magnetically and lightweight relevant compared to the other magnets, but due to their temperature sensitivity they may be not interesting for reaching high specific power. Also, Hairpin conductors are relevant for high copper filling and reduced end-winding, however, they are a disadvantage for high speed operating.

We have also surveyed the improvement of some technologies currently either proposed or carried out for overcome some thermal, mechanical and electromagnetic limits. However, most of them are still under research. Eventually, considering the current limits, establishing trade-offs between technologies is suggested for reaching targets.

The next chapter presents a tool which allows assessing these technologies for hybrid aircraft propulsion. This tool also allows to make trade-offs on specific power and efficiency.

References

Project Framework

- [All_17] Jean-François Allias, AIRBUS HASTECS deliverable 2017, July 2017
- [All_18] Jean-François Allias, AIRBUS HASTECS deliverable 2018, July 2018
- [Hor_20] Horizon 2020: 'Hybrid Aircraft; academic research on Thermal and Electrical Components and Systems'[Available Online]: <https://cordis.europa.eu/project/rcn/205619/factsheet/fr>
- [Wor_18] Workshop dissemination 29th Oct 2019, http://www.laplace.univlse.fr/IMG/pdf/hastecs_workshop_dissemination_program-2.pdf
- [Dis_18] <https://www.cleansky.eu/power-trip-hastecs-energizes-the-path-to-hybrid-powered-flight-0>
- [Air_19] <https://www.airbus.com/innovation/future-technology/electric-flight/e-fan-x.html>

Machines performances

- [Gie_10] J. F. Gieras, 'Permanent Magnet Motor Technology: Design and Applications', 3rd edition, Taylor and Francis Group, Chapter 3, pp. 104-106, 2010.

Magnets materials

- [Con_04] S. Constantinides, D. Guilck, 'NdFeB for High Temperature Motor Applications', SMMA Fall Technical Conference, Arnolds Magnetic, 3rd-5th November 2004
- [Vac_14] Rare earth permanent magnets Vacodynam and Vacomax', Vacuumschmelze Catalogue, https://vacuumschmelze.com/Assets-Web/VACODYM-VACOMAX-PD002_2015_in_pdf

Conductors

- [Rog_18] S. Roggia, M. Iacchetti, 'Multi-physics analysis of electric vehicles (EV) power train' *Tutorial in IEEE International Conference Electrical Machines 2018*, 3-6 Sept 2018, Alexandroupoli, Greece. <http://www.globalevents.gr/2018/icem/tutorial/ICEM-Tutorials-MultiphysicsEV.pdf>
- [Sto_04] G. C. Stone, E. A. Boulter, I. Culbert, H. Dhirani, 'Electrical Insulation for Rotating Machines, Design, Evaluation, Aging, Testing, and Repair', IEEE Press and John Wiley and Sons, INC, 2008
- [Bur_17] T. Burress, 'Electrical Performance, Reliability Analysis, and Characterization', Oak Ridge National Laboratory National Transportation Research Center June 6, 2017
- [Liu_19] Y. Liu, 'Rectangular conductor winding for electric motor with high performance and high production volume', Report of Swedish Electromobility Center, Chalmers University of Technology 25 June, 2019
- [Deu_19] D. Deurell, V. Josefsson, 'FEA study of proximity effect in hairpin windings of a PMSM for automotive applications' Master thesis, CHALMERS UNIVERSITY OF TECHNOLOGY, Sweden 2019
- [Rhy_15] Se-Hyun Rhyu and *al.*, 'Design of the end-coil structure with square conductor for automobile ISG', *International Electric Vehicle Symposium and Exhibition*, KINTEX, Korea, May 3-6, 2015
- [Mil_19] D. Miljavec, 'Integrated Modular Distributed Drivetrain for Electric & Hybrid Vehicles DRIVEMODE Project', Report on considered electrical motor technologies, evaluation matrix, concept decision, <https://ec.europa.eu/research/participants/documents/downloadPublic?documentIds=080166e5c18d75cf&appId=PPGMS>
- [Yoo_16] A. Yoon, X. Yi, J. Martin, Y. Chen, K. Haran, 'A high-speed, high-frequency, air-core PM Machine for Aircraft Application', *IEEE Power and Energy Conference (PECI)*, 19-20 Feb. 2016, USA
- [Mar_17] J. Martin, A. Yoon, A. Jin, K. S. Haran, 'High-Frequency litz "Air-Gap" windings for high-power density electrical machines', *Electric Power Components and Systems Journal*, Issue. 7, Vol. 45, May 2017
- [Kha_14] H.V. Khang, J. Saari, A. Arkkio, 'Form-wound Stator Winding for High-Speed Induction Motors', *IEEE International Conference on Electrical Machines*, 2-5 Sept 2014, Germany
- [Mer_14] J. Merwerth, 'The Hybrid-Synchronous Machine of the New BMWi3 and i8: Challenges with electric traction drives for vehicles workshop university lund', BMW Presentation, April 2014, http://hybridfordonscentrum.se/wp-content/uploads/2014/05/20140404_BMW.pdf
- [Bia_18] N. Bianchi, G. Berardi, 'Analytical Approach to design Hairpin Windings in High Performance Electric Vehicle Motors', *IEEE Energy Conversion Congress and Exposition (ECCE)*, 23-27 Sept. 2018, USA
- [Gla_20] T. Glaessel, J. Seefried, A. Kuel, J. Franke, 'Skinning of insulated copper wires within the production chain of hairpin windings for electric traction drives', *Int. J. Mech. and Rob. Research* vol.9, no.2, March 2020
- [Dub_18] C. Du-Bar, A. Mann, O. Wallmark, M. Werke, 'Comparison of performance and manufacturing aspects of an insert winding and a hairpin winding for an automotive machine application', *IEEE 8th International Electric Drives Production Conference (EDPC)*, 4-5 Dec. 2018.
- [Ber_18] G. Berardi, N. Bianchi, 'Design Guideline of an AC Hairpin winding', *IEEE International Conference on Electrical Machine (ICEM)*, 3-6 Sept 2018, Greece.
- [Rey_16] Dominique Rey, 'Tooth coils with litz wire: Advantages for E-Drives', Von Roll Schweiz AG presentation in CWIEME 2016, Berlin 2016

Chapter I: State of the art

- [Hen_14] J. R. Hendershot, 'Electric traction machine choices for hybrid and electric vehicles', Presentation in Florida International University, 20th Nov.2014, <https://site.ieee.org/miami/files/2014/11/Hendershot-FIU-Lecture.pdf>
- [Ast_cat] Available website: <http://www.ast-austria.com/en/roebel-bars.html>.
- [CerCat] Cerafil, 'Miniature ceramic insulation conductor wire for very high temperatures: -90°C to +500°C, peak +1000°C', available website: <http://www.cables-cgp.com/en/produits/high-temperature-miniature-ceramic-wires/>.

Insulations

- [Cha_08] M. Chapman, N. Frost, R. Bruetsch, 'Insulation systems for rotating low-voltage machines', Conference Record of the 2008 IEEE International Symposium on Electrical Insulation, 9-12 June 2008, Canada
- [Dupcat] 'Setting the standard for electrical insulation' DuPont Catalogue, 2008
- [Nema] 'NEMA Magnet Wire Thermal Class Ratings'
- [Pyrh_08] J. Pyrhönen, T. Jokinen, V. Hrbovcová, 'Design of rotating electrical machines', 2nd edition, John Wiley and Sons, 2008, pp.429-455
- [Sto_04] G. C. Stone, E. A. Boulter, I. Culbert, H. Dhirani, 'Electrical Insulation for Rotating Machines, Design, Evaluation, Aging, Testing, and Repair', IEEE Press and John Wiley and Sons, INC, 2008
- [Len_18] J. D. Lenz, N. J. Renner, X. Yi, K. S. Haran, 'Insulation considerations in from-wound armature windings for high-frequency electric machines', *IEEE Power and Energy Society General Meeting (PESGM)* 5-10 August 2018, USA
- [AxaCat] Axalta Electrical Insulation Materials, https://www.axalta.com/electricalinsulation_global/en_US/wire_enamels/what-are-wire-enamels.html
- [ElaCat] Elantas wire enamel, <https://www.elantas.com/tongling/products-services/wire-enamels/polyimide-enamels.html>
- [Hem_19] R. Hemmati, F. Wu, A. El-Refaie, 'Survey of Insulation Systems in Electrical Machines', IEEE International Electric Machines & Drives Conference (IEMDC), 12-15 May 2019, USA
- [Data]<https://plastics.ulprospector.com/generics/45/c/t/polyurethane-pur-properties-processing>
- [Data2] Database of thermal materials: https://www.engineeringtoolbox.com/thermal-conductivity-d_429.html
- [VitCat] Victrex High Performance Polymers Catalogue: Victrex PEEK 450G, https://www.victrex.com/~/media/datasheets/victrex_tds_450g.pdf
- [Oht_85] S. Ohta, 'Temperature Classes of Electrical Insulators', Three Bond Technical News, Issued 1st Dec. 1985

Winding

- [Ref_10] A. M. El-Refaie 'Fractional slot concentrated-windings synchronous permanent magnet machines: opportunities and challenges', *IEEE Trans. On. Indus. Electr.*, vol.57, no.1, pp.107-121, January 2010

Bearing

- [Mal_06] J. Malinowski, D. R. Snyder, 'Choosing an antifriction bearing', *IEEE Industry Applications Magazine*, vol.12, iss.6, pp.49-56, 2006
- [TimPr] Timken presentation 'Bearing basics', Available website: <http://dumbelt.com/palestra-29-04-2016/1.%20Apres%20ANFITEATRO%20Pav%20Mec%20II.pdf> [SKFCat] <https://www.skf.com/fr/index.html>
- [Le_16] Y. Le, K. Wang, 'Design and optimization method of magnetic bearing for high-speed motor considering eddy current effects', *IEEE Transactions on Mechatronics*, vol.21, no.4, pp.2061-2072, August 2016

Sleeves

- [Zha_15] F. Zhang, G. Du, T. Wang, G. Liu, W. Cao, 'Rotor retaining sleeve design for a 1.12-MW High-Speed PM Machine', *IEEE Trans. On. Indus. Appl.*, vol. 51, no. 5, pp. 3675-3685, Sept/Oct 2015
- [Gie_10] J. F. Gieras, 'Permanent magnet motor technology: design and applications', 3rd edition CRC Press 2010
- [Fan_15] H. Fang, R. Qu, J. Liu, P. Zheng, X. Fan, 'Rotor design for a high-speed high-power permanent-magnet synchronous machine', *IEEE Energy Conversion Congress and Exposition (ECCE)*, 2015

Cooling

- [Yan_17] Y. Yang, B. Bilgin, M. Kasprzak, S. Nalakath, H. Sadek, M. Preindl, J. Cotton, N. Schofield, A. Emadi, 'Thermal management of electric machines', *IEEE IET Electr. Syst. in Transp.* pp.1-13. May 2016
- [Satru_17] M. Satrustegui, M. Martinez-Iturralde, J. C. Ramos, P. Gonzalez, G. Astarbe, I. Elosegui, 'Design criteria for water cooled systems of induction machines', *Applied Thermal Engineering Journal*, vol.114, pp.1018-1028, 2017
- [Dav_15] T. Davin, J. Pelle, S. Harmand, R. Yu, 'Experimental study of oil cooling systems for electric motors', *Applied Thermal Engineering Journal*, vol.75, pp.1-13, 2015
- [Lud_17] D. C. Ludois, 'Brushless and Permanent Magnet Free Wound Field Synchronous Motors for EV Traction', Technical report, University of Wisconsin-Madison, Illinois Institute of Technology, 2017, doi:10.2172/1349258

Chapter I: State of the art

- [Sem_14] S. A. Semidey, J. R. Mayor, 'Experimentation of an Electric Machine Technology Demonstrator Incorporation Direct Winding Heat Exchangers', *IEEE Trans. On. Ind. Electr.* vol.61, no.10, October 2014
- [Sch_15] M. Scheifer, M. Doppelbauer, 'Indirect Slot Cooling for High-Power-Density Machines with Concentrated Winding', *IEEE International Electric Machines & Drives Conference (IEMDC)*, USA, 10-13 May 2015
- [Rhe_15] C. Rhebergen, B. Bilgin, A. Emadi, E. Rowan, J. Lo, 'Enhancement of Electric Motor Thermal Management through Axial Cooling Methods: A materials approach', IEEE Energy Conversion Congress and Exposition (ECCE 2015), Canada, 20-24 Sept 2015
- [Lin_16] P. M. Lindh, I. Petrov, R. S. Semken, M. Niemelä, J. J. Pyrhönen, L. Aarniovuori, T. Vaimann, A. Kallaste, 'Direct Liquid Cooling in low-power electrical machines: proof of concept', *IEEE Trans. On. Ener. Conv.* Vol.31, no.4., Dec.2016, pp. 1257-1266
- [Tig_16] C. Tighe, C. Gerada, S. Pickering, 'Assessment of cooling methods for increasing power density in electrical machines', *IEEE XXII International Conference on Electrical Machines (ICEM)*, 4-7 Sept.2016
- [Rei_14] A. Reinap, F.J. Marquez-Fernandez, R. Andersson,C. Hogmark, M. Alakula, A. Goransson, 'Heat Transfer Analysis of a traction machine with directly cooled laminated windings', IEEE [4th International Electric Drives Production Conference \(EDPC\)](#), 30 Sept-1 Oct 2014, Germany
- [Pol_14] M. Polikarpova, P. M. Lindh, J. A. Tapia, J. J. Pyrhönen, 'Application of potting material for 100kW radial flux PMSM', *IEEE International Conference on Electrical Machines (ICEM)*, 2-5 Sept. 2014, Germany
- [Min_17] M. Liu, Y. Li, H. Ding, B. Sarlioglu, 'Thermal management and cooling of windings in electrical machines for electric vehicle and traction application', *IEEE Transportation Electrification Conference and Exposition (ITEC)*, 22-24 June 2017, USA
- [Tuy_17] A. Tuysuz, F. Meyer, M. Steichen, C. Zwyssig, J. W. Kolar, 'Advanced cooling methods for high-speed electrical machines', *IEEE Trans. On. Ind. Appl.*, vol.53, no.3., May/June 2017, pp.2077-2087
- [Ch_15] Yew Chuan Chong, 'Thermal Analysis and air flow modelling of electrical machines' PhD thesis manuscript, The University of Edinburgh, 2015
- [Kim_17] J. H. Kim *et al.* "Design and analysis of cooling structure on advanced air-core stator for megawatt-class HTS Synchronous Motor" *IEEE Trans. On. Applied Supercond.*, vol.4, June 2017.
- [Wei_14] Wei Tong 'Mechanical design of electric motors', chapter 6: Motor Cooling, CRC Press Taylor and Francis group, edition 2014
- [Gia_17] Y. Gia, M. Kimiaeigui, J. D. Widmer, Y. C. Chong, J. Goss, U. San Andres, D. A. Staton, 'Shaft cooling and the influence on the electromagnetic performance of traction motors', *IEEE International Electric Machines and Drives Conference (IEMDC)*, 21-24 May 2017, USA
- [Has_12] T. Hassett, M. Hodowanee, 'Electric motor with heat pipes', Patent n° US8134260B2, 2012, <https://patents.google.com/patent/US8134260B2/en>
- [Tes_13] L. Fedoseyev, E. Marcum Pearce Tesla motor patent 'Rotor Assembly with Heat Pipe Cooling System', , Patent n°US20140368064A1, 2013, <https://patents.google.com/patent/US20140368064A1/in> pdf

Actual specific power

- [Zha_18] X. Zhang, C. L. Bowman, T. C. O'Connell, K. S. Haran, 'Large electric machines for aircraft electric propulsion', *IET Electr. Power Appl.*, vol. 12, Iss. 6, pp. 767-779, 2018
- [Jan_17] R. H. Jansen, C. Bowman, A. Jankovsky, R. Dyson, J. Felder, 'Overview of NASA Electrified Aircraft Propulsion Research for Large Subsonic Transports', *Aircraft Electrical Propulsion*, AIAA 2017-4701 <https://arc.aiaa.org/doi/abs/10.2514/6.2017-4701> , July 2017
- [Sar_17]B. Sarlioglu, C. T. Morris, D. Han, S. Li, '[Driving Toward Accessibility: A Review of Technological Improvements for Electric Machines, Power Electronics, and Batteries for Electric and Hybrid Vehicles](#)', *IEEE Ind. Appl. Magazine*, vol.23, issue.1, 2017
- [Hend_14] J. R. Hendershot 'Electric traction machine choices for hybrid and electric vehicles', Nov 2014, <https://site.ieee.org/miami/files/2014/11/Hendershot-FIU-Lecture.pdf>
- [Bin_14] A. Binder, W-R. Canders, 'Tutorial "High Speed Drives" ', *IEEE International Conference on Electrical Machines*, 2nd-5th September 2014, Germany
- [Bur_12] T. Burress, 'Benchmarking of competitive technologies', Oak Ridge National Laboratory, 15th May 2012, https://www.energy.gov/sites/prod/files/2014/03/f10/ape006_burress_2012_p.pdf
- [Sta_17] D. Staton, J. Goss, 'Open source electric motor models for commercial EV and Hybrid Traction Motors', CWIEME Berlin 2017, https://www.coilwindingexpo.com/berlin/_media/pages/Tutorial-1-D--Staton-&-J--Goss-MDL.PDF

- [Pet_15] K. Petermaier, Transformative Vertical Flight Workshop, 'Electric propulsion components with high power densities for aviation' Siemens presentation, 8th march 2015, <https://nari.arc.nasa.gov/sites/default/files/attachments/Korbinian-TVFW-Aug2015.pdf>
- [Che_17] Y. Chen, R. Sanchez, A. Yoon, K. Sivasubramanian, 'Mechanical design considerations of an "Ironless" high-specific-power electric machine', *IEEE Transaction On Transportation Electrification*, vol.3, no.4, Dec.2017
- [Aab_14] S. Al Aabid, Y. Lefevre, J. F. Llibre, 'Assessment of electric motor technologies for long-term aircraft propulsion', Internal report, Electromagnetism Research Group Laplace Laboratory, July 2014

Limits for increasing specific power

- [Sin_12] S. Singal, 'Vibration and rotor dynamics of large high-speed motors driving compressors in the oil and gas industry', Petroleum and Chemical Industry Technical Conference, 2012 Record of Conference Papers Industry Applications Society IEEE
- [Bor_10] A. Borisavljevic, H. Polinder, J.A. Ferreira, On the speed limits of Permanent Magnet Machines, *IEEE Transaction On Industrial Electronics*. vol. 57, no.1, January 2010
- [Can_14] W. R. Canders, J. Hoffmann, 'Tutorial on High Speed Drives, Part two-mechanical aspects', *IEEE International Conference on Electric Machines*, Germany, 1st-5th Sept 2014
- [Bra_92] E. L. Brancato, "Estimation of Lifetime Expectancies of Motors", *IEEE Electrical Insulation Magazine*, vol. 8, Issue 3, May-June 1992, pp.5-13
- [Dri_05] J. Driesen, R. Belmans, 'Specific problems of high-speed electrical drives', Micro Gas Turbines, p. 12–1, 2005.

Chapter II: Target Setting Tool

Contents

Introduction	34
I.4 Load concepts in electrical machines.....	34
I.5 Sizing model of electric motors.....	35
I.2.9 Electromagnetic torque, fundamental waves and tangential stress.....	35
I.2.10 Magnetic flux balance.....	36
I.2.11 Electric current balance.....	39
I.2.12 Power balance.....	40
I.2.13 Main sizes of electric motor.....	40
I.2.14 Electric motor weight.....	42
I.2.15 Specific power and torque.....	44
I.6 Loss assessment models.....	44
I.3.4 Analytical model of Joule losses.....	44
I.3.5 Analytical model of iron losses.....	44
I.3.6 Semi-empirical models of mechanical losses.....	45
I.7 Thermal constraint.....	48
I.8 Mechanical constraint.....	48
I.9 Inputs and outputs of Target Setting Tool.....	49
Conclusion.....	51
Appendices.....	52
References.....	54

Introduction

In the previous chapter, different technologies employed in electrical machines were overviewed. Besides, their advantages and drawbacks were presented to identify the main limitations for increasing specific power of electric motor with its cooling system. In this chapter, a Target Setting Tool will be developed to make quick trade-offs on the specific power including the technological levels. For the purpose, loadability concept will be firstly reminded. Afterward, sizing model of nonsalient radial flux of ideal sinewave electric motors based on magnetic flux, electrical current densities and thermal balances will be developed to assess main sizes, active part volumes and weights from material choices. Losses of electric motor will be assessed by analytical models. As well specific power, specific torque and efficiency will be assessed. Sizing model will be implemented in Target Setting Tool. Finally, inputs, outputs and validity conditions of Target Setting Tool will be evoked.

II. 1 Load concepts in electrical machines

From well-designed AC electric motors, manufactures have drafted some ranges of both magnetic and electric loads for given thermal class and cooling method [Pyr_08]:

- **Magnetic loads** indicate flux densities in airgap, stator and rotor cores allowed by the soft and hard magnetic materials. Table II. 1 gives varying ranges of flux densities for various standard induction and synchronous electric machines.
- **Electric loads** indicate current densities in stator and rotor windings allowed by the cooling methods. These densities ranges are summarized in Table II. 2.
- **Electromagnetic loads** indicate the tangential stress in airgap allowed by the soft, hard magnetic materials, the insulation materials and the cooling methods as presented in Table II. 3.

Magnetic and electric loads characterize the technologies involved in electric motors as well as their performances as mentioned in [Gee_15] [Mar_15]. Therefore, to reach high specific powers of electric motors, load concepts may constitute baselines to identify the most promising technologies.

Table II. 1: Allowed flux densities for various standard induction and synchronous electrical machines [Pyr_08]

Flux density	Salient-pole		Nonsalient-pole synchronous machines
	Induction machines	Synchronous machines	
Airgap	0.7-0.9	0.85-1.05	0.8-1.05
Stator yoke	1.4-1.7	1.0-1.5	1.1-1.5
Stator tooth	1.4-2.1	1.6-2.0	1.5-2.0
Rotor yoke	1-1.6	1.0-1.5	1.3-1.6
Pole core	-	1.3-1.8	1.1-1.7

Table II. 2: Allowed RMS values of current and linear current "j_{rms} and A_{rms}" densities for various standard induction and synchronous electrical machines and according to cooling method [Pyr_08]

Cooling method	Induction machines	Salient-pole synchronous machines	Nonsalient-pole synchronous machines		
			Indirect		Direct
			Air	Hydrogen	
Current density j _{rms} [A.mm ⁻²]					
- Stator winding	3-8	4-6.5	3-5	4-6	7-10
- Rotor winding	3-8	2-3.5	-	-	13-18
Linear current density A _{rms} [A.mm ⁻¹]	30-65	35-65	30-80	90-110	150-200
Max current density product A _{rms} ×j _{rms} [A ² .m ⁻³]	9×10 ¹⁰ -52×10 ¹⁰	14×10 ¹⁰ -42.5×10 ¹⁰	9×10 ¹⁰ -40×10 ¹⁰	36×10 ¹⁰ -66×10 ¹⁰	1.05×10 ¹² -2×10 ¹²

Table II. 3: Allowed tangential stress values for various standard induction and synchronous electrical machines and according to cooling method [Pyr_08]

Cooling method	Induction machines	Salient-pole synchronous machines	Nonsalient-pole synchronous machines		
			Indirect		Direct
			Air	Hydrogen	
Linear current density A _{rms} [A.mm ⁻²]	30-65	35-65	30-80	90-110	150-200
Airgap flux density B _m [T]	0.7-0.9	0.85-1.05	0.8-1.05	0.8-1.05	0.8-1.05
Tangential stress σ [Pa]					
- Minimum value	12000	21000	17000	51000	85000
- Maximum value	33000	48000	59500	81500	148500

II. 2 Sizing model of the electric motors

Until recently, modelling for the purpose of sizing electric motors remains complex and often inaccurate in the case of nonconventional structures or in the case of salient electric motors. In contrast, nonsalient radial flux electric motors supplied with sinewave currents are usually fairly modelled and sized. Their windings are assumed sinewave distributed. Moreover, flux density in the airgap is assumed sinewave to simplify expressing model and design [Sle_94] [Hen_94]. To develop a Target Setting Tool, the emphasis will be paid, in this thesis, only on sizing model of nonsalient radial flux sinewave electric motors. However, it could be extended for instance to the radial flux square-wave electric motors.

II.2.1.Electromagnetic torque, fundamental waves and tangential stress

Electromagnetic torque of an electric machine results from interaction between two fundamental space-time waves on the stator bore [Han_94] [Sle_94] [Hen_94] [Gie_10]. The first fundamental wave is radial airgap flux density due to the rotor magnetic sources $B_{rs}(\theta, t)$. The second fundamental wave is the axial surface current density due to the stator currents $K(\theta, t)$. The electromagnetic torque can be calculated using *Maxwell stress tensor* or using *Lorentz force*. Thereby, the general expression of transient electromagnetic torque of a radial flux electric machine is given by:

$$T_{em}(t) = \iint_{S_b} R^2 B_{rs}(\theta, t) K(\theta, t) d\theta dz \quad (\text{II- 1})$$

Where: R is the radius of stator bore, S_b is the inner stator surface as shown in Figure II. 1, θ is the angular position, t is the time and z is the axial direction.

Ideal sinewave electric machine is characterized by sinewave distributed winding and sinewave airgap flux density as illustrated in Figure II. 2. They are expressed by:

$$\begin{cases} K(\theta, t) = K_m \cos(p\Omega t - p\theta + \alpha_{dis}) \\ B_{rs}(\theta, t) = B_m \cos(p\Omega t - p\theta) \end{cases} \quad (\text{II- 2})$$

Where: K_m is the maximum amplitude of the surface current density, B_m is the maximum amplitude of the airgap flux density, p is the number of pole pairs, Ω is the rotor speed and α_{dis} is the electric angular displacement.

Therefore, from equations (II-1) and (II-2), the electromagnetic torque leads to the well-known constant torque of non-salient pole electric motor.

$$T_{em} = \pi R^2 L_m K_m B_m \cos(\alpha_{dis}) \quad (\text{II- 3})$$

Where: L_m is the axial active length.

Mechanically, it is possible to define approximatively the maximum electromagnetic torque from the forces applied over the rotor and then from the tangential stress σ (cf. Figure II. 3) as written in the following equation:

$$T_{em_{max}} = R_r S_{rot} \sigma \quad (\text{II- 4})$$

With:

$$S_{rot} = 2\pi R_r L_m$$

Where: S_{rot} is the rotor surface and R_r is the external rotor radius.

Thereby, from the equations (II-3), (II-4) and using the following approximation:

$$R \approx R_r \quad (\text{II- 5})$$

The tangential stress can be then deduced:

$$\sigma = \frac{B_m K_m}{2} = B_{rms} K_{rms} \quad (\text{II- 6})$$

Where: B_{rms} and K_{rms} are the root mean square values of the airgap flux density and the surface current density respectively.

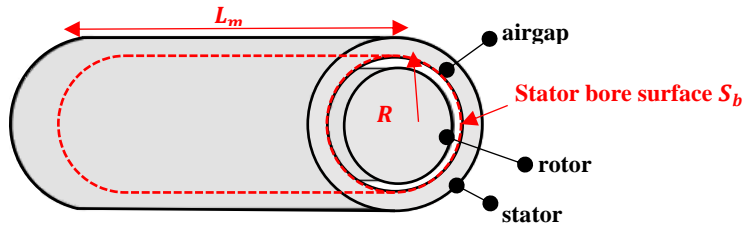


Figure II. 1. Stator bore of a radial flux electric machine

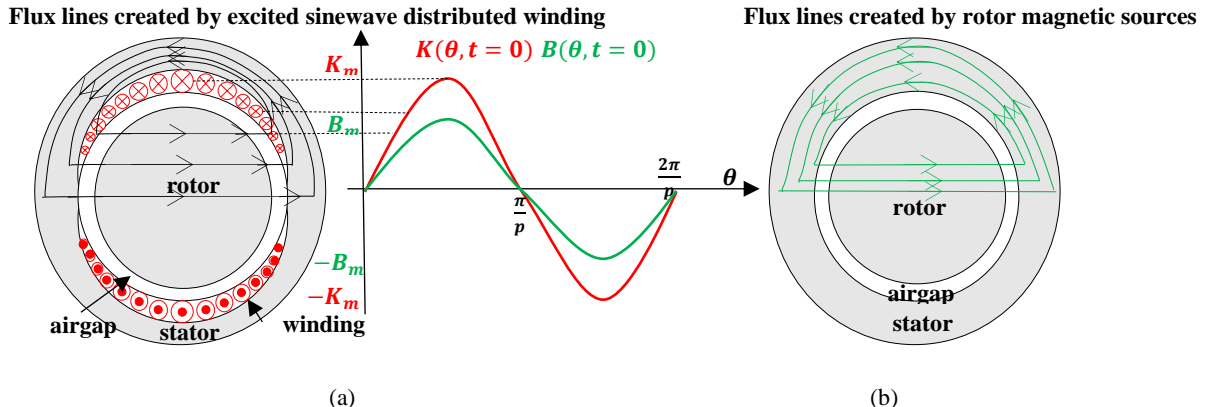


Figure II. 2. (a) Two-pole sinewave distributed winding, (b) two-pole sinewave airgap flux density [Hen_94]

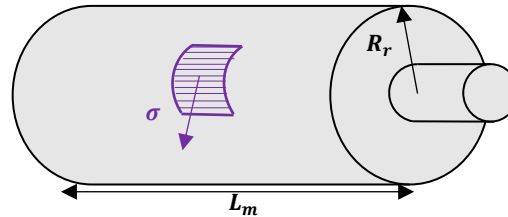


Figure II. 3. Tangential stress applied to the rotor surface

II.2.2. Magnetic flux balances

Due to magnetic nature of stator and rotor laminations, the magnetic flux crosses the rotor to the stator through teeth and closes through the stator yoke as illustrated in Figure II. 4. Therefore, the magnetic flux conservation and the balances in stator yoke and teeth can be applied. For the purpose, some assumptions are made:

- ✓ the magnetic leakage fluxes mainly crossing in the airgap and the end-winding are neglected,
- ✓ the slot effect is not taking into account,
- ✓ the saturation of magnetic sheets is not taking into account.

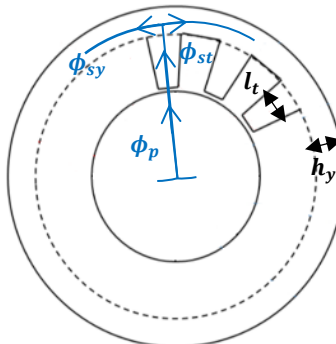


Figure II. 4. Magnetic Flux path in radial electric motor

a. Magnetic flux per pole

By applying Gauss law, the magnetic flux per pole is given by integration of the magnetic airgap flux density resulting from stator and rotor sources on the airgap surface as demonstrated in the following equation:

$$\phi_p = \iint_{S_b} (\overrightarrow{B_{ss}} + \overrightarrow{B_{rs}}) \cdot \overrightarrow{dS} = \iint_{S_b} B_{tot} dS \quad (\text{II- 7})$$

Where: B_{ss} is the flux density resulting from the stator currents, B_{tot} is the amplitude of the total flux density in airgap, S_b is the inner stator surface and $dS = L_m R d\theta$.

The flux density per pole resulting from the stator source can be deduced from the *Maxwell's equations* (equations II-8 and II-9) applied on the study domain shown in Figure II. 5.

$$\overrightarrow{\text{rot}}(\vec{H}) = \vec{0} \quad (\text{II- 8})$$

$$\text{div}(\vec{B}) = 0 \quad (\text{II- 9})$$

and knowing that:

$$\vec{B} = \mu \vec{H} \quad (\text{II- 10})$$

Where: \vec{B} is the magnetic field, \vec{H} is the magnetic field strength and μ is the permeability.

Equation II-9 leads to the definition of the magnetic vector potential \vec{A} :

$$\vec{B} = \overrightarrow{\text{rot}}(\vec{A}) \quad (\text{II- 11})$$

Therefore, previous equations (II-8, 9, 10, 11) can be reduced to:

$$\overrightarrow{\text{rot}}(\overrightarrow{\text{rot}}(\vec{A})) = \vec{0} \quad (\text{II- 12})$$

In cylindrical coordinates, equation (II-12) can be expressed by:

$$\text{For } R_r < r < R \quad \frac{\partial^2 A_z}{\partial r^2} + \frac{1}{r} \frac{\partial A_z}{\partial r} + \frac{1}{r^2} \frac{\partial^2 A_z}{\partial \theta^2} = 0 \quad (\text{II- 13})$$

Where: A_z is the z component of magnetic potential vector.

Boundary conditions in study domain are given by:

$$\begin{cases} H_\theta(R, \theta, t) = -\frac{1}{\mu_0} \frac{\partial A_z}{\partial r} \Big|_{r=R} = K_m \cos(p\Omega t - p\theta + \alpha_{dis}) \\ H_\theta(R_r, \theta, t) = -\frac{1}{\mu_0} \frac{\partial A_z}{\partial r} \Big|_{r=R_r} = 0 \end{cases} \quad (\text{II- 14})$$

Therefore, the general solution of a partial differential equation (II-13) is governed by:

$$A_z(r, \theta, t) = \left(C_1 r^p + \frac{C_2}{r^p} \right) \cos(p\Omega t - p\theta + \alpha_{dis}) \quad (\text{II- 15})$$

Where: C_1 and C_2 are constants given by boundary conditions (II-14) as expressed by:

$$\begin{cases} C_1 R^{p-1} - C_2 R^{-p-1} = -\frac{\mu_0 K_m}{p} \\ C_1 R_r^p - C_2 R_r^{-p} = 0 \end{cases} \quad (\text{II- 16})$$

Then, constants C_1 and C_2 are:

$$\begin{cases} C_2 = -\frac{\mu_0 K_m}{p} \frac{R^{p+1}}{(R^{2p} - R_r^{2p})} R_r^{2p} \\ C_1 = -\frac{\mu_0 K_m}{p} \frac{R^{p+1}}{(R^{2p} - R_r^{2p})} \end{cases} \quad (\text{II- 17})$$

Therefore, magnetic vector potential is given by:

$$A_z(r, \theta, t) = \frac{\mu_0 K_m R^{p+1}}{p} \left(\frac{R_r^{2p} r^{-p} + r^p}{R_r^{2p} - R^{2p}} \right) \cos(p\Omega t - p\theta + \alpha_{dis}) \quad (\text{II- 18})$$

The flux density resulting from the stator currents is given by:

$$B_{ss}(R, \theta, t) = \frac{1}{r} \frac{\partial A_z}{\partial \theta} \Big|_{r=R} = \mu_0 K_m \left(\frac{R_r^{2p} + R^{2p}}{R_r^{2p} - R^{2p}} \right) \sin(p\Omega t - p\theta + \alpha_{dis}) \quad (\text{II- 19})$$

Thus, the magnetic flux per pole at $t = 0$ and $\alpha_{dis} = 0$:

$$\phi_p = \iint_{S_p} B_{tot} dS = \iint_{S_p} \left(B_m \cos(p\theta) + \mu_o K_m \left(\frac{R^{2p} + R_r^{2p}}{R^{2p} - R_r^{2p}} \right) \sin(p\theta) \right) dS \quad (\text{II- 20})$$

After calculation:

$$\phi_p = \iint_{S_p} B_{mtot} \cos(p\theta - \psi) dS \quad (\text{II- 21})$$

Where: $\psi = \arctan \left(\frac{\mu_o K_m}{B_m} \left(\frac{R^{2p} + R_r^{2p}}{R^{2p} - R_r^{2p}} \right) \right)$ and $B_{mtot} = \sqrt{B_m^2 + \mu_o^2 K_m^2 \left(\frac{R^{2p} + R_r^{2p}}{R^{2p} - R_r^{2p}} \right)^2}$

Then:

$$\phi_p = RL_m \int_{-\frac{\pi}{2p} + \frac{\psi}{p}}^{\frac{\pi}{2p} + \frac{\psi}{p}} B_{mtot} \cos(p\theta - \psi) d\theta \quad (\text{II- 22})$$

Therefore, the magnetic flux per pole is deduced by:

$$\phi_p = \frac{2RL_m B_{mtot}}{p} \quad (\text{II- 23})$$

By setting the x ratio defined as:

$$x = \frac{R_r}{R} \quad (\text{II- 24})$$

Finally, the magnetic flux per pole is given by:

$$\phi_p = \frac{2RL_m}{p} \sqrt{B_m^2 + \mu_o^2 K_m^2 \left(\frac{1+x^{2p}}{1-x^{2p}} \right)^2} \quad (\text{II- 25})$$

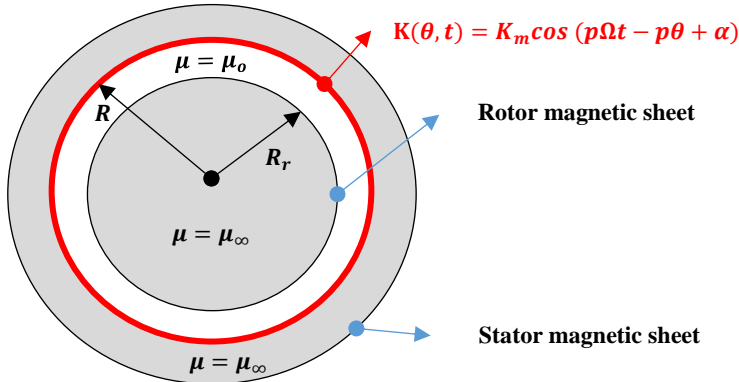


Figure II. 5. Study domain of magnetic flux per pole

b. Magnetic flux in stator yoke

Through the conservation of magnetic flux (cf. Figure II. 4), the magnetic flux in stator yoke can be expressed by:

$$\phi_{sy} = \frac{\phi_p}{2} = \frac{L_m R}{p} \sqrt{B_m^2 + \mu_o^2 K_m^2 \left(\frac{1+x^{2p}}{1-x^{2p}} \right)^2} \quad (\text{II- 26})$$

On other hand, using Gauss law, the magnetic flux in stator yoke can be written by:

$$\phi_{sy} = B_{sy} S_{sy} \quad (\text{II- 27})$$

Where: B_{sy} is the mean flux density in stator yoke, S_{sy} is the surface of stator yoke (with $S_{sy} = h_y L_m$) and h_y is the stator yoke thickness.

Hence, the magnetic flux balance in stator yoke is:

$$B_{sy} h_y = \frac{R}{p} \sqrt{B_m^2 + \mu_o^2 K_m^2 \left(\frac{1+x^{2p}}{1-x^{2p}} \right)^2} \quad (\text{II- 28})$$

c. Magnetic flux in stator teeth

Likewise, the total magnetic flux in stator teeth is deduced from the conservation of magnetic flux in electrical machines:

$$N_t \phi_{st} = 2p\phi_p \quad (\text{II- 29})$$

With:

$$\phi_{st} = B_{st}S_{st} = B_{st}l_tL_m \quad (\text{II- 30})$$

The magnetic flux balance in stator teeth is deduced by:

$$B_{st}N_t l_t = 4R \sqrt{B_m^2 + \mu_o^2 K_m^2 \left(\frac{1+x^{2p}}{1-x^{2p}} \right)^2} \quad (\text{II- 31})$$

Where: B_{st} is the mean flux density in stator yoke, S_{st} is the tooth surface crossed by the flux, N_t is the number of teeth, l_t is the tooth width.

In fact, magnetic flux balances established in stator yoke and tooth (equations II-28 and II-31) allow to determine the stator sizes from the flux density level of the soft materials and from flux density level in the airgap.

II.2.3. Electric current balances

a. Current density

By applying the Ampere law, the rms current density is expressed by:

$$j_{rms} = \frac{I_{rms}}{S_{cond}} = \frac{N_{cs}I_{rms}}{k_{fill}k_{sc}S_{slot}} \quad (\text{II- 32})$$

With:

$$N_{cs} = \frac{N_c}{N_s} , \quad S_{slot} = h_s l_s \quad \text{and} \quad S_{cond} = \frac{S_{tot-cond}}{N_{cs}} = \frac{k_{sc}k_{fill}S_{slot}}{N_{cs}} \quad (\text{II- 33})$$

Where: I_{rms} is the rms value of current, S_{cond} is the cross section of a conductor and S_{slot} is the slot cross section. N_c is the total number of conductors, N_s is the number of slots (with $N_s = N_t$). So N_{cs} is the total number of conductors per slot connected in series. $S_{tot-cond}$ is the total cross section of conductors in one slot. k_{fill} is the fill factor which represents the ratio of the conductor area over the total slot area. k_{sc} is a coefficient that takes into account the elliptical cross-section of the conductors generated by twisting and splitting [Tan_03] as it is shown in Figures II. 6 and II. 7.

At high frequency, current density is nonuniform distributed in the conductor cross-section due to the skin and proximity effects. Skin effect is caused by the magnetic field induced by the own current flowing inside the conductor. Proximity effect is caused by magnetic fields induced by currents circulating in adjacent conductors [Pyr_08] [Gia_10] [Hen_94] [Han_94]. Usually, splitting and twisting conductors into several wires connected in parallel allow to reduce Ohmic losses due to these effects. Nevertheless, twisting and splitting conductors requires more conductor length and more outer conductor surface. A coefficient k_{lc} is introduced to take into account this conductor length in regards to a lay length (cf. Figure II. 7).

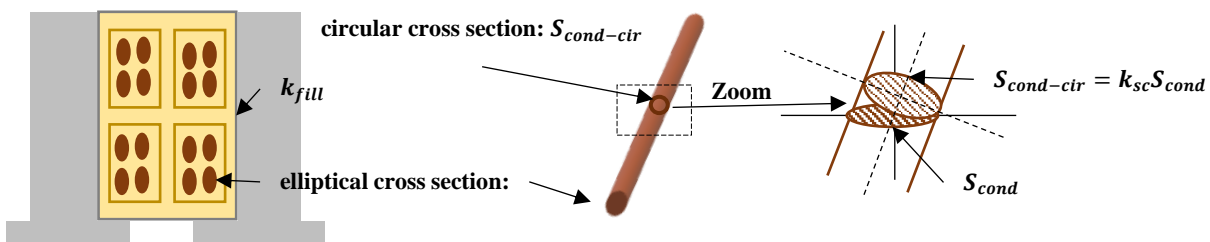


Figure II. 6. Slot and conductor cross section showing the slot filling and elliptical and circular cross sections of conductor

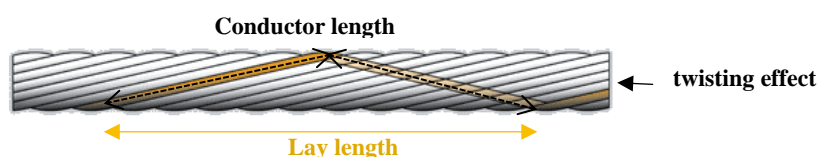


Figure II. 7. Twisting of conductors

b. Linear and surface current density

Linear current density expressed in [A/m], may be defined from the total number of conductors and from sinewave current by the following equation:

$$A_{rms} = \frac{N_c I_{rms}}{2\pi R} \quad (\text{II- 34})$$

According to [Sle_94], linear current density can be linked to the surface current density by:

$$A_{rms} = \frac{K_m}{\sqrt{2} k_w} = \frac{\sqrt{2}\sigma}{k_w B_m} \quad (\text{II- 35})$$

Where: k_w is the winding coefficient.

c. Current density product

From equations (II-32) and (II-34), the current density product is obtained by:

$$A_{rms} j_{rms} = \frac{k_{sc} k_{fill} h_s N_s l_s j_{rms}^2}{2\pi R} \quad (\text{II- 36})$$

Knowing that:

$$N_s l_s + N_t l_t = 2\pi R \quad (\text{II- 37})$$

and using equation (II-31), equation (II-36) can be written by:

$$A_{rms} j_{rms} = k_{sc} k_{fill} h_s j_{rms}^2 \left(1 - \frac{2}{\pi} \sqrt{\left(\frac{B_m}{B_{st}}\right)^2 + \mu_o^2 \left(\frac{K_m}{B_{st}}\right)^2 \left(\frac{1+x^{2p}}{1-x^{2p}}\right)^2} \right) \quad (\text{II- 38})$$

Therefore, winding and slot sizes can be deduced from the levels of linear surface current density A_{rms} , current density j_{rms} , airgap flux density B_m and flux density in stator teeth B_{st} .

II.2.4.Power balance

a. Electromagnetic, mechanical and electric powers

Electromagnetic power developed by electric motor is given by:

$$P_{em} = T_{em} \Omega \quad (\text{II- 39})$$

According to the power balance applied to an electric motor, mechanical power at the shaft level and input electric power are given by:

$$P_{mech} = P_{em} - (P_{mech-loss} + P_{rot-loss}) \quad (\text{II- 40})$$

and

$$P_{ele} = P_{em} + P_{js} + P_{fs} \quad (\text{II- 41})$$

Where: $P_{mech-loss}$ are the total mechanical losses, $P_{rot-loss}$ are the total electromagnetic rotor losses, P_{js} is the stator joule losses and P_{fs} is the stator iron losses.

b. Efficiency

Efficiency of an electric motor is evaluated by:

$$\eta = \frac{P_{mech}}{P_{ele}} \quad (\text{II- 42})$$

In the thesis context, mechanical power at the shaft level is set as our baseline specification.

II.2.5.Main sizes of electric motor

Main sizes of an ideal sinewave electric motor having unspecified winding and rotor structures include:

- the stator bore radius " R ",
- the active length of active part " L_m ",
- the slot height " h_s ",
- the stator yoke thickness " h_y ", as shown in Figure II. 8.

As demonstrated through electric and magnetic balances previously established, for given electromagnetic power " P_{em} " and given rotational speed " Ω ", the main sizes are linked to the magnetic, electric, thermal and mechanical loads:

- Max airgap flux density " B_m "

- Flux density in teeth " B_{st} "
- Flux density in yoke " B_{sy} "
- Tangential stress " σ "
- Current density " j_{rms} ".

Moreover, for given parameters as:

- number of pole pairs " p ",
- fill factor " k_{fill} ",
- shape coefficient " $\lambda = 2R/L_m$ ", these sizes can be deduced by the following equations:

$$R = \sqrt[3]{\left(\frac{\lambda}{4\pi\sigma}\right) \frac{P_{em}}{\Omega}} \quad (\text{II- 43})$$

$$L_m = \left(\frac{2}{\lambda}\right) \sqrt[3]{\left(\frac{\lambda}{4\pi\sigma}\right) \frac{P_{em}}{\Omega}} \quad (\text{II- 44})$$

$$h_y = \frac{R}{p} \sqrt{\left(\frac{B_m}{B_{sy}}\right)^2 + \mu_o^2 \left(\frac{K_m}{B_{sy}}\right)^2 \left(\frac{1+x^{2p}}{1-x^{2p}}\right)^2} \quad (\text{II- 45})$$

$$h_s = \frac{\sqrt{2}\sigma_t}{k_w B_m j_{rms}} \frac{1}{k_{sc} k_{fill} \left(1 - \frac{2}{\pi} \sqrt{\left(\frac{B_m}{B_{st}}\right)^2 + \mu_o^2 \left(\frac{K_m}{B_{st}}\right)^2 \left(\frac{1+x^{2p}}{1-x^{2p}}\right)^2}\right)} \quad (\text{II- 46})$$

From these main sizes, external stator radius is given by:

$$R_{out} = R + h_y + h_s \quad (\text{II- 47})$$

and ratio between tooth length to bore radius can be given:

$$r_{tooth} = \frac{N_t l_t}{2\pi R} = \frac{2}{\pi} \sqrt{\left(\frac{B_m}{B_{st}}\right)^2 + \mu_o^2 \left(\frac{K_m}{B_{st}}\right)^2 \left(\frac{1+x^{2p}}{1-x^{2p}}\right)^2} \quad (\text{II- 48})$$

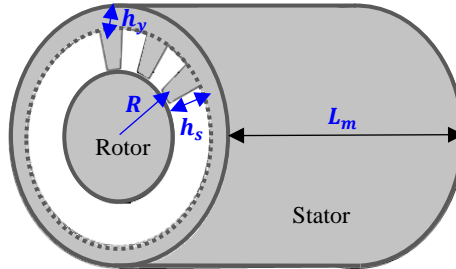


Figure II. 8. Main sizes of an electric motor

To obtain more intrinsic sizes as the end-winding length, the axial length of electric motor, the airgap of thickness and the radius of shaft, some approximations are made:

• *Approximation on end-winding length*

Stator winding is composed from two parts: the first one is located inside slot in the active part, the second one is located on the end-side of the electric motor as illustrated in Figure II. 9. End-winding length depends on winding configurations as mentioned in Chapter I. It can be measured in terms of active length L_m and a half-turn length l_{ht} as expresses the end-winding coefficient k_{tb} :

$$k_{tb} = l_{ht}/L_m \cong L/L_m \quad (\text{II- 49})$$

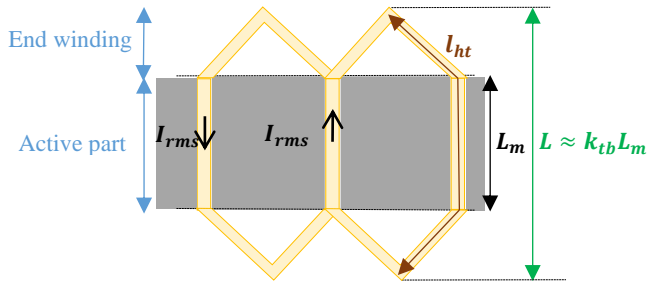


Figure II. 9. End-winding sizes

- *Approximation on the airgap length and the rotor radius*

Airgap length e_g can be approximated using the airgap ratio x_e :

$$e_g = x_e R \quad (\text{II- 50})$$

Therefore, external rotor radius R_r is obtained by:

$$R_r = R - e_g \quad (\text{II- 51})$$

- *Approximation on shaft radius*

To assess mechanical losses, sizes of shaft should be determined although rotor structure is not defined. For the purpose, shaft radius is approximated by:

$$R_{sh} \approx \frac{1}{3} R_r \quad (\text{II- 52})$$

- *Approximation on frame sizes*

To estimate the frame sizes, a benchmarking has been established on Etel TMB and TMK electric motors with air and water cooling method [EteCat]. These motors have been chosen given that more data of electric motors are available. The benchmarking on frame allows to obtain ratio τ_r between external frame radius R_{fr} and external stator radius R_{out} as established in [Lef_19]. Frame sizes expressed using ratio τ_r are shown in Figure II. 10.a. The ratio between external frame radius R_{fr} and external stator radius R_{out} is given by equation (II-53). Figure II. 10.b shows its variation according to R_{out} .

$$\tau_r(R_{out}) = \begin{cases} 0.7371 R_{out}^2 - 0.580 R_{out} + 1.1599 & \text{for } R_{out} \leq 400\text{mm} \\ 1.04 & \text{for } R_{out} > 400\text{mm} \end{cases} \quad (\text{II- 53})$$

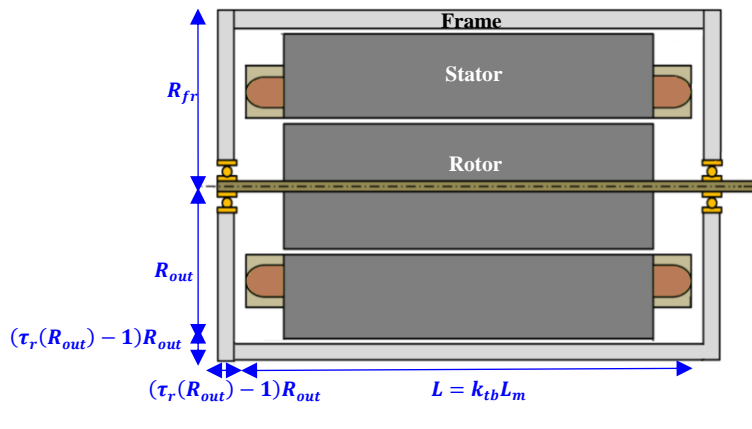


Figure II. 10. (a) Frame sizes, (b) ratio function of housing diameter to external stator radius [Lef_19]

II.2.6. Electric motor weight

a. Stator weight

Once stator sizes are determined, stator weight can be evaluated from chosen conductor, insulation and magnetic soft materials previously introduced (cf. Chapter I). The following equations summarized the weight of stator core and stator winding:

- **stator core**

$$W_{stat-core} = [\pi L_m (R_{out}^2 - R^2) - (h_s L_m N_s l_s)] \rho_{sf} \quad (\text{II- 54})$$

Where: ρ_{sf} is the density of soft magnetic material.

- **stator winding**

$$W_{stat-wind} = [k_{tb} k_{lc} h_s L_m N_s l_s] [k_{fill} \rho_c + (1 - k_{fill}) \rho_{insl}] \quad (\text{II- 55})$$

Where: ρ_c is the density of conductor material and ρ_{insl} is the density of insulation material.

Therefore, the weight of stator is deduced by:

$$W_{stat} = W_{stat-core} + W_{stat-wind} \quad (\text{II- 56})$$

b. Rotor weight

Usually, rotor is mainly composed of shaft, rotor core and winding or magnets depending to electric motor topology. Rotor components are made with different materials. Assess of rotor weight is difficult if the rotor structure is not specified. In our case, only external rotor volume is known. To overcome this difficulty, benchmarking established on Etel TMB and TMK electric motors can be used since more than one hundred detailed electric motors with large range of number of pole pairs are available. Moreover, benchmarking on large number of pole pairs allows to fit all rotor possible shapes. On other side, the available details are enough for establishing equivalent rotor density as illustrated in Figure II. 11. Equivalent of rotor density ρ_{rot} is given by [Lef_19]:

$$\rho_{rot}(p) = \begin{cases} -431.67p + 7932 & \text{for } p \leq 10 \\ 1.09p^2 - 117.45p + 4681 & \text{for } 10 < p \leq 50 \\ 1600 & \text{for } p > 50 \end{cases} \quad (\text{II- 57})$$

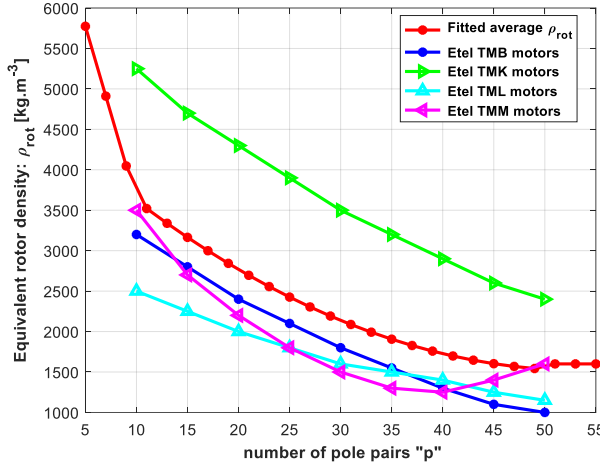


Figure II. 11. Equivalent rotor density vs number of pole pairs [Lef_19]

Therefore, rotor weight is given by:

$$W_{rot} = \pi R_r^2 L_m \rho_{rot}(p) \quad (\text{II- 58})$$

c. Frame weight

Through estimation on frame sizes, the weight frame is:

$$W_{frame} = \rho_{fr} (\pi L_m k_{tb} (R_{fr}^2 - R_{out}^2) + 2\pi(\tau_r(R_{out}) - 1) R_{out} R_{fr}^2) \quad (\text{II- 59})$$

Where: ρ_{fr} is the density of the frame.

Eventually, electric motor weight is:

$$W_{mot} = W_{rot} + W_{stat} + W_{frame} \quad (\text{II- 60})$$

II.2.7. Specific power and specific torque

Specific power and specific torque of an electric motor expressed in [W/kg] and [Nm/kg] respectively, are deduced by:

$$S_P = \frac{P_{mec}}{W_{mot}} \quad (\text{II- 61})$$

and

$$S_T = \frac{T_{emmax}}{W_{mot}} \quad (\text{II- 62})$$

In this sizing model of the electric motor, specific power and torque take into account the all parts of the electric motor without the cooling system.

II. 3 Loss assessment models

Losses in electrical machines are mainly composed of Joule losses in winding, iron losses in magnetic core and mechanical losses. These losses are consistently critical to reach high performances especially specific power as well as efficiency. Therefore, their assessment is mandatory for sizing electric machines. The following sections presents the analytical models used for assessing losses.

II.3.1. Analytical model of Joule losses

Joule losses are often the first largest losses in electric motors [Pyr_08] [Hen_94] [Han_94]. They arise mainly due to Ohmic heating in conductors supplied by current. At low operating speed, current density is uniformly distributed in the cross-section of conductors. Joule losses are governed by:

$$P_J = qR_s I_{rms}^2 \quad (\text{II- 63})$$

With:

$$R_s = \frac{N_c}{q} \rho_{cu}(T_{win}) \frac{l_c}{S_{cond}} \quad \text{and} \quad \rho_{cu}(T_{win}) = \rho_{cu20^\circ} (1 + \alpha_{th}(T_{win} - 20^\circ)) \quad (\text{II- 64})$$

Where: q is the number of phase, I_{rms} is the rms current and R_s is the resistance. ρ_{cu20° is the copper electric resistivity at 20°C, T_{win} is the winding temperature, α_{th} is the temperature coefficient resistance (for copper $\alpha_{th} = 3,81 \cdot 10^{-3} \text{ K}^{-1}$). l_c is the length of one conductor of a half-turn ($l_c = k_{tb}k_{lc}L_m$) and S_{cond} is the conductor cross section.

Using equations (II-32) and (II-34), Joule losses can be also written by:

$$P_J = \rho_{cu}(T_{win})k_{tb}k_{lc}L_m 2\pi R A_{rms} j_{rms} \quad (\text{II- 65})$$

II.3.2. Analytical model of Iron losses

In electric motors, iron losses arise from the variation of magnetic flux density in magnetic core. They are the second largest losses after Joule losses [Pyr_08] [Gie_10]. Variations of magnetic flux density usually induce two losses namely hysteresis losses and eddy current losses. Variation of flux density in magnetic core is cyclically due to hysteretic characteristic of magnetic core (cf. Chapter I). Each cyclic variation induces "hysteresis" losses proportional to enclosed hysteresis area [Lip_04] [Pyr_08]. Eddy current losses induce current occurring in magnetic core at the same frequency as the variation in magnetic flux density [Mil_02] [Pyr_08]. Iron losses are difficult to accurately estimate. However, there are several proposed models to estimate them: [Ber_85] [Mil_02] [Zha_12] [Egg_12] [Roy_16] [Ion_16]. From among, Bertotti model [Ber_85] is the well-known and the most used in the finite element analysis software. His corresponding equation is given by:

$$P_f = k_h f B_m^2 + k_c f^2 B_m^2 + k_e f^{3/2} B_m^{3/2} \quad (\text{II- 66})$$

Where: B_m is the maximum magnetic flux density, f is the frequency, k_h is the hysteresis loss coefficient, k_c is the eddy loss coefficient and k_e is the excess loss coefficient.

Figure II. 12 shows a comparison of specific iron losses given by manufacturers and specific iron losses modeled using Bertotti formulation. Indeed, Bertotti model gives specific losses close to those given experimentally by manufacturers as shown for "Vacodur 49" in Figure II. 12.a. However, specific losses of "Vacoflux 48" given by Bertotti model are less close to those given by manufacturers (cf. Figure II. 12.b). Moreover, usually specific iron loss data given by manufacturers are not enough for modelling using Bertotti model. For the purpose, new formulation of iron losses based on Least Square Method is proposed:

$$P_f = \sum_{i=1}^{i=4} \sum_{j=1}^{j=4} a_{ij} (\sqrt{B_m})^j (\sqrt{f})^i \quad (\text{II- 67})$$

Where: a_{ij} is the iron loss coefficient determined by the Least Square Method.

The results using equation (II-67) are shown in Figure II. 13. More results are given in Appendix A.

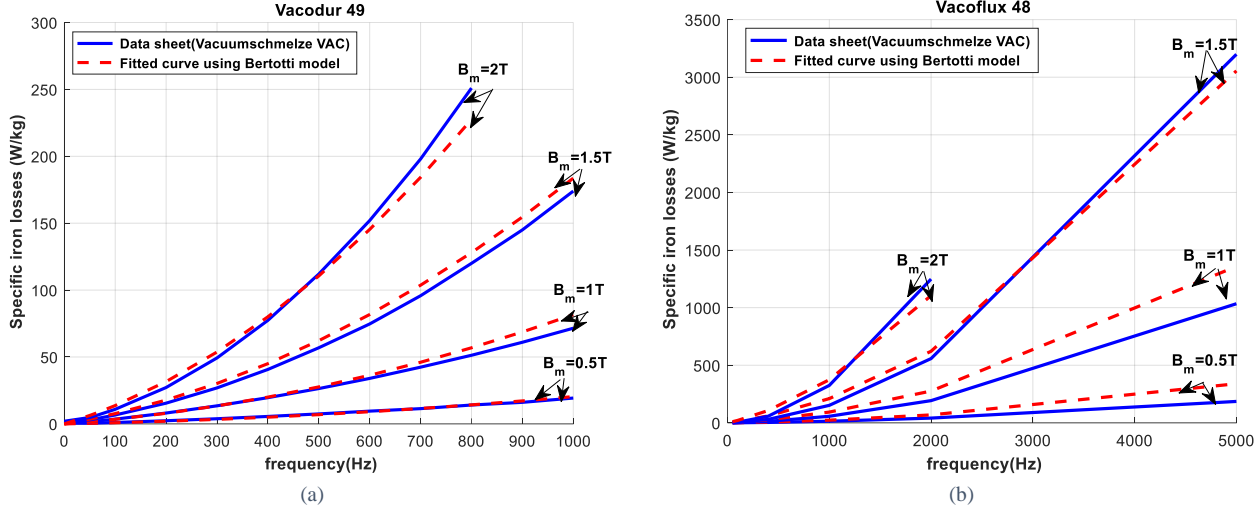


Figure II. 12. Specific iron losses using Bertotti model

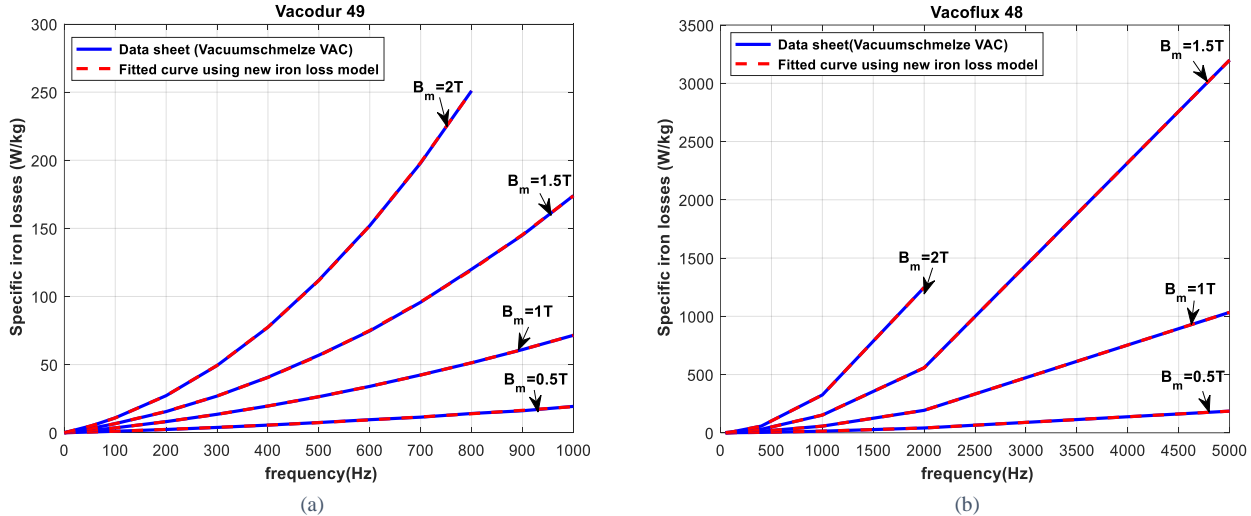


Figure II. 13. Specific iron losses using proposed model

II.3.3. Semi-empirical models of mechanical losses

Mechanical losses are consequence of frictions between gas and rotating solid or between rotating solid and stationary solid. We distinguish then two losses in electric motors: windage losses and friction bearing losses. Therefore, total mechanical losses are given by (II-68). At high rotational speed these losses may be very significant. The following sections provide more detail to estimate them.

$$P_{\text{mech-loss}} = P_{\text{windage}} + 2P_{\text{friction}} \quad (\text{II- 68})$$

Where: P_{windage} is the total windage losses, P_{friction} is the friction losses in one bearing.

a. Windage losses

Windage losses are due to friction between the air and rotor surfaces. These frictions occur in airgap and in rotor ends as shown in Figure II. 14. The rotating movement of rotor gives to air a tangential velocity component. This component affects the friction windage torque and then generated losses. [Saa_98] has proposed formulas

of windage losses for high speed electrical motors which are used by several authors [Lip_04] [Ner_08] [Pyr_08] [Luo_09] [Rei_10] [Kol_11] [Hua_16].

Total windage losses are given by:

$$P_{windage} = P_{windage-airgap} + 2P_{windage-rotor} \quad (\text{II- 69})$$

where $P_{windage-airgap}$ is the windage losses in airgap and $P_{windage-rotor}$ is the windage losses in one rotor ends.

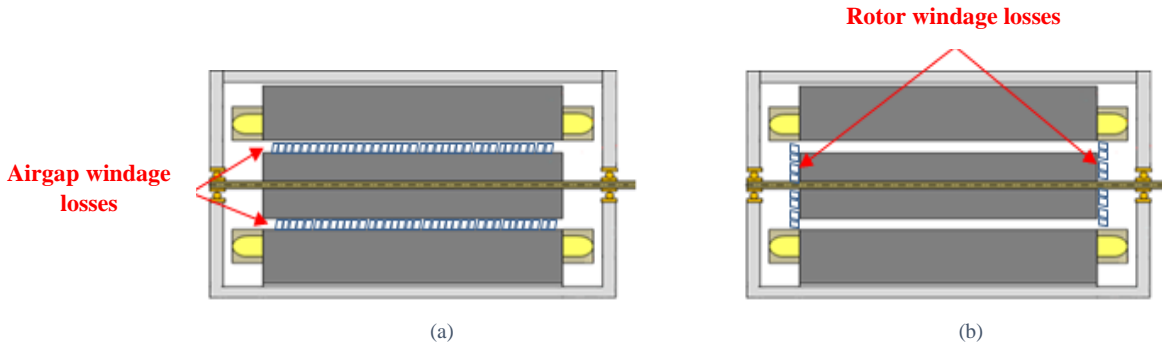


Figure II. 14. Windage losses in electrical motors (a) airgap, (b) rotor ends

- Windage losses in airgap

The windage losses in airgap can be estimated by the following equation:

$$P_{windage-airgap} = k_1 C_{fa} \pi \rho_{air} \Omega^3 R_r^4 L \quad (\text{II- 70})$$

Where: k_1 is the roughness coefficient. $k_1=1$ for smooth rotor and stator surfaces, $k_1=2$ to 4 for other type of surfaces.

ρ_{air} is the air density given by:

$$\rho_{air}(T, pr) = 1.293 \times \frac{273.15}{T} \times pr \quad (\text{II- 71})$$

With: T is the air temperature [K] and pr is the air pressure [atm].

C_{fa} is the friction coefficient depending on the flow regimes.

The nature of flow is determined by the Reynolds number R_{ea} by:

$$Re_a = \frac{\rho_{air} R_{re} e_g}{\mu_{air}} \Omega \quad (\text{II- 72})$$

With:

For laminar flow $500 < R_{ea} < 10^4$:

$$C_{fa} = 0.515 \frac{(e_g/R_r)^{0.3}}{Re_a^{0.5}} \quad (\text{II- 73})$$

For turbulent flow $R_{ea} > 10^4$:

$$C_{fa} = 0.0325 \frac{(e_g/R_r)^{0.3}}{Re_a^{0.2}}$$

Where: μ_{air} is the air dynamic viscosity given at 1 atm by:

$$\mu_{air}(T, p = 1\text{atm}) = 8.88 \cdot 10^{-15} T^3 - 3.23 \cdot 10^{-11} T^2 + 6.26 \cdot 10^{-8} T + 2.35 \cdot 10^{-6} \quad (\text{II- 74})$$

- Windage losses rotor end

The windage losses in rotor ends can be estimated by:

$$P_{windage-rotor} = \frac{1}{2} C_{fr} \pi \rho_{air} \Omega^3 (R_r^5 - R_{sh}^5) \quad (\text{II- 75})$$

As for the airgap, the friction coefficient C_{fr} depends on the flow regime:

For laminar flow $R_{e rot} < 3 \cdot 10^5$:

$$C_{fr} = \frac{3.87}{R_{e\text{rot}}^{0.5}} \quad (\text{II- 76})$$

For turbulent flow $R_{e\text{rot}} > 3.10^5$:

$$C_{fr} = \frac{0.146}{R_{e\text{rot}}^{0.2}}$$

with $R_{e\text{rot}}$ is the Reynolds number of the flow in rotor ends. It can be calculated by:

$$R_{e\text{rot}} = \frac{\rho_{air} R_r^2}{\mu} \Omega \quad (\text{II- 77})$$

b. Friction bearing losses

The friction in bearings comes from surface contacts between rolling elements and raceways, between the rolling elements and cage, and between the rolling elements. The bearing losses depend on the loads and several other factors such as bearing type, lubrication type, bearing sizes and rotational speed. Therefore, it is hard to accurately define the friction losses in bearings. However, bearing manufacturers propose often models for estimating friction losses such as SKF proposes in the condition of good lubrication and normal operating conditions [Skf_13-Skf_16]:

$$P_{\text{friction}} = \frac{1}{2} C_f P d \Omega \quad (\text{II- 78})$$

Where: C_f is the friction coefficient which depends on the type bearing (cf. Table II. 4), d is the bearing bore diameter, Ω is the speed and P is the equivalent dynamic bearing load (cf. Figure II. 15) expressed by:

$$\vec{P} = \vec{F_a} + \vec{F_r} \quad (\text{II- 79})$$

Where: $\vec{F_a}$ is the axial load and $\vec{F_r}$ is the radial load.

Usually bearings for radial flux electric machines are subjected to both radial and axial loads. To approximate the calculation of equivalent dynamic bearing load, only radial load is considered. Therefore, radial load can be approximated by the rotor weight (ie. $\vec{P} = W_{\text{rot}} \vec{g}$ with \vec{g} is the gravitational force).

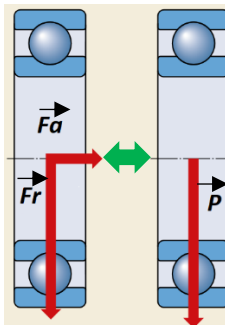


Figure II. 15. Axial and radial loads applied on rotor [Skf_16]

Table II. 4: Friction coefficient according to the bearing types used mainly to withstand the radial loads [Skf_13-Skf_16]

Bearing types	Friction coefficient C_f
Deep groove ball bearings	0.0015
Cylindrical roller bearings	
- with cage	0.0011
- full complement	0.0020
Spherical toroidal roller bearings	0.0018
CARB toroidal roller bearings	0.0016
Angular contact ball bearings	
- single row	0.0020
- double row	0.0024
- four-point contact	0.0024
Hybrid bearings	-

In other conditions and for more advanced calculation of friction bearing losses, SKF proposes a model of the calculation of different friction torques generated in surface contacts. This model is detailed in [Skf_16].

II. 4 Thermal constraint

To not exceed the thermal limits in sizing of electric motors, thermal constraint based on the current density product definition is introduced in the sizing model of electric motor. In [Pyr_08], it has been demonstrated that current density j_{rms} and linear current density A_{rms} depend only on the effectiveness of cooling system and not on the sizes of electric motor. [Pyr_08] has demonstrated it from the Joule losses relationship (equation II-65). To take into account all losses, we propose as thermal constraint the equivalent current density product evaluated by bringing them to the bore stator surface as it shown in Figure II. 16. This equivalent current density product allows also to quantify the cooling effort required to reach targeted specific power.

$$\langle A_{eq} \rangle = \frac{P_{js} + P_{fs} + P_{mech-loss} + P_{rot-loss}}{2\pi R k_{tb} L_m \rho_{cu}(T_{win})} \quad (\text{II- 80})$$

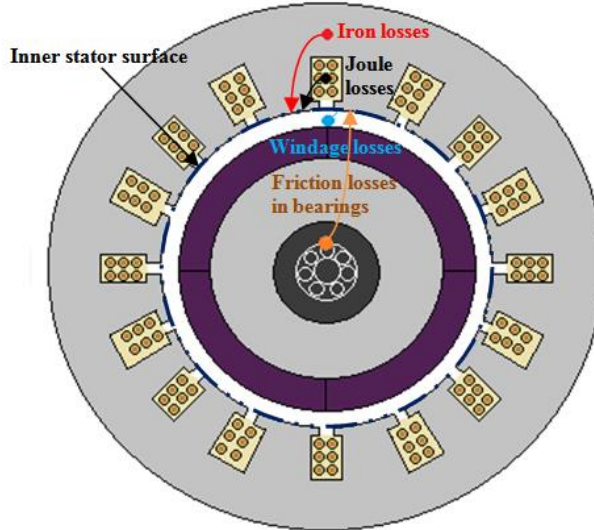


Figure II. 16. Losses taken back to the bore stator surface

II. 5 Mechanical constraint

Regarding to not exceed static and dynamic mechanical limits in sizing high speed electric motors requires a mechanical constraint (cf. Chapter I). It will be obtained through a combination between these both limits.

- **Static mechanical limit**

The maximum mechanical stress generating by the centrifugal forces applying on the external rotor surface (cf. Figure I. 48.a) is given by:

$$\sigma_m = C \rho_{rot} R_r^2 \Omega^2 \quad (\text{II- 81})$$

It can be also written using maximum peripheral speed $V_{p_{max}}$:

$$\sigma_m = C \rho_{rot} V_{p_{max}}^2 \quad (\text{II- 82})$$

With:

$$V_{p_{max}} = R_r \Omega \quad (\text{II- 83})$$

Where: C is a coefficient depending of rotor shape, $C = \frac{3+\nu}{8}$ for a smooth homogeneous cylinder, $C = \frac{3+\nu}{4}$ for a cylinder with small bore, ν is the Poisson's ratio, R_r is the maximum rotor radius and ρ_{rot} is the rotor density.

Therefore, maximum rotor radius can be expressed by maximum mechanical stress:

$$R_r = \sqrt{\frac{\sigma_m}{C \rho_{rot}}} \frac{1}{\Omega} \quad (\text{II- 84})$$

- **Dynamic mechanical limit**

Axial length of rotor is limited by the critical rotational speeds (cf. Figure I. 48.b). According to [Bor_11] [Lah_02] [Bin_07] [Aho_07] [Mul_99] [Can_14] [Sin_12] [Bor_10] [Pyr_08], these critical speeds are defined by:

$$\Omega_{cr}^* = n^2 \Omega_{cr} = n^2 \sqrt{\frac{96}{5} \frac{E}{\rho_{rot} k_p^2 L_m^2}} \frac{k_a R_r}{k_p^2 L_m^2} \quad (\text{II- 85})$$

Where: n is the order of the critical rotor speed, E is the young's modulus of the rotor material, k_a is the ratio between shaft radius and rotor radius ($k_a = \frac{R_{sh}}{R_r}$) and k_p is the ratio between axial length L and the active length L_m ($k_p = \frac{L}{L_m}$)

By matching the 1st order critical rotational (i.e. Equation (II-85)) with rotational speed expressed with the maximum mechanical stress (i.e. Equation (II-81)):

$$\Omega \leq \Omega_{cr} \quad (\text{II- 86})$$

The ration between rotor radius is obtained by:

$$k_p \sqrt{\frac{1}{k_a} \sqrt{\frac{\sigma_m}{C} \frac{5}{6E}}} \leq \frac{2R_r}{L_m} \quad (\text{II- 87})$$

And knowing that:

$$\lambda \cong \frac{2R_r}{L_m} \quad (\text{II- 88})$$

Mechanical constraint can be written as follows:

$$k_p \sqrt{\frac{1}{k_a} \sqrt{\frac{\sigma_m}{C} \frac{5}{6E}}} \leq \lambda \quad (\text{II- 89})$$

By taking: $k_p = 1.4$, $k_a = \frac{1}{3}$ and the mechanical properties of rotor materials as " Silicon Iron Alloy":

- $E = 160\text{GPa}$
- $\sigma_m = 250\text{MPa}$
- $\nu=0.33$
- $C = \frac{3+\nu}{4} = 0.83$

Finally, mechanical constraint for high and low rotational speeds is given by:

$$0.4 \leq \lambda \quad (\text{II- 90})$$

Equation (II-90) is obtained from the superposition of the static and dynamic mechanical limits at high rotational speed ($V_p \geq 100\text{m/s}$) and at low rotational speed ($V_p \leq 100\text{m/s}$) as illustrated in Appendix B.

II. 6 Inputs and outputs of Target Setting Tools

Equations (II-1) to (II-90) developed previously, can be organised on a Tool having inputs and outputs to assess the technology levels. For the purpose, inputs should be specifications, loads, geometrical and material choices. For outputs should be sizes, weights, specific power and torque, and further intrinsic parameters as listed in Table II. 5. Graphic user interface can be also programed in Matlab software as illustrated in Figure II. 17.

Table II. 5: Target Setting Tool inputs/outputs list

TST inputs	TST outputs
Mechanical specifications	Main sizes
<ul style="list-style-type: none"> - Electromagnetic power "P_{em}" - Rotational speed "Ω" 	<ul style="list-style-type: none"> - External stator radius "R_{out}" - Stator bore radius "R" - Active length "L_m" - Stator yoke height "h_y" - Tooth (or slot) height "h_s"
Thermal specifications	Weight
<ul style="list-style-type: none"> - Winding temperature "T_{win}" 	<ul style="list-style-type: none"> - Stator magnetic core weight "$W_{stat-core}$" - Winding stator weight "$W_{stat-wind}$" - Rotor weight "W_{rot}" - Frame weight "W_{frame}" - Total motor weight "W_{mot}"
Magnetic and electric loads	Specific power and torque
<ul style="list-style-type: none"> - Tangential stress "σ" - Current density "J_{rms}" - Max airgap flux density "B_m" - Flux density in yoke "B_{sy}" - Flux density in teeth "B_{st}" 	<ul style="list-style-type: none"> - Specific power "S_P" - Specific torque "S_T"
Geometrical choice	Further intrinsic parameters
<ul style="list-style-type: none"> - Shape coefficient "$\lambda = 2R/L_m$" - Fill factor "k_{fill}" - End-winding coefficient "k_{tb}" - Number of pole pairs "p" 	

Chapter II: Target Setting Tool

Materials library - Magnetic soft material (Iron Cobalt alloys (CoFe) and Silicon Iron alloys (SiFe))	- Peripheral speed " V_p " - Joule losses " P_{js} " - Iron losses " P_{fs} " - Mechanical losses " $P_{mech-loss}$ " - Efficiency " η "
--	---

Inputs		Magnetic, electric technological levels	Geometrical choice	Material library
Mechanical specifications Power Power (W) <input type="text" value="0.9e6"/> Speed (rpm) <input type="text" value="20000"/>	Thermal specifications Thermal level T_{air} temperature (°C) <input type="text" value="100"/>	Typical electromagnetic values depending on cooling type and selected materials Tangential stress (Pa) <input type="text" value="38000"/> Current density (A/m ²) <input type="text" value="11e6"/> Max air gap flux density 'Bm(T)' <input type="text" value="1"/> Teeth flux density 'Bt(T)' <input type="text" value="1.3"/> Yoke flux density 'By (T)' <input type="text" value="1"/> Linear current density (A/m): 59711.2 Current densities product Arms ² Jrms(A ² m ³): 6.56824e+11	Geometric choices Lambda 'DrotL' <input type="text" value="0.5"/> Fill factor 'kfill' <input type="text" value="0.5"/> Winding head coefficient <input type="text" value="1.4"/> Pole pair number <input type="text" value="2"/>	Material Choice <input type="text" value="Vacoflux48"/>
<input type="button" value="Validation"/>				
Output data				
Main sizes Geometric parameters External stator radius (m) <input type="text" value="0.136217"/> Inner stator radius (m) <input type="text" value="0.0766279"/> Active length (m) <input type="text" value="0.306512"/> Yoke height (m) <input type="text" value="0.0383139"/> Teeth height (m) <input type="text" value="0.0212752"/> Teeth length to rotor perimeter percentage (%) <input type="text" value="48.9708"/>	Weights Weights Weight of stator iron (kg) <input type="text" value="82.622"/> Weight of stator copper (kg) <input type="text" value="10.0039"/> Stator weight (kg) <input type="text" value="92.6259"/> Rotor weight (kg) <input type="text" value="39.9675"/> Casing weight (kg) <input type="text" value="18.2325"/> Epoxy glue weight (kg) <input type="text" value="1.68227"/> Total weight (kg) <input type="text" value="152.508"/>	Specific power, specific torque Power and torque densities Specific power (W/kg) <input type="text" value="5901.32"/> Specific torque (N.m/kg) <input type="text" value="2.81768"/>	Further intrinsic parameters Peripheral speed Peripheral speed (m/s) <input type="text" value="160.489"/> Losses Joule losses (W) <input type="text" value="14754.7"/> Iron losses (W) <input type="text" value="2683.15"/> Windage losses (W) <input type="text" value="1498.79"/>	
<input type="button" value="Save"/> <input type="button" value="Print"/> <input type="button" value="Return to homepage"/> <input type="button" value="Close"/>				

Figure II. 17. Graphic user interface of Target Setting Tool "TST"

Conclusion

This chapter deals with a model elaborated for the assessment electric motor technologies. It uses the loadability concepts tying set of magnetic, electric, mechanical loads and cooling methods to the different technologies involved in electric motors. Also, it involves an analytical model of non-salient sinewave electric machines. This model helps to identify the most promising technological levels allowing to achieve high targets.

The performances targeted result mainly from the used magnetic and electric balance equations which determine the main sizes and weights without needing to describe the stator and rotor structure. So that leads us to avoid selecting one given electric motor topology while disqualifying the others. Hence, the model deals the strong feature of the developed model since that the topology is usually beforehand selected by the electric motor designers. Moreover, in this context, loadability concepts are very useful.

In order to not exceed the limits, we have introduced two constraints in this performed model: a thermal constraint and a mechanical constraint.

We have programmed in Matlab software the model's equations as a tool called **Target Setting Tool "TST"**. Within TST, it gives as inputs the specifications, loads and materials library and gives as outputs set of data such as main sizes, weights, losses, efficiency, specific power and torque. Target Setting Tool inputs are very few compared to the many given outputs. Therefore, TST allows to provide results in a short time which is very useful.

Through sizing electric motors for Hastecs targets, Target Setting Tool could be validated. This led us to develop another more precise sizing tool in the next chapter.

Appendices

- Appendix A: Iron losses in magnetic cores fitted by the new proposed equation

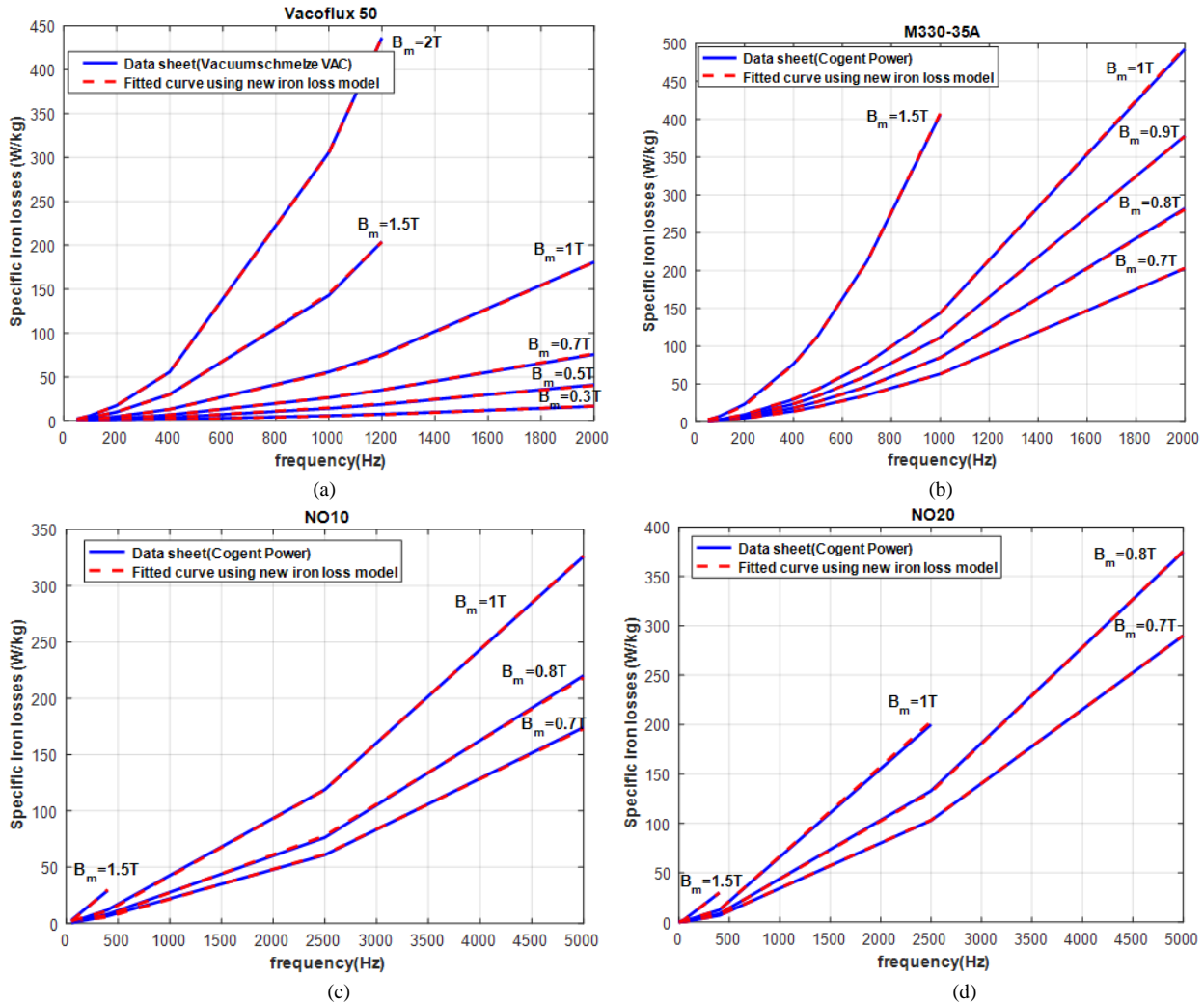
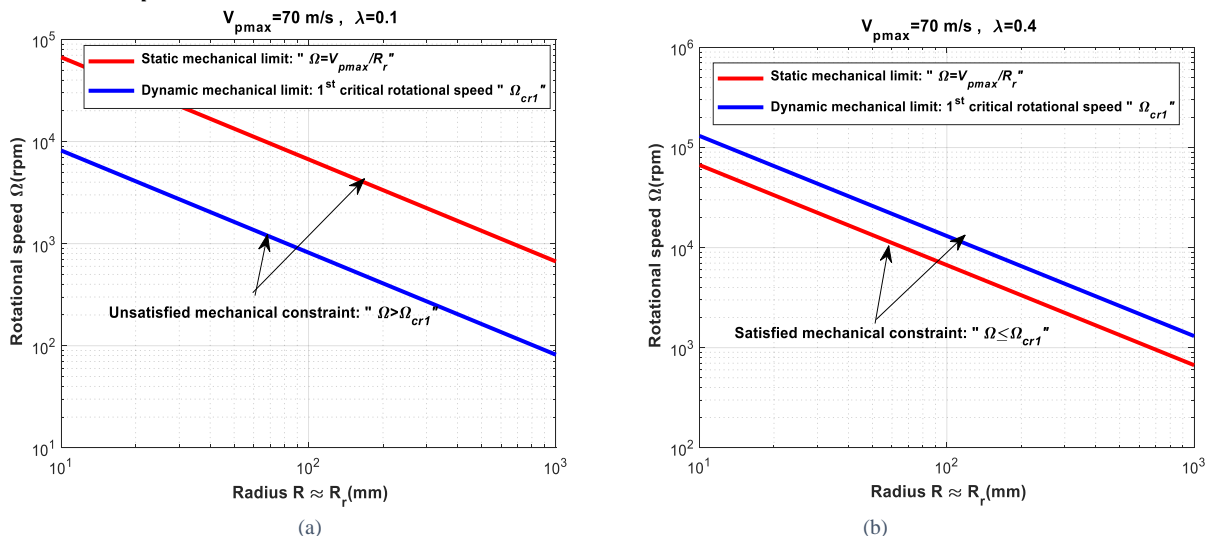


Figure II. 18: specific iron losses using new model: (a) Iron Cobalt alloy (Vacoflux 50)-0.35mm (b) Silicon Iron alloy (M330-35A)-0.35mm, (c) Silicon Iron alloy (NO20)-0.20mm , (d) Silicon Iron alloy (NO10)-0.10mm

- Appendix B: Mechanical constraint at low rotational speed ($V_{pmax} < 100 \text{ m/s}$) and high rotational speed ($V_{pmax} \geq 100 \text{ m/s}$)



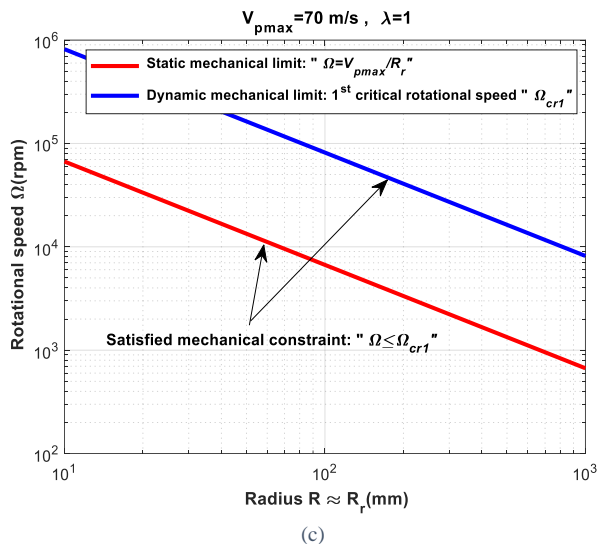


Figure II. 19: Mechanical constraint at low rotational speed $V_{pmax} < 100m/s$: (a) $\lambda = 0.1$, (b) $\lambda = 0.4$, (c) $\lambda = 1$

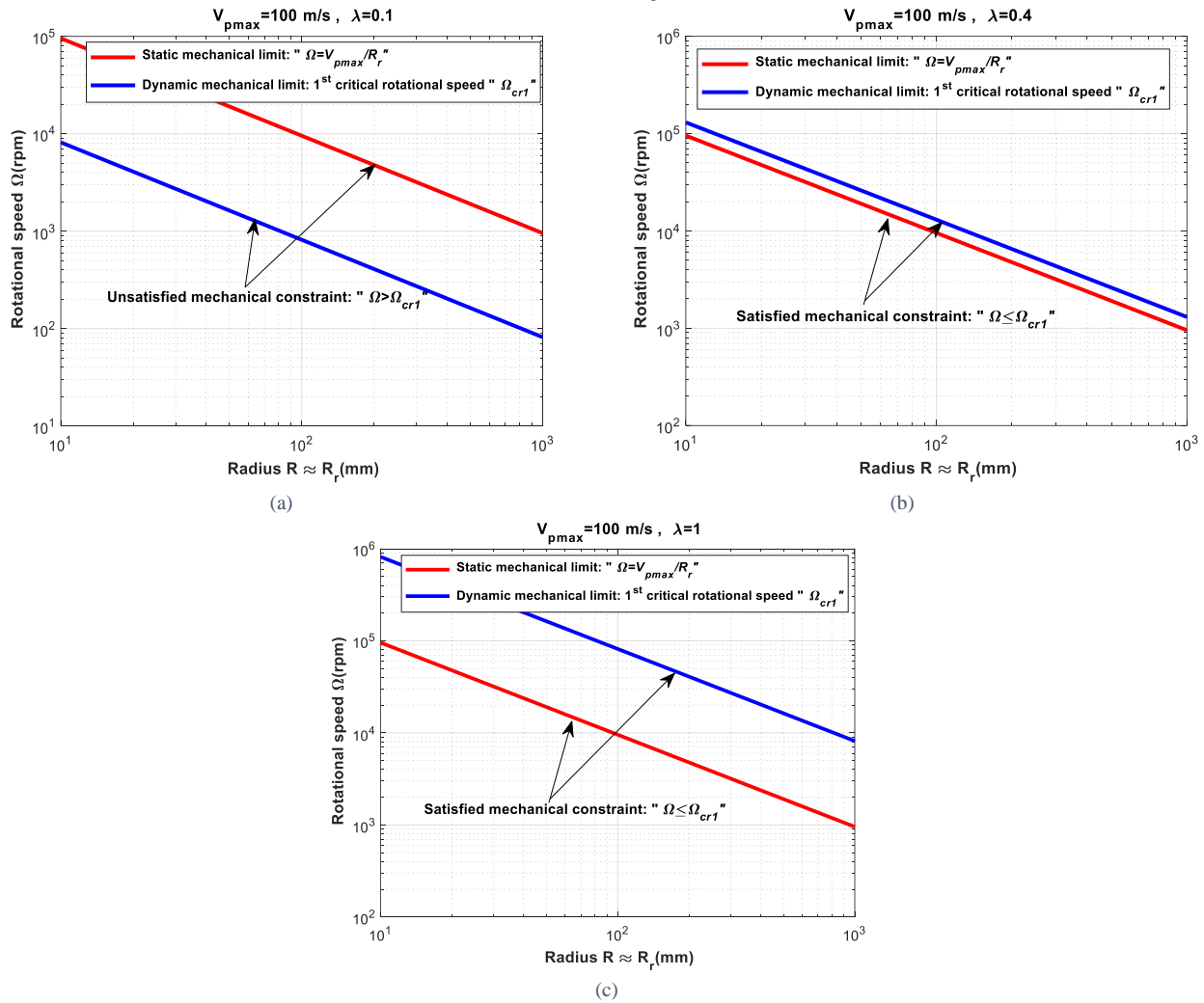


Figure II. 20: Mechanical constraint at high rotational speed $V_{pmax} \geq 100m/s$: (a) $\lambda=0.1$, (b) $\lambda=0.4$, (c) $\lambda=1$

References

Load concept of electrical machines

- [Pyr_08] J. Pyrhönen, T. Jokinen, V. Hrbovcovà, 'Design of rotating electrical machines', Edition John Wiley 2008.
- [Gee_15] M. Van der Geest, H. Polinder, J.A. Ferreira, M. Christmann, 'Power density limits and design trends of high-speed permanent magnet', *IEEE Transaction On Transportation Electrification*, vol.1, Issue. 3, pp.266-276, Oct. 2015
- [Mar_15] M. Van der Geest, 'Design and modelling of high performance Permanent Magnet Synchronous Machines', PhD thesis manuscript, Delft University of Technology, 2015

Analytical model of no salient sinewave electric machines

- [Hen_94] J. R. Hendershot Jr, THE Miller, 'Design of Brushless Permanent-Magnet Motors', Magna Physics and oxford science publications, edition 1994
- [Sle_94] G. R. Slemon, 'On the design of High-Performance Surface-Mounted PM Motors', *IEEE Transactions On Industry Applications*, vol.30, no.1, pp. 134-140, January/February 1994
- [Gie_10] J. F. Gieras, 'Permanent Magnet Motor Technology: Design and Applications', 3rd edition, Taylor and Francis Group, Chapter 3, pp. 104-106, 2010
- [Han_94] D. C. Hanselman, 'Brushless Permanent-Magnet Motor Design' McGraw-Hill, Inc., Chapter 2, pp 20-24, 1994.
- [Lip_04] T. A. Lipo, 'Introduction to AC Machine design', University of Wisconsin-Madison, 2nd edition 2004.
- [EteCat] ETEL Motors Catalogue, www.etel.ch/torque-motors/overview/
- [Lef_19] Y. Lefevre, S. El Aabid, J. F. Llibre, C. Henaux, S. Touhami, 'Performance assessment tool based on loadability concepts', *International Journal of Applied Electromagnetics and Mechanics*, vol.59, no.2, pp.687-694, 2019. <https://oatao.univ-toulouse.fr/21430/>

Twisting

- [Tan_03] X. Tang, C. R. Sullivan, 'Stranded wire with uninsulated strands as a low-cost alternative to litz wire', *IEEE 34th Annual Conference on Power Electronics Specialist*, 15-19 June 2003.

Analytical model of iron losses

- [Ber_85] G. Bertotti, 'Physical interpretation of eddy current losses in ferromagnetic materials, I. Theoretical considerations', *Journal of Applied Physics*, vol. 57, no.6, pp.2110-2117, March 1985.
- [Zha_12] H. Zhao, Y. Luo, H. Wang Ren, B. Peter, 'A complete model for iron losses prediction in electric machines including material measurement, data fitting, FE Computation and Experimental Validation', *Przeglad Elektrotechniczny*, 2012.
- [Roy_16] R. Roy, A. Dalal, P. Kumar, 'Prediction of high frequency core loss for electrical steel using data provided by manufacturer', *Journal of Magnetism and Magnetic Materials*, vol. 410, pp.248-256, 2016.
- [Mil_02] TJE Miller, 'Speed's electric motors', University of Glasgow 2002.
- [Egg_12] D. Eggers, S. Steentjes K. Hameyer, Advanced Iron-Loss estimation for nonlinear material behaviour, *IEEE Transactions on magnetics*, vol.48, no.11, pp.3021- 3024, November 2012.
- [Ion_06] D.M. Ionel, M. Popescu, S. J. Dellinger, T. J. E. Miller, R. J. Heideman and M. I. McGilp, 'On the Variation with flux and frequency of the core loss coefficients in electrical machines', *IEEE Transactions On Industry Applications*, vol. 42, no.3, May/June 2006.

Analytical model of windage losses

- [Saa_98] J. Saari, 'Thermal analysis of high-speed induction machines', PhD Dissertation, Helsinki University Technology, Espoo, Finland, 1998.
- [Ner_08] J. Nerg, M. Rilla, J. Pyrhönen, 'Thermal analysis of radial-flux electrical machine with a high power density', *IEEE Transactions On Industrial Electronics*, vol.55, no.10, October 2008.
- [Luo_09] J. Luomi, C. Zwyssig, A. Looser, J. W. Kolar, 'Efficiency optimization of a 100W-500000r/min permanent magnet machine including air-friction losses', *IEEE Transactions On Industry Applications*, vol.45, no.4, July/August 2009.
- [Rei_10] B. Reimer, M. Lebmann, K. Hameyer, 'Rotor design of a high-speed permanent magnet synchronous machine rating 100000rpm at 10kW', *IEEE Energy Conversion Congress and exposition*, 2010.
- [Gie_10] J. F. Gieras, 'Permanent magnet motor technology', 3rd edition CRC Press Taylor & Francis Group 2010, pp.565-574.
- [Kol_11] Z. Kolondzovski, A. Arkkio, J. Larjola, P. Sallinen, 'Power limits of high-speed permanent-magnet electrical machines for compressor applications', *IEEE Transactions On Energy Conversion*, vol.26, no.1, pp.73-82 March 2011.

[Hua_16] Z. Huang, J. Fang, X. Liu, B. Han, 'Loss calculation and thermal analysis of rotors supported by active magnetic bearing for high-speed permanent magnet electrical machines', *IEEE Transactions On Industrial Electronics*, vol.63, no.4, April 2016.

Analytical model of friction bearing losses

[Skf_13] Rolling bearings and seals in electric motors and generators, SKF datasheet publication 5320E, August 2013.

[Skf_05] Bearings handbook for electric motors, SKF datasheet publication 140-430, 2005.

[Skf_04] Rolling bearings in electric motors and generators, SKF datasheet publication 5230E, 2004.

[Skf_01] Hybrid bearings for electrical machinery electrically insulating higher speeds longer grease life, SKF datasheet publication 5128E, 2001.

[Skf_16] Rolling bearings, SKF datasheet publication Pub/P110000/3E, August 2016.

Mechanical limits

[Lah_02] J. Lähtennmäki, 'Design and voltage supply of high-speed induction machines', PhD thesis manuscript, Helsinki University of Technology, Finland, 2002.

[Mul_99] B. Multon, J. Bonal, 'Les entraînements électromécaniques directs: diversité, contraintes et solutions', La conversion électromécanique direct, "<https://hal.archives-ouvertes.fr/hal-00674081>".

[Bin_07] A. Binder, T. Schneider, 'High-speed inverter-fed AC drives', *IEEE International Aegean Conference on Electrical Machines and Power Electronics*, 10-12 Sept. 2007.

[Aho_07] T. Aho, 'Electromagnetic design of a solid steel rotor motor for demanding operation environments', Lappeenranta University of Technology, Finland 2007.

[Bor_11] A. Borisavljevic, 'Limits, modeling and design of high-speed permanent magnet machines', PhD thesis manuscript, Delft University of Technology, Netherlands, 2011.

[Can_14] W. R. Canders, J. Hoffmann, 'Tutorial on high speed drives, part-two mechanical aspects', *IEEE International Conference on Electric Machines*, Germany, 1st -5th Sept 2014.

[Sin_12] S. Singal, 'Vibration and rotor dynamics of large high-speed motors driving compressors in the oil and gas industry', *IEEE Petroleum and Chemical Industry Technical Conference, Record of Conference Papers Industry Application Society*, 2012.

[Bor_10] A. Borisavljevic, H. Polinder, J. A. Ferreira, 'On the speed limits of Permanent Magnet Machines', *IEEE Transactions On Industrial Electronics*, vol.57, no.1, pp.220-227, January 2010.

Chapter III: Surface Mounted Permanent Magnet Synchronous Motor Tool

Contents

Introduction	57
I.10 Motivation for choosing Surface Mounted Permanent Magnet Synchronous Motor Topology.....	57
I.11 Assumption and study domain.....	58
I.12 Analytical model of surface mounted permanent magnet synchronous motor.....	58
III.3.1 Rotor configuration.....	58
III.3.1.1 Analytical 2D magnetic field model.....	58
III.3.1.2 Permanent magnet thickness calculation.....	61
III.3.1.3 Halbach permanent magnet design.....	64
III.3.2 Stator configuration.....	67
III.3.2.1 Conductor distribution function.....	67
III.3.2.2 Surface current density function.....	68
III.3.2.3 Winding coefficient.....	69
I.13 Stator and rotor additional sizes.....	69
III.4.1 Additional stator sizes.....	69
III.4.2 Additional rotor sizes.....	69
I.14 Electric parameters of surface mounted permanent magnet synchronous motor.....	70
III.5.1 Noload magnetic flux.....	70
III.5.2 Electromotive force.....	71
III.5.3 Resistance, self and mutual inductances.....	71
III.5.4 Electromagnetic torque.....	72
I.15 Inputs and outputs of SM-PMSM Tool.....	72
Conclusion.....	74
Appendices.....	75
References.....	79

Introduction

Usually, designers of electric motors early chose and fixed the electric motor topology in sizing procedure. Nevertheless, using Target Setting Tool "TST" the topology becomes an option of second level required only to give more details and specifications of the electric motors such as intrinsic electric parameters. In this chapter, these last ones will be given from an analytical model established on a chosen topology of electric motor. Motivations to choose the topology will be firstly outlined. Then, the analytical model with its study domain and its assumptions of chosen topology will be illustrated. Also, the performances and the intrinsic electric parameters will be deduced. Eventually, the analytical model will be implemented in a new sizing tool by specifying its inputs and outputs.

III.1 Motivation for choosing Surface Mounted Permanent Magnet Synchronous Motor Topology

As demonstrated in previous chapter, the main sizes of a radial flux electric motor satisfying the TST assumptions can be deduced from the electric, the magnetic and the thermal loads. The other sizes can be obtained only if the topology of electric motor is specified. In this context, several electric motor topologies satisfying TST assumptions can be selected mainly as the synchronous and asynchronous electric motor topologies (cf. Chapter I). Nowadays, several research works try to develop more accurate analytical models towards to size these electric motors. Only the analytical model of permanent magnet synchronous motors that is most accurate and less complex. Indeed, wound rotor synchronous motors are often sized by means of numerical models [Lel_18]. Moreover, this topology is excluded given that could not be beneficial for reaching a high specific power. Besides, due to the significant electromagnetic transient state of asynchronous motors, their analytical modelling remains more complex and less accurate.

There are several permanent magnet synchronous motor topologies, we can quote, namely:

- Surface mounted permanent magnet synchronous motors,
- Buried permanent magnet synchronous motors,
- Interior permanent magnet synchronous motors.

Surface Mounted-Permanent Magnet Synchronous Motor "SM-PMSM" topology includes the classical mounted permanent magnet and the bread loaf permanent magnet illustrated respectively in Figure III.1. a and b. This topology can ensure flux density in airgap very close to the sine wave with very low saliency due to the shape and polarization of permanent magnets.

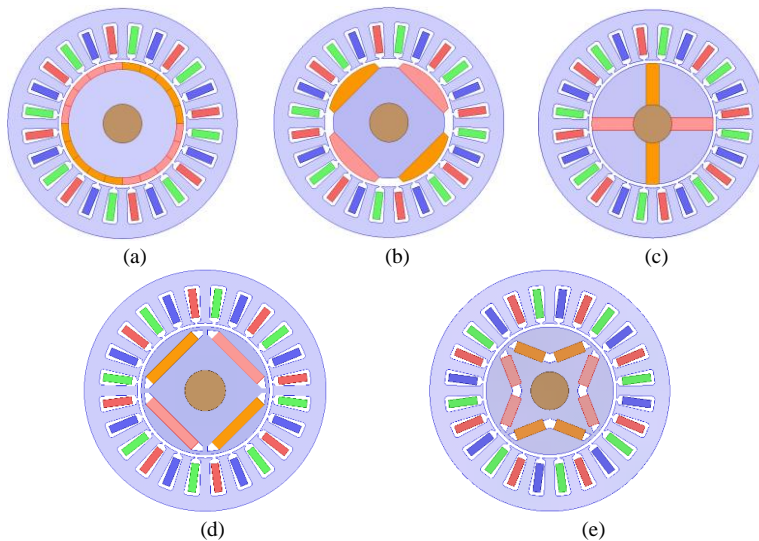


Figure III. 1. Permanent Magnet Synchronous Motors:(a) Surface Mounted Halbach Permanent Magnet, (b) Bread Loaf Permanent Magnet, (c) Buried Permanent Magnet, (d) Interior Permanent Magnet, (e) Interior Folded Permanent Magnet

Buried and interior permanent magnet synchronous motor topologies presented respectively in Figure III.1.c, d and e can also ensure flux density in airgap close to the sine wave with highest value of the airgap flux density. Moreover, these topologies are characterized by an important salience. Indeed, all these permanent magnet synchronous machine topologies can be candidate for sizing using TST,

whereas, due to the salience that is not taking into account in the TST, only surface mounted permanent magnet with Halbach structure topology is selected (cf. Figure III.1.a)

III.2 Assumptions and study domain

To establish the 2D analytical model of SM-PMSM on three regions (cf. Figure III. 2) some assumptions are made for simplifying the conception of the analytical model, such as:

- The slot effect is not taking into account,
- The permeability of stator and rotor magnetic sheets is infinite.

The region I is the permanent magnet, the region II is the airgap and the region III is the rotor magnetic sheet.

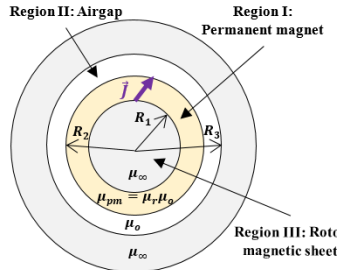


Figure III. 2. Study domain for general 2D analytical field model

III.3 Analytical model of Surface Mounted Permanent Magnet Synchronous Motor

Establishing analytical model allows to determine further sizes and to assess further performances by choosing rotor and stator configurations. The following sections will describe the analytical model applied on the rotor and airgap regions to analyse the magnetic field created by Permanent Magnets and the stator winding design.

III.3.1 Rotor configuration

III.3.1.1 Analytical 2D magnetic field model

a. General 2D Analytical Field Model

To analyse the magnetic field created by the PM in SM-PMSM, only airgap and permanent magnet regions are considered. For these both regions, the magnetic flux density B and the magnetic field strength H vectors are respectively expressed as:

$$\begin{cases} \overrightarrow{B^I} = \mu_{pm} \overrightarrow{H^I} + \vec{J} \\ \overrightarrow{B^{II}} = \mu_o \overrightarrow{H^{II}} \end{cases} \quad (\text{III- 1})$$

Where μ_o is the airgap permeability, μ_{pm} is the PM permeability ($\mu_{pm} = \mu_o \mu_r$), μ_r is the relative permeability and J is the polarization vector of PM.

The polarization vector of permanent magnet can be written in cylindrical coordinates and by using Fourier's series:

$$\vec{J} = \begin{cases} J_r = \sum_{n=1}^{n=\infty} J_{rcn} \cos(np\theta) + J_{rsn} \sin(np\theta) \\ J_\theta = \sum_{n=1}^{n=\infty} J_{\theta cn} \cos(np\theta) + J_{\theta sn} \sin(np\theta) \\ J_z = 0 \end{cases} \quad (\text{III- 2})$$

Where: J_{rcn} , J_{rsn} , $J_{\theta cn}$ and $J_{\theta sn}$ are the Fourier's series components of the radial and tangential polarization J_r , J_θ respectively, p is the pole pair number and n is the harmonic rank.

In region I and II, Maxwell's equations are given by:

$$\begin{cases} \overrightarrow{\text{rot}}(\overrightarrow{H^I}) = \vec{0} \\ \overrightarrow{\text{rot}}(\overrightarrow{H^{II}}) = \vec{0} \end{cases} \quad (\text{III- 3})$$

Using equation (III-1), equation (III-3) can be rewritten as follow:

$$\begin{cases} \overrightarrow{\text{rot}}(\overrightarrow{B^I}) = \overrightarrow{\text{rot}}(\vec{J}) \\ \overrightarrow{\text{rot}}(\overrightarrow{B^{II}}) = \vec{0} \end{cases} \quad (\text{III- 4})$$

With vector potential definition in cylindrical coordinates \vec{A} (cf. Chapter II equation (II-11)), equation (III- 4) can be expressed as:

$$\begin{cases} \frac{\partial^2 A_z^I}{\partial r^2} + \frac{1}{r} \frac{\partial A_z^I}{\partial r} + \frac{1}{r^2} \frac{\partial^2 A_z^I}{\partial \theta^2} = \frac{1}{r} \frac{\partial J_r}{\partial \theta} - \frac{J_\theta}{r} - \frac{\partial J_\theta}{\partial r} \\ \frac{\partial^2 A_z^{II}}{\partial r^2} + \frac{1}{r} \frac{\partial A_z^{II}}{\partial r} + \frac{1}{r^2} \frac{\partial^2 A_z^{II}}{\partial \theta^2} = 0 \end{cases} \quad (\text{III- 5})$$

Where: A_z^I and A_z^{II} are the vector potential in the permanent magnet and airgap respectively. The general solution of A_z^I and A_z^{II} are obtained by solving equations (III-5):

$$\begin{cases} A_z^I(r, \theta) = \sum_{n=1}^{\infty} \left(\left[C_{1n} r^{np} + \frac{C_{2n}}{r^{np}} + k_{cn}(r) \right] \cos(np\theta) + \left[S_{1n} r^{np} + \frac{S_{2n}}{r^{np}} + k_{sn}(r) \right] \sin(np\theta) \right) \\ A_z^{II}(r, \theta) = \sum_{n=1}^{\infty} \left(\left[E_{1n} r^{np} + \frac{E_{2n}}{r^{np}} \right] \cos(np\theta) + \left[E_{3n} r^{np} + \frac{E_{4n}}{r^{np}} \right] \sin(np\theta) \right) \end{cases} \quad (\text{III- 6})$$

With:

$$\begin{cases} k_{cn}(r) = \begin{cases} \frac{np J_{rsn} - J_{\theta cn}}{1 - n^2 p^2} r & np \neq 1 \\ \frac{J_{rs1} - J_{\theta c1}}{2} r \ln(r) & np = 1 \end{cases} \\ k_{sn}(r) = \begin{cases} -\frac{np J_{rcn} + J_{\theta sn}}{1 - n^2 p^2} r & np \neq 1 \\ -\frac{J_{rc1} + J_{\theta s1}}{2} r \ln(r) & np = 1 \end{cases} \end{cases} \quad (\text{III- 7})$$

And: C_{1n} , C_{2n} , S_{1n} , S_{2n} and $E_{1n...4n}$ are constants determined by boundary conditions and continuity conditions on interfaces as expressed by:

$$\begin{cases} H_\theta^I(r = R_1, \theta) = 0 \\ H_\theta^{II}(r = R_3, \theta) = 0 \\ H_\theta^I(r = R_2, \theta) = H_\theta^{II}(r = R_2, \theta) \\ B_r^I(r = R_2, \theta) = B_r^{II}(r = R_2, \theta) \end{cases} \quad (\text{III- 8})$$

The value of these constants C_{1n} , C_{2n} , S_{1n} , S_{2n} and $E_{1n...4n}$ are given in Appendix A.

After determining A_z^I and A_z^{II} , we can write:

$$\begin{cases} B_r^I(r, \theta) = \frac{1}{r} \frac{\partial A_z^I}{\partial \theta} \\ H_\theta^I(r, \theta) = -\frac{1}{\mu_{pm}} \frac{\partial A_z^I}{\partial r} - \frac{J_\theta}{\mu_{pm}} \\ B_r^{II}(r, \theta) = \frac{1}{r} \frac{\partial A_z^{II}}{\partial \theta} \\ H_\theta^{II}(r, \theta) = -\frac{1}{\mu_o} \frac{\partial A_z^{II}}{\partial r} \end{cases} \quad (\text{III- 9})$$

B_r^I , H_θ^I , B_r^{II} and H_θ^{II} are the radial flux density and the tangential magnetic field of the permanent magnet and the airgap regions respectively:

$$\begin{cases} B_r^I(r, \theta) = \sum_{n=1}^{\infty} B_{mc}^I(r) \cos(np\theta) + B_{ms}^I(r) \sin(np\theta) \\ B_r^{II}(r, \theta) = \sum_{n=1}^{\infty} B_{mc}^{II}(r) \cos(np\theta) + B_{ms}^{II}(r) \sin(np\theta) \\ H_\theta^I(r, \theta) = \sum_{n=1}^{\infty} H_{mc}^I(r) \cos(np\theta) + H_{ms}^I(r) \sin(np\theta) \\ H_\theta^{II}(r, \theta) = \sum_{n=1}^{\infty} H_{mc}^{II}(r) \cos(np\theta) + H_{ms}^{II}(r) \sin(np\theta) \end{cases} \quad (\text{III- 10})$$

Where:

$$\begin{cases} B_{mc}^I(r) = \frac{np}{r} \left(S_{1n} r^{np} + \frac{S_{2n}}{r^{np}} + k_{sn}(r) \right) \\ B_{ms}^I(r) = -\frac{np}{r} \left(C_{1n} r^{np} + \frac{C_{2n}}{r^{np}} + k_{cn}(r) \right) \\ B_{mc}^{II}(r) = \frac{np}{r} \left(E_{3n} r^{np} + \frac{E_{4n}}{r^{np}} \right) \\ B_{ms}^{II}(r) = -\frac{np}{r} \left(E_{1n} r^{np} + \frac{E_{2n}}{r^{np}} \right) \\ H_{mc}^{II}(r) = -\frac{1}{\mu_o} \frac{np}{r} \left(E_{1n} r^{np} - \frac{E_{2n}}{r^{np}} \right) \\ H_{ms}^{II}(r) = -\frac{1}{\mu_o} \frac{np}{r} \left(E_{3n} r^{np} - \frac{E_{4n}}{r^{np}} \right) \end{cases} \quad (\text{III- 11})$$

With:

$$\begin{cases} H_{mc}^I(r) = -\frac{np}{\mu_{pm} r} \left(C_{1n} r^{np} - \frac{C_{2n}}{r^{np}} + \frac{k_{cn}(r) + r J_{\theta cn}}{np} \right) & \text{for } np \neq 1 \\ H_{ms}^I(r) = -\frac{np}{\mu_{pm} r} \left(S_{1n} r^{np} - \frac{S_{2n}}{r^{np}} + \frac{k_{sn}(r) + r J_{\theta sn}}{np} \right) & \text{for } np \neq 1 \\ H_{mc}^I(r) = -\frac{1}{\mu_{pm} r} \left(C_{1n} r - \frac{C_{2n}}{r} + k_{c1}(r) + \frac{J_{rs1} + J_{\theta c1}}{2} r \right) & \text{for } np = 1 \\ H_{ms}^I(r) = -\frac{1}{\mu_{pm} r} \left(S_{1n} r - \frac{S_{2n}}{r} + k_{s1}(r) + \frac{J_{\theta s1} - J_{rc1}}{2} r \right) & \text{for } np = 1 \end{cases}$$

b. Radial, tangential and parallel polarizations

There are three types of permanent magnet polarization: radial polarization, tangential polarization and parallel polarization as shown in Figure III. 3.

→ *Radial polarization* characterized by polarization only along radial axis (cf. Figure III.3. a) as given by the equation:

$$\vec{J} = \begin{cases} J_r = \frac{J\beta p}{\pi} \sum_{n=1}^{\infty} (1 - (-1)^n) \frac{\sin(0.5np\beta)}{0.5np\beta} \cos(np(\theta - \alpha)) \\ J_\theta = 0 \\ J_z = 0 \end{cases} \quad (\text{III- 12})$$

Where: J is the polarization amplitude, β is the angular width, α is the angular center of permanent magnet.

→ *Tangential polarization* characterized by polarization only along angular axis (cf. Figure III. 3. b) as given by the equation:

$$\vec{J} = \begin{cases} J_r = 0 \\ J_\theta = \frac{J\beta p}{\pi} \sum_{n=1}^{\infty} (1 - (-1)^n) \frac{\sin(0.5np\beta)}{0.5np\beta} \cos(np(\theta - \alpha)) \\ J_z = 0 \end{cases} \quad (\text{III- 13})$$

→ *Parallel polarization* characterized by polarization parallel-oriented from the center of permanent magnet α with γ angle as shown in Figure III.3. c. Parallel polarization is governed by:

$$\vec{J} = \begin{cases} J_r = \frac{J\beta p}{\pi} \sum_{n=1}^{\infty} \frac{\sin(0.5m_1\beta)}{0.5m_1\beta} \cos(np(\theta - \alpha) + \gamma) + \frac{\sin(0.5m_2\beta)}{0.5m_2\beta} \cos(np(\theta - \alpha) - \gamma) \\ J_\theta = \frac{J\beta p}{\pi} \sum_{n=1}^{\infty} \frac{\sin(0.5m_1\beta)}{0.5m_1\beta} \sin(np(\theta - \alpha) + \gamma) - \frac{\sin(0.5m_2\beta)}{0.5m_2\beta} \sin(np(\theta - \alpha) - \gamma) \\ J_z = 0 \end{cases} \quad (\text{III- 14})$$

With: $m_1 = 1 + np$ and $m_2 = 1 - np$.

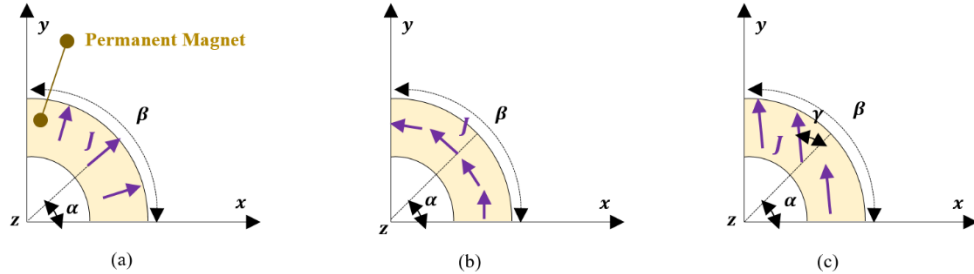


Figure III. 3. Permanent Magnet Polarizations: (a) Radial polarization, (b) Tangential polarization, (c) Parallel polarization

c. Ideal Halbach Permanent Magnet

According to [Zhu_10] sine wave airgap flux density is ensured by an ideal Halbach Permanent Magnet.

The last one is characterized in cylindrical coordinates by sine wave polarization as expressed in equation (III-15). Ideal Halbach PM polarization can be either internal or external as shown in Figure III. 4. Practically, it is hard to manufacturer ideal Halbach PM, for the purpose, Halbach PMs are often segmented into some number of segments having different parallel polarizations.

$$\overrightarrow{J(\theta)} = \overrightarrow{J_r(\theta)} + \overrightarrow{J_\theta(\theta)} = \begin{cases} J_r(\theta) = J \cos(p\theta) \\ J_\theta(\theta) = \pm J \sin(p\theta) \end{cases} \quad (\text{III- 15})$$

"+" being for internal field Halbach and "-" for external field Halbach.

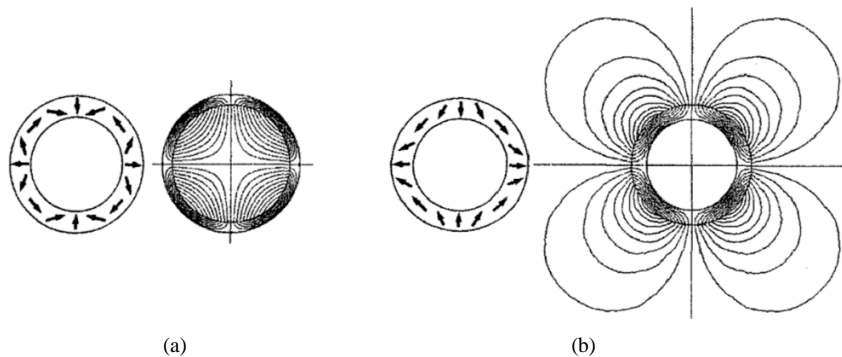


Figure III. 4. Ideal Halbach Permanent Magnet in 2 pole pairs:
(a) internal field Halbach, (b) external field Halbach [Zhu_01]

III.3.1.2 Permanent magnet thickness calculation

From definition of an ideal Halbach PM, sizes and structure of Halbach PM with external field can be deduced. Indeed, for a desired maximum airgap sine wave flux density B_m and from a given value of airgap thickness $e_g = R_3 - R_2$, the thickness of a Halbach Permanent Magnet $e_{pm} = R_2 - R_1$ can be analytically determined by using the 2D general analytical field model and by considering only the fundamental harmonic ($n = 1$).

Thereby from equation (III-11), the radial flux density and the tangential magnetic field in airgap and PM can be reduced to:

$$\begin{cases} B_r^I(r, \theta) = B_{mc}^I(r) \cos(p\theta) + B_{ms}^I(r) \sin(p\theta) \\ H_\theta^I(r, \theta) = H_{mc}^I(r) \cos(p\theta) + H_{ms}^I(r) \sin(p\theta) \\ B_r^{II}(r, \theta) = B_{mc}^{II}(r) \cos(p\theta) \\ H_\theta^{II}(r, \theta) = H_{ms}^{II}(r) \sin(p\theta) \end{cases} \quad (\text{III- 16})$$

As the airgap flux density is desired equal to $B_m \cos(p\theta)$, the $B_{ms}^{II}(r)$ should be null. For the purpose, E_{11} and E_{21} should be null. Therefore, $H_{mc}^{II}(r)$ becomes null.

With:

$$\begin{cases} B_{mc}^I(r) = p \left(S_{11} r^{p-1} + \frac{S_{21}}{r^{p+1}} + \frac{k_{s1}(r)}{r} \right) \\ B_{ms}^I(r) = -p \left(C_{11} r^{p-1} + \frac{C_{21}}{r^{p+1}} \right) \\ B_{mc}^{II}(r) = p \left(E_{31} r^{p-1} + \frac{E_{41}}{r^{p+1}} \right) \\ H_{ms}^{II}(r) = \frac{-p}{\mu_0} \left(E_{31} r^{p-1} - \frac{E_{41}}{r^{p+1}} \right) \end{cases} \quad (\text{III- 17})$$

With:

$$\begin{cases} H_{mc}^I(r) = \frac{-p}{\mu_{pm} r} \left(C_{11} r^p - \frac{C_{21}}{r^p} + \frac{k_{c1}(r)}{p} \right) & \text{for } p \neq 1 \\ H_{ms}^I(r) = \frac{-p}{\mu_{pm} r} \left(S_{11} r^p - \frac{S_{21}}{r^p} + \frac{k_{s1}(r)}{p} - \frac{J}{p} r \right) & \text{for } p \neq 1 \\ H_{mc}^I(r) = \frac{-1}{\mu_{pm} r} \left(C_{11} r - \frac{C_{21}}{r} + k_{c1}(r) \right) & \text{for } p = 1 \\ H_{ms}^I(r) = \frac{-1}{\mu_{pm} r} \left(S_{11} r - \frac{S_{21}}{r} + k_{s1}(r) - J r \right) & \text{for } p = 1 \end{cases}$$

And:

$$\begin{cases} k_{c1}(r) = 0 \\ k_{s1}(r) = \begin{cases} \frac{J}{1+p} r & p \neq 1 \\ 0 & p = 1 \end{cases} \end{cases} \quad (\text{III- 18})$$

By applying boundary conditions and continuity conditions on interfaces (i.e. Equations III-8 and III-9) we obtain:

$$\begin{cases} H_\theta^I(r = R_1, \theta) = 0 \\ H_\theta^{II}(r = R_3, \theta) = 0 \\ H_\theta^I(r = R_2, \theta) = H_\theta^{II}(r = R_2, \theta) \\ B_r^I(r = R_2, \theta) = B_r^{II}(r = R_2, \theta) \end{cases} \quad (\text{III- 19})$$

Then $\forall p$:

$$\begin{cases} S_{11} R_1^{p-1} - \frac{S_{21}}{R_1^{p+1}} + \frac{k_{s1}(R_1)}{R_1 p} - \frac{J}{p} = 0 \\ C_{11} R_1^{p-1} - \frac{C_{21}}{R_1^{p+1}} = 0 \\ E_{31} R_3^{p-1} - \frac{E_{41}}{R_3^{p+1}} = 0 \\ S_{11} R_2^{p-1} - \frac{S_{21}}{R_2^{p+1}} + \frac{k_{s1}(R_2) - R_2 J}{R_2 p} = \mu_r E_{31} R_2^{p-1} - \mu_r \frac{E_{41}}{R_2^{p+1}} \\ C_{11} R_2^{p-1} - \frac{C_{21}}{R_2^{p+1}} + \frac{k_{c1}(R_2)}{R_2 p} = 0 \\ S_{11} R_2^{p-1} + \frac{S_{21}}{R_2^{p+1}} + \frac{k_{s1}(R_2)}{R_2} = E_{31} R_2^{p-1} + \frac{E_{41}}{R_2^{p+1}} \\ C_{11} R_2^{p-1} + \frac{C_{21}}{R_2^{p+1}} + \frac{k_{c1}(R_2)}{R_2} = 0 \end{cases} \quad (\text{III- 20})$$

Furthermore, knowing that:

$$B_{mc}^{II}(R_3) = B_m \quad (\text{III- 21})$$

To obtain permanent magnet thickness, radius R_1 should be determined. For the purpose, only S_{11} , S_{21} , E_{31} , E_{41} coefficients should be calculated function of R_3 and R_2 , therefore only 3rd, 4th and 7th equations of (III-20) and equation (III-21) are considered as:

$$\begin{cases} E_{31}R_3^{p-1} - \frac{E_{41}}{R_3^{p+1}} = 0 \\ E_{31}R_3^{p-1} + \frac{E_{41}}{R_3^{p+1}} = \frac{B_m}{p} \\ S_{11}R_2^p + \frac{S_{21}}{R_2^p} + k_{s1}(R_2) = E_{31}R_2^p + \frac{E_{41}}{R_2^p} \\ S_{11}R_2^p - \frac{S_{21}}{R_2^p} + \frac{k_{s1}(R_2) - R_2J}{p} = \mu_r E_{31}R_2^p - \mu_r \frac{E_{41}}{R_2^p} \end{cases} \quad (\text{III- 22})$$

Therefore,

- For $p \neq 1$:

$$\begin{cases} E_{31} = \frac{B_m}{2p} R_3^{1-p} \\ E_{41} = \frac{B_m}{2p} R_3^{1+p} \\ S_{11} = \frac{(1+\mu_r)}{4p} R_3^{1-p} B_m + \frac{(1-\mu_r)}{4p} \frac{R_3^{1+p}}{R_2^{2p}} B_m \\ S_{21} = \frac{(1-\mu_r)}{4p} R_3^{1-p} R_2^{2p} B_m + \frac{(1+\mu_r)}{4p} R_3^{1+p} B_m - \frac{R_2^{p+1}}{p+1} J \end{cases} \quad (\text{III- 23})$$

- For $p = 1$:

$$\begin{cases} E_{31} = \frac{B_m}{2} \\ E_{41} = \frac{B_m}{2} R_3^2 \\ S_{11} = \frac{(1+\mu_r)}{4} B_m + \frac{(1-\mu_r)}{4} \frac{R_3^2}{R_2^2} B_m + \frac{J}{2} \\ S_{21} = \frac{(1-\mu_r)}{4} R_2^2 B_m + \frac{(1+\mu_r)}{4} R_3^2 B_m - \frac{R_2^2}{2} J \end{cases}$$

Consequently, thickness of permanent magnet can be deduced from the following equation:

$$\begin{cases} S_{11}R_1^{p-1} - \frac{S_{21}}{R_1^{p+1}} + \frac{k_{s1}(R_1)}{R_1 p} - \frac{J}{p} = 0 & \text{for } p \neq 1 \\ S_{11} - \frac{S_{21}}{R_1^2} - J = 0 & \text{for } p = 1 \end{cases} \quad (\text{III- 24})$$

Then:

$$\begin{cases} S_{11}R_1^{2p} - S_{21} - R_1^{p+1} \frac{J}{1+p} = 0 & \text{for } p \neq 1 \\ R_1 = \sqrt{\frac{S_{21}}{S_{11}-J}} & \text{for } p = 1 \end{cases} \quad (\text{III- 25})$$

Knowing that:

$$e_{pm} = R_2 - R_1 \quad (\text{III- 26})$$

Where: e_{pm} is the thickness of permanent magnet.

Equation (III-25) becomes:

$$\begin{cases} S_{11}R_2^{2p} \left(1 - \frac{e_{pm}}{R_2}\right)^{2p} - S_{21} - R_2^{p+1} \left(1 - \frac{e_{pm}}{R_2}\right)^{p+1} \frac{J}{1+p} = 0 & \text{for } p \neq 1 \\ e_{pm} = R_2 - \sqrt{\frac{S_{21}}{S_{11}-J}} & \text{for } p = 1 \end{cases} \quad (\text{III- 27})$$

By using the Newton-Raphson's method in the case of $p > 1$ of the equation (III-27), the PM thickness can be directly deduced as given below:

- For 1st order approximation

$$\begin{cases} \left(1 - \frac{e_{pm}}{R_2}\right)^{2p} \approx 1 - 2p \frac{e_{pm}}{R_2} \\ \left(1 - \frac{e_{pm}}{R_2}\right)^{p+1} \approx 1 - (p+1) \frac{e_{pm}}{R_2} \end{cases} \quad (\text{III- 28})$$

Then, the thickness of permanent magnet at the 1st order approximation:

$$e_{pm} = \frac{R_2^{p+1} J - S_{11}(1+p)R_2^{2p} + S_{21}(1+p)}{R_2^p J(1+p) - 2pS_{11}(1+p)R_2^{2p-1}} \quad (\text{III- 29})$$

- For 2nd order approximation:

$$\begin{cases} \left(1 - \frac{e_{pm}}{R_2}\right)^{2p} \approx 1 - 2p \frac{e_{pm}}{R_2} + \frac{2p(2p-1)}{2} \left(\frac{e_{pm}}{R_2}\right)^2 \\ \left(1 - \frac{e_{pm}}{R_2}\right)^{p+1} \approx 1 - (p+1) \frac{e_{pm}}{R_2} + \frac{(p+1)p}{2} \left(\frac{e_{pm}}{R_2}\right)^2 \end{cases} \quad (\text{III- 30})$$

Then:

$$\frac{1}{2} D_2 e_{pm}^2 - D_1 e_{pm} + D_0 = 0 \quad (\text{III- 31})$$

With: $D_2 = 2p(2p-1)S_{11}R_2^{2p-2} - JpR_2^{p-1}$, $D_1 = 2pS_{11}R_2^{2p-1} - JR_2^p$, and $D_0 = S_{11}R_2^{2p} - S_{21} - \frac{JR_2^{p+1}}{p+1}$

Then, the thickness of permanent magnet at the 2nd order approximation is:

$$e_{pm} = \frac{D_1 + \sqrt{D_1^2 - 2D_0 D_2}}{D_2} \quad (\text{III- 32})$$

III.3.1.3 Halbach permanent magnet design

a. Direct design of segmented Halbach permanent magnet

The realization of the polarization of PM Halbach, illustrated in Figure III. 4, is very difficult. For the purpose, the discretization method is often the used solution. Discretization of PM Halbach can be approached by several equal length PM blocs with different parallel polarizations (cf. Figure III. 5) or can be approached by several optimized PM blocs. The parallel polarization approached by several equal lengths PM blocs is governed by the following equation:

$$\overrightarrow{J(\theta_k)} = \begin{cases} J_r(\theta_k) = J \cos(p\theta_k) \\ J_\theta(\theta_k) = \pm J \sin(p\theta_k) \end{cases} \quad \text{with} \quad \theta_k = \theta_{k-1} + \frac{\delta\theta}{2} \quad (\text{III- 33})$$

Where: θ_k is the angle at the center of PM bloc k , θ_{k-1} is the angle at the center of PM bloc $k-1$, $\delta\theta$ is the PM bloc angular width ($\delta\theta = \pi/pn_b$), n_b is the number of segments, $J(\theta_k)$ is the polarization of PM bloc k , $J_r(\theta_k)$ and $J_\theta(\theta_k)$ are the radial and tangential components of the polarization of PM block. Indeed, to get closer to an ideal Halbach PM, the number of blocs should be increased as shown in the resulting airgap flux density Figure III. 6.

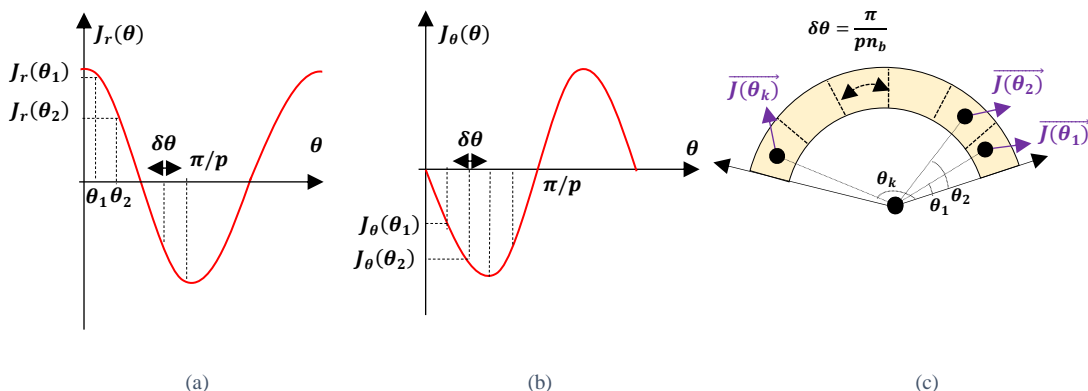


Figure III. 5. Discretized ideal Halbach PM:

(a) radial component of polarization, (b) tangential component of polarization, (c) segmented Halbach PM

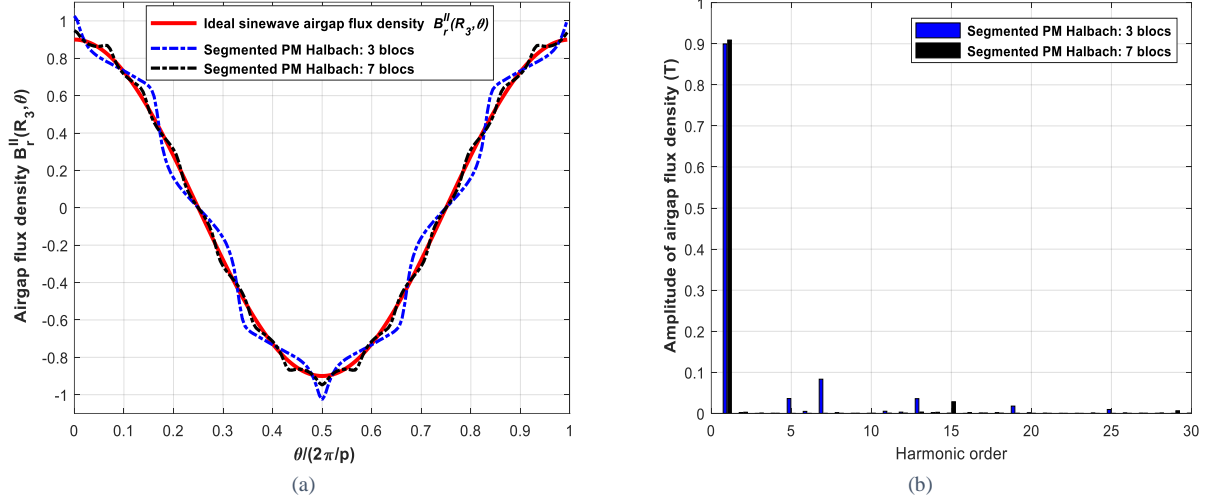


Figure III. 6. (a) Resulting airgap flux density of discretized Halbach PM, (b) harmonic analysis of resulting airgap flux density

b. Design of segmented Halbach permanent magnet using optimization

For different polarization types of Halbach PM, design is often carried out using optimization procedures [Chen_17] [Mel_07] [Hua_18] [Mar_09]. Indeed, airgap flux density can be written as linear superposition of elementary airgap flux densities generated by each polarization of PM bloc. For instance, airgap flux density can be written as linear superposition of elementary airgap flux density generated by unit radial $J_{rk}(\theta)$ and unit tangential $J_{\theta k}(\theta)$ polarizations in each PM segment as given by:

$$B_r^{II}(R_3, \theta) = \sum_k (J_r^k b_{rk}^{II}(R_3, \theta) + J_\theta^k b_{\theta k}^{II}(R_3, \theta)) \quad (\text{III- 34})$$

Where: J_r^k is the amplitude of radial polarization of k PM segment, J_θ^k is the amplitude of tangential polarization of k PM segment, b_{rk}^{II} and $b_{\theta k}^{II}$ are the elementary airgap flux densities generated by unit radial and unit tangential polarization in each segment k as illustrated in Figure III.7.

Therefore, Halbach PM can be optimized by taking as variables the polarizations and the sizes of all PM segments. Sequential Quadratic Programming Method (SQPM) optimization can be used given that it is the most used optimization method. In fact, thanks to the linear superposition applied to the airgap flux density, Least Squares (LS) method can be used inside (SQPM) to reduce the number of optimization variables. (LS) method allows finding the required radial and tangential polarizations of segmented PM Halbach of each optimization solution of SQPM. SQPM allows finding the required sizes of segmented PM Halbach as illustrated in Figure III.8. This procedure is characterized by reduced time computation although sizes and polarizations are variables. This optimization procedure can be suitable for all PM polarization types. Figure III. 9 compares the direct designed segmented PM Halbach with the one optimized segmented PM Halbach. Direct design gives result close to the one obtained using optimization.

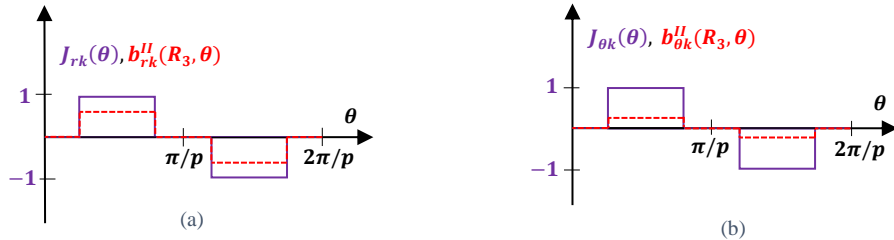


Figure III. 7. (a) Unit radial polarization with its resulting elementary airgap flux density, (b) Unit tangential polarization with its resulting elementary airgap flux density

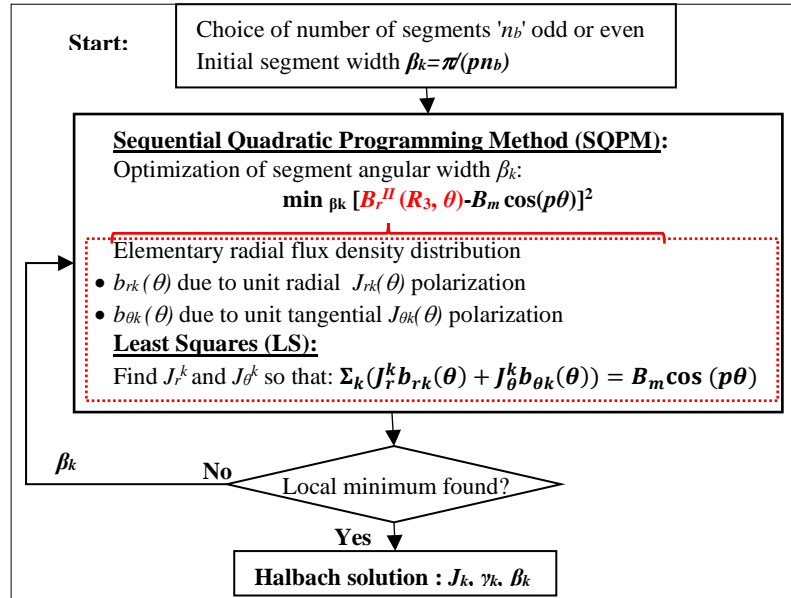


Figure III. 8. Optimization procedure: LS method inside the SQPM

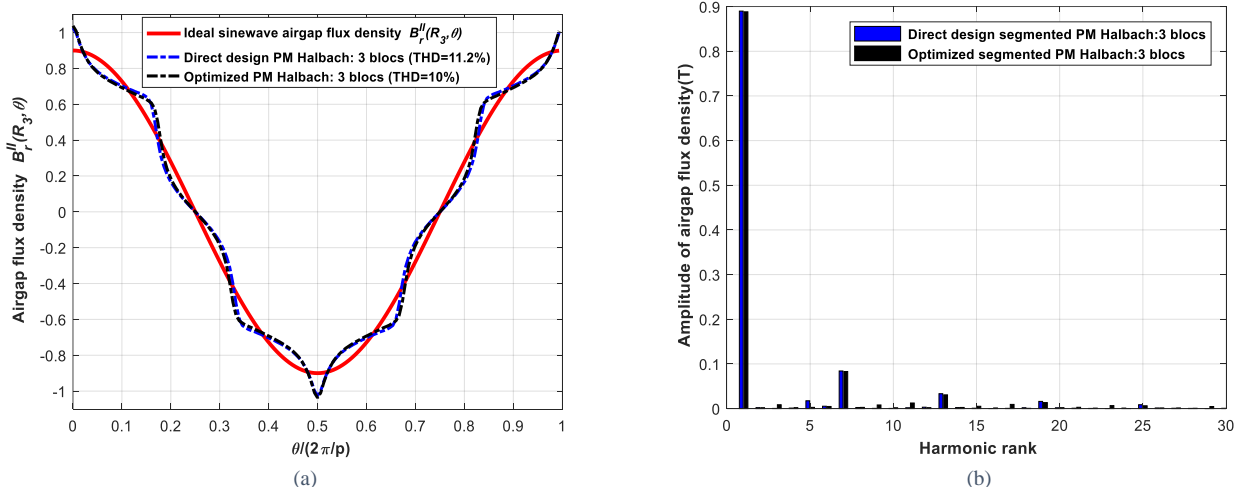


Figure III. 9. Comparison of optimized and direct design Parallel Polarization of segmented Halbach PM: (a) airgap flux density, (b) harmonic analysis of airgap flux density

III.3.2 Stator configuration

As it is hard to realize ideal Halbach PM, sine wave stator winding is also difficult to realize. However, it can be designed as closer as possible to a sine wave stator winding by means of conductor distribution functions. The following section will describe these functions. These last ones are useful to determine the surface current density function.

III.3.2.1 Conductor distribution functions

Basically, conductor distribution functions are not often employed for sizing winding. It's rather the Magnetomotive Force (MMF) functions which are mostly used. Although conductor distribution functions are the real winding functions. They are given by:

$$C(\theta) = \frac{1}{R\chi} N(\theta) \quad (\text{III- 35})$$

Where: $N(\theta)$ is the winding distribution function expressed by the number of conductors, R is the stator bore radius and χ is the opening slot angle.

MMF are the integrated function of conductor distribution functions as demonstrated in Appendix B. Conductor distribution functions can be described for all winding configurations as distributed and concentrated windings. In our analysis we will focus only on the distributed winding.

a. Elementary coil with full pitch

An elementary coil with full pitch is characterized by go-conductors placed in one slot and return-conductors placed in a slot located at angle π/p from the go-conductors as shown in Figure III.10. a. Hence, the winding function of elementary coil with full pitch can be expressed using Fourier's series:

$$N_e(\theta) = \sum_{k=1}^{k=\infty} \frac{4N_{cs}}{\pi} \frac{\sin(0.5(2k-1)p\chi)}{(2k-1)\chi} \cos((2k-1)p\theta) \quad (\text{III- 36})$$

Where: N_{cs} is the number of conductor per slot and k is the harmonic rank.

The conductor distribution function of elementary coil with full pitch (cf. Figure III.10. b) is expressed by:

$$C_e(\theta) = \sum_{k=1}^{k=\infty} \frac{4N_{cs}}{\pi R} \frac{\sin(0.5(2k-1)p\chi)}{(2k-1)\chi} \cos((2k-1)p\theta) \quad (\text{III- 37})$$

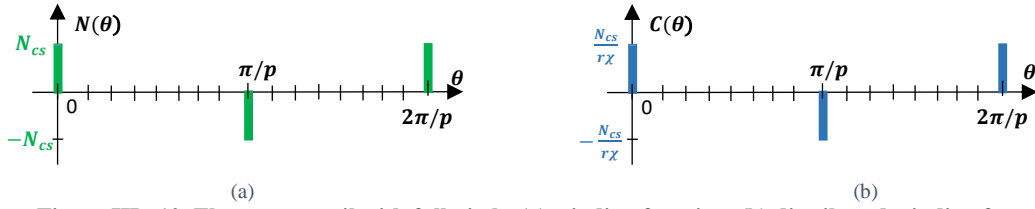


Figure III. 10. Elementary coil with full pitch: (a) winding function, (b) distributed winding function

b. Full pitch distributed winding: several coils per poles and per phases

For full pitch distributed winding with several coils per pole and per phase as shown in Figure III.11, the winding function can be deduced from the winding function of elementary coil by:

$$N(\theta) = \sum_{j=1}^{j=m} \sum_{k=1}^{k=\infty} \frac{4N_{cs}}{\pi} \frac{\sin(0.5(2k-1)p\chi)}{(2k-1)\chi} \cos((2k-1)p(\theta - (j-1)\gamma)) \quad (\text{III- 38})$$

Where: m is the number of slots per pole and per phase (i.e.: $m = N_s/(2pq)$), N_s is the number of slots, q is the number of phases and γ is the angular step between two neighboring coils of the same phase.

Using equation (III-35), the conductor distribution function is given by:

$$C(\theta) = \sum_{k=1}^{k=\infty} \frac{4N_{cs}}{\pi R} \frac{\sin(0.5(2k-1)p\chi)}{(2k-1)\chi} \frac{\sin(0.5(2k-1)pmy)}{\sin(0.5(2k-1)p\gamma)} \cos((2k-1)p\theta) \quad (\text{III- 39})$$

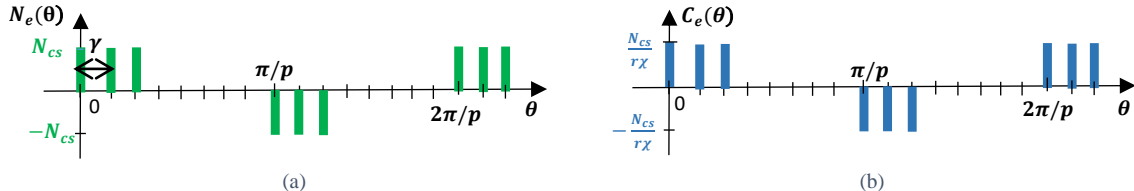


Figure III. 11. Full pitch distributed winding "several coils per poles and per phases": (a) winding function, (b) distributed winding function

c. Full pitch distributed winding: several coils per poles and per phases with several layers

For winding with several layers (cf. Figure III. 12), the winding function can be deduced from equation (III-38) by:

$$N(\theta) = \sum_{l=1}^{l=n_l} \sum_{k=1}^{k=\infty} \frac{4N_{cs}}{\pi n_l} \frac{\sin(0.5(2k-1)p\chi)}{(2k-1)\chi} \frac{\sin(0.5(2k-1)mpl\gamma)}{\sin(0.5(2k-1)p\gamma)} \cos((2k-1)p(\theta - (l-1)\xi)) \quad (\text{III- 40})$$

Where: ξ is the angular step between two layers of the same phase and n_l is the number of layers.

The corresponding conductor distribution function is given by:

$$C(\theta) = \sum_{k=1}^{k=\infty} \frac{4N_{cs}}{\pi R n_l} \frac{\sin(0.5(2k-1)p\chi)}{(2k-1)\chi} \frac{\sin(0.5(2k-1)pmy)}{\sin(0.5(2k-1)p\gamma)} \frac{\sin(0.5(2k-1)n_l p\xi)}{\sin(0.5(2k-1)p\xi)} \cos((2k-1)p\theta) \quad (\text{III- 41})$$

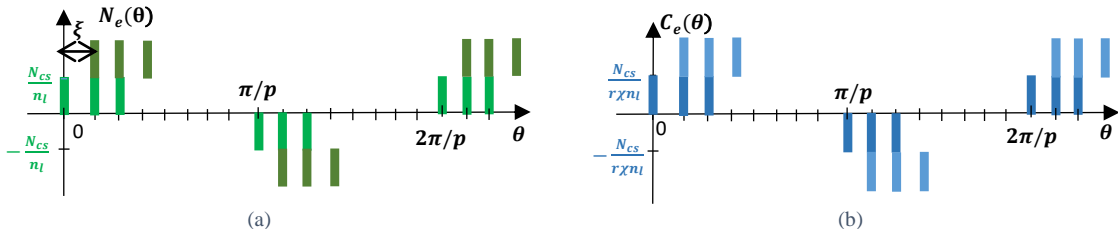


Figure III. 12. Full pitch distributed winding "several coils per poles and per phases with several layers": (a) winding function, (b) distributed winding function

d. Several phases

The conductor distribution functions of a winding with q phases, N_{cs} number of conductors per slot, m number of slots per pole and per phase and n_l number of layers are governed by:

$$C_i(\theta) = \sum_{k=1}^{k=\infty} A_{2k-1} D_{2k-1} L_{2k-1} \cos\left((2k-1)\left(p\theta - \frac{(i-1)2\pi}{q}\right)\right) \quad (\text{III- 42})$$

With:

$$\begin{aligned} A_{2k-1} &= \frac{2pN_{cs}}{\pi R} \frac{\sin(0.5(2k-1)p\chi)}{0.5(2k-1)p\chi} \\ D_{2k-1} &= \frac{\sin(0.5(2k-1)p\gamma)}{\sin(0.5(2k-1)p\gamma)} \\ L_{2k-1} &= \frac{\sin(0.5(2k-1)p n_l \xi)}{n_l \sin(0.5(2k-1)p\xi)} \end{aligned} \quad (\text{III- 43})$$

Where: A_{2k-1} expresses the full pitch winding, D_{2k-1} expresses the distributed winding and L_{2k-1} expresses winding having several layers.

III.3.2.2 Surface current density function

As mentioned in previous chapter (cf. § II.2.2), the surface current density is useful to take into account the armature reaction field in the 2D magnetic vector potential model of electric motors. Surface current density wave can be defined by the separation of space functions of the conductor distribution functions along stator bore and time functions of currents:

$$K(\theta, t) = \sum_{i=1}^q C_i(\theta) \times I_i(t) \quad (\text{III- 44})$$

Where: $I_i(t)$ is the time function of the q of the i phase current.

For three phase sine wave currents, the surface current density function is then given by:

$$K(\theta, t) = \sum_{i=1}^{i=3} \sum_{k=1}^{k=\infty} A_{2k-1} D_{2k-1} L_{2k-1} \cos\left[(2k-1)\left(p\theta - \frac{(i-1)2\pi}{3}\right)\right] I_m \cos\left[\omega t - \frac{(i-1)2\pi}{3}\right] \quad (\text{III- 45})$$

With: I_m is the amplitude of current, ω is the electrical pulse and t is the time.

For fundamental component ($k = 1$), equation (III-45) is reduced to:

$$K_1(\theta, t) = \sum_{i=1}^{i=3} A_1 D_1 L_1 I_m \cos\left(p\theta - \frac{(i-1)2\pi}{3}\right) \cos\left(\omega t - \frac{(i-1)2\pi}{3}\right) \quad (\text{III- 46})$$

Where:

$$\begin{cases} A_1 = \frac{2pN_{cs}}{\pi R} \frac{\sin(0.5p\chi)}{0.5p\chi} \\ D_1 = \frac{\sin(0.5pm\gamma)}{\sin(0.5p\gamma)} \\ L_1 = \frac{\sin(0.5pn_l\xi)}{n_l \sin(0.5p\xi)} \end{cases} \quad (\text{III- 47})$$

Therefore, the fundamental component of surface current density wave is governed by:

$$K_1(\theta, t) = K_{m1} \cos(p\theta - \omega t) \quad (\text{III- 48})$$

With:

$$K_{m1} = \frac{3A_1 D_1 L_1 I_m}{2} \quad (\text{III- 49})$$

Where: K_{m1} is the fundamental amplitude of the surface current density.

III.3.2.3 Winding coefficient

Winding coefficient characterizes the harmonic content of a winding configuration. It is therefore involved in performances of electric motors namely electric parameters. Classically, winding coefficient is defined using fundamental component of MMF [Pyr_14] by:

$$k_w = k_d k_{pi} k_s \quad (\text{III- 50})$$

With:

$$\begin{cases} k_d = \frac{\sin(0.5pm\gamma)}{m \sin(0.5p\gamma)} \\ k_{pi} = \sin\left(\frac{\tau\pi}{2}\right) \\ k_s = \frac{\sin\left(\frac{s\pi}{2}\right)}{\frac{s\pi}{2}} \end{cases} \quad (\text{III- 51})$$

Where: τ is the short pitch factor, s is the skewing factor, k_d is the distribution winding coefficient, k_{pi} is the pitch coefficient and k_s is the skewing coefficient.

Using conductor distribution functions, winding coefficient is defined [Sle_94] by:

$$k_w = \frac{K_m}{A_m} \quad (\text{III- 52})$$

Where A_m is the amplitude of linear current density defined by:

$$A_m = \frac{N_s N_{cs} I_m}{2\pi R} \quad (\text{III- 53})$$

Therefore, according to equations (III-47) and (III-49), the winding coefficient is given by:

$$k_w = \frac{\sin(0.5p\chi)}{0.5p\chi} \frac{\sin(0.5pm\gamma)}{m \sin(0.5p\gamma)} \frac{\sin(0.5pn_l\xi)}{n_l \sin(0.5p\xi)} \quad (\text{III- 54})$$

Equation (II-54) can be written also as: $k_w = \frac{D_1 B_1}{m L_1}$ with $B_1 = \frac{2pN_{cs}A_1}{\pi R}$. For small opening slot and one-layer winding, winding coefficient calculated using conductor distribution function is equal to the winding coefficient calculated using MMF (cf. also to the Appendix B).

III.4 Stator and rotor additional sizes

Main sizes of the surface mounted permanent magnet synchronous motor have been previously determined in Chapter II. By considering a chosen winding configuration, a chosen magnetic flux density level in rotor yoke and polarization in permanent magnets, the additional stator and rotor sizes will be determined in the next sections. This allows to accurate, consequently, the assessment of specific power of electric motor.

III.4.1 Additional stator sizes

Additional stator sizes can be obtained by choosing a winding configuration set by:

- a number of phases "q",
- a number of slots per poles and per phases "m",
- a number of conductors per slot " N_{cs} ",
- a full pitch winding " $\tau = 1$ " or a short pitch winding " $\tau < 1$ ".

With taking into account rectangular geometry for slots, the slot and tooth widths with their corresponding surfaces are assessed by:

$$l_s = (1 - r_{tooth}) \frac{2\pi R}{N_s} \quad (\text{III- 55})$$

$$l_t = r_{tooth} \frac{2\pi R}{N_s} \quad (\text{III- 56})$$

$$S_{slot} = \pi h_s (h_s + 2R)/N_t - S_{slot} \quad (\text{III- 57})$$

With S_{slot} is the slot surface (cf to equation (II-33)), N_t is the number of teeth and it's equal to the number of slots N_s given by:

$$N_s = 2pqm \quad (\text{III- 58})$$

Where: r_{tooth} is the ratio between tooth length to bore radius determined by equation (II-48) and h_s is the slot height determined by equation (II-46).

Indeed, once the winding configuration is chosen, end winding sizes can be accurately assessed by means of " k_{tb} ". It is given by:

$$k_{tb} = \frac{l_{ht}}{L_m} = 1 + \frac{\tau\pi}{p} \frac{R}{L_m} + \frac{\pi r_{tb}}{L_m} \quad (\text{III- 59})$$

With:

$$r_{tb} = \frac{2\pi R}{N_s} \quad (\text{III- 60})$$

Where: l_{ht} is the length of one half turn (cf. Figure III. 13).

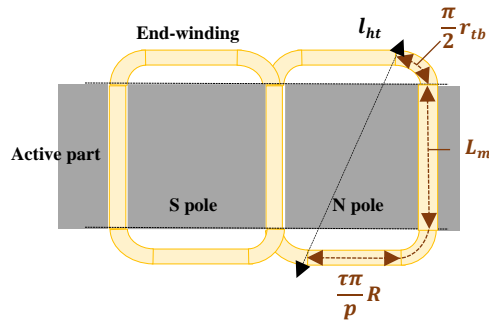


Figure III. 13. Approximated end winding geometry

III.4.2 Additional rotor sizes

Likewise, additional rotor sizes can be obtained by choosing some parameters and materials such as:

- Magnetic flux density in rotor yoke " B_{ry} " to specify the rotor yoke thickness,
- Rotor magnetic sheets: " Silicon Iron alloys" or "Iron Cobalt alloys",
- Magnetic polarization and relative permeability of permanent magnets "J" and " μ_r " to assess the Halbach PM thickness (cf. § III.3.1.2),
- Permanent magnets: "Samarium-Cobalt" or "Neodymium Iron Boron".

By neglecting the leakage flux, rotor yoke thickness can be deduced using the flux conservation principle:

$$h_{ry} = \frac{B_{sy}}{B_{ry}} h_y \quad (\text{III- 61})$$

Where: h_y is the stator yoke thickness calculated using equation (II-45) and B_{sy} is the flux density in stator yoke.

Hence, shaft radius is governed by:

$$R_{sh} = R_r - e_{pm} - h_{ry} \quad (\text{III- 62})$$

Where: R_r is the external rotor yoke.

III.5 Electric parameters of surface mounted permanent magnet synchronous motor

III.5.1 Noload magnetic flux

Considering the fundamental component of conductor distribution function $C_1(\theta)$ and the fundamental component of magnetic potential vector at the stator bore $A_z^{II}(R_3, \theta)$ due to Halbach PM source with adequate rotor position (i.e. $\frac{\pi}{2}$ for maximum torque) , the magnitude of no-load flux is written as:

$$\Phi_{vm} = R_3 L_m \int_0^{2\pi} A_{z_1}^{II}(R_3, \theta) \times C_1(\theta) d\theta \quad (\text{III- 63})$$

With:

$$\begin{cases} C_1(\theta) = A_1 D_1 L_1 \cos(p\theta) \\ A_{z_1}^{II}(R_3, \theta) = \left(E_{31} R_3^p + \frac{E_{41}}{R_3^p} \right) \sin\left(p\theta + \frac{\pi}{2}\right) \end{cases} \quad (\text{III- 64})$$

And

$$\begin{cases} E_{31} = \frac{B_m}{2p} R_3^{1-p} \\ E_{41} = \frac{B_m}{2p} R_3^{1+p} \end{cases} \quad (\text{III- 65})$$

Then:

$$\Phi_{vm} = R_3 L_m \int_0^{2\pi} \frac{B_m}{p} R_3 \cos(p\theta) \times A_1 D_1 L_1 \cos(p\theta) d\theta \quad (\text{III- 66})$$

Therefore, the magnitude of the no-load flux is:

$$\Phi_{vm} = \frac{\pi L_m B_m R_3^2 A_1 D_1 L_1}{p} \quad (\text{III- 67})$$

With: $R_3 = R$, R is the stator bore radius. By using equations (III-47) and (III-54), the magnitude of the no-load flux can be written:

$$\Phi_{vm} = 2 L_m B_m R_3 m N_{cs} k_w \quad (\text{III- 68})$$

Or:

$$\Phi_{vm} = \frac{2L_m B_m R_3 N_{ts} k_w}{p} \quad (\text{III- 69})$$

With: N_{ts} is the number of turns per phase connected in series and defined as $N_{ts} = pmN_{cs}$. The fundamental component of no-load flux wave given per phase is:

$$\Phi_{vi}(\theta) = \Phi_{vm} \cos\left(p\theta - \frac{(i-1)2\pi}{q}\right) \quad (\text{III- 70})$$

III.5.2 Back-electromotive force

The back-electromotive force per phase can be then derived from the no-load flux using the Faraday's law:

$$E_i = -\frac{d\Phi_{vi}(\theta)}{d\theta} \dot{\theta} = \omega \Phi_{vm} \sin\left(p\theta - \frac{(i-1)2\pi}{q}\right) \quad (\text{III- 71})$$

Where: ω is the electric pulse ($\omega = p\dot{\theta}$).

III.5.3 Resistance, self and mutual inductances

Resistance per phase is directly derived from the Joule losses (cf. equation (II-64)) by:

$$R_s = 2N_{ts}\rho_{cu}(T_{win}) \frac{k_{lc}k_{tb}L_m}{S_{cond}} \quad (\text{III- 72})$$

Where: ρ_{cu} is the resistivity of copper at temperature T_{win} , k_{lc} is a coefficient which takes into account the twisting of conductors or wires (its calculation is presented in Chapter IV), S_{cond} is the cross section of conductor (calculated in equation (II-33)).

Self and mutual inductances can be calculated from the flux linkage or from the stored energy although they are more complex to evaluate due to the magnet flux [Lip_04]. Self and mutual inductances have mainly three components which are linked to the airgap linkage flux, the slot leakage flux and the end-winding leakage flux [Hen_94]. Usually, the component linked to the airgap linkage flux is the main component of self and mutual inductances. Therefore, we will focus only on the calculation of this component to approximate the evaluation of self and mutual inductances.

The self-inductance calculated using the total airgap linkage flux per phase is given by:

$$L_s = \frac{\Psi_g}{I_m} \quad (\text{III- 73})$$

Where: I_m is the amplitude of current and Ψ_g is the total airgap linkage flux.

The total airgap linkage flux per phase calculated in the stator bore is given by:

$$\Psi_g = p \int_0^{\pi} \phi_p(\theta) N_s(\theta) d\theta \quad (\text{III- 74})$$

Where: $\phi_p(\theta)$ is the flux per pole given by:

$$\phi_p(\theta) = \frac{2RL_m}{p} B_{ss} \cos(p\theta) \quad (\text{III- 75})$$

And: B_{ss} is the flux density produced by the supplied conductors as given by the following equation:

$$B_{ss} = \mu_o H_g \quad (\text{III- 76})$$

With: H_g is the magnetic field strength calculated by the Ampere's law applied on the magnetic flux lines established by the sinewave distributed conductors $N_{sin}(\theta)$ as illustrated in Figure III.14:

$$2(e_{pm} + e_g)H_g = \frac{N_{tsin}}{p} I_m \quad \text{with } \mu_r \approx 1 \quad (\text{III- 77})$$

And:

$$N_{sin}(\theta) = \frac{N_{tsin}}{2} \cos(p\theta) \quad (\text{III- 78})$$

With: N_{tsin} is the max number of turns of sine wave distributed conductor.

Therefore, using the equations (III-76) to (III-79) the total airgap linkage flux per phase for sine wave distributed conductors can be deduced by:

$$\Psi_g = \frac{\pi}{4} \mu_o \left(\frac{N_{tsin}}{p} \right)^2 \frac{RL_m}{(e_{pm} + e_g)} I_m \quad (\text{III- 79})$$

The self-inductance per phase for sine wave distributed conductors is:

$$L_s = \frac{\pi}{4} \mu_o \left(\frac{N_{tsin}}{p} \right)^2 \frac{R}{e_{pm} + e_g} L_m \quad (\text{III- 80})$$

Practically, the actual number of turns is linked to the sine wave distributed conductors by the following equation according to [Hen_94]:

$$N_{tsin} = \frac{4}{\pi} k_w N_{ts} \quad (\text{III- 81})$$

Eventually, the self-inductance per phase for the real winding is approximated by:

$$L_s = \frac{4}{\pi} \mu_o \left(\frac{k_w N_{ts}}{p} \right)^2 \frac{R}{e_{pm} + e_g} L_m \quad (\text{III- 82})$$

Moreover, according to [Hen_94] for waves close to sine wave the mutual inductance for three phase winding can be approximated by:

$$M \approx -\frac{L_s}{2} \quad (\text{III- 83})$$

Therefore, the cyclic inductance can be deduced by:

$$L_{cs} = L_s - M \quad (\text{III- 84})$$

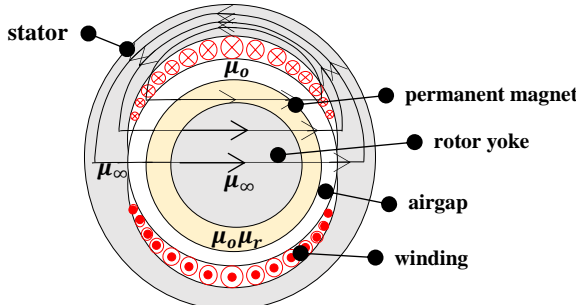


Figure III. 14. Magnetic flux lines established by the sinewave distributed winding

III.5.4 Electromagnetic torque

According to equation (II-3) and using established equation (III-49), the maximum average electromagnetic torque can be expressed also by:

$$T_{em_{max}} = \frac{3}{2} \pi R^2 L_m A_1 D_1 L_1 I_m B_m \quad (\text{III- 85})$$

III.6 Inputs and outputs of SM-PMSM Tool

Figure III.15 summarizes the inputs and outputs of SM-PMSM. As SM-PMSM is based on TST assumptions it takes as inputs:

- The main sizes of electric motor,
- Some parameters defining the stator and the rotor configurations that are close to TST assumptions.

Therefore, SM-PMSM gives as outputs the additional rotor and stator sizes. Those will consequently modify the approximate weights assessed by TST to more accurate weights of SM-PMSM. For chosen rotor materials, the weights are recalculated in SM-PMSM Tool using equations (II-54) to (II-60). Moreover, the specific power and torque are revisited using equations (II-61) and (II-62). In contrast to TST, winding parameters such as winding and end-winding coefficients are accurately calculated in SM-PMSM Tool. Electric parameters are calculated for different number of conductors per slots. And lastly, performances and equivalent current density product are also recalculated by using equations (II-65) to (II-78) and (II-80) respectively.

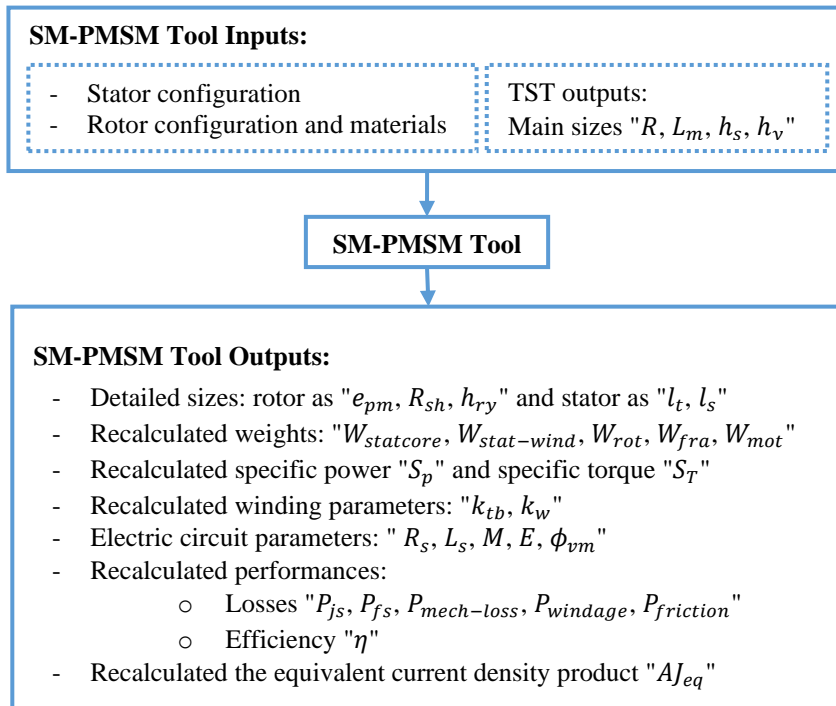


Figure III. 15. Inputs and outputs of SM-PMSM Tool

Conclusion

Surface Mounted Permanent Magnet Synchronous Motor "SM-PMSM" structure is chosen due to its simple analytical model at hand and also to satisfy the Target Setting Tool assumptions. Analytical model is developed to give more details of electric motor which allows more accurate sizing.

Firstly, we have determined the additional stator sizes from the chosen winding configuration. From chosen rotor configurations and materials we have determined the rotor sizes. To ensure sinewave airgap flux density (i.e. TST assumption), we have chosen the Halbach structure for permanent magnets.

Thickness of permanent magnets is calculated from the ideal Halbach definition and from the analytical model. We have determined Halbach polarization using the two proposed methods: a direct design method and optimization method.

Therefore, we have updated in SM-PMSM model some Target Setting Tool outputs namely the weights, the specific power and the specific torque, the winding parameters, the performances and the thermal constraint.

The conductor distribution functions were permitting us to determine the electric circuit parameters, namely: the inductances, the no-load flux and the back electromotive force. We have also updated the Joule losses considering that end-winding size is more defined.

We have programmed in Matlab software the SM-PMSM model's equations as a tool called SM-PMSM tool. It considers set of inputs: the main sizes of electric motor, the stator and rotor configurations and gives set of outputs, namely: the additional sizes, the weights, the electric parameters and the performances. These outputs are required to the other work packages (WP2, 3, 5 and 6).

As well as for Target Setting Tool, SM-PMSM Tool will be validated in the next chapter through sizing electric motors for medium and long term targets.

Appendices

- Appendix A: "Constants of potential vector in airgap and permanent magnet regions"

$$\begin{bmatrix} R_1^{np} & -R_1^{-np} & 0 & 0 & 0 & 0 & 0 & 0 \\ 0 & 0 & R_1^{np} & -R_1^{-np} & 0 & 0 & 0 & 0 \\ R_2^{np} & R_2^{-np} & 0 & 0 & -R_2^{np} & -R_2^{-np} & 0 & 0 \\ 0 & 0 & R_2^{np} & R_2^{-np} & 0 & 0 & -R_2^{np} & -R_2^{-np} \\ \mu_r R_2^{np} & -\mu_r R_2^{-np} & 0 & 0 & -R_2^{np} & R_2^{-np} & 0 & 0 \\ 0 & 0 & \mu_r R_2^{np} & -\mu_r R_2^{-np} & 0 & 0 & -R_2^{np} & R_2^{-np} \\ 0 & 0 & 0 & 0 & R_3^{np} & -R_3^{-np} & 0 & 0 \\ 0 & 0 & 0 & 0 & 0 & 0 & R_3^{np} & -R_3^{-np} \end{bmatrix} = \begin{bmatrix} C_{1n} \\ C_{2n} \\ S_{1n} \\ S_{2n} \\ E_{1n} \\ E_{2n} \\ E_{3n} \\ E_{4n} \end{bmatrix} = \begin{bmatrix} \frac{k_{cn}(R_1) + R_1 J_{\theta cn}}{np} \\ \frac{k_{sn}(R_1) + R_1 J_{\theta sn}}{np} \\ k_{cn}(R_1) \\ k_{sn}(R_1) \\ \frac{k_{cn}(R_1) + R_2 J_{\theta cn}}{np} \\ \frac{k_{sn}(R_1) + R_2 J_{\theta sn}}{np} \\ 0 \\ 0 \end{bmatrix}$$

- For $np \neq 1$

$$\begin{cases} E_{1n} = \frac{\mu_r (J_{tcn} - np J_{rsn}) (R_2 R_1^{2np} - R_2^{2np+1}) - (J_{rsn} - np J_{tcn}) (R_2 R_1^{2np} + R_2^{2np+1}) + 2\mu_r R_1^{np+1} R_2^{np} (J_{rsn} - np J_{tcn})}{(n^2 p^2 - 1) ((1 + \mu_r) R_2^{2np} (R_1^{2np} - R_3^{2np}) + (1 - \mu_r) (R_2^{3np} - R_2^{np} R_1^{2np} R_3^{2np}))} \\ E_{2n} = E_{1n} R_3^{2np} \\ E_{3n} = \frac{\mu_r (J_{tsn} + np J_{rcn}) (R_2 R_1^{2np} - R_2^{2np+1}) + (J_{rcn} + np J_{tsn}) (R_2 R_1^{2np} + R_2^{2np+1}) - 2\mu_r R_1^{np+1} R_2^{np} (J_{rcn} + np J_{tsn})}{(n^2 p^2 - 1) ((1 + \mu_r) R_2^{2np} (R_1^{2np} - R_3^{2np}) + (1 - \mu_r) (R_2^{3np} - R_2^{np} R_1^{2np} R_3^{2np}))} \\ E_{4n} = E_{3n} R_3^{2np} \\ \\ C_{1n} = \frac{(J_{rsn} - np J_{tcn}) (\mu_r R_1^{np+1} (R_2^{2np} + R_3^{2np}) + R_1^{np+1} R_2^{2np} - R_1^{np+1} R_3^{2np} - R_2^{3np+1} R_3^{2np}) - (J_{tcn} - np J_{rsn}) R_2^{np+1} (R_2^{2np} - R_3^{2np})}{(n^2 p^2 - 1) ((R_1^{2np} R_2^{2np} - R_2^{2np} R_3^{2np}) (1 + \mu_r) + (R_2^{4np} - R_1^{2np} R_3^{2np}) (1 - \mu_r))} \\ C_{2n} = \frac{(J_{rsn} - np J_{tcn}) (\mu_r R_1^{np+1} R_2^{2np} (R_2^{2np} + R_3^{2np}) - R_2^{4np} R_1^{np+1} + R_1^{np+1} R_2^{2np} R_3^{2np} - R_2^{2np} R_2^{3np+1} - R_1^{2np} R_2^{3np+1} R_3^{2np}) - (J_{tcn} - np J_{rsn}) R_1^{2np} R_2^{np+1} (R_2^{2np} - R_3^{2np})}{(n^2 p^2 - 1) ((R_1^{2np} R_2^{2np} - R_2^{2np} R_3^{2np}) (1 + \mu_r) + (R_2^{4np} - R_1^{2np} R_3^{2np}) (1 - \mu_r))} \\ S_{1n} = \frac{-(J_{rcn} + np J_{tsn}) (\mu_r R_1^{np+1} (R_2^{2np} + R_3^{2np}) + R_1^{np+1} R_2^{2np} - R_1^{np+1} R_3^{2np} - R_2^{3np+1} R_3^{2np}) - (J_{tsn} + np J_{rcn}) R_2^{np+1} (R_2^{2np} - R_3^{2np})}{(n^2 p^2 - 1) ((R_1^{2np} R_2^{2np} - R_2^{2np} R_3^{2np}) (1 + \mu_r) + (R_2^{4np} - R_1^{2np} R_3^{2np}) (1 - \mu_r))} \\ S_{2n} = \frac{-(J_{rcn} + np J_{tsn}) (\mu_r R_1^{np+1} R_2^{2np} (R_2^{2np} + R_3^{2np}) - R_2^{4np} R_1^{np+1} + R_1^{np+1} R_2^{2np} R_3^{2np} - R_2^{2np} R_2^{3np+1} - R_1^{2np} R_2^{3np+1} R_3^{2np}) - (J_{tsn} + np J_{rcn}) R_1^{2np} R_2^{np+1} (R_2^{2np} - R_3^{2np})}{(n^2 p^2 - 1) ((R_1^{2np} R_2^{2np} - R_2^{2np} R_3^{2np}) (1 + \mu_r) + (R_2^{4np} - R_1^{2np} R_3^{2np}) (1 - \mu_r))} \end{cases}$$

- For $np = 1$

$$\begin{cases} E_{11} = \frac{R_2 (R_2^2 + R_1) (J_{rs1} + J_{tc1} + ln(R_2) (J_{rs1} - J_{tc1})) - R_1 \mu_r (R_2^2 + R_2) (J_{rs1} + J_{tc1} + ln(R_1) (J_{rs1} - J_{tc1})) + R_2^2 ln(R_2) \mu_r (R_1 - R_2) (J_{rsn} - J_{tcn})}{2 (R_2 (R_1 - R_3 \mu_r) + R_2^2 (R_1 \mu_r - R_3) + R_2^3 (1 - \mu_r) - R_1 R_3 (1 - \mu_r))} \\ E_{21} = R_3 E_{11} \\ E_{31} = \frac{-R_2 (R_2^2 + R_1) (J_{rc1} - J_{ts1} + ln(R_2) (J_{rc1} + J_{ts1})) + R_1 \mu_r (R_2^2 + R_2) (J_{rc1} - J_{ts1} + ln(R_1) (J_{rc1} + J_{ts1})) - R_2^2 log(R_2) \mu_r (R_1 - R_2) (J_{rcn} + J_{tsn})}{2 (R_2 (R_1 - R_3 \mu_r) + R_2^2 (R_1 \mu_r - R_3) + R_2^3 (1 - \mu_r) - R_1 R_3 (1 - \mu_r))} \\ E_{41} = R_3 E_{31} \\ \\ C_{11} = \frac{R_2 (R_2^2 + R_3) (J_{rs1} + J_{tc1} + ln(R_2) (J_{rs1} - J_{tc1})) - R_1 (J_{rs1} + J_{tc1} + ln(R_1) (J_{rs1} - J_{tc1})) (\mu_r R_2^2 + R_2 + R_3 (\mu_r - 1)) - R_2^2 ln(R_2) (R_2 - R_3) (J_{rs1} - J_{tc1})}{2 (R_2 (R_1 - R_3 \mu_r) + R_2^2 (R_1 \mu_r - R_3) + R_2^3 (1 - \mu_r) - R_1 R_3 (1 - \mu_r))} \\ C_{2n} = R_1 \frac{R_2 (R_2^2 + R_3) (J_{rs1} + J_{tc1} + ln(R_2) (J_{rs1} - J_{tc1})) - R_2 (J_{rs1} + J_{tc1} + ln(R_1) (J_{rs1} - J_{tc1})) (R_2 R_3 + R_2^2 (\mu_r - 1) + R_3 \mu_r) - R_2^2 ln(R_2) (R_2 - R_3) (J_{rs1} - J_{tc1})}{2 (R_2 (R_1 - R_3 \mu_r) + R_2^2 (R_1 \mu_r - R_3) + R_2^3 (1 - \mu_r) - R_1 R_3 (1 - \mu_r))} \\ S_{1n} = \frac{R_1 (J_{rc1} - J_{ts1} + ln(R_1) (J_{rc1} + J_{ts1})) (\mu_r R_2^2 + R_2 - R_3 + R_3 \mu_r) - R_2 (R_2^2 + R_3) (J_{rc1} - J_{ts1} + ln(R_2) (J_{rc1} + J_{ts1})) + R_2^2 ln(R_2) (R_2 - R_3) (J_{rc1} + J_{ts1})}{2 (R_2 (R_1 - R_3 \mu_r) + R_2^2 (R_1 \mu_r - R_3) + R_2^3 (1 - \mu_r) - R_1 R_3 (1 - \mu_r))} \\ S_{2n} = R_1 \frac{-R_2 (R_2^2 + R_3) (J_{rc1} - J_{ts1} + ln(R_2) (J_{rc1} + J_{ts1})) + (J_{rc1} - J_{ts1} + ln(R_1) (J_{rc1} + J_{ts1})) R_2 (R_2 R_3 + R_2^2 (\mu_r - 1) + R_3 \mu_r) + R_2^2 ln(R_2) (R_2 - R_3) (J_{rc1} + J_{ts1})}{2 (R_2 (R_1 - R_3 \mu_r) + R_2^2 (R_1 \mu_r - R_3) + R_2^3 (1 - \mu_r) - R_1 R_3 (1 - \mu_r))} \end{cases}$$

- Appendix B: "Magnetomotive force functions (MMF)"

The magnetomotive force (MMF) is linked to the distribution conductor $C(\theta)$ by the following equation:

$$MMF(\theta) = IR \int C(\theta) d\theta \quad (\text{III- 86})$$

Where: θ is the angular position, I is the current, R is the airgap bore radius

- Elementary full pitch winding

The magnetomotive force (MMF) waveform of an elementary full pitch winding is illustrated in Figure III.16.

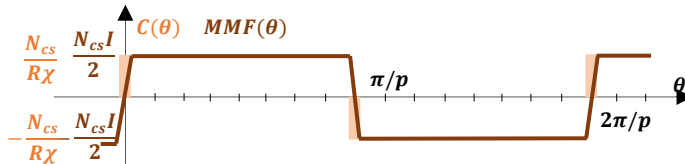


Figure III. 16: Elementary full pitch winding: distribution conductor and magnetomotive force functions

Due to the periodicity of MMF, it can be expressed by the Fourier's series decomposition by:

$$MMF(\theta) = \sum_{n=1}^{n=\infty} b_n \sin(np\theta) \quad (\text{III- 87})$$

Where: n is the harmonic rank, p is the pole pair number, b_n is the Fourier's series component defined by:

$$b_n = \frac{2p}{\pi} \int_0^{\frac{\pi}{p}} mmf(\theta) \sin(np\theta) d\theta \quad (\text{III- 88})$$

Where: $mmf(\theta)$ is magnetic force defined between 0 and $\frac{\pi}{p}$, it given by:

$$mmf(\theta) = \begin{cases} mmf_1(\theta) = \frac{N_{cs}I}{\chi} \theta & \text{for } 0 \leq \theta \leq \frac{\chi}{2} \\ mmf_2(\theta) = \frac{N_{cs}I}{2} & \text{for } \frac{\chi}{2} \leq \theta \leq \frac{\pi}{p} - \frac{\chi}{2} \\ mmf_3(\theta) = -\frac{N_{cs}I}{\chi} \theta + \frac{N_{cs}\pi}{\chi p} & \text{for } \frac{\pi}{p} - \frac{\chi}{2} \leq \theta \leq \frac{\pi}{p} \end{cases} \quad (\text{III- 89})$$

with: N_{cs} is the number of conductors per slot, χ is the angular opening slot, p is the pole pair number.

Using equation (III-89) in equation (III-88), we obtain:

$$b_n = \frac{2p}{\pi} \left[\int_0^{\frac{\chi}{2}} mmf_1(\theta) \sin(np\theta) d\theta + \int_{\frac{\chi}{2}}^{\frac{\pi}{p}-\frac{\chi}{2}} mmf_2(\theta) \sin(np\theta) d\theta + \int_{\frac{\pi}{p}-\frac{\chi}{2}}^{\frac{\pi}{p}} mmf_3(\theta) \sin(np\theta) d\theta \right] \quad (\text{III- 90})$$

By calculation the 1st integration of equation (III-90), we have:

- 1st integration is:

$$\int_0^{\frac{\chi}{2}} mmf_1(\theta) \sin(np\theta) d\theta = \frac{N_{cs}I}{\chi} \int_0^{\frac{\chi}{2}} \theta \sin(np\theta) d\theta = \frac{N_{cs}I}{\chi np} \left[-\theta \cos(np\theta) + \frac{1}{np} \sin(np\theta) \right]_0^{\frac{\chi}{2}}$$

then:

$$\int_0^{\frac{\chi}{2}} mmf_1(\theta) \sin(np\theta) d\theta = \frac{N_{cs}I}{\chi np} \left[-\frac{\chi}{2} \cos\left(\frac{np\chi}{2}\right) + \frac{1}{np} \sin\left(\frac{np\chi}{2}\right) \right]$$

- 2nd integration is:

$$\int_{\frac{\chi}{2}}^{\frac{\pi}{p}-\frac{\chi}{2}} mmf_2(\theta) \sin(np\theta) d\theta = \int_{\frac{\chi}{2}}^{\frac{\pi}{p}-\frac{\chi}{2}} \frac{N_{cs}I}{2} \sin(np\theta) d\theta = \frac{N_{cs}I}{2} \left[-\frac{\cos(np\theta)}{np} \right]_{\frac{\chi}{2}}^{\frac{\pi}{p}-\frac{\chi}{2}}$$

then:

$$\int_{\frac{\chi}{2}}^{\frac{\pi}{p}-\frac{\chi}{2}} mmf_2(\theta) \sin(np\theta) d\theta = \frac{N_{cs}I}{2np} [1 - (-1)^n] \cos\left(\frac{np\chi}{2}\right)$$

- 3rd integration is:

$$\int_{\frac{\pi}{p}-\frac{\chi}{2}}^{\frac{\pi}{p}} mmf_3(\theta) \sin(np\theta) d\theta = \int_{\frac{\pi}{p}-\frac{\chi}{2}}^{\frac{\pi}{p}} \left[-\frac{N_{cs}I}{\chi} \theta + \frac{N_{cs}I\pi}{\chi p} \right] \sin(np\theta) d\theta = \frac{N_{cs}I}{\chi np} \left[[\theta \cos(np\theta)]_{\frac{\pi}{p}-\frac{\chi}{2}}^{\frac{\pi}{p}} - \right. \\ \left. \left[\frac{\sin(np\theta)}{np} \right]_{\frac{\pi}{p}-\frac{\chi}{2}}^{\frac{\pi}{p}} \right] + \frac{N_{cs}I\pi}{np\chi} [\cos(np\theta)]_{\frac{\pi}{p}-\frac{\chi}{2}}^{\frac{\pi}{p}} \\ \int_{\frac{\pi}{p}-\frac{\chi}{2}}^{\frac{\pi}{p}} mmf_3(\theta) \sin(np\theta) d\theta = \frac{N_{cs}I}{2np} \left[\cos\left(\frac{np\chi}{2}\right) - \frac{2(-1)^n}{np\chi} \sin\left(\frac{np\chi}{2}\right) \right]$$

Equation (III-88) becomes:

$$b_n = \frac{N_{cs}I}{n\pi} [1 - (-1)^n] \frac{\sin\left(\frac{np\chi}{2}\right)}{\frac{\chi np}{2}} \quad (\text{III- 91})$$

Therefore:

$$b_n = \begin{cases} 0 & \text{when } n = 2k \\ \frac{4N_{cs}I}{(2k-1)\pi} \frac{\sin(0.5(2k-1)p\chi)}{(2k-1)p\chi} & \text{when } n = 2k-1 \end{cases} \quad (\text{III- 92})$$

Eventually, MMF of elementary full pitch winding:

$$MMF(\theta) = \sum_{k=1}^{k=\infty} \frac{4N_{cs}I}{(2k-1)\pi} \frac{\sin\left(\frac{(2k-1)p\chi}{2}\right)}{(2k-1)p\chi} \sin((2k-1)p\theta) \quad (\text{III- 93})$$

Equation (III-93) can be also written by:

$$MMF(\theta) = \sum_{k=1}^{k=\infty} \frac{RI}{(2k-1)p} A_{2k-1} \sin((2k-1)p\theta) \quad (\text{III- 94})$$

With: $A_{2k-1} = \frac{4N_{cs} \sin(0.5(2k-1)p\chi)}{\pi R (2k-1)\chi}$

- Distributed winding with full pitch

The MMF of a full pitch distributed winding is shown in Figure III.17. From the MMF of an elementary full pitch winding, the MMF of distributed winding can be deduced by:

$$MMF(\theta) = \sum_{j=1}^m \sum_{k=1}^{k=\infty} \frac{RI}{(2k-1)p} A_{2k-1} \sin((2k-1)p(\theta - (j-1)\gamma)) \quad (\text{III- 95})$$

where γ is the angular step between two neighboring coils of the same phase.

with $D_{2k-1} = \frac{\sin(0.5(2k-1)p\gamma)}{\sin(0.5(2k-1)p\gamma)}$, equation (III-95) can be written by:

$$MMF(\theta) = \sum_{k=1}^{\infty} \frac{RI}{(2k-1)p} A_{2k-1} D_{2k-1} \sin((2k-1)p\theta) \quad (\text{III- 96})$$

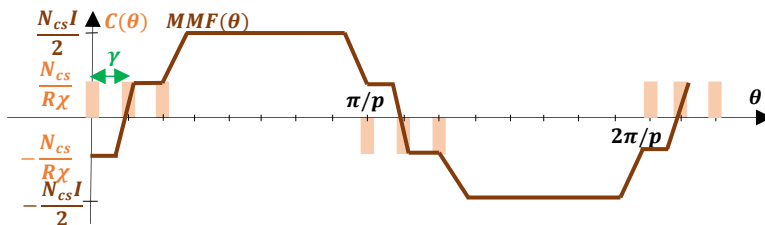


Figure III. 17: Distributed winding: distribution conductor and magnetomotive force functions

- Distributed winding with several layers

Distributed winding with layers has MMF function illustrated in Figure III.18. By considering the layers of winding shifted an angular step between two layers ξ , $MMF(\theta)$ function is expressed by:

$$MMF(\theta) = \sum_{l=1}^{l=n_l} \sum_{k=1}^{\infty} \frac{RI}{(2k-1)p} A_{2k-1} D_{2k-1} \sin((2k-1)p(\theta - (l-1)\xi)) \quad (\text{III- 97})$$

with $L_{2k-1} = \frac{\sin(0.5(2k-1)p n_l \xi)}{n_l \sin(0.5(2k-1)p \xi)}$, the MMF function can be written

$$MMF(\theta) = \sum_{k=1}^{k=\infty} \frac{RI}{(2k-1)p} A_{2k-1} D_{2k-1} L_{2k-1} \sin((2k-1)p\theta) \quad (\text{III- 98})$$

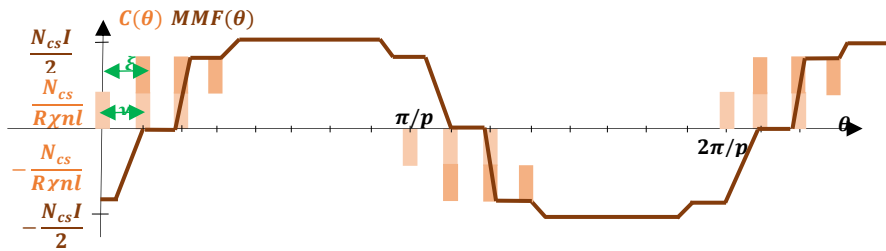


Figure III. 18: Distributed winding with several layers: distribution conductor and magnetomotive force functions

References

- [Lel_18] Houng Thao Le Luong, 'Conception optimale d'un moteur synchrone à rotor bobiné modulaire à hautes performances pour une application embarqué', PhD manuscript, University of Toulouse, 2018
- [Zhu_01] Z. Q. Zhu, D. Howe, 'Halbach permanent magnet machines and applications: a review', *IEE Proc. Electr. Power Appl.*, vol. 148, no.4, pp.299-308, July 2001.
- [Che_17] Y. Chen, R. Sanchez, A. Yoon, K. Sivasubramniam, 'Mechanical design considerations of an Ironless high specific power electric machine,' *IEEE Trans. on Transp. Elect.*, vol.3, no.4, Dec 2017.
- [Mel_07] P. H. Mellor, R. Wrobel, 'Optimization of a multipolar permanent-magnet rotor comprising two arc segments per pole,' *IEEE Trans. Ind. Appl.*, vol.43, no.4, pp.951-942, Jul/Aug 2007.
- [Hua_18] H. Huang, R. Qu, D. Li, 'Analysis and application of discrete Halbach magnet array with unequal arc lengths and unequally changed magnetization directions,' *IEEE Trans. Appl. Supercond*, vol. 28, no.3, Apr 2018.
- [Mar_09] M. Markovic, Y. Perriard, 'Optimization deisgn of a segmented halbach permanent-magnet motor using an analytical model,' *IEEE Trans. On. Magn.*, vol.45, no.7, July 2009.
- [Pyr_14] J. Pyrhönen, T. Jokinen, V. Hrbcovcà, "Design of rotating electrical machines," 2nd Edition, John Wiley & Sons, 2014
- [Sle_94] G. R. Slemon, "On the design of high-performance surface-mounted PM motors," *IEEE Trans. Ind. App.*, vol.30, no.1, Jan/Feb 1994, pp.134-141
- [Hen_94] J. R. Hendershot Jr, TJE Miller, 'Design of brushless permanent-magnet motors', GNA Physics Publications, Oxford Science Publications, 1994
- [Lip_04] T. A. Lipo 'Introduction to AC Machine Design', Wisconsin Power Electronics Research Center University of Wisconsin, 2nd edition, 2004.

Chapter IV: Sizing of Electrical Motors for Medium and Long Term Targets

Contents

Introduction.....	81
IV.1 Specifications and choice of sizing point.....	81
IV.2 Sizing procedure.....	81
IV.3 Sizing electric motor for medium term target 2025.....	83
IV.3.1 Issues, limitations and strategy to achieve target 2025.....	83
IV.3.2 Choice of technological levels.....	83
IV.3.3 Assessment of electric motor technologies: Target Setting Tool.....	84
IV.3.4 Sizing electric motor: Surface Mounted Permanent Magnet Synchronous Motor.....	85
IV.3.5 Validation with Finite Element Analysis.....	86
IV.3.5.1. Slotless model.....	87
IV.3.5.2. Slotted model.....	90
IV.3.6 Thermal behaviour and cooling system design.....	96
IV.4 Sizing electric motor for long term target 2035.....	99
IV.4.1 Issues, limitations and strategy to achieve target 2035.....	99
IV.4.2 Choice of technological levels.....	100
IV.4.3 Assessment of electric motor technologies: Target Setting Tool.....	100
IV.4.4 Sizing electric motor: Surface Mounted Permanent Magnet Synchronous Motor.....	101
IV.4.5 Validation with Finite Element Analysis.....	102
IV.4.5.1. Slotless model.....	102
IV.4.5.2. Slotted model.....	105
IV.4.6 Thermal behaviour and cooling system design.....	110
Conclusion.....	113
Appendices.....	115
References.....	120

Introduction

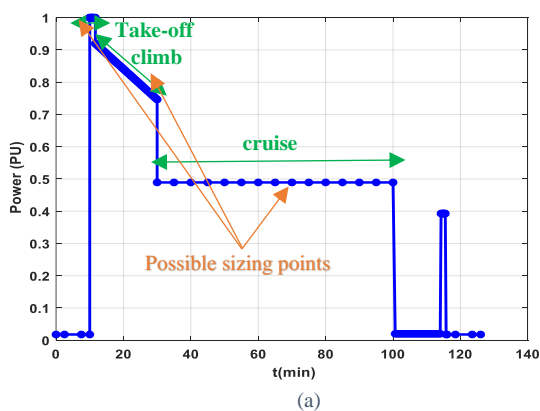
After introducing the assessment and sizing tools of electric motors, sizing surface mounted permanent magnet synchronous motors satisfying the medium and long term targets will be performed in this chapter. Specifications of targeted electric motors with their cooling systems will be firstly reminded. Besides, considering the flying profiles, the choice of sizing point will be discussed. Secondly, a sizing procedure will be proposed for reaching targets. It includes tools using for the assessment electric motor technologies, for sizing electric motors and for sizing cooling systems. Thereupon, sizing electric motor for medium term target 2025 will be given. It will be validated using finite element analysis. Moreover, thanks to close interaction with WP3 the sizing cooling system as well as whole thermal behaviour of electric motor with its cooling will be illustrated. To exceed the medium term target 2025 for reaching the long term target 2035, several technological promising solutions will be discussed and identified to overcome issues and limitations of increasing specific power. Besides, a highlight will be payed to the differences between the electric motor targeted for medium term target 2025 with the one targeted for long term target 2035. Thereafter, sizing electric motor for long term target 2035 will be given with validation using finite element analysis. Still with WP3 interaction, sizing cooling system with thermal behaviour for long term target will be illustrated.

IV.1 Specifications and choice of sizing point

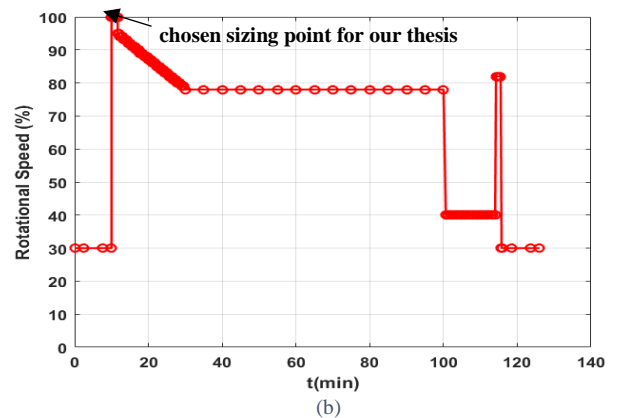
In terms of specific power and efficiency, sizing electric motors with their cooling systems should be performed to reach:

- Specific power 5kW/kg with efficiency at cruise point must be greater than 96% and efficiency at design point greater than 94.5% for medium term target 2025,
- Specific power 10kW/kg with efficiency at cruise point must be greater than 98.5% and efficiency at design point greater than 97% for long term target 2035.

On the other hand, electric motors should be sized for providing during a flying mission a mechanical power ranging from 0.018PU to 1PU with rotational speed ratio ranging from 30% to 100% as represented in Figure IV.1. It is therefore important to define the sizing point for electric motors with their cooling system. In other terms, to set the levels of mechanical power and rotational speed ratio on which sizing will be carried out. Indeed, according to the power flying mission three flying phases which sizing can be considered, namely take-off phase, climb phase and cruise phase as indicated in Figure IV.1. Take-off flying phase is the most thermally critical phase in contrast to the climb and cruise flying phases for electric motors. Due to the lack of time, we study the sizing for medium and long term targets only at take-off flying phase considering that sizing at climb and cruise flying phases will require several loopbacks to check the most thermal critical phase (i.e. the take-off flying phase). Besides, sizing electric motors at another sizing point does not change the used method in this manuscript.



(a)



(b)

Figure IV. 1 (a) Power profile vs flying time , (b) Rotational speed profile per unit vs flying time with sizing point

IV.2 Sizing procedure

As mentioned in Chapter I, sizing electric motors is strongly linked to cooling methods. Furthermore, design of cooling system depends on the sized electric motors. For the purpose, we propose a sizing procedure including in a loop the sizing of electric motor and the design of cooling system. We recall

that design of cooling system is carried out by WP3². Therefore, this procedure expresses the strong interaction between the 1st and 3rd WP. To reach high specific power, sizing procedure consists of six steps:

- Step 1: consists of assessing the electric motor technologies required to reach high specific power and high efficiency using the Target Setting Tool.
- Step 2: consists to size Surface Mounted Permanent Magnet synchronous motor using the SM-PMSM tool for specific power of electric motor well above to the target.
- Step 3: checks thermal constraint according to cooling method chosen in the 1st step and check the efficiency at cruise point.
- Step 4: assesses the temperature inside electric motor by using Lumped Parameter Thermal Model.
- Step 5: designs cooling system taking into account the temperature assessing.
- Step 6: assesses the total weight of electric motor with its cooling system as illustrated in Figure IV.2.

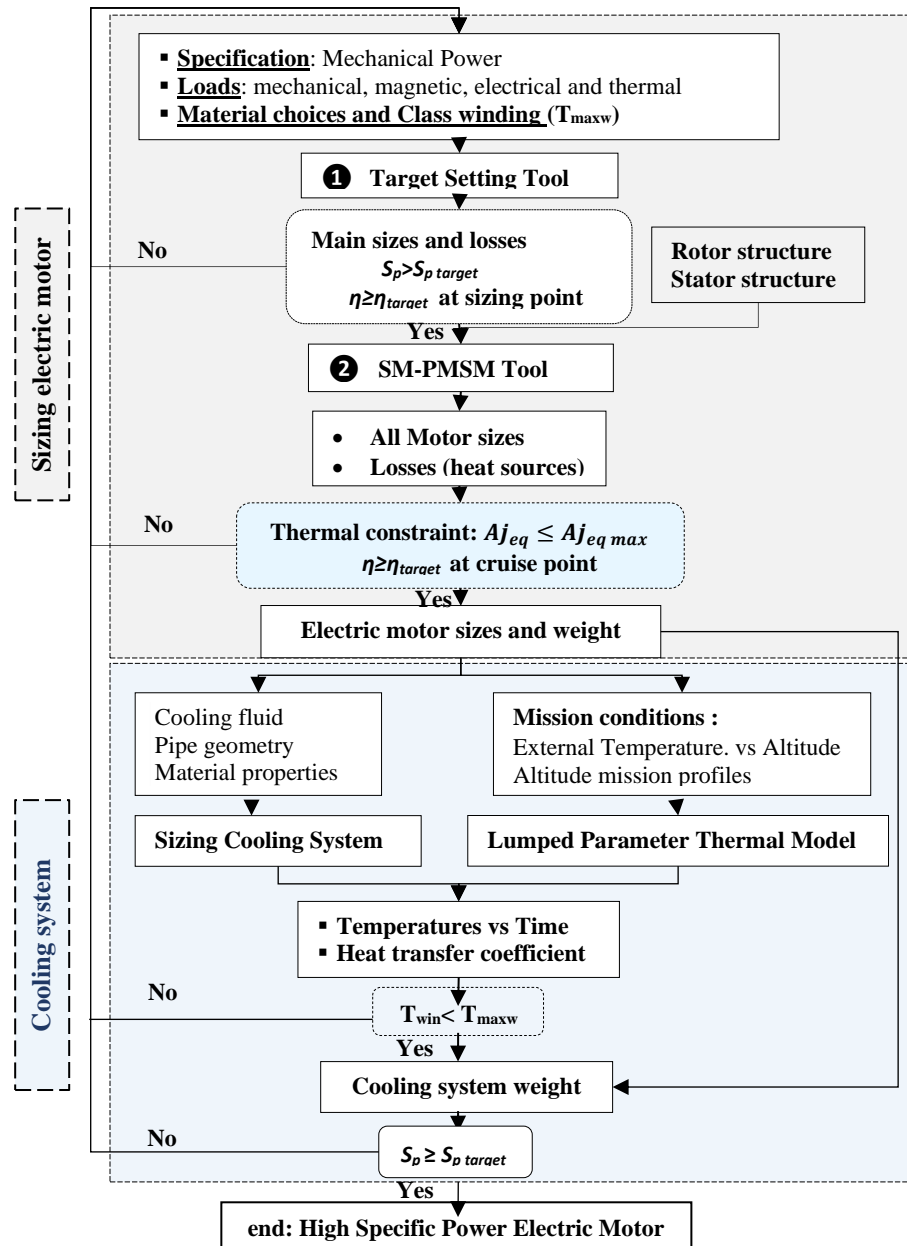


Figure IV. 2. Sizing procedure of high specific electric motor with its cooling system

Sized electric motor using this procedure allows, on the other hand, to provide the needed data for the other work packages especially 2nd and 5thWPs as illustrated in Figure IV.3. Synchronous frequency and

²"Thermal modelling and cooling of an electric motor. Application to a Hybrid Aircraft Propulsion", PhD thesis prepared by Amal Zeaiter and Supervised by Matthieu Fénot and Etienne Videcoq, Ecole Nationale Supérieure de Mécanique et d'Aéronautique ENSMA, France, <https://www.theses.fr/s174528>.

electric parameters of electric motor are required for sizing power converters of the hybrid electric aircraft power chain. Data relating to winding, for instance, the conductor voltages and the slot sizes are required for partial discharge study of the electric motor. Regarding to the 6th WP, it is rather the assessment and sizing tools of electric motors which are provided.

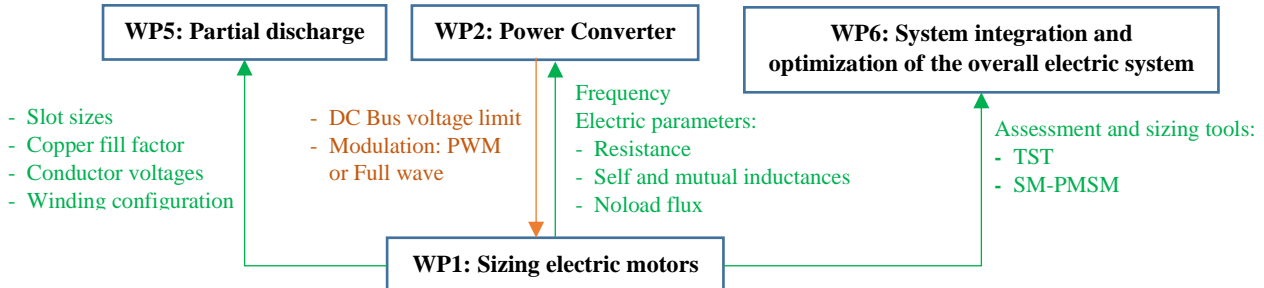


Figure IV. 3. Interaction sizing electric motor work package with others WPs

IV.3 Sizing of electric motor for medium term target 2025

IV.3.1 Issues, limitations and strategy to achieve target 2025

In electric motors, tangential stress level in airgap quantifies the electromagnetic torque as expressed in (II-4):

$$T_{em\max} = R_r S_{rot} \sigma$$

Increasing magnetic, electric, thermal and mechanical loads, for instance, the rotational speed allows decreasing rotor volume and thus its weight. Simultaneously, it leads to increase iron, Joule and mechanical losses (cf. Equations (II-65) to (II-69)) and thus temperatures and decrease efficiency.

Usually, insulation and permanent magnet materials are the most critical parts in electric motors as mentioned in Chapter I. As insulation materials are thermally bad conductors, the evacuation of the heat generated due to losses through winding is the main limitation for increasing specific power of electric motors.

Despite of issues and limitations for increasing specific power and efficiency, it is wise to increase loads and decrease losses. Moreover, reducing losses not only increases efficiency but also reduces the cooling system weight of the cooling system. In other words, our work will consist of identifying the most promising available technologies that allow us to achieve our 2025 goals.

For the purpose, our first strategy is to select, according to the actual cooling technologies, a conventional cooling method for medium term target 2025: external liquid cooling method performed through the frame for stator cooling and internal liquid cooling method through the shaft for rotor cooling. Joule losses are usually the hardest losses to extract and to evacuate, their limitation is crucial for 2025 target. Joule losses can be limited, for this target, by using stranded and twisted conductors.

The second strategy consists of identifying the other magnetic material technological levels according to the chosen conventional cooling method. This identification will be performed using Target Setting Tool. Afterward sizing of surface mounted permanent magnet synchronous motor will be carried out using SM-PMSM. Finite Element Analysis will be used to validate the sizing of electric motor. The thermal behaviour of the latter will be given with its cooling system design.

IV.3.2 Choice of technological levels

Electric, magnetic and thermal loads are linked to the materials used in electric machine as it illustrated in the previous Chapters. For reaching and satisfying both Hasteecs targets and specifications, the choice of loads should be wise considering the all limitations. Therefore, the choice of loads involves material selecting that allow achieving the chosen loads. Electric motor designers [Pyr_14] have been draft typical values of loads according to the cooling method as presented in Table IV.1. The loads given in this table are drafted for non-salient synchronous machines. Since, we are going to size for 1st and 2nd Hasteecs targets, surface mounted permanent magnet synchronous motors, loads given in this table will constitute a good basic for identifying the required technologies in TST and SM-PMSM.

Table IV. 1:Magnetic, electric and thermal loads of Non-salient pole synchronous machines

Loads	Indirect air cooling	Indirect hydrogen cooling	Direct water cooling
Airgap flux density B_m [T]		0.8-1.05	
Stator yoke flux density B_{sy} [T]		1.1-1.5	
Stator tooth flux density B_{st} [T]		1.5-2.0	
Current density j_{rms} [A.mm ⁻²]	3-5	4-6	7-10
Linear current density A_{rms} [A.mm ⁻¹]	30-80	90-110	150-200
Max tangential stress σ [Pa]	17000-59500	50000-81500	85000-148500
Current density product $A_{rms} \times j_{rms}$ [A ² .m ⁻³]	9×10^{10} - 40×10^{10}	36×10^{10} - 66×10^{10}	1.05×10^{12} - 2×10^{12}

IV.3.3 Assessment of electric motor technologies: Target Setting Tool

For sizing electric motor, we define a range values of electric, magnetic and thermal loads on which we will make several trade-offs on losses, efficiency and specific power. Table IV.2 summarizes the used range value of electric, magnetic and thermal loads. These range values are defined from the typical values given in Table IV.1. Range values of magnetic loads such as flux density levels in airgap, yoke and tooth are chosen the same as typical values.

Range values of tangential stress, current density and linear current density are chosen from the typical values corresponding to the direct water and indirect hydrogen cooling methods although the chosen cooling method for the 1st target is conventional with liquid coolant. This choice is carried out in order to not underestimate the thermal limit expressed by equivalent current density product in Target Setting Tool.

Table IV. 2:Range values of electric, magnetic and thermal loads for medium term target 2025

Loads	Range values
Airgap flux density B_m [T]	0.8-1.05
Stator yoke flux density B_{sy} [T]	1.1-1.5
Stator tooth flux density B_{st} [T]	1.5-2.0
Current density j_{rms} [A.mm ⁻²]	4-10
Linear current density A_{rms} [A.mm ⁻¹]	80-200
Max tangential stress σ [Pa]	50000-148500
Current density product $A_{rms} \times j_{rms}$ [A ² .m ⁻³]	0.32×10^{12} - 2×10^{12}

In the 1st step of sizing procedure, we apply at the beginning

- limited values of loads,
- high rotational speed,
- high number of pole pairs,
- high thermal class such as 200°C,
- high copper fill factor,
- shape coefficient greater than the limit value (i.e. $\lambda \geq 0.4$) in order to assess the maximum reached specific power regardless of resulting losses.

If the achieved specific power is not enough greater than the target, we increase again the speed and number of pole pairs until to exceed 5kW/kg. Once it is done, we adjust these loads, speed, the number of pole pairs and copper fill factor in order to decrease the losses while controlling the specific power and efficiency by using some technological solutions:

→ Using twisted strands in order to reduce Joule losses resulting in less skin and proximity effects (i.e. $R_{AC}/R_{DC}=1$ at high frequency) as shown in Figure IV. 4. These strands are splitted and twisted such as: $k_{lc} = 1.25$ and $k_{sc}k_{fill} = 0.5$.



Figure IV. 4. Twisted strands

- Using Vacoflux 48 with thickness of 0.35mm for stator and rotor yokes considering that has the lower specific iron losses (cf. to Figure I. 14);
- Halbach permanent magnet with radial and axial segmentation to ensure sinewave airgap flux density to reduce eddy current losses.

On the other hand, these loads, the speed and the number of pole pairs are adjusted in order to ensure a loss distribution suitable to the chosen cooling method and not to exceed the thermal limit (i.e. $A_{eq} \leq 2 \times 10^2 \text{ A}^2 \cdot \text{m}^{-3}$). For this target, as stator is cooled through its frame, Joule losses should be well distributed in the stator surface. Furthermore, to not exceed mechanical limit, using of Fiber Carbon Sleeve for retaining permanent magnets at high rotational speed is required. In this manuscript, sleeve will not be modelled, however the airgap will be sized largely enough to take into account the sleeve thickness.

Table IV.3 illustrates the adjusted loads, rotational speed, number of poles pairs, copper fill factor and others adjusted parameters which allow achieving target without exceeding thermal and mechanical limits. The main sizes, weights of electric motor and further intrinsic parameters are also summarized in this table.

Table IV. 3: Target Setting Tool inputs/outputs for medium term target 2025

Target Setting Tool inputs	Target Setting Tool outputs
Mechanical specifications	Main sizes
<ul style="list-style-type: none"> - Electromagnetic power "$P_{em}=1\text{PU}$" - Rotational speed "$\Omega=15970\text{rpm}$" 	<ul style="list-style-type: none"> - Frame external stator radius "$R_{fr}=172.9\text{mm}$" - External stator radius "$R_{out}=162.9\text{mm}$" - Stator bore radius "$R=92.5\text{mm}$" - Active length "$L_m=317.4\text{mm}$" - Stator yoke height "$h_y=34.3\text{mm}$" - Tooth (or slot) height "$h_s=36.1\text{mm}$" - Airgap thickness "$e_g=2.77\text{mm}$"
Thermal specifications	Weights
<ul style="list-style-type: none"> - winding temperature "$T_{win}=180^\circ\text{C}$" 	<ul style="list-style-type: none"> - Stator magnetic core weight "$W_{stat-core}=115.4\text{kg}$" - Winding stator weight "$W_{stat-wind}=33.8\text{kg}$" - Rotor weight "$W_{rot}=56.7\text{kg}$" - Frame weight "$W_{fra}=19.7\text{kg}$"
Magnetic and electric loads	Specific power and torque of electric motor
<ul style="list-style-type: none"> - Tangential stress "$\sigma=50000\text{Pa}$" - Current density "$j_{rms}=8.1\text{A/mm}^2$" - Max surface current density "$K_m=111.1\text{kA/m}$" - RMS linear current density: "$A_{rms}=81.4\text{kA/m}$" - Current density product "$A_{rms}j_{rms}=6.59 \times 10^{11} \text{ A}^2 \cdot \text{m}^3$" - Max airgap flux density "$B_m=0.9\text{T}$" - Flux density in teeth "$B_{st}=1.3\text{T}$" - Flux density in yoke "$B_{sy}=1.2\text{T}$" 	<ul style="list-style-type: none"> - Specific power "$S_p=6.3\text{kW/kg}$" - Specific torque "$S_T=3.8\text{Nm/kg}$"
Geometrical choice	Further intrinsic parameters
<ul style="list-style-type: none"> - Shape coefficient "$\lambda=0.6$" - Slot copper fill factor "50%" - End-winding coefficient "$k_{tb}=1.4$" - Number of pole pairs "$p=2$" 	<ul style="list-style-type: none"> - Peripheral speed "$V_p=150\text{m/s}$" - Joule losses "$P_{js}=5960\text{W}$" - Iron losses "$P_{fs}=3620\text{W}$" - Mechanical losses "$P_{mech-loss}=1740\text{W}$" - Efficiency "$\eta=98\%$"
Material of stator electrical sheet: "Vacoflux 48- 0.35mm"	Equivalent current density product "$A_{eq}=1.565 \times 10^{12} \text{ A}^2 \cdot \text{m}^3$" Electromagnetic torque " $T_{em}=1\text{PU}$ " Synchronous frequency " $f_s=532\text{Hz}$ "

In fact, there are several other load combinations allowing to achieve our target such as: low rotational speed with high number of pole pairs, high current density with low flux density levels, etc. For instance, low rotational speed with high number of pole pairs leads to design electric motor at low speed without gearbox which can be an interesting solution for removing the gearbox from the hybrid power chain. In contrast, in power converter point of view this solution could be not interesting given that it leads to electric motor with low cyclic inductance (i.e. electric motor with small sizes of stator magnetic sheet parts).

IV.3.4 Size electric motor: Surface Mounted Permanent Magnet Synchronous Motor

After determining the main sizes of electric motor in the 1st step of sizing procedure, the structure of electric motor is defined by choosing the winding and rotor configurations. Although it is difficult to carry out sinewave winding, we choose conventional winding having full pitch winding, single layer, three phases and two slot per pole and per phases as summarized in Table IV.4. This corresponds to stator with 24 slots. For rotor, we select Samarium Cobalt "SmCo" for permanent magnets due to its less temperature sensitivity (cf. Appendix B) and Iron Cobalt magnetic sheet "Vacoflux 48" for rotor yoke. Flux density in rotor yoke and polarization of permanent magnets are given in Table IV.4.

Outputs as further sizes, recalculated weight and recalculated losses of surface mounted permanent magnet synchronous motor are given in Table IV.5. Deviations between TST and SM-PMSM on weights, losses, specific power and torque are less than 15% although TST takes many assumptions. In Table IV.5, performances as electric parameters are given for example for one conductor per slot.

Table IV. 4: SM-PMSM Tool Inputs for medium term target 2025

Stator configuration	Rotor configuration
<ul style="list-style-type: none"> - Full pitch winding "$\tau=1$" - Number of layers "$n_l=1$" - Number of phases "$q=3$" - Number of slots per pole and per phase "$m=2$" 	<ul style="list-style-type: none"> - Flux density in rotor yoke "$B_{ry}=1.4T$" - Polarization of permanent magnets "$J=1.16T$"

Table IV. 5: SM-PMSM Tool Outputs for medium term target 2025

Further sizes	Electric parameters for "$N_{cs}=1$"						
<ul style="list-style-type: none"> - Permanent magnet thickness "$e_{pm}=9mm$" - Rotor yoke thickness "$h_{ry}=29.72mm$" - Rotor shaft radius "$R_{sh}=50.98mm$" - Stator slot width "$l_s=13.48mm$" - Stator tooth width "$l_t=10.73mm$" 	<ul style="list-style-type: none"> - Resistance "$R_s=0.62m\Omega$" - Self-inductance "$L_s=14.89\mu H$" - Mutual inductance "$M=-7.44\mu H$" - Rms back electromotive force "$E_i=241.32V$" - No-load magnetic flux "$\varphi_{vm}=0.1021Wb$" 						
Recalculated winding parameters	Recalculated the equivalent current density product						
<ul style="list-style-type: none"> - Winding coefficient "$k_w=0.9659$" - End winding coefficient "$k_{tb}=1.6974$" 	<ul style="list-style-type: none"> - Equivalent current density product "$A_{eq}=1.522\times 10^{12}A^2/m^3$" 						
Recalculated weights	Recalculated specific power and specific torque (without cooling system)						
<ul style="list-style-type: none"> - Stator magnetic core weight "$W_{stat-core}=115.4kg$" - Winding stator weight "$W_{stat-wind}=41kg$" - Rotor weight "$W_{rot}=80.14kg$" - Frame weight "$W_{fra}=22.4kg$" 	<ul style="list-style-type: none"> - Specific power "$S_p=5.5kW/kg$" - Specific torque "$S_T=3.30Nm/kg$" 						
Recalculated performances:							
<ul style="list-style-type: none"> - Joule losses "$=7213W$" - Iron losses "$=3621W$" - Mechanical losses "$=2507W$" - Efficiency "$\eta=98\%$" 	<table border="1"> <tr> <td>Joule loss</td> <td>54%</td> </tr> <tr> <td>Iron loss</td> <td>27%</td> </tr> <tr> <td>Mechanical loss</td> <td>19%</td> </tr> </table>	Joule loss	54%	Iron loss	27%	Mechanical loss	19%
Joule loss	54%						
Iron loss	27%						
Mechanical loss	19%						

Efficiency at sizing point is greater than the targeted efficiency at sizing point. Performances such as electric parameters and losses will be validated by Finite Element Analysis in the next paragraph.

IV.3.5 Validation with Finite Element Analysis

Classically to validate the analytical models, numerical methods as finite element analysis are the most used. Ansys Maxwell software is one of these numerical tools. It is increasingly used due to its fast time solving and its compatibility with other software. Therefore, we will use it for analysing and validation. According to assumptions used in TST and SM-PMSM Tool, two models will be performed in Finite Element Analysis namely: slotless and slotted models. The first one will be performed in order to check the TST and SM-PMSM formula, given that these latter are based on slotless model assumptions. The second one will be performed to evaluate the deviations on loads and performances due to the slot effect. In all finite element analysis, simulations will be carried out for one conductor per slot.

IV.3.5.1. Slotless model

As the analytical model established in Target Setting Tool is based on the slotless model (cf. Chapter II), no-load and load 2D simulations will be performed to validate the electric machine performances. The structure of slotless model is represented by one-layer current at the airgap bore, segmented Halbach permanent magnet and magnetic rotor yoke. Due to the pole periodicity and the axisymmetric of the structure, 2D numerical model can be performed as shown in Figure IV.5.a. Therefore, the employed boundary conditions are illustrated in Figure IV.5.b. Within, master and slave boundary conditions employed on the model extremities are used for ensuring the periodicity and zero flux boundary

condition (or the Dirichlet boundary condition i.e. $A = 0$) applied on shaft bore radius for ensuring the closure of the flux lines in slotless model.

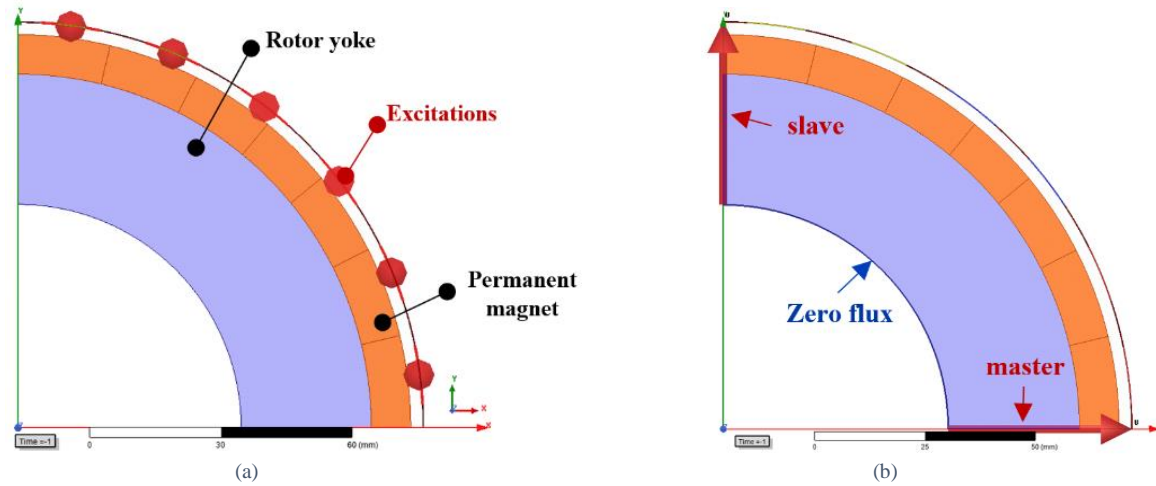


Figure IV. 5. Slotless model electric motor of medium term target 2025: (a) Slotless model structure on one pole, (b) boundary conditions applied on one pole structure

a. No-load simulation

No-load simulation consists to ensure and to validate the airgap flux density set as an input of TST and the performances calculated by SM-PMSM such as the no-load magnetic flux and the back electromotive force.

In order to obtain a sinusoidal waveform of the airgap magnetic flux density, we determine the width using the direct design (cf. Table IV.5) and the orientation of segmented Halbach PMs by optimization established in Chapter III. For 7 segments of Halbach PMs and max airgap flux density equal to 0.9T, the structure of segmented Halbach PMs is given in Table IV. 6 and shown in Figure IV.6.a. The airgap flux density waveform is validated in Figure IV.6.b.

The resulting no-load magnetic flux and back electromotive force are shown in Figure IV.7. We notice that they are quasi-sinusoidal and their amplitudes are close to those calculated by SM-PMSM (cf. equations (III-70) and (III-71)).

Table IV. 6: Electric motor of medium term target 2025: Structure of 7 segment Halbach PMs

Segment	1	2	3	4	5	6	7
Orientation γ (°)	74	50	24	0	-24	-50	-74
Angular width: $\frac{\beta}{\pi/p}$ (%)	15.09	14.85	13.89	12.34	13.89	14.85	15.09

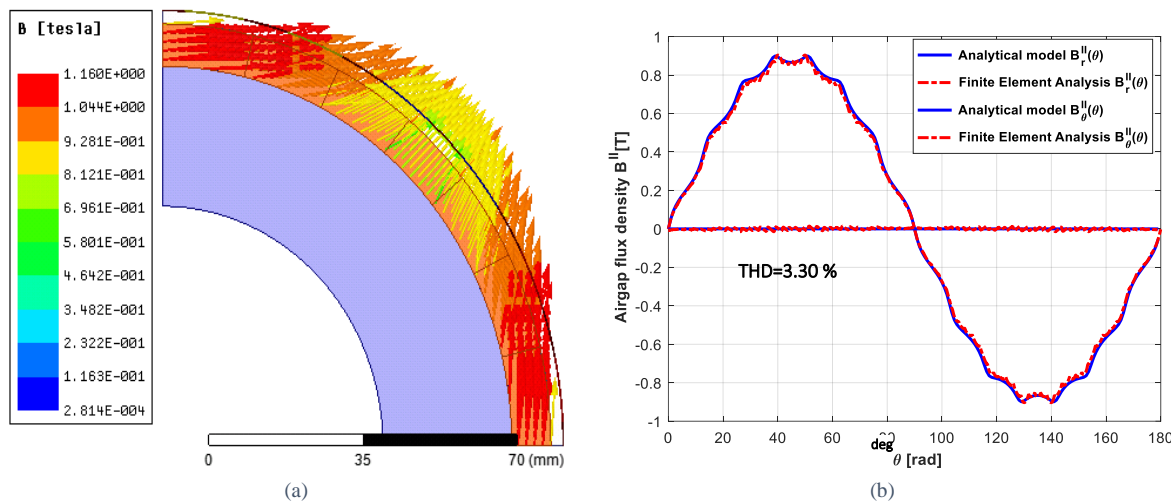


Figure IV. 6. (a) Halbach array 7 segment PMs, (b) Airgap flux density

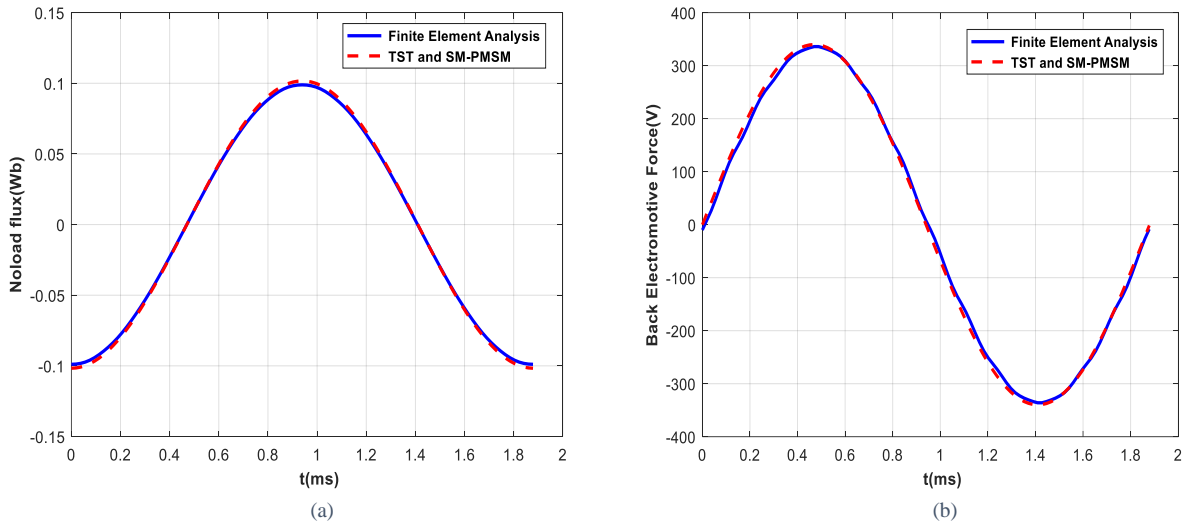


Figure IV. 7. Slotless model: (a) No-load magnetic flux, (b) Back electromotive force

b. Load simulation

Load simulation consists to validate the airgap flux density due to the armature reaction and the performances as:

- the self, mutual and cyclic inductances,
- the electromagnetic torque.

The airgap flux density due to the Halbach PMs and the armature reaction is shown in Figure IV.8. By considering the fundamental component of the airgap flux density given by finite element analysis we notice that the analytical model performed in TST and SM-PMSM is validated (cf. equation (II-21)).

Figure IV.9 shows the comparisons of the self, mutual and cyclic inductances given by finite element analysis and those calculated by analytical model of SM-PMSM (cf. equations (III-82), (III-83) and (III-84)). The values of inductances given by finite element analysis are respectively $15.7\mu\text{H}$, $-6.208\mu\text{H}$ and $21.91\mu\text{H}$. The deviations on self, mutual and cyclic inductances are respectively 5%, 20% and 2%. Deviation on mutual inductance remains allowable considering that deviation on cyclic inductance is insignificant.

The electromagnetic torque calculated in SM-PMSM results from the interaction of the surface current density and the airgap flux density as presented in Figure IV.10.a. The electromagnetic torque given by finite element analysis is compared to the analytical electromagnetic torque in Figure IV.10.b. The average electromagnetic torque given by simulation is 0.98PU. The deviation on electromagnetic torque is 2%. In slotless model, deviation on efficiency will not be assessed considering that iron losses in stator are not analysed. It can be evaluated only in slotted model.

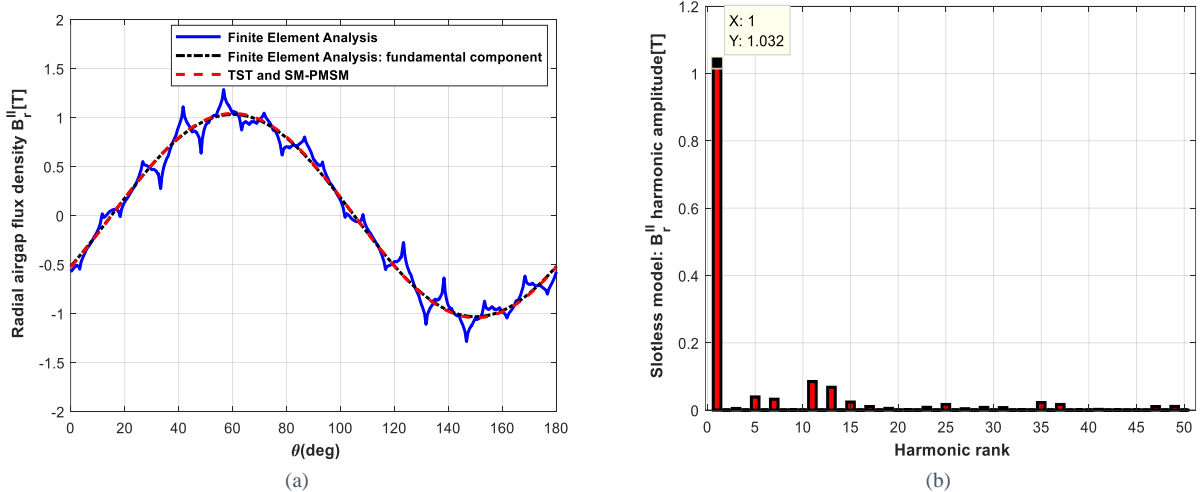


Figure IV. 8. Slotless model: (a) Airgap flux density, (b) harmonic analysis

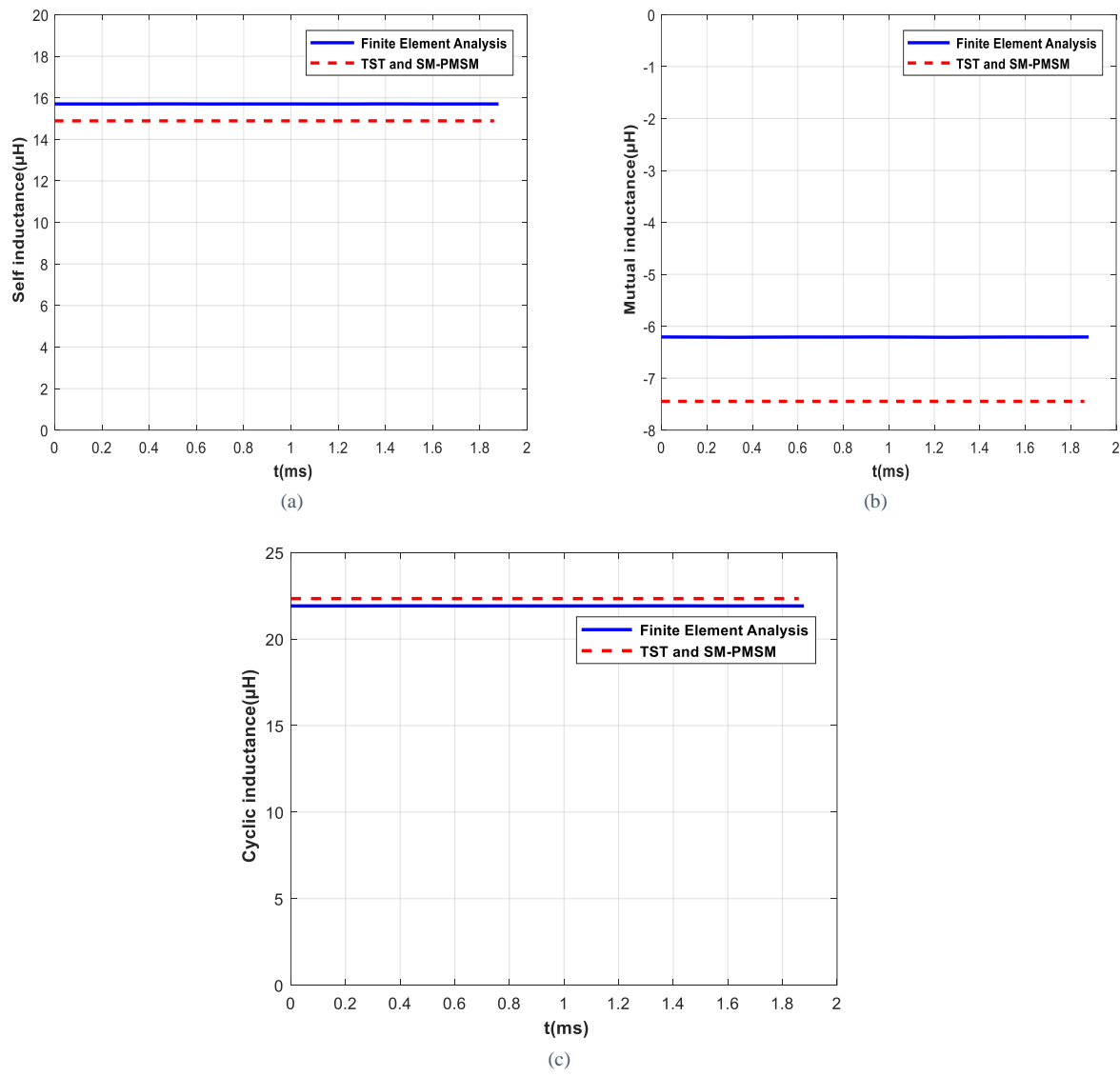


Figure IV. 9. Slotless model: (a) Self-inductance, (b) Mutual inductance, (c) cyclic inductance

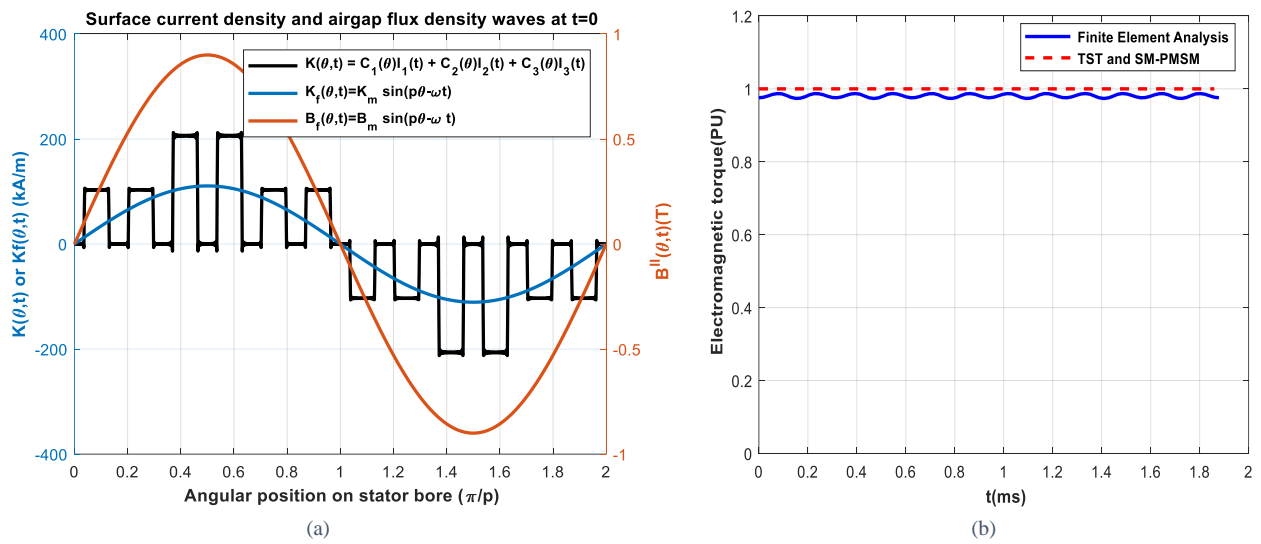


Figure IV. 10. Slotless model: (a) Surface current density and airgap flux density waves, (b) The electromagnetic torque

IV.3.5.2. Slotted model

After dealing the slotless model, this part is devoted to the slotted model of the electric motor. Slotted model is the most representing structure of electric motor in contrast to slotless model. Slotted model allows to assess deviations due to slot effect on performances between the slotless model which SM-PMSM is based on it and the real electric motor structure. Figure IV.11.a shows the 2D structure of electric motor on one pole. The corresponding boundary conditions are illustrated in Figure IV.11.b.

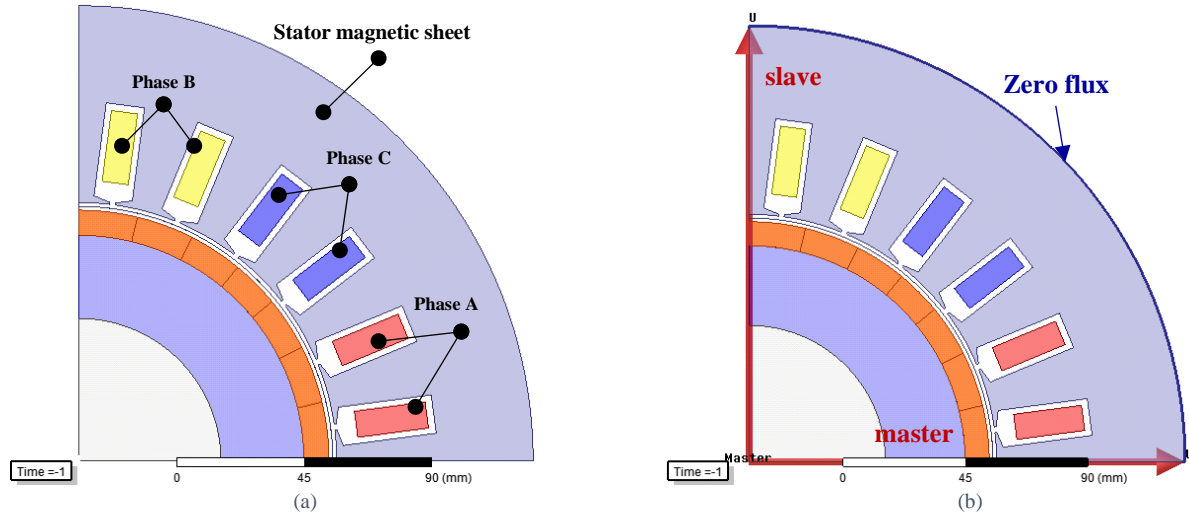


Figure IV. 11. Slotted model electric motor of medium term target 2025: (a) Slotted model structure on one pole, (b) boundary conditions on one pole structure

a. No-load simulation

The airgap flux density at no-load simulation is presented in Figure IV.12. We notice that airgap flux remains close to the sinewave despite of slot effect structure as indicated by the harmonic analysis. The amplitude of fundamental component is equal to 0.88, therefore it is close to TST target. Stator yoke and tooth flux densities can be checked by integrating potential vector on the magnetic paths as shown on Figure IV.13.a. The resulting flux densities are presented in Figure IV.13.b and c. These peak flux densities (i.e. 1.18T for yoke flux density and 1.33T for tooth flux density) are very close to those set in TST.

The no-load magnetic flux and back electromotive force are presented in Figure IV.14. Compared to SM-PMSM results, we notice that slot effect on no-load magnetic flux and back electromotive is insignificant.

At no-load simulations, it is interesting to assess the cogging torque although it does not contribute to the rated electromagnetic torque. Cogging torque arises from the magnetic interaction between rotor permanent magnets and slotted stator at no-load. Figure IV.15 shows the cogging torque. Its maximum ripple is $\Delta T_{cogging} = 1.9 \text{ Nm}$. This value is low compared to the average electromagnetic torque. Figure IV.16 shows the magnetic flux and the flux line distributions. The mean magnetic flux density in teeth is about 1.25T. In yoke, the mean magnetic flux density is 1.09T.

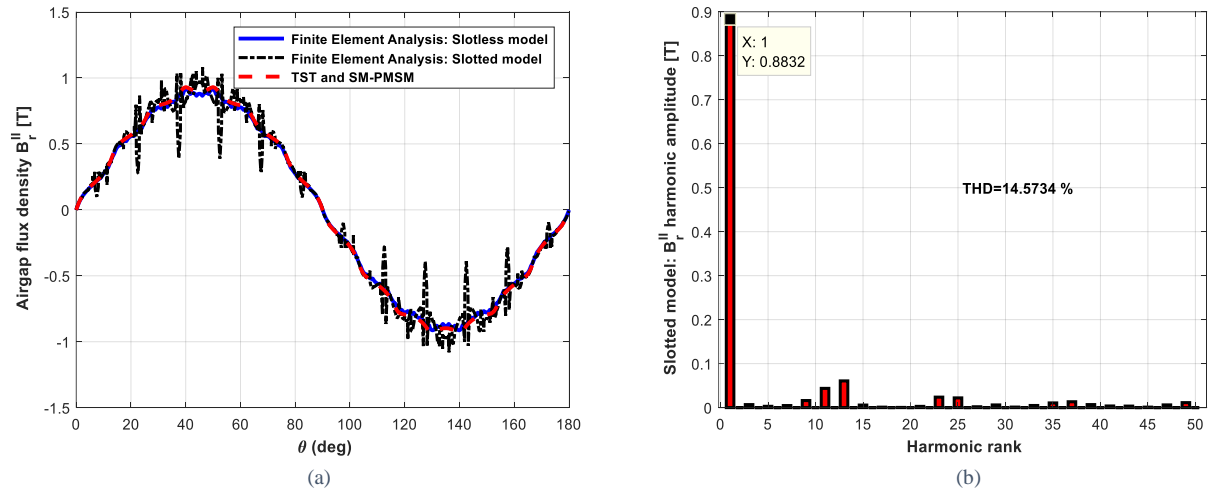


Figure IV. 12. Airgap flux density at no-load: (a) slotless and slotted models, (b) harmonic analysis

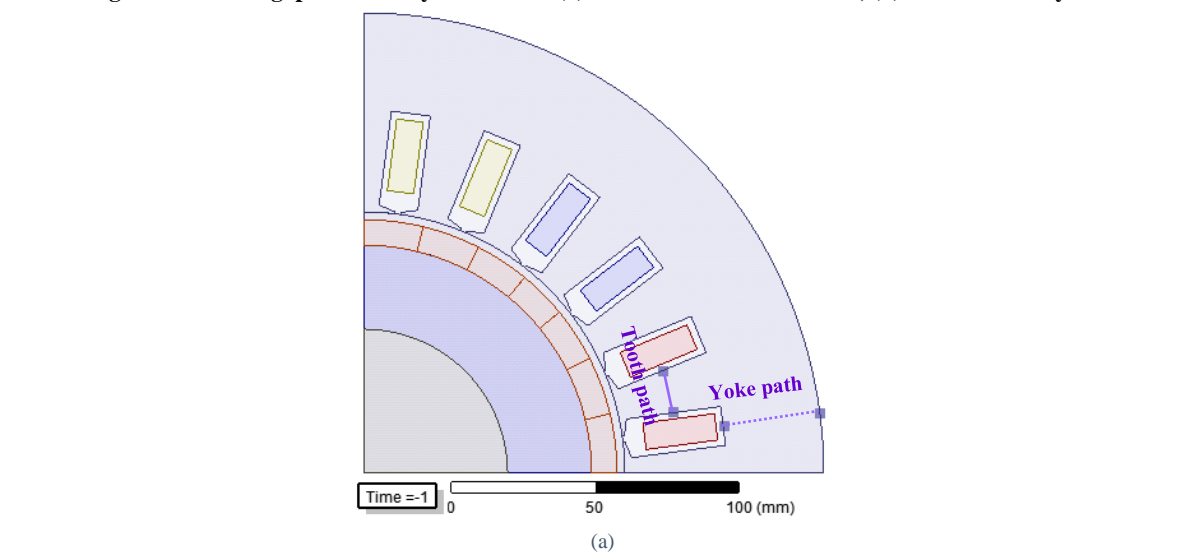


Figure IV. 13. Slotted model at no-load: (a) Magnetic paths, (b) tooth flux density, (c) stator yoke flux density

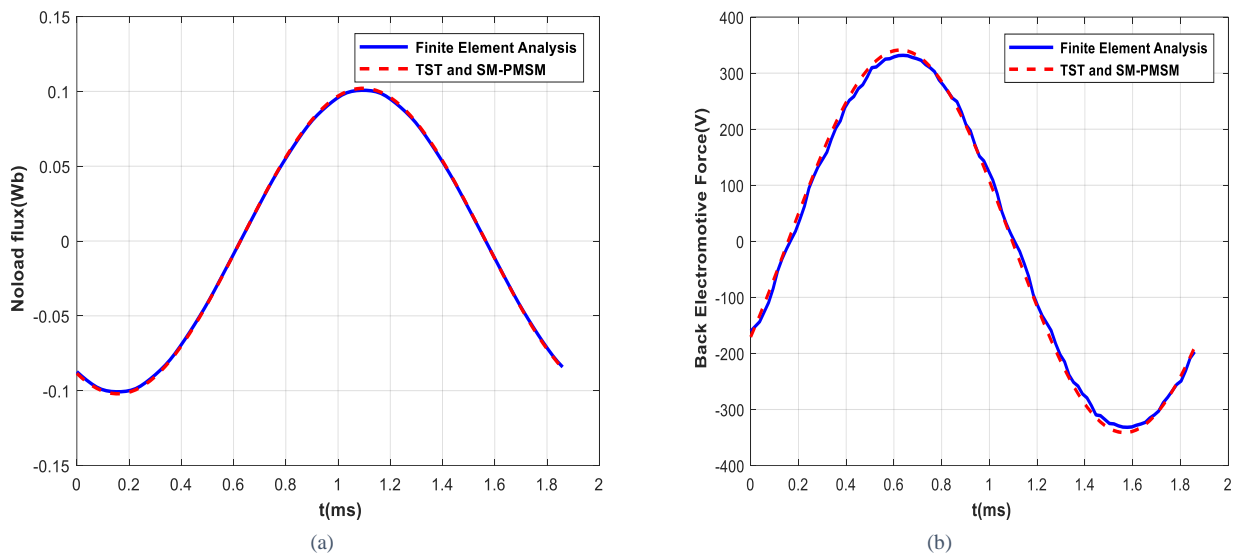


Figure IV. 14. Slotted model: (a) No-load magnetic flux, (b) Back electromotive force

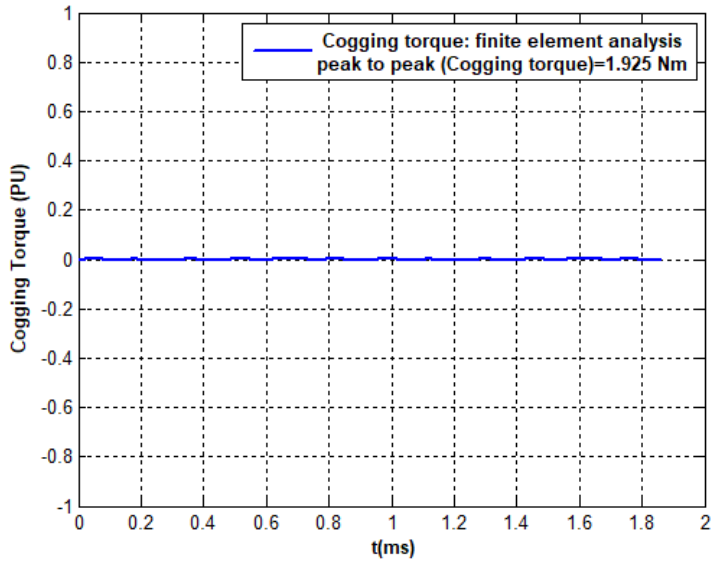


Figure IV. 15. Noload simulation: cogging torque

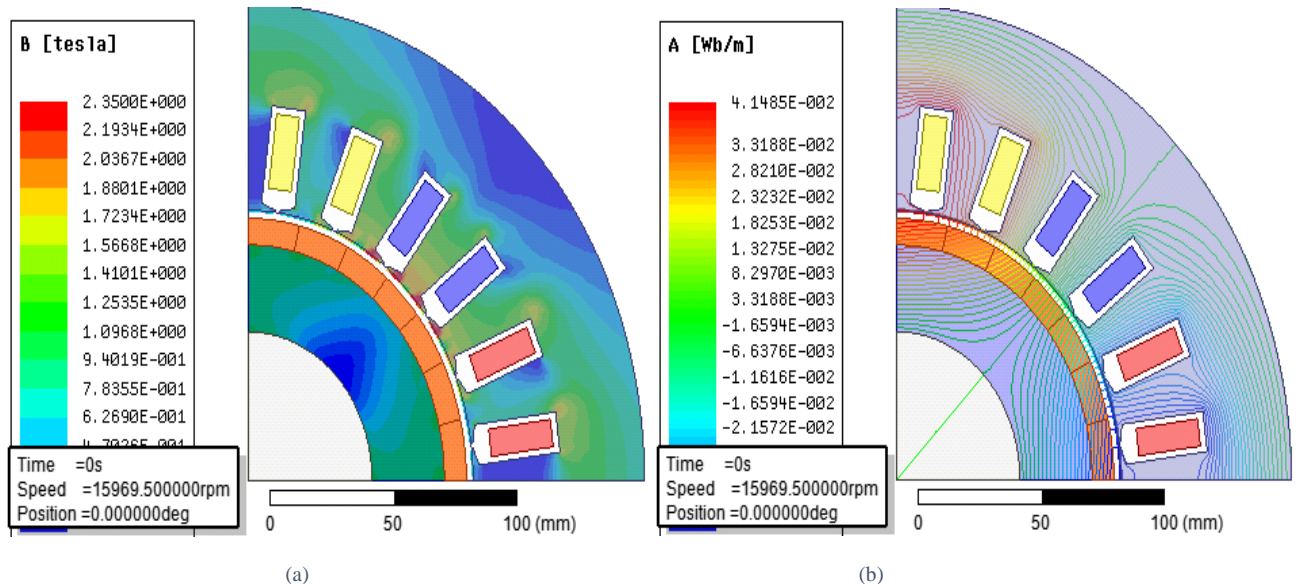


Figure IV. 16. Slotted model at no-load simulation: (a) Magnetic flux density distribution, (b) Flux line distribution

b. Load simulation

Airgap flux density taking into account the armature reaction is presented in Figure IV.17. By comparison to the no-load simulation we notice that the influence of the armature reaction on the airgap flux density is negligible (increasing of 0.1T due to the armature reaction). Moreover, we notice that the airgap flux density taking into account the armature reaction analytically calculated in TST and SM-PMSM is close to that given by simulation of slotted model.

Taking the same paths of stator tooth and yoke, the assessing of flux densities is illustrated in Figure IV.18. By comparison to the no-load simulation, we find that flux densities in stator tooth and stator yoke increase respectively by 0.16T and 0.36T from the values obtained by the no-load simulation. The reached peak values are 1.49T and 1.54T respectively in stator tooth and stator yoke.

The self, mutual and cyclic inductances given by slotted model are shown in Figure IV.19. They have saliency around their average values. Saliency can be explained by mildly noteworthy saturation in the bottom teeth as shown in Figure IV.20. The average values are respectively 22 μ H, -6.2 μ H and 28.2 μ H. By comparison to the inductances calculated in SM-PMSM, we observe deviations which may be the consequence of not taking into account the inductances due to leakage fluxes in TST and SM-PMSM. The electromagnetic torque is given in Figure IV.21. Its average value is equal to 0.97PU which is close to the value calculated in analytical model of TST and SM-PMSM.

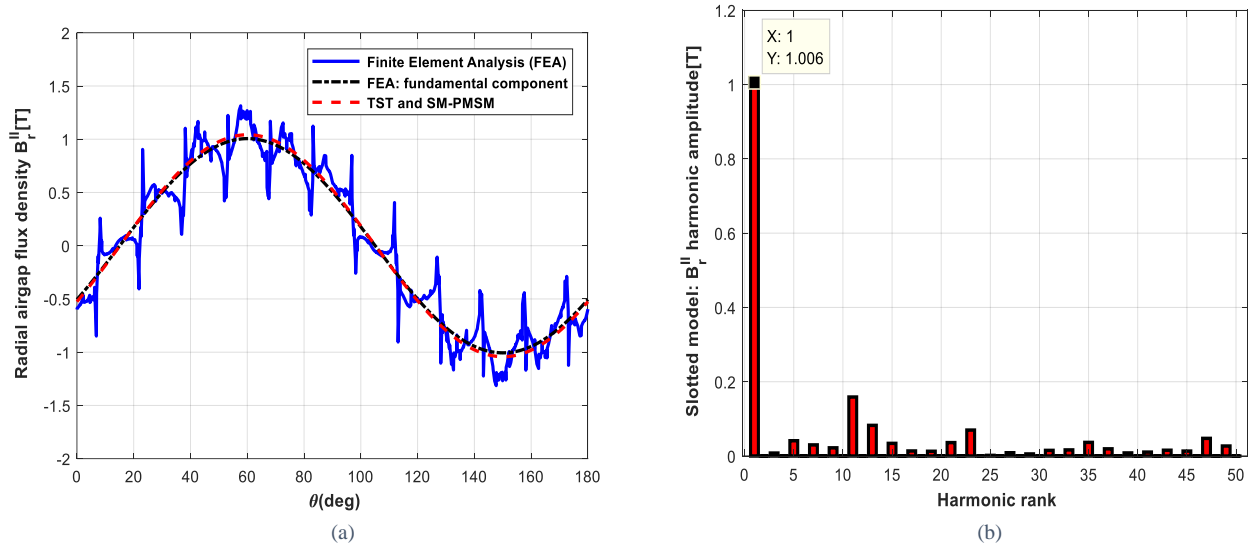


Figure IV. 17. Slotted model at load: (a) airgap flux density, (b) harmonic analysis

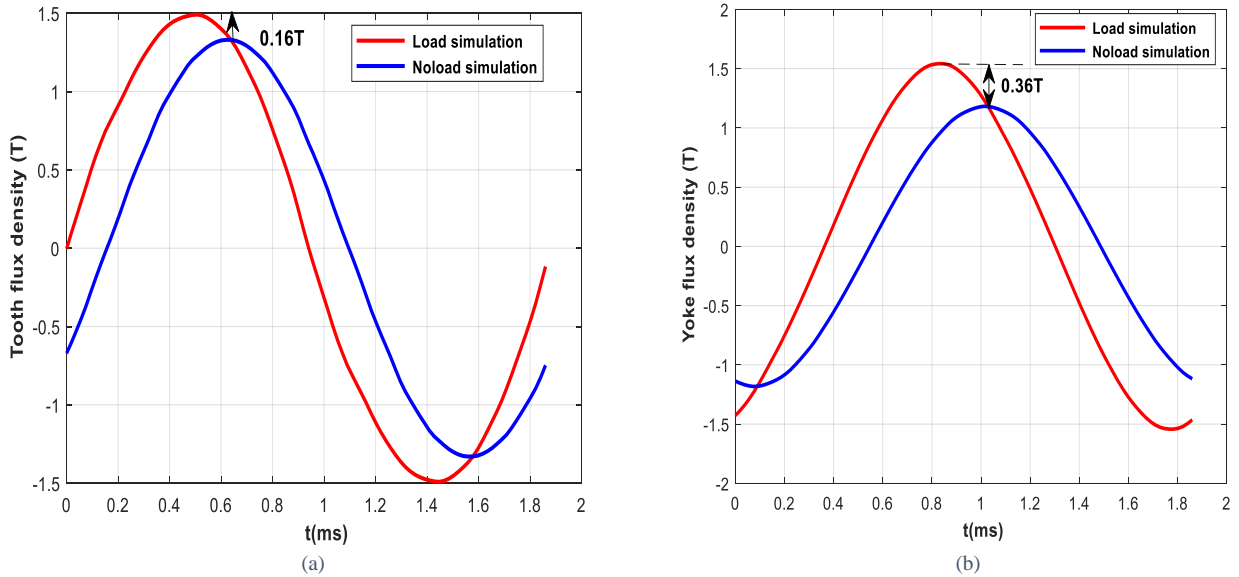


Figure IV. 18. Slotted model at load: (a) tooth flux density, (b) stator yoke flux density

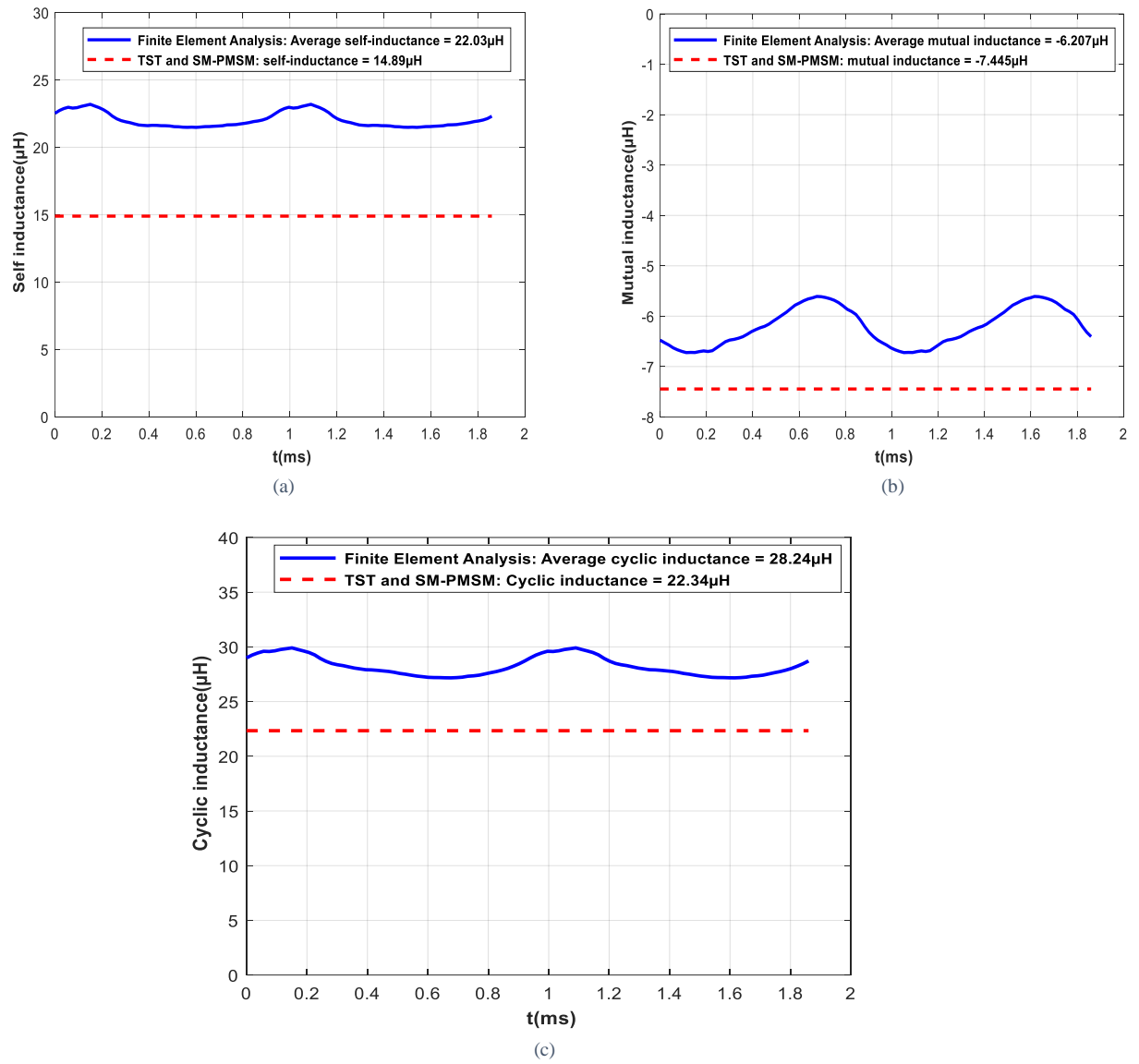


Figure IV. 19. Slotted model: (a) Self-inductance, (b) Mutual inductance, (c) cyclic inductance

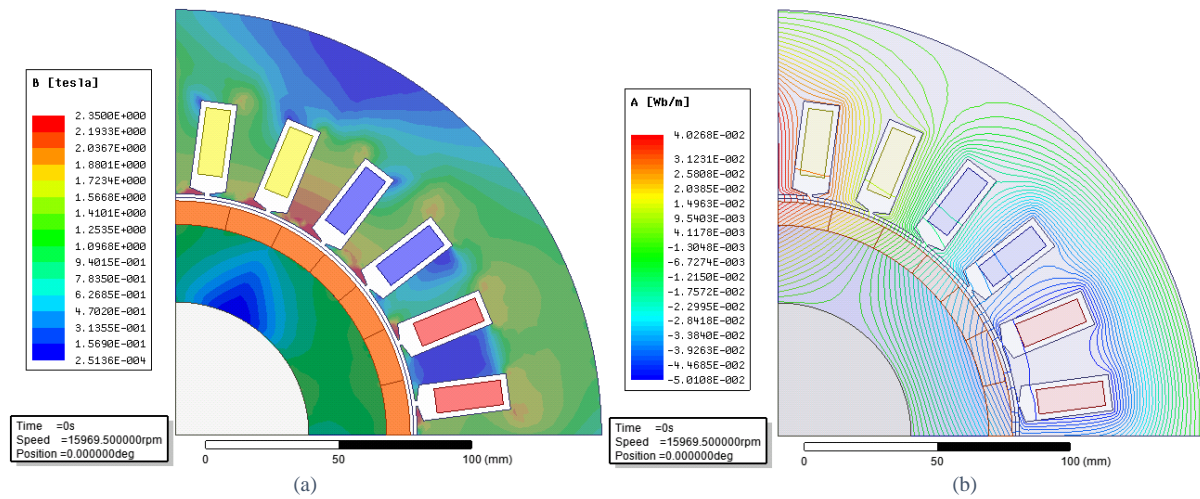


Figure IV. 20. Slotted model at load simulation: (a) Magnetic flux density distribution, (b) Flux line distribution

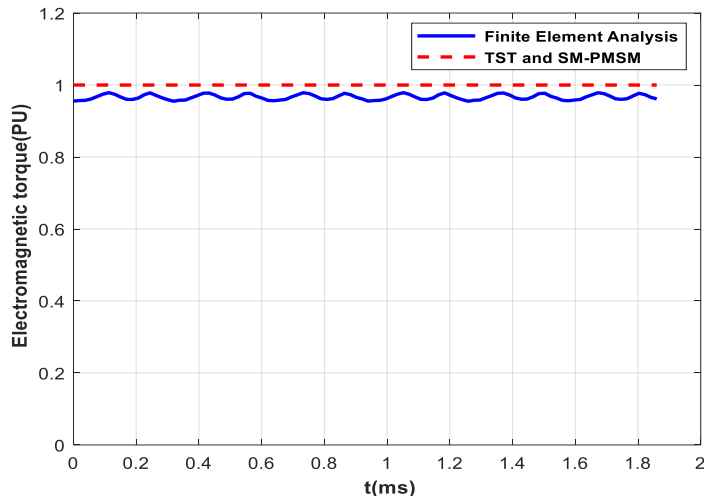


Figure IV. 21. Slotted model: The electromagnetic torque

In TST and SM-PMSM, iron losses are assessed by assuming that flux density distribution is homogeneous in the magnetic sheets. However, through finite element analysis flux density distribution is not homogeneous considering that often magnetic sheet saturates in some areas as shown in Figure IV.20. Therefore, it is interesting to compare the iron losses assessed by finite element analysis which takes into account the saturation with those assessed in TST and SM-PMSM. Figure IV.22 shows a comparison of iron losses calculated using analytical model of TST and SM-PMSM with those calculated by finite element analysis. At synchronous frequency, iron losses in rotor yoke are zero which is quite obvious. The mean value of iron losses in stator magnetic sheet is 7.5kW. This value is significantly higher than the one calculated by TST and SM-PMSM. This deviation can be explained firstly by the difference of basic iron loss model used in TST and SM-PMSM (cf. equation II-67 and Appendix A) with the one used in Finite Element Analysis (cf. equation II-66 and Appendix A). Secondly, the deviation can be explained by the deviation of flux density levels in stator magnetic sheet set in TST with those checked by finite element analysis. Thirdly, deviations can come from the nonlinear behaviour of magnetic material. In addition, from the electromagnetic torque and the iron losses analysed using FEA, efficiency is recalculated. Its value is closer to 98%, it remains higher than targeted efficiency at sizing point. Deviation on efficiency is quasi-zero.

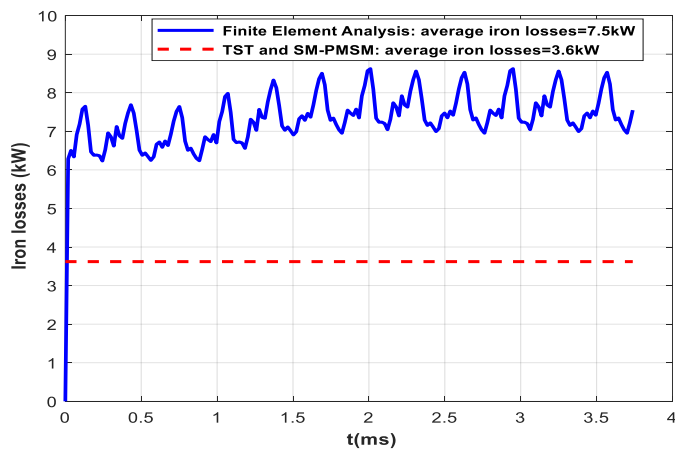


Figure IV. 22. Slotted model: Iron losses

To conclude the comparison, Table IV.7 summarizes the deviations of electric motor 2025 performances between TST and SM-PMSM with finite element analysis. Deviations between these tools is less than 4% for no-load magnetic flux, for back-electromotive force and for electromagnetic torque. In contrast, deviations between these tools is 32% for self-inductance, 21% for mutual and cyclic inductance. These deviations are significant by reason of ignoring the leakage flux in inductance calculations in TST and SM-PMSM. In contrast, deviations of slotless model of TST and SM-PMSM with slotless model of finite element analysis are negligible.

Table IV. 7: Electric motor of medium term target 2025: summary comparison of performances between analytical tools and finite element analysis

Performances	TST	SM-PMSM	Finite Element Analysis		Slotless model deviation	Slotted model deviation
			Slotless model	Slotted model		
Max. No-load magnetic flux " $\Phi_{vm}[\text{Wb}]$ "	-	0.102	0.10	0.10	2%	2%
Rms Back-Electromotive Force " $E_i[\text{V}]$ "	-	241	238	236	1%	2%
Electromagnetic torque " $T_{em}[\text{PU}]$ "	1	1	0.98	0.97	2%	3%
Self-inductance " $L_s[\mu\text{H}]$ "	-	14.89	15.7	22.03	5%	32%
Mutual inductance " $M[\mu\text{H}]$ "	-	-7.44	-6.20	-6.20	20%	20%
Cyclic inductance " $L_{cs}[\mu\text{H}]$ "	-	22.34	21.91	28.24	2%	21%

IV.3.6 Thermal behaviour and cooling system design

Cooling system proposed by WP3 is mainly based on: *ambient air cooling* and *cooling primary circuit*. Ambient air cooling consists of taking the outside ambient air as cold source considering that its maximum temperature at cruise is -12°C and at ground is 38°C [All_18].

Cooling primary circuit is composed of a heat exchanger placed near to the cold source, a hydraulic circuit and a pump. Heat exchanger allows the evacuation of heat generated by electric motor to the outside air through plate embedded around the nacelle. It is composed of pipes and a cold plate. The heat evacuation is carried out mainly by conduction heat transfer between the pipes and cold plate (i.e. nacelle) and then by convection heat transfer between the nacelle and the air as presented in Figure IV.23.

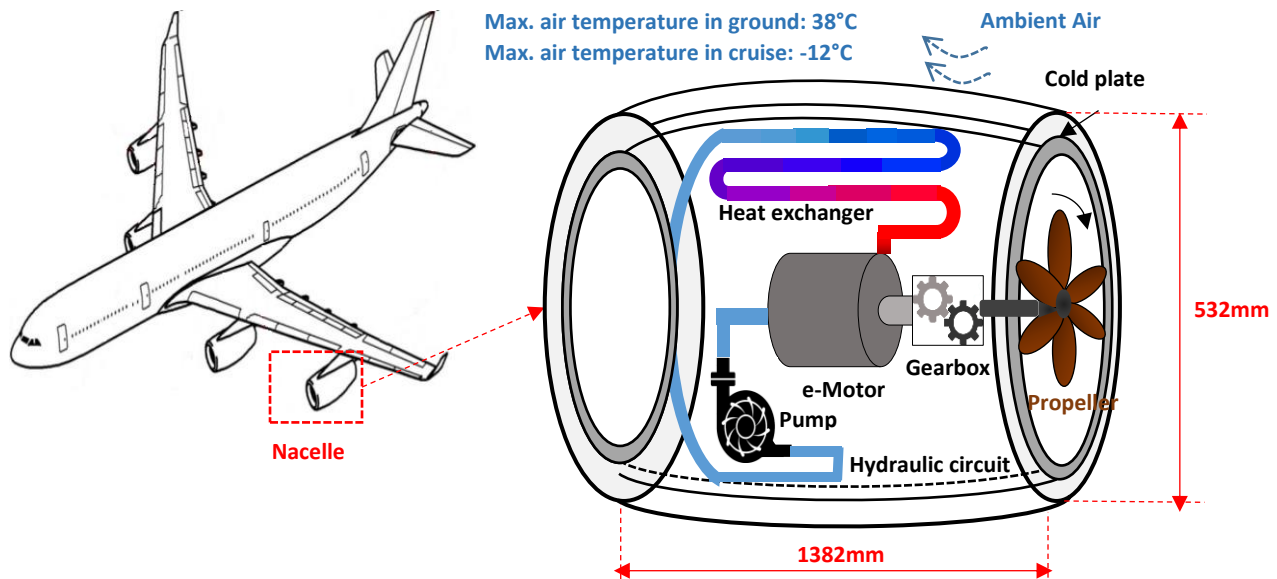


Figure IV. 23. Nacelle architecture: electric motor with its cooling circuit

Hydraulic circuit is used to extract the heat flux generated by electric motor losses to the heat exchanger. Hydraulic circuit is composed of pipes which coolant as Ethylene Glycol Water 50/50 (cf. Table IV.8) circulates inside them using a hydraulic pump.

Table IV. 8. Characteristics of Ethylene Water-Glycol 50/50 [Ton_14]

Characteristics	Water-Glycol 50/50
Density [kg.m^{-3}]	1065
Thermal conductivity [$\text{W.m}^{-1}.K^{-1}$]	0.3937
Specific heat [$\text{J.kg}^{-1}.K^{-1}$]	3361
Dynamic viscosity [$\text{kg.m}^{-1}.s^{-1}$]	2.2564×10^{-3}
Freezing temperature	-37°C
Boiling temperature	107.2°C

This coolant extracts and evacuates the heat flux by circulating inside cooling channels performed in frame and inside cooling channel performed in shaft as shown in Figure IV.24. This cooling method aims to cool stator through the frame, and rotor through the shaft.

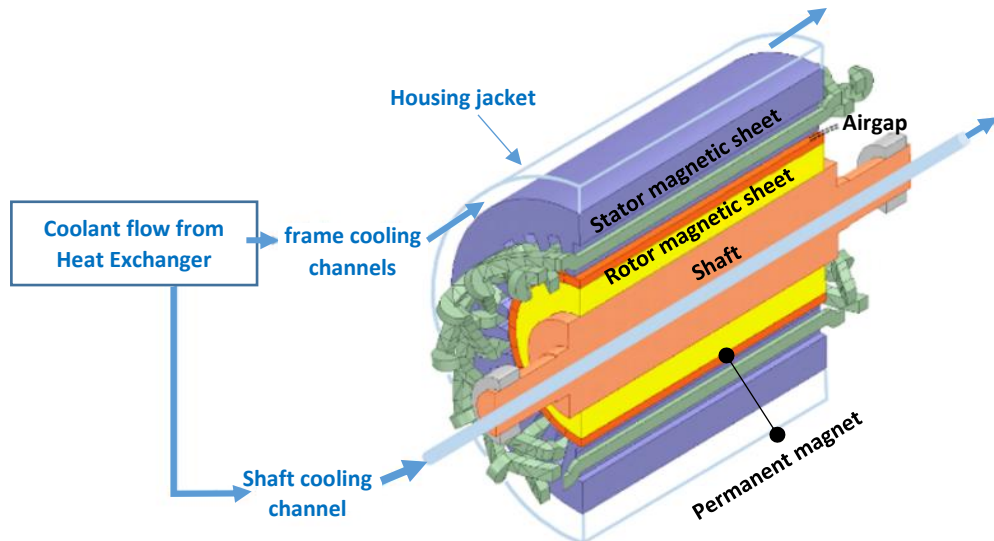


Figure IV. 24. Medium term target 2025: Electric motor with its cooling channels

WP3 sizes cooling system and takes as thermal limits the maximum allowed winding and permanent magnet temperatures (220°C for winding and 150°C for permanent magnet). For the purpose, WP1 gives to WP3 the losses profiles function of time flying (cf. Figure IV.25, maximum total losses which WP3 should be evacuated are 16.8kW) for sizing cooling system and to take into account its transient thermal behaviour. In these loss profiles, iron losses are assessed using finite element analysis whereas Joule and mechanical losses are assessed using analytical models established in TST and SM-PMSM. The characteristics of cooling system sized by WP3 are summarized in Table IV.9. Indeed, as cooling in frame and shaft are designed, assessment of electric motor weight is recalculated. Cooling system weight includes pipes of heat exchanger, coolant and hydraulic pump. Total weight of cooling system is 32kg, therefore, the specific power of the electric motor with its cooling system is almost 5kW/kg. This achieved target can be improved with more optimized cooling system.

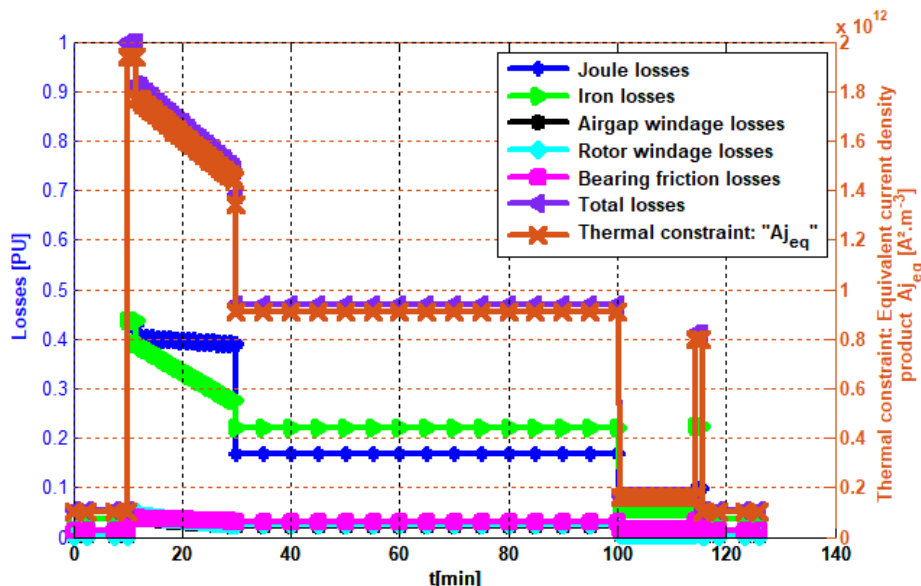


Figure IV. 25. Medium term target 2025: Losses profiles and equivalent current density product function of time flying

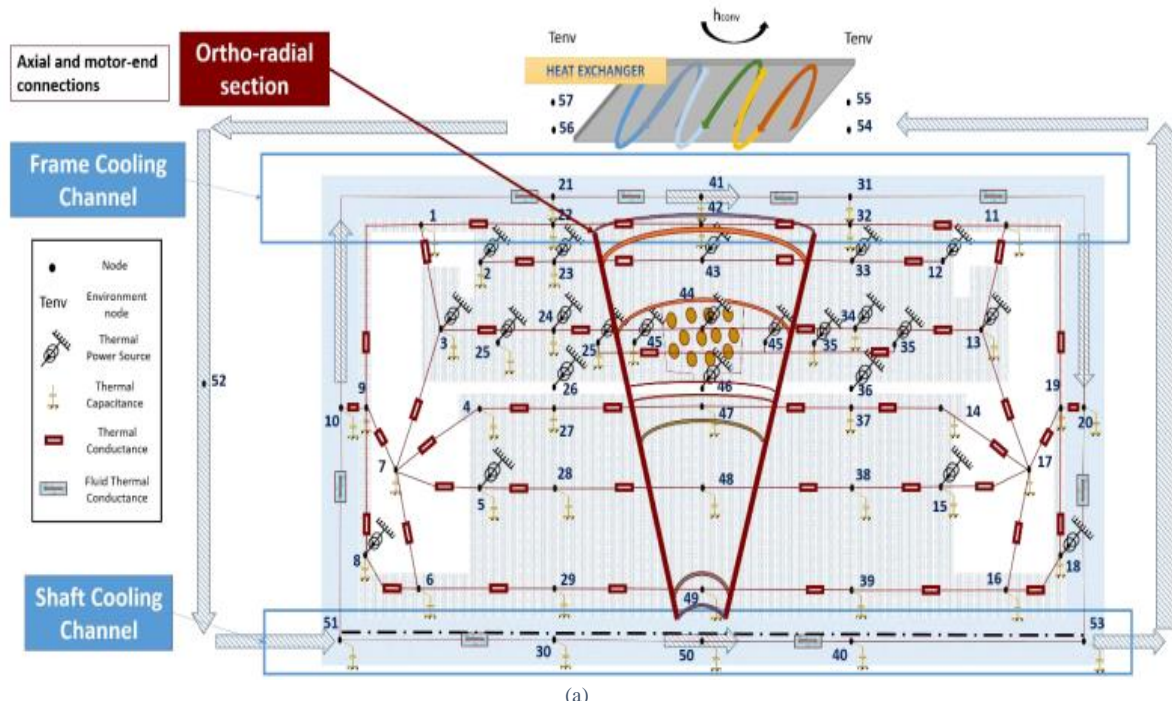
Table IV. 9: Medium term target 2025: Cooling system characteristics given by WP3

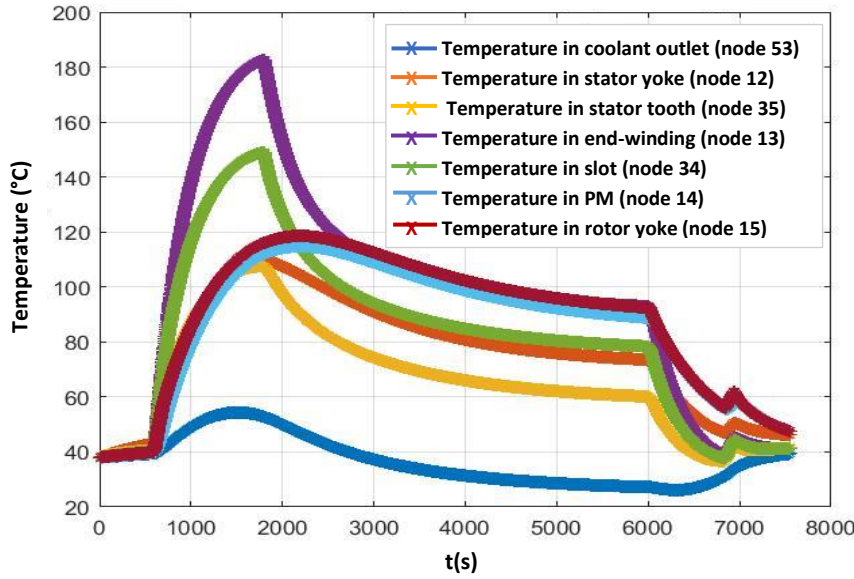
Cooling channels inside housing jacket and shaft

Parameters of cooling channels	Housing jacket	Shaft		
Hydraulic diameter [mm]	45	14		
Flow rate [$\text{m}^3.\text{s}^{-1}$]	4.2×10^{-3}	10^{-4}		
Heat transfer coefficient [$\text{W}.\text{m}^{-2}.\text{K}^{-1}$]	3900	1000		
Heat exchanger				
Parameters	Pipes	Cold plate		
Material	"Aluminium"			
Thickness[mm]	1	3		
Flow rate [$\text{m}^3.\text{s}^{-1}$]	4.3×10^{-3}	-		
Hydraulic diameter [mm]	45	-		
Hydraulic Pump				
Normal operating pressure [bars]	206			
Maximum speed [rpm]	3646			
Length [cm]	26.16			
Height [cm]	21.84			
Width [cm]	17.27			
Weight [kg]	14			
Coolant				
"Ethylene Glycol Water 50/50"				

The thermal electric motor behaviour is given using the Lumped Parameter Thermal Model [Zea_18] developed by WP3 as shown in Figure IV.26.a. The resulting thermal behaviour according to the mission profile is given in Figure IV.26.b. Within, temperatures in most critical zones are given as temperature in winding (node 34 for slot and 13 for end winding), permanent magnet (node 14), magnetic sheets (nodes 12 and 35 for stator and 14 for rotor) and in the outlet coolant on the electric motor side (node 53). Temperature in end-winding is the hotspot zone in electric motor, however, its temperature remains below the winding thermal class.

To exceed the first targeted specific power (i.e. 5kW/kg), loads should be more increased. Consequently, it is important to further improve cooling by adding, for instance, another cooling inside or near to the winding.





(b)

Figure IV. 26. Medium term target 2025: (a) Axial and ortho-radial section of SM-PMSM including its cooling system with Lumped Parameter Thermal Model LPTM nodes location, and axial and motor-end connections, (b) Temperature evolution during flying mission in the sized electric motor [Zea_18][Tou_20]

IV.4 Sizing of electric motor for long term target 2035

IV.4.1 Issues, limitations and strategy to achieve target 2035

As well as for the medium term target 2025, issues for long term target 2035 are the same. Besides, limitations for long term target 2035 are huger than those medium term target 2025. To achieve long term target 2035: specific power of 10kW/kg and efficiency at sizing point greater than 97%, loads, speed, number of pole pair, copper fill factor, thermal class should be further increased. Considering the thermal limitations, new cooling methods are mainly the key solution for exceeding, for instance, the chosen loads for medium term target. These new cooling methods will involve new thermal limit. The latter will hence be higher than the thermal limit of medium term target. Table IV.10 reminds chosen loads, speed, number of pole pairs, thermal class and technological solutions carried out for medium term target 2025. Therefore, for reaching long term target 2035, technological choices will be improved compared to those given in Table IV.10.

Table IV. 10: Technological choices performed for medium term target 2025

Loads, speed, number of pole pair and slot fill factor	Technological solutions
<ul style="list-style-type: none"> - Tangential stress "$\sigma=50000\text{Pa}$" - Current density "$j_{rms}=8.1\text{A/mm}^2$" - Max surface current density "$K_m=111.1\text{kA/m}$" - RMS linear current density "$A_{rms}=81.4\text{kA/m}$" - Current density product "$A_{rms}j_{rms}=6.5948\times10^{11}\text{ A}^2/\text{m}^3$" - Max airgap flux density "$B_m=0.9\text{T}$" - Flux density in teeth "$B_{st}=1.3\text{T}$" - Flux density in yoke "$B_{sy}=1.2\text{T}$" - Rotational speed "$\Omega=15970\text{rpm}$" - Number of pole pairs "$p=2$" - Slot fill factor is 0.5% 	<ul style="list-style-type: none"> - Stranded and twisted conductors - Magnetic sheet: "Vacoflux 48- 0.35mm" - Halbach permanent magnet with radial and axial segmentation to ensure sinewave airgap flux density to reduce eddy current losses - Carbon Fiber Sleeve

By following the same sizing approach, technologies will be firstly selected and assessed for reaching the targeted specific power and efficiency (i.e. 10kW/kg and 97%) using TST. By choosing the same electric motor structure, the sizing will be performed using SM-PMSM and validated by Finite Element Analysis. With WP3 interaction, the sizing will be finished by the sizing of cooling system.

IV.4.2 Choice of technological levels

We define another range values of loads for this 2nd Hastecs target as presented in Table IV.11. Mainly, flux density in stator tooth and yoke and current density are expanded respectively to 2.35T (cf. Appendix A) and to 25A/mm² corresponding to the high saturation flux density level and to achieved current density for inner cooling method (cf. Chapter I, Table I. 16).

Table IV. 11:Range values of electric, magnetic and thermal loads for long term target 2035

Loads	Range values
Airgap flux density B_m [T]	0.8-1.05
Stator yoke flux density B_{sy} [T]	1.2-2.35
Stator tooth flux density B_{st} [T]	1.2-2.35
Current density j_{rms} [A.mm ⁻²]	8-25
Linear current density A_{rms} [A.mm ⁻¹]	80-200
Max tangential stress σ [Pa]	50000-148500
Current density product $A_{rms} \times j_{rms}$ [A ² .m ⁻³]	0.64×10 ¹² -5×10 ¹²

Therefore, according to range values of loads, some technological levels are kept same as those used in 1st Hastecs target such as:

- cooling methods in shaft and in frame,
- material choices of magnetic sheets, permanent magnet and sleeve,

and some technological solutions are added as:

- direct inner cooling method for stator winding cooling,
- potting materials around end-windings for improving their cooling (cf. Chapter I),
- insulation materials with 240°C thermal class by using inorganic insulation materials. It allows increasing of current density and frequency levels;
- Litz wires to reduce winding losses at very high frequency (i.e. $R_{AC}/R_{DC} \approx 1$ for very high frequency 400Hz to 5kHz) unlike to the stranded conductors where R_{AC}/R_{DC} can be greater than 1 at frequency > 1kHz. Compacted Litz wire conductor illustrated in Appendix C is used as conductor reference for this motor.

IV.4.3 Assessment of electric motor technologies: Target Setting Tool

In the same way, we apply at the beginning the limited values of loads (cf. Table. IV.11), high rotational speed ($\Omega > 16000$ rpm), high number of pole pairs ($p > 2$) and high copper fill factor in order to assess the maximum reached specific power regardless of resulting losses. If the achieved specific power is not enough greater than the target, we increase again the speed and the number of pole pairs until to exceed 10kW/kg. Once it is done, we adjust these loads, speed, the number of pole pairs and the copper fill factor in order to decrease the losses while controlling the specific power and efficiency.

Table IV.12 shows the adjusted loads, rotational speed, number of poles pairs, copper fill factor and others adjusted parameters which allow achieving targets (i.e. specific power >10kW/kg and efficiency >97%). The main sizes, weights of electric motor and further intrinsic parameters are also summarized in Table IV.12.

By comparison between the 1st and 2nd Hastecs targets, we notice significant increasing of:

- Current density from 8A/mm² to 20A/mm²,
- Linear current density from 80kA/m to 110kA/m,
- Tangential stress from 50000Pa to 70000Pa,
- Rotational speed increases from 15970rpm to 20000rpm,
- Number of pole pairs from 2 to 4. They therefore allow duplicating specific power of electric motors.

However, although the partial discharges are allowed for 2nd Hastecs target, the fill factor is eventually adjusted to equal to 1st Hastecs target since cooling is chosen inside slots.

Table IV. 12: Target Setting Tool inputs/outputs for long term target 2035

Target Setting Tool inputs	Target Setting Tool outputs
Mechanical specifications	Main sizes
<ul style="list-style-type: none"> - Electromagnetic power "$P_{em}=1\text{PU}$" - Rotational speed "$\Omega=20000\text{rpm}$" 	<ul style="list-style-type: none"> - Frame external stator radius "$R_{fr}=123.6\text{mm}$" - External stator radius "$R_{out}=111.9\text{mm}$" - Stator bore radius "$R=72.9\text{mm}$" - Active length "$L_m=292\text{m}$" - Stator yoke height "$h_y=14.1\text{mm}$" - Tooth (or slot) height "$h_s=25\text{mm}$" - Airgap thickness "$e_g=3.06\text{mm}$"
Thermal specifications	Weights
<ul style="list-style-type: none"> - winding temperature "$T_{win}=180^\circ\text{C}$" 	<ul style="list-style-type: none"> - Stator magnetic core weight "$W_{stat-core}=39.9\text{kg}$" - Winding stator weight "$W_{stat-wind}=14.22\text{kg}$" - Rotor weight "$W_{rot}=27.7\text{kg}$" - Frame weight "$W_{fra}=12.53\text{kg}$"
Magnetic and electric loads	Specific power and torque of electric motor
<ul style="list-style-type: none"> - Tangential stress "$\sigma=70000\text{Pa}$" - Current density "$j_{rms}=20\text{A/mm}^2$" - Max surface current density "$K_m=155.5\text{kA/m}$" - RMS linear current density: "$A_{rms}=110\text{kA/m}$" - Current density product "$A_{rms}j_{rms}=2.199\times10^{12}\text{ A}^2/\text{m}^3$" - Max airgap flux density "$B_m=0.9\text{T}$" - Flux density in teeth "$B_{st}=1.25\text{T}$" - Flux density in yoke "$B_{sy}=1.25\text{T}$" 	<ul style="list-style-type: none"> - Specific power "$S_p=15.121\text{kW/kg}$" - Specific torque "$S_T=7.22\text{Nm/kg}$"
Geometrical choice	Further intrinsic parameters
<ul style="list-style-type: none"> - Shape coefficient "$\lambda=0.5$" - Slot copper fill factor "50%" - End-winding coefficient "$k_{tb}=1.4$" - Number of pole pairs "$p=4$" 	<ul style="list-style-type: none"> - Peripheral speed "$V_p=146.3\text{m/s}$" - Joule losses "$P_{js}=13.293\text{kW}$" - Iron losses "$P_{fs}=6.468\text{kW}$" - Mechanical losses "$P_{mech-loss}=1.086\text{kW}$" - Efficiency "$\eta=98\%$"
Material of stator electrical sheet: "Vacoflux 48- 0.35mm"	Equivalent current density product " $Aj_{eq}=3.978\times10^{12}\text{ A}^2/\text{m}^3$ " Electromagnetic torque " $T_{em}=1\text{PU}$ " Synchronous frequency " $f_s=1.333\text{kHz}$ "

In the sizing of electric motor for 2nd HasteCS target, we deliberately place our target above 10kW/kg considering that cooling system is not taken into account in TST. Moreover, electric motor weight is approximately calculated in TST (electric motor structure is not defined) as it has been shown in the electric motor of 2025.

IV.4.4 Size electric motor: Surface Mounted Permanent Magnet Synchronous Motor

Using the main sizes given by TST, the further sizes are given by choosing the stator and rotor configurations as summarized in Table IV.13. Since that cooling is inner, the number of slots is chosen similar to the previous electric motor (i.e. 24 slots). For the purpose, the number of slots per pole and per phase is 1. For the rotor, configuration is kept similar to the one chosen for medium term target. Table IV.14 presents the outputs as further sizes, recalculated weight and recalculated losses of surface mounted permanent magnet synchronous motor. Deviations between TST and SM-PMSM on weights, specific power and torque are less than 14%.

Table IV. 13: SM-PMSM Tool Inputs for long term target 2035

Stator configuration	Rotor configuration
<ul style="list-style-type: none"> - Full pitch winding "$\tau=1$" - Number of layers "$n_l=1$" - Number of phases "$q=3$" - Number of slots per pole and per phase "$m=1$" 	<ul style="list-style-type: none"> - Flux density in rotor yoke "$B_{ry}=1.4\text{T}$" - Polarization of permanent magnet "$J=1.16\text{T}$"

Table IV. 14: SM-PMSM Tool Outputs for long term target 2035

Further sizes	Electric parameters for " $N_{cs}=1$ "
<ul style="list-style-type: none"> - Permanent magnet thickness "$e_{pm}=7.84\text{mm}$" - Rotor yoke thickness "$h_{ry}=16.66\text{mm}$" - Rotor shaft radius "$R_{sh}=45.36\text{mm}$" - Stator slot width "$l_s=9.71\text{mm}$" - Stator tooth width "$l_t=9.38\text{mm}$" 	<ul style="list-style-type: none"> - Resistance "$R_s=1.01\text{m}\Omega$" - Self-inductance "$L_s=3.12\mu\text{H}$" - Mutual inductance "$M=-1.56\mu\text{H}$" - Rms back electromotive force "$E_i=226.77\text{V}$" - No-load magnetic flux "$\varphi_{vm}=0.0383\text{Wb}$"
Recalculated winding parameters	Recalculated equivalent current density product
<ul style="list-style-type: none"> - Winding coefficient "$k_w=1$" - End winding coefficient "$k_{tb}=1.402$" 	<ul style="list-style-type: none"> - Equivalent current density product "$Aj_{eq}=4.065\times10^{12}\text{ A}^2/\text{m}^3$"

Recalculated weights	Recalculated specific power and specific torque (without cooling system)
<ul style="list-style-type: none"> - Stator magnetic core weight "$W_{stat-core}=39.9\text{kg}$" - Winding stator weight "$W_{stat-wind}=14.24\text{kg}$" - Rotor weight "$W_{rot}=42.58\text{kg}$" - Frame weight "$W_{fra}=12.6\text{kg}$" 	<ul style="list-style-type: none"> - Specific power "$S_p=13\text{kW/kg}$" - Specific torque "$S_T=6.25\text{Nm/kg}$"
Recalculated performances:	
<ul style="list-style-type: none"> - Joule losses "$=13.312\text{kW}$" - Iron losses "$=6.468\text{kW}$" - Mechanical losses "$=1.557\text{kW}$" - Efficiency "$\eta=98\%$" 	<p>Joule loss: 63% Iron loss: 30% Mechanical loss: 7%</p>

By comparison to the medium term target, we notice that resulting mechanical losses of long term target are less than those resulting of medium term target although speed is increased. It may be explained by the rotor size which is reduced. It may then lead to decrease mechanical losses as indicated in equations (II-70, II-75 and II-78).

Efficiency at sizing point is greater than the targeted efficiency at sizing point. Performances such as electric parameters and losses will be validated by Finite Element Analysis as will be given in the next paragraph.

IV.4.5 Validation with Finite Element Analysis

For the 2nd Hastecs target, validation with finite element analysis is essential for quantifying the sizing validation range of TST and SM-PMSM. In fact, this validation will mainly allow us to check on one hand the performances such as losses, torque and inductances. On the other hand, validation allow us to check the saturation risk in stator magnetic sheet given that loads are significant. For the purpose, the slotless and slotted models will be used.

VI.4.5.1. Slotless model

Slotless model conditions for simulations of the 2nd Hastecs targeted electric motor are the same as conditions (cf. Figure IV.27) taken for slotless model of the 1st Hastecs targeted electric motor.

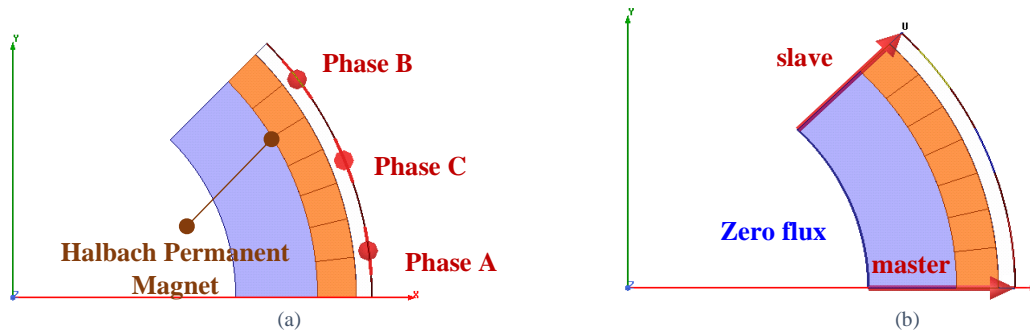


Figure IV. 27. Slotless model electric motor of long term target 2035: (a) Slotless model structure on one pole, (b) boundary conditions applied on one pole structure

a. No-load simulation

Structure of segmented Halbach permanent magnet obtained by optimization is summarized in Table IV.15. Its polarization is shown in Figure IV.28.a. Validation of airgap flux density, no-load magnetic flux and back-emf are illustrated respectively in Figure IV.28.b, Figure IV.29.a and b. Total harmonic distortion calculated on the airgap flux density confirms that the latter are closer to sinewaves.

Table IV. 15: Electric motor of long term target 2035: seven segment Halbach PMs

Segment	1	2	3	4	5	6	7
Orientation $\gamma(^{\circ})$	76.13	48.56	22.77	0	22.77	48.56	76.13
Angular width: $\frac{\beta}{\pi/p} (%)$	15.00	14.449	13.781	13.538	13.781	14.449	15.00

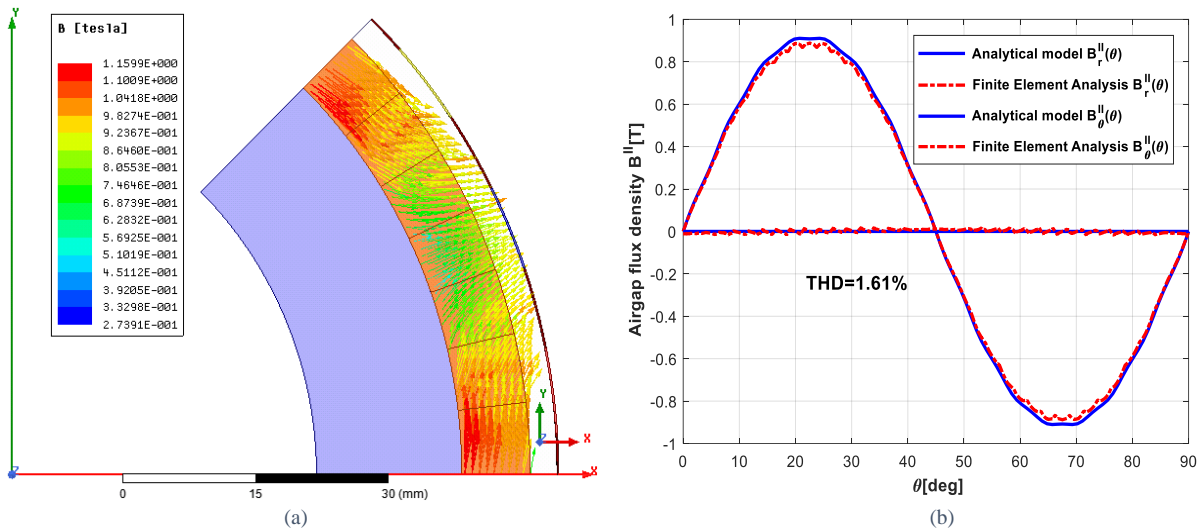


Figure IV. 28 Electric motor of long term target 2035 (a) Halbach array 7 segment PMs, (b) Airgap flux density

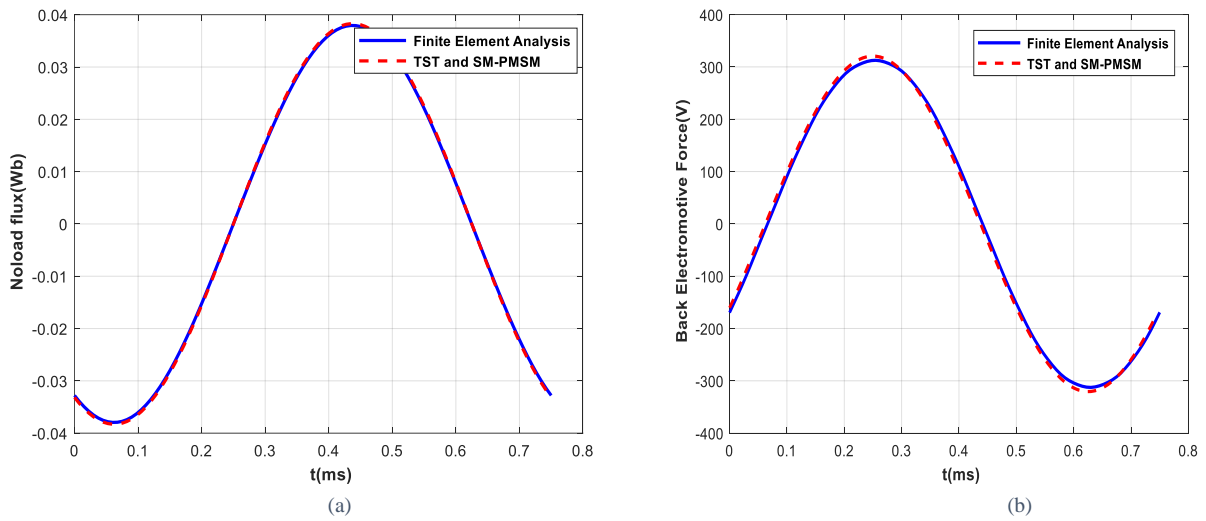


Figure IV. 29. Slotless model: (a) No-load magnetic flux, (b) Back electromotive force

b. Load simulation

Airgap flux density resulting of the stator current and the rotor permanent magnets is represented in Figure IV.30. Through comparison between models and at the fundament component, we validate again the airgap flux density analytically calculated. Figure IV.31 shows the comparison between inductances analytically calculated and inductances calculated by finite element analysis. The last ones have values of $4.034\mu\text{H}$ on self-inductance, $-1.211\mu\text{H}$ on mutual inductance and $5.245\mu\text{H}$ on cyclic inductance. Hence, we notice a deviation of 23% on self-inductance, deviation of 29% on mutual inductance and a deviation of 11% on cyclic inductance. Figure IV.32 shows the simulated electromagnetic torque. Its mean value is about 0.988PU which is close to 1PU, the value calculated using the surface current density and airgap flux density waves. Therefore, deviation on electromagnetic torque is 1.2%.

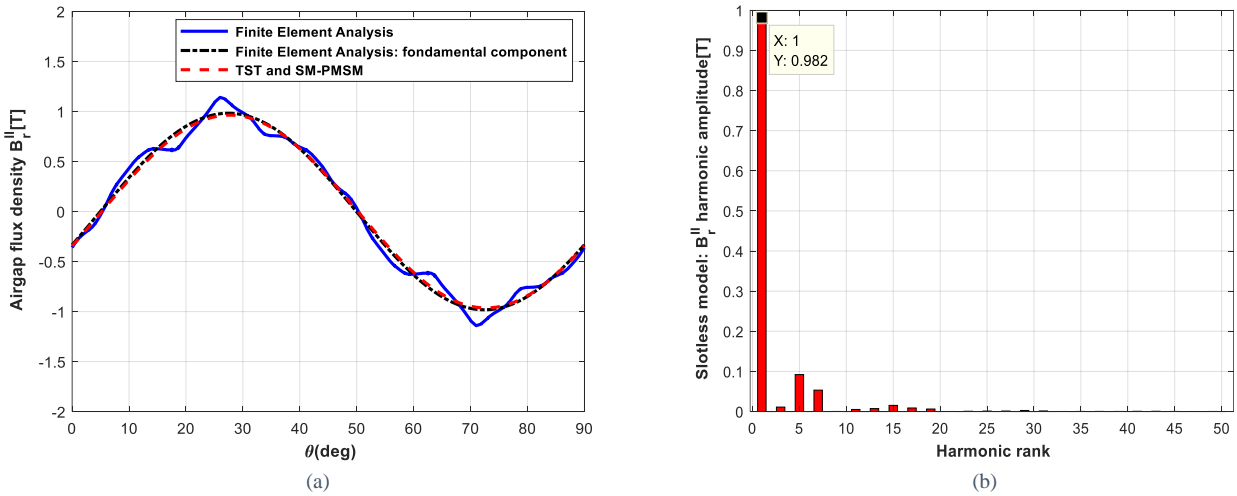


Figure IV. 30. Slotless model: (a) Airgap flux density, (b) harmonic analysis of airgap flux density given by Finite Element Analysis

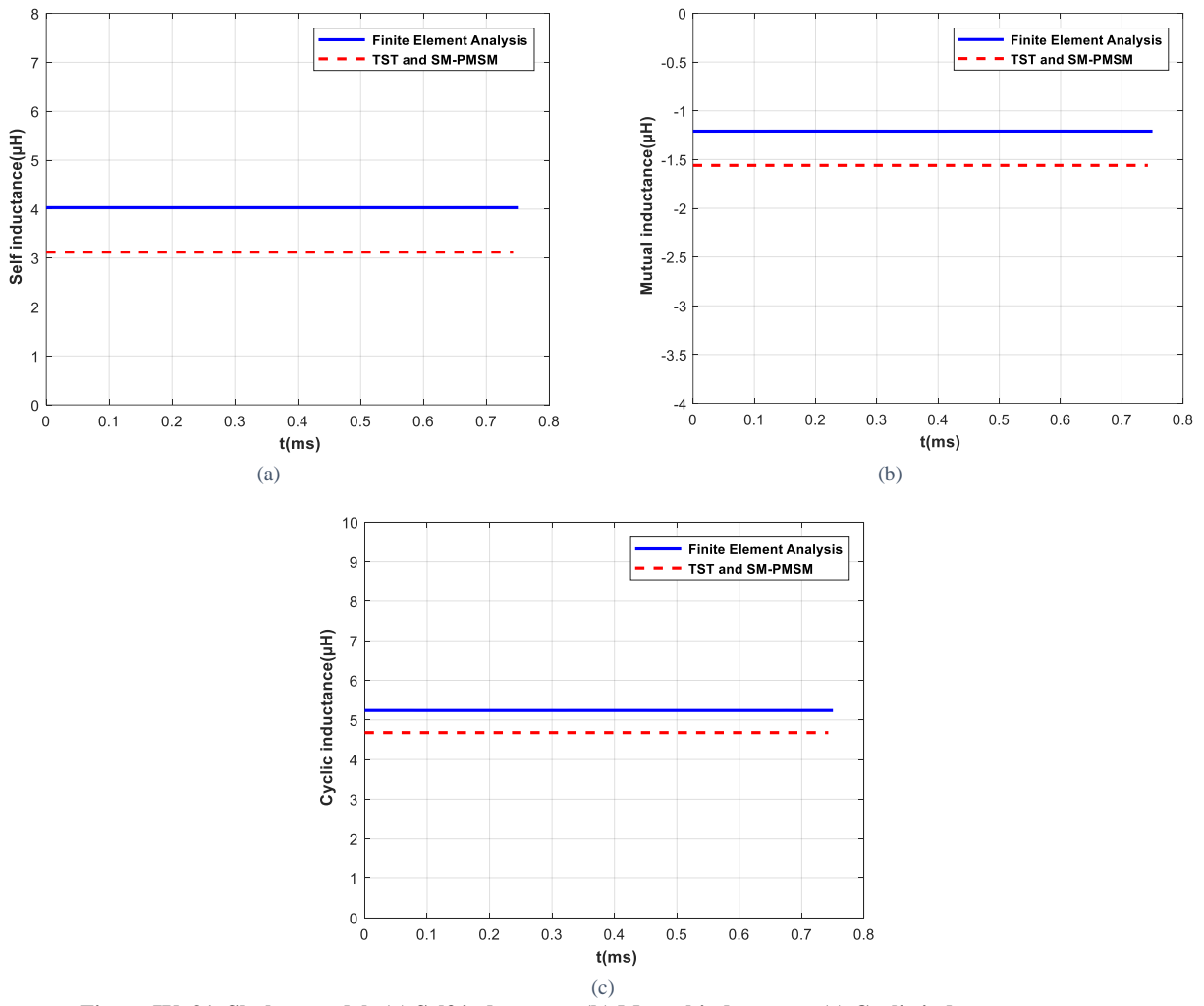


Figure IV. 31. Slotless model: (a) Self-inductance, (b) Mutual inductance, (c) Cyclic inductance

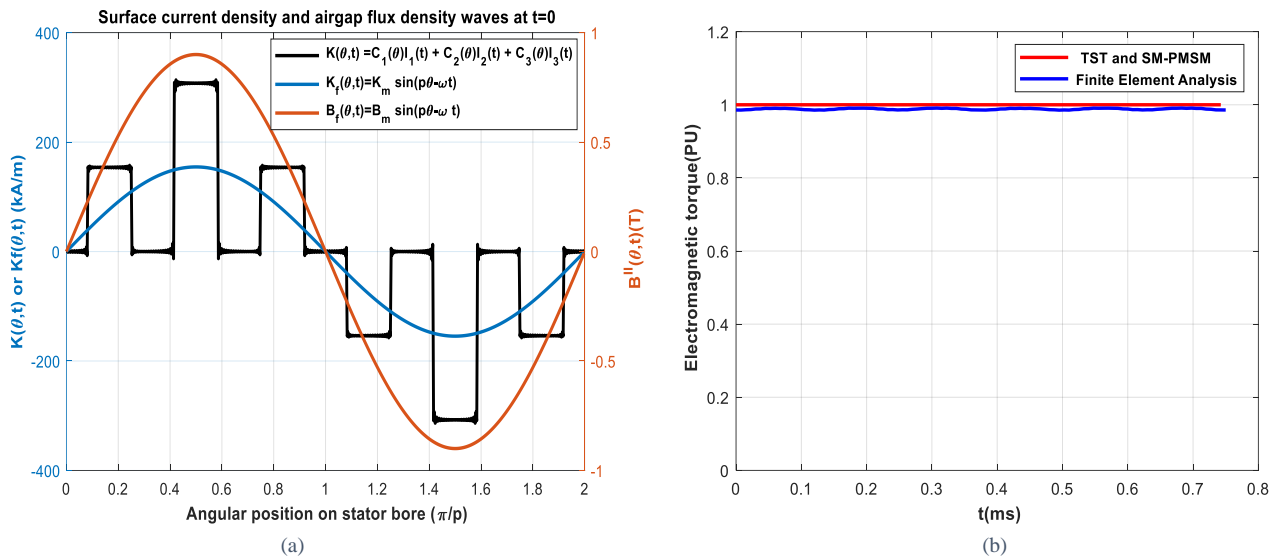


Figure IV. 32. Slotless model: (a) Surface current density and airgap flux density waves, (b)The electromagnetic torque

VI.4.5.2. Slotted model

Slotted structure of electric motor is represented on one pole as shown in Figure IV.33. Performances will be calculated for one conductor per slot and will be compared to those given by TST and SM-PMSM.

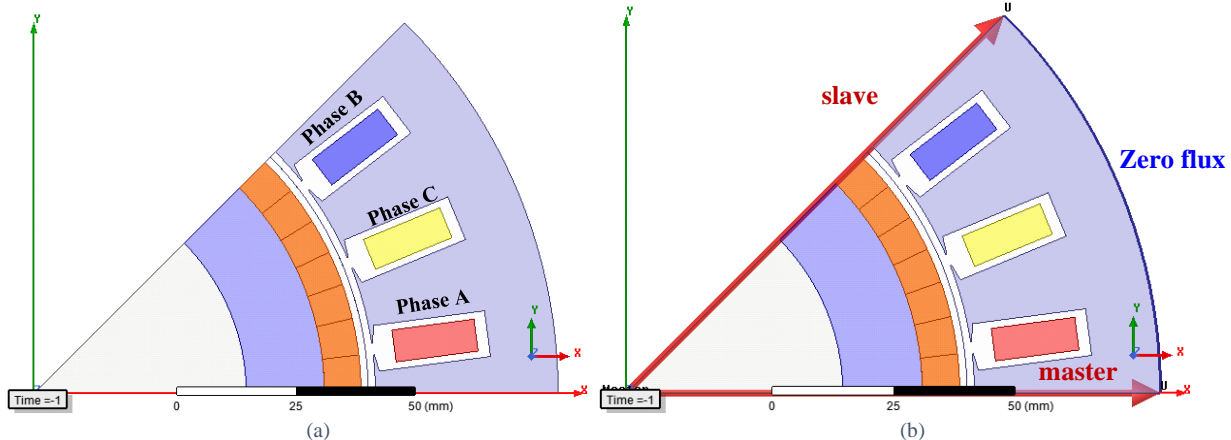


Figure IV. 33. Slotted model electric motor of long term target 2035: (a) Slotted model structure on one pole, (b) boundary conditions applied on one pole structure

a. No-load simulation

Figure IV.34.a presents the airgap flux density resulting from permanent magnet with and without slot effect. The harmonic analysis of airgap flux density (cf. Figure IV.34.b) obtained by slotted model indicates that it remains close to the sinusoidal waveform. Moreover, the amplitude of fundamental component is 0.9T. Therefore, slot effect on airgap flux density is negligible.

Flux densities in tooth and stator yoke resulting from rotation of permanent magnet at rated speed are illustrated in Figure IV.35. Their maximum respective values are 1.256T and 1.159T. No-load magnetic flux and back-electromotive force are shown in Figure IV.36. They are very close to those calculated using TST and SM-PMSM. Cogging torque resulting from magnetic interaction of permanent magnets and slotted stator is shown in Figure IV.37. Its peak to peak value is 9.08Nm about 1.3% of rated electromagnetic torque.

Figure IV.38.a shows the magnetic flux density distribution and Figure IV.38.b the flux lines at no-load. Slight saturation in the tooth bottom can be observed. The maximum local magnetic flux density in tooth is about 0.9T to 2.35T. In rotor yoke, the mean flux density is about 0.8T.

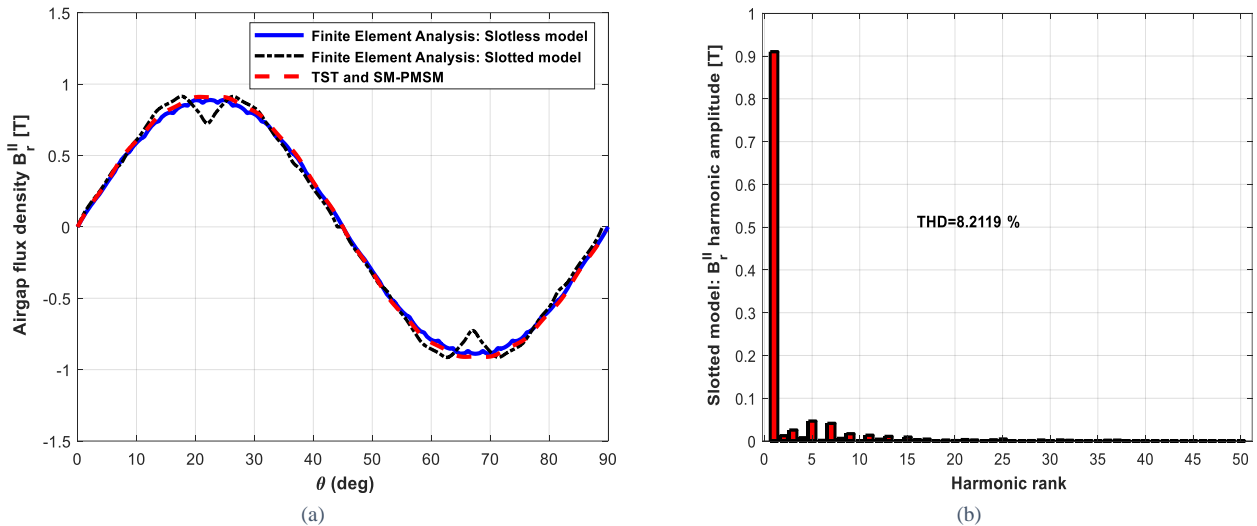


Figure IV. 34. Airgap flux density at no-load: (a) slotless and slotted models, (b) harmonic analysis

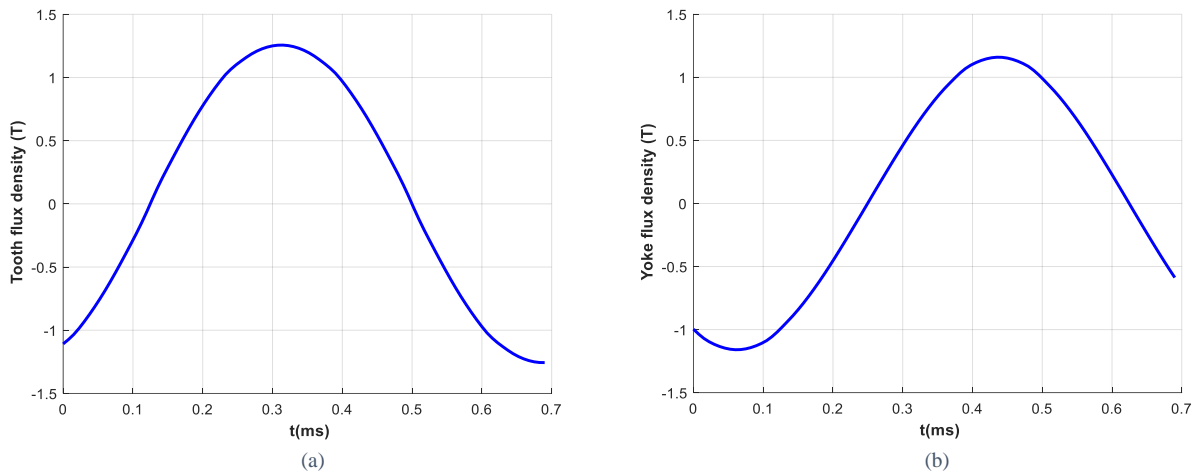


Figure IV. 35. Slotted model at no-load: (a) tooth flux density, (b) stator yoke flux density

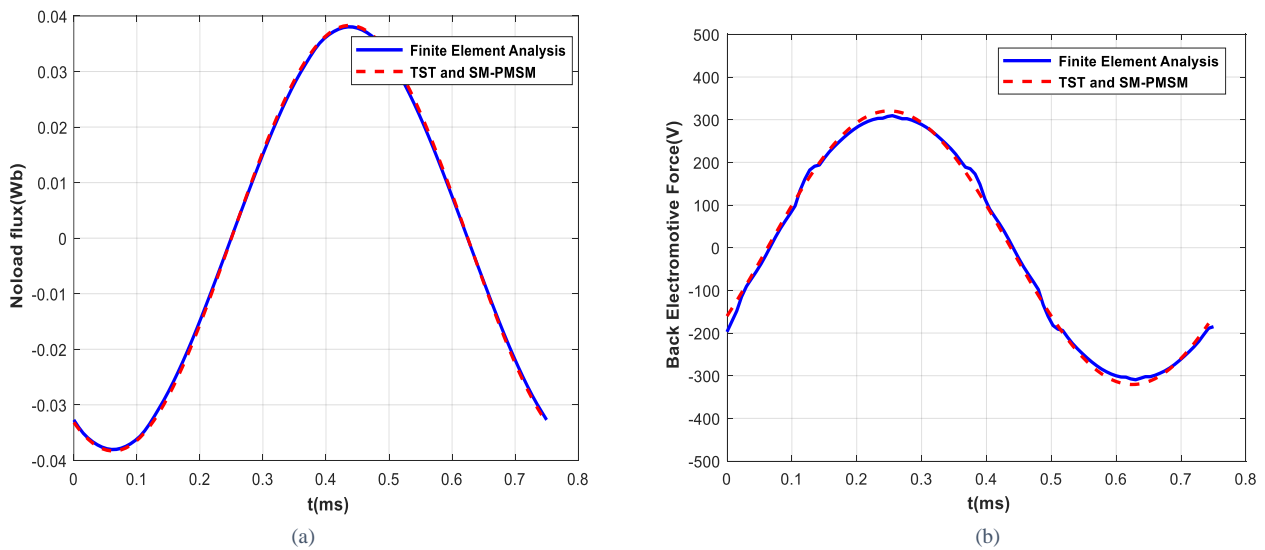


Figure IV. 36. Slotted model: (a) Noload magnetic flux, (b) Back electromotive force

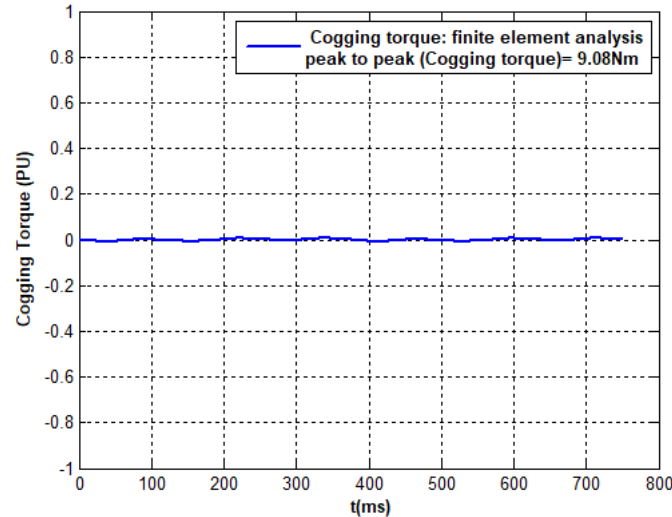


Figure IV. 37. No-load simulation: cogging torque

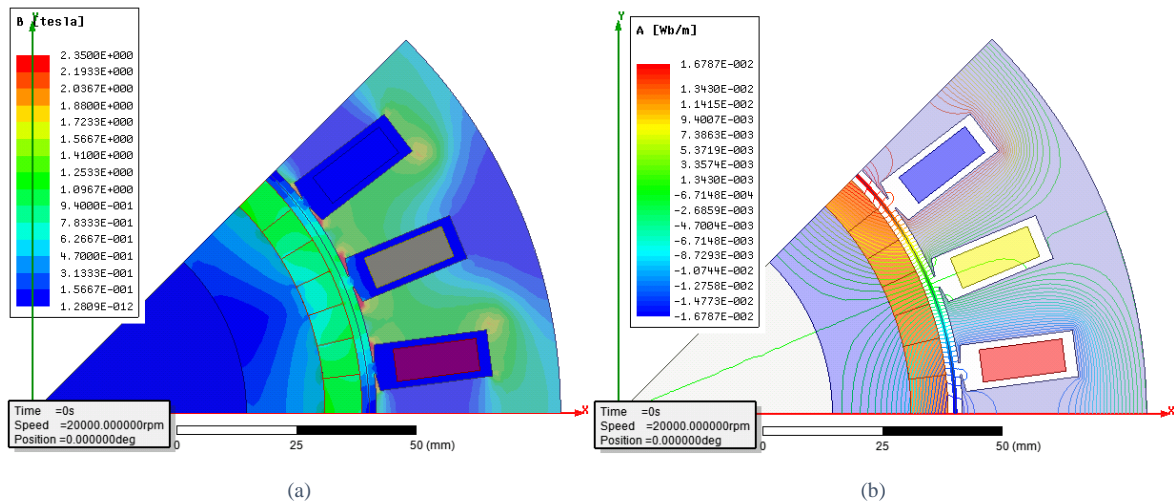


Figure IV. 38. Slotted model at no-load simulation: (a) Magnetic flux density distribution, (b) Flux line distribution

b. Load simulation

In load simulation, the airgap flux density and its harmonic analysis are given in Figure IV.39. Fundamental component obtained by FEA is aligned to the one calculated analytically in TST and SM-PMSM. According to its amplitude, the airgap flux density due to armature reaction is less than 0.06T. Increasing of flux densities in stator tooth and yoke due to the armature reaction is about 0.27T and 0.31T respectively (cf. Figure IV.40).

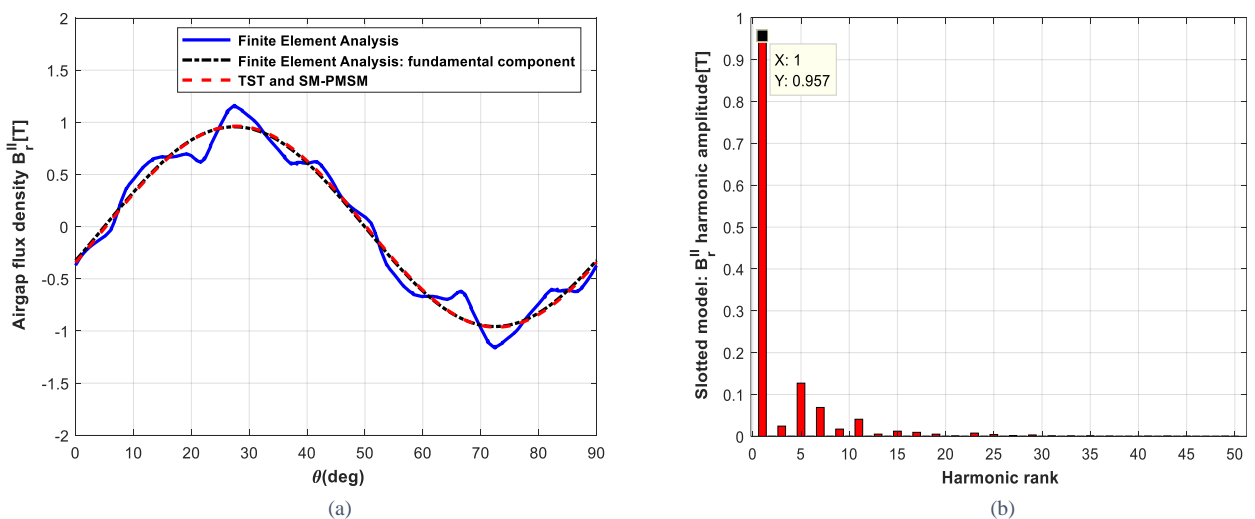


Figure IV. 39. Slotted model at load: (a) airgap flux density, (b) harmonic analysis

Magnetic flux density distribution and flux lines are presented in Figure IV.41. In teeth, the maximum local magnetic flux density is about 1.4T to 2.35T. In yoke, the maximum local magnetic flux density is about 1.25T to 1.88T for stator and 0.7T to 1.25T for rotor.

Self, mutual and cyclic inductances obtained by finite element analysis are illustrated in Figure IV.42. Their respective mean values are $7.9\mu\text{H}$, $-1.2\mu\text{H}$ and $9.2\mu\text{H}$. They have ripples which can be due to the magnetic saturation. We notice deviations around 30% between inductances calculated in SM-PMSM and those obtained by finite element analysis. These deviations are mainly due to the ignoring flux leakages.

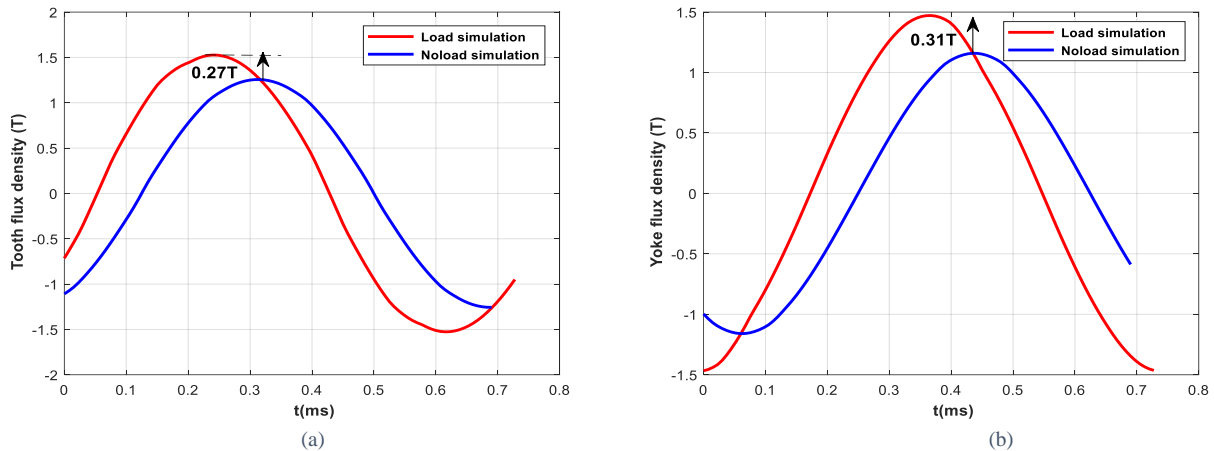


Figure IV. 40. Slotted model at load: (a) tooth flux density, (b) stator yoke flux density

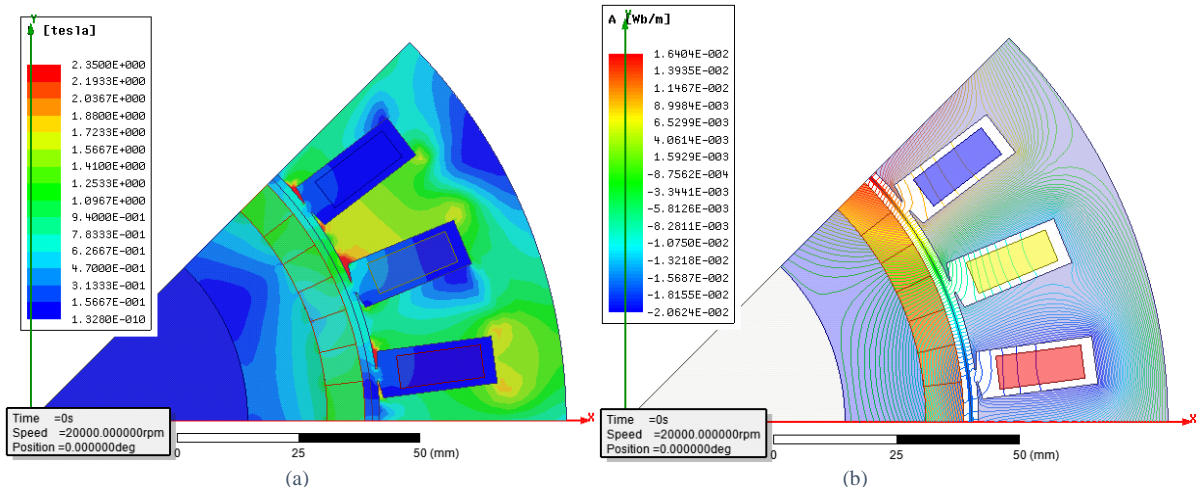
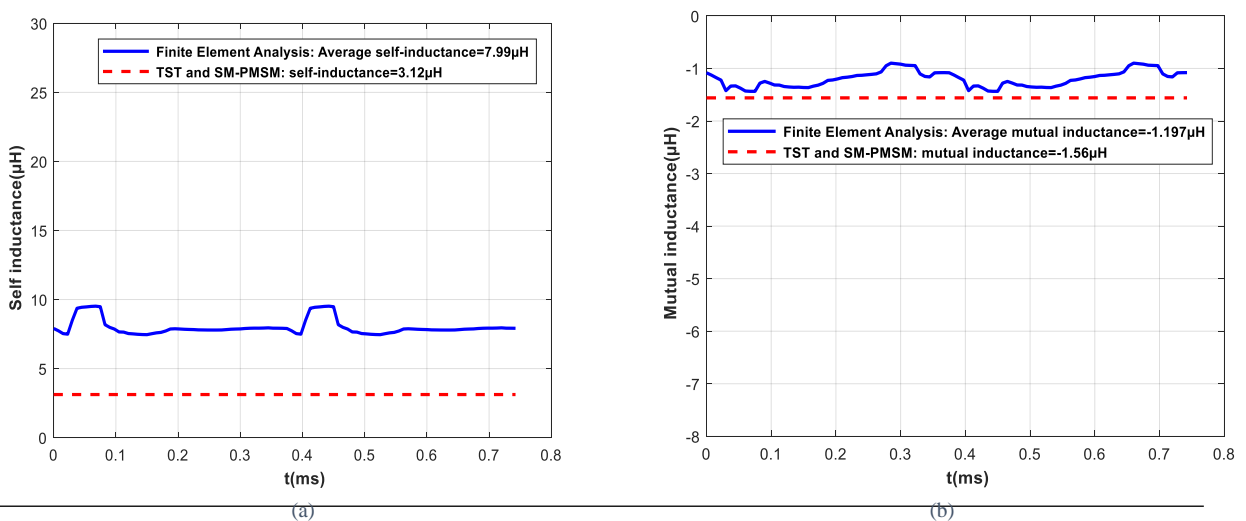


Figure IV. 41. Slotted model at load simulation: (a) Magnetic flux density distribution, (b) Flux line distribution



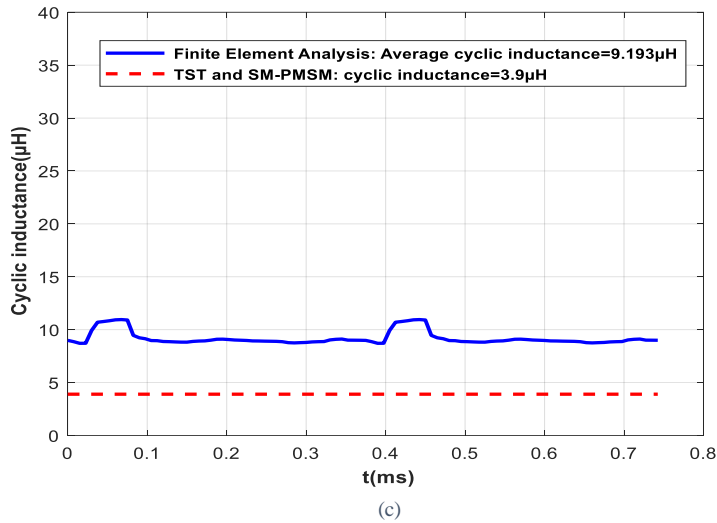


Figure IV. 42. Slotted model: (a) Self-inductance, (b)Mutual inductance, (c) Cyclic inductance

Figure IV.43 shows the rated electromagnetic torque. The mean value is 0.99PU which is close to the rated value calculated in TST and in SM-PMSM. Thus, deviation is 1%.

The iron losses in electric motor are shown in Figure IV.44. The mean value of these losses is 13.45kW. It is twice greater than the losses calculated in TST and in SM-PMSM. Likewise, for the 1st electric motor, the analytical model of iron losses remains imprecise mainly due to the nonlinear behaviour of magnetic stator and rotor sheets.

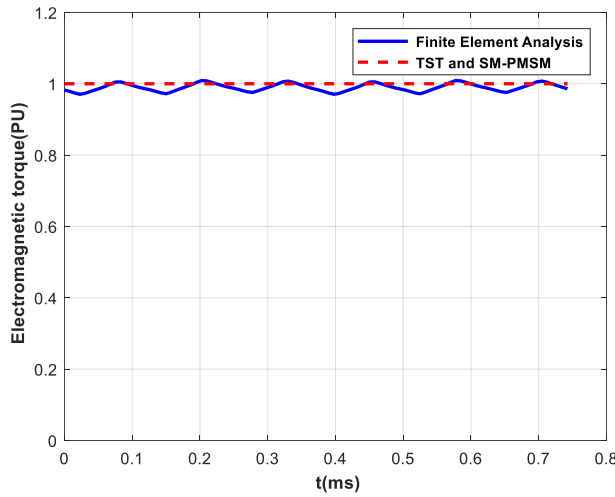


Figure IV. 43. Slotted model: The electromagnetic torque

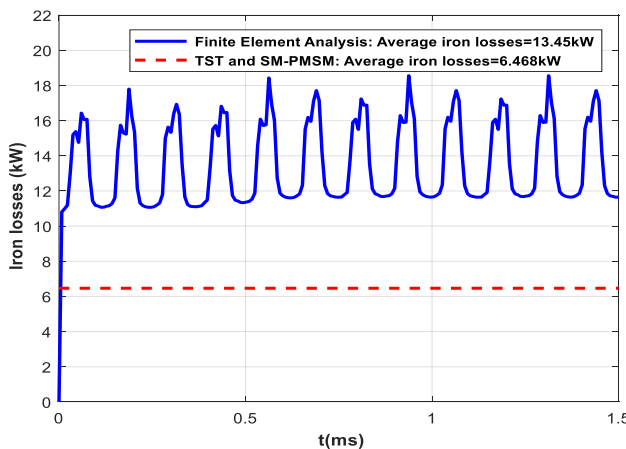


Figure IV. 44. Slotted model: Iron losses

In summary of these comparisons, performances as electromagnetic torque, no-load flux and back electromotive force are well validated as shown in Table IV.16. In contrast, analytical inductances are relatively validated only with slotless model. Due to the neglecting of flux leakages and the nonlinear behaviour of magnetic material, calculation of inductances and iron losses in TST and SM-PMSM remain relatively imprecise. From the electromagnetic torque and the iron losses analysed using FEA, efficiency is recalculated. Its value is closer to 98%, it remains higher than targeted efficiency at sizing point. Deviation on efficiency is quasi-zero.

Table IV. 16: Electric motor of long term target 2035: summary comparison of performances between analytical tools and finite element analysis

Performances	TST	SM-PMSM	Finite Element Analysis		Slotless model deviation	Slotted model deviation
			Slotless model	Slotted model		
Max. Noload magnetic flux " $\Phi_{vm}[\text{Wb}]$ "	-	0.0383	0.0379	0.0381	1%	0.5%
Rms Back- electromotive force " $E_i[\text{V}]$ "	-	226.77	224.13	223.5	1.2%	1.4%
Electromagnetic torque " $T_{em}[\text{PU}]$ "	1	1	0.98	0.99	2%	1%
Self-inductance " $L_s[\mu\text{H}]$ "	-	3.12	4.034	7.996	23%	61%
Mutual inductance " $M[\mu\text{H}]$ "	-	-1.56	-1.211	-1.1972	29%	30%
Cyclic inductance " $L_{cs}[\mu\text{H}]$ "	-	4.68	5.245	9.1933	11%	49%

IV.4.6 Thermal behaviour and cooling system design

As for electric motor of 1st target, cooling system of 2nd target is designed from heat flows generated by magnetic, electric and mechanical losses. Figure IV.45 illustrates losses profiles obtained for operating at maximum torque (Appendix D). In these loss profiles, iron losses are assessed using finite element analysis whereas Joule and mechanical losses are assessed using analytical models established in TST and SM-PMSM. Thermal constraint expressed by equivalent current density is also shown in Figure IV.45. Based on these losses, the maximum equivalent current density is equal to $5 \cdot 10^{12} \text{ A}^2/\text{m}^3$. It indicates the required cooling effort. Maximum total losses which WP3 should be evacuated are 28kW.

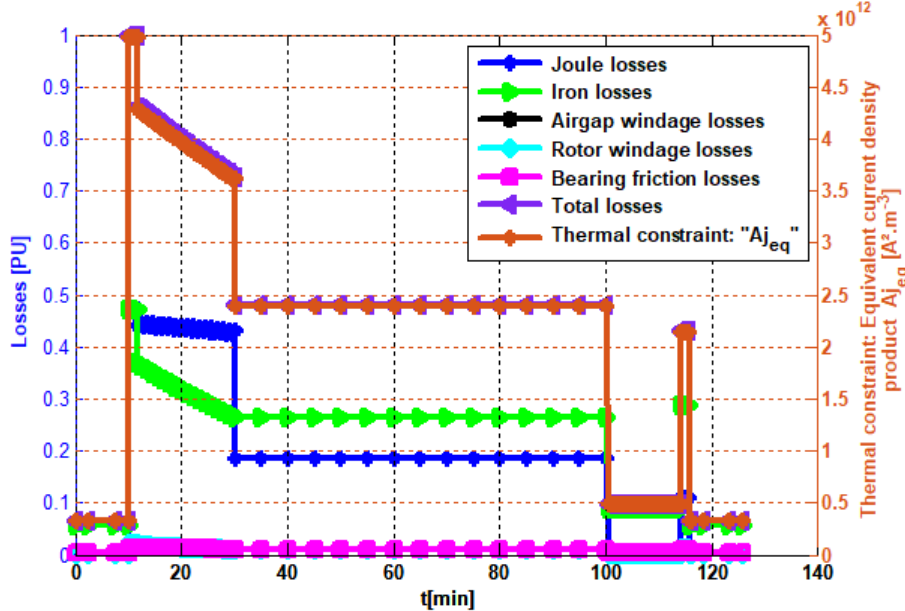


Figure IV. 45. Long term target 2035: Losses profiles and equivalent current density product function of time flying

As for 1st targeted electric motor, cooling circuit is composed of heat exchanger, hydraulic circuit and hydraulic pump for evacuating losses (cf. Figure IV.23). Joule losses are the highest losses compared to other losses, indeed their extraction and evacuation in small zones is a huge challenge. For the purpose, inner cooling method in winding is added to the cooling methods employed in 1st targeted electric motor. Inner cooling method is performed by two cooling channels embedded in slots as presented in Figure IV.46. These cooling channels are designed in order to respect copper fill factor of 50%.

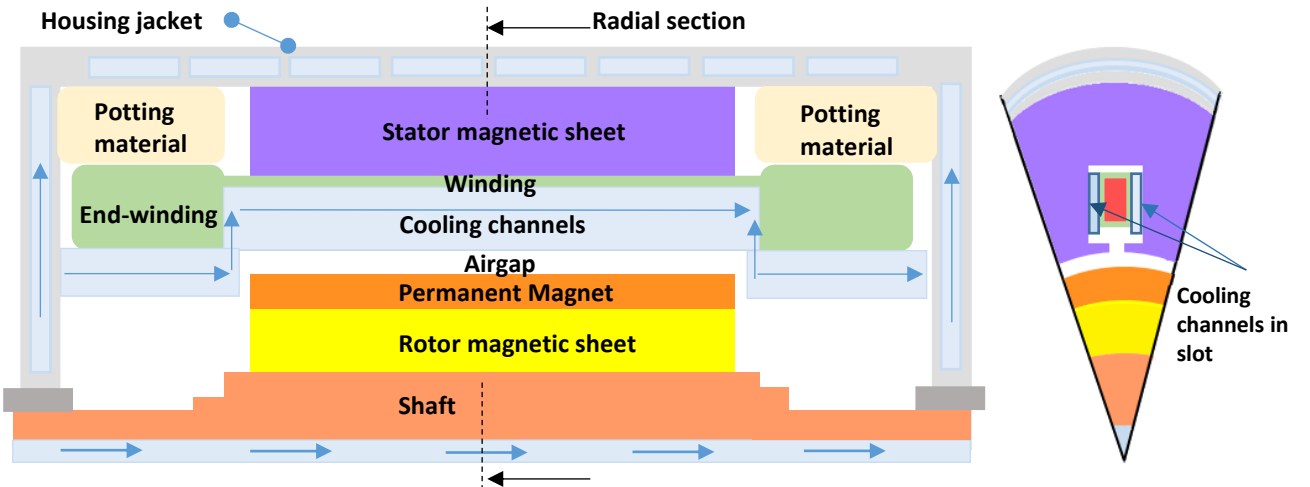
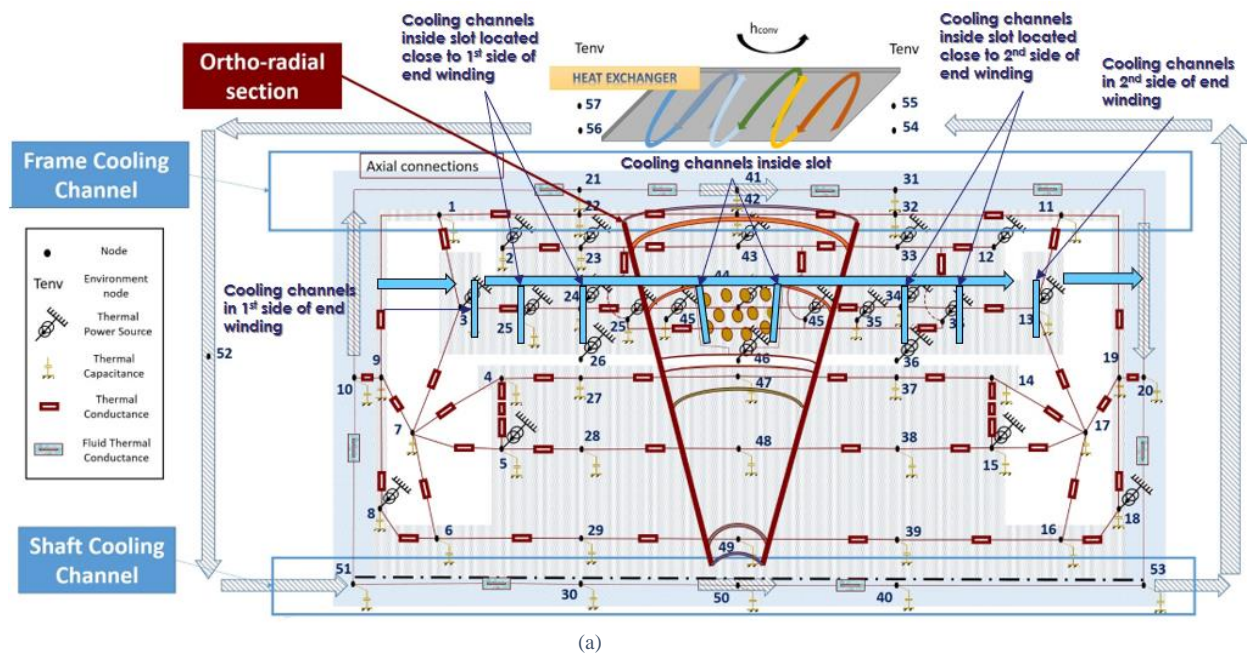


Figure IV. 46. Long term target 2035: axial and radial sections of electric motor and its cooling channels

Iron and mechanical losses are extracted using cooling housing jacket and using cooling channel implemented in rotor shaft. Therefore, to take into account the inner cooling method in winding, WP3 proposed another lumped parameter thermal model given in Figure IV.47.a. Lumped parameter thermal model associated to the cooling system design model allows to evaluate temperatures in electric motor with its cooling system during flying mission as shown in Figure IV.47.b. We notice that temperature in slot does not exceed 160°C due to the direct cooling effort performed in slot. In end-winding, temperature achieves maximum value of 190°C (in take-off flying phase). The latter is lower than to the thermal class chosen in §VI.4.1. Moreover, due to both cooling efforts in shaft and in slots, temperature in permanent magnet does not exceed 130°C which thus leads sustaining the electromagnetic performances of targeted electric motor. The cooling system weight given by WP3 is 33kg with 10kg for the pump weight and 23kg for the coolant, the pipes, the potting materials and the pipes of the heat exchanger. Then the motor with its cooling system reached almost 10kW/kg. Characteristics of cooling system designed by WP3 are summarized in Table IV.13. By comparison to the cooling system of targeted electric motor 2025, we notice that cooling effort performed in winding allows to reduce on one side the winding temperature especially in slot and on the other side reducing the cooling efforts performed in shaft and in frame as indicate the heat transfer convections (cf. Tables IV.7 and IV.13).



(a)

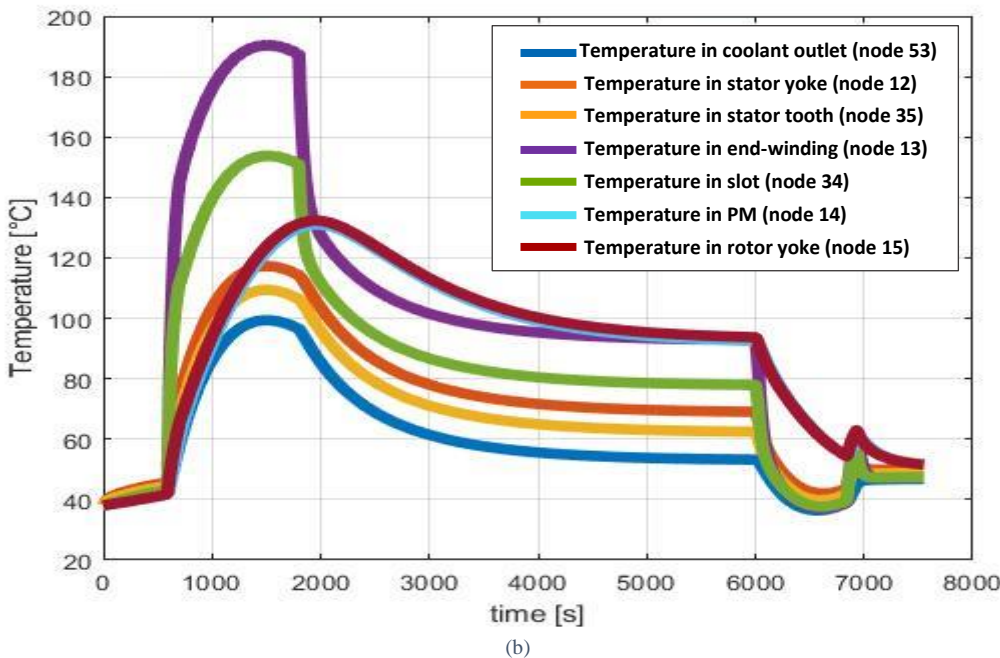


Figure IV. 47. Long term target 2035: (a) Axial and ortho-radial section of SM-PMSM including its cooling system with Lumped Parameter Thermal Model LPTM nodes location, and axial and motor-end connections, (b) Temperature evolution during flying mission in the sized electric motor

Table IV. 17: Long term target 2035: Cooling system characteristics given by WP3

Cooling channels inside housing jacket and shaft

Parameters of cooling channels	Housing jacket	Shaft
Hydraulic diameter [mm]	7.1	9.1
Flow rate [$\text{m}^3 \cdot \text{s}^{-1}$]	1×10^{-4}	5×10^{-5}
Heat transfer coefficient [$\text{W} \cdot \text{m}^{-2} \cdot \text{K}^{-1}$]	250	1600

Heat exchanger

Parameters	Pipes	Cold plate
Material	"Aluminium"	
Thickness[mm]	1	3
Hydraulic diameter [mm]	42	-
Flow rate [$\text{m}^3 \cdot \text{s}^{-1}$]	2.55×10^{-3}	-
Heat transfer coefficient [$\text{W} \cdot \text{m}^{-2} \cdot \text{K}^{-1}$]	3300	-

Cooling channels inside slots: inside winding

Material	"Silicone rubber"
Section [mm^2]	2.415
Thickness [mm]	0.2
Flow rate [$\text{m}^3 \cdot \text{s}^{-1}$]	5×10^{-5}
Heat transfer coefficient [$\text{W} \cdot \text{m}^{-2} \cdot \text{K}^{-1}$]	4700

Coolant "Ethylene Glycol Water 50/50"

Potting material "CoolThermTM EP - 3500"

Thermal conductivity [$\text{W} \cdot \text{m}^{-1} \cdot \text{K}^{-1}$]	3.3
---	-----

Hydraulic Pump

Normal operating pressure [bars]	206
Maximum speed [rpm]	4420
Length [cm]	26.42
Height [cm]	19.05
Width [cm]	17.78
Cooling total weight[kg]	33

Conclusion

This chapter aims to identify the most promising electric motor technologies for achieving medium and long term targets using Target Setting Tool developed in Chapter II. It aims also to size the electric motors with their cooling systems using Surface Mounted Permanent Magnet Synchronous Motor Tool developed in Chapter III and cooling design models performed by WP3. For sizing electric motors taking into account interactions with WP3 and WP5, we have slightly overrated the targeted specific power and slightly underrated the fill factor in TST and SM-PMSM for including subsequently the cooling system and the insulation respectively.

This chapter provides the following conclusions:

- Increasing specific power of electric motor is mainly based on the improving material properties and cooling effort, as it is illustrated in the summary table given below.
- Using external cooling method carried through the frame, using ambient external air as cooled source and with stranded and twisted conductors and high performance materials, the medium term target of 5kW/kg is achieved.
- Using inner cooling method in winding in electric motor, thermal limit set for medium term target is exceeded. Therefore, long term target of 10kW/kg is achieved
- Thermal limit expressed as equivalent current density product represents a good indicator to design high specific power electric motors.
- Thermal limit expressed by the equivalent current density does not exceed $2.10^{12} \text{A}^2/\text{m}^3$ and $5.10^{12} \text{A}^2/\text{m}^3$ for respectively medium term target and long term target. These given values can be taken as good hybrid propulsion chain optimization constraints for the two targets.
- For medium term target winding insulation materials should be 220°C thermal class and for long term target winding insulation materials should be 240°C thermal class.
- Although for a given specific power, there are sizing solutions at low speed with high pole pairs, these solutions are similar in terms of electric frequency to sizing solutions at high speed and low number of pole pairs.

Medium term target 2025	Long term target 2035
Loads, speed, number of pole pair and slot fill factor	
<ul style="list-style-type: none"> - Tangential stress "$\sigma = 50000 \text{Pa}$" - Current density "$j_{rms} = 8.1 \text{A/mm}^2$" - Max surface current density "$K_m = 111.1 \text{kA/m}$" - RMS linear current density: "$A_{rms} = 81.4 \text{kA/m}$" - Current density product "$A_{rms}j_{rms} = 6.5948 \times 10^{11} \text{ A}^2/\text{m}^3$" - Max airgap flux density "$B_m = 0.9 \text{T}$" - Flux density in teeth "$B_{st} = 1.3 \text{T}$" - Flux density in yoke "$B_{sy} = 1.2 \text{T}$" - Rotational speed "$\Omega = 15970 \text{rpm}$" - Number of pole pairs "$p = 2$" - Slot fill factor is 0.5 	<ul style="list-style-type: none"> - Tangential stress "$\sigma = 70000 \text{Pa}$" - Current density "$j_{rms} = 20 \text{A/mm}^2$" - Max surface current density "$K_m = 155 \text{kA/m}$" - RMS linear current density: "$A_{rms} = 110 \text{kA/m}$" - Current density product "$A_{rms}j_{rms} = 2.199 \times 10^{12} \text{ A}^2/\text{m}^3$" - Max airgap flux density "$B_m = 0.9 \text{T}$" - Flux density in teeth "$B_{st} = 1.25 \text{T}$" - Flux density in yoke "$B_{sy} = 1.25 \text{T}$" - Rotational speed "$\Omega = 20000 \text{rpm}$" - Number of pole pairs "$p = 4$" - Slot fill factor is 0.5
Technological solutions	
<ul style="list-style-type: none"> - Stranded and twisted conductors (frequency <1kHz) - Magnetic sheet: "Vacoflux 48- 0.35mm" - Halbach permanent magnet with radial and axial segmentation to ensure sinewave airgap flux density to reduce eddy current losses - Carbon Fiber Sleeve - Thermal winding class 220°C 	<ul style="list-style-type: none"> - Compacted rectangular litz wires conductors (frequency >1kHz) - Magnetic sheet: "Vacoflux 48- 0.35mm" - Halbach permanent magnet with radial and axial segmentation to ensure sinewave airgap flux density to reduce eddy current losses - Carbon Fiber Sleeve - Thermal winding class 240°C
Cooling methods	
<ul style="list-style-type: none"> - Conventional direct cooling method performed in the frame and shaft - Thermal limit: equivalent current density product is $2 \cdot 10^{12} \text{A}^2/\text{m}^3$ 	<ul style="list-style-type: none"> - Conventional direct cooling method performed in the frame and shaft - direct inner cooling method for stator winding cooling, - potting materials around end-windings for improving their cooling - Thermal limit: equivalent current density product is $5 \cdot 10^{12} \text{A}^2/\text{m}^3$
<ul style="list-style-type: none"> → Speed: 15970rpm → Cooling system weight: 32kg 	<ul style="list-style-type: none"> → Speed: 20000rpm → Cooling system weight: 33kg

Chapter IV: Sizing of Electrical Motors for Medium and Long Term Targets

→ Specific power: 5kW/kg
→ Efficiency >97%

→ Specific power: 10kW/kg
→ Efficiency >97%

Despite of tools developed in Chapters II and III are based on huge assumptions, they are suitable for sizing electric motors with tolerable deviations. They are developed in Matlab for becoming useful for hybrid propulsion chain optimization (WP6) given that they need very few input data. Therefore, they provide results in a short time.

Appendices

- Appendix A: Magnetic sheet Iron Cobalt "FeCo: Vacoflux 48-0.35mm"

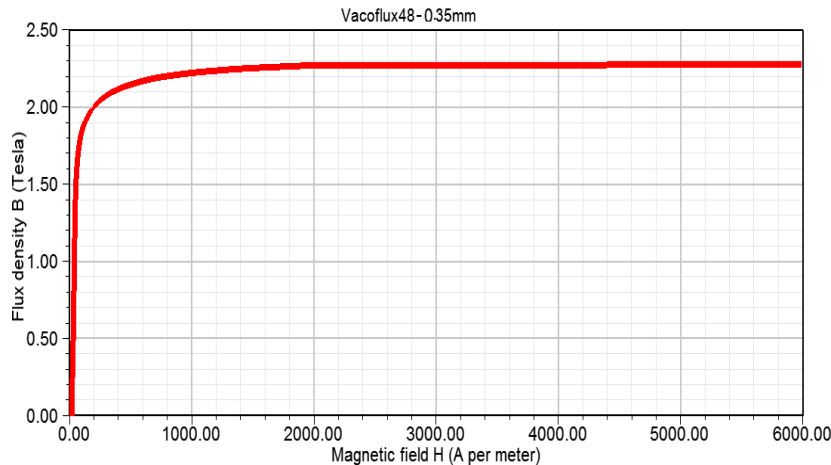


Figure IV. 48: B(H) characteristic of iron cobalt magnetic sheet: Vacoflux 48-0.35mm

Table IV. 18: Bertotti model of iron loss for Vacoflux 48-0.35mm : equation (II-66)

Iron loss coefficients	Hysteresis loss coefficient "k _h " [W.s.T ⁻² .kg ⁻¹]	Eddy loss coefficient "k _c " [W.s ² .T ⁻² kg ⁻¹]	Excess loss coefficient "k _e " [W.(s/T) ^{3/2} .kg ⁻¹]
	0.049058	4.44997.10 ⁻⁵	0

Table IV. 19: New formulation of iron loss for Vacoflux 48-0.35mm : equation (II-67)

Iron loss coefficients	"a ₁₁ "	"a ₁₂ "	"a ₁₃ "	"a ₁₄ "	"a ₂₁ "	"a ₂₂ "	"a ₂₃ "	"a ₂₄ "
	4.369	-13.65	13.66	-4.33	-0.705	2.193	-2.17	0.688
	"a ₃₁ "	"a ₃₂ "	"a ₃₃ "	"a ₃₄ "	"a ₄₁ "	"a ₄₂ "	"a ₄₃ "	"a ₄₄ "
	0.0308	-0.0966	0.098	-0.0317	-0.0006	0.001985	-0.002217	0.00085743

- Appendix B: Permanent Magnet Samarium Cobalt (SmCo) "Recoma33E"

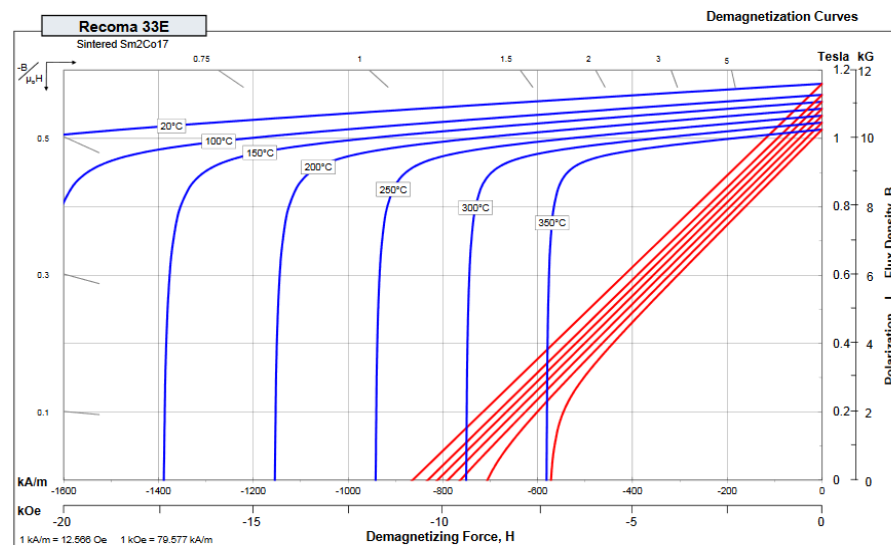


Figure IV. 49 Demagnetization curves of Samarium Cobalt (Sm₂Co₁₇): "Recoma 33E [ArnCat]

Table IV. 20: Magnetic properties of Samarium Cobalt (Sm₂Co₁₇): "Recoma 33E" [ArnCat]

Properties	Minimum	Nominal
Residual induction "B _r "	1.14 T	1.16 T
Coercivity "H _{Cb} "	845kA/m	865kA/m
Intrinsic coercivity "H _{cj} "	1750kA/m	2100kA/m
Maximum energy product "BH _{max} "	238kJ/m ³	251kJ/m ³

Table IV. 21: Physical properties of Samarium Cobalt ($\text{Sm}_2\text{Co}_{17}$): "Recoma 33E" [ArnCat]

Thermal properties	Value
Reversible temperature coefficient induction " α_B "	-0.035
Reversible temperature coefficient coercivity " α_H "	-0.25
Thermal conductivity	$10\text{W.m}^{-1}\cdot\text{K}^{-1}$
Specific heat	$350\text{J.kg}^{-1}\cdot\text{K}^{-1}$
Max. recommended use temperature	350°C
Curie temperature	825°C
Density	8300kg/m^3
Electrical resistivity	$90\mu\Omega\cdot\text{cm}$

- **Appendix C: "Rectangular compacted litz wires"**

- *Rectangular compacted litz wires "New England Wire Technologies Catalogue"*

According to New England Wire Technologies Catalogue, rectangular compacted Litz wire type 8 (cf. Figure IV.50) is the particular suitable conductor for high frequency electric machines. Rectangular compacted litz conductor is designed with 60 to 75 of copper filling. Table IV.22 presents some characteristics of rectangular compacted litz wires.

Table IV. 22. Rectangular compacted litz wire type 8 [NewCat]

Equivalent AWG	Circular Mil Area	Number of wires	AWG of wire	Film coating	Nominal width	Nominal thickness	Nominal linear inductance	Direct Current Resistance	Construction
Unit	Cmils	-	-	-	inch	inch	Lbs/1000ft	Ohms/1000ft	-
Recommended operating frequency- 400Hz to 5kHz									
4	46403	7	12	H*	0.327	0.152	140.0	0.262	7×12
2	79548	12	12	H	0.533	0.152	240.0	0.153	12×12
1	106064	16	12	H	0.704	0.152	320.0	0.115	16×12
1/0	119322	18	12	H	0.789	0.152	361.0	0.102	18×12
6	28763	7	14	H	0.262	0.121	88.0	0.416	7×14
4	41090	10	14	H	0.374	0.121	126.0	0.291	10×14
1	82180	20	14	H	0.700	0.121	251.0	0.146	20×14

(*) Heavy film coating insulation, cmils= $6.4516 \cdot 10^{-4}\text{mm}^2$, inch= $2.54 \cdot 10^{-2}\text{m}$, lbs= 0.4536kg , ft= 304.8mm



Figure IV. 50. Rectangular compacted litz-wire type 8 [NewCat]

- *Chosen conductor for long term target: "Compacted rectangular compacted Litz wires: 18×AWG12"*

Characteristics of chosen conductor for long term target are shown in bold in Table IV.22. This conductor is composed of 18 wires of AWG 12. Characteristics of AWG 12 wire is given in Table IV.23. Rectangular compacted litz has nominal width of 20mm for 9 wires in one row and nominal thickness of 3.86mm with two rows of nine wires (i.e. 9×2 arrangement) as shown in Figure IV.51.

Table IV. 23. Copper whole AWG12 of Essex Magnet Wire Catalogue [EssCat]

Round wire data	Bar wire	Single Build Film-Insulated wire	Heavy Build Film-Insulated Wire	Triple Build Film-Insulated Wire
Bar wire diameter [mm]	2.052	2.052	2.052	2.052
Bar wire cross section [mm ²]	3.3081	3.3081	3.3081	3.3081
Bar wire weight [kg/m]	29.44	29.44	29.44	29.44
Bar wire resistance [Ω/m]	0.005212	0.005212	0.005212	0.005212
Insulated thickness [μm]	-	21.590	43.18	60.959
Insulated wire weight [kg/km]	-	0.18	0.380	0.550
Insulated material density [kg/m^3]	-	1279	1337	1359
Overall wire diameter [mm]	-	2.0955	2.138	2.174
Overall wire cross section [mm ²]	-	3.4488	3.592	3.7128
Film-insulated wire weight [kg/km]	-	29.589	29.789	29.959
Film-insulated wire resistance [Ω/m]	-	0.005216	0.005216	0.005218

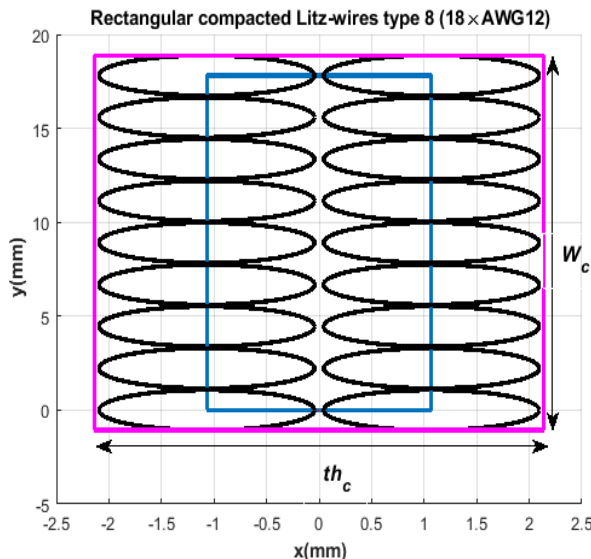


Figure IV. 51. Arrangement of rectangular compacted Litz wires type 8 [NewCat]

- Calculation of "k_{lc}" taking into account the twisting effect

In rectangular compacted Litz wires, wires are twisted with an angle β_e on the lay length as illustrated in Figure IV. 52. Indeed, wires have circular cross-section in perpendicular plan of twisting direction which leads elliptical cross-section as shown in Figure IV.53. Therefore, the angle between circular and elliptical cross-sections is none other than the β_e angle. It can be calculated by the following equation:

$$\cos(\beta_e) = \frac{D_{iw}}{W_c/n_{w1}} \quad (\text{IV- 1})$$

With:

$$n_{w1} = \frac{n_w}{n_{w2}} \quad (\text{IV- 2})$$

Where: D_{iw} is the insulated wire diameter (cf. Table IV.23), W_c is the width of rectangular compacted Litz wire (cf. Table IV.22), n_w is the total number of wires (for chosen rectangular compacted Litz wire $n_w = 18$), n_{w1} is the number of wires in y direction (for chosen conductor $n_{w1} = 9$), n_{w2} is the number of wires in the x direction (for chosen conductor $n_{w2} = 2$).

Then the lay length shown in Figure IV.52.b can be given by:

$$\text{lay length} = 2 \times \frac{\left(\frac{n_{w1}-1}{n_{w1}}\right) W_c}{\tan(\beta_e)} \quad (\text{IV- 3})$$

Thus, the length of a wire can be deduced by:

$$l_w = 2 \times \left(\frac{0.5 \text{ lay length}}{\cos(\beta_e)} + D_{wi} \right) \quad (\text{IV- 4})$$

The coefficient taking into account the twisting effect is governed by:

$$k_{lc} = \frac{l_w}{\text{lay length}} \quad (\text{IV- 5})$$

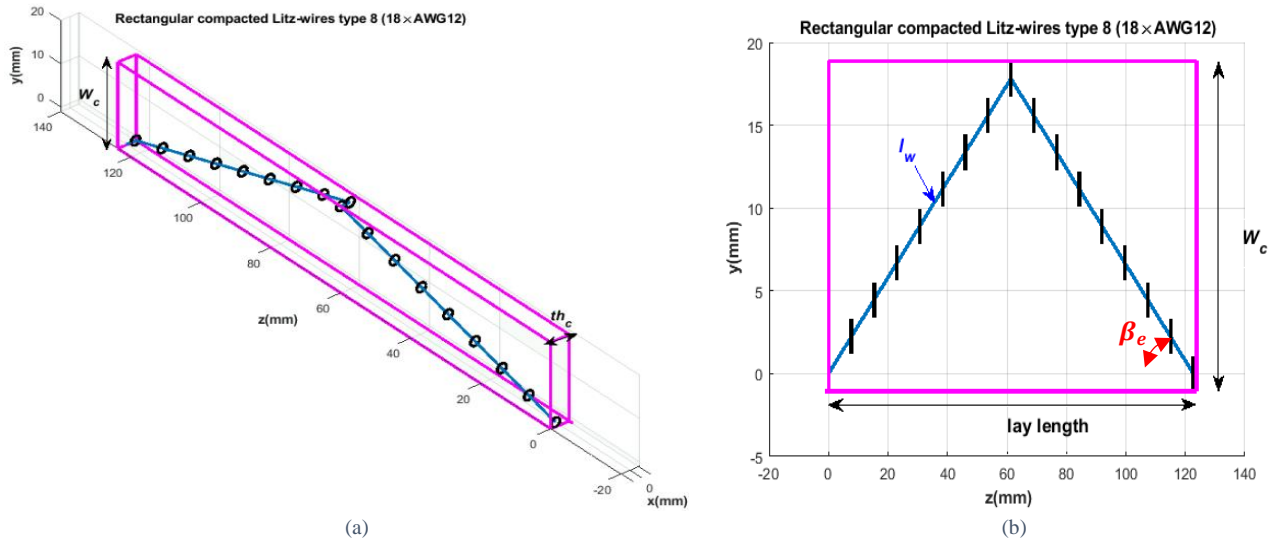


Figure IV. 52. Rectangular compacted Litz-wires type 8: (a) 3D view, (b) YZ view

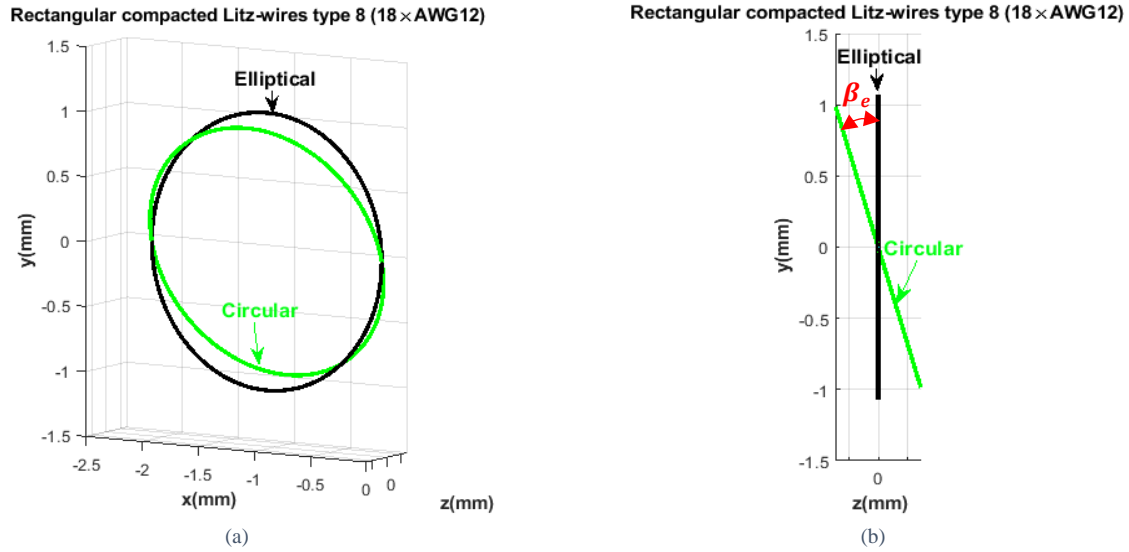


Figure IV. 53. Circular and elliptical cross sections: (3D) view, YZ view

- Calculation of "k_{sc}" which takes into account the elliptical cross section of conductors

Coefficient "k_{sc}" is governed by:

$$k_{sc} = \frac{S_w}{S_{elliptical}} \quad (\text{IV- 6})$$

With: S_{elliptical} is the elliptical cross-section of wire:

$$S_{elliptical} = \frac{S_w}{\cos(\beta_e)} \quad (\text{IV- 7})$$

Where: S_w is the circular cross section of wire ($S_w = \frac{\pi}{4} D_{wi}^2$).

- Calculation of fill factor of conductor "k_{fillcond}"

Copper filling of conductor is given by:

$$k_{fillcond} = \frac{n_w S_{elliptical}}{w_c th_c} \quad (\text{IV- 8})$$

Eventually, rectangular compacted Litz wire 18×12AWG are characterized by:

$$\begin{cases} \beta_e = 29.89^\circ \\ k_{sc} = 86.69\% \\ k_{lc} = 1.153 \\ k_{fillcond} = 71.67\% \end{cases} \quad (\text{IV- 9})$$

- Appendix D: "Control strategy of permanent magnet synchronous motor"

For controlling electric machines, model using Park transformation is often employed. Park transformation aims to transform three phase model of electric machines into two phases in quadratic reference noted by dq (d is the direct axis; q is the quadratic axis) [Kim_17] [Oun_16]. Park model of permanent magnet synchronous motor expresses the voltage equations given in direct axis (d) and quadrature axis (q) by:

$$\begin{cases} V_d = R_s I_d + L_{cs} \frac{dI_d}{dt} - L_{cs} I_q \omega \\ V_q = R_s I_q + L_{cs} \frac{dI_q}{dt} + L_{cs} I_d \omega + E \end{cases} \quad (\text{IV- 10})$$

Where: V_d , V_q are respectively direct and quadratic voltages, I_d and I_q are respectively the direct and quadratic currents, ω is the electric pulsation, L_{cs} is the cyclic inductance and R_s is the resistance.

In steady state, equation (IV-10) can be written by:

$$\begin{cases} V_d = R_s I_d - L_{cs} I_q \omega \\ V_q = R_s I_q + L_{cs} I_d \omega + E \end{cases} \quad (\text{IV- 11})$$

Permanent magnet synchronous motor can operate at either constant torque mode or at constant power mode according to control strategies applied to the inverter. Figure IV.54 illustrates the torque-speed characteristic and the two operation modes of permanent magnet synchronous motor.

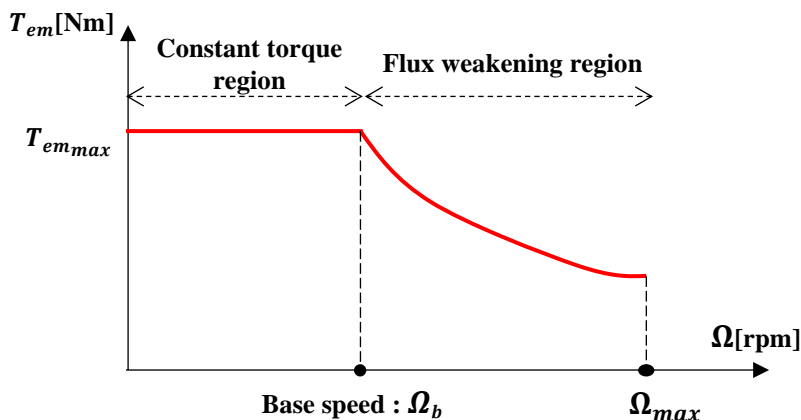


Figure IV. 54. Torque-speed characteristic of SM-PMSM

Electric power using dq voltages and currents is given by:

$$P_{ele} = V_q I_q + V_d I_d \quad (\text{IV- 12})$$

By using equation (IV-10), equation (IV-11) can be written by:

$$P_{ele} = R_s (I_d^2 + I_q^2) + EI_q \quad (\text{IV- 13})$$

Knowing that:

$$P_{ele} = P_j + P_{em} \quad (\text{IV- 14})$$

And

$$E = \omega \phi_{vm} \quad (\text{IV- 15})$$

By identification:

$$P_{em} = EI_q \quad (\text{IV- 16})$$

Therefore, the electromagnetic torque using quadratic current is:

$$T_{em} = \frac{P_{em}}{\Omega} = p \phi_{vm} I_q \quad (\text{IV- 17})$$

References

- [Pyr_14] J. Pyrhönen, T. Jokinen, V. Hrbovcovà, "Design of rotating electrical machines," 2nd Edition, John Wiley & Sons, 2014.
- [All_18] Jean-François Allias, AIRBUS HASTECS deliverable 2018, July 2018.
- [Tou_20] S. Touhami, A. Zeaiter, M. Fénot, Y. Lefevre, J. F. Libre, E. Videcoq, "Electrothermal Models and Design Approach for High Specific Power Electric Motor for Hybrid Aircraft", 1st Edition of the Aerospace Europe Conference AEC 2020, Bordeaux, France, 25th-28th February 2020.
- [Zea_18] A. Zeaiter, M. Fénot, "Thermal sensitivity analysis of a high power density electric motor for aeronautical application", 2018 IEEE International Conference on Electrical Systems for Aircraft Railway, Ship Propulsion and Road Vehicles and International Transportation Electrification Conference (ESARS-IETC), Nottingham, United Kingdom, 7-9 Nov 2018.
- [Ton_14] Wei Tong, "Mechanical Design of Electric Motors", CRC Press, Taylor and Francis Group, LLC, 2014.
- [ArnCat] "Arnold Magnetic Technologies' Catalogue", <https://www.arnoldmagnetics.com>
- [NewCat]"New England Wire Technologies",http://www.litzwire.com/nepdfs/Rectangular_Compacted_Litz_Catalog.pdf
- [EssCat]"Essex Magnet Wire Catalogue", <https://prod.essexwire.com/sites/essexwire.com/files/2017-08/Essex-Wire-Engineering-Data-Handbook-EN.pdf>
- [Oun_16] H. Ounis, "Conception intégrée par optimisation multicritère multi-niveau d'un système d'actionnement haute vitesse pour l'avion plus électrique", PhD thesis, Toulouse University, November 2016.
- [Kim_17] Sang-Hoon Kim, "Electric Motor Control: DC, AC and BLDC Motor", Elsevier Science, 2017, <https://books.google.fr/books?id=ewKqDQAAQBAJ>

General conclusion and perspectives

In this manuscript, we were interested in the development of models and tools allowing to identify the most promising actual and future technologies and breakthroughs which need to be overcome for increasing specific power of electric motors dedicated to serial hybrid aircraft propulsion. These models and tools are carried out as part of the HASTECS project which set two high specific power targets for H2020 Horizon (i.e. 5kW/kg for 2025 and 10kW/kg for 2035). They have been carried out, on the one hand, to be integrated in global optimization study of hybrid propulsion chain and on the other hand for supplying details required for sizing the further components and for studying partial discharges.

To satisfy our thesis goal, we have drafted, in the first Chapter, a wide panorama on the electric motor current and future technologies in order to situate the actual specific power and to identify used technologies. Several materials, electric motor topologies and cooling technologies have been studied and compared to emphasize on their advantages and disadvantages in terms of weights, loads and limits. It results that is difficult, in this phase, to identify the most promising materials, the most cooling technology and the best electric motor topology. Considering the strengths and weaknesses of each technology, establishing trade-offs on the wide technology panorama is essential. It results also that thermal constraints are the major limitations for reaching the HASTECS targets.

In the second chapter, we have focused on the development of model and tool for the assessment electric motor technologies. For the purposes, we firstly reminded the loadability concepts which characterize the technological levels. Afterward, we have introduced loadability concepts on the analytical model of non-salient sinewave electric machines for carrying out tool for assessing performances without describing the topology. Indeed, this presents the strong and original features. To consider limits, two constraints have been introduced the first one is thermal expressed from the concept of current density product and the second one is mechanical expressed from rotor shape factor. We have developed this tools in Matlab software as a tool called **Target Setting Tool "TST"**. It takes as inputs: the specifications, loads and materials library and gives as outputs set of data such as main sizes, weights, losses, efficiency, specific power and torque. Developed model of TST is in fact an inverse model.

Surface Mounted Permanent Magnet Synchronous Motor "SM-PMSM" is one of the topology satisfying TST assumptions. In Chapter II, a sizing tool based on this topology provides additional data for the other packages. It is most accurate than TST Tool while remaining an uncomplicated analytical model. As well as for TST, we have programmed SM-PMSM in Matlab software. To ensure sinewave airgap flux density we have chosen Halbach structure for permanent magnets. Therefore, we have established analytical model for determining the polarization and additional rotor sizes using direct design and using an optimization. By choosing distributed winding configurations we have determined the additional stator sizes and the electric circuit parameters by means of established conductor distribution functions. Moreover, as structure is defined, we have updated some data mainly weights and performances (i.e. losses, specific power and specific torque).

In the last Chapter, we have sized through interaction with WP3, two electric motors including their cooling systems for HASTECS targets. This sizing allowed us on the one hand to identify for each target the most promising technologies and on the other hand to validate the assessment tool "TST" and sizing tool "SM-PMSM". From flying mission profiles (i.e. mechanical power and speed) given by AIRBUS, we have firstly discussed on the choice of sizing point given that electric motors should be satisfying specifications (mainly mechanical power between kW to MW). As a result, choice was made on the take-off phase given that is the most critical flying phase for electric motors. Thereafter, as sizing cooling systems strongly depends on the sizing of electric motor, we have proposed a sizing procedure which involves all tools and models performed in Chapters II and III and in those developed by WP3. For each target, we reminded the issues and limitations in order to define the strategies to be followed before starting the sizing. We have therefore proposed two strategies: the first one consists to define the involved cooling methods according to the actual/future cooling technologies. The second one consists to define the involved materials according to the chosen cooling methods. For the 1st target (2025), sizing was based on the actual technological levels whereas for 2nd target (2035) sizing was based on the actual and future technological levels. For reaching high specific power for the two targets, we have increased

General conclusion and perspectives

loads while making sure we don't exceed thermal limits (i.e. expressed by the equivalent current density product). We have decreased losses by using high performance materials and using design technology solutions that allow it.

According to actual technology, we have introduced in TST and SM-PMSM a set of loads and parameters which allowing to reach 5kW/kg, namely:

- Tangential stress " $\sigma = 50000\text{Pa}$ "
- Current density " $j_{rms} = 8.1\text{A/mm}^2$ "
- Max surface current density " $K_m = 111.1\text{kA/m}$ "
- RMS linear current density: " $A_{rms} = 81.4\text{kA/m}$ "
- Current density product " $A_{rms}j_{rms} = 6.6 \times 10^{11}\text{ A}^2/\text{m}^3$ "
- Max airgap flux density " $B_m = 0.9\text{T}$ "
- Flux density in teeth " $B_{st} = 1.3\text{T}$ "
- Flux density in yoke " $B_{sy} = 1.2\text{T}$ "
- Rotational speed " $\Omega = 15970\text{rpm}$ "
- Number of pole pairs " $p = 2$ "
- Slot fill factor is 0.5,

and this is for the following technological choices:

- Using external cooling method carried out frame for cooling stator
- Using ambient external air as cooled source
- Using inner cooling method in rotor shaft for cooling rotor
- Using stranded and twisted conductors to limit AC joule losses at high frequency
- Using Halbach PM radially and axially segmented for decreasing eddy current losses and to ensure sinewave airgap flux density.
- Using high thermal classes in insulation winding: 220°C
- Using high performance materials: Vacoflux 48, Samarium Cobalt SmCo, Carbon fiber sleeve...etc.

Through interaction with WP3, the thermal limit obtained for the specific power 5kW/kg with the used cooling methods is $2.10^{12}\text{A}^2/\text{m}^3$. Using finite element analysis, we have validated with tolerable deviations the assessment tool TST and the sizing tool SM-PMSM even they are based on huge assumptions especially TST.

Based on the sizing electric motor of the 1st target, we have increased some loads in TST and SM-PMSM and we have kept the others in order to double the achieved specific power (i.e. for reaching 10kW/kg):

- Tangential stress " $\sigma = 70000\text{Pa}$ "
- Current density " $j_{rms} = 20\text{A/mm}^2$ "
- Max surface current density " $K_m = 155\text{kA/m}$ "
- RMS linear current density: " $A_{rms} = 110\text{kA/m}$ "
- Current density product " $A_{rms}j_{rms} = 2.2 \times 10^{12}\text{ A}^2/\text{m}^3$ "
- Flux density in yoke " $B_{sy} = 1.25\text{T}$ "
- Rotational speed " $\Omega = 20000\text{rpm}$ "
- Number of pole pairs " $p = 4$ ",

this is for the following new technological choices specially in winding, insulation and stator cooling:

- Adding inner cooling method in winding to improve cooling stator because thermal limit set for 1st target is exceeded
- Using litz-wires to limit AC joule losses at very high frequency ($>1\text{kHz}$)
- Using very high thermal classes in insulation winding: 240°C , the technologies of the other electric machine parts remain same.

Always with WP3 interaction on this target 10kW/kg, thermal limit should be not exceeding $5.10^{12}\text{A}^2/\text{m}^3$.

Once again, we have validated with tolerable deviations the assessment tool TST and the sizing tool SM-PMSM. In conclusion of these two sizing electric motors, reaching 2nd Hasteecs target strongly relies on the using cooling method (in our studied motor winding should be directly cooled).

After sizing electric motors with their cooling systems and validation of tools, it would be interesting for future works to carry out an optimization using developed tools (i.e. using only TST or using both

General conclusion and perspectives

TST and SM-PMSM) in order to determine the most critical points for increasing the specific power given that for instance, these two motors have been sized for high speed rotation.

List of publications

Conferences with HASTECS Project Acknowledgement

- Yvan Lefèvre, Sami El Aabid, Jean-François Llibre, Carole Henaux, **Sarah Touhami**, Performance assessment tool based on loadability concepts, the 18th International Symposium on Applied Electromagnetics and Mechanics, France September 2017.
- **Sarah Touhami**, Yves Bertin, Yvan Lefèvre, Jean-François Llibre, Carole Henaux, Matthieu Fénot, Lumped Parameter Thermal Model of Permanent Magnet Synchronous Machines, International Conference Electrimacs, Transactions of IMACS Mathematics and Computers in Simulation (special issue), Toulouse July 2017.
- **Sarah Touhami**, Yvan Lefèvre, Jean François Llibre. Joint Design of Halbach Segmented Array and Distributed Stator Winding. IEEE Proceedings of the XXIII International Conference on Electrical Machines (ICEM'18), Alexandroupoli, Greece September 2018.
- Philippe Colin, **Sarah Touhami**, David Malec, Yvan Lefèvre, Jean-François Llibre, Design of Electric Machine Taking into Account the Partial Discharges Phenomena for Future Hybrid Propelled Aircrafts, More Electric Aircraft (MEA 2019) Conference, Toulouse February 2019.
- **Sarah Touhami**, Yvan Lefèvre, Jean François Llibre, Original Optimization Procedures of Halbach Permanent Magnet Segmented Array, 19th International Symposium on Electromagnetic Fields in Mechatronics Electrical and Electronic Engineering, 29-31 August 2019, Nancy-France.
- **Sarah Touhami**, Amal Zeaiter, Matthieu Fenot, Yvan Lefèvre, Jean-François Llibre, Electro-thermal Models and Design Approach for High Specific Power Electric Motor for Hybrid Aircraft, Aerospace Europe Conference 2020, 25-28 February 2020, Bordeaux, France.
- Matthieu Pettes-Duler, Xavier Roboam, Bruno Sareni, **Sarah Touhami**, Yvan Lefèvre, Jean François Llibre, Sensitivity Analysis of a Hybrid-Electric Aircraft Powertrain Based on Sobol Indices, Aerospace Europe Conference 2020, 25-28 February 2020, Bordeaux, France.
- **Submitted and accepted conference abstract:** **Sarah Touhami**, Yvan Lefèvre, Jean François Llibre, Effects of Splitting and Twisting Conductor on the AC Joule losses, 19th IEEE Conference on Electromagnetic Field Computation, CEFC 2020, November 16-19, Pisa Italy.

Journal

Yvan Lefèvre, Sami El Aabid, Jean-François Llibre, Carole Henaux, **Sarah Touhami**, Performance assessment tool based on loadability concepts, International Journal of Applied Electromagnetics and Mechanics, IOS Press, vo. Pre-press, no. Pre-press, December 2018.

Other submitted journal papers

- **Sarah Touhami**, Amal Zeaiter, Matthieu Fenot, Yvan Lefevre, Jean-François Llibre, Etienne Videcoq, Electrothermal models and Design Approach for High Specific Power Electric Motor for Hybrid Aircraft Propulsion, **Submitted to CEAS Aeronautical Journal Springer**.
- **Sarah Touhami**, Yvan Lefevre, Jean-François Llibre, Direct and Optimisation Based Designs of an Halbach Permanent Magnet Segmented Array, **Submitted to the International Journal for Computation and Mathematics in Electrical and Electronic Engineering**.
- **Sarah Touhami**, Yvan Lefevre, Jean-François Llibre, Pré-dimensionnement d'un Moteur Electrique de Très Forte Puissance Spécifique pour Avion Hybride, **Submitted to Revue de l'Electricité et de l'Electronique (REE)**.

HASTECS Acknowledgement

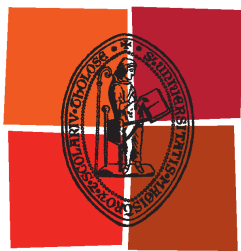


This project has received funding from the CleanSky2 Joint Undertaking under the European Union's Horizon 2020 research and innovation program under grant agreement No 715483.

List of publications

Other conference paper

- Theo Capri, Maxime Bonnet, **Sarah Touhami**, Yvan Lefevre, Jean-François Llibre, Unified Sizing Model Approach for Radial and Axial Flux Permanent Magnet Machines, IEEE Proceedings of the XXIV International Conference on Electrical Machines (ICEM'20), Gothenburg, Sweden, 23rd-26th August 2020.



Université
de Toulouse

THÈSE

En vue de l'obtention du

DOCTORAT DE L'UNIVERSITÉ DE TOULOUSE

Délivré par :

Institut National Polytechnique de Toulouse (Toulouse INP)

Discipline ou spécialité :

Génie Electrique

Présentée et soutenue par :

Mme NAJOUA ERROUI

le vendredi 15 novembre 2019

Titre :

High power conversion chain for hybrid aircraft propulsion

Ecole doctorale :

Génie Electrique, Electronique, Télécommunications (GEET)

Unité de recherche :

Laboratoire Plasma et Conversion d'Energie (LAPLACE)

Directeur(s) de Thèse :

M. GUILLAUME GATEAU

M. NICOLAS ROUX

Rapporteurs :

M. ERIC LABOURE, SUPELEC

M. YVES LEMBEYE, UNIVERSITE GRENOBLE 1

Membre(s) du jury :

Mme XUEFANG LIN-SHI, INSA LYON, Président

M. GUILLAUME FONTES, TOULOUSE INP, Invité

M. GUILLAUME GATEAU, TOULOUSE INP, Membre

M. JEAN-FRANCOIS ALLIAS, AIRBUS FRANCE, Invité

M. NICOLAS ROUX, TOULOUSE INP, Membre

Remerciements

Ces travaux ont été réalisés au sein du laboratoire LAPLACE (Laboratoire Plasma et Conversion d'Energie) à Toulouse et s'intègrent aux travaux de recherche du groupe CS (Convertisseurs Statiques) et GENESYS (Groupe Energie Electrique et Systémique).

Je tiens à remercier en premier lieu mes directeurs de thèse Nicolas Roux et Guillaume Gateau d'avoir dirigé cette thèse. Nos interactions ont été très riches et j'ai beaucoup appris grâce à vous.

Je souhaite remercier aussi les différents membres du jury : Mme Xuefang LIN-SHI pour sa participation en tant que présidente du jury ainsi que pour l'intérêt qu'elle a montré pour mon travail, MM. Eric LABOURE et Yves LEMBEYE pour avoir rapporté cette thèse ainsi que pour leurs commentaires lors de la soutenance ainsi que MM. Jean-François ALLIAS et Guillaume FONTES.

Je voudrais également remercier tous mes collègues du projet HASTECS pour toutes les discussions constructives notamment Falvio, Matthieu, Sarah, Philippe, Amal, Maillys et Malik.

Je voudrais aussi remercier les permanents du laboratoire pour leur aide et leur bienveillance et que j'ai côtoyé avec plaisir durant ces trois années de thèse. En particulier Didier Flumian, Jacques Benaioun, Xavier Roboam, Frédéric Richardieu, Marc Cousineau, Eric Bru, Henri Schneider, Amine Jaafar, Nicolas Rouger, Philippe Ladoux, Hubert Piquet, Christophe Turpin, Sébastien Vinnac. Merci également à Jessica Toscano pour son aide sur les démarches administratives. Je tiens aussi à remercier Jean-Marc Blaquier pour son aide pour la conception des bus bar et pour ses conseils techniques.

Merci à tous mes amis et collègues doctorants pour vos discussions et votre soutien : Kepa, Vanesa, Vinicius, Yazan, Youness, François, Timothé, Clément, Olivier, Andallah, Davin, Andrea V., Andrea E., Jaime, Frederico, Plinio, Hugo, Tiago, Guilhermé, Rémi, Jordan, Quentin, Jessica, Lucille, Morgane, Joseph, Alvaro, Kamil, Sami, Abdelkader, Khaled, Alexandre, Andy et Yann. J'en oublie tant d'autres, je vous prie de m'excuser.

Un grand merci à Miguel et Bernard d'avoir partagé avec moi les moments de joies et surtout ceux de déprime pendant ces trois années. Merci à Victor et Bouazza pour vos conseils précieux et votre soutien.

Merci à Anne et Arnaud C. qui étaient à mon écoute dans mes périodes de doute et m'ont toujours soutenu dans les moments les plus difficiles.

Un énorme merci à Soukaina, Youness et Reda d'avoir été à mes côtés dans les bons moments et ceux un peu plus stressants.

Je remercie infiniment ma deuxième famille : Maxime, Guillaume, Isabelle, Clément, Léa, Chloé, Adrien, Ichrak, Mathieu, Arnaud J. et Estelle qui ont toujours été à mes côtés et m'ont encouragé pour aller au bout de cette aventure.

Pour finir, je remercie mes parents et ma famille qui m'ont toujours soutenu et sans qui je n'aurai jamais pu prendre ce chemin. Ils ont su faire preuve de patience et sans lesquels je n'en serais pas là aujourd'hui. J'espère que vous êtes fiers de moi.

A ma famille

Résumé

Ces dernières années, l'utilisation des systèmes de transport aérien s'est considérablement amplifiée. Par conséquent, les considérations environnementales actuelles poussent à réduire leur utilisation. Des projets tels que Clean Sky 2 tentent d'apporter une réponse à ce problème, en proposant une réduction des émissions de CO₂ et des nuisances sonores. Le recours à l'hybridation de la propulsion des avions réduirait ces émissions en réduisant la taille et la masse des systèmes et en utilisant des systèmes électriques plus efficaces ce qui permettrait d'augmenter le nombre de passager. Cela permettrait de réduire la consommation de carburant et donc les émissions polluantes.

Ces travaux s'inscrivent dans le cadre du projet européen HASTECS Clean Sky 2 qui vise à optimiser l'ensemble de la chaîne électrique de l'avion à propulsion hybride en intégrant toutes les contraintes aéronautiques telles que les décharges partielles pour les équipements électriques placés en zone non pressurisée. Le projet HASTECS s'est fixé le défi de doubler la densité de puissance des machines électriques pour passer de 5 kW/kg à 10 kW/kg, y compris leur refroidissement, tandis que pour l'électronique de puissance, avec son système de refroidissement, le but sera de passer à 15 kW/kg en 2025 et à 25 kW/kg en 2035.

Pour augmenter la densité de puissance, la masse du système de refroidissement doit être diminuée dans un premier temps soit en optimisant ses composants, ce qui est fait par le 4^{ème} lot de travail (WP4), soit en réduisant les pertes. La réduction des pertes de l'onduleur pourrait être obtenue en utilisant de semi-conducteurs de faible calibre en tension, en jouant sur les stratégies de modulation ou en utilisant des semi-conducteurs plus performants. La première option peut être faite en utilisant des architectures multi-niveaux pour éviter l'association en série direct. Contrairement à l'association directe en série, l'association parallèle est plus facile à gérer en termes de commande d'interrupteurs, ce qui a été autorisé dans nos études. Plusieurs topologies d'onduleurs (topologies à 2, 3 et 5 niveaux) et stratégies de modulation (PWM, injection de troisième harmonique, PWM discontinu et pleine onde) ont été comparées en utilisant plusieurs technologies de semi-conducteurs pour choisir la solution la plus performante en termes de rendement et de densité de puissance. Pour le profil de mission considéré, l'onduleur pourrait être dimensionné pour le point de puissance maximum (décollage) ou la phase de vol la plus longue (croisière). Une étude comparative des stratégies de modulation a été réalisée pour mettre en évidence la structure et la modulation présentant les meilleures performances afin de minimiser les pertes pour les points de dimensionnement choisis en utilisant les topologies les plus intéressantes pour le profil de mission étudié en utilisant deux configurations différentes de bobinage du moteur électrique proposées par le WP1.

Mots clés

Propulsion aéronautique hybride, Onduleur multiniveaux, Stratégies de modulation, Semi-conducteurs, Electronique de puissance.

Abstract

Recently, the use of air transport systems has increased considerably. Therefore, the current environmental considerations are pushing to reduce their ecological impact. Projects such as Clean Sky 2 provide an answer to this problem, by proposing a reduction in CO₂ emissions and noise pollution. The development of a hybrid-electric aircraft would reduce these emissions by reducing the size and weight of the systems and using more efficient electrical systems. This would reduce fuel consumption and therefore pollutant emissions.

This work takes part into HASTECS Clean Sky 2 European project which aims to optimize the complete electrical chain of the hybrid aircraft integrating all aeronautical constraints such as partial discharges for electrical equipment placed in the non-pressurized zone. HASTECS project has set itself the challenge of doubling the specific power of electric machines including their cooling from 5 kW/kg to 10 kW/kg, while the power electronics, with their cooling system, would evolve from 15 kW/kg in 2025 to 25 kW/kg in 2035.

To increase the specific power, the cooling system mass should be decreased either by optimizing its components which is done by the 4th work package (WP4) or by reducing power losses. Inverter losses reduction could be achieved by using small voltage rating components, by playing on modulation strategies or by using more performant semiconductors. The first option could be done by using multilevel architectures to avoid the direct series association. Unlike direct series association, the parallel one is easier to manage in terms of switches command so it was allowed in our studies. Several inverter topologies (2-, 3- and 5-level topologies) and modulation strategies (PWM, third harmonic injection, discontinuous PWM and full-wave) were compared using several semiconductors generations to choose the most performant solution in terms of efficiency and specific power. For the considered mission profile, the inverter could be sized for the maximum power point (takeoff) or the most extended flight phase (cruise). A comparative study of modulation strategies was carried out to highlight the structure and modulation presenting the best performance to minimize the losses for the chosen sizing points using most interesting topologies for the studied mission profile using two electrical motor windings configurations proposed by WP1.

Key words

Hybrid aircraft propulsion, Multi-level inverter, Modulation strategies, Semiconductors, Power electronics.

Contents

Remerciements	1
Résumé	3
Abstract	5
Contents.....	7
List of figures	9
List of tables	14
List of acronyms.....	17
General introduction.....	19
I. State of the art and context.....	21
1. Hybrid-electric propulsion aircraft	21
i. Hybrid and electric propulsion aircraft evolution	23
ii. Hybrid-electric architectures	25
iii. Energy management for the studied solution	27
2. Problematic and objectives	27
i. HASTECS project	27
ii. Hybrid-electric components specific power targets	28
iii. Flight mission profile	29
iv. HASTECS work packages	30
v. Work Package 2 (WP2)	33
3. Reference case: 2-level PWM inverter solution	34
4. Conclusion	36
II. Simulation tool	39
1. Software organization	40
2. Power losses and thermal modeling	42
i. Modeling principle	42
ii. Needed parameters	45
iii. Example of the method for determining the formulas of switching and conduction currents	46
3. Semiconductors Database	48
i. Components' families	50
ii. Generated components	50
iii. Comparison of real and generated components	53
4. Capacitor sizing	57
i. DC bus capacitor	57
ii. Flying capacitor	60
iii. Selecting the capacitor from the database	61
5. Model validation using <i>Plecs</i>	62
i. Multilevel Flying Capacitor topology (FC):	63
ii. 3-level Neutral clamped point topology (NPC):	64
iii. 5-level Active neutral clamped point topology (ANPC):	65
iv. Multilevel Stacked Multicell Converter topology (SMC):	65
6. Introduction of Multilevel Necessity	66
7. Conclusion	69
III. Comparison of possible solutions sized for the maximal power point	71
1. Comparison of topologies with PWM modulation strategy	72
i. Multilevel inverter topologies	72

ii.	Studied topologies	74
iii.	Comparison of studied topologies and DC bus voltage definition	80
2.	Modulation strategies	87
i.	Multilevel SPWM	89
ii.	Discontinuous PWM (DPWM)	90
iii.	Third Harmonic injection PWM (THIPWM ¼)	91
iv.	Full-wave modulation	91
v.	Comparison of modulation strategies	97
3.	Comparison of component generations and technology with a chosen strategy and topology	98
i.	7 th generation IGBTs	98
ii.	6 th generation IGBT vs 7 th Generation IGBT (Mitsubishi)	99
iii.	Silicon Carbide (SiC) vs Silicon (Si) components	101
4.	Total weight repartition	102
i.	3D inverter design	103
ii.	Specific power comparison	106
iii.	Module packaging for bus bar reduction and capacitor weight reduction	107
5.	Conclusion	109
IV.	Performance of the chosen solutions during the mission profile	111
1.	DC bus voltage sizing and components choice depending on the voltage mission profile and control strategy	112
2.	Inverter performances during the mission profile	113
i.	Strategy 1: Sine PWM and THIPWM	114
ii.	Strategy 2: THIPWM versus DPWM	115
iii.	Strategy 3: Full-wave modulation	117
iv.	Strategy 4: hybrid modulation using Sine PWM and FW	119
v.	Strategy 5: DPWMMAX and FW modulation	121
vi.	Overview of control strategies	123
3.	Conclusion	126
	Conclusion & perspectives.....	127
	Appendix	131
	Résumé en français.....	139
	References	159

List of figures

Fig. I-1. Global air travel 1936-2016 [2].....	21
Fig. I-2. CO ₂ Emissions Trends from International Aviation, 2005 to 2050	22
Fig. I-3. Airbus electro-mobility roadmap [24] [25]	24
Fig. I-4. Series hybrid propulsion system [27].....	25
Fig. I-5. Parallel hybrid propulsion system [27]	26
Fig. I-6. General propulsion schematic system during a mission of an aircraft [28]	27
Fig. I-7. Baseline architecture for assessments	28
Fig. I-8. Voltage and current RMS mission profile.....	30
Fig. I-9. HASTECS consortium structure	31
Fig. I-10. Electrical PMSM model (single phase), Vector diagram of the PMSM for a maximum torque.....	32
Fig. I-11. Hybrid Electric propulsion system configuration	33
Fig. I-12. Inverter weight distribution for different used voltage rating components.....	36
Fig. II-1. Studied electric system	39
Fig. II-2. Software organization	40
Fig. II-3. Available component selection algorithm	41
Fig .II-4. IGBT current and voltage waveforms during switching and conduction and switching losses	43
Fig. II-5. IGBT and Diode equivalent electric circuit	43
Fig. II-6. <i>Eon</i> datasheet parameters' extraction (ABB's 5SNA 1200E330100 IGBT)	44
Fig. II-7. Equivalent thermal model of an IGBT component with antiparallel diode [30] [32]	45
Fig. II-8. Output voltage & current waveforms of a single phase 5-level ANPC obtained by <i>Plecs</i> simulation	47
Fig. II-9. Waveforms of ANPC semiconductors commands and currents obtained by simulation in <i>Plecs</i>	47
Fig. II-10. ANPC 5L Converter schematics: 3-level FC + Switcher (2-level, DC)	48

Fig. II-11. Efficiency for several topologies using available database components	49
Fig. II-12. Voltage and current ratings of semiconductor devices in the database	50
Fig. II-13. Variation of Aon, Bon et Con versus voltage rating and E _{on} versus the current	52
Fig. II-14. Real versus generated components efficiencies, maximal junction temperatures and parallel and series associated switches number for fixed calibers	54
Fig. II-15. Real versus generated components efficiencies and maximal junction temperatures for fixed voltage calibers and adapted current calibers	55
Fig. II-16. Thermal resistance for real and generated used components.....	55
Fig. II-17. Efficiency and maximal junction temperature for real and generated 3300 V components for a power sweep	56
Fig. II-18. Real versus generated components efficiencies and used Silicon ratio for adapted voltage and current calibers.....	56
Fig. II-19. DC bus link types.....	58
Fig. II-20. Inverter input and output currents.....	59
Fig. II-21. Series and parallel capacitor association.....	62
Fig. II-22. Efficiency for 2-level inverters with different voltage rating components for DC bus voltage sweep	67
Fig. II-23. Efficiency for 2-level inverters with different voltage rating components for DC bus voltage sweep with adapted switching frequency	67
Fig. II-24. DC bus optimal voltage value depending on components voltage rating and topologies level number	68
Fig. II-25. Number of topology level to use for 1.7 kV DC bus voltage	68
Fig. III-1. Specific power increasing study line	71
Fig. III-2 : Direct series component association	72
Fig. III-3 : Parallel component association	73
Fig. III-4 : Multilevel converter classification [41].....	74
Fig. III-5. 2-level 3-phase inverter	75
Fig. III-6. 3-level FC inverter's leg	76
Fig. III-7. 3-level NPC inverter.....	77

Fig. III-8. 3-level single phase ANPC	78
Fig. III-9. 5-level ANPC single phase inverter	78
Fig. III-10. 5-level SMC 2x2 single phase inverter.....	79
Fig. III-11. Generated components response for DC bus sweep for 2-, 3- an 5-level topologies	81
Fig. III-12. 2-,3- and 5-level topologies performances for a DC bus voltage sweep with adapted switching frequency	82
Fig. III-13. Specific power for studied topologies using generated components and adapted switching frequency	83
Fig. III-14. Weight distribution for studied topologies with generated components	84
Fig. III-15. Specific power for studied topologies using a switching frequency of 5.8 kHz using real components.....	85
Fig. III-16. Efficiencies of studied topologies for DC voltage and power parametric sweeps	86
Fig. III-17. Multilevel inverter modulation classification.....	87
Fig. III-18. Studied modulation strategies.....	88
Fig. III-19. Output desired voltage and current 3-level PWM waveforms	88
Fig. III-20. PWM triangular carrier and sine reference.....	90
Fig. III-21. DPWMMIN with phase opposition and DPWMMAX with phase disposition triangular carrier and sine reference.....	90
Fig. III-22. 3-level THIPWM1/4 modulation.....	91
Fig. III-23. Switching cell combinations for 3-level NPC and output desired voltage waveform	92
Fig. III-24. T1 and T2 3-level NPC control signals	92
Fig. III-25. Switching cell command schematic	93
Fig. III-26. Full wave 1 used switches combination	93
Fig. III-27. 0 voltage level switches combination for full wave 2	94
Fig. III-28. FW2 State machine.....	94
Fig. III-29. T1 and T2 3-level FC full wave 2 control signals	95

Fig. III-30. Switching at high frequency between the two possible configurations.....	95
Fig. III-31. Voltage and current waveforms for 3-level FC using full wave 3 for an apparent switching frequency of 60 kHz	96
Fig. III-32. Staircase or selective harmonic elimination modulation strategy	97
Fig. III-33. Losses repartition for 3-level FC	98
Fig. III-34. NX and std Mitsubishi modules Type packaging.....	99
Fig. III-35. Packaging structure (std Type)	99
Fig. III-36. 3D single phase 3-level FC inverter	103
Fig. III-37. CPLIP concept scheme [32]	104
Fig. III-38. Module/evaporator assembly.....	104
Fig. III-39. Bus bar configuration for a 3-level FC single phase	105
Fig. III-40. Bus bar leakage inductance	105
Fig. III-41. 3-level DPWMMAX FC (left) and 3-level DPWMMAX NPC (right) weight distribution	106
Fig. III-42. 3-level NPC weight distributions	107
Fig. III-43. 3-level NPC weight distributions with the new sized capacitor	107
Fig. III-44. Design of a 3-level ANPC inverter power module.....	108
Fig. III-45. Lower (left) and upper (right) power modules placed on the evaporator.....	108
Fig. III-46. 3-level 3-phase NPC inverter with new power modules	108
Fig. III-47. 3-level NPC weight distributions with the new sized capacitor and power modules	109
Fig. IV-1. Electrical power mission profile.....	111
Fig. IV-2. Needed machine voltage during the flight mission with the first e-motor winding configuration	112
Fig. IV-3. Needed machine voltage during the flight mission with the second e-motor winding configuration	112
Fig. IV-4. 3-level FC and NPC efficiencies using PWM strategies with both e-motor winding configurations	114

Fig. IV-5. 3-level NPC current repartition during Taxi out phase	115
Fig. IV-6. 3-level FC and NPC efficiencies using THIPWM and DPWMMAX strategies with both e-motor winding configurations	116
Fig. IV-7. 3-level FC and NPC efficiencies using DPWMMAX and DPWMMIN strategies for the 1 st e-motor winding configuration	116
Fig. IV-8. 3-level FC and NPC efficiencies using FW strategy with the 1 st motor winding configuration	117
Fig. IV-9. Current waveforms for Taxi out, take off, cruise and descent using the 1 st motor winding configuration	118
Fig. IV-10. 3-level FC and NPC efficiencies using FW strategy with the 2 nd motor configuration	119
Fig. IV-11. 3-level FC and NPC efficiencies using FW and PWM strategies with 1700 V IGBTs	120
Fig. IV-12. 3-level FC and NPC efficiencies using FW and PWM strategies with 1200 V IGBTs	120
Fig. IV-13. 3-level FC and NPC efficiencies using FW and PWM strategies with 1700 V IGBTs for the 2 nd e-motor	121
Fig. IV-14. 3-level FC and NPC efficiencies using FW and DPWMMAX strategies with 1700 V IGBTs	122
Fig. IV-15. 3-level FC and NPC efficiencies using FW and DPWMMAX strategies with 1200 V IGBTs	122
Fig. IV-16. 3-level FC and NPC efficiencies using FW and DPWMMAX strategies with 1700 V IGBTs for the 2 nd e-motor	123
Fig. IV-17. Output voltage for 3-level FC during the cruise using DPWMMAX and PWM	125
Fig. V-1. Power rating and converter architecture	129

List of tables

TABLE I-1. Hybrid-electric aircraft characteristics [8], [9],[10]	23
TABLE I-2. Full electric aircraft characteristics [8], [9],[10].....	24
TABLE I-3. Advantages and disadvantages of series and parallel hybrid propulsion architectures	26
TABLE I-4. Electric components specific power state of the art and research targets [29]....	29
TABLE I-5. Electric components HASTECS specific power targets.....	29
TABLE I-6. HASTECS inverter efficiency targets	30
TABLE I-7. Used specification.....	35
TABLE I-8. 2-level inverter performances	35
TABLE II-1. Current distribution during an operating period.....	48
TABLE II-2. Needed parameters dependency	51
TABLE II-3. Summary of generated parameters	52
TABLE II-4. Inverter and capacitor currents calculation comparison.....	60
TABLE II-5. Summary of flying capacitor number and voltage value	61
TABLE II-6. 2-level power losses comparison using analytic analysis (<i>Matlab</i>) and <i>Plecs</i> simulation.....	63
TABLE II-7. 3-level FC power losses comparison using analytic analysis (<i>Matlab</i>) and <i>Plecs</i> simulation.....	63
TABLE II-8. 5-level FC power losses comparison using analytic analysis (<i>Matlab</i>) and <i>Plecs</i> simulation.....	64
TABLE II-9. 7-level FC power losses comparison using analytic analysis (<i>Matlab</i>) and <i>Plecs</i> simulation.....	64
TABLE II-10. 3-level NPC power losses comparison using analytic analysis (<i>Matlab</i>) and <i>Plecs</i> simulation.....	64
TABLE II-11. 3-level NPC outer diode switching losses	65
TABLE II-12. 5-level ANPC power losses comparison using analytic analysis (<i>Matlab</i>) and <i>Plecs</i> simulation	65

TABLE II-13. 3-level SMC power losses comparison using analytic analysis (<i>Matlab</i>) and <i>Plecs</i> simulation	66
TABLE II-14. 5-level SMC power losses comparison using analytic analysis (<i>Matlab</i>) and <i>Plecs</i> simulation	66
Table III-1. Summary of topology properties	79
TABLE III-2. Maximal power density for 2-level, 3-level FC, 5-level FC and 5-level ANPC with generated components.....	83
TABLE III-3. Maximal power density for 2-level, 3-level FC, 5-level FC and 5-level ANPC with real components with adapted switching frequency	85
TABLE III-4. Maximal output voltage magnitude as function of DC bus voltage and modulation strategy	89
TABLE III-5. 3-level FC performances for different modulation strategies	97
TABLE III-6. 6 th vs 7 th generation std type module characteristics.....	100
TABLE III-7. 6 th vs 7 th generation 1700 V/ 600 A IGBTs	100
TABLE III-8. 6 th vs 7 th generation 1200V IGBTs	101
TABLE III-9. 7 th generation 1200V vs 1700V IGBTs	101
TABLE III-10. 6 th and 7 th generation 1200V/600A IGBTs vs 1200V/600A SiC module....	102
TABLE III-11. Efficiencies for the two studied topologies and modulation strategies.....	102
TABLE III-12 Specific power the two studied topologies using DPWMMAX modulation strategy	106
TABLE IV-1. Maximal output voltage as function of DC bus voltage and control strategy	113
TABLE IV-2. DC bus voltage value for the different studied modulation strategies and electric motor winding configurations	113
TABLE IV-3. THD for some mission profile points for the 3-level FC using DPWMMAX modulation for the 1 st e-motor winding configuration	117
TABLE IV-4. THD and harmonics amplitudes for some mission profile points for the 3-level FC using full wave modulation	118
TABLE IV-5. THD and harmonics amplitudes for some mission profile points for the 3-level FC using full wave modulation with the 2 nd motor configuration	119
TABLE IV-6. THD and harmonics amplitudes for some mission profile points for the 3-level FC using full wave and PWM modulation for the 2 nd e-motor configuration	121

TABLE IV-7. Efficiencies for different mission profile points for the NPC topology 1 st e-motor	123
TABLE IV-8. Efficiencies for different mission profile points for the NPC topology 2 nd e-motor	124
TABLE IV-9. Efficiencies for different mission profile points for the FC topology 1 st e-motor	124
TABLE IV-10. Efficiencies for different mission profile points for the FC topology 2 nd e-motor	124
TABLE IV-11. Target and achieved efficiencies during takeoff and cruise.....	125
TABLE. VI-1. Conduction Mode average and RMS current	131
TABLE. VI-2. Switching Mode average current formulas	132
TABLE. VI-3. Conduction Mode average and RMS current	132
TABLE. VI-4. Switching Mode average current formulas	133
TABLE. VI-5. Conduction Mode average and RMS current	134
TABLE. VI-6. Switching Mode average current formulas	134
TABLE. VI-7. Conduction Mode average current formulas	135
TABLE. VI-8. Conduction Mode RMS current formulas	136
TABLE. VI-9. Switching Mode average current formulas	136
TABLE. VI-10. Switching Mode RMS current formulas	137

List of acronyms

ANPC: Active Neutral Clamped Point topology

Avg: average

Cond: conduction

DPWM: Discontinuous Pulse Width Modulation

EMF: electromotive force

FC: Flying capacitor topology

FW: Full Wave modulation

GT: Gas turbines

HASTECS: Hybrid Aircraft reSearch on Thermal and Electric Components & Systems

MTOW: Maximum Take-Off Weight

NPC: Neutral Clamped Point topology

PMSM: Permanent Magnet Synchronous Motor

PWM: Pulse Width Modulation

RMS: Root Mean Square

SMC: Stacked Multicell Converter topology

SW: switching

THD: Total Harmonic Distortion

THIPWM: Third Harmonic Injection Pulse Width Modulation

WP: work package

General introduction

The environmental and ecological footprint of transport systems, particularly aircraft, has been increasing steadily in recent years. Current environmental considerations are, therefore, pushing to reduce their ecological impact. Projects such as the Clean Sky 2 project offer an answer to this problem, by proposing a reduction in CO₂ emissions and noise pollution. The development of a hybrid-electric propulsion aircraft would reduce these emissions by reducing the size and mass of systems and using more efficient electrical systems. This would reduce fuel consumption and thus pollutant emissions. It would also improve system reliability and reduce design and operating costs.

This work takes part in HASTECS Clean Sky 2 European project, which studies the possibility of series electric propulsion hybridization in an aircraft, and aimed to develop a simulation tool to pre-size inverters meant to drive hybrid-electric propulsion aircraft's motor. To do so, power electronics topologies, smart control and modulation strategies and also semiconductor technologies were taken into account.

To increase the specific power, the cooling system mass should be decreased either by optimizing its components which is done by the 4th work package or by reducing power losses. Inverter losses reduction could be achieved by using small voltage rating components, by playing on modulation strategies or by using more performant semiconductors.

The first chapter presents the main problem related to current aviation and the opportunities that hybrid-electric propulsion aircraft offers. Hybrid-electric propulsion aircraft principle and necessity will be shown due to the evolution of the commercial aircraft industry and environmental needs in addition to the Clean Sky 2 European project HASTECS goals. The problematic and objectives of this work will be presented in this chapter as well as the used load model.

In chapter II, the software organization and used power losses and thermal models will be presented. The used semiconductor database will also be discussed. This work aims to develop a simulation tool which allows to pre-size converters. It computes different results for different conversion architectures. Its entries are the design constraints, the foreseen converter topologies, and the semiconductor family or manufacturer choice from the available components database. The results such as the efficiency, number of semiconductor devices, maximal junction temperature, switching and apparent frequencies, total losses, and semiconductors, heat exchanger, DC bus capacitor and flying capacitor weights, and also the power density are shown as figures for different parameters of different architectures behaviors.

The studied inverter topologies and modulation strategies will be presented in chapter III. Then the performances will be compared using several semiconductors to choose the most performant solution in terms of efficiency and specific power. The main factor to increase the specific power that was identified in the first chapter is decreasing the cooling system mass,

optimizing its components which is a part of WP4 work or by reducing power losses. Inverter power losses reduction could be achieved either by using small components or by playing on modulation strategies or by using more performant semiconductors.

The main objective of chapter IV is to evaluate several power converter architectures and associated modulation strategies to power the electric machine used for the aircraft propulsion. A comparative study of modulation strategies was carried out to highlight the structure and modulation presenting the best performance to minimize the losses for the sizing point using 3-level topologies using two electrical motor windings configurations; 2 and 3 conductors per slot.

I. State of the art and context

Aviation undoubtedly brings economic and social benefits to society. However, related activities also contribute to climate change, environmental degradation, noise, and local air pollution. The aviation industry contributes about 2 % of the world's global carbon dioxide (CO₂) emissions [1], and this is set to rise so it is under pressure to reduce these emissions, even if air travel continues to gain popularity around the world as shown in Fig. I-1. To reduce the impact of air transport, new technologies are being studied. One solution could be to transpose the hybrid propulsion developed for land vehicles using batteries or fuel cells as an additional energy source to reduce fuel.

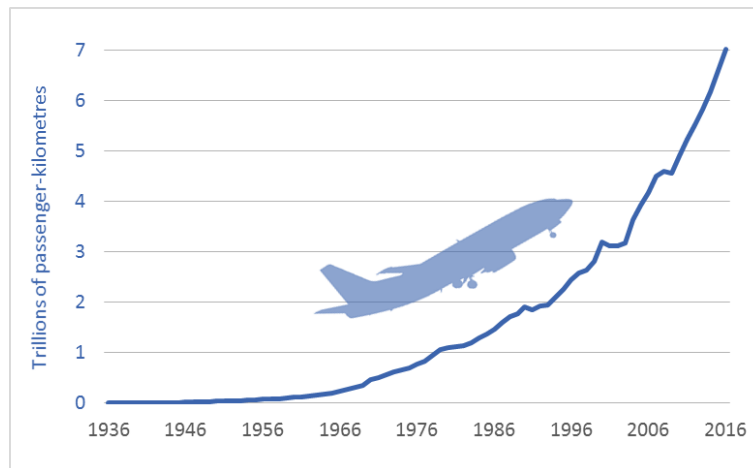


Fig. I-1. Global air travel 1936-2016 [2]

This chapter will present the main problem related to current aviation and the opportunities that hybrid-electric propulsion aircraft offers. To do so, the hybrid-electric propulsion aircraft principle and necessity will be shown due to the evolution of the commercial aircraft industry and environmental needs. These needs were set as the Clean Sky 2 European project HASTECs goals. This work takes part into this project [3] which aims to optimize the complete electrical chain of the hybrid aircraft integrating all aeronautical constraints such as partial discharges for electrical equipment placed in the non-pressurized zone or, in case of high operating voltage, even in the pressurized area. The problematic and objectives of this work will be presented in this chapter as well as the used motor model. To choose an adapted inverter topology, a regular 2-level inverter with a regular PWM was sized for the maximal power point to get a reference in terms of efficiency and specific power using a simple solution which will help to identify the areas to be worked on to reach the targets.

1. Hybrid-electric propulsion aircraft

Each year, about 37 million commercial aircraft carry 4 billion passengers[4], connecting 20,000 city pairs. Commercial aircraft now consume more than 270 million tons of jet fuel per year and thus produce more and more CO₂ emissions [5] as shown in Fig. I-2. Therefore, any discussion on reducing carbon emissions from commercial aircraft will have to be applicable

and effective at this scale. A clean sky is the objective of recent developments and research carried out by all aircraft manufacturers.

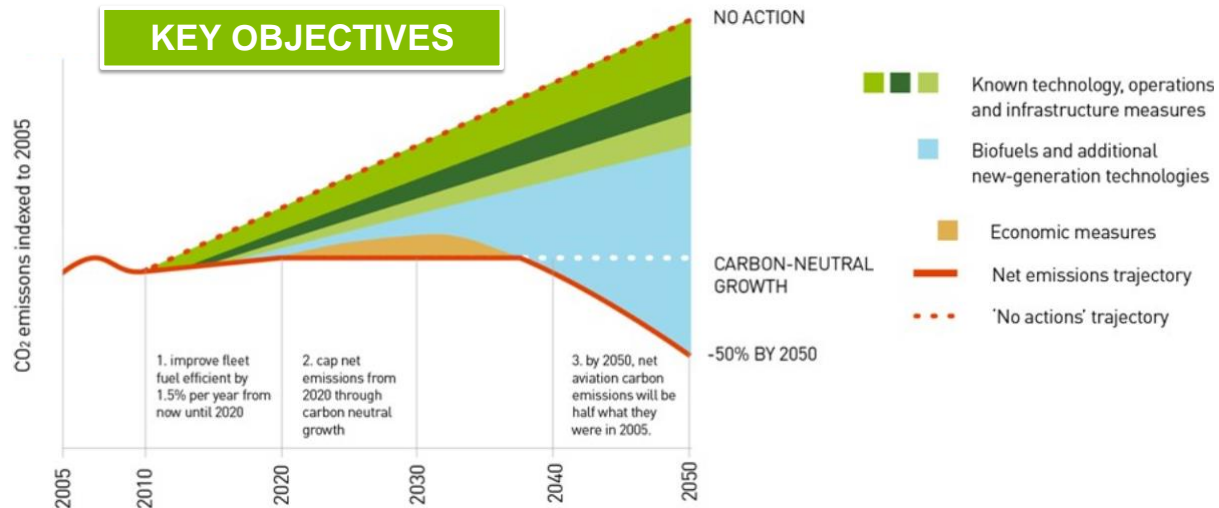


Fig. I-2. CO₂ Emissions Trends from International Aviation, 2005 to 2050

CO₂ emissions from a commercial aircraft can be reduced by reducing the energy required to fly the aircraft by reducing its weight or by improving the propulsion system efficiency or by reducing the amount of drag. This must include total life-cycle carbon emissions during fuel production. For electrical aircraft, this also would include carbon emissions generated by the power source, either on the ground for battery-powered aircraft or onboard electric aircraft equipped with a generator.

The desired overall objective of hybrid and fully electric transport vehicles/aircraft is to limit/cancel the CO₂ emissions caused by internal combustion engines to drive the propeller of the system. Weight may not be a desired optimized parameter in the terrestrial vehicle system, but on the other hand, for space vehicles, it is a highly recommended optimized parameter, because less mass means fewer energy requirements.

Electric propulsion has the potential to revolutionize flight: from cleaner and quieter travel to completely new vehicles, the benefits could be enormous. Faced with estimations that air traffic will double every 15 to 20 years, Airbus believes that electric and hybrid propulsion can offer a viable solution that allows their industry to grow sustainably while reducing its impact on the environment [6]. The international organization ATAG (Air Transport Action Group) in the aviation sector set objectives to have a cleaner sky. It wants to reduce fuel consumption by an average of 1.5 % per year from 2009 to 2020, and to cap CO₂ emissions with carbon-neutral growth from 2020 onwards, as well as to reduce net CO₂ emissions from aviation activities by half by 2050.

These objectives cannot be achieved with current technologies. That is why several projects on research and development of electric and hybrid-electric propulsion technologies are held. In addition to the obvious benefits of reducing CO₂ emissions and noise levels, electrification also makes it possible to completely re-evaluate the design of an aviation vehicle. Different range of vehicles will take advantage of the electrification. One of them concerns the low-capacity and limited-range urban air mobility demonstrators which are developed by Airbus: Vahana and CityAirbus, for intra-urban flights. These are all-electric air vehicles with a capacity of one to four passengers. In the longer term, Airbus believes that hybrid-electric propulsion will probably be installed on larger civil aircraft before becoming fully electric, as the power-to-weight ratios of battery technology are still far from being sufficient [7].

i. Hybrid and electric propulsion aircraft evolution

TABLE I-1 and TABLE I-2 summarize characteristics of some hybrid and electric propulsion aircraft that could be found in the literature.

This table shows a wide range of electric and hybrid propulsion aircrafts. There are mostly small power range aircraft. The small general aviation aircraft using the electric and hybrid propulsion systems are already flying. Indeed, small aircraft can be useful for testing in-flight new technologies. However, not all technologies suitable for general aviation aircraft are scalable to the large dimensions, long flight distances and high operational rates that are key characteristics of large commercial aircrafts.

The Boeing Sugar Volt has the closest power range to our studied case. However, the battery specific energy target reported by Boeing seems high compared to the other ones.

TABLE I-1. Hybrid-electric aircraft characteristics [8], [9],[10]

Name	Architecture	Max power (kW)	Maximum Take-Off Weight (kg)	Battery energy (Wh/kg)	Year
Boeing Sugar Volt [11], [12]	Parallel hybrid	1300-5300	70k-85k	750	2008
ENFICA – FC [13]	Series hybrid	40	550	100	2010
Siemens/Diamond E- Star [14]	Series hybrid	70	800	-	2011
Embry-Riddle Eco-Eagle	Parallel hybrid	105	1075	125	2011
Siemens/Diamond E- Star 2	Series hybrid	80	800	-	2013
Hypstair [15]	Series hybrid	200	-	-	2014
Cambridge SOUL[16], [17]	Parallel hybrid	20	235	144	2014
Airbus E-Fan 1.2	Series hybrid	60	600	-	2016

TABLE I-2. Full electric aircraft characteristics [8], [9],[10]

Name	Maximum power (kW)	MTOW (kg)	Battery energy (Wh/kg)	Year
Lange Antares [18]	42	660	136	2003
Fishman Electraflyer C [19]	13.5	283	-	2008
Yuneec E430 [20]	40	470	154	2009
Pipistrel Taurus Electro G2 [20]	40	450	-	2011
Pipistrel Taurus Electro G4 [21]	150	1500	180	2011
FB Stuttgart eGenius [21]	60	950	204	2011
Chip Yates Long ESA	192	680	-	2012
Airbus E-Fan	60	600	207	2014
Nasa X-57 Maxwell [12], [22]	132	1360	-	2014
Pipistrel Alpha Electro	60	550	171	2015
Siemens Extra 300 (330LE) [23]	260	1000	-	2016

Unlike Boeing who developed its hybrid-electric propulsion aircraft in 2008, Airbus began its journey to electric flight later. Fig. I-3 presents Airbus electro-mobility roadmap starting from 2010. As noticed in Fig. I-3, in only 10 years, the needed power is 100 times higher than for the single-seat Cri-Cri that was designed to fly 30 minutes. There is a multitude of challenges that must be researched and mastered to design the new single-aisle aircraft requiring 20 MW.

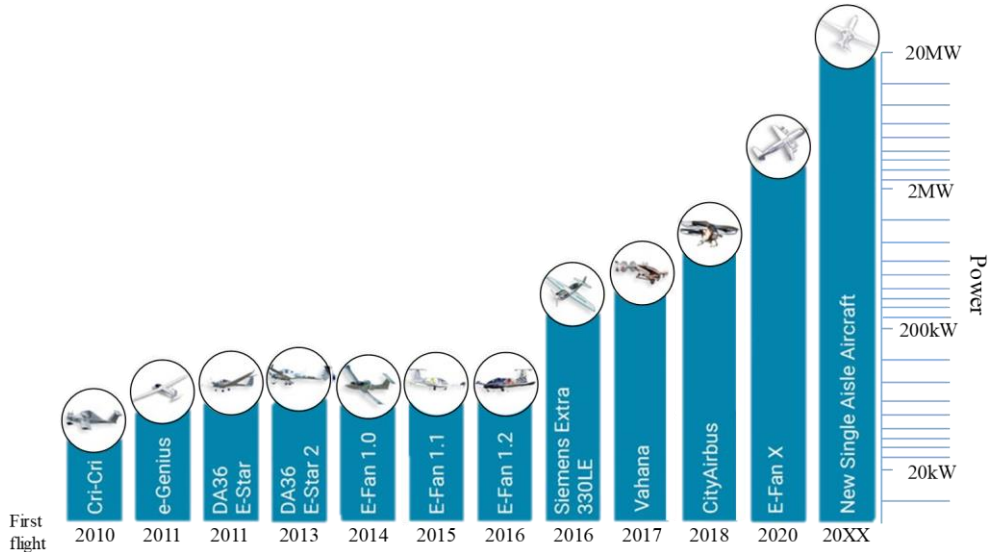


Fig. I-3. Airbus electro-mobility roadmap [24] [25]

The E-Fan family of aircraft allowed Airbus to learn many lessons from the hundreds of flights performed. In November 2017, Airbus launched the E-Fan X with its partners Siemens and Rolls-Royce which aims to replace only one propeller of the four by a hybrid-electric one. In June 2019, Rolls-Royce took over Siemens' e-Aircraft division, so Siemens is no longer involved in this project. This partnership aims to accelerate and take the technological maturity and performance of hybrid-electric propulsion to a new level. The E-Fan X is an ambitious technology demonstrator project that will be a decisive step towards the manufacture of a hybrid

electric civil aircraft on the scale of today's single-aisle aircraft. The consortium will use a BAe146 as a flight test platform for a hybrid serial architecture by 2020, consisting of a 2 MW electric motor, a gas turbine with integrated 2 MW generator and a 2 MW battery controlled by a control unit called "e-supervisor". E-fan X has the same power range as the one studied in our project presented later in this chapter.

ii. Hybrid-electric architectures

Recently, the idea to use hybrid architecture in aircraft propulsion has expanded. This idea is similar to what can be found in Hybrid Electrical Vehicles (HEV). Three different hybrid architectures exist: Series, Parallel and Series/Parallel systems, presented below. Each type of them has its benefits and criteria that differ from the others [26]. However, all three types share the idea of using a storage system that separates the thermal engine operating point (Gas Turbine, Electrical Generator or Auxiliary Power Unit (APU)) from the propulsion, thereby optimizing the efficiency of the thermal engine.

- Series Hybrid Propulsion:

In the series hybrid-electric architecture, the Gas turbines (GT) or the engine as in Fig. I-4 runs at constant RPM and drives a mechanically-coupled electrical generator that produces electric power. This power is then delivered to the system where it is combined with the electric power coming from the auxiliary power sources. To supply the AC electric motor, the DC power supply from the batteries and/or generator must be converted to AC power, which is done by power converters so that it can finally operate the electric motor that drives the propeller.

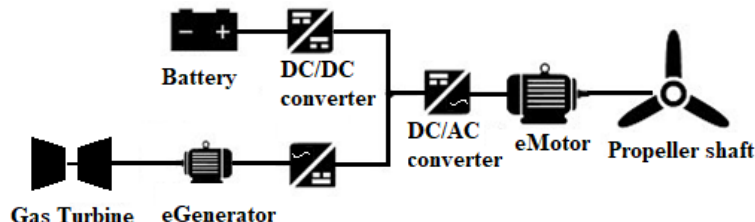


Fig. I-4. Series hybrid propulsion system [27]

- Parallel Hybrid Propulsion:

The parallel hybrid-electrical architecture (Fig. I-5) is more complex than that of the series. Indeed, to be able to have the propeller-driven simultaneously by the GT and the electric motor, a complex gearbox is required. Besides, the GT does not always operate at its maximum efficiency point but rather is required to operate at a wide range of speeds, which generally makes it less efficient. Conversely, the parallel architecture has the advantage that the electric motor can be less powerful and therefore smaller and lighter than in series architecture since it does not have to provide the maximum power required for the propeller alone. Since it is not necessary to convert the GT mechanical power into electrical power, the electrical generator is not present, but the advantages of getting rid of it are reduced by the need for the complex

mechanical transmission and gearbox part used to distribute the mechanical power between the electric motor, the GT and the propeller.

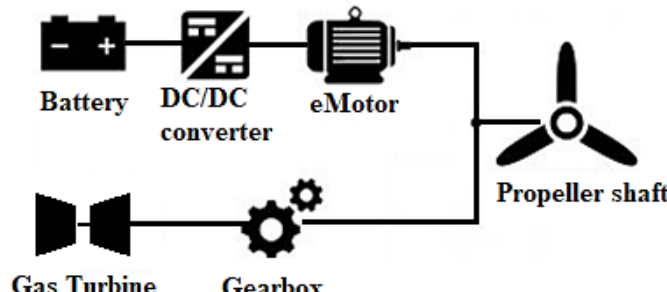


Fig. I-5. Parallel hybrid propulsion system [27]

- Combined Hybrid, mixed or association of Parallel/Series Hybrid Propulsion:

This architecture merges the two series and parallel types. The main advantages of this architecture are that it allows a smaller gas turbine to operate optimally and directly during the cruise mission phase, and also to charge the batteries, a possibility that traditional parallel architectures do not allow. This powertrain architecture is widely used in the automotive industry.

TABLE I-3 sums up the advantages and disadvantages of both series and parallel hybrid architectures. The series-parallel configuration benefits from most of the advantages of both configurations. The engine propulsion power is divided into two power-flows, which are transmitted to the propeller over a mechanical and an electrical branch. However, this configuration is more complex to design and control.

TABLE I-3. Advantages and disadvantages of series and parallel hybrid propulsion architectures

Architecture	Series	Parallel
Pros	<ul style="list-style-type: none"> • E-motor configuration is relatively simple to control • Engine able to operate at its maximum efficiency point • Gas turbine is more efficient at low speed and high load 	<ul style="list-style-type: none"> • A small engine and motor help reduce vehicle mass • Performs well in high average power and high load conditions • higher transmission efficiency due to the mechanical connection
Cons	<ul style="list-style-type: none"> • Low transmission efficiency 	<ul style="list-style-type: none"> • complex mechanical transmission • The design and control is relatively more complex than the series configuration

iii. Energy management for the studied solution

Only the series propulsive system is taken into account in the scope of this study.

The general schematic of the system during different phases of a mission is shown in Fig. I-6. In the meantime, our study considers only the power conversion for motor driving. There are two main phases in this mission profile; the takeoff which represents the maximal power point and the cruise which is the longest phase of the flight mission. Taxi out and in and descent could be powered using full electric energy given by auxiliary electric source either the batteries or the fuel cell. During these sequences, the power demand is low and the turboshafts could be relieved by electric power sources which are more efficient. This scenario corresponds to a light hybridization. The gas turbine could be sized for the cruise power point and auxiliary electric source could be used to help the gas turbine to supply the needed electric power for the takeoff.

This study does not cover hybridization and energy generation but focuses mainly on the inverter that feeds the electric motor connected to the propeller.

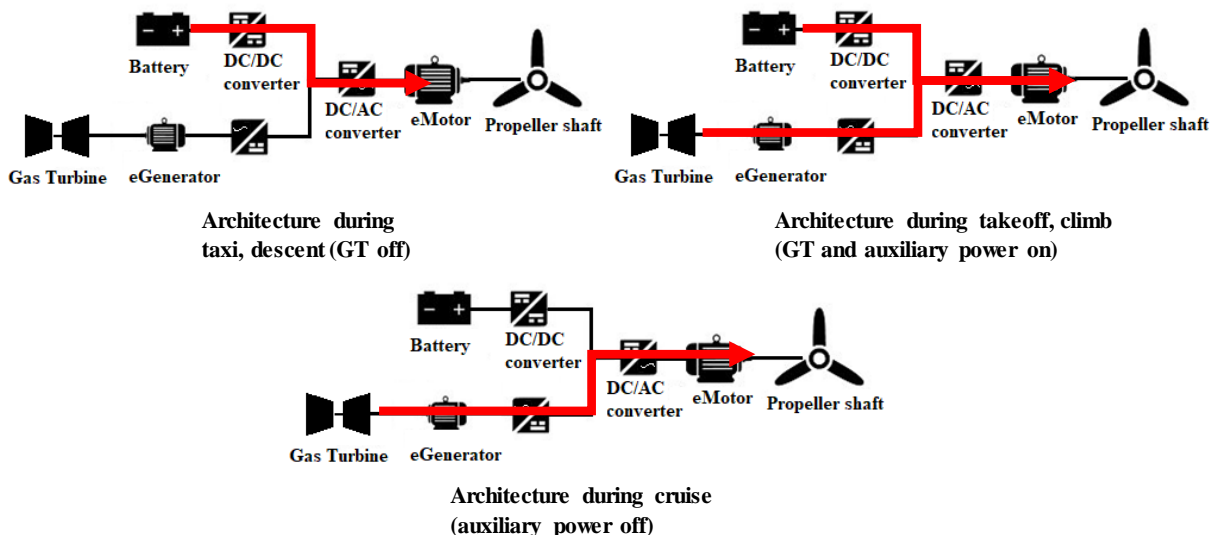


Fig. I-6. General propulsion schematic system during a mission of an aircraft [28]

2. Problematic and objectives

i. HASTECS project

The overall objective of the HASTECS (Hybrid Aircraft: Academic research on thermal & Electric Components & Systems) project is to support a hybrid-electric demonstration by developing models and tools that can help designers evaluate the main benefits of architectures and energy management. The assessments will be integrated at system level and will include the design and analysis of the main components of the hybrid energy chain: electrical machines and their cooling, cables, power electronics and associated thermal management taking into

account the main environmental constraints, including partial discharges due to the new high power and ultra-high voltage standards.

To this end, the various working groups will try to optimize the performance of electrical and thermal components in terms of specific power (kW/kg) or specific energy for batteries or fuel cells. The energy efficiency of the components and the entire system with its energy management is a second major objective. The performance evaluation will be based on the "basic architecture" presented in Fig. I-7 and extrapolations will, of course, be made to generalize our results to other architectures and other power levels.

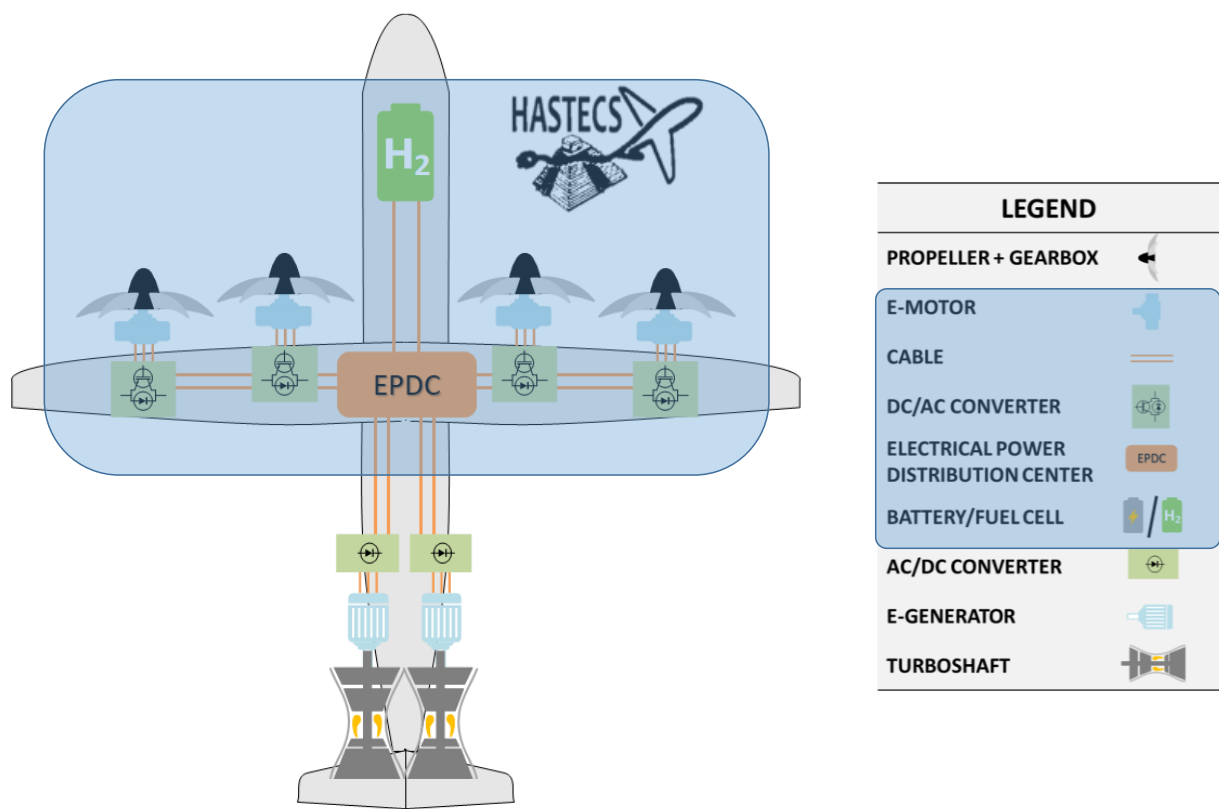


Fig. I-7. Baseline architecture for assessments

The "brakes on innovation" and the subsequent physical limitations that would make it difficult to achieve performance objectives will be identified, and a sensitivity analysis will be carried out to select the most significant impact on technologies and components taking into account the environmental constraints. These constraints are mainly partial discharges and thermal cooling systems and they depend on environmental conditions (external temperature, pressure, humidity, air velocity) in the nacelle as well as in the fuselage.

ii. Hybrid-electric components specific power targets

The power chain needs careful design to minimize the weight of the whole system. This last element is directly linked to the weight of the converter but also the losses through the weight

of the heat exchanger. To obtain an aircraft with a propulsive system weight similar to the current one, some research projects have set targets in terms of specific power for the different components of the power chain as reported in TABLE I-4. Based on this specific power values, our project sets its targets that will be detailed in the project presentation.

TABLE I-4. Electric components specific power state of the art and research targets [29]

	Motor & Generator	Power Electronics	Battery		
	Power (MW)	Specific Power (kW/kg)	Power (MW)	Specific Power (kW/kg)	Specific Energy (Wh/kg)
Current state of the art (2016)					
Non cryogenic	0.25	2.2	0.25	2.2	200-250
Cryogenic	1.5	0.2			
Research goals (2016)					
NASA 10-year goals	1-3	13	1-3	15	
NASA 15-year goals	5-10	16	5-10	19	
US Air Force 20-year goals	1	5	1	5	400-600
Ohio State University 5-year goals	2	15	2	23	

However, this project sets two main objectives in terms of specific power. The first is the "medium-term objective of 2025" which corresponds to 15 kW/kg for power electronics including their cooling system and 5 kW/kg for electrical machines including cooling. The second is the "2035 long-term objective" which corresponds to 25 kW/kg for the power electronics and 10 kW/kg for electrical machines including their cooling systems (TABLE I-5).

TABLE I-5. Electric components HASTECS specific power targets

	Electric motor Specific Power (kW/kg)	Inverter Specific Power (kW/kg)
HASTECS targets (2016)		
2025	5	15
2035	10	25

Achieving these objectives would have major positive consequences for the environment, with a constant reduction in fuel consumption in flight and a reduction in ground noise thanks to entirely electric taxiing.

iii. Flight mission profile

The flight mission profile, in terms of electric motor voltage and current, considered in the project is shown in Fig. I-8. The maximum power is in the range of MW and due to confidentiality issues, the value of the maximum power cannot be given: all power values will be given in per unit.

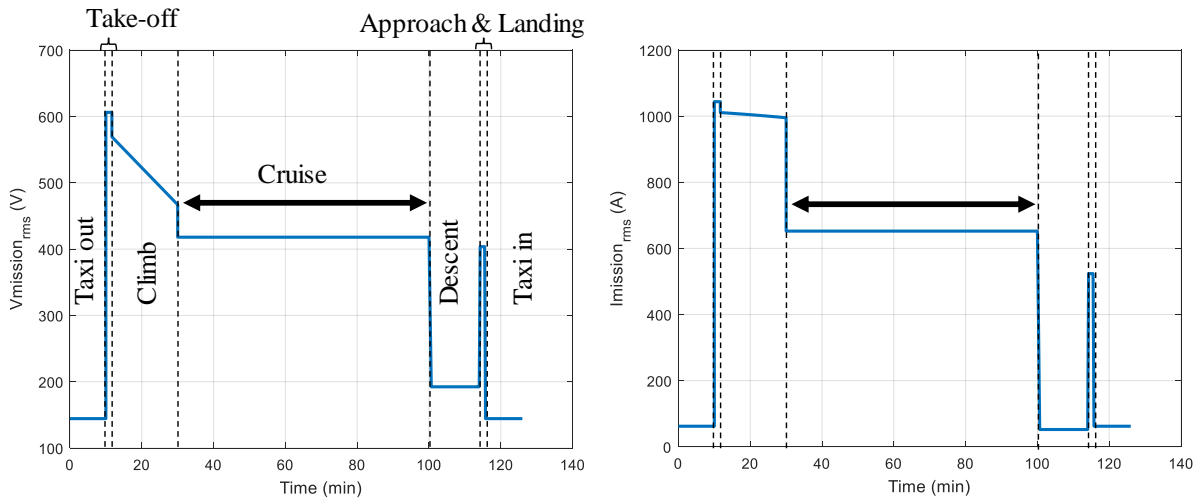


Fig. I-8. Voltage and current RMS mission profile

Two targets in term of efficiency for the power electronics were set by HASTECS project. For the 2025 target, the efficiency should be higher than 98 % for the cruise point and higher than 96.5 % for the maximal power point. On the other hand, for the 2035 target, the efficiency should be higher than 99.5 % for the cruise point and higher than 99 % for the maximal power point (TABLE I-6).

TABLE I-6. HASTECS inverter efficiency targets

	Take-off Efficiency (%)	Cruise Efficiency (%)
HASTECS targets (2016)		
2025	96.5	98
2035	99	99.5

iv. HASTECS work packages

To achieve these objectives, the INPT has assembled a consortium of 3 research laboratories with experience in the preliminary design of electrical and thermal components and architectures for aerospace applications:

- Laboratory on Plasma and Energy Conversion (LAPLACE), Toulouse (FR)
- Research and Engineering Institute for Transport and Environment (P'), Poitiers (FR)
- Inter-university Material Research and Engineering Centre (CIRIMAT), Toulouse (FR)

To achieve these general objectives, the HASTECS project has identified six technical work packages derived from the baseline architecture (Fig. I-9). It started in September 2016 and will last for 5 years and it includes 6 Ph.D. thesis and 2 post-doctoral positions. Each work package objectives are detailed below.

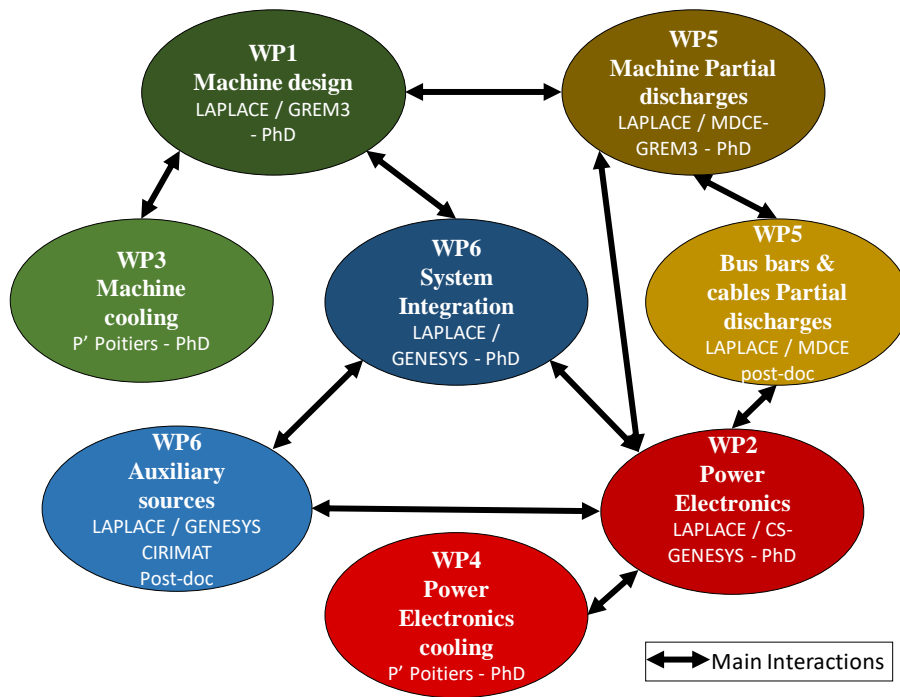


Fig. I-9. HASTECS consortium structure

WP 1: develop a target-setting tool to help evaluate the design of electric machines for hybrid-electric propulsion. The main objective is to analyze the phenomena that limit the specific power of electrical machines and to propose technological and structural innovations (geometry);

WP 2: develop sizing trends of static converters for a hybrid-electric propulsion system. Define two or three levels of DC bus standards for which every component will be designed; the first at a “moderated voltage” (~700 V); the second (and potentially third) at few kV (<7 kV); and develop a design tool for the estimation of power electronics performances;

WP 3: propose and analyze original machine cooling solutions;

WP 4: provide cooling and heat exchanger system solutions for power electronic converters;

WP 5: take into account the partial discharges phenomenon and assess impacts in the design of the power electronics and electric machines of the Hybrid Electric Propulsion System;

WP 6: develop simplified models for the most promising technologies of auxiliary sources (Lithium-Ion batteries, fuel cells) for 2035; and integrate technological bricks (machines, power electronics, cables, storage components, cooling system) and new concepts proposed in other WPs, then optimize the overall hybrid chain integrating its power management strategy.

For example, for our work package (WP2) strong links with the other WPs (Fig. I-9) exist, detailed below for each one.

- WP4: converter losses and components heat fluxes in W/cm² will impact heat exchanger system sizing and the transient capacity of this latter will influence converter sizing point.
- WP5: the voltage variation generated by the change of switch state, both in static and dynamic, will represent the stress of bus bars, cables and motor windings leading to possible partial discharges.
- WP6: to optimize the whole architecture, the WP2 needs to develop equations and models representing the trends studied in the “system integration” task.

WP1: To design the power electronics converter, a machine model is needed. Moreover, the switching frequency has a great impact on motor losses and current waveform.

Many possible electrical motors can be used in the scope of aircraft propulsion system design. Recent applications in the transportation domains are mostly using Permanent Magnet Synchronous Motor (PMSM) due to many specifications mainly high power density. This work does not highlight the mechanical solution of the system design since this part is a main study of WP1.

The simplified electrical model of a PMSM consists of the synchronous inductor with a resistor and the electromotive force (EMF) in series which is presented in Fig. I-10. The iron losses are not represented but have been taken into account in the sizing by WP1. The choice here is to maximize the torque, so the current is in phase with the EMF (non-salient pole rotor). This results in the vector diagram of Fig. I-10. The current is not in phase with the output voltage, leading to a power factor not equal to one and an oversizing of the inverter. Equations (I-1) and (I-2) can be determined.

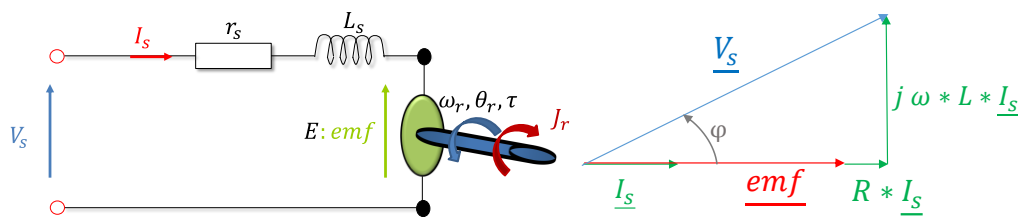


Fig. I-10. Electrical PMSM model (single phase), Vector diagram of the PMSM for a maximum torque

$$V_s = R * \underline{I}_s + jL \omega \underline{I}_s + \underline{emf} \quad (I-1)$$

$$emf(t) = \Phi_{no_load} * \omega * \sin(\omega t) \quad (I-2)$$

So the given parameters from WP1 are R and L the stator resistance and inductance and Φ_{no_load} the no-load flux and ω the electric pulsation or the frequency.

v. Work Package 2 (WP2)

The work package focuses only on the inverter used to power the electric motor that drives the propeller.

WP2's goal is to develop a software tool that determines the best static converter architectures for hybrid-electric propulsion shown in Fig. I-11, taking into account both environmental and cooling constraints. The tool must evaluate the efficiency of the chosen solution, its weight and other factors for the medium term (2025) or the future (2035). In order to facilitate the integration tasks of the WP6 system, an output model representing the design trends will be provided to process them in an optimization cycle. The proposed study will be based in particular on the post-doctoral study "High power conversion chain for aircraft hybrid propulsion" carried out by Mohammad IBRAHIM [28] in cooperation with Airbus FPO.

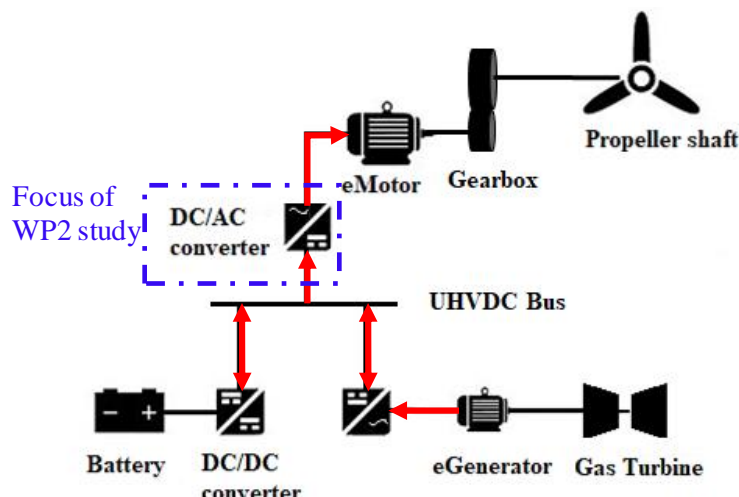


Fig. I-11. Hybrid Electric propulsion system configuration

Even if the system is inside the fuselage (i.e. in a pressurized area), the cruise cabin altitude is higher than the limit given by manufacturers of the high-power modules for ground equipment. Besides, the ability to extract heat losses from the converter is a huge problem: for example, a 1 MW converter with 95 % efficiency will have 50 kW of losses!

Compared to the static converters used today in aeronautical electrical networks, the nominal power of the converters will increase significantly (more than 1 MW). Therefore, the bus voltage value must also increase above 700 V, which will be critical in the event of partial discharge.

The variation of the operating point during flight sequences as shown in Fig. I-8 represents a serious issue that should be investigated. Maximum power is only required during the "take-off" and "climb". The cruise power requirement is lower (half the maximum power) and represents more than half the duration of the mission. Thus, if the converter is sized for maximum power, it will be mainly used at operating points where its efficiency is not optimized. This is a major difference compared to the electric propulsion of land vehicles. The

study will, therefore, attempt to optimize the choice of converter sizing points to be able to accept peak consumption while having the highest efficiency throughout the mission (especially during the cruise).

If the sizing power of the converter is close to the take-off power, solutions to increase the efficiency of the converter when it is used at low power can be studied: for example, the number of converter legs or switches in parallel can be changed according to the desired power (because the power is directly linked to the current, the speed of the machine being close to constant). Of course, such a solution will lead to a heavier sizing, only used at its nominal capacity during a short period (take-off). Another possibility is to use two or more converters. In the case of two converters, both are operated during take-off. Then, only one is connected to the motor, the other one being used for other non-propulsive functions.

Several converter architectures will be evaluated according to the value of the DC bus and the sizing power, through different criteria (weight, losses, output frequency, passive components weight, etc.), using today silicon components as IGBTs, which are the most suitable for the needed power, voltage and frequency ranges, with the first target around 2025. But since the project is designing the aircraft of the future (long term target for 2035), a sizing with silicon carbide components (SiC) or other new technologies will also be made.

To study all aspects and to achieve these objectives, WP2 was composed of two successive tasks. The first one deals with the study and design of a unique power converter for the whole power needed by the application. It will take into account the possible value for the DC Bus and different architectures of the power converter based on silicon power devices. The second one was devoted to the study of power converter architectures using components based on new generations and technologies and several control strategies. Moreover, in this study, the filters are not considered since network quality constraints are not taken into account as well as their potential impact on the mass of the system.

3. Reference case: 2-level PWM inverter solution

To choose an adapted inverter topology, a regular 2-level inverter with a sine PWM was sized for the maximal power point to get an idea about what could be achieved in terms of specific power using a simple solution.

For this study case, the DC voltage (V_{DCBus}) is chosen to deliver the needed maximal voltage of the electric machine ($V_{out_{max}}$) as in TABLE I-7. The inverter is sized for the maximal power point with a 2 kV DC bus and a switching frequency of 5.8 kHz which represents approximately 11 times the PMSM nominal frequency parameter given by WP1. To estimate the inverter specific power including the heat exchanger, a 0.34 kW/kg coefficient is taken into account which translates the power losses directly into cooling system weight. This value is used as a base value issued from the specification dossier. The passive components weight, capacitors, in this case, are also taken into account.

TABLE I-7. Used specification

Fundamental frequency (Hz)	532.3
$V_{out_{max}}$ (V)	857.3
$I_{out_{RMS}}$ (A)	1054
Modulation index	0.86
Power factor	0.78

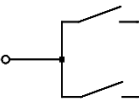
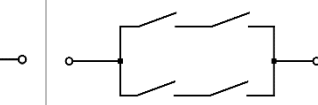
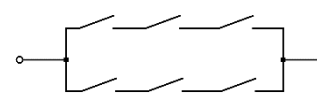
To withstand the current imposed by the machine, semiconductors are put in parallel if the needed current rating exceeds the maximally available one. On the other hand, to withstand the voltage depending on the voltage using rate (K_v), components may be associated in series (n_{series}). The components are used up to 100 % of their current rating.

$$n_{series} = \frac{2*K_v}{V_{rating}} * V_{DCBus} \quad (\text{I-3})$$

If the direct series association is not allowed and the components should be used up to 50 % of their nominal voltage, only one component rating could be used which is 6500 V. However, these components are not adapted to the used high switching frequency. If the second largest voltage rating components (3300 V) are to be used, they should be used up to 61 % of their rating in order to use only one component in series.

The first study case uses two 3300 V / 800 A Infineon components associated in parallel to withstand the current and are used at 61 % of their voltage caliber. The second one uses two 1700 V / 600 A Infineon components associated in parallel and two components in series used at 59% of their voltage caliber even if the direct series association is hard to realize. For the third case, two 1200 V / 600 A Infineon components are associated in parallel and three components in series used at 56 % of their voltage caliber. TABLE I-8 sums the main inverter performances for these three study cases.

TABLE I-8. 2-level inverter performances

Components voltage ratings	3300 V	1700 V	1200 V
$\eta(\%)$	92.55	98	98.54
Junction temperature (°C)	244	307	98
Specific Power (kW/kg)	3.39	8.86	9.23
Series and parallel associations (per switch)			
Total number of semiconductors (per phase)	4	8	12

For the 3.3 kV components, the obtained efficiency is very low so as the specific power compared to smaller components. The maximal junction temperature exceeds the limit of 150 °C for the 3.3 kV and 1.7 kV components. If the efficiency is higher so the cooling system mass is lower, which leads to a higher specific power. But these results are still far from the targets. To have an acceptable solution using the 3.3 kV components, the switching frequency should be reduced to 2 kHz (3.8×532 Hz) whereas for the 1.7 kV ones it is not possible even if the switching frequency is equal to the machine fundamental frequency (532 Hz).

Fig. I-12 shows the inverter weight distribution for the different used voltage rating components. The cooling system mass, which is a direct image of the power losses through the coefficient given by Airbus, is the predominant weight of the inverter. The bus bar comes in second place and will be dominant if the heat exchanger weight is reduced.

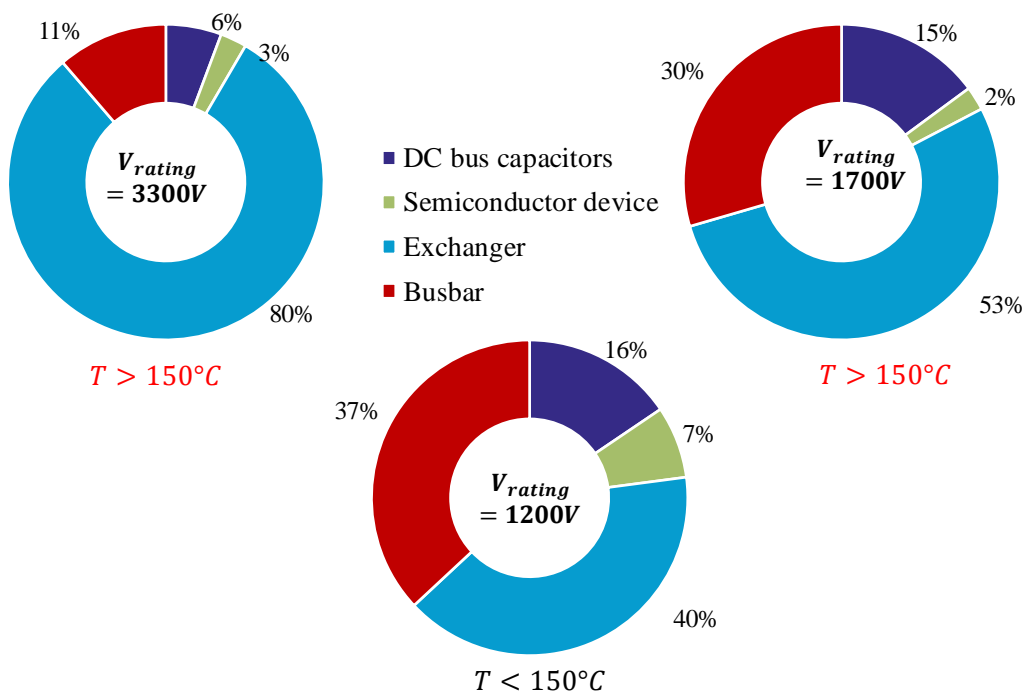


Fig. I-12. Inverter weight distribution for different used voltage rating components

Small rating components have of course better performances, but the direct series association is hard to realize so using multilevel topologies could be a solution. From these examples, the main factors to increase power density are identified. The first one is decreasing the cooling system mass, optimizing its components or by reducing power losses. The second one will be to optimize the bus bar weight.

4. Conclusion

HASTECS project studies the possibility of electric propulsion hybridization in an aircraft. Besides the global architecture, the different work packages aim to increase the specific power of the different components of a high-power electric chain incorporating a high-voltage DC

bus, its wiring and power electronics interfacing the bus and the electric motor to have a solution that can be fitted in an aircraft.

This study will lead to an optimization of the complete chain that will propose the interesting structures integrating all aeronautical constraints such as partial discharges for electrical equipment placed in a non-pressurized zone or case of high operating voltage even in a pressurized zone. In this Ph.D., power electronics topologies, smart control, and modulation strategies and also semiconductor technologies will be taken into account. This work objective is to design a highly integrated power electronics inverter with a specific power of 15 kW/kg for 2025 target and 25 kW/kg for 2035 target including its cooling system.

Our work package focuses on the power electronics converter. To guide the work of the various work packages of the project, a first step is to define an optimal DC bus voltage range. This has a direct impact on the study of partial discharges but also in the design of motor windings. This will be done using a developed simulation tool, detailed in Chapter II, which uses the conventional inverter topologies model and components from the available database, to compute the inverter performances as efficiency, maximal junction temperature, and total weight.

Then, it is necessary to compare the efficiency and power density of several multilevel topologies, modulation strategies and components technologies which will be evaluated in Chapter III, to find the optimal solution. A 3D inverter model will be designed to estimate more accurately the total inverter weight including the bus bar. This study will lead to the inverter topologies choice for the given specification.

In chapter IV the chosen inverter topologies will be evaluated for two electric motor configuration for the entire flight mission. A comparative study of modulation control strategies will be carried out to highlight the structure and modulation presenting the best performance to minimize the losses.

II. Simulation tool

This work aims to develop a pre-design tool which allows to pre-size the converters and their components for a DC to AC 3 phases inverter as in Fig. II-1. It computes different performance results for different conversion architectures. Its main entries and results are as follows:

Entries:

- Specification (DC bus voltage, output power, load power factor...),
- Inverter topologies,
- Modulation strategy,
- Switching frequency,
- Semiconductor manufacturer,
- Heat exchanger coefficient is given by WP4 that translates power losses to cooling system weight.

Results:

- Efficiency
- Semiconductor power losses (conduction and switching),
- Number of semiconductors associated in series and in parallel,
- Maximal junction temperature,
- Semiconductors, capacitors and cooling system weights,
- Specific power.

The results are shown as figures for different parameters of different architectures behaviors.

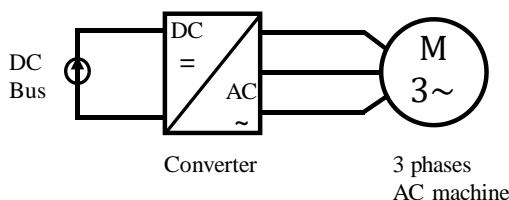


Fig. II-1. Studied electric system

In this chapter, the organization of the software will be presented. In this software, the inverter topologies and modulation strategies are fixed so that the user can choose his inputs from those available. It calculates the power losses and junction temperature for each selected case according to the model that will be detailed later in this chapter using the parameters of the selected semiconductor. This semiconductor device is selected from the available database or can be generated in such a way as to adapt to the necessary current and voltage calibers if the user so decides, according to the generation principle which will be described and validated below. The sizing of the capacitor will then be explained. The loss models will then be validated using a time simulation on *Plecs* for several inverter topologies. These models and the generated components will then help to define the voltage range of the DC bus, which corresponds to the first step of the WP2's work.

1. Software organization

The tool makes it possible from a specification to size the converter according to the chosen topology. It also makes it possible to carry out parametric studies by varying the DC bus voltage, the requested power or the modulation index to determine the optimum operating point. It can also take into account a mission profile that allows checking the performances of the converter for a given mission[28].

Then the tool computes the different results. It is realized in *Matlab* object programming to model converters architectures and is based on analytical calculations of the losses in the semiconductor components for the various integrated multilevel architectures considering several modulation strategies. These losses result in heating up the semiconductors. The thermal rising in the semiconductor will affect its functionality and its lifetime, however, this was not taken into account in this work. Moreover, the losses impact the size of the cooling system needed in the design.

For example, to size a 3-level FC inverter using the user specifications, the tool defines firstly the needed voltage and current components ratings for semiconductors, DC bus and flying capacitors. Then, from the available database, using a database manager program, chooses the most appropriate components and uses their parameters to compute the inverter performances including the power losses, efficiency, maximal junction temperature and also the total weight.

To get an image of the object-oriented principle used to model the converters topologies in *Matlab*, a diagram in Fig. II-2 is established. It illustrates the class diagram of the proposed model. Hence we can distinguish all the links and dependencies between objects.

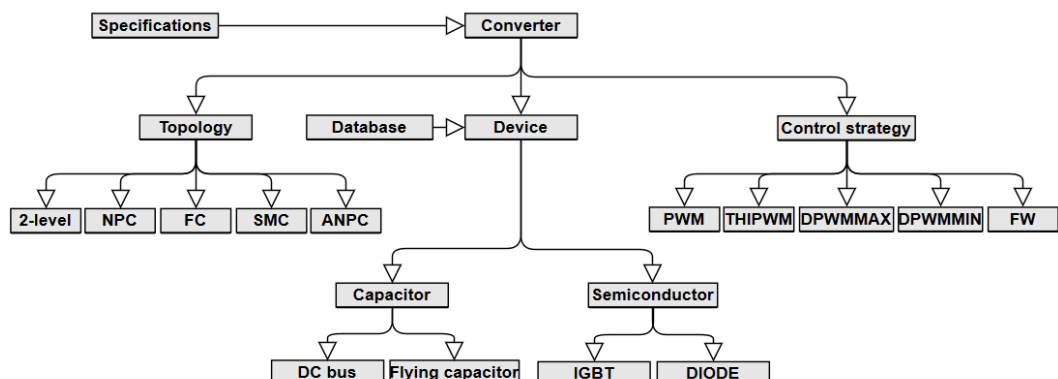


Fig. II-2. Software organization

The ‘Device’ object, for example, is a class that can be linked to a database. This element can then be characterized as a semiconductor, capacitor, or any other type of item. For example, inductors are integrated to the software as a Device object and not used in this work but it could be used if necessary, for example, as a filtering components. So the software is completely modular and could be easily modified to add new objects. Each element has a number of

associated properties and methods. For a semiconductor element, an object of either type IGBT or type DIODE is created.

Furthermore, an object of type converter is proposed and can be characterized into multiple topologies (2-level topology, FC, NPC, SMC or ANPC). This converter object is then linked with a specification object and a set of semiconductor and capacitor elements. It is also composed of control or modulation strategies that uses the selected topology and devices parameter to evaluate the power losses. Each block may contain one *Matlab* m-file script or multiple ones. Moreover, each script has data and characteristics of classes and their properties; the scripts are named as the including class inside them. These converter components will be detailed in Chapter III.

For each design point, it selects from the available database, the most appropriate semiconductor components that fit well the desired voltage and current. In order to do so, an adapted algorithm was developed (Fig. II-3).

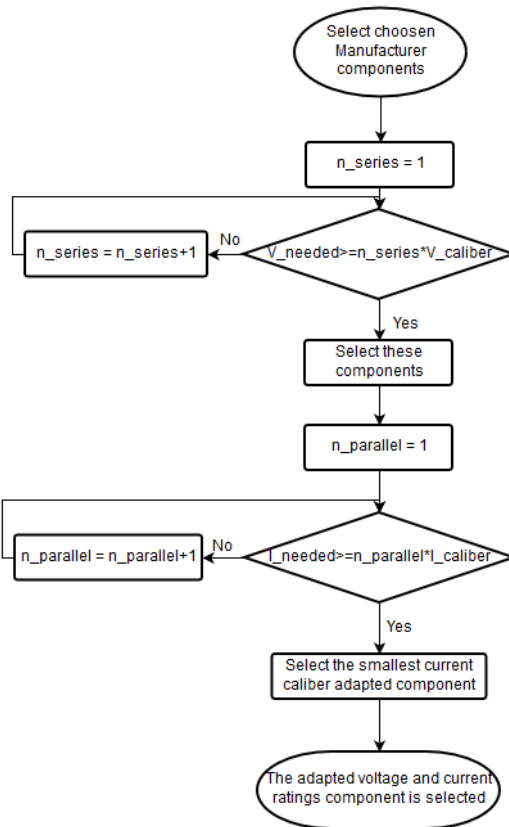


Fig. II-3. Available component selection algorithm

The first step of this algorithm is selecting the manufacturer chosen by the user to extract the corresponding components from the database. It is then determined whether the requested voltage rating can be achieved by the available components. If none of the components is adapted and therefore the biggest component is too small, components are connected in series to obtain the desired voltage. Otherwise, if several component calibers are suitable, the smallest caliber is chosen among those which are suitable so to have the best performing component as

noticed in Chapter I. for the current caliber, if the required current is higher than the largest current rating component, components are associated in parallel. Otherwise, if several components are adapted, the smallest one is selected.

This software allows great flexibility and a large degree of freedom for different designs and their behaviors during studies. This adds many advantages regarding multiple methods implementations and desired parametric sweep modeling.

2. Power losses and thermal modeling

After selecting the components, the next step is to compute the power losses to evaluate the inverter efficiency. They will also be used to calculate the maximal junction temperature. These losses and junction temperature are computed using a simplified models presented below.

i. Modeling principle

In order to model the losses in the semiconductor, we need to calculate the switching and conduction losses. Both losses depend on the circuit parameters and device characteristics. In order to simplify the calculation of the losses caused by power semiconductors, a number of preliminary assumptions have been made. In this case, the used semiconductor are only silicon IGBTs and diodes. These are set out below:

- The modulation depth is represented by the index k which value is between 0 and 1. Only the sine PWM power losses will be presented in this chapter;
- The load is considered linear: the load current is sinusoidal with an RMS value depending on the voltage value applied;
- Current and voltage ripples are neglected;
- The system is considered to be in steady state;
- The load (PMSM sized by WP1 presented in Chapter 1) is always inductive so the phase shift θ between the phase current and the associated single voltage belongs to the interval $[0, \pi/2]$.
- No dead time on IGBT drive orders.

For the power losses model, the current and voltage characteristics of a transistor during a switching period are represented in Fig .II-4. There are two types of power losses, switching and conduction losses.

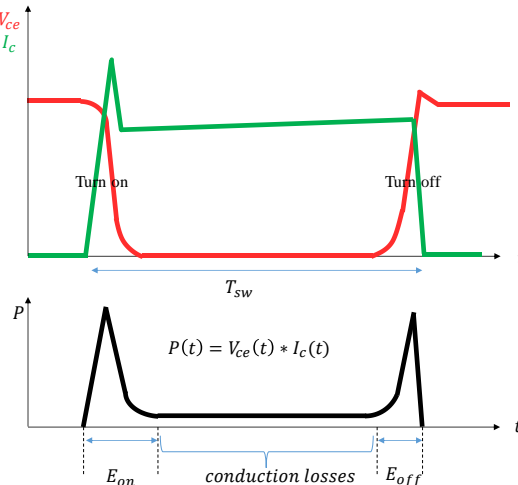


Fig .II-4. IGBT current and voltage waveforms during switching and conduction and switching losses

The power losses are compute using the current-voltage product. To calculate the conduction ones, the IGBT and diode can be modeled by a voltage drop and an internal resistance connected in series considering only a positive current[30] [31]. The voltage is obtained with the formula (II-1).

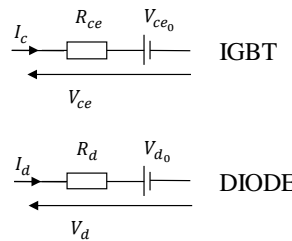


Fig. II-5. IGBT and Diode equivalent electric circuit

$$V_{ce} = V_{ce_0} + R_{ds0n} * I_c \quad (\text{II-1})$$

Then the conduction losses can be computed using (II-2):

$$P_{cond} = \frac{1}{T_{modulation}} \int_0^{T_{modulation}} V_{ce}(t) * I_c(t) dt \quad (\text{II-2})$$

The switching losses are neglected for the conduction losses calculation.

$$P_{cond} = V_{ce_0} * I_{c\ average} + R_{ds0n} * I_{c\ rms}^2 \quad (\text{II-3})$$

Where $I_{c\ average}$ and $I_{c\ rms}$ are respectively the average and RMS values of the current.

To calculate the switching losses, the curves of the energy losses versus the switched current given for a switched voltage, present in the datasheets (Fig. II-6), are used. They can be approximated by a second-order equation with three parameters A_x , B_x , and C_x as shown in Fig. II-6.

$$E_x = A_x + B_x * I + C_x * I^2 \quad (\text{II-4})$$

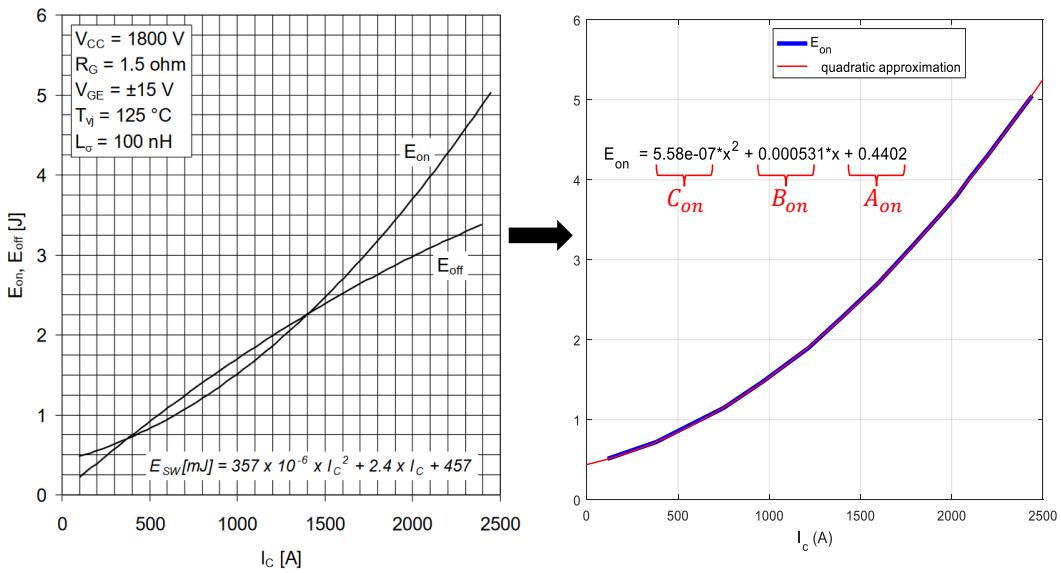


Fig. II-6. E_{on} datasheet parameters' extraction (ABB's 5SNA 1200E330100 IGBT)

For a switching frequency f_{sw} and a modulation period $T_{modulation}$, the switching losses are computed with:

$$P_{sw} = \frac{1}{T_{modulation}} \frac{1}{T_{sw}} \int_{t_1}^{t_2} \frac{V_{sw}}{V_{def}} E_{V_{def}}(I_{load}) \cdot dt \quad (\text{II-5})$$

$$P_{sw} = f_{sw} * \frac{V_{sw}}{V_{def}} * (A \frac{\Delta_{sw}}{T_{modulation}} + B * I_{sw\ average} + C * I_{sw\ rms}^2) \quad (\text{II-6})$$

Where $I_{sw\ average}$ and $I_{sw\ rms}$ are respectively the average and RMS values of the switched load current, V_{sw} is the switched voltage of the semiconductor that depends on the topology, V_{def} is determined from the datasheet and is often equal to the half of the component voltage rating ($V_{def} = \frac{V_{rating}}{2}$). Δ_{sw} is the switching time interval $[t_1, t_2]$ in which the semiconductor switches ($\Delta_{sw} = t_2 - t_1$).

The previous equations for the conduction and switching losses are also valid for the diode, knowing that the diode has only recovery losses as switching losses. The total losses are the sum of conduction and switching losses for both IGBT and diode.

$$P_{total} = P_{cond} + P_{sw} \quad (\text{II-7})$$

Because of the semiconductors losses, a thermal model is needed in order to determine and manage the chip temperature. As for the electrical circuit analysis, the thermal analysis integrates power sources which represent the losses, temperature at different nodes and thermal resistors depending on the thermal conductivity and chip sizes. This is a steady-state study so the thermal capacitances are not taken into account.

In our architecture, a single power switch contains a transistor with an antiparallel diode that ensures a path for the reverse current. So the thermal model circuit will include two thermal resistors as in Fig. II-7. Each resistor has a heat energy flow caused by the losses of each component. The temperatures of the different points in the switch package can be determined using the following equations:

$$T_{\text{Transistor}} = P_{\text{losses}_{\text{transistor}}} \cdot R_{\text{th}_{\text{jc}} T} + T_{\text{case}} \quad (\text{II-8})$$

$$T_{\text{Diode}} = P_{\text{losses}_{\text{diode}}} \cdot R_{\text{th}_{\text{jc}} D} + T_{\text{case}} \quad (\text{II-9})$$

$$T_{\text{case}} = (P_{\text{losses}_{\text{transistor}}} + P_{\text{losses}_{\text{diode}}}) \cdot R_{\text{th}_{\text{ch}}} + T_{\text{heatsink}} \quad (\text{II-10})$$

Where $R_{\text{th}-\text{jc}}$ is the junction to case thermal resistance, $R_{\text{th}-\text{ch}}$ is the case to heatsink thermal resistance and $R_{\text{th}-\text{ha}}$ is the heatsink to ambient thermal resistance in K/W . Here, the heatsink to ambient resistance is not considered because of the fixed heat sink temperature (70°C - 90°C in our example). The used cooling system has a non-constant heatsink to ambient thermal resistance ($R_{\text{th}-\text{ha}}$) which makes it possible to set the heatsink temperature. This resistance is defined by the 4th work package evaporator conductance in function of the power losses per module as in Fig. II-7.

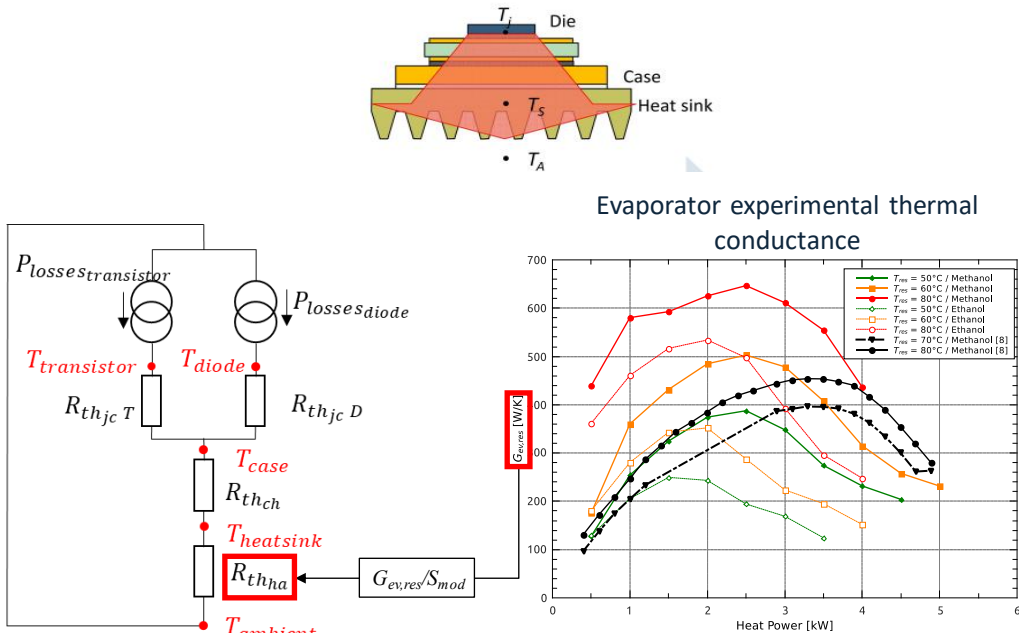


Fig. II-7. Equivalent thermal model of an IGBT component with antiparallel diode [30] [32]

ii. Needed parameters

In order to evaluate losses and components temperature, we need the following parameters:

- Thermal resistance: $R_{\text{th}-\text{jc}_T}$, $R_{\text{th}-\text{jc}_D}$, $R_{\text{th}-\text{ch}}$
- Conduction parameters for IGBT: $V_{\text{ce}0}$ R_{dson} , and diode: V_d , R_d .
- Switching losses parameters (E_{on} , E_{off} et E_{rec}): A_x , B_x and C_x

- Component surface: Surface (mm^2) needed to calculate the heat flux in W/cm^2 in order to size the heat exchanger and the cooling system.

These parameters are extracted from semiconductor manufacturer datasheets and used to create the semiconductor database.

iii. Example of the method for determining the formulas of switching and conduction currents

To calculate the switching and conduction losses, the currents need to be defined. To find the conduction and switching losses, a simulation is done using *Plecs* to identify the switching intervals for each switch. In this part, an example will be shown to illustrate this method.

The output current absorbed by the source is supposed to be sinusoidal with a θ phase shift as in the equation (II-11). The considered load is a 3-phase electric motor model presented in Chapter I.

$$I_{out}(x) = \sqrt{2}I \sin(x - \theta), \quad x = \omega \cdot t \quad (\text{II-11})$$

As a case study to show how to derive the currents values of a converter during its different mode of functionality, the 5-level ANPC architecture schematic shown in Fig. II-10 is considered. This topology will be studied in detail in the next chapter and it is used here to illustrate the power losses calculation method. The specificity of this converter is that it combines a 3-level FC one working at high frequency and a 2-level one working at a low frequency. The connection of both elements gives this ANPC five levels output voltage and an output frequency with a multiplication of two times the switching frequency. As Switcher semiconductors switch only half of one cycle of conduction phase at low frequency so the switching losses are lower than if it was switching at high frequency.

The current waveforms for each switch of the low and high frequencies part of the converter are shown in Fig. II-9. In this figure, only one semiconductor current waveform of the FC part is shown (T_1) due to the symmetry of this topology. On the other hand, for the low switching frequency part, two semiconductors current waveforms are shown (T_5, T_6) and the other two remaining have similar waveforms.

This will help in the determination of the limits of the integrations used in the losses derivations equations and hence proper results as validated in the tables shown later in this chapter.

The command functions of the firing gates signal shown in Fig. II-9 are expressed by:

$$\text{3-level FC: } f(x)_{T_1, T_3} = 1 - f(x)_{T_2, T_4} = \begin{cases} k * \sin(x), & 0 \leq x < \pi \\ 1 + k * \sin(x), & \pi \leq x \leq 2\pi \end{cases} \quad (\text{II-12})$$

$$\text{Switcher: } f(x)_{T_5, T_7} = 1 - f(x)_{T_6, T_8} \begin{cases} 1, & 0 \leq x < \pi \\ 0, & \pi \leq x \leq 2\pi \end{cases} \quad (\text{II-13})$$

With k the modulation index.

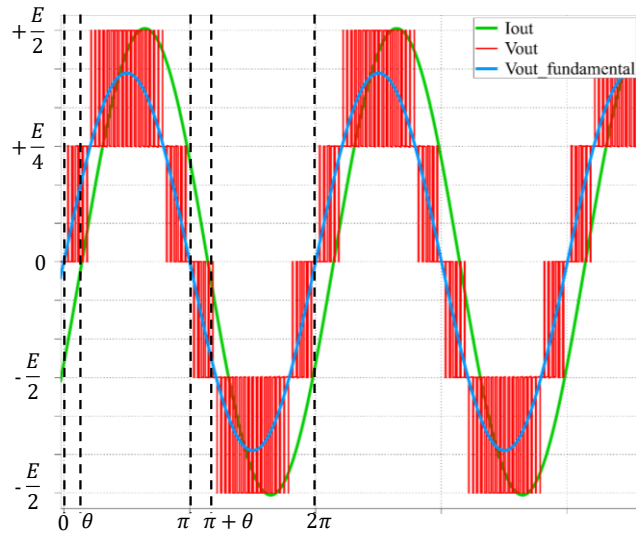


Fig. II-8. Output voltage & current waveforms of a single phase 5-level ANPC obtained by *Plecs* simulation

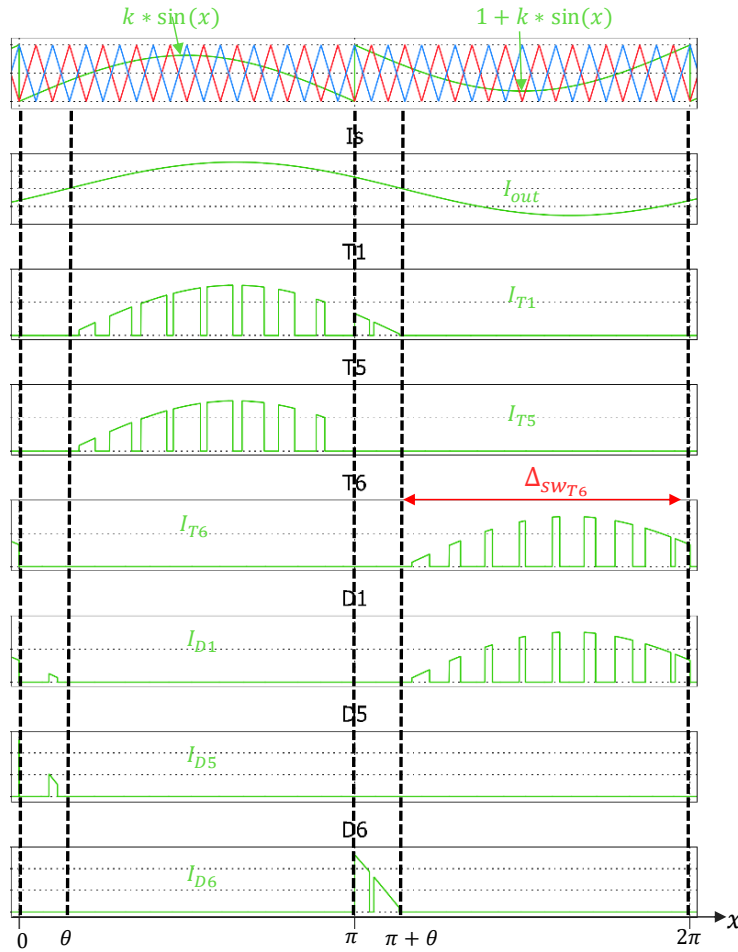


Fig. II-9. Waveforms of ANPC semiconductors commands and currents obtained by simulation in *Plecs*

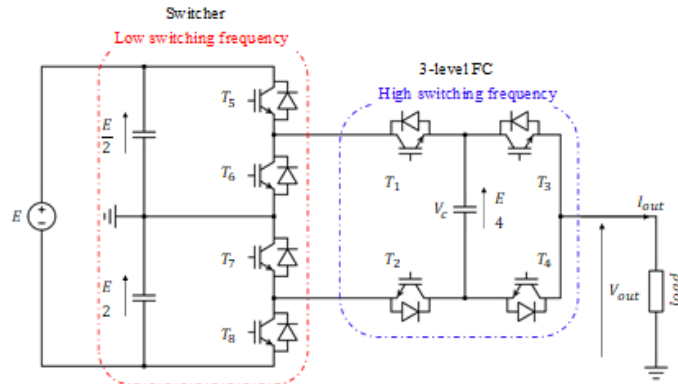


Fig. II-10. ANPC 5L Converter schematics: 3-level FC + Switcher (2-level, DC)

TABLE II-1 summarizes the operation properties of ANPC converter with its characteristics and function modes durations which are issued from the simulation current waveforms.

TABLE II-1. Current distribution during an operating period

Current Direction	Active components	Intervals	Output Voltage
$I_{out} > 0$	T_1, T_3, T_5	$[\theta, \pi + \theta]$	$+E/2$
	T_1, T_5, D_4	$[\theta, \pi]$	$+E/4$
	T_3, D_2, D_8	$[\pi, \pi + \theta]$	$-E/4$
	T_1, T_3, D_6	$[\theta, \pi]$	0
$I_{out} < 0$	T_4, T_2, D_7	$[\pi + \theta, 2\pi + \theta]$	0
	T_2, T_8, D_3	$[\pi + \theta, 2\pi]$	$-E/4$
	D_1, T_4, D_5	$[0, \theta]$	$+E/4$
	T_2, T_4, T_8	$[\pi + \theta, 2\pi]$	$-E/2$

Following the formulas presented in the previous section with the help of the waveforms shown in Fig. II-9; the calculations for average & RMS conduction and switching currents for each semiconductor can be found appendix 1. For more converters topologies waveforms simulation results and currents derivations, they could be found in [2] and [4] and could be resumed in the appendix.

3. Semiconductors Database

The simulation tool uses a created database that sums up the semiconductors technological parameters obtained from the manufacturer datasheets. The components are classified as families according to their manufacturer. In this case, only Silicon IGBT components are studied in the first part of the project.

Our work package (WP2) focuses on the static converters and the DC bus design. In order to help the work of the other work packages of the project, a first step is to determine an optimal DC bus voltage range. This will have a direct impact on the study of partial discharges but also in the design of motor windings. Then, it is necessary to compare the efficiency and power density of several multilevel topologies. Using the simulation tool and the available database, the efficiency is plotted for 2-level inverter in green in Fig. II-11 and the used voltage calibers are reported below the efficiency curves. The noticed jumps of efficiency are due to the change in the used component voltage calibers. These jumps are also present for the other studied topologies as noticed in Fig. II-11.

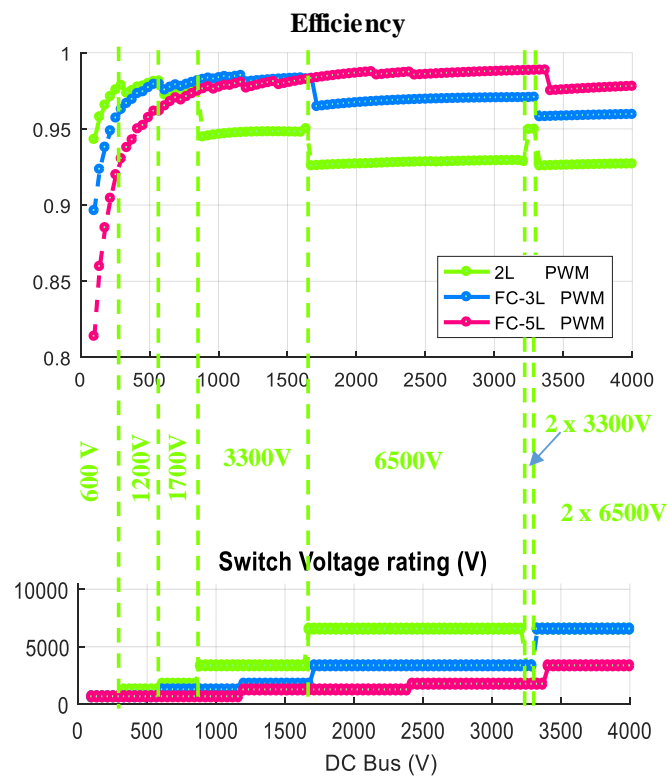


Fig. II-11. Efficiency for several topologies using available database components

Therefore, it is made difficult to find the optimal DC bus voltage due to the discretization of available voltage ratings. To overcome this problem, we created a continuous components database that suits the needed voltage rating by fitting and extrapolating the existing database components. Of course, these components may never exist, but it allows to see the effect of the choice of static conversion architecture on the efficiency over the voltage range considered while removing a bias (discretization of ratings).

This solution will help us explore several possible solutions. Validation of the results will be done by simulation so as not to limit the number of proposed architectures. The experiment will be done in a second time, after this project, to verify the solutions that will come from the overall optimization.

For these study cases, the switching frequency is chosen in order to eliminate subharmonics components. Therefore, it should be higher than 7 times the fundamental frequency as stated in [33]. In our case, the switching frequency was set to 4 kHz which represents about 7 times the electric machine fundamental frequency.

i. Components' families

Semiconductor manufacturers can offer relatively low IGBT devices rates but can reach as high as 6.5 kV/0.75 kA.

As shown in Fig. II-12, the used database has two families of silicon components. The first consists of ABB components with four available voltage ratings (1700 V, 3300 V, 4500 V, and 6500 V). Current ratings vary from 250 to 1600 A.

The second family is made up of Infineon components whose voltage ratings are: 600 V, 1200 V, 1700 V, 3300 V and 6500 V. For current calibers, they are smaller than those of the previous family and range from 200 to 800 A.

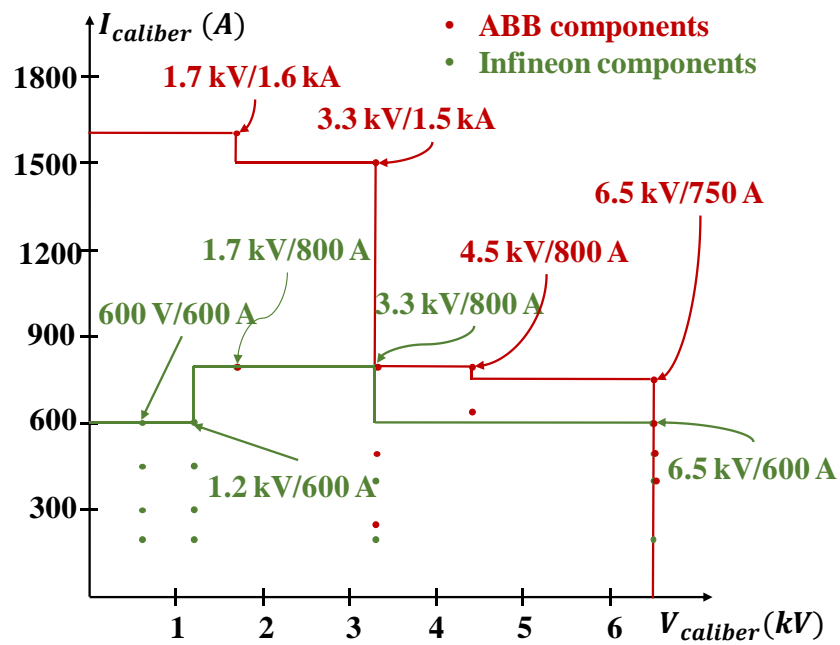


Fig. II-12. Voltage and current ratings of semiconductor devices in the database

ii. Generated components

There are discontinuities in the first resulted curves (Fig. II-11) due to the discretization of the components shown in Fig. II-12. These jumps are due to the change in component size used since the selected family (ABB components, for example) has a limited number of calibers (1700 V, 3300 V, 4000 V, and 6500 V).

The manufacturer does not make a customized component. However, using discrete components in our simulation brings up jumps in the resulted performances curves which will

be problematic for the global system optimization. Since it is an exploratory study, it is interesting to have components for all voltage and current ratings which will involve determining component parameters for sizes that vary continuously. In order to have a continuous database, we have to create components for the different desired ranges. The user will still have the choice of using real components instead of the created ones.

To create a component that does not exist in our database, we first select the family or manufacturer to which the created component will belong. For this purpose, all the parameters of the components belonging to this family are extracted from the *Matlab* file. The closest voltage and current ratings components are selected to be used in the extrapolation.

Once the various components have been selected, they will be used to generate the parameters of the desired component. The laws of variation of all the parameters are then identified as a function of the voltage caliber or current-voltage calibers product as stated in TABLE II-2 and then applied to the desired one.

TABLE II-2. Needed parameters dependency

Generated parameter	Depending parameter
Switching losses parameters A_x , B_x and C_x	Voltage rating
Conduction parameters for IGBT and Diode V_{ce0} R_{dson} , V_d , R_d .	Voltage rating * Current rating
Thermal resistance R_{th-jc_T} , R_{th-jc_D} and R_{th-ch}	Voltage rating * Current rating
Surface	Voltage rating * Current rating

For the switching energies E_{on} , E_{off} and E_{rec} , we can model the variation of their parameters (A_x , B_x , and C_x seen in equation (II-4)) using a polynomial function which is the function that fits the best our data as in Fig. II-13. Variation of A_{on} , B_{on} et C_{on} versus voltage rating and E_{on} versus the current. In this figure, the blue asterisks stand for the real components parameters and the red curve the approximation function. Variation of A_{on} , B_{on} et C_{on} versus voltage rating and E_{on} versus the current. Second-degree polynomial functions are chosen because we do not have enough points in order to pick higher degree polynomial functions. In the fourth figure, the turn-on energy is plotted using both real and generated components and as noticed, our approximation fits well the real components and allows to go beyond the available current and voltage ratings.

The same method is used to generate the IGBT and the diode, we need the on-state voltage drop at zero current condition and resistive elements and the thermal resistors (heatsink-case, junction-case for both transistor and diode) as a function of the voltage and current calibers.

In order to generate the surface of the component, we search for a function that fits the variation of this parameter depending on the current-voltage calibers. We can approximate this parameter

also with a polynomial function. The value of the created component surface will be very helpful to design the cooling system allowing the computation of the thermal density.

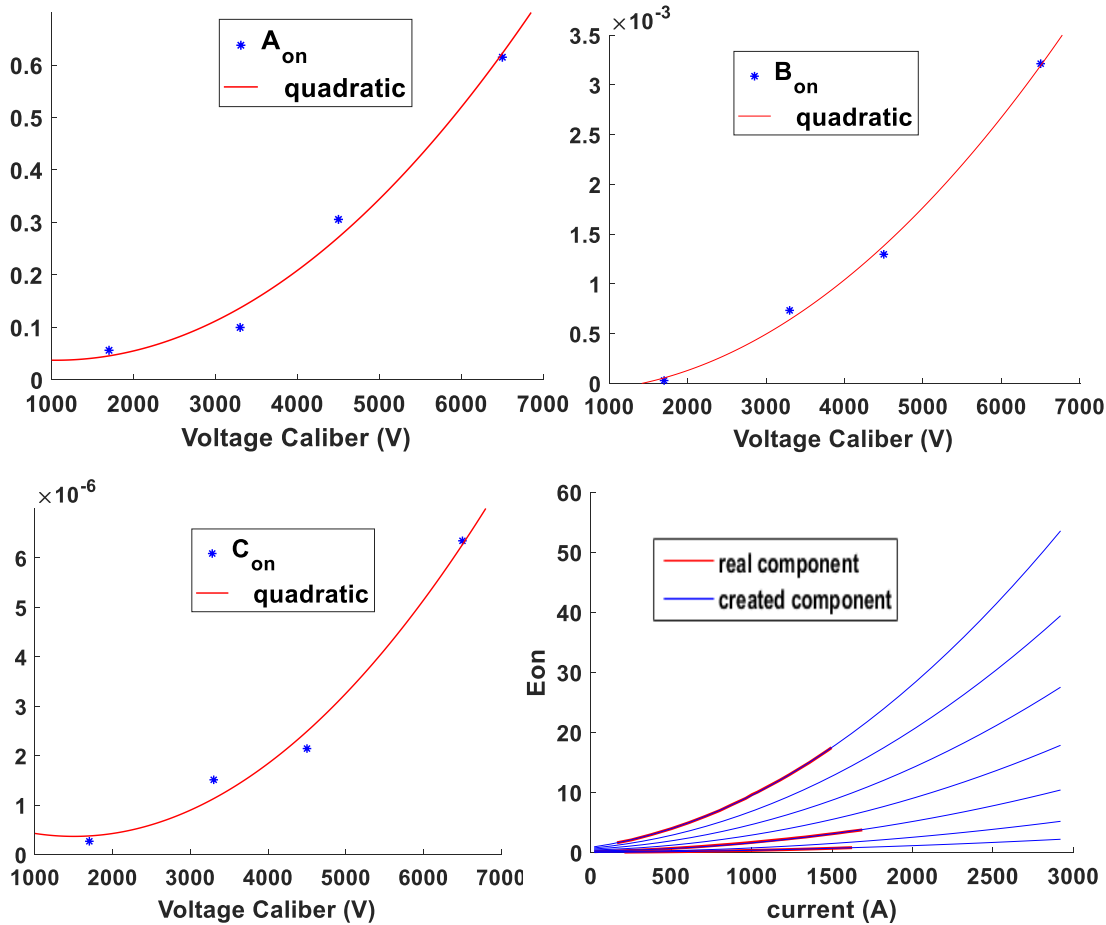


Fig. II-13. Variation of A_{on} , B_{on} et C_{on} versus voltage rating and E_{on} versus the current

TABLE II-3 summarizes the order of the polynomial functions for the different parameters modeled.

TABLE II-3. Summary of generated parameters

Generated parameter	Depending parameter	Approximation function
Switching losses parameters A_x , B_x and C_x	Voltage rating	Second-degree polynomial $f(x) = ax^2 + bx + c$
Conduction parameters for IGBT and Diode V_{ce0} , R_{ds0n} , V_d , R_d .	Voltage rating * Current rating	First-degree polynomial $f(x) = ax + b$
Thermal resistance R_{th-jc_T} , R_{th-jc_D} and R_{th-ch}	Voltage rating * Current rating	Second-degree power $f(x) = ax^b + c$
Surface	Voltage rating * Current rating	First-degree polynomial $f(x) = ax + b$

The generated semiconductor components will make it possible to compare the different parameters of the studied topologies in order to choose the optimum voltage range which will minimize the losses and increase the power density.

These generated components will be useful for the global hybrid-electric propulsion system optimization which will be done by the 6th work package.

iii. Comparison of real and generated components

The first studies will verify that the results with the generated components are coherent with the ones obtained with the real components. A DC voltage sweep is carried out using Infineon components and the component choice is fixed manually in the simulation tool. Due to the limitation of the existing voltage calibers, the sweep range is limited to 4000 V due to the limitation of the existing components' voltage calibers which corresponds to 6500 V so a definition voltage of 3600 V using a 2-level inverter topology. The power is fixed to 1 per unit.

With these generated components, several options are available. The first one could be setting a voltage and current calibers which will be done in the first test in order to compare these components to the real ones. The second option is to set only the voltage rating so the direct series association would be allowed and using the adapted current rating in order to avoid parallel association. The third one consists of generating adapted voltage and current rating components and compare them to the case of using only available components calibers associated in series and parallel so to withstand the needed voltage and current required by the load.

1. Fixed component choice

For this study case, the voltage and current calibers are fixed for both real and generated components in order to check the validity of the generated components and also compare the impact of component calibers on the inverter performances. Real and generated with same calibers, side-by-side, will be compared under the same conditions. Both components calibers are fixed for both real and generated components. Fig. II-14 represents the efficiency for fixed components allowing direct series association.

In order to have the adapted component, series and parallel connection are made if the needed component ratings are beyond the available current and voltage rating. The series connection is used to adapt the input voltage while the parallel connection is needed to adapt the current of the transferred power.

For the tested components, the generated components have the same properties as the real ones. The difference between components conduction losses remains low compared to switching losses which is higher for larger voltage caliber components.

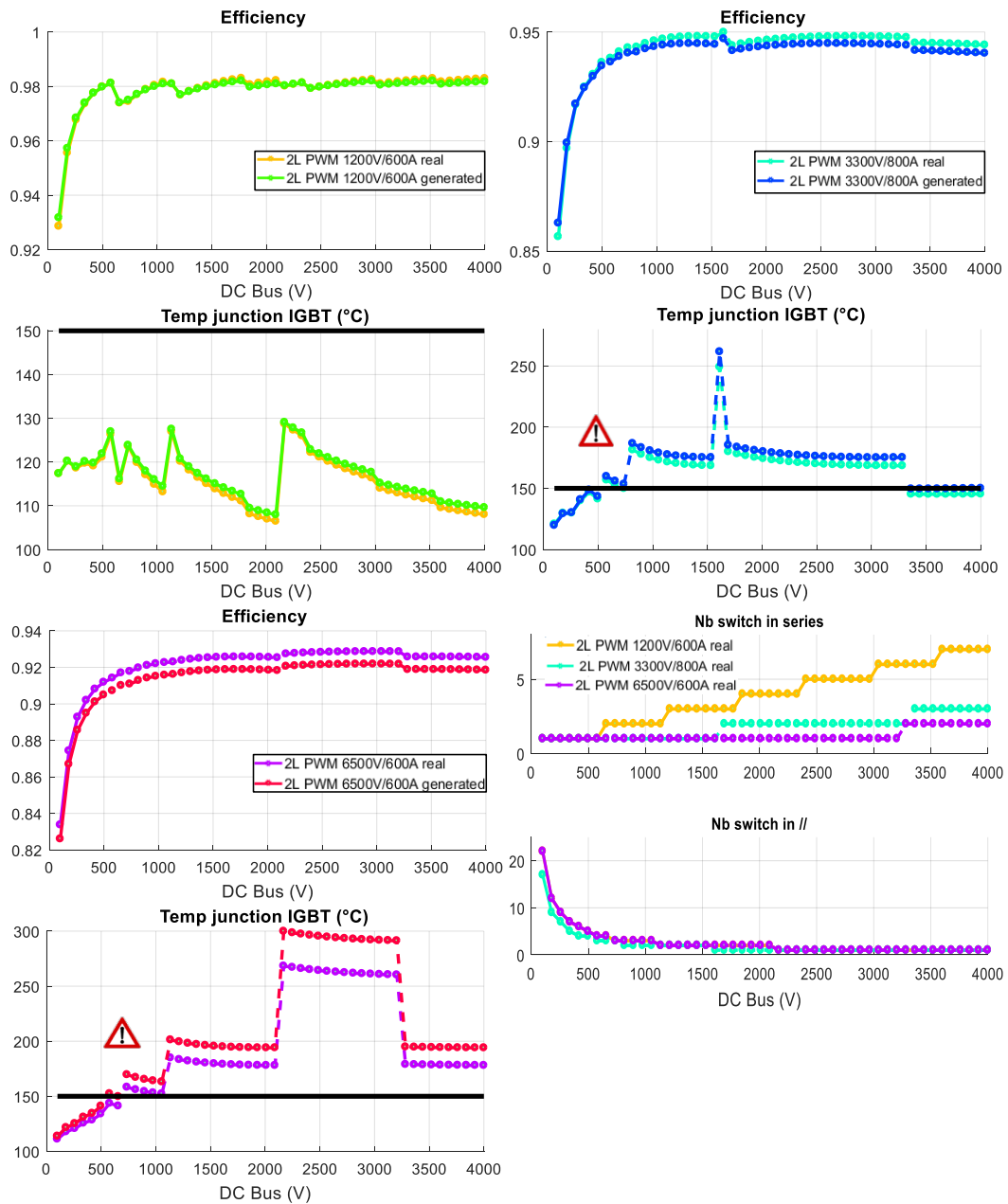


Fig. II-14. Real versus generated components efficiencies, maximal junction temperatures and parallel and series associated switches number for fixed calibers

2. Fixed choice of the components' voltage caliber and adapted current

For the next simulation, the voltage calibers are fixed however the current ones are chosen in order to respond to the needed current with both real and generated components, so the last ones will always have good use of the Silicon surface. In this case, the real components are used at their nominal current.

In this case, the real components have smaller thermal density due to the surface of the component which is bigger than the generated components ones. The bigger surface is, the lowest the current density is so the component junction temperature will be lower.

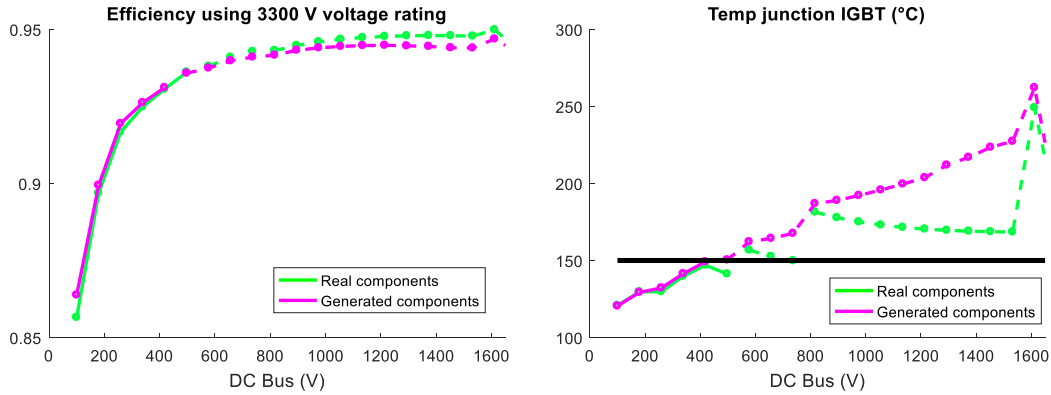


Fig. II-15. Real versus generated components efficiencies and maximal junction temperatures for fixed voltage calibers and adapted current calibers

The jumps noticed for the temperature of the generated components are mainly due to the thermal resistor which does not correspond to the optimal value. The generated components have a higher thermal resistance as shown in Fig. II-16. This is linked to the distribution of the thermal resistances that do not follow an obvious mathematical law. This data spread is related to the gap between the selected components which result in noise, sampling errors and nonlinearity of the distribution law.

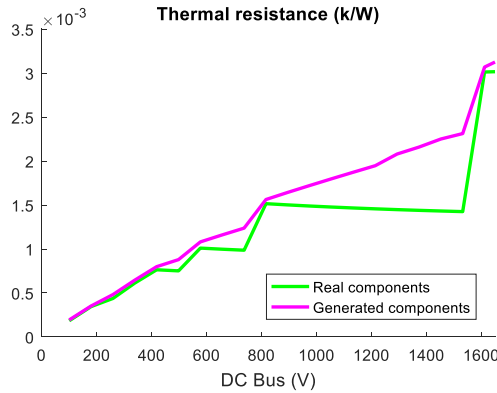


Fig. II-16. Thermal resistance for real and generated used components

In order to see the effect of the current caliber, the efficiency and maximal junction temperature are plotted as function of the power (Fig. II-17). The 3300 V components were used for a DC bus of 1600 V so to be used at 48% of their rating.

The current rating variation is not as important as the voltage one in terms of efficiency jumps. However, it has a great effect on the thermal resistances and therefore the maximal junction temperature.

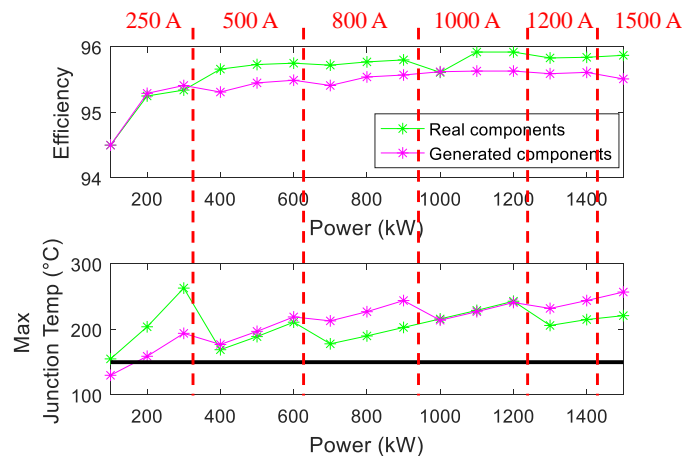


Fig. II-17. Efficiency and maximal junction temperature for real and generated 3300 V components for a power sweep

3. Adapted voltage and current calibers

For the third case, the voltage and current calibers are chosen in order to respond to the needed voltage and current to both real and generated components.

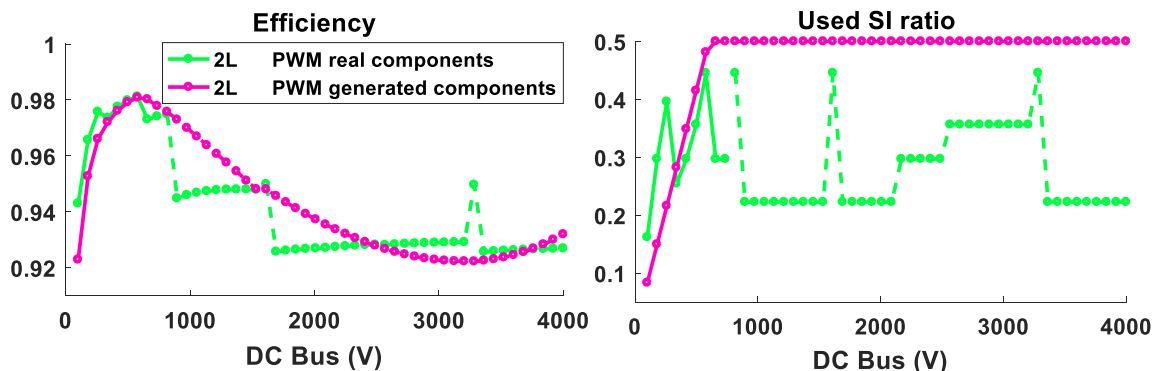


Fig. II-18. Real versus generated components efficiencies and used Silicon ratio for adapted voltage and current calibers

The very high switching losses and maximal junction temperature for the first points of the simulation are due to the very low voltage calibers (100 to 500 V) that are lower than the smallest available caliber which is 600 V.

The efficiency curves overlap for the points that match a used Silicon ratio of 50% for the real components. This ratio is computed as follows:

$$Used_{Si_ratio} = \frac{V_{DCbus} * I}{n_{switch} * \frac{V_{caliber}}{2} * I_{caliber}} \quad (II-14)$$

Where V_{DCbus} is the DC bus voltage, I is the load current, n_{switch} is the number of the used switches depending on the studied topology.

The generated components are optimized in order to use 50% of the installed Silicon (50% of voltage rating and 100% of current one) since the recommended ratio is between 50 % and 70 % so to have an optimal efficiency and an acceptable over-voltage. The same remarks about the junction temperature can be made again.

The generated components can be used to replace the real components in our study so to avoid the efficiency jumps. Although these jumps could still be present for the maximal junction temperature.

These components will be used for to define the optimal DC bus voltage to use for each multilevel topology in Chapter III.

4. Capacitor sizing

Capacitors are key components of the power electronics that are used as part of the electric motor drive system. In the state of the art inverters, the capacitors are the largest components and essentially determine the inverter volume. Consequently, an increase in the energy storage density of capacitors would have a huge impact on the size and power density of power electronics.

The capacitor value could be calculated from the stored energy as shown in the following equations.

$$Energy = \frac{1}{2} \frac{Q^2}{C} = \frac{1}{2} CV^2 \quad (\text{II-33})$$

$$Q = CV \quad (\text{II-34})$$

But $\Delta Q = I\Delta t$, then

$$I\Delta t = C\Delta V \Rightarrow \frac{I}{f} = C\Delta V \quad (\text{II-35})$$

$$C = \frac{I}{f * \Delta V} \quad (\text{II-35})$$

To define the capacitance value, the current, frequency and voltage ripples are needed. In this part, the capacitor current will be evaluated for two capacitor types. The first one is the DC bus capacitor that is needed by all the topologies and the second one is the flying capacitor which is used in some 3-level and 5-level topologies. These capacitors are selected form an available database according to a selection process detailed below.

i. DC bus capacitor

Picking a DC link capacitor is decided by two constraints: one is the capacitance which is determined by the voltage ripple, the other one is the RMS current ripple across the capacitor

for the worst case, which will cause the capacitor internal temperature rise and has to be under a certain value to ensure the proper operation of the capacitors. This ripple depends on the switching depending on the control type (with or without homopolar injection), modulation index, frequency and the load phase.

Therefore, an algorithm was developed to estimate the worst case, assuming that the filtering is perfect and that only the non DC part goes through the capacitor. There are two types of DC bus capacitor depending on the used inverter topology. The first one is the 2-level type capacitor and the second one is the NPC one as in Fig. II-19.

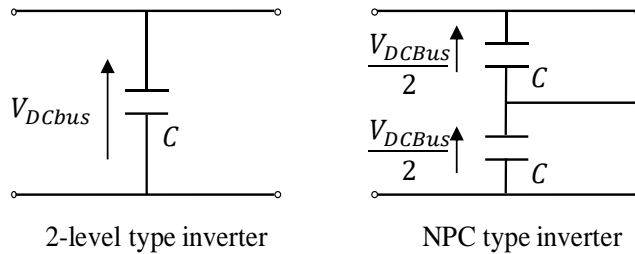


Fig. II-19. DC bus link types

The sizing method is similar for both cases; however, the current calculation is not. The used method to find out the capacitor value is described in detail in [34]. The algorithm developed determines the worst case. It scans different parameters: the load phase (0° to 90°), modulation depth from 0 to 1.15 and zero-sequence control strategies (nothing, harmonic 3, SVM).

In order to choose the most appropriate component from the datasheet, the capacitor current is needed. The RMS current in the DC bus capacitors is analytically calculated for sine wave output currents with arbitrary phase shift angles $\text{acos}(P_f)$ and modulation factors k . With pulse width modulation (PWM), the three sinusoidal desired curves are compared with the triangle modulation one.

For both cases, the capacitor RMS current value could be calculated using the inverter average and RMS currents as follows:

$$I_{capaRMS} = \sqrt{I_{invRMS}^2 - I_{invavg}^2} \quad (\text{II-15})$$

For the first DC bus type, according to [34] the capacitor RMS current can be calculated as follows:

$$I_{invavg} = \frac{3}{4}\sqrt{2}I_{outrms}k * P_f \quad (\text{II-16})$$

$$I_{invRMS} = \sqrt{2}I_{outrms}\sqrt{\left(\frac{\sqrt{3}k}{4\pi}\right) * (1 + 4 * P_f^2)} \quad (\text{II-17})$$

With I_{outrms} the inverter output RMS current imposed by the 3-phase electric motor.

From equations (II-16), (II-17) and (II-18), the capacitor current is defined in equation (II-18).

$$I_{capaRMS} = \sqrt{2} I_{outrms} \sqrt{\sqrt{3} \frac{k}{4\pi} + (\sqrt{3} \frac{k}{\pi} - 9 * \frac{k^2}{16}) * P_f^2} \quad (\text{II-18})$$

For the second DC bus type, for each angular sector $\frac{\pi}{3}$, we look at one switch current in each phase knowing that the inverter current is the composition of the three (Fig. II-20) and are represented in the following equations by functions f_1 to f_6 . To obtain the RMS value, the

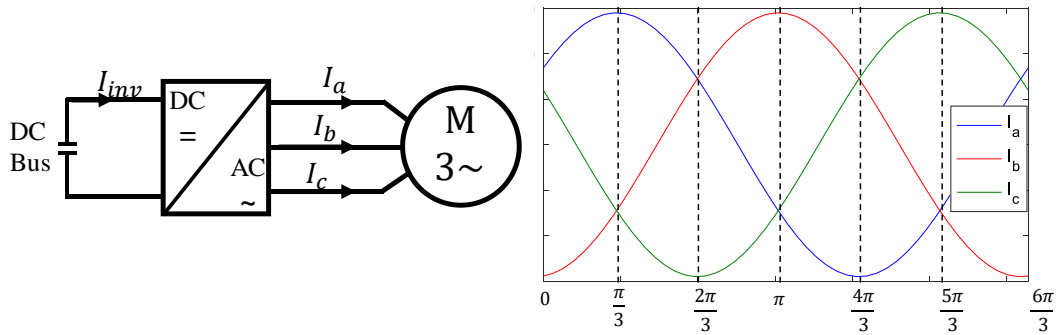


Fig. II-20. Inverter input and output currents

square currents are then modulated by taking into account the double product.

The RMS and average current values depend on the 3 phases currents (I_a, I_b, I_c), the modulation index and ω the electric pulsation or the frequency.

$$I_{invRMS} = \sqrt{\frac{1}{2\pi} * (\int_0^{\frac{\pi}{3}} f_1 + \int_{\frac{\pi}{3}}^{\frac{2\pi}{3}} f_2 + \int_{\frac{2\pi}{3}}^{\pi} f_3 + \int_{\pi}^{\frac{4\pi}{3}} f_4 + \int_{\frac{4\pi}{3}}^{\frac{5\pi}{3}} f_5 + \int_{\frac{5\pi}{3}}^{2\pi} f_6)} \quad (\text{II-19})$$

The six $\frac{\pi}{3}$ sectors currents are defined by the following functions:

$$f_1 = k * (I_a^2 * \sin(\omega t) + I_c^2 * \sin(\omega t - 4\pi/3) + 2 * (I_a * I_c) * \sin(\omega t) * k * \sin(\omega t - 4\pi/3)) \quad (\text{II-20})$$

$$f_2 = k * I_a * \sin(\omega t) \quad (\text{II-21})$$

$$f_3 = k * (I_a^2 * \sin(\omega t) + I_b^2 * \sin(\omega t - 2\pi/3) + 2 * (I_a * I_b) * \sin(\omega t) * k * \sin(\omega t - 2\pi/3)) \quad (\text{II-22})$$

$$f_4 = k * I_b^2 * \sin(\omega t - 2\pi/3) \quad (\text{II-23})$$

$$f_5 = k * (I_c^2 * \sin\left(\omega t - \frac{4\pi}{3}\right) + I_b^2 * \sin\left(\omega t - \frac{2\pi}{3}\right) + 2 * (I_b * I_c) * \sin\left(\omega t - \frac{4\pi}{3}\right) * (k * \sin(\omega t - 2\pi/3))) \quad (\text{II-24})$$

$$f_6 = k * I_c^2 * \sin(\omega t - 4\pi/3) \quad (\text{II-25})$$

Now, the average current will be calculated. It could be calculated using each function above in the right section over one period $[0, 2\pi]$.

$$\begin{aligned} I_{inv\ avg} = & \frac{1}{2\pi} * \left(\int_0^{\frac{\pi}{3}} f_{1\ avg} + \int_{\frac{\pi}{3}}^{\frac{2\pi}{3}} f_{2\ avg} + \int_{\frac{2\pi}{3}}^{\pi} f_{3\ avg} + \int_{\pi}^{\frac{4\pi}{3}} f_{4\ avg} + \int_{\frac{4\pi}{3}}^{\frac{5\pi}{3}} f_{5\ avg} \right. \\ & \left. + \int_{\frac{5\pi}{3}}^{2\pi} f_{6\ avg} \right) \end{aligned} \quad (\text{II-26})$$

The used function $f_{1\ avg}$ to $f_{6\ avg}$ are as follows:

$$f_{1\ avg} = k * (I_a * \sin(\omega t) + I_c * \sin(\omega t - 4\pi/3)) \quad (\text{II-27})$$

$$f_{2\ avg} = k * (I_a * \sin(\omega t)) \quad (\text{II-28})$$

$$f_{3\ avg} = k * (I_a * \sin(\omega t) + I_b * \sin(\omega t - 2\pi/3)) \quad (\text{II-29})$$

$$f_{4\ avg} = k * (I_b * \sin(\omega t - 2\pi/3)) \quad (\text{II-30})$$

$$f_{5\ avg} = k * (I_c * \sin(\omega t - 4\pi/3) + I_b * \sin(\omega t - 2\pi/3)) \quad (\text{II-31})$$

$$f_{6\ avg} = k * (I_c * \sin(\omega t - 4\pi/3)) \quad (\text{II-32})$$

For example, for a 3-level NPC inverter with a 2 kV DC bus and 1024 A RMS output current, the inverter currents are as follows in TABLE II-4. The RMS capacitor current obtained using the previous equations with the inverter simulation current values equals to 547 A versus 521 A obtained by using *Plecs* simulation. This difference is due to *Plecs* RMS measure which is discrete in *Plecs* so the results varies with the sample number. Yet, the obtained values using the analytic analysis are comparable to the *Plecs* ones.

TABLE II-4. Inverter and capacitor currents calculation comparison

	Analytic analysis	Plecs simulation
$I_{inv\ avg}$ (A)	740.73	742.1
$I_{inv\ RMS}$ (A)	852.76	922
$I_{capa\ RMS}$ (A)	422.51	521

ii. Flying capacitor

If the used converter structure needs flying capacitors to maintain a proper blocking voltage sustained by the power switches in order to have a correct output voltage, these capacitors could be sized according to the stored energy. So normally the nearest capacitor to DC bus is the largest one. However, for an industrial point of view, a hypothesis is taken to have the same flying capacitance for all capacitors within the architecture. It could also be sized according to the ripple voltage across the capacitor ($\Delta V_{C_{FY}} \approx 10\%$).

The flying capacitor sees only switching frequency current harmonic components so it is sized using this frequency.

$$C_{FY} = \frac{I_{out_max}}{\Delta V_{C_{FY}} * V_C * f_{sw}} \quad (\text{II-36})$$

The value V_C depends on the converter topology, and here is taken to be equal the value of the nearest capacitor voltage in the topology as stated before. TABLE II-5 summarizes the values of the worst case V_C for different topologies which are in the scope of our study.

TABLE II-5. Summary of flying capacitor number and voltage value

Topology	Number of C_{FY}	V_C (largest)
FC N Cells	$N - 1$	$(N - 1)E/N$
SMC $n \times p / 6$ SWs	$(n - 1) \times p$	$(n - 1)E/(n \times p)$
SMC $n \times p / 4$ SWs	$(n - 1) \times p$	$(n - 1)E/(n \times p)$
ANPC including (FC N Cells)	$N - 1$	$(N - 1)E/N/2$

The capacitor sizing was validated by comparing our results to the *Powerforge* [35] which is a software based on frequency analysis.

iii. Selecting the capacitor from the database

To select the adapted capacitor from the available database two methods are possible. The first one consists of using the capacitor total energy and the second one depends on the required voltage and current.

If the first method is chosen, according to the manufacturer's data, the coefficients K_{vol} and K_{weight} can be defined by the following equations.

$$\begin{cases} Volume (cm^3) = \frac{1}{2} \cdot C(\mu F) \cdot V^2 \cdot K_{vol} \\ Weight (kg) = \frac{1}{2} \cdot C(\mu F) \cdot V^2 \cdot K_{weight} \end{cases} \quad (\text{II-37})$$

These coefficients are almost constant for a given technology depending on the operating frequency (high or low frequency). So a customized capacitor could be easily made by the manufacturer, unlike the semiconductors.

The sizing algorithm will give a desired capacitor value C_{des} and an operating voltage V_{des} . If these ranges are not available, series or parallel associations will be made.

To withstand the maximum RMS current through the capacitor, a parallel connection is needed as in equation (II-38).

$$n_{pC} = \frac{I_{rms}}{I_{rms,max; DataSheet}} \quad (\text{II-38})$$

It is necessary that the capacitor should be able to hold an overvoltage of $(1 + \Delta V_C) * V_{DCbus}$ before its breakdown. The data sheet covers a range of maximum capacitor voltage up to 3000V. So to overcome a needed overvoltage higher than 3000V, a series connection of small standard capacitors can be implemented, and so form a bank capacitor association as shown in Fig. II-21.

$$n_{sC} = \frac{V_C}{V_{C,max; DataSheet}} \quad (\text{II-39})$$

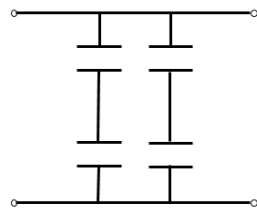


Fig. II-21. Series and parallel capacitor association

As the value of C is known, the next step is to look for a proper capacitor technology in the capacitor file that includes different capacitors datasheets and their tendencies. The foreseen technologies of the capacitors are Film Capacitors (Polypropylene (PP), Polyethylene Terephthalate Polyester (PET), etc....). This step is done manually, hence increasing the degree of freedom of the designer for the choice of C . The calculation will then indicate values for the size and volume of the chosen capacitor(s).

If the desired voltage exceeds the range, n_s capacitors are put in series of the value $n_s * C_{des}$ in order to keep the same capacitance value. The capacitors will see a voltage V_{des} divided by n_s . To ensure the capacitance, parallel association may also be used. This gives total energy of:

$$E_{tot} = n_s * \frac{1}{2} n_s \cdot C_{des} \left(\frac{V_{des}}{n_s} \right)^2 = n_p * \frac{1}{2} \cdot \frac{C_{des}}{n_p} V_{des}^2 = \frac{1}{2} C_{des} \cdot V_{des}^2 \quad (\text{II-40})$$

5. Model validation using *Plecs*

In order to validate the converters losses' models, the results obtained with the *Matlab* tool are compared to *Plecs* simulations. To simulate converters in *Plecs*, we use the components from

the same database as for the *Matlab* tool. It allows having the same data on *Matlab* and *Plecs* so to compare the results of both tools. Then we compare the results for different topologies. For the *Plecs* simulations, we have the same assumptions as for the analytic analysis.

As an example, the results will be compared using the following parameters, which does not correspond to our specification.

- DC bus voltage : 600 V
- I_{out_rms} : 214 A
- Switching frequency : 5 kHz
- modulation depth : 0.8165
- power factor : 0.9
- Used component : FF300R06KE3 (600 V, 300 A)

TABLE II-6. 2-level power losses comparison using analytic analysis (*Matlab*) and *Plecs* simulation

2-level	Switching losses (W)		Conduction losses (W)	
	<i>Matlab</i>	<i>Plecs</i>	<i>Matlab</i>	<i>Plecs</i>
IGBT	145	145.37	114.67	114.8
Diode	111	111.23	28.85	28.88

We note in TABLE II-6 that we have the same losses unlike the results of the study carried out in [2] which did not give the same losses by conduction. This error was due to not using identical components losses parameters on *Matlab* analytic analysis and *Plecs*.

For the other used topologies that will be presented in detail in the next chapter, the power losses analytic analysis was validated for several points and case scenario using *Plecs* simulation.

i. Multilevel Flying Capacitor topology (FC):

For this topology, we will compare the results for different number of FC cells. The first one to be simulated is a 3-level FC with the same parameters as for the 2-level presented above.

TABLE II-7. 3-level FC power losses comparison using analytic analysis (*Matlab*) and *Plecs* simulation

3-level FC	Switching losses (W)		Conduction losses (W)	
	<i>Matlab</i>	<i>Plecs</i>	<i>Matlab</i>	<i>Plecs</i>
IGBT	26	26.25	113	112.94
Diode	12.04	12.01	27.22	27.25

Similar results with both tools are noticed for both cases.

Secondly, a 5-level FC is simulated keeping the same parameters as for the FC 3 levels with a switching frequency of 2.5 kHz (10 kHz/4 switching cells) to keep an apparent frequency of 10 kHz.

TABLE II-8. 5-level FC power losses comparison using analytic analysis (*Matlab*) and *Plecs* simulation

5-level FC	Switching losses (W)		Conduction losses (W)	
	<i>Matlab</i>	<i>Plecs</i>	<i>Matlab</i>	<i>Plecs</i>
IGBT	6.55	6.65	113	112.95
Diode	3.01	2.95	27	27.26

Then, a 7-level FC is simulated keeping the same parameters as for the previous case with a switching frequency of 1.67 kHz (10 kHz/6 switching cells).

TABLE II-9. 7-level FC power losses comparison using analytic analysis (*Matlab*) and *Plecs* simulation

7-level FC	Switching losses (W)		Conduction losses (W)	
	<i>Matlab</i>	<i>Plecs</i>	<i>Matlab</i>	<i>Plecs</i>
IGBT	2.91	2.97	113	112.92
Diode	1.34	1.29	27	28.02

For the FC topology overall, the results are similar in both cases and allow validating the analytical analysis carried out with *Matlab*.

ii. 3-level Neutral clamped point topology (NPC):

For the 3-level NPC topology, we used the same case-study as for the FC using the FF450R06ME3 (600 V, 450 A) switch and 10 kHz as the switching frequency.

TABLE II-10. 3-level NPC power losses comparison using analytic analysis (*Matlab*) and *Plecs* simulation

3-level NPC	Switching losses (W)		Conduction losses (W)	
	<i>Matlab</i>	<i>Plecs</i>	<i>Matlab</i>	<i>Plecs</i>
Clamping Diode	20	20.3	49	49.54
IGBT (outer)	54	53.8	71	70.95
Diode (outer)	1.15	1.91	0.63	0.63
IGBT (inner)	4.14	4.25	118	118.23
Diode (inner)	0.77	1.88	0.63	0.63

For this topology, we notice that there is an imbalance between the diodes' losses because the analytical analysis considers that the diodes see an $\frac{E}{2}$ voltage during the overlap, which is not

the case in *Plecs* simulation. In the simulation, the closest diode to the current source (Inner Diode) sees $0.2 \times E$ while the other one (Outer Diode) sees $0.3 \times E$.

We changed the switching voltages on the *Matlab* file for the diodes in order to match the *Plecs* ones and we got the following results:

TABLE II-11. 3-level NPC outer diode switching losses

3-level NPC	Switching losses (W)	
	<i>Matlab</i>	<i>Plecs</i>
Diode (outer)	1.15	1.16
Diode (inner)	0.77	0.77

iii. 5-level Active neutral clamped point topology (ANPC):

We check the 5-level ANPC topology results for the same input data as for the 3-level NPC and a 5 kHz switching frequency.

This inverter combines a 3-level FC switching at high frequency (5 kHz) and a 2 cells 2-level switching at a low frequency (50 Hz) which gives a 5-level output voltage and 10 kHz as the apparent frequency. As Switcher switches at low frequency, the switching losses of this cell are very low.

TABLE II-12. 5-level ANPC power losses comparison using analytic analysis (*Matlab*) and *Plecs* simulation

5-level ANPC	Switching losses (W)		Conduction losses (W)	
	<i>Matlab</i>	<i>Plecs</i>	<i>Matlab</i>	<i>Plecs</i>
IGBT(FC)	15	14.54	75.02	75.11
Diode(FC)	6	5.57	45.45	45.51
IGBT (Switcher outer)	0.27	0.16	70.87	70.94
Diode (Switcher outer)	0.01	0	0.63	0.63
IGBT (Switcher inner)	0.27	0.3	43.08	43.12
Diode (Switcher inner)	0	0	4.67	4.67

iv. Multilevel Stacked Multicell Converter topology (SMC):

Using the same input data as before and a 10 kHz switching frequency, we first simulate the 3-level SMC 1x2.

TABLE II-13. 3-level SMC power losses comparison using analytic analysis (*Matlab*) and *Plecs* simulation

SMC 1x2	Switching losses (W)		Conduction losses (W)	
	<i>Matlab</i>	<i>Plecs</i>	<i>Matlab</i>	<i>Plecs</i>
IGBT inner	4.14	4.13	47	47.28
Diode inner	20.41	20.49	49	49.54
IGBT outer	26.93	26.96	71	70.95
Diode outer	0.96	0.99	0.63	0.63

Then we simulate a 5-level SMC 2x2:

TABLE II-14. 5-level SMC power losses comparison using analytic analysis (*Matlab*) and *Plecs* simulation

SMC 2x2	Switching losses (W)		Conduction losses (W)	
	<i>Matlab</i>	<i>Plecs</i>	<i>Matlab</i>	<i>Plecs</i>
IGBT inner	1.03	1.03	49.17	47.28
Diode inner	5.1	5.08	51.84	49.54
IGBT outer	6.73	6.75	69.9	70.88
Diode outer	0.24	0.24	0.63	0.63

For the SMC topologies, we have the same losses with both tools.

The data show that the analytic analysis using *Matlab* and the simulation using *Plecs* have the same results so we can validate the analytic analysis.

6. Introduction of Multilevel Necessity

The first step of the project defined in Chapter I was to define the DC bus voltage. As seen in the part 3 of this chapter (Fig. II-18), using the adapted generated component for a 2-level inverter implies an optimal DC bus voltage around 600 V. If real components meant to be used for this DC bus voltage, the number of semiconductors in parallel would be important.

To define the DC bus voltage using real components, the limits of components voltage and current ratings and the high switching frequency should be taken into account. For a two-level inverter, a DC bus voltage sweep was done using several real components and plotted the efficiency in Fig. II-22. For 6500 V and 3300 V components that are not adapted to 6 kHz switching frequency, the losses are high so is the temperature. With the used switching frequency, these components cannot be used. For 1700 V components, the efficiency is higher and gets better with 1200 V ones. If we want to use a 4 kV DC bus, for example, we should use several components associated in series. But in these cases, the direct series association is allowed, unlike the red curve. The shadowed part of the curves cannot be realized without direct series association.

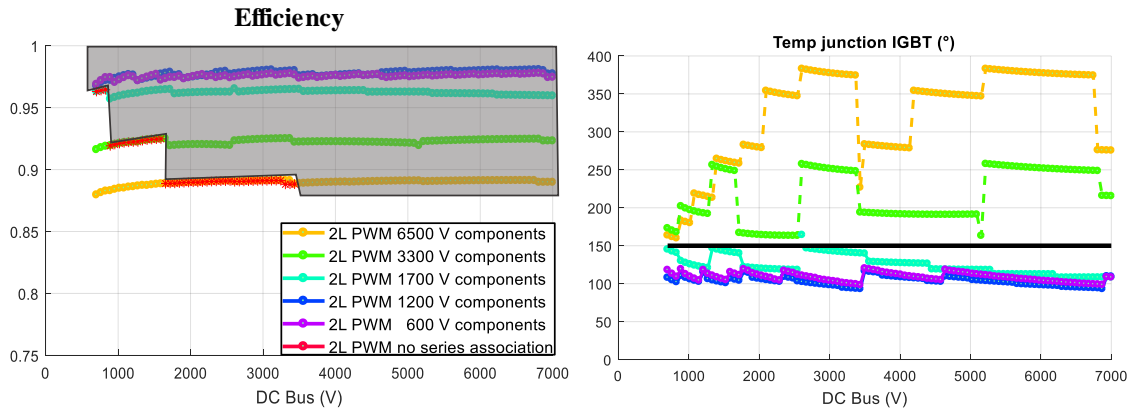


Fig. II-22. Efficiency for 2-level inverters with different voltage rating components for DC bus voltage sweep

Fig. II-23 shows the efficiency of the 2-level inverters studied above with an adapted switching frequency so to keep the maximal junction temperature under 150 °C. For the 6500 V and 3300 V components, the switching frequency should be nearly equal to the electric motor fundamental frequency (around 500 Hz) which will create current harmonics that should be eliminated by using a filter. The big switching frequency jumps correspond to the series association. For example, for the 1700 V components, around 1000 V, the inverter goes from 4 components in parallel and one in series to 3 in parallel et 2 in series. As the DC bus voltage increases, the needed current decreases for the same power. If the installed silicon is not optimally used, it results in more losses so the component heats up and the temperature exceeds the thermal limit so the switching frequency has to be reduced.

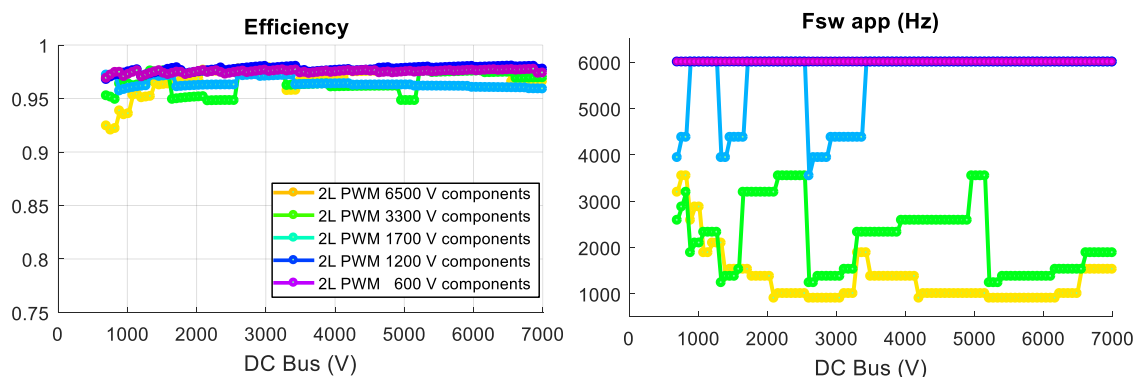


Fig. II-23. Efficiency for 2-level inverters with different voltage rating components for DC bus voltage sweep with adapted switching frequency

To choose the optimal DC bus voltage, using the available component voltage ratings, we estimated the possible DC bus voltages to use fully the available Silicon considered here as 60% of the component rating. This value was chosen so to have optimal use of the 1200 V and 1700 V components with an acceptable overvoltage. With the 5-level topologies, we can go up to 7 kV however with 2-level one, 2 kV is still high for the available components as it is noticed in Fig. II-24. The shadowed points are not feasible due to the high switching frequency which implies a high junction temperature.

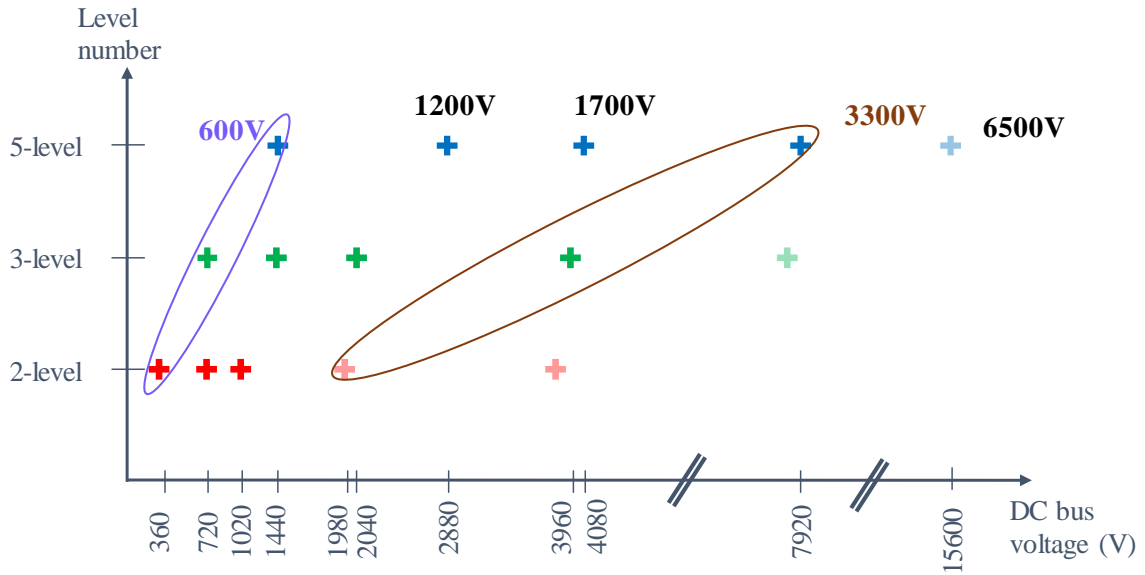


Fig. II-24. DC bus optimal voltage value depending on components voltage rating and topologies level number

If a 1.7 kV DC bus voltage, which seems to be an optimal value, is considered, the possible topology and components associations to withstand this voltage value are shown in Fig. II-25.

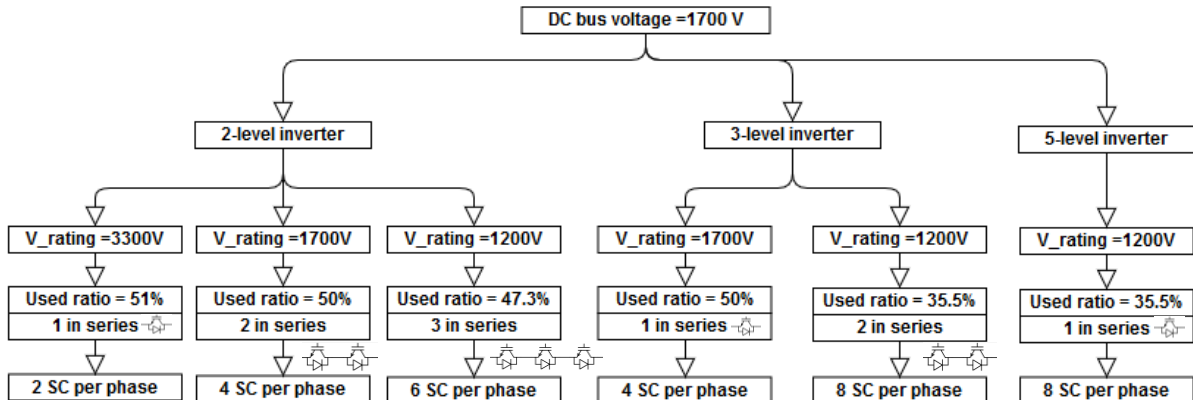


Fig. II-25. Number of topology level to use for 1.7 kV DC bus voltage

If direct series association is not allowed, a 3.3 kV component can be used with a 2-level inverter, or 1.7 kV one with 3-level topologies or 1.2 kV components with 5-level topologies. However, the 1200 V components are not fully used in this case.

So to use small voltage rating components, multilevel topologies must be used and the selected topologies will be shown in the Chapter III.

7. Conclusion

To size the power converter used to feed the electrical motor for the aircraft propulsion, a pre-design tool was developed. This tool is developed using *Matlab* object-oriented programming and is based on analytic analysis of the inverter power losses so to evaluate the efficiency and components temperatures to respond to our specification. The used power losses and thermal models were presented in this chapter. These models need several components such as capacitors and semiconductors parameters that are issued from the available database or generated based on it so to satisfy the current and voltage requirements. These components were validated using several study case scenarios and would help to define the DC bus voltage which is the first task of this work.

The available semiconductors voltage ranges limit the DC bus voltage that could be chosen if the 2-level topology was to be used without allowing direct series association. The high switching frequency represents also a constraint to the large voltage caliber components that were not meant to operate at these frequency levels due to the high switching losses. With all this said, using smaller voltage rating components but with high DC bus voltage to reduce the needed current rating would be more interesting. This could be done by using multilevel topologies.

The studied multilevel topologies will be presented in the next chapter as well as the different control strategies. The used components technologies will also be compared so to choose the optimal solution in terms of efficiency and specific power.

III. Comparison of possible solutions sized for the maximal power point

The main factor to increase the specific power that was identified in Chapter I is decreasing the cooling system mass by optimizing its components which is a part of WP4 work or by reducing power losses. Inverter power losses reduction could be achieved either by using small components or by playing on modulation strategies or by using more performant semiconductors (Fig. III-1). The first option, which is using small voltage rating components, could be done by using multilevel architectures to avoid the direct series association.

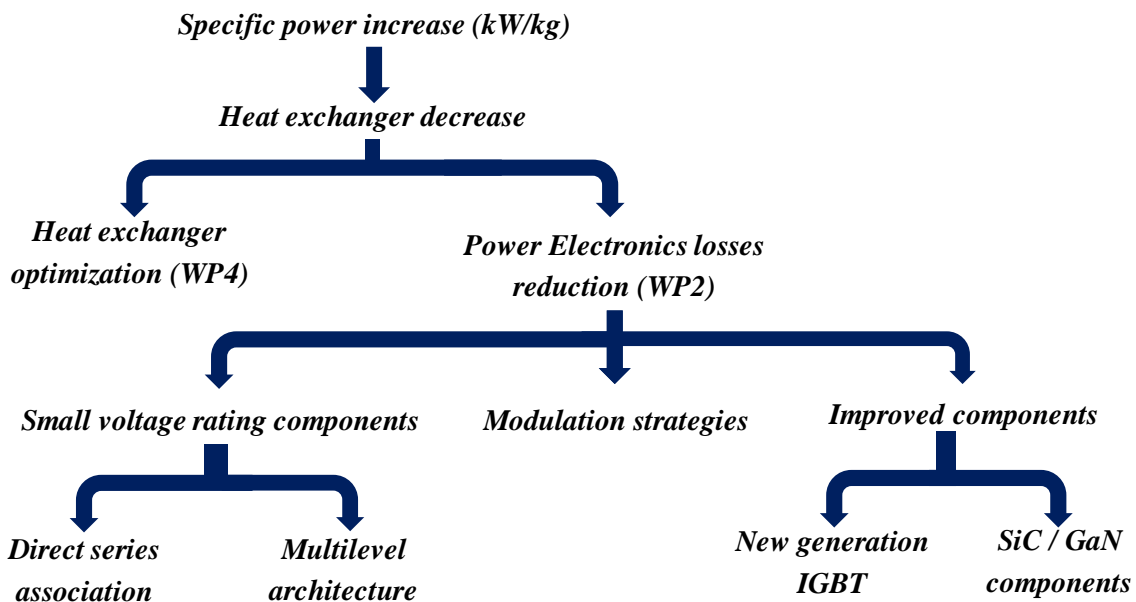


Fig. III-1. Specific power increasing study line

To design and compare power inverters to choose the most suitable solution, the simulation tool presented and developed in the previous chapter was used. It can easily compute different results for different power converters architectures. It takes into account the design constraints (DC bus voltage, output power, ...), the foreseen converter topologies, and the semiconductor family choice from the included components database. The study results such as efficiency, number of semiconductor devices, voltage rating selection, maximal junction temperature, losses, cooling system mass, DC bus capacitor, and specific passive elements (such as flying capacitor weights), as well as the power density, are shown as figures for different parameters of different architectures performances.

The power chain needs careful design to minimize the mass of the whole system which is directly linked to the mass of the converter and also the losses through the weight of the cooling system.

In this chapter, the studied inverter topologies and modulation strategies will be presented. Then the performances will be compared using several semiconductors to choose the most performant solution in terms of efficiency and specific power. For this Chapter, the considered design point

is the maximal power point which corresponds to the takeoff shown in the mission profile in Chapter I.

1. Comparison of topologies with PWM modulation strategy

i. Multilevel inverter topologies

The need in terms of power electronics has evolved and tends to increase power or usage voltage and to decrease the needed current to reduce losses and cables mass. However, this is not possible with a conventional two-level structure since the semiconductor ranges are limited in voltage to 6500 V which corresponds to a maximum blocking voltage of about 3600 V. The performance of these components is reduced for high voltages since the components are slower, which means more switching losses. These power electronics topologies are used in the medium-voltage drive application. For a marine propulsion for example [36], the onboard DC grid system contains a 1 kV DC bus and 2 x 4.5 MW propellers with 2 x 6.6 MVA low-voltage inverters. For this type of application, ABB uses the ACS1000 which contains a three-level inverter, without series or parallel connected power semiconductors, that is one of the least complex, most robust and efficient drive topologies [37].

To address the voltage needed levels, two solutions are possible and will be detailed below and are as follows:

- Split up the voltage or current constraints
- Use cell or converters associations.

1. *Split components' constraints*

The first possibility is the direct series association of the components (Fig. III-2), which makes it possible to split the voltage constraint and to use combinations of cells or converters.

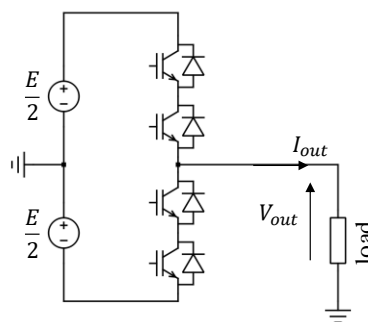


Fig. III-2 : Direct series component association

This method increases the voltage while keeping the voltage range of the component low which is more performant than high voltage rating components. This association also makes it possible to increase the switching frequency since the constraint is divided over components associated in series but does not improve the waveforms and the distribution of the dynamic constraints.

The spontaneous balancing of the constraints can't be guaranteed without additional components such as resistors. The switches do not commute exactly at the same time and therefore a switch must be able, in the worst-case scenario, to handle twice its sizing voltage which leads to its breakdown. In static, the association works very well even if, in dynamic, there may be a delay in the turn-on or blocking of the switch. It is then necessary to guarantee the constraints balance using, for example, intelligent drivers.

The second possibility is the parallel association of the components (Fig. III-3) which makes it possible to increase the current. This method does not improve output waveforms.

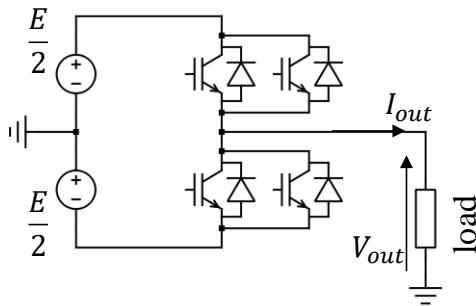


Fig. III-3 : Parallel component association

In this case, the sizing is the same as for a conventional two levels and the balancing depends on the ship temperature coefficient that can lead to a self-balancing or divergence. In this case, for the dynamic aspect, the switch must support the twice current if there is a delay in starting or blocking, which causes the temperature to rise, which could lead to thermal breakage. However, the static balancing is not guaranteed as for the voltage constraint stated above. But this solution is less penalizing than direct serialization thanks to thermal inertia.

2. Multilevel inverters

Even if the multi-level converters are used for high power medium voltage drive applications, they seem to be the best option to reduce the weight of the converter and still have high efficiency with smaller DC bus voltage.

More and more applications that require medium-voltage use multilevel topologies. With this type of inverters, the output voltage harmonics quality can be improved. The multilevel inverter is also used for renewable energy generation such as wind or solar that are medium and high power applications [38].

However, using a multilevel inverter to approximate sinusoidal waveforms from stepped waveform have sharp voltage transitions which create harmonics in addition to the fundamental frequency of the sinusoidal waveform [39]. The power quality and THD are affected by these harmonics. However, the generated harmonics are high-frequency one so they could be easily

filtered compared to the low frequency ones. So the multilevel inverter is more advantageous than a conventional two-level inverter.

The more levels the inverter has, the less THD will be. However, the limit of levels number is fixed by the voltage balancing problems, voltage clamping requirement circuit layout and packaging constraints [40]. The main disadvantage of this type of structure is the numbers of used switches and maintaining the voltage balanced in the voltage sources.

The high power converters could be classified as in Fig. III-4. In this work, the chosen converter topologies are medium voltage high power multilevel voltage source ones. The studied topologies will be the Neutral Point Clamped (NPC), the Flying Capacitor (FC), the Stacked Multicellular Converter (SMC) and the Active NPC topology (ANPC) [28].

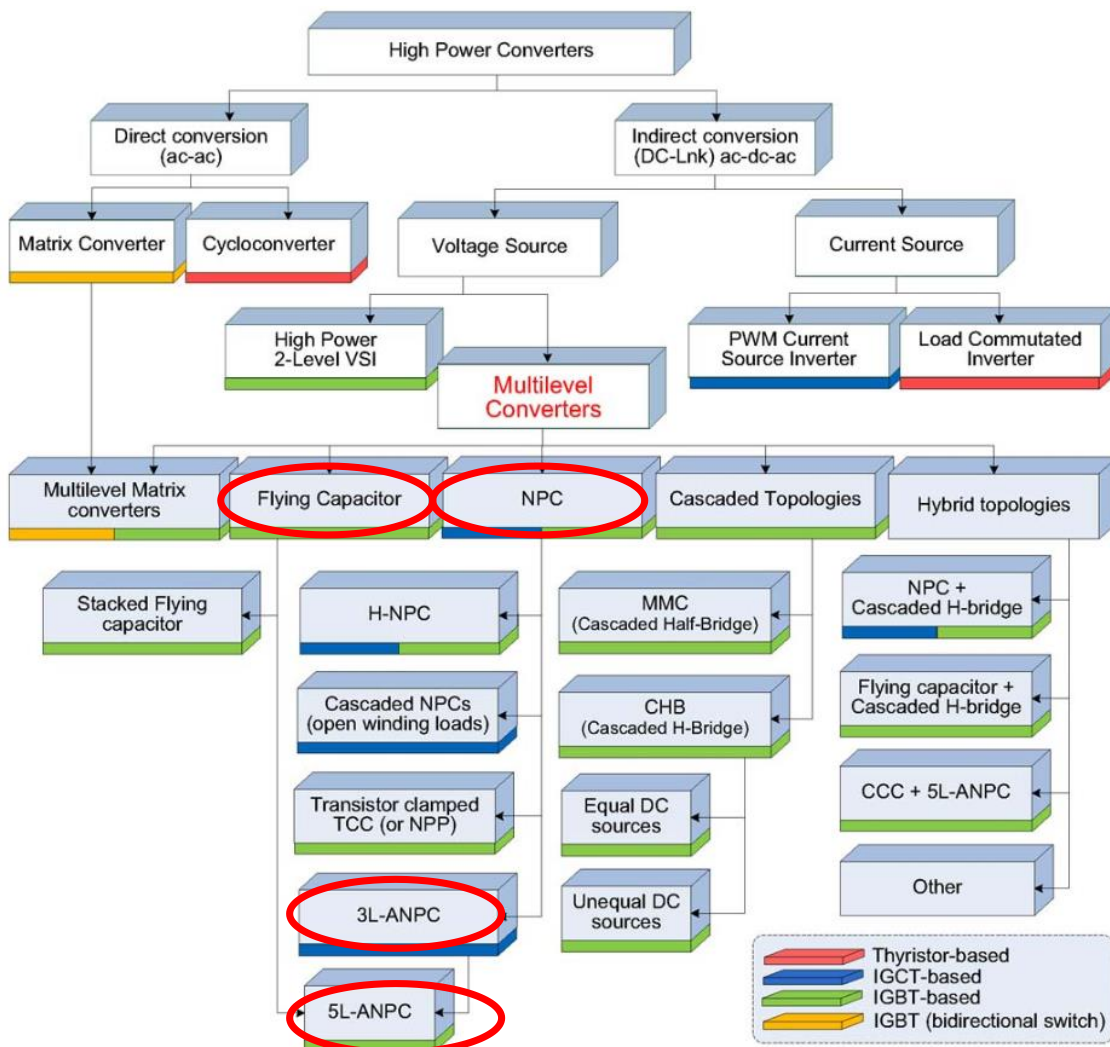


Fig. III-4 : Multilevel converter classification [41]

ii. Studied topologies

Several studied conventional topologies will be presented in this part. The chosen topologies are mainly 3 and 5-level ones as shown in Chapter II based on the DC bus choice according to

the components voltage ratings. Firstly, the 2-level inverter topology is presented so to have reference for comparison. Then Neutral Clamped Point, Flying Capacitor and Stacked Multi-Cell inverter topologies are shown. For each topology, the properties such as the components voltage rating (V_{rating}) and apparent switching frequency (F_{swapp}) will be stated.

1. Two level inverter topology

The two-level voltage inverter for the 3-phase configuration is composed of six active switches with a freewheel diode in parallel with each switch. Fig. III-5 represents the 3-phase two-level inverter.

This structure is widely used for low voltage application (under 900 V) [42] but it can be extended to medium voltage high power applications.

The two-level inverter has several advantages such as the simplicity of its control. The conventional carrier-based sinusoidal modulation or space vector modulation scheme could be implemented for this inverter.

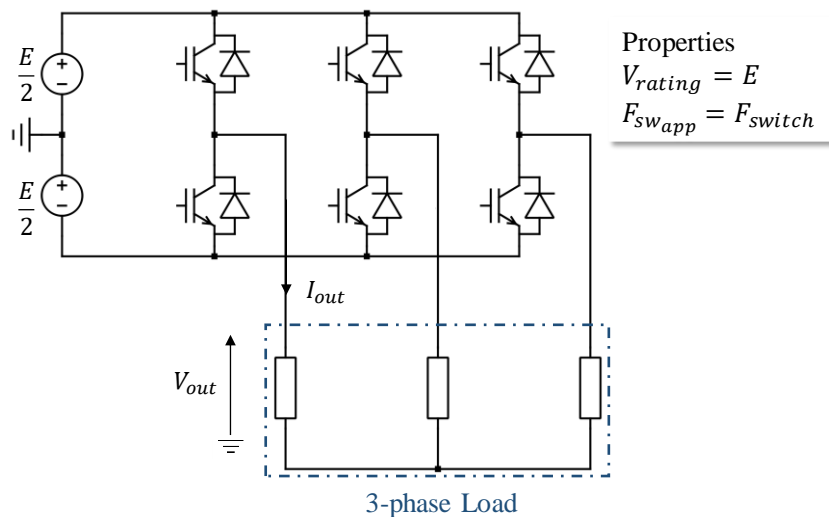


Fig. III-5. 2-level 3-phase inverter

However, there are some drawbacks associated with the two-level inverter such as the high $\frac{dV}{dt}$ in the output voltage due to the fast switching speed of the IGBT. This could lead to premature failure of motor winding insulation, early bearing failure and wave reflection. It could also generate high harmonic distortion in the stator voltage and current if it operates at a low switching frequency. These harmonics produce additional power losses in the motor.

These problems could be solved by adding an LC filter between the inverter and the motor. However, the use of the LC filter can increase the inverter weight and fundamental voltage drops.

2. Flying Capacitor inverter topology (FC)

The flying capacitor inverters have evolved from the two-level and based on a direct series association by adding an intermediate flying capacitor between two switching cells associated in series to fix the switches voltage and allows to split the input voltage by combination [43]. There are two complementary switch pairs in each commutation cell of the 3-level inverter (highlighted in red and blue in Fig. III-6).

The flying-capacitor inverter in Fig. III-6 can produce a phase voltage with three voltage levels.

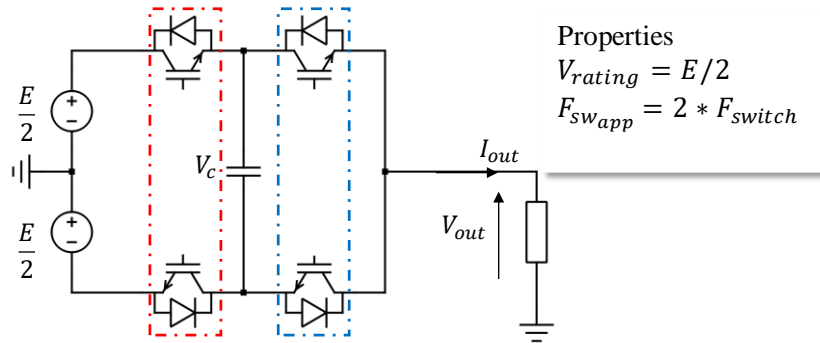


Fig. III-6. 3-level FC inverter's leg

In this case, it is necessary to guarantee the balancing of the voltage across this flying or floating capacitor. Some voltage levels can be obtained by more than one switching state. The voltage level 0, for instance, can be produced by two sets of different switching states. The switching state redundancy is a common phenomenon in multilevel converters, which provides great flexibility for the switching pattern design and control of intervals states variables.

As for the NPC, as a result of the serial connection, this structure thus makes it possible to divide the sizing voltage of the switches, in addition to that, it makes it possible to increase the apparent switching frequency at the output and to reduce the current ripple or the size of the inductance at the output, which makes it possible to improve the output performances.

Since the FC inverter topology is derived from the two-level inverter, it carries the same features as the two-level inverter such as a modular structure for the switching devices. It is also a multilevel inverter, producing the voltage waveforms with reduced $\frac{dV}{dt}$ and THD. However, the flying-capacitor inverter has some drawbacks such as their voltage balancing issues and also a large number of capacitors needed which take up a very large volume of the inverter.

3. Neutral Point Clamped (NPC) and Active NPC (ANPC) inverter topologies

The neutral point clamped inverter employs clamping diodes and cascaded DC capacitors to produce alternative voltage waveforms with multiple levels. The inverter can generally be configured as a 3, 4, or 5-level topology, but only the three-level inverter has found wide

application in medium voltage high power drives [44] [45]. Fig. III-7 represents the 3-phase three-level NPC inverter.

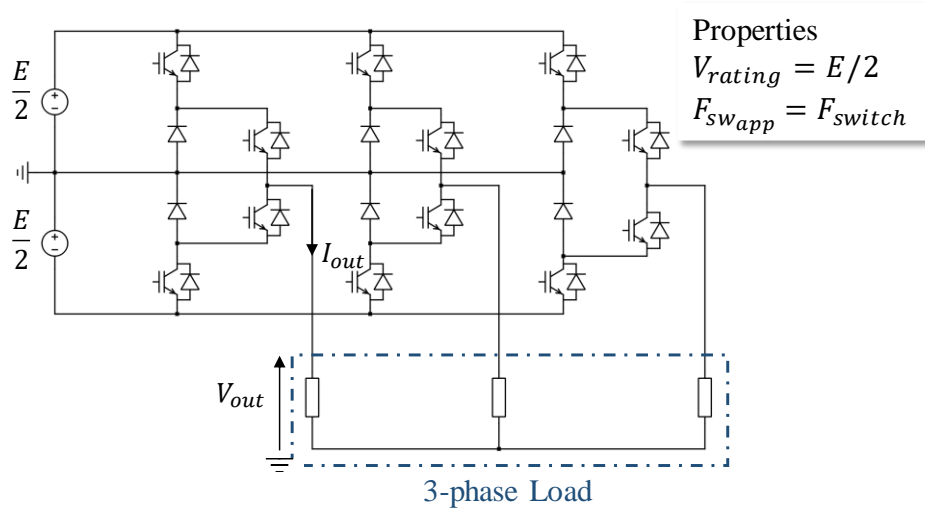


Fig. III-7. 3-level NPC inverter

This structure is based on a direct series association by adding a clamp to fix the switches voltage and allows to divide the input voltage. This structure does not improve the inverter output apparent switching frequency and the clamping circuit is a little complex to realize for 5 and above level topologies.

The main advantage of this structure is the reduced $\frac{dV}{dt}$ and output harmonics compared to the two-level inverter working at the same DC bus voltage and switching frequency. Yet, it needs additional clamping diodes and possible deviation of neutral point voltage which should be taken into account using this structure [46].

There is another NPC inverter type called Active NPC (ANPC) that overcomes the drawback of the unequal current distribution and has additional active switches in antiparallel to the clamping diodes as in Fig. III-8. So to balance the losses distribution, this topology offers multiples command strategies. The first one consist of switching the part in the red dotted frame at low frequency and the blue one at a high frequency so to use the switches near the voltage source as a switcher. The second strategy would be to use the reverse strategy which means switching at low frequency the switches near the load. The third strategy consists of switching both red and blue frames components at high frequency which will lead to double the output apparent frequency, but with higher switching losses [47], [48].

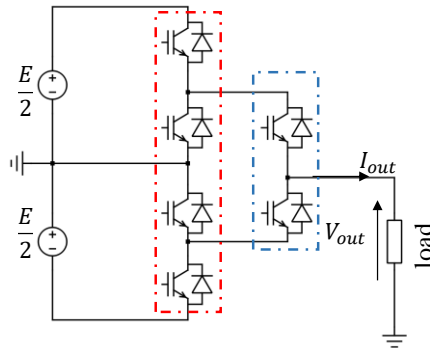


Fig. III-8. 3-level single phase ANPC

The 5-level active neutral point clamped inverter shown in the figure below (Fig. III-9) was developed by ABB to increase the voltage level without highly increasing the price. The idea was based on connecting converters in series. A three-level DC supply alone cannot supply five voltage levels, and so the circuit does require an additional capacitor per output phase. But the solution ABB ingeniously created keeps this capacitor charged without the need for dedicated control circuitry [49].

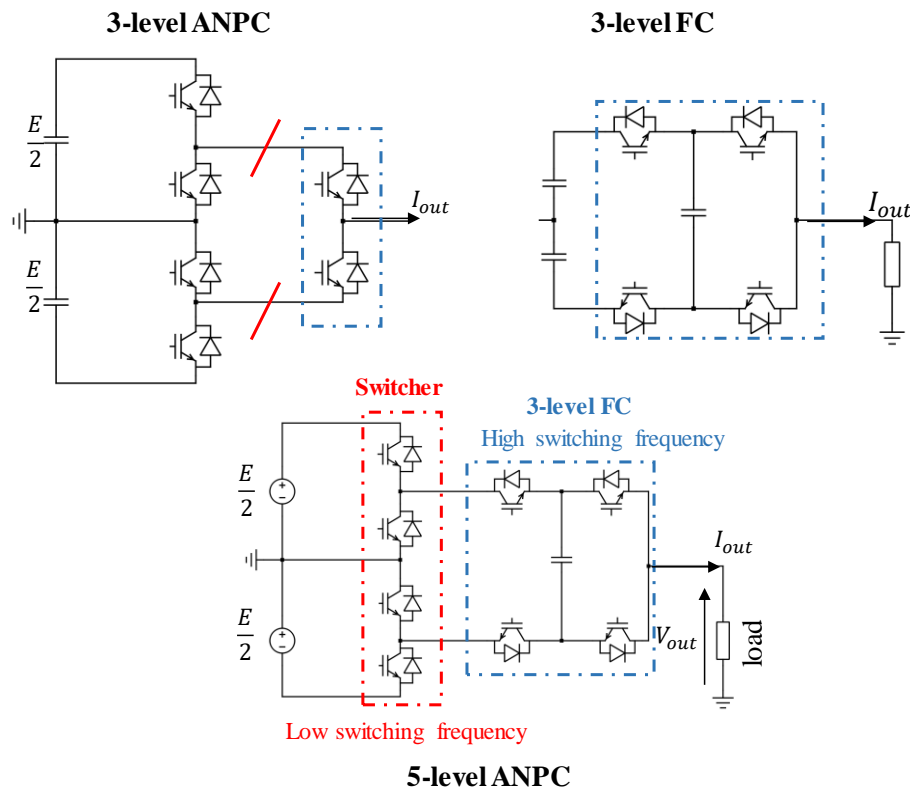


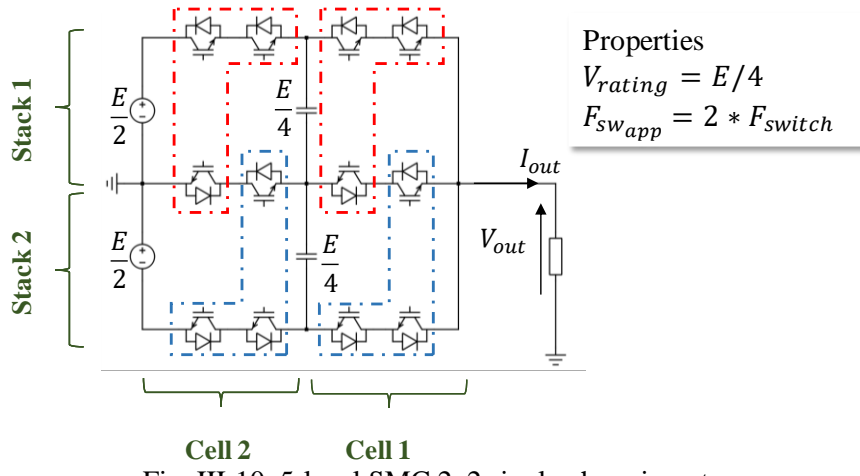
Fig. III-9. 5-level ANPC single phase inverter

The flying capacitor is kept charged to half the voltage of the capacitors in the DC link, one-quarter of the total DC-link voltage. The overall principle of the circuit can be considered as a three-level NPC converter plus an additional capacitor. This phase capacitor is switched in series with the three-level converter as required and provides two additional intermediate output levels (Fig. III-9). Moreover, it requires only one more capacitor and two switches per phase than an ANPC three-level converter.

4. Stacked Multicell Converter inverter topology (SMC)

The stacked multicell converter is based on a hybrid association of elementary switching cells as shown in Fig. III-10 for 2×2 SMC. An SMC $p \times n$ inverter has p switching cells in series and n stacks [50].

As for the FC topology, this topology enables to share the voltage constraint between several switches and also improves the output waveforms of the converter in terms of the number of levels and switching frequency.



Although the SMC requires more switches than an FC, it reduces the stored energy in the converter and thus the size of the flying capacitors proportionally to the number of stacks [50].

The following table sums up the studied topologies properties.

Table III-1. Summary of topology properties

Topology	number of levels	SC rating	Voltage	Output Frequency f_{out}	Switching Frequency f_{sw}	Passive components
2 levels	2		2E		f_{sw}	-
FC N Cells ($N \geq 2$)	$N + 1$		$\frac{2E}{N}$		$N * f_{sw}$	(N-1) Capacitors
3-level NPC	3		E		f_{sw}	-
SMC 1×2	3		E		f_{sw}	-
SMC $n \times p$	$n \times p + 1$		$\frac{2E}{n \times p}$		$n * f_{sw}$	n Capacitors
ANPC including FC 2 Cells	5		$\frac{E}{2}$		FC: $2 * f_{sw}$ Switcher: f_{low_freq}	1 Capacitor

where: E is the DC Bus input Voltage, $n \times p$ is Cell \times Stack numbers of the SMC topology.

iii. Comparison of studied topologies and DC bus voltage definition

These topologies performances will be compared so to define the best operating parameters for our specifications.

The first step of this work was to find out the DC bus voltage by taking into account the problem of partial discharges which limits the possibility of increasing the voltage level if the conductors are placed in the non-pressurized zone. To choose an optimal bus voltage range, it is necessary to compare the efficiency of several multilevel topologies. However, it is difficult to do so due to the discretization of available voltage ratings. To overcome this problem, the generated components database developed in Chapter II, that suits the needed voltage caliber by fitting and extrapolating the existing database are going to be used.

For the first phase of the project, the study will be based on the topologies shown before with silicon components and a standard machine. The DC voltage of the hybridization bus (0.7-7kV) must, therefore, be set [51]. The optimum voltage range will be defined by comparing the results of the parametric study for the various topologies studied using the available components database.

In this first approach, the evolution of converters specifications is studied for different DC bus voltages. The converters under study are: 2L (PWM), 3-level FC (PWM), 5-level FC (PWM) and 5-level ANPC. A parametric sweep of the DC bus voltage is implemented starting from 100 V to 4 kV for an imposed power of 1 p.u. which corresponds to the first specification. Due to the limitation of the existing components' voltage calibers which corresponds to 6500 V so a definition voltage of 3600 V, for the low-level topologies, the results for higher DC bus voltage should not be taking into account.

As regards the switching frequency, a ratio of 10 between the electric motor fundamental frequency and the apparent switching frequency was maintained. This study was done based on the first specification.

1. Comparison of 2-, 3- and 5-level topologies

To verify earlier conclusions concerning the use of low-voltage components, three topologies using small and large voltage calibers for each topology are compared. Using ABB component available in our database, 2-level, 3 and 5-level topologies performances were estimated for a DC bus sweep from 700 V to 7 kV with a switching frequency of 5.8 kHz and the maximal power point with a fixed case temperature of 80 °C. Fig. III-11 shows the inverter efficiency, power losses, maximal junction temperature and number of total used switches for the studied topologies. The generated components are used at 50 % of their voltage rating and 100 % of their current rating.

The high voltage components that are used for the 2-level topology have more switching losses due to their properties and also to the high switching frequency which is lower for 3 and 5-level topologies.

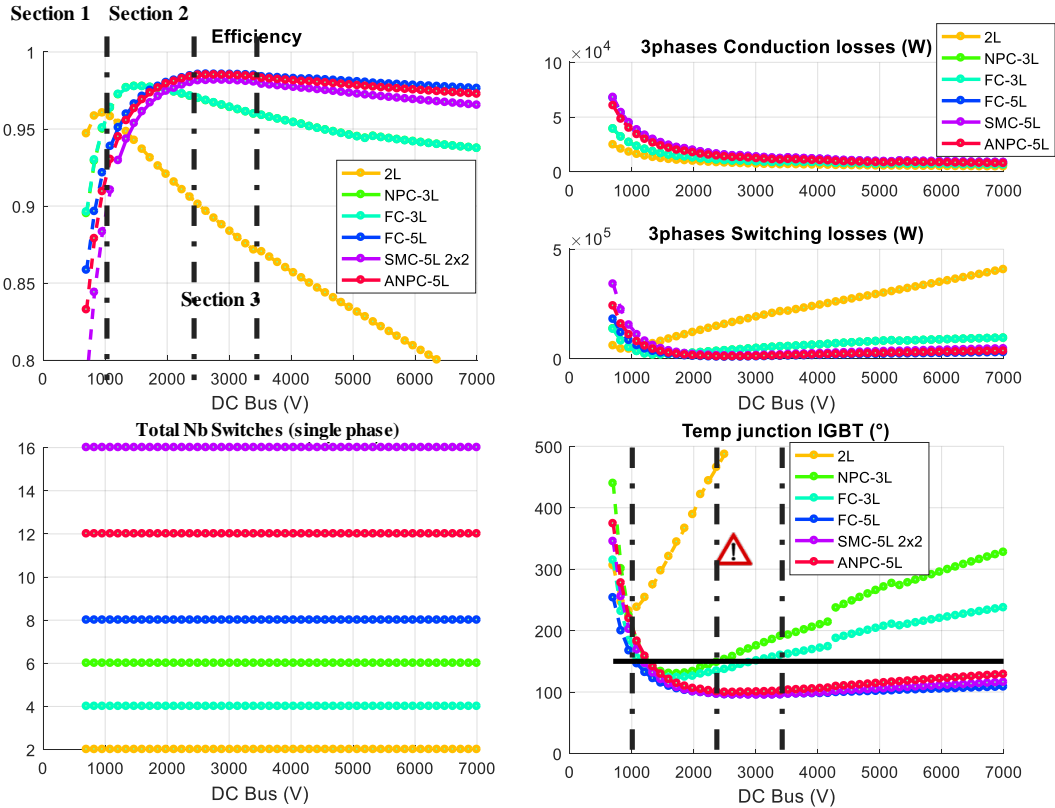


Fig. III-11. Generated components response for DC bus sweep for 2-, 3- an 5-level topologies

In the first section ($700 \text{ V} \leq V_{DCBus} \leq 1 \text{ kV}$), the 2-level topology has higher efficiency than the other ones, however, if this solution is selected, it would be disadvantaged by the number of needed components in parallel to withstand the needed current. Above 700 V, the maximal junction temperature of the used semiconductors is higher than the 150°C limit.

In the second section ($1 \text{ kV} \leq V_{DCBus} \leq 2.4 \text{ kV}$), the 3-level topology efficiency is slightly better than the 5-level topologies so no need to use them. In the third section ($2.4 \text{ kV} \leq V_{DCBus} \leq 3.5 \text{ kV}$), both 3 and 5-level topologies are equivalent in terms of efficiency. For a DC bus voltage higher than 3.5 kV, the maximal junction temperature of the 3-level topology semiconductors is higher than the thermal limit so only the 5-level topologies are interesting for this voltage range in terms of efficiency and maximal junction temperature.

Multilevel topologies use more components than a 2-level one but have better performances and lower maximal junction temperature. As seen before, the high voltage components have more switching losses due to their properties and also to the high switching frequency that is lower for 3 and 5-level topologies. They have therefore lower junction temperature even if they are use more semiconductors.

2. Switching frequency impact study

The purpose of this part is to verify if the switching frequency value can change the tendencies seen in the previous part, namely that the use of the multilevel structures makes it possible to improve the efficiency by using components with smaller voltage rating in spite of their greater number. The high voltage components are not meant to be used at high switching frequencies which lead to great losses that heat the components and their junction temperature exceeds the thermal limit of 150 °C.

Fig. III-12 shows the previously studied topologies for a DC bus voltage sweep using an adapted switching frequency so to have an acceptable maximal junction temperature. The apparent or output switching frequency was limited to the electric motor fundamental frequency of 532.3 Hz (represented in black limit in the figure) so it can't be lower than this value. The relation between the switching frequency and apparent one depends on the topology. For example, if the apparent or output switching frequency is 5 kHz for the 3-level NPC, it is then 2.5 kHz for the 3-level FC and 1.25 kHz for the 5-level FC.

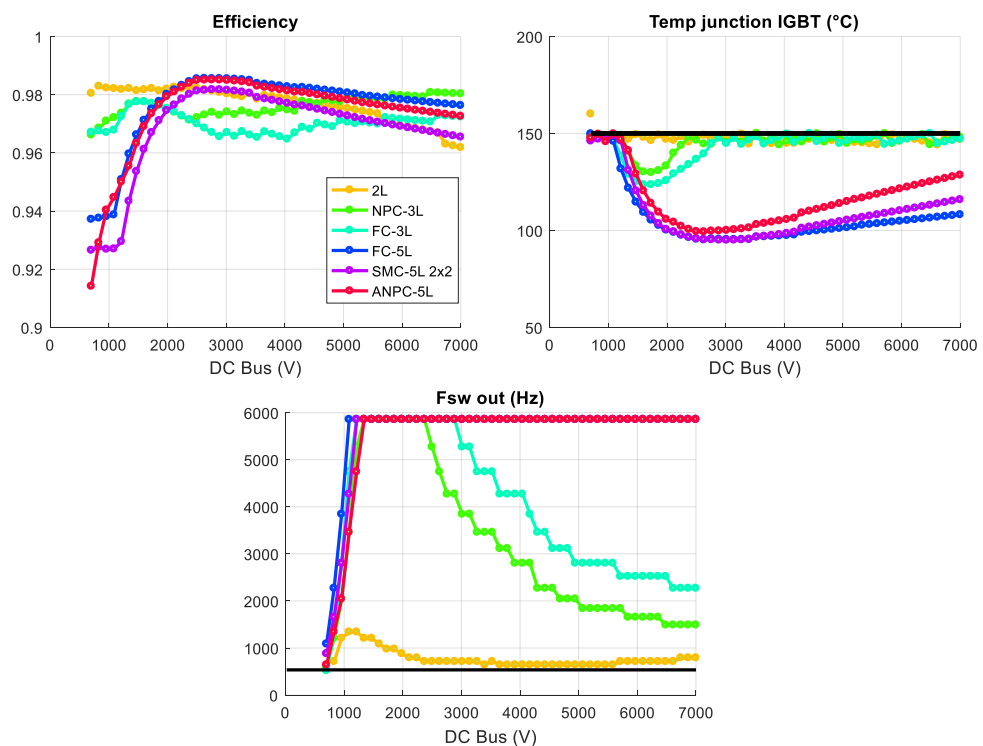


Fig. III-12. 2-,3- and 5-level topologies performances for a DC bus voltage sweep with adapted switching frequency

The 2-level topology should operate at a low switching frequency so to have an acceptable maximal junction temperature. Above 2.4 kV, the switching frequency should be reduced to keep the 3-level topologies temperature under the 150 °C limit unlike the 5-level ones that have acceptable temperature starting from 1 kV DC bus voltage.

The multilevel converters are the best solution to keep an acceptable junction temperature with a high efficiency whatever is the switching frequency. This conclusion is even stronger when the switching frequency is higher, the efficiency gap between the structures increasing.

3. Specific power

To estimate the specific power, the total weight of the inverter including the DC bus capacitor, the semiconductors, the heat exchanger coefficient given in the specification dossier (0.34 kW/kg) and the flying capacitors is calculated for 3- and 5-level studied topologies using the generated components. Fig. III-13 shows the specific power for the studied topologies as a function of the DC bus voltage value using generated components.

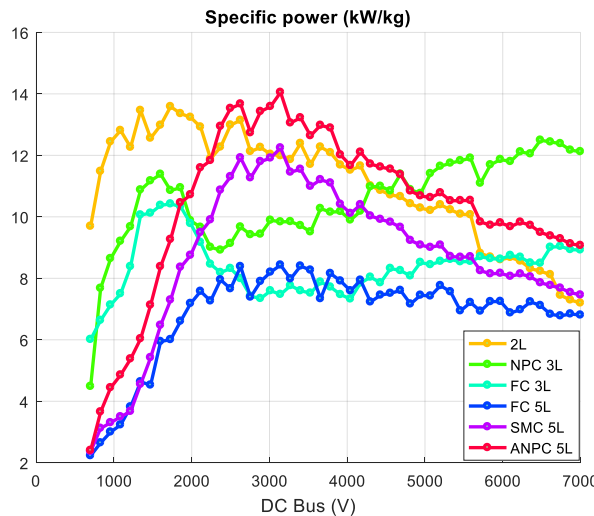


Fig. III-13. Specific power for studied topologies using generated components and adapted switching frequency

The following table sums up the maximal power density and the corresponding DC bus voltage and efficiency using generated components. The 2-level is written in red since its maximal junction temperature is higher than the thermal limit with a 5.8 kHz switching frequency. Its switching frequency is then adapted to satisfy the thermal constraint.

TABLE III-2. Maximal power density for 2-level, 3-level FC, 5-level FC and 5-level ANPC with generated components

Switching frequency (Hz)	Topology	Maximal specific power (kW/kg)	Corresponding DC bus voltage (V)	Efficiency (%)
5855	2-level	6.73	957	96.04
	3-level NPC	11.39	1600	97.76
	3-level FC	10.42	1730	97.77
	5-level FC	8.43	3143	98.53
	5-level SMC	12.24	3143	98.12
	5-level ANPC	14.05	3143	98.47
879	2-level	14.98	1986	98.19

Fig. III-14 represents the total weight repartition for the studied topologies using generated components for the points corresponding to the highest specific power with a maximal junction temperature lower than 150 °C. The cooling system represents the predominant weight for almost all the topologies except for the 5-level FC in which the flying capacitors represent 36 % of the total weight. Using multilevel topologies makes it possible to reduce the total weight at least by 20 % compared to the 2-level one.

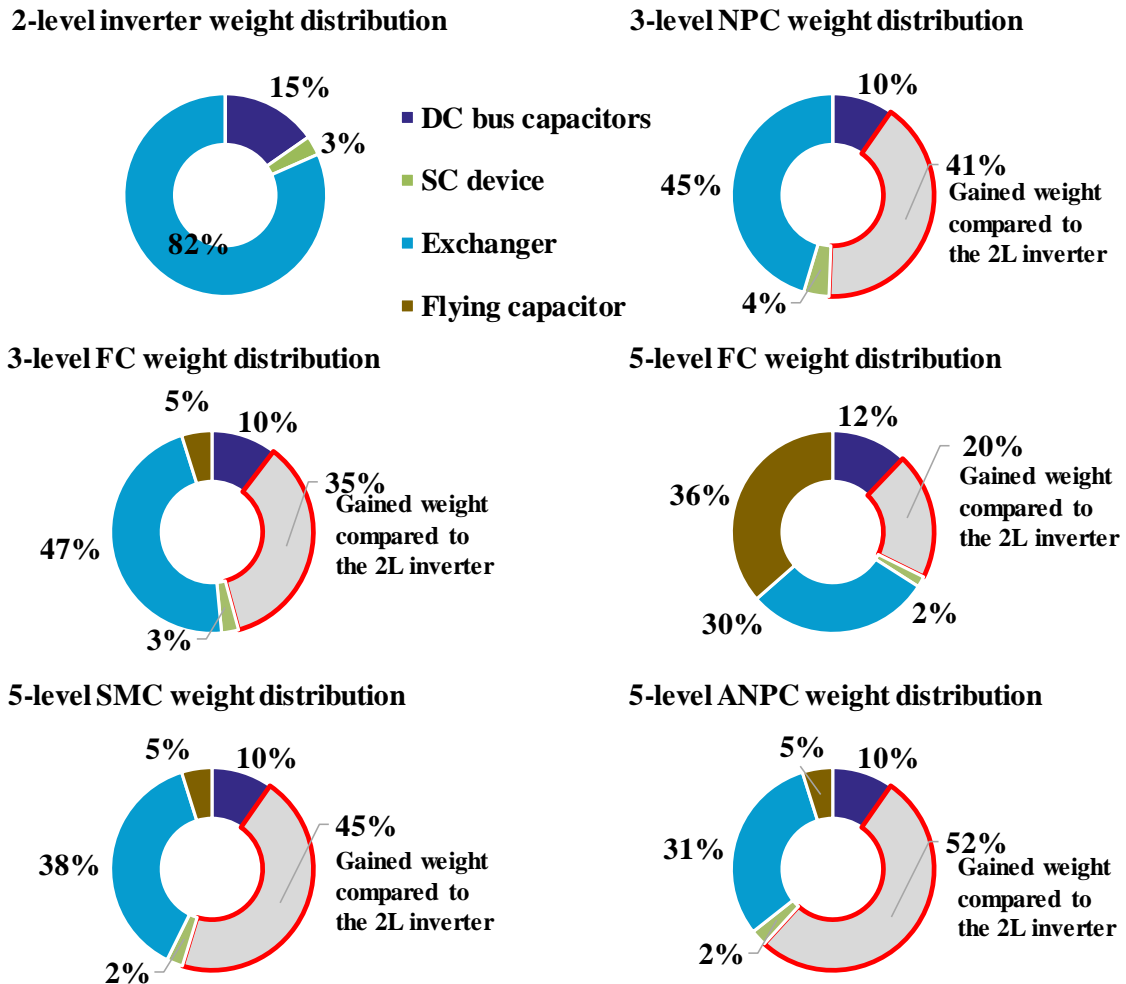


Fig. III-14. Weight distribution for studied topologies with generated components

Due to the flying capacitors weight, the FC topologies have lower power density than the other multilevel topologies even if their efficiency is high. To go beyond the 2025 target, the 5-level ANPC seems to be the best option if it is used at a low switching frequency. The 3-level NPC is also to be considered to reach this target even with the high switching frequency.

Now let's see what could be achieved using real components. Fig. III-15 shows the specific power for the studied topologies as a function of the DC bus voltage value using real components and shows only the points satisfying the thermal limit condition. For the 2-level topology, the switching frequency should be reduced to have a maximal junction temperature under 150 °C.

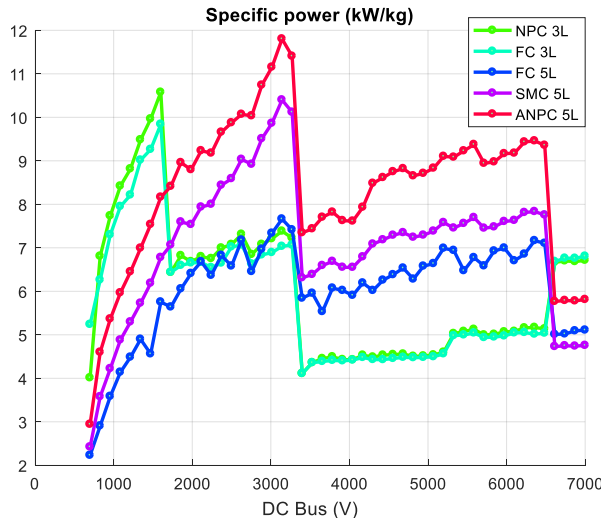


Fig. III-15. Specific power for studied topologies using a switching frequency of 5.8 kHz using real components

In TABLE III-3, the maximal specific power using real components is at the same range as for the generated components. With the 2-level topology, the specific power is the closest to the 2025 target of 15 kW/kg, however, the switching frequency is so low that it could degrade the THD and output waveforms.

TABLE III-3. Maximal power density for 2-level, 3-level FC, 5-level FC and 5-level ANPC with real components with adapted switching frequency

Switching frequency (Hz)	Topology	Maximal specific power (kW/kg)	Corresponding DC bus voltage (V)	Efficiency (%)
577	2-level	13.05	2886	98.29
5855	3-level NPC	10.58	1600	97.67
5855	3-level FC	9.84	1600	97.67
5855	5-level FC	7.66	3143	98.27
5855	5-level SMC	10.40	3143	97.85
5855	5-level ANPC	11.80	3143	98.22

To achieve the specific power targets, the used topology will mainly be a 3-level one which is the most adapted for the used voltage and power ranges. 5-level could be an option if the DC bus voltage was to be increased ($\geq 2kV$) to optimize the whole power chain. However, flying capacitor topologies are penalized by the added capacitor weight. The bus bar weight will also be taken into account, in the part 4 of this study, to get a more accurate estimation of the inverter specific power.

4. Design for different power values

Another study is done using two parametric sweeps of the DC voltage [700 V – 7 kV] and power [25 - 1500 kW] considering a fixed apparent frequency (5.8 kHz). The simulation results

are shown in Fig. III-16 with taking into account the thermal limit using generated components. These figures give an impression of the efficiency tendencies of each studied topology. For all the topologies, the efficiency is very low for low power because the used components are not adapted to this power range.

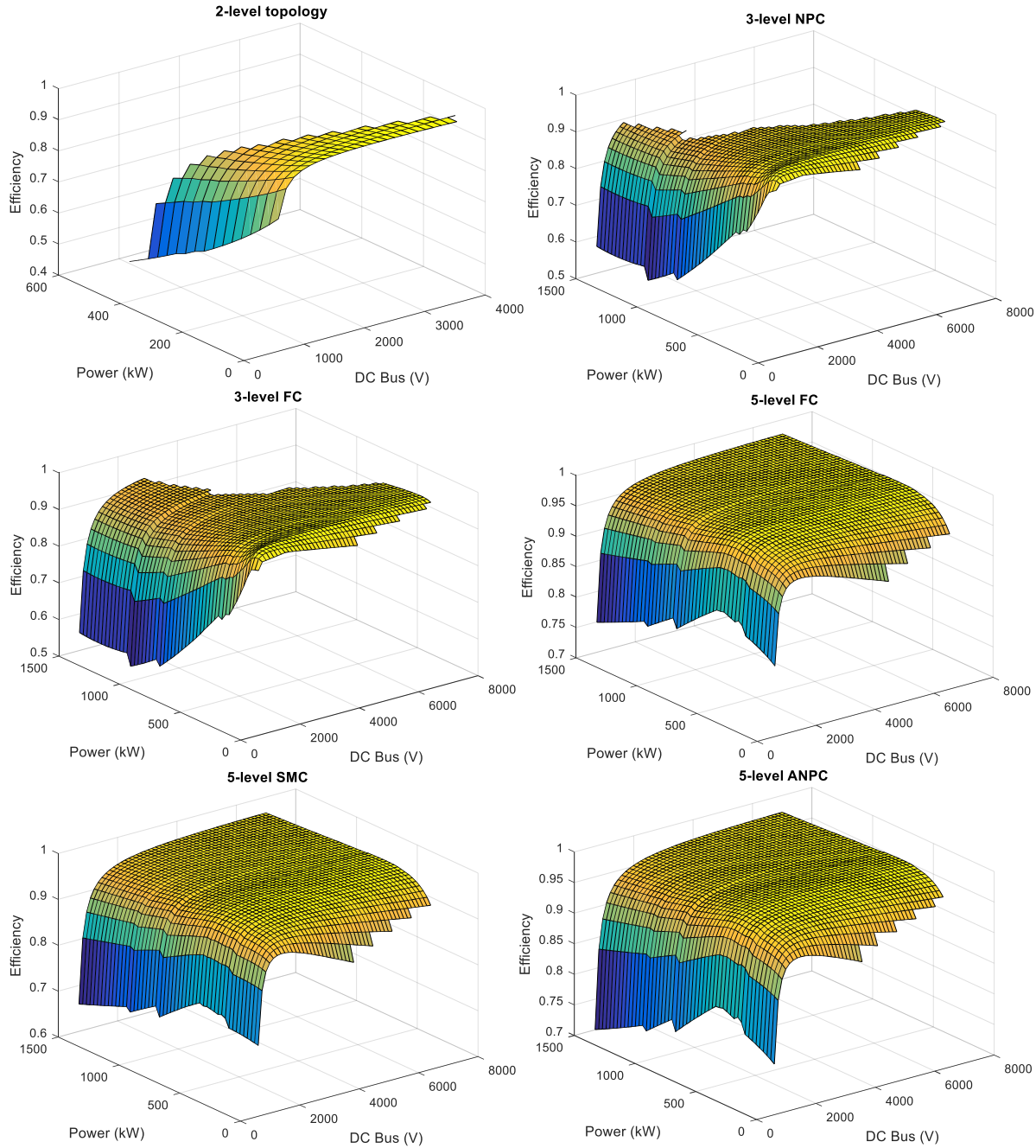


Fig. III-16. Efficiencies of studied topologies for DC voltage and power parametric sweeps

More power means more absorbed current by the load for a DC bus voltage, thus more losses in the semiconductors. This leads to increase junction temperature due to the high thermal resistance related to the needed high current rating which heats up of the components. Hence larger and heavier exchanger and cooling dissipation system are needed.

The 2-level inverter could only be used at low power with a DC bus voltage that decreases with the used power for the used switching frequency. So this inverter does not seem to be the best option for our application as stated before. The 3-level inverters could be used up to 2 kV all over the studied power range and they have an optimal efficiency between 1 kV and 2 kV. However, for the 5-level topologies, they have an optimal efficiency between 3 kV and 4 kV. It can be drawn that for these topologies, from the efficiency graphs, that the optimal efficiency is for a DC Bus voltage is between 1 kV and 4 kV.

2. Modulation strategies

Modulation strategies aim to get an output voltage that approximates a sinusoidal waveform with adjustable amplitude or frequency. Each strategy has its switching configuration which generates control reference and keeps the voltage sources balanced. The multilevel modulation techniques could be classified as in Fig. III-17 [52].

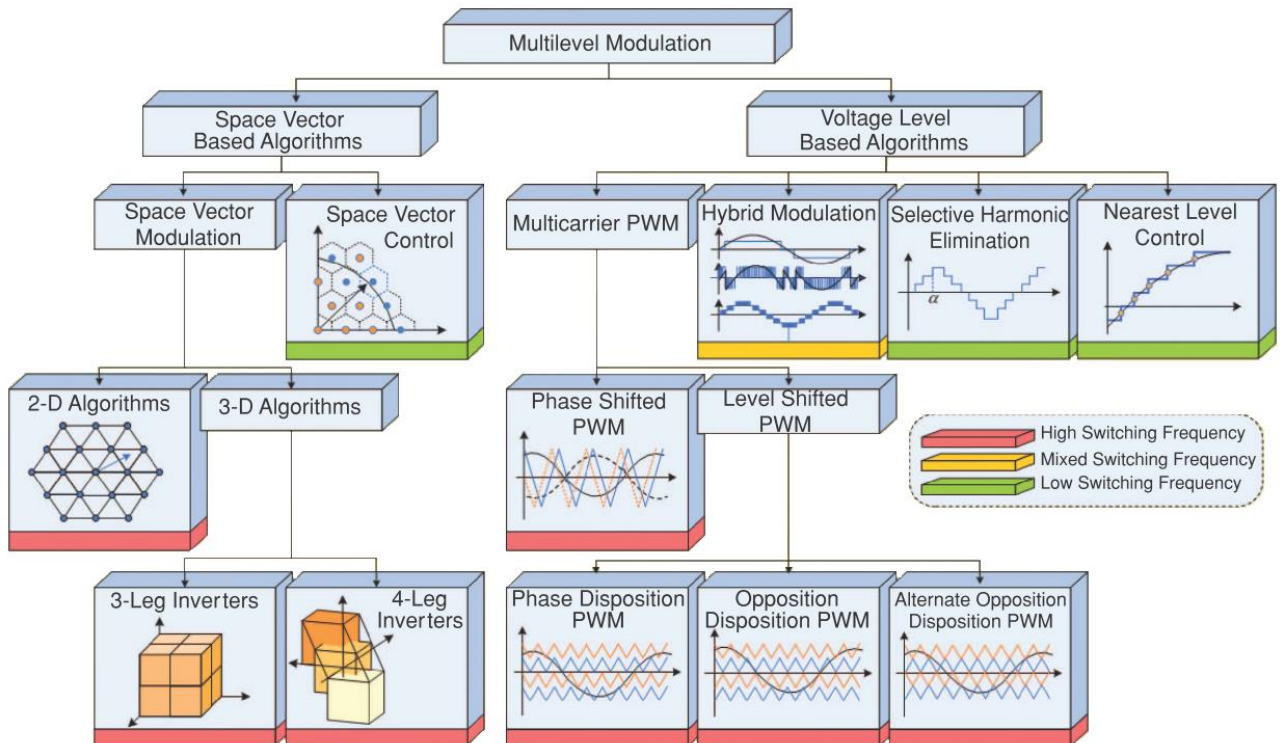


Fig. III-17. Multilevel inverter modulation classification

Modulation algorithms are divided into two main groups. The first one corresponds to the space vector, in which the operating principle is based on the generation of the voltage vector, and the second one corresponds to the time domain, in which the method is based on the generation of the voltage level over a given period. The different methods could be sorted as a function of the switching frequency they produce. In general, low switching frequency methods are preferred for high power applications due to the high voltage components' low switching speed, while the higher output power quality and bandwidth of high switching frequency algorithms are better suited for high dynamic range applications. They can also be classified according to

switching frequency [53]. The switching frequency is at least 7 times higher than the fundamental frequency so to have acceptable waveforms [33].

The studied multilevel modulations are based on the voltage level algorithms and could be classified as in Fig. III-18. They can be grouped into two types of modulation based on the used switching frequency. The first one, based on high switching frequency, is the Pulse Width Modulation including three options: the regular sine PWM, third harmonic injection PWM, and discontinuous PWM. The second one, based on low switching frequency, is the Full-Wave Modulation. These modulation strategies will be presented in detail later in this chapter.

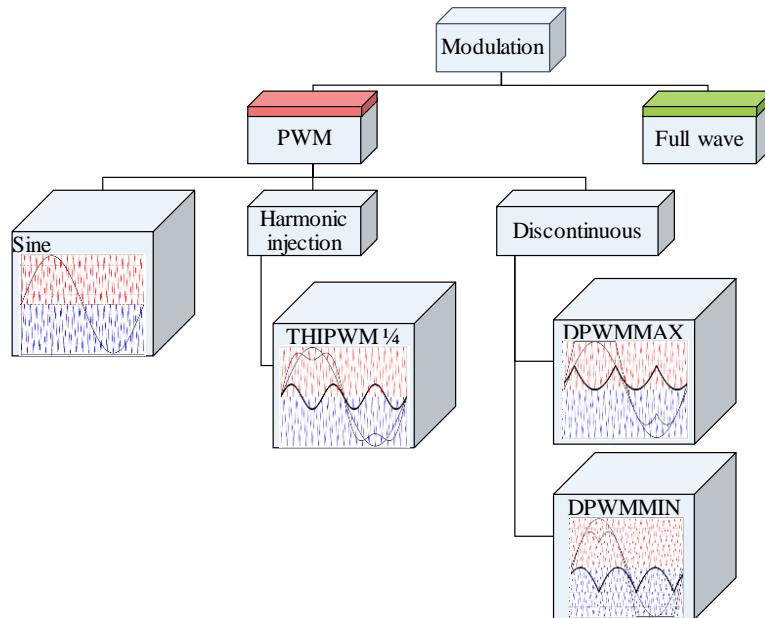


Fig. III-18. Studied modulation strategies

To have a point of reference, results using the sine PWM are given with a 3-level inverter. The voltage is not purely sinusoidal because of the switching and we will also plot the fundamental as in Fig. III-19. This fundamental will be controlled since the machine will filter the harmonics to obtain an almost sine wave current.

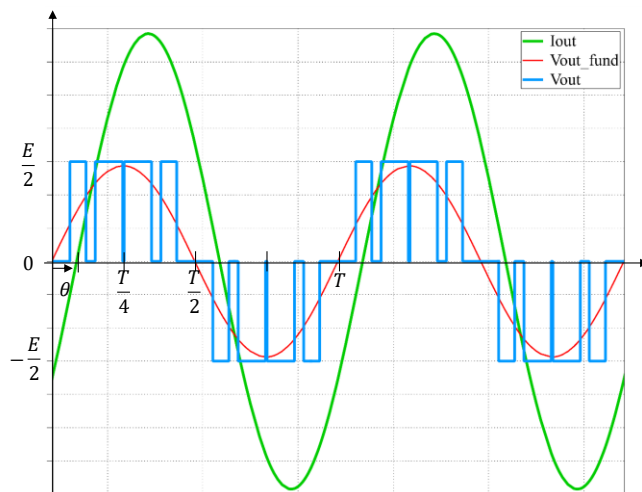


Fig. III-19. Output desired voltage and current 3-level PWM waveforms

The switching losses account for a significant amount of the total power losses in this type of inverters. Unlike conduction losses, they can be reduced by reducing the switching frequency without reducing the current or changing the used component parameters. Moreover, the cooling system represents a large part of the mass. Reducing the cooling requirements by reducing the losses in the converter would decrease the global weight of the system, also reducing its physical size and manufacturing cost. It would also increase the specific power. The switching loss minimization can be done by using a full-wave modulation. However, the reduction of switching frequency generally causes an increase in harmonic distortion of the line- and motor-side waveforms of the drive which will be the case of the full-wave modulation. THD must be monitored.

The full-wave, discontinuous and harmonic injection PWM methods will also allow generating more output voltage to feed the machine as in TABLE III-4. Using the Full wave modulation provide 30 % more voltage than a sine PWM which will able us to reduce the DC bus voltage for the same needed output voltage.

However, to take into account the dead time, the required time delay for the conduction of the transistors, to ensure that their complementary transistors have had time to lock, the maximal modulation index for PWM was fixed to 0.9 and not 1.

TABLE III-4. Maximal output voltage magnitude as function of DC bus voltage and modulation strategy

	PWM	THIPWM / DPWM	Full wave
V_{out_max}	$\frac{V_{DCbus}}{2}$	$1.15 * \frac{V_{DCbus}}{2}$	$1.3 * \frac{V_{DCbus}}{2}$

To define the needed DC bus voltage and appropriate modulation strategy, the output needed voltage during the flight mission profile which will be developed in Chapter IV.

i. Multilevel SPWM

Sinusoidal pulse width modulation is the most popular method where a high-frequency triangular carrier wave is compared with a sinusoidal reference of the desired frequency. The switching or commutation instants are defined by the intersection of both waves. For this modulation, the harmonics are around the switching frequency. This was the method used so far for this project [28].

Fig. III-20 shows a phase-shifted PWM two cells carrier and sine reference that will be compared to generate the switches command signal for a 3-level inverter. Other strategies as carrier phase opposition and phase disposition could be used depending on the used topology and the desired output performances.

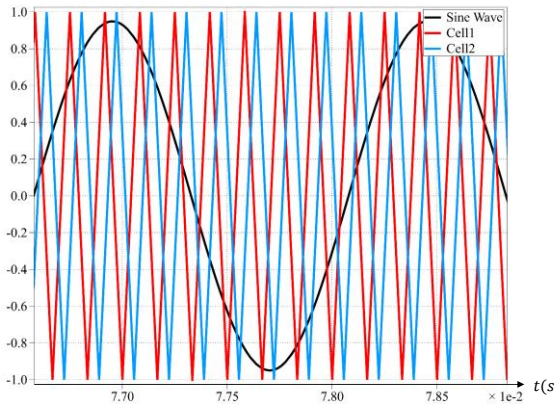


Fig. III-20. PWM triangular carrier and sine reference

ii. Discontinuous PWM (DPWM)

Discontinuous PWM method is an effective strategy to reduce switching losses. DPWM involves locking each phase leg to a fixed DC voltage level for 120° per fundamental cycle while the remaining two-phase legs are pulse width modulated [54]. Theoretically, DPWMs reduce about 33% of the inverter switching losses compared to continuous PWMs [55].

The easiest approach for discontinuous modulation of a multilevel inverter is to simply lock particular phase legs to the upper or lower voltage rails for fractions of the fundamental cycle [33].

To do so, a signal is added to the sinusoidal reference which results in the new reference (equations III-1) represented in black in Fig. III-21 that is compared to the triangular carrier, in which the switching cell does not switch for a third of the modulation period.

$$\begin{cases} V_{off,DPWMMIN}(t) = -\left(1 + \min(V_{1N,ref}(t), V_{2N,ref}(t), V_{3N,ref}(t))\right) \\ V_{off,DPWMMAX}(t) = -\left(1 + \max(V_{1N,ref}(t), V_{2N,ref}(t), V_{3N,ref}(t))\right) \\ V_{1N,ref,DPWM} = V_{1N,ref}(t) + V_{off,DPWM}(t) \end{cases} \quad (\text{III-1})$$

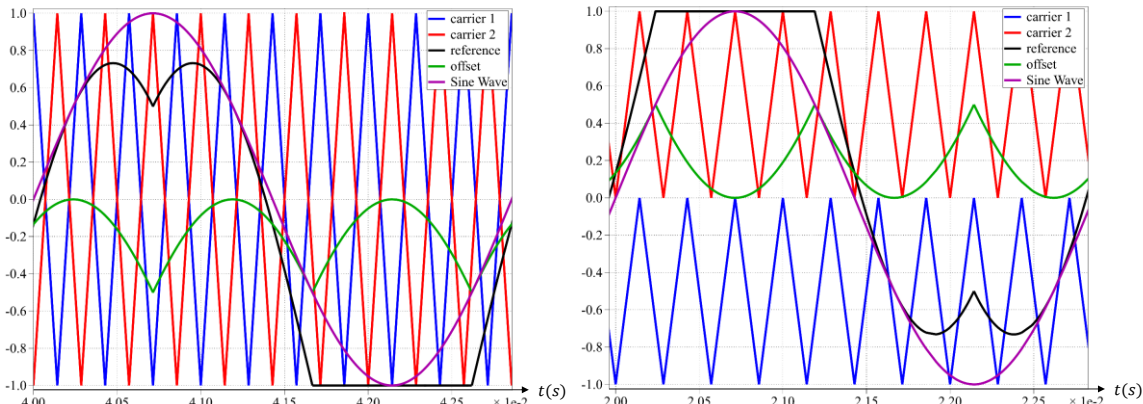


Fig. III-21. DPWMMIN with phase opposition and DPWMMAX with phase disposition triangular carrier and sine reference

iii. Third Harmonic injection PWM (THIPWM 1/4)

The sinusoidal pulse width modulation does not fully utilize the DC bus voltage. So, the third harmonic injection pulse width modulation strategy was developed to increase the inverter output voltage fundamental magnitude for the same DC bus voltage as for a Sine PWM.

The third harmonic injection PWM (THIPWM) method is suitable for three-phase inverters. To obtain the modulation reference, a triangular homopolar component is added to the sine wave which is the commonly used method, equivalent to the Space Vector strategy.

$$\begin{cases} MAX = \max(V_{1N,ref}(t), V_{2N,ref}(t), V_{3N,ref}(t)) \\ MIN = \min(V_{1N,ref}(t), V_{2N,ref}(t), V_{3N,ref}(t)) \\ V_{off(t)} = -\frac{MAX+MIN}{2} \\ V_{1N,ref,SVPWM} = V_{1N,ref}(t) + V_{off}(t) \end{cases} \quad (\text{III-2})$$

However, in our study, a sinusoidal homopolar at three times the fundamental frequency and amplitude $\frac{1}{4}$ of the fundamental (equations (III-3)) is used instead of the triangular one as in Fig. III-22.

$$\begin{cases} V_{off}(t) = \frac{M_{ref}}{4} \sin(3 * \omega * t) \\ V_{1N,ref,THIPWM} = V_{1N,ref}(t) + V_{off}(t) \end{cases} \quad (\text{III-3})$$

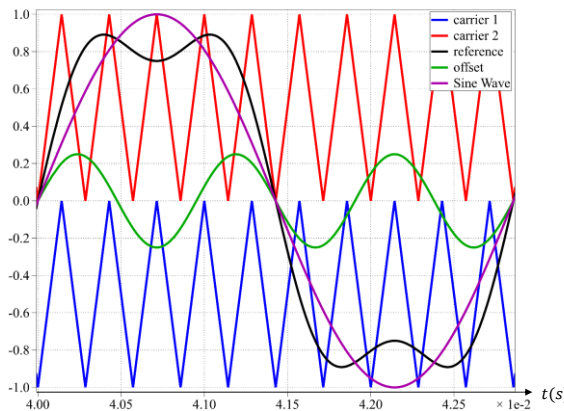


Fig. III-22. 3-level THIPWM1/4 modulation

iv. Full-wave modulation

The full-wave modulation is a low-frequency method which is interesting for high power applications as each semiconductor switches twice per period in which losses minimization is crucial. However, this method has a main drawback which is the low-frequency range harmonics contents. In this part, several full-wave strategies will be shown for 3-level NPC and FC topologies.

1. Full Wave modulation 1 (FW1)

The considered full wave modulation is a 3-level wave ($+E/2, 0, -E/2$) in which, the 0 level duration or α (equation III-4) is used to control the supplied RMS voltage ($V_{s_{rms}}$) or amplitude value ($V_{s_{max}}$), with E the DC bus voltage value (Fig. III-23). The considered switching cell are consisting of components T1 and T3 for the first one and T2 and T4 for the second one. The switches of a switching cell have complementary states ($T3 = \overline{T1}$, $T4 = \overline{T2}$).

$$\alpha = \frac{1}{\pi} * \arcsin\left(\frac{V_{s_{max}}}{2 * \frac{E}{\pi}}\right) \quad (\text{III-4})$$

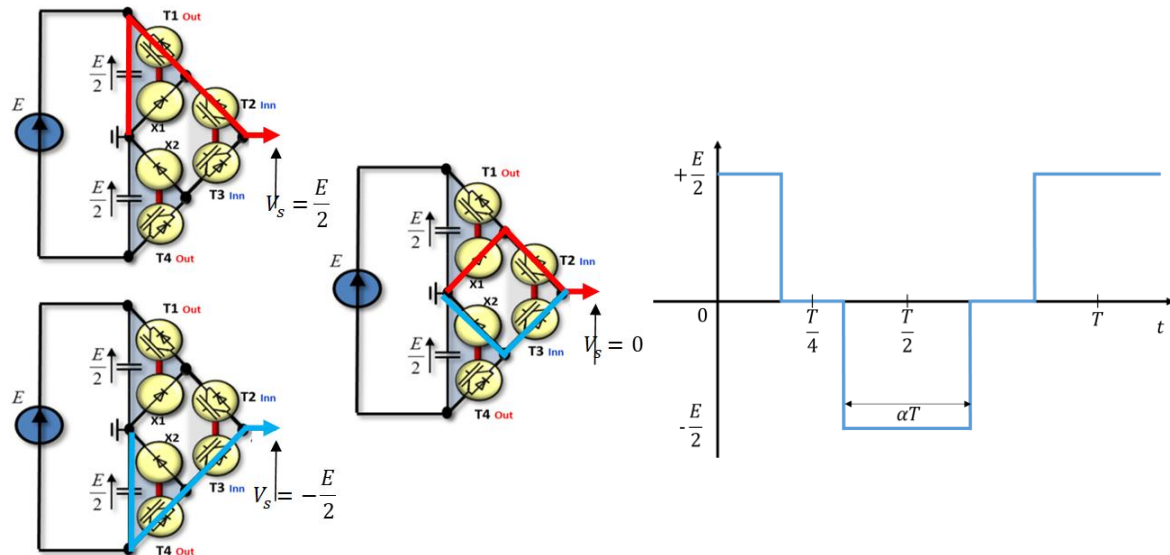


Fig. III-23. Switching cell combinations for 3-level NPC and output desired voltage waveform

This modulation will generate the desired voltage and current waveforms with only low-frequency switching which will reduce the overall power losses of the inverter. Simulation results will be presented later in this chapter. The generated control signals are shown in the following figure (Fig. III-24).

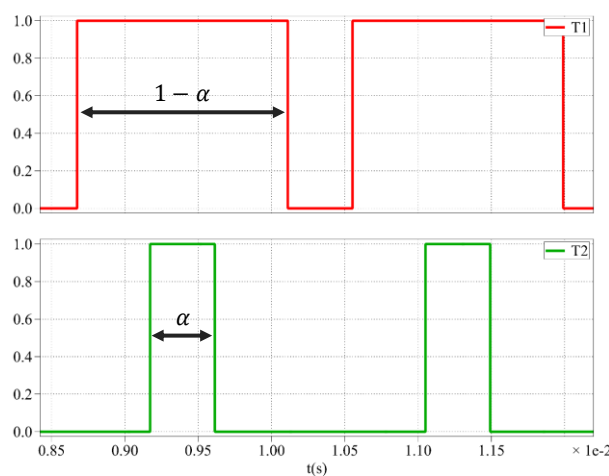


Fig. III-24. T1 and T2 3-level NPC control signals

To obtain the desired output voltage waveform, the two switching cells' control signals are issued of comparison of a constant α (III-4), and a low-frequency triangular wave for the first cell and a half a period delayed triangular wave for the second cell as in Fig. III-25.

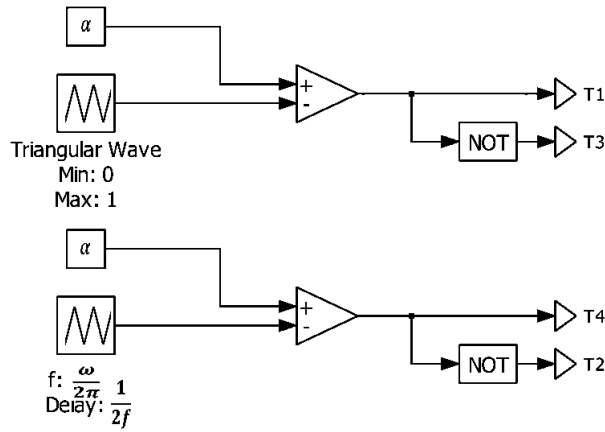


Fig. III-25. Switching cell command schematic

For the 3-level FC topology, we still have the 4 switches states to deal with (same switching cells defined above) in addition to the flying capacitor voltage. Various modulation strategies have been implemented to improve the operation of this inverter, loss distribution and voltage regulation of the flying capacitor. In this simulation, the converter is studied using perfect voltage sources instead of flying capacitors assuming that the voltage of the flying capacitor is perfectly controlled.

For the full-wave modulation called "Full Wave 1", the control of both switching cells are centered, and the duty cycle is chosen to control the RMS voltage value (Fig. III-24). Fig. III-26 shows the different states obtained and the voltage then generated and that this leads to a fixed 0 state which was chosen as in the figure. This leads to an imbalance in the flying capacitor voltage which is only compensated for at the scale of the low frequency period with the current direction inversion. This method unbalances the losses of the switches of this topology, which prevents us from taking advantage of one of the key strengths of this structure, which is the balanced distribution of losses.

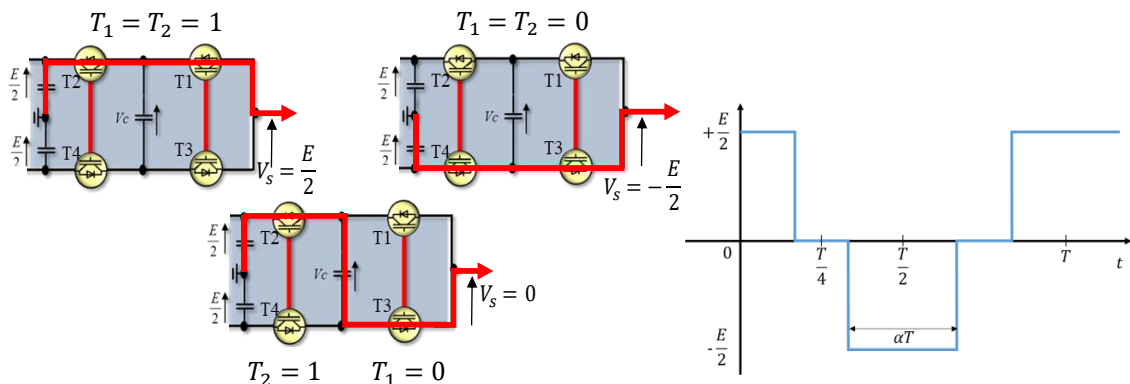


Fig. III-26. Full wave 1 used switches combination

For a DC bus voltage of 2 kV, the needed flying capacitor value is 13.4 mF which is more important than the DC bus capacitor of 1.07 mF. In this case, the flying capacitor is sized according to the low-frequency component of the current with a voltage ripple of 10 %. For the capacitors sizing, chapter II formulas were used.

2. Full wave modulation 2 (FW2)

The second modulation idea consists of adding to the "Full Wave 1" command, the combination of the two possible configurations for the 0 voltage level (Fig. III-27), and thus be able to balance the losses of the two switching cells over two periods.

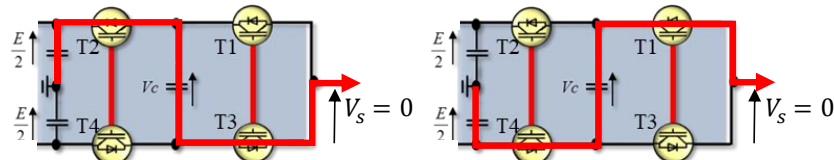


Fig. III-27. 0 voltage level switches combination for full wave 2

The full-wave modulation called "Full Wave 2" is designed as over a first period, switch T1 is primed, and T2 is blocked to create the voltage level at 0 V, and in the following one, switch T2 is primed, and T1 is blocked to generate the 0 V as mentioned in the state machine in Fig. III-28. This command, therefore, balances the losses in the switches over two periods.

This modulation strategy uses the same state machine as for a regular PWM, however, the switching frequency corresponds to the fundamental one.

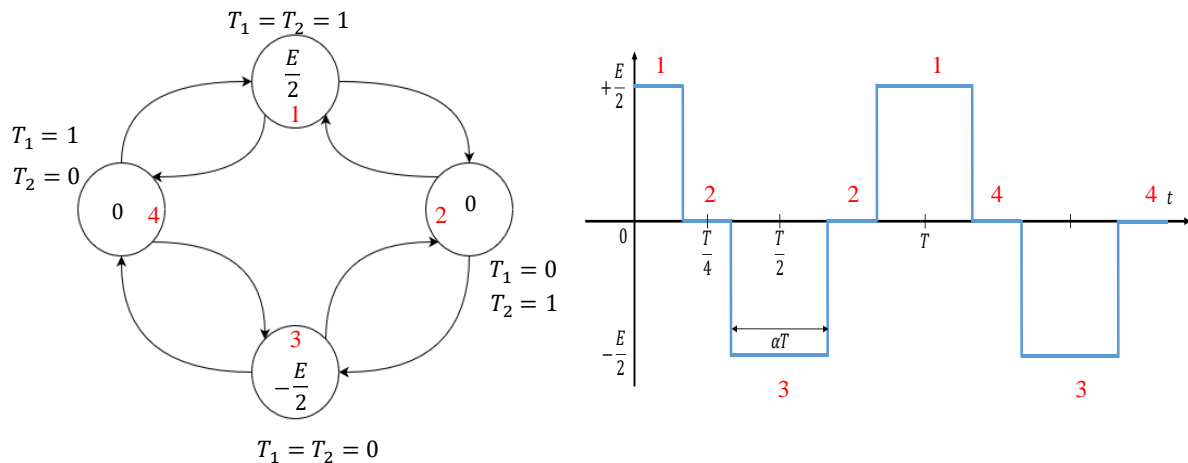


Fig. III-28. FW2 State machine

Fig. III-29 shows the switches T_1 and T_2 control signals that correspond to the previous state machine.

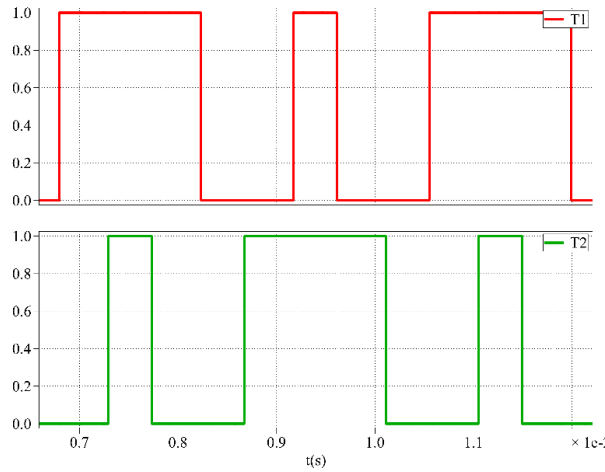


Fig. III-29. T1 and T2 3-level FC full wave 2 control signals

For this modulation, the flying capacitor sizing does not change since the capacitor voltage balancing is done over two low-frequency periods.

3. Full wave modulation 3 (FW3)

Following the idea of the previous case, as to improve the losses balancing over a single period, but with a smaller flying capacitor, the “Full Wave 3” was developed. It consists in switching the two switches combinations (over the same period) in high frequency to make the output voltage level at 0 V as shown in Fig. III-30. This will result in a zero average current in the flying capacitor which will help to maintain its voltage at an average value of $\frac{E}{2}$. It also allows a reduction of the size of the flying capacitor.

To maximize the reduction of the flying capacitor weight, the 0 V level could be achieved by switching at a high frequency of 6 kHz which corresponds to about 11 times the electrical machine frequency. This switching frequency engenders a flying capacitor of 1.34 mF as for the PWM strategy.

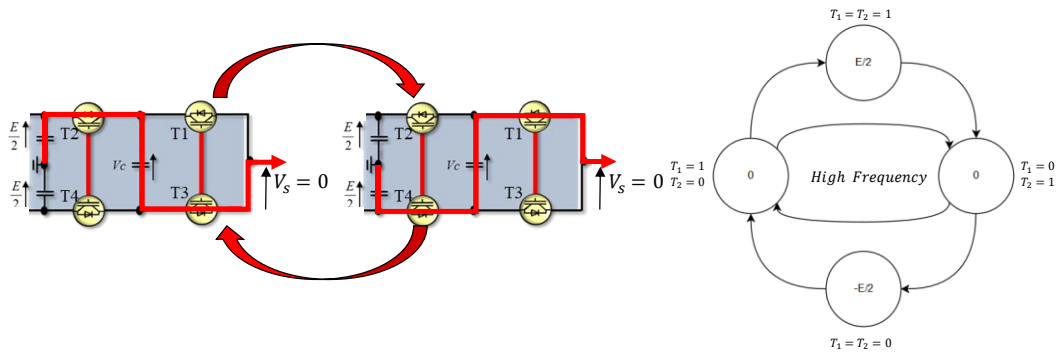


Fig. III-30. Switching at high frequency between the two possible configurations

In this case, using about 6 kHz switching frequency will not be interesting due to the high value of the electrical machine frequency (532 Hz, $T = 1.88 \text{ ms}$) and the duration of the 0 V level

which is very short ($\left(\frac{1}{2} - \alpha\right) * T$ with $\alpha = 0.45$). The 0 level lasts for 0.09 ms which is in the same range of the half switching period (0.083 ms) if the used apparent switching frequency is 6 kHz so the 0 level does not appear clearly to include changes of state. The ratio between the two frequencies must be higher for this method to be interesting.

To have more than two commutations, the switching frequency should be higher than 32 kHz. That is why a second example is given in Fig. III-31 with a switching frequency of 60 kHz. This switching frequency engenders a flying capacitor of 0.23 mF.

For the FC topology using full-wave modulation, the study was realized using perfect voltage sources instead of flying capacitors. Flying capacitors' voltage balancing should be taken into consideration. The 0 voltage level phase of the output voltage can be used to balance the flying capacitor voltage at high frequency actively since the current sign is not the same for both configurations. However, this will not change the output waveforms.

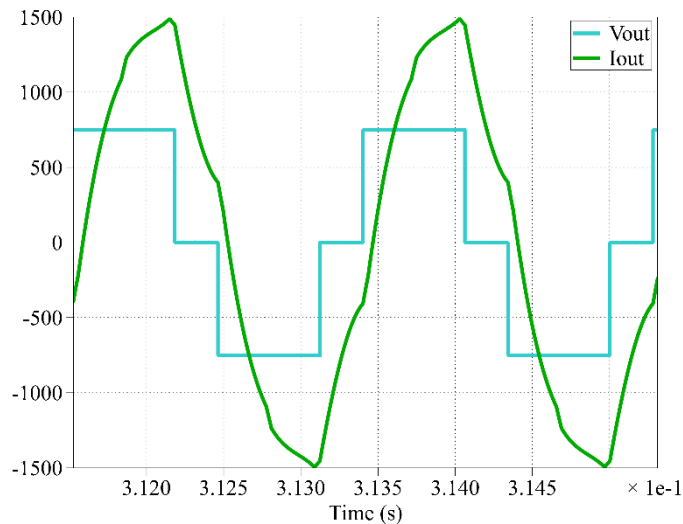


Fig. III-31. Voltage and current waveforms for 3-level FC using full wave 3 for an apparent switching frequency of 60 kHz

The full-wave modulation effect on the THD will be studied in the Chapter IV. To improve this THD, the selective harmonic elimination could be considered as a solution. It is based on harmonic elimination theory. It allows eliminating some low order harmonics by varying the commutation instants. This modulation generates a staircase output voltage waveform. Using this modulation reduces switching losses because each switch is turned ON /OFF once in a switching cycle and switching angles are usually chosen based on specific harmonic elimination or minimization of THD in the output voltage [53]. The control is done by determining the angles α_i (Fig. III-32).

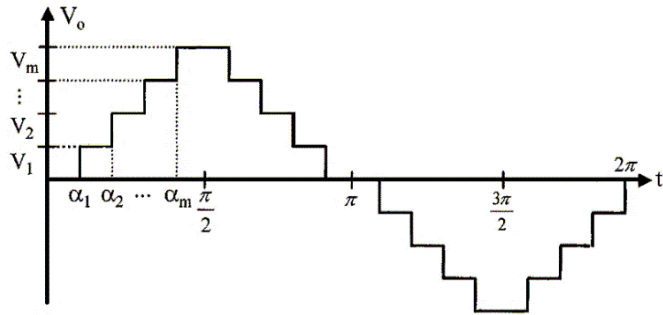


Fig. III-32. Staircase or selective harmonic elimination modulation strategy

v. Comparison of modulation strategies

To compare the different modulation strategies, the following specifications are taken and the results for the 3-level Flying capacitor topology are shown below. The inverter was sized for a DC bus of 2 kV which result in a DC bus capacitor of 2.5 mF using Chapter 2 sizing method.

As noticed in TABLE III-5, DPWM and full-wave strategies have better efficiency. However, for the full-wave modulation, the flying capacitor is sized for the low frequency which results in a bigger capacitor. For the third harmonic injection and discontinuous PWM, the DC bus voltage was sized taking into account the additional 15 % output voltage than the sine PWM and the FW one was sized taking into account the additional 30 % output voltage for the same power point as the sine PWM.

TABLE III-5. 3-level FC performances for different modulation strategies

Topology	3-level Flying Capacitors			
Modulation Strategy	PWM	THIPWM1/4	DPWMMAX	Full wave 2
η (%)	96.54	97.80	97.85	98.09
Temperature (°C)	122	132	137	112
C_{FC} (mF)	1.35			5.7

Fig. III-33 shows the losses repartition for the previous modulation strategies. The switching losses could be decreased by changing the used modulation method. However, the conduction losses depend on the components parameters and are not very much affected by the modulation strategy.

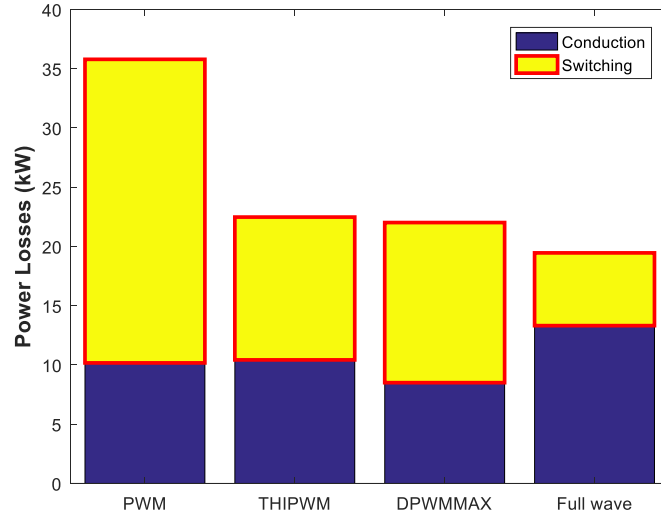


Fig. III-33. Losses repartition for 3-level FC

To optimize the inverter efficiency during the cruise, changing the inverter modulation strategy during the flight could be considered. For example, the inverter could be sized for the cruise with PWM and FW could be used for the takeoff and climb or it could be done using only FW which will be studied in Chapter IV.

3. Comparison of component generations and technology with a chosen strategy and topology

The component choice has a great impact on the inverter performances since the power losses depend on the semiconductor conduction and switching parameters. Several components are available on the market due to the increased demand in the recent years for industrial equipment such as inverters for UPS, wind power and photovoltaic power generation, and due to the rising demand for more efficient and longer lifetime equipment.

i. 7th generation IGBTs

To achieve high efficiency and reliability, Mitsubishi has developed the 7th generation modules that include new thinner IGBT chips and RFC (Relaxed Field of Cathode) diode chips (1200 V, 1700 V products) mounted and an improved internal structure of the unit which reduces power losses. This new generation also maintains a compact and lightweight packaging.

In the 7th generation IGBT module, a new structure is adopted for the NX and std types respectively as in Fig. III-34. The NX type are more compact and lighter than std ones. The internal structure is shown in Fig. III-35. The NX and std types have a low inductance reduced by 30 % compared to conventional models by optimizing the internal layout of the module. The optional pre-applied phase changes thermal interface material and eliminates the grease coating

process. Besides, the NX types are simpler to assembly. The NX and std models offer a wide range of breakdown voltages from 650 V, 1200 V, and 1700 V.



Fig. III-34. NX and std Mitsubishi modules Type packaging

To reduce conduction and switching losses leading to improved module energy-saving performance, the structure of the seventh generation IGBT and MOS charge storage chips has been optimized using thinner wafers. The 7th generation diode chip was manufactured with a thinner wafer which means lower resistance.

ii. 6th generation IGBT vs 7th Generation IGBT (Mitsubishi)

To compare the performances of the Mitsubishi IGBT last generations, Fig. III-35 shows the std type packaging structure evolution and TABLE III-6 sums the main characteristics improvements.

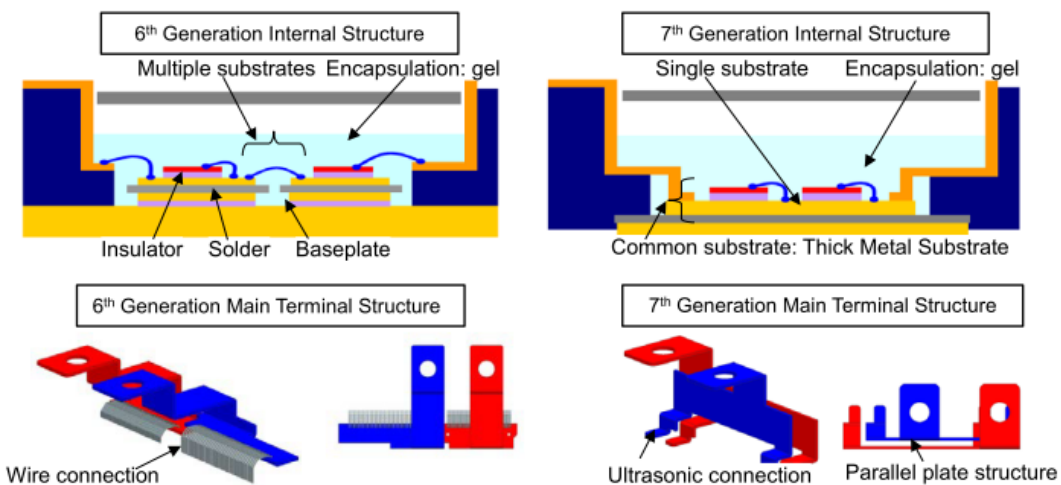


Fig. III-35. Packaging structure (std Type)

By adopting a unique substrate structure and Mitsubishi bonding technology, the mounting surface of the chips has been extended and the nominal current improved in the same housing. The 1200 V / 600 A module, for example, is replaced by a 20 % smaller packaging and the weight is reduced by 45 % compared to the 6th generation.

For the NX type packaging, the same module has been kept and the weight has been reduced by 15 % thanks to a new internal structure. In addition, by increasing the thickness and width of the copper circuit inside the module and using a single optimized substrate structure instead of several conventional insulating substrates, the mounting surface of the chips is expanded to improve the rated current in the same package.

TABLE III-6. 6th vs 7th generation std type module characteristics

Item	6 th gen	7 th gen	Improvement
Thermal resistance (ratio)	1	0.5	Reduction of 50%
Inductance (ratio)	1	0.7	Reduction of 30%
Package size (W*D*H)	110*80*29 mm	108*62*30 mm	Reduction of 20%
Weight (g)	580	320	Reduction of 45%
Power losses (ratio)	1	0.85	Reduction of 15%

To compare both generations and choose the most suitable component, we started with the 1700 V ones, with a DC bus of 2 kV to fully use the 1700 V module (60 % as mentioned in the Datasheet) in a 3-level architecture. The components are compared using a 3-level NPC with a sine PWM modulation strategy and associating two components in parallel to withstand the imposed current. The inverter performances are shown in TABLE III-7.

TABLE III-7. 6th vs 7th generation 1700 V/ 600 A IGBTs

	6 th generation	7 th generation
Efficiency (%)	97.62	98.94
Conduction losses (kW)	11.05	10.87
Switching losses (kW)	25.60	5.17
Temp junction max (°C)	129	121

Compared to the 6th generation IGBT module, the 7th one has significantly less switching losses for the same specifications. Similar results were obtained for the other studied topologies and modulation strategies. For the same specifications, the losses were reduced by more than 50 % with the 7th generation IGBT modules compared to the 6th one.

To see the difference between the 6th and 7th generation components, a comparison will be done using the 1200 V components which are mostly used in industry and therefore optimized compared to the 1700 V ones, were compared, for a DC bus of 1440 V to use them at 60 % of their voltage rating. The compared results are for a 3-level NPC using a DPWMMAX modulation strategy and associating three components in parallel to withstand the imposed current to withstand the voltage. The obtained results are reported in TABLE III-8.

TABLE III-8. 6th vs 7th generation 1200V IGBTs

	6 th gen	7 th gen
Efficiency (%)	98.64	98.88
Conduction losses (kW)	13.96	11.30
Switching losses (kW)	6.78	5.73
Temp junction max (°C)	112	110

The difference between 6th and 7th generation 1200V components is not huge compared to the previous case due to the lower switching losses as a result of the discontinuous used PWM. However, the 7th generation is still better.

To choose the adapted component, the 1200 V components, which are mostly used in industry and therefore optimized compared to the 1700 V ones, were compared, for DC bus voltages that make them work at 60 % of their rating to fully use installed Silicon. The compared results are for a 3-level NPC using a DPWMMAX modulation strategy and associating three components in parallel to withstand the imposed current for the 1200 V components versus two for the 1700 V ones. The obtained results are reported in TABLE III-9. The 1200 V modules are the best for this application but the 1700 V 7th generation are still interesting; since we will avoid adding one more component in parallel to withstand the current.

 TABLE III-9. 7th generation 1200V vs 1700V IGBTs

	1200 V 7 th gen 3 in parallel 1 in series	1700 V 7 th gen 2 in parallel 1 in series
Efficiency (%)	98.88	98.80
Conduction losses (kW)	11.30	11.55
Switching losses (kW)	5.73	6.38
Temp junction max (°C)	110	121
Total switches number per phase	18	12

The 1700 V modules are adapted to our application and allow to use fewer modules which will reduce the inverter weight and volume.

iii. Silicon Carbide (SiC) vs Silicon (Si) components

To compare both generations to SiC modules and choose most suitable technology, the inverter is designed using 1200 V / 600 A modules, with a DC bus of 1.2 kV to fully use the module (50 % as mentioned in the Datasheet). The compared results are for a 3-level NPC using a sine

PWM modulation strategy and associating two components in parallel to withstand the imposed current. The power was adapted to use only two components in parallel since the DC bus voltage was reduced.

TABLE III-10. 6th and 7th generation 1200V/600A IGBTs vs 1200V/600A SiC module

	1200 V 6th gen 2 in parallel 1 in series	1200 V 7th gen 2 in parallel 1 in series	1200 V SiC 2 in parallel 1 in series
Efficiency (%)	98.53	98.84	98.51
Conduction losses (kW)	11.4	8.95	14.48
Switching losses (kW)	3.52	2.81	0.679
Temp junction max (°C)	95.6	90.6	111.3

For our specification, the 1200 V Full SiC module does not add much to our solution. Even if the switching losses are low, the conduction losses remain higher than the total losses of the 7th generation module. The used switching frequency is low because it is not necessary to have sinus currents so we do not take fully advantage of SiC technology. Moreover, the thermal resistance is higher for the SiC module so is the junction temperature. Furthermore, SiC technology is only at its beginning and therefore is less advanced than Silicon and may be an interesting option in the future.

4. Total weight repartition

Using the shown topologies, modulation strategies, and 7th generation components, the inverter is designed for the maximal power point and 2 kV DC bus. The efficiencies for 3-level FC and NPC with sine and Discontinuous PWM are shown in TABLE III-11.

TABLE III-11. Efficiencies for the two studied topologies and modulation strategies

Topology	3-level FC		3-level NPC	
Modulation	PWM	DPWMMAX	PWM	DPWMMAX
Efficiency (%)	98.81	99.01	98.85	98.98

The obtained efficiencies are higher than the 2-level one (92.5 %) shown in chapter I and both 3-level topologies have similar efficiencies. The decisive point will be their total weight which will be compared below.

i. 3D inverter design

To more accurately estimate the total mass, 3D models of the inverter was done on **Inventor** to evaluate the weight of the needed bus bar and also the volume of a single phase. The 3D model of the FC inverter is shown in Fig. III-36.

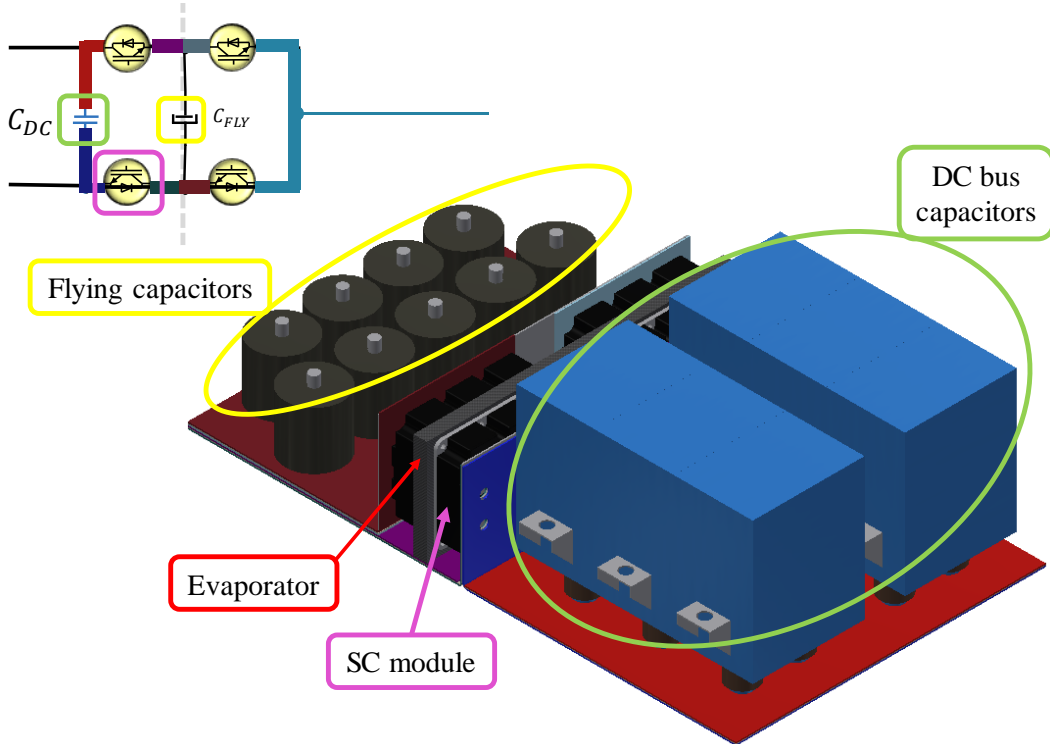


Fig. III-36. 3D single phase 3-level FC inverter

To design the inverter, several constraints should be taken into account. The first one concerns the heat exchanger and the cooling system designed by WP4.

The increasing power and the miniaturization of electronic components make the classical cooling solutions inadequate to evacuate the thermal load generated by chips. It is thus necessary to find and use more efficient and easy-to-integrate solutions [56]. In general, the choice of cooling technology depends on efficiency and performance requirements. The Capillary Pumped Loop for Integrated Power (CPLIP) shown in Fig. III-37, allows a temperature range controllability, like a classical CPL without all the instabilities. High heat flux removing capability is undeniable for this kind of loop. It has a theoretical thermal evacuation capability up to $40 \text{ W} \cdot \text{cm}^{-2}$, in our case, we are around $35 \text{ W} \cdot \text{cm}^{-2}$. Accorinti et al. [57] have deeply explained the ability to maintain a constant operating temperature on the evaporator walls, where electronics power modules are installed, for any cold source temperature variation and power cycle with large amplitude heat load steps. In particular, Accorinti et al. [32] showed, changing cold source temperature from 5 to 40°C, at constant applied thermal power, that the evaporator wall temperature change was negligible. Moreover, it was demonstrated, parametrizing the reservoir temperature, at constant cold source

temperature and heat power, that it is possible to control the evaporator wall temperature and so to fix the junction temperature.

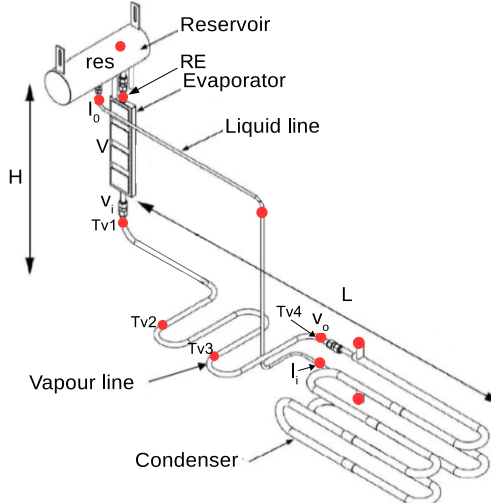


Fig. III-37. CPLIP concept scheme [32]

The four semiconductor module that constitutes one 3-level FC inverter phase, are placed on both evaporator sides as shown in Fig. III-38. This was recommended by WP4 to take advantage of both the evaporator side to evacuate the thermal losses and balance the constraints on both sides. This solution will also help to reduce the volume and weight of the inverter since it creates a more compact inverter and divides by 2 the number evaporators compared to when using only one side of the evaporator. In this case, we end up with 3 evaporators in parallel for the three phases instead of 6.

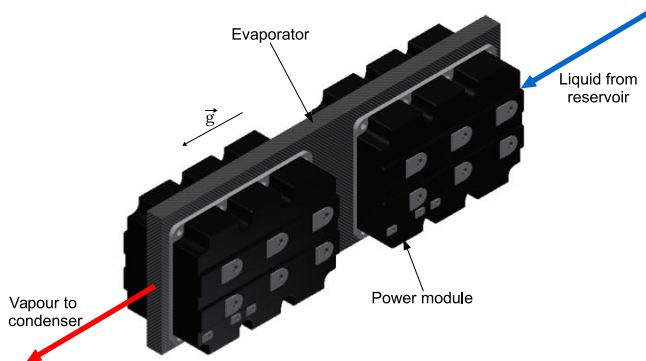


Fig. III-38. Module/evaporator assembly

The second constraint concerns the partial discharge (PD) risk estimated by WP5. Fig. III-39 shows the bus bar points that may be problematic from a PD aspect. The bus bar consists of copper flat bars (2 mm-thick each) connecting input bus capacitors, power modules, and flying capacitors. The DC bus is powered by a 2 kV input voltage. PTFE films are sandwiched between each copper bus bars pairs. In such topology, many triple points (area in the air with both metal and insulator in the neighboring) appear in bus bars/PTFE/air interfaces. These points are well known to be weak points, as the electric field is enhanced in such a particular area. Both confinement and power densities increasing expose electric insulation systems to

more PD risks. Added to materials defects, these partial discharge inception locally increase the stress within the dielectric material. This stresses change the intrinsic material properties and reliability, with the consequence of an irreversible insulators damage that can affect the whole insulation system.

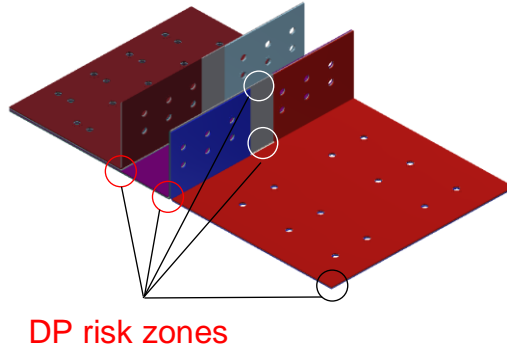


Fig. III-39. Bus bar configuration for a 3-level FC single phase

So to reduce these risks the dielectric used between the copper layers should be thicker. However, if it is thicker this would increase the bus bar stray inductance. This parasitic inductance is responsible for DC bus overshoots and overvoltage spikes across the power semiconductors during switching [58]. As a result, semiconductor device losses increase. In our case, no devices such as snubbers were considered to reduce the overvoltage generated by the leakage inductance.

This inductance could be estimated using *ANSYS Electronic Desktop* and the bus bar CAD model. The evolution of this inductance as a function of the dielectric thickness is represented in Fig. III-40. A trade-off has been made and the dielectric thickness was set to 2 mm.

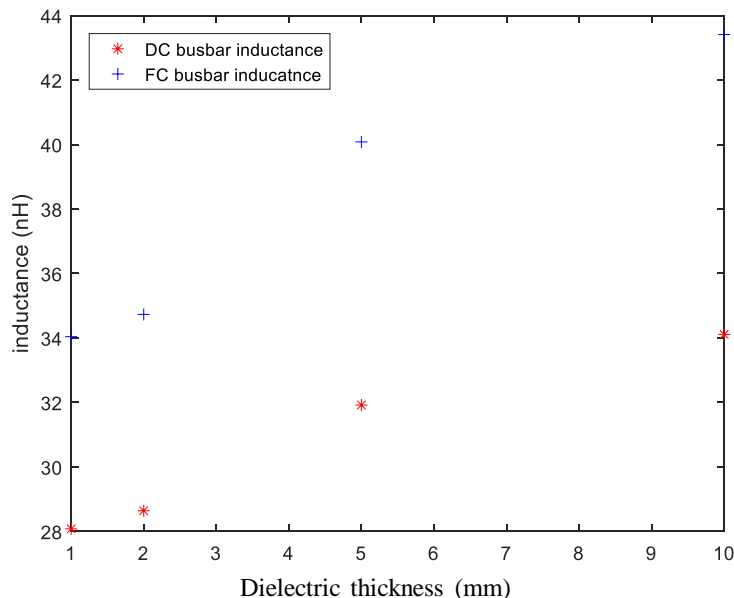


Fig. III-40. Bus bar leakage inductance

As a result of the WP5 study, rounded edges are to be used so to reduce PD risks. A solution without a bent bus bar would be better, however, to use both sides of the evaporator, the bus bar has to be bent.

ii. Specific power comparison

The DC bus capacitors are represented in Fig. III-36 in blue and account for a large amount of the total volume and thus its weight. The used bus bar is made of copper which is mostly used in similar range inverters.

For the weight distribution, it changed and the exchanger is not the predominant anymore but instead, the Bus bar and capacitors are the heaviest components (see Fig. III-41). The cooling system weight accounted for 11 times the semiconductors one for the 3-level NPC (Fig. III-14) versus only 2 times for the last solution using the same inverter topology (Fig. III-41).

Compared to the FC inverter, the NPC one is 26% lighter due to the lower capacitor (less flying capacitors) and bus bar weights (17 % less bus bar). It results to a specific power of 14.10 kW/kg for the 3-level that does not match the 2025 target of 15kW/kg unlike the 3-level NPC (19.01 kW/kg) (TABLE III-12).

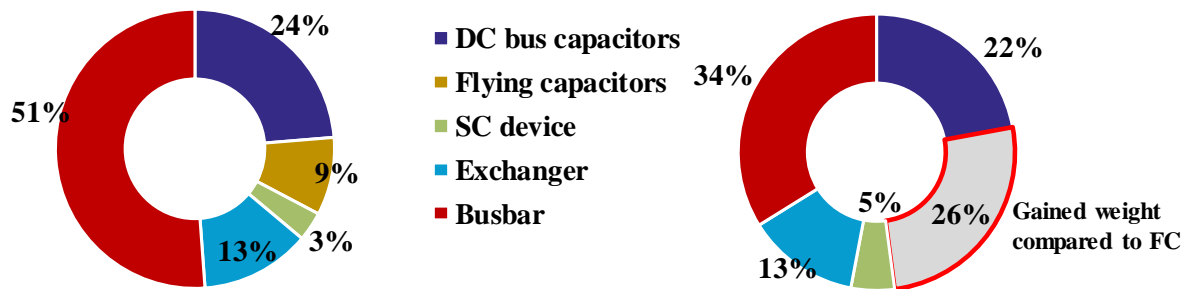


Fig. III-41. 3-level DPWMMAX FC (left) and 3-level DPWMMAX NPC (right) weight distribution

TABLE III-12 Specific power the two studied topologies using DPWMMAX modulation strategy

	3-level DPWMMAX FC	3-level DPWMMAX NPC
Specific Power (kW/kg)	14.10	19.01

To compare, for the same topology, the effect of the modulation strategy, used semiconductor and the cooling system weight coefficient, a simulation was done using a 3-level NPC inverter. Both sine PWM and DPWMMAX were compared combined with the 6th generation IGBTs for the first one and 7th generation for the second one. The heat exchanger coefficient went from 0.34 to 1.3 kW/kg thanks to the work of WP4 due to the CPLIP properties [56]. The obtained weight distribution is shown in Fig. III-42. The specific power went from 9.77 kW/kg to 19.01 kW/kg and the 2025 target is reached. However, we are still far from the 2035 one which was 25 kW/kg.

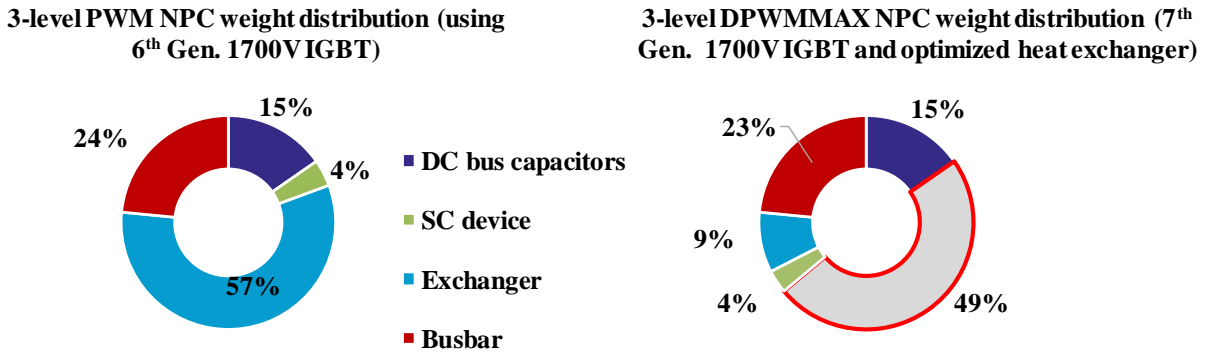


Fig. III-42. 3-level NPC weight distributions

To reach efficiency targets and have a higher efficiency during the cruise, changing the inverter modulation strategy during the flight could be interesting which will be discussed in detail in the next chapter.

iii. Module packaging for bus bar reduction and capacitor weight reduction

Even if there are no power losses in the semiconductors (no need for a heat exchanger), a specific power of 23 kW/kg is reached. In order to achieve the 2035 target (25 kW/kg) the bus bar and the capacitors weights have to be optimized.

To reduce the capacitor weight, it is now designed according to the desired voltage ripple which corresponds here to 5 % instead of sizing it depending on the energy as shown in Chapter II. In this case, the specific power goes from **19.01 kW/kg** to **23.29 kW/kg** for the 3-level DPWM MAX NPC. Moreover, the percentage of the DC bus capacitor weight represents 5.86 % instead of 15.31 % as noticed in Fig. III-43.

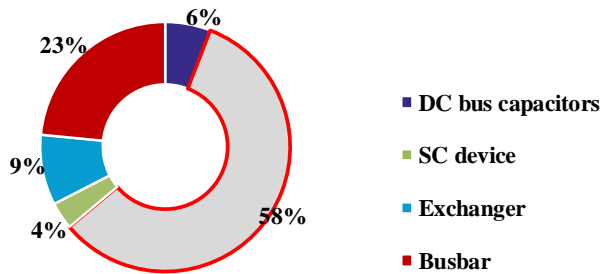


Fig. III-43. 3-level NPC weight distributions with the new sized capacitor

To reduce the Bus bar weight, creating a single-phase power module will remove the bus bar between the power modules and all that remains is the connection between the module and the DC bus capacitors and between the module and the motor phase. This study was carried out in collaboration with **Deep Concept**. They designed a specific power module for a 3-level single-phase NPC and carried out a 3D design taking into account schematic, dimensional and environmental constraints. Then they did an EMC simulation of the module by finite elements to evaluate the loop inductances and current distribution.

The designed module includes half a phase of the 3-level ANPC or NPC type inverter.

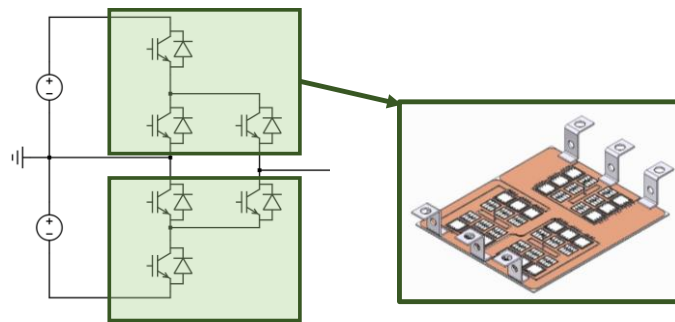


Fig. III-44. Design of a 3-level ANPC inverter power module

The obtained modules are placed on each side on the evaporator as in Fig. III-45.



Fig. III-45. Lower (left) and upper (right) power modules placed on the evaporator

These power modules are so compact that the final 3-phase inverter assembly is smaller as noticed in the different views in Fig. III-46. The bus bar weight is reduced by 56 %.

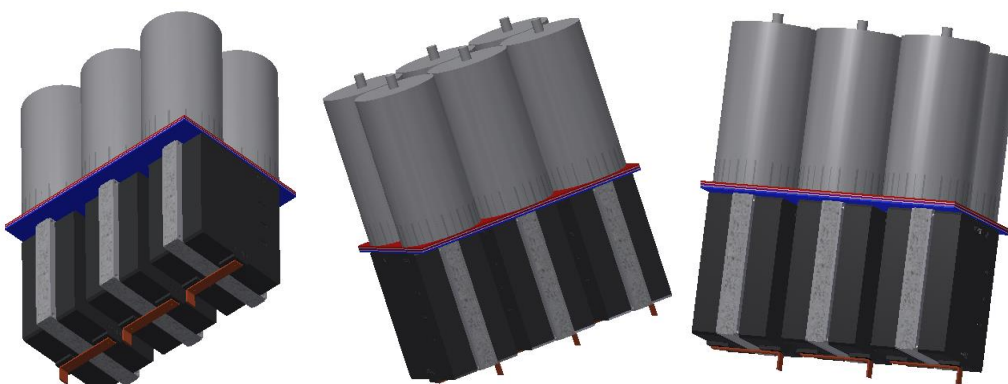


Fig. III-46. 3-level 3-phase NPC inverter with new power modules

The module weight was estimated from the available module that has the same dimensions which is 1.5 kg per module which lead to a total semiconductor devices weight of 9 kg. Fig. III-47 represents the new weight repartition compared to the sine PWM 3-level NPC using 6th generation IGBTs and non-optimized cooling system. The weight is reduced by 83 % which lead to a specific power of 57.59 kW/kg for the inverter including only its cooling system, bus bars, semiconductor modules and DC bus capacitor. The heat exchanger coefficient for this solution is set to 4.5 kW/kg.

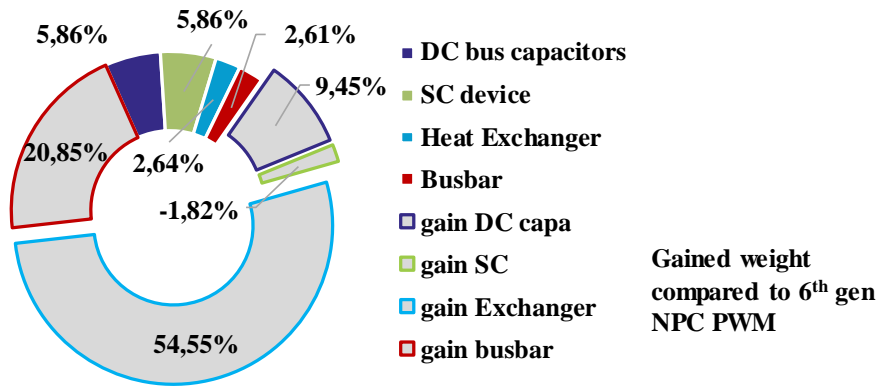


Fig. III-47. 3-level NPC weight distributions with the new sized capacitor and power modules

The obtained specific power seems high but it does not take into account several inverter components such as drivers, snubbers, components attaching elements, etc. To have a more accurate estimation, these parameters should be included. Filters are not also take into account since we do not have network quality constraints to be fulfilled.

5. Conclusion

The main factor to increase the specific power was identified in Chapter I. two options were conceivable. The first one was decreasing the cooling system mass by optimizing its components which was done by WP4 work. The second one was reducing power losses which is a part of our work package (WP2) tasks. Using the simulation tool developed in Chapter II, the inverter design was conducted.

The first point that was covered was the inverter topologies. Inverter power losses reduction could be achieved by using small rating components. This was done by using multilevel architectures to avoid the direct series association. The used topologies were 2, 3 and 5 levels ones. They were compared using DC bus voltage sweeps to find the optimal DC bus voltage range for each group of topologies. If the DC bus voltage is between 700 V and 1 kV, the 2-level topology could be used, however, in this case, to withstand the machine current, several components should be associated in parallel which will increase the inverter weight and volume. If the DC bus voltage is between 1 and 2.4 kV, the 3-level topologies have the best efficiencies for this voltage this range. However, if the DC bus voltage is between 2.4 and 3.5 kV, the 5-level ones must be recommended. This voltage range depends also on the used switching frequency. This parameter is very important especially for the high voltage components that were used and have a great impact on the power losses and therefore the semiconductors maximal junction temperature. The 3-level topologies and the 5-level ANPC seemed to be the most adapted ones to our specification. This study showed also that, so to use some topologies such as 2-level or 3-level ones, they should be used with a low switching frequency so to have an acceptable junction temperature. This means that the sine PWM strategy is not adapted in some cases.

This leads to the second covered point in this chapter which is the modulation strategies. The multilevel modulation techniques could be classified according to switching frequency. High switching frequency modulations have higher switching losses but less impact on the machine current since the high-frequency filtering is better than low-frequency one. Therefore, with low switching frequency methods, efficiency is higher. In this work, four modulation strategies, which are sine PWM, Third Harmonic Injection PWM, Discontinuous PWM MIN and MAX, and Full Wave adapted to 3-level inverter topologies, were studied and compared in terms of efficiency so to find the most performant. The sine PWM had the lowest efficiency among all the topologies but still near to the others' performances. The DPWMMAX was the one with the highest efficiency for both studied 3-level topologies.

The third tackled point was semiconductors technologies. The component choice has a great impact on the inverter performances since the power losses depend on the semiconductor conduction and switching parameters. The market evolution of silicon components seemed to be saturated in recent years. However, with the new Mitsubishi 7th generation IGBT module, this is not the case anymore. These components have fewer losses and come in a compact light-weighted packaging. These components were compared to the previous IGBT generation and also to SiC modules with the same current and voltage calibers and seems to be the best option for our specifications.

Using these components, the DPWMMAX modulation and an optimized cooling system with a 3-level NPC topology, the 15 kW/kg specific power target was exceeded (23.29 kW/kg) but it stills far from the 2035 one which is 25 kW/kg. To reach the second target, a specific power module was designed so to integrate half a phase in a single module. This solution reduced the used bus bar and make it possible to achieve a specific power of 57.59 kW/kg for the 3-phase inverter taking into account only the bus bar, DC bus capacitor, semiconductors and its cooling system. To have a more accurate estimation, parameters such as drivers and components attaching elements should be included.

As noticed in the mission profile presented in Chapter I, three sizing points can be considered, however in this chapter only the takeoff power point was considered. In the next chapter, several modulation strategies and sizing points will be studied so to find out the best scenario for the 3-level inverter modulation strategies taking into account the flight mission.

IV. Performance of the chosen solutions during the mission profile

The developed tool presented in Chapter II makes it possible, from a specification to size the converter according to the chosen topology and carry out parametric studies to determine the optimum sizing point by varying: the DC bus voltage, the requested power or the modulation index. It can also take into account the aircraft mission profile that allows checking the performances of the converter as a function of time [28].

The considered power mission profile is shown in Fig. IV-1. Three sizing points can be considered. The first one consists of sizing the inverter for the take-off which corresponds to the maximum power along the profile; the second one would be the cruise phase which represents the most extended phase of the flight mission; a middle point for the third case (climb phase). The maximum power is in the range of MW and due to confidentiality issues, the value of the maximum power cannot be given: all values will be given in per unit.

Two targets in term of efficiency for the power electronics were set by HASTECS project. For the 2025 target, the efficiency should be higher than 98 % for the cruise point and higher than 96.5 % for the maximal power point. On the other hand, for the 2035 target, the efficiency should be higher than 99.5 % for the cruise point and higher than 99 % for the maximal power point.

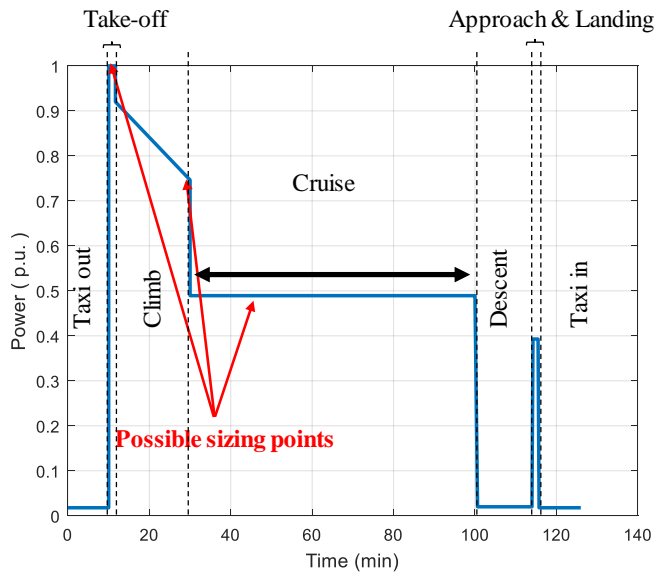


Fig. IV-1. Electrical power mission profile

The main objective of this chapter is to evaluate the chosen inverter topologies and associated modulation strategies to power the electric machine used for the aircraft propulsion. A comparative study of modulation control strategies is carried out to highlight the structure and modulation presenting the best performance to minimize the losses for the chosen sizing point associated 3-level FC and NPC topologies.

1. DC bus voltage sizing and components choice depending on the voltage mission profile and control strategy

To define the needed DC bus voltage and appropriate modulation strategy, the output needed voltage magnitude during the flight mission profile was plotted for two electric motors winding configurations sized by WP1 (Fig. IV-2 and Fig. IV-3). The first configuration uses two conductors per slot and needs less voltage but more current than the second one (3 conductors per slot) since they are both sized for the same power.

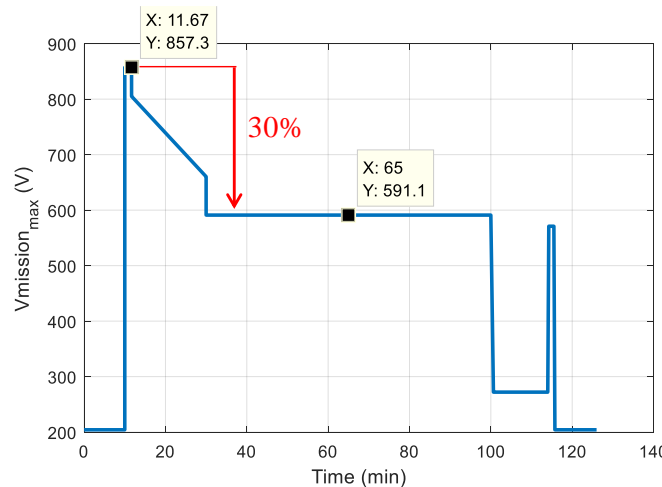


Fig. IV-2. Needed machine voltage during the flight mission with the first e-motor winding configuration

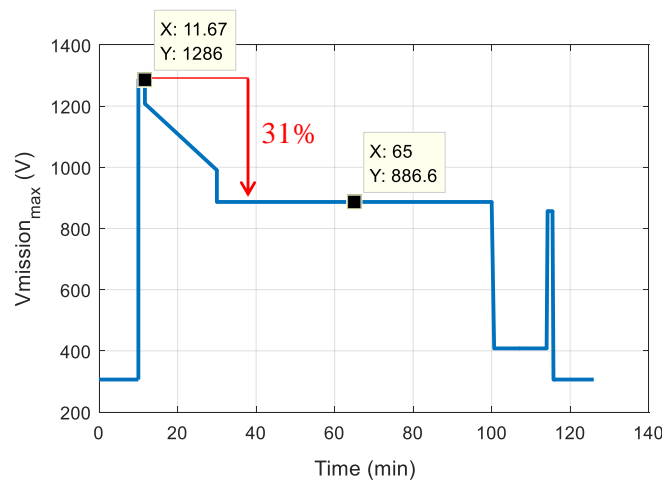


Fig. IV-3. Needed machine voltage during the flight mission with the second e-motor winding configuration

A 30 % voltage difference between the maximal power point which corresponds to the take-off and the cruise is noticed for both studied electric motor winding configurations. Based TABLE III-4, using full-wave modulation for the take-off and climb phases and PWM for the cruise could be considered to optimize the efficiency during the longest phase which is the cruise.

The DC bus voltage, as in equation (IV-1), is defined so to be able to provide the maximal needed voltage and the modulation index which based on the used modulation strategy as in TABLE IV-1.

$$V_{DCbus} = \frac{2*V_{out_max}}{mod_index} \quad (IV-1)$$

TABLE IV-1. Maximal output voltage as function of DC bus voltage and control strategy

	PWM	THIPWM / DPWM	Full wave
V_{out_max}	$\frac{V_{DCbus}}{2}$	$1.15 * \frac{V_{DCbus}}{2}$	$1.3 * \frac{V_{DCbus}}{2}$

For the first electric motor, if only PWM is used which corresponds to a modulation index of 0.9 to take into account the dead time of the switching operations, the DC bus voltage should be equal to 1.9 kV versus 1.5 kV if third harmonic injection or discontinuous PWMs were to be used. However, if the full-wave modulation is used for the maximal power point, the DC bus voltage should be around 1350 V.

For the second electric motor configuration, if only PWM is used, the DC bus voltage should be around 2300 V versus 2250 V if third harmonic injection or discontinuous PWMs were to be used. If the full-wave modulation was to be used for the maximal power point, the DC bus voltage should be around 2 kV.

TABLE IV-2 sums up the required DC bus voltage values for both machine configuration depending on the used modulation strategy.

TABLE IV-2. DC bus voltage value for the different studied modulation strategies and electric motor winding configurations

		PWM	THIPWM / DPWM	Full wave
V_{DCbus}	1 st e-motor	1900 V	1500 V	1350 V
	2 nd e-motor	2300 V	2250 V	2000 V

2. Inverter performances during the mission profile

In this part, the studied modulation strategies performances will be compared for the entire mission profile. The adapted DC bus voltage and semiconductors choice will be explained for each case.

The first studied cases will be done using PWM strategies. So to not oversize the inverter, it will be sized for the maximal power point (takeoff) using the third harmonic injection PWM which will be used during takeoff and climb and Sine PWM will be used for the remaining parts of the flight mission (cruise, taxi out and in and descent).

The second study case compares two modulation strategies that have the same required DC bus voltage which are THIPWM and discontinuous PWM. The third one will be using only full-wave modulation for the whole flight mission and then used in combination with other PWM strategies to find the most efficient combination for these inverters the flight mission.

i. Strategy 1: Sine PWM and THIPWM

For the PWM strategy, the DC bus voltage is fixed to 1500 V to have a modulation index of 1.15 at the maximal power point. For the take-off and climb, third harmonic injection PWM will be used. Fig. IV-4 represents the efficiencies of 3-level FC and 3-level NPC inverters during the mission profile.

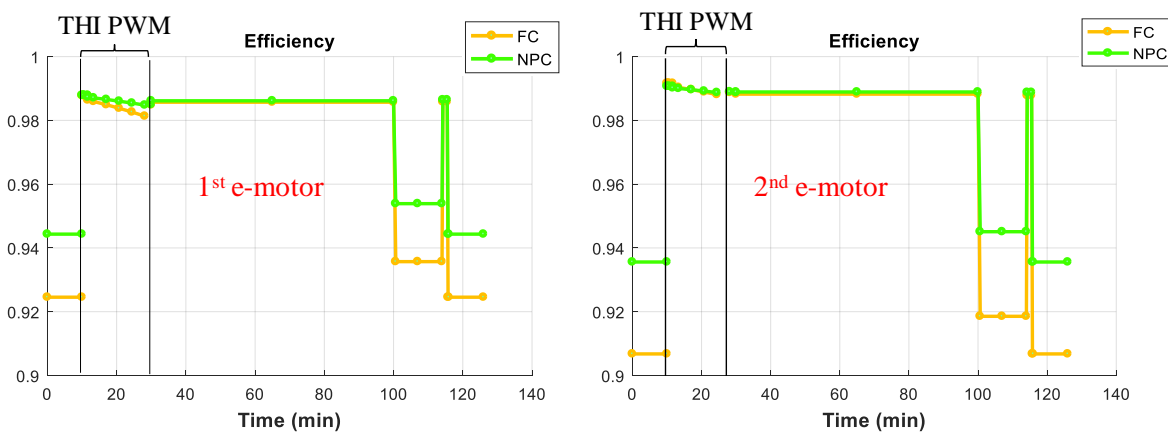


Fig. IV-4. 3-level FC and NPC efficiencies using PWM strategies with both e-motor winding configurations

By sizing the inverter for the maximal power point with a THIPWM, the efficiency in the cruise phase is maximized. For this sizing, 1700 V IGBTs are used at 44 % of their voltage rating for a 1500 V DC bus voltage for the first e-motor and used at 66 % for a DC bus voltage of 2250 V.

The difference between both topologies is negligible for the take-off, climb and cruise phases, however for the taxi out and in, the difference is more important. This is due to the switching losses that are 35 % higher for the FC than the NPC topology in this particular case. For the first point of the mission profile, which corresponds to the taxi-out phase, the total IGBTs' equivalent losses are similar for both topologies. However, for the Diodes, only the conduction losses are similar. The reverse recovering losses are 7 times higher for the FC topology; 709 W versus 101 W for the NPC topology. Several parameters could be leading to this situation. The main reason is the higher switched current and its repartition in the different diodes which is not symmetrically done in the NPC. It is also due to the current-voltage phase shift which depends on the electric machine parameters. The current-voltage phase shift which depends on the electric machine parameters in this phase is almost equal to 0. In this case, only the IGBTs and clamping diodes are used to create the 3-level voltage waveform as in Fig. IV-5. To create the high level ($+\frac{E}{2}$) the current is positive and goes through T1 and T2. For the 0 level with a positive current, it goes through the clamping diode X1 and T2. If the current is negative, it

goes through X2 and T3 and to create the low level ($-\frac{E}{2}$), the current is still negative and goes through T3 and T4. So the D1, D2, D3, and D4 diodes do not see the current therefore don't have additional losses.

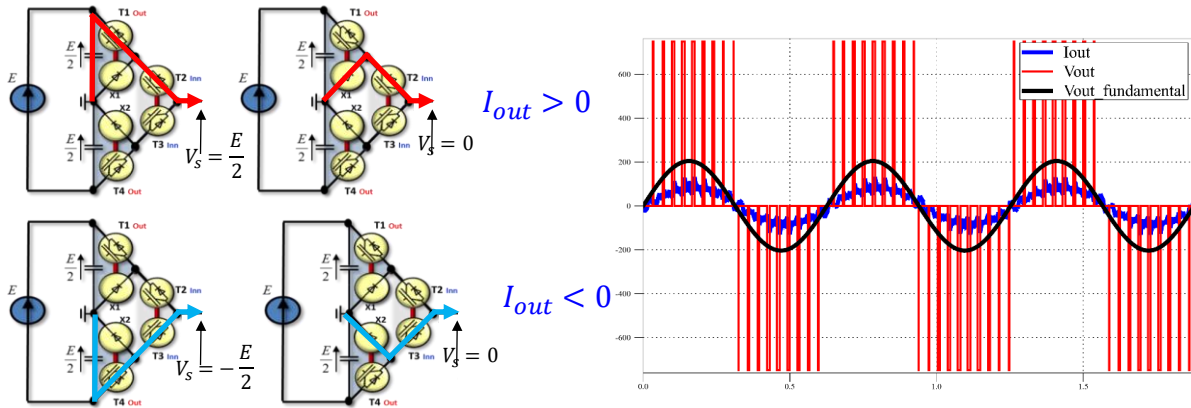


Fig. IV-5. 3-level NPC current repartition during Taxi out phase

The use of the second machine parameters increases the efficiency of the inverter since for the same power, the used DC bus voltage is higher and therefore the current is lower, which reduces power losses in semiconductors.

ii. Strategy 2: THIPWM versus DPWM

For the third harmonic injection and discontinuous PWMs, the modulation index could reach 1.15 so the chosen DC bus voltage is 1500 V as for the previous case using the 2-conductor per slot machine parameters. However, this time, these modulations are used during the whole flight mission to find out the best one to use for each flight phase.

Fig. IV-6 presents the efficiencies of 3-level FC and NPC topologies using third harmonic injection PWM and discontinuous PWM max strategies. The last one has better results overall the mission profile. This is due to the conduction losses that are higher for the first strategy. Yet, the difference or the gap between both inverter topologies during low power phases is still noticeable no matter what modulation strategy was used. However, for the DPWMMAX, the situation is reversed; the NPC has higher losses than the FC which is due to the unbalanced power losses and currents repartition caused by this control strategy that reduces significantly the switching power losses.

For the second motor winding configuration, the overall efficiencies are better than the previous case but still, the same remarks apply to this case as above. In this case, the 1700 V IGBTs are used for about 66 % of their voltage rating they are slightly overused. However, the maximal junction temperature does not increase much due to the low losses. For the high power phases; take off, climb and cruise, the efficiencies are higher compared to the previous machine ones because the components are optimally used as the manufacturer advises to use it around 60 % of its voltage rating and the conducted and switched currents are lower.

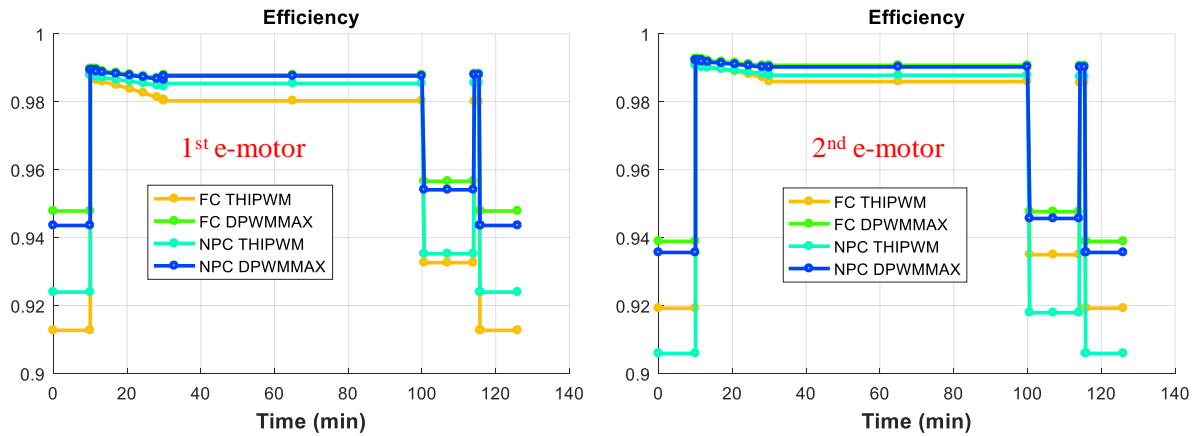


Fig. IV-6. 3-level FC and NPC efficiencies using THIPWM and DPWMMAX strategies with both e-motor winding configurations

We propose now to compare only the discontinuous strategies (Fig. IV-7).

For the FC topology, the converter is fully symmetric so if the modulating signal is saturated in the top or bottom it will not have an impact on the converter operation which is exactly what was obtained and shown in the efficiency plot below. On the other hand, for the NPC, the current sign determines its path used for the current, this implies that the losses are not symmetrically distributed in the inverter. In this studied case, the DPWMMAX has better performances than the MIN for the 3-level NPC.

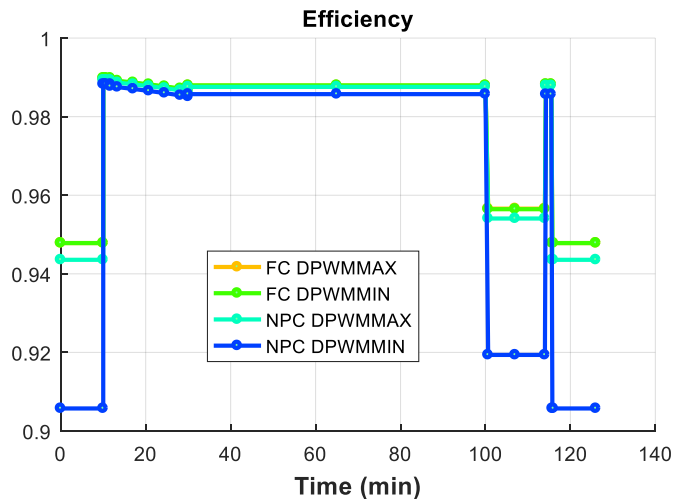


Fig. IV-7. 3-level FC and NPC efficiencies using DPWMMAX and DPWMMIN strategies for the 1st e-motor winding configuration

So the best modulation to use to minimize the overall power losses is the DPWMMAX.

The current THD, which is calculated as in equation (IV-2), is then evaluated for the 3-level FC using the DPWMMAX and reported in TABLE IV-3. The obtained THD values remain acceptable.

$$THD = \frac{\sqrt{\sum I_n^2}}{I_1} \quad (\text{IV-2})$$

With I_1 the current fundamental amplitude and I_n the amplitudes of the harmonics.

TABLE IV-3. THD for some mission profile points for the 3-level FC using DPWMMAX modulation for the 1st e-motor winding configuration

Flight phase	Current THD
Taxi out & in	0.13
Take-off	0.05
Cruise	0.08
Descent	0.76

This modulation strategy has a low current THD so it will not degrade the output waveforms.

iii. Strategy 3: Full-wave modulation

For the 3rd strategy, the DC bus voltage is fixed to 1350 V to have an equivalent modulation index of 1.30 for the maximal power point. Fig. IV-8 shows the efficiencies of both inverters during the mission profile using only full-wave modulation. In this case, the 1700 V IGBTs will be used for about 40 % of their installed silicon so they will be underused and will not have optimal efficiency. The low efficiency is due also to the high conducted and switched current which is a consequence of the lower DC bus voltage for the same needed power.

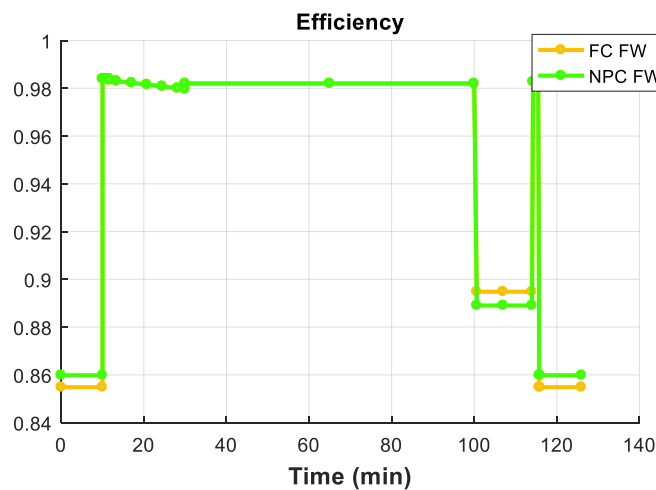


Fig. IV-8. 3-level FC and NPC efficiencies using FW strategy with the 1st motor winding configuration

The FW modulation strategy is a low-frequency modulation strategy, therefore, the output current waveforms are impacted which can lead to more low-frequency harmonic components. This can deteriorate the current THD that is calculated using equation (IV-2), which will increase the electric motor losses.

The efficiencies during the taxi out & in and descent (low power and speed phases) are low compared to the PWM results for the same points. The current waveforms for the different flight mission phases are shown in Fig. IV-9. The losses and current THD are high due to the 5th and 7th harmonic components as noticed in TABLE IV-4. For the takeoff and cruise, the full-wave modulation does not alter the THD unlike what was expected. This is due to the used high-speed synchronous machine thanks to its low inductance that results in a higher reactance and to the electromotive force presence.

TABLE IV-4. THD and harmonics amplitudes for some mission profile points for the 3-level FC using full wave modulation

Flight phase	THD	Fundamental amplitude (A)	5 th harmonic amplitude (A)	7 th harmonic amplitude (A)
Taxi out & in	4.03	97.55	303.3	165
Take-off	0.059	1633	78.61 (4.8%)	31.64 (1.93%)
Cruise	0.078	1021	74.24 (7.2%)	53.38 (5.22%)
Descent	1.14	81.97	57.99	59.56

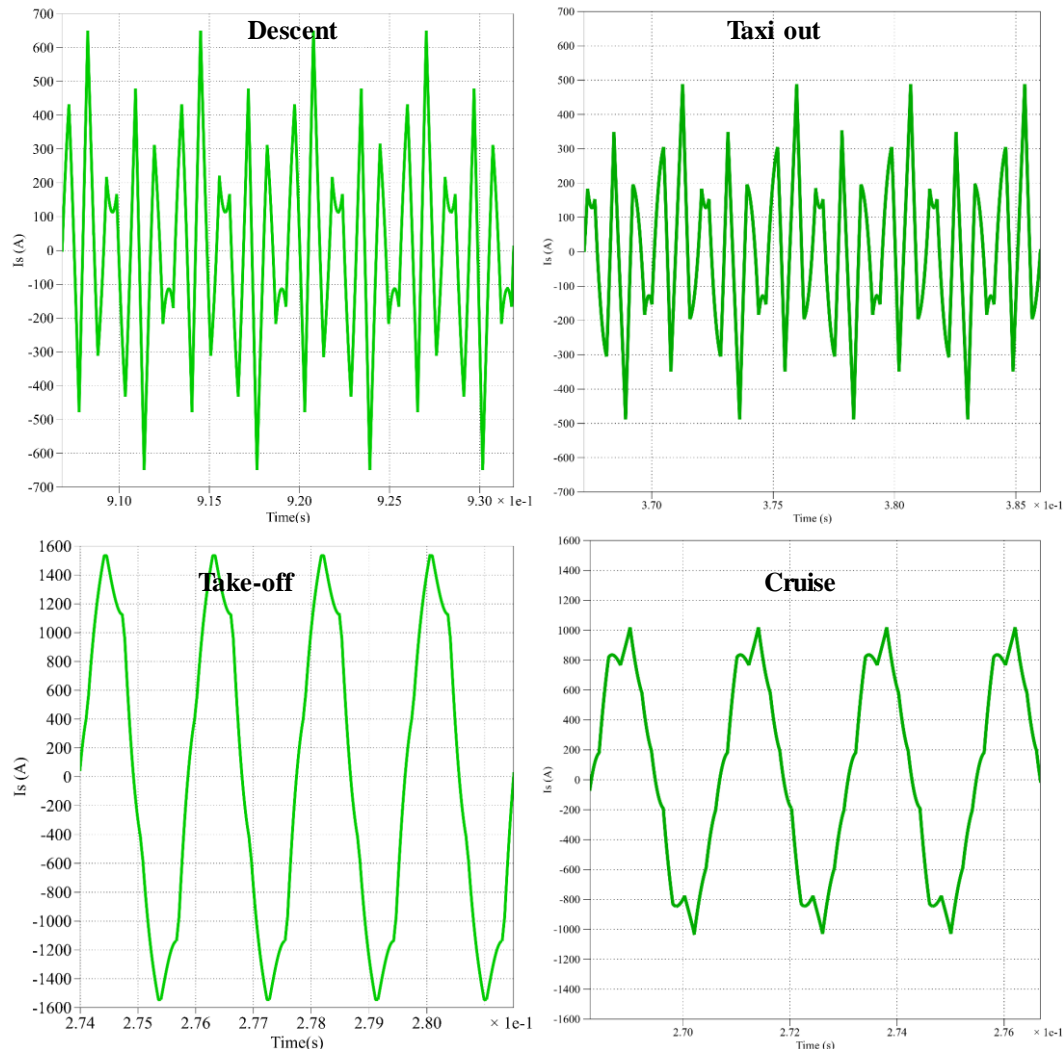


Fig. IV-9. Current waveforms for Taxi out, take off, cruise and descent using the 1st motor winding configuration

For the second studied machine configuration, the DC bus voltage is fixed to 2 kV to have a modulation index of 1.28 for the maximal power point. Fig. IV-10 presents the efficiencies of both inverters during the mission profile using only FW modulation.

In this case, the 1700 V IGBTs will be used for about 59 % of their installed silicon. For the high power phases (take off, climb and cruise), the efficiencies are higher compared to the previous machine ones because the components are optimally used as the manufacturer advises to use it around 60 % of its voltage rating. The low efficiencies during the taxi out & in and descent are due to the high losses and 5th and 7th harmonic current components as shown in TABLE IV-5 as for the previously studied machine.

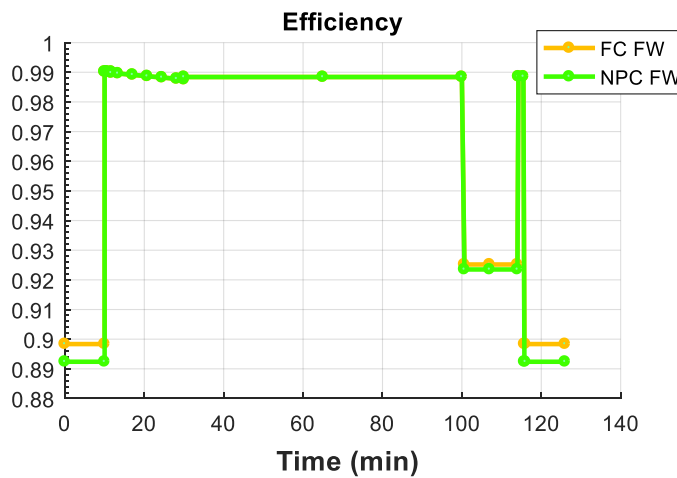


Fig. IV-10. 3-level FC and NPC efficiencies using FW strategy with the 2nd motor configuration

TABLE IV-5. THD and harmonics amplitudes for some mission profile points for the 3-level FC using full wave modulation with the 2nd motor configuration

Flight phase	THD	Fundamental amplitude (A)	5 th harmonic amplitude (A)	7 th harmonic amplitude (A)
Taxi out & in	4.01	57.70	201	108
Take-off	0.078	965.2	64.35 (6.6%)	32.8 (3.3%)
Cruise	0.106	605.77	52.7 (8.6%)	33.12 (5.4%)
Descent	3.6	48.47	160.6	62.1

The full-wave modulation strategy increases efficiency during the takeoff, climb, and cruise. However, during the low power, the efficiency is very low as well as the current THD due to the high 5th and 7th harmonic components that are a result of the low modulation strategy.

iv. Strategy 4: hybrid modulation using Sine PWM and FW

For the 4th strategy, the 1st electric machine configuration was considered and thus the DC bus voltage was fixed to 1350 V to have a modulation index of 1.3 for the maximal power point and a modulation index around 0.9 during the cruise. For the take-off and climb, full-wave modulation will be used and PWM for the remaining parts of the mission so to have better

waveforms than during these phases. The same semiconductors are used even if they are oversized (Fig. IV-11). For the first case, 1700 V components are used to compare it to the previously studied cases.

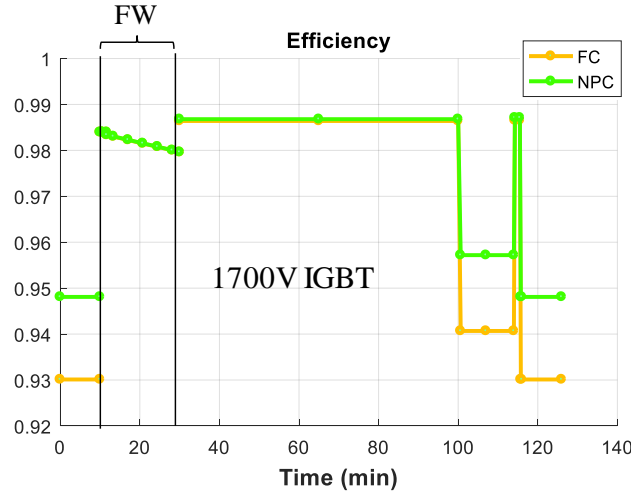


Fig. IV-11. 3-level FC and NPC efficiencies using FW and PWM strategies with 1700 V IGBTs

Compared to the third harmonic injection which had an efficiency of 98.79 % for the 3-level FC during the takeoff, the FW has lower efficiency (98.4 %). However, if more adapted components are used as in Fig. IV-12, the takeoff efficiency is slightly 98.81 %. The overall efficiency is better than the sine PWM combined with third harmonic injection. The 1200 V IGBTs are used up to 56 % of their voltage rating. Even if they are slightly overused, the maximal junction temperature (< 110 °C) is still lower than the manufacturer's thermal limit of 150 °C.

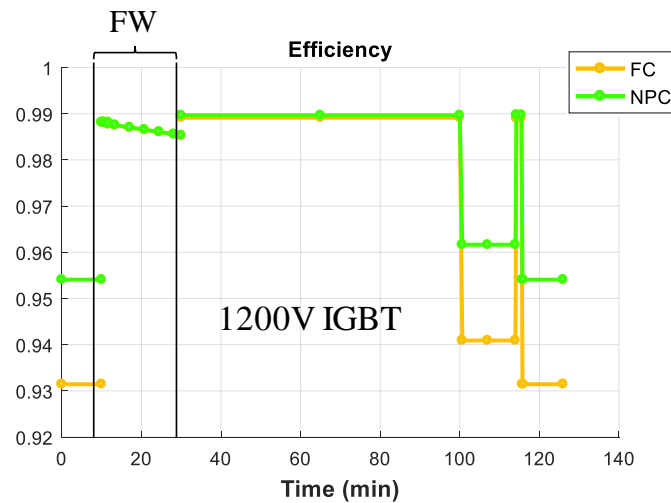


Fig. IV-12. 3-level FC and NPC efficiencies using FW and PWM strategies with 1200 V IGBTs

For the 2nd electric machine configuration, the DC bus voltage was fixed to 2 kV to have a modulation index of 1.28 for the maximal power point and a modulation index around 0.9 during the cruise. As for the 1st machine configuration, full-wave modulation is used for the take-off and climb and PWM for the remaining parts of the mission (Fig. IV-13). Compared to

the third harmonic injection (3-level FC efficiency during the takeoff 99.07 %), the FW has lower efficiency for the take-off (99.02 %) and climb but the cruise efficiency using PWM with this DC bus voltage and components is better which was the one needed to be optimized. For the cruise, the efficiency with this configuration is 98.97 % for the 3-level FC which is higher than the one for the first strategy (THIPWM + PWM) which was equal to 98.89 %.

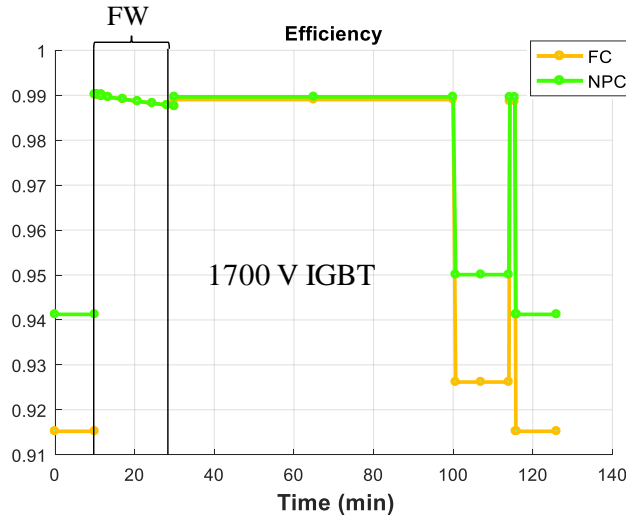


Fig. IV-13. 3-level FC and NPC efficiencies using FW and PWM strategies with 1700 V IGBTs for the 2nd e-motor

TABLE IV-6 shows the current THD and 5th and 7th harmonics amplitudes for the 2nd electric machine configuration using full-wave for the take-off and climb and sine PWM for the remaining parts of the mission profile. We can clearly see that using the combination of both strategies for the studied mission profile improves the overall current THD and inverter efficiency.

TABLE IV-6. THD and harmonics amplitudes for some mission profile points for the 3-level FC using full wave and PWM modulation for the 2nd e-motor configuration

Flight phase	THD	Fundamental amplitude (A)	5 th harmonic amplitude (A)	7 th harmonic amplitude (A)
Taxi out & in (PWM)	0.82	57.70	0.015	0.014
Take-off (FW)	0.078	965.2	64.35	32.8
Cruise (PWM)	0.077	605.77	0.25	0.49
Descent (PWM)	1.15	48.47	0.03	0.03

The FW strategy combined with a sine PWM improves the inverter efficiency during the cruise which was our objective. This reduces also the current THD during the low power phases which improve the waveforms.

v. Strategy 5: DPWMMAX and FW modulation

For this 5th strategy, the 2-conductor per slot electric machine configuration was considered and thus the DC bus voltage was fixed to 1350 V to have a modulation index of 1.3 for the

maximal power point. For the take-off, full-wave modulation will be used and DPWMMAX for the remaining part of the mission (Taxi out and in, climb, cruise and descent). The 1700 V semiconductors are used even if they are oversized (Fig. IV-14). These components are used at 40 % of their voltage rating.

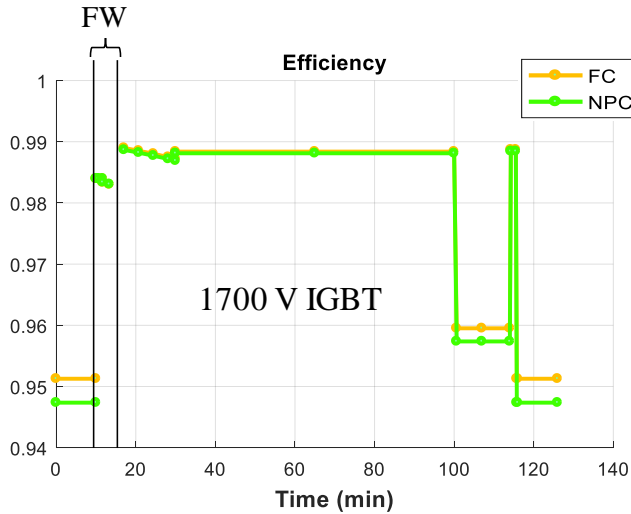


Fig. IV-14. 3-level FC and NPC efficiencies using FW and DPWMMAX strategies with 1700 V IGBTs

The efficiency is higher than for the previous combination (FW + sine PWM), which was 98.64 % during the cruise for the NPC topology and is equal to 98.84 % with this strategy. However, if 1200 V components that are more adapted to this voltage are used at 56 % of their rating as in Fig. IV-15, the efficiency is even better due to this component's parameters and is equal to 99.06 %. The maximal junction temperature is still lower than the manufacturer's thermal limit of 150 °C as for the previously studied case.

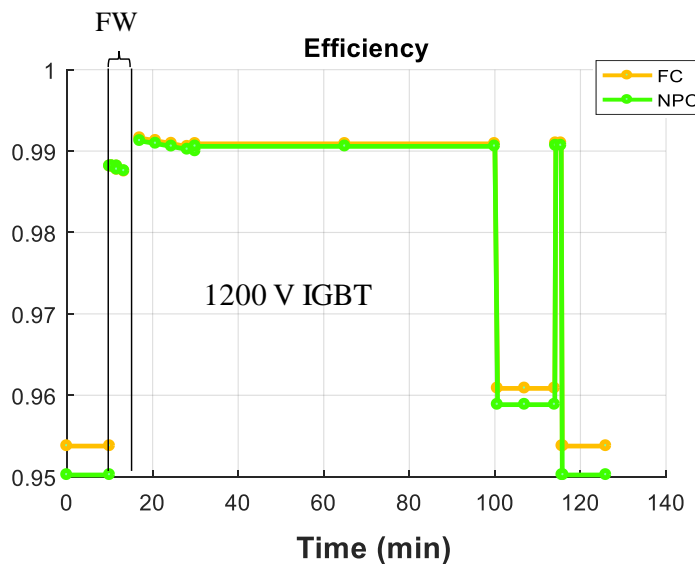


Fig. IV-15. 3-level FC and NPC efficiencies using FW and DPWMMAX strategies with 1200 V IGBTs

For the second electric machine configuration, the DC bus voltage was fixed to 2 kV to have a modulation index of 1.28 for the maximal power. For the take-off, full-wave modulation will

be used and DPWMMAX for the remaining part of the mission (Fig. IV-16). Compared to the third harmonic injection, the FW has lower efficiency for the takeoff than if only the DPWMMAX was used (99.02 % vs 99.26 % for the NPC) however, with DPWMMAX, the efficiency is higher during the cruise (99.09 % vs 99.07 % for the NPC) which meant to be optimized.

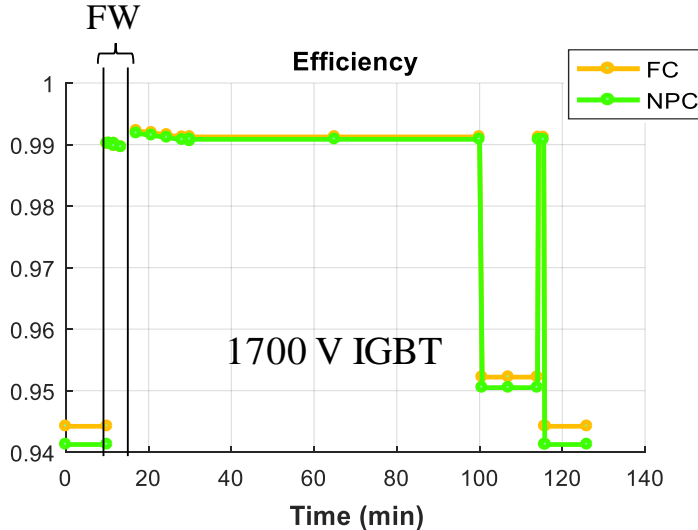


Fig. IV-16. 3-level FC and NPC efficiencies using FW and DPWMMAX strategies with 1700 V IGBTs for the 2nd e-motor

Using the combination of both strategies for the studied mission profile improves the overall inverter efficiency.

vi. Overview of control strategies

TABLE IV-7 to TABLE IV-10 sum up the different studied control strategies for the 3-level NPC topology sized for the appropriate strategy using 1700 V components and TABLE IV-9 and TABLE IV-10 sums up those for the FC topology. The worst efficiencies backgrounds are in red and the best ones are in green. The global efficiency presents the overall inverter efficiency during the flight mission.

TABLE IV-7. Efficiencies for different mission profile points for the NPC topology 1st e-motor

Flight phase	PWM+ THIPWM (Takeoff)	DPWM MAX	FW	PWM + FW (Takeoff / Climb)	DPWMMAX + FW (Takeoff)
Design strategy for P_{max}	THIPWM	DPWM MAX	FW	FW	FW
Taxi out	94.43%	94.36%	85.98%	93.01%	94.74%
Takeoff	98.79%	98.93%	98.39%	98.39%	98.39%
Cruise	98.61%	98.76%	98.20%	98.64%	98.81%
Descent	95.39%	95.41%	88.91%	94.07%	95.74%
Global efficiency	97.62%	97.72%	95.26%	97.20%	97.76%

TABLE IV-8. Efficiencies for different mission profile points for the NPC topology 2nd e-motor

Flight phase	PWM+ THIPWM (Takeoff)	DPWM MAX	FW	PWM + FW (Takeoff / Climb)	DPWMMAX + FW (Takeoff)
Design strategy for P_{max}	THIPWM	DPWM MAX	FW	FW	FW
Taxi out	93.56%	93.56%	89.24%	91.52%	94.42%
Takeoff	99.07%	99.22%	99.02%	99.02%	99.02%
Cruise	98.89%	99.02%	98.84%	98.90%	99.12%
Descent	94.51%	94.56%	92.35%	92.62%	95.22%
Global efficiency	97.59%	97.69%	96.62%	97.05%	97.92%

 TABLE IV-9. Efficiencies for different mission profile points for the FC topology 1st e-motor

Flight phase	PWM+ THIPWM (Takeoff)	DPWM MAX	FW	PWM + FW (Takeoff / Climb)	DPWMMAX + FW (takeoff)
Design strategy for P_{max}	THIPWM	DPWM MAX	FW	FW	FW
Taxi out	92.46%	94.78%	85.48%	94.81%	95.13%
Takeoff	98.78%	98.98%	98.39%	98.39%	98.39%
Cruise	98.57%	98.80%	98.20%	98.68%	98.84%
Descent	93.57%	95.66%	89.48%	95.72%	95.95%
Global efficiency	97.08%	97.84%	95.24%	97.69%	97.86%

 TABLE IV-10. Efficiencies for different mission profile points for the FC topology 2nd e-motor

Flight phase	PWM+ THIPWM (Takeoff)	DPWM MAX	FW	PWM + FW (Takeoff / Climb)	DPWMMAX + FW (Takeoff)
Design strategy for P_{max}	THIPWM	DPWM MAX	FW	FW	FW
Taxi out	90.68%	93.89%	89.83%	94.12%	94.12%
Takeoff	99.16%	99.26%	99.02%	99.02%	99.02%
Cruise	98.82%	99.07%	98.84%	98.97%	99.09%
Descent	91.86%	94.76%	92.52%	95.01%	95.05%
Global efficiency	96.81%	97.80%	96.74%	97.77%	97.84%

Since the ratio between the switching frequency and the machine frequency is not very high, the full-wave control does not have much interest in this case compared to the discontinuous PWM modulation. For the Taxi out, Cruise and Descent, the DPWMMAX efficiencies and THD are close to the sine PWM ones due to the low switching frequency as noticed in Fig. IV-17. However, the best compromise would be to size the inverter for the takeoff using the

FW and use the DPWMMAX for the other flight mission phases which improve the global inverter efficiency.

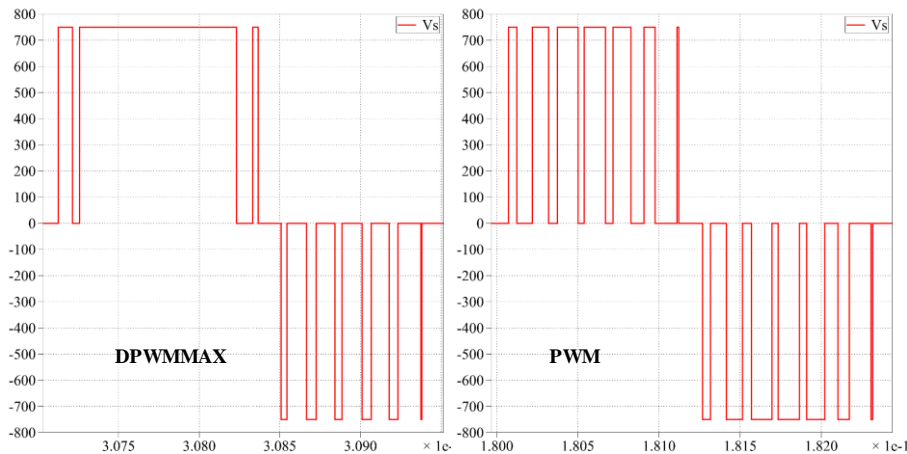


Fig. IV-17. Output voltage for 3-level FC during the cruise using DPWMMAX and PWM

The highest efficiency for these studied scenarios corresponds to the 2nd machine configuration with hybrid FW + DPWMMAX for both 3-level FC and NPC topologies.

TABLE IV-11 sums the target efficiencies during takeoff and cruise phases and achieved ones using the 5th strategy which is the DPWMMAX + FW which has the best results for the cruise phase.

TABLE IV-11. Target and achieved efficiencies during takeoff and cruise

Flight phase	2025 Target	2035 Target	DPWMMAX + FW (takeoff)			
			FC 1 st e-motor	NPC 1 st e-motor	FC 2 nd e-motor	NPC 2 nd e-motor
Takeoff	96.5%	99%	98.39%	98.39%	99.02%	99.02%
Cruise	98%	99.5%	98.84%	98.81%	99.09%	99.12%
Global Efficiency	-	-	97.86%	97.76%	97.84%	97.92%

The 2025 efficiency targets were achieved only by using a regular sine PWM and the 1st machine winding configuration. However, for 2035 efficiency objectives, even with the 2nd machine winding configuration and DPWMMAX, the efficiency is lower than the cruise power point objective and for the maximum power point, the objective was reached with the 3-level FC using a DPWMMAX control strategy. Nevertheless, the specific power of the FC topology is significantly lower than the NPC one due to the additional flying capacitors weight.

3. Conclusion

This chapter evaluates the efficiency of the chosen 3-level inverter topologies, which are the FC and NPC, for different modulation strategies during the flight mission so to find the best option to improve the efficiency during the cruise. This study was carried for two electric motor winding configurations.

The first studied strategy was to use the THIPWM during the takeoff and climb so to fully use the sine PWM during the cruise. This strategy enhances the overall inverter efficiency. The second one compares the THIPWM and DPWM both MIN and MAX. The DPWMMAX stands out from this comparison for both inverter topologies and both machine configurations. The third one is using FW for the entire mission profile. In this case, the efficiency is enhanced however, since the FW is a low modulation strategy, the THD is high for low power and frequency phases due to the low harmonic components. To avoid this problem, the 4th and 5th strategies were studied. These strategies use FW in combination with sine PWM for the 4th one and DPWMMAX for the 5th one. This improves efficiency and THD during the low power phases.

For all the modulation strategies, the use of the second machine parameters increases the efficiency of the inverter since for the same power, the used DC bus voltage is higher and therefore the current is lower, which reduces power losses in semiconductors.

So the most interesting strategy would be to size the inverter for the takeoff using the FW and use the DPWMMAX for the other flight mission phases. This strategy makes it possible to achieve the first targets set by HASTECS project in terms of efficiency. However, the cruise 2035 efficiency target (99.5 %) is still not reached (99.12 %).

Another solution to improve the efficiency during the cruise could be to use two or more converters. In the case of two converters, both are operated during take-off. Then, only one is connected to the motor. This solution could be considered to reach the 2035 targets. However, the inverter weight could be increased which will reduce the specific power.

Conclusion & perspectives

The main objective of this manuscript has been to size a highly integrated power electronic inverter that will feed an electric motor connected to an aircraft propeller with a specific power of 15 kW/kg for 2025 target and 25 kW/kg for 2035 target including its cooling system. It takes part in the second work package of HASTECS Clean Sky 2 European project that aims to study the possibility of electric propulsion hybridization in an aircraft which was presented in detail in Chapter I. In this Ph.D. study, power electronics topologies, smart control, and modulation strategies as well as semiconductor technologies were investigated.

As a result of a first simple sizing for a 2-level inverter, the main factor to increase the specific power was identified in Chapter I, decreasing the weight of the cooling system. Two options were conceivable. The first one was decreasing the cooling system mass by optimizing its components which was done by WP4 work. The second one was reducing power losses which is a part of our work package (WP2) tasks.

To size the power converter used to feed the electrical motor for the aircraft propulsion, a pre-design tool was developed. This tool uses *Matlab* object-oriented programming and is based on analytic analysis of the inverter power losses so to evaluate the efficiency and components temperatures to respond to our specification detailed in chapter II. The used power losses and thermal models were also presented in the second chapter. These models need several components such as capacitors and semiconductors parameters that are issued from the available database or generated based on it so to satisfy the current and voltage requirements. These components were validated using several study case scenarios and would help to define the DC bus voltage which is the first task of this work.

The available semiconductors voltage ranges limit the DC bus voltage that could be chosen if the 2-level topology was to be used without allowing direct series association. The high switching frequency represents also a constraint to the large voltage caliber components that were not meant to operate at these frequency levels due to the high switching losses. With all this said, using smaller voltage rating components but with high DC bus voltage to reduce the needed current rating would be more interesting. This could be done by using multilevel topologies.

In Chapter III, the inverter topologies, modulation strategies, and components technologies were presented. As noticed in chapter II, the inverter power losses reduction could be achieved by using small rating components. This was done by using multilevel architectures to avoid the direct series association. The used topologies were 2, 3 and 5 levels ones. They were compared using DC bus voltage sweeps to find the optimal DC bus voltage range for each group of topologies. If the DC bus voltage is between 700 V and 1 kV, the 2-level topology could be used, however, in this case, to withstand the machine current, several components should be associated in parallel which will increase the inverter weight and volume. If the DC bus voltage is between 1 and 2.4 kV, the 3-level topologies have the best efficiencies for this voltage this

range. However, if the DC bus voltage is between 2.4 and 3.5 kV, the 5-level ones must be recommended. This voltage range also depends on the used switching frequency. This parameter is very important especially for the high voltage components that were used and have a great impact on the power losses and therefore the semiconductors maximal junction temperature. The 3-level topologies and the 5-level ANPC seemed to be the most adapted ones to our specification. This study showed also that, so to use some topologies such as 2-level or 3-level ones, they should be used with a low switching frequency so to have an acceptable junction temperature.

This leads to the second covered point of chapter III which was the study modulation strategies. The multilevel modulation techniques could be classified according to switching frequency. High switching frequency modulations have higher switching losses but less impact on the machine current since the high-frequency filtering is better than low-frequency one. Therefore, with low switching frequency methods, efficiency is higher. In this work, four modulation strategies, which are sine PWM, Third Harmonic Injection PWM, Discontinuous PWM MIN and MAX, and Full Wave adapted to 3-level inverter topologies, were studied and compared in terms of efficiency so to find the most performant one. The sine PWM had the lowest efficiency among all the topologies but still close to the others' performances. The DPWMMAX was the one with the highest efficiency for both studied 3-level topologies.

The third tackled point in chapter III was semiconductors technologies. The component choice has a great impact on the inverter performances since the power losses depend on the semiconductor conduction and switching parameters. The market evolution of silicon components seemed to be saturated in recent years. However, with the new Mitsubishi 7th generation IGBT module, this is not the case anymore. These components have fewer losses and come in a compact light-weighted packaging. These components were compared to the previous IGBT generation and also to SiC modules with the same current and voltage calibers and seem to be the best option for our specifications.

Using these components, the DPWMMAX modulation and an optimized cooling system with a 3-level NPC topology, the 15 kW/kg specific power target was exceeded (23.29 kW/kg) but it stills far from the 2035 one which is 25 kW/kg. To reach the second target, a specific power module was designed so to integrate half a phase in a single module. This solution reduced the used bus bar and make it possible to achieve a specific power of 57.59 kW/kg for the 3-phase inverter taking into account only the bus bar, DC bus capacitor, semiconductors, and its cooling system. To have a more accurate estimation, parameters such as drivers, filters and components attaching elements should be included.

In chapter IV, several modulation strategies and sizing points have been studied to find out the best scenario for the 3-level FC and NPC inverters modulation strategies taking into account the flight mission. This study was carried for two electric motor winding configurations.

The first studied strategy was to use the THIPWM during the takeoff and climb so to fully use the sine PWM during the cruise. This strategy enhances the overall inverter efficiency. The second one compares the THIPWM and DPWM both MIN and MAX. The DPWMMAX stands out from this comparison for both inverter topologies and both machine configurations. The third one is using FW for the entire mission profile. In this case, the efficiency is enhanced however, since the FW is a low modulation strategy, the THD is high for low power low-speed phases due to the low harmonic components. To avoid this problem, the 4th and 5th strategies were studied. These strategies use FW in combination with sine PWM for the 4th one and DPWMMAX for the 5th one. This improves efficiency and THD during the low power phases.

So the most interesting strategy would be to size the inverter for the takeoff using the FW and use the DPWMMAX for the other flight mission phases. This strategy makes it possible to achieve the targets set by HASTECS project in terms of efficiency for the takeoff. However, for the cruise, the reached efficiency is 99.12 % with the second machine configuration and the 2035 target was 99.5 %. For all the modulation strategies, the use of the second machine parameters increases the efficiency of the inverter since for the same power, the used DC bus voltage is higher and therefore the current is lower, which reduces power losses in semiconductors.

One way to improve inverter efficiency during the cruise could be to use two or more converters. In the case of two converters, both are operated during takeoff. Then, only one is connected to the motor. This solution could be considered to reach the 2035 targets. However, the inverter weight could be increased which would reduce the specific power. Fig. V-1 represents some ideas that were meant to be explored:

- Possibility to increase the number of converter leg if using a multi-motor (Fig. V-1.D) or “multi stator” (double or more) machine (Fig. V-1.E-F), by dividing the required current to power the motor by the number of phases;
- Possibility to interleave the converter legs by inductors (Fig. V-1.B-C). To reduce the size of the inductors, coupling devices can be used or the stator itself can be used as a coupling device (multi-phase or multi-stator Fig. V-1.E-F-G). In each case, the losses inside the converter will change and due to the change in output waveforms, motor performance and partial discharge effect would be affected;
- Impact of the power splitting on the architecture redundancy and fault tolerance issues.

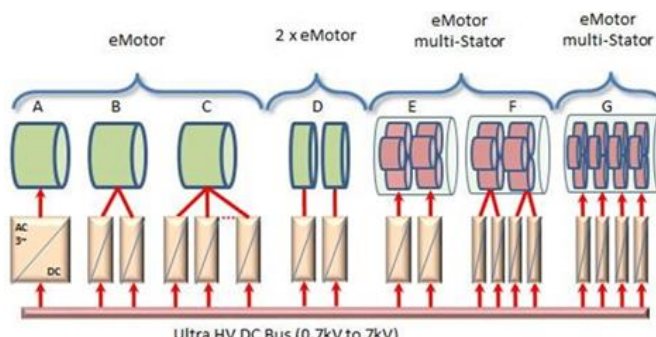


Fig. V-1. Power rating and converter architecture

Appendix

The considered output current (1) absorbed by the electrical motor is supposed to be sinusoidal with a phase shift θ and ω is the electric motor pulsation.

$$I_{out}(x) = \sqrt{2} * I_{rms} * \sin(x - \theta) \text{ with } x = \omega t \quad (1)$$

The command function depends on the used modulation strategy and is as follows:

$$f(x) = \begin{cases} k * \sin(x) & , \text{ Sine PWM} \\ k * \sin(x) + \frac{1}{4} * \sin(3x), & \text{THIPWM} \end{cases} \quad (2)$$

With k the modulation index.

1. 3-level FC topology

The considered topology is shown in Fig. VI-1. The switched and conducted average and RMS current expressions are given for the sine PWM and THIPWM modulation strategies. These expressions are deduced from a *Plecs* simulation used to define the switching intervals and the connection function.

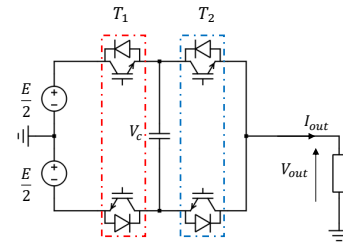


Fig. VI-1. 3-level FC inverter leg

i. PWM

For the sine PWM, the losses are balanced for this topologies so the current are calculated only for one IGBT and one Diode.

TABLE. VI-1. Conduction Mode average and RMS current

Avg	$\bar{I}_{T_1} = \bar{I}_{T_2} = \bar{I}_{T_3} = \bar{I}_{T_4} = \frac{1}{2\pi} \left[\int_{\theta}^{\pi+\theta} I_{out}(x) (1 + f(x)) dx \right]$ $\bar{I}_{D_1} = \bar{I}_{D_2} = \bar{I}_{D_3} = \bar{I}_{D_4}$ $= \frac{1}{2\pi} \left[\int_0^{\theta} I_{out}(x) (1 + f(x)) dx + \int_{\pi+\theta}^{2\pi} I_{out}(x) (1 + f(x)) dx \right]$
RMS	$I_{rms T_1} = I_{rms T_2} = I_{rms T_3} = I_{rms T_4} = \sqrt{\frac{1}{2\pi} \left[\int_{\theta}^{\pi+\theta} I_{out}^2(x) (1 + f(x)) dx \right]}$ $I_{rms D_1} = I_{rms D_2} = I_{rms D_3} = I_{rms D_4} = \sqrt{\frac{1}{2\pi} \left[\int_0^{\theta} I_{out}^2(x) (1 + f(x)) dx + \int_{\pi+\theta}^{2\pi} I_{out}^2(x) (1 + f(x)) dx \right]}$

TABLE. VI-2. Switching Mode average current formulas

	Interval Δ^{SW}	Current
Avg	$\frac{1}{2}$	$\bar{I}_{T_1}^{SW} = \bar{I}_{T_2}^{SW} = \bar{I}_{T_3}^{SW} = \bar{I}_{T_4}^{SW} = \frac{1}{2\pi} \left[\int_{\theta}^{\pi+\theta} I_{out}(x) dx \right]$
	$\frac{1}{2}$	$\bar{I}_{D_1}^{SW} = \bar{I}_{D_2}^{SW} = \bar{I}_{D_3}^{SW} = \bar{I}_{D_4}^{SW} = \frac{1}{2\pi} \left[\int_{\theta}^{\pi+\theta} I_{out}(x) dx \right]$
RMS	$\frac{1}{2}$	$I_{rms T_1}^{SW} = I_{rms T_2}^{SW} = I_{rms T_3}^{SW} = I_{rms T_4}^{SW}$ $= \sqrt{\frac{1}{2\pi} \left[\int_{\theta}^{\pi+\theta} I_{out}(x) dx \right]}$
	$\frac{1}{2}$	$I_{rms D_1}^{SW} = I_{rms D_2}^{SW} = I_{rms D_3}^{SW} = I_{rms D_4}^{SW}$ $= \sqrt{\frac{1}{2\pi} \left[\int_0^{\theta} I_{out}(x) dx + \int_{\theta+\pi}^{2\pi} I_{out}(x) dx \right]}$

ii. THIPWM1/4

For the THIPWM, the losses are symmetric so the current are calculated for one upper and one lower IGBT and Diode.

TABLE. VI-3. Conduction Mode average and RMS current

Avg	$\bar{I}_{T_1} = \bar{I}_{T_2} = \frac{1}{2\pi} \left[\int_{\theta}^{\pi} I_{out}(x) dx + \int_{\pi}^{\pi+\theta} I_{out}(x) (1 + f(x)) dx \right]$ $\bar{I}_{T_3} = \bar{I}_{T_4} = \frac{1}{2\pi} \left[\int_{\theta}^{\pi} I_{out}(x) * f(x) dx \right]$ $\bar{I}_{D_1} = \bar{I}_{D_2} = \frac{1}{2\pi} \left[\int_0^{\theta} I_{out}(x) dx + \int_{\pi+\theta}^{2\pi} I_{out}(x) (1 + f(x)) dx \right]$ $\bar{I}_{D_3} = \bar{I}_{D_4} = \frac{1}{2\pi} \left[\int_0^{\theta} I_{out}(x) * f(x) dx \right]$
RMS	$I_{rms T_1} = I_{rms T_2} = \sqrt{\frac{1}{2\pi} \left[\int_{\theta}^{\pi} I_{out}^2(x) dx + \int_{\pi}^{\pi+\theta} I_{out}^2(x) * (1 + f(x)) dx \right]}$
	$I_{rms T_3} = I_{rms T_4} = \sqrt{\frac{1}{2\pi} \left[\int_{\theta}^{\pi} I_{out}^2(x) * f(x) dx \right]}$
	$I_{rms D_1} = I_{rms D_2} = \sqrt{\frac{1}{2\pi} \left[\int_0^{\theta} I_{out}^2(x) dx + \int_{\pi+\theta}^{2\pi} I_{out}^2(x) * (1 + f(x)) dx \right]}$
	$I_{rms D_3} = I_{rms D_4} = \sqrt{\frac{1}{2\pi} \left[\int_0^{\theta} I_{out}^2(x) * f(x) dx \right]}$

TABLE. VI-4. Switching Mode average current formulas

Interval Δ^{SW}	Current
Avg	$\bar{I}_{T_1}^{SW} = \bar{I}_{T_2}^{SW} = \frac{1}{2\pi} \left[\int_{\pi}^{\pi+\theta} I_{out}(x) dx \right]$
	$\bar{I}_{T_1}^{SW} = \bar{I}_{T_2}^{SW} = \frac{1}{2\pi} \left[\int_{\theta}^{\pi} I_{out}(x) dx \right]$
	$\bar{I}_{D_1}^{SW} = \bar{I}_{D_2}^{SW} = \frac{1}{2\pi} \left[\int_{\pi+\theta}^{2\pi} I_{out}(x) dx \right]$
	$\bar{I}_{D_3}^{SW} = \bar{I}_{D_4}^{SW} = \frac{1}{2\pi} \left[\int_0^{\theta} I_{out}(x) dx \right]$
RMS	$I_{rms T_1}^{SW} = I_{rms T_2}^{SW} = \sqrt{\frac{1}{2\pi} \left[\int_{\pi}^{\pi+\theta} I_{out}^2(x) dx \right]}$
	$I_{rms T_3}^{SW} = I_{rms T_4}^{SW} = \sqrt{\frac{1}{2\pi} \left[\int_{\theta}^{\pi} I_{out}^2(x) dx \right]}$
	$I_{rms D_1}^{SW} = I_{rms D_2}^{SW} = \sqrt{\frac{1}{2\pi} \left[\int_{\pi}^{\pi+\theta} I_{out}^2(x) dx \right]}$
	$I_{rms D_3}^{SW} = I_{rms D_4}^{SW} = \sqrt{\frac{1}{2\pi} \left[\int_0^{\theta} I_{out}^2(x) dx \right]}$

2. 3-level NPC topology

The considered 3-level NPC topology is shown in Fig. VI-2. The switched and conducted average and RMS current expressions are given for the sine PWM but are the same for the THIPWM since they don't have the same connection function f .

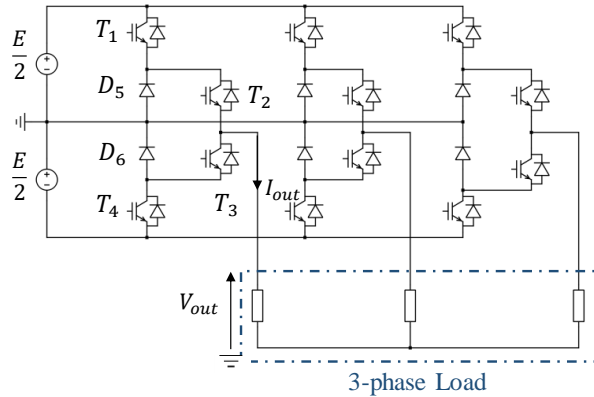


Fig. VI-2. 3-level NPC inverter

TABLE. VI-5. Conduction Mode average and RMS current

Avg	$\bar{I}_{T_1} = \bar{I}_{T_3} = \frac{1}{2\pi} \left[\int_{\theta}^{\pi} I_{out}(x) f(x) dx \right]$ $\bar{I}_{T_2} = \bar{I}_{T_4} = \frac{1}{2\pi} \left[\int_{\theta}^{\pi} I_{out}(x) dx + \int_{\pi}^{\pi+\theta} I_{out}(x) (1 + f(x)) dx \right]$ $\bar{I}_{D_1} = \bar{I}_{D_3} = \frac{1}{2\pi} \left[\int_0^{\theta} I_{out}(x) f(x) dx \right]$ $\bar{I}_{D_2} = \bar{I}_{D_4} = \frac{1}{2\pi} \left[\int_0^{\theta} I_{out}(x) f(x) dx \right]$ $\bar{I}_{D_5} = \bar{I}_{D_6} = \frac{1}{2\pi} \left[\int_{\theta}^{\pi} I_{out}(x) (1 - f(x)) dx + \int_{\pi}^{\pi+\theta} I_{out}(x) (1 + f(x)) dx \right]$
RMS	$I_{rms T_1} = I_{rms T_3} = \sqrt{\frac{1}{2\pi} \left[\int_{\theta}^{\pi} I_{out}^2(x) f(x) dx \right]}$ $I_{rms T_2} = I_{rms T_4} = \sqrt{\frac{1}{2\pi} \left[\int_{\theta}^{\pi} I_{out}^2(x) dx + \int_{\pi}^{\pi+\theta} I_{out}^2(x) * (1 + f(x)) dx \right]}$ $I_{rms D_1} = I_{rms D_3} = \sqrt{\frac{1}{2\pi} \left[\int_0^{\theta} I_{out}^2(x) f(x) dx \right]}$ $I_{rms D_2} = I_{rms D_4} = \sqrt{\frac{1}{2\pi} \left[\int_0^{\theta} I_{out}^2(x) f(x) dx \right]}$ $I_{rms D_5} = I_{rms D_6} = \sqrt{\frac{1}{2\pi} \left[\int_{\theta}^{\pi} I_{out}^2(x) (1 - f(x)) dx + \int_{\pi}^{\pi+\theta} I_{out}^2(x) * (1 + f(x)) dx \right]}$

TABLE. VI-6. Switching Mode average current formulas

	Interval Δ^{SW}	Current
Avg	$\frac{\pi - \theta}{2\pi}$ $\frac{\theta}{2\pi}$ $\frac{\theta}{2\pi}$ $\frac{\theta}{2\pi}$ $\frac{\pi - \theta}{2\pi}$	$\bar{I}_{T_1}^{SW} = \bar{I}_{T_3}^{SW} = \frac{1}{2\pi} \left[\int_{\theta}^{\pi} I_{out}(x) dx \right]$ $\bar{I}_{T_2}^{SW} = \bar{I}_{T_4}^{SW} = \frac{1}{2\pi} \left[\int_{\pi}^{\pi+\theta} I_{out}(x) dx \right]$ $\bar{I}_{D_1}^{SW} = \bar{I}_{D_3}^{SW} = \frac{1}{2\pi} \left[\int_0^{\theta} I_{out}(x) dx \right]$ $\bar{I}_{D_2}^{SW} = \bar{I}_{D_4}^{SW} = \frac{1}{2\pi} \left[\int_0^{\theta} I_{out}(x) dx \right]$ $\bar{I}_{D_5}^{SW} = \bar{I}_{D_6}^{SW} = \frac{1}{2\pi} \left[\int_{\theta}^{\pi} I_{out}(x) dx \right]$

RMS	$\frac{\pi - \theta}{2\pi}$	$I_{rms\ T_1}^{SW} = I_{rms\ T_3}^{SW} = \sqrt{\frac{1}{2\pi} \left[\int_{\theta}^{\pi} I_{out}^2(x) dx \right]}$
	$\frac{\theta}{2\pi}$	$I_{rms\ T_2}^{SW} = I_{rms\ T_4}^{SW} = \sqrt{\frac{1}{2\pi} \left[\int_{\pi}^{\pi+\theta} I_{out}^2(x) dx \right]}$
	$\frac{\theta}{2\pi}$	$I_{rms\ D_1}^{SW} = I_{rms\ D_3}^{SW} = \sqrt{\frac{1}{2\pi} \left[\int_0^{\theta} I_{out}^2(x) dx \right]}$
	$\frac{\theta}{2\pi}$	$I_{rms\ D_2}^{SW} = I_{rms\ D_4}^{SW} = \sqrt{\frac{1}{2\pi} \left[\int_0^{\theta} I_{out}^2(x) dx \right]}$
	$\frac{\pi - \theta}{2\pi}$	$I_{rms\ D_5}^{SW} = I_{rms\ D_6}^{SW} = \sqrt{\frac{1}{2\pi} \left[\int_{\theta}^{\pi} I_{out}^2(x) dx \right]}$

3. 5-level ANPC PWM

The considered 5-level ANPC topology is shown in Fig. VI-3. The switched and conducted average and RMS current expressions are given only for the sine PWM.

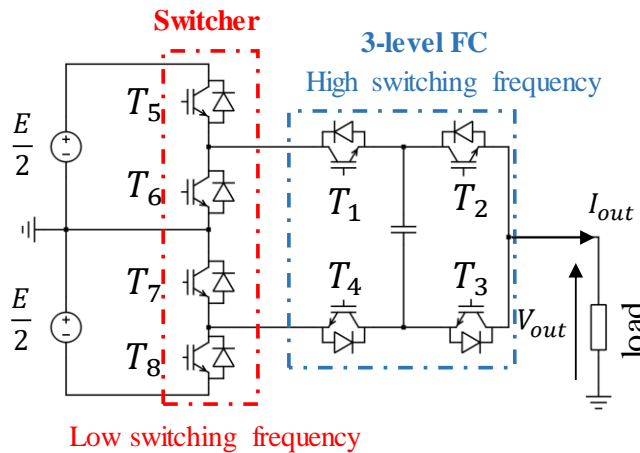


Fig. VI-3. 5-level ANPC topology

TABLE. VI-7. Conduction Mode average current formulas

FC	$\bar{I}_{T_1} = \bar{I}_{T_2} = \bar{I}_{T_3} = \bar{I}_{T_4}$ $= \frac{1}{2\pi} \left[\int_{\theta}^{\pi} I_{out}(x) f(x) dx + \int_{\pi}^{\pi+\theta} I_{out}(x) (1 + f(x)) dx \right]$ $\bar{I}_{D_1} = \bar{I}_{D_2} = \bar{I}_{D_3} = \bar{I}_{D_4}$ $= \frac{1}{2\pi} \left[\int_0^{\theta} I_{out}(x) f(x) dx + \int_{\pi+\theta}^{2\pi} I_{out}(x) (1 + f(x)) dx \right]$
----	---

Switcher $\bar{I}_{T_5} = \bar{I}_{T_8} = \frac{1}{2\pi} \left[\int_{\theta}^{\pi} I_{out}(x) dx \right]$ $\bar{I}_{D_5} = \bar{I}_{D_8} = \frac{1}{2\pi} \left[\int_0^{\theta} I_{out}(x) dx \right]$ $\bar{I}_{T_6} = \bar{I}_{T_7} = \frac{1}{2\pi} \left[\int_{\pi+\theta}^{2\pi} I_{out}(x) dx \right]$ $\bar{I}_{D_6} = \bar{I}_{D_7} = \frac{1}{2\pi} \left[\int_{\pi}^{\pi+\theta} I_{out}(x) dx \right]$

TABLE. VI-8. Conduction Mode RMS current formulas

FC $I_{rms T_1} = I_{rms T_2} = I_{rms T_3} = I_{rms T_4} = \sqrt{\frac{1}{2\pi} \left[\int_{\theta}^{\pi} I_{out}^2(x) f(x) dx + \int_{\pi}^{\pi+\theta} I_{out}^2(x)(1+f(x)) dx \right]}$ $I_{rms D_1} = I_{rms D_2} = I_{rms D_3} = I_{rms D_4} = \sqrt{\frac{1}{2\pi} \left[\int_0^{\theta} I_{out}^2(x) f(x) dx + \int_{\pi+\theta}^{2\pi} I_{out}^2(x)(1+f(x)) dx \right]}$
Switcher $I_{rms T_5} = I_{rms T_8} = \sqrt{\frac{1}{2\pi} \left[\int_{\theta}^{\pi} I_{out}^2(x) dx \right]}$ $I_{rms D_5} = I_{rms D_8} = \sqrt{\frac{1}{2\pi} \left[\int_0^{\theta} I_{out}^2(x) dx \right]}$ $I_{rms T_6} = I_{rms T_7} = \sqrt{\frac{1}{2\pi} \left[\int_{\pi+\theta}^{2\pi} I_{out}^2(x) dx \right]}$ $I_{rms D_6} = I_{rms D_7} = \sqrt{\frac{1}{2\pi} \left[\int_{\pi}^{\pi+\theta} I_{out}^2(x) dx \right]}$

TABLE. VI-9. Switching Mode average current formulas

Interval ΔSW	Average Currents
FC T_1, T_4 D_1, D_4	$\bar{I}_{T_1}^{SW} = \bar{I}_{T_2}^{SW} = \bar{I}_{T_3}^{SW} = \bar{I}_{T_4}^{SW}$ $= \frac{1}{2\pi} \left[\int_{\theta}^{\pi} I_{out}(x) dx + \int_{\pi}^{\theta+\pi} I_{out}(x) dx \right]$ $\bar{I}_{D_1}^{SW} = \bar{I}_{D_2}^{SW} = \bar{I}_{D_3}^{SW} = \bar{I}_{D_4}^{SW}$ $= \frac{1}{2\pi} \left[\int_0^{\theta} I_{out}(x) dx + \int_{\theta+\pi}^{2\pi} I_{out}(x) dx \right]$

Switcher		
T_5, T_8	$\frac{\pi - \theta}{2\pi}$	$\bar{I}_{T_5}^{SW} = \bar{I}_8^{SW} = \frac{1}{2\pi} \left[\int_{\theta+\pi}^{2\pi} I_{out}(x) dx \right]$
D_5, D_8	$\frac{\theta}{2\pi}$	$\bar{I}_{D_5}^{SW} = \bar{I}_{D_8}^{SW} = \frac{1}{2\pi} \left[\int_0^{\theta} I_{out}(x) dx \right]$
T_6, T_7	$\frac{\pi - \theta}{2\pi}$	$\bar{I}_{T_6}^{SW} = \bar{I}_{T_7}^{SW} = \frac{1}{2\pi} \left[\int_{\theta}^{\pi} I_{out}(x) dx \right]$
D_6, D_7	$\frac{\pi - \theta}{2\pi}$	$\bar{I}_{D_6}^{SW} = \bar{I}_{D_7}^{SW} = \frac{1}{2\pi} \left[\int_{\theta+\pi}^{2\pi} I_{out}(x) dx \right]$

TABLE. VI-10. Switching Mode RMS current formulas

	Interval Δ^{SW}	RMS Currents:
FC		
T_1, T_4	$\frac{1}{2}$	$I_{rms T_1}^{SW} = I_{rms T_2}^{SW} = I_{rms T_3}^{SW} = I_{rms T_4}^{SW}$ $= \sqrt{\frac{1}{2\pi} \left[\int_{\theta}^{\pi} I_{out}(x) dx + \int_{\pi}^{\theta+\pi} I_{out}(x) dx \right]}$
D_1, D_4	$\frac{1}{2}$	$I_{rms D_1}^{SW} = I_{rms D_2}^{SW} = I_{rms D_3}^{SW} = I_{rms D_4}^{SW}$ $= \sqrt{\int_0^{\theta} I_{out}(x) dx + I_{out}(x) dx}$
Switcher		
T_5, T_8	$\frac{\pi - \theta}{2\pi}$	$I_{rms T_5}^{SW} = I_{rms T_8}^{SW} = \sqrt{\frac{1}{2\pi} \left[\int_{\theta+\pi}^{2\pi} I_{out}^2(x) dx \right]}$
D_5, D_8	$\frac{\theta}{2\pi}$	$I_{rms D_5}^{SW} = I_{rms D_8}^{SW} = \sqrt{\frac{1}{2\pi} \left[\int_0^{\theta} I_{out}^2(x) dx \right]}$
T_6, T_7	$\frac{\pi - \theta}{2\pi}$	$I_{rms T_6}^{SW} = I_{rms T_7}^{SW} = \sqrt{\frac{1}{2\pi} \left[\int_{\theta}^{\pi} I_{out}^2(x) dx \right]}$
D_6, D_7	$\frac{\pi - \theta}{2\pi}$	$I_{rms D_6}^{SW} = I_{rms D_7}^{SW} = \sqrt{\frac{1}{2\pi} \left[\int_{\pi+\theta}^{2\pi} I_{out}^2(x) dx \right]}$
T_5, T_8	$\frac{\pi - \theta}{2\pi}$	$\bar{I}_{T_5}^{SW} = \bar{I}_{T_8}^{SW} = \frac{1}{2\pi} \left[\int_{\theta+\pi}^{2\pi} I_{out}^2(x) dx \right]$

Résumé en français

Introduction

L'empreinte environnementale et écologique des systèmes de transport, en particulier des avions, n'a cessé de croître ces dernières années. Les considérations environnementales actuelles poussent donc à réduire leur impact écologique. Des projets tels que le projet Clean Sky 2 apportent une réponse à ce problème, en proposant une réduction des émissions de CO₂ et des nuisances sonores. La mise au point d'un avion hybride à propulsion électrique réduirait ces émissions en réduisant la taille et la masse des systèmes et en utilisant des systèmes électriques plus efficaces. Cela permettrait de réduire la consommation de carburant et donc les émissions polluantes.

Ces travaux s'inscrivent dans le cadre du projet européen HASTECS Clean Sky 2, qui étudie la possibilité d'hybridation de la propulsion d'un avion régional et vise à développer un outil de simulation pour pré-dimensionner les onduleurs destinés à piloter les moteurs électriques connectés aux hélices pour propulser l'avion. Pour ce faire, les topologies de l'électronique de puissance, les stratégies de contrôle et de modulation ainsi que les technologies des semi-conducteurs ont été prises en compte. Le projet HASTECS s'est fixé le défi d'augmenter la densité de puissance de l'électronique de puissance et de son système de refroidissement pour atteindre 15 kW/kg en 2025 puis 25 kW/kg en 2035. Cela permettrait de réduire la masse de l'onduleur ainsi que celle de la chaîne de propulsion, ce qui se traduirait par une réduction de la consommation de carburant. Deux objectifs en termes de rendement pour l'électronique de puissance ont été fixés également par les avant-projets. Pour l'objectif de 2025, le rendement devrait être supérieur à 98 % pour la phase de croisière et supérieur à 96.5 % pour le point de puissance maximal. En revanche, pour l'objectif de 2035, le rendement devra être supérieur à 99.5 % pour la phase de croisière et supérieur à 99 % pour le point de puissance maximal.

Pour augmenter la densité de puissance, la masse de l'ensemble du système de conversion de puissance doit être diminué et en particulier la masse du système de refroidissement qui sera validé par le WP4. La réduction des pertes de l'onduleur peut être obtenue en utilisant des composants de faible calibre en tension, en jouant sur les stratégies de modulation ou en utilisant des semi-conducteurs plus performants. La première option pourrait être faite en utilisant des architectures multi-niveaux afin d'éviter l'association série directe. Contrairement à l'association série directe, l'association parallèle est plus facile à gérer en termes de commande de interrupteurs, ce qui a été autorisé dans nos études. Plusieurs topologies d'onduleurs (topologies à 2, 3 et 5 niveaux) et stratégies de modulation (PWM, injection de troisième harmonique, PWM discontinu et pleine onde) ont été comparées en utilisant plusieurs générations de semi-conducteurs pour choisir la solution la plus performante en termes de rendement et de densité de puissance. Pour le profil de mission de vol considéré, l'onduleur peut être dimensionné pour le point de puissance maximum (décollage) ou pour la phase de vol la plus longue (croisière). Une étude comparative des stratégies de contrôle de modulation a été réalisée pour mettre en évidence la structure et la modulation présentant les meilleures performances afin de minimiser

les pertes pour les points de dimensionnement choisis en utilisant les topologies les plus intéressantes pour le profil de mission étudié avec deux configurations de bobinages du moteur (2 et 3 conducteurs par encoche).

Le premier chapitre présente le principal problème lié à l'aviation actuelle et les opportunités offertes par les avions à propulsion hybride électrique. Le principe et la nécessité des avions à propulsion hybride-électrique seront démontrés en raison de l'évolution de l'industrie aéronautique commerciale et des besoins environnementaux, en plus des objectifs du projet européen Clean Sky 2 HASTECS. La problématique et les objectifs de ce travail seront présentés dans ce chapitre ainsi que le modèle de charge utilisé.

Dans le chapitre II, l'organisation du logiciel et les modèles thermiques et de pertes dans les convertisseurs de puissance utilisés seront présentés. La base de données des semi-conducteurs utilisés sera également abordée. Ce travail vise à développer un outil de simulation permettant de pré-dimensionner les convertisseurs. L'outil calcule différents résultats pour différentes architectures de conversion. Ses entrées sont les contraintes de conception, les topologies prévues des convertisseurs, et le choix de la famille de semi-conducteurs ou du fabricant à partir de la base de données des composants disponibles. Les résultats tels que le rendement, le nombre de semi-conducteurs, la température maximale de jonction, les pertes, les fréquences de découpages, les masses des semi-conducteurs, l'échangeur de chaleur, les éléments passifs internes au convertisseur, ainsi que la densité de puissance sont présentés sous forme de figures pour différents paramètres des différents comportements d'architecture.

Les topologies d'onduleurs et les stratégies de modulation étudiées seront présentées au chapitre III. Les performances seront ensuite comparées en utilisant plusieurs semi-conducteurs pour choisir la solution la plus performante en termes de rendement et de densité de puissance.

Dans le chapitre IV, les topologies d'onduleur choisies seront évaluées pour deux configurations de bobinages du moteur électrique pour l'ensemble de la mission de vol. Une étude comparative des stratégies de modulation sera réalisée pour mettre en évidence la structure et la modulation présentant les meilleures performances pour minimiser les pertes.

Chapitre I : Etat de l'art et contexte

Un ciel plus propre est l'objectif des développements récents et des recherches menées par tous les constructeurs aéronautiques. Cependant, les avions commerciaux consomment aujourd'hui plus de 270 millions de tonnes de kérosène par an et produisent donc de plus en plus d'émissions de CO₂.

La propulsion électrique a le potentiel de révolutionner le vol : des voyages plus propres et plus silencieux, les avantages pourraient être énormes. De plus, les estimations prévoient un doublement du trafic aérien tous les 15 à 20 ans. L'organisation internationale ATAG (Air Transport Action Group) s'est fixé des objectifs pour un ciel plus propre. Elle souhaite réduire la consommation de carburant de 1.5 % par an en moyenne entre 2009 et 2020, et plafonner les émissions de CO₂ par une croissance neutre en carbone à partir de 2020, ainsi que réduire de moitié les émissions nettes de CO₂ des activités aériennes d'ici 2050.

Ces objectifs ne peuvent être atteints avec les technologies actuelles. C'est pourquoi plusieurs projets de recherche et développement sur les technologies de propulsion électrique et hybride-électrique sont menés. Outre les avantages évidents de la réduction des émissions de CO₂ et des niveaux sonores, l'électrification permet également de réévaluer complètement la conception d'un aéronef. Différentes gammes de véhicules profiteront ainsi de l'électrification. À plus long terme, Airbus estime que la propulsion hybride-électrique sera probablement installée sur les avions civils de plus grande taille avant de devenir entièrement électrique, car les rapports puissance/masse de la technologie des batteries sont encore loin d'être suffisants.

Récemment, l'idée d'utiliser l'architecture hybride dans la propulsion aéronautique s'est développée. Cette idée est similaire à celle que l'on retrouve dans les véhicules électriques hybrides en automobile (VEH). Trois architectures hybrides différentes existent : hybridation série, parallèle et série/parallèle. Chaque type a ses avantages et ses critères qui diffèrent les uns des autres. Cependant, les trois types partagent l'idée d'utiliser un système de stockage qui sépare le point de fonctionnement du moteur thermique (turbine à gaz, générateur électrique ou groupe auxiliaire de puissance (APU)) de la propulsion, optimisant ainsi le rendement du moteur thermique. Seule l'hybridation série sera prise en compte dans le cadre de cette étude.

1. Présentation du projet HASTECS

Le projet HASTECS étudie la possibilité d'hybridation du système de propulsion d'un avion régional (Figure 1). Outre l'architecture globale, les différents lots de travail (work package WP) visent à augmenter la densité de puissance des différents composants de la chaîne électrique haute puissance. Cette étude conduira à une optimisation de l'ensemble de la chaîne qui proposera des structures intéressantes intégrant toutes les contraintes aéronautiques telles que les décharges partielles pour les équipements électriques placés en zone non pressurisée.

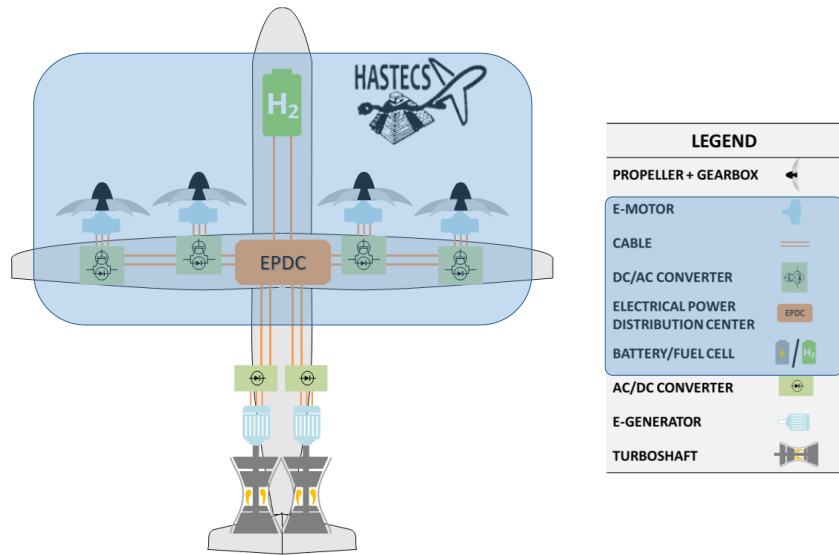


Figure 1. Architecture de base du projet HASTECS

Cette thèse se concentre uniquement sur l'onduleur utilisé pour alimenter le moteur électrique qui entraîne l'hélice (Figure 2). Pour cela, les topologies de l'électronique de puissance, les stratégies de modulation, ainsi que les technologies des semi-conducteurs seront prises en compte. Ceci a pour but de concevoir un onduleur hautement intégré d'une densité de puissance de 15 kW/kg pour la cible de 2025 et de 25 kW/kg pour la cible de 2035, incluant son système de refroidissement. Deux objectifs en termes de rendement pour l'électronique de puissance ont été fixés par le projet HASTECS. Pour l'objectif 2025, le rendement devrait être supérieur à 98 % pour la croisière et supérieur à 96.5 % pour le point de puissance maximal qui correspond au décollage. En revanche, pour l'objectif 2035, le rendement devrait être supérieur à 99.5 % pour la croisière et supérieur à 99 % pour le point de puissance maximal.

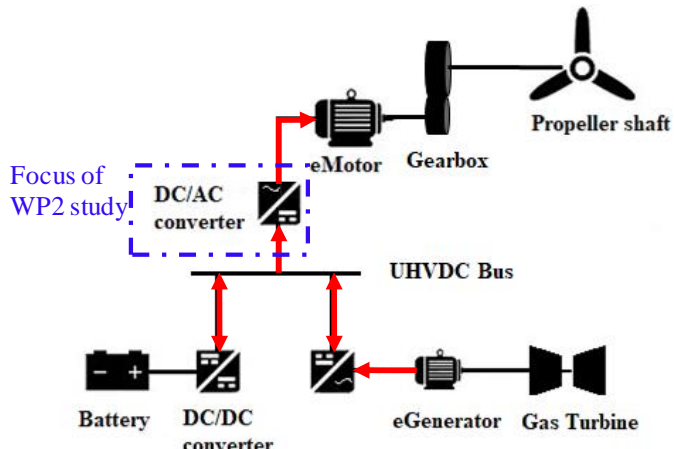


Figure 2. Configuration du système de propulsion hybride électrique

2. Cas de référence

Un onduleur régulier à 2 niveaux avec une PWM sinusoïdal a été dimensionné pour le point de puissance maximal afin de se faire une idée de ce qui pourrait être réalisé en termes de densité de puissance avec une solution basique.

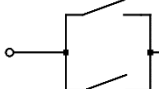
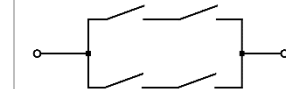
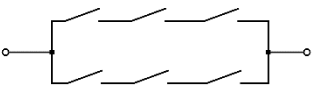
Pour ce cas d'étude, la tension du bus DC est choisie pour fournir la tension maximale nécessaire de la machine électrique ($V_{out_{max}}$) comme dans le Tableau 1. L'onduleur est dimensionné pour le point de puissance maximale avec un bus DC de 2 kV et une fréquence de découpage de 5.8 kHz qui représente environ 11 fois la fréquence nominale PMSM donné par le WP1. Pour estimer la densité de puissance de l'onduleur, y compris le système de refroidissement, on prend en compte un coefficient de 0.34 kW/kg qui traduit directement les pertes en masse du système de refroidissement. Cette valeur est utilisée comme valeur de base issue de l'état de l'art du partenaire Airbus. La masse des composants passifs tels que les condensateurs dans ce cas, sont également pris en compte.

Tableau 1. Paramètres de l'étude

Fréquence fondamentale (Hz)	532.3
$V_{out_{max}}$ (V)	857.3
$I_{out_{RMS}}$ (A)	1054
Indice de modulation	0.86
Facteur de puissance	0.78

Nous proposons de tester l'utilisation de trois calibres de composants différents afin de comparer les performances du convertisseur étudié. Pour ce premier cas d'étude, il est possible d'utiliser deux composants Infineon 3300 V / 800 A associés en parallèle pour s'adapter au niveau de courant imposé par la machine (utilisés à 61 % de leur calibre en tension). Le second utilise deux composants Infineon 1700 V / 600 A associés en parallèle et deux composants en série utilisés à 59% de leur calibre de tension même si l'association directe en série est difficile à réaliser. On suppose dans ce cas que l'on sait résoudre par la commande la problématique de la mise en série. Dans le troisième cas, deux composants Infineon 1200 V / 600 A sont associés en parallèle et trois composants en série utilisés à 56 % de leur calibre de tension. Le Tableau 2 résume les principales performances des onduleurs pour ces trois cas d'étude.

Tableau 2. Performances du convertisseur 2 niveaux

Calibre en tension	3300 V	1700 V	1200 V
η (%)	92.55	98	98.54
Température de jonction (°C)	244	307	98
Densité de puissance (kW/kg)	3.39	8.86	9.23
Associations séries et parallèles (par interrupteur)			
Nombre total de semi-conducteurs par phase	4	8	12

La Figure 3 montre la répartition de la masse de l'onduleur pour les différents cas étudiés. La masse du système de refroidissement, qui est une image directe des pertes en utilisant les composants de puissance à travers le coefficient d'échange initial, est la masse prédominante de l'onduleur. Le bus bar vient alors en deuxième position et sera dominant si la masse de l'échangeur thermique est réduite.

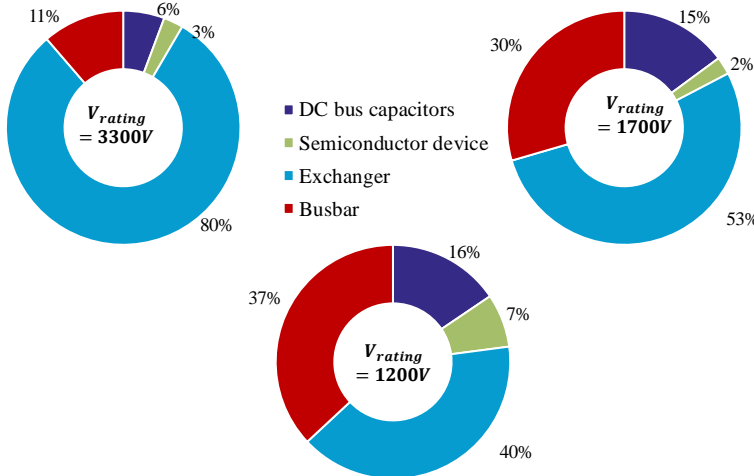


Figure 3. Répartition de la masse de l'onduleur pour les différents composants étudiés

Le convertisseur utilisant les composants possédants un petit calibre en tension a un meilleur rendement mais l'association en séries directe est difficile à réaliser, donc l'utilisation de topologies multi-niveaux pourrait être une solution. À partir de ces exemples, les principaux facteurs d'augmentation de la densité de puissance sont identifiés. Le premier consiste à diminuer la masse du système de refroidissement, en optimisant ses composants ou en réduisant les pertes de puissance. Le deuxième sera donc d'optimiser le bus bar.

Chapitre II : Outil de simulation

Ce chapitre vise à présenter l'outil de simulation développé qui permet de pré-dimensionner les convertisseurs et leurs composants pour un onduleur triphasé. Dans cet outil, les topologies des onduleurs et les stratégies de modulation sont fixées afin que l'utilisateur puisse choisir ses entrées parmi celles disponibles. Il calcule les pertes et la température de jonction pour chaque cas sélectionné selon le modèle qui sera détaillé dans ce chapitre en utilisant les paramètres du semi-conducteur sélectionné. Ce semi-conducteur est sélectionné dans la base de données disponible ou peut être généré de manière à s'adapter aux calibres de courant et tension nécessaires si l'utilisateur le décide, selon le principe de génération qui sera décrit et validé ci-dessous. Le dimensionnement du condensateur sera ensuite expliqué. Les modèles de perte seront ensuite validés à l'aide d'une simulation temporelle sur *Plecs* pour plusieurs topologies d'onduleurs. Ces modèles et les composants générés aideront ensuite à définir la plage de tension du bus DC au chapitre III, qui correspond à la première étape du travail du WP2.

1. Organisation de l'outil

L'outil permet à partir d'un cahier des charges donné de dimensionner le convertisseur en fonction de la topologie choisie. Il permet également de réaliser des études paramétriques en faisant varier la tension du bus DC, la puissance demandée ou l'indice de modulation pour déterminer le point de fonctionnement optimal. Il peut également prendre en compte un profil de mission qui permet de vérifier les performances du convertisseur pour une mission donnée.

Cet outil est réalisé en programmation orientée objet sur *Matlab*. Il est basé sur des calculs analytiques des pertes dans les composants semi-conducteurs pour les différentes architectures multiniveaux intégrées en considérant plusieurs stratégies de modulations. Chaque partie du convertisseur est représenté par un objet ou une classe.

Un objet de type convertisseur, par exemple, peut être caractérisé en topologies multiples (topologie à 2 niveaux, FC, NPC, SMC ou ANPC). Cet objet convertisseur est ensuite relié à un objet de spécification et à un ensemble d'éléments semi-conducteurs et condensateurs. Il est également composé de stratégies de modulation qui utilisent la topologie sélectionnée et les paramètres des dispositifs pour évaluer les pertes de puissance. Chaque bloc peut contenir un ou plusieurs scripts m-file *Matlab*. De plus, chaque script possède des données et des caractéristiques de classes et de leurs propriétés ; les scripts sont nommés comme la classe incluse à l'intérieur. Ces composants du convertisseur seront détaillés au chapitre III.

Pour chaque point de dimensionnement, l'outil sélectionne, à partir de la base de données disponible, les composants semi-conducteurs les plus appropriés qui conviennent le mieux à la tension et au courant désirés. Pour ce faire, un algorithme adapté a été développé. La première étape de cet algorithme consiste à sélectionner le fabricant choisi par l'utilisateur pour extraire les composants correspondants de la base de données. Il est ensuite déterminé si les composants disponibles permettent d'atteindre la tension nominale demandée. Si aucun des composants n'est adapté et que le composant le plus gros est donc trop petit, les composants sont connectés en série pour obtenir la tension souhaitée. Sinon, si plusieurs calibres de composants sont appropriés, le plus petit calibre est choisi parmi ceux qui sont appropriés pour avoir le composant le plus performant comme indiqué au chapitre I. Pour le calibre courant, si le courant requis est supérieur au plus grand calibre en courant, les composants sont associés en parallèle. Sinon, si plusieurs composants sont adaptés, le plus petit est sélectionné.

Ce logiciel permet une grande flexibilité et un grand degré de liberté pour le dimensionnement et l'étude des convertisseurs pour différents scénarios possibles.

2. Modélisations des pertes et de la thermique

Après avoir sélectionné les composants, l'étape suivante consiste à calculer les pertes pour évaluer le rendement de l'onduleur. Elles seront également utilisées pour calculer la température

maximale de jonction. Ces pertes et la température de jonction sont calculées à l'aide des modèles simplifiés présentés ci-dessous.

Pour modéliser les pertes dans le semi-conducteur, nous devons calculer les pertes par commutation et par conduction. Les deux pertes dépendent des paramètres du composant et des courants et tensions appliqués à ce dernier. Afin de simplifier le calcul des pertes dans les semi-conducteurs, un certain nombre d'hypothèses préliminaires ont été formulées qui sont présentées en détail dans le chapitre II. Dans ce cas, les semi-conducteurs utilisés sont uniquement des IGBT et des diodes en silicium.

Les pertes sont calculées à l'aide du produit courant-tension. Pour calculer les pertes par conduction, l'IGBT et la diode peuvent être modélisés par une chute de tension et une résistance interne connectée en série ne considérant qu'un courant positif (eq. (1)).

$$V_{ce} = V_{ce_0} + R_{dson} * I_c \quad (1)$$

$$P_{cond} = \frac{1}{T_{modulation}} \int_0^{T_{modulation}} V_{ce}(t) * I_c(t) dt \quad (2)$$

$$P_{cond} = V_{ce_0} * I_{caverage} + R_{dson} * I_{crms}^2 \quad (3)$$

Avec $I_{caverage}$ et I_{crms} sont respectivement les valeurs moyenne et efficace du courant.

Pour calculer les pertes par commutation, on utilise les courbes des pertes d'énergie en fonction du courant pour une tension commutée, présentes dans les fiches techniques. Elles peuvent être approximées par une équation du second ordre avec trois paramètres Ax, Bx et Cx.

$$E_x = A_x + B_x * I + C_x * I^2 \quad (4)$$

$$P_{sw} = \frac{1}{T_{modulation}} \frac{1}{T_{sw}} \int_{t_1}^{t_2} \frac{V_{sw}}{V_{def}} E_{V_{def}}(I_{load}). dt \quad (5)$$

$$P_{sw} = f_{sw} * \frac{V_{sw}}{V_{def}} * (A \frac{\Delta_{sw}}{T_{modulation}} + B * I_{swaverage} + C * I_{swrms}^2) \quad (6)$$

Avec f_{sw} la fréquence de découpage, $T_{modulation}$ la période de modulation, $I_{swaverage}$ et I_{swrms} respectivement les courants moyen et efficaces découplés, V_{def} la tension d'utilisation du composant et $\Delta_{sw} = t_2 - t_1$ l'intervalle de commutation.

À partir des pertes dans la diode et l'IGBT, la température de jonction peut être définie. Dans notre architecture, un seul interrupteur de puissance contient un transistor avec une diode antiparallèle qui assure un chemin pour le courant inverse. Le modèle thermique comprendra donc deux résistances thermiques. Chaque résistance a un flux d'énergie thermique causé par les pertes de son composant respectif. Les températures des différents points de l'ensemble de commutation peuvent être déterminées à l'aide des équations suivantes :

$$T_{\text{Transistor}} = P_{\text{losses}_{\text{transistor}}} \cdot R_{\text{th}_{\text{jc}} T} + T_{\text{case}} \quad (7)$$

$$T_{\text{Diode}} = P_{\text{losses}_{\text{diode}}} \cdot R_{\text{th}_{\text{jc}} D} + T_{\text{case}} \quad (8)$$

$$T_{\text{case}} = (P_{\text{losses}_{\text{transistor}}} + P_{\text{losses}_{\text{diode}}}) \cdot (R_{\text{th}_{\text{ch}}} + R_{\text{th}_{\text{ha}}}) + T_{\text{ambient}} \quad (9)$$

3. Base de données des semi-conducteurs

L'outil de simulation utilise une base de données qui résume les paramètres des semi-conducteurs obtenus à partir des fiches techniques des fabricants. Les composants sont classés en familles selon leur fabricant. Dans ce cas, seuls les composants en silicium sont étudiés.

WP2 se concentre sur les convertisseurs statiques et la définition de la tension du bus DC. Pour faciliter le travail des autres groupes de travail du projet, une première étape consiste à déterminer une plage de tension optimale pour le bus DC. À l'aide de l'outil de simulation et de la base de données disponible, le rendement ainsi que les calibres de tension utilisés lors d'une étude paramétrique qui dépendent de la tension du bus DC sont indiqués sur la Figure 4. Les sauts de rendement constatés sont dus au changement des calibres de tension des composants utilisés.

Par conséquent, il est difficile de trouver la tension optimale du bus DC en raison de la discréétisation des tensions nominales disponibles. Pour surmonter ce problème, nous avons créé une base de données continue de composants qui s'adapte aux calibres souhaités en ajustant et en extrapolant les composants existants de la base de données. Bien sûr, ces composants peuvent ne jamais exister, mais cela permet de voir l'effet du choix de l'architecture de conversion statique sur le rendement sur la plage de tension considérée tout en éliminant l'effet dû à la discréétisation.

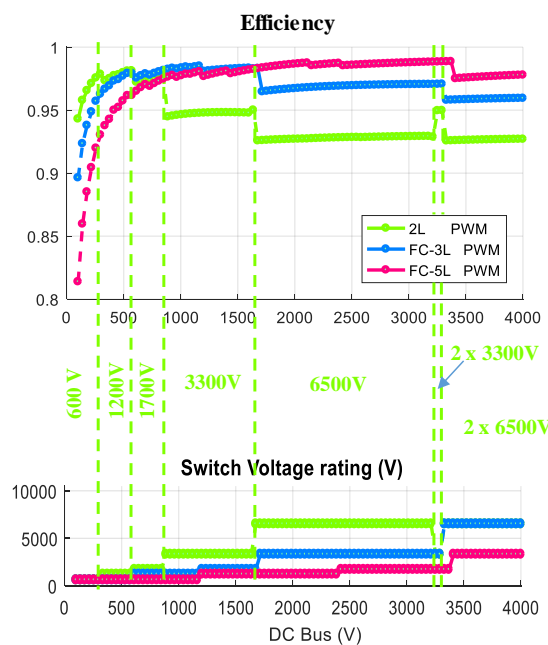


Figure 4. rendement de différentes topologies étudiées en utilisant les composants de la base de données

Pour créer un composant qui n'existe pas dans notre base de données, nous sélectionnons d'abord la famille ou le fabricant auquel le composant créé appartient. Pour cela, tous les paramètres des composants appartenant à cette famille sont extraits du fichier *Matlab*. Les composants de calibre en tension et en courant les plus proches sont sélectionnés pour être utilisés dans l'extrapolation. Une fois les composants sélectionnés, ils seront utilisés pour générer les paramètres du composant désiré. Les lois de variation de tous les paramètres sont ensuite identifiées en fonction du calibre de tension ou du produit calibres tension-courant comme indiqué dans le Tableau 3 et ensuite appliquées aux calibres souhaités.

Tableau 3. Paramètres générés

Paramètres générés	Dépendance	Fonction d'approximation
Pertes par commutation A_x , B_x and C_x	Calibre en tension	Polynôme du deuxième ordre $f(x) = ax^2 + bx + c$
Pertes par Conduction V_{ce0} R_{dson} , V_d , R_d .	Calibre en tension * Calibre en courant	Polynôme du premier ordre $f(x) = ax + b$
Résistances thermiques R_{th-jc_T} , R_{th-jc_D} and R_{th-ch}	Calibre en tension * Calibre en courant	Polynôme du deuxième ordre $f(x) = ax^b + c$
Surface	Calibre en tension * Calibre en courant	Polynôme du premier ordre $f(x) = ax + b$

4. Condensateurs

Les condensateurs sont des composants clés de l'électronique de puissance. Dans l'état de l'art des onduleurs, les condensateurs sont les plus grands composants et déterminent essentiellement le volume de l'onduleur. Par conséquent, une augmentation de la densité de stockage d'énergie des condensateurs aurait un impact énorme sur la taille et la densité de puissance de l'électronique de puissance.

Pour définir la valeur de la capacité, des informations sur les ondulations de courant, la fréquence et la tension sont nécessaires. Dans cette partie, le courant du condensateur est évalué pour deux types de condensateurs. Le premier est le condensateur de bus DC qui est nécessaire pour toutes les topologies et le second est le condensateur flottant qui est utilisé dans certaines topologies à 3 et 5 niveaux. Ces condensateurs sont sélectionnés à partir d'une base de données disponible selon un processus de sélection détaillé au chapitre II.

5. Nécessité des topologies multiniveaux

En utilisant les calibres en tension de composants disponibles, nous avons estimé les tensions de bus DC possibles pour utiliser pleinement le silicium disponible considéré ici comme 60% de leur calibre en tension. Cette valeur a été choisie de manière à permettre une utilisation optimale des composants 1200 V et 1700 V avec une surtension acceptable. Avec les topologies à 5 niveaux, on peut aller jusqu'à 7 kV mais avec les topologies à 2 niveaux, 2 kV est encore élevé pour les composants disponibles comme on peut le voir sur la Figure 5. Les points floutés ne sont pas réalisables en raison de la fréquence de découpage élevée qui implique une température de jonction élevée.

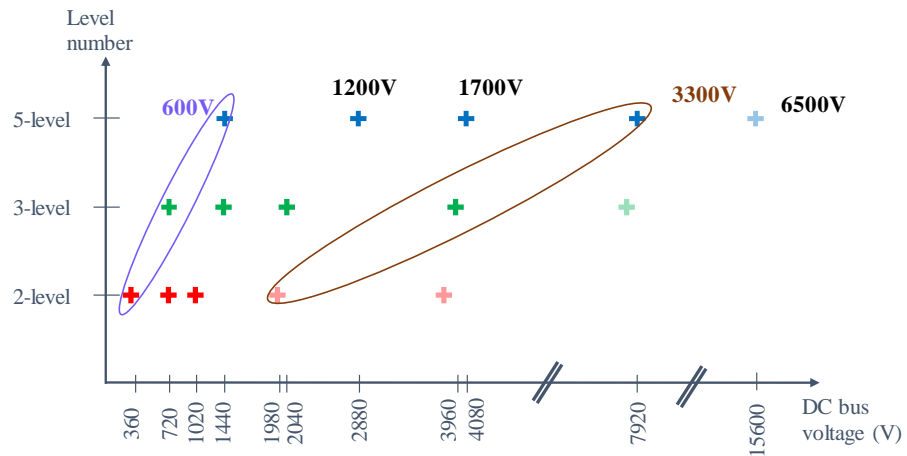


Figure 5. Tension optimale du bus DC en fonction du calibre en tension des composants et du nombre de niveaux de topologies

Les plages de tension des semi-conducteurs disponibles limitent la tension du bus continu qui pourrait être choisie si la topologie à deux niveaux devait être utilisée sans permettre une association directe en série. La fréquence de commutation élevée représente également une contrainte pour les composants de grand calibre de tension qui ne sont pas conçus pour fonctionner à ces niveaux de fréquence en raison des pertes par commutation élevées. Il serait donc plus intéressant d'utiliser des composants de calibre en tension plus petits mais avec une tension de bus DC élevée pour réduire le courant nominal nécessaire. Cela pourrait être fait en utilisant des topologies multi-niveaux. Les topologies sélectionnées seront présentées dans le chapitre III.

Chapitre III : Comparaison des solutions possibles dimensionnées pour le point de puissance maximal

Le principal facteur pour augmenter la densité de puissance identifié au chapitre I est la diminution de la masse du système de refroidissement en optimisant ses composants qui fait partie du travail du WP4 ou en réduisant les pertes. La réduction des pertes de l'onduleur peut être obtenue soit en utilisant de petits composants, soit en jouant sur des stratégies de modulation ou bien en utilisant des semi-conducteurs plus performants (Figure 6). La première option, qui consiste à utiliser de petits composants de tension nominale, pourrait être réalisée en utilisant des architectures multiniveaux pour éviter l'association série directe.

Dans ce chapitre, les topologies d'onduleurs et les stratégies de modulation étudiées sont présentées. Les performances sont ensuite comparées en utilisant plusieurs technologies de semi-conducteurs pour choisir la solution la plus performante en termes de rendement et de densité de puissance. Pour ce chapitre, le point de conception considéré est le point de puissance maximal qui correspond au décollage indiqué dans le profil de mission du chapitre I.

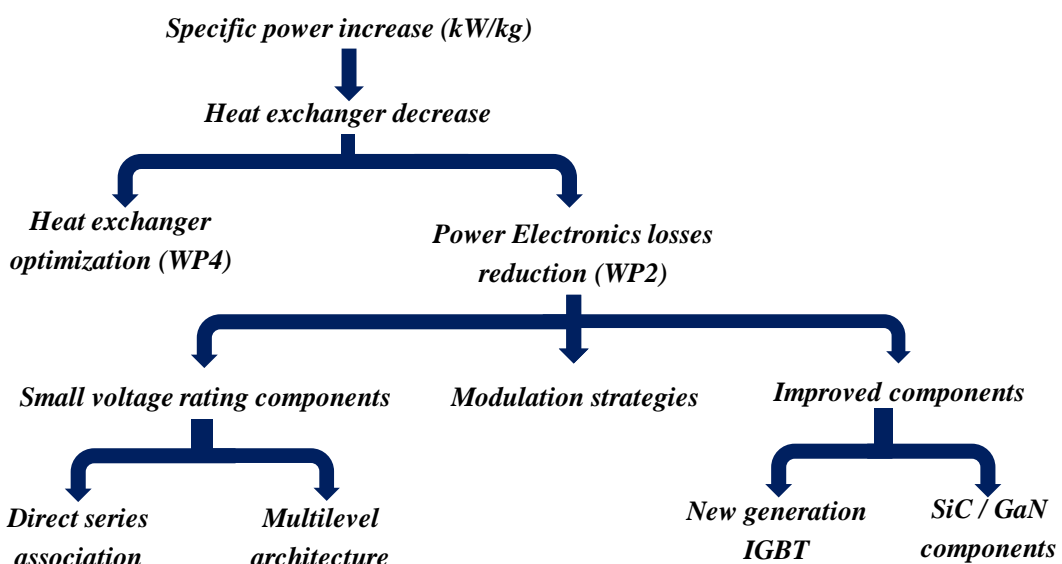


Figure 6. Ligne d'étude d'augmentation de densité de puissance

1. Comparaison des topologies multiniveaux

Dans cette thèse, les topologies de convertisseurs choisies sont des topologies multiniveaux de moyenne tension et de haute puissance. Les topologies étudiées sont le *Neutral Point Clamped* (NPC), le *Flying Capacitor* (FC), le *Stacked Multicellular Converter* (SMC) et l'*Active NPC topology* (ANPC).

Pour vérifier les conclusions antérieures concernant l'utilisation de composants de faible calibre en tension, trois types de topologies sont comparées. En utilisant le composant ABB disponibles dans notre base de données, les performances des topologies à 2, 3 et 5 niveaux ont été estimées

pour un balayage de bus DC de 700 V à 7 kV avec une fréquence de découpage apparente de 5.8 kHz et le point de puissance maximal avec une température de semelle fixée à 80 °C. Les composants générés sont utilisés à 50 % de leur tension nominale et à 100 % de leur courant nominal.

À l'issue de cette étude, les intervalles de tension du bus DC pour chaque topologie ont été définis. L'onduleur à 2 niveaux ne pourrait être utilisé qu'à faible puissance avec une tension de bus DC qui diminue avec la puissance utilisée pour la fréquence de découpage utilisée. Cet onduleur ne semble donc pas être la meilleure option pour notre application comme indiqué précédemment. Les onduleurs à 3 niveaux peuvent être utilisés jusqu'à 2 kV sur toute la gamme de puissance étudiée et ont un rendement optimal entre 1 kV et 2 kV. Cependant, pour les topologies à 5 niveaux, ils ont un rendement optimal entre 3 kV et 4 kV. On peut en conclure que pour ces topologies, à partir des graphiques de rendement, le rendement est optimal pour une tension de bus DC comprise entre 1 kV et 4 kV.

2. Comparaison des stratégies de modulation

Dans ce chapitre, quatre stratégies de modulation ont été étudiées. La modulation à largeur d'impulsion (PWM) sinusoïdale, la PWM avec injection de la troisième harmonique, la PWM MIN et MAX discontinu (DPWM) et la modulation pleine onde (FW) adaptée aux topologies d'onduleurs à 3 niveaux, ont été étudiées et comparées en termes de rendement.

Pour comparer les différentes stratégies de modulation, les résultats topologie pour la FC à 3 niveaux sont présentés ci-dessous. L'onduleur a été dimensionné pour un bus DC de 2 kV, ce qui donne un condensateur de bus DC de 2.5 mF selon la méthode de dimensionnement du chapitre II.

Comme l'indique le Tableau 4, les stratégies DPWM et la FW sont plus intéressantes. Cependant, pour la modulation pleine onde, le condensateur flottant est dimensionné pour la basse fréquence, ce qui donne un condensateur plus gros. Pour la THIPWM et la DPWM, la tension du bus DC a été dimensionnée en tenant compte de 15 % de tension de sortie supplémentaire par rapport au la PWM sinusoïdal et celle du FW a été dimensionnée en tenant compte de 30 % de tension de sortie supplémentaire pour le même point de puissance que la PWM.

Tableau 4. Performances d'un FC à 3 niveaux pour différentes stratégies de modulation

Topologie	Flying Capacitors 3 niveaux			
Stratégie de modulation	PWM	THIPWM1/4	DPWMMAX	FW 2
η (%)	96.54	97.80	97.85	98.09
Température (°C)	122	132	137	112
C_{FC} (mF)		1.35		5.7

3. Comparaison des 6^{ème} et 7^{ème} générations d'IGBT et les composants SiC

Le choix des composants a un impact important sur les performances de l'onduleur car les pertes dépendent des paramètres de conduction et de commutation du semi-conducteur. L'évolution du marché des composants en silicium semble avoir été saturée ces dernières années. Cependant, avec le nouveau module IGBT Mitsubishi de 7^{ème} génération, ce n'est plus le cas. Ces composants ont moins de pertes et ont un emballage compact et léger.

Pour comparer la 6^{ème} et la 7^{ème} génération aux modules SiC et choisir la technologie la plus appropriée, l'onduleur est conçu en utilisant des modules 1200 V / 600 A, avec un bus DC de 1.2 kV pour utiliser pleinement le module (50 % du calibre en tension comme indiqué dans la fiche technique). Les résultats sont comparés pour un NPC à 3 niveaux utilisant une stratégie de modulation PWM sinusoïdale et associant deux composantes en parallèle pour satisfaire le niveau de courant imposé. La puissance a été adaptée pour n'utiliser que deux composants en parallèle puisque la tension du bus DC a été réduite.

Tableau. IGBT 1200V/600A de 6^{ème} et 7^{ème} génération vs module SiC 1200V/600A

	6 ^{ème} génération IGBT	7 ^{ème} génération IGBT	SiC
$\eta(\%)$	98.53	98.84	98.51
Pertes par conduction (kW)	11.4	8.95	14.48
Pertes par commutation (kW)	3.52	2.81	0.679
Température jonction max (°C)	95.6	90.6	111.3

Pour notre spécification, le module 1200 V Full SiC n'est pas pertinent par rapport à notre solution. Même si les pertes par commutation sont faibles, les pertes par conduction restent supérieures aux pertes totales du module de 7^{ème} génération. La fréquence de découpage utilisée est faible car il n'est pas nécessaire d'avoir une fréquence élevée afin de garantir des courants sinusoïdaux dans la machine. Nous ne profitons donc pas pleinement des avantages de la technologie SiC. De plus, la résistance thermique du module SiC est plus élevée, augmentant la température de jonction. En plus, la technologie SiC n'en est qu'à ses débuts et est donc moins avancée que la technologie Silicium et pourrait être une option intéressante à l'avenir.

4. Modèle onduleur en 3D

En utilisant ces composants de 7^{ème} générations, la modulation DPWMMAX et un système de refroidissement optimisé avec une topologie NPC à 3 niveaux, l'objectif de densité de puissance de 15 kW/kg a été dépassé (23.29 kW/kg) mais on est encore loin de celui de 2035 qui est 25 kW/kg.

Pour réduire la masse du bus bar, la création d'un module intégré monophasé enlève le bus bar entre les modules de semi-conducteurs et tout ce qui reste est la connexion entre le module et les condensateurs du bus DC et entre le module et la phase du moteur. Un module de puissance a été conçu pour un NPC monophasé à 3 niveaux (Figure 7) en prenant en compte les contraintes schématiques, dimensionnelles et environnementales.

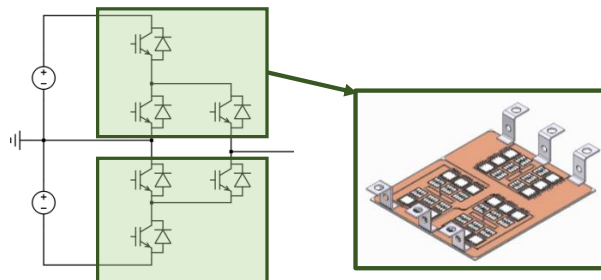


Figure 7. Conception d'un module de puissance pour un onduleur ANPC à 3 niveaux

Le convertisseur complet (3 phases) est représenté dans la Figure 8.

Cette solution a permis de réduire le bus bar utilisé et d'atteindre une densité de puissance de 57.59 kW/kg pour l'onduleur triphasé en ne prenant en compte que le bus bar, le condensateur du bus DC, les semi-conducteurs et son système de refroidissement dont le coefficient considéré est 4.5 kW/kg. Pour obtenir une estimation plus précise, il faut inclure des paramètres tels que les drivers et les éléments de fixation des composants.

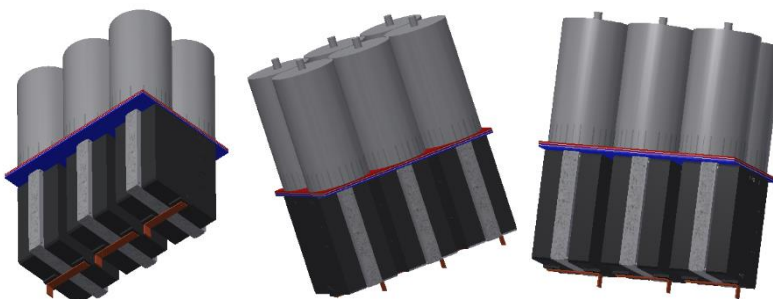


Figure 8. Onduleur NPC triphasé à 3 niveaux avec nouveaux modules de puissance

Chapitre IV : Performances des solutions choisies au cours du profil de mission

Le profil de mission de puissance considéré est illustré à la Figure 9. Trois options de dimensionnement peuvent être prises en compte. La première consiste à dimensionner l'onduleur pour le décollage qui correspond à la puissance maximale du profil. La seconde serait de le dimensionner pour la phase de croisière qui représente la phase la plus longue de la mission de vol. La troisième est de dimensionner pour un point milieu de la phase de montée. La puissance maximale est de l'ordre du MW et, pour des raisons de confidentialité, la valeur exacte ne peut être donnée : toutes les valeurs de puissance ont été normalisées par rapport à la puissance maximale.

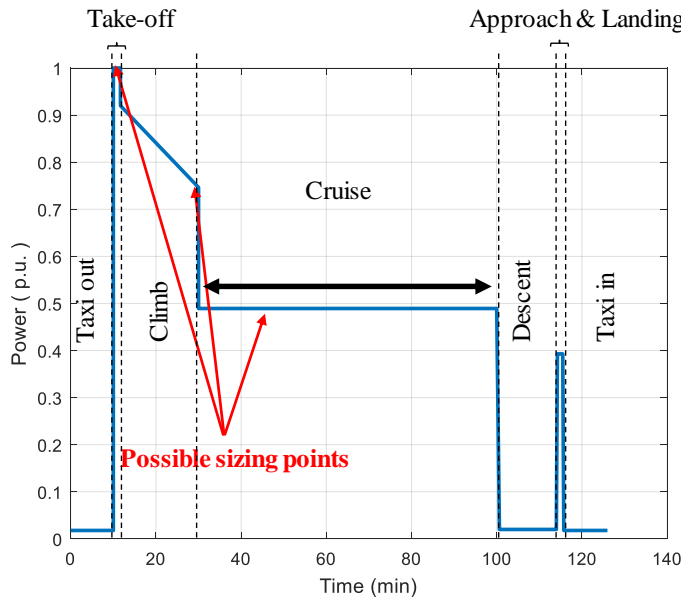


Figure 9. Profil de mission de puissance

Deux objectifs en termes de rendement pour l'électronique de puissance ont été fixés par le projet HASTECS. Pour l'objectif de 2025, le rendement devrait être supérieur à 98 % pour le point de croisière et supérieur à 96.5 % pour le point de puissance maximal. En revanche, pour l'objectif de 2035, le rendement devrait être supérieur à 99.5 % pour le point de croisière et supérieur à 99 % pour le point de puissance maximal.

L'objectif principal de ce chapitre est d'évaluer les topologies d'onduleurs choisies et les stratégies de modulation associées pour alimenter la machine électrique utilisée pour la propulsion de l'avion. Une étude comparative des stratégies de modulation est réalisée pour mettre en évidence la structure et la modulation présentant les meilleures performances afin de minimiser les pertes pour le point de dimensionnement choisi associé aux topologies FC et NPC à 3 niveaux.

Le rendement le plus élevé pour les scénarios étudiés correspond à la 2^{ème} configuration machine (3conducteurs par encoche) avec DPWMMAX+ FW hybride pour les topologies FC 3 niveaux et NPC. La stratégie FW est alors utilisée pour le décollage et la DPWMMAX pour le reste de la mission de vol. Le Tableau 5 résume les objectifs en terme de rendement pendant les phases de décollage et de croisière et ceux obtenus en utilisant la 5^{ème} stratégie qui est la DPWMMAX + FW qui a les meilleurs résultats pour la phase de croisière.

Tableau 5. Cibles et résultats atteints pour le rendement au décollage et en croisière

Phase de vol	Objectif 2025	Objectif 2035	DPWMMAX + FW (décollage)			
			FC 1 ^{er} e-moteur	NPC 1 ^{er} e-moteur	FC 2 ^{ème} e-moteur	NPC 2 ^{ème} e-moteur
Décollage	96.5%	99%	98.39%	98.39%	99.02%	99.02%

Croisière	98%	99.5%	98.84%	98.81%	99.09%	99.12%
Rendement global	-	-	97.86%	97.76%	97.84%	97.92%

Les objectifs de rendement pour 2025 ont été atteints en utilisant simplement la PWM sinusoïdal avec la première configuration de bobinage de la machine. Cependant, pour les objectifs de 2035, même avec la 2^{ème} configuration de bobinage de la machine et la DPWMMAX, le rendement reste inférieur à celui désiré pour la croisière tandis que pour le décollage, l'objectif a été atteint avec le FC 3 niveaux. Néanmoins, la densité de puissance de la topologie FC est nettement inférieure à celle du NPC en raison de la masse supplémentaire des condensateurs flottants.

Conclusion et perspectives

L'objectif principal de ce manuscrit était de dimensionner un onduleur de puissance hautement intégré pour alimenter un moteur électrique d'une densité de puissance de 15 kW/kg pour la cible 2025 et de 25 kW/kg pour la cible 2035, incluant son système de refroidissement. Il fait partie du WP2 du projet européen HASTECS Clean Sky 2 qui vise à étudier la possibilité d'hybridation de la propulsion d'un avion régional et qui a été présenté en détails au chapitre I.

Suite à un premier dimensionnement simple pour un onduleur à 2 niveaux, le facteur principal pour augmenter la densité de puissance a été identifié au chapitre I. Deux options étaient envisageables. La première était de diminuer la masse du système de refroidissement en optimisant ses composants, ce qui a été fait par le WP4. Le deuxième était la réduction des pertes, qui fait partie des tâches du WP2.

Pour dimensionner le convertisseur de puissance, un outil de préconception a été développé. Cet outil est développé à l'aide de la programmation orientée objet sous *Matlab* et est basé sur le calcul analytique des pertes de l'onduleur afin d'évaluer le rendement et les températures des composants. Le calcul des pertes et les modèles thermiques utilisés ont également été présentés dans le deuxième chapitre. Ces modèles ont besoin de plusieurs paramètres de composants semi-conducteurs qui sont issus de la base de données disponible ou générés à partir de celle-ci afin de satisfaire les exigences en courant et en tension. Ces composants générés ont été validés à l'aide de plusieurs scénarios de cas d'étude et ont aidé à définir la tension du bus DC qui est la première tâche de ce travail.

Les calibres en tension des semi-conducteurs disponibles limitent la tension du bus continu qui pourrait être choisie si la topologie 2 niveaux devait être utilisée sans autoriser l'association série directe. La fréquence de découpage élevée représente également une contrainte pour les composants de grand calibre en tension qui ne sont pas conçus pour fonctionner à ces niveaux de fréquence. Ceci dit, il serait plus intéressant d'utiliser des composants de faible calibre en tension mais avec une tension de bus DC élevée pour réduire le courant nécessaire pour le même niveau de puissance. Cela pourrait être fait en utilisant des topologies multiniveaux.

Dans le chapitre III, les topologies d'onduleur, les stratégies de modulation et les technologies des composants semi-conducteurs ont été présentées. Comme indiqué au chapitre II, la réduction des pertes de l'onduleur pourrait être obtenue en utilisant des composants de faible calibre en tension. Ceci a été fait en utilisant des architectures multi-niveaux pour éviter l'association série directe. Les topologies utilisées étaient des topologies à 2, 3 et 5 niveaux. Elles ont été comparées à l'aide de balayages de tension de bus DC pour trouver la plage de tension de bus DC optimale pour chaque groupe de topologies. Si la tension du bus DC est comprise entre 700 V et 1 kV, la topologie à deux niveaux peut être utilisée, mais dans ce cas, plusieurs composants doivent être associés en parallèle pour supporter le courant imposé mais cela augmente la masse et le volume de l'onduleur. Si la tension du bus DC est comprise entre 1 et 2.4 kV, les topologies à 3 niveaux ont les meilleurs rendements pour cette plage de tension.

Cependant, si la tension du bus DC est comprise entre 2.4 et 3.5 kV, les convertisseurs 5 niveaux sont recommandés. Cette plage de tension dépend également de la fréquence de découpage utilisée. Ce paramètre est très important surtout pour les composants de fort calibre en tension et a un grand impact sur les pertes et donc la température maximale de jonction des semi-conducteurs. Les topologies à 3 niveaux et l'ANPC à 5 niveaux semblent être les plus adaptées à notre cahier des charges. Cette étude a également montré que, pour utiliser certaines topologies telles que les topologies à 2 ou 3 niveaux, elles doivent être utilisées avec une faible fréquence de découpage afin d'avoir une température de jonction acceptable.

Cela nous amène au deuxième point abordé au chapitre III, à savoir les stratégies de modulation. Les techniques de modulation multiniveaux pourraient être classées en fonction de la fréquence de découpage. Les modulations à haute fréquence de découpage ont des pertes par commutation plus élevées mais moins d'impact sur le courant de la machine puisque le filtrage haute fréquence est meilleur que celui en basse fréquence. Par conséquent, avec les méthodes à basse fréquence, le rendement est plus élevé. Dans ce travail, quatre stratégies de modulation, qui sont la PWM sinusoïdale, la PWM à injection de troisième harmonique, la PWM MIN et MAX discontinu et la pleine onde (FW) adaptée aux topologies d'onduleurs à 3 niveaux, ont été étudiées et comparées en termes de rendement afin de trouver la plus performante. La PWM sinusoïdale a le rendement le plus faible mais toujours proche des performances des autres. Le DPWMMAX est la meilleure en termes de rendement pour les deux topologies 3 niveaux sélectionnées.

Le troisième point abordé au chapitre III concerne les technologies des semi-conducteurs. Le choix des composants a un impact important sur les performances de l'onduleur car les pertes dépendent des paramètres de conduction et de commutation du semi-conducteur. Les nouveaux modules IGBT Mitsubishi de 7^{ème} génération ont moins de pertes et ont un emballage compact et léger. Ces composants ont été comparés à la génération IGBT précédente ainsi qu'aux modules SiC avec les mêmes calibres de courant et de tension et semblent être la meilleure option pour notre cas.

En utilisant ces composants, la modulation DPWMMAX et un système de refroidissement optimisé avec une topologie NPC à 3 niveaux, l'objectif de densité de puissance de 15 kW/kg a été dépassé (23,29 kW/kg) mais le résultat est encore loin de la cible de 2035 qui est 25 kW/kg. Pour atteindre cette cible, un module de puissance a été conçu pour intégrer une demi phase de l'onduleur NPC 3 niveaux dans un seul boîtier. Cette solution a permis de réduire la masse du bus bar utilisée et d'atteindre une densité de puissance de 57.59 kW/kg pour l'onduleur triphasé en ne tenant pas compte que le bus bar, le condensateur du bus DC, les semi-conducteurs et le système de refroidissement. Pour obtenir une estimation plus précise, il faut inclure des paramètres tels que les drivers et les éléments de fixation des composants.

Dans le chapitre IV, plusieurs stratégies de modulation et points de dimensionnement ont été étudiés afin de trouver le meilleur scénario pour les stratégies de modulation des onduleurs à 3 niveaux FC et NPC en tenant compte de la mission de vol. Cette étude a été réalisée pour

deux configurations de bobinage du moteur électrique. La première stratégie étudiée était d'utiliser le THIPWM pendant le décollage et la montée afin d'utiliser pleinement le PWM sinusoïdal pendant la croisière. Cette stratégie améliore le rendement global de l'onduleur. La seconde compare la THIPWM et la DPWM MIN et MAX. La DPWMMAX se distingue de cette comparaison pour les deux topologies d'onduleurs et les deux configurations de la machine. La troisième utilise la FW sur tout le profil de mission. Dans ce cas, le rendement est amélioré, puisque la FW est une stratégie à faible fréquence de commutation, le THD est élevé pour les phases de faible puissance en raison de la présence des composantes harmoniques de basse fréquence. Pour éviter ce problème, les 4^{ème} et 5^{ème} stratégies ont été étudiées. Ces stratégies utilisent la FW en combinaison avec la PWM pour la 4^{ème} et DPWMMAX pour la 5^{ème} stratégie. Ceci améliore le rendement et le THD pendant les phases de faible puissance.

La stratégie la plus intéressante serait donc de dimensionner l'onduleur pour le décollage en utilisant la FW et d'utiliser la DPWMMAX pour les autres phases de la mission de vol. Cette stratégie permet d'atteindre les objectifs fixés par le projet HASTECS en termes de rendement pour la phase de décollage. Tandis que pour la croisière, le rendement obtenu est 99.12 % en utilisant un NPC 3 niveaux et la seconde machine alors que la cible de 2035 est 99.5 %. Pour toutes les stratégies de modulation, l'utilisation des paramètres de la seconde machine augmente le rendement de l'onduleur puisque pour la même puissance, la tension du bus DC utilisé est plus élevée et donc le courant plus faible, ce qui réduit les pertes dans les semi-conducteurs.

Pour améliorer le rendement de l'onduleur pendant la croisière, une autre solution peut être envisageable et qui est l'utilisation de deux convertisseurs ou plus. Dans le cas de deux convertisseurs, les deux peuvent être utilisés pendant le décollage. Ensuite, un seul est connecté au moteur pour le reste de la mission de vol. Cette solution pourrait être envisagée pour atteindre les objectifs de 2035. Cependant, la masse de l'onduleur pourrait être augmenté, ce qui réduirait la densité de puissance.

Il y a aussi la possibilité d'augmenter le nombre de bras d'onduleur en cas d'utilisation d'une machine multi moteur ou "multi stator" (double ou plus), en divisant le courant nécessaire pour alimenter le moteur par le nombre de phases. La deuxième option est d'entrelacer les bras du convertisseur par des inductances. Pour réduire la taille des inductances, des dispositifs de fixation peuvent être utilisés ou le stator lui-même peut être utilisé comme dispositif d'accouplement (multi phase ou multi stator). Dans chaque cas, les pertes du convertisseur changeront et, en raison de la modification des formes d'onde de sortie, les performances du moteur et l'effet des décharges partielles seront affectés.

References

- [1] R. Hotten, “Could aviation ever be less polluting?,” 10-May-2019.
- [2] D. Qualman, “Too much tourism: Global air travel and climate change,” *Darrin Qualman*, 07-Feb-2017. .
- [3] N. Didelot, “Hastecs : un projet pour développer la propulsion hybride des avions du futur.,” *AeroMorning.com*, 27-Dec-2016.
- [4] “Planetoscope - Statistiques : Vols d'avions dans le monde.” [Online]. Available: <https://www.planetoscope.com/Avion/109-vols-d-avions-dans-le-monde.html>. [Accessed: 16-May-2019].
- [5] “ICAO Environmental Report 2016.” [Online]. Available: <https://www.icao.int/environmental-protection/Documents/ICAO%20Environmental%20Report%202016.pdf>. [Accessed: 03-Sep-2019].
- [6] “Future of electric flight,” *Airbus*. [Online]. Available: <https://www.airbus.com/newsroom/news/en/2017/06/Future-of-electric-flight.html>.
- [7] “Powering the next generation of aircraft,” *Airbus*. [Online]. Available: <https://www.airbus.com/newsroom/news/en/2017/04/powering-the-next-generation-of-aircraft.html>.
- [8] “Project MAHEPA - D1.1: Concept of Modular Architecture for Hybrid Electric Propulsion of Aircraft.” Dec-2017.
- [9] “MAHEPA Newsletter 2018/1,” *Mahepa*, 05-Jul-2018. .
- [10] B. J. Brelje and J. R. R. A. Martins, “Electric, hybrid, and turboelectric fixed-wing aircraft: A review of concepts, models, and design approaches,” *Prog. Aerosp. Sci.*, vol. 104, pp. 1–19, Jan. 2019.
- [11] M. K. Bradley and C. K. Droney, “Subsonic ultra green aircraft research,” 2011.
- [12] M. K. Bradley and C. K. Droney, “Subsonic Ultra Green Aircraft Research: Phase 2. Volume 2; Hybrid Electric Design Exploration,” 2015.
- [13] “ENFICA-FC: Preliminary Survey & Design of 2-Seat Aircraft Powered by Fuel Cells Electric Propulsion | Aviation Technology, Integration, and Operations (ATIO) Conferences.” [Online]. Available: <https://arc.aiaa.org/doi/10.2514/6.2007-7754>. [Accessed: 21-May-2019].
- [14] “Diamond Aircraft proudly presents the world's first serial hybrid electric aircraft ‘DA36 E-Star,’” *Diamond Aircraft Industries*. [Online]. Available: <https://www.diamondaircraft.com/en/about-diamond/newsroom/news/article/diamond-aircraft-proudly-presents-the-worlds-first-serial-hybrid-electric-aircraft-da36-e-star/>.
- [15] “Hypstair home.” [Online]. Available: <http://www.hypstair.eu/>.

- [16] C. Friedrich and P. a. Robertson, "Hybrid-Electric Propulsion for Aircraft," *J. Aircr.*, vol. 52, no. 1, pp. 176–189, May 2014.
- [17] "Watts up - aeroplanes go hybrid-electric | University of Cambridge." [Online]. Available: <https://www.cam.ac.uk/research/news/watts-up-aeroplanes-go-hybrid-electric>. [Accessed: 21-May-2019].
- [18] L. A. Costello, "State of the Art of Piloted Electric Airplanes, NASA's Centennial Challenge Data and Fundamental Design Implications," 2011.
- [19] "ElectraFlyer.com - Home of the ElectraFlyer - Electric Aircraft Corporation." [Online]. Available: <http://www.electraflyer.com/>. [Accessed: 21-May-2019].
- [20] C. E. D. Riboldi and F. Gualdoni, "An integrated approach to the preliminary weight sizing of small electric aircraft," *Aerospace Sci. Technol.*, vol. 58, pp. 134–149, Nov. 2016.
- [21] J. W. Langelaan *et al.*, "Green Flight Challenge: Aircraft Design and Flight Planning for Extreme Fuel Efficiency," *J. Aircr.*, vol. 50, no. 3, pp. 832–846, 2013.
- [22] K. . Chau and Y. . Wong, "Overview of power management in hybrid electric vehicles," *Energy Convers. Manag.*, vol. 43, no. 15, pp. 1953–1968, Oct. 2002.
- [23] SIEMENS AG, "Aerobatic Airplane 'Extra 330LE,'" 2016. [Online]. Available: <https://www.siemens.com/press/pool/de/events/2016/corporate/2016-12-innovation/inno2016-aerobatic-airplane-e.pdf>. [Accessed: 21-May-2019].
- [24] "Airbus, Rolls-Royce and Siemens develops Hybrid-Electric demonstrator - Leeham News and Analysis." [Online]. Available: <https://leehamnews.com/2017/11/29/airbus-rolls-royce-siemens-develops-hybrid-electric-demonstrator/>. [Accessed: 21-May-2019].
- [25] "Airbus' Urban Air Mobility Roadmap leads to an electric future." [Online]. Available: <https://newatlas.com/airbus-urban-air-mobility-roadmap-electric-aircraft/50113/>.
- [26] F. Roy, "Optimisation énergétique de chaînes de traction électrifiées," PhD Thesis, Paris 6, 2015.
- [27] "Modeling the Capabilities of Hybrid-Electric Aviaton Propulsion Systems | Engineering360." [Online]. Available: <https://insights.globalspec.com/article/10609/modeling-the-capabilities-of-hybrid-electric-aviaton-propulsion-systems>. [Accessed: 20-May-2019].
- [28] M. Ibrahim, "High Power Conversion System for Aircraft Hybrid Propulsion: Multilevel Converters Design Conception, Analysis Study, and Optimization," Laboratoire Laplace, Toulouse, France, 2016.
- [29] Committee on Propulsion and Energy Systems to Reduce Commercial Aviation Carbon Emissions, Aeronautics and Space Engineering Board, Division on Engineering and Physical Sciences, and National Academies of Sciences, Engineering, and Medicine,

- Commercial Aircraft Propulsion and Energy Systems Research: Reducing Global Carbon Emissions.* Washington, D.C.: National Academies Press, 2016.
- [30] A.-M. Lienhardt, “Etude de la Commande et de l’Observation d’une Nouvelle Structure de Conversion d’Energie de type SMC (Convertisseur Multicellulaire Superposé),” Institut National Polytechnique de Toulouse, 2006.
- [31] V. Dargahi, A. K. Sadigh, and K. Corzine, “Analytical determination of conduction losses for modified flying capacitor multicell converters,” in *2016 IEEE Applied Power Electronics Conference and Exposition (APEC)*, 2016, pp. 2840–2846.
- [32] F. Accorinti, V. Ayel, and Y. Bertin, “Steady-state analysis of a Capillary Pumped Loop for Terrestrial Application with methanol and ethanol as working fluids,” *Int. J. Therm. Sci.*, vol. 137, pp. 571–583, Mar. 2019.
- [33] D. G. Holmes and T. A. Lipo, *Pulse width modulation for power converters: principles and practice*. Hoboken, NJ: John Wiley, 2003.
- [34] F. Renken, “Analytic Calculation of the DC-Link Capacitor Current for Pulsed Single-Phase H-Bridge Inverters,” *EPE J.*, vol. 13, Jan. 2004.
- [35] “PowerForge user documentation — PowerForge documentation.” [Online]. Available: <https://powerforge.powerdesign.tech/userguide/index.html#>. [Accessed: 29-Aug-2019].
- [36] “Technical publication - Feasibility of Electric Propulsion for Semi-submersible Heavy Lift Vessels.” [Online]. Available: <http://search.abb.com/library/Download.aspx?DocumentID=9AKK105713A2139&LanguageCode=en&DocumentPartId=&Action=Launch>.
- [37] “ACS1000 brochure.” [Online]. Available: <https://search-ext.abb.com/library/Download.aspx?DocumentID=3BHT490400R0001&LanguageCode=en&DocumentPartId=&Action=Launch>.
- [38] U. S. Ragupathy, R. Uthirasamy, and V. Kumar Chinnaian, “Structure of boost DC-link cascaded multilevel inverter for uninterrupted power supply applications,” *IET Power Electron.*, vol. 8, no. 11, pp. 2085–2096, Nov. 2015.
- [39] J. N. Chiasson, L. M. Tolbert, K. J. McKenzie, and Zhong Du, “Control of a multilevel converter using resultant theory,” *IEEE Trans. Control Syst. Technol.*, vol. 11, no. 3, pp. 345–354, May 2003.
- [40] A. Nabae, I. Takahashi, and H. Akagi, “A New Neutral-Point-Clamped PWM Inverter,” *IEEE Trans. Ind. Appl.*, vol. IA-17, no. 5, pp. 518–523, Sep. 1981.
- [41] S. Kouro *et al.*, “Recent Advances and Industrial Applications of Multilevel Converters,” *IEEE Trans. Ind. Electron.*, vol. 57, no. 8, pp. 2553–2580, Aug. 2010.
- [42] Y. Shakweh, “New breed of medium voltage converters,” *Power Eng. J.*, vol. 14, no. 1, pp. 12–20, Feb. 2000.

- [43] M. F. Escalante, J. C. Vannier, and A. Arzande, “Flying capacitor multilevel inverters and DTC motor drive applications,” *IEEE Trans. Ind. Electron.*, vol. 49, no. 4, pp. 809–815, Aug. 2002.
- [44] J. Shen and N. Butterworth, “Analysis and design of a three-level PWM converter system for railway-traction applications,” *IEE Proc. - Electr. Power Appl.*, vol. 144, no. 5, pp. 357–371, Sep. 1997.
- [45] Y.-H. Lee, B.-S. Suh, and D.-S. Hyun, “A novel PWM scheme for a three-level voltage source inverter with GTO thyristors,” *IEEE Trans. Ind. Appl.*, vol. 32, no. 2, pp. 260–268, Mar. 1996.
- [46] B. Wu and M. Narimani, *High-Power Converters and AC Drives*. John Wiley & Sons, 2016.
- [47] D. Floricau, C.-L. Popescu, M.-O. Popescu, E. Floricau, and L. Spataru, “A comparison of efficiency for three-level NPC and active NPC voltage source converters,” in *Compatibility and Power Electronics, 2009. CPE'09.*, 2009, pp. 331–336.
- [48] L. Parvulescu, D. Floricau, and M. Covrig, “A new control method for the three level active neutral point clamped converter for low speed applications,” *Przeglad Elektrotechniczny Electr. Rev. ISSN*, pp. 0033–2097, 2011.
- [49] F. Kieferndorf, M. Basler, L. A. Serpa, J. H. Fabian, A. Coccia, and G. A. Scheuer, “ANPC-5L technology applied to medium voltage variable speed drives applications,” in *SPEEDAM 2010*, 2010, pp. 1718–1725.
- [50] G. Gateau, T. A. Meynard, and H. Foch, “Stacked multicell converter (SMC): properties and design,” in *2001 IEEE 32nd Annual Power Electronics Specialists Conference (IEEE Cat. No.01CH37230)*, 2001, vol. 3, pp. 1583–1588 vol. 3.
- [51] N. Erroui, N. Roux, and G. Gateau, “Pré-dimensionnement de Convertisseur de Très Forte Puissance pour une Application à la Propulsion Aéronautique Hybride,” *JCGE*, May 2017.
- [52] L. Franquelo, J. Rodriguez, J. Leon, S. Kouro, R. Portillo, and M. Prats, “The age of multilevel converters arrives,” *IEEE Ind. Electron. Mag.*, vol. 2, no. 2, pp. 28–39, Jun. 2008.
- [53] J. Rodriguez, Jih-Sheng Lai, and Fang Zheng Peng, “Multilevel inverters: a survey of topologies, controls, and applications,” *IEEE Trans. Ind. Electron.*, vol. 49, no. 4, pp. 724–738, Aug. 2002.
- [54] Z. Zhang, O. C. Thomsen, and M. A. E. Andersen, “Discontinuous PWM Modulation Strategy With Circuit-Level Decoupling Concept of Three-Level Neutral-Point-Clamped (NPC) Inverter,” *IEEE Trans. Ind. Electron.*, vol. 60, no. 5, pp. 1897–1906, May 2013.

- [55] L. Asiminoaei, P. Rodriguez, F. Blaabjerg, and M. Malinowski, “Reduction of switching losses in active power filters with a new generalized discontinuous-PWM strategy,” *IEEE Trans. Ind. Electron.*, vol. 55, no. 1, pp. 467–471, 2008.
- [56] F. Accorinti *et al.*, “High-efficiency cooling system for highly integrated power electronics for hybrid propulsion aircraft,” in *2019 IEEE 28th International Symposium on Industrial Electronics (ISIE)*, 2019, pp. 870–877.
- [57] F. Accorinti, N. Blet, V. Ayel, S. Dutour, and Y. Bertin, “Experimental and Numerical Analysis of Start-up of a Capillary Pumped Loop for Terrestrial Applications,” 2018.
- [58] M. C. Caponet, F. Profumo, R. W. D. Doncker, and A. Tenconi, “Low stray inductance bus bar design and construction for good EMC performance in power electronic circuits,” *IEEE Trans. Power Electron.*, vol. 17, no. 2, pp. 225–231, Mar. 2002.

THESE

Pour l'obtention du Grade de

DOCTEUR DE L'ECOLE NATIONALE SUPERIEURE DE MECANIQUE ET D'AEROTECHNIQUE (Diplôme National – Arrêté du 25 mai 2016)

Ecole Doctorale :
Sciences et Ingénierie en Matériaux, Mécanique, Energétique

Secteur de Recherche : Energétique, Thermique et Combustion

Présentée par :

Amal ZEAITER

THERMAL MODELING AND COOLING OF ELECTRIC MOTORS. APPLICATION TO THE PROPULSION OF HYBRID AIRCRAFT

Directeurs de thèse :

**Matthieu FÉNOT
Etienne VIDECOQ**

Soutenue le 13 octobre 2020

devant la Commission d'Examen :

JURY

Présidente :

Eva DORIGNAC, Professeure des Universités, Université de Poitiers

Rapporteurs :

Julien PELLÉ, Professeur des Universités, ENSIAME, Valenciennes

Charbel HABCHI, Assistant Professor, Notre Dame University, Louaizé

Membres :

Xavier ROBOAM, Directeur de Recherche CNRS, ENSEEIHT, Toulouse

Matthieu FÉNOT, Maître de Conférences, ISAE-ENSMA de Poitiers

Etienne VIDECOQ, Maître de Conférences, ISAE-ENSMA de Poitiers

Time is way too long for us now... but it was too short with you.

You have given me the support, the encouragement, and everything I needed to begin the journey of my doctoral thesis, but you were not here when I've finished. Yet, your virtual presence is still inspiring me!

You deserve a lot more than the dedication of the present work to acknowledge your past existence in this life for all your sacrifices.

This one is for you...

I love you DAD <3

ACKNOWLEDGMENTS

En commençant la thèse, à part ce sentiment de fierté de pouvoir contribuer à l'avancement de la science ou du monde, on passe par une phase où l'on se projette dans le futur, au moment de la fin, mais on n'imagine pas le lot d'événements et de circonstances que l'on va traverser pendant ces quelques années. Je voudrais bien remercier de tout mon cœur toutes les personnes qui m'ont accompagnée, celles qui m'ont soutenue, et celles qui ont participé à la réalisation de la thèse jusqu'à la soutenance, voire au-delà.

Je tiens tout d'abord à présenter mes plus amples remerciements à **M. Matthieu FÉNOT**, qui a encadré ce travail de thèse, et à qui je suis profondément reconnaissante. Merci Matthieu pour tes conseils, ta confiance, tes recommandations judicieuses, mais surtout pour ta façon d'échanger sur les problématiques scientifiques. C'est avec beaucoup d'émotions que j'écris ces quelques lignes qui ne représentent que très peu de ce que j'ai à te dire pour te remercier encore, autant sur le niveau académique de la recherche que sur le niveau humain. J'ai eu la chance de te connaître et d'avoir effectué la thèse sous ta direction.

Je remercie profondément **M. Etienne VIDECOQ** tout d'abord pour son co-encadrement de thèse. Je suis consciente que tout le travail que nous avons effectué et les échanges scientifiques fructueux que nous avons eus m'ont permis d'avancer efficacement dans mon travail. Pourtant, si je tiens à te remercier, Etienne, c'est aussi pour avoir été présent durant la thèse surtout aux moments les plus délicats, pour avoir été patient mais toujours critique pour perfectionner le travail, et pour avoir donné les remarques pertinentes et suggestions scientifiques sincères et adaptées. Je te remercie également pour tout ce que j'ai appris de toi.

Merci Matthieu et Etienne d'être vous, parce que vous êtes des vrais encadrants, et je n'ai jamais arrêté d'apprendre de vous, de votre pédagogie, et surtout de l'intégrité scientifique et de l'esprit de progression pour le développement que vous portez en vous.

J'adresse mes remerciements aux rapporteurs de la thèse **M. Julien PELLÉ** et **M. Charbel HABCHI**. Je vous remercie d'avoir pris le temps d'évaluer le travail, de votre lecture très attentive du mémoire ainsi que de vos remarques précieuses. Je vous remercie également d'avoir participé au jury de soutenance. Grâce à cette participation, j'ai reçu des avis d'experts que j'apprécie infiniment et que je garderai dans mon esprit scientifique pour le futur.

Ce n'est pas toujours le cas dans un jury de soutenance d'avoir des chercheurs qui travaillent dans des domaines assez variés. Je remercie **Mme Eva DORIGNAC** et **M. Xavier ROBOAM** d'avoir participé à ce jury et d'être venus partager leurs avis, leurs connaissances et leurs

expertises sur différents points de vue : thermique, énergétique, électrotechnique et intégration de systèmes. Je remercie également **M. Yvan LEFEVRE** et **M. Jean-François ALLIAS** pour leur participation au jury en tant qu'invités.

Pour nos échanges collaboratifs, un grand merci à la famille du projet HASTECS, de l'institut Pprime, **M. Yves BERTIN**, **M. Vincent AYEL** et **M. Flavio ACCORINTI**, ainsi que du Laboratoire Laplace et d'Airbus. Particulièrement, à toi **Sarah**, je voudrais te dire plus qu'un merci... J'ai gagné une vraie amie et j'apprécie énormément cette amitié et tous les échanges que nous avons eus durant ces années de thèse.

Merci également à l'Union Européenne pour le financement de la thèse, à **l'ISAE-ENSMA** de m'avoir accueillie en tant que doctorante, ainsi que l'**Institut Pprime** et l'École Doctorale **SIMME**, membres, directions et personnel administratif. Merci aux membres de l'équipe de thermique de Pprime, ceux avec qui j'ai eu des discussions et j'ai partagé des moments conviviaux qui resteront gravés dans mon cœur.

Mes remerciements vont aux personnes charmantes que j'ai côtoyées et connues à Poitiers et qui m'ont accueillie à différents endroits dans cette ville assez originale et élégante : A l'ENSMA, **Mme Jocelyne BARDEAU**, cette dame attachante et aimable, et dans ma grande famille à l'ASPTT, **Mme Geneviève DELACHAUME** et **M. Gilles CATALOT**, ainsi que tous les membres et instructeurs de l'aéroclub. Merci à la Team Pilates pour votre accueil chaleureux et convivial, et pour les moments sportifs, spirituels et humains que nous avons partagés. Je remercie les amis que j'ai connus ici, pour tous les beaux souvenirs que nous avons créés. Merci surtout à celles et ceux qui réussissent toujours à avoir un esprit positif et à rehausser le moral, merci pour leur compréhension lorsque la situation était compliquée.

Un merci du fond du cœur va à ma petite famille, mes frères et ma sœur, et à mes amis, sans votre support je ne serais pas arrivée à tenir le coup, j'espère que vous êtes fiers aujourd'hui de cet aboutissement.

A ma maman que j'aime infiniment, je ne pourrai jamais te dire autant de 'merci' que tu le mérites. Merci pour m'avoir supportée et soutenue toujours dans les hauts et les bas, surtout ces deux dernières années.

Si je veux remercier la personne qui a eu le plus grand impact sur mon arrivée à ce stade de mon parcours académique, c'est sans doute toi papa. Ton absence me laisse sans mots, mais pour tous tes sacrifices et pour ton encouragement infini, je vais garder la force et la motivation que tu m'avais léguées pour avancer toujours.

CONTENTS

ACKNOWLEDGMENTS.....	iii
CONTENTS	v
NOMENCLATURE.....	ix
CHAPTER 1 ELECTRIC MOTORS FOR AIRCRAFT PROPULSION	1
1.1 Introduction	2
1.2 HASTECS: The Project under CleanSky II	2
1.3 Why Hybrid Aircraft?.....	5
1.3.1 Environmental Issues, Reality or Myth?	5
1.3.2 Towards Transportation Electrification and Hybridization	8
1.4 Electric Motors for Vehicle Propulsion.....	10
1.4.1 Overview of Electric Motors Types	12
1.4.2 From Ground to Air Vehicles Examples.....	19
1.4.3 Electric Motors, Suitable but?	24
1.5 Thermal Issues in Electric Motors.....	25
1.6 Purpose and Thesis Contents	25
CHAPTER 2 E-MOTOR THERMAL MANAGEMENT STATE OF THE ART	27
2.1 Introduction	28
2.2 Heat Transfer in Electric Machinery	28
2.2.1 Conduction Mode	29
2.2.2 Convection Mode	33
2.3 Electric Motor Cooling Methods	48
2.3.1 External Cooling Methods	49
2.3.2 Internal Cooling Methods.....	59
2.4 Conclusion	73

CHAPTER 3 LUMPED PARAMETER THERMAL MODELING	75
3.1 Introduction	76
3.2 LPTM Approach.....	76
3.3 Electric Motor System Definition.....	80
3.3.1 E-Motor Geometry and Materials Properties	81
3.3.2 Boundary conditions	82
3.3.3 Electric Motor Losses (Heat Sources).....	82
3.3.4 Initial Conditions.....	87
3.4 Modeling Assumptions.....	87
3.4.1 Geometry	87
3.4.2 Symmetry and Periodicity for Model Reduction	88
3.4.3 Temperature-Independent Media Physical Properties	89
3.5 LPTM Construction	89
3.5.1 Thermal Conductance Matrix G	89
3.5.2 Thermal Capacity Matrix C	91
3.5.3 Heat Sources and Heat Sinks Vector Ψ	91
3.5.4 Space Discretization and Nodal Network	91
3.6 Thermal Properties of Components	95
3.6.1 Equivalent Properties of Heterogeneous Components.....	96
3.6.2 Contact Thermal Resistance	101
3.7 Validation with Experimental Results	103
3.8 Conclusion	106
CHAPTER 4 THERMAL MANAGEMENT OF DESIGNED E-MOTORS	107
4.1 Introduction	108
4.2 Electric Motor Design for 2025 (EM2025)	108
4.2.1 Thermal Constraint Evaluation	109
4.2.2 Motor Design and Sizing.....	112

4.2.3	Thermal and Physical Properties	115
4.2.4	Dynamical Profile of Power	116
4.3	Cooling System.....	118
4.3.1	Thermal Resistance Analysis	119
4.3.2	Nodal Network	124
4.3.3	Cooling technology	126
4.3.4	Heat Exchanger of Cooling System	128
4.4	Thermal Behavior of the System	135
4.4.1	Thermohydraulic Parameters and Characteristics	136
4.4.2	Results and Analysis	138
4.4.3	Influence of Thermophysical Parameters Variation.....	147
4.4.4	Fluid Choice	150
4.4.5	Exchanger Surface and Coolant Flows	154
4.5	Case-studies	157
4.5.1	Influence of Flight Mission Scenarios	157
4.6	Electric Motor for 2035	158
4.6.1	Motor Cooling System Choice	159
4.6.2	First Motor Design and Results.....	161
4.6.3	Second Design for EM2035	165
4.7	Conclusion	171
CHAPTER 5	MODEL INVESTIGATION AND INVERSE METHOD	173
5.1	Introduction	174
5.2	Sensitivity of Motor Temperature to Losses	174
5.3	Losses Identification using an Inverse Method	178
5.3.1	Interest and Background.....	178
5.3.2	Heat Transfer Equation	179
5.3.3	State-Space Representation	179

5.3.4	Inverse Problem Solution	181
5.3.5	Results and Analysis	185
5.4	Conclusion	195
CHAPTER 6 CONCLUSIONS AND PERSPECTIVES		197
6.1	Conclusions	198
6.2	Perspectives	200
FUNDING ACKNOWLEDGMENT		203
CHAPTERS' SUMMARIES IN FRENCH		205
BIBLIOGRAPHY		213

NOMENCLATURE

Variables and Parameters

T	temperature	$^{\circ}C$
h	convection heat transfer coefficient	$W \cdot m^{-2} \cdot K^{-1}$
D	diameter	m or mm
c, c_p	specific heat	$J \cdot K^{-1} \cdot kg^{-1}$
g	gravitational acceleration	$m \cdot s^{-2}$
L or l	length	m
u	velocity	$m \cdot s^{-1}$
r	radius	m or mm
\dot{Q}_i	heat generation in motor system	W
V	volume	m^3
P	electric losses	W
H	hydraulic losses	m
S	surface	m^2
s	section	m^2
t	time	s
Δt	time step	s
q	flow rate	$m^3 \cdot s^{-1}$
\dot{m}	mass flow rate	$kg \cdot s^{-1}$
A	linear surface current density	$kA \cdot m^{-1}$
J	current density	$A \cdot mm^{-2}$
R	thermal resistance	$K^{-1} \cdot W$
\mathcal{R}	electrical resistance	Ω
N	number of nodes	
\mathcal{C}	moment coefficient (for friction)	
n_f	number of future times for specification function	
n_p	number of heat sources	
n_q	number of outputs	
n_t	number of time steps	

Greek symbols

φ	heat flux density	$W \cdot m^{-2}$
λ	thermal conductivity	$W \cdot m^{-1} \cdot K^{-1}$
ω	rotational velocity	RPM
Φ	heat flux	W
μ	dynamic viscosity	$kg \cdot m^{-1} \cdot s^{-1}$
ρ	density	$kg \cdot m^{-3}$
ϱ	electrical resistivity	$\Omega \cdot m$
ν	kinematic viscosity	$m^2 \cdot s^{-1}$
β	coefficient of thermal expansion	K^{-1}
Γ	system boundary	

σ_U	mean quadratic error for U	W
σ_Y	main quadratic error for Y ,	$^{\circ}C$
χ	characteristic space function	
Ω	system domain	

Matrices and vectors

G	conductance matrix	$W \cdot K^{-1}$
ψ	heat sink vector	W
C	thermal capacity matrix	$J \cdot K^{-1}$
Ψ	vector representing heat generation term in the matrix form	W
$A (N,N)$	state matrix	
$B_c (N)$	command vector relative to environment	
$B_p (N,n_p)$	command matrix relative to heat sources	
$C_o (n_q,N)$	output matrix	
I	identity matrix	
P	heat source vector	W
U	vector of unknown heat sources	W
K	vector of known heat sources	W
V	vector of known inputs	W
vol	volume	m^3
$Y (n_q)$	output vector	

Dimensionless numbers

Nu	Nusselt number
Pr	Prandtl number
Re	Reynolds number
Gr	Grashof number
Ra	Rayleigh number
Ta	Taylor number

Abbreviations

WP	Work-Package
EV	Electric Vehicle
HEV	Hybrid-Electric Vehicle
HASTECS	Hybrid Aircraft Academic reSearch on Thermal and Electrical Components Systems
MTOW	Maximum Take-Off Weight
MEW	Maximum Empty Weight
DC	Direct Current
AC	Alternating Current
PU	Per-Unit

NdFeB	Neodymium Iron Boron
Sm2Co17	Samarium Cobalt
LPTM	Lumped Parameter Thermal Model
PMSM	Permanent Magnet Synchronous Machine
SM	Surface Mounted
PCM	Phase Changing Material
EM2025	Electric Motor for year 2025
EM2035	Electric Motor for year 2035
FTS	Future Time Steps

Subscripts

<i>cv</i>	convective
<i>w</i>	wall
<i>ref</i>	reference
<i>h</i>	hydraulic
<i>p</i>	at constant pressure
<i>cr</i>	critical
<i>ext</i>	exterior
<i>k</i>	time index
<i>f</i>	for fluid at a surface
<i>rs</i>	rotor-stator
<i>r</i>	with respect to radius
<i>el</i>	for electrical
<i>ag</i> or <i>g</i>	for airgap
<i>ax</i>	for axial
<i>rad</i>	for radial direction
<i>ang</i>	for angular direction
<i>lam</i>	for laminations
<i>ins</i>	for insulation material
<i>cu</i>	for copper
<i>ch</i>	for channel

Superscripts

*	noisy temperature
[^]	estimated value
<i>T</i>	transposition sign
<i>-1</i>	inverse of a matrix
<i>cond</i>	for conduction
<i>conv</i>	for convection
<i>f</i>	for fluid
<i>radial</i>	for radial direction
<i>axial</i>	for axial direction
<i>eq</i>	for equivalent properties

CHAPTER 1 ELECTRIC MOTORS FOR AIRCRAFT PROPULSION

Synopsis:

A presentation of the subject area of the thesis and its problematics is developed in this chapter. Moreover, electric motors main characteristics and issues are summarized to focus on the topic of electric propulsion of aircrafts.

1.1 Introduction

Electric propulsion of vehicles is being increasingly investigated recently for a possible reduction in gas emissions and particulates. Besides the challenge of switching to a new architecture that goes with this goal, constraints relative to electric motors are defying the design of electric propulsion systems. Indeed, due to limited space and weight in vehicles, high-performance compact motors are strongly required. Fortunately, the technological advancements in materials and technologies have enabled the development of a new generation of high specific power motors (up to a few kW/kg). Generally in the transportation sector (ground, marine, and aeronautical applications) and specifically for cars, a turning point in the electric machinery domain has been registered during the last decade, highlighted by the rising interest in developing Electric Vehicles (EV) and Hybrid-Electric Vehicles (HEV). While propulsion electrification and hybridization are considered a promising solution for environmental pollution, electric motors in the aeronautical domain are constrained by several issues such as performance, weight, altitude, external conditions, safety, etc.

The objective of this chapter is to approach the thesis topic, by defining some important concepts and clarifying the basics in this subject area.

1.2 HASTECS: The Project under CleanSky II

This work is carried out within the framework of a project called **HASTECS** (*Figure 1.1*), standing for **H**ybrid **A**ircraft **a**cademic reSearch on **T**hermal & **E**lectrical **C**omponents and **S**ystems). This project kick-started in September 2016 and is currently running until 2021.



Figure 1.1 : HASTECS Project logo.

The hybrid-electric propulsion model consists of several inputs for electrical and thermal engines' systems (i.e. Mach number and altitude as a function of time) that contribute to determining the Maximum Take-Off Weight (MTOW) of the plane at each iteration in a global optimization process as depicted in *Figure 1.2*. The Maximum Empty Weight (MEW) is given by Airbus, and the loopback on this weight is performed using a simplified function, subject to specific constraints (for instance, the drag effect not taken into account). HASTECS project is located at the electric propulsion units' design and studies, aiming to reach the propulsion target in terms of weight.

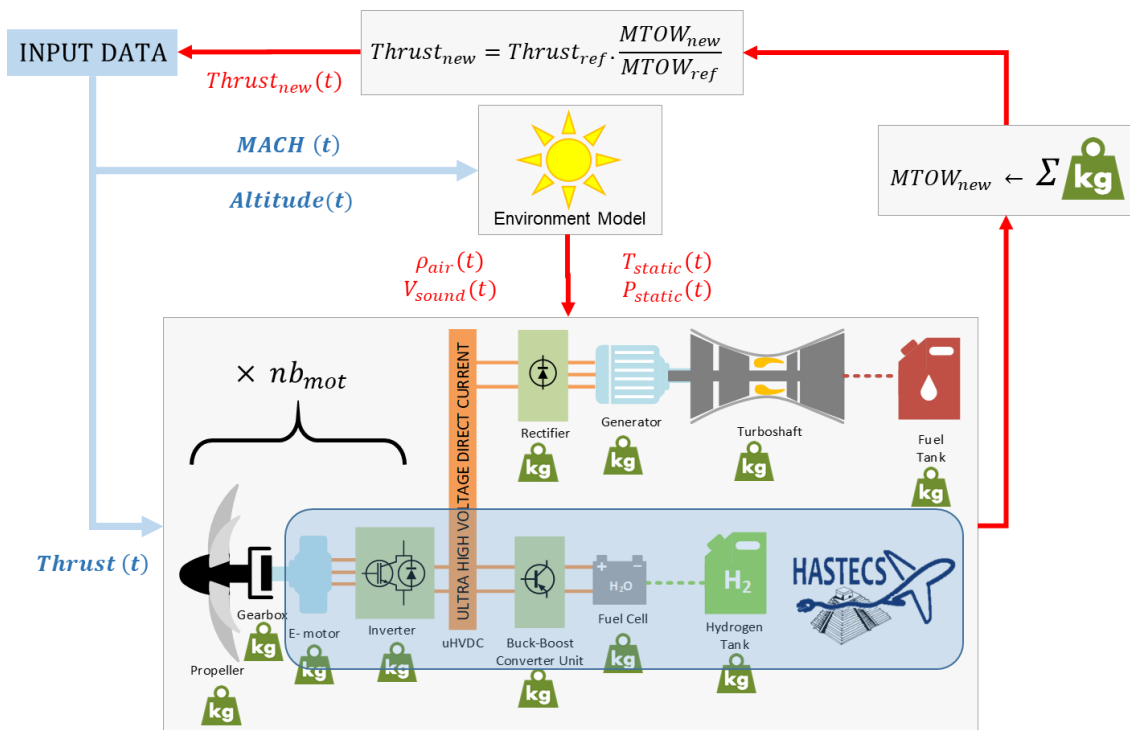


Figure 1.2 : Hybrid Aircraft power chain with HASTECS project-area [HASTECS Workshop October 2018].

The general objective of HASTECS project, indicated in the project proposal, is to support Hybrid Electric Aircraft propulsion demonstration by developing electro-thermal models and tools to assess the main benefits of different hybrid propulsion architectures and power management for short/medium-range aircraft.

These means will help to design propulsive electrical architectures for radical aircraft, by setting specific objectives for different Work-Packages (WPs). System-level integration of the assessments is the task assigned to the Work-Package 6 of the project (WP6) from main components design and analysis of the hybrid power chain (see *Figure 1.3*). This chain consists

of electric machine designs (WP1), associated cooling systems (WP3), power electronics and cables (WP2, 5), and associated thermal management (WP4). It considers the main environmental constraints, especially the partial discharges (WP5) due to high-power-ultra-high voltage new standards.

The project is funded by the CleanSky2 Joint Undertaking under the European Union's Horizon 2020 research and innovation program. For short and long-term targets, objectives have been fixed in terms of specific powers considering reasonable possible development in materials choices, and technologies. The specific power of electric machines is doubled from 5 kW/kg for 2025 to 10 kW/kg for 2035, while specific powers of converters must be increased from 15 kW/kg for 2025 to 25 kW/kg for 2035. For instance in electric machinery, the properties of new insulators, impregnation materials, and magnets, are currently being investigated in industries and research institutes to be applied in the long-term future, while it is confirmed for other promising materials that they will be available to use in electric machinery in the short-term future.

The current thesis is registered to work on WP3. The electric machines specialists of WP1 provide multiple designs of motors to match the short-term and long-term targets (2025 e-motor and 2035 e-motor). A strong interaction between our Work-Package (WP3) and WP1 has been developed during the project running time. Both workgroups have been collaborating to harmonize tools and models to meet the specific power density targets considering the electrical and thermal constraints and motor efficiencies.

To exceed the existing limits of motor specific power density, HASTECS electric machine and heat transfer specialists mutualized their electromagnetic and thermal investigations to find genuine technological solutions. From a thermal point of view, the interaction requires first a definition of some basic points: electric motor types, the specificity of electric motor for propulsion, the limiting constraints in terms of temperature and weight, origins of thermal problems in these motors, and possible configurations that could be suitable in this groundbreaking application.

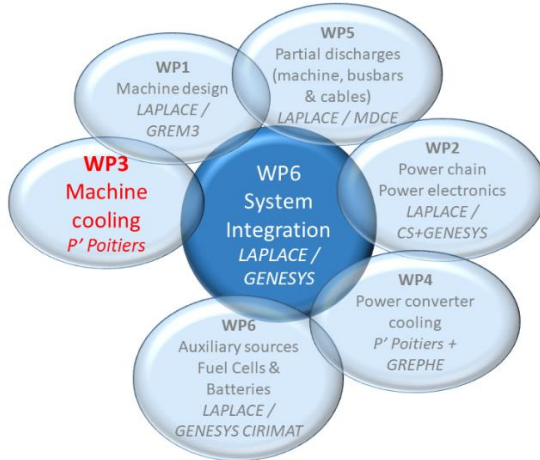


Figure 1.3 : HASTECS Project Work-Packages scheme for interactions.

In this framework, the objective of this thesis, concisely termed ‘Electric Motor Cooling’ or WP3, is to elaborate thermal models for super-high specific power electric motors, conceived in the project, and to configure suitable cooling systems. It aims to design and assess adequate techniques for the thermal management of such motors. With the existing technologies, the electric motors compactness and power are toughly limited by thermal constraints that should be respected. Also, with the high targets of global performance and specific power, motors for aeronautical propulsion should be investigated acutely from electro-technical as well as thermal points of view.

These points are the topic lead-ins of our study and will be developed successively in the thesis.

1.3 Why Hybrid Aircraft?

1.3.1 Environmental Issues, Reality or Myth?

The increased carbon footprint is challenging scientists, researchers, and environment specialists to raise interest and investigate other sustainable energy supply sources. The resulting anomaly is alarming with an increasing average land-sea temperature. This will change the global vital conditions on earth, together with higher frequency and intensity of heatwaves, hazardous fire weather, and drought conditions in multiple zones of the earth [1].

Many are the indicators of climate change and global warming, could it be the air temperature, ocean warming and sea-level rise, extreme weather events, or the changing rainfall patterns resulting from the changing global water cycle and intensifying with a warming climate. NASA [2] provided data on global temperature variations, as depicted in *Figure 1.4*. The rising temperature curves in the past decades prove that the warming effect on earth is rapidly growing. The climate models are developed, according to intermittent factors, to simulate and predict the responses of environment temperatures to all influencing factors [3]. Ignoring the alerting signs indicates that global surface warming will follow the trend line indicated in red in *Figure 1.5*.

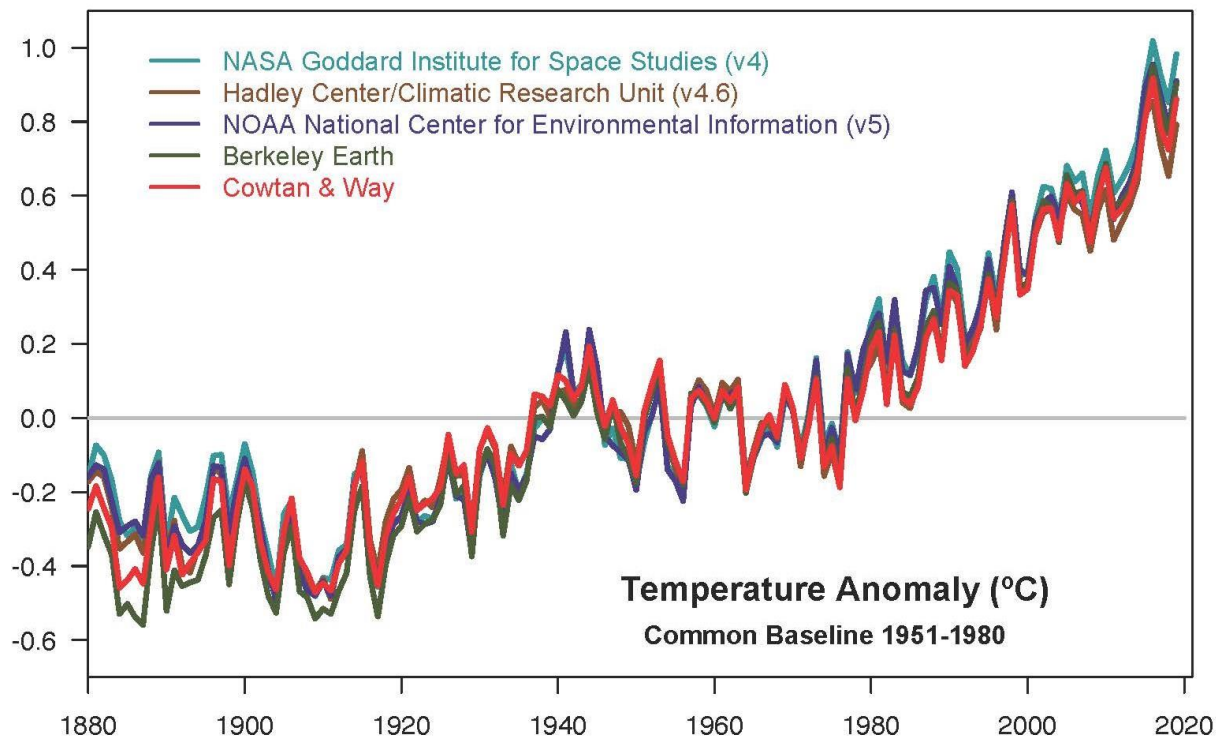


Figure 1.4 : Yearly temperature anomalies from 1880 to 2019 [2].

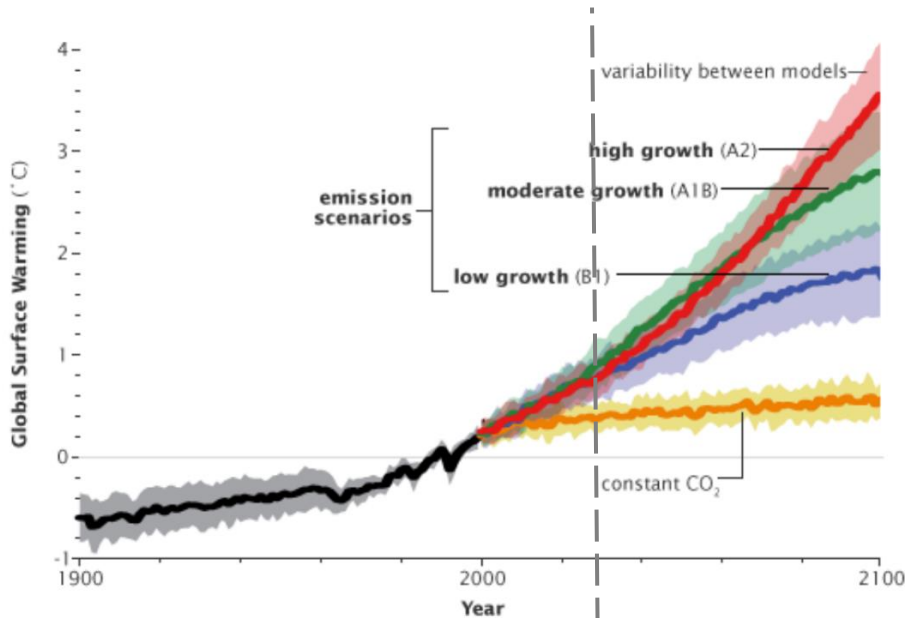


Figure 1.5 : Global surface warming evolution in time with future projection scenarios [3].

It is thought that if no concrete actions are adopted to reduce greenhouse gas emissions considering plausible emission scenarios, by the end of the current century, the average temperature could increase between 2 °C and 6 °C.

The European Union is committed to meet technical environmental goals set in the European Commission's Flighthpath 2050 Vision for Aviation, which is to reduce by 75% CO₂ and by 90% NOx emissions, and by 65% the noise. Data and statistics of the International Energy Agency 'IEA' [4] show that actually 'transport' sector accounts for around a quarter of global CO₂ emissions in the world, as seen in the diagram of *Figure 1.6*.

With that being said, the transportation sector, implying broad private companies and industries, is now seeking sustainability for propulsion power systems mainly, and for other deployments as well. One can cite, for instance, the CO₂ roadmap at Airbus. They, among other companies in this sector, are willing to achieve sustainable air travel soon, through greater decarbonization (a reduction of 50% of the net aviation carbon emissions by 2050 compared to what they were in 2005), by improving environmental performance and adopting sustainable supply chain, etc [5].

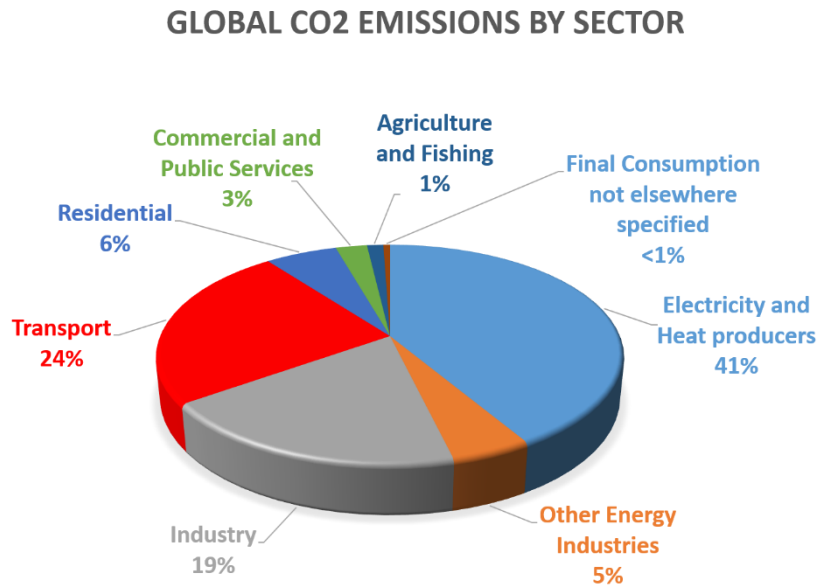


Figure 1.6 : Global CO₂ emissions by sector in 2017 [4].

A key objective is to conceive and produce transportation means that consume less fuel or other « new » and cleaner energy sources and therefore reduce toxicity emission levels.

1.3.2 Towards Transportation Electrification and Hybridization

Vehicles have been powered, for a long time, predominantly by fuel of fossil - or biomass - origins that ignite in their heat engines emitting pollutant substances and gases. As for cars and ground vehicles, propulsion hybridization is thought to be an ecological solution for planes as well.

Aircraft hybridization (with solar power such as Sunseeker II [6] or electric power such as the Pipistrel Taurus Electro G2.5 [7]), and aircraft electrification (Siemens' electric aircraft designs [8] as an example) was recently investigated as a solution to enable achieving the aforementioned environmental goals. To accelerate electrification, Rolls Royce Company - in partnership with YASA electric motor and controller manufacturer and Electroflight aviation start-up - has started an initiative called ACCEL[9], within which an all-electric powered aircraft with zero-emissions was unveiled in late December 2019 in an Iron Bird test airframe as shown in *Figure 1.7*. This plane, characterized by its high speed (over 480 km/h), is scheduled to take off in 2020. On the other hand, the first flight of the largest commercial all-electric aircraft (flying testbed) took place on May 28, 2020, with a Cessna 208B Grand

Caravan from AeroTEC company [10]. With a propelling electric motor from MagniX of 560 kW power, the zero-emissions flight lasted 30 minutes at a maximum of 2500 ft .



Figure 1.7 : ACCEL Iron Bird test airframe [9].

These light aircraft units and prototypes showed the extent and the limits of using less-pollutant energy types for propulsion. However, the tough environmental objectives suggest taking firmer actions and pushing the boundaries as far as enabling hybridization of regional aircraft in the same standard. The aerospace companies and industries are investigating the use of electric power for hybrid-electric propulsion of commercial aircraft. Electricity is retained as a potential candidate for hybridization in the aeronautical transportation sector, with the lack of other powerful energy sources.

Receiving funds from the Boeing Company and the state of Washington, Zunum Aero [11] is working on the development of a hybrid electric private jet. NASA STARC-ABL [12] is the established concept of Single-Aisle Turboelectric Aircraft with an Aft-Boundary-Layer propulsor, to be more fuel-efficient than existing aircraft designs. With a large turbofan engine on the rear of the aircraft and generators added to wing-mounted turbofans supplying the back engine with generated electricity, this plane is designed to use 10% less fuel, promoting longer ranges of aircrafts for a long-term goal of two decades. NASA researchers are still carrying out tests on future turboelectric (and besides hybrid-electric) concepts of electrical components and systems (PEGASUS [13]). Airbus, Rolls Royce, and Siemens engaged to switch to hybrid electric propulsion of commercial air vehicles. Airbus company is thought to be a major player and enabler to reduce considerably the emissions of CO₂, NO_x, and particulate [14]. Their

E-Fan project aims to develop an e-system architecture and other related electrical propulsion technologies. Spotted with the launching of the E-Fan X hybrid-electric aircraft demonstrator [15] (see design in *Figure 1.8*), the year 2019 has also witnessed many transportation electrification events sponsored by the primary actors in the aircraft design industry (chiefly, but not limited to, Airbus and Boeing companies). Recently, the E-Fan X project was canceled during the COVID-19 pandemic.



Figure 1.8 : E-Fan X demonstrator design [15].

Those major advancements in electrification and hybridization of commercial aviation are being led towards a less polluted environment and more sustainable actions in the air transportation sector.

Before getting through more details, let us comprehend the possibility of switching to electrical propulsion and its limitations, by getting through some general definitions and conventions.

1.4 Electric Motors for Vehicle Propulsion

In addition to their environmental benefits, electric motors have a proven advantage over gasoline engines, which is their higher specific torque. The curves from [16] in *Figure 1.9a* show the performance characteristics, in terms of torque and power, of two Internal Combustion Engine (ICE) that propel Renault Fluence 1.6 16V 110 and Renault Fluence dCi 105. The electric motor propelling the same vehicle model: Renault Fluence Z. E. battery electric vehicle,

is compared. Torque and power diagrams as function of speed are simultaneously depicted in *Figure 1.9b*. At certain conditions of grades, the performance of the EV is higher. Furthermore, *Figure 1.9a* and *Figure 1.9b* prove that at low speed the electric motor supplies a satisfactory torque for starting, which is not the case for thermal engines.

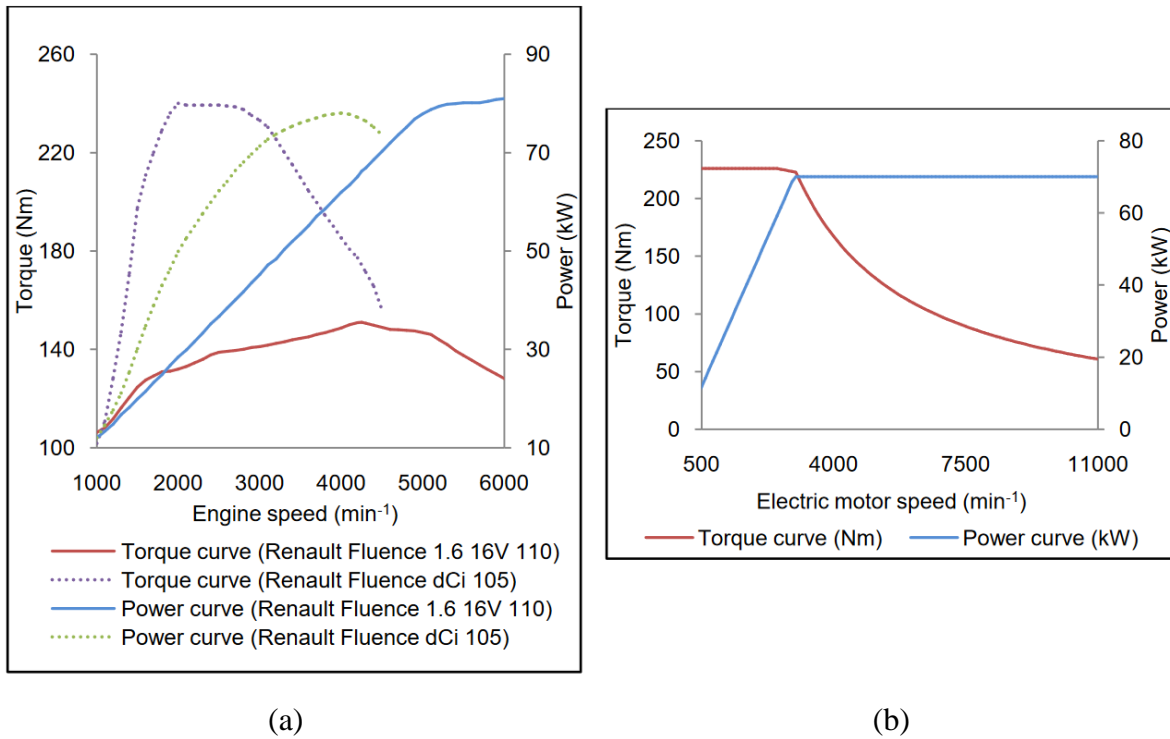


Figure 1.9 : Comparison between performance characteristics of (a) petrol ICE, diesel ICE, and (b) electric motor. Motors are used to propel the variants of the same vehicle model: Renault Fluence 1.6 16V 110, Renault Fluence dCi 105, and Renault fluence Z. E. respectively.

With the arising tendency to switch to electrified propulsion, the electric drive systems are one of the major components in the chain, provided that the electricity powering these drives is safely and continuously supplied. The development of these drives and motors belongs to the electric machinery and power systems industry. As the thesis concerns only the electric motor area, it is important to understand the topology of these machines. Herein, the first subsection overviews the main electric motor types, and the second subsection focuses on propulsion application types. Since technical information has not been published for air vehicles application, only electric motors developed for ground vehicles are presented. Besides, information is given on how these motor types can be derived for aircraft propulsion application.

1.4.1 Overview of Electric Motors Types

Back to the basics, electric motors are by definition devices that convert electrical energy into mechanical energy. This conversion is based on an electromagnetic process similar to a rectangular loop conductor placed in a magnetic field and through which a current passes. It will rotate due to the generated force applied to it, whose direction is determined based on Fleming's left-hand rule. Electric motors are classified as rotary electrical machines that require to be fed with electricity as input energy, and their application relies mainly on the resultant rotating motion as kinetic energy output. In their topology, a rotor and a stator are the main two parts of electric motors. Classically, the rotor is mounted on bearings so that the rotational motion is applied to a mechanical system (or load). The electrical energy supplying these motors can derive from Direct Current (DC) sources or Alternating Current (AC) sources.

From these statements, one can figure out that there are as many types of electric motors as there are operation principles and types of electrical energy sources. Two important categories depending on the electrical current type are presented hereafter which are the DC motors and AC motors. Other motor types are grouped in other electric motors' category, which are motors with special characteristics that cannot be included in any of the former two categories. Motors types are presented briefly and characterized accordingly. The differences between the presented motor types are clarified. Besides, some examples of applications are given.

1.4.1.1 *Direct Current Motors*

DC motors are electric motors that are supplied with direct current electrical energy. The working mechanism is based on Faraday's law of energy conservation from electrical to mechanical form. It is the first motor form working on the principle that when a voltage is applied to a conductor coil in a magnetic field, an electromagnetic force (Lorentz force) will be applied to the conductor driving it to rotate and producing a torque. There are different DC motors types: Shunt, separately excited, series, Permanent-Magnet DC, and compound.

The topology of these motors consists of the following parts: rotor, stator, airgap, winding, and brushed commutator. The airgap is the space that separates the rotor from the stator in which the magnetic field circulates. Winding is the coil made of wound conductors through which the current passes. The commutator in DC motors is the device that keeps switching the current direction in the rotor coil to ensure that the rotor will keep turning indefinitely in the static field,

i.e. the resulting force applied to the coil should change its direction every half rotation to lead to a rotating motion. Commutators consist of metallic segments and brushes mounted in a cylinder. Segments are connected by direct contact to rotor windings applying to them the electric current. Brushes are mounted on the commutator cylinder and are used to reverse the current direction.

The DC motors types are presented below:

❖ Shunt Motor

A shunt motor has its rotor and stator windings, respectively named armature and field windings, electrically connected in parallel. A DC shunt motor is characterized by maintaining a constant speed regardless of the applied load.

❖ Separately Excited Motor

The electrical energy supply is given from separate sources to field and armature windings. The DC voltage applied to the armature coil has a different source than the voltage source in the field winding. Coils are isolated from each other.

As for shunt motors, the electric current passing through the field coil in separately excited motors is constant and the field flux is also considered constant. However, with this latter type, it is possible to control the motor, compared to shunt motors where it is not possible.

Separately excited motors are used in industrial applications such as actuators.

❖ Series Motor

In series wound DC motor, armature, and field windings are connected in series and the current flowing through both windings is the same. The main difference between these motors and shunt motors is that for series motors the speed varies with load. The torque is proportional to the squared current value. Thus, they are characterized by the highest obtained torque among all other motor types for the same current ratio. Series motors can be applied as starter motors in the automotive sector and as elevators' motors.

❖ Permanent-Magnet DC Motor

Permanent-Magnet DC motors (PMDC) have winding in the rotor (armature winding) but have magnetized permanent magnets mounted on the inner side of the stator to produce the field flux instead of windings (no field windings). The required flux density provided by magnets will be therefore constant, and permanent magnets are chosen in the construction phase accordingly. Their advantage is mainly their smaller size compared to other types of DC motors; their disadvantage is their low applied torque.

❖ Compound Motor

In a compound wound DC motor, the connection between stator and rotor is a combination of connections of shunt and series excited DC motor windings. The field winding is connected both in parallel and in series to the armature winding. Two field coils are used for a compound working mechanism. These motors combine the efficient speed regulation property of shunt-wound motors and the high starting torque of series motors.

1.4.1.2 Alternating Current Motors

Alternating Current (AC) motors are electric motors supplied with AC voltage. There are two main types of AC motors: Induction (or asynchronous) motors and synchronous motors.

❖ Induction Motors (IM)

Induction motors or asynchronous motors are AC electric motors operating based on the principle that an induced current is created in a conductor (of the rotor) when placed in a rotating magnetic flux from the stator. The rotor induced current and stator current interact to produce a torque on the rotor.

Rotor part: The conductor is part of the rotor structure that is typically in the form of a squirrel cage with multiple conductor bars of aluminum or copper, connected cylindrically at both ends by rings (see *Figure 1.10a*). The bars are short-circuited by the rings, which allows the creation of the induced current. Inside the cage, steel laminations are stacked around the shaft. The rotating magnetic field from the stator and the induced current in the rotor drives this latter into rotation due to the generated force.



Figure 1.10 : Squirrel cage rotor (a) and stator (b) of an Induction Motor

Stator part: The construction of the induction motor stator, as depicted in *Figure 1.10b* verifies the role of this part in inducing the magnetic field that penetrates the rotor. Its main part is made up of a laminated core (stack of laminations sheets) and one or more windings depending on the number of phases. Windings are encapsulated in slots and they carry supply current.

When starting the motor, the rotor begins to rotate in the same direction and at the speed of the rotating magnetic field of the stator. To keep up its rotation, electrically wise, it is crucial to vary either the induced current in conductors or the magnetic flux. In AC induction motors, the latter one is changed. Since the rotation at synchronism speed will not produce torque at the rotor mechanical connection, there should be a ‘slip’ between rotor speed and synchronous speed i.e. the rotor operates at a slightly lower speed. When a load is applied, the motor will adapt its speed to the load torque. As a resulting drawback, slip losses are generated in the rotor and these losses reduce the efficiency and lifespan of motors [17].

This motor type is generally known to require low-maintenance, to be easily constructed, and to be robust. It can be coupled to variable frequency drive-in applications that require controlling a load velocity and displacement. The induction machine can be applied as both generator and motor.

❖ Synchronous Motors

In synchronous motors (SM), the rotor speed is equal to the stator current rotation speed. From an electromagnetic point of view, the rotor will be continuously lining up with the rotating magnetic field in the stator i.e. there is no slip between motor and stator current rotations.

The major difference between synchronous and induction motors is that synchronous motors have their rotors magnetized by external excitation (Wound-Rotor Synchronous Motor WRSM) or self-magnetization (Permanent-Magnet Synchronous Motor PMSM).

The stator of synchronous motors is structured similarly to that of an induction motor. The difference is in the rotor structure. There are two main SM rotor configurations: either with a wound rotor made with laminations and winding (also called electro-magnet) excited from a DC source or with permanent magnets within or at the surface of a laminated core.

They are used for devices of high precision positioning such as robots, as well as in powering elevators when coupled to variators. Their key advantages are their very high power factor (real power/apparent power ~ 1) and the constant motor speed regardless of the applied load. Permanent-Magnet motors support high overload current for fast kick-starting phase, while wound rotor synchronous motors are reversible electrical machine: they can operate as motors and as generators.

One of the drawbacks of synchronous machines is their operation failure in the case of overload torque.

1.4.1.3 Other Electric Motors

❖ Stepper Motor

A stepper motor is a DC motor that discretizes one rotation or revolution into multiple steps. Its stator is formed with a number of coils. Each winding group forms a phase. The steps are controlled by a computer, which gives them high precision characteristics in operation. There is a variety of stepper motors depending on the application requirement. Among these motors, one can site Permanent-Magnet or hybrid stepper motors, 2-phase bipolar or 4-phase unipolar.

❖ Brushless DC Motor

Brushless DC motors as their name suggests, are brush-free and their operation is owed to an integrated electronic controller. They achieve higher performance and efficiency levels. The electronic controller eliminates the friction losses of a brushed commutator. They can be better adapted to applications. Brushless DC motors have a smaller size than AC motors of similar performance. They have a higher torque-to-weight ratio than brushed motors.

❖ Hysteresis Motor

The hysteresis motor is a special synchronous self-starting electric motor without DC excitation. The stator rotating-field acts on the rotor as in induction motors. The hysteresis and eddy current induced in the rotor produce the torque. The stator of hysteresis motors is wound with coils similar to that of an induction motor. The rotor is made up of hardened steel laminations mounted on a nonmagnetic shaft [18]. The motor starts as in induction motors and runs as in synchronous motors. The motor has a smooth rotor with no teeth and no windings and operates soundlessly. The main drawbacks of this type are low efficiency and low output torque. It is generally used in sound equipment.

❖ Reluctance Motor

Reluctance Motors (RM) are electric motors that produce torque through magnetic reluctance. The magnetic reluctance quantifies the opposition or resistance of a magnetic circuit to magnetic field penetration. In this motor type, the rotor is made from soft magnetic material without windings. The stator has multiple projecting electromagnet poles (or salient poles). The rotor laminations have multiple projections that act as salient poles through reluctance. Their number is lower than the number of stator salient poles to allow the generation of torque. They can be either synchronous reluctance or variable (or switched) reluctance (which are a subtype of stepper motors). Reluctance motors can reach high power density; they have low cost and easy maintenance features and have various applications from computer hard disk drive to electric vehicle propulsion as in Tesla Model 3.

❖ Universal Motor

A universal motor is an electric motor that runs either on AC or DC source. Its stator consists of an electromagnet. Field and armature coils are connected in series. It has a wound rotor and a commutator with brushes. The motor structure is similar to the DC motors, but their stator and rotor are laminated to minimize eddy current losses. Universal motors are characterized by high starting torque similar to series DC motors. They can be found integrated into home appliances.

1.4.1.4 Summary of E-Motors Characteristics

In this subsection, *Table 1.1* sums up the main advantages and disadvantages of each electric motor type that is applied in electrified vehicle propulsion based on [19].

Motor type	Advantage	Disadvantage
Brushed DC Motor	+ Maximum torque at low speed	- Bulky structure - Low efficiency - Heat generation at brushes
Permanent Magnet Brushless DC Motor	+ No rotor copper loss + More efficiency than induction motors + Lighter + Smaller + Better heat dissipation + More reliability + More torque density + More specific power	- Short constant power range - Decreased torque with increase in speed - High cost because of PM
Permanent Magnet Synchronous Motor	+ Operable in different speed ranges without using gear systems + Efficient + Compact + Suitable for in-wheel application + High torque even at very low speeds	- Huge iron losses at high speeds during in-wheel operation
Induction Motor	+ The most mature commutatorless motor drive system + Can be operated like a separately excited DC motor by employing orientation control	- Very noisy - Low efficiency - Larger and heavier than PM machines - Complex design and control - Problems in controllability and manufacturing - Low power factor
Reluctance Motor	+ Simple and robust construction + Low cost + High speed + Less chance of hazard + Long constant power range + High power density + Robust + Fault-tolerant + Efficient + Small	-
PM assisted Synchronous Reluctance Motor	+ Greater power factor than Synchronous Reluctance Motors + Free from demagnetizing problems observed in PM	-

Table 1.1 : Advantages and disadvantages of electric motors according to their types [19].

1.4.2 From Ground to Air Vehicles Examples

The modern era has been marked by a substantially increased interest in Electric Vehicle (EV) and Hybrid-Electric Vehicle (HEV) concepts in the ground transportation sector. These concepts have been emerging for over a century now but have become recently a driving trend. Vehicles' propulsion electrification is shaping the future of the automotive industry with exponential development. Reviews of technologies used, benchmarking and an exhaustive database of these concepts are found in [20]–[24].

Vehicles' industries and manufacturers have been developing EV and HEV to reduce both, emissions and fuel consumption. Tesla Models (3, S and X), Jaguar I-Pace, General Motor EV1, BMW i3, Hyundai kona and ioniq, Audi e-tron, Nissan Leaf, Renault Zoe, Hybrid Toyota Camry and Prius, Hybrid Honda Accord are, among others, examples of EV and HEV. Actually, with this revolution over the combustion engines, and their replacement in part or total with batteries, the type of electric motor is one of the major choices to be made in this field of investigation. Indeed, with the wide variety of options, it has been proved – based on the diversity of the adopted types in existing electrified vehicles - that a suitable type depends on the technological targets aimed to be reached and some economic constraints (mainly motor construction cost).

Once an electric motor category and type seem to fit the specifications and requirements, researchers launch a process of design and optimization. This same procedure is conducted for air vehicles or planes as well. However, constraints and targets are quite different since external conditions and issues at altitudes are not similar, and objective loads are by far greater.

The typical types of electric machines used in traction applications are presented in *Figure 1.11* in assembled and exploded views. One can find that mainly the three presented types (Permanent-Magnet, Induction, and Switched-Reluctance machines) are the most suitable types for electrified powertrains allowing the engine to operate closer to its peak efficiency areas, lowering fuel consumption in hybrid vehicles [25].

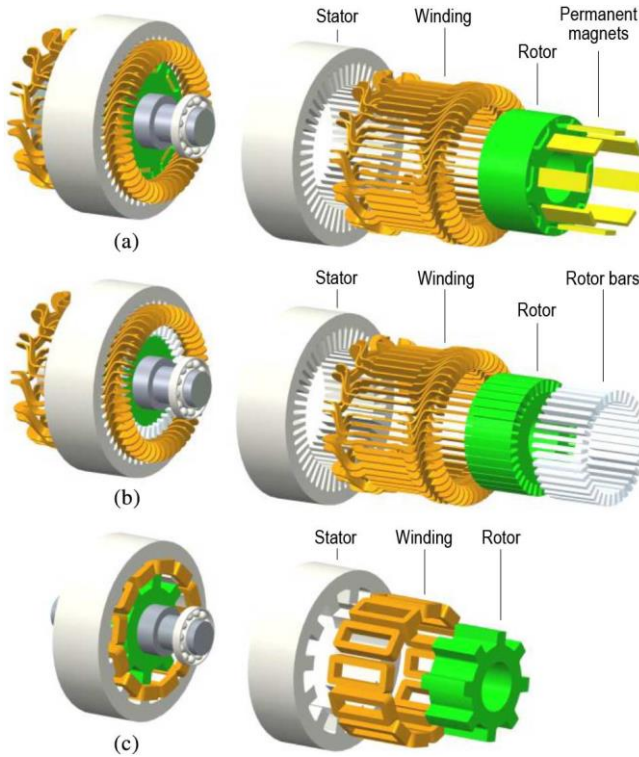


Figure 1.11 : Typical electric machines for traction applications, (a) PMSM (with interior magnets configuration), (b) IM, (c) SRM [25].

Statistics on electric motors technology for EV and HEV propulsion during the last twenty years are depicted in *Figure 1.12*.

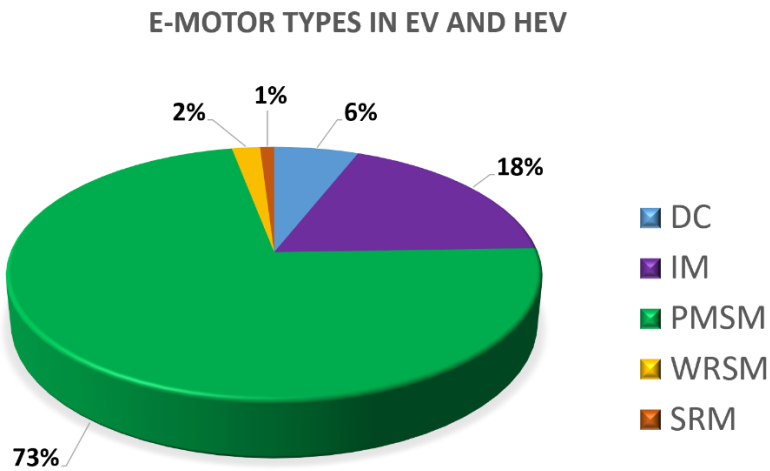


Figure 1.12 : The percentage distribution of electric machine technology in EV and HEV during the last twenty years, 'dc' (for DC), 'IM', 'PMSM', 'SRM', and 'WRSM' (Wound-Rotor Synchronous Machine) based on [22].

Data from [22] show that over the last twenty years, the PMSM type is widely used for electric propulsion vehicles (73% of vehicles with electrified propulsion). With the addition of 2% of wound-rotor SM type, Synchronous Machine type has globally 75% of the share. IM machines were selected for around 18% of EV and HEV. DC machines are less employed because of their maintenance requirements [21] (6%). SRM are used for 1% of the existing vehicles' electric propulsion. Their external control is more complex than equivalent induction and DC motors [26].

The e-motor types used commonly in electrified propulsion of ground vehicles existing in the automotive market so far are listed hereafter with examples of each:

- ❖ IM (Induction Motor): Tesla Model S 2012, Ford Think City 2008, and Honda Fit EV 2011, General Motors EV1 1996.
- ❖ PMSM (Permanent-Magnet Synchronous Motor): Lexus LS 600h 2008, Toyota Prius 2010, Toyota Camry Hybrid 2007, Hyundai Sonata 2011, Nissan Leaf 2012, Honda Jazz 2012.
- ❖ WRSM (Wound-Rotor Synchronous Motor): Renault ZOE 2011.
- ❖ PM assisted SynRM (Permanent-Magnet assisted Synchronous Reluctance Motor): BMW i3 2012 [19] (hybrid Synchronous Motor type).
- ❖ DC Motor: Peugeot Partner 1999 (Separately excited DC), Nice Mega City 2006.
- ❖ RM (Reluctance Motor): Tesla Model 3 2017 (Interior Permanent-Magnet Synchronous Reluctance), Holden ECOmmodore 2000 (Switched Reluctance).

PMSM type has been used increasingly for electric-propulsion vehicles in ongoing decades, because of the high machine performances in terms of torque-to-power ratio [28]. Common examples of EV and HEV with axial-field PMSM are Toyota Camry Hybrid 2007, Lexus LS 600h 2008, Toyota Prius 2010, Hyundai Sonata 2011, and Nissan Leaf 2012. Their stators' laminations are depicted in *Figure 1.13*.

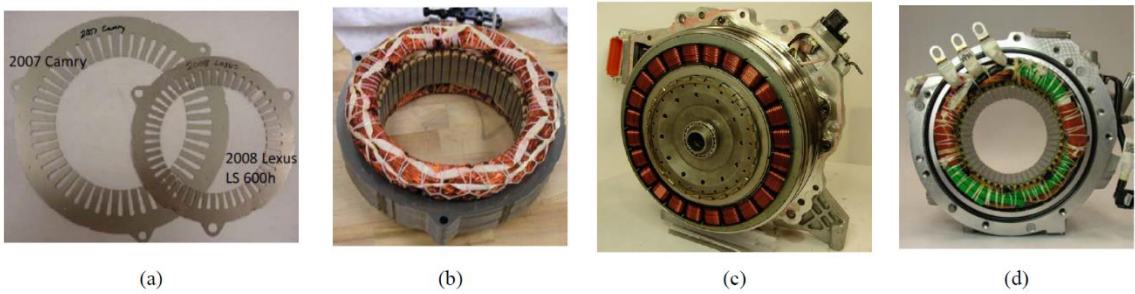


Figure 1.13 : Stator and stator laminations of (a) Camry and LS 600h, (b) Prius, (c) Sonata, (d) Leaf [28].



Figure 1.14 : Rotor laminations of different PM Machines in EV and HEV [23].

Rotor laminations and details of PM machines and other types used in vehicles' propulsion are found in the benchmarking of [23]. According to the authors, a trend is noticed in the use of electric motors with higher rotational speed. This is mainly due to the fact that with higher speeds, motors with less weight, and a lower volume of structure are needed, to achieve the same power targets.

Targets of powerful motors with less weight, existing in ground vehicles, are indicated by the specific power of the motor. For air vehicles, more attention is drawn to this indicator since higher values should be achieved. The existing motors in ground vehicles (mostly including the cooling system) have their specific power values grouped in *Table 1.2.* from [29]. Lexus LS 600h (2008) is equipped with one of the highest specific power motors of around 2.5 kW/kg [24].

Vehicle model	2012 Leaf	2012 Sonata	2011 Sonata HSG 23	2010 Prius	2008 Lexus LS600h	2007 Camry	2006 Honda Accord	2004 Prius
Power (kW)	80	8.5	30	60	110	70	12	50
Specific power (kW/kg)	1.4	1.9	1.1	1.6	2.5	1.7	0.5	1.1

Table 1.2 : Comparison between specific density of electric motor in EV and HEV based on [29].

Based on their multiple advantages in hybrid propulsion of vehicles, Permanent-Magnet Synchronous Motor type is considered suitable for our project's application and targets (as a reminder: 5 kW/kg for the year 2025 and 10 kW/kg for the year 2035).

The selected motor for our project is of SM-PMSM type that is enclosed in a case. Laminations are made from soft-magnetic Co-Fe alloy. Materials are investigated and chosen at WP1 and some characteristics are extracted from catalogs. The rotor consists of laminated core and surface mounted Samarium-Cobalt magnets. NdFeB magnets could be an option for the machine unless simulations show that the temperature field in the magnet could exceed the maximum allowed value. The stator is made up of a laminated core with teeth-and-slots configuration and distributed windings in slots. The shaft consists of a steel rod. The motor frame is made of aluminum. In a modeling approach, a simplified motor section is depicted in *Figure 1.15.*

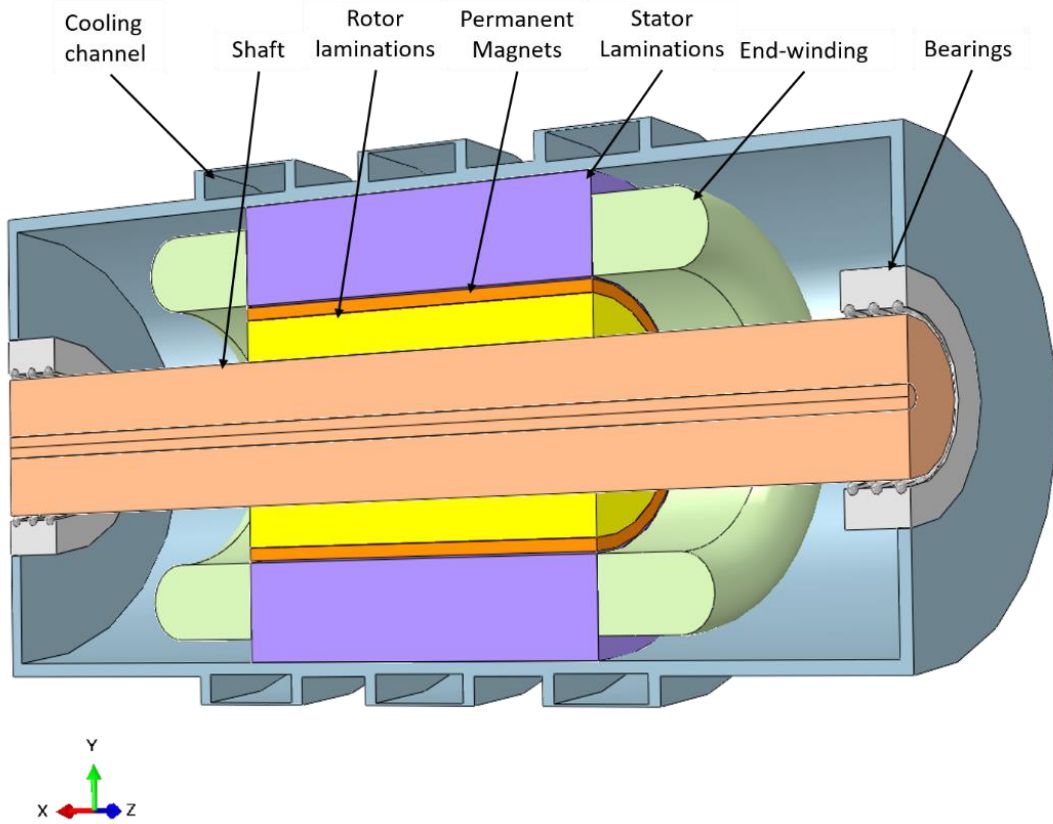


Figure 1.15 : Section of a simplified electric motor geometry for modeling.

1.4.3 Electric Motors, Suitable but?

One of the challenges met in e-motors with high performance, for power traction applications, for instance, is the thermal concern. When high performance is targeted, loads should be increased and the heat produced due to losses increases correspondingly as well. Since the heat flux in a system influences its thermal behavior, the e-motor temperature evolution depends on these losses. To reach high specific power values, required to maximize motor power and minimize its weight for propulsion application, loads should be increased wisely such that acceptable motor operating conditions are respected. Vice versa, loads are limited by motor thermal conditions, specifically, the maximum allowed temperature in winding insulation and the maximum operating temperature of permanent magnets. The excessive temperature increase may irreversibly demagnetize magnets [30] or could lead to shortening motor lifetime due to overheated electric insulation material [31]. Consequently, electrical machine cooling is becoming recently one of the biggest issues in the electrical machinery industry. The thermal issue in such high specific power density machines is brought back to the huge heat fluxes

generated in confined zones. The solution resides in a configuration where the produced heat is extracted from the motor core and simultaneously evacuated to a secondary cooling circuit. Extraction and evacuation of the heat through a cooling medium should be adapted efficiently so that the aforementioned limits are not exceeded, and no hot spot points are induced in motor sensitive parts.

1.5 Thermal Issues in Electric Motors

Stating that the emerging technologies aiming to increase specific power of motors and their efficiency and performance while economizing in production cost, has issued a serious thermal problem, researchers in electric machinery sector are concerned in finding suitable cooling solutions. To overcome the resulting thermal problem in electric motors and maintain acceptable temperatures in their critical components, some cooling techniques have been developed. In classical electric machines, traditional cooling methods managed to give satisfactory results in terms of temperature being maintained far below the limits. The machine cooling was handled sometimes with the simple natural convection as in Totally Enclosed Non-Ventilated (TENV) machines or with forced air-cooling through a fan as in Totally Enclosed Fan-Cooled (TEFC) type. These techniques rely on the machine ‘global cooling’ concept, which is adopted regardless of the heat generation location.

The developed e-motors, or prototypes being investigated, for the electrified vehicles’ propulsion, should have more sophisticated cooling than a global cooling concept, such as forced air or liquid cooling on specific areas. These techniques fall under the ‘specific and efficient cooling’ approach. During the design stage, motor cooling techniques and circuits must be accurately considered and integrated into thermal models to get reliable temperature results. This procedure requires sophisticated and detailed analysis and integration of coolant circuits’ to genuinely assessing the motor thermal behavior.

1.6 Purpose and Thesis Contents

The purpose of the present study is to thermally model specific motors designed in HASTECS project (Work-Package 1) for the propulsion of a hybrid aircraft and to find cooling solutions that could be integrated into this specific environment and context. To do so, we will start with

a presentation of the thermal characteristics and phenomena encountered in an electric motor in the following *Chapter 2*. Then, existing and future cooling solutions in electric machinery are reviewed and analyzed, to qualify their adaptability to our case-study motors.

Chapter 3 introduces the method that we will use for our model, which is the nodal network modeling method, also termed Lumped Parameter Thermal Modeling. Based on the general energy balance equation, the general matrix form of the numerical model is displayed, for application on electric motors. The bare model of the motor system is built and validated on an existing industrial motor, as close as possible to the studied motors.

In *Chapter 4*, the two target motors of the project are presented and investigated. Based on the provided electromagnetic design, the electric motor for 2025 is thermally assessed. A double liquid-cooling system in frame and shaft and an end-windings potting are adopted to maintain temperatures below the imposed limits. The resulting temperature evolutions in the motor are discussed. Besides, multiple studies are carried out on this motor to investigate the effect of some parameters and particular scenarios on the thermal behavior of the overall system. The weight of the motor with its cooling system is computed to ensure reaching the targeted value of specific power for this short-term. Whereas, for the long-term target (electric motor for 2035), several electric motor designs were assessed, and two of them are presented in this chapter for comparison purposes. The second design is adopted, and the cooling system is configured accordingly. It consists of the same cooling circuit as the electric motor for 2025, with an additional liquid cooling circuit in windings slots.

Finally, *Chapter 5* presents a study with slightly different objectives. The main goal of this chapter is to test and develop an inverse method based on the thermal model developed in *Chapter 3* and *Chapter 4* to predict motor losses using noisy temperatures. Indeed motor losses are generally difficult or impossible to measure directly. A thermal method allowing their identification would be a significant gain in the design and fabrication processes. A sensitivity study of motor temperatures to losses is conducted. It allowed determining the suitable locations of output data for each type of losses. Then, the sequential inverse method is presented. A regularization using Beck's function specification technique is applied to get losses dynamical profiles in real-time. Different cases of unknown losses are tested, and low-accessibility temperatures are predicted with high precision using the determined losses in the forward model. The method gives accurate results proving its reliability and efficiency in terms of computation time.

CHAPTER 2 E-MOTOR THERMAL MANAGEMENT STATE OF THE ART

Synopsis:

In this chapter, a literature review on the thesis topic is developed and a detailed theoretical background of the thermal management of e-machines is given.

2.1 Introduction

Conceiving the conceptual electric motors for aircraft propulsion with some tough specifications presented in *Chapter 1* comes out with multiple issues related to the thermal constraints and the cooling concepts. A detailed review of all existing techniques used for the thermal management of these motors is crucial to initiate the investigation of this topic. Great time investment was accorded to create a full state of the art on e-motor thermal management and apprehend the thermal phenomena inside the motor. In literature, suggestions can be found for global and specific cooling solutions to deal with the encountered problems. Classical approaches as well as recent advancements in thermal management are both reviewed to choose the most adapted technologies for the targeted motors. Since our motors to be conceived should have a super-high specific power, it is expected to have specific zones with hot spot temperatures. Therefore, particular attention to cooling methods of targeted parts of the machine should be drawn, particularly for zones where global cooling methods seem to be less effective, and where promising solutions are required.

The main physically dissociated parts of the electric motor are the rotor, the stator, and the frame. Hereby, a state of the art on heat transfer (conduction and convection modes) and heat extraction in electrical machines is detailed. The issue of radiation heat transfer will be discussed later in this thesis. This review consists of the following parts:

- i. Conduction heat transfer in the motor components
- ii. Convection phenomenon specifically in airgap and end windings
- iii. Renowned and groundbreaking cooling methods existing so far or being investigated for future application in electric machinery.

For simplification purposes, the symbols and letters used for variables in this chapter are not included in the Nomenclature section but are defined when mentioned.

2.2 Heat Transfer in Electric Machinery

Conduction and convection modes of heat transfer occurring in electric motors and their related issues are developed in this section. A general description of these modes and the definition of some important dimensionless numbers are presented.

2.2.1 Conduction Mode

The conduction mode of heat transfer is based on diffusion phenomena in a physical medium. Further information on the theory of heat transfer is found in [32], [33]. Studying the thermal conduction issue in an electric motor is related to assessing mainly the solid components of the motor. This assessment requires first specifying the adequate material for each component. Each material is chosen based on many criteria to meet the overall intended performance. The motor material composition and related conduction heat transfer occurring in the electric machines are known to be a complex and challenging problem that was investigated for decades. It is specifically challenging at some specific zones where hot spot temperatures, due to the low efficiency of conduction heat transfer, are encountered. When such problems occur at these levels, there will be no significant impact of optimizing other heat transfer modes (such as convection) on the thermal behavior of electric machines. Changing the materials, their ratios in heterogeneous elements, or even their dimensions would make a difference. However, any change in these characteristics will influence the loads of the machine and can affect its electrical performance. A trade-off decision is required between thermal and electromagnetic constraints.

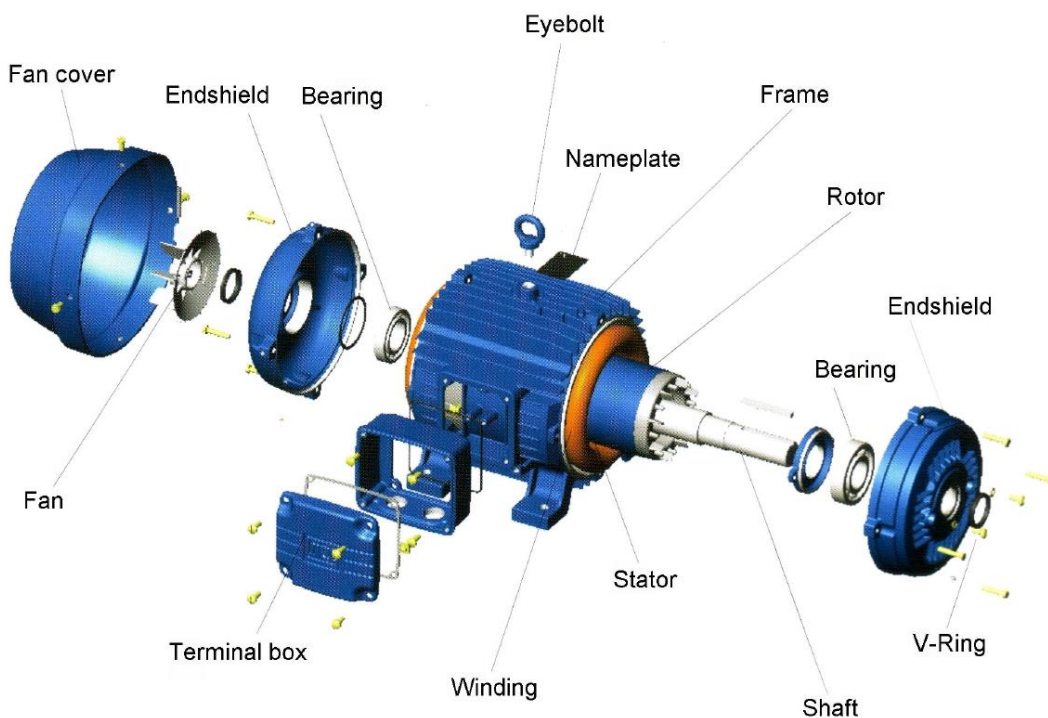


Figure 2.1 : Dissociated components of an electric motor [34].

The structure of the electrical machine consists of different parts as presented in *Figure 2.1*. In this configuration, the main machine components are the following: windings (made of coils), stator laminations, rotor laminations, motor housing (or frame), and eventually the magnets (in electrical machines with permanent magnets)

Each component will be described and studied from a thermal point of view. It will help to understand the element composition and structure and will allow figuring out the modeling of the conduction heat transfer in the motor.

2.2.1.1 Windings

The windings are formed with metallic coils covered by electrical insulation material(s), which can be generally a coat of insulator around the coil, traditionally a varnish, and lately, other constituents are added such as epoxy resin for impregnation. At the end-motor sides, the windings are coiled around the teeth, which creates a shape of wreaths that cover the stator at the cavities' sides. These wreaths are called end-windings.

According to [35], the impregnation material of the end windings and stator slots affects quite significantly the thermal behavior in electric machinery. Their experimental data show that around these two regions, the temperature reaches a serious peak value. In this same context, the authors explained that the hot spot temperature found in one of these two regions is essentially due to the low thermal conductivity of the impregnation material. The filling insulation material of the windings prohibits an efficient heat extraction from the conductors. What is practically occurring in these zones is that the heat produced due to Joule losses, hardly extracted from the metal, will result in temperature rise and will require more cooling effort. For this purpose, deep investigations of these two parts (the end winding and stator slots) are conducted. Materials are classified according to their characteristics and properties: electric properties (especially resistivity, which is directly related to electrical resistance), density, and thermal properties (mainly specific heat capacity and thermal conductivity).

Nategh et al. [36] used varnish and epoxy (named Epoxylite, which is a specific trademark of Elantas PDG, Inc., St. Louis, MO, USA) for winding impregnation in their studied motors. They presented a practical approach to model the thermal effects in directly-cooled electric machines. But later the authors in [35] studied the SbTCM, a silicone-based material, with higher thermal conductivity than epoxy and varnish ($3.2 \text{ W}\cdot\text{m}^{-1}\cdot\text{K}^{-1}$ compared to $0.85 \text{ W}\cdot\text{m}^{-1}\cdot\text{K}^{-1}$ for epoxy and $0.25 \text{ W}\cdot\text{m}^{-1}\cdot\text{K}^{-1}$ for varnish). They concluded that there is no change in thermal, mechanical, and electrical properties for the SbTCM under medium-term

tests (>1000 hours) at 150 °C. *Table 2.1* groups the material characteristics considered for comparison. An evident reduction of the hot spot temperatures of electric machines was observed for the machines manufactured using SbTCM compared to those with varnish and epoxy.

Material	SbTCM	Epoxylite	Varnish
Thermal conductivity ($W \cdot m^{-1} \cdot K^{-1}$)	3.2	0.85	0.25
Dielectric Strength ($kV \cdot mm$)	10	20	80
Price (PU)	4	2	1

Table 2.1 : Some characteristics of the materials used for impregnation [35].

This result can be justified by the relatively high thermal conductivity that SbTCM has. Despite the thermal gain obtained when using the SbTCM, this material is widely less reassuring from electric and economic sides, but deeper investigations proved that using materials with higher thermal conductivities, such as SbTCM, leads to increase torque densities, machine reliability, and machine efficiency (regardless of the impact of slot fill factor on the produced copper losses). This is the reason why the SbTCM can be considered as a promising solution for the thermal hot spots encountered in the end windings and stator slots in electric motors. The SbTCM was adopted in the work of [37] consisting of the cooling of traction electric motors.

2.2.1.2 Metallic Materials

Multiple parts of the electric machine, more specifically the synchronous electric motor, are made, totally or mostly, from metals. These parts are the housing (frame), the end-caps, the stator laminations, the conductors in windings, and the rotor. In general, for the stator laminations, the FeSi alloy is mostly used which is an iron-based alloy with silicone, in addition to other iron alloys that can be used. The winding conductors are commonly made of copper coils.

In an electric machine, there is a noticed interest in using aluminum (Al) in the structure of the housing, made classically of rolled-steel. Beginning with the mechanical features, Al metal gives high structural strength due to the stress and vibration resistance property of this material. Besides, Al frame motors are characterized by their lightweight compared to rolled-steel frame motors. On the other hand, from a thermal point of view, it is evident that Al has advantages over steel for the exceptional heat dissipation capacity and structural integrity of this metal that Siemens [38], one of the leading industry in motors, produced electric motors with aluminum coils.

Aluminum has a much better thermal conductivity than steel, but the former can be used at much higher temperatures than Al, which becomes soft above 400 °C temperature.

In [39], the authors reviewed the modern heat extraction systems for electrical machines. In their work, they compared Al and Cu from a thermal viewpoint. This comparison of properties is reported in *Table 2.2* showing the higher specific heat and lower density of Aluminum against Copper.

Material	Copper	Aluminum 99.9%
Electric resistivity at 20 °C ($\Omega \cdot m$)	1.724×10^{-8}	2.826×10^{-8}
Thermal conductivity ($W \cdot m^{-1} \cdot K^{-1}$)	386	205
Density ($kg \cdot m^{-3}$)	8890	2700
Specific heat ($kJ \cdot kg^{-1} \cdot K^{-1}$)	0.385	0.833

Table 2.2 : Copper and aluminum characteristics [39].

❖ Laminations

The stator of an electric motor consists of laminations of ferromagnetic material separated alternatively by insulator sheets. The stator laminations are usually made of magnetic alloys to reduce the induced Foucault currents. The iron is responsible for the low resistivity of the sheets while the added materials work on increasing this resistivity with a maintained level of polarization. Three main alloys were investigated in the literature [40]: Iron-Silicone (FeSi), Iron-Cobalt (FeCo), and Iron-Nickel (FeNi). The latter (FeNi) is the less dissipative. However, this alloy has relatively high permeability and average values of density and crack resistance. FeCo is the most dissipative alloy. As previously mentioned, FeSi is the alloy of preponderant use regarding the low resulting iron losses, the high resistivity, and its moderate density. However, those three alloys have many problems looking from economic and environmental sides.

The investigation of promising materials led to finding the Soft Magnetic Compound-(SMC), which is a kind of micro-dimensional granules or powder that deals with the technical and economic requirements. It was used in electric motors investigations such as in [41].

❖ Magnets

The rare-earth-based hard magnetic material Neodymium Iron Boron (NdFeB) is the most commonly used material for the permanent magnet of electric motors. Since Hybrid Electric Vehicles (HEV) have emerged, this material has offered the possibility to get higher performance of machines. The motor technology that uses NdFeB has allowed the development

of compact electric traction motors with higher torque and higher power density [42]. Besides, the demagnetization of magnets is a possible failure mechanism in the electric motor. The demagnetization curve has a strong dependence on magnets' temperature. Sm₂Co₁₇ (Samarium-Cobalt) magnets are also used in electric machinery. They show a relatively high resistivity to temperature compared to NdFeB, which makes them appropriate for use in high specific power synchronous machines where high temperatures may be easily attained.

2.2.2 Convection Mode

In this paragraph, we are interested in presenting the numerical and experimental models (and resulting reliable correlations) elaborated by authors for setting the thermal parameters for convection heat transfer in the machine internal cavities. These cavities refer to the internal spaces between the rotor-stator configuration and the motor housing (black areas in *Figure 2.2*).

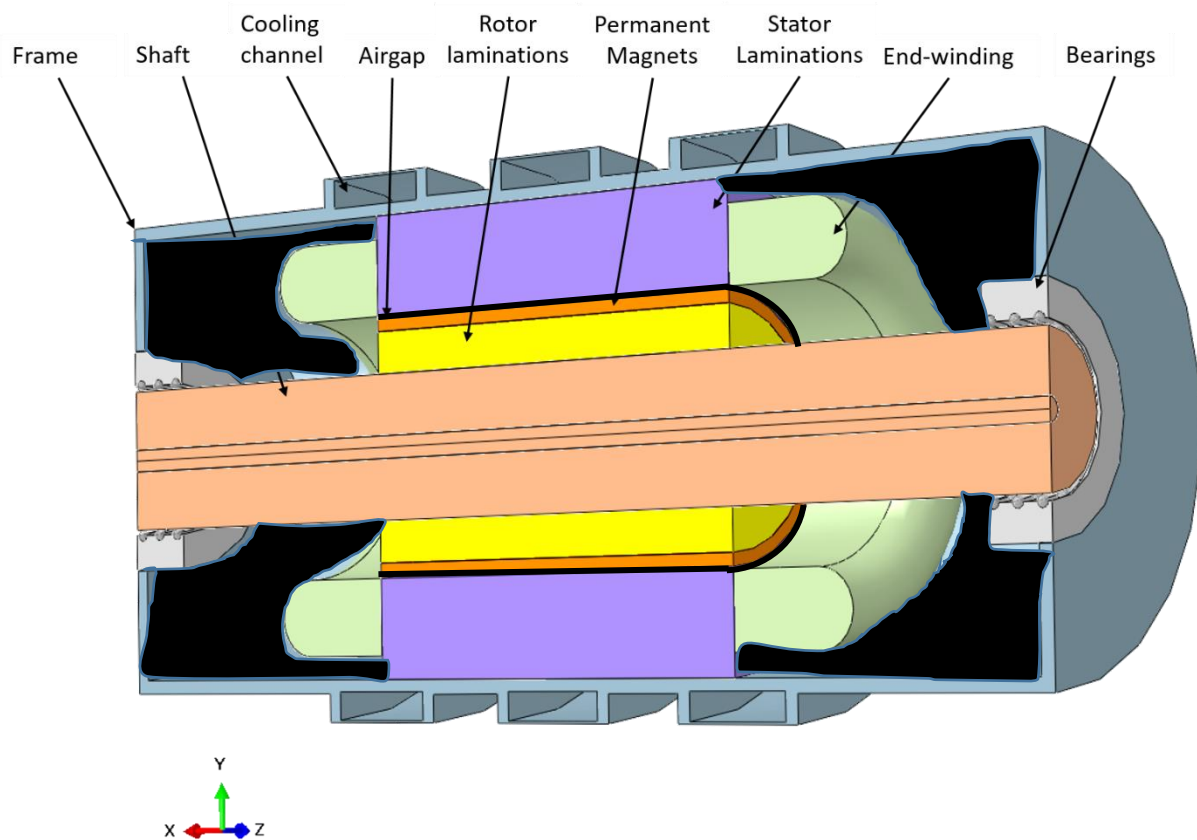


Figure 2.2 : 3-D section of a permanent magnet synchronous e-motor showing in black color the air spaces inside the machine.

The convection transfer inside the motor is divided into three main regions of convection in the motor:

- iv. The airgap between rotor and stator,
- v. The rotor end-disk,
- vi. The end-space regions (mainly the end-windings and the frame inner surfaces at both motor sides).

Let us begin with general definitions in this field. Essentially, convection is the heat transfer mode where a fluid interacts with a surface such that the fluid and the surface exchange thermal energy. Three types of convection exist: natural, forced, and mixed convection types. In natural convection, the fluid motion is due entirely to the buoyancy forces arising from density variations in the fluid, while in a forced convection system, an external force causes the fluid motion. Mixed convection is when both phenomena occur simultaneously and comparably (i.e. a density variation accompanied with imposed velocity).

In the electric motor, we distinguish external convection at the motor external surfaces, and the internal convection, which often takes place in a confined area (the closed area not connected to the atmosphere and where specific conditions are imposed), for example in the airgap [43]. The heat transfer law of convection (Newton's law) is defined by:

$$\varphi_{cv} = h(T_w - T_{ref}) \quad (2.1)$$

Where φ_{cv} is the heat flux, h is the convection heat transfer coefficient, T_w is the surface temperature, and T_{ref} is fluid reference temperature. Kreith et al. [44] presented the range of values generally reached by h , depending on the fluid nature, its physical state, and the convection type and characteristics (see *Table 2.3*).

Fluid	Convection Heat Transfer Coefficient	
	W/m ² K	Btu/h ft ² °F
Air, free convection	6–30	1–5
Superheated steam or air, forced convection	30–300	5–50
Oil, forced convection	60–1,800	10–300
Water, forced convection	300–18,000	50–3,000
Water, boiling	3,000–60,000	500–10,000
Steam, condensing	6,000–120,000	1,000–20,000

Table 2.3 : Order of magnitude of the convection heat transfer coefficient [44].

Some dimensionless numbers are used to characterize the convection phenomenon according to its type. Above all, the Nusselt number allows the determination of the convection coefficient and is defined by:

$$Nu = \frac{hL_{ref}}{\lambda_f} \quad (2.2)$$

Where L_{ref} is the characteristic length of the surface of heat exchange, also called hydraulic diameter D_h , and λ_f is the fluid thermal conductivity. When a circular channel is the fluid domain, the D_h is the channel diameter, in other cases, D_h is computed as: $D_h = 4 \times \text{channel section/wetted perimeter}$.

Other dimensionless numbers are often used in convection defined by:

$$\text{Prandtl number } Pr = \frac{c_p \mu}{\lambda}$$

- Forced and mixed convective:

$$\text{Axial Reynolds number } Re_{L_{ref}} = \frac{\rho u L_{ref}}{\mu}$$

$$\text{Rotational Reynolds number (mainly for rotational flows): } Re_\omega = \frac{\omega r_i L_{ref}}{\nu}$$

- Natural and mixed Convections:

$$\text{Grashof number } Gr = \frac{\beta g \Delta T \rho^2 L_{ref}^3}{\mu^2}$$

$$\text{Rayleigh number } Ra = Gr \cdot Pr$$

Where:

μ is the fluid dynamic viscosity,

ρ is the fluid density,

c_p is the fluid specific heat capacity,

u is the fluid velocity,

ΔT is the temperature difference between surface and fluid,

L_{ref} is the length,

ω is the rotational velocity,

ν is the kinematic viscosity,

r_i is the outer radius of the inner cylinder (rotor)

β is the fluid coefficient of thermal expansion, equals to $1/(273+T_{Fluid}^{\circ C})$ for perfect gases,

g is the gravitational acceleration.

Through literature, the calculation of convection coefficient is mainly based on the empirical formulations, as stated by [45], and convection correlations from [32], [33], specifically for common geometries. Nowadays, due to the complexity of the flow dynamics and the geometries investigated, the coefficient h is often determined through numerical (CFD) and/or experimental methods. In our study, we were based on correlations from literature to compute these coefficients.

2.2.2.1 *Stator-Rotor Airgap Convection*

The stator-rotor airgap in an electric machine is the space between the rotor external surface and the stator inner surface. The geometry in the electric machine could be assimilated to two coaxial cylinders where the inner one is in rotation while the outer one is fixed. The space between rotor and stator in an electric motor is relatively thin and the thermal effects are generally critical on windings and magnets. This region creates a radial heat path between stator and rotor and could have either a negative impact on hot spot temperature (when a significant heat flux is dissipated due to friction in this area) or a positive impact by a possible air-cooling axial flow (mainly in the case of open-motor configuration). The flow dynamics analysis in this region is crucial for obtaining temperature gradients. It helps in finding the heat transfer coefficient h . Some authors studied the airgap convection specifically in rotating electrical machines for annular case ([46] and [47]) and non-annular (or slotted) case ([48]). Other authors reviewed both annular and non-annular airgap cases ([43], [49]). Since in our case, the PMSM has surface-mounted magnets that cover the whole rotor surface to form a cylindrical shape, only an annular airgap flow case is considered, and the corresponding heat transfer studies are presented.

The governing flow in a closed machine is the Taylor-Couette flow, while in an open machine, where there is an additional axial cross flow, it is rather the Taylor-Couette-Poiseuille flow. The distinction between the two cases is that for the former, there is only the effect of the rotor rotation while for the latter there is also the external force of the axial flow acting on the fluid. As the motor is applied in specific environmental conditions, a closed configuration is maintained for this aeronautical application and a brief review of the annular airgap case without axial flow is presented.

This current study concerns the Taylor-Couette flow (normally with no or slight axial flow), for which a dimensionless number characterizes the importance of centrifugal forces, which is the Taylor number Ta , defined by:

$$Ta = \frac{\omega^2 (r_e - r_i)^3 r_i}{\nu^2} \quad (2.3)$$

Where r_e and r_i are respectively the inner stator diameter and outer rotor diameter.

Bertin et al. [47], Fasquelle [43] and Fénot et al. [49] adopted a slightly different correlation for a modified Taylor number Ta_m as follows:

$$Ta_m = \frac{\omega^2 (r_e - r_i)^3 r_m}{\nu^2 F_g} \quad (2.4)$$

where $r_m = (r_e - r_i) / \ln(r_e/r_i)$, and F_g is the geometrical factor that has many definitions depending on the airgap type and form (annular, slotted, with or without axial flow [50]) and is around the value of 1 for a narrow airgap. In [47], the authors suggested the computation of this factor as follows:

$$F_g = \left(\frac{\pi^4}{1697 P_g} \right) \left(\frac{r_e + r_i}{2r_i} \right) \quad (2.5)$$

Where P_g is calculated as a function of e and r_i based on the following:

$$P_g = 0.0571 \left[1 - 0.652 \left(\frac{e}{r_i} \right) \right] + 0.00056 \left[1 - 0.652 \left(\frac{e}{r_i} \right) \right]^{-1} \quad (2.6)$$

Fénot et al. [49] unified the formulations of the three parameters: Taylor number, the characteristic length, and Nusselt number, to compare results from different authors' works. The dynamical property that defines the flow regime, in this case, is the rotor speed (referred to as the inner cylinder rotational velocity) ω . Besides, the channel performance coefficient (also called aspect ratio of the radial cylindrical gap) is defined by: $\eta = \frac{r_i}{r_e}$. Based on [51], for low rotor speeds, the flow is steady and laminar (Couette flow). There is a critical Taylor number Ta_{cr} corresponding to a critical speed ω_{cr} , for which the torque transmitted to the fluid begins to increase faster, as the rotational speed increases [49]. Above this value, the flow is a Taylor vortex flow and vortices (called Taylor vortices) appear as can be seen in *Figure 2.3*. These vortices are in an axially centered disk form. Coles et al. [52] described that when further increasing the velocity and exceeding the critical Taylor number to reach a ratio of $Ta/Ta_{cr} =$

1.2 with a narrow gap ($\eta = 0.95$), a wavy mode appears (Figure 2.3) with azimuth waves [53]. Then the number of waves increases with velocity to reach a constant maximum for a range of values of the ratio: $4.5 < Ta/Ta_{cr} < 25$. The critical Taylor number in the case of two co-axial cylinders is determined by [51] as: $Ta_{cr} = 1700$.

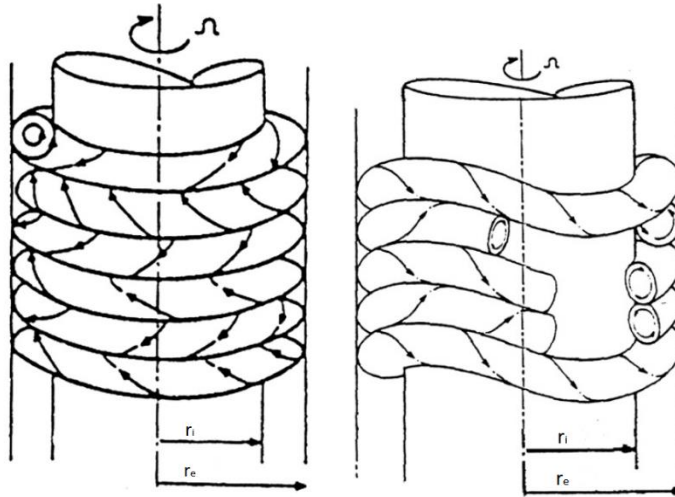


Figure 2.3 : Taylor Vortices (left) and Azimuth waves (right) [53].

In a Taylor-Couette flow, [49] focused on three types of flows: Couette, Taylor vortex, and turbulent flows, and provided heat transfer correlations to well define the heat transfer phenomena happening between two co-axial cylinders. For a closed annulus system with a rotating inner cylinder in both laminar and turbulent flow modes without axial flow, [53] proposed the following expression of the global Nusselt number:

$$Nu_{D_h} = \frac{D_h h_{rs}}{\lambda_{air}} \quad (2.7)$$

Where the characteristic length is D_h is the hydraulic diameter of the airgap, λ_{air} is the thermal conductivity of the air, and h_{rs} is the heat transfer coefficient between rotor and stator defined by:

$$h_{rs} = \frac{\Phi_{rs}}{S_m(T_r - T_s)} \quad (2.8)$$

Where S_m is the average surface between rotor and stator ($S_m = \frac{S_{rotor} + S_{stator}}{2}$), T_r and T_s are respectively the rotor and stator temperatures, Φ_{rs} is average flux density between the rotor and stator. The hydraulic diameter D_h is defined as:

$$D_h = 4s_{ag}/P_{gm}$$

Where s_{ag} is the airgap section and P_m is the wetted perimeter of the airgap area.

Herein, the thermophysical properties of the fluid are calculated at the average air-film temperature T_f :

$$T_f = \frac{T_w + T_\infty}{2} \quad (2.9)$$

Where T_w is the wall (surface) temperature and T_∞ is the air temperature in airgap.

Below the critical Ta number, heat transfer across the gap is quasi-conductive. In this same strategy, and for the Couette flow part ($Ta < 1700$), the constant value of the Nusselt number found by some authors ([54]) was: $Nu = 1$. Becker et al. [55], Gazleyet al. [53] and Bjorklund et al. [56] determined a value of Nusselt number of 2, when a laminar and stable flow type is considered. This specific value corresponds obviously to the radial conduction phenomenon in the air driven into rotation in the annular space between the rotor and stator.

When Taylor number is increased with increasing the rotational speed until reaching Taylor vortex flow and then turbulent flows, it was concluded from previous studies that Nu increases with Ta , which means a higher heat transfer. Authors in [55], [57]–[59] described another transition at $Ta = 10^4$ corresponding to a minimum of wavelength. Fénot et al. [49] explained that the lack of information about this second transition in some authors' results is due to two possible factors: either the difference in experimental settings or the relatively small range of Ta values before the transition. Tachibana et al. [54], [60] observed one additional transition for $Ta = 10^8$ when working with relatively high Taylor numbers. *Figure 2.4* depicts the comparison between different authors correlations from [49] according to a common definition for Nusselt number calculation. In this comparative graph, variation in line slope is observed for the high Ta region.

As previously presented, there are general forms of empirical formulations (elaborated from experiments) of the Nusselt number as a function of the Ta reported to be: $Nu = K_b Ta^{n_b}$

Where K_b and n_b are constants depending on the values of a geometrical factor (radial cylindrical gap aspect ratio).

Nusselt number expressions for Taylor vortex flows are used by several authors ([43], [53], [56]), based on Taylor [61]. It is expressed according to Taylor number ranges as in equation (2.10).

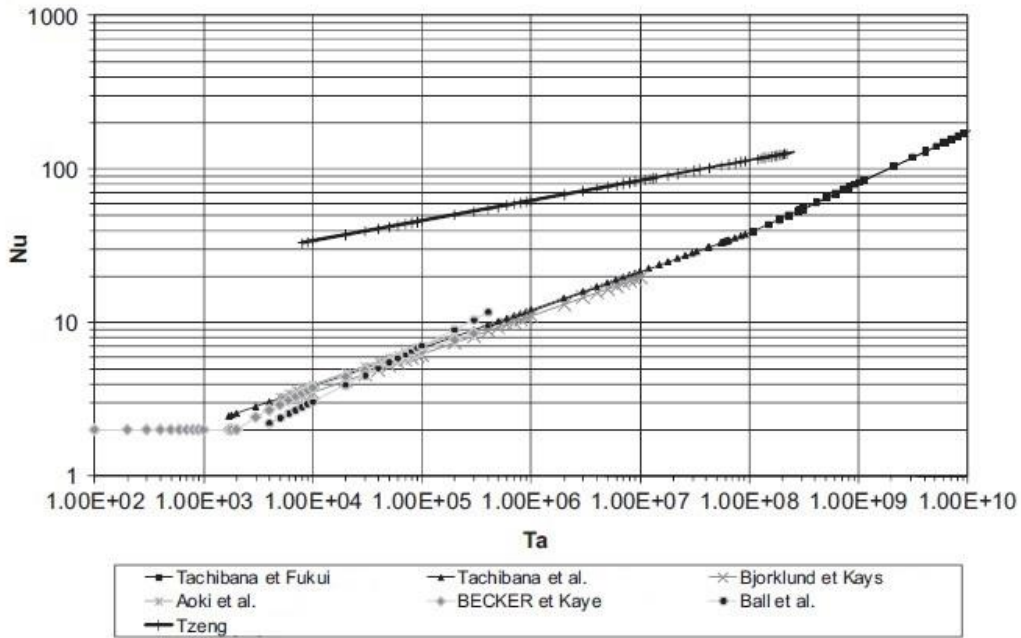


Figure 2.4 : Comparison of the evolution curves of Nusselt number (modifying its definition to have coincidence between authors' results) with respect to Taylor number [49].

$$\begin{aligned} Nu &= 0.128 Ta^{0.365} \text{ for } 1700 < Ta < 10^4 \\ Nu &= 0.409 Ta^{0.241} \text{ for } 10^4 < Ta < 10^7 \end{aligned} \quad (2.10)$$

2.2.2.2 Rotor End-Disk Convection

The convection heat transfer issue at the rotor end-caps in each side of the motor facing the lateral frame surfaces can be solved using a simple modeling approach. The configuration is thought to be comparable to the geometry of a rotating disk in an air domain. For the electric machine, the disk is enclosed in an air cavity of thickness ϵ (see *Figure 2.5*). The determination of the corresponding coefficient should be performed according to the case of a rotating disk in a closed space [47].

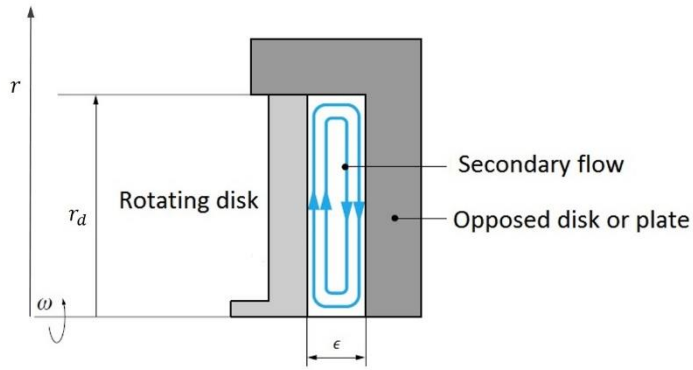


Figure 2.5 : Lateral view of the enclosed rotating disk [47].

For the rotating disk, a local Reynolds number and a global Reynolds number, Re_r and Re_ω respectively, are defined as follows:

$$Re_r = \frac{\omega r^2}{\nu} \quad (2.11)$$

$$Re_\omega = \frac{\omega r_d^2}{\nu} \quad (2.12)$$

Where r is the radial coordinate and r_d is the disk radius.

The authors of [46], [47], [62] reviewed the configuration of a disk in closed space (shroud cylinder covering it). Critical Reynolds numbers were ranged in [63] for the flow transition (from laminar to turbulent) according to literature, between 1.8×10^5 and 3.6×10^5 . From the authors' works, there are general correlations forms for the local and average Nusselt numbers respectively as follows:

$$Nu_r = c_1 \times Re_r^{d_1} \quad (2.13)$$

$$\overline{Nu}_{r_d} = c_2 \times Re_\omega^{d_2} \quad (2.14)$$

where the indices r and r_d are relative to the radial coordinate and the radius of the disk, respectively. As explained in [62], coefficients c_1 and c_2 depend on the flow regime, Prandtl number Pr , and radial temperature distribution on the disk; for laminar and turbulent flows they are highly affected by the temperature profile. Whereas d_1 and d_2 are only influenced by the flow regime (Re number). For laminar flows and isothermal disk surface, $d_1 = d_2 = 0.5$, and $c_1 = c_2 = 0.28$ to 0.38 ; for transient (laminar to turbulent) flows, coefficients are grouped in Table 2.4 from [64]–[66]. Finally for turbulent flows and isothermal surface, $d_1 = d_2 = 0.8$, $c_1 = 0.0179$ to 0.0197 , and $c_2 = 0.015$ (evaluation of all constants is for $Pr = 0.72$).

Authors	Correlation	Lowest Re	Highest Re
Popiel et al.[64]	$Nu_r = 10 \times 10^{-20} Re_r^4$	1.95×10^5	2.5×10^5
Elkins et al. [65]	$Nu_r = 2.65 \times 10^{-20} Re_r^4$	2.9×10^5	3.6×10^5
Cardone et al. [66]	$Nu_r = 8.01 \times 10^{-14} Re_r^{2.8}$	2.6×10^5	3.5×10^5

Table 2.4 : Local Nusselt numbers over a rotating disk for transitional flows [62].

Kreith et al. [67] found, from the experimental data obtained, a correlation for Nusselt number of a rotating disk in a closed space (Nu) compared to that in a free space (Nu_∞). Bertin et al. [47] reported the equation of the free space case and its corresponding coefficients (Table 2.5); this equation is as follows:

$$Nu_\infty = \frac{4a}{2b_1 + 1} Re_\omega^{b_1} Pr^{b_2} \quad (2.15)$$

Application Domain	Wall conditions	a	b ₁	b ₂	Flow regime
$Re < 1.8 \times 10^5$	-	0.41	0.5	0.44	Laminar
$Re < 2.5 \times 10^5$	uniform T	0.024	0.8	0.6	Turbulent
	uniform φ	0.031	0.8	0.6	

Table 2.5 : Coefficients of the correlation equation (3.26) of Nu_∞ depending on the flow type [67].

In Figure 2.6 the ratio Nu/Nu_∞ is represented as a function of the aspect ratio of the cavity G (ratio of the cavity thickness to the disk radius: ϵ/r_d). It is evident that when this geometrical coefficient is above the value $\epsilon/r_d = 0.2$, the Nusselt number is equal to Nu_∞ .

In [44], the Nusselt number is evaluated with respect to the disk radius $r_d = r_0$ and a critical value r_c of the radial coordinate (indicating the radial limit between flow regions: laminar and turbulent) as follows:

$$\overline{Nu}_{r_0} = 0.36 \left(\frac{\omega r_0^2}{\nu} \right)^{0.5} \left(\frac{r_c}{r_0} \right)^2 + 0.015 \left(\frac{\omega r_0^2}{\nu} \right)^{0.8} \left(1 - \left(\frac{r_c}{r_0} \right)^{2.6} \right) \quad (2.16)$$

They described the different flows and transition radii as well as the different boundary layers for each flow type as presented in Figure 2.7.

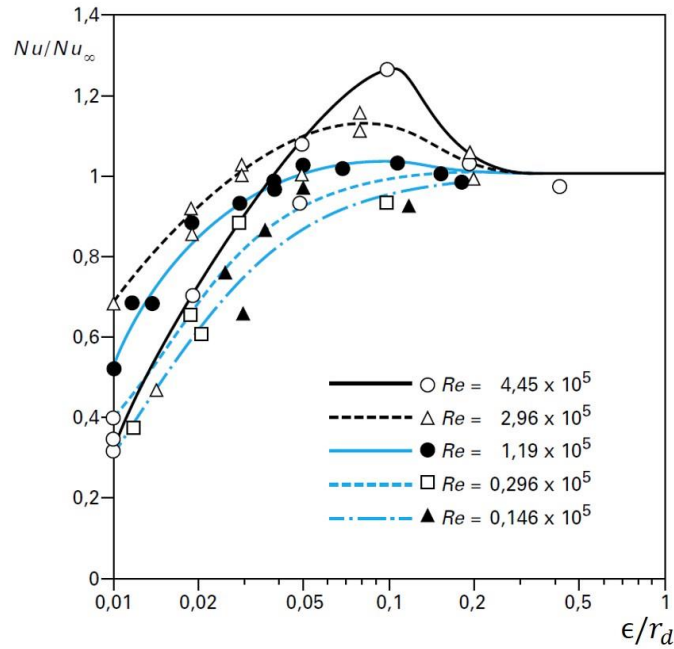


Figure 2.6 : Nu/Nu_{∞} as function of geometric ratio ϵ/r_d and Re [67].

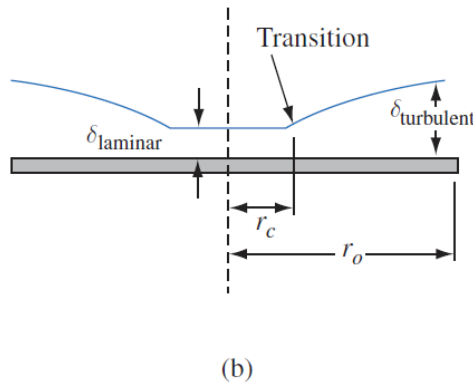


Figure 2.7 : The rotating disk velocities' profiles and transition radii and their impact on boundary layer thickness δ [44].

Four flow regimes are deduced in [68] from their experimental and theoretical study of an enclosed rotor-stator. The graph of *Figure 2.8* represents the four different flow regimes as regions, separated by the partition curves and governed by the two parameters $G_c = \epsilon/r_d$ and Re number. They reported the moment coefficient ($\$M$) correlations based on the torque measurement. Moreover in [69], the authors evaluated Nusselt number (Nu) according to the region to which the flow belongs (*Table 2.6*).

Regions	\mathbb{C}_M from Daily [68]	Nu from Vasilescu [69]
I	$\pi G_c^{-1} Re_\omega^{-1}$	$0.6119 G_c^{-1}$
II	$1.85 G_c^{0.1} Re_\omega^{-0.5}$	$0.2195 G_c^{0.1} Re_\omega^{0.5}$
III	$0.04 G_c^{-0.167} Re_\omega^{-0.25}$	$0.00823 G_c^{-1/6} Re_\omega^{0.75}$
IV	$0.051 G_c^{0.1} Re_\omega^{-0.2}$	$0.0092 G_c^{0.1} Re_\omega^{0.8}$

Table 2.6 : Torque and Nusselt number correlations according to the flow regions.

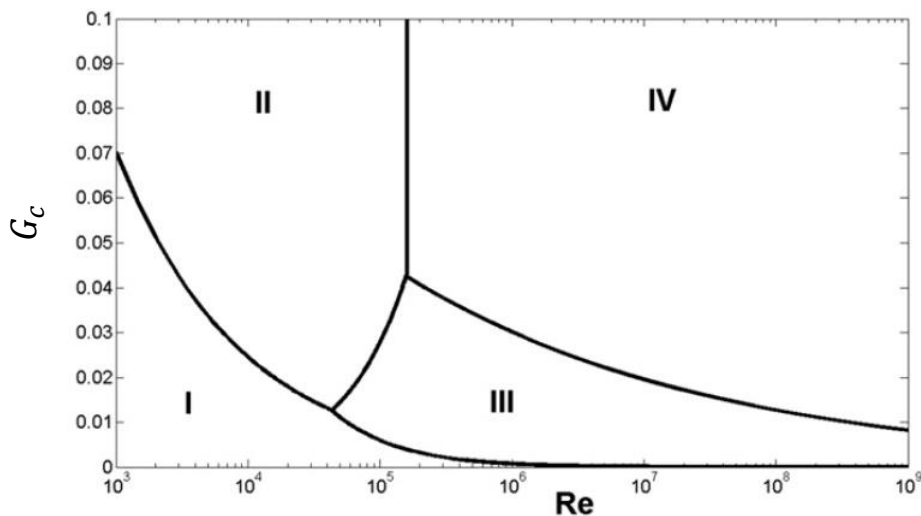


Figure 2.8 : Flow regions in an enclosed stator-rotor cavity according to G and Re (rotational). I --> laminar merged boundary, II --> laminar unmerged boundary, III --> turbulent merged boundary, and IV --> turbulent unmerged boundary [68].

In our motor application, depending on G_c value, the corresponding correlation is adopted to evaluate the convection coefficient in rotor end-disk. The aspect ratio G_c depends on the geometry of the machine, subject to multiple variations throughout the thesis.

2.2.2.3 End-Space Regions Convection

The correlations for the coefficient of convective heat transfer in the end-space regions of an electric machine (especially end windings and cavities' internal surfaces) and the thermal problems related to these regions are elaborated through some bibliographical reviews and publications. Generally, several authors ([44], [45], [70]–[72]) based their electric motors studies on the following correlation, for the convection phenomenon at the end-space region:

$$h = k_1 [1 + k_2 u^{k_3}] \quad (2.17)$$

Where k_1 , k_2 , and k_3 are curve fit coefficients and u is the average air velocity.

❖ End Windings

In [47], the authors studied forced convection around the end-windings and suggested the correlation of Nusselt number found by [73] for the cooling of end-windings of small electrical machines in different geometrical forms as a function of the end windings Reynolds number (Re_{ew}):

$$Nu = K_1 Re_{ew}^{0.8} \quad \text{for } 25000 < Re_{ew} < 125000 \text{ and } 0.031 < K_1 < 0.04 \quad (2.18)$$

In the thesis of [74], they investigated experimentally and numerically the heat transfer coefficients at the end-winding surface according to each end-winding part. They grouped their results from experiments and simulations for thick and thin end-windings (*Figure 2.9*), and it is concluded from these results that at the far end of the end-windings (the zone where coils are folded), there are the lowest heat transfer coefficients. Pickering and their co-authors [75]–[78] worked on the heat transfer in different end winding configurations. In [79], they investigated the heat transfer in a high-voltage strip-wound 4-pole induction motor ventilated with a fan mounted on the motor rear end (air outlet end). They found that the overall heat transfer coefficient in the fan side of the end windings was much higher than that at the air inlet end. Furthermore, they studied the effect of removing the wafers (which is an additional device mounted on the rotor used for changing the airflow inside the motor) on this coefficient and obtained the results in *Figure 2.10*. These results show an unexpected effect of wafers removal on the overall heat transfer coefficients at the fan end where a strong circulation of the flow is developed. The authors concluded that the wafers are thermally beneficial at the inlet end but they affect negatively the heat transfer at the motor end to fan side where the convection coefficient increases thoroughly when removing them, especially on the outer surfaces of the end-windings.

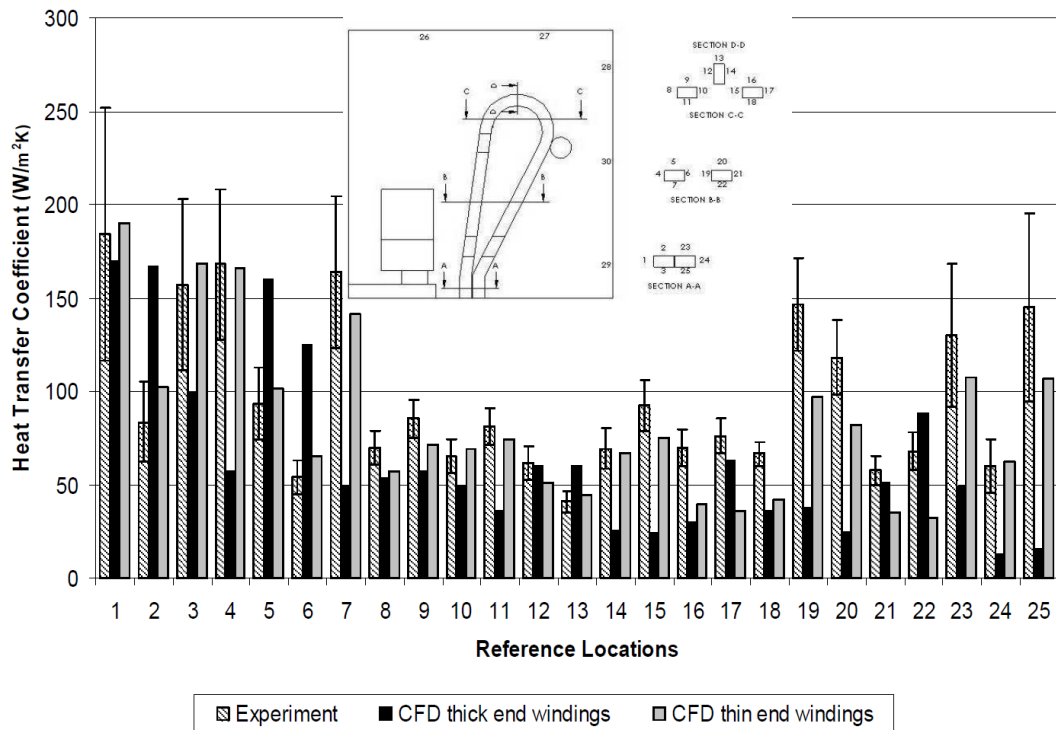


Figure 2.9 : Resulting heat transfer coefficient according to location, at the end-winding region [74].

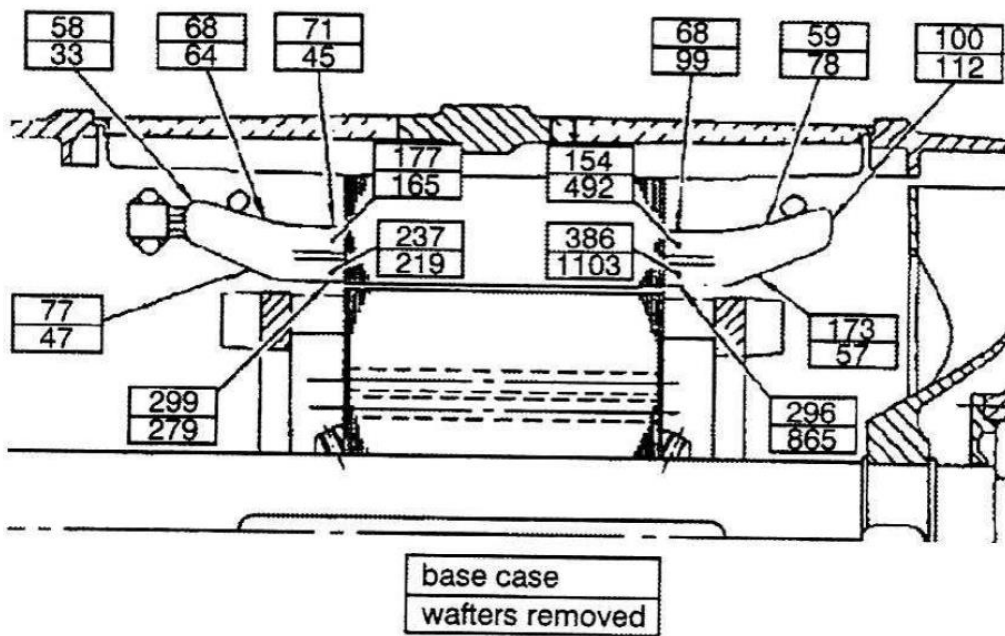


Figure 2.10 : End-winding heat transfer coefficients found by [79].

In our case, there are no wafers at the rotor surfaces and an estimated average value from the results of [74] between the lower bound of $50 \text{ W}\cdot\text{m}^{-2}\cdot\text{K}^{-1}$ and the upper bound $170 \text{ W}\cdot\text{m}^{-2}\cdot\text{K}^{-1}$, is considered for the whole end-winding.

❖ Frame Inner Surface

As shown in *Figure 2.11* from [45], the frame lateral inner surfaces are part of the circumferential surfaces of the e-motor air cavities (white spaces). For the convection in the frame internal static surfaces, the authors in [69] used the same correlations of the heat transfer coefficient as those of the rotor end-disk.

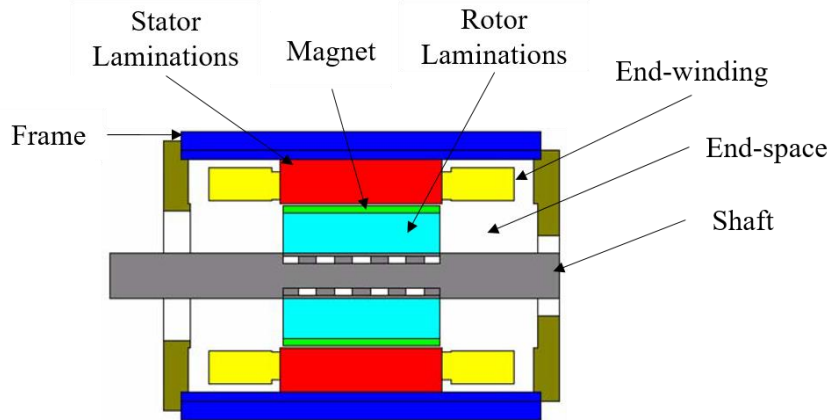


Figure 2.11 : Electric motor axial view [45].

Based on the work in [68], the authors of [80] assumed that the rotor acts as a fan, and the airflow in this end-space is turbulent due to rotor speed. They analyzed the motor thermal behavior by evaluating the Nusselt number as follows:

$$\begin{cases} Nu = \frac{3.87}{2\pi} Re_{\omega}^{0.5} Pr & Re_{\omega} < 3 \times 10^5 \\ Nu = \frac{0.146}{2\pi} Re_{\omega}^{0.8} Pr & Re_{\omega} \geq 3 \times 10^5 \end{cases} \quad (2.19)$$

$$h_{cavity} = \frac{\lambda_{air}}{r} Nu \quad (2.20)$$

λ_{air} is the air thermal conductivity, r is the rotor radius.

The authors in [70] studied also the convection coefficient at the bearing level of enclosed asynchronous machines to determine the convection coefficient: $h = 20 (1 + 0.0425 u^{0.7})$

Later, in [72], the study of the electric motor design was improved to find out a more accurate form of the correlation as follows:

$$h_{cavity} = 40 (1 + 0.1 u) \quad (2.21)$$

In [50], the authors assimilated the geometry of the cavity in electric machines to the space between two vertical or horizontal disks where one disk is heated. They used the correlations of [44] for the Nusselt number relative to the cavity's thickness (as the characteristic length).

2.3 Electric Motor Cooling Methods

The thermal study and cooling of an electric machine designed to achieve promising electrical objectives have a critical influence on its performance. We can cite from [81]: ‘The analysis of heat transfer and fluid flow in electric machines is actually more complex, more nonlinear, and more difficult than the electromagnetic behavior. Bertin [82] has studied the main heat evacuation possibilities and issues in electric machines.

Nowadays the importance of finding modern solutions for acceptable maximum temperatures in the machine and uppermost heat dissipation to surrounding areas is rising. In fact, these machines are required to provide high-efficiency and huge power values specifically when applied for propulsion in the aeronautical domain, compared to what was designed in the previous decades. Similarly, automotive motors main constraint is the high specific power density. The works of researchers in this domain are studied in [83]. They have set out, explained, and evaluated different cooling schemes and methods for automotive traction motors.

Two possible strategies can be adopted to solve the thermal problems encountered. The first strategy consists of finding critical physical parameters that influence the heat transfer (for instance, it could be the structure materials used in motor construction, geometrical factors, or properties of cooling fluids, etc.), and working on optimizing them to fit with the adequate machine thermal design (passive cooling). The other strategy is to focus on developing cooling techniques allowing the highest heat dissipation (active cooling). Through literature, it is remarked that authors essentially worked on one of the two strategies for possible improvement in heat extraction methods and few of them studied both. Some parts of the machine that are classically cooled must be accurately studied in different electrical and environmental

conditions, such that their cooling will be adapted to the electrical performance of the machine and will enhance its overall efficiency. Those parts are mainly the stator, the frame, and the rotor. In this section, we will be interested in reviewing the motor cooling methods, separated into two categories: external cooling without inflowing to the motor structure and internal cooling methods when cooling media are directly cooling the inside of the motor core.

2.3.1 External Cooling Methods

The external cooling allows cooling the motor skin (the frame in this case) by creating areas of heat exchange or equipment for thermal energy release. These cooling methods do not require, in most of the cases, modifications inside the motor. They are easily mounted outside the motor but are consequently far from hot spot zones. The heat flux must get through the different parts of the motor to reach the heat sink. However, they are still used widely in electric machinery to evacuate heat through the frame. Several techniques are employed, mainly convective air-cooling through fins and liquid-cooling with water jackets.

2.3.1.1 *External Cooling through Fins*

The frame of an electric machine, or directly its stator sometimes, can be equipped with fins that are mounted to increase the surface of air convection of the motor stator and to improve the heat transfer (by creating a flow with forced convection for instance). Many authors raised interest in studying the effect of motor cooling through fins and their optimization as in [31], [84], [85].

On the other hand, through literature, a great number of research investigations focused on the heat transfer through fins depending on their configurations. Deployed in multiple applications (turbines, fans, heat exchangers...), numerous fins' designs can be conceived. Optimization of their shapes is proposed for finned-tube heat exchangers in [86].

Generally, the efficiency of fins depends, among other factors, on the flow nature around the stator. Both natural and forced convection types around motor finned frame are reviewed.

❖ Natural Convection with Fins

Natural Convection is one of the less expensive cooling methods since no extra components neither further consideration of the cooling system design are needed. However, an important drawback of this system is the small rate of heat transfer achieved, as detailed in heat transfer

books [32], [44]. Based on these books and other advancements in this field, the authors of [71] proposed the use of the following general correlation for natural convection in the case of electric motor application:

$$Nu = a(GrPr)^b \quad (2.22)$$

Where Gr is Grashof number calculated as follows: $Gr = \frac{\beta g \Delta T \rho^2 L_{ref}^3}{\mu^2}$, and Pr is Prandtl number determined as follows: $Pr = \frac{c_p \mu}{\lambda_f}$, a and b are given constants depending essentially on the nature of the flow and the surface shape.

Natural convection through the housing surface is mainly a function of the temperature difference between the structure and the fluid.

The total enclosed non ventilated electric machine (TENV) housing thermal behavior depends on surface characteristics. According to [45], a few examples of housings types are designed and they are usually smooth. However, the housing can be designed with fins to increase the convection surface but in a well-oriented design suitable for optimal convection cooling (i.e. without disturbing natural airflow). As suggested by [45], radial fins are suitable for vertical mounted TENV motors.

❖ Forced Convection with Fins

Improvement of heat transfer can be provided by mounting a fan on the motor shaft that induces turbulent airflow in the longitudinal direction of the motor housing. The total enclosed fan-cooled (TEFC) motor has sometimes a smooth housing, for which the Nusselt number can be obtained in terms of axial Reynolds (Re_a) and Prandtl numbers with well-known correlations for a configuration of flow over flat plate [32], [33], as follows:

- Laminar flow ($Re_a < 5 \times 10^5$ and $0.6 < Pr < 50$):

$$Nu = 0.664 Re_a^{0.5} Pr^{0.33} \quad (2.23)$$

- Turbulent flow ($Re_a > 5 \times 10^5$):

$$Nu = (0.037 Re_a^{0.8} - 871) Pr^{0.33} \quad (2.24)$$

However, motor housing is generally finned, and geometries vary according to requirements and constraints to get optimized convection cooling.

The authors of [31] studied experimentally the effect of finned casing modifications on the thermal behavior of the motor when its external surface is subjected to a flow. The authors compared commercial and prototype motors' thermal behavior and deduced that a considerable reduction in temperature due to the improvement of geometry and flow characteristics. According to [87] who conducted tests on finned induction motors and considered a turbulent flow due to existing fans and cowlings, the convection heat transfer coefficient h for semi-open channels made with axial fins is given by:

$$h = \frac{\rho c_p D_h u_a}{4 L_a} (1 - e^{-m}) \quad (2.25)$$

And m is calculated as follows:

$$m = 0.1448 \frac{L_a^{0.946}}{D_h^{1.16}} \left(\frac{\lambda_a}{\rho c_p u_a} \right)^{0.214} \quad (2.26)$$

Where L_a is the axial length of the finned frame, u_a is the airflow velocity, D_h is the hydraulic diameter of the channel; ρ , c_p , and λ_a are respectively the density, the specific heat capacity, and the thermal conductivity of the air at the average air temperature in each channel.

Based on these correlations, the finned housing of a TEFC electric machine was recently investigated by [85]. In this work, the authors were concerned in optimizing the cooling fin design by elaborating a conjugate heat transfer model validated by CFD results and used then to evaluate whether a fine or a coarse engineering tolerance is required for the casting of motor housing. In *Figure 2.12*, the geometry shape of the studied finned motor housing is depicted.

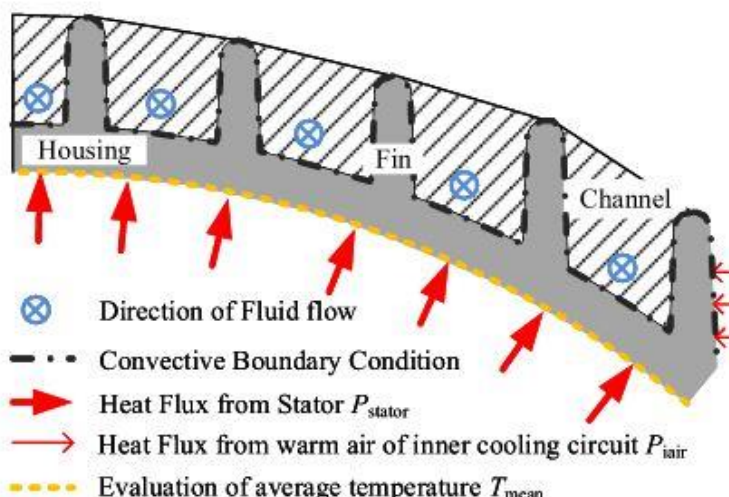


Figure 2.12 : Heat and fluid flow conditions for motor finned housing [85].

Their method consists of evaluating many possible designs of fins using a novel algorithm that allows a great reduction of candidate geometries for CFD simulations.

2.3.1.2 Frame Channels and Pipes

Intending to bring cooling closer to the heat sources in the stator, some authors propose to create a fluid circulation through stator channels. Examples are found in [36], [45], [47], [88]–[90]. Some authors investigated the fluid flow in multiple geometries of the cooling channels [47], [91]. In this latter research, the authors simulated motor behavior with different duct sections (*Figure 2.13*) and, based on this study, they recommended an oval shape for a traction motor application in a hybrid electric vehicle or zero-emission vehicle. In most cases, water is used as a coolant fluid and the technique is commonly known as water jacket cooling. Channels are classified into two groups: smooth channels and channels with perturbations (ribs). In [92] (evaluation of the 2008 Lexus LS 600H hybrid synergy drive system), oil is used as a coolant in the cooling channels of the motor, and ethylene glycol/water for heat exchanger. Cooling channels are made with Aluminum. Based on the works of [93], the authors of [89] developed a model simulating the thermal behavior of a TEFC induction machine with empirical direct lamination cooling (where cooling tubes are implemented within the frame).

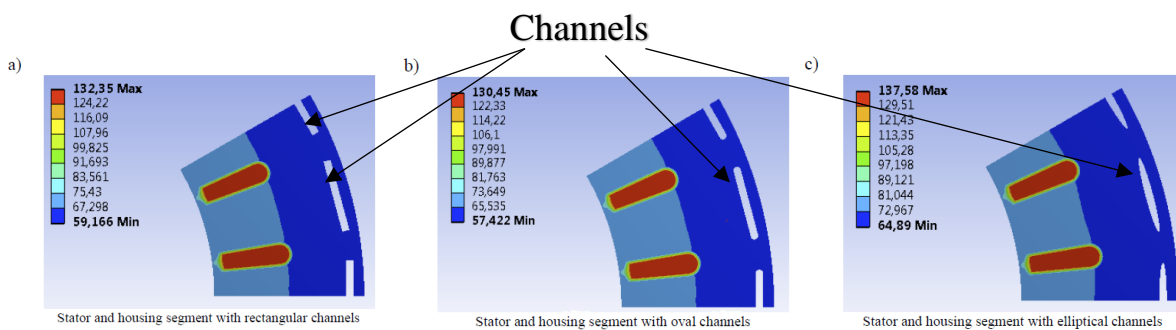


Figure 2.13 : Different geometries of channels simulated in CFD [91].

The frame or stator channels of electric machines have generally a specific geometry (curved duct). Throughout literature, flow in stator channel geometry has not been widely studied analytically, while numerous correlations concern another panel of duct geometries. [88] proposed the simplified rectangular form as in *Figure 2.14*, which shows the actual curved channel form (with respective internal and external diameters R_i and R_e) and the rectangular duct representation (with height H and width W). Physical parameters for hydraulic and thermal calculations for this geometry are defined in *Table 2.7*.

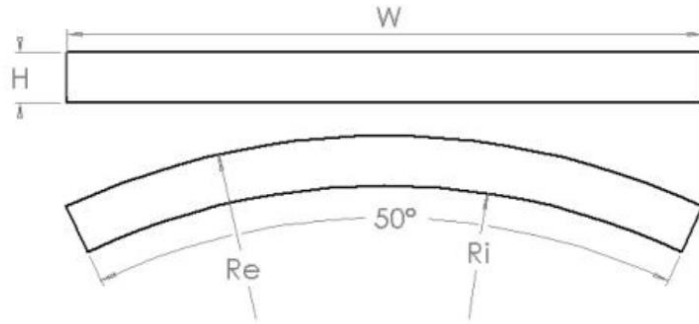


Figure 2.14 : Rectangular section of the cooling channel compared to its effective form [88].

Parameter	Expression
Channel length	L_{ch}
Hydraulic Diameter	$D_h = 4WH/2(W + H)$
Channel aspect ratio	W/H
Channel length to hydraulic diameter ratio	L_{ch}/D_h

Table 2.7 : Geometrical parameters of the stator channel [88].

❖ Smooth Channels

The study is divided into two parts according to the flow type: laminar or turbulent.

For laminar flow ($Re_{D_h} < 2000$): In dynamic developing, and based on correlation from [94], the ratio of the dynamic development length (L_m) to the hydraulic diameter is given by:

$$\frac{L_m}{D_h} = 0.0575 Re_{D_h} \quad (2.27)$$

According to [47], for a circular channel of isothermal wall, where the flow is dynamically fully developed and for which temperature and velocity profiles are developing, the thermal developing length L_{th} can be expressed by:

$$\frac{L_{th}}{D_h Re_{D_h} Pr} = 0.05 \quad (2.28)$$

When $L_{ch} < L_{th}$, Nusselt number :

$$Nu_{D_h}(x) = 1.86 \left[Re_{D_h} Pr / (x/D_h) \right]^{1/3} \quad (2.29)$$

Different correlations of Nusselt number are provided by [32] depending on channel shape.

For a circular channel:

$$Nu_{D_h} = 3.66 + \frac{0.065 Re Pr D_h / L_{ch}}{1 + \left[0.04 \left(\frac{Re Pr D_h}{L_{ch}} \right)^{2/3} \right]} \quad (2.30)$$

For concentric cylinders:

$$Nu_{D_h} = 7.54 + \frac{0.03 Re_{D_h} Pr D_h / L_{ch}}{1 + \left[0.016 \left(\frac{Re_{D_h} Pr D_h}{L_{ch}} \right)^{2/3} \right]} \quad (2.31)$$

For turbulent flow: In their thesis [88], where the author adopted an effective channel section, as in *Figure 2.14*, they considered for airflow in channels that in stator channels the flow typically found is turbulent developed corresponding to a Reynolds number between 2×10^4 and 2.5×10^4 . Bertin et al. [47] distinguished between two possible cases, relatively to the ratio of the channel length to the hydraulic diameter (L_{ch}/D_h), around the critical value of 60.

For $\frac{L_{ch}}{D_h} > 60$, Dittus-Boelter correlation is used consequently for a circular channel's section as follows:

If $0.7 < Pr < 100$ and $Re_{D_h} > 2000$

$$Nu_{D_h} = A_n Re_{D_h}^{0.8} Pr^{n_{pr}} \quad (2.32)$$

$A_n = 0.024$ and $n_{pr} = 0.4$ for heating, $A_n = 0.026$ and $n_{pr} = 0.3$ for cooling.

For liquids, the temperature effect is taken into account in the correlation of Sieder and Tate [95]:

$$Nu_{D_h} = 0.027 Re_{D_h}^{4/5} Pr^{1/3} \left(\frac{\mu_m}{\mu_p} \right)^{0.14} \quad (2.33)$$

The corrected form, that considers the length of the channel, is:

$$Nu_{D_h} = 0.0243 Re_{D_h}^{0.8} Pr^{0.4} (1 + k D_h / L_{ch}) \quad \text{with } k = 0.067 Re_{D_h}^{0.25} \quad (2.34)$$

Mc Adams [96] gives a general form of the correlation for cooling and heating:

$$Nu_{D_h} = 0.023 Re_{D_h}^{0.8} Pr^{0.4} \quad (2.35)$$

For $\frac{L_{ch}}{D_h} < 60$, [47] proposed the computation of Nusselt number using another equation that considers the channel length:

$$Nu_{D_h}(L_{ch}) = 0.036 Re_{D_h}^{0.8} Pr^{n_{pr}} \left(\frac{D_h}{L_{ch}} \right)^{1/18} \quad (2.36)$$

Where $n_{pr} = 0.4$ for heated gas, $n_{pr} = 0.3$ for cooled gas and $n_{pr} = 0.5$ for water.

The authors of [97] used a modified equation of Dittus-Boelter in their studies:

$$Nu = 0.023 Re_{D_h}^{0.8} Pr^{0.4} \left(\frac{2R_{av}}{D_e} \right)^{-0.2} \quad (2.37)$$

$$\text{Where } \left(\frac{2R_{av}}{D_e} \right) = \left(\frac{\frac{1.156 + \frac{W}{H} - 1}{\frac{H}{W}}}{\frac{W}{H}} \right) \quad \text{for } 2500 \leq Re_{D_h} \leq 1.24 \times 10^5$$

Gnielinski correlation used to find the Nusselt number takes into consideration the average temperatures of the fluid and the solid surfaces, respectively T_{fm} and T_{pm} . It is noted that this correlation slightly underestimates the convection heat transfer and is stated as follows:

$$Nu = 0.0214 (Re^{0.8} - 100) \left\{ 1 + \left(\frac{D_h}{L_{ch}} \right)^{0.66} \right\} \left(\frac{T_{fm}}{T_{pm}} \right)^{0.45} Pr^{0.4} \quad \text{for } 2300 \leq Re \leq 10^6 \quad (2.38)$$

The author in [88] noted that the Nusselt number depends on the ratio of the heated length along the channel to the hydraulic diameter L_{ch}/D_h , which explains the difference between authors.

In [32], [33], [45], researchers calculated analytically the Nusselt number for fully developed flow, considering the friction coefficient f (detailed subsequently) even for a smooth channel wall, as follows:

$$Nu = \frac{\left(\frac{f}{8} \right) (Re - 1000) Pr}{1 + 12.7 \left(\frac{f}{8} \right)^{2/3} \left(Pr^{2/3} - 1 \right)} \quad \text{for } 3000 < Re < 10^6 \quad (2.39)$$

Where $f = [0.79 \ln(Re) - 1.64]^{-2}$

❖ Friction coefficient

In any channel configuration, it is important to determine the friction coefficient function f . The expression of this coefficient relates the fluid flow to the thermal behavior and differs throughout literature. In general, the researchers in this field ([98]–[100]) used the modified Blasius expression function of Reynolds number which is supposed to underestimate the friction coefficient for low Reynolds number (compared to experimental results of [99]); The friction coefficient is defined by:

$$f = 0.085 Re^{-0.25} \quad (2.40)$$

Bhatti and Shah Correlation fits better with the experimental results, covering a larger domain of Reynolds number; the friction coefficient is determined with respect to the Reynolds number criterion, and the friction coefficient of a circular section channels f_c :

$$f = \left(1.0875 - 0.1125 \frac{H}{W} \right) f_c \quad (2.41)$$

f_c is defined in terms of Reynolds number as follows:

$$\begin{aligned} f_c &= 0.0054 + 2.3 \times 10^{-8} Re^{1.5} && \text{for } 2300 \leq Re \leq 4000 \\ f_c &= 1.28 \times 10^{-3} + 0.1143 Re^{-0.311} && \text{for } 4000 \leq Re \leq 10^7 \end{aligned} \quad (2.42)$$

Karwa et al. [101] suggested the following correlation:

$$f = 0.0791 Re^{-0.25} \quad \text{for } 4000 \leq Re \leq 10^5 \quad (2.43)$$

While the authors in [102] used for the entire domain:

$$f = 0.046 Re^{-0.2} \quad (2.44)$$

In reference [88], they found that generally, the friction coefficient decreases when the Reynolds number increases, except for $2300 \leq Re \leq 4000$ in the Bhatti and Shah correlation, and that this decrease becomes less rigorous for high Reynolds numbers.

❖ Channels with Perturbations

It is commonly known that the use of disruptive elements or ribs at the flow surfaces of heated channels (as in *Figure 2.15*) increases the convection phenomenon in these regions. Perturbations in the cooling system channels are used to increase the thermal efficiency of the system by increasing the coefficient of heat transfer.

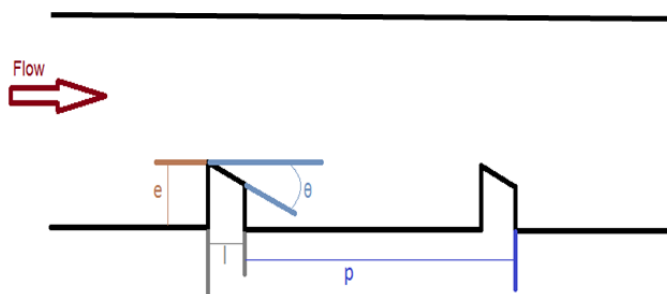


Figure 2.15 : ribs geometrical parameters in a rectangular channel.

However, adding ribs to the channel will also affect the fluid flow mechanics by increasing the friction and thus the coefficient of hydraulic losses specifically for liquid cooling. This will require more pumping power for the operation of the system. In [88], the author was interested specifically in air-cooling through channels. They investigated different configurations of perturbations in channels and provided a detailed literature review from which we can sum up some correlations of Reynolds number computation according to roughness function Rg .

$$Rg = \sqrt{\frac{2}{f}} + 2.5 \ln\left(\frac{e}{D_h}\right) + E \quad (2.45)$$

Where E is a geometrical constant depending on the channel configuration.

2.3.1.3 External Heat Pipes and Two-Phase Loop

- ❖ Heat Pipes

A heat pipe is a cooling device that is based on phase-changing to transfer heat between two interface structures. Heat pipes are solid structures relatively static to their environment and are composed of three parts: the evaporator at one side, the condenser at the other side, and the adiabatic part at the center. The working principle relies on the temperature difference between the two ends of the pipe. When one end is heated, the working fluid inside the pipe at that end evaporates and increases the vapor pressure inside the cavity of the heat pipe. The latent heat of evaporation absorbed by the vaporization of the working fluid reduces the temperature at the hot end of the pipe (*Figure 2.16*). At the other end of the pipe, the cold sink (namely the condenser) absorbs the heat by the condensation of the vapor. The working fluid flows back to the hot end due to temperature differences. A typical heat pipe consists of a sealed pipe or tube made of a material that is compatible with the working fluid such as copper for water heat pipes, or aluminum for ammonia heat pipes. They are used in many engineering applications (spacecraft, computer systems, ventilation heat recovery...); a wealth of studies were conducted on their operation and performance. Chen et al.[103] stated that Heat Pipes are characterized by a high thermal conductivity, a high efficiency (with no electric energy consumed), and a suitable working temperature for electric devices.

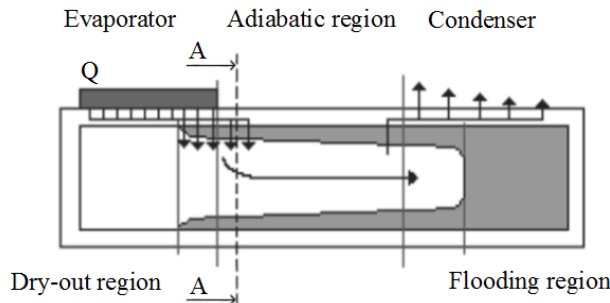


Figure 2.16 : Heat Pipe axial section showing the different regions [103].

Some authors were interested in studying the electric motors cooling using heat pipes [104]–[107]. Recently, authors of [108] investigated a new design of L-shaped heat pipes placed at the surface of the motor housing. Their objective was to determine experimentally the performance of the electric motor. In the design, heat sinks are mounted to each condenser side to increase heat transfer to the ambient air as in *Figure 2.17*.

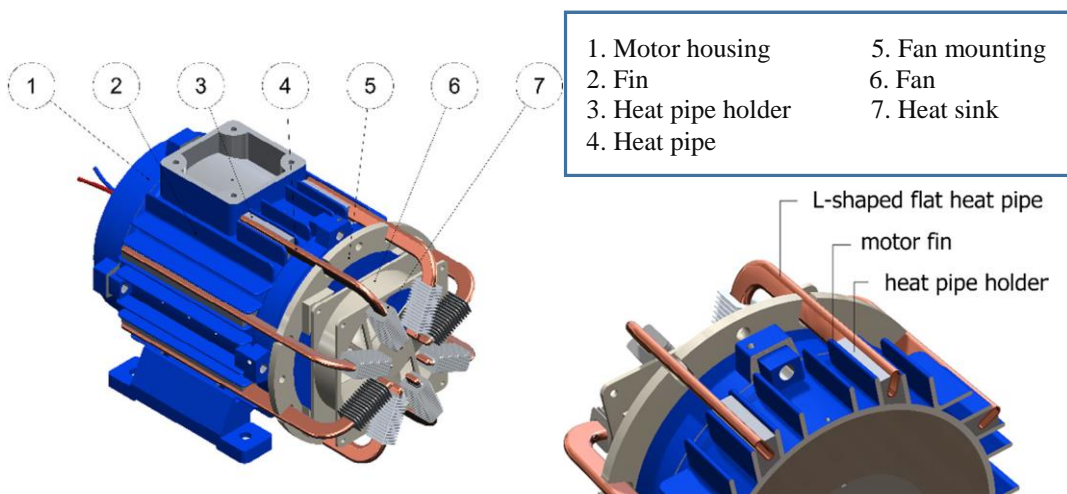


Figure 2.17 : Electric motor prototype cooled with L-shaped heat pipes [108].

Putra et al. [108] reported that the use of heat pipes was capable of reducing the motor housing temperature less than the classical solutions (water jackets, hollow shaft), but the authors mentioned that the surface of heat exchange with ambient air in the studied motor is smaller.

Two-phase loop cooling technologies are based on the same principle as heat pipes, but with liquid and vapor phases circulating in different areas of the circuit. Though, these systems can dissipate greater heat flux densities. Among these cooling technologies, one can cite Loop Heat

Pipe, Looped Pulsating Heat Pipes, and Capillary Pumped Loop. Recently, many authors investigated these systems [109]–[115] and their industrial applications in gas turbines, energy savings applications, solar power (photovoltaic) applications, reactors, and others. Besides, they are widely applied in electronics cooling. The possibility of applying these techniques in electric machinery has not been yet explored. However, their efficacy in evacuating heat fluxes incites to investigate their possible deployment in high specific power electric motors for promising cooling results.

It is nevertheless important to consider the geometrical characteristics of the heated system, specifically lengths since they are one of the main factors that define the operation of heat pipes and two-phase loops.

2.3.2 Internal Cooling Methods

In internal cooling, the components where hot spot temperatures are encountered inside the motor are directly cooled. Actually, in this review cooling is performed by different means: through convection in a single-phase (air: jet impinging or flowing, liquid: jet impinging or spraying), eventually two-phase (internal heat pipes), or another physical phenomenon (phase-changing materials).

2.3.2.1 End-Space Potting

Motor potting has been recently investigated in the electric machines industry as a solution to improve heat evacuation in electric motors [116], [117]. This technique consists of adding a high thermally conductive potting material such as epoxy resin with $3.5 \text{ W}\cdot\text{m}^{-1}\cdot\text{K}^{-1}$ of thermal conductivity or silicone with $3.2 \text{ W}\cdot\text{m}^{-1}\cdot\text{K}^{-1}$ to connect hot spot zones, more specifically the end-winding, to the frame. According to [116] a reduction in winding temperature of a potted motor goes up to 50°C at a given power, while at a given temperature, an increase in power output by 15–25% has been shown. In their study, they described the potting process, beginning with motor sealing, hardener, and resin mixing then degassing, applying the potting mixed material to the end winding (*Figure 2.18*), and the final product after curing. Machines were potted with two materials of different thermal conductivities ($1.1 \text{ W}\cdot\text{m}^{-1}\cdot\text{K}^{-1}$ and $3.5 \text{ W}\cdot\text{m}^{-1}\cdot\text{K}^{-1}$). Temperature decrease between potted and unpotted machines is found sensitive to the machine active length as shown in *Figure 2.19*.



Figure 2.18 : Potting technique processing [116].

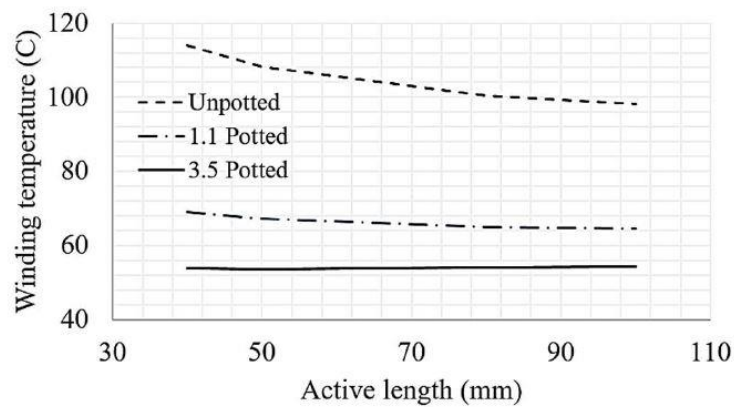


Figure 2.19 : Comparison of motor winding temperature for unpotted and potted (with different types of epoxy) motor end-space [116].

Besides, other potential advantages characterize potting: more uniform distribution of the temperature throughout the windings and lower overheating risk.

2.3.2.2 Metallic Bars

The complexity of heat extraction from electrical machines motivated researchers to find some original and advanced cooling techniques. Pyrhönen et al. [117] proposed some heat transfer improvement methods in an axial-flux permanent magnet synchronous machine by introducing copper bars in stator teeth transferring heat to a “liquid cooling pool”. Using a 1-copper-bar per tooth, the authors noticed that end windings temperature diminishes by 15 °C. In their study, they also used potting of end-windings (as illustrated in *Figure 2.20*) and liquid jackets around the machine.

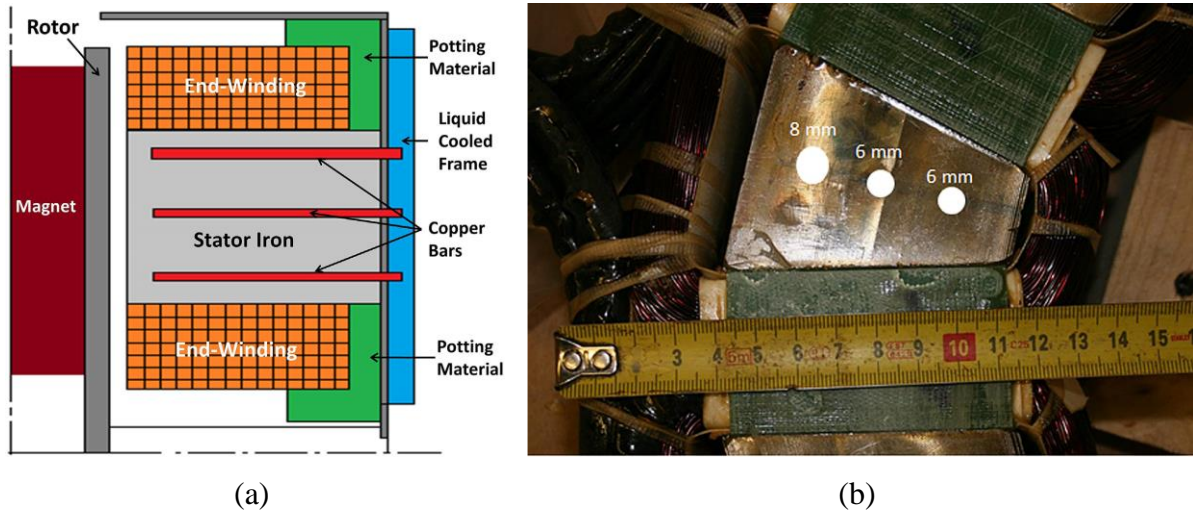


Figure 2.20 : Improved e-motor cooling from [117] using copper bars, potting, and frame liquid cooling (a) schematic e-motor radial section and (b) photo view section.

For 3-copper-bars with end winding potting, a further reduction of the end-winding temperature by approximately 10°C with respect to the 1-copper-bar case. The results showed that both improved internal cooling techniques are efficient in decreasing hot spot temperatures provided that the machine has liquid jacket cooling.

2.3.2.3 Phase-Changing Materials (PCM) Cooling

The investigation of Belletre et al. [118] is one of the rare works on the use of Phase-Changing Materials (PCM) in the cooling of electric machines. In their design, they considered a low power auto-synchronous machine with eighteen slots. Two models were considered in the simulation procedures: the first model with one side of the end-windings covered with PCM (*Figure 2.21a*) and the second is when the material covers the whole end-windings surfaces (*Figure 2.21b*). The authors remarked that when radiation heat transfer is considered, the hot spot and conductor temperatures decrease. Their study shows that the hot spot temperature decreases when the PCM thermal conductivity, its thermal inertia, and its latent heat of melting increase and when its melting temperature decreases.

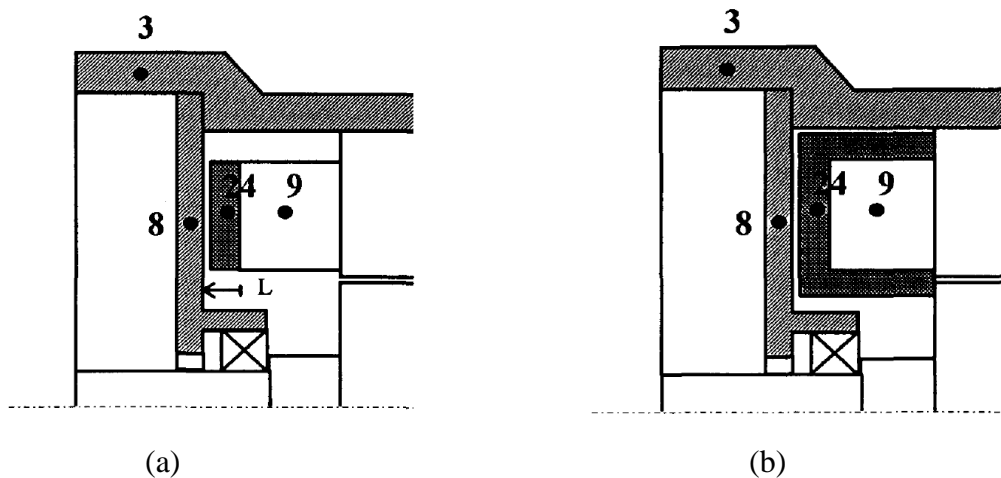


Figure 2.21 : PCM in solid-state node 24 (a) in one end-winding side (b) covering the whole end-windings cavity [118].

As reported in the work, the modeling considers four stages of PCM cooling which are described herein:

The first stage is the pre-melting where the interface temperature is calculated. The second stage is for the melting phenomenon when the heat flows at a constant temperature and the liquid-solid phase temperatures are determined by solving corresponding equations. The melted mass is assumed based on the heat flux difference at the solid-liquid interface.

Rayleigh number (Ra) is calculated at each step ($Ra = Gr Pr$, characterizing natural convection) until reaching a certain value in terms of a geometrical parameter. Reaching this value indicates the beginning of the third stage where natural convection starts. The corresponding heat transfer coefficient is computed according to Seki correlation:

$$h = 0.096 Pr^{0.051} Ra^{0.3} \quad (2.46)$$

Finally, a fourth and last stage takes place where a post-melting of PCM is noticed. It is similar to the first stage but with a PCM in a liquid state.

Depending on PCM properties, the end-windings temperature is reduced by either increasing conductivities, thermal inertia, and latent heat of melting or decreasing melting temperature. End-winding cooling can be achieved also by increasing the stator thermal inertia (15% is equivalent to 69 K cooling with gallium PCM or 14 K with P116 paraffin PCM).

2.3.2.4 Air Cooling

Despite the development and application of multiple fluid cooling technologies aiming to dissipate the increasing heat fluxes in electronic and electrical industries, air-cooling is still

used significantly and on a large scale as a classical cooling solution in electrical machines. Different configurations are used for air cooling of the electric motors and can be separated into two categories according to motor type: closed motor and open motor.

The closed motor refers to the electric machine implemented in a confined area where no environmental flow circulates in any of the machine's internal spaces (*Figure 2.22a*). It is complex to determine the convection inside the motor, and consequently, its global thermal behavior and the level of temperatures reached; it is due to many factors that affect the fluid flow inside the machine (surface finish of the rotor end sections, turbulence effect due to the rotational speed, wafers..) [45]. Usually, different types of heat dissipation can be added passively to the rotor movement providing an improved heat transfer between solid components and spaces. For example, wafers can be added to the rotor giving a fanning effect useful for end-space cooling, i.e. improving heat transfer by creating turbulent effects and therefore increasing the heat transfer coefficient. It is worth mentioning that inside the closed motor, the flow is Taylor-Couette and correlations correspond to natural convection.

In an open motor, fluid flows (usually air) through the machine, where cooling channels may exist (or simply through open space: airgap, end-space..), and the cooling process is well-improved by convection heat transfer (*Figure 2.22b*). The flow is Taylor-Couette-Poiseuille (see *subsection 2.2.2.1*).

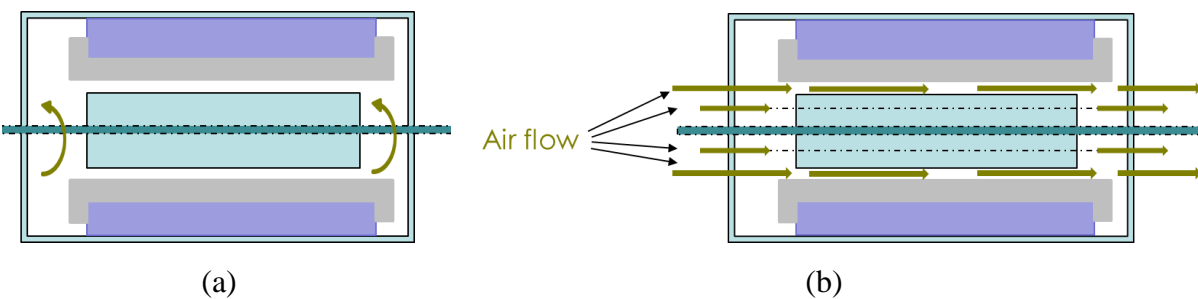


Figure 2.22 : Schematic representation of an axial section of (a) a closed electric motor and (b) an open electric motor.

At the stator level, the authors in [90] proposed the vortex tube (also known as Ranque-Hilsch vortex tube) cooling method to be used in cooling the stator with an air flowing at -40 °C. It is based on the temperature separation phenomenon and consists of converting normal pressurized gas, injected into a swirl chamber through a nozzle, into two gas streams: hot gas and cold gas, with a specific nozzle geometry allowing the transfer of energy between the two gas streams. As described in their work, the technique needs no coolant, is made of a compact and lightweight system, has a low cost of application, does not need maintenance, and presents no

spark or explosion hazard. Compared to a water-cooled machine, this method provides, in transient-state and at low speeds (~up to 3000 RPM), a reduction in stator temperature up to 60 °C, but on the other hand, there is no reduction noted at the windings level (*Table 2.8*).

	Water Cooling	Vortex Cooling	
	3000 rpm	8000 rpm	3000 rpm
			8000 rpm
<i>Temp_Slot (°C)</i>	121,55	140,26	113,15
<i>Temp_Teeth (°C)</i>	77,51	95,65	83,29
<i>Temp_Teeth_2 (°C)</i>	69,02	86,37	57,94
<i>Temp_Yoke (°C)</i>	48,38	57,90	41,49
			90,73

Table 2.8 : Comparison of vortex cooled machine with the water-cooled machine [90].

❖ Air Jet Impingement

Martin [119] provided a literature review on air submerged jets. In [120], theoretical studies on air-jet impingements were conducted. Single and multiple impinging air jets are widely used in many industrial applications because of the high heat and mass transfer coefficients which are developed in the impingement region. Generally, they are either circular (or axisymmetric jets), or slotted (or two-dimensional jets). Jet configuration and influencing factors on heat transfer coefficient (mainly Reynolds number, nozzle-to-surface distance...) are currently under investigation. Recently authors of [62], [121], [122] investigated the air impingement cooling on different parts that are similar to some specific motor parts.

❖ Air Jet Impingement on Rotating Disk

The adequate cooling of the rotor end-disks will enhance the reduction of rotor temperature. Hamdan et al. [62] reviewed the case of the geometry of a rotating disk facing a stationary one, with an air jet. They focused on the case where a confined (closed surrounding space) round jet impinged onto the rotating disk from the center of the stationary one, at a flow rate q_j and through a diameter D_j , which is expected to improve the heat transfer process. Since the same fluid is impinged through the cavity then this is a submerged jet (*Figure 2.23*). They found that only few groups of researchers focused on the study of the rotating disk with jet impingement. In [123], the authors studied experimentally shrouded parallel disks with both rotation and

coolant through-flow and visualized the flow and the heat transfer for the different values of the following parameters: Gr , Re_ω and $Cw = q_j/(v_j r_d)$ (flow rate coefficient) in *Table 2.9*.

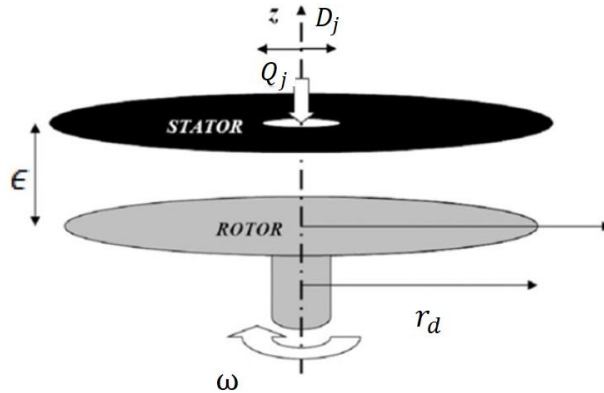


Figure 2.23 : Configuration of a disk rotating at ω and facing stationary one with impinging jet [62].

Parameter	Value		
G_c	4/9	8/9	2
Re_ω	1.8×10^5	5.4×10^5	1.1×10^6
Cw	23560	37700	73830

Table 2.9 : Parametric study values for Re_Ω and Cw [123].

Nusselt number is found to be increasing with the rotation rate as well as with the flow-rate but decreasing with G_c . Otherwise, in the laminar flow regime, Nu is not influenced by the variation of Cw . Haynes et al. [124] extended the investigation adding other values of the parameters of the previous study: the shroud clearance ($G_c = \epsilon_c/r$, ϵ_c is the axial clearance between the shroud cylinder and the rotor), with two values $G_c = 0.0033$ and $G_c = 0.0067$.

$$Cw_{min} = 0.61G_c Re_\omega \quad (2.47)$$

It was deduced that the average Nusselt number and the axial clearance are inversely related and that for small rotational Reynolds number, the rotational speed rate seems to not affect the results, while for large values the case is similar to that of a free disk. For a range of rotational Reynolds number Re_ω and jet Reynolds numbers ($Re_j = u_j D_j / v_j$ respectively, where u_j is the jet velocity, D_j is the jet diameter and v_j is the kinematic viscosity of the jet fluid, which is the air in this case), the correlations of the average Nusselt number at the rotor surface \overline{Nu}_{r_d} , proposed by [121] for different aspect ratio values, can be grouped in *Table 2.10*. Harmand et al. [62] considered also the multiple jets solution for the cooling study of this component, considering two possible interactions: the first between every two successive jets and the second

between the impinging jets and the flow formed by the fluid of the neighboring jets. They deduced that the correlations obtained for a single jet based on the dimensionless numbers are not enough for the case of multiple jets.

G	[0.01; 0.02]	[0.04; 0.08]	0.16
Re_j	$\leq 4.17 \times 10^4$		
Re_ω	$[2 \times 10^4; 5.16 \times 10^5]$		
$\overline{Nu_{r_d}}$	$0.08G^{-0.07}Re_j^{0.5}Re_\omega^{0.25}$	$0.006G^{-0.07}Re_j^{0.5}Re_\omega^{0.5}$	$0.006Re_j^{0.25}Re_\omega^{0.25}$

Table 2.10 : Average Nusselt number in the rotor for different aspect ratio according to Re_ω and Re_j [121].

Lallave et al. [125] suggested the following correlation for averaged Nusselt number of rotating disk under confined jet impingement cooling:

$$\overline{Nu_{r_d}} = 1.97619 \left(\frac{t_{noz}}{D_j} \right)^{0.0909} \left(\frac{4Q_j}{\pi v_j D_j} \right)^{0.75} \left(\frac{v_j}{4\omega r_d^2} \right)^{-0.1111} \left(\frac{\lambda_s}{\lambda_f} \right)^{-0.9} \quad (2.48)$$

Where t_{noz} is the distance from the rotor disk to the nozzle, λ_s and λ_f are the thermal conductivities of the solid and the fluid respectively.

❖ Air Jet Impingement on Windings

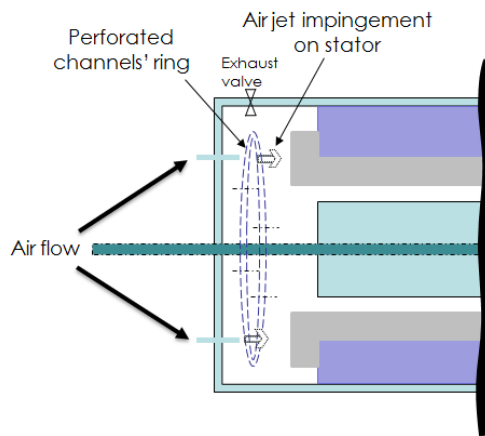


Figure 2.24 : Schematic representation of an open electric motor jet impingements on stator windings.

A possible air jet cooling technique applied at the surface of the end-windings is depicted in Figure 2.24. This technique aims mainly to improve the convection coefficient in this area and to create a circulation of fresh air arriving at the surface of these hot spot zones. These two factors will significantly help to extract heat from the motor windings efficiently (see subsection 2.2.2.3 for end-windings end-space convection).

2.3.2.5 Liquid Cooling

Many authors investigated liquid cooling in electrical machines as water jackets around the stator [80], [126] or refrigerant cooling of the stator [127], [128]. Liquid cooling can be applied to rotor [83] or both stator and rotor [107].

❖ Internal Flow Liquid Cooling

Electric motor cooling through channels has been the subject of many patents [129]–[132].

Most of the concerned authors suggested using oil as a coolant in internal liquid channels for electric safety reasons. To improve the performance at low speed and high torque of a 43 kW induction motor (TEFC machine with turbine fitted on the external part of the shaft and housing fins), Assaad et al. [133] proposed to integrate an oil cooling circuit in a hollow shaft having three holes inside the motor. These holes are used for oil injection directly on motor active parts and are illustrated in *Figure 2.25*.

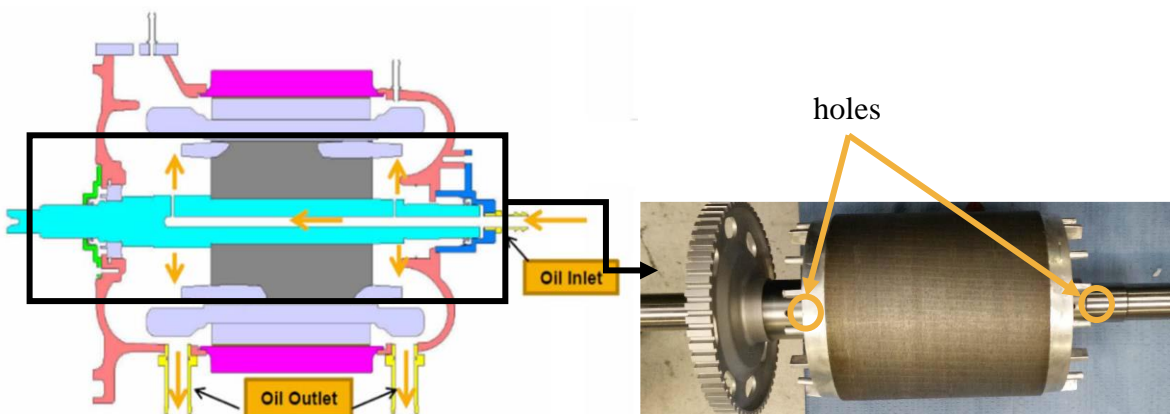


Figure 2.25 : Motor oil cooling, (left) circuit illustration, (right) with rotor and shaft with holes [133].

Nategh et al. [36] proposed oil jackets used for both stator and end-windings cooling. They simulated and tested experimentally two machines made respectively with two different impregnation materials (varnish and epoxy) and under different cooling conditions and losses levels. In their system, after flowing in the stator channels, the oil drops off on the outer surface of the end winding body and is then collected at the bottom side of the housing. The collected oil is emptied using two outlets mounted in both end shields. Based on [32], [33], they used the following correlation for Nusselt number calculation in the model (considering laminar flow and rectangular channel of *Figure 2.14*):

Heat transfer from stator back to the oil of thermal conductivity k_{oil} :

$$Nu_{D_h} = 7.49 - 17.02 \left(\frac{H}{W} \right) + 22.43 \left(\frac{H}{W} \right)^2 - 9.94 \left(\frac{H}{W} \right)^3 + \frac{0.065 Re_{D_h} Pr D_h / L_{Ch}}{1 + \left[0.04 \left(\frac{Re_{D_h} Pr D_h}{L_{Ch}} \right)^{2/3} \right]} \quad (2.49)$$

Where L_{Ch} is the length of each cooling channel.

Heat transfer from the end-winding surface to the oil (laminar flow in a flat surface):

$$Nu_{D_h} = 0.664 Re_{D_h}^{0.5} Pr^{1/3} \quad (2.50)$$

$$h = Nu k_{oil} / D_h$$

❖ Liquid Jets and Sprays

From a general point of view, liquids provide a better heat transfer coefficient than air, therefore some electric motor designers and researchers have focused recently on studying liquid cooling methods. In some works [134], [135], the authors compared jet and spray cooling using water, and found that the same global heat transfer is achieved by spray at a lower flow rate. Other authors [136]–[138] investigated oil jets and sprays for electric machine cooling and searched for improving heat transfer by modifying corresponding parameters. In their theses, [43], [139] studied the oil cooling of the motor airgap. Besides, patents were granted to some original works in this area, such as those in [140], [141].

❖ Liquid Jets

Jet impingements offer a good solution for surface cooling. Impingement cooling schemes may be classified according to whether they involve unconfined or semi-confined jets, crossflow effects associated with neighboring jets, circular or rectangular (slot) jets, and free-surface or submerged jets. Unconfined free surface and submerged jets are shown in *Figure 2.26* [142]. Depending on these conditions and properties, correlations for Nusselt number are presented to study convection heat transfer by jet cooling.

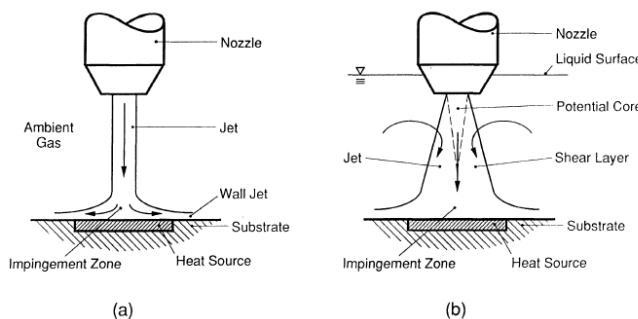


Figure 2.26 : Schematic representation of unconfined (a) free surface and (b) submerged jets impinging on a discrete heat source [142].

Zheng and his co-authors [143]–[145] conducted their studies on submerged and free jets using different liquids (transformer oil, ethylene glycol) and compared results of measurements or prediction of heat transfer coefficient. Jet impingements are recently used in the cooling of electric traction drive machines in some vehicles and the cooling is accomplished by impinging automatic transmission fluid (ATF) directly onto the copper windings [92]. According to [138] the dielectric property of the ATF makes it a good choice for removing heat by direct cooling but no major studies are available regarding direct cooling of end-windings by ATF. The authors approached concentrated ATF jets for a temperature T ranging between 50 °C and 90 °C. They tested jet impingements with different surface features with sandpaper polished baseline and other samples are made with wire bundles with radii corresponding to American wire gauge AWG. Highlighting the effect of the surface topology, they found a coefficient of heat transfer, depending on the jet velocity ranging between $1000 \text{ W}\cdot\text{m}^{-2}\cdot\text{K}^{-1}$ and $10000 \text{ W}\cdot\text{m}^{-2}\cdot\text{K}^{-1}$ for a jet velocity from $0.5 \text{ m}\cdot\text{s}^{-1}$ up to $10 \text{ m}\cdot\text{s}^{-1}$. They concluded also that the pressure drop across the nozzle was found to be decreasing with increasing fluid temperature (lower viscosity values). According to [146] and based on [147], the average Nusselt number for an unconfined circular free jet on a surface equivalent diameter (D_s much larger than nozzle diameter (d_n) (i.e. $D_s/d_n \gg 1$), is correlated as follows:

$$\text{For } 2.2 \times 10^3 \leq Re_{d_n} \leq 1.4 \times 10^5, 3 \leq Pr \leq 150, 1.75 \leq \frac{D_s}{d_n} \leq 25.1, 1 \leq \frac{d_s}{d_n} \leq 3$$

$$\overline{Nu}_{D_s} = 2.74 \left(Re_{d_n}\right)^{0.348} \left(Pr\right)^{0.487} \left(\frac{D_s}{d_n}\right)^{-0.774} \left(\frac{\mu_s}{\mu_\infty}\right)^{-0.37} \quad (2.51)$$

Where d_s is the surface to nozzle distance, μ is the dynamic viscosity, subscripts s and ∞ correspond respectively to the surface and the free-stream condition.

❖ Liquid Sprays

Since it was first applied in electronic system technology and despite being based on a complex phenomenon, spray cooling (*Figure 2.27*) was able to provide a great balance of high heat flux removal capability, iso-thermal property, and fluid inventory, compared to other liquid cooling methods [148]. Some works focused on spray cooling under multiple conditions. Mudawar and their co-authors [149]–[153] and more recently Wang and their co-authors [154]–[156] examined spray cooling in different modes and under different conditions (single-phase convection, which is found to be the primary heat transfer mechanism and two-phase convection, beyond and within critical heat flux (CHT)..). Wang et al. [154] studied the effect of varying the orifice-to-surface distance and the spray inclination, on the performance of the

cooling, in a non-boiling regime. They found the optimum distance between orifice and test square surface for the best heat transfer efficiency (6 mm , 3.5 mm , and 2.1 mm) corresponding to each spray inclination angle adopted for optimum results (28° , 42° , and 49°). Besides, they developed in this work an empirical correlation for the Nusselt number based on the experimental study (equation (2.52)).

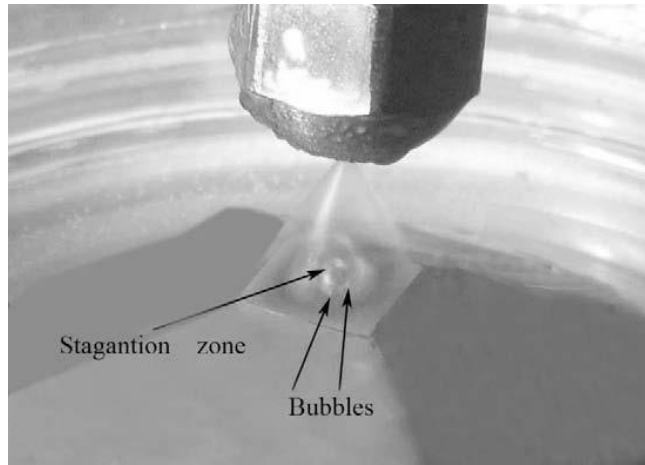


Figure 2.27 : Spray cooling over a square test surface in stagnation at 0° angle inclination and 8.66 mm standoff distance [154].

This correlation is a function of Reynolds number and the non-dimensional temperature $\xi = \frac{T_s}{T_{boiling} - T_e}$ where T_s is the surface temperature, $T_{boiling}$ is the liquid boiling temperature and T_e is the environment temperature. The authors also provided correlations of the Reynolds number and the average heat flux with taking into account inclination that produces elliptical spray area.

$$Nu = 7.144 Re^{0.438} \xi^{0.9016} \quad (2.52)$$

The authors in [148], [157], in combination with data from [153], adopted the following correlation (2.53) for Nusselt number on the targeted surface of sprays in single-phase regime for the PF-5052 coolant, which is an ozone-depleting substance:

$$Nu_{d_{32}} = 4.7 Re_{d_{32}}^{0.61} Pr_f^{0.32} \quad (2.53)$$

With:

$$Nu_{d_{32}} = \frac{q''}{T_s - T_i} \frac{d_{32}}{k_l} \quad (2.54)$$

And:

$$Re_{d_{32}} = \frac{\rho_l \overline{Q''} d_{32}}{\mu_l} \quad (2.55)$$

Where $\overline{Q''}$ is the average volumetric flux, k_l , ρ_l and μ_l are respectively the thermal conductivity, density, and viscosity of the liquid, d_{32} is the Sauter mean diameter which is the droplet diameter with the same volume to surface ratio as the entire spray, expressed by:

$$d_{32} = \frac{\sum n_i d_i^3}{\sum n_i d_i^2} \quad 0.6 \times 10^{-3} < Q'' < 9.96 \times 10^{-3} \quad (2.56)$$

These expressions are defined for surface temperatures below 400°C.

Few authors examined spray cooling in the electric machine case. The interesting work of Lim et al. [158] in this area concerns a 35 kW in-wheel electric motor oil cooling. Based on their numerical analysis and experiments, they found that oil spray cooling injected from a hollow shaft to coil/stator core, bearings, and reduction gear (as shown in *Figure 2.28*), has better thermal performance compared to conventional models where oil stagnates in the lower end of the machine.

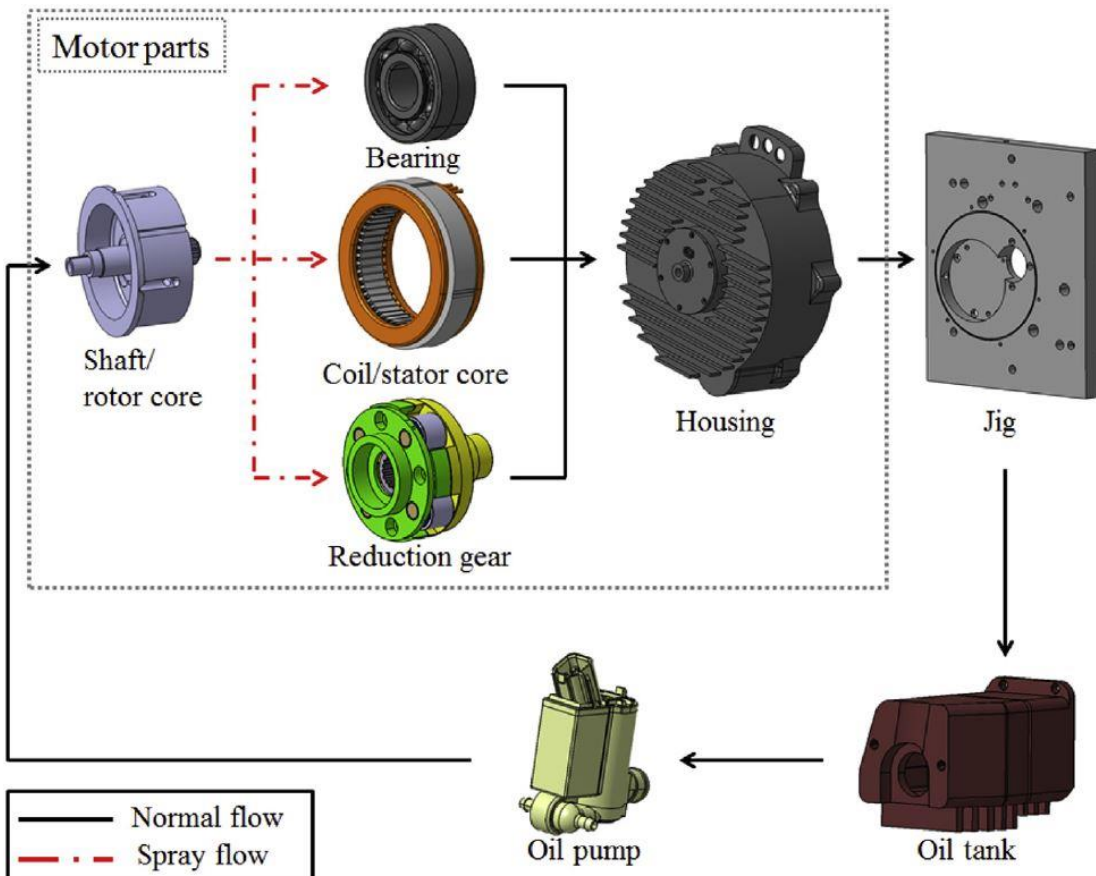


Figure 2.28 : Flow circuit of an in-wheel motor cooling system [158].

They deduced that the windings temperature is reduced and that this cooling technique demonstrates a more uniform inner temperature distribution.

2.3.2.6 *Internal Heat Pipes and Two-Phase Loop*

Heat Pipes and Two-Phase Loops technology integrated to electric motors has been recently the object of many patents (approved or under revision), yet very few studies investigated two-phase cooling in this configuration. In 2009, research on Heat Pipes has led to initiate and incite investigations of these cooling devices and their installation inside the motor. The aim is to cool directly the machine's internal part with a more efficient and more compact system. Through the patent [104] with publication number US 7569955 B2 entitled: "Electric Motor with Heat Pipes", the authors were based on using straight heat pipes and placing the evaporator part in the stator laminated core, and the condenser in a cooling chamber containing a coolant circulating using a pump (*Figure 2.29a*). In this conception, there are many difficulties to mention. First, the risk of leakage of heat pipes inside the motor, second the possible maintenance that is difficult to perform, and finally the power supply required to circulate the coolant. Later on, the invention of [105] has been granted a patent in this field with publication number US 8368265 B2, entitled: "Electric Motor Having Heat Pipes" also using straight heat pipes. The heat pipes are placed around the motor shaft while the condenser is on the impeller. In this technique, the disadvantage is that any leakage in the heat pipes will risk damaging the motor in addition to the difficulty of repairing eventual damage. The work of [106] has been granted a patent for the invention entitled: "Cooling of an Electric Motor via Heat Pipes", patent with publication number US 9561716 B2 in which straight heat pipes were used. The evaporator section was installed in the motor housing and the condenser in the cooling tank. Also, [107] considered another model for electric motor cooling with heat pipes under patent number US 9331552 B2 entitled: "Rotor Assembly with Heat Pipe Cooling System". It was based on putting the evaporator in the shaft and the condenser equipped with cooling fins outside the motor (*Figure 2.29b*). Here also, the drawback is that any leak in heat pipes may cause damage to the motor construction since they are put inside the shaft and a special design is required.

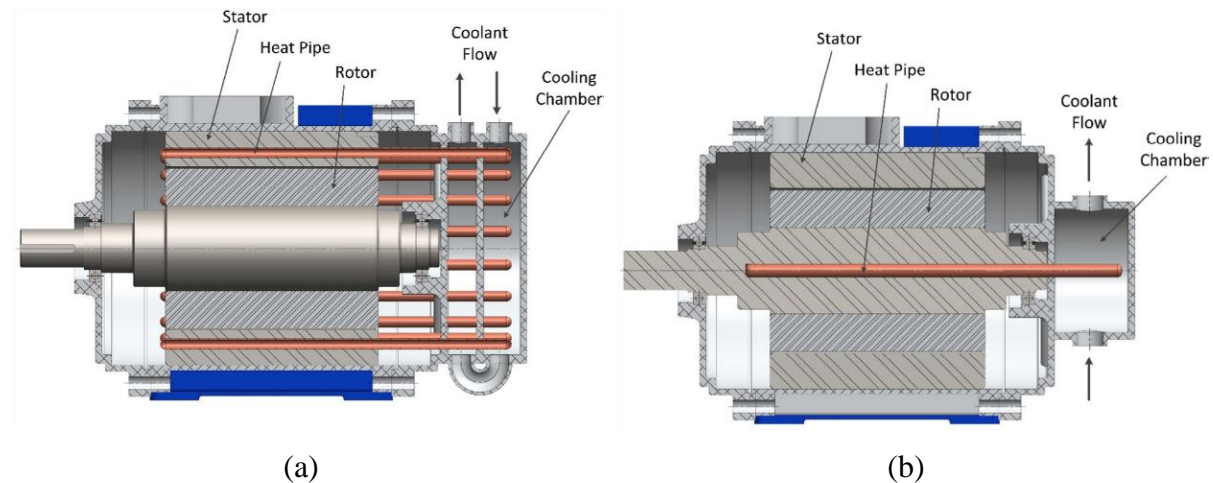


Figure 2.29 : Electric motor internal Heat Pipes: (a) Electric Motor with Heat Pipes [104]

(b) Rotor Assembly with Heat Pipe Cooling System [105].

2.4 Conclusion

A review of the existing methods for e-motor thermal management was presented based on the literature. In this review, the basics of heat transfer phenomena in electric machines are assessed and the existing cooling solutions are presented with corresponding descriptions and information. Efficient techniques are relative to the motor design, but the major conclusion is that liquid cooling provides higher heat extraction for high specific power machines. An important point as well is that critical temperature found in end windings of these machines encouraged researchers to bring cooling techniques closer to these zones, which helped to reach higher performance through windings direct cooling.

CHAPTER 3 LUMPED PARAMETER THERMAL MODELING

Synopsis:

Given the general notions and characteristics of a permanent-magnet synchronous electric motor, the numerical thermal model of the system is constructed using nodal modeling method. Elaboration of the main model components and details on the construction procedure are presented hereafter.

3.1 Introduction

Based on the literature [93], [159], among many thermal modeling techniques, the Lumped Parameter Thermal Modeling (LPTM) is considered an interesting method to assess electric motor thermal behavior. This method can be applied to solve steady-state and transient thermal problems and their relative equations for the whole machine. It is often used in electrical problems as well as in thermal and heat transfer problems thanks to the analogy between electrical and thermal quantities.

In addition to the time-based efficiency of this technique (compared to other solutions such as Finite Element Modeling or Computational Fluid Dynamics), for e-motor application, this technique is also characterized by other features. The main feature of LPTM is the possibility to model components of multiple dimensions. Moreover, the model can be integrated into other systems and/or aspects i.e. the electromagnetic and mechanical models, the simple fluid dynamics, connection to system control, and others. LPTM is also a multiscale modeling technique that allows considering thermal resistance for structures of different scales from micro-scale (contact resistance) to a higher one (conduction along rotor axis).

3.2 LPTM Approach

The lumped parameter analysis is a modeling method that consists of discretizing a distributed system to apprehend its behavior. It will be applied to the electric motor system to investigate its thermal behavior and proceed with its thermal management. Also called Nodal Network Modeling, this technique is based on certain assumptions reducing the system and presented thereafter. Being a nodal network, the main components in the thermal nodal network are the thermal conductance between two nodes that defines the heat transfer between them, the thermal capacity of each node for transient analyses, and the heat sources or heat sinks at each node. To address the determination of these components, a direct approach to heat transfer modes and principles to proceed with LPTM is presented. Further description of the LPTM method, as well as thermal modeling theories and equations, can be found in [160].

The heat transfer in LPTM is modeled based on the thermal energy balance. The equation governing heat diffusion in a domain Ω , including the mass transport term, is written as follows:

$$\rho c_p \left[\frac{\partial T}{\partial t} + \vec{u} \cdot \vec{\nabla} T \right] = \vec{\nabla} \cdot (\lambda \vec{\nabla} T) + \dot{q} \quad (3.1)$$

Where $\vec{u} \cdot \vec{\nabla} T$ is the mass transport term, $\vec{\nabla} \cdot (\lambda \vec{\nabla} T)$ is the diffusion term, \dot{q} is the heat production density. T is the temperature at a point in the domain, ρ is the density, c_p is the specific heat, λ is the thermal conductivity, and \vec{u} is the velocity field. This latter equation is associated with the following general boundary condition at the boundary Γ of domain Ω , and initial condition respectively:

$$\lambda \vec{\nabla} T \cdot \vec{n} = h(T_{ref} - T) + \varepsilon \sigma (T_p^4 - T^4) \quad (3.2)$$

$$T(t = 0) = T_{init} \quad (3.3)$$

The term $h(T_{ref} - T)$ is the heat flux density exchanged through convection mode, where h denotes the convection coefficient and T_{ref} is the reference temperature of the fluid media. The term $\varepsilon \sigma (T_p^4 - T^4)$ is the heat flux density relative to radiation heat transfer mode, where ε is the emissivity of the surface, σ is the constant of Stefan-Boltzmann, and T_p is the temperature of the body surface with which the surface Γ exchanges heat by radiation.

To proceed with LPTM, a discretization of the domain into N finite volumes V_i must be performed. Each volume is represented by a node i at its center, to which a temperature T_i , a thermal capacity $C_i = (\rho c_p)_i V_i$, and a heat source \dot{Q}_i representing the generated heat through this volume, are assigned. Assuming that each finite volume is homogeneous and isothermal and that the heat is produced uniformly through that volume, the equation of thermal energy balance can be expressed as follows:

$$(\rho c_p)_i V_i \frac{dT_i}{dt} = \sum_k \Phi_{i k, \text{ conduction}} + \sum_l \Phi_{i l, \text{ convection}} + \sum_m \Phi_{i m, \text{ radiation}} + \sum_p \Phi_{i p, \text{ mass transport}} + \dot{Q} \quad (3.4)$$

Where the sums $\sum_k \Phi_{i k, \text{ conduction}}$, $\sum_l \Phi_{i l, \text{ convection}}$, $\sum_m \Phi_{i m, \text{ radiation}}$, and $\sum_p \Phi_{i p, \text{ mass transport}}$ are the sums of exchanged heat fluxes through conduction, convection, radiation, and mass transport modes respectively between node i and its surroundings.

If radiation phenomenon is to be considered directly in the nodal network model, problem linearization is needed, since a nonlinear equation characterizes this heat transfer mode. In

numerical models, this requires some specific considerations and assumptions (view factors, surface properties, and grey or black bodies hypotheses) and many iterative procedures.

According to [161], radiation heat transfer for e-motors could be negligible when forced cooling is occurring. In our case, radiation is assumed negligible during the first-time simulation, and then the obtained temperatures in end-windings and surrounding surfaces are extracted to evaluate the probable radiation heat flux. This flux will be compared to the preeminent heat flux in this area - mainly convection heat flux – and the assumption of neglecting this phenomenon is either maintained or rejected in the subsequent simulations.

Therefore, a system of N Ordinary Differential Equation (ODE) is obtained, and equation (3.4) is expressed for each node as follows:

$$C_i \frac{dT_i}{dt} = \sum_{j,i \neq j} G_{ij}(T_j - T_i) + \dot{Q}_i \quad \text{for } j: 1 \dots N \quad (3.5)$$

Where G_{ij} is the thermal conductance characterizing the heat transfer in both solid and fluid regions between volumes of nodes i and j (index j corresponds to the adjacent node connected to node i). For diffusion and convection processes, heat transfer is reciprocal, hence: $G_{ji} = G_{ij}$.

It can be more convenient in a nodal representation to formulate the previous equation without exhibiting the temperature difference $T_j - T_i$, as follows:

$$C_i \frac{dT_i}{dt} = \left(- \sum_{j,i \neq j} G_{ij} \right) T_i + \sum_{j,i \neq j} G_{ij} T_j + \dot{Q}_i \quad (3.6)$$

When i is connected to reference temperature T_{ref} , a corresponding conductance appears $G_{i,ref}$, and an additional heat sink term for the evacuation of heat ($\psi_{i,ext} = G_{i,ref} T_{ref}$) is added to the equation as follows:

$$C_i \frac{dT_i}{dt} = \left(-G_{i,ref} - \sum_{j,i \neq j} G_{ij} \right) T_i + \sum_{j,i \neq j} G_{ij} T_j + \dot{Q}_i + \psi_{i,ext} \quad (3.7)$$

\dot{Q}_i and $\psi_{i,ext}$ stand respectively for heat sources (motor losses in our case) and heat sinks (coming out from boundary conditions for heat evacuation by convection). To solve the first-order linear differential equation of temperature, they can be summed in one term: $\Psi_i = \psi_{i,ext} + \dot{Q}_i$.

As it was evoked, fluidic connections by mass transport can also be represented in the model, for which the appropriate expression of conductance between two fluid nodes i and j depends on the flow and its direction. There is no reciprocal relation in thermal conductance when both nodes are fluidic.

This allows writing a matrix form of the thermal balance equation of the overall domain discretized into N nodes as follows:

$$C \frac{dT}{dt} = G T + \Psi \quad (3.8)$$

Where C and G are $N \times N$ matrices representing capacity and conductance matrices, and T and Ψ are vectors (of dimension N) representing temperature and heat generation vectors in the system. These matrices and vectors are structured as follows:

$$C = \begin{pmatrix} & & 0 \\ & \ddots & \\ & & C_i \\ & & 0 \end{pmatrix},$$

$$G = \begin{pmatrix} G_{i1} & & -G_{i,ref} - \sum_{\substack{j=1 \\ j \neq i}}^n G_{ij} & G_{in} \end{pmatrix}$$

$$T = \begin{pmatrix} \cdot \\ \cdot \\ \cdot \\ T_i \\ \cdot \\ \cdot \\ \cdot \\ \cdot \end{pmatrix} \quad \text{and} \quad \Psi = \begin{pmatrix} \cdot \\ \cdot \\ \cdot \\ \dot{Q}_i + \psi_{i,ext} \\ \cdot \\ \cdot \\ \cdot \\ \cdot \end{pmatrix}$$

An implicit Euler time-scheme will be used to solve Equation (3.8) in the transient regime. Whereas the steady-state temperature vector T can be obtained by inverting the matrix G : $T = -G^{-1} \Psi$. The heat flux Φ_{ij} between nodes i and j is computed using the following equation:

$$\Phi_{ij} = G_{ij}(T_j - T_i) \quad (3.9)$$

In both transient regime and steady-state, the thermal conductance matrix G and the heat generation vector Ψ should be defined according to the geometry structure and the system characteristics. The thermal capacity matrix C is only defined to solve transient regimes, allowing the prediction of temperature evolution as a function of time. LPTM of the motor system requires specific input parameters, which are extracted from the motor geometry, materials and their properties, initial and boundary conditions, and machine losses generating the heat inside the motor. The following section points out the definition of electric motor system composition.

3.3 Electric Motor System Definition

The case-study system consists mainly of the electric motor structure and its subsystems including cooling techniques, heat generation, etc... These parts should be defined to proceed with LPTM configuration and simulation based on Equation (3.8). Therefore, this requires the definition of many parameters and conditions to enable system modeling and get representative results of the thermal analysis: determination of motor temperatures, detection of thermal problems, finding appropriate cooling solutions, and others.

These parameters and conditions include:

- Geometry and relative data
- Structure materials and properties
- Fluid properties (namely air and liquid coolant if applied)
- Initial and boundary conditions, such as surrounding temperature
- Heat sources distribution, location, and values

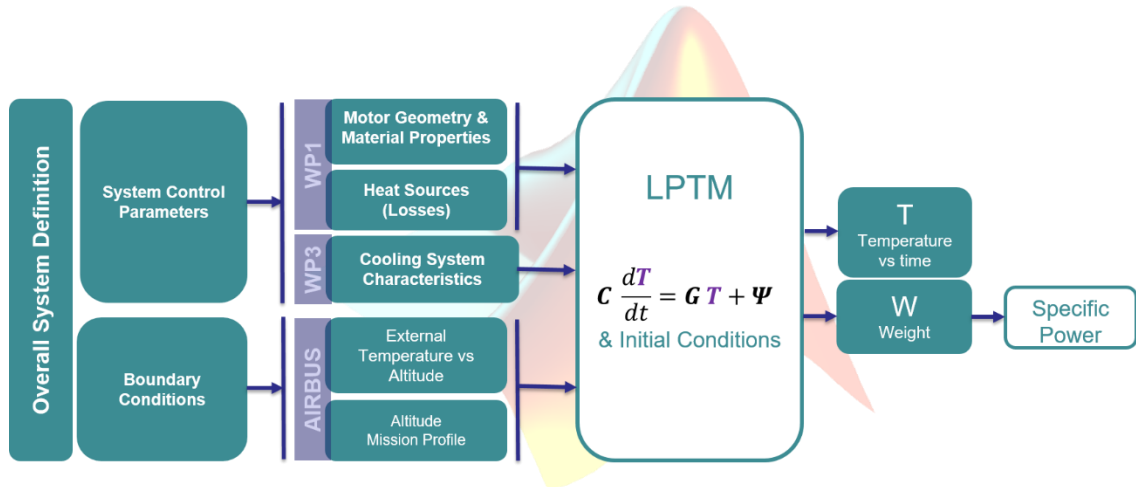


Figure 3.1 : Overall system definition of e-motor LPTM.

The overall system definition of e-motor LPTM is suggested as in *Figure 3.1*. The system control parameters defined at WP1 and WP3 are related to electric machine design and cooling and can be modified upon the given specifications and targets. Boundary conditions are provided by our industrial partner Airbus to represent the outside motor operating conditions and can be modified accordingly. The outputs of the model are mainly the temperatures of the components. On the other hand, in the specific context of the present study (electric motor for the propulsion of transportation means and more specifically in the aeronautical sector), the system weight has major importance. Consequently, the results of our model (called *ATHEM*) will include the system weight calculation, particularly the cooling system weight (taking into account the cooling fluid weight and the pipe weight for instance). The system definition and outputs are detailed in the following subsections.

3.3.1 E-Motor Geometry and Materials Properties

For the motor system discretization into finite volumes, it is crucial to define a geometry design that includes all data on motor components and their dimensions, materials properties, and some mechanical and electrical data. Depending on these electro-technical design data, the cooling system design can be proposed and modeled. Several questions may be asked to help to define the possible cooling type consequently, for instance: is the motor open or close? In other words, is it directly connected to the outside medium or totally enclosed? is it possible to integrate an external flow inside the machine? Actually, on one hand, the motor type, design, and geometry

determine the electro-magnetic and mechanical phenomena (that take place in the e-motor to allow converting electrical energy into other energy forms) and define by this way the generated heat fluxes of the motor system. On the other hand, the motor geometry influences the cooling techniques that could be selected for thermal management. Materials' physical properties should be defined to determine conduction thermal conductances and thermal capacities. When recalling the geometry of the case-study motor type: SM-PMSM (Surface Mounted-Permanent Magnet Synchronous Motor) presented earlier in *Chapter 1*, it is revealed that motor parts are made up of many materials with various physical properties. Some motor components are heterogeneous and made out of multiple micro-structures (up to hundreds of copper wires in the winding for example), whose geometries are generally not accurately known (e.g. precise position and configuration of wires in the winding slot). For time-optimization reasons, these components are better considered homogeneous with equivalent properties. Therefore, all motor components geometry, dimensions, and materials must be defined to solve the motor model and find suitable cooling solutions, and in an advanced step, optimize the motor thermal management.

3.3.2 Boundary conditions

Boundary conditions are defined as boundary temperatures (termed reference temperatures T_{ref}) and convection Heat Transfer Coefficients (HTC) for external nodes connected to some system nodes. In general, the electric motor heat sinks depend on cooling solutions. It could be one or more heat exchangers (to which reference temperatures and heat convection coefficients are set), with or without forced air convection. Along with the adapted modeling of the motor, the location and type of these boundary conditions are determined.

The value of HTC between the motor structure and its surroundings depends on the motor environment and can be determined based on [32], [33], [61], [74] as detailed in the previous *Chapter 2*.

3.3.3 Electric Motor Losses (Heat Sources)

The high heat dissipation inside the electric motor is due to the losses resulting from electro-magnetic phenomena and aerothermal effects due to high rotational speed. Generally, these

losses are categorized for the PMSM type as follows: **Joule Losses** (in windings), **Magnetic Losses** (Iron Losses and Permanent-Magnets Losses), and **Mechanical Losses** due to friction (Windage Losses in Airgap and Rotor End-caps, and Bearings Losses). Magnetic losses in the rotor are neglected based on electro-technical data (iron losses in the rotor are neglected to assume the hypothesis of first harmonic). Windage or aerothermal losses in rotor result from friction between air and rotor surfaces. They can be quite significant in the case of high-speed rotation. They are located mainly in airgap and rotor end-caps and are estimated based on correlations.

It is commonly known in PMSM machinery that stator losses are highly significant and lead to serious thermal problems that can end up with real damage to the motor if heat dissipation is not well treated.

In the rotor, thermal constraints on magnets can be critical even when losses in this motor area are relatively low. Due to the relatively low allowed maximum temperature in magnets ($100\text{--}150\text{ }^{\circ}\text{C}$ against $200\text{ }^{\circ}\text{C}$ for other motor parts).

Since the heat sources in the system correspond to these losses, it is important that an accurate distribution and allocation of the thermal input sources could be defined in the thermal model. In the nodal network, these heat sources are injected into nodes according to where losses occur. Surface losses are assigned to surface nodes, particularly at the extremities while volume losses are correspondingly allocated to volume nodes. Moreover, due to the dynamical change of required power during the flight mission losses have resultant profiles in terms of time. This aspect will be considered in the electric motor design (WP1 expertise area- see *Chapter 1*) and in the cooling system definition and sizing in the present work. In the thermal model, losses variation in terms of flight time will be taken into account instantly to take advantage of the thermal inertia of some motor components. This transient effect may help to reduce the increase in temperature in the motor core and consequently decreasing the required cooling effort.

Let us first briefly define the PMSM losses and the physical phenomena behind them. For each type of losses, the corresponding definition, determination, and distribution of heat production in the motor model are presented.

3.3.3.1 Joule Losses

Joule losses (or winding losses in our case-study motor) are located in copper conductors and can also be called copper losses. As their name reveals, they result from Joule effect and are produced due to current circulation in windings resulting from the electrical potential difference between each of the stator ends. Since these losses are the main reason behind temperature rise in windings, they are considered as the primary threat to windings damage and thus the operation failure of motors of PMSM type. Motor Joule losses resulting from an electrical current I_{el} in the winding coils having an electrical resistance \mathcal{R}_{el} , are calculated in terms of the number of phases n_{ph} as follows:

$$P_{Joule} = n_{ph} \mathcal{R}_{el} I_{el}^2 \quad (3.10)$$

Electrical resistance is calculated, considering Direct Current (DC) circulation, as a function of the conductor temperature T_{cu} as follows: $\mathcal{R}_{el} = \rho_{cu,T_0} (1 + \alpha_{el}(T_{cu} - T_0)) l_c / S_c$, where ρ_{cu,T_0} is the electrical resistivity of copper at 20 °C, α_{el} is the temperature coefficient resistance ($\alpha_{el}=3.93\times10^{-3} K^{-1}$), l_c is the conductor length and S_c is the conductor cross-section.

An existing effect in conductors called skin effect results from the circulation of Alternating Current (AC) in windings once surrounded by the magnetic field (in the stator, in airgap...) and will lead to additional Joule losses. Due to the magnetic field in a conductor, the proximity effect occurs as well in the other neighboring conductors. The calculation of Joule losses of a PMSM with alternating current circulation should take into consideration skin and proximity effects. Estimation of these losses depends on the AC electrical resistance \mathcal{R}_{AC} . In this case $\mathcal{R}_{el} = \mathcal{R}_{AC}$ is used in the previous equation (3.10) to determine Joule losses. This resistance is defined by its ratio to the DC electrical resistance: $\mathcal{R}_{AC}/\mathcal{R}_{DC}$. This ratio is function of many parameters and is roughly estimated by the analytical approach since it strongly depends on the effective configuration of coils in the slots. These parameters are mainly geometrical depending on the slot dimensions, number of conductors in the slot, their height and width for rectangular copper wires, and the spacing of conductors. There are also physical factors mainly copper electrical conductivity and current frequency. These effects can be neglected in some configuration cases (Litz wires or ultra-thin insulator conductors are examples of these cases).

In the PMSM Thermal model, these losses are injected into stator slots enclosing the windings and to end-winding parts at each motor side (front and rear).

3.3.3.2 Iron Losses

Iron losses are produced in ferromagnetic materials. In PMSM, they are found in laminations and can be sometimes more significant in value than Joule losses, and can be estimated according to their category (Hysteresis, eddy current resulting from Faraday's law, and excess losses) based on [162] as follows:

$$P_{Iron} = k_h f_{el} B_m^2 + k_c f_{el}^2 B_m^2 + k_e f_{el}^{3/2} B_m^{3/2} \quad (3.11)$$

Where B_m is the maximum magnetic flux density, f_{el} is the frequency, k_h is the hysteresis loss coefficient, k_c is the eddy loss coefficient and k_e is the excess loss coefficient.

Iron losses are very important to consider in the thermal management of e-motors. Based on the aforementioned assumptions (neglecting the rotor laminations losses), they are mainly located in the stator laminations and are considered uniformly distributed between teeth and other areas.

3.3.3.3 Airgap Losses

Windage losses in airgap are relative to rotor movement creating tangential velocity components. The friction of rotating air to surfaces and between its fluid layers, creates significant heat dissipation, These losses are estimated according to [163] based on [164] by:

$$P_{Airgap} = k_r \mathbb{C}_{M,airgap} \pi \rho_{air} \omega^3 r_{rotor}^4 L_{airgap} \quad (3.12)$$

Where k_r is the roughness coefficient. According to [163]: $1 < k_r < 4$, depending on rotation speed and surface smoothness. To estimate these losses WP1 of the project used the value $k_r=1$ considering smooth rotor and stator surfaces. $\mathbb{C}_{M,airgap}$ is the friction coefficient in airgap depending on flow characteristics. It is defined at WP1 by:

$$\mathbb{C}_{M,airgap} = 0.515 \frac{(e_g/r_{rotor})^{0.3}}{Re_{ag}^{0.5}} \text{ for } 500 < Re_{ag} < 10^4 \quad (3.13)$$

$$\mathbb{C}_{M,airgap} = 0.325 \frac{(e_g/r_{rotor})^{0.3}}{Re_{ag}^{0.2}} \text{ for } Re_{ag} > 10^4 \quad (3.14)$$

Where e_g is the airgap thickness and Re_{ag} is the rotational Reynolds number relative to airgap considering rotor speed ω defined by: $Re_{ag} = \frac{\rho_{air} r_{rotor} e_g \omega}{\mu_{air}}$

3.3.3.4 Rotor End-caps Losses

At the end-caps of the rotor, there are windage losses at each side due to friction between these rotating ends and the surrounding air layer in motor cavities. These losses are estimated by [163] as in equation (3.15):

$$P_{Rotor} = \frac{1}{2} \mathbb{C}_{M,rotor} \pi \rho_{air} \omega^3 (r_{rotor}^5 - r_{shaft}^5) \quad (3.15)$$

$\mathbb{C}_{M,rotor}$ is the friction coefficient at the rotor end-caps deduced from the coefficient of moment relative to torque presented earlier in *Chapter 2*. WP1 used the following correlations to compute the friction coefficient:

$$\mathbb{C}_{M,rotor} = \frac{3.87}{Re_{\omega}^{0.5}} \text{ for } 500 < Re_{\omega} < 10^4 \quad (3.16)$$

$$\mathbb{C}_{M,rotor} = \frac{0.146}{Re_{\omega}^{0.2}} \text{ for } Re_{\omega} > 10^4 \quad (3.17)$$

Re_{ω} is the rotational Reynolds number relative to rotor radius defined in *Chapter 2*.

3.3.3.5 Bearings Losses

Bearings of high specific power electric motors are subject to high loads in different directions (radial, thrust). Due to the loads applied to bearings along with their rotation motion, friction losses occur at this level. In addition to loads factor, other factors such as the solids' friction coming out from surface contact between bearings elements and the adjacent elements (cage, raceways, and other rolling elements) will influence these losses. These non-negligible losses produce heat dissipation in the bearings ending up increasing their temperature above their operating limits. Heat may also be transferred through diffusion or convection to the motor rotor, frame, or even end-windings. This might raise the temperature of some degrees in the motor.

$$P_{Bearing} = \frac{1}{2} \mathbb{C}_{M,bearing} F_b d_b \omega \quad (3.18)$$

Where $\mathbb{C}_{M,bearing}$ is the bearings friction coefficient whose value depends on the bearing type, F_d is the equivalent dynamic bearing load, d_b is the bearing bore diameter, and ω is the rotation speed.

3.3.4 Initial Conditions

Solving the system equation in transient regime provides the temperature evolution during the flight mission considering the thermal capacity matrix of the motor system, and any variation in input data such as the external temperature and power profile (generating motor losses profiles). An initial condition, in terms of system variables, has to be set to solve the LPTM equation system in transient regime. For the aeronautical application of the motor, this condition corresponds to the initial temperature of the motor environment (or simply the motor temperature at time=0).

3.4 Modeling Assumptions

The numerical model based on the LPTM method is a low-order reduced model. To exhibit the motor thermal behavior in an efficient representative way, the corresponding calculations should be executed in the fastest yet accurate possible procedure. Thus, some modeling assumptions could be considered based on the motor and cooling system configurations.

3.4.1 Geometry

In *Chapter 1*, a global geometry of motor chosen for our application was depicted (see *Figure 3.2*). It is a Surface Mounted – Permanent-Magnet Synchronous Motor (SM-PMSM) characterized by its rotor geometry, compared to other AC motor types. The rotor is made of iron laminations tightly packed with permanent magnets mounted at the surface.

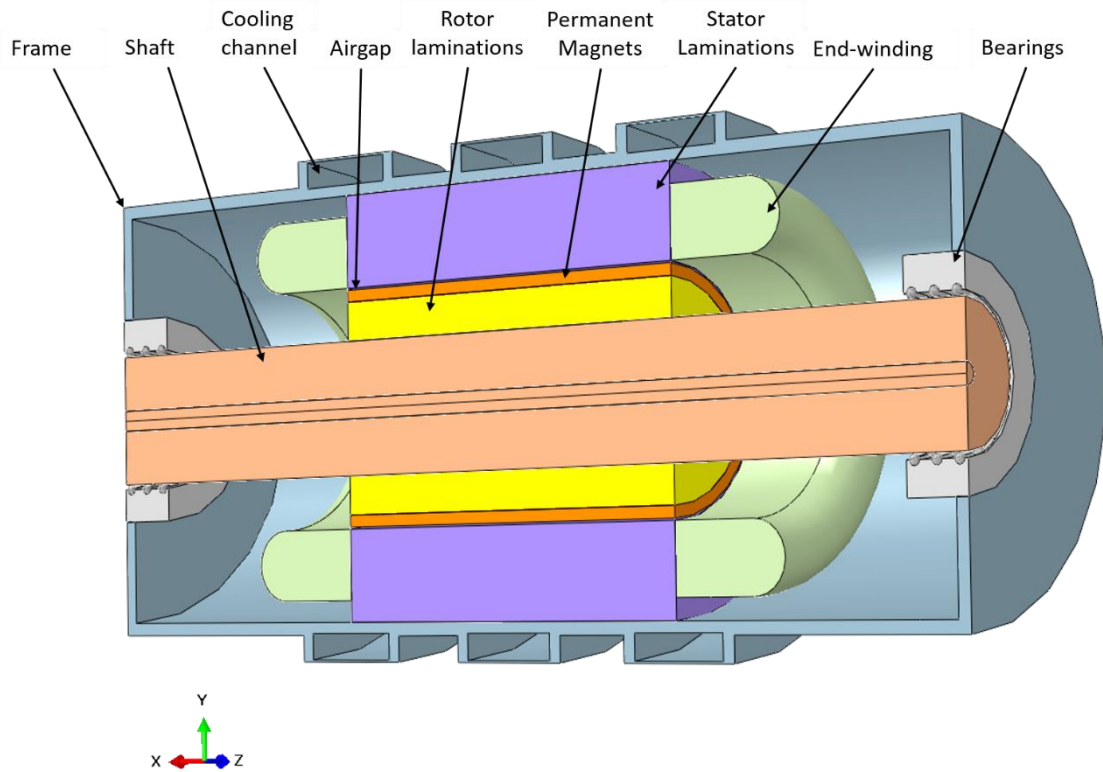


Figure 3.2 : An example of a simplified geometry design of SM-PMSM used for numerical modeling.

As in other motors, the stator has windings inserted into the slots of an iron structure of ferromagnetic laminations. Since the motor has a cylindrical geometry, it is convenient to consider cylindrical coordinates and sections.

3.4.2 Symmetry and Periodicity for Model Reduction

The solid configuration of the SM-PMSM machine adopted for the thermal model is homogeneous in an axisymmetric rotor section since the rotor consists of one type of material for each radial dimension. In the stator, a periodicity is considered due to the alternation of winding slots and teeth. This is depicted in a real stator geometry (see stator of AC motors in *Chapter 1*), as well as in the modeled e-motors designs. The core motor structure is axially symmetric with respect to the middle section of the motor.

3.4.3 Temperature-Independent Media Physical Properties

The system's thermophysical properties are considered temperature-independent. These properties refer particularly to thermal conductivity, specific heat capacity, density, viscosity, and electrical resistivity of copper conductors. Sensitivity studies are carried out and, in a further approach, some media properties are varied in terms of the temperature evolution of each medium.

3.5 LPTM Construction

To solve the problem and get temperature results, the differential equation system (equation (3.8)) should be elaborated. For this purpose matrices G and C , and vector Ψ should be constructed for the motor model.

3.5.1 Thermal Conductance Matrix G

Based on the thermal conductivities of materials, and the boundary conditions, the conductance matrix G can be evaluated. To sum up, *Table 3.1* gathers the expressions of the thermal conductance for each heat transfer mode.

Conduction connections are referred to two configurations: axial and radial, since our electric motor can be represented in cylindrical coordinate system for which components' volumes are connected radially, while volumes of the same component are connected considering axial conductance expressions.

Considering temperature-independent conductivities for each element, in the case study electric motor, the anisotropic property of the material and the cylindrical configurations of the motor structure and main parts motivated us to use a 3D representation of the equation of conduction heat transfer with constant conductivities in each direction (radial (r), angular (θ) and axial (x)).

Heat Transfer Mode	Heat Flux Expression	Conductance
Conduction (axial and ortho-radial)	$\frac{\lambda S_{ij}}{L_{ij}} (T_j - T_i)$	$G_{ij}^{cond,axial} = \frac{\lambda S_{ij}}{L_{ij}}$
Conduction (radial)	$\frac{2\pi \lambda H}{\ln(r_j/r_i)} (T_j - T_i)$	$G_{ij}^{cond,radial} = \frac{2\pi \lambda H}{\ln(r_j/r_i)}$
Convection	$h S_i (T_f - T_i)$	$G_{S_i}^{conv} = h S_i$
Fluidic Flow	$\dot{m} c_p (T_j - T_i)$	$G_{ij}^f = \dot{m} c_p$

S_{ij} is the surface of heat transfer between volumes represented by nodes i and j

S_i is the surface of V_i exposed to convection heat transfer

T_f is the average temperature of the fluid surrounding surface S_i

L_{ij} is the distance between nodes i and j

H is the height of the cylindrical object

\dot{m} is the fluid flow rate

r_i is the radius of node i from motor axis

$r_j > r_i$ (radii)

Table 3.1 : Flux and conductance expressions for each heat transfer mode.

Where:

$G_{ij}^{cond,axial}$ and $G_{ij}^{cond,radial}$ are respectively axial and radial conduction conductances in cylindrical systems between two volumes represented by nodes i and j

$G_{S_i}^{conv}$ is the convection conductance between surface S_i of node i and the fluid surrounding this surface.

G_{ij}^f is the fluidic conductance which represents the energy transfer through mass transport between two fluid elements from node j to node i .

As one can see in subsection 3.2, additional elements of matrix G are assigned for boundary nodes connected to the cold media of heat evacuation.

3.5.2 Thermal Capacity Matrix C

The heat capacity C of a volume is the product of the average mass m of the volume and specific heat capacity c_p ¹ of the material of which the volume is made: $C = m c_p = \rho V c_p$, where ρ is the material density. Matrix C is diagonal and contains the C_{ii} elements of the heat capacity of each V_i of node i , calculated based on the physical property of the volume.

3.5.3 Heat Sources and Heat Sinks Vector Ψ

The vector Ψ of heat sources and heat sinks consists of adding heat production vector to heat evacuation thanks to boundary conditions heat exchange as explained in *paragraph 3.2* of LPTM approach. \dot{Q} vector is integrated using the values of different losses injected to nodes correspondingly. Heat sinks correspond to the values of the extracted heat through the cold plate or heat exchanger. Therefore, they are injected to heat exchanger nodes.

3.5.4 Space Discretization and Nodal Network

To assess thermally the complete front-to-rear motor structure, it is important to consider several sections along the motor shaft axis, specifically when a coolant flow is integrated, which may create a temperature gradient between the two motor ends. This probable temperature difference suggests using many radial sections all motor long.

In our model, the nodal network created according to the assumptions, with nodes locations, is displayed in *Figure 4.5*.

¹ For solids, the specific heat capacity is not a pressure-constant property, since the pressure is not an influencing parameter. However, the “ p ” subscript is maintained for text uniformity reasons.

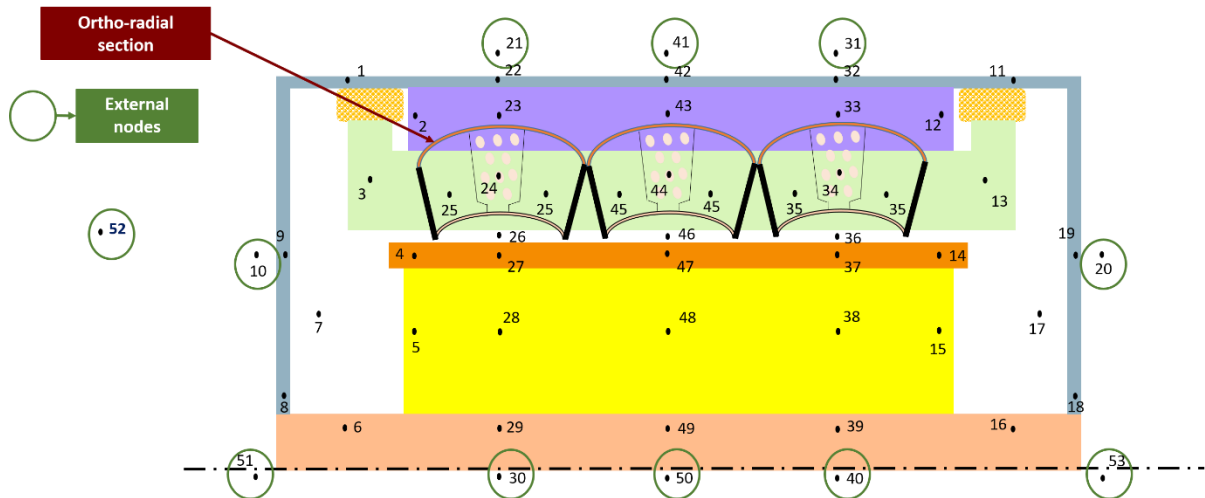


Figure 3.3 : Electric motor axial section showing nodes' location for nodal network model.

To represent the motor block, three sections along the axial direction at three different positions, symmetrically to the middle of the motor core, are considered (front side: nodes 22 to 29, middle section: nodes 42 to 49, and rear side: nodes 32 to 39). In addition to those three sections, each extremity (front and rear) of each motor component is assigned one node (nodes 1 to 6 and nodes 11 to 16), which connect motor parts to air cavities' nodes.

Due to the periodicity of the slots in the stator and to ortho-radial homogeneity in other motor parts, ortho-radial sections of the motor instead of radial ones consisting of one tooth-step are adopted. Consequently, the model is reduced radially to an angle $\alpha = 2\pi/(\text{slots' number})$. In each section, each motor part is represented by at least one node. The conductance connections in the ortho-radial section (front side) are shown in *Figure 3.4(a)*.

Each of the three tooth-nodes (25, 45, and 35) is relative to the teeth adjacent to each corresponding slot volume. Due to symmetry and periodicity in the stator, we assumed that this node is at the same temperature on each side. Hence, it is considered as one node, and the connection between these nodes and the winding nodes is computed based on this assumption with parallel conductances.

Axial and extremity connections of a quarter motor section are depicted in *Figure 3.4(b)*.

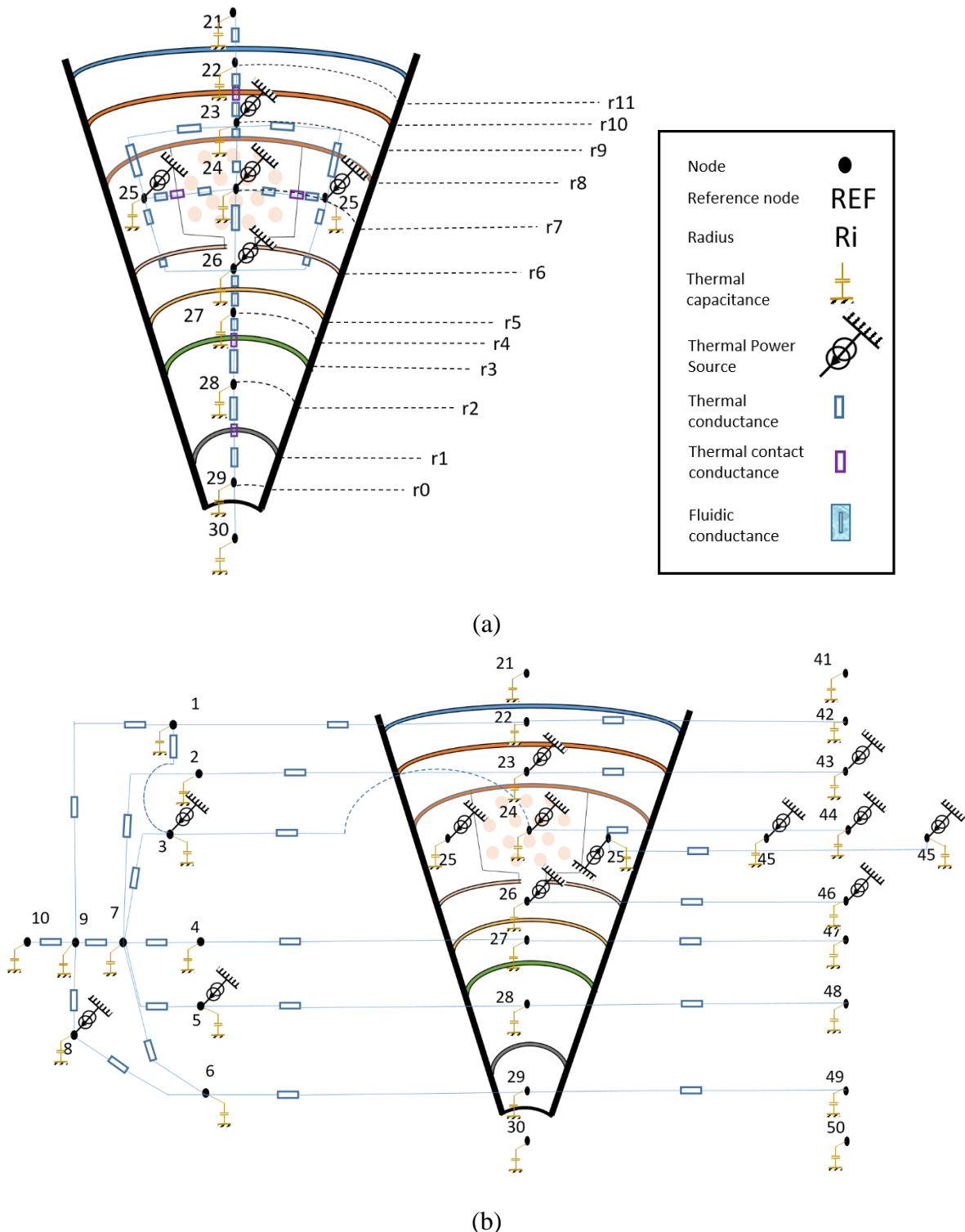


Figure 3.4 : Conductance connections of the motor nodal network. (a) Radial and ortho-radial connections of ortho-radial section. (b) Axial and Extremity connections of a quarter of the motor.

The nodes in each of the three motor axial sections are repeated for each component as follows:

Shaft nodes 29, 49, and 39;

Rotor laminations nodes 28, 48, and 38;

Magnets nodes 27, 47, and 37;

Airgap nodes 26, 46, and 36

Teeth nodes 25, 45, and 35;

Windings nodes 24, 44, and 34;

Stator laminations nodes 23, 43, and 33;

Frames nodes 22, 42, and 32.

Extremities' nodes are important in the lumped circuit for two main reasons. On one hand, they represent the convection heat transfer occurring in end-space regions with air in each cavity. Indeed, all extremities' nodes, at the front and rear sides, are connected to the air node in the cavity correspondingly. On the other hand, some of these nodes receive surface heat sources such as aerothermal losses due to friction (mainly found at rotor end-caps). Normally, these surface nodes should have a tiny axial dimension. The air in each cavity is considered homogeneous in terms of properties and temperature (which is generally the case due to the mixing process produced by the rotation) and is thus assigned one node at each motor end (nodes 7 and 17).

Bearings at each side are assigned nodes 8 and 18 connecting them to the frame lateral sides and shaft.

The frame, in the radial direction, takes part of the three sections (nodes 22, 32, and 42). It has also extremities' nodes (nodes 1 and 11). Both lateral frame surfaces are represented each by one node (node 9 for front side and node 19 for rear side) connected to air cavities' nodes and to radial frame nodes.

The complete nodal network of the motor with axial and extremity connections and external nodes is presented in *Figure 3.5*.

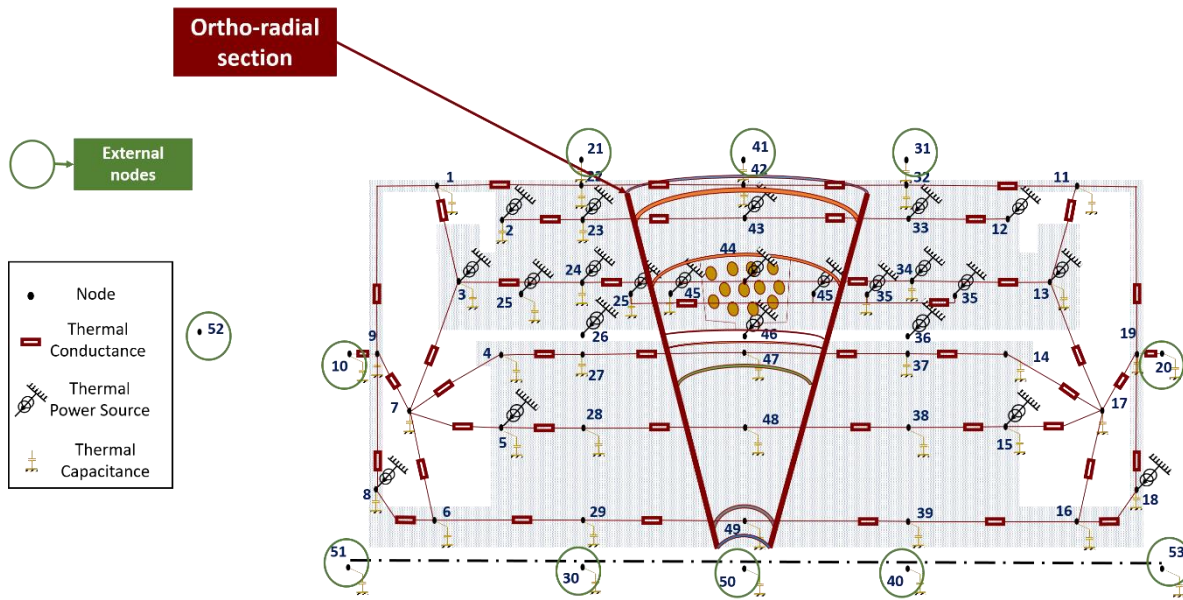


Figure 3.5 : Nodal network of e-motor with axial and extremity connections including the external nodes.

External nodes are added to the model to represent the surrounding environment of the motor: in the shaft, there are nodes 30, 40, and 50 (hollow shaft case), and around the motor frame, there are nodes 10 and 20 and nodes 51 to 53.

3.6 Thermal Properties of Components

Before going further in lumped model construction, we have to define the thermophysical properties of motor components implied in the system. In the model, materials are defined in terms of their properties; namely: thermal conductivities, densities, and specific heat capacities.

As described for the motor type applied, windings are mainly made of copper wires impregnated in an epoxy resin and wrapped with a polyimide film insulator. The motor stator has slots, wound with distributed windings. Rotor and stator iron cores are made of axially stacked ferromagnetic sheets alternatively with insulator disks. Permanent Magnets are made from rare-earth magnetic alloys. The shaft and frame are made of metallic materials or alloys.

As one can remark, some components of the motor are not homogeneous and have their structure made of two or more materials, such as the windings and laminated core of both rotor and stator. One of the advantages of LPTM is that multi-scale components can be modeled in

the same system. However, when detailed and delicate modeling requires longer computation time, which normally lowers the time-based efficiency of solving and may not be needed, it is more convenient to optimize the solution by determining and setting equivalent properties for these assemblies. The thermal and physical properties of both homogeneous and heterogeneous elements have to be defined in the nodal network model.

3.6.1 Equivalent Properties of Heterogeneous Components

In this section, methods for the determination of equivalent properties of the heterogeneous e-motor parts are elaborated. The two main heterogeneous components in the e-motor are the windings and the laminations.

3.6.1.1 Windings Equivalent Properties

The high heat dissipation existing in slots (spaces between every two consecutive teeth of stator filled with wound coils) and end-windings, due to Joule losses, and the confined character of these components encapsulated in low-conductivity materials, explain why this motor part in the motor reaches the high temperatures. The maximum allowed winding temperature depends on the impregnation thermal class. A non-uniform heat dissipation characterizes this part since it is made of multiple dissipative and non-dissipative materials. It is then crucial to find an accurate thermal model that takes into account the equivalent properties of winding coils.

❖ Equivalent Thermal Conductivity

The first approach is to determine the thermal conductivity of these elements based on the thermal conductivities of the constituents and the slot fill factor. The axial conductivity (along the motor shaft direction) of the windings is much greater than the radial one (relative to the radial direction in the motor). The coils are wound around the teeth parallel to the motor axis with a copper fill factor. In the axial direction, thermal resistances of copper wires and resin layers are parallel, while in the radial direction they are in series. When the copper thermal conductivity is hundreds of times greater than that of impregnation material, the approximate equivalent thermal conductivity of a series-set of equal proportions is closer to that of the more

resistant material. Thus, the heat flux propagation is limited mainly by the thermal conductivity of the impregnation material.

For the radial and ortho-radial thermal conductivities, some authors evaluated this conductivity for a two-material component $\lambda_{rad}^{eq,2}$ using homogenization formula from the work of Milton [165] (consisting of studying two-material composite structure properties). It was assumed a two-material microstructure, with cylindrical fibers (copper coils), distributed in an isotropic way in a matrix material (resin in this case). Then another computation from Mori [166] is adopted to evaluate the three-material slot thermal conductivity $\lambda_{rad}^{eq,3}$ (addition of varnish). These configuration approaches are respectively expressed in equations (3.19) and (3.20).

$$\lambda_{rad}^{eq,2} = \lambda_{res} \frac{(1 + \tau)\lambda_{cu} + (1 - \tau)\lambda_{res}}{(1 - \tau)\lambda_{cu} + (1 + \tau)\lambda_{res}} \quad (3.19)$$

$$\lambda_{rad}^{eq,3} = \lambda_{res} \frac{(2\lambda_{res} + \lambda_{cu})(\tau_2(2\lambda_{res} + \lambda_{var} + 3\tau_3\lambda_{var}) + 3\tau_1\lambda_{cu}(2\lambda_{res} + \lambda_{var}))}{\tau_2(2\lambda_{res} + \lambda_{cu})(2\lambda_{res} + \lambda_{var}) + 3\lambda_{res}(\tau_1(2\lambda_{res} + \lambda_{var}) + \tau_3(2\lambda_{res} + \lambda_{cu}))} \quad (3.20)$$

Where λ_{res} , λ_{cu} and λ_{var} are the resin, copper, and varnish conductivities respectively, τ is the slot fill factor of copper in the case of a two-material slot ($\tau = \text{ratio of copper volume in the slot to total slot volume}$). τ_1 , τ_2 and τ_3 are the ratios of the volume of each material (respectively copper, resin, and varnish) in the slot to the total volume of the slot (can be the section ratios in an axis-orthogonal section). The thickness of the insulator layer (varnish here) used to cover each coil is generally set to be around $0.25 \mu\text{m}$ as an approximation.

To determine the axial equivalent conductivity of the slots λ_{ax}^{eq} , Lutun [167] used a simple approach. It consists of the linear combination in the following equation:

$$\lambda_{ax}^{eq} = s_{cu} \lambda_{cu} + s_{var} \lambda_{var} + s_{res} \lambda_{res} \quad (3.21)$$

Where s_{cu} , s_{var} and s_{res} are the volume percentages of copper, varnish, and resin respectively.

Two nomographs from General Electric [168] and Rohsenow [169] consisting of heterogeneous materials as a function of the slot fill factor (*Figure 3.6* and *Figure 3.7*) are generally used. The assumptions to determine the radial and ortho-radial conductivities of the windings for their case were: steady-state (or permanent regime), homogeneous impregnation material, highly conductive conductors, thermal flux along the winding axis, and negligible boundary effects. In these nomographs, λ_e is the winding equivalent thermal conductivity and λ_i is the resin thermal conductivity.

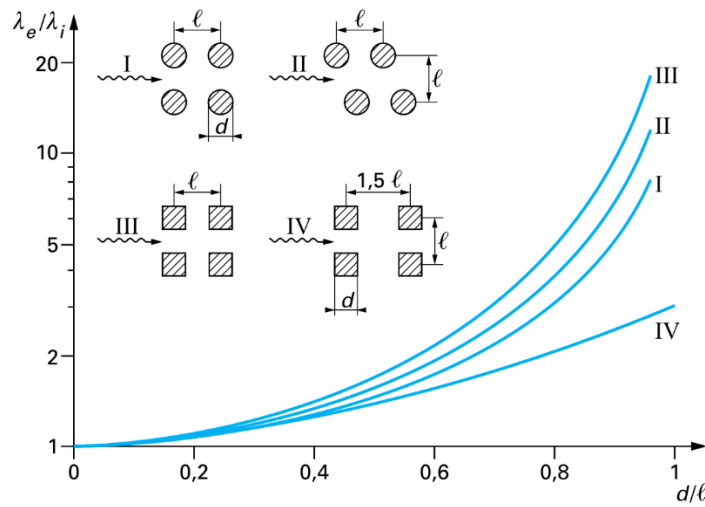


Figure 3.6 : Rohsenow nomograph [169] for equivalent thermal conductivity in heterogeneous materials with different configurations from [47].

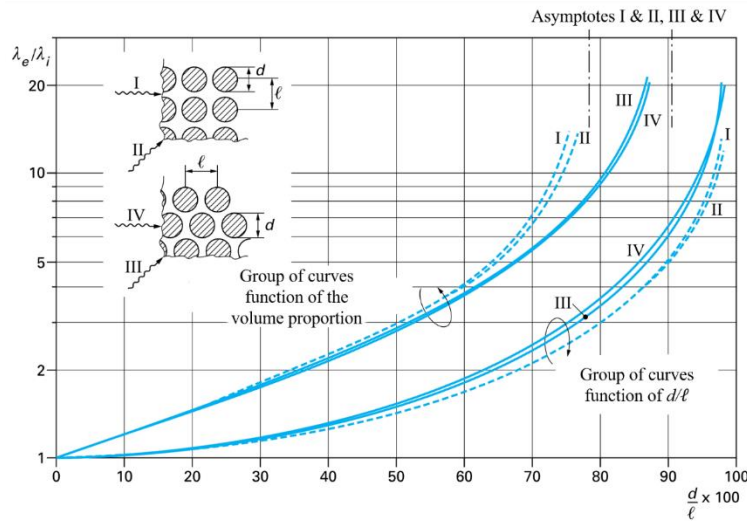


Figure 3.7 : General Electric nomograph for the thermal equivalent conductivity in heterogeneous materials with different configurations [47].

Renard [170] maintained the value of the equivalent winding conductivity in the radial direction from the linear regression for 8 circular coils ($0.42 \text{ W} \cdot \text{m}^{-1} \cdot \text{K}^{-1}$), with a slot, fill factor of 54.8% for windings and 65.1% for wreaths (end-windings). While for transverse (angular) and axial conductivities for a slot fill factor of 38%, the values are obtained from Finite Element (FE) model simulation on I-DEAS software considering that the heat is produced only in copper wires. Based on the numerical FEM simulation, they found for the adopted configuration case the following values: $\lambda_{ang} = 0.33 \text{ W} \cdot \text{m}^{-1} \cdot \text{K}^{-1}$ and $\lambda_{ax} = 203 \text{ W} \cdot \text{m}^{-1} \cdot \text{K}^{-1}$.

Subsequently, based on the sensitivity analysis to thermal parameters [171] conducted in our work, the accurate thermal conductivity of the slot in the radial plan is considered an important parameter. Therefore, it has been determined through FE analysis corresponding to heat production inside the slot. A complete parametric two-dimensional study of the thermal conductivity of winding in radial and ortho-radial directions has been conducted during the thesis. This study takes into account the dissipative character of coils impregnated in the resin and wrapped with an insulator sheet. Multiple parameters were considered in this analysis. Based on wide ranges of possible parameters values and options, correlations were elaborated to estimate more accurately this conductivity in each direction. The full study [172] was presented at the 2018 International Conference on Electrical Machines. We have extracted a polynomial correlation with two different sets of coefficients respectively to the two mentioned directions as in equation (3.22) with coefficients in *Table 3.2*.

$$\lambda_{rad,ang}^{eq} = A^{eq} + B^{eq}\lambda_{res} + C^{eq}\tau + D^{eq}\tau\lambda_{res} + E^{eq}\tau^2 \quad (3.22)$$

Coefficient	A^{eq}	B^{eq}	C^{eq}	D^{eq}	E^{eq}
Radial direction: λ_{rad}^{eq}	2.05	0	-12.14	4.39	17.4
Angular direction: λ_{ang}^{eq}	0.23	1.17	0.94	0.56	-0.57

Table 3.2 : Coefficients for winding thermal conductivity expression in equation (3.22).

❖ Equivalent Density

Similarly to thermal conductivity, considering that the variation of physical properties with temperature is negligible, the equivalent density of the winding, ρ_{wind} is calculated, based on the densities of copper and resin (ρ_{cu} and ρ_{res}) and the fill factor, as in the following equation:

$$\rho_{wind} = [\rho_{cu}\tau + \rho_{res}(1 - \tau)] \quad (3.23)$$

❖ Equivalent Specific Heat Capacity

Considering the temperature-independent property of the motor constituents, the heat (or thermal) capacity of volume V_i in the system is the product of the average weight of V_i and the

specific heat capacity of the material. In the electric motor, the equivalent heat capacity of the overall winding, c_{wind} , is related to its two main elements: coil and impregnation material. It is determined, based on specific heat capacities of copper and resin (c_{cu} and c_{res}) and the fill factor, as follows:

$$c_{wind} = c_{cu}\tau \frac{\rho_{cu}}{\rho_{wind}} + c_{res}(1 - \tau) \frac{\rho_{res}}{\rho_{wind}} \quad (3.24)$$

Where ρ_{cu} and ρ_{res} are respectively the copper and resin densities, ρ_{wind} is the winding equivalent density and τ is the slot fill factor.

3.6.1.2 Laminations Equivalent Thermal Conductivity

The equivalent thermal conductivity is calculated for the stator and rotor laminations in terms of the conductance of lamination and insulators sheets, as parallel in the angular and radial directions, or in series in the axial direction. For the sheets' plane direction, the conductivity is close to that of the ferromagnetic sheets since in parallel, the equivalent conductance is the sum of all conductances, and for the same dimensions, the total thickness of insulator sheets is negligible compared to the thickness of ferromagnetic sheets. In the direction of the sheets' thickness, the conductivity is a function of the interface connection and its thermal contact resistance [47]. In [170], the authors considered that the radial and angular conductivities are similar. They used equation (3.25) to evaluate these thermal conductivities for the stator and rotor laminations of an electric motor made up of ferromagnetic sheets with 0.65 mm thickness of FeSi (Iron-Silicon material) and insulator sheets of 1 μm thickness each. These equivalent conductivities are computed as the sum of the thermal conductivities of all components considered in parallel. Besides, the axial thermal conductivity is evaluated using a series approach between the insulator and ferromagnetic sheets' conductivities as in equation (3.26):

$$\lambda_{rad} = \lambda_{ang} = \frac{\ell_{ins} \cdot \lambda_{ins} + \ell_{lam} \cdot \lambda_{lam}}{\ell} = 41.9 \text{ W} \cdot \text{m}^{-1} \cdot \text{K}^{-1} \quad (3.25)$$

$$\lambda_{ax} = \frac{\ell \cdot \lambda_{ins} \cdot \lambda_{lam}}{\ell_{ins} \cdot \lambda_{lam} + \ell_{lam} \cdot \lambda_{ins}} = 25.6 \text{ W} \cdot \text{m}^{-1} \cdot \text{K}^{-1} \quad (3.26)$$

Where ℓ denotes the total thickness of all insulator sheets and laminations, λ is the thermal conductivity property, ℓ_{ins} and ℓ_{lam} are the thicknesses of insulator sheets and laminations respectively.

3.6.2 Contact Thermal Resistance

It is important to note that the equivalent lumped model of any system depends strongly on physical factors, one of which is the nature of the connection between different elements. In particular, the complex nature of the interface region between two different elements (presence of residual impurities, air...) influences the thermal behavior of the electric motor at some locations in the stator (*Figure 3.8*) as well as in rotor (for instance, between magnets and rotor core). For an imperfect surface contact, calculating the total conductance between machine elements consists of adding directly or indirectly a contact thermal conductance representing the interface.

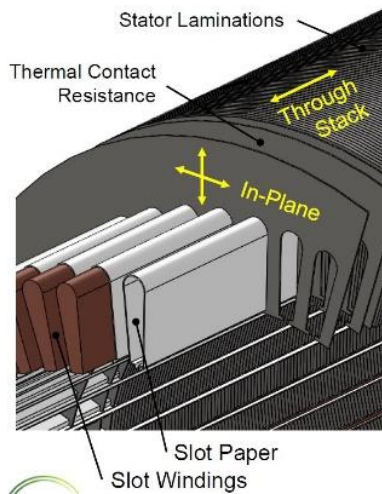


Figure 3.8 : Electric motor stator geometry showing slot coils and papers and thermal contact resistance of laminations [138].

Bertin [47] suggested some values of the contact conductance at some locations for different electric motor types, depending on the pressure applied to the contact region, surface roughness, materials properties, and connection type and technique. For each region, the contact conductance is reported in the following subsections.

3.6.2.1 Between Coil and Slot Walls

An insulator sheet separates the contact region between coils and the slot surface to protect the conductors. This contact region between the sheet and the coils is not fully adherent, and the connection problem is modeled as a thermal conductance existing between each slot surface and the corresponding coils. Bennion [138] found a surface contact conductance between slot liner paper and the coil of around $555 \text{ W}\cdot\text{m}^{-2}\cdot\text{K}^{-1}$, which is equal or smaller than the paper same property alone ($597 \text{ W}\cdot\text{m}^{-2}\cdot\text{K}^{-1}$). Bertin [160] found experimentally a value of $333 \text{ W}\cdot\text{m}^{-2}\cdot\text{K}^{-1}$, lately adopted by Thieblin [173], which is equivalent to an insulator sheet of 0.67 mm of thickness. This value of the surface contact conductance will be used in our case to account for the contact effect in radial and angular directions according to contact surfaces.

3.6.2.2 Between Stator Laminations and Frame

Renard [170] considered a value of $1500 \text{ W}\cdot\text{m}^{-2}\cdot\text{K}^{-1}$ for the surface contact conductance between stator and frame. In their application, an alterno-starter consists of a closed compact machine for which the model was recalibrated according to the contact thermal conductances and to ambient temperature. Due to aluminum and iron dilatation, a value of $5000 \text{ W}\cdot\text{m}^{-2}\cdot\text{K}^{-1}$ is found more adequate at an ambient temperature of $35 \text{ }^{\circ}\text{C}$ and $2000 \text{ W}\cdot\text{m}^{-2}\cdot\text{K}^{-1}$ at an ambient temperature of $70 \text{ }^{\circ}\text{C}$.

3.6.2.3 Between Magnet and Rotor Laminations

Permanent magnets of the rotor are directly bonded to the rotor laminations. Thieblin [173] considered a 0.05 mm adhesive thickness assuming a perfect contact of adhesion. Depending on the temperature difference value and sign between laminations and magnets in the rotor assembly of the motor, this contact property is classified to be a major or minor, positive or negative factor, or even insignificant.

However, in this thesis a contact conductance is added and is extracted from the value range found in [170], stating that for rough contact with undulations, the surface thermal resistance value is located between $10^{-3} \text{ m}^2\cdot\text{K}\cdot\text{W}^{-1}$ to $10^{-4} \text{ m}^2\cdot\text{K}\cdot\text{W}^{-1}$, and for simply rough contact, the

value ranges between $2 \times 10^{-4} \text{ m}^2 \cdot \text{K} \cdot \text{W}^{-1}$ to $10^{-5} \text{ m}^2 \cdot \text{K} \cdot \text{W}^{-1}$. In our case, an average value of $10^{-4} \text{ m}^2 \cdot \text{K} \cdot \text{W}^{-1}$ is adopted considering a rough surface contact.

3.6.2.4 Between Rotor Laminations and shaft

According to [170], and according to the range of values mentioned in subsection 3.6.2.3 for rough contact type, we have decided to use a penalizing value of $10^{-3} \text{ m}^2 \cdot \text{K} \cdot \text{W}^{-1}$ to consider the surface contact resistance between rotor laminations and shaft. This will affect the heat flux path from the rotor to the shaft.

3.7 Validation with Experimental Results

Before sizing the high specific power electric motor cooling system, it is crucial to validate the thermal model core (inner motor thermal model). An electric motor of the same type as the one to be conceived has been chosen. It is a permanent magnet synchronous machine designed for automotive propulsion designed and optimized for a hybrid-electric vehicle [174]. Experiments are conducted on the machine, and results were used to validate the elaborated small thermal network (eight-node model), which was used for sensitivity analysis in [52] as well.

The experimental PMSM is liquid-cooled in the stator, with water jackets and a coolant flow temperature of $16 \text{ }^\circ\text{C}$. Stator, rotor, and frame structural materials are listed in *Table 3.3*. Motor power data and losses distribution are grouped in *Table 3.4*. Motor characteristics and dimensions are found in *Table 3.5*.

The experimental temperatures are given at an operating point with 6000 RPM speed corresponding to an output power of the motor of 50 kW . The total losses are around 2.3 kW .

Motor part	Structural material	Density ($kg \cdot m^{-3}$)	Thermal conductivity ($W \cdot m^{-1} \cdot K^{-1}$)	Specific heat capacity ($J \cdot kg^{-1} \cdot K^{-1}$)
Lamination	EBG, NO20	7600	38	460
Coil	Copper (Cu)	8900	395	385
Frame	Aluminum (Al)	2705	230	900
Shaft	Steel	7800	51	460
Magnets	NdFeB	7500	9	-
Winding impregnation	Unsaturated polyester	1350	0.2	1700
Slot insulation	Mylar film	-	0.2	-

Table 3.3 : Experimental PMSM structural material data used in the model[174].

Size	Value	Unit
Shaft power	49	kW
Maximum speed	6021	RPM
Terminal current	170	A
Supply frequency	201	Hz
Winding losses	822	W
End-winding losses	513	W
Stator yoke losses	464	W
Stator teeth losses	387	W
Rotor losses	22	W
Friction losses	90	W
Total losses	2.298	kW

Table 3.4 : Experimental PMSM power data and losses [174].

The specific power of the motor with the cooling is around 1 kW/kg , which is less than the targeted motor in the current project but can be considered for motor model comparison.

The motor design is applied to the thermal model and steady-state results have been compared against the measured temperatures in the stator.

This comparison shows a strong agreement of the simulated and measured data (the relative errors considering the coolant temperature are around 3.2% for the end-windings and 1.2% for the coils). The results of this comparison are presented in *Table 3.6*.

Motor type	PMSM	
Cooling type	Water cooling of stator frame	
Application	Hybrid Electric Vehicle	
Dimension	Value	Unit
Stator core length	231	mm
Lamination filling factor	0.965	mm
Stator inner diameter	110	mm
Stator outer diameter	189	mm
Number of stator slots	48	-
Yoke thickness	16.4	mm
Tooth width	3.5	mm
Tooth height	20.4	mm
Slot area	89.8	mm ²
Number of pole pairs	2	-
Slot filling factor	0.45	-
Mechanical airgap	0.3	mm
Magnet thickness	5	mm
Rotor core outer diameter	107.1	mm
Rotor core inner diameter	64.6	mm
Retaining sleeve thickness	0.75	mm

Table 3.5 : Experimental PMSM characteristics and dimensions [174].

Node	Temperature	Measured [174] (°C)	Computed (Nodal Network) (°C)
End-windings		72	70.2
Coil Sides		51	51.7
Coolant inlet		16	16

Table 3.6 : Comparison between experimental and numerical resulting temperature.

Consequently, the developed thermal model could reasonably be considered for a high specific power permanent magnet motor.

3.8 Conclusion

The basics of the LPTM technique and its application to our study were addressed. The structure and general characteristics of the electric motor system (PMSM type) are described and detailed to elaborate a global thermal model network. Compared against experimental data, the developed motor model core is stated valid for subsequent investigations. Hence, the model can be used in different context studies for the same motor type. In the following chapter, the motor designs provided by WP1 are simulated. A description of the electric machine and the configuration of the associated thermal model considerations and cooling system are discussed, and thermal results are analyzed and processed.

CHAPTER 4 THERMAL MANAGEMENT OF DESIGNED E-MOTORS

Synopsis:

After elaborating the model of the e-motor core, the cooling systems of e-motors are integrated to the numerical model. Simulation results are displayed and analyzed. Then, sensitivity studies and investigations on the motor thermal behavior are carried out. Considering the thermal constraints, a final design for each e-motor is selected, with electromagnetic and thermal data. The designs of the e-motor fulfill the conditions and project targets, mainly the specific power values.

4.1 Introduction

In HASTECS project, several configurations of the propulsion of the hybrid aircraft have been investigated. In particular, two configurations were specifically investigated with high specific power motors, inducing complex electrical and thermal problems. For each of the project targets (Target 1 for 2025 and Target 2 for 2035), a sizing point of the propeller power is adopted to which a suitable electric motor design is elaborated and verified according to the required mechanical power. The objective is to find a suitable cooling configuration for each motor design. The motors should have high specific power densities of at least 5 kW/kg for Target 1 and 10 kW/kg for Target 2. Electric motors designed in this framework are thermally assessed to deal with hot spot temperatures through cooling techniques. A global design procedure of high specific power electric motors based on an equivalent thermal constraint value is presented.

Based on the model presented in the previous chapter, cooling techniques and circuits are simulated for each machine design correspondingly. The targeted specific power of each motor takes into consideration the weight of the motor with the cooling installed in the system. Temperature limits are the main constraints of the numerical model.

To find the most efficient and light cooling technology that maintains motor temperatures below the maximum allowed values, several strategies and investigations are conducted for each of the two electric motor targets.

4.2 Electric Motor Design for 2025 (EM2025)

The first objective of the current work is to manage the thermal behavior of the future electric motor for the first target of the project. The electromagnetic design calculations are performed by WP1 and the provided data needed for thermal management design are integrated into the thermal model (LPTM).

4.2.1 Thermal Constraint Evaluation

The issue of reaching high specific power targets for electric motors of hybrid propulsion requires a complex procedure. With that being added to several constraints, both the electric motor and its cooling system are subject to investigation and mutual effort in the design phase. For this purpose, in collaboration with the WP1 team, a sizing approach using electro-thermal models is proposed and defined. This study is detailed in [176]. Although all electromagnetic design parameters are provided by WP1, some interesting criteria related to thermal management have to be taken into account.

A thermal constraint has been introduced in the design process by the joint work of WP1 and WP3 of the project to make sure motor temperatures could be maintained below the limits. This constraint is equivalent to a current density product called Aj , which is a parameter that depends only on the effectiveness of the cooling system (Aj expressed in $[A^2 \cdot m^{-3}]$). It is the product of the linear surface current density (A or A_{rms} [$kA \cdot m^{-1}$]) by the current density (j or j_{rms} [$A \cdot mm^{-2}$]). It reflects the allowed values of electromagnetic loads and their limits according to the cooling technology. Each electric motor type has specifically permitted values of the electromagnetic loads depending on the cooling technology used [177]. In the case of direct water cooling, Aj attains essentially higher values. *Table 4.1* categorizes the value ranges of these two loads parameters (A and j) and their product, according to the machine cooling technique for low rotational speed non-salient synchronous machine. Knowing that this product considers only Joule losses and intending to find a global thermal constraint that takes into account all losses [176], an equivalent product Aj_{eq} [$A^2 \cdot m^{-3}$] (defined as the thermal constraint for the electromagnetic design of our motors) is evaluated as follows:

$$\langle Aj_{eq} \rangle = \frac{\sum \text{Motor Losses}}{2\pi R_{stator} L_m \rho_{cu}(T) k_{tb}} \quad (4.1)$$

Where R_{stator} is the inner stator radius, L_m is the active length, $\rho_{cu}(T)$ is the copper electrical resistivity as a function of winding temperature, and k_{tb} is the end-windings coefficient (equals to the ratio of machine total length to machine active length).

Electric loads	Indirect cooling		Direct water cooling
	Air	Hydrogen	
$j_{rms} (A \cdot mm^{-2})$	3-5	4-6	7-10
$A_{rms} (kA \cdot m^{-1})$	30-80	90-110	150-200
$A_{rms} j_{rms} (A^2 \cdot m^{-3})$	$10.5-40 \times 10^{10}$	$36-66 \times 10^{10}$	$1.05-2 \times 10^{12}$

Table 4.1 : Permitted values of electromagnetic loads for non-salient synchronous machines according to cooling technology [177].

The organigram in *Figure 4.1* models the interaction between the electromagnetic and thermal models developed by WP1 and WP3.

The design procedure consists of six steps enumerated below:

Step 1: assess the electric motor technologies required using WP1 model called Target Setting Tool (TST) for high specific power electric motor design.

Step 2: size the surface-mounted permanent magnet synchronous motor using WP1 tool called SM-PMSM for this electric motor type.

Step 3: check the value of the thermal constraint according to the cooling method chosen in step 1.

Step 4: determine the electric motor temperatures and verify that no motor parts are overheated.

Step 5: get the sizing of the cooling system.

Step 6: compute the total weight and verify that the specific power target is obtained.

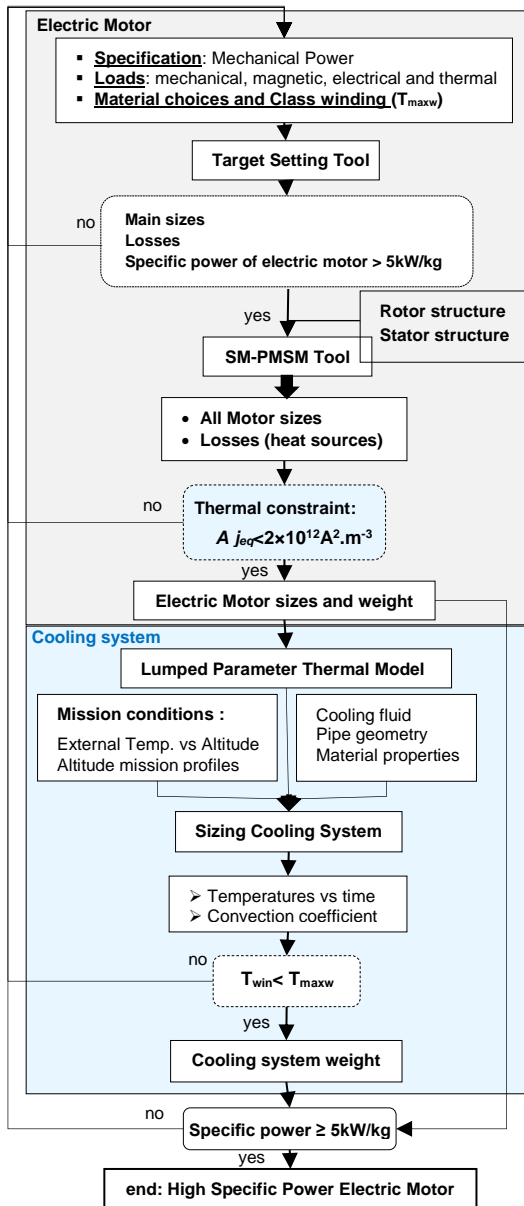


Figure 4.1 : Interaction between electro-thermal models for sizing high specific electric motors with their cooling system [176].

This joint work of both Work-Packages allowed the determination of a maximum value of this equivalent thermal constraint according to cooling configurations to design high-specific motors (EM2025 and EM2035). The proposed cooling for EM2025 and EM2035 respectively enabled the design of a high specific power electric motor with $2 \times 10^{12} A^2 \cdot m^{-3}$ and $5 \times 10^{12} A^2 \cdot m^{-3}$ as thermal constraint values.

4.2.2 Motor Design and Sizing

A three-dimensional (3D) section of the Electric Motor for 2025 (EM2025) designed for the first target provided by WP1 is depicted in *Figure 4.2*. The electric motor design is of SM-PMSM type with distributed windings forming a wreath at each extremity.

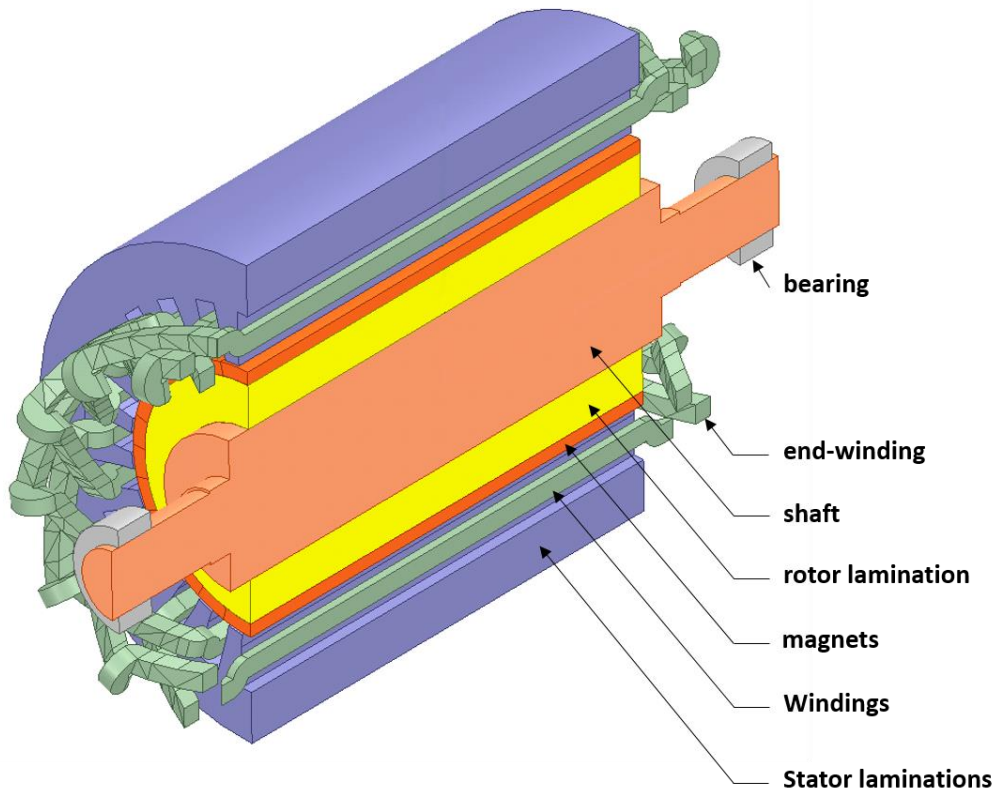


Figure 4.2 : Electric Motor 3D section view (from WP1).

The motor section shows the core geometry of the e-motor with its components. E-motor data are presented thereafter.

4.2.2.1 Electric Motor Characteristics

Developed by the WP1 group, the electrical design of the motor and corresponding data with their maximum values are gathered in *Table 5.1*.

The losses values in *Table 5.1* are the maximum level of heat sources in the thermal model. For a steady-state simulation, they can be used to estimate a continuous full-power operating motor. A dynamical profile for each losses type is presented thereafter.

The machine geometrical dimensions are grouped in *Table 4.3*. With a motor power around 1.5 MW , tens of kW of losses are estimated at a full power operation of the machine.

The EM2025 is characterized by a high rotation rate. It should have a minimum specific power of 5 kW/kg which is the ratio of the power to the weight. The overall weight of the bare motor without the frame is kept confidential. These weights are optimized to achieve the specific power target. Confidential values of losses are expressed in Per-Unit (PU) with respect to motor total losses (equal to 1 PU).

Characteristic	Unit	Value
Mechanical speed	RPM	15696
Number of phases	-	3
Number of slots	-	24
Winding losses	PU	0.25
End-winding losses	PU	0.18
Stator yoke losses	PU	0.30
Stator teeth losses	PU	0.13
Windage losses	PU	0.10
Friction losses	PU	0.04

Table 4.2 : PMSM Power Data and losses from WP1.

Main size	Unit	Value
External stator radius	mm	162.87
Inner stator radius	mm	92.47
Stator yoke height	mm	34.29
Slot height	mm	36.11
Tooth width	mm	10.58
Slot width	mm	13.48
Airgap thickness	mm	1.53
Permanent magnet thickness	mm	9.00
Rotor yoke height	mm	29.72
Shaft radius	mm	50.98
Active length	mm	317.33
Motor length	mm	538.6

Table 4.3 : Main dimensions of the electric motor without cooling system [176].

4.2.2.2 Specific Characteristics (Maximum Temperatures)

The maximum temperatures in the motor are set as constraints for our machine. They are mainly due to the operation conditions of the windings and permanent magnets. These two components are particularly sensitive to temperature, once exceeding a certain maximum allowed level, they can undergo serious electrical and magnetic malfunctioning. Through repeated cycles of reaching these maximum temperatures, this malfunctioning leads to total motor failure. The temperature constraint is defined according to the material properties constituting these components. For windings, each degree above the allowed maximum temperature will shorten the motor lifetime exponentially. Permanent magnets are subject to demagnetization in the case of temperature overshoot. This specificity must be taken into consideration when defining the motor and cooling system design.

For EM2025, the temperature limits are given in *Table 4.4*. The adopted winding thermal class defining the insulation material's maximum temperature is class 220 °C, which allows reaching 180 °C considering the safety margin set by WP1. The permanent magnet used in the motor is the Samarium-Cobalt alloy with a maximum limit of the temperature of 150 °C, which practically gives 135 °C depending on materials, with a safety margin according to WP1.

Component	Temperature limit for Target 1
Windings	180 °C
Permanent magnet	135 °C

Table 4.4 : Temperature limits for EM2025 critical components.

4.2.3 Thermal and Physical Properties

Thermal and physical properties of media should be defined to run the model simulation. They are determined based on the components' materials. Rotor and stator laminations are made of a soft magnetic material: cobalt iron alloy. Permanent magnets are samarium-cobalt rare earth magnets. The shaft is made of steel and finally, the frame is made of aluminum. Properties of different materials of the e-motor are grouped in *Table 4.5*. They are assumed constant relatively to the changing component temperature in this numerical study.

Material		Properties			Data Source
		Density (kg·m ⁻³)	Thermal conductivity (W·m ⁻¹ ·K ⁻¹)	Specific Heat Capacity (J·kg ⁻¹ ·K ⁻¹)	
Winding	Copper	8920	360-400	390	WP1/WP5
	Resin	1500	1	1700	
Stator/Rotor Laminations	Soft Magnetic Alloy Co-Fe	8120	Axial: 25 Radial: 46 Angular: 42	460	Material choice: WP1. Properties' definition: literature [170], [174]
Permanent Magnets	Sm2Co17	8400	10	370	WP1
Shaft	Steel	8100	45	502	WP1
Frame	Aluminum	2700	200	900	Set by WP3
Bearings	Steel	8100 (70% filled)	45	502	Set by WP3

Table 4.5 : Material properties of EM2025 at ambient temperature.

The thermal conductivity of resin applied for impregnation of windings is $1 \text{ W}\cdot\text{m}^{-1}\cdot\text{K}^{-1}$ for EM2025. As a perspective for the year 2025, these materials will be available for application.

Based on the study presented in *Chapter 3*, the resulting winding thermal conductivities are $2.53 \text{ W}\cdot\text{m}^{-1}\cdot\text{K}^{-1}$ and $2 \text{ W}\cdot\text{m}^{-1}\cdot\text{K}^{-1}$ respectively in radial and angular directions. After defining these parameters, the thermal model can be configured for the electric motor EM2025. These properties' values are used as constants then a sensitivity study is conducted to determine whether their variation due to temperature could change significantly the resulting maximum temperature in each motor part (see *subsection 4.4.3*).

4.2.4 Dynamical Profile of Power

4.2.4.1 Mission Profile

Based on hybrid chain studies of the aircraft propulsion system analyzed and investigated by our project partners, a mission profile of the power required at the shaft level for one propeller has been delivered by Airbus. This dynamical profile is depicted in *Figure 4.3*.

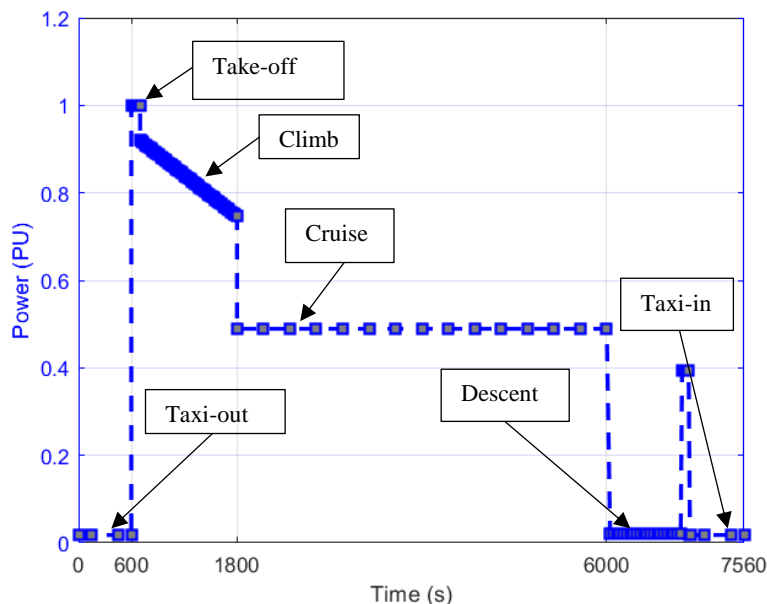


Figure 4.3 : Mission profile provided by Airbus.

During the first and last phases of taxiing, a low level of power is needed, while full power is required for the take-off phase. After this short phase, a decreasing power level is depicted in this profile during the climb phase reaching around its half at the beginning of the following

phased of the cruise. A constant value is applied during the whole cruise phase until the descent phase where a decreasing profile of power is required.

4.2.4.2 Losses Profiles

In this work, losses profiles dissipated in the designed electric motor are obtained from electrical, magnetic, and mechanical equations based on power profile at maximum torque. These losses – equivalent to heat sources - are provided by WP1 as a function of the flight mission, and the resulting graph is depicted in *Figure 4.4* accordingly. The plot gives the dynamical profiles of losses according to their types (total of 5) in percentages (%), with respect to the total losses value at full power.

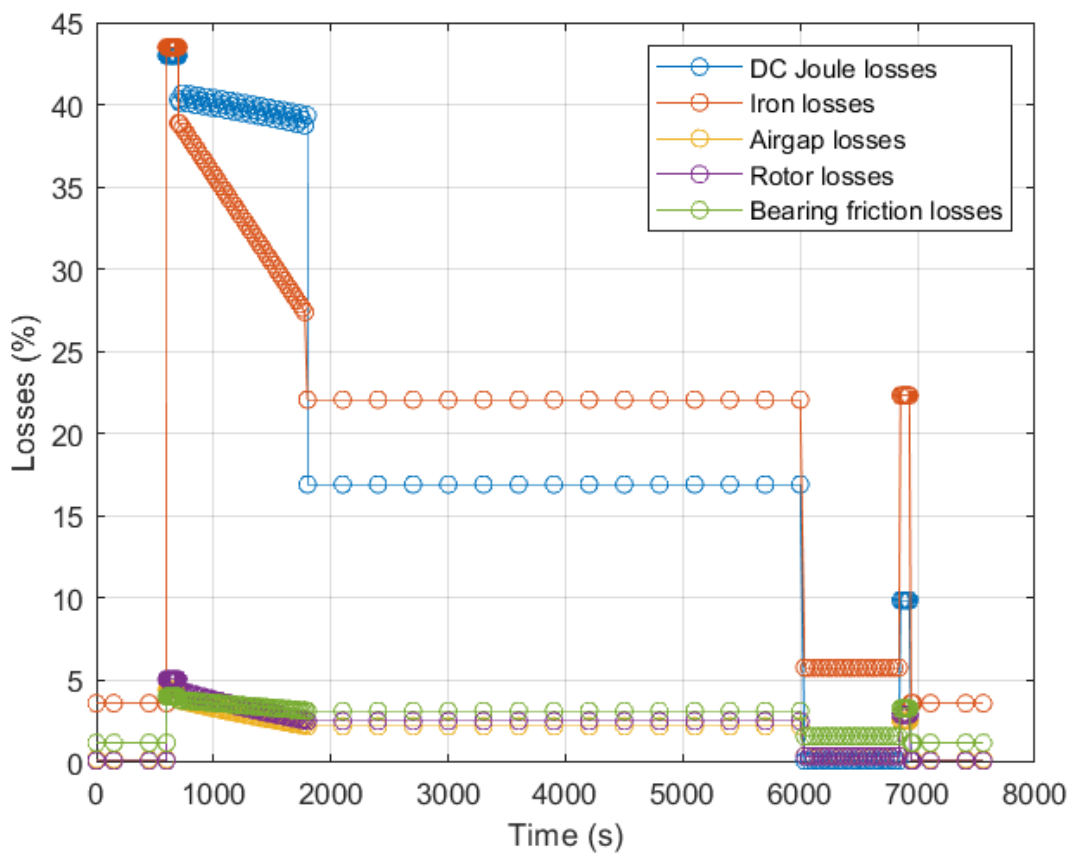


Figure 4.4 : Losses profile of EM2025 in % with respect to maximum total value from WP1.

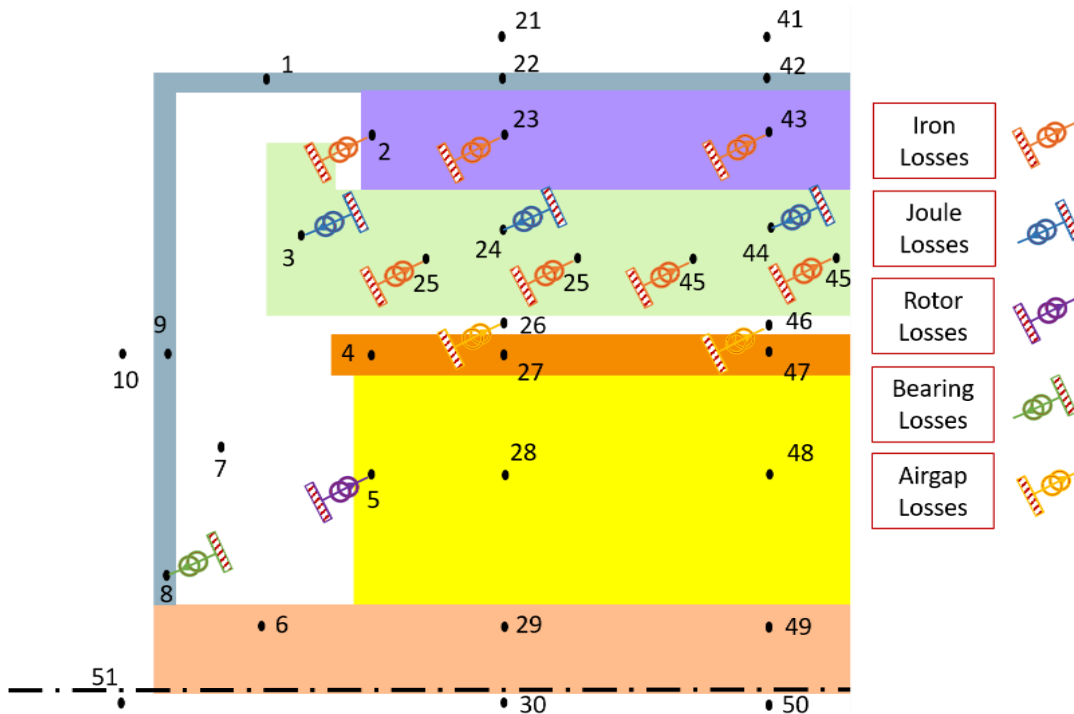


Figure 4.5 : losses location in a quarter e-motor axial section.

Figure 4.5 shows the location of generated losses. Losses are injected uniformly between the different nodes of a given motor part. Due to symmetry in the electric motor structure, half of the axial section is represented in this figure. In the model, Joule losses are injected into windings nodes in both the slot parts and the end-windings. Iron losses are computed for the stator iron part since rotor iron losses are neglected. Mechanical losses due to friction are considered as follows: airgap losses in the airgap, rotor windage losses at the rotor endcaps (surface heat sources), and bearing friction losses injected into both front and rear bearings.

4.3 Cooling System

Cooling technology choice is a matter of the required effort to reduce the temperature of each critical part. This effort should be proportional to temperature rise during the motor operating process. The objective is always to maintain temperature and weight below the limits. Therefore, excessive cooling penalizes the weight and hence it decreases the specific power that should be at least equal to 5 kW/kg . Investigations and analyses concern mainly the heat paths towards the outside environment. Based on the heat transfer equation, these heat paths depend on the thermal resistance values between the elements and the heat sink or more

specifically the specific cooling media. Consequently, possible cooling solutions and techniques are drawn from these analyses.

4.3.1 Thermal Resistance Analysis

To determine suitable cooling methods, a preliminary analytical study of thermal global resistances helped us choosing the cooling techniques for specific motor zones by analyzing heat fluxes paths. It is based on steady-state heat transfer calculations oriented towards eliminating some inefficient methods.

The main thermal constraint of the electric motor is in the windings, which are limited by their maximum acceptable temperature. Moreover, the windings generate the highest heat dissipation in the motor. Their conductors are isolated from the surrounding parts with an insulation material of low thermal conductivity (impregnation material). Permanent magnets have also a constraint related to their maximum allowed temperature. All of these facts lead us to investigate finding an optimum way to extract heat through cooling. Windings and rotor parts are the main studied areas.

Our LPTM consists of considering one-twenty-fourth (one over the slots number) of the motor. Volumes, surfaces, and heat sources, are required to calculate the temperature rise in the motor core

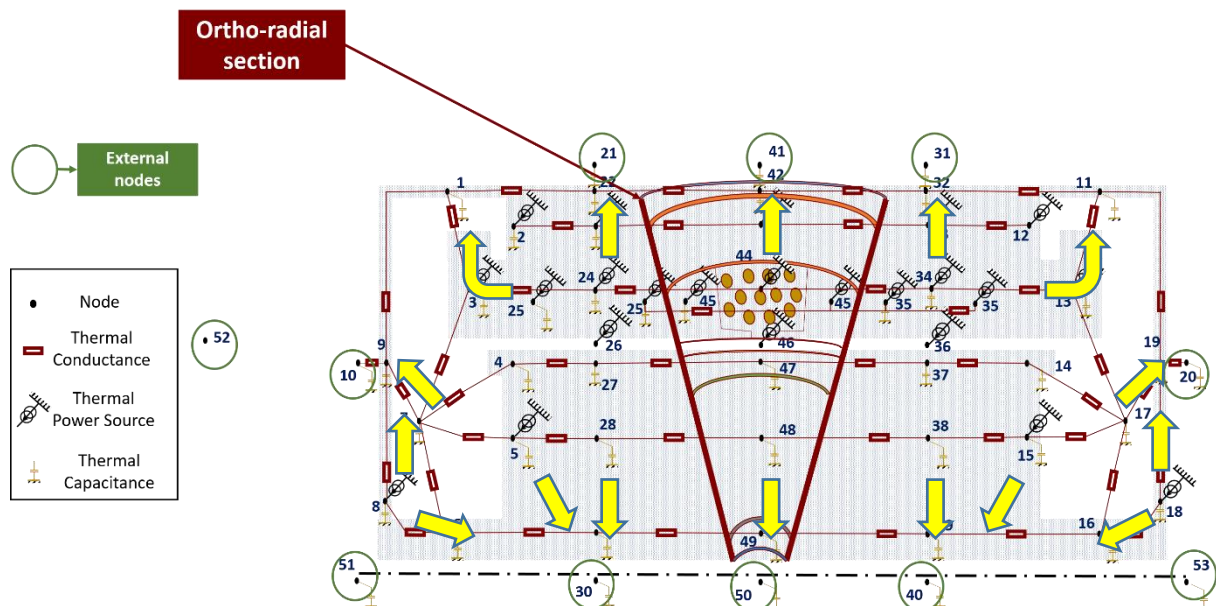


Figure 4.6 : Nodal network of the electric motor with emphasis on heat paths (yellow arrows) through external nodes connections.

For this purpose, the analysis based on the nodal network and heat path connections with external nodes (*Figure 4.6*) is conducted for the main critical hot spot zones: windings and rotor magnets. The total value of maximum heat dissipations is considered for steady-state temperatures.

4.3.1.1 Analysis for Winding Case

Before analyzing heat paths and resistances in windings material, it seems practical to separate motor windings into two main parts: slot part representing the windings inside slots and end-windings or winding wreaths at each of the motor sides.

On external nodes (in green in *Figure 4.6*), heat transfer coefficients have been imposed assuming forced air cooling ($200 \text{ W}\cdot\text{m}^{-2}\cdot\text{K}^{-1}$) or forced liquid cooling ($2000 \text{ W}\cdot\text{m}^{-2}\cdot\text{K}^{-1}$). The windings in the slot and the end-windings are studied, based on a simplified network depicted in *Figure 4.7*.

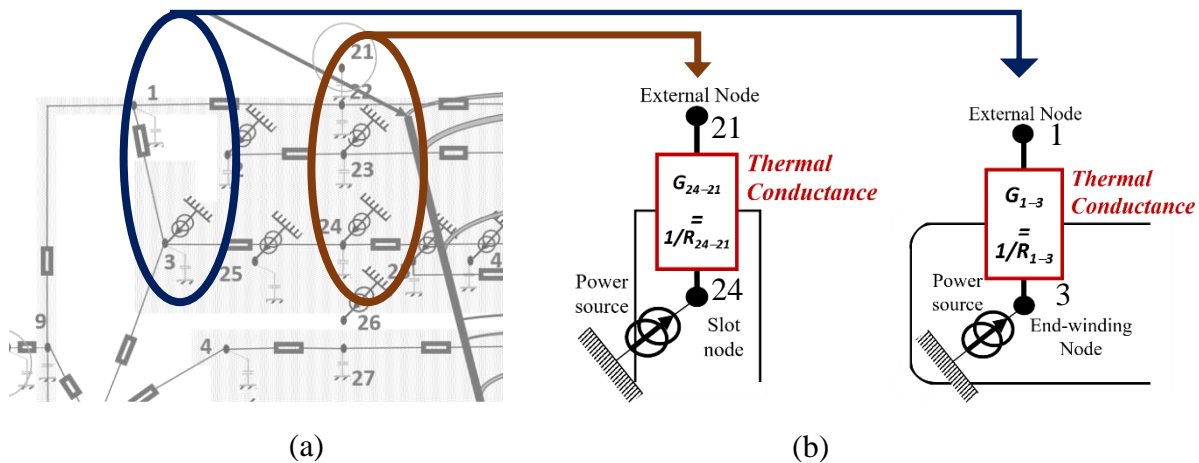


Figure 4.7 : (a) Nodal network near the stator zone at front motor side. (b) Thermal resistances between external nodes and slot node (left) and end-winding node (right).

For slot node 24 in our LPTM, we have considered connecting the central winding node, to the external node representing the cooling medium (air in the case of air cooling). The total heat path through a corresponding thermal resistance in permanent full power regime results in heating the windings to a maximum temperature that we will call: $T_{w,max}$.

The simplest way for the generated heat to evacuate from windings to the outside is through the housing radial part depicted in *Figure 4.7b (left)*. The thermal resistances are calculated for two possible cases: air cooling and liquid cooling. Knowing that the difference is mainly in the convection coefficient, the thermal conduction resistance remains the same for both cases. This resistance is calculated between slot node 24 and frame node 22 in the studied ortho-radial section for the corresponding volumes. It corresponds to two series resistances R_{24-23} (of $5.435 \text{ K}\cdot\text{W}^{-1}$) and R_{23-22} (of $0.095 \text{ K}\cdot\text{W}^{-1}$). The estimation gives the equivalent resistance of these two series resistances: $R_{24-22}=5.53 \text{ K}\cdot\text{W}^{-1}$, which is close to the slot-to-laminations resistance value due to the low thermal conductivity of windings compared to other high-conductivity materials.

The remaining thermal resistance in the path corresponding to cooling, which stands in series with the previous resistance, is R_{22-21} connecting node 22 to external node 21. A total thermal resistance called $R_{slot-ext}$ corresponding to R_{24-21} is calculated for each coolant option.

In the case of air at a temperature of 38°C (the ground temperature at ISA+23), with $200 \text{ W}\cdot\text{m}^{-2}\cdot\text{K}^{-1}$ of convection coefficient, $R_{22-21}=0.633 \text{ K}\cdot\text{W}^{-1}$, and $R_{slot-ext}=6.163 \text{ K}\cdot\text{W}^{-1}$. In this case a temperature $T_{w,max}=403^\circ\text{C}$ is found.

For liquid cooling with water-glycol jackets providing around ten times the previous coefficient of convection heat transfer ($\sim 2000 \text{ W}\cdot\text{m}^{-2}\cdot\text{K}^{-1}$), the resistance between nodes 22 and 21 is reduced by nearly the same ratio and $R_{22-21}=0.085 \text{ K}\cdot\text{W}^{-1}$. The total resistance between the slot node and the external node is $R_{slot-ext}=5.61 \text{ K}\cdot\text{W}^{-1}$, which can reduce the winding temperature by at least 30°C ($T_{w,max}=370^\circ\text{C}$). This temperature difference of 30°C is significant with respect to the maximum allowed temperatures in the motor. Thus, the liquid cooling solution with a jacket around the stator will be privileged.

The same calculation methodology is applied for the end-winding zone (also generating heat). The value of thermal resistance R_{ew-ext} between end-winding and the external node is analyzed. In the case of air convection at the end-winding end-space, this resistance is approximated as $R_{ew-ext}=8.6 \text{ K}\cdot\text{W}^{-1}$ with a convection coefficient of $110 \text{ W}\cdot\text{m}^{-2}\cdot\text{K}^{-1}$. It leads to an end-winding steady-state temperature $T_{ew,max}=571^\circ\text{C}$. A novel technique detailed in literature consists of potting the end-windings with highly conductive material (see *Chapter 2*). Thanks to this

technique the thermal resistance is reduced to $R_{ew-ext}=7.1\text{ K}\cdot\text{W}^{-1}$ (since thermal conduction, in this case, is more significant than air-convection). This results in a temperature decrease of around $100\text{ }^{\circ}\text{C}$. Obviously, in this motor design, potting is more efficient than air cooling in the case of winding wreaths with high heat dissipation.

As might be expected, the level of $T_{w,max}$ and $T_{ew,max}$ is very high in steady-state. As can be seen in *Figure 4.4*, the maximum losses are imposed during a very short time. Moreover, during this phase (take-off), the outside air temperature decreases rapidly due to the plane climb phase. Consequently, we decided to get profit from the system inertia to maintain the temperatures below the limits with an optimized cooling configuration.

4.3.1.2 Analysis for Rotor Case

The critical temperature in the rotor is that of magnets. The thermal resistance between rotor and external node (or nodes), $R_{rotor-ext}$, depends on the heat paths to outside as depicted in *Figure 4.8*.

For the front motor side, near the rotor, a focused network scheme is depicted in *Figure 4.8a*.

Two ways of heat extraction are possible according to the nodal network in this area. It can be either the heat path through the air cavity node (through node 7 to external node 10 in the lateral side of the frame) or the shaft and along the channel (towards node 30, the cooling node in the hollow shaft).

As for stator channels, two cooling techniques are evaluated for the rotor, which are liquid cooling and air cooling with similar heat transfer coefficient values: $200\text{ W}\cdot\text{m}^{-2}\cdot\text{K}^{-1}$ for air case and $2600\text{ W}\cdot\text{m}^{-2}\cdot\text{K}^{-1}$ for the liquid case. With forced liquid cooling (with water-glycol for instance), a high convection coefficient can be obtained, and thus the dominant heat path is through the shaft axial channel.

The simplified connections network is depicted in *Figure 4.8b* between rotor node 5 and the external nodes 10 and 30.

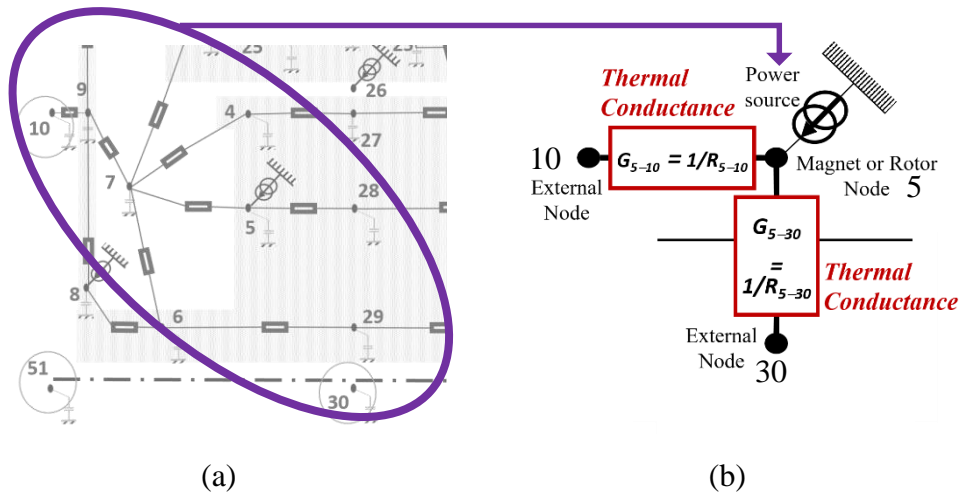


Figure 4.8 : (a) Nodal network near the rotor zone at front motor side. (b) Thermal resistances between external nodes and rotor or magnet node for the evacuation of heat.

The heat dissipation from windage losses at the rotor end-caps is assigned to the rotor laminations surface since magnets have a relatively low thickness in radial direction compared to the rotor radial surface. This results in approximately the same temperature levels in these elements since there is a low conduction resistance from laminations to magnets.

For air-cooling, $R_{5-30}=R_{rotor-ext,1}=24.43 \text{ K}\cdot\text{W}^{-1}$.

Liquid cooling gives $R_{5-30}=R_{rotor-ext}=5.14 \text{ K}\cdot\text{W}^{-1}$ for the corresponding volumes in the ortho-radial section.

The other thermal resistance through the air cavity is $R_{5-10}=R_{rotor-ext,2}=15.52 \text{ K}\cdot\text{W}^{-1}$.

In this steady-state analysis and considering the maximum losses, the average estimated maximum temperature reaches $360 \text{ }^{\circ}\text{C}$ with air cooling, while in the same conditions it reaches $210 \text{ }^{\circ}\text{C}$ with liquid cooling. This result means that a temperature decrease of around $150 \text{ }^{\circ}\text{C}$ is possible.

The liquid cooling technology provides a significant improvement in thermal results with a high-temperature reduction. Therefore, this solution will be adopted for motor cooling and the LPTM will be extended accordingly.

4.3.2 Nodal Network

Liquid cooling of the motor requires that a model that takes into account the temperature increase of the liquid in the axial direction of the motor, be developed. Moreover, a heat sink or exchanger allows transferring the extracted heat from the motor to the environment (outside air). This model is particularly important with regards to the significance of time and inertia factors in our application. As stated previously, the maximum losses occur during a short period. Thus, the optimization of the cooling system has to consider the liquid temperature variation during the mission.

In the nodal network of the motor core, the three radial sections along the e-motor shaft axis, allow taking into account the variation of coolant temperature when flowing from front side to rear one. Between the inlet and the outlet, the fluid temperature increases and influences the temperature of each radial section connected to each fluid node.

An illustration of the complete LPTM nodes' locations is depicted in *Figure 4.9*. This schematic representation shows half of the axial section of the motor.

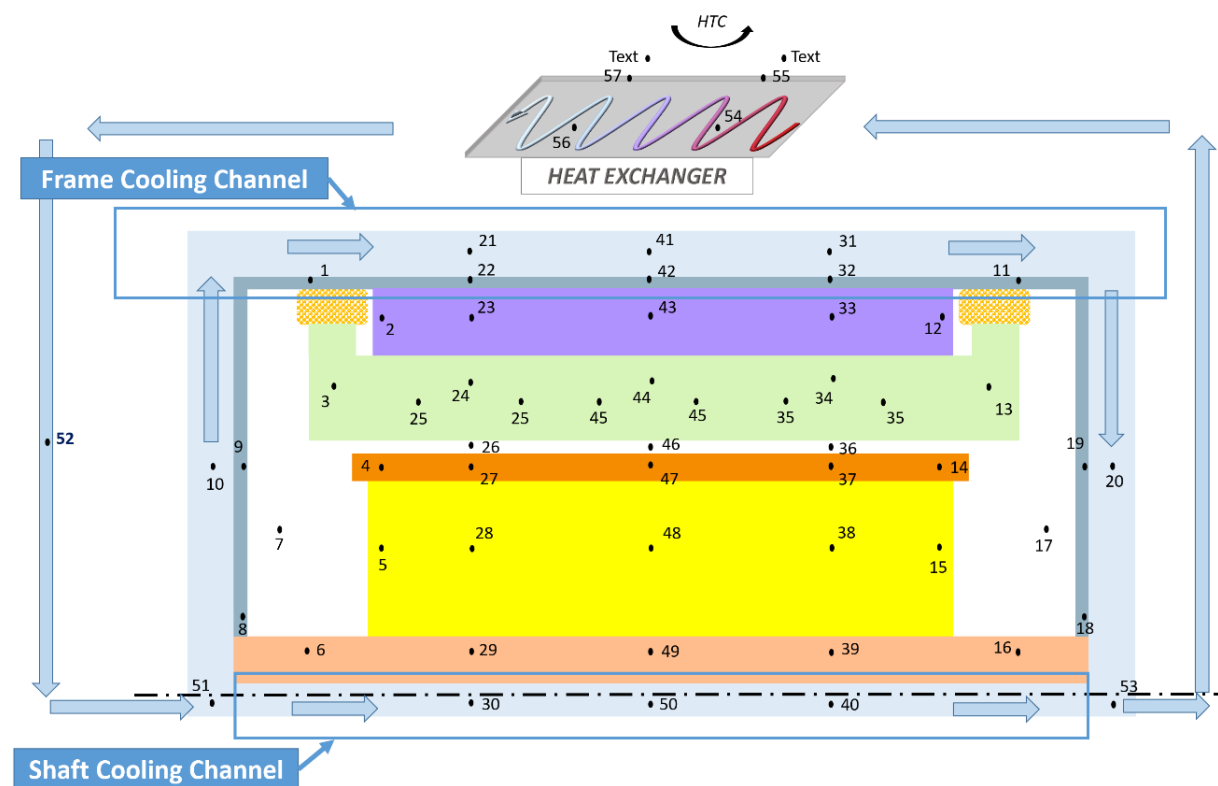


Figure 4.9 : LPTM nodes of the motor and its heat exchanger and the end-windings potting.

A connected heat exchanger plate is represented regardless of the actual shape and design used in our application. The full connections and nodes characteristics are set to the LPTM. *Figure 4.10* shows radial and ortho-radial connections and *Figure 4.11* shows the axial and end-space connections.

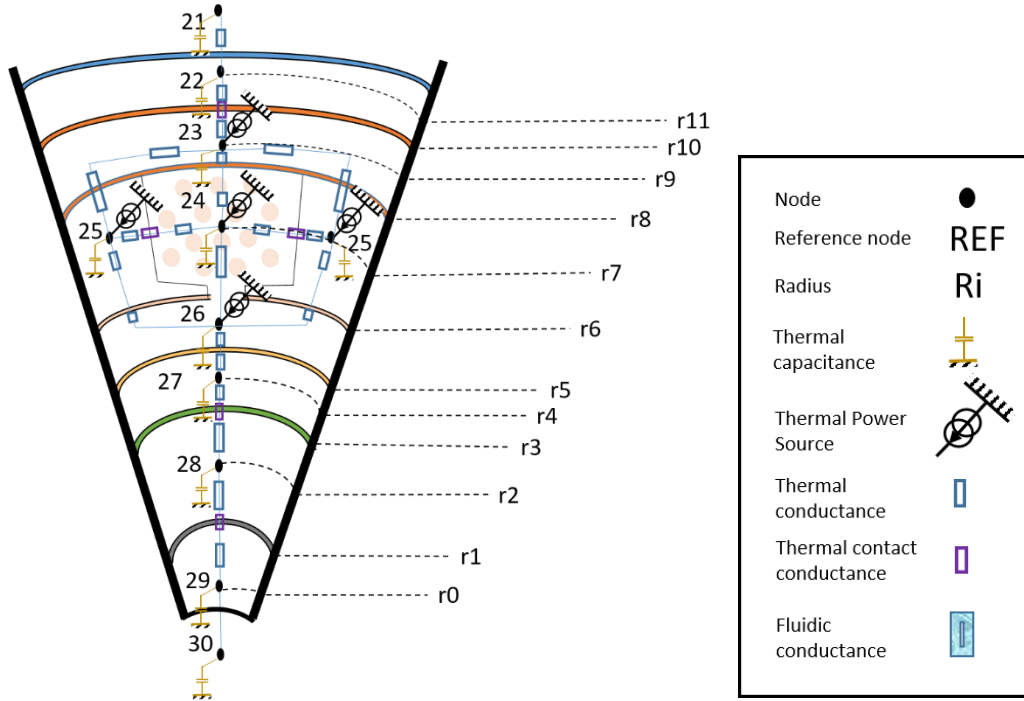


Figure 4.10 : Radial and ortho-radial connections of the motor nodal network.

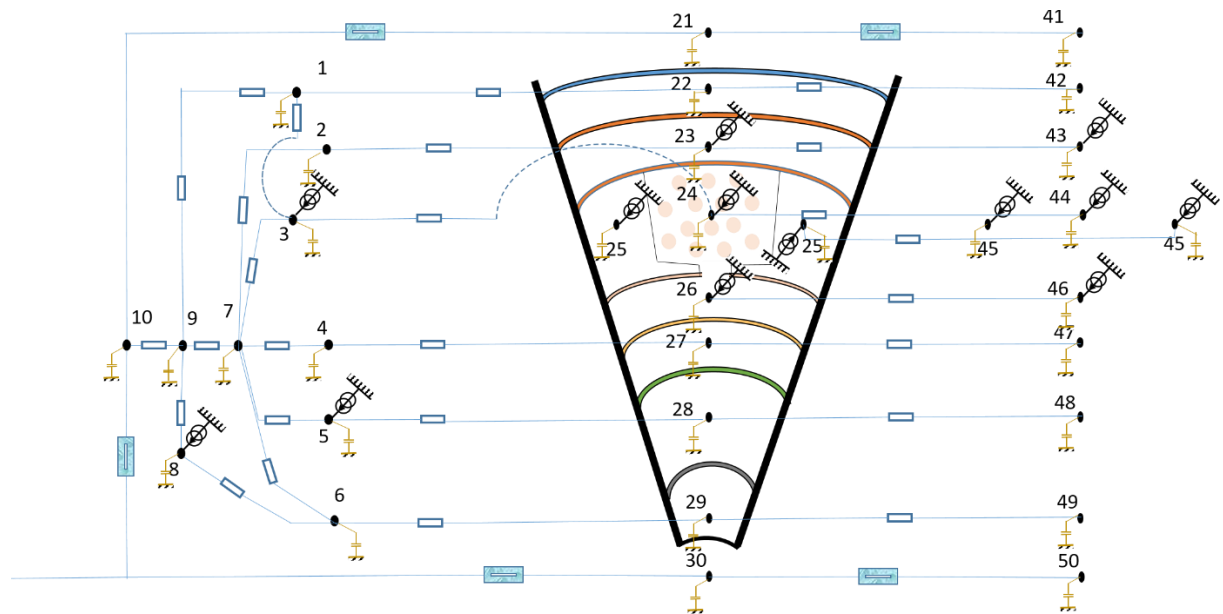


Figure 4.11 : Axial and extremity connections of the motor nodal network.

The model is simulated on MATLAB software and can be adapted to the motor dimensions to give temperature evolution. The cooling circuit, the heat exchanger, and the connections will be specifically described in the following subsections.

4.3.3 Cooling technology

The thermal issue and cooling solutions are defined based on the analytical study in subsection 4.3.1. To maintain the motor temperatures below the limits, the cooling system focuses on frame liquid cooling with liquid jackets around the motor core, a possible rotor liquid cooling through the motor shaft, and end-windings potting.

- ❖ Cooling Channels in Motor

The coolant circulation in motor channels is illustrated in *Figure 4.12*. A cooling circuit has been chosen consisting of a water-glycol jacket with the internal liquid flow around the motor and possibly a liquid flow inside the shaft (examples of such technology is found in [178], [179]).

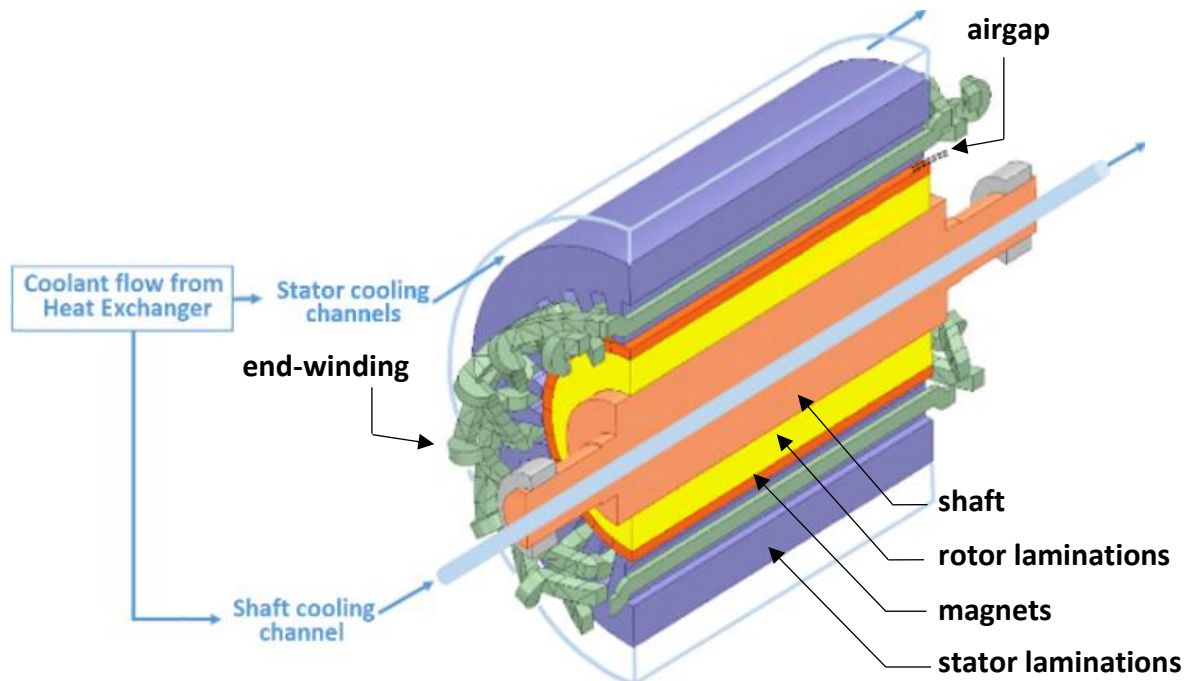


Figure 4.12 : Illustration of an electric motor 3-D section with cooling system channels.

Through these liquid channels, the coolant will flow to absorb the thermal flux, and the outside environment acts as a heat evacuation medium to dissipate the absorbed heat. DOWTHERM SR-1 Fluid at 50% Ethylene Glycol has been chosen as a coolant in the circuit for multiple properties and in particular its low solidification temperature. Even if cases with low outside temperatures will not be tested, the aircraft could encounter such environment.

In the stator channel, the liquid flows axially from the front to the rear sides of the motor. The frame structure, in which the channel is located, has a total thickness equal to 5% of the stator outer diameter. The channel has hence an annular shape whose height is equal to 3% of this latter diameter.

From one motor end to the other, we have considered three coolant nodes in the radial plans numbered 21, 41, and 31. The liquid in the channel gets in and out through the frame lateral surfaces at the front and rear sides respectively nodes 51 and 53. This improves the heat transfer from motor cavities to the coolant directly through these latter surfaces. The corresponding coolant nodes in the network are numbered 10 and 20 respectively. An annular shape channel is not structurally realistic but corresponds to a less advantageous case than a multi-channel configuration from a thermal point of view.

In the rotor, the possible cooling channel has a circular section with a diameter D_{rot-ch} of 5% of shaft diameter. As in the stator channel, the considered flow is axial along the motor rotation axis from the front side to the rear side of the motor. Three corresponding nodes in the shaft are numbered as follows: 30, 50, and 40.

The coolant pipe from the exchanger is connected to the motor channels at the inlet node 51 and outlet node 53 for thermal behavior evaluation in simulations.

❖ Potting

End-winding potting is adopted to lower the temperature in the end-winding critical zone. Thus, a solid connection between end-windings and the frame is made out of highly conductive epoxy resin (with $3.5 \text{ W}\cdot\text{m}^{-1}\cdot\text{K}^{-1}$ of thermal conductivity) allowing efficient conduction of heat through the potting material. As a reminder of *Chapter 2* review, this technique is investigated in [116].

Since this technique is applied to create a heat path to the frame, only the upper surface of each end-winding is encapsulated with potting material. The annular potting has a length equal to that of end-windings, an internal radius R_8 in *Figure 4.10*, and external radius equal to stator outer radius.

Finally, the heat flux extracted through liquid cooling should be evacuated to the outside environment. This job is accomplished using an efficient heat exchanger designed for this purpose.

4.3.4 Heat Exchanger of Cooling System

For the targeted hybrid aircraft, the nacelle is used to hold, cover, and protect the propulsion power units and components; it offers also an aerodynamical shape to these systems. Nacelle dimensions are defined by the project industrial partner Airbus as seen in *Figure 4.13*. It has a cylindrical revolved form of 532 mm central diameter and a total of 1382 mm length. It will enclose the propulsion components and could be used for other purposes in the design process of the hybrid propulsion chain for aeronautical application.

In the current study, the nacelle of the propulsion system will be employed as a heat sink plate to help to design a heat exchanger at minimum weight. For this purpose, a pipe is wound to the internal surface of this nacelle. A sketch is depicted in *Figure 4.14*.

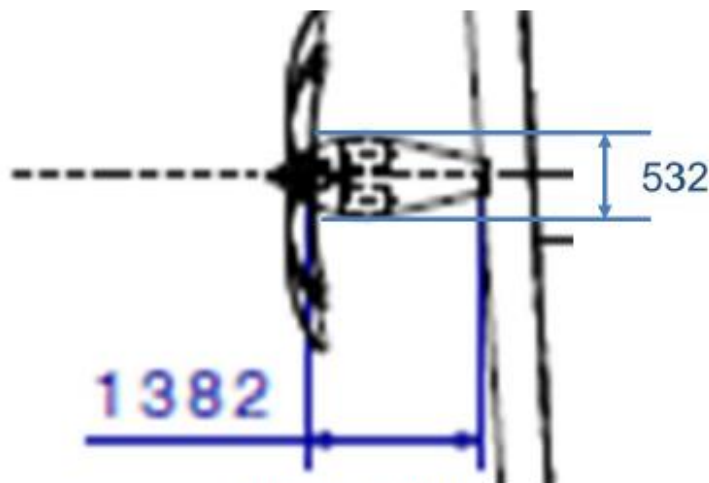


Figure 4.13 : Nacelle size with dimensions in mm from Airbus deliverable.

The calculations must include convection heat transfer and hydraulic calculations that are crucial to simulate our thermal model. In the model, the external dynamical conditions are considered to get accurate results and design a reduced cooling system with an optimum size.

The transient effects in power command during the mission enable us to conceive the cooling system with adapted size. Besides, the outside temperature variation of the environment air around the nacelle T_{env} should be considered during the flight mission time. The dynamical model should consider as well the inertia of the overall system to guaranty an optimized cooling system weight along with the safety of the motor operation.

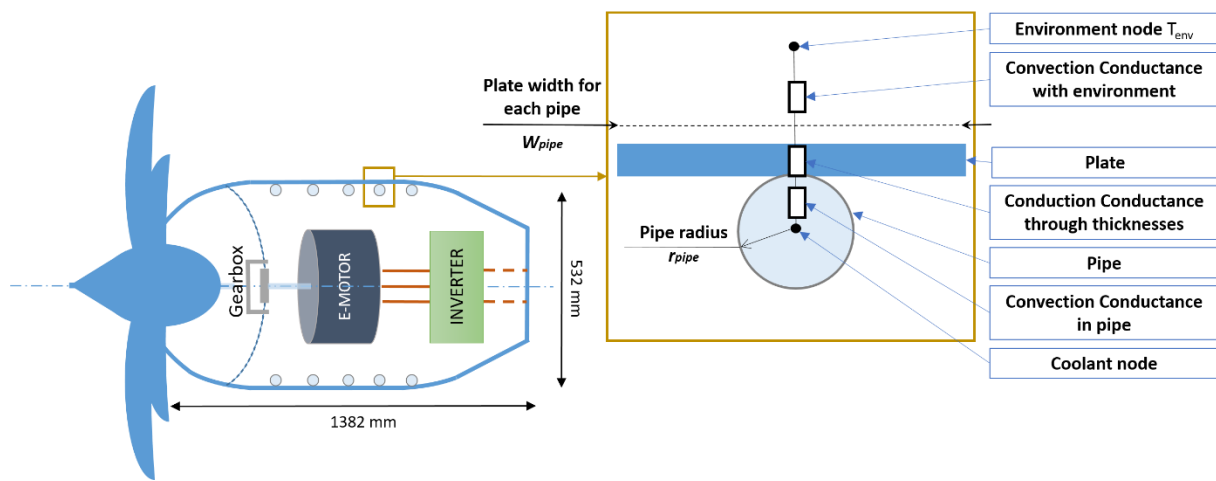


Figure 4.14 : Nacelle sketching view with radial sections used as heat exchanger cold plate.

Therefore, *ATHEM* model is developed to integrate in addition to the core motor system and design, the cooling system and hydraulic circuits and components required in thermal simulations and weight computation. The heat exchanger and cooling circuit integration in the model will be displayed subsequently.

4.3.4.1 Characteristics

During the flight, the motor conditions of temperature and pressure depend on the surrounding conditions (internal and external conditions of the nacelle behind the propeller).

The project industrial partner, Airbus, defines the conditions of the flight mission. Their specifications on the flight include the aircraft mission profile and the external conditions of the atmosphere during the flight.

This allows determining the temperature dynamical evolution during the complete aircraft mission from taxi-out to taxi-in. *Figure 4.15* shows the altitude profile during the flight mission. *Figure 4.16* gives the temperature as a function of altitude. Temperature conditions are considered at the ISA+23 °C Norm level according to Airbus. The ISA is the International Standard Atmosphere: 15 °C temperature and 1013 hPa pressure, whose level is displayed with a red line in *Figure 4.16*. The resulting temperature dynamical profile during the considered flight is depicted in *Figure 4.17*.

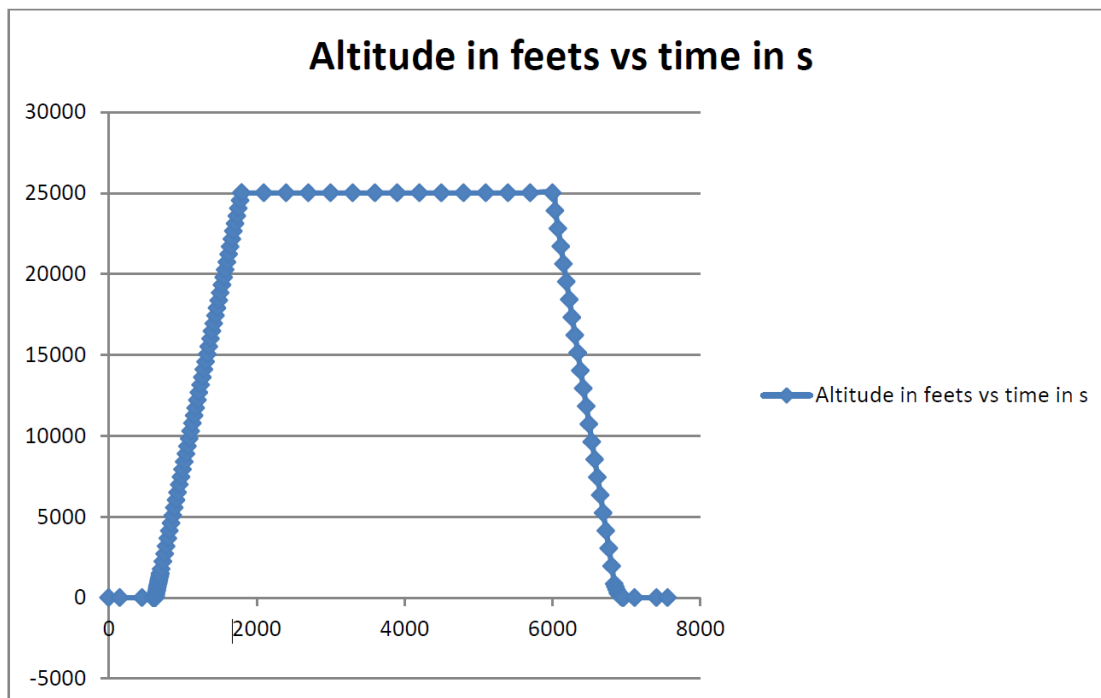


Figure 4.15 : Altitude (ft.) vs time (s) for a flight mission according to Airbus specifications.

Based on the ISA+23 °C level, ground temperature around the nacelle is equal to 38 °C, and the atmospheric air temperature T_{ext} decreases with altitude reaching -12 °C at the end of the climb phase.

The coolant circulating in the pipe transfers the heat to the ambient air through the nacelle wall at the rate of the external air convection Heat Transfer Coefficient HTC.

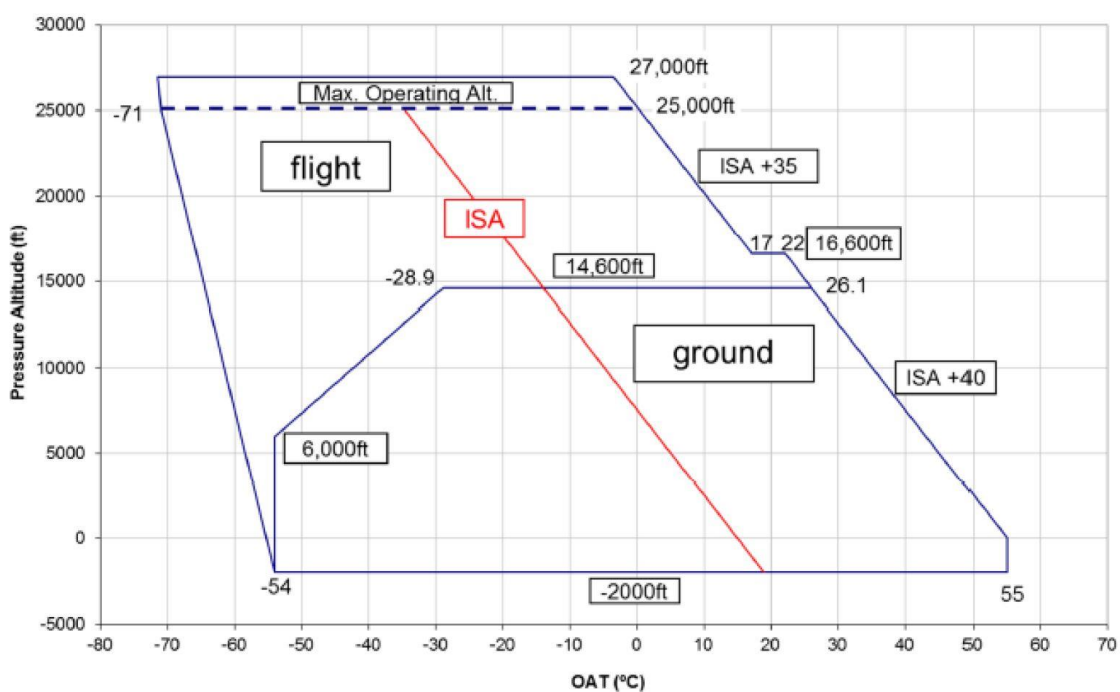


Figure 4.16 : External conditions of pressure altitude and temperature from Airbus deliverable.

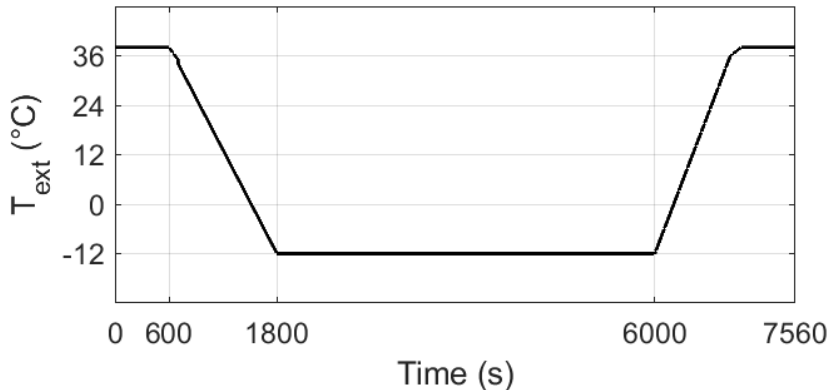


Figure 4.17 : Outside temperature's profile during aircraft mission.

The evacuation of the extracted heat from the motor is consequently limited by the nacelle surface, the HTC as well as the cooling circuit characteristics (coolant, flow rate, pipe geometry).

❖ Nodal Network at Exchanger Level

The nodal connection in *Figure 4.14* depicts three thermal conductances associated with three heat transfer phenomena: convection inside the exchanger pipe, conduction through the pipe, and plate thicknesses (t_{pipe} and t_{plate} respectively), and outside air convection at the exchanger plate surface.

The convection inside the pipe depends mainly on the coefficient of convection deduced from coolant flow type and properties and on pipe diameter ($d_{pipe}=2 r_{pipe}$) and length (l_{pipe}).

The conduction through the structure thickness depends on two characteristics: the thermal conductivity of the material and the thickness value. It is also a matter of how wide is the portion of the exchanger surface allocated to dissipate heat along the pipe length. Since the thickness value could be relatively low and the thermal conductivity is high ($200 \text{ W}\cdot\text{m}^{-1}\cdot\text{K}^{-1}$), the conduction conductance has less impact on thermal data than the other ones.

The last conductance concerns the heat transfer with external air through the total surface of the heat exchanger, which is the nacelle surface $S_{nacelle}$ with a total available surface of 2.3 m^2 .

For pipe diameter, the thermal conductance depends on a percentage $S_{nac-pipe}$ of this surface such that: $S_{nac-pipe}=W_{pipe} l_{pipe}$, and on the external Heat Transfer Coefficient (HTC) with the plate. This coefficient determines how the process of evacuation of thermal flux to the surrounding atmosphere occurs. Behind the propeller, HTC depends on the airflow velocity and characteristics. With the poorly known velocity profile around the nacelle behind the propeller, an intermediate value of this coefficient, of $140 \text{ W}\cdot\text{m}^{-2}\cdot\text{K}^{-1}$, has been used. It falls between the two values: $135 \text{ W}\cdot\text{m}^{-2}\cdot\text{K}^{-1}$ from empirical flat plate correlation (in turbulent regime based on from *Chapter 2* with an approximate take-off velocity) and $185 \text{ W}\cdot\text{m}^{-2}\cdot\text{K}^{-1}$ from the literature [180]. Finally, for W_{pipe} we have assumed that the heat will be evacuated from the coolant in the pipe through the corresponding width as follows: $W_{pipe}=\pi\times d_{pipe}$. The pipe length in the exchanger l_{pipe} required for motor cooling is deduced from the surface of the exchanger plate and the fixed distance between adjacent pipes (equal to W_{pipe}).

The thermophysical properties of exchanger components are also integrated into the model according to the values found in *Table 4.6*. Aluminum is chosen for pipes and plates based on the attractive properties it has thermally and physically compared to other materials (high thermal conductivity, corrosion resistance, lightness, a strength-to-weight ratio higher than steel..).

Material Property	Component	
	Pipe	Plate
	Aluminum	
Density ρ	2699 kg·m ⁻³	
Thermal conductivity λ	200 W·m ⁻¹ ·K ⁻¹	
Specific heat c_p	900 J·kg ⁻¹ ·K ⁻¹	
Thickness t	2 mm	3 mm

Table 4.6 : Pipe and plate properties.

These values are based on classical data existing in the market. Some considerations are taken into account for this specific aeronautical application such as lightness (weight), aerodynamics (shape), and thermal performance.

4.3.4.2 Thermal and Hydraulic Formulas

❖ Pipe Internal Convection Heat Transfer Coefficient

According to the theoretical and bibliographical correlations, the cooling channels' Nusselt number (Nu) expression (based on Prandtl and Reynolds numbers, respectively Pr and Re) is used to determine the coefficient of convection heat transfer in each pipe or channel (correlations in *Chapter 2*). Reynolds number is computed based on the flow dynamic characteristics which are the flow velocity u (determined by $u = \text{volumetric flow rate}/\text{channel section}$) and the coolant dynamic viscosity μ , in addition to coolant density ρ and the hydraulic diameter D_h . In the case of the non-circular channel section, the hydraulic diameter used in computation is defined by $4 \times \text{channel cross-section}/\text{wetted perimeter}$; otherwise, the real diameter of the channel is used.

Fluid connections can be represented as a one-way flow-pass that permits a heat flux transfer through the mass transport phenomenon. In *Chapter 3*, the fluidic connection between fluid nodes is detailed. Thus, a heat path is created in the coolant flow, which will define the temperature level in the coolant medium and consequently in the motor.

❖ Hydraulic Losses, Pump Power, and Weight Calculations

The adopted cooling system consisting of the exchanger, the pipes, and the pump, is evaluated according to hydraulic equations and motor specifications. Mainly, the exchanger pipe and plate are determined respecting surface and volume constraints in the application.

The total flow rate of the coolant circulating in the system and the properties of this latter are used to determine the hydraulic losses and consequently the pump power, according to equations (4.2) to (5.1). The total value of hydraulic losses is the sum of dynamic and static losses. Dynamic losses are the sum of major losses (which are linear losses along the circuit) and minor losses (which characterizes the singular losses occurring at specific points).

Major losses H_M are obtained based on the following equation:

$$H_M = \frac{K_{pipe} u^2}{2g} \quad (4.2)$$

Where K_{pipe} is the major losses coefficient computed as follows:

$$K_{pipe} = \frac{f_{pipe} L_{pipe}}{d_{pipe,int}} \quad (4.3)$$

Detailed explanation, nomographs, and numerous correlations corresponding to hydraulic specifications and properties related to minor losses H_m are found in [181]. Since specifications on positions and configuration of hydraulic components (such as Tees, valves, elbows,...) are not fixed, an approximation of the minor losses by half of the major losses value is adopted.

❖ Friction Coefficient and Pump Head

Friction coefficient f and pump head H_{pump} are calculated as in the following equations respectively:

$$f = \frac{1}{\left(\ln \left(\frac{k}{3.7 d_{pipe,int}} \right) + \left(\frac{5.74}{Re_{pipe}} \right)^{0.9} \right)^2} \quad (4.4)$$

$$H_{pump} = H_{dynamic} + H_{static} \quad (4.5)$$

The dynamic head $H_{dynamic}$ is the sum of the major and minor heads (or losses). In our application, static head H_{static} is considered negligible assuming that there is no significant difference in horizontal levels of the hydraulic components.

$$H_{dynamic} = H_m + H_M \quad (4.6)$$

$$H_{static} = 0 \quad (4.7)$$

Finally, the pump power P_{pump} is computed as follows:

$$P_{pump} = \frac{\dot{m} H_{pump} g}{\eta_{pump}} \quad (4.8)$$

Classically, the pump efficiency η_{pump} is considered around 60% and the roughness coefficient of the channel is $k=3\times10^{-4} m$. The gravity acceleration is considered constant at the ground level $g = 9.81 m \cdot s^{-2}$. Pump weight is evaluated according to its power P_{pump} mass flow rate \dot{m} in $kg \cdot s^{-1}$, and hydraulic losses (pump head) H_{pump} .

4.4 Thermal Behavior of the System

The model of our motor system can simulate the thermal behavior of the motor considering the dynamical profile of boundary conditions (see *Figure 4.18*). Therefore, steady-state analysis is far from being realistic when a full power use of the motor is required only during the take-off phase lasting a hundred seconds. Actually, during the longest phase, which is the cruise phase, less than half of this power is involved. Besides, during the aircraft mission (specifically climb and cruise phases), the outside air temperature change is significant (see *Figure 4.17*).

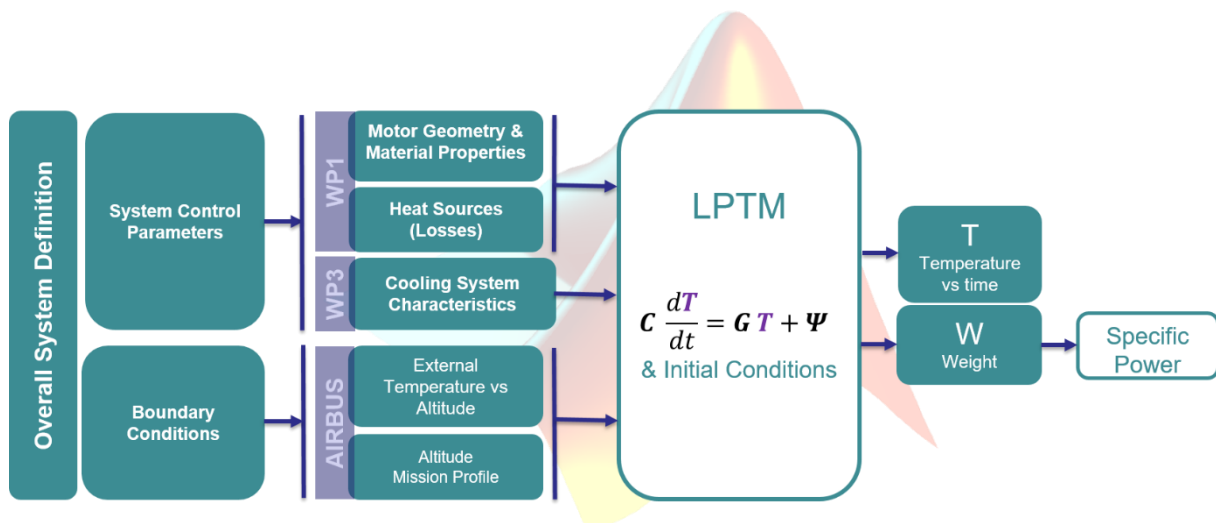


Figure 4.18 : Overall system definition of e-motor LPTM.

It influences the peak temperatures results in the motor since it affects the cooling system exchanger. The LPTM of the EM2025 is simulated using *ATHEM* model and the results are progressively displayed and analyzed.

4.4.1 Thermohydraulic Parameters and Characteristics

The parameters of the overall system of EM2025 are categorized into control parameters and boundary conditions.

Now that the motor is designed and that aircraft mission and boundary conditions have been presented, the missing characteristics of the cooling system will be filled out. The applied cooling system is defined by some control parameters that affect the temperature in the motor. They are mainly related to the hydraulic circuit in the motor and are prone to variation in the sizing process. They concern the coolant properties, channels and pipes dimensions in motor and exchanger, and flow rates in channels. The resultant characteristics coming out are mainly the convection coefficients, the pipe length in exchanger, and the hydraulic losses in order to compute pump head and power.

In our motor application, a water-glycol mixture (DOWTHERM SR-1 Fluid) is chosen as a coolant. Water-glycol mixtures present some interesting features over other possible fluids, mainly high specific heat. Moreover, this coolant can stand a wider range of temperatures than other liquids (such as pure water) before phase changing. Its liquid state belongs to a wider temperature interval (-33°C to 107°C) for the chosen mixture at 50% water to ethylene-glycol). Actually, with the outside air temperature dropping down to -12°C during the cruise phase, the coolant temperature will be directly impacted and could run a risk of falling to a negative level. Besides, high temperatures in motor stator due to high heat dissipations (up to 180°C allowed in windings for EM2025) with the thermal resistances between stator nodes and jackets are deemed able to raise significantly the coolant temperature. That being said, other possible choices of liquids will be investigated later in this chapter to test their efficiency given the dynamical profiles during the mission.

The properties of the selected solution of water-glycol at 40°C are grouped in *Table 4.7*.

Coolant Property	Unit	Value for water-glycol
Density ρ	$\text{kg}\cdot\text{m}^{-3}$	1065
Thermal conductivity λ_{fluid}	$\text{W}\cdot\text{m}^{-1}\cdot\text{K}^{-1}$	0.3937
Specific heat c_p	$\text{J}\cdot\text{kg}^{-1}\cdot\text{K}^{-1}$	3361
Dynamic viscosity μ	$\text{kg}\cdot\text{m}^{-1}\cdot\text{s}^{-1}$	2.2564×10^{-3}

Table 4.7 : Properties of water-glycol coolant at 40 °C.

In the following study, these properties will be considered constant with respect to temperature.

Hydraulic diameters, coolant flow rates, and channels or pipe lengths characterize the stator and shaft channels on one hand and the heat exchanger on the other hand. The resultant convection coefficients are computed according to these characteristics based on the presented thermal and hydraulic correlations. The stator convection coefficient value is applied to corresponding conductances connected to nodes: 10, 20, 21, 31, and 41. For the shaft, the convection coefficient value is used in the convection conductances connected to nodes 30, 40, and 50. Finally, the exchanger convection coefficient characterizes the convection in the pipe nodes 54 and 56.

In *Table 4.8*, the values of the hydraulic diameters, the flow rates, the channel lengths, and the convection coefficients h are grouped for each corresponding zone. The total flow rate of coolant in the exchanger channel is $q_{exch} = 4.1 \times 10^{-3} \text{ m}^3 \cdot \text{s}^{-1}$. The following results of temperatures are obtained considering that 65% of the nacelle surface is engaged. Later on, an advanced study on the effect of exchanger surface variation on motor cooling is developed in *subsection 4.4.5*.

Zone	Stator	Shaft	Exchanger
Hydraulic diameter D_h (mm)	10.2	5.1	35
Flow rate q ($\text{m}^3\cdot\text{s}^{-1}$)	4×10^{-3}	10^{-4}	4.1×10^{-3}
Channel length l (m)	0.5386	0.5386	10.62
Convection coefficient h ($\text{W}\cdot\text{m}^{-2}\cdot\text{K}^{-1}$)	1500	1000	6700

Table 4.8 : Cooling system parameters in channels according to motor zones and exchanger.

Even if no rigorous optimization process is conducted, those values have been chosen after a comparison of several configurations with numerous values. The weight of the cooling system without the pump is around 19 kg .

With these parameters, the motor temperatures are obtained and the cooling system hydraulic calculations are performed to estimate hydraulic losses and deduce pump power.

4.4.2 Results and Analysis

With these values of the parameters and characteristics and a total flow rate in exchanger of $q_{exch} = 4.1 \times 10^{-3} \text{ m}^3 \cdot \text{s}^{-1}$, the model is simulated and the maximum temperatures are verified according to each critical zone. The rear-end-nodes of the motor have higher temperatures than the front motor side. In *Figure 4.19*, the nodes of extracted temperatures are indicated in red circles in the nodal network. They are as follows:

- $T_{coolant\ outlet}$ is the outlet cooling temperature of the coolant node 53,
- T_{stator} corresponds to node 33,
- T_{teeth} is the temperature at node 35,
- Stator windings hottest point $T_{windings}$ is given at node 34,
- The highest temperature of end-windings $T_{end-windings}$ is given at node 13,
- Rotor temperatures, T_{pm} of permanent magnet and T_{rotor} of iron structure, are given at nodes 14 and 15, and
- Shaft temperature T_{shaft} is given at node 16.

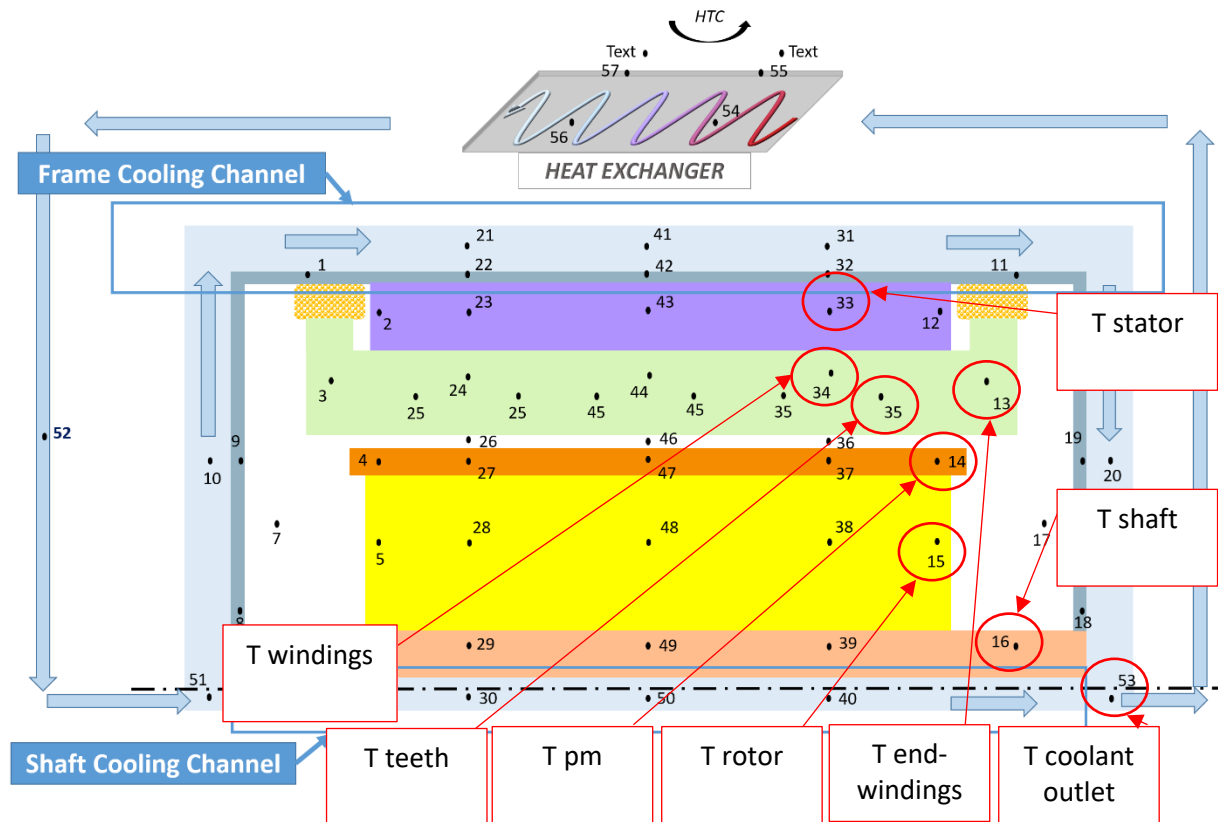


Figure 4.19 : Nodal network with the positions of extracted temperatures.

According to this simulation, the motor will exhibit the temperature profiles depicted in *Figure 4.20*. This figure shows the group of temperature evolution curves at indicated nodes. Separate graphs for stator and rotor temperatures are displayed in *Figure 4.21* and *Figure 4.22*.

The first evidence in this graph is that the temperatures in the stator and rotor have a dynamical evolution all mission long without reaching a definite steady-state. This proves that thermal inertia has an important influence on temperature profiles in the motor.

When analyzing the temperature profiles, it is remarked from the plots that there are two types of thermal behavior. The first set of curves represents the stator parts temperatures evolution and a second set represents rotor lamination and permanent-magnets temperatures response.

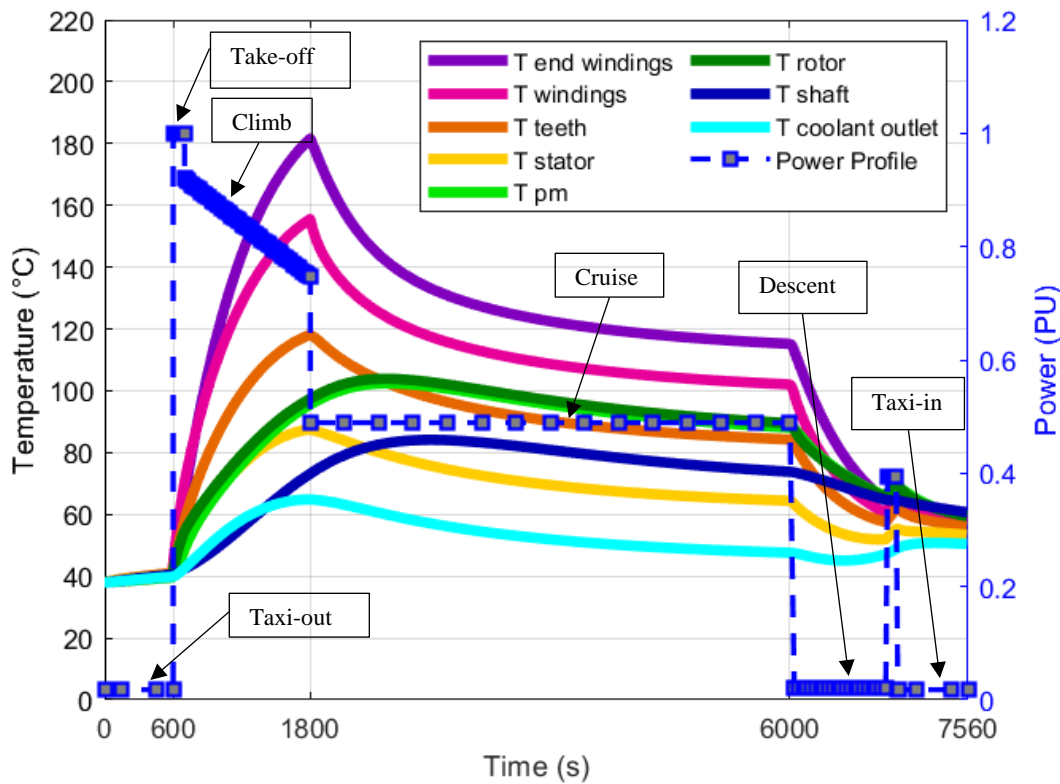


Figure 4.20 : Temperature profile of motor EM2025 parts with corresponding power profile.

4.4.2.1 Stator Behavior

For stator behavior, the temperature rise in the observed parts is very slight during the taxi-out phase, and then a significant increase is exhibited during take-off and climb phases.

Almost all of the stator components reach their maximum temperatures at the end of the climb phase, which is 1800 s after the mission start-off. Actually, the spike observed in these temperature profiles indicates that the steady-state was not reached. Then, a temperature drop follows an exponential decay during the cruise phase where the motor is running at only half of its full power. The losses profiles in this phase record a sharp decrease of Joule and iron losses (see Figure 4.4).

Consequently, the maximum temperature in each stator part would attain significantly higher values if the motor was kept on running at a high power rate for a longer time. In fact, these evolutions in temperature depend strongly on the boundary conditions during the motor functioning. Indeed, the heat profiles and levels influencing this motor part and creating these curves of temperature, are those produced due mainly to Joule losses and also to iron losses.

Another two exponential decays are observed for the power drop after the cruise phase for descent and taxi-in phases. Amidst the last two phases, a brief and moderate shot of 40% power-on pushes the evolution of the temperatures up to a sharp spike before resuming its last decrement from that point. The temperature decrement continues its way down until reaching a low level that is slightly higher than the ground temperature surrounding the nacelle, at the end of the aircraft mission. The significant losses reduction during these two phases acts as the major player in the evolution of the resulting temperatures. Thus, despite the increasing outside temperature, the reduction of the influencing losses has a much higher effect on temperature for these last two phases, as seen in the stator temperature curves of *Figure 4.20*.

Globally, one more evidence is noticed in the graph, which is the peak temperature zones. The end-windings are the hottest points found in the motor all mission long as seen in *Figure 4.20*. This was an expected result according to previous studies. Actually, this is due to high Joule losses in all windings part and the high thermal resistances between the end-windings core and the surrounding environment. While these parts dissipate a great percentage of Joule losses (as much flux density as windings), they are thermally more isolated than the slot part. In fact, the thermal resistance between this part and the frame through the air in the cavity is at least 3 times the one between the winding in the slot and the frame through adjacent teeth. Besides, the thermal resistance connecting the end-windings to the frame through potting (between nodes 1 and 3 for instance) is around 1.3 times higher than the thermal resistance between the winding core in the slot and the frame in the radial direction (between nodes 22 and 24 for instance).

It can be remarked that in this configuration, the temperatures of the hot-spot zone remain below the thermal limit ($180\text{ }^{\circ}\text{C}$) with the adopted cooling techniques for the chosen winding impregnation thermal class.

In *Figure 4.21*, the speed of increase of four temperatures in the stator with respect to time is displayed with their corresponding evolutions. For windings and end-windings, a peak of around $20\text{ }^{\circ}\text{C}/\text{min}$ is noticed for take-off, which is a crucial speed to consider in controlling the evolution of motor temperatures. Moreover, during the climb phase, a significant decrease of this speed is observed.

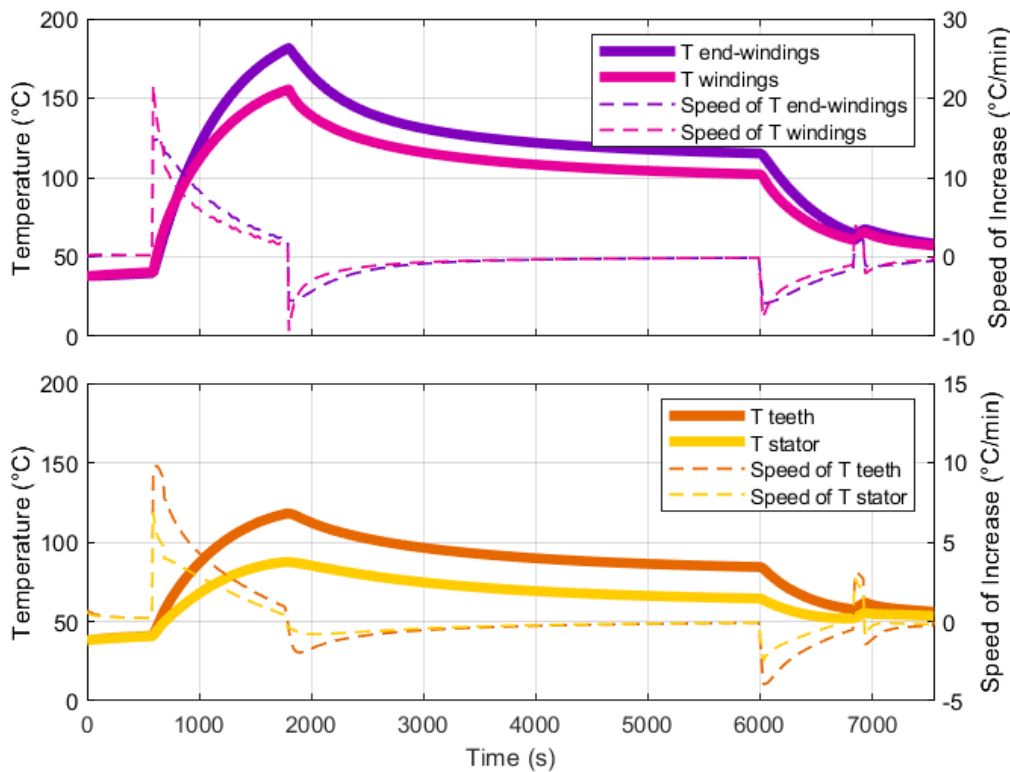


Figure 4.21 : Evolution of four stator temperatures and their speed of increase during the mission.

The breaking point of the slopes of temperature curves between the end of the climb and the beginning of the cruise induces a change in the aspect of the speed curve since the speed becomes negative. Also, the same behavior is noticed between the end of the cruise phase and the beginning of the descent phase.

For stator and teeth temperatures, their speeds of temperature increase follow the same evolution as previous graphs with a ratio of 0.5 and a peak of around $10\text{ }^{\circ}\text{C}/\text{min}$.

4.4.2.2 Rotor Behavior

For the rotor, the upper graph of *Figure 4.22* demonstrates that the stator evolution of temperature exhibited during the mission does not apply to the rotor behavior.

Moreover, the graphs show a similar evolution and levels of temperatures in the rotor laminations *T rotor* and permanent magnets *T pm*.

For permanent magnets, the maximum is around $100\text{ }^{\circ}\text{C}$, which prevents magnets from overheating. At the beginning of each phase, these elements exhibit a quite different transient

evolution than rotor laminations due to their thermal inertia. However, since the rotor tends to stabilize into a steady-state in the critical phases, the end temperature result is quite similar.

During taxi-out, a similar temperature evolution is observed for all motor parts, due to the low heat dissipations occurring at this level. At the end of this low-power phase, the sudden full power for take-off phase and high-power level for the climb phase afterward, the stator and rotor behaviors are quite different. Actually, the rotor reaches its maximum temperatures at a delayed time relatively to the stator temperatures peak. This delay is justified by a group of parameters that controls the rotor peak time, mainly losses in the rotor environments (end-caps, airgap..) maintaining almost the same level between end of climb and cruise phases. For the stator, the location of the maximum temperature at the end of the climb is due to the losses significantly reduced: Joule losses by more than 50% and Iron losses by around 25%. Other factors lead to this time difference, which are the coolant temperature extremely influenced by the stator temperatures. Besides, rotor temperatures display a smoother peak curvature, specifically in permanent magnets and rotor laminations zones. The maximum for these two latter parts is obtained at 2500 s after the beginning of the mission. A very slight decrease is noticed in the cruise since the losses are constant in this phase while only the drop in outside air temperature affects the temperature evolution.

Afterward, the descent phase starting at 6000 s is marked by a sudden drop of heat sources (losses). The reduction of windage and bearings losses (influencing the rotor) is less pronounced than that of Joule and iron losses (influencing the stator). Therefore, the rotor temperatures in this phase pursue a decrease with a lower slope than that of the stator temperatures curve.

For the last two phases, the temperature evolutions in the stator and rotor are similar due to the same relative heat dissipations in the components.

On the other side, the evolutions of the rotor and coolant speed of temperature increase are depicted in *Figure 4.22*.

As rotor and permanent magnets temperatures have almost the same evolution, the peaks of speed are in phase, with a higher level noticed for rotor (maximum of 12 °C/min) due to its lower thermal capacity.

For the shaft, it is remarked from *Figure 4.22* that the scale of the increased speed is notably reduced by ten times compared to other motor parts with a smoother curve aspect.

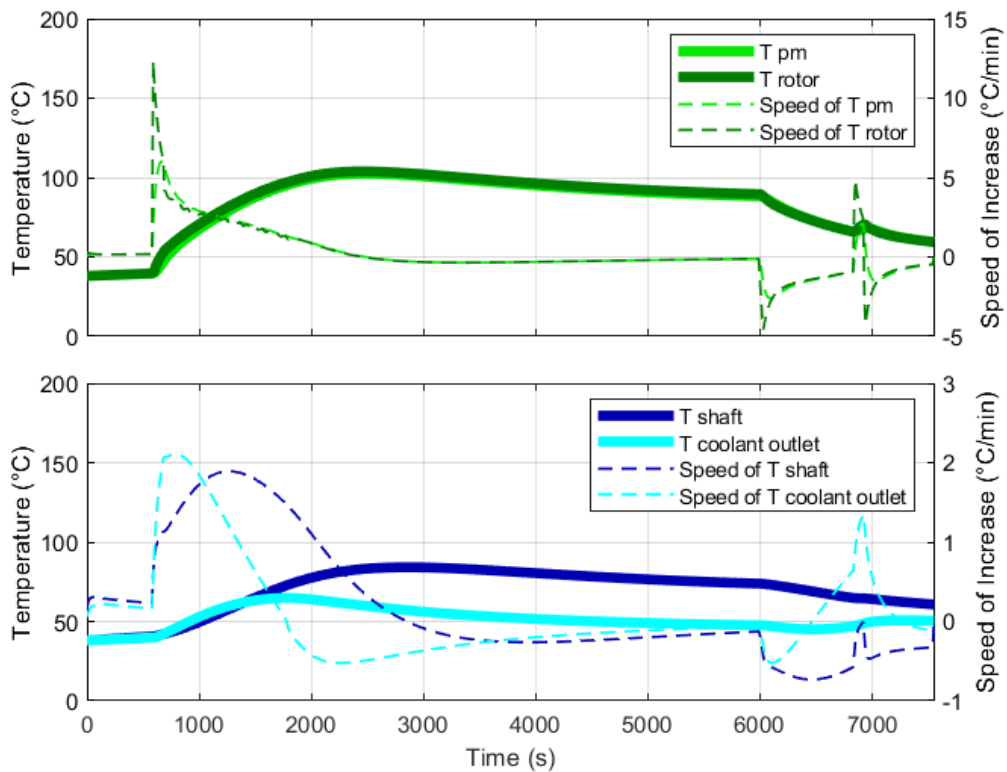


Figure 4.22 : Evolution of rotor and coolant temperatures and their speed of increase during the mission.

Besides the evolution of the speed of increase of the coolant outlet temperature follows the dynamics associated with the adopted cooling system characteristics. Here, with the weight, the mass flow rate, the exchange surface, and the convection coefficients, we notice a maximum speed of increase of around $2\text{ }^{\circ}\text{C}/\text{min}$ during the take-off phase.

4.4.2.3 Influence of Outside Air Temperature

The coolant evolution seems to follow the stator temperature dynamics with a variation between $38\text{ }^{\circ}\text{C}$ and $70\text{ }^{\circ}\text{C}$. The heat is mainly extracted from the stator (around 85% of the total losses at full power) through the coolant medium. High heat dissipations in this motor part influence the coolant outlet temperature considerably. During take-off and climb phases, the water-glycol mixture exhibits a continuous temperature increase. The high heat extracted from the motor is evacuated through the nacelle surface to the outside with a convection coefficient HTC . Since the exchanger surface is limited and the coefficient HTC is relatively low, the process of heat evacuation is limited and the coolant temperature increases.

The convection coefficient of the plate with outside air is a limiting factor since the corresponding thermal resistance is the highest among the three main resistances between coolant and outside air in the heat exchanger (see *subsection 4.3.4.1*). Finally, the ending phases (descent and taxi-in) of the mission are marked by an outside air temperature that increases significantly, which influences the coolant temperature evolution, in addition to the dynamical profiles of losses during these phases.

The temperature of the outside air during the mission is another influencing factor acting on the stator temperatures. The dynamically changing temperature of external air at the heat exchanger level is critically important to avoid oversizing of the exchanger. If a constant outside air temperature is considered during the mission, the hot spot temperatures would follow the curves depicted in *Figure 4.23* and *Figure 4.24* for 38 °C and 53 °C constant values respectively.

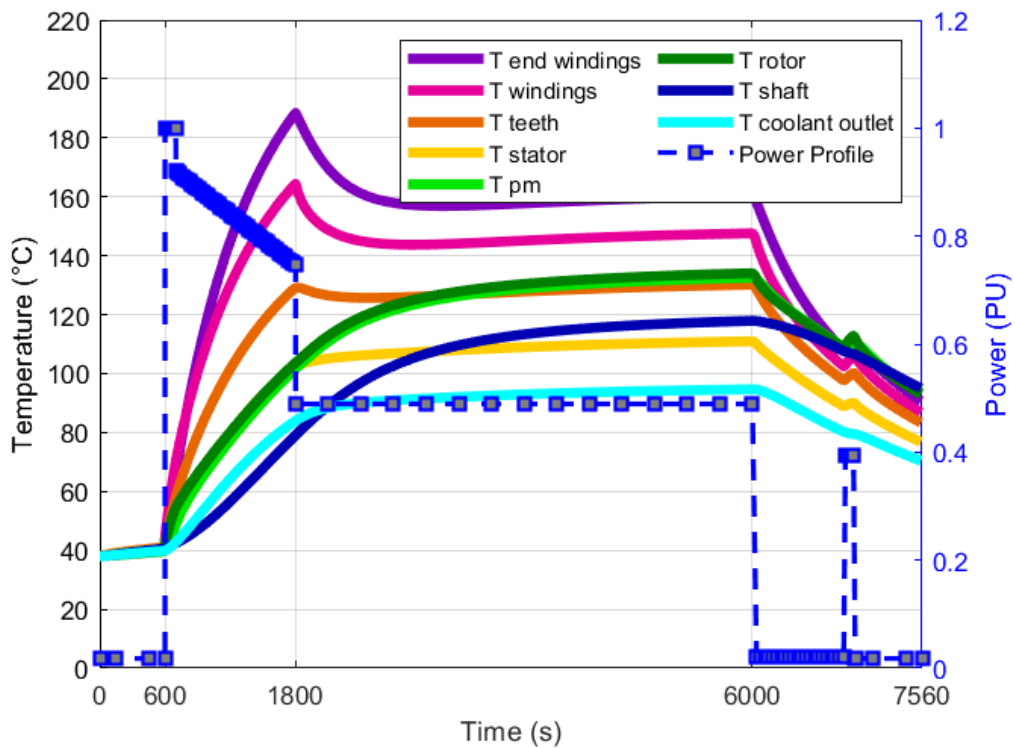


Figure 4.23 : Temperature profile of motor EM2025 parts with a constant outside temperature of 38°C.

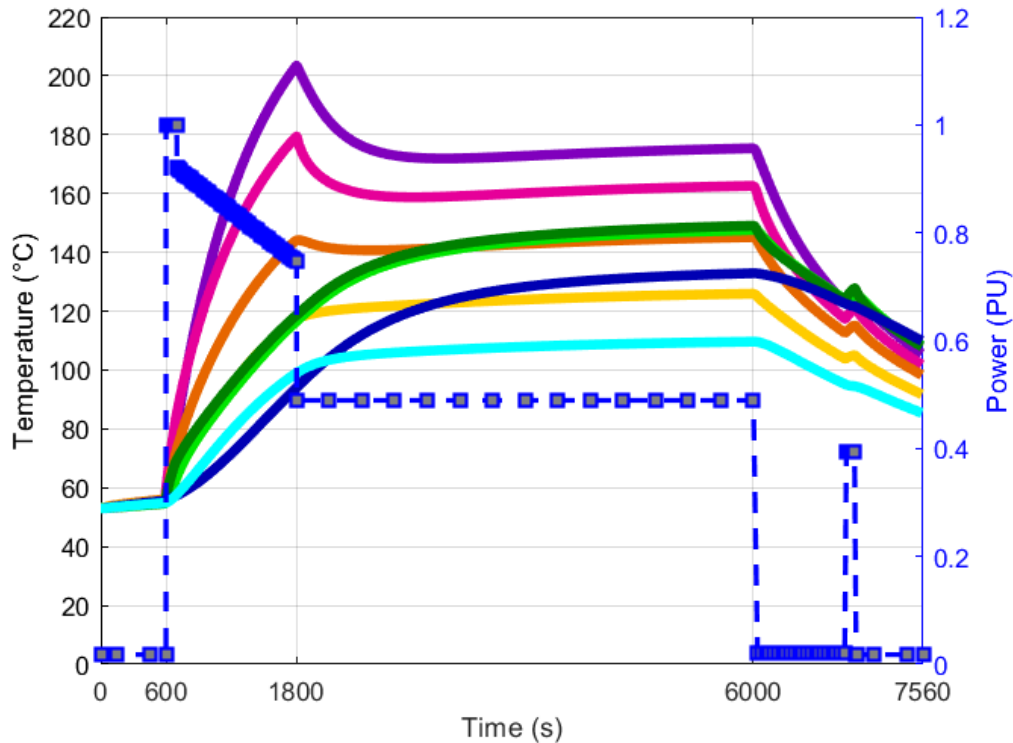


Figure 4.24 : Temperature profile of motor EM2025 parts with a constant outside temperature of 53°C (same legend as Figure 4.23).

In these two cases, the maximum temperatures at end-windings increase by 5°C and 20°C respectively. It is noticed that the temperatures rise in the rotor is in the range of 30°C to 40°C , which brings the maximum temperatures in laminations and permanent magnets close to (or above) the allowed limits. Besides, in this case, the coolant temperatures increased since they are highly dependent on the heat evacuation rate in the exchanger. Actually, the outside air temperature (which is the fluid in the secondary cooling circuit) controls directly the efficacy of the cooling system by controlling the coolant temperature at the motor inlet.

Moreover, we can notice that the vaporization temperature is not reached. The maximum temperature of the liquid even remains far below 100°C . Hence, the main reason to use water-glycol instead of water is the lower bound of its temperature for the liquid phase of -33°C that allows the aircraft traveling in northern countries.

4.4.2.4 Hydraulic Losses and Pump

The resulting hydraulic losses H_L are presented in *Table 4.9*. The pump characteristics (mainly pump head H_{pump} and flow rate q) should allow the identification of the pump weight and properties according to the catalog of hydraulic pumps from Parker Pumps and Motor Division [182]. An adequate pump has the characteristics found in *Table 4.10*.

Zone	Stator	Shaft	Exchanger
Hydraulic major losses $H_L(m)$	0.06	3.89	2.54

Table 4.9 : Resulting hydraulic major losses in channels according to motor zones and exchanger.

Pump		
Characteristic	Unit	Value
Normal Operating Pressure	bar	206
Maximum Speed	RPM	3646
Length	cm	26.16
Height	cm	21.84
Width	cm	17.27
Weight	kg	14

Table 4.10 : Pump characteristics (AP27V) from [182].

4.4.3 Influence of Thermophysical Parameters Variation

Due to the temperature evolution of motor parts, some physical parameters' values might be subject to variation, whereas in the model we have assumed the values of thermophysical properties of motor materials as constant. Therefore, a focused sensitivity study has been conducted to verify that this assumption does not lead to faulty thermal results.

To proceed with this study, we were interested in evaluating the impact of a 10% increase in two thermal properties of each motor part on motor maximum temperatures. The properties are thermal conductivity and specific heat capacity. It is worth mentioning that variation of specific heat capacity in the model is equivalent to that of the density since the product of these two properties is considered in thermal capacity calculation. The material properties of the following motor components were successively changed: the frame, the permanent magnet, the windings (or resin impregnation material), the shaft, and the laminations.

The temperatures of several motor zones are included in this study: end-space (node 17), rotor (node 15), permanent magnets (node 14), stator yoke (node 33), teeth (node 34), windings (node 35), and end-windings (node 13). The decrease in temperature for each motor zone is displayed in graphs of *Figure 4.25* and *Figure 4.26* for thermal conductivity and specific heat capacity respectively.

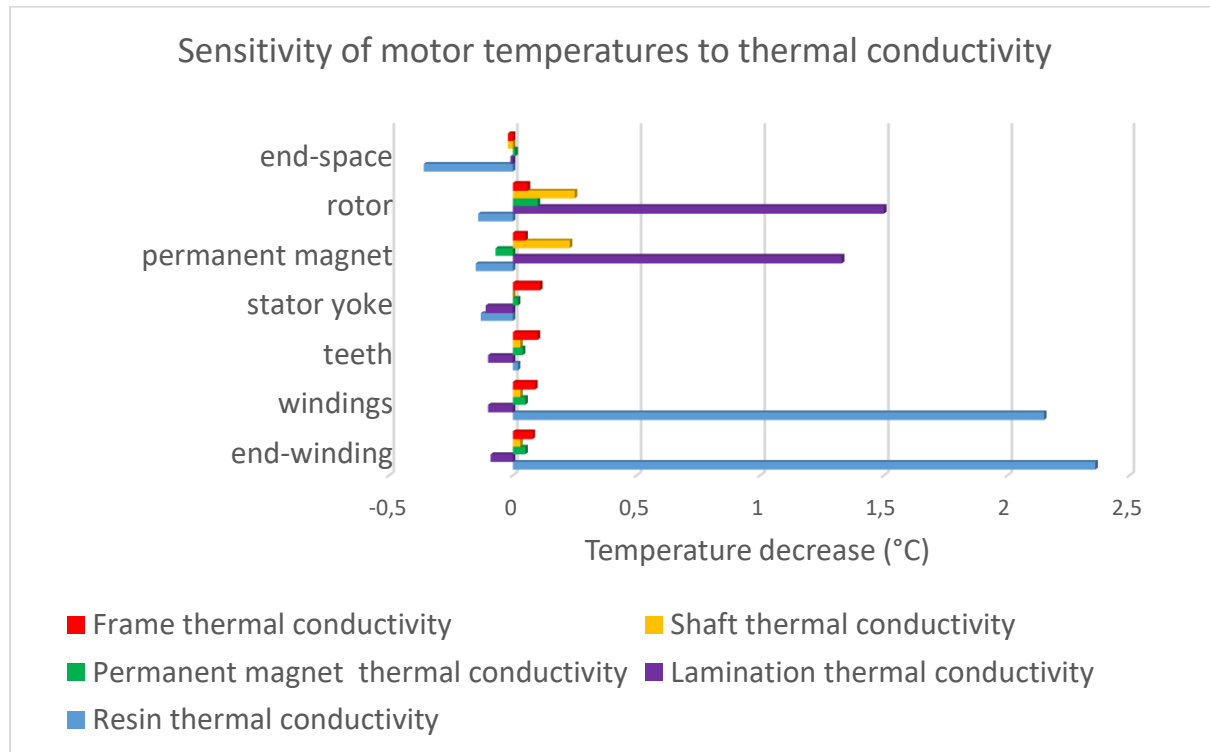


Figure 4.25 : Maximum temperature difference of motor parts with 10% variation in thermal conductivity of motor materials.

As depicted in these figures, the temperature decrease is slight or insignificant. Therefore, only high temperatures' differences will be analyzed hereafter.

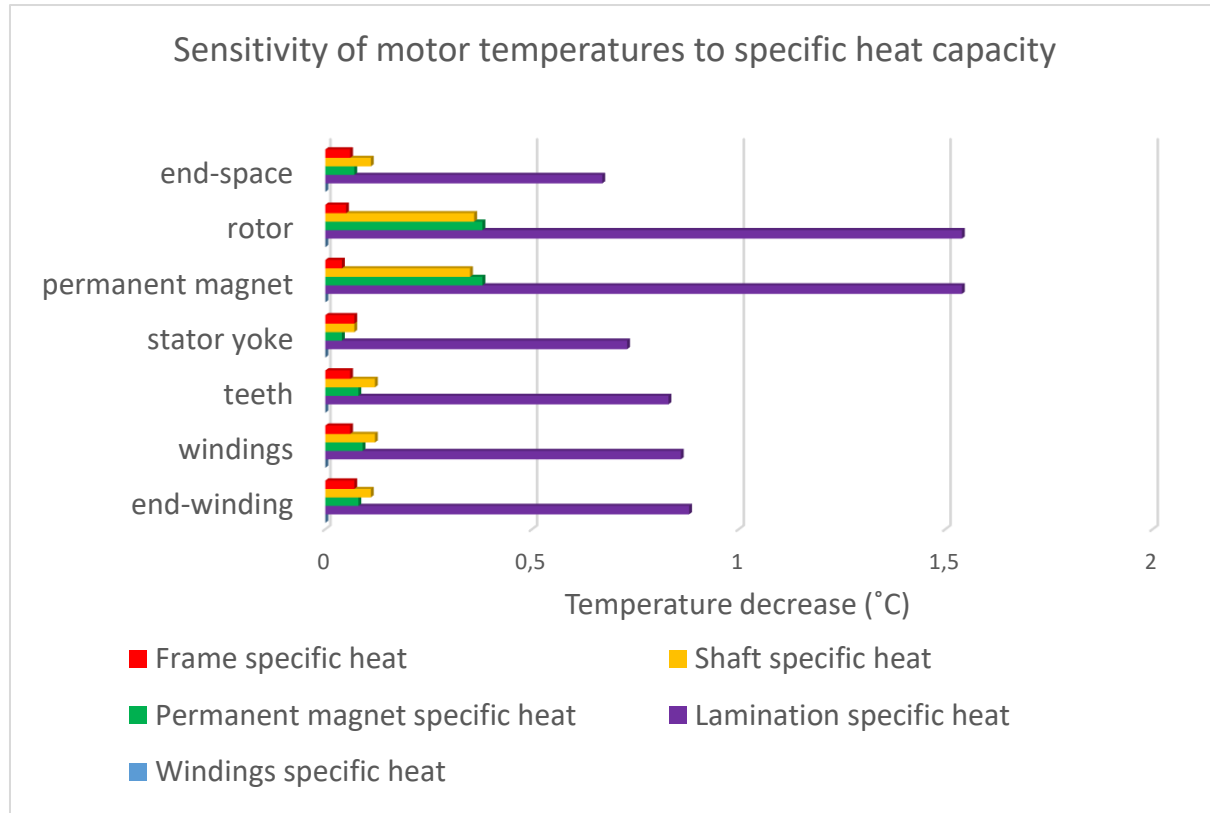


Figure 4.26 : Maximum temperature difference in motor parts with 10% variation in specific heat capacity of different motor materials.

4.4.3.1 Influence of Thermal Conductivity

The thermal conductivity of resin as impregnation material applied in windings influences the windings and end-windings temperatures the most (decrease of $2.2\text{ }^{\circ}\text{C}$ and $2.4\text{ }^{\circ}\text{C}$ respectively) relative to $135\text{ }^{\circ}\text{C}$ and $180\text{ }^{\circ}\text{C}$ of allowed maximum temperatures. A minor effect of this variation is noticed on end-space and rotor temperatures (decrease of $0.4\text{ }^{\circ}\text{C}$ and $0.2\text{ }^{\circ}\text{C}$ respectively). However, this indirect effect is justified by the enhanced heat evacuation path from the stator to the cavity, specifically from the end-windings heat dissipation zones.

For laminations, the variation of thermal conductivity has the most significant impact on the rotor temperatures ($1.3\text{-}1.5\text{ }^{\circ}\text{C}$) since the conduction is the main mode of heat transfer to the shaft coolant medium, considering that the convection coefficient is optimized for cooling the rotor.

The thermal conductivity variation of shaft material has around much lower effect (around ten times lower) on temperatures than that of laminations.

4.4.3.2 *Influence of Specific Heat*

The specific heat of stator and rotor laminations dominantly influences all temperatures. In fact, among all other materials, the specific heat property of laminations concerns the larger volumes of motor components. Besides, in the rotor, we observed a temperature difference around twice that in the stator for the same increase in laminations specific heat.

Actually, we notice that the temperature difference relative to the maximum increase in its temperature (i.e. temperature rise with respect to initial temperature condition) for rotor and stator laminations are proportional.

Permanent magnet specific heat has a more significant impact on rotor maximum temperatures than on other motor components (around 5 times the effect on these latter ones). However, the global effect on the motor thermal behavior and temperature evolution in all components is comprehensively explained by the fact that permanent magnets are the point of connection between heat flux paths from rotor and stator. The heat flux is conducted through the thermal conductances with the airgap area, considered in the numerical model.

Finally, these diagrams allow stating a frank conclusion that a variation of 10% of these properties gives a maximum temperature difference (between 1.5 °C and 2.4 °C) is observed for lamination specific heat and thermal conductivity variations, and resin thermal conductivity variation. This remains an acceptable temperature oscillation compared to motor temperature levels.

4.4.4 Fluid Choice

The water-glycol mixture was adopted as a coolant in the design of the liquid cooling system. This fluid exhibits interesting thermal properties cited earlier in this chapter. Water, in general, is known to be by far one of the most beneficial and performant coolant in single-phase circuits (purely used or combined with other liquids to improve boiling and/or freezing points). However, other potential candidates can be advantageous in hybrid aircraft motor application for industrial reasons (compatibility, maintenance, cost...) or for some of their advantages (low dielectric property, phase changing possibility under particular conditions...). Herein, two fluids will be tested hereafter to verify their efficiency, provided that they demonstrate a pronounced interest.

The coolants tested are namely: industrial oil and pure water. Oil as a coolant in electrical machines is recently being investigated in winding cooling techniques since some types of this fluid are safe to use in the case of direct contact with electrical wires and are more beneficial in convection cooling of end-windings than air convection. While pure water will be tested to compare the temperature results to those with water-glycol. It is known that water temperatures in the circuit should not fluctuate beyond the margins corresponding to the liquid phase state (above 0 °C and below 100 °C).

Properties of the coolants applied in this investigation, oil and water respectively, are grouped in *Table 4.11* and *Table 4.12*.

Coolant Property	Unit	Value for oil
Density ρ	$\text{kg}\cdot\text{m}^{-3}$	835
Thermal conductivity λ_{fluid}	$\text{W}\cdot\text{m}^{-1}\cdot\text{K}^{-1}$	0.133
Specific heat c_p	$\text{J}\cdot\text{kg}^{-1}\cdot\text{K}^{-1}$	1970
Dynamic viscosity μ	$\text{kg}\cdot\text{m}^{-1}\cdot\text{s}^{-1}$	3.17×10^{-2}

Table 4.11 : Oil coolant properties at 40 °C.

Coolant Property	Unit	Value for water
Density ρ	$\text{kg}\cdot\text{m}^{-3}$	995
Thermal conductivity λ_{fluid}	$\text{W}\cdot\text{m}^{-1}\cdot\text{K}^{-1}$	0.628
Specific heat c_p	$\text{J}\cdot\text{kg}^{-1}\cdot\text{K}^{-1}$	4178
Dynamic viscosity μ	$\text{kg}\cdot\text{m}^{-1}\cdot\text{s}^{-1}$	6.51×10^{-4}

Table 4.12 : Water coolant properties at 40 °C [183].

Definitely, the same conditions of flow rate are applied. Therefore, the resulting hydraulic losses are different for every change in coolant type. The objective is to test the heat extraction efficiency of the coolant.

The results are depicted in *Figure 4.27* and *Figure 4.29* respectively for oil and water as coolants.

Figure 4.27 shows that oil, as a coolant, does not act efficiently in cooling the motor with the applied configuration. As seen in the graph, the oil temperatures have an increasing tendency all mission long despite the outside air temperature decrease between take-off moment and the

end of the cruise phase. This continuous increase in coolant temperature proves that the heat exchanger is not sized adequately to evacuate all the heat generated in the motor.

Moreover, the motor temperatures increase with a higher slope – which means more rapidly – than the coolant curve. This is an indicator that the heat transfer in motor channels (stator and rotor) between coolant and motor parts does not occur efficiently due to the lower specific heat of oil compared to water-glycol.

Finally, the convection coefficients are not sufficiently high: $170 \text{ W}\cdot\text{m}^{-2}\cdot\text{K}^{-1}$ for stator channel and $140 \text{ W}\cdot\text{m}^{-2}\cdot\text{K}^{-1}$ for rotor channel (see *Table 4.8* for water-glycol convection coefficients). To obtain these results (even not acceptable for temperature limits), the generated hydraulic losses are more than twice those obtained with water-glycol (23.9 m against 9.6 m), and the pump power is more than twice that required with water-glycol coolant. The use of oil will result in increasing significantly the weight of the pump while not providing efficiency in cooling the motor parts.

Actually, the oil being viscous, either channels' geometries or flow rates or both together, should be adapted to provide the required coefficients of convection and block the temperature rise in the motor. However, the thermally suitable hydraulic and geometrical parameters will lead to much higher hydraulic losses and higher pump head and power.

Another test of oil is conducted with twenty times the old flow rate in the stator channel and fifty times that in the rotor channel. The resulting temperatures' profiles with oil as coolant are presented in *Figure 4.28*. The stabilization of coolant and motor temperatures during the cruise proves that the heat flux extraction from the motor is quite efficient. Whereas, the high flow rates applied require a huge pump head and super-high pump power, which is industrially not applicable. This specificity lowers the efficiency of using oil as a coolant when other performant cooling fluids can be used and are completely safe for the motor application.

Using oil would be interesting only if the flow is directly injected into the critical part (as a way to reduce the thermal resistance).

Water as a coolant in the hydraulic circuit has a positive impact on reducing motor temperatures compared to other liquids since it has higher thermal conductivity and specific heat. However, compared to the water-glycol mixture applied in the reference model, there is no significant variation in temperatures when pure water is utilized.

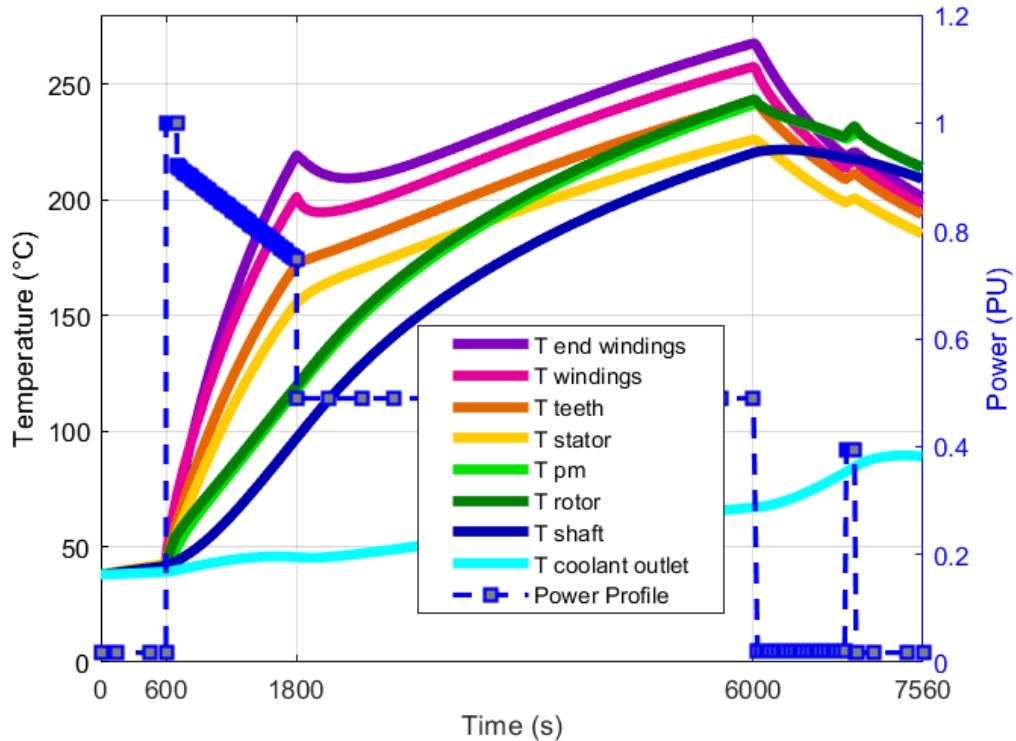


Figure 4.27 : Temperatures profiles in different motor parts with oil as coolant with initial flow rates.

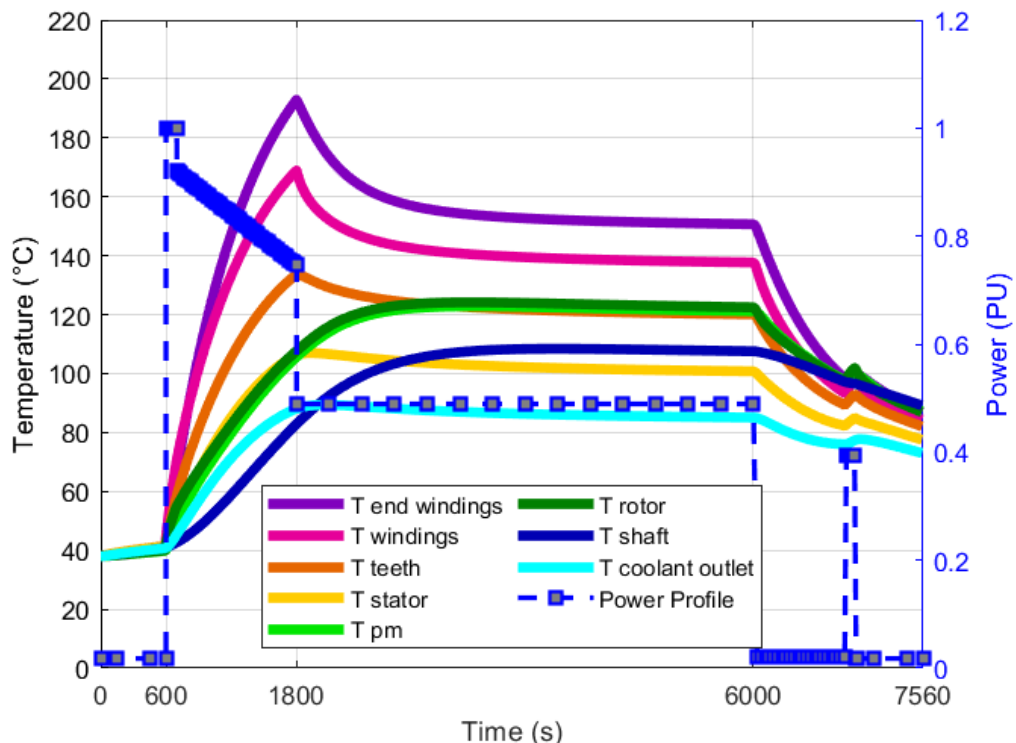


Figure 4.28 : Temperatures profiles in different motor parts with oil as coolant with higher flow rates.

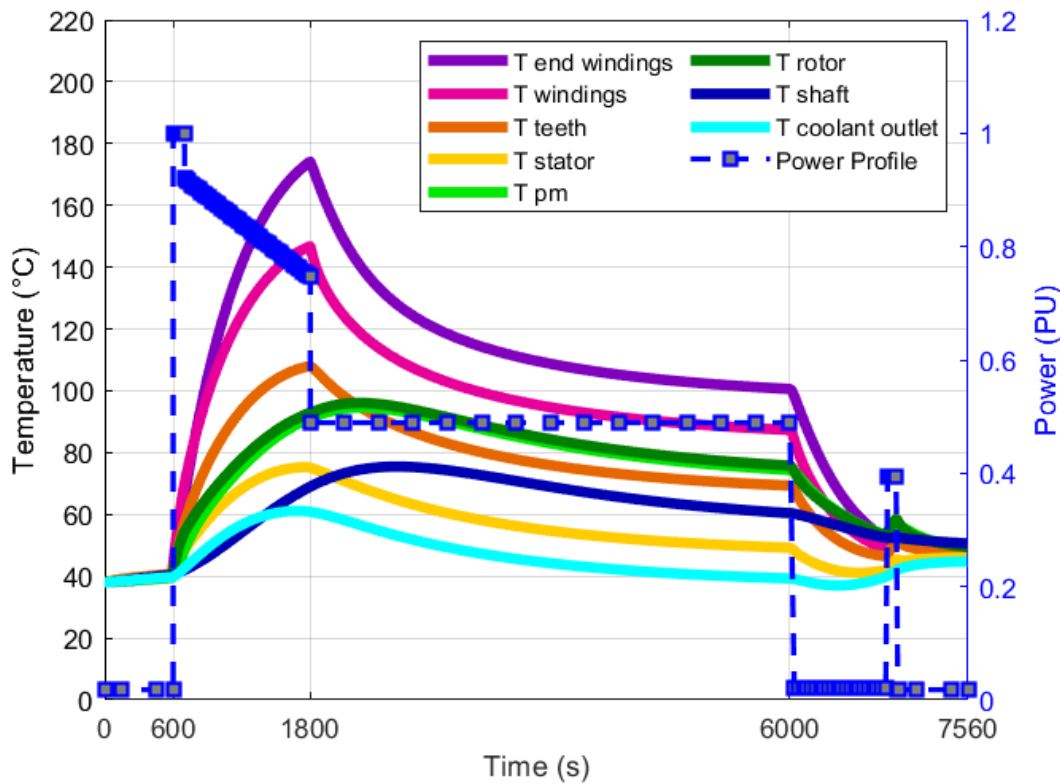


Figure 4.29 : Temperatures profiles of different motor parts with water as a coolant.

In addition to the water-glycol mixture features, this fluid has more advantageous properties than water when system temperatures are strongly changing, i.e. the operating temperature range (freezing to boiling points) are [0 °C to 100 °C] for water and [-33 °C to 107 °C] for the water-glycol adopted solution.

Some unpredictable circumstances that might take place during flight operation (for instance an overheated motor due to a lasting full power regime or freezing outside temperature during cruise lower than that considered in the profile) would expose the coolant to different ranges of temperatures. In these cases, the water-glycol mixture has a significant advantage over pure water. Besides, the DOWTHERM SR-1 Fluid solution contains industrial corrosion inhibitors.

4.4.5 Exchanger Surface and Coolant Flows

The exchanger plate involved in the cooling system can be a proportion of the nacelle. A variation in the exchanger surface is proportional to a variation of the exchanger pipe length since the pipe is assigned a plate proportion all-long. The surface of the plate could vary between 35% and 95% of $S_{nacelle}$. Variations of the shaft flow rate and stator flow rate are also

evaluated. The flow rates values that were tested are as follows: for the stator, the flow rates vary from $84 \times 10^{-5} \text{ m}^3 \cdot \text{s}^{-1}$ up to $84 \times 10^{-4} \text{ m}^3 \cdot \text{s}^{-1}$ and for shaft flow the rate variation is between $2 \times 10^{-5} \text{ m}^3 \cdot \text{s}^{-1}$ and $2 \times 10^{-4} \text{ m}^3 \cdot \text{s}^{-1}$. The separate cooling of rotor and stator, the low level of losses in the rotor with respect to those in the stator, and the geometry of channels influencing the flow rate of the shaft that is by far lower than stator one are all factors to be kept in mind in analyzing the results of this study.

Note that actually, the shaft channel flow rate variation has no significant impact on T_{\max} since the hottest point is in the stator as it can be seen in *Figure 4.30*. Hence only the first two parameters (exchanger surface and stator flow rate) are investigated. The corresponding response surface is depicted in *Figure 4.31*. In the response surface displayed, two discontinuous levels of temperatures corresponding to two sets of points are seen.

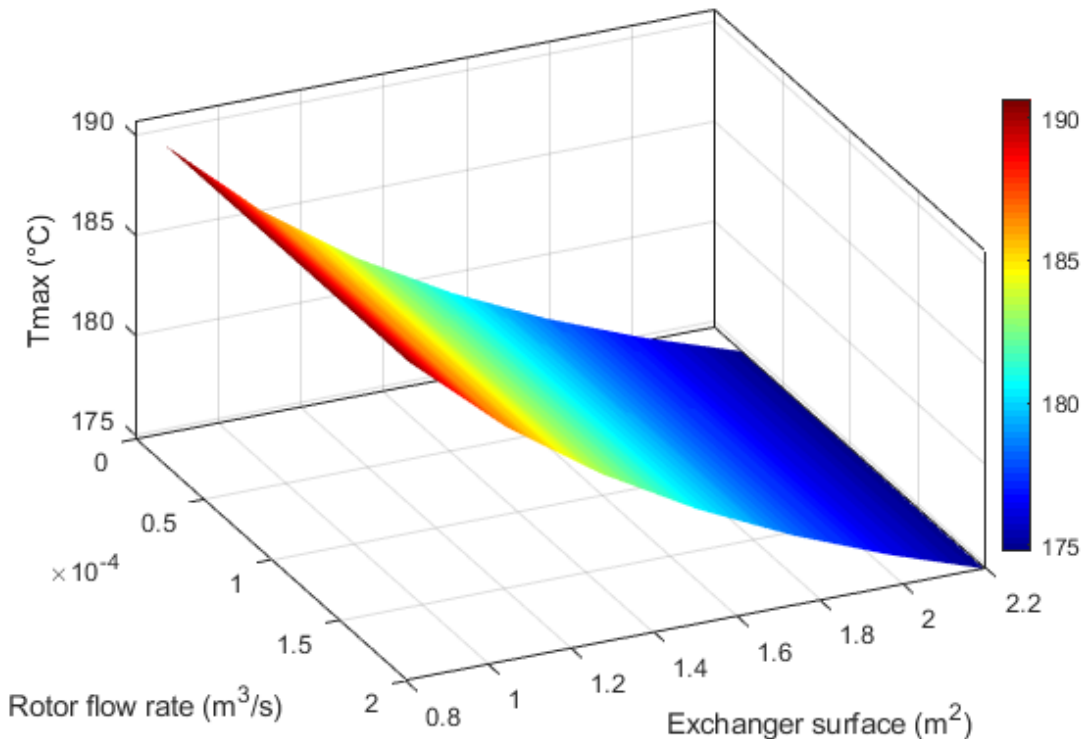


Figure 4.30 : Surface response of temperature to variation of exchanger surface and rotor flow rate

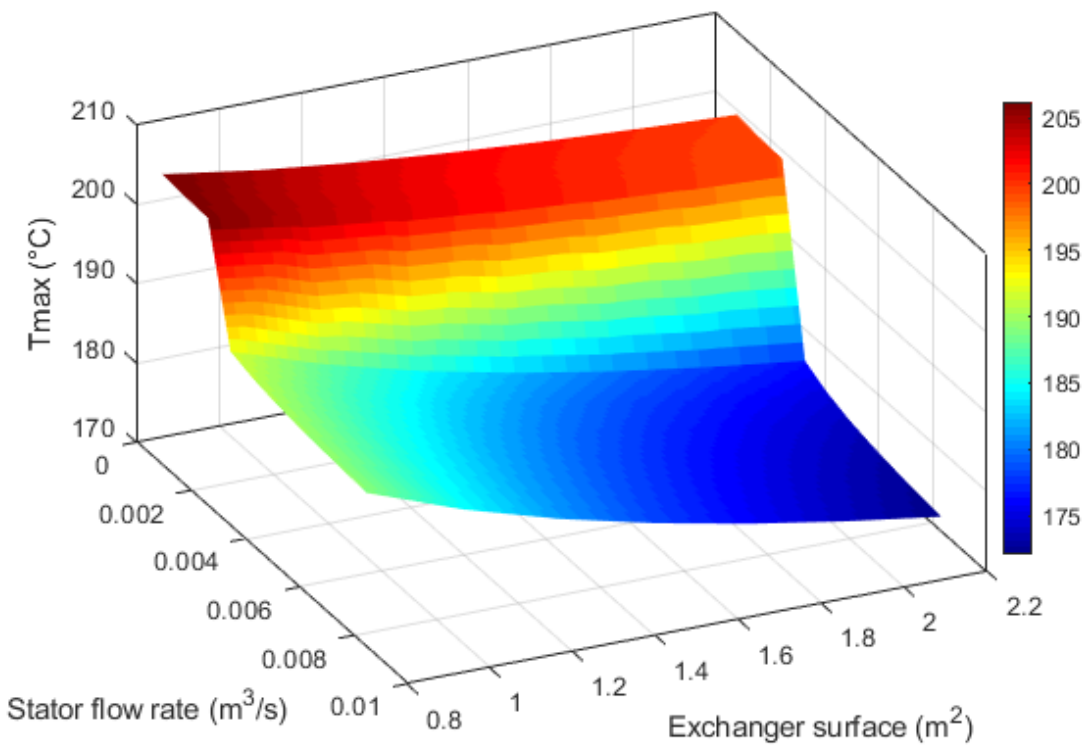


Figure 4.31 : Surface response of temperature to variation of exchanger surface and stator flow rate.

The maximum temperature difference reaches $30 \text{ } ^{\circ}C$. This is justified by a switch between laminar and turbulent flows when changing the flow rate value. Turbulent flow provides a higher convection coefficient and helps to extract more efficiently the heat from the motor, and thus lowering temperatures in the critical zone. This flow corresponds to the lower set of points.

Moreover, the effect of exchanger surface reduction is less pronounced in laminar flows (the upper set of points) than turbulent flows. Finally, in this latter flow type, the stator flow rate has a more significant impact on temperature reduction at high exchanger surface (around $5 \text{ } ^{\circ}C$) than at reduced surfaces ($2-3 \text{ } ^{\circ}C$).

4.5 Case-studies

4.5.1 Influence of Flight Mission Scenarios

In this same configuration, we have tested the model in an emergency condition that calls the motor to run under continuous full power after the take-off phase. The resulting evolution of temperatures in the motor is depicted in *Figure 4.32*. The simulation shows that the maximum temperature reached is 282 °C. The total time before reaching the limit of 180 °C at end-windings after the end of the taxiing phase is 900 s. if we consider the real maximum allowed temperature of winding without considering the safety margin, the time to reach 220 °C is around 1600 s from the same reference point. For the rotor temperatures, the limit with the safety margin is touched in 1400 s after take-off and without this margin in 2100 s.

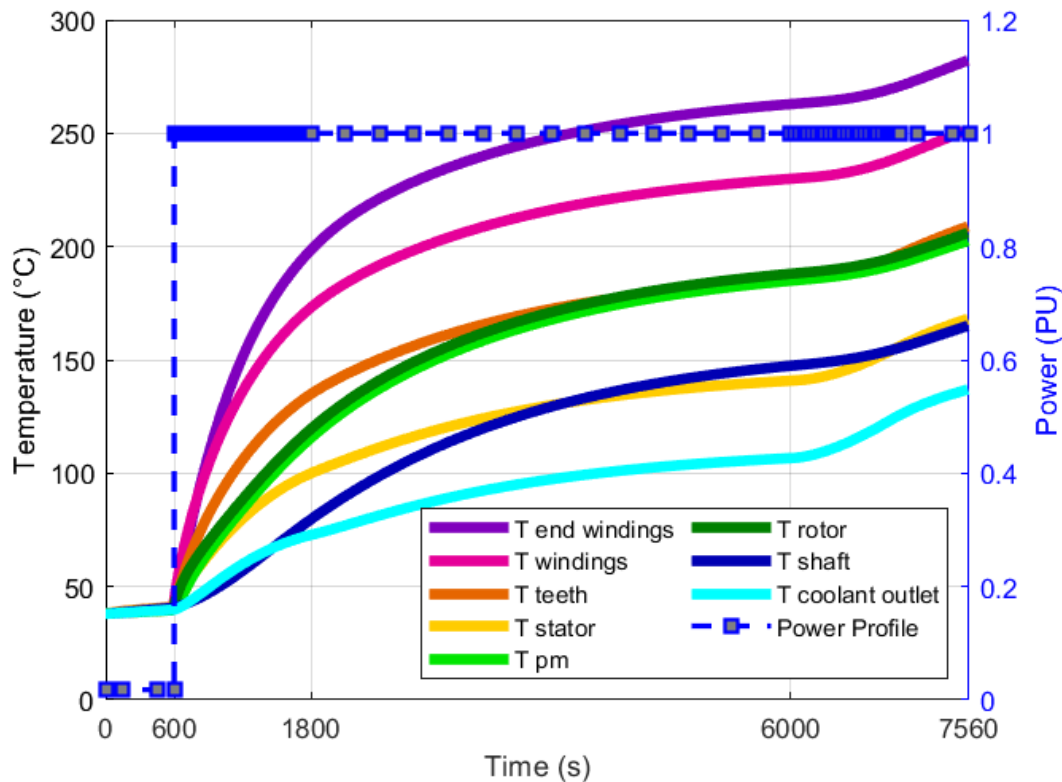


Figure 4.32 : Motor temperatures evolution for a continuous full-power regime after take-off.

The effect of outside temperature decrease during climb and cruise phases and increase during descent and landing phases, prohibit the steady-state to take place. However, the objective of this simulation is not to approve maintaining a flight mission under these severe conditions but to determine the time-to-damage duration of the electric motor and prevent any failure risk.

This duration should be strictly considered in the case of full-power application to keep motor temperatures within the safe margins.

4.6 Electric Motor for 2035

The second objective is to design a motor with higher specific power (10 kW/kg) that could be used for aircraft propulsion in the year 2035.

Actually, for the electric design of this motor, several technological solutions are proposed, investigated, and assessed (such as inorganic insulation materials of class 240°C , carbon fiber sleeves having high permissible stresses, Litz wires to reduce windings losses [176]).

Once more, the electro-magnetic design and data are provided by our project partners at WP1.

Hence, adapted thermal management of this motor design is required. It must include several considerations and modifications in the inputs of the thermal model. The cooling strategy is modified accordingly.

Practically, a preliminary study has been conducted upon estimations of the influence of these modifications (mainly losses) brought to the design of EM2025. Actually, with the same motor power as that of EM2025, the EM2035 has considerably higher total losses, with the same distribution in the machine. The minimum specific power should be 10 kW/kg , which means that the machine must not weigh more than half of the weight of EM2025.

Logically, with the same power and a lower weight, the motor will exhibit higher temperatures due to lower thermal capacities. Besides, the doubled specific power value generates higher motor losses than EM2025, and a different distribution of motor losses.

Hence, we have begun the investigation with increasing losses (specifically Joule losses), with respect to the recommendations of electric machine specialists to obtain first temperatures' results. Based on the resulting profiles and hot spots, we have elaborated a provisional cooling system design guaranteeing its efficiency on the modified EM2025 model. The procedure at this stage implies a brand-new motor design from WP1 for the long-term hybrid aircraft propulsion.

Since many inputs of WP1 design tools can be tuned to optimize the system (specifically loads and material choice), multiple electric motor designs of EM2035 were provided and tested

successively throughout a complementary work process between our Work-Package and WP1. A synthesis study of only two motors is presented hereafter. The second design was adopted and its cooling system was developed accordingly. Nevertheless, the results and issues of the first design are discussed before getting to the final design of EM2035.

4.6.1 Motor Cooling System Choice

Before presenting the possible cooling system of EM2035, a variation in the thermal conductivity of resin applied for the impregnation of windings is made in the model.

The cooling system choice for EM2035 is based on the maximum allowed temperatures set as constraints as for EM2025. However, the values of these temperatures for critical motor parts are quite different. For windings, the insulation class is $240\text{ }^{\circ}\text{C}$, which allows a limit of $200\text{ }^{\circ}\text{C}$ in the numerical model. The magnets limit is similar to that of the EM2025 case, as reminded in *Table 4.13*. The modified temperature is based on the probable use of different techniques of winding.

Component	Temperature limit for Target 2
Windings	$200\text{ }^{\circ}\text{C}$
Permanent magnet	$135\text{ }^{\circ}\text{C}$

Table 4.13 : Temperature limits for EM2035 critical components.

The thermal conductivity of the impregnation material remains the same around $1\text{ W}\cdot\text{m}^{-1}\cdot\text{K}^{-1}$.

To allow the evacuation of the generated heat to the outside, the cooling system of the EM2025 is maintained. It focuses on frame liquid cooling with liquid jackets around the motor core and a possible rotor liquid cooling and end-windings potting. In addition to these solutions, the high heat dissipation in windings and surroundings (due to Joule and iron losses) and based on first results, ‘direct’ cooling of windings through internal channels in slots is a necessity.

The cooling of windings consists of two channels integrated into each slot at the sides as depicted in *Figure 4.33*. A proportion of 25% of the slot is reserved for these channels. Thus, the two channels occupy this proportion in width while their height is only a proportion of 75% of the slot height. Each channel is made of a plastic material electrically insulating with 0.1 mm thickness and thermal conductivity of $0.5\text{ W}\cdot\text{m}^{-1}\cdot\text{K}^{-1}$.

At the end-windings, the channels cover the lateral sides of the geometry (rectangular in the model). Since we consider an ortho-radial section, the corresponding surfaces of contact between channels and end-windings are numerically computed. Practically, at each motor side (front and rear), all of the windings channels will be connected into an annular channel covering the end-winding surface in the parallel plan to motor radial view.

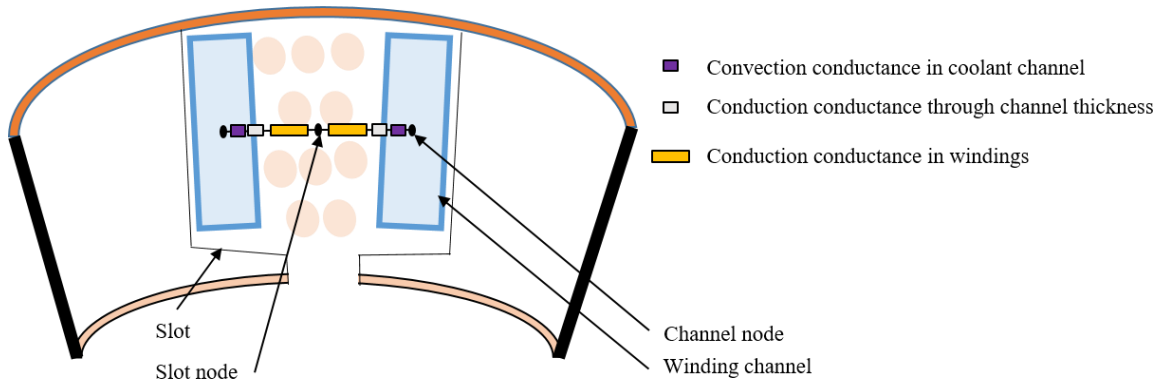


Figure 4.33 : Slot channels illustration with corresponding thermal resistances.

Five nodes are added in the nodal network for EM2035 (nodes 58 to 62). An illustration of the new LPTM with channels location is depicted in *Figure 4.34*, showing half of the axial section of the motor.

With the added nodes, the developed LPTM is a 62-node-base network. The data entry and general composition of discretized volumes follow the same process applied to develop the EM2025 model. The coolant is the same water-glycol mixture (DOWTHERM SR-1 Fluid).

The use of potting at end-windings was maintained for first results, and has been evaluated afterwards.

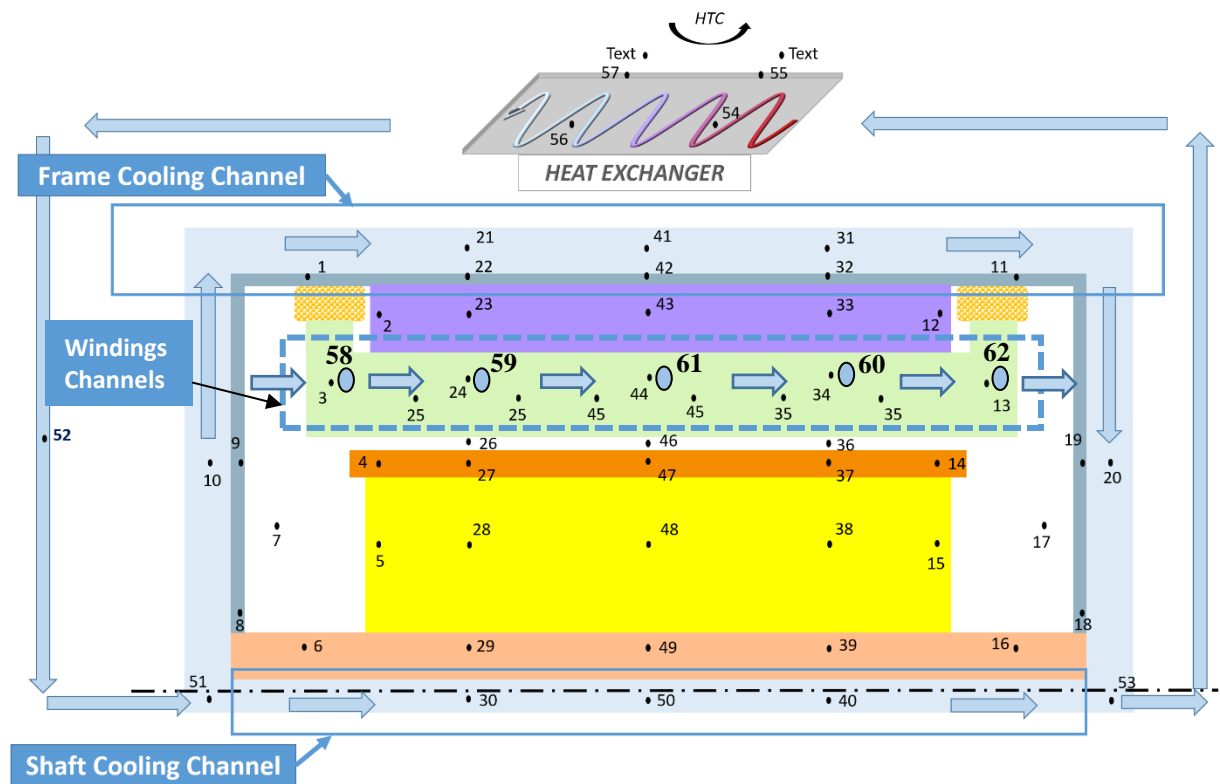


Figure 4.34 : LPTM nodes of the motor EM2035 with windings channels locations and added nodes.

4.6.2 First Motor Design and Results

A first motor design is presented for comparison with the adopted final EM2035 motor.

4.6.2.1 Data and Dimensions

The corresponding data for the first design of the motor with their maximum values are gathered in *Table 4.14* (including losses levels). The machine geometrical dimensions are grouped in *Table 4.15*. For this first design, the corresponding losses profiles are given in *Figure 4.35*.

Losses data in this first design configuration exhibit a disproportional distribution of Joule and iron losses. The iron losses are more than twice the Joule losses all along the mission.

Characteristic	Unit	Value
Mechanical speed	RPM	29000
Number of phases	-	3
Number of slots	-	24
Winding losses	PU	0.26
Stator iron losses	PU	0.59
Windage losses	PU	0.13
Friction losses	PU	0.02

Table 4.14 : Data of first design of EM2035 from WP1.

The interaction between WP1 and our Work-Package WP3 induced a strategy consisting of reducing Joule losses to a minimum since the windings are confined areas with low thermal conductivity in radial and ortho-radial direction. This has logically been compensated in other losses, mainly iron losses.

Main size	Unit	Value
External stator radius	mm	120.84
Inner stator radius	mm	72.09
Stator yoke height	mm	18.82
Slot height	mm	29.93
Tooth width	mm	11.50
Slot width	mm	7.38
Airgap thickness	mm	3.03
Permanent magnet thickness	mm	7.56
Rotor yoke height	mm	15.92
Shaft radius	mm	45.58
Active length	mm	288.38
Motor length	mm	404.30

Table 4.15 : Main dimensions of the first design of EM2035 from WP1.

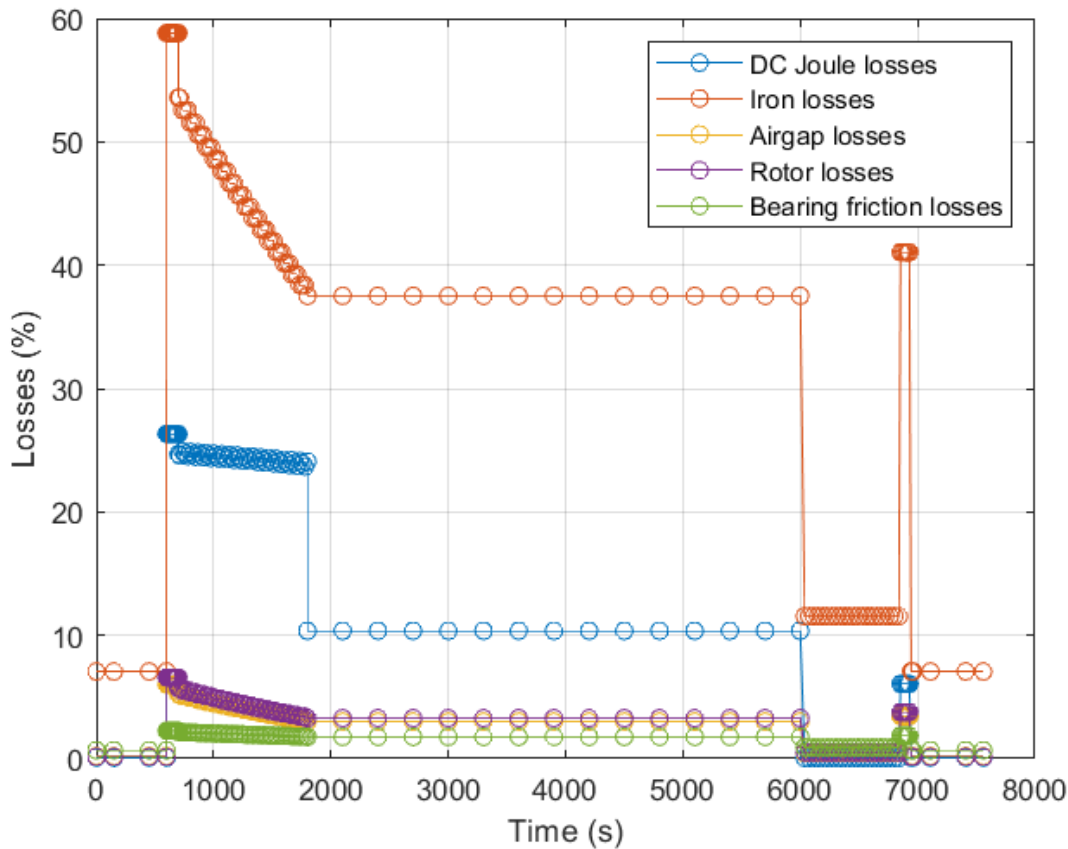


Figure 4.35 : Losses Profiles for the first design of EM2035 from WP1.

This should have a big influence on hot spot temperatures found at windings and end-windings since the reduced Joule losses strongly control these regions. Besides, the cooling focusing on this same region will help further reduction of temperatures.

The distribution of flow rates in the motor is shown in *Table 4.16* as well as the corresponding hydraulic diameters and channels' lengths. It is worth to remind that the results of temperatures are obtained considering that the entire nacelle surface is engaged.

Zone	Stator	Shaft	Winding	Exchanger
Hydraulic diameter D_h (mm)	7.1	9.1	1.9	42
Flow rate q ($m^3 \cdot s^{-1}$)	1×10^{-4}	5×10^{-5}	5×10^{-5}	2.55×10^{-3}
Channel length l (m)	4.09×10^{-1}	4.09×10^{-1}	4.09×10^{-1}	17.5
Convection coefficient h ($W \cdot m^{-2} \cdot K^{-1}$)	250	1600	4700	3300

Table 4.16 : Cooling system parameters in channels according to motor zones and exchanger.

4.6.2.2 Results

The simulation results are depicted in *Figure 4.36*. With this first design features, and the marked increase of iron losses, a significant increase of temperatures in rotor and magnets (around 180 °C) is noted during the take-off phase, far above the maximum allowed temperature.

The windage losses, affecting mainly the rotor, are estimated to around 13% of total losses, which is a high proportion for this motor configuration and temperature limits (10% in EM2025 configuration). The profile and magnitude of losses at this level have led to high magnets temperatures rapidly after take-off and until the descent phase. Even if the nacelle surface is entirely engaged, temperatures increase drastically.

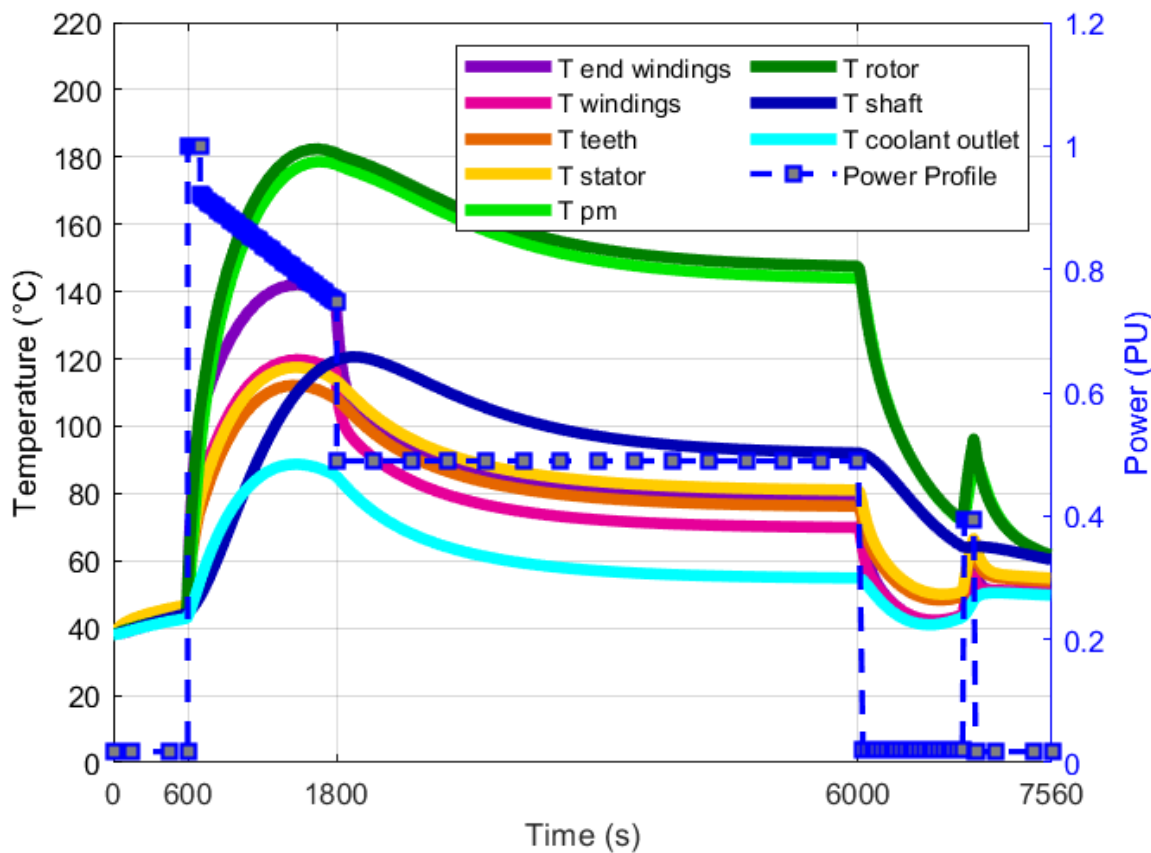


Figure 4.36 : Resulting temperatures profiles for the first design of EM2035.

Whereas other temperatures, specifically end-windings, exhibit low temperatures during the mission and a low peak value ($140\text{ }^{\circ}\text{C}$). This is induced by the low Joule losses in this first design of the motor (26% of total losses compared to 43% in the EM2025).

It is interesting also to mention that the magnets peak value is reached earlier in this case compared to the EM2025 configuration and before the shaft peak.

Even with a significant increase in mass flow rate in the shaft channel or an increase in channel diameter, rotor maximum temperatures cannot be maintained below $135\text{ }^{\circ}\text{C}$ all mission long due to the high thermal resistance between the rotor surface and the channel. Hence, this design configuration is not adapted to our application and is rejected.

Finally, another motor design is therefore proposed. An enhancement is required, mainly in losses profile with a reduction of at least 50% of windage losses, by reducing the rotational speed (variation of windage losses is proportional to ω^3) and providing a new motor geometry.

4.6.3 Second Design for EM2035

A second design of EM2035 is presented herein. The created heat paths in the motor as well as the exchanger characteristics are optimized. The thermal analysis of data and results are briefly exposed since the main issue is to provide a design that answers the specifications and target of electric motor for the time-target (EM2035).

4.6.3.1 Motor Design Data

As for the previous design, the corresponding data of the motor design with their maximum values are gathered in *Table 4.17*. The geometrical dimensions are grouped in *Table 4.18*. Losses profiles are given in *Figure 4.37*.

Characteristic	Unit	Value
Mechanical speed	RPM	20000
Number of phases	-	3
Number of slots	-	24
Winding losses	PU	0.5
Stator iron losses	PU	0.44
Windage losses	PU	0.05
Friction losses	PU	0.01

Table 4.17 : Data of final design of EM2035 from WP1.

Main size	Unit	Value
External stator radius	mm	111.94
Inner stator radius	mm	72.92
Stator yoke height	mm	14.07
Slot height	mm	24.95
Tooth width	mm	9.38
Slot width	mm	9.71
Airgap thickness	mm	3.06
Permanent magnet thickness	mm	7.84
Rotor yoke height	mm	16.66
Shaft radius	mm	45.36
Active length	mm	291.67
Motor length	mm	408.90

Table 4.18 : Main dimensions of the final design of EM2035 [184].

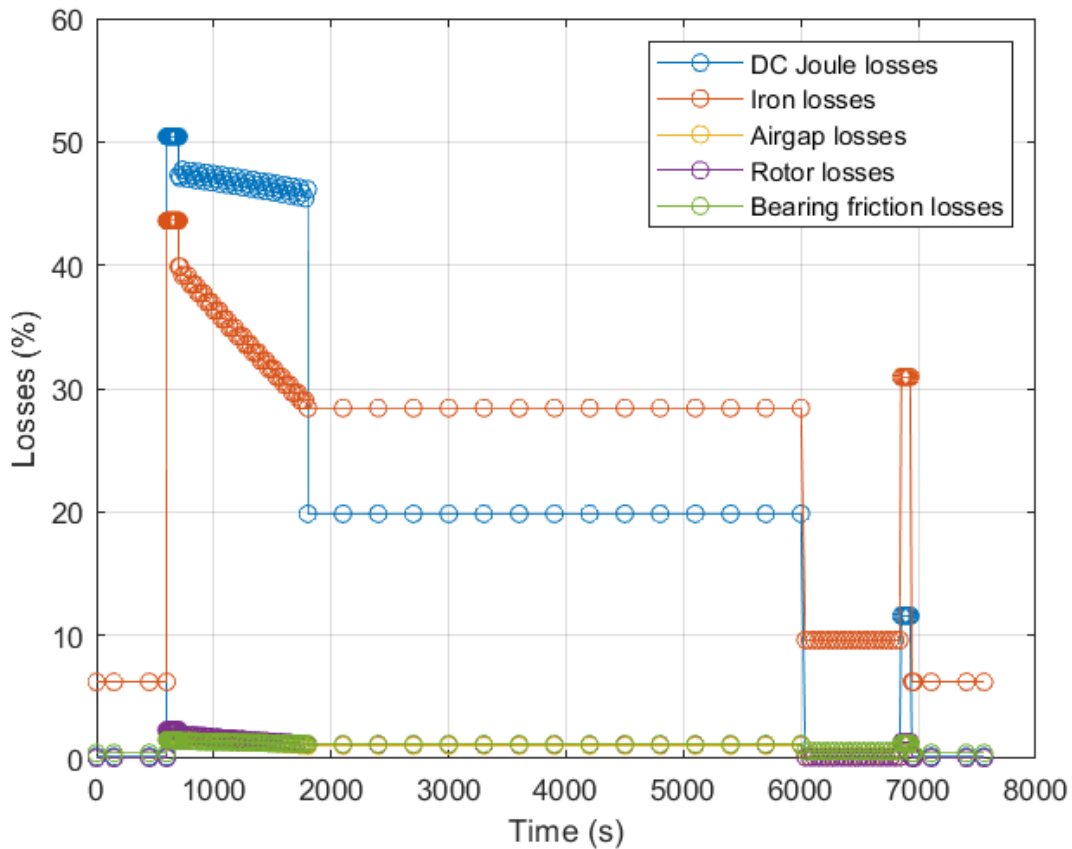


Figure 4.37 : Losses Profiles for the final design of EM2035 [184].

The corresponding profiles of EM2035 losses (resulting from different loads' sets in the design tool of WP1) show a significant reduction of rotor losses with windage losses around 4.5% of total motor losses.

4.6.3.2 Results and Analysis

The resulting profiles of motor temperatures are depicted in *Figure 4.38*. Thanks to the losses distribution, different thermal behavior is exhibited in the machine. As seen in the figure, the thermal response of the motor with this design and these losses profiles is dissimilar from the previous configuration. Unlike the first design, the magnets and windings temperatures retrieved a dynamical evolution similar to that found in EM2025 adopted design, with a maximum temperature of 133 °C.

According to the model results, stator behavior is consistent in all parts and the peaks (188 °C for end-windings and 155 °C for windings) are reached before the end of the climb phase

(1540 s), while the rotor peaks are obtained afterward during the beginning of the cruise phase (1980 s). This time difference corresponds to the difference in the evolution between losses.

Beginning with a slight temperature rise during the taxi-out phase, then a spike increase during take-off and climb phases. The reduction of 50% of power during the cruise phase and the drop in outside air temperature, associated with an efficient cooling system allow reaching a steady-state at the end of this phase. The temperature evolutions during the last two phases are typically similar to that noticed in EM2025 behavior and correspond to the losses profiles according to motor zones. Attention should be paid to coolant temperature, which reaches a maximum of 100 °C.

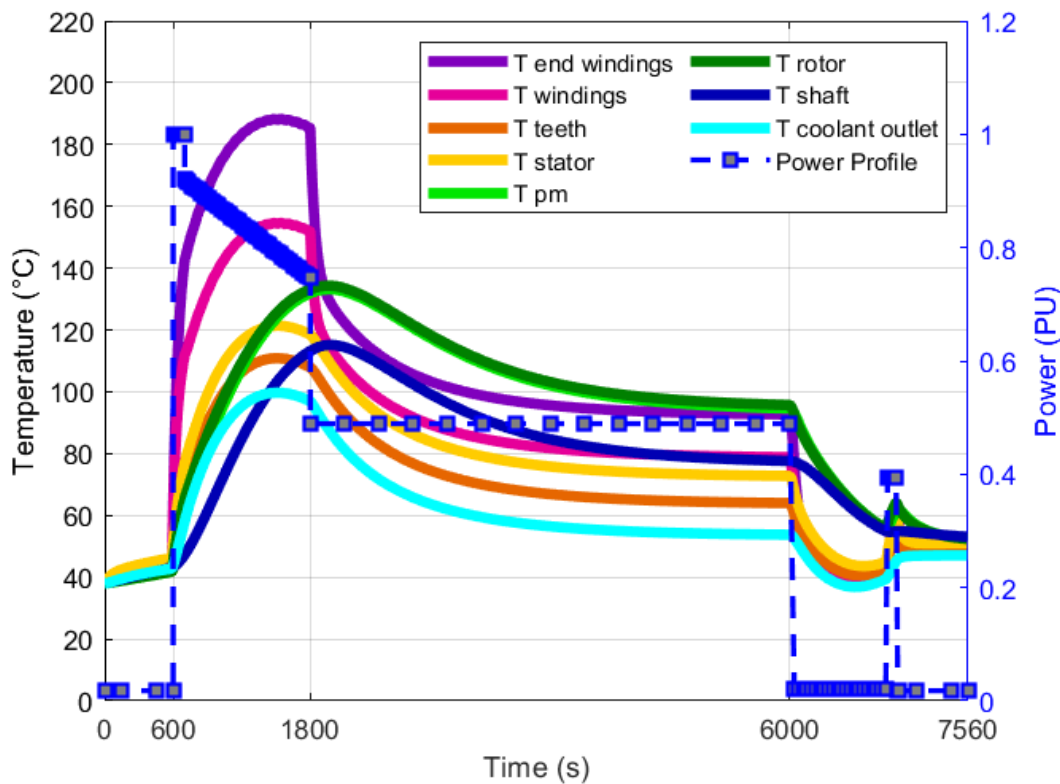


Figure 4.38 : Resulting temperatures profiles for the final design of EM2035 with potting.

Since the resulting end-winding maximum temperature is below the limit of 200 °C, the potting could be useless in this design. A simulation of the model is carried out without end-windings potting to check if this additional technique is required. The resulting graphs of *Figure 4.39* depict the temperature evolution in the motor without potting. In both cases, motor behavior is

quite similar. A temperature increase of very few degrees is observed. However, the limit is not reached for end-winding temperature. This result allows choosing to remove the potting option from the EM2035 configuration.

The thermal behavior of the motor in this configuration approves the heat extraction and evacuation techniques. The temperature values are below the maximum limits and are acceptable. Hence, this design is adopted.

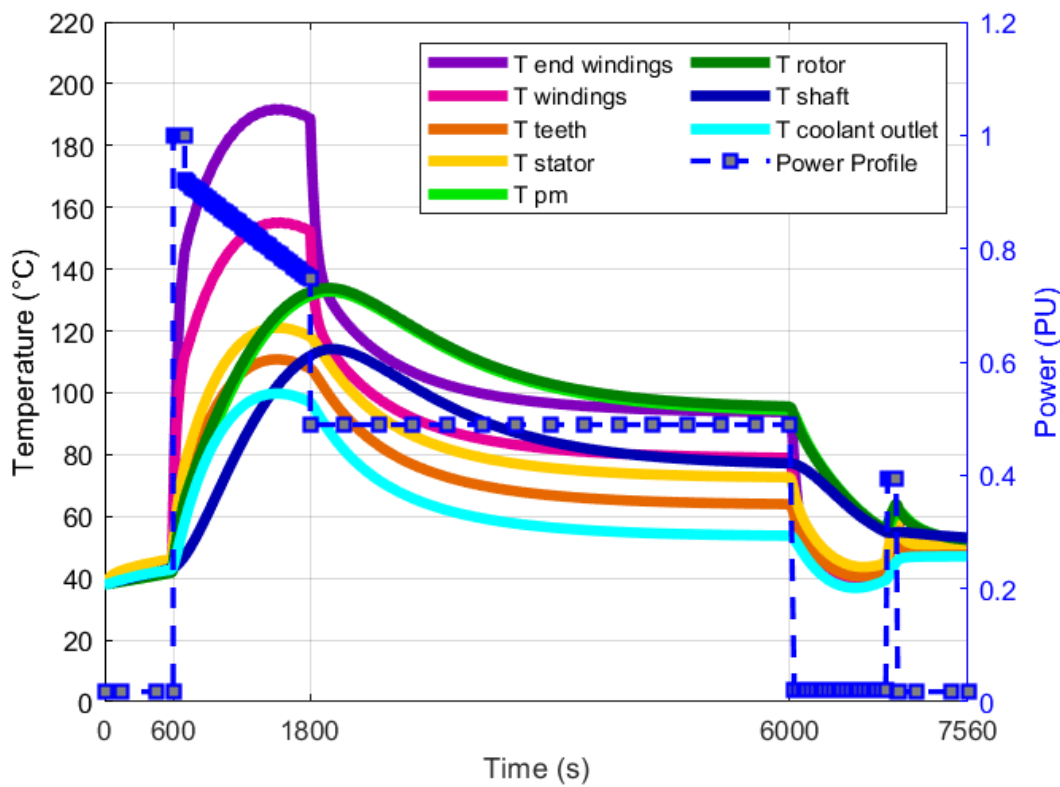


Figure 4.39 : Resulting temperatures profiles for the final design of EM2035 without potting.

4.6.3.3 Cooling System Sizing

In *Table 4.16*, the values of the hydraulic diameters, the flow rates, and the channel lengths are grouped for each corresponding zone. To optimize the pump weight, a convenient total flow rate of $2.55 \times 10^{-3} \text{ m}^3 \cdot \text{s}^{-1}$ has been chosen.

The resulting hydraulic losses H_L in each motor zone and in exchanger are grouped in *Table 4.19*. The pump is selected from the catalog of hydraulic pumps from Parker Pumps and Motor Division [182]. An adequate pump has the characteristics found in *Table 4.20*. The pump weight is integrated into the calculation of the total weight of the motor and its cooling system, and the specific power target is met.

Zone	Stator	Shaft	Winding	Exchanger
Hydraulic major losses H_L (m)	0.021	0.061	3.707	0.493

Table 4.19 : Resulting hydraulic major losses in channels according to motor zones and exchanger for EM2035.

Pump		
Characteristic	Unit	Value
Normal Operating Pressure	bar	206
Maximum Speed	RPM	4420
Length	cm	26.42
Height	cm	19.05
Width	cm	17.78
Weight	kg	11.34

Table 4.20 : Pump characteristics (AP15V) for EM2035 from [182].

The weight of the cooling system without pump is around 30 kg. The overall cumulative weights of the motor and its cooling system - including the coolant weight and the pump - respect the limits to reach 10 kW/kg of motor specific power target.

4.7 Conclusion

Electric motors for the project targets are thermally assessed in this chapter. Two designs of SM-PMSM have been finally adopted for the first and second time-frames respectively.

The design of Electric Motor Target 1 (EM2025) is investigated using the developed numerical tool: *AThEM* model. The cooling system, adequately chosen for the motor configuration, is integrated into this model and the expected temperatures' results are elaborated. Corresponding calculations are presented. A double liquid cooling with water jackets and shaft channel and a potting of end-windings provided satisfactory results. The hot spot levels of temperatures and weight values for the motor and cooling system are obtained allowing reaching 5 kW/kg of specific power for the motor and its cooling system.

For the Electric Motor for 2035 (EM2035), an assessment of many motor designs has been carried out. Based on the thermal studies, a direct liquid cooling of winding is strongly required to maintain motor temperatures below the limits during the mission. Thus, additional cooling channels for windings are integrated into the motor model, covering a part of end-windings. Simulations and analyses have proved that high windage losses (specifically at rotor level) induce overheating of magnets. Among several case-study motor designs, two were presented. The second configuration with corresponding losses distribution is found adequate for EM2035. The resulting temperatures' profiles are presented showing acceptable peak values in hot spot zones.

Consequently, from the studies, it is deduced that in this motor type (high specific power synchronous machine), adapted configurations of geometry, losses distribution, and cooling technique, altogether, should be tuned to reach a reliable and optimized electric motor design.

CHAPTER 5 MODEL INVESTIGATION AND INVERSE METHOD

Synopsis:

Since the developed Lumped Parameter Thermal Model has the advantage of having few degrees of freedom, it will be applied to identify motor losses by solving an inverse problem. Once identified, these losses will be used to monitor temperatures at unreachable critical points.

5.1 Introduction

Our numerical model LPTM is now developed, validated, and adapted to the targeted motor type. In this motor type and in electric motors in general, losses are generally hardly determined. The identification of motor heat sources through an inverse method, based on thermal measurements, is proposed using the same LPTM model; which is an adapted choice because of the small number of degrees of freedom. Beforehand, a sensitivity study to losses has been carried out to distinguish the impact of losses types on motor values.

Finally, based on optimal losses and external measurements, it is possible to predict rapidly low-accessibility temperatures to prevent exceeding critical temperature.

5.2 Sensitivity of Motor Temperature to Losses

Before carrying out the losses determination through the inverse technique, a sensitivity study of motor temperatures to losses has been conducted on EMT1 (Electric Motor Target 1). This study aims to determine which losses are critical, and on which motor parts each type of losses has a significant impact.

Figure 5.1 reminds of the position of each losses type in the nodal network of the motor in a symmetric cut at the middle of the machine scheme.

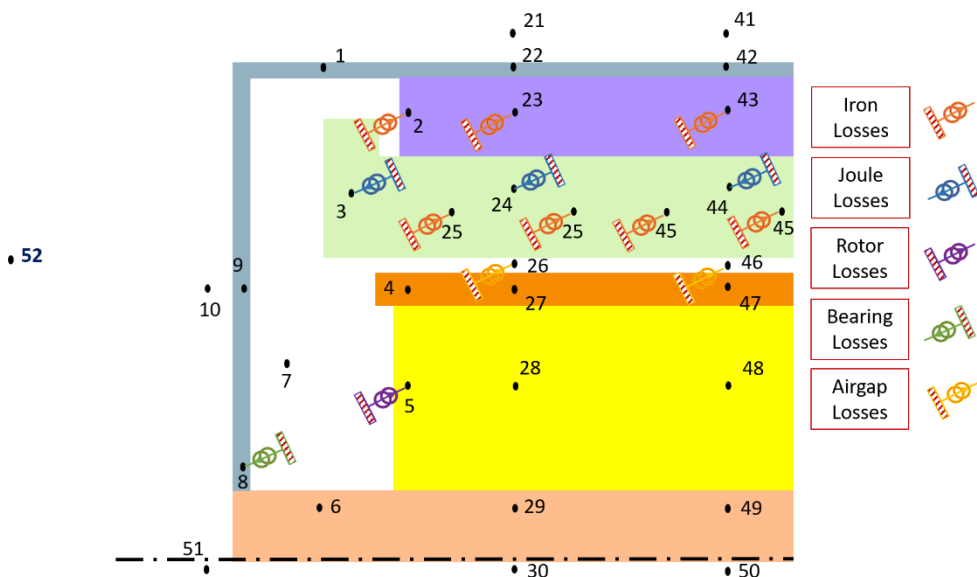


Figure 5.1 : E-motor losses locations in the nodal network symmetric cut according to nodes.

According to zones, the results of a 10% decrease in each type of losses (equivalent to heat sources) are depicted in *Figure 5.2*. Variations of losses in bearings, airgap, rotor, iron/yoke part, iron/teeth part, and windings (Joule losses) are examined.

Figure 5.2a represents the temperature decrease ΔT_{sen} resulting from each variation in losses as: $\Delta T_{sen} = T_{initial} - T_{variation}$. In *Figure 5.2b*, the relative temperature decrease ε_T is calculated for each motor zone, and is given by: $\varepsilon_T = 100 \times \Delta T_{sen}/T_{initial}$.

For each zone, the corresponding temperatures in the network are taken according to nodes positions as follows:

- Node 17 for end-space,
- Node 15 for rotor (laminations),
- Node 14 for permanent magnets,
- Node 33 for stator yoke (laminations),
- Node 34 for teeth,
- Node 35 for windings,
- Node 13 for end-windings.

The temperature decrease depends mainly on the zone to which the losses are injected. The closer the losses are to the zone, the higher is the drop in this zone temperature. Globally, stator losses (iron and Joule losses) are extremely significant in the determination of stator temperatures. The maximum allowed temperatures are $180\text{ }^{\circ}\text{C}$ and $120\text{ }^{\circ}\text{C}$ respectively for winding and permanent magnets.

Joule losses in windings and end-windings are highly critical to almost all motor temperatures. Their impact is significant on all stator temperatures but also on rotor temperatures. An average of $10\text{ }^{\circ}\text{C}$ of reduction in winding and end-winding temperatures (6% of temperature variation) is noticed when decreasing Joule losses by 10%. As a result, the stator teeth temperatures are simultaneously reduced by around $4\text{ }^{\circ}\text{C}$ in stator teeth temperature (4% of temperature variation) for the same variation in Joule losses. Actually, an interesting heat path for Joule losses is made through the teeth to the stator iron and the cooling medium due to the small slot width compared to its height. The significant effect of Joule losses on windings can be justified by the very high thermal resistance between the slots and the stator laminations, making it more complicated for the generated heat to be extracted from this area. This makes the windings zone ultimately sensitive to the heat resulting from Joule losses.

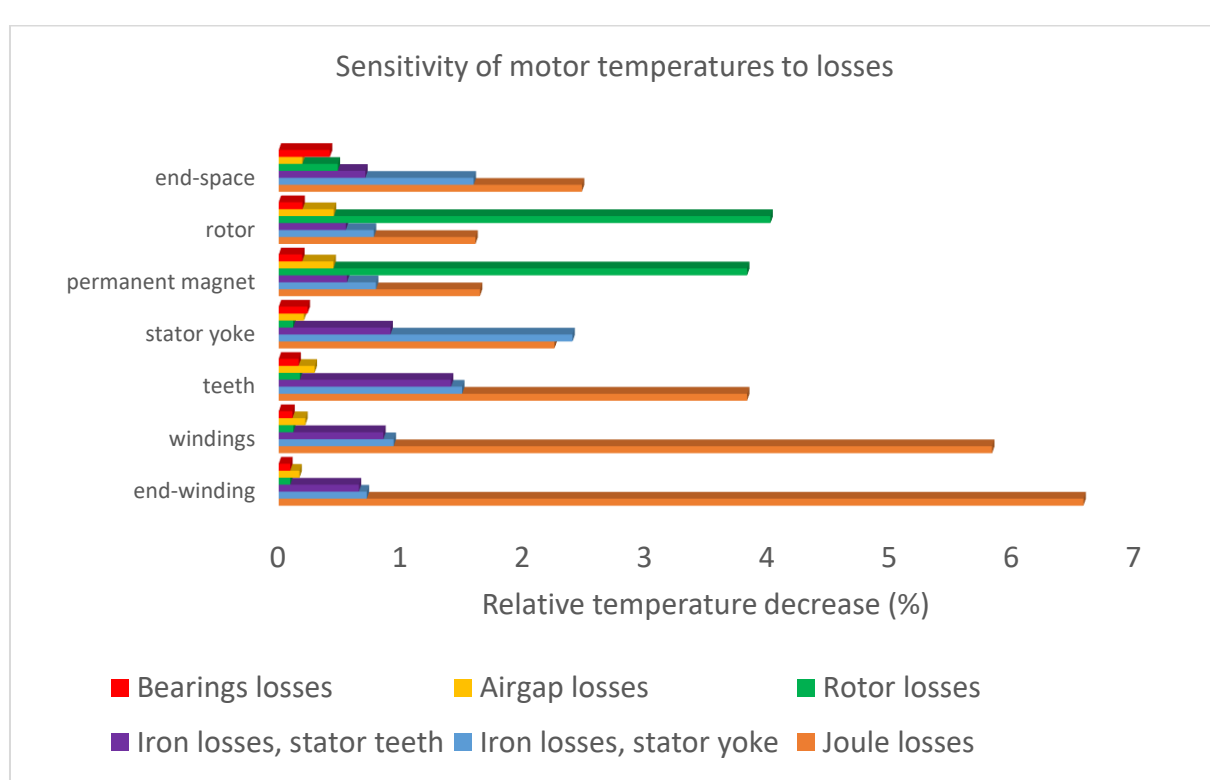
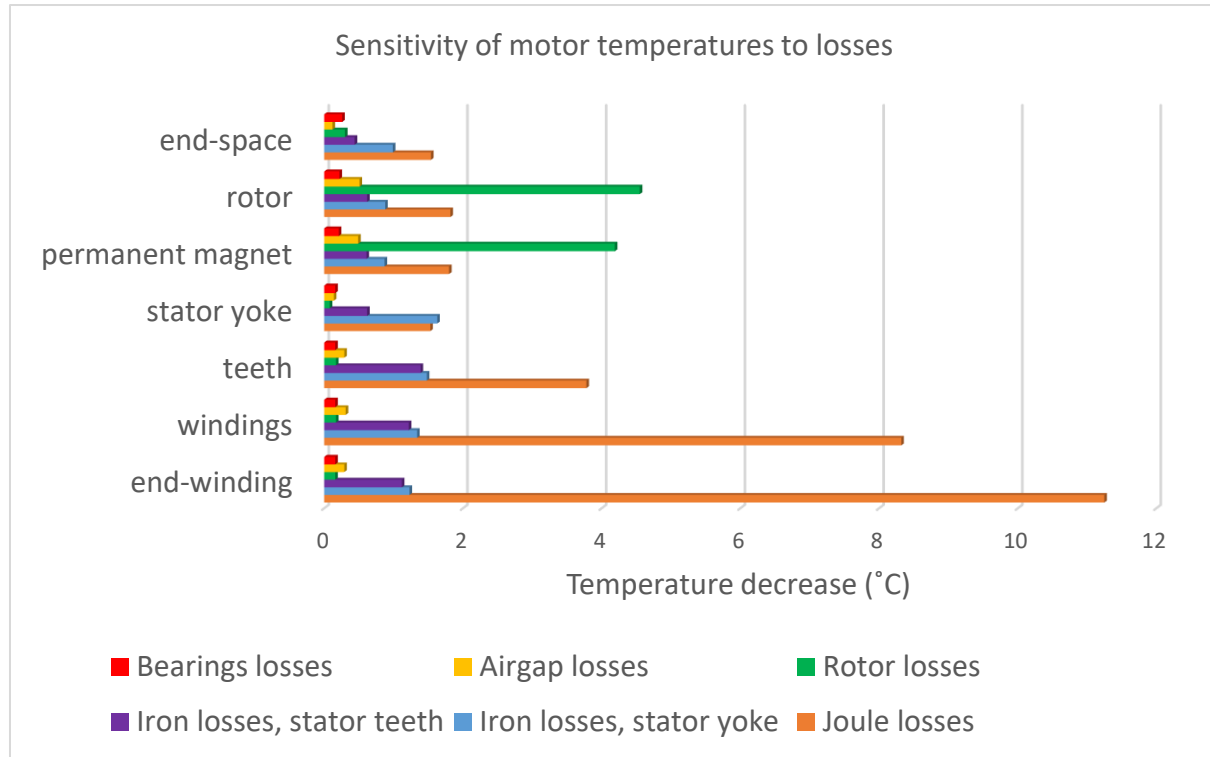


Figure 5.2 : Sensitivity of motor temperature to 10% of losses variation, (a) temperature decrease in (°C), (b) relative temperature decrease in %.

Although these losses are produced in the stator part, the rotor will be indirectly affected by any variation at this level. This results from the coolant arriving at the rotor and the air inside the cavities. Those are the only two fluid media connecting the rotor to the outside heat sink.

The major finding in the rotor sensitivity to losses is that losses injected at the rotor end-caps have the sharpest influence on permanent-magnets and rotor yoke temperatures (up to 4% of temperature variation). Besides, it is noticed that iron and Joule losses variations can have a slightly higher impact on rotor temperatures than bearings and airgap losses: $1\text{ }^{\circ}\text{C}$ to $2\text{ }^{\circ}\text{C}$ (up to 1.6% of temperature variation) for the former two types compared to less than $1\text{ }^{\circ}\text{C}$ (less than 0.5% of temperature variation) for the latter two types. End-space is influenced by the percentage of variation in stator electromagnetic losses rather than the variation of the same percentage in mechanical losses (up to 1.5% of temperature variation). This can be justified by the losses level in windings and their temperatures, which are both higher than those of rotor end-caps and their sensitivity. In fact, this end-space air is contacting both end-motor surfaces.

Finally, rotor losses affect considerably the hot spot in permanent magnets temperature: more than $4\text{ }^{\circ}\text{C}$ of variation is observed for rotor temperatures when reducing these losses by 10%, which corresponds to around 4% of temperature variation.

Decreasing the rotor end-caps losses by 10% has four times more significant impact on decreasing rotor temperatures than the airgap losses reduction by the same percentage (more than 4% of temperature decrease against less than 0.5%). This is due to the nodes connections in airgap where a part of the heat flux has its path towards the stator, which creates less influence on rotor temperatures than the losses injected to end-caps directly. Practically, reducing the rotor or airgap losses by 10% represents a reduction of 2.5% of actual RPM or exactly 345 RPM fewer for the full power regime of EMT1.

The sensitivity of all stator temperatures (teeth and yoke) to iron losses injected to stator yoke is extremely similar. The radial thermal conductivity of laminations is quite high in this direction and the heat injected tends to follow a path towards the outside. This creates a kind of homogenization of temperatures in stator laminations. Moreover, Joule losses and iron losses variations have relatively the same impact on stator yoke thermal behavior (~2.3% of temperature variation).

To sum up, one can conclude that in the case-study motor configuration, efficient distribution of losses should take into account the greater influence of Joule losses reduction compared to decreasing other stator losses. In the rotor, friction losses at the rotor end-caps have the highest impact on permanent-magnets temperature.

5.3 Losses Identification using an Inverse Method

5.3.1 Interest and Background

Besides being hardly evaluated with analytical and some computational methods, it is believed that even with a motor prototype, determination of the different losses and distinguishing their types or origins are quite complicated. Generally, such information can be barely obtained with long iterative methods. A possible solution to identify electric motor losses is to measure temperatures inside the motor and then use an inverse method. Such methods need a thermal model with a quick solving process. The thermal nodal network developed in this thesis could be a good choice because of the few degrees of freedom.

Being mathematically ill-posed, the solution of the inverse problem may be unstable and not unique. Hence, several regularization techniques have been developed by researchers to ensure stable solutions [185]. Some examples of inverse problems for electric machines can be found in the literature. Let us cite hereafter some of these works. In [186], the authors propose an inverse problem in order to identify a set of 9 design parameters (geometric and magnetic parameters) for a permanent magnet brushless motor. The results show that the density of the magnetic flux in the air gap is increased, as well as motor efficiency. A 3D inverse heat conduction problem is presented by [187] to estimate the generated heat fluxes for a high-speed electric motor. An inverse method for the identification of heat convection coefficients on coil end-windings from experimental data is presented in [137]. An interesting algorithm is developed and described for this nonlinear inverse heat conduction problem using a lumped parameter model. In [188], a low-order model is built in the first stage to estimate a set of thermal parameters. In the second stage, this model is used to identify thermal losses in the stator of an axial flux PM machine. A prediction of the strength of the heat source field in an induction motor is also carried out in [189] using a steady-state thermal model.

Considering these studies, it seems possible to determine losses using our low-order model LPTM and specific thermal measurements. To verify this, a numerical study has been conducted, starting with only one unknown source to be determined and then increasing the number of losses to finally calculate all losses. Moreover, as comparison criteria, we have also included the prediction of temperatures at unreachable critical parts. This study can be found in [190].

5.3.2 Heat Transfer Equation

The temperature distribution within the motor is determined by solving the Lumped Parameter Thermal Model (LPTM). The heat equation governing heat diffusion and convection in the domain Ω associated with initial and boundary conditions can be written as a system of N Ordinary Differential Equation (ODE), where N is the total number of nodes. Our system model equation is detailed in *Chapter 3* and can be written as follows:

$$C(M) \frac{dT(M, t)}{dt} = G(M) T(M, t) + \Psi(t) \quad \forall M \in \Omega \quad (5.1)$$

Where $T(M, t)$ is the temperature at a point M in the domain representing a volume, C is the thermal capacity of this volume, G is the thermal conductance connecting M to other points, Ψ is the heat source or heat sink in the corresponding volume.

The initial condition is:

$$T(M, 0) = T_{init} \quad \forall M \in \Omega \quad (5.2)$$

Boundary conditions are determined based on the external temperature T_{ext} and the external coefficient of convection.

5.3.3 State-Space Representation

The developed LPTM, discretizing the domain into N nodes and having a relatively low number of parameters, is used to solve the problem. Matrix C being invertible, equation (5.1) can be written as follows:

$$\dot{T}(t) = C^{-1}GT(t) + C^{-1}\Psi(t) \quad (5.3)$$

To adapt the heat transfer equation to this study, the thermal stress term $C^{-1}\Psi$ is separated into two terms representing respectively the heat sinks due to the convective mode and heat sources generated in the motor: $C^{-1}\Psi = B_c T_{ext} + B_p P$, where B_c and B_p are two command matrices relative to convective boundary conditions and heat sources respectively.

Hence, equation (5.3) can be rewritten as follows:

$$\dot{T}(t) = AT(t) + B_c T_{ext}(t) + B_p P(t) \quad (5.4)$$

Where $T(t)$ (dimension N) is the vector of temperatures, a function of time t , at the N discretization nodes, $\dot{T}(t)$ is its derivative with respect to time ($\frac{dT(t)}{dt}$). Matrix $A = C^{-1}G$ (dimension N,N) is the state matrix that connects temperatures at discretization nodes and contains diffusion and transport terms, as well as terms related to convective boundary conditions. The vector B_c is associated with these latter conditions and links corresponding nodes to environment nodes. Matrix B_p (dimension N,n_p) associated discretization nodes to internal heat sources gathered in vector function $P(t) = [P_{Joule} \ P_{Iron} \ P_{Rotor} \ P_{Airgap} \ P_{Bearings}]^T$ (dimension n_p).

In what follows, let us separate vector P into two sets: unknown heat sources included in U (dimension n_U) and known heat sources included in K (dimension (n_p-n_U)). The command matrix B_p can also be split into two matrices as: $B_p = [B_K \ B_U]$. By defining a vector V as: $V = B_c T_{ext} + B_K K$, the state space representation takes the following form:

$$\begin{cases} \dot{T}(t) = AT(t) + V(t) + B_U U(t) \\ Y(t) = C_o T(t) \end{cases} \quad (5.5) \quad (5.6)$$

Where an observation matrix C_o (dimension n_q, N) allows to select n_q temperatures in the whole temperature field $T(t)$ and to store them in vector function $Y(t)$.

In this study, a maximum of nine temperature locations will be used as outputs. These temperatures are depicted in *Figure 5.3*, and are located in the stator lamination (Ts1, Ts2, and Ts3), in the end-winding (Tw) at the surface of the end-winding (Tsw), on the surface of the stator in the airgap (Ta), in the cavity between the rotor end-cap and the frame (Tc), in the bearings (Tb), and in the magnets (Tm).

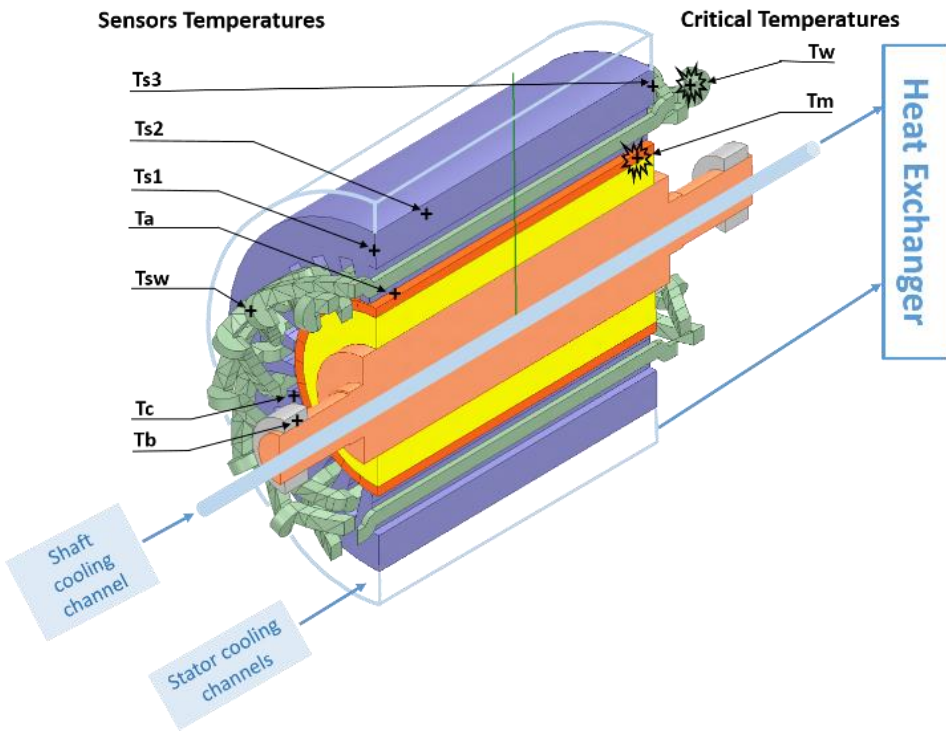


Figure 5.3 : E-motor schematic section with specific locations of temperatures.

These locations have been chosen given the heat sources but also considering plausible experimental measurement system positions. The temperature in the static part of the motor could be obtained using thermocouples (T_{s1} , T_{s2} , T_{s3} , T_{sw} , T_a , T_b , and T_c). The rotor flange temperature could be obtained by infrared measurement. T_m and T_w are the critical temperatures difficult to obtain experimentally due to their locations, i.e. T_w inside the end-windings is confined and thought to be the hottest point and T_m requires a slip ring due to the rotor in rotational motion.

5.3.4 Inverse Problem Solution

The form of the heat transfer model, developed in subsection 5.3.3, is convenient to be used now in the inverse procedure. The inverse problem aims at finding an estimation \hat{U} of the input vector U from measured temperatures Y^* . Note that, in this study, real temperature measurements are not available. The temperatures included in the vector Y^* derive from the direct problem with known heat sources. In order to simulate measurement errors, each temperature is altered with an additive Gaussian error, whose standard deviation is given by σ .

Subsequently, to have simplified and clear annotations, we will write U_k for $U(t_k)$, $U(t_k)$, T_k for $T(t_k)$, Y_k for $Y(t_k)$.

A sequential estimation method is adopted. Having the vector of measured temperatures Y_{k+1}^* , and an estimated \hat{U}_k of U_k , an estimation of \hat{U}_{k+1} is then computed.

Using the Euler implicit scheme with a time step Δt , equation (5.5) becomes:

$$\dot{T} = \frac{T_{k+1} - T_k}{\Delta t} = AT_{k+1} + V_{k+1} + B_U U_{k+1} \quad (5.7)$$

Then:

$$T_{k+1} = (I - A\Delta t)^{-1}[T_k + \Delta tV_{k+1} + \Delta tB_U U_{k+1}] \quad (5.8)$$

Hence, according to equation (5.6):

$$Y_{k+1} = C_o(I - A\Delta t)^{-1}[T_k + \Delta tV_{k+1} + \Delta tB_U U_{k+1}] \quad (5.9)$$

Due to the lagging and damping effects of heat diffusion and convection, a variation of heat source strength does not immediately affect the sensors. To take into account these effects, Future Time Steps (FTS) [191]–[194] are used. It means that sensor information at further times t_{k+2}, t_{k+3}, \dots are used to correctly estimate \hat{U}_{k+1} .

If nf is the number of FTS, then:

for $1 \leq f \leq nf$, equation (5.9) is written for $k+1+f$ instead of $k+1$. A temporary approximation of U_{k+1+f} is therefore needed to look for \hat{U}_{k+1} . In this study, a constant value is chosen:

$$U_{k+1+f} = U_{k+1} \text{ for } 1 \leq f \leq nf \quad (5.10)$$

Hence, a global matrix formulation is obtained as in equation (5.11):

$$Y_{k+1}^* = S U_{k+1} + D_k \quad (5.11)$$

With:

$$\mathbf{Y}_{k+1}^* = \begin{bmatrix} Y_{k+1}^* \\ Y_{k+2}^* \\ \vdots \\ Y_{k+1+f}^* \\ \vdots \\ Y_{k+1+nf}^* \end{bmatrix} \quad (5.12)$$

$$\mathbf{S} = \begin{bmatrix} C_o(I - A\Delta t)^{-1}B_U\Delta t \\ C_o[(I - A\Delta t)^{-1} + (I - A\Delta t)^{-2}]B_U\Delta t \\ \vdots \\ C_o \left[\sum_{j=1}^{f+1} (I - A\Delta t)^{-j} \right] B_U\Delta t \\ \vdots \\ C_o \left[\sum_{j=1}^{nf+1} (I - A\Delta t)^{-j} \right] B_U\Delta t \end{bmatrix} \quad (5.13)$$

And:

$$\mathbf{D}_k = \begin{bmatrix} C_o(I - A\Delta t)^{-1}[T_k + V_{k+1}\Delta t] \\ C_o(I - A\Delta t)^{-2}[T_k + V_{k+1}\Delta t] + C_o(I - A\Delta t)^{-1}V_{k+2}\Delta t \\ \vdots \\ C_o(I - A\Delta t)^{-(f+1)}[T_k + V_{k+1}\Delta t] + C_o \left[\sum_{j=1}^f (I - A\Delta t)^{-j} \right] V_{k+2+f-j}\Delta t \\ \vdots \\ C_o(I - A\Delta t)^{-(nf+1)}[T_k + V_{k+1}\Delta t] + C_o \left[\sum_{j=1}^{nf} (I - A\Delta t)^{-j} \right] V_{k+2+nf-j}\Delta t \end{bmatrix} \quad (5.14)$$

The size of vector \mathbf{Y}^* is $((nf + 1) \times n_q, 1)$ and matrix \mathbf{S} is of size $((nf + 1) \times n_q, n_U)$. The objective is to identify the pseudo-solution $\widehat{\mathbf{U}}_{k+1}$ of the inverse problem, such that $\mathbf{Y}^* - \mathbf{Y} \approx 0$, where \mathbf{Y} is the temperature vector computed by LPTM. As matrix \mathbf{S} is not square due to the addition of future time steps, the least square method is used to solve equation (5.11) and leads to the sequential solution:

$$\widehat{\mathbf{U}}_{k+1} = (\mathbf{S}^T \mathbf{S})^{-1} \mathbf{S}^T (\mathbf{Y}_{k+1}^* - \mathbf{D}_k) \quad (5.15)$$

In order to evaluate the accuracy of the estimations for the different studied cases, a mean quadratic discrepancy between exact heat sources (vector \mathbf{U}^{exact}) and estimated ones (vector $\widehat{\mathbf{U}}$) is defined as follows:

$$\sigma_U = \left[\frac{1}{n_U \times (nt - nf)} \sum_{i=1}^{n_U} \sum_{k=1}^{nt-nf} (\hat{U}_{i,k} - U_{i,k}^{exact})^2 \right]^{1/2} \quad (5.16)$$

Where nt is the number of time steps in the inverse problem.

It is worth to remind that, in a practical application, this quantity is not reachable. Similarly, for each output Y_i , a mean quadratic error between measured temperatures and those computed with the estimated set of heat sources strengths is defined as follows:

$$\sigma_{Y_i} = \left[\frac{1}{(nt - nf)} \sum_{k=1}^{nt-nf} (\hat{Y}_{i,k} - Y_{i,k+1}^*)^2 \right]^{1/2} \quad (5.17)$$

When the unknown heat sources \hat{U}_{k+1} are identified, they will be used as inputs in the direct problem to predict the temperature in inaccessible parts of the motor, for instance, the critical temperatures T_{crit} in windings or magnets. The complete procedure is illustrated in the block diagram of *Figure 5.4*.

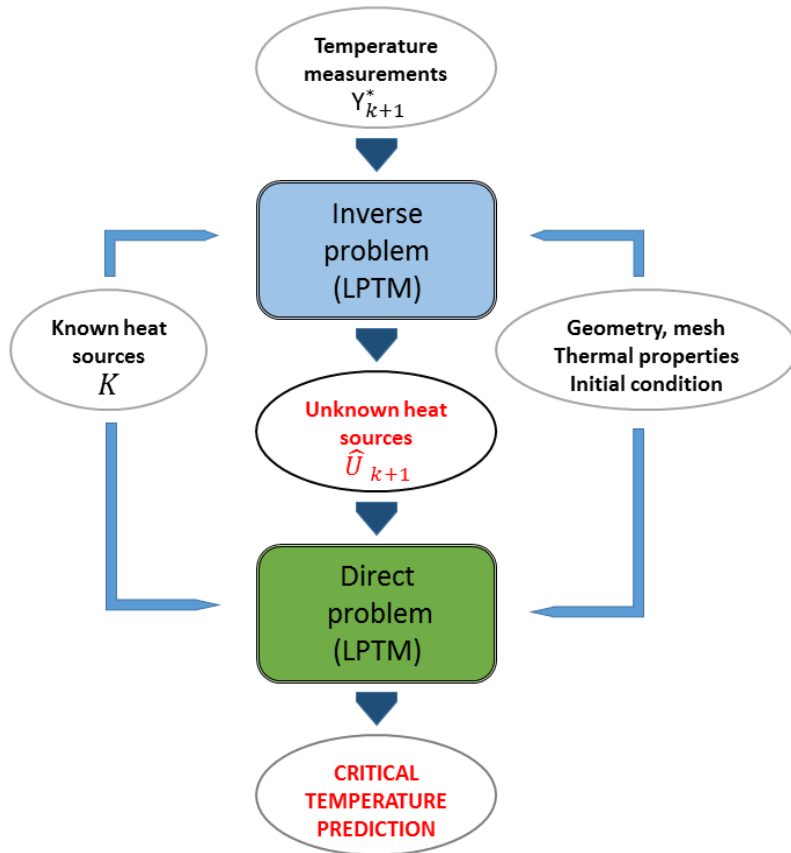


Figure 5.4 : Block diagram: use of LPTM for both inverse and forward problems.

At each time-step, the model is solved in the inverse problem approach to get motor losses. The inputs for inverse LPTM are the temperature measurements equivalent to sensors' output temperatures at accessible points.

Then, forward LPTM is used to determine indicated critical temperatures.

5.3.5 Results and Analysis

A scenario of motor operation is chosen corresponding to a profile mission in an aircraft flight application as in *Figure 5.5*. This profile is different from the proposed mission flight in the project since the objective of this investigation is testing the efficiency of the inverse technique on the motor model independently from the profile used. The flight phases correspond to the taxi-out phase (0 to 450 s), take-off and climb (450 s to 900 s), cruise flight (900 s to 2250 s), descent and landing (2250 s to 2700 s), and taxi-in (2700 s to 3600 s).

Besides, the corresponding outside temperature profile during the flight is an input of the model. It is given by T_{ext} as function of time as in *Figure 5.6*.

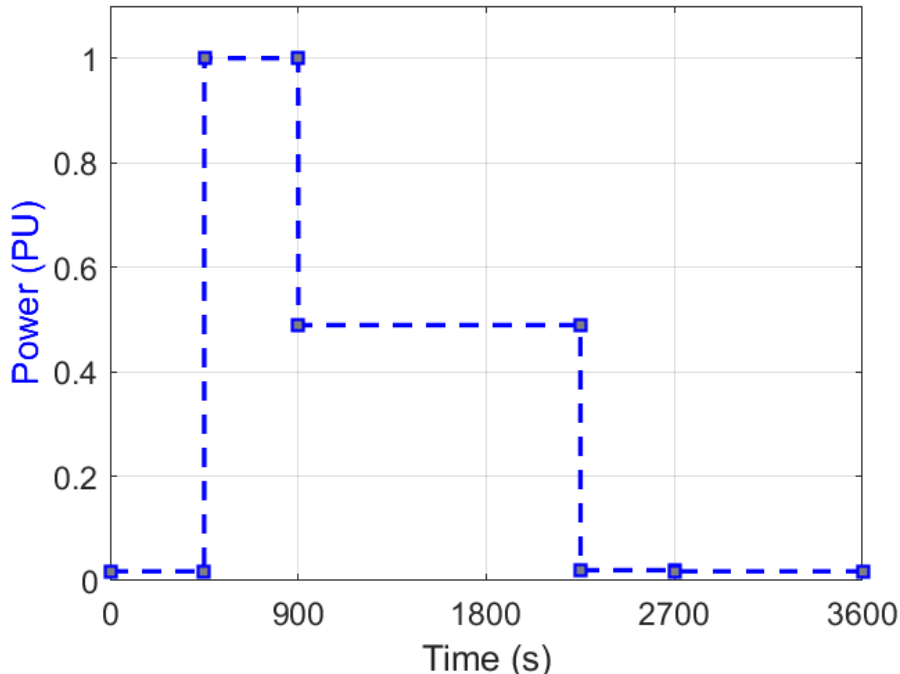


Figure 5.5 : Power profile for losses profile model in the inverse technique.

The corresponding profiles of heat sources generated in the motor (motor losses) are depicted in *Figure 5.7* during the mission profile of 3600s. For confidentiality reasons, all losses (or heat sources) are expressed in Per-Unit (PU) with respect to total losses value.

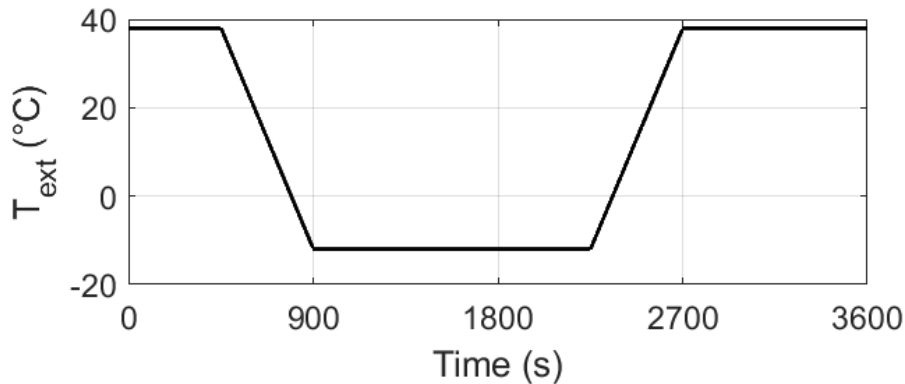


Figure 5.6 : Outside temperature variation as function of time during mission profile corresponding to the current application.

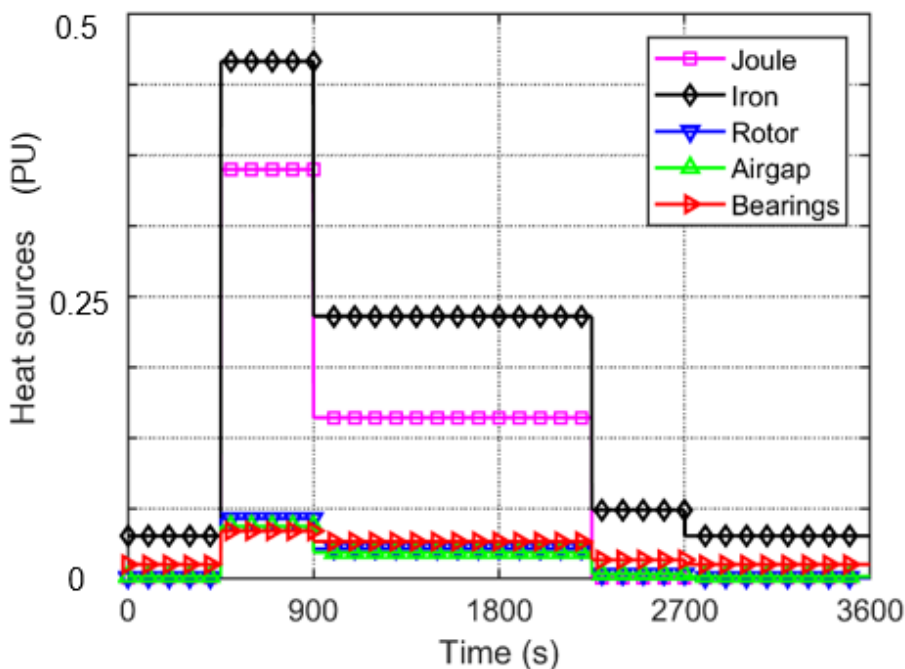


Figure 5.7 : PMSM heat sources evolution as function of time.

Rotor, Airgap, and Bearings losses remain relatively low and are at the same level all mission long, whereas Joule and Iron losses change significantly. Those losses are particularly high during the take-off phase as they are linked to propulsion power. Airgap and Bearings losses

depend principally on the rotor rotation speed, which varies slightly between take-off and cruise, and is very low during taxi phases.

Temperatures are then computed using LPTM and a time step equal to one second. Among these temperatures, a set of observables is chosen depending on the different case studies (see subsection 5.3.3). A noise of standard deviation equal to $\sigma = 0.1^\circ\text{C}$ is added to these observables so that they are used as temperature measurements in various inverse problem cases.

5.3.5.1 Identification of Iron Losses

In this first case, among the five heat sources, four are supposed to be known ($P_{Joule} P_{Rotor} P_{Airgap} P_{Bearings}$) and only iron losses ($P_{Iron}(t)$) have to be identified. Figure 5.8a shows the evolution of temperature T_{s1} with respect to time.

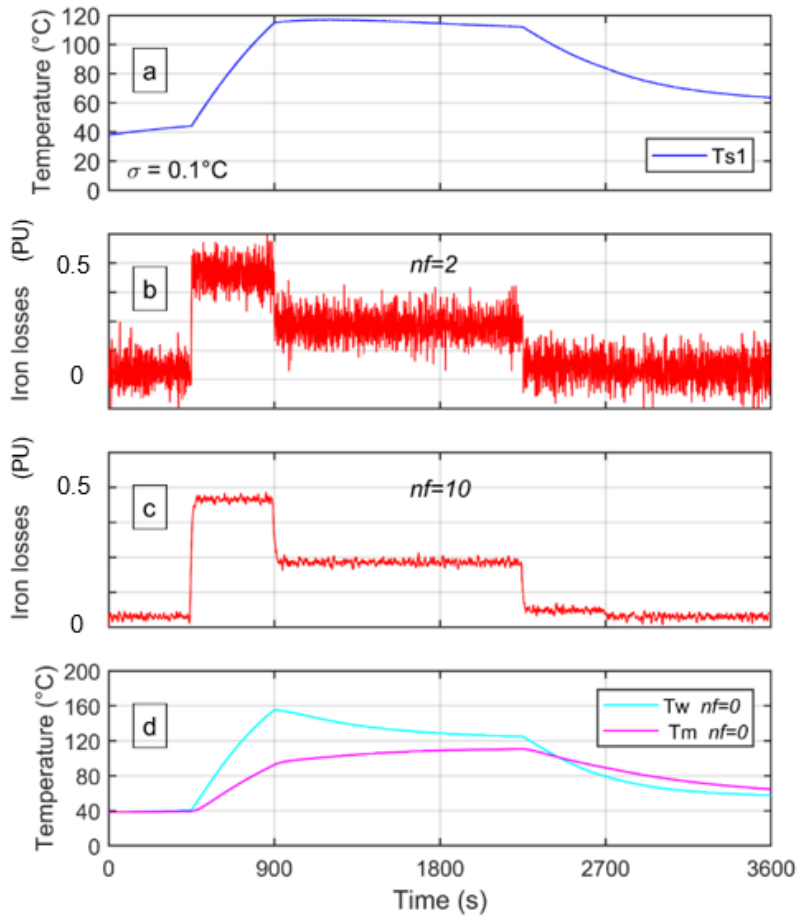


Figure 5.8 : Iron losses identification from sensor T_{s1} with $nf=2$ and $nf=10$ and computation of critical temperatures T_w and T_m .

From this temperature, the inverse problem is solved to identify $P(t) = P_{Iron}(t)$ knowing $K(t) = [P_{Joule} P_{Rotor} P_{Airgap} P_{Bearings}]^T$. Hence, for this case, $n_q = n_U = 1$.

The procedure is sequential, as mentioned before, expressed in equation (5.15), and depends on the number of future time steps. Results of identification are presented in *Figure 5.8b* and *Figure 5.8c* for respectively $nf = 2$ and $nf = 10$. It is remarkable that, without regularization ($nf = 0$), the oscillations of $P_{Iron}(t)$ are huge. Hence, we have chosen to draw $P_{Iron}(t)$ for $nf = 2$ in *Figure 5.8b*.

It appears that the number of future time steps filters the oscillations of P_{Iron} , which is confirmed by the quadratic criterion σ_U in *Table 5.1*. The main criterion, and the only one to be computed in a real case, is σ_Y . Its evolution with respect to nf is quite interesting. For $nf = 0$, even if the problem is ill-posed, large oscillations in \hat{U} allow to follow exactly the evolution of the noisy temperature. Hence, as indicated in *Table 5.1*, $\sigma_Y \approx 0^\circ\text{C}$. When nf increases, regularization tends to damp the time evolution of \hat{U} , leading to a bias in the temperature computation. We choose then the number nf for which $\sigma_Y \geq \sigma$ to “get out” of the noise level. The identification of $P_{Iron}(t)$ for $nf = 10$ is depicted in *Figure 5.8c* and shows a very good agreement with the exact evolution of these losses drawn in *Figure 5.7*.

nf	$\sigma_U (W)$	$\sigma_{Ts1} (\text{ }^\circ\text{C})$
0	5303.1	3e-14
2	936.7	0.0871
4	451.3	0.0935
6	304.7	0.0964
8	249.4	0.0988
10	229.2	0.1009
12	224.0	0.1034

Table 5.1 : Inversion results for iron losses identification from Ts1; bold lines correspond to results shown in Figure 5.8.

Once P_{Iron} is identified, the aim is to predict temperatures T_w and T_m in inaccessible parts of the electric motor. They have been computed for the different values of nf and are shown in *Figure 5.8d* for $nf = 0$. Note that for $nf = 0$, temperature prediction occurs without any delay whereas it is executed with a 10 s delay with $nf = 10$ since the time step Δt is equal to 1 s. For any value of nf the temperature evolution in critical zones is the same, since oscillations in \hat{U} are damped by the thermal path and inertia of the system. Same as in equation (5.16), critical temperatures T_w and T_m are compared to the exact temperatures computed with the exact

inputs. For $nf = 0$, a quadratic error $\sigma_{T_{crit}} = 0.003 \text{ } ^\circ\text{C}$ is obtained, which gives a very accurate prediction.

Now, a new test is carried out using a second measurement point Ts2 located in the stator. Graphical results are summarized in *Figure 5.9*.

It appears obvious that the oscillations of $P_{Iron}(t)$ decreased compared to *Figure 5.8*, which is confirmed by *Table 5.2* where σ_U goes from 229 W to 200 W for $nf = 10$.

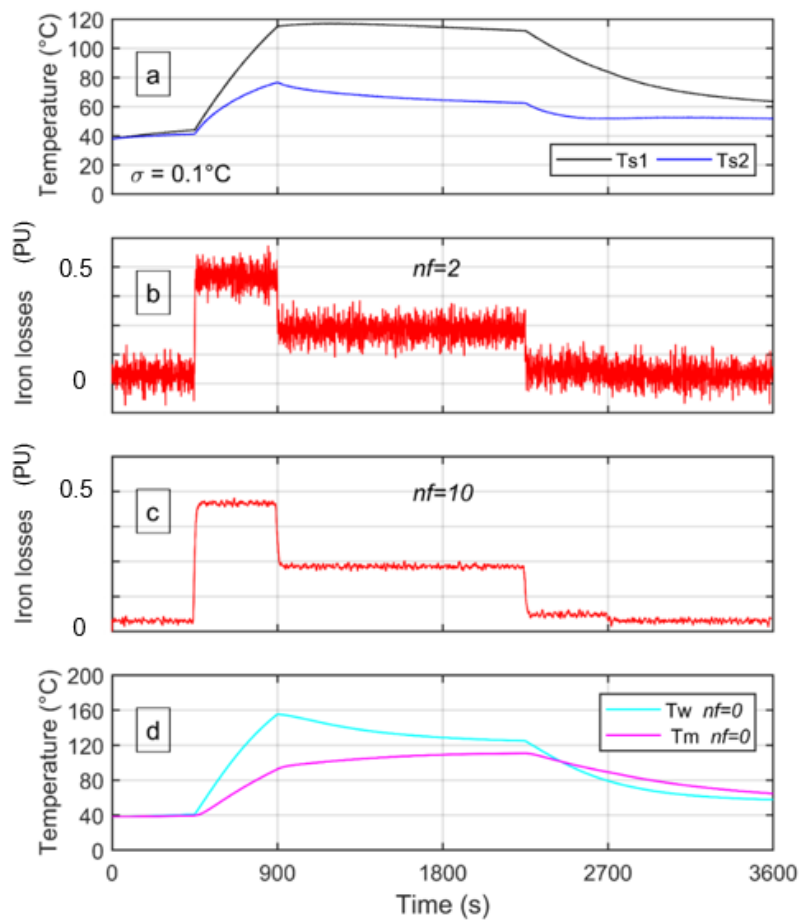


Figure 5.9 : Iron losses identification from sensors Ts1 and Ts2 with $nf=2$ and $nf=10$ and computation of critical temperatures T_w and T_m .

nf	$\sigma_U (W)$	$\sigma_{Ts1} (\text{°C})$	$\sigma_{Ts2} (\text{°C})$
0	3713.2	0.0690	0.0700
2	673.8	0.0921	0.0929
4	336.0	0.0957	0.0960
6	237.5	0.0976	0.0975
8	205.1	0.0992	0.0987
10	200.1	0.1011	0.1001
12	205.0	0.1034	0.1020

Table 5.2 : Inversion results for iron losses identification from Ts1 and Ts2; bold lines correspond to results shown in Figure 5.9.

It is interesting to observe that in this case ($n_q = 2$, $n_U = 1$) it is not possible to obtain $\sigma_Y \approx 0^\circ\text{C}$ for each of the two sensors from only one heat source $P_{Iron}(t)$. The temperature prediction in windings and magnets is also very accurate with an error $\sigma_{Tcrit} = 0.002^\circ\text{C}$ for $nf = 0$.

5.3.5.2 Identification of Joule and Iron Losses

For the second case, Joule losses (P_{Joule}) are also unknown. The evolutions of $P_{Joule}(t)$ and $P_{Iron}(t)$ have to be identified. Firstly, sensors Ts1 and Tsw located in the stator and at the winding surface are used. It can be remarked in Figure 5.10 and Table 5.3 that both heat sources are well identified when increasing the number of future time steps.

In this case, $nf = 12$ gives $\sigma_Y \geq \sigma$ for each sensor, as calculated in Table 5.3.

The condition number of the matrix $\mathbf{S}^T \mathbf{S}$ to invert is also indicated. It is noteworthy that this last one decreases when the number of future time steps increases, which confirms the regularization effect of the function specification, knowing that in case 1, $\mathbf{S}^T \mathbf{S}$ is a scalar, hence its condition number is equal to 1.

Compared to the first case, the winding temperature is quite sensitive to the oscillations in Joule losses identification, hence the error increases: $\sigma_{Tcrit} = 1.161^\circ\text{C}$ for $nf = 0$.

On the other hand, by adding two other sensors Ts2 and Ts3, located in the stator, better inversion results are again obtained, as depicted in Figure 5.11 and Table 5.4, since σ_U goes from 200 W to 180 W.

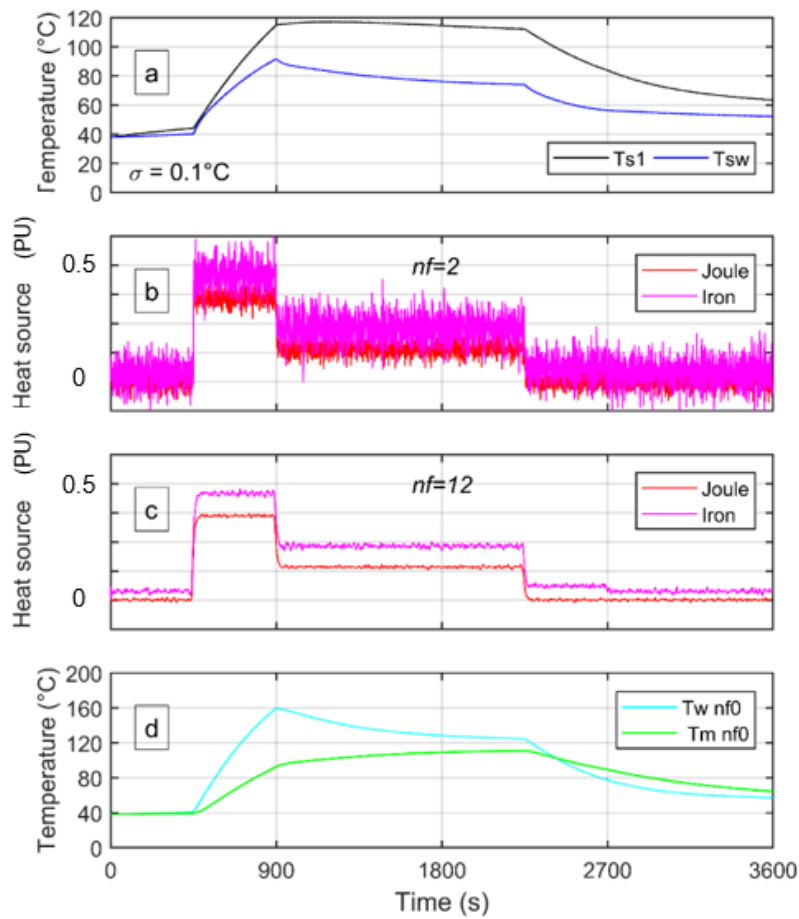


Figure 5.10 : Joule and iron losses identification and computation of critical temperatures from sensors T_{s1} and T_{sw} with $nf=2$ and $nf=12$.

nf	$\sigma_U (W)$	$\sigma_{Ts1} (\text{°C})$	$\sigma_{Tsw} (\text{°C})$	$CN(\mathbf{S}^T \mathbf{S})$
0	4125.2	3e-14	6e-15	3.74
2	741.2	0.0859	0.0869	3.64
4	359.2	0.0926	0.0931	3.54
6	246.4	0.0949	0.0971	3.45
8	209.3	0.0970	0.1007	3.36
10	198.9	0.0992	0.1051	3.28
12	200.4	0.1017	0.1104	3.20
14	207.9	0.1047	0.1168	3.12

Table 5.3 : Inversion results for Joule and iron losses identification from T_{s1} and T_{sw} ; bold lines correspond to results shown in Figure 5.10.

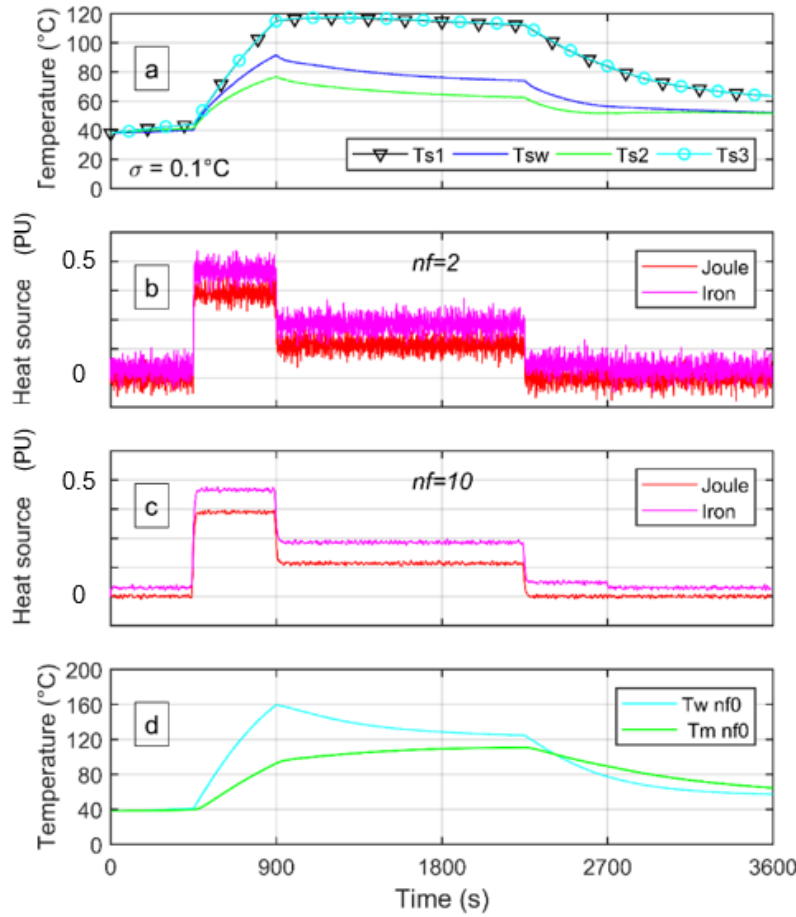


Figure 5.11 : Joule and iron losses identification and computation of critical temperatures from sensors Ts_1 , T_{sw} , Ts_2 , and Ts_3 with $nf=2$ and $nf=10$.

nf	$\sigma_U (W)$	$\sigma_{Ts1} (\text{°C})$	$\sigma_{T_{sw}} (\text{°C})$	$\sigma_{Ts2} (\text{°C})$	$\sigma_{Ts3} (\text{°C})$	$CN(S^T S)$
0	2849.0	0.0803	3e-5	0.0832	0.0816	1.26
2	518.4	0.0941	0.0867	0.0974	0.0952	1.23
4	262.6	0.0964	0.0937	0.0994	0.0974	1.21
6	194.5	0.0976	0.0975	0.1004	0.0987	1.18
8	179.2	0.0990	0.1012	0.1012	0.0999	1.16
10	180.3	0.1007	0.1055	0.1025	0.1016	1.13
12	188.3	0.1028	0.1109	0.1040	0.1038	1.11

Table 5.4 : Inversion results for Joule and iron losses identification from Ts_1 , T_{sw} , Ts_2 , and Ts_3 ; bold lines correspond to results shown in Figure 5.11.

The addition of sensors acts as a filter in the inversion procedure and the condition number of the matrix $\mathbf{S}^T \mathbf{S}$ decreases as well. The temperature prediction in windings and magnets remains relatively accurate with an error $\sigma_{T_{crit}} = 1.158 \text{ }^\circ\text{C}$ for $nf = 0$.

5.3.5.3 Identification of all Losses

In this third case, the five heat sources altogether are considered unknown and have to be identified simultaneously from five sensors T_{s1} , T_c , T_{sw} , T_a , and T_b , whose temperature evolutions are given in *Figure 5.12a*.

These sensors are located in the stator, in the cavity, on the surface of the windings, in the airgap, and on the bearings respectively. It can be remarked that the temperature magnitude is very different according to the locations of the sensors.

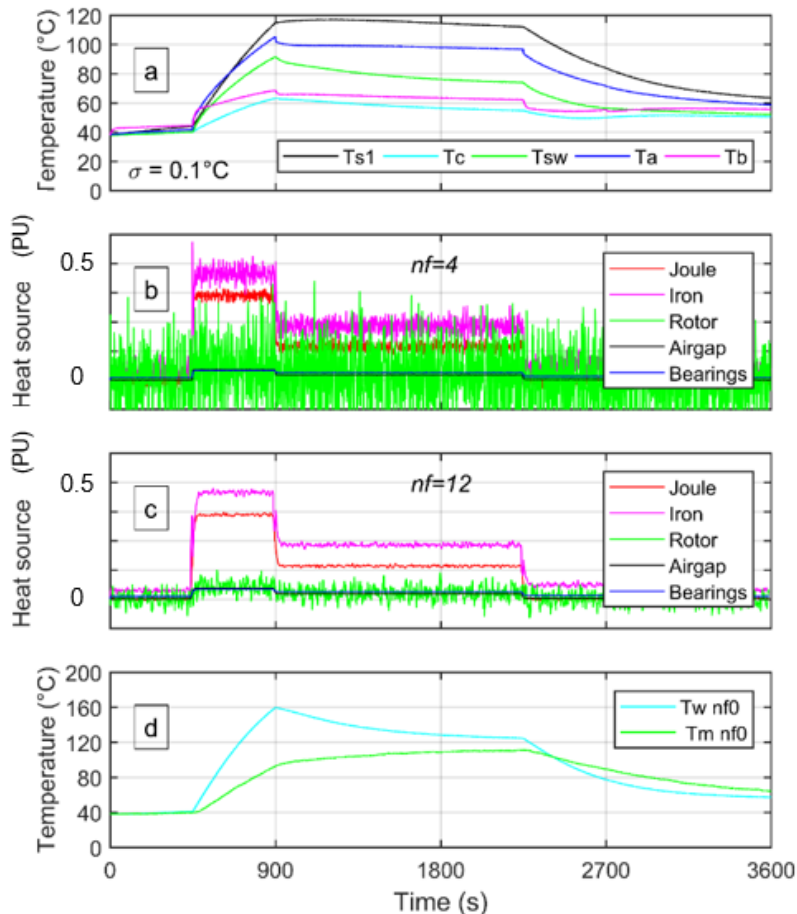


Figure 5.12 : Identification of all the heat sources and computation of critical temperatures from sensors T_{s1} , T_c , T_{sw} , T_a , and T_b with $nf=4$ and $nf=12$.

As for previous cases, the quadratic errors and the condition number are given in *Table 5.5* with respect to the number of future time steps.

nf	$\sigma_U (W)$	$\sigma_{Ts1} (\text{°C})$	$\sigma_{Tc} (\text{°C})$	$\sigma_{Tsw} (\text{°C})$	$\sigma_{Ta} (\text{°C})$	$\sigma_{Tb} (\text{°C})$	$CN(\mathbf{S}^T \mathbf{S})$
0	11990.5	3e-14	1e-14	6e-15	2e-14	2e-14	2.46e6
2	1859.6	0.0881	0.0861	0.0842	0.1213	0.0876	4.48e5
4	859.3	0.0973	0.0930	0.0913	0.1639	0.0996	1.82e5
6	529.7	0.1038	0.0959	0.0952	0.1982	0.1129	9.90e4
8	382.1	0.1100	0.0975	0.0990	0.2282	0.1295	6.23e4
10	305.8	0.1169	0.0987	0.1037	0.2557	0.1490	4.85e4
12	263.9	0.1243	0.1000	0.1096	0.2816	0.1712	4.29e4
14	240.1	0.1326	0.1014	0.1167	0.3061	0.1950	3.82e4

Table 5.5 : Inversion results for all losses identification from $Ts1$, Tc , Tsw , Ta , and Tb ; bold lines correspond to results shown in Figure 5.12.

In this case, the condition number of the matrix $\mathbf{S}^T \mathbf{S}$ is very high, hence, the noise in temperature measurements may be greatly amplified by the inverse problem. As in previous cases, $nf = 0$ corresponds to a square case ($n_q = n_U = 5$), thus, even if the problem is ill-posed, large oscillations in \hat{U} allow to follow exactly the noisy temperature evolutions.

Hence, as indicated in *Table 5.5*, $\sigma_Y \approx 0 \text{ °C}$. An increase of nf leads to $\sigma_Y > \sigma$ for all sensors for $nf = 12$. *Figure 5.12c* shows large oscillations in P_{Rotor} due to the fact that the sensors are located far from this heat source. But, these oscillations are damped when increasing nf , as depicted in *Figure 5.12c*.

Concerning the temperature prediction in windings and magnets (*Figure 5.12d*), the error is reasonably acceptable with $\sigma_{Tcrit} = 1.178 \text{ °C}$ for $nf = 0$.

5.4 Conclusion

In this chapter, the numerical model developed earlier in this work is applied to assess the losses identification in high specific power electric motors design.

Being a critical problem in electric machinery, electric motor losses are major players in temperature evolution. An inverse method has been developed to enable determining these losses based on easily accessed temperatures. Firstly, a sensitivity study of temperatures to losses has been carried out to determine the influence of each losses type on motor thermal behavior to adapt the losses identification procedure.

Then, the low-order Lumped Parameter Thermal Model (LPTM) has been used to solve both inverse and direct problems. The method is sequential and includes regularization with the function specification technique. Different configurations have been tested according to the number of heat sources to be identified. For each case, the influence of the required number of sensors to be used to solve the inverse problem, and the number of future time steps were analyzed.

The technique gives also an accurate prediction of the temperature in unreachable critical parts of the motor and is computationally efficient: only 10^{-3} s at each time step is needed for identification of the heat sources and prediction of the motor temperatures.

CHAPTER 6 CONCLUSIONS AND PERSPECTIVES

Synopsis:

General conclusions are given hereafter, in addition to some perspectives from academic and industrial points of view.

6.1 Conclusions

Electric Motors are nowadays crucial systems for different applications in multiple domains. In the recent era of electrification of vehicles, these components have a major role to play. Indeed, to meet the requirements of reaching the aimed reduction in gas emissions and noise, solutions of electrification and hybridization in the transportation sector are proposed.

In the domain of aeronautics, many industries, institutes, and researchers are moving forward on working on a hybrid aircraft with electric motors as a step towards less polluting air transportation means. However, such transition in propulsive power requires detailed and specific studies on electrical and thermal issues. Actually, the aircraft targets in terms of weight are almost not reachable with the existing technologies. On the other hand, electric motor high targets of specific powers and efficiencies are limited by, among other factors, the thermal constraints. Those constraints result from super-high losses induced by such motors and the relatively low allowed maximum temperatures of specific components. In fact, these components' lifetimes are subject to variations at each cycle of overshooting of temperature, leading to a drastic reduction of motor operational time or even a total motor failure. Pushing the technological limits suggests advancements in the motor design and cooling solutions so that the temperatures do not exceed the allowed maximum values.

The framework of this thesis is a CleanSky II project aiming to design propulsive electrical architectures for aircraft with specific targets and multiple Work-Packages. The objective of our Work-Package is the thermal assessment of high specific power electric motors, with high efficiencies, designed in the same framework. These motors are Surface Mounted-Permanent Magnet Synchronous Machines with issues in thermal behavior, in addition to their temperature limits.

First, a state of the art, reviewing thermal characteristics and cooling techniques applied to electric motors, has been elaborated to comprehend the cooling issue and solutions. Based on this review, some methods were selected for their feasibility and adaptability to the motor type and geometry.

A thermal modeling approach based on the nodal network method is adopted to design the motors with their cooling systems. The developed numerical model consisting of a nodal network, of a relatively low number of nodes, allows a rapid assessment of the temperatures and fluxes in the motor. It takes into account the motor electromagnetic and mechanical losses

(Joule losses, iron losses, bearings losses, and windage losses of two types) that generate the heat. The proposed designs of the targeted motors have been tested. The exchanger and the cooling circuit are integrated into the model. Actually, the nacelle surface is used as a cold plate in the heat exchanger. Hence, the boundary conditions in terms of outside temperature at the nacelle external surface are implemented in the model. Besides, the heat sources' dynamic profiles are injected to corresponding nodes where losses occur.

Strong interaction with the Work-Package working on the electromagnetic design of the motor was required to get an optimized distribution of losses in the motor. This interaction has been the topic of several synergies and public contributions.

Motors for two time-target (5 kW/kg then 10 kW/kg of specific powers) were investigated using the developed model, and cooling solutions consisting mainly of a liquid cooling jacket and motor channels were proposed. These investigations allowed reaching relatively optimal designs for the two target motors.

❖ Studies on Electric Motor of 5 kW/kg

For this intermediate specific power value, the motor cooling consists of a liquid shaft channel for rotor heat extraction, a liquid jacket cooling of the stator in the frame structure, and a potting of the end-windings with high thermal conductivity impregnation material. The liquid coolant used is a mixture of Water-Ethylene-Glycol. The resulting temperatures, taking into account the mission dynamical profile, for heat sources injected, and the outside air-temperatures show two different behaviors for rotor and stator components. Other fluids are tested and compared, whereas the first adopted mixture seems to be the most convenient. A scenario of full power application after the aircraft take-off is tested to show the limits of the design and cooling efficiency. Then, a parametric investigation on the heat exchanger's main parameters (coolant flow rates and plate surface) is carried out to verify the optimum operating point. Moreover, a sensitivity study of thermophysical properties to temperatures is performed.

❖ Studies on Electric Motor of 10 kW/kg

For this high specific power motor, simulations show that winding direct cooling is inevitable given the current density (producing high Joule losses) in this confined area. Two motor designs were investigated in *Chapter 4*, one with relatively low Joule losses and high iron and rotor

losses, and the other with comparable levels of Joule and iron losses. The results suggested that the second design is more suitable for the specific power target in terms of cooling system weight since the first design exhibited a serious issue.

❖ Losses Identification through an Inverse Method

Finally, using the elaborated motor thermal model, an inverse method has been developed to enable determining the motor losses based on temperature data at relatively easy-accessed points. First, a sensitivity study of temperatures to losses has been carried out to determine the influence of each losses type on motor thermal behavior to adapt the losses identification procedure. Then, a sequential technique, that uses Beck's function specification for regularization, was developed. Different configurations, with increasing complexity in unknown losses, have been tested. For each of these configurations, the influence of the required number of sensors to be used to solve the inverse problem, and the number of future time steps were analyzed. The method seems efficient in identifying the losses and in predicting temperatures in poorly accessible critical parts.

6.2 Perspectives

Industrial Aspects

❖ Multiphysics model for optimization

The LPTM technique offers a great ability to be adapted to other models since the tool is built by coding concepts and can be combined with the electromagnetic tools and specific environment models. Optimization of the design of the motor or the overall aircraft propulsion architecture can be enabled by such multiphysics models.

❖ Current density product

In collaboration with WP1, the equivalent current density product has been introduced as a constraint for the design of high-specific power electric motors. It takes into account the electromagnetic and thermal issues. A further investigation of this constraint can allow

designing motors of different specific power values or different types (for example the induction motor, or the synchronous motor with wound rotor).

❖ Larger integration of the thermal system

The cooling system could be better integrated into the plane at several levels. For instance, the extracted heat could be used for specific applications such as anti-icing or air-conditioning. Moreover, a single thermal system could be used to cool different systems.

Academic Research Aspects

❖ Validation of the inverse method on an experimental bench

The concept of the technique allowing identifying losses through thermal measurements has been only tested numerically. This first step must be followed by an experimental validation that would take into account issues related to measuring process and uncertainties.

❖ Testing the method on other motor types

The inverse method has been developed for the identification of losses in a Surface Mounted-Permanent Magnet Synchronous Machine. It is possible to test the method on other topologies. However, the method can be adapted to other motor types. With the new field of research on electric motors thermal aspects, the proposed technique interests the electrical machines specialists and motor designers, especially with the lack of other methods that allow the determination of losses or poorly accessed temperatures.

❖ Other regularization technique (drawbacks of the proposed one)

The regularization technique used in this thesis to solve the inverse problem of the identification of heat sources is the Future Time Step (FTS) method. Its only drawback in real-time consists of requiring temperature measurements at subsequent times, which causes a slight delay (depending on the number of FTS) in the identification of unknowns. Hence, it would be very interesting to find other real-time identification methods that allow however minimizing the propagation of the noise in the inversion process.

FUNDING ACKNOWLEDGMENT

This project has received funding from the European Union's Horizon 2020 (Cleansky 2 JTI) research and innovation program, 2014-2024 under grant agreement No 715483.

CHAPTERS' SUMMARIES IN FRENCH

Chapitre 1

La propulsion électrique des moyens de transport connaît récemment un progrès inédit lié à l'intérêt sérieux que portent les acteurs du secteur du transport à réduire les émissions de gaz nocifs et les nuisances sonores. Maintenant que le développement de voitures électriques et hybrides prend une place importante dans le transport terrestre afin de réduire la consommation d'énergie fossiles, vient le tour des avions hybrides électriques.

Outre le défi de passer à une architecture différente de propulsion, les aspects contraignants de l'électrification du secteur du transport aéronautique sont multiples. Effectivement, du fait des limites de poids et de volume des aéronefs, une puissance élevée de moteurs, suffisamment compacts et légers, est exigée. Ces moteurs électriques de propulsion d'avions doivent vérifier alors un cahier des charges contraignant de densités de puissance.

Grâce aux avancées technologiques réalisées sur les matériaux, qui sont de plus en plus adaptés à ces applications, une remarquable nouvelle génération de ces moteurs est en cours de développement.

Pourtant, au vu des forts flux de chaleur dissipés dans ces machines ainsi que des limites de température pour certains de leurs composants, de nouvelles contraintes thermiques apparaissent dans la phase de dimensionnement de machines, et la mise en place d'un système d'extraction de chaleur efficace et optimisé devient inévitable. En effet, au-delà de certaines valeurs critiques de température, le fonctionnement nominal du moteur ne peut plus être assuré.

Le présent travail fait partie d'un projet européen de Clean Sky 2 décomposé en plusieurs Work-Packages (WP) et impliquant de nombreux partenaires des milieux académique et industriel (tels que le laboratoire Laplace et Airbus). Notre partie constitue le WP3 visant en particulier à étudier le comportement thermique de moteurs électriques pour la propulsion d'avions hybrides.

En plus de la performance et du poids, d'autres aspects contraignants des machines électriques apparaissent dans la propulsion aéronautique, que l'on devrait considérer dans ce genre d'étude multiphasique. On peut citer notamment l'altitude, les conditions externes de l'environnement, la sécurité de fonctionnement, les matériaux à proscrire, etc.

Le travail consiste à modéliser le moteur, trouver des techniques de refroidissement adaptées et à optimiser le moteur et son système de refroidissement pour répondre aux cahiers des charges respectivement pour les années 2025 et 2035. Dans cette étude, les conditions de vol en termes de profil de puissance ainsi que de conditions extérieures de température sont considérées.

Chapitre 2

Dans la conception de moteurs électriques à forte densité de puissance, du fait de l'existence de points chauds critiques, le choix de techniques de refroidissement adaptées est incontournable. Ce choix est fait en se basant sur l'étude des aspects thermiques dans la machine ainsi que sur les méthodes d'extraction de chaleur possibles, ce que l'on va appeler management thermique du moteur.

Une étude bibliographique est détaillée dans le *Chapitre 2* portant sur la thermique du moteur électrique. Cette étude a été développée de la manière la plus exhaustive possible pour la création d'un rapport complet sur le management thermique de ces machines. Pour cela, une partie du chapitre est dédiée au transfert de chaleur ayant lieu à l'intérieur, comme autour de la machine par différents modes. Ensuite, les approches classiques de refroidissement de moteurs électriques à haute densité de puissance ainsi que les dernières innovations sur ce sujet sont présentées.

Les études concernent parfois des moteurs de densités de puissance relativement faibles, mais qui présentent suffisamment de similarités avec les moteurs de plus fortes densités de puissance pour que leurs études restent intéressantes.

Cet état de l'art a notamment permis de classifier les méthodes de refroidissement en deux catégories : le refroidissement global de toute la machine et le refroidissement spécifique de certains composants.

Une attention particulière a été accordée aux parties du moteur qui sont sensibles à la température, et où un refroidissement global ne serait pas suffisamment efficace.

L'état de l'art sur la thermique du moteur électrique est divisé en 3 grands paragraphes :

- i. Le transfert par conduction dans les composants du moteur ;

- ii. Le transfert par convection, particulièrement dans l'entrefer entre le rotor et le stator et sur les têtes de bobines ;
- iii. Les méthodes de refroidissement connues et classiquement utilisées dans ces machines ainsi que celle considérées prometteuses et qui sont en cours d'évaluation pour des applications futures.

Ce chapitre a permis de trouver les technologies de refroidissement les plus prometteuses pour notre application. Un point important à signaler est que le refroidissement doit être adapté au design du moteur. Enfin, le refroidissement liquide, assurant une extraction de chaleur significativement plus importante que le refroidissement par air, est fortement suggéré pour refroidir des points chauds internes du moteur notamment les têtes de bobines et les aimants afin de pouvoir atteindre des densités de puissances élevées.

Chapitre 3

Le Chapitre 3 présente la méthode de travail choisie pour l'étude des moteurs électriques des objectifs 2025 et 2035 du projet.

Parmi les différentes techniques de modélisation thermique, la méthode nodale ou LPTM (pour Lumped Parameter Thermal Model) a été considérée comme la plus adaptée à la modélisation et à l'étude du comportement thermique de nos moteurs électriques et de leurs systèmes de refroidissement. Cette méthode permet de résoudre l'équation de la chaleur en régimes transitoire et permanent en discrétilisant spatialement le système à étudier. Elle se base sur l'analogie entre les quantités électriques et thermiques et permet une représentation de la thermique par des composants électrique (conductances, condensateurs...).

Dans la pratique, cette méthode consiste à définir des nœuds correspondants à chaque volume discrétilisé du moteur. Chacun de ses nœuds est affecté une capacité thermique et, le cas échéant, une source ou un puits de chaleur. Les nœuds sont connectés les uns aux autres par des conductances thermiques représentant les échanges de chaleur entre nœuds adjacents. Un réseau nodal peut être désormais créé.

La structure des moteurs à étudier est du type synchrone à aimants permanents. Dans ce cadre, les entrées thermiques sont de plusieurs natures : les pertes dans le moteur (Joule, fer, roulements, entrefer, flasques du rotor) fonction du profil de puissance, ainsi que la température

et les échanges avec l'extérieur. Ces entrées thermiques variant dans le temps seront considérées afin d'étudier le comportement en régime transitoire du moteur durant un vol type.

Partant de certaines hypothèses et considérations relatives à la géométrie et aux spécificités du moteur électrique en question (comme l'axisymétrie au niveau du rotor du fait de l'homogénéité des matériaux dans la direction azimutale, la périodicité au niveau du stator, etc..), un nombre réduit de nœuds (57 à 62 nœuds) est utilisé pour modéliser le moteur et son système de refroidissement.

Une fois les matrices de capacités thermiques et de conductances thermiques, et le vecteur des sollicitations thermiques assemblés, le modèle devient un système de N équations différentielles ordinaires en temps, où N est le nombre de nœuds de la discréétisation spatiale.

La méthode de résolution par Euler implicite est utilisée pour trouver la distribution de températures dans la machine. La modélisation est effectuée sous le logiciel Matlab, et un modèle appelé *AThEM* se basant sur le LPTM est développé.

Afin de valider le code, les résultats de simulation du modèle sont comparés à des résultats expérimentaux issues d'essais sur un moteur similaire à ceux envisagées pour la propulsion aéronautique avec un refroidissement liquide autour du moteur. Pour le point de fonctionnement du moteur considéré, le maximum d'écart entre les températures simulées et les températures expérimentales est de 3,2% ($\sim 1,8 \text{ }^{\circ}\text{C}$) au niveau des têtes de bobines et dans le bobinage, ce qui permet de valider les hypothèses faites lors de la modélisation.

Des modèles similaires vont être utilisés dans le chapitre suivant pour simuler le comportement thermique des moteurs propulsifs envisagés pour l'avion hybride (à échéance 2025 et 2035).

Chapitre 4

Une procédure itérative a été mise en place avec le Work-Package 1 (WP1), qui s'occupe de l'électrotechnique du moteur, du fait du fort couplage électrotechnique/thermique nécessaire à l'optimisation des moteur notamment en terme de densité de puissance (kW/kg).

Au modèle précédemment validé de moteur synchrone à aimants permanents (type choisi pour nos moteurs), une extension comprenant tout le circuit de refroidissement et notamment l'échangeur permettant au liquide de refroidissement d'évacuer vers l'air extérieur la chaleur prise au moteur a été développée. En effet, d'une part, le poids du système de refroidissement

doit être pris en compte dans la densité de puissance. D'autre part, du fait de notre modélisation en régime transitoire, son inertie doit être prise en compte. Un vol complet fourni par Airbus est simulé, allant du taxi-out au taxi-in avec une phase de décollage de quelques minutes où la puissance requise du moteur est à 100% de la valeur nominale. Cette phase est suivi d'une phase de montée durant laquelle on observe une décroissance de la puissance jusqu'environ 78% de la puissance maximale requise, et à la fin de laquelle une chute de puissance aux alentours de 50% correspond à la phase de croisière.

Pour le premier objectif du projet (pour l'année 2025), le moteur a une densité de puissance de 5 kW/kg . Après plusieurs itérations avec le WP1, un design optimal et des stratégies de refroidissement adéquates sont considérés pour le moteur électrique. Un double refroidissement par canaux d'eau glycolée au niveau de la carcasse du stator et dans l'arbre du rotor, ainsi qu'un encapsulant sur les têtes de bobines ont donné des résultats satisfaisants pour maintenir les températures du moteur en dessous des valeurs seuils critiques. La température maximale durant ce vol est atteinte à la fin de la phase de montée, et est obtenue aux têtes de bobines et aux bobinages. Les températures maximales au rotor sont décalées par rapport à celle du stator. Nous avons pu maintenir les températures en-dessous des valeurs seuils critiques en jouant sur l'inertie du moteur et sa variation de puissance ainsi que sur la baisse de température extérieure durant la montée.

Une optimisation du poids du système de refroidissement a permis également d'atteindre la densité de puissance demandée dans le cahier des charges. Des études de sensibilité sont menées sur ce modèle pour évaluer l'influence de certains paramètres thermophysiques et électriques sur le maximum de températures à l'intérieur de la machine.

Plusieurs designs de moteurs ont été également étudiés pour le second objectif du projet pour 2035 afin de trouver un dimensionnement adapté permettant d'avoir une densité de puissance doublée de 10 kW/kg . La machine choisie est assez similaire au moteur précédent (celui de l'année 2025) en termes de pertes et de caractéristiques physiques. Cette machine a une densité de pertes plus importante que la précédente et alors présente des températures plus élevées si on utilise le même refroidissement. Nous avons donc adapté notre système de refroidissement de façon à compenser cette augmentation, en rapprochant l'écoulement liquide d'une source principale de pertes localisées au niveau du bobinage et des têtes de bobines. Ainsi, un troisième circuit de refroidissement en contact avec le bobinage a été choisi constitué par des canaux dans les encoches du stator. En conséquence, le système de refroidissement choisi est formé par le double refroidissement du stator (externe) et du rotor (dans l'arbre) précédemment considéré,

et d'un circuit de refroidissement avec du liquide dans le bobinage. Nous avons alors été amenés à modifier notre modèle LPTM au travers de nœuds supplémentaires pour intégrer les canaux du bobinage. D'autre part, ce système a rendu inefficace la présence d'encapsulant qui ne sera plus considéré pour ce moteur. Les températures trouvées à partir du modèle numérique sont parfaitement acceptables, surtout au niveau des zones critiques. Finalement, la cible de 10 kW/kg en densité de puissance pour ce design de moteur a pu être satisfaite.

Chapitre 5

Après avoir développé le code du modèle numérique du moteur en adaptant et intégrant le refroidissement et après avoir obtenu les résultats en termes de températures du moteur en simulation directe, nous allons nous intéresser dans ce dernier chapitre à une extension de l'utilisation du LPTM. Il s'agit d'estimer les puissances dissipées dans le système à partir de quelques observables en températures par résolution d'un problème inverse. Dans un second temps, ces pertes estimées serviront à calculer les températures à des endroits inaccessibles à la mesure.

Il s'agit ici de profiter du faible nombre de degrés de liberté du LPTM afin de résoudre le problème inverse en temps réel.

A partir du vecteur de température complet, quelques observables vont être choisis convenablement et ensuite bruités pour reproduire une mesure expérimentale. Ces températures seront utilisées à travers le LPTM pour identifier les entrées inconnues qui sont les pertes dans ce cas. Mathématiquement, ce problème inverse est délicat à résoudre. Il est dit mal posé car sa solution n'est pas unique, ni stable en particulier avec un bruit de mesure.

Par conséquent, il a été nécessaire eu nécessité d'adoindre une méthode de régularisation. Pour cela, parmi les techniques existantes, la méthode des pas de temps futurs de Beck très bien adaptée à la résolution séquentielle a été choisie. Trois cas de configurations, de complexité croissante allant jusqu'à chercher toutes les pertes simultanément, sont étudiés et montrent la fiabilité de la méthode pour l'identification des pertes du moteur. Cela permet de remonter aux températures inaccessibles dans le moteur, via le LPTM. Dans chaque cas, l'influence des pas de temps futurs est étudiée.

Finalement, les résultats trouvés sont très satisfaisants et la procédure d'identification est très rapide à chaque itération, ce qui rend la technique « temps réel ». Le temps nécessaire pour chaque itération est de 10^{-3} s.

Chapitre 6

Cette thèse s'intéresse à la gestion thermique de moteurs électriques de fortes densités de puissance, appliqués à la motorisation électrique des avions hybrides. Elle s'inscrit dans le projet européen de Clean Sky2 appelé HASTECS, qui porte sur l'hybridation d'avions futurs à travers le développement d'outils électrothermiques et l'étude de différentes architectures hybrides avec des objectifs respectifs pour les années 2025 et 2035.

Etant donné les densités de puissance très élevées des moteurs électriques de propulsion, ces derniers dissipent de fortes densités de puissance qu'il faut évacuer efficacement. Ce travail concerne alors la conception de moteurs avec leurs systèmes de refroidissement. La gestion thermique comprend alors une étape de création du modèle du moteur pour simuler son comportement thermique et une étape de choix de solutions et techniques de refroidissement adaptées ainsi que leur intégration au modèle.

La thèse est composée de 5 chapitres comme suit :

Premièrement, le sujet et ses contours sont présentés afin de créer une base scientifique pour le travail et permettre de comprendre les problématiques à résoudre.

Ensuite, une recherche bibliographique a permis de construire un état de l'art sur le transfert de chaleur et les techniques de refroidissement, ainsi que d'évaluer les solutions prometteuses pour extraire la chaleur des moteurs.

La modélisation du moteur est présentée dans le troisième chapitre. Elle a permis d'obtenir des températures dans le moteur en fonction des conditions initiales et des conditions aux limites à partir de la simulation du modèle de base.

Les moteurs des deux objectifs d'avions hybrides sont maintenant modélisés et un design optimal pour chacun est déterminé après échange avec les spécialistes de moteurs électriques. Les cahiers des charges contraignants sont respectés en termes de densité de puissance.

Enfin, une méthode inverse a été développée pour l'identification des pertes dans le moteur et pour la supervision de températures inaccessibles à la mesure, surtout aux points chauds critiques du moteur.

BIBLIOGRAPHY

- [1] “Average temperature anomaly,” *Our World in Data*. <https://ourworldindata.org/grapher/temperature-anomaly> (accessed Oct. 24, 2019).
- [2] “Scientific Consensus: Earth’s Climate is Warming,” *Climate Change: Vital Signs of the Planet*. <https://climate.nasa.gov/scientific-consensus> (accessed Jul. 20, 2020).
- [3] “Global Warming,” Jun. 03, 2010. <https://earthobservatory.nasa.gov/features/GlobalWarming/page5.php> (accessed Jan. 22, 2020).
- [4] “Global Energy & CO₂ Status Report 2019 – Analysis,” *IEA*. <https://www.iea.org/reports/global-energy-and-co2-status-report-2019> (accessed Jan. 22, 2020).
- [5] “Environment,” *Airbus*. <https://www.airbus.com/company/sustainability/environment.html> (accessed Jul. 20, 2020).
- [6] “SUNSEEKER II,” *Solar Flight*. <https://www.solar-flight.com/sunseeker-ii/> (accessed Oct. 24, 2019).
- [7] “Taurus Electro – Pipistrel.” <https://www.pipistrel-aircraft.com/aircraft/electric-flight/taurus-electro/> (accessed Oct. 24, 2019).
- [8] Siemens, “Electric propulsion components with high power densities for aviation,” presented at the Transformative Vertical Flight Workshop, Mar. 08, 2015.
- [9] “Rolls-Royce unveils all-electric YASA powered plane targeting the record books | YASA Limited.” https://www.yasa.com/news/rolls-royce_accel_unveiling/ (accessed Dec. 30, 2019).
- [10] “magniX and AeroTEC Announce Successful First Flight of the World’s Largest All-Electric Aircraft,” *AeroTEC*, May 28, 2020. <https://www.aerotec.com/magnix-and-aerotec-announce-successful-first-flight-of-the-worlds-largest-all-electric-aircraft/> (accessed Jul. 19, 2020).
- [11] “ZUNUM Aero – JetBlue Technology Ventures.” <https://www.jetblueventures.com/portfolio/zunum-aero/> (accessed Oct. 24, 2019).
- [12] J. Welstead and J. L. Felder, “Conceptual Design of a Single-Aisle Turboelectric Commercial Transport with Fuselage Boundary Layer Ingestion,” presented at the 54th AIAA Aerospace Sciences Meeting, San Diego, California, USA, Jan. 2016, doi: 10.2514/6.2016-1027.
- [13] K. R. Antcliff and F. M. Capristan, “Conceptual Design of the Parallel Electric-Gas Architecture with Synergistic Utilization Scheme (PEGASUS) Concept,” in *18th AIAA/ISSMO Multidisciplinary Analysis and Optimization Conference*, American Institute of Aeronautics and Astronautics.
- [14] “Airbus Group Electrical Aircraft Program, The E-Fan Project | AIAA Propulsion and Energy Forum.” <https://arc.aiaa.org/doi/abs/10.2514/6.2016-4613> (accessed Oct. 23, 2019).
- [15] “E-Fan X,” *Airbus*. <https://www.airbus.com/innovation/future-technology/electric-flight/e-fan-x.html> (accessed Dec. 11, 2019).
- [16] S. Beganovic, “Comparison of Dynamic Characteristics of Electric and Conventional Road Vehicles,” Sep. 2012, pp. 149–155, Accessed: Feb. 04, 2020. [Online]. Available: https://www.academia.edu/3401454/Comparison_of_Dynamic_Characteristics_of_Electric_and_Conventional_Road_Vehicles.
- [17] Environmental Potentials, “Reducing Slip Losses in Motors,” 2009. http://ep2000.com/uploads/EP_WhitePaper-SlipLosses.pdf (accessed Jan. 03, 2020).

- [18] B. R. Teare, "Theory of hysteresis-motor torque," *Electrical Engineering*, vol. 59, no. 12, pp. 907–912, Dec. 1940, doi: 10.1109/EE.1940.6435257.
- [19] F. Un-Noor, S. Padmanaban, L. Mihet-Popa, M. N. Mollah, and E. Hossain, "A Comprehensive Study of Key Electric Vehicle (EV) Components, Technologies, Challenges, Impacts, and Future Direction of Development," *Energies*, vol. 10, no. 8, p. 1217, Aug. 2017, doi: 10.3390/en10081217.
- [20] J. de Santiago *et al.*, "Electrical Motor Drivelines in Commercial All-Electric Vehicles: A Review," *IEEE Transactions on Vehicular Technology*, vol. 61, no. 2, pp. 475–484, Feb. 2012, doi: 10.1109/TVT.2011.2177873.
- [21] A. M. Bazzi, "Electric machines and energy storage technologies in EVs and HEVs for over a century," in *2013 International Electric Machines Drives Conference*, May 2013, pp. 212–219, doi: 10.1109/IEMDC.2013.6556255.
- [22] A. M. Bazzi, Y. Liu, and D. S. Fay, "Electric Machines and Energy Storage: Over a Century of Technologies in Electric and Hybrid Electric Vehicles," *IEEE Electrification Magazine*, vol. 6, no. 3, pp. 49–53, Sep. 2018, doi: 10.1109/MELE.2018.2849900.
- [23] B. Sarlioglu, C. T. Morris, D. Han, and S. Li, "Benchmarking of electric and hybrid vehicle electric machines, power electronics, and batteries," in *2015 Intl Aegean Conference on Electrical Machines Power Electronics (ACEMP), 2015 Intl Conference on Optimization of Electrical Electronic Equipment (OPTIM) 2015 Intl Symposium on Advanced Electromechanical Motion Systems (ELECTROMOTION)*, Sep. 2015, pp. 519–526, doi: 10.1109/OPTIM.2015.7426993.
- [24] T. Burress and S. Campbell, "Benchmarking EV and HEV power electronics and electric machines," in *2013 IEEE Transportation Electrification Conference and Expo (ITEC)*, Jun. 2013, pp. 1–6, doi: 10.1109/ITEC.2013.6574498.
- [25] B. Bilgin *et al.*, "Making the Case for Electrified Transportation," *IEEE Transactions on Transportation Electrification*, vol. 1, no. 1, pp. 4–17, Jun. 2015, doi: 10.1109/TTE.2015.2437338.
- [26] N. Zabihi and R. Gouws, "A review on switched reluctance machines for electric vehicles," in *2016 IEEE 25th International Symposium on Industrial Electronics (ISIE)*, Jun. 2016, pp. 799–804, doi: 10.1109/ISIE.2016.7744992.
- [27] A. Cassidy, *English: Cutaway view of the electric motor which powers the Tesla Model S*. 2013.
- [28] R. Benlamine, F. Dubas, C. Espanet, S. A. Randi, and D. Lhotellier, "Design of an Axial-Flux Interior Permanent-Magnet Synchronous Motor for Automotive Application: Performance Comparison with Electric Motors Used in EVs and HEVs," in *2014 IEEE Vehicle Power and Propulsion Conference (VPPC)*, Oct. 2014, pp. 1–6, doi: 10.1109/VPPC.2014.7007043.
- [29] J. M. Miller, "Oak Ridge National Laboratory Annual Progress Report for the Power Electronics and Electric Motors Program," 2013. [Online]. Available: <https://info.ornl.gov/sites/publications/files/Pub46377.pdf>.
- [30] T. de Paula Machado Bazzo, J. F. Kölzer, R. Carlson, F. Wurtz, and L. Gerbaud, "Multiphysics Design Optimization of a Permanent Magnet Synchronous Generator," *IEEE Transactions on Industrial Electronics*, vol. 64, no. 12, pp. 9815–9823, Dec. 2017, doi: 10.1109/TIE.2017.2726983.
- [31] K. Farsane, P. Desevaux, and P. K. Panday, "Experimental study of the cooling of a closed type electric motor," *Applied Thermal Engineering*, vol. 20, no. 14, pp. 1321–1334, Oct. 2000, doi: 10.1016/S1359-4311(99)00094-0.
- [32] A. F. Mills, *Heat Transfer*. Englewood Cliffs, NJ: Prentice-Hall, 1999.
- [33] Incropera and De Witt, *Fundamentals of heat and mass transfer*. John Wiley Sons, 1985.

- [34] C. Cezário, M. Verardi, S. Borges, J. Silva, A. Antônio, and M. Oliveira, “Transient thermal analysis of an induction electric motor,” presented at the 18th International Congress of Mechanical Engineering, Ouro Preto, MG, Nov. 2005.
- [35] S. Nategh, A. Krings, O. Wallmark, and M. Leksell, “Evaluation of Impregnation Materials for Thermal Management of Liquid-Cooled Electric Machines,” *IEEE Transactions on Industrial Electronics*, vol. 61, no. 11, pp. 5956–5965, Nov. 2014, doi: 10.1109/TIE.2014.2308151.
- [36] S. Nategh, Z. Huang, A. Krings, O. Wallmark, and M. Leksell, “Thermal Modeling of Directly Cooled Electric Machines Using Lumped Parameter and Limited CFD Analysis,” *IEEE Transactions on Energy Conversion*, vol. 28, no. 4, pp. 979–990, Dec. 2013, doi: 10.1109/TEC.2013.2283089.
- [37] M. rabie Guéchi, “Etude numérique et expérimentale du refroidissement de moteurs de traction électriques,” 2014.
- [38] “SIMOTICS Motors,” [siemens.com Global Website](https://new.siemens.com/global/en/products/drives/electric-motors.html). <https://new.siemens.com/global/en/products/drives/electric-motors.html> (accessed May 05, 2020).
- [39] M. Popescu, D. Staton, A. Boglietti, A. Cavagnino, D. Hawkins, and J. Goss, “Modern heat extraction systems for electrical machines - A review,” in *2015 IEEE Workshop on Electrical Machines Design, Control and Diagnosis (WEMDCD)*, Mar. 2015, pp. 289–296, doi: 10.1109/WEMDCD.2015.7194542.
- [40] Y. Alhassoun, “Étude et mise en oeuvre de machines à aimantation induite fonctionnant à haute vitesse,” thesis, Toulouse, INPT, 2005.
- [41] C. Henaux, B. Nogarede, and D. Harribey, “A New Concept of Modular Permanent Magnet and Soft Magnetic Compound Motor Dedicated to Widespread Application,” *IEEE Transactions on Magnetics*, vol. 48, no. 6, pp. 2035–2043, Jun. 2012, doi: 10.1109/TMAG.2011.2181530.
- [42] J. D. Widmer, R. Martin, and M. Kimiabeigi, “Electric vehicle traction motors without rare earth magnets,” *Sustainable Materials and Technologies*, vol. 3, pp. 7–13, Apr. 2015, doi: 10.1016/j.susmat.2015.02.001.
- [43] A. Fasquelle, “Contribution à la modélisation multi-physique : électro-vibro-acoustique et aérothermique de machines de traction,” Nov. 2007, Accessed: Oct. 16, 2019. [Online]. Available: <https://tel.archives-ouvertes.fr/tel-00196574>.
- [44] F. Kreith, R. M. Manglik, and M. S. Bohn, *Principles of heat transfer*, 7th edition, Cengage Learning, Inc. 2011.
- [45] D. A. Staton and A. Cavagnino, “Convection Heat Transfer and Flow Calculations Suitable for Electric Machines Thermal Models,” *IEEE Transactions on Industrial Electronics*, vol. 55, no. 10, pp. 3509–3516, Oct. 2008, doi: 10.1109/TIE.2008.922604.
- [46] D. A. Howey, A. S. Holmes, and K. R. Pullen, “Measurement and CFD Prediction of Heat Transfer in Air-Cooled Disc-Type Electrical Machines,” *IEEE Transactions on Industry Applications*, vol. 47, no. 4, pp. 1716–1723, Jul. 2011, doi: 10.1109/TIA.2011.2156371.
- [47] Y. Bertin, “Refroidissement des machines électriques tournantes,” *Techniques de l'ingénieur Généralités sur les machines électriques tournantes*, vol. base documentaire : TIB250DUO., no. ref. article : d3460, 1999, [Online]. Available: <https://www.techniques-ingenieur.fr/base-documentaire/energies-th4/generalites-sur-les-machines-electriques-tournantes-42250210/refroidissement-des-machines-electriques-tournantes-d3460/>.
- [48] M. Nili-Ahmabadi and H. Karrabi, “Heat transfer and flow region characteristics study in a non-annular channel between rotor and stator,” *Thermal Science*, vol. 16, no. 2, pp. 593–603, 2012.
- [49] M. Fénot, Y. Bertin, E. Dorignac, and G. Lalizel, “A review of heat transfer between concentric rotating cylinders with or without axial flow,” *International Journal of Thermal*

- Sciences*, vol. 50, no. 7, pp. 1138–1155, Jul. 2011, doi: 10.1016/j.ijthermalsci.2011.02.013.
- [50] B. Assaad, “Contribution à la prise en compte des aspects thermiques des machines électriques dans un environnement mécatronique,” Ph.D. Thesis, UTC, 2015.
- [51] G. I. Taylor, “Stability of a viscous liquid contained between two rotating cylinders,” *Philosophical Transactions of the Royal Society of London. Series A, Containing Papers of a Mathematical or Physical Character*, vol. 223, no. 605–615, pp. 289–343, Jan. 1923, doi: 10.1098/rsta.1923.0008.
- [52] D. Coles, “Transition in circular Couette flow,” *Journal of Fluid Mechanics*, vol. 21, no. 3, pp. 385–425, Mar. 1965, doi: 10.1017/S0022112065000241.
- [53] C. Gazley, “Heat-Transfer Characteristics of the Rotational and Axial Flow Between Concentric Rotating Cylinders,” *Transactions ASME*, vol. 80, pp. 79–90, 1958.
- [54] F. Tachibana and S. Fukui, “Convective Heat Transfer of the Rotational and Axial Flow between Two Concentric Cylinders,” *Bulletin of JSME*, vol. 7, no. 26, pp. 385–391, 1964, doi: 10.1299/jsme1958.7.385.
- [55] K. M. Becker and J. Kaye, “The Influence of a Radial Temperature Gradient on the Instability of Fluid Flow in an Annulus With an Inner Rotating Cylinder,” *J. Heat Transfer*, vol. 84, no. 2, pp. 106–110, May 1962, doi: 10.1115/1.3684306.
- [56] I. S. Bjorklund and W. M. Kays, “Heat Transfer Between Concentric Rotating Cylinders,” *J. Heat Transfer*, vol. 81, no. 3, pp. 175–183, Aug. 1959, doi: 10.1115/1.4008173.
- [57] B. T. Nijaguna and B. Mathiprakasam, “HEAT TRANSFER IN AN ANNULUS WITH SPIRAL FLOWS,” presented at the International Heat Transfer Conference 7, 1982, doi: 10.1615/IHTC7.1540.
- [58] M. Bouafia, Y. Bertin, J. B. Saulnier, and P. Ropert, “Analyse expérimentale des transferts de chaleur en espace annulaire étroit et rainuré avec cylindre intérieur tournant,” *International Journal of Heat and Mass Transfer*, vol. 41, no. 10, pp. 1279–1291, May 1998, doi: 10.1016/S0017-9310(97)00317-7.
- [59] M. Bouafia, A. Ziouchi, Y. Bertin, and J.-B. Saulnier, “Étude expérimentale et numérique des transferts de chaleur en espace annulaire sans débit axial et avec cylindre intérieur tournant,” *International Journal of Thermal Sciences*, vol. 38, no. 7, pp. 547–559, Jul. 1999, doi: 10.1016/S0035-3159(99)80035-X.
- [60] F. Tachibana, S. Fukui, and H. Mitsumura, “Heat Transfer in an Annulus with an Inner Rotating Cylinder,” *Bulletin of JSME*, vol. 3, no. 9, pp. 119–123, 1960, doi: 10.1299/jsme1958.3.119.
- [61] G. I. Taylor, “Statistical Theory of Turbulence,” *Proceedings of the Royal Society of London. Series A, Mathematical and Physical Sciences*, vol. 151, no. 873, pp. 421–444, 1935.
- [62] S. Harmand, J. Pellé, S. Poncet, and I. V. Shevchuk, “Review of fluid flow and convective heat transfer within rotating disk cavities with impinging jet,” *International Journal of Thermal Sciences*, vol. 67, pp. 1–30, May 2013, doi: 10.1016/j.ijthermalsci.2012.11.009.
- [63] I. V. Shevchuk, “Convective heat and mass transfer in rotating disk systems,” *Springer Verlag*, Berlin, Heidelberg, pp. 1–239, 2009.
- [64] Cz. O. Popiel and L. Bogusławski, “Local heat-transfer coefficients on the rotating disk in still air,” *International Journal of Heat and Mass Transfer*, vol. 18, no. 1, pp. 167–170, Jan. 1975, doi: 10.1016/0017-9310(75)90020-4.
- [65] C. J. Elkins and J. K. Eaton, “Heat transfer in the rotating disk boundary layer,” Stanford University, Department of Mechanical Engineering, Thermosciences Division Report TSD-103, 1997.
- [66] G. Cardone, T. Astarita, and G. M. Carlomagno, “Infrared heat transfer measurements on rotating disk,” *Optical Diagnostics in Engineering 1*, pp. 1–7, 1996.

- [67] F. Kreith, "Convection Heat Transfer in Rotating Systems," in *Advances in Heat Transfer*, vol. 5, T. F. Irvine and J. P. Hartnett, Eds. Elsevier, 1969, pp. 129–251.
- [68] J. W. Daily and R. E. Nece, "Chamber Dimension Effects on Induced Flow and Frictional Resistance of Enclosed Rotating Disks," *J. Basic Eng.*, vol. 82, no. 1, pp. 217–230, Mar. 1960, doi: 10.1115/1.3662532.
- [69] C. Vasilescu, "Modélisation du transfert de chaleur au sein des machines électriques tournantes: dimensionnement et optimisation de leur système de refroidissement," Université Paris 6, 2003.
- [70] E. Schubert, "Heat transfer coefficients at end winding and bearing covers of enclosed asynchronous machines," *Elektric*, vol. 22, pp. 160–162, 1968.
- [71] D. Staton, A. Boglietti, and A. Cavagnino, "Solving the More Difficult Aspects of Electric Motor Thermal Analysis in Small and Medium Size Industrial Induction Motors," *IEEE Transactions on Energy Conversion*, vol. 20, no. 3, pp. 620–628, Sep. 2005, doi: 10.1109/TEC.2005.847979.
- [72] A. Di Gerlando and I. Vistoli, "Improved thermal modelling of induction motors for design purposes," in *1993 Sixth International Conference on Electrical Machines and Drives (Conf. Publ. No. 376)*, Sep. 1993, pp. 381–386.
- [73] O. Oslejsek, "The cooling of the endwindings of small enclosed electric machines," *Elektrotech*, vol. 61, no. 10, 1972.
- [74] C. Micallef, "End winding cooling in electric machines," 2006. <http://eprints.nottingham.ac.uk/10260/> (accessed Jun. 05, 2018).
- [75] S. J. Pickering, D. Lampard, N. Hay, and T. F. Roylance, "Heat transfer from the stator end-windings of a low voltage concentric-wound induction motor," in *1995 Seventh International Conference on Electrical Machines and Drives (Conf. Publ. No. 412)*, Sep. 1995, pp. 477–481, doi: 10.1049/cp:19950918.
- [76] S. J. Pickering, D. Lampard, N. Hay, and T. F. Roylance, "Heat transfer in a high voltage, through-ventilated 4-pole induction motor," in *1997 Eighth International Conference on Electrical Machines and Drives (Conf. Publ. No. 444)*, Sep. 1997, pp. 11–15, doi: 10.1049/cp:19971028.
- [77] J. Mugglestone, S. J. Pickering, and D. Lampard, "Prediction of the heat transfer from the end winding of a TEFC strip-wound induction motor," in *IEEE International Electric Machines and Drives Conference. IEMDC'99. Proceedings (Cat. No.99EX272)*, May 1999, pp. 484–486, doi: 10.1109/IEMDC.1999.769153.
- [78] J. Mufflestone, S. J. Pickering, and D. Lampard, "Effect of geometric changes on the flow and heat transfer in the end region of a TEFC induction motor," in *1999. Ninth International Conference on Electrical Machines and Drives (Conf. Publ. No. 468)*, Sep. 1999, pp. 40–44, doi: 10.1049/cp:19990987.
- [79] S. J. Pickering, D. Lampard, N. Hay, and T. F. Roylance, "Heat transfer in a through-ventilated induction motor," *IEE Proceedings - Electric Power Applications*, vol. 145, no. 5, pp. 429–433, Sep. 1998, doi: 10.1049/ip-epa:19982169.
- [80] B. Zhang, R. Qu, W. Xu, J. Wang, and Y. Chen, "Thermal model of totally enclosed water-cooled permanent magnet synchronous machines for electric vehicle applications," in *2014 International Conference on Electrical Machines (ICEM)*, Sep. 2014, pp. 2205–2211, doi: 10.1109/ICELMACH.2014.6960490.
- [81] J. R. Hendershot and T. J. E. Miller, *Design of Brushless Permanent-magnet Motors*. Magna Physics Pub., 1994.
- [82] Y. Bertin, "Refroidissement des machines tournantes. Études paramétriques," *Techniques de l'ingénieur Généralités sur les machines électriques tournantes*, vol. base documentaire : TIB250DUO., no. ref. article : d3462, 2006, [Online]. Available: <https://www.techniques-ingeneur.fr/base-documentaire/energies-th4/generalites-sur-les->

- machines-electriques-tournantes-42250210/refroidissement-des-machines-tournantes-
etudes-parametriques-d3462/.
- [83] Y. Gai *et al.*, “Cooling of Automotive Traction Motors: Schemes, Examples, and Computation Methods,” *IEEE Transactions on Industrial Electronics*, vol. 66, no. 3, pp. 1681–1692, Mar. 2019, doi: 10.1109/TIE.2018.2835397.
 - [84] M. Grabowski, K. Urbaniec, J. Wernik, and K. J. Wołosz, “Numerical simulation and experimental verification of heat transfer from a finned housing of an electric motor,” *Energy Conversion and Management*, vol. 125, pp. 91–96, Oct. 2016, doi: 10.1016/j.enconman.2016.05.038.
 - [85] S. Ulbrich, J. Kopte, and J. Proske, “Cooling Fin Optimization on a TEFC Electrical Machine Housing Using a 2-D Conjugate Heat Transfer Model,” *IEEE Transactions on Industrial Electronics*, vol. 65, no. 2, pp. 1711–1718, Feb. 2018, doi: 10.1109/TIE.2017.2748051.
 - [86] H. Nemati, M. A. Moghimi, P. Sapin, and C. N. Markides, “Shape optimisation of air-cooled finned-tube heat exchangers,” *International Journal of Thermal Sciences*, vol. 150, p. 106233, Apr. 2020, doi: 10.1016/j.ijthermalsci.2019.106233.
 - [87] F. Heiles, “Design and arrangement of cooling fins,” *Elektrotechnik und Maschinenbau*, vol. 69, no. 14, 1952.
 - [88] A. Giret, “Transferts thermiques convectifs dans le cadre de machines tournantes,” thesis, Chasseneuil-du-Poitou, Ecole nationale supérieure de mécanique et d'aéronautique, 2009.
 - [89] M. M. Baggu, H. L. Hess, and K. Rink, “Thermal modeling of ‘direct lamination cooling (DLC)’ induction motor for hybrid electric vehicle applications,” in *2005 IEEE Vehicle Power and Propulsion Conference*, Sep. 2005, pp. 468–472, doi: 10.1109/VPPC.2005.1554564.
 - [90] A. Nollau and D. Gerling, “A new cooling approach for traction motors in hybrid drives,” in *2013 International Electric Machines Drives Conference*, May 2013, pp. 456–461, doi: 10.1109/IEMDC.2013.6556136.
 - [91] Z. Huang, S. Nategh, V. Lassila, M. Alaküla, and J. Yuan, “Direct oil cooling of traction motors in hybrid drives,” in *2012 IEEE International Electric Vehicle Conference*, Mar. 2012, pp. 1–8, doi: 10.1109/IEVC.2012.6183163.
 - [92] T. A. Burress *et al.*, “Evaluation of the 2008 Lexus LS 600H Hybrid Synergy Drive System,” 2009, doi: 10.2172/947393.
 - [93] P. H. Mellor, D. Roberts, and D. R. Turner, “Lumped parameter thermal model for electrical machines of TEFC design,” *IEE Proceedings B Electric Power Applications*, vol. 138, no. 5, p. 205, 1991, doi: 10.1049/ip-b.1991.0025.
 - [94] J. HUETZ and J.-P. PETIT, “Notions de transfert thermique par convection,” *Ref: TIP100WEB - “Plastiques et composites,”* Aug. 10, 1990. <https://www.techniques-ingenieur.fr/base-documentaire/archives-th12/archives-plastiques-et-composites-tiaam/archive-1/notions-de-transfert-thermique-par-convection-a1540a/> (accessed May 11, 2020).
 - [95] E. N. Sieder and G. E. Tate, “Heat Transfer and Pressure Drop of Liquids in Tubes,” *Ind. Eng. Chem.*, vol. 28, no. 12, pp. 1429–1435, Dec. 1936, doi: 10.1021/ie50324a027.
 - [96] W. H. McAdams and National Research Council. Committee on Heat Transmission, *Heat Transmission*. London: McGraw-Hill, 1942.
 - [97] A.-M. Ebrahim Momin, J. S. Saini, and S. C. Solanki, “Heat transfer and friction in solar air heater duct with V-shaped rib roughness on absorber plate,” *International Journal of Heat and Mass Transfer*, vol. 45, no. 16, pp. 3383–3396, Jul. 2002, doi: 10.1016/S0017-9310(02)00046-7.
 - [98] A. Chaube, P. K. Sahoo, and S. C. Solanki, “Analysis of heat transfer augmentation and flow characteristics due to rib roughness over absorber plate of a solar air heater,”

- Renewable Energy*, vol. 31, no. 3, pp. 317–331, Mar. 2006, doi: 10.1016/j.renene.2005.01.012.
- [99] A. R. Jaurker, J. S. Saini, and B. K. Gandhi, “Heat transfer and friction characteristics of rectangular solar air heater duct using rib-grooved artificial roughness,” *Solar Energy*, vol. 80, no. 8, pp. 895–907, Aug. 2006, doi: 10.1016/j.solener.2005.08.006.
- [100] J. L. Bhagoria, J. S. Saini, and S. C. Solanki, “Heat transfer coefficient and friction factor correlations for rectangular solar air heater duct having transverse wedge shaped rib roughness on the absorber plate,” *Renewable Energy*, vol. 25, no. 3, pp. 341–369, Mar. 2002, doi: 10.1016/S0960-1481(01)00057-X.
- [101] R. Karwa, S. C. Solanki, and J. S. Saini, “Heat transfer coefficient and friction factor correlations for the transitional flow regime in rib-roughened rectangular ducts,” *International Journal of Heat and Mass Transfer*, vol. 42, no. 9, pp. 1597–1615, May 1999, doi: 10.1016/S0017-9310(98)00252-X.
- [102] G. Tanda, “Heat transfer in rectangular channels with transverse and V-shaped broken ribs,” *International Journal of Heat and Mass Transfer*, vol. 47, no. 2, pp. 229–243, Jan. 2004, doi: 10.1016/S0017-9310(03)00414-9.
- [103] X. Chen, H. Ye, X. Fan, T. Ren, and G. Zhang, “A review of small heat pipes for electronics,” *Applied Thermal Engineering*, vol. 96, pp. 1–17, Mar. 2016, doi: 10.1016/j.applthermaleng.2015.11.048.
- [104] T. Hassett and M. Hodowanec, “Electric motor with heat pipes,” US7569955B2, Aug. 04, 2009.
- [105] R.-J. Owng, C.-W. Ruan, Y.-T. Wei, and M.-C. Liao, “Electric motor having heat pipes,” US8368265B2, Feb. 05, 2013.
- [106] S. Ruby and J.-P. L. Lagadec, “Cooling of an electric motor via heat pipes,” US9561716B2, Feb. 07, 2017.
- [107] L. Fedoseyev and E. M. P. JR, “Rotor Assembly with Heat Pipe Cooling System,” US20140368064A1, Dec. 18, 2014.
- [108] N. Putra and B. Ariantara, “Electric motor thermal management system using L-shaped flat heat pipes,” *Applied Thermal Engineering*, vol. 126, pp. 1156–1163, Nov. 2017, doi: 10.1016/j.applthermaleng.2017.01.090.
- [109] A. Faghri, “Review and Advances in Heat Pipe Science and Technology,” *J. Heat Transfer*, vol. 134, no. 12, Dec. 2012, doi: 10.1115/1.4007407.
- [110] D. Bugby, C. Stouffer, J. Garzon, M. Beres, and A. Gilchrist, “Advanced Devices for Cryogenic Thermal Management,” *AIP Conference Proceedings*, vol. 823, no. 1, pp. 1790–1798, Apr. 2006, doi: 10.1063/1.2202608.
- [111] Yu. F. Maydanik, “Loop heat pipes,” *Applied Thermal Engineering*, vol. 25, no. 5, pp. 635–657, Apr. 2005, doi: 10.1016/j.applthermaleng.2004.07.010.
- [112] F. Mena, W. Supper, and C. Puillet, “Design and Development of Loop Heat Pipes,” SAE International, Warrendale, PA, SAE Technical Paper 2000-01-2315, Jul. 2000. doi: 10.4271/2000-01-2315.
- [113] A. A. M. Delil, V. Baturkin, G. Gorbenko, P. Gakal, and V. Ruzaykin, “Modeling of a Miniature Loop Heat Pipe with a Flat Evaporator,” *SAE Transactions*, vol. 111, pp. 315–322, 2002.
- [114] T. Kaya and J. Ku, “Experimental Investigation of Performance Characteristics of Small Loop Heat Pipes,” in *41st Aerospace Sciences Meeting and Exhibit*, American Institute of Aeronautics and Astronautics.
- [115] H. Jouhara, A. Chauhan, T. Nannou, S. Almahmoud, B. Delpech, and L. C. Wrobel, “Heat pipe based systems - Advances and applications,” *Energy*, vol. 128, pp. 729–754, Jun. 2017, doi: 10.1016/j.energy.2017.04.028.

- [116] S. Nategh, D. Barber, A. Boglietti, D. Lindberg, O. Aglen, and R. Brammer, “A Study on Thermal Effects of Different Potting Strategies in Traction Motors,” in *2018 IEEE International Conference on Electrical Systems for Aircraft, Railway, Ship Propulsion and Road Vehicles & International Transportation Electrification Conference (ESARS-ITEC)*, Nottingham, Nov. 2018, pp. 1–6, doi: 10.1109/ESARS-ITEC.2018.8607600.
- [117] J. Pyrhönen, P. Lindh, M. Polikarpova, E. Kurvinen, and V. Naumanen, “Heat-transfer improvements in an axial-flux permanent-magnet synchronous machine,” *Applied Thermal Engineering*, vol. 76, pp. 245–251, Feb. 2015, doi: 10.1016/j.applthermaleng.2014.11.003.
- [118] J. Bellettre, V. Sartre, F. Biais, and A. Lallemand, “Transient state study of electric motor heating and phase change solid-liquid cooling,” *Applied Thermal Engineering*, vol. 17, no. 1, pp. 17–31, Jan. 1997, doi: 10.1016/1359-4311(96)00026-9.
- [119] H. Martin, “Heat and Mass Transfer between Impinging Gas Jets and Solid Surfaces,” in *Advances in Heat Transfer*, vol. 13, J. P. Hartnett and T. F. Irvine, Eds. Elsevier, 1977, pp. 1–60.
- [120] S. kakaç, “Introduction to ASI on Cooling of Electronic Systems,” in *Cooling of Electronic Systems*, S. Kakaç, H. Yüncü, and K. Hijikata, Eds. Dordrecht: Springer Netherlands, 1994, pp. 1–15.
- [121] J. Pellé and S. Harmand, “Heat transfer study in a rotor–stator system air-gap with an axial inflow,” *Applied Thermal Engineering*, vol. 29, no. 8, pp. 1532–1543, Jun. 2009, doi: 10.1016/j.applthermaleng.2008.07.014.
- [122] M. Fénot, J.-J. Vullierme, and E. Dorignac, “A heat transfer measurement of jet impingement with high injection temperature,” *Comptes Rendus Mécanique*, vol. 333, no. 10, pp. 778–782, Oct. 2005, doi: 10.1016/j.crme.2005.08.002.
- [123] J. P. Yu, E. M. Sparrow, and E. R. G. Eckert, “Experiments on a shrouded, parallel disk system with rotation and coolant throughflow,” *International Journal of Heat and Mass Transfer*, vol. 16, no. 2, pp. 311–314, Feb. 1973, doi: 10.1016/0017-9310(73)90060-4.
- [124] C. M. Haynes and J. M. Owen, “Heat Transfer From a Shrouded Disk System With a Radial Outflow of Coolant,” *J. Eng. Power*, vol. 97, no. 1, pp. 28–35, Jan. 1975, doi: 10.1115/1.3445907.
- [125] J. C. Lallave, M. M. Rahman, and A. Kumar, “Numerical analysis of heat transfer on a rotating disk surface under confined liquid jet impingement,” *International Journal of Heat and Fluid Flow*, vol. 28, no. 4, pp. 720–734, Aug. 2007, doi: 10.1016/j.ijheatfluidflow.2006.09.005.
- [126] A. Tüysüz, F. Meyer, M. Steichen, C. Zwyssig, and J. W. Kolar, “Advanced Cooling Methods for High-Speed Electrical Machines,” *IEEE Transactions on Industry Applications*, vol. 53, no. 3, pp. 2077–2087, May 2017, doi: 10.1109/TIA.2017.2672921.
- [127] T. Woolmer, “Wheel-hub motor cooling,” US20130187492A1, Jul. 25, 2013.
- [128] H. Fujita, A. Itoh, and T. Urano, “Newly Developed Motor Cooling Method Using Refrigerant,” *World Electric Vehicle Journal*, vol. 10, no. 2, p. 38, Jun. 2019, doi: 10.3390/wevj10020038.
- [129] P. Zhou, N. R. Kalayjian, G. D. Cutler, and P. K. Augenbergs, “Liquid cooled rotor assembly,” US7489057B2, Feb. 10, 2009.
- [130] T. Miyamoto and K. NAGATA, “Rotating electrical machine cooling system,” US8912691B2, Dec. 16, 2014.
- [131] T. Miyamoto, S. Matsusaka, and K. Kato, “Cooling structure of rotary electric machine,” US9729027B2, Aug. 08, 2017.
- [132] S. H. Swales, P. F. Turnbull, B. Schulze, F. R. Poskie, W. J. Omell, and W. C. Deneszcuk, “Oil cooled motor/generator for an automotive powertrain,” US8169110B2, May 01, 2012.

- [133] B. Assaad, K. Mikati, T. V. Tran, and E. Negre, “Experimental Study of Oil Cooled Induction Motor for Hybrid and Electric Vehicles,” in *2018 XIII International Conference on Electrical Machines (ICEM)*, Sep. 2018, pp. 1195–1200, doi: 10.1109/ICELMACH.2018.8507058.
- [134] K. Oliphant, B. W. Webb, and M. Q. McQuay, “An experimental comparison of liquid jet array and spray impingement cooling in the non-boiling regime,” *Experimental Thermal and Fluid Science*, vol. 18, no. 1, pp. 1–10, Sep. 1998, doi: 10.1016/S0894-1777(98)10013-4.
- [135] N. Karwa, S. R. Kale, and P. M. V. Subbarao, “Experimental study of non-boiling heat transfer from a horizontal surface by water sprays,” *Experimental Thermal and Fluid Science*, vol. 32, no. 2, pp. 571–579, Nov. 2007, doi: 10.1016/j.expthermflusci.2007.06.007.
- [136] T. Davin, J. Pellé, S. Harmand, and R. Yu, “Experimental study of oil cooling systems for electric motors,” *Applied Thermal Engineering*, vol. 75, pp. 1–13, Jan. 2015, doi: 10.1016/j.applthermaleng.2014.10.060.
- [137] T. Davin, J. Pellé, S. Harmand, and R. Yu, “Motor Cooling Modeling: An Inverse Method for the Identification of Convection Coefficients,” *Journal of Thermal Science and Engineering Applications*, vol. 9, no. 4, pp. 041009–041009–13, Apr. 2017, doi: 10.1115/1.4036303.
- [138] K. Bennion, E. Cousineau, X. Feng, C. King, and G. Moreno, “Electric Motor Thermal Management R&D,” presented at the IEEE Power & Energy Society General Meeting, Denver, CO, USA, Jul. 2015, [Online]. Available: <https://www.ieee-pes.org/presentations/gm2015/PESGM2015P-002837.pdf>.
- [139] G. R. G. Guemo, “Modélisation et caractérisation thermique de machines électriques synchrones à aimants permanents,” phdthesis, INSA de Lyon, 2014.
- [140] T. Kikuchi, S. Kitada, and Y. Kaneko, “Motor/generator with equalized coolant distribution,” US6515384B1, Feb. 04, 2003.
- [141] K. Chen, A. Masrur, S. Ahmed, and V. K. Garg, “Jet impingement cooling of electric motor end-windings,” US6639334B2, Oct. 28, 2003.
- [142] S. J. Slayzak, R. Viskanta, and F. P. Incropera, “Effects of interaction between adjacent free surface planar jets on local heat transfer from the impingement surface,” *International Journal of Heat and Mass Transfer*, vol. 37, no. 2, pp. 269–282, Jan. 1994, doi: 10.1016/0017-9310(94)90098-1.
- [143] X. C. Lee, C. F. Ma, Q. Zheng, Y. Zhuang, and Y. Q. Tian, “Numerical study of recovery effect and impingement heat transfer with submerged circular jets of large Prandtl number liquid,” *International Journal of Heat and Mass Transfer*, vol. 40, no. 11, pp. 2647–2653, Jul. 1997, doi: 10.1016/S0017-9310(96)00263-3.
- [144] C. F. Ma, Q. Zheng, S. C. Lee, and T. Gomi, “Impingement heat transfer and recovery effect with submerged jets of large Prandtl number liquid—I. Unconfined circular jets,” *International Journal of Heat and Mass Transfer*, vol. 40, no. 6, pp. 1481–1490, Apr. 1997, doi: 10.1016/S0017-9310(96)00069-5.
- [145] C. F. Ma, Q. Zheng, and S. Y. Ko, “Local heat transfer and recovery factor with impinging free-surface circular jets of transformer oil,” *International Journal of Heat and Mass Transfer*, vol. 40, no. 18, pp. 4295–4308, Nov. 1997, doi: 10.1016/S0017-9310(97)00054-9.
- [146] D. H. Wolf, F. P. Incropera, and R. Viskanta, “Jet Impingement Boiling,” in *Advances in Heat Transfer*, vol. 23, J. P. Hartnett and T. F. Irvine, Eds. Elsevier, 1993, pp. 1–132.
- [147] D. E. Metzger, K. N. Cummings, and W. A. Ruby, “Effects of Prandtl Number on Heat Transfer Characteristics of impinging Liquid Jets,” presented at the International Heat Transfer Conference 5, 1974, doi: 10.1615/IHTC5.1680.

- [148] J. Kim, "Spray cooling heat transfer: The state of the art," *International Journal of Heat and Fluid Flow*, vol. 28, no. 4, pp. 753–767, Aug. 2007, doi: 10.1016/j.ijheatfluidflow.2006.09.003.
- [149] K. A. Estes and I. Mudawar, "Comparison of Two-Phase Electronic Cooling Using Free Jets and Sprays," *J. Electron. Packag.*, vol. 117, no. 4, pp. 323–332, Dec. 1995, doi: 10.1115/1.2792112.
- [150] I. Mudawar and K. A. Estes, "Optimizing and Predicting CHF in Spray Cooling of a Square Surface," *J. Heat Transfer*, vol. 118, no. 3, pp. 672–679, Aug. 1996, doi: 10.1115/1.2822685.
- [151] M. Visaria and I. Mudawar, "Theoretical and experimental study of the effects of spray inclination on two-phase spray cooling and critical heat flux," *International Journal of Heat and Mass Transfer*, vol. 51, no. 9, pp. 2398–2410, May 2008, doi: 10.1016/j.ijheatmasstransfer.2007.08.010.
- [152] I. Mudawar, D. Bharathan, K. Kelly, and S. Narumanchi, "Two-Phase Spray Cooling of Hybrid Vehicle Electronics," *IEEE Transactions on Components and Packaging Technologies*, vol. 32, no. 2, pp. 501–512, Jun. 2009, doi: 10.1109/TCAPT.2008.2006907.
- [153] I. Mudawar and W. S. Valentine, "Determination of the local quench curve for spray-cooled metallic surfaces," *J. Heat Treating*, vol. 7, no. 2, pp. 107–121, Sep. 1989, doi: 10.1007/BF02833195.
- [154] Y. Wang, M. Liu, D. Liu, K. Xu, and Y. Chen, "Experimental study on the effects of spray inclination on water spray cooling performance in non-boiling regime," *Experimental Thermal and Fluid Science*, vol. 34, no. 7, pp. 933–942, Oct. 2010, doi: 10.1016/j.expthermflusci.2010.02.010.
- [155] Y. Wang, M. Liu, D. Liu, and K. Xu, "Heat Flux Correlation for Spray Cooling in the Nonboiling Regime," *Heat Transfer Engineering*, vol. 32, no. 11–12, pp. 1075–1081, Oct. 2011, doi: 10.1080/01457632.2011.556505.
- [156] M. Liu, Y. Wang, D. Liu, K. Xu, and Y. Chen, "Experimental study of the effects of structured surface geometry on water spray cooling performance in non-boiling regime," *Front. Energy*, vol. 5, no. 1, pp. 75–82, Mar. 2011, doi: 10.1007/s11708-010-0014-0.
- [157] J. R. Rybicki and I. Mudawar, "Single-phase and two-phase cooling characteristics of upward-facing and downward-facing sprays," *International Journal of Heat and Mass Transfer*, vol. 49, no. 1, pp. 5–16, Jan. 2006, doi: 10.1016/j.ijheatmasstransfer.2005.07.040.
- [158] D. H. Lim and S. C. Kim, "Thermal performance of oil spray cooling system for in-wheel motor in electric vehicles," *Applied Thermal Engineering*, vol. 63, no. 2, pp. 577–587, Feb. 2014, doi: 10.1016/j.applthermaleng.2013.11.057.
- [159] A. Boglietti, A. Cavagnino, D. Staton, M. Shanel, M. Mueller, and C. Mejuto, "Evolution and Modern Approaches for Thermal Analysis of Electrical Machines," *IEEE Transactions on Industrial Electronics*, vol. 56, no. 3, pp. 871–882, Mar. 2009, doi: 10.1109/TIE.2008.2011622.
- [160] Y. Bertin, "Analyse des transferts de chaleur dans un moteur électrique asynchrone : développement d'un environnement CAO et modélisations thermoédrauliques," thesis, Poitiers, 1987.
- [161] A. Boglietti, A. Cavagnino, M. Parvis, and A. Vallan, "Evaluation of radiation thermal resistances in industrial motors," *IEEE Transactions on Industry Applications*, vol. 42, no. 3, pp. 688–693, May 2006, doi: 10.1109/TIA.2006.873655.
- [162] G. Bertotti, "Physical interpretation of eddy current losses in ferromagnetic materials. I. Theoretical considerations," *Journal of Applied Physics*, vol. 57, no. 6, pp. 2110–2117, Mar. 1985, doi: 10.1063/1.334404.

- [163] J. Saari, *Thermal analysis of high-speed induction machines*. Helsinki University of Technology, 1998.
- [164] J. E. Vrancik, *Prediction of windage power loss in alternators*. Washington, DC: National Aeronautics and Space Administration, 1968.
- [165] G. W. Milton, “Concerning bounds on the transport and mechanical properties of multicomponent composite materials,” *Appl. Phys. A*, vol. 26, no. 2, pp. 125–130, Oct. 1981, doi: 10.1007/BF00616659.
- [166] K. Mori *et al.*, “Thermal transport and magnetic properties of $\text{GdBa}_2\text{Cu}_3\text{O}_7-\text{y}$ superconductor,” *Physica C: Superconductivity*, vol. 153–155, pp. 1515–1516, Jun. 1988, doi: 10.1016/0921-4534(88)90398-X.
- [167] J. Lutun, “Modélisation thermique des alternateurs automobiles,” Jan. 2012, Accessed: Oct. 16, 2019. [Online]. Available: <https://tel.archives-ouvertes.fr/tel-00742950>.
- [168] General Electric, *Heat transfer and fluid flow data book*. 1981.
- [169] W. M. Rohsenow, J. P. Hartnett, and E. N. Ganic, “Handbook of heat transfer fundamentals (2nd edition),” Jan. 1985, Accessed: Oct. 15, 2019. [Online]. Available: <https://www.osti.gov/biblio/5892601>.
- [170] B. Renard, “Etude expérimentale et modélisation du comportement thermique d’une machine électrique multi-fonctions : application à un alterno-démarreur intégré,” Poitiers, 2003.
- [171] A. Zeaiter and M. Fénöt, “Thermal Sensitivity Analysis of a High Power Density Electric Motor for Aeronautical Application,” in *2018 IEEE International Conference on Electrical Systems for Aircraft, Railway, Ship Propulsion and Road Vehicles International Transportation Electrification Conference (ESARS-ITEC)*, Nov. 2018, pp. 1–6, doi: 10.1109/ESARS-ITEC.2018.8607393.
- [172] A. Zeaiter, M. Fénöt, and D. Saury, “Numerical Approach to Determining Windings’ Thermal Conductivity,” in *2018 XIII International Conference on Electrical Machines (ICEM)*, Alexandroupoli, Sep. 2018, pp. 1291–1296, doi: 10.1109/ICELMACH.2018.8506692.
- [173] S. Thieblin, “Analyse et modélisation du comportement thermique d’un moteur électrique soumis à des régimes de charge et de vitesse variables - application au moteur de traction d’un véhicule électrique,” Ph. D. Thesis, Université de Poitiers, 1997.
- [174] J. Lindström, “Thermal Model of a Permanent-Magnet Motor for a Hybrid Electric Vehicle,” Department of Electric Power Engineering Chalmers University of Technology, Göteborg, Sweden, 1999.
- [175] K. Bennion and J. Cousineau, “Sensitivity analysis of traction drive motor cooling,” in *2012 IEEE Transportation Electrification Conference and Expo (ITEC)*, Jun. 2012, pp. 1–6, doi: 10.1109/ITEC.2012.6243512.
- [176] S. Touhami, A. Zeaiter, M. Fénöt, Y. Lefèvre, J.-F. Libre, and E. Videcoq, “Electro-thermal Models and Design Approach for High Specific Power Electric Motor for Hybrid Aircraft,” presented at the Aerospace Europe Conference, Bordeaux, France, Feb. 2020, Accessed: Apr. 22, 2020. [Online]. Available: <https://aerospace-europe2020.eu/>.
- [177] J. Pyrhönen, T. Jokinen, and V. Hrabovcová, *Design of rotating electrical machines*. John Wiley & Sons, Ltd, 2008.
- [178] “Liquid cooled rotor assembly - US 7,579,725 B2 - PatentSwarm.” <https://patentswarm.com/patents/US7579725B2> (accessed May 28, 2020).
- [179] K.-H. Lee, H.-R. Cha, and Y.-B. Kim, “Development of an interior permanent magnet motor through rotor cooling for electric vehicles,” *Applied Thermal Engineering*, vol. 95, pp. 348–356, Feb. 2016, doi: 10.1016/j.applthermaleng.2015.11.022.
- [180] R. Christie, A. Dubois, and J. Derlaga, “Cooling of Electric Motors Used for Propulsion on SCEPTOR,” presented at the AIAA Aviation and Aeronautics Forum and Exposition;

- 13-17 Jun. 2016, Washington, DC; United States, Jun. 13, 2016, [Online]. Available: <https://ntrs.nasa.gov/archive/nasa/casi.ntrs.nasa.gov/20170001724.pdf>.
- [181] I. E. Idelchik, *Handbook of Hydraulic Resistance*, 3rd ed. New York: Begell House Inc., 1996.
- [182] “Catalog of hydraulic pumps,” *Parker Hannifin Corporation*. <https://www.parker.com/> (accessed Jun. 03, 2020).
- [183] E. R. G. Eckert, E. R. G. Eckert, and R. M. Drake, *Analysis Of Heat And Mass Transfer*. Taylor & Francis, 1986.
- [184] S. Touhami, “Analytical Sizing Models to Assess the Performances of High Specific Power Electric Motors for Hybrid Aircraft,” These en préparation, Toulouse, INPT, 2016.
- [185] K. A. Woodbury, *Inverse Engineering Handbook*. CRC Press, 2002.
- [186] M. Khelifa, M. Mordjaoui, and A. Medoued, “An inverse problem methodology for design and optimization of an interior permanent magnetic BLDC motor,” *International Journal of Hydrogen Energy*, vol. 42, no. 28, pp. 17733–17740, Jul. 2017, doi: 10.1016/j.ijhydene.2017.02.017.
- [187] C.-H. Huang and H.-C. Lo, “A three-dimensional inverse problem in estimating the internal heat flux of housing for high speed motors,” *Applied Thermal Engineering*, vol. 26, no. 14, pp. 1515–1529, Oct. 2006, doi: 10.1016/j.applthermaleng.2005.12.009.
- [188] H. Vansompel, A. Yarantseva, P. Sergeant, and G. Crevecoeur, “An Inverse Thermal Modeling Approach for Thermal Parameter and Loss Identification in an Axial Flux Permanent Magnet Machine,” *IEEE Transactions on Industrial Electronics*, vol. 66, no. 3, pp. 1727–1735, Mar. 2019, doi: 10.1109/TIE.2018.2838089.
- [189] D. G. Nair and A. Arkkio, “Inverse Thermal Modeling to Determine Power Losses in Induction Motor,” *IEEE Transactions on Magnetics*, vol. 53, no. 6, pp. 1–4, Jun. 2017, doi: 10.1109/TMAG.2017.2661381.
- [190] A. Zeaiter, E. Videcoq, and M. Fénöt, “Determination of electric motor losses and critical temperatures through an inverse approach,” *Electr Eng*, Sep. 2020, doi: 10.1007/s00202-020-01098-0.
- [191] J. V. Beck, B. Blackwell, and C. R. St. Clair, *Inverse heat conduction: ill-posed problems*. New York: Wiley, 1985.
- [192] E. Videcoq, D. Petit, and A. Piteau, “Experimental modelling and estimation of time varying thermal sources,” *International Journal of Thermal Sciences*, vol. 42, no. 3, pp. 255–265, Mar. 2003, doi: 10.1016/S1290-0729(02)00025-X.
- [193] J. V. Beck, B. Blackwell, and A. Haji-Sheikh, “Comparison of some inverse heat conduction methods using experimental data,” *International Journal of Heat and Mass Transfer*, vol. 39, no. 17, pp. 3649–3657, Nov. 1996, doi: 10.1016/0017-9310(96)00034-8.
- [194] G. Blanc, M. Raynaud, and T. H. Chau, “A guide for the use of the function specification method for 2D inverse heat conduction problems,” *Revue Générale de Thermique*, vol. 37, no. 1, pp. 17–30, Jan. 1998, doi: 10.1016/S0035-3159(97)82463-4.

MODELISATION THERMIQUE ET REFROIDISSEMENT DE MOTEURS ELECTRIQUES. APPLICATION A LA PROPULSION D'UN AVION HYBRIDE

Résumé :

Le travail présenté dans ce mémoire concerne la modélisation thermique de moteurs électriques de forte densité de puissance. Le but est de trouver les techniques de refroidissement efficaces et adaptées aux moteurs conçus pour application à la propulsion de l'avion hybride du futur. Deux cibles de densité de puissance, 5 kW/kg pour le court terme (année 2025) et 10 kW/kg pour le long terme (année 2035), sont abordées avec leurs propres exigences. Les moteurs électriques étudiés sont de type synchrone à aimants permanents montés en surface du rotor. Ce type de moteur est caractérisé par un rendement élevé et contraint par les températures maximales admissibles relativement faibles de son bobinage et de ses aimants. Une fois atteintes, ces valeurs de température entraînent le dysfonctionnement du moteur ou la limitation de sa durée de vie. En outre, avec un design fermé imposé et des densités élevées de flux de chaleur dissipées dans la machine, une optimisation du refroidissement est incontournable.

Pour se familiariser avec le problème, un état de l'art détaillé sur le refroidissement des machines électriques est réalisé. En conséquence, les différentes techniques utilisées et les avancements technologiques récents sont analysés vis-à-vis de notre cas d'application. Ensuite, afin de prédire le comportement thermique du moteur et d'assurer le suivi des températures critiques (surtout au bobinage et aux aimants), un modèle nodal transitoire est mis en place et résolu sous Matlab. Ce dernier est construit en considérant l'intégralité du système moteur avec son circuit de refroidissement. Les conditions externes liées à l'environnement sont prises en compte, en particulier la variation de la température d'air extérieur en fonction de l'altitude et le profil de mission de vol de l'avion. En effet, les pertes dans le moteur, qui constituent les sources de chaleur, varient en fonction de la puissance pendant le vol. Afin d'identifier précisément les paramètres intrinsèques du modèle, une étude par éléments finis a été menée et des corrélations permettant l'estimation de la conductivité thermique du bobinage en sont déduites par interpolation polynomiale. Plusieurs études ont ensuite été menées concernant l'influence des propriétés thermophysiques, de la température extérieure, de la nature du liquide de refroidissement, de son débit ainsi que la surface extérieure de l'échangeur sur les réponses en température du modèle. Plusieurs designs du moteur sont étudiés grâce à ce modèle afin de proposer des solutions de refroidissement adaptées. Pour chacune des cibles, une configuration optimale du moteur avec son système de refroidissement a été adoptée.

Par ailleurs, les pertes électromagnétiques et mécaniques étant difficiles à estimer dans ces machines, un chapitre est consacré à leur identification par résolution d'un problème inverse. La technique est séquentielle et utilise la spécification de fonction de Beck comme méthode de régularisation. Trois cas, de complexité croissante, sont étudiés et montrent la fiabilité de la méthode qui permet également d'estimer les températures inaccessibles dans le moteur. C'est finalement ce modèle nodal à faible nombre de degré de liberté qui nous permet d'assurer, en temps réel, le suivi des points chauds.

Mots clés : Avions--Moteurs, Conductivité thermique, Moteurs électriques--Construction et conception, Moteurs électriques--Refroidissement, Problèmes inverses, Moteur synchrone à aimants permanents, Modélisation thermique méthode nodale, Pertes moteur.

THERMAL MODELING AND COOLING OF ELECTRIC MOTORS. APPLICATION TO THE PROPULSION OF HYBRID AIRCRAFT

Abstract :

The concern of this thesis is the thermal modeling of high-specific power electric motors. The aim is to allow finding the efficient and adequate cooling solutions of the motors designed for hybrid aircraft propulsion application. Two specific power values, 5 kW/kg for the short-term (year 2025) and 10 kW/kg for the long-term (year 2035), are targeted, each with specific requirements. The investigated type of electric motors is the synchronous machine with surface-mounted permanent magnets. This motor type is constrained by relatively low values of maximum allowed temperatures in windings and magnets. Once reached, these temperature values lead to a failure in motor operation or at least to shortening its lifetime. Moreover, with a closed motor design and high heat fluxes generated, the optimization of the cooling is essential.

To become acquainted with the issue, a detailed state of the art on electric machine cooling is elaborated. Then, the commonly used techniques and the recent technological advancements are analyzed with respect to our case study. Afterward, in order to predict motor thermal behavior and ensure the monitoring of critical temperatures (windings and magnets), a nodal transient model is implemented and solved on Matlab software. This latter is built for the whole system of the motor and cooling circuit. Specific conditions of the flight are taken into account, particularly the outside air temperature variation in terms of altitude and the flight mission profile. Actually, the motor losses, generating the heat in the machine, vary depending on the motor power during the mission. For the identification of crucial parameters, a Finite-Element study was conducted and corresponding correlations were elaborated to estimate the windings thermal conductivity through polynomial interpolation.

Several studies were carried out involving the influence of the thermo-physical properties, the outside temperature, the coolant nature, its flow rate as well as the exchanger surface, on the temperature response of the model. This model has allowed studying several motor designs and proposing adequate cooling solutions. For each target, a final optimal configuration of the motor with its cooling system was adopted.

Besides, since the electromagnetic and mechanical losses are hardly estimated in this machine type, a chapter was dedicated to identifying them through an inverse approach. A sequential technique, that uses Beck's function specification for regularization, was developed. Three cases of unknown losses, with increasing complexity, were studied, proving the method's reliability. Finally, using the same developed low-order model, the real-time procedure also allows monitoring low-accessibility motor temperatures (specifically hot spots).

Keywords : Airplanes--Motors, Thermal conductivity, Electric motors--Design and construction, Electric motors--Cooling, Inverse problems, Permanent-magnet synchronous motor, Nodal network thermal modeling, Motor losses.



Two-Phase Power Electronics Cooling Solution Design in Air Context Answering to the Objectives of the Hybrid Aircraft 2035

Flavio Accorinti

► To cite this version:

Flavio Accorinti. Two-Phase Power Electronics Cooling Solution Design in Air Context Answering to the Objectives of the Hybrid Aircraft 2035. Other. ISAE-ENSMA Ecole Nationale Supérieure de Mécanique et d'Aérotechique - Poitiers, 2020. English. NNT: 2020ESMA0005 . tel-02993195

HAL Id: tel-02993195

<https://tel.archives-ouvertes.fr/tel-02993195>

Submitted on 6 Nov 2020

HAL is a multi-disciplinary open access archive for the deposit and dissemination of scientific research documents, whether they are published or not. The documents may come from teaching and research institutions in France or abroad, or from public or private research centers.

L'archive ouverte pluridisciplinaire **HAL**, est destinée au dépôt et à la diffusion de documents scientifiques de niveau recherche, publiés ou non, émanant des établissements d'enseignement et de recherche français ou étrangers, des laboratoires publics ou privés.

THESE

Pour l'obtention du Grade de
**DOCTEUR DE L'ECOLE NATIONALE SUPERIEURE DE MECANIQUE ET
D'AEROTECHNIQUE**
(Diplôme National – Arrêté du 25 mai 2016)

Ecole Doctorale :
Sciences et Ingénierie en Matériaux, Mécanique, Énergétique

Secteur de Recherche : **Énergétique, Thermique et Combustion**

Présentée par : **Flavio ACCORINTI**

**TWO-PHASE POWER ELECTRONICS COOLING SOLUTION DESIGN IN AIR CONTEXT
ANSWERING TO THE OBJECTIVES OF THE HYBRID AIRCRAFT 2035**

**Directeur de thèse : Yves BERTIN
Co-encadrants : Vincent AYEL, Sébastien DUTOUR**

Soutenue le 05 Juin 2020

devant la Commission d'Examen

JURY

Président et rapporteur :

HARMAND Souad, Professeur, Université de Valenciennes

Rapporteur :

PLATEL Vincent, Maître de conférences, Université de Pau et des Pays de l'Adour

Membres du jury :

GATEAU Guillaume, Professeur, Institute LAPLACE, INP-ENSEEIHT

DUTOUR Sébastien, Maître de conférences, Institute LAPLACE, Université Toulouse

AYEL Vincent, Maître de conférences, Institute Pprime, ISAE-ENSMA

BERTIN Yves, Professeur, Institute Pprime, ISAE-ENSMA

A Marina

This project has received funding from the [European Union's Horizon 2020 (Cleansky 2 JTI) research and innovation program, 2014-2024] under grant agreement No 715483.



Remerciements

Je souhaite tout d'abord remercier Yves Bertin et Vincent Ayel, maîtres de science et de vie, pour m'avoir suivi pendant ces trois années, pour m'avoir conseillé et pour avoir participé à mon développement professionnel et personnel. Merci pour leur confiance ! Je veux remercier Vincent pour la deuxième fois de m'avoir dédié du temps même quand il n'avait pas de temps et de m'avoir donné envie d'aller plus loin quand je pensais : « ça sert à rien... ». Je souhaite remercier Sébastien Dutour pour m'avoir posé les bonnes questions aux bons moments. Je le remercie car ses questions, toujours appropriées, m'ont permis de prendre du recul pour améliorer mes travaux !

Mes remerciements vont à mes rapporteurs, Prof. Harmand et Prof. Platel qui ont pris le temps de lire ce manuscrit, malgré sa longueur et la langue anglaise. Je voudrais aussi les remercier pour leurs remarques et leurs conseils ainsi que pour les mots d'appréciation qu'ils ont voulu exprimer pour moi et mon travail. Je voudrais remercier tout le jury pour avoir assisté (en visio) à ma soutenance malgré les conditions « atypiques »....

Je tiens à remercier le consortium HASTECS. D'abord je veux remercier Najoua, toujours disponible à échanger par téléphone, même pendant des heures, et pour sa capacité d'alterner une blague à un calcul. C'était un plaisir de travailler avec elle, c'était une très belle collaboration ! Merci à toute l'équipe d'électroniciens (WP2). Merci à l'équipe WP6 : à Matthieu, avec qui j'ai eu le plaisir de partager des bières et des moments en dehors du boulot, pour son sourire, et à son chef, Xavier R., le « big boss » d'HASTECS, pour sa confiance. Merci à Sarah, Amal et Philippe. Merci à AIRBUS et plus en particulier à Jean-François pour sa contribution, son intérêt envers mon travail et sa confiance.

Je voudrais remercier Dominique Couton pour m'avoir mis à disposition le logiciel GRETh (EchTherm) sans lequel le chapitre sept de cette thèse n'existerait qu'en partie...

Merci à tous ceux qui m'ont accompagné pendant mon parcours. Bastien G. pour ses conseils et sa bonne humeur contagieuse, pour son amitié, pour les bons moments qu'on a partagé et pour ceux à venir ! Merci à Yann B. pour son soutien et... ses conseils ; à Florian M. pour son ouverture d'esprit et pour les longues discussions autour de la cuisine.

Merci à Filippo, avec qui j'ai partagé le bureau pendant deux années, pour tous les

échanges qu'on a eu ; merci à Maksime qui est toujours là, même quand il est à Paris ! Merci Arun. Merci à Tung et à tous les déjà docteurs et aux doctorants du labo. Merci à vous tous.

Merci aux italiens à Poitiers (d'hier et d'aujourd'hui) : Nathan (même si tu n'es pas italien ;), Antonio, Vincenzo, Barbara, Federico, Eleonora, Battista, Giuseppe, Marco, Carolina.

Merci à Jonathan Cormier, à Jean-Marie Petit, à Adel et Etienne pour leur bonheur.

Un remerciement spécial va à Gildas, avec qui j'ai partagé mon expérience sur BATH, avant cette aventure, et des cours. Il m'a donné les bons conseils aux bons moments. Peut-être que sans lui je ne serais pas là à tous vous remercier ! Merci à Eva pour sa bonne humeur et son sourire.

Je tiens à remercier toutes les gens qui font partie du labo, en particulier un grand merci va à Catherine L. sans laquelle tout serait à l'arrêt. Merci aux gens de l'équipe technique, qui m'ont « filé un coup de pouce » quand j'en ai eu besoin et pour les nombreux échanges en terrasse pendant la pause. Merci à Christophe qui a toujours répondu (positivement) à mes demandes d'installation de nouveaux logiciels. Merci à Catherine F., Nicolas P., Cyril, Jean-Christophe, Hervé, Sébastien...

Bien sûr, mes plus grands remerciements vont à Marina, ma femme et compagne de vie, à qui j'ai voulu dédicacer cette thèse. Merci de m'avoir toujours soutenu tout au long de mon parcours et surtout merci pour sa patience... Je veux enfin remercier mes parents et mon frère, Bitto, pour avoir toujours cru en moi !

Pendant cette expérience j'ai rencontré des gens inoubliables, et les journées passées avec vous tous je les apporterais pour toujours avec moi.

Merci à tous !

Contents

Remerciements	iii
List of Figures	xvi
List of Tables	xviii
Symbols and Abbreviations	xix
Résumé étendu (Français)	1
I HASTECS	
Hybrid Aircraft Academic reSearch on Thermal and Electrical Components and Systems	19
Introduction	21
1 Hybrid aircraft power electronics cooling issue	25
1.1 Why power electronics cooling?	25
1.2 The aircraft mission profile	28
1.3 A not constant cold source temperature	29
1.4 The cold source	32
1.4.1 Skin heat exchanger	33
1.4.2 RAM-air	35
II Hybrid aircraft power electronics cooling: from the state of the art to system selection	39
2 Overview of existing cooling solutions	41
2.1 Active cooling systems	44
2.1.1 Single phase cooling systems	45
2.1.1.1 Transport lines	45
2.1.1.2 The pump and the expansion tank	46

2.1.1.3	Heat sink heat transfer	48
2.1.1.4	The cold heat exchanger (HXG)	49
2.1.2	Two-phase active cooling systems	53
2.1.2.1	Pumped two-phase technologies	53
2.1.2.2	Vapour compression technologies	55
2.2	Passive cooling systems	58
2.2.1	Thermosyphons and Heat pipes	58
2.2.1.1	Thermosyphons	58
2.2.1.2	Heat pipes	60
2.2.1.3	Pulsating heat pipes (PHP)	64
2.2.2	Two-phase passive loops	65
2.2.2.1	Loop Heat Pipe (LHP)	65
2.2.2.2	Capillary Pumped Loop (CPL)	67
2.2.2.3	Capillary Pumped Loop for Integrated Power (CPLIP) .	68
2.2.3	First comparison between two-phase passive cooling systems	70
2.3	Conclusion	70
3	Power electronics cooling: state of the art of heatsinks	73
3.1	Direct cooling systems: jet impingement and spray cooling	74
3.2	Indirect cooling systems	78
3.2.1	Cold plate	78
3.2.2	Mini and Microchannels	80
3.2.3	Porous media and metal foams	83
3.3	Conclusion	86
4	Technology choice	89
4.1	Comparison of high performance cooling systems	89
4.1.1	Technology screening	93
4.2	System selection	95
4.2.1	Cold source technology comparison	96
4.2.2	First approximation evaluation of mass and power coefficient . . .	98
4.2.3	Cooling technology comparison	104
4.3	Conclusion	107

III CPLIP in HASTECS context	109
5 Capillary Pumped Loop for Integrated Power (CPLIP): working principle, experimental facility and numerical tool	111
5.1 CPLIP generalities and working principle	111
5.1.1 Evaporator	113
5.1.2 Condenser	115
5.1.3 Reservoir	117
5.1.4 Transport lines	118
5.2 Experimental facility	118
5.2.1 CPLIP 1.1: the experimental facility	119
5.3 Numerical models	122
5.4 CPLIP model	123
5.4.1 Navier-Stokes equations	124
5.4.1.1 General case (vapour and liquid lines, condenser)	125
5.4.1.2 Reservoir	126
5.4.1.3 Evaporator	133
5.4.2 Thermal/electrical analogy	134
5.5 Conclusion	137
6 CPLIP answer to HASTECS requirements: thermal characterisation	139
6.1 CPLIP experimental steady-state test campaigns	139
6.1.1 Operating conditions	139
6.1.2 CPLIP thermal response to different heat power levels	141
6.2 Post-processing tool and CPLIP real thermodynamic cycle	142
6.3 CPLIP thermal characterisation for HASTECS specifications	146
6.3.1 Steady-state experimental results and thermal conductance analysis	146
6.3.2 Evaporator-power module numerical analysis	151
6.3.2.1 Power electronics modules characteristics	151
6.3.2.2 Evaporator configuration	152
6.3.2.3 Finite volume analysis of power electronics module	153
6.3.3 Experimental thermal mission profile	157
6.4 Influence of vapour line pressure drop on the thermal response of the CPLIP	159
6.5 Conclusion	164
7 CPLIP optimisation for 2025 and 2035 requirements	167
7.1 Design point	167

7.2 CPLIP optimisation	169
7.2.1 Condenser optimisation	170
7.2.2 Condenser general characteristics	173
7.2.2.1 A condenser for 2025	174
7.2.2.2 A condenser for 2035	182
7.3 Back to design point	186
7.4 Overall power coefficient	188
7.5 Conclusion	189
IV CPLIP behaviour under severe transient conditions	191
8 Severe transient phases: Start-up	193
8.1 Experimental operating conditions	193
8.2 Start-up behaviour	195
8.2.1 A severe start-up condition	195
8.2.2 Low intensity power load step: experimental analysis	198
8.3 Vapour front velocity evaluation	200
8.4 Discussion	202
8.5 Experimental and numerical results comparison	204
8.5.1 Effect of vapour line wall temperature	204
8.5.2 Effect of vapour line wall thermal inertia	206
8.6 Conclusion	208
9 CPLIP behaviour under sudden and violent acceleration stages	211
9.1 Accelerations in civil flight applications	212
9.2 Simulation conditions	213
9.3 CPLIP behaviour under perturbed transient acceleration field	214
9.4 Parametric study	221
9.5 Conclusion and perspectives	225
V Conclusion and Perspectives	227
10 General conclusion	229
11 Perspectives	237
11.1 General perspectives	237
11.2 A newer technology: Capillary Jet Loop (CJL)	238

Bibliography	241
Appendix	257
A Working fluid discussion	259
B First approximation design	261
B.1 Active single phase (liquid cooling) first approximation design	261
B.1.1 The cold plate	261
B.1.2 Pump selection	262
B.1.3 Transport lines	262
B.1.4 Single phase cold heat exchanger	263
B.1.4.1 Skin heat exchanger first approximation design	263
B.1.4.2 Cold heat exchanger in a bank configuration	266
B.2 Two-phase solution first approximation design	268
B.2.1 The evaporator	268
B.2.2 Condenser design	268
B.2.2.1 Skin heat exchanger for a two-phase internal flow: condenser first approximation design	268
B.2.2.2 Condenser design in tube bank configuration	273
C GRETh (EchTherm)	275
C.1 Continuous finned heat exchangers	275
C.1.1 Limits and hypothesis	275
C.1.2 Correlations	275
C.1.2.1 External side	275
C.1.2.2 Internal side	277
C.2 Louvered fins & microchannels heat exchanger	281
C.2.1 Limitations and hypothesis	281
C.2.1.1 External side	281
C.2.1.2 Internal side	282
D Heavy duty tests	285

List of Figures

0.1	Involved Labs	21
0.2	WPs and their interactions	22
1.1	Electric power losses scheme	26
1.2	Mass distribution of a 3-level PWM NPC electronic system (using 6th gen. 1700 V IGBT) equipped by a classical air forced convection cooling system [1].	27
1.3	Qualitative thermal mission profile and altitude variation as a function of time.	29
1.4	ISA diagram for pressure and temperature as a function of the altitude [2]	31
1.5	Cooling system loop as a broker	33
1.6	Skin heat exchanger 3D scheme [3]	34
1.7	Skin heat exchanger scheme [4]	34
1.8	Positioning scheme of skin heat exchanger [4]	35
1.9	RAM air.	36
2.1	Cooling systems classification.	41
2.2	General scheme of an active cooling system	44
2.3	Single phase cooling system concept scheme	45
2.4	Expansion vessels typologies	47
2.5	Heat transfer mechanism simplified scheme in the heat sink.	48
2.6	Co-current heat exchanger qualitative operating diagram	50
2.7	Cold side heat exchanger concept scheme	52
2.8	Air mass flow rate as a function of the external air temperature and altitude.	52
2.9	Pumped two-phase cooling system concept scheme.	54
2.10	Vapour compression concept diagram scheme.	56
2.11	Scheme of principle of an active two-phase thermal system equipped by a MMPS solution [5].	57
2.12	Thermosyphon [6]	59
2.13	Heat Pipe. [6]	61
2.14	Heat pipes application example	62

2.15 Pulsating heat pipes [6]	64
2.16 Loop Heat Pipe Scheme and thermodynamic cycle	66
2.17 Principle scheme and thermodynamic cycle of CPL and LHP loops	68
2.18 CPLIP scheme [7]	69
3.1 Spray cooling	75
3.2 Typical spray cooling curve [8]	76
3.3 Cold plate for electronic cooling [9]	79
3.4 Thermal and hydraulic performances of water, fuel and oil [9]	80
3.5 Microchannels	81
3.6 Metal foam example [10]	84
3.7 Micrographs of sintered porous medium (a), compressed metal foam (b) and metal foam (c)	84
4.1 Historical trend of heat flux density and thermal evacuation capability for active and passive technologies.	90
4.2 Maximal total thermal load and heat flux density histogram of active cooling techniques.	91
4.3 Maximal total thermal load and heat flux density histogram of passive cooling systems. [11].	91
4.4 Technology comparison [11]	92
4.5 Transport distance for different passive technologies	94
4.6 Unladen, fluid and total mass comparison for the considered technologies.	105
4.7 Mass composition of different cooling technologies	106
5.1 Scheme of principle of CPLIP	112
5.2 CPLIP thermodynamic cycle [12]	112
5.3 Evaporator assembly	113
5.4 Evaporator sections	114
5.5 Schematic of evaporation in a porous wick.	115
5.6 Condensation flow regimes [13]	116
5.7 Reservoir concept scheme	118
5.8 Schematic of the CPLIP 1.1 [12, 14, 15]	120
5.9 Evaporator concept scheme (sec. A-A)	120
5.10 Staggered grid	124
5.11 Reservoir schematic	127
5.12 Reservoir lower part discretisation	127

5.13 Reservoir higher part thermo-hydraulic model	131
5.14 Evaporator discretisation	133
5.15 Thermal/hydraulic-electrical analogy networks [16]	136
6.1 Example of NCG absence verification (methanol)	141
6.2 CPLIP temperature evolution as a function of the time, for different heat power applied to the evaporator (methanol, $T_{res} = 70^\circ\text{C}$ and $T_{sec} = 20^\circ\text{C}$) [12].	142
6.3 CPLIP thermodynamic cycle: comparison at $Q = 0.5 \text{ kW}$ and $Q = 5 \text{ kW}$ (methanol, $T_{res} = 70^\circ\text{C}$ and $T_{sec} = 20^\circ\text{C}$) [12].	144
6.4 CPLIP thermodynamic cycle: comparison at $T_{res} = 50; 60$ and 70°C (methanol, $Q = 1.5 \text{ kW}$ and $T_{sec} = 20^\circ\text{C}$) [12].	145
6.5 CPLIP thermodynamic cycle: comparison at $T_{sec} = 5; 20$ and 40°C (methanol, $Q = 1.5 \text{ kW}$ and $T_{res} = 70^\circ\text{C}$).	146
6.6 Evaporator thermal conductance, $G_{ev,res}$, based on the reservoir saturation temperature as a function of the thermal load (ethanol and methanol, $T_{res} = 50; 60; 70$ and 80°C , $T_{sec} = 20^\circ\text{C}$).	147
6.7 Mean diffuser wall temperature, \bar{T}_{diff} ; evaporator saturation temperature, T_V , as a function of the thermal load (methanol, $T_{sec} = 5; 20$; and 40°C , $T_{res} = 70^\circ\text{C}$) [12].	149
6.8 $G_{ev,res}$ and $G_{ev,V}$ comparison as a function of the thermal power (methanol, $T_{sec} = 5; 20$; and 40°C , $T_{res} = 70^\circ\text{C}$)	150
6.9 $HTC_{ev,V}$ and $HTC_{ev,res}$ comparison as a function of the thermal power (methanol, $T_{sec} = 20^\circ\text{C}$, $T_{res} = 70^\circ\text{C}$).	150
6.10 7th Generation Mitsubishi module	151
6.11 Evaporator configuration example [1].	152
6.12 Power module scheme and boundary conditions	153
6.13 Mesh example	154
6.14 Mesh independence temperature distribution (methanol, $T_{res} = 70^\circ\text{C}$)	155
6.15 Temperature map CASE 1 (junction view): $Q_{th,D} = 155 \text{ W}$; $Q_{th,I} = 0 \text{ W}$ (methanol, $T_{res} = 70^\circ\text{C}$).	156
6.16 Temperature map CASE 1 (evaporator-module interface view, according to Fig. 6.15): $Q_{th,D} = 155 \text{ W}$; $Q_{th,I} = 0 \text{ W}$ (methanol, $T_{res} = 70^\circ\text{C}$).	156
6.17 Temperature map CASE 2 (junction view): $Q_{th,D} = 12 \text{ W}$; $Q_{th,I} = 133 \text{ W}$ (methanol, $T_{res} = 70^\circ\text{C}$).	157
6.18 Temperature map CASE 2 (evaporator-module interface view, according to Fig. 6.17): $Q_{th,D} = 12 \text{ W}$; $Q_{th,I} = 133 \text{ W}$ (methanol, $T_{res} = 70^\circ\text{C}$).	157

6.19	Experimental thermal mission profile (methanol, $T_{sec} = 20^\circ\text{C}$, $T_{res} = 70^\circ\text{C}$).	158
6.20	Time dependent diagram of temperature evolution of the CPLIP for increasing vapour line pressure drop (methanol, $Q_{th} = 1\text{ kW}$, $T_{sec} = 20^\circ\text{C}$).	160
6.21	Thermodynamic cycle comparison between the highest and the lowest valve overture: $N/N_{max} = 0.25$ and $N/N_{max} = 1$ (methanol, $Q_{th} = 1\text{ kW}$, $T_{res} = 70^\circ\text{C}$ and $T_{sec} = 20^\circ\text{C}$).	161
6.22	\bar{T}_{diff} as a function of N/N_{max} and for different thermal loads (methanol, $T_{res} = 70^\circ\text{C}$; $T_{sec} = 20^\circ\text{C}$).	162
6.23	Temperature differences as a function of the valve overture (ethanol and methanol, $T_{res} = 70^\circ\text{C}$; $T_{sec} = 20^\circ\text{C}$).	162
6.24	Thermal conductance as a function of the pressure drop (ethanol and methanol, $T_{res} = 70^\circ\text{C}$; $T_{sec} = 20^\circ\text{C}$).	163
6.25	Overall pressure drop as a function of valve opening (N/N_{max}) and for different thermal loads (ethanol and methanol, $T_{res} = 70^\circ\text{C}$; $T_{sec} = 20^\circ\text{C}$).	164
7.1	Design point choice	168
7.2	Passive two-phase mass distribution (three parallel evaporators CPLIP: —CERBERE—)	169
7.3	Optimisation process of a heat exchanger.	171
7.4	Fin configurations used for 2025 solution [17]	173
7.5	Circular fins geometric characteristics	175
7.6	Condenser mass and thermal power coefficient as a function of fin thickness, δ	176
7.7	Continuous fins geometric characteristics	177
7.8	Condenser mass distribution for optimised and not optimised solution	180
7.9	Cooling system overall mass and thermal power coefficient as a function of the thermal load	181
7.10	Components mass distribution for 16 kW CPLIP	181
7.11	Louvered fin condenser	183
7.12	Louvered fins and microchannels condenser mass distribution example	185
7.13	Louvered fin-microchannels equipped CPLIP mass distribution	186
7.14	Mass and thermal power coefficient as a function of the thermal load (2035)	186
7.15	Thermal load shape and temperature increase due to not treated thermal energy	187
7.16	Global power coefficient trends for 2025 and 2035 solutions	189

8.1	CPLIP: experimental facility	194
8.2	Heating process of the vapour line solid walls (methanol, $T_{res} = 70^\circ\text{C}$)	195
8.3	0 – 5 kW cold start-up (methanol, $T_{res} = 70^\circ\text{C}$, $T_{sec} = 20^\circ\text{C}$)	196
8.4	0 – 4 kW hot start-up failure (methanol, $T_{res} = 70^\circ\text{C}$, $T_{sec} = 20^\circ\text{C}$)	197
8.5	Cold start-up (methanol, $T_{res} = 70^\circ\text{C}$, $T_{sec} = 20^\circ\text{C}$)	199
8.6	Hot start-up (methanol, $T_{res} = 70^\circ\text{C}$, $T_{sec} = 20^\circ\text{C}$)	199
8.7	Qualitative sigmoid profile as a function of the time	201
8.8	Temperature profiles as a function of the time, fitted curves for $Q_{th} = 2\text{ kW}$ (methanol, $T_{res} = 70^\circ\text{C}$, $T_{sec} = 20^\circ\text{C}$)	202
8.9	Experimental and numerical comparison for a cold start-up (methanol, $Q_{th} = 0.4\text{ kW}$, $T_{res} = 70^\circ\text{C}$ $T_{sec} = 20^\circ\text{C}$)	205
8.10	Vapour front qualitative shapes: real (up), numerical (piston shape, down)	205
8.11	Vapour line temperature profiles with (continuous lines) and without (dashed lines) solid wall thermal inertia (methanol, $Q_{th} = 0.4\text{ kW}$, $T_{res} = 70^\circ\text{C}$, $T_{sec} = 20^\circ\text{C}$)	206
8.12	Mass flow rate profiles with (continuous lines) and without (dashed lines) solid wall thermal inertia (methanol, $Q_{th} = 0.4\text{ kW}$, $T_{res} = 70^\circ\text{C}$, $T_{sec} =$ 20°C)	207
8.13	Vapour quality profiles with (continuous lines) and without (dashed lines) solid wall thermal inertia (methanol, $Q_{th} = 0.4\text{ kW}$, $T_{res} = 70^\circ\text{C}$, $T_{sec} =$ 20°C)	207
8.14	Real start-up condition $3 \times 0.8\text{ kW}$ (methanol, $T_{res} = 70^\circ\text{C}$, $T_{sec} = 20^\circ\text{C}$) .	209
9.1	Qualitative diagram of acceleration impulse used for study	214
9.2	Total pressure variation diagram during acceleration impulse (methanol, $Q_{th} = 1\text{ kW}$, $T_{res} = 70^\circ\text{C}$, $T_{sec} = 20^\circ\text{C}$, $3g$, $H = 90\text{ cm}$)	215
9.3	Mass flow rate variation diagram during acceleration impulse ($Q_{th} = 1\text{ kW}$, $T_{res} = 70^\circ\text{C}$, $T_{sec} = 20^\circ\text{C}$, $3g$, $H = 90\text{ cm}$)	216
9.4	Condenser inlet to outlet pressure (top) and mass flow rate (bottom) dif- ference during acceleration impulse (methanol, $Q_{th} = 1\text{ kW}$, $T_{res} = 70^\circ\text{C}$, $T_{sec} = 20^\circ\text{C}$, $3g$, $H = 90\text{ cm}$)	217
9.5	Two-phase length variation during acceleration impulse (methanol, $Q_{th} =$ 1 kW , $T_{res} = 70^\circ\text{C}$, $T_{sec} = 20^\circ\text{C}$, $3g$, $H = 90\text{ cm}$)	219
9.6	Vapour quality variation during acceleration impulse (methanol, $Q_{th} =$ 1 kW , $T_{res} = 70^\circ\text{C}$, $T_{sec} = 20^\circ\text{C}$, $3g$, $H = 90\text{ cm}$)	219
9.7	Temperature variation during acceleration impulse (methanol, $Q_{th} = 1\text{ kW}$, $T_{res} = 70^\circ\text{C}$, $T_{sec} = 20^\circ\text{C}$, $3g$, $H = 90\text{ cm}$)	220

9.8 Acceleration impulsion time duration, Δt_{gp} , effect condenser outlet mass flow rate (methanol, $Q_{th} = 1 \text{ kW}$, $T_{res} = 70^\circ\text{C}$, $T_{sec} = 20^\circ\text{C}$, $\mathbf{H} = 80 \text{ cm}$, 3g)	222
9.9 Qualitative diagram of accumulated liquid mass during perturbation perturbation (area Ξ) and returning mass during settling (area Γ)	223
9.10 Condenser-to-reservoir height difference effect on condenser outlet mass flow rate (methanol, $Q_{th} = 1 \text{ kW}$, $T_{res} = 70^\circ\text{C}$, $T_{sec} = 20^\circ\text{C}$, $\Delta t_{gp} = 0.25 \text{ sec}$, 3g)	224
9.11 Acceleration impulse intensity effect on the reversed mass flow rate and condensation length (methanol, $Q_{th} = 1 \text{ kW}$, $T_{res} = 70^\circ\text{C}$, $T_{sec} = 20^\circ\text{C}$, $\Delta t_{gp} = 0.25 \text{ sec}$, $\mathbf{H} = 30 \text{ cm}$)	225
9.12 Pressure at condenser outlet for different acceleration intensity (methanol, $Q_{th} = 1 \text{ kW}$, $T_{res} = 70^\circ\text{C}$, $T_{sec} = 20^\circ\text{C}$, $\Delta t_{gp} = 0.25 \text{ sec}$, $\mathbf{H} = 30 \text{ cm}$)	225
11.1 Capillary Jet Loop concept [18]	238
11.2 Injector principle scheme [19]	239
11.3 Scheme of principle of C JL adapted for HASTEC requirements	240
A.1 Comparison between different fluid using Mouromtseff number	259
A.2 Fluid to water comparison	260
B.1 Single phase cooling system scheme	261
B.2 Two different cold plate configurations	262
B.3 Skin heat exchanger	264
B.4 Hypothesis	265
B.5 Mesh configuration	266
B.6 Moody diagram	267
B.7 Tube bank configuration	268
B.8 Mesh configuration for two-phase flow	269
D.1 Heavy duty test (methanol, $T_{res} = 70^\circ\text{C}$, $T_{sec} = 20^\circ\text{C}$, $Q_{th} = 2 \text{ kW}$)	285
D.2 Saturation conditions in the reservoir before and after the tests (methanol, $T_{res} = 70^\circ\text{C}$)	286

List of Tables

1.1	Temperature specifications [2]	31
2.1	Single phase cooling system synthesis	53
2.2	Synthesis of the main characteristics of CPL, LHP and CPLIP.	70
2.3	Pros and drawbacks comparison between passive cooling systems	71
3.1	Comparison of different porous media characteristics [20]	85
3.2	Active cooling systems pro & drawbacks	88
4.1	Main characteristics of the cooling systems	93
4.2	Technology generalities.	98
4.3	Cooling system main geometrical dimensions.	100
4.4	Single phase cooling system mass evaluation (first approximation design).	101
4.5	Pumped two-phase cooling system mass evaluation (first approximation design).	102
4.6	Two-phase passive cooling system mass evaluation (first approximation design of a three-evaporators-CPLIP).	103
4.7	Two-phase passive cooling system mass evaluation (first approximation design of three different one-evaporator-CPLIP).	103
4.8	Cooling systems geometrical characteristics.	104
6.1	Summary of experimental tests [12]	140
7.1	Thermal energy ratios during take-off and cruise stage	169
7.2	Individually finned condenser geometrical parameters for different fin pitches and thickness	175
7.3	Parametric study of continuous fins condenser.	177
7.4	Condenser configurations comparison.	177
7.5	Optimised solution geometry, 2025	179
7.6	Optimised solution thermo-hydraulic characteristics, 2025 (C: condensation zone; S: subcooling zone; G: global; F: fin)	179
7.7	Optimised results for the proposed electronic topologies (2025) [1, 21]	182

7.8	Optimised solution geometry, 2035	183
7.9	Optimised solution thermo-hydraulic characteristics, 2035 (C: condensation zone; S: subcooling zone; G: global; F: fin)	184
8.1	Successful and unsuccessful start-up synthesis	198
8.2	Thermocouples distances	201
8.3	Velocity evaluation for hot and cold start up at 0.5 kW and a 2 kW power steps	202
9.1	Acceleration modules, wing zone up to O/B engine	213
9.2	Performed simulations	222

Symbols and Abbreviations

Abbreviations

CHF Critical Heat Flux

CHT Conjugated Heat Transfer

CLT Closed Loop Thermosyphon

CPL Capillary Pumped Loop

CPLIP Capillary Pumped Loop for Integrated Power

CPLTA Capillary Pumped Loop for Terrestrial Applications (see CPLIP)

FPHP Flat Plate Heat Pipe

GHP Grooved Heat Pipe

HP Heat Pipe

HT Heat Transfer

HTC Heat Transfer Coefficient

IGBT Insulated Gate Bipolar Transistor

ISA International Standard Atmosphere

LHP Loop Heat Pipe

MFR Mass Flow Rate

NCG Non condensable Gases

PHP Pulsating Heat Pipe

PPI Pore per Inch

Th Thermosyphon

VC Vapour Chamber

WHF Wall Heat Flux

Greek Symbols

α	Fraction	
α_g	Vapour void fraction	[−]
β	Fluid Compressibility Factor	
Ω	Control Volume	
ρ	Density	[kg · m ^{−3}]
σ	Surface Tension	[N · m ^{−1}]
θ	Wetting Angle	[−]

Roman Symbols

ΔP	Pressure Drop or Pressure Head	[Pa]
\dot{Q}	Heat	[W]
\dot{W}_{comp}	Work	[J]
h	Altitude	[m]
A	Heat transfer surface area	[m ^{−2}]
C_v	Valve Flow Coefficient	[−]
D	Diameter	[m]
d_i	Internal Diameter	[m]
E	Energy	[J]
G	Mass flow rate per unit area	[kg · s ^{−1} · m ^{−2}]
g	Gravity acceleration	[m · s ^{−2}]
$G_{ev,res}$	Evaporator thermal conductance based on the reservoir saturation temperature	[W/K]

$G_{ev,V}$	Evaporator's conductance based on the evaporator saturation temperature [W/K]	
H	Height	[m]
h	Enthalpy	[J · kg ⁻¹]
h	Heat Transfer Coefficient	[W · m ⁻² · K ⁻¹]
$h_{l,v}$	Latent Heat	[J · kg ⁻¹]
j_g^*	Dimensionless Vapour Mass Velocity	[−]
k	Thermal Conductivity	[W · m ⁻¹ · K ⁻¹]
K_V	Volumetric Heat Transfer Coefficient	[W · m ⁻³ · K ⁻¹]
L	Length	[m]
m	Mass	[kg]
N	Valve Number of Turns	
P_V	Evaporator's saturation pressure	[Pa]
Q	Thermal Power [Unless otherwise indicated]	[W]
R	Curvature Radius	[m]
R_p	Pore Radius	[m]
T_V	Evaporator's saturation temperature	[°C]
V	Volume	[m ³]
Fr	Froude number	[−]
We	Weber number	[−]

Subscripts

c	Condenser	
cap	Capillary	
ci	Cold fluid at the inlet of the heat exchanger	
co	Cold fluid at the outlet of the heat exchanger	

<i>D</i>	Diode
<i>diff</i>	Diffuser (wall)
<i>el</i>	Electrical
<i>ext</i>	External (side)
<i>f</i>	frictional
<i>g</i>	Gas (Phase)
<i>go</i>	Gas (vapour) only
<i>hi</i>	Hot fluid at the inlet of the heat exchanger
<i>ho</i>	Hot fluid at the outlet of the heat exchanger
<i>I</i>	IGBT
<i>I</i>	Inlet
<i>int</i>	Internal (side)
<i>l</i>	Liquid (Phase)
<i>lo</i>	Liquid only
<i>max</i>	Maximum
<i>O</i>	Outlet
<i>res</i>	Reservoir
<i>s</i>	Solid (Phase)
<i>sec</i>	Secondary side (cold source)
<i>sns</i>	Sensible (heat)
<i>th</i>	Thermal
<i>tot</i>	Total
<i>v</i>	Vapour (Phase)

Résumé étendu (Français)

Le projet HASTECS (Hybrid Aircraft academic reSearch on Thermal and Electrical Components and Systems) est un projet européen Clean Sky 2 financé par H2020-EU.3.4.5.1. L'objectif de ce projet est le développement d'outils pour la conception et le développement de l'avion du futur à propulsion hybride. En particulier le projet est concentré sur la recherche de la génération, distribution, conversion et management thermique de la chaîne de puissance électrique. Plusieurs instituts de recherche français participent au consortium HASTECS. Par exemple, les sujets liés à l'électronique de puissance et au moteur électrique concernent l'Institut LAPLACE à Toulouse, tandis que leur refroidissement est étudié à l'Institut Pprime à Poitiers. Le partenaire industriel du projet est AIRBUS. Six différentes équipes, associées aux différents WPs (Work Packages), travaillent sur le projet, chacune avec des tâches et objectifs différents. WP1 a pour but la recherche d'une technologie adaptée au moteur électrique (eMotor) ; WP2 travaille sur l'électronique de puissance. Ces engins sont utilisés pour convertir le courant électrique continu (DC) en courant alterné (AC) pour l'alimentation du moteur électrique à la fréquence appropriée : l'équipe doit trouver une technologie de rupture et développer un modèle pour le design des modules de puissance. Le management thermique des eMoteurs et de l'électronique de puissance sont abordées respectivement par le WP3 et le WP4. Tous deux doivent trouver une solution de rupture pour le refroidissement des équipements associés. Au WP3 est demandé le développement d'un modèle à intégrer dans l'outils d'optimisation globale, tandis que le but du WP4, entre autres, est la recherche, la conception, l'optimisation, le développement et l'étude d'une solution d'avant-garde pour le refroidissement de l'électronique de puissance. Ce dernier work package devrait alimenter le WP2 avec des outils de conception simplifiés qui devront être intégrés dans le modèle de conception et d'optimisation globale de la chaîne de conversion hybride. Ainsi, WP2 et WP4 sont fortement couplés entre eux. Ensuite, le WP5 a pour but l'étude des décharges partielles, bus-bars et câbles et, pour finir, la tâche du WP6 est l'étude de l'intégration des sources auxiliaires : piles à combustible et batteries, pour une optimisation de la masse embarquée dans l'avion. Tous les WPs convergent vers le WP6. Le but du sujet présenté dans ce travail (WP4), principalement numérique, est de rechercher, concevoir, et optimiser une solution pour le refroidissement de l'électronique de puissance en

contexte aérien. Un tel système de refroidissement devrait être capable d'évacuer la chaleur tout en assurant le contrôle de température au niveau de la semelle des composants électroniques, et répondant aux contraintes de masse imposées par AIRBUS. À cet effet, des modèles ont été développés et certains, déjà existants, ont été modifiés et adaptés. Les principales problématiques stationnaires et transitoires ont été abordées et résolues et, quand cela a été possible, comparées avec des résultats issus de tests expérimentaux. La thèse est divisée en cinq parties. Ici, les problématiques scientifiques et technologiques d'ingénierie ont été abordées dans le but de proposer une solution robuste et fiable.

La problématique du refroidissement de l'électronique de puissance pour l'avion hybride

Le refroidissement de l'électronique de puissance est l'un des problèmes majeurs de la gestion des nouvelles motorisations électriques du futur. L'augmentation de la puissance électrique des composants a mené à l'augmentation de la puissance thermique à évacuer. Dans le passé, la problématique du refroidissement des composants électroniques a été sous-évaluée car les technologies classiques de refroidissement (convection forcée à air) étaient plus ou moins capables d'évacuer la puissance thermique tout en maintenant la température des composants électroniques à des niveaux raisonnables. Un grand effort a été fait pour augmenter l'efficacité des composants électroniques, mais comme cela était facilement prévisible, l'asymptote a été atteinte et les technologies de refroidissement n'ont pas évolué ! Dans le même temps, certaines technologies encore plus performantes n'étaient pas accessibles car les pertes thermiques étaient encore trop importantes. L'efficacité électrique ne devrait pas être vue comme un nombre à maximiser à tout prix : à n'importe quelle transformation d'énergie, des pertes thermiques y sont associées (qui peuvent être réduites mais pas annulées) et donc, quel que soit le système, le rendement sera toujours inférieure à 1. Si la puissance demandée par les moteurs électriques est $Q_{el} = 1.5 \text{ MW}$, en considérant une efficacité des modules de puissance $\eta_{el} = 99\%$, la puissance totale à fournir est de $Q_{el} = 1.515 \text{ MW}$, et les pertes associées de $Q_{th} = 15 \text{ kW}$. Cette valeur est bien loin d'être négligeable et un système de refroidissement capable d'évacuer cette puissance thermique est donc nécessaire. Dans le cas des applications à puissance électrique élevée, le problème est encore plus évident car les pertes doivent être évacuées en maximisant l'efficacité globale du système (électrique + thermique). L'optimisation n'est plus limitée à la simple optimisation de chaque composant du système, mais il est nécessaire de considérer le système dans sa globalité pour augmenter l'efficacité, calculée sur la base d'un indice. Dans le cas des applications aéronautiques, le système doit répondre aussi à des contraintes de masse et de volume occupé. Pour mesurer la légèreté d'un système, par rapport à son utilité, on introduit le concept

de coefficient de puissance, C_c [$\text{kW}\cdot\text{kg}^{-1}$]. Ce dernier représente la puissance électrique convertie pour chaque kg de masse du système, y compris du refroidissement. Deux objectifs ont été donnés pour résoudre le problème. Le premier objectif, à l'horizon 2025 est d'obtenir $C_{c,2025} = 15 \text{ kW}\cdot\text{kg}^{-1}$, tandis que celui à l'horizon 2035 est d'atteindre $C_{c,2035} = 25 \text{ kW}\cdot\text{kg}^{-1}$, a minima ! L'énergie demandée à la chaîne de propulsion d'un avion n'est pas constante dans le temps, mais varie en fonction des différentes phases de vol. Comme pour la puissance mécanique demandée aux moteurs électriques, la puissance que les modules de puissance doivent convertir et, par conséquence, la puissance thermique à évacuer, changent dans le temps. A partir d'un profil de mission type, cinq phases de vol peuvent être distinguées. Pendant la première phase, l'avion reste au sol et les pertes thermiques sont les plus faibles. La deuxième phase, de « take-off & climb » (décollage et ascension), peut être divisée en deux sous-phases : le take-off, qui représente le moment où l'avion accélère sur la piste et où la puissance maximale est demandée aux moteurs pour faire décoller l'avion, et l'ascension, où l'avion monte jusqu'à atteindre la hauteur h_{max} . La phase de croisière est presque stationnaire, la puissance thermique à évacuer est constante dans le temps et sa durée est d'environ 70 minutes. De façon identique à la deuxième phase, la phase de descente et atterrissage peut être divisée en deux sous-phases. Pendant la descente l'avion plane jusqu'à l'approche et c'est là qu'un pique de puissance est demandé. Enfin, pendant la phase de « taxi-in », la puissance thermique à évacuer est la même que pendant la phase de « taxi-out ». La variation dans le temps de la puissance thermique à évacuer est aussi accompagnée par une variation de température de l'air ambiant et donc de la source froide. Le lien entre l'altitude et la température de l'air est exprimée par le NASA's Earth Atmosphere Model [22], selon lequel, dans la troposphère ($h \leq 11\,000 \text{ m}$), le lien entre les deux grandeurs est linéaire. Les systèmes de communication radio, les systèmes embarqués et autres systèmes électroniques installés à bord sont aussi refroidis en utilisant directement ou indirectement l'air extérieur comme source froide. Comme la plupart de ces systèmes, l'idée développée au cours de cette thèse est d'utiliser l'air extérieur comme source froide, en utilisant une boucle de refroidissement pour transporter la chaleur de la source chaude à la source froide où la puissance thermique est définitivement évacuée. De plus, l'utilisation de « heatsinks » plus performantes, permettrait d'augmenter l'efficacité de l'échange thermique en atteignant des coefficients d'échange d'ordre de grandeur plus élevés que ceux liés à la simple convection forcée à air. Deux différentes technologies sont ici considérées comme sources froides : l'échangeur à peau (skin heat exchanger) qui introduit une résistance additionnelle à cause de la présence d'une paroi solide entre la tuyauterie de la boucle de refroidissement et l'air externe : la peau de l'avion ; et le système RAM-air qui permet un

contact direct entre l'air ambiant et les tubes de l'échangeur de chaleur. L'échangeur à peau peut être vu comme faisant déjà partie de l'avion, les tuyaux passent à l'extérieur de la couche isolante de l'avion. Pang et al. [4] ont analysé cette technologie pour un avion volant à Mach 0.9, et à 10 km d'altitude. En considérant deux emplacements différents pour l'échangeur à peau, ils ont trouvé une position défavorable, où le coefficient d'échange thermique était entre $45 - 51 \text{ W} \cdot \text{m}^{-2} \cdot \text{K}^{-1}$, tandis que pour la position la plus favorable le coefficient d'échange était entre $80 - 66 \text{ W} \cdot \text{m}^{-2} \cdot \text{K}^{-1}$. Le système RAM-air représente la technologie la plus ancienne permettant d'amener l'air extérieur à bord de l'avion pour être utilisé comme source froide pour le refroidissement des systèmes électroniques ou autres. Il est composé par une entrée d'air de type NACA, un diffuseur, le côté secondaire de l'échangeur de chaleur, une tuyère (simplement convergent) et la sortie d'air. Ce système est caractérisé, bien sûr, par un encombrement plus grand que celui de l'échangeur à peau, mais il est capable d'assurer des coefficients d'échange thermique bien plus élevés que ce dernier.

Solutions de refroidissement existantes

A cause de la complexité des systèmes de refroidissement, du nombre de composants, des différentes principes physiques liés à leur fonctionnement, il n'existe pas de classification universelle. Les performances dépendent, bien sûr, du système de refroidissement et de son architecture, ainsi que de la typologie du « heatsink » (module de refroidissement situé au niveau de la source chaude) utilisé. En général, un système de refroidissement est utilisé pour maintenir la température du dispositif à refroidir contrôlée tout en évacuant la puissance thermique. Dans ce but, deux différentes méthodes sont utilisées :

- refroidir le dispositif en utilisant directement l'air externe (refroidissement à air ou, plus généralement, circuits de refroidissement ouverts)
- refroidir le dispositif en utilisant une boucle à circuit fermé (refroidissement liquide ou, plus en général, circuits de refroidissement fermés).

Dans le premier cas, à cause du fait que l'air extérieur est utilisé directement comme fluide caloporteur, en particulier dans le domaine aéronautique, il est nécessaire de considérer certaines contraintes comme la variabilité de la température, de la pression et de la masse volumique de l'air extérieur. Tous ces facteurs ont un impact pas tout à fait négligeable sur le coefficient d'échange thermique et donc sur les performances du système de refroidissement. La seconde méthode est plus pertinente. En effet, grâce à l'utilisation d'un circuit intermédiaire entre la source froide et le dispositif à refroidir, il y a un dé-couplage entre le coefficient d'échange de l'échangeur secondaire et celui au niveau du « heatsink ». Tout ça est encore plus vrai lorsque l'on considère les systèmes de refroidisse-

ment diphasiques, actifs ou passifs. Dans ce cas, le coefficient d'échange du « heatsink » dépend de la technologie utilisée (microcanaux, mousse métalliques ou autres) et non pas des caractéristiques de l'air extérieur. Un circuit fermé est donc le choix le mieux adapté. Les systèmes à circuit fermé peuvent être divisés entre systèmes actifs et passifs. Dans les systèmes actifs l'utilisation d'une pompe ou d'un compresseur (selon la typologie) est nécessaire pour permettre le mouvement du fluide caloporteur dans la boucle. Les systèmes passifs, en revanche, utilisent la gravité ou la capillarité pour générer l'écoulement nécessaire au fluide de refroidissement. Dans les systèmes actifs, la pompe (ou compresseur dans le cas de systèmes à compression de vapeur), doit être conçue pour contrebalancer toutes les pertes de charge dans le circuit et assurer le bon débit pour l'évacuation de la chaleur. Un vase d'expansion est utilisé pour amortir des instabilités éventuelles (coup de bâlier ou dilatation du fluide caloporteur due à l'augmentation de température). Les systèmes actifs peuvent être mono ou diphasique et, même si les principes de fonctionnement sont profondément différents, les composants sont peu ou prou identiques et jouent le même rôle. La technologie des systèmes actifs monophasiques est sans doute la plus ancienne, aussi connue comme "refroidissement à liquide", son utilisation est très étendue à cause de sa simplicité et de la bonne connaissance de phénomènes à la base de son fonctionnement. Le fluide est chauffé dans le "heatsink", puis s'écoule dans la ligne de transport et, finalement, il arrive dans l'échangeur froid où la chaleur est évacuée. Selon la disponibilité de la source froide, l'une des technologies présentées dans le premier chapitre peut être utilisée. L'une des principales limitations liées à l'utilisation de cette technologie est la forte dépendance entre la température de la source froide et la température de la source chaude et, par conséquence, de la température de jonction du composant. On démontre très facilement que la température de jonction a un lien direct avec la température d'entrée de l'air dans l'échangeur de chaleur, ce qui peut limiter l'application de cette technologie à notre cas. En effet, à cause des changements de température de l'air extérieur en fonction de l'altitude (ici on ne considère pas les changements de la masse volumique et de pression), la capacité de maintenir la température de jonction fixe, quelle que soit la condition opératoire, devient très difficile. Cependant, il est possible de garder cette caractéristique, mais au prix de pouvoir faire varier soit le débit du fluide caloporteur soit celui de l'air, en rajoutant un système de vannes et d'autres accessoires compliquant fortement le système de refroidissement et sa régulation. Dans les systèmes diphasiques, les chaleurs latente et sensible du fluide sont utilisées pour évacuer la chaleur : le "heatsink" est alors un évaporateur tandis que l'échangeur froid est un condenseur (avec sous-refroidissement). Le liquide sous-refroidi en provenance du condenseur/échangeur froid s'écoule vers l'évaporateur. Le fluide chaud

rejoint à nouveau le condenseur/échangeur froid où la chaleur est définitivement évacuée vers l'air extérieur et le cycle recommence. Les systèmes actifs diphasiques sont divisés en deux catégories : les systèmes pompés dont l'évaporateur opère forcement à une température plus élevée que le condenseur et où une pompe est installée sur la ligne liquide ; les systèmes à compression de vapeur dont l'évaporateur peut opérer à des températures plus basses que le condenseur (grâce à l'utilisation d'un cycle de Rankine) et où un compresseur est installé sur la ligne vapeur. Le liquide sous-refroidi provenant du condenseur, et traversant le réservoir, où les conditions de saturation sont imposées, rentre dans l'évaporateur où les chaleurs sensible (marginale) et latente sont évacuées. Dans cette technologie, le titre de vapeur en sortie de l'évaporateur est $x_{sortie} < 1$ tandis que la différence entre la température de saturation, T_{sat} , et la température d'entrée, T_{in} , est normalement négligeable ($T_{in} \leq T_{sat}$). De surcroît, si la surchauffe de la vapeur est absente on a $T_{out} = T_{sat}$. Le fluide ainsi complètement ou partiellement évaporé s'écoule dans la ligne vapeur jusqu'au condenseur. Ici la vapeur est condensée et sous-refroidie jusqu'à que sa température soit proche de celle d'entrée du fluide froid T_{ci} . Les systèmes à compression de vapeur permettent à l'évaporateur de travailler à une température plus faible que celle du condenseur. Dans ces systèmes, la vapeur en sortie de l'évaporateur doit être surchauffée pour ne pas avoir la dite « compression humide ». Si la surchauffe change à cause des changements des conditions opératoires, la valve de régulation agit pour conserver des conditions thermodynamiques constantes pour la vapeur. Ces technologies sont hautement performantes et avec des rendements très élevés, mais elles sont encore considérées comme prématurées pour la plupart des auteurs. Les systèmes passifs ne nécessitent quant à eux aucune forme d'énergie externe pour permettre l'écoulement du fluide dans la boucle. Dans les trente dernières années ces systèmes se sont imposés comme standards dans les applications spatiales, en particulier pour le refroidissement des systèmes radio et dissipatifs des satellites. Dans la suite, une très rapide explication des différentes technologies considérées dans ces travaux est reportée. Le thermosiphon est composé par un tube hermétiquement fermé à des deux extrémités et rempli d'une petite quantité de liquide. Quand la puissance thermique est appliquée au niveau de la partie inférieure (évaporateur), le fluide s'évapore et la vapeur s'écoule (à travers la section adiabatique) vers la partie supérieure : le condenseur. Ici, la vapeur se condense et le liquide s'écoule par gravité vers l'évaporateur où le cycle recommence. La condition nécessaire pour que ce système puisse fonctionner est que le condenseur se trouve au-dessus de l'évaporateur. Les caloducs capillaires sont, sous certains aspects, proches des thermosiphons. En effets, ils gardent la même structure que les thermosiphons, mais leur paroi interne est recouverte de tout son long d'une structure capillaire (rainures,

poreux frittés ou à mèche). Dans ce cas, le condensat est ramené par capillarité vers l'évaporateur. Ce mode de fonctionnement permet de dépasser la problématique liée à l'installation du condenseur au-dessus de l'évaporateur dans les thermosiphons. Les caloducs sont utilisés avec succès dans le cadre du refroidissement de la microélectronique, là où les distances de transport ne sont pas trop importantes (voir refroidissement puces d'ordinateurs ou de smartphones). Plusieurs typologies de caloducs sont décrites dans le manuscrit, le lecteur est invité à consulter la version intégrale du texte pour plus de détails. Parmi les systèmes passifs, citons les boucles passives à pompage capillaire. La Loop Heat Pipe (LHP) et la Capillary Pumped Loop (CPL) sont composées d'un évaporateur, d'un condenseur et d'un réservoir. La différence principale entre les deux systèmes est liée à la position de ce dernier : directement accolé à l'évaporateur pour les LHP. Cette configuration permet des échanges de masse et de chaleur entre les deux composants, ce qui permet la transmission d'une partie de la chaleur depuis l'évaporateur vers le réservoir. C'est le flux thermique qui modifie les conditions de saturation dans le réservoir même, en donnant lieu à la capacité d'autorégulation typique de cette boucle. Les CPL sont quant à elles caractérisées par un découplage entre l'évaporateur et le réservoir, qui est installé sur la ligne vapeur et relié à cette dernière à travers un petit tube dont le diamètre ne permet pas trop facilement des échanges de masse avec le reste de la boucle. Dans ce cas, les conditions de saturation y sont maintenues par un réchauffeur électrique. Ce principe de fonctionnement permet bien sûr de contrôler la température opératoire, mais le découplage entre le réservoir et l'évaporateur donne lieu à des instabilités et des oscillations, en particulier pendant les phases de démarrage. Ces deux technologies n'ont pas été retenues dans le cadre du projet HASTECS à cause de leurs limites. En revanche, un nouveau type de boucle, la Boucle Gravitaire à Pompage Capillaire ou CPLIP (Capillary Pumped Loop for Integrated Power) permet de dépasser toutes ces limitations et est parfaitement adaptée au refroidissement de l'électronique de puissance, ce pour quoi elle a été imaginée depuis 2006. Son principe de fonctionnement est décrit en détail dans le texte.

Refroidissement de l'électronique de puissance : état de l'art des “heatsinks”

Dans le chapitre 3 les différentes technologies disponibles pour les “heatsinks” sont présentées, telles que l'impact de jet, les microcanaux, les milieux poreux et mousses métalliques, pour donner une idée des technologies utilisables dans le cadre du projet HASTECS. Tous les systèmes caractérisés par un contact direct entre la surface à refroidir et le fluide de refroidissement appartiennent à la catégorie des systèmes à refroidissement direct. Ils sont donc caractérisés par l'absence d'une résistance thermique entre le fluide caloporteur et les composants électroniques. Ces sont des systèmes très

performants, dont le coefficient d'échange thermique est l'un des plus élevés. En général leur utilisation est justifiable quand la résistance convective du système direct est inférieure à la somme des résistances d'un système direct. Les systèmes à impact de jet et le refroidissement par spray ("spray cooling") ont des mécanismes d'échange thermique très complexes, et les phénomènes liés à leur fonctionnement ne sont pas complètement compris. Certains auteurs ne sont pas toujours d'accord pour ranger les deux systèmes dans la même catégorie, on peut tout de même affirmer que le concept de refroidissement par spray représente une extension du concept d'impact de jet. En général on peut dire que la différence tient du fluide caloporteur utilisé. Dans le "spray cooling" un mélange gaz/liquide est souvent utilisé pour permettre l'atomisation du fluide pendant son écoulement dans l'atomiseur, tandis que dans le cas de l'impact de jet l'échange thermique est strictement lié à la vitesse du fluide, souvent monophasique, canalisé vers la surface à refroidir. Au contraire des systèmes directs, dans les systèmes indirects il n'y a pas de contact entre le fluide de refroidissement et la semelle du composant électronique. A cette catégorie appartiennent les plaques à eau, les microcanaux, les mousses métalliques et les milieux poreux. Tous les systèmes ici nommés peuvent à la fois être utilisés dans des systèmes de refroidissement mono ou diphasiques. La plaque à eau est la configuration la plus basique, bien connue et beaucoup utilisée en raison de sa simplicité, en particulier dans sa configuration monophasique. Selon l'environnement, différentes fluides peuvent être utilisés, et logiquement les performances et la masse finale du système de refroidissement en dépendent aussi. Par exemple, Sakanova et al. [9] ont étudié trois fluides caloporteurs monophasiques (eau, huile et fioul) dans un tel système, pour des applications aéronautiques, et ont conclu que l'utilisation du fioul était le meilleur compromis entre performances et masse du système. L'une des technologies les plus prometteuses pour l'évacuation de densités de flux de chaleur très élevées à partir le composants électroniques de petite taille : les « heatsinks » à microcanaux sont composés de matériaux à très faible résistance thermique traversés par une série de canaux parallèles dont le diamètre hydraulique est inférieur ou égal à 1 mm. Il est possible d'utiliser différents matériaux, mais le silicium est l'un des plus utilisés. Par exemple Colgan et al. [23] ont réussi à évacuer une densité de flux de $300 \text{ W} \cdot \text{cm}^{-2}$. Malgré la perte de charge élevée liée à cette technologie, ils ont démontré que son utilisation est valable en particulier pour sa capacité à maintenir une température plus ou moins uniforme au niveau de la puce à refroidir. En revanche, concernant la physique de ce système, actuellement il n'y a pas de modèle thermo-hydrodynamique universellement accepté et les résultats des différentes études de la littérature sont souvent contradictoires. Quoi qu'il en soit, les performances des microcanaux mono ou diphasiques sont indéniables, et les échangeurs de chaleur qui uti-

lisent cette technologie sont caractérisés par des coefficients d'échange volumétriques qui peuvent atteindre $10^8 \text{ W}\cdot\text{m}^{-3}\cdot\text{K}^{-1}$ contre des valeurs typiques des échangeurs classiques de $100 \text{ W}\cdot\text{m}^{-3}\cdot\text{K}^{-1}$ [24] ! Les milieux poreux et les mousses métalliques représentent une alternative valable aux microcanaux, en particulier si les densités de flux thermiques sont très élevées. Les mousses métalliques sont caractérisées par des surfaces d'échange thermique très élevées en raison de leur structure complexe et tortueuse constituée d'un matériau à très haute conductivité thermique. Le fluide s'écoule dans un « chemin » tortueux à travers la structure tridimensionnelle qui augmente ainsi la surface mouillée. La présence d'une mousse métallique n'augmente pas que la surface d'échange thermique, mais aussi la conductivité thermique effective des “heatsinks”. Sa présence favorise l'homogénéisation du champ de température sur la surface du « heatsink » grâce à un effet diffusif propre à ce type de milieu. Ces effets de diffusion thermique sont différents selon que l'on considère des milieux poreux frittés ou non, étant donné que les contacts solide-solide et solide-liquide jouent un rôle fondamental dans les transferts de chaleur. En général, on peut dire que les milieux frittés sont caractérisés par des propriétés de diffusion thermique bien meilleures que les mousses ou les milieux non frittés. Ce phénomène les rend plus efficaces d'un point de vue de l'évacuation de la chaleur, mais le prix à payer est lié aux pertes de charges associées à ces systèmes. Même si on les considère dans une configuration diphasique, avec une réduction du débit nécessaire pour l'évacuation de la même quantité de chaleur, les pertes de charge associées à une telle configuration ne se réduisent pas par rapport à leur contrepartie monophasique.

Choix de la technologie

Il s'agit dans le chapitre 4 de choisir la solution la mieux adaptée aux besoins du refroidissement de l'électronique de puissance dans le cadre du projet HASTECS, tant du point de vue système que local au niveau de la source chaude. Tous les systèmes présentés précédemment sont capables d'évacuer la charge thermique requise tout en assurant des performances importantes, mais il est nécessaire que le système choisi soit capable de répondre aux contraintes de masse imposées dans le cadre du projet HASTECS pour permettre au système de voler. Pour bien choisir le système le plus adapté à répondre aux objectifs imposés, le choix va être basé sur une conception de première approximation et sur une comparaison des masses des systèmes : le plus léger sera celui qui sera choisi et optimisé par la suite. Deux systèmes actifs, mono et diphasique, équipés d'une plaque à eau, et un système passif à pompage capillaire, la CPLIP, seront donc comparés. Un certain nombre d'hypothèses, dont une explication détaillée est reportée dans le manuscrit, ont été faites. Bien évidemment toutes les conditions opératoires et conditions limites pour le dimensionnement sont maintenues constantes et identiques pour les trois

systèmes comparés. Le système monophasique est considéré dans sa forme la plus simple : les vannes et les autres accessoires de régulation ont été négligés dans cette première approximation. Les lignes de transport, chaude et froide, ont une longueur de 1 et 1,2 m et ont la même section transversale. Les trois « heatsinks » (six composants d'électronique de puissance à refroidir en parallèle) sont installés en parallèle et en position verticale, et sont traversés par neuf canaux parallèles, dont la section est de 0,8 cm, dans lesquels le fluide caloporteur s'écoule. L'échangeur froid air-liquide non-aileté à courants croisés a une longueur totale de 80 m. Il est composé de 5×20 tubes dont la section transversale est égale à celle des lignes de transports. La pompe est dimensionnée pour assurer un débit de $11,35 \text{ litres} \cdot \text{min}^{-1}$ et une pression de 590 kPa. Comme pour le système monophasique, le système diphasique actif a été conçu dans sa forme la plus simple. Il est aussi constitué de trois « heatsinks » installés en parallèle et verticalement. Comme déjà expliqué dans le chapitre 2, cette technologie ne nécessite pas la complète évaporation du fluide caloporteur, mais pour ne pas condamner a priori cette solution avec un débit plus élevé que nécessaire, il a été choisi un titre de vapeur $x = 1$ en sortie de l'évaporateur. Les lignes de transport ont la même longueur que celles du système monophasique, mais leur section transversale est différente. La ligne vapeur a un diamètre de 21,2 mm tandis que celui de la ligne liquide est de 3,5 mm. Le condenseur conserve la même configuration que l'échangeur de la technologie monophasique, 5×20 tubes dont la section transversale est celle de la ligne vapeur, mais sa longueur est de 50 m. Le débit qui s'écoule est d'un ordre de grandeur inférieure à celui demandé par le système monophasique. Pour des raisons de choix de pompe (consulter le manuscrit original pour plus d'infos), les « heatsinks » sont traversés par un seul canal à serpentin dont le diamètre hydraulique de la section transversale est de 12 mm. Pour la comparaison reportée dans ce chapitre, la CPLIP a été considérée selon deux configurations : une première utilisant une seule boucle équipée de trois évaporateurs installés en parallèle, et une deuxième utilisant trois boucles distinctes équipées d'un seul évaporateur, et dont la puissance thermique de chacune est un tiers de la puissance totale à évacuer. Dans tous les cas, les dimensions des évaporateurs sont proportionnelles à celles des modules de puissance installés. Ils sont équipés d'un milieux poreux en nickel dont la porosité est 73% et le diamètre moyen des pores est $6,2 \mu\text{m}$. Les lignes de transport, dans la configuration avec trois évaporateurs en parallèle, ont les mêmes dimensions que celles du système diphasique pompé. Les systèmes actifs monophasiques sont en général plus légers que les systèmes actifs diphasiques. Les deux technologies sont caractérisées par une même masse à vide, mais une quantité de fluide plus importante est contenue dans le système diphasique. Une telle quantité de fluide est justifiée par un volume du condenseur plus important et donc par un volume

du réservoir plus grand. Les systèmes actifs sont fortement impactés dans leur masse par la présence de la pompe, dont la masse est respectivement de 19% de la masse totale de la boucle monophasique et de 27% de la boucle diphasique. Ceci est la principale raison pour laquelle la CPLIP peut assurer une économie en masse d'au moins 20%. C'est la technologie dont la masse est assurément la plus faible et, même si elle n'a pas encore été optimisée, dont le coefficient de puissance ($\text{kW}\cdot\text{kg}^{-1}$) est le plus proche de celui imposé pour l'horizon 2025.

CPLIP : principe de fonctionnement, dispositif expérimental et modèle numérique

La boucle diphasique passive CPLIP est composée d'un évaporateur, d'un condenseur et d'un réservoir. En conditions stationnaires, la chaleur en provenance des modules de puissance installés sur l'évaporateur arrive aux niveaux des ménisques liquide/vapeur par conduction à travers le milieu poreux et déclenche la vaporisation au niveau de ces interfaces. La vapeur, en sortie de l'évaporateur, s'écoule à travers la ligne vapeur vers le condenseur où a lieu la désurchauffe, la condensation et le sous-refroidissement du liquide. Le liquide sous-refroidi s'écoule dans la ligne liquide vers le réservoir, divisé en deux parties séparées par une plaque. Même si, en conditions stationnaires, il n'y a pas d'échanges de masse entre les parties haute et basse du réservoir, le liquide en provenance du condenseur est chauffé par conduction à travers la plaque de séparation et par convection à travers le liquide contenu dans le réservoir. Le liquide s'écoule ainsi vers l'évaporateur, où il mouille à nouveau le milieu poreux et, chauffé par la chaleur dégagée par les chauffeurs électriques, vaporise en faisant recommencer le cycle. Le dispositif expérimental utilisé dans le cadre de cette thèse, aussi appelée CPLIP 1.1, a été à l'origine développé en 2006 pour des études liées au refroidissement de modules d'électronique de puissance pour des applications ferroviaires. Toute la boucle est en acier à l'exception de l'évaporateur, composé de différentes matériaux pour assurer un transfert de chaleur adéquate entre les corps chauffants et le milieu poreux (ce dernier étant en nickel). Le réservoir est cylindrique, a un diamètre externe de 99,6 mm et une longueur de 308 mm. La hauteur de la plaque de séparation est de 6mm. La température et la pression de saturation du réservoir sont imposées par une cartouche chauffante installée dans la partie haute de ce dernier. Le bâti de l'évaporateur est en acier et nickel, et contient le milieu poreux en nickel dont la porosité est de 73%, le diamètre moyen des pores de $6,8 \mu\text{m}$ et la perméabilité de $6,53 \cdot 10^{-13} \text{ m}^2$. Trois artères liquides y assurent l'alimentation du liquide en provenance du réservoir. Le condenseur est un échangeur de type « tube-in-tube » dont la longueur est de 4,04 m, alimenté au secondaire par un mélange eau-glycol à 30%, refroidi par un cryostat d'une puissance nominale de 8 kW. Sur la ligne vapeur, en acier elle aussi, est installée une valve à travers laquelle il est possible d'augmenter les pertes

de charges afin d'étudier de quelle manière le comportement thermique de la boucle est influencé par un changement des caractéristiques hydrauliques. Le modèle, quant à lui, introduit au cœur de ce chapitre [25] est celui qui va être utilisé tout au long des chapitres suivants pour des études à la fois stationnaires et transitoires. Le modèle est du type monodimensionnel et homogène. Il résout les équations de conservation de la masse, de la quantité de mouvement et de l'énergie à travers l'analogie thermique-électrique en utilisant le solveur d'ESACAP®. Le fluide est considéré compressible tandis que la phase vapeur est considérée comme un gaz parfait. Les équations de conservation de la masse et de la quantité de mouvement sont résolues à travers deux maillages décalés pour permettre une stabilité numérique grâce au fait que les variables de pression et de vitesse ne se trouvent pas sur le même nœud et réduisant les erreurs dues aux propriétés thermophysiques basées sur les valeurs d'enthalpie et de pression. L'équation de l'énergie est résolue sous une forme enthalpique plutôt qu'en utilisant la température comme variable d'état. Ce choix permet d'aller au-delà des limitations liées à la définition de l'état physique du fluide à travers la température, qui autrement présenterait une discontinuité en correspondance à la température de saturation. Le modèle prend en charge la modélisation du réservoir, à la fois dans sa partie haute et sa partie basse. Les deux parties sont modélisées chacune à l'aide d'un seul nœud. En particulier, l'hypothèse d'homogénéité entre les deux phases fluides est respectée dans la partie basse, mais pas dans la partie haute, à cause de la coexistence des phases liquide et vapeur et de la présence d'une interface, mobile, qui les sépare. Les échanges de masse et d'énergie dans l'évaporateur sont très complexes et pas encore bien connus. Une approche de type « microscopique » serait trop complexe et onéreuse d'un point de vue du temps de calcul ; c'est pourquoi les auteurs [25] (et [26] avant lui) ont décidé d'utiliser des paramètres empiriques. Les valeurs des conductances expérimentalement obtenues seront donc utilisées dans ce but. La façon dont l'analogie thermique-électrique est utilisée pour la résolution du modèle est abordée à la fin du chapitre.

La réponse de la CPLIP aux contraintes d'HASTECS

L'analyse reportée dans ce chapitre est de type expérimental. Elle se base sur deux différentes campagnes de tests dont le but était de caractériser des points de vue thermique et hydraulique la CPLIP en régime stationnaire. L'étude paramétrique a pour but la connaissance de l'influence que la puissance thermique appliquée à l'évaporateur, \dot{Q} , la température de consigne au réservoir, T_{res} , et la température de la source froide, T_{sec} , ont sur le comportement de la boucle. En plus de ces trois paramètres thermiques, une étude hydraulique sur la réponse thermique de la boucle a été menée, dont le but était de connaître quelle influence ont les pertes de charge de la vapeur introduites à travers

la fermeture d'une vanne dont les caractéristiques hydrauliques sont connues. Dans le souci d'évaluer le coefficient d'échange à l'évaporateur, les valeurs des conductances thermiques ont été obtenues sur la base de la différence de température entre la paroi de l'évaporateur et la température de saturation du réservoir ($T_{diff} - T_{res}$) et entre la température de paroi de l'évaporateur et la température d'évaporation ($T_{diff} - T_V$). À cause de l'impossibilité de mesurer directement cette dernière, un outil de post-traitement basé sur la reconstruction du cycle thermodynamique a été utilisé se basant sur les valeurs de température mesurées. Les paramètres manquants ont été calculés en utilisant la relation entre pression et température sur la courbe de saturation. Les caractéristiques principales de la boucle ont été expliquées en utilisant ces cycles thermodynamiques simplifiés, qui montrent bien les raisons pour lesquelles la CPLIP s'est avérée particulièrement intéressante dans le cadre du projet HASTECS. Par exemple, la température de paroi de l'évaporateur ainsi que sa perte de charge sont fortement dépendantes de la puissance thermique appliquée, tandis qu'il n'y a pas de dépendance entre la température de la source froide et la température de l'évaporateur. Cette dernière caractéristique rend la CPLIP particulièrement efficace pour ce type d'applications où la température de la source froide varie, y compris de manière significative, mais nécessitant une température constante de la source chaude, telle que dans ce contexte aéronautique. Dans le même temps, il est possible de contrôler sa température en agissant sur la température de consigne imposée au réservoir. Bien évidemment, cela a un impact non négligeable sur les valeurs des conductances thermiques, qui varie aussi en fonction de la puissance appliquée à l'évaporateur et du fluide utilisé. Bien qu'il existe une différence entre les valeurs de conductances thermiques, selon si elles sont basées sur la différence ($T_{diff} - T_{res}$) : $G_{ev,res}$, ou sur ($T_{diff} - T_V$) : $G_{ev,V}$, il a été observé que pour des puissances élevées les différences entre ces dernières deviennent négligeables tandis que pour des basses puissances les valeurs divergent. Sur la base des valeurs de conductance mesurées il a été possible de mener une étude numérique aux volumes finis dans le but d'obtenir la carte des températures sur les modules de puissance dans les pires conditions opératoires. Le module choisi par l'équipe d'électroniciens a donc été précisément reproduit numériquement et des simulations 3D stationnaires ont été faites en résolvant l'équation de l'énergie. Bien évidemment, une étude de sensibilité sur la dimension du maillage a été également menée. Sur la base de la puissance appliquée sur les diodes et les IGBT, et rapportée aux dimensions des composants, il a été trouvé une densité de flux thermique atteignant respectivement $242 \text{ W}\cdot\text{cm}^{-2}$ et $92 \text{ W}\cdot\text{cm}^{-2}$. Malgré ces densités de flux les températures des composants les plus sollicités (les diodes) ne dépassent pas 130°C pour une température maximale de 150°C conseillée par les constructeur des modules.

La CPLIP est donc capable de maintenir la température contrôlée bien en-dessous du seuil indiqué. Pour ce qui concerne le régime transitoire, et dans le souci d'exploiter le comportement de la boucle pendant un profil de mission réel, la CPLIP 1.1 a été testée expérimentalement pour observer sa réponse en particulier pendant les phases les plus critiques : augmentation soudaine de la puissance thermique évacuée par les composants électroniques pendant la phase de décollage ; réduction violente de la puissance évacuée entre la fin de la phase de décollage et le début de la croisière. La boucle a démontré pendant ces tests être bien adaptée à de tels variations de puissance et les valeurs de température enregistrées collaient parfaitement avec les prévisions des modèles. L'étude du comportement de la boucle suivant des changements des caractéristiques hydrauliques a été abordée en utilisant la même méthodologie expérimentale et outil de post-traitement déjà décrits. La première impression est que l'augmentation des pertes de charge dans la ligne vapeur a le même impact que l'augmentation de la puissance thermique. Les températures ne dépendent pas que de la puissance appliquée à l'évaporateur, mais aussi des pertes de charges. La longueur de la ligne vapeur, la configuration de la boucle, la typologie et la configuration du condenseur, et le fluide caloporteur ont un impact sur la réponse de la boucle et en particulier les conductances thermiques sont particulièrement sensibles aux caractéristiques hydrauliques.

Optimisation de la CPLIP pour 2025 et 2035

Les résultats de l'optimisation d'une CPLIP aux horizons 2025 et 2035 sont présentés dans le chapitre sept. En se basant sur la distribution de masses de la CPLIP à trois évaporateurs en parallèle, il a été observé que le composant le plus critique était le condenseur. Sa masse à vide est le 40% du totale, et ses dimensions ont un impact sur la masse totale de fluide contenu dans la boucle (48% de la masse totale), et sur la masse à vide du réservoir (9%) dont le volume interne est égal aux volumes du condenseur et de la ligne vapeur cumulés. La réduction des dimensions du condenseur est donc la priorité si l'on veut obtenir les résultats demandés dans le cadre du projet HASTECS. Pour rappel, la solution retenue pour la source froide était une solution de type RAM-air, dont l'air s'écoule, dans la pire condition opératoire à une vitesse de $10 \text{ m} \cdot \text{s}^{-1}$ et une température de 33°C . Pour la solution 2025 deux différentes typologies de condenseur ont été étudiées et comparées afin de choisir la mieux adaptée. La solution la plus simple, celle qui prévoyait l'utilisation d'ailettes circulaires a été enfin écartée car elle ne permettait pas de parvenir à des masses « acceptables » selon les contraintes imposées par le projet HASTECS. En revanche, le condenseur à ailettes continues a permis de baisser la masse du condenseur même et de réduire sa longueur ainsi que le volume de fluide contenu. Dans la solution optimisée, la CPLIP est caractérisée par une masse d'environ 11 kg pour

l'évacuation d'environ $16 \text{ kW}_{\text{th}}$. Si l'on considère le système dans sa totalité (électronique de puissance + refroidissement) le coefficient de puissance totale obtenu est supérieur à $19 \text{ kW} \cdot \text{kg}^{-1}$ relativement à une cible imposée pour l'horizon 2025 de $15 \text{ kW} \cdot \text{kg}^{-1}$. Dans le but d'améliorer la solution de refroidissement à l'horizon 2035, une nouvelle technologie de condenseur à coupler avec la CPLIP a été proposée : le condenseur à microcanaux et ailettes à persienne permet une augmentation du coefficient d'échange externe de 3 à 5 fois celui d'un condenseur classique et une réduction du volume du fluide. Les résultats portant sur l'optimisation de la CPLIP équipée avec ce condenseur démontrent une augmentation des pertes de charge liées à cette technologie, mais malgré tout, elles restent en dessous de la capacité de pompage capillaire maximale $\Delta P_{\text{cap},\text{max}}$. Si cette augmentation est par ailleurs comparée à l'augmentation de performances (dans ces travaux considérés comme la réduction en masse), on peut observer une réduction significative de la masse du système de refroidissement, qui est autour de 5 kg pour l'évacuation d'environ $16 \text{ kW}_{\text{th}}$. Dans ce cas, le coefficient de puissance imposé à l'horizon 2035 a été plus que doublé !

Conditions transitoires sévères : démarrage

Dans le but de mieux comprendre les limitations de la CPLIP, dans le chapitre 8 une étude sur son démarrage est proposée. En particulier, il est très intéressant d'exploiter comment les conditions environnementales, telles que la température initiale de la ligne vapeur, en plus des paramètres classiques (puissance appliquée à l'évaporateur) peuvent influencer le comportement de la boucle pendant ses phases de démarrage. L'analyse présentée ici est basée sur des résultats expérimentaux et numériques effectués sur le modèle et le dispositif expérimental présentés dans le cinquième chapitre. Comme dit précédemment, l'attention est portée sur la température initiale de la ligne vapeur, tandis que tous les autres paramètres, tels que la température de consigne au réservoir et la température de la source froide, sont fixés (70°C et 20°C respectivement). Par mesure de simplicité, les définitions de démarrage à froid et à chaud ont été utilisées pour indiquer un démarrage dont la température initiale de la ligne vapeur est respectivement égale ou supérieure à la température ambiante (20°C). À partir des résultats expérimentaux, on a observé que la boucle a pu démarrer à froid sans problèmes particuliers jusqu'à des échelons de puissance de 0-5 kW, tandis qu'à chaud, même pour une puissance de démarrage plus faible, la CPLIP a échoué dans son démarrage. L'analyse expérimentale effectuée sur un démarrage à froid et à chaud à faible puissance a démontré, dans le cas chaud, une augmentation importante de la vitesse du front de vapeur dans la ligne vapeur, qui peut être un ordre de grandeur plus élevée pendant le démarrage à chaud qu'à froid. La plus faible vitesse du front de vapeur, pendant le démarrage à froid, est

due à l'énergie échangée entre le fluide et les parois solides de la ligne vapeur, entraînant une recondensation de la vapeur issue de l'évaporateur. Pendant le démarrage à chaud, une plus faible différence de température entre la vapeur et les parois solides atténuent ce phénomène et rendent les démarriages plus violents. Si cette quantité d'énergie est calculée pour un démarrage à chaud et à froid, on peut observer que l'énergie relâchée par la vapeur dans le atteint environ 5 kJ dans le premier cas et 9 kJ dans le deuxième. Ces valeurs d'énergie ne sont pas négligeables, car elles correspondent à une puissance de 0,5 kW appliquée à l'évaporateur pendant un temps de quasiment 20 s et 10 s respectivement. La plus petite quantité de vapeur re-condensée pendant le démarrage à chaud amène à des vitesses du front de vapeur plus élevées, ce qui peut entraîner un décrochage de la boucle. Pour mieux comprendre les enjeux, les résultats expérimentaux ont été comparés avec des résultats numériques où l'énergie thermique des parois solides a été modifiée en agissant sur l'inertie thermique des parois solides qui a été supprimée pour vérifier et valider l'observation du comportement hydraulique expliqué expérimentalement.

Comportement de la CPLIP sous conditions d'accélérations sévères

La vérification sous condition de vibrations sévères est plus que naturelle dans le secteur de l'aéronautique, c'est pourquoi une étude sur l'influence d'accélérations sévères sur le comportement de la CPLIP est abordée dans le dernier chapitre. En absence d'un banc expérimentale permettant l'étude de ce comportement, une étude numérique a été réalisée, dont les limitations sont bien expliquées dans le texte. L'étude est divisée en deux parties, une première liée à la compréhension des phénomènes, et une deuxième étude paramétrique. Dans tous les cas, pour des raisons de stabilité numérique, une impulsion d'accélération dont l'intensité et la durée dans le temps sont variables a été appliquée à la CPLIP pendant ses opérations en régime stationnaire. L'influence la plus remarquable de la présence d'un champ d'accélération sévère qui perturbe le comportement de la CPLIP est bien sur liée aux caractéristiques hydrauliques de la boucle. Il a été observé une forte variation du champ de pression tout au long de la CPLIP qui amène à un débit négatif de liquide qui s'écoule du réservoir vers l'évaporateur. Ce comportement, anomalie, est responsable d'une réduction de longueur de condensation car le liquide en provenance du réservoir repousse le front de vapeur en arrière, en modifiant aussi les conditions de saturations dans le condenseur même. Malgré ces modifications très importantes dans le comportement hydraulique de la boucle, sa réponse thermique ne semble pas être affectée de manière significative : la vapeur continue à être produite dans l'évaporateur et poussée vers le condenseur. Les paramètres qui ont une influence au premier ordre sur le comportement hydraulique de la boucle sont la durée dans le temps de la perturbation, la différence de hauteur entre le condenseur et le réservoir, et bien sûr l'intensité de la

perturbation. Si, d'une part, il n'est pas possible de contrôler ni la durée ni l'intensité des perturbations, de l'autre part il est nécessaire de garder, en phase de conception la moindre distance entre le condenseur et le réservoir. En effets ce dernier a un impact relevant sur le terme $\rho(k \cdot g) H$ ainsi que sur le temps de stabilisation de la boucle en conditions stationnaires.

Part I

HASTECS Hybrid Aircraft Academic reSearch on Thermal and Electrical Components and Systems

The first part of this work is an introduction to the issues which HASTECS project faces with. After a general introduction to the project and the teams that are giving their contribution for the development of future hybrid aircraft, the attention is focused on high density power electronics cooling issue. The data and the challenges to successfully solve the problem are here introduced.

Introduction: HASTECS project

HASTECS (Hybrid Aircraft academic reSearch on Thermal and Electrical Components and Systems) is a Clean-Sky 2 European Project financed by H2020-EU.3.4.5.1. It has the purpose to develop innovative tools and models to be used by European aircraft constructors for the design and the development of future hybrid propulsion aircrafts. HASTECS project is especially focused on research of generation, distribution, conversion and thermal management of electric power.

HASTECS consortium involves different French Research Institutes. It is at LAPLACE institute, in Toulouse, where power electronics and electrical motors are studied while at Pprime Institute in Poitiers, their adjoined cooling systems are researched. AIRBUS is the main industrial partner of the project.



Figure 0.1: Involved Labs

Six different teams, so called WPs (Work Packages), work on the project and each of them has different tasks and objectives. WP1 has the purpose to find a technology to be used for electrical motor (eMotor). It has the purpose to develop a complete model to

be used for its design. WP2 team works on power electronics. Such devices are used to convert electrical direct current (DC) to alternating current (AC) to supply eMotors with the required electrical frequency. The purpose of WP2 is to find a disrupting technology and to develop a model for converters design. Thermal management of eMotor and power electronics converters is handled by WP3 and WP4, respectively. Both teams have the purpose to propose cutting-edge technologies for thermal management. To WP3, in particular, is required the development of a model to be integrated in the optimisation tool. WP4's aim, rather, is to find, design, optimise, develop and study an *avant-gard* solution for power electronics cooling. It should supply WP2 with simplified tools for the development of a unique model for electronic converters and their cooling system. Such model will be finally integrated into the overall one for the optimisation of the conversion chain. WP2 and WP4 are strongly coupled between them. WP5 has the purpose to analyse partial discharges, bus-bars and cables. Finally, WP6's task is to study system integration and auxiliary sources: fuel cells and batteries. All work packages converge to WP6 system integration.

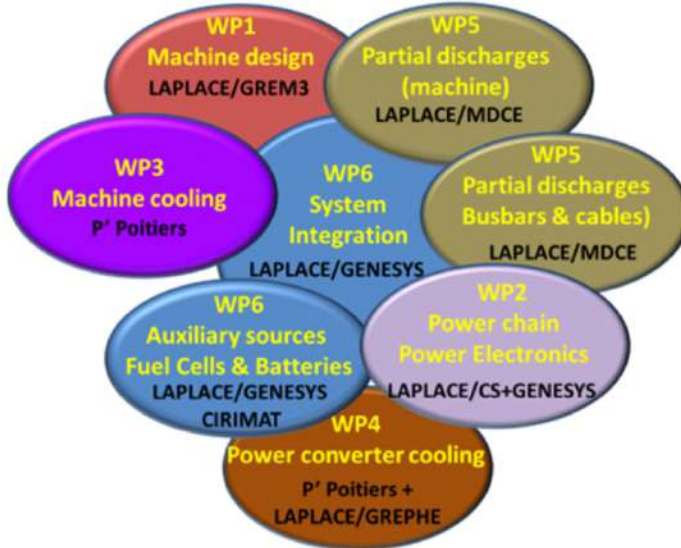


Figure 0.2: WPs and their interactions

“[...] The electric motors and power converters are designed by LAPLACE Laboratory in Toulouse while innovative solutions for cooling of these devices are proposed by the Pprime institute in Poitiers. Some prospective study on future high energy density auxiliary sources (batteries, Lithium Ion) are currently being developed in LAPLACE with the expertise of the CIRIMAT Centre. [...] Finally, the overall system will be analyzed and even optimised thanks to an integrated design model which is currently built which

involves the whole power system. This system level design tool couples the devices models (efficiency and weights) with the whole weight of the aircraft and subsequently with power and thrust needs to fly the mission“ [cit.] [27].

The aim of the research presented in this thesis (WP4), mainly numerical, is to find, design and optimise a technology for high power density electronics cooling. Such cooling solution should be able to evacuate the required thermal power from power electronics converters, ensuring temperature control at level of chips and responding to the requirements imposed by AIRBUS to let the entire system fly. Such constraints are especially related to the mass of the whole system: power electronics converters and adjoined cooling system. For the purpose, models have been developed, and existing ones adapted and modified to fit the requirements of the project. Steady-state and transient issues have been numerically addressed and, when possible, compared to experimental results. Design and optimisation softwares have been used to finally solve the problem and to propose the best possible performing solution.

This thesis is divided in five parts where technological, engineering and scientific issues are addressed to solve the problem and to propose a robust and reliable solution.

The first part is an introduction to explain why do we need a high performing cooling system in the context of this project.

The second part, composed by three chapters, reports a wide extent state of the art of electronics cooling technologies. In particular, due to the complexity of the existing cooling systems, such state of art has been divided in two. The first part, reported in the second chapter, is an overview of cooling systems using a system approach. Closed loop cooling systems and their components are here introduced, and pros and drawbacks, related to their use, highlighted. Active single and two-phase, and passive two-phase, cooling systems are here outlined, reporting the actual limits of each technology as well. The third chapter, instead, addresses the issue related to local heat evacuation from electronic components. Here, the attention is focused on the hot side of the cooling systems. Different technologies are introduced and analysed on the basis of current literature results. Finally, the fourth chapter represents a technology screening. The most adapted technologies will be compared on the basis of a first approximation design, and the choice will be done using the mass of the overall cooling system as index.

In the third part, the retained technology will be analysed. Working principle, experimental facility and numerical model of CPLIP will be introduced in the fifth chapter. A thermal characterisation of the CPLIP, based on experimental data, will be presented in the sixth chapter to show how it is able to answer to HASTECS requirements. Finally, optimisation of CPLIP is proposed in the seventh chapter to achieve the best

configuration for 2025 and 2035.

In the fourth part, the attention is focused on CPLIP behaviour during severe and harsh start-up phases — chapter eight — and during severe and sudden acceleration stages — chapter nine —.

Finally, general conclusions and perspectives are addressed in the fifth part.

Hybrid aircraft power electronics cooling issue

1.1 Why power electronics cooling?

Power electronics cooling problem is one of the main technological issues by which modern society is facing with. The increasing electrical power to be processed by power electronics components, inevitably bring to increasing thermal load to be evacuated. In the past, power electronics cooling issue has been underestimated because of the capability (more or less) of classic air forced convection heatsinks to evacuate the thermal power by maintaining controlled the temperature at level of chips. Great efforts have been done, from an electronic point of view, to optimise electronic components and architectures, and to increase their efficiency. As it was easily foreseeable, the efficiency asymptote has been reached and the electric power to be processed continued to increase. At the same time, some high-efficiency power electronics configurations were not accessible because of still high thermal losses related with.

Electric efficiency¹ should be not seen just as a number to be reached and maximised. In any case the efficiency is lower than one, and one must be aware *because any kind of energy transformation is related to inevitable thermal losses and so, whatever the system, the efficiency cannot never be equal to unity!*

To give the reader an idea on how important losses are, even in the case of high electrical efficiency, lets make a simple example based on the issue we are going to discuss in this work.

On the basis of the scheme reported in Fig. 1.1, starting by the hypothesis that power electronics efficiency is $\eta_{el} = 99\%$, the adjoined thermal losses linked to this particular system are $(1 - \eta_{el}) = 1\%$.

From the knowledge of the electrical power to be supplied to electrical motors Q_{el} ²,

¹The electric efficiency is defined as the ratio between the power to be converted and the total power necessary to converters: electronics components outlet to inlet power ratio.

²The discussion in this work is “only” limited to power electronics and its adjoined cooling system. Here we do not face with electrical motors issues.

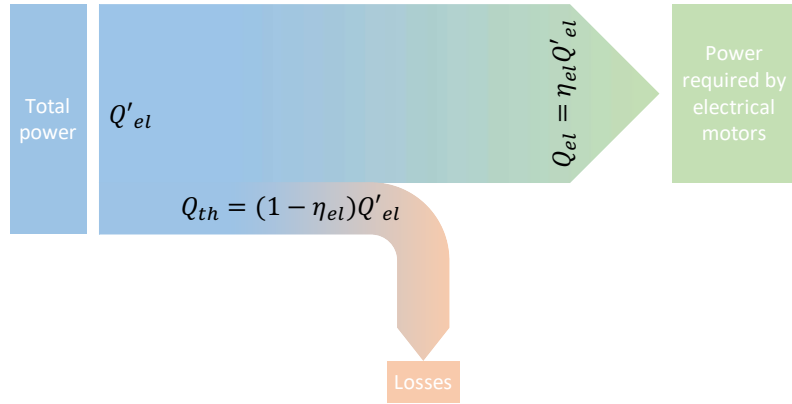


Figure 1.1: Electric power losses scheme

power electronics converters need to be supplied with an electrical power, Q'_{el} , calculated as:

$$Q'_{el} = \frac{Q_{el}}{\eta_{el}} \quad (1.1)$$

so, the related thermal losses are:

$$Q_{th} = (1 - \eta_{el}) Q'_{el} \quad (1.2)$$

Now, if the power required by electrical motors is $Q_{el} = 1.5 \text{ MW}$ [27], considering the above cited electric efficiency ($\eta_{el} = 99\%$), the total power to be supplied to electronics converters is 1.515 MW (from eq. 1.1), and the adjoined thermal power losses are $Q_{th} = 15 \text{ kW}$ (from eq. 1.2). This value is obviously far to be negligible and a cooling system, able to evacuate this quantity of energy, is required!

Thermal and electronics issues nowadays go hand in hand and researchers of both subjects need to converge after some iterations to let modern technologies work well.

In the case of high-power applications the problem is more evident and, even if electric efficiency is pretty high, thermal losses are not negligible: they need to be treated in the best way to increase the overall system efficiency. Optimisation process is not limited to get the highest electric efficiency possible but, on the base of an index, the best overall performances for the whole system should be found, by also considering the cooling technology that inevitably is related with. At the same time, the system should be designed to be fully integrated in the aircraft system and to maximise the total vehicle's performance and efficiency. A system must be so considered into the architecture where it should be placed [28].

The problem is not only related to the “simple” heat evacuation, but some constraints

are applied in the case of aeronautics field. In fact, to let power electronics and the adjoined cooling system fly, they should be as lightweight and compact as possible.

To have a measure on how lightweight the system is, let's now introduce the concept of *power coefficient*, C_c . The latter, measured in $[\text{kW}\cdot\text{kg}^{-1}]$, indicates the total power that power electronics modules are able to convert per each kilogram of system mass, including the whole cooling system. Obviously, the higher the power coefficient, the better the performance of the system. Two different targets have been imposed for minimum power coefficient value. The first objective, referred to the year 2025, is to design and optimise power electronics and their associated cooling system with the purpose to obtain an overall power coefficient, $C_{c,2025} = 15 \text{ kW}\cdot\text{kg}^{-1}$, while a power coefficient, $C_{c,2035} = 25 \text{ kW}\cdot\text{kg}^{-1}$ has to be reached for 2035! To show how far from the targets a classical solution is, let's now consider as an example a classical power electronics configuration (3-level PWM NPC), optimised at the best, and its adjoined cooling system, but using a classical forced air convection technology. The perceptual mass distribution of each component in the system is reported in Fig. 1.2 [1].

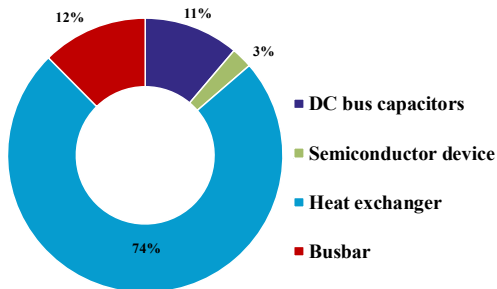


Figure 1.2: Mass distribution of a 3-level PWM NPC electronic system (using 6th gen. 1700 V IGBT) equipped by a classical air forced convection cooling system [1].

As one can notice from the pie chart, almost three-quarters of the entire system mass is due to the cooling system (heat exchanger in the diagram). Because of the low heat transfer coefficient (HTC) related to air forced convection technology, the high mass is due to extended heat transfer surface area related to the use of finned surfaces. In this case the adjoined power coefficient, less than $9 \text{ kW}\cdot\text{kg}^{-1}$, is too low if compared with the minimum admissible value (2025) and no warranties are given on the capability to limit the temperature of electronic components. The latter are in fact characterised by different maximal temperature requirements following chips constituting material. For example, pure Si components maximal temperature is limited to about 150°C , SiC components may in general withstand up to 175°C , but GaN components maximal temperature

is much lower than 150°C ³. To overcome such limitations, great efforts have to be done to ensure the evacuation of thermal load, to control the temperature of electronics components, and to reduce the mass of the cooling system!

1.2 The aircraft mission profile

The energy required to propulsion chain of the aircraft is not constant with time due to variation of mechanical power required by motors and following the different flying stages. Due to linear relation between supplied electrical power and thermal losses in power electronics converters system, the same shape of mission profile can be identified in both cases. Referring to thermal losses, five different stages can be identified in the mission profile, qualitatively reported in Fig. 1.3:

- I. Taxi-out
- II. Take-off and climb
- III. Cruise
- IV. Descent and landing
- V. Taxi-in

During the first stage, between the time t_0 and t_I , very limited in time, thermal power losses are the lowest ones (Q_{min}) and the aircraft remains on the ground (see the corresponding altitude profile reported above the mission profile in Fig. 1.3). The second stage (take-off and climb) can be divided in two different sub-stages: the take-off sub-stage, corresponding to the aircraft acceleration on the runway until detachment, and the climb sub-stage. In the first sub-stage, the maximal power is required during acceleration, so a high amplitude power step is applied (from Q_{min} to Q_{max}). During the climb sub-stage the power required slightly decreases until Q_{II} at the end of this phase. From t_I to t_{II} (almost 20 min) the altitude continues to increase. Once the maximal altitude, h_{max} , is reached, thermal power suddenly decreases from Q_{II} to Q_{III} : cruise begins. The latter, from t_{II} to t_{III} , is characterised, in theory, by steady-state operation. Its duration is, in this case, in the order of 70 min; the thermal power evacuated by power modules is almost one half of that evacuated during the very beginning of take-off stage and the altitude does not change. Like take-off and climb stage, descent and landing stage can be divided in two sub-stages: the descent is characterised by a decrease of the

³In the following of this work only SiC components will be considered.

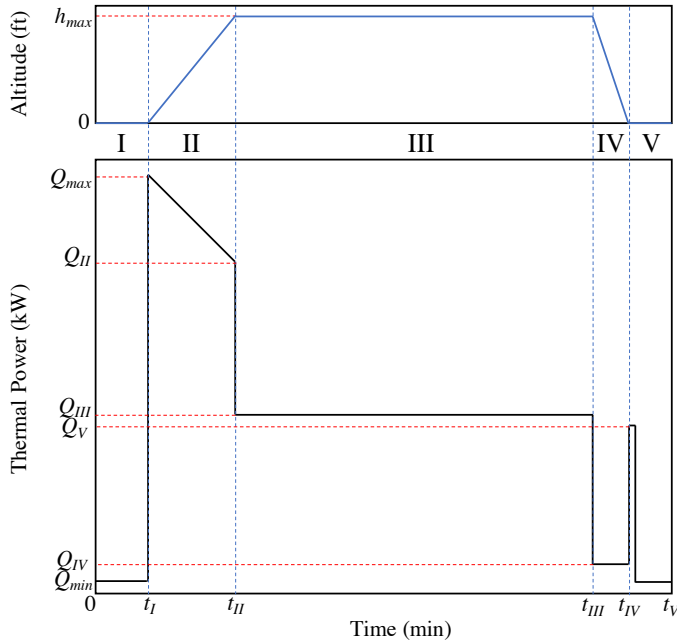


Figure 1.3: Qualitative thermal mission profile and altitude variation as a function of time.

thermal power (from Q_{III} to Q_{IV}) and the airplane planes until approaching. When the aircraft approaches, a power peak, characterised by a maximal intensity (Q_V) almost equal to that of cruise stage, is produced. Finally, during the taxi-in, the thermal power to be evacuated is the same as taxi-out.

As shown in Fig. 1.3, during the mission, the altitude changes as a function of time, and so air temperature, density and pressure change as well. This inevitably impacts the cooling system choice and temperature operating range. In the following sections, a discussion on temperature variation as a function of altitude is reported and two different methods to use external air as cold source are proposed. Also, in the following chapters, the mission profile will be quantitatively shown and analysed, for different power electronics configurations. A method based on an energetic analysis is reported to calculate the cooling system design point.

1.3 A not constant cold source temperature

As already mentioned in the previous section, when talking about aircraft, the air temperature is not constant as a function of time and different conditions are encountered during the mission: the air thermodynamic conditions (temperature, T ; pressure, p and air density, ρ) change as a function of altitude. By considering the NASA's Earth At-

mosphere Model [22], temperature, pressure and density, in Celsius degrees, kPa and $\text{kg}\cdot\text{cm}^{-3}$, respectively, are related to the altitude, h [m], by the following relations⁴:

Temperature

$$T = 15.04 - 0.00649 h \quad (1.3)$$

Pressure

$$p = 101.29 \left[\frac{(T + 273.15)}{288.08} \right]^{5.256} \quad (1.4)$$

Density

$$\rho = \frac{p}{0.2869 (T + 273.15)} \quad (1.5)$$

Referring to the altitude diagram, reported above the mission profile in Fig. 1.3, during stage I, the operating condition corresponds to the ground one. In this case, temperature of air (before and during the taxi-out and during and after the taxi-in stages) is obviously dependent on the geographical location, the season and the time of the day. From the beginning to the end of stage II and from the beginning to the end of stage IV, temperature varies as a function of altitude and so as a function of the time, as shown in Fig. 1.3. During the cruise, temperature is considered stationary: the flight altitude does not change.

The ISA (International Standard Atmosphere) diagram (see fig. 1.4) graphically relates temperature and altitude. Temperatures are reported on the abscissa, while altitude, in feet (ft), on the ordinates. The red line is the definition of ISA temperature as a function of altitude for standard ground temperature condition ($h = 0$ m, $P = 1$ atm, $T = 20^\circ\text{C}$), while each parallel line defines the value ISA($\pm T$) following the changes due to the place, the season and the time of the day.

In the following of this document, a value of ISA(+18) °C is assumed as input for cold source calculations. This value, in fact, well agrees with thermodynamic conditions realised on the ground for 60-65% of the airports in the world [2].

⁴Here, are reported only the laws relating the thermodynamic condition to the altitude, h , in the troposphere ($h \leq 11\,000$ m).

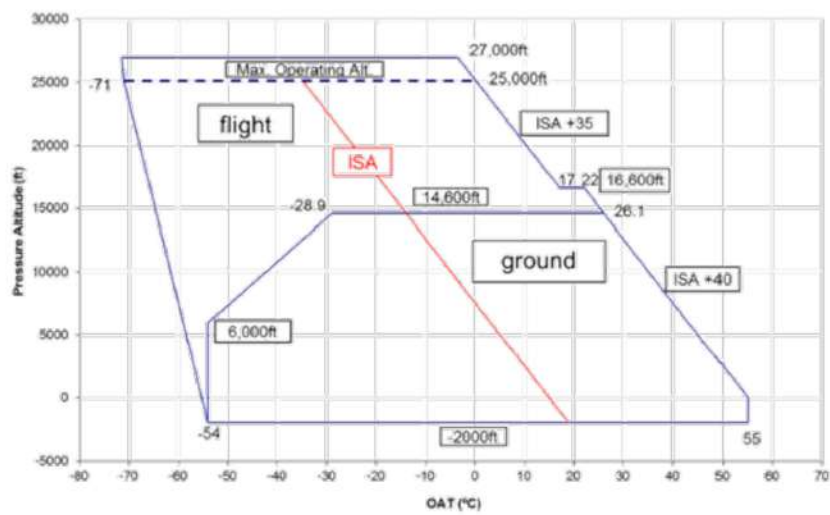


Figure 1.4: ISA diagram for pressure and temperature as a function of the altitude [2]

This choice is not related to a showstopper or to an infeasibility of the HXG design for a higher ISA value, covering a larger number of the airports in the world, but to specification requirement [2]. Such ISA value, in fact, allows to cover 100% of the airports in the Northern Europe, such as the Norwegian market, for which the hybrid aircraft is at first previewed. In particular, from specification data sheet [2], in table 1.1, the temperature boundary conditions for ground and high altitude flight phase are reported.

Flight phase	Normal ground operating conditions	Normal flight operating conditions	Severe operating conditions (low temperature condition)
Temperature (°C)	+33	+28	-15
Flight phase	Severe operating conditions (High temperature condition)	Operating during start-up after soak at low temperature	Operating during start-up after soak at high temperature
Temperature (°C)	+53	-40	+53

Table 1.1: Temperature specifications [2]

Table 1.1 details: normal operating conditions, related to external environment; severe

operating conditions, related to temperature values that may be realised in some unpressurised and non-temperature controlled position of the aircraft. To impose the boundary conditions to solve the problem — especially for the determination of real heat transfer coefficient values on the external side of the cold-heat-exchanger/condenser —, the following hypothesis have been assumed⁵:

1. The temperature of cold air at the inlet of the nacelle or the temperature of the air flowing upon the fuselage, in the worst operating condition, is equal to ambient temperature (33°C , as indicated in table 1.1)
2. The velocity of the air at the inlet of the nacelle⁶ or upon the fuselage, corresponds to the aircraft velocity during taxi-out stage (I): $10 \text{ m} \cdot \text{s}^{-1}$.

1.4 The cold source

Radio communication, avionics system and other electronics equipments installed on board are cooled by using directly or indirectly external air as cold source (it depends if a closed loop circuit is inserted between the cold source and the components to be cooled). Like these systems, the idea developed in this work is to use the same cold source to cool the power electronics modules, but in a smarter way. It is so necessary to find a link between power electronics modules and cold source where heat will be definitively evacuated to the external ambient.

The general idea, as shown in fig. 1.5, is to use a closed loop cooling system to transport heat from the hot source⁷ (heatsink), where power modules are installed on, to the cold source. The use of a vector loop allows to evacuate in a more efficient and smart way the thermal power generated by chips. Moreover, the use of an intermediate cooling loop allows to use higher efficiency heatsinks, such as microchannels, porous media or metal foams. In fact, the higher the quality of the heatsink, the higher the efficiency of the system itself, as observed by Dolley *et al.* [28, 29].

A cooling system is, in most cases, a way to transport heat from the source to another location where its evacuation is in general simpler, while the use of external air as a secondary fluid in a heat exchanger is the easiest way to definitively evacuate the thermal

⁵Considering that the power electronics and its adjoined cooling system can be placed in the fuselage (PIF) or in the nacelle (PIN), the cold source nature changes as a function of the position in the aircraft.

⁶Only in the case where the nacelle is considered, the value of air intake equivalent diameter is calculated to respect the desired dynamic conditions (point 2), on the first heat-exchanger tube-rank.

⁷A definition for heatsink is given in chap. 2 page 42.

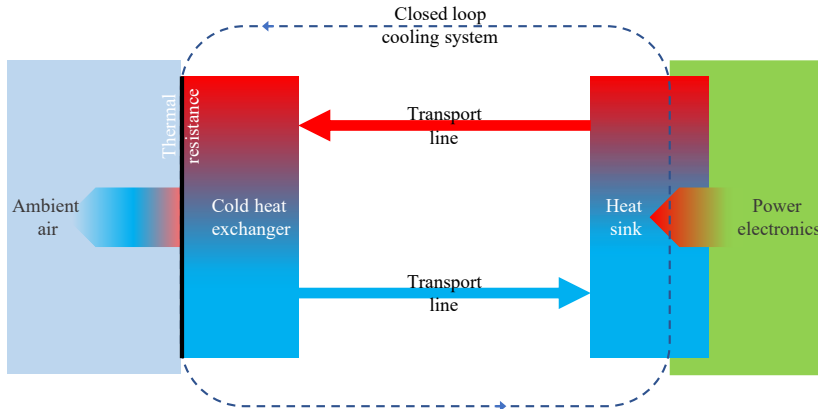


Figure 1.5: Cooling system loop as a broker

load transported by the coolant fluid. However, the use of the latter is related to air temperature and thermal resistance on the secondary side (see Fig. 1.5).

Two different technologies are introduced here: skin heat exchanger (see sec. 1.4.1), which introduces an additional resistance, due to the presence of a solid wall, between external air and cold heat exchanger's tubes; and RAM air (see sec. 1.4.2), which allows a direct contact between the external air and the tubes of the cold heat exchanger.

In the past, both technologies have been used, as they are, to cool embedded systems (“air cooling”) and rarely an intermediate closed loop circuit was added between them and the chips to be cooled [30]. In particular, in the case of RAM air, the problem is strongly related to air temperature and velocity, so to heat transfer coefficient, variation.

1.4.1 Skin heat exchanger

The skin heat exchanger is an “already-integrated-system”, today used on aircrafts, such as the CL-600 Challenger [31], to cool avionics equipment⁸.

In 1989, Howard (McDonnell Douglas Corporation) deposited a patent on skin heat exchanger [3]. The system was described as able to provide cooling and ensuring required heat evacuation for avionics systems. In fig. 1.6 a simplified scheme taken from the Howard’s patent of his skin heat exchanger is reported.

A skin heat exchanger, as shown in Fig. 1.6 and Fig. 1.7, is a part of the aircraft itself and is installed outside of the aircraft insulation layer. It is composed by the low thermal resistance aircraft skin, fin and base panel (23 and 27, respectively, in Fig. 1.6). Hot

⁸For “already integrated system” the inventor means a system that does not need extremely weight-expensive radiator systems, metal fasteners, rivets and so on, on the outer side of the skin of the vehicle [3]

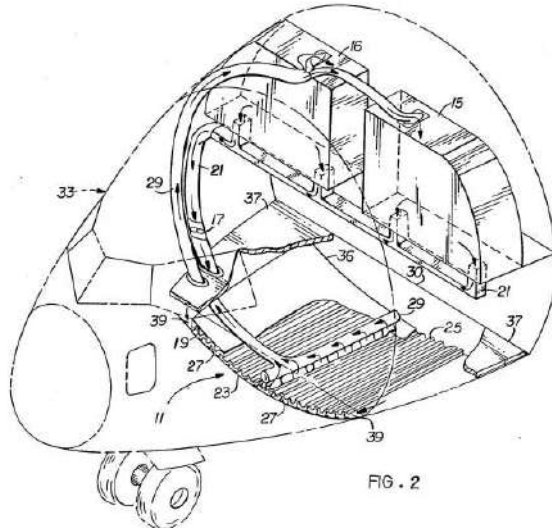


Figure 1.6: Skin heat exchanger 3D scheme [3]

cabin air flows into the hot side, while the “cold source” is the cold air available outside of the aircraft [4]. On the hot side, the air is forced, by using some fans, for example, to enter the cabin where electronic systems are installed. Hot air, flowing in the tube, reaches the heat exchanger.

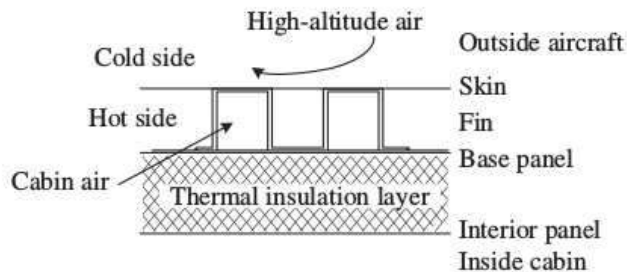


Figure 1.7: Skin heat exchanger scheme [4]

Pang *et al.* [4] have analysed, assuming an aircraft cruising at Mach 0.9, at 10 km of altitude, the behaviour of a skin heat exchanger positioned in two different positions, as reported in Fig. 1.8.

Position 1, defined as unfavourable, is relative to a parallel flow of external air with the skin heat exchanger, while position 2, defined as favourable, is relative to a windward angle. They obtained an overall heat transfer coefficient (HTC), in the less favourable position of skin heat exchanger, of $45 - 51 \text{ W} \cdot \text{m}^{-2} \cdot \text{K}^{-1}$, while in the most favourable position the HTC ranges between 66 and $80 \text{ W} \cdot \text{m}^{-2} \cdot \text{K}^{-1}$. This kind of technology,

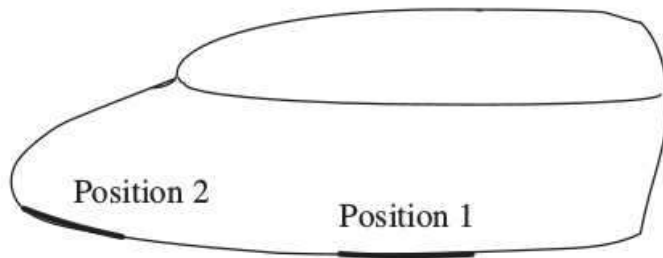


Figure 1.8: Positioning scheme of skin heat exchanger [4]

already used for electronics cooling, has been already considered, as secondary side of a LHP condenser for the same purpose [32]. A reduction of the heat transfer coefficient as a function of the altitude, principally due to a reduction of air density, was also observed by Fleming *et al.* [32]. As reported by them, even if the HTC increases as a function of the Mach number, over 40 000 ft ($\simeq 12\,200$ m) the dependence of HTC on the velocity is negligible. However, the results of Fleming *et al.* [32] show the capability to maintain temperature controlled and to evacuate the heat power because of positive heat flux (from the aircraft skin to the external air). Otherwise, for high Mach numbers and low altitudes, one assists to an inversion of the heat flux direction principally due to a higher adiabatic wall temperature than the skin temperature. This phenomenon is mainly due to aerodynamic heating effects [32]. Using this technology, Ashemi *et al.* [33] numerically studied electronics equipment cooling. A heat transfer rate higher than 15 kW had to be evacuated in their case, by maintaining the temperature controlled at 105°F (40.56°C).

1.4.2 RAM-air

“When air is taken aboard an aircraft in flight, it undergoes an increase of pressure which is called the —ram effect—, and a cooling system which uses such air is called a RAM-air cooling system.” [34]. RAM-air is maybe the oldest technology, used in aircraft applications, to bring external air on board⁹. Its working principle is simple and the number of components limited. In Fig. 1.9b a principle scheme of this technology is reported. It is composed by an air intake, obtained on the aircraft structure, which shape can be NACA type to reduce the influence on the lift to drag ratio; an heat exchanger, where air coming from the intake is heated by the devices to be cooled and, finally, an air outlet, where air is released to external environment. The air, entering from intake diffuser, is subject to a pressure and temperature increase: the air temperature at the exit of the intake diffuser is almost equal to the total temperature of ambient air; while

⁹It was mostly used with air cooling heatsinks.

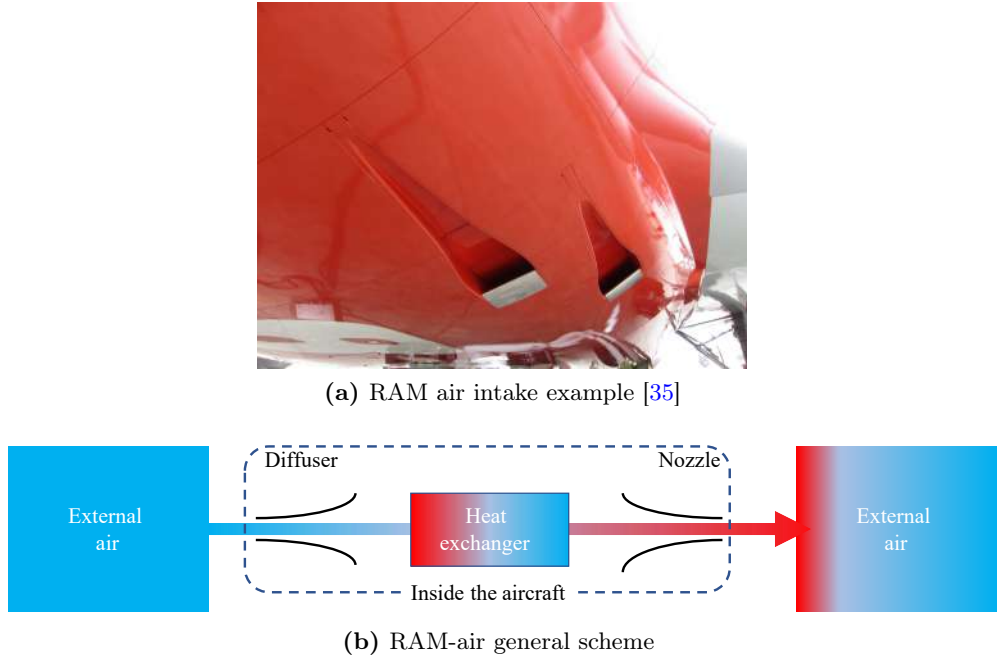


Figure 1.9: RAM air.

the static pressure is lower than the total pressure of atmospheric air. The diffuser has the purpose to reduce and stabilise the air flow velocity. In the heat exchanger, heat is evacuated by the coolant fluid and air, flowing within a nozzle, is rejected to the ambient through the outlet duct. The outlet duct conveys the air to the outlet of the system where the exit nozzle is used to expand air and so to generate thrust to partially damp lift losses due to the presence of air intake [30]. RAM-air cooling system is the simplest way to use external air as a secondary side heat exchanger (see Fig. 1.9b). However, its influence on the aerodynamics characteristics of the aircraft could be not negligible and so, it should not be used on such aircrafts which mission is limited in time (less than thirty minutes) [34]. The additional mass related to the use of this kind of system is mostly due to the presence of the inlet diffuser, ducts and outlet nozzle. RAM air may be characterised by a quite large volume encumber: other than diffuser and nozzle, the duct has to be designed to avoid any high flow resistance, due to supersonic flows that may be realised in some flight conditions, during the entire mission [30]. Grabow and Kazan [36] designed, in 1996, a high performing cooling system, using this technology as cold source for the secondary side of a liquid-to-air and a air-to-air heat exchanger. They were able to evacuate up to 5 kW of thermal load by requiring a maximum electrical power of 2 kW to let the whole cooling system work. Because of the dimensions and the complexity of the equipment to cool (fighter aircraft pod), their system was equipped by a series of

“accessories” such as valves and by-passes, and different fans to drive the airflow to the different heat exchangers. Finally a ACM (Air Cycle Machine¹⁰) was positioned between the air inlet and the outlet, where compressor and blower were respectively installed. The highest advantage of a ACM driven RAM-air cooling system is the capacity to decrease the temperature of air at the inlet of the heat exchanger on the secondary side. It has to be noted that, in the case analysed in ref. [36], more extreme conditions, typical of military applications, were encountered in the air intake because of extreme aircraft velocity (up to Mach 1.2)¹¹. The compressor is used to increase the air pressure, after heat exchanges, before the expansion in the nozzle to minimise the effects on the lift losses. Before Grabow and Kazan, Grabow *et al.* [37] have done a similar study for fighter avionic’s pods cooling. Instead of using a unique technique based on the ACM-driven RAM-air, they used a coupling of a direct RAM-air system and a driven-RAM air intake. To avoid problems linked to high Mach numbers flights ($\text{Ma} > 1$), especially related to the lowering of the mass flow rate into the RAM-air intake, they programmed to use the direct RAM-air for low Mach numbers/low altitude flights and the RAM-driven technique for high Mach numbers/high altitude flights. This solution allowed them to provide the adequate avionics cooling in a huge range of operating conditions.

RAM-air seems to be the most performing solution, ensuring the lowest temperature available at any time of the mission profile. However, problems are mostly related to heat exchangers, that should be as compact as possible, and to the ducts which impose a not neglecting penalty to volume encumber. Some solutions are thought to embed RAM air heat exchanger within the engine inlet [28]. However this solution is more adapted in conventional propulsion aircraft in which bleed air can be extracted from fan.

Both skin heat exchanger and RAM-air seem to be suitable technologies to evacuate the thermal load generated by electronics components. They have to be coupled with a “liquid cooling system” to have a better control of the cooling rate. Skin heat exchanger is characterised by lower overall performances. It is mainly due to presence of an additional thermal resistance, and to difficulties in use of fins to increase the heat exchanger surface area. Higher heat exchanger dimensions are surely related to this technology if compared with RAM-air one. On the other side, RAM-air is a more flexible solution to be used on the cold source side. It allows the use of a finned, and so compact, heat exchanger. Moreover, the duct dimensions can be controlled, during design process, to control and optimise the air velocity to maximise the HTC.

In the following chapters, a research of high performing and efficient cooling loops is

¹⁰A turbo-compressor system.

¹¹At such velocities the air entering from the ram air is subject to a temperature increase due to the isentropic transformations.

reported to finally select the best solution adapted to solve the problem. Its thermal and hydraulic characteristics in steady and transient conditions will be exploited.

Part II

Hybrid aircraft power electronics cooling: from the state of the art to system selection

The part two of this work is focused on the analysis of different solutions that potentially could help to solve the problem related to high power density electronics cooling. Composed by three chapters, in this part, active single and two-phase and passive two-phase cooling systems will be analysed at first using a system approach, by considering all the main components of such system. So, the attention will be focused on the hot side, introducing and analysing different high performing heatsink technologies. Finally, on the basis of a first approximation design, a comparison is introduced to choose the most adapted cooling system for the application discussed in this work.

Overview of existing cooling solutions

Due to the high complexity of cooling systems, the number and typology of components and the physical phenomena at the base of their working principle, it does not exist a universal way to classify them. In fact, different point of views are considered when talking about. Actually, with the word cooling system one can either indicate the hot heat exchanger (HXG), where the thermal load is transferred to the coolant, or the whole system, by considering transport lines, pumps or compressor if any, accessories and so on. Different performances characterise cooling systems following their typology. However, they may be classified on the base of their general working principle and main physical characteristics of heatsinks.

To try to give a classification, by considering either installation and heat transfer mechanism occurring in the hot side, or heatsink as it will be called in this work for simplicity, in Fig. 2.1 a diagram based on the main heat transfer mechanisms, thermodynamic principles, and hydraulic characteristics is reported.

In general, a cooling system is used to maintain the temperature controlled on the device to be cooled by evacuating the required thermal load. To accomplish this job two different methods can be used:

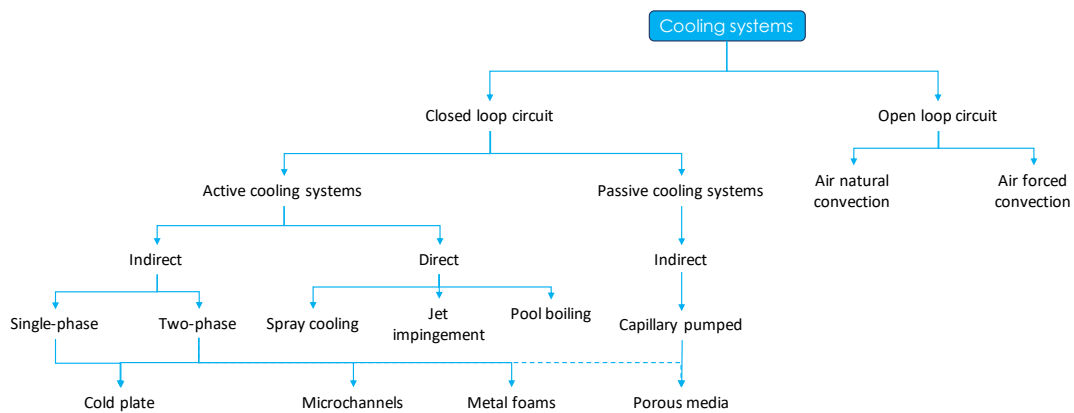


Figure 2.1: Cooling systems classification.

- Cool the device by directly using external air (air cooling, or in general called open loop circuits).
- Cool the device by using an intermediate circuit (liquid cooling, or in general called closed loop circuits).

In the first case, due to the fact that external air is directly used as coolant, in particular in aeronautics fields, one has to face with some issues, such as the variability of ambient air temperature, velocity and density on which the heat transfer coefficient (HTC) depends. The second method, which is also usually called “liquid cooling”, uses a closed loop circuit to transfer the heat to another point where its extraction is simpler. In this case, it is possible to overcome the limitations of air cooling by, for example, using some kind of regulating valves. This allows to maintain the temperature controlled on the device to be cooled, even when cold source condition changes are significative during the mission of the aircraft. As it will be observed later in this chapter, some kind of technologies do not need any kind of controlling system because of their “auto-regulating” ability. It is the case of some passive two-phase systems. Other cooling technologies, instead, need regulating accessories which could be, in some cases, detrimental in this application field (it is the case of active single-phase systems).

However, a closed loop circuit behaves as a “smart broker” between the heatsink, where heat is evacuated from the device to be cooled to the working fluid, and the cold source (heat exchanger), where heat is definitively evacuated to the external ambient air. In order to have smarter and more efficient solutions, only closed loop circuits will be considered here and the following definitions will be used:

- **Heat sink** the device through which the thermal power is evacuated from the base plate of power electronics modules to the coolant (hot source).
- **Coolant** or working fluid, is the fluid used to transport the thermal load from the hot to the cold source.
- **Cold source** is the heat exchanger used to evacuate the thermal load from the coolant to the ambient air.

According to Fig. 2.1, closed loop circuits cooling systems can be divided in two categories: active and passive. Active cooling systems are characterised by the presence of a pump or a compressor, following the technology, to move the fluid into the circuit. Passive cooling systems use gravity or capillary forces to make the fluid flow into the loop. The difference is obviously in the amount of energy required by the cooling system to operate.

With reference to the heatsink, active cooling systems can be classified in different ways. A first classification is about direct and indirect. Direct cooling systems are characterised by a direct contact between coolant and electronic components. The heat exchange mechanism depends on temperature and heat flux ranges. Forced or natural convection, or evaporation/boiling, are the main heat exchange mechanisms. In general, in this kind of systems, particular attention has to be payed to the choice of the coolant, in contact with the electronic devices: dielectric fluids must be used. In the case of indirect cooling systems, the coolant is confined into a case (usually made of a high conductivity material) in which the fluid can flow. So, because of the presence of an interface between the electronics components and the working fluid, an additional thermal resistance is added. The heat transfer mechanism is conduction between the base plate and the heatsink and forced or natural convection, or boiling/evaporation, between the heatsink and the working fluid. Either direct and indirect cooling systems can be single or two-phase and, following the efficiency and thermo-hydraulic requirements of the problem to be solved, different heat sink technologies may be used¹. Otherwise, due to the use of gravity or capillary phenomena to move the fluid into the loop, all passive solutions are liquid/vapour two-phase systems. Capillarity only occurs in presence of a porous medium. So, a confinement is necessary in two-phase passive cooling systems which may thus only be indirect.

All active cooling systems can be divided in single and two-phase according to the heat transfer mechanism. In single phase case, sensible heat is used to transfer the thermal load from the heat sink to the working fluid, which is subject to a temperature increase from the inlet to the outlet. In two-phase case, sensible heat-rate is usually negligible and latent heat is used to allow a phase change of the working fluid (generally evaporation). In this case, a difference in vapour quality occurs between the inlet and the outlet of the heatsink.

In this work, two different approaches are used to show the state of the art of the actual cooling technologies. In this chapter, a discussion about active single and two-phase cooling loops and capillary pumped (passive two-phase) technologies is presented. Working principles and concept schemes of such technologies are introduced to explain how they work and to analyse pros and drawbacks of each one.

In chapter 3, instead, the attention will be focused on the heatsink. Different heat extraction mechanisms and technologies will be compared, the working principle explained and actual performance level introduced.

¹An overview of different heatsink technologies is presented in chapter 3.

2.1 Active cooling systems

Systems requiring an external source of energy to move the fluid into the loop are defined as active cooling systems. The general operating scheme is reported in figure 2.2 where the main components of the loop may be distinguished.

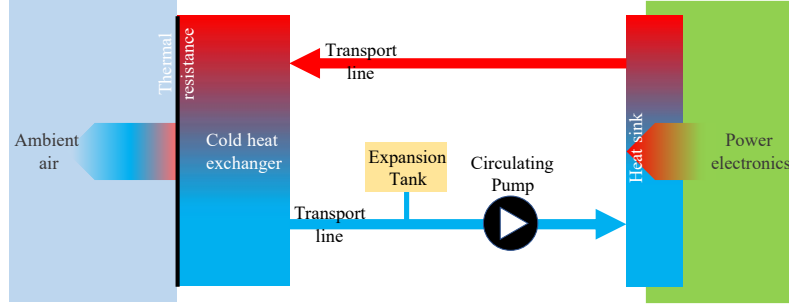


Figure 2.2: General scheme of an active cooling system

The circulating pump, or the compressor in the case of vapour compression technologies, has to be designed to counterbalance all the pressure drops in the loop and to maintain the necessary mass flow rate to evacuate the thermal load from the heatsink, where thermal load is transferred to the coolant. In the cold heat exchanger, heat is definitively evacuated to the external ambient. An expansion tank is used to prevent fluid expansion, eventual water-hammers and other instabilities to mechanically damage loop's components.

Active cooling systems can be single or two-phase. Even if heat transfer mechanisms are quite different between them, the constituting components play the same role. In two-phase systems either latent and sensible heats are used: the heatsink is an evaporator and the cold source becomes the condenser (with sub-cooling). Referring to the scheme reported in fig. 2.2, and for standard two-phase pumped circuits, in steady state conditions, the sub-cooled fluid coming from the cold heat exchanger/condenser, flows to the heatsink. Hot fluid or vapour reaches the cold heat exchanger or condenser where heat is definitively evacuated to the external ambient. Through the return transport/liquid line, sub-cooled liquid return to the evaporator where the loop starts again. The expansion tank is also used to impose and regulate saturation conditions, but this point will be better approached in the following. In other cases, the pump is replaced by a compressor, the tank suppressed and an expansion valve mounted on the liquid line, obtaining a Rankine vapour compression cycle.

In the case where a direct contact technology is used, such as jet-impingement/spray-cooling, the scheme reported in figure 2.2 is also valid, but a collecting tank must be

provided to ensure that fluid is in liquid state before its return to the evaporator.

2.1.1 Single phase cooling systems

Single phase cooling systems, also called “liquid cooling”, are maybe the simplest and most used configuration. The physical principle of this technology is relatively simple and, in its “classical configuration”, is the best-known technology.

The working fluid, heated in the heatsink, flows within the transport lines, ideally adiabatic, to the cold heat exchanger. A pump is used to move the fluid into the loop and it has to be designed to ensure the adequate mass flow rate and the necessary pressure head to counterbalance for all the pressure drops in the circuit. Some accessories, such as expansion vessel and valves have to be provided to ensure the smooth functioning. In fig. 2.3 a concept scheme is reported.

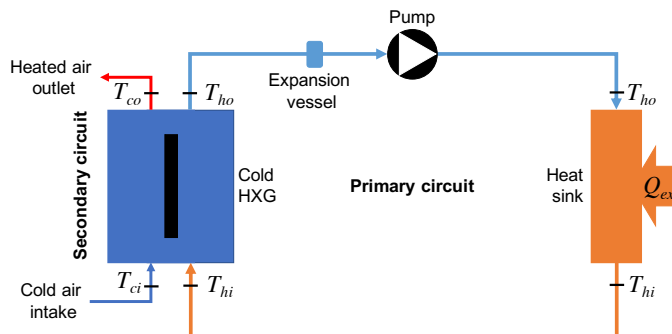


Figure 2.3: Single phase cooling system concept scheme

Starting from the heat sink, the sensible heat, evacuated by the devices to be cooled, let the working fluid temperature to increase from T_{ho} to T_{hi} . The working fluid joins the cold heat exchanger (Cold HXG) where, in steady-state condition, it transfers sensible heat to the secondary fluid. The primary circuit working fluid temperature decreases from T_{hi} to T_{ho} while the secondary circuit working fluid temperature increases from T_{ci} to T_{co} .

Depending on the availability of the cold source and the performance requirements, one of the technologies introduced in sec. 1.4 may be used.

2.1.1.1 Transport lines

Transport lines are simply tubes. They should allow the fluid to flow with the lowest distributed pressure drop possible and minimising heat losses.

For single-phase flows, transport line design is based on the assumption that liquid velocity should be limited to $u_{max} = 2 \text{ m}\cdot\text{s}^{-1}$. This assumption is in general used in industrial and building application for two main reasons. The first one, purely mechanical, is to avoid erosion of tubes that may occur for pretty high liquid velocities. The second one, fluid-dynamics in nature, is to avoid high pressure drops and instabilities, such as water hammers and subsequent mechanical danger and noise due the exaggerate liquid velocity in the ducts.

Starting from the required mass flow rate, tube internal diameter is calculated as:

$$D_i = \sqrt{\frac{4 \dot{m}_l}{\rho_l \pi u}} \quad (2.1)$$

where u is the fluid mean velocity through the tube having cross-sectional diameter D_i .

In literature, two methods are used to calculate the maximum velocity as a function of the flow typology. In the case of laminar flow, because of the parabolic velocity profile along the cross section of tube, the liquid maximum velocity is calculated in correspondence of the tube axis: $u_{max} = 2u$. In the case of turbulent flow, because of high velocity gradients in the boundary layer, the maximum velocity is related to the mean one as $1.3u \leq u_{max} \leq 1.5u$.

In general, if no phase change occurs, the tube inner diameter is the same for both hot and cold lines and thermophysical properties change is usually neglected. Any eventual volume variation, as it occurs during operations and due to the working fluid temperature difference, is dumped by the expansion tank.

2.1.1.2 The pump and the expansion tank

The pump is the component that allows the liquid flow within the primary circuit. It has to be designed to ensure the required mass flow rate to evacuate the thermal power and the necessary pressure head to cross over all the pressure drops in the loop.

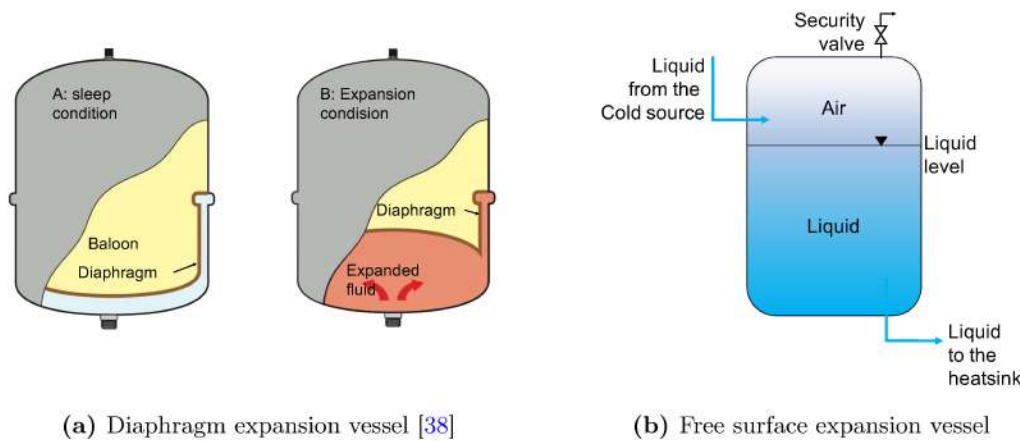
The electric power to drive the pump is calculated as:

$$P_{elec} = \frac{\rho_l \dot{V}_l \Delta P_{tot}}{\eta_{pump}} \quad (2.2)$$

where \dot{V}_l is the working fluid volumetric mass, ΔP_{tot} the total pressure drops in the loop (considering both distributed and localised one) and η_{pump} the pump efficiency which rarely is higher than 40%. The higher the pumping power, the higher the pump's mass. They are used in either single and two-phase active cooling systems and are chosen in

the same way.

The expansion tank is used in all closed loop circuits to reduce any kind of instability related to pressure oscillations or fluid expansions due to temperature variations. In this last case, in fact, the fluid expands or reduces its volume. If volume variations are not considered and contained during design stage, they can lead to serious mechanical damages all over the circuit. Two of the most used kinds of expansion vessels are diaphragm expansion vessels, showed in Fig. 2.4a, and free surface expansion vessels, shown in Fig. 2.4b. Even if the purpose is the same, different operating principles characterise these two typologies.



(a) Diaphragm expansion vessel [38]

(b) Free surface expansion vessel

Figure 2.4: Expansion vessels typologies

Diaphragm expansion vessel is only “activated” when a pressure change of the fluid occurs consequently to a volume variation. It is composed by a gas charged, usually nitrogen (N), balloon; a diaphragm, separating the nitrogen and the working fluid, and a metallic case. When liquid expansion occurs, the latter enters in the vessel and deforms the elastic membrane until pressure equilibrium between nitrogen contained in the balloon and liquid into the circuit is reached.

Free surface expansion vessel (Fig. 2.4b) is characterised by the presence of air in the upper-side of the vessel and liquid in the bottom-side. In this case, a direct contact between liquid and air occurs. The liquid, coming from the cold source, always enters in the vessel and, in the case where a pressure variation in the circuit takes place, it is dumped by air. In this case, the free surface of liquid changes its position until pressure equilibrium. This kind of expansion tank is the one used in cars’ engines cooling systems and, as it will be better explained later, it is also used in two-phase cooling systems. In the latter, air is mixed with vapour of the working fluid and saturation condition are

imposed.

However, a security valve, usually a spring-loaded pressure relief valve, is used to protect the circuit from exaggerate pressure increases that can occur in some cases (usually due to design error). If pressure in the expansion vessel is higher than the setting value of the valve, the latter opens and pressure is released to the ambient.

2.1.1.3 Heat sink heat transfer

Following the efficiency requirements, the heatsink (discussed in chap. 3) has to be able to ensure the adequate cooling of electronics devices allowing control of their surface temperature.

Due to sensible heat exchange, a strong dependency between mass flow rate and heat-sink temperature exists in single-phase case.

From the knowledge of thermal power evacuated by the electronic components, Q_{th} , the mass flow rate, \dot{m}_l , can be evaluated by eq. (2.3):

$$Q_{th} = \dot{m}_l c_{p,l} (T_{hi} - T_{ho}) \quad (2.3)$$

Under the hypothesis of adiabatic transport lines and in absence of any kind of regulation system, the temperature of the liquid at the inlet of the heat sink, T_{ho} , is imposed by the cold heat exchanger primary side outlet².

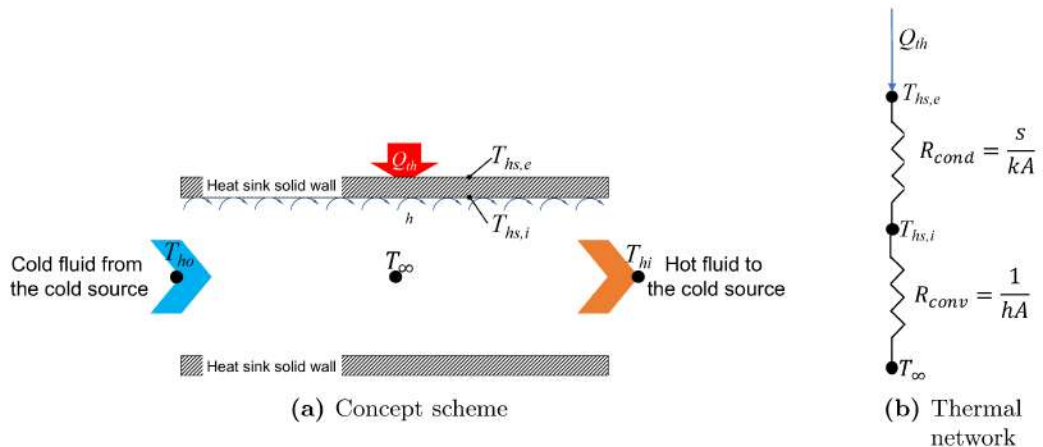


Figure 2.5: Heat transfer mechanism simplified scheme in the heat sink.

²All the variables are referred to the cold heat exchanger, with respect of the convention reported in fig. 2.3

According to schemes reported in Fig. 2.5 (where a schematic of transversal section of the heatsink is reported with the related heat transfer mechanism and the associated thermo-electrical network, respectively Fig. 2.5a and Fig. 2.5b), the coolant side heat sink wall temperature $T_{hs,i}$, can be simply obtained by the Newton's law:

$$Q_{th} = h A (T_{hs,i} - T_{\infty}) \quad (2.4)$$

where, h is the fluid equivalent heat transfer coefficient (calculated on the base of the electronic baseplate), A is the heat transfer surface area and T_{∞} the working fluid bulk temperature (calculated as the arithmetic mean between the plate's inlet and outlet temperature, T_{ho} and T_{hi} , respectively).

By combining equation 2.3 and 2.4, the bulk to wall temperature difference can be written as:

$$(T_{hs,i} - T_{\infty}) = \frac{\dot{m} c_{p,l} (T_{hi} - T_{ho})}{h A} \quad (2.5)$$

The heatsink external wall temperature, related by relation $(T_{hs,e} - T_{hs,i}) = \frac{Q_{th}}{\frac{kA}{s}}$, is calculated as:

$$T_{hs,e} = [\dot{m} c_{p,l} (T_{hi} - T_{ho})] \left[\frac{1}{\frac{kA}{s}} + \frac{1}{h A} \right] + T_{\infty} \quad (2.6)$$

From eq. (2.6) one may notice that to maintain a constant heatsink wall temperature, $T_{hs,e}$, at constant T_{hi} and T_{ho} , the mass flow rate, \dot{m}_l , and the heat transfer coefficient, h , need to change contemporarily. As it will be shown in sec. 2.1.1.4, for the cold source temperature differences realised in this application, up to $\simeq 80$ K, MFR (mass flow rate) adjustment is not a practical way.

2.1.1.4 The cold heat exchanger (HXG)

The cold heat exchanger allows evacuation of thermal load from the working fluid, flowing in the primary side circuit, to the secondary side one. Even in this case, the heat transfer mechanism is based on sensible heat exchange between hot and cold fluid. The hot fluid, flowing in the primary side, releases the thermal power to the cold source (secondary side) which nature, in this particular study case, is limited to one of the technologies presented in section 1.4. The logarithmic mean temperature difference method is used to obtain the heat exchanger geometrical dimensions and, a posteriori, the NTU method is used to calculate the heat exchanger efficiency ε .

Considering a co-current heat exchanger, its operating diagram is qualitatively reported in fig. 2.6. There, heatsink inlet to outlet temperature difference, ΔT_{hs} , under the hypothesis of adiabatic transport lines, and the secondary fluid inlet to outlet temperat-

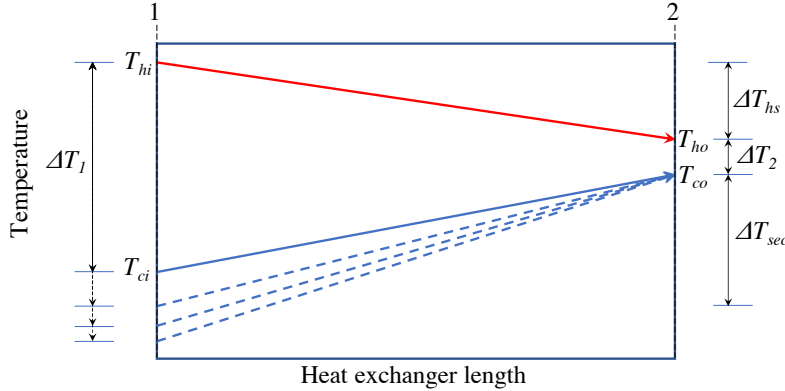


Figure 2.6: Co-current heat exchanger qualitative operating diagram

ure difference, ΔT_{sec} , on which the following discussion is based are also reported.

The primary circuit working fluid enters in the heat exchanger at temperature T_{hi} . It evacuates the thermal load, Q_{th} , to the cold fluid which temperature increases from T_{ci} (corresponding to the RAM-air inlet temperature, for example) to T_{co} . Hot fluid leaves the heat exchanger at temperature T_{ho} . — The heatsink inlet temperature, T_{ho} , depends on T_{ci} .

In classical applications, where the cold source temperature is fixed and does not change as a function of time, unless minor temperature change occurs (for example a night/day temperature oscillation in the case of an air-cooler HXG), the heat exchanger works at constant T_{ci} , so no T_{ho} change occurs. In this case, thermal transformations are only verified following the continuous lines in Fig. 2.6. In aeronautics field, on the contrary, according to the mission profile, the cold source inlet temperature, T_{ci} , is not constant, but it cyclically changes as a function of the altitude (see section 1.3). Temperature differences up to about 80 K may occur and such temperature change may impact the mean logarithmic temperature difference (LMTD) unless a regulating system is used on the primary or secondary side to control heatsink inlet condition.

Considering the design equation of a heat exchanger, the heat power to be evacuated is calculated as:

$$Q_{th} = U A \Delta T_{lm} \quad (2.7)$$

where: A is the heat transfer surface area; U the global heat transfer coefficient and ΔT_{lm} the logarithmic mean temperature difference, calculated as:

$$\Delta T_{lm} = \frac{\Delta T_1 - \Delta T_2}{\ln \frac{\Delta T_1}{\Delta T_2}} \quad (2.8)$$

When a change in T_{ci} occurs, two different scenarios are realised.

In the first case, mass flow rate rules. No regulating equipments are available on the circuit, neither on the primary or the secondary side. For given Q_{th} , ΔT_{hs} is fixed by the primary fluid mass flow rate (eq. 2.3) and ΔT_{lm} is fixed: in eq. (2.7), heat exchanger heat transfer area and overall heat transfer coefficient are fixed by design conditions. The whole heat exchanger diagram, in this case, will readapt its working point to maintain constant temperature differences, but changing heatsink working temperatures range. For constant inlet to outlet heatsink temperature difference, ΔT_{hs} , heatsink wall temperature, $T_{hs,e}$, and consequently junction temperature, change as a function of altitude/time. This solution is the simplest one, but not acceptable. In fact, the junction temperature is limited to an operating range, that, in most cases, is not compatible with external high-altitude ambient air temperature. Often, the junction temperature should be maintained as constant as possible, independently from the cold source temperature, to ensure power modules reliability and lifetime. To avoid such problems, a mass flow rate control system may be used to maintain the junction temperature regulated and fixed. On the basis of heat exchange on the secondary side, the air mass flow rate is calculated by eq. (2.9):

$$Q_{th} = \dot{m}_{air} c_{p,air} (T_{co} - T_{ci}) \quad (2.9)$$

Combining eq. (2.3) and eq. (2.9), it is:

$$\dot{m}_l c_{p,l} (T_{ho} - T_{hi}) = \dot{m}_{air} c_{p,air} (T_{co} - T_{ci}) \quad (2.10)$$

From relation (2.10), according to Fig. 2.7, one can observe that for fixed T_{hi} and ΔT_{hs} , to maintain the heatsink temperature as constant as possible, the air mass flow rate, \dot{m}_{air} , needs to be adjusted for any variation of T_{ci} . So, during climb and descent stages, a continuous regulation of external mass flow rate, \dot{m}_{air} , is required. Moreover, external air velocity variations occurring during taxi-out and take-off and climb stages transitions should be considered as well: they impact the air mass flow rate at the inlet of the heat exchanger.

To show required air mass flow rate variation as a function of altitude (to evacuate a thermal load of 15 kW and to maintain a fixed temperature difference on the heatsink, $\Delta T_{hs} = 12$ K), it has been calculated for three different working fluids (methanol, ethanol and water) as reported in Fig. 2.8. There, only temperature variations are considered.

The higher the altitude and the lower the external air temperature, the lower the required mass flow rate. A regulation of this type is not ease-to-implement. It might be strongly problematic and it could imply the use of valves and other regulation systems,

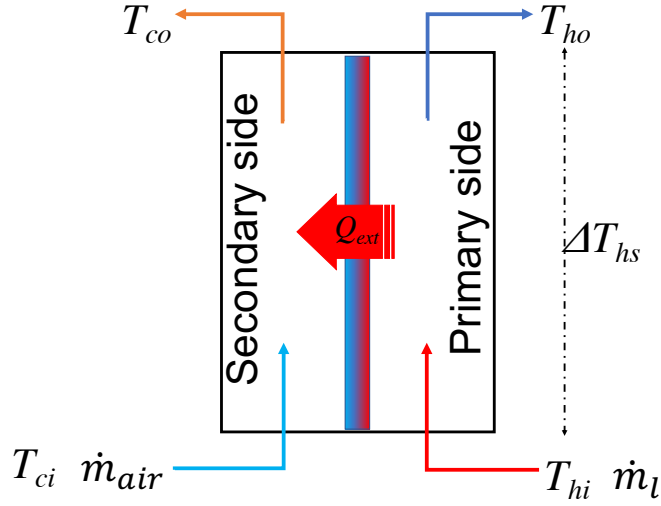


Figure 2.7: Cold side heat exchanger concept scheme

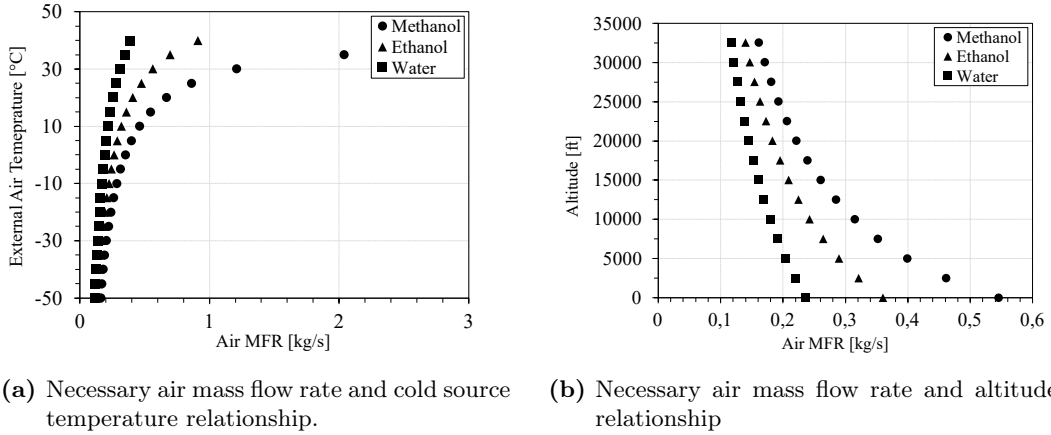


Figure 2.8: Air mass flow rate as a function of the external air temperature and altitude.

such as variable section nozzles. In order to respect the efficiency requirements in the context of HASTECS project, this is an option that cannot be retained. However, considering that the most part of radio communication and embedded systems are today cooled using this kind of technology, it will be considered for comparison purposes. In alternative to secondary air mass flow rate regulation, primary liquid mass flow rate regulation should be considered to maintain a constant heatsink temperature. In this case, a regulation valve such as a three-way-valve or a variable-speed-pump should be considered, but reducing the efficiency of the whole cooling system and increasing the overall mass.

Pros	Drawbacks
Very well known physics phenomena	Heatsink inlet temperature dependent on the cold source temperature
Easy to design	Strongly dependence on the operating point
-	Heatsink temperature dependent on the mass flow rate
-	Not flexible
-	Necessity of regulation accessories

Table 2.1: Single phase cooling system synthesis

2.1.2 Two-phase active cooling systems

Pumped two phase cooling systems are divided in two categories with different physical working principles and thermodynamic characteristics. In *pumped two-phase* technology the evaporator operates at higher temperature than condenser and a pump is installed on the liquid line. In *vapour compression* technology, because of the use of Rankine cycle, the evaporator can operate at lower temperature than condenser and a compressor is used on the vapour line.

2.1.2.1 Pumped two-phase technologies

Two-phase pumped cooling systems are the most effective way to evacuate the thermal load by increasing the overall efficiency of the cooling system itself.

Most of the authors that analysed this kind of technology focused their attention on performances, heat transfer efficiency and heat recovery requirements. When talking about electronics cooling, in fact, the attention is in particular paid to chips and data server cooling, which are characterised by quite high heat flux densities, but pretty small heat transfer surfaces. In this case, despite the really high heat flux densities, the heat rate to be evacuated is limited if compared with application analysed in this work.

The effectiveness of this kind of technologies has been demonstrated by Thome and Brunch [39]. By comparing two-phase pumped systems with single-phase ones, they showed that, to maintain constant chip temperature, the use of two-phase technology allows sensitive pumping power saving and using a lower coolant mass flow rate. If, instead, the same pumping power than active single-phase technology is used, a temperature difference of 13 K is realised in favour of two-phase one.

Such solutions are currently designed to fit the thermal evacuation requirements of military aircrafts. In those cases, very high thermal power, up to hundreds of kilowatts, with peaks in the order of thousands of kilowatts, must be evacuated [40]. The American society ACT develops two-phase technologies to be used for civil and military applications. They ensure a lowering of overall system mass due, in particular, to the reduction of the mass flow rate and pumping power [41].

Even if the concept scheme for this kind of technology is similar to the one related to single-phase cooling systems, the operating principle is completely different. Here, latent heat is used to extract heat by hot source.

In Fig. 2.9 the concept scheme of a pumped two-phase cooling system is reported.

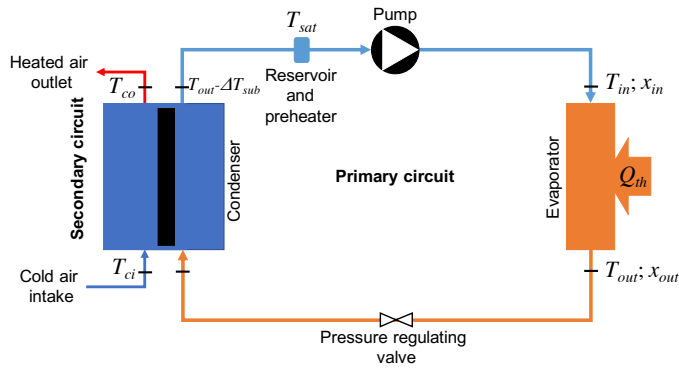


Figure 2.9: Pumped two-phase cooling system concept scheme.

In the case where a free surface tank is used as a reservoir, where saturation conditions are imposed, subcooled liquid coming from the condenser enters in it. The liquid flows within the liquid line to the evaporator, where heat is exchanged according to eq. (2.11).

$$Q_{th} = \dot{m} h_{l,v} (x_{out} - x_{in}) + \dot{m}_l c_{p,l} (T_{sat} - T_{in}) \quad (2.11)$$

Usually the vapour quality at the exit of the evaporator, x_{out} , is lower than unity and the temperature difference between the saturation temperature, T_{sat} , and the liquid entering in the evaporator, T_{in} , is usually negligible ($T_{in} \leq T_{sat}$). Sensible heat exchange in eq. (2.11) is negligible and, if no superheating occurs, vapour leaves the evaporator at saturation temperature, $T_{out} = T_{sat}$. The partially or completely evaporated fluid flows within the vapour line to the condenser, where heat is rejected and liquid subcooled before returning to the pump. Liquid temperature depends on the undercooling level imposed to the heat exchanger and so on the cold source temperature, T_{ci} . Subcooled liquid flows within the reservoir where it is heated until saturation condition and the cycle

starts again [41]. More generally, the reservoir, used to impose the saturation conditions, is separated from the circuit and is linked to it by a tube. No subcooled liquid flows within it, and in this case liquid temperature is $T_{in} < T_{sat}$.

If superheating occurs in the evaporator, the scheme of principle needs to be modified according to the fluid temperature change occurring into the evaporator. In this case no pressure regulating valve is needed on the vapour line. The superheated vapour directly flows to the condenser which has to be designed to ensure the necessary length, either for condensing and sub-cooling.

However, the position and the configuration of the circuit are imposed by system requirements. For example, in the case of Marcini *et al.* [42], a variable speed pump was used to regulate the fluid mass circulating into the circuit and a stepper motor valve, installed just before the evaporator, was used to control vapour quality through MFR regulation. In other cases, the sub-cooler may be separated from the condenser, usually valid for heat exchangers operating at fixed temperatures, this configuration avoids to use an electric heater in the reservoir and saturation conditions are imposed in heat exchanger as a function of T_{ci} . This kind of configuration requires to the evaporator to operate at higher temperature than in the condenser.

2.1.2.2 Vapour compression technologies

Vapour compression technology allows to evaporator to work at lower temperature than condenser. A concept scheme of this particular technology is presented in Fig. 2.10. Superheated gas, at the exit of the evaporator, is compressed up to the pressure corresponding to condenser's operating temperature. Once subcooled liquid condition is reached at the condenser outlet, the liquid flows through an expansion valve decreasing the fluid static pressure and bringing it to saturated vapour condition. So, the fluid flows to the evaporator and the cycle re-starts.

Because of the thermodynamics characteristics of these kind of systems, the vapour compression technology is able to lower the evaporator temperature below the condensing one. If in two-phase pumped systems, the liquid must be subcooled before entering the pump, installed on the liquid line, in this case, to avoid "wet compression", the vapour has to be superheated before its entering in the compressor [40, 43]. If the superheating required by the evaporator changes, due to a change of operating characteristics, the expansion valve regulates the superheating level to maintain fixed operating conditions. Even if some authors describe this technology as premature, especially for problems related to micro-compressors reliability and efficiency [44], when applied to electronics, it is successfully used in aeronautics fields for military applications.

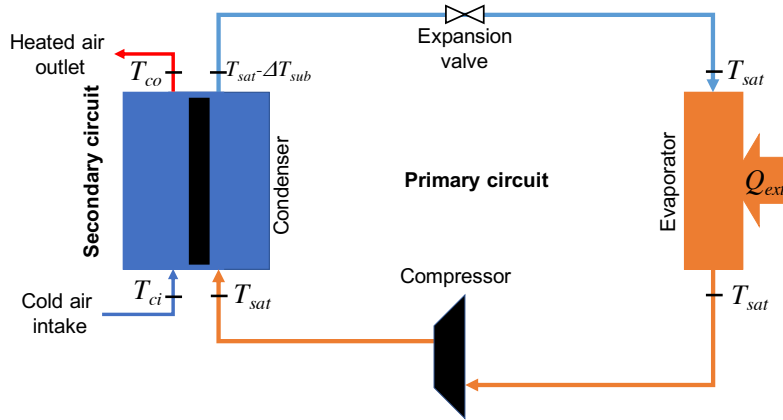


Figure 2.10: Vapour compression concept diagram scheme.

Mancin *et al.* [45] studied a vapour cycle system used to cool high heat flux density electronic components in avionic packages: a cold plate was used as evaporator and a tube-in-tube heat exchanger, supplied by two independent water flow rates controlled in temperature, was used as condenser. They obtained a coefficient of performance, COP, between 1.05 and 5.80. Trutassanawin's [46] refrigeration system was able to evacuate a $40 - 75 \text{ W} \cdot \text{cm}^{-2}$ on a 1.9 cm^2 chip and maintaining its temperature lower than 85°C . Comparing vapour compression technologies to the most promising cooling techniques, this is the only technology³ able to lower the junction temperature below the cold source temperature. However, they are affected by some integration difficulties. Today, the challenge is the compressor miniaturisation and efficiency increasing, especially at small scales, to make them more flexible and to reduce vibration and noise [44].

This technology is described as reliable enough in steady state applications, but during sudden and violent transient phases it demonstrates its biggest limitations. The latter are in particular related to instabilities concerning the entering of liquid phase into vapour compressor. This is true during severe transient phases related to sudden and violent variable-gravity stages. As reported by Chen *et al.* [5], the major issue is mostly related to multi-evaporator configuration. To solve the problem, they introduced a system, reported in Fig. 2.11, able to suppress flow instabilities, separating liquid and vapour phase in a two-phase flow, by using a Microchannel Membrane Phase Separator (MMPS). A first MMPS is installed after the evaporators. It separates liquid and vapour phase of an eventual two-phase flow at the exit of the evaporators. The liquid is sent back to the evaporators inlet, where an ejector⁴ is installed, driving the liquid in the recirculation

³Unless Peltier cells are considered.

⁴Ejectors are passive devices able to generate a pressure difference. They require a sufficient momentum to the fluid to raise the suction flow pressure.

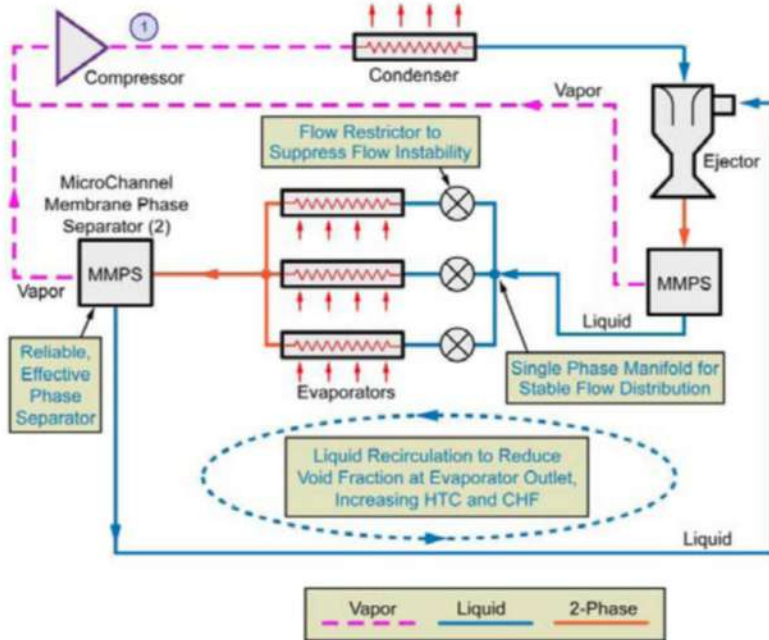


Figure 2.11: Scheme of principle of an active two-phase thermal system equipped by a MMPS solution [5].

loop. An other MMPS is installed before evaporators and separates eventual liquid and vapour phases at the exit of the ejector. In this case, vapour phase is sent to the compressor inlet, while the liquid phase to the evaporators inlet. A great complexity characterises this kind of system, in which it is not possible to control each phase of the flow without using a by-pass control loop.

Even if vapour compression technology is able to lower the evaporator temperature below the condenser's one, it has to be underlined that, because of the higher specific volume of vapour, compared with liquid one, the work required to vapour compression technology is higher than that required to *pumped* two-phase cooling systems to provide the same differential pressure between compressor/pump inlet an outlet. Marcinichen *et al.* [42] proposed three different kind of “two-phase cooling cycle”. They compared the performance of a liquid pumped two-phase technology, a vapour compression cycle and a hybrid one. They used a variable speed pump to control MFR in the circuit, while a stepper motor valve was used to control vapour quality at the outlet of the evaporator.

The scheme of principle of this kind of technology is not so different than that of single-phase one.

Even if this technology is one of the most promising, flexible and potentially efficient, its use in aeronautical field could be a gamble, even due to its instabilities during some

transient stages. On the other hand, pumped two-phase cooling systems will be retained to be compared with other promising technologies introduced in the following.

2.2 Passive cooling systems

In contrast to active cooling systems, passive cooling systems do not require any external source of energy to move the coolant. Neglecting systems using natural convection because of its low heat transfer coefficient, here we will only refer to two-phase passive technologies.

During the latest thirty years passive cooling systems, such as *heat pipes*, *thermosyphons*, CPLs (*Capillary Pumped Loops*) and LHPs (*Loop Heat Pipes*), began to be used in aeronautical and aerospace fields [47]. The main advantages of these systems are their simplicity, adaptability and efficiency. Some of them, such as thermosyphons, have been used since a long time in terrestrial applications, such as railway field, for IGBTs cooling, while other ones have begun to be used since the latest ten years [48, 49, 50].

2.2.1 Thermosyphons and Heat pipes

Heat pipes (HP) and thermosyphons are successfully used in applications do not requiring high transport distances. Generally, they are able to transport heat powers from a few dozens of Watt up to 1 kW for distances ranging between 10 cm and few meters. They are today used for thermal control, temperature homogenisation or as thermal diodes [51]. They are particularly useful when the heat sink and the cold source are located up to a few meters. Today, capillary heat pipes are effective to evacuate heat flux up to $100 \text{ W} \cdot \text{m}^{-2}$ and reducing hot-spot influence by flattening the temperature field on the surface to be cooled. Vapour chamber has been successfully used as heat spreader, to reduce temperature gradients on electronic components and evacuating heat flux densities up to $220 \text{ W} \cdot \text{cm}^{-2}$ as Reyes *et al.* reported [52].

2.2.1.1 Thermosyphons

A thermosyphon is a finite closed tube filled with a small quantity of fluid at saturated state. Its higher and lower ends are closed and sealed, while air is sucked-out. When thermal load is applied to the lower end (evaporator), the working fluid evaporates and vapour flows within the adiabatic length to the condenser. Here, heat is evacuated and condensed fluid flows back to the evaporator, thanks to gravity forces, sliding on the lateral walls of the device. The essential condition that allows a thermosyphon to operate is obviously the ability for the condensate to flow back to the evaporator.

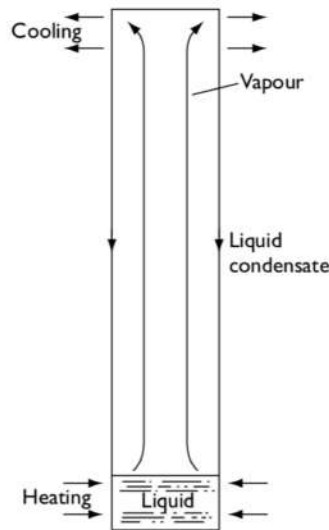


Figure 2.12: Thermosyphon [6]

A vertical installation or any other kind of favourable direction is so necessary to allow the condenser to be positioned over the evaporator.

At the evaporator, three different heat transfer mechanism occur following the intensity of the heat flux and the liquid/vapour phase distribution. The working fluid stratifies in the evaporator, it is so affected by three different behaviours: liquid pool, liquid film and vapour. For small heat fluxes, natural convection occurs in the liquid pool; for medium and high heat fluxes, mixed convection and nucleate boiling may take place. Different factors, such as filling ratio (FR, the liquid over the evaporator volume ratio), inclination angle, heat power load, and aspect ratio influence the performance of the thermosyphon. Among them, the most important is the filling ratio. A small amount of liquid contained in the thermosyphon easily bring the device to dry-out. This is a detrimental condition that leads to failure of the device. A pretty high amount of liquid may cause flooding in the evaporator. In this case the liquid remains in the condenser or in adiabatic section and is no more able to return back to the evaporator. However, this is not the only condition that prevents the liquid to flow back to the evaporator. In fact, if thermal load to the evaporator is too high, violent boiling can prevent the liquid to flow back to the evaporator and chocking occurs if vapour velocity is higher than the sonic limit. In this case, vapour, flowing in the centre of the thermosyphon, experiences a shockwave and the device stops to work. When vapour expansion is violent, instabilities may occur due to reduction of hydraulic head (geyser boiling). This phenomenon does not limit thermal and hydraulic operations of the device, but, due to vibrations related to, this phenomenon can be detrimental from a mechanical point of view [53, 54]. For

example, using water as working fluid, Ong and Lim [53] experimentally observed that the best performing condition for the thermosyphon is vertical condition with a filling ratio equal to unity. Abou-Ziyan *et al.* [55] investigated the performances of a vibrated and a stationary thermosyphon with water and R134a as working fluids. The heat flux densities were measured from 4 to $28 \text{ W}\cdot\text{cm}^{-2}$ with water and from 1.6 to $3.8 \text{ W}\cdot\text{cm}^{-2}$ with R134a. They found that the adiabatic length, like the filling ratio, deeply influences the behaviour of the device. The maximum heat transport capability is influenced by the working fluid: a difference of one order of magnitude was found between water, characterised by the best performances, and R134a. Filippeschi and Franco [56] experimentally investigated, using water and ethanol as working fluids, the influence of the main parameters on a thermosyphon. They did not observe an important influence of the filling ratio if water was used as working fluid while, using ethanol, a higher sensitivity to the FR was tracked down other than higher instabilities.

As well as instabilities, thermosyphons are strongly limited by their inability to work whatever the position. For this reason, capillary driven technology, such as HP, LHP and CPL are worth of attention, more than thermosyphon, here introduced just for completeness.

2.2.1.2 Heat pipes

Capillary Heat Pipes (HP) are under certain aspects close to thermosyphons, but thanks to capillary pumping liquid is sucked back from condenser to evaporator. This, obviously, allows HPs to potentially well operate whatever their orientation.

According to Fig. 2.13a, heat pipes are composed by a tube internally coated with a thin layer of porous material (wick) and closed at the higher and lower ends. A small quantity of liquid is inserted and air is sucked out.

As thermosyphons, HP can be divided in three different thermal sections: evaporator, where the thermal load is applied, adiabatic zone and condenser. In the evaporator, vapour is formed and naturally flows within the adiabatic zone (into vapour space, see Fig. 2.13b) to the condenser section. Here, vapour condensates and liquid come back to the evaporator thanks to capillary forces caused by the menisci curvature in the porous wick. Heat pipes are characterised by high thermal performances, and can be used in several applications. Beyond the classical use, for cooling purposes, they are successfully used as thermal diodes and thermal switches (for variable conductance HPs) [6] as soon as heat spreaders. According to their design, they can operate over a wide range of temperatures (from 4K to 2300K) and for pretty high heat flux densities, up to $20 \text{ kW}\cdot\text{cm}^{-2}$ with lithium used as working fluid [6]. However, HPs began to be widely used in electronics

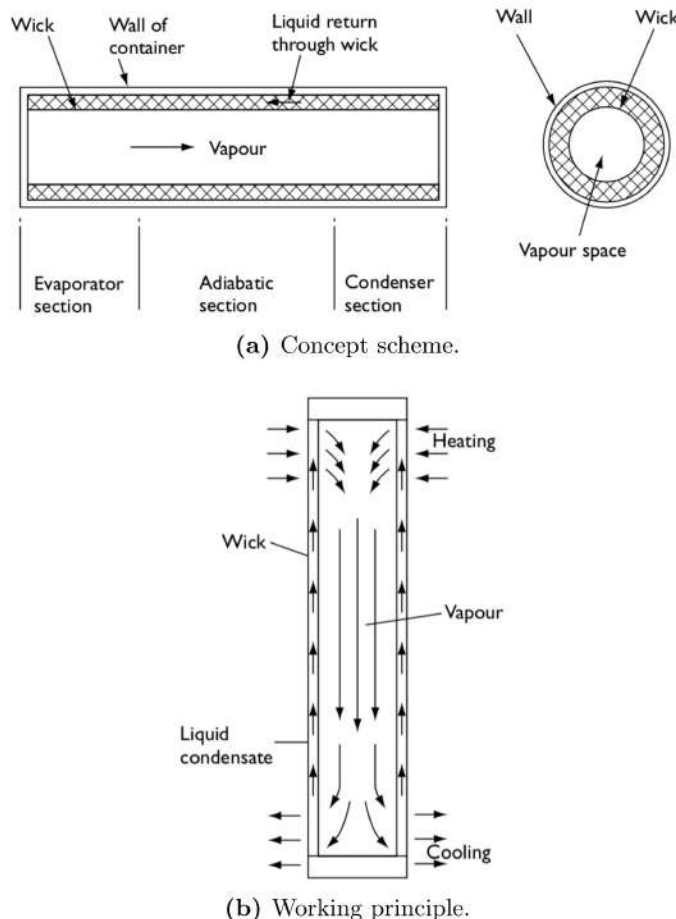


Figure 2.13: Heat Pipe. [6]

cooling because of their adaptability to the geometry to be cooled, easy integration, as well as their capability to maintain a uniform temperature field on the surface to be cooled and their property to transport heat to another point where the evacuation is simpler. In particular, according to geometry, different kind of heat pipes exist, from flat heat pipe (FHP) to micro heat pipes. The latter are used in array configuration allowing a direct concurrence to microchannels (see sec. 3.2.2). A typical application concerns chips cooling of “smart devices” we every day use and everybody has in his pocket (see Fig. 2.14a). Sometimes they are used by devices constructors for advertising purposes (Fig. 2.14a and 2.14a) [57, 58].

Ray and Kew [6] classify HP in five categories. Including Loop Heat Pipes (LHP), the other categories are tubular, flat plate, micro heat pipes and direct contact systems. Tubular HPs represent the “basic” category of heat pipes and different design features may be used in particular in electronics application field. For example, for power electronics

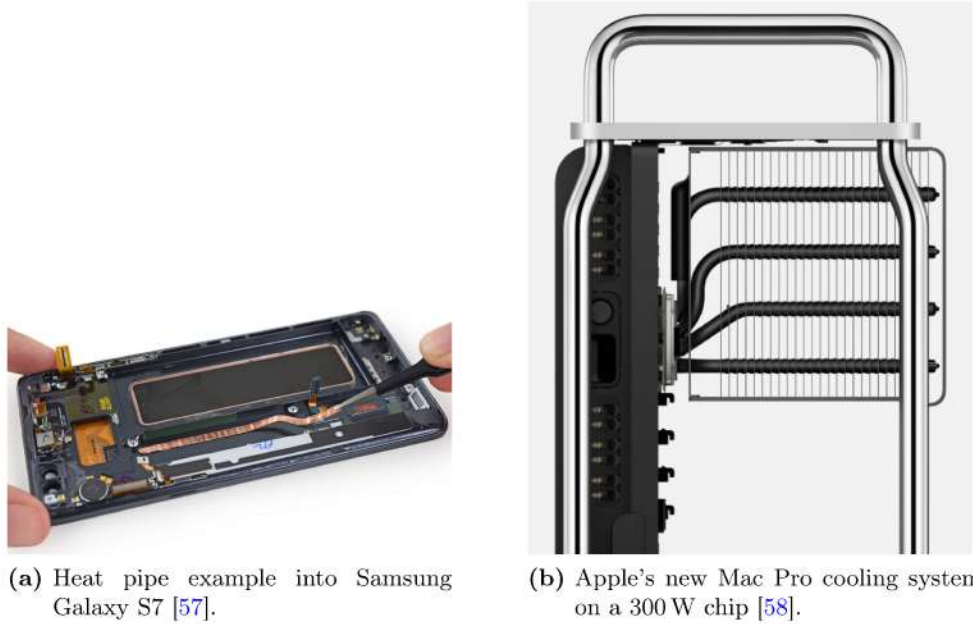


Figure 2.14: Heat pipes application example

cooling on high speed trains, their adiabatic section is electrically insulated. The ceramic insulation insert is able to hold-off very high electric voltage, in the order of kilovolts [6].

Flat plate heat pipes (Fig. 2.14a) are the mostly used, in particular for micro-electronics cooling purposes for their particular ability to flatten the temperature field and so, to obtain a nearly isothermal surface on the device to be cooled [6]. The electronics chips can be directly mounted on HP. In this case, a heat conducting electric insulation layer is used between chips and HP evaporator. In other cases, electronic components are mounted on heat pipes using such heat spreader or any other kind of structural component [59]. Flat plate heat pipes FPHP may be bended as they can fit into small devices, as is the example of laptop computers. However, bending angle of FPHP should be optimised, as well as HP length because of decreasing thermal performances. Chen and Chou [60] experimentally observed a bell shape thermal conductivity behaviour as a function of thermal power. By exploiting different bending angles of adiabatic length, they observed an increase in thermal conductivity of almost 3 times: from $2 \text{ kW} \cdot \text{m}^{-1} \cdot \text{K}^{-1}$ at a bending angle $\alpha = 0^\circ$ to over $6 \text{ kW} \cdot \text{m}^{-1} \cdot \text{K}^{-1}$ at a bending angle $\alpha = 90^\circ$.

Micro and miniature HPs are widely used in electronics components cooling and are worthy of attention because of their efficiency, lightweight and passivity. They are characterised by diameter in the range $0.3 - 6 \text{ mm}$. They can work in thermosyphon mode,

without a wick coating, or in HP mode when a sintered powder, a metal-fibre or a grooved wick are being used. Different working fluids can be used, from pure water to ethanol, methanol or dielectric fluids [6, 59]. They are successfully used to evacuate thermal power up to 250 W on distances up to 200 mm. Low thermal resistances characterise this particular technology, from $1.5 \text{ K} \cdot \text{W}^{-1}$ for lower outer diameter HPs to $0.6 \text{ K} \cdot \text{W}^{-1}$ for higher diameters HP [59]. As reported by Chen *et al.* [61], the smaller the channel transversal section of HPs, the higher the heat transfer coefficient (HTC) and the higher the heat transfer surface area per unit flow volume. For this reason, micro heat pipes (MHP) were worth of attention other than for their ability to evacuate thermal heat flux densities up to $1 \text{ kW} \cdot \text{cm}^{-2}$ (for small heat sources). However, they are no longer used for small transport distances, in the order of centimetres, because of their low thermal performances. In fact, at such little transport lengths, at which MHPs were used, conduction heat transfer mechanism gets the upper hand on two-phase heat transfer one, undermining HPs themselves. If a temperature flattening is required and so the thermal heat flux needs to be reduced, by increasing the heat dissipating surface, from the dissipating device, the heatsink can also be equipped by a vapour chamber which can be characterised by very high thermal conductivities, up to $800 \text{ W} \cdot \text{m}^{-1} \cdot \text{K}^{-1}$ [59].

However, strong limitations may affect HPs. If, for example, the temperature at evaporator is quite low, no vapour menisci are formed and so no fluid circulation occurs in the device: the pressure difference between the evaporator and the condenser is not sufficient (vapour viscous limit) for the liquid to come back to the evaporator by capillary effect. As the temperature increases, the vapour velocity increases as well, but it is limited to sonic limit to avoid chocking. Capillary limit occurs when the capillary pressure is too low to counterbalance the overall pressure losses due to the fluid flow: $\Delta P_{cap} < \Delta P_{tot}$. The capillary pressure head ΔP_{cap} , reported in eq. (2.12), is a function of the surface tension of the working fluid, σ , and of the curvature radius, R , of the liquid-vapour interface in pores of the wick.

$$\Delta P_{cap} = \frac{2\sigma \cos \theta}{R} \quad (2.12)$$

The total pressure drop, ΔP_{tot} , is the sum of the frictional pressure drop in the porous wick, viscous pressure drop of vapour during its path from the evaporator to the condenser, internal and gravity pressure drops .

However, it exists a maximum value of capillary pressure head, $\Delta P_{cap,max}$: as well as the thermal load increases, the curvature radius R tends to decrease until it reaches its

minimum value, $R = R_p$. The maximal capillary pressure head is so defined as:

$$\Delta P_{cap,max} = \frac{2\sigma}{R_p} \quad (2.13)$$

When the minimal value of R_p is reached, any eventual augmentation of thermal load at evaporator will lead to a regression of the liquid/vapour front in the primary wick, with the consequent system failing [62]: dry-out occurs and HP stops to work.

2.2.1.3 Pulsating heat pipes (PHP)

Pulsating Heat pipes (PHP) belong to the category of wickless heat pipes. In this particular devices, heat is transferred under the form of latent heat through the vapour and sensible heat through the liquid slugs. The working principle is different than that of classic HP. In this case, the fluid flow is not imposed by a capillary structure in which capillary forces take place to push the liquid from the condenser to the evaporator. Its pattern is imposed by surface tension effects in a smooth tube causing phase separation resulting in the formation of slugs of liquid dispersed into vapour bubbles. As one can observe in Fig. 2.15, the device is formed by a serpentine, partially filled of liquid, which cross section dimension is in the order of capillary dimension.

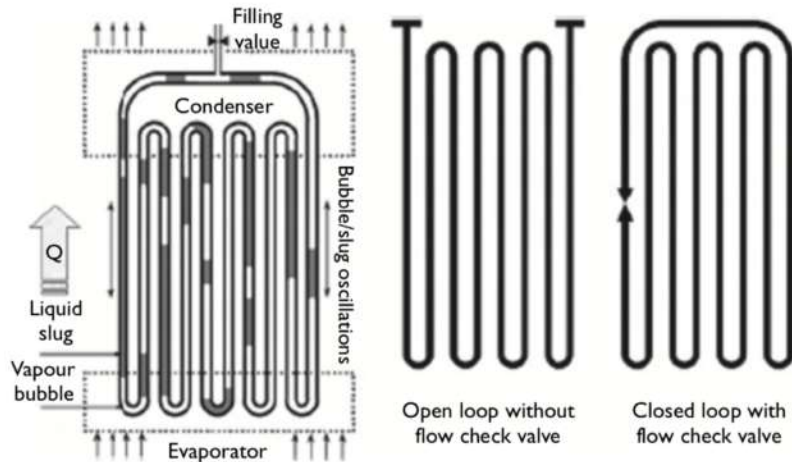


Figure 2.15: Pulsating heat pipes [6].

When thermal load is applied to evaporator, the working fluid evaporates and vapour pressure increases bringing to vapour bubbles growing in the evaporation zone. The liquid slugs and vapour bubbles are so pushed to the condenser where lowering of the vapour pressure occurs and condensation takes place. Bubbles growing and collapsing bring to the typical oscillating motion of liquid into the adiabatic section of the PHP.

Despite the simplicity of this technology, the working principle is not completely known, but its potentialities, in particular for electronics device cooling are undeniable. Fundamental and applied studies are currently in progress to increase the knowledge about this particular technology such as in refs. [63, 64, 65, 66, 67, 68, 69, 70].

2.2.2 Two-phase passive loops

LHP and CPL belong to the category of two-phase passive loops and are characterised by a decoupling between liquid and vapour lines. The same components constitute LHP and CPL: evaporator, composed by a porous wick confined in a metallic housing; reservoir, condenser and transport lines. The difference between the two loops is the position of two-phase reservoir. LHPs are characterised by a *hydraulic* and a *thermal* coupling between the evaporator and the reservoir. It is due to a direct contact between the two components, that are connected together, to allow heat and mass exchanges between them. The two-phase reservoir is installed immediately before the evaporator and receives a part of the heat flux. A buffer volume is directly linked with the porous wick in the evaporator. So, an eventual surplus of vapour can return into the reservoir.

CPLs are characterised by a *hydraulic decoupling* between the reservoir and the evaporator, as explained by Nikitkin [47], Lossouarn [50] and Blet [71]. The reservoir is installed on the liquid line, and linked to it by a little tube [47]. This particular configuration does not facilitate hydraulic exchanges between the two components [50]. Because of such decoupling between the two entities, CPL is characterised by a slower time constant (so called “thermal” time constant) during transient operations. There are strong operating differences between the two systems. LHPs are characterised by robustness and auto-regulation ability, while the direct coupling between reservoir and evaporator does not easily allow regulation of saturation point [71] that is one of CPL characteristics.

Nikitkin and Cullimore [47] described the difference between the two loops, and said that between them many technologies could be imagined and developed.

2.2.2.1 Loop Heat Pipe (LHP)

Loop Heat Pipes (LHP) can be seen as an extension of the concept of classic heat pipes. LHP are characterised, as HPs, by the presence of an evaporator and a condenser, but a decoupling between vapour and liquid line exists. Beyond the separated transport line feature, LHP is characterised by the presence of a reservoir where saturation conditions (temperature and pressure) are “automatically” established [6]. Despite the fact that the LHPs represent an “evolution” of HPs, they are characterised by higher capillary

pumping head if compared to HPs, allowing transport of heat for several meters (up to 21 meters) [72].

Loop heat pipes are characterised by a direct coupling between the evaporator and the reservoir. The direct link between the two components makes possible the transmission of a part of the heat flux from the one to the other. The heat flux modifies the saturation conditions in the reservoir. The equilibrium between the saturation conditions in the reservoir and the flow of cold fluid at the inlet makes possible its typical auto-regulation capacity. Moreover, the contact between the porous mesh and the reservoir walls increases the robustness of the system: the liquid at the inlet of the porous wick is directly provided by the reservoir.

To explain the loop operating principle, we will refer to the scheme and the thermodynamic diagram reported in Fig. 2.16.

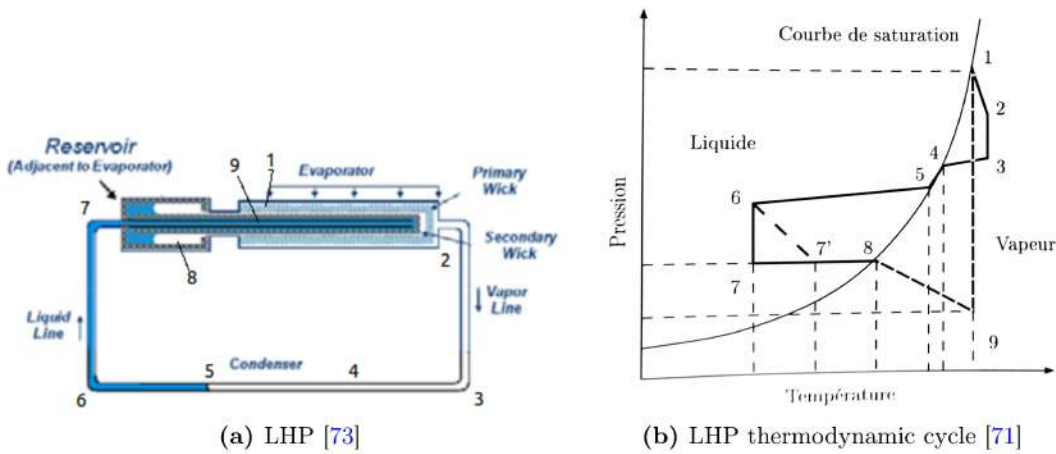


Figure 2.16: Loop Heat Pipe Scheme and thermodynamic cycle

When the thermal load is applied to the evaporator wall, it reaches the liquid menisci in the porous wick and triggers the evaporation (point 1). Vapour pressure increases and vapour leaves the evaporator slightly superheated by evaporator walls (point 2). Vapour flows through the vapour line into the condenser (point 3) where it is initially cooled until saturation condition is reached (point 4 on the saturation curve), so condensed (4-5) and undercooled (5-6). Subcooled liquid flows through the liquid line to reservoir inlet (point 7). Here, it is heated by a fraction of the heat flux received by the thermal load until saturation conditions are reached (point 8, corresponding to the reservoir thermodynamic conditions at equilibrium). Then, liquid flows through the porous wick until the liquid/vapour menisci (point 9), where capillary forces take place and the cycle starts again. Saturation conditions in the reservoir are not imposed, but depends on

heat balance. A change of the thermal load leads to a change of saturation conditions in the reservoir, displacing the point 8 on the saturation curve and modifying the whole thermodynamic cycle. The loop adapts the operating point to respect the global balance of the loop [26].

Gravitational effects influence the loop behaviour and must be taken into account. In fact, the presence of a gravity field modifies the fluid distribution, in particular between the compensation chamber and the evaporator core [62]. Two important parameters have to be considered when a LHP operates in gravity fields. The *elevation*, which is the relative position between the evaporator and the condenser, and the *tilt*, which represents the relative position between the evaporator and the compensation chamber. A modification of tilt can modify the liquid distribution between the evaporation core and the compensation chamber. In adverse tilt conditions, the evaporation core is filled with vapour, so, it could lead to an increase of the operating temperatures of the loop [62]. At positive tilt, the evaporation core is completely flooded with liquid.

2.2.2.2 Capillary Pumped Loop (CPL)

Capillary pumped loops (CPL) use the same mechanisms than LHP to let the fluid flow into the loop, so equations (2.12) and (2.13) are still valid in this case. As said above, the differences between the two loops is the position of the reservoir which modifies the operating characteristics and the behaviour of the whole system. In CPLs, the saturation point in the reservoir is generally fixed by using an electric heater. So, in this case, the reservoir is used as a compensation chamber where the reference point for the thermodynamics cycle is constant and has to be controlled during operations.

To explain CPL working principle, even in this case, the concept scheme and the thermodynamic cycle will be used (see Fig. 2.17).

Comparing thermodynamic cycles of LHP and CPL reported in Fig. 2.16b and 2.17b, no difference exists between the thermodynamic states (1 to 7). On CPLs, a change of thermal load applied to the evaporator will lead to a temperature change of evaporator itself. On the other hand, a shift of the whole cycle on the saturation curve takes place: thermodynamic states will change respecting the saturation conditions constraint imposed to the reservoir (point 8). It is worth of attention that a change of heat load at the evaporator leads to a change of condensation length in the condenser. So, its conductance adapts itself maintaining a constant temperature in the loop [25]. This is one of the most important CPLs characteristics: the temperature level control capacity, that makes of CPLs one of the most flexible system. On the other hand, due to the decoupling between reservoir and evaporator, they are characterised by high instabilities

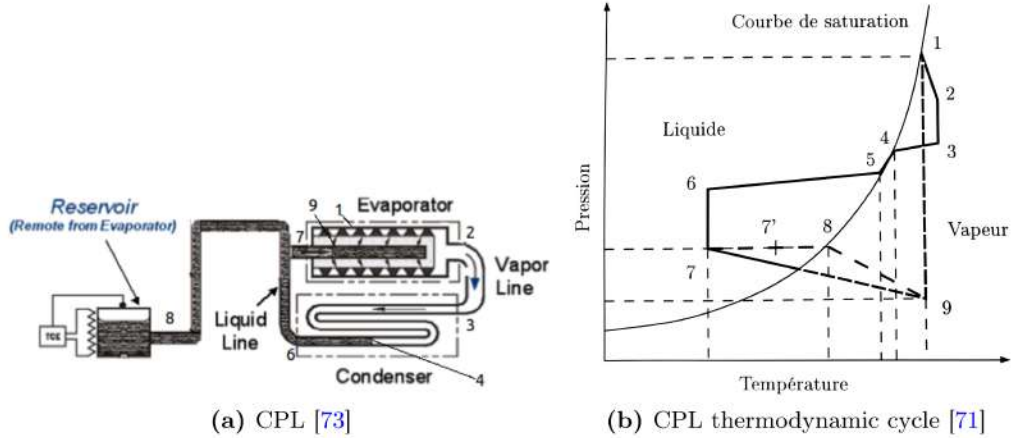


Figure 2.17: Principle scheme and thermodynamic cycle of CPL and LHP loops

and oscillations [50], in particular during start-up stages [74].

The described systems are characterised by a great robustness and auto-adaptability, in the case of LHPs, and by an undeniable temperature levels regulation ability in the case of CPLs.

2.2.2.3 Capillary Pumped Loop for Integrated Power (CPLIP)

During the last years, a new loop typology has been developed to solve the problems related to the use of CPLs and having the reliability and robustness of LHPs. The Capillary Pumped Loop for Terrestrial Applications (CPLTA), or Capillary Pumped Loop for Integrated Power (CPLIP), is not really a CPL-LHP operating conditions mixing, but it is another kind of loop. It is more similar to a CPL, but with a higher energetic and mass coupling between reservoir and evaporator thanks to gravity forces. It was designed for the first time by the Belgian society EHP (Euro Heat Pipe) for power electronics thermal control for the railway field purposes [50].

The CPLIP, which a concept scheme is reported in Fig. 2.18, is characterised by a particular architecture that makes possible hydraulic and thermal couplings between reservoir and evaporator. The reservoir (R) is installed above the evaporator (E) and the two components are linked by a liquid line, continuously supplying⁵ the evaporator with liquid. If eventual vapour bubbles are formed in the wick, they are evacuated flowing up to reservoir while the liquid is forced by gravity to enter the evaporator. In this case, especially during the start-up stages, compared to classical CPLs, loop crisis are absent [50] and system reliability is high.

⁵During normal operating conditions.

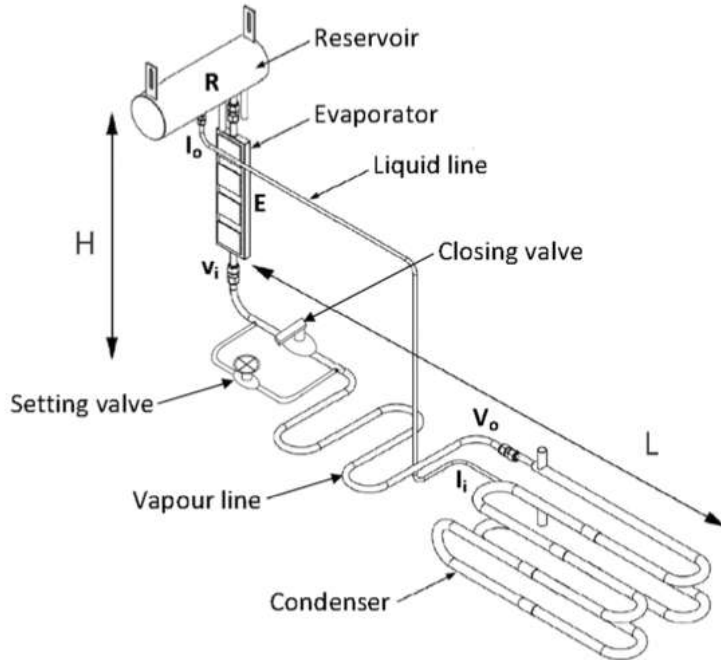


Figure 2.18: CPLIP scheme [7]

The reservoir is physically divided in two parts. The higher part, having the higher volume, contains the liquid-vapour interface. The height of the interface changes as a function of loop operating regimes: “variable conductance mode”. Like in classical CPLs, it is possible to control the saturation conditions in the reservoir and so, the evaporation temperature [49]. The lower part, directly linked to the liquid line and characterised by a smaller volume than the higher part, contains the under-cooled liquid coming from the condenser. The two parts of reservoir communicate through a small opening which makes possible mass transfer between both volumes and so pressure and energy balances. The controllability of reservoir temperature, by using an electric heater, makes possible a great stability of the loop especially during transient regimes such as start-ups [74].

Like CPLs and LHPs, the evaporator contains a porous wick, which, using capillarity effect, described in sec. 2.2.1.2, is able to pump the liquid into the whole loop. Different materials may be used for this component. In such cases the use of a Nickel porous wick determines the reduction of the particles size, leading to an increase of ΔP_{cap} and so to an increase of the performances of the whole loop.

Like CPLs, the condenser must be designed to allow complete condensation and the adequate subcooling of working fluid to avoid two-phase flow in the liquid line and so vapour bubbles at the inlet of reservoir. A too small condenser has not a sufficient length

to ensure liquid under-cooling, while a too long one could lead to quite large pressure drop, determining in some cases the failure of the loop. It has been demonstrated that the condenser has the ability to adapt its conductance to maintain a constant evaporating temperature [14, 12] by adapting the condensing length to the thermal load that has to be evacuated. This point will be better and deeply explained in chapter 6.

It has to be noted that the loop is successfully used today to cool the power electronics components on a train operating on the RATP line in Paris [48] since 2012, by evacuating heat flux densities from $20 \text{ W} \cdot \text{cm}^{-2}$ up to $40 \text{ W} \cdot \text{cm}^{-2}$.

2.2.3 First comparison between two-phase passive cooling systems

In tables 2.2 and 2.3 the main pros and drawbacks of most important passive technologies are reported.

A first comparison between CPL and LHP has been made by Delalandre [26] and his table has been completed by adding the CPLIP characteristics (table 2.2). In table 2.3 a comparison between the passive cooling technologies is reported, considering their pros and drawbacks.

Properties	CPL	LHP	CPLIP
Regulation	+	-	+
Robustness	-	+	+
Integration	+	+	(~)+
Maturity	+	+	±

Table 2.2: Synthesis of the main characteristics of CPL, LHP and CPLIP.

2.3 Conclusion

Due to complexity, intrinsic characteristics and possible configurations, it is difficult to classify cooling systems. However, in this chapter, a possible classification was proposed by splitting them in different categories and by grouping them on the basis of their basic physics and working principles. Starting from general point of view, on the basis of the thermodynamics operating principles beyond each cooling loop, they were divided in active and passive cooling systems.

Active and passive loop circuits were introduced, considering the whole system and their basic physics. So, the main components of such cooling circuit were analysed under a thermo-hydraulic point of view. Pros and drawbacks were introduced to easily

Technology	Pro	Drawback
<i>LHP</i>	Auto-regulation capacity	Incapability to control temperatures
	Robustness	
<i>CPL</i>	Temperature regulation possibility	Instabilities Slow start-up
	High stability [75]	
	Independence between cold source and junction temperature	External source of energy required
	Heat flux densities up to $40 \text{ W} \cdot \text{cm}^{-2}$	
<i>CPLIP</i>	Heat transport capacity up to 10 m [75]	
	Highly performing up to $100 \text{ W} \cdot \text{cm}^{-2}$ (HP)	Low transport distance on the ground
	High performances as heat spreaders [51] (Vapour chamber case)	
	High versatility	
<i>HP</i>	Simplicity in construction	Instabilities (geyser effect)
		Favourable position mounting (condenser above the evaporator)
		Highly influenced by accelerations
<i>Thermosyphons</i>		

Table 2.3: Pros and drawbacks comparison between passive cooling systems

understand, even in the following of this work, why a system can be retained and why another is not adapted for this particular application case.

Active single phase cooling systems are not, in general, able to maintain a constant temperature level during operation if the secondary side temperature changes as a function of time, unless such a kind of control system is added on the circuit. However, this kind of technology is today widely used, because of its simplicity, for electronics cooling purposes, so it is worthy of attention for comparison purposes. Two-phase active cooling systems are a rising technology, and in particular vapour compression cycle is an interesting solution that begins to be used in aeronautics field. Despite its performances, and its ability to lower the evaporator temperature below the cold source one, this technology is unfortunately at its early stages, and some problems, in particular related

to compressor's hydraulics, have to be solved. Moreover, to damp instabilities naturally related to this application field, the use of complex regulating systems is necessary.

The attention was also focused on passive two-phase cooling systems. In particular working principle of thermosyphons, heat pipes, loop heat pipes and capillary pumped loop (with particular attention to a new kind of gravity CPL) were introduced. Literature results were considered in terms of thermal resistance, transport distance, heat evacuation capability to understand which system is the most adapted for this particular application field.

Passive two-phase technologies began to be used for electronics cooling purpose since the thermal heat flux densities became too high and the air forced convection showed its limitations. Heat pipes are able to evacuate high heat fluxes densities, but heat transport capability is limited. They are not an interesting technology for this application case. Loop heat pipes (LHP) and capillary pumped loop (CPL) are worthy of attention, and in particular the CPLIP (Capillary Pumped Loop for Integrated Power) because of its ability to maintain a constant operating temperature to the evaporator whatever the cold source temperature.

With reference to active cooling systems, and considering only the heatsink, in the following chapter different "brand new" heat evacuation technologies, considering the heat transfer characteristics at the level of the hot source base plate, will be introduced and compared with the purpose to understand if one of them is worthy of attention to compete with passive two-phase technologies in terms of evaporator/hot source thermal and hydraulic performances.

Classic cold plates, micro and mini channels, porous media and metal foams, as well as jet impingement and spray cooling, will be analysed, independently from their systems and in their single and two-phase version.

Power electronics cooling: state of the art of heatsinks

In the previous chapter the attention was focused on the whole cooling system, to introduce the working principle of different kinds of cooling loops. Here, a different point of view is used, in fact, performances of a cooling loop change following the typology of the heatsink used. Over the last thirty years, many research teams have worked on the issue and different technologies have been continuously compared and studied. In general, it is not possible to argue that it exists a better solution than another, but the choice depends on necessity and performance requirements. A trade-off has to be found in most cases. Cooling system performances strongly depend on the ability to evacuate the required thermal load with the lower mass flow rate possible: in other words the HTC needs to be maximised. In fact, the higher the HTC, the lower the mass flow rate required and the higher the cooling system efficiency: the cooling system performances and its ability to maintain the temperature of the electronics components controlled depends on the performances of the heat sink itself. The latter is, in fact, the first stage where the thermal load is evacuated by electronics components to the coolant. Single-phase and some active two-phase cooling systems can be studied by decoupling the heatsink performances from the rest of the system. In this case, it is possible to analyse the behaviour of the heat sink, its performances and characteristics, independently from the nature and performances of the cold source or any other component in the loop. In the following, efforts have been made to classify heatsinks in two categories: direct cooling systems, for which the cooling fluid is directly in contact with the electronic baseplate; and indirect cooling systems where the coolant is confined in a separated circuit (no contact occurs between the working fluid and the electronic components in this case). In this chapter the most suitable heatsink configurations are analysed, the basic physics of the different technologies explained, and pros and drawbacks of each one underlined.

3.1 Direct cooling systems: jet impingement and spray cooling

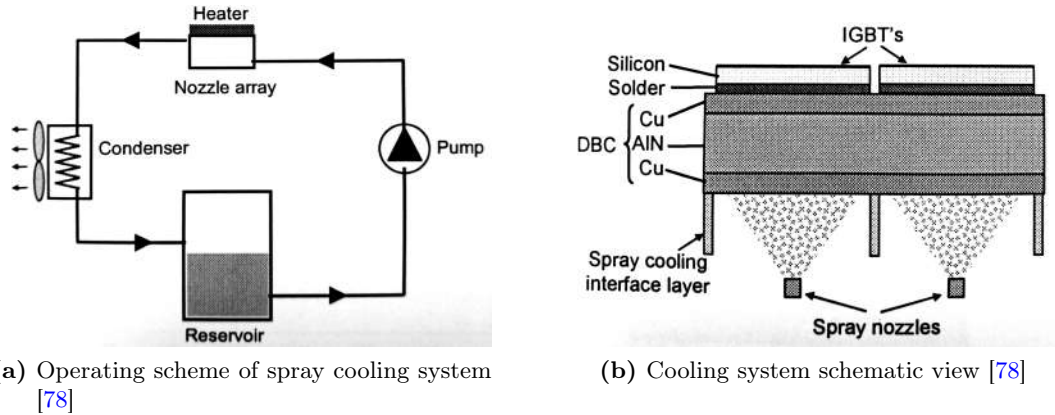
As already explained in the previous chapter, direct cooling system are characterised by the absence of a thermal resistance (material layer) between the device to be cooled and the coolant. However, the use of direct cooling technology is affordable only when the direct cooling convective thermal resistance is lower than the sum of all resistances related to an indirect cooling system [76]. In this work only jet impingement and spray cooling technologies will be analysed and no other direct cooling technologies, such as pool boiling¹, will be considered.

The line separating the spray cooling from the jet cooling technology is thin. However, both are characterised by a great complexity in heat transfer mechanisms and the governing phenomena are not fully known today. Some authors put spray cooling and jet impingement into different categories, while others (put them) in the same one [20]. However, it can be said that spray cooling represents an extension of impingement cooling concept [77]. The difference between the two systems essentially comes from the nature of the working fluid. In general, spray cooling systems use a gas/liquid mixture to assist the atomisation of the fluid when flowing within the atomiser (nozzle). In the case of jet impingement, only one-phase fluid (liquid or gas) is used and the heat transfer rate is strongly related to fluid velocity.

Spray cooling The mechanism of spray cooling is based on the principle of shattering the cooling fluid when passing into a very small orifice. A dispersion of fine droplets that impact the heated surface is so created. Depending on the surface temperature, droplets evaporate or form a liquid thin film able to remove, thanks to latent heat of evaporation in addition to conventional single phase heat removal mechanisms, a large amount of energy. In general, it has been observed that this technology is very attractive because of its capability of high heat flux removing (up to $10^3 \text{ W}\cdot\text{cm}^{-2}$), with extremely high overall convective Heat Transfer Coefficients (HTC), higher than $5 \times 10^5 \text{ W}\cdot\text{m}^{-2}\cdot\text{K}^{-1}$. It is so able to maintain a uniform temperature field on the cooled surface (if an array is used) with pressure drop values up to 250 kPa, but requiring high MFR (up to 44.2 $\text{Liters}\cdot\text{min}^{-1}$) [20]. This technology is characterised by the absence of any kind of thermal resistance, such as a solid wall, and the suppression of the thermal grease layer between the components and the cooling fluid on the base of IGBTs [78].

The operating circuit, in a closed loop, is the same presented in figure 2.2, with the

¹Pool boiling will be not considered in the context of the present study because of the difficulties related to the integration of such technology in the aircraft environment.

**Figure 3.1:** Spray cooling

addition (of a series) of filters to avoid fouling, and consequently, obstruction of the very small orifices. In figure 3.1a and in Fig. 3.1b a simplified operating scheme of the loop and a schematic operating principle of a spray cooling heatsink are respectively reported.

The pump has to be powerful enough to ensure the necessary pressure at the inlet of the nozzles. In fact, the cooling efficiency of the system strongly depends on droplet dimensions: the lower the droplet diameter, the higher the system performances. Lower droplets diameter requires higher pressure difference between the nozzle inlet and outlet. Pressure is not the only parameter on which droplet size depends. In fact, it also depends on the mass flow rate and nozzle geometry. In general, there is a unique relation between the required inlet to outlet nozzle pressure difference, and the necessary mass flow rate to reach the desired droplet dimensions. As well as droplet diameter, other parameters influencing the cooling efficiency are droplet distribution and velocity, impact angle and roughness of impacting surface.

Wang *et al.* [79] carried out a study on the influence of different surface characteristics and different additives in the cooling fluid, using different heating powers. By comparing drilled, finned and a combination of both surface geometries, they concluded that combined surface is the best trade-off to obtain a good heat transfer efficiency. To avoid formation of stagnation regions that can occur under the hollow cone spray nozzle, and so to increase the heat transfer rate, it is possible to increase the inclination angle. Kim *et al.* [8] reported that it exists an optimal angle between the impinging surface and the spray direction that should not exceed the value of 40° C. Lin *et al.* [80] performed experiments to study the behaviour of a spray cooling pattern on an up to $490 \text{ W}\cdot\text{cm}^{-2}$ heated source equipped by lateral walls. They observed that the droplets impinge the hot surface and “splash” on the lateral sides. The splashed liquid is restricted by the

walls and forced to rebound the space surrounding the sprays. They concluded that the interaction between the spray and the surrounding fluid is stronger in the case of multiple nozzles, making a more uniform HTC.

Single and two-phase heat transfer mechanisms may take place depending on temperature of the wall to be cooled and wall heat flux [8]. In figure 3.2 an example of a typical spray cooling curve is reported. As reported by Kim [8], it is possible to divide the curve in two parts: the first one is characterised by a linear dependency between the wall temperature and the heat flux. As the latter increases, phase change occurs and becomes more important until dry-out outside of the impact area.

Because of the contact between the coolant fluid and the electronic component, this particular technology needs the use dielectric fluids. One assists to a deterioration of cooling system performances [20] due to the lower thermal conductivity, specific heat and latent heat of vaporisation of this kind of fluids.

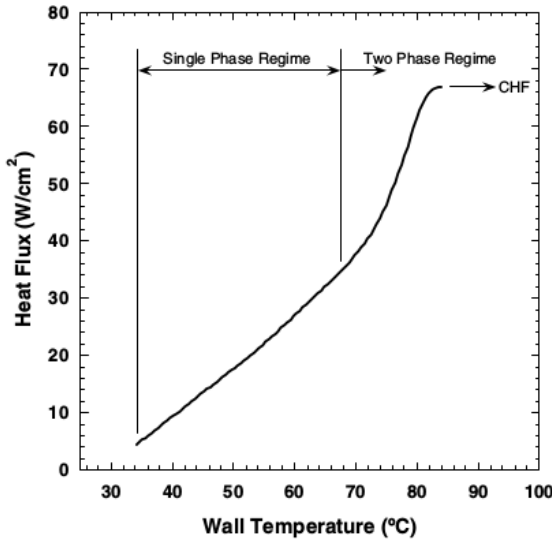


Figure 3.2: Typical spray cooling curve [8]

Jet impingement Jet impingement generally uses air or liquid as working fluids, so forced convection is the main heat transfer mechanism. Even if thermal properties make of air a less performing fluid, if compared to liquids, its high velocity in the impinging zone determines very high HTCs, that tend to quickly decrease out of this zone [20]. Molana and Banooni [81] divide the jet dynamics in three zones. The first one, called “free jet zone”, is situated from the outlet of the nozzle until the target. The second one is where a deceleration of the impinging fluid occurs due to the interaction between

the fluid and the heated solid zone. The third zone is where the fluid wets the target and flows on it. The dynamics of jet impingement do not change so much if a gas or a liquid are used as working fluids. The main difference is due to the amount of fluid that does not participate to the heat transfer process because of the “loss” of liquid after the impingement. In this case, in fact, droplets splat and do not participate to the heat transfer process, lowering the heat transfer performances [81]. Comparing spray cooling, with no phase change, and jet impingement, thermal performances of both technologies are quite different. Oliphant *et al.* [77] performed a comparison between the two technologies in single phase configuration concluding that, for the same heat transfer rate than jet impingement, the liquid mass flow rate of “non-boiling” spray impingement is one order of magnitude lower. According to them, very different heat transfer mechanisms occur between single-phase spray cooling and jet impingement. Different boundary layer thicknesses were recorded. In fact, if liquid jet impingement forms a “well defined” boundary layer that rapidly moves outwards the heated surface, the spray-impingement boundary layer thickness is definitely lower ($0.1 - 0.5$ mm for liquid jet impingement and $10 - 30 \mu\text{m}$ for single-phase spray cooling) [77]. However, it has been found that jet impingement is characterised by the highest heat transfer coefficient for single-phase heat exchange, as reported by Whelan and Robinson [82]. They found HTC values up to almost $50 \text{ kW}\cdot\text{m}^{-2}\cdot\text{K}^{-1}$ using high mass flow rate (over than $20 \text{ Liters}\cdot\text{s}^{-1}$) and with pressure drop up to 70 kPa (for the highest mass flow rate). Despite the high pressure drop registered, they concluded that the performance benefits, in terms of HTC, are higher than the penalty introduced by high pressure losses. Even if air is used as working fluid, this technology is able to reach high performances due to high Nusselt numbers deriving by high Reynolds numbers (one more time the velocity is the main factor for HTC increasing) [83]. Guo *et al.* [83] numerically and experimentally studied the transient behaviour of a 120 mm -diameter circular stainless steel plate, cooled by an air-jet, to find the influence of the Reynolds number on the heat transfer. They obviously found that the higher the Re, the higher the Nu number and that the latter increases as a function of time (starting from zero at time 0 s) until the assessment that occurred after almost 50 s.

Both for jet impingement and spray cooling, the use of an array of nozzles [84] or a coupling with other solutions, such as the combination with a transversal air flow [85], is suitable to have a more uniform heat transfer coefficient and so to obtain better performances. Ionic wind, for example, is used in addition to jet impingement for this purpose. This technology uses an interaction between ions and neutral molecules to perturb the hydrodynamic boundary layer and to enhance the heat transfer coefficient of

an existing flow. The interaction between ions and neutral molecules is called ion-drag, and is defined using a body force equation consisting of Coulombic force (force due to permittivity gradient and electrostriction force). In other words, a corona discharge is used to generate ions and to perturb the higher boundary layer [86].

Worth of attention is the work of Oliveira and Barbosa [76]. They have successfully inserted this kind of technology into a vapour compression cycle. By using R-134a as working fluid they were able to evacuate up to 160 W from a 6.36 cm^2 heated surface ($\phi \simeq 25 \text{ W} \cdot \text{cm}^{-2}$), maintaining the temperature controlled up to 35°C and reaching HTC values up to $14 \text{ kW} \cdot \text{m}^{-2} \cdot \text{K}^{-1}$. Oliveira and Barbosa moreover exploited the influence of the reservoir (saturation temperature) on the overall performances of their system. They concluded that the increase of saturation temperature lowers the overall performances of the system. This is due to an increase of the compressor electrical consumption and to lower condenser performances due to a reduction of the subcooling rate; while, it almost not impacts the temperature of the cooled surface.

Despite their performances, the drawbacks related to their physics and working principle represent a limiting factor to the use of such cooling technologies. In particular, in the case of jet impingement, high liquid or air velocities are necessary to evacuate the heat, so corrosion is one of the main limiting factor. Integration problems affect these technologies in this application field. For example, the use of a collector tank, necessary to fetch the liquid after the impinging on the surface to be cooled, could not be a practical way for HASTECS application case.

3.2 Indirect cooling systems

Indirect cooling systems are characterised by the presence of a “solid wall” between the working fluid and the electronic baseplate. This leads to the presence of a supplementary thermal resistance between them. In the following, three different technologies are introduced. Starting from the most classical one, the cold plate, for which only single-phase heat transfer is here considered, microchannels and forced convection into porous media are introduced considering both single and two-phase heat transfer mechanisms for the latter.

3.2.1 Cold plate

Cold plate is one of the most simple existing technologies. It is composed of a simple tube or channel, directly mounted under the plate to be cooled, in which the coolant flows. Its simplicity and low cost makes of it one of the most used technologies in liquid



Figure 3.3: Cold plate for electronic cooling [9]

cooling of electronic equipments. In fig. 3.3 an example of cold plate is reported.

Sensible heat is used to evacuate the thermal load from the plate. So, the fluid enters into the tube below the base plate (at temperature T_{ho}) and it leaves the heat sink at higher temperature (T_{hi})²:

$$Q_{th} = \dot{m}_l c_{pl} (T_{ho} - T_{hi}) \quad (3.1)$$

Different fluids can be used depending on environment, thermal performance and mass requirements. In order to achieve a good trade-off between performances, compatibility (between fluid and tube material) and system mass, Sakanova *et al.* [9] experimentally and numerically investigated thermal performances of different fluids, according to mass requirement, of a cold plate to be used for high power density electronics converters in “future” aircrafts (see Fig. 3.4). They studied thermal and hydraulic performances of oil, fuel and water, by changing the number of fluid passages in the plate, and to evacuate an amount of thermal losses between 0.5 and 2% of the 50 kW_e-power converters ($0.25 \leq Q_{th} \leq 1 \text{ kW}_{\text{th}}$). On one hand, they concluded that water is the best choice because of its thermal performances, but, on the other hand, this fluid is not used anywhere else for this purpose on board, so the additional required weight determines a mass penalty for the overall system. Pressure drops related to the use of oil are too high, “unless a less viscous oil is used” and the thermal resistance due to the use of this fluid does not allow its application: it was not able to meet the specifications regarding the maximum junction temperature requirements of power modules. They concluded that fuel could be the best trade-off between thermal and hydraulic performances in such applications [9].

The major problem of cold plate heatsinks is the strong dependency among the amount of heat to be extracted, the mass flow rate and the cold plate-inlet-temperature, as also

²The same notation of Fig. 2.3 is used.

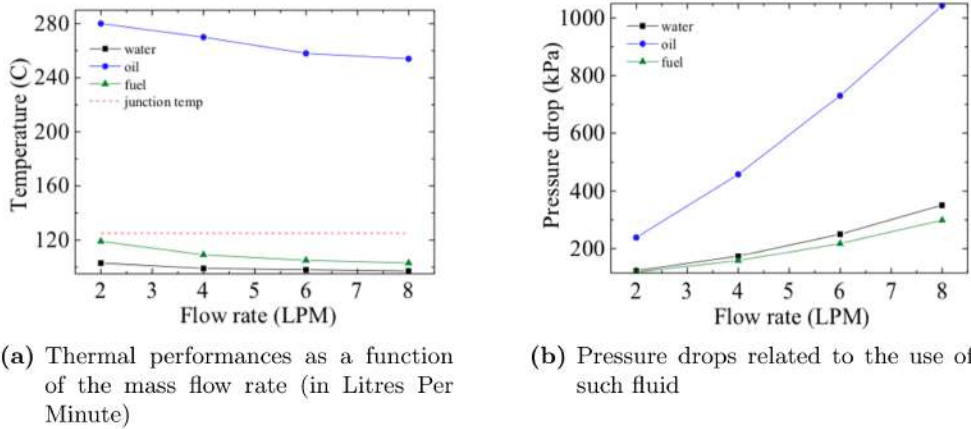


Figure 3.4: Thermal and hydraulic performances of water, fuel and oil [9]

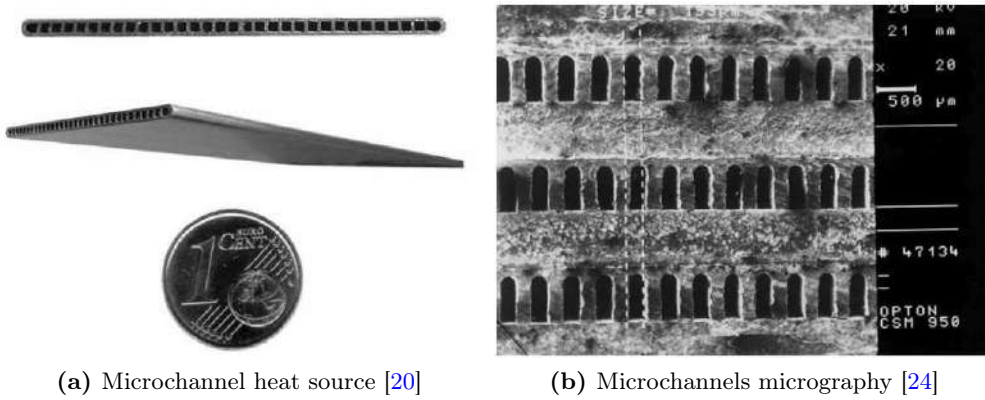
underlined by Douchet *et al.* [87]. Obviously, because of upper and lower limits of working fluid temperature, to avoid icing or evaporation, the higher is the heat flux to be extracted, the higher is the required mass flow rate (eq. 3.1). Moreover, heat sink temperature is also dependent on the mass flow rate, so a some kind of regulation system, such as regulating valves are necessary to maintain a constant temperature if the cold source temperature changes during operations (see sec. 1.3).

3.2.2 Mini and Microchannels

Single-phase microchannels This is one of the most promising technology, and it is the direct concurrent of micro heat pipes arrays, for high heat flux density evacuation. Microchannels heat sinks are formed by a very low thermal-resistance-material traversed by a series of parallel channels which hydraulic diameter is lower or equal than 1 mm. In figure 3.5a, and 3.5b, are respectively shown a typical microchannel heatsink and a typical example of microchannels micrography.

Different materials may be used for microchannels, but silicon is from far one of the most used one. Colgan *et al.* [23], for example, used a silicon heat sink with water as working fluid applying a heat flux density of $300 \text{ W} \cdot \text{cm}^{-2}$. They demonstrated that, despite the high pressure drop induced by microchannels, it is possible to cool a chip with very high performances and maintaining a more or less constant temperature on the baseplate of the electronic components!

Concerning the physics of such system, actually there are not generally and accepted heat transfer models and physics laws to be applied in this field of thermo-fluid-dynamics, and the results between different authors are sometimes strongly contradictory [88]!

**Figure 3.5:** Microchannels

For example, according to Avramenko [89], in the case of very small hydraulic diameters of the channels, the behaviour of the fluid cannot be modelled by using the classical laws of the fluid *continuum*. This is essentially due to the reduced length scale of the flow. Fluid flow in microchannel is regulated by “sophisticated” fluid mechanisms and thermal processes that take part on the fluid-solid walls interface. Nevertheless, researches made in this field demonstrate that classical relations for Nusselt number calculations remain appropriate and may give accurate results [24]. Grohamann [88] made an experimental and theoretical research, validated by the application of different correlations, on single and two-phase flows in microchannels. He observed that, regarding single-phase heat exchange, there are no differences between the heat transfer mechanisms between micro and macro scale tubes. The increase of the heat transfer coefficient is given by a greater influence of rugosity on the channel surface. The smaller the dimension of the channel, the higher the influence of rugosity, because of the greater perturbation in the fluid-dynamics length scales. On the contrary, Alm *et al.* [90], by comparing results of classical heat exchanger theory with experimental ones, obtained that, on a ceramic microchannels heat exchanger, classical correlations underestimate the heat transfer coefficient value. At the same manner, while applying the *LMTD* method to predict the heat transfer rate, Koyama and Asako [91] found a good agreement between experimental and theoretical results. Experimental pressure drop measurements were almost 10 times higher than those obtained by applying classical correlations.

However, thermal performances of microchannels are undeniable. In fact, they are characterised by very high exchange-surface per volume ratio, and very high volumetric heat transfer coefficients, up to $10^8 \text{ W} \cdot \text{m}^{-3} \cdot \text{K}^{-1}$, when compared to classical-heat exchangers-values (around $100 \text{ W} \cdot \text{m}^{-3} \cdot \text{K}^{-1}$) [24]. The volumetric heat transfer coefficient, K_V , is

based on the volume of the heat exchanger, V , the heat exchanger correction factor, ψ , the heat power and logarithmic mean temperature difference respectively, Q and ΔT_{lm} . It is calculated as reported in eq. (3.2) [24]:

$$K_V = \frac{Q}{V \psi \Delta T_{lm}} \quad (3.2)$$

The high volumetric heat transfer coefficient value is not only due to the particular flow characteristics, but also to the high aspect ratio in the transversal section. This allows the solid walls to behave as fins. Heat transfer coefficient up to $22 \text{ kW} \cdot \text{m}^{-2} \cdot \text{K}^{-1}$ can be reached, even if pressure drops may reach values up to 7 bar for a 12-millimeters-long heat exchanger [90] (it has to be noted that pressure drop is strongly related to channels transversal section dimensions, material and construction process as reported by some authors, [90, 91]). This technology is being used in electronic chips cooling, because of its compactness and ease-to-integrate property. Zhang *et al.* [92] used microchannels to study the cooling of a $12 \times 12 \text{ mm}^2$ chip footprint. By applying a heat flux up to $136 \text{ W} \cdot \text{cm}^{-2}$, they obtained a very low value of thermal resistance ($0.44 \text{ K} \cdot \text{W}^{-1}$). They also found very high pressure drop: increase of mass flow rate of about 50% leads to increase of pressure drop value of about 120%, while decrease of thermal resistance is not significative (about 6%). Agostini *et al.* [20] reported Genert *et al.*'s. system, developed to cool desktop computers, able to operate below 0°C evacuating a thermal heat flux up to $250 \text{ W} \cdot \text{cm}^{-2}$. By using this technology, Ljubisa *et al.* [93] were able to maintain a constant IGBT junction temperature at 52°C and a diode junction temperature at 75°C .

Despite thermal performances, extremely high pumping powers are required [20], limiting the use of this technology for the application field considered in this study.

Two-phase microchannels In the latest few years, two-phase flows studies for microchannels evolved, and then heat extraction capability has exceeded $100 \text{ W} \cdot \text{cm}^{-2}$ and actually is going to achieve $300 - 500 \text{ W} \cdot \text{cm}^{-2}$. This technology, unfortunately, and more than single-phase case, is particularly affected by contradictory models describing the physical phenomena. Many authors [20, 94, 95] agree on the fact that the flow boiling models, related to macro-scale, are not adequate to extrapolate the phenomenon in micro-scales. So, this kind of micro-heat exchangers technology is affected by a lack of prediction, design and optimisation methods. For example, according to Agostini *et al.* [20], the heat transfer coefficient is strongly dependent on heat flux and vapour quality, while Yen *et al.* [94] and Grohamann [88] agree on the fact that it is weakly dependent on vapour quality. However, heat flux is the most influential parameter for heat transfer coefficient: a too low value of the latter could cause instabilities during the transition

from single to two-phase flow [88]. Instabilities have been also observed by Agostini and Bontemps [96] when vapour quality x becomes higher than 0.4. In this case, a decreasing value of heat transfer coefficient has been observed due to intermittent dry-out. During this phenomenon the wall is periodically dried and re-wetted because of the passage of liquid slugs: the liquid layer in correspondence of the tube wall is thinned down by vapour bubble passage. This high frequency phenomenon occurs before reaching the CHF. The heat transfer coefficient decreases as the vapour quality increases, then remains constant towards vapour quality $x = 1$. They also suggest that, for high mass flow rates (MFR), the probability for dry-out to occur is higher because of the higher liquid film that is dragged out from the walls. This behaviour is obviously the opposite than the one observed in traditional/small-size tubes where HTC increases while wall heat flux (WHF) and MFR increase.

Beyond all the problems related to the flow boiling in microchannels, their use in electronic devices cooling is very performing. Actually, a maximum heat flux of $350 \text{ W} \cdot \text{cm}^{-2}$ has been achieved with a more than one order of magnitude decreasing pressure drop value if compared with single phase microchannels technology.

3.2.3 Porous media and metal foams

Porous media and metal foams are an alternative to microchannels, especially for high thermal heat flux evacuations. Both are characterised by porosity ε (empty to total volume ratio) and mean particle size diameter.

Metal foams are characterised by a very high heat transfer surface due to the presence of the “mesh”, generally made of high conductivity material. The fluid is subject to a tortuous path, in the foam structure, that increases the wetted surface and so the “interstitial” heat transfer. An example of foam is reported in Fig. 3.6, while in Fig. 3.7, micrographs of sintered porous medium, metal foam and compressed metal foam are reported.

The presence of the mesh in porous media not only increases the heat transfer surface, if compared to that of “only fluid”, but also the effective thermal conductivity of the medium itself.

This phenomenon leads to the homogenisation of temperature field on the heated surface [98]. Different thermal behaviours have been observed between sintered and non-sintered porous media. First of all, spreading and heat diffusion in sintered and non-sintered materials are quite different. It is mainly dependent on the solid-to-solid and solid-to-liquid interfaces between heatsink walls and porous medium, and among porous medium/heatsink walls and working fluid. In general sintered meshes are characterised

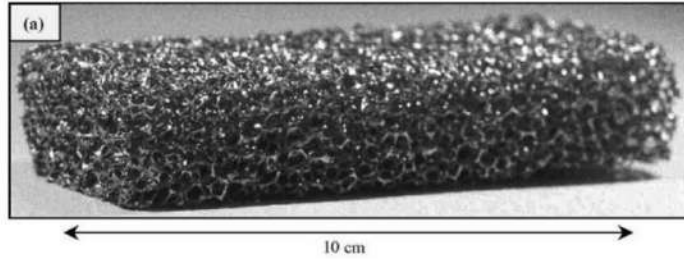
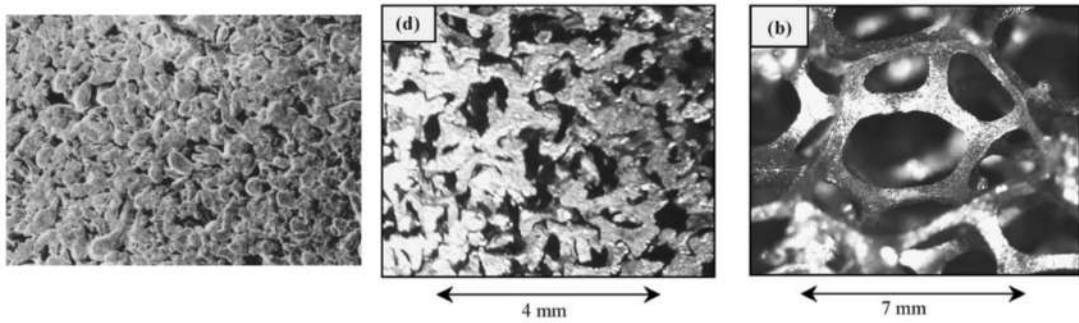


Figure 3.6: Metal foam example [10]



(a) Sintered porous medium [97] (b) Compressed metal foam [10] (c) Metal foam [10]

Figure 3.7: Micrographs of sintered porous medium (a), compressed metal foam (b) and metal foam (c)

by a higher spreading property. It is mainly due to a “densified network” of solid particles, due to sintering process, and to a higher contact surface with the heatsink walls: lower void fraction. In general, the greater the contact surface between the porous structure and the heat source wall, the smaller the contact thermal resistance. So, heat exchange becomes more efficient [99]. Hetsroni *et al.* [97] studied a porous heat sink characterised by a 32% porosity and a pores average diameter of $20\text{ }\mu\text{m}$. Using water as working fluid, they evacuated a heat flux density up to $600\text{ W}\cdot\text{cm}^{-2}$ with a bulk-to-wall temperature difference of 55 K^3 . By making a comparison between their *Aluminium* foam and a sintered porous material, they found that sintered material is more performing than the foam, because of a “better” contact between particles in the media. Zhang *et al.* [100] made an experimental study on the influence of porosity on heat exchanges in copper foam materials. They studied copper foams with porosities from 60% to 90% and pore densities ranging from 60 PPI (pores per inch) to 100 PPI. All the foams with porosity

³Even though the very high thermal heat flux densities, all the experiments here reported have been done by using reduced heating surfaces, in the millimetre magnitude order. In this case a $5 \times 2\text{ mm}^2$ heating surface was used.

between 80 and 90% and pore density in the range 60 – 100 PPI, were not sintered. They concluded that thermal resistance reduction is due to the particular structure and composition of the porous medium. In table 3.1 a comparison between two porous media characteristics and their heat transfer capabilities is reported⁴.

Porous medium typology	Porosity	Heat sink material	Thermal resistance [K·cm ² ·W ⁻¹]	$\Delta P/\Delta L$ [MPa·m ⁻¹]	Q_{max} [W·cm ⁻²]
Sintered particle [24]	47%	Copper	0.166 ÷ 0.752	32	-
Sintered particle [99]	46%	Bronze	0.667	0.74	-
Sintered particle [97]	32%	Stainless Steel	0.092	232	600
Foam [100]	80%	Copper	0.134	2	41.7
Compressed Foam [10]	67%	Aluminium alloy	0.463	7.2	68.8

Table 3.1: Comparison of different porous media characteristics [20]

On one hand, very high heat flux densities have been evacuated with this cooling technology, but, on the other hand, awfully high pressure drops characterise it. Boomsma *et al.* [10] performed an experimental research on metal foam heat exchanger performances. Despite the high heat flux density evacuation capability, $\simeq 69 \text{ W}\cdot\text{cm}^{-2}$ (1100 W on a $4 \times 4 \text{ cm}^2$ surface), they obtained high pressure drop values: over $70 \text{ bar}\cdot\text{m}^{-1}$ in some cases. Many authors took into account pressure drop and made some researches about this specific topic. Jiang *et al.* [24] compared the performances of microchannel heat exchangers with sintered porous media ones. By taking into account both thermal and hydraulic performances, they concluded that, despite the higher thermal performances of porous media heat exchangers, pressure drops of microchannels heat exchanger are lower. Using the same mass flow rate in both technologies, they observed that, for a ratio of 2.25 between the volumetric heat transfer coefficients of porous media and microchannels, respectively, the corresponding porous-media-to-microchannel pressure drop ratio was 5. They concluded that, despite the strong gap existing between the two technologies in terms heat exchange performances, it should be better to use microchannels because of their lower pressure drop.

By considering two-phase heat exchange mechanism applied to this particular technology, it was observed that despite the lower mass flow rates necessary to evacuate the

⁴It has to be underlined that the pressure drop is a function of the working fluid, the mass flow rate, the porous typology and so on.

thermal load, pressure drops do not decrease. Peterson *et al.* [101] conducted a study on two-phase porous channels. They found, at constant liquid velocity, increasing pressure drop consequent to increasing heat flux. This was essentially due to the increase of vapour quality. The highest pressure drop was obviously related to the lowest particle diameter in the wick. They observed the pressure drop difference between an empty channel and a wick equipped one (supplied at constant inlet liquid velocity and constant heat flux) to be up to two orders of magnitude. According to Peterson *et al.*, Chen *et al.* [102] found, at constant liquid velocity, an increase in pressure drop consequent to a reduction of mean particle diameter and to an increase of thermal heat flux (at constant flow rate and heat flux).

3.3 Conclusion

In this chapter, the problem related to the extraction of heat load from the heatsink has been dealt. Only technologies related to active cooling systems have been here introduced. In fact, for these particular cooling techniques it is possible to split the hot from the cold side of the cooling system and to analyse the behaviour of the heat sink independently from the rest of the circuit. Here, only technologies adapted for HASTECs specifications were introduced and analysed. Particular attention was paid to micro and minichannels, porous media and metal foams. Even if for the sake of completeness jet impingement and spray cooling have been here introduced, this particular technologies, despite the very high thermal and hydraulic performances have not been retained. The main reason of the exclusion of jet impingement technology, whatever its form, is mainly related to integration difficulties and a such kind of corrosion. In fact, in this case, it necessary to use a collection tank to collect the fluid. This is not a practical choice for the problem we are facing in this work.

Cold plate heatsink is up to now the most used technology, even in active two-phase/vapour compression technology configurations, but its limitations in heat transfer coefficient and strong dependence of thermal performances on mass flow rate, do not make of it a suitable technology in its single-phase configuration.

Microchannels and metal foams represent the best solution to be used in active cooling system configuration. In fact, they allow high heat transfer coefficients and almost independence of thermal performance on mass flow rate. Unlike, the high pressure drops can represent a strong limitation. It has to be also considered that the higher pressure drops, in particular for microchannels technology, are strongly related to the material and production processes. These technologies give the best in active-two-phase config-

uration, where pressure drop are up to two orders of magnitude lower than single-phase configuration. In such case heat transfer coefficient is higher.

Sintered porous media are not suitable neither in single and in two-phase configuration. Pressure drop are quite high and, despite heatsink thermal performances, the required pumping power should be extremely high. However, their use is necessary in the case of two-phase passive cooling system, because of capillarity effect related to the use of sintered porous media in two-phase systems.

In the following chapter, a comparison of just introduced heat sink technologies will be done, in terms of heat evacuation capability and heat transfer coefficient, also observing the evolution of such technology during the years. Passive two-phase cooling systems will be compared to show the current state of the art.

To finally choose the most adapted solution in context of HASTECS project, the mass of a single-phase and of an active two-phase cooling systems, both equipped with a cold plate, calculated on the basis of a first approximation design, will be compared with a Capillary Pumped Loop for Integrated Power, CPLIP.

Technology	Pro	Drawback
<i>Single-phase Microchannel</i>	High cooling performance	Pressure drops up to $22 \text{ Mpa}\cdot\text{m}^{-1}$
		High temperature gradients along the plate (if compared with two-phase MC) [20]
<i>Two-phase Microchannel</i>	Low required Mass Flow Rate [20]	Back-flow and instabilities
	High HTC and increasing with temperature	Lacking in thermal exchange mechanisms
	Low pressure drop if compared with single-phase MC [20]	
<i>Cold Plate</i>	High simplicity	Junction temperature strongly dependent on cold source temperature
		High dependency on MFR
		Weight and size strongly dependent on working fluid properties
<i>Porous media</i>	High cooling performance	Pressure drops up to up to $227 \text{ MPa}\cdot\text{m}^{-1}$ [97]. Required very high pump power! [24]
	Very good temperature distribution	
	Heat transfer surface extremely extended	
	Very low thermal resistance especially in sintered materials	Performances highly dependent on CHF [103]
	Heat transfer enhancement	
	Smaller wall super-heats than microchannels	
<i>Jet impingement/Spray cooling</i>	Very high heat transfer coefficient	Lower performances of dielectric fluids [20]
	Very high heat removal capacity	Necessity of a compatibility study between the fluid and the electronic components
	Very low temperature gradients in on heat source	Non-uniform HTC if one jet is used
	No thermal interfaces required	Erosion
		Lack of physical model for Heat Transfer prediction

Table 3.2: Active cooling systems pro & drawbacks

Technology choice

4.1 Comparison of high performance cooling systems

In the previous chapters the most promising cooling technologies have been studied to understand their operating principles and to analyse their main pros and drawbacks. The purpose is not only to research the best lightweight available solution to evacuate the thermal load, but also the one able to ensure the temperature requirements at junction level.

Thermal performances All analysed systems are able to evacuate high heat flux densities, ensuring good thermal performances and high HTC. Some of them are today successfully used¹.

The number of studies has incredibly increased during the latest thirty years, pushed by a continuous increase of the electrical power and the miniaturisation of electronic components. Observing this evolution as a function of time, according to figures 4.1a and 4.1b, it may be noticed that either active and passive technologies are characterised by the same trend and the performances increase during the time.

By analysing literature data, in some cases great importance is given to heat flux density (Fig. 4.1a) and low thermal powers are often applied to small heat transfer surface areas (in the order of 1 mm^2). In other cases, the attention is focused on the total heat power to be evacuated (Fig. 4.1b), but not considering the thermal power per surface unit. The way of presenting results is after all due to the purpose of the single study: — the end justifies the means —. For example, the majority of the studies related to active techniques (jet impingement/spray cooling, microchannels and porous media/ metal foams) are focused on heat flux density. This is maybe related to small dimensions of the chips mounted on the heatsinks, or even to limit the pressure drop on the hot side and consequently the required pumping power. No pumps are required in the case of passive cooling systems. Performances of a given capillary driven technology

¹Let's mention heat pipes used in smart devices and computer/server chips cooling because of their compactness and adaptability (see bendable FPHP), for example.

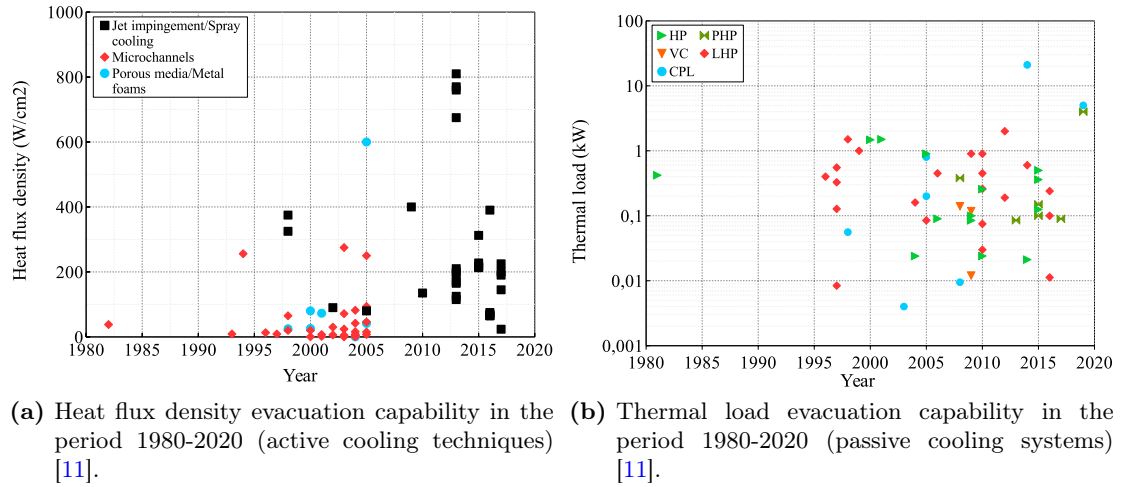


Figure 4.1: Historical trend of heat flux density and thermal load evacuation capability for active and passive technologies.

are strictly related to capillary pressure head of the porous wick and so to the heat transferred and the transport distance. Larger evaporators may be used, sometimes in the order of tens centimetres. In those cases, even if pretty high thermal powers are applied to the evaporator, the thermal-power to surface ratio decreases.

Therefore, comparing the results related to a given technology, significative variations may be noticed depending on the points of view. In Fig. 4.2, the highest heat flux density and the highest thermal load related to each active cooling technique are reported for comparison purposes. Considering for example the porous heatsink, if the heat flux density is used to evaluate its performances, Hetsroni *et al.* [97] reached the best results (evacuating about $600 \text{ W} \cdot \text{cm}^{-2}$, but using a quite small thermal load). If the thermal load is considered instead, the best results are related to the work of Chen *et al.* [102] who evacuated 0.4 kW , but obtaining a heat flux density one order of magnitude lower ($80 \text{ W} \cdot \text{cm}^{-2}$) than Hetsroni *et al.* Faulkner *et al.* [104] evacuated $275 \text{ W} \cdot \text{cm}^{-2}$ using microchannels, but the highest thermal load, evacuated by Lazarek and Black [105], was 11.5 kW . The latter corresponds to a heat flux density of $38 \text{ W} \cdot \text{cm}^{-2}$. At the same way, considering jet impingement, the highest heat flux density evacuated by Zhang *et al.* [106] was $810 \text{ W} \cdot \text{cm}^{-2}$, corresponding to a total thermal load of 1045 W , using water as working fluid. This result does not match with the most performing technology, measured using the thermal load. In fact, Ortiz and Gonzalez [107] evacuated a total thermal power of almost 60 kW , obtaining less than one-half of Zhang's heat flux density ($375 \text{ W} \cdot \text{cm}^{-2}$) and using the same working fluid.

In fig. 4.3, heat transfer evacuation capability of most researched passive technologies

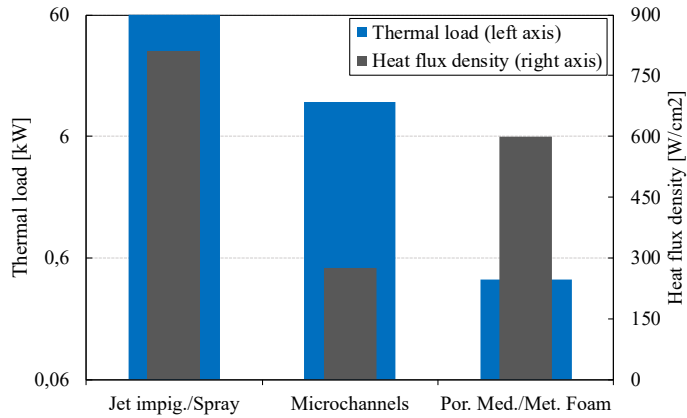


Figure 4.2: Maximal total thermal load and heat flux density histogram of active cooling techniques.

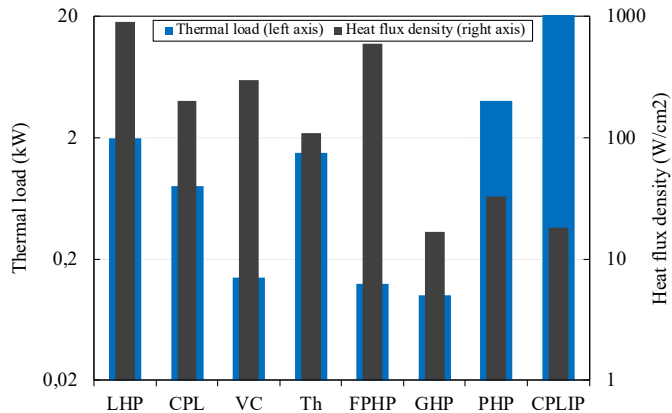


Figure 4.3: Maximal total thermal load and heat flux density histogram of passive cooling systems. [11].

is reported. The solution presented by Maydanik *et al.* [108] is worth of attention. He presented an experimental research on a flat plate evaporator LHP heated with two different heaters (one of 9 cm^2 and another of 1 cm^2) on which the heat load has been varied from 5 to 900 W. He reached a maximal evaporator temperature of 275°C applying the highest thermal load on the smallest heater surface. Because of the spreading effect related to the use of the same evaporator, whatever the heater dimension, he registered a maximal heat flux density of $900\text{ W}\cdot\text{cm}^{-2}$. This result does not match on the thermal load side. In this case, the highest thermal load evacuated was that of Kang in 2012 [109]: about 2 kW. The same differences have been found analysing CPL's literature data. Meyer *et al.* [110] evacuated a heat flux density of $200\text{ W}\cdot\text{cm}^{-2}$ using a heat power of just

4 W, but the highest power evacuation observed is related to a CPL for Integrated Power (CPLIP), characterised by a theoretical thermal load of 21 kW in railway application field [48]. In figure 4.4 equivalent *HTC* against heat power evacuation capability for such technologies is reported. The same results together with other system characteristics (thermal load, thermal power, transport distance etc.), resulting from literature data, are reported in table 4.1.

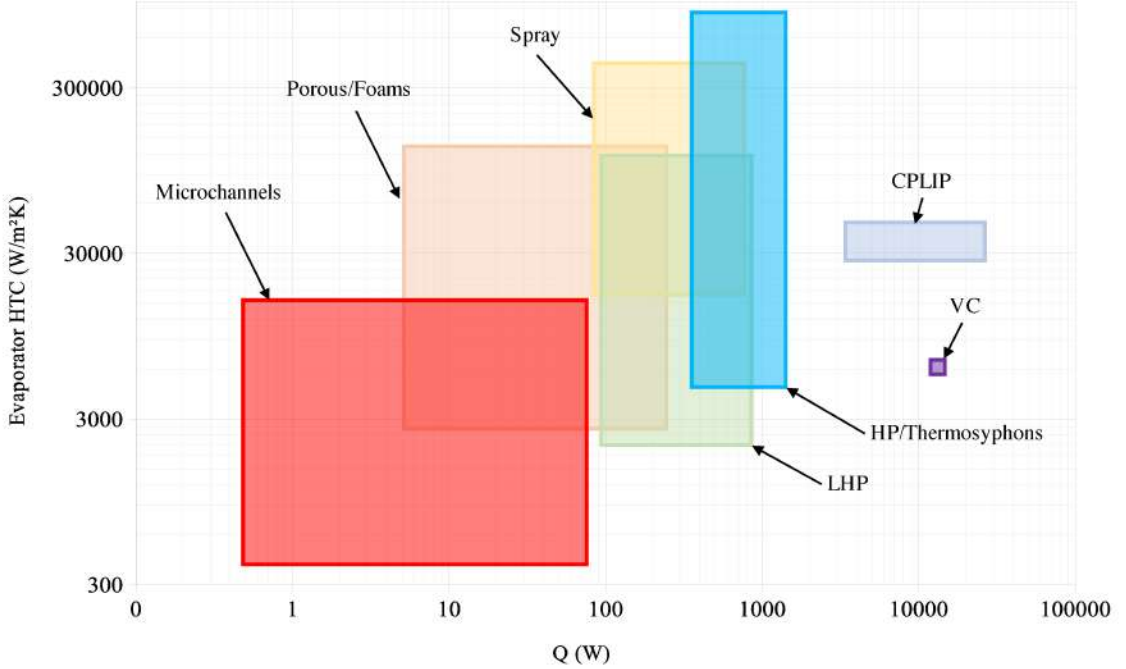


Figure 4.4: Technology comparison [11]

Transport distance Observing table 4.1 it may be noticed that active cooling systems are related to pressure drops, while passive ones are related to transport distance L [m]. Either in active and passive cooling systems, pressure drops are obviously dependent, *inter alia*, on the circuit length. On one hand, for active ones, pumping power can be increased according to overall pressure drop in the circuit, and without changing the thermal characteristics of the heatsink. On the other hand, for passive cooling systems, the loop length is limited by capillary pressure head or gravity pressure drop. In Fig. 4.5 the heat power as a function of transport length is reported for such passive technologies. From there one can notice in a more clear way that some technologies, like CPL or LHP, due to higher heat transport length, are more adapted than others for power electronics cooling in aeronautics field: the higher transport distance, the higher the flexibility of such solution.

Technology	\dot{Q}_{max} [W · cm $^{-2}$]	HTC_{eq} [W · m $^{-2}$ K $^{-1}$]	Pressure drop [MPa · m $^{-1}$]	L [m]
<i>Single-phase HT in microchannels</i> [23]	up to 300	10 000 - 100 000	1.8	-
<i>Single-phase HT in porous media</i> [97]	up to 600	25 000 - 100 000	232	-
<i>Two-phase HT in microchan- nels</i> [Kosar et al.][20]	up to 250	60 000 - 150 000	0.309	-
<i>Two-phase HT in porous media</i> [102]	up to 80	40 000 - 10 000	2.2	-
<i>Jet impingement</i> [20]	up to 1820	300 000	0.241	-
<i>Mini vapour cycle</i> [45]	76	25	-	-
<i>Ionic wind enhancement</i> [86]	30	400	-	-
<i>Cold-plate</i> [9]	7.46	2750	-	-
<i>LHP</i> [72, 108]	130 - 900	30 000	-	30
<i>CPL</i> [75]	100	-	-	2 - 5
<i>CPLIP</i> [48, 75]	20 ÷ 40	27 000	-	up to 10
<i>HP</i>	100	30 000	-	up to 0.5

Table 4.1: Main characteristics of the cooling systems

4.1.1 Technology screening

The best performing technology does not exist, but the choice of a system depends on the particular requirements of the issue to be solved. For the specifications assigned to this work package in the frame of HASTECS project, a good candidate solution should:

1. be as lightweight as possible;
2. ensure the lowest energy consumption for its operations;
3. ensure the highest cooling performances;
4. be easily integrable;
5. ensure the highest transport length possible (in the case of passive cooling systems)

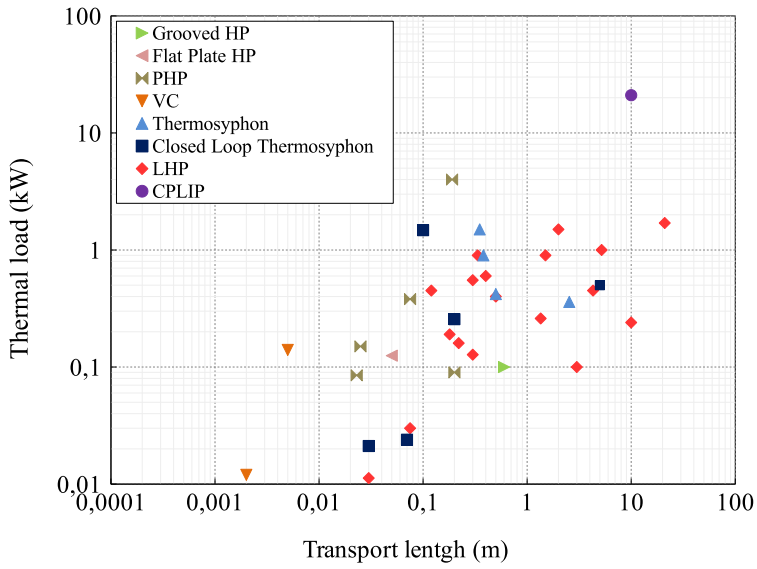


Figure 4.5: Transport distance for different passive technologies

or, in the case of an active technique, a good trade-off between pressure drops and pump-power-consumption;

6. ensure temperature controllability to the heat sink;
7. ensure high reliability.

All the enumerated points need to be respected to obtain a full working power electronics cooling system for hybrid propulsion aircraft in the context of HASTECS project (operating conditions are described in chap. 1).

By considering the length that the heatsink should have in the direction of the fluid flow, in the order of 10 cm, due to the high pressure drops related to, neither microchannels and porous media can be retained for active single-phase configuration. The high pressure drops related to such heatsink could heavily impact the overall system performances: the mass of the pump is proportional to the overall pressure drops in the circuit. At the same way, considering these technologies as part of a two-phase pumped cooling system, pressure drops are still high, even if lower than their liquid-cooling counterparts. This kind of cooling technique cannot be retained at the moment. Despite their high thermo-hydraulic overall performances, jet impingement and spray cooling cannot be retained, a priori, for integration issues. Moreover, the HTC is strongly dependent on the droplet dimension and so, on the pressure difference between the inlet and the outlet of the nozzles. Even in this case, high pumping powers are required. Vapour compression

is promising and it is the only technology (except for Peltier cells) able to lower the heat-sink temperature below the cold source one. Unfortunately it is moving its first steps in this application field, so it will be not considered at this stage. Phase Change Materials (liquid/solid), PCMs, have not been considered for the purposes of this work. They are in general used to stock thermal energy to be re-used after. After an analysis² based on an energy criterion to approach the design of an undersized, “conventional”, cooling system installed in parallel to a PCM able to damp the amount of not treated energy, it was concluded that the mass penalty introduced by the PCM is higher than the mass saving deriving from the undersizing of the cooling system itself.

Despite its low overall thermal and hydraulic performances, cold plates (in single phase configuration) are nowadays used in most applications, even in aeronautics field. This technology is worth to be considered at the first stage of the present research to demonstrate how a “brand-new” technology overcomes the limitations of a “classical” one.

None of the wicked or wickless HPs (classic HP, FPHP, GHP, micro-HP, PHP, thermosyphons and CLT) ensure the requirements, because of their limited transport distance (lower than one meter). However, passive cooling systems are promising and some of them respond to all requirements! Loop heat pipes and capillary pumped loops seem to be the best candidates for such purpose. Despite the very high thermal and hydraulic performances, LHPs are not able to ensure the required temperature controllability. CPLs suffer of instabilities, in particular during their long start-up stages, but CPLIP has a very good behaviour, even during severe transient phases [1, 111]. The latter satisfies most of the enumerate conditions: it is efficient, passive, stable and robust. It allows temperature controllability, thanks to the fixed saturation point in the reservoir. It appears to be the best candidate to solve the problem.

In the following, a deep comparison between three technologies (CPLIP, single-phase and active two-phase cooling systems, both equipped by a cold plate) is reported to analyse, under an engineering stand point, pros, drawbacks and limitations related to such technologies.

4.2 System selection

The mass of the cooling system is the index used to select the most appropriate solution for hybrid propulsion aircraft power electronics cooling issue. —*The purpose of the work is after all to find a cut-off technology, able to work in the most critical cases, with the lowest energy requirement and the lowest mass possible*—. Single phase cooling solution

²Different PCMs characterised by different melting temperatures have been exploited

is considered to compare the results of two-phase active and passive technologies, and to have an evaluation of the mass saving related to the use of the latter. Moreover, with the purpose of choosing the best cold source technology, between those presented in sec. 1.4, a heat exchanger is in the following designed, independently from the rest of the system, to evaluate its performances³.

4.2.1 Cold source technology comparison

To choose the best adapted cold source technology, a design of a heat exchanger is here proposed to quantitatively compare skin heat exchanger and a tube bank HXG inserted in a RAM-air circuit (see also section 1.4).

To remind, a skin heat exchanger uses the external skin of the aircraft to cool the primary side fluid. No contact obviously occurs between the external air and the tubes, because of the presence of a low thermal resistance layer (the aircraft skin) between them. *A priori*, this solution is the best candidate to be used if power electronics and the adjoined cooling system emplacement is the fuselage (PIF - Power electronics In the Fuselage).

On the other hand, RAM-air allows the use of a crossed-flow air-liquid HXG. The latter is composed by staggered and equispaced tubes. Air velocity in correspondence of the first tube rank can be better controlled (during the design process), allowing higher heat transfer coefficient than skin HXG.

In accordance to models presented in Appendix B.1.4.1 and B.1.4.2 a design based comparison is here reported for both technologies. The heat exchanger will be designed to evacuate a thermal load of 15 kW and to ensure a temperature difference of 40 K (from 80 °C at the inlet to 40 °C at the outlet). Even if, at this stage, only the heat exchanger is considered, the same conclusion are also valid for condenser.

Skin heat exchanger During the mission of the aircraft, pretty high differences occur in air density (see sec. 1.3) and velocity between the ground stage and the high altitude flight. The design of a heat exchanger needs to be considered in steady state [17], so the worst operating conditions are used for the purpose. The latter are obviously realised for the lowest air velocity flowing on the external side of the fuselage, during taxi-out and taxi-in stages, and for the highest external air temperature, T_∞ , and the lowest air density.

Considering all these parameters, the external side HTC, h_{ext} , may be obtained in a quite similar way of an airflow flowing on a flat-plate which curvature radius is pretty

³All calculation details are reported in Appendix B

large. So, according to Pang *et al.* [4], correlation (4.1) may be used to calculate the external Nu number:

$$\text{Nu}_{\text{ext}} = 0.2948 \text{Re}_L^{0.5} \quad (4.1)$$

In this case, a very small value of HTC was found, about $5 \text{ W}\cdot\text{m}^{-2}\cdot\text{K}^{-1}$, corresponding to an airflow flowing on a 1.5-meter-long flat-plate at $10 \text{ m}\cdot\text{s}^{-1}$. The resulting heat exchanger length is in the order of $2\cdot 10^3 \text{ m}$ and, consequently, pressure drops related to such dimension are fairly high. The total heat transfer surface area, corresponding to the $2.2 \cdot 10^3$ -meter-long heat exchanger tube having a diameter of 10.5 mm, to ensure a maximum liquid velocity of $2 \text{ m}\cdot\text{s}^{-1}$, is about 73 m^2 , while the aircraft skin surface area is just below 62 m^2 . This is a nonsense! To check the just obtained values, let's simply apply the Newton's law to evaluate the necessary heat transfer surface area to evacuate $Q_{th} = 15 \text{ kW}$ for a wall to air temperature difference $(T_w - T_\infty) \simeq 40 \text{ K}$. If the previously obtained heat transfer coefficient value is used ($5 \text{ W}\cdot\text{m}^{-2}\cdot\text{K}^{-1}$), the resulting heat transfer surface area is 75 m^2 , according with calculation from the model. A whole aircraft is not enough to evacuate such thermal load.

The skin heat exchanger, the potentially most adapted solution to be used in an eventual PIF configuration, is absolutely not adapted for the purpose!

Tube rank configuration (RAM-air) The same boundary conditions expressed before were used even in this case. The heat exchanger configuration (assigned *a priori*) is a staggered not finned tube bank composed by 5×20 tubes, spaced of 1.5 times the condenser-tube-diameter and with a single-tube-length of 0.8 m. Because of the heat exchanger configuration, the external side heat transfer coefficient is $144 \text{ W}\cdot\text{m}^{-2}\cdot\text{K}^{-1}$, so the corresponding tube total length is⁴ 80 m!

Comparisons are not necessary in this case. A staggered tube bank is the best configuration for the heat exchanger/condenser. RAM-air configuration answers to requirements. RAM-air intakes are usually installed in the centre of the aircraft, and so it could be also used when power electronics and its cooling systems need to be installed in the fuselage. However, it has to be underlined that an installation in the nacelle (Power electronics in the Nacelle - PIN) is suggested to take advantage of an eventual and maybe larger air intake.

More studies are required, in particular related to aerodynamics, to weigh up pros and drawbacks related to the use of a RAM-air system or a nacelle air intake.

⁴For more details about the relations used in this case, the interested reader can find more informations in sec. B.1.4.2.

4.2.2 First approximation evaluation of mass and power coefficient

To remind, the overall power coefficient is:

$$C_{c,tot} = \frac{Q_{el}}{m_{el} + m_{th}} \quad (4.2)$$

Being the mass of the whole electronic system equal to 60 kg (as described by WP2 [21]), the cooling system should have a maximum mass, $m_{th} = 40$ kg, to satisfy the power coefficient requirement for 2025 ($C_{c,2025} = 15 \text{ kW}\cdot\text{kg}^{-1}$).

In table 4.2 the main characteristics of the below analysed cooling techniques are reported.

Technology	Evaporator	Condenser	Cold source
Liquid cooling	Cold plate (parallel channels)		
Pumped two-phase	Cold plate (serpentine)	Not finned tube bank	RAM-air
Capillary pumped (CPLIP)	Sintered porous medium		

Table 4.2: Technology generalities.

For comparison purpose, the same constituting materials, working fluid⁵ and boundary conditions will be used for all considered technologies.

To simplify the first approximation design, either for active and passive two-phase technologies, the condenser will be designed by neglecting subcooling section. However, the sensible heat rate necessary to lower the primary fluid temperature close to the external air one is 5-10% of the total thermal power. The related subcooling length does not exceeds 5 m and all the obtained HXG/condenser dimensions are rounded-up to the closest higher round value, sometimes exceeding such length.

The comparison is based on the following assumptions:

- The heat power to be evacuated is 15 kW;
- RAM-air is considered as cold source.
- Either two-phase, active and passive, and single phase solutions are considered using the same heat exchanger configuration (not finned tube bank⁶).

⁵A discussion and a comparison between the working fluids is reported in Appendix A

⁶see Appendix. B.1.4.2 for more details.

- The air frontal velocity on the first HXG tube rank is equal to the aircraft velocity during taxi-out-and-in stages ($10 \text{ m}\cdot\text{s}^{-1}$).
- The cold fluid temperature at the inlet of the cold side corresponds to the worst operating condition: 33°C , realised on the ground during the taxi-out and in stages.
- Three parallel heatsinks are used to evacuate the thermal load;
- Stainless steel is used as solid material;
- Methanol is used as working fluid for all compared technologies⁷;
- All tubes: transport lines and heat exchanger/condenser have the same thickness ($t = 0.6 \text{ mm}$);
- Liquid velocity is limited to $2 \text{ m}\cdot\text{s}^{-1}$ in the liquid lines (both for single and two-phase systems) and vapour velocity is limited to $20 \text{ m}\cdot\text{s}^{-1}$ into vapour line of two-phase systems;
- The evaporator to condenser distance is supposed to be 1 m and the reservoir to condenser height difference is 20 cm. Vapour and liquid line lengths⁸ are respectively 1 and 1.2 m.
- Eq. (2.3) and eq. (2.11) are respectively used for single and two-phase fluid mass flow rate estimation, and in the last case assuming a vapour quality $x = 1$ at the exit of the evaporator;
- Fluid thermophysical properties are assumed to be constant for a given fluid-phase;
- Fouling is not considered.

In table 4.3 the main geometrical dimensions of the considered cooling systems are reported.

Single phase cooling system Single phase cooling system is considered in its simplest form. No regulating valves or other accessories are taken into account. The 1-meter and the 1.2-meter-long transport lines (hot and cold respectively), are characterised by the same transversal section, imposed by fixed coolant velocity and mass flow rate. The

⁷Except water, that is the most performing fluid, but limited by its high freeze point and for compatibility issues, methanol is a good candidate for single-phase cooling solution as well. In Appendix A is reported a detailed comparison between different working fluids.

⁸In absence of information about dimensions, integration and environmental constraints the transport line length has been, arbitrary, chosen to simplify the calculations.

	Liquid cooling	Two-phase active	Two-phase passive
Hot/vapour line length (m)	1	1	1
Hot/vapour line diameter (mm)	10.5	21.2	21.2
Cold/liquid line length (m)	1.2	1.2	1.2
Cold/liquid line diameter (mm)	See hot/vapour line	3.5	3.5
Condenser diameter (cm)	Same than hot/vapour line diameter		
Heatsink dimensions (cm^2)	12.4×12.2	12.4×12.2	12.4×12.2
Reservoir/condenser height difference (m)	0.2	0.2	0.2

Table 4.3: Cooling system main geometrical dimensions.

three parallel vertically mounted heatsinks have dimensions of $12.4 \times 12.2 \text{ cm}^2$ and are equipped by four power electronics modules installed face-to-face (in couple of two). They are traversed by nine 0.8 cm-side-squared parallel channels in which the coolant flows (allowing a theoretical temperature difference between the inlet and the outlet of 40 K). The 80-meters-long air-liquid crossed-flow cold HXG is not finned on its external side. The staggered tube bank is composed by 5 raws of 20 tubes (the tube distance is imposed to be 1.5 times the condenser-tube-diameter) and a single-tube-length of 0.8 m. The pump is designed to ensure the required pressure head (590 kPa) and mass flow rate ($11.35 \text{ Liters} \cdot \text{min}^{-1}$). It has been selected from a wide range of pumps used for aeronautics field. The loop is completely fulfilled of liquid and should be pressurised to avoid boiling issues in heatsink channels.

In table 4.4, results, in terms of mass for each component constituting the single phase cooling system, are reported. The unladen mass is more than three times the mass of the fluid contained in the system, and about 35% of the unladen mass is due to the pump. Considering the obtained system mass, the thermal power coefficient, $C_{c,th}$, is just above $0.3 \text{ kW} \cdot \text{kg}^{-1}$. Considering electronics components total mass equal to 60 kg, the total power coefficient C_c is $13.8 \text{ kW} \cdot \text{kg}^{-1}$. The latter is close to HASTECS' target for 2025 ($15 \text{ kW} \cdot \text{kg}^{-1}$)⁹, but all previously explained issues related to low efficiency and temperature control inability cannot be neglected!

⁹If water was used as working fluid, mass saving related to its use is lower than 5% and its impact on the power coefficient negligible.

	Fluid Volume (m ³)	Fluid Mass (kg)	Solid Volume (m ³)	Unladen mass (kg)	Total mass: solid+fluid (kg)
Hot line	9.15E-05	0.07	2.15E-05	0.17	0.23
Cold HXG	7.32E-03	5.35	1.72E-03	13.40	18.75
Cold line	9.15E-05	0.07	2.15E-05	0.17	0.23
Expansion tank	7.41E-03	5.42	3.59E-04	2.80	8.22
Heatsink	2.11E-04	0.15	3.34E-04	7.81	7.96
Pump	-	-	-	13.00	13.00
<i>Total</i>	1.51E-02	11.06	2.45E-03	37.35	48.41

Table 4.4: Single phase cooling system mass evaluation (first approximation design).

Active two-phase cooling system Like single-phase, active two-phase solution has been designed in its simplest form (reported in Fig. 2.9). Even in this case a three parallel-heatsink-evaporator was considered. The latter is vertically mounted and its external dimensions are related, as always, to power electronics modules ones. This technology generally does not require the complete evaporation of the working fluid at the outlet of the heatsink, so a vapour quality x lower than 1 should be imposed for mass flow rate calculation ($\dot{m} = Q/h_{lv}\Delta x$). If a vapour quality $x < 1$ is chosen, the corresponding mass flow rate is higher than that required for the complete evaporation of the working fluid, negatively impacting pump mass, tube cross sections and so the overall loop mass. For comparison purposes a vapour quality $x = 1$ has been adopted at the outlet of the heat-sink to not *a priori* “condemn” this technology. The mass flow rate value is one order of magnitude lower than single phase solution. A serpentine configuration has been chosen for the cold plate to avoid too low liquid velocities. The 12-millimetre-side squared-section serpentine traverses ten times the heat sink. The 1-meter-long vapour line and the 1.2-meter-long liquid line are characterised by a hydraulic diameter of 21.2 mm (twice than single phase solution) and 3.5 mm-hydraulic-diameter, respectively. The fifty-meter-long condenser has the same hydraulic diameter than the vapour line. It is considered using the same configuration described before: 5 tube raws of 20 tubes each, but with single tube length of 0.5 m. Due to the one order of magnitude lower mass flow rate than single phase solution, no pumps in aeronautics family were available. A general purpose pump has been used in this case. Like single-phase solution, a height difference of 20 cm between the condenser outlet and the reservoir inlet is considered. The results of the mass evaluation for this kind of cooling technology are reported in table 4.5.

Two phase cooling systems are characterised by a reservoir total volume equal to the cumulated volumes of fluid contained in the condenser and in the vapour line. This

	Fluid Volume (m ³)	Fluid Mass (kg)	Solid Volume (m ³)	Unladen mass (kg)	Total mass: solid+fluid (kg)
Vapour line	4.62E-04	0.34	4.69E-05	0.37	0.70
Condenser	2.17E-02	15.89	2.20E-03	17.18	33.06
Liquid line	9.41E-06	0.01	7.65E-06	0.06	0.07
Reservoir	2.22E-02	4.06	5.18E-04	4.04	8.09
Evaporator	5.27E-04	0.00	1.99E-04	1.55	1.55
Pump	-	-	-	10.43	10.43
<i>Total</i>	0.04	20.29	0.00	33.62	53.91

Table 4.5: Pumped two-phase cooling system mass evaluation (first approximation design).

explains the high fluid mass characterising this kind of technology (double than single phase system). However, due to a reduction of the pump mass and to a lower unladen mass, the higher amount of fluid has a small impact on the global power coefficient, C_c , that, in this case, is about $13.6 \text{ kW}\cdot\text{kg}^{-1}$.

Passive two-phase cooling system: CPLIP Two different configurations are here considered for comparison purposes: three parallel evaporators CPLIP, also called CERBERE [71], and three parallel CPLIPs: each one designed to evacuate a single-electrical-phase thermal losses.

Three parallel evaporators configuration: CERBERE

At first, the three parallel evaporators configuration is considered. Neglecting the sensible heat rate and because of the complete evaporation of the fluid, the same mass flow rate than two-phase active solution has been obviously obtained. The two-millimetres-thick nickel evaporator casing has the same external dimensions than other technologies (depending on the power electronics modules installed on). The nickel porous wick is characterised by a porosity of 73% and a mean pore-diameter of $6.3 \mu\text{m}$. Vapour and liquid line dimensions are the same than active-two-phase solution. In table 4.6 the mass evaluation for this configuration is reported. Due to the same mass flow rate value than two-phase active technology, the same tube vapour line and so condenser transversal section is used.

By using the just obtained cooling system mass to calculate the global power coefficient, it results $C_c = 14.3 \text{ kW}\cdot\text{kg}^{-1}$! This value is the closest one to the 2025 target ($C_{c,2025} = 15 \text{ kW}\cdot\text{kg}^{-1}$). Anyway, this solution needs to be optimised: an increase of the power coefficient is thus expected.

	Fluid Volume (m ³)	Fluid Mass (kg)	Solid Volume (m ³)	Unladen mass (kg)	Total mass: solid+fluid (kg)
Vapour line	4.62E-04	0.34	4.69E-05	0.37	0.70
Condenser	2.17E-02	15.89	2.20E-03	17.18	33.06
Liquid line	9.41E-06	0.01	7.65E-06	0.06	0.07
Reservoir	2.22E-02	4.06	5.18E-04	4.04	8.09
Evaporator	1.07E-04	0.08	2.12E-04	0.86	2.82
<i>Total</i>	4.45E-02	20.37	2.99E-03	22.50	44.75

Table 4.6: Two-phase passive cooling system mass evaluation (first approximation design of a three-evaporators-CPLIP).

Three parallel loops

Assuming the case where three parallel loops work independently, each one cooling one electrical-phase, each CPLIP should be designed to evacuate one-third of the total thermal losses. In this case, the total mass of the cooling system is obviously given by the sum of the masses of all CPLIPs. Smaller components dimension than CERBERE characterises this solution. Vapour and liquid lines have the same lengths (defined in table 4.3) than its three-heads counterpart, but smaller hydraulic diameters: respectively 14 and 2 mm. The 23-meter-long condenser has the same configuration than before, but due to the smaller hydraulic diameter the heat transfer surface area is obviously lower. In this case, the condenser staggered tube bank has 5-raws of 6 tubes each, a single-tube-length of 0.8 m and a tube distance 1.5 times the condenser hydraulic diameter. The mass evaluation of three-parallel CPLIPs configuration is reported in table 4.7. Actually, if this last result is used to calculate the power coefficient, a value of $C_c = 16 \text{ kW}\cdot\text{kg}^{-1}$ is obtained: higher than the target 2025!

	Fluid Volume (m ³)	Fluid Mass (kg)	Solid Volume (m ³)	Unladen mass (kg)	Total mass: solid+fluid (kg)
Vapour line	1.54E-04	0.11	2.75E-05	0.21	0.33
Condenser	3.54E-03	2.59	6.33E-04	4.94	7.53
Liquid line	3.14E-06	0.00	4.90E-06	0.04	0.04
Reservoir	3.70E-03	0.68	2.14E-04	1.67	2.35
Evaporator	1.07E-04	0.08	2.12E-04	0.86	0.94
<i>Total</i>	7.50E-03	3.46	1.09E-03	7.72	11.18/CPLIP

Table 4.7: Two-phase passive cooling system mass evaluation (first approximation design of three different one-evaporator-CPLIP).

4.2.3 Cooling technology comparison

A comparison of the characteristics resulting from the first approximation design are reported in table 4.8. Despite the already expressed low efficiency and strong dependency between operating temperature range and mass flow rate, single phase cooling system is in general lighter than two-phase active technology (see Fig. 4.6). Both technologies are characterised by almost the same unladen mass, but a two times higher quantity of fluid is contained in two-phase active solution.

Higher condenser and vapour line internal tube diameters (two times than those of single phase solution), and a greater reservoir volume justify the higher amount of fluid in two-phase solution. Both technologies are, as expected, strongly impacted by the pump that, in active single and two-phase technologies are, respectively, 27% and 19% of the total mass (see Fig. 4.7). So the use of a CPLIP can ensure a mean mass saving of about 23%.

	Liquid cooling	Two-phase active	CERBERE	3×CPLIP
Thermal load [kW]	15	15	15	3×5
Total MFR [$\text{kg}\cdot\text{s}^{-1}$]	0.14	0.014	0.014	3×0.0046
Heatsink configuration	9 parallel squared channels; $D_h = 8 \text{ mm}$	Single-channel serpentine; 10 passages; $D_h = 12 \text{ mm}$	Porous wick	Porous wick
Condenser length [m]	80	50	50	3×23
Condenser diameter [mm]	11	24	24	14
Cold HXG/condenser configuration	Staggered tube bank; 5×20 tubes of 0.8 m; equispaced 1.5 diameters	Staggered tube bank; 5×20 tubes of 0.5 m; equispaced 1.5 diameters	Staggered tube bank; 5×20 tubes of 0.5 m; equispaced 1.5 diameters	Staggered tube bank; 5×6 tubes of 0.8 m; equispaced 1.5 diameters
Reservoir volume [m^3]	7.13E-03	2.22E-02	2.22E-02	$3 \times 3.70\text{E}-03$
Total mass (kg)	48.4	53.9	44.7	33.6
First approximation global power coefficient, C_c ($\text{kW}\cdot\text{kg}^{-1}$)	13.8	13.2	14.3	16

Table 4.8: Cooling systems geometrical characteristics.

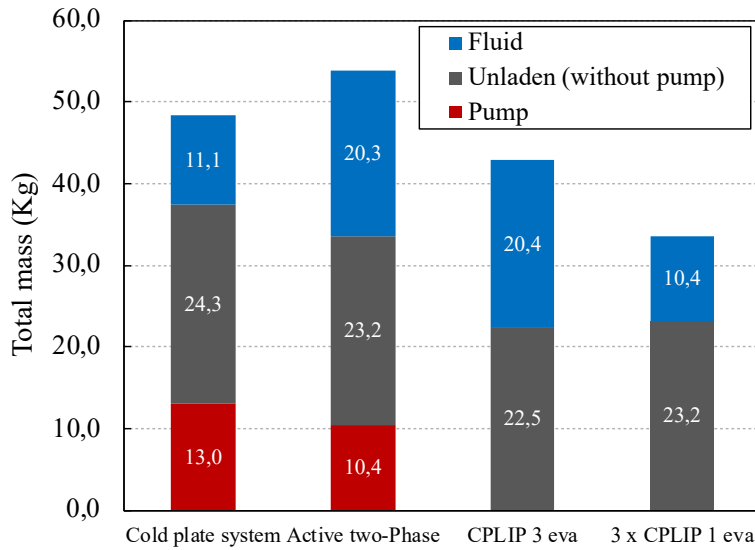


Figure 4.6: Unladen, fluid and total mass comparison for the considered technologies.

Cold-heat-exchanger/condenser and fluid are the second and the third heaviest components in active technologies.

Despite the great difference in terms of unladen mass, the quantity of fluid filling the pumped two-phase technology and the CPLIP is almost the same. Pumped two-phase cooling system and CPLIP, with three parallel evaporators, share the same components dimensions, but their working principle is quite different in nature. They share condenser configuration and dimensions as well as vapour line, liquid line and reservoir dimensions. Evaporator of pumped two phase technology (cold plate) is lighter than CPLIP's one (wicked). The difference is mainly due to the presence of the nickel porous wick in the capillary pumped solution, while empty channels compose the evaporator of active two-phase technology. If in pumped two phase cooling system, no fluid fills the evaporator in stand-by condition, in the case of the CPLIP, the evaporator is filled with liquid.

The use of three different CPLIPs allows a significative mass saving (about 26%) than CERBERE, but some integration issues may be solved. In this case, in fact, three independent loops need to be installed side by side and electronic components, positioned on the evaporators, have to be linked between them. Even if the mass of CERBERE configuration is higher than the maximum mass requirement, it has to be considered that this solution is not optimised yet.

CPLIP is mostly impacted by condenser and fluid mass. In this last case the fluid mass is almost 50% of the total mass and the 40% is due to the condenser. Obviously,

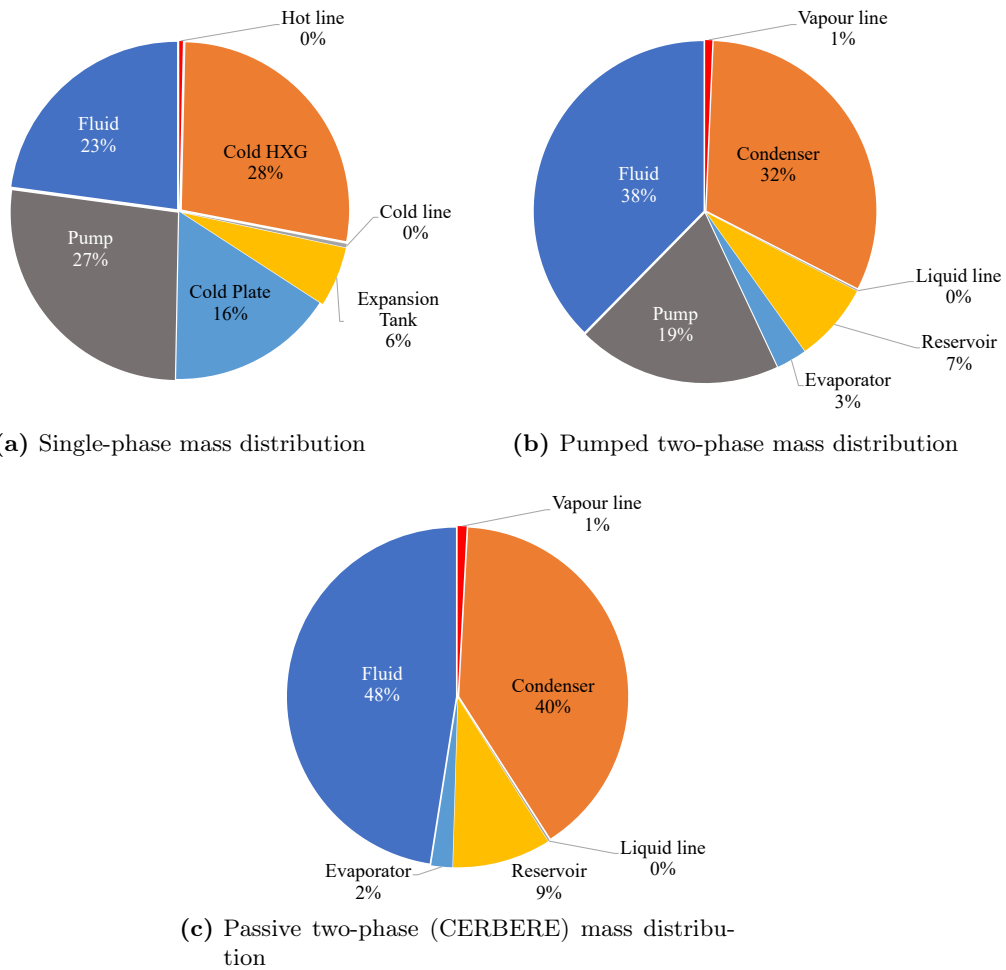


Figure 4.7: Mass composition of different cooling technologies

the lower the unladen mass, the higher the perceptual weight of fluid in the cooling system. However, the fluid is mostly present in the condenser, the longest component for all analysed technologies. So, the smaller the condenser, the lower the quantity of fluid filling the loop and also the lower the reservoir volume. The condenser is the main component on which the optimisation process should be focused. Note that liquid and vapour line masses are negligible for all systems.

Actually, between the compared technologies only the CPLIP is the one able to ensure the closest value of the power to mass ratio [$\text{kW}\cdot\text{kg}^{-1}$] to the minimal requirements.

4.3 Conclusion

In this chapter a comparison between different cooling devices was introduced, considering the heat evacuation capability, the maximal HTC and the evolution of each technology.

Jet impingement and spray cooling, microchannels and, porous media and metal foams were compared to have a broad knowledge of the actual state of the art concerning electronics cooling. Considering either single and two-phase exchange mechanisms, the latter is the best choice to ensure higher HTC as well as lower pressure drop on the hot side. The main problems related to the use of these particular cooling techniques is, in fact, related to their pressure drops. The higher the pressure drop, the higher the energy required by the cooling system to work and so the lower the power coefficient that should be proportionally reduced to consider the pump efficiency.

Passive two phase cooling systems are nowadays widely used for the same purposes and their performances increase time by time. These technologies are today able to ensure the adequate cooling with relatively high transport distances, as is the case for two-phase passive loops (see LHP/CPL/CPLIP).

A first approximation design and a comparison was also introduced in this chapter to finally choose the most adapted cooling solution for the purpose of this work. Actually, neither classic liquid cooling systems and active two-phase technologies are able to ensure, following the first approximation design, the mass requirement. On the other hand, CPLIP, is able to ensure the mass requirement, and, even if optimisation is needed this technology crosses over, in a particular configuration, the minimal power to mass ratio, C_c . Three separate parallel CPLIPs configuration represents the more lightweight solution, ensuring a power coefficient higher than $15 \text{ kW}\cdot\text{kg}^{-1}$ (2025 target). Its volume encumber could be higher than a CERBERE and some integration issues could affect such arrangement. For CERBERE, the power coefficient is slightly lower than that required for 2025, but an optimisation must be performed.

CPLIP seems to well responds to power electronics requirements either for the targets of 2025.

CPLIP's working principles, characteristics, numerical models and experimental facility will be introduced. Experimental tests and numerical simulations will be used to show how this loop is able to ensure the temperature and mass requirements. A particularly fine CPLIP optimisation will be so presented to check if this technology, coupled to the electronic components, is able to answer to requirements of 2035.

Part III

CPLIP in HASTECS context

After an introduction on the state of the art of the Capillary Loop for Integrated Power (CPLIP), its working principle, the experimental facility and the numerical model used in this study, are here introduced. CPLIP will be experimentally characterised from a thermal and hydraulic point of view to analyse its behaviour in presence of high heat flux densities, to know if it meets HASTECS requirements and to evaluate evaporator thermal conductances. An experimental stress test, based on the response of the loop in a real aircraft mission profile cycle is introduced to show its capabilities. Finally, it will be designed and optimised, according to power electronics requirements, to evaluate its performances in terms of power coefficient, C_c , either for targets 2025 and 2035.

Capillary Pumped Loop for Integrated Power (CPLIP): working principle, experimental facility and numerical tool

The Capillary Pumped Loop for Integrated Power (CPLIP), or CPLTA (Capillary Pumped Loop for Terrestrial Applications) as it is also called, is a two-phase passive loop which design has been enhanced from classical CPLs. In the latter, no mass exchanges are possible because of the small diameter of the tube linking the liquid line and the reservoir [47]. Low stability during harsh transient stages and long response time during loop start-up [74] characterise CPLs. Thanks to gravity and a higher thermo-hydraulic coupling between the compensation chamber and the evaporator, linked by a vertical tube, problems affecting CPLs were solved in CPLIP. Mass exchanges are so possible: the liquid contained in the reservoir is forced by gravity to come down to the evaporator, and if vapour bubbles are formed in the latter, they can return-up to reservoir.

In this chapter, an introduction on the CPLIP is presented and its working principle discussed. The physical phenomena governing its components are explained and the experimental facility introduced. Finally, the numerical model used in this study is presented.

5.1 CPLIP generalities and working principle

Like other capillary pumped systems, CPLIP is constituted by evaporator, condenser, compensation chamber (or reservoir) and transport lines (vapour and liquid). The thermodynamic working principle is explained using the scheme reported in Fig. 5.1 according to the qualitative thermodynamic cycle of Fig. 5.2.

In steady state conditions, the heat coming from the evaporator walls, point E_i , (where the hot source is installed) reaches the liquid menisci by conduction through the porous wick particles and the vapour contained in it. Vaporisation occurs at the liquid/vapour interface (point V) following the pressure difference between reservoir (res) and the

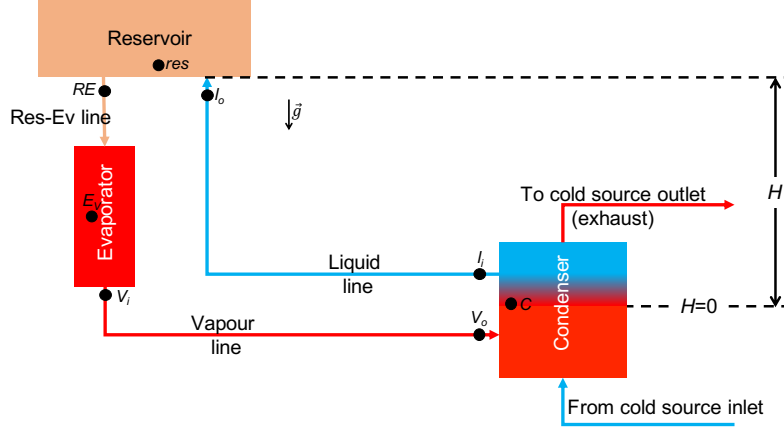


Figure 5.1: Scheme of principle of CPLIP

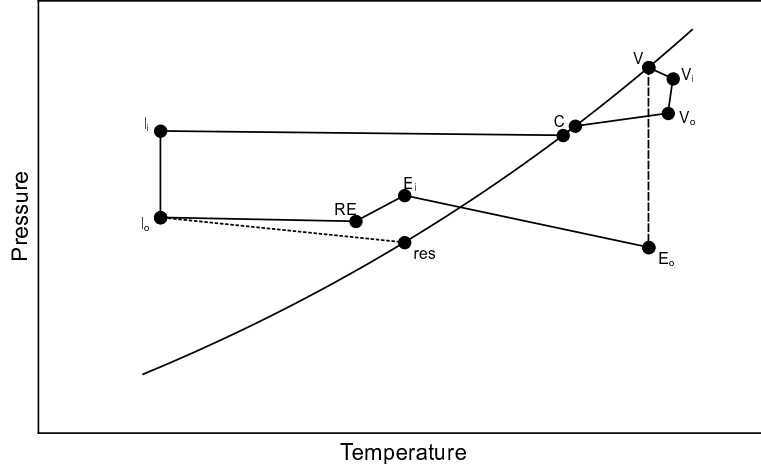


Figure 5.2: CPLIP thermodynamic cycle [12]

evaporator itself. Vapour, subject to a small pressure drop in the evaporator, reaches the inlet of the vapour line slightly superheated by evaporator walls (point V_i) and, subject to viscous pressure drop, flows to the condenser within the vapour line (point V_o). In the condenser, vapour temperature decreases, from superheated to saturated condition (on the saturation curve), until condensation occurs (point C). Oversizing of this last component is necessary to allow the required sub-cooling: the liquid should quit the condenser as close as possible to the cold source inlet temperature. Subcooled liquid enters the liquid line in the condition l_i , it flows within it and enters in the reservoir in condition l_o . In CPLIP, pressure drops in the liquid line are mostly due to gravity, $\rho_l g H$ (given the difference of height, H , between the condenser outlet and the reservoir inlet),

and marginally to viscous effect. In reservoir, saturation conditions are imposed using an electric cartridge heater and controlled using a PID regulator and a thermocouple, so that the point *res* is fixed on the diagram. Liquid, entering in the reservoir in condition l_o , flows within its lower part. Due to convective and conductive heat exchanges between the higher and the lower part of the reservoir, liquid quits it in condition *RE* (hotter than l_o point). It enters into the evaporator by gravity, where it wets the porous wick. Here, liquid is heated from the temperature corresponding to condition *RE* until the evaporator's saturation one. Finally, evaporation, and so mass transfer from liquid to vapour phase, takes place. Pressure head, due to capillary effect, allows the fluid to flow into the loop making the cycle to start again.

Even if a system approach is here used to describe the behaviour of the CPLIP, a description of each component is reported to give the reader an overview of the different phenomena occurring in this kind of loop.

5.1.1 Evaporator

The evaporator, the component where the most complex physical phenomena take place, is the “engine” of the CPLIP. Energy exchanges and mass transfer, from liquid to vapour phase, occur here to evacuate the thermal load, while capillarity generates the fluid motion in the loop.

The evaporator is constituted by a low thermal resistance enclosure which contains a sintered porous wick. Even if different materials can be used for the purpose, high thermal conductivity wick materials are preferred to obtain a heat spreading from the enclosure walls to the centre of the wick itself. Evaporator assembly and transversal sections are respectively reported in Fig. 5.3 and Fig. 5.4.

The liquid, forced by gravity, enters in the arteries (see Fig. 5.4a and Fig. 5.4c) and

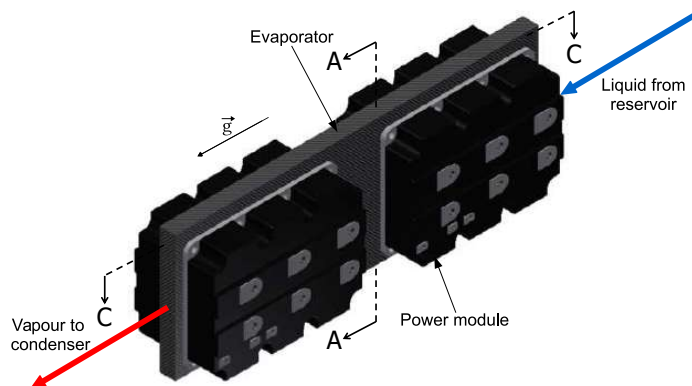


Figure 5.3: Evaporator assembly

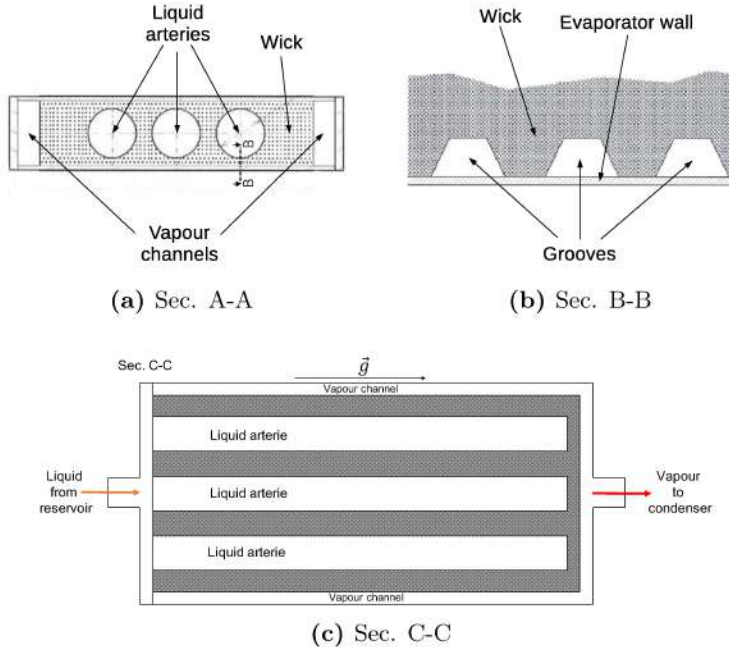


Figure 5.4: Evaporator sections

penetrates the porous wick. The evaporator, vertically mounted, is uniformly heated from two opposite sides. When the heat flux is applied to the (vertical) bounding surfaces, the wick temperature increases. By conduction, the heat is transferred to the wick particles and the wetting liquid. When the latter reaches and crosses-over the saturation temperature, according to reservoir conditions, evaporation occurs in the wick (see Fig. 5.5). The interface between the liquid and the vapour phases is constituted by menisci supported by the porous structure. In correspondence of the point where solid, liquid and gaseous phases are in contact (triple line), a force field is created and the system evolves towards a new equilibrium generating a curvature in the meniscus profile. The liquid below the meniscus is depressurised (P_l) relatively to the vapour phase (P_v) above the interface. Such differential pressure, also called capillary pressure head, created between the two phases of the fluid is due to the presence of superficial tension forces (σ) able to counterbalance the overall pressure drop in the loop. Considering the meniscus curvature radius r_m , the capillary pressure ($P_v - P_l$) is defined by the Young-Laplace law:

$$P_v - P_l = \Delta P_{cap} = \frac{2\sigma}{r_m}$$

Due to the geometrical relations between the meniscus-curvature-radius, r_m , and the pore capillary radius, r_c , through the contact angle, θ_m : $2/r_m = 2\cos\theta_m/r_c$, the maximum

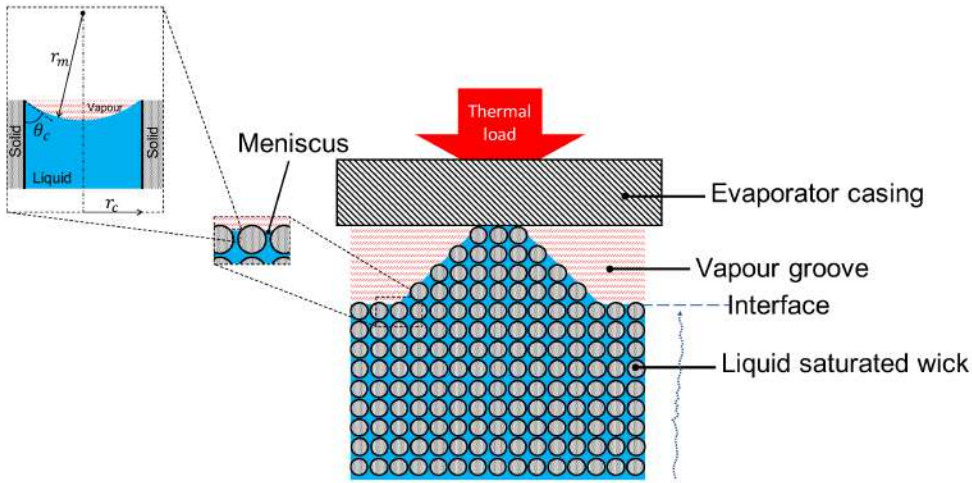


Figure 5.5: Schematic of evaporation in a porous wick.

capillary pressure head, $\Delta P_{cap,max}$, is defined by a meniscus curvature radius, r_m , tending to the capillary pore radius, r_c . The contact angle θ_m , characteristic of the couple solid-liquid, is an important indicator of the wettability of the porous wick: the way on which the liquid phase spreads onto the solid surface. $\theta_m \leq \pi/2$ indicates a wetting liquid, while $\theta_m > \pi/2$ characterises a non-wetting liquid.

Factors, in general, influencing the behaviour of the porous wick [112] are the geometrical characteristics of the wick, such as matrix structure, pore number and dimensions, and matrix topology. Beyond the geometrical ones, other influencing factors are the fluid-solid interactions (see also θ_c).

In general, the complexity of evaporation process into the porous media do not allow a simple modelling of this component of the loop. To simplify the task, a 2D flow has been assumed for the resolution of the fluid flow, but great differences exist between 2D and 3D results. In some cases 2D results are related to “false phenomena” that in reality do not occur, as in particular underlined by Mottet *et al.* [113, 114].

5.1.2 Condenser

The condenser is the component where heat is definitively evacuated to the external environment. In general, it is a classic heat exchanger where latent and sensible heats are exchanged between external and internal fluids to evacuate the thermal load. Classically, in the first part of the condenser only latent heat is exchanged between the primary and the secondary fluid and, if sub-cooling is required, sensible heat is exchanged in the

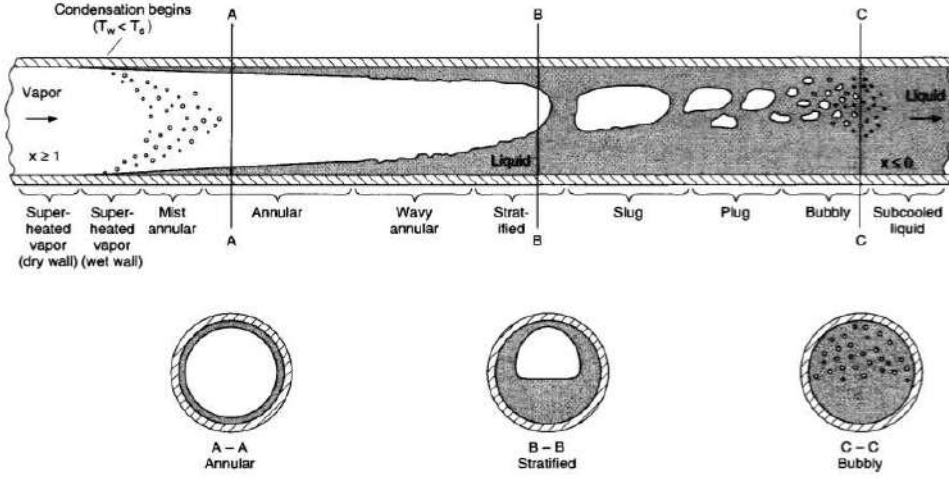


Figure 5.6: Condensation flow regimes [13]

remaining part to lower the temperature of the condensed fluid.

Condensation is, together with evaporation in the porous structure, one of the most complex phenomena occurring in the loop. A qualitative scheme of condensation occurring in a tube is reported in Fig. 5.6. When the wall temperature is lower than the local saturation one, condensation starts on the tube walls, but the fluid bulk remains in superheated conditions. Due to mass exchanges from vapour to liquid phases, a thin film of liquid begins to be formed on the tube walls: annular flow. The velocity of the fluid decreases because of the higher density of the liquid compared to the vapour one. Depending on the orientation of the condenser and the shear to gravity force ratio, one can assist or not to a stratification of the liquid in the lower part of the tube. Waves can be formed on the liquid film and they could become big enough to form slugs (slug flow). Slugs of liquid will intermittently push the plugs of vapour towards the exit of the condenser. So, after a bubbly flow, depending on the condenser length, sub-cooled liquid leaves the condenser. In this last section of the condenser only single phase heat transfer occurs, and, as a function of the heat flux density, the fluid temperature can be easily calculated from sensible heat transfer and single phase (liquid) correlations. Due to the complexity of the flow pattern, different models exist to predict the fluid behaviour. On the basis of the dimensionless vapour mass velocity, j_g^* (see eq. (5.1), where apart from the already known parameters, G [$\text{kg} \cdot \text{s}^{-1} \cdot \text{m}^{-2}$] is the mass flow rate per unit area), the flow pattern can be identified as [13]:

$$j_g^* = \frac{xG}{[g\rho_g(\rho_l - \rho_g)d_i]^{1/2}} \quad (5.1)$$

If $j_g^* < 0.5$, stratified condensation occurs. Because of the presence of gravity, vapour, condensed in top part of the tube, drop-off around the tube walls. The liquid is collected in the lower part (see sec. B-B of fig. 5.6) where, due to the presence of shear forces, it axially flows forward. In this case, the calculation of the heat transfer coefficient is not dependent on the stratified part which contribution may be in general neglected [13]. It is the case of Chato correlation, for example.

If the vapour velocity becomes high enough, the influence on the heat transfer coefficient of the stratified liquid in the lower part of the tube cannot be neglected anymore, and the interfacial vapour shear stress can influence the heat transfer coefficient of the fluid film in the higher part of the tube wall. In this case, either the liquid accumulated in the lower part of the tube and the vapour need to be considered for HTC calculation.

Finally, when the vapour velocity is pretty high, *i.e.* $j_g^* > 1.5$, laminar flow model is no more adapted and turbulence models have to be used for HTC prediction: gravitational effects become almost negligible and no more stratification occurs. In this case the fluid regime is more similar to the annular one (showed in sec. A-A reported in fig. 5.6).

Condenser design is not easy and, because of the presence of all these complex phenomena, numerical methods should be used to predict condenser behaviour and its internal HTC.

5.1.3 Reservoir

Reservoir position and internal structure distinguish the CPLIP from a classical CPL. This component deeply influences the operation of the loop and its behaviour. In Fig. 5.7 a schematic of the reservoir is reported. A separation plate divides the reservoir in two parts. Lower and higher parts communicate through an orifice allowing mass and energy exchanges between them. An electric cartridge heater is used to control saturation temperature, and so saturation pressure, by controlling the electrical power supplied.

In steady-state conditions, sub-cooled liquid, coming from the condenser, flows within the reservoir lower part and no mass exchanges occur with the higher part. There, it is pre-heated until the outlet temperature, T_{RE} , before flowing towards the evaporator (see Fig. 5.1). If loop operating conditions change, mass and energy exchanges between the two sections of the reservoir occur adapting its thermo-hydraulic conditions to the new working point. During transient phases, liquid mass exchanges through the orifice lead to a change of the height of liquid-vapour interface and so to variation of the saturation conditions in the reservoir higher part. Generally, transient phenomena of evaporation and condensation are fast enough to consider the thermodynamic state of the reservoir at nearly constant saturation conditions [25].

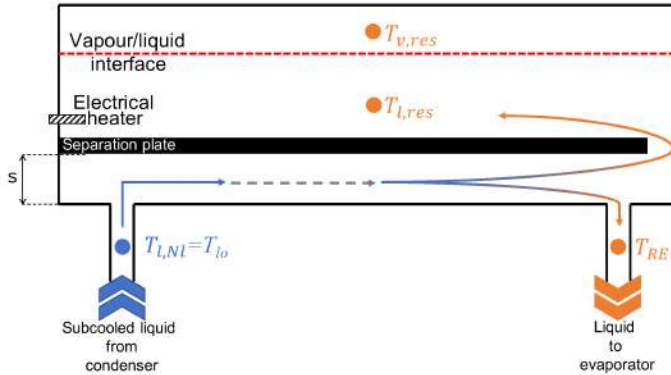


Figure 5.7: Reservoir concept scheme

5.1.4 Transport lines

Except quite smooth internal tube walls requirements, to ensure the lowest pressure drop possible, and particular constraints related to weight-saving or transport distance, transport lines do not require particular characteristics.

Vapour, generated in the evaporator, flows within the vapour line. Due to higher vapour velocity than that related to the liquid flow in the liquid line¹, viscous pressure losses are generally higher. It is so necessary to verify that distributed pressure drops (cumulated with all other ones in the loop), for a given tube diameter and length, are lower than the maximal capillary pressure head in the porous wick. In general, the vapour line diameter should be dimensioned to ensure the lower vapour velocity possible: the one that minimise the pressure drops according to the highest MFR realisable, corresponding to the highest thermal load.

In the liquid line, the undercooled liquid flows from the outlet of the condenser to the reservoir inlet (point represented with the subscript l, Nl in Fig. 5.7 and corresponding to the point lo in Fig. 5.2). Some instabilities could occur if liquid velocity is too high. In general, like all industrial applications, the liquid line diameter is calculated to limit the maximal velocity to $2 \text{ m} \cdot \text{s}^{-1}$, in the case where the maximal mass flow rate occurs (maximal thermal power applied to the evaporator).

5.2 Experimental facility

Over the last decade, Capillary Pumped Loop for Terrestrial Applications have been studied by different authors and for many research purposes [1, 14, 48, 71, 26, 74, 115].

¹In steady state condition $\dot{m} = \rho_v A_v u_v = \rho_l A_l u_l$ in the vapour line (v), and the liquid line (l), respectively.

Prior to the experimental facility used in this study, CPLIP was developed for terrestrial applications. Its purpose was to solve problems related to the use of classical CPLs: low robustness, slow start-up and instabilities during this transient phase. CPLIP was developed for the first time in 2006 for thermal control of power electronics in railways field, whence the name Capillary Pumped Loop for Integrated Power. The first prototype, called “CPLIP 1.0” was built by Euro Heat Pipes (EHPTM) to perform feasibility studies related to power electronics cooling. Power electronics modules were installed on the evaporator and, because of its ability to ensure the temperature requirements on the electronic components, a second prototype (with the same characteristics than the first one) has been built for the same purposes. The latter, like the first one, was equipped by an air-to-liquid condenser to ensure as realistic as possible operating conditions. A maximal air mass flow rate of $125\text{l}\cdot\text{s}^{-1}$ was supplied by a blower to the secondary side of the condenser, which tubes were equipped by 4 mm-spaced-fins generating a maximal external pressure drop of 400 Pa [15].

5.2.1 CPLIP 1.1: the experimental facility

In 2008 a new prototype has been built by EHPTM and Pprime Institute at the ISAE-ENSMA. The CPLIP 1.1, studied for the first time by D. Lossouarn during his Ph.D thesis [15], has been modified (suppressing some measurement equipments) for educational purposes and is still wondrously operating (as it will be shown later) —despite, sometimes, “mistreatments” from students—.

Referring to fig. 5.8, a detailed description of the experimental facility used in this work (CPLIP 1.1) is reported in the following.

The whole loop is made of stainless steel, with the exception of the evaporator where different materials are used to ensure the adequate heat transfer from the heating bodies to the porous wick (see Fig. 5.9).

Reservoir is cylindrical with an external diameter $D_{res} = 99.6\text{ mm}$ and a length $L_{res} = 308\text{ mm}$. Its total volume is $V_{res} = 2398.5\text{ cm}^3$. The height of the separating plate from the reservoir lower wall (s in Fig. 5.7) is 6 mm, so, its volume is $V_{res,low} = 58.7\text{ cm}^3$. The saturation conditions are imposed using a heating cartridge in the higher part of the reservoir in the liquid phase. Here, on the base of the temperature measurement, it is possible to set the operating point and to control the saturation temperature to the desired value using a PID controller. A temperature platinum sensor has an accuracy of $\pm 0.1^\circ\text{C}$, while the pressure sensor, used to measure the absolute pressure in the reservoir (GE druck PDCR3500), has an accuracy of $\pm 0.1\%$ in the operating range, 0 – 5 bar. The coupling of both sensors allows to measure and control the saturation conditions and, as

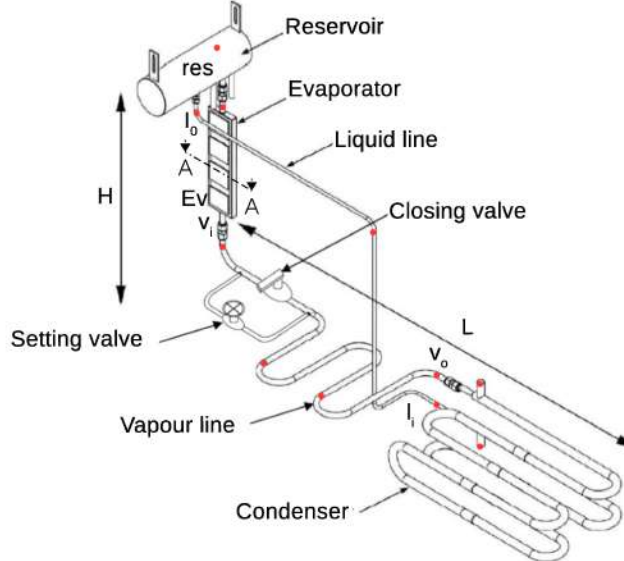


Figure 5.8: Schematic of the CPLIP 1.1 [12, 14, 15]

it will be better explained later, to verify the absence of non condensable gases.

The evaporator is constituted by a stainless steel enclosure, overall dimensions of $296 \times 83 \times 18 \text{ mm}^3$, which contains the nickel porous wick (dimensions $283 \times 68 \times 16 \text{ mm}^3$). The latter (transversal sections reported in Fig. 5.4a and Fig. 5.4b) is characterised by a porosity of 73%, an average pore diameter of $6.8 \mu\text{m}$, a permeability of $6.53 \cdot 10^{-13} \text{ m}^2$ and an effective thermal conductivity of $5 \text{ W} \cdot \text{m}^{-1} \cdot \text{K}^{-1}$. As shown in fig. 5.4a and 5.4c, three liquid arteries allow to supply the liquid coming from the reservoir. The trapezoidal vapour grooves (see fig. 5.4b), which dimensions are 1.2 mm-major, 0.6 mm-minor base and 0.6 mm-height, allow the evacuation of the vapour. The stainless-steel enclosure (see Fig. 5.9) is equipped by eight thermal diffusers (four on each side) positioned face-

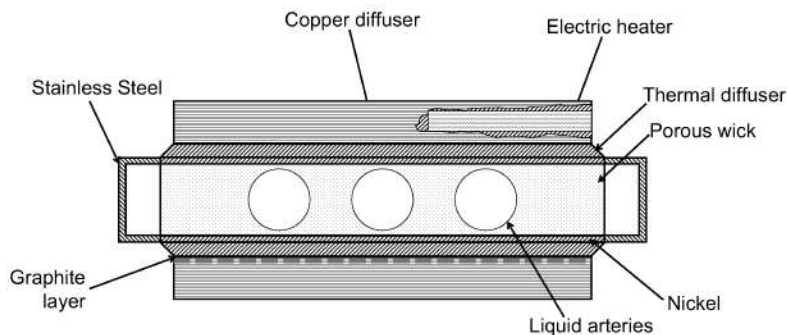


Figure 5.9: Evaporator concept scheme (sec. A-A)

to-face (height 4 mm). Each diffuser is equipped by four thermocouples inserted into external grooves. A copper diffuser is installed on each of them allowing the insertion of the cylindrical heating resistances (two per each one) to simulate the heat sources. A thermal graphite layer (TIM) is used between the first and the second diffuser [50]. The thirty-two evaporator's wall type-T thermocouples have an accuracy of $\pm 0.5^\circ\text{C}$. The evaporator heating resistances are linked to the electrical power supplier (Xantrex, up to 300 V and 30 A) that allows a regulation of the thermal power up to about 8 kW.

The condenser is installed in a favourable position, under the evaporator at a height of 50 cm. It is a 4.04-meter-long, tube-in-tube, heat exchanger supplied on the secondary side by a mass flow rate, up to $20 \text{ kg}\cdot\text{s}^{-1}$ [50], of 30%-ethylene-glycol-water solution cooled by an up to 8 kW thermo-cryostat. The primary fluid side tube has an external diameter of 14 mm and the secondary one has an external diameter of 21.3 mm. Tube thicknesses are 1 and 1.5 mm, respectively.

Vapour and liquid lines are made of stainless-steel like the rest of the loop. The 2.05-meter-long vapour line has the same condenser primary side tube diameters (12 and 14 mm-internal and external-side-diameter, respectively). The liquid line (1.5 m long) has an internal diameter of 6 mm and a thickness of 1 mm. Transport lines are insulated, with a stainless-steel to insulating layer thermal resistance ratio of $2 \cdot 10^{-4}$. Bends are included in the vapour line to make it longer.

As one can observe on the scheme reported in fig. 5.8, the vapour line is equipped by a settling valve that allows to regulate vapour pressure drop, by reducing the fluid flow section. The valve flow coefficient, C_v , depends on the number of turns, N , following the polynomial law:

$$C_v = F_c[0.0103N^4 + 0.0909N^3 + 0.178N^2 + 0.3766N + 0.0016] \quad (5.2)$$

with the conversion factor $F_c = 0.116$.

The vapour mass flow rate is related to the flow coefficient as reported in eq. (5.3):

$$\dot{m}_v = 22.4 C_v \sqrt{\Delta P \cdot p_{sat}} \quad (5.3)$$

Red points in fig. 5.8 indicate the position of the 0.1-millimeter-diameter T-type thermocouples installed all over the CPLIP. In particular, in addition to the saturation temperature platinum sensor (T_{res}), the reservoir is equipped by other two thermocouples in its lower and higher parts (named T_{RL} and T_{RV} , respectively). The vapour line is equipped by four thermocouples (named T_{v1} to T_{v4} from the evaporator to the condenser, respectively). The first one is installed at 8 cm from the evaporator outlet and

the others distanced of 49, 69 and 79 cm. The liquid line is equipped by three thermo-couples, named T_{l1} to T_{l3} , respectively positioned at the outlet of the condenser, in the middle of the line and at the end. The condenser secondary fluid side thermocouples are installed at the inlet and outlet of the condenser itself [111].

5.3 Numerical models

The complexity of the phenomena regulating the working principle of capillary pumped systems makes of modelling one of the most complex tasks. Other than the classical Navier-Stokes equations (continuity, momentum and energy equations), phase change phenomena have to be considered during this job. In the case of the porous wick, the task is more arduous because of the not well known thermo-fluid dynamic laws.

Many studies have been conducted to model the thermo-fluid dynamic behaviour of a porous wick in which phase change phenomena occur. Mottet *et al.* [113] modelled the behaviour of a LHP's capillary wick in which evaporation occurs. Using the finite volume method, with ammonia as working fluid, they got more realistic results with 3D simulations and obtained the classical bell-shape thermal conductance curve. Beyhaghi *et al.* [116] developed a novel analytical model, using different working fluids (a series of alkaline) and a polycarbonate wick to study the variation of the characteristics of the porous wick (porosity and mean bead radius) to obtain the optimal design.

However, none of the models cited above is adapted for its use in a system approach, that should consider all the phenomena occurring in a capillary pumped loop in a “reasonable” calculation time. Even if numerical results well agree with experimental ones, CFD is a too expensive method to be used during design and optimisation of the overall loop — especially for industrial applications —.

Actually, for a CPLIP, it does not exist a standard commercial tool for its design and to estimate its performances. Although many efforts have been done to model this loop to find a good way to design it and predict its behaviour in many configurations and operating conditions [16, 49, 26, 25, 117]. Modelling results well agree with experimental ones, and some models, such as the Blet's one [25], are able to predict with a good agreement the real behaviour of the loop. Unfortunately, this model needs some empirical entries (evaporator and reservoir thermal conductances) to evaluate the thermal behaviour of the loop.

Thanks to the completeness and some peculiarities of the Blet's model, it was used for the purposes related to the present work after adaptation and modification. In particular, as it will be better explained in the following, both steady and transient simulations were

performed to analyse and understand some experimentally observed phenomena. In the following a simplified explanation of the Blet's model is reported.

5.4 CPLIP model

Blet's model [25] is an evolution of Delalandre's model [26]. While the second one [26] was created to study the CPLIP in a single evaporator configuration, the first one [25] represents an adaptation and an improvement of the previous one with the purpose to study a three parallel evaporators configuration of the CPLIP. Thanks to the use of a more advanced reservoir model, and the ability to predict any kind of negative mass flow rate (reversed flow) into the loop², the Blet's model is an important upgrade of the previous one, able to overcome all the limitations and instabilities of Delalandre's model.

The fluid is considered compressible and the vapour phase is considered as a perfect gas. Enthalpy is used instead of temperature as variable in the energy equation. This choice allows to overcome the limitations related to the use of the temperature to define the physical state of the fluid. In fact, if temperature is used, the fluid thermophysical properties present a discontinuity in correspondence of the saturation temperature. Thanks to the hypothesis of homogeneous fluid, the different fluid properties can be defined as a function of the vapour mass fraction, x , and considering the enthalpy. No more discontinuities are related to the physic state of the fluid in correspondence of the saturation temperature. According to McAdams formulation, in fact, the phase change is managed as follows:

$$\begin{cases} h < h_{l,sat}(P) & x = 0 & \text{(liquid phase)} \\ h_{l,sat}(P) \leq h \leq h_{v,sat}(P) & x = \frac{h-h_{l,sat}(P)}{h_{v,sat}(P)-h_{l,sat}(P)} & \text{(two-phase)} \\ h > h_{v,sat}(P) & x = 1 & \text{(vapour phase)} \end{cases}$$

All fluid's thermophysical properties, in single or two-phase state, are so evaluated from pressure, P , and enthalpy, h , as well as the fluid temperatures.

Beyond the just cited assumptions, other strong hypothesis on which the model is based are [25]:

- conduction thermal resistance is neglected in the radial direction in the transport lines;

²This particular characteristic will be particularly useful during the study of the CPLIP in a cycle of sudden and violent accelerations.

- the higher part of the reservoir is always in two-phase state and the vapour phase is always considered in saturation condition: the reservoir higher part is the only “place” where the hypothesis of homogeneity of the fluid is not respected, so vapour and liquid phases always co-exist here;
- the porous wick is always filled of liquid, so the liquid/vapour interface is always positioned in correspondence of the mesh. The fluid-flow in the latter is considered fully developed and one dimensional in the direction of the wick thickness.

A staggered grid (see fig. 5.10) is used to model mass, momentum and energy exchanges in the loop.

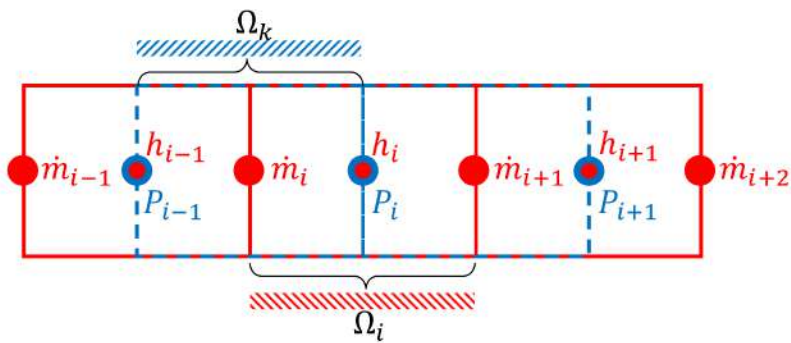


Figure 5.10: Staggered grid

Mass nodes, belonging to Ω_i (red volume in fig. 5.10), are positioned on the bounds of the cell, while enthalpy nodes, belonging to the same volume, Ω_i , are positioned in the centre of red grid. This last position also corresponds to pressure nodes, positioned on the bounds of Ω_k (blue volume in fig. 5.10), shifted by one-half control volume than mass nodes. This configuration allows the minimisation of errors related to the calculation of the fluid thermophysical properties (based either on P and h) and reduces instabilities related to the presence of velocity and pressure variables on the same node [25].

The numerical model has been developed to use the thermal-hydraulic/electrical analogy on ESACAP^(C) solver [16]. Mass, momentum and energy equations have been re-written in order to be consistent with the required network formalism. A finite volume method was used to discretise the Navier-Stokes equations in their 1D form [25]³.

5.4.1 Navier-Stokes equations

Except the higher part of the reservoir, all over the domain the fluid is supposed homogeneous and the control volumes fixed and constant. The general form of Navier-Stokes

³For more details about this model, the interested reader is invited to read ref. [25].

equations integrated on such control volume Ω delimited by the surface Σ , are directly used for single and two-phase fluid state. The integral form of mass conservation equation is:

$$\frac{D}{Dt} \int_{\Omega} \rho d\omega = 0 \quad (5.4)$$

The momentum equation in its integral form is:

$$\frac{D}{Dt} \int_{\Omega} \rho \vec{v} d\omega = \oint_{\Sigma} P \vec{n}_i d\sigma + \int_{\Omega} \rho \vec{g} d\omega + \oint_{\Sigma} \bar{\tau} \cdot \vec{n}_i d\sigma \quad (5.5)$$

Finally the integral form of the energy equation on the previously defined control volume is:

$$\frac{D}{Dt} \int_{\Omega} \rho h d\omega = \dot{Q}_{ext} + \frac{D}{Dt} \int_{\Omega} P d\omega - \int_{\Omega} P \operatorname{div}(\vec{v}) d\omega + \int_{\Omega} \bar{\tau} : \bar{D} d\omega \quad (5.6)$$

With reference to the grid structure reported in Fig. 5.10, the discretised form of conservation equations (continuity, momentum and energy) related to the transport lines and the condenser is reported in the following.

5.4.1.1 General case (vapour and liquid lines, condenser)

Continuity equation Considering a fixed and constant control volume Ω_i , the mass conservation equation can be written in its one-dimensional form, according to the discretisation reported in fig. 5.10 as:

$$\Omega_i \frac{d\rho_i}{dt} = \dot{m}_i - \dot{m}_{i+1} \quad (5.7)$$

Momentum equation Referring to the discretisation reported in Fig. 5.10, eq. (5.5) can be rewritten to agree with the used formalism [25].

As said before, one of the most important characteristics of the Blet's model is the ability to take into account reversed flows into the loop. Momentum equation can be so written in two different forms following the flow direction. Considering, as an example, the control volume Ω_{k+1} , for $\dot{m}_{i+1} \geq 0$ it is [25]:

$$\begin{aligned} \frac{L_i + L_{i+1}}{2} \frac{d\dot{m}_{i+1}}{dt} + \dot{m}_{i+1} \frac{\frac{1}{2}(\dot{m}_{i+1} + \dot{m}_{i+2})}{\frac{\rho_i \Omega_i + \rho_{i+1} \Omega_{i+1}}{\Omega_i + \Omega_{i+1}} S_{i+1}} - \dot{m}_i \frac{\frac{1}{2}(\dot{m}_i + \dot{m}_{i+1})}{\frac{\rho_{i-1} \Omega_{i-1} + \rho_i \Omega_i}{\Omega_{i-1} + \Omega_i} S_i} \\ + (P_{i+1} - P_i) S_{eq,i/i+1} \pm \frac{\rho_i H_i S_i + \rho_{i+1} H_{i+1} S_{i+1}}{2} g \\ + \frac{1}{2} (|\Delta P_{vis,i}| S_i + |\Delta P_{vis,i+1}| S_{i+1}) = 0 \end{aligned} \quad (5.8)$$

and for $\dot{m}_{i+1} < 0$ it is [25]:

$$\frac{L_i + L_{i+1}}{2} \frac{d\dot{m}_{i+1}}{dt} + \dot{m}_{i+2} \frac{\frac{1}{2}(\dot{m}_{i+1} + \dot{m}_{i+2})}{\frac{\rho_{i+1}\Omega_{i+1} + \rho_{i+2}\Omega_{i+2}}{\Omega_{i+1} + \Omega_{i+2}} S_{i+1}} - \dot{m}_{i+1} \frac{\frac{1}{2}(\dot{m}_i + \dot{m}_{i+1})}{\frac{\rho_i\Omega_i + \rho_{i+1}\Omega_{i+1}}{\Omega_i + \Omega_{i+1}} S_i} \\ + (P_{i+1} - P_i) S_{eq,i/i+1} \pm \frac{\rho_i H_i S_i + \rho_{i+1} H_{i+1} S_{i+1}}{2} g \\ - \frac{1}{2} (|\Delta P_{vis,i}| S_i + |\Delta P_{vis,i+1}| S_{i+1}) = 0 \quad (5.9)$$

Where S is the transversal section, normal to the flow, and H the height. Either in eq. (5.8) and (5.9) the sign used for the hydrostatic losses (second-to-last term on the left side) depends on the position of the control volume with respect of the \vec{g} direction.

Energy balance Referring to the control volume Ω_i , in the mesh example reported in Fig. 5.10, the discretised form of the energy equation, if $\dot{m}_i \geq 0$, is [25]:

$$\rho_i \Omega_i \frac{dh_i}{dt} = \dot{m}_i (h_{i-1} - h_i) + \dot{Q}_{ext,i} + \dot{W}_{comp,i} \quad (5.10)$$

and in the reversed flow case ($\dot{m}_i < 0$):

$$\rho_i \Omega_i \frac{dh_i}{dt} = \dot{m}_{i+1} (h_i - h_{i+1}) + \dot{Q}_{ext,i} + \dot{W}_{comp,i} \quad (5.11)$$

In eq. (5.10) and (5.11), $\dot{W}_{comp,i}$ is the term related to the work compression. Blet demonstrated that the latter is about 3% of $\dot{Q}_{ext,i}$, so to simplify the model it has been neglected [25]. $\dot{Q}_{ext,i}$ is heat flux density received by node i from adjacent nodes, considering conduction, convection and radiative exchanges. To calculate such term it is necessary to introduce a thermal network (see also Fig. 5.15d) relating the fluid with the solid walls and the external environment. For its resolution, the thermal network model uses the temperature field obtained by the enthalpy-mass and pressure networks as boundary conditions.

5.4.1.2 Reservoir

Due to its separation in two sections, different formulations have to be used to model this component. In the lower part of the reservoir, the fluid is considered homogeneous. The same formulation as the rest of the loop is used. The higher part requires the use of a non-homogeneous model because of the co-existence of the two fluid phases at every moment.

5.4.1.2.1 Reservoir lower part A schematic of the reservoir, on which the discretisation of Fig. 5.12 is based, is reported in Fig. 5.11. The lower part of the reservoir is discretised using just one node, defined as *res, low* in Fig. 5.12 and positioned between the last node of the liquid line (*l, Nl*) and the node of the reservoir-evaporator tube (*RE*).

Mass balance For the mass balance equation, mass exchanges occurring between the lower and the higher part of the reservoir have to be considered. So, the mass flow rate flowing through the orifice, \dot{m}_{res} , is defined as:

$$\dot{m}_{res} = \dot{m}_{res,I} - \dot{m}_{res,O} \quad (5.12)$$

Where the inlet and outlet fluid mass flow rates, $\dot{m}_{res,I}$ and $\dot{m}_{res,O}$, respectively, are evaluated from the overall mass flow network related to the whole loop.

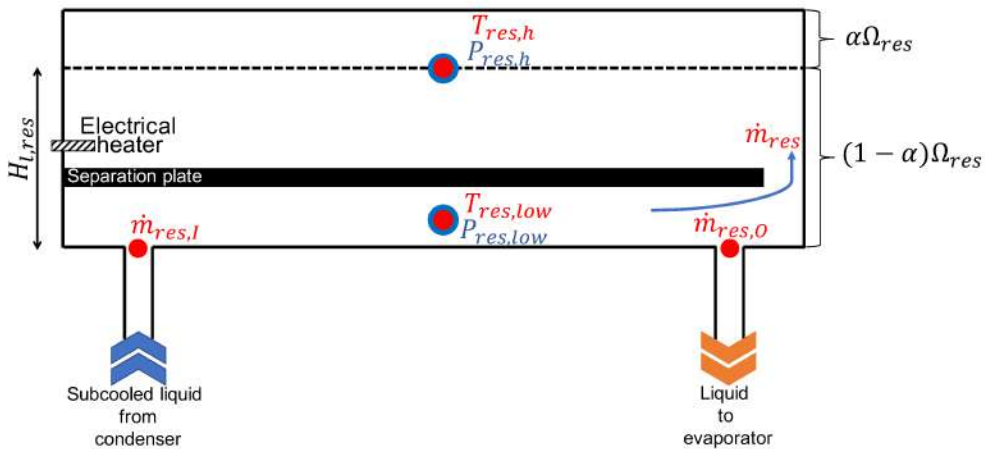


Figure 5.11: Reservoir schematic

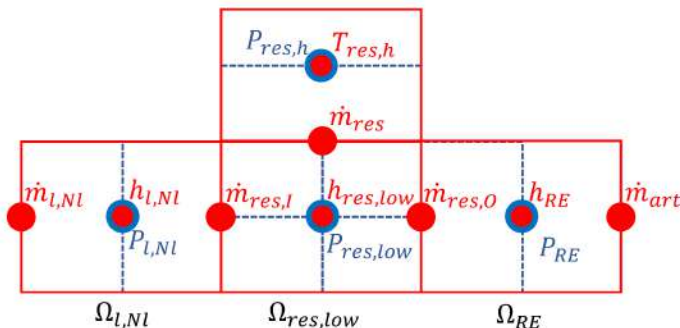


Figure 5.12: Reservoir lower part discretisation

Momentum balance Like transport lines and condenser, in the reservoir's lower part, momentum balance is dependent on the flow direction. Because of the presence of the mass flow rate exchanged between the lower and the higher part, \dot{m}_{res} , the momentum equation has to be written either for inlet and outlet nodes to consider such difference (also defined by eq. (5.12)). Three different cases can be so realised following the direction of the mass flow rate at the inlet, $\dot{m}_{res,I}$, the outlet, $\dot{m}_{res,O}$, and through the orifice, \dot{m}_{res} . In the first case, a positive mass flow rate flows within the inlet and the outlet of the reservoir and, at the same time, a liquid mass flow rate flows from the lower to the higher part. The second case is realised when a positive mass flow rate flows either through the reservoir inlet and outlet, but a negative mass flow rate flows through the orifice (the liquid contained in the higher part flows to the evaporator). These first two cases are realised during normal operations of the loop when a change in its operating conditions occurs: in the first case the required thermal load has been increased and in the second case decreased, for example. The third case, critical, is realised when the liquid contained in the higher part is reversed to the lower section, but exiting from the reservoir either through the outlet and the inlet nodes. The reservoir inlet becomes a “second exit” and the loop does not operate in a “conventional” way. This case, as it will be shown in chap. 9, is realised, for example, during harsh transient accelerations stages or, as explained by Blet, during severe thermal unloads [25]. To consider the described phenomena, discretised momentum equations are reported for the inlet and the outlet nodes of the reservoir [25]. The reservoir inlet considers the semi-volume including the node l, Nl and the reservoir outlet includes the node RE .

At the inlet of the reservoir, between the nodes $P_{l,Nl}$ and $P_{res,low}$, the momentum equation, for $\dot{m}_{res,I} \geq 0$, is:

$$\begin{aligned} \frac{L_{l,Nl}}{2} \frac{d\dot{m}_{res,I}}{dt} + & \frac{\dot{m}_{res,I}^2}{\frac{\rho_{l,Nl}\Omega_{l,Nl} + \rho_{res,low}\Omega_{res,low}}{\Omega_{l,Nl} + \Omega_{res,low}} S_L} \\ & - \dot{m}_{l,Nl} \frac{\frac{1}{2}(\dot{m}_{l,Nl} + \dot{m}_{res,I})}{\frac{\rho_{l,Nl-1}\Omega_{l,Nl-1} + \rho_{l,Nl}\Omega_{l,Nl}}{\Omega_{l,Nl-1} + \Omega_{l,Nl}} S_L} + (P_{res,low} - P_{l,Nl}) S_L \\ & + \frac{\rho_{l,Nl} H_{l,Nl} S_L}{2} g + \frac{1}{2} |\Delta P_{vis,l,Nl}| S_L = 0 \quad (5.13) \end{aligned}$$

and for $\dot{m}_{res,I} < 0$ it is:

$$\frac{L_{l,Nl}}{2} \frac{d\dot{m}_{res,I}}{dt} + \frac{\dot{m}_{res,I}^2}{\frac{\rho_{res,low}\Omega_{res,low} + \rho_{res,h}\Omega_{res,h}}{\Omega_{l,Nl} + \Omega_{res,low}} S_L}$$

$$\begin{aligned}
& - \dot{m}_{res,I} \frac{\frac{1}{2}(\dot{m}_{l,Nl} + \dot{m}_{res,I})}{\frac{\rho_{l,Nl}\Omega_{l,Nl} + \rho_{res,low}\Omega_{res,low}}{\Omega_{l,Nl} + \Omega_{res,low}} S_L} + (P_{res,low} - P_{l,Nl}) S_L \\
& \quad + \frac{\rho_{l,Nl} H_{l,Nl} S_L}{2} g - \frac{1}{2} |\Delta P_{vis,l,Nl}| S_L = 0
\end{aligned}$$

For the outlet node, between the nodes $P_{res,low}$ and P_{RE} , considering $\dot{m}_{res,I} \geq 0$ and $\dot{m}_{res} \geq 0$, the momentum equation is in the form:

$$\begin{aligned}
& \frac{L_{RE}}{2} \frac{d\dot{m}_{res,O}}{dt} + \dot{m}_{res,O} \frac{\frac{1}{2}(\dot{m}_{res,O} + \dot{m}_{art})}{\frac{\rho_{RE}\Omega_{RE} + \rho_{res,low}\Omega_{res,low}}{\Omega_{RE} + \Omega_{res,low}} S_{RE}} \\
& \quad - \frac{\dot{m}_{res,O}^2}{\frac{\rho_{l,Nl}\Omega_{l,Nl} + \rho_{res,low}\Omega_{res,low}}{\Omega_{l,Nl} + \Omega_{res,low}} S_{RE}} + (P_{RE} - P_{res,low}) S_{RE} \\
& \quad - \frac{\rho_{RE} H_{RE} S_{RE}}{2} g + \frac{1}{2} |\Delta P_{vis,RE}| S_{RE} = 0 \quad (5.14)
\end{aligned}$$

while, for the same mass flow direction, but $\dot{m}_{res} < 0$, it becomes:

$$\begin{aligned}
& \frac{L_{RE}}{2} \frac{d\dot{m}_{res,O}}{dt} + \dot{m}_{res,O} \frac{\frac{1}{2}(\dot{m}_{res,O} + \dot{m}_{art})}{\frac{\rho_{RE}\Omega_{RE} + \rho_{res,low}\Omega_{res,low}}{\Omega_{RE} + \Omega_{res,low}} S_{RE}} \\
& \quad - \frac{\dot{m}_{res,O}^2}{\frac{\rho_{l,Nl}\Omega_{l,Nl} + \rho_{res,low}\Omega_{res,low} + \rho_{res,h}\Omega_{res,h}}{\Omega_{l,Nl} + \Omega_{res,low} + \Omega_{res,h}} S_{RE}} + (P_{RE} - P_{res,low}) S_{RE} \\
& \quad + \frac{\rho_{RE} H_{RE} S_{RE}}{2} g + \frac{1}{2} |\Delta P_{vis,RE}| S_{RE} = 0 \quad (5.15)
\end{aligned}$$

Finally, if an inversion of the flow occurs ($\dot{m}_{res,I} < 0$) and $\dot{m}_{res} < 0$, it is:

$$\begin{aligned}
& \frac{L_{RE}}{2} \frac{d\dot{m}_{res,O}}{dt} + \dot{m}_{res,O} \frac{\frac{1}{2}(\dot{m}_{res,O} + \dot{m}_{art})}{\frac{\rho_{RE}\Omega_{RE} + \rho_{res,low}\Omega_{res,low}}{\Omega_{RE} + \Omega_{res,low}} S_{RE}} \\
& \quad - \frac{\dot{m}_{res,O}^2}{\frac{\rho_{res,low}\Omega_{res,low} + \rho_{res,h}\Omega_{res,h}}{\Omega_{res,low} + \Omega_{res,h}} S_{RE}} + (P_{RE} - P_{res,low}) S_{RE} \\
& \quad - \frac{\rho_{RE} H_{RE} S_{RE}}{2} g + \frac{1}{2} |\Delta P_{vis,RE}| S_{RE} = 0 \quad (5.16)
\end{aligned}$$

Energy balance Considering the flow direction, even for energy balance, two different equations have to be written for this case. When $\dot{m}_{res,I} \geq 0$, the energy equation has the form:

$$\rho_{res,low} \Omega_{res,low} \frac{dh_{res,low}}{dt} = \dot{m}_{res,I} (h_{l,Nl} - h_{res,low}) + \dot{Q}_{ext_{res,low}} + \dot{W}_{comp_{res,low}} \quad (5.17)$$

Due to the absence of the hypothesis of fluid homogeneity in the higher part of the reservoir, if $\dot{m}_{res,I} < 0$ the energy equation is written using the temperature instead of the enthalpy formulation. In this case, eq. (5.17) becomes:

$$\rho_{res,low} \Omega_{res,low} \frac{dh_{res,low}}{dt} = \dot{m}_{res,I} c_{pl} (T_{res,low} - T_{res,h}) + \dot{Q}_{ext_{res,low}} + \dot{W}_{comp_{res,low}} \quad (5.18)$$

where the compression work is $\dot{W}_{comp_{res,low}} = \Omega_{res,low} \frac{dP_{res,low}}{dt}$, and

$$dh = c_p dT + \frac{1}{\rho} (1 - \beta T) dP$$

with β the compressibility factor of the fluid.

5.4.1.2.2 Reservoir higher part In this section of the reservoir, liquid and vapour phases, separated by a well defined interface, co-exist. Because of the just cited reason, the hypothesis of homogeneous fluid cannot be applied anymore and a different approach has to be used to model this part of the loop. In this case, Blet chose to use a “macroscopic” approach.

The reservoir is an expansion tank in which the height of the liquid/vapour interface changes as a function of the working point in order to absorb any volume variation of the fluid in the loop. To consider such volume variation, the volume fraction of vapour in the reservoir, α , is introduced. The latter is defined as the ratio between the volume occupied by the vapour, $\Omega_{v,res}$, and the total reservoir volume, Ω_{res} :

$$\alpha = \frac{\Omega_{v,res}}{\Omega_{res}} \quad (5.19)$$

The mass balance equation assumes the form of a differential equation solved in α . Either liquid and vapour densities are so considered. The mass flow rate exchanged between the lower and the higher part of the reservoir is defined by eq. (5.20):

$$(\rho_{l,res} - \rho_{v,res}) \Omega_{res} \frac{d\alpha}{dt} + \Omega_{res} \frac{d\rho_{v,res}}{dt} \alpha = \dot{m}_{res} \quad (5.20)$$

As the reservoir lower part is modelled using a single node, the pressure in this part of the expansion tank is constant all along the lower part. Moreover, under the hypothesis of saturating vapour in the higher part, the pressure corresponds to the saturation one: $P_{res,h} = P_{sat}(T_{res,h})$. Considering the height of the liquid/vapour interface, $H_{l,res}$, the pressure in the reservoir lower part, $P_{res,low}$ is calculated considering the hydrostatic

pressure:

$$P_{res,low} = P_{res,h} + \rho_{l,res} g H_{l,res} \quad (5.21)$$

The complexity related to the modelling of this component requires the use of some empiric conductances. In Fig. 5.13, the complex thermo-hydraulic model developed by Blet [25], to obtain the thermal and hydraulic couplings in the reservoir higher part, is reported.

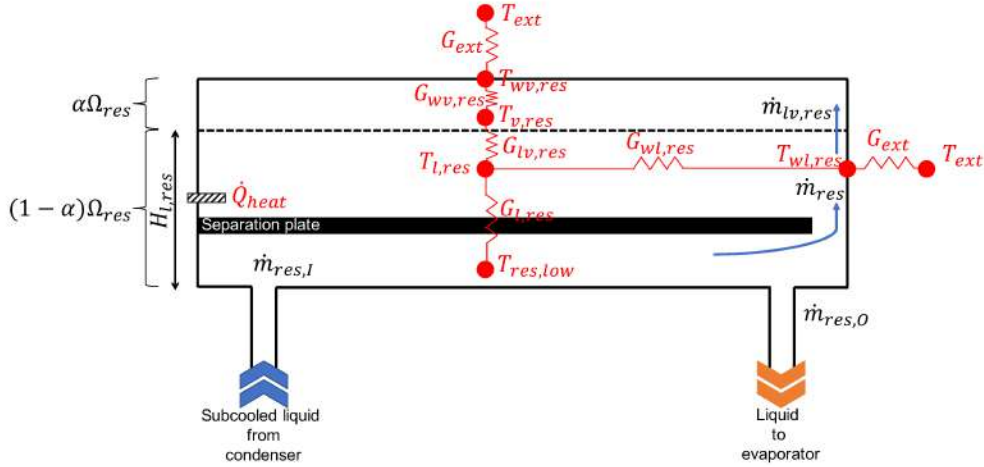


Figure 5.13: Reservoir higher part thermo-hydraulic model

The empiric thermal conductance $G_{l,res}$, coupling the liquid temperature in the higher and the lower part of the reservoir, $T_{l,res}$ and $T_{res,low}$, respectively, considers: the convective heat exchanges between the liquid in the low reservoir and the separation plate; the convective heat exchanges in the higher part of the reservoir, considering the stratification and the heating cartridge, and, finally, the conductive heat transfer through the separation plate and the reservoir walls [25]. The thermal conductance $G_{lv,res}$, considers the conductive heat exchanges within the liquid and the stratification system. The empiric thermal conductances between the wall and the liquid phase and between the wall and the vapour phase, $G_{wl,res}$ and $G_{wv,res}$, respectively, are assumed constant and dependent on the saturation temperature [25].

Considering the model reported in Fig. 5.13, the saturated vapour temperature in the reservoir higher part can be calculated as:

$$\begin{aligned} \rho_{v,res} c_{p_{v,res}} \alpha \Omega_{res} \frac{dT_{v,res}}{dt} = \\ G_{lv,res} (T_{l,res} - T_{v,res}) + G_{wv,res} (T_{wv,res} - T_{v,res}) \end{aligned}$$

$$+ \Omega_{res} \frac{d(P_{v,res} \alpha)}{dt} - \dot{m}_{lv,res} h_{lv} \quad (5.22)$$

The evaporation heat flow rate term, $\dot{m}_{lv,res} h_{lv}$, is considered if and only if $\dot{m}_{lv,res} \geq 0$. $\dot{m}_{lv,res}$ is defined as the sum between the mass flow rate flowing within the orifice, \dot{m}_{res} , and the time dependent variation of the vapour volume fraction:

$$\dot{m}_{lv,res} = \dot{m}_{res} + \rho_{l,res} \Omega_{res} \frac{d\alpha}{dt}$$

The liquid temperature in the higher part of the reservoir, $T_{l,res}$, like $T_{v,res}$, is calculated considering the compression work, $\dot{W}_{comp,l}$ and the heating power \dot{Q}_{ext} as well as the thermal network:

$$\begin{aligned} \rho_{l,res} c_{p_{l,res}} (1 - \alpha) \Omega_{res} \frac{dT_{l,res}}{dt} = \\ G_{l,res} (T_{res,low} - T_{l,res}) + G_{lv,res} (T_{v,res} - T_{l,res}) + G_{wl,res} (T_{wl,res} - T_{w,res}) \\ + \dot{Q}_{heat} + \dot{W}_{comp,l} + \dot{m}_{res}^* c_{p_{l,res}} (T_{res,low} - T_{l,res}) - \dot{m}_{lv,res} h_{lv} \end{aligned} \quad (5.23)$$

Where, in eq. (5.23), the term $\dot{m}_{res}^* = \dot{m}_{res}$ if $\dot{m}_{res} \geq 0$, and $\dot{m}_{res}^* = 0$ else. So, the evaporation heat flow rate term, $\dot{m}_{lv,res} h_{lv}$, in eq. (5.23) is only considered when $\dot{m}_{lv,res} < 0$. The energy balance due to the mass flow rate flowing within the orifice from the lower to the higher part of the reservoir is considered for positive or null values of \dot{m}_{res} .

To have a better modelling related to the momentum balance, the pressure in the higher part has to be considered by taking into account the pressure of the liquid and the pressure of the vapour at the interface, $P_{l,res}$ and $P_{v,res}$, respectively. So, following the hypothesis of saturated vapour⁴, it is:

$$P_{v,res} = P_{sat}(T_{v,res})$$

The momentum balance in the higher liquid part is defined as a function of the variation of the height of the liquid/vapour interface, $H_{l,res}$, related to the mass flow rate flowing within the orifice, \dot{m}_{res} :

$$\frac{d(\dot{m}_{res} H_{l,res})}{dt} + \frac{\dot{m}_{res,O}^2}{\rho_{l,res} S_{RE}} - \frac{\dot{m}_{res,I}^2}{\rho_{l,res} S_L} +$$

⁴In ref. [71], it has been observed that the time constant of evaporation/condensation in the higher part of the reservoir is negligible if compared to those of eq. (5.20), (5.22) and (5.23). So, the return to saturated equilibrium is considered instantaneous in the vapour volume of the reservoir.

$$\left(\frac{\dot{m}_{lv,res}}{\rho_{l,res} S_{lv,res}} + \frac{dH_{l,res}}{dt} \right) \dot{m}_{lv,res} + |\Delta P_{vis,res}| S_{eq,res} + \rho_{l,res} g H_{l,res} S_{eq,res} + (P_{l,res} - P_{res,low}) = 0 \quad (5.24)$$

The momentum balance equation in correspondence of the liquid/vapour interface is:

$$P_{l,res} - P_{v,res} = \frac{\dot{m}_{lv,res}^2}{S_{lv,res}^2} \left(\rho_{v,res}^{-1} - \rho_{l,res}^{-1} \right) \quad (5.25)$$

5.4.1.3 Evaporator

Due to complex thermo-hydraulic phenomena occurring there, a “microscopic” approach to model the evaporator behaviour, at pore level of the porous wick, leads to high computation time. Moreover, pretty high difficulties are related to the coupling of such model to the rest of the loop. To solve the problem, Delalandre [26], before, and Blet [71], after, decided to use some empiric parameters for its modelling.

The thermal load, \dot{Q}_{evap} , applied to the evaporator is used to heat the casing and the porous wick, to warm the liquid arriving from the reservoir (until saturation condition in correspondence of the liquid/vapour interface —sensible heat exchange—), for liquid-vapour phase change (latent heat exchange) and for vapour superheating. Introducing the empiric thermal conductance, G_V , and the conductances G_{ch} and G_{chlat} , relying the temperature of the casing, T_C , respectively with the saturation temperature in the porous wick T_V , the fluid temperature in the grooves T_{ch} (Fig. 5.4b) and the fluid temperature in the lateral grooves T_{chlat} (vapour channels), in steady-state conditions eq. (5.26) has to be verified.

$$\dot{Q}_{evap} - \dot{Q}_{loss} = \dot{Q}(G_V) + \dot{Q}(G_{ch}) + \dot{Q}(G_{chlat}) \quad (5.26)$$

Four control volumes are considered for evaporator modelling (see Fig. 5.14). In particular, the volumes are related to the (three) liquid arteries, Ω_{art} , to the whole porous wick, Ω_{por} , to the grooves, Ω_{ch} and to the lateral vapour channels, Ω_{chlat} (see also Fig. 5.4).

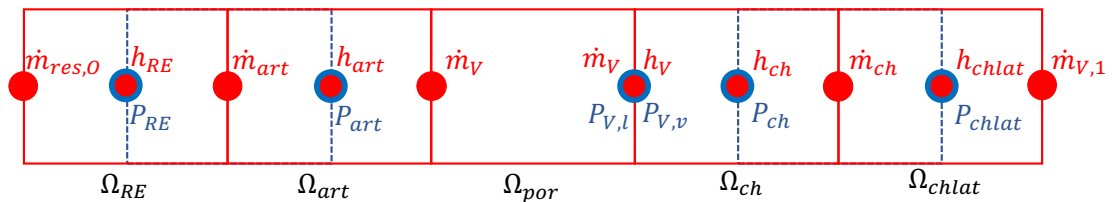


Figure 5.14: Evaporator discretisation

Due to the hypothesis of fully developed 1-D fluid flow in the direction of the thickness of the wick, and complete filling of the latter, the mass flow rate entering and exiting the porous wick is always equal to the evaporating mass flow rate \dot{m}_V . Moreover, the enthalpy is always dependent on the saturation pressure: $h_V = h_{v,sat}(P_{ch})$.

The mass conservation equation, due to the strong hypothesis of complete filling of the wick, assumes the same form of eq. (5.7). The mass flow rate \dot{m}_V is so imposed following the energy balance on the node related to the wick (*por*):

$$\dot{m}_V = \frac{\dot{Q}(G_V)}{\left(h_{lv} \Big|_{T_V} + c_{p,l}(T_V - T_{art}) \right)} \quad (5.27)$$

The equation related to the momentum balance assumes the same form of eq. (5.13). In correspondence of the volume related to the wick where the liquid is pumped, following the hypothesis of fully developed flow as well as the hypothesis whereby the liquid/vapour interface is considered to be always positioned on the surface of the wick, the pressure difference is given by the Darcy law:

$$P_{art} - P_{V,l} = \frac{\mu_l e_{por}}{\kappa \rho_l S_{por}} \dot{m}_V \quad (5.28)$$

where κ is the permeability of the porous wick and provided by the evaporator manufacturer [50].

The energy balance equation related to the fluid is similar to eq. (5.10) and (5.11), while for the solid part it is:

$$\begin{aligned} \rho_C \Omega_C c_{p,C} \frac{dT_C}{dt} = & \\ & \dot{Q}_{eva} - \dot{Q}_{loss} + G_V(T_V - T_C) + G_{ch}(T_{ch} - T_C) \\ & + G_{chlat}(T_{chlat} - T_C) \end{aligned} \quad (5.29)$$

where the thermal conductances G_{ch} and G_{chlat} are calculated as a function of the heat transfer coefficients h_{ch} and h_{chlat} , and in turn calculated using standard correlation for a uniformly heated flat plate.

5.4.2 Thermal/electrical analogy

Mass, momentum and energy equations are solved using the electric analogy. The model has been adapted to agree with the formalism used by ESACAP^(TM) [25] that allows a robust resolution of strongly coupled differential equation systems by using the

thermal/electrical analogy. On its basis, temperature and pressure difference in thermal and hydraulic domains can be compared with the voltage difference of an electrical system, while thermal heat flux and mass flow rate can be compared with current variable.

According to the nodal method, each elemental control volume Ω_i , is supposed isothermal and characterised, in the centre, by a thermal capacity $C_i = \rho_i c_{p,i} \Omega_i$. If the thermal conductance $G_{i,j}$ between two adjacent nodes, i and j , is considered, the thermal heat flux exchanged can be generally written, if the thermal heat flux is directed from the node j to the node i , in the form:

$$\dot{Q}_{i,j} = G_{i,j}(T_j - T_i) \quad (5.30)$$

Vice-versa, $\dot{Q}_{i,j} = G_{i,j}(T_i - T_j)$ if the heat flux is lost by the node i towards the node j . The energy balance equation, considering conductive, convective and radiative heat transfer as well as the k -th heat source heat generation, \dot{q}_k , in the node i , can be so written as:

$$C_i \frac{dT_i}{dt} = \sum_j \dot{Q}_{i,j}^{cond} + \sum_j \dot{Q}_{i,j}^{conv} + \sum_j \dot{Q}_{i,j}^{rad} + \sum_k \dot{q}_k \quad (5.31)$$

When a fluid flow occurs in the system, as well as $\dot{Q}_{i,j}^{cond}$, $\dot{Q}_{i,j}^{conv}$, $\dot{Q}_{i,j}^{rad}$, it is necessary to add to the right term of eq. (5.31) the heat flux related to mass exchange between the node $i - 1$ and the node i . So that, according to the enthalpy formulation used in this model, the heat transported by the fluid is defined as:

$$\dot{Q}_{i-1,i} = \dot{m}_i (h_{i-1} - h_i) \quad (5.32)$$

and eq. (5.31) assumes the form:

$$\rho_i \Omega_i \frac{dh_i}{dt} = \dot{m}_i (h_{i-1} - h_i) + \dot{Q}_{i,j}^{rec} \quad (5.33)$$

where $\dot{Q}_{i,j}^{rec}$ is the “cumulated” thermal flux received by the volume Ω_i due to internal heat generation, \dot{q}_k , and conduction, convection and radiation heat transfer ($\dot{Q}_{i,j}^{cond}$, $\dot{Q}_{i,j}^{conv}$, $\dot{Q}_{i,j}^{rad}$). The particular property of reciprocity related to the heat flux direction in eq. (5.30) is no more valid in eq. (5.32). According to fluid direction, the heat may only be transferred in one direction: from the node $i - 1$ to the node i . The fluidic conductance GF_i , related to the mass flow rate \dot{m}_i , is thus strictly dependent on the flow direction, and for mono-directional flows it is $GF_i = \dot{m}_i$.

The formulation related to eq. (5.33) needs to be modified to consider any change in

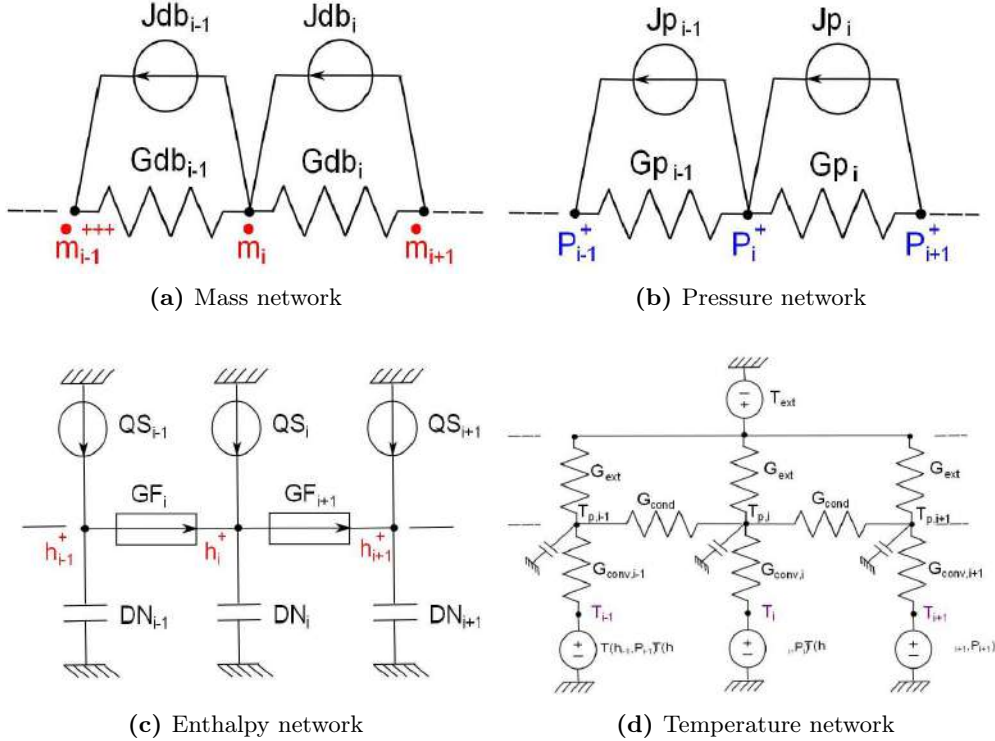


Figure 5.15: Thermal/hydraulic-electrical analogy networks [16]

the mass flow direction. In such case, in fact, $GF_i^{\leftrightarrow} = (\dot{m}_i; \dot{m}_{i+1})$ and eq. (5.33) becomes:

$$\dot{Q}(GF_i^{\leftrightarrow}) = \dot{m}_i^* (h_{i-1} - h_i) + \dot{m}_{i+1}^* (h_i - h_{i+1}) \quad (5.34)$$

Where, $\dot{m}_i^* = \dot{m}_i$ if $\dot{m}_i \geq 0$ and $\dot{m}_{i+1}^* = \dot{m}_{i+1}$ if $\dot{m}_{i+1} < 0$, otherwise they are null: the first term on the right side of eq. (5.34) is related to a positive MFR (from node $i - 1$ to i) and the second term is related to a negative mass flow rate (from node $i + 1$ to i).

Examples of networks used in Blet's model are reported in Fig. 5.15. There, the mass network (fig. 5.15a), related to the continuity equation solution; the pressure network (see fig. 5.15b), related to momentum equation; the mass enthalpy network (see fig. 5.15c), related to the energy balance equation, are shown. Finally, the temperature network (fig. 5.15d) used to relate the fluid model to external (thermal) conditions such as tube wall temperature, ambient temperature, heat power and cold source temperature.

5.5 Conclusion

In this chapter, the main characteristics of the CPLIP were described focusing the attention on the physical phenomena governing its operations. CPLIP working principle was explained on the base of the thermodynamic transformation shown on (P, T) diagram and an explanation of the governing physics of each component of the loop has been given to understand its potentials and limitations. After a brief history about the Capillary Pumped Loop for Integrated Power, the experimental facility, used in the context of this work, has been introduced to explain its mechanical, hydraulic and thermal characteristics. A deep description of the measure sensors equipping the experimental loop has been also done to give an idea of the accuracy of measurements that will be presented during the entire description and analysis of this work. It has to be underlined that to increase the quantity of the measurement, more sensors would be required, but such experimental facility is also used for educational purposes. Any kind of modification to the CPLIP 1.1 could not be actually considered. Moreover, although the loop is used by students, after several years, it keeps its characteristics and potentialities. This is, as it will be observed later, one of the main characteristics of these systems: high reliability and robustness. Finally, the numerical model used in this work was described. Obviously, in the model, not all physical phenomena, such as mass and energy exchanges in the evaporator, are considered because of their complexity. It is, after all, a model that describes the loop behaviour using a “system approach”, and it is used to have a quantitative evaluation of the thermal and hydraulic magnitude. Initially, this model was developed to study the behaviour of a three parallel evaporators CPLIP and a validation has been done in this particular configuration. A good agreement between the numerical and the experimental results was observed in this particular case [25]. However, after an adaptation of the described model to the experimental facility here introduced, numerical and experimental results will be compared to show the agreement with new experimental results presented in this study, by adapting the conductances G_V , G_{res} and vapour, condenser, and liquid line geometry, as well as the reservoir one to the experimental facility used in the course of this study.

In the following, the CPLIP behaviour, either in steady and in transient conditions will be numerically and experimentally analysed. In particular, in the next chapter, it will be shown how this kind of cooling system is able to ensure the temperature requirements for power electronics modules. The evaporator thermal conductance will be experimentally obtained and coupled with a finite volume model to obtain the temperature field on electronics components.

CPLIP answer to HASTECS requirements: thermal characterisation

The analysis reported in this chapter is related to steady-state behaviour of the CPLIP. It will be experimentally analysed to understand how the different parameters, such as reservoir and cold source temperature, applied thermal load and vapour line pressure drop, influence the stationary behaviour of the loop. The results related to the use of two different working fluids, ethanol and methanol, are also presented.

A theoretical post-processing tool is used with the purpose to study the influence of the thermal load and the impact of the cold source temperature variation on the thermal conductance. Thermodynamic cycles are built on the base of the real evaporation temperature in the porous wick.

Starting from experimentally obtained thermal conductance curves of evaporator base plate, numerical 3D results of a finite volume model will be introduced to obtain the 3D temperature map and the effective temperature distribution of a real power electronics module.

Finally, the loop transient behaviour will be experimentally studied during an entire mission profile to show how this technology is also able to ensure temperature requirements and to successfully cool the power electronics modules.

6.1 CPLIP experimental steady-state test campaigns

6.1.1 Operating conditions

Using methanol as working fluid, comparing the results obtained by Ayel *et al.* [7, 14] for ethanol and in presence of non condensable gases (NCG) in the case of methanol, a detailed overview of the loop behaviour in different cases is presented. On the basis of the triplet: reservoir temperature, T_{res} ; cold source temperature, T_{sec} and applied thermal power to the evaporator, Q_{th} , a parametric study is introduced by changing the just cited parameters. Furthermore, in order to analyse how thermal response of the loop,

and in particular the evaporator behaviour, is impacted by vapour line pressure losses, the latter will be increased until loop failure, by gradually closing the valve from open to closed condition. Results will be analysed, even in this case, by using an appropriate post-processing tool by which the thermodynamic cycles are constructed.

A synthesis of the tests performed during the two different campaigns is reported in table 6.1.

	T_{res} [°C]	T_{sec} [°C]	\dot{Q} [kW]	N/N_{max}
Influence of thermal load	50	20	0.5 to 5	1
	60	20	0.5 to 5	1
	70	20	0.5 to 5	1
	80	20	0.5 to 5	1
	70	5	0.5 to 5	1
	70	40	0.5 to 5	1
Influence of pressure drop	60	20	1 to 2	1 to 0.25
	70	20	1 to 2	1 to 0.25
	80	20	1 to 2	1 to 0.25

Table 6.1: Summary of experimental tests [12]

During the first test campaign (to study the influence of thermal load), the reservoir temperature, T_{res} , was changed from 50 to 80 °C at constant cold source temperature, $T_{sec} = 20$ °C. For each value of T_{res} , the thermal power has been changed from the minimum to the maximum admissible value (from 0.5 to 5 kW stepping by 0.5 kW). Also, for a reservoir temperature, T_{res} , of 70 °C, two more different cold source temperatures were exploited, 5 and 40 °C, to observe their impact on the thermodynamic cycle.

During the second test campaign (to study the influence of vapour line pressure drop), three different reservoir temperatures were exploited: 60, 70 and 80 °C, at constant cold source temperature ($T_{sec} = 20$ °C) and, for each of them, the number of valve turns was changed from the maximal value ($N/N_{max} = 1$, corresponding to fully opened valve condition —no pressure drop—) to the minimal one ($N/N_{max} = 0.25$, corresponding to the maximum pressure drop possible avoiding the complete occlusion of the line¹). A thermal power applied to the evaporator from 1 to 2 kW was exploited at constant reservoir temperature and for each vapour line pressure drop group.

Non condensable gases (NCG) For each test, the absence of NCG was verified by comparing the actual saturation conditions in the reservoir with the theoretical ones on

¹The value $N/N_{max} = 0$ corresponds to the total closure of the valve.

the saturation curve. The Clausius-Clapeyron relation was used to compare theoretical and experimental points (see Fig. 6.1).

In Fig. 6.1, an example of verification of absence of NCG is reported. The error bars on the tested points indicate a maximal error of $\pm 0.6\%$ due to the accuracy of the platinum sensor. In particular, other than a base accuracy of $\pm 0.1\%$, an accuracy loss of $\pm 0.05\%/\text{year}$ is considered.

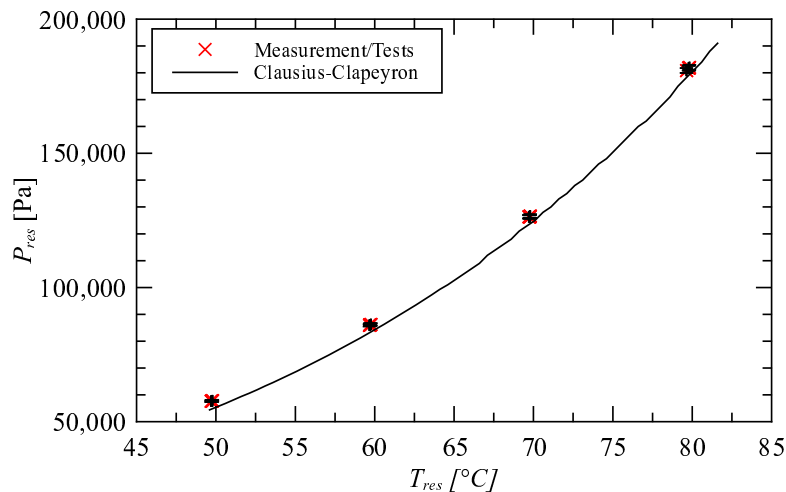


Figure 6.1: Example of NCG absence verification (methanol)

6.1.2 CPLIP thermal response to different heat power levels

In Fig. 6.2, a typical test with methanol as working fluid is reported. The analysis here introduced is based on the assumption of steady-state operating condition for each heat power step² (+0.5 kW).

From the diagram reported in Fig. 6.2, one can trivially notice that, for any heat power load step, the reservoir saturation temperature, T_{res} (black line), remains almost constant as a function of time. A slight temperature lowering occurs during the start-up stage, due to the inlet of cold liquid mass coming from the condenser through the liquid line³.

Red, grey and green lines on the diagram are related to temperature measurement in different positions of the evaporator wall ($T_{\text{diff},\text{max}}$ and $T_{\text{diff},\text{min}}$, in Fig. 6.2), where a

²For each heat power load variation to the evaporator, the complete stabilisation of the loop was attained before the successive heat power step.

³The behaviour of the Capillary Pumped Loop for Integrated Power during the start-up stage is widely discussed in chapter 8.

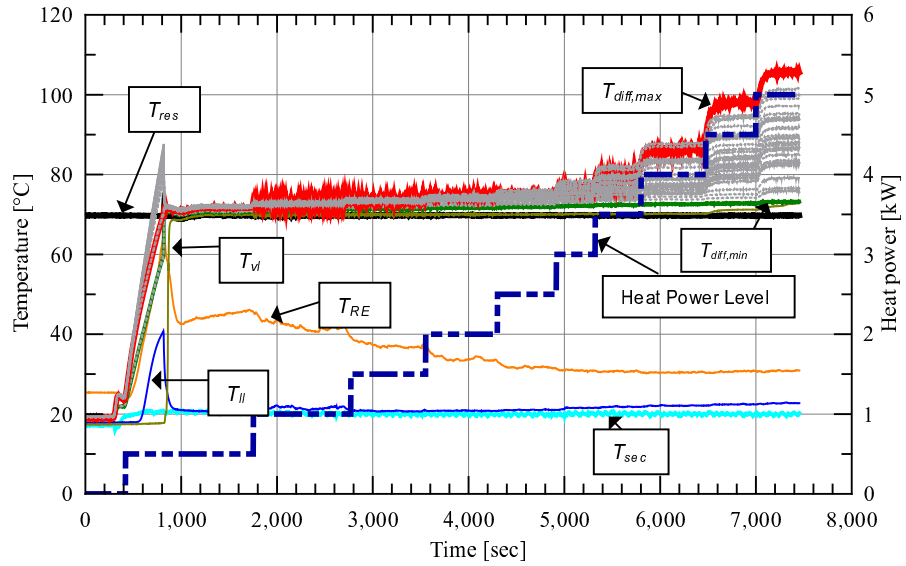


Figure 6.2: CPLIP temperature evolution as a function of the time, for different heat power applied to the evaporator (methanol, $T_{res} = 70^\circ\text{C}$ and $T_{sec} = 20^\circ\text{C}$) [12].

temperature gradient is evident. Temperature distribution decreases progressively from higher temperatures at the top to lower temperatures at the bottom. Accorinti *et al.* [111] associated such temperature gradient to gravity pressure drop that leads to a progressive recession of the evaporation front in the porous wick as soon as the thermal load is increased. That's why $T_{diff,max}$ to $T_{diff,min}$ temperature difference increases with thermal load. For thermal loads over than 2.5 kW, the slight temperature increase of the liquid line, T_{ll} , could be due to a pretty slight condenser undersizing.

6.2 Post-processing tool and CPLIP real thermodynamic cycle

In order to obtain the thermal conductance value, based on the evaporator-wall to saturation temperature difference, $G_{ev,V}$, the post-processing tool, described in ref. [14], was used to estimate the real values of evaporation temperature in the porous wick, T_V , by reconstructing the thermodynamic diagram of the CPLIP for a given working point. The tool is based on the reconstruction of a quite simplified version of CPLIP thermodynamic cycle (like that reported in Fig. 6.3) using experimental temperature values as entry. The missing parameters are calculated using the relationship between pressure and temperature on the saturation curve. In steady-state condition, on the basis of the

qualitative thermodynamic cycle reported in Fig. 5.2, the pressure difference between P_V and P_{E_0} represents the capillary pressure head. The latter should be equal to the cumulated viscous pressure losses in the vapour line ΔP_v ⁴, in the liquid line ΔP_l and those due to gravity ΔP_g :

$$P_V - P_{E_0} = \sum \Delta P_v + \sum \Delta P_l + \sum \Delta P_g \quad (6.1)$$

From the knowledge of: experimental values of temperature and pressure in the reservoir (respectively T_{res} and P_{res}), vapour and liquid line inlet and outlet temperatures (T_{vi} , T_{vo} and T_{li} , T_{lo} respectively) and reservoir-evaporator tube temperature T_{RE} , according to Ayel *et al.* [14], the missing parameters can be identified by using the following assumptions:

- The vapour pressure losses in the porous wick may be neglected, because of the equivalent length to the exit (as also shown by Mottet *et al.* [113]);
- Single phase distributed and local pressure drops are calculated using standard correlations;
- In the condenser, two-phase pressure drops were estimated by only considering vapour phase on the condensation length;
- The condenser internal side HTC is calculated on the base of the Chato's correlation (see eq. (B.14) to (B.16));
- The liquid height in the reservoir is considered constant. As also shown in [14], variations of liquid/vapour interface corresponding to thermal power variation are pretty small.

For a given thermal load applied to the evaporator, the mass flow rate flowing within the loop can be computed as:

$$\dot{m} = \frac{Q_{el} - Q_{loss}}{h_{l,v} + c_{p,l}(T_V - T_{RE})} \quad (6.2)$$

where the evaporator to ambient thermal losses term, Q_{loss} , is evaluated by using an empty test as described by Ayel *et al.* [14], and the evaporation temperature in the evaporator (T_V) is iteratively calculated until convergence: mass, pressure and temperature balances on the saturation curve.

⁴Condenser pressure drops are supposed to be only related to vapour flow until condensation length and included into vapour line pressure drops.

Thermodynamic cycles and main thermal characteristics In Fig. 6.3, thermodynamic cycles are reported for two different CPLIP operating conditions and using methanol as working fluid, with constant reservoir and cold source temperatures, $T_{res} = 70^\circ\text{C}$ and $T_{sec} = 20^\circ\text{C}$ respectively, at 0.5 and 5 kW.

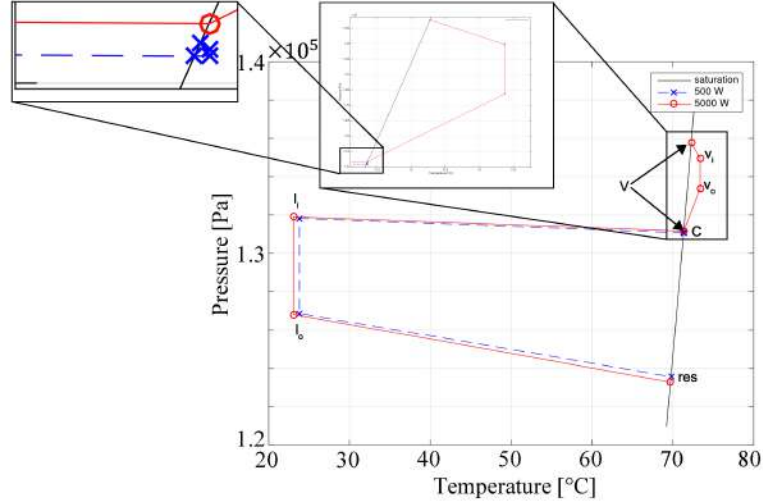


Figure 6.3: CPLIP thermodynamic cycle: comparison at $Q = 0.5 \text{ kW}$ and $Q = 5 \text{ kW}$ (methanol, $T_{res} = 70^\circ\text{C}$ and $T_{sec} = 20^\circ\text{C}$) [12].

At 0.5 kW, pressure variations in the evaporator grooves, in the vapour line and the condensation front are pretty small when compared to those at 5 kW. In fact, for the lowest thermal load, the pressure variation between the evaporation point (V in the diagram) and the vapour line outlet, v_o , are one order of magnitude lower than those related to the highest thermal power test. At 5 kW, the pressure difference from the evaporator to the condensation front (points V and C on the diagram) is almost the same than gravity pressure losses in the liquid line ($P_{l_i} - P_{l_o}$): the latter is mainly due to a height difference, $H_l = 0.7 \text{ m}$, affecting the gravity term ($\Delta P_{g,ll} = \rho_l g H_l$).

As soon as reservoir temperature changes, and consequently saturation pressure in the reservoir changes as well, for a fixed thermal power applied to the evaporator, a translation of the thermodynamic cycle on the saturation curve occurs, as shown in Fig. 6.4. Here, the divergence of thermodynamic cycles for the exploited three different reservoir temperatures ($T_{res} = 50, 60, 70^\circ\text{C}$), at constant thermal power and cold source temperature, is shown. For any variation of T_{res} , a translation of operating points occurs while the overall pressure difference remains almost the same for all the three analysed cases.

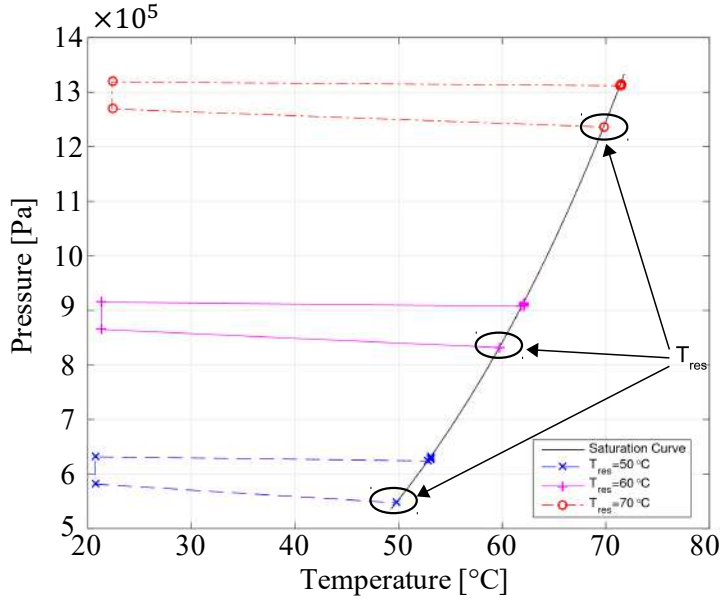


Figure 6.4: CPLIP thermodynamic cycle: comparison at $T_{res} = 50$; 60 and 70 °C (methanol, $Q = 1.5 \text{ kW}$ and $T_{sec} = 20^\circ\text{C}$) [12].

One of the key characteristics of this kind of cooling system is evident when the diagram reported in Fig. 6.4 is observed: at constant heat power supplied to the evaporator, its temperature can be controlled by choosing the operating point, fixed as saturation condition in the reservoir. The slight cold source temperature divergence between the three analysed cases, may be attributed to the slight, previously cited, undersizing of condenser (not sufficient subcooling). Even if too small to be appreciated, the difference between the saturation pressure in the evaporator and the condenser inlet is similar for the three analysed cases.

Worth of attention is the response of the loop related to a variation of the cold source temperature. In fact, the latter is relevant when a temperature change occurs during the different stages of the aircraft mission. When the cold source temperature variation, T_{sec} , is observed at constant thermal load and reservoir temperature, T_{res} , no significative changes in evaporation one, T_V , are noticeable, as it can be easily observed from the diagram reported in Fig. 6.5. Here, three different cold source temperatures are compared at constant thermal load ($Q = 1.5 \text{ kW}$) and reservoir temperature, $T_{res} = 70^\circ\text{C}$. Except quite small variations, no significative alterations of evaporator saturation temperature are evident. Such variations could be due to pretty small changes of liquid line pressure losses consequent to a change of liquid thermophysical properties (ρ_l , μ_l) with temperature. The nearly independence between evaporator and cold source temperature is due

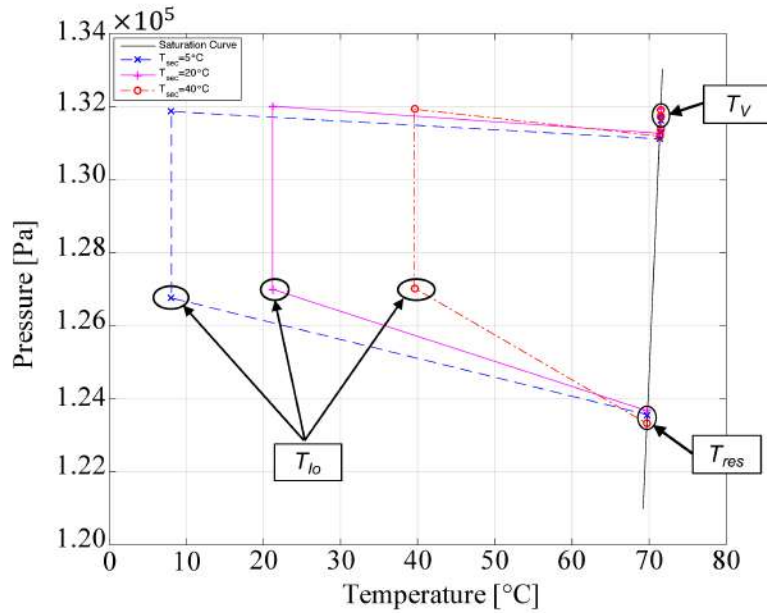


Figure 6.5: CPLIP thermodynamic cycle: comparison at $T_{sec} = 5$; 20 and 40 °C (methanol, $Q = 1.5 \text{ kW}$ and $T_{res} = 70 \text{ }^{\circ}\text{C}$).

to a re-adaptation of the condensation length related to the cold source temperature variation. The change in sensible heat (heating of liquid from T_{lo} to T_V) is damped by heat exchanges in the lower part of the reservoir and in the evaporator. Such difference is not apparent at the scale of the position of T_V on the thermodynamic diagram. The independence between the cold source and the saturation temperature in the evaporator makes this kind of technology particularly suitable for all applications where the secondary side temperature changes continuously. Obviously, as underlined by Accorinti *et al.* [12], this is an intrinsic characteristics of two-phase heat exchange, where saturation conditions are imposed.

6.3 CPLIP thermal characterisation for HASTECS specifications

6.3.1 Steady-state experimental results and thermal conductance analysis

Based on the reservoir to evaporator-wall temperature difference, $(\bar{T}_{diff} - T_{res})$, the “rough” evaporator conductance, $G_{ev,res}$, can be obtained from experimental data. Due to the impossibility to directly measure the saturation temperature in the porous wick, T_V , and so to calculate the real thermal conductance, from a purely engineering standpoint

it may be assumed that the reservoir temperature is not so far from the evaporator saturation one. This is the most practical and easy method to obtain the evaporator thermal conductance and to use it for applicative purposes. The latter, measured in $[W \cdot K^{-1}]$ can be so calculated as:

$$G_{ev,res} = \frac{Q_{th} - Q_{loss}}{\bar{T}_{diff} - T_{res}} \quad (6.3)$$

Other than the already known symbols, in eq. (6.3), \bar{T}_{diff} is the mean evaporator wall temperature, calculated as the average value of the thirty-two temperature sensors installed on the evaporator wall ($\bar{T}_{diff} = \frac{1}{32} \sum_{i=1}^{32} T_{diff,i}$, see sec. 5.2.1).

By applying eq. (6.3), it is possible to obtain the evolution of evaporator thermal conductance, $G_{ev,res}$, as a function of the thermal load and for different reservoir temperatures and working fluids, as reported in Fig. 6.6. Here, thermal conductance values related to ethanol [14] and methanol [12] are reported, and for the latter the case of presence of NCG [15] is considered as well.

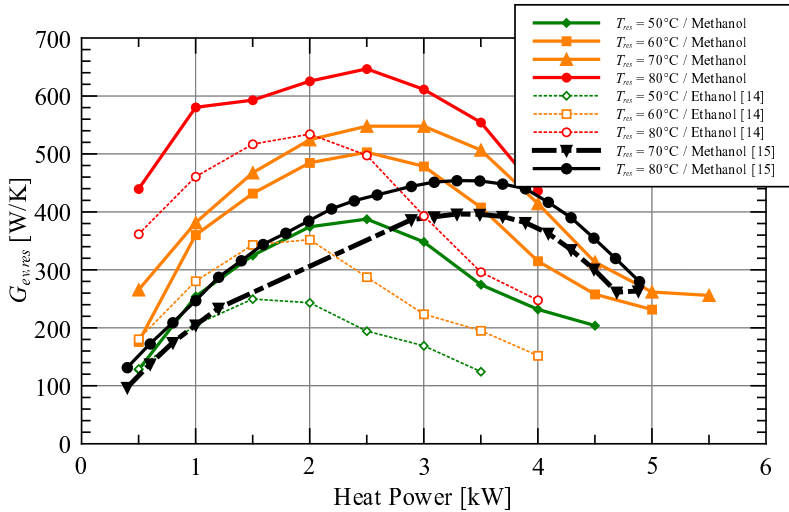


Figure 6.6: Evaporator thermal conductance, $G_{ev,res}$, based on the reservoir saturation temperature as a function of the thermal load (ethanol and methanol, $T_{res} = 50; 60; 70$ and 80°C , $T_{sec} = 20^{\circ}\text{C}$).

Observing Fig. 6.6, the classical bell-shape can be identified for all curves, independently from the reservoir temperature, working fluid and even in presence of NCG. At constant T_{res} and thermal power, methanol is characterised by higher conductance values than ethanol. Obviously, this difference impacts the evaporator HTC that is related to the thermal conductance through the heat transfer surface area of thermal diffusers.

Evaporator performance are strongly impacted by the presence of NCG, as one can notice considering the curves related to methanol (black curves), also reported by Ayel *et al.* [14]. Their presence in the reservoir, in fact, tends to lower the evaporator thermal conductance and entails a shift of the maximum point of thermal conductance curve to higher power values. At constant thermal load, Q_{th} , the increase of reservoir saturation temperature consequent to higher saturation pressure, related to the presence of NCG, makes the difference $T_{diff} - T_{res}$ rise, leading to lower $G_{ev,res}$ values. Thermal conductance and mean wall temperature strongly depend on the saturation temperature imposed in the reservoir. This is due to the link between T_{res} and T_V on the saturation curve, coupled by the overall pressure drops between the same points, and the vapour mass transfer through the dried part of the porous wick [12].

To calculate the evaporator thermal conductance, but based on the real evaporator saturation temperature, T_V , it is necessary to consider: the thermal load applied to the evaporator, Q_{th} , the losses to the ambient, Q_{loss} , as well as the sensible heat rate, Q_{sns} . In this case, the thermal conductance is calculated as:

$$G_{ev,V} = \frac{Q_{th} - Q_{loss} - Q_{sns}}{\bar{T}_{diff} - T_V} \quad (6.4)$$

and the sensible heat is defined by the difference between the saturation temperature in the evaporator, T_V , and the liquid in the reservoir-evaporator tube, T_{RE} :

$$Q_{sns} = \dot{m} c_{p,l} (T_V - T_{RE}) \quad (6.5)$$

To observe the differences between reservoir-temperature-based and evaporator temperature based thermal conductances, $G_{ev,res}$ and $G_{ev,V}$ respectively, the divergence between T_V and T_{res} must be weighed-up in addition to thermal losses and sensible heat considered in eq. (6.4). In Fig. 6.7, reservoir and evaporator saturation temperatures divergence are reported as a function of thermal load.

T_V remains higher than T_{res} and almost constant for any Q_{th} lower than 3.5 kW. Then, it starts to slightly deviate. In fact, as mentioned above, for an increasing thermal power, the reservoir temperature does not obviously change, while a slight increase in the evaporator saturation temperature, T_V , is noticeable. Despite significative variation of viscous pressure drop corresponding to an increase of power load (see Fig. 6.3), the corresponding temperature change is pretty small. This is due to the link between temperature and pressure on the saturation curve: to a high pressure variation corresponds a small temperature change. This explains why T_V to T_{res} temperature difference is in the order of 1 K at 0.5 kW and about 2.3 K at 5 kW despite the corresponding pressure

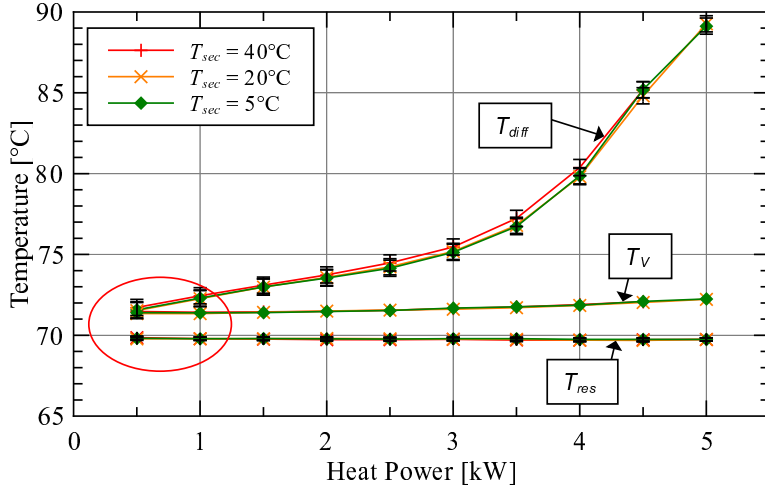


Figure 6.7: Mean diffuser wall temperature, \bar{T}_{diff} ; evaporator saturation temperature, T_V , as a function of the thermal load (methanol, $T_{sec} = 5$; 20; and 40°C , $T_{res} = 70^\circ\text{C}$) [12].

difference is one order of magnitude higher (or more) for the same power ranges.

The error bars showed in Fig. 6.7 and related to evaporator wall diffuser temperature. They are based on an accuracy of $\pm 0.5\%$ of the measured temperature values. Observing the mean evaporator wall temperature related to the lowest heat power (red circle), the wall to saturation temperature difference in the evaporator is in the same order than the accuracy value. For such low thermal loads, great differences are noticeable in $G_{ev,V}$ calculation, which value is only reliable when upper-bounds of error bars are considered. In fact, if \bar{T}_{diff} tends to T_V , the evaporation-temperature based thermal conductance, $G_{ev,V}$, tends to infinite and the calculation is no more reliable! This is the main reason why, in Fig. 6.8, the $G_{ev,V}$ values are blackened for such low thermal loads. Observing thermal conductance curves (Fig. 6.8), either the ones based on T_{res} and those based on T_V , neglecting the lowest thermal load for which temperature measurements are not reliable, either curve groups have the same trend. When the difference $(\bar{T}_{diff} - T_V)$ is high enough to make the temperature difference $(T_V - T_{res})$ no more significative, the difference $(G_{ev,V} - G_{ev,res})$ tends to zero. Also, worth of attention is the independence between the thermal conductance and the cold source temperature, as already explained in section 6.2. In fact, either for $G_{ev,res}$ and $G_{ev,V}$ curves, no significative differences are noticeable as a function of the cold source temperature.

Dividing the thermal conductance values, G_{ev} , by the evaporator heat transfer surface area, S_{ev} , it is possible to determine the evaporator equivalent heat transfer coefficient ($HTC_{ev} = G_{ev}/S_{ev}$) — particularly useful in the case of modelling heat exchanges

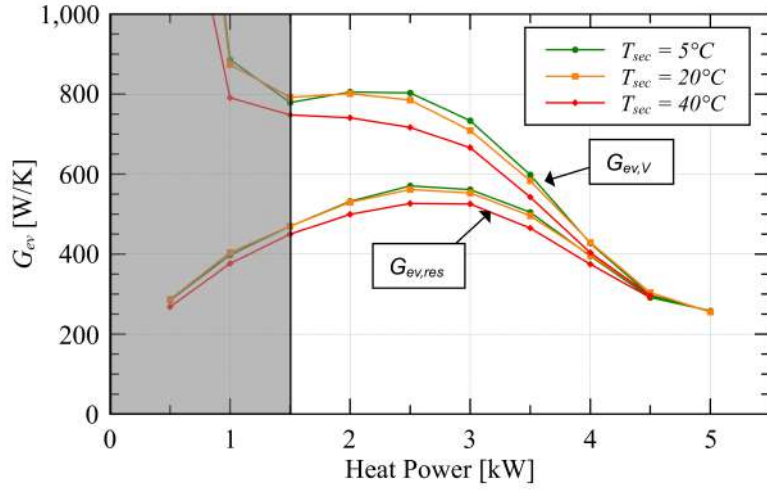


Figure 6.8: $G_{ev,res}$ and $G_{ev,V}$ comparison as a function of the thermal power (methanol, $T_{sec} = 5$; 20; and $40^\circ C$, $T_{res} = 70^\circ C$)

between the evaporator and the power electronics modules, for example —. If HTC_{ev} is plotted as a function of thermal heat flux density, as reported in Fig. 6.9, it is possible to observe, even in this case, the characteristic “bell-shape”, as also shown by Mottet *et al.* [113] at the scale of the porous medium. Error bars indicate an error based on the uncertainty due to thermocouples and electrical power supply used during the tests. Even in this case the lowest $HTC_{ev,V}$ values are blackened for the same reason explained above.

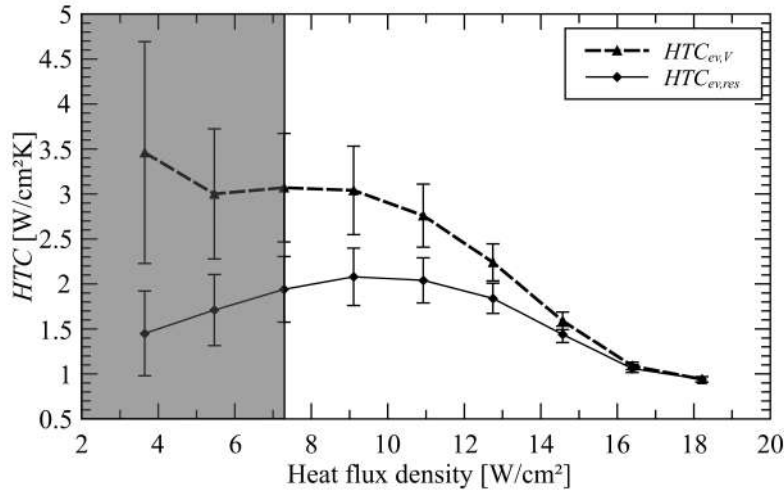


Figure 6.9: $HTC_{ev,V}$ and $HTC_{ev,res}$ comparison as a function of the thermal power (methanol, $T_{sec} = 20^\circ C$, $T_{res} = 70^\circ C$).

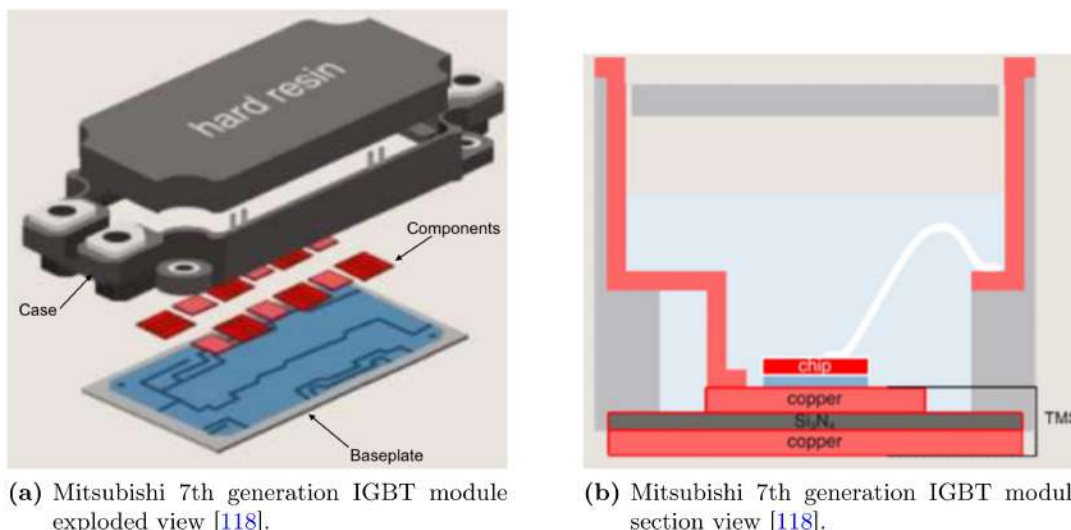
6.3.2 Evaporator-power module numerical analysis

As previously shown, it exists an independence between the cold source temperature (condenser operating conditions and its configuration) and the evaporator. It is thus possible to analyse the evaporator behaviour independently from the rest of the cooling system. In this section, the attention is focused on the evaporator and in particular on the temperature distribution on the junction of electronic components.

Using a commercial software (Star-CMM+), a finite volume analysis has been performed to obtain the temperature distribution on an exact numerical reproduction of power modules base. In particular, on the basis of experimentally obtained thermal conductance (see Fig. 6.6) as well as the evaporator geometry, dependent on the power modules dimensions, evaporator HTC has been calculated and used as boundary condition. Temperature map on the junction of electronic components was then obtained when they operate in the most critical electrical condition (highest electrical conversion power, lowest electrical efficiency).

6.3.2.1 Power electronics modules characteristics

Following the power electronics modules chosen by WP2 team [21], the *Mitsubishi 7th generation IGBT modules NC-type*, shown in exploded view in Fig. 6.10a, are considered. The proposed power module has baseplate dimensions of $6.2 \times 12.2 \text{ cm}^2$, and is characterised by only three layers between the chips and the baseplate (see Fig. 6.10b). This allows a reduction of the thermal resistance, declared to be 30% lower than previous



(a) Mitsubishi 7th generation IGBT module exploded view [118].

(b) Mitsubishi 7th generation IGBT module section view [118].

Figure 6.10: 7th Generation Mitsubishi module

generation one [118]. Only one layer of Si_3N_4 is inserted between the two copper layers, as it is possible to observe from Fig. 6.10b.

The thermal resistances and the different layer thicknesses, diodes and IGBTs distribution and their number, are reported in the data sheet in ref. [118, 119].

6.3.2.2 Evaporator configuration

In Fig. 6.11, a schematic of the evaporator and its adjoined electronics power modules is reported. The power modules, installed face to face, are mounted in block of two or three (depending on the electronic configuration) on each side of the evaporator, which dimensions are consequent to the power modules ones.

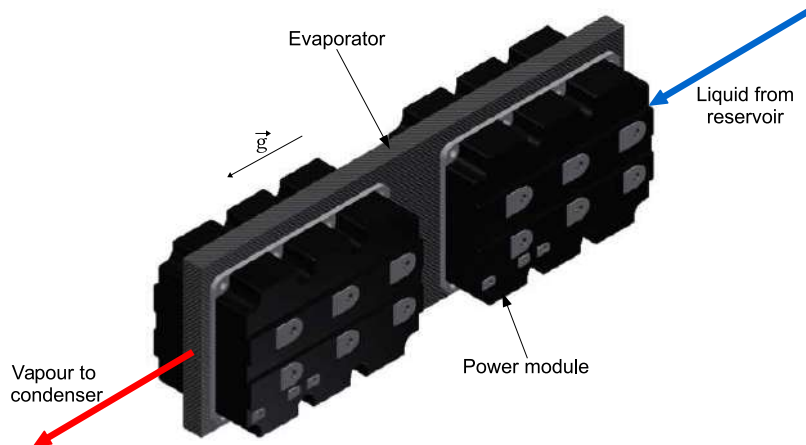


Figure 6.11: Evaporator configuration example [1].

The evaporator is vertically mounted, along \vec{g} direction, and the fluid coming from the reservoir (blue arrow) wets the porous wick contained in it. The nickel evaporator case has a thickness of 1 mm, and the total surface⁵ where power modules are mounted is $18.6 \times 12.2 \text{ cm}^2$. The total evaporator thickness is 1.8 cm. A nickel porous wick with a porosity of 73%, an average pore diameter of $6.3 \mu\text{m}$ and a thickness of 1.4 cm, is contained into the evaporator case, as in [12, 14]. The choice of the same evaporator characteristics is related to the fact that the experimentally obtained thermal conductance values, $G_{ev,res}$, already take into account the evaporator wall thermal resistance.

⁵The discussion reported in this section is referred to the case where three power electronics modules are installed on each side of the evaporator, and three evaporators are used in parallel.

6.3.2.3 Finite volume analysis of power electronics module

On the basis of the data reported on the module specification data-sheet, the module was numerically reproduced⁶. A schematic of power electronic baseplate is reported in Fig. 6.12a.

Finite volume model and boundary conditions Boundary conditions and material layers are schematically reported in Fig. 6.12b.

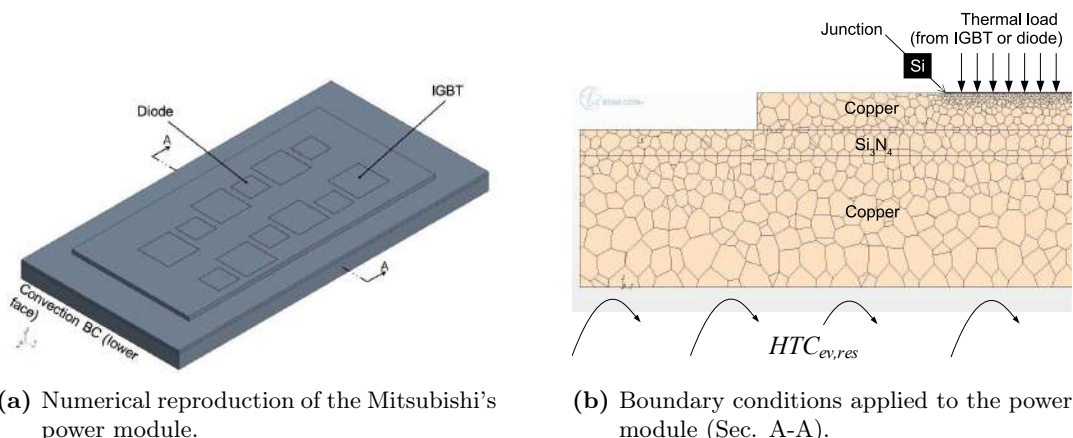


Figure 6.12: Power module scheme and boundary conditions

All the side-walls of the power module are supposed to be adiabatic and the black casing containing the resin layer neglected. A convection boundary condition is applied to the downside wall. Here, the equivalent heat transfer coefficient (HTC) is defined as $HTC_{ev,res} = G_{ev,res}/S_{mod}$, with S_{mod} the module baseplate surface area and $G_{ev,res}$ the reservoir based thermal conductance experimentally obtained (see Fig. 6.6)⁷. The so called “environmental” temperature is equal to the reservoir saturation one: $T_{res} = 70^\circ\text{C}$. A thermal load is applied on the sockets of electronic components and depends on the electronic configuration. NPC (Neutral Point Clamped) is the configuration suggested by WP2 team [21]. The latter allows the power modules to switch differentially: only diodes or only IGBTs work in each power module. In this case, on the basis of the scheme reported in Fig. 6.11, for example, the module positioned in the upper side works using

⁶The plastic case and the hard resin layer (black component in Fig. 6.10a) above IGBTs and diodes have been not considered. No information are given about geometry and thermal characteristics of such layer. It usually is not considered in thermal calculations and no information are reported in data sheet.

⁷The use of $G_{ev,res}$ allows *inter alia* to obtain more conservative junction temperature values because $G_{ev,res} \leq G_{ev,V}$ (see Fig. 6.8)

only IGBTs (largest components in Fig. 6.12a) while the one positioned in the lower side works only using diodes (smallest components in Fig. 6.12a). In this configuration each diode evacuates a thermal power of 155 W and each IGBT a thermal power of 0 W, for the module that uses only diodes. While in power module that only uses IGBT, the thermal power to be evacuated by each diode is just 12 W, but 133 W must be evacuated from each IGBT. The total thermal load to be evacuated is so 16.2 kW (six modules per evaporator), in the configuration here considered.

For simplicity, in the following, $Q_{th,D}$ is the thermal power applied to the diodes and $Q_{th,I}$ is the one applied to IGBTs. We will refer to:

- CASE 1: for the module in which only diodes work ($Q_{th,D} = 155$ W; $Q_{th,I} = 0$ W)
- CASE 2: for the module in which only IGBTs work ($Q_{th,D} = 12$ W; $Q_{th,I} = 133$ W)

A 3D steady-state solver is assumed considering that the high switching frequency (thermal load/unload cycle on the electronic chips), in the order of MHz, is dumped by thermal inertia of the materials constituting power modules and evaporator. Only the energy equation is solved using a multi-domain solver to consider the Conjugated Heat Transfer resolution (CHT) through the different layers of material constituting the power module.

Mesh independence analysis and results A mesh example is reported in Fig. 6.13, where the upside and the downside (interface between the power module and the evaporator wall) views of the power module are respectively reported.

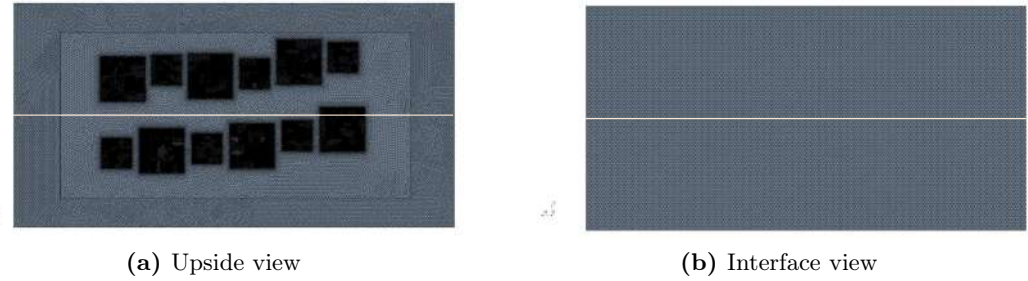


Figure 6.13: Mesh example

A structured polyhedral mesh⁸ was used. It has been refined in correspondence of the electronic component sockets and in correspondence of interfaces between the different material layers. Here, in fact, it is expected to have a heat spreading effect. For each

⁸The polyhedral mesh is a kind of proprietary structured mesh in the used commercial tool (StarCCM+).

studied case, three different mesh dimensions were used: from the coarser to the finer one, they are defined as $M1\dots M3$, respectively. For mesh independence calculation, between two successive grids, a maximal temperature difference of 2% has been defined as acceptable⁹. The first grid ($M1$), characterised by about $2.5 \cdot 10^5$ cells and having the lowest resolution, was compared with the medium dimension grid (about $5 \cdot 10^5$ cells). The difference in the temperature distribution is about 3% in this case. The comparison between the medium and the finer mesh, characterised by about $1.3 \cdot 10^6$ elements, gives a difference lower than 2% in the temperature distribution, which curve is reported in Fig. 6.14. The temperature profiles plotted in Fig. 6.14 are distributed along the light-pink line, shown in Fig. 6.13a and Fig. 6.13b, respectively, on the upside copper surface and at the interface between the evaporator and the power module.

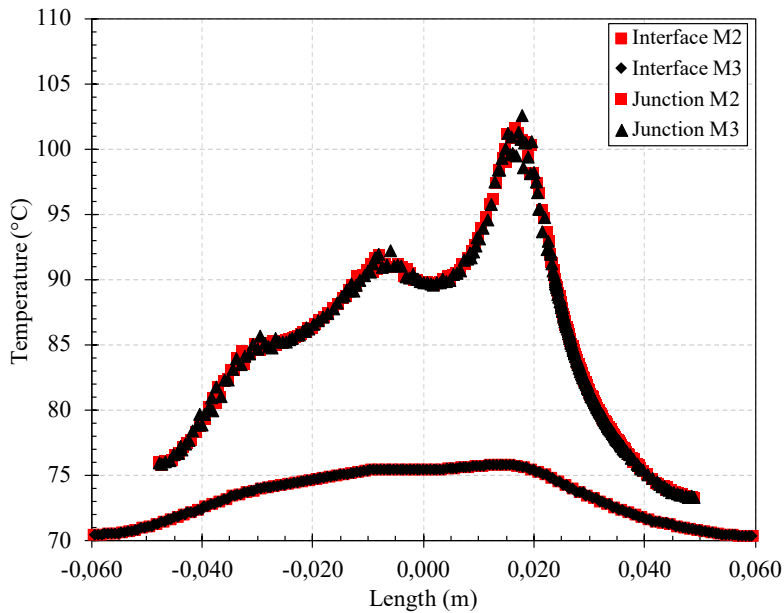


Figure 6.14: Mesh independence temperature distribution (methanol, $T_{res} = 70^\circ\text{C}$)

By using a minimum convergence criterion of 10^{-10} for residuals of energy equation, temperature maps for CASE 1 are reported in Fig. 6.15 and Fig. 6.16. Diodes have side dimension of 0.8 cm, so a thermal heat flux density of about $242 \text{ W}\cdot\text{cm}^{-2}$ is evacuated by each of them. Thanks to the spreading property of copper and Si_3N_4 layers, constituting the power module's base plate, the equivalent heat flux density at the interface between the module and the evaporator is reduced to almost $12.5 \text{ W}\cdot\text{cm}^{-2}$. Despite the presence

⁹Temperature difference is calculated at the same position for two grids, M_n and M_{n-1} , is $\frac{T_{M_{n-1}} - T_{M_n}}{\Delta T_{ref}}$, with $\Delta T_{ref} = T_{M_{n-1}} - T_{ref}$ and $T_{ref} = T_{res}$.

of hot-spots in correspondence of diodes or IGBTs, a flattening of the temperature distribution can be observed in correspondence of the base of the module, from the junction to the interface (see Fig. 6.14).

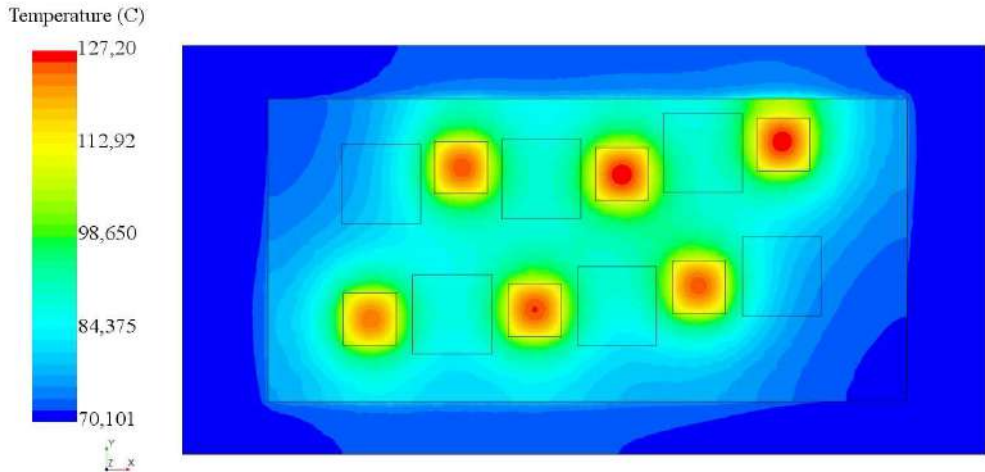


Figure 6.15: Temperature map CASE 1 (junction view): $Q_{th,D} = 155 \text{ W}$; $Q_{th,I} = 0 \text{ W}$ (methanol, $T_{res} = 70^\circ\text{C}$).

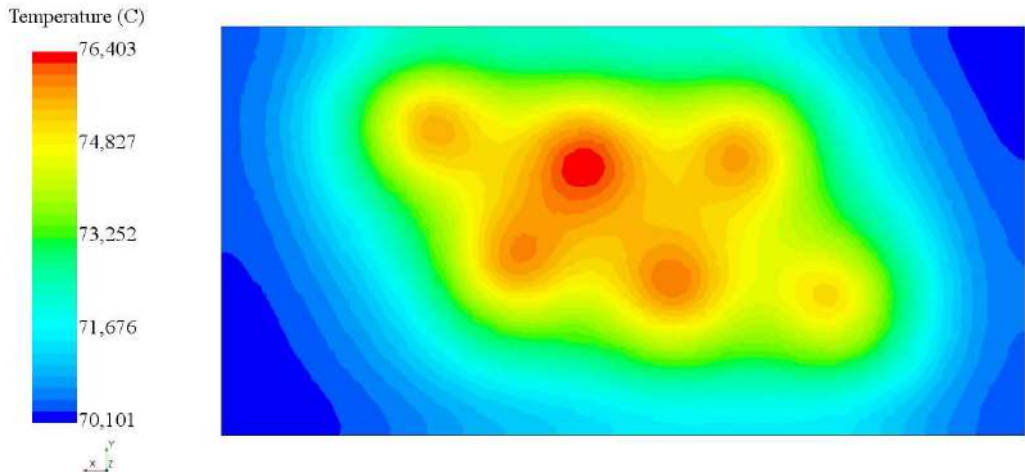


Figure 6.16: Temperature map CASE 1 (evaporator-module interface view, according to Fig. 6.15): $Q_{th,D} = 155 \text{ W}$; $Q_{th,I} = 0 \text{ W}$ (methanol, $T_{res} = 70^\circ\text{C}$).

The same thermal behaviour may be noticed for CASE 2 (see figures 6.17 and 6.18). In this case, for a thermal heat flux density of about $92.5 \text{ W}\cdot\text{cm}^{-2}$ and $18.75 \text{ W}\cdot\text{cm}^{-2}$ applied on each IGBT and diode socket, respectively, the equivalent heat flux density

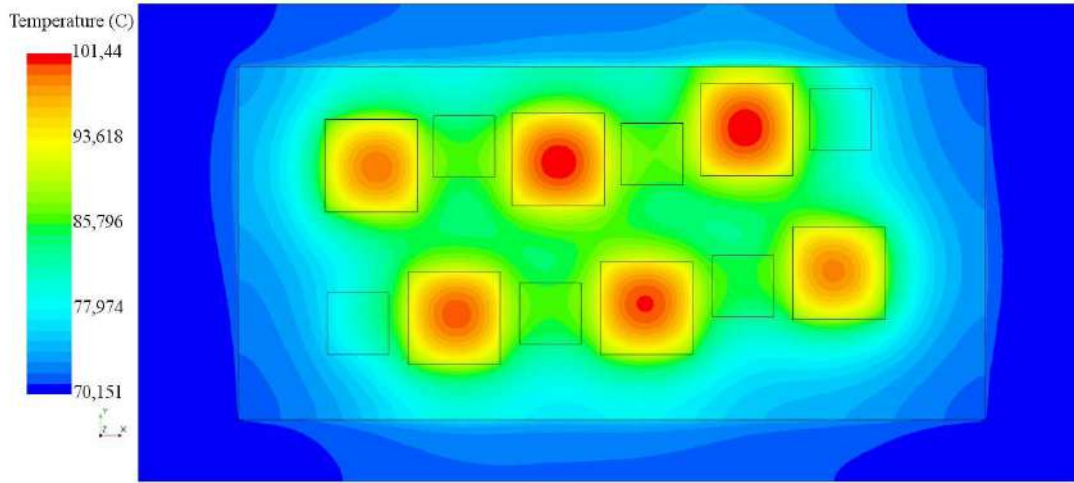


Figure 6.17: Temperature map CASE 2 (junction view): $Q_{th,D} = 12\text{ W}$; $Q_{th,I} = 133\text{ W}$ (methanol, $T_{res} = 70^\circ\text{C}$).

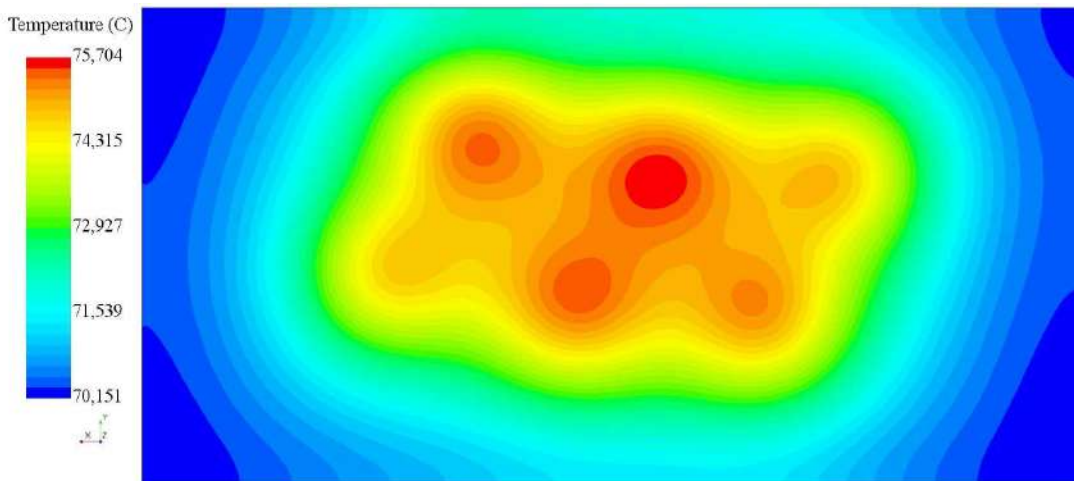


Figure 6.18: Temperature map CASE 2 (evaporator-module interface view, according to Fig. 6.17): $Q_{th,D} = 12\text{ W}$; $Q_{th,I} = 133\text{ W}$ (methanol, $T_{res} = 70^\circ\text{C}$).

at the evaporator/power module interface is $11.5\text{ W}\cdot\text{cm}^{-2}$. The maximum temperature values are 127°C and 101°C for the CASE 1 and the CASE 2 respectively, lower than the maximal allowed junction temperature given by modules constructor (150°C) [118].

6.3.3 Experimental thermal mission profile

To explore the behaviour of the CPLIP in more realistic operating conditions, the mission profile was experimentally tested using the experimental facility described in sec. 5.8. The purpose is to test the CPLIP during severe transient stages of the mission profile,

such as the sudden power increase that occurs between stage I and stage II, for example (see Fig. 6.19).

Considering the electrical configuration NPC-DPWMMAX¹⁰, the maximal total thermal load to be evacuated is $Q_{th} = 16.2 \text{ kW}$ in three-phase: $5.4 \text{ kW}/\text{phase}$.

Fig. 6.19 depicts the experimental results for one-electrical phase thermal losses mission profile using the same experimental facility used in [1, 12, 14] and [111].

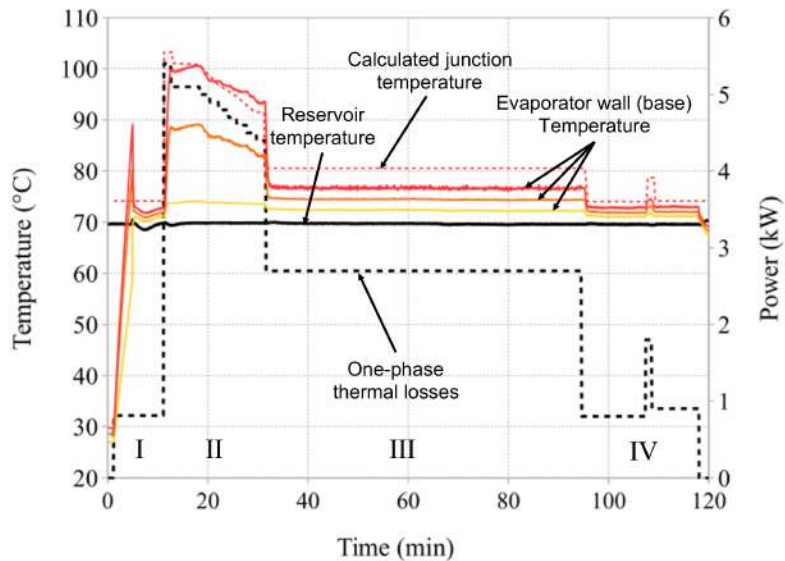


Figure 6.19: Experimental thermal mission profile (methanol, $T_{sec} = 20^\circ\text{C}$, $T_{res} = 70^\circ\text{C}$).

From the stand-by position¹¹ (before stage I), as the power load is applied to the evaporator, 0.8 kW , at the time $t = 0$, a sudden temperature overshoot occurs in correspondence of the evaporator walls (the behaviour of the CPLIP during start-up is widely treated in chap. 8 and in ref. [111]) until start-up of loop operations, triggered by nucleation bubbles in the evaporator. After this point, the evaporator wall temperature suddenly decreases reaching an almost uniform value along the evaporator wall. During the taxi-out stage (I) the thermal load evacuated by the electronic components is constant for about 10 min. At the beginning of the take-off stage (II) the power peak (5.4 kW) is applied to the evaporator. Wall temperature suddenly increases, small perturbations occur in the reservoir: here the temperature slightly decreases before settling to the imposed value. This could be due to a higher liquid mass flow rate that flows from the condenser to the reservoir. The maximal power peak is very limited in time

¹⁰Such electrical configuration is the one retained by WP2 [21] for its efficiency and lightweight.

¹¹No thermal load is applied to the evaporator; the reservoir is maintained at fixed thermodynamic conditions: $T_{res} = 70^\circ\text{C}$; and the cold source temperature is at $T_{sec} = 20^\circ\text{C}$.

and, due to the evaporator thermal inertia, the temperature peak is reached only when the thermal power starts to decrease. Despite the lower thermal load, the evaporator wall temperature continues to increase, but with a lower slope. Once reservoir conditions are stabilised, again, evaporator wall temperature decreases, gradually, following power unload until the end of the climb stage ($t = 30$ min). At beginning of the cruise stage (III), temperature follows a constant power profile and, all along this phase, temperatures are stabilised. CPLIP works in steady state conditions until the end of the cruise at $t = 95$ min, when descent stage begins. Observing temperature distribution on the evaporator walls, a difference can be noticed between the highest and the lowest one (red to yellow line difference). As explained before, this difference could be due to a pressure gradient, between the evaporator inlet and outlet, due to evaporator pressure drop. At the same way, it is expected to observe the same temperature difference on the power electronic module bases. Temperature distribution follows the same shape of thermal load during the remaining stages of the mission profile. Due to the lower power load applied to the evaporator, a lower temperature gradient can be observed on the evaporator walls.

Note that the dashed red curve on the experimental diagram, representing the calculated junction temperature¹², shows the temperature prediction based on the simplified model developed by power electronics team [21, 111] and based on experimental thermal conductance values obtained along this chapter (Fig. 6.9). A slight over-estimation of temperature prediction may be observed during the steady state stages. This could be due to the use of the reservoir-based conductance values, more conservative than evaporator saturation temperature-based ones. However, it is worth of attention that temperature values, in correspondence of power peak, about 103 °C, well agree with the predictions based on CFD and is lower than the value suggested by power module constructor (150 °C).

6.4 Influence of vapour line pressure drop on the thermal response of the CPLIP

The same methodology and post-processing tool were used to analyse the thermal response of the CPLIP to variations of hydraulic characteristics: vapour line pressure drop.

By following the same methodology and post-processing tool explained above, pressure drop in the vapour line, following the closure of the valve, $\Delta P_{v, valve}$ (see eq. 6.6), must

¹²A simplified mono-dimensional electrical analogy based model has been developed by WP2 [21] according to CPLIP's thermal characteristics explained in this chapter.

be added to the overall pressure drop equation, (6.1):

$$\Delta P_{v, valve} = \left[\frac{\dot{m}}{C_v \rho_v \left(1 - \frac{2\Delta P_{v, valve}}{3P_{vi}} \right)} \right]^2 \frac{G_v T_{vi}}{P_{vi}} \times 10^{10} \quad (6.6)$$

where C_v is the flow coefficient relating the pressure drop to the valve number of turns, N , following the relation:

$$C_v = F_c [0.0103 N^4 + 0.0909 N^3 + 0.178 N^2 + 0.3766 N + 0.0016] \quad (6.7)$$

The conversion factor is $F_c = 0.0116$, and the evolving vapour mass flow rate is calculated as:

$$\dot{m}_v = 22.4 C_v \sqrt{\Delta P \cdot P_{sat}} \quad (6.8)$$

For a given and constant thermal load applied to the evaporator, Q_{th} , reservoir and cold source temperature, T_{res} and T_{sec} , respectively, pressure drop in the vapour line has been gradually increased by closing the setting valve (see Fig. 5.8) and attempting steady-state conditions in each case. To give the reader an idea of the global behaviour of the CPLIP corresponding to pressure drops increase, the time dependent diagram of temperature evolution, during a test, is reported in Fig. 6.20 (methanol and constant heat power, $Q_{th} = 1\text{ kW}$). There, valve overture, indicated on the right side axis, are shown as the ratio N/N_{max} . N is the actual number of turns and N_{max} is the number

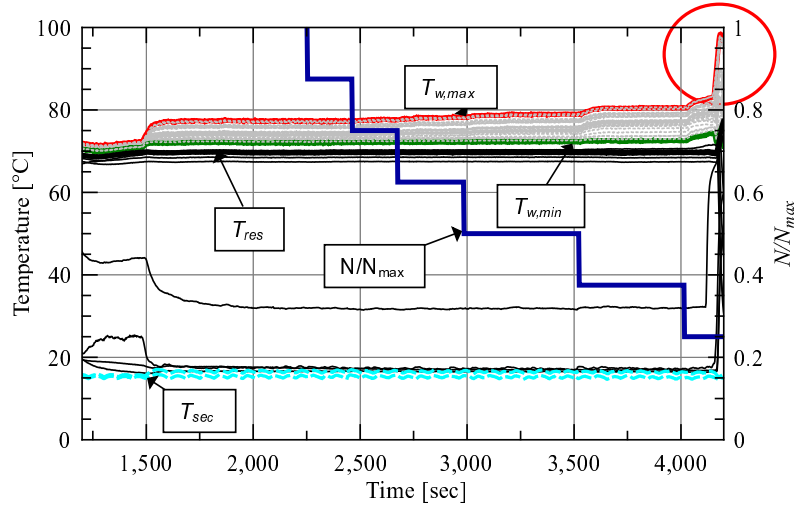


Figure 6.20: Time dependent diagram of temperature evolution of the CPLIP for increasing vapour line pressure drop (methanol, $Q_{th} = 1\text{ kW}$, $T_{sec} = 20^\circ\text{C}$).

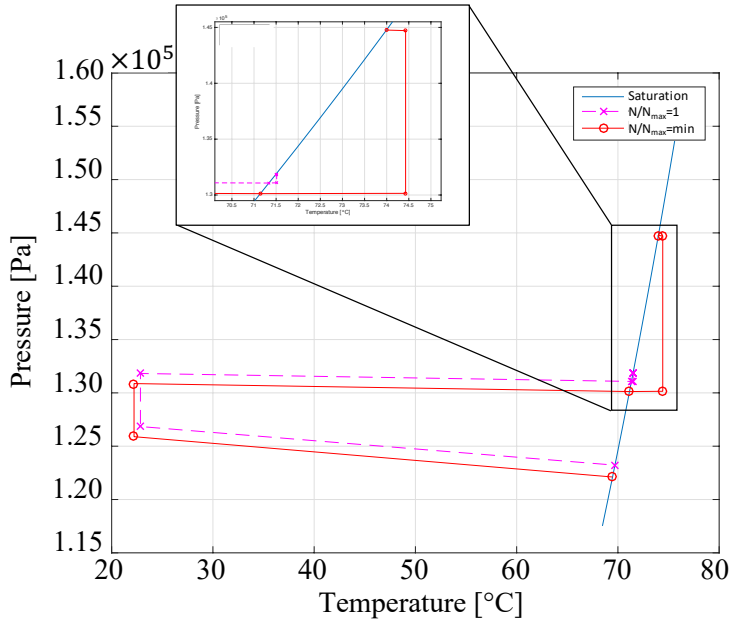


Figure 6.21: Thermodynamic cycle comparison between the highest and the lowest valve overture: $N/N_{max} = 0.25$ and $N/N_{max} = 1$ (methanol, $Q_{th} = 1\text{ kW}$, $T_{res} = 70^\circ\text{C}$ and $T_{sec} = 20^\circ\text{C}$).

of turns corresponding to the fully open condition. The first impression one has, observing the diagram in Fig. 6.20, is that the impact of increasing pressure drop is almost comparable with that of increasing thermal load to the evaporator: the evaporator temperature increases. This behaviour can also be noticed from the thermodynamic diagram comparison reported in Fig. 6.21 where the lowest pressure drop possible ($N/N_{max} = 1$) and the highest one ($N/N_{max} = \min = 0.25$, corresponding to the lowest value of N before loop failure) are compared. The loop failure due to valve closing is highlighted by a red circle in Fig. 6.20. In this case, the overall pressure drop in the loop exceeds the capillary limit of the porous wick [7, 12], see eq. (6.1). The latter is thus no more able to supply the adequate pressure head, no more fluid flows in the loop and dry out occurs in the wick. Evaporator temperature goes out of control.

Temperatures are not only dependent on the applied thermal load, but also on the pressure drops. Vapour line length, loop configuration, condenser typology and configuration and working fluid affect overall pressure drops and consequently the loop response.

By comparing ethanol and methanol as working fluids, considering the mean evaporator wall temperature, \bar{T}_{diff} , from Fig. 6.22, the lowest wall temperatures and lowest sensitivity to vapour line pressure drop are recorded for methanol. Increasing the thermal load, Q_{th} , curve depletion quickens proportionally to valve closure, so CPLIP demonstrates a

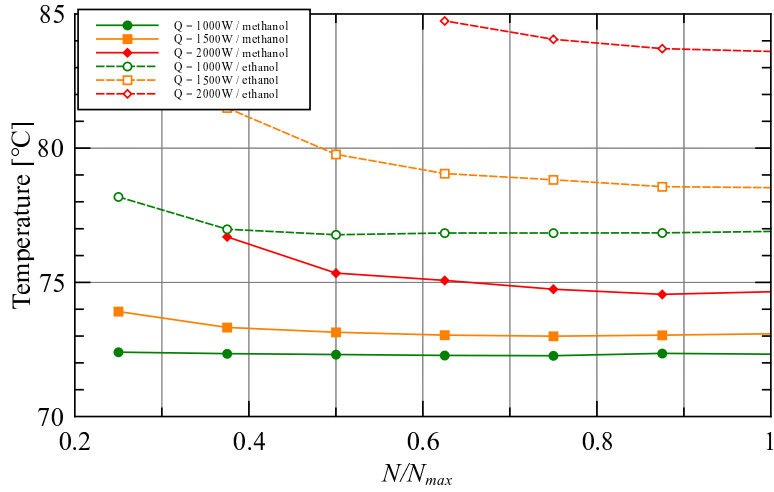


Figure 6.22: \bar{T}_{diff} as a function of N/N_{max} and for different thermal loads (methanol, $T_{res} = 70^\circ\text{C}$; $T_{sec} = 20^\circ\text{C}$).

higher sensitivity to pressure drops: curve slopes increase.

The mean diffuser to reservoir temperature difference, $(\bar{T}_{diff} - T_{res})$, and the mean diffuser to evaporator temperature difference, $(\bar{T}_{diff} - T_V)$, are considered, for comparison purposes, as a function of N/N_{max} , for different thermal loads and for methanol and ethanol (see Fig. 6.23). Basically, at constant thermal load, \bar{T}_{diff} decreases as N/N_{max} increases (see Fig. 6.22). Being the reservoir temperature constant, whatever the position of the valve, the difference $(\bar{T}_{diff} - T_{res})$ decreases as well, either for ethanol and methanol (see Fig. 6.23a). At the same manner, as reported in Fig. 6.23b, because of

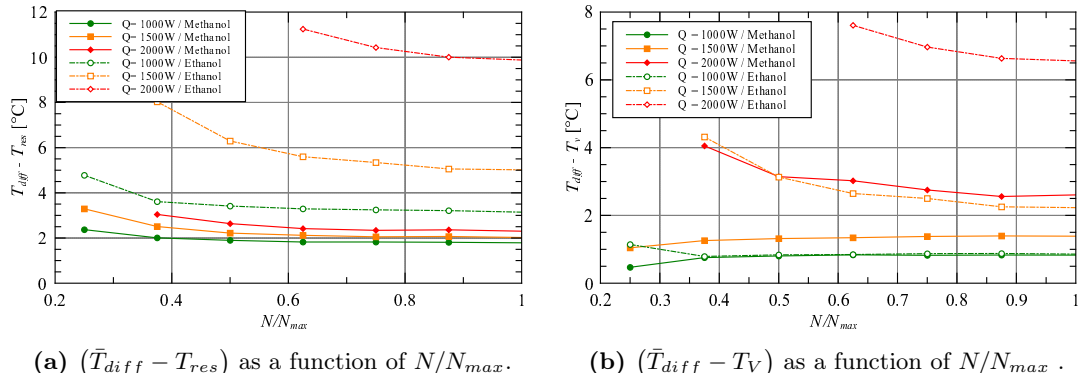


Figure 6.23: Temperature differences as a function of the valve overture (ethanol and methanol, $T_{res} = 70^\circ\text{C}$; $T_{sec} = 20^\circ\text{C}$).

the lowering of the evaporator temperature, T_V , as a function of N/N_{max} , $(\bar{T}_{diff} - T_V)$ decreases too. This behaviour may be justified by a recession of menisci in the porous wick between the interface and the diffuser. In fact, the higher the thermal load, the higher the temperature difference and the slope of the curve because of the presence of an increasing dried portion of the porous wick. The pressure difference around the menisci increases and the evaporation front recesses. As reported by Accorinti *et al.* [12], this could be the reason of the final failure of the loop for high pressure drop at high thermal loads.

As expected, both temperature differences are characterised by the same trend for each working fluid and almost all thermal loads. However, as observed in Fig. 6.7, for low thermal loads, at low N/N_{max} (highest pressure drops), $(T_{diff} - T_V)$ is in the same order of the temperature sensor accuracy. Measurements are no more reliable in this range (see methanol at 1 and 1.5 kW for example). This justifies the change in the slope observed for such curves.

Finally, if the thermal conductance values, based on the real evaporator temperature, are calculated as a function of the pressure drops in the vapour line, the highest conductance value is obtained, as expected, for the lowest thermal load and the highest pressure drop, as reported in Fig. 6.24 (being the curve at 1000 and 1500 W in the range of high uncertainty given by the blackened area of Fig. 6.8).

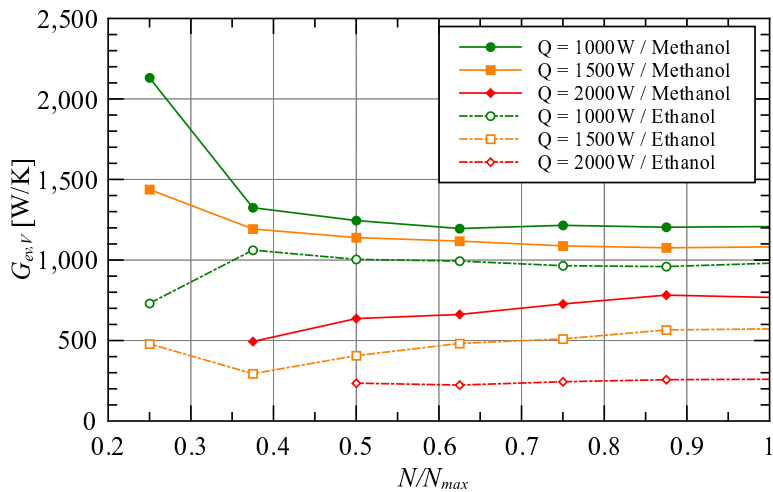


Figure 6.24: Thermal conductance as a function of the pressure drop (ethanol and methanol, $T_{res} = 70^\circ\text{C}$; $T_{sec} = 20^\circ\text{C}$).

Considering the overall pressure drop ΔP as a function of the valve overture and for different power levels (see Fig. 6.25), obviously the lower the thermal power, the higher

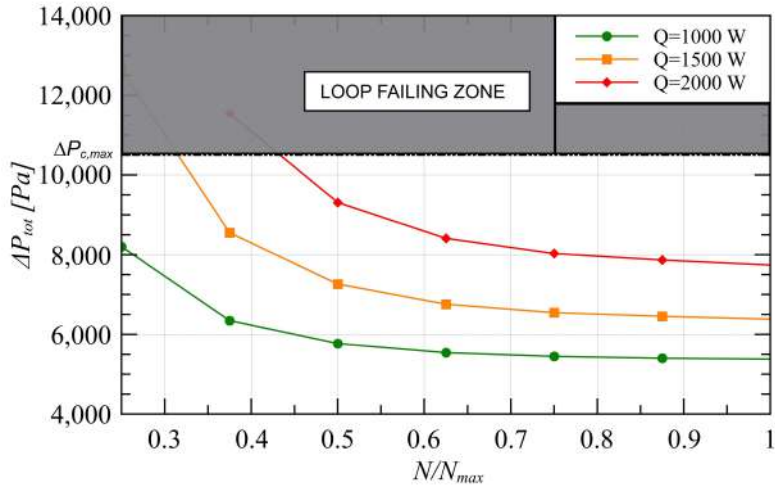


Figure 6.25: Overall pressure drop as a function of valve opening (N/N_{max}) and for different thermal loads (ethanol and methanol, $T_{res} = 70^\circ\text{C}$; $T_{sec} = 20^\circ\text{C}$).

the pressure drop at which the loop can operate without failing. But the higher the thermal power, the higher the pressure gradient. It means that, for the highest thermal loads, the loop failure occurs before low ones, as the prediction of pressure drops above the $\Delta P_{c,max}$ line shows!

6.5 Conclusion

In this chapter, the behaviour of the CPLIP in many experimental operating conditions was introduced. In particular, acting on its thermal and hydraulic characteristics, a detailed explanation of different behaviour of the CPLIP was presented. This chapter was, fundamentally, divided in four parts. In the first part, a thermal characterisation of the CPLIP, using methanol and ethanol as working fluids, has been carried on to understand CPLIP limits and potentialities. A widely extended experimental parametric study was presented to understand the influence of such parameter on the CPLIP working conditions. Due to the inability to directly measure the evaporation temperature in the porous wick, an adapted post-processing tool was used to obtain all the missing parameters on the thermodynamic cycle. In particular, a first study on the influence of different parameters on the thermodynamic cycle was presented to explain, in a more clear way, the main CPLIP working characteristics. It was observed that, due to the intrinsic characteristics of such two-phase cooling system, where saturation conditions are imposed and controlled, an independency between cold source temperature and the

evaporator operating one exists. So, evaporator conductance values are also independent from the secondary side temperature. This behaviour renders this system particularly adapted for the application studied in the context of HASTECS project. Evaporator conductances were experimentally obtained, based either on the reservoir and evaporator temperatures. On the basis of experimentally obtained thermal conductances, it was possible to numerically study the temperature field on a real power module. Based on the finite volume method (on StarCCM+), the energy equation was solved to obtain steady-state temperature distribution in the worst efficiency case and operating condition for the power modules. Despite the very high heat flux density evacuated by electronic chips, the CPLIP, characterised by a very high evaporator HTC, is able to maintain temperature controlled and lower than the maximum value allowed by power-electronics-module constructor. Thanks to spreading behaviour of used power electronics modules, one assists to flattening of the temperature field in correspondence of the base plate (interface between the evaporator and the power module).

To explore the CPLIP behaviour during an entire mission profile cycle, the latter has been successfully tested. The CPLIP is able to evacuate the supplied thermal load, and temperatures on the evaporator walls remain controlled even during the most critical phases (transition between taxi-out and take-off stages, for example). The experimentally obtained temperatures were compared with those obtained by WP2 team from a mono-dimensional electrical analogy based model. It allows to verify, *inter alia*, the temperature prediction. A slight overestimation was found. This allows, however, to be more conservative during design stage of electrical components and its adjoined cooling system.

Finally, to know which is the influence of the vapour line pressure drops and to relate them to the transport distance, a parametric study was conducted, acting on the hydraulic characteristics of the CPLIP. It was found that increasing pressure drops in the vapour line has some similarities with thermal load variation to the evaporator. Methanol and ethanol have the same qualitative behaviour, but, due to the differences in thermophysical properties, they are quantitatively different. Ethanol, in particular, is more sensitive to heat power increase or vapour line pressure drops.

Some differences could exist between CPLIP's behaviour tested in laboratory and real operating conditions. They could be mainly due to a difference in transport lines length and/or a different nature of the condenser. Moreover, in this experimental study, the evaporator was uniformly, and quasi ideally heated by heating resistances, so, some differences could be also due to the use of real switching power modules, having a lower thermal inertia than copper diffuser used in the experimental facility.

CPLIP optimisation for 2025 and 2035 requirements

Capillary Pumped Loop for Integrated Power (CPLIP), seems to be the best solution for power electronics cooling in the context of HASTECS project. From first approximation design (see chapter 4), the power coefficient of three parallel evaporators CPLIP was quite close to target 2025! With the purpose to reduce its mass, in this chapter, its optimisation is proposed either for 2025 and 2035.

7.1 Design point

When talking about system design, the first issue to solve is related to the choice of design point. The latter not only impacts the mass of the system, but also its thermo-hydraulic behaviour. If the cooling system is oversized, its mass will be higher than the one actually required. As a result, it will be under-exploited. On the contrary, in the case of undersizing, the system is not able to ensure the required cooling and consequences may be catastrophic.

Due to the high variability of thermal losses as a function of time, the choice of design point is impacted by the shape of the mission profile. An energy approach is necessary to choose the best one. The mission profile is divided in five stages, as usual (see Fig. 7.1), and the amount of thermal energy evacuated during each stage is calculated. Taxi out-and-in and landing phases (I, IV and V) are characterised by a quite small amount of thermal losses and their duration in time is relatively short: they will be not considered for the purpose. During the remaining flight stages (II and III), whichever the design point, thermal losses will be surely higher than previous ones. The harsh transient take-off stage (II) is critical. At the very beginning of this phase, power converters work at their maximum power for a quite limited time, almost three minutes (red circle), but a pretty high amount of thermal energy has to be evacuated from electronics components. After that, thermal losses slightly decrease until point D (Fig. 7.1). Thermal losses during cruise stage (III), stationary, are no particularly high, but it lasts longtime.

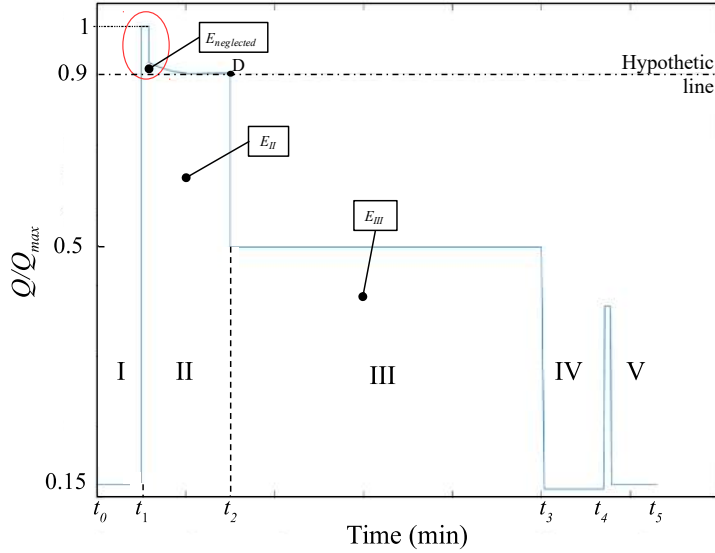


Figure 7.1: Design point choice

Referring to Fig. 7.1, considering only take-off (II) and cruise (III) stages and the hypothetic line¹, three different critical areas can be distinguished on the diagram. The area related to take-off and climb stage, below the line (E_{II}); the area belonging to take-off and climb stage, above that line ($E_{neglected}$); the whole area related to the cruise stage (E_{III}). Considering the four electronic architectures proposed by WP2 [21] for the solution 2025 (FC-DPWMMAX and FC-PWM — Flying Cap Discontinuous Pulse Width Modulation MAX and Flying Cap Discontinuous Pulse Width Modulation respectively—, and NPC-DPWMMAX and NPC-PWM — Neutral Point Clamped—), due to the different efficiency of each electronic configuration², a different amount of heat must be evacuated. In table 7.1, thermal energy calculations are reported for the four electronic topologies in the previously mentioned areas of the mission profile. Thermal energy to be evacuated during take-off stage, E_{II} , is almost 50% than that related to cruise stage, E_{III} . As expected, the design point should consider stage II. Despite the amount of neglected energy, $E_{neglected}$, is between 1.6 and 2% of E_{II} , its absolute value is not negligible and, if point D is chosen as design point, it has to be verified that cooling system thermal inertia is able to damp such amount of not “treated” energy.

¹The line corresponding to the thermal load to be evacuated at the end of stage II (take-off and climb).

²For confidentiality issues is not possible to give any information related to the exact amount of thermal losses to be evacuated for each electronic configuration.

Power electronic topology	E_{II} [MJ]	E_{III} [MJ]	$E_{neglected}$ [kJ]	E_{II}/E_{III}	E_{neg}/E_{II}
FC-DPWMMAX	16.2	36.1	369.5	44.9%	2.2%
FC-PWM	19.4	44.1	395.2	44.0%	2.0%
NPC-DPWMMAX	16.9	38.2	267.3	44.1%	1.6%
NPC-PWM	18.8	42.0	356.5	44.6%	1.9%

Table 7.1: Thermal energy ratios during take-off and cruise stage

After cooling system optimisation, on the basis of precise mass calculation, temperature increase due to amount of neglected energy will be evaluated.

7.2 CPLIP optimisation

To remind, the mass distribution of a three parallel evaporators CPLIP resulting from first approximation design is reported in Fig. 7.2 (see sec. 4.2.3). The resulting first attempt value of thermal power coefficient was $C_{c,th} = 0.33 \text{ kW}\cdot\text{kg}^{-1}$.

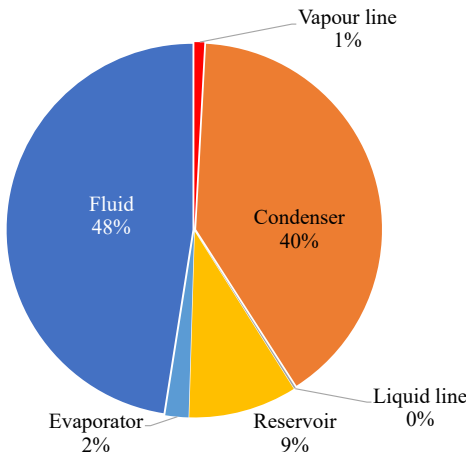


Figure 7.2: Passive two-phase mass distribution (three parallel evaporators CPLIP: — CERBERE—)

As one can notice, condenser, fluid and reservoir are the heaviest components in the loop. Due to the impact of condenser on the fluid and reservoir mass, optimisation process is particularly focused on it to reduce its overall dimensions: the smaller the condenser internal volume, the lower the fluid and reservoir volumes. Moreover, a significant mass reduction can be achieved by using a lightest material than the one used during first approximation design. For compatibility issues between fluid (methanol) and solid material, aluminium cannot be considered. Titanium, already used in aeronautics applications for

similar purposes, has been chosen as constituting material of loop components.

Transport lines geometrical dimensions, which mass is negligible if compared with all other components, cannot be modified furthermore (for mechanical resistance issues, their thickness cannot be reduced below 0.6 mm).

The evaporator dimensions are proportional to power module ones, so this component cannot be modified unless different power modules are used.

7.2.1 Condenser optimisation

The problem of heat exchanger design is not ease-to-solve and involves a multidisciplinary approach. Qualitative and quantitative design considerations and experience-based judgements are necessary to define the optimal heat exchanger (HXG) geometry. During design and optimisation process, thermo/hydraulic approach is only “one side of the coin”. Most decisions are related to manufacturing and economic considerations as well as mechanic and dynamic (vibration) analysis. A trade-off is necessary to reach the optimal heat exchanger final geometry. For given thermo/hydraulic requirements, the solution is not unique, and different optimum solutions exist.

Two different approaches are related to heat exchanger problem. The first one, related to design, is usually called *sizing problem*. It faces with the research of optimal geometric characteristics of a HXG for given industrial process. Materials, heat exchanger configuration, flow arrangement, thermal calculations (HTC, heat transfer surface area), pressure drop *etc.* are related to such process as well. The second approach, usually called *rating problem*, instead, is different in nature. It faces with thermo/hydraulic verification of an already existing heat exchanger or an already designed one to verify if it “answers” to process requirements.

Neglecting mechanical and economic parameters, a scheme of design process is reported in Fig. 7.3 to show how complex this task is. Strong interactions between the different stages of design process make it arduous. The task is based on the assignation of a first attempt geometry, trial, calculation, verification, change of different parameters, and re-trials until a satisfying geometry is reached. The latter is verified by using *trade-off factor(s)*, based on the requirements of the problem, and eventually re-iteration until the satisfaction of all requirements.

Diagram 7.3 can be fundamentally divided in three sections and each of them is representative of a single part of the design task. Process section is related to “problem entries”. It defines heat transfer rate; fluid mass flow rate and temperatures; maximal allowable pressure drops (both for internal and external sides). Operating conditions, HXG architecture, configuration and solid materials are defined here as well. Key char-

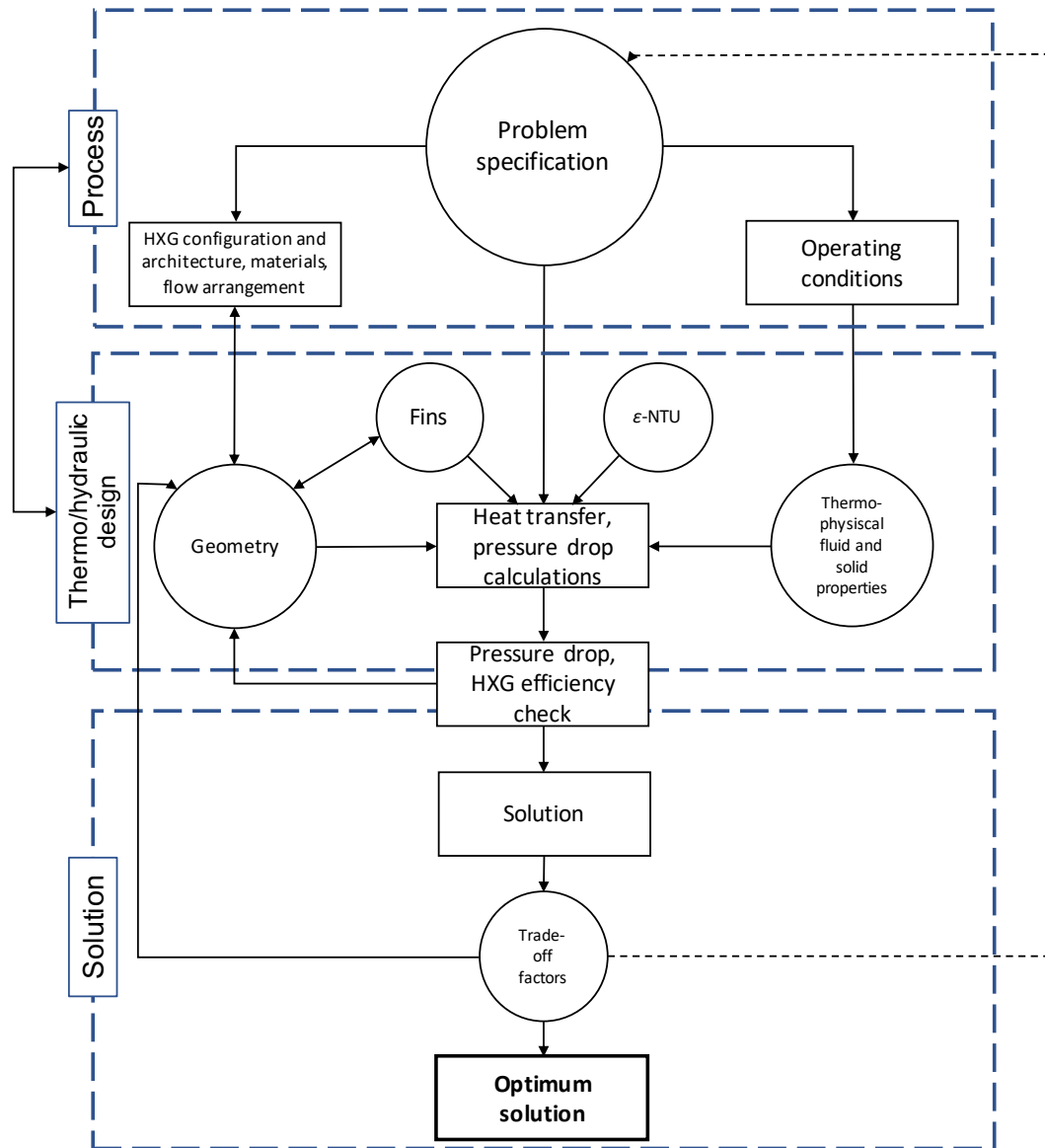


Figure 7.3: Optimisation process of a heat exchanger.

acteristics of heat exchanger, such as flow arrangement, are assigned in this section *a priori* and verified *a posteriori*.

Thermo-hydraulic design section is related to geometry, such as number, geometry and distribution of tubes and fins. Fluid thermophysical properties and resolution method are defined in this section to obtain, on the base of the previously defined parameters, the thermal and hydraulic characteristics of the heat exchanger. Once thermal and hydraulic calculations are executed, the solution is rejected or accepted based on hydraulic and

thermal requirements such as actual-to-allowed pressure-drop ratio and heat exchanger overall efficiency, for example. In the case of rejection of the solution, the process is repeated until global efficiency and pressure drops factors are verified. During this stage, it is sometimes necessary to change some process parameters, such as fluid arrangement to obtain an acceptable solution. Once a possible solution has been obtained, trade-off factors are used to verify if it is the optimum one. If not, once again, geometric characteristics, fluid arrangement, and sometimes operating conditions are re-defined until satisfaction of trade-off factors.

Process is repetitive and based on trials. Solutions must be analysed, at each step, and compared with previous ones. Geometric parameters and configuration have to be changed one by one. Moreover, due to non-linearity between thermo-hydraulic characteristics of the heat exchanger and its geometrical parameters, the process is hard to automate. Designer has to take decisions at each step of the design process until the optimum solution is reached.

Condensers design process is similar to heat exchangers one, but due to difficulties in prediction of two-phase flow pattern (see sec. 5.1.2), it is much more complicated. Different heat transfer mechanisms (desuperheating if any, condensation, subcooling) have to be considered as well as the complex geometries (external and sometimes internal) and the eventual presence of non-condensable-gases.

The continuous variation of the flow pattern inevitably affects the internal heat transfer coefficient and so the overall one. This is the reason why condenser design usually considers an approximate form of the heat transfer rate equation:

$$Q = \check{U} A \Delta T_{lm} \quad (7.1)$$

where the overall heat transfer coefficient \check{U} and the logarithmic mean temperature difference ΔT_{lm} are calculated as:

$$\check{U} = \frac{1}{A} \int_A U dA \quad (7.2)$$

and

$$\Delta T_{lm} = \frac{Q}{\int_A U dA} \quad (7.3)$$

The two last parameters are calculated by integrating equation (7.4).

$$dQ = U \Delta T dA \quad (7.4)$$

Due to such strong variability of temperature and vapour quality, the total condenser heat load is divided in different sub-heat-duty zones (or incremental zones) and, for each

of them, energy balance is solved using the enthalpy formulation, instead of temperature one. Finally, the total heat transfer area is calculated as the sum of areas related to all sub-heat-duty zones:

$$A = \sum_i \frac{Q_i}{U_i \Delta T_{lm,i}}$$

This method is the one usually implemented in the majority of heat exchangers design softwares [17]. To avoid pretty complex calculations related to condenser optimisation process, a commercial software (GRETh-EchTherm³) has been used to design and optimise this component of the CPLIP.

7.2.2 Condenser general characteristics

Ram air is the solution retained as cold source to evacuate the thermal load. The same external air conditions used for first approximation design will be used for the optimisation of the condenser. To remind, for the external side: $u_{air} = 10 \text{ m}\cdot\text{s}^{-1}$, $T_{air(land)} = 33^\circ\text{C}$ (see sec. 1.3) and for the internal side, $T_{sat} = 70^\circ\text{C}$.

Fins must be obviously used to increase condenser external heat transfer surface area. They are generally used on the external side of tubes. Finned tubes heat exchangers are categorised in *individually finned tubes* and *tube-finned exchangers*. In the first case (see Fig. 7.4a), fins, usually circular or pseudo-circular, are installed on each tube. In the second case (see Fig. 7.4b) fins are continuous, flat, unique and rely all tubes in the bank. Fins may be installed on the tube using different mechanical technologies: press

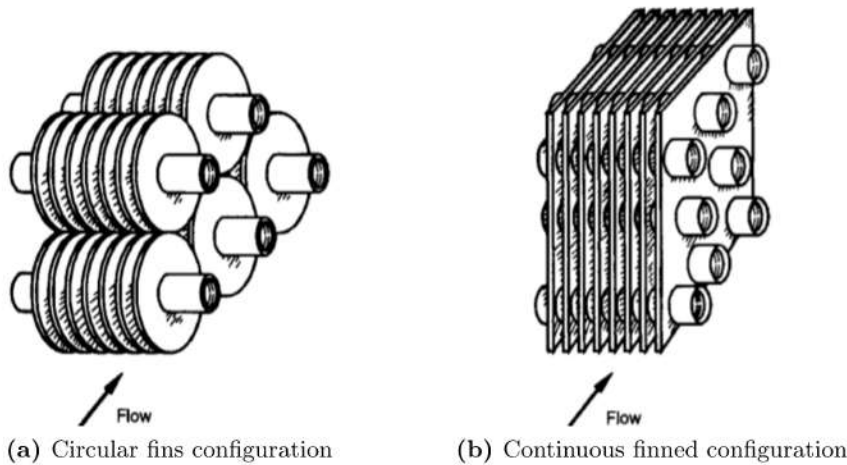


Figure 7.4: Fin configurations used for 2025 solution [17]

³see Appendix C for more information about the used correlations

fit, tension winding, adhesive bonding, soldering, brazing, welding or extrusion [17]. Fin density can vary from 250 to 800 fins/m and their thickness is in general between 0.08 and 0.25 mm. Pressure drop introduced by these devices and their mass should be as low as possible to not negatively influence the drag to lift ratio of the aircraft and the overall power coefficient, C_c [$\text{kW}\cdot\text{kg}^{-1}$]. Fins require the use of a high thermal conductivity material to evacuate as easily as possible the thermal load from the tube to external air. For this reason, a coupling of titanium ($k_{\text{Ti}} \simeq 20 \text{ W}\cdot\text{m}^{-1}\cdot\text{K}^{-1}$), for tubes, and aluminium ($k_{\text{Al}} \simeq 210 \text{ W}\cdot\text{m}^{-1}\cdot\text{K}^{-1}$), for fins, has been chosen⁴. Two different condenser configurations are proposed for 2025 and 2035 solutions.

7.2.2.1 A condenser for 2025

At first, for 2025 solution, circular and continuous fins were compared. A parametric study has been made to chose the configuration minimising pressure drop and mass penalty. A different kind of condenser will be introduced for the solution 2035.

Circular fins Geometrical characteristics of circular fins installed in a staggered configuration are reported in Fig. 7.5. All fin geometric characteristics and their configuration have a strong impact on the air-flow characteristics: Reynolds number and heat transfer coefficient [120, 121]. As a consequence, the condenser length is impacted as well. To show the importance of such geometric parameters, fin thickness and fin pitch (δ and f_p) and number of tubes in the bundle (in the transversal and longitudinal directions, X_l and X_t) have been changed, as well as tubes diameter and flow arrangement, to modify the condenser dimensions. Considering a constant thermal power of 15 kW as well as the oversizing to allow subcooling and referring to the geometrical characteristics reported in Fig. 7.5, the results of such parametric study are reported in table 7.2.

Each geometric characteristic of the condenser deeply impacts its behaviour and the change of just one of them leads to a different condenser configuration. External air pressure drop, for example, is impacted by number of ranks, bundle depth and fins geometry. At constant values of δ , l , f_p and longitudinal distance, X_l , the higher the number of ranks, the higher the pressure drop on the air side. This is the reason why the number of ranks should be maintained as low as possible. If fin thickness is increased of 100 μm , the number of tubes per rank should be increased as well to maintain all other geometric characteristics, including condenser total length, unchanged. Observing, for example, the geometry related to a bundle width of 0.3 m (see table 7.2), increasing the

⁴The contact resistance between tubes and fins is not considered neither for solution 2025 nor for 2035 one.

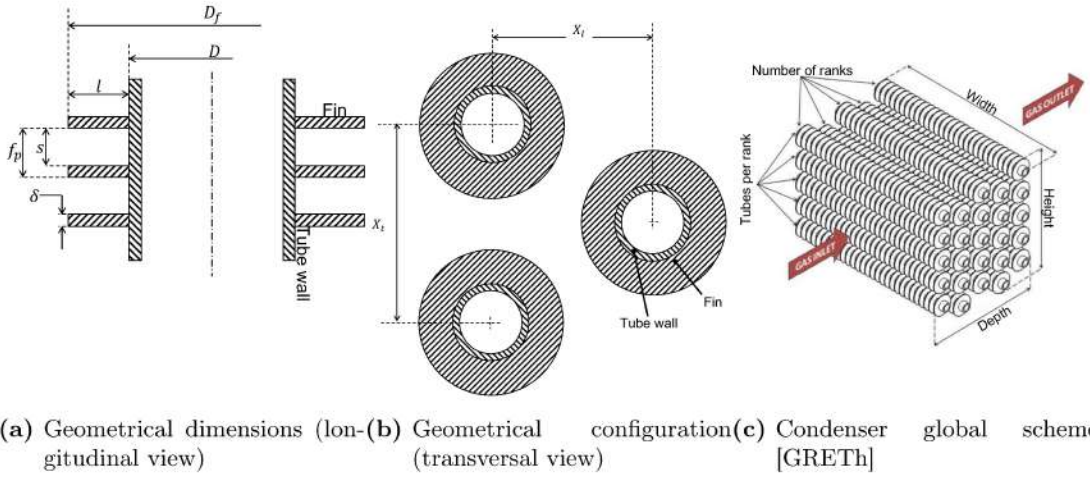


Figure 7.5: Circular fins geometric characteristics

$\delta(\mu\text{m})$	l (mm)	f_p (mm)	Bundle width (m)	Bundle height (m)	Bundle depth (m)	Nbr of ranks	Tubes per rank	Total Length (m)
100	10	1	0.3	0.132	0.67	3	7	17.1
			0.5	0.179	0.35	4	9	18.5
			0.7	0.084	0.47	2	12	17.0
200	10	1	0.3	0.132	0.67	3	17	17.2
			0.4	0.179	0.4	4	10	16.7
			0.7	0.084	0.5	2	12	16.3
300	10	2	0.3	0.132	0.79	3	20	16.5
			0.5	0.084	0.75	2	19	17.2
			0.7	0.084	0.55	2	14	17.5
400	10	2	0.3	0.179	0.56	4	15	16.2
			0.5	0.132	0.51	3	13	16.9
			0.7	0.084	0.55	2	14	17.5
500	15	4	0.4	0.112	1.28	2	24	21.1
600	15	5	0.3	0.112	1.7	2	32	21.9
700	15	6	0.3	0.112	1.8	2	34	23.4
800	15	6	0.3	0.112	1.8	2	34	23.4

Table 7.2: Individually finned condenser geometrical parameters for different fin pitches and thickness

fin thickness, δ , from 100 to 200 μm , the number of tubes per rank increases from 7 to 17! Due to constant bundle height, tubes transversal distance, X_t , decreases: fins are closer and air maldistribution increases. This reduces the overall HXG efficiency and

introduces a pressure drop penalty. Again, comparing results for $\delta = 200$ and $300 \mu\text{m}$, a slight reduction of condenser length is possible by increasing the fin pitch, f_p , of 1 mm. Bundle depth increases as well and a higher number of tubes per rank is required.

All solutions in table 7.2 are equivalent from a thermal point of view (all of them are able to evacuate the same thermal load), but not from a hydraulic standpoint. Fin thicknesses higher than $400 \mu\text{m}$ are not suitable because of pretty high overall condenser volume: one assists to a significative increase of bundle length. In Fig. 7.6 condenser mass and thermal power coefficient are reported as a function of fin thickness, δ , for such solutions of table 7.2 minimising the overall condenser mass. As expected, the increase of fin thickness leads to the increase of the overall condenser mass.

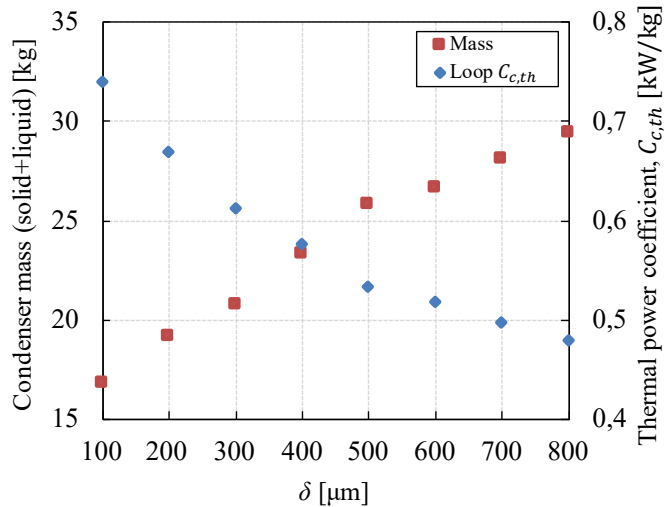


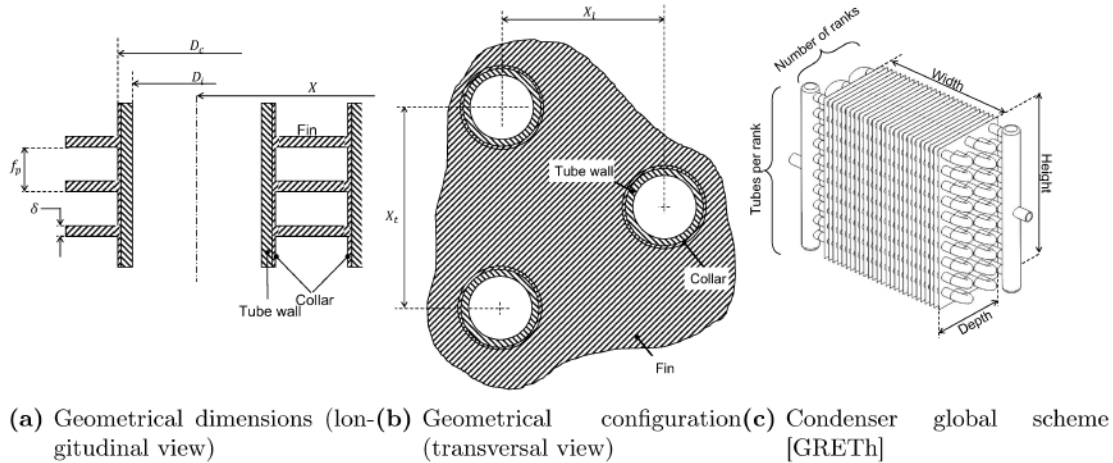
Figure 7.6: Condenser mass and thermal power coefficient as a function of fin thickness, δ .

Continuous finned tubes Mechanical construction of this configuration is quite different than the previous one. Geometric characteristics and tube configuration are reported in Fig. 7.7.

Tubes are inserted in a casing, called *collar*⁵, on which rectangular fins are brazed on. Collar and fins are made of the same material. Tubes are forced to enter into the collar to reduce the contact resistance between them. This configuration is the most used in transport applications such as automobiles radiators. Air is forced to flow among fins and can only interact with tube sections along its path. A thermal interaction between adjacent tubes can occur due to conduction on the fin in X_l and X_t directions. Condenser

⁵Collar internal diameter is the same than tube external one; collar external diameter, D_c , is the tube external diameter + collar thickness (sometimes assumed equal to fin thickness).

design for a thermal load of 15 kW is reported in table 7.3 for different fin thicknesses and pitches (δ and f_p). Condenser behaviour is impacted at the same way than the previous fins typology.



(a) Geometrical dimensions (longitudinal view)
(b) Geometrical configuration (transversal view)
(c) Condenser global scheme [GRETh]

Figure 7.7: Continuous fins geometric characteristics

$\delta(\mu\text{m})$	D_c (mm)	f_p (mm)	Bundle height (m)	Bundle depth (m)	Bundle width (m)	Nbr of ranks	Tubes per rank	Length (m)
1000	1.3	9	0.32	0.155	1.50	2	40	24
100	1.3	2	0.32	0.155	0.95	2	25	15
100	1.3	2	0.32	0.076	1.00	2	28	16.8

Table 7.3: Parametric study of continuous fins condenser.

A comparison of optimised configuration of both typologies, using a fin thickness of 100 μm , is reported in table 7.4. Continuous fins allow a reduction of the condenser mass as well as a reduction of external side pressure drop and a slightly higher heat exchanger efficiency. This configuration is the one used for 2025.

Configuration	$\delta(\mu\text{m})$	Mass (kg)	Volume (m^3)	Loop C_c ($\text{kW}\cdot\text{kg}^{-1}$)
Individually finned	100	16.6	0.026	0.67
Continuous finned	100	13.3	0.044	0.74

Table 7.4: Condenser configurations comparison.

7.2.2.1.1 Optimised solution for 2025

Condenser Optimised geometric and thermo-hydraulic characteristics are reported in table 7.5 and 7.6, respectively, for a continuous finned condenser⁶.

The same tube thickness of transport lines, 0.6 mm, has been used for all optimised solutions. A fluid arrangement of four fluid passages has been previewed independently from thermal load and number of tubes composing the condenser. Fins and bank geometric characteristics (δ , f_p and X_l , X_t respectively) are unchanged as well, while condenser external dimensions vary as a function of length and number of tubes to adapt condenser thermo-hydraulic characteristic to the thermal load to be evacuated. On the internal side, the resolution method reported in sec. C.1 is used by the software for thermo-hydraulic resolution. Actually, for thermal calculation, Thome's condensation heat transfer model [122, 123] (see C.1.2.2) is used, but no outputs are given about the resulting condensation regime. The reason of constant internal heat transfer coefficient as a function of thermal power are not known.

Considering the mass of the cooling system as trade-off factor, as usual, if just fins geometrical characteristics were modified it could be very difficult to achieve an optimum solution. In fact, to a reduction of fin mass corresponds a proportional increase of tubes mass to damp the lower heat transfer surface area and the HTC reduction. To better understand, let's analyse two condenser solutions. Both are designed to evacuate a nominal thermal load of 16 kW, but using two different fin densities.

The first one, corresponding to the optimum solution (reported in tables 7.5 and 7.6), has a fin density of 833 fins/m (corresponding to a fin pitch $f_p = 1.2$ mm). The second one, with a fin density of 416 fins/m, is identical to the first one, except for the fin pitch which is the double ($f_p = 2.4$ mm). An increase in fin pitch, f_p , leads to condenser undersizing of 27%, if all other geometrical dimensions remain unchanged. Such undersizing is obviously due to a not sufficient heat transfer surface area and to a slight lower HTC. To damp such fin pitch, f_p , variation, the number of tubes per rank should be increased from 22 to 32 and the single tube length from 0.55 to 0.62 m. The condenser is almost 8 m longer! In Fig. 7.8 a comparison of condenser mass distribution is reported for optimised and not optimised solutions (Fig. 7.8a and 7.8b, respectively). A reduction of fin mass leads to an increase of the volume of fluid due to additional tube length and, considering titanium density (used for tubes), almost double than aluminium one (used for fins), the additional mass is significantly higher. The condenser total mass increases of about

⁶With the purpose to provide WP6 (optimisation team, see chap. I) with CPLIP mass trend as a function of power electronics thermal losses, the cooling system has been optimised in the range 5 – 30 kW.

Nominal thermal power (kW)	$\delta(\mu\text{m})$	D_{int} (mm)	D_c (mm)	f_p (mm)	Bundle width (m)	Bundle height (m)	Bundle depth (m)	Nbr of ranks	Tubes per rank	X_t (mm)	X_l (mm)
6	100	3.8	5.2	1.2	0.3	0.265	0.099	8	15	17.7	12.4
8	100	3.8	5.2	1.2	0.37	0.283	0.099	8	16	17.7	12.4
10	100	3.8	5.2	1.2	0.47	0.283	0.099	8	16	17.7	12.4
12	100	3.8	5.2	1.2	0.5	0.319	0.099	8	18	17.7	12.4
14	100	3.8	5.2	1.2	0.61	0.300	0.099	8	17	17.7	12.4
16	100	3.8	5.2	1.2	0.55	0.389	0.099	8	22	17.7	12.4
18	100	3.8	5.2	1.2	0.61	0.389	0.099	8	22	17.7	12.4
20	100	3.8	5.2	1.2	0.69	0.389	0.099	8	22	17.7	12.4
25	100	3.8	5.2	1.2	0.72	0.46	0.0992	8	26	17.7	12.4

Table 7.5: Optimised solution geometry, 2025

Effective thermal power (kW)	Thermal efficiency (%)		HTC_{int} ($\text{W}\cdot\text{m}^{-2}\cdot\text{K}^{-1}$)		HTC_{ext} ($\text{W}\cdot\text{m}^{-2}\cdot\text{K}^{-1}$)		ΔP_{int} (Pa)	ΔP_{ext} (Pa)	Area (m ²)
	C	S	G	F	C	S			
6	0.45	87.65	87.04	2383	224.3	92.53	57.54	120.8	11.54
7.97	0.60	87.58	86.97	2383	224.3	93.21	101.9	122.9	15.18
10.05	0.76	87.67	87.06	2383	224.3	92.39	214.9	120.3	19.28
12.02	0.91	87.65	87.04	2383	224.3	92.53	266.8	224.3	23.08
13.99	1.06	87.59	86.98	2383	224.3	93.17	497.8	122.8	26.59
16.06	1.21	87.70	87.09	2383	224.3	92.1	350.4	119.4	31.02
18.03	1.361	87.62	87.01	2383	224.3	92.83	495	121.7	34.41
20.11	1.52	87.71	87.11	2383	224.3	91.92	689.9	118.8	38.92
25.02	1.89	87.64	87.03	2383	224.3	81.17	784.9	1210	48.00

Table 7.6: Optimised solution thermo-hydraulic characteristics, 2025 (C: condensation zone; S: subcooling zone; G: global; F: fin)

23%, from 7.8 to 10.1 kg (fluid included), and the total loop mass increases from 11.8 to 15 kg⁷: it's about 21%! —Once optimal fins geometry has been found it is better to act on the bank configuration to achieve required results—.

Optimisation results Except the evaporator, which dimensions are related to power electronics modules⁸, CPLIP components mass increases as a function of thermal load.

⁷Overall loop mass increase is also due to reservoir volume mass augmentation.

⁸2025's power module dimensions, evaporator characteristics and configuration have been deeply explained in sec. 6.3.2

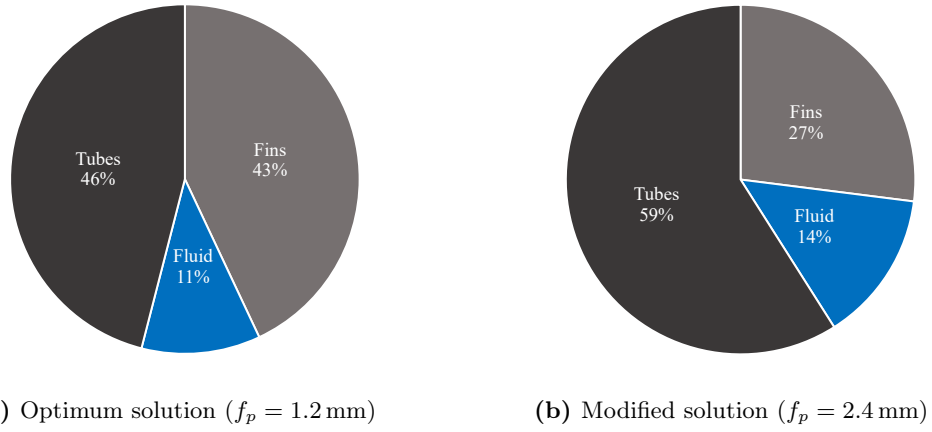


Figure 7.8: Condenser mass distribution for optimised and not optimised solution

Fig. 7.9 depicts the overall loop mass (Fig. 7.9a) and thermal power coefficient (Fig. 7.9b) variation as a function of power electronics thermal losses for solution 2025. As expected, the higher the thermal power to be evacuated, the higher the mass of the cooling system. One may notice that, m_{th} , is linearly related to the thermal load, Q_{th} , as:

$$m_{th} = a Q_{th} + b \quad (7.5)$$

where coefficients a and b are respectively 0.5681 and 2.7323. In particular, the presence of coefficient b is due to a constant evaporator mass whatever the thermal load⁹.

Thermal power coefficient, $C_{c,th}$, has a hyperbolic trend and is characterised by the same coefficients than eq. (7.5):

$$C_{c,th} = \frac{Q_{th}}{m_{th}} = \frac{Q_{th}}{a Q_{th} + b} \quad (7.6)$$

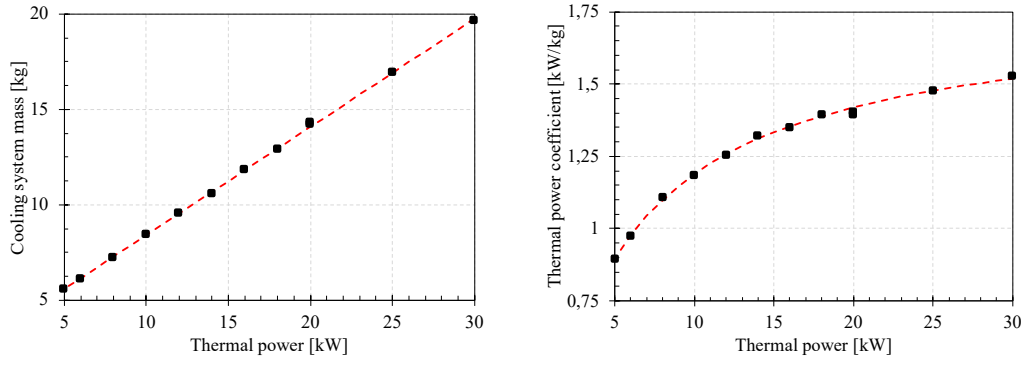
An important mass reduction than first approximation design is evident observing both mass and thermal power coefficient diagrams. Optimisation has led to a significative reduction of the cooling system overall mass, obtaining a thermal power coefficient of $1.33 \text{ kW}\cdot\text{kg}^{-1}$ for the 15-kW-CPLIP¹⁰.

An example of mass distribution for a 16-kW-CPLIP is reported in Fig. 7.10. The smaller condenser leads to a reduction of total fluid and reservoir masses, while the evaporator perceptual-weight has obviously increased due to total weight reduction.

Considering the four electronic topologies proposed by WP2 team [21] for 2025, the

⁹The value of coefficient b agrees with the evaporator total mass.

¹⁰This thermal losses amount has been used of the first approximation design in chap. 4.



(a) CPLIP mass variation as function of the thermal load (2025)

(b) Thermal power coefficient (C_{Cth}) trend as function of the heat power (2025)

Figure 7.9: Cooling system overall mass and thermal power coefficient as a function of the thermal load

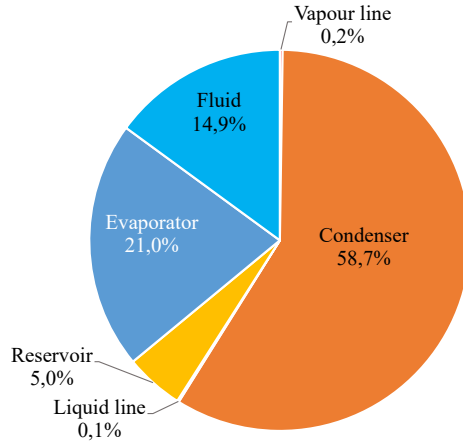


Figure 7.10: Components mass distribution for 16 kW CPLIP

related cooling system optimised results are reported in table 7.7. The highest power coefficient ($> 19 \text{ kW}\cdot\text{kg}^{-1}$, higher than the $15 \text{ kW}\cdot\text{kg}^{-1}$ required for target 2025) was reached for the NPC-DPWMMAX topology [1]. The latter, from an electronic point of view, is characterised by the lowest mass, and the highest electric efficiency: the one that minimises the thermal losses. —Considering the whole system, power electronics and its adjoined cooling *apparatus*, the best solution is not the one composed by two optimised subsystems, but the one characterised by the best trade-off—.

Power electronics topology	Cooling system mass (kg)	Power electronic mass (kg)	$C_{c,th}$ (kW·kg ⁻¹)	C_c (kW·kg ⁻¹)
FC-DPWMMAX	10.5	83	1.29	16.04
FC-PWM	14.0	83	1.16	15.46
NPC-DPWMMAX	11.1	65	1.26	19.71
NPC-PWM	12.3	65	1.27	19.41

Table 7.7: Optimised results for the proposed electronic topologies (2025) [1, 21]

7.2.2.2 A condenser for 2035

2025 solution is characterised by a condenser which has been optimised to minimise as much as possible the whole mass of the loop, but its perceptual weight in CPLIP distribution is still high. With the purpose to further reduce the overall cooling system mass for 2035, another condenser technology must be selected. Such technology has to be characterised by the highest external HTC possible to reduce the solid mass. Moreover, it should contain the lowest amount of fluid with the purpose to reduce the reservoir volume and its fluid content.

Louvered fin heat exchangers (see Fig. 7.11) are characterised, on the external side, by a complex, “interrupted” fin geometry. The “breaking” of the fins allows, of course, to an increase of heat transfer surface area, but it is marginal if compared to the heat transfer coefficient enhancement.

Other than the already known dimensions, in common with “conventional” fins (fin pitch, height and thickness), louvered fins are characterised by the louver angle, louver pitch and louver height, L_α , L_p and L_h , respectively, in Fig. 7.11b.

To enhance the external side heat transfer coefficient, the physics principle beyond louvered fins is based on the rupture of the fluid boundary layer passing through two fins. A portion of air flows through two adjacent fins while another portion deviates flowing through louvers. Among them, boundary layer is broken creating counter-rotating recirculation zones respectively to the leading edge and the detachment bound of the louver itself. Thanks to them, heat transfer coefficient can increase up to three times the one of a not interrupted surface [124]. As one may easily guess, this kind of technology is characterised by higher pressure drops than conventional ones.

With the purpose to reduce the volume of fluid in the condenser and to increase the overall condenser performances, microchannels are used on the internal side. Despite the high pressure drops related to such technology (see. chap. 3.2.2), they are lower than the residual pressure drop calculated considering $\Delta P_{cap,max}$ (see eq. (2.13)) for any exploited

thermal power. Based on the same optimisation criterion used for the solution 2025, and following the same methodology, optimised condenser geometry and thermo-hydraulic characteristics for different thermal loads are reported in table 7.8 and 7.9.

Like the 2025 solution, titanium is the material used for tubes and aluminium is the

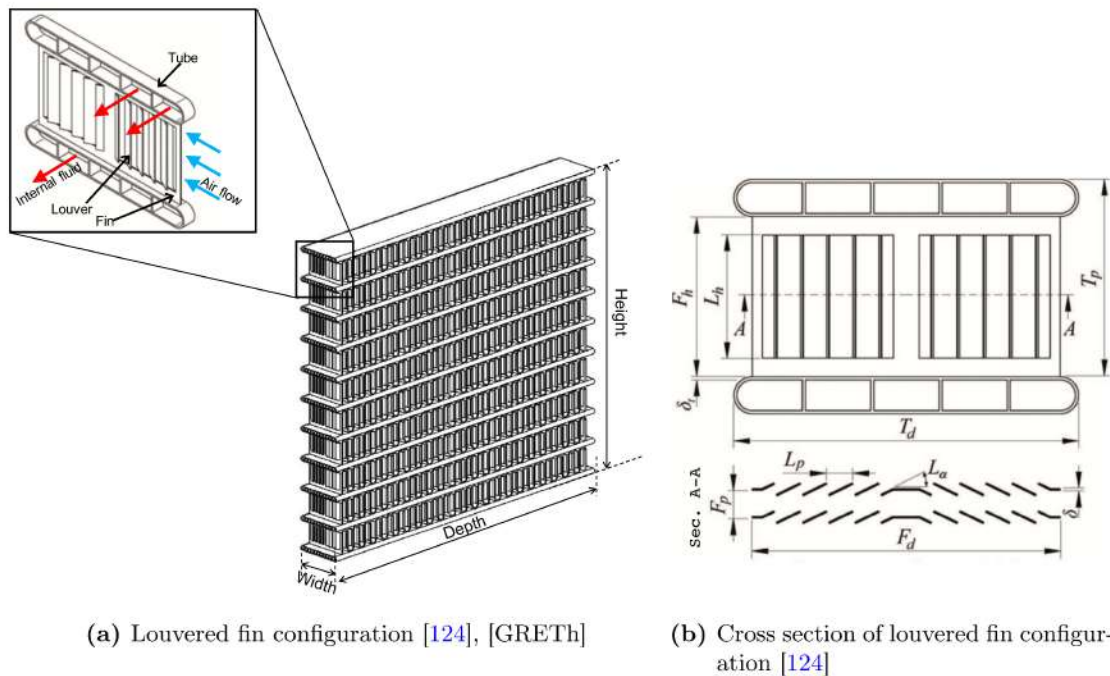


Figure 7.11: Louvered fin condenser

Nominal thermal power (kW)	Fins			Louver			Bank				
	δ (μm)	f_p (mm)	F_h (mm)	L_h (mm)	Height (mm)	L_p (mm)	Width (m)	Height (m)	Depth (m)	N tubes	M. chs/tube
6	100	1	8	7	0.35	0.5	0.04	0.105	0.175	12	30
8	100	1	8	7	0.35	0.5	0.0364	0.133	0.23	15	30
10	100	1	8	7	0.35	0.5	0.04	0.152	0.24	17	33
12	100	1	8	7	0.35	0.5	0.0364	0.171	0.265	19	30
14	100	1	8	7	0.35	0.5	0.0364	0.180	0.35	20	30
16	100	1	8	7	0.35	0.5	0.0364	0.189	0.37	21	30
18	100	1	8	7	0.35	0.5	0.0376	0.199	0.38	22	31
20	100	1	8	7	0.35	0.5	0.040	0.208	0.31	23	33
25	100	1	8	7	0.35	0.5	0.0424	0.282	0.35	23	35

Table 7.8: Optimised solution geometry, 2035

Effective thermal load (kW)		Thermal efficiency (%)		HTC_{int} ($\text{W} \cdot \text{m}^{-2} \cdot \text{K}^{-1}$)		HTC_{ext} ($\text{W} \cdot \text{m}^{-2} \cdot \text{K}^{-1}$)	ΔP_{int} (Pa)	ΔP_{ext} (Pa)	Area (m ²)
C	S	G	F	C	S				
5.027	0.466	-	-	3707	1238	320.7	228.2	884	1.39
7.977	0.698	-	-	4239	1538	320.3	423.3	749.3	2.11
10.05	0.880	-	-	4254	1238	321.1	584.5	877	2.76
12.02	1.051	-	-	4543	1572	322.4	888.6	758.4	3.12
13.99	1.223	-	-	4728	1592	324.0	1165	768.1	3.61
16.06	1.405	-	-	4900	1630	326.6	1419	784.9	4.06
18.03	1.577	-	-	4972	1672	330.4	1598	854	4.54
20.11	1.759	-	-	4977	1712	341.2	1633	1034	4.90
25.02	2.189	-	-	5308	1851	354.5	2461	1271	5.86

Table 7.9: Optimised solution thermo-hydraulic characteristics, 2035 (C: condensation zone; S: subcooling zone; G: global; F: fin)

one foreseen for fins. Rectangular, 0.2-millimetres-thick tubes are equipped by 1 mm-side-microchannels, spaced of 0.2 mm, which number varies as a function of the thermal load. The internal fluid traverses the condenser in two passages. $N - 1$ tubes are fed-up in parallel, so that the mass flow rate is fairly shared among them (1st passage), while for the second passage, the total amount of fluid is conveyed to flow within the last tube. A manifold is used at the inlet to supply the $N - 1$ tubes and at the outlet to receive the subcooled liquid from the last tube just before the CPLIP's liquid line. Such asymmetry in the mass flow arrangement allows a significative reduction of the overall condenser mass whatever the thermal load. Despite the high pressure drop, either on the internal and on the external side, the condenser is significantly performant if compared to the solution proposed for 2025. In fact, as one can notice from table 7.9, the use of louvered fins allows a significant increase of external HTC, three times higher than the one of 2025 (see tab. 7.6). Such high values of HTC lead to the decrease of the heat transfer surface area, allowing a significative mass saving. Considering the 16 kW solution, for example, the required heat transfer surface area is almost eight times lower for the louvered finned microchannel condenser. Mass distribution of the condenser (see Fig. 7.12) is almost the same than the classical solution, but its total mass is pretty lower.

Optimisation results The same electronic configuration than 2025 has been previewed by WP2 for the solution 2035 (NPC-DPWMMAX) [21]. Power electronics thermal losses are the same, but a different kind of power module is employed with the purpose to make the entire electronic system lighter. Power modules are larger than 2025 ones, they

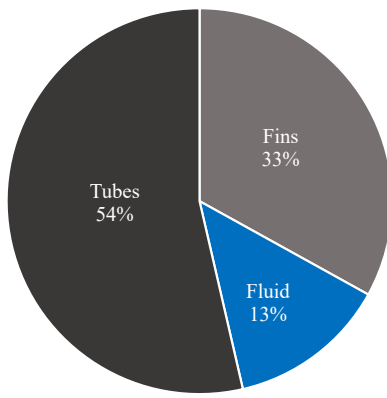


Figure 7.12: Louvered fins and microchannels condenser mass distribution example

are squared ($160 \times 160 \text{ mm}^2$), and only two power modules per electric phase are used. This configuration, under an electronic standpoint, allows mass saving due to reduction of electrical capacities [21]. Even in this case power modules are installed on the evaporator face-to-face resulting in a three parallel evaporators CPLIP. As result, considering the thermal losses related to this electronic configuration, the adjoined cooling system mass, equipped by a louvered fin-microchannels condenser, is just 5.5 kg and, taking into account a power electronics system mass of 22 kg [21], the related global power coefficient¹¹, C_c , overcomes $54 \text{ kW} \cdot \text{kg}^{-1}$! If the main issue of solution 2025 was related to the reduction of condenser mass, in this case, room for improvement are no longer possible. Condenser is the smallest possible while the evaporator represents the critical component. In fact, observing Fig. 7.13, where a 16-kW-optimised CPLIP components mass distribution is reported, the evaporator is about 72% of total mass, while the cumulated mass of all other components is almost one quarter of total! This solution is the closest to the ideal case: the mass of the entire cooling system is concentrated where power modules are positioned. Cooling system overall mass and thermal power coefficient trends as a function of the thermal load are reported in Fig. 7.14a and 7.14b respectively. The same trends than 2025 has been obviously found, but they are quantitatively different. This solution allows a mass lowering up to six times the 2025's solution with the consequent “boosting” of the thermal power coefficient up to three times.

¹¹2035 target is $25 \text{ kW} \cdot \text{kg}^{-1}$

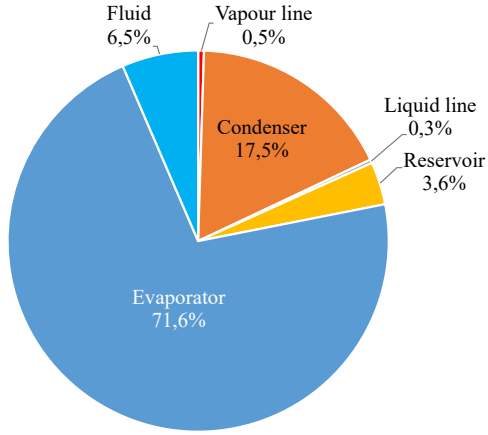
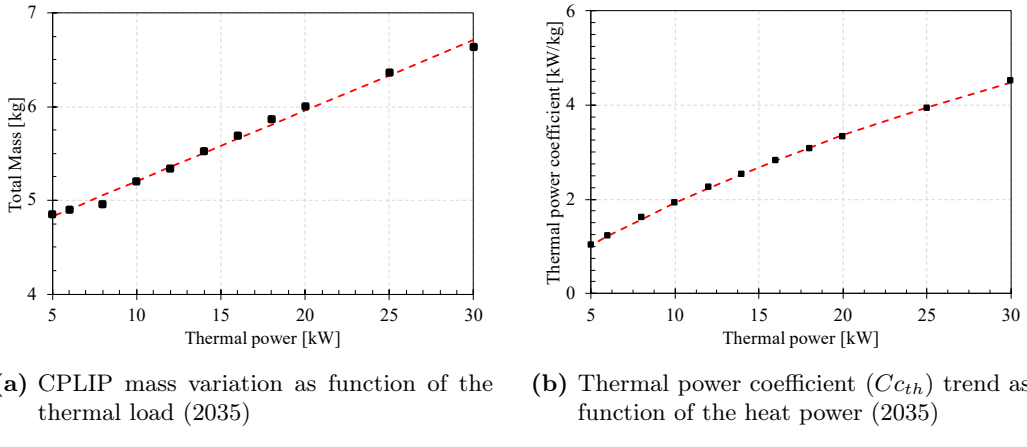


Figure 7.13: Louvered fin-microchannels equipped CPLIP mass distribution



(a) CPLIP mass variation as function of the thermal load (2035) (b) Thermal power coefficient ($C_{c_{th}}$) trend as function of the heat power (2035)

Figure 7.14: Mass and thermal power coefficient as a function of the thermal load (2035)

7.3 Back to design point

To chose the design point, it was necessary to consider the entire mass of the cooling system to check if its thermal inertia could be used to damp the lack of neglected energy, $E_{neglected}$, during the take-off stage (see sec. 7.1 and Fig. 7.1).

In general, if no cooling is foreseen, the thermal energy accumulated in a given interval of time is:

$$E_{neglected} = \int_{t_1}^{t_2} Q_{th}(t) dt \quad (7.7)$$

and also,

$$E_{neglected} = C_{eq} \Delta T \quad (7.8)$$

where the equivalent thermal capacity, C_{eq} , is given by the parallel of thermal capacities of the whole CPLIP (solid and filling liquid)¹²:

$$C_{eq} = m_s c_{p,s} + m_l c_{p,l} \quad (7.9)$$

Combining eq. (7.7) and (7.8), the temperature increase, ΔT , due to the absence of the cooling system to evacuate the thermal load, $Q_{th}(t)$, may be obtained as:

$$\Delta T = \frac{\int_{t_0}^{t_1} Q_{th}(t) dt}{C_{eq}} \quad (7.10)$$

Considering the four electronics topologies proposed by WP2, and considering the design point marked by the letter D in Fig. 7.1, the neglected thermal load shape as a function of time, $Q_{th}(t)$, is reported in Fig. 7.15a. Under the hypothesis that the neglected thermal energy, $E_{neglected}$, is accumulated by the entire mass of the cooling system, the temperature increase due to not evacuated thermal load (calculated according to eq. (7.10)) as a function of time is reported in Fig. 7.15b.

Even if, for the best performing electronic configuration (the one characterised by the best efficiency, NPC-DPWMMAX, grey lines on diagrams 7.15), the quantity of neglected thermal energy is about 2% of the take-off one (see table 7.1), at the end of take-off the system is subject to a temperature rise higher than 30 K.

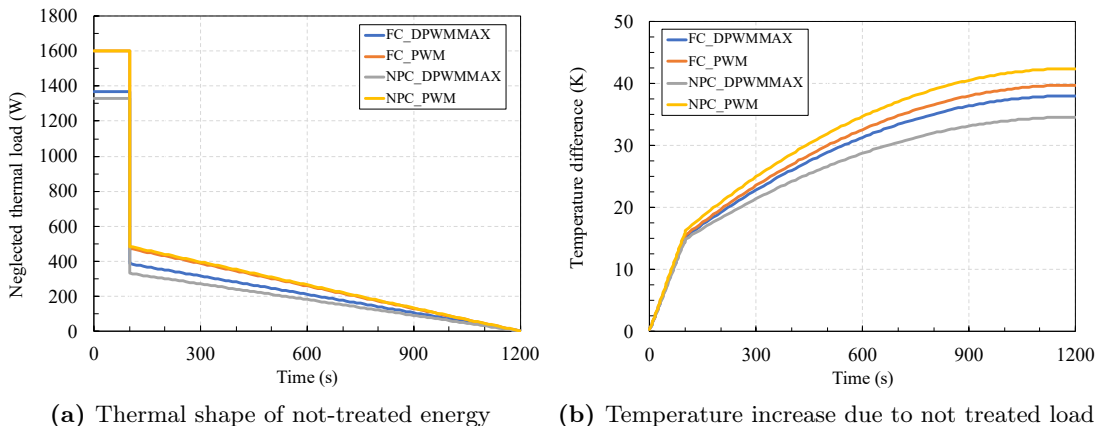


Figure 7.15: Thermal load shape and temperature increase due to not treated thermal energy

CPLIP's thermal inertia cannot damp such amount of neglected energy, $E_{neglected}$, and, to avoid catastrophic consequences, the highest value of thermal losses must be chosen

¹²In reality only evaporator, vapour line and condenser solid and liquid parts should be considered for the purpose. The entire CPLIP mass has been used here to be conservative.

as cooling system design point!

7.4 Overall power coefficient

Targets to be achieved for power electronics and its adjoined cooling system either for 2025 and 2035 are stated here to remind:

- 2025: $15 \text{ kW} \cdot \text{kg}^{-1}$
- 2035: $25 \text{ kW} \cdot \text{kg}^{-1}$

Power coefficient trend as a function of thermal load, for constant power electronics mass, m_{el} , and constant electrical power to be converted, Q_{el} , is here proposed with the purpose to study the variation of total power coefficient, $C_{c,tot}$, as a function of thermal losses, Q_{th} . Considering that cooling system mass, m_{th} , is linearly related to them, see eq. (7.5), the total power coefficient, expressed by the ratio $C_{c,tot} = \frac{Q_{el}}{m_{el} + m_{th}}$, assumes the hyperbolic form described by eq. (7.5). Due to such relation, power coefficient trend is characterised by a decreasing hyperbolic shape.

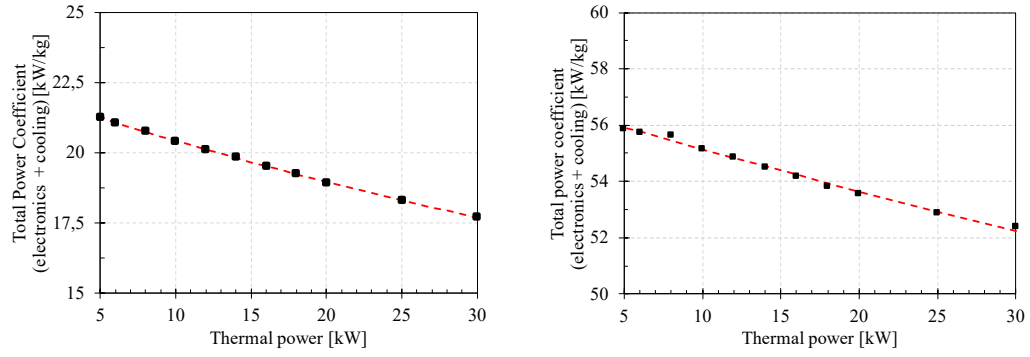
$$C_{c,tot} = \frac{Q_{el}}{m_{el} + (a Q_{th} + b)} \quad (7.11)$$

Fig. 7.16 shows power coefficient interpolated data for different thermal losses and for 2025 and 2035 solutions. Here, power electronics mass, m_{el} , is considered constant whatever the thermal losses: 65 and 22 kg, for 2025 and 2035 solutions, respectively. Moreover, the total electrical power is also considered constant, $Q_{el} = 1500 \text{ kW}$.

As one can easily notice both solutions overcome the target imposed in the context of the HASTECS project!

Solutions for 2025 and 2035 are similar considering the cooling technique. Both solutions share the same components and materials, but not the condenser technology. In 2025 solution, the condenser was the heaviest component allowing room for improvement for 2035 solution, while in the latter the evaporator is the most critical component in the loop. Also, after optimisation, the difference in terms of mass, between 3 independent CPLIPs and three parallel heads CPLIP, is absolutely negligible. Thanks to the use of a cutting-edge technology, allowing to boost condenser external HTC and to increase the compactness of the heat exchanger, requirements of 2035 have been overtaken!

In this work the attention is only focused on thermal and hydraulic issues, and mechanical ones are not addressed. Thus, mass calculations do not consider fixation devices, mechanical construction and other kind of accessories that obviously lead to an increase



(a) Global power coefficient (C_{ctot}) trend as function of thermal losses (2025): $Q_{el} = \text{const} = 1500 \text{ kW}_e$; $m_{el} = \text{const} = 65 \text{ kg}$

(b) Global power coefficient (C_{ctot}) trend as function of thermal losses (2035): $Q_{el} = \text{const} = 1500 \text{ kW}_e$; $m_{el} = \text{const} = 22 \text{ kg}$

Figure 7.16: Global power coefficient trends for 2025 and 2035 solutions

of the overall mass. It has to be underline that, however, the obtained results allow room for manoeuvre!

7.5 Conclusion

In this chapter CPLIP was designed and optimised following the HASTECs' requirements for 2025 and 2035. After a discussion about the complex optimisation process linked to the condenser, and about the most suitable fin configurations to be used, optimised CPLIP results for 2025 have been presented for the four electronics configurations. Each of them is characterised by a different efficiency. Considering either electronics components and the adjoined cooling system, the configuration allowing the highest mass saving was the NPC-DPWMMAX. In this case, the obtained power coefficient was pretty higher than requirement for 2025 ($> 19 \text{ kW}\cdot\text{kg}^{-1}$).

With the purpose to further reduce the mass of the cooling system, a louvered fins-microchannels condenser was selected for the solution 2035. The latter allows a reduction of the solid mass thanks to enhancement of external side HTC, and a reduction of the fluid amount in the loop thanks to the use of microchannels. The cooling solution proposed for 2035 is “impressive”. Despite the electronic configuration is the same than 2025 (the same thermal power must be evacuated), the overall CPLIP mass has been sensibly reduced. Overall power coefficient boosting comes from either electronic and cooling system mass reduction. It is more than twice than the requirement for 2035! However, no accessories and fixation system are considered in calculation at this stage, but the results are encouraging and allows room for manoeuvre.

Part IV

CPLIP behaviour under severe transient conditions

This part is related to the transient behaviour of CPLIP. Its start-up and its response to sudden and violent accelerations are here introduced. The previously introduced numerical model will be used to explain and to understand the phenomena experimentally observed during start-up of the CPLIP in different initial conditions. In the second case, harsh acceleration stages are numerically studied. Weakness and the critical components of this particular cooling system together with a physical explanation of the different phenomena are introduced in this part.

Severe transient phases: Start-up

CPLIP's start-up is worth of attention, as observed in sec. 6.3.3. To have a deeper knowledge of limitations related to this kind of technology, in this chapter a transient study on start-up phases is proposed. In particular, it is interesting to exploit how environmental conditions, such as vapour line initial temperature, affect thermo/hydraulic CPLIP behaviour during this critical stage.

An analysis based on experimental and numerical results is proposed. The same experimental facility used in previous chapters (5 and 6) and works (see ref. [1, 7, 12, 14, 49, 111, 115]) is used here (see Fig. 8.1)¹. Experimental observations are backed up by precise numerical results, based on 1D model, already described in chap. 5, allowing a better understanding of different phenomena occurring during this critical and delicate stage. The attention is in particular focused on vapour line solid walls, to get quantitative evaluation of the influence of their initial temperature and so of energy exchanges between them and vapour. As it will be shown in the following, thermal load applied to the evaporator is not the only parameter to be considered during CPLIP's start-up.

8.1 Experimental operating conditions

The attention is focused on vapour line initial temperature and how the latter influences energy exchanges between vapour, flowing in it, and solid walls. In other terms, solid walls thermal inertia plays a fundamental role in successful start-up of the CPLIP. To consider thermal inertia influence, from a numerical stand point, it is sufficient to suppress tube thermal capacity, inhibiting the solid specific heat, c_p , but from an experimental point of view it is necessary to act on walls initial temperature to modify the amount of energy exchanged between the fluid and the solid itself.

By keeping fixed and constant reservoir saturation and cold source temperatures, respectively $T_{res} = 70^\circ\text{C}$ and $T_{sec} = 20^\circ\text{C}$, start-up of the loop has been exploited applying different intensities of thermal load steps to the evaporator and using two vapour line

¹The setting valve will be not used in this study, which is why it is not represented in the scheme.

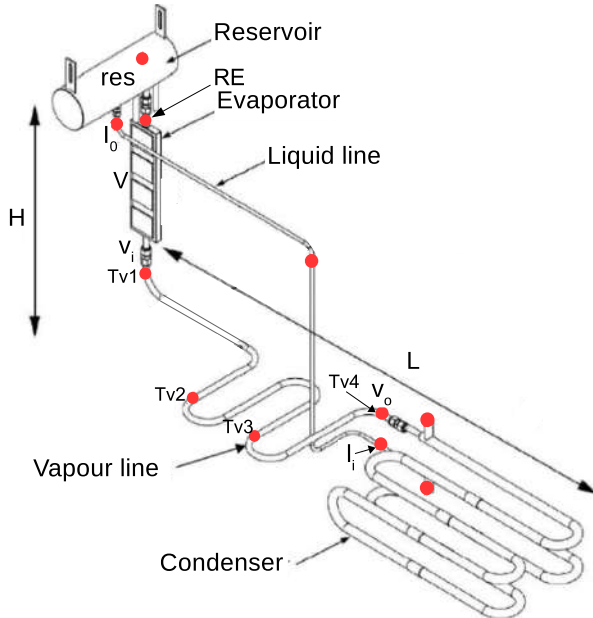


Figure 8.1: CPLIP: experimental facility

solid-wall initial thermal conditions. For simplicity, in the following the definition of cold and hot start-up will be used.

Cold-start-up Start-up condition using vapour line solid walls initial temperature equal to the environmental one (around 20 °C);

Hot-start-up Start-up condition using vapour line solid walls initial temperature higher than the environmental one (between 30 and 60 °C).

In order to experimentally investigate the influence of vapour tube initial temperature, the latter should be modified to reach the expected value. According to this, the complex heating process of vapour line walls is shown in Fig. 8.2. Such process, for practical purposes, has been divided in four stages: I to III (+hot start-up — IV —).

During stage I the loop is in stand-by position. No thermal load is applied to the evaporator, reservoir is kept to desired saturation conditions and cold source temperature is maintained fixed. In order to heat the vapour line, at the beginning of stage II, power supplied to the evaporator is turned-on and secondary side condenser temperature is set-up to desired vapour line solid wall temperature (50 °C for example in this case). The heating process starts here. Condenser cold source temperature increases up to its imposed value and liquid temperature at the outlet of the condenser consequently

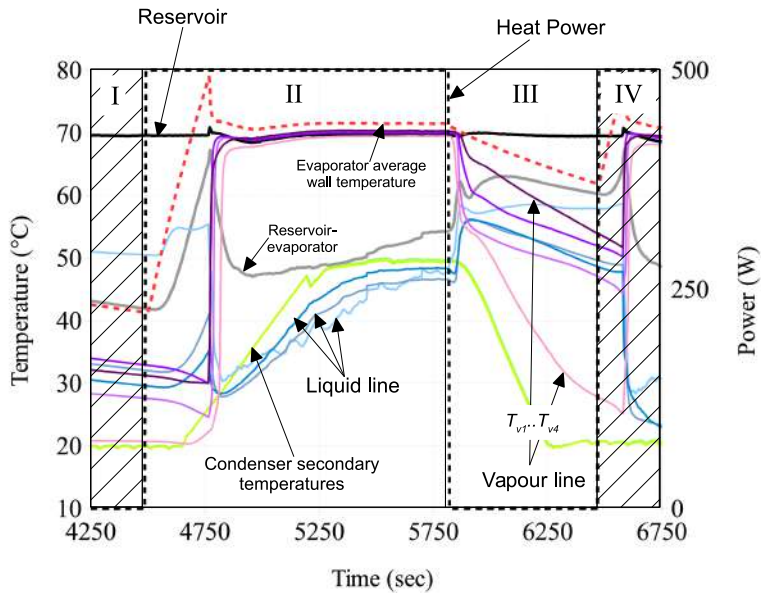


Figure 8.2: Heating process of the vapour line solid walls (methanol, $T_{res} = 70^\circ\text{C}$).

follows such increase. Once steady-state conditions reached, power supply is cut-off and cold source temperature is set-up to the desired value (20°C): stage III begins. Liquid flows back from the reservoir heating the liquid line (blue curves) and subcooled liquid, which temperature is by now close to the cold source one (around 50°C at the end of stage II), flows back and invades condenser and vapour line. At this stage, vapour line solid walls temperature suddenly decreases up to liquid temperature, so they are slightly cooled down. Once the vapour line temperatures have reached the required value, the hot test can begin. Unfortunately, a temperature gradient is present along the vapour line, from the inlet to the outlet. It depends on the proximity of such components like evaporator or condenser. As soon as the cold source temperature has reached the desired value (20°C in this case), power load step is applied to the evaporator: hot start-up test begins (phase IV).

8.2 Start-up behaviour

8.2.1 A severe start-up condition

The response of the CPLIP to a high intensity heat load step, from 0 to 5 kW, during a cold start-up at fixed reservoir and cold source temperature, respectively, $T_{res} = 70^\circ\text{C}$ and $T_{sec} = 20^\circ\text{C}$, is described in this section. The diagram of the response of the

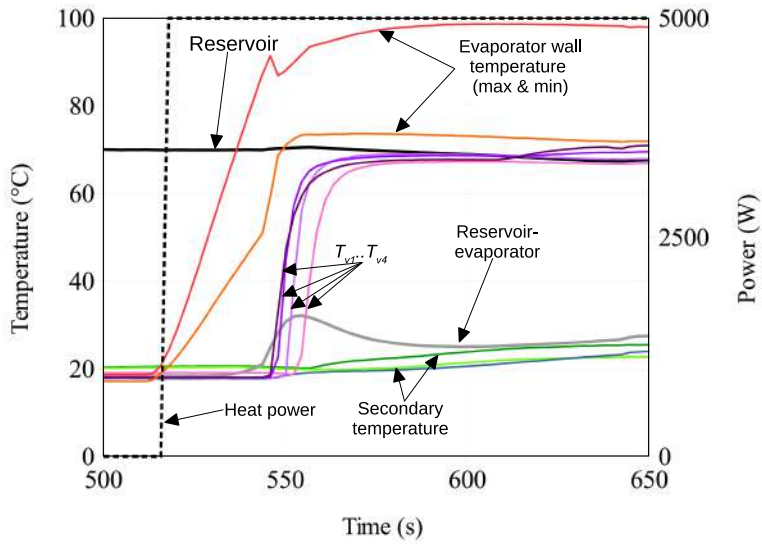


Figure 8.3: 0 – 5 kW cold start-up (methanol, $T_{res} = 70^\circ\text{C}$, $T_{sec} = 20^\circ\text{C}$).

loop is reported in Fig. 8.3². As the power step is applied to the evaporator, the wall temperature increases as quickly as severe the power step is. The evaporator wall temperature continues to rise until vapour is formed in the wick. Evaporator wall is characterised by a temperature difference, red to orange curves' gap (see Fig. 8.3). Following the height of the evaporator, such difference may be attributed to pressure variation between the inlet and the outlet of the evaporator itself: gravity pressure drops lead to progressive recession of evaporation front in the porous wick as a function of temperature levels [111] (see also sec. 6.1.2). When the bottom of the evaporator experiences a temperature peak, due to the onset of nucleation in the wick, its higher part is subject to a fast change in temperature profile. At the same time, temperature increases into reservoir-evaporator tube (grey curve). During start-up, as well as “thermosyphon effect”, from evaporator through the reservoir-evaporator tube, some vapour bubbles percolate the porous wick and flow back to the reservoir. However, no dry-out occurs and liquid, permanently supplied by gravity from reservoir, continues to wet the porous wick. Once saturation conditions stabilised, the temperature difference on evaporator wall stops changing (red to orange curve gap) and vapour, finally, abruptly leaves the evaporator flowing within the vapour line to the condenser. Vapour front transit, through the different sections of the vapour line, may be followed by temperature rise registered by the thermocouples installed on it, one-by-one, from T_{v1} to T_{v4} (dark to light violet

²To simplify the reading, liquid line temperatures were intentionally omitted. They are not relevant for the phenomena here considered.

curves in the diagram). Vapour line is initially filled of liquid at “ambient” conditions ($\simeq 20^\circ\text{C}$), so vapour front passage (pushing-out the liquid) thorough a given section is characterised by a solid wall temperature rise. Sensors register such increase that, as a function of time, has a sigmoid-like shape (as it will be seen in sec. 8.3).

Once vapour front has left the evaporator and liquid has reached the condenser, sub-cooled liquid flows at first in the liquid line and so in the lower part of the reservoir where it is slightly heated. From there, it flows to the evaporator inlet cooling down the reservoir evaporator tube walls until its value is more or less stabilised to the cold source one. The slight increase of inlet and outlet cold source temperatures (light and dark green curves, respectively) is due to slow response of the cryostat. The latter, in fact, is not fast enough to compensate for the occurring high thermal power variation [111].

The loop is able to starts its operations with no particular problems if a high amplitude heat load step (0 – 5 kW) is applied to the evaporator at “low” initial vapour line solid wall temperature. On the contrary, increasing vapour line initial temperature, the loop is not longer able to boot, even in the case of a one-kilowatt-lower load step. In Fig. 8.4, a failing hot start-up of a four-kilowatts-heat power step is reported.

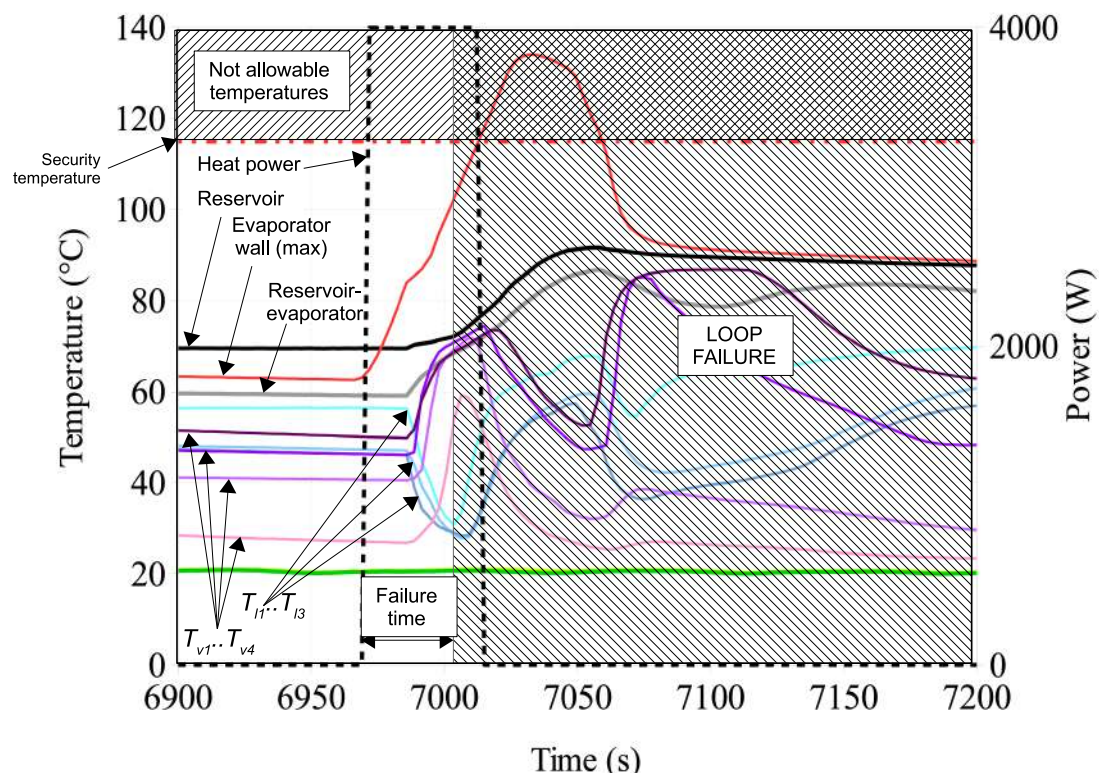


Figure 8.4: 0 – 4 kW hot start-up failure (methanol, $T_{res} = 70^\circ\text{C}$, $T_{sec} = 20^\circ\text{C}$).

Like the first case, after power charge, evaporator wall temperature³ (red line in the diagram) increases, but as the vapour front leaves the evaporator (dark violet curve rise) its shape is slightly modified, but ever growing. At this stage, reservoir saturation temperature (black curve) is modified: vapour bubbles percolate and flow back from the evaporator warming the liquid contained in its lower part. Vapour front flows within the vapour line (all temperature sensors record vapour front passage) and liquid line temperature lowers. At the end of failure time, slope of temperature profiles in the vapour line changes for the first three sections while liquid line temperature rises — no more subcooled liquid is supplied by the condenser —. Continuous percolation from evaporator heavily modifies saturation conditions in the reservoir: reservoir-evaporator line temperature increases (grey line). Once thermal load has been cut-off by security system, evaporator temperature continues to rise due to copper diffusers thermal inertia. The rise of reservoir temperature continues until new saturation conditions are reached. At this moment, in presence of new equilibrium condition the loop seems to re-start! This is testified by the sudden lowering of evaporator walls temperature (red curve), by vapour front passage recorded through the sections of the vapour line (violet curves temperature increase) and by the lowering of liquid line temperature. Cool liquid has reached the lower part of reservoir finally stopping its temperature rising. No thermal load is applied to the evaporator and vapour flow ceases when its saturation conditions reach the reservoir ones. Reservoir and evaporator temperatures slightly decrease, weakly cooled down by natural convection heat exchanges with the external ambient air.

Different tests have been performed to know the start-up limit conditions. In table 8.1, a synthesis of the successful and unsuccessful start-ups is reported.

Power step intensity (kW)	0-0.5	0-2	0-4	0-5
Cold start-up	OK	OK	OK	OK
Hot start-up	OK	OK	X	X

Table 8.1: Successful and unsuccessful start-up synthesis

8.2.2 Low intensity power load step: experimental analysis

Let's now give a look to a working hot start-up and compare it to its cold counterpart. To show how vapour line tubes' thermal discharge influences the overall loop behaviour, a low thermal load power step is used. It has to be considered that all the analyses here introduced are also valid for higher intensity load steps, while the loop is obviously

³For readability issues only the maximal evaporator wall temperature is in this case reported.

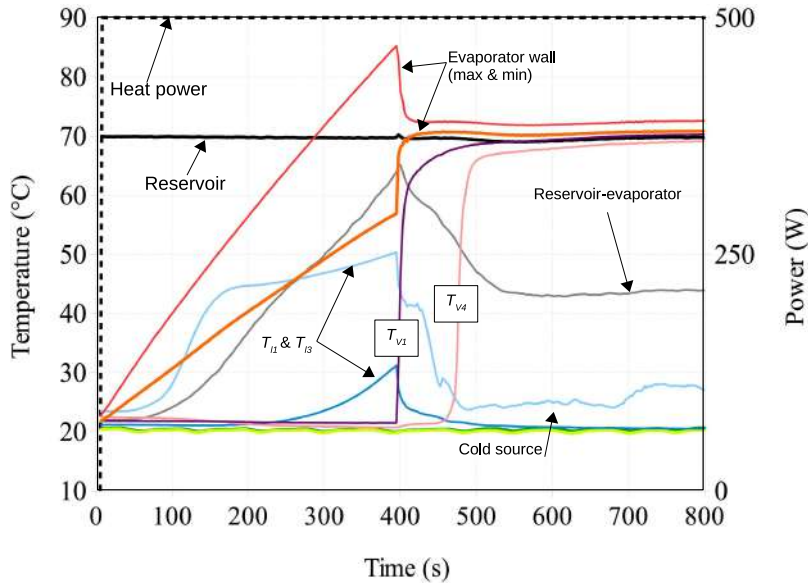


Figure 8.5: Cold start-up (methanol, $T_{res} = 70^{\circ}\text{C}$, $T_{sec} = 20^{\circ}\text{C}$)

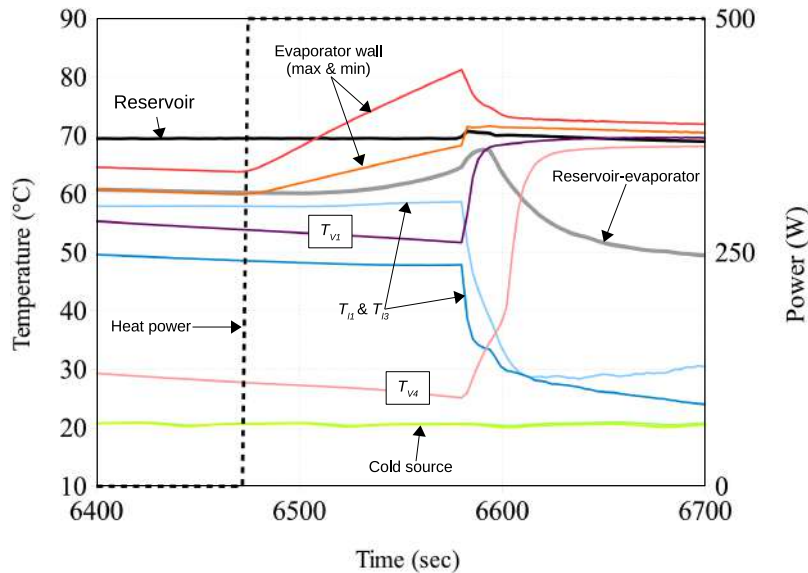


Figure 8.6: Hot start-up (methanol, $T_{res} = 70^{\circ}\text{C}$, $T_{sec} = 20^{\circ}\text{C}$)

still operating. Cold and hot start-ups for a heat load step of 0.5 kW, with methanol as working fluid, are reported in Fig. 8.5 and Fig. 8.6, respectively.

As the power step begins, even in this case a temperature gradient is present on evaporator wall, from the bottom to the top (red and orange lines on the diagrams). Temperature on evaporator wall continues to rise until vaporisation of the liquid occurs in the porous wick, after a sufficient superheating highlighted by the temperature peak.

Comparing the start-ups at 5 kW and 0.5 kW, the evaporator wall temperature obviously increases more slowly in the case of low thermal loads (400 s versus 40 s respectively). During this first stage, the reservoir-evaporator temperature (grey curve) rises. Like the previous case, this is mainly due to natural convection effect occurring in the loop before evaporation in the porous wick. The liquid, heated by the evaporator, flows back to the reservoir and, from there, into the liquid line by gravity. This explains the temperature increase recorded in the liquid line from the moment when the power load is applied to the evaporator, to the time when evaporation occurs. Once vapour front has left the evaporator and the liquid is pushed in the good direction, one assists to a lowering of reservoir-evaporator and liquid line temperatures: subcooled liquid flows from the condenser to the reservoir. Temperatures are stabilised and the loop works in steady-state condition.

In Fig. 8.6 the behaviour of the CPLIP is reported in the case of a hot start-up with an initial vapour line temperature between 30 and 60 °C and using the same operating conditions than before. Even in this case, as the thermal load is applied to the evaporator walls, one assists to a slight temperature rise of reservoir-evaporator tube and liquid line due to thermosyphon effect. The slope of the temperature gradient on the evaporator wall is the same than the cold case, but as the vapour quits the evaporator, the progression time of the vapour front through its line is much lower than before⁴. Vapour front takes about 68 s in the cold case (Fig. 8.5) and 18 s in the hot case (Fig. 8.6) to cross the whole vapour line from the inlet to the outlet. A velocity variation has occurred. The vapour front-flow in the hot case is quicker than the cold one. It is interesting to evaluate vapour front velocities, for different thermal loads applied to the evaporator and for different vapour line temperatures to investigate which phenomena are at the basis of the loop failure for pretty high heat load steps.

8.3 Vapour front velocity evaluation

To remind, vapour front evolution in the vapour line can be followed by observing temperature profile in correspondence of a given section. Temperature profiles are characterised by a sigmoid-like shape, whatever the heat load and the section. Such shape is well described by eq. (8.1) and qualitatively reported in Fig. 8.7.

$$T_{v,n} = T_0 + \frac{\Delta T}{b + c e^{-(\Delta \cdot t + f)}} \quad (8.1)$$

⁴One can notice that the time scale (*x*-axis) in Fig. 8.6 is reduced if compared to Fig. 8.5.

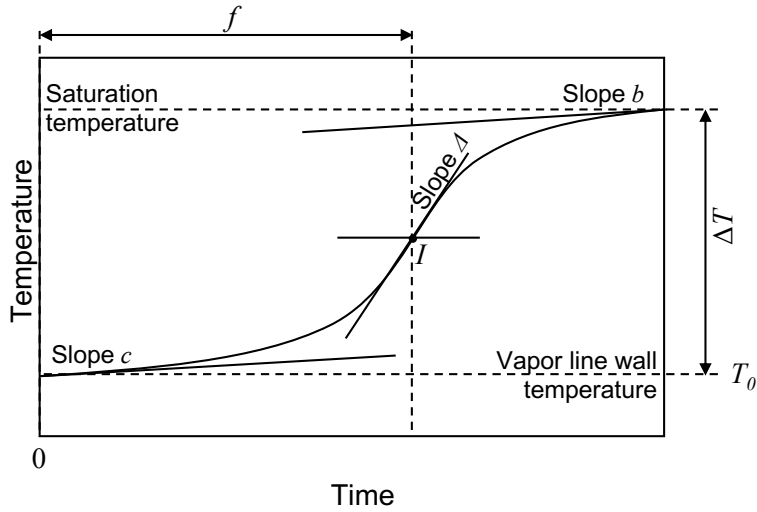


Figure 8.7: Qualitative sigmoid profile as a function of the time

ΔT is the temperature difference between saturation and vapour line initial wall temperature, T_0 , respectively; b and c are tangent values above and below the inflection point I , which slope is Δ . Finally, f is the time that elapses between the power load application and the point corresponding to I .

Experimental vapour front velocity evaluation in different start-up conditions is obtained by fitting temperature measurements in correspondence of the different sections where the thermocouples are installed, and measuring the time difference between the inflection points, I . So, from the knowledge of thermocouple distances, reported in table 8.2, vapour front velocity value is simply obtained as:

$$v = \frac{\Delta x}{\Delta t} \quad (8.2)$$

Range	Distance [cm]
Evaporator outlet- T_{v1}	8
$T_{v1} - T_{v2}$	49
$T_{v2} - T_{v3}$	69
$T_{v3} - T_{v4}$	79

Table 8.2: Thermocouples distances

Curve fitting, on the basis of eq. (8.1), for 2 kW-hot and cold start-up tests are reported in Fig. 8.8.

Resulting velocities for 0.5 and 2 kW-hot and cold tests are reported in table 8.3.

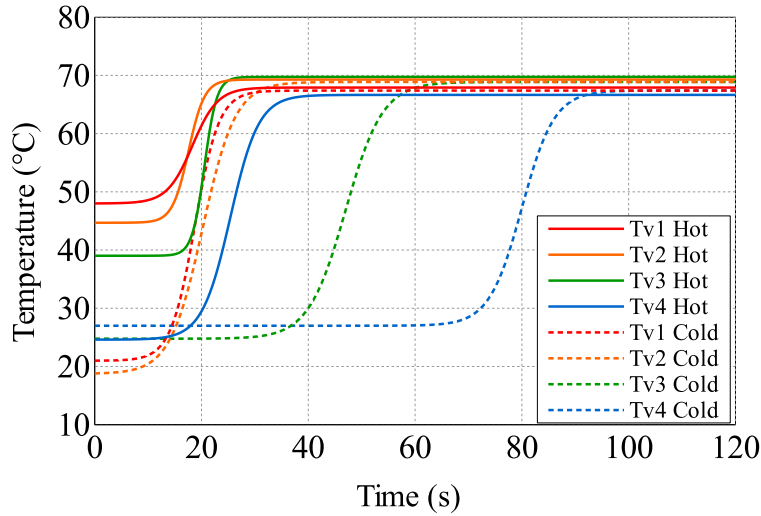


Figure 8.8: Temperature profiles as a function of the time, fitted curves for $Q_{th} = 2 \text{ kW}$ (methanol, $T_{res} = 70^\circ\text{C}$, $T_{sec} = 20^\circ\text{C}$).

Range	Velocity [$\text{cm}\cdot\text{s}^{-1}$]			
	0-0.5 [kW]		0-2 [kW]	
	Cold	Hot	Cold	Hot
$T_{v2} - T_{v3}$	2.3	10.3	2.6	24.6
$T_{v3} - T_{v4}$	2.1	7.0	2.4	14.5

Table 8.3: Velocity evaluation for hot and cold start up at 0.5 kW and a 2 kW power steps

As one can observe from table 8.3, vapour front velocity is more impacted by initial vapour line temperature than applied thermal load. During cold start-up, either 0.5 and 2 kW load steps are characterised by nearly same velocity values. On the contrary, during hot start-up, a one order of magnitude higher velocity value was found. The higher the initial vapour line temperature, the higher the vapour front velocity during the start-up. Vapour front velocity variation from cold to hot start-up could be the reason of unsuccessful start-ups of the loop for quite high heat power steps (4 and 5 kW).

8.4 Discussion

The lower vapour front velocity, during the cold start-up, is due to a higher amount of energy exchanged between the fluid and the solid walls of the vapour line.

During hot start-ups, the increase of vapour front velocity may be due to a reduction of the energy of vapour re-condensation during its flow in a colder tube. In this case,

in fact, vapour temperature decreases below the equilibrium, so it condensates. Vapour pressure decreases as well as vapour front velocity. So, a lower energy of condensation during the loop start-up can be attributed to still high wall temperatures. This leads to a lowering of the hydraulic time constant.

During discharging phase, the amount of energy accumulated by vapour line tube walls can be calculated by eq. (8.3):

$$\begin{aligned} E_t &= (\rho c_p)_{tube} \pi (r_e^2 - r_i^2) \int_{x=0}^{L_v} [T_{fin}(x) - T_0(x)] dx \\ &\simeq (\rho c_p)_{tube} \pi (r_e^2 - r_i^2) L_v \Delta T_v \end{aligned} \quad (8.3)$$

where, r_e and r_i are vapour line external and internal radii respectively, L_v its length and $T_0(x)$ the initial tube temperature at time $t = 0$, and $T_{fin}(x)$ the final tube temperature reached by vapour line in steady state condition. In particular, it can be assumed that, in steady state condition, the latter is almost equal to reservoir saturation temperature, T_{res} , as it may be observed from Fig. 8.8.

If eq. (8.3) is applied to the cold start-up case, which initial tube temperature, T_0 , is 20°C , and the final one is $T_{fin} \simeq T_{res} = 70^\circ\text{C}$, the energy, E_t , released by vapour to tube walls is:

$$E_t|_{T_0=20^\circ\text{C}} \simeq 8.8 \text{ kJ}$$

Assuming a thermal load, $Q_{th} = 0.5 \text{ kW}$, the latter should be supplied for a delay of 17.5 s to obtain such amount of energy, E_t . At the same way, calculating the equivalent amount of energy for the hot start-up case, the energy, E_t , released by vapour is obviously lower:

$$E_t|_{T_0=40^\circ\text{C}} \simeq 5.3 \text{ kJ}$$

This corresponds to a delay of 10.5 s for a thermal load of 0.5 kW supplied to the evaporator. The highest amount of energy is extracted by the fluid, about 9 kJ during the cold start-up, to heat the tube walls and consequently to condensate the vapour flowing within the vapour line. The lowest amount of energy required during hot-start up, about 5 kJ , leads to a lower amount of condensing vapour within the vapour line.

The lower amount of condensed vapour, during hot start-up, leads to higher vapour front velocities. Pressure drop in the vapour line is proportional to the square of velocity. For pretty high vapour front velocities the pressure in the line could be higher than $\Delta P_{c,\max}$ (loop failing zone in Fig. 6.25), leading to loop start-up failure.

It has to be underlined that the presence of the insulating foam installed on the external side of the vapour line tube wall does not impact the solid thermal capacity. In fact,

the thermal capacity of the tube metallic wall is 10^3 times higher than the insulating expanded foam one.

8.5 Experimental and numerical results comparison

8.5.1 Effect of vapour line wall temperature

For the comparison reported in this section, the model presented in section 5.4 is used and results obtained by simulations are compared with experimental ones. The purpose, here, is to explain how thermal inertia of solid tube wall influences vapour distribution in the vapour line. In fact, as observed in sec. 8.3, the behaviour of the vapour front is strictly related to solid walls thermal inertia: the higher or the lower amount of energy used to heat the vapour line tube wall influences the amount of condensing vapour impacting the velocity distribution of the vapour front.

To validate numerical results, the same boundary and initial conditions used during experimental tests were applied. In Fig. 8.9 a comparison between experimental and numerical curves is reported. There, temperature profiles are reported for positions where thermocouples are installed, $T_{v1 \rightarrow v4}$, for experimental (continuous lines) and numerical (dotted lines) curves and using the same operating conditions: $Q_{th} = 0.4 \text{ kW}$, $T_{res} = 70^\circ\text{C}$ and $T_{sec} = 20^\circ\text{C}$.

Experimental and numerical temperature shapes well agree at least for the last two thermocouples, $T_{v3} - T_{v4}$, while a substantial difference is evident observing temperature profiles of the first two thermocouples, $T_{v1} - T_{v2}$ ⁵. It is evident that both temperature sensors record a *quasi-instantaneous* temperature rise, while after a certain time temperature profile of section T_{v2} diverges from T_{v1} . This behaviour could be related either to vapour front shape and vapour line solid wall thermal inertia. In fact, as vapour is formed into the evaporator it enters the vapour line. At this point, a sudden inclusion of vapour into the liquid contained in the vapour line occurs. Because of the violence of this phenomenon, the first two thermocouples are apparently affected, at the same time, by the temperature rise due to the vapour front passage (dotted circle). The latter, flowing within the vapour line becomes flatter and, far from the vapour line inlet, the amount of liquid tends to increase because of the vapour re-condensation. On the other hand, observing temperature profiles resulting from numerical simulations, one can observe a more “relaxed” start-up behaviour. In this case, the vapour front passes through the analysed sections, crossing them one by one, and no particular interesting phenomena may be noticed. Divergence between experimental and numerical results is due to va-

⁵Even if at the end of the process, T_{v2} experimental curve well fits with the numerical one.

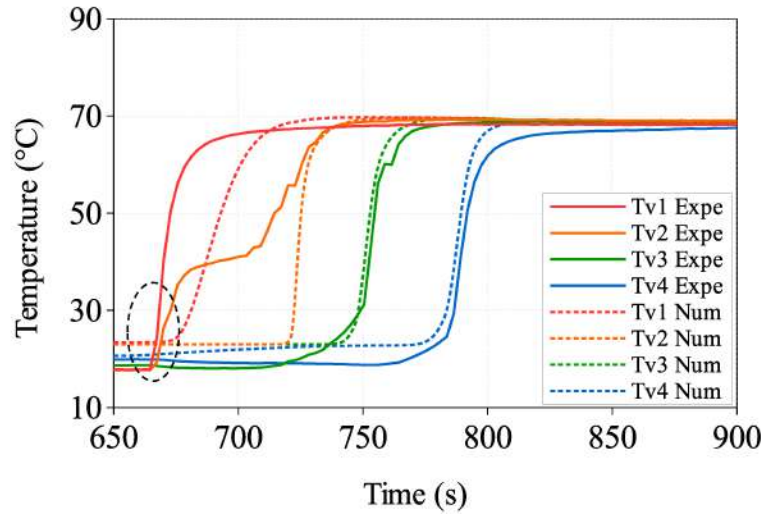


Figure 8.9: Experimental and numerical comparison for a cold start-up (methanol, $Q_{th} = 0.4 \text{ kW}$, $T_{res} = 70^\circ\text{C}$ $T_{sec} = 20^\circ\text{C}$).

pour front shape, modelled as a *piston shape* in the numerical tool, being the model one dimensional and homogeneous. In reality, vapour front shape is much more complicated (see Fig. 8.10) especially at the very beginning of the process. However, today, the causes of the divergence occurring between the measurements of the thermocouples T_{v1} (red line) and T_{v2} (orange line) after a given lapse of time are not well known. This could

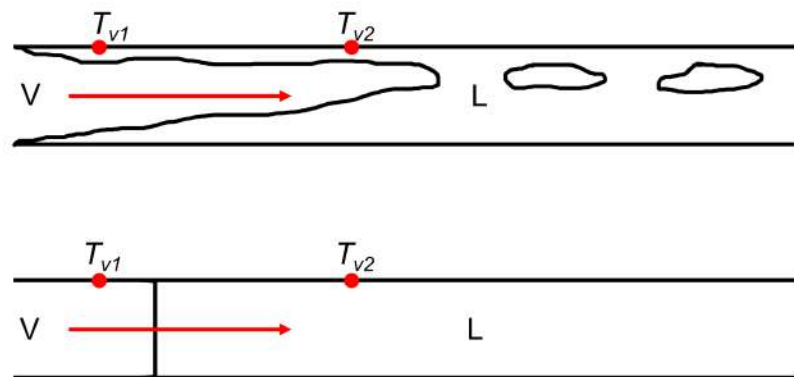


Figure 8.10: Vapour front qualitative shapes: real (up), numerical (piston shape, down)

be due to an expansion, followed by a contraction of the vapour front during the first moments of start-up, but it is just a speculation that may be only confirmed by optical visualisations.

8.5.2 Effect of vapour line wall thermal inertia

As expected, a strict connection between hydraulic and thermal characteristics of the CPLIP exists. A different distribution of fluid phases determines a different pressure field distribution that consequently impacts the velocity field. This is the cause of velocity variations if initial vapour line temperature conditions are modified. For this reason, in order to assess vapour line initial temperature influence on the dynamic response of the loop, a new theoretical study has been performed: numerical calculations have been done taking into account and not walls thermal inertia. From a numerical point of view, this can be easily done by suppressing solid thermal capacities from the thermal network model (see Fig. 5.15d).

In Fig. 8.11, results of simulations with (continuous lines) and without (dashed lines) thermal inertia are reported. Temperature profiles are largely affected by the solid wall thermal capacity, and at the same way than experimental results for hot and cold start-ups (see Fig. 8.8). In fact, as soon as solid walls thermal inertia is not considered, one assists to a reduction of time required by vapour front to cross the vapour line,

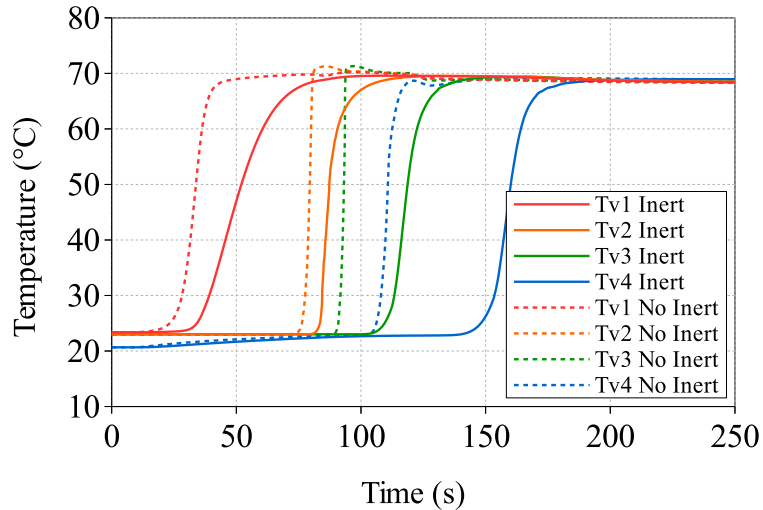


Figure 8.11: Vapour line temperature profiles with (continuous lines) and without (dashed lines) solid wall thermal inertia (methanol, $Q_{th} = 0.4 \text{ kW}$, $T_{res} = 70^\circ\text{C}$, $T_{sec} = 20^\circ\text{C}$)

temperature profiles are stepper and have, at least for the last three thermocouples, a temperature overshoot. Such slight superheating is recorded just before the assessment to the final temperature value. On the contrary, the first thermocouple is impacted by heat conduction from evaporator and its thermal inertia, damping the temperature overshoot that should be present as well.

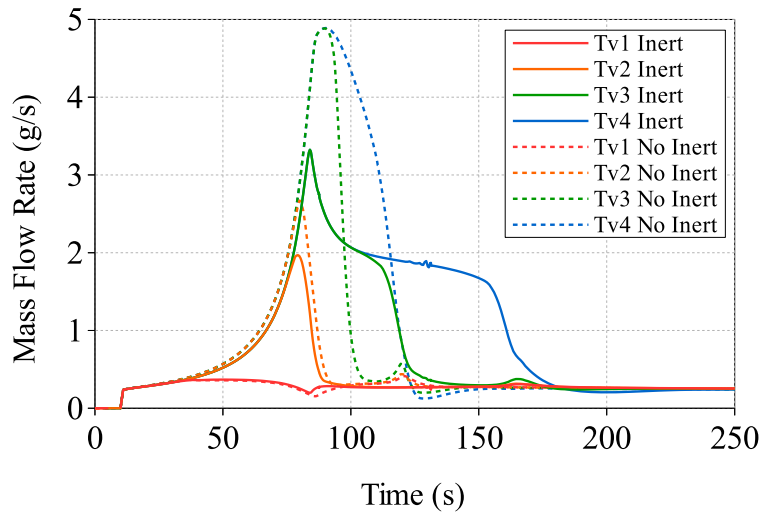


Figure 8.12: Mass flow rate profiles with (continuous lines) and without (dashed lines) solid wall thermal inertia (methanol, $Q_{th} = 0.4 \text{ kW}$, $T_{res} = 70^\circ\text{C}$, $T_{sec} = 20^\circ\text{C}$)

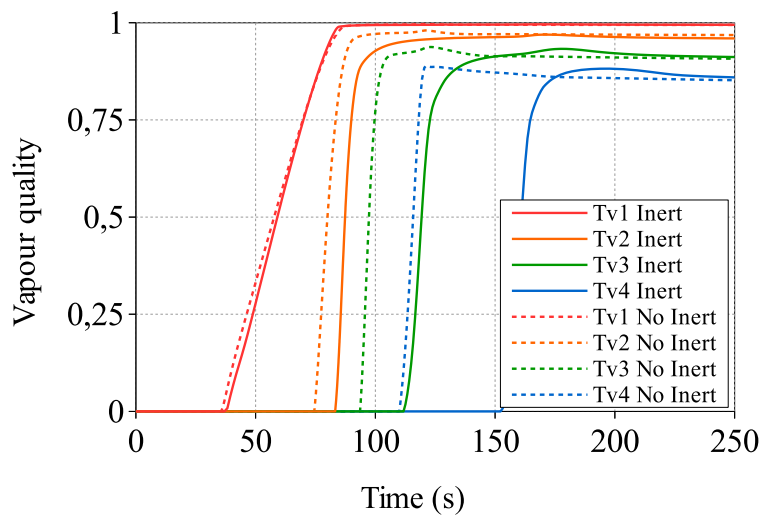


Figure 8.13: Vapour quality profiles with (continuous lines) and without (dashed lines) solid wall thermal inertia (methanol, $Q_{th} = 0.4 \text{ kW}$, $T_{res} = 70^\circ\text{C}$, $T_{sec} = 20^\circ\text{C}$)

The mass flow rate evolving in the loop, at constant thermal power applied to the evaporator, $Q_{th} = 0.4 \text{ kW}$, at $T_{res} = 70^\circ\text{C}$ and $T_{sec} = 20^\circ\text{C}$, with and without thermal inertia is reported in Fig. 8.12. During the very beginning of start-up stage, vapour pushes the liquid within the vapour line to the condenser. Vapour and liquid phases have thus the same velocity. In a given section of the vapour line, due to higher density of the liquid, the mass flow rate value increases up to its maximum value. As soon as liquid fraction decreases, the density decreases as well and mass flow rate experiences a lowering until settling to steady state condition. Both vapour quality and mass flow rate diagrams are influenced by energy exchanges between fluid and solid walls. In particular, observing vapour quality (see Fig. 8.13), thermal inertia decelerates the settling process to the steady vapour quality value for a given section: curves are smoother. This phenomenon is due to vapour re-condensation mechanism described before. By considering no thermal inertia curves in Fig. 8.11 (dashed lines), temperature overshoot, observed in correspondence of section T_{v2} , T_{v3} , and T_{v4} may be attributed to mass flow rate reduction occurring due to lower density of vapour. The minimum mass flow rate occurs when the maximum vapour quality is reached all over the vapour line: CPLIP is stabilised and it operates in steady-state conditions.

8.6 Conclusion

In this chapter, an analysis of the start-up behaviour of a CPLIP is presented in order to have a better understanding of the phenomena occurring during this complex phase. Experimental tests were performed using methanol as working fluid. Results for different vapour line initial conditions were compared to evaluate the influence of thermal inertia on the vapour front behaviour during the loop start-up. Numerical simulations were compared with experimental results during cold start-ups to testify the correctness of interpretation of experimental data. For all experimental tests and numerical simulations, a constant reservoir temperature of 70°C was used. To understand the differences between “relaxed” and extremely severe start-up conditions, CPLIP was pushed up to reach its operating limits during some specific start-ups. The comparison between a severe (5 kW) and a more relaxed (0.5 kW or 2 kW) cold start-up showed that vapour front velocity values are similar for low power step cases, while for high intensity heat power step start-up velocity is one-order-of-magnitude higher. To understand and justify such results for hot and cold cases, an energy based analysis, considering the importance of thermal inertia of vapour line tubes, was performed. It was observed that the variation of vapour front velocity is due to a recondensation of the vapour on the vapour line wall,

more significant during cold start-ups due to a higher difference between fluid and tube initial temperatures. So, as the initial vapour line temperature is low, the vapour front velocity decreases, resulting in higher settling times and quicker vapour quality increases. The vapour line initial temperature determines the quantity of energy that is dissipated by the fluid to the tube walls. This energy, directly related to the recondensation phenomenon on the tube walls, has an impact on the pressure and mass distributions of the vapour phase and, so, on the vapour front velocity and shape. Further studies need to be performed, particularly in terms of experimental visualisations and numerical volume of fluid simulations (of the vapour flow in the vapour line during such transient start-ups) in order to completely validate the assessments given in this chapter from the obtained results.

It has to be underlined that, in the context of HASTECS project, the most critical phases are realised, on the basis of the actually held data, on the ground, where the CPLIP is required to boot at temperatures lower than 40 °C. Also, observing Fig. 8.14, where the initial and the final phases of the experimentally exploited mission profile are reported, one may notice that start-up occurs at the beginning of the taxi out stage at low thermal load. In such conditions no particular problems are related to loop start-up.

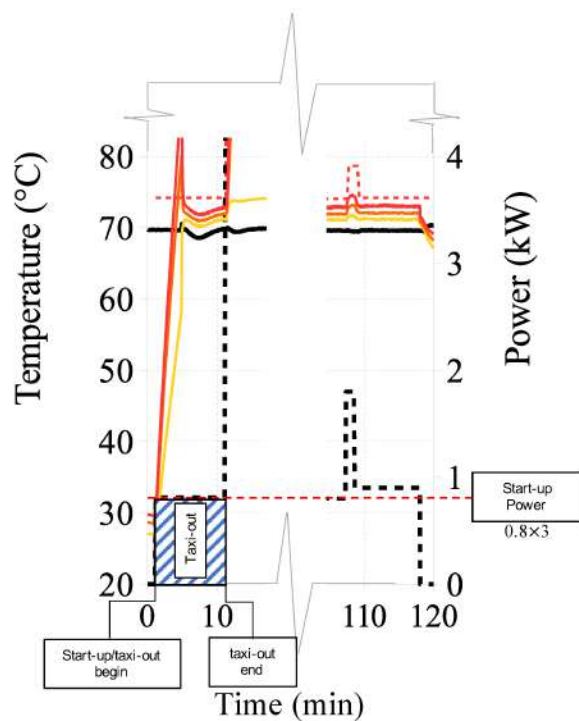


Figure 8.14: Real start-up condition 3×0.8 kW (methanol, $T_{res} = 70$ °C, $T_{sec} = 20$ °C)

CPLIP behaviour under sudden and violent acceleration stages

Equipment verification in presence of violent acceleration fields is necessary for such systems that will be installed on flying vehicles. During “turbulence” stages, in fact, equipments are strongly stressed for a limited lapse of time. In this brief and last chapter, an introduction to CPLIP behaviour during such sudden and violent acceleration stages is described. Starting from a simple acceleration impulse, hydraulic behaviour of CPLIP will be numerically analysed, using the already described model (see chap. 5), to understand which components of the loop are mostly impacted. An acceleration peak of a given intensity is used for the study to explain hydraulic and thermal effects on the loop. Finally, to have a first overview of the most impacting parameters on CPLIP behaviour, a parametric study is proposed, changing impulse time duration, amplitude and condenser-to-reservoir height difference.

Limitations of the present study *It is expected to have more questions than answers at the end of this chapter!* This study should be seen as an introduction to a pretty higher difficult research subject related to the study of transient and violent acceleration fields perturbing the operations of the CPLIP.

Strong limitations are related to the nature of the model and to the absence of validation of results. The model here used, the Blet’s one [25], is a 1-D finite volume homogeneous model, in which the evaporator is modelled by using a macroscopic approach. So, any effect of acceleration field modification on the wick operating mechanisms, unfortunately, cannot be observed using this model. Any thermo-hydraulic effect, like, for example, bubbles back-flow to the reservoir lower part, potentially leading to loop failure, cannot be assessed. Similarly, the way the acceleration field variation modifies the fluid distribution in the evaporator and how it behaves in such cases, will remain an open question. In fact, the way the liquid phase spreads in the evaporator is surely impacted by acceleration field variation and changes in turn the way the porous wick behaves. The reservoir-evaporator tube is characterised by a gravity driven liquid flow. The discretisa-

tion of such component by using just one volume, results in a strong limiting condition, and does not allow to observe “what really is going on”. In fact, a change in gravity field could lead to a different pressure distribution at the inlet and at the outlet of the tube, and being the latter related to the evaporator, it could often play a role, on its behaviour.

On reservoir side, despite the ability to take into account mass and energy exchanges between reservoir higher and lower parts, and between the lower part and the liquid line, the reservoir lower part is modelled by just one node, and the fluid flow is one-dimensional. To be clear, “the reservoir lower part is modelled as a 0.3-meter-long tube characterised by just one node”. Even in this case, a difference in pressure distribution could not be taken into account neither at the inlet nor at the outlet of this component.

Due to the use of empirical conductances, any change in their value, consequent to a transient acceleration field, may be not considered as well¹.

Two-phase flow homogeneity hypothesis represents a limiting factor as well. Following the definition given by Goncalves and Patella: “[...] in homogeneous model the phases are assumed to be in kinematic and thermodynamic equilibrium: they share the same pressure, P , temperature, T , and velocity, u [...]” [125]. During sudden transient stages, homogeneity of two-phase flow is not ensured and such equilibrium is broken!

Actually, either numerical and physical problems have to be assessed during this study and nowadays it is difficult to say if divergence issues encountered during the study come from a “not well posed condition” or by a physical danger for the loop. To avoid any kind of instability, a low thermal load (1 kW) has been used to complete the following study.

However, despite all its limitations — in this application case — the model is able to give “acceptable” results, suggesting basic and qualitative behaviour of the loop during sudden acceleration stages. The attention will be especially focused on hydraulics effects, such as competition between the liquid back-flow into the condenser and the vapour phase compression in the vapour line. In particular, this study allows to identify most delicate components in the loop during such critical stages.

9.1 Accelerations in civil flight applications

Acceleration field maximal intensity depends on the position of the equipment on the aircraft and on its operating requirements. The latter are divided in three categories (A, B and C), defined by data sheet and applicable to equipments:

A which are not required to work during manoeuvre stage.

¹It should be also reminded that the definition itself of thermal conductance requires its measurement in steady state conditions.

B which are required to reliably operate in manoeuvre stage.

C which are required to operate after an emergency landing.

Local acceleration field intensity is strongly influenced by the position of the equipment in the aircraft. Information are so given depending on the position: VTP (Vertical Tail Plane), HTP (Horizontal Tail Plane), fuselage and, finally, wing zone. The latter is divided in up to engine and after the engine. Table 9.1 reports, as an example, the acceleration modules for an equipment installed on the wing up to the engine, as the solution retained in this work has been considered to be placed in the nacelle. Acceleration values are given for forward (FWD), toward (AFT), UP, DOWN and lateral (LAT) directions. Moreover, arbitrary and non-arbitrary mounted equipments should be considered as well.

The cooling system retained during this work is supposed to be installed in the nacelle and acceleration intensity field is considered for an up-to-engine non-arbitrary mounted equipment. Under the hypothesis that the CPLIP is not required to surely work after an emergency landing, but it must, during manoeuvre state, category B has been chosen for acceleration levels.

	Arbitrary Mounted	Non-arbitrary mounted			
		FWD	AFT	UP	DOWN
Functional test Category A & B	8g	8g	2g	2g	5.5g
Functional test Category C	13g	13g	9g	8.5g	6g
Structural test	13g	9g	3g	8.5g	6g
					4.5g

Table 9.1: Acceleration modules, wing zone up to O/B engine

However, no information are given about the time lasting of such acceleration stage. In absence of such information, time will be arbitrarily chosen.

9.2 Simulation conditions

For simulations, the previously described Blet's model [25] (see chap. 5) has been modified in order to agree with the requirements of the problem.

According to the qualitative diagram reported in Fig. 9.1, once the CPLIP operates in steady-state conditions, an acceleration impulse is applied to the loop at the time t_{init} . Acceleration field increases from normal gravity state to the maximum acceleration value: $\vec{a} = k \vec{g}$ with $1 \leq k \leq 8.5$. After the peak, at time t_{gp} , acceleration value decreases

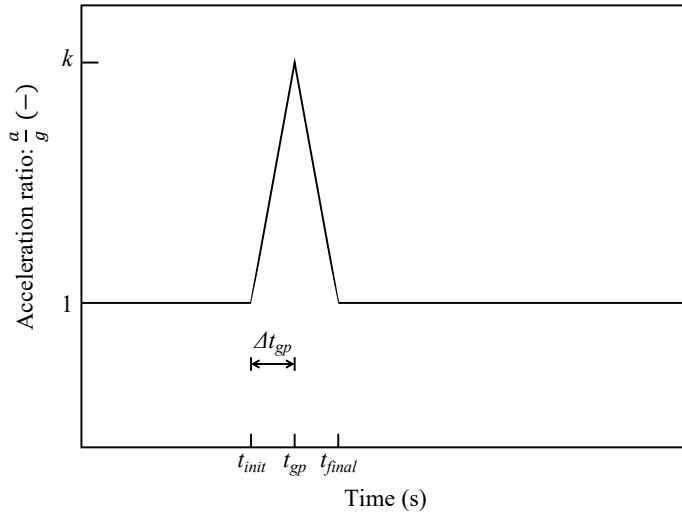


Figure 9.1: Qualitative diagram of acceleration impulse used for study

down to normal gravity at time t_{final} . From this moment, the loop continues — if it can — to operate in normal conditions.

For all the cases presented in this chapter, the thermal load², Q_{th} , applied to the evaporator is constant and equal to 1 kW, while reservoir and cold source temperatures are, respectively, $T_{res} = 70^\circ\text{C}$ and $T_{sec} = 20^\circ\text{C}$.

9.3 CPLIP behaviour under perturbed transient acceleration field

Hydraulics To study the influence of sudden acceleration stages on CPLIP behaviour, an impulsion intensity of $3g$ will be considered for a time duration $\Delta t_{gp} = 0.5$ s. Perturbed acceleration stage starts³ at 2130 s and lasts 1 s. The gravity term, $\rho g H$, responsible for the highest pressure drop in the loop (see eq. 6.1) for the fluid phase characterised by the highest density, ρ , is obviously impacted by acceleration variation.

In Fig. 9.2, pressure profiles at the inlet and the outlet of vapour and liquid lines are reported for such acceleration value. Vapour line inlet to outlet pressure difference (circled and crossed red lines in the diagram), $\Delta P_{vapour\ line}$, is quite small when compared

²Due to some stability issues of the model, which reason are not today known, the thermal load has been chosen to be the highest possible, allowing to reach a value of $8.5g$ during the parametric study. However, being this parameter constant during all the present discussion, it will not influence understanding of phenomena and conclusion.

³The beginning time has been arbitrary chosen with the only condition that it should be far enough from start-up and so to allow full steady operations before the acceleration impulse.

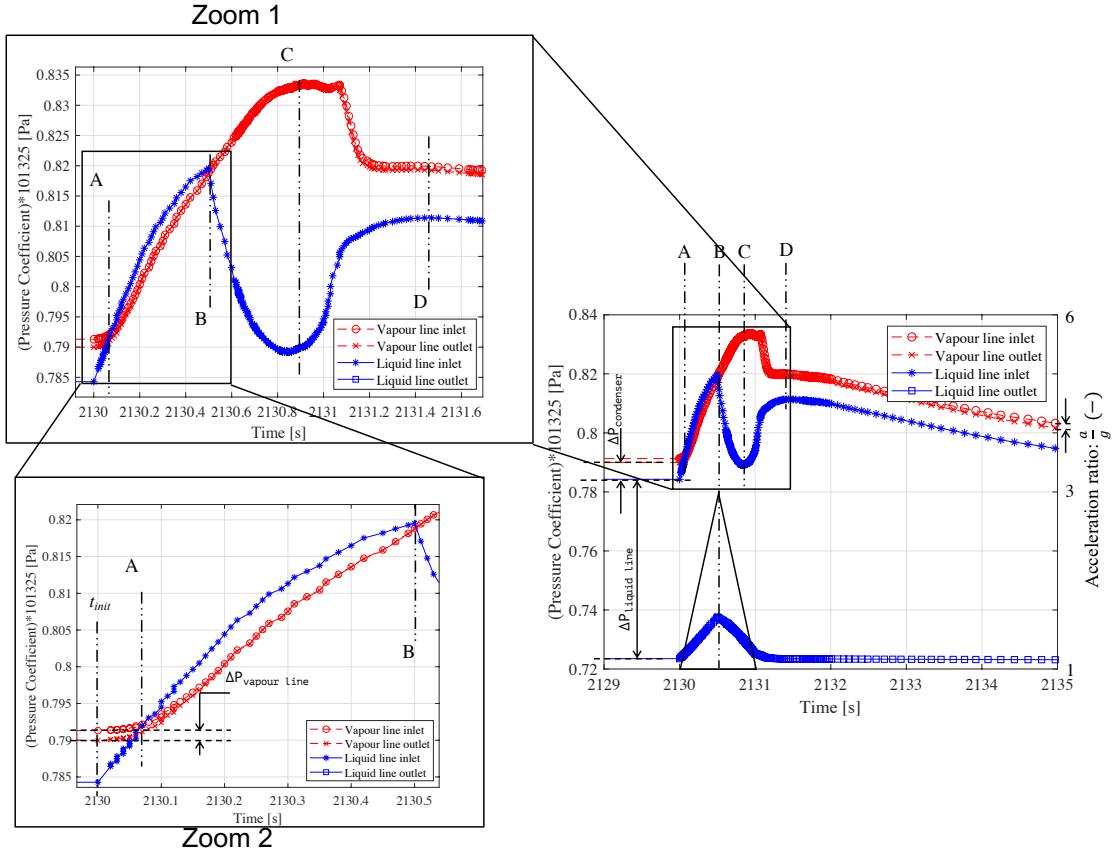


Figure 9.2: Total pressure variation diagram during acceleration impulse (methanol, $Q_{th} = 1 \text{ kW}$, $T_{res} = 70^\circ\text{C}$, $T_{sec} = 20^\circ\text{C}$, $3g$, $H = 90 \text{ cm}$)

to liquid line one (star and squared blue lines), $\Delta P_{liquid \ line}$, where the weight of gravity pressure drop is much higher than viscous one. Pressure drops in the condenser (vapour line outlet to liquid line inlet pressure difference), $\Delta P_{condenser}$, are reported as well.

To understand the phenomena occurring during sudden acceleration stages, the pressure diagram in Fig. 9.2 has been divided in five stages. The first stage, starting at 2130 sec (corresponding to the perturbation beginning time, t_{init}) and ending in A, is characterised by a range of pressure values at the inlet of liquid line (blue curve) lower than those at the outlet of vapour line (red line — see also Zoom 2 in Fig. 9.2 —). During this stage, pressure at condenser outlet rises faster than pressure at condenser inlet until intersection in correspondence of point A. The latter has been chosen as the point where the liquid pressure at the outlet of the condenser becomes higher than the pressure at the inlet, demonstrating a transition to a counterflow after the beginning of the acceleration perturbation. Between points A and B, the pressure at the outlet of the condenser

remains higher than the one at the inlet. Once the acceleration peak reached (point B is positioned in correspondence of such peak), the pressure at the outlet of the condenser decreases and re-becomes lower than the one at the inlet. Point B also corresponds to the maximal pressure achieved at condenser outlet. Between B and C, pressure at condenser outlet falls down (blue curve), while at the inlet it continues to rise (red curve). In correspondence of point C, the pressure drop in the condenser is the highest possible (during the transient stage): the pressure at the inlet reaches its maximum, while the one at the outlet reaches its minimum. After point C, acceleration impulse influence is going to run out and pressures at inlet and outlet of the condenser get close until point D. The latter corresponds to the maximum pressure value reached at the outlet of the condenser before the slow return to steady state conditions. Equilibrium is re-established in the condenser, at the inlet and at the outlet. Despite both curves decrease, they run alongside until settling in steady state conditions and their difference is constant. Pressure difference between vapour line inlet and outlet is also re-established, testifying that vapour is still flowing in the line. Observing liquid line outlet shape (squared blue curve), one may notice, instead, that the time variation of pressure simply follows acceleration impulse shape. As the reader has surely noticed, during sudden acceleration stages the condenser is the key component driving the behaviour of the CPLIP.

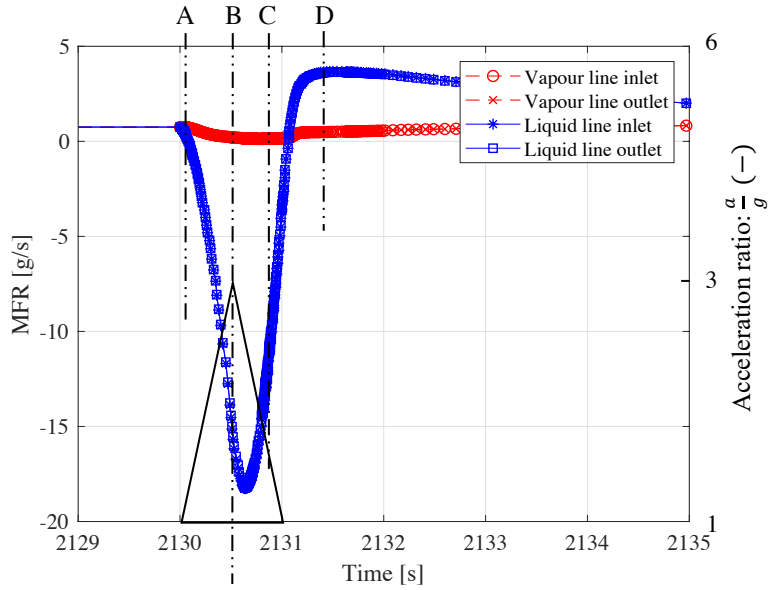


Figure 9.3: Mass flow rate variation diagram during acceleration impulse ($Q_{th} = 1 \text{ kW}$, $T_{res} = 70^\circ\text{C}$, $T_{sec} = 20^\circ\text{C}$, $3g$, $H = 90 \text{ cm}$)

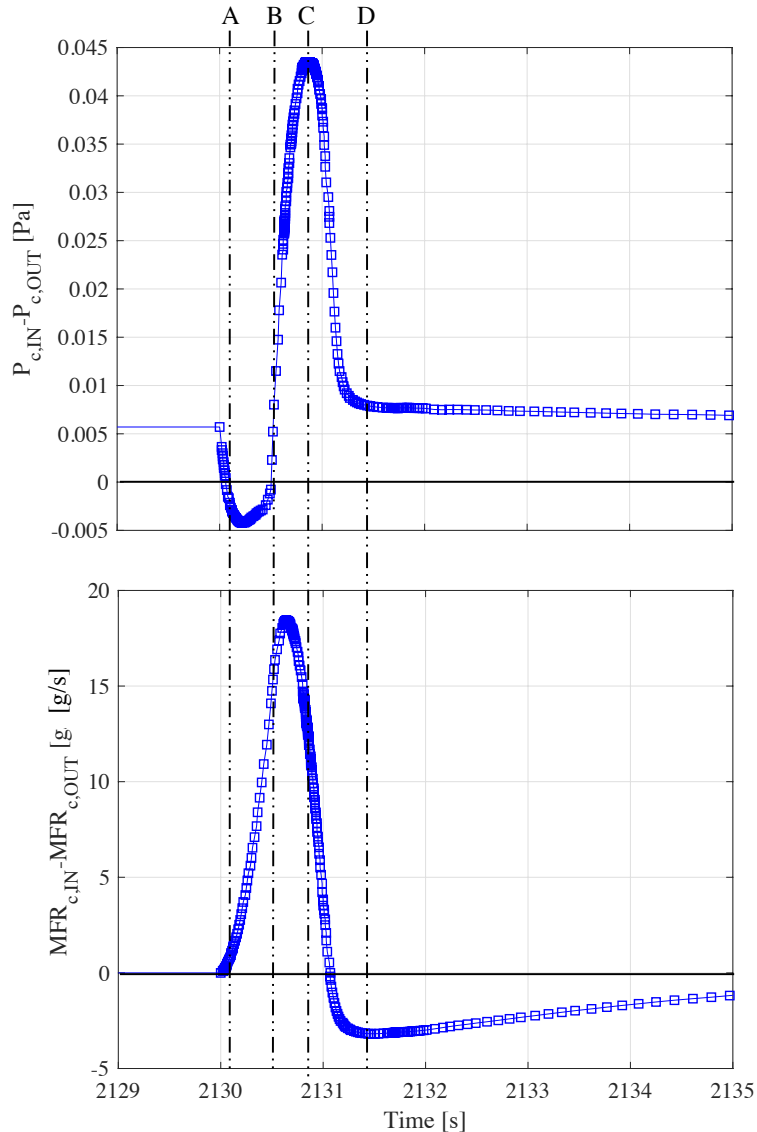


Figure 9.4: Condenser inlet to outlet pressure (top) and mass flow rate (bottom) difference during acceleration impulse (methanol, $Q_{th} = 1\text{ kW}$, $T_{res} = 70^\circ\text{C}$, $T_{sec} = 20^\circ\text{C}$, $3g$, $H = 90\text{ cm}$)

Liquid and vapour mass flow rate behaviour are reported in Fig. 9.3 for the same positions than Fig. 9.2. While in Fig. 9.4, condenser inlet to outlet pressure and mass flow rate difference relations are graphically reported. There, the same division has been used as well.

From the beginning of the acceleration impulse (2130 sec), the pressure difference, $P_{C,IN} - P_{C,OUT}$, decreases and becomes negative after point A and condenser inlet to

outlet mass flow rate difference, $MFR_{C,IN} - MFR_{C,OUT}$, increases. A mass of liquid flows back from reservoir to the condenser while vapour flows in the positive direction⁴. Masses of fluid enter in the condenser both from the inlet (vapour) and the outlet (liquid), so the condition $|\dot{m}_{C,OUT}| > |\dot{m}_{C,IN}|$ is verified all along the duration of the perturbation. The MFR of liquid, flowing from the reservoir, continues to rise until point B, corresponding to the condition $P_{C,IN} = P_{C,OUT}$. There, the mass flow rate, after a slight delay (time occurring between point B and maximum liquid MFR entering the condenser) reaches its maximum value. Despite the reversed flow of liquid, vapour phase continues to flow from the evaporator to the condenser. Its mass flow rate decreases with time and, according to the vapour line inlet-to-outlet pressure difference, observed in Fig. 9.2, it never becomes negative. It reaches its minimum in C where the pressure drop in the condenser is the highest one. The mass flow rate difference continues to drop until it intersects one more time the zero axis (equivalence between inlet and outlet mass flow rates). It temporarily re-becomes negative: liquid mass flow rate exiting the condenser is higher than the vapour entering one (piston flow). Once point D reached, the mass flow rate difference is the lowest one, and the first “zero-gradient point” in pressure difference diagram is reached. From now the system is going to be settled until normal gravity steady conditions.

The increasing amount of liquid, flowing back from reservoir to condenser, naturally pushes back the vapour, impacting condensation length as well as the vapour mass flow rate (due to its pressure increase). Recession of condensation front in the condenser is shown in Fig. 9.5 (two-phase length). As acceleration peak begins, vapour is pushed back by the mass of liquid flowing from the reservoir. As soon as acceleration peak is reached, liquid phase continues to expands back. Vapour is still compressed by liquid, until the pressure of the latter decreases (from point B to C). Expansion of liquid continues during gravity discharge and, just before the end of the impulse, the pressure in vapour line settles as soon as the negative mass flow rate of liquid diminishes. The increase in vapour pressure continues during the discharging phase as well as the liquid pressure lowering. As soon as the positive liquid mass flow rate is re-established, condensation length slowly increases, driven by the re-established pressure equilibrium between vapour at condenser inlet and subcooled liquid at the outlet. The liquid thrust during the transient stage is responsible of the recession of condensation front in the condenser. During such liquid expansion within the condenser, vapour is compressed, its mass flow rate slightly decreases all along the duration of the acceleration impulse, but it never becomes zero (as it may be seen in Fig. 9.3).

⁴From the evaporator to the condenser.

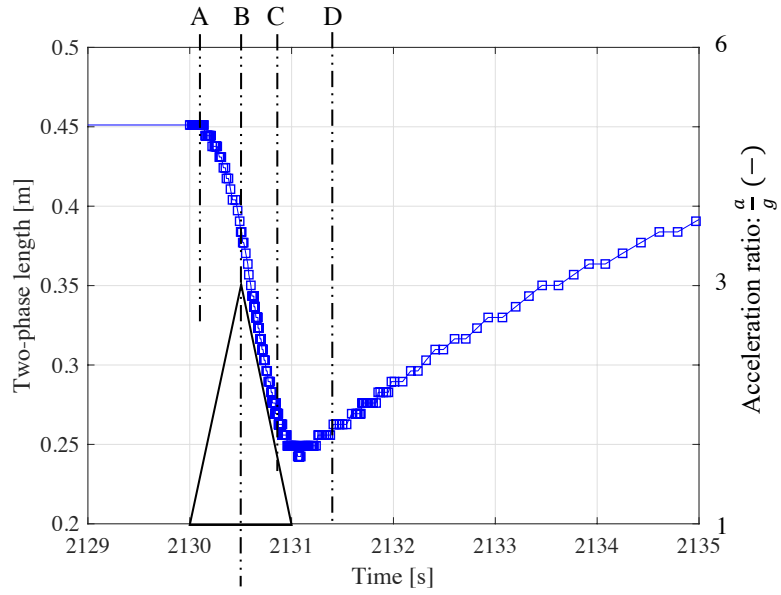


Figure 9.5: Two-phase length variation during acceleration impulse (methanol, $Q_{th} = 1 \text{ kW}$, $T_{res} = 70^\circ\text{C}$, $T_{sec} = 20^\circ\text{C}$, $3g$, $H = 90 \text{ cm}$)

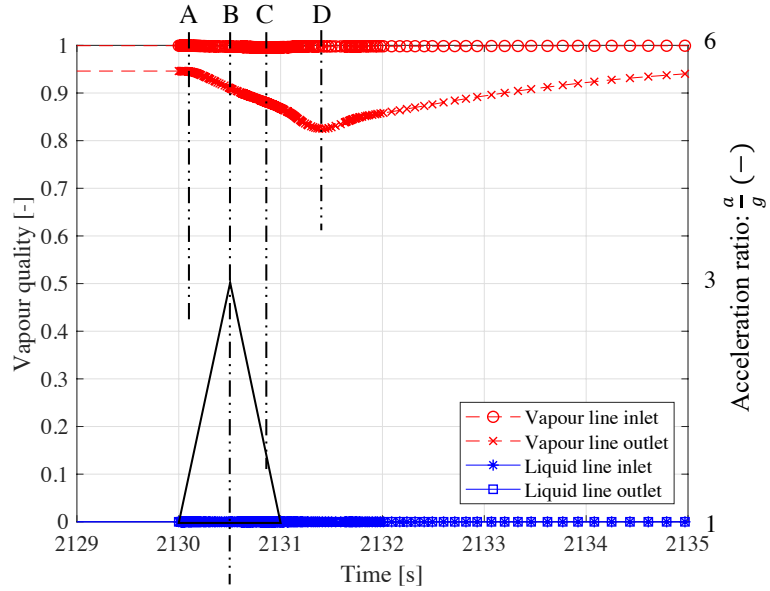


Figure 9.6: Vapour quality variation during acceleration impulse (methanol, $Q_{th} = 1 \text{ kW}$, $T_{res} = 70^\circ\text{C}$, $T_{sec} = 20^\circ\text{C}$, $3g$, $H = 90 \text{ cm}$)

Indeed, as vapour is still produced in the wick, it continues to flow in the vapour line. Vapour quality at vapour line inlet is not affected by acceleration stage, but at the outlet, as expected, its value decreases (see Fig. 9.6). This behaviour could be due to

recession of condensation front (see Fig. 9.5) pushed back by liquid. The condensation length reduction could be not only due to liquid thrust, but also to a higher vapour pressure. In fact, after the maximum in acceleration peak, vapour pressure increases due to reversed liquid flow rate, but its temperature slightly increases allowing a higher amount of condensing vapour due to increasing equivalent saturation temperature. The higher pressure makes the vapour to condensate faster, so a new mass of liquid is formed. Once the point D is reached, vapour quality slightly comes back to “normal” values.

Temperatures Fig. 9.7 depicts temperature variations in the evaporator and in the reservoir-evaporator tube as well as in all the previously considered sections and for the same acceleration impulse. As the reader surely notices, the temperature variation as a function of time is no particularly relevant for the evaporator, for the reservoir-evaporator tube and the vapour line inlet, but a small change in temperature shape at inlet and outlet sections of the vapour line is worth of attention. Such small temperature augmentation at vapour line, inlet and outlet (red lines), could be due to the increase in pressure generated by the vapour compression due to liquid back-flow. To a higher vapour pressure corresponds a higher saturation temperature but, due to evaporator thermal inertia, the following augmentation of the evaporator temperature is slower. The saturation temperature temporarily becomes close to the evaporator one and this causes

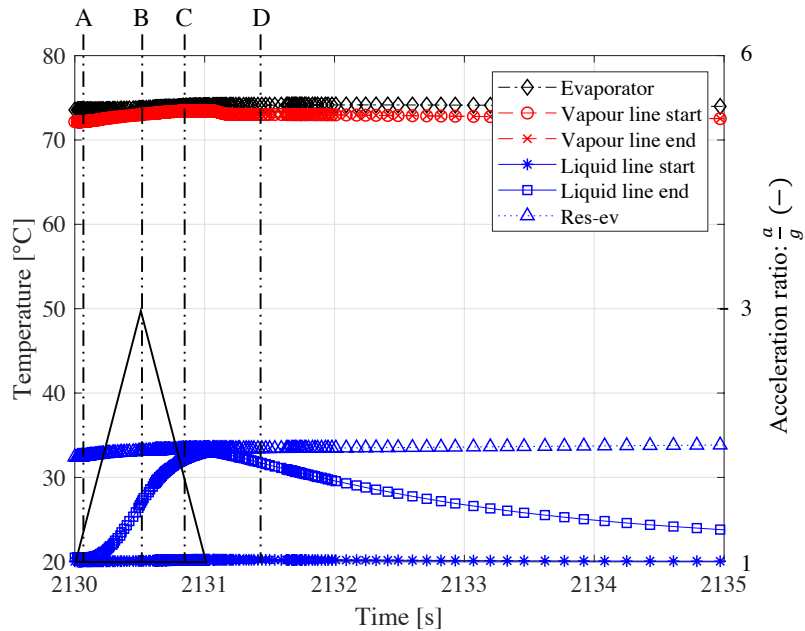


Figure 9.7: Temperature variation during acceleration impulse (methanol, $Q_{th} = 1 \text{ kW}$, $T_{res} = 70^\circ\text{C}$, $T_{sec} = 20^\circ\text{C}$, $3g$, $H = 90 \text{ cm}$)

the vapour mass flow rate diminution observed in Fig. 9.3. Liquid line outlet temperature significantly changes. An amount of liquid flows through the reservoir orifice, from the higher part. A part of hot liquid flows from the reservoir to the evaporator, while another part flows back to the liquid line. The last section of the tube is thus gradually heated. Obviously, due to higher thermal time constants, this phenomenon is slightly slower than the hydraulic one. Once the liquid mass flow rate re-starts to flow from the condenser to the reservoir, subcooled liquid cools down the reservoir inlet section until settling to steady-state equilibrium and its stabilisation to cold source value.

9.4 Parametric study

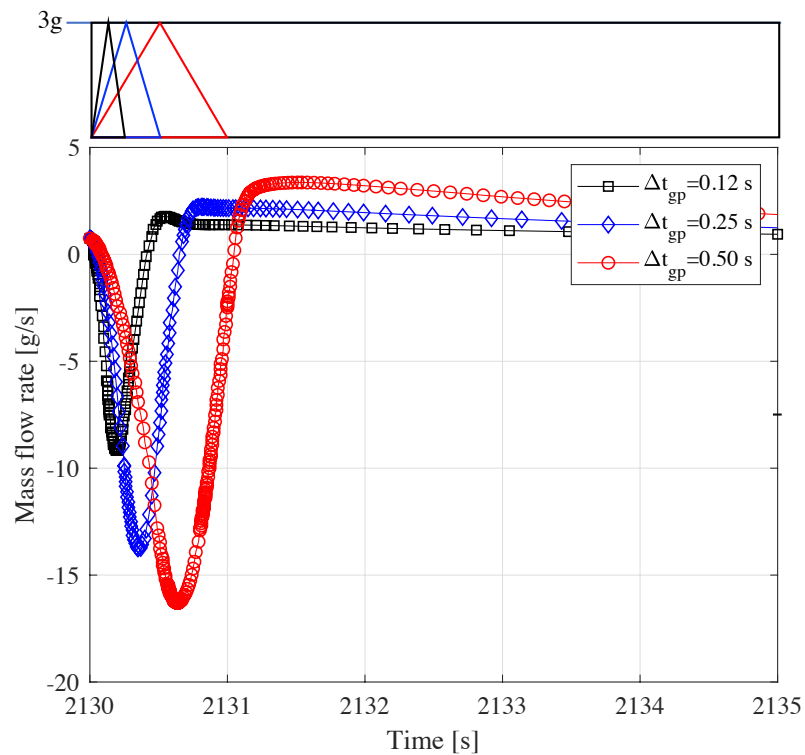
The three parameters, acceleration intensity, k , time duration, Δt_{gp} , and difference of height between condenser and reservoir, H , influence the behaviour of the CPLIP during such transient stage. As explained in chap. 5, in CPLIP, liquid line pressure drop is more impacted by gravity forces than viscous ones. Due to the difference of height between condenser and reservoir, this section of the loop is the mostly influenced by gravity field modification (expressed as $\rho(kg)H$). Likewise the factor k , the response of the loop is impacted by the height between the condenser and the reservoir, H , that is a design parameter⁵. To have an idea on how each parameter affects the loop, three different condenser to reservoir height differences, H , were exploited: 30, 60 and 80 cm; and acceleration values from 2 to 8.5 g were studied at different heights, H . In table 9.2 a synthesis of the performed simulations is reported. For the study, acceleration values up to 8.5g have been considered, stepping by 0.5g. For numerical stability issues⁶, the height H has been gradually reduced for an increasing value of factor k . Finally, to explore the effect of the duration of acceleration perturbation, Δt_{gp} , values of 0.12, 0.25 and 0.5 sec have been explored.

It has been observed that, consequently to acceleration perturbation, the liquid backflow to the condenser results from the amount of liquid flowing through the orifice from the higher part of the reservoir within the lower part and, finally, to the liquid line. Reservoir inlet becomes an outlet realising the issue described in sec. 5.4.1.2. All the three parameters considered in this chapter influence the amount of liquid flowing back to condenser. First of all, let's analyse the influence of impulse duration, Δt_{gp} .

⁵Obviously, the “tilt” or “inclination”, could change the equivalent height between the reservoir and the evaporator, but in this work such parameter is just considered as a design parameter.

⁶Up to date, the reasons of calculation divergence for high acceleration values and high heights are not known. Such divergence could be either due to numerical stability or to physical reasons.

$k \cdot g \text{ (m} \cdot \text{s}^{-2}\text{)}$	Acceleration $k \cdot g \text{ (m} \cdot \text{s}^{-2}\text{)}$	Height, H (cm)
2g	2g	30, 60, 80
2.5g	2.5g	30, 60, 80
3g	3g	30, 60, 80
3.5g	3.5g	30, 60, 80
4g	4g	30, 60
4.5g	4.5g	30, 60
5g	5g	30, 60
5.5g	5.5g	30
6g	6g	30
6.5g	6.5g	30
7g	7g	30
7.5g	7.5g	30
8g	8g	30
8.5g	8.5g	30

Table 9.2: Performed simulations**Figure 9.8:** Acceleration impulsion time duration, Δt_{gp} , effect condenser outlet mass flow rate (methanol, $Q_{th} = 1 \text{ kW}$, $T_{res} = 70^\circ\text{C}$, $T_{sec} = 20^\circ\text{C}$, $H = 80 \text{ cm}$, $3g$)

In Fig. 9.8, such parameter variation is reported at constant thermal load, reservoir and cold source temperature, condenser to reservoir height difference, H , and acceleration factor, k . The more the acceleration impulse lasts, the higher the amount of liquid flowing from reservoir to the condenser. Once the acceleration perturbation ends up, the settling time depends on the fluid mass accumulated in a lapse of time: the smaller the amount of fluid flowing back to the condenser (the lower the Δt_{gp}), the shorter the settling time (from the mass flow rate overshoot to the complete stabilisation of the flow). Perturbations lasting more, need a longer time for settling (see 0.12 s — black — to 0.50 s — red — curve difference for example). Thus, the settling time depends on the equivalence between the areas $\Xi = \Gamma$ (see Fig. 9.9), representing the amount of fluid mass accumulated during the perturbation and the mass of fluid that has to return.

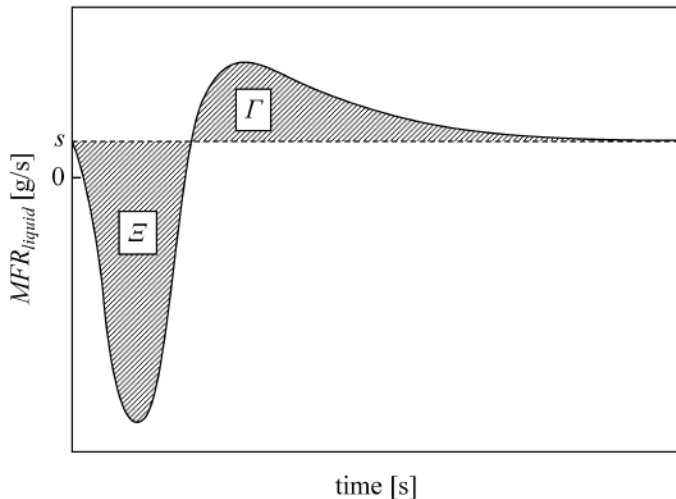


Figure 9.9: Qualitative diagram of accumulated liquid mass during perturbation (area Ξ) and returning mass during settling (area Γ)

The difference of height between condenser and reservoir obviously influences the amplitude of the reversed flow rate during the acceleration impulse (Fig. 9.10). The higher the difference of height between condenser and reservoir, H , the larger the pressure drop and so the amount of mass flow rate flowing back in the liquid line. Actually, the difference of height plays a significant role on acceleration term of pressure drop, $\rho (k g) H$. This impacts back-flowing liquid mass flow rate and condensation length.

Finally, in Fig. 9.11, parametrisation of acceleration intensity factor, k , at constant condenser-to-reservoir height difference and impulse duration, is reported. As expected, according to Fig. 9.11a, the higher the acceleration intensity, the higher the back-flow amplitude and so the settling time necessary for the loop to return to steady state

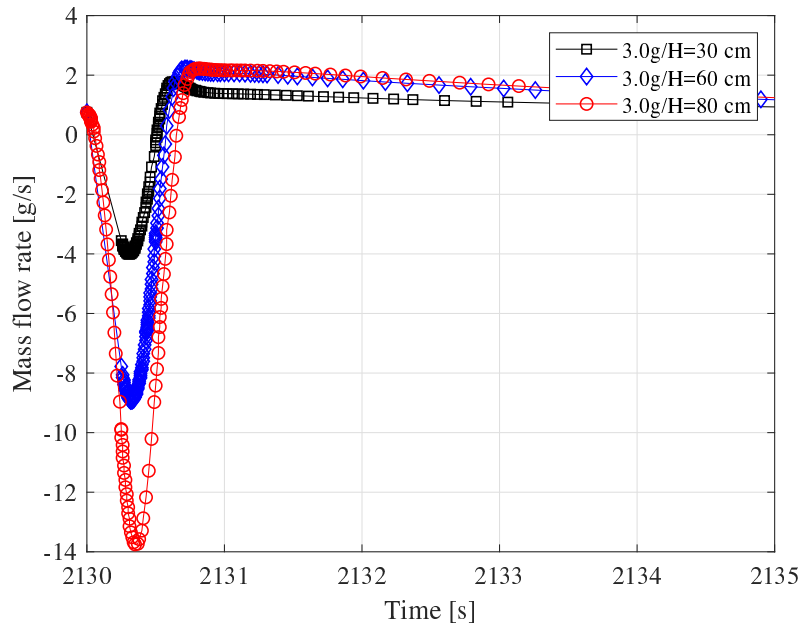


Figure 9.10: Condenser-to-reservoir height difference effect on condenser outlet mass flow rate (methanol, $Q_{th} = 1 \text{ kW}$, $T_{res} = 70^\circ\text{C}$, $T_{sec} = 20^\circ\text{C}$, $\Delta t_{gp} = 0.25 \text{ sec}$, 3g)

conditions. Also, according to Fig. 9.11b, the higher the acceleration impulse, the higher the condensation length reduction.

Observing pressure variation as a function of acceleration intensity (see Fig. 9.12), pressure shape does not change with acceleration intensity but, obviously, like mass flow rate and condensation length, the higher the acceleration amplitude, the higher the pressure perturbation at the exit of the condenser and the longer the time necessary for settling in steady state conditions. The same pressure shape than Fig. 9.2 may be noticed, but due to a smaller Δt_{gp} and, according to acceleration impulse value, it appears to be more “stretched”.

For the highest value of acceleration impulse, the highest total pressure drop (temporarily introduced by the fast acceleration perturbation) has been compared with the maximum capillary pressure head, resulting in $\Delta P_{8.5g} < \Delta P_{c,max}$ ($\Delta P_{8.5g} = 7500 \text{ Pa}$ for $\Delta P_{c,max} = 10700 \text{ Pa}$). It seems that capillary pumping capacity is not affected by the chosen height, $H = 30 \text{ cm}$, coupled with the maximum acceleration intensity and for a time lasting impulse of 0.25 sec. Moreover no liquid has been attained at the inlet of the condenser during the highest intensity impulse. However, it should be underlined that a transient phenomenon is considered here and more precise studies are needed.

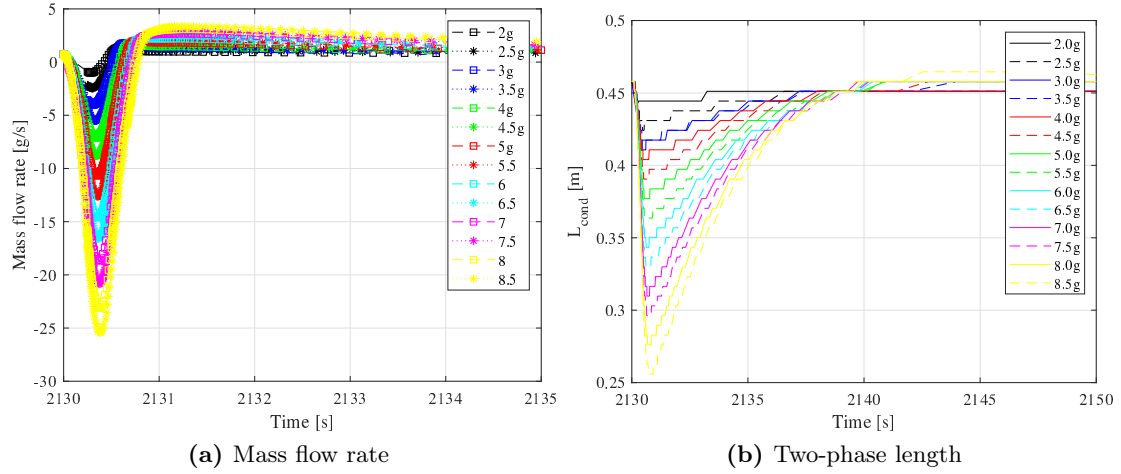


Figure 9.11: Acceleration impulse intensity effect on the reversed mass flow rate and condensation length (methanol, $Q_{th} = 1\text{ kW}$, $T_{res} = 70^\circ\text{C}$, $T_{sec} = 20^\circ\text{C}$, $\Delta t_{gp} = 0.25\text{ sec}$, $H = 30\text{ cm}$)

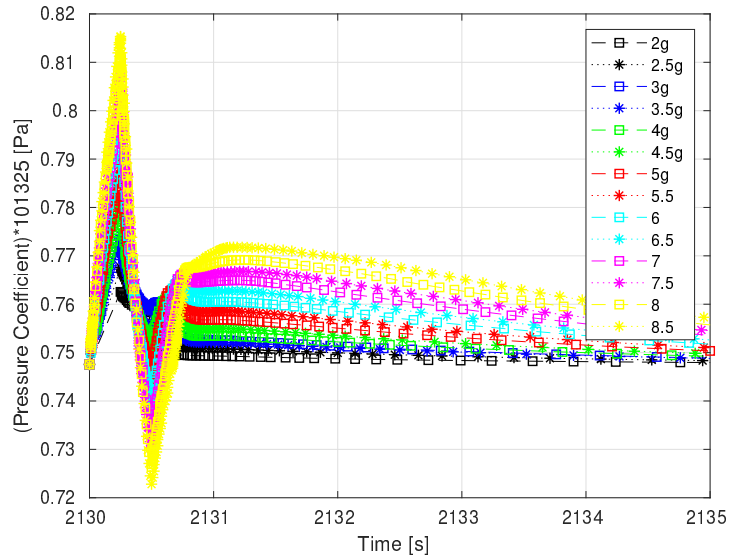


Figure 9.12: Pressure at condenser outlet for different acceleration intensity (methanol, $Q_{th} = 1\text{ kW}$, $T_{res} = 70^\circ\text{C}$, $T_{sec} = 20^\circ\text{C}$, $\Delta t_{gp} = 0.25\text{ sec}$, $H = 30\text{ cm}$)

9.5 Conclusion and perspectives

In this chapter a brief study on transient acceleration stages has been proposed. The purpose was to identify the main components in the CPLIP that are mostly influenced by sudden and violent acceleration stages. Because of the impossibility to experimentally

validate the numerically observed phenomena, this chapter should be seen as introduction and inspiration for future studies.

After an introduction about sever acceleration stages occurring in aeronautics field⁷, to have a better comprehension of phenomena occurring in the loop, a simple case study has been considered. By using an acceleration impulse, hydraulic effects and, to a lesser extent, thermal effects on the loop were studied. Finally, a parametric study has been used to understand the effect of each influencing parameter such as acceleration impulse intensity and time lasting, and difference of height between condenser and reservoir.

From the results obtained, it was observed a strong effect on hydraulics of the loop, but its thermal behaviour seems to be weakly influenced by acceleration impulse. As expected, the first effect of variation of acceleration field has been observed in the liquid line. This component is, in fact, characterised by the higher gravity pressure drop, due to the flow of the highest density fluid. The stronger effect was related to liquid spilling from the reservoir higher part, and within the lower part to the liquid line. The amount of liquid coming from the reservoir participates to condensation length reduction, vapour compression in the vapour line, as well as vapour flow reduction. Vapour seems to be pushed in the vapour line by the capillary forces in the evaporator, but, due to limitations related to evaporator model, actually it is not well known what's going on in the wick. Influencing parameters are, other than acceleration intensity, time duration and condenser to reservoir height difference. An increase of all just expressed parameters negatively influences the loop behaviour. In fact, the higher the acceleration intensity, or its duration or the height difference, the higher the back-flowing mass flow rate. From an engineering stand point the presence of non-return valve at the inlet of the reservoir should be exploited. The latter could help to prevent liquid back-flow effects on the loop during such violent stages.

Further studies are strongly needed on the issue, particularly interesting in the context of HASTECS project. The study presented in this chapter is far to define if the CPLIP is able to resist to turbulence acceleration stages during flight, but it represents a fundamental study to identify the weakest components in the loop. Experimental study is required, as well as a numerical one, using CFD⁸, to analyse the most interesting components to better understand the phenomena that in this chapter we have begun to observe.

⁷The discussion is here only focused on civil aviation. It has to be underlined that Defence and space applications are surely related to higher and different acceleration constraints than those here described.

⁸First CFD calculations has been performed during the last period of this study, but results are not satisfying and are not worthy to be considered in this document.

Part V

Conclusion and Perspectives

This final part of the work is related to general conclusion, perspectives and suggestions for future researches. In particular, in perspectives a newer technology is introduced. The latter is particularly adapted for coupling of power electronics and eMotor coolings.

General conclusion

Issue dealing with heat extraction from high power density electronics components for hybrid propulsion aircraft has been analysed in this work. Despite the high efficiency of such electronics components, the main difficulty is related to the high amount of thermal power losses. The higher the mechanical power required by eMotors, the higher the electrical power to be supplied by power electronics and, even when electric efficiencies are significant, thermal losses are far to be negligible.

Due to the constraints related to low-mass requirements, classical air forced convection cooling systems are not adapted for the purpose! The use of the latter would make the whole system, power electronics and adjoined cooling system, too heavy for its use in a high technological aircraft like the hybrid aircraft might be. Consequently, the use of a cutting-edge technology is necessary to solve the problem.

To find the best cooling system, able to work in critical conditions, like those realised during the mission of an aircraft, a study, focused on different cooling technologies and heat extraction techniques, has been carried out. The high amount of thermal losses to be evacuated and the high required thermal efficiency, made necessary the use of closed loop circuit to transport heat from hot to cold source.

Problem solving can be fundamentally synthesised in three “sub-issues”, each of which is related to a section of the cooling system. In order from the hot to the cold source they are:

1. Research of an adapted technology to extract heat, in the most efficient way (maximising the HTC), and to ensure temperature requirement at level of chips.
2. Research of adapted closed loop circuit: heat transport from hot to cold sources. Such technology should require pretty low amount of energy for its operations and ensure temperature controllability on the hot side whatever the cold source temperature variation. Finally it should be stable, reliable and robust.
3. Research of most performing cold source technology. The latter should be characterised by low thermal resistance between primary side (closed loop circuit side)

and the secondary side (external air circuit). The last condition is necessary to reduce as far as possible heat exchanger dimensions.

Cold plate heatsink is up to now the most used technology in active single and two-phase pumped/vapour-compression technologies. Its working principle is well known, it is ease-to-design and to integrate, but its limitations, related to low heat transfer coefficient and strong dependency of thermal performances on the mass flow rate, do not make of it a suitable technology for HASTECS project. Nowadays different technologies allow to maximise heat exchange rate from chips to coolant to obtain pretty high heat transfer coefficients on the hot side. Jet impingement and spray cooling, microchannels, porous media and metal foams, were compared to have a broad knowledge of current state of the art concerning electronics cooling. Such cooling technologies are successfully used to cool small-dimensions and high performing electronics components. Literature research has demonstrated their effectiveness, but it comes at steep price. The main problems related to the use of these particular cooling techniques is, in fact, related to their pressure drops. Microchannels and metal foams, for example, represent the best solution to be used in active cooling system configuration. They allow high heat transfer coefficients and almost independence of thermal performance on mass flow rate. Otherwise, their related high pressure drops represent a strong limitation. These technologies give their best in active-two-phase configuration, where pressure drop are lower, up to two orders of magnitude compared to single-phase configuration. Actually, sintered porous media are not suitable neither in single nor in two-phase configuration. Pressure drop are higher than those related to microchannels and metal foams. Despite quite high heatsink thermal performances, the required pumping power is extremely high. The higher the pumping power, the higher the pump mass and so the lower the power coefficient, C_c [$\text{kW}\cdot\text{kg}^{-1}$] — being the latter the main constraint in aeronautics field —.

Considering the whole cooling system, active and passive closed loop circuits were introduced. The main components of such circuit have been analysed under a thermo-hydraulic point of view. Pros, drawbacks and potentialities of each solution were introduced. Active single phase cooling systems are not, in general, able to maintain constant temperature level during operation if the secondary side temperature changes as a function of time (how it occurs during the mission of the aircraft), unless a kind of control system is used (regulating valves, variable speed pumps and so on). However, due to high simplicity, well known physical phenomena and design methods, this kind of technology is today widely used. This is the reason why it has been used for comparison purposes. Two-phase active cooling systems are rising technology, and especially vapour compression is quite interesting and begins to be used in aeronautics field. Despite its per-

formances and its ability to maintain the evaporator temperature below the cold source one, this technology is unfortunately at its early stages, and some problems, especially related to compressor hydraulics, and its behaviour during sever acceleration stages, must be solved. Actually, complex regulating systems are required for their operations. The attention was also focused on passive two-phase cooling systems. Working principles of thermosyphons, heat pipes, loop heat pipes and capillary pumped loops (with particular attention to a new kind of gravity CPL) were introduced. Literature results were considered in terms of thermal resistance, transport distance and heat evacuation capability to understand which technology should be the most adapted.

Passive two-phase technologies began to be used for electronics cooling purpose since the thermal heat flux densities became too high. Their performances increase time by time and they are today able to ensure the adequate cooling with relatively high transport distance, as is the case of two-phase passive loops (see LHP/CPL/CPLIP). Loop heat pipes (LHP) and capillary pumped loop (CPL) are worth of attention. Especially, a particular configuration of CPL, the CPLIP (Capillary Pumped Loop for Integrated Power), is able to maintain a constant operating temperature to the evaporator whatever the cold source one and ensuring stability, robustness and reliability.

When talking about aircraft, the choice of the cold source is limited. If heat recovery in the fuel is not considered, only skin heat exchanger and RAM-air are candidates for the cold source. Their coupling with a closed loop cooling system may ensure a better control of cooling rate. Skin heat exchanger is characterised by lower overall performances. It is mainly due to difficulties in use fins to increase the heat exchanger surface area or in general to increase the external side HTC. Higher heat exchanger dimensions characterise this technology if compared with RAM-air one. On the other side, RAM-air is more flexible. It allows the use of a finned, and so more compact, heat exchanger. Moreover, secondary-side duct dimensions can be controlled, during design process, to control and optimise air velocity and maximising the external HTC.

Active single and two-phase cooling systems and passive capillary driven ones, have been compared on the basis of a first approximation design and using the total mass of the cooling system as index, to make the final choice. Actually, neither classic liquid cooling systems nor active two-phase technologies are able to ensure the mass requirement, while not yet optimised CPLIP crosses over the minimal C_c condition.

CPLIP is thus the best solution to be used in the context of this work.

CPLIP main characteristics were described focusing the attention on the physical phenomena governing its operations. An existing experimental facility, used in the context of this work, has been introduced to explain its mechanical, hydraulic and thermal charac-

teristics. An extent description of the measuring sensors equipping the experimental loop has been also done to give an idea of the measurements accuracy presented during the entire description and analysis of this work. — To testify one of the main characteristics of CPLIP: high reliability and robustness, one has to think that, despite the loop is used by students for educational purposes, after several years it keeps its characteristics and potentialities unchanged —.

Numerical model used in this work was also described. Such model, using a “system approach”, has been used to obtain quantitative evaluation of thermal and hydraulic characteristics of the loop and to explain the experimentally observed phenomena. Adaptation of such model to the used experimental facility has been done, modifying evaporator and reservoir thermal conductances G_{ev} , G_{res} ; and vapour, condenser, and liquid line geometries, as well as the reservoir and evaporator ones. Numerical and experimental results have been compared, in transient and steady conditions, to show the agreement [111].

Behaviour of CPLIP in many operating conditions was experimentally studied, and in particular its thermal and hydraulic characteristics were exploited. From widely extended experimental parametric study, thermal characterisation of CPLIP, using methanol and ethanol as working fluids, has been carried out. Because of the inability to directly measure the evaporation temperature in the porous wick, an adapted post-processing tool was used to obtain all missing parameters on simplified thermodynamic cycle. It was observed, that, due to the intrinsic characteristics of two-phase cooling system, where saturation conditions are imposed and controlled, an independence between cold source temperature and evaporator operating temperature exists. Consequently, evaporator thermal conductance values are independent on the secondary side temperature. This behaviour makes this system particularly adapted for the application studied in the context of HASTECS project. Evaporator thermal conductances were experimentally obtained, based either on the reservoir and evaporator temperature. The typical bell shape was got as a function of the heat power. On the base of the experimentally obtained thermal conductances (related to evaporator HTC by the electronics modules base plate surface area) it was possible to numerically study the temperature field on a numerical reproduction of real electronic power module. Based on the finite volume method on StarCCM+, energy equation was solved to obtain temperature distribution in the worst operating condition for power electronics modules and for the less performing electronics configuration (the one characterised by the lowest efficiency). Despite the very high heat flux density evacuated by electronic chips, CPLIP, characterised by quite high evaporator HTC, is able to maintain the temperature value lower than the one allowed by

power-electronics-module constructor! Thanks to spreading behaviour of power-module-layers, one assists to a flattening of temperature field in correspondence of the base plate (interface between the evaporator and the power module) reducing the effect of hot-spots in correspondence of evaporator walls. CPLIP behaviour was experimentally explored during an entire mission profile cycle¹. This technology is able to evacuate the supplied thermal load, and temperatures on the evaporator walls remain controlled even during the most critical phases (transition between the taxi-out and take-off stage for example). The experimentally obtained temperatures were compared with those resulting from WP2's mono-dimensional electrical analogy model, based on the thermal characterisation presented in this work. Such test allowed to verify the good agreement between calculated temperatures and experimentally obtained ones. Results are quite satisfying, even if slight overestimation of junction temperature was found in the model. This, however, allows to be more conservative during the design process of electrical components and their adjoined cooling system.

Some differences could exist between laboratory tested behaviour and real operating conditions. They could be mainly due to a difference in transport lines length and/or a different nature of the condenser. Moreover, in this experimental study, the evaporator was uniformly, and quasi ideally heated by electrical resistances, so, some differences could be due to the use of real switching power modules. In fact, they are surely characterised by pretty different values of thermal inertia than copper, actually used for the thermal diffusers.

To know the influence of the vapour line pressure drops, to relate them to the transport distance, a parametric study was conducted, acting on the hydraulic characteristics of the CPLIP. It was found that the increasing pressure drops in the vapour line have a similar effect than changing the thermal load to the evaporator. Methanol and ethanol have the same qualitative behaviour, but, due to their different thermophysical properties, they bring to quantitatively different results. Ethanol, in particular, is more sensitive to heat power step-up or vapour line pressure drops.

CPLIP was designed and optimised following the HASTECS' requirements for 2025 and 2035. After a discussion about the complex optimisation process linked to the condenser, and about the most suitable fin configurations to be used, optimised CPLIP results for 2025 have been presented for the four electronics configurations proposed by WP2. Each of them is characterised by a different efficiency. Considering either electronics components and the adjoined cooling system, the configuration allowing the highest

¹One third of the maximal thermal load has been here used (5.4 kW, also corresponding to the thermal load of one electrical phase).

mass saving was the NPC-DPWMMAX. In this case, the obtained power coefficient was higher than requirement for 2025 ($> 19 \text{ kW}\cdot\text{kg}^{-1}$, target 2025: $15 \text{ kW}\cdot\text{kg}^{-1}$). With purpose to further reduce the mass of the cooling system, a louvered fins-microchannels condenser was selected for the solution 2035. The latter allows a reduction of the solid mass thanks to enhancement of external side HTC, over three times, and a reduction of the fluid amount in the loop thanks to the use of microchannels. The cooling solution proposed for 2035 is “impressive”! Despite the same electronic configuration than 2025 (NPC-DPWMMAX), the overall CPLIP mass has been sensibly reduced. Cooling system mass related to 2035 solution is one order of magnitude lower than 2025 solution! Overall power coefficient boosting comes, in fact, from either electronic and cooling system mass reduction. It is more than twice the 2035 requirement: over $50 \text{ kW}\cdot\text{kg}^{-1}$, for a target of $25 \text{ kW}\cdot\text{kg}^{-1}$. It has to be underlined that no accessories and fixation system have been considered in calculation at this stage, but the results are encouraging and allow room for manoeuvre.

CPLIP well responds to power electronics cooling requirements either for the targets of 2025 and 2035!

Finally, CPLIP was experimentally and numerically analysed when critical harsh transient conditions occur. The attention was focused on high heat power step start-ups and harsh acceleration stages. Experimental tests using methanol as working fluid were performed changing vapour line initial temperature to evaluate its influence on the vapour front behaviour during start-ups. Numerical simulations were compared to experimental results during cold start-ups to testify the correctness of interpretation of experimental data. To understand the differences between “relaxed” and extremely severe start-up conditions, CPLIP was pushed up to reach its operating limits during some specific start-ups stages. The comparison between a severe (5 kW) and a more relaxed (0.5 kW or 2 kW) cold start-ups showed that vapour front velocity values in the vapour line are similar for the relaxed cases, while in the case of a severe start-up its velocity is one-order-of-magnitude higher. To understand and justify such results for hot and cold cases, an energy based analysis, considering the importance of heat accumulated, due thermal inertia of vapour line tubes, was performed. It was observed that the variation of vapour front velocity is due to recondensation of the vapour on the internal side of vapour line wall. This phenomenon is more significant during cold start-ups due to a higher difference between fluid and tube-initial temperatures. So, as the initial-vapour line-temperature is low, the vapour front velocity decreases, resulting in higher settling times and quicker vapour quality increases. The vapour line initial temperature determines the quantity of energy dissipated by the fluid to the tube walls. Such amount of energy exchanged,

directly related to the recondensation phenomenon on the tube walls, has an impact on pressure and mass distributions of vapour phase and, so, on the vapour front velocity and shape. Further studies need to be performed, particularly in terms of experimental visualisations and numerical volume of fluid (VOF) simulations (of the vapour flow in the vapour line during such transient start-ups) in order to completely validate the assessments given in this work.

It has to be underlined that in the context of HASTECS project, the most critical phases are realised, on the basis of the actually held data, on the ground where the CPLIP is required to boot at temperatures lower than 40 °C and with an applied thermal load of about 2.4 kW (0.8 kW/ePhase). On the basis of results obtained, no particular problems are related to loop start-up in such conditions.

Finally, like all equipments which is required to fly, CPLIP behaviour has been studied during sudden and violent acceleration stage, with the purpose to identify the weakest and the most impacted components in the loop. The study performed in this work should be seen as a beginning for a wider and more complex research on the subject. The study has been fundamentally divided in two parts: a simple case study has been considered to understand the phenomena occurring and to identify how CPLIP is hydraulically and thermally impacted; and a parametric study to understand the effect of each influencing parameter such as acceleration intensity and time lasting, and difference of height between condenser and reservoir.

From results obtained, it was observed a strong effect on hydraulics of the loop, while its thermal behaviour seems to be weakly influenced by acceleration impulse. As expected, the first effect of variation of acceleration field has been observed in the liquid line. This component is, in fact, characterised by the higher gravity pressure drop, due to the flow of the highest density fluid. The stronger effect was related to liquid spilling from the reservoir higher part, and within the lower part to the liquid line. The amount of liquid coming from the reservoir participates to condensation length reduction, vapour compression in the vapour line, and somehow to the vapour mass flow rate reduction into the vapour line. Influencing parameters are, other than acceleration intensity, time duration and condenser to reservoir height difference. An increase of all just expressed parameters negatively influences the loop behaviour. In fact, the higher the acceleration intensity, or its duration or the height difference, the higher the back-flowing mass flow rate. More studies are strongly suggested on the subject, both from experimental and numerical points of view, to continue the assessments of this work.

CPLIP seems to be the best choice for power electronics cooling in the context of HASTECS project, but other studies are required. It could be interesting to experiment-

ally study the behaviour of the CPLIP, in the configuration 2035, to compare the results introduced in this work with experimental ones.

Perspectives

11.1 General perspectives

Capillary Pumped Loop for Integrated Power, CPLIP, is a valuable solution for power electronics cooling in the context of HASTECS project. As observed all along the study, this solution is able to evacuate high power density thermal load from power electronics modules by ensuring temperature requirements and respecting the power to mass ratio constraints, C_c . Actually, this kind of capillary driven loop crosses-over the imposed power coefficient values either for targets 2025 and 2035!

Outstanding questions remain at the end of this study, and they should be retained as input for future researches and development.

The evaporator is the CPLIP's key component. In this study a nickel porous wick has been used, because of its high performances, in terms of HTC, measured on the existing experimental facility. However, it should be interesting to exploit the use of different materials for porous mesh for issues related to the mass of the loop. The use a less dense material could help to further reduce CPLIP overall mass and consequently increase the power coefficient value, C_c . Especially for 2035 solution, that is mostly influenced by evaporator mass.

All experimental tests were performed using heating resistances to simulate the presence of power modules. However, new tests involving the presence of real power electronics converters could be done in order to compare the thermal inertia of actual copper diffusers with real converters one. Moreover, as laboratory conditions are quite different than real operating ones, CPLIP behaviour equipped by an air-liquid condenser should be considered for tests, instead of the coaxial liquid-to-liquid condenser used in the tests. Especially, 2035's condenser configuration should be explored. In this last case, in fact, either external (louver side) and internal side (condensation in microchannels) should be exploited to observe the difference between estimated thermo-hydraulic behaviour and real one. In this case, in fact, the used technology ensures the highest possible internal and external HTC, but pressure drops should be measured to obtain a more precise evaluation.

A joint adventure with a hypothetic aerodynamics team could lead to a better integration of the cooling system into the aircraft, a more accurate knowledge of limitations, related to condenser external side configuration and its impact on lift to drag ratio. Such cooperation could lead to more “appropriate results”. — For a such high technological aircraft, like the hybrid one, it will be necessary to build the aircraft around the sub-system (power electronics cooling in this case), and of course to adapt the latter to be integrated at the best! —

Finally, with the purpose to propose a solution able to merge power electronics and eMotor cooling, a new promising technology should be exploited: Capillary Jet Loop (CJL).

11.2 A newer technology: Capillary Jet Loop (CJL)

Basic principle of CJL is similar to a CPL (Capillary Pumped Loop) in which reservoir has been replaced by a “flow ring”, obviously without, cartridge heater to impose saturation conditions. CJL can be divided in two subsystems, also called rings [18]: two-phase ring, capillary driven, and single phase ring, injector driven. At the end of the vapour line the injector is used to transfer momentum from hot vapour, flowing in the vapour line, to the liquid in the liquid ring. From the liquid ring, where different heat sources may be installed, heat is definitively evacuated through the subcooler. In Fig. 11.1 a schematic of CJL is introduced.

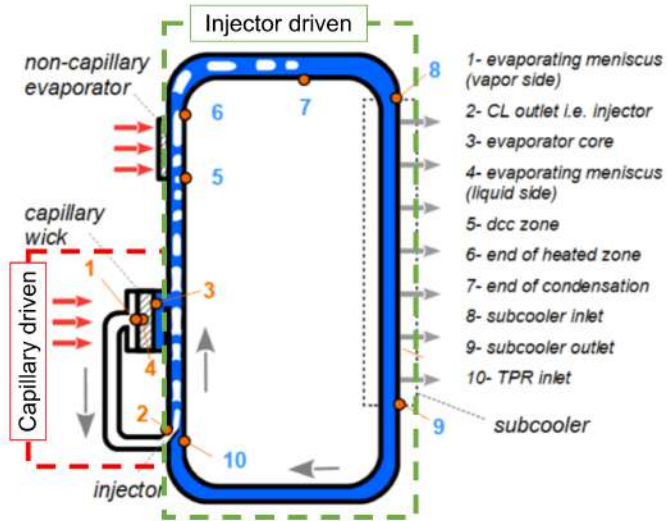


Figure 11.1: Capillary Jet Loop concept [18]

Referring to Fig. 11.1, thermal load is applied to the capillary wicked evaporator

(point 1). There, capillary forces take place allowing vapour flow within the vapour line to the injector (point 2). In the latter, which physical phenomena are quite delicate and complex, vapour kinetic energy is used to transfer momentum to liquid in the external ring (from point 2 to 10). “*Steam injector (SI) is a passive jet pump without moving parts or machineries [...]”* [cit.] [19]. In other words, injector is able to generate an additional pressure head allowing the liquid flow. Injector is in general composed by coaxial liquid and vapour inlet nozzles, mixing section and diffuser (see Fig. 11.2). Following the fluid phase flowing in the inner nozzle as well as the external nozzle inlet

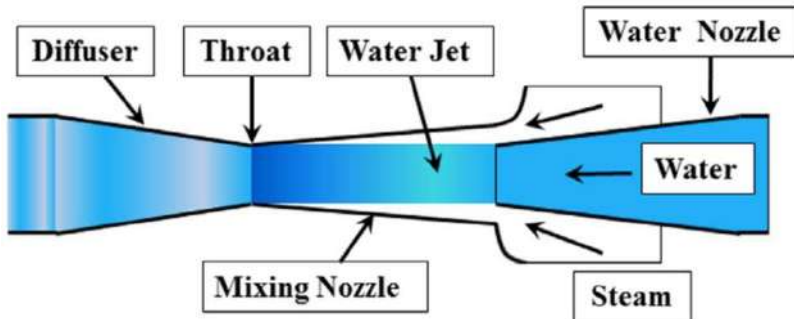


Figure 11.2: Injector principle scheme [19]

direction (coaxial or perpendicular to nozzle axis) different shapes may be used for the inner part. The mixing nozzle, usually converging, allows direct contact condensation of vapour, coming from evaporator, in the liquid phase. In centred liquid jet injectors, interesting for their application in CJL, the vapour nozzle is external and annular. Here, superheated vapour adiabatically expands reaching sonic conditions at the exit of the nozzle: its enthalpy is converted in kinetic energy [126, 19]. At the same time subcooled liquid velocity increases from the inlet to the outlet of liquid nozzle. A high velocity liquid jet is so created. In the mixing nozzle direct contact condensation of vapour occurs due to contact with the high velocity liquid jet. Mass, energy and momentum exchanges occur in correspondence of the interface between the two fluid phases, due to condensation and to quite high temperature and velocity differences between vapour and liquid phases. Complete condensation of vapour should occur in this section of injector. If not, the injector is not working in the appropriate condition [127]. The region where the complete condensation takes place is called *condensation shock* [19]. The latter is violent and, on the contrary of gas-dynamics' shock waves its thickness is significative and comparable with channel diameter [126]. The final section of the injector is the diffuser, allowing to increase fluid pressure from the throat to the exit section — injectors are used in a quite large range of applications. Actually they are particularly interesting to

passively pump coolant in nuclear reactors in emergency cases, for example —. Finally, in the diffuser (divergent section), condensed sub-cooled liquid at the exit of the mixing nozzle decelerates and its pressure further increases from the inlet to the outlet¹. At point 3, a part of liquid wets the porous wick allowing evaporation and capillary pumping to let the vapour cycle to re-start, while another part of the liquid flows to the secondary heat source. In the latter, sensible heat is exchanged increasing the fluid temperature between points 5 and 6. From point 7, liquid flows to the heat exchanger: subcooler. Here, only sensible heat is exchanged with external environment and definitively evacuating the thermal load. From point 9, subcooled liquid flows to point 10, corresponding to the injector inlet. Here, pressure head takes place to let the cycle start again.

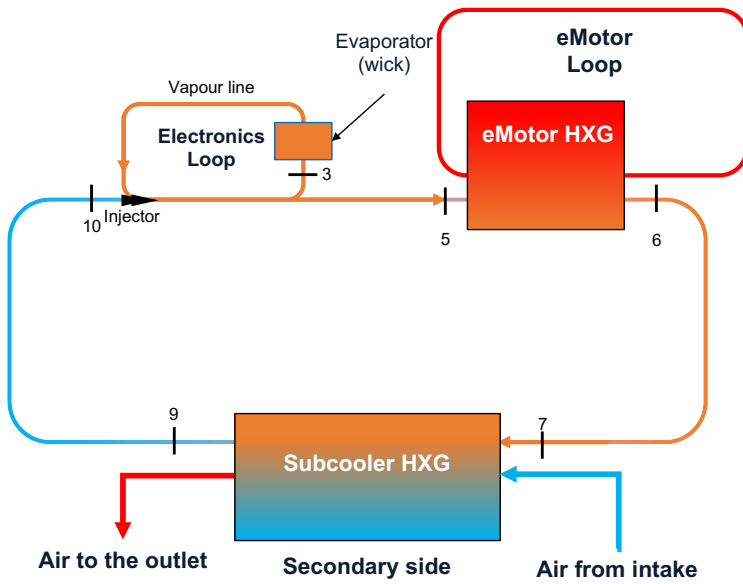


Figure 11.3: Scheme of principle of CJL adapted for HASTEC requirements

¹For the interested reader, references [126, 19, 127] are strongly suggested.

As the reader has surely noticed, this loop does not require any form of external source of energy for its operations: no cartridge heater is used to impose saturation conditions that are so dependent on the subcooler outlet temperature. It follows that any variation of the cold source temperature would impact the internal fluid temperature. The design of this technology is quite complex and should consider some phenomena that up to date still represent an open issue. The injector should be designed and chosen with pretty high attention to maximise its efficiency and to exploit all the potential of this component [126].

A possible scheme of principle of this technology applied to HASTEC project is reported in Fig. 11.3. This technology is worth of attention. Efforts have to be made to design it and to let it work for power electronics and eMotor cooling in the context of Hybrid aircraft. Power coefficients shall be re-thought according to coupling of power electronics modules, eMotor and their adjoined cooling systems. If on one hand louvered fins-microchannels HXG may represent a valuable solution for the subcooler, some efforts have to be done to research the best heat exchanger solution to be used on eMotor side according to performance and mass requirements of aeronautics fields.

Bibliography

- [1] F. Accorinti, N. Erroui, V. Ayel, G. Gateau, Y. Bertin, N. Roux, S. Dutour, M. Miscevic, High-efficiency cooling system for highly integrated power electronics for hybrid propulsion aircraft, in: 28th IEEE International Symposium on Industrial Electronics (ISIE), 2019, pp. 870–877. [doi:10.1109/ISIE.2019.8781086](https://doi.org/10.1109/ISIE.2019.8781086).
- [2] J.-F. Allias, Specification dossier for HASTECS (AIRBUS) (January 2018).
- [3] H. R. W. (McDonnell Douglas Corporation Long Beach Calif.), Skin Heat Exchanger, United States Patent 4819720.
- [4] L.P. Pang, X. Dang, J. Cheng, Study on heat transfer performance of skin heat exchanger, *Experimental Heat Transfer* (28) (2015) 317–327.
- [5] W. Chen, D. W. Fogg, M. Izenson, C. Kurwitz, A highly stable two-phase thermal management system for aircraft, Tech. rep., SAE Technical Paper (2012).
- [6] D. Ray, P. Kew, *Heat Pipes - Theory, Design and Applications*, fifth edition Edition, BH, 2006.
- [7] V. Ayel, L. Lachassagne, Y. Bertin, C. Romestant, Experimental study on the effect of the vapour pressure losses on a capillary pumped loop for terrestrial application, in: 16th International Heat Pipe Conference, Lyon, France, 2012.
- [8] J. Kim, Spray cooling heat transfer: the state of art, *International Journal of Heat and Fluid Flow* 28 (2007) 753–767.
- [9] A. Sakanova, C. F. Fong Tong, A. Nawawi, R. Simanjorang, K. Tseng, A. K. Gupta, Investigation on weight consideration of liquid coolant system for power electronics converter in future aircraft, *Applied Thermal Engineering* (104) (2016) 603–615.
- [10] K. Boomsma, D. Poulikakos, F. Zwick, [Metal foams as compact high performance heat exchangers](#), *Mechanics of Materials* 35 (12) (2003) 1161 – 1176. [doi:<https://doi.org/10.1016/j.mechmat.2003.02.001>](https://doi.org/10.1016/j.mechmat.2003.02.001).
URL <http://www.sciencedirect.com/science/article/pii/S0167663603001029>

- [11] Y. Bertin, F. Accorinti, F. Pagnoni, Systèmes diphasiques pour le contrôle thermique de l'électronique de puissance, in: Journée Thématique, SFT (Société Française de Thermique), Toulouse - March 29, 2018.
- [12] F. Accorinti, V. Ayel, Y. Bertin, [Steady-state analysis of a capillary pumped loop for terrestrial application with methanol and ethanol as working fluids](#), International Journal of Thermal Sciences 137 (2019) 571 – 583. [doi:<https://doi.org/10.1016/j.ijthermalsci.2018.10.036>](https://doi.org/10.1016/j.ijthermalsci.2018.10.036).
URL <http://www.sciencedirect.com/science/article/pii/S1290072918300681>
- [13] P. J. Marto, Handbook of Heat Transfer (Third Edition), McGraw-Hill, 1998, Ch. 14, pp. 1–54.
- [14] V. Ayel, L. Lachassagne, Y. Bertin, C. Romestant, D. Lossouarn, Experimental analysis of a capillary pumped loop for terrestrial application, Journal of thermophysics and heat transfer 25 (4) (2011) 561–571.
- [15] D. Lossouarn, Etude théorique et expérimentale du refroidissement diphasique à pompage capillaire des convertisseurs de puissance à haute densité de flux de chaleur pour la traction ferroviaire, Ph.D. thesis, ISAE-ENSMA (2008).
- [16] N. Blet, V. Ayel, Y. Bertin, C. Romestant, V. Platel, Transient modeling of cpl for terrestrial applications. part a: Network concept & influence of gravity on the cpl behavior, Vol. India, Kampur, 2013, pp. 263–270.
- [17] R. K. Shah, D. P. Sekulic, Handbook of Heat Transfer (Third Edition), McGraw-Hill, 1998, Ch. 17, pp. 1–65.
- [18] V. Dupont, B. Paran, S. Van Oost, C. Billet, Capillary jet loop, in: Joint 19th IHPC and 13th IHPS, Pisa, Italy, June 10-14, 2018.
- [19] S. Miwa, H. Endo, T. Moribe, H. Sakashita, M. Mori, T. Hibiki, [Investigation of the thermal-hydraulic characteristics of supersonic steam injector](#), Applied Thermal Engineering 109 (2016) 261 – 271. [doi:<https://doi.org/10.1016/j.applthermaleng.2016.08.069>](https://doi.org/10.1016/j.applthermaleng.2016.08.069).
URL <http://www.sciencedirect.com/science/article/pii/S1359431116314235>
- [20] B. Agostini, M. Fabbri, J. E. Park, L. Wojtan, J. Thome, B. Michel, State of art of high heat flux cooling technologies, Heat Transfer Engineering 28 (4) (2007) 258–281.

- [21] N. Erroui, High power conversion chain for hybrid aircraft propulsion, Ph.D. thesis, Laboratoire plasma et conversion d'énergie (ENSEEIHT) (2019).
- [22] Nasa, [Earth atmosphere model](https://www.grc.nasa.gov/WWW/k-12/airplane/atmosmet.html) (2019).
URL <https://www.grc.nasa.gov/WWW/k-12/airplane/atmosmet.html>
- [23] E. G. Colgan, F. Bruce, M. Gaynes, W. S. Graham, N. C. LaBianca, J. H. Magerlein, R. J. Polastre, M. B. Rothwell, R. J. Bezama, R. Choudhary, K. C. Marston, H. Toy, J. Wakil, J. A. Zitz, R. R. Schmidt, A Practical Implementation of Silicon Microchannel Coolers for High Power Chips, *IEEE Transactions on Components and Packaging Technologies* 30 (2).
- [24] P.-X. Jiang, M.-H. Fan, G.-S. Si, Z.-P. Ren, Thermal-hydraulic performance of small scale micro-channel and porous-media heat-exchanger, *International Journal of Heat and mass Transfer* (44) (2001) 1039–1051.
- [25] N. Blet, Analyse expérimentale et par voie de modélisation d'une boucle gravitaire à pompage capillaire multi-évaporateurs, Ph.D. thesis, ISAE-ENSMA (2014).
- [26] N. Delalandre, Analyse par voie de modélisation du comportement thermohydraulique instationnaire des boucles diphasiques à pompage capillaire en environnement gravitaire: application au refroidissement de composants électroniques de puissance soumis à des sollicitations sévères, Ph.D. thesis, ISAE-ENSMA (2011).
- [27] [Power trip: Hasteecs energizes the path to hybrid-powered flight](#) [online].
- [28] R. W. Newman, M. Dooley, C. Lui, Efficient propulsion, power, and thermal management integration, in: 49th AIAA/ASME/SAE/ASEE Joint Propulsion Conference, 2013, p. 3681.
- [29] M. Dooley, N. Lui, R. Newman, C. Lui, Aircraft thermal management-heat sink challenge, Tech. rep., SAE Technical Paper (2014).
- [30] R. H. Zimmerman, W. Robinson, Equipment cooling systems for aircraft, part 1, Tech. Rep. 54-359, The Ohio State University Research Foundation (September 1954).
- [31] A. Hashemi, E. Dyson, Performance Characterization of High-Power Electronic Equipment onboard an aircraft, *Heat Transfer Engineering* 21 (2000) 15–24.
- [32] J. F. Andrew, H. L. Quinn, L. Y. Kirk, J. E. Levi, Aircraft thermal management using loop heat pipes: Experimental simulation of high acceleration environments

- using the centrifuge table test bed, Air Force Research Laboratory and SAE International.
- [33] A. Hashemi, E. Dyson, J. Nigen, Aircraft skin-cooling system for thermal management of onboard high-power electronics, *Journal of thermophysics and heat transfer* 13 (14) (1999) 529–536.
 - [34] M. R. Moroney, Ram-air cooling systems for aircraft generators, *Transactions of the American Institute of Electrical Engineers, Part II: Applications and Industry* 76 (4) (1957) 217–221. [doi:10.1109/TAI.1957.6367231](https://doi.org/10.1109/TAI.1957.6367231).
 - [35] [link].
URL https://upload.wikimedia.org/wikipedia/commons/1/1f/Air_intakes_of_RAM_air_for_environmental_control_systems_of_Boeing_747-8I.jpg
 - [36] Design of a ram air driven air cycle cooling system for fighter aircraft pods, AIAA, Thermophysiscs Conference, American Institute of Aeronautics and Astronautics, Inc., June 17-20, 1996.
 - [37] R. M. Grabow, T. W. Kreter, G. E. Limberg, [A ram air driven air cycle cooling system for avionics pods](#), in: SAE Technical Paper, SAE International, 1986. [doi:10.4271/860912](https://doi.org/10.4271/860912).
URL <https://doi.org/10.4271/860912>
 - [38] Caleffi, [Vasi di espansione](#) (2019).
URL https://www.caleffi.com/sites/default/files/file/01079_it.pdf
 - [39] J. Thome, A. Bruch, Refrigerated cooling of microprocessors with micro-evaporation heat sinks: new development and energy conservation prospects for green datacenters, Proceedings Institute of refrigeration (IOR).
 - [40] J. Homitz, R. Scaringe, G. Cole, Evaluation of a vapor-compression thermal management system for reliability while operating under thermal transients, Tech. rep., SAE Technical Paper (2010).
 - [41] ACT, [Pumped two phase resources](#) (2019) [cited 2019].
URL <https://www.1-act.com/resources/pumped-two-phase-cooling/>
 - [42] J. B. Marcinichen, J. R. Thome, B. Michel, [Cooling of microprocessors with micro-evaporation: A novel two-phase cooling cycle](#), *International Journal of Refrigeration* 33 (7) (2010) 1264 – 1276. [doi:https://doi.org/10.1016/j.ijrefrig](https://doi.org/10.1016/j.ijrefrig).

2010.06.008.

URL <http://www.sciencedirect.com/science/article/pii/S0140700710001271>

- [43] J. Homitz, R. P. Scaringe, G. S. Cole, A. Fleming, T. Michalak, Comparative analysis of thermal management architectures to address evolving thermal requirements of aircraft systems, Tech. rep., SAE Technical Paper (2008).
- [44] J. R. Barbosa, G. B. Ribeiro, P. A. Oliveira, A state-of-art review of compact vapor compression refrigeration systems and their applications, Heat Transfer Engineering 33 (4-5) (2012) 356–374.
- [45] S. Mancin, C. Zilio, G. Righetti, L. Rossetto, Mini vapor cycle system for high density electronic applications, International Journal of Refrigeration (36) (2013) 1191–1202.
- [46] S. Trutassanawin, E. A. Groll, S. V. Garimella, L. Cremaschi, Experimental investigation of a miniature-scale refrigeration system for electronics cooling, IEEE Transactions on Components and Packaging Technologies 29 (3) (2006) 678–687.
[doi:10.1109/TCAPT.2006.881762](https://doi.org/10.1109/TCAPT.2006.881762).
- [47] Mikhail Nikitkin, B. Cullimore, CPL and LHP Technologies: What are the Differences, What are the Similarities, Society of Automotive Engineers.
- [48] V. Dupont, S. V. O. Oost, L. Barremaecker, S. Nicolau, Railwais qualification tests of capillary pumped loop on a train, in: 17th International Heat Pipe Conference, 2013, pp. 311–318.
- [49] L. Lachassagne, Y. Bertin, V. Ayel, C. Romestant, Steady-state modeling of Capillary Pumped Loop in gravity field, International Journal of Thermal Sciences 64 (2013) 62–80.
- [50] L. Vasiliev, D. Lossouarn, C. Romestant, A. Alexandre, Y. Bertin, Y. Piatsiushyk, V. Romanenkov, Loop heat pipes for cooling of high-power electronic components, International Journal of Heat Transfer 52 (2009) 301–308.
- [51] N. Blet, S. Lips, V. Sartre, Heat pipes for temperature homogenization: a literature review, Applied Thermal Engineering 118 (2017) 490–509.
- [52] M. Reyes, D. Alonso, J. R. Arias, A. Velazquez, Experimental and theoretical study of a vapour chamber based heat spreader for avionics applications, Applied Thermal Engineering (37) (2012) 51–59.

- [53] K.-S. Ong, C. Lim, Performance of water filled thermosyphons between 30-150oc, *Frontiers in Heat Pipes (FHP)* 6 (1).
- [54] D. Jafari, A. Franco, S. Filippeschi, P. Di Marco, Two-phase closed thermosyphons: a review of studies and solar applications, *Renewable and Sustainable Energy Reviews* 53 (2016) 575–593.
- [55] H. Abou-Ziyan, A. Helali, M. Fatouh, M. A. El-Nasr, Performance of stationary and vibrated thermosyphon working with water and R134a, *Applied Thermal Engineering* (21) (2001) 813–830.
- [56] S. Filippeschi, A. Franco, Experimental analysis of the instabilities effect on the thermal performance of a closed loop two-phase thermosyphon, *Heat Pipe Science and Technology, An International Journal* 5 (1-4).
- [57] [link].
URL <https://samsungrumors.net/samsung-galaxy-s8-will-heatpipe-like-s7/>
- [58] [link].
URL <https://www.apple.com/fr/mac-pro/>
- [59] Sergii Khairnasov, A. Naumova, Heat pipes application in electronics thermal control systems, *Frontiers in Heat Pipes (FHP)* 6 (6).
- [60] J.-S. Chen, J.-H. Chou, The length and bending angle effect on the cooling performance of flate plate heat pipes, *International Communications in Heat and Mass Transfer* 90 (2015) 848–856.
- [61] X. Chen, H. Ye, X. Fan, T. Ren, G. Zhang, A review of small heat pipes for electronics, *Applied Thermal Engineering* 96 (2016) 1–17.
- [62] Stéphane Launay, V. Sartre, J. Bonjour, Parametric analysis of loop heat pipe operation: a literature review, *International Journal of Thermal Sciences* (46) (2007) 621–636.
- [63] J. Gu, M. Kawaji, R. Futamata, Effects of gravity on the performance of pulsating heat pipes, *Journal of Thermophysics and Heat Transfer* 18 (3) (2004) 370–378.
- [64] V. Ayel, Y. Bertin, C. Romestant, G. Burban, Experimental study of pulsating heat pipes tested in horizontal and vertical positions, in: Proc. 15th International Heat Pipe Conference (Clemson, South Carolina, USA, 25-29 April 2010), Vol. 8, 2010, p. 26.

- [65] G. Burban, V. Ayel, A. Alexandre, P. Lagonotte, Y. Bertin, C. Romestant, [Experimental investigation of a pulsating heat pipe for hybrid vehicle applications](#), Applied Thermal Engineering 50 (1) (2013) 94 – 103. [doi:<https://doi.org/10.1016/j.applthermaleng.2012.05.037>](https://doi.org/10.1016/j.applthermaleng.2012.05.037).
URL <http://www.sciencedirect.com/science/article/pii/S1359431112004152>
- [66] V. Ayel, C. Romestant, Y. Bertin, V. Manno, S. Filippeschi, Visualisation of flow patterns in flat plate pulsating heat pipe: influence of hydraulic behaviour on thermal performances, Heat pipe science and technology, An International Journal 5 (2016) 377–384.
- [67] H. Han, X. Cui, Y. Zhu, S. Sun, A comparative study of the behavior of working fluids and their properties on the performance of pulsating heat pipes (php), International Journal of Thermal Sciences 82 (2014) 138–147.
- [68] V. Ayel, L. Araneo, A. Scalambra, M. Mameli, C. Romestant, A. Piteau, M. Marengo, S. Filippeschi, Y. Bertin, [Experimental study of a closed loop flat plate pulsating heat pipe under a varying gravity force](#), International Journal of Thermal Sciences 96 (2015) 23 – 34. [doi:<https://doi.org/10.1016/j.ijthermalsci.2015.04.010>](https://doi.org/10.1016/j.ijthermalsci.2015.04.010).
URL <http://www.sciencedirect.com/science/article/pii/S1290072915001349>
- [69] D. Mangini, M. Mameli, D. Fioriti, S. Filippeschi, L. Araneo, M. Marengo, Hybrid pulsating heat pipe for space applications with non-uniform heating patterns: ground and microgravity experiments, Applied Thermal Engineering 126 (2017) 1029–1043.
- [70] S. Lips, A. Bensalem, Y. Bertin, V. Ayel, C. Romestant, J. Bonjour, [Experimental evidences of distinct heat transfer regimes in pulsating heat pipes \(php\)](#), Applied Thermal Engineering 30 (8) (2010) 900 – 907. [doi:<https://doi.org/10.1016/j.applthermaleng.2009.12.020>](https://doi.org/10.1016/j.applthermaleng.2009.12.020).
URL <http://www.sciencedirect.com/science/article/pii/S1359431110000037>
- [71] N. Blet, Y. Bertin, V. Ayel, C. Romestant, V. Platel, Experimental analysis of a capillary pumped loop for terrestrial applications with several evaporators in parallel, Applied Thermal Engineering 93 (2016) 1304–1312.
- [72] Y. Maydanik, Loop Heat Pipes, Applied Thermal Engineering (25) (2005) 635–657.

- [73] D. Bugby, T. Miller, J. Baker, Multi-Evaporator Two-Phase Loop Cooling System, in: 4th International Energy Conversion Engineering Conference and Exhibit (IECEC), San Diego (California), 2006.
- [74] A. Kaled, S. Dutour, V. Platel, J. Lluc, Experimental study of a Capillary Pumped Loop for cooling power electronics: Response to high amplitude heat load steps, *Applied Thermal Engineering* 89 (2015) 169–179.
- [75] V. Dupont, J.-C. Legros, S. V. Oost, L. Barremaecker, Experimental investigation of CPL pressurized with NCG inside a centrifuge up to 10 G., in: 17th International Heat Pipe Conference, 2013, pp. 303–310.
- [76] P. A. de Oliveira, J. R. Barbosa, Effect of jet length and ambient temperature on the performance a two-phase jet impingement heat sink refrigeration system, *International Journal of Refrigeration* 75 (2017) 331–342.
- [77] K. Oliphant, B. W. Webb, M. Q. McQuay, An experimental comparison of liquid jet array and spray impingement cooling in the non-boiling regime, *Experimental Thermal and Fluid Sciance* (18) (1998) 1–10.
- [78] H. Bostanci, D. V. Ee, B. A.Saarloos, D. P. Rini, L. C. Chow, Spray cooling of power electronics using high temperature coolant and enhanced surface, ISBN: 978-1-4244-2601-0/09 IEEE.
- [79] Y. Wang, N. Zhou, Z. Yang, Y. Jiang, Experimental investigation of aircraft spray cooling system with different heating surfaces and different additives, *Applied Thermal Engineering* 103 (2016) 510–521.
- [80] L. Lin, R. Ponnappan, Heat transfer characteristics of spray cooling in a closed loop, *International Journal of Heat and Mass Transfer* 46 (2003) 3737–3746.
- [81] M. Molana, S. Banoooni, Investigation of heat transfer processes involved liquid impingement jets: A review, *Brazilian Journal of Chemical Engineering* 30 (3) (2013) 413–435.
- [82] B. P. Whelan, A. J. Robinson, Nozzle geometry effects in liquid jet array impingement, *Applied Thermal Engineering* (29) (2009) 2111–2221.
- [83] Q. Guo, Z. Wen, R. Duo, Experimental an numerical study on the transient heat-transfer characteristics of circular air-jet impingement on a flat plate, *International Communications in Heat and Mass Transfer* 104 (2017) 1177–1188.

- [84] B. Horacek, K. T. Kiger, J. Kim, Single nozzle spray cooling heat transfer mechanisms, *International Journal of Heat and Mass Transfer* 48 (2005) 1425–1438.
- [85] C. Wang, L. Wang, Bengt Sundén, A novel control of jet impingement heat transfer in cross-flow by vortew generatorpair, *International Journal of heat and Mass Transfer* 88 (2015) 82–90.
- [86] D. Go, R. A. Maturana, T. Fisher, S. Garimella, Enhancement of external forced convection by ionic wind, *International Journal of heat and Mass Transfer* (51) (2008) 6047–6053.
- [87] F. Douchet, D. Nortershauser, S. L. Masson, P. Gouannec, Experimental study of water cold plate for datacom equipment, in: ASME-ATI-UIT 2015 Conference on thermal energy systems: Production, storage, utilization and environment, 2015.
- [88] S. Grohamann, Measurement and modeling of single-phase and flow-boiling heat transfer in microtubes, *International Journal of Heat and Mass Transfer* 48 (2005) 4073–4089.
- [89] A. Avramenko, A. Tyrinov, I. Shevchuk, N. Dmitrenko, A. Kravchuck, V.I.Shevchuk, Mixed convection in a vertical flat microchannel, *International Journal of Heat and Mass Transfer* 106 (2017) 1164–1173.
- [90] B. Alm, U. Imke, R. Knitter, U. Schygulla, S. Zimmermann, Testing and simulation of ceramic micro heat exchangers, *Chemical Engineering Journal* 135S (2008) S179–S184.
- [91] K. Koyama, Y. Asako, Experimental investigation on heat transfer characteristics of a gas-to-gas counterflow microchannel heat exchanger, *Experimental Heat Transfer* 23 (2010) 130–143.
- [92] H. Y. Zhang, D. Pinjala, Y. K. Joshi, T. Wong, K. C. Toh, M. K. Iyer, Fluid Flow and Heat Transfer in Liquid Cooled Foam Heat Sinks for Electronic Packages, *IEEE Transactions on Components and Packaging Technologies* 28 (2).
- [93] L. D. Stevanovic, R. A. Beaupre, A. V. Gowda, A. G. Pautsch, S. A. Solovitz, Integral Micro-channel Liquid Cooling for Power Electronics, in: *Applied Power Electronics Conference and Exposition (APEC), Twenty-Fifth Annual IEEE*, 2010.
- [94] T.-H. Yen, N. Kasagi, Y. Suzuki, Forced convective boiling heat transfer in micro-tubes at low mass and heat fluxes, *International Journal of Multiphase Flow* 29 (2003) 1771–1792.

- [95] J. Lee, I. Mudawar, Two-phase flow in high-heat-flux micro-channel heat sink for refrigeration cooling applications: Part II-Heat transfer characteristics, International Journal of Heat and Mass Transfer (48) (2005) 941–955.
- [96] B. Agostini, A. Bontemps, Vertical flow boiling of refrigerant R134a in small channels, International Journal of Heat and Fluid Flow 27 (2005) 296–306.
- [97] G. Hetsroni, M. Gurevich, R. Ronzenblit, Sintered porous medium heat sink for cooling of high-power mini-devices, International Journal of Heat and Fluid Flow (27) (2006) 259–266.
- [98] P.-X. Jiang, X.-C. Lu, Numerical simulation of fluid flow and convection heat transfer in sintered porous plate channels, International Journal of Heat and Mass Transfer (49) (2006) 1685–1695.
- [99] P.-X. Jiang, M. Li, T.-J. Lu, L. Yu, Z.-P. Ren, Experimental research on convection heat transfer in sintered porous plate channels, International Journal of Heat and Mass Transfer (47) (2004) 2085–2096.
- [100] H. Zhang, D. Pinjala, T. Wong, K. Toh, Y. Joshi, Single-phase liquid cooled microchannel heat sink for electronic packages, Applied Thermal Engineering 25 (2005) 1472–1487.
- [101] G. P. Peterson, C. S. Chang, Two-phase heat dissipation utilizing porous-channels of high-conductivity material, Journal of Heat Transfer 1 (120) (1998) 243–252.
- [102] Z. Chen, P. Cheng, T. Zhao, [An experimental study of two phase flow and boiling heat transfer in bi-dispersed porous channels](#), International Communications in Heat and Mass Transfer 27 (3) (2000) 293 – 302. doi:[https://doi.org/10.1016/S0735-1933\(00\)00110-X](https://doi.org/10.1016/S0735-1933(00)00110-X).
URL <http://www.sciencedirect.com/science/article/pii/S073519330000110X>
- [103] T.S. Zhao, Q. Liao, On capillary-driven flow and phase-change heat transfer in a porous structure heheat by a finned surface: measurements and modeling, International Journal of Heat and Mass Transfer (43) (2000) 1141–1155.
- [104] D. Faulkner, M. Khotan, R. Shekarriz, Practical Design of a 1000 W/cm^2 Cooling System, in: 19th IEEE SEMI-THERM Symposium, 2003.
- [105] G. Lazarek, S. Black, [Evaporative heat transfer, pressure drop and critical heat flux in a small vertical tube with r-113](#), International Journal of Heat and Mass Transfer

- 25 (7) (1982) 945 – 960. doi:[https://doi.org/10.1016/0017-9310\(82\)90070-9](https://doi.org/10.1016/0017-9310(82)90070-9).
URL <http://www.sciencedirect.com/science/article/pii/0017931082900709>
- [106] Z. Zhang, J. Li, P.-X. Jiang, Experimental investigation of spray cooling on flat and enhanced surfaces, *Applied Thermal Engineering* 51 (1-2) (2013) 102–111.
- [107] L. Ortiz, J. E. Gonzalez, Experiments on steady-state high heat fluxes using spray cooling, *Experimental Heat Transfer* 12 (3) (1999) 215–233.
- [108] Y. F. Maydanik, S. Vershinin, Development and investigation of copper-water loop heat pipes with high operating characteristics, *Heat Pipe Science and Technology, An International Journal* 1 (2).
- [109] S. S. Kang, Advanced cooling for power electronics, in: 2012 7th international conference on integrated power electronics systems (cips), IEEE, 2012, pp. 1–8.
- [110] L. Meyer, S. Dasgupta, D. Shaddock, J. Tucker, R. Fillion, P. Bronecke, L. Yorinks, P. Kraft, A silicon-carbide micro-capillary pumped loop for cooling high power devices, in: Ninteenth Annual IEEE Semiconductor Thermal Measurement and Management Symposium, 2003., IEEE, 2003, pp. 364–368.
- [111] F. Accorinti, N. Blet, V. Ayel, S. Dutour, Y. Bertin, *Experimental and Numerical Analysis of Start-Up of a Capillary Pumped Loop for Terrestrial Applications*, *Journal of Heat Transfer* 141 (9), 091813. doi:[10.1115/1.4044276](https://doi.org/10.1115/1.4044276).
URL <https://doi.org/10.1115/1.4044276>
- [112] M. Kaviany, *Handbook of Heat Transfer* (Third Edition), McGraw-Hill, 1998, Ch. 9, pp. 1–82.
- [113] L. Mottet, T. Coquard, M. Prat, Three dimensional liquid and vapour distribution in the wick of capillary evaporators, *International Journal of Heat and Mass Transfer* 83 636–651.
- [114] C. Figus, Y. Le Bray, S. Bories, M. Prat, Heat and mass transfer with phase change in aporous structure partially heated: continuum model and pore network simulations, *International Journal of Heat and Mass Transfer* 42 (14) (1999) 2557–2569.
- [115] L. Lachassagne, V. Ayel, C. Romestant, Y. Bertin, Experimental study of capillary pumped loop for integrated power in gravity field, *Applied Thermal Engineering* 35 (2012) 166–176.

- [116] S. Beyhaghi, S. Geoffroy, M. Prat, K. M. Pillai, Wicking and evaporation of liquids in porous wicks: a simple analytical approach to optimization of wick design ., AIChE Journal 60 (5) 1930–1940.
- [117] N. Blet, V. Ayel, Y. Bertin, C. Romestant, V. Platel, Transient modeling of cpl for terrestrial applications, part b reservoir modeling, Vol. India, Kampur, 2013, pp. 263–270.
- [118] Mitsubishi, 7th Generation IGBT Modules – Standard-Type, Mitsubishi Electric.
- [119] [Mitsubishielectric.com cm600dx-34t/cm600dpx-34t igt modules](http://Mitsubishielectric.com/cm600dx-34t/cm600dpx-34t) [online].
- [120] P. Wais, [Correlation and numerical study of heat transfer for single row cross-flow heat exchangers with different fin thickness](#), Procedia Engineering 157 (2016) 177 – 184, selected Papers from IX International Conference on Computational Heat and Mass Transfer (ICCHMT2016). [doi:
https://doi.org/10.1016/j.proeng.2016.08.354](https://doi.org/10.1016/j.proeng.2016.08.354).
URL <http://www.sciencedirect.com/science/article/pii/S1877705816325292>
- [121] P. Wais, [Fin-tube heat exchanger optimization](#), in: J. Mitrovic (Ed.), Heat Exchangers, IntechOpen, Rijeka, 2012, Ch. 13. [doi:
10.5772/33492](https://doi.org/10.5772/33492).
URL <https://doi.org/10.5772/33492>
- [122] J. E. Hajal, J. Thome, A. Cavallini, [Condensation in horizontal tubes, part 1: two-phase flow pattern map](#), International Journal of Heat and Mass Transfer 46 (18) (2003) 3349 – 3363. [doi:
https://doi.org/10.1016/S0017-9310\(03\)00139-X](https://doi.org/10.1016/S0017-9310(03)00139-X).
URL <http://www.sciencedirect.com/science/article/pii/S001793100300139X>
- [123] J. Thome, J. E. Hajal, A. Cavallini, [Condensation in horizontal tubes, part 2: new heat transfer model based on flow regimes](#), International Journal of Heat and Mass Transfer 46 (18) (2003) 3365 – 3387. [doi:
https://doi.org/10.1016/S0017-9310\(03\)00140-6](https://doi.org/10.1016/S0017-9310(03)00140-6).
URL <http://www.sciencedirect.com/science/article/pii/S0017931003001406>
- [124] L. B. Erbay, B. Dogan, M. M. Ozturk, [Comprehensive study of heat exchangers with louvered fins](#), in: S. M. S. Murshed, M. M. Lopes (Eds.), Heat Exchangers, IntechOpen, Rijeka, 2017, Ch. 4. [doi:
10.5772/66472](https://doi.org/10.5772/66472).
URL <https://doi.org/10.5772/66472>

- [125] E. G. da Silva, R. F. Patella, Numerical simulation of cavitating flows with homogeneous models, *Computers and Fluids* 38 (9) (2009) 1682–1696. [doi:10.1016/j.compfluid.2009.03.001](https://doi.org/10.1016/j.compfluid.2009.03.001).
- [126] K. ?mierciew, A. Pawluczuk, J. Gagan, D. Butrymowicz, [Thermodynamic analysis of two-phase injector for various working fluids](#), *Applied Thermal Engineering* 157 (2019) 113713. [doi:<https://doi.org/10.1016/j.applthermaleng.2019.113713>](https://doi.org/10.1016/j.applthermaleng.2019.113713).
URL <http://www.sciencedirect.com/science/article/pii/S135943111930225X>
- [127] K. Smierciew, D. Butrymowicz, T. Przybyli?ski, A. Pawluczuk, [Investigations of heat and momentum transfer in two-phase injector operating with isobutane](#), *Applied Thermal Engineering* 127 (2017) 1495 – 1505. [doi:<https://doi.org/10.1016/j.applthermaleng.2017.08.160>](https://doi.org/10.1016/j.applthermaleng.2017.08.160).
URL <http://www.sciencedirect.com/science/article/pii/S1359431117326054>
- [128] product-selection.grundfos.com/catalogue [online].
- [129] C.-C. Wang, K.-Y. Chi, C.-J. Chang, [Heat transfer and friction characteristics of plain fin-and-tube heat exchangers, part ii: Correlation](#), *International Journal of Heat and Mass Transfer* 43 (15) (2000) 2693 – 2700. [doi:\[https://doi.org/10.1016/S0017-9310\\(99\\)00333-6\]\(https://doi.org/10.1016/S0017-9310\(99\)00333-6\)](https://doi.org/10.1016/S0017-9310(99)00333-6).
URL <http://www.sciencedirect.com/science/article/pii/S0017931099003336>
- [130] GRETh, Transfert de chaleur dans les tubes de section circulaire - TM2 (Novembre 1987).
- [131] GRETh, Pertes de pression régulière dans les conduites rectilignes des section uniforme - TM1 (Novembre 1987).
- [132] GRETh, Pertes de pression dans les canaux de section uniforme (June 1999).
- [133] GRETh, Les pertes de pression singulières (1999).
- [134] Y.-J. Chang, C.-C. Wang, [A generalized heat transfer correlation for louver fin geometry](#), *International Journal of Heat and Mass Transfer* 40 (3) (1997) 533 – 544. [doi:\[https://doi.org/10.1016/0017-9310\\(96\\)00116-0\]\(https://doi.org/10.1016/0017-9310\(96\)00116-0\)](https://doi.org/10.1016/0017-9310(96)00116-0).
URL <http://www.sciencedirect.com/science/article/pii/0017931096001160>
- [135] Y.-J. Chang, K.-C. Hsu, Y.-T. Lin, C.-C. Wang, [A generalized friction correlation for louver fin geometry](#), *International Journal of Heat and Mass Transfer* 43 (12)

- (2000) 2237 – 2243. [doi:`https://doi.org/10.1016/S0017-9310\(99\)00289-6`](https://doi.org/10.1016/S0017-9310(99)00289-6).
URL <http://www.sciencedirect.com/science/article/pii/S0017931099002896>
- [136] N. Berrada, Transfert de chaleur et pertes de pression dans les minis-canaux, Tech. rep., GRETh (2011).
- [137] A. Cavallini, L. Doretti, M. Matkovic, L. Rossetto, [Update on condensation heat transfer and pressure drop inside minichannels](#), Heat Transfer Engineering 27 (4) (2006) 74–87. [arXiv:`https://doi.org/10.1080/01457630500523907`](https://doi.org/10.1080/01457630500523907), [doi:10.1080/01457630500523907](https://doi.org/10.1080/01457630500523907).
URL <https://doi.org/10.1080/01457630500523907>

Appendix

APPENDIX A

Working fluid discussion

The choice of the working fluid is one of the most important aspects for efficient cooling systems. It also affects and limits the choice of the material to be used for the cooling system and its components (fluid/solid compatibility issue) as well as global performances. Different working fluids have been studied and compared on the basis of literature data.

Fluids used in single phase cooling systems can be compared using the Mouromtseff number (Mo), defined as:

$$Mo = \frac{\rho^a k^b c_p^d}{\mu^e}$$

where coefficients a , b , d , e depend on the nature of fluid flow (for internal turbulent flows: $a = 0.908$, $b = 0.13$, $d = 0.092$ and $e = 0.038$). The higher the Mouromtseff number, the higher the fluid performances. In Fig. A.1 the value of Mouromtseff number for different working fluids is reported as a function of temperature.

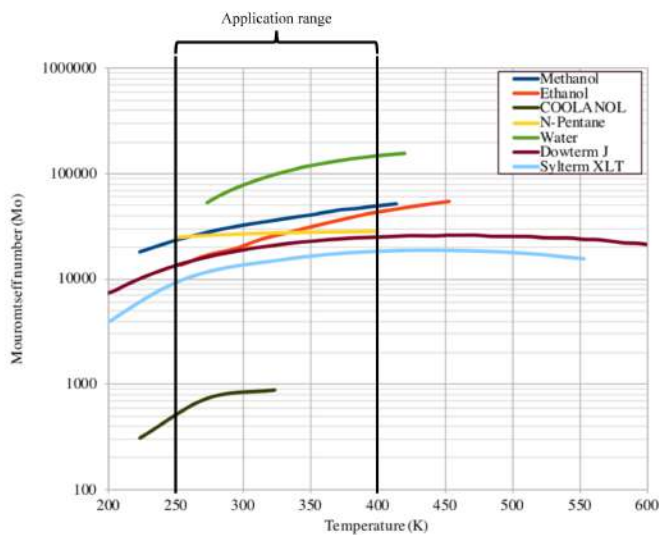


Figure A.1: Comparison between different fluid using Mouromtseff number

As one can notice, water, characterised by the highest value of the Mouromtseff num-

ber, is in absolute the most performing fluid. Despite its performances, water freeze point (0°C at atmospheric pressure) limits its use in aeronautics field. Methanol, ethanol and n-pentane are characterised by quite good performances and low freeze point. This makes these fluids adapted for this application. Especially in the range $250 - 400\text{ K}$ (Fig. A.1), methanol is the one characterised by better performances than ethanol and n-pentane. In Fig. A.2 a fluid-to-water comparison in terms of thermal conductivity and Mouromtseff number, for each analysed fluid, is reported.

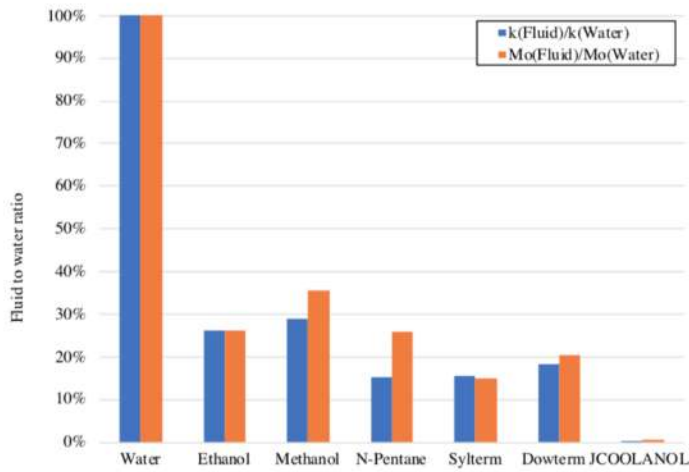


Figure A.2: Fluid to water comparison

Comparison of fluid thermal conductivity could be a good performance indicator. In the example reported in Fig. A.2 Mouromtseff number and fluid thermal conductivity, k , at 60°C are compared for different working fluids and water. The Mouromtseff number could be a good reference to evaluate the performances of a given fluid in single-phase systems. Concerning two-phase systems, active and passive, at our knowledge it does not exist a reference to evaluate fluid performances (except for heat pipes for which the merit number is used). However, the comparison between fluid density and thermal conductivity for liquid and vapour phases are a good index. Experimental studies, based on evaluation of evaporator thermal conductance, such those conducted by Ayel *et al.* [14] and Accorinti *et al.* [12] to evaluate the performances of methanol, ethanol and n-pentane in a CPLIP may give good indications about the fluid choice in two-phase cooling systems.

First approximation design

B.1 Active single phase (liquid cooling) first approximation design

In Fig. B.1, a schematic of single phase cooling system is reported.

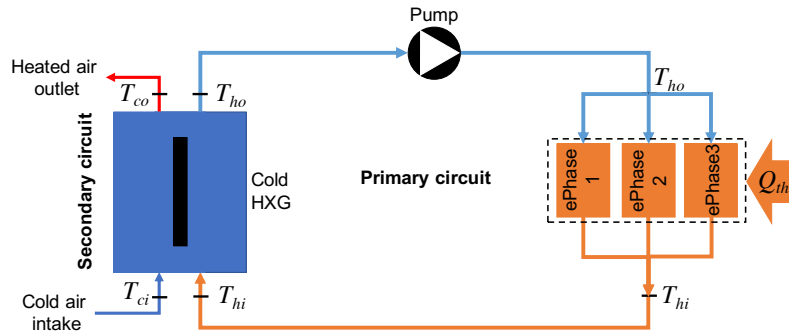
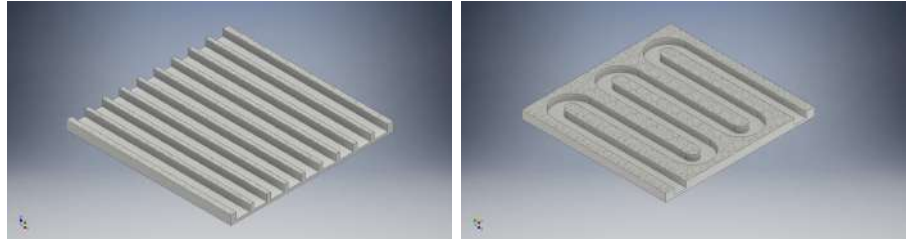


Figure B.1: Single phase cooling system scheme

Three parallel cold plates, one per each electrical phase, are considered.

B.1.1 The cold plate

Cold plate dimensions are related to modules number dimensions. Here, four modules, which dimensions are $12.2 \times 6.2 \text{ cm}^2$ [21], are installed on the cold plate in couple of two and face to face. The thermal load applied on each cold plate is simply given by the total thermal load divided by three. A thermal load of 5 kW is so applied on each cold plate. considering the modules dimensions, the cold plate, reported in Fig. B.2 has dimension $12.4 \times 12.2 \text{ cm}^2$ and thickness of 1.4 cm. Each cold plate is traversed by 1 cm-side-squared section channels. Two different configurations of the cold plate have been considered. The first one, characterised by nine parallel channels, which section is reported in Fig. B.2a and a second configuration, which section is reported in Fig. B.2b, characterised by the presence of the serpentine.



(a) Parallel channels cold plate

(b) Serpentine cold plate

Figure B.2: Two different cold plate configurations

The channels configuration, obviously impacts the temperature distribution on the surface of the cold plate and the pressure drop of the fluid flowing in the cold plate. Lower pressure drop characterises the first configuration and ensures a more uniform temperature distribution from the inlet of the coolant to the outlet. If in the first case, the coolant flow is symmetrical with respect to longitudinal plane, the second configuration is characterised by a non symmetrical flow and an increasing temperature gradient on the surface of the cold plate, from the inlet to the outlet. The mass flow rate, necessary to evacuate the thermal load, is calculated using the eq. (2.3), on the base of a temperature difference of 40°C ($T_{\text{inlet}} = 40^{\circ}\text{C}$ and $T_{\text{outlet}} = 80^{\circ}\text{C}$). In this stage of the work, the second configuration of the cold plate is assumed, because of the lower pressure drop values.

B.1.2 Pump selection

Pump selection is based on the overall loop pressure drop in the loop and the required mass flow rate.

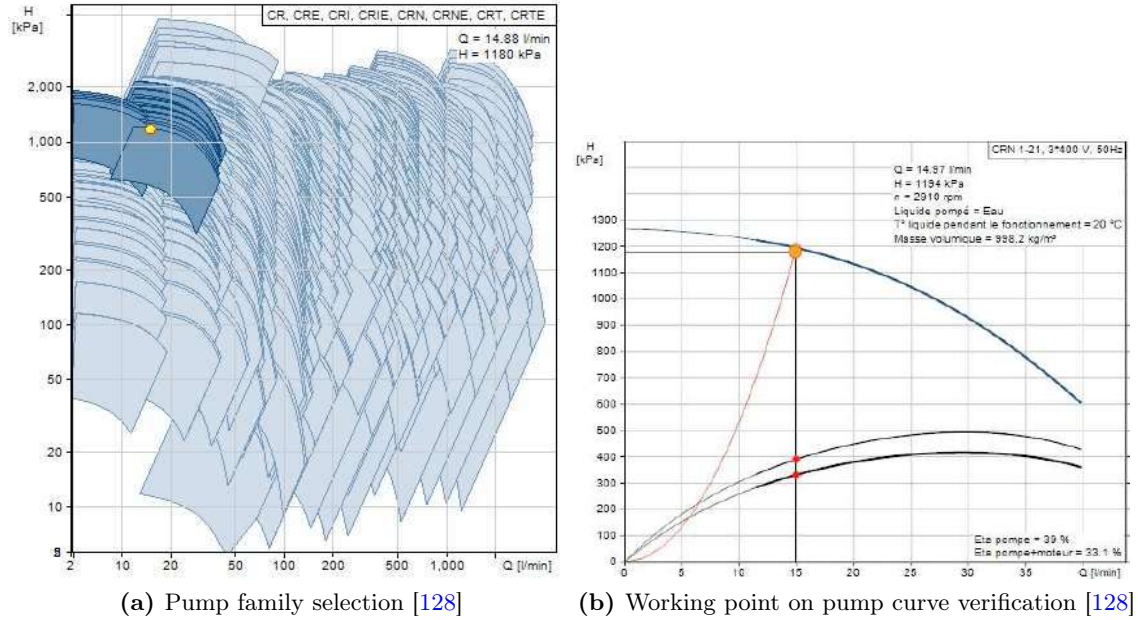
Pump family is chosen on a classical selection diagram like the one showed (see Fig. B.3a), and pump work point verification is done using the pump curve reported in Fig. B.3b.

This procedure is today automated thanks to web applications available on manufacturer web sites¹.

B.1.3 Transport lines

Either hot and liquid line are characterised by the same hydraulic diameter, calculated by eq. (2.1). The fluid velocity is assumed to be constant into the transport lines, at

¹Diagrams reported in this section are an example to show how the choice is made, and they are absolutely not representative of pumps used in this work, chosen by using the already cited web application.



each temperature (the liquid density is assumed constant at the working temperatures), and equal to $2 \text{ m} \cdot \text{s}^{-1}$ to avoid instabilities and eventual corrosion of the tubes due to too high liquid velocities.

B.1.4 Single phase cold heat exchanger

Here, the first approximation design model for the cold HXG of a single-phase cooling system is presented. Two different configurations of cold source will be here introduced. In particular skin heat exchanger, the most adapted solution to evacuate the thermal load in the case where the electronics components are installed in the fuselage (power electronic in the fuselage, PIF), will be designed and compared with RAM-air. The latter is particularly adapted to cases where an intake is needed. In this last case, components to be cooled may be installed in the nacelle (power electronics in the nacelle, PIN) for example. However, it should be considered that RAM-air is the most flexible solution allowing either a configuration in the nacelle or in the fuselage.

B.1.4.1 Skin heat exchanger first approximation design

As already explained in sec. 1.4.1, this technology is characterised by the presence of a tube, in which the hot fluid flows and evacuates the thermal load through the aircraft skin to the external ambient air. A schematic of skin heat exchanger is reported in Fig. B.3a. The sensible heat exchange mechanism is convection from the hot fluid to the tube

walls and from the tube walls to the aircraft skin. So, convection from the skin to the external ambient air. In Fig. B.3b the equivalent electrical network for the skin heat exchanger is reported.

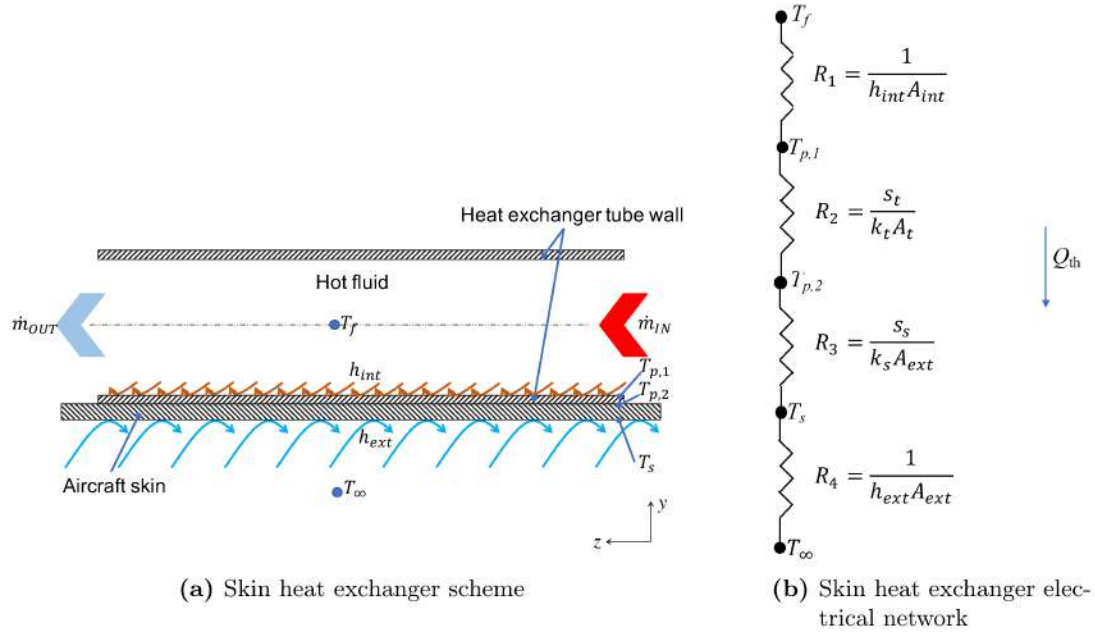


Figure B.3: Skin heat exchanger

To design the skin heat exchanger, a finite volume method, based on the electrical analogy, was used under the following hypothesis and on the base of the schematic reported in Fig. B.4 :

- No heat exchanges between the tube wall and the internal environment of the aircraft (the upside of the tube is adiabatic);
- The heat transfer surface area, for the internal and the external tube side is assumed to be equal ($A_{int} = A_{ext} = \pi D_m dz$): a thermal diffuser is used to spread the heat;
- The conductive resistances are neglected: $(R_1 \wedge R_4) \gg (R_2 \wedge R_3)$;
- Solid thermal capacities are neglected;
- The ambient air temperature does not change as the skin temperature does (the external ambient air is large enough to respect this condition).

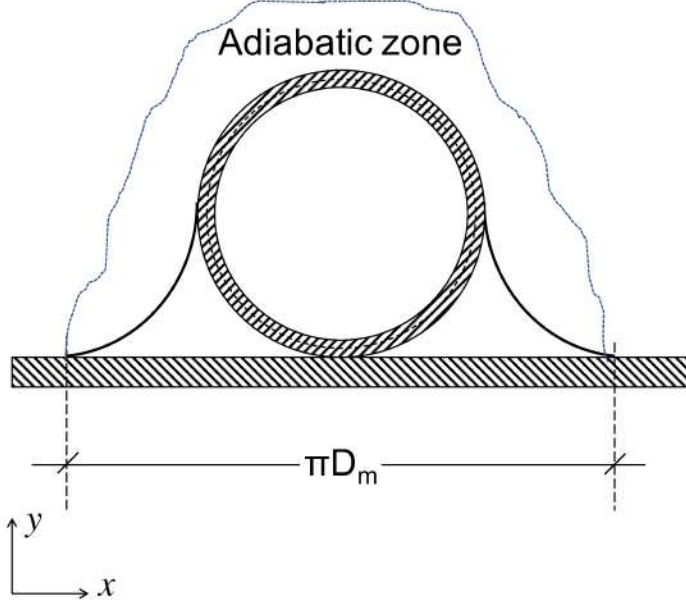


Figure B.4: Hypothesis

- The external heat transfer coefficient is calculated using a modified correlation for the flat plate flow, according to Pang *et al.* [4]:

$$\text{Nu}_{\text{ext}} = 0.2948 \text{ Re}_L^{0.5} \quad (\text{B.1})$$

- The internal side heat transfer coefficient is calculated using the following correlation, according to Pang *et al.* [4] that found a good agreement with experimental results:

$$\text{Nu}_{\text{int}} = 0.021 \text{ Re}_D^{0.94} \quad (\text{B.2})$$

Under the following hypothesis and discretising using the mesh reported in Fig. B.5, the energy balance equations considered to solve the problem are reported in the system (B.3):

$$\begin{cases} \Delta q_i = \dot{m}_f c_p (T_{f,i} - T_{f,i+1}) \\ \Delta q_i = h_{\text{int}} \pi D_m \Delta z (\bar{T}_{f,i} - T_{s,i}) \\ \Delta q_i = h_{\text{ext}} \pi D_m \Delta z (T_{s,i} - T_{\infty}) \end{cases} \quad (\text{B.3})$$

Where, in eq. (B.1) and (B.2) the Reynolds number is respectively calculated on the base of flat plate length and the heat exchanger internal diameter. The mean fluid bulk

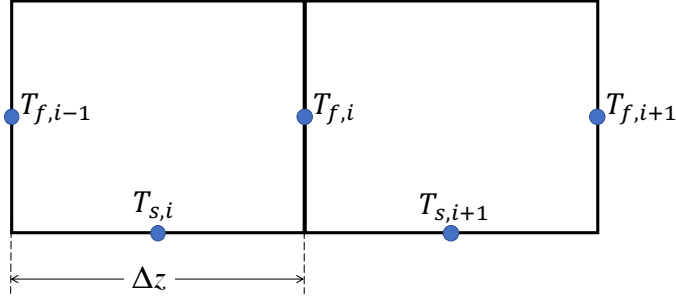


Figure B.5: Mesh configuration

temperature, $\bar{T}_{f,i}$, is the corresponding temperature in the centroid of the cell and calculated as the average between the cell inlet and outlet temperature ($\bar{T}_{f,i} = \frac{T_{f,i} + T_{f,i+1}}{2}$).

The linear system (B.3) may be so easily solved, three equations for three unknown factors: the wall temperature $T_{s,i}$; the cell outlet temperature, $T_{f,i+1}$ and the heat exchanged between the hot and the cold fluid Δq_i .

While the cell outlet temperature is higher or equal to the cold plate inlet temperature, corresponding to 40 °C the system is solved and the parameters found. Obviously, the total skin heat exchange length is given by the sum of all the Δz_i :

$$L_{tot} = \sum_{i=1}^n \Delta z_i \quad (\text{B.4})$$

and the energy balance must be verified :

$$Q_{th} = \sum_{i=1}^n \Delta q_i \quad (\text{B.5})$$

Pressure drops Pressure drops for a single phase flow into a smooth tube, can be calculated by applying the relation:

$$\Delta P = \xi \frac{L_{tot}}{D} \frac{1}{2} \rho u^2 \quad (\text{B.6})$$

where the friction factor, ξ , can be obtained, for a turbulent flow, from the Moody diagram (see Fig. B.6).

B.1.4.2 Cold heat exchanger in a bank configuration

If the skin heat exchanger requires a contact between the heat exchanger tube(s) and the aircraft skin, RAM-air configuration requires the use of a bank of tubes. In this case,

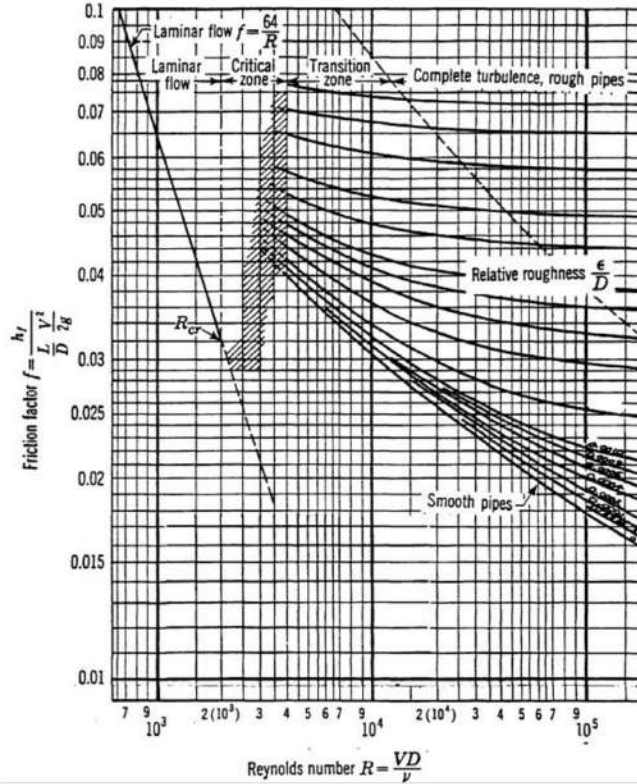


Figure B.6: Moody diagram

the external air velocity can be better controlled, during the design phase, to ensure the adequate heat transfer coefficient.

The configuration used for the first approximation design of the tube bank is reported in Fig. B.7. Here, other than the hypothesis detailed in sec. B, the hypothesis of not externally finned tubes is introduced to simplify the design process.

In this case, the same correlation for the internal side heat transfer coefficient evaluation is used (eq. B.2), while, for the external side, the not finned tube bench correlation is adopted [13]:

$$\text{Nu}_{\text{ext}} = 1.04 \text{Re}_{\text{D}_{\text{ext}}}^{0.4} \text{Pr}_{\text{air}}^{0.36} \quad \text{if } 1 < \text{Re}_{\text{D}_{\text{ext}}} < 500 \quad (\text{B.7})$$

$$\text{Nu}_{\text{ext}} = 0.71 \text{Re}_{\text{D}_{\text{ext}}}^{0.5} \text{Pr}_{\text{air}}^{0.36} \quad \text{if } 500 < \text{Re}_{\text{D}_{\text{ext}}} < 10^3 \quad (\text{B.8})$$

$$\text{Nu}_{\text{ext}} = 0.35 \left(\frac{X_t}{X_{ls}} \right)^{0.2} \text{Re}_{\text{D}_{\text{ext}}}^{0.6} \text{Pr}_{\text{air}}^{0.36} \quad \text{if } 10^3 < \text{Re}_{\text{D}_{\text{ext}}} < 2 \cdot 10^5 \quad (\text{B.9})$$

$$\text{Nu}_{\text{ext}} = 0.031 \left(\frac{X_t}{X_{ls}} \right)^{0.2} \text{Re}_{\text{D}_{\text{ext}}}^{0.8} \text{Pr}_{\text{air}}^{0.36} \quad \text{if } 2 \cdot 10^5 < \text{Re}_{\text{D}_{\text{ext}}} < 2 \cdot 10^6 \quad (\text{B.10})$$

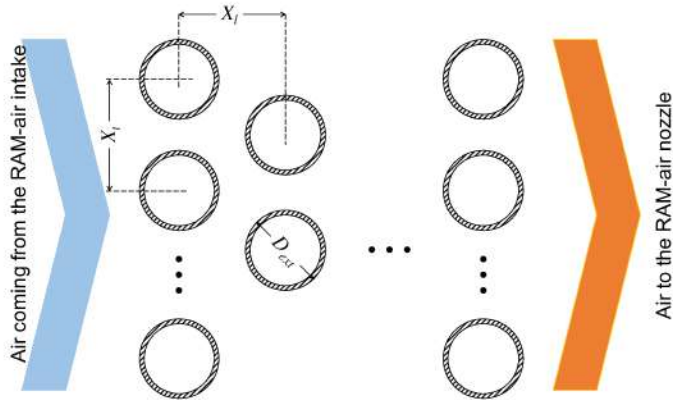


Figure B.7: Tube bank configuration

Where in relations (B.9) and (B.10) $X_{ls} = X_l/D_{ext}$ according to Fig. B.7.

B.2 Two-phase solution first approximation design

B.2.1 The evaporator

As for single phase cold plate, for pumped two phase cooling system, the same simplest evaporator configuration is considered to minimise pressure drops and to not condemn a priori such technology. In fact, even if more performing technologies should be used, such as metal foams or non-sintered porous media, to increase the heat transfer coefficient, here a parallel macro channel evaporator is considered.

B.2.2 Condenser design

B.2.2.1 Skin heat exchanger for a two-phase internal flow: condenser first approximation design

It has been observed that this particular technology is not able to reasonably satisfy the requirements of the problem that is being solved in this work. However, for completeness, a condenser first approximation design, assuming that all the thermal load is used for condensation only and under the hypothesis already detailed in sec. B, is here presented.

Two-phase flows are much complicated than single phase flow. In this case, to solve the problem and to find the appropriate condensing length, it is necessary to find the correct vapour quality change Δx_i for each control volume Δz_i .

The energy balance Δq_i for the control volume Δz_i can in general be expressed as [13]:

$$\Delta q_i = h_{int} A_{int} (T_{sat} - T_{w,k}) = \dot{m} \lambda_{l,v} \Delta x_i \quad (\text{B.11})$$

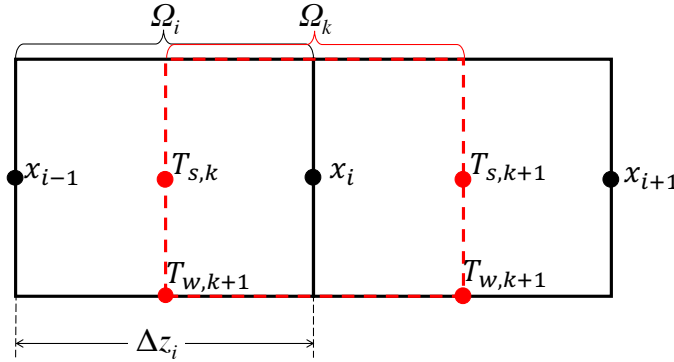


Figure B.8: Mesh configuration for two-phase flow

or

$$\frac{\Delta x}{\Delta z} = \frac{\pi D_c h_{ext} (T_\infty - T_w)}{\dot{m} \lambda_{l,v}} \quad (\text{B.12})$$

Two different shifted grids need to be used in this case: the saturation temperature and the wall temperature are so calculated in correspondence of the grid k , while the inlet and outlet vapour quality in a given control volume are referred to the grid i . Even in this case, the average value in a given control volume Ω_i is given by the mean value between the inlet and the outlet in correspondence of the same control volume.

$$\begin{cases} \Delta q = h_{ext} A_{ext} (T_w - T_\infty) \\ \Delta q = h_{int} A_{int} (T_{sat} - T_w) \\ \Delta q = \dot{m} \lambda_{l,v} \Delta x \end{cases} \quad (\text{B.13})$$

In this case, other than the unknown values of the incremental thermal power exchanged, Δq , the wall temperature, T_w , and the vapour quality change within the control volume, Δx , the internal side heat transfer coefficient is also unknown. The closure equation which may be used is the Chatot's correlation:

$$h_{int,m} = \Omega \left[\frac{\rho_l (\rho_l - \rho_v) g \lambda_{l,v} k_l^3}{\mu_l (T_{sat} - T_w) D_{int}} \right]^{\frac{1}{4}} \quad (\text{B.14})$$

where the coefficient Ω , dependent on the fraction of the tube circumference in which vapour is stratified, is related to the void fraction, α_g , following the relation:

$$\Omega = 0.728 \alpha_g^{\frac{3}{4}} \quad (\text{B.15})$$

with:

$$\alpha_g = \frac{1}{1 + \left(\frac{x-1}{x}\right) \left(\frac{\rho_v}{\rho_l}\right)^{\frac{2}{3}}} \quad (\text{B.16})$$

The system composed by eq. (B.13) and eq. (B.14) in this case is non-linear and coupled. To solve the problem, the Newton-Raphson's method will be used.

The wall temperature $T_{w,k}$ can be either calculated from the external side, considering the external HTC, h_{ext} , and from the internal side, considering the internal HTC, h_{int} . In particular, from the external side:

$$T_{w,k}^+ = \left(\frac{\dot{m} \lambda_{l,v}}{\pi D_c h_{ext}} \right) \left(\frac{\Delta x}{\Delta z} \right) + T_\infty \quad (\text{B.17})$$

and from the internal side, considering equations (B.14), (B.15) and (B.16):

$$T_{w,k}^- = T_{sat} - \left(\frac{\dot{m} \lambda_{l,v}}{\pi D_c h_{int}} \right) \left(\frac{\Delta x}{\Delta z} \right) \quad (\text{B.18})$$

where, the h_{int} value is iteratively calculated by changing at each iteration j the vapour quality difference Δx . In particular, imposing a fixed value of the control volume dimension Δz , the initial vapour quality difference Δx is initially related to the spatial dimension by the ratio $\Delta x = 10^{-3} \cdot \Delta z$. Imposing a forbearance value, ε , small enough and in the order of 10^{-8} , the ratio $\frac{\Delta x}{\Delta z}$ is updated at each iteration j as, $\frac{\Delta x}{\Delta z}|_{j+1} = \frac{\Delta x}{\Delta z}|_j + \varepsilon$ while the residual wall temperature difference, $R = T_{w,k}^- - T_{w,k}^+$, is small enough and in the order of 10^{-3} . Only when the convergence is reached for the wall temperature, the control volume counter is updated to the next one until the vapour quality at the exit of the control volume n -th is $x_{i=n} = 0$.

Even in this case, as for single phase HXG, relations (B.4) and (B.5) must be verified.

Pressure drop For two-phase pressure gradient, neglecting gravity, pressure losses may be written in terms of frictional and acceleration components [13]. In particular in differential terms, it can be written as:

$$\frac{dP}{dz} = \left(\frac{dP}{dz} \right)_f + G^2 \frac{d}{dz} \left[\frac{(1-x)^2}{\rho_l (1-\alpha_g)} + \frac{x^2}{\rho_v \alpha_g} \right] \quad (\text{B.19})$$

Where G [$\text{kg} \cdot \text{m}^{-2} \cdot \text{s}^{-1}$] = $\frac{4\dot{m}}{\pi D_c^2}$ is the mass flow rate per unit area and the frictional pressure gradient term, $\left(\frac{dP}{dz} \right)_f$, can be related to a single phase flow, but using the adapted multiplier ϕ . Being the methanol liquid to vapour viscosity ratio, $\frac{\mu_l}{\mu_g} < 1000$, it is possible to use the Friedel's correlation [13]. In this case, the frictional term is defined

as:

$$\left(\frac{dP}{dz} \right)_f = \phi_{lo}^2 \left(\frac{dP}{dz} \right)_{lo} \quad (\text{B.20})$$

The frictional multiplier is defined as:

$$\phi_{lo}^2 = E + \frac{(3.23F H)}{\text{Fr}^{0.045} \text{We}^{0.035}} \quad (\text{B.21})$$

and the liquid only pressure gradient is defined as:

$$\left(\frac{dP}{dz} \right)_{lo} = \frac{2 f_{lo} G^2}{\rho_l D_c} \quad (\text{B.22})$$

where the friction factor is $f = 0.079 \text{Re}^{-0.25}$, calculated for vapour phase only and for liquid phase only using respectively the Re number of the given phase.

In eq. (B.21), E is defined as:

$$E = (1 - x)^2 + x^2 \frac{\rho_l f_{go}}{\rho_v f_{lo}} \quad (\text{B.23})$$

F is defined as:

$$F = x^{0.78}(1 - x)^{0.224} \quad (\text{B.24})$$

and H :

$$H = \left(\frac{\rho_l}{\rho_v} \right)^{0.91} \left(\frac{\mu_v}{\mu_l} \right)^{0.19} \left(1 - \frac{\mu_v}{\mu_l} \right)^{0.7} \quad (\text{B.25})$$

The Froude number is calculated as:

$$\text{Fr} = \frac{G^2}{g D_c \rho_h} \quad (\text{B.26})$$

and the Weber number is obtained in the following manner:

$$\text{We} = \frac{G^2 D_c}{\rho_h \sigma} \quad (\text{B.27})$$

The equivalent density ρ_h is defined as:

$$\rho_h = \frac{\rho_v \rho_l}{x \rho_l + (1 - x) \rho_v} \quad (\text{B.28})$$

The evaluation of the frictional term, in each control volume Ω_i is so relatively simple, using the relations from (B.20) to (B.28).

Let's now rewrite the second term of the expression (B.19) to derivate it in a more

simple way:

$$\frac{d}{dz} \left[\frac{(1-x)^2}{\rho_l(1-\alpha_g)} + \frac{x^2}{\rho_v\alpha_g} \right] = \frac{d}{dz} (A + B) \quad (\text{B.29})$$

where obviously

$$A = \frac{(1-x)^2}{\rho_l(1-\alpha_g)} \quad (\text{B.30})$$

and

$$B = \frac{x^2}{\rho_v\alpha_g} \quad (\text{B.31})$$

So, the term:

$$\frac{dA}{dz} = \frac{-\left(\frac{dx}{dz}\right)x - \left(\frac{dx}{dz}\right)(x-1)}{x^2} \left(\frac{\rho_v}{\rho_l}\right)^{\frac{2}{3}} \quad (\text{B.32})$$

and

$$\frac{dB}{dz} = \frac{\frac{d}{dz}(x^2)\rho_g\alpha_g - \frac{d}{dz}(\alpha_g)x^2}{(\rho_g\alpha_g)^2} \quad (\text{B.33})$$

Rewriting eq. (B.32) and (B.33) in a discrete form, it is obtained:

$$\frac{d}{dz} (A + B) = A' + B'$$

where

$$A' = \frac{2(1-X)(-\Delta x)\rho_l(1-\mathfrak{A}_g) - [\rho_l(-\Delta\alpha_g)](1-X)^2}{[\rho_l(1-\mathfrak{A}_g)]^2} \quad (\text{B.34})$$

and

$$B' = \frac{2X\rho_v\mathfrak{A}_g - \Delta\alpha_g X^2}{(\rho_v\mathfrak{A}_g)^2} \quad (\text{B.35})$$

In eq. (B.34) and (B.35), the term X represents the vapour quality value in a given control volume and calculated in the centroid of the cell, so like the temperature, the vapour quality is $X = \frac{x_i+x_{i+1}}{2}$. At the same manner, the void fraction of vapour calculated in the centroid of a given cell is $\mathfrak{A}_g = \frac{\alpha_{g,k-1}+\alpha_{g,k}}{2}$.

It is now possible to calculate the two-phase pressure drop in each control volume ΔP_i , calculated from the discretised form of eq. (B.19), and to obtain the total pressure drop as the cumulated pressure drop of the n control volumes. The total pressure drop is so calculated as:

$$\Delta P_{c,tot} = \sum_{i=1}^n \Delta P_i$$

Discussion The external side heat transfer coefficient is strictly related to the aircraft velocity. Even in this case the lowest velocity value, realised during the taxi stages, is considered for the external HTC (h_{ext}). The same external heat transfer coefficient is so applied to this case.

From the thermal calculations, even in the case of condenser design, the use of the skin heat exchanger is not adapted to this study case. In fact, a total length of 920 m was obtained from the calculations and pressure drops too high to let this solution to be retained.

B.2.2.2 Condenser design in tube bank configuration

The same assumptions than those of the single phase heat exchanger are here used. A not finned tube bank configuration is here considered to be inserted in the same RAM-air system, which intake conduits are designed to ensure a minimal air velocity of $10 \text{ m} \cdot \text{s}^{-1}$ during the taxi stages of the aircraft.

In this case, the same correlation from (B.7) to (B.10) are used to evaluate the heat transfer coefficient. In this case, due to the higher tube diameter, and so higher X_t and X_l , see Fig. B.7, the heat transfer coefficient increases up to a value of $110 \text{ W} \cdot \text{m}^{-2} \cdot \text{K}^{-1}$. So a length of 46 m is in this case necessary to completely condense the fluid. The heat transfer surface area corresponding to a condenser tube diameter of 0.021 m is about 3 m^2 to evacuate a total thermal power of 15 kW. If sub-cooling is considered to lower the liquid temperature up to 37°C , about 6.5% of the thermal load is used, requiring an additional condenser length lower than 4 m.

APPENDIX C

GRETh (EchTherm)

GRETh (Groupement pour la Recherche sur les Echangeurs Thermiques) EchTherm is a calculation software for heat exchanger design and verification. It is based on iterative resolution of appropriate correlations, following the typology of heat exchanger. In this chapter only known characteristics of the software for continuous finned and for louvered fin-microchannels condensers are reported.

C.1 Continuous finned heat exchangers

The external fluid is single phase while condensation and subcooling occur for internal fluid. As better explained in Chap. 7, to have more accurate results, the heat exchanger is divided in different sub-heat duty zones and for each of them all thermo-hydraulic parameters (internal and external HTC, internal and external pressure drops, HXG's efficiency) are calculated.

C.1.1 Limits and hypothesis

As declared by GRETh, the following hypothesis and limitations have to be considered when using such software:

1. In general, fluid thermo-physical properties are evaluated at inlet and outlet temperature and pressure as well as in saturation conditions.
2. Pressure drops at inlet and outlet collectors are not considered
3. For wet air, a constant humidity is considered.

C.1.2 Correlations

C.1.2.1 External side

On the external side (fin side) correlations reported in ref. [129] are used. The Colburn factor, $j = \frac{Nu}{Re Pr^{\frac{1}{3}}}$, depends on the number of raws, N , in the heat exchanger. For $N \geq 2$

it is:

$$j = 0.086 \text{Re}_{D_c}^{P3} N^{P4} \left(\frac{F_p}{D_c} \right)^{P5} \left(\frac{F_p}{D_h} \right)^{P6} \left(\frac{F_p}{P_t} \right)^{-0.93} \quad (\text{C.1})$$

where $P3$ is calculated as:

$$P3 = -0.361 - \frac{0.042N}{\ln(\text{Re}_{D_c})} + 0.1581 \ln \left(N \left(\frac{F_p}{D_c} \right)^{0.41} \right) \quad (\text{C.2})$$

$P4$ is a function of $P1 = 1.9 - 0.23 \ln \text{Re}_{D_c}$, and it is calculated as:

$$P4 = -1.224 - \frac{0.076 \left(\frac{P1}{D_h} \right)^{1.42}}{\ln \text{Re}_{D_c}} \quad (\text{C.3})$$

Factor $P5$ in eq. (C.1) is:

$$P5 = -0.083 + \frac{0.058N}{\ln \text{Re}_{D_c}} \quad (\text{C.4})$$

and finally $P6$ is:

$$P6 = -5.735 + 1.21 \ln \frac{\text{Re}_{D_c}}{N} \quad (\text{C.5})$$

Following the same reference, the airside friction factor is calculated as:

$$f = 0.0267 \text{Re}_{D_c}^{F1} \left(\frac{P_t}{P_l} \right)^{F2} \left(\frac{F_p}{D_c} \right)^{F3} \quad (\text{C.6})$$

where P_t and P_l are transversal and longitudinal tube pitch respectively. The factors $F1$, $F2$ and $F3$ are defined as follow:

$$F1 = -0.764 + 0.739 \frac{P_t}{P_k} + 0.177 \frac{F_p}{D_c} - \frac{0.00758}{N} \quad (\text{C.7})$$

$$F2 = -15.689 + \frac{64.021}{\ln \text{Re}_{D_C}} \quad (\text{C.8})$$

$$F3 = 1.696 + \frac{15.695}{\ln \text{Re}_{D_C}} \quad (\text{C.9})$$

As reported by Wang *et al.* [129], eq. (C.1) can correlate almost 89% of experimental Colburn factors within an error of 15%, while eq. (C.6) can describe almost 85% of experimental data within an error of 15%.

C.1.2.2 Internal side

Single phase

Heat transfer Single phase heat transfer coefficient is calculated on the basis of relations reported in ref. [130]. For laminar flows and short pipes, in which $0.1 < \text{Re} \text{Pr} \frac{D}{L} < 10^4$, Schlünder's correlation is used:

$$\text{Nu} = \left(3.66 + 1.61^3 \text{Re} \text{Pr} \frac{D}{L} \right)^{\frac{1}{3}} \quad (\text{C.10})$$

or, alternatively, Haussen's correlation may be used in the same range:

$$\text{Nu} = 3.66 + \frac{0.19 \left(\text{Re} \text{Pr} \frac{D}{L} \right)^{0.18}}{1 + 0.117 \left(\text{Re} \text{Pr} \frac{D}{L} \right)^{0.467}} \quad (\text{C.11})$$

If $100 < \text{Re} < 2100$, $L/D < 0.1 \text{Re} \text{Pr}$ and $0.6 < \text{Pr} < 100$, Sieder-Tate correlation is applied:

$$\text{Nu} = 1.86 \left(\text{Re} \text{Pr} \frac{D}{L} \right)^{0.33} \left(\frac{\mu}{\mu_p} \right)^{0.14} \quad (\text{C.12})$$

For very short pipes, $L/D < 10$, Pohlhausen's equation is used:

$$\text{Nu} = 0.664 \frac{1}{\text{Pr}^{\frac{1}{6}}} \left(\text{Re} \text{Pr} \frac{D}{L} \right)^{\frac{1}{2}} \quad (\text{C.13})$$

Between transition and turbulent regimes, the empiric form of Nusselt number is valid:

$$\text{Nu} = a \text{Re}^b \text{Pr}^n \quad (\text{C.14})$$

In this case, classical relations may be applied:

- Dittus-Boelter if $0.7 < \text{Pr} < 120$; $10^4 < \text{Re} < 1.2 \cdot 10^5$ and $L/D > 60$, with $n=0.3$ or 0.4 if the liquid in the tube is respectively cooled or heated.
- Colburn if $0.7 < \text{Pr} < 120$.
- Petukhov and Gnielinki if $0.6 < \text{Pr} < 2000$; $2300 < \text{Re} < 10^6$ and $0 < L/D < 1$:

$$\text{Nu} = \frac{\Lambda/8 (\text{Re} - 1000) \text{Pr}}{1 + 12.7 \left(\text{Pr}^{\frac{2}{3}} - 1 \right) \sqrt{\frac{\Lambda}{8}}} \left[1 + \left(\frac{D}{L} \right)^{\frac{2}{3}} \right] \quad (\text{C.15})$$

where Λ is the Darcy's coefficient.

Pressure drops Here only correlations for smooth and circular-section tubes are reported. As usually, pressure drops are calculated as [131]:

$$\Delta P = \Lambda \left(\frac{L}{D_h} \right) \frac{1}{2} \rho u^2 \quad (\text{C.16})$$

For laminar regimes the Darcy's coefficient is classically [131]:

$$\Lambda = \frac{64}{\text{Re}} \quad (\text{C.17})$$

For turbulent flows, if $2300 < \text{Re} < 100\,000$ it is:

$$\Lambda = \frac{0.3164}{\text{Re}^{\frac{1}{4}}} \quad (\text{C.18})$$

if $2 \cdot 10^4 < \text{Re} < 10^6$, Herman or Filonenko's relation may be used indifferently [131]. According to Herman:

$$\Lambda = 0.00540 + \frac{0.3964}{\text{Re}^{0.3}} \quad (\text{C.19})$$

and according to Filonenko:

$$\Lambda = (1.83 \log \text{Re} - 1.64)^{-2} \quad (\text{C.20})$$

Finally, if $\text{Re} > 10^6$ Karman-Nikuradze's relation is used:

$$\frac{1}{\sqrt{\Lambda}} = -0.8 + 2 \log \left(\text{Re} \sqrt{\Lambda} \right) \quad (\text{C.21})$$

Two-phase

Heat transfer For heat transfer calculations in the case of two-phase heat exchange, Thome's condensation heat transfer model [122, 123] is used. It is based on:

1. Determination of void fraction, ε , using the logarithmic mean void fraction method (LM ε):

$$\varepsilon = \frac{\varepsilon_h - \varepsilon_{ra}}{\ln \frac{\varepsilon_h}{\varepsilon_{ra}}} \quad (\text{C.22})$$

where

$$\varepsilon_h = \left[1 + \left(\frac{1-x}{x} \right) \left(\frac{\rho_v}{\rho_l} \right) \right]^{-1} \quad (\text{C.23})$$

and

$$\varepsilon_{ra} = \frac{x}{\rho_v} \left\{ [1 + 0.12 (1 - x)] \left[\frac{x}{\rho_v} + \frac{1 - x}{\rho_l} \right] + \frac{1.18 (1 - x) [g \sigma (\rho_l - \rho_v)]^{0.25}}{G \rho_l^{0.5}} \right\} \quad (\text{C.24})$$

2. Determination of local flow pattern. Such task is pretty complex and requires the application of a quite wide range of relations and iterative resolution of some equations. It is suggested to consult ref. [122] for more details. Thanks to this task it is possible to identify with a pretty good approximation the flow pattern of each sub-heat-duty zone of the condenser (see sec. 7.2.1).
3. Flow pattern identification. Based on it, different relation must be applied.
- a) If flow pattern is annular, condensation HTC has the form:

$$h_c = c \text{Re}_l^n \text{Pr}_l^m \frac{\lambda_l}{\delta} f_i \quad (\text{C.25})$$

where, λ_l is the liquid thermal conductivity and the liquid film Reynolds number is calculated as:

$$\text{Re}_l = \frac{4 G (1 - x) \delta}{(1 - \epsilon) \mu_l} \quad (\text{C.26})$$

The annular liquid film thickness is obtained from:

$$A_l = \frac{2 \pi - \theta}{8} \left[d^2 - (d - 2 \delta)^2 \right] \quad (\text{C.27})$$

with d internal diameter of the tube, A_l the cross sectional area occupied by liquid phase, and θ the upper-side angle of the tube not wetted by stratified liquid.

Interfacial roughness correction factor, f_i , is calculated as:

$$f_i = 1 + \left(\frac{u_v}{u_l} \right)^{\frac{1}{2}} \left(\frac{(\rho_l - \rho_v) g \delta^2}{\sigma} \right)^{\frac{1}{4}} \quad (\text{C.28})$$

In eq. (C.28), liquid and vapour velocities are $u_l = \frac{G(1-x)}{\rho_l(1-\varepsilon)}$ and $u_v = \frac{Gx}{\rho_v \varepsilon}$ respectively.

- b) If flow pattern is stratified-wavy, convective condensation heat transfer coefficient, h_c ; heat transfer coefficient of condensing film on top perimeter of the tube, h_f , and local perimeter condensing fluid, h_{tp} , have to be considered. h_c

is calculated with eq. (C.25). h_f is:

$$h_f = 0.655 \left[\frac{\rho_l (\rho_l - \rho_v) g h_{lv} \lambda_l^3}{\mu_l dq} \right] \quad (\text{C.29})$$

where dq is the applied heat flux on analysed sub-heat-duty zone. Finally, local perimeter heat transfer coefficient, h_{tp} , is defined as a function of internal radius:

$$h_{tp} = \frac{h_f r \theta + h_c r (2\pi - \theta)}{2\pi r} \quad (\text{C.30})$$

c) If flow pattern is fully stratified, the angle θ_{strat} is calculated from:

$$A_l = \frac{d^2}{8} [(2\pi - \theta_{strat}) - \sin(2\pi - \theta_{strat})] \quad (\text{C.31})$$

or

$$\begin{aligned} \theta_{strat} = & 2\pi - 2 \left\{ \pi(1 - \varepsilon) + \left(\frac{3\pi}{2}\right)^{1/3} \left[1 - 2(1 - \varepsilon) + (1 - \varepsilon)^{1/3} - \varepsilon^{1/3} \right] \right. \\ & \left. - \frac{1}{200} \varepsilon (1 - \varepsilon) [1 - 2(1 - \varepsilon)] \left[1 + 4((1 - \varepsilon)^2 + \varepsilon^2) \right] \right\} \end{aligned} \quad (\text{C.32})$$

h_c is calculated from eq. (C.25), but considering the roughness correction factor, f_i , calculated as:

$$f_i = 1 + \left(\frac{u_v}{u_l} \right)^{\frac{1}{2}} \left(\frac{(\rho_l - \rho_v) g \delta^2}{\sigma} \right)^{\frac{1}{4}} \left(\frac{G}{G_{strat}} \right) \quad (\text{C.33})$$

h_f and h_{tp} are calculated from eq. (C.29) and (C.30) respectively.

Pressure drops Pressure drops are calculated as reported in ref. [132]. The same method than cf. B.2.2.1 is used to calculate total two-phase pressure drops. Sum of frictional pressure losses, $(\frac{dP}{dz})_f$, acceleration pressure losses, $(\frac{dP}{dz})_a$ and gravity pressure losses, $(\frac{dP}{dz})_g$, are considered for the purpose. Friction pressure losses are calculated as [132]:

$$-\left(\frac{dP}{dz} \right)_f = -0.09 (1 + 2.85 X^{0.523})^2 \frac{\mu_v^{0.2} (\dot{m} x)^{1.8}}{\rho_v d^{1.2}} \quad (\text{C.34})$$

where the factor X^2 is defined as:

$$X^2 = \frac{(\frac{dP}{dz})_{f,l}}{(\frac{dP}{dz})_{f,v}}$$

Acceleration term is calculated as:

$$-\left(\frac{dP}{dz}\right)_f = -\frac{\dot{m}^2}{\rho_v} \frac{dx}{dz} \left[2x + (1-2x) \left(\frac{\rho_v}{\rho_l}\right)^{\frac{1}{3}} + (1-2x) \left(\frac{\rho_v}{\rho_l}\right)^{\frac{2}{3}} - (2-2x) \left(\frac{\rho_v}{\rho_l}\right) \right] \quad (\text{C.35})$$

and gravity term is:

$$-\left(\frac{dP}{dz}\right)_g = g \sin \theta [\varepsilon \rho_v + \rho_l (1-\varepsilon)] \quad (\text{C.36})$$

Classical relations are used for localised pressure losses, that are calculated as reported in ref. [133].

C.2 Louvered fins & microchannels heat exchanger

C.2.1 Limitations and hypothesis

Even in this case fluid thermo-physical properties are calculated at inlet, outlet and saturation conditions. In this case, pressure drops related to collectors (or manifold) are considered in calculation, only two passages may be considered for calculation.

C.2.1.1 External side

Heat transfer For louvered fins, correlation reported in [134] is used. Such correlation agrees with experimental data at about 89%, within $\pm 15\%$ and gives a mean deviation of 7.6% [134]. The Colburn factor is:

$$j = \text{Re}_{L_p}^{0.49} \left(\frac{\theta}{90}\right)^{0.27} \left(\frac{F_p}{L_p}\right)^{-0.14} \left(\frac{F_l}{L_p}\right)^{-0.29} \left(\frac{T_d}{L_p}\right)^{-0.23} \left(\frac{L_l}{L_p}\right)^{0.68} \left(\frac{T_p}{L_p}\right)^{-0.28} \left(\frac{\delta_f}{L_p}\right)^{-0.05} \quad (\text{C.37})$$

where θ is the louver angle; L_h , L_l , L_p are respectively louver height, length and pitch. δ is the thickness of the tube, while T_p and T_d tube pitch and tube depth respectively.

Pressure drop Correlation presented in ref. [135] is used for air side friction factor calculation. Such correlation agrees with experimental data at 83.1% within $\pm 15\%$ and presents a mean deviation of 9.2%.

The friction factor is calculated as:

$$f = f_1 f_2 f_3 \quad (\text{C.38})$$

where:

$$f_1 = \begin{cases} 14.39 \text{Re}_{Lp}^{(-0.805 \frac{F_p}{F_l})} \left[\ln \left(1 + \frac{F_p}{L_p} \right) \right]^{3.04} & \text{Re}_{Lp} < 150 \\ 4.97 \text{Re}_{Lp}^{(0.6049 - \frac{1}{\theta^{0.2}})} \left[\ln \left(\left(\frac{F_t}{F_p} \right)^{0.5} + 0.9 \right) \right]^{-0.527} & 150 < \text{Re}_{Lp} < 5000 \end{cases} \quad (\text{C.39})$$

$$f_2 = \begin{cases} \left[\ln \left(\left(\frac{F_t}{F_p} \right)^{0.48} + 0.9 \right) \right]^{-1.435} \left(\frac{D_h}{L_p} \right)^{-3.01} \ln^{-3.01}(0.5 \text{Re}_{Lp}) & \text{Re}_{Lp} < 150 \\ \left[\ln(0.5 \text{Re}_{Lp}) \frac{D_h}{L_p} \right]^{-2.966} \left(\frac{F_p}{L_l} \right)^{-0.7931 \frac{T_p}{T_h}} & 150 < \text{Re}_{Lp} < 5000 \end{cases} \quad (\text{C.40})$$

$$f_3 = \begin{cases} \left(\frac{F_p}{L_l} \right)^{-0.308} \left(\frac{F_d}{L_l} \right)^{-0.308} \left(e^{-0.1167 \frac{T_p}{D_m}} \right) \theta^{0.35} & \text{Re}_{Lp} < 150 \\ \left(\frac{T_p}{D_m} \right)^{-0.0446} \ln^{-3.553} \left(\frac{L_p}{F_p} \right)^{\frac{1}{4}} \theta^{-0.477} & 150 < \text{Re}_{Lp} < 5000 \end{cases} \quad (\text{C.41})$$

C.2.1.2 Internal side

Single-phase

Pressure drops

The study [136] reports relations implemented for friction factor, f , evaluation in Ech-Therm. For laminar regimes:

$$4 f = \frac{4 C_{f,l}}{\text{Re}^{1.98}}$$

and for turbulent regimes:

$$4 f = \frac{4 C_{f,l}}{\text{Re}^{1.72}}$$

Two-phase Both used heat transfer and pressure drop relations are taken from ref. [137]. The same method presented in cf. B.2.2.1 has to be applied for pressure drop estimation in mini or microchannels. Cavallini *et al.* [137] presented a method, based on Friedel parameters (cf. B.2.2.1), to calculate frictional pressure gradient in annular flow.

Frictional pressure gradient is:

$$\left(\frac{dP}{dz} \right)_f = \phi_{lo}^2 \left(\frac{dP}{dz} \right)_{f,lo} = \frac{2 \phi_{lo}^2 f_{lo} G}{D_h \rho_l} \quad (\text{C.42})$$

where

$$\phi_{lo}^2 = Z + 3.595 F H W (1 - E)^W = 1.398 P_R \quad (\text{C.43})$$

$$Z = (1 - x)^2 + x^2 \left(\frac{\rho_l}{\rho_v} \right) \left(\frac{\mu_l}{\mu_v} \right)^{0.2} \quad (\text{C.44})$$

$$F = x^{0.9525} (1 - x)^{0.414} \quad (\text{C.45})$$

$$H = \left(\frac{\rho_l}{\rho_v} \right)^{1.132} \left(\frac{\mu_v}{\mu_l} \right)^{0.44} \left(1 - \frac{\mu_v}{\mu_l} \right)^{3.542} \quad (\text{C.46})$$

The coefficient E is calculated as:

$$E = 0.015 + 0.44 \log \left[\left(\frac{\rho_{gc}}{\rho_l} \right) \left(\frac{\mu_l j_G}{\sigma} \right)^2 \cdot 10^4 \right] \quad (\text{C.47})$$

if $E < 0.95$, else $E = 0.95$. In eq. (C.42), the factor f_{lo} is:

$$f_{lo} = 0.046 \left(\frac{G D_h}{\mu_l} \right)^{-0.2} \quad (\text{C.48})$$

Once calculated pressure losses from Cavallini's model, the heat transfer coefficient, h_{an} , may be calculated as follows:

$$h_{an} = \frac{\rho_l c_{p,l} \sqrt{\frac{\tau}{\rho_l}}}{T^+} \quad (\text{C.49})$$

where the liquid-vapour interfacial shear stress is calculated as:

$$\tau = \left(\frac{dP}{dz} \right)_f \frac{1}{4} D_h$$

In eq. (C.49), T^+ is defined as follow

$$T^+ = \begin{cases} \delta^+ \Pr_l & \delta^+ \leq 5 \\ 5 \left\{ \Pr_l + \ln \left[1 + \Pr_l \left(\frac{\delta^+}{5} - 1 \right) \right] \right\} & 5 < \delta^+ < 30 \\ 5 \left\{ \Pr_l + \ln [1 + 5 \Pr_l] + 0.495 \ln \left(\frac{\delta^+}{30} \right) \right\} & \delta^+ \geq 30 \end{cases} \quad (\text{C.50})$$

and

$$\delta^+ = \begin{cases} \sqrt{\frac{\text{Re}_l}{2}} & \text{Re}_l \leq 1145 \\ 0.0504 \text{Re}_l^{\frac{7}{8}} & \text{Re}_l > 1145 \end{cases}$$

and

$$\text{Re}_l = \frac{G(1-x)(1-E)D_h}{\mu_l}$$

APPENDIX D

Heavy duty tests

With the purpose to check CPLIP's resistance and reliability to long duration load, heavy duty tests have been performed. Test campaigns lasted seven days and CPLIP worked at constant thermal load applied to the evaporator up to 9 hours/day. Every day the same thermal load was applied to the evaporator, $Q_{th} = 2 \text{ kW}$, with reservoir and cold source temperatures of $T_{res} = 70^\circ\text{C}$ and $T_{sec} = 20^\circ\text{C}$, respectively. In Fig. D.1 an example of heavy duty test is reported. There, only maximal and minimal evaporator

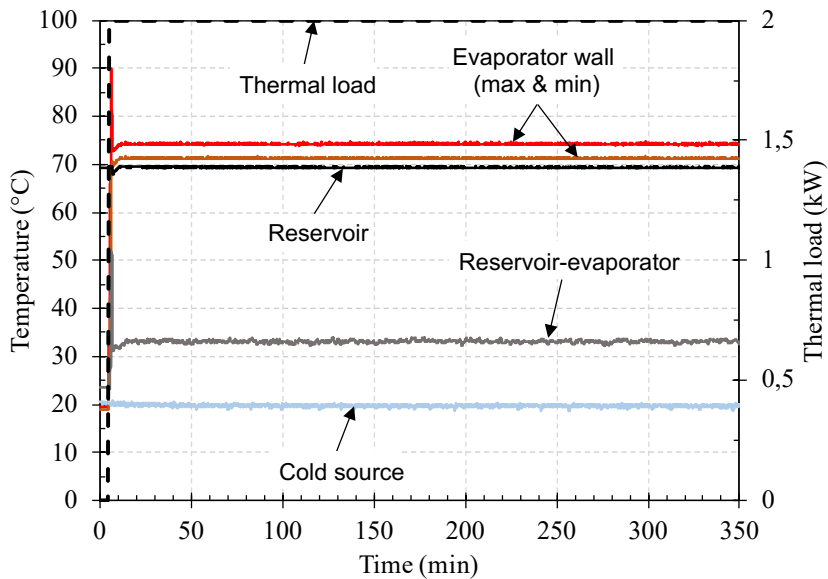


Figure D.1: Heavy duty test (methanol, $T_{res} = 70^\circ\text{C}$, $T_{sec} = 20^\circ\text{C}$, $Q_{th} = 2 \text{ kW}$)

wall, reservoir, reservoir-evaporator line and cold source temperatures are reported for clarity of reading.

During the whole test campaign the loop does not encountered any kind of problem, continuing to work all the time.

Apparently, no chemical reactions occurred in the evaporator, as NCG check demonstrates.

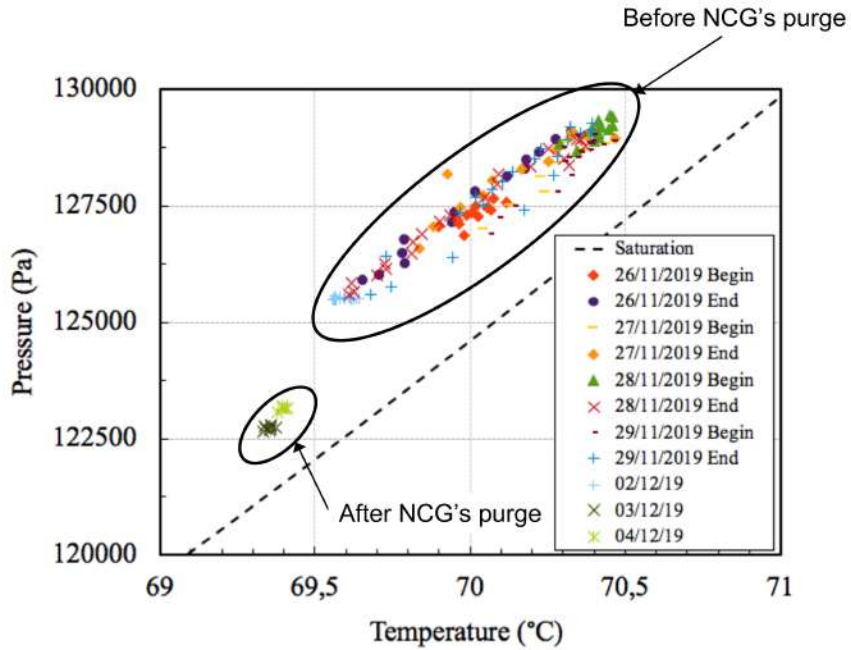


Figure D.2: Saturation conditions in the reservoir before and after the tests ($T_{res} = 70^\circ\text{C}$)

Presence of non-condensable-gases was checked at the beginning and at the end of each test. No particular phenomena are noticeable as one may observe in Fig. D.2. Pressure and temperature at the beginning and at the end of each test are quite similar. A slight amount of NCG were present in the CPLIP reservoir at the beginning of the test campaign.

CONCEPTION DE SOLUTIONS DE REFROIDISSEMENT PAR VOIE DIPHASIQUE D'ELECTRONIQUE DE PUISSANCE EN CONTEXTE AERIEN REPONDANT AUX OBJECTIFS DE L'AVION HYBRIDE 2035

Le monde aérien est lui aussi destiné à réduire drastiquement son empreinte environnementale. Cela passe pour partie par l'innovation technologique et la réduction de l'énergie nécessaire à la propulsion. Dans cet objectif, les travaux relatifs dans ce mémoire s'inscrivent dans un projet de recherche (Clean Sky 2-HASTECs) visant le développement de propulsion hybride mettant à profit les performances d'une chaîne électrique. Les puissances mises en jeu requièrent de revisiter les solutions de refroidissement pour atteindre les spécifications de puissance massique envisagées à l'horizon 2035. Nous nous intéressons ici à la gestion thermique de l'électronique de puissance qui vise une puissance massique de 25kW/kg à cet horizon. Le travail effectué, essentiellement numérique, est lié à la recherche, au dimensionnement, à l'optimisation, et à l'analyse d'une technologie de refroidissement efficace, caractérisée par une faible masse et capable de contrôler la température des composants électroniques dans les conditions opératoires les plus drastiques. Différentes technologies de refroidissement, actives mono et diphasiques et passives, à pompage capillaire, ont été analysées et comparées sur la base de données disponibles dans la littérature et d'un dimensionnement de première approximation : la solution la plus adaptée a été choisie en utilisant comme critère sa masse spécifique. La solution finalement retenue et présentant le meilleur indice de masse spécifique global est une boucle diphasique CPLIP (Capillary Pumped Loop for Integrated Power), par ailleurs pourvues des caractéristiques thermiques et hydrauliques uniques. Après son dimensionnement, la CPLIP a été optimisée pour répondre aux objectifs à deux horizons successifs, 2025 et 2035 (mentionnons un travail itératif avec les chercheurs responsables du développement de l'électronique permettant une optimisation mutuelle). L'attention a été en particulier concentrée sur le condenseur, le composant le plus lourd de la boucle. La solution 2025 est caractérisée par un condenseur classique air-méthanol, et a démontré sa capacité d'aller au-delà du seuil de 15 kW/kg demandé. La solution 2035, caractérisée par un concept de condenseur innovant : à micro-canaux et à ailettes à persiennes, a permis d'obtenir, après ce travail de co-dimensionnement thermique-électronique, des valeurs de puissance spécifique doubles par rapport à l'objectif 2035. Dans cette thèse, les caractéristiques hydrauliques et thermiques de la boucle CPLIP ont été analysées expérimentalement sur un prototype issu d'études antérieures, et numériquement à l'aide d'un modèle CFD ainsi qu'à l'aide d'un modèle 0D innovant. Les résultats démontrent l'aptitude de la CPLIP à gérer thermiquement l'électronique de puissance pour des cycles de mission d'un avion court ou moyen-courrier, caractérisés par des changements brutaux de puissance thermique, tout en assurant le contrôle de la température des modules électroniques. Enfin, une étude a été conduite portant sur le comportement transitoire de la boucle, en particulier lors des démarrages sévères à très hautes puissances, ainsi que pendant des cycles d'accélérations sévères qui caractérisent ce champ d'application. Dans le premier cas, une étude expérimentale et numérique a été menée pour démontrer la capacité de la boucle à démarrer dans les conditions thermiques et environnementales les plus difficiles (haute puissance de démarrage et haute température environnementale). Dans le deuxième cas, une étude numérique a été utilisée pour comprendre quel est le comportement de la boucle quand des champs d'accélérations, jusqu'à 10g, perturbent ses conditions opératoires. Ce travail ouvre des perspectives très intéressantes tant du point de vue de l'application que vis-à-vis de la nécessité aujourd'hui d'adopter des approches de recherche couplées pour dimensionner simultanément thermiquement et électriquement l'électronique de puissance.

Mots clés : (Appareils électroniques--Température--Régulation, Électronique de puissance, Simulation par ordinateur, Moteurs hybrides, Avion hybride, Refroidissement, Boucle à pompage capillaire)

TWO-PHASE POWER ELECTRONICS COOLING SOLUTION DESIGN IN AIR CONTEXT ANSWERING TO THE OBJECTIVES OF THE HYBRID AIRCRAFT 2035

Technological innovation and reduction of the energy required for propulsion is necessary to reduce aircrafts environmental impact. The present work is part of the research project Clean Sky 2 – HASTECs, which purpose is the development of a hybrid propulsion aircraft. The high powers involved make classical cooling solutions obsolete, in terms of efficiency, and not suitable for the power to mass ratio required for the target 2035. In particular, the problem related to power electronics cooling is assessed in this work with the purpose to achieve a performance coefficient of 25 kW/kg. This work, essentially numerical, is linked to the research, design, optimisation and analysis of a high efficiency cooling system, able to control power electronics components temperature, operating in pretty severe conditions (high thermal power density, >15kW; cyclic variation of cold source temperature and severe transient phases) and which has to be lightweight to ensure performance coefficient requirements. Different cooling technologies, active single and two-phase and passive capillary driven, have been analysed and compared on the basis of literature data and of a first approximation design: the most adapted solution has been chosen on the base of its specific power [kW/kg]. The solution that has been finally retained is a Capillary Pumped Loop for Integrated Power (CPLIP), which thermal characteristics are quite interesting and unique. After its design, the loop has been optimised to answer to objectives of 2025 and 2035. It is worth of attention the work carried out in collaboration with power electronics team of the same project to achieve a mutual optimisation of the systems. Concerning the thermal side, the attention was focused on the condenser, the heaviest component in the loop. The 2025's solution is characterised by a classical flat plate air-methanol condenser which allowed to cross over the threshold of 15kW/kg for 2025. 2035's solution, on the contrary, is characterised by an innovative condenser typology, using microchannels on methanol side and louvered fins on air side, allowing to obtain more than double of the power coefficient required! In this work, thermal and hydraulic characteristics of the CPLIP have been experimentally analysed, using a prototype deriving from previous studies, and by using CFD and a 0D model. Results show the ability of the CPLIP to control the temperature of power electronics modules during a short and medium-range aircraft mission profile, characterised by sudden changes of thermal load and cyclic variations of the cold source temperature. Finally, a study focused on the transient behaviour of the loop has been carried out. In particular, the start-up of the CPLIP and its behaviour during sudden and violent acceleration stages, characterising this application field, have been exploited. In the first case, an experimental and a numerical study were carried out to demonstrate the ability of the loop to start its operation in the most difficult thermal and environmental conditions (high thermal load and high environmental temperature). In the second case, a numerical study has been performed to understand the behaviour of the loop when an acceleration field up to 10g perturbs its operations. This work opens new interesting perspectives stand points concerning the application itself and the necessity to adopt a multidisciplinary approach to simultaneously thermally and electronically design new generation power electronics.

Keywords: (Electronic apparatus and appliances--Temperature control, Power electronic, Computer simulation, Hybrid aircraft, Cooling, Capillary pumped loop)

THÈSE

En vue de l'obtention du
DOCTORAT DE L'UNIVERSITÉ DE TOULOUSE

Délivré par l'Université Toulouse 3 - Paul Sabatier

Présentée et soutenue par
Philippe COLLIN

Le 03 novembre 2020

Design, taking into account the partial discharges phenomena, of the Electrical Insulation System (EIS) of high power electrical motors for hybrid electric propulsion of future regional aircrafts

Ecole doctorale : **GEET – Génie Electrique Electronique et Télécommunications :**
du système au nanosystème

Spécialité : **Génie Electrique**

Unité de recherche :
LAPLACE - Laboratoire PLasma et Conversion d'Energie - CNRS-UPS-INPT

Thèse dirigée par
David MALEC et Yvan LEFEVRE

Jury

Stéphane DUCHESNE, Professeur au LSEE – Université d'Artois, Rapporteur

Olivier GALLOT-LAVALLEE, Maître de conférence HDR au G2ELab – Université Grenoble-Alpes, Rapporteur
Anca PETRE, Maître de conférences au SIAME – Université de Pau et des Pays de l'Adour, Examinateuse

Pierre BIDAN, Professeur au LAPLACE – Université de Toulouse, Examinateur

David MALEC, Professeur au LAPLACE – Université de Toulouse, Directeur de thèse

Yvan LEFEVRE, Chargé de recherche HDR au CNRS – LAPLACE, Co-directeur de thèse

Thierry LEBEY, Responsable des recherches sur la haute tension et les technologies associées – SAFRAN, Invité
Laurent ALBERT, Project Manager – IRT Saint-Exupéry, Invité
Jean François ALLIAS, R&T Program Engineer – AIRBUS, Invité

Résumé

La réduction des émissions de CO₂ est un enjeu majeur pour l'Europe dans les années à venir. Les transports sont en effet aujourd'hui à l'origine de 24% des émissions mondiales de CO₂. L'aviation ne représente cependant que 2-3% des émissions globales de CO₂ mais le trafic aérien est en pleine expansion et, déjà, des inquiétudes apparaissent légitimement. A titre d'exemple, en Suède, depuis les années 1990, les émissions de CO₂ dues au trafic aérien ont augmenté de 61%. Ce constat explique l'apparition du mouvement « Flygskam » qui se repend dans de plus en plus de pays Européens.

C'est dans ce contexte que l'Union Européenne a lancé en septembre 2016 le projet **Hybrid Aircraft academic reSearch on Thermal and Electrical Components and Systems (HASTECS)**. Le consortium regroupe différents laboratoires ainsi que l'avionneur Airbus. Ce projet s'inscrit dans le programme « H2020 Clean Sky 2 » qui vise à développer une *aviation plus verte*. L'objectif ambitieux est de réduire de 20% les émissions de CO₂ ainsi que le bruit produit par les avions, d'ici 2025. Pour cela, le consortium a décidé d'étudier une architecture hybride de type série. La propulsion est assurée par une motorisation électrique pour laquelle deux cibles ont été définies. En 2025, les moteurs devront en effet atteindre une densité de puissance de 5kW/kg, système de refroidissement inclus. En 2035, cette densité de puissance devra être doublée (10kW/kg). Pour atteindre ces cibles, le niveau de tension sera considérablement augmenté, probablement au-delà du kilovolt. Le risque d'apparition de décharges électriques dans les stators des moteurs électriques sera considérablement accru et doit être pris en compte dès la phase de conception du moteur.

L'objectif de cette thèse est de mettre au point un outil d'aide au design du Système d'Isolation Electrique (SIE) primaire du stator des moteurs électriques qui seront pilotés par convertisseurs. Le manuscrit qui synthétise les travaux effectués est découpé en cinq parties.

La première partie commencera par préciser les enjeux et défis d'une aviation plus verte. La constitution du SIE d'un stator de moteur électrique sera ensuite développée. Enfin, les contraintes qui s'appliquent sur le SIE dans l'environnement aéronautique seront identifiées.

La deuxième partie présentera les différents types de décharges électriques que l'on peut retrouver dans les dispositifs électriques. Le principal risque vient des Décharges Partielles (DP) qui détériorent peu à peu le SIE. Le principal mécanisme permettant d'expliquer l'apparition des DP est l'avalanche électronique. Le critère de Paschen permet d'évaluer le Seuil d'Apparition des Décharges Partielles (SADP). Différentes techniques permettent de détecter et mesurer l'activité des DP. Des modèles numériques permettent d'évaluer le SADP.

La troisième partie présentera une méthode originale pour déterminer les lignes de champ électrique dans un problème electrostatique. Elle n'utilisera qu'une formulation en potentiel scalaire.

La quatrième partie présentera une étude expérimentale pour établir une correction du critère de Paschen. En effet, un bobinage de moteur électrique est très loin des hypothèses dans lesquelles ce critère a été originellement défini.

Enfin, la cinquième partie sera consacrée à l'élaboration de l'outil d'aide au design du SIE. Des abaques seront construits afin de fournir des recommandations sur le dimensionnement des différents isolants dans une encoche de stator. Une réduction du SADP due à une variation combinée de la température et de la pression sera également prise en compte.

Mots clefs : Décharges partielles, théorie de Paschen, Modélisation, Eléments finis, Champ électrique, Dimensionnement, Diélectriques, Isolation électrique, SADP.

Abstract

Reducing CO₂ emissions is a major challenge for Europe in the forthcoming years. Nowadays, transport represents 24% of the world CO₂ emissions. Aviation accounts for only 2-3% of these world CO₂ emissions. However, air traffic is booming and concerns are legitimately emerging. As an example, CO₂ emissions from air traffic have increased by 61% in Sweden since the 90s. This explains the emergence of the "Flygskam" movement which is spreading in more and more European countries.

It is in this context that the European Union launched in September 2016 the project **Hybrid Aircraft academic reSearch on Thermal and Electrical Components and Systems (HASTECS)**. The consortium brings together different research laboratories and Airbus. This project is part of the program "H2020 - Clean Sky 2" which aims to develop a *greener aviation*. Its ambitious goal consists in reducing CO₂ emissions and noise produced by aircraft by 20%, by 2025. To do that, the consortium has decided to study a serial hybrid architecture. Propulsion is provided by electric motors. Two targets have been defined. In 2025, the engines must reach a power density of 5kW/kg, including the cooling system. In 2035, this power density of the engines will have to be doubled (10kW/kg). To reach these targets, the voltage level will be considerably increased, probably beyond one kilovolt. The electric discharges appearance risk will be considerably increased and need to be considered right from the motor design stage. The objective of this thesis is then to develop a tool in order to help the designer of electric motors fed by a converter when he will deal with its primary Electrical Insulation System (EIS). This manuscript is organized into five parts.

The first part will begin by clarifying both issues and challenges of a greener aviation. The EIS composition in electric motors will then be developed. Finally, the constraints withstood by the EIS in an aeronautical environment will be identified.

The second part will present the different types of electric discharges that can be found in electric devices. The main risk comes from Partial Discharges (PD) which gradually deteriorate the EIS. The main mechanism for explaining the appearance of PD is the electronic avalanche. The Paschen criterion makes it possible to evaluate the Partial Discharge Inception Voltage (PDIV). Different techniques may be used to detect and measure the activity of these PD. Numerical models may also be used to evaluate the PDIV.

The third part will present an original method for determining the electric field lines in an electrostatic problem. It only uses a scalar potential formulation.

The fourth part will present an experimental study to establish a correction of the Paschen criterion. Indeed, an electric motor winding is very far from the assumptions in which this criterion was originally defined.

Finally, the fifth part will be devoted to the development of the SIE design aid tool. Graphs will be generated to provide recommendations on the sizing of the various insulators in a stator slot. A reduction in the PDIV due to a combined variation in temperature and pressure will also be taken into account.

Keywords: *Partial discharges, Paschen, Modelling, Finite elements, Electric field, Sizing, Dielectrics, Electrical insulation, PDIV.*

Remerciements

Ces travaux de thèse ont été réalisés au laboratoire LAPLACE (Laboratoire PLasma et Conversion d'Energie). Ils ont été financés par l'Union Européenne dans le cadre du programme H2020.

Je tiens tout d'abord à grandement remercier mes deux directeurs de thèse David Malec et Yvan Lefevre. Ils m'ont accompagné tout au long de cette aventure tant humaine que scientifique. Je garde de très bon souvenirs de nos escapades aux cours des différentes conférences auxquelles j'ai eu la chance de participer. Je suis très heureux de l'amitié qui nous lie désormais. Egalement merci aux membres des deux équipes du laboratoire qui m'ont accueilli chaleureusement : le MDCE sur le site université Paul Sabatier et le GREM 3 sur le site INPT-ENSEEIHT.

Je tiens à remercier Stéphane Duchesne (LSEE, Université d'Artois) et Olivier Gallot-Lavalée (G2ELab, Université Grenoble-Alpes) d'avoir accepté d'être rapporteurs de ma thèse. Merci également aux autres membres du jury, Anca Petre (SIAME, Université de Pau et des Pays de l'Adour), Pierre Bidan (LAPLACE, Université de Toulouse) pour l'évaluation de ce travail en tant qu'examinateurs. Merci à Thierry Lebey (SAFRAN), Laurent Albert (IRT Saint-Exupéry) et Jean François Allias (AIRBUS) d'avoir pris part au jury en tant que membres invités. Je vous suis très reconnaissant d'avoir pris le temps pour évaluer mon travail et pour la richesse des échanges que nous avons eu lors de la soutenance de cette thèse.

Je voudrais remercier Sorin Dinculescu, Zarel Valdez-Nava, Vincent Bley, Céline Combettes, Benoit Lantin, Benoit Schlegel, Pierre Hernandez et Nofel Merbahi pour leur aide à la réalisation de mes travaux expérimentaux.

Merci également à tous les doctorants, post-doctorants et stagiaires qui ont fait un passage dans le bureau porte 102 du bâtiment 3R3 : Mallys Banda, Fernando Pedro, Riccardo Albani, Kemas M Tofani, Imadeddine Benfridja, Youcef Kemari, Paweł Piotr Pietrzak, Trong Trung Le et bien d'autres ! Il y a toujours eu une bonne ambiance dans ce bureau !

Un grand merci aussi aux doctorants et docteurs du troisième étage sur le site ENSEEIHT : Maxime Bonnet, Théo Carpi, Mateus Carvalho Costa, Jessica Neumann, Jordan Stekke, Youness Rtimi. C'était toujours un plaisir de passer vous dire bonjour et de squatter un siège et votre café !

Merci à tous mes collègues du projet HASTECS. Aux doctorants : Sarah Touhami, Najoua Erroui, Amal Zeaiter, Flavio Accorinti, Malik Tognan et Matthieu Pettes-Duler. J'ai passé d'excellents moments en votre compagnie ce qui a rendu mon travail encore plus agréable. Bon courage à toi Matthieu qui est le dernier à soutenir !

Je tiens à remercier tous mes compères de l'Association des Lapaciens (ADeL) que j'ai eu le plaisir de présider : Marjorie Morvan, Aurélien Pujol, Plinio Bau, Bojan Djuric et Matthieu Pettes-Duler (encore toi !). On a vraiment fait du bon boulot et on s'est bien éclaté !

Merci aussi aux nombreux doctorants et docteurs du PRHE avec lesquels j'ai passé beaucoup de bon temps : Cyril Van de Steen, Julien Cosimi, Maxime Bafoil, Tristan Gouriou, Aurélie Marches, Eléna Griset, Valentin Ferrer. Je pense aussi à d'autres gens bien sympas : Maxime Castelain, Aurélie Tokarski, Benoit Prochet, Nicolas Millet, Davin Guedon, Andréa Al Haddad.

Remerciements

Merci à mes anciens camarades de l'ENSEEIHT : Thomas Longchamps, Etienne Farman, Yoann Scotto, Baptiste Genet et tous les autres pour les très bons moments passés même après l'obtention de notre diplôme d'ingénieur.

Je remercie ma famille étendue (les Collin et les Chauvin) pour leur soutien pendant ces années de thèse.

Enfin je dédie mes derniers remerciements à ma compagne Julie Chauvin. Tu es toujours à mes côtés pour me supporter et pour me donner la force d'aller de l'avant. Je t'aime!

Table of contents

Résumé	3
Abstract	4
Remerciements	5
General Introduction	13
Chapter 1: Toward full-electric transportation	17
1 Implications and challenges	19
1.1 Sustainable transportation.....	19
1.1.1 International context.....	19
1.1.2 European and France contexts.....	21
1.2 The “Flygskam” movement	21
2 Toward more electric aircrafts	22
2.1 Classic aircraft architecture.....	22
2.1.1 Pneumatic network	22
2.1.2 Hydraulic network	22
2.1.3 Mechanical power	23
2.1.4 Electrical network.....	23
2.2 Projects of more electric aircrafts	24
2.2.1 E-FanX.....	25
2.2.2 CityAirbus	26
3 HASTECS project	26
3.1 Targets.....	26
3.2 Serial hybrid configuration	27
3.3 Work packages	27
3.3.1 Work Package 1 (WP1)	28
3.3.2 Work Package 2 (WP2)	29
3.3.3 Work Package 3 (WP3)	30
3.3.4 Work Package 4 (WP4)	32
3.3.5 Work Package 5	33
3.3.5.1 DC busbar	33
3.3.5.2 Motor Electrical Insulation System (EIS)	35
3.3.6 Work Package 6	35
4 Electric motors electrical insulation	36
4.1 Low voltage machine.....	36
4.1.1 Turn-to-turn insulation.....	38

4.1.2	Phase-to-phase insulation	41
4.1.3	Turn-to-slot insulation.....	41
4.1.4	Slot impregnation	42
4.2	High voltage machine	44
5	Thermal aspect	46
5.1	Cooling strategies	46
5.2	Thermally enhanced polymers	47
6	Impact of power electronics.....	49
6.1	Pulse Width Modulation (PWM) basis	49
6.2	Power feeding cable	51
6.3	Frequency increase.....	55
6.4	Voltage distribution.....	57
	Chapter 2: Physics of Partial Discharges (PD).....	61
1	Different kinds of discharges.....	63
1.1	Discharges in non-vented cavities	64
1.2	Discharges in vented cavities	65
1.3	Discharges on the surface	66
1.4	Corona discharge.....	67
1.5	PD consequences on stator insulation	68
2	Physics of plasma.....	69
2.1	Townsend mechanism.....	69
2.1.1	First Townsend's coefficient.....	70
2.1.2	Second coefficient	73
2.2	Paschen's law	74
2.3	Impact of aeronautics conditions.....	75
2.3.1	Environmental variations	75
2.3.2	Impact of temperature	77
2.3.3	Impact of humidity	80
3	PD analysis.....	82
3.1	Experimental detection of PD activity.....	82
3.1.1	Radio-frequency detection.....	83
3.1.2	Optical detection	83
3.1.3	Power factor/capacitance tip-up test.....	84
3.1.4	Used electric detection.....	84
3.2	Parameters linked to PD.....	85
3.2.1	Partial Discharge Inception Voltage (PDIV)	85

3.2.2	Partial Discharge Extinction Voltage (PDEV)	86
3.2.3	Apparent charge	86
3.3	Statistical processing of the results.....	87
4	Degradation of the polymer insulation in aeronautic environment	90
4.1	Pressure.....	91
4.2	Humidity	92
4.3	Temperature.....	93
4.4	Frequency and voltage	94
4.5	Lifetime evaluation.....	96
5	Modelling partial discharges activity.....	98
5.1	Streamer criterion	98
5.2	Paschen's criterion	100
	Chapter 3: Electric field lines computation	103
1	Introduction.....	105
2	The electrostatic problem	105
2.1	Presentation of the field of study.....	105
2.2	Electrostatic equations and formulations	106
2.3	Advantages and disadvantages of each formulation	108
2.3.1	Vector potential.....	108
2.3.2	Scalar potential.....	109
3	Electric field lines computation derived from a scalar potential formulation	109
3.1	Ballistic method	109
3.2	Flux tubes based method	113
4	Proposed method.....	116
4.1	Electric field and electric flux	116
4.2	Equipotential lines.....	118
4.3	Flux function.....	120
4.4	Illustrative examples.....	122
5	Another method using <i>Matlab</i> functions.....	124
5.1	Building the additional mesh.....	124
5.2	Electric field	125
5.3	Comparison with the proposed method	126
6	Conclusion	128
	Chapter 4: Correction of the Paschen's criterion.....	129
1	Motivations	131
1.1	Configuration different from the initial one.....	131

1.2	Experimental observation	131
2	Experimental approach	133
2.1	Samples	133
2.2	Experimental protocol.....	135
3	Results	136
3.1	PDIV results	136
3.2	Dielectric constant measurements	139
4	Mixed experimental and numerical approaches.....	141
5	Single layer insulation.....	144
6	Secondary electron emission coefficients.....	146
6.1	Impact of the incoming angle of bombarding ions	147
6.2	Influence of the enamel chemistry	149
7	Additional experimentation	150
7.1	Set up.....	150
7.2	Results	152
8	Conclusions and perspectives	154
	Chapter 5: Tool to predict PD activity in machine slot.....	157
1	Dielectric constant evolution with temperature and frequency	159
2	Partial Discharge Evaluation Criterion.....	160
3	Partial Discharge Inception Voltage (PDIV) decrease for a combined variation of temperature and pressure	161
4	Wire design graphs.....	162
4.1	Simple analytical model for electric field in air gap computation.....	162
4.2	Validation of Simple Analytical Model with finite elements	164
4.3	Enamel thickness as a function of applied voltage	165
4.4	Copper diameter as function of computed enamel thickness	167
4.5	Validation	168
5	Slot insulation design graphs.....	170
5.1	Simple analytical model for electric field in air gap computation.....	170
5.2	Validation of Simple Analytical Model with finite elements	171
5.3	Slot liner thickness as a function of applied voltage and insulation materials	172
5.3.1	First imbrication	173
5.3.2	Second imbrication.....	174
5.3.3	Third imbrication	175
5.4	Validation	175
6	Evaluation of the electric stresses under normal temperature and pressure conditions	176

6.1	Turn/turn electric stress	176
6.2	Turn/slot electric stress.....	178
7	Partial Discharge Evaluation Tool (PDET)	178
7.1	PDET algorithm	179
7.2	Inputs.....	180
8	Illustrative example	181
9	Conclusion	186
	General conclusion and perspectives.....	189
	Publications	193
	Annex.....	195
	References:.....	197

General Introduction

Aircrafts manufacturers such as Airbus, Boeing and Bombardier are engaged in the competition to develop more- and full- electric aircrafts. That incoming revolution takes place in a context where more and more people and countries are expecting a much greener air transportation. The first step of this change is to progressively replace turboshafts by electric motors to ensure the propulsion of the aircraft. More and more on-board electric power is consequently required.

The risk of electric discharges in propelling electric motors will then increased, as the feeding voltage will probably be higher than one kilovolt. The Electric Insulation System (EIS) ensures the protection of a machine against electric hazards. It can be divided into two categories. Type I is used in low-voltage rotating machine. The International Electric Commission (IEC) considers a machine with a phase-to-phase voltage lower than $700 \text{ V}_{\text{rms}}$ as a low-voltage machine. Type I insulation is almost exclusively made of polymer materials. These are also called organic materials. On the other hand, Type II insulation is used in machine with phase-to-phase voltage upper than $700 \text{ V}_{\text{rms}}$. It uses inorganic materials such as fibber glass, mica, ceramics, composite materials,... These are more expensive materials which lifespan is increased in presence of electric discharges. Type I insulation is also used in machines fed by voltages higher tan $700 \text{ V}_{\text{rms}}$, as the EIS has been designed to be free from electric discharges.

Since the introduction of power electronic power supplies, that provides easy control of the machine rotational speed, the electrical insulation of such motors faces new hazards. Fast changing supply voltage, with high dV/dt , may cause the apparition of partial discharges (PD), that results in accelerated insulation aging and often leads to premature failure of the motors. In low voltage rotating machines, the stator insulation system is multi-level. Its first component (primary insulation) is the polymer enamel on the magnet wire, among the others: inter-phase insulation, slot insulation and impregnation varnish. Depending on the desired thermal properties, there are several types of polymers being used nowadays in enameled wires: polyamide (PA), polyamide-imide (PAI), polyester-imide (PEI) and polyimide (PI). Inorganic nano-particles (SiO_2 , Al_2O_3 , ZnO ,...) may also be used as fillers to obtained *corona-resistant* enamels. In random-wound stators powered by power inverters, in comparison with sinusoidal power supply, the magnet wire insulation is far more endangered. Hence, the objective is to concentrate on this primary insulation. Once the voltage exceeds the Partial Discharge Inception Voltage (PDIV), electronic avalanches will take place in the EIS, leading to:

- an ions bombardment of the insulator surfaces;
- an increase in temperature the the area submitted to PD;

General Introduction

- a chemical degradation of the insulators.

All these actions will strongly increase the insulator degradation rate. Usually, there are three ways used to avoid and/or to resist to such damage. Firstly, the use of corona-resistant enameled wires, especially formulated to increase the lifetime under PD attacks. Secondly, a suitable design of the primary electrical insulation: choice of right enamel wires (size and shape), insulation thickness (grade), choice of wires arrangement in the slots... Third, the use of both of these two solutions.

A non-closed motor embedded in an aircraft is submitted to severe environmental variations. These are mainly the temperature, the pressure, the humidity and vibration. These environmental parameters have a significant impact on the physics describing PD. It is for example known that a combined temperature increase and pressure decrease in dry air reduces the PDIV.

The objective of this thesis is to develop an automatic tool, based on PD physics, in order to help the machine designer to better design and size the EIS of rotating machines fed by inverters. The scope of investigation of the tool is limited to the stator slot. It considers only one phase per slot (an upgrade could be considered thereafter to treat more than one phase per slot). Therefore, the turn/turn and turn/slot electric stresses are studied. First, a criterion to evaluate PDIV in both configuration is established. It is a correction of the Paschen's criterion, taking into account the dielectric over-coating and a combined variation of temperature and pressure in micro gaps. Simple Analytical Models (SAM) are developed and validated with 2D-Finite Elements Models (2D-FEM). Graphs are derived from parametric studies to size the EIS in order to withstand electric stress without PD in turn/turn and turn/slot configurations.

This thesis is founded by the **Hybrid Aircraft reSearch on Thermal and Electrical Components and Systems (HASTECS)** project. It is part of the “H2020 - Clean Sky 2” European program. It is a consortium composed of public laboratories and Airbus. The PhD research work takes place in the LAPlace Laboratory on PLasma and Conversion of Energy (LAPLACE) in Toulouse. The works in LAPLACE were conducted in collaboration between 2 research teams: the *Dielectrics Materials in the Energy Conversion* (MDCE) group and the *Research Group in Electrodynamics* (GREM3). MDCE has provided the facilities for the experimental studies, whereas GREM3 has provided the license and expertise on Ansys finite elements software.

This PhD dissertation is divided into five chapters. A short description of each chapter is given in the following.

Chapter I: Toward full electric transportations

Chapter I will start by presenting the challenges on the road toward a green aviation, based on Worldwide and European scales. Then, a classic aircraft architecture will be detailed. Projects of more electric aircrafts will be introduced alongside the HASTECS project with its serial-hybrid electric architecture. Chapter I will continue with the explanation of a motor EIS composition for Type I and Type II machines. It will finish by identifying power electronics impacts on electric stresses occurring at the motor terminals.

Chapter II: Physics of Partial Discharges

Chapter II will begin with a presentation of the different kinds of electric discharges. The electronic avalanche will be identified as the main mechanism involved in PD. It will be described by the Paschen's law. The impact of aeronautical conditions on Paschen's law will be detailed. Chapter II will then describe the experimental methods to detect and measure a PD activity in an electric device. The parameters impacting the insulation lifespan will be identified. Finally, two main numerical models to evaluate PD activity will be introduced; each of them uses a different criterion.

Chapter III: Electric field lines computation

This chapter will be dedicated to the electrostatic problem composed by two enamelled round wires in close contact. The formulations in both vector and scalar potential will be presented. It will come that the scalar formulation is the easiest to handle. It will be consequently used to propose an original method to compute field lines. The proposed method will be compared to a ballistic method implanted in Matlab software. The field lines geometry and the scalar potential distribution are required for the application of the PDIV evaluation criterion based on Paschen's law.

Chapter IV: Correction of Paschen's criterion

Paschen's criterion has been experimentally established for a configuration which is completely different from the ones found in a machine stator slot. Therefore, the validity of this criterion will be investigated. Experimental observations of PD degradation between enamelled round wires in close contact has revealed that the Paschen's law shape is conserved. The dielectric over-coating has been found to simply increase the PDIV level. An experimental study coupled with a 2D-FEM will be performed to evaluate the secondary electron coefficient value in the presence of a dielectric over-coating.

Chapter V

This chapter will present in detail the tool to implement the EIS design in order to avoid any PD in stator slots. It will start by giving the assumptions used in the different models. A focus will be on turn/turn and turn/slot configurations. Parametric studies on the impacting parameters will be realized using SAM. Sizing graphs will be derived from these studies. These graphs will then be implanted in a Partial Discharge Evaluation Tool (PDET). The interest and efficiency of the developed PDET will finally be proved with an illustrative example.

Finally, conclusions as well as perspectives for future works will be proposed.

Chapter 1: Toward full-electric transportation

1 IMPLICATIONS AND CHALLENGES

1.1 SUSTAINABLE TRANSPORTATION

1.1.1 International context

The role of transportation in the world sustainable development was firstly pointed out during the 1992 United Nation's Earth Summit at Rio de Janeiro [1]. Since then, the strong role of transportation in climate change, raw material depletion, human health and ecosystems equilibrium is as important as ever. Indeed, the transportation sector:

- is responsible of 24% of world CO₂ emissions [2]. Every person on our planet produces, on average, 1.5t of CO₂ emissions per year, just for being on the move [3]. Both passengers and freight road vehicles are responsible of 74% of the total transportation CO₂ emissions, while both aviation and shipping reach 22% and rail 1.3%;
- remains the largest consumer of oil : 57% of the global demand [4], i.e. : 55.8 Mb/day where road represents 78.1%, air 11.4%, sea 7.3% and rail 3.2% ;
- is responsible of 12-70% of the total tropospheric air pollution mix [5]: Asia, Africa and the Middle East suffer more due to the use of old and inefficient vehicles. Outdoor air pollution (O₃, NO_x, SO₂, CO, PM₁₀, PM_{2.5},...) kills more than 8 million people across the world every year. Transportations, mainly road ones, *would be* responsible of almost 50% of these premature deaths [6] ;
- is responsible of direct and indirect damages, or major changes, on ecosystems (air, marine and earth), which are often unpredictable [7].

In order to identify guidelines, different scenarii such as the *Sustainable Development Scenario* (SDS), the *Clean Air Scenario* and the *Future is Electric Scenario* have been established by using the World Energy Model developed by the International Energy Agency [8]. As an example, Figure 1 shows the CO₂ emissions SDS targets versus transportation sectors ; direct transport emissions must peak around 2020 and then fall by more than 9% by 2030.

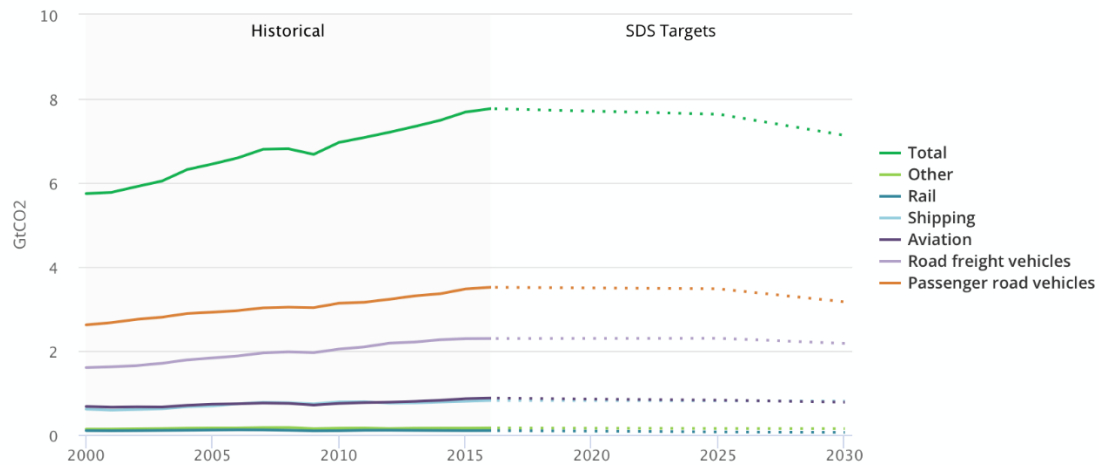


Figure 1: CO₂ emissions versus transportation sectors (past evolution and SDS targets) [2]

In order to put global warming, human health and environmental impacts of transportation on track to meet all 2030 goals, different efforts must be undertaken or pursued in all kind of transport by increasing even more:

- 1) the efficiency of existing ICE (Internal Combustion Engine) powertrains: lower fuel consumption, use of bio- or low carbon-fuels, better decontamination of exhaust gas, ... ;
- 2) the electrification of ICE powertrains: hybridization or full electrification;
- 3) the capacity, the efficiency, the lifetime and the hybridization of embedded power sources;
- 4) the efficiency of existing powertrains, traditionally electric ;
- 5) the good consumer's behaviours (better transportation planning, carpooling,...) and the voluntary city transport policies.

The transportation sector has now entered a critical transition period where existing measures listed below must be deepened and extended in order to reach the environmental goals, whereas in the meantime the need in this sector is continuously growing. This process will need to be set in motion over the next decade. Any delay would require stricter measures beyond 2030, which could noticeably increase the cost of reaching environmental and health targets. This must be accompanied, of course, by the power sector decarbonisation since 41% of world CO₂ emissions is due to electricity generation [2]. Among all the measures listed below, items 2), 3), 4) and 1) for electric-assisted solutions, are essentially dependent on R&D efforts in the field of both Electrical and Electrochemical (-applied to energy) Engineering.

1.1.2 European and France contexts

In the European Union (EU), more and more societies aim to be greener; fossils energies are more and more substituted by sustainable ones. As an example, in France, the proportion of sustainable energy into the total energy consumption has increased by about 69% from 1990 to 2016 [9]. It represents 16% of the total consumption of energy in France in 2018. With the *Accord de Paris* and the *Climate Plan*, EU aims to increase this proportion up to 27% in 2030 [9].

There are several motivations for the energy transition. It is first economic. Nowadays, fossil energies still represent 81.7% of total energy consumption in the World. Oil remains the most used [10]. It mainly comes from the Middle East. Due to both repeated politic tensions and commercial monopoly, the oil barrel price is unstable. Figure 2 presents the evolution of the oil barrel cost (in US \$) from 1970 to 2015 [11].

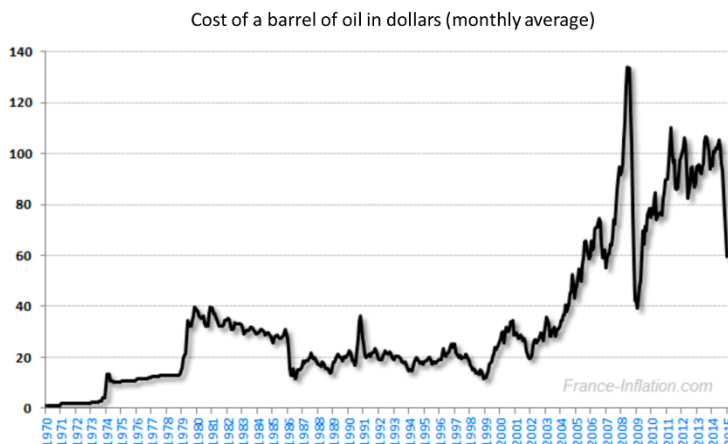


Figure 2: Evolution of the oil barrel cost (in US dollars) [11]

The second motivation is the society awareness on both contamination and climate change. Political actions are undertaken to reduce carbon emissions, especially in the transportation field. As an example, the EU Horizon 2020 project aims to a 23% reduction of greenhouse gas emissions from road transport in 2030 compared to 2005 [12]. In 2016, road transport represented nearly 21% of EU's total emissions of carbon dioxide [12].

1.2 THE “FLYGSKAM” MOVEMENT

Aviation is only responsible of 2-3% of global CO₂ emissions according to the International Air Transport Association (IATA) [13]. It represents 11-12% of the total emission due to transportation [14]. There, the total CO₂ emissions have decreased by 24% from 1990 while the emissions due to aviation have increased by 61% [14]. These data have particularly rang a bell in Sweden where people are

increasingly abandoning air planes for internal trips; internal flights have decreased by 3% from January to September 2018 [14]. This movement that has received the name “Flygskam”, literally *the shame to take the plane*, is growing in other countries.

2 TOWARD MORE ELECTRIC AIRCRAFTS

2.1 CLASSIC AIRCRAFT ARCHITECTURE

Multiple sources of energy are present in an aircraft. It includes mechanical, electrical, hydraulic and pneumatic energies. Figure 3 illustrates the implantation of a conventional power distribution [15].

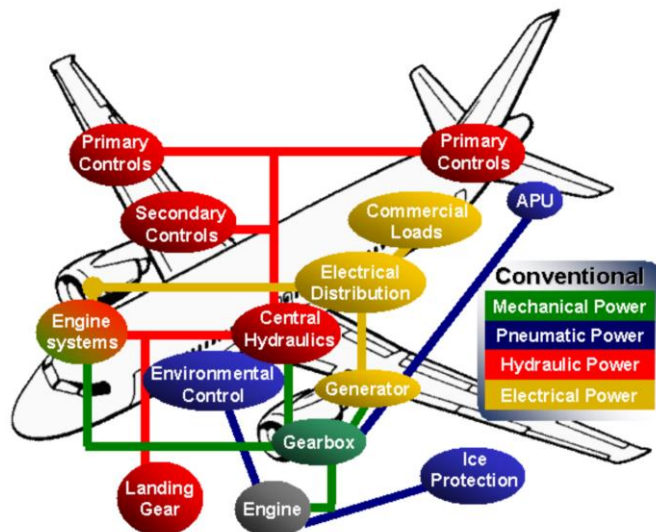


Figure 3: Schematic of a conventional power distribution in aircrafts [15]

2.1.1 Pneumatic network

The pneumatic power is bled from the engine high-pressure compressor. It is commonly used to power the Environmental Control System (ECS). It also supplies hot air for Wing Ice Protection System (WIPS). The major drawback of air bleeding from the engine is that it reduces thrust efficiency.

2.1.2 Hydraulic network

The hydraulic power is provided by a central hydraulic pump. The power is transferred to actuation systems (primary and secondary flight control), landing gears, engine actuation, thrust reversal system and several other auxiliary systems.

As an example, the A320 hydraulic system is composed of three fully independent circuits: Green, Yellow and Blue (see Figure 3) . The normal hydraulic source on the blue circuit is the electrical pump. The auxiliary source is the Ram Air Turbine (RAT), used in case of a huge electrical power failure. On the green and yellow circuits, the normal hydraulic source is the Engine Driven Pump (EDP). The auxiliary source is the Power Transfer Unit (PTU). It is a hydraulic motor pump which transfers hydraulic power between the green and yellow systems without transfer of fluid [16].

The main drawback of a hydraulic power is the economic cost in maintenance due to the system complexity.

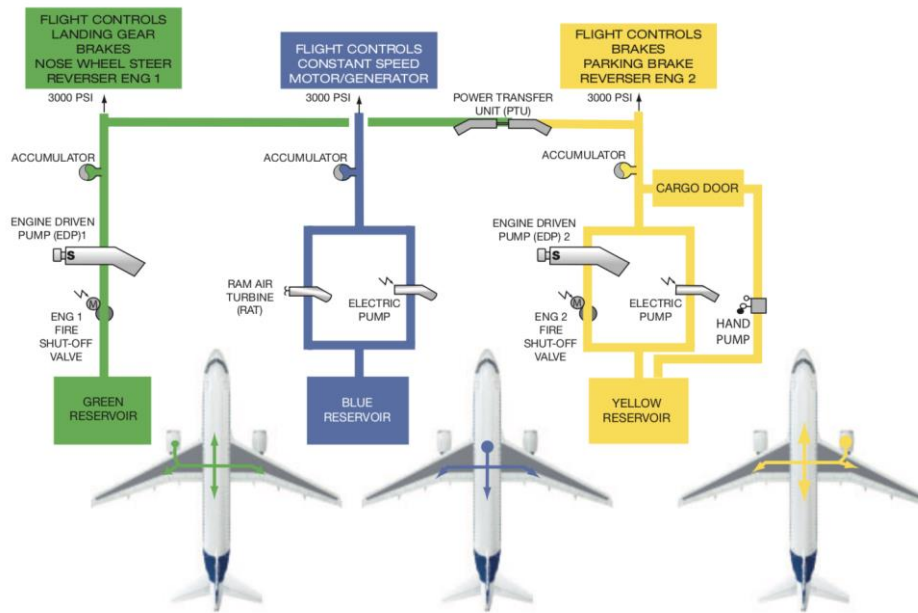


Figure 4: Green, Blue and Yellow A320 hydraulic circuits [16]

2.1.3 Mechanical power

The gearbox is the heart of the mechanical power transmission. It transfers the power from the engines to central hydraulic pumps, to local pumps for engine equipment, to other mechanically driven subsystems and to the main electrical generator [15].

2.1.4 Electrical network

The proportion of on board electric power has continuously increased in aircrafts. The electric power tends to replace more and more systems which were powered by either pneumatic or hydraulic power. Figure 5 illustrates the increasing of inboard electrical equipment demand in commercial aviation [17].

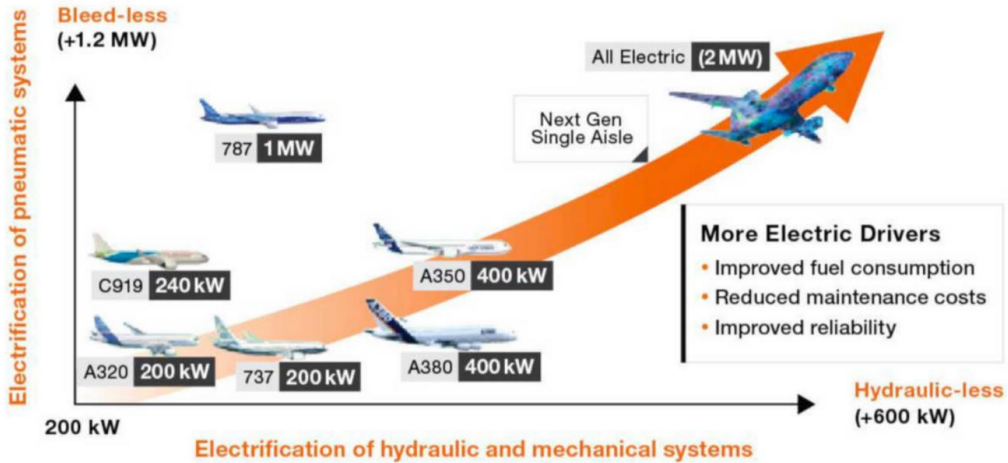


Figure 5: Increasing on board electrical equipment demand in commercial aviation [17]

The former on board electric bus first provided both constant voltage and frequency to the aircrafts devices. An Integrated Drive Generator (IDG) was used to change the variable speed of the jet engine to constant speed [18]. Between 1936 and 1946, the voltage supply has increased from 14.25 VDC to 28 VDC [19].

In recent aircrafts such as Airbus A380, Airbus A350 and Boeing 787, there is no more IDG. A gearbox is used to directly couple the engine generator to the jet engine. An alternative voltage of 115/200 VAC is produced with a frequency range from 350 to 800 Hz [18].

The interest to replace pneumatic and hydraulic system with electric ones is mainly economic. Moreover, electric aircrafts have a lower maintenance cost.

2.2 PROJECTS OF MORE ELECTRIC AIRCRAFTS

Almost ten years ago, focusing in EU, Airbus revealed its first full electric aircraft. Up to now, new demonstrators try to develop and optimize the electric propulsion technology.

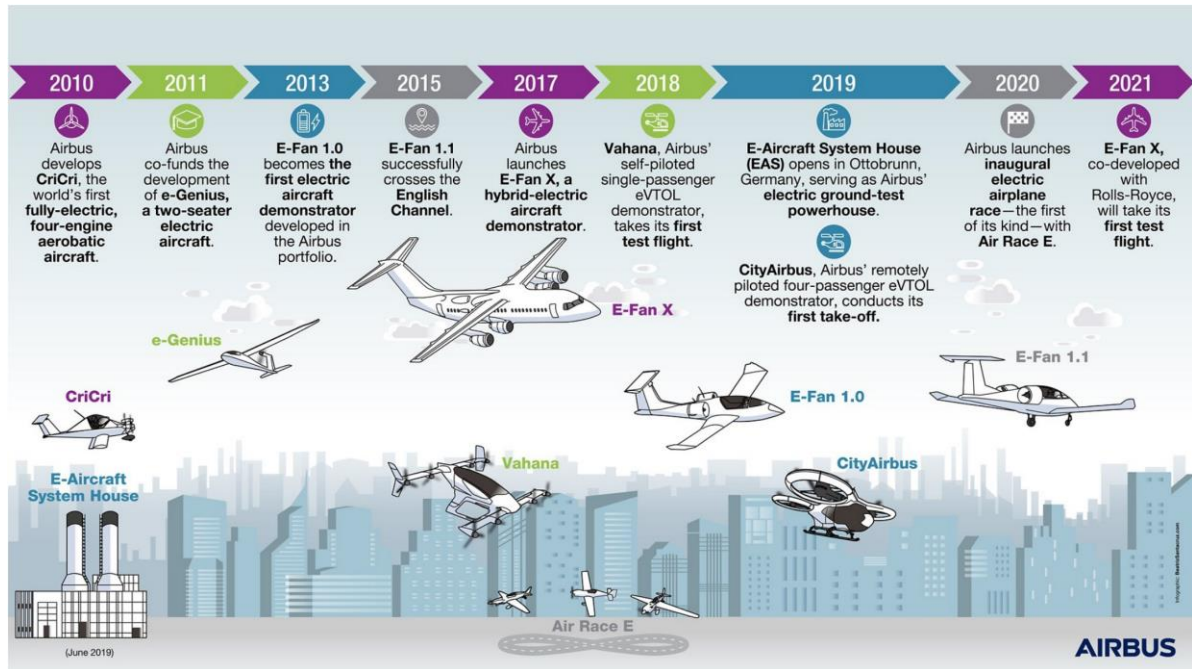


Figure 6: A timeline of Airbus's achievement in electric propulsion [20]

2.2.1 E-FanX

The E-FanX is the last Airbus-Rolls Royce project dealing with airplanes electrification. The objective is to develop a flight demonstrator testing a 2MW hybrid-electric propulsion system on a 100 seat regional jet. One of the four jet engines will be replaced with a 2 MW electric motor fed by a 3 kVDC electrical distribution. The flight testing should have started by the end of 2020 but, due to the corona virus pandemic, it has been stopped until further notice [21].



Figure 7: Airbus-Rolls Royce E-FanX (in green : the electric propeller) [21]

2.2.2 CityAirbus

The CityAirbus is an all-electric four-seat multicopter vehicle demonstrator. It is an **electric Vertical Take-Off and Landing** vehicle (eVTOL). It is remotely piloted. The CityAirbus demonstrator first take-off happened in May 2019. This vehicle produces less noise and zero emission compared to a classic helicopter.

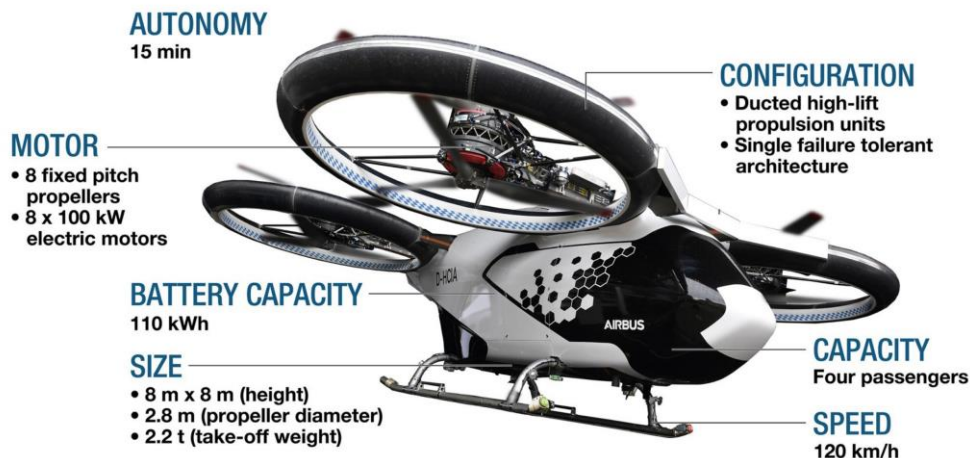


Figure 8: CityAirbus technical data [22]

3 HASTECS PROJECT

3.1 TARGETS

The **Hybrid Aircraft academic reSearch on Thermal and Electrical Components and Systems (HASTECS)** is part of the “H2020 - Clean Sky 2” program. It is a heavy EU aeronautics research program which aims to reduce by 20% the CO₂ emissions and the noise produced by airplanes by 2025. It regroups several laboratories, including LAPLACE, in partnership with Airbus Toulouse.

HASTECS objectives are to identify the most promising technological breakthrough solutions and to develop tools to considerably increase the efficiency of the electric hybrid powertrain systems. The final objective is to obtain both fuel consumption and noise contamination significant saves as it is currently the case for road vehicles (cars, buses, trucks). To successfully achieve such objectives, the specific powers will have to be increased.

HASTECS consortium aims to double the specific power of electric motors including cooling system. The targets are 5 kW/kg by 2025 and 10kW/kg by 2035. Concerning the power electronics, the specific power, including cooling, aims to be 15kW/kg by 2025 and 25kW/kg by 2035. These targets are to be achieved despite challenging environmental conditions such as harsh environmental conditions.

This technological breakthrough should reduce by 1.8 ton the weight of a 1.5MW inverter-motor powertrain. Consequently, 3.5% fuel save should be achieved on a 300 nautical miles' regional flight.

The kick-off meeting on September 13th 2016 has marked the start of HASTECS project for five years. It involves six PhD students and two post-doctoral students for a total funding of 1.5 M€ [23].

3.2 SERIAL HYBRID CONFIGURATION

There are several possible architectures for an electric hybrid powertrain [24]. HASTECS consortium has retained the serial hybrid one. It has mainly been selected because it is the architecture of the future Airbus demonstrator eFanX [21]. It is illustrated in Figure 9.

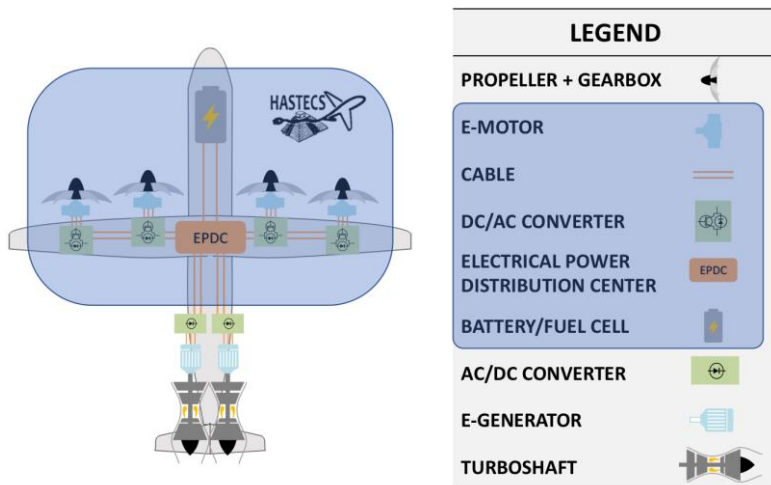


Figure 9: Serial hybrid powertrain [25]

Gas turboshafts driving electric generators are the main sources of power. Rectifiers supply an ultra-high DC voltage. Bus voltages are in the range of kVs [26]. The power is directed toward the Electrical Power Distribution Center (EPDC). Auxiliary power is delivered by batteries and/or fuel cells. The power supplies inverter fed motors. The propellers are driven through gearboxes.

HASTECS perimeter is composed of the batteries/fuel cells, the high voltage DC bus, the power electronics and the inverter fed motors. The tasks are dispatched between six Work Packages (WP).

3.3 WORK PACKAGES

Figure 10 below illustrates the tasks carried by each WP and the possible interactions.

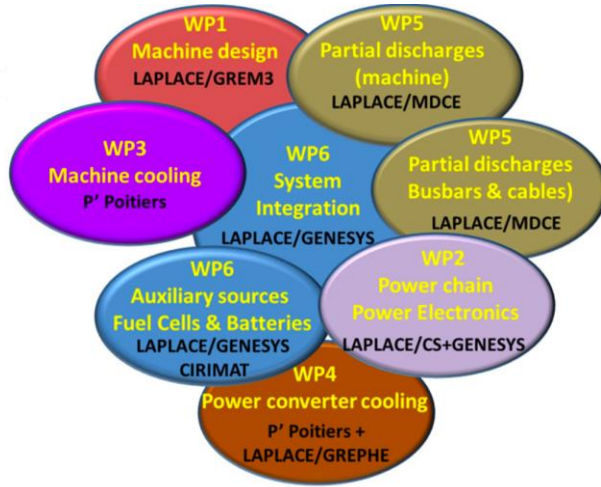


Figure 10: HASTECS work packages [23]

3.3.1 Work Package 1 (WP1)

This WP focuses on the electromechanical sizing of the electric motors. The first target for 2025 is a 5 kW/kg specific power, including cooling. The second target for 2035 is to reach 10 kW/kg. WP1 strongly interacts with WP3 (thermal study) and WP5 (partial discharges study). To choose the motor architecture, an analytic calculation tool has been developed [27]. It makes quick trade-offs of high specific torque electric motors using the loadability concepts developed by designers. The loadability concepts are mainly the electric, magnetic and thermal loads (see Table 1). Such loads are introduced in the tool as inputs to get the main sizes, weight and performances of the electric motor. The main interest is that there is no need to specify neither the stator winding configuration, nor the rotor structure. Additional inputs data such as the mechanical power or the rotational speed are required [28].

Load	Parameter	Description	Constraint
Magnetic loading	B_m	Magnetic flux in air gap	Magnetic materials
Electric loading	K_m	Surface current density	Insulation materials Cooling technology
Electromagnetic loading	$\sigma_t = \frac{B_m * K_m}{2}$ $T_{em} = 2 * \sigma_t * \pi * R^2 * L$	σ_t : tangential stress in airgap T_{em} : maximum electromagnetic torque R: inner stator radius L: motor active length	Magnetic materials Insulation materials Cooling technology

Table 1: Electric machine loads [28]

3.3.2 Work Package 2 (WP2)

The task of this WP is to develop a tool to facilitate high-power converters design in a limited time to analyse and compare several conversion topologies to power the motorization system. The first objective for 2025 is to size a 15 kW/kg power converter, including cooling. The second objective for 2035 is to increase this value to 25 kW/kg. To reach such high values, the power converter losses have to be minimized.

First, this WP determines an optimal DC bus voltage. This key parameter is determinant in both machine sizing and partial discharges study. The efficiency and power density of different multilevelled topologies are investigated using a developed tool and real semiconductors datasheets (Figure 11).

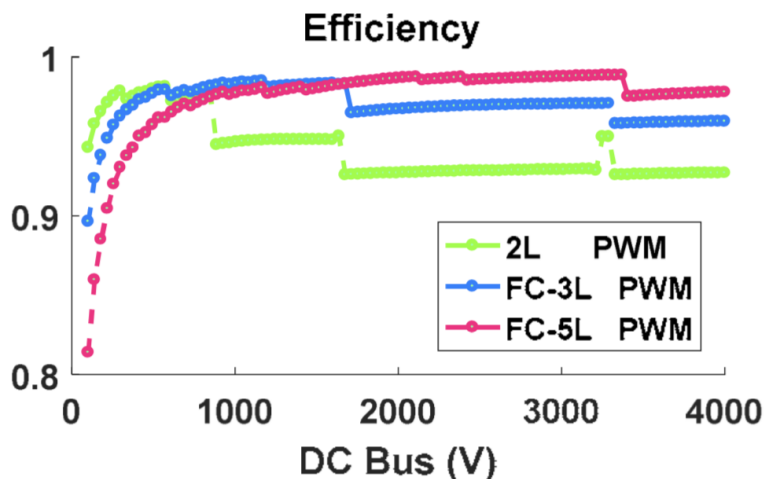


Figure 11: Power electronics efficiency for several topologies using available database components [29]. 2L PWM: 2 Layers Pulse Width Modulation, FC-3L PWM: Flying Cap-3 Layers Pulse Width Modulation, FC-5L PWM: Flying Cap-5 Layers Pulse Width Modulation

This WP carried out a work to develop a simulation tool for pre-sizing converters. It makes it possible to size a converter from a chosen topology. Parametric studies by varying the DC bus voltage, the requested power or the modulation index make it possible to determine the optimum operating point. An algorithm was developed to select the best suited component for both desired voltage and current values [29]. The performances are being computed based on analytical calculations of the losses in the semiconductors components for multiple multilevel architectures. Pulse Width Modulation (PWM) control is mainly considered [29].

Discontinuities in the results (see Figure 10) are due to discontinuities in component calibres and have been overcome by generating virtual components with continuous calibres. Components parameters

variation laws are identified as a function of the voltage or current-voltage product calibres and then applied to the desired one [29]. Figure 12 illustrates the efficiency as a function of DC bus voltage for a real two layers PWM components versus the generated ones [29] .

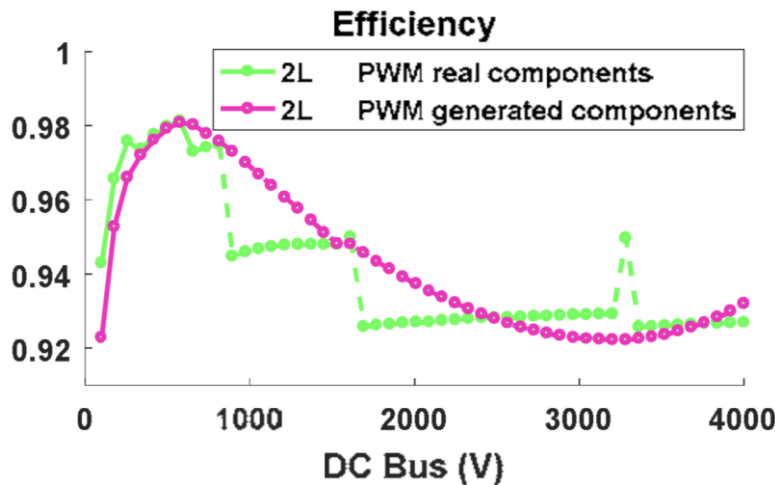


Figure 12: Real versus generated components efficiencies for adapted voltage and current calibres [29]

3.3.3 Work Package 3 (WP3)

This WP deals with the electric motors cooling technology. Thermal limitations are mainly imposed by both magnetic components and insulation materials. Besides, there are multiple losses in the electric motor that increase its temperature [30], [31]:

- iron losses in both stator and rotor laminations;
- Joule's losses in windings and end-windings;
- aero-thermal losses in air-gap;
- mechanical losses in the bearings.

An analytically Lumped Parameter Thermal Model (LPTM) has been used. It enables a quick parametric study. The motor is discretized in nodes (Figure 13); the thermal energy balance on each nodes is computed [30].

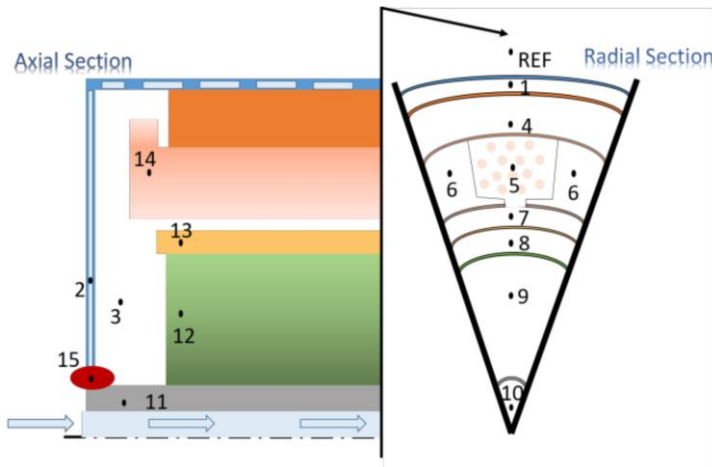


Figure 13: Motor nodes locations in axial and radial sections [30]

The connections between nodes (Figure 14) depends on material properties such as thermal conductance.

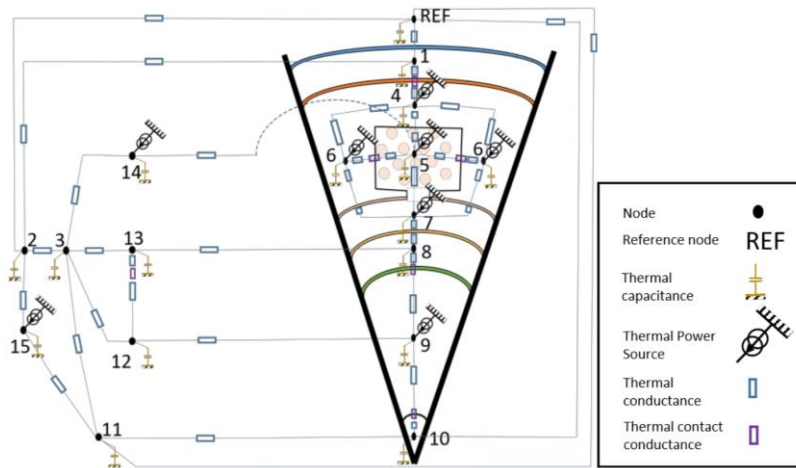


Figure 14: Motor nodal network [30]

As an example, for a motor configuration similar to the Lexus 2008 [32] and considering a water jacket cooling solution [30], the hot spots have been identified (see Figure 15):

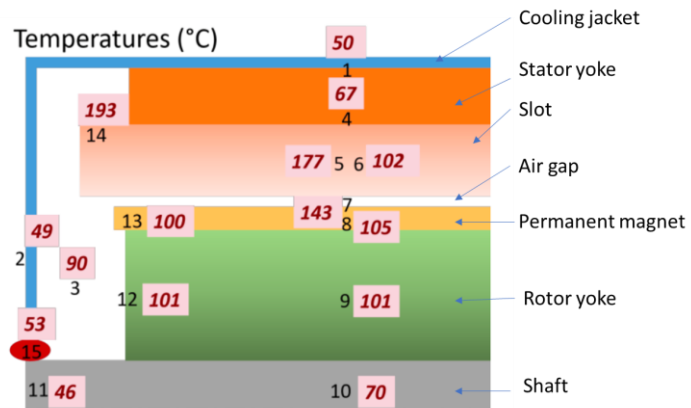


Figure 15: Resulting temperatures in different locations inside a motor. Adapted from [30].

The hot spots are located in the winding and end-winding where the thermal conductivities are the lowest [30], [32].

3.3.4 Work Package 4 (WP4)

This WP aims to design and to optimize solutions to cool the electric power converters. The cooling solution also has to provide a constant operating temperature for the whole mission of the aircraft. Climb and descent stages are the most stressful. The temperature difference between ground and flight can reach 40 °K [33]. The Capillary Pumped Loop for Integrated Power (CPLIP) cooling solution has been chosen. It suits the Power electronics In the Nacelle (PIN) configuration. Figure 16 illustrates the CPLIP concept [33]:

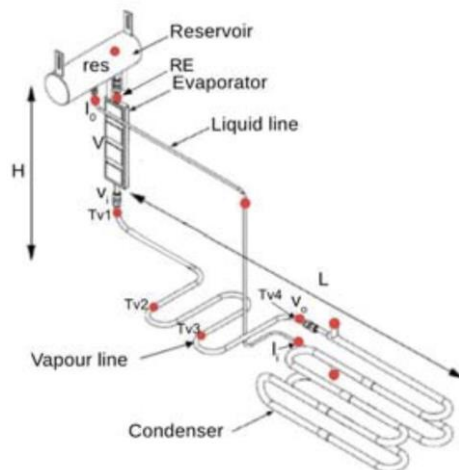


Figure 16: CPLIP concept schema [33]

The power electronic is set up around the evaporator wall. A tank delivers the liquid at ambient temperature to the evaporator. In this porous component, there is a heat exchange occurring between the power electronics and the fluid. The fluid then turns to vapour and is directed toward the condenser through the vapour line. In the condenser, the vapour is cooled and turns back to liquid. The liquid is sent back to the reservoir through the liquid line.

The choice of the design point is particularly sensitive as it influences the weight of the cooling system. It has been chosen at the beginning of the take-off and climb stage [33]. Whatever the selected power converter topology, the energy to be evacuated during the take-off and climb stage represent 44% to 45% of the energy to be evacuated in the cruise stage but in a much smaller amount of time [33].

Figure 17 gives the results obtained from an experimental test in a mission profile of a single-phase fed power converter [33]. The maximal losses to be evacuated are Q_{max} greater than 15 kW. It can be seen that the power converter temperature (evaporator wall) is maintained lower than 150 °C which is the highest temperature the components can withstand.

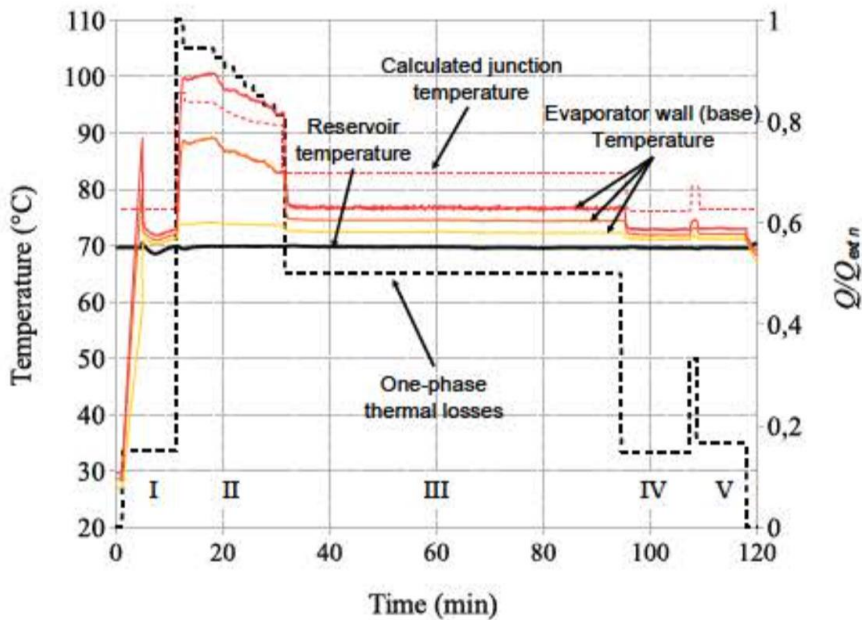


Figure 17: Diagram resulting from an experimental test in a mission profile of a single-phase fed power converter. Stages: taxi out (I), take-off and climb (II), cruise (III), descent and landing (IV), taxi in (V) [33]

3.3.5 Work Package 5

This WP deals with partial discharges (PD) that may occur. Two systems are studied by this WP: the Electrical Insulation System (EIS) of the DC busbar powering the power electronic and the motor EIS design.

3.3.5.1 DC busbar

Concerning the EIS busbar design, the main results/achievements are:

- the evidence that the risk of PD appearance in busbars is high at triple points areas;
- simulations to evaluate and to prevent the PD appearance.

The power converter topology is based on a design provided by WP2. It is made of seven busbars slats. The DC bus voltage is 2.5 kV and the insulation is made of Polytétrafluoroéthylène (PTFE) film located between the slats [34]. Such configuration results in multiple triple points busbars/PTFE/air interfaces. PD are more likely to appear at these points due to a local electric field reinforcement. Figure 18 is a schematic view of power busbars embedded inside a power converter [34].

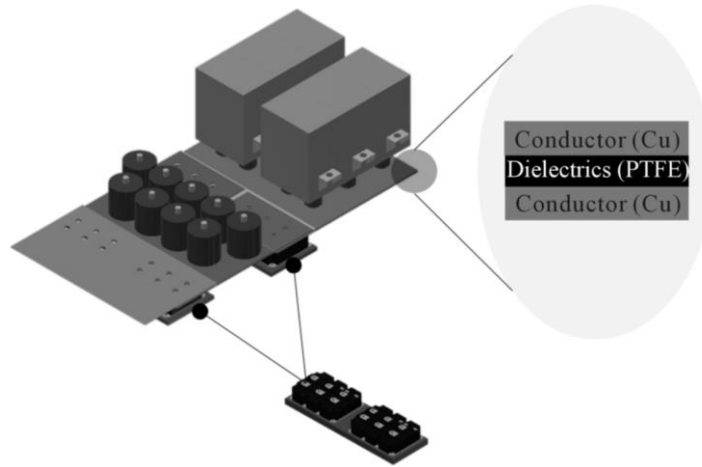


Figure 18: Schematic view of power busbars embedded inside a power electronics converter; example of triple point [34]

2D-finite elements study of a characteristic triple point has been done. It has pointed out the sensitivity of the charge accumulation in the dielectric interfaces on the air gap electric field. There are two possible scenarios:

- firstly, the charges accumulated in the insulator near the interfaces have the same sign than the conductor polarities: these are so called homo-charges. The electric field in the triple point is then reduced. The gaps are larger than 1 mm, thus the air will breakdown if the electric field exceeds 3kV/mm. Figure 19 displays the numerical results for a configuration without any dielectric charge density and with an homo-charges absolute charge density of 1 C/m^3 [34].

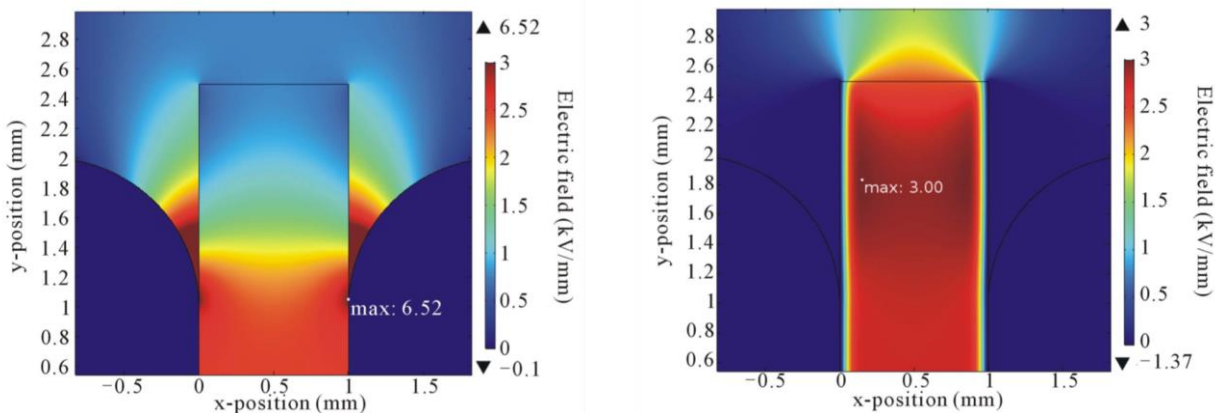


Figure 19: Simulated electric field associated to homo-charges; left) Absolute charge density of 0 C/m^3 ; right) Absolute charge density of 1 C/m^3 [34]

With the dielectric uncharged (left) the electric field in the triple point reaches the air breakdown threshold (3kV/mm). PD are more likely to occur. However, with the dielectric charged with homo-charges with an absolute density of 1 C/m^3 , the electric field in the triple point areas is decreased under

the breakdown threshold. The electric field is reinforced inside the dielectric. However, such material has a higher dielectric strength than air: classical values are 60-100 kV/mm.

- The other scenario is that the charges accumulated in the insulator near the interfaces are of opposite signs than the conductors. These are so called hetero-charges. In such case, the numerical results are less optimistic concerning PD in the triple points (Figure 20).

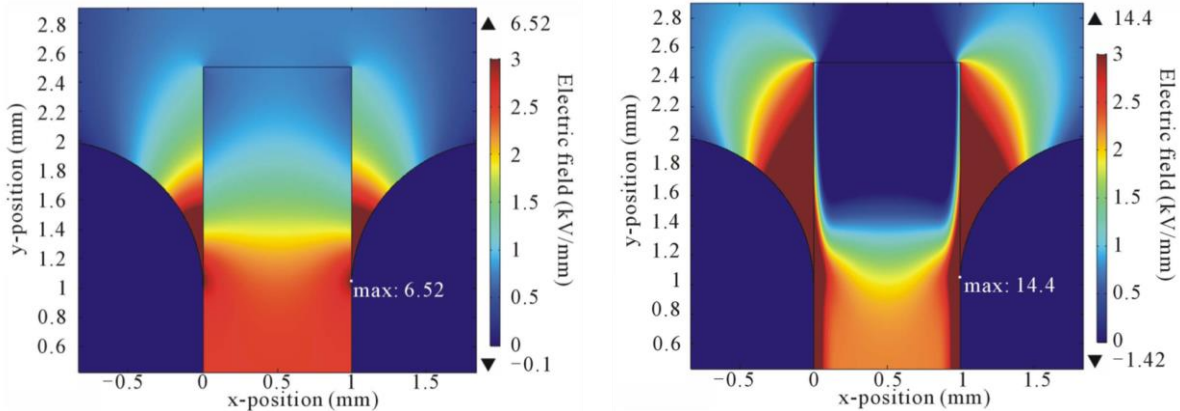


Figure 20: Simulated electric field associated to hetero-charges; left) Absolute charge density of 0 C/m³; right) Absolute charge density of 1 C/m³ [34]

In such case, the electric field is reinforced in the triple points area and the electric field exceeds the breakdown threshold.

This work has shown that the charging of the dielectric has hazardous consequences on the electric field at triple points areas. One conclusion is the special care to design a non-charged insulation system, for example by using insulators well known to accumulate a low amount of charges.

3.3.5.2 Motor Electrical Insulation System (EIS)

This task is the research subject of this PhD dissertation. The aim is to provide a tool to help the machine designers to avoid or to reduce PD that may occur in the EIS of inverter fed motors. The work has mainly been focused on the Paschen's criterion application in the context of electric motor working under aeronautics conditions.

3.3.6 Work Package 6

This WP centralises the multiple models developed by the others WP. It realizes the global optimization of the whole powertrain. From an input data set and given environmental conditions (temperature, pressure, aircraft speed,...) "surrogate" models are used to quickly assess the efficiencies and masses

from each devices to the whole powertrain. The regional aircraft structure is fixed, only the propulsive system can be modified thanks to an implicit loop as pictured in Figure 21.

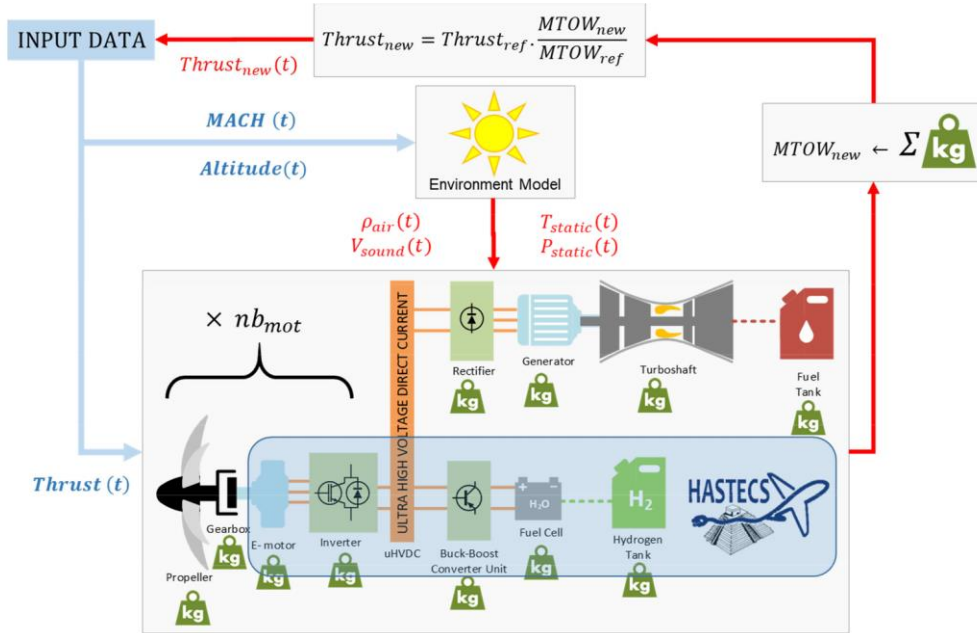


Figure 21: Implicit looped integrated process [26]

This WP has also realized a state of the art and prospects on auxiliary sources (batteries and fuel cells).

4 ELECTRIC MOTORS ELECTRICAL INSULATION

4.1 LOW VOLTAGE MACHINE

The electric insulation of electric motors is generally made of organic materials. These are the polymers; they are mainly found in the motor as foils, papers, varnishes and resins.

The primary electrical insulation of Low Voltage (LV) rotating machine stators is composed of three main insulation layers. These are the turn-to-turn, turn-to-ground and phase-to-phase insulations.

Figure 22 is a sketch of the three insulation layers of a stator.

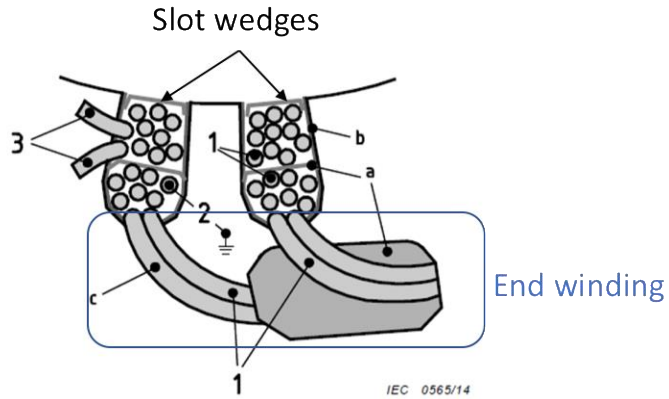


*Figure 22: Electric stresses: 1) phase-to-phase, 2) turn-to-ground, 3) turn-to-turn
Insulation layer: a) phase separator, b) slot liner, c) enamelled turn – adapted from [35]*

The slot is impregnated with a resin and generally closed with edges. The end winding insulation is reinforced. The following table gives some common materials used for the electric insulation of LV motors:

Component	Insulation Material
Enamelled wire	<ul style="list-style-type: none"> • Polyurethane • Polyether • Polyester-imide • Polyamide-imide • Poly-imide • With Self-bonding overcoat • Litz wires (for HF applications)
End winding tape	<ul style="list-style-type: none"> • Glass cloth • Polyester • Silicon Carbide Coating
Slot insulation	<ul style="list-style-type: none"> • Impregnated PET felt/film/felt • Impregnated polyaramid paper • PET film/mica/PET film
Impregnating resin	<ul style="list-style-type: none"> • Epoxy • Silicone • Polyester-imide • Polyamide-imide • Poly-imide
Wedges/closure	<ul style="list-style-type: none"> • Glass mat with epoxy resin • Glass fabric bonded with epoxy resin

Table 2: Insulating materials for low-voltage motors based on [19][36]

The choice of the material is determined by four criteria. They are given in order of importance:

- 1) Dielectric strength. Usually expressed in [kV/mm]. It represents the maximum electric field amplitude the material is able to endure. Most of the organic materials of dozens of micrometers in thickness have dielectric strength of the order of 100 kV/mm.
- 2) Maximum working temperature. It defines the maximum temperature at which the material ensures its insulating function. The best organic materials have maximum working temperature up to 240 °C.
- 3) Mechanical properties for the implementation of the material inside the stator slot.
- 4) Thermal conductivity. It characterises the ability of the material to evacuate the heat flux toward the cooling system. Organic materials have thermal conductivity of the order of 0.1-0.3 W.m⁻¹.K⁻¹.

4.1.1 Turn-to-turn insulation

It is made with a polymer enamel coating the conductor core, generally made of copper. The thickness of the enamel varies from some micro-meters to dozens of micro-meters for turn copper diameter up to 5mm [37].

Anton [38] detailed the enamel technology and realized a comparative study of the common polymers used as enamel.

The enamel is the result of a varnish being cured. The varnish is a complex mix in which are present: the solvent, a polymer precursor, the cross-linking agents and some additives.

The solvent prevents the polymer precursor from polymerizing. It represents between 60-80% of the total solution. It is mainly composed of a mix of phenol and cresylic acid. The solvent is evaporated during the curing process. Some additives such as naphtha or xylene are added to the solvent to adjust the viscosity of the varnish. The polymer precursors represent 18-40% of the solution.

The enamel overcoat is made of multiple layers which are successively polymerized at high temperature in an oven. The first layers (i.e.: the closest to the copper) goes much more in the oven than the external layers. The cross-linking is therefore not uniform in the whole enamel thickness. The process to get an enamelled wire is illustrated in Figure 23.

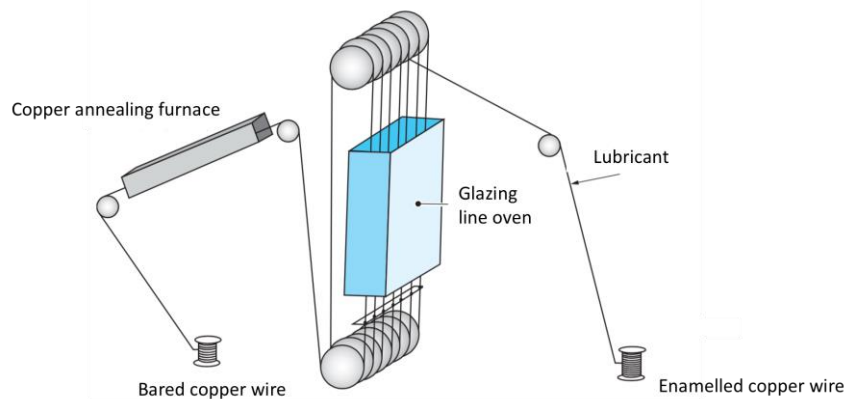


Figure 23: Enameled wires glazing line process [38]

Multiple polymers are generally found in the enamel coating. The enamel has to resist the biggest thermal stress present in a motor slot due to its location just over the copper wire, which is the main heat source. Besides, it is surrounded by the resin which impregnates the whole slot. The choice of the polymers thus strongly depends on the temperature and the chemical compatibility with the impregnation resin. The insulation power of polymers is highly affected by the temperature. They are distributed into thermal classes. They define the higher temperature at which the polymer is able to ensure its insulation function up to 20 000 hours. Some are presented in Table 3.

Thermal class	Y	A	E	B	F	H	N	-	-	-
Temperature (°C)	90	105	120	130	155	180	200	220	240	280*

Table 3: Some thermal classes [39]

(*) 280°C thermal class is obtained by adding non-organic nano-fillers in a PI matrix [40]

Here are the different materials commonly used:

- Polyvinyl formal: thermal class 120 °C, they have very good mechanical properties. They are particularly used on big round wires or flat wires in transformer application due to their good resistance to hydrolysis.

- Polyurethane (PUR): thermal class 180 °C, they are used on thin wires (from 0.02 to 2 mm). One can find them in household appliances, television or phone.

- Polyester imide (PEI): thermal class 180 °C, they are very flexible and they have a good grip on copper. They are applied on wires from 0.03 to 0.8 mm.

- Polyester THEIC (TriHydroxyEthyl IsoCyanurate): thermal class 200 °C. They are usually used as undercoat of polyamides imides in order to improve their mechanical properties (flexibility, grip) while keeping a good heat resistance. They are used on diameter from 0.5 to 5 mm.

- Polyester imide THEIC: thermal class 200 °C, they have a good heat resistance and a good chemical resistance. They are also used as undercoat of polyamides imides.

- Polyamide imide (PAI): they have a very good thermal stability, a very good resistance to thermal shock and very good mechanical properties. Used as full coat, they have a thermal class of 220 °C and are used with diameters from 0.1 to 1.3 mm. Because of their high cost, they are generally used as upper layer of polyester imides THEIC to get wires of thermal class of 200 °C with diameters from 0.1 to 5 mm.

- Polyimide (PI): they have a very good heat resistance (up to 240 °C) and a very good resistance to thermal shock. They are used on wires from 0.05 to 6 mm diameter.

These properties are summarized in Table 4.

Properties	Formal	PUR	PEI	PET-THEIC + PAI	PEI-THEIC + PAI	PAI	PI
Thermal class [°C]	120	155	180	200	200	220	240
Copper diameters [mm]	0.6 - 5	0.02 - 2	0.05 - 2	0.05 - 5	0.1 - 5	0.1 – 1.3	0.05 – 6
Electric strength (EIC V/µm)	170	180	175	180	180	180	180
Abrasion	(2)		(3)	(2)	(2)	(2)	(5)
Grip	(2)		(2)	(1)	(2)		
Flexibility	(2)					(2)	(2)
Solvent resistance	(3)			(2)	(2)	(2)	
Thermal conductivity [W.m⁻¹.K⁻¹]	Mainly between 0.1-0.3 [41]						
Properties: (1): excellent, (2): very good, (3) good, (5): very bad							

Table 4: Main properties of standard enamel wires adapted from [38]

The thermal conductivity characterizes the behaviour of a material to a heat flux. The lowest this value, the more difficult the heat flux cross over and evacuation from the winding. For comparison, the thermal conductivity of iron is $80 \text{ W.m}^{-1}.\text{K}^{-1}$. Conductivity values of standards enamel materials are very low compared to iron.

4.1.2 Phase-to-phase insulation

The phase-to-phase insulation ensures the electrical insulation between different phases in the end winding and/or into the slots (if there is more than one phase by slot). Depending on the number of different phases which overlaps and the winding configuration, such insulation has to resist up to twice a phase peak voltage.

It is mainly composed of porous fabric from aramid fibers. This porous material is impregnated with resin, during the winding impregnation step. Aramid fibers have also good both heat and humidity resistances [42].

4.1.3 Turn-to-slot insulation

The slot insulation ensures the electrical insulation between the winding and the stator slot. Mainly, the stator frame is grounded. This insulation has to be able to resist the whole phase peak voltage.

It is inserted inside the slot before the winding operation. It also protects the wires during their insertion in the slot against stator abrasion. Slot insulation is mainly formed with paper, film or flexible materials. It is also used to ensure a physical separation between the end winding and the stator slot. The common materials used are mica and/or aramid. Slot wedges are an additional protection which increases the mechanical handling of the winding.



Figure 24: Slot wedges and phase insulation seen with the winding in place; one wedge is partially inserted [43]

		Tensile strength [N/mm ²]	Operation temp. [°C]	Moisture absorb. (% by weight)	Chemical strength; Graded 0-4			Voltage strength [kV/mm]	Trade names
					Acid s	Alkali s	Organic solvent		
Insulating foils	Polyester PETP	140-160	130	0.5	2	1	4	150	Mylar Melinex Hostaphan
	Polyimide	180	220	3	3	0	4	280	Kapton
	Polysulfone PS	90	180	1.1	3	3	1	175	Folacron PES
Fiber insulator	Cotton fibers	250-500	105 (impregnated)	10	1	2	4	-	-
	Polyester fibers	500-600	155	0.4	2	1	4	-	-
	Glass fibers	1000-2000	130-200 (depending the impregnant)	-	4	3	4	-	-
	Aramid paper	1250	210	7-9	3	3	4	20 (1min, 50Hz test)	Nomex

Table 5: Characteristics of foils and fiber insulators [39]

4.1.4 Slot impregnation

The slot is filled with a resin. It aims to electrically insulate the whole slot. It also holds the winding in place and improve the heat dissipation toward the stator cylinder head. Impregnation resins are mainly composed of both solvent and polymer precursor. The solvent prevents the precursor from polymerizing. That is the reason why it is necessary to heat the resin during impregnation. The solvent evaporates and the precursors assemble to form the polymer.

The main function of the resin is to mechanically hold the winding in place (to avoid damage due to friction between the winding and the core) and to protect it against moisture, pollution and dust in the case of an open motor. It is not in direct contact with the copper so it does not have to resist such a high temperature as the enamel. It has to be chemically stable.

Several process exist to fix the resin. They have been documented by [44] in his PhD dissertation:

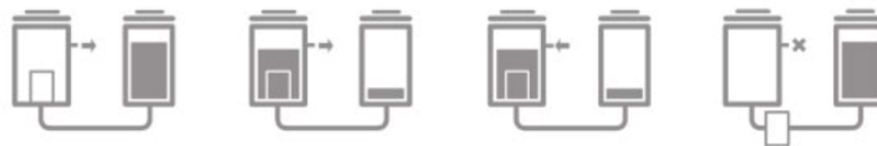
- **drop by drop method.** The resin is slowly deposited on the winding so that it impregnates the winding by capillarity. It is the most employed method in the industry. However, it is quite possible that some parts of the winding may not well be impregnated.

- **brush method.** The impregnation is done during the manufacturing of hand-made windings. The resin is repeatedly applied with a brush. The repartition of the resin is more uniform than the one obtained with the drop by drop method. The resin is directly put in the middle of the winding. This method is only applied to specific machine for small series production.

- **soaking method.** The machine is slowly lowered in a tank full of resin. It stays here a while so that the air trapped between the wires is extracted. The machine is then slowly pulled up and drained.

- **Vacuum Pressure Impregnation (VPI) method.** It is composed of different steps:

- Preheating: the motor is placed in an oven that heats it and allows moisture to evaporate. This will also help the resin better penetrate the material;
- Dry Vacuuming: the motor is removed from the oven and placed into a vacuum chamber to remove air and any remaining moisture;
- Filling: the chamber is filled with resin, coating the part and filling in all the gaps of the EIS;
- Wet Vacuuming: the vacuum levels is reduced and hold it for a set period of time;
- Pressure: the pressure is increased within the chamber using dry air (nitrogen for example) to allow deeper penetration of the resin;
- Draining: the pressure is vented and the motor is removed;
- Curing: the motor is finally placed into an oven to cure the impregnating resin.



- | | | | |
|---|---|--|---|
| 1.
Transfert
preheated
object to
vacuum vessel.
Pull vacuum. | 2.
Transfert resin
under vacuum
(the vacuum
pump must be
closed). Allow
time to soak. | 3.
Release vacuum.
Apply positive
pressure. | 4.
Transfer resin back to
storage tank. Put
object back in oven
and cure. |
|---|---|--|---|

Figure 25: Vacuum impregnation steps given by Von Roll [45]

This method is found to be better than the others.

- double VPI: the vacuum impregnation steps are done twice to reinforce the holding of the winding. It is used when a high quality of impregnation is required.

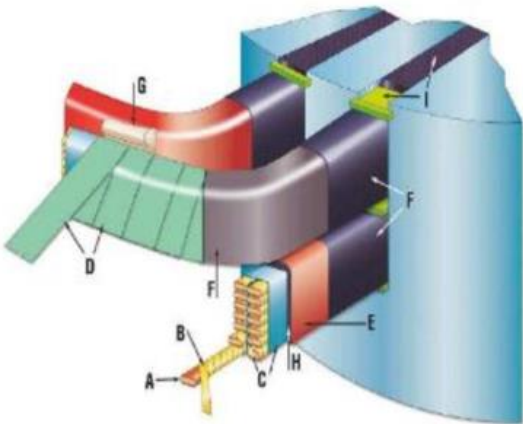
Table 6 gives the common varnishes characteristics.

	Mechanical strength; Grades 0-4	Operation temperature [°C]	Moisture resistance; Grades 0-4	Chemical strength; Grades 0-4	Typical materials
Impregnating varnishes	3	155	3	3	Alkyd polyester
	1	180	3	3	Silicone epoxy
Impregnating resins	3	155	3	3	Polyester alkyd Epoxy
	4	180	4	4	Polyester Epoxy
Coating (surface) varnishes	2	130	3	3	Alkyd Polyruethane
	2	155	4	4	Alkyd Polyruethane
	1	180	4	3	Alkyd Silicone Epoxy

Table 6: Characteristics of varnishes and resins [39]

4.2 HIGH VOLTAGE MACHINE

Machines powered with a phase to phase voltage higher than 700Vrms are considered as high voltage machines [35]. When the applied voltage is more than a few kV, these machines have to work doubtless with partial discharges. Their EIS is consequently reinforced by using non-organic materials. Figure 26 illustrates a classical EIS used in such high voltage machines.



- Winding wire (A)
- Conductor insulation (B)
- Stack insulation (C)
- Main wall insulation: Mica tape (D) + VPI resin (H)
- Conductive paint or tape (F)
- Stress grading paint or tape (F)
- Finishing or sealing tapes (E)
- Bracing materials (G)
- Slot wedging materials (I)

Figure 26: High voltage machine electrical insulation system [46]

In most high voltage motors the winding is composed of enamelled copper bars. It is well organized in the slot. Bars reduce the end winding congestion outside the slot. For high frequency application, the bars are subdivided. This is to prevent frequency losses such as skin and proximity effects.

Some specifications for high voltage motor insulation are given in [39]. Mica tape wound is widely used in layers around the conductors due to its very good partial discharge resistance. On the end windings, stress grading tapes are applied on the bars extremity close to the slot end. The most common stress grading materials are a semi-conductive silicon carbide tape or paint. It aims to progressively reduce the electric field at the area where the stator cylinder head, the insulation tape and the surrounding air meet together (triple point). That is a weak spot in the system which is susceptible to easily lead to electric discharges [34].

The groundwall insulation is usually made out from natural resins and mineral used as fillers. The resins include refined petroleum oils, waxes, asphalts, etc. Minerals include mica, asbestos or quartz [47].

In this PhD dissertation, we consider that the level of the applied voltage (i.e.: 2.5 kV) allows to find solution leading to PD-free working conditions. This is the reason why the following chapters will deal with an organic EIS. However, if partial discharges appear, the methodology that will be developed may be applied just by changing both size and permittivity of the EIS components.

5 THERMAL ASPECT

5.1 COOLING STRATEGIES

There are two main strategies to cool an electric motor. The first one consists in evacuating the heat on the stator cylinder head. A thermal exchange takes place between the hot stator cylinder head and the coolant. The coolant can either be a gas such as air or a liquid such as water. In the case of a high power density electric motor for aeronautical application, a water jacket seems to be the best suited solution [30]. An example of water jacket configuration extracted from [48] is presented in Figure 27. The housing oil channel is used to deliver the oil to the stator oil channels. After running in the channels, the oil is cooled at the end windings and goes back to the tank.

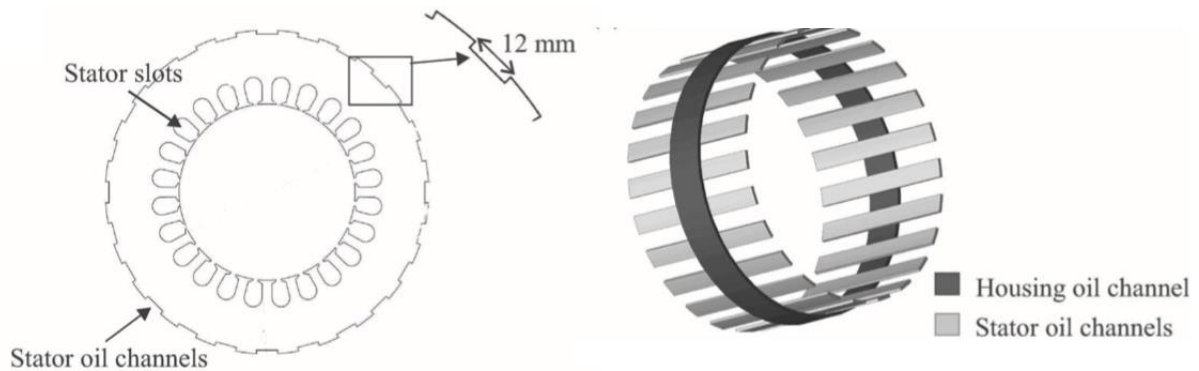


Figure 27: Left) Stator design; right) Cooling system structure [48]

The thermal conductivity of polymers used in the electrical insulation of motors is mainly between $0.1\text{-}0.5 \text{ W.m}^{-1}\text{.K}^{-1}$. That represents a real difficulty when using external cooling system such as water jacket. The heat flux has to cross the enamel overcoat, the impregnation resin and the slot liner. Such low thermal conductive materials retain the heat inside the slot and then reduce the cooling efficiency.

Another strategy consists in directly cooling the conductors inside the slot. The authors in [49] presented a Direct Winding Heat exchangers (DWHX) made using a 3D printer (see Figure 28).

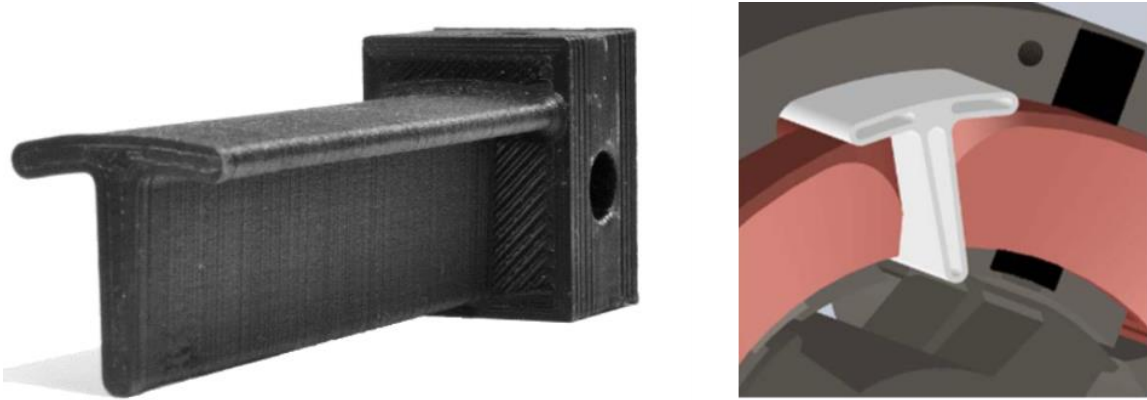


Figure 28: left) 3D-DWHX CF-Nylon prototype for heat transfer testing; right) 3D-DWHX shown in the stator slot of a motor equipped with permanent magnets [49]

The numerical results of the maximum temperature in several spots obtained by using only water jacket, only the 3D-DWHX and the combination of both are presented on Table 7:

	Maximum Temperature [°C]		
	Winding	Stator iron	Magnet
Water Jacket	30.1	22.5	21.1
3D-DWHX	58.1	67.6	37.3
Combined	16.9	15	18.6

Table 7: Comparison of stator cooling strategies involving 3D-DWHX [49]

The worst performance is obtained by using 3D-DWHX alone. This can be explained by the low thermal conductivity of the Nylon constituting the DWHX and of the winding. However, significant temperature reduction is obtained combining both cooling solutions, especially in the winding.

5.2 THERMALLY ENHANCED POLYMERS

Hitachi and Hitachi Chemical has developed an enhanced thermal epoxy resin [50]. They change the amorphous molecular structure into a crystal-like structure (see Figure 28). These liquid crystal molecules are called *mesogens*. They form a highly ordered structure which increase both thermal conductivity and flexibility of the resin. The enhanced thermal conductivities can reach $0.96 \text{ W.m}^{-1}\text{.K}^{-1}$, which is up to 5 times greater than classic epoxy resin.

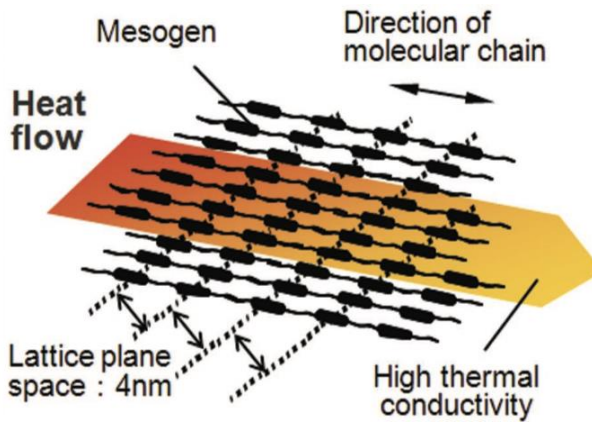


Figure 29: Structure of a new high thermal properties epoxy resin [50]

The authors in [48] compared the maximal temperature in a water cooled machine using three different impregnation materials. The main thermal and electric properties are summarized in Table 8.

Materials	Varnish	Epoxylite	SbTCM
Thermal conductivity [W.m ⁻¹ .K ⁻¹]	0.25	0.85	3.20
Dielectric strength [kV/mm]	80	20	10

Table 8: Materials used by [48]

SbTCM stands for silicone-based thermally conductive material. The simulation results obtained for a coolant flow rate of 2.5 L/min are presented on Figure 30. The temperature decrease compared to classic varnish at 3.2 A is of around 20% for Epoxylite and 30% for SbTCM. The current amplitude is at the stator winding.

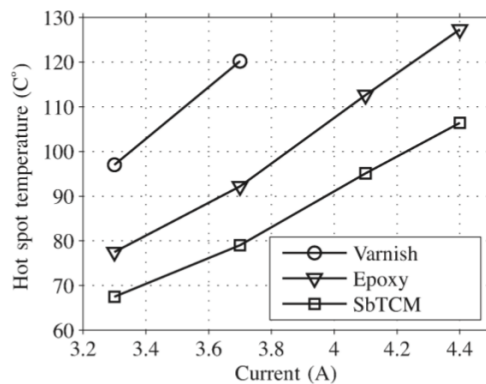


Figure 30: Simulation results: comparison between the hot spot temperature in electric machines using different impregnation materials at different current magnitude (at the stator winding). The inlet coolant flow rate is assumed to be 2.5L/min [48]

The drawback of such efficient thermal properties for SbTCM is a reduction of a factor 8 of the dielectric strength compared to classic varnish. SbTCM looks attractive but for some application, such as high power density motors, its dielectric strength may be too low.

Other high thermal conductivity composites have been reported by [51] (Table 9).

Properties	PA 66		PPS		PPA		LCP		PEEK	
	Std	Enh	Std	Enh	Std	Enh	Std	Enh	Std	Enh
Thermal conductivity [W.m ⁻¹ .K ⁻¹]	0.24	20-32	0.08-0.29	10-20	0.15	20	0.0837	20	0.25	10
Tensile strength [MPa]	95	65-117	48-86	45-70	76	44-83	110-186	80	70-103	70
Elongation %	15-90	0.75-1.5	1-6	0.31-0.75	30	0.6-1	1.3-4.5	0.25	30-150	0.5

Table 9: Comparison of standard (Std) versus thermally enhanced (Enh) polymer composites material properties [51]

As shown in Table 9, very high thermal conductivity are reached. However, the enhanced composites are much more mechanically fragile than the standard ones: the elongation is much lower. The enhanced materials are closer to ceramics than polymers.

On the other hand in [52] the Direct Current electric properties of polyimide/boron nitride (PI/BN) nano-composites for a large range of nanoparticle size and filler content have been investigated. It was shown that an efficient control of the charge carrier mobility allows a huge enhancement of the insulating properties of PI films.

6 IMPACT OF POWER ELECTRONICS

6.1 PULSE WIDTH MODULATION (PWM) BASIS

Power electronic offers a wide range of possibilities in machine control. AC motors now replace DC motors in application that require to control the machine rotation speed. AC motors are less expensive in particular due to less wearing parts. However, the power has to be converted from DC to AC. This is done via an inverter. Figure 31 illustrates such a classic electromechanical chain.

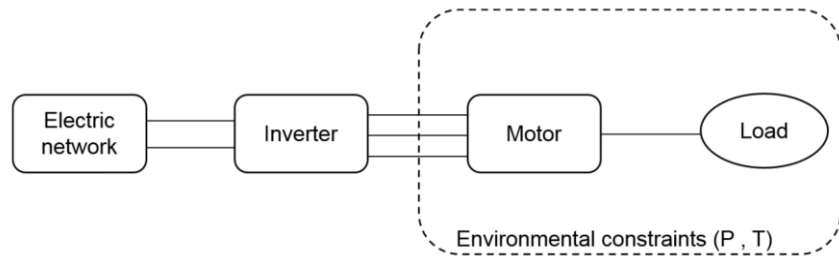


Figure 31: Diagram of an electromechanical chain [53]

If one considers the application of an electric aircraft, the load would be a fan. In case the motor is not pressurized, the group composed of the motor and the fan will be submitted to pressure (P) and temperature (T) variations.

An example of classic three phase inverter architecture is presented in Figure 32.

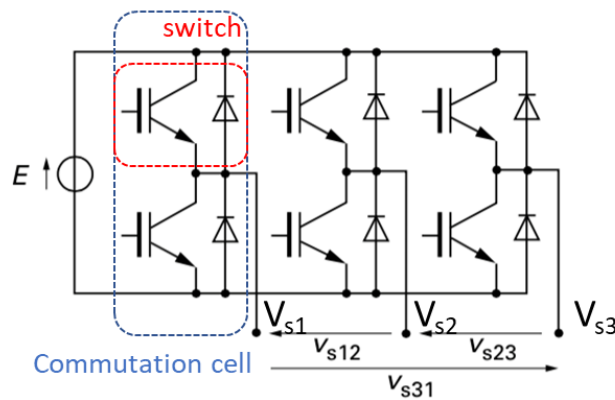


Figure 32: Classic three-phase inverter based from [54]

It is composed of three commutation cells. One cell is made of two switches. A switch is composed of a switching semi-conductive component, such as MOSFET or IGBT, and its anti-parallel diode. The two switches composing a cell are complementary. When the one at the top is ON (i.e.: the electric current can flow through it) the one below is OFF (i.e.: the electric current cannot pass). A commutation function f_m is defined. It equal either 0 or 1 depending on which switch is ON or not. So, for the commutation cell on phase 1, the output voltage is:

$$V_{s1} = f_{m1} * E$$

One of the most common command of PWM is the intersective one. It consists in comparing the modulant to a carrier signal. The modulant defines the shape of the wanted output signal. The carrier generally has a triangular shape. Its frequency is much higher than the modulant frequency. Figure 33 illustrates the principle of three-phase sinusoidal PWM.

Two sinusoidal waveform modulants signals are represented. These are the ideal voltage on phases 1 and 2. The phase shift between the two signals is 120° . The output of f_{m1} is equal to 1 if the phase 1 modulant has a larger amplitude than the one of the carrier and 0 otherwise. It is the same for f_{m2} but comparing the phase 2 modulant to the carrier. The frequency of f_{m1} and f_{m2} pulses is constant. Only the width of the pulse changes. The phase to phase voltage is simply the difference of the cells output voltages. So, the resulting modulated phase to phase voltage between phase 1 and 2 is obtained by subtracting the f_{m1} and f_{m2} signals.

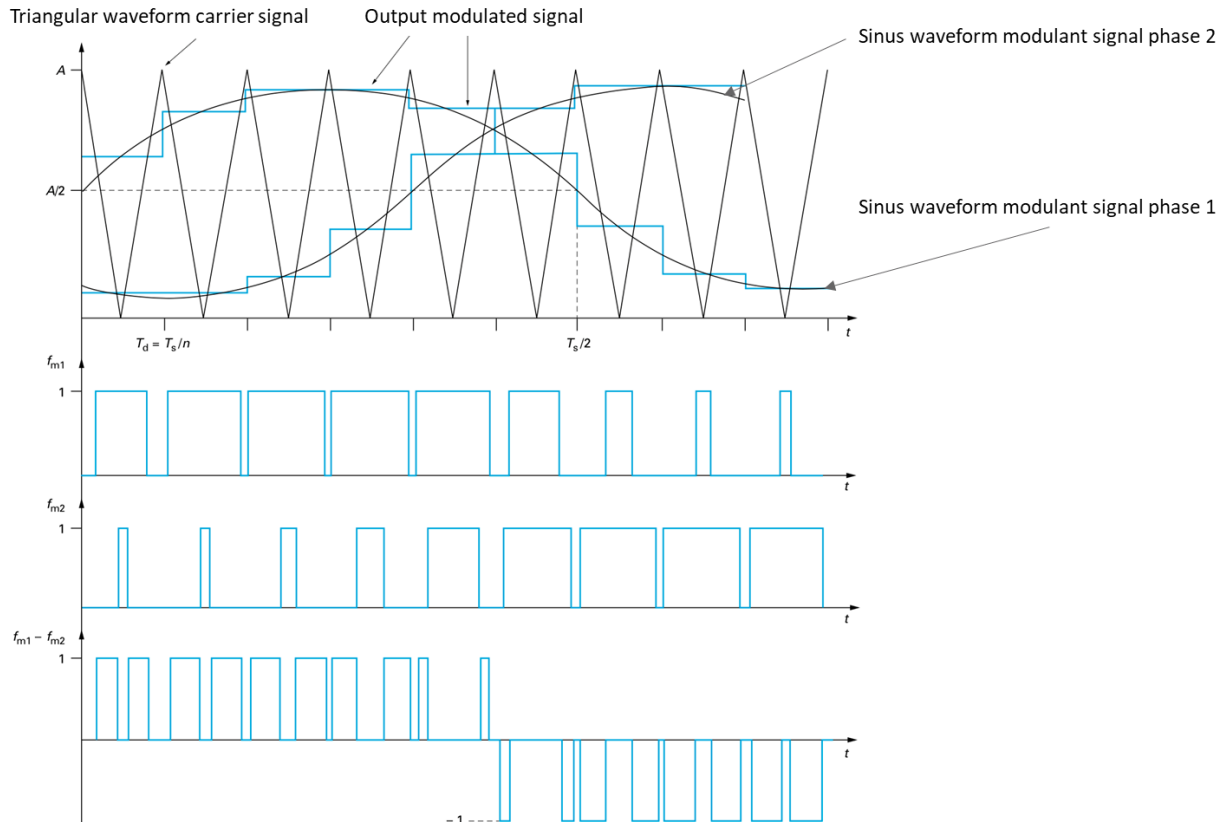


Figure 33: Example of three-phase sinusoidal PWM based from [54]

6.2 POWER FEEDING CABLE

The power cable connects the inverter to the motor. It has an impact on the overshoot that happen at the motor terminals. This cable is generally modelled using a transmission line harness [53],[55].

Figure 34 illustrates the single conductor transmission line model. It corresponds to a phase-to-ground connection. It is a repetition of infinitesimal elements. The number of elements to used depend on the line length and the frequency of the output inverter signal.

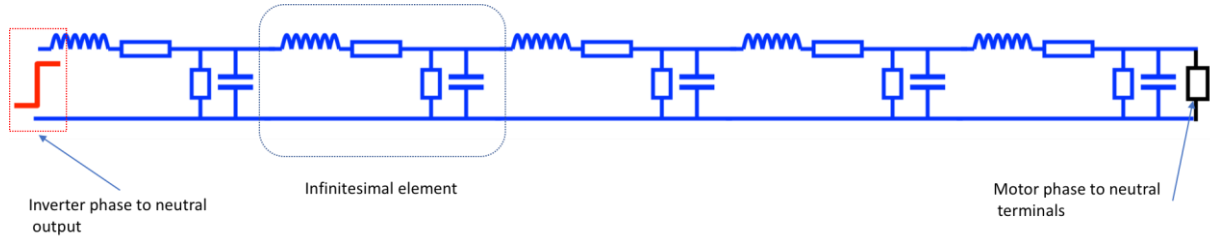


Figure 34: Transmission line phase to neutral model

Figure 35 details the constitutive elements of an infinitesimal line element. The line behaves as a global inductive behaviour modelled with a per-unit-length inductance (L^*dx). Joule's losses are modelled by a per-unit-length resistance (R^*dx) in serial with the per-unit-length inductance. The capacitive coupling between the line and the ground is modelled connecting a per-unit-length capacitor (C^*dx). The dielectric losses in the insulation of the line are modelled with a per-unit-length resistance (G^*dx) in parallel with the line capacitor.

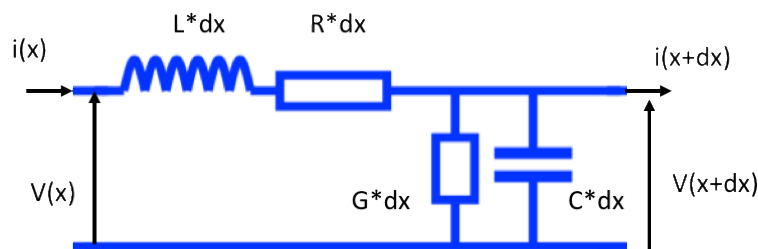


Figure 35: Transmission line elementary cell

Let us designate by Z_c , Z_m and Z_i the impedances of respectively the power cable, the motor and the inverter. As these three impedances are different, there are reflexions of the input voltage waveform in the cable. At each time step, the voltage at a point along the cable is the sum of the reflected voltage waveforms toward the inverter and toward the motor. The reflexion of the voltage waveform toward the inverter output is characterized by the reflexion coefficient Γ_{ri} :

$$\Gamma_{ri} = \frac{Z_i - Z_c}{Z_i + Z_c} \quad Eq\ 1$$

The reflexion of the voltage waveform toward the motor is similarly characterized by the reflexion coefficient Γ_{rm} :

$$\Gamma_{rm} = \frac{Z_m - Z_c}{Z_m + Z_c} \quad Eq\ 2$$

The impedance of the cable Z_c is function of its dimensions. It can be computed from both its per-unit-length inductance L (H/m) and per-unit-length capacity C (F/m):

$$Z_c = \sqrt{\frac{L}{C}} \quad Eq\ 3$$

The voltage at the motor terminals is submitted to damped oscillations. The first oscillation has the biggest amplitude. Figure 36 adapted from [56] presents the phase-to-ground and first stator coil maximum voltage amplitudes. It can be seen in this example that the overshoot can reach 1.5 the DC voltage bus for a cable of 25m.

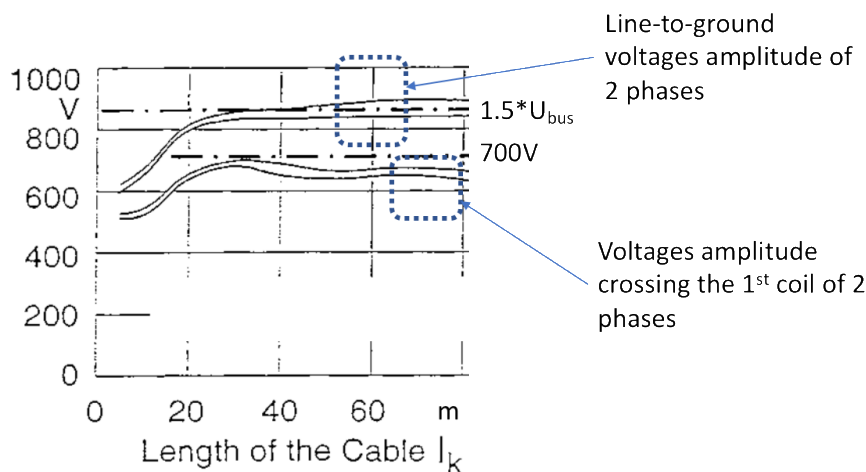


Figure 36: Maximum motor terminal voltage during PWM inverter operation depending on the cable length. Pulse frequency 9kHz, $U_{bus}=560V$, 4kW induction motor, rise time $t_r=100ns$. Adapted from [56]

The authors in [57] has proposed an improved model for computing the phase-to-phase voltage overshoots at a motor terminals. An equivalent two phase model of the electromechanical chain (inverter+cable+motor) is considered (Figure 37), where j is the complex operator and w is the angular frequency. The model is composed of classic RLCG($j\omega$) elements and a propagation function $\gamma_c(jw)$.

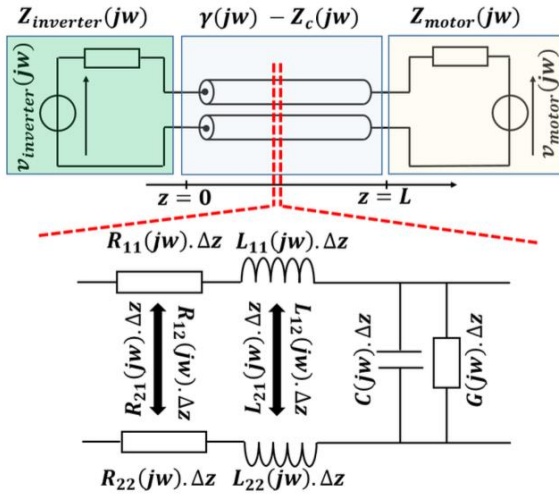


Figure 37: Proposed equivalent two-phase model of an electromechanical chain [57]

Figure 38 presents the computed phase-to-phase motor terminals overshoots as a function of the cable length. Different transistor gate resistance (R_g) values were used. This resistance modulates the output rising time. The biggest the R_g value, the slowest the rising time. It can be seen that the phase-to-phase voltage overshoot increases considerably for cable length higher than 2 m. For the biggest R_g values, it happens for length superior to 3 m. Besides, compared to Figure 36, the phase-to-phase high overshoots occur for cable length much shorter than in the case of phase-to-ground or coil-to-ground overshoot. For phase-to-phase, one can consider a critical cable length of 2 m whereas for phase-to-ground and coil-to-ground the critical cable length is about 20 m.

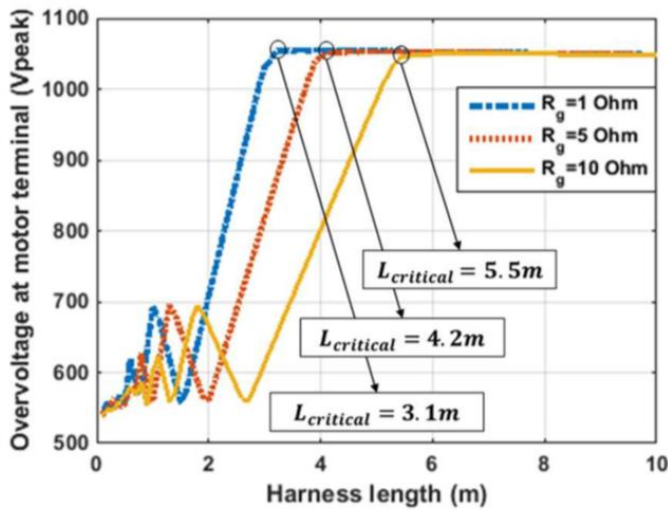


Figure 38: Maximal overvoltage at motor terminals for different harness lengths, obtained by simulation using trapezoidal inverter waveforms [57]

6.3 FREQUENCY INCREASE

New semi-conductive components based on SiC and GaN technologies permit power electronics to switch higher levels of voltage in shorter time than classic silicon components [58]. Besides, SiC components have a bigger energy gap. That means that at a fixed temperature, an electron in a SiC component will need more energy to cross the gap than in a silicon component. Therefore, SiC technology enables to work at higher temperature [59].

The rise of inverters switching frequencies lead to faster rising time on the machine terminals. It is the time interval in which the voltage amplitude goes from 10% to 90% of the peak voltage. Figure 39 illustrates an incoming voltage front wave at motor terminals fed by a PWM inverter.

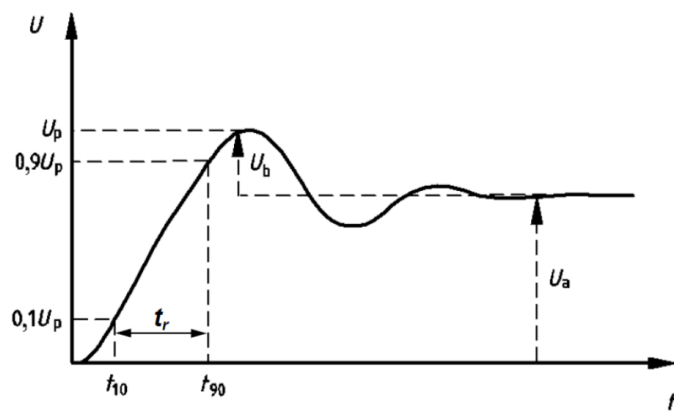


Figure 39: Voltage front wave at a machine terminal fed with PWM inverter [35]

The author in [60] has investigated the impact of the voltage front coming from an inverter over the overshoot at the stator winding. A 41 turns coil has been powered by a pulse generator with rising times of 10 ns and 85 ns. The results are displayed in Figure 40. It can be seen that for the front of 10 ns the overshoot is 1.73 times the DC bus voltage. However, there is barely no overshoot for a slower rising time of 85 ns.

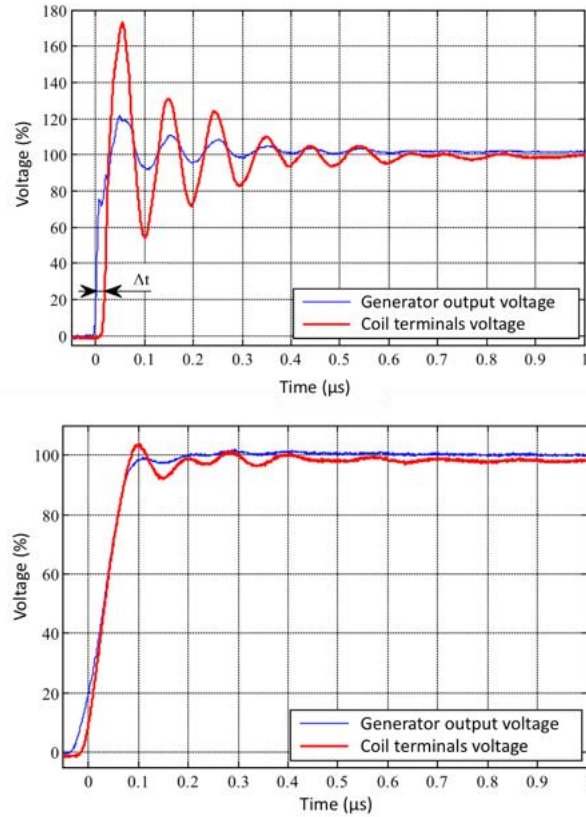


Figure 40: Voltage at a 41 turns coil terminals; top) rising time 10ns; below) rising time 85ns [60]

An evaluation of the overvoltage at the motor terminals as a function of both rising time and cable length is proposed in EIC Standard (60034-18-41). On Figure 41, the overvoltage factor defined by the ratio of the phase-to-phase peak voltage over the pulse voltage is given versus cable length and rising time. The results obtained by [57] on Figure 38 are coherent with the EIC Standard evaluation.

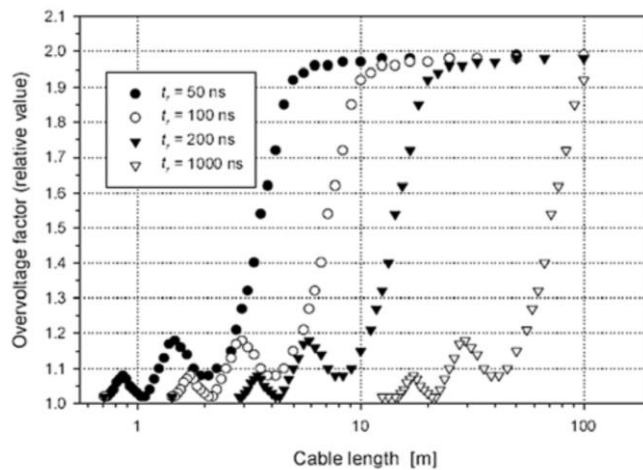


Figure 41: Overvoltage ratio in function of cable length and rising time proposed in EIC Standard (60034-18-41)

However, it is no more the case when considering fast switching frequency of a SiC inverter. A complex ringing phenomena may happen for cable length lower than 3 m [61]. This ringing phenomena is attenuated with the increase in the power cable length. Figure 42 illustrates the overvoltage at the motor terminals powered with a silicon based inverter (dashed blue lines) versus a SiC inverter (red line).

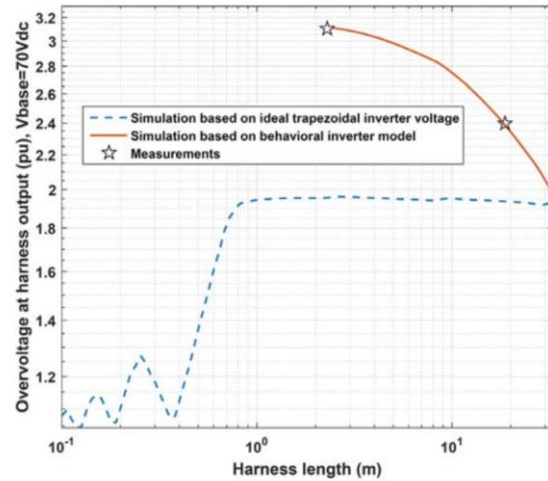


Figure 42: Overvoltage ratio as a function of both cable length and rising time (dashed blue curve: $tr=50\text{ns}$, red curve: $tr=8\text{ns}$) [61]

6.4 VOLTAGE DISTRIBUTION

Figure 43 presents the voltage waveforms measured between 5 coils constituting one phase. A step voltage amplitude E has been used. The coil number one is the first to receive the incoming voltage front. The first coil receives a much bigger overshoot (top). After the transient regime the voltage is uniformly distributed between the coils (below). However, during transient, the voltage between the coils can be of the same magnitude than the step voltage.

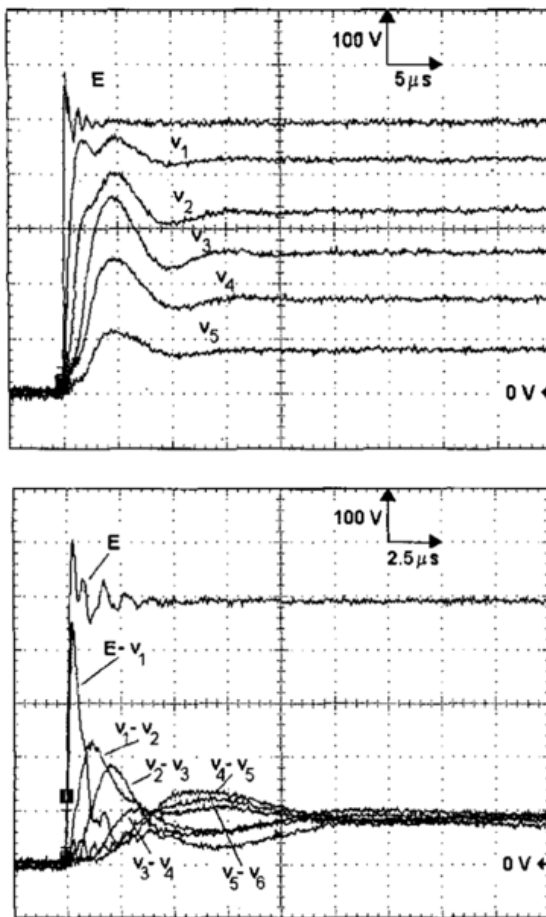


Figure 43: Overvoltage measured in a stator coils. Top) voltage distribution; Below) voltage between coils turns [62]

The voltage crossing the first coil as a function of the incoming front rising time has been investigated by [56]. It is expressed as a percentage of the phase-to-neutral motor terminal voltage. Figure 44 shows that for rising time lower than 50 ns, the first coil is susceptible to get more than 70% of the maximum phase-to-neutral motor voltage.

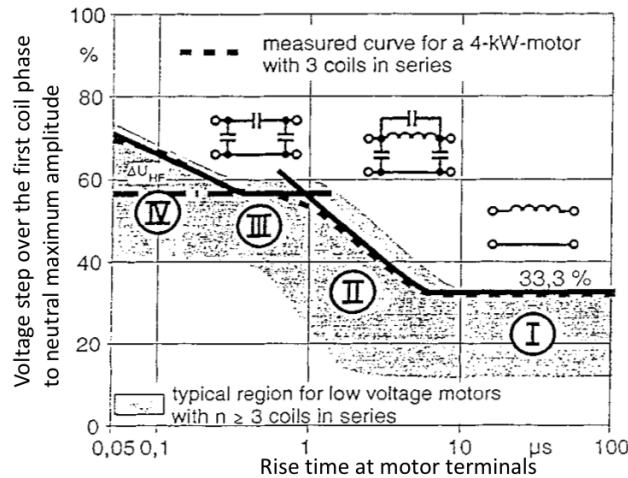


Figure 44: Percentage of the voltage across the first coil phase as a function of the rise time [56]

Works have been done to evaluate the non linear voltage repartition within the winding. The author in [60] modelled a coil by using a RLC circuit model. The parameters have been determined either by experimental measurements or 2D-finite elements computation. Figure 45 compares the results obtained with the RLC circuit and the experimental measurements. A 41 turns coil is considered. It is powered by a 300V DC bus voltage. The top figure shows the response of the coil terminals to a voltage front. The bottom picture represents the maximal turn to turn voltage drop obtained between turns 4 and 9. The RLC model provides a good evaluation of the first peak.

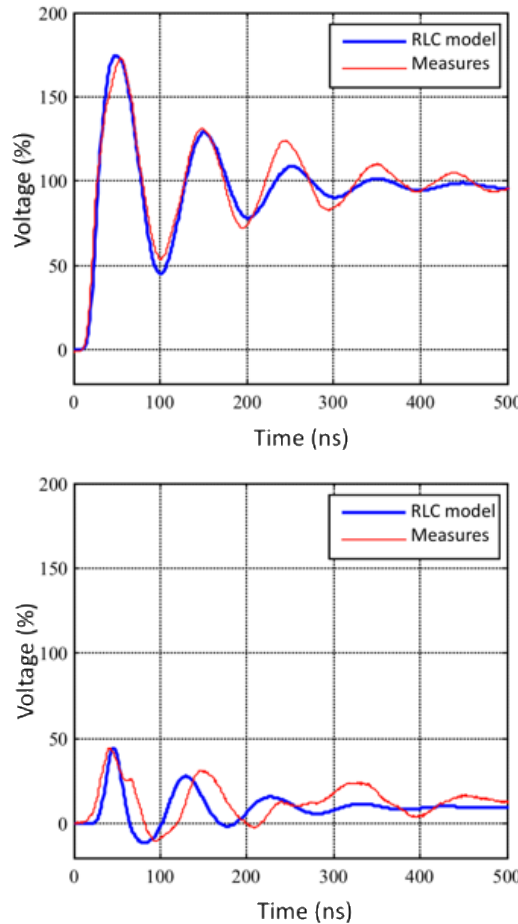


Figure 45: top) voltage at a 41 turns coil; below) voltage drop between turns 4 and 9 (% of 300V DC bus voltage) [60]

Both motor terminal overshoots and non linear voltage distribution within stator winding in transient regimes are the main cause of partial discharges (PD) appearance. In the next chapter, the behaviour of PD will be investigated. It aims to a better understanding of the phenomenon in order to evaluate PD on stator winding of inverter fed motors.

This chapter has presented the implication and challenges for more electric aircrafts. It has introduced the serial hybrid architecture under study for the HASTECS project. The insulation of the stator of an electric machine has been detailed. The impact of power converter switching frequency and of the power harness length on the voltage distribution in the winding has been pointed out. The next chapter presents the partial discharges and how they are affected by the components of the powertrain.

Chapter 2: Physics of Partial Discharges (PD)

Chapter 2: Physics of Partial Discharges (PD)

This chapter is dedicated to Partial Discharges (PD). It will start with the definition of a PD and the explanation of the mechanism which ignites it. Then, the experimental techniques to detect and measure PD activity will be presented. The effect of aeronautical environment on PD will be then considered. Finally, the principle of common numerical models to evaluate PD will be introduced.

1 DIFFERENT KINDS OF DISCHARGES

There are different ways to classify electric discharges. For instance in [63] the discharges were classified depending on their nature. The nature of the discharge varies depending on the voltage and current characteristics.

Another way to sort discharges is to classify them by the location where they take place. In [64] the discharges are sorted in four main categories: inner discharges, surface discharges, corona discharges and treeings. Treeings take place during ageing, so that this kind of discharge will not be considered in our study. Figure 46 illustrates the three kinds of discharges that may take place in machines during a PDIV measurement.

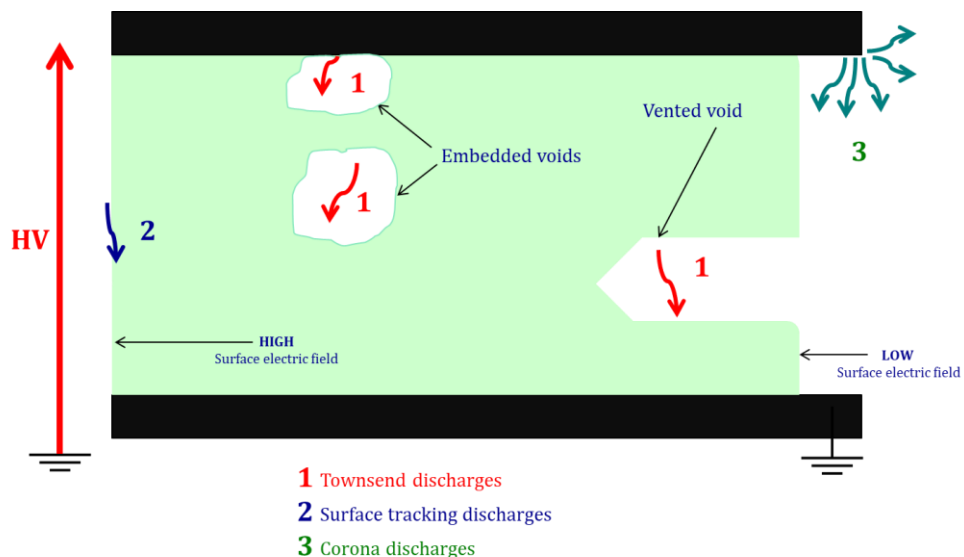


Figure 46: Different kinds of discharges depending on their location: 1) Townsend discharges in both embedded and vented voids, 2) surface tracking discharges, 3) corona discharges

In this paragraph the discharges sorted in the way of [64] are developed.

1.1 DISCHARGES IN NON-VENTED CAVITIES

These discharges happen inside the insulation material. It is due to the presence of defects in the insulator (Figure 47). These defects can be introduced during the manufacturing process (air bubbles) or during the polymer aging (delamination).. Additional defects may be introduced during the winding operation mainly because of mechanical stress. Besides, at working conditions, there can be displacement of insulating materials due to both vibration and thermal cyclings. Air gaps are then introduced between insulators and metallic parts of the EIS. As these gaps are not vented (they are embedded inside the EIS), PD are not sensitive to the environmental working conditions (temperature, humidity, dust, fluids, ...).

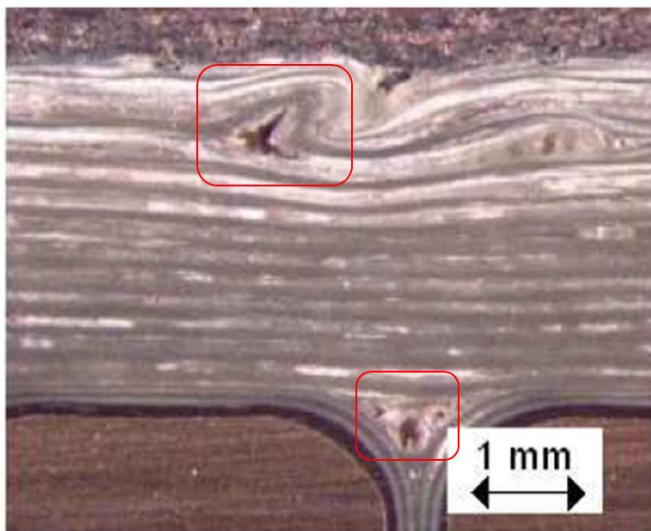


Figure 47: Mica insulation showing various defects (red rectangles) – adapted from [65]

The PD activity causes the insulator structure damage by ions bombardments, heat, physico-chemical attacks, UV and other radiations effects. With the repetition of PD, electrical trees can grow inside the polymer (Figure 48). At term, some branches go through the whole insulator thickness, leading to its electric breakdown.

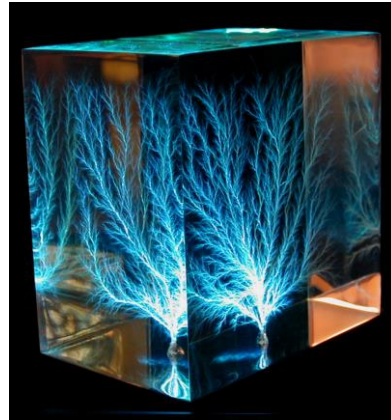


Figure 48: 3D electrical treeing in a block of clear acrylic [66]

In the presence of humidity inside a hydrophilic insulator, so called water treeing are ignited at much lower electric field amplitude. The author in [67] reported an amplitude around 10 kV/mm for water treeing and around 100 kV/mm for normal treeing.

1.2 DISCHARGES IN VENTED CAVITIES

Most of electric motors are not hermetic. That means that the air is free to circulate all over the stator winding and that it is submitted to the external air. The authors in [68] investigates the impact of air flow on a two-dimensional array of integrated coaxial micro-hollow coplanar DBD in air at atmospheric pressure. It is shown that the discharge is considerably impacted by the air flow as presented on Figure 49, as this air flow modifies the physics on the insulator surface.

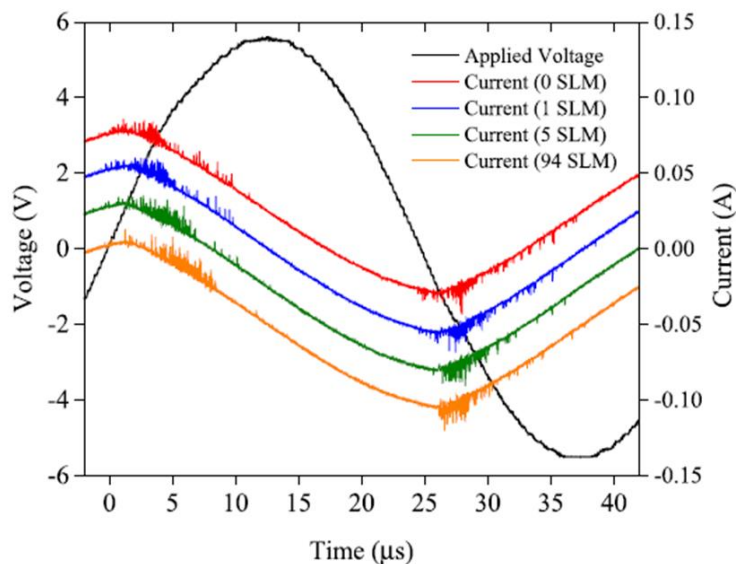


Figure 49: Typical current and voltage waveforms of the 2D-micro-discharges in air. The peak-to-peak applied voltage is identical for all the flow rates [68]

In [69] the impact of pressure on the stator winding PDIV was investigated. Figure 50 indicates a decrease of PDIV when the pressure decreases.

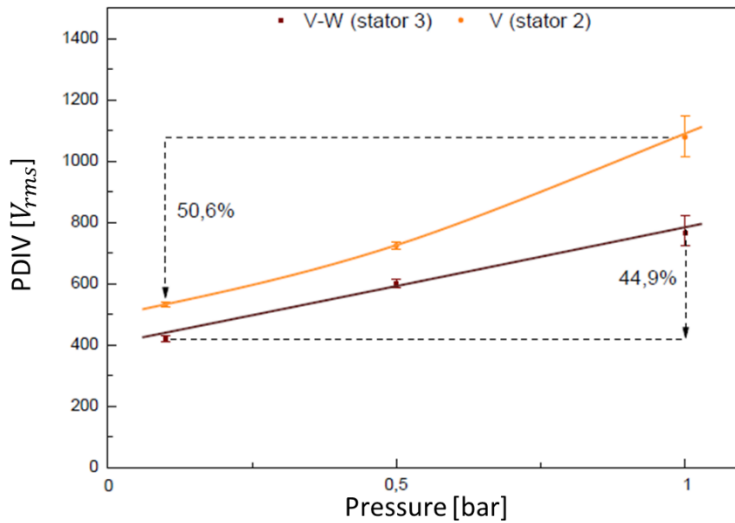


Figure 50: PDIV as a function of pressure (temperature 25°C, relative humidity 50%) - 2 stators are tested [69]

In our research project, an open motor will be considered. So the impact of environmental conditions on PDIV have to be taken into account. These are detailed further.

1.3 DISCHARGES ON THE SURFACE

These kind of discharges occur when a high tangential electric field appear at the insulator surface (surface tracking PD type). If contaminants, moisture,... are present on the insulator surface, discharges can be triggered with lower electric field. This phenomenon may be increased when it takes place at a triple point (in an area where air, polymer and metal are present). The partial surface discharges propagate on the insulator surface and cause damage on it (Figure 51). When the propagation link two conductors, the discharge switches from a partial to a total one.

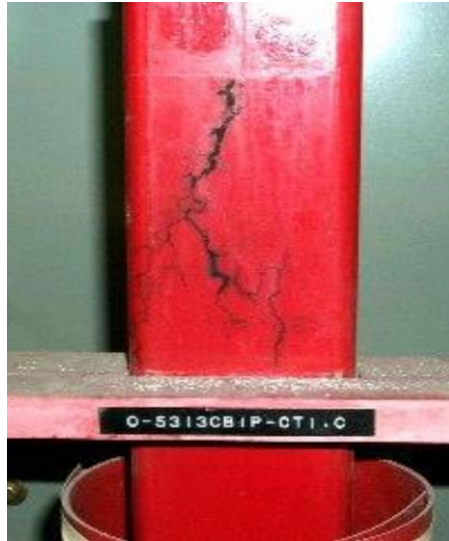


Figure 51: Example of surface tracking discharges effects on an insulator due to contamination/humidity [70]

The end windings of high voltage electric motors are more susceptible to trigger such surface discharges. It is possible to limit such discharges by a suitable design, the choice of insulators having high surface resistivity and by adding a semi-conductive paint on the winding close to the stator slot edge [71]. This additional overcoat will gradually decrease the electric field.

1.4 CORONA DISCHARGE

This kind of discharges takes place in strongly non uniform electric field zone. These are needle-plane or cylinder wire–plane configuration. The electric field is very high in a small region directly surrounded the needle, the wire, the busbar, the junction... and remains weak in the rest of the domain. The size of the electrodes has to be very small compare to the gap between electrodes. They represent a great deal on high voltage power line design (Figure 52).

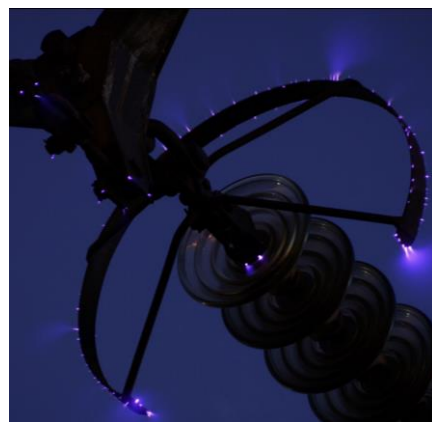


Figure 52: Corona discharge on an insulator string of a 500 kV overhead power line [72]

1.5 PD CONSEQUENCES ON STATOR INSULATION

Three types of solid insulator dielectric breakdown due to high electric field can be distinguished. These can combine each other:

- Electromechanical breakdown: an electrostatic pressure is applied by the conductors on the insulators. This leads to a decrease of the slot insulation thickness or a creation of cracks in it. This phenomenon can lead to an irreversible electromechanical rupture of the material. Moreover, initial cracks existing in the insulator (defects) may lead to a filamentary electromechanical breakdown.

- Thermal breakdown: it occurs when the material conductivity increases due to a high current density. That causes additional losses and therefore heating by Joule's effect. Thermal runaway can then cause a dielectric breakdown, call thermal breakdown. As for electromechanical breakdown, filamentary thermal breakdown may take place in insulators.

- Electronic breakdown: a sufficiently high electric field may cause different breakdown mechanisms, each initiated by electrons: electronic avalanche, field effect emission, free volume effect. These phenomena all lead to the breakdown by generating a large amount of electrons that transform the insulator in a conductor.

PD activity is responsible of premature failure. A PD generates erosion (by ions bombardment), heat but also ozone. Ozone rapidly attack polymers and reduce its lifetime [73]. This PD activity slowly degrade the insulators and at term can lead to a complete failure of the motor.

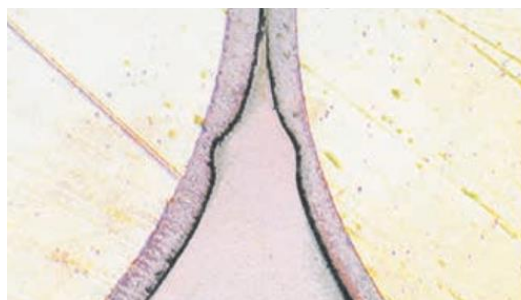


Figure 53: Consequences of PD on a stator winding insulation; left) Corroded enamel layer [40]; right) Slot liner flashover [74]

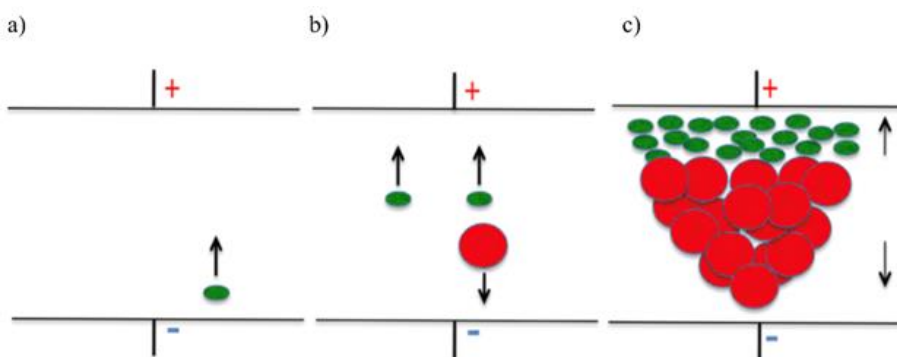
2 PHYSICS OF PLASMA

Townsend type PD happen in cavities (embedded bubble, delamination) inside the polymer or in the surrounding air submitted to a high electric field (vented voids). If the field intensity exceeds a critical value, the air is ionized. Negatively and positively charged particles are then present in such proportion that the air remains electrically neutral. The air is in an another physical state: it is a so called plasma.

The evaluation of the PD activity is extremely dependent on the formation of this plasma. In this paragraph, the predominant mechanism, supposed to take place in our motors EIS, will be presented.

2.1 TOWNSEND MECHANISM

It describes the ionization of a gas between two metallic plane electrodes. It was established by John Townsend in 1901, following the empirical discovery by Friedrich Paschen in 1889 [75]. The electric breakdown of the gas results from an electronic avalanche (Figure 54). It requires that an initial free electron is present in the gas gap (the germ electron). This electron is submitted to an uniform electric field produced by the voltage applied to the electrodes. The electron is accelerated by this electric field. During its motion in the gas gap, impacts occur with gas neutral particles. Additional electrons are then pulled from the impacted particles. The neutral particles then turn to positive ions. If the electric field is strong enough, there is an electronic flow toward the positive electrode and a positive ionic flow toward the negative electrode. An electric current is established in the gas gap. This leads consequently to the gas electric breakdown.



Electronic avalanche process: a) electron acceleration, b) ionization collision, c) electronic avalanche

Figure 54: Electronic avalanche mechanism; green circles are electrons, red circles are positive ions [76]

Two coefficients mainly impact on the described mechanism, as described below.

2.1.1 First Townsend's coefficient

The first Townsend's coefficient is commonly designated as α . It represents the quantity dn of electrons generated by n electrons moving along a distance dx during the avalanche process (4). The solution of Eq 4 is of the form given by Eq 5.

$$dn = \alpha \cdot n \cdot dx \quad Eq\ 4$$

$$n = n_0 \cdot \exp(\alpha \cdot x) \quad Eq\ 5$$

With n_0 being the initial number of electrons at $x = 0$.

The α coefficient describes the formation of additional electrons by the collision of a single initial electron with the other particles in the gas. It is mainly dependent from the chemical composition of the gas and the energy of the incoming electron. Different outputs may result from a collision. In some cases, an additional electron is generated but in others it is simply absorbed by the impacted particle. Table 10 summarizes some reactions which happen in the plasma between gas particles (A and B) and colliding electrons (e^-).

Process	Reactions
Ionization by electronic collision	$e^- + A \rightarrow 2e^- + A^+$
Excitation by electronic collision	$e^- + A \rightarrow e^- + A^*$
Radiative recombination	$e^- + A^+ \rightarrow A^* + h\nu$
Three corpses recombination	$e^- + A^+ + B \rightarrow B + A^*$
Detachment by electronic collision	$e^- + A^- \rightarrow 2e^- + A$
Three corpses attachment	$e^- + A + B \rightarrow B^- + A$
Dissociative ionization	$e^- + AB \rightarrow 2e^- + A + B^+$
Dissociation by electronic collision	$e^- + AB \rightarrow e^- + A + B$

Table 10: Main collision reactions in a plasma. Adapted from [76] [75]; * symbol designates an excited state of the particle, $h\nu$ indicates light emission

Collisions are characterised by the notion of effective cross-section. Let us consider an electron moving at the speed v toward N particles contained in an elementary volume of gas designated by the product $\sigma \cdot dx$. The particles are moving at a speed much slower than the electron one (v). Let's define v_r as the relative speed of the electron compared to the particles speed. Thus, the surface σ is dependent of the relative speed v_r and the species in interaction [77]. The surface σ is the so called effective cross-section.

Figure 55 illustrates the concept of effective cross-section.

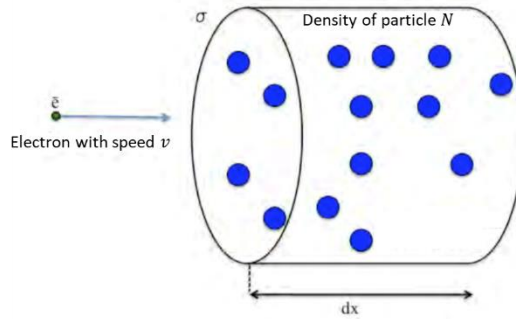


Figure 55: Effective cross-section.

The number of collision n_c is defined as:

$$n_c = N \cdot \sigma \cdot dx \quad Eq\ 6$$

The density N of the gas can be derived from the perfect gas law:

$$p = N \cdot k \cdot T \quad Eq\ 7$$

With p the gas pressure, k the Boltzmann's constant and T the gas temperature.

The electron mean free path λ is a notion derived from the number of collision n_c and the travelled length in the plasma dx :

$$\lambda = \frac{dx}{n_c} = \frac{1}{N \cdot \sigma} \quad Eq\ 8$$

Let us consider one electron ($n = 1$) travelling over the distance dx and doing one single collision ($n_c = 1$) which generates one electron ($dn = 1$). Combining Eq 4, Eq 6 and Eq 8 one gets:

$$\alpha = \frac{1}{\lambda} \quad Eq\ 9$$

The diminution of the number of free paths dn_λ travelled through a unit of length dx due to n_c collisions is expressed by Eq 10. The solution is given by Eq 11.

$$dn_\lambda = -n_\lambda \cdot n_c = -n_\lambda \cdot N \cdot \sigma \cdot dx \quad Eq\ 10$$

$$dn_\lambda = -\frac{1}{\lambda} \cdot n_\lambda \cdot dx$$

$$n_\lambda = n_{\lambda,0} \cdot \exp\left(\frac{-x}{\lambda}\right) \quad Eq\ 11$$

With $n_{\lambda,0}$ the total number of free path.

Let us consider that an electron which ionizes an atom starts with a zero speed in the direction of the electric field between two collisions. The electron then transfers all its kinetic energy to the impacted atom. The probability of ionizing the atom is taken as 1 as long as the electron kinetic energy is equal or above the atom ionizing energy. This is written as:

$$e \cdot E \cdot \lambda_i \geq e \cdot V_i \quad Eq\ 12$$

$$E \cdot \lambda_i \geq V_i$$

With e the electron's charge, E the electric field amplitude, λ_i the electron minimal free path, eV_i is the atom ionizing energy.

The probability for an electron free path being superior to the minimal free path λ_i is expressed as the variation of the number of free paths, which length is at least of λ_i , over dx compared to the total number of free paths $n_{\lambda,0}$. Combining Eq 10 and Eq 11 one gets:

$$\frac{n_\lambda(\lambda_i) - n_\lambda(\lambda_i + dx)}{n_{\lambda,0}} = -\frac{dn_\lambda(\lambda_i)}{n_{\lambda,0}} = \frac{1}{\lambda} \cdot \exp\left(\frac{-\lambda_i}{\lambda}\right) \cdot dx \quad Eq\ 13$$

By definition, this probability also represents the number of electrons generated by electronic avalanche per unit of length which is in fact the α coefficient itself. So Eq 13 can be written as:

$$\alpha = \frac{1}{\lambda} \cdot \exp\left(\frac{-\lambda_i}{\lambda}\right) \quad Eq\ 14$$

Combining Eq 8 and Eq 7, it has been demonstrated that the mean free path λ is proportional to the ratio T/p with T the plasma temperature and p the pressure. One can now get to the well-known formula:

$$\frac{\alpha}{p} = A \cdot \exp\left(\frac{-B \cdot p}{E}\right) \quad Eq\ 15$$

With:

$$\frac{1}{\lambda} = A(T) \cdot p$$

$$B = A(T) \cdot V_i$$

The authors in [78] gives the value of A and B, at normal temperature and pressure conditions, for different gases. The results are presented on Table 11:

Gas	A [Torr ⁻¹ .cm ⁻¹]	B [V.Torr ⁻¹ .cm ⁻¹]	Validity domain of E/p [V.Torr ⁻¹ .cm ⁻¹]
H ₂	5	130	150-600
N ₂	12	342	100-600
CO ₂	20	466	500-1000
Air	15	365	100-800
H ₂ O	13	290	150-1000
HCl	25	380	200-1000
He	3	34	20-150
Ne	4	100	100-400
Ar	14	180	100-600
Kr	7	240	100-1000
Xe	26	350	200-800
Hg	20	370	200-600

Table 11: A and B constants values for different gases [78]

2.1.2 Second coefficient

The second coefficient is commonly designated with γ . It characterises the emission of secondary electrons in the gap due to ions impacting the cathode (Figure 54.c). However, not all the electrons being ejected from the cathode will participate to the electronic avalanche. Some will be absorbed by atoms, others may be recaptured by the cathode and others may leave the gap [79].

In the Townsend's mechanism, the γ coefficient represents the part of electrons which are ejected from the cathode and which participate to the electronic avalanche over the number of ions bombing the cathode. For a metallic plane electrode in air, a common value found in the literature for this coefficient is $\gamma = 0.01$ [78] [55] [44]. The value of this coefficient strongly depend on the gas composition and the electrode geometry and chemical composition [80].

Let us consider an air gap of length d . Initially, only one electron is present in the gap ($n_0 = 1$). The total number of electrons present in the gap due to electronic avalanche is given by Eq 5. So, the number of electrons generated by electronic avalanche initialized by the one present electron is:

$$e^{\alpha \cdot d} - 1$$

Eq 16

It is also the number of generated positive ions.

The Townsend's mechanism considers the electronic avalanche to be self-maintained. The ions bombing the cathode have to eject at least one electron which will ignite another avalanche. This condition is expressed as:

$$\gamma \cdot (e^{\alpha \cdot d} - 1) = 1 \quad Eq\ 17$$

$$\alpha \cdot d = \ln\left(\frac{1}{\gamma} + 1\right)$$

2.2 PASCHEN'S LAW

In 1889, Friedrich Paschen investigated the breakdown of air located between two metallic plane electrodes [81]. The authors in [82] represented the Paschen's curve in different gases based on multiple data sources. The Paschen's curve in air at normal temperature and humidity conditions is shown in Figure 56.

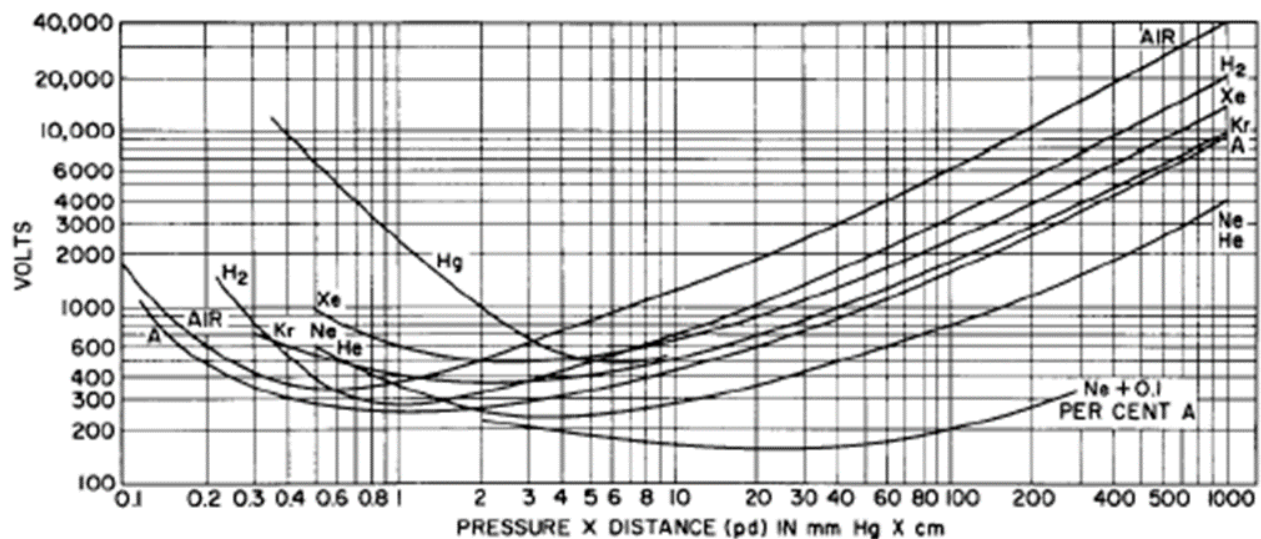


Figure 56: Paschen's curve for various gases [83]

The abscissa axis corresponds to the product of the air pressure p times the gap length d . It is expressed in torr.mm in Figure 56. The ordinate axis indicates the voltage level (peak value, not rms value) at which the electric breakdown of the air gap due to a self-maintained electronic avalanche occurs. At such voltage level, the equation Eq 17 is verified.

The Paschen's curves can be plot using the following equation:

$$V = \frac{B * p * d}{C + \ln(p * d)} \quad Eq\ 18$$

With:

$$C = \ln\left(\frac{A}{\ln\left(1 + \frac{1}{\gamma}\right)}\right)$$

The Paschen's curve is displayed in logarithmic scale. It presents a minimum voltage of about 306 V_{peak} for a product $pd=0.01\text{bar}.\text{mm}$. The presence of this minimum can be explained by simply considering a fixed d gap length and keeping in mind that the electronic avalanche breakdown is the only mechanism represented by this curve. On the left of the minimum, the pressure p decreases. That means that the density of atoms decreases too. The less atoms in the gap, the more important the probability for an electron to cross the gap without impacting any atom. Thus, it is more difficult to get an electronic avalanche and consequently the breakdown voltage increases. On the right of the minimum, the pressure p increases and so does the density of atoms. The number of collisions increases but the energy of the electron between two collisions decreases. A higher energy is required for an electron to travel through the gap without being absorbed. So the breakdown voltage increases.

At air pressure of 1 bar the minimum is obtained for an air gap of 8 μm width. This correspond to the order of magnitude of big air bubbles trapped in the secondary insulation (impregnation resin) [31], [55].

2.3 IMPACT OF AERONAUTICS CONDITIONS

The aeronautics conditions impact on PD appearance have been studied in [1] and [11]. Thus, the results and figures displayed in the following paragraph are mainly extracted from these works.

2.3.1 Environmental variations

The Pashen's curve has originally been computed under normal condition of temperature and humidity [81] [82]. This means a temperature of 20 °C and an absolute humidity of 11 g/m³.

In the aeronautical context, the environmental conditions may change, especially for equipment located in non-pressurized areas of the fuselage, the wings, the landing gears and the nacelles. The ground temperature amplitude can go from – 40 °C (polar climate) up to + 50 °C (arid desert climate). During the aircraft climb, the temperature is considered to decrease of 2 °C per 300 m. At 15 000 m (about 49 000 ft) the external temperature is about - 60°C. However, the calculated temperature within

the winding in the HASTECS motors will be around 180 °C (result of motor Joule's heating and cooling system). The DO160 standard provides test procedures to characterise an equipment for a given mission profile. Figure 57 illustrates the kind of considered temperature variations.

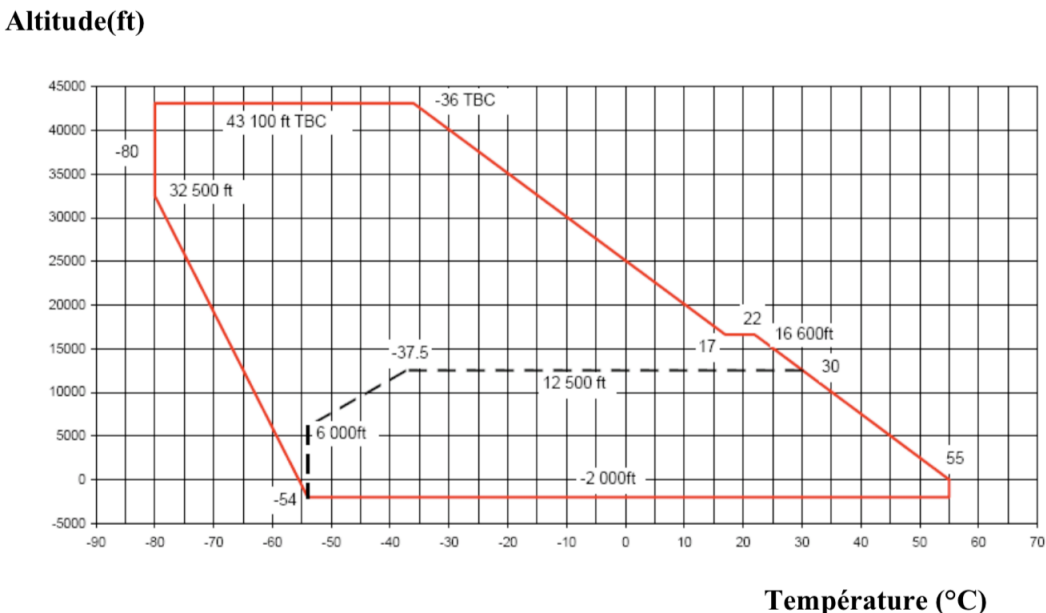


Figure 57: Temperature variation in aeronautic environment – DO160 [85]

Figure 58 displays the humidity variation as a function of the altitude. Multiple mission types are considered; Polar Mission (PM), Tropical Mission (TM), Allowable Maximum Hot Day (AMHD), Structural Maximum Hot Day (SMHD), Standard Day (SD). The humidity is defined by the ratio r of water quantity over dry air quantity. This ratio r is expressed in [g/kg]. The data were provided by Airbus.

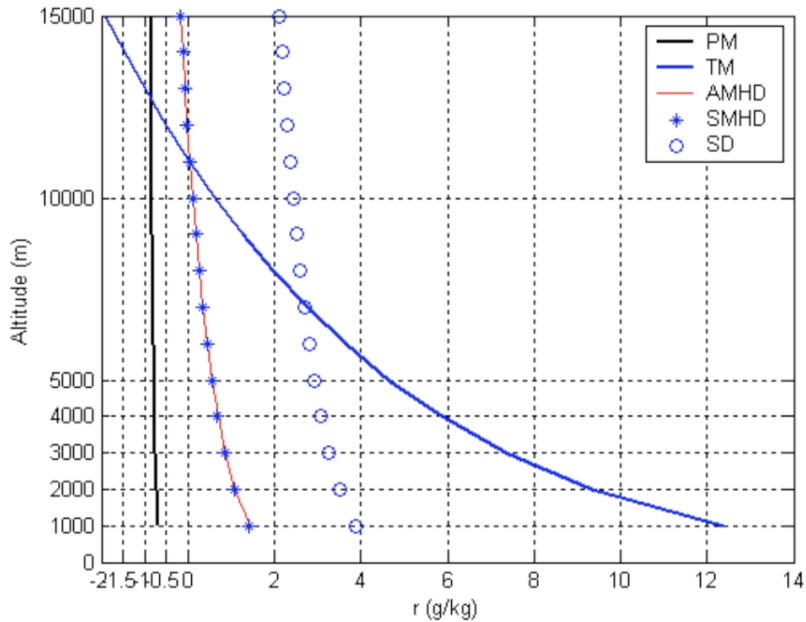


Figure 58: Humidity profile in altitude [76] [84]

For a tropical mission (TM), the humidity level changes significantly as a function of the altitude. For the other missions, the humidity can be considered as constant whatever the altitude.

2.3.2 Impact of temperature

Two main corrections are used to consider the impact of the temperature in dry air on the original Paschen's curves. These are the Peek's [86] and Dunbar's [87] corrections.

The Peek's correction introduces a factor δ . It is an image of the air density. The breakdown voltage level V for a considered temperature T and pressure p is deduced from the breakdown voltage V_0 at standard temperature $T_0= 293 K$ and pressure $p_0= 760 Torr$

$$V(p, T, H_{r0}) = \delta * V(p_0, T_0, H_{r0}) \quad Eq\ 19$$

$$\delta = \frac{293}{T[K]} * \frac{p[Torr]}{760}$$

With H_{r0} : the standard humidity rate 11 g/m^3 . Temperatures are expressed in K and pressures in Torr .

The Peek's correction moves the original Paschen's curve along the ordinate axis (Figure 59).

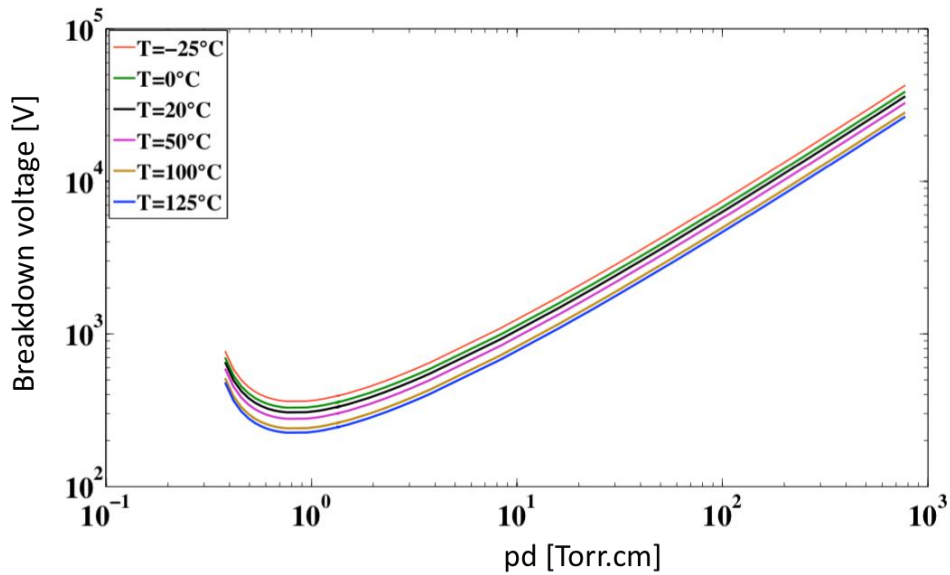


Figure 59: Corrected Paschen's curves computed with Peek's correction [76]

The higher the temperature, the lower the breakdown voltage. The temperature is an image of the particles energy. An electron in a 125 °C air gap is more energetic than one in a - 25 °C air gap. Due to that initial amount of energy, such electron requires less energy to ignite an electronic avalanche mechanism. Thus, a lower electric field is required in the air gap (i.e.: a lower voltage drop).

On the other hand, the correction proposed by Dunbar [87] is derived from the perfect gas law Eq 7. For a constant volume of air gap, the pressure is proportional to the temperature. It is then possible to extract an equivalent pressure p_{eq} in the air gap due to the temperature T starting from initial conditions (p_0, T_0).

$$p_{eq} = p_0 * \frac{273 + T[\text{°C}]}{273 + T_0[\text{°C}]} \quad \text{Eq 20}$$

Where the temperatures are expressed in [°C].

The Dunbar's correction thus moves the original Paschen's curve along the abscissa axis because the impact of temperature is taken into account by defining the resulting equivalent pressure p_{eq} . It is displayed on Figure 60:

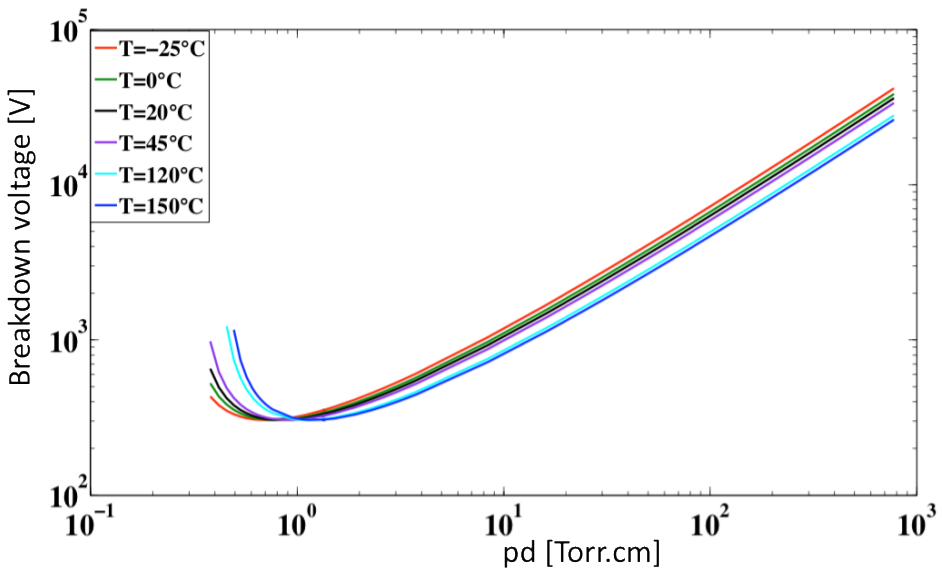


Figure 60: Corrected Paschen's curves computed with Dunbar's correction [76]

At higher temperature the curves are shifted to the right because it results in higher equivalent pressure in the air gap.

In her PhD work, Sili [76] identified the domain of validity of both Peek's and Dunbar's corrections. Peek's correction is validated for pressure or distance variations at temperatures lower than 25 °C. Dunbar's correction is validated for variations of distance at atmospheric pressure at temperatures upper than 25 °C. However, if both the temperature and pressure varies, Dunbar correction is no more validated. A new empirical formulation for breakdown voltage computation has then been proposed. This formulation is validated for temperatures upper than 35 °C.

Table 12 recaps the different corrections in temperatures and give their domains of validity.

Experimental conditions	Domain of validity	Correction
<ul style="list-style-type: none"> • p=760Torr • d varies or <ul style="list-style-type: none"> • p varies • d= 1 mm 	T<25°C	Peek: $V(p, T, H_{r0}) = \delta * V(p_0, T_0, H_{r0})$ $\delta = \frac{293}{T[K]} * \frac{p[Torr]}{760}$
<ul style="list-style-type: none"> • p=760Torr • d varies 	T>25°C	Dunbar: $p_{eq} = p_0 * \frac{273 + T[^\circ C]}{273 + T_0[^\circ C]}$

<ul style="list-style-type: none"> • p varies • d=1mm 	T>35°C	Sili: $V_T = \frac{V_{\text{Paschen},\text{mod}}}{K_T}$ With $\begin{cases} \frac{B*p*d}{c+\ln(p*d)} & \text{for } p * d > p * d_{\min} \\ 306V & \text{for } p * d < p * d_{\min} \end{cases}$ $K_T = a \cdot \delta^b$ $\begin{cases} a = 0.0226 * T(K) - 6.13 \\ b = 0.0027 * T(K) - 0.74 \end{cases}$
---	--------	---

Table 12: Temperature corrections of the Paschen's curve

2.3.3 Impact of humidity

Figure 61 displays the evolution of the breakdown voltage of air as a function of the relative humidity [84]. Three temperatures have been considered: 10 °C, 20 °C and 30 °C.

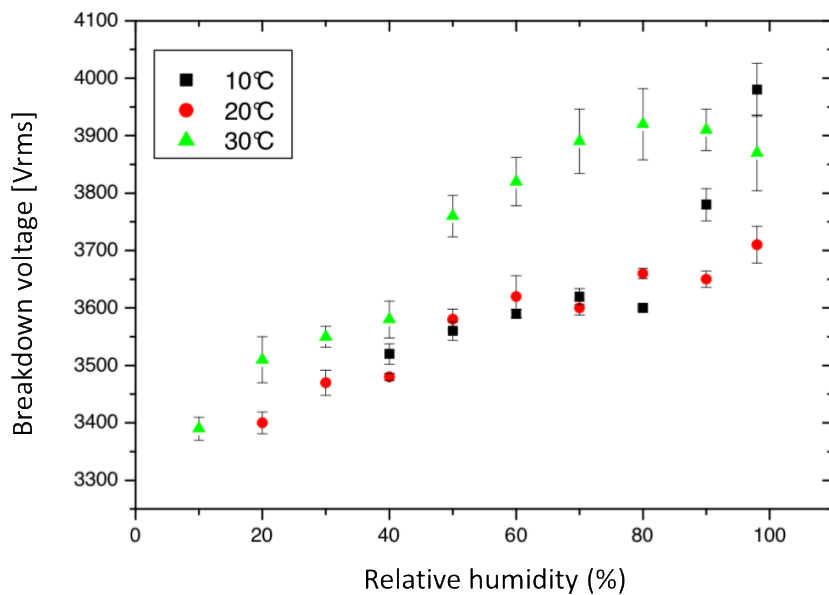


Figure 61: Impact of relative humidity versus air breakdown voltage for different temperatures [84]

Globally, an increase in humidity leads to an increase in breakdown voltage. Water molecules in the gap produce a screen effect. Thus, more energy is required for the electrons to ionize the particles.

Chapter 2: Physics of Partial Discharges (PD)

One can also notice that, in presence of humidity, the breakdown voltage increases with the temperature. This observation is in opposition with the conclusions in dry air presented in the previous paragraph. This can be explained by other mechanisms which are now introduced by the presence of humidity and which dynamic may be dependant on the temperature [88].

A correction can be found in the literature to take into account the humidity alone in the Paschen's theory [89]:

$$V_h = V_{NCTP} * \left(1 + \frac{K_h}{100} * (h - h_{NCTP})\right) \quad Eq\ 21$$

With:

- V_h is the corrected breakdown voltage for an absolute humidity h compared to the standard absolute humidity $h_{NCTP} = 11\ g/m^3$.
- V_{NCTP} is the breakdown voltage under normal condition of temperature and pressure given by the IEC Publication 60 (1970).

The K_h coefficient is linked to the humidity. For a gap smaller than 1 m, IEC suggests that it does not depend on the gap length:

$$K_h = \left(1 + \frac{h - h_{NCTP}}{100}\right) \quad Eq\ 22$$

Table 13 gives the correspondence between some absolute humidity and the corresponding relative humidity at a fixed temperature (from Mollier's diagram):

Relative humidity %	Absolute humidity [g/m^3]
20%	4
40%	8.29
52.5%	11
60%	12.56
80%	16.7
90%	18

Table 13: Correspondence between absolute humidity and relative humidity at 25°C

Figure 62 displays the corrected breakdown voltages for absolute humidity of $4\ g/m^3$, $11\ g/m^3$ and $18\ g/m^3$ [44].

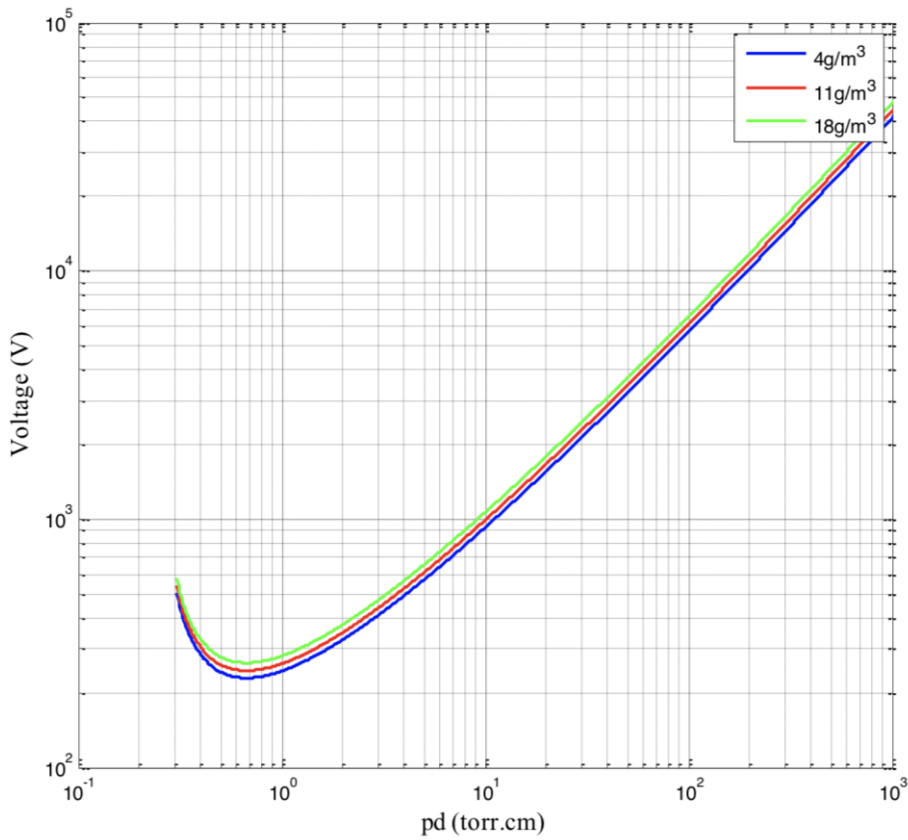


Figure 62: Corrected Paschen's curve versus absolute humidity values at atmospheric pressure and room temperature [44]

In the case of a closed motor (pressurized or not) the air may be considered as dry.

3 PD ANALYSIS

3.1 EXPERIMENTAL DETECTION OF PD ACTIVITY

Partial discharges (PD) consist in repetitive current pulses. These generate electromagnetic interferences, audible noise, light emission, chemical species (from gas breakdown), pressure waves, heat and dielectric losses [42]. PD detection methods consist in measuring variations of one or more of these quantities. They can be divided into two main categories: the indirect and direct methods. In an indirect method, the sensor is located outside the circuit where the sample/device is. In a direct method, the sample and the sensor are located in the same electric circuit.

In this paragraph, two main indirect commonly used PD detection methods will be introduced: radio-frequency detection and optical detection. Common electric direct detections will then be detailed.

3.1.1 Radio-frequency detection

It consists in capturing the electromagnetic PD induced interference by using an antenna. The signal can be visualised by connecting an oscilloscope. The main difficulty consists in separating the PD wave signature from surrounding electromagnetic interferences. Consequently, some devices use complex algorithms to recognize real partial discharges signatures [90]. This method cannot be used in electromagnetically polluted area.

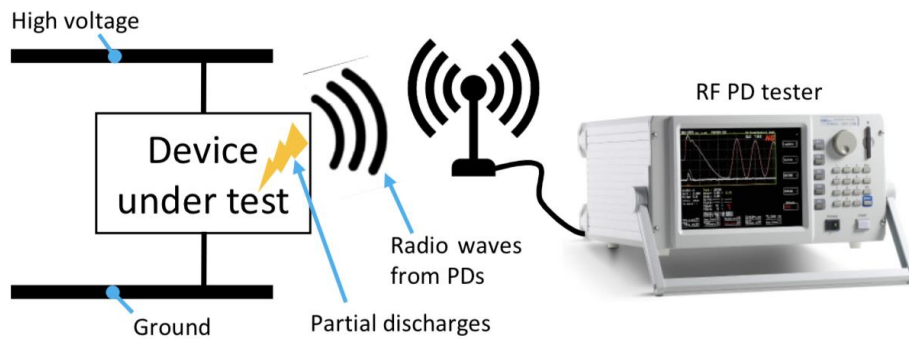


Figure 63: Setup for PD radio-frequency detection [91]

3.1.2 Optical detection

It is possible to detect PD occurring on the surface or in gas thanks to its induced light emission. It is measured using a photomultiplier tube using a photon-counting technique [42]. It results in a frequency distribution graph whose amplitude correspond to the total number of photon count per second collected by the optical sensor. The main advantage of this technique is that it is not perturbed by surrounding electromagnetic interferences. Its main disadvantage is that it cannot detect PD in embedded areas where no light may be detected from outside.

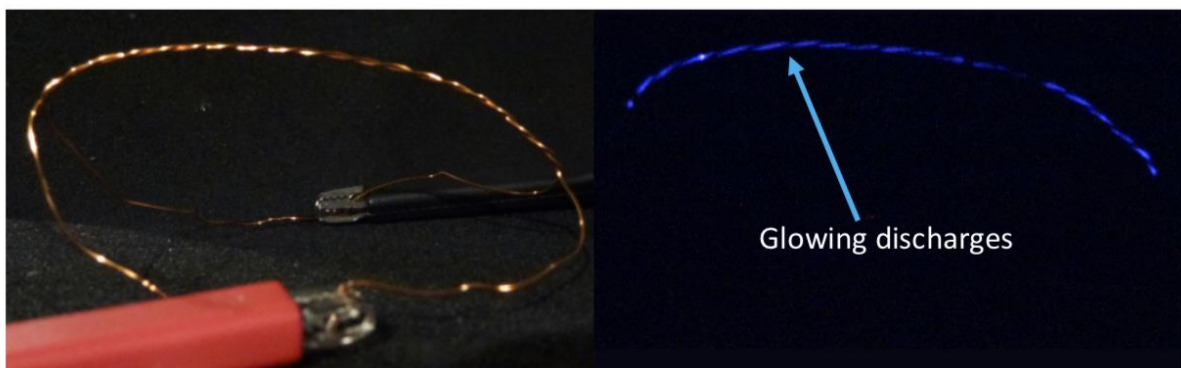


Figure 64: PD light emission (on the right) on a twisted pair made with two enamelled wires sample [91]

3.1.3 Power factor/capacitance tip-up test

This test is commonly used to determine the quality of a coil or a bar ground insulation. It uses the fact that the power factor (also called dissipation factor) or the capacity of such insulation will change with applied AC voltage if defects (voids, delaminations) exist. Indeed, when applying high voltage, PD will take place in these defects leading to an increase in the dissipation factor (PD induce losses) and a decrease in the capacity (PD short-circuit the defects). The difference between low and high voltage values gives an indication of how void-free that insulation is.

In high voltage machines, two measurements are performed at 25% and 100% of the rated line-to-ground voltage. For new coils, it is suggested that the power factor tip-up should be < 0.5% and the capacitance tip-up should be < 1% for new machines and < 4% for old generation machines [47].

3.1.4 Used electric detection

The detection is operated with a non-destructive electric measurements under a 50 Hz sine voltage. A high-pass RLC filter is employed, allowing the measurement of high frequency current pulses by considerably reducing the low frequency current signature from the power source.

Figure 65 illustrates the whole setup for a direct electric PD detection. A high voltage transformer (220 V / 20 kV - PD free) is used to applied high voltage to the sample. A low frequency generator (FX 1641A) coupled with a low frequency amplifier deliver the power to the high voltage transformer in order to be fully independent from the power network and its perturbations. The whole detection circuit is located inside a Faraday cage to avoid surrounding electromagnetic perturbations. The coupling capacity C_k associated with the measurement impedance Z_m are used to detect PD. For each PD occurring in the sample or in the air gap surrounding it, image charges at both sample electrodes are modified. As the external circuit (C_k, Z_m) has a very low high frequency impedance, these image charges change leads to a pulse current in the detection circuit. A voltage measurement is performed at the measurement impedance terminals. The acquisition is done on an oscilloscope.

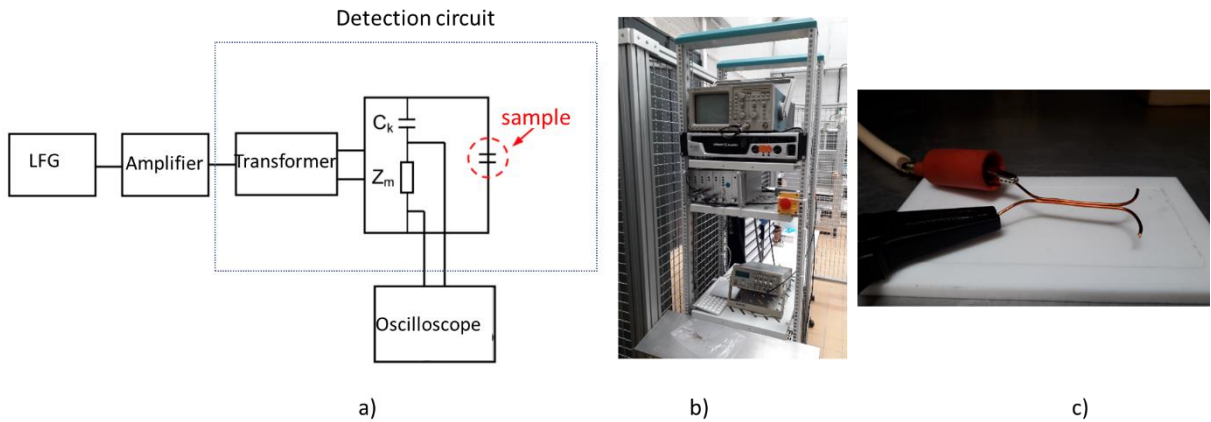


Figure 65: Setup for PD electric detection; a) Schematic of the PD measurement circuit, b) LFG: Low Frequency Generator, amplifier and oscilloscope, c) Sample inside the Faraday cage

3.2 PARAMETERS LINKED TO PD

3.2.1 Partial Discharge Inception Voltage (PDIV)

The PDIV is defined as the lowest voltage value at which PD are ignited and remain maintained. Indeed, during a first PDIV test, surface discharges may occur, corresponding to the ionization of dust, moisture or contaminant on the sample surface. These kind of PD quickly disappear and the corresponding voltage do not have to be considered as the PDIV. IEC standard recommends that the PDIV corresponds to the lowest voltage at which a measured quantity exceeds a predefined threshold. We will not used these definition but the one described before. Figure 66 illustrates a PD pattern obtained at the PDIV.

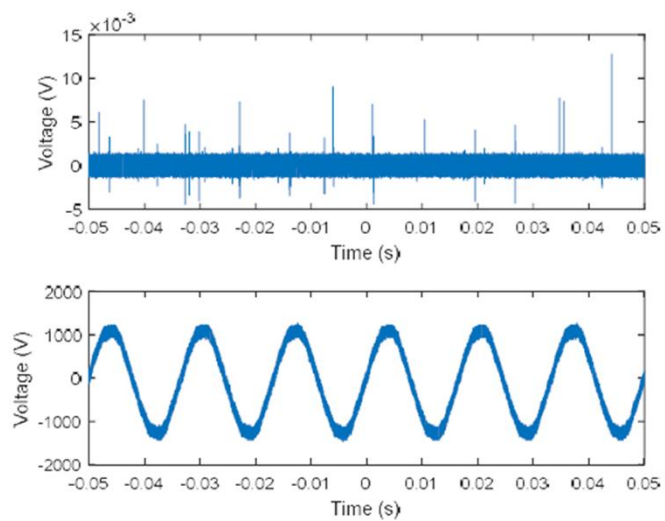


Figure 66: Illustration of PD detection; below) Applied voltage, top) PD signals [92]

3.2.2 Partial Discharge Extinction Voltage (PDEV)

The PDEV is the voltage at which PD disappear when progressively reducing the applied voltage from PDIV. Practically, PD continue to be maintained when the voltage is decreasing from the PDIV up to a value from which they disappear.

3.2.3 Apparent charge

A PD between electrodes at different voltage results in a release of charges. The charges move in the gap between the electrodes. Such displacement of charges over the thickness of the electrodes induces either a transient voltage pulse at the electrodes terminals or a transient current pulse (this is our case). This phenomenon is attributed to the so called apparent charge. The evaluation of the apparent charge quantity is required for the PD quantification. However, the apparent charge does not correspond to the total charge locally released by the PD. It is affected by the electrodes geometries, the material properties, the measurement circuit impedance.... Thus, the real PD charge cannot be directly measured.

Considering the work in [93], it is possible to get the real charge from the measurable charge. Let us consider two plane parallel electrodes at a voltage V separated by air. A discharge occurs and results in a charge q being present in the gap. Figure 67 illustrates the considered configuration.

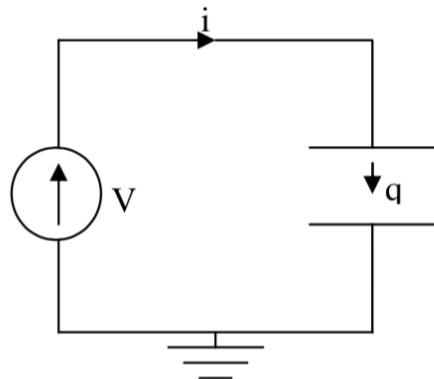


Figure 67: Charge circulation in an air gap between two plane parallel electrodes [84]

When travelling a dx length in the gap, the charge q submitted to the electric field E realise a work W . This work is provided by the power source.

$$W = q * E * dx = i * V * dt \quad Eq\ 23$$

$$\text{With } \begin{cases} E = E * u \\ dx = dx * u \\ \|u\| = 1 \end{cases}$$

Let us consider that a displacement of charge q over a length dx results in a voltage drop ΔV . The apparent charge q_{app} in the circuit is given by (24).

$$q_{app} = \int_0^{\Delta t} i * dt = \frac{q}{V} * \int_0^{\Delta x} E * dx \quad \text{Eq 24}$$

$$q_{app} = q * \frac{\Delta V}{V}$$

The apparent charge is only a part of the charge released by the PD.

3.3 STATISTICAL PROCESSING OF THE RESULTS

PDIV experimental evaluations always present dispersions in the results from one sample to another one. It comes from difference in the manufacturing process, dimensions tolerance and incertitude from the measurement equipment. Dispersion may also be expected when reproducing the same measurement successively on the same sample. This is due to the fact that PD do not exactly take place in the same area from one test to another. Despite the same breakdown mechanism (electronic avalanche), the PDIV values (and thus the breakdown electric field values) will consequently be different and need to be treated by a statistical analysis.

The Weibull's distribution, commonly used to treat dielectric strength data, has been used for the statistical processing of PDIV values. It is also applicable with lifetime data processing. First, the results are distributed into n_i intervals. A probability density $P(E)$ is defined. This function is obtained when the width of the n_i intervals tend to zero and when the number of intervals tend to the infinite. In other words, $P(E)$ is the continuous distribution of the discontinuous data. Figure 68 illustrates an example of data distribution and the associated $P(E)$ function.

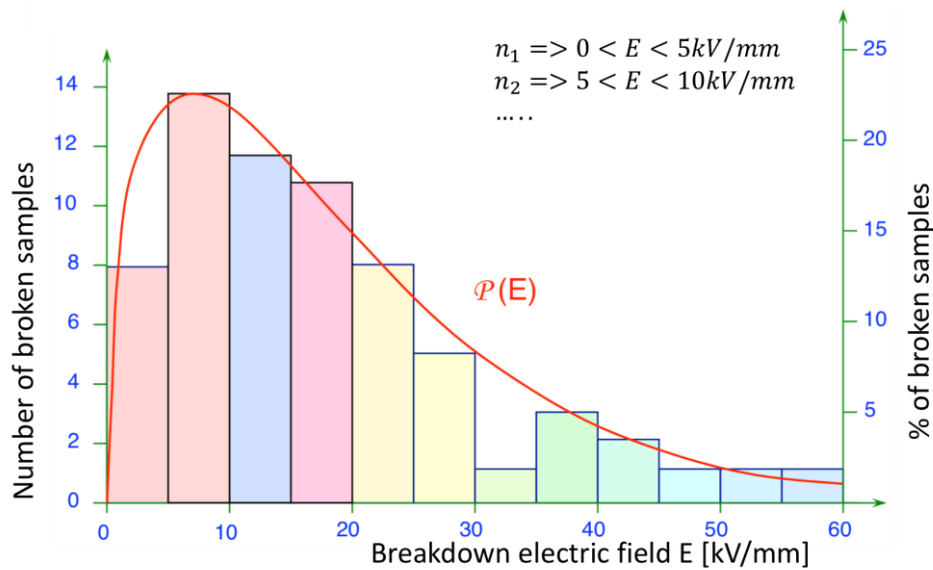


Figure 68: Illustration of PDIV data distribution

The cumulative probability density $P_C(E)$ is computed as follow:

$$P_C(E) = \int_0^E P(E) * dE \quad Eq\ 25$$

Figure 69 illustrates the P_C cumulative probability. It comes from different results than the one presented on Figure 68.

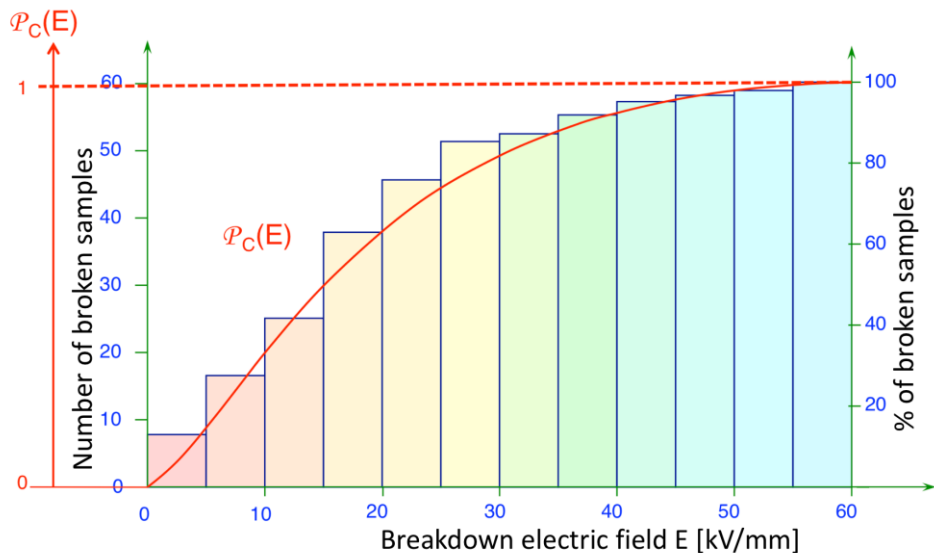


Figure 69: Example of P_C cumulative probability

A good and simple approximation of $P_C(E)$ is recommended by EIC 62539 standard and given by [94]:

$$P_C(i, n) = \frac{i - 0.44}{n + 0.25} \quad Eq\ 26$$

With

- i : breakdown value in ascendant order;
- n : total number of breakdown values.

Experimental PDIV data show that $P_C(E)$ is generally of the form:

$$P_C(E) = 1 - (\exp(\frac{E}{\alpha})^\beta) \quad Eq\ 27$$

With β the shape parameter and α the characteristic breakdown field value such that:

$$P_C(\alpha) = 63.2\% \quad Eq\ 28$$

By manipulating Eq 27 with log operator on can gets:

$$\log\left(\log\left(\frac{1}{1 - P_C(E)}\right)\right) = \beta * \log(E) - \beta * \log(\alpha) \quad Eq\ 29$$

By taking an axis system $\log\left(\log\left(\frac{1}{1 - P_C(E)}\right)\right) = f(\log(E))$ the points can be interpolated with a slope β .

Figure 70 illustrates an example of $P_C(E)$ evolution in the particular axis system defined by Eq 29.

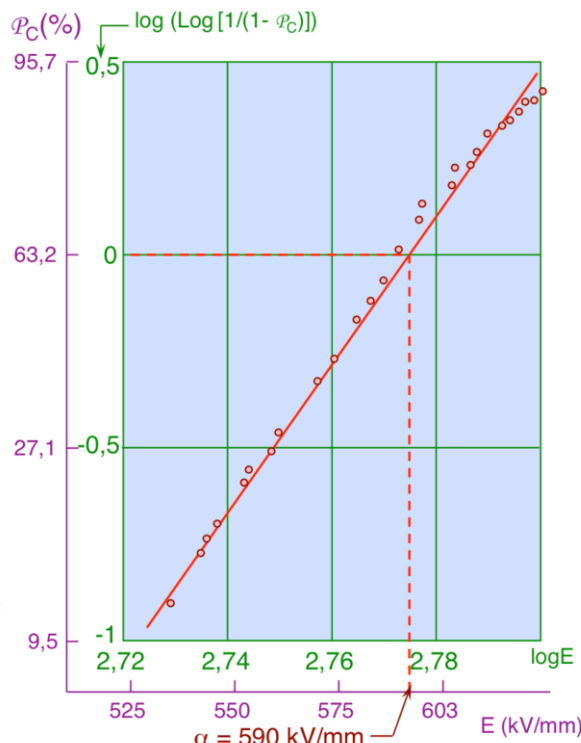


Figure 70: $P_C(E)$ evolution in the axis system defined by (26)

Another way to determine the α and β coefficients is through computation. This approach is based on least square regression and used weighting coefficients given by White in [95]. Let us apply the following change of variable:

$$X_i = \log(-\log(1 - P_c(i))) \quad Eq\ 30$$

$$Y_i = \log(E_i)$$

Where the index i refers to sample i .

First, the weighted averages of X_i and Y_i are computed Eq 31 and Eq 32. It is considered that all the samples are used: there is no sample excluded due any sample defect or artefact occurring during the experimental measurements.

$$X_m = \frac{\sum_{i=1}^n w_i * X_i}{\sum_{i=1}^n w_i} \quad Eq\ 31$$

$$Y_m = \frac{\sum_{i=1}^n w_i * Y_i}{\sum_{i=1}^n w_i} \quad Eq\ 32$$

With w_i the weighted coefficient associated to the broken sample i given by [95]. Samples are sorted in ascendant breakdown values.

The α and β coefficients are finally computed in Eq 33 and Eq 34:

$$\beta = \frac{\sum_{i=1}^n w_i * (X_i - X_m)^2}{\sum_{i=1}^n w_i * (X_i - X_m) * (Y_i - Y_m)} \quad Eq\ 33$$

$$\alpha = \exp(Y_m - \frac{X_m}{\beta}) \quad Eq\ 34$$

4 DEGRADATION OF THE POLYMER INSULATION IN AERONAUTIC ENVIRONMENT

There are different mechanisms which may impact the time to failure of dielectrics under an electric field [96]. The intrinsic failure of a polymer mainly results from electrical, thermal and mechanical mechanisms, sometimes acting simultaneously. A PD activity does not lead to an instantaneous breakdown of the polymer: the time to failure can goes from seconds to days. It is an extrinsic stress which degrades the polymer insulation progressively up to the final breakdown. The extrinsic time to failure, occurring above the PDIV, is always lower than the intrinsic one. It has been introduced in the

Chapter 2- §1 that some PD take place in cavities inside the polymer. The author in [67] have established a link between thermal and mechanical stresses over the apparition of cavities inside the polymer. This indicates that during its lifetime, PD may occur after ageing in initially healthy samples. This paragraph focuses on electric degradation of polymer in aeronautic environment.

4.1 PRESSURE

The impact of pressure on machine winding PD magnitude has been investigated in [97]. The measurements have been done on twisted pair samples. Figure 71 displays the evolution of the discharge magnitude as a function of the applied voltage at different pressure levels. The temperature value is not given.

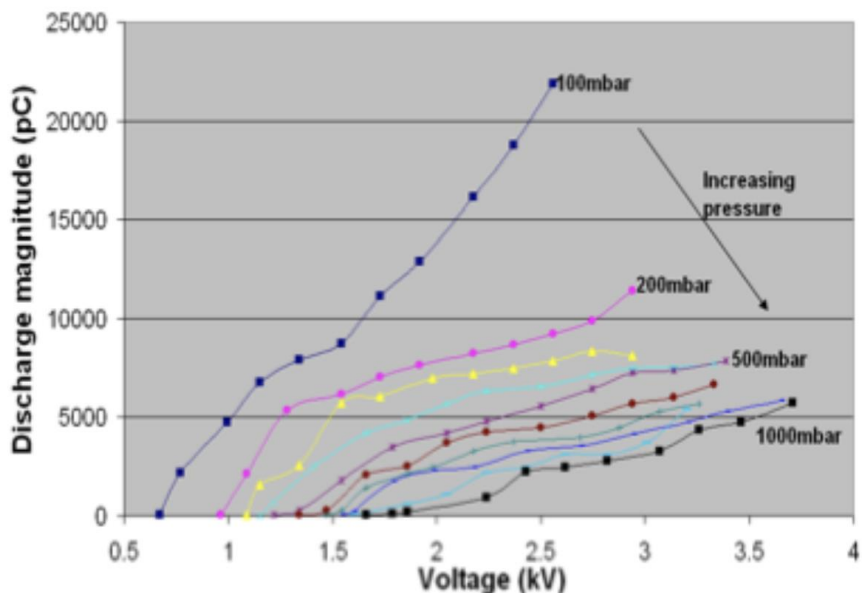


Figure 71: PD magnitudes at different voltage and pressure levels [97]

The discharges magnitude can be interpreted as a stress indicator. The higher the discharge magnitude level, the more stressed the polymer. At fixed voltage and temperature, the discharge magnitude increases when the pressure decreases. Thus, the stress on the polymer increases when the pressure decreases. A faster degradation of the polymer can be expected at low pressure.

4.2 HUMIDITY

Humidity changes the degradation of the polymer into two opposite directions whether considering surface discharges or inner discharges. The authors in [98] have investigated the effect of exposure to ambient relative humidity on the dielectric degradation. Figure 72 displays the evolution of the time to failure as a function of the electric field applied to the dielectric for different relative humidity exposure. The magnitudes are in arbitrary unit (AU).

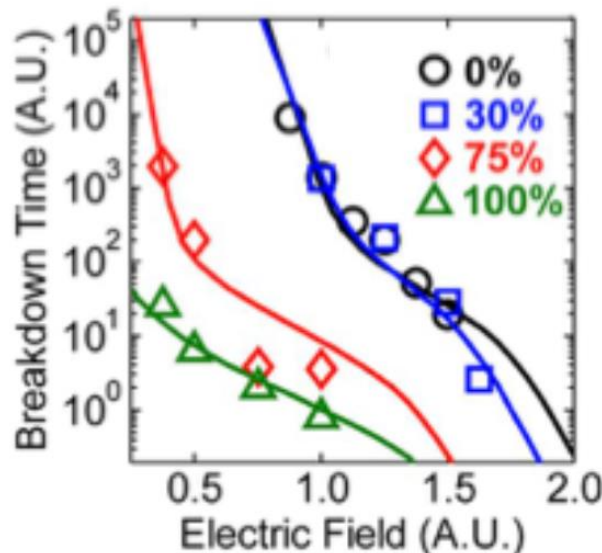


Figure 72: Time to failure as a function of the electric field for different humidity - 60Hz AC voltage [98]

In this experiment, samples have been exposed to different humidity levels for two weeks. The higher the humidity level, the higher the humidity inside the dielectric sample. At a fixed electric field amplitude, the time to failure decreases when the humidity inside the dielectric increases. This can be explained by a failure due to water treeing as presented by [67] and/or by the increase in dielectric losses due to humidity.

In [99] the degradation of polyethylene under corona discharges is studied at different external humidity level. Here, there is no humidity inside the dielectric. Figure 73 displays the obtained results.

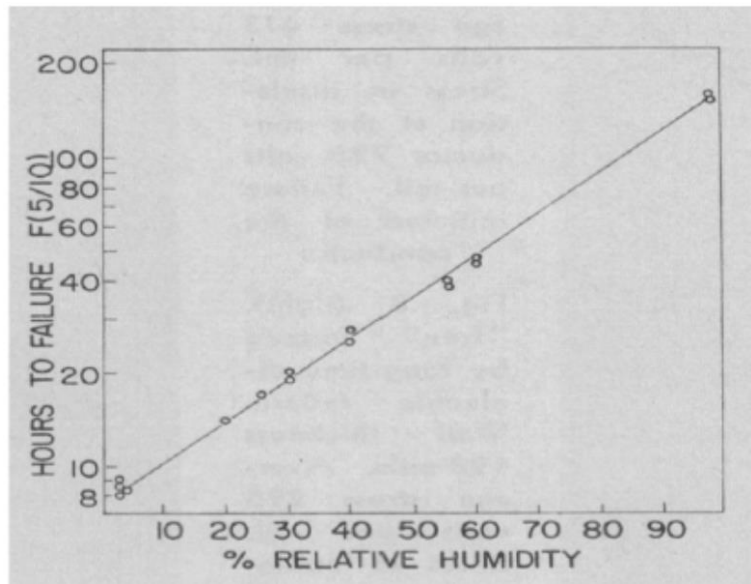


Figure 73: Polyethylene failure time as a function of the external relative humidity under corona discharges ($E=8\text{kV/mm}$, $f=60\text{Hz}$) [99]

In the case of corona discharge, the time to failure extends with the augmentation of the humidity. In fact, water particles act as a screen effect which shielded the polymer.

4.3 TEMPERATURE

The impact of temperature over electrical tree development inside a dielectric has been studied in [100]. Figure 74 presents the trees average growth rate in Low Density Polyethylene (LDPE) and branched LDPE (BPEQ) as a function of the applied voltage for temperatures ranging from 20 °C to 50 °C.

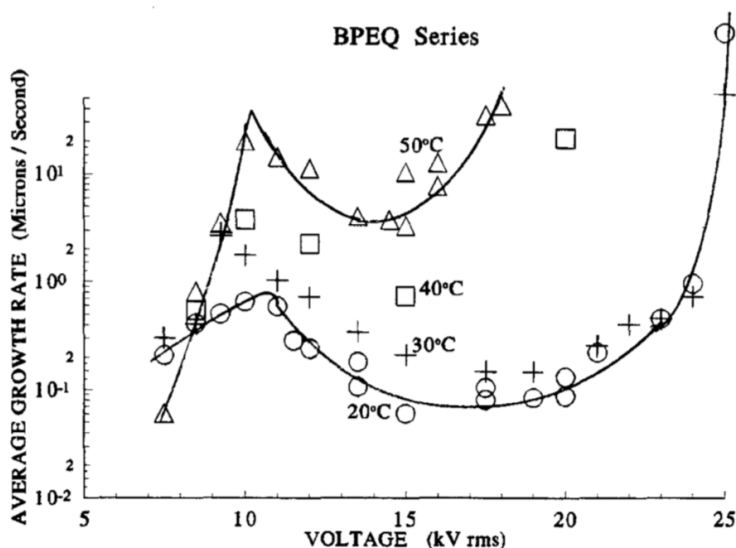


Figure 74: Average tree growth rate as a function of voltage and temperature in LDPE and branched LDPE (BPEQ) [100]

At a fixed voltage, the tree growth accelerates when the temperature increases. This can be explained by an increase of cavities formation inside the dielectric due to the temperature [67]. The time to failure of the dielectric due to tree is thus decreased.

It has been presented Chapter 2 §2.3 that an elevation of temperature reduces the PDIV level (at a fixed pressure). Due to that, PD are ignited at lower voltage and thus for a given voltage, the higher the temperature, the higher the dielectric degradation rate. Figure 75 displays the lifespan evolution of enamelled twisted pairs, showing the strong impact of temperature [101].

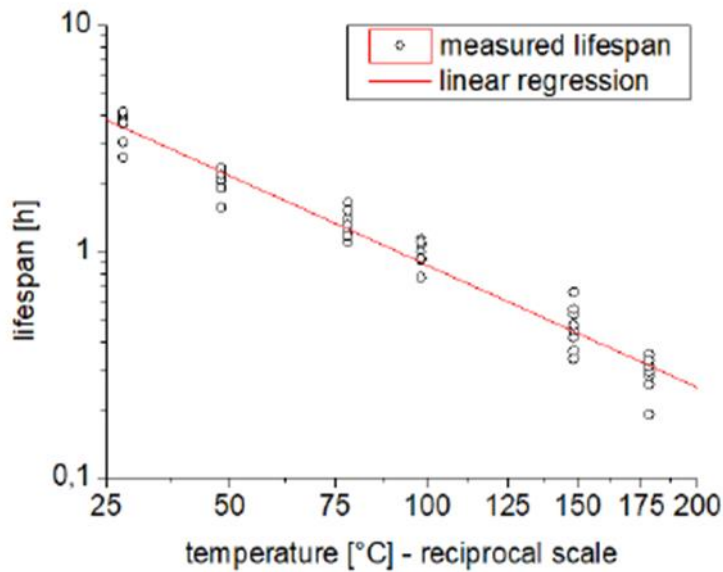


Figure 75: Lifespan of twisted pairs under PD versus temperature; copper diameter: 1.12mm, grade 2, PEI/PAI 200°C corona resistant magnet wire, V=1.75kV, f=10kHz [101]

4.4 FREQUENCY AND VOLTAGE

In Chapter 1 §6, it has been pointed out that power electronics increases the electric stress on the motor EIS, especially when overvoltages appear at the motor terminals. The level of the voltage, as well as the switching frequency of the converter, are stressful parameters [69], [101]. Figure 76 displays two examples of twisted pairs lifespan reduction due to an increase in voltage or frequency.

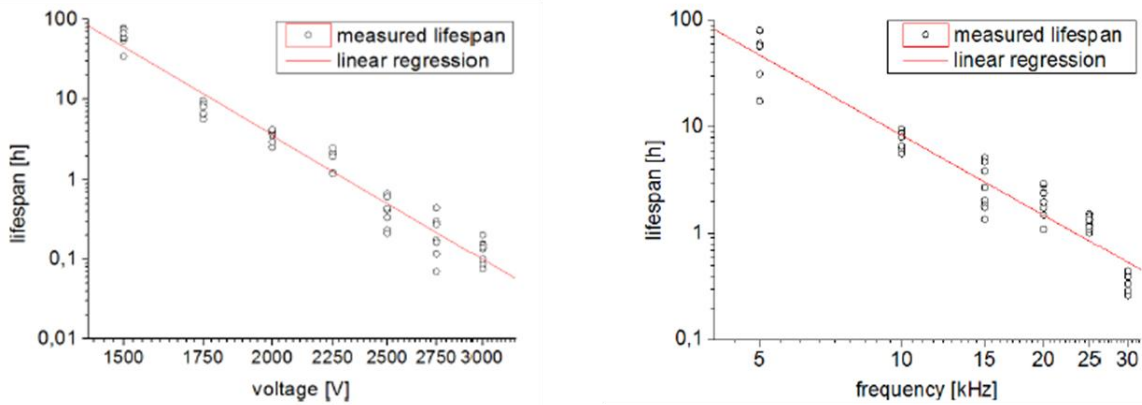


Figure 76: Lifespan of twisted pairs under P. Left) Lifespan versus voltage ($f=10\text{kHz}$, $T=30^\circ\text{C}$), Right) Lifespan versus frequency ($V=1.75\text{kV}$, $T=30^\circ\text{C}$); copper diameter: 1.12mm, grade 2, PEI/PAI 200°C corona resistant magnet wire [101]

Besides, the introduction of wide-band gap materials such as SiC or GaN rises some interrogation on the impact of the dV/dt slope on the dielectric ageing. The impact of all these parameters on the ageing of the electric insulation is investigated in [57], [61], [102].

In [102], two voltage signals were used: a sinusoidal one and a square-wave voltage. The applied voltage amplitudes, frequencies and duty cycles are the same for both signals. Figure 77 displays the main results. As expected, at a fixed frequency, the lifetime decreases when the voltage increases whereas at fixed voltage, the lifetime decreases when the frequency increases. Finally, the slope of the applied voltage seems to have no significant impact on the lifetime as under the same conditions, the measured lifetimes by applying a sine or a square wave voltage are very close together.

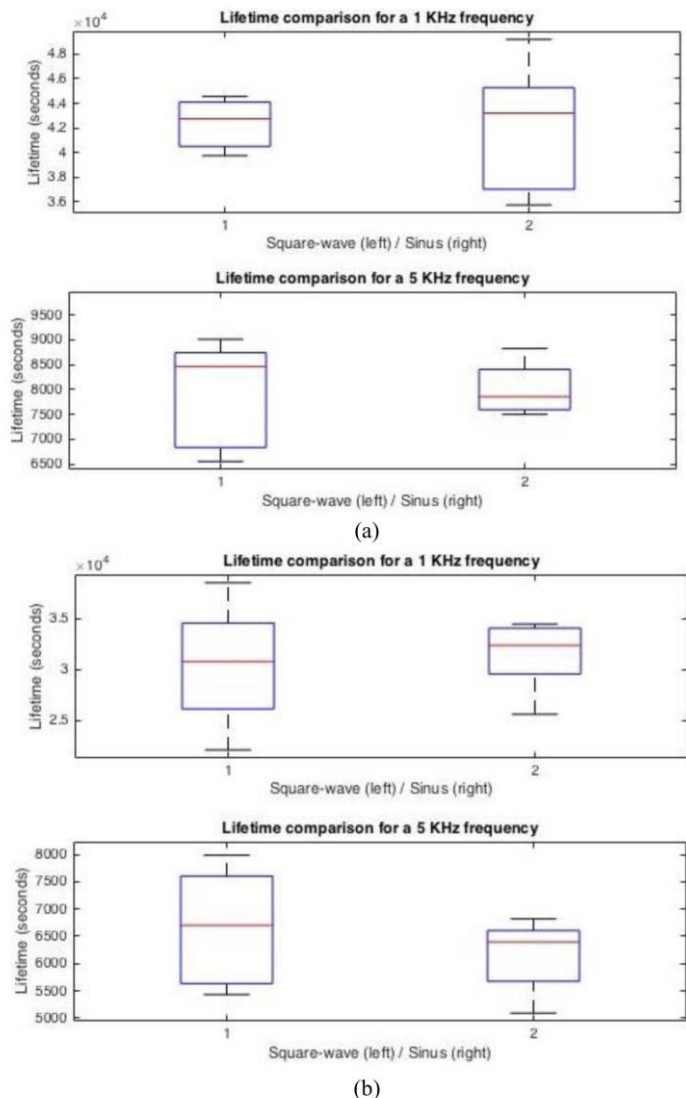


Figure 77: Comparison between square and sine voltage effect on lifetime under PD. Boxplots representing lifetimes (median, quartiles, extrema): (a) $V=1445 \text{ V}_{\text{peak}}$ (50%) (b) $V=1540 \text{ V}_{\text{peak}}$ (60%) [102]

4.5 LIFETIME EVALUATION

There are different models to predict the lifespan of a sample. The simplest ones take only one constraint into account. The commonly used are the Inverse Power Model and the Exponential Model [103]. Table 14 presents the equations used.

Model	Parameters	Equation
Inverse Power Model	L: time to failure at voltage V V: voltage k: constant N: constant	$L = k * V^{-N}$

Exponential Model	L : time to failure at voltage V V: voltage c: constant k: constant	$L = c * \exp(-k * V)$
-------------------	--	------------------------

Table 14: Inverse power model and exponential model for lifetime under PD evaluation; adapted from [103]

The authors in [104] studied the combined impact of temperature, voltage and frequency on the lifetime. Concerning the electrical stresses (i.e.: voltage and frequency) an inverse power model was applied. For the temperature, an exponential model was applied.

Stress	Parameters	Model
Electrical	E_V : constant derived from both the material and power law applied to voltage V V: voltage E_F : constant derived from both the material and power law applied to frequency F F: frequency L: time to failure	$\begin{cases} \log(L) = E_V * \log(V) \\ \log(L) = E_F * \log(F) \end{cases}$
Thermal	E_T and b: constants derived from the material and obtained from lifetime data under electro-thermal stress T: temperature	$\log(L) = E_T * \exp(-b * T)$

Table 15:Lifetime models applied for electrical and thermal stresses; adapted from [104]

The model which couples the electrical and thermal stresses is expressed in Eq 35.

$$\begin{aligned} \log(L) \sim & M + E_V * \log(V) + E_F \\ & * \log(F) + E_T * \exp(-b * T) + E_{FV} \\ & * \log(V) * \log(F) + E_{VT} \\ & * \log(V) * \exp(-b * T) + E_{FT} \\ & * \log(F) * \exp(-b * T) + E_{VFT} \\ & * \log(V) * \log(F) * \exp(-b * T) \end{aligned} \quad \text{Eq 35}$$

The first four terms in Eq 35 correspond respectively to the averaged lifetime M , the impact of voltage alone, the impact of frequency alone and the impact of temperature alone. The terms five to seven coupled two by two temperature, voltage and frequency. For example, the constant E_{FV} is attached to the coupling frequency-voltage term. Finally, the last term couples all three parameters (i.e.: temperature, frequency and voltage).

The design of experiment regression has been applied to characterise the influence of each terms on the lifetime [104].

On board electrical motors are usually designed to have a lifetime of several ten thousand hours. It will be obviously too much money and time consuming to check its lifetime under nominal working conditions. An alternative is to use accelerated lifetime tests. It consists in testing the machine at higher stress levels. Stresses can be the voltage, frequency, current, temperature or pressure. Stresses level have to remain under maximum values defined by standards [105] [106] in order not to produce irrelevant degradation mechanisms (for example testing at a temperature above the thermal class). The results are then treated using regression methods. A survey of several regression methods is presented in [107]. These are the design of experiments, response surface, multilinear and robust regression. Each method has its advantages. As an example, design of experiments is accurate with a limited experimental cost.

5 MODELLING PARTIAL DISCHARGES ACTIVITY

5.1 STREAMER CRITERION

This approach considers that the mechanism at the origin of the discharge is the ionization of the gas. It introduces the effective ionization α_{eff} . It corresponds to the rate of net production of free electrons in the gas. This coefficient strongly depends on the electric field amplitude E . The function varies depending the gas. This function is given in air by [108]:

$$\alpha_{eff}(E) = p * \left[k * \left(\frac{E}{p} - \Lambda \right)^2 - A \right] \quad Eq\ 36$$

With $k = 1.6\ mm.\ bar/kV^2$, $\Lambda = 2.2\ kV/(mm.\ bar)$ and $A = 0.3\ 1/(mm.\ bar)$. p is the pressure in [bar]. $\alpha_{eff}(E) > 0$ for $E > 2.6\ kV/mm$. That is the critical field strength at which there is a net production of free electrons.

Figure 78 displays the evolution of this reduced coefficient as a function of the reduced electric field. Three different sets of experimental data points are used [108].

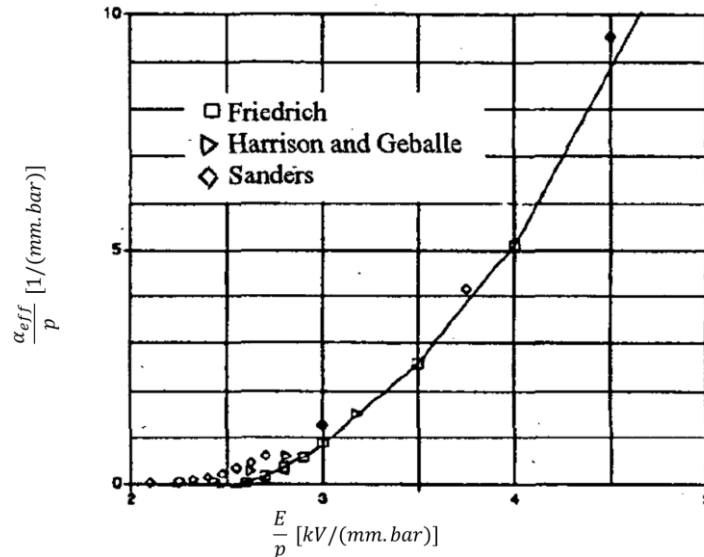


Figure 78: reduced effective ionization as a function of reduced electric field in air [108]

It is assumed that a streamer occurs along a field line on which the density of electrons is high enough for the electronic avalanche to happen. The condition of self-sustained avalanche is given in [109]:

$$\int \alpha_{eff}(E) \cdot dl > C_{crit} \quad Eq\ 37$$

The integral is computed along field lines on which $\alpha_{eff} > 0$. The critical value C_{crit} is usually in the range of 9–18 [108]–[110]. At this point two scenarios are possible:

- Firstly, $\alpha_{eff} > 0$ on the entire field line. The fulfilment of Eq 37 will lead to breakdown across the gap;
- Secondly, there are parts along the line where $\alpha_{eff} < 0$. It is still possible to go to breakdown if the electric field in front the streamer head is so high that it makes the streamer goes forward. This is kind of a suction effect. This is the so called streamer propagation. It requires that the average electric field $\langle E \rangle$ along the line satisfied the following equation given by [109]:

$$\langle E \rangle = \frac{U}{L} > \frac{U_0}{L} + E_0 \quad Eq\ 38$$

With U the voltage difference between electrodes, L the field line length, $U_0 \approx 10 - 30\ kV$ is an empirical constant and $E_0 \approx 0.5\ kV/mm$ for a discharge starting from positive electrode and $E_0 \approx 1.2\ kV/mm$ for a discharge starting from the negative electrode [109].

This methodology has been implanted in COMSOL [110]. Figure 79 presents an application of COMSOL Particle Tracing Module for the evaluation of field lines starting from a positive electrode where Eq 37 is verified and on which a streamer is likely to appear.

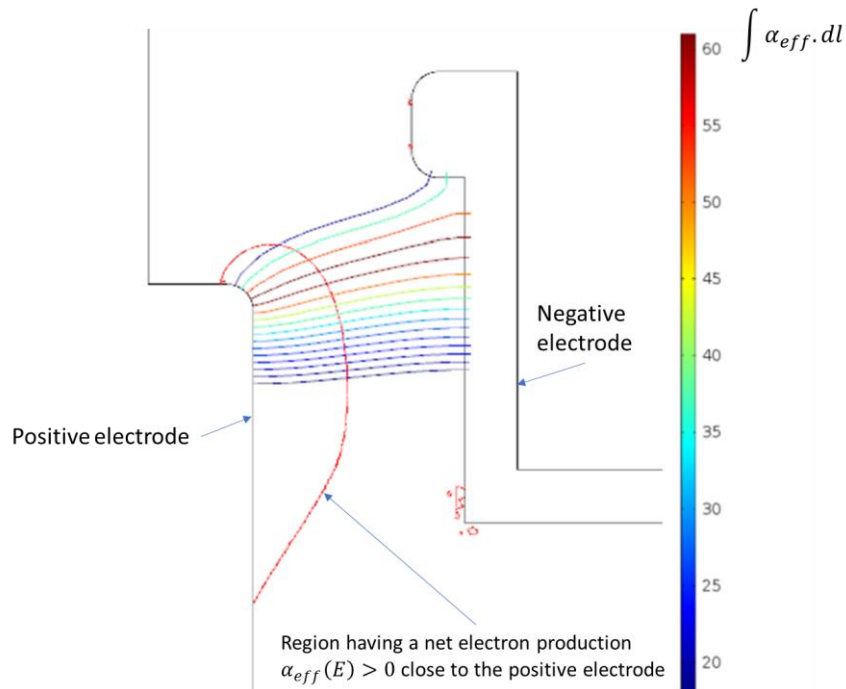


Figure 79: Field lines satisfying the streamer propagation condition (Eq 37) for discharges starting from the positive electrode [110]

The main advantage of this method is that it does not require an uniform electric field along the field line.

5.2 PASCHEN'S CRITERION

Another approach consists in using the Paschen's criterion. It requires the computation of the field lines. The electric field has to be uniform along a field line. This approach was used in [55] to determine the PDIV between two enamelled round copper wires. The field lines are considered as straight lines. They are computed using geometrical relations. Figure 80 displays the used 2D-model.

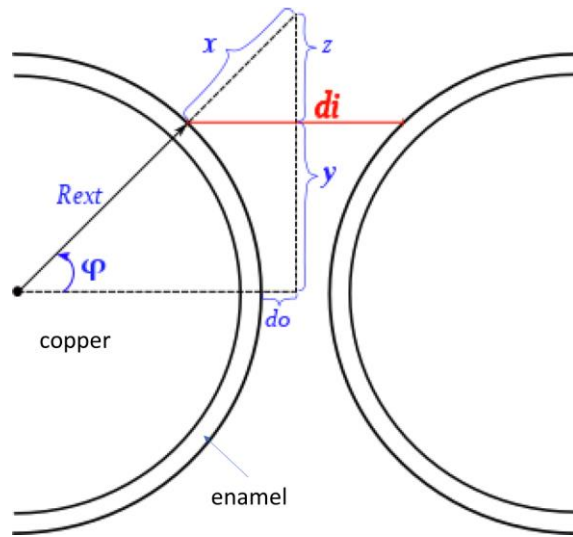


Figure 80: Parallel enamelled round wires; 2D-model [55]

This model is solved using finite elements. The voltage is then available on the whole model. The voltage difference at the extremities of a field line d_i is computed. The results are displayed in a Paschen's plot as presented in Figure 81. The abscissa axis is the product pd ($p = 1 \text{ bar}$) (i.e.: the field line length) and the ordinate axis is the voltage difference.

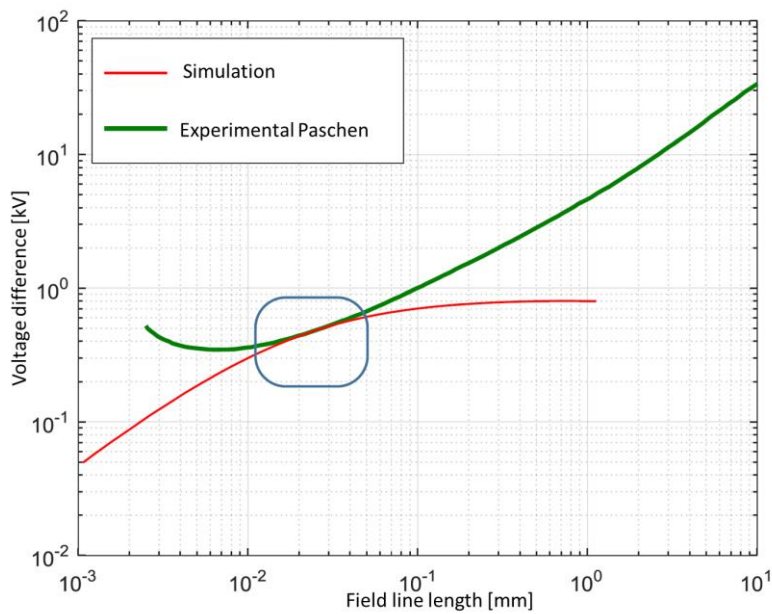


Figure 81: Example of simulated results versus the experimental Paschen's criterion [55]

Chapter 2: Physics of Partial Discharges (PD)

The intersection of the simulated curve (red line) with the Paschen's curve (green line) indicates that the field line at this intersection is probably subject to PD. In this case the field line of length $20 \mu\text{m}$ is the one on which PD may occur.

This approach is selected to evaluate PD activity in this work. That choice is made for mainly three reasons. First, it is simple to code. Second, it gives precise results. Third, only uniform fields are considered in this work. Chapter III will present the original developed method for precise field lines computation. Chapter IV will then detail an experimental study on the Paschen's criterion and will propose a correction adapted to enamelled round wires configurations. Finally, Chapter V will present the integration of the field lines computation module and the corrected Paschen's curve in an automatic tool to evaluate PD activity inside an electric motor slot under aeronautical environment.

This chapter has detailed the Partial Discharges (PD). The Paschen's law and some deviations which take into account the aeronautic environmental conditions have been given. The different experimental set-ups to detect and analysis the PD have been given. Results concerning the impact of frequency, voltage and temperature on insulation lifespan have been presented. At the end of this chapter two methods have been presented to evaluate the Partial Discharge Inception Voltage (PDIV). The Paschen's criterion has been retained. The next chapter deals with the computation of electric field lines. Field lines geometry and voltage drop are required to apply the Paschen's criterion.

Chapter 3: Electric field lines computation

1 INTRODUCTION

Our research for the evaluation of Partial Discharges (PD) leads us to the computation of electric field lines using *Matlab* software. However, in some configuration, strange results have been observed. These are field lines which are not perpendicular to iso-potential lines. In order to investigate the cause of such weirdness and to fully understand the methods used in *Matlab* software, we have to reinforce our knowledge on numerical methods used for the electric field lines computation in an electrostatic problem composed of both conductors and dielectric materials.

After the presentation of electrostatic formulations, the Whitakker's method is illustrated on a simple example. From the presentation of the Horowitz's method, we propose an improvement in the computation of field lines. This improvement makes it possible to present a more synthetic field map: the field lines are drawn so that their density is proportional to the intensity of the electric field. Finally, an example is treated with the Whitakker's method implemented in *Matlab* and the proposed method which allows them to be compared.

2 THE ELECTROSTATIC PROBLEM

2.1 PRESENTATION OF THE FIELD OF STUDY

The problem consists of two enameled round wires in close contact in air. It is a configuration representative of a contact between two adjacent wires in a stator slot in the presence of a default (air bubble or bad impregnation) in the surrounding impregnating resin.

The copper areas are obviously not modelled since there is no electric field in conductor materials. Boundary conditions (i.e.: voltages) are applied on the copper areas contours.

The air and the enamel are considered charge carrier free.

The wires are considered infinitely long in the machine active length dimension and the voltage drops are neglected. Due to invariance along this dimension and symmetries the problem is reduced to a 2D-electrostatic problem with only a quarter of the wires being modelled.

Figure 82 displays the 2D-problem.

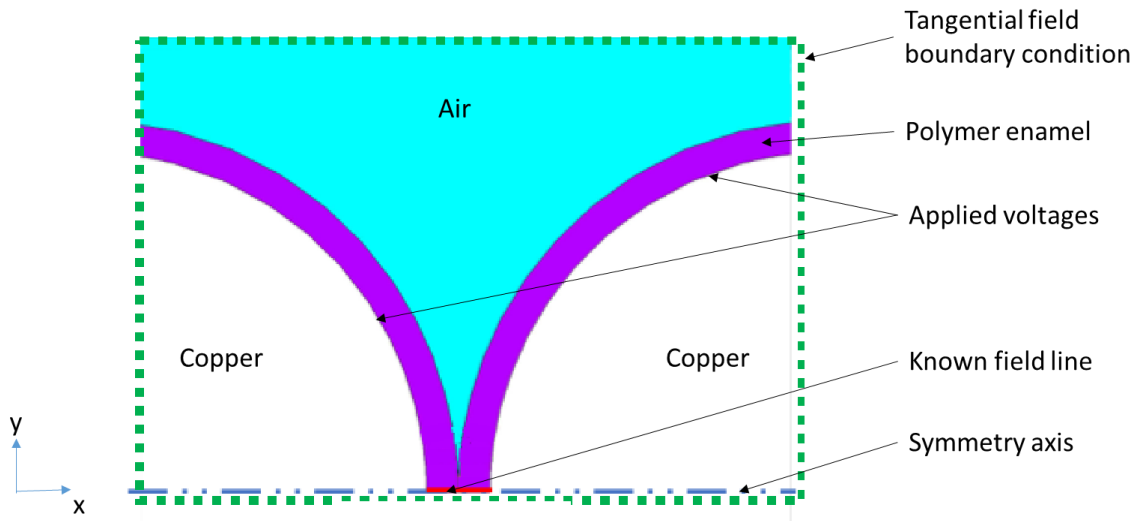


Figure 82: Enamelled wires 2D-electrostatic problem

In such electrostatic problem, the materials are characterized with their dielectric constant. The dielectric constant of air is 1. The dielectric constant of the enamel is greater than 1 and depends on the polymer used. In this chapter, the dielectric constant of the enamel will be taken as 3.5.

2.2 ELECTROSTATIC EQUATIONS AND FORMULATIONS

The basis of electromagnetism are the Maxwell's equations. These are recap in Table 16.

$\text{Curl } \vec{H} = \vec{J} + \frac{\partial \vec{D}}{\partial t}$	<i>Eq 39</i>
$\text{Curl } \vec{E} = -\frac{\partial \vec{B}}{\partial t}$	<i>Eq 40</i>
$\text{div } \vec{B} = 0$	<i>Eq 41</i>
$\text{div } \vec{D} = \rho$	<i>Eq 42</i>

Table 16: Complete Maxwell's equations [42]

Five field vectors are introduced: the electric field intensity \vec{E} , the magnetic field intensity \vec{H} , the electric flux density \vec{D} , the magnetic flux density \vec{B} and the current density \vec{J} . The volume charge density of the dielectric medium in which the field is considered is noted ρ .

The fields produced by a power frequency alternating voltage are not electrostatic. However, they are considered quasi-stationary: the fields time variation is neglected. Besides, in this work both air and

polymer insulation materials are considered free of charge carrier. Table 17 gives the simplified Maxwell's equations which comes into play in the considered electrostatic problem.

$\text{curl } \vec{E} = 0$	<i>Eq 43</i>
$\text{div } \vec{D} = 0$	<i>Eq 44</i>

Table 17: Maxwell's equations used for a charge carrier free electrostatic problem

Because \vec{E} is curl free, it can be expressed as a gradient of a scalar potential. This scalar is the electric potential V :

$$\vec{E} = -\text{grad } V \quad \text{Eq 45}$$

The electric flux density \vec{D} is derived from the electric field intensity \vec{E} and the medium properties:

$$\vec{D} = \epsilon_r * \epsilon_0 * \vec{E} = \epsilon * \vec{E} \quad \text{Eq 46}$$

With ϵ_0 the vacuum dielectric constant, ϵ_r the medium relative dielectric constant (equals 1 in air). The medium is considered isotropic thus ϵ is a constant.

By injecting Eq 45 and Eq 46 into Eq 44 one gets:

$$\text{div}(\epsilon * (-\text{grad } V)) = 0 \quad \text{Eq 47}$$

$$\text{div}(\text{grad } V) = 0$$

$$\nabla^2 V = 0$$

Equation Eq 47 is called the Poisson's equation. It is the scalar potential formulation of a charge carrier free electrostatic problem.

As \vec{D} is divergent free it thus can be expressed as the curl of an electric vector potential \vec{u} :

$$\vec{D} = \text{curl } \vec{u} \quad \text{Eq 48}$$

By injecting Eq 48 in Eq 43 one gets:

$$\text{curl}(\text{curl } \vec{u}) = 0 \quad \text{Eq 49}$$

$$\text{grad}(\text{div } \vec{u}) - \nabla^2 \vec{u} = 0$$

The Coulomb's gauge applied to the vector potential \vec{u} is defined as follow:

$$\text{div}(\vec{u}) = 0 \quad \text{Eq 50}$$

Applying the Coulomb's gauge in Eq 49 results in:

$$\nabla^2 \vec{u} = 0 \quad Eq\ 51$$

Equation Eq 51 is the vector potential formulation of a charge carrier free electrostatic problem.

There are thus two formulations for solving the electrostatic problem. The first uses a scalar potential V . The second uses a vector potential \vec{u} . Each formulation has its advantages and disadvantages.

2.3 ADVANTAGES AND DISADVANTAGES OF EACH FORMULATION

2.3.1 Vector potential

In case of a 2D-problem in a (x,y) plane, the electric vector potential \vec{u} is written as:

$$\vec{u} = u \cdot \vec{z} \quad Eq\ 52$$

With:

$$\|\vec{z}\| = 1$$

The main advantage of the vector potential is that it directly gives the electric field lines. Field lines are in fact level curves (i.e.: contour) of a scalar function u . Such function is usually called the stream function [111]. By injecting Eq 52 in Eq 48 one gets:

$$\begin{cases} \frac{du}{dx} = -D_y \\ \frac{du}{dy} = D_x \end{cases} \quad Eq\ 53$$

Using the relationship between the electric field \vec{E} and the electric flux density \vec{D} (Eq 46), Eq 53 can be expressed under the form:

$$\begin{cases} \frac{du}{dx} = -\varepsilon * E_y \\ \frac{du}{dy} = \varepsilon * E_x \end{cases} \quad Eq\ 54$$

With E_x and E_y respectively the projections of \vec{E} along \vec{x} and \vec{y} axis in a 2D-system.

The vector potential formulation is complex to execute in an electrostatic problem with multiple conductors. It requires to put in place a network of branches and cuts all across the field of study [112], [113]. However, [113], [114] have successfully put in application that formulation to solve an electrostatic problem with multiple conductors. Their work has been done almost at the same time we started our researches on this topic.

Besides, none of the software at our disposal uses the vector potential formulation.

2.3.2 Scalar potential

The formulation with the scalar potential V is the simplest to use. Contrary to the vector potential u , there is no need to introduce cuts if multiple conductors are present in the domain of study. That is because the solution using a V formulation is unique. The scalar potential is also easy to handle for the computation of equipotential lines.

The main inconvenient of the V formulation is that it does not give directly the electric field lines. Additional steps are consequently required. Two main methods were found in the literature to compute field lines by using a numerical calculation software (such as *Matlab*) from the scalar potential solution.

The formulation with the scalar potential V was finally chosen for several reasons. First, the finite elements software at our disposal (*Ansys Emag*, *Ansys Maxwell*, *Femm* or *Jmag*) are using the scalar potential formulation. Then, it is simple to manipulate. Finally, methods exist in the literature to compute field lines from the scalar potential solutions. They constitute a strong base to start our work.

3 ELECTRIC FIELD LINES COMPUTATION DERIVED FROM A SCALAR POTENTIAL FORMULATION

3.1 BALLISTIC METHOD

The first method to compute field lines from a scalar potential formulation solution is presented by [115]. By definition, the electric field \vec{E} is parallel to a field line \vec{l} . In a direct orthonormal system, the cross-product of these two quantities is null:

$$\vec{l} \times \vec{E} = 0 \quad Eq\ 55$$

$$l_x * E_y - l_y * E_x = 0$$

With l_x and l_y respectively the projections of \vec{l} along \vec{x} and \vec{y} axis in a 2D-system.

From Eq 55 it comes:

$$\frac{E_y}{E_x} = \frac{l_y}{l_x} \quad Eq\ 56$$

E_x, E_y are the field components over the mesh. These are known.

Starting at any point, the field line \vec{l} can be computed by incrementing Eq 56 given an arbitrary displacement Δ_x along x axis. Thus, the vertical displacement Δ_y along y axis is expressed as follow:

$$\Delta_y = \Delta_x * \frac{E_y}{E_x} \quad Eq\ 57$$

Let us express equation Eq 57 between two consecutive points $M_i(x_i, y_i)$ and $M_{i+1}(x_{i+1}, y_{i+1})$:

$$(y_{i+1} - y_i) = (x_{i+1} - x_i) * \frac{E_{y,i}}{E_{x,i}} \quad Eq\ 58$$

Let us define a constant step increase Δ_{step} at each iteration, so that:

$$\Delta_{step} = \frac{(y_{i+1} - y_i)}{E_{y,i}} = \frac{(x_{i+1} - x_i)}{E_{x,i}} \quad Eq\ 59$$

It is thus possible to express the $M_{i+1}(x_{i+1}, y_{i+1})$ coordinates from $M_i(x_i, y_i)$ data (coordinates and field components) and Δ_{step} :

$$x_{i+1} = x_i + \Delta_{step} * E_{x,i} \quad Eq\ 60$$

$$y_{i+1} = y_i + \Delta_{step} * E_{y,i}$$

When chosen arbitrary, the starting point may not be the start of the field line. It is then necessary to integrate Eq 60 backward to complete the line.

This method is called a ballistic method. The mesh is swept and field lines are started in elements which do not already contain a field line. The field lines are computed by integration. The integration process is stopped if one of the following condition is checked:

- the field line enters a forbidden region (for instance the limit of the domain);
- the field line reaches a null field;
- the field line loops back onto itself;
- the field line has too many segments. This is a safety measure in case the previous conditions do not work properly.

By doing so, there is the same density of field line all over the model. It does not allow to represent the electric field intensity.

As an illustration, let us consider an electrostatic problem made of two infinitely long cylinder oppositely. Due to the symmetries, only a quarter of the field of study is considered as displayed on Figure 83. The mesh is represented with black crosses. It is made of rectangular elements (dotted red line). The blue line delimits the conductor contour.

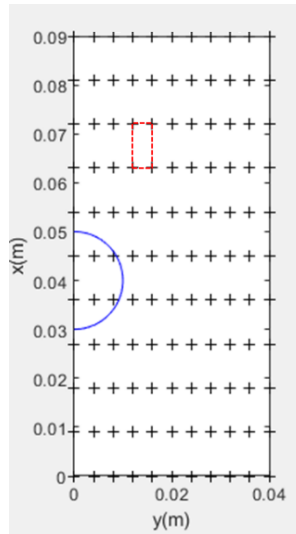


Figure 83: System of 2 infinite cylinders oppositely charged - field of study represents one quarter of the system - mesh (dots) and half conductor contour (blue)

Let us apply the Whittaker ballistic method on that system. The algorithm noted above is implanted in a Matlab script.

The orientation vector of the electric field is computed on all mesh nodes, except for the ones located inside the conductor. The starting points are chosen on the contour of the domain. Figure 84 displays the computed orientation vectors and the starting points (circles). The starting points are arbitrary chosen on the limit of the field of study.

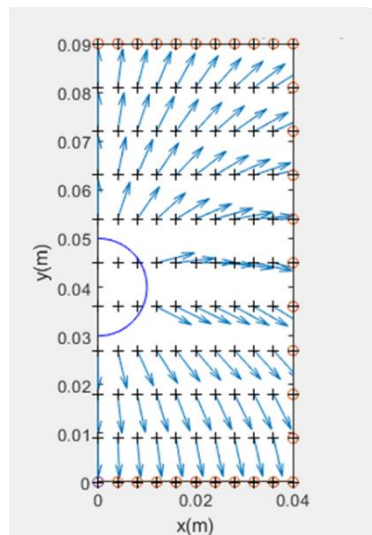


Figure 84: Electric field orientation vectors and starting points (red circles)

Let us designate the starting point $Q(x_0, y_0)$ of a field line. Then, the next point on the line $M_1(x_1, y_1)$ is computed by iteration from point Q . The iteration is backward because the starting points are on the end of the field lines:

$$x_1 = x_0 - \Delta_{step} * E_{x,0} \quad \text{Eq 61}$$

$$y_1 = y_0 - \Delta_{step} * E_{y,0}$$

With $E_{x,0}$ and $E_{y,0}$ the electric field orientation vector components along x and y axis respectively on starting point Q . The step increase Δ_{step} at each iteration is taken equal to the grid spacing along x axis dx . Figure 85 displays the field lines after one iteration backward from starting points.

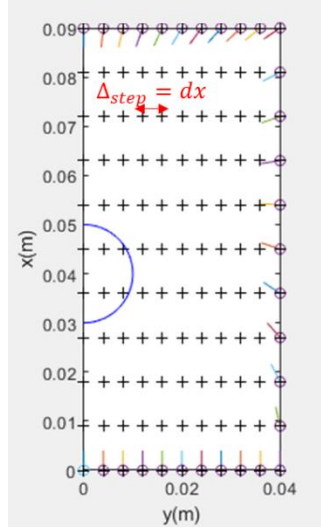


Figure 85: Field lines after a first iteration backward

It can be seen that the M_1 points do not coincide with a mesh node. The electric field orientation vectors are interpolated on the extra M_1 points using the *interp2* function.

At each iteration, the field lines extend. The i^{th} iteration between two consecutive points $M_i(x_i, y_i)$ and $M_{i+1}(x_{i+1}, y_{i+1})$ correspond to:

$$x_{i+1} = x_i - \Delta_{step} * E_{x,i} \quad Eq\ 62$$

$$y_{i+1} = y_i - \Delta_{step} * E_{y,i}$$

The computed field lines after 11 iterations are displayed on Figure 86.

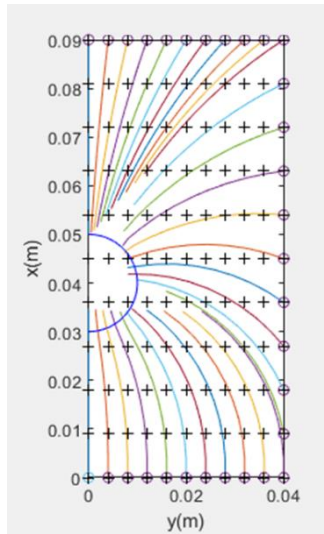


Figure 86: Computed field lines after 11 backward iterations

In this method, the starting points are chosen arbitrarily. In the next presented method, the choice of the starting points is a key step in order to represent a field intensity with the density of field lines.

3.2 FLUX TUBES BASED METHOD

The objective is to represent the strength of the electric field by the density of the electric flux lines [111]. The core of the method is the choice of the field lines starting points.

A predetermined amount of flux $\delta\phi$ has to be present between two adjacent lines a and b :

$$\delta\phi = \int_a^b E \cdot n \cdot ds \quad Eq\ 63$$

Where n is the normal vector and s is the path between the lines a and b . This path is chosen as the contour of scalar potential V . Figure 87 illustrates the equation Eq 63.

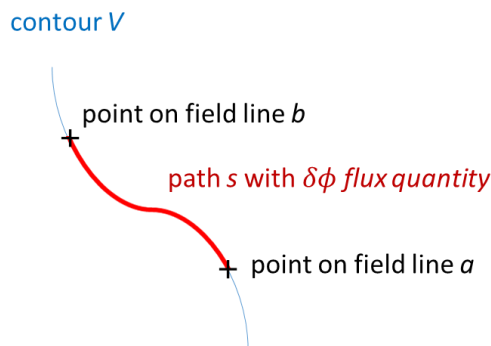


Figure 87: Illustration of flux quantity $\delta\phi$ located between two consecutive field lines a and b

Such as in Whittaker's method, a uniform mesh is applied. The electric field is calculated on the whole meshed domain using linear interpolations. In a simple case, all the field lines pass through a single V contour. The contour results in a series of points $s_i = \{x_i, y_i\}; i=1, \dots, I$. The total flux through the contour of potential V is:

$$\phi_V = \int_{s_1}^{s_I} E ds = \frac{1}{2} \sum_{i=1}^I (E_i + E_{i+1}) |s_{i+1} - s_i| \quad Eq\ 64$$

Figure 88 displays the contour V discretization in a uniform meshed domain. Here the total number of points is $I=5$.

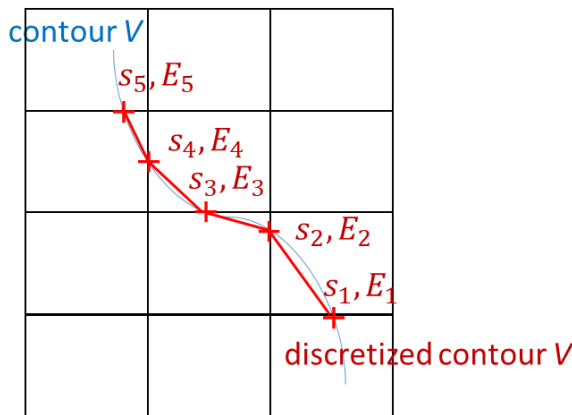


Figure 88: Contour discretization in an uniform mesh

The field lines starting points on contour V results in a second series of points $s_j = \{x_j, y_j\}; j=1, \dots, N$. Such points satisfy the following equation:

$$\int_{s_j}^{s_{j+1}} E ds = \delta \Phi \quad Eq\ 65$$

Starting from the s_1 point of the contour V , the s_i contour point which is in proximity of the next field line starting point is identified by this equation:

$$\int_{s_1}^{s_i} E ds < \delta \Phi < \int_{s_1}^{s_{i+1}} E ds \quad Eq\ 66$$

The s_j field line starting point on contour V segment s_i, s_{i+1} is defined as:

$$\int_{s_i}^{s_j} E ds = \delta \Phi - \int_{s_1}^{s_i} E ds = \phi_0 \quad Eq\ 67$$

Then one can express Eq 67 as:

$$\frac{1}{2} (E_i + E_j) |s_j - s_i| = \phi_0 \quad Eq\ 68$$

Let $a = \frac{|s_j - s_i|}{|s_{i+1} - s_i|}$ be the fractional distance from contour point s_i to field line starting point s_j . As the electric field \vec{E} is linear along the grid, one finally gets Eq 69 [111]:

$$a = \phi_0/E_i |s_{i+1} - s_i| \quad Eq\ 69$$

Starting points s_j of field lines on contour V are finally determined [111]:

$$s_j = \{x_j, y_j\} \quad Eq\ 70$$

$$s_j = \{(1 - a) * x_i + a * x_{i+1}, (1 - a) * y_i + a * y_{i+1}\}$$

The field lines are then built from their starting point by integrating as in Whittaker's method [111]. As the same flux quantity $\delta\Phi$ is present between two adjacent lines, the electric field strength is represented by the concentration of field lines. The same termination criteria as in Whittaker's method are used.

However, an electric machine slot filled with conductors is a more complex case. It mainly happens that all the field lines do not pass through a single V contour. Let us consider two conductors at potential of V_1 and V_2 respectively. A field line starting from V_1 contour is identified by $l_{n1}^1; n1=1,...,N1$. The same procedure described in the simple case is applied to V_1 contour. However, the intersections of l_{n1}^1 field lines with V_2 contour have to be tracked. To do that, each segment of l_{n1}^1 is checked to verify whether or not it intersects with V_2 contour. The intersection points are added to V_2 contour points series. Now, one can apply the same procedure with V_2 contour adding some steps:

Step 1: choose as a starting point of field lines from V_2 contour ($l_{n2}^2; n2=1,...,N2$) one of the intersection point of a l_{n1}^1 field line with V_2 contour;

Step 2: integrate from that point until (a) another intersection point of a l_{n1}^1 field line with V_2 contour is reached or (b) the integral exceed the fixed flux quantity $\delta\Phi$. In case (b), the next point as to be determined the same way s_j point is in the simple case;

Step 3: repeat step 2 until the whole V_2 contour is swept;

Step 4: integrate backward from the first intersection point to find the remaining starting points.

Figure 89 illustrates the field lines computed between two conductors at potential V_1 and V_2 using the presented algorithm.

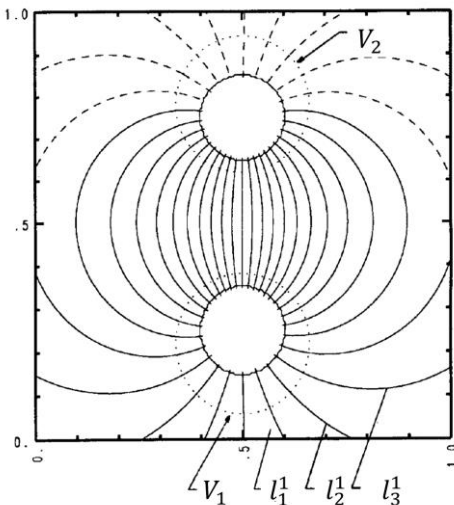


Figure 89: Electric field lines from two infinitely long wires of opposite charge in free space. V_1 and V_2 are potential contours. The solid field lines were drawn from V_1 . The dashed field lines were drawn from V_2 [111]

4 PROPOSED METHOD

The proposed method we developed is an upgrade of the method presented by Horowitz [111]. A flux function is built from the electric field components on all the nodes. The field lines correspond to iso-values of this scalar function. The proposed method does not require a uniform mesh. The calculation is done on the same mesh on which the scalar potential V is computed.

4.1 ELECTRIC FIELD AND ELECTRIC FLUX

The 2D-finite element model on Ansys Mechanical APDL uses 8 nodes elements. On each element, the coordinates and the scalar potential solution are expressed as a combination of each nodes data with a defined shape function. Shape functions are expressed in the local coordinate system (u, v) of the element. It is a coordinate system attached to the element which define the location of each node.

$$\begin{cases} x_e(u, v) = \sum_{i=1}^8 N_i(u, v) \cdot x_e(i) \\ y_e(u, v) = \sum_{i=1}^8 N_i(u, v) \cdot y_e(i) \\ V_e(u, v) = \sum_{i=1}^8 N_i(u, v) \cdot V_e(i) \end{cases} \quad Eq\ 71$$

With:

$$\begin{cases} N_i(u, v) = 1 \text{ at node } i \\ N_i(u, v) = 0 \text{ elsewhere} \end{cases}$$

With x_e and y_e the coordinates in the global coordinate system (x, y) of the nodes of an element e . For an 8 nodes elements, the shape functions N are given in [116].

The electric field on the nodes of an element is derived from the voltage values on the node using Eq 45. It requires the expression of partial derivatives in the global system.

First, the partial derivatives of a function in the local system (u, v) can be expressed from its partial derivatives in the global system (x, y) :

$$\begin{pmatrix} \frac{\partial}{\partial u} \\ \frac{\partial}{\partial v} \end{pmatrix} = \begin{bmatrix} \frac{\partial x}{\partial u} & \frac{\partial y}{\partial u} \\ \frac{\partial x}{\partial v} & \frac{\partial y}{\partial v} \end{bmatrix} \begin{pmatrix} \frac{\partial}{\partial x} \\ \frac{\partial}{\partial y} \end{pmatrix} = J \begin{pmatrix} \frac{\partial}{\partial x} \\ \frac{\partial}{\partial y} \end{pmatrix} \quad \text{Eq 72}$$

With:

$$J = \begin{bmatrix} J_{11} & J_{12} \\ J_{21} & J_{22} \end{bmatrix}$$

With J the Jacobian matrix. It is computed from the known shape functions partial derivatives in the local system when putting Eq 71 in Eq 72.

Then, the partial derivatives of a function in the global system (x, y) can be expressed from its partial derivatives in the local system (u, v) :

$$\begin{pmatrix} \frac{\partial}{\partial x} \\ \frac{\partial}{\partial y} \end{pmatrix} = \begin{bmatrix} \frac{\partial u}{\partial x} & \frac{\partial v}{\partial x} \\ \frac{\partial u}{\partial y} & \frac{\partial v}{\partial y} \end{bmatrix} \begin{pmatrix} \frac{\partial}{\partial u} \\ \frac{\partial}{\partial v} \end{pmatrix} = I \begin{pmatrix} \frac{\partial}{\partial u} \\ \frac{\partial}{\partial v} \end{pmatrix} \quad \text{Eq 73}$$

With:

$$I = \begin{bmatrix} I_{11} & I_{12} \\ I_{21} & I_{22} \end{bmatrix}$$

$$I = J^{-1}$$

It is matrix I which is use in practise because the data have to be expressed in the global system. It is computed as follow:

$$I = J^{-1} = \frac{1}{\det(J)} \begin{bmatrix} J_{22} & -J_{12} \\ -J_{21} & J_{11} \end{bmatrix} \quad \text{Eq 74}$$

With:

$$\det(J) = J_{11}J_{22} - J_{12}J_{21}$$

The electric field components on the nodes of an element e can finally be expressed in the global system by combining Eq 71 and Eq 73:

$$\begin{cases} E_{x,e} = -\frac{\partial V_e}{\partial x} = -\sum_{i=1}^8 \left(I_{11} \frac{\partial N_i}{\partial u} + I_{12} \frac{\partial N_i}{\partial v} \right) \cdot V_e(i) \\ E_{y,e} = -\frac{\partial V_e}{\partial y} = -\sum_{i=1}^8 \left(I_{21} \frac{\partial N_i}{\partial u} + I_{22} \frac{\partial N_i}{\partial v} \right) \cdot V_e(i) \end{cases} \quad Eq\ 75$$

The electric flux components are computed from electric field components using Eq 46.

4.2 EQUIPOTENTIAL LINES

The next step consists in forming equipotential lines. These are contours on which the voltage value is constant. Equipotential lines are obtained by regrouping nodes with the same voltage value. Let us see the steps to compute an equipotential line at voltage V .

A test is done on each edge of each element to check whether or not it is crossed by the equipotential line V . As can be seen on Figure 90, each edge is composed of three nodes. There are three possible outcomes:

- The voltage V is lower or bigger than any of the three nodes voltage. The edge is not intersected by the equipotential line V ;
- The voltage V is equal to one of the three nodes voltage. The equipotential line intersects the edge at the corresponding node of voltage V ;
- The voltage V is between any of the three nodes voltage. The edge is intersected by the equipotential line at a point which is interpolated.

Figure 90 illustrates an equipotential intersecting two edges of an element. On one edge the intersection point is an already existing node (node 6). The second edge intersection point has to be interpolated (red cross). The local numbering of the nodes is rearranged compared to Ansys 8 nodes reference element to facilitate the programming.

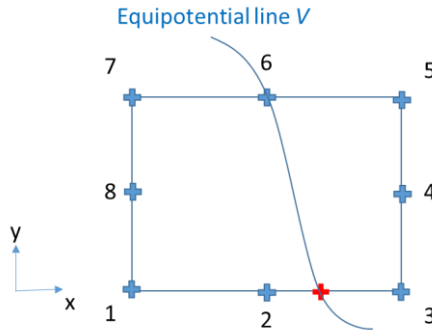


Figure 90: Equipotential line V intersecting an element edges

A second order polynomial is used for the interpolation. The following equation gives the parametric expression of the polynomial:

$$z(t) = a_{1,z} + a_{2,z} * t + a_{3,z} * t^2 \quad Eq\ 76$$

With:

$$t \in [0,1]$$

The parameter t represents the edge on which the interpolation is performed.

Figure 91 displays Eq 76 along a parameterized edge:

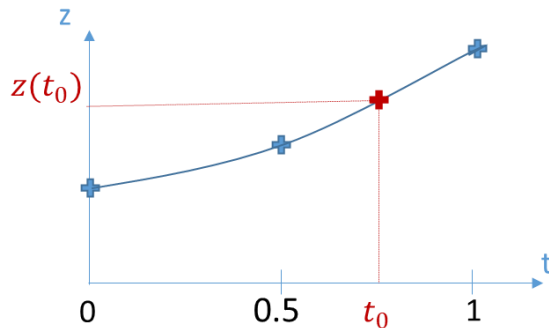


Figure 91: Illustration of a second order polynomial interpolation over a parameterized edge

For instance, on Figure 90 the interpolation is done on the edge containing the nodes (1,2,3). The nodes are parameterized according to the local numbering order: $t=0$ for node 1, $t=0.5$ for node 2 and $t=1$ for node 3. By solving Eq 76 in term of voltage it is possible to derived the polynomial coefficients:

$$V(t) = a_{1,V} + a_{2,V} * t + a_{3,V} * t^2 \quad Eq\ 77$$

With:

$$\begin{cases} V(0) = a_{1,V} = V_0 \\ V(0.5) = a_{1,V} + a_{2,V} * 0.5 + a_{3,V} * 0.25 = V_{0.5} \\ V(1) = a_{1,V} + a_{2,V} + a_{3,V} = V_1 \end{cases}$$

In the considered example, $(V_0, V_{0.5}, V_1)$ are respectively the finite elements voltage solution on nodes (1,2,3) in Figure 90. The three polynomial coefficients $(a_{1,V}, a_{2,V}, a_{3,V})$ are thus determined.

$$V(t_0) = V = a_{1,V} + a_{2,V} * t_0 + a_{3,V} * t_0^2 \quad Eq\ 78$$

With V the voltage of the considered equipotential line V .

The obtained parameter t_0 is injected back into Eq 77 to determine the interpolated node coordinates, electric field components and electric flux components. As in Eq 78, the associated polynomial coefficients are deduced from the known nodes data.

4.3 FLUX FUNCTION

At this point, equipotential lines made of nodes at the same scalar potential V are determined. The coordinates and fields components are determined on all these nodes. The number of equipotential lines depends on the accuracy from which the electric scalar potential problem is solved. The finer the mesh used to solve the problem, the higher the number of equipotential lines that can be accurately determined.

For each equipotential line a geometrical reference is defined on its barycentre. The points on the line are located by using polar coordinates in this reference. A starting point Q is chosen for instance by means of the angular coordinates. Figure 92 illustrates the barycentre reference attached to an equipotential line V . Point G is the barycentre. A point M located on the equipotential line is identified by its curvilinear abscissa $s(M)$.

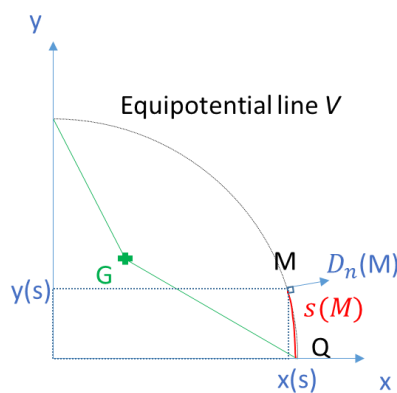


Figure 92: Barycentre system associated to an equipotential line V

A flux function $\Phi(M)$ of points on each equipotential is defined as the flux per meter crossing the line between the starting point Q and point M :

$$\Phi(M) = \int_Q^M D_n ds \quad Eq\ 79$$

D_n is the normal electric flux density on the equipotential line, ds is the elemental curvilinear length of the equipotential line. Each point M on the line is parameterized by the curvilinear abscissa $s(M)$ and:

$$\begin{cases} s(M) = \int_Q^M ds \\ x(M) = x(s) \\ y(M) = y(s) \\ \Phi(M) = \Phi(s) \end{cases} \quad Eq\ 80$$

The trace of a flux tube on the equipotential line is delimited by two points P_i and P_{i+1} which are given by the predetermined flux per meter $\delta\Phi$:

$$\delta\Phi = \int_{P_i}^{P_{i+1}} D_n ds \quad Eq\ 81$$

The properties of these points are:

$$\begin{cases} P_1 = Q \\ \Phi(P_1) = 0 \\ \Phi(P_i) = \Phi(P_{i-1}) + \delta\Phi = (i-1)\delta\Phi \end{cases} \quad Eq\ 82$$

All the points P_i on the equipotential line are determined by inverting the previous functions:

$$s(P_i) = \Phi^{-1}((i-1)\delta\Phi) \quad Eq\ 83$$

Figure 93 illustrates the flux tubes computation using Eq 80, Eq 81, Eq 82 and Eq 83:

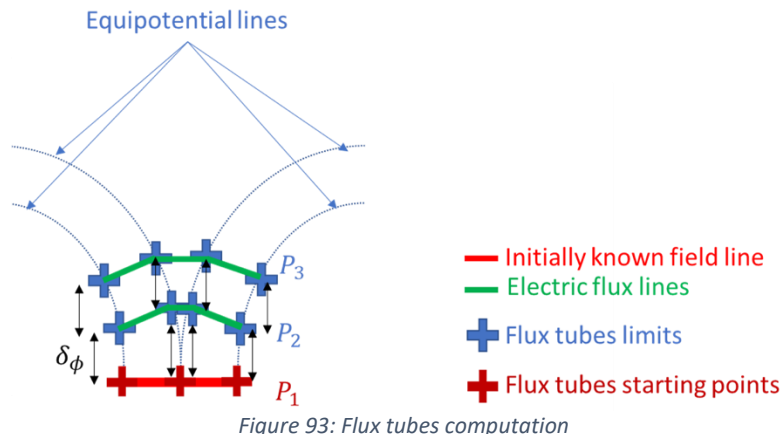


Figure 93: Flux tubes computation

The determination of points P_i is done on all equipotential lines. If the starting point Q on each equipotential line is correctly chosen then the electric flux lines are defined by iso- Φ lines. The starting point has to be chosen on a field line crossing all the equipotential lines present in the domain.

4.4 ILLUSTRATIVE EXAMPLES

In this paragraph the proposed method is used to compute electric field lines in the studied electrostatic problem. Table 18 gives the parameters used.

Wires' parameters		
R_{int}	Round wire copper radius	0.75 mm
e	Enamel overcoat thickness	$70 \mu m$
ε_r	Enamel dielectric constant	3.5
Applied voltages		
V_1	Left wire voltage amplitude	1000 V
V_2	Right wire voltage amplitude	0 V
Equipotential lines parameters		
V_{imp}	Imposed potentials intervals	$[0; \frac{V_1}{4}; \frac{2 * V_1}{4}; \frac{3 * V_1}{4}; V_1]$
N_{imp}	Imposed number of computed equipotential lines on each potential interval	[25; 25; 25; 25]

Table 18: Parameters used in the illustrative example

It can be seen that there are one hundred equipotential lines which will be formed. The voltage amplitude is divided into four intervals. A same number of twenty-five equipotential lines per voltage interval is chosen.

The finite element software used is *Ansys Mechanical APDL*. The used mesh is displayed on Figure 94. The computation time is given as an order of magnitude. It is obtained using tic-toc on *Matlab*. It changes depending on the system computing speed. Thus, the computation time presented on Figure 94 is the sum of the loading times of data transfer between *Ansys* and *Matlab*, the meshing time and the resolution time.

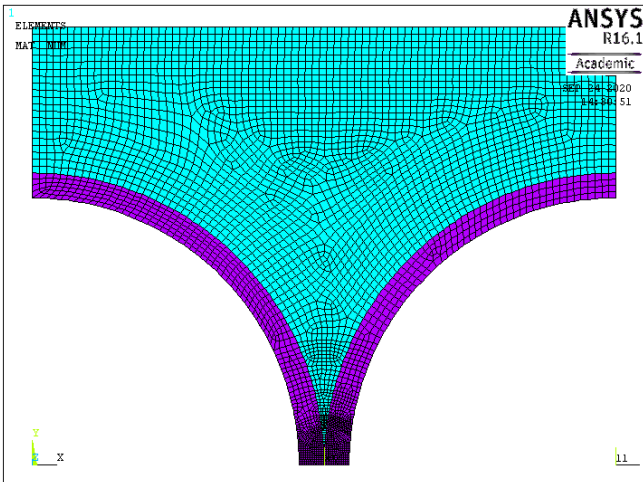
Mesh		Number of elements: 4144
		Computation time: 12.6 s

Figure 94: Used mesh (white: copper, purple: enamel, green: air)

The significant results are given on Figure 95 and Figure 96

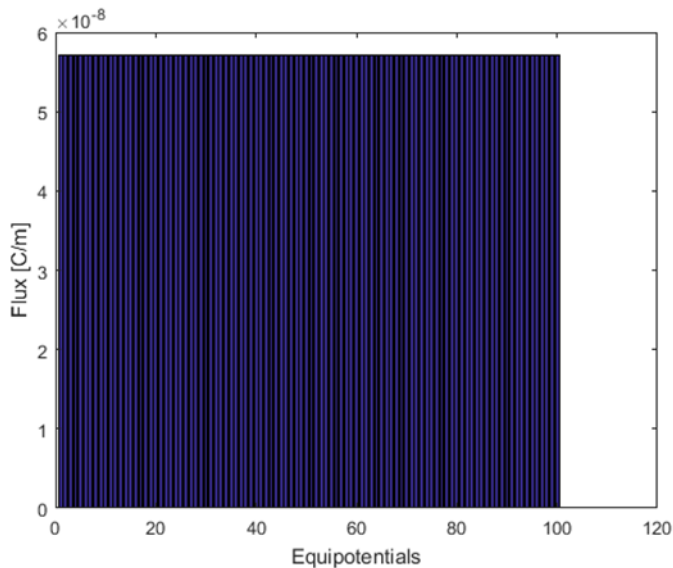


Figure 95: Total electric fluxes crossing each equipotential line

The electric flux across each equipotential line is constant. The starting point of the twenty field lines displayed on Figure 96 are chosen by dividing the total electric flux crossing each equipotential line by nineteen. That is because there is already one known field line that is the reference line chosen on the symmetry axis.

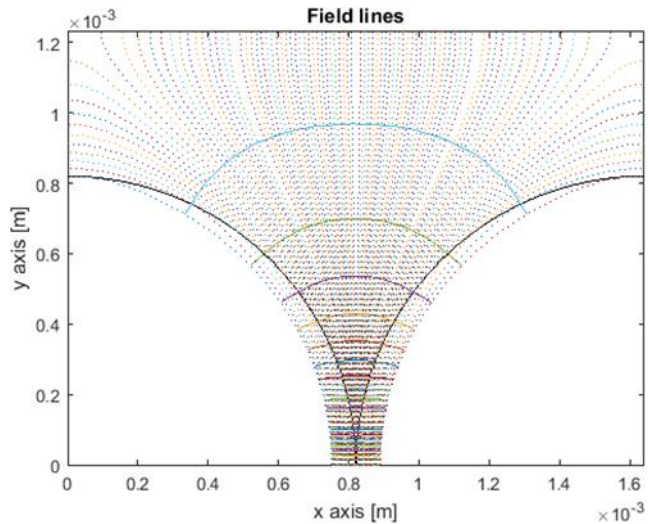


Figure 96: Electric field lines obtained with the mesh of Figure 94

The post processing time is the time required to build the field lines starting from the finite elements solution. It is of 9.11 s.

In this approach, the density of the field lines is linked to the electric field amplitude.

5 ANOTHER METHOD USING MATLAB FUNCTIONS

Another method to plot electric field lines from scalar potential solution is developed using *Matlab* functions. It is likely a Whittaker based approach [115]. The different steps in order to obtain such results are presented.

5.1 BUILDING THE ADDITIONAL MESH

The mesh created by the finite element software cannot be used directly by *Matlab* functions. Indeed, it has to be uniform. So the first step consists in building a second uniform mesh. The finite element (FEM) computed nodes coordinates (X, Y) and scalar potential V lists are imported. Axis vectors X_a, Y_a are built from X, Y lists such that:

- $X_a \in [X_{min}, X_{max}]$ and $Y_a \in [Y_{min}, Y_{max}]$
- X_a and Y_a results in a N uniformly spaced values

The *linspace* function is used so that:

$$X_a = \text{linspace}(X_{min}, X_{max}, N)$$

$$Y_a = \text{linspace}(Y_{min}, Y_{max}, N)$$

A new mesh is generated from these axis vectors. It is made of identical rectangles.

The *meshgrid* function is used:

$$[X_g, Y_g] = \text{meshgrid}(X_a, Y_a)$$

The X_g, Y_g matrix contain the coordinate of all the points of the new mesh. This mesh is referred as *Matlab* mesh.

5.2 ELECTRIC FIELD

The *Matlab* mesh is different from the one generated with the FEM software. Multiple points of the FEM mesh are deleted. Besides, the *Matlab* mesh adds some points. The voltage solution on these points are linearly interpolated from the existing ones.

The *griddata* function is used:

$$V_g = \text{griddata}(X, Y, V, X_g, Y_g, 'linear')$$

The V_g matrix contain the scalar potential values on all points in *Matlab* mesh.

The electric field components over the *Matlab* mesh is computed based on Eq 45.

The *gradient* function is used. It computes only the voltage drops over the mesh between two consecutive points.

$$[\delta V_{g,x}, \delta V_{g,y}] = \text{gradient}(-V_g)$$

Field lines starting points are chosen on one of the wire external contour (i.e.: on the enamel overcoat).

The starting points coordinates are designated by (X_0, Y_0) .

The field lines are built using the *stream2* function. This function generates field lines over the Matlab mesh following Whittaker methodology [115].

$$\text{FieldLines} = \text{stream2}(X_g, Y_g, \delta V_{g,x}, \delta V_{g,y}, X_0, Y_0)$$

5.3 COMPARISON WITH THE PROPOSED METHOD

The proposed method and the method based on *Matlab* functions are compared. The parameters are given in Table 18. The Figure 94 mesh configuration is used. For *Matlab* functions, the additional mesh generated with *meshgrid* has a resolution of 600*600.

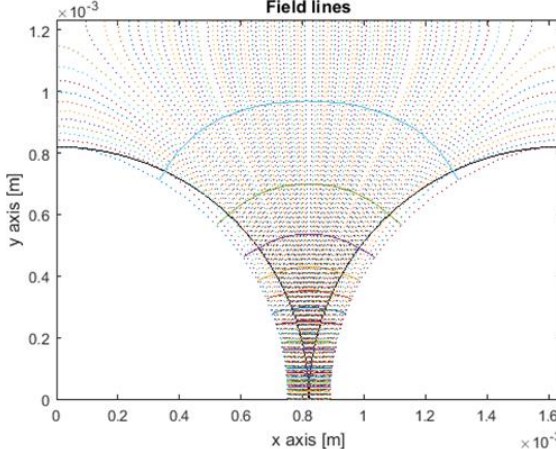
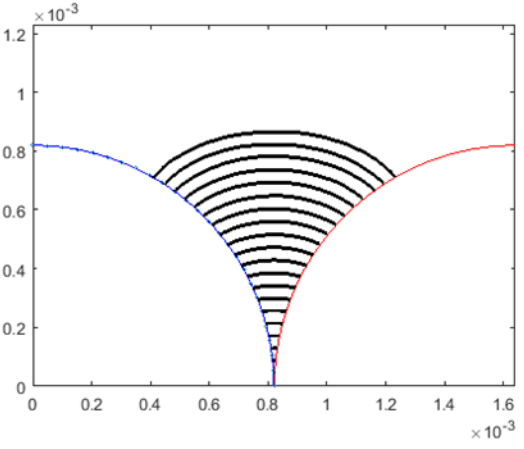
Proposed method	Matlab functions
	
20 field lines	20 field lines
Post processing time: 9.11 s	Post processing time: 1.4 s

Figure 97: Proposed method versus *Matlab* functions to obtain electric field lines

The post process refers to all the steps from the finite element solution to the field lines. *Matlab* algorithm is much more efficient than the developed approach. It is almost ten time faster.

In PD evaluation, only the part of the electric field line in the air gap is considered. Besides, the electric field along the field lines has to be uniform. Figure 98 displays the electric field amplitude. It can be seen that the electric field in the air gap is quite constant along the obtained field lines.

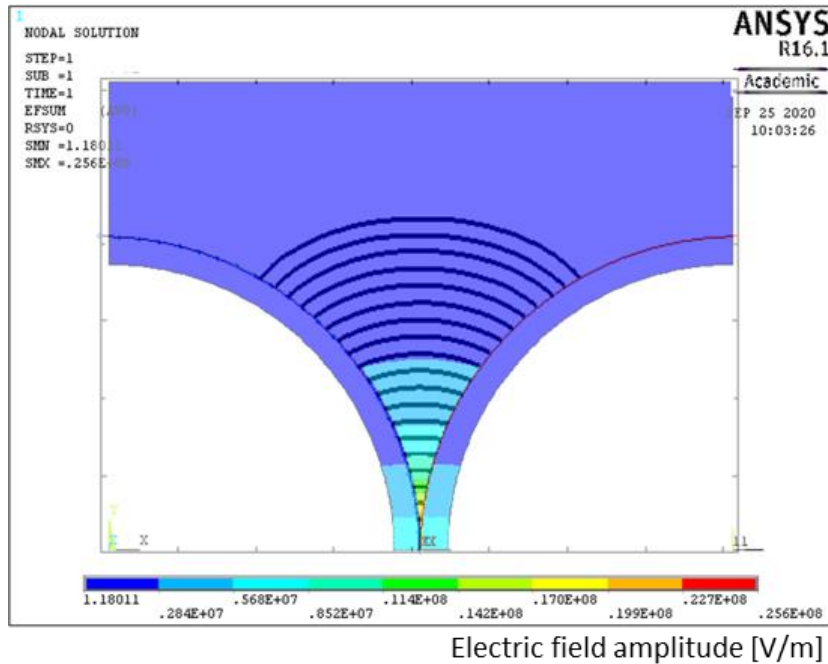


Figure 98: Electric field amplitude [V/m] obtained with finite elements

So the Paschen's criterion could be applied on the part of the field lines in the air gap to evaluate the PDIV. The PDIV is evaluated at 1040 V at 20°C, 1 bar pressure. The voltage on the enamel overcoat contours at the interface with the air is picked up at PDIV. Figure 99 displays the computed voltage drops along each part of field lines in air for the two approaches. The points intersecting with the Paschen's curve indicates field lines on which PD activity is likely to occur.

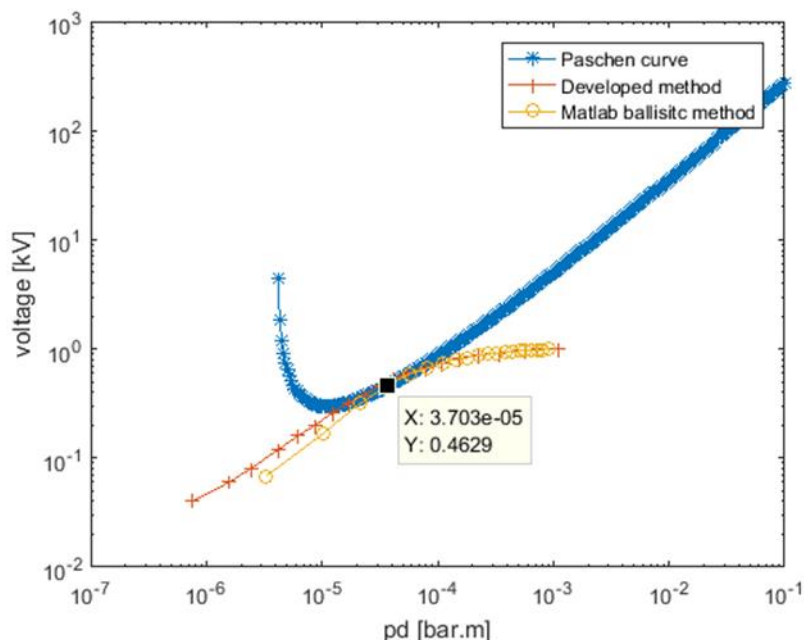


Figure 99: Computed voltage drops along field lines in air ($p=1$ bar) obtained with the two compared methods; $y=0.01$

The results coincide for field lines longer than $10 \mu m$. Both methods evaluate a PD activity on the field line of $37 \mu m$ length in the gap. The additional inflection point on the orange curve for field lines of a few micrometers length could be due to a resolution issue and do not have to be taken into consideration.

In the tool to evaluate PD risk, the *Matlab* approach will be used. It is much faster than the developed method and gives similar results for the field lines of interest (i.e.: a few dozens of micrometers). However, *Matlab* functions are black boxes. Strange results have already been obtained with some configuration due to numerical errors. Numerical errors are much easier to deal with in the developed method because there is no black box. The whole code is accessible and modifiable.

6 CONCLUSION

The method using *Matlab* functions to plot electric field lines is most likely based on Whittaker's approach [115]. The work presented in this chapter clarifies the functions used by *Matlab*.

The method presented by Horowitz [111] make it possible to plot field lines with the electric field strength being represented by the density of lines. In this chapter, this method has been upgraded. A flux function is defined which iso-values directly give the field lines. For now, starting with the scalar potential solution obtained with Ansys Emag and using our proposed method, the computation times are long. However, it must be possible to significantly reduce the computation time by implanting the proposed method in a field calculation code. The main advantage of the proposed method is that it reuses the initial *Ansys Emag* mesh on which the scalar solution is first obtained.

Due to high computation times, the method using *Matlab* functions is used for now to derive field lines on a simplified problem with two conductors. The results given by the two methods are in good agreement for field lines in air longer than $10 \mu m$. In the evaluation of PD using the Paschen's criterion, smaller field lines are not of interest.

In the next chapter, the validity of the Paschen's criterion for a configuration of two enamelled round wires in contact is investigated.

Chapter 4: Correction of the Paschen's criterion

1 MOTIVATIONS

1.1 CONFIGURATION DIFFERENT FROM THE INITIAL ONE

The Paschen's criterion has been presented in Chapter 2. It defines the required electric field strength in a gas gap in order to produce a self-maintained electronic avalanche. This criterion has been established for two metallic plane electrodes facing each other in an uniform electric field [81], [82].

In the literature, the Paschen's criterion has been widely used to determine the Partial Discharges Inception Voltage (PDIV) in the Electrical Insulation Systems (EIS) of electric devices (rotating machines, power electronics, connectors,...) [44], [55], [117], [118]. A representative configuration encountered in rotating machines EIS is two round enamelled wires in close contact. A 2D-finite elements model has been developed with *Ansys Mechanical APDL* (Figure 82). It has provided results showing non-uniform electric field in some air gap areas, as presented on Figure 98. Consequently, the conditions in which the Paschen's criterion has been established are not present in all the air gap surrounding the two neighbouring wires. The use of this criterion in the configuration of two enamelled wires in close contact, as it is the case in stator slots, is then questionable and need to be clarified.

1.2 EXPERIMENTAL OBSERVATION

Figure 100 confronts the observation of PD induced damage between two enamelled round wires in close contact in air (under normal pressure and temperature conditions) and the well-known Paschen's curve.

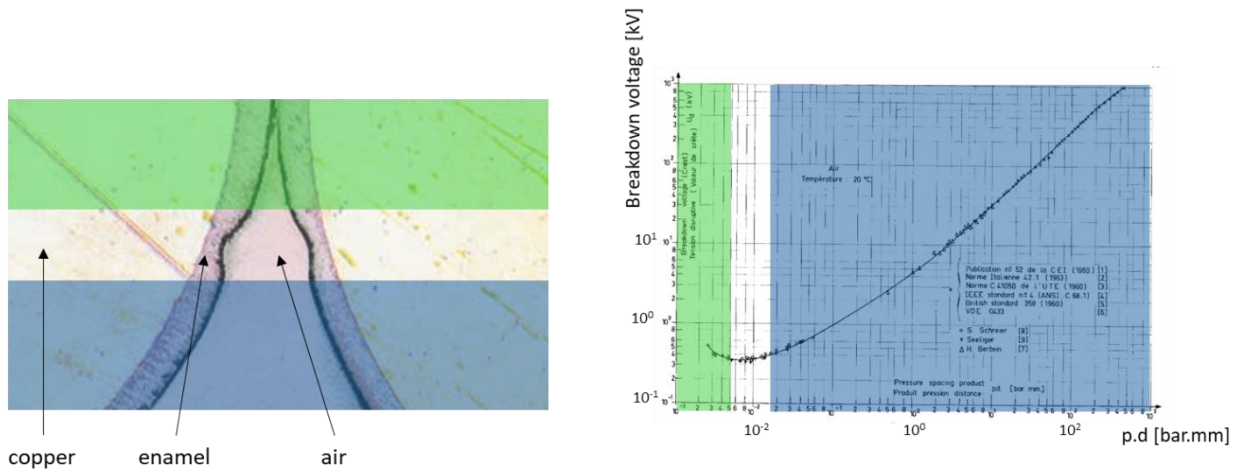


Figure 100: Left) Round enamelled wires damaged by PD [40]. Right) Paschen's curve in air [81]

As clearly shown in Figure 100, PD damage is neither located in small air gap zones (coloured in green) nor in large ones (coloured in blue), but in the intermediate air gap zone (coloured in white). This is coherent with the existence of a minimum which is well known in the Paschen's curve.

However differences have been observed by [44] between experimental and theoretical results obtained by using a 2D-finite element model. A correction was proposed by fitting the original Paschen's curve by coupling the numerical model with experimental results. This approach uses the secondary electron emission coefficient γ as a parameter, as it could be different from a material to another (Figure 101).

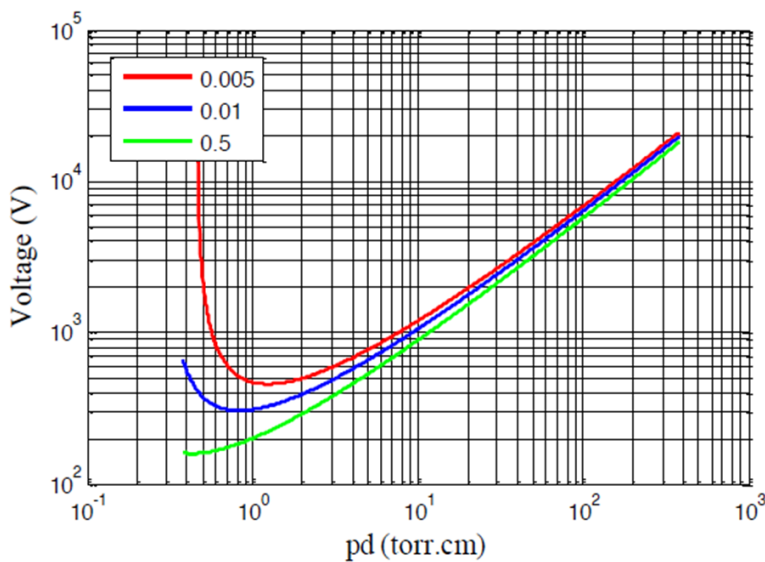


Figure 101: Paschen's curves in air plotted for three different γ values [44]

The introduction of two polymer layers may modify the mechanisms brought out by Paschen. This could even change the well-known Paschen's curve shape. However, in this work, the hypothesis consists in considering that the Paschen's curve shape is conserved (the theory is considered to be always applicable). In that case, the enamel layers only modify the breakdown voltage values. Such vertical translation of the Paschen's curve (at a given temperature and humidity rate) depends on the secondary electronic emission coefficient. In that way, the study will be focused on the evolution of the electronic secondary emission coefficient γ (also referred as Townsend's second coefficient) as a function of the copper diameters and the enamel nature used by the wire manufacturers.

2 EXPERIMENTAL APPROACH

2.1 SAMPLES

Investigation over four different enamelled copper wires were performed with (see Table 19):

- a (THEIC) Polyester-imide enamelled copper wire, overcoated with Polyamide-imide;
- a (THEIC) Polyester-imide enamelled copper wire, overcoated with a Polyamide-imide layer and overcoated with a self-bonding Polyamide layer;
- a Polyamide-imide copper, overcoated with a corona resistant Polyamide-imide layer;
- a Polyamide-imide copper, overcoated with a corona resistant Polyester-imide layer;

Three different copper diameters were investigated: 0.5 mm, 0.71 mm and 1 mm. Table 19 recaps the wires designations and layers order. The first named layer is in contact with the copper, the last named is the external layer, in contact with the air. These four magnet wires are overcoated with an external layer made with different polymers: Polyamide-imide, self-bonding Polyamide, corona-resistant Polyamide-imide and corona-resistant Polyester-imide.

Item	Polymer coating	Designation (number of layer)	Thermal class [°C]
Magnetemp CA 200	THEIC-modified Polyesterimide / Polyamide imide	PEI-THEIC / PAI (2)	200
Magnebond CAR-200	THEIC-modified Polyesterimide/Polyamide imide/self-bonding aromatic Polyamide	PEI-THEIC / PAI / self-bond PAI (3)	210
KMKED 22A	Polyamide-imide/ corona resistant Polyamide imide	PAI / PAI-PD (2)	220
KMKED 20E	Polyamide-imide / corona resistant Polyesterimide	PAI / PEI-PD (2)	220

Table 19: Recap of tested magnet wires

The samples consist in two parallel enamelled round wires in close contact. Their length is approximatively 3.5 cm. These kind of samples has been chosen instead of twisted pairs that are too complex samples. Indeed the contacts (gaps) between the wires are not well controlled and may vary along the wire and also from one sample to another. Moreover, this needs a 3D-modelling that is too complex and time-consuming to perform.

On one extremity of each wire, the enamel is removed in order to connect the samples to the high voltage power supply (and to the earth for the second wire). Three samples per diameter were tested. At both extremities of the samples, the gaps between the wires are filled with a glue, in order to avoid any discharge in this area and to be sure that PD will occur only just along the part of the wires in contact. The samples have been carefully examined by using a digital microscope (Keyence VHX1000) in order to verify whether there is no air gap between the two wires (Figure 102.b). If any small gap is detected, the sample is removed and a brand new one is built up and examined again. To detect small gaps, the sample is illuminated from below and carefully examined on all its length. If any bubble (where PD may appear) is observed in the the glue at both sample extremities, the sample is removed as well.

Figure 102 shows a typical sample. We may notice that small 'particles' are observed on the surface of the samples. This is not dust, as the samples have been carefully dusted off by blowing and cleaned with ethanol before testing. These are *protrusions* in the external layer of the wires. These protrusions appear during the wire manufacturing process presented in Chapter 1 paragraph 4.1.1 Turn-to-turn insulation. Such protrusions, that may reach $40 \mu\text{m}$ length and $20 \mu\text{m}$ tall for the larger ones, may probably modify the field distribution in air and consequently reduce the PDIV. We may however take them into account, as they are representative of defects in commercial wires, but when bigger ones are located close to the contact area, the sample is rejected. All these precautions are needed to obtain samples close to ideal ones modelled in our 2D-finite element simulations.

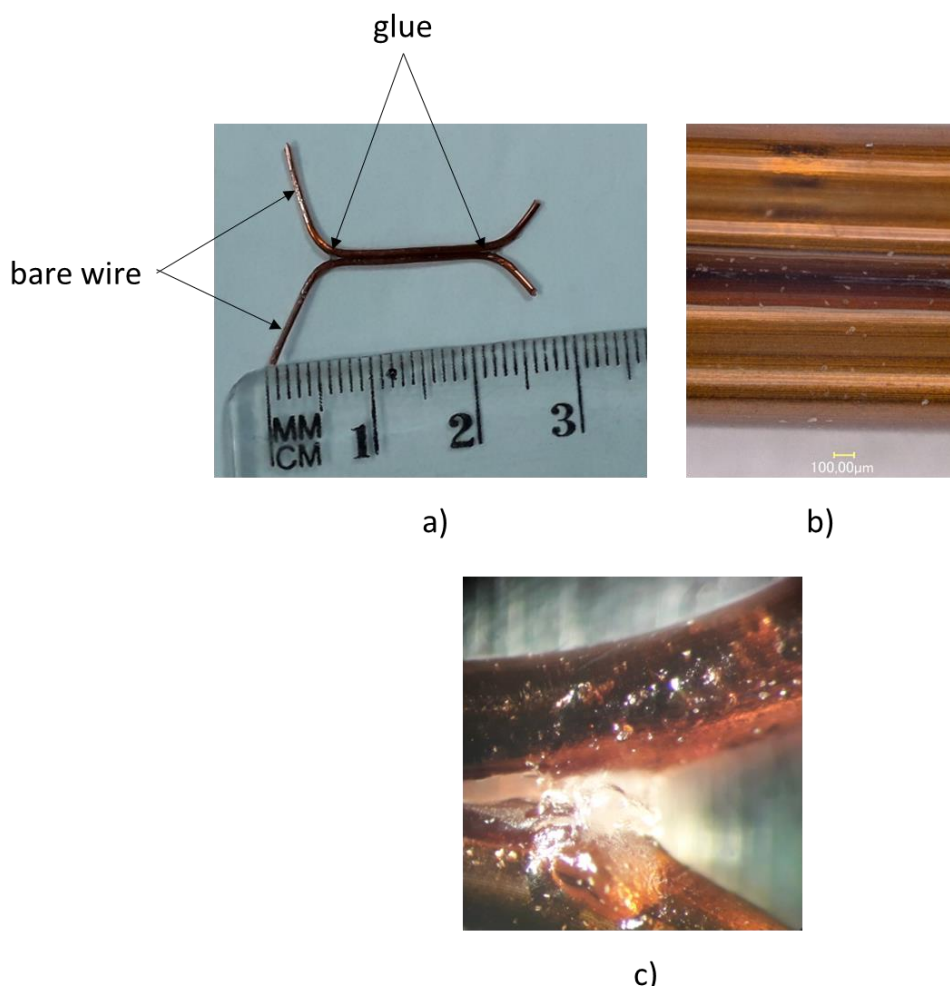


Figure 102: a) 0.71 mm 200°C studied sample; b) zoom on contact between the 2 wires; c) zoom on one glued extremity

2.2 EXPERIMENTAL PROTOCOL

Samples were tested under normal pressure and temperature conditions in a Faraday's cage to measure their respective PDIV. The experimental set-up followed, as well as we can, the IEEE standard [119]. Figure 65 displays the used setup for PD electric detection.

In order to compare both measurement and simulation, it is absolutely necessary to get the real sizes of each wire (copper diameter, enamel thickness, eccentricity) to introduce them into the simulation. These data may indeed vary from one sample to another (the standard allows a tolerance in the enamel thickness – see Annex 1). After each PDIV measurements, all samples were consequently encapsulated in Varykleer (Buehler) acrylic resin under pressure (2 bar) during twenty minutes. Encapsulated samples were then cut by using a circular saw (STRUERS SECOTOM 10) equipped with Buehler's grinder (ref 11-4217-010). Finally, the sections were polished by using at first 68 μm grains

diameters, then 22 μm ones. Samples were then observed with a digital microscope in order to get the exact sizes. Figure 103 shows an example of an observed sample.

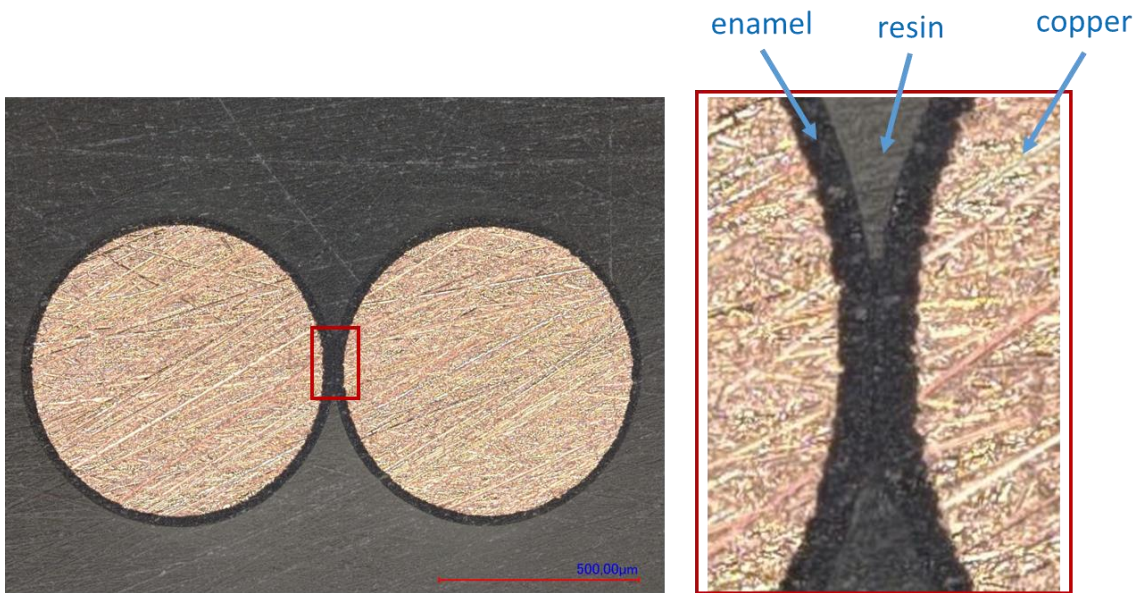


Figure 103: left) Encapsulated 200°C 0.71 mm magnet wires sample; right) Zoom in the contact area

The treatment of PDIV data were done using a two-parameters Weibull's law code [120]. A mixed numerical and finite element method [28], [121] was used to fit the original Paschen's curve with the obtained Weibull's PDIV for samples with the same copper diameter and for the same wire manufacturer. The finite element model was built with *Ansys APDL*. The enamel profile is modelled by picking out the enamel thickness of the samples every 10 degrees by using the microscope. A spline is used to connect the points. The finite element modelling thus represents the true experimental configuration. The nodal voltage solution of this model is exported to a numerical calculation code developed on *Matlab* 2017. This code computes the electric field lines and the voltage drops along field lines. These voltage drops are then compared to the Paschen's curve to determine whether or not there is a risk of PD appearance. The method iterates the secondary electron emission coefficient (γ) until the Paschen's curve intersects the computed voltage drops along the field lines curves

3 RESULTS

3.1 PDIV RESULTS

The PDIV (50Hz sine waveform - rms values) of the studied samples are presented in Table 20:

Manufacturer	Copper diameter [mm]	Sample number	PDIV [Vrms]
Magnetemp CA 200	0.5	1	541; 552; 559; 536; 546; 539; 530; 559
		2	549; 534; 558; 554; 553; 563; 556; 556
		3	561; 566; 533; 557; 541; 543; 523; 544
	0.71	1	524; 539; 546; 529; 535; 541; 538; 533
		2	572; 568; 579; 580; 566; 570; 581; 574
		3	582; 588; 641; 600; 602; 631; 634; 687
	1	1	676; 696; 667; 686; 682; 702; 710; 679
		2	717; 685; 751; 737; 748; 787; 778; 749
		3	691; 713; 747; 735; 720; 759; 704; 730
KMKED 20E	0.5	1	572; 567; 546; 547; 558; 536; 530; 555
		2	546; 548; 518; 537; 539; 532; 539; 519
		3	548; 544; 539; 533; 537; 538; 541; 546
KMKED 22A	0.5	1	595; 629; 622; 604; 617; 625; 640; 631
		2	560; 575; 611; 565; 613; 607; 580; 641
		3	568; 545; 526; 559; 579; 543; 595; 549
Magnebond CAR-200 NAT	0.5	1	674; 698; 717; 719; 733; 748; 763; 788
		2	666; 672; 684; 690; 690; 691; 712; 716
		3	767; 775; 781; 805; 817; 822; 825; 877

Table 20: Experimental PDIV versus wire diameter and kind of enamel ($T=23^\circ\text{C}$, $RH=36\%$)

Eight measurements for each sample have been done successively. When the PDIV is reached, the voltage is no longer maintained in order to avoid any damage cause by PD that may modified the enamel surface and then the other remaining measurements.

For each sample, the experimental PDIV were analysed by using a two-parameters Weibull's code [122]. It gives the PDIV characteristic values (i.e.: at 63.2% of probability) and the corresponding regressive voltage with 90% confidence bounds. For each manufacturer and for a fixed copper diameter, the confidence intervals are displayed and the estimated Weibull's PDIV is determined. Such plot is shown on Figure 104 that gives an example for three 200 °C samples made with the same magnet wires (copper diameter: 0.5 mm).

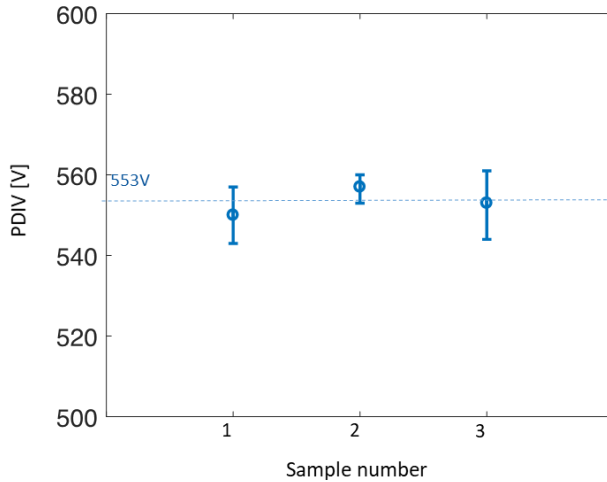


Figure 104: Measured PDIV - 0.5mm copper diameter (PEI overcoated with PAI, 200°C wire, T=23°C; RH=36%)

The PDIV values reported in Figure 104 show three characteristic PDIV close together. The average value is determined (dotted line). The average PDIV for each copper diameter and each wire manufacturer are recapitulated on Table 21.

Enamel	Copper diameter [mm]	Average PDIV [Vrms]
PEI-THEIC/PAI	0.5	553
	0.71	580
	1	721
PEI-THEIC/PAI/PA-self-bonding	0.5	768
PAI/PAI-PD	0.5	588
PAI/PEI-PD	0.5	546

Table 21: Average PDIV versus manufacturer and copper diameter

It should be noticed that the highest PDIV value is obtained with the 0.5 mm copper diameter PEI-THEIC/PAI/PA self-bonding wire. That wire has three layers of insulation leading to a higher enamel thickness, then the higher PDIV. The external additional layer is used as a varnish and may be polymerized by different technics (self heating by Joule's effect, oven, UV).

These average PDIV values will be applied as boundary conditions on the 2D-finite element model in the proposed method (Figure 106).

3.2 DIELECTRIC CONSTANT MEASUREMENTS

The equivalent dielectric constant of each enamel were measured by using a Novocontrol Alpha-A dielectric spectrometer [123]. This device is able to determine the dielectric constant in a wide range of temperature and frequency.

We used our magnet wires samples. For that, they were metallized (gold sputtering - pressure 10^{-5} mbar) in order to form a cylindrical coaxial capacitor as illustrated on Figure 105. It is a vacuum metallization; the resulting gold deposit has a thickness of about 125 nm.



Figure 105: Gold metallization of an enamelled copper wire. Left) Equivalent 2D-coaxial capacitor - R_1 : external radius; R_2 : copper radius; e : enamel whole thickness.; Right) Real sample for test in the Novocontrol.

At first, the parasitic capacitance is evaluated using both 2D- and 3D-finite elements model. Due to the limitation in the number of elements, a wire of 100 μm length is considered.

The capacitance values are derived from the total electric energy of the models:

$$C_{2D}[\text{F.m}] = \frac{2 * E_{2D} [\text{J.m}]}{V^2} \quad \text{Eq 84}$$

$$C_{3D}[\text{F}] = (C_{2D} + C_{par}) = \frac{2 * E_{3D} [\text{J}]}{V^2} \quad \text{Eq 85}$$

In these relationships, C_{2D} and E_{2D} are the respectively the linear capacitance and the electric energy on the 2D-model, V is the applied voltage peak value. C_{3D} and E_{3D} are the capacitance and electric energy in the 3D-model. C_{par} represents the parasitic capacitance.

Let us consider one configuration presented in Table 22.

Copper radius	522 μm
Enamel thickness	36 μm
Enamel dielectric constant	4.07
Applied voltage	1 Vrms
Wire length	$L_{tot} = 100 \mu\text{m}$

Table 22: Test configuration for parasitic capacitance evaluation

The C_{2D} and C_{3D} are computed using Eq 84 and Eq 85. The main results are given in the Table 23 below:

	2D-model	3D-model
Electric energy	$E_{2D}=0.339497 \cdot 10^{-8} \text{J.m}$ $E_{2D} * L_{tot}=0.339497 \cdot 10^{-12} \text{J}$	$E_{3D}=0.36652 \cdot 10^{-12} \text{J}$
Capacitance	$C_{2D} * L_{tot} = 0.34 \text{pF}$	$C_{3D} = 0.37 \text{pF}$

Table 23: 2D- and 3D-capacitance evaluations

The parasitic capacitance is low (8% of the total capacitance) for a 100 μm -long wire, so that we can reasonably neglect it in the case of wire length of several centimetres. So the results given by the Novocontrol are directly the wanted coaxial equivalent capacitance.

The voltage (1 Vrms) is applied to the copper core via the pin. The sample is deposit on a grounded electrode. The sample is adapted to the Novocontrol electrode dimensions, that is the reason why in Figure 105 it is bent. The equivalent capacitor corresponds to a coaxial capacitor of total length $L_{tot} = 2 * L$.

To get a good measurement with the Novocontrol, the sample capacitance has to be bigger than 100 pF. The 2D-finite element model of the enamelled wire is used to determine the required total length L_{tot} . With $L_{tot}=5 \text{ cm}$, the evaluated capacitance is 170 pF, considering an enamel with a dielectric constant of 3.5.

A coaxial capacitor analytical formulation is given by Eq 86. The parameters are defined on Figure 105.

$$C = \epsilon_0 * \epsilon_r * \frac{2 * \pi * L_{tot}}{\ln(\frac{R_1}{R_2})} \quad \text{Eq 86}$$

With C the capacity of the sample, ϵ_r the wanted enamel dielectric constant.

However, to the Novocontrol requires a diameter D because it considers a disc capacitor Eq 87:

$$C = \epsilon_0 * \epsilon_r * \frac{\pi * (\frac{D}{2})^2}{e} \quad \text{Eq 87}$$

With e being the enamel thickness.

By identification, it comes that the equivalent diameter of the sample seen by the Novocontrol is:

$$D = 2 * \sqrt{\frac{2 * e * L}{\ln(\frac{R_1}{R_2})}} \quad Eq\ 88$$

This value is given to the Novocontrol prior to the measurements.

Finally, the dielectric constant is derived from the capacitance computation Eq 87. The enamel thickness e is obtained using a digital microscope. Table 24 gives the computed dielectric constants at 20°C and 50 Hz :

Wire (0.5 mm)	Polymer coating	ε_r ($20^\circ\text{C}, 50\text{ Hz}$)	Capacitance ($20^\circ\text{C}, 50\text{ Hz}$) [pF]
Magnetemp CA 200	PEI-THEIC/PAI	3.3	162.81
Magnebond CAR-200 NAT	PEI-THEIC/PAI/PA self-bonding	4.4	122.27
KMKED 22A	PAI/PAI-PD	3.8	108.08
KMKED 20E	PAI/PEI-PD	4.2	126.84

Table 24: Samples computed dielectric constants at $20^\circ\text{C}, 50\text{ Hz}$

These values are in range to the ones found in the literature [124]. The measured dielectric constants will be introduced into the 2D-finite element model in the proposed method (Figure 106).

4 MIXED EXPERIMENTAL AND NUMERICAL APPROACHES

The experimental data are introduced into a numerical code which iterates the secondary electron emission coefficient value γ in order to make the Paschen's curve intersect the simulated voltage drop across field lines length curves. The experiments were conducted under normal temperature and pressure conditions. Thus, the computed γ are only valid at atmospheric pressure and 20°C .

The algorithm of the mixed experimental and numerical proposed approach is presented in Figure 106.

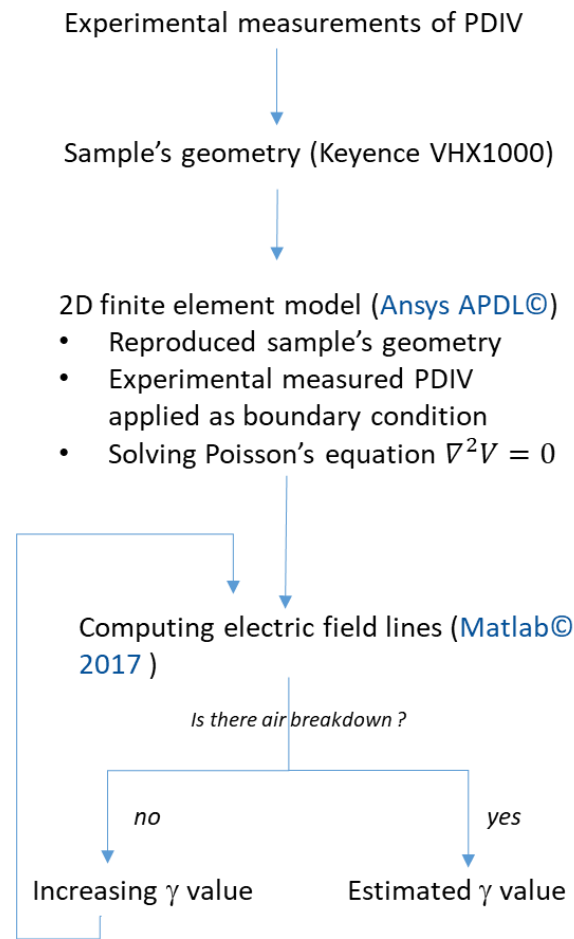


Figure 106: Algorithm, combining experimental and numerical approaches, used to determine γ

Field lines are computed by using Matlab approach presented in Chapter 3, paragraph 5: Another method using *Matlab* functions. Figure 107 displays an example of field lines between two 0.71 mm copper diameter wires in close contact.

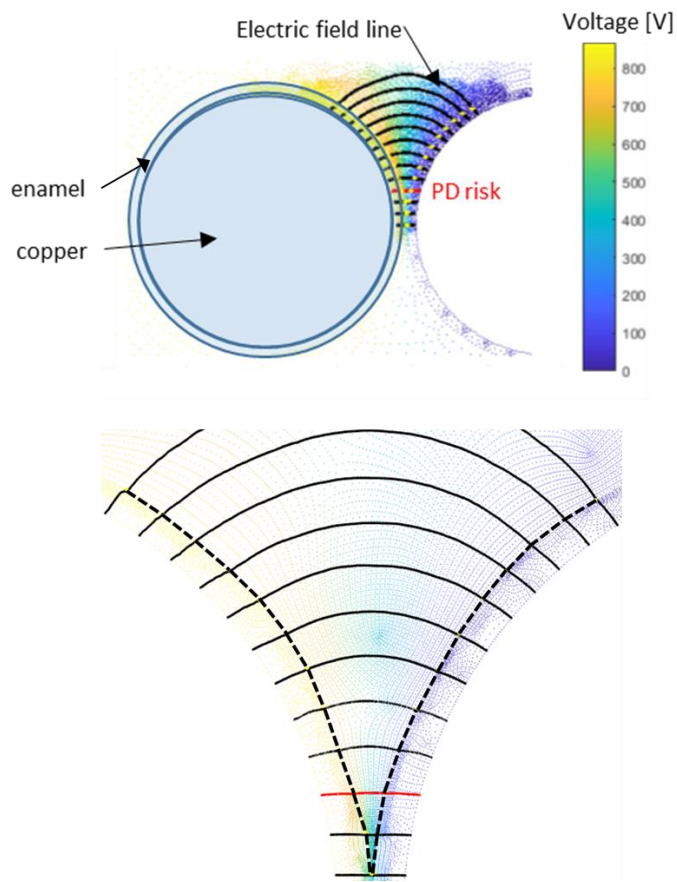


Figure 107: Top) Electric field lines. Bottom) Zoom. 0.71 mm copper diameter wire meshing. Dot lines represent the external wire contour

Figure 108 displays the corresponding voltage drop versus field lines length in the Paschen's plot ($p=1$ bar, $T=20$ °C). Two Paschen's curves computed with two values of γ are displayed. For $\gamma=1.1 \cdot 10^{-3}$ the Paschen's curve intersects the simulated one for an applied voltage corresponding to the experimental PDIV. Thus, PD appear on the red field line corresponding to the intersection point (Figure 109-bottom).

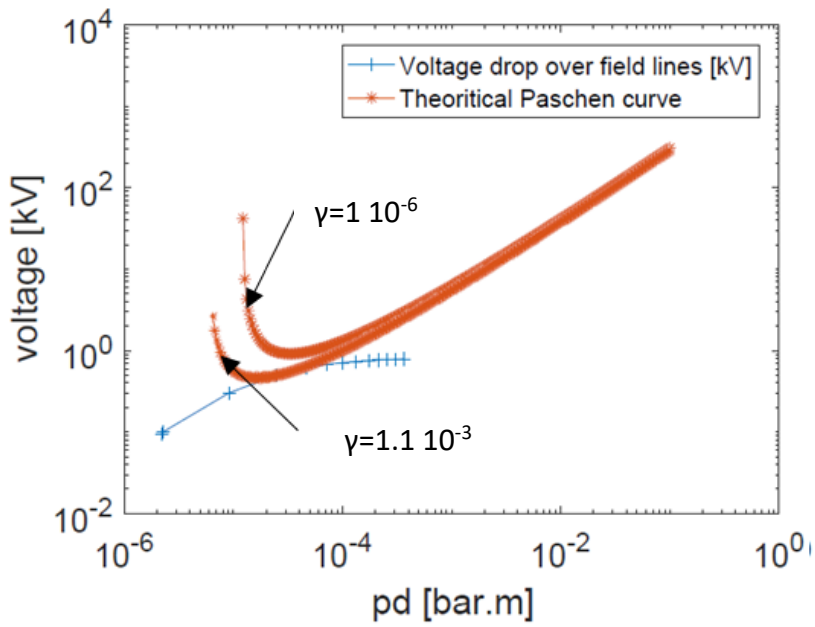


Figure 108: Corresponding voltage drop versus field lines length (in air, $p=1$ bar, $T=20^\circ\text{C}$)

5 SINGLE LAYER INSULATION

Most of the commercial enamel overcoating the copper wires are composed of multiple layers of polymers. The dielectric constant of each layer may be different. The slot insulation may also be multi-layered. Previously, we have considered a unique insulating layer, taking into account the equivalent global permittivity of all the layers. In order to verify whether this assumption is valid, we have estimated the PDIV for a multi layers insulation and a single one (with an equivalent dielectric constant). The simulated system is composed of two enamelled round wires in close contact, as presented in Figure 82. Table 25 gives the parameters values.

Parameter	Value
Copper diameter	0.5 mm
Enamel thickness	31.5 μm
Multi layered configuration:	
• Dielectric constant layer 1	• 3.5
• Dielectric constant layer 2	• 4.5
Single layered configuration:	
• Equivalent dielectric constant	• 3.94

Table 25: Multi layers versus single layer enamel parameters

In the case of multi-layered enamel, each layer has the same thickness. The given enamel thickness in Table 25 is the total thickness (layer 1 + layer 2).

The equivalent dielectric constant is derived from the capacitance calculation. The capacitance associated to layer 1 ($C_{layer\ 1}$) and layer 2 ($C_{layer\ 2}$) of the enamel are connected in series. The equivalent capacitance (C_{eq}) is expressed as follow:

$$\frac{1}{C_{eq}} = \frac{1}{C_{layer\ 1}} + \frac{1}{C_{layer\ 2}} \quad Eq\ 89$$

In both configurations, 2-layers and 1-layer, the same geometry has been considered. The capacitances $C_{layer\ 1}$ and $C_{layer\ 2}$ are computed on half the enamel thickness. In the capacitance computation, the only variable is the material dielectric constant. Eq 89 can be written as follow:

$$\frac{1}{\varepsilon_{eq}} = \frac{1}{2 * \varepsilon_{layer\ 1}} + \frac{1}{2 * \varepsilon_{layer\ 2}} \quad Eq\ 90$$

The PDIV for both configurations was evaluated under normal temperature and pressure conditions by using the 2D-finite element model introduced in Chapter 3 and a secondary electron emission coefficient $\gamma=9\ 10^{-4}$. Figure 109 displays the voltage drop across the field lines at 1 bar.

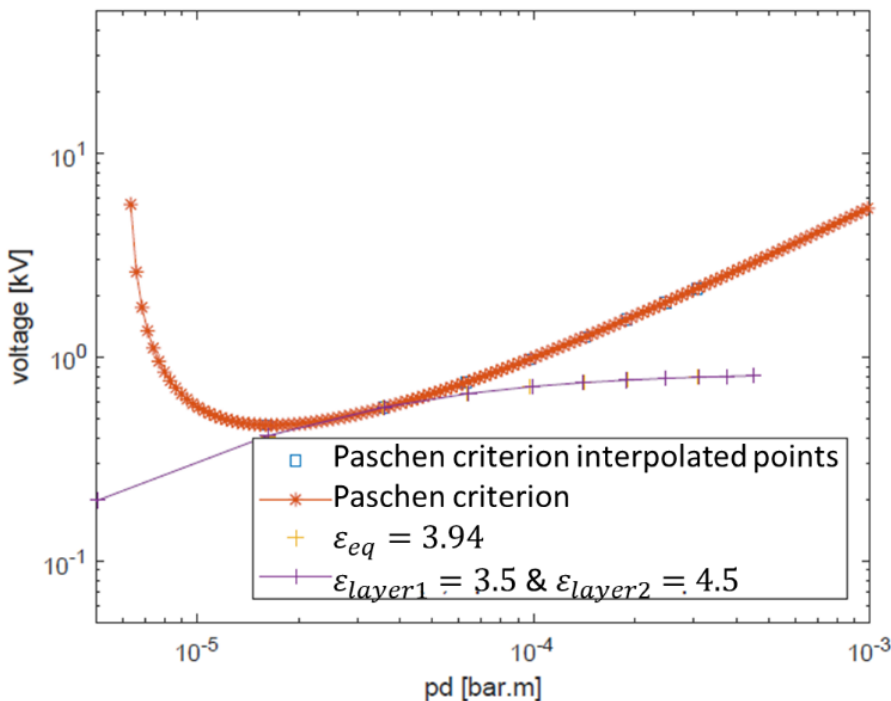


Figure 109: Voltage drop across field lines in air gap with a multi-layers enamel versus an equivalent single layered enamel.
Applied voltage is 840 V_{peak}

Clearly, the results given by the model in the air gap by considering an equivalent single layer insulation are the same that the one considering a multi-layered one (the dots are superimposed).

In the PD evaluation tool, the multi-layered enamel and the multi-layered slot insulation will thus be considered as an equivalent single layer, as this do not affect the voltage repartition in the air, so that

the PDIV is unchanged. However, slot insulation may be composed of different layers having great differences between their permittivity, i.e.: organic (polymer) and non-organic layers (polymer filled with ceramic, mica,...). In that case, the same modelling has to be performed to be sure of the veracity of one layer assumption.

6 SECONDARY ELECTRON EMISSION COEFFICIENTS

The impact of the wire radius in the secondary electron emission coefficient γ is presented in Figure 11 for a Magnetemp CA 200 wire. The γ coefficient is computed for three different copper diameters: 0.5 mm, 0.71 mm and 1 mm. The γ values displayed in Figure 110 result from a Weibull's law applied to treat the γ values computed of all samples for each copper diameter.

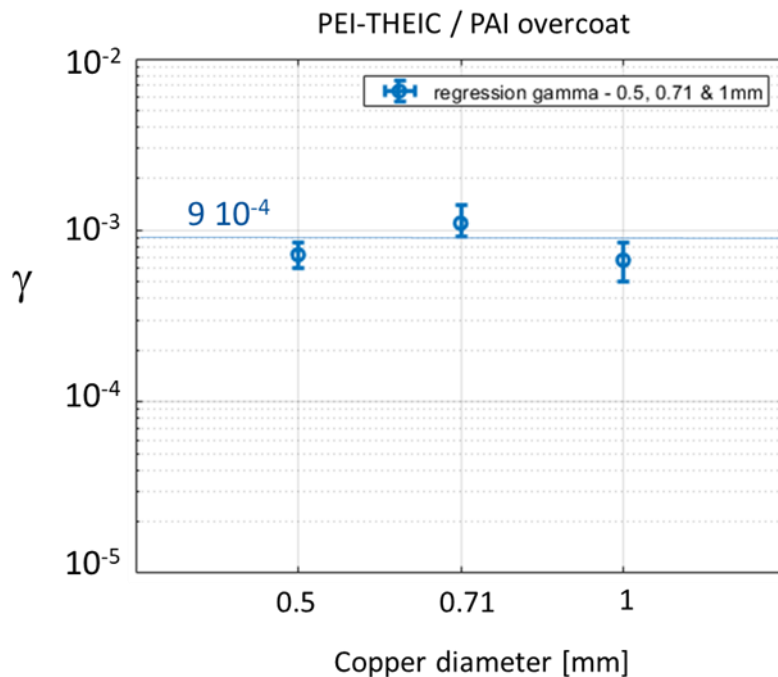


Figure 110: Secondary electron emission coefficient for 0.5 mm, 0.71 mm and 1 mm copper diameter (PAI overcoat, $T=23^\circ\text{C}$, $RH=36\%$)

The three γ coefficients found for a PAI overcoat enamel are close together. The observed differences may be due to the random distribution of defects (protusions) and the difference in the external layer structure (even if they are made with the same monomer, the final structure depend on the deposit and polymerization process that may be different versus wire diameter). In Figure 111 we have drawn the effect of changing the γ value on the Paschen's curve. As clearly shown, from 6.7×10^{-4} to 11×10^{-4} , the resulting Paschen's curve is quite the same (Figure 111). The difference between the lowest an

highest Paschen's minimum values is less than 7% (i.e.: 32V). The mean value is $\gamma_{PAI}=9 \cdot 10^{-4}$. It is almost one decade lower than the traditional γ value found in the literature for metallic electrodes ($\gamma = 0.01$). A similar value is obtained by [125].

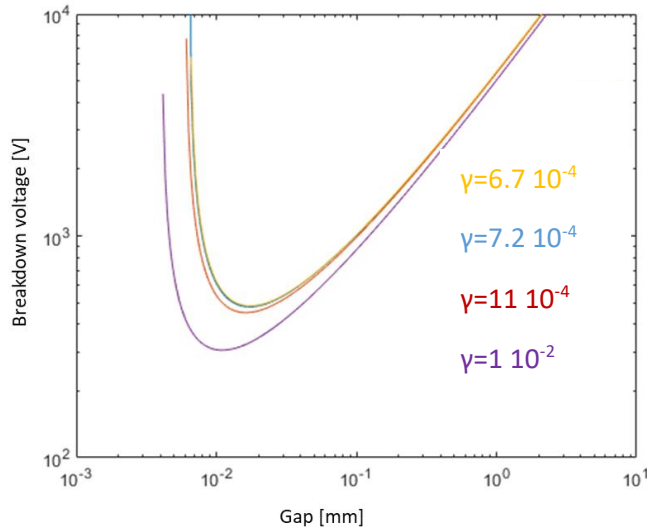


Figure 111: Paschen's curves in air for 3 γ coefficients

6.1 IMPACT OF THE INCOMING ANGLE OF BOMBARDING IONS

The impact of the ions incident angle of attack has been investigated in [126]. A monochromatic H_g^+ ion beam was used to bomb different kinds of electrodes. The energy of the incoming ion beam was adjusted from 5 to 25keV. Three angles of attack were tested: 0°, 30° and 45°. The higher the angle, the higher γ . The difference is amplified with the energy of the incoming ion beam.

In our experiments, it is assumed that the positive ions move along the field lines. Therefore, they are impacting the wire with a null incidence angle (i.e.: perpendicular to the bombarded area). We have investigated the incidence angle (Δ) of straight lines. It is calculated between the straight field line and the normal to the tangent at the point of impact. Copper diameters from 0.5 to 5mm were investigated. Figure 112 displays the field lines in the air gaps computed using the 2D-numerical model. The red field lines are subject to PD. The incoming angle Δ is introduced. Table 26 recaps the evolution of the incoming angle as a function of the wire copper diameter. It appears that the bigger the wire diameter, the closer to a straight line the field line in the air gap where PD occur.

However, it is not certain that the positive ions move along the electric field lines. Their trajectory may be perturbed by complex interactions and by particles distribution in the air gap. Their mass may also reinforce these perturbations.

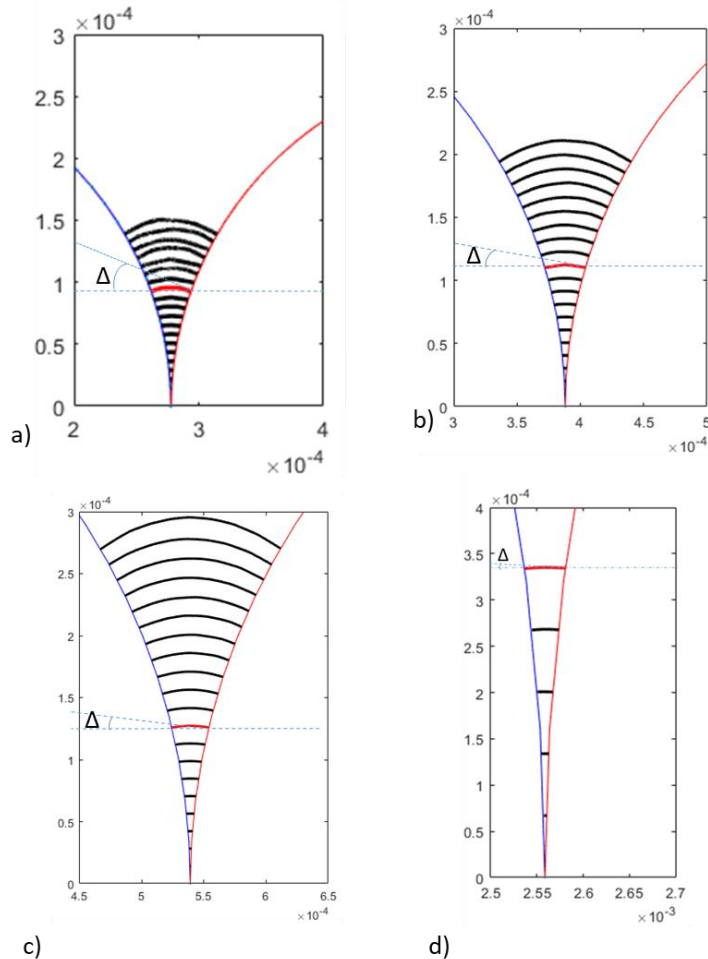


Figure 112: Field lines in air gap between two enameled copper wires; Red lines are subject to PD; Δ is the incidence angle of positive ions following a straight field line ; Copper diameters of 0.5 mm (a), 0.71 mm (b), 1 mm (c) and 5 mm (d); Axes are in meter

Copper diameter [mm]	Length of the field line where PD occur	Incidence angle Δ (with straight field line) [degree]
0.5	32 μm	23°
0.71	32 μm	11°
1	37 μm	8°
5	43 μm	4°

Table 26: Incidence angles for copper diameters between 0.5 and 5mm - Evaluated at PDIV considering an average grade 2 insulation thickness (see Annex 1)

Let us evaluate the energy of a positive ion impacting the enamel layer for the configuration corresponding to Figure 112 c). The enamel thickness is $e=39.25 \mu\text{m}$ and the evaluated PDIV is 970 Vpeak. The resulting voltage drop in the air gap is evaluated using Eq 92 and equals 604 Vpeak. A

positive nitrogen ion N_2^+ is considered in the air gap. We suppose that this ion is accelerated from one side of the air gap to the other without any collision. Thus, only the electric force is applied to this ion. That force is a conservative one, so the mechanical energy of the ion is constant. The mechanical energy is the sum of the kinetic energy and of the potential energy. Initially, we consider that the ion starts with zero kinetic energy. Thus, the mechanical energy equals the potential energy alone. The potential electric energy of the ion is of 604 eV. That energy is fully converted to kinetic energy when the ion crashes on the enamel layer on the other side of the air gap. In [126], a 30° incidence angle has an impact on the γ coefficient for an energy bigger than 5 keV. We may reasonably consider that for enamelled wires of diameters ranging from 0.5 to 5 mm, γ will only depend on the external layer chemistry (and do not depend on the copper wire diameter). Consequently, if γ is estimated from an experiment performed with one wire, this value may be used for enamelled wires having the same external polymer layer but having another copper diameter.

6.2 INFLUENCE OF THE ENAMEL CHEMISTRY

The influence of the enamel chemistry is presented in Figure 113 for 0.5 mm enamelled wires. Different wires were tested with different external layers ($p=1$ bar; $T = 23$ °C). The results show that γ naturally depends on the enamel overcoat. From left to right, γ values are: $7.2 \cdot 10^{-4}$, $5.5 \cdot 10^{-4}$, $6.2 \cdot 10^{-4}$ and $5.5 \cdot 10^{-5}$.

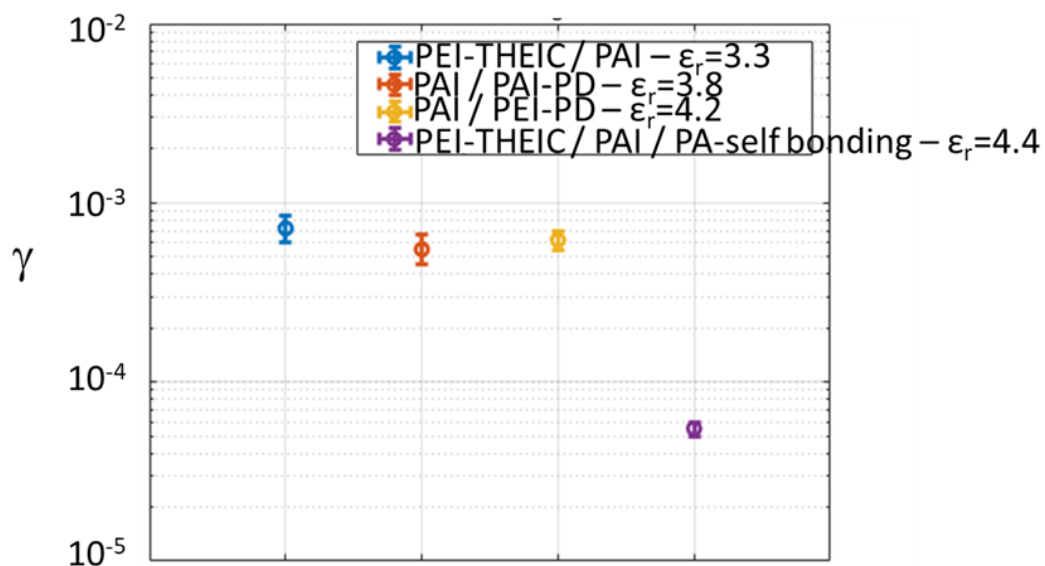


Figure 113: γ versus external enamel layer nature - copper diameter 0.5 mm – $T=23^\circ\text{C}$, $RH=34\%$

For PAI, PAI-PD and PEI-PD external overcoats, the obtained values are very close together while for self-bonding PA it is almost one decade lower. In the particular case of self-bonding PA, the polymerization is not achieved. We can reasonably consider that this value may change after the curing process.

As a conclusion, preliminary measurements of such important coefficient has to be performed prior to any modelling.

7 ADDITIONAL EXPERIMENTATION

In the experiments previously described, no proof has been found to dismiss the Paschen's theory in our samples. However, another experimentation has been performed in order to check that both Paschen's theory and our proposed methodology are applicable. The idea consisted in determining the PDIV between two enamelled round wires in parallel to rebuilt the Paschen's curve.

7.1 SET UP

Samples were prepared with 3 mm copper diameter wires overcoated with PAI (wire length about 3 cm). The choice of the diameter was mainly due to the great rigidity of the samples, allowing an easy manipulation. The two pieces of enamelled wires were manually positioned and glued. One on the micrometre screw and the other on the support (see Figure 114). The screw and the support are

electrically isolated. The gap is approximatively obtained by interleaving wedges of the wanted thickness in between the wires. Then the two wire samples are glued on the micrometre screw measuring contacts. Once the glue is dry, the wedge was removed and the potential was brought by two needles to the copper cores on the edge. The needles were equipped with small springs to ensure a good electrical contact with the copper. Some glue was finally applied at each wire extremities to avoid any discharge in these areas. If bubbles were found inside the glue, the sample was removed. It is assumed that the wires are infinitely long so that the 2D-finite element model is relevant to determine the field lines and the voltage drops in air for the corresponding gap value. A particular attention was also paid to be sure that the two wires were perfectly parallel. This has been checked by using an electronic microscope. In this condition, the electric field may still be calculated with a 2D-finite element model, while if the wires are not parallel, the electric field is strongly modified and need to be modelled by a 3D-finite element model (see an example in Figure 115).

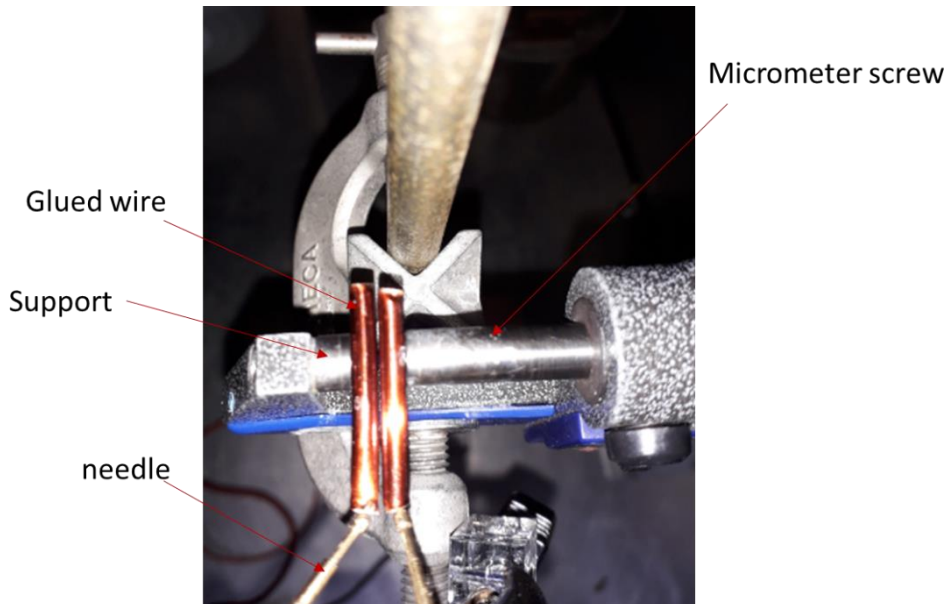


Figure 114: Experimental sample holder for rebuilding the Paschen's curve with two parallel enamelled wire samples

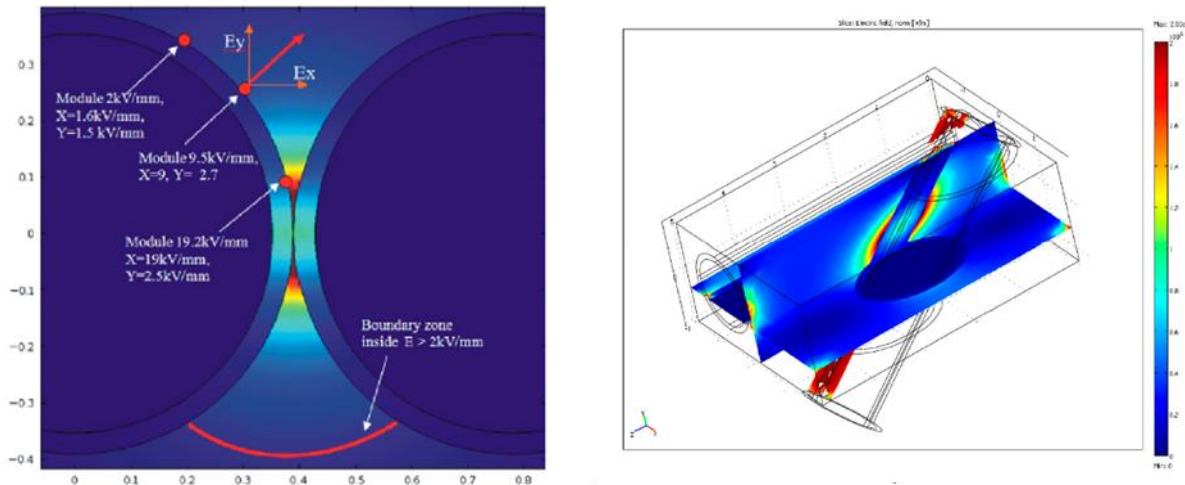


Figure 115: Electric field calculation between two enameled wires in close contact [127]. Left) parallel wires: $E_{max}=19.2$ kV/mm; Right) non-parallel wires: $E_{max}=2$ kV/mm. 0.7 mm enameled wires; enamel thickness: 100 μm ; dielectric constant: 4.2; Applied voltage: 2 kVpeak.

The micrometre screw was used to obtain the parallelism. If the wires were not satisfactorily fixed (as shown in Figure 116 where the gap is not constant), they were removed to built-up another ones. A very large number of attempts were necessary to obtain suitable samples!

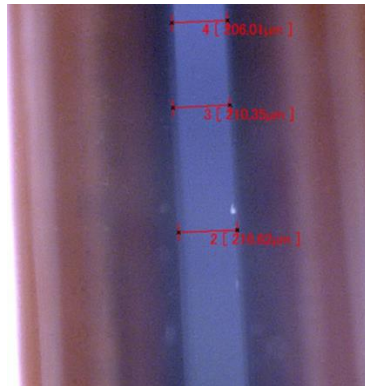


Figure 116: Gap observed with an electronic microscope in between two non-rigorously parallel enamelled wires

7.2 RESULTS

The measured PDIV and the corresponding gap values are presented in Table 27.

Measured gap [$\mu\text{m} +/- 2\mu\text{m}$]	PDIV [Vrms]
30 μm	634; 589; 631; 616; 593; 611; 619; 600
100 μm	887; 859; 893; 921; 885; 880; 922; 942
140 μm	985; 1033; 1080; 972; 1007; 993; 1014; 1004
210 μm	1318; 1319; 1221; 1301; 1299; 1253; 1191; 1248

Table 27: Experimental PDIV for different values of the gap in between the two parallel enamelled wires

Figure 117 displays a cross section of the tested 3mm diameter PAI overcoated wires. The enamel thickness entered in the numeric model is close to 50 μm (see Figure 117). The dielectric constant is taken equal to 3.5.

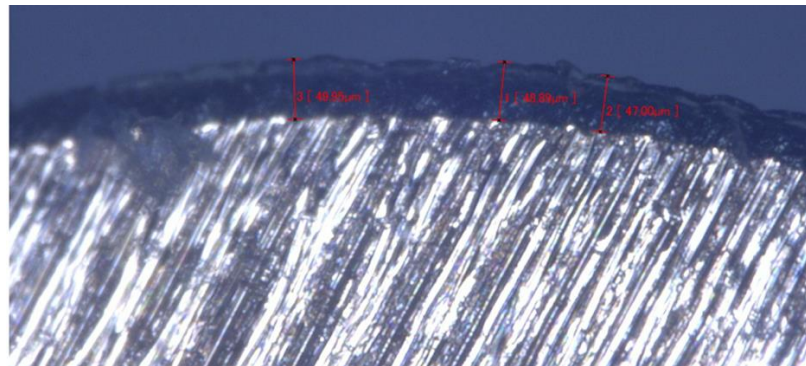


Figure 117: Cross section of a 3mm copper diameter wire (PAI overcoat)

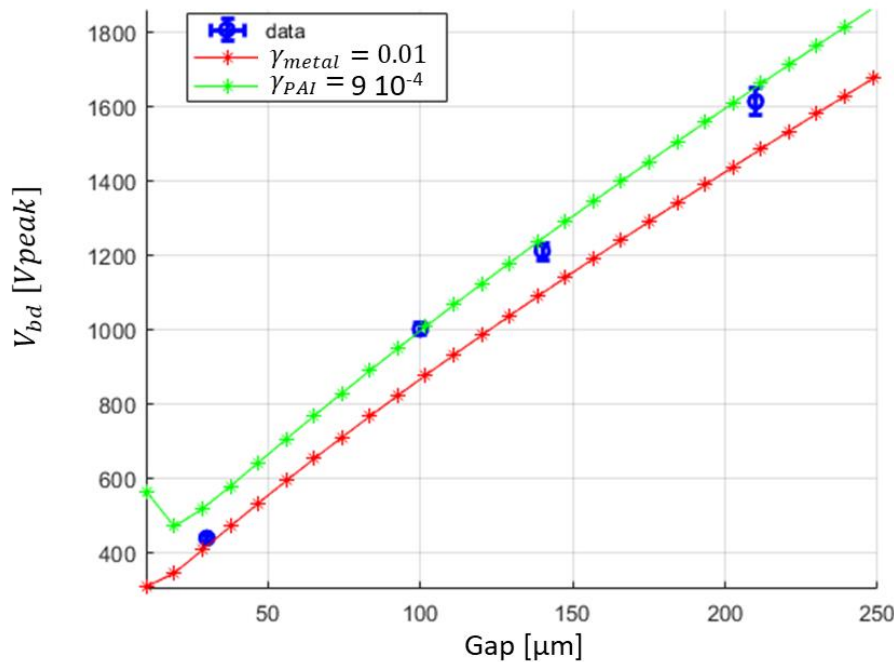
The experimental PDIV were treated using the 2 parameters Weibull's law. The characteristic PDIV at 63% along with the 90% boundary intervals were determined. These data were entered in the previously introduced numeric model. The electric field lines was thus computed. The voltage drops along the field line crossing the air gap were collected. It is designated as the breakdown voltage V_{bd} .

Table 28 recaps the voltage drops (peak values) of the field lines crossing the air gaps.

Measured gap [μm]	V_{bd} in air [Vpeak]
30	437
100	1000
140	1210
210	1612

Table 28: Breakdown voltages of air gap between parallel enamelled wires versus gap thickness

Figure 118 displays two Paschen's curves plotted with two γ values coefficients: $\gamma_{metal} = 0.01$ and $\gamma_{PAI}=9 \cdot 10^{-4}$ (mean value calculated for different diameter of PAI overcoated wires – see Figure 110). The computed air breakdown voltages, calculated from the measured PDIV, are positioned on the graph.

Figure 118: V_{bd} of air gap between parallel enamelled wires versus gap thickness

As clearly shown in Figure 118, experimental air breakdown voltage data obtained with PAI overcoated wires fit well with the theoretical Paschen's curve plotted by using the γ value obtained with this kind of wire. Concerning the measurement performed for the lower gap (i.e.: 30 μm), the effect of surface irregularities and/or defects may strongly affect (by lowering) the PDIV. This value should not be considered in the same way as the others.

8 CONCLUSIONS AND PERSPECTIVES

In this chapter it has been demonstrated that the Paschen's criterion is still valid in a configuration of two enamelled round wires in close contact. A methodology to determine the secondary electron emission coefficient of enamelled round wires was proposed. It combines both experimental data and numerical models. This coefficient is obtained by fitting the Paschen's curve with a computed voltage drops along straight field lines curve. Close results have been obtained for the same overcoating enamel (PAI) with different copper diameters, i.e.: $\gamma=7.2, 11$ and $6.7 \cdot 10^{-4}$ for 0.5, 0.71 and 1 mm respectively. It can be concluded that if a secondary electron emission coefficient is found by using this proposed method on a sample having a given copper diameter, this coefficient could be used to predetermine the PDIV of wires having others copper diameters but made with the same overcoating enamel. This study has also shown that this method has to be applied each time the wire enamel

Chapter 4: Correction of the Paschen's criterion

chemistry is changed or if the same thermal class wire is used but provided by different manufacturers. However, the developed numerical model is a static one. Physical dynamic effects, such as memory effect [128], are not taken into account in the model. Our model is thus only valid when the first discharges occur.

In the next chapter, the corrected Paschen's criterion is used to evaluate PDIV and compute sizing graphs for the insulation layers.

Chapter 5: Tool to predict PD activity in machine slot

This chapter presents the Partial Discharge Evaluation Tool (PDET) that has been developed. It has been coded with Matlab. It provides recommendations regarding the sizing of the Electrical Insulation System inside a stator slot. As it is considered only one phase per slot, the hot spot for Partial Discharges (PD) activity are turn/turn and turn/slot contacts. It could be naturally upgraded to treat the case of slots embedding more than a single phase.

This chapter starts by considering the impact of both temperature, frequency and pressure. Then the Partial Discharge Evaluation Criterion (PDEC) will be given. It will take into account the variable environmental conditions which should be withstood by the motor in a non-pressurized area. Simplified Analytical Models (SAMs) of turn/turn and turn/slot contacts will be developed. These SAMs will be validated with 2D Finite Elements Models (2D FEMs). Parametric studies will be done by using the SAMs in order to compute design graphs for the enamel and slot liner insulation design. Finally, the graphs will be arranged into the PDET. The solutions provide the minimal thicknesses necessary to withstand the determined electric stresses in both turn/turn and turn/slot contacts.

1 DIELECTRIC CONSTANT EVOLUTION WITH TEMPERATURE AND FREQUENCY

In inverter fed motors, the dielectric properties of insulators may change as a function of both working temperature and converter frequency. To study the impact on the PDIV, some enamelled wires have been characterised by using a dielectric spectrometer (Novocontrol Alpha-A). The measurement method was presented in Chapter 4. Figure 119 displays the evolution of the dielectric constant as a function of both applied temperature and frequency for two different enamelled wires.

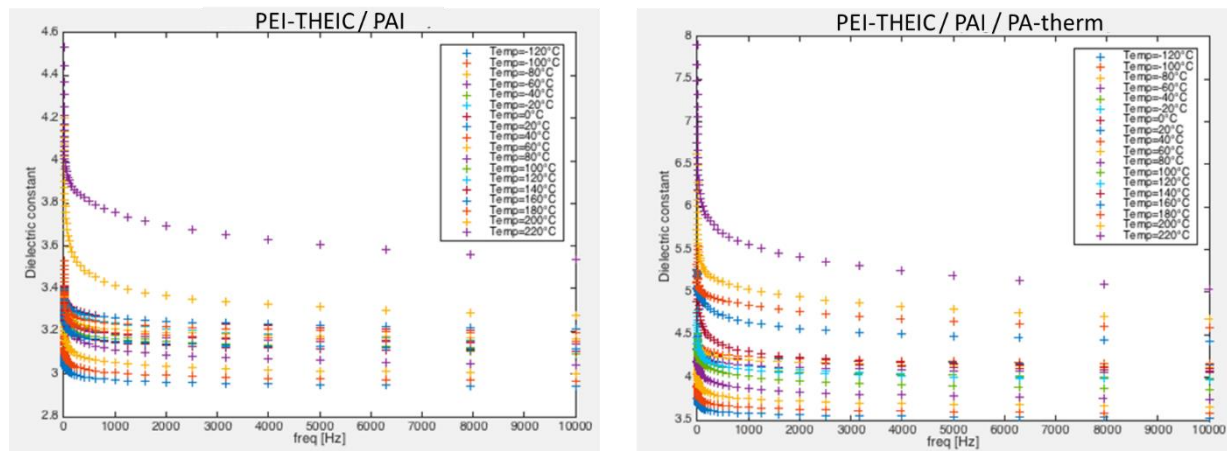


Figure 119: Evolution of the dielectric constant as a function of both applied temperature and frequency for two enamelled wires (PEI-THEIC/PAI and PEI-THEIC/PAIS/PA-therm)

It can be seen that the dielectric constant ϵ_r is classically inversely dependent on the frequency. This evolution is strongly dependent on the nature of the material. Thus, it is absolutely necessary to characterise the dielectric materials following a similar approach presented on Chapter 4, prior to any

modelling, as no general model can be used. Even if the data sheets of different commercial enamelled wires indicate that they are made with the same enamels, it is necessary to proceed to such dielectric characterization as it is well known that polymers properties are strongly dependent on their thermo-mechanical history which may be different from one manufacturer to another.

2 PARTIAL DISCHARGE EVALUATION CRITERION

In stator slot, where enamelled wires having diameters ranging from 0.5 to 5 mm are used under normal conditions of temperature and pressure, the PD risk was evaluated to take place in gaps of about $30 \mu\text{m}$ length (Chapters 2,3 and 4).

The strong environmental variations along the mission profile of an aircraft have been highlighted in Chapter 2. Some deviations to the Paschen's curve are then taken into account (Table 12). Such deviations have been verified experimentally for gaps of about 1 mm with a variable pressure. However, it has been pointed out that for a same pd product (with p the pressure in the gap and d the gap length) the breakdown voltage is not the same either the gap length is fixed and the pressure varies or the pressure is fixed and the gap length varies [129]. Moreover, deviations to the Paschen's curve have been observed for micro gaps smaller than $10 \mu\text{m}$ at room temperature [130], [131].

The authors in [132] have presented an approach to evaluate the PDIV in a planar geometry with many length scales. It was experimentally observed that for small pressure values the breakdown voltage versus pd product curve shows an extended flat region rather than a narrow dip. Multiple curves are plotted, each one associated to a gap length.

The corrected Paschen's criterion implanted in the PDET was derived from [132]. The standard Paschen's equation was used. However, the narrow dip on the left of the minimum is replaced by a flat region. The temperature was taken into account by defining an equivalent pressure as recommended by Dunbar [87]. Figure 120 displays the breakdown voltage as a function of pressure curves for different gap length at a temperature of 180°C . The secondary electron emission coefficient is taken equals to 0.01 for further comparison with experimental data obtained with metallic electrodes (Figure 121).

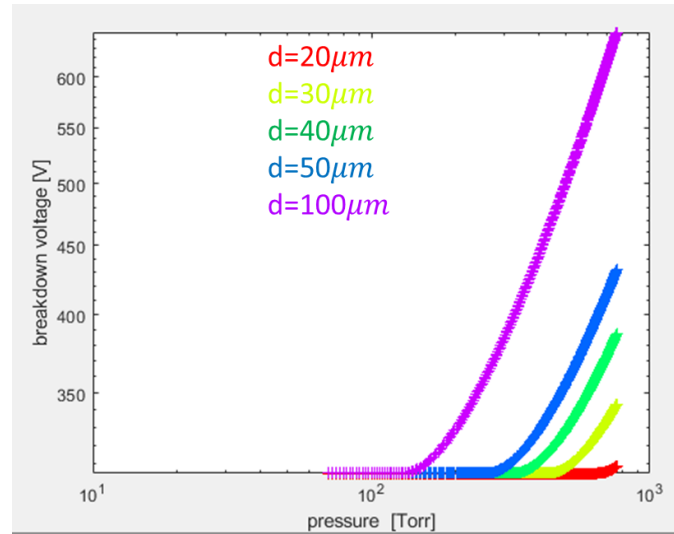


Figure 120: Breakdown voltage as a function of pressure for several gap length ($T = 180^\circ\text{C}$ - $\gamma = 0.01$)

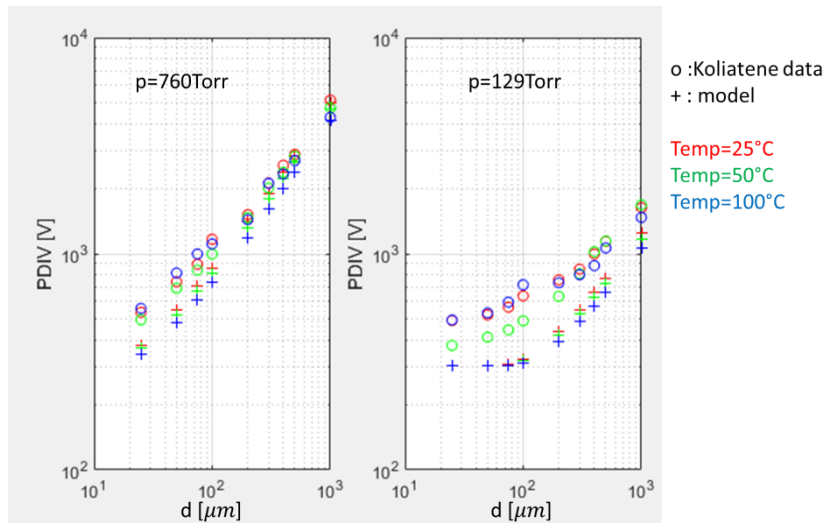


Figure 121: Comparison between the corrected Paschen's criterion and experimental data from [84] - $\gamma = 0.01$

The model is in good agreement with the experimental data.

The criterion is defined with $\gamma_{PA} = 9 \cdot 10^{-4}$. The criterion is designated as the Partial Discharge Evaluation Criterion (PDEC).

3 PARTIAL DISCHARGE INCEPTION VOLTAGE (PDIV) DECREASE FOR A COMBINED VARIATION OF TEMPERATURE AND PRESSURE

The Partial Discharge Evaluation Criterion (PDEC) was used to produce a graph which indicates the decrease in PDIV level due to a combined variation of temperature and pressure (Figure 122). The

system into consideration was composed of two enamelled round wires in close contact. That was designated as turn/turn close contact. The copper diameter of the wire was 0.5 mm, the enamel thickness overcoating the copper was $30\mu\text{m}$. The enamel dielectric constant was 3.5.

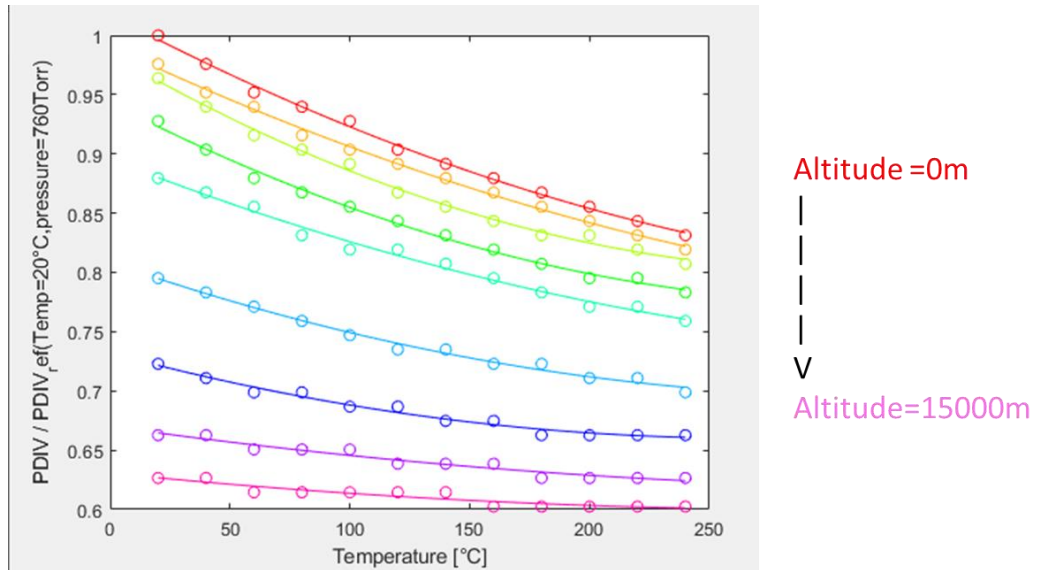


Figure 122: PDIV decrease for a combined variation of temperature and pressure

The PDIV is maximum at normal temperature and pressure conditions (i.e.: 20 °C, 760 Torr). This PDIV is designated as PDIV_{ref} . Using the graph in Figure 122, it is possible to evaluate the PDIV level between two enamelled round wires in close contact for any point on the mission profile. It is directly derived from PDIV_{ref} obtained with a numerical model.

It was assumed that the decrease of the PDIV level with temperature and pressure is the same considering the turn/slot close contact.

4 WIRE DESIGN GRAPHS

4.1 SIMPLE ANALYTICAL MODEL FOR ELECTRIC FIELD IN AIR GAP COMPUTATION

A Simple Analytical Model (SAM) was developed. It is a simplified vision of the 2D-Finite Elements Model (2D FEM) of turn/turn close contact. It requires no finite element computation that makes it much faster. The electric field line where PD takes place was approximated to a straight line. The lines length in the gap between two round conductors was determined by using geometric relations. The field line was delimited with a tube. The tube was considered thin enough so that the materials are considered as planar capacitances. Figure 123 illustrates the idea of flux tube and the resulting analytical circuit model representing the turn to turn configuration. We must notice that this

assumption is consider as valid only at PDIV, as for applied voltages much higher than the PDIV, electric field lines involved in the PD area may not necessary be all straight lines.

The wire grade refers to the standard enamel thickness applied on a wire given the copper radius. In the model, grades 1, 2 and 3 were considered. The data were taken from catalogue [36].

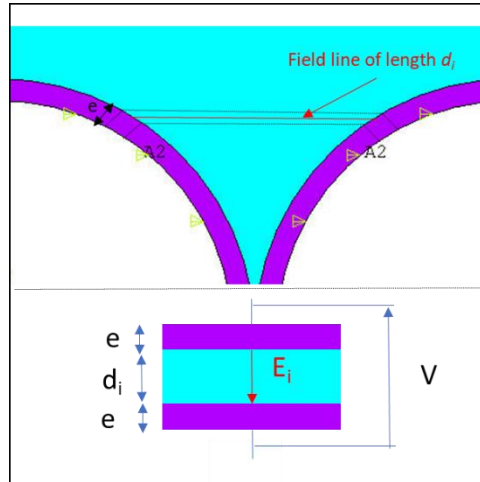


Figure 123: Top) example of straight field line and associated tube; below) resulting SAM circuit model

In the analytical model, the electric field \vec{E} and electric field density \vec{D} are purely normal. They are noted E and D respectively. The D field is conservative on the interfaces air/polymer:

$$D_{air} = D_{diel} \quad \text{Eq 91}$$

$$E_{air} \cdot \epsilon_0 = E_{diel} \cdot \epsilon_0 \cdot \epsilon_{r, \text{enamel}}$$

With E_{air} and E_{diel} the electric field respectively in the air gap and in the dielectric overcoating the conductors, D_{air} and D_{diel} the electric field density in the air gap and the dielectric respectively, ϵ_0 and ϵ_r the dielectric constants of vacuum and the dielectric respectively.

It is thus possible to derive the electric field in the air gap as a function of the applied voltage V , the geometric and dielectric parameters:

$$E_{air} = \frac{V}{d_i + 2 \cdot e \cdot \frac{1}{\epsilon_{r, \text{enamel}}}} \quad \text{Eq 92}$$

The copper radius comes in the computation of d_i . Field lines length in air d_i are computed using geometrical relations as in [55].

4.2 VALIDATION OF SIMPLE ANALYTICAL MODEL WITH FINITE ELEMENTS

Figure 124 displays the evaluation of the PDIV as a function of the enamel thickness for both 2D FEM and SAM. The wire copper radius and associated enamel thicknesses are extracted from [36]. The enamel dielectric constant was $\epsilon_{r,ename} = 3.5$. The PDIV was evaluated under normal temperature and pressure conditions (i.e.: 20 °C, 760 Torr) by using the PDEC.

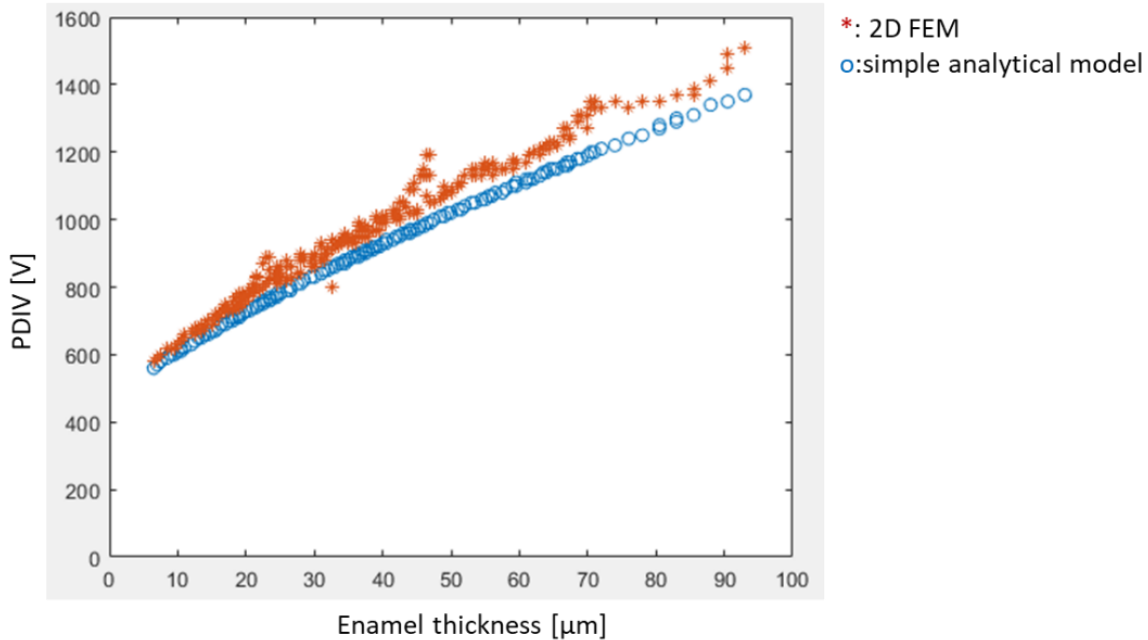


Figure 124: Evaluation of the PDIV as a function of the enamel thickness - 2D-FEM model versus SAM - $\epsilon_{r,ename} = 3.5$

Field lines from 2D-FEM are computed by using Matlab approach presented in Chapter 3, paragraph 5: Another method using *Matlab* functions. It can be seen important variations on some consecutive 2D FEM points. These are due to numerical errors mainly introduced by:

- the same mesh used for each configuration.
- the variation of the field lines length for each configuration. This is due to, firstly, to the same number of field lines to be computed, and secondly, the same angular coordinate of each field line starting point. In some configurations, field lines that lengths are close to the Paschen's minimum, may not be computed. That leads to an overestimated PDIV value.

The SAM gives an evaluation of the PDIV very close to the one obtained with the 2D-FEM. Besides, the SAM returns undervalued results compared to the 2D-FEM. It means that the design choices resulting from the SAM will be slightly oversized. As an example, for an enamel thickness of 30 μm, the oversize is about 3%, at 90 μm, it is about 10%.

The main advantage of the SAM is its speed of execution. The results presented on Figure 124 requires only few minutes of computation compared to dozens of hours in the case of 2D-FEM ! To study the impact of parameters presented on Table 2 on the wire design, multiple variations have to be tested. Therefore, the simple analytical model was used in this chapter for the computation of the wire design model.

4.3 ENAMEL THICKNESS AS A FUNCTION OF APPLIED VOLTAGE

The SAM was used to realize a parametric study on the impacting parameters for the turn/turn insulation design. These parameters are indicated on Table 29:

Parameters	Designation
Partial Discharge Inception Voltage	PDIV
Enamel dielectric constant	$\epsilon_{r,ename}$
The grade of the wire	grade

Table 29: Impacting parameters in wire insulation design

The parameter *grade* in the model takes into account this standardized overcoat thickness associated to a copper diameter. It is defined as follow:

Grade	Tolerance
0	min grade 1
1/5	max grade 1
2/5	min grade 2
3/5	max grade 2
4/5	min grade 3
1	max grade 3

The catalogue [36] was swept. For each configuration of copper radius and enamel thickness, the maximal voltage that the wire can stand was evaluated with the simple analytical model illustrated on Figure 123. The impact of the material was investigated by changing the dielectric constant values. Figure 125 displays the evolution of the enamel thickness as a function of the PDIV occur in the air gap. The PDIV in the air gap were evaluated using the introduced Partial Discharge Evaluation Criterion (PDEC) under normal conditions of temperature and pressure with the secondary electron emission coefficient $\gamma = 9 \cdot 10^{-4}$.

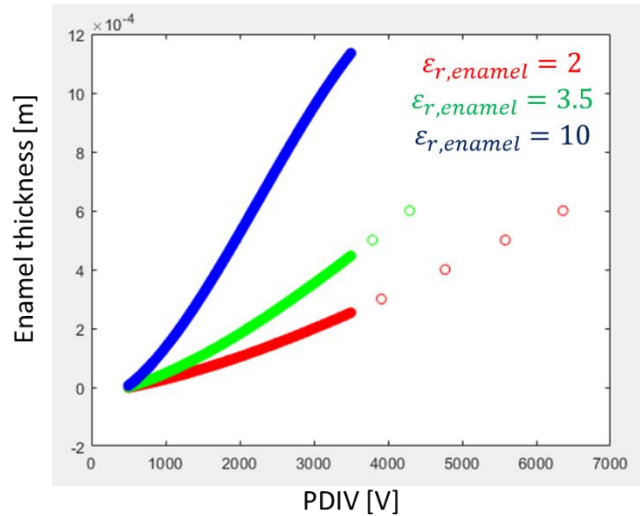


Figure 125: Enamel thickness as a function PDIV - PDIV evaluated using the PDEC under normal temperature and pressure conditions – ($\gamma = 9 \cdot 10^{-4}$)

The required enamel thickness e was interpolated over the $PDIV$ domain using a 3rd order polynom.

The polynom coefficients are dependant on the material dielectric constant.

$$e = a_1(\varepsilon_{r,enamel}) * PDIV^3 + a_2(\varepsilon_{r,enamel}) * PDIV^2 + a_3(\varepsilon_{r,enamel}) * PDIV + a_4(\varepsilon_{r,enamel}) \quad Eq\ 93$$

The evolution of the a_i ($i \in [1:4]$) polynomial coefficients was investigated for dielectric constant values ranging from 1 to 10. Most of the polymer used for the enamel overcoat have dielectric constant in this interval. Figure 126 displays the evolution of the a_i polynomial coefficients as a function of the dielectric constant. It was obtained under normal temperature and pressure conditions (i.e.: 20 °C, 760 Torr).

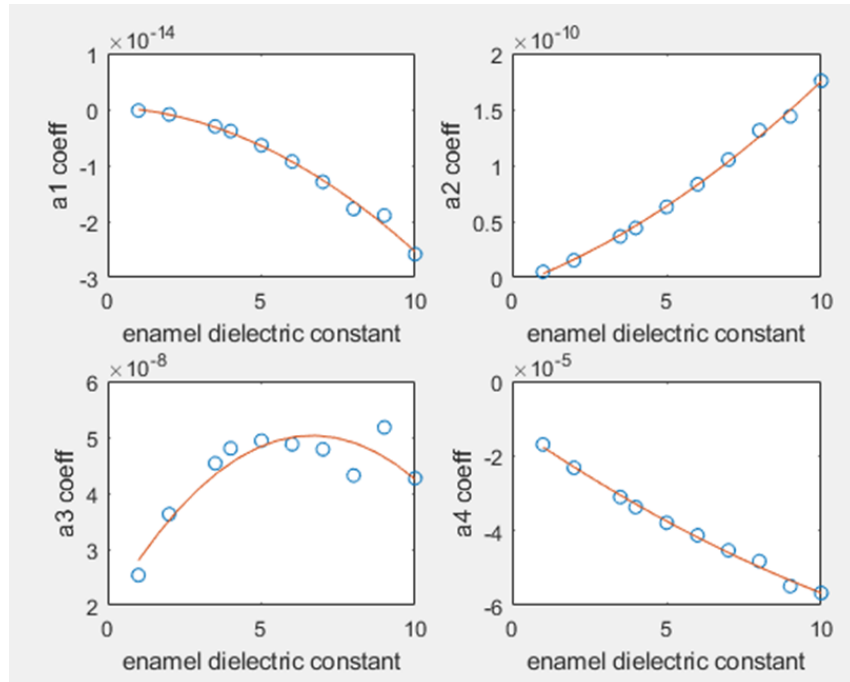


Figure 126: Evolution of a_i polynomial coefficients as a function of enamel dielectric constant – (20°C, 760Torr)

A second order polynom (red line) was used to interpolate the evolution of a_i coefficients (blue dots) over the domain of dielectric constant. The dependency of the a_i coefficients with the enamel dielectric constant $\epsilon_{r, \text{enamel}}$ is expressed as follow:

$$a_i = c_{i,1} * \epsilon_{r, \text{enamel}}^2 + c_{i,2} * \epsilon_{r, \text{enamel}} + c_{i,3} \quad \text{Eq 94}$$

With: $i \in [1,4]$

$$\epsilon_{r, \text{enamel}} \in [1,10]$$

4.4 COPPER DIAMETER AS FUNCTION OF COMPUTED ENAMEL THICKNESS

Figure 127 displays the copper radius as a function of the enamel thickness given by the grade tolerance (min/max). The data were taken from catalogue [36].

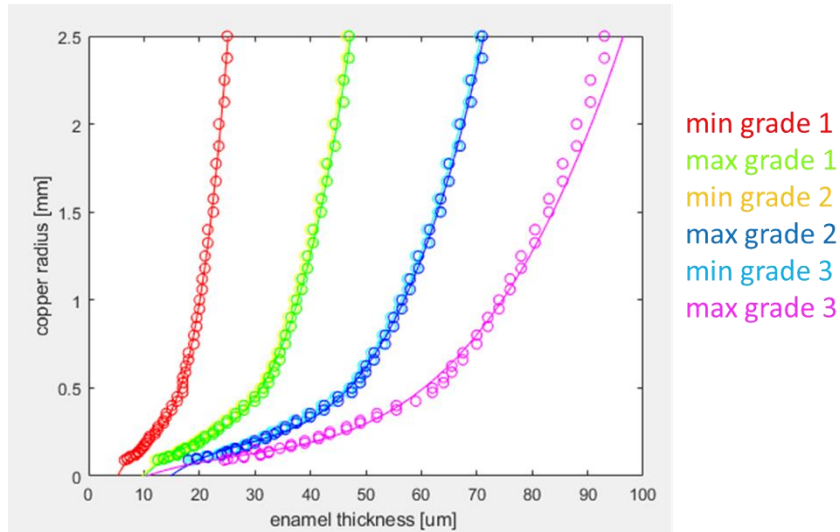


Figure 127: Copper radius versus enamel thickness for all grade tolerances in [36]

It can be seen that the tolerances max grade 1 and min grade 2 are overlapping. It is the same for the tolerances max grade 2 and min grade 3.

The discrete data from the catalogue (dots) can be interpolated with a 3rd order polynom. The coefficients of such polynom are dependent on the wire grade.

$$R_{copper} = b_1(\text{grade}) * e^3 + b_2(\text{grade}) * e^2 + b_3(\text{grade}) * e + b_4(\text{grade}) \quad \text{Eq 95}$$

4.5 VALIDATION

The results given by the wire design model were confronted to the ones using the simple analytical model. The catalogue [36] was swept considering a min grade 2 insulation, (i.e.: grade=2/5). The enamel dielectric constant was taken as $\varepsilon_{r, \text{enamel}} = 4.2$.

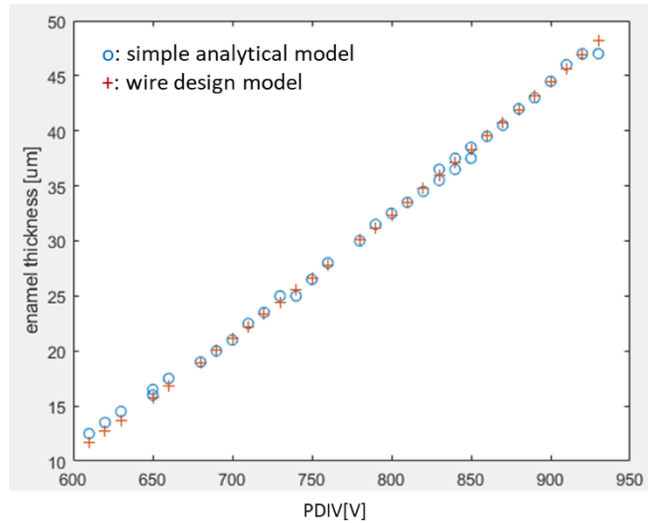


Figure 128: Enamel thickness as a function of PDIV - blue circles are simple analytical model results; red crosses are wire design model results – (grade=2/5; $\epsilon_{r, \text{enamel}} = 4.2$)

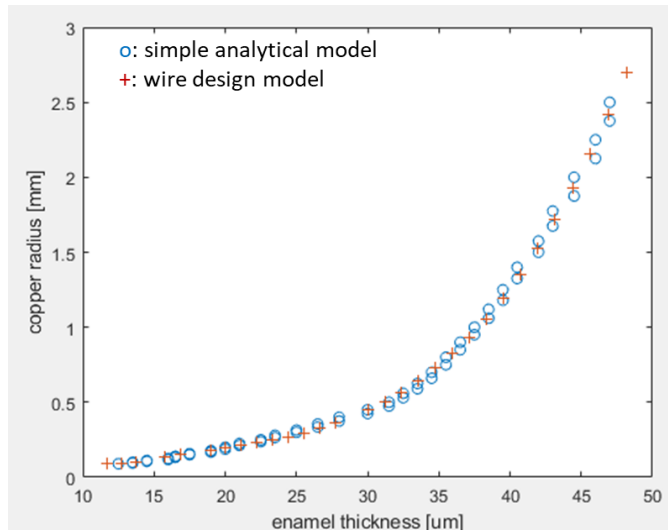


Figure 129: Copper radius as a function of the enamel thickness - blue circles are simple analytical model results; red crosses are wire design model results – (grade=2/5; $\epsilon_{r, \text{enamel}} = 4.2$)

Figure 128 and Figure 129 shows that the wire design model generated using polynomial forms gives results in very good agreement with the ones obtained using the simple analytical model.

The main advantage of the wire design graphs is that they directly return an enamel thickness whatever the inputs and, in addition, the applied voltage domain is continuous.

5 SLOT INSULATION DESIGN GRAPHS

The same approach was carried on for the slot liner design evaluation. This case is more complex due to the presence of two different insulation materials: the enamel and the slot liner. Table 30 presents the impacting parameters on the slot liner thickness choice.

Parameters	Designation
Partial Discharge Inception Voltage	$PDIV$
Enamel dielectric constant	$\epsilon_{r,ename}$
The grade of the wire	$Grade$
Enamel thickness	E
Slot liner dielectric constant	$\epsilon_{r,liner}$

Table 30: Impacting parameters on slot insulation design

5.1 SIMPLE ANALYTICAL MODEL FOR ELECTRIC FIELD IN AIR GAP COMPUTATION

The electric field lines in this model were approximated to straight line too. The lines length in the gap between a round conductor and the slot liner was determined using geometric relations, as in [55]. The field lines were delimited with a tube. The tube is considered thin enough so that the materials are considered as planar capacitances. Figure 130 illustrates the idea of flux tube and the resulting Simple Analytical Model (SAM) representing the turn/slot configuration.

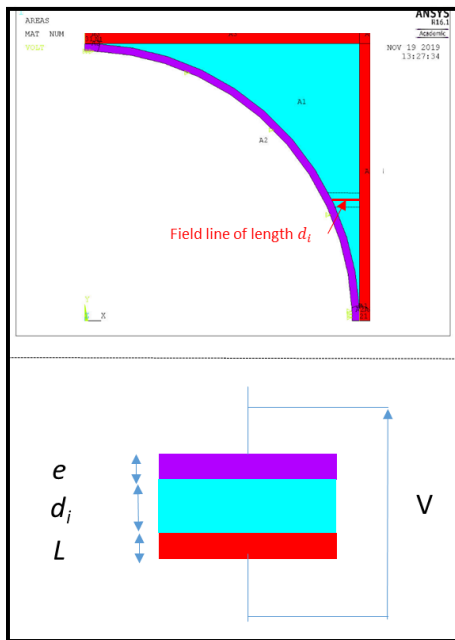


Figure 130: Top) Example of straight field line and its associated tube; below) SAM. (red: slot insulator, purple: enamel, blue: air)

In the SAM, the electric field \vec{E} and electric field density \vec{D} are purely normal. They are noted E and D respectively. The D field is conservative on the interfaces air/polymer:

$$\begin{aligned} D_{air} &= D_{enamel} \\ E_{air} \cdot \varepsilon_0 &= E_{enamel} \cdot \varepsilon_0 \cdot \varepsilon_{r,enamel} \end{aligned} \quad Eq\ 96$$

$$\begin{aligned} D_{air} &= D_{liner} \\ E_{air} \cdot \varepsilon_0 &= E_{liner} \cdot \varepsilon_0 \cdot \varepsilon_{r,liner} \end{aligned}$$

With E_{air} , E_{enamel} and E_{liner} the electric fields respectively in the air gap, in the enamel and in the slot liner, D_{air} , D_{enamel} and D_{liner} the electric field densities in the air gap, the enamel and the liner respectively, ε_0 , $\varepsilon_{r,enamel}$ and $\varepsilon_{r,liner}$ the dielectric constants of vacuum, enamel and liner respectively.

Based on Eq 96 it is possible to derive the electric field in the air gap as a function of the applied voltage V , the geometric and dielectric parameters:

$$E_{air} = \frac{V}{d_i + e \cdot \frac{1}{\varepsilon_{r,enamel}} + L \cdot \frac{1}{\varepsilon_{r,liner}}} \quad Eq\ 97$$

5.2 VALIDATION OF SIMPLE ANALYTICAL MODEL WITH FINITE ELEMENTS

Figure 131 presents a comparison between the simple analytical model (solid lines) and the 2D-finite element model (FEM) in the evaluation of the PDIV as a function of insulation configuration. The wire configuration was fixed. The wire copper radius was 0.5 mm, the enamel thickness was $e = 40\mu m$ and the enamel dielectric constant was $\varepsilon_{r,enamel} = 3.5$. The PDIV was determined under normal temperature and pressure conditions using the PDEC.

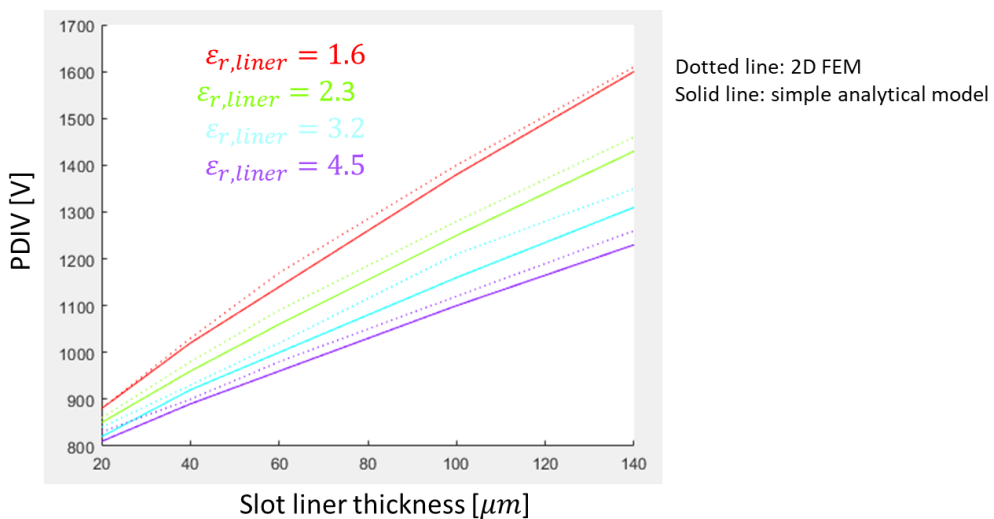


Figure 131: Evaluation of the PDIV as a function of the slot liner thickness - 2D-FEM model versus simple analytical model – ($e=40\mu m$, $\varepsilon_{r,enamel} = 3.5$)

The simple analytical model gives results close to the one obtained with the 2D-FEM. The evaluation of the PDIV is slightly undervalued compared to 2D FEM. As an example, for $\varepsilon_{r,liner} = 3.2$, the oversize is only 4% for a 140 μm -thick slot liner. The simple analytical model was used in this chapter for the study of the impacting parameters on the slot liner design mainly because of its fast computation time.

5.3 SLOT LINER THICKNESS AS A FUNCTION OF APPLIED VOLTAGE AND INSULATION MATERIALS

Figure 132 displays the evaluation of the required slot liner thickness depending on the PDIV and the wire insulation parameters. The wire insulation parameters are its enamel dielectric constant $\varepsilon_{r,enamel}$ and its thickness e . The slot liner dielectric constant was fixed at $\varepsilon_{r,liner} = 4.5$. The PDIV was determined under normal temperature and pressure conditions using the PDEC.

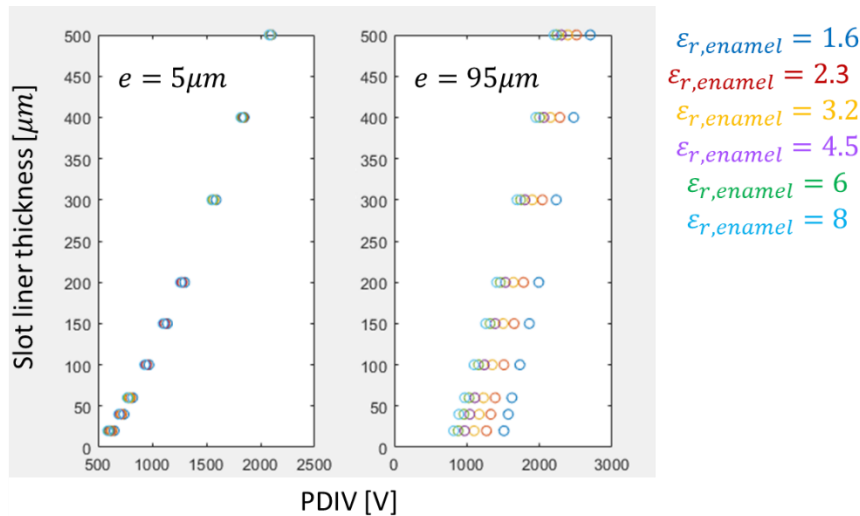


Figure 132: Evaluated slot liner insulation as a function of PDIV for different wire insulation configurations (thickness e and permittivity $\varepsilon_{r,enamel}$) ($\varepsilon_{r,liner} = 4.5$)

A 2nd order polynom was used to interpolate the slot liner thickness L as a function of the PDIV. The polynomial coefficients are dependent on the enamel thickness e and dielectric constant $\varepsilon_{r,enamel}$ and of the slot liner dielectric constant $\varepsilon_{r,liner}$.

$$L = a_1(e, \varepsilon_{r,enamel}, \varepsilon_{r,liner}) * PDIV^2 + a_2(e, \varepsilon_{r,enamel}, \varepsilon_{r,liner}) * PDIV + a_3(e, \varepsilon_{r,enamel}, \varepsilon_{r,liner}) \quad \text{Eq 98}$$

The polynomial coefficients are dependent on three parameters. Therefore, three imbrications were required to fully spell out Eq 98.

The first imbrication expresses the a_i ($i \in [1: 3]$) polynomial coefficients as a function of $\varepsilon_{r, liner}$. A polynomial form was also used here. The polynomial coefficients are named “first imbrication polynomial coefficients”.

The second imbrication expresses the “first imbrication polynomial coefficient” as a function of e . Another polynomial has been used, resulting in the apparition of “second imbrication polynomial coefficients”.

Finally, the third imbrication expresses the “second imbrication polynomial coefficients” as a function of $\varepsilon_{r, enamel}$.

By going up from the third imbrication to the first one, equation Eq 98 was fully determined.

Figure 133 illustrates the described imbrications:

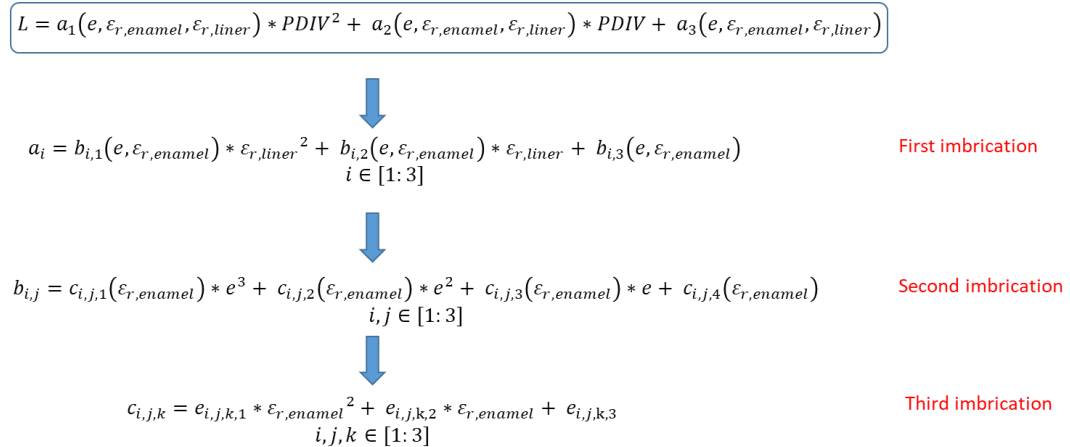


Figure 133: Imbrications equations

5.3.1 First imbrication

Figure 134 displays the evolution of a_i ($i \in [1: 3]$) polynomial coefficients present in Eq 98 as a function of $\varepsilon_{r, liner}$. The enamel thickness is $e = 5\mu m$.

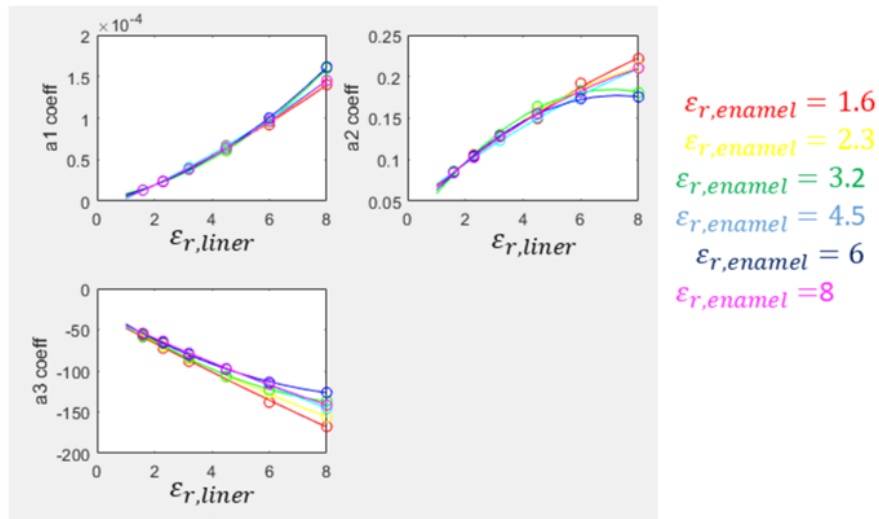


Figure 134: a_i ($i \in [1:3]$) polynomial coefficients as a function of $\varepsilon_{r, liner}$ - $e=5\mu m$

The a_i ($i \in [1:3]$) coefficients are interpolating over the $\varepsilon_{r, liner}$ domain using a second order polynom.

$$a_i = b_{i,1}(e, \varepsilon_{r, enamel}) * \varepsilon_{r, liner}^2 + b_{i,2}(e, \varepsilon_{r, enamel}) * \varepsilon_{r, liner} + b_{i,3}(e, \varepsilon_{r, enamel}) \quad Eq\ 99$$

With $i \in [1:3]$

The $b_{i,j}$ ($i, j \in [1:3]$) are the “first imbrication polynomial coefficients”.

5.3.2 Second imbrication

Figure 135 displays as an example the evolution of $b_{1,1}$ coefficient presents in Eq 99 as a function of the enamel thickness e for different $\varepsilon_{r, enamel}$.

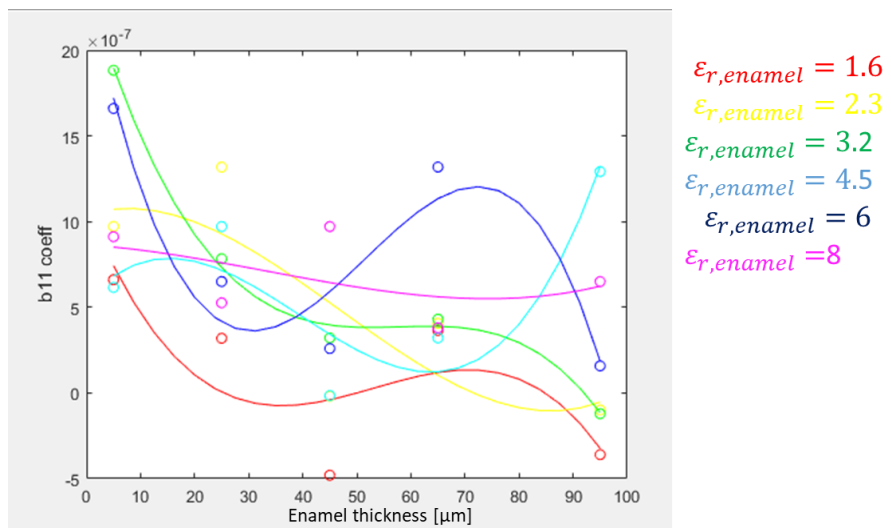


Figure 135: $b_{1,1}$ coefficients as a function of enamel thickness

The $b_{i,j}$ ($i \in [1:3]$) coefficients were interpolating over the $\varepsilon_{r, liner}$ domain using a third order polynom.

$$b_{i,j} = c_{i,j,1}(\varepsilon_{r,ename}) * e^3 + c_{i,j,2}(\varepsilon_{r,ename}) * e^2 + c_{i,j,3}(\varepsilon_{r,ename}) * e + c_{i,j,4}(\varepsilon_{r,ename}) \quad Eq\ 100$$

With $i, j \in [1: 3]$

The $c_{i,j,k}$ ($i, j \in [1: 3]$ and $k \in [1: 4]$) are the “second imbrication polynomial coefficients”.

5.3.3 Third imbrication

Figure 136 presents as an example the evolution of $c_{3,j,k}$ ($j \in [1: 3]$ and $k \in [1: 4]$) coefficients in Eq 100 as a function of $\varepsilon_{r,ename}$.

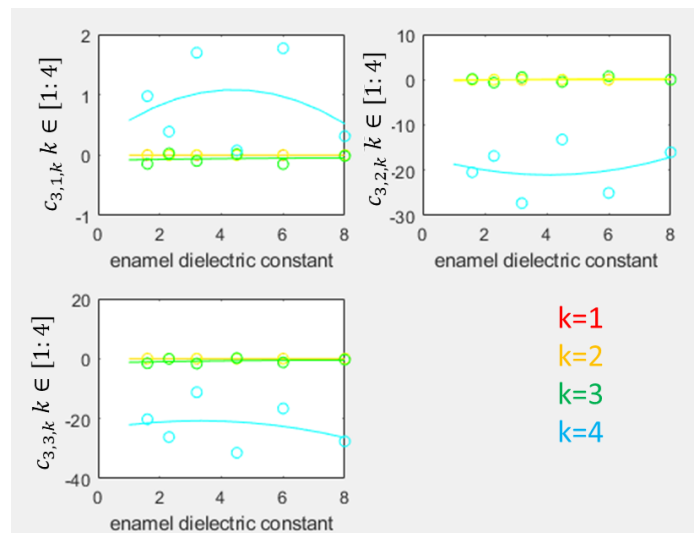


Figure 136: $c_{3,j,k}$ coefficients as a function of $\varepsilon_{r,ename}$

The $c_{i,j,k}$ ($i, j \in [1: 3]$ and $k \in [1: 4]$) are finally interpolated over $\varepsilon_{r,ename}$ using second order polynomial forms.

5.4 VALIDATION

The results given by the slot insulation design model were then compared to the ones using the simple analytical one. The wire copper radius was $R_{copper} = 0.5\ mm$, the enamel thickness was $e = 31.5\ \mu m$ and the enamel dielectric constant was $\varepsilon_{r,ename} = 4.2$. The slot insulation was taken as $\varepsilon_{r,liner} = 3.5$.

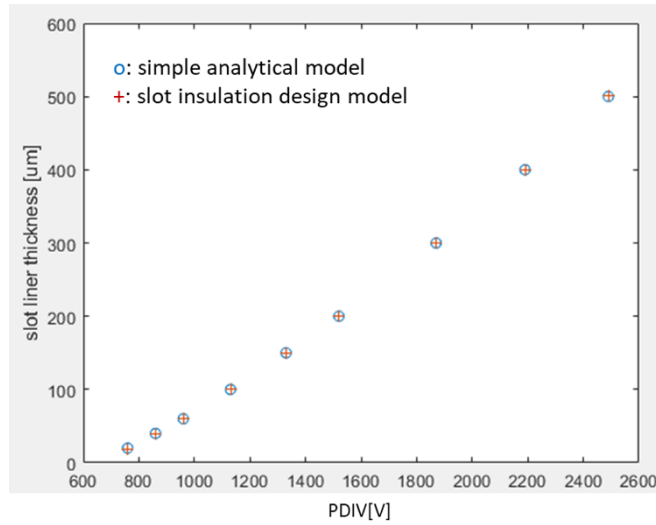


Figure 137: Slot liner thickness versus PDIV - blue circles are simple analytical model results; red crosses are wire design model results - $R_{copper} = 0.5 \text{ mm}$; $e = 31.5 \mu\text{m}$; $\epsilon_{r,ename} = 4.2$; $\epsilon_{r,liner} = 3.5$

Figure 137 shows that the results given by the slot insulation design model are in very good agreement with the ones given by the simple analytical model.

As for turn/turn insulation, the main advantages of the slot insulation design model is that it directly returns a slot liner thickness whatever the inputs and moreover the applied voltage domain is continuous. An abacus can therefore be produced.

6 EVALUATION OF THE ELECTRIC STRESSES UNDER NORMAL TEMPERATURE AND PRESSURE CONDITIONS

6.1 TURN/TURN ELECTRIC STRESS

The transient regime determines the maximum turn/turn electric stress. In transient regime, voltage phase terminals have to withstand pulses train of amplitude V_{step} as illustrated in Figure 138.

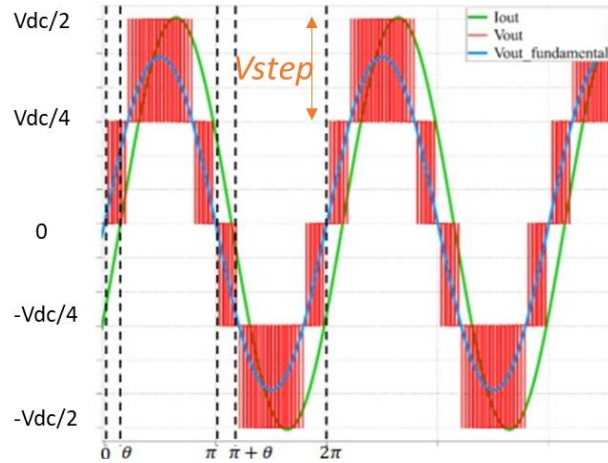


Figure 138: Example of both output voltage (phase to ground) and current waveforms of a 5-level ANPC obtained with PLECS software. V_{dc} is the bus voltage.

The effect of the impacting parameters on the motor terminals overshoots have been presented in Chapter 1, paragraph 6 Impact of power electronics. The power cable length between the inverter output and the motor terminals is considered shorter than 1 m. Thus, only the rising time remains impacting. In the example of Figure 138, the multilevel converter enables to reduce the voltage pulse amplitude.

The impact of the rising time of inverter voltage pulse was derived from [60] results. Figure 139 presents a simple evaluation of voltage overshoot at phase terminals expressed as a percentage of the inverter voltage pulse amplitude.

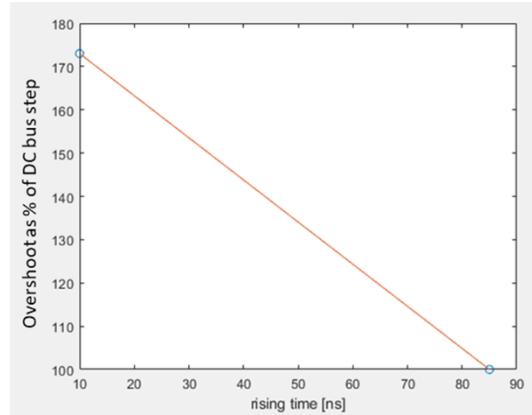


Figure 139: Overshoot at phase terminals expressed as a percentage of inverter voltage pulse amplitude as a function of the rising time

Overshoot starts to appear for rising time shorter than 80 ns. It was considered that during transient the first conductor of the phase receives 70% of the transient phase voltage [56]. The voltage front does not reach the other conductors during a fraction time of transient regime [62].

6.2 TURN/SLOT ELECTRIC STRESS

The maximal electric stress between turn and slot insulation is the nominal phase peak voltage.

A linear voltage repartition was considered all over a phase. There was one single phase per slot. The number of conductors inside a slot represent the number of passing of the phase inside the slot. The machine active length was considered long enough so that the end winding length was neglected.

The voltage on the i^{th} conductor of the phase in the slot is expressed as:

$$V_{cond,i} = V_{peak} * \left(1 - \frac{L_i}{L_{tot}}\right)$$

With L_i the length of the phase in the slot lugs for the i^{th} conductor, L_{tot} the total phase length and V_{peak} the phase to neutral peak voltage.

7 PARTIAL DISCHARGE EVALUATION TOOL (PDET)

The perimeter of the PDET is only the stator slot. The PDET provides solution(s) in order to get a PD-free stator slot. These(this) correspond(s) to minimal required insulation thicknesses to withstand the electric stresses in both turn/turn and turn/slot close contacts.

The solutions are derived from graphs computed using the presented Simple Analytical Model (SAM) validated with 2D-Finite Elements Model (2D FEM) in the case of a uniform electric field.

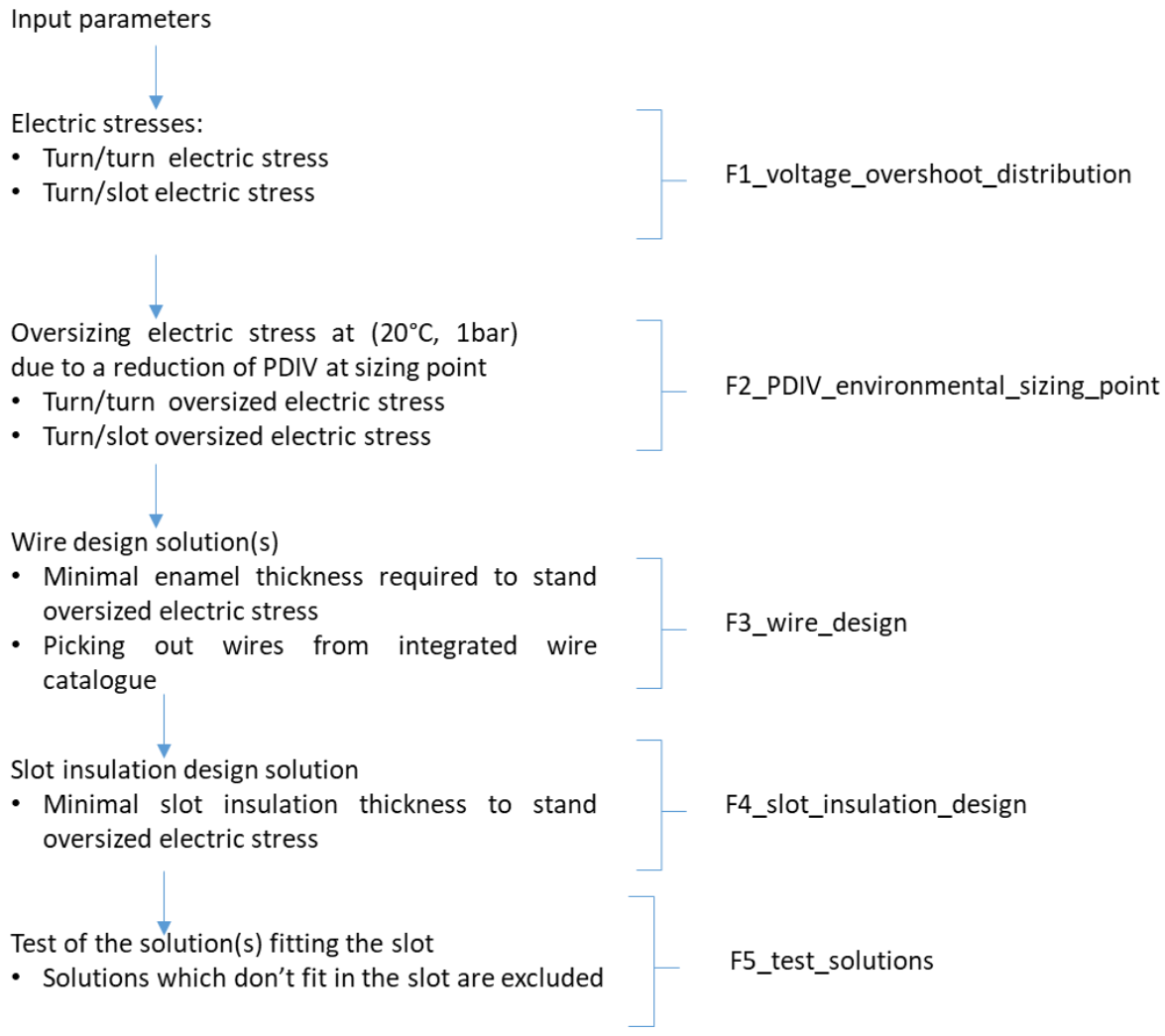
The developed PDET scope is:

- inside a rectangular stator slot;
- only one phase in the slot;
- considered slot is the phase entrance;
- round enamelled wires constitute the turns;
- turns in close contact with each other and with the slot insulation;
- a catalogue of round enamelled copper wires is already integrated.

Obviously, the scope of this study may be changed to take into account other configurations: flat wires, trapezoidal slots, more than one phase per slot,...

7.1 PDET ALGORITHM

Figure 140 illustrates the PDET organigram. There are five main steps. Each step is managed by a function. These steps are automatically executed when PDET is running.



F3_wire_design and *F4_slot_insulation_design* uses the graphs above presented. In *F2_PDIV_environmental_sizing_point* function, the graph on Figure 122 is applied on turn/turn and turn/slot evaluated electric stresses. It comes the oversized electric stresses at (20°C, 1bar) to ensure that the solution takes into account the decrease in PDIV with temperature increase and pressure decrease.

7.2 INPUTS

The inputs are listed on Table 31.

Input	Description	Unit
Motor		
<i>nb_phase</i>	Number of electric phases of the motor	
<i>nb_slot</i>	Total number of slots in the stator	
<i>nb_cond</i>	Number of conductors per slot. The conductors are the passages of a phase in the slot	
<i>L_slot</i>	Slot width	[m]
<i>h_slot</i>	Slot height	[m]
<i>kfill</i>	Filling factor	
Converter		
<i>ma</i>	Maximal modulation width	
<i>Vemot_max_cond1</i>	Equivalent 1 conductor / slot / phase peak voltage	[V]
<i>nb_level</i>	Number of levels of the converter	
<i>rise_time</i>	Switch component rise time	[ns]
Sizing point		
<i>Temp0</i>	Stator operating temperature	[°C]
<i>h0</i>	Operating altitude	[m]
Material		
<i>val_epsr_enamel</i>	Enamel dielectric constant	
<i>val_epsr_cale</i>	Slot insulation dielectric constant	
<i>val_cale_min</i>	Minimal slot insulation thickness	[μm]
Wire		
<i>R_cu</i>	Copper radius – 0 if no selected wire (default)	[m]
<i>e</i>	Enamel thickness – 0 if no selected wire (default)	[m]

Table 31: PDET inputs

The user may use the tool with a pre-selected wire configuration. PDET will then check that the selected wire can withstand turn/turn electric stress. It will design the slot insulation to withstand the electric stress between turn/slot. It will finally check that the solution fits in the slot.

The DC bus voltage is evaluated from the parameters *Vemot_max_cond1*, *ma* and *nb_cond*. At iso power, increasing the number of conductors of the phase reduces the current density on the conductors. On the other hand, the phase voltage increases.

$$\begin{aligned}
 V_{emot_max} &= V_{emot_max_cond1} * nb_{cond} \\
 V_{inv_max} &= V_{emot_max} / ma \\
 V_{dc} &= 2 * V_{inv_max}
 \end{aligned} \tag{Eq 101}$$

The wires are in close contact with each other and with the slot liner. That is because of the assumptions made for the elaboration of the wire design and slot insulation graphs. These graphs are established for round enamelled wires.

A default minimal slot liner thickness is fixed at $20\mu\text{m}$. It may be a constraint given by the user.

8 ILLUSTRATIVE EXAMPLE

As an example, let us consider the configuration presented on Table 32. No wire is preselected.

	Parameters	Designation	Value
Inverter	Maximal modulation width	<i>ma</i>	1.15
	Equivalent 1 conductor / slot / phase peak voltage	<i>Vemot_max_cond1</i>	450 V
	Number of levels	<i>nb_level</i>	5
	Voltage pulse amplitude		
	Voltage pulse rising time	<i>rise_time</i>	200 ns
Motor	Number of phases	<i>nb_phase</i>	3
	Number of slots	<i>nb_slot</i>	36
	Number of conductors	<i>nb_cond</i>	4
	Slot width	<i>L_slot</i>	8 mm
	Slot pitch	<i>h_slot</i>	46 mm
Sizing point	Filling factor	<i>kfill</i>	0.5
	Temperature	<i>Temp</i>	180°C
Materials	Altitude	<i>h0</i>	8000 m
	Enamel dielectric constant	<i>ε_{r,enamel}</i>	3.5
	Slot liner dielectric constant	<i>val_epsr_enamel</i>	4.5
	Minimal slot liner thickness	<i>val_epsr_cale</i>	20 μm

Table 32: Tool inputs - Example values

Referring to PDET organigram in Figure 140, the first step is the determination of the electric stresses for turn/turn and turn/slot contacts. That is detailed in above §6: Evaluation of the electric stresses under normal temperature and pressure conditions. The second step is to determine the overvalued electric stresses at (20 °C, 1 bar) corresponding to the impact of the sizing point. For that, the graph on Figure 122 is used.

Figure 141 displays PDET window where the electric stresses are computed. The tab pages on the top (Inputs, Electric stresses, Wire design, Slot liner design and Solutions) are the steps to compute in successive order. The DC bus voltage computed using Eq 101 is $V_{dc}=3130$ V. The inverter voltage pulse amplitude is $V_{step}=782.6$ V. The turn/turn and turn/slot electric stresses are respectively designated by *PDIV0_turn_turn* and *PDIV0_turn_slot*. The rise time of 200 ns is slow enough so that no additional overshoot is considered. The turn/turn electric stress thus correspond to 70% of V_{step} . The turn/slot electric stress is the nominal voltage of the first conductor. The graph on Figure 141 displays the PDIV evolution as a function of the temperature on the ground (triangles) and at 8000 m (crosses). The blue

curves correspond to turn/slot contact, the red curves to turn/turn contact. To be able to stand the identified electric stresses at 180°C, 8000 m (green circles) the insulation has to be oversized at 20 °C, on the ground (purple circles). Table 33 gives the electric stresses and the resulting overvalued stresses at (20°C, 1bar) due to the sizing point environmental conditions.

Interface	Electric stresses	Oversized electric stresses at (20°C, 1bar) due to sizing point impact
Turn/turn	547.8 V	807.8 V
Turn/slot	1800 V	2640 V

Table 33: Calculated overvalued voltages

The third step is the evaluation of wire solution(s). Figure 142 displays PDET Wire design window.

The left graph on Figure 142 is the enamel thickness design graph corresponding to the used material. The right graph is the used catalogue. For each copper radius, there are six possible enamel thicknesses. These correspond to the tolerances min and max of grade 1, grade 2 and grade 3 wires. PDET returned a required enamel thickness of 27.65 µm using the left graph. That results in five possible wires configuration (Table 34). Each configuration has an enamel thickness close to the required one.

Copper radius [mm]	Enamel thickness [μm]	Grade
0.425	29.5	0.2 (i.e.: max grade 1)
0.3750	28	0.4 (i.e.: min grade 2)
0.1675	28	0.6 (i.e.: max grade 2)
0.1675	28.5	0.8 (i.e.: min grade 3)
0.1060	28	1 (i.e.: max grade 3)

Table 34: Wire solutions

The two solutions corresponding to a copper radius of 0.1675 mm are quite the same as explained with Figure 127. The enamel thickness given by PDET is the minimal required thickness to withstand both overshoot and sizing point conditions.

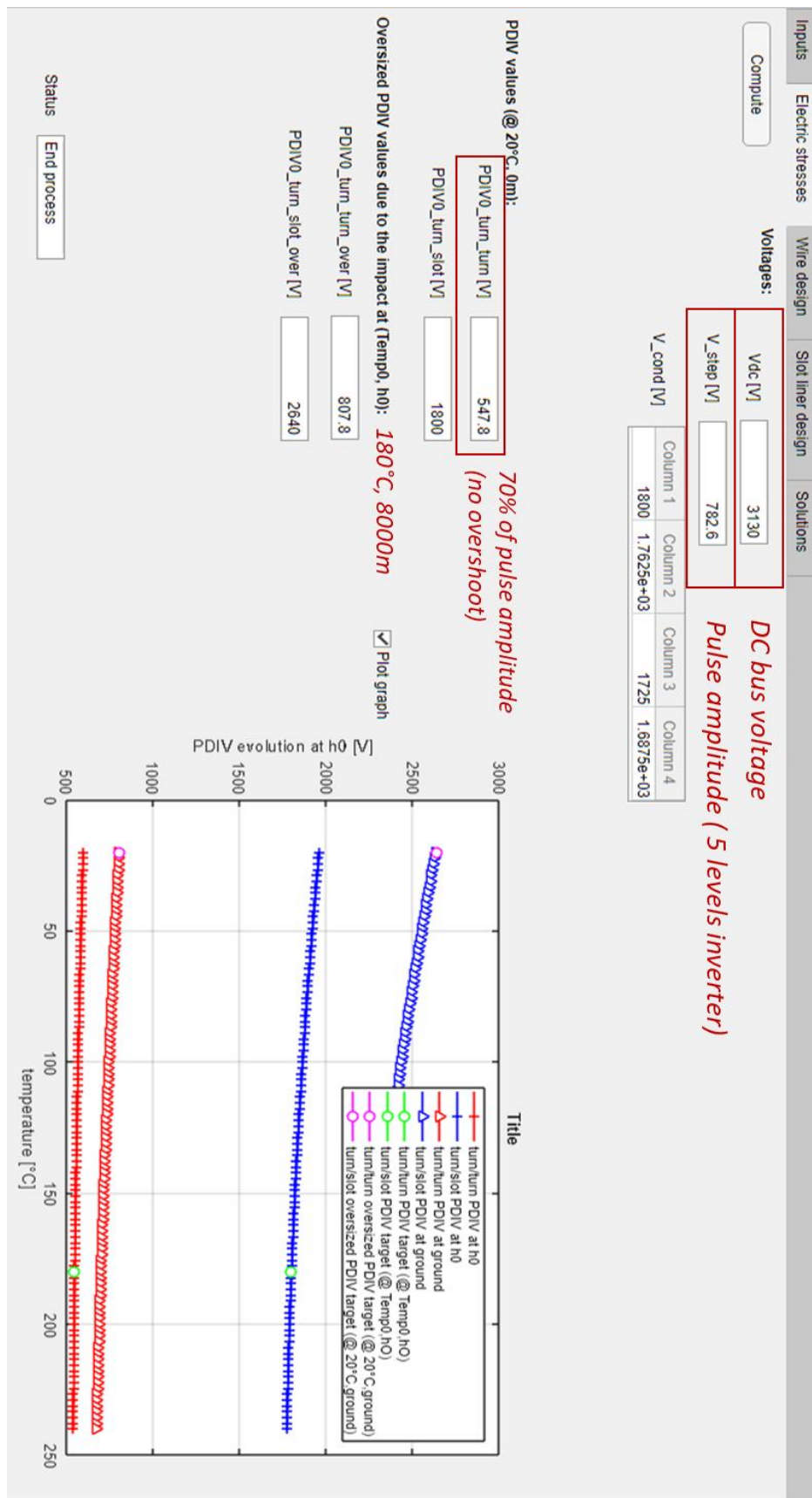


Figure 141: PDET - Electric stresses window

Chapter 5: Tool to predict PD activity in machine slot

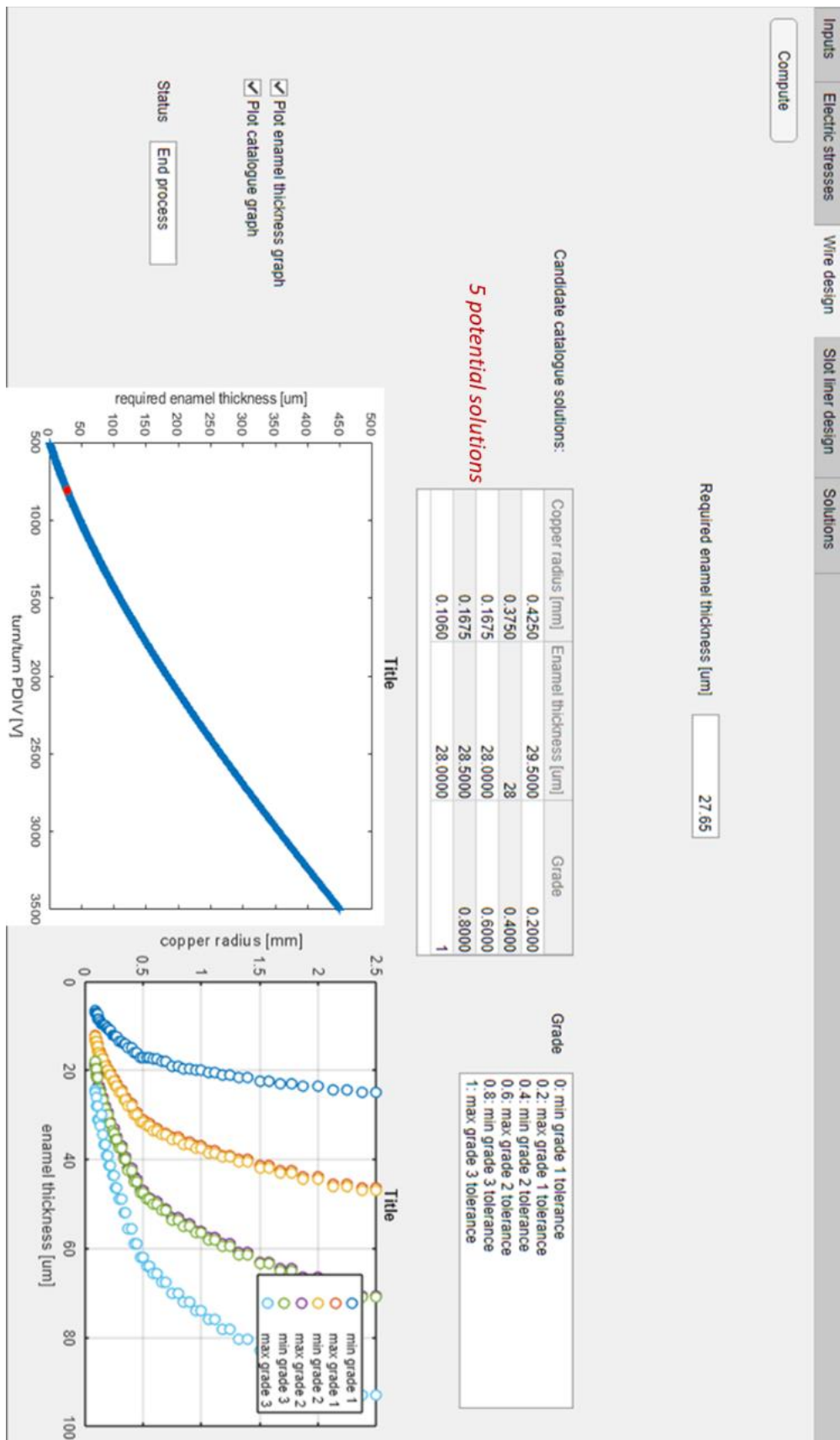


Figure 142: PDET - Wire design window

Chapter 5: Tool to predict PD activity in machine slot

The fourth step is the evaluation of the minimal required liner thickness to withstand the turn/slot electric stress at sizing point conditions. Figure 143 displays PDET Slot liner design window. The graph provides a slot liner thickness of 716.4 μm .

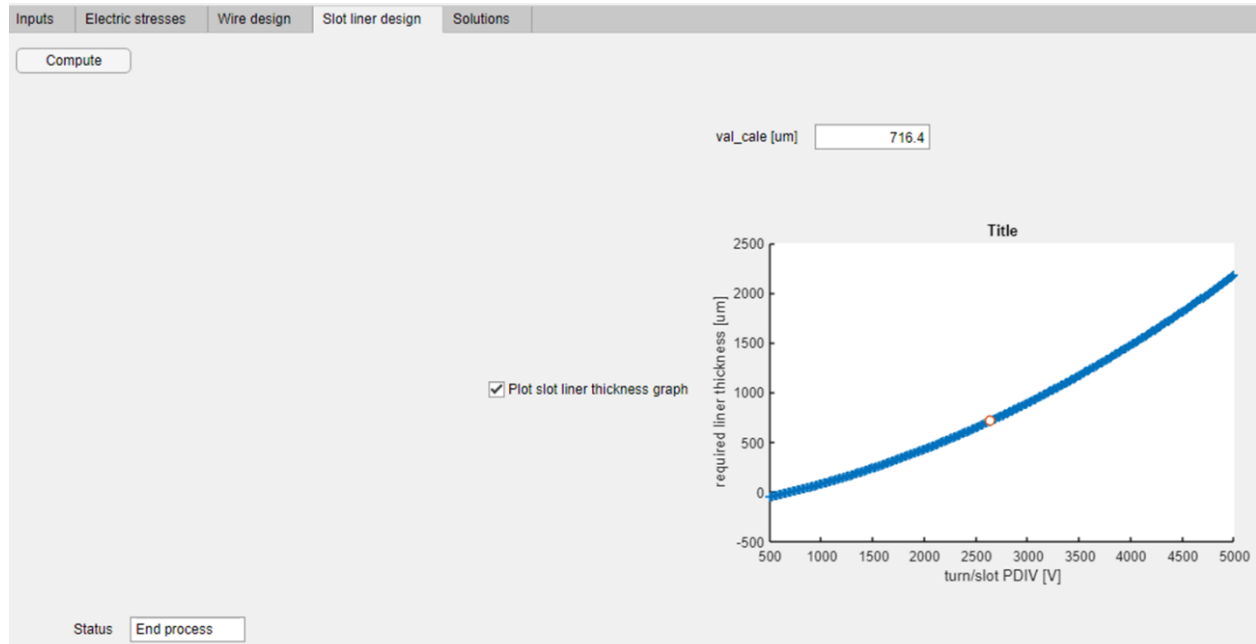


Figure 143: PDET - Slot liner design window

The final step consists in checking if the wire solutions are fitting in the slot considering a liner thickness of 716.4 μm . The fitting solutions are displayed on Figure 144:

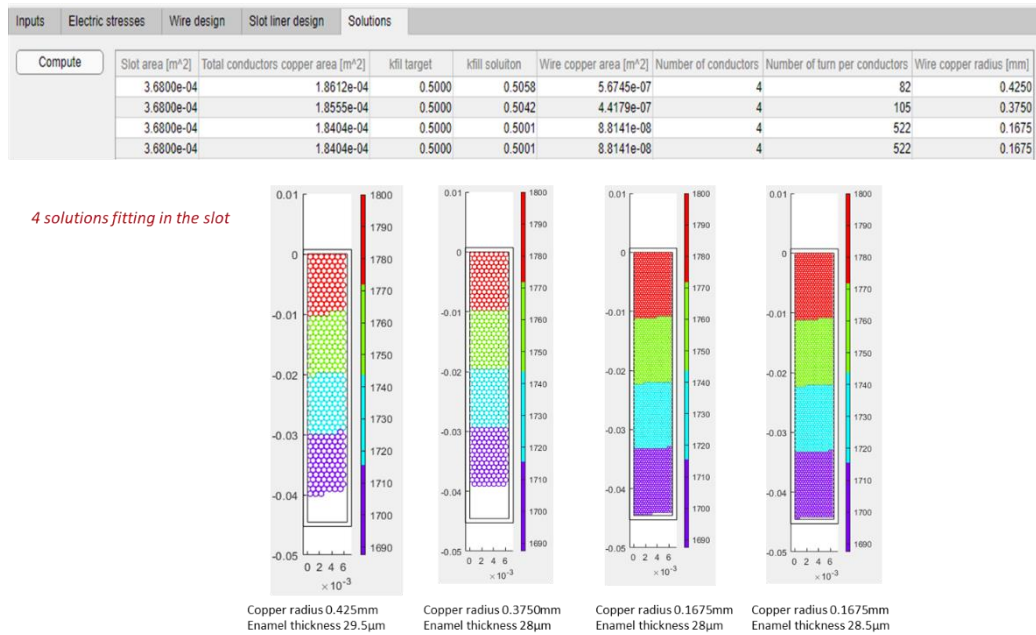


Figure 144: PDET - Solutions window

The color bar on the plots represent the nominal voltage [V] on each conductor. As four conductors are considered in this example, there are four colors. The outer rectangle is the slot. The inner rectangle is the free space in the slot once the liner is inserted. Each blank circle is the copper area of the wires. The colored contour is the enamel overcoat. Each conductor is subdivided depending the copper radius of the solution so that the filling factor is close to 0.5. From the five original solutions only four fit in the slot.

Table 35 recap the solutions:

	Copper radius [mm]	Enamel thickness [μm]	Grade	Number of wires per conductor
Wire	0.425	29.5	0.2 (i.e.: max grade 1)	82
	0.3750	28	0.4 (i.e.: min grade 2)	105
	0.1675	28	0.6 (i.e.: max grade 2)	522
	0.1675	28.5	0.8 (i.e.: min grade 3)	522
Liner		Liner thickness		
		716.4 μm		

Table 35: PDET solutions

In case no solution fits the slot, different actions are possible:

- Changing the material parameters alone (i.e.: the insulation materials) ;
- Changing inverter parameters alone;
- Changing motor parameters alone;
- Changing sizing point alone;
- A combination of the previous four possible actions.

Therefore, several actions to suppress PD have an impact on the whole powertrain sizing. The strong connection with the other WP has been clearly shown.

9 CONCLUSION

This chapter has presented the tool coded on *Matlab* which automatically size the insulation in a stator slot to avoid PD risk. First, the criterion to evaluate PDIV was presented. That criterion takes into account a combined variation of temperature and altitude for different field lines length. That criterion has been used to produce a graph to quantify the PDIV decrease (compared to 20 °C, 1 bar conditions) due to changing environmental conditions (sizing point).

Chapter 5: Tool to predict PD activity in machine slot

Then, Simple Analytical Models (SAMs) of the turn/turn and turn/slot contacts have been presented and validated by 2D-Finite Element Models (2D-FEMs). The SAMs have been used to compute graphs which give the minimal required insulation thickness to withstand electric stresses considering the chosen materials and taking into account a transient voltage overshoot. Besides, the electric stresses are overestimated in order to take into account the decrease in PDIV at the sizing point.

Finally, it came out that multiple actions are possible to avoid PD. Some of them may actually have a real impact on the whole powertrain sizing.

General conclusion and perspectives

This PhD work has consisted in studying the Electrical Insulation System (EIS) of rotating machines fed by inverters that will equip future hybrid propulsion aircrafts. It is a part of the European H2020 project HASTECs (**H**ybrid **A**ircraft **r**e**S**earch on **T**hermal and **E**lectrical **C**omponents and **S**ystems).

Partial Discharges (PD) phenomenon represents a great deal in the design of future rotating machines fed by inverter. On one hand, new faster components made out of SiC and GaN technologies will considerably improve the performances of the inverters. On the other hand, they will generate harder voltage fronts at the motor terminals which lead to higher transient voltage overshoots. PD will be more likely to appear and the insulation lifespan will be reduced due to both voltage overshoots and high switching frequency. That is the reason why it is absolutely necessary to take into account such a phenomenon when designing the motor to avoid any PD appearance, rather than searching for solutions in a motor already produced to remove them.

It was appeared relevant in this project to integrate both inverters and motors in the nacelles. That will reduces the voltage overshoots at motor terminals by using a power harness length shorter than 2 m. Nevertheless, in an aeronautical non-pressurized environment where equipment are submitted to great temperature and pressure variations, the Partial Discharge Inception Voltage (PDIV) will be considerably affected, as it is very sensitive to them.

It has appeared that the choices for the EIS will considerably impact the design of the cooling system. Polymer materials widely used in EIS have very low thermal conductivity. Therefore, an oversizing of the EIS results in much more thermal resistance in the path of the heat flux to be evacuated by the cooling system. New insulating materials having higher thermal conductivity are nowadays under study (not only for aircraft electric devices). These are composites made of a polymer matrix in which ceramic particles are inserted. Such particles are used in micro- or nano-sizes. The proportion of ceramic introduced in the polymer material is completely adjustable. It improves thermal properties but also have a negative impact on mechanical properties.

Experimental works about the relevant use of the well-known Paschen's criterion in motor EIS design have been carried on during this PhD work. PDIV measurements have been performed on samples of PEI/PAI overcoated round copper wires (polymers able to support the estimated motors working temperature). A correction of the secondary electron emission coefficient has been proposed for the configuration of two parallel enamelled round copper wires in close contact (representative of two neighbouring conductors in a machine slot). This corrected coefficient has been found to be almost

General conclusion and perspectives

ten times lower compare to the value found in the literature obtained with metallic planar electrodes. That leads to higher PDIV levels in the case of enamelled round wires.

The Paschen's criterion requires the complete knowledge of electric field lines geometry. A numerical code has then been developed on Matlab to drawn electric field lines from a 2D-Finite Elements (2D-FEM) solution of an electrostatic problem. The originality of the proposed method is that only the scalar potential solution is required and the density of displayed lines is analogous to the field intensity. It has been compared to a ballistic approach already implanted on Matlab. It results that the Matlab function is much faster. Both methods give similar results for the considered 2D-electrostatic problem. The development of the proposed method provided better understanding on scalar potential formulation and the notions of electric flux tubes.

Simple Analytical Models (SAM) of the turn/turn and turn/slot configurations have been established. Results given by the SAM have been verified with the corresponding 2D-FEM. The SAM enabled parametric studies which has lead to design graphs. They indicate the minimal insulation thicknesses to ensure a PD-free slot in order to withstand the nominal electric stresses.

Finally, the design graphs have been implanted in tool specifically developed in this work: the Partial Discharge Evaluation Tool (PDET). It is a fully automatic tool which dimensions the EIS inside a stator slot to avoid PD appearance. This tool can be implanted in an optimization loop of the whole powertrain. For now, the tool perimeter is inside a stator slot with only one phase, but it may be upgraded to treat more than one phase per slot. The conductors are made of enamelled round wires in close contacts. The hot spots are the turn/turn and turn/slot electric stresses. The stresses were automatically evaluated from the inverter and motor parameters. The decrease in PDIV due to a combined variation of pressure and temperature was also considered.

PDET provides PD-free solutions for Type I-EIS motors. It is obviously transposable to Type II-EIS motors (high voltage motors). In case of Type II-EIS motors (able to support PD), the PDET will provide an EIS design that will limit the PD amplitude.

The work carried on during this PhD work offers multiple perspectives:

- The use of flat wire for windings. In such geometry, SAM are not valid anymore. Besides, the electric field is slightly non uniform. Design graphs will have to be derived from 2D-FEM and the degree of uniformity of the electric field will have to be carefully checked in order to apply the corrected Paschen's criterion.

General conclusion and perspectives

- The consideration of multiple phases per slot. An additional insulation layer will be required to insulate the different phases. The maximum electric stress will be now found between two different phases.
- The addition of cooling pipes embedded in the slot for a more efficient cooling inside the winding. The coolant may be composed of glycooled water, which is an electric insulating liquid. However, the pipes are usually conductors. That will add new zones where the electric stress has to be carefully investigated. Hollow wires may also be investigated.
- The end winding is the zone where electric stress may also be high. Indeed, in this area, the different phases overlap. Besides, there is triple points at the exit of the slot between the metallic carcass of the motor, the air, and the insulation. Tackle such configuration will need to develop a 3D-modelling.

General conclusion and perspectives

Publications

P. Collin, D. Malec, Y. Lefevre, "Tool to Design the Primary Electrical Insulation System of Low Voltage Rotating Machines Fed by Inverters", In 2018 IEEE Electrical Insulation Conference (EIC) (pp. 8-13). IEEE

P. Collin, D. Malec, Y. Lefevre, "Outil d'aide au design du système d'isolation primaire de machines tournantes basse tension alimentées par onduleur", In SFE Grenoble 2018

"Design of Electric Machine Taking Into Account the Partial Discharges Phenomena for Future Hybrid Propelled Aircrafts", P.Collin, S.Touhami, D.Malec, Y.Lefevre, J.F.Llibre, More Electric Aircraft, February 6-7, 2019, Toulouse

"Concernant la pertinence de l'utilisation du critère de Paschen pour l'estimation de la tension d'apparition des décharges partielles (TADP) lors du design du système d'isolation électrique de moteurs alimentés par onduleur", P. Collin, D. Malec, Y. Lefevre, Jeunes Chercheurs en Génie Electrique, 11-14 juin, 2019, Olérons

"About the relevance of using Paschen's criterion for partial discharges inception voltage (PDIV) estimation when designing the electrical insulation system of inverter fed motors", P. Collin, D. Malec, Y. Lefevre, Electrical Insulation Conference, June 16-19, 2019, Calgary

"A general method to compute the electric flux lines in the slots of electric machines for the evaluation of partial discharges risk", P. Collin, D. Malec, Y. Lefevre, Compumag, July 15-19, 2019, Paris

"Tool to predict and avoid Partial Discharges in stator slot of rotating motors fed by inverter", P. Collin, D. Malec, Y. Lefevre, Aerospace Europe Conference, February 25-28, 2020, Bordeaux

Publications

Annex

Nominal conductor diameter [mm]	Minimum increase due to the insulation thickness [mm]			Maximal overall diameter [mm]		
	Grade 1	Grade 2	Grade 3	Grade 1	Grade 2	Grade 3
0,180	0,013	0,025	0,036	0,204	0,217	0,229
0,190	0,014	0,027	0,039	0,216	0,228	0,240
0,200	0,014	0,027	0,039	0,226	0,239	0,252
0,212	0,015	0,029	0,043	0,240	0,254	0,268
0,224	0,015	0,029	0,043	0,252	0,266	0,280
0,236	0,017	0,032	0,048	0,267	0,283	0,298
0,250	0,017	0,032	0,048	0,281	0,297	0,312
0,265	0,018	0,033	0,050	0,297	0,314	0,330
0,280	0,018	0,033	0,050	0,312	0,329	0,345
0,300	0,019	0,035	0,053	0,334	0,352	0,360
0,315	0,019	0,035	0,053	0,349	0,367	0,384
0,335	0,020	0,038	0,06	0,372	0,391	0,408
0,355	0,020	0,038	0,057	0,392	0,411	0,428
0,375	0,021	0,040	0,060	0,414	0,434	0,453
0,400	0,021	0,040	0,060	0,439	0,459	0,478
0,425	0,022	0,042	0,064	0,466	0,488	0,508
0,450	0,022	0,042	0,064	0,491	0,513	0,533
0,475	0,024	0,045	0,067	0,519	0,541	0,562
0,500	0,024	0,045	0,068	0,544	0,566	0,587
0,530	0,025	0,047	0,071	0,576	0,600	0,623
0,560	0,025	0,047	0,071	0,606	0,630	0,653
0,600	0,027	0,050	0,075	0,649	0,674	0,698
0,630	0,027	0,050	0,075	0,679	0,704	0,728
0,670	0,028	0,053	0,080	0,722	0,749	0,774
0,710	0,028	0,053	0,080	0,762	0,789	0,814
0,750	0,030	0,056	0,085	0,805	0,834	0,861
0,800	0,030	0,056	0,085	0,855	0,884	0,911
0,850	0,032	0,060	0,090	0,909	0,938	0,968
0,900	0,032	0,060	0,090	0,959	0,989	1,081
0,950	0,034	0,063	0,095	1	1	1,074
1,000	0,034	0,063	0,095	1,062	1,094	1,124
1,060	0,034	0,065	0,098	1,124	1,157	1,188
1,120	0,034	0,065	0,098	1,184	1,217	1,248
1,180	0,035	0,067	0,100	1,246	1,279	1,311
1,250	0,035	0,067	0,100	1,316	1,349	1,381
1,320	0,036	0,069	0,103	1,388	1,422	1,455
1,400	0,036	0,069	0,103	1,468	1,502	1,535
1,500	0,038	0,071	0,107	1,570	1,606	1,640
1,600	0,038	0,071	0,107	1,670	1,706	1,740
1,700	0,039	0,073	0,110	1,772	1,809	1,844
1,800	0,039	0,073	0,110	1,872	1,909	1,944
1,900	0,040	0,075	0,113	1,974	2,012	2,048
2,000	0,040	0,075	0,113	2,074	2,112	2,148
2,120	0,041	0,077	0,116	2,196	2,235	2,272
2,240	0,041	0,077	0,116	2,316	2,355	2,392
2,360	0,042	0,079	0,119	2,438	2,478	2,516
2,500	0,042	0,079	0,119	2,578	2,618	2,656
2,650	0,04	0,081	0,123	2,730	2,772	2,811

Annex

2,800	0,043	0,081	0,123	2,880	2,922	2,961
3,000	0,045	0,084	0,127	3,083	3,126	3,166
3,150	0,045	0,084	0,127	3,233	3,276	3,316
3,350	0,046	0,086	0,130	3,435	3,479	3,521
3,550	0,046	0,086	0,130	3,635	3,679	3,721
3,750	0,047	0,089	0,134	3,838	3,883	3,926
4,000	0,047	0,089	0,134	4,088	4,133	4,176
4,250	0,049	0,092	0,138	4,341	4,387	4,431
4,500	0,049	0,092	0,138	4,591	4,637	4,681
4,750	0,050	0,094	0,142	4,843	4,891	4,936
5,000	0,050	0,094	0,142	5,093	5,141	5,186

Annex 1: Enamel thickness tolerances picked from [37]

References:

- [1] ‘Agenda 21 (Rio Declaration on Environment and Development)’, 1992, p. 79.
- [2] ‘IEA World energy outlook 2018’. International Energy Agency, Jul. 2018.
- [3] ‘ITF Transport outlook 2017’. International Transport Forum , OECD iLibrary, 2017.
- [4] ‘OPEC World Oil Outlook 2040’. Organization of the Petroleum Exporting Countries, Sep. 2018.
- [5] ‘WHO Health and sustainable development - Transport and health risks’. World Health Organization, 2019.
- [6] ‘The cost of air pollution – Health impacts of road transport’. ISBN 978-92-64-210448, OECD iLibrary, 2014.
- [7] J. P. RODRIGUE, C. COMTOIS, and B. SLACK, *The geography of transports systems*, 4th edition. New York Routledge Edition, 2017.
- [8] ‘World Energy Model’. International Energy Agency, Version 2018.
- [9] ‘Les énergies renouvelables en France : les chiffres clés 2018’. Ministère de la Transition écologique et solidaire, May 24, 2018.
- [10] ‘Quelle est la source d’énergie la plus utilisée dans le monde ?’ ENGIE, Mar. 29, 2019.
- [11] ‘Historique évolution du cours du baril (159 litres) de pétrole WTI’. france-inflation.com, 2020.
- [12] ‘Road transport: Reducing CO₂ emissions from vehicles’. European Comission, 2019.
- [13] ‘Aviation carbon offset programmes’. IATA, 2008.
- [14] E. Férard, ‘En Suède, la “honte de prendre l’avion” pousse les voyageurs à favoriser le train’. Géo, Apr. 16, 2019.
- [15] L. Faleiro, J. Herzog, B. Schievelbusch, and T. Seung, ‘INTEGRATED EQUIPMENT SYSTEMS FOR A MORE ELECTRIC AIRCRAFT – HYDRAULICS AND PNEUMATICS’, *Hydraul. Pneum.*, p. 10.
- [16] M. Palomeque, ‘A320 - Dual hydraulic loss’. Safety first #4, Jun. 2017.
- [17] J. Robinson, ‘Collins Aerospace building \$67M electric aircraft lab’, *Wings Mag.*, Apr. 2019.
- [18] B. Sarlioglu and C. T. Morris, ‘More Electric Aircraft: Review, Challenges, and Opportunities for Commercial Transport Aircraft’, *IEEE Trans. Transp. Electrification*, vol. 1, no. 1, pp. 54–64, Jun. 2015, doi: 10.1109/TTE.2015.2426499.
- [19] R. Hemmati, F. Wu, and A. El-Refaie, ‘Survey of Insulation Systems in Electrical Machines’, in *2019 IEEE International Electric Machines & Drives Conference (IEMDC)*, San Diego, CA, USA, May 2019, pp. 2069–2076, doi: 10.1109/IEMDC.2019.8785099.
- [20] ‘Electric flight - Bringing zero-emission technology to aviation’. Airbus.
- [21] ‘The future is electric’. Airbus, Jul. 17, 2018.
- [22] ‘CityAirbus’. Airbus.
- [23] ‘HASTECS’. <http://www.laplace.univ-tlse.fr/HASTECS> (accessed Jan. 09, 2020).
- [24] J. Thauvin, ‘Exploring the design space for a hybrid-electric regional aircraft with multidisciplinary design optimisation methods’, Institut National Polytechnique de Toulouse, 2018.
- [25] ‘Hybrid Aircraft Academic reSearch on Thermal & Electrical Components and Systems (HASTECS), Project selected from CFP in CleanSky II (H2020) framework’ .
- [26] M. Pettes-Duler, X. Roboam, and B. Sareni, ‘Integrated design process and sensitivity analysis of a hybrid electric propulsion system for future aircraft’, Salerno, Italy, May 2019.
- [27] Y. Lefevre, S. El-Aabid, J.-F. Llibre, C. Henaux, and S. Touhami, ‘Performance assessment tool based on loadability concepts’, *Int. J. Appl. Electromagn. Mech.*, vol. 59, no. 2, pp. 687–694, Mar. 2019, doi: 10.3233/JAE-171059.
- [28] P. Collin, S. Touhami, D. Malec, Y. Lefevre, and J. F. Llibre, ‘Design of Electric Machine Taking Into Account the Partial Discharges Phenomena for Future Hybrid Propelled Aircrafts’, 2019.

References:

- [29] N. Erroui, G. Gateau, and N. Roux, ‘Continuous-caliber semiconductor components’, in *2018 IEEE International Conference on Industrial Technology (ICIT)*, Lyon, Feb. 2018, pp. 658–663, doi: 10.1109/ICIT.2018.8352256.
- [30] A. Zeaiter and M. Fenot, ‘Thermal Sensitivity Analysis of a High Power Density Electric Motor for Aeronautical Application’, in *2018 IEEE International Conference on Electrical Systems for Aircraft, Railway, Ship Propulsion and Road Vehicles & International Transportation Electrification Conference (ESARS-ITEC)*, Nottingham, Nov. 2018, pp. 1–6, doi: 10.1109/ESARS-ITEC.2018.8607393.
- [31] R. Wrobel, S. J. Williamson, J. D. Booker, and P. H. Mellor, ‘Characterizing the in situ Thermal Behavior of Selected Electrical Machine Insulation and Impregnation Materials’, *IEEE Trans. Ind. Appl.*, vol. 52, no. 6, pp. 4678–4687, Nov. 2016, doi: 10.1109/TIA.2016.2589219.
- [32] S. Touhami, Y. Bertin, Y. Lefèvre, J.-F. Llibre, C. Henaux, and M. Fenot, ‘Lumped Parameter Thermal Model of Permanent Magnet Synchronous Machines’, p. 7.
- [33] F. Accorinti *et al.*, ‘High-efficiency cooling system for highly integrated power electronics for hybrid propulsion aircraft’, in *2019 IEEE 28th International Symposium on Industrial Electronics (ISIE)*, Vancouver, BC, Canada, Jun. 2019, pp. 870–877, doi: 10.1109/ISIE.2019.8781086.
- [34] M. E. Banda, D. Malec, and J.-P. Cambronne, ‘Simulation of Space Charge Impact on Partial Discharge Inception Voltage in Power Busbars Dedicated to Future Hybrid Aircrafts’, *Circuits Syst.*, vol. 09, no. 11, pp. 196–212, 2018, doi: 10.4236/cs.2018.911018.
- [35] ‘EIC 60034-18-41, “Partial discharge free electrical insulation systems (Type I) used in rotating electrical machines fed from voltage converters – Qualification and quality control tests,” 2014.’
- [36] ‘Enamelled copper wire, SONA’..
- [37] ‘enamled_copper_wire.pdf’.
http://www.universalmetals.com.pk/pdf/enamled_copper_wire.pdf (accessed Jan. 15, 2020).
- [38] A. Anton, ‘Émaux isolants et fils émaillés’, *Tech. Ing.*, vol. D2330, p. 19, 2009.
- [39] J. Pyrhonen, T. Jokinen, and V. Hrabovcová, *Design of rotating electrical machines*. Chichester, West Sussex, United Kingdom ; Hoboken, NJ: Wiley, 2008.
- [40] ‘Magnet Wire – Selection and Use Directions for Magnet Wire’,
https://www.ecmenzies.com.au/images/productpdf/COROCUdatasheet_1.pdf.
- [41] Y. Agari, A. Ueda, and S. Nagai, ‘Thermal conductivity of a polymer composite’, *J. Appl. Polym. Sci.*, vol. 49, no. 9, pp. 1625–1634, Sep. 1993, doi: 10.1002/app.1993.070490914.
- [42] R. Arora and W. Mosch, ‘High Voltage and Electrical Insulation Engineering’. A John Wiley & Sons, Inc., Publication, 2011.
- [43] M. Chapman, N. Frost, and R. Bruetsch, ‘Insulation Systems for Rotating Low-Voltage Machines’, in *Conference Record of the 2008 IEEE International Symposium on Electrical Insulation*, Vancouver, BC, Jun. 2008, pp. 257–260, doi: 10.1109/ELINSL.2008.4570323.
- [44] J. Moeneclaey, ‘Méthode de conception des bobinages des actionneurs électriques adaptés aux nouvelles contraintes de l'avionique’, University of Artois, Béthune, 2015.
- [45] ‘Resins and Varnishes 2013 - VON ROLL - PDF Catalogs | Technical Documentation | Brochure’.
<https://pdf.directindustry.com/pdf/von-roll/resins-varnishes-2013/12485-556569.html> (accessed Jan. 21, 2020).
- [46] ‘Design and Testing of Insulation for Adjustable Speed Drives - PDFHALL.COM’.
https://pdfhall.com/design-and-testing-of-insulation-for-adjustable-speed-drives_5b69f350097c4775388b45ee.html (accessed Jan. 22, 2020).
- [47] G. C. Stone, Ed., *Electrical insulation for rotating machines: design, evaluation, aging, testing, and repair*. Piscataway, NJ : Hoboken, NJ: IEEE ; Wiley-Interscience, 2004.
- [48] S. Nategh, A. Krings, O. Wallmark, and M. Leksell, ‘Evaluation of Impregnation Materials for Thermal Management of Liquid-Cooled Electric Machines’, *IEEE Trans. Ind. Electron.*, vol. 61, no. 11, pp. 5956–5965, Nov. 2014, doi: 10.1109/TIE.2014.2308151.

References:

- [49] W. Sixel, M. Liu, G. Nellis, and B. Sarlioglu, ‘Cooling of Windings in Electric Machines via 3D Printed Heat Exchanger’, in *2018 IEEE Energy Conversion Congress and Exposition (ECCE)*, Portland, OR, Sep. 2018, pp. 229–235, doi: 10.1109/ECCE.2018.8557845.
- [50] Y. Ohki, ‘Development of epoxy resin composites with high thermal conductivity’, *IEEE Electr. Insul. Mag.*, vol. 26, no. 1, pp. 48–49, Jan. 2010, doi: 10.1109/MEI.2010.5383936.
- [51] P. Rodgers, V. Eveloy, and L. El Sayed, ‘Candidate thermally enhanced polymer composite materials for cooling of electronic systems’, in *20th International Workshop on Thermal Investigations of ICs and Systems*, Greenwich, London, United Kingdom, Sep. 2014, pp. 1–6, doi: 10.1109/THERMINIC.2014.6972495.
- [52] S. Diaham, ‘Modulation of the dielectric breakdown strength in polyimide nanocomposites by deep traps tailoring in interphase regions’, *IEEE Trans. Dielectr. Electr. Insul.*, vol. 26, no. 1, pp. 247–252, Feb. 2019, doi: 10.1109/TDEI.2018.007540.
- [53] C. Abadie, T. Lebey, and T. Billard, ‘On-line non-intrusive partial discharges detection in aeronautical systems’, Université Toulouse 3 Paul Sabatier, 2017.
- [54] H. Foch, F. Forest, and T. Meynard, ‘Onduleurs de tension - Structures. Principes. Applications’, p. 21, 1998.
- [55] L. Benmamas, ‘Méthodes d’évaluation du risque de décharges partielles dans le bobinage de machines électriques destinées à la traction automobile’, University of Paris-Saclay, Gif-sur-Yvette, 2017.
- [56] M. Kaufhold, H. Aninger, M. Berth, J. Speck, and M. Eberhardt, ‘Electrical stress and failure mechanism of the winding insulation in PWM-inverter-fed low-voltage induction motors’, *IEEE Trans. Ind. Electron.*, vol. 47, no. 2, pp. 396–402, Apr. 2000, doi: 10.1109/41.836355.
- [57] B. Taghia, B. Cougo, H. Piquet, D. Malec, A. Belinger, and J.-P. Carayon, ‘Advanced analysis of transient overvoltage in electromechanical chain fed by SiC inverter’, *Electrimacs 2017*, p. 8, 2017.
- [58] A. Ong, J. Carr, J. Balda, and A. Mantooth, ‘A Comparison of Silicon and Silicon Carbide MOSFET Switching Characteristics’, in *2007 IEEE Region 5 Technical Conference*, Fayetteville, AR, USA, Apr. 2007, pp. 273–277, doi: 10.1109/TPSD.2007.4380318.
- [59] L. Dupont, S. Lefebvre, and Z. Khatir, ‘Characterisationof Silicon Carbide Schottky diodes and COOLMOSTMtransistors at high temperature’, *35th Annu. IEEE Power Electron. Spec. Conf.*, p. 6, 2004.
- [60] V. Mihaila, ‘Nouvelle Conception des bobinages statoriques des machines à courant alternatif pour réduire les effets négatifs des dV/dt .’, Artois, 2011.
- [61] B. Taghia, B. Cougo, H. Piquet, D. Malec, A. Belinger, and J.-P. Carayon, ‘Overvoltage at motor terminals in SiC-based PWM drives’, *Math. Comput. Simul.*, vol. 158, pp. 264–280, Apr. 2019, doi: 10.1016/j.matcom.2018.09.009.
- [62] P. Bidan, T. Lebey, and C. Neacsu, ‘Development of a new off-line test procedure for low voltage rotating machines fed by adjustable speed drives (ASD)’, *IEEE Trans. Dielectr. Electr. Insul.*, vol. 10, no. 1, pp. 168–175, Feb. 2003, doi: 10.1109/TDEI.2003.1176584.
- [63] R. Bartnikas and E. McMahon, ‘Engineering dielectrics - Volume 1 - Corona measurements and interpretation’, *Am. Soc. Test. Mater.*, no. STP669, 1979.
- [64] F. H. Keuger, ‘Partial discharge detection in high voltage equipment’, *Butterworth-Heinemann*, pp. 78–85, 1990.
- [65] R. Bruetsch, M. Tari, K. Froehlich, T. Weiers, and R. Vogelsang, ‘Insulation Failure Mechanisms of Power Generators’, p. 7.
- [66] ‘Lichtenberg figure’, *Wikipedia*. Jan. 25, 2020, Accessed: Feb. 12, 2020. [Online]. Available: https://en.wikipedia.org/w/index.php?title=Lichtenberg_figure&oldid=937573574.
- [67] C. Mayoux, ‘Aging of polymeric insulating materials in power cables’, *IEEE Trans. Dielectr. Electr. Insul.*, vol. 4, no. 6, pp. 665–673, Dec. 1997, doi: 10.1109/94.654573.
- [68] G. Nayak, Y. Du, R. Brandenburg, and P. J. Bruggeman, ‘Effect of air flow on the micro-discharge dynamics in an array of integrated coaxial microhollow dielectric barrier discharges’, *Plasma Sources Sci. Technol.*, vol. 26, no. 3, p. 035001, Feb. 2017, doi: 10.1088/1361-6595/aa56a4.

References:

- [69] M. Q. Nguyen, ‘Etude de l’impact des contraintes aéronautiques sur les systèmes d’isolation des moteurs de conditionnement d’air’, University of Toulouse, Toulouse, 2012.
- [70] G. Stone, ‘Partial Discharges in Electrical Insulation’..
- [71] J. Kurimský, I. Kolcunová, and R. Cimbala, ‘Understanding surface partial discharges in HV coils and the role of semi-conductive protection’, *Electr. Eng.*, vol. 92, no. 7–8, pp. 283–289, Dec. 2010, doi: 10.1007/s00202-010-0184-0.
- [72] ‘Corona discharge’, *Wikipedia*. Feb. 03, 2020, Accessed: Feb. 13, 2020. [Online]. Available: https://en.wikipedia.org/w/index.php?title=Corona_discharge&oldid=938928794.
- [73] ‘Ozonation of Polymers’. <https://polymerdatabase.com/polymer%20chemistry/Ozone.html> (accessed Feb. 13, 2020).
- [74] ‘Failures in Three-Phase Stator Windings’. <https://easa.com/resources/failures-in-three-phase-stator-windings> (accessed Feb. 13, 2020).
- [75] C. Julie, ‘Etude des mécanismes anti-cancéreux induits par milieux activés par jet de plasma froid : vers une nouvelle approche thérapeutique.’, Toulouse 3 Paul Sabatier, 2018.
- [76] E. SILI, ‘Etude et caractérisation des décharges partielles et du vieillissement du polyimide en environnement aéronautique’, Toulouse 3 Paul Sabatier, 2012.
- [77] C. Van De Steen, ‘Modélisation des propriétés de transport des ions moléculaires de krypton et xénon pour l’optimisation des générateurs de plasma froids utilisant les gaz rares’, Université Toulouse 3 Paul Sabatier, Toulouse, 2018.
- [78] I. Popescu and E. Badareu, *Gaz Ionisés, Décharges Electriques dans les Gaz*, Dunod. Paris, 1968.
- [79] E. R. B. Adamson and A. Dissertation, ‘SECONDARY ELECTRON EMISSION COEFFICIENT FROM LEXAN: THE LOW ENERGY CROSSOVER’, p. 78.
- [80] O. Eichwald, M. Yousfi, and O. Ducasse, ‘Breakdown criteria in air: an overview supported by predictive simulations’, p. 6.
- [81] F. Paschen, ‘Ueber die zum Funkenübergang in Luft, Wasserstoff und Kohlensäure bei verschiedenen Drucken erforderliche Potentialdifferenz’, *Ann. Phys.*, vol. 273, no. 5, pp. 69–96, 1889, doi: 10.1002/andp.18892730505.
- [82] T. W. Dakin, G. Luxa, G. Oppermann, J. Vigreux, G. Wind, and H. Winkelkemper, ‘Breakdown of Gases in Uniform Fields Paschen Curves for Nitrogen, Air and Sulfur Hexafluoride’, *Electra*, 1974.
- [83] H. H. Wittenberg, ‘Gas Tube Design’, *Electron Tube Des. RCA Electron Tube Div.*, pp. 792–817, 1962.
- [84] F. Koliatene, ‘CONTRIBUTION A L’ETUDE DE L’EXISTENCE DES DECHARGES DANS LES SYSTEMES DE L’AVIONIQUE’, Toulouse 3 Paul Sabatier, 2009.
- [85] ‘RTCA DO-160, Environmental Conditions and test Procedures for Airborne Equipment’..
- [86] F. W. Peek, *Dielectric Phenomena in High Voltage Engineering*, McGraw Hill. 1929.
- [87] W. G. Dunbar and J. W. Seabrook, ‘High Voltage Design Guide for Airborne Equipment’, *Boeing Aerosp. Co.*, p. 217, 1976.
- [88] V. L. Bychkov, S. A. Volkov, and I. V. Kochetov, ‘Ionization process in the humid air of the lower troposphere’, *Russ. J. Phys. Chem. B*, vol. 5, no. 6, pp. 940–945, Dec. 2011, doi: 10.1134/S1990793111060054.
- [89] P. Mikropoulos, C. Stassinopoulos, and B. Sarigiannidou, ‘Positive Streamer Propagation and Breakdown in Air: the Influence of Humidity’, *IEEE Trans. Dielectr. Electr. Insul.*, vol. 15, no. 2, pp. 416–425, Apr. 2008, doi: 10.1109/TDEI.2008.4483460.
- [90] G. Robles, J. Fresno, J. Martínez-Tarifa, J. Ardila-Rey, and E. Parrado-Hernández, ‘Partial Discharge Spectral Characterization in HF, VHF and UHF Bands Using Particle Swarm Optimization’, *Sensors*, vol. 18, no. 3, p. 746, Mar. 2018, doi: 10.3390/s18030746.
- [91] B. Cella, ‘On-line partial discharges detection in conversion systems used in aeronautics’, University of Toulouse, 2015.
- [92] T. Balachandran, S. Sirimman, A. Jin, and K. S. Haran, ‘Partial Discharge Testing of Form-Wound Air-Core Armature Windings for a High-Frequency PMSM for Electric Aircraft Applications’, in *2018 IEEE International Conference on Information and Automation for*

References:

- Sustainability (ICIAfS)*, Colombo, Sri Lanka, Dec. 2018, pp. 1–6, doi: 10.1109/ICIAfS.2018.8913342.
- [93] J. M. Wetzer and P. C. T. van der Laan, ‘Prebreakdown currents: Basic interpretation and time-resolved measurements’, *IEEE Trans. Electr. Insul.*, vol. 24, no. 2, pp. 297–308, Apr. 1989, doi: 10.1109/14.90288.
- [94] R. Ross, ‘Graphical methods for plotting and evaluating Weibull distributed data’, in *Proceedings of 1994 4th International Conference on Properties and Applications of Dielectric Materials (ICPADM)*, Brisbane, Qld., Australia, 1994, vol. 1, pp. 250–253, doi: 10.1109/ICPADM.1994.413986.
- [95] J. S. White, ‘The Moments of Log-Weibull Order Statistics’, *Technometrics*, pp. 373–386, 1969.
- [96] J. C. Fothergill, ‘Ageing, Space Charge and Nanodielectrics: Ten Things We Don’t Know About Dielectrics’, in *2007 IEEE International Conference on Solid Dielectrics*, Winchester, UK, Jul. 2007, pp. 1–10, doi: 10.1109/ICSD.2007.4290739.
- [97] R. Rui and I. Cotton, ‘Impact of low pressure aerospace environment on machine winding insulation’, in *2010 IEEE International Symposium on Electrical Insulation*, San Diego, CA, USA, Jun. 2010, pp. 1–5, doi: 10.1109/ELINSL.2010.5549718.
- [98] S. Palit, D. Varghese, H. Guo, S. Krishnan, and M. A. Alam, ‘The Role of Dielectric Heating and Effects of Ambient Humidity in the Electrical Breakdown of Polymer Dielectrics’, *IEEE Trans. Device Mater. Reliab.*, vol. 15, no. 3, pp. 308–318, Sep. 2015, doi: 10.1109/TDMR.2015.2431998.
- [99] E. McMahon and J. Perkins, ‘Surface and Volume Phenomena in Dielectric Breakdown of Polyethylene’, *IEEE Trans. Power Appar. Syst.*, vol. 82, no. 69, pp. 1128–1136, Dec. 1963, doi: 10.1109/TPAS.1963.291505.
- [100] J. V. Champion, S. J. Dodd, A. S. Vaughan, and S. J. Sutton, ‘THE EFFECT OF VOLTAGE, TEMPERATURE AND MORPHOLOGY ON ELECTRICAL TREEING IN POLYETHYLENE BLENDS’, *IEEE Dielectr. Mater. Meas. Appl. Conf. Publ.*, no. 473, p. 6, 2000.
- [101] M. Szczepanski, ‘Development of methods allowing the test and the comparison of low-voltage motors insulation systems running under partial discharges (fed by inverter)’, p. 214.
- [102] R. Acheen, C. Abadie, T. Lebey, T. Billard, and S. Duschesne, ‘Comparison of the Electrical Ageing Under Sinusoidal and Square-Wave Stresses’, San Antonio, TX, 2018, pp. 353–356.
- [103] ‘IEEE Guide for the Statistical Analysis of Electrical Insulation Voltage Endurance Data’. ANSI/IEEE Std 930, 1987.
- [104] N. Lahoud, J. Faucher, D. Malec, and P. Maussion, ‘Electrical Aging of the Insulation of Low-Voltage Machines: Model Definition and Test With the Design of Experiments’, *IEEE Trans. Ind. Electron.*, vol. 60, no. 9, pp. 4147–4155, Sep. 2013, doi: 10.1109/TIE.2013.2245615.
- [105] ‘Qualification and type tests for Type I electrical insulation systems used in rotating electrical machines when fed from voltage converters’. IEC 60034-18-CD International Standard, 2012.
- [106] ‘Qualification and acceptance tests for partial discharge resistant electrical insulation systems (Type II) used in rotating electrical machines when fed from voltage converters’. IEC 60034-18-42 TS, International Standards, 2008.
- [107] P. Maussion, A. Picot, M. Chabert, and D. Malec, ‘Lifespan and aging modeling methods for insulation systems in electrical machines: A survey’, in *2015 IEEE Workshop on Electrical Machines Design, Control and Diagnosis (WEMDCD)*, Torino, Italy, Mar. 2015, pp. 279–288, doi: 10.1109/WEMDCD.2015.7194541.
- [108] K. Petcharaks, ‘A contribution to the streamer breakdown criterion’, in *11th International Symposium on High-Voltage Engineering (ISH 99)*, London, UK, 1999, vol. 1999, pp. v3-19-v3-19, doi: 10.1049/cp:19990689.
- [109] A. Pedersen, T. Christen, A. Blaszczyk, and H. Boehme, ‘Streamer inception and propagation models for designing air insulated power devices’, in *2009 IEEE Conference on Electrical Insulation and Dielectric Phenomena*, Virginia Beach, VA, USA, Aug. 2009, pp. 604–607, doi: 10.1109/CEIDP.2009.5377740.

References:

- [110] G. Eriksson, ‘Easy Evaluation of Streamer Discharge Criteria’, *Proc. 2012 COMSOL Conf. Milan*, p. 7, 2012.
- [111] E. J. Horowitz, ‘A general field-line plotting algorithm’, *Comput. Phys.*, vol. 4, no. 4, p. 418, 1990, doi: 10.1063/1.168384.
- [112] Z. Ren, ‘2-D dual finite-element formulations for the fast extraction of circuit parameters in VLSI’, *IEEE Trans. Magn.*, vol. 39, no. 3, pp. 1590–1593, May 2003, doi: 10.1109/TMAG.2003.810548.
- [113] G. Parent, S. Duchesne, and P. Dular, ‘Determination of Flux Tube Portions by Adjunction of Electric or Magnetic Multivalued Equipotential Lines’, *IEEE Trans. Magn.*, vol. 53, no. 6, pp. 1–4, Jun. 2017, doi: 10.1109/TMAG.2017.2661401.
- [114] G. Parent, M. Rossi, S. Duchesne, and P. Dular, ‘Determination of Partial Discharge Inception Voltage and Location of Partial Discharges by Means of Paschen’s Theory and FEM’, *IEEE Trans. Magn.*, vol. 55, no. 6, pp. 1–4, Jun. 2019, doi: 10.1109/TMAG.2019.2902374.
- [115] T. M. Whittaker, *Mon Weather.*, 1977.
- [116] G. Dhatt and G. Touzot, *Une présentation de la méthode des éléments finis*, Les Presses de l’Université Laval. Québec, et Maloine, Paris, 1981.
- [117] F. Pauli, N. Driendl, L. Yang, and K. Hameyer, ‘Corona resistant enameled wires as a solution for electrical motor winding systems supplied by high du/dt inverter voltage: An insulation life-time estimation’, *IEEE Submitt.*, p. 7, 2019.
- [118] N. Hayakawa and H. Okubo, ‘Partial discharge characteristics of inverter-fed motor coil samples under ac and surge voltage conditions’, *IEEE Electr. Insul. Mag.*, vol. 21, no. 1, pp. 5–10, Jan. 2005, doi: 10.1109/MEI.2005.1389265.
- [119] ‘IEC 60270 (2000-12), High-voltage test techniques — Partial discharge measurements’.
- [120] W. Weibull, ‘A Statistical Distribution Function of Wide Applicability’, *J. Appl. Mech.*, no. 18, pp. 293–297, 1951.
- [121] P. Collin, D. Malec, and Y. Lefevre, ‘Tool to Design the Primary Electrical Insulation System of Low Voltage Rotating Machines Fed by Inverters’, *2018 IEEE Electr. Insul. Conf. EIC*, pp. 8–13, 2018, doi: 10.1109/EIC.2018.8481037.
- [122] M. Szczepanski, D. Malec, P. Maussion, B. Petitgas, and P. Manfe, ‘Prediction of the lifespan of enameled wires used in low voltage inverter-fed motors by using the Design of Experiments (DoE)’, in *2017 IEEE Industry Applications Society Annual Meeting*, Cincinnati, OH, Oct. 2017, pp. 1–6, doi: 10.1109/IAS.2017.8101798.
- [123] H. Xu, Y. Zhang, and F. Zheng, ‘Study on measuring method of dielectric spectroscopy for polymer dielectrics’, in *2009 IEEE 9th International Conference on the Properties and Applications of Dielectric Materials*, Harbin, China, Jul. 2009, pp. 922–925, doi: 10.1109/ICPADM.2009.5252247.
- [124] F. Aymonino, ‘Contribution à l’étude du comportement des systèmes d’isolation des machines tournantes à courant alternatif fonctionnant sous très hautes températures (200-400°C)’, University of Toulouse Paul Sabatier, Toulouse, 2008.
- [125] M. G. D. L. Calle, J. M. Martínez-Tarifa, Á. M. G. Solanilla, and G. Robles, ‘Uncertainty Sources in the Estimation of the Partial Discharge Inception Voltage in Turn-to-Turn Insulation Systems’, *IEEE Access*, vol. 8, pp. 157510–157519, 2020, doi: 10.1109/ACCESS.2020.3018870.
- [126] H. Ismail, ‘Étude du taux de pulvérisation et du coefficient d’émission électronique secondaire de cibles métalliques polycristallines bombardées par des ions Hg+, dans un domaine d’énergie allant de 5 à 30 keV’, *Rev. Phys. Appliquée*, vol. 5, no. 5, pp. 759–764, 1970, doi: 10.1051/rphysap:0197000505075900.
- [127] M. Florkowski, B. Florkowska, and P. Zydrón, ‘Partial Discharges in Insulating Systems of Low Voltage Electric Motors Fed by Power Electronics—Twisted-Pair Samples Evaluation’, *Energies*, vol. 12, no. 5, p. 768, Feb. 2019, doi: 10.3390/en12050768.
- [128] N. Naudé, A. Belinger, S. Dap, and N. Gherardi, ‘Memory effects in Atmospheric Pressure Townsend Discharges in N₂ and air’, p. 4, 2015.

References:

- [129] D. Marić, N. Škoro, P. D. Maguire, C. M. O. Mahony, G. Malović, and Z. L. Petrović, 'On the possibility of long path breakdown affecting the Paschen curves for microdischarges', *Plasma Sources Sci. Technol.*, vol. 21, no. 3, p. 035016, Jun. 2012, doi: 10.1088/0963-0252/21/3/035016.
- [130] P. G. Slade and E. D. Taylor, 'Electrical breakdown in atmospheric air between closely spaced (0.2 μm -40 μm) electrical contacts', *IEEE Trans. Compon. Packag. Technol.*, vol. 25, no. 3, pp. 390–396, Sep. 2002, doi: 10.1109/TCAPT.2002.804615.
- [131] A. Peschot, N. Bonifaci, O. Lesaint, C. Valadares, and C. Poulain, 'Deviations from the Paschen's law at short gap distances from 100 nm to 10 μm in air and nitrogen', *Appl. Phys. Lett.*, vol. 105, no. 12, p. 123109, Sep. 2014, doi: 10.1063/1.4895630.
- [132] P. Carazzetti and H. R. Shea, 'Electrical breakdown at low pressure for planar microelectromechanical systems with 10- to 500- μm gaps', vol. 8, p. 9.



[Open Archive Toulouse Archive Ouverte](#)

OATAO is an open access repository that collects the work of Toulouse researchers and makes it freely available over the web where possible

This is an author's version published in: <http://oatao.univ-toulouse.fr/28466>

Official URL :

To cite this version:

Banda Gnama Mbimbiangoye, Mallys Elliazar  and Malec, David  and Cambronne, Jean-Pascal  *Partial discharge (DP) prevention within power converter busbars dedicated to hybrid aircraft propulsion.* (2021) .
(Unpublished)

Any correspondence concerning this service should be sent
to the repository administrator: tech-oatao@listes-diff.inp-toulouse.fr

1. Introduction

The postdoctoral position associated to this WP covered the period from January to December 2018. It was focused on the second aim of WP5, dedicated to better understanding of partial discharge inside power electronics converters designed for the future hybrid aircrafts expected to 2025/2035 period.

For this aim, many tasks were performed to achieve the free-charge objectives under DC electric field and power density increase requirements. Firstly, from WP2, a preliminary study based on various topologies of power busbars were analysed. In second, some simulation studies were performed to prevent them inside power electronics systems through a focalization on power busbars.

2. Context and problematic

The key expectations intended on this post-doc (O5) was the simulation/modelling studies of DP risk appearances within the busbars dedicated to the power converters and more widely within electrical insulating systems surrounding power electronics medias. This would run by:

- Providing information that can help to the design of connectors, busbars, power modules and cables, by minimizing PD risks;
- Assessing of electrical constraints minimizing the DP risks within the power converters as well as at the motor terminals;
- Studying the optimal conditions leading to the free-PD EIS under operating conditions.

3. Main results in stationary case

3.1. Topology and triple point

Figure 1 shows a view of the studied power converter topology on which this study is based. It consists in seven busbars slats (2 mm-thick) mounted between input bus capacitors and fly output capacitors. Electronic component ships are

packaged inside power modules embedded in below. The DC bus is powered by a DC 2.5 kV input voltage. PTFE films are sandwiched between each busbars pairs. In such topology, many triple points appear in bus-bars/PTFE/air interfaces.

In power busbars application case, these triple point are the busbars-insulator-air junction point. De facto, the both confinement and power densities increasing expose electric insulation systems to more partial discharge risks. Added to materials defects (structural and chemical defects, electronic traps distributions, trapping level...), these partial discharge inception locally increase the electric field within the dielectric material. This local increase in electric field changes the intrinsic material properties and reliability, with the consequence of an irreversible insulators damage of dielectric that can affect the insulation system and then expose the power converters on which the propulsion depends on [1].

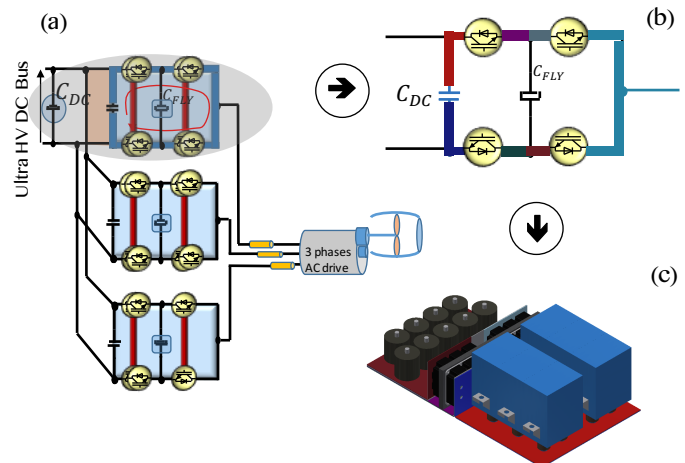


Fig. 1 : Power converter "FC-3 levels topology" model. (a) Structural view of converter, (b) Equivalent electric scheme by phase, (c) Designed packaging.

The triple point, corresponding to the one with greatest potential difference, is zoomed in Figure 1 (at the right). Since this point is the one submitted to highest electric stress, it is also the most exposed to partial discharge risk, as well for transient as steady state, especially during strong electrical stress during flight phases (take-off and landing). For this reason, the study focuses on the estimation of partial discharges risks through electric field assessment in this triple point to characterize the insulation behaviour of busbars for this applied electric specification. Based on simulation results highlighted around this triple

point, partial discharge risks incurred on this one would also reveal those expected on other triple points, since other triple points support lower electric potential differences.

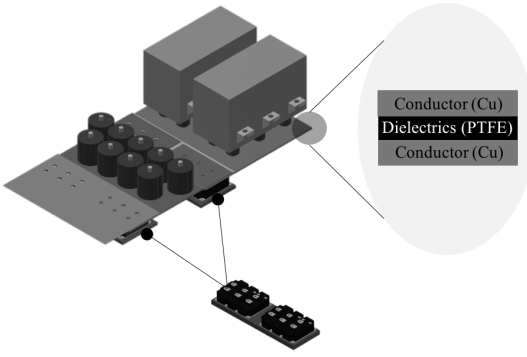


Fig. 2 : Schematic view of power busbars embedded inside a power electronics converter.

3.1. Simulation conditions

A common way to evaluate if partial discharges occur between two conductor materials consists in comparison of Paschen theoretical and experimental curves obtained in considered gas where Paschen's assumptions are applicable (uniformity of the electric field, plan/plan geometry of conductors, preponderance of electronic avalanche mechanism, ...) [2]. For air gaps greater than 1 mm (linear part of the Paschen curve), another alternative way would consist to assess the electric field distribution in a considered medium and to estimate the partial discharges risks by taking into account the breakdown threshold in air. This last way is the one used in this study. Figure 3 shows a schematization of the considered calculation domain.

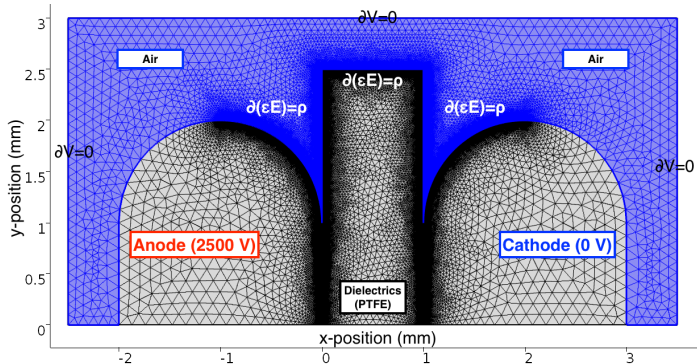


Fig. 3 : Calculation domain meshing for simulation studies.

The electric field is computed through finite elements method by solving Poisson's equation in both air and dielectrics domains:

$$\frac{\partial E(x,y)}{\partial x \partial y} = \frac{\rho(x,y)}{\epsilon_0 \epsilon_r} \quad (1)$$

Where E is related to electric potential V such as :

$$E = -\nabla V \quad (2)$$

ρ is the space charge density, ϵ_0 and ϵ_r the vacuum and relative permittivity, respectively. A zero flux was applied in air boundaries according to relation:

$$n \cdot (\epsilon_0 \epsilon_r E) = 0 \quad (3)$$

Where n is surface unit vector. The calculation domain was non-uniformly meshed. To increase calculation precision of electric field and charge at the interfaces, refinement was added to both boundaries and in triple points as shown in Figure 3. The total meshing was sized in 7.5×10^5 finite elements.

3.2. Main Results

Simulated electric field due to gradual homocharges densities: Figure 4 shows the cartographies of simulated electric field obtained in the case of homocharges implantation near to dielectrics surface with charge densities ranging from 0 C/m³ to 1 C/m³.

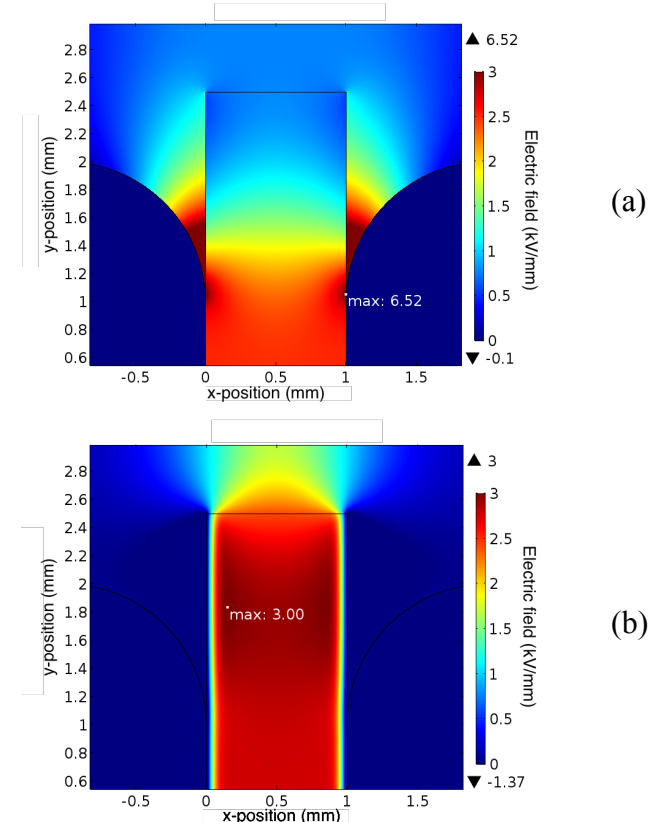


Fig. 4 : Simulated electric field at triple points under DC voltage. Stationary simulation. Absolute homocharges density of (a) 0 C/m³, (b) 1 C/m³.

These results highlight that more homocharges accumulation near dielectric surface seems to decrease electric field at the triple points (for

densities greater than 1 C/m^3). As well for static implantation near busbars/insulator interfaces as for spatial ranging of their distribution inside insulator, accumulation of heterocharges within insulating material sandwiched between busbars would qualitatively and quantitatively affects distribution electric field in the dielectric. It would seem that for a charge density below 0.5 C/m^3 , the electric field due to heterocharges would not be sufficient to impact the total electric field in material and consequently at the triple points, although this threshold would not be the unique conditions to generate a partial discharge in air since other physical and electronic processes should also be met [3]. However, it appears that partial discharge risks would be attenuated with higher heterocharges accumulation (above 0.5 C/m^3) at insulators/busbars interfaces.

Simulated electric field due to gradual heterocharges densities: The same simulation, performed in same condition with heterocharges implantation give the reverse results such exposed in Figure 5.

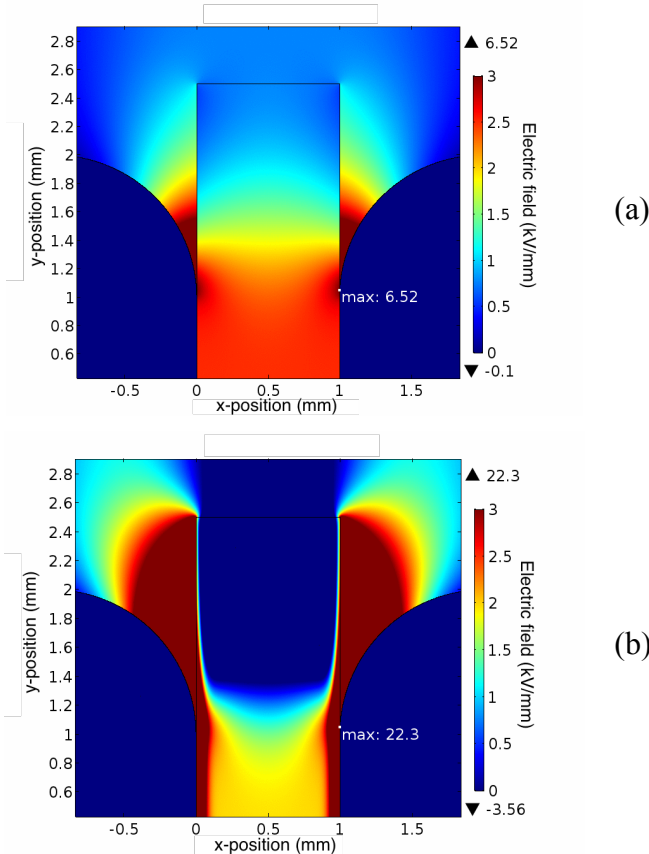


Fig. 5 : Simulated electric field at triple points under DC voltage. Stationary simulation. Absolute heterocharges density of (a) 0 C/m^3 , (b) 1 C/m^3 .

In presence of heterocharges close to the dielectric surface, the electric field rapidly grows in triple points and at dielectric surface. This increasing depends on charge density, while it decreases considerably in the volume of the insulator. This

behaviour is the contrary of what observed with homocharges (Figure 4).

Various mechanisms could cause heterocharges accumulation in such solid insulating material polarized between busbars in a DC electric field. These heterocharges could be generated through natural traps within insulator, trapping distribution in dielectrics bulk, electrode/dielectrics interface defaults but also directly by extraction of charges towards busbars conductors due to a favourable internal electric field, chemical defaults or by detrapping processes induced by thermal activation through potential barrier. All these physical mechanisms that would make possible heterocharges accumulation would therefore be favourable to partial discharges inception in busbars environment [4, 5]. For this reason, although polarization in busbars configuration presented in this power circuit topology would not permit direct injection of heterocharges, prediction of their accumulation at busbar/insulator interface would require to carefully rethink industrial chain of insulators design dedicated to power converters intended to hybrid aircraft, in order to prevent partial discharge risks as highlighted by this study.

4. Time-dependent simulation of PD risks

Another part of these postdoctoral focused on simulation of PD-risks in time-dependent conditions. The main outputted results, based on generation and transport equations of charge mobility as function of electric field, reveal some difference in homocharge behaviour at insulator(PTFE)/conductor interfaces under DC electric field (cf. Figure 6).

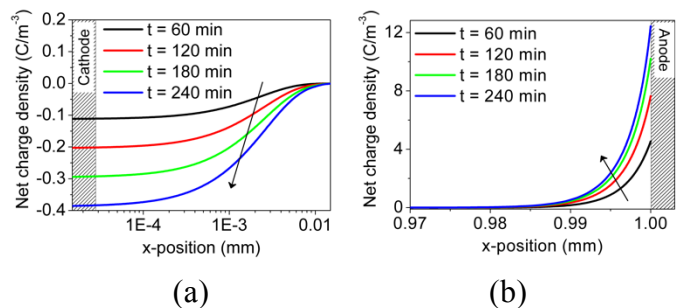


Figure 6. Net charge densities as a function of x-position within PTFE film in $y = 1 \text{ mm}$ (i.e.: at triple points level). (a) Negative charges arising from cathode electrode; (b) Positive charges arising from anode electrode.

By considering the net charge densities associated with total electric field (i.e.: net fluxes of mobile and trapped charges injected at the electrodes) we observe that more holes are injected/trapped at the anode and the injected/trapped electrons are dominant at the cathode. The electrons distribution

is extended over approximately 10 µm while the holes distribution is extended over 2 µm. Quantitatively, the holes density injected from the anode, and trapped near the surface of the dielectric, is thirty times greater than electrons injected and trapped at the cathode.

Beyond 180 minutes, simulations seem to confirm the hypothesis of a very weak electron injection within the PTFE, for the electric field considered. The significant decrease of the electric field within the triple point positioned at the anode would confirm a progressive accumulation of holes injected at the anode. These positive charges, of the same sign as the applied voltage, form a homocharges area which will promote a reduction of the electric field at the PTFE/conductor interfaces. On the other hand, a very weak injection of negative charges at the cathode does not induce the creation of a large zone of negative homocharges. De facto, the electric field is less affected at the cathode triple point. These observations are in agreement with experimental ones that measure a larger injection of holes than electrons in PTFE films [6, 7], even for a highest DC electric field.

5. Conclusion

This reporting period through this postdoctoral position was efficiently used to develop some preventive tools in order to prevent the partial discharge risks within power busbars dedicated to hybrid aeronautical converter systems. Not only this study confirms that presence of space charges within a solid insulator generates an internal increase of electric field that impacts total electric field distribution, but it also highlights that for an applied electric field of 2.5 kV/mm, accumulation of small charges density in dielectrics ($\sim 0.01 \text{ C/m}^3$), induced by example by some chemical defaults, thermal, pressure or mechanical stress, would be sufficient to anticipate partial discharges in air surrounding power busbars dedicated to aircraft. Moreover, according to the sign of these charges, the risks of discharges would be differently appreciable. In case of homocharges accumulation at the busbars/insulator interfaces, electric field would tend to strengthen in dielectrics. This is less advantageously the case when these homocharges are transported in the volume of the dielectrics. On the contrary, heterocharges accumulation at busbar/insulator interfaces would reinforce the total electric field at insulator surface, leading to the greater risks of partial discharges resulting to the confinement of electric field at triple points. This situation would be accentuated as well by surface heterocharges

density as their transport within the insulator bulk. Although PTFE is considered among the lower charging insulators, this study, applicable to other polymer insulators, reveals above all that charge accumulation of a few C/m³ would generate various mechanisms sufficient to age or activate degradation of insulators [4, 7].

In the intended case of hybrid-propulsion aircraft, electrical insulation system will be more exposed to partial discharge risks if insulation systems operate in thermal, humidity and pressure environmental conditions. In such condition, heterocharges accumulation would offer favourable conditions for partial discharges inception whose material, human and financial consequences could be irreversible. It is necessary to design non-charged insulation system in accordance to electrical strength intended for busbars to avoid any discharge inception. An alternative solution could be to screen busbars to ensure non-penetration of electric field in air gap, although this solution would increase weight density [8].

6. References

- [1] Bilodeau, T. M., Dunbar, W. G. and Sarjeant, W. J. (1989) High-voltage and partial discharge testing techniques for space power systems. *IEEE Electrical Insulation Magazine*, **5**, 12-21.
- [2] Cotton, I., Nelms, A. and Husband, M. (2008) Higher voltage aircraft power systems. *IEEE Aerospace and Electronic Systems Magazine*, **23**, 25-32.
- [3] Niemeyer, L. (1995) A generalized approach to partial discharge modeling. *IEEE transactions on Dielectrics and Electrical insulation*, **2**, 510-528.
- [4] Tanaka, T. (1986) Internal partial discharge and material degradation. *IEEE Transactions on Electrical Insulation*, **6**, 899-905.
- [5] Wang, W., Takada, T., Tanaka, Y. and Li, S. (2017) Space charge mechanism of polyethylene and polytetrafluoroethylene by electrode/dielectrics interface study using quantum chemical method. *IEEE Transactions on Dielectrics and Electrical Insulation*, **24**, 2599-2606.
- [6] Min, D., Cho, M., Li, S., & Khan, A. R. (2012) Charge transport properties of insulators revealed by surface potential decay experiment and bipolar charge transport model with genetic algorithm. *IEEE Transactions on Dielectrics and Electrical Insulation*. **19**.
- [7] Wang, W., Takada, T., Tanaka, Y., & Li, S. (2017) Space charge mechanism of polyethylene and polytetrafluoroethylene by electrode/dielectrics interface study using quantum chemical method. *IEEE Transactions on Dielectrics and Electrical Insulation*, **24**, 2599-2606.
- [8] Pretzsch, G. (1983) Charge state of PTFE thermoelectrets. *Physica Status Solidi (a)*, **79**, K139-K142.



Hybrid **A**ircraft
Academic re**S**earch on **T**hermal
& **E**lectrical **C**omponents and **S**ystems



Mars 2019

Malik Tognan, Christophe Turpin (Laplace)
Patrice Simon (Cirimat)



Preliminary delivery Battery & Fuel
Cell metamodels; “HASTECS M6.1”
Technical report



AIRBUS

SUMMARY

1.	Introduction.....	1
2.	State of the art of the power and energy densities of battery / fuel cell systems for embedded applications today and tomorrow.....	2
2.1.	Preliminary definitions	2
2.2.	State of the art of battery specific power and energy performances in mobile applications (automotive and aeronautical).....	2
2.2.1.	Overview of the general battery performances statements today and tomorrow in scientific articles and reviews.....	3
2.2.2.	Selection of three technologies (LTO, NMC, Li-S) and review of emblematic datasheets for each of them	7
2.2.3.	Overview of the battery weight integrating factor values assessed in the literature	12
2.3.	State of the art of FC stacks and systems power densities and H ₂ storage systems energy densities for mobile applications (automotive and aeronautical)	13
2.3.1.	Pre-selection of the FC technologies and H ₂ storage methods.....	14
2.3.2.	State of the Art of the FC stack and system power densities: High Temperature / Low Temperature PEM FC and Solid Oxide FC	14
2.3.3.	Overview of the gravimetric and volumetric performances of the H ₂ storage methods	23
2.4.	Summary of the performances assessments made for the selected technologies	30
2.4.1.	Battery: specific energies, C _{rate} capabilities and cyclability assessments	30
2.4.2.	Fuel Cell stacks and systems specific power / H ₂ storage performances	32
2.4.3.	First comparison at the system scale between FC and batteries on a particular case.....	35
3.	Mass estimations based on a simplified light hybridization mission and modeling developments for the Battery / Fuel Cell block.....	36
3.1.	Power profile mission(s) taken as reference(s).....	37
3.2.	First level mass estimations	38
3.3.	Second level mass estimations and modeling developments	42
3.3.1.	Battery behavior modeling	42
3.3.2.	Fuel Cell system modeling and potential trade-offs.....	46
4.	Conclusion – Perspectives.....	48

5.	APPENDIX	49
5.1.	Appendix A.....	49
5.2.	Appendix B.....	51
5.3.	Appendix C.....	53
5.4.	Appendix D.....	54
6.	BIBLIOGRAPHY	56

ABBREVIATIONS / SYMBOLS

BMS: Battery Management System

BoP: Balance of Plants

DOD: Depth Of Discharge (%)

DOE: Department of Energy

FC: Fuel Cell

HT / LT: High Temperature (140 – 180 °C) / Low Temperature (60 – 80 °C)

LH₂: Liquid H₂

LHV: Lower Heating Value of hydrogen (33.3 kWh/kg)

LiS: Lithium Sulfur

LTO: Lithium Titanate Oxide (anode material)

MEA: Membrane Electrode Assembly

MLI: Multi-Layer Insulation

NMC: Nickel Manganese Cobalt (cathode material)

PEM FC: Proton Exchange Membrane Fuel Cell

SOC: State Of Charge (%)

SOFC: Solid Oxide Fuel Cell

SSB: Solid State Battery (also referred as All solid state)

TNO: Titanium Niobium Oxide (anode material)

1. INTRODUCTION

The work presented in this document is a part of the Hastecs project (Hybrid aircraft Academic reSearch on Thermal & Electrical Components and Systems) dedicated to the development of models and tools that can support the demonstration of radical aircraft configurations. More specifically, the case of a hybrid-electric aircraft with a serial-hybrid configuration (all the energy conversion chain is electrified) is treated here. Inside this project divided in six Work Packages (WPs), the Work Package n°6 is dedicated to the global system integration (Matthieu Pettes-Duller pHD work) and to the auxiliary source which is going to hybridize the main power source (the gas turbines). The report developed here, conclusion of a one year post-doctorate work, is treating the case of this auxiliary source consisting of a Battery and/or a Fuel Cell (FC) with a H₂ storage system.

Two objectives are followed in this study:

- A state of the art of the current and future performances of battery and fuel cell systems in aeronautic and more generally in embedded applications (especially automotive ones).
- The development of modeling tools to identify the behavior of the hybrid source and to estimate its mass.

Obviously the two objectives are intimately linked, as the development of modeling tools relies on empirical data coming from the state of the art. In this report, a particular focus is laid on the state of the art while the modeling developments are summarized in a more synthetical way. A selection of Li-ion battery technologies, from high power type to very high energy type, as well as a selection of FC technologies is firstly considered for the state of the art step in order to assess typical performances values in terms of specific energies and powers. H₂ storages media are as well considered regarding their gravimetric efficiencies performances. Various articles and datasheet are scanned in order to assess average values and progression margin for the next decades. A specific attention is given to the contextualization of all the power and energy specific values regarding parameters such as charge and discharge speed capabilities (C_{rate}) for the different battery technologies, or FC system structure regarding the different auxiliary components for the FC technologies.

A first-level modeling based on simplified equations is then proposed to assess different sizing and system mass estimations of the auxiliary source considering two emblematic power missions corresponding to a light-hybridization scenario. Thereafter, second-level modeling developments are introduced in order to refine the previous results and to provide more insights into the auxiliary source behavior regarding parameters such as efficiency, State of Charge, auxiliary components parasitic consumptions, etc. Conclusions are finally given considering the state of the art values and the masses assessment for the different technologies.

2. STATE OF THE ART OF THE POWER AND ENERGY DENSITIES OF BATTERY / FUEL CELL SYSTEMS FOR EMBEDDED APPLICATIONS TODAY AND TOMORROW

Two different kinds of assessments have to be done for both battery and FC systems: whereas a battery system exhibits an intrinsic coupling between its energy and power capabilities, a FC system is separated between its power conversion stage and its energy storage (H_2 storage). Consequently, separate assessments of FC stacks power performances on one hand and H_2 storage capabilities on the other hand need to be addressed.

The following paragraphs will thus detail separately the states of the art of current battery performances on one hand, and of FC stacks and systems together with H_2 storage systems capabilities on the other hand.

2.1. Preliminary definitions

In order to quantify the battery/FC performances, a few parameters are going to be scanned:

- The gravimetric and volumetric energy densities (specific energy) – $e_m(Wh/kg)$ and $e_v(Wh/L)$ – represent for a given energy source or energy container its intrinsic energy content with respect respectively to its mass and volume.
- The gravimetric and volumetric power densities (specific power) – $p_m(W/kg)$ and $p_v(W/L)$ – represent, in a complementary manner, for a given power source its intrinsic ability to deliver a certain power with respect to its mass and volume.
- The C_{rate} expresses the speed of charge/discharge of a battery: a C_{rate} is independent of the battery capacity (size) and current and is homogeneous to a frequency (h^{-1}). For instance, a battery discharge at a C_{rate} of 1 C means that the battery will be discharged in one hour, at 0.2 C in 5 hours, at 2 C in 30 minutes... The C_{rate} capabilities of a battery are thus closely linked to its specific power performances: the ability to charge/discharge at a certain C_{rate} a certain amount of energy is equivalent to a power capability.
- For the H_2 storages medias: the gravimetric index – $\eta_m(-)$ often expressed as “wt. %” – represent the amount of H_2 kg that can be stored with respect to the total mass (including the H_2 contained inside) of the storage system:

$$\eta_m = \frac{kg_{H_2}}{kg_{storage\ system}} \quad (1)$$

2.2. State of the art of battery specific power and energy performances in mobile applications (automotive and aeronautical)

Battery performances do not only consist in its specific energy and/or power but also rely on cyclability aspects (how the battery capacity / internal resistance are going to decline with the accumulation of working cycles). Even if these aspects are of first importance they may not be treated as well as those mentioned earlier, mainly because cyclability data is often less

available or incomplete. Also, several battery technologies – such as Lead-acid, Ni-Zn, flow batteries... – will not be considered in the global overview considering their too small energy densities.

2.2.1. Overview of the general battery performances statements today and tomorrow in scientific articles and reviews

In a first attempt to evaluate the battery performance assessments made in the literature, it can be relevant to have a look on how these assessments are actually made in articles exploring themes close to the main study thematic (hybrid-electric propulsion, electric flight...). More specifically, the idea is to aggregate, between the articles investigating on a future electrical propulsion or on the integration of battery systems in aircrafts, the values of the batteries specific gravimetric and volumetric energy/power densities taken as references, as well as the technologies mentioned.

2.2.1.1. Assumptions made in articles investigating on the electric flight and/or studying hybrid-electric aircraft concepts

In [KUH-12], the authors investigate the fundamental prerequisites for electric flying and the potential of hybrid power systems for air transport. A review of battery negative and positive electrode material is made in order to highlight the different combinations possible and the most energetic ones theoretically achievable (Figure 1).

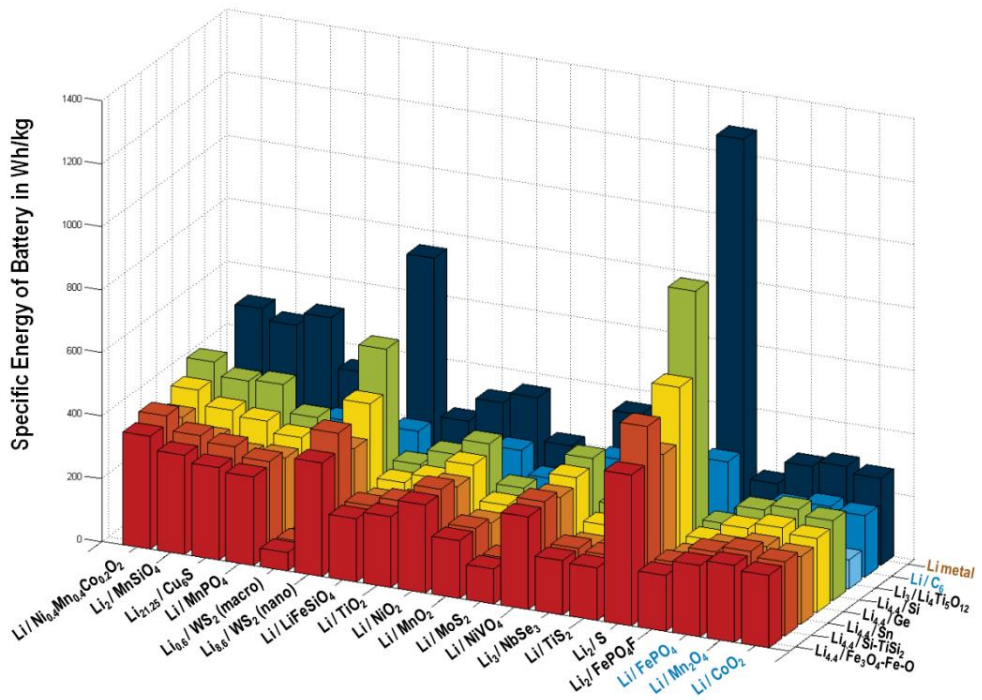


Figure 1 - Combinatory analysis of different materials for negative (right axis) and positive (left axis) electrodes with their corresponding theoretical specific energies (y-axis); picture from [KUH-12]

The authors highlight for instance that while graphite is still today the most used material for the negative electrode, materials such as Silicon are the most promising to increase the

electrode capacity. Even if the Li metal negative electrode is supposed to bring the best specific energies on the paper (Figure 1), the authors underline that for safety reasons (dendrites build-up risks) this option is not used in commercial cells. For the positive electrode, materials such as Sulfur and Nickel Manganese Cobalt (NMC) metal oxides are mentioned as the most promising ones to increase the cell specific energy. The authors assert that with a combination of these materials, a maximum of about 350 Wh/kg can be easily achieved at the cell scale (with a limit at 1 kWh/kg). For the high power capabilities, Lithium Iron Phosphate (LFP) batteries are said to present very impressive specific powers (up to 90 kW/kg at 200 C) by the same authors. Nevertheless, Lithium Titanate Oxide technologies show today better power performance and safety (only small SEI), and more potential gain in performance in the future (LFP is close to its maximal performances).

Several studies ([HEP-12] and [STU-12]), also focused on the potential of electric flight, mention technologies such as Lithium Sulfur and Lithium-Air as the most promising for the future, with specific energies rising up to 1700 Wh/kg in 2025-2030 for the latest (Lithium-Air) at the cell level. This value is used as well in [POR-15], where concepts of hybrid electric flights are also investigated. More recently, publications anticipating the future performances of battery systems respectively in 2030 and 2035, such as [HOE-18] or [MUE-18], mention as well the Lithium-Air and the Lithium-Sulfur technologies. The development of the Lithium-Air seems however quite challenging today because of superoxide productions.

The high expectations are put up to 1 kWh/kg (with 1 kW/kg for the power capabilities) in [HOE-18] for Lithium-Air and 0.65 kWh/kg / 1 kW/kg for Lithium-Sulfur, while [MUE-18] focus only on Lithium-Sulfur with values such as 0.5 kWh/kg (0.6 kWh/L) / 1 kW/kg (all these values are considered at the system scale, including the packaging and cooling mass).

Unlike the previous studies, [KUH-12] seems more cautious with the Lithium-Air battery, pointing out practical limits such as a 600Wh/kg barrier for the specific energy and also a very poor specific power (in the range of mW/kg). **These poor power capabilities of the Lithium-Air battery are, for the authors, a clear showstopper for aviation applications.**

After this first overview of the battery performances assumptions taken by prospective studies on electrified aircraft, a closer look will be given on papers exclusively focused on the different available battery technologies and their current and expected performances.

2.2.1.2. Reviews focused on the battery performances evolution and trends

In their review, Le Cras and Bloch ([LEC-15]) give an overall picture of the development of Lithium-ion battery technologies in the last decades and show in one of their tables some orders of magnitudes for embedded batteries in the automotive context (Figure 2).

This first list gives us some insights about the current performances of embedded Li-ion battery systems: from 89 Wh/kg for a “power type” battery such as Lithium Titanate Oxide (LTO) to 233 Wh/kg for High Energy type like Nickel Cobalt Aluminum (NCA). The authors

underline furthermore current trends of investigation to increase the cell specific energy: the use of Li-metal for the negative electrode, as well as Sulfur or Air for the positive one.

Tableau 4 – Différents types de cellules Li-ion pour VE ou VEH commercialisés en 2015									
Fabricant	Chimie (anode/cathode)	Capacité (Ah)	Type	Tension (V)	Masse (kg)	Volume (L)	Densité d'énergie (Wh/L) (Wh/Kg)	Utilisé dans : Fabricant Modèle	
AESC	G/LMO-NCA	33	Polymère	3,75	0,80	0,40	309	155	Nissan Leaf
LG Chem	G/NMC-LMO	36	Polymère	3,75	0,86	0,49	275	157	Renault Zoe
Li-Tec	G/NMC	52	Polymère	3,65	1,25	0,60	316	152	Daimer Smart
Li Energy Japan	G/LMO-NMC	50	Prismatique	3,7	1,70	0,85	218	109	Mitsubishi i-MiEV
Samsung	G/NMC-LMO	64	Prismatique	3,7	1,80	0,97	243	132	Fiat 500
Lishen Tianjin	G/LFP	16	Prismatique	3,25	0,45	0,23	226	116	Coda EV
Toshiba	LTO/NMC	20	Prismatique	2,3	0,52	0,23	200	89	Honda Fit
Panasonic	G/NCA	3,1	Cylindrique	3,6	0,05	0,02	630	233	Tesla Modèle S

Figure 2 - List of Li-ion cells chemistries used in electrical or hybrid-electrical vehicle in 2015 ([LEC-15])

In [PER-18], among the description of technologies such as Lead-acid, Ni-Mh, Ni-Zn, several orders of magnitude are given for Li-ion batteries (up to 250 Wh/kg at the cell scale) as well as for Lithium Sulfur (300 Wh/kg at the cell scale with reachable targets between 400 – 600 Wh/kg). The author highlights the poor cyclability of the Lithium Sulfur (not more than 300 cycles to date). The all solid state battery, composed of a solid electrolyte, Li-metal on the negative electrode instead of graphite, and the same chemistry as the usual Li-ion ones – NMC, NCA... – for the positive electrode, is also mentioned as an upcoming technology, even if the main limitation seems to be the working temperature of the electrolyte (usually a high temperature because of the polymer electrolyte). For the all solid state battery, values such as 400 Wh/kg can be expected according to the author.

As reported in [MIS-18], current performances for high energy Li-ion battery such as NMC are today around 250 Wh/kg at the cell level and 150 Wh/kg at the system scale (Tesla is said to have reached the best specific energy – 170 Wh/kg – at the pack level). Changing the anode material for Li-metal or the use of silicon-base composite (few at% of Si) together with a high Ni NMC cathode (Ni-rich) should, according to the author, bring specific energies up to 350 Wh/kg at the cell scale in the next decade. Unlike [HOE-18] or [MUE-18], **the author affirm that the value of 1 kWh/kg is not seemingly possible even in the next 20, 30 years.**

In [FUS-15], a large overview of the different battery technologies for future aircraft propulsion is given as well as a concrete state of the art and projected numbers of specific energies, specific powers, energy density and cyclability. The author underlines particularly the current limits of high energy Li-ion batteries (around 220-280 Wh/kg_{cell}), as well as some orders of magnitude for high power Li-ion batteries (from 2 to 7 kW/kg_{cell} for technologies such as LFP and/or using Lithium Titanate Oxide – LTO anodes). The global review highlights some global tendencies such as the good cyclability of high power batteries compared to the high energy ones.

The poor cyclability of LiS is also mentioned as well as its low volumetric energy and specific power. Interestingly, the author presents some roadmaps for the high energy / high

power batteries from today to 2020-2025: the following table details briefly some information contained in these roadmaps (Table 1).

		Li-ion High Energy	Li-ion High Power	Li-S
Today	Cell scale	< 250 Wh/kg (300 Wh/kg under development)	50 Wh/kg ; 2 kW/kg ; >10000 cycles	~ 300 Wh/kg (C/10) ; ~ 300-400 Wh/L ; 10-50 cycles
	System scale	~ 150 Wh/kg ; 230 Wh/L ; 750 cycles	—	—
Tomorrow (2020 or 2025)	Cell scale	500 Wh/kg ; 1500 Wh/L ; (2025)	70 Wh/kg ; 6 kW/kg ; 10000 cycles (2020)	600 Wh/kg ; 700 Wh/L ; 2000 cycles (2025)
	System scale	290 Wh/kg ; (< 270 Wh/kg) 375 Wh/L ; 200-500 cycles (2020)	—	400 Wh/kg ; (< 330 W/kg) 300-500 cycles (2025)

Table 1 - High Energy / High Power Li-ion technologies roadmap synthesis from [FUS-15]

As the table presents a compilation of some values seen in three or four roadmaps, all the data (number of cycles, energy volumetric density...) are not systematically available for each kind of Li-ion batteries. The perspectives at the cell and system scale for the “High Energy” column are quite high (500 Wh/kg_{cell} and 290 Wh/kg_{system} for 2025 and 2020 respectively) and correspond to the projections for the solid-state Li-metal batteries (not mature yet). For non-solid-state technologies, there is today a consensus about the values: 350 Wh/kg_{cell} with same cyclability (>1,000) and so on seems to be the maximal reachable. With lower cyclability (<1,000), 400 Wh/kg_{cell} can be reachable with Si anode. For the “High Power” column, the data refer to LTO technologies. The Lithium Sulfur (LiS) column is also added to the table as it represents the Li-ion technology with the highest predicted specific energy together with Li-Air. The projections for the Li-Air battery (not mentioned in Table 1) are lower than in [HEP-12] and [STU-12], with a value such as 500 Wh/kg_{system} expectable around 2035.

To sum up, similar orders of magnitude are given in all these reviews ([FUS-15], [MIS-18], [PER-18], [LEC-15]) for the current performances of High-Energy Li-ion batteries (250 Wh/kg_{cell} and 150 Wh/kg_{system}) and other technologies such as Li-S (300 Wh/kg_{cell} achievable today and 400-600 Wh/kg_{cell} in the next decade).

Even if a global consensus is coming from the values seen in all the reviews mentioned (except for the long term projections of Li-Air), it is sometimes hard to contextualize them: what is the exact behavior of each Li-ion technologies when changing the C_{rate} in terms of specific energy and durability? What are the specific power values exactly referring to (max peak power or continuous discharge/charge power)?

Some of these interrogations remain a bit cloudy and would require more precise insight through discharge/charge characteristics of specific cells for example.

Several technologies for each type of Li-ion batteries have also been mentioned in a recurrent manner:

- Very high energy: Li-S, Lithium-Air, Li-metal anode with high energy cathode
- High energy: NMC, NCA, Li-rich cathodes
- High power: LTO anode, LFP

In order to refine the bibliographic review and to have a concrete look on each type of Li-ion batteries, three typical technologies are selected: Li-S for the very high energy type, NMC for the high energy type and LTO for high power type.

2.2.2. Selection of three technologies (LTO, NMC, Li-S) and review of emblematic datasheets for each of them

The following paragraphs will detail current performances of the selected Li-ion technologies through some datasheets as well as forecasts coming from scientific publications and reviews.

2.2.2.1. Lithium Titanate Oxide anode based Lithium battery (LTO) – High Power

As mentioned previously, the LTO technology is a “High power” one, with very impressive C_{rate} capabilities (up to 10C continuous charge/discharge) and a very good cyclability (up to 20000 cycles). As LTO is used instead of graphite on the anode, the nominal cell voltage is usually around 2.3-2.4 V, which explains the relatively low specific energies (50-90 Wh/kg) compared to classic Li-ion cells. However, 100 % charge/discharge cycles are possible (contrary to the classical 80 % margin usually taken to preserve the battery from electrolyte degradation reactions) without degrading the performances. The high potential of the anode (1.5 V vs Li) limits the degradation mechanisms usually occurring with graphite anodes, allowing very good results in terms of cyclability even at high C_{rate} s. An illustration of these two aspects is visible on Figure 3 (from [TOS-17])) with discharge and cycling characteristics of a 20 Ah LTO cell developed by Toshiba (SCiB).

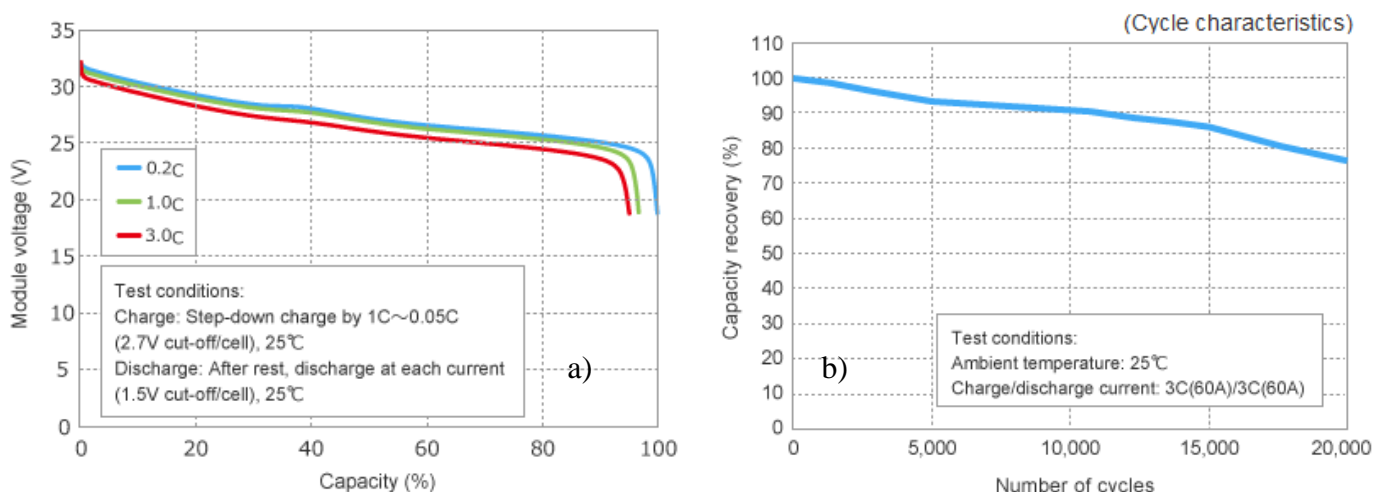


Figure 3 – a) Discharge curves characteristic of a SCiB Toshiba module 2P12S (20 Ah LTO cells); b) Cycling performances of a 20 Ah SCiB Toshiba cell at 3C/3C 100 % charge/discharge cycles ([TOS-17])

The “high power” aspect of this technology, issued from the spinel structure of the LTO anode which offer tunnels for fast Li ion mobility, is clearly highlighted here (Figure 3 a)): a high C_{rate} discharge is possible, and thus a high power output, without impacting much the available battery capacity and energy.

Table 2 synthetizes the current performances of three different manufacturers (Kokam, Leclanché and Toshiba) producing LTO cells and modules (the modules contain at least the packaging and BMS). The power capabilities are highlighted with the maximum possible continuous charge/discharge, at high rates such as 3C/4C in charge and discharge, here mentioned under the specific energies.

		Kokam ([KOK-14])	Leclanché ([LEC-14])	Toshiba SCiB ([TOS-17])
Cell type		Pouch	Pouch	Prismatic
Cell level	Wh/kg	77 Wh/kg	70-80 Wh/kg	47-96 Wh/kg
	Max continuous C_{rate}	4C charge / 8C discharge	3C / 3C	4C / 4C
	Wh/L	148 Wh/L (1.9 kg/L)	-	88-176 Wh/L (1.8 kg/L)
System level (module)	Cycling life (20 % capacity loss)	20000 charge / discharge cycles at 1C and 80 % DOD	15000-20000 cycles at 4C and 100 % DOD	15000 cycles at 3C and 100 % DOD
	Wh/kg	-	42 Wh/kg	78 Wh/kg
	Wh/L	-	46 Wh/L (1.1 kg/L)	128 Wh/L (1.6 kg/L)

Table 2 - Performances of current LTO technology at the cell and module level ([LEC-14], [KOK-15], [TOS-17])

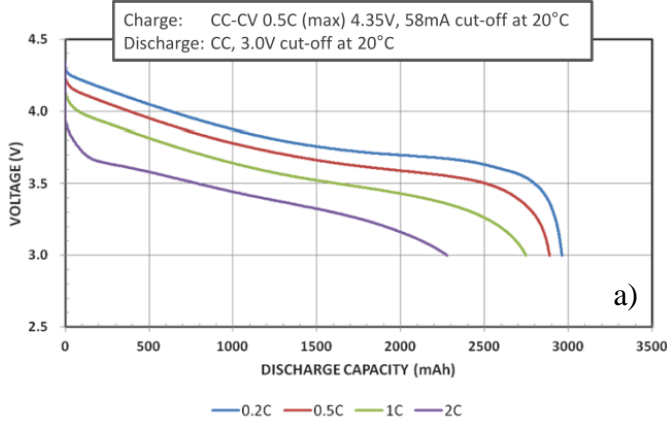
A recent study ([TAK-18]) led by Toshiba, presents very impressive **perspectives** for this technology by changing the anode composition from LTO to mixed valency Ti-Nb oxide TNO ($TiNb_2O_7$) and thus increasing the specific capacity of the anode. The authors claims that the specific energy of this cell (TNO/NMC cell) can be improved to reach values such as 140 Wh/kg and 350 Wh/L, while keeping approximately the same C_{rate} and cyclability capabilities as LTO cells (up to 10C discharge and 14000 cycles at 100 % 1C charge/discharge cycles).

2.2.2.2. High Energy – Nickel Manganese Cobalt cathode based Lithium battery (NMC)

Unlike the LTO, the so-called NMC Li-ion battery refers to chemistries using NMC as cathode material and classically graphite for the anode material, allowing a higher cell voltage (hence a higher energy content) but also less power and cyclability capabilities (the high C_{rate} s charges/discharges are more impactful in terms of durability and degradations).

The aspects previously mentioned are clearly observable on Figure 4, where discharge curves as well as cycling characteristics are exposed for a Panasonic cylindrical NMC cell (ref UR18650ZTA, [PAN-18]).

Discharge Characteristics (by rate of discharge)



Cycle Life Characteristics

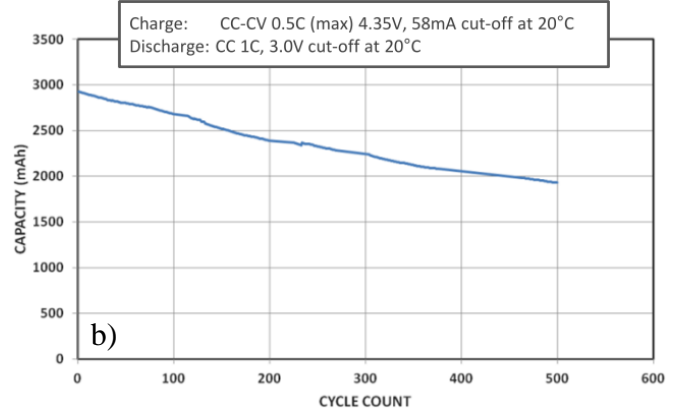


Figure 4 – a) Discharge curves characteristic of a Panasonic cylindrical cell (UR18650ZTA); b) Cycling performances of the Panasonic cell at 0.5C/1C charge/discharge cycles ([PAN-18])

If we compare Figure 4 and Figure 3, we can clearly see the different behavior of the high energy cell when increasing the C_{rate} compared to the high power one: the voltage curve is collapsing much faster when increasing the discharge current than with the LTO cell. If we look concretely the energy available for each discharge current, the actual specific energy at 2C is 158 Wh/kg vs 230 Wh/kg at 0.2C (32 % drop) for the Panasonic cell, while for the Toshiba cell the specific energy at 3C is 82 Wh/kg vs 90 Wh/kg at 0.2C (9 % drop). This little calculation underlines the relativity of the specific energy values: if the demanded power exceeds a certain value with respect to the energy contained inside the battery (the theoretical energy usually available at a low C_{rate}), the energy delivered will be lower than expected (depending on the battery technology). In other words, a single value associated to the specific energy cannot describe accurately the actual energy available in all situations, and depends on the C_{rate} at which the battery is used.

Several orders of magnitude have already been given previously (cf. Figure 2 and Table 1) for the high energy NMC cells (max 260 Wh/kg_{cell} and 150 Wh/kg_{system}). Table 3 presents, in order to give more concrete details, some key parameters of NMC cells from three different manufacturers (Kokam – Li-ion polymer cell, Leclanché, Panasonic) in terms of specific energies, C_{rate} limitations and cyclability. Through the observation of this table, we can see that even if some discrepancies are visible between the three cells, especially in terms of cyclability, the global specific energies reached, as well as the maximum continuous discharge rates, show good agreements between them (~ 200 Wh/kg and 2C max discharge). Despite the 18650 Panasonic cell ([PAN-18]) only have a poor cyclic life, LGchem 18650 NMC cell reach today more than 300 cycles with specific energies up to 260 Wh/kg_{cell}.

		Kokam ([KOK-15], [KOK-17])	Leclanché ([LEC-14], [LEC-14(2)])	Panasonic ([PAN-18])
Cell type		Pouch (Li-ion polymer)	Pouch	Cylindric
Cell level	Wh/kg	192 Wh/kg	120-200 Wh/kg	230 Wh/kg
	Max continuous C _{rate}	2C discharge (charge not precised)	2.3C (discharge) / 1C (charge)	2C (discharge) / 0.5C (charge)
	Wh/L	407 Wh/L (2.12 kg/L)	-	620 Wh/L (2.7 kg/L)
System level (module)	Cycling life	-	8000 cycles at 80 % DOD (1C/1C)	20 % capacity loss after 200 cycles (33 % after 500 cycles)
	Wh/kg	150 Wh/kg (@ C/2) (direct liquid cooling system included)	74 Wh/kg	-
	Wh/L	172 Wh/L (1.14 kg/L)	106 Wh/L (1.43 kg/L)	-

Table 3 – Performances of current NMC technology at the cell and module level ([LEC-14], [LEC-14(2)], [KOK-14], [KOK-17], [PAN-18])

In terms of prospects, one of the area of investigation is today focused on the **all solid-state technology with the use of a Li-metal anode** in order to increase the anode specific capacity, hence the cell specific energy. The key parameter linked with the change of the graphite anode to Li-metal is the constitution of the electrolyte ([SE-18]): it should be safe and not suffer from a lack of conductivity (which is the case of the polymer electrolytes, imposing high working temperatures precisely in order to increase their conductivity). Manufacturers such as Solid Energy ([SE-18]) or Sion Power ([SIO-18]) have already communicated about products presenting the same features (Li-metal/NMC cells with very high energy density). Sion Power is already announcing values such as 500 Wh/kg_{cell} and 1000 Wh/L_{cell} on their website with their Licerion® technology ([SIO-18]), but without giving complete information (no datasheet actually available).

However, Solid Energy has already published one datasheet (Hermès, [SE-18(2)]) detailing current performances of such type of cell with values up to 450 Wh/kg_{cell}, 1200 Wh/L_{cell}, 2C max continuous discharge and a working temperature range between -20 °C and 45 °C (complementary information is available on Appendix A). If we have a look on the datasheet published by Solid Energy (Appendix A), the main drawback seems to be the poor cyclability of the Li-metal/NMC cell: 10 % capacity loss after 100 cycles at 0.1C charge and 0.5C discharge. Another disadvantage of this technology should be as well its power capabilities for temperatures below 25 °C.

SSB (solid state batteries) will use polymer or ceramic solid electrolytes. Ceramic is the best route to follow in terms of safety. A target at 650 Wh/kg_{cell} should be reachable for 2035 if the

interface issues coming with the use of ceramic electrolyte and the Li anode and cathode (which in this case will both need coatings to stabilize the solid electrolyte) are solved, while using a bipolar design. There is today no guarantee that ceramic electrolyte-based SSB will come out, but many companies are working in this area. Finally, one thing to keep in mind is that ceramic-based SSB stacks will need to be kept under pressure to operate, to avoid loss of contacts between the electrode and the electrolyte, due to mechanical stress. This may affect the energy density. Another option is the use of solid polymer electrolytes to assemble SSBs. In this case, differently from the Blue Solution Lithium Metal Polymer battery, those polymers will operate at room temperature and below. This is highly challenging; however, it seems that a company (Ionic Materials) may have achieved a significant breakthrough in the field and raised > 100 US\$ millions from big companies. However, to date, only plots are available and no detail on the chemistry has been disclosed. This company has to be tracked for the near future.

2.2.2.3. Lithium Sulfur battery (Li-S) – Very High Energy

The Li-S cells (also often featuring Li-metal anode) are very high energy cells, recurrently mentioned when forecasting the future of battery performances as the most promising in terms of energy density (cf. 2.2.1). However, there are nowadays few manufacturers producing Li-S cells and fewer Li-S battery racks or modules, hence it can be a bit delicate to assess the actual level of performances of this technology. In [BRU-12], the authors describe the main drawbacks of Li-S associated with each cell component: safety and cycling efficiency problems (linked to the Li-metal anode), limited rate capabilities and a poor volumetric efficiency (cf. Figure 5). Calendar aging can also be quite important according to [FRA-18] with non-negligible self-discharge effects.

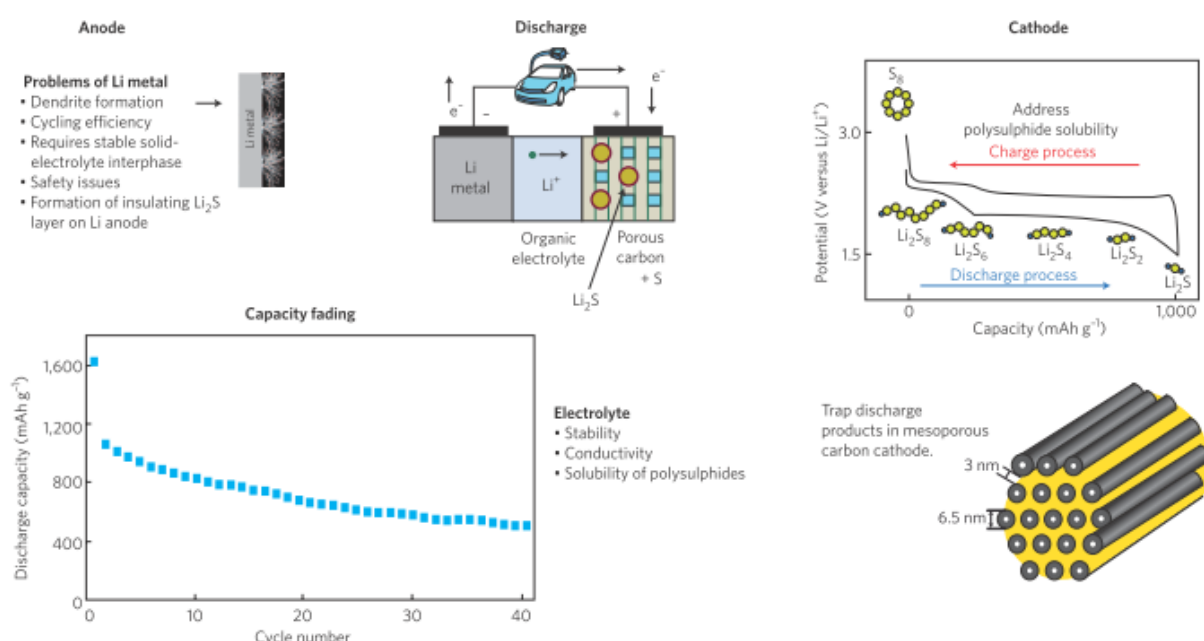


Figure 5 - Picture taken from [BRU-12] illustrating some issues faced by Li-S cells (rapid capacity loss, soluble sulfur as redox shuttles, electrolyte impedance behavior...)

Another study ([FOT-17]) corroborates the information given in [BRU-12] especially on the specific power limitations of this technology, underlining that above 1C, the specific capacity can drop dramatically.

Manufacturers such as Sion Power and Oxis Energy have already published some datasheet of Li-S cells ([SIO-08], [OXI-17]), whose main information are synthetized on Table 4.

Manufacturer	Oxis Energy (Appendix B) Pouch cell (POA0217)	Sion Power (Appendix C) Prismatic cell
Cell gravimetric energy	400 Wh/kg	350 Wh/kg
Cell volumetric energy	300 Wh/L (0.75 kg/L)	320 Wh/L (0.9 kg/L)
Cycling life (20 % capacity loss)	< 100 cycles at 80 % DOD	-

Table 4 - Main features of Lithium Sulfur cells developed by Oxis Energy and Sion Power ([SIO-08], [OXI-17])

Oxis Energy announces on his website that the target of 400 Wh/kg_{cell} has already been reached and that 500 Wh/kg_{cell} is on their roadmap for 2019. The company also manufactures currently Lithium Sulfur battery packs (datasheet available on Appendix B), reaching 120 Wh/kg and 73 Wh/L and reaching 1400 cycles at 80 % DOD for a capacity loss of 40 %.

In terms of **prospects**, the manufacturer projection already mentioned ([OXI-17]) target 500 Wh/kg_{cell} / 500 Wh/L_{cell} with improved cyclability (1000 cycles at 80 % DOD) for 2019 (cf. Appendix B). Other forecasts for this technology with a longer-term horizon have already been exposed in Table 1 (values taken from [FUS-15]).

2.2.3. Overview of the battery weight integrating factor values assessed in the literature

Without having much specification on a concrete integration case, it is quite difficult to make an accurate estimation of the weight impact of the different components necessary to make the step from the cell to the battery system. Nevertheless, a rough estimation can be made using a simple formula with a weight integrating factor f_m :

$$m_{\text{system}} = m_{\text{cell}} * f_m \quad (2)$$

Several orders of magnitude for this weight impact can already be deducted from the previous tables when going from the cell level line to the system line (cf. Table 2 and Table 3). However the “system” level mentioned can refer to different set of components (cells, connections, packaging, BMS, cooling system) and the cells used to make the packs are not necessarily the exact cells mentioned on the upper line (cell level), so the estimation of the auxiliary components weight impact through this way can be rather uncertain.

A few articles and publications quantifying this weight impact when passing from the cell level to the system level (adding the connections, sensors, cables, BMS, cooling system and packaging) have been reviewed and are synthetized on Table 5.

Considering the values referenced in this table as well as the aeronautical context of the study, the upper limit of $f_m = 2$ is taken as reference in order to estimate the weight impact factor of the packaging, BMS and cooling mass.

Looking the volume impact on the system integration (parameter f_v), there is unfortunately fewer information in the studies quoted in Table 5 than for the weight impact: from [FUS-15] it appears that this parameter is apparently higher with values up to 2.5 – 3. It must be precised here that, being rigorous, the f_m and f_v factors should depend on parameters such as the battery technology employed, the cell type (pouch, prismatic or cylindrical) or the power mission profile and temperature conditions for instance.

The final assumptions made on the specific energies / powers / cycling life corresponding to the previously mentioned technologies (current performances and forecast) are exposed in a synthetic way in the 2.4 section.

Reference	Weight integrating factor (f_m) estimation	Comments
[PER-18]	1.4	Cell to pack
[BIR-10]	1.43	Automotive context – mild-hybrid – Cell to system (including cooling)
LG chemistry pack (Zoé/Renault)	1.8	Cell to system (automotive context)
[MUE-18]	1.43	Cell to system (future aeronautical context assessment)
[TAR-16]	2	Cell to system (charger, casing, sensing circuitry) – aeronautical context
[STU-12]	2	Cell to system (including cooling and BMS) – aeronautical context
[FUS-15]	1.6 – 2	Cell to system – aeronautical context

Table 5 - Non-exhaustive overview of weight integrating factor assessments in different studies

2.3. State of the art of FC stacks and systems power densities and H₂ storage systems energy densities for mobile applications (automotive and aeronautical)

After having detailed in the previous part a state of the art of the current performances of several battery technologies, the next paragraphs will focus on the Fuel Cell performances and on their associated H₂ storage systems.

The objective of this section is, as well as for the battery part, to collect relevant orders of magnitude of the current and future performances of such devices in terms of power densities, weight impact of the fuel cell auxiliaries and H₂ storage gravimetric/volumetric efficiencies.

2.3.1. Pre-selection of the FC technologies and H₂ storage methods

In an attempt to limit the potential technologies considered, a first selection of the fuel cell technologies has been made and is summarized Table 6.

Fuel Cell technologies considered							
Low Temperature Proton Exchange Membrane Fuel Cell (LT PEM FC) Temperature: ~ 60 – 80 °C	High Temperature Proton Exchange Membrane Fuel Cell (HT PEM FC)		Solid Oxide Fuel Cell (SOFC)	Temp.: ~ 600 – 1000 °C			

Table 6 – List of the pre-selected Fuel Cell technologies

Among the three FC technologies, the Low Temperature PEM FC is the most mature one (industrially speaking) and the most popularized in markets such as the automotive market, with products currently commercialized and available such as the Honda Clarity or the Toyota Mirai ([YOS-15], [MAT-09]).

The High Temperature PEMFC and SOFC present both less maturity than the LT PEMFC and show for most of them lower power conversion efficiencies at the stack scale (~ 0.5 at 0.2 A/cm² vs 0.5 at 1-1.5 A/cm² for the LT PEMFC). Nevertheless, other advantages linked to their working temperatures can make their integration easier in several contexts. The HT PEMFC does not need any humidification system for instance, whereas LT PEMFC stacks usually need it in order to monitor the cell's membranes hydration level. In a similar vein, contrary to the LT PEMFC, the very high working temperature of the SOFC allows several possibilities for the system implementation (like coupling with gas turbines) as well as a higher tolerance to contaminants or other fuel mix.

Regarding the energy storage, H₂ storage methods are also pre-selected (Table 7):

H ₂ storage technologies considered		
Compressed H ₂ (350 bara and 700 bara) composite tanks	Liquid H ₂ cryogenic tanks (20 K)	Solid H ₂ storage (metal hydrides)

Table 7 – List of the pre-selected H₂ storage technologies considered

2.3.2. State of the Art of the FC stack and system power densities: High Temperature / Low Temperature PEM FC and Solid Oxide FC

Due to the abundance of available information in the literature on current LT PEMFC performances on one hand and to the lack of information on current HT PEMFC and SOFC performances on the other hand, the following parts will mainly focus on the LT PEMFC. As a matter of fact, most studies on HT PEMFC and SOFC systems are focused on future integration concepts and rarely give some insights into their concrete performances in terms of global power densities at the stack and system scale. Also, the FC system power densities mentioned in the next paragraphs is related to the **power conversion part only (FC stacks and auxiliaries)** and does not account for the H₂ storage mass or volume.

2.3.2.1. Low Temperature Proton Exchange Membrane FC (LT PEMFC)

A lot of developments and improvements on LT PEMFC stacks and systems have already been done to this day, mainly driven by the automotive industry for the embedded applications. The DOE (Department of Energy) is actually fixing the global targets for the embedded applications accordingly to the automotive systems requirements where, for instance, the stack gravimetric power density target of 2 kW/kg for 2020 ([DOE-16]) is already reached and the volumetric power density target of 2.5 kW/L is well surpassed as well since 2014 ([YOS-15]).

Figure 6 illustrates the development tendency of Toyota LT PEMFC stacks from 2002 to 2017 as well as the volumetric and gravimetric DoE targets marked with green dotted lines.

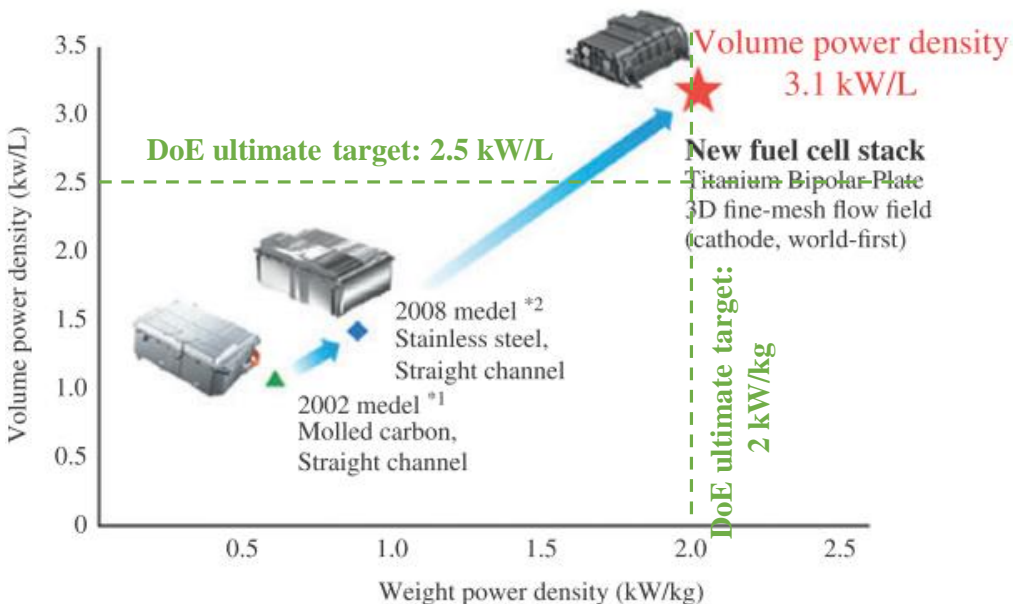


Figure 6 - Past and current performances of Toyota LT PEMFC stacks (power densities), [NON-17] - Ultimate targets of the DoE for transportation FC stacks (in green), [DOE-16]

FC systems usually feature some Balance of Plants (BoP) components (also called auxiliary components or simply auxiliaries) providing to the FC stack appropriated environmental conditions to work properly (air and H₂ supply and fluidic management, thermal control, humidity control...).

Between all these auxiliary components, a few can be mentioned without being exhaustive:

- An air delivery unit usually featuring an air compressor, a regulator and an appropriate circuitry (tubes, pipes)
- A hydrogen fluidic control system (pressure and flow); it can be with or without any recirculator unit
- A humidification system in order to monitor the stack's cells hydration
- A cooling system to monitor the stack working temperature (depending on the cooling method, it can feature a condenser, radiators, a cooling pump, tubes, valves...).

Although, as we will observe later, not all these BoP components are necessarily presents in all the FC systems, they can appear regularly depending on the constructor and the environmental constraints. An illustrative example of a FC system is proposed on Figure 7 to highlight the different loops and circuits (air, H₂ and cooling) as well as the auxiliary components surrounding a FC stack. In this automotive example (Toyota Mirai case, [KOJ-15]), the humidification system is for instance eliminated thanks to several improvements at the cell scale (very thin membranes enhancing the water crossover) and on the H₂ recirculation system, allowing an efficient self-humidification and internal water loop inside the stack ([HAS-16]).

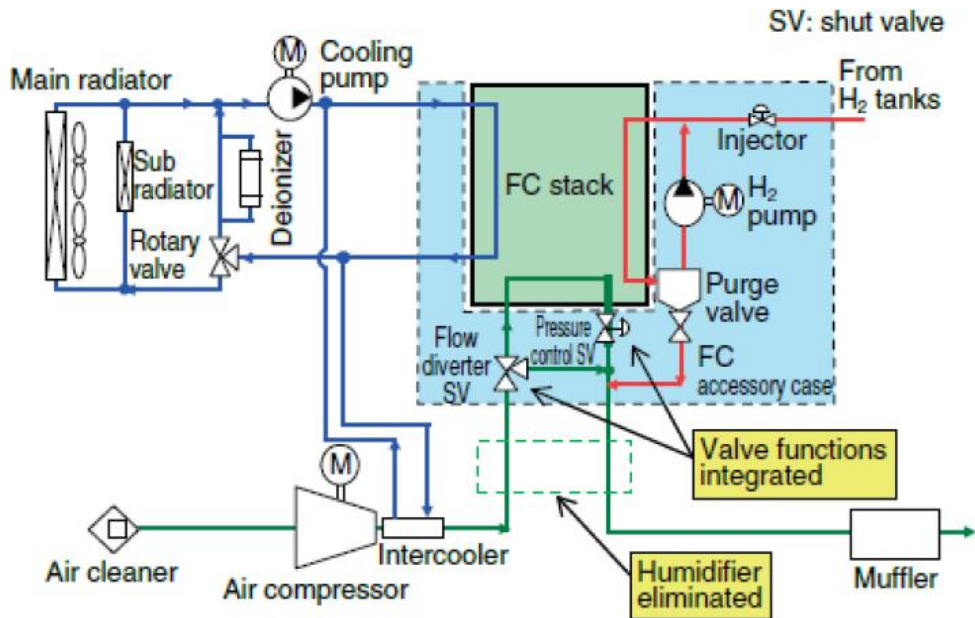


Figure 7 - Illustrative example of a FC system in an automotive embedded case (Toyota Mirai) - Picture taken from [KOJ-15]

As all the auxiliary components are not passive elements, some will consume a parasitic part of the whole power generated by the FC stack to work properly (mainly the air compressor). Based on this observation, a distinction can be made between the power generated by the FC stack, the gross power (P_{gross}), and the power delivered by the FC system, the net power (P_{net}), which is the actual usable power after considering the auxiliary parasitic power consumption (P_{aux}) as described on eq. (3).

$$P_{net} = P_{gross} - P_{aux} \quad (3)$$

As mentioned previously, automotive constructors such as Honda, General Motors or Hyundai already commercialize FC electrical vehicles comprising a fuel cell stack, stack auxiliaries like a cooling loop with a radiator, and a compressed H₂ storage unit (700 bara composite tanks). Furthermore, a few manufacturers, such as Ballard, Hydrogenics, Intelligent Energy or PowerCell between others, propose mature products (stacks and systems) for high power mobility applications (cars, busses, boats...).

In an attempt to reference the performances of such devices, Table 8 summarizes some data in terms of power densities at the stack and system scale published by these different manufacturers or visible in scientific publications. For the sake of simplicity, and in order to consider numbers at a power scale relatively close to the one of the auxiliary mission (a few hundreds of kW), only high power stacks and systems are mentioned. As it can be seen in this table, it is sometimes delicate to associate values at the stack and at the system scale: some information are often given in an incomplete manner (a stack power density without the corresponding system power density for instance).

Moreover, the FC “system” appellation is often quite ambiguous and can lead to several misunderstandings: quite often, the so called FC system will feature a FC stack and some auxiliary components but not all of them. For instance, the cooling system mentioned in some modules will often be incomplete and won’t include the external radiator; hence, one can underestimate the global weight and volume of the actual system while thinking the global cooling loop mass and volume are considered.

Nevertheless the comparison of these numbers, especially for the last lines of Table 8, highlight quite impressively the actual impact of the transition from the stack scale to the system scale regarding the power density. The data from [POW-16(1)], [POW-16(2)] and [IE-15] allow a fair comparison of the performances before and after the integration of the stack into a system and show a huge impact for this integration (from 2.9 kW/kg to 0.74 kW/kg for the PowerCell stack and system for instance). Regarding the system description, the module presented by Intelligent Energy on the last line of the table (Appendix D) is the most complete one (the mass and volume information contain all the auxiliary components, including the condenser in the cooling unit). For this module, the specific power drops from 3 to 0.667 kW/kg (0.22 factor) when jumping from the stack to the system scale.

The decrease in power density from the FC stack to the FC system scale can be explained not only by the weight impact of the auxiliaries but also by their parasitic power consumption decreasing the overall power available, which is highlighted in eq. (3), (4) and (5).

$$p_m^{gross/FC} \left(\frac{kW}{kg} \right) = \frac{P_{FC} (= P_{gross})}{m_{FC}} \quad (4)$$

$$p_m^{net/system} \left(\frac{kW}{kg} \right) = \frac{P_{system} (= P_{net})}{m_{system}} = \frac{P_{FC} - P_{aux}}{m_{FC} + m_{aux}} \ll p_m^{gross} \quad (5)$$

With $p_m^{gross/FC}$ and $p_m^{net/system}$ being respectively the gravimetric power densities at the FC stack and at the system scale, and m_{FC} , m_{aux} and m_{system} respectively the FC stack, auxiliaries and system masses.

Hence, the challenge in terms of system power density increase does not only rely on lighter auxiliaries but as well on minimizing their power consumption.

Reference	Power densities (gravimetric – p_m – and volumetric – p_v)		Comments / remarks
	Stack scale	System scale	
[HYD-16]	-	0.430 kW/kg (p_m)	Hydrogenics HD-30 module with complete BoP components ($\sim 30 \text{ kW}_{\text{net}}$). p_m value: without coolant pump mass.
	-	0.410 kW/L (p_v)	p_v value: without coolant pump and air delivery volume.
[HYD-16]	-	0.275 kW/kg	Hydrogenics HD-180 module ($\sim 200 \text{ kW}_{\text{net}}$). p_m and p_v assessments without some BoP components (cf. HD-30 module – upper line).
	-	0.167 kW/L	
[BAL-16]	> 0.350 kW/kg	0.256 kW/kg	Ballard FCveloCity Heavy-Duty module HD-100 ($\sim 100 \text{ kW}_{\text{net}}$). Assessments of p_m and p_v at the system scale consider the FC module plus the air and cooling subsystems (normally deliberately dissociated to improve the system flexibility).
	> 0.190 kW/L	0.130 kW/L	
[FON-13]	-	0.434 kW/kg	CEA estimation for automotive embedded FC systems (including stack, auxiliaries and connections).
[MAT-09]	1.5 kW/kg	-	Honda FCX Clarity (2009) Fuel Cell stack ($\sim 100 \text{ kW}_{\text{gross}}$) power densities.
	2 kW/L	-	
[NON-17], [ESA-18]	2 kW/kg	$\sim 0.7 \text{ kW/kg}$	Toyota Mirai (2014) Fuel Cell stack ($\sim 114 \text{ kW}_{\text{gross}}$) power densities. Assessment at the system scale by ESA.
	3.1 kW/L	-	
[POW-16(1)], [POW-16(2)]	2.91 kW/kg	0.740 kW/kg	PowerCell S3 FC stack ($\sim 125 \text{ kW}_{\text{gross}}$) and MS 100 ($\sim 100 \text{ kW}_{\text{net}}$) FC system. Assessments of p_m and p_v values are made without considering the external radiator (liquid cooling) and the air filter.
	3.37 kW/L	0.333 kW/L	
[IE-15] (Appendix D)	3 kW/kg	0.667 kW/kg	Intelligent Energy Evaporative Cooling automotive Fuel Cell system ($\sim 100 \text{ kW}_{\text{net}}$). Assessments of p_m and p_v values are made considering complete BoP components, including the condenser radiator, the air delivery system (with the compressor)...
	3.5 kW/L	0.595 kW/L	

Table 8 – Overview of LT PEMFC stacks and systems performances in terms of power densities: p_m and p_v (highlighted with a blue background)

Prospects regarding LT PEMFC power densities:

In terms of prospects, many improvements have already been done at the stack scale (cf. Figure 6) with a doubling of the stack power density in less than 10 years.

As can be seen in Table 8, power densities of around 3 kW/kg are already achieved ([IE-15]), by changing the stack traditional architecture and the stack cooling system. More precisely, as the stack is evaporatively cooled with the direct injection of liquid water in the cathode compartments of the stack's cells, there are no cooling channels neither cooling plates usually used with classic direct cooling structures. Very thin single piece bipolar plates can then be employed ([IE-18]) and further reduction of the overall stack weight can be achieved, increasing the power density. Such method can pave the way to future weight reductions of LT PEMFC stacks and bring even higher power densities.

Moreover, in order to reach the target of 2 kW/kg (previous model reached 0.83 kW/kg – [KOJ-15]), Toyota ([NON-17]) achieved an increase of the stack areal power density (W/cm^2) by a factor of 2.3 by boosting the catalyst activity and using revolutionary air channels structures (3D fine-mesh flow field structure), together with a reduction of some of the stack constitutive material (20 % thinner membranes) and the use of titanium for the bipolar plates (weight reduction by almost 40 %).

According to [HAS-15] (Nissan research center), future performances of LT PEMFC stacks could reach in the short-term (2025) a target of around 5 kW/kg and 8.5 kW/kg in the mid-term (2030-2035) with improvements focusing on, on one hand increasing the areal current densities (up to 2 to 3 A/cm^2), and on the other hand decreasing the cell pitch (enhancing more in this case the volumetric power density).

Kadyk et al. ([KAD-18]), exploring potential FC systems for aviation, assert that power densities up to 10 kW/kg at the stack level could be reached in the future by the same means described in [HAS-15] and [NON-17] (changing the graphite bipolar plates for metallic ones with carbon coating in order to avoid corrosion on one hand and increasing the areal power density on the other hand), with 8 kW/kg at the system level.

2.3.2.2. Weight impact of the auxiliaries

As mentioned earlier, the auxiliaries have a double weight impact on the overall system power density: because they add a burden to the system and because they consume a part of the power generated by the FC stack. If the parasitic power consumption of such components can be estimated looking to the system efficiency, it is sometimes delicate to find a direct reference to their masses in the previous sources quoted Table 8.

Several publications such as [HAS-15] estimate approximately the total mass of the auxiliary components proportionally to the FC stack mass with a range between 100 and 300 % of the FC stack mass, while others simply estimate empirically the auxiliary weight proportionally to the FC stack gross power ([POG-18]).

Regarding the two ways of assessing the weight of the auxiliary components (proportionally to the stack mass or to the FC stack power), the second one seems the most appropriate since the mass of the auxiliaries mainly depends on their own parasitic power consumption or on the FC stack heat to evacuate. Indeed, the air compressor for instance will be designed regarding its pressure conversion ratio and its airflow rate, while in return this airflow rate should be proportional to the FC stack power generation and efficiency. Considering a fixed efficiency on the design point, the compressor size (hence its mass and volume) will thus mainly depend on the FC gross power. The same argument can be applied to the Hydrogen recirculation pump. Moreover, the cooling system size will depend (all the environmental conditions being fixed) on the heat generated by the stack which is proportional to the FC stack power and to its efficiency. In the end, even if the approximation is not completely rigorous, we make the hypothesis that the auxiliary mass is directly proportional to the FC stack gross power. An empirical parameter called the auxiliaries specific weight impact, p_m^{aux} (p_v^{aux} in its volumetric declination), is thus introduced to highlight this link (equation (6)).

$$p_m^{aux} \left(\frac{kW}{kg} \right) = \frac{P_{FC} (= P_{gross})}{m_{aux}} \quad (6)$$

The parameter is homogeneous to a gravimetric specific power even if in this case the power mentioned is obviously not coming from the auxiliary components but from the FC stack.

If we take back the equation (5), the system specific power p_m^{system} can now be reformulated this way:

$$p_m^{system} = \frac{P_{net}}{m_{FC} + m_{aux}} = \frac{P_{net}}{P_{FC}} * \frac{1}{\frac{m_{FC}}{P_{FC}} + \frac{m_{aux}}{P_{FC}}} \quad (7)$$

$$p_m^{system} = \frac{P_{net}}{P_{FC}} * \frac{1}{\frac{1}{p_m^{FC}} + \frac{1}{p_m^{aux}}} \quad (8)$$

Looking the equation (8), we see that we can link together p_m^{system} , p_m^{FC} and p_m^{aux} which are only power coefficients between them, if we can estimate the P_{net}/P_{gross} ratio. If these information are not available, the ratio can be estimated from the FC stack and system power conversion efficiencies respectively η_{FC}^{stack} and η_{FC}^{system} as developed in equations (9), (10), (11).

$$\eta_{FC}^{stack} = \frac{P_{FC}}{P_{H2} (= \dot{m}_{H2}^{in} * LHV)} \quad (9)$$

$$\eta_{FC}^{system} = \frac{P_{net}}{P_{H2}} \quad (10)$$

$$\frac{P_{net}}{P_{gross}} = \frac{\eta_{FC}^{system}}{\eta_{FC}^{stack}} \quad (11)$$

With LHV the Lower Heating Value of H₂ (33.3 kWh/kg), \dot{m}_{H2}^{in} the hydrogen input mass flow (kg/h) and P_{H2} the hydrogen chemical power (kW). Knowing either the gross and net power, either the FC stack and FC system power conversion efficiencies, p_m^{aux} can be deduced from η_m^{system} and η_m^{FC} . Interestingly, these information are given one way or another for the three FC systems given in the last lines of Table 8:

- For the Toyota Mirai FC system, the efficiencies η_{FC}^{stack} and η_{FC}^{system} at maximum power are already known from [LOH-17] (respectively 0.5 and 0.42), as well as p_m^{system} (ESA estimation, [ESA-18]) and p_m^{FC} ([NON-17]).
- For the PowerCell S3 high power stack and MS 100 FC system ([POW-16(1)], [POW-16(2)]), the stack polarization curve is available allowing a close estimation of the FC stack conversion efficiency η_{FC}^{stack} around 0.55 at full power. The system global efficiency at full power ($\eta_{FC}^{system} = 0.5$) is also given.
- For the Intelligent Energy module (Appendix D), the system global efficiency is given as well (0.4). A hypothesis on the FC stack efficiency ($\eta_{FC}^{stack} = 0.5$) is made to complete the picture.

Additionally, based on experimental data from the Hy4 small airplane (using LT PEMFC stacks – 4 stacks at 45 kW each – and a Li-ion battery for the propulsion system [Hy4]), an estimation of the auxiliary components mass is given by [POG-18] for a 150 kW_{gross} / 133.5 kW_{net} FC system: an estimation of p_m^{aux} , moreover in an aeronautical context, can then be made. Also, some values of p_m^{FC} and p_m^{system} can be assessed from [POG-18] and compared to the ones already mentioned Table 9: $p_m^{FC} = 2$ kW/kg and $p_m^{system} = 0.731$ kW/kg.

A final overview of the values of p_m^{aux} (and p_v^{aux} when possible) estimated for these four sources is given Figure 8. As it can be seen, the estimations show globally a good agreement between them despite the systems have different scales and are designed for different operation (Toyota Mirai vs Hy4 for instance) with values around 1.13 and 1.43 kW/kg for the auxiliaries gravimetric impact p_m^{aux} . Due to the lack of information, it is however more delicate to assess coherent values for the auxiliary volumetric impact p_v^{aux} : the two values estimated (0.41 and 0.94 kW/L) show great difference. In this case, the evaluation of p_v^{aux} for the Intelligent Energy module (0.94 kW/L) should be more reliable than the one made for the MS 100 PowerCell FC system because the IE module features absolutely all BoP components.

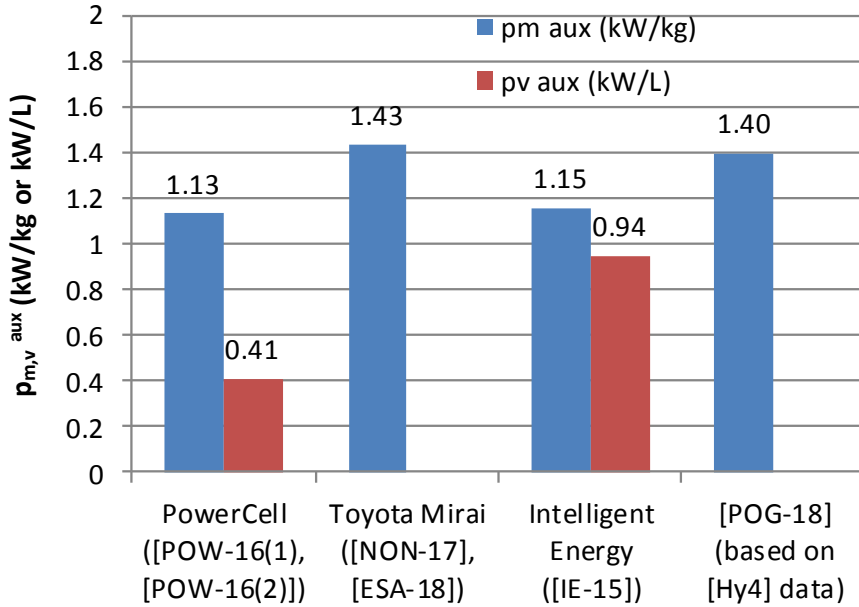


Figure 8 - Summary of the estimated value of p_m^{aux} (kW/kg) in blue and p_v^{aux} (kW/L) in red

2.3.2.3. High Temperature PEM FC and Solid Oxide FC

As discussed in the introduction of the 2.3.2, due to the lack of maturity of the HT PEMFC and the SOFC compared to the LT PEMFC it is quite delicate to assess their actual level of performances. This being said, a few studies presenting HT PEMFC or SOFC system concepts or even demonstrations for transport applications ([EEL-04], [REN-16]) have already been published underlining the potential advantages of such technologies in various contexts. Mainly because of their high working temperatures, they inherently present easier integration aspects with respect to their cooling system ([ROS-17]), as well as a better tolerance to contaminants (such as CO for instance). On the other hand, their high working temperature (especially for the SOFC), bring as well some constraints in terms of start-up time: the temperature raise from the ambient temperature to the operating temperature should not be too quick in order to minimize the mechanical stresses inside the stack in the SOFC case for example.

In [REN-16], the authors present a 1 kW HT PEMFC stack designed for a high altitude operation (10 km) in an UAV (Unmanned Aerial Vehicle) with an appropriate air cooling system. Their stack reaches a power gravimetric density of about **0.3 kW/kg** at its maximum power point and around 0.16 kW/kg at the FC system scale which is, at least for this example, highlighting a great gap between LT and HT PEM FC performances at the moment. However, in [NEO-17], the authors claim to have reached a maximum gravimetric power density of about **0.8 kW/kg** with a 5 kW HT PEMFC stack designed for a telecom satellite.

Regarding the SOFC, in [EEL-04], [RAJ-08], [MIS-18], concepts for the hybrid electric propulsion or for the Auxiliary Power Unit (APU) in an aeronautical context are presented, and interesting trade-offs between SOFC systems and Gas Turbines are shown (an example of potential benefits resulting from such an association for the APU is shown Figure 9). In this

case ([RAJ-08]), a fuel reformer is used to feed the SOFC and the products of the SOFC (high temperature exhaust air and syngas) are further reemployed in a Gas Turbine. As the global system energetic efficiency is improved compared to the use of a gas turbine, the global fuel consumption is reduced, but in return the target presented in terms of system gravimetric power density should be $> 0.5 \text{ kW/kg}$ for the entire SOFC system. Regarding the estimation of the SOFC gravimetric power density, [ROT-10] gives an estimation for the current performances around **0.33 kW/kg** which is, at least for the previous study case ([RAJ-08]), rather pessimistic.

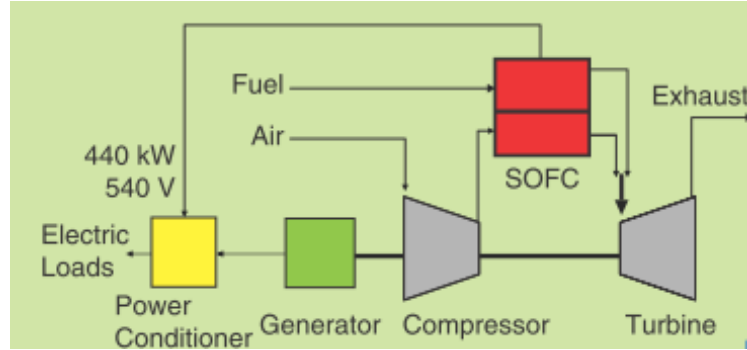


Figure 9 - Simplified example of a SOFC-GT concept for the APU (picture taken from [RAJ-08])

In conclusion, even if concepts of HT PEMFC and SOFC systems in the aeronautical context seem to be promising (HT PEMFC in the mid-term and SOFC in the long-term), it is still quite delicate to assess the actual level of performances of such technologies due to the lack of maturity and feedback from current system performances. The only few values of present gravimetric power density of HT PEMFC or SOFC stacks observed in the different articles reviewed, seem for the moment way behind LT PEMFC ones. At the system scale, clear benefits could appear in terms of implementation in an airplane when using such technologies, but again hardly quantifiable regarding their current level of maturity.

2.3.3. Overview of the gravimetric and volumetric performances of the H₂ storage methods

After a focus on the evaluation of current and future FC stack and system performances, this part is going to deal with the energy storage brick, i.e. the H₂ storage methods. As detailed in Table 7, three storage methods are considered: compressed H₂ composite tanks, liquefied H₂ tanks and metal hydrides.

2.3.3.1. Compressed H₂ tanks

Between all the H₂ media storages, composite tanks containing compressed H₂ are among the preferential options in the automotive industry (option chosen – 700 bara tanks – for the Toyota Mirai or the Honda Clarity between others), because of their lightness and reduced volume. Such type of H₂ storage has quite improved its gravimetric performances during the past years: an increase of the gravimetric efficiency from 4.6 wt. % to 5.7 wt. % between 2008 and 2014 has for instance been achieved with 700 bara composite tanks by Toyota (the value of 5.7 wt. % is a world record in 2014, [NON-17]). The H₂ volumetric capacity of these

current composite tanks of the Toyota Mirai is around $0.041 \text{ kg}_{\text{H}_2}/\text{L}$. In terms of energy density, such tanks would thus reach about 1.88 kWh/kg and 1.35 kWh/L considering the LHV of hydrogen (without taking into account the efficiency of the energy converter i.e. the Fuel Cell). In small aerial vehicles, such storage systems have already been used ([Hy4], [REN-16]) coupled with a FC, but with lower storage pressures.

Indeed, depending on the tank pressure, the two values (gravimetric efficiency and H_2 volumetric capacity) can vary in a non-negligible way. Using as reference products from Hexagon Composite (compressed H_2 storage composite tanks manufacturer) in [HEX-17], one can see the evolution of these two parameters depending on the storage pressure in Figure 10.

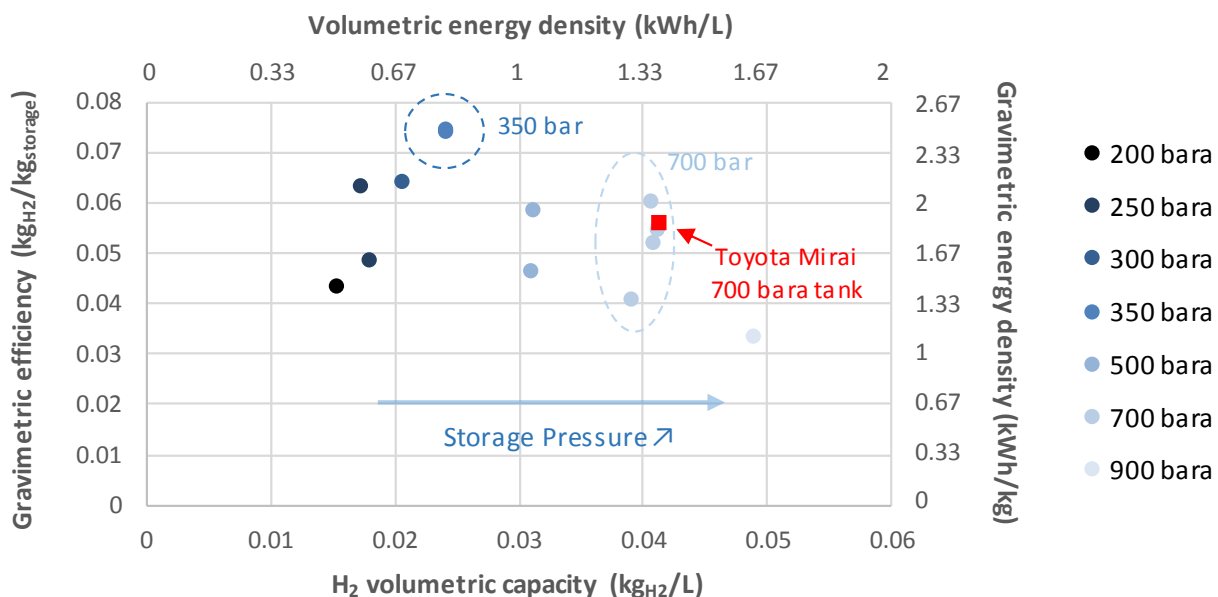


Figure 10 - Gravimetric and volumetric performances of composite storage tanks (type IV) containing compressed H_2 (data from Hexagon Composite manufacturer, [HEX-17])

Obviously, when the storage pressure increases, the H_2 volumetric capacity increases as well: a maximum of $0.05 \text{ kg}_{\text{H}_2}/\text{L}$ is almost reached at 900 bara. However, there are no gain visible (at least for this data) after 350 bara regarding the gravimetric efficiency: moreover the gravimetric efficiencies drop after 350 bara (where a maximum of 7.5 wt. % is reached).

With respect to the energetic cost of the H_2 compression operation, a multi-stage 700 bara compression would require around $4.5 \text{ kWh/kg}_{\text{H}_2}$ while $3.3 \text{ kWh/kg}_{\text{H}_2}$ would be used for a 350 bara compression ([MAK-17]). These values represent respectively 13 % and 10 % of the LHV of hydrogen, which should be kept in mind when considering the overall energy balance.

Although tanks of compressed H_2 are an attractive option for the energy storage (taking into account its maturity, lightness and energy density), it should be kept in mind that putting high-pressure tanks in an airplane is a high challenge in terms of compliance to the specific aeronautic safety requirements.

2.3.3.2. Liquid H₂ tanks

Due to its intrinsic properties, H₂ in its liquid form (LH₂) presents obvious advantages in terms of energy density (70.9 kg/m³ – 2.34 kWh/L – at 1 atm and ~ 20K) compared to compressed H₂. When looking to its gravimetric and volumetric energy capabilities with respect to kerosene, one can see that while LH₂ present a higher gravimetric energy density (33.3 kWh/kg vs 12 kWh/kg for kerosene), its volumetric energy density is much less than the kerosene one (respectively 2.34 kWh/L vs 9.7 kWh/L). The Figure 11 highlights the proportion differences in mass and volume for the same energy content between LH₂ and kerosene to illustrate these aspects.

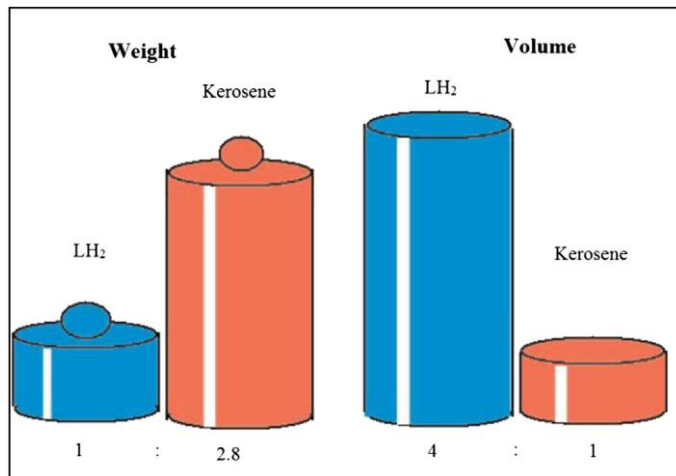


Figure 11 - LH₂ and Kerosene weight and volume comparison for a given energy content ([NOJ-09])

To make a fair comparison in terms of gravimetric and volumetric energy densities between the two elements (LH₂ and kerosene), one should nevertheless consider the impact of the tank weight and volume on the energy storage system (higher in the case of LH₂ than for kerosene, [WIN-18]). Such comparison between kerosene and LH₂ is made in studies such as [WES-03] (Cryoplane project), [HAG-06], [VER-10], [KHA-13], when considering LH₂ as a potential candidate to replace kerosene in direct combustion engines for aviation applications.

In [VER-10] and [WIN-18] in particular, the authors investigate potential LH₂ tank designs for aviation applications (regional airliner) by taking into account various parameters such as the tank geometrical shape, the H₂ venting pressure inside the tank (maximal acceptable H₂ pressure before venting), the insulation type (between other factors). Such tanks generally feature a double-wall structure (inner and outer wall) with an insulating layer between the two walls, as well as a venting pipe and a filling pipe. Regarding the insulation methods to maintain the ~ 20 K necessary to keep the H₂ in liquid state and limit the boil-off of LH₂, three possibilities are often mentioned ([KHA-13], [VER-10]):

- A Multi-Layer Insulation (MLI), consisting of a superposition of metallic foils and insulating thin material (polyester or glass fiber for instance) to avoid metal-to-metal contact. The MLI insulation should act as a shield for the thermal radiations ([KHA-13]), however the layer density should not be too high in order not to increase the conduction

effects between the two walls. To minimize gas conduction, MLI has to operate at ~ 12 mbar pressures ([VER-10]).

- A vacuum insulation: while [KHA-13] underlines that it is theoretically the best option, the authors add that it is practically impossible to maintain a vacuum without additional venting equipment (pumps to suck the air and maintain the vacuum).
- A foam insulation, consisting of a foam layer put between the two walls. As the thermal conductivity of such foams is higher than the MLI under very low pressures, the thickness of the insulation layer should be higher as well, and thus increase the overall system weight and volume. Nevertheless, as the walls have to be thicker (thus heavier) in the vacuum-insulation and MLI case, in order to feature a higher mechanical resistance to the pressure difference, this weight penalty is somehow the same in both cases.

Such possible insulating systems based on foams or MLI are visible on Figure 12, where the two designs studied by [VER-10] are exposed. Indeed, a combination of the three methods described previously can be imagined to develop the tank insulating system (the “MLI” design of [VER-10] uses for instance an MLI layer as well as a foam layer).

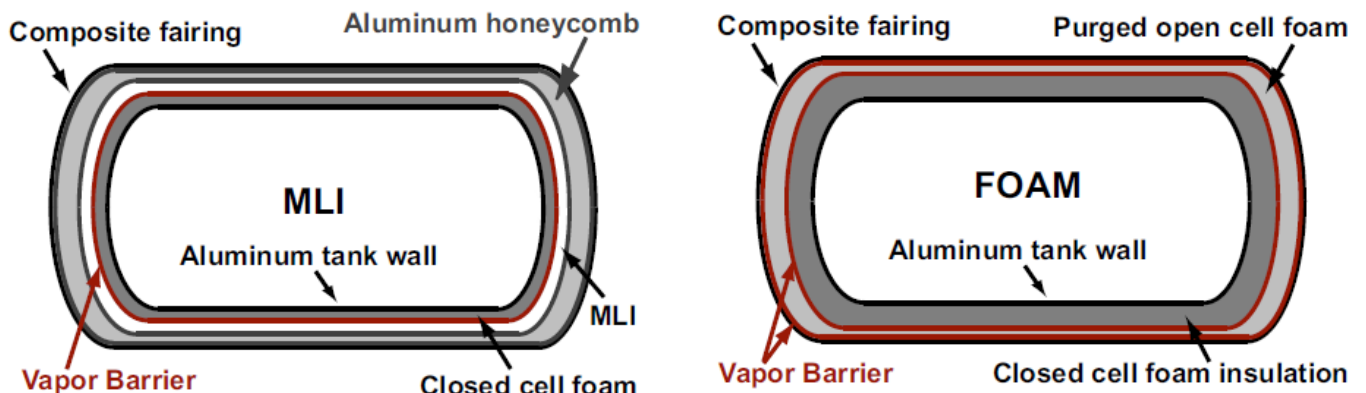


Figure 12 – Two possible insulating structures for LH₂ tanks (MLI and FOAM) investigated in [VER-10] for regional aircraft

Studies investigating on the design of future tanks for aircraft applications such as [VER-10] or [WIN-18], show that gravimetric index up to 71 wt. % ([VER-10]) and 64 – 70 wt. % ([WIN-18]) could be reached for regional aircraft (vs. 75 wt. % in the case of kerosene tanks, [WIN-18]). These high values should nevertheless be contextualized with respect to the amount of H₂ stored in these tanks (~ 1150 kg_{H2} in the [VER-10] study).

Indeed, **the weight of the tank is proportional to the wall surface** (the wall thickness depends on the insulating method and on the heat leak but not on the tank volume or surface), whereas **the weight of the embedded LH₂ is proportional to the tank volume**. Hence, **the higher the H₂ embedded mass is, the higher the gravimetric efficiency of the tank will be** (cf. equation (1)).

While these theoretical studies are concentrated on the design and potential use of LH₂ tanks for future aircrafts (without demonstration prototypes or experimental values available), a LH₂ storage system has already been embedded in a small UAV coupled with a LT-PEMFC ([STR-14]). Despite the small quantity of H₂ stored inside the tank (1.34 kg_{H2}), the

gravimetric efficiency of the storage system reached 23 wt. % and the H₂ volumetric capacity 0.036 kg_{H2}/L. The authors used there an MLI and vacuum insulation system between a double-wall structure (cf. Figure 13), as well as a heater and pressure relief valves (MPRV and SPRV for Mechanical and Solenoid Pressure Relief Valves on the figure) to manage the boil-off and the H₂ pressure inside the tank as well as the FC H₂ feed.

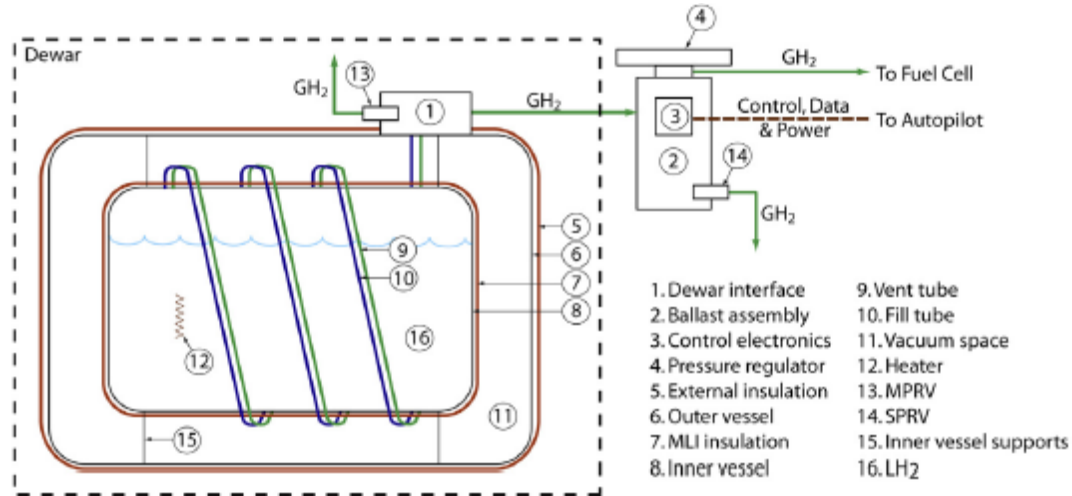


Figure 13 - LH₂ storage system (schematic) used in [STR-14] (Ion Tiger UAV)

One of the issue underlined by the authors ([STR-14]) is the H₂ loss due to LH₂ boil-off during the mission: even with a small heat leak, H₂ has to be vented regularly if it is not consumed by the FC. In [WIN-18], the authors underline that this issue could be somehow compensated by imposing an adequate power load to the FC: as the evaporated H₂ would be consumed continuously through the FC, the pressure rise inside the tank would be limited and thus the H₂ loss through venting as well.

The spatial field has already been using liquid hydrogen, for the famous NASA Apollo's missions for instance ([BOW-06]). Liquid H₂ tanks were there embedded together with alkaline fuel cells (employed as power and water producing units). For this application, spherical tanks containing up to ~ 42 kg_{H2} each and showing a gravimetric efficiency of ~ 30 wt. % and a H₂ volumetric capacity of ~ 0.051 kg_{H2}/L were used (tank weight and volume of 98 kg and 820 L – outside diameter of 1.16 m, [BOW-06]).

Cryogenic LH₂ tanks have also been considered in automotive applications as an alternative fuel for direct combustion, especially by BMW. The BMW Hydrogen 7 sedan who has reached the series development step ([MUL-07]), features for instance LH₂ tanks (with a vacuum + MLI insulation) containing ~ 8 kg_{H2} each. Such tank and LH₂ storage system is well described in [AMA-06], as well as the different procedures to fill the tank, to manage the H₂ boil-off and the H₂ pressure inside the tank, and to control the H₂ feed to the combustion engine (cf. Figure 14). According to [DIC-18], the LH₂ tanks used in the BMW series 7 cars reach gravimetric efficiencies around 14.2 wt. % and H₂ volumetric capacities of 0.042 kg_{H2}/L (51.5 kg and 200 L tanks with a venting pressure of 5 bara).

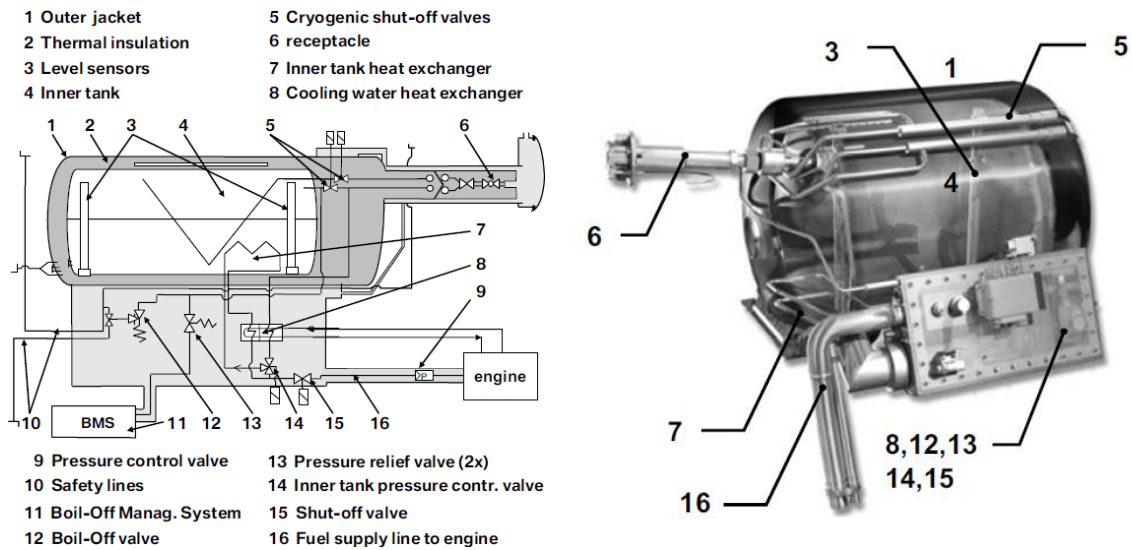


Figure 14 - BMW series 7 LH₂ storage system diagram and constitution ([AMA-06])

Air Liquide also developed various LH₂ tanks in collaboration with BMW ([MIC-06], [MIC-08]), particularly with a cylindrical LH₂ lightweight tank prototype reaching a gravimetric efficiency of 15 wt. % and a H₂ volumetric capacity of 0.04 kg_{H2}/L (the tank contains ~ 11.7 kg_{H2} with an empty weight of 66 kg and a volume of 291 L). Such value (15 wt. % gravimetric efficiency) is often referred to as an emblematic value for LH₂ storage systems when considering stored H₂ quantities in this order of magnitude (~ 10 kg_{H2}), for instance in [BEN-15].

Taking into account some of the LH₂ storages mentioned previously, a quick comparison with Figure 10 is made in Figure 15, where LH₂ storage systems performances are plotted in addition to the compressed H₂ composite storages.

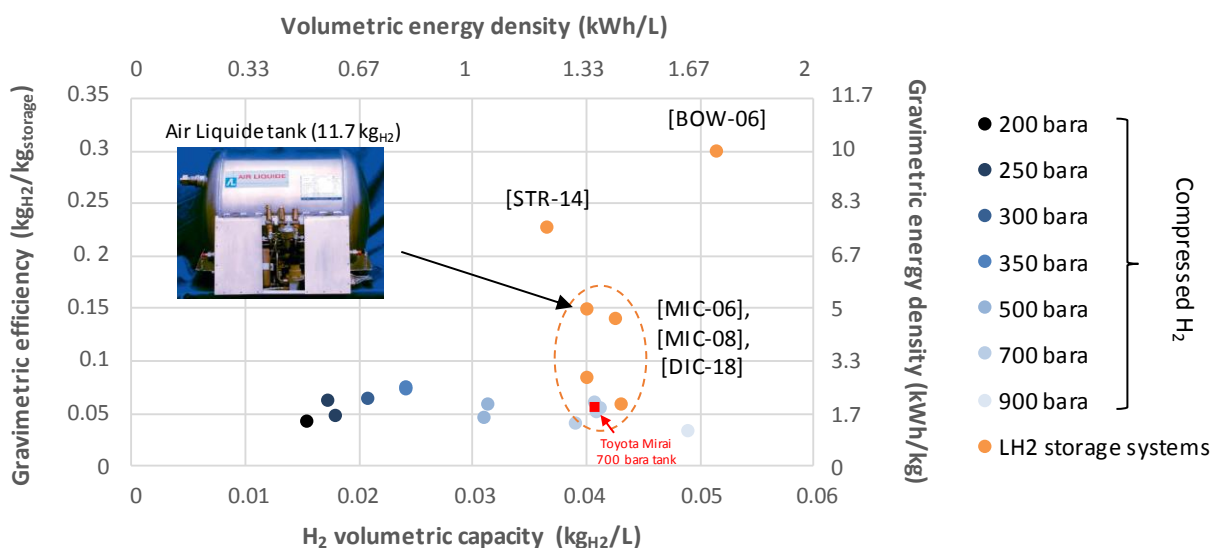


Figure 15 - Gravimetric efficiencies and H₂ volumetric capacity of different H₂ storages (derived from Figure 10)
Compressed H₂ storage data from [HEX-17]

Even if to be completely rigorous, other parameters like the H₂ mass stored in each tank should be precised when comparing such numbers, the graphic underlines the higher potential of LH₂ compared to compressed H₂ in terms of embedded mass and volume.

Regarding the energetic cost to liquefy H₂, [DIC-18] affirms that almost 40 % of the H₂ specific energy (LHV) is needed for the liquefaction process, which would be around 13.3 kWh/kg_{H2}. In [SIN-17], the authors mentioned a lower proportion of 30 – 33 % of the H₂ specific energy needed for the liquefaction (~ 10.5 kWh/kg_{H2}). Such values are much higher than the values mentioned previously (2.3.3.1) for the H₂ compression energetic cost (4.5 kWh/kg_{H2} for a compression at 700 bara); nevertheless, one work ([SAD-17]) claims that a much lower value of 4.41 kWh/kg_{H2} could be reached with a novel refrigeration process.

To sum up, very promising theoretical studies focused on future LH₂ storage systems for aeronautical applications, whether or not in order to be used as a fuel for direct combustion ([VER-10], [KHA-13]) or through a fuel cell ([WIN-18]), announce today possible gravimetric efficiencies in the order of 60 – 70 wt. % (in systems embedding more than 1000 kg_{H2}). Besides, such storage systems have already reached values up to 30 wt. % ([BOW-06]) in spatial applications. This value should however be considered with caution as the durability requirements are not the same in spatial and aeronautical applications (i.e. the LH₂ tanks were not designed to endure several duty cycles). On a specific application ([STR-14]), a value of 23 wt. % could be reached with a demonstration prototype storing a small H₂ quantity (1.34 kg_{H2}). In addition to these studies, the automotive industry has already been driving the development of LH₂ storage systems up to the serial production step and has consequently brought some important information about the actual level of performances of such storage systems ([MIC-06], [MIC-08], [AMA-06]). Considering these sources, values in the range of 14 – 15 wt. % for the gravimetric efficiency and 0.04 kg_{H2}/L for the H₂ volumetric capacity have already been demonstrated and can be considered as references for H₂ storage systems embedding H₂ masses around 10 kg_{H2}.

2.3.3.3. Metal Hydrides

Although compressed and liquid H₂ constitute today the most mature methods to embed hydrogen, storing H₂ through solid material can also be mentioned when scanning the different H₂ storage methods. Such approaches often use material like reversible metal hydrides that will have the ability to adsorb H₂ and to release it through chemisorption mechanisms driven by pressure and temperature cycles. These materials offer great performances in terms of H₂ volumetric capacity (0.05 kg_{H2}/L, [YOU-04]) but poor performances in terms of gravimetric efficiency (1.5 wt. %, [YOU-04]), behind the performances of compressed H₂ or Liquid H₂ storages. According to [BUS-16], values up to 7 wt. % and 0.045 kg_{H2}/L (and an availability of 90 % for the stored H₂) have been recently reached using sodium borohydrides material in an application with an UAV.

Despite the last value showing that there is room for improvement and interesting perspectives with this storage method with respect to the gravimetric efficiency and the H₂

volumetric capacity, some uncertainties remain concerning the ability of the material employed to withdraw large quantities of H₂ ([WIN-18]).

For this reason, and because to date state-of-the-art performances of such storages are behind compressed and liquid H₂ storages in terms of mass efficiency, metal hydrides and solid storages will not be considered further in this study.

2.4. Summary of the performances assessments made for the selected technologies

After having detailed some information about different technologies of battery, FC, and H₂ storages, considered in this study as potential parts of the auxiliary sources hybridizing the gas turbines in a future regional aircraft, this part will attempt to **summarize in a very synthetic way several values** representatives of their current and future (if evaluable) performances.

More specifically, typical values of specific energies, C_{rate} maximal limits and cycle life will be given on one hand for the battery technologies scanned in the 2.2.2 part (High power: LTO/TNO, High Energy: NMC, Very high energy: all solid state NMC and LiS); while on the other hand, estimated state of the art values of FC stacks specific power, auxiliaries specific weight / volume impact factor (for the LT PEMFC case) and H₂ storages gravimetric efficiencies and volumetric capacities (2.3.2 and 2.3.3 parts), will be assessed.

Two dates will be considered for the future performances evaluation: the years 2025 and 2035. Obviously, the collection of information as well as the lack of visibility on the development of several technological aspects (on the battery side and on the FC / H₂ storage side) is not necessarily providing clear answers for these projections, hence some blanks can appear in the forecast tables.

2.4.1. Battery: specific energies, C_{rate} capabilities and cyclability assessments

The first tables (Table 10 and Table 11) summarize the information scanned in the 2.2.2 part, respectively in terms of gravimetric and volumetric energy density for the selected technologies (LTO – high power, NMC – high energy and LiS – Very High Energy). In addition, two others technologies mentioned as well previously were added: the TNO on the high power side and the all solid state battery on the very-high-energy side.

Specific energy e _m (Wh/kg @ <u>cell scale</u>)	Today	2025	2035
High Power: LTO / TNO	~ 90 – 140 Wh/kg _{cell}	~ 160 – 180 Wh/kg _{cell}	~ 180 – 200 Wh/kg _{cell}
High Energy: NMC	~ 250 Wh/kg _{cell}	~ 350 Wh/kg _{cell}	~ 500 Wh/kg _{cell}
Very-high Energy: All Solid State (NMC)	~ 450 Wh/kg _{cell}	~ 550 Wh/kg _{cell}	~ 650 Wh/kg _{cell}
Very-high Energy: LiS	~ 500 Wh/kg _{cell}	~ 600 Wh/kg _{cell}	~ 650 Wh/kg _{cell}

Table 10 - Gravimetric energy density assessments (Wh/kg) for the selected technologies at the cell scale (cf. 2.2.2)

A few comments can be made regarding Table 10:

- LTO / TNO: the two technologies are put together because they feature a lot of common characteristics (nominal cell voltage, cyclability, C_{rate} performances...).
- NMC: the perspectives (2025 and 2035) are given considering the capabilities of cells using Si for the anode electrode.
- All solid state: we include with this term technologies using a Li metallic anode and a solid electrolyte (polymer) or a semi-solid electrolyte (ceramic + liquid electrolyte) with a high energy cathode (NMC).

Specific energy e_v (Wh/L @ cell scale)	Today	2025	2035
High Power: LTO / TNO	~ 180 – 350 Wh/L _{cell}	~ 320 – 450 Wh/L _{cell}	~ 360 – 500 Wh/L _{cell}
High Energy: NMC	~ 650 Wh/L _{cell}	~ 900 Wh/L _{cell}	~ 1250 Wh/L _{cell}
Very-high Energy: All Solid State (NMC)	~ 900 – 1000 Wh/L _{cell}	~ 1150 Wh/L _{cell}	~ 1300 Wh/L _{cell}
Very-high Energy: LiS	~ 300 Wh/L _{cell}	~ 600 Wh/L _{cell}	~ 650 Wh/L _{cell}

Table 11 - Volumetric energy density assessments (Wh/L) for the selected technologies at the cell scale (cf. 2.2.2)

Regarding the estimation of the volumetric energy density forecasts on Table 11, the following hypothesis was taken: if no specific information was available, a constant kg/L ratio was considered at the cell scale to evaluate the Wh/L_{cell} future projections. To jump from the cell to the system scale assessments of the gravimetric and volumetric energy densities, constant integrating factor parameters (f_m and f_v) are considered, as developed in the 2.2.3 section. Their values are estimated to be respectively **$f_m = 2$ and $f_v = 2.5$** .

The power capabilities of the selected technologies are appraised in Table 12 where the C_{rate} performances are put for the charge and discharge options. Indeed, the values specified here refer to the C_{rate} limits given by some manufacturers (cf. 2.2.2) for the maximum continuous charge and/or discharge speeds. The information displayed here does not specify however the peak power capabilities of each technology (which will be higher than the maximum continuous charge/discharge power).

C_{rate} capabilities (charge / discharge)	Today	2025	2035
High Power: LTO / TNO	3 – 10C / 3 – 10C	-	-
High Energy: NMC	0.5C / 2C	-	-
Very-high Energy: All Solid State (NMC)	0.2C / 2C	-	-
Very-high Energy: LiS	0.2C / 1C	-	-

Table 12 - C_{rate} capability assessments for the selected technologies (cf. 2.2.2)

Additionally, the charge / discharge speed will have an impact on the available energy for a given battery mass, and therefore the expected energy/power will somehow be different depending on the charge/discharge characteristics of each technology. Let's assume for

instance that 1 kWh of battery is embedded and that this battery maximal continuous discharge speed is about 2C: the expected 1 kWh / 2 kW capabilities of the embedded battery will quite probably be lower, due to the battery discharge speed (through the effect of the electrochemical losses and/or Peukert effect on the battery capacity). This aspect will be further developed in the next part (cf. 3.3.1), through a modeling approach based on the Tremblay-Dessaint equations ([TRE-09]).

Information collected about the typical cycling life of the different battery technologies is reported in Table 13. The cycling numbers specified here refer to the charge/discharge cycles (if not specified: up to 80 % DoD) that can be reached until a 20 % capacity loss.

Cyclability (charge / discharge cycles)	Today	2025	2035
High Power: LTO / TNO	Up to 15000 cycles (100 % DoD)	Up to 20000 cycles (100 % DoD)	-
High Energy: NMC	> 300 cycles	-	-
Very-high Energy: All Solid State (NMC)	200 cycles	-	-
Very-high Energy: LiS	100 cycles	500 – 1000 cycles	-

Table 13 - Cyclability assessments for the selected technologies (cf. 2.2.2)

The charge / discharge speeds associated to this cycling life are often at nominal conditions (cf. Appendix A for instance), however in the case of LTO/TNO cells the charge/discharge speeds were much higher during the cycling tests (15000 cycles at 3C/3C for the LTO for instance, [TOS-17]).

Also, even if this aspect is not much covered in this work, one should as well take into account the thermal performances of the selected technologies as well as the dependence of the other performances indicators to the working temperature (cell specific energy / C_{rate} capabilities / cyclability).

2.4.2. Fuel Cell stacks and systems specific power / H₂ storage performances

Looking the different technologies of Fuel Cell stacks and systems considered here, Table 14 proposes a summary of the different datasheets and articles reviewed in the 2.3.2 part. The FC stack specific power values refer to the ratio between the FC stack output power and its mass / volume, whereas the FC system specific power values refer to the ratio between the FC system net output power (considering the FC stack auxiliaries parasitic power consumption) and the total system mass / volume (the denomination “system” referring here to the power conversion part, i.e. without considering the energy storage brick).

Indeed, as already precised previously, it is quite delicate to assess current and future level of performances of the HT PEMFC and SOFC technologies at the stack and at the system level, due to their lack of maturity. For the LT PEMFC, more information are available at the stack and at the system scale. Although a certain uncertainty remains concerning the current LT

PEMFC system power performances (as all the auxiliary components are not compulsorily included in all the datasheets or articles reviewed, cf. Table 8), several values can be estimated around 0.6 and 0.7 kW/kg_{system} by looking to the few communications bringing information at the system scale including all the Balance of Plants components ([IE-15], [POG-18]).

FC stack and system specific power densities p_m / p_v (kW/kg and kW/L)	Today	2025	2035
LT PEMFC	$\sim 2 - 3$ kW/kg _{stack} $\sim 0.6 - 0.7$ kW/kg _{system}	~ 4 kW/kg _{stack} ~ 1 kW/kg _{system}	> 5 kW/kg _{stack} > 1.1 kW/kg _{system}
	$\sim 3 - 3.5$ kW/L _{stack} $\sim 0.3 - 0.6$ kW/L _{system}	~ 5 kW/L _{stack} ~ 0.8 kW/L _{system}	> 6 kW/L _{stack} > 0.9 kW/L _{system}
HT PEMFC	$\sim 0.4 - 0.8$ kW/kg _{stack}	~ 1 kW/kg _{stack}	-
SOFC	~ 0.33 kW/kg _{stack}	-	-

Table 14 - Fuel Cell stack / system (gravimetric and volumetric) specific power densities (cf. 2.3.2.1 & 2.3.2.3)

The projections values (~ 1 kW/kg_{system} for 2025) are estimated not only by updating the estimations of the stack specific powers, but also the auxiliary specific weight / volume impact (presented Table 15), and by considering improvements of the FC stack and system efficiencies at nominal power: from 0.5 (today) to 0.55 (2025 and 2035) for the FC stack efficiency η_{FC}^{stack} and from 0.42 to 0.5 for the FC system efficiency η_{FC}^{system} .

The auxiliaries specific weight and volume impact factor (p_m^{aux} and p_v^{aux} respectively) are estimated according to the calculations made in 2.3.2.2 and displayed in Table 15. It should be emphasized here that these rough estimations are made for LT PEMFC systems and that the p_m^{aux} and p_v^{aux} values should vary when considering HT PEMFC or SOFC systems (and probably increase, i.e. the auxiliaries mass should decrease). Also, it is precised here again that these values represent respectively the ratio between the FC stack output power (P_{gross}) and the auxiliaries mass and volume (cf. equation (6)).

Auxiliary specific weight / volume impact parameter (p_m^{aux} / p_v^{aux})	Today	2025	2035
LT PEMFC	1.15 kW _{gross} /kg 0.94 kW _{gross} /L	1.5 kW _{gross} /kg 1.2 kW _{gross} /L	1.75 kW _{gross} /kg 1.4 kW _{gross} /L

Table 15 - Auxiliaries specific weight / volume impact parameter (cf. 2.3.2.2)

In order to estimate some projections for 2025 and 2035, improvements of respectively 30 % and 50 % were assessed on the cooling system mass and volume as well as on the other auxiliary components (compressor and H₂ recirculator masses and volumes).

In addition to the previous tables focused on the power conversion part, Table 16 summarizes the current performances and forecasts for the H₂ storage brick. In order to give some orders

of magnitude in terms of specific energies, two values are added (each associated to the different storage methods considered): a “gross” value based on the gravimetric efficiency of the storage method and on the H₂ LHV (kWh_{gross}/kg_{storage}), and a “net” value taking additionally into account the conversion efficiency of the FC system block and representing thus a “useable” specific energy (kWh_{net}/kg_{storage}).

H ₂ storage gravimetric efficiencies (-) and specific energy (Wh/kg based on H ₂ LHV)	Today	2025	2035
Compressed H ₂ (700 and 350 bara)	~ 5 – 7.5 wt. % ~ 1.67 – 2.5 kWh/kg (0.7 – 1 kWh/kg*)	~ 10 wt. % ~ 3.3 kWh/kg (1.67 kWh/kg**)	> 10 wt. % > 3.3 kWh/kg
Liquid H ₂ (~ 20 K)	~ 15 wt. % ~ 5 kWh/kg (2.1 kWh/kg*)	~ 20 wt. % ~ 6.6 kWh/kg (3.3 kWh/kg**)	> 20 wt. % > 6.6 kWh/kg
Solid (metal hydrides)	~ 2 – 3 wt. % ~ 0.67 – 1 kWh/kg (0.28 – 0.42 kWh/kg*)	~ 7 wt. % ~ 2.3 kWh/kg (1.15 kWh/kg**)	> 7 wt. % > 2.3 kWh/kg > 1.15 kWh/kg**

* useful energy assuming a FC system efficiency of 0.42 ; ** useful energy assuming a FC system efficiency of 0.5

Table 16 - H₂ storage gravimetric efficiencies (wt. %) and specific energies (kWh/kg) – cf. 2.3.3 & Figure 15

Regarding the H₂ volumetric capacity (kg_{H2}/L_{storage}), the values of compressed H₂ composite tanks are already closed to the theoretical value of the H₂ densities under such pressures, i.e. 0.024 kg_{H2}/L (~ 0.8 kWh_{gross}/L and 0.3 – 0.4 kWh_{net}/L considering a FC system efficiency η_{FC}^{system} around 0.4 – 0.5) at 350 bara and 0.041 kg_{H2}/L (~ 1.36 kWh_{gross}/L and 0.6 kWh_{net}/L considering a FC system efficiency η_{FC}^{system} around 0.4 – 0.5) at 700 bara. These numbers cannot obviously be improved in the next decades for physical reasons (density of compressed H₂). For LH₂ storages, values up to 0.04 kg_{H2}/L (~ 1.33 kWh_{gross}/L and 0.6 kWh_{net}/L considering a FC system efficiency η_{FC}^{system} around 0.4 – 0.5) are reached today for H₂ quantities around 10 kg with automotive tanks (cf. Figure 15), while the theoretical limit is around 0.071 kg_{H2}/L. In the same way as for the gravimetric efficiencies, these values are of course highly dependent on the stored H₂ quantity: the more H₂ is carried, the higher the volumetric capacity is. In terms of perspectives, if we assume a constant H₂ quantity, the only way to improve the H₂ volumetric capacity is to reduce the insulation thickness which seem however quite challenging. Also, it should be taken into account that due to venting pressures superiors to 1 bara, the actual H₂ density inside the LH₂ tank will be lower than 0.071 kg_{H2}/L ([WIN-18]), decreasing as well the theoretical target limit.

High H₂ volumetric capacities are reached today with the solid storages based on metal hydrides (cf. 2.3.3.3) with values up to 0.045 – 0.05 kg_{H2}/L (~ 1.66 kWh_{gross}/L and 0.7 – 0.8 kWh_{net}/L considering a FC system efficiency η_{FC}^{system} around 0.4 – 0.5). Although such technologies could be the most promising in terms of H₂ volumetric capacity, it is quite

delicate to estimate some future projections due to their lack of maturity. In addition, their poor gravimetric efficiency is to date a showstopper for weight sensitive applications such as aeronautical ones.

2.4.3. First comparison at the system scale between FC and batteries on a particular case

Anticipating a little bit on part 3, this section will try to make a **short first comparison at the system scale between the different battery technologies and a LT PEMFC + LH₂ association**, in terms of specific energy and specific power (Table 17 & Table 18).

As there are no intrinsic values of specific energy or specific power linked with any association of one FC technology with one H₂ storage method (both values depend on the specific mass of each part of the system – the power conversion part and the energy storage part – which in returns depends on the energy and power requirements of the mission), a particular case is considered here. More specifically, a light hybridization scenario (cf. 3.1) is taken as reference with a maximal power requirement of 280 kW and a total energy requirement of 157 kWh.

For the sake of simplicity, only one {FC + H₂ storage} association is considered: the one presenting the best current performances respectively for the FC system power conversion part (LT PEMFC) and for the H₂ storage gravimetric efficiency (LH₂ tank(s)).

Specific energy at the system scale (Wh/kg)	Today	2025	2035
High Power: LTO/TNO	~ 70 Wh/kg	~ 90 Wh/kg	~ 100 Wh/kg
High Energy: NMC	~ 150 Wh/kg	~ 225 Wh/kg	~ 250 Wh/kg
Very-High Energy: All solid state (NMC)	~ 225 Wh/kg	~ 275 Wh/kg	~ 325 Wh/kg
Very-High Energy: LiS	~ 250 Wh/kg	~ 300 Wh/kg	~ 325 Wh/kg
LT PEMFC + LH₂*	~ 300 Wh/kg	~ 480 Wh/kg	~ 550 Wh/kg

* Study case: assuming 280 kW and 157 kWh needs to estimate the LT PEMFC + LH₂ system case

Table 17 - Evaluation of specific energies at the system scale between batteries and a {LT PEMFC + LH₂ storage} potential association (cf. Table 10, Table 14, Table 15 & Table 16)

In order to evaluate the values presented Table 17 & Table 18, several hypotheses are assumed:

- On the battery side, the specific energies at the system scale are assessed by dividing the specific energies at the cell scale (presented Table 10) by the integrating factor f_m (f_m = 2). Regarding the specific powers at the system scale (Table 18), at first approximation their values are assessed by multiplying the specific energies at the system scale with the maximal C_{rate} capacities associated to the battery technologies (in **continuous discharge** mode here). The actual values should nevertheless be lower due to the different losses presents during the energy conversion, lowering both the specific energies and specific powers values.

- On the FC side, based on Table 14, Table 15 & Table 16, the FC system mass and H₂ storage mass are first assessed with respect to the mission requirements (280 kW and 157 kWh), and in a second time the specific energy and power at the system scale can be evaluated knowing the power and energy capabilities of the system with respect to its total mass.

Specific power at the system scale (kW/kg)	Today	2025	2035
High Power: LTO/TNO	~ 0.7 kW/kg	~ 0.9 kW/kg	~ 1 kW/kg
High Energy: NMC	~ 0.25 kW/kg	~ 0.35 kW/kg	~ 0.5 kW/kg
Very-High Energy: All solid state (NMC)	~ 0.45 kW/kg	~ 0.55 kW/kg	~ 0.65 kW/kg
Very-High Energy: LiS	~ 0.25 kW/kg	~ 0.3 kW/kg	~ 0.32 kW/kg
LT PEMFC + LH₂*	~ 0.53 kW/kg	~ 0.85 kW/kg	~ 1 kW/kg

* Study case: assuming 280 kW and 157 kWh needs to estimate the LT PEMFC + LH₂ system case

Table 18 – Evaluation of specific powers at the system scale between batteries and a {LT PEMFC + LH₂ storage} potential association (cf. Table 10, Table 12, Table 14, Table 15 & Table 16)

Even if these tables are focused on a particular case and based on roughly estimated numbers, they allow a first comparison between the battery technologies and FC capacities. This first appraisal shows better results on the FC side for missions showing such energy and power requirements (regarding the current and future performances) with all the hypotheses taken previously.

In order to go deeper into the evaluation of the hybrid auxiliary source mass, as well as to investigate its behavior in terms of aspects such as efficiency, heat release, impact of the C_{rate} on the available energy for the battery case for instance, the next part is going to present several modeling developments on the battery and FC sides.

3. MASS ESTIMATIONS BASED ON A SIMPLIFIED LIGHT HYBRIDIZATION MISSION AND MODELING DEVELOPMENTS FOR THE BATTERY / FUEL CELL BLOCK

While part 2 proposed a review of different battery, FC system and H₂ storages, considered as potential candidates for the auxiliary source in a hybrid-electrical aircraft, this part is going to investigate more concretely on the auxiliary source modeling and on its mass evaluation accordingly to the objectives presented during the introduction.

In order to consider a specific case, an emblematic power mission is going to be firstly detailed (corresponding to the evaluation made in 2.4.3). Modeling developments will be presented further to assess some masses corresponding to the power missions presented, and to give some insights into the auxiliary source behavior during the mission (regarding parameters such as efficiency, heat release...). The modeling developments will be first introduced with a simplified approach giving a “first level” evaluation of the auxiliary source mass, while a more refined approach (“second level” estimation of the masses) will be given afterwards.

3.1. Power profile mission(s) taken as reference(s)

As already briefly specified in the 2.4.3 part, the reference mission is corresponding to a “light hybridization” scenario case: the auxiliary source is exclusively used during the taxi phases (taxi-in and taxi-out) and during the descent step, while the gas turbines handle the rest of the mission. Assuming that the non-propulsive loads can be estimated to a constant 140 kW, the entire power mission corresponding to a light hybridization scenario can be assessed and is presented Figure 16.

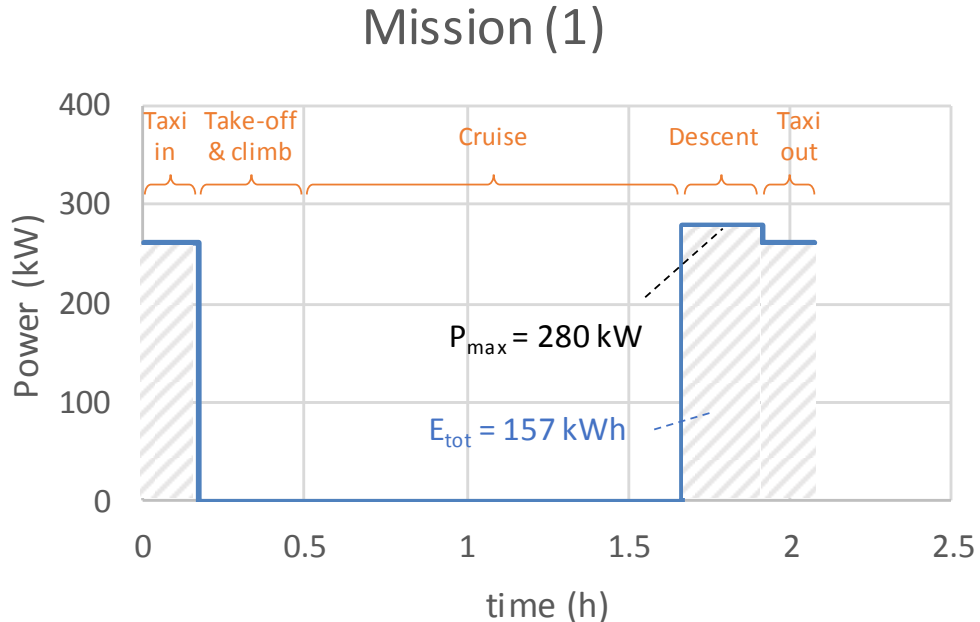


Figure 16 - Auxiliary source power mission (“light hybridization” scenario) - Mission (1): taxi in and out and descent phases (considering constant non-propulsive loads of 140 kW)

Such mission – referred to as Mission (1) – would require from the auxiliary source an amount of energy of ~ 157 kWh with a max power of 280 kW. As batteries are considered as a potential auxiliary source in this study, an alternative version of this light hybridization scenario is also considered with a recharge phase during the cruise period. This alternative version of the light hybridization scenario only concerning batteries is presented in Figure 17. In this particular case, the amount of energy provided by the auxiliary source (i.e. the battery here), not originate from the recharge (energy from the kerosene combustion), would decrease from 157 to 113 kWh.

Obviously, the two missions presented here are not necessarily representing an optimal power sharing strategy regarding the overall kerosene consumption or any other global design parameters, but they constitute fixed examples to illustrate the modeling developments purpose. In a complementary step, the modeling tools presented further are meant to be used as analytic tools in order to investigate the sensitivity of some global systemic parameters (such as the overall kerosene consumption during the mission) to the power sharing strategy and the auxiliary source power mission. The reader is referred to the Matthieu Pettes-Duller PhD work (WP6), for deeper developments on these aspects.

Mission (2)

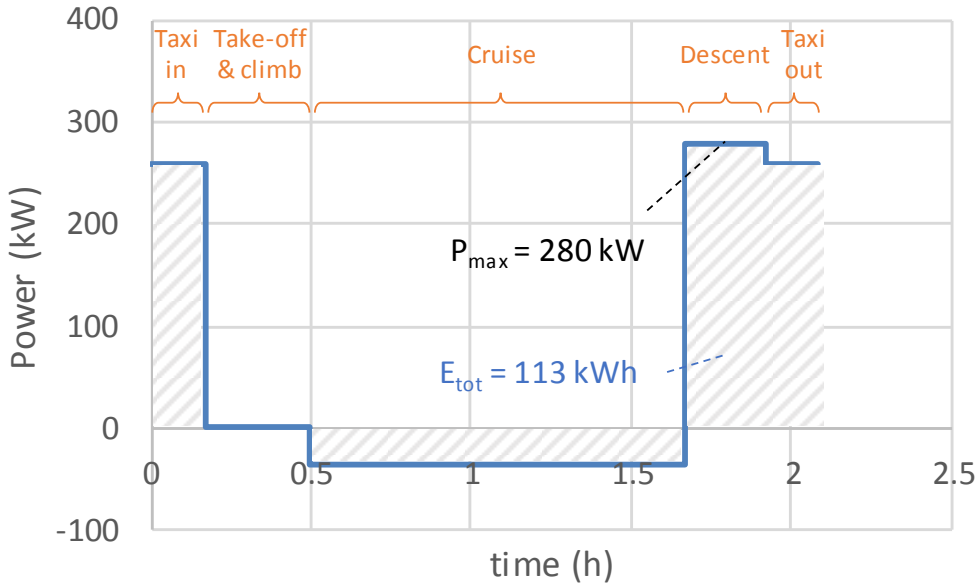


Figure 17 - Auxiliary source power mission (battery case only) - Mission (2): taxi in and out and descent phases (considering constant non-propulsive loads of 140 kW) with a recharge during the cruise

Note: even if temporal dynamic aspects are not examined in this work, one should however consider beside the main energy source the presence of a buffer device – such as a supercapacitor pack and/or a high power type battery (LTO for instance) – in order to handle the load dynamic variations. If we take for instance the FC system case, a slow dynamic response of the air compressor to the power steps Figure 16 could limit the dynamic capacities of the entire FC system, and the presence of a buffer device would be therefore necessary.

3.2. First level mass estimations

In order to give a rough estimation of the auxiliary source mass depending on the power mission requirements and on the different technologies selected, two equations (eq. (12) and (13)) are used respectively for the battery block and for the FC system & H₂ storage block. The expressions are presented here only for the mass evaluation of the auxiliary source in order to keep the document to a reasonable size, however the parameters used (f_m , e_m , η_m , p_m^{FC} , p_m^{aux}) can be as well transposed in their volumetric form (f_v , e_v , η_v , p_v^{FC} , p_v^{aux}) to evaluate the auxiliary source volume.

$$m_{Battery} = \max \left(\frac{E_{tot}}{e_m} * f_m ; \frac{P_{max}}{(C_{rate}^{max}) * e_m} * f_m \right) \quad (12)$$

$$m_{\{H_2 \text{ storage / FC system}\}} = \frac{E_{tot}}{(\eta_m * LHV * \eta_{FC}^{system})} + \left(\frac{P_{max}}{p_m^{FC}} + \frac{P_{max}}{p_m^{aux}} \right) * \frac{\eta_{FC}^{stack}}{\eta_{FC}^{system}} \quad (13)$$

Some parameters used in these equations have already been introduced previously (cf. equations (1) to (11) and 2.1), however for the sake of clarity they are listed again below:

- E_{tot} (kWh) and P_{max} (kW) correspond respectively to the auxiliary source energy requirement and maximal power requirement (in absolute value for the battery charge case) for the given power mission.
- e_m (expressed here in kWh/kg) is the battery gravimetric energy density at the cell scale.
- f_m (kg_{system}/kg_{cell}) is the battery weight integrating factor accounting for the mass of the battery packaging, BMS and cooling system.
- C_{rate}^{max} (h⁻¹) is the battery maximal continuous charge/discharge (corresponding to the P_{max} sign) rate.
- η_m is the H₂ storage gravimetric efficiency (kg_{H2}/kg_{storage}) and LHV is the Lower Heating Value of H₂ (33.3 kWh/kg_{H2}).
- η_{FC}^{stack} and η_{FC}^{system} (-) are respectively the FC stack and FC system power conversion efficiencies at maximal power (equations (9) and (10)).
- p_m^{FC} (kW/kg) is the gravimetric power density of the FC stack.
- p_m^{aux} (kW_{FC}/kg_{aux}) is the FC auxiliaries specific weight impact (with respect to the FC gross power).

These two equations ((12) and (13)) represent basic sizing rules based on the bibliographic review made in part 2.

For the battery mass expression (equation (12)), two sizings are compared:

- An “energy” one ($\frac{E_{tot}}{e_m} * f_m$): the energy requirement of the mission (maximal energy charged/discharged by the battery during the mission) is the sizing criterion.
- A “power” one ($\frac{P_{max}}{(C_{rate}^{max}) * e_m} * f_m$): the maximal power (in charge and discharge mode) and the corresponding maximal continuous charge/discharge rate are the sizing criteria: the battery is sized in order not to exceed the C_{rate}^{max} limit in charge or discharge mode.

The maximum value between both evaluations is finally the mass estimation of the battery block. Obviously, several simplifying hypotheses are underlaid in this expression: no battery losses are considered for instance which not only consists in assuming a 100 % battery conversion efficiency but also in assuming that the C_{rate} has no impact on the energy and power capacities of the battery. Also, no margin are taken regarding the SOC limits during the mission and the impact of the packaging and cooling system mass is integrated using a simple multiplying factor f_m .

For the {FC system + H₂ storage} mass equation (eq. (13)), the H₂ storage part is evaluated with respect to the mission energy requirement E_{tot} , the FC system conversion efficiency and the H₂ storage gravimetric efficiency, while the FC system part depends not only on the stack gravimetric power density and the auxiliaries weight impact factor, but also on the power

requirement at the stack scale (hence on the mission maximal power requirement and the efficiencies at the stack and at the system scale). Obviously, as for the battery mass equation, a few hypotheses are underlaid in equation (13): the H₂ storage gravimetric efficiency is considered constant and independent on the H₂ mass stored for instance, and fixed efficiencies at the system and stack scale are assumed. Furthermore, as already developed previously (2.3.2.2), a single parameter (p_m^{aux}) is considered for the auxiliary mass evaluation. Furthermore, for the whole FC system part it is assumed that the design point is the stack maximum power point (the stack maximum power capacity is equal to its maximal power requirement during the mission), while one could imagine moving this design point to impact the overall system mass and maybe minimize it, as it will be developed in 3.3.2.

Using these two equations and the values summarized in 2.4 (Table 10, Table 12 for the battery equation, and Table 14, Table 15, Table 16 for the FC one), it is possible to make a first assessment for the auxiliary source mass depending on the technology considered.

Regarding the FC technologies, only the LT PEMFC results associated with two H₂ storage technologies, compressed H₂ (CH₂) at 700 bara and LH₂, are shown. Results of these masses evaluations are presented in Figure 18 for the two missions (respectively in blue and red for Mission (1) and (2)). It is worth noting that the results presented for Mission (1) in this figure are the ones corresponding to the values of gravimetric energies and powers densities displayed in Table 17 and Table 18.

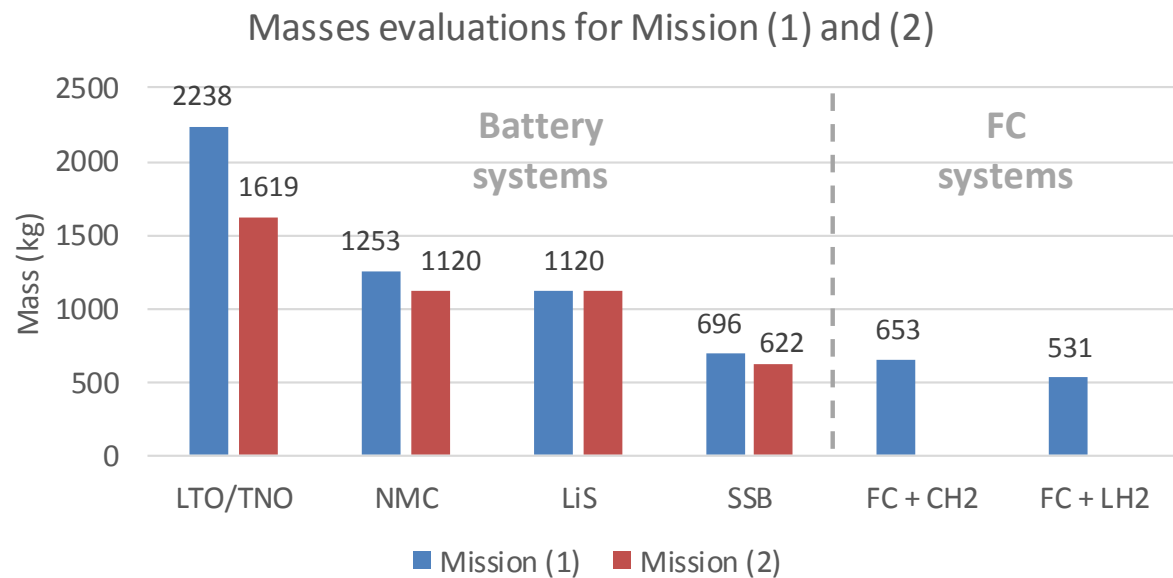


Figure 18 - Masses evaluations of the Battery / {FC + H₂ storage} systems for the missions presented Figure 16 and Figure 17 (today values)

A global overview of these results shows at first sight (and considering all the simplifying hypotheses detailed previously) a superiority of the FC systems compared to the battery ones in terms of mass for these power missions. A minimum of around 531 kg is especially reached with the {FC + LH₂} combination for Mission (1). On the battery side, these results obviously

confirm that the more energetic technologies – i.e. LiS and SSB – have better results than NMC and LTO/TNO for the energy/power requirements of these missions (SSB mass is lower than LiS mass because SSB C_{rate}^{max} value – 2C – is higher than LiS C_{rate}^{max} value – 1C). Besides these estimations, one should however consider the cyclability aspects already mentioned in part 2.2.2. Indeed, there is a clear trend showing that the most energetic technologies are often the technologies with the worst cyclability (Table 13): **it should be highlighted here that the best solutions regarding the mass Figure 18, are at the same time the ones showing the poorest cyclability.**

Obviously the mass results can widely vary depending on the two mission parameters in equations (12) and (13) – E_{tot} and P_{max} : the P_{max}/E_{tot} ratio, which could be considered as a mean equivalent C_{rate} , is actually a key parameter to understand what technology can be the best appropriated for a given mission profile in terms of mass. In order to illustrate this point, a case study assuming an energy requirement E_{tot} of 1 kWh and varying values of the P_{max}/E_{tot} ratio can be considered: Figure 19 show in particular the evolution of the different masses with the P_{max}/E_{tot} ratio and according to equations (12) and (13).

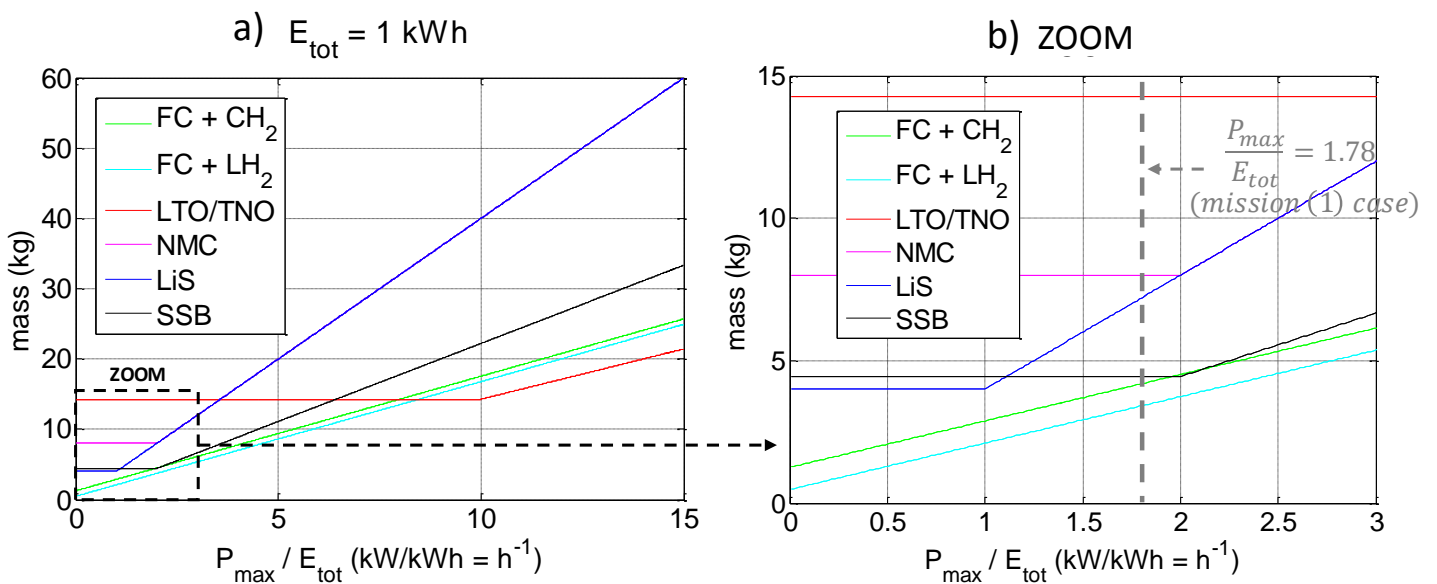


Figure 19 - Evolution of the battery / FC system masses (eq. (12) and (13)) with the P_{max}/E_{tot} ratio considering an energy requirement $E_{tot} = 1 \text{ kWh}$ / zoom for low values of P_{max}/E_{tot} in b)

The juxtaposition of the masses variations for each technology, depending on the P_{max}/E_{tot} ratio, highlights in Figure 19 that the minimum mass is not always reached by the same technology: in some areas ($P_{max}/E_{tot} > 8.5$), technologies such as LTO/TNO are lighter than the FC options, while for lower P_{max}/E_{tot} values (zoom Figure 19 – b)), FC systems and SSB technologies are the lightest options.

The graphics in Figure 19 highlights also for each battery technology a break in the curve when $P_{max}/E_{tot} > C_{rate}^{max}$, i.e. where the “power” sizing $\frac{P_{max}}{(C_{rate}^{max}) * e_m} * f_m$ becomes superior to the “energy” one $\frac{E_{tot}}{e_m} * f_m$ (cf. equation (12)).

In order to provide more insights into the auxiliary source behavior during the mission, as well as to give a more refined estimation of its mass, several aspects related to the auxiliary source modeling are investigated in the following paragraphs. Knowing the simplifying hypotheses associated to the first level mass model presented in equations (12) and (13), some aspects are especially scrutinized for these modeling developments:

- On the battery side: a loss model integrating the dependence between parameters such as the SOC, the C_{rate} , the discharge / charge power or the conversion efficiencies seems compulsory in order to understand the battery electrical and thermal behavior (in a global way), as well as the actual sizing criterion (SOC, max discharge/charge current, or voltage limits).
- On the FC side: the understanding of the dependencies between the FC stack and system efficiencies and the stack size as well as the couplings between the auxiliary systems and the FC stack seem to be a compulsory step in order to improve the understanding of such systems during the mission.

3.3. Second level mass estimations and modeling developments

The battery modeling developments will be exposed together with the battery block sizing method in a first time, while the FC system and H₂ storage modeling and sizing method will be detailed after.

3.3.1. Battery behavior modeling

In order to describe, for each battery technology, the evolution of the battery conversion losses with parameters such as the State of Charge (SOC) or the C_{rate} , the Tremblay-Dessaint based equations are used ([TRE-09]). The equation (14) developed in [TRE-09] (without including dynamic effects here), express in the discharge mode the battery voltage (V_{bat}) dependence to the battery discharged capacity (it in Ah) and discharge current (i in A) with 6 parameters: E0 (V) the nominal voltage, A (V) and B ((Ah)⁻¹) respectively the exponential zone amplitude and time constant, K_{pol} (V/Ah) and K_{res} (Ω) the polarization constant and resistance and R the internal resistance (Ω). Q represents here the battery capacity (Ah).

$$V_{bat} = E0 + A * e^{-B * it} - K_{pol} * it * \frac{Q}{Q - it} - R * i - K_{res} * i * \frac{Q}{Q - it} \quad (14)$$

In order to associate these six parameters (E0, A, B, K_{pol}, K_{res} and R) to each battery technology introduced previously, emblematic cells are chosen for each technology: Toshiba cells (20 Ah SCiB cell and Toshiba R&D cell, [TAK-18]) for LTO and TNO, Panasonic cell (reference UR18650ZTA, [PAN-18]) for NMC, Oxis Energy pouch cell (POA0217, Appendix B) for LiS and Solid Energy (“Hermès” cell, Appendix A) for the SSB. For each of the technologies considered, the different sets of parameters are identified using available discharge curves characteristics of the reference cells, and through an optimization step minimizing the sum of the squared errors between the model and the measures. Figure 20

illustrates the modeling results for two technologies (TNO and NMC), after this identification step and the fitting accuracies (mean error < 2 %). The Tremblay-Dessaint equation is able to model quite faithfully all the discharge/charge behavior for the technologies selected, except for the LiS one, where the discharge/charge patterns are drastically different compared to the other technologies.

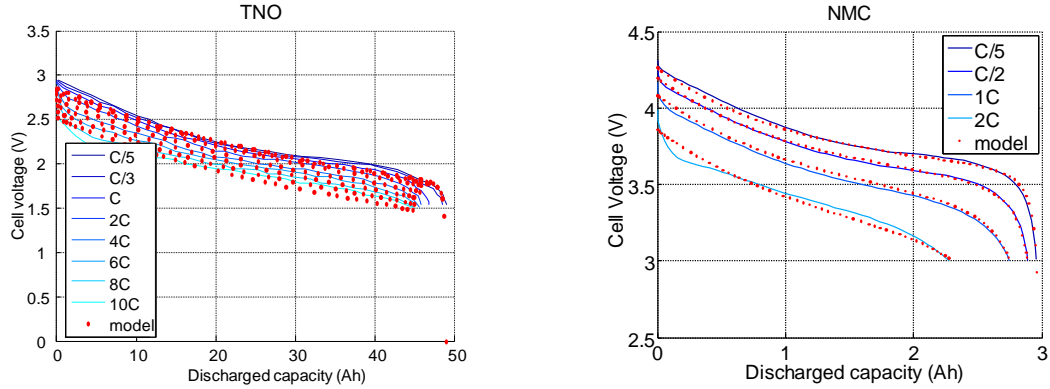


Figure 20 - Examples of modeling results (mean error < 2 %) with the Tremblay-Dessaint equation for two of the battery technologies considered (TNO and NMC)

Thanks to the parameters identification, the battery behavior during any power mission can be modeled and hence, a battery sizing can be evaluated. More precisely, a recursive algorithm is developed in order to find the minimal necessary cell number / mass able to fulfill a certain set of constraints: **voltage constraints** (the cells should stay in a certain voltage working range), **C_{rate} constraints** (the cells should not be discharged/charged faster than certain speeds, cf. Table 12) and **SOC constraints** (some technologies – NMC, SSB, LiS – cannot be fully discharged and a margin – usually 20 % – should be kept). A first sizing step (oversizing the battery on purpose) initialize the sizing loop, then the number of cells is decreased step by step, and the minimal necessary cell number is identified to the last cell number respecting all the sizing constraints. Knowing the cell number, the cell mass and the system mass can be identified (by multiplying the cell mass with the integrating factor f_m).

The sizing results are presented Figure 21 for the LTO, TNO, NMC and SSB (for the LiS case, no results are displayed as the modelling approach was not adapted to the LiS behavior):

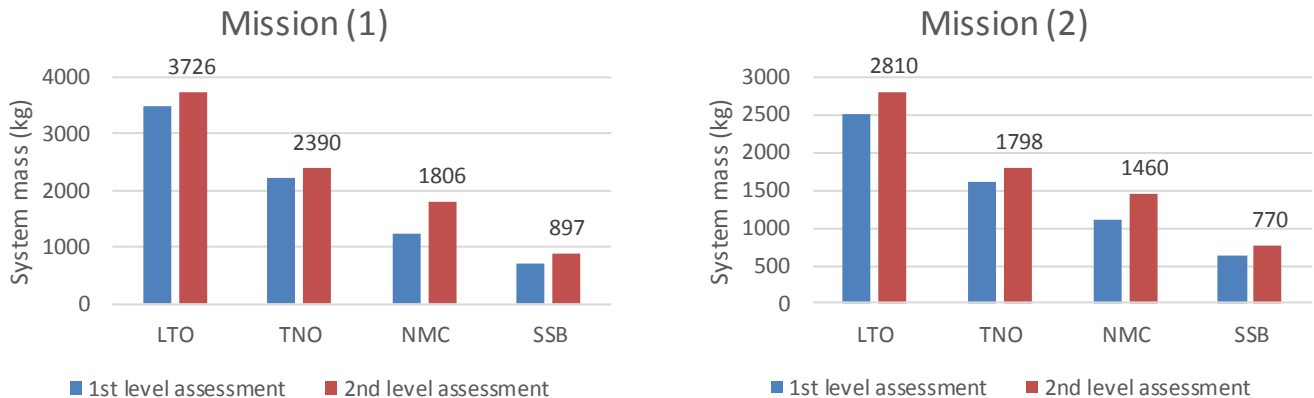


Figure 21 - Sizing results (in red) compared to the 1st assessment estimation (in blue)

In addition to the numerical simulations performed in order to assess the battery system masses, graphical tools in the Energy/Power plane are used to characterize each technology behavior during the missions. Thanks to the Tremblay-Dessaint equation (eq. (14)), iso-power charge and discharge characteristics are simulated and plotted in the Energy/power plane, considering the constraints detailed previously (voltage, C_{rate}^{max} , SOC), for each technology.

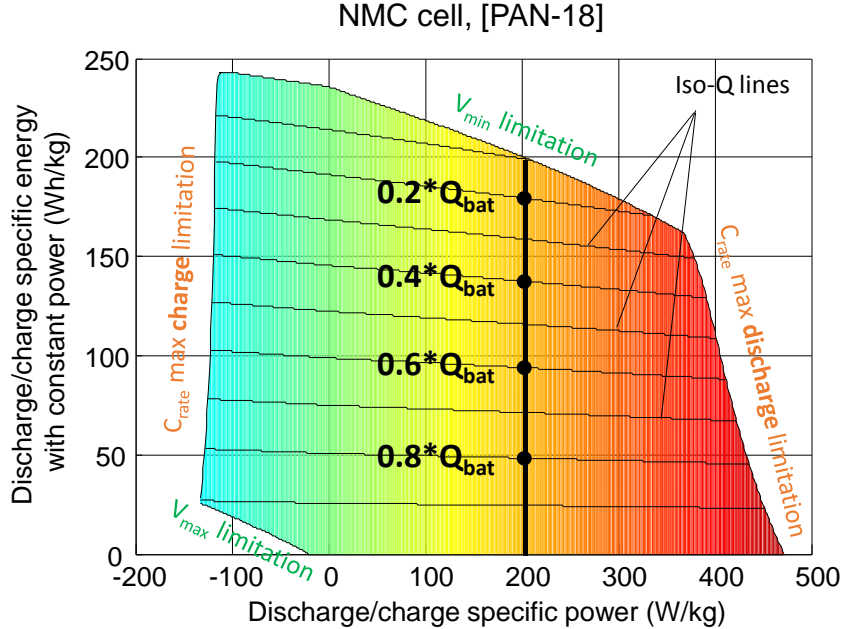


Figure 22 - NMC Panasonic cell ([PAN-18]) Energy/Power plot at constant discharge/charge powers

In Figure 22, an Energy/power plot for constant discharge/charge powers is shown for the NMC reference cell ([PAN-18]); values are normalized with respect to the cell mass in order to read directly the specific power and energy. In this plot, constant discharge/charge trajectories correspond to vertical lines, as highlighted in black for the 200 W/kg constant discharge from a fully charged state (discharged specific energy is equal to zero), to a maximum discharged specific energy of 200 Wh/kg for this discharge specific power (the minimum voltage constraint is in this example the dominant constraint if we don't consider the traditional SOC minimum margin of 20 %). This kind of plot illustrate in a graphic way how the available energy will vary with the charge/discharge power and the battery C_{rate} . Obviously, different plot shapes appear according to the battery technology. Also, as the available discharge specific energies depend on the discharge specific power, iso-Q (as well iso-SOC) lines (in black) are not horizontal lines in this plot: depending on the discharge power, the amount of energy that is delivered for a same amount of charge (Ah or SOC %) will vary.

The energy and power margin of each battery technology when the sizing is done can as well be analyzed thanks to this method. Figure 23 shows specifically such an Energy/Power plot for the final NMC sizing (1806 kg) with the Mission (1) power trajectory. As can be seen, the power trajectory fits in the Energy/Power pattern and the sizing constraint is here the minimum SOC (20 %). Such a plot can provide quick insight about how the battery technology “fits” for a given power mission and how it would be possible, in a next step, to adapt the power mission in order to optimize the battery utilization for a given sizing.

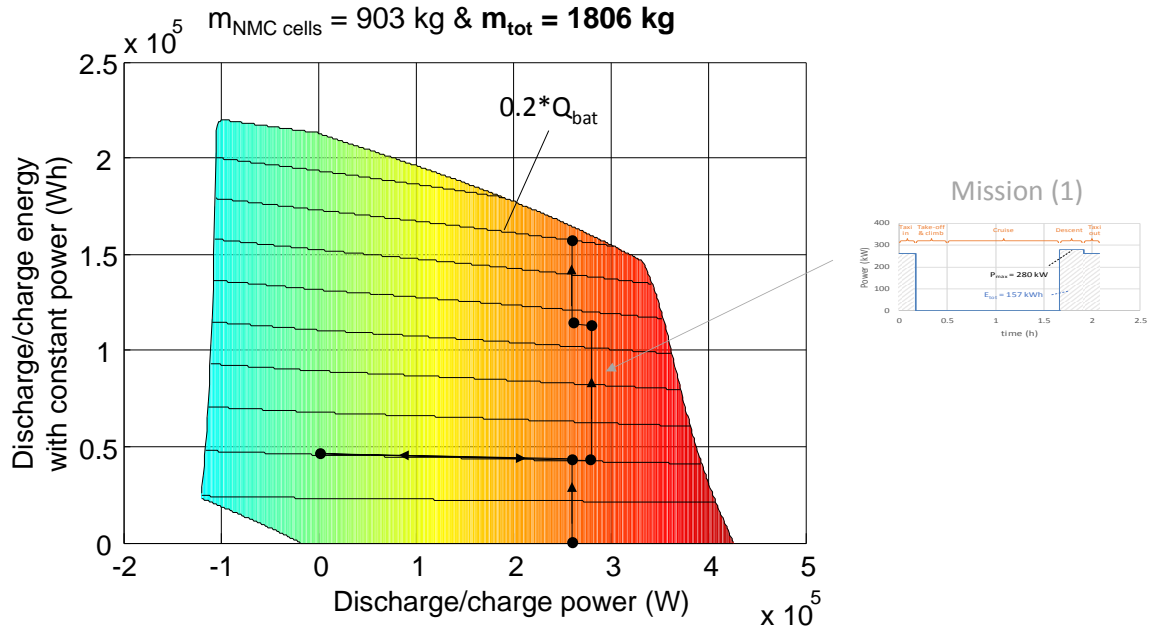


Figure 23 - Energy/Power plot for constant charge/discharge power (final sizing) with mission (1) trajectory

As the battery losses during the mission are here considered, as well as SOC margin for the NMC and BSS cases (LTO and TNO batteries can be fully discharged), the masses estimated Figure 21 are substantially higher than those presented Figure 18. To sum up the global approach, Figure 24 proposes finally a graphical illustration in four steps of the battery modelling and sizing strategy previously described.

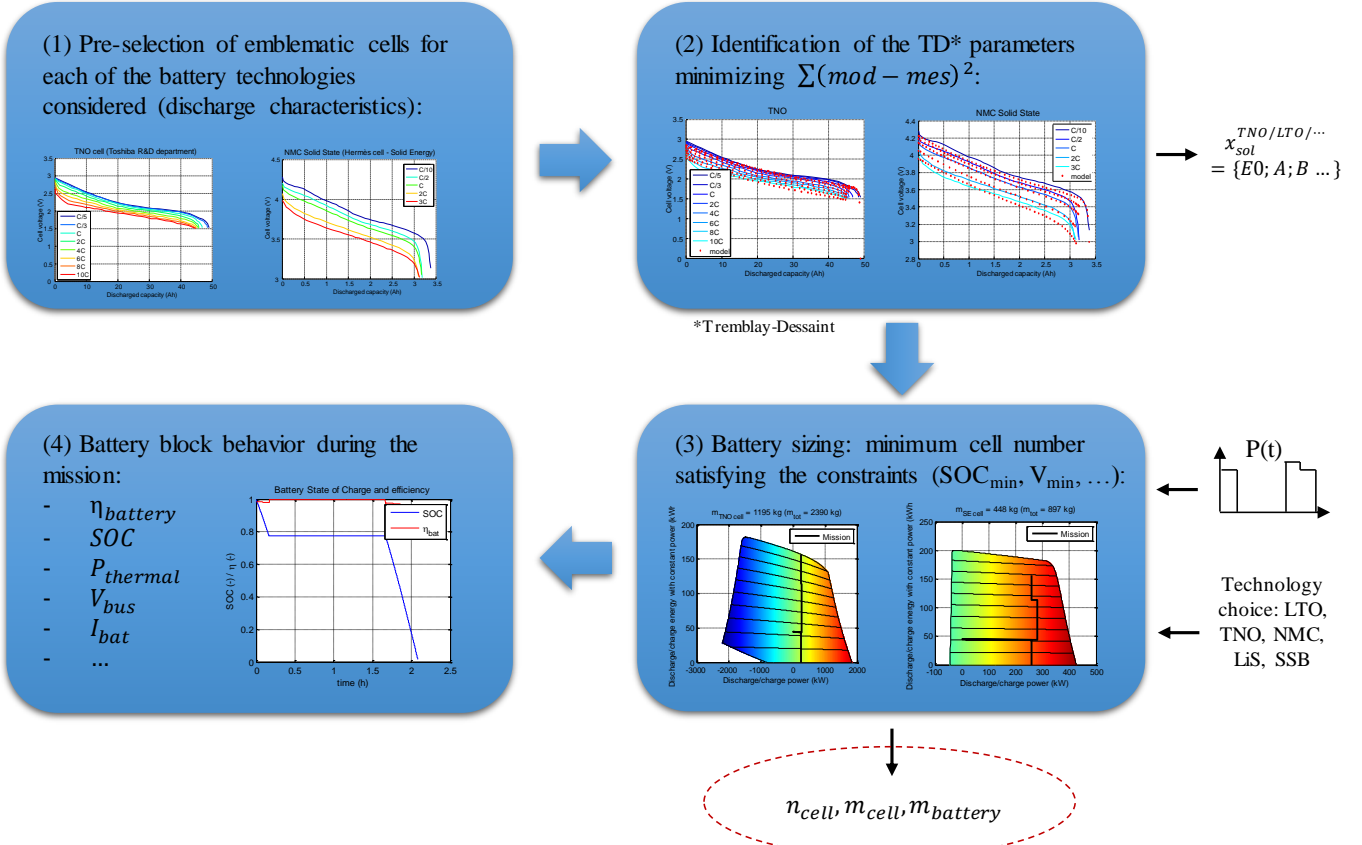


Figure 24 – Recapitulative sketch of the battery modeling and sizing strategies

3.3.2. Fuel Cell system modeling and potential trade-offs

As the state of the art highlights an advanced maturity for LT PEMFC systems as well as the best performances in terms of gravimetric and volumetric power densities, the modeling approach is focused on LT PEMFC systems. In the same vein, a LH₂ storage is considered here as the bibliographic review shows for these H₂ storages the best gravimetric efficiencies. For the FC block, a simplified structure is assumed with one/several FC stack(s), air compressor(s) for the air delivery, H₂ recirculator(s) and a cooling system. A cylindrical LH₂ tank is considered for the H₂ storage as first approximation. Numerous communications are today available on the Toyota Mirai FC car and especially on the FC stack and system. As the Toyota Mirai FC arrangement is today one of the most technologically advanced LT PEMFC embedded system ([YOS-15]), the modeling developments rely largely on information based on this system.

A simplified model of the FC stack mass and volume, depending on the cell number and on the stack surface area, is developed thanks to publications providing insights into the Toyota Mirai stack constitution ([JAM-12], [KOM-15], [BOR-18]). For the performance modeling of the FC stack, a quasi-static equation is employed and its parameters are identified thanks to a communication on the Mirai FC stack performances ([LOH-17]). Knowing the stack voltage, current and efficiency, the FC stack air input mass flow and the H₂ input mass flow can be deduced and used to evaluate the air compressor and the H₂ pump parasitic power consumptions, thanks to respectively a thermodynamic formula (assuming a constant compressor efficiency of 0.55) and an empirical law based on data from [LOH-17]. The FC stack and system efficiencies η_{FC}^{stack} and η_{FC}^{system} are at this step compared with experimental data ([LOH-17]) to validate the whole modeling framework in Figure 25 (the model – in blue – is projected further for higher power values):

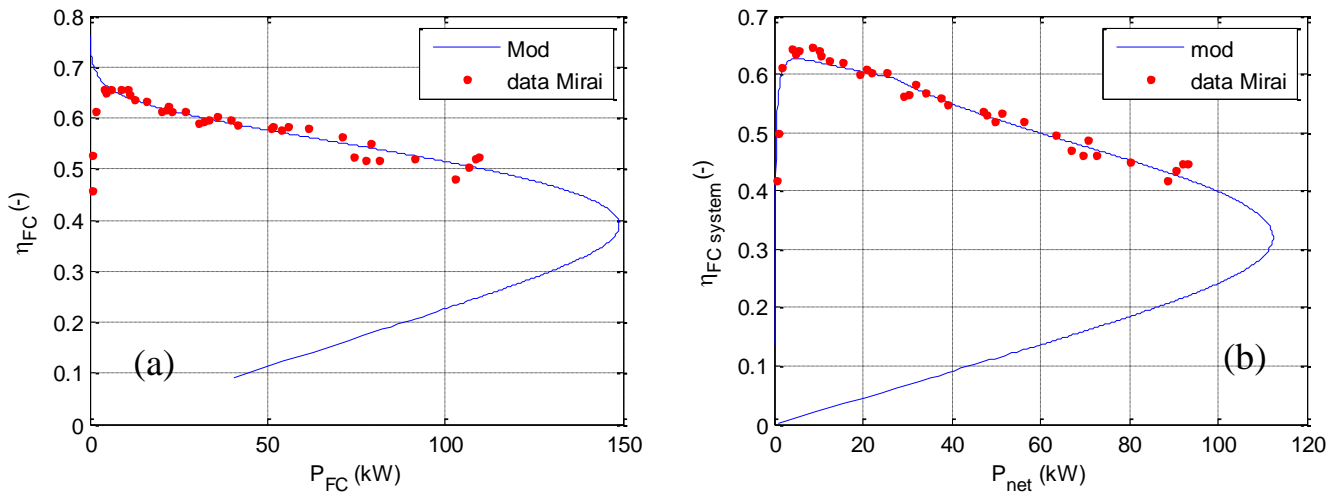


Figure 25 - η_{FC}^{stack} vs P_{FC} (a) and η_{FC}^{system} vs P_{net} (b) characteristics of the Mirai FC stack and system – Model (blue curves) vs experimental data (red points)

The cooling system mass is deduced from the FC stack efficiency (the heat release can be calculated) and an empirical coefficient of $\sim 1.3 \text{ kW}_{\text{thermal}}/\text{kg}$ (identified from Appendix D). For the LH₂ tank mass and volume model, a simplifying hypothesis is made assuming one

cylindrical geometrical design with a constant length to radius ratio (~ 2.35). Based on [MIC-06], a wall equivalent surface density is assessed, and a tank mass can be calculated knowing the H_2 density inside the tank (a bit lower than the theoretical 71 kg/m^3 , as a fraction of the stored H_2 is on gaseous state) and the embedded H_2 mass. Thanks to these modeling developments, a more accurate estimation of the FC system and H_2 storage masses can be made, and interesting couplings can appear inside the FC system between the FC stack size and other parameters, such as the auxiliary parasitic power consumption (hence the system global efficiency), the cooling system mass, the H_2 stored mass for instance. Indeed, when increasing the FC stack size, its efficiency increases, and spillovers effects can be visible on other parts of the system: as lower air and H_2 input flows are necessary, the parasitic consumption of the air compressor and the H_2 recirculation pump decrease and the FC system efficiency increase. Also, the cooling mass decreases as well as the H_2 storage mass when the FC stack efficiency increases. These coupling effects are highlighted in Figure 26, where for a same mission power profile (Mission (1)), several configurations are tested while varying the total number of cells (stack(s) size and number).

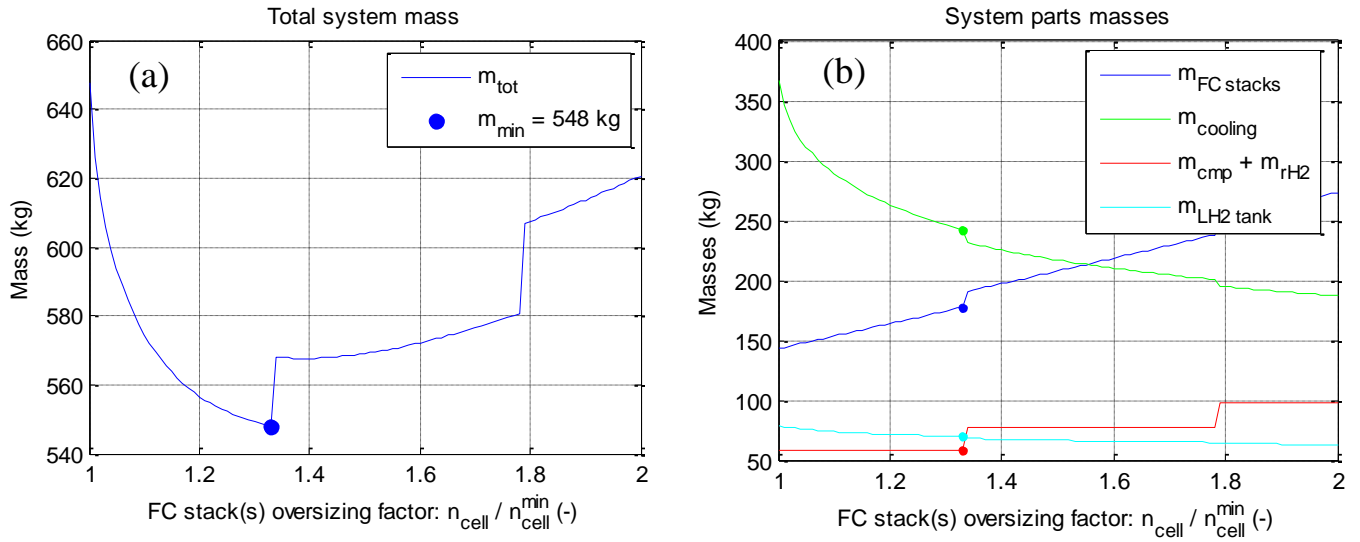


Figure 26 - Evolution of the FC total system mass (a) and of individual parts (b) with the FC stack size for Mission (1)

In this example, a limit is set on the maximal cell number allowed per stack (400 cells in these simulations). For this reason, discontinuities appear when looking to the evolution of the global system mass (and also the individual FC system parts) when one additional stack is added (mainly because of the ending plates weight impact). Interestingly, the system mass shows a non-monotonous variation with the stack oversizing factor (Figure 26 (a)), and reveal the existence of an optimum FC stack design point minimizing the overall system mass.

4. CONCLUSION – PERSPECTIVES

A state of the art of the current performances and future prospects of potential auxiliary sources for the hybrid propulsion has been done. A selection of Li-ion battery technologies, from high power type to very high energy type, as well as a selection of FC technologies has been considered and numerous publications have been scanned in order to assess typical performances values in terms of specific energies and powers. H₂ storages media have as well been investigated regarding their gravimetric efficiencies performances. The bibliographic review showed that reaching maximal values such as 650 Wh/kg_{cell} and 325 Wh/kg_{system} (LiS and/or SSB technologies) may be possible for 2035, but in return, aspects such as C_{rate} capabilities and cyclability will be difficult to improve and may constitute showstoppers for these applications. Although HT PEMFC and SOFC constitute very promising technologies for aviation applications (due to their high working temperature), their current level of maturity and progression margin remains cloudy for the next decades. On the contrary, LT PEMFC is today reaching a certain maturity thanks to the automotive industry and may reach at the system scale values up to 1 kW/kg_{system} in the next decades. On the H₂ storage side, Liquid H₂ storage tanks show the best gravimetric efficiencies and have already been deeply considered in numerous studies for potential aviation applications. Values up to 20 % wt. may be reachable (for H₂ quantities around 10 kg) in the next decades and could highly increase if the H₂ stored quantities increase as well ([VER-10] mention values up to 78 % wt. for H₂ quantities ~1000 kg).

Some masses evaluations have been done considering “light hybridization” scenarios for {FC + H₂ storage} and battery systems, showing the best results for an association between a LT PEMFC and a LH₂ storage. Other modeling developments and more refined masses estimations (visible on Figure 27), on the battery and on the FC sides, show higher values but the same tendencies: the lightest options seem to be the LT PEMFC options (especially with an LH₂ association).

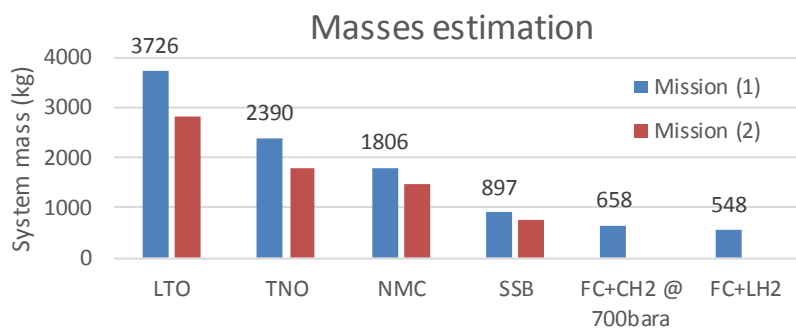


Figure 27 - Battery / FC systems masses estimation for Mission (1) and Mission (2)

Modeling developments have been proposed on the battery and FC sides and have highlighted interesting results regarding potential design trade-offs and sizing procedures.

5. APPENDIX

5.1. Appendix A

Hermes™

High Energy Rechargeable Metal Cells for Space

LMP063767



SolidEnergy Systems developed advanced high-energy lithium-metal rechargeable battery technology, which delivers best-in-class energy density characteristics and cycling performance. This product is ideally suited for applications requiring very high gravimetric and volumetric energy densities that have battery-weight and dimension constraints, such as aeronautics and space, consumer electronics, and EVs.

Electrical Characteristics

Nominal Voltage	3.8 V
Typical Capacity (C10, 25°C)	3.4 Ah
Nominal Energy	13 Wh

Mechanical Characteristics

Height	66 ± 1 mm
Width	37 ± 1 mm
Thickness	6.35± 0.3 mm
Typical Weight	29 g
Cell Volume	0.015 L

Operating Conditions

Charge Method	Constant Current / Constant Voltage
Charge Voltage	4.3 ± 0.05V
Maximum Recommended Charge Current	0.68 A (0.2 C Rate)
Charge Temperature Range	0°C to 45°C
Charge Time at 20°C	Function of the Charge Current C Rate → 1.5 – 2 Hr C/2 Rate → 2.5 – 3 Hr C/5 Rate → 6 – 7 Hr
Maximum Continuous Discharge Rate	6.8 A (2C Rate)
1kHz ACR, Ω (50%SOC, RT)	<18 mΩ
Pulse Discharge Rate	Up to 16 A (5C Rate)
Discharge Cut-off Voltage	3 V
Discharge Temperature Range	-20°C to 45°C

*Electric protection circuits within battery packs may limit the maximum charge/discharge current available. Contact SES.

Benefits

- World's lightest rechargeable battery
- Ultra-high volumetric energy Density of 1200 Wh/L
- Ultra-high gravimetric energy density of 450 Wh/kg
- High Voltage
- Flexible, customizable design
- Recommended for weight constraint applications

Key Features

- Excellent capacity retention and long cycle life
- High pulse charge rate
- High continuous discharge rate
- Great high-altitude performance
- Practical operating temperature range
- High cycling efficiency

Main Applications

- High-altitude drones
- Commercial drones
- Electric autonomous flying transportation
- Consumer electronics
- Power tools
- Small UPS
- Transportation

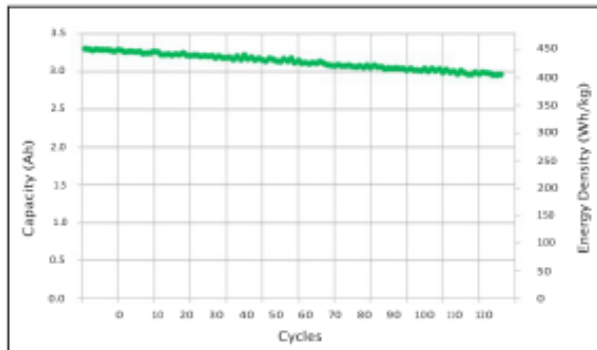
Hermes™

High Energy Rechargeable Metal Cells for Space

Performance Characteristics

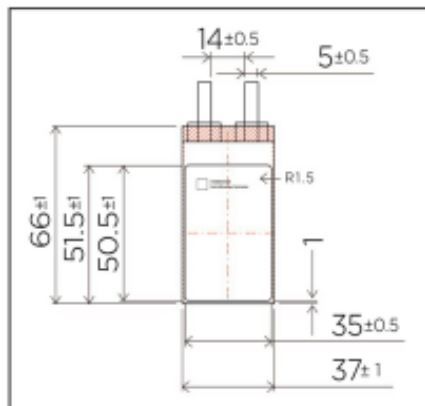
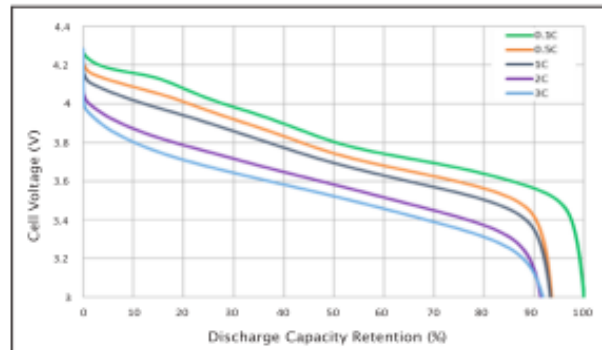
Cycle Life Characteristics

Charge: CC-CV 0.1C (std.) 4.3V, C/20A cut-off at 25°C
Discharge: CC 0.5C, 3V cut-off at 25°C



Discharge Rate Characteristics

Charge: CC-CV 0.1C(std.) 4.3V, C/20A cut-off at 25°C
Discharge: CC 0.1C/ 0.5C /1C/ 2C/ 3C, 3V cut-off at 25°C



Use dimensions for reference only.
For your cell/battery needs please contact SolidEnergy's application engineers.

Discharge Characteristics at 25°C	0.1 C	0.5 C	1.0 C	2.0 C	3.0 C
Capacity, Ah	3.4	3.2	3.2	3.1	3.1
Capacity Retention, %	100	93	93	91	92
Energy, Wh	13.0	12.0	11.8	11.2	11.0
Gravimetric Energy Density, Wh/kg	450	415	408	386	381
Volumetric Energy Density, Wh/L	1157	1068	1050	996	979

Technology

Ultra-thin lithium metal anode

Proprietary ultra-light anode current collector

High Ni content NMC cathode

Ceramic-filled separator

Solvent-in-salt electrolyte

Flexible, customizable design

Storage and Handling

- Store in a dry place at room temperature (preferably <30°C)
- Do not disassemble or incinerate
- Do not short terminals
- For long-term storage, keep the cell within a 30% state of charge

SolidEnergy Systems Corporation

Product Development & Marketing

35 Cabot Road

Woburn, MA 01801 - USA

Tel. +1 339-298-8304

Web: www.solidenergysystems.com

Data in this document are subject to change without notice and become contractual only after written confirmation by SolidEnergy Systems.



5.2. Appendix B



Ultra Light Lithium Sulfur Pouch Cell

Ultra Light



High gravimetric energy density, Rechargeable Li-S Pouch Cell

Key Features

- ◆ Extremely lightweight: >400 Wh/kg already proven
- ◆ Safe
- ◆ Full 100% Discharge Capability
- ◆ High Power type for Aviation and Automotive
- ◆ High Energy type for HAPS
- ◆ Bespoke cell sizes available

Ultra Light Cell Technology Specifications

Type	High Power	High Energy
Part Number	POA0343	POA0412
Availability	Evaluation Sample	
Operating Voltage (V)	1.9-2.6	
Nominal Voltage (V)	2.1	
Typical Capacity (Ah) 0.2C discharge at 20°C to 1.9V	19.5	14.7
Gravimetric Energy (Wh/kg)	300*	400**
Max. Peak Discharge (C) <30s, 50% SoC, 20°C	6	3
Max. Continuous Discharge (C)***	2	1
Max. Charge Rate (Hours)	4	
Cycle Life (Cycles) 100% DoD****, 80% BoL	80-100	60-100
Cycle Life (Cycles) 80% DoD, 60% BoL	~200	
Operating Temperature (°C)*****	0 to 30	
Storage Temperature (°C)	-30 to 30	
Pouch Format (mm) Length x width x thickness	151x118x10.5	145x78x10
Tab Dimensions (mm) Length x width x height	27x20x0.1	
Cell Weight (g)	137	85
Abuse Safety Testing	In-House to IEC62133 standard	

Notes:

* Figure obtained at 0.2C discharge at 30°C

** Figure obtained at 0.1C discharge at 20°C

*** Maximum discharge rates are expressed as a C-Rate, defined as a ratio of the maximum discharge power (W) to the typical cell capacity (Wh).

**** Depth of Discharge (DoD) is the percentage of the cell's rated capacity discharges relative to a fully charged condition.

***** The same range applies for both charge and discharge.

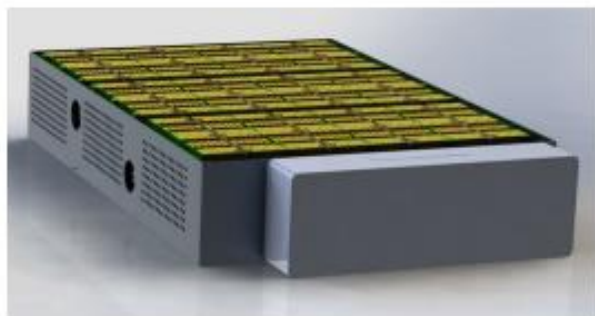
Notice to Readers:

OXIS Energy Ltd reserves the right to make changes to this document and without prior notice.

We do not support orders from consumers, please see our website for details about our cell production and battery design partners

V4.08 (Oct-18)

PRODUCT DATA SHEET
Rechargeable Lithium Sulfur Rack Mounted Battery



- State-of-the-art Lithium Sulfur technology
- 19" rack-mount battery with only a 3U profile
- Nominal 48V / 3 kWh Lithium Sulfur pack
- For Energy Storage and Vehicle applications
- Fully scalable to large MWh solutions
- Lightweight – only 25 kg
- Extremely safe - no acids or risk of fire
- Reduced environmental impact
- Advanced Battery Management System providing safe operation, control and status

Description:

The unit is based on OXIS Energy's unique Lithium Sulfur (Li-S) technology, offering a superior gravimetric energy density resulting in a very lightweight battery. Furthermore, compared to other lithium based chemistries, OXIS cells are very robust and safe when subject to abuse such as over-discharge, over-charge and high temperatures.

The active ingredients of the Li-S cells are sulfur - a recycled waste product from the oil industry - and lithium. Unlike lithium-ion our cells do not contain manganese, cobalt, lead or other harmful metals.

The battery is designed to easily install into 19" racking, allowing a scalable solution to both cabinet and large container size systems.

Communication ports are included, providing full diagnostics, status indication, health and usage monitoring. The on-board communication allow users access to various battery information including cell fault report, data logging, voltage, battery State of Charge (SoC) and historical data.

The advanced Battery Management System provides the measurement and safe control of cells, ensuring that they are closely matched and balanced during charging.

Parameter	Performance
Nominal Voltage	48 V
Rated Capacity	3000 Wh
Weight	25 kg
Max. Continuous Discharge	3000 W
Max Peak (30 sec) Discharge	9000 W
Dimensions	H = 130 mm W = 482 mm D= 650 mm
Charge Time	4 Hours
Cycle life (80% DoD, 60% BoL)	1,400
Operating Temperature range	0 to +60 °C
Communication Interface	CANbus, RS485, Ethernet
Approval	CE Designed to meet UN DoT38.3
Safety and Protection	The unit incorporates electronic protection, including: <ul style="list-style-type: none">• Over-charge protection• Over-discharge protection• External short circuit protection• Over temperature monitoring

oxiS ENERGY
Next Generation Battery Technology

5.3. Appendix C



Lithium Sulfur Rechargeable Battery Data Sheet

Lithium sulfur has the highest theoretical specific and volumetric energy densities of any rechargeable battery chemistry (2550 Wh/kg and 2862 Wh/l theoretically). SION Power has learned how to unlock this potential and has created a unique rechargeable battery system. This patented technology is enabling new applications for rechargeable batteries and replacing existing primary and rechargeable batteries in applications where weight is a critical factor.

Typical applications include:

- Unmanned Vehicle Systems
- Weight sensitive electronic applications
- Military communication systems
- Sensors

Electrical Specifications:

Nominal Voltage:	2.15V
Maximum Charge Voltage:	2.5V
Minimum Voltage on Discharge:	1.7V
Nominal Capacity @ 25°C:	2.5 Ah @ C/5
Maximum continuous discharge rate:	2C
Maximum charge rate:	C/5
Specific Energy:	350 Wh/kg
Energy Density:	320 Wh/l
Cell Impedance:	25 mΩ

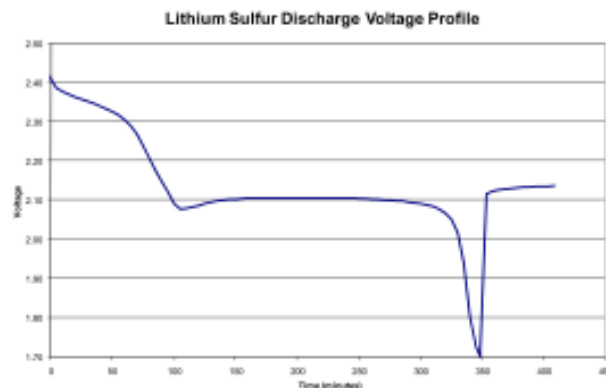


Mechanical Specifications:

Configuration:	Prismatic
Length:	55 mm (top flanged folded)
Width:	37 mm
Thickness:	11.5 mm
Weight:	~16 g

Environmental Specifications:

Discharge Temperature:	-20°C to +45°C
Charge Temperature:	-20°C to +45°C
Storage Temperature:	-40°C to +50°C



SION Power Inc., 2900E. Elvira Rd., Tucson, AZ 85756 Tel: +1.520.799.7500 Fax: 1.520.799.7501
www.sionpower.com

All specifications are subject to change without notice. The information contained here is for reference only and does not constitute a warranty of performance.

Date: 10/3/08 - Supersedes: 09/28/05

5.4. Appendix D



Data sheet

100kW EC Automotive Fuel Cell System

The Intelligent Energy 100kW fuel cell architecture has been developed in response to increasing market demand for next generation high power automotive fuel cell solutions.

The 100kW platform takes full advantage of Intelligent Energy's superior stack technology which offers world leadership in power density.

A history of 25 years in fuel cell technology development has produced compact and power-dense fuel cells which offer robust and cost-effective power systems for the automotive market.

Features:

- Patented EC fuel cell technology
- No cooling required – simplified balance of plant
- World-class stack power density
- Designed for ease of integration into automotive applications

Includes:

- Fuel cell stack featuring Intelligent Energy's proprietary EC technology
- Hydrogen regulation
- Air management system including compressor and controller
- Water management and recovery system
- Stack thermal management system
- Low voltage control module
- HV interface

100kW Fuel Cell Power Unit

Description	A hydrogen fuelled PEM fuel cell power unit, designed to automotive standards for both mobile and stationary applications, for example as an automotive FCEV power plant, or stationary DC generator.	
System architecture	Fuel cell system	Including fuel cell stack, fuel management, air management, water management, thermal management and control module
	Fuel cell stack	Intelligent Energy proprietary evaporatively-cooled fuel cell stack – demonstrated at 3.0kW/kg and 3.5kW/L
Electrical output	Rated continuous net power output	100kWe
	Maximum voltage	320 VDC
	Minimum voltage	180 VDC
Physical system	Mass	150kg ^[1]
	Maximum dimensions	400 (W) x 700 (D) x 600 (H) mm
Environment	Operating ambient temperature range	-20°C to 30°C nominal -40°C to 85°C derated
	Storage / shipment	-40°C to 85°C
Fuel	Type	Gaseous hydrogen ISO14687:2 Grade D
	Efficiency at rated power ^[2]	40% ^[2]
	Peak efficiency	55% ^[2]
	Fuel flow rate at rated power	7.5kg/h
	Hydrogen supply pressure	6 to 10BarG
Interfaces	Electrical	1 off high voltage power output with integral interlock 1 off low voltage interface (11 to 14V DC) bi-directional earthing point for chassis ground
	Control	CAN 2.0B bus

^[1] Complete system mass including condenser.

^[2] Efficiency of system at 25°C, 100kPa, including balance of plant and condenser.

© Intelligent Energy Limited 2015. All Rights Reserved. The Intelligent Energy name, logo, and other trade brands/names referenced herein are trademarks or registered trademarks of Intelligent Energy Ltd or its group companies.

Disclaimer: The information contained in this publication is intended only as a guide and is subject to change as a result of the constant evolution of the Intelligent Energy's business and its technology. This publication and its contents (i) are not definitive or contractually binding; (ii) do not include all details which may be relevant to particular circumstances; and (iii) should not be regarded as being a complete source of information. To the fullest extent permitted by law, Intelligent Energy offers no warranty as to the accuracy of the content of this publication, shall not be liable for the content of this publication and no element of this publication shall form the basis of any contractual relationship with a third party or be used by any third party as the basis for its decision to enter into a contractual relationship with Intelligent Energy. Published by: Intelligent Energy Ltd, Chamwood Building, Holywell Park, Ashley Road, Loughborough LE11 3GB (Registered in England with company number:03958217). Printed May 2015.

For more information please visit: www.intelligent-energy.com

6. BIBLIOGRAPHY

- [AMA-06] Amaseder, F., & Krainz, G. (2006). Liquid hydrogen storage systems developed and manufactured for the first time for customer cars (No. 2006-01-0432). SAE Technical Paper.
- [BAL-16] [Ballard FCveloCity® specifications \(2016\). \(\[http://www.ballard.com/docs/default-source/motive-modules-documents/fcvelocity_hd_family_of_products_low_res.pdf\]\(http://www.ballard.com/docs/default-source/motive-modules-documents/fcvelocity_hd_family_of_products_low_res.pdf\)\)](http://www.ballard.com/docs/default-source/motive-modules-documents/fcvelocity_hd_family_of_products_low_res.pdf)
- [BEN-15] Bensadoun, E. (2015). Hydrogen Storage on board aeronef and ground infrastructure. *Air Liquide Advanced Technologies - Workshop on aeronautical applications of fuel cell and hydrogen technologies*. Lampholdshausen, Germany.
- [BIR-10] Birke, P. (Continental). Electric Battery Actual and future Battery Technology Trends (2010).
- [BOR-18] Borup, Rodney L., et al. PEM Fuel Cell Catalyst Layer (MEA) Architectures. No. LA-UR-18-24447. Los Alamos National Lab.(LANL), Los Alamos, NM (United States), 2018.
- [BOW-06] Bowman Jr, R. C. (2006, May). Roles of hydrogen in space explorations. In AIP Conference Proceedings (Vol. 837, No. 1, pp. 175-199). AIP.
- [BOW-12] Bowman, B., & Klebanoff, L. (2012). Historical Perspectives on Hydrogen, Its Storage, and Its Applications. *Hydrogen Storage Technology: Materials and Applications*, 65.
- [BUS-16] [BusinessWire New. Solid hydrogen-on-demand fuel cell from HES energy systems flies ST Aerospace UAV for record 6 hours. February 2016. \(<http://www.businesswire.com/news/home/20160216006857/en/Solid-Hydrogen-on-Demand-Fuel-Cell-HES-Energy-Systems>\)](http://www.businesswire.com/news/home/20160216006857/en/Solid-Hydrogen-on-Demand-Fuel-Cell-HES-Energy-Systems)
- [DIC-18] Dicks, A., & Rand, D. A. J. (2018). Fuel cell systems explained. Chapter 11: Hydrogen Storage. New York: Wiley.
- [DOE-16] [Department of Energy \(2017\). Fuel Cell Technologies Office Multi-Year Research, Development, and Demonstration Plan. \(\[https://www.energy.gov/sites/prod/files/2017/05/f34/fcto_myrrd_fuel_cells.pdf\]\(https://www.energy.gov/sites/prod/files/2017/05/f34/fcto_myrrd_fuel_cells.pdf\)\)](https://www.energy.gov/sites/prod/files/2017/05/f34/fcto_myrrd_fuel_cells.pdf)
- [EEL-04] Eelman, S., y de Poza, I. D. P., & Krieg, T. (2004). fuel cell APU'S in commercial aircraft an assessment of SOFC and PEMFC concepts. In 24th international congress of the Aeronautical sciences, ICAS 2004.
- [ESA-18] ESA Roadmap of activities (2018). CNES, COMET, Batteries, constraints, challenges and perspectives, Toulouse.
- [FON-13] Da Fonseca, R. (2013). Optimization of the sizing and energy management strategy for a hybrid fuel cell vehicle including fuel cell dynamics and durability constraints. *These de doctorat de l'Institut National des Sciences Appliquées de Lyon*.

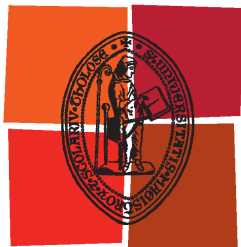
- [FOT-17] Fotouhi, A., Auger, D., O'Neill, L., Cleaver, T., & Walus, S. (2017). Lithium-sulfur battery technology readiness and applications—a review. *Energies*, 10(12), 1937.
- [FRA-18] Fraunhauser institute / Thales Arena (2018). Management of a Li-S battery for space applications. CNES, COMET, *Batteries, constraints, challenges and perspectives*, Toulouse.
- [FUS-15] Fusalba, F. (2015). Key Drivers for Aerospace Batteries: Today and Future Aircraft Electrically Powered. In *Proceedings of the EU-Japan Symposium “Electrical Technologies for the Aviation of the Future*.
- [HAG-06] Haglind, F., Hasselrot, A., & Singh, R. (2006). Potential of reducing the environmental impact of aviation by using hydrogen Part I: Background, prospects and challenges. *The Aeronautical Journal*, 110(1110), 533-540.
- [HAS-15] Hasegawa, T., Nissan research center, (2015). Airbus symposium: future perspectives on fuel cell technologies. *Europe-Japan Symposium Electrical Technologies for the Aviation of the Future*, Tokyo, March 2015.
- [HAS-16] Hasegawa, T., Imanishi, H., Nada, M., and Ikogi, Y., "Development of the Fuel Cell System in the Mirai FCV," SAE Technical Paper 2016-01-1185, 2016, doi:10.4271/2016-01-1185.
- [HEP-12] Hepperle, M. (2012). Electric flight-potential and limitations.
- [HEX-17] [Hydrogen storage and transportation systems. Hexagon Composite brochure \(2017\). \(<http://www.hexagonlincoln.com/resources/brochures>\)](http://www.hexagonlincoln.com/resources/brochures)
- [HOE-18] Hoelzen, J., Liu, Y., Bensmann, B., Winnefeld, C., Elham, A., Friedrichs, J., & Hanke-Rauschenbach, R. (2018). Conceptual design of operation strategies for hybrid electric aircraft. *Energies*, 11(1), 217.
- [Hy4] [Hy4 Fuel Cell aircraft website. \(<http://hy4.org/hy4-technology>\)](http://hy4.org/hy4-technology)
- [HYD-16] [Hydrogenics \(2016\). HyPM-HD POWER MODULES for light and heavy duty mobility, technical specifications. \(<https://www.hydrogenics.com/wp-content/uploads/HyPM-HD-Brochure.pdf>\)](https://www.hydrogenics.com/wp-content/uploads/HyPM-HD-Brochure.pdf)
- [IE-15] Intelligent Energy 100 kW EC Automotive Fuel Cell System datasheet (2015).
- [IE-18] [Intelligent Energy official website, Evaporatively Cooled technology page. \(<https://www.intelligent-energy.com/evaporatively-cooled-technology/>\)](https://www.intelligent-energy.com/evaporatively-cooled-technology/)
- [JAM-12] James, Brian D., and Andrew B. Spisak. "Mass production cost estimation of direct H₂ PEM fuel cell systems for transportation applications: 2012 update." report by Strategic Analysis, Inc., under Award Number DEEE0005236 for the US Department of Energy 18 (2012).
- [KAD-18] Kadyk, T., Winnefeld, C., Hanke-Rauschenbach, R., & Krewer, U. (2018). Analysis and Design of Fuel Cell Systems for Aviation. *Energies*, 11(2), 375.

- [KHA-13] Khandelwal, B., Karakurt, A., Sekaran, P. R., Sethi, V., & Singh, R. (2013). Hydrogen powered aircraft: the future of air transport. *Progress in Aerospace Sciences*, 60, 45-59.
- [KOJ-15] Kojima, K., & Fukazawa, K. (2015). Current status and future outlook of fuel cell vehicle development in TOYOTA. *ECS Transactions*, 69(17), 213-219.
- [KOK-15] [KOKAM Li-ion / Polymer cell brochure \(http://kokam.com/cell/\)](http://kokam.com/cell/)
- [KOK-17] [Kokam battery solution - Transportation application / Kokam modular pack - For High Energy E-mobility \(http://kokam.com/data/Kokam_EV_Pack_Brochure_V_1.6.pdf\)](http://kokam.com/data/Kokam_EV_Pack_Brochure_V_1.6.pdf)
- [KON-15] Konno, Norishige, Seiji Mizuno, and Hiroya Nakaji. "Development of compact and high-performance fuel cell stack." *SAE International Journal of Alternative Powertrains* 4.1 (2015): 123-129.
- [KUH-12] Kuhn, H., & Sizmann, A. (2012). *Fundamental prerequisites for electric flying*. Deutsche Gesellschaft für Luft-und Raumfahrt-Lilienthal-Oberth eV.
- [LEC-14(2)] <http://www.leclanche.com/technology-products/products/graphitenmc-racks/>
- [LEC-14] <http://www.leclanche.com/technology-products/leclanche-technology/lithium-ion-cells/>
- [LEC-15] Le Cras, F., Bloch, D. (2015). De Volta aux accumulateurs Li-ion - Développement des batteries au Lithium. *Techniques de l'ingénieur, Réf: BE8620*.
- [LOH-17] Lohse-Busch, H., Stutenberg, K., Duoba, M., & Iliev, S. (2018). *Technology Assessment Of A Fuel Cell Vehicle: 2017 Toyota Mirai* (No. ANL/ESD-18/12). Argonne National Lab.(ANL), Argonne, IL (United States).
- [MAK-17] Makridis, S. (2017). Hydrogen storage and compression. arXiv preprint arXiv:1702.06015.
- [MAT-09] Matsunaga, M., Fukushima, T., & Ojima, K. (2009). Powertrain system of Honda FCX Clarity fuel cell vehicle. *World Electric Vehicle Journal*, 3(4), 820-829.
- [MIC-06] Michel, F., Fieseler, H., & Allidieres, L. (2006, June). Liquid hydrogen technologies for mobile use. In Proceedings of WHEC (Vol. 16, pp. 13-16).
- [MIC-08] Michel, F. (2008). Cryogenic Reservoirs. In *Hydrogen Technology* (pp. 311-333). Springer, Berlin, Heidelberg.
- [MIS-18] Misra, A. (2018). Energy Storage for Electrified Aircraft: The Need for Better Batteries, Fuel Cells, and Supercapacitors. *IEEE Electrification Magazine*, 6(3), 54-61.
- [MUE-18] Mueller, J. K., Bensmann, A., Bensmann, B., Fischer, T., Kadyk, T., Narjes, G., ... & Hanke-Rauschenbach, R. (2018). Design considerations for the electrical power supply of future civil aircraft with active high-lift systems. *Energies*, 11(1), 179.

- [MUL-07] Müller, C., Fürst, S., & von Klitzing, W. (2007). Hydrogen Safety: New challenges based on BMW Hydrogen 7. In Proceedings.
- [NEO-17] Neophytides, S., Daletou, M. K., Athanasopoulos, N., Gourdoupi, N., De Castro, E., & Schautz, M. (2017). High Temperature PEM Fuel Cell Stacks with Advent TPS Meas. In E3S Web of Conferences (Vol. 16, p. 10002). EDP Sciences.
- [NOJ-09] Nojoumi, H., Dincer, I., & Naterer, G. F. (2009). Greenhouse gas emissions assessment of hydrogen and kerosene-fueled aircraft propulsion. *International journal of hydrogen energy*, 34(3), 1363-1369.
- [NON-17] Nonobe, Y. (2017). Development of the fuel cell vehicle mirai. *IEEJ Transactions on Electrical and Electronic Engineering*, 12(1), 5-9.
- [OXI-17] [Datasheet Ultra-light Lithium Sulfur pouch cell Oxis Energy \(available on: https://oxisenergy.com/products/\)](https://oxisenergy.com/products/)
- [PAN-18] [Panasonic UR18650ZTA cylindrical cell datasheet \(https://industrial.panasonic.com/ww/products/batteries/secondary-batteries/lithium-ion/cylindrical-type/UR18650ZTA\)](https://industrial.panasonic.com/ww/products/batteries/secondary-batteries/lithium-ion/cylindrical-type/UR18650ZTA)
- [PER-18] Perdu, F. (2018). OVERVIEW OF EXISTING AND INNOVATIVE BATTERIES, CEA Liten, *Science and energy scenarios*.
- [POG-18] Poggel, S., Aptsiauri, G., Flade, S., Schirmer, S. (2018). Electric powertrain technology for fixed-wing aircraft. *International Hydrogen and Fuel Cell Conference*, Trondheim.
- [POR-15] Pornet, C., & Isikveren, A. T. (2015). Conceptual design of hybrid-electric transport aircraft. *Progress in Aerospace Sciences*, 79, 114-135.
- [POW-16(1)] [PowerCell S3 stack \(2016\) datasheet. \(https://www.powercell.se/wordpress/wp-content/uploads/2018/12/powercell-s3-datasheet-pdf-190129.pdf\)](https://www.powercell.se/wordpress/wp-content/uploads/2018/12/powercell-s3-datasheet-pdf-190129.pdf)
- [POW-16(2)] [PowerCell MS 100 FC System \(2016\). \(https://www.powercell.se/wordpress/wp-content/uploads/2018/12/powercell-ms100-datasheet-pdf.pdf\)](https://www.powercell.se/wordpress/wp-content/uploads/2018/12/powercell-ms100-datasheet-pdf.pdf)
- [RAJ-08] Rajashekara, K., Grieve, J., & Daggett, D. (2008). Hybrid fuel cell power in aircraft. *IEEE Industry Applications Magazine*, 14(4), 54-60.
- [REN-16] Renau, J., Barroso, J., Lozano, A., Nueno, A., Sánchez, F., Martín, J., & Barreras, F. (2016). Design and manufacture of a high-temperature PEMFC and its cooling system to power a lightweight UAV for a high altitude mission. *International Journal of Hydrogen Energy*, 41(43), 19702-19712.
- [ROS-17] Rosli, R. E., Sulong, A. B., Daud, W. R. W., Zulkifley, M. A., Husaini, T., Rosli, M. I., ... & Haque, M. A. (2017). A review of high-temperature proton exchange membrane fuel cell (HT-PEMFC) system. *International Journal of Hydrogen Energy*, 42(14), 9293-9314.
- [ROT-10] Roth, B., & Giffin, R. (2010, July). Fuel cell hybrid propulsion challenges and opportunities for commercial aviation. In 46th AIAA/ASME/SAE/ASEE Joint Propulsion Conference & Exhibit (p. 6537).

- [SAD-17] Sadaghiani, M. S., & Mehrpooya, M. (2017). Introducing and energy analysis of a novel cryogenic hydrogen liquefaction process configuration. International Journal of Hydrogen Energy, 42(9), 6033-6050.
- [SE-18(2)] [Solid Energy - Li-metal/NMC cell datasheet \(Hermès\) / \(<http://www.solidenergysystems.com/hermes/>\)](http://www.solidenergysystems.com/hermes/)
- [SE-18] [Solid Energy - how solid Energy is transforming the future of transportation and connectivity \(<http://www.solidenergysystems.com/athena/>\)](http://www.solidenergysystems.com/athena/)
- [SHA-15] Sharifzadeh, S., Verstraete, D., & Hendrick, P. (2015). Cryogenic hydrogen fuel tanks for large hypersonic cruise vehicles. International Journal of Hydrogen Energy, 40(37), 12798-12810.
- [SIN-17] Sinigaglia, T., Lewiski, F., Martins, M. E. S., & Siluk, J. C. M. (2017). Production, storage, fuel stations of hydrogen and its utilization in automotive applications-a review. International journal of hydrogen energy, 42(39), 24597-24611.
- [SIO-08] Datasheet SionPower prismatic Lithium Sulfur cell
- [SIO-18] <https://sionpower.com/products/>
- [STR-14] Stroman, R. O., Schuette, M. W., Swider-Lyons, K., Rodgers, J. A., & Edwards, D. J. (2014). Liquid hydrogen fuel system design and demonstration in a small long endurance air vehicle. international journal of hydrogen energy, 39(21), 11279-11290.
- [STU-12] Stückl, S., van Toor, J., & Lobentanzer, H. (2012, September). VOLTAIR—the all electric propulsion concept platform—a vision for atmospheric friendly flight. In *28th International Congress of the Aeronautical Sciences (ICAS)*.
- [TAK-18] Takami, N., Ise, K., Harada, Y., Iwasaki, T., Kishi, T., & Hoshina, K. (2018). High-energy, fast-charging, long-life lithium-ion batteries using TiNb₂O₇ anodes for automotive applications. *Journal of Power Sources*, 396, 429-436.
- [TAR-16] Tariq, M., Maswood, A. I., Gajanayake, C. J., & Gupta, A. K. (2016). Aircraft batteries: current trend towards more electric aircraft. *IET Electrical Systems in Transportation*, 7(2), 93-103.
- [TOS-17] [Toshiba rechargeable battery SCiB™ - datasheet cells and module \(<https://www.scib.jp/en/product/index.htm>\)](https://www.scib.jp/en/product/index.htm)
- [TRE-09] Tremblay, O., & Dessaint, L. A. (2009). Experimental validation of a battery dynamic model for EV applications. *World electric vehicle journal*, 3(2), 289-298.
- [VER-10] Verstraete, D., Hendrick, P., Pilidis, P., & Ramsden, K. (2010). Hydrogen fuel tanks for subsonic transport aircraft. *International journal of hydrogen energy*, 35(20), 11085-11098.
- [WES-03] Westenberger, A. (2003). Liquid hydrogen fuelled aircraft-system analysis. *CRYOPLANE, The European Commission, Brussels, Belgium, Report No. GRD1-1999-10014*.

- [WIN-18] Winnefeld, C., Kadyk, T., Bensmann, B., Krewer, U., & Hanke-Rauschenbach, R. (2018). Modelling and designing cryogenic hydrogen tanks for future aircraft applications. *Energies*, 11(1), 105.
- [YOS-15] Yoshida, T., & Kojima, K. (2015). Toyota MIRAI fuel cell vehicle and progress toward a future hydrogen society. *The Electrochemical Society Interface*, 24(2), 45-49.
- [YOU-04] Young, R. C., Chao, B., Li, Y., Myasnikov, V., Huang, B., & Ovshinsky, S. R. (2004). A hydrogen ICE vehicle powered by Ovonic metal hydride storage. SAE transactions, 348-358.



Université
de Toulouse

THÈSE

En vue de l'obtention du

DOCTORAT DE L'UNIVERSITÉ DE TOULOUSE

Délivré par :

Institut National Polytechnique de Toulouse (Toulouse INP)

Discipline ou spécialité :

Génie Electrique

Présentée et soutenue par :

M. MATTHIEU PETTES-DULER

le vendredi 23 avril 2021

Titre :

Conception intégrée optimale du système propulsif d'un avion régional
hybride électrique

Ecole doctorale :

Génie Electrique, Electronique, Télécommunications (GEETS)

Unité de recherche :

Laboratoire Plasma et Conversion d'Energie (LAPLACE)

Directeur(s) de Thèse :

M. XAVIER ROBOAM

M. BRUNO SARENI

Rapporteurs :

M. FREDERIC GILLON, ECOLE CENTRALE DE LILLE

M. SALVY BOURGUET, UNIVERSITE DE NANTES

Membre(s) du jury :

MME DELPHINE RIU, INP DE GRENOBLE, Président

M. BRUNO SARENI, TOULOUSE INP, Membre

M. JEAN-FRANCOIS ALLIAS, AIRBUS FRANCE, Invité(e)

M. JEAN-FRANCOIS LLIBRE, TOULOUSE INP, Invité(e)

M. MARC BUDINGER, INSA TOULOUSE, Membre

M. XAVIER ROBOAM, TOULOUSE INP, Membre

RÉSUMÉ

En 2019, le transport était le secteur qui connaissait la croissance la plus rapide au niveau mondial, contribuant du même coup à la dégradation de l'environnement. Trouver des solutions durables moins polluantes est un élément clé pour résoudre ce problème, en particulier pour le secteur aéronautique, qui représente environ 2 % des émissions mondiales de CO₂. Avec l'apparition de la Covid-19, le trafic aérien semble assez durablement interrompu, mais cette pandémie renforce la nécessité d'aller vers « un ciel plus propre » et respectueux de l'environnement, ce qui constitue l'objectif du programme Clean Sky2 (H2020 EU), contexte dans lequel le projet "HASTECS" et notre thèse se situent.

L'objectif principal d'HASTECS (Hybrid Aircraft Academic reSearch on Thermal and Electrical Components and Systems) est de coupler études thermiques et électriques au sein de la chaîne de propulsion hybrides électrique d'un avion régional, ceci en intégrant les contraintes d'environnement (en particulier les décharges partielles) spécifiques au secteur aérien. Le but est d'identifier les technologies et ruptures les plus prometteuses et de mettre au point les outils qui permettront d'accroître de manière significative la compacité et l'efficacité des processus électriques au sein de la chaîne de propulsion hybride. Dans notre cas, seule l'architecture électrique hybride série a été étudiée dans ce projet, car elle conduit à une grande puissance de dimensionnement maximisant les contraintes technologiques sur la chaîne.

Les cibles technologiques fixées dans HASTECS, considérées sous deux horizons (2025 puis 2035), sont les suivantes :

	Cible 2025	Cible 2035
Moteur électrique + refroidissement		
Densité de Puissance	5 kW/kg	10 kW/kg
Rendement en phase de croisière	96%	98.5%
Rendement au point nominal	94.5%	97%
Électronique de puissance + refroidissement		
Densité de puissance	15 kW/kg	25 kW/kg
Rendement en croisière	98%	99.5%
Rendement au point nominal	96.5%	99%

Dans le cadre de ce projet, notre thèse vise la conception par optimisation de la chaîne de propulsion complète intégrant en particulier les modèles issus des développements technologiques des constituants majeurs (électroniques de puissance, câblage et architecture de distribution, actionnement) tout en considérant, à partir d'une gestion d'énergie simplifiée, l'hybridation d'une source principale (thermique) et auxiliaire (électrique).

Un premier objectif de notre thèse a concerné le développement d'un modèle d'environnement. Ces conditions étant fixées, l'intégration système consiste à bâtir une suite de modèles réduits dont la granularité permet l'évaluation globale (systémique) des rendements énergétiques et des masses de chaque composant jusqu'à la chaîne de propulsion

complète. Le système propulsif est conçu, via un processus itératif estimant, selon les choix de conception, les variations de masses et leurs conséquences sur la poussée : cette approche de conception intégrée permet entre autre d'évaluer les effets boules de neige dont l'influence est majeure en aéronautique. En effet, l'ajout de masse sur un dispositif entraîne des conséquences sur la structure et le carburant embarqué.

Après un état de l'art situant le contexte de l'étude, nous proposons une suite de « modèles réduits » intégrables au sein d'un processus d'optimisation de la chaîne complète (avec un temps de calcul raisonnable) : ces modèles sont issus :

- D'études antérieures : turbines à gaz, sources électriques auxiliaires (batteries, piles à combustible), réducteur de vitesse, hélice ;
- Ou d'une adaptation (réduction) des modèles technologiques issus des work packages d'HASTECS : électroniques de puissance et leur refroidissement, moteurs électriques et leur refroidissement, contraintes de décharges partielles.

Avant de progresser vers l'intégration système et l'optimisation du dimensionnement, un chapitre est consacré à l'analyse de sensibilité dont l'objectif est de préciser les degrés de liberté (variables de décision) les plus sensibles vis-à-vis des principaux objectifs (réduction de masse et des pertes) de la conception. Des techniques d'analyse de sensibilité basées sur les indices de Sobol sont en particulier exploitées.

Enfin, la dernière partie et l'objectif final de ce projet concerne la conception optimale de la chaîne complète intégrant une gestion d'énergie propre à l'architecture hybride électrique. Cette étude démarre par des études locales sur les constituants majeurs (chaîne d'actionnement) pour progresser vers l'intégration système et la chaîne complète. De nombreux résultats mettent en évidence l'émergence de couplages systèmes qui n'apparaissent pas dans l'assemblage d'optima locaux.

ABSTRACT

In 2019, transportation was the fastest growing sector, contributing to environmental degradation. Finding sustainable solutions that pollute less is a key element in solving this problem, particularly for the aviation sector, which accounts for around 2% of global CO₂ emissions. With the advent of Covid-19, air traffic seems to have come to a fairly permanent halt, but this pandemic reinforces the need to move towards a "cleaner sky" and respect for the environment, which is the objective of the Clean Sky2 program (H2020 EU), the context in which the HASTECS project and our thesis are set.

The main objective of HASTECS (Hybrid Aircraft Academic reSearch on Thermal and Electrical Components and Systems) is to couple thermal and electrical studies within the hybrid electric propulsion chain of a regional aircraft, by integrating the environmental constraints (in particular partial discharges) specific to the aviation sector. The aim is to identify the most promising technologies and breakthroughs and to develop the tools that will significantly increase the compactness and efficiency of the electrical processes within the hybrid propulsion chain. In our case, only series hybrid electric architecture was studied in this project, as it leads to a high dimensioning power maximizing the technological constraints on the chain.

The technological targets set in HASTECS, considered under two horizons (2025 then 2035), are the following:

	2025 target	2035 target
Electric motor + cooling system		
Specific power	5 kW/kg	10 kW/kg
Cruise efficiency	96%	98.5%
Maximal design point efficiency	94.5%	97%
Power electronics + cooling system		
Specific power	15 kW/kg	25 kW/kg
Cruise efficiency	98%	99.5%
Maximal design point efficiency	96.5%	99%

In the framework of this project, our thesis aims at the design by optimization of the complete propulsion chain integrating in particular the models resulting from the technological developments of the major components (power electronics, wiring and distribution architecture, actuation) while considering, from a simplified energy management, the hybridization of a main (thermal) and auxiliary (electrical) source.

A first objective of our thesis concerned the development of an environment model. Once these conditions are set, the system integration consists in building a suite of scale models whose granularity allows the global (systemic) evaluation of the energy yields and masses of each component up to the complete propulsion chain. The propulsion system is designed via an iterative process estimating, according to the design choices, the mass

variations and their consequences on thrust: this integrated design approach allows, among other things, to evaluate the snowball effects, which have a major influence in aeronautics. Indeed, the addition of mass on a device has consequences on both the structure and onboard fuel.

After a state of the art and context study, we propose a series of "scale models" that can be integrated into an optimization process of the complete chain (with a reasonable computing time). These models are derived from:

- Previous studies: gas turbines, auxiliary electrical sources (batteries, fuel cells), speed reducer, propeller;
- Or from an adaptation (reduction) of technological models from HASTECS work packages: power electronics and their cooling, electric motors and their cooling, partial discharge constraints.

Before moving on to system integration and design optimization, a chapter is devoted to sensitivity analysis, the objective of which is to specify the most sensitive degrees of freedom (decision variables) with respect to the main objectives (mass and loss reduction) of the design. Sensitivity analysis techniques based on Sobol indices are used in particular.

Finally, the last part and the final objective of this project concerns the optimal design of the complete chain integrating clean energy management in hybrid electric architecture. This study starts with local studies on the major components (drive chain) in order to progress towards system integration and the complete chain. Many results highlight the emergence of system couplings that do not appear in the assembly of local optima.

REMERCIEMENTS

Les travaux de recherche présentés dans ce mémoire ont été effectués à l’Institut National Polytechnique de Toulouse, dans le laboratoire Plasma et Conversion d’Energie LAPLACE, au sein du Groupe de Recherche en Energie Electrique et Systémique.

Je souhaite dans un premier temps remercier les membres du jury. Madame Delphine Riu, pour le grand plaisir qu’elle m’a fait en présidant ce jury. Monsieur Salvy Bourguet et monsieur Frédéric Gillon, pour le temps et l’attention qu’ils ont accordés à la relecture de mon manuscrit, ainsi que pour leurs remarques pertinentes sur mon travail en qualité de rapporteur. Merci à Jean-François Libre d’avoir suivi mes travaux de thèse. Enfin, merci à AIRBUS et particulièrement Jean-François Allias pour s’être intéressé à mes travaux et m’avoir fait confiance.

J’adresse de chaleureux remerciement à mes directeurs de thèse, Xavier Roboam et Bruno Sareni. Merci à vous de m’avoir fait confiance dès mon projet de fin d’étude, cela m’a permis d’aborder plus sereinement le sujet de thèse. Je vous remercie également pour vos conseils avisés, nos interactions ont été riches et j’ai beaucoup appris à vos côtés. Je n’étais pas le « premier de la classe » mais l’encadrement a été bienveillant et ma motivation sans faille. Merci également pour vos qualités humaines qui ont veillé au bon déroulement de ce projet de recherche. J’espère enfin pouvoir fêter tout cela autour d’un bon petit repas avec vous.

Je tiens également à remercier tous les collègues du projet HASTECS, mes travaux sont également les vôtres, de beaux résultats découlent de cette thèse et c’est grâce à vous : Flavio, Najoua, Philippe, Sarah, Amal, Maillys et Malik.

Un grand merci aux personnes qui constituent le LAPLACE, au-delà d’un laboratoire à la pointe, cette « famille » est bienveillante et assure la bonne ambiance dans les bureaux. Merci à vous tous pour m’avoir mis la pression dans certains moments, accompagné dans les démarches, ou encore fait rire.

Un immense merci à toutes les « forces contractuelles de recherche » du LAPLACE. Tout d’abord merci à Jérôme, de m’avoir permis d’utiliser tes modèles ; Jo, Théo et Robin pour les parties de baby-foot sans fin, et autres activités ludiques. Merci à Sami, Abdelkader et Khaled pour votre accueil dans votre bureau. Merci à Yazan, Plinio, Andrea, Quentin, Hugo, Davin et les autres pour tous ces bons moments passés en votre compagnie. Je suis heureux d’avoir fait votre connaissance.

Enfin mes remerciements, s’adressent à ma famille qui a toujours été là pour moi. Je remercie mes parents, David et Cathy, pour leur soutien pendant toute la durée de mes études, je ne pensais pas aller jusque là ! Merci à ma sœur, Aurélie, de m’avoir supporté et encouragé pendant ces années.

Je finirai par remercier ma compagne, Elise. Je remercie le destin d’avoir croisé ton chemin ; tu as su m’écouter et me faire confiance, je t’en suis reconnaissant. Je suis heureux d’être à tes côtés pour commencer cette nouvelle vie qui nous attend.

ACKNOWLEDGMENTS



This project has received funding from the [European Union's Horizon 2020 (cleansky 2 JTI) research and innovation program, 2014-2024] under grant agreement No 715483.

TABLE OF CONTENTS

INTRODUCTION	1
CHAPTER I. The electric revolution impacts aviation.....	5
<i>I.1 Why are (hybrid-)electric aircrafts headed for a takeoff?</i>	6
I.1.1 An air traffic growth that was not ready to stabilize before COVID-19.	6
I.1.2 Flygskam or flight shame.....	8
I.1.3 Towards a new revolution in the aviation industry?	8
I.1.4 Enemy number one in aeronautics: weight!	10
<i>I.2 Potential hybridization gains of the hybrid-electric aircraft propulsive system.....</i>	13
I.2.1 A complicated hybridization of the propulsive system.....	13
I.2.2 Turboshaft design gains (performance and fuel burn).....	17
I.2.2.1 Optimal design of gas turbines.	17
I.2.2.2 Intelligent use of gas turbines.	17
I.2.3 Aerodynamic gains.	18
I.2.3.1 The distributed propulsion (blown wing).	18
I.2.3.2 The Boundary Layer Ingestion propulsion (BLI).	20
I.2.4 Energy gains: how to operate high electric efficiency in a hybrid-electric propulsion?.....	22
I.2.4.1 Parallel hybrid electric propulsive system (PH).	23
I.2.4.2 Propulsion Series/Parallel Partial Hybrid (SPPH).	25
I.2.4.3 Partial Turbo electric propulsive system (PT).	26
I.2.4.4 Turbo Electric propulsive system (TE).....	27
I.2.4.5 Series Hybrid propulsive system (SH).	27
I.2.4.6 All-electric propulsion (AE).	30
I.2.5 Towards greener aircrafts: hydrogen power, a huge challenge that seems reachable	32
<i>I.3 Presentation of the HASTECS Project and thesis objectives.</i>	41
I.3.1 Input data.....	42
I.3.2 Project description	45
I.3.3 A major “snowball effect” involving an integrated looped process	47
I.3.4 About sensitivity of technologies on both max take off weight and fuel burn.	48
I.3.5 Thesis objectives.	52
CHAPTER II. Modeling for multidisciplinary design optimization of the overall propulsion system.....	55
<i>II.1 Reference models out of the HASTECS scope.....</i>	57
II.1.1 Propeller model.....	57
II.1.2 Gearbox model.....	59
II.1.3 Turboshaft model.	60
II.1.4 Cable model.	60
<i>II.2 “HASTECS” MODELS.....</i>	61
II.2.1 Electric motor design model.	61
II.2.1.1 Presentation of the electromechanical analytic model, modeling process and results.	61
II.2.1.2 Adaptation of the PMSM analytical model for system optimization.....	63
II.2.2 Electric machine cooling system.	71
II.2.2.1 Presentation of the e-motor cooling research team model.	71
II.2.3 Modeling of partial discharges.	73
II.2.3.1 Presentation of the partial discharges model.....	73
II.2.3.2 Adaptation for system optimization.	75

II.2.4	Power Electronics design model.	76
II.2.4.1	Presentation of the power electronics model and results.	76
II.2.4.2	Adaptation for system optimization.	77
II.2.5	Power converter cooling system.	81
II.2.5.1	Presentation of the power electronics cooling model.	81
II.2.5.2	Adaptation for system optimization.	82
II.2.6	Fuel cell and battery model.	83
CHAPTER III.	Sensitivity analysis on the hybrid-electric aircraft.	87
III.1	<i>New technologies that broaden the scope of possibilities.</i>	88
III.1.1	Reference aircraft.	88
III.1.2	Preliminary target results (2025 – 2035)....	88
III.1.2.1	TEA (TurboElectric aircraft).	89
III.1.2.2	HEA (Hybrid-electric aircraft).	89
III.1.2.3	Global sensitivity analysis of target assessments on global weight and fuel burn.	92
III.2	<i>Sobol indices-based sensitivity analysis.</i>	93
III.2.1	An overview of Sobol indices.	94
III.2.2	Calculation process of the Sobol indices.	95
III.2.3	Whole sensitivity analysis based on specific power assessments.	96
III.3	<i>Sobol indices based sensitivity analysis at component level.</i>	98
III.3.1	Analysis of 1st order Sobol indices on the design-oriented electric motor model.	100
III.3.2	Revisited sensitivity analysis with total indices and refined bounds (e-motor level).	101
III.3.3	Sensitivity analysis of the electromechanical powertrain (propeller, gearbox, electric-motor).	103
III.3.3.1	Sensitivity analysis without feasability constraint fulfilment.	105
III.3.3.2	Sensitivity analysis with feasability constraint fulfilment.	108
III.4	<i>Conclusion.</i>	111
CHAPTER IV.	Multi-disciplinary design optimization of the hybrid-aircraft powertrain.....	113
IV.1	<i>Optimal design of the electric motor weight.</i>	114
IV.1.1	The cooling system: the main challenge.	114
IV.1.2	Electric motor optimization results.	115
IV.1.2.1	Electric motor optimization with the steady state thermal model.	117
IV.1.2.2	Electric motor optimization with the transient state thermal model.	119
IV.1.2.3	Comparison of motor optimization between steady state and transient state thermal models with reference to the electric motor sized by the WP1.	121
IV.2	<i>Hybrid-electric aircraft design with a “light hybridization scenario”.</i>	128
IV.2.1	Optimization of aircraft fuel burn with a “light hybridization scenario”.....	130
IV.2.2	Adaptation of sizing models to formulate a system optimization problem.....	131
IV.2.3	Optimization results and analysis.....	133
IV.3	<i>Integrated design of a hybrid-electric aircraft coupled with its energy management system.....</i>	138
IV.4	<i>Exploration of the performance of a hybrid-electric aircraft taking account of technological advances in electrical components (target 2035).</i>	147
IV.4.1	Optimization of the eMotor weight (2025 vs 2035 assessments).....	147
IV.4.2	System optimization including energy management strategies	150
IV.5	<i>Conclusion.</i>	158
CONCLUSION	161

REFERENCES	167
APPENDIX.....	177
APPENDIX A. ENVIRONMENT MODEL.....	179
APPENDIX B. PROPELLER MODEL.....	181
<i>B.1 Sizing model:</i>	182
<i>B.2 Disk Actuator Theory:</i>	182
<i>B.3 Saturation function:</i>	183
<i>B.4 Constraint:</i>	184
APPENDIX C. GEARBOX MODEL.....	185
<i>C.1 Sizing model:</i>	186
<i>C.2 Performance model:</i>	187
APPENDIX D. TURBOSHAFT MODEL	189
<i>D.1 PSLS computation:</i>	190
<i>D.2 Fuel estimation:</i>	191
<i>D.3 Sizing model:</i>	192
<i>D.4 Power constraint:</i>	192
APPENDIX E. CABLE MODEL	193
APPENDIX F. ELECTRIC MOTOR MODEL	195
<i>F.1 Sizing model.</i>	196
F.1.1 1rst harmonic air gap flux density	196
F.1.2 Electric motor geometry.	196
F.1.3 Centrifugal pressure and peripheral speed.....	198
F.1.4 Electric motor winding configuration.....	198
F.1.5 Electric parameters.	198
<i>F.2 Sizing constraints.</i>	199
<i>F.3 Performance model.</i>	200
F.3.1 Field weakening control	200
F.3.2 Losses model	203
<i>F.4 Performance constraints.....</i>	204

APPENDIX G. ELECTRIC MOTOR COOLING MODEL 205

<i>G.1 Sizing model.</i>	206
G.1.1 Winding channel model for internal cooling (2035 target).	206
G.1.2 Water Jacket and shaft cooling design (2025 and 2035).	207
G.1.3 Fluid convection coefficients computation.	208
G.1.4 Computation of air convection coefficients.	209
G.1.4.1 Air gap.	209
G.1.4.2 End-space frame.	209
G.1.4.3 End-space rotor.	210
G.1.4.4 End-space windings.	210
<i>G.2 Lumped parameter thermal model.</i>	213
Thermal conductance matrix G.	213
<i>G.3 Constraints.</i>	214

APPENDIX H. PARTIAL DISCHARGES IN THE SLOT..... 215

<i>H.1 Calibration model.</i>	216
<i>H.2 Slot component definition model.</i>	217
H.2.1 Wire definition model.	217
H.2.2 Liner definition model.	219
<i>H.3 Winding layout model.</i>	219
<i>H.4 Constraints.</i>	221

APPENDIX I. POWER ELECTRONICS AND ITS COOLING 223

<i>I.1 Power Electronics model.</i>	224
I.1.1 Semiconductor sizing model.	224
I.1.2 Capacitor sizing model.	225
I.1.3 Loss model.	226
I.1.4 Mass and efficiency.	226
<i>I.2 Cooling model.</i>	227

APPENDIX J. FUEL CELL SYSTEM AND BATTERY MODEL..... 231

<i>J.1 Fuel cell model.</i>	232
<i>J.2 Battery model.</i>	233
<i>J.3 Auxiliary electrical power source choice.</i>	233

APPENDIX K. RECTIFIER AND GENERATOR EFFICIENCY AND WEIGHT ASSESSMENTS 235

<i>K.1 Sizing model.</i>	236
--------------------------------	-----

APPENDIX L. MULTIDISCIPLINARY DESIGN OPTIMIZATION PROCESS OF A HYBRID ELECTRIC AIRCRAFT PROPULSION SYSTEM 237

LIST OF FIGURES

Fig. I-1: Air traffic evolution since 1977 and estimate to 2037 (Source AIRBUS GMF 2019 [5]).	6
Fig. I-2: Schematic CO ₂ emissions reduction roadmap (Source IATA [8]).	7
Fig. I-3: CO ₂ emissions evolution in % from 1940 to 2015 (Source Roland Berger[9]).	8
Fig. I-4: Electric propulsion is finally on the map (or hybrid-electric aviation) (Source Roland Berger [11]): number of electric or hybrid electric aviation projects.	9
Fig. I-5: Evolution of the number of projects aimed at taking off electric planes according to the type of aircraft (Source Roland Berger[11]).	9
Fig. I-6: "Snowball effect" on conventional architecture fixed aircraft mass additions and fuel consumption effects.	10
Fig. I-7: Safran aircraft electrification roadmap [13].	11
Fig. I-8: Determination of a minimal value of battery specific energy function of the design range according to EIS of three different MTOW aircrafts (Source: J. Th PhD Thesis[12]).	12
Fig. I-9: Aircraft geometry comparison for a 400nm design range and a 2030+ EIS (Source: J. Th PhD Thesis [12]).	13
Fig. I-10: Example of different PHP missions.	14
Fig. I-11: Example of two same-PHP value missions with different EHP values.	15
Fig. I-12: Ragone Plan – electric energy storage comparison (specific energy and specific power).	15
Fig. I-13: Interactions during a complete aircraft design (Source: J. Th PhD Thesis [12]).	16
Fig. I-14: Start-up TURBOTECH products: Turbogen and Turboprop.	17
Fig. I-15: Racer European project concept and its ecomode presentation.	18
Fig. I-16: Specific fuel consumption of a gas turbine versus the output power rating.	18
Fig. I-17: Tecnam P2006T (conventional wing) – NASA X-57 Maxwell (distributed powered wing).	19
Fig. I-18: Illustration of a yaw control (Source : J. Th PhD Thesis [12]).	19
Fig. I-19: AMPERE european project studied by ONERA.	20
Fig. I-20: Boundary Layer Ingestion Principle (BLI) - Source ONERA [27].	20
Fig. I-21: Starc-ABL and N3X NASA projects.	21
Fig. I-22: DRAGON European project studied in ONERA.	22
Fig. I-23: Hybrid-electric propulsive system state of the art (NASA [29]).	23
Fig. I-24: 804 Project - UTAP parallel hybrid-electric propulsion system.	24
Fig. I-25: Ampaire Electric EEL.	25
Fig. I-26: Eco-Pulse project (Series/Parallel Partial Hybrid).	25
Fig. I-27: VOLTAERO Cassion hybrid-electric aircraft.	26
Fig. I-28: VTOL Aurora Lightning Strike.	27
Fig. I-29: E-fan X description and its propulsive system [43].	28
Fig. I-30: E-fan X architecture description.	28
Fig. I-31: ZA10 description concept [44].	29
Fig. I-32: VTOL Bell NEXUS propulsive system description from SAFRAN [45].	29
Fig. I-33: Airbus E-fan [46], [47] and Siemens Extra 330LE all electric aircraft.	30
Fig. I-34: Eviation Alice (Paris Air Show 2019).	30

Fig. I-35: Successful Flight of World's First Commercial Electric Airplane (Harbour Air – magniX [49]–[51]).....	31
Fig. I-36: ACCEL project (Rolls-Royce)	31
Fig. I-37: CityAirbus [55]	32
Fig. I-38: Element One (Hydrogen powered aircraft).....	33
Fig. I-39: Hydrogen aviation vision by ZeroAvia.	33
Fig. I-40: Cryogenic hydrogen powered aircraft NASA project.	34
Fig. I-41: EUROCONTROL draft Traffic scenarios (European aviation).....	34
Fig. I-42: Commuter aircraft powered by fuel cells.....	35
Fig. I-43: Regional aircraft powered by fuel cells.	36
Fig. I-44: Avion Mauboussin fuel cell powered aircraft concept (AlcyonM3c)[59].	36
Fig. I-45: Airbus ZEROe aircraft concepts[60].	37
Fig. I-46: Alaka'i Skai Hydrogen powered VTOL air taxi[61].	37
Fig. I-47: Toyota Mirai 1 & 2 (hydrogen powered car).....	38
Fig. I-48: Hydrogen Motive Company: the Hopium Machina.	38
Fig. I-49: Hynova yachts: hydrogen propulsion system	38
Fig. I-50: Hybrid electric aircraft representation considering hybridization power degree and hybridization energy degree.	40
Fig. I-51: HASTECS project reference aircraft.....	42
Fig. I-52: Altitude, Mach, Thrust, Aircraft power profile missions.	43
Fig. I-53: Environmental aircraft flight domain conditions (OAT: Outside Air Temperature). 43	
Fig. I-54: Speed triangle (<i>Aircraft speed = Va ; tangential rotation speed = VT;</i> <i>blade tip speed = Vb</i>).	44
Fig. I-55: Nacelle and propeller sizes.....	44
Fig. I-56: Interactions between the system integration work package and the others.....	46
Fig. I-57: Academic HASTECS project perimeter (universities and laboratories).....	46
Fig. I-58: Implicit looped integrated process.....	47
Fig. I-59: Validation of the looped process by comparison of aerodynamic and looped models	48
Fig. I-60: Hybrid power train mass sharing.	50
Fig. I-61: Power distribution between sources.	50
Fig. I-62: Fuel burn variation versus technological improvement of the electric propulsion system from the 2025 target.....	51
Fig. I-63: MTOW variation versus technological improvement of the electric conversion chain from the 2025 target.....	51
Fig. II-1: Five levels of optimization from "technologies" to "aircraft".....	56
Fig. II-2: Description of the total hybrid-electric powertrain.....	57
Fig. II-3: Schematic model of disk actuator (dotted line = location of the propeller).....	58
Fig. II-4: Transmission and lubrication system weight correlation [79].....	59
Fig. II-5: Turboshaft data regression.	60
Fig. II-6: Four popular motors in Hybrid Electric Vehicle: direct current machines (DC), Induction machines (IM), permanent magnet synchronous machines (PMSM) and switched reluctance machines (SRM) [82].	61
Fig. II-7: Power balance of the permanent magnet synchronous motor (PMSM).....	62
Fig. II-8: Electromagnetic model design process.....	62
Fig. II-9: Air gap flux density at no load (a) slotless and slotted models, (b) harmonic analysis [83][83]	63

Fig. II-10: First results considering the overall powertrain.	64
Fig. II-11: 20 independent run solutions.	64
Fig. II-12: Process to determine the real value of flux density in the air gap and magnet thickness (Original model and the new one).	65
Fig. II-13: 15 independent run solutions after the first model modification.	66
Fig. II-14: 6 independent run solutions after the second model modification.	67
Fig. II-15: Torque/speed characteristic(left) - Emotor mass (objective function)(right).	67
Fig. II-16: Behn-Eschenburg diagrams (without and with field weakening).	68
Fig. II-17: Set of solutions of Eq (10) in the torque speed plan for an example of electric motor characteristic and given a sizing voltage	69
Fig. II-18: Differences between the new model and the original model.	70
Fig. II-19: Cooling systems classification [88].	71
Fig. II-20: Nacelle architecture (electric machine and its cooling system) [83], [87]....	72
Fig. II-21: Cross section of the electric motor schematic (with its cooling system) [83], [87].	72
Fig. II-22: Paschen curve in air gap between plane electrodes at normal conditions and at p =760 Torr.	73
Fig. II-23: WP5 tool outputs: (a) FEA software mesh; (b) & (c) electric field and voltage drops along fields lines (p=1bar).	74
Fig. II-24: WP5 tool process (left), example of a PD free solution with 6 conductors (right) .	74
Fig. II-25: Decrease of PDIV for a combined variation of pressure and temperature.	75
Fig. II-26: Voltage phase overshoot evaluation as a function of the switch rise time.....	75
Fig. II-27: Multilevel converter classification.	76
Fig. II-28: Simulation tool organisation.	77
Fig. II-29: Comparison of possible solutions sized [94].	78
Fig. II-30: 3-level NPC inverter.....	78
Fig. II-31: 5-level ANPC single phase inverter.....	79
Fig. II-32: Voltage rule for determining the topology and the component to be used.	79
Fig. II-33: CPLIP schematic [88].	81
Fig. II-34: Module/evaporator assembly [93].	82
Fig. II-35: CPLIP mass variation as function of the heat power (2025 Target).	82
Fig. II-36: CPLIP mass variation as function of the heat power (2035 Target).	83
Fig. II-37: Technological comparison in terms of specific energy given the mission profile. ..	85
Fig. III-1: Reference aircraft architecture (REF).....	88
Fig. III-2: Turbo-Electric aircraft architecture (TEA).	89
Fig. III-3: Symmetrical Hybrid Electric Aircraft (HEASYM) with the Energy management.....	90
Fig. III-4: ATR 72-600 datasheet [65]	90
Fig. III-5: Asymmetrical architecture (HEA ASYM) with an energy management.....	91
Fig. III-6: One Engine architecture (HEA-1GT) with one energy management.	91
Fig. III-7: Summary of results versus reference aircraft with both targets.	93
Fig. III-8: Comparison of two Sobol indices estimation methods.	95
Fig. III-9: Integrated design process flow chart.....	96
Fig. III-10: First order Sobol indices for three hybrid-electric architectures regarding the fuel mass; bar colors are related to the 3 compared architectures.	97
Fig. III-11: First order Sobol indices for three hybrid-electric architectures regarding the MTOW; bar colors are related to the 3 compared architectures.	98
Fig. III-12: Process to determine Sobol Indices for the electric motor sensitivity analysis.	99

Fig. III-13: First order Sobol indices calculated by the two estimation methods. Output variable: efficiency. Input variables: motor parameters.....	100
Fig. III-14: First order Sobol indices calculated by the two estimation methods. Output variable: mass. Input variables: motor parameters	100
Fig. III-15: First order (pale color) and total order (dark color) Sobol indices and its effects on the e-motor efficiency.....	102
Fig. III-16: First order (pale color) and total order (dark color) Sobol indices and its effects on the e-motor mass.	103
Fig. III-17: Electromechanical powertrain sensitivity analysis process.	104
Fig. III-18: First order (pale color) and total order (dark color) Sobol indices with e-motor efficiency as output without considering constraint fulfillment.	106
Fig. III-19: First order (pale color) and total order (dark color) Sobol indices with e-motor mass as output without considering constraint fulfillment.....	106
Fig. III-20: First order (pale color) and total order (dark color) Sobol indices with the e-motor peripheral speed as output without considering constraint fulfillment.....	107
Fig. III-21: First order (pale color) and total order (dark color) Sobol indices on the thermal constraint as output without considering constraint fulfillment.....	108
Fig. III-22: First order (pale color) and total order (dark color) Sobol indices with e-motor efficiency as output by considering constraint fulfillment.	108
Fig. III-23: First order (pale color) and total order (dark color) Sobol indices with e-motor mass as output by considering constraint fulfillment.....	109
Fig. III-24: First order (pale color) and total order (dark color) Sobol indices with the e-motor peripheral speed as output by considering constraint fulfillment.	110
Fig. III-25 : First order (pale color) and total order (dark color) Sobol indices with the e-motor thermal constraint as output by considering constraint fulfillment.....	110
Fig. IV-1: Temperature evolution(left) and losse profile (right) during flight mission [84] ..	115
Fig. IV-2: MDO formulation process.....	116
Fig. IV-3: Cross section of the electric motor (optimization with steady thermal model)	118
Fig. IV-4: e-Motor temperatures (optimization with steady state thermal) during the flight mission.....	119
Fig. IV-5: Cross section of the electric motor (optimization with transient state thermal model)	119
Fig. IV-6: e-Motor temperatures (optimization with transient state thermal model) during the flight mission.....	120
Fig. IV-7: e-Motor temperatures (optimization with transient state thermal model – steady state display) during the flight mission.	121
Fig. IV-8: Cross sections of three electric motors (left: steady state optimization, middle: WP1 e-motor design , right: transient state optimization).	122
Fig. IV-9: Torque - Speed characteristic (blue steady state (SS) optimization, red transient state (TS) optimization and yellow WP1 electric motor).	122
Fig. IV-10: Joules and Iron loss profiles.	123
Fig. IV-11: Current, current density and voltage in the three electric motors.	124
Fig. IV-12: Relative size deviations versus the maximum values.	124
Fig. IV-13: Relative radius deviations versus the maximum values.	125
Fig. IV-14: Relative mass deviations to the maximum values.	126
Fig. IV-15: Electric circuit parameter deviations to the maximum values.	126

Fig. IV-16: Both values giving the best objective function for both optimizations (blue and red), compared to with the e-motor designed made by the team in charge of WP1.....	127
Fig. IV-17: Decision variables giving the best objective function for both optimizations (blue and red), compared with the e-motor designed by the team in charge of WP1.....	127
Fig. IV-18: Symmetrical Hybrid Electric Aircraft (HEASYM) with the Energy management...	130
Fig. IV-19: Presentation of the multifields loop approached by the MDO of the hybrid-electric powertrain.....	132
Fig. IV-20: Three optimization results on the fuel burn.....	133
Fig. IV-21: Three optimization results on the specific power of the electric motor and the inverter (including cooling.)	133
Fig. IV-22: Efficiency of the electro-propulsion chain during the flight mission (propeller -> inverter).....	134
Fig. IV-23: Optimization result on propeller and gearbox input variables.....	134
Fig. IV-24: Propulsion system mass distribution	135
Fig. IV-25: Final decision variables giving the best objective function for the three optimizations.....	136
Fig. IV-26: Electric motor torque-speed characteristic for the fuel mass optimization.....	137
Fig. IV-27: Electric motor torque-speed characteristic for the e-motor mass optimization.	137
Fig. IV-28: Hybridization ratio over the flight mission.	139
Fig. IV-29: Power management system over the flight mission per unit.....	139
Fig. IV-30: Design variables for the snowball effect, the propeller, the gearbox and the fuel cell stack nominal power for both scenario (green: optimization including fuel cell stak power in the decision variable set – grey: “light hybridization”)......	141
Fig. IV-31: Propulsion system mass distribution for the 2025 HASTECS target.....	141
Fig. IV-32: Optimisation comparison (green: optimal hybridization ratio – grey: light hybridization scenario).....	142
Fig. IV-33: Geometrical comparison (green: optimal hybridization ratio – grey: light hybridization scenario).....	142
Fig. IV-34: Torque-Speed characteristic for the 2025 optimum results (including FC stack sizing).....	143
Fig. IV-35: Torque-Speed characteristic for the 2025 light hybridization scenario results....	143
Fig. IV-36: Specific power of the electrical components.....	144
Fig. IV-37: Comparison of the fuels required for the mission.....	144
Fig. IV-38: Hybridization ratio and consequence on the power management of the propulsion system (green background: optimal hybridization scenario – grey background: light hybridization scenario).....	145
Fig. IV-39: Relative deviations in MTOW and fuel mass with respect to the reference aircraft	146
Fig. IV-40: e-Motor temperature (2035 target) over time.....	147
Fig. IV-41: Geometrical comparison (blue: optimal 2025 emotor – red: optimal 2035 emotor).	148
Fig. IV-42: Optimisation comparison (blue: optimal 2025 emotor – red: optimal 2035 emotor).....	148
Fig. IV-43: Torque-Speed characteristic for the 2025/ 2035 optimum results.....	149
Fig. IV-44: e-Motor temperature (2035 target for both optimisations) over time.....	150
Fig. IV-45: Geometrical comparisons of three electric motors.....	151
Fig. IV-46: Comparison between 2025 target and 2035 target.	152

Fig. IV-47 : Torque-speed plan of the electromechanical actuators obtained by optimization of 2025 and 2035 (optimal hybridization scenario)	154
Fig. IV-48 : 2025 and 2035 dashboard of optimization constraints (optimal hybridization scenario)	155
Fig. IV-49: Specific power of the electrical components found by optimization of 2025 and 2035 (optimal hybridization scenario).	156
Fig. IV-50: Relative deviations in MTOW and fuel mass with respect to the reference thermal aircraft	157
Fig. A-1: Process chart of the model.	179
Fig. B-1: Process chart of the propeller model.....	181
Fig. B-2: Comparison of propeller performance models for a 6-bladed propeller of 3.93 m diameter rotating at maximum tip speed at sea level [12].	183
Fig. C-1: Process chart for the gearbox model.	185
Fig. C-2: Propeller rotation speed profile.....	186
Fig. C-3: Transmission and lubrication system weight correlation from Nasa.	186
Fig. D-1: Example of gas turbine.....	189
Fig. D-2: Process chart of the turboshaft model.	189
Fig. E-1: Process chart for the cable model.....	193
Fig. F-1: Process chart of the electric motor.	195
Fig. F-2: Cross section of an electric motor with each variable name.	197
Fig. F-3: Description of the slot length calculation.....	197
Fig. F-4: Circuit parameters of the PMSM and its electric equivalent circuit.	199
Fig. F-5: Behn-Eschenburg model (left: without field weakening $\Psi =0^\circ$)(right: with field weakening $\Psi >0^\circ$)	200
Fig. F-6: Field-weakening operation. (a) Power/torque versus rotational speed plane. (b) Analysis in the d-q plane. Two representations of actuator circles (blue circle: maximum torque per ampere strategy, with $Id = 0$, green circle: field-weakening strategy, with increased speed and constant limited voltage).	201
Fig. F-7: Field weakening control description.	202
Fig. G-1: Process chart of the electric motor cooling model.....	205
Fig. G-2: Winding channel layout details in the cross section of the slot.	206
Fig. G-3: Cross section of the electric motor with water jacket and shaft cooling representation.....	207
Fig. G-4: Fluid convection coefficient calculation process.	208
Fig. G-5: Air gap convection coefficient calculation process.	209
Fig. G-6: End-space frame convection coefficient calculation process.....	209
Fig. G-7: Lumped parameter thermal network of the motor and its heat exchanger.....	211
Fig. G-8: Lumped parameter thermal network detailed.....	212
Fig. H-1: Process chart of the partial discharge model in the slot.	215
Fig. H-2: PASCHEN abacus: PDIV decrease for a combined variation of temperature and pressure.....	216
Fig. H-3: 5-level PE voltage and current curves.....	217
Fig. H-4: Enamel thickness as a function $PDIV_{windingsref}$ ($T=20^\circ\text{C}$, $P = 760$ Torr).	218
Fig. H-5: Copper radius versus enamel thickness for all grade tolerances ($T=20^\circ\text{C}$, $P = 760$ Torr).	218
Fig. H-6: Slot liner thickness as a function of $PDIV_{linerref}$ and enamel thickness ($T=20^\circ\text{C}$, $P = 760$ Torr).	219

Fig. H-7: Example of winding layout.....	220
Fig. H-8: WP5 detailed process.	221
Fig. I-1: Process chart of the models.	223
Fig. I-2: Topology and IGBT choice process.....	224
Fig. I-3: Representation the equivalent thermal model of a single module.	227
Fig. I-4: New equivalent thermal model for the power electronics.....	228
Fig. I-5: Cooling system mass estimation (LEFT: 2025 TARGET and RIGHT: 2035 TARGET)...	228
Fig. J-1: Process chart of the electric source model.....	231
Fig. J-2: Stack/system efficiencies versus the net power to supply per unit.	232
Fig. J-3: Stack and system efficiencies.....	233
Fig. K-1: Process chart for the rectifier/e-generator model.	235
Fig. L-1: Weight optimization process for electric motor.	238
Fig. L-2: Integrated optimal design process of a hybrid electric powertrain.	239

LIST OF TABLES

Table I-1: Electrical component assumptions according to EIS (Source: J. Th PhD Thesis)	12
Table I-2: Profile mission comparison (Source: J. Th PhD Thesis[12]).	16
Table I-3: Listing of hybrid-electric propulsive system thanks to energy and power ratio.	23
Table I-4: HASTECS electric component targets.....	41
Table I-5: Flight phase duration.	43
Table I-6: Electric component assessments.	49
Table II-1 : Summary of changes between the initial sizing model and the integrated model used in optimization.....	70
Table II-2: Summary of converter topology properties.	80
Table II-3: Electrochemical source assumptions.	83
Table II-4: Fuel cell specific power assessments.	84
Table II-5: H ₂ storage specific energy assessments.	84
Table III-1: Electric component assessments.	92
Table III-2: 1rst sensitivity analysis input variables and their bounds	99
Table III-3: 2nd sensitivity analysis input variables and their bounds	102
Table IV-1: Decision variables (11) for optimization with their respective bounds.....	117
Table A-1: Environmental model.....	180
Table B-1: Propeller design model	182
Table B-2: Detailed saturation function.	183
Table C-1: Input/output variables used in the gearbox model.	185
Table C-2: Gearbox mass estimation.....	187
Table D-1: Input/output variables for the turboshaft model.	189
Table D-2: Turboshaft mechanical power functions.	190
Table D-3: Fuel estimation model	191
Table E-1: Input/output variables for the cable model.	193
Table F-1: Input/output variables for the electric motor sizing model.	195
Table F-2: First harmonic flux density computation process.	196
Table F-3: Geometry of the electric permanent magnet synchronous machine.....	196
Table F-4: Slot sizes details.....	197
Table F-5: Mechanical constraints calculation.	198
Table F-6: Winding factors description.	198
Table F-7: Circuit parameter equations.	199
Table F-8: Sizing constraints.	199
Table F-9: Initialization of the field weakening control.	200
Table F-10: PMSM electric parameters and flux densities.	202
Table F-11: Inverter parameters	203
Table F-12: Electric engine losses description.	203
Table F-13: Performance constraints.	204
Table G-1: Input/output variables for the electric motor cooling model.	205
Table G-2: Winding channel sizes.....	206
Table G-3: Differences between 2025 and 2035 targets	207
Table G-4: Water-jacket design equations.....	207
Table G-5: Shaft cooling design equations.....	207

Table G-6: Heat exchanger tube design equations.....	208
Table G-7: Reynolds and Prandtl number used in the fluid convection coefficients computation.....	208
Table G-8 : Prandtl and Taylor number in the air gap.....	209
Table G-9: Prandtl and Nusselt number in the end-space rotor.....	210
Table G-10: Convection coefficient in the end-space windings.....	210
Table G-11: Flux and conductance expressions for each heat transfer mode.	213
Table G-12: Performance constraints.	214
Table G-13: Differences between 2025 and 2035 targets.	214
Table H-1: Input/output variables for the partial discharges model in the slot.	215
Table H-2: Calibration factor determined by the PASCHEN abacus.	216
Table H-3: Detailed wire definition model.	217
Table H-4: Detailed liner definition model.	219
Table H-5: Detailed winding layout model.	219
Table H-6: Constraints.	221
Table I-1: Input/output variables for the power electronics model.	223
Table I-2: Current and electric frequency computation.	224
Table I-3: Switching frequency seen by IGBT and definition of the number of semiconductors per phase.	225
Table I-4: Capacitor sizing model.	225
Table I-5: Conduction and switching losses description.	226
Table I-6: Mass table.	226
Table I-7: Efficiency table.	226
Table I-8: Thermal equations related to the Fig. I-3.	227
Table I-9: Cooling system mass linear function.	228
Table I-10: Differences between 2025 and 2035 targets.	229
Table I-11: Total inverter mass.	229
Table J-1: Input/output variables for the fuel cell and the battery.	231
Table J-2: Fuel cell system mass estimation.	232
Table J-3: Linear function of the fuel cell efficiencies.	233
Table J-4: Mass estimation considering the discharge energy and the C-rate (Power).	233
Table K-1: Input/output variables for the rectifier and the e-generator.	235
Table K-2: Assumptions for the electric device fed by the turboshaft.	236
Table K-3: Mass and power estimation for the rectifier and the e-generator.	236

LIST OF ACRONYMS

ACARE	Advisory Council for Aeronautical Research in Europe
AE	All-Electric (aircraft)
ANPC	Active Neutral Clamped Point topology
ANOVA	Analyze Of VAriance
BLI	Boundary Layer Ingestion
CORAC	Council of Civil Aeronautical Research
CPU	Central Processing Unit
DPWM	Discontinuous Pulse Width Modulation
EIS	Entry Into Service / Electrical insulation System
FEA	Finite Element Analysis
FC	Flying Capacitor topology
GHG	GreenHouse Gas
GSA	Global Sensitivity Analysis
HASTECS	Hybrid Aircraft reSearch on Thermal and Electric Components and Systems
IATA	International Air Transport Association
ICAO	International Civil Aviation Organization
IM	Induction machine
ISA	International Standard Atmosphere
LEAPTECH	Leading Edge Asynchronous Propeller TECHnology
MDO	Multidisciplinary Design Optimization
MTOW	Max Take-Off Weight
NASA	National Aeronautics and Space Administration
NPC	Neutral Clamped Point topology
OAD	Overall Aircraft Design
OEI	One Engine Inoperative
ONERA	Office National d'Etudes et de Recherche Aérospatiale
PAX	Passengers
PE	Power Electronics
PH	Parallel Hybrid (electric aircraft)
PT	Partial Turboelectric (aircraft)
EHP	Energy Hybridization Potential
PHP	Power Hybridization Potential
RMS	Root Mean Square
SFC	Specific Fuel Consumption
SH	Series Hybrid (electric aircraft)
SMC	Stacked Multicell Converter topology
SM-PMSM	Surface-Mounted Permanent Magnet Synchronous Machine
SPPH	Serie- Parallel Partial Hybrid (electric aircraft)
SRM	Synchronous Reluctance Machine
Starc-ABL	Single-aisle Turbo-electric AiRCraft with an Aft Boundary Layer propulsor
TE	TurboElectric(aircraft)
VTOL	Vertical Take-Off and Landing
WP	Work Package

INTRODUCTION

Since the 1950s, the aviation industry has made incredible progress in increasing both the power and efficiency of its internal combustion engines. However, recent studies suggest that the technology of these engines is approaching the thermodynamic limits of the amount of energy it is capable of extracting from a carbon-based fuel at a lower cost. This means that the more flights and airplanes there are, the more fuel consumption and greenhouse gas emissions will increase, unless a suitable substitute is found for fossil fuels, such as hybrid and electric airplanes. The electrification of propulsion functions expands the aircraft design space by introducing new configurations. Several hybridizations are possible with more or less advanced hybridization ratios in power and energy depending on the chosen topology.

This thesis deals with series hybrid-electric propulsion, all the propulsion is provided by electric motors, only the sources are dimensioned according to the associated missions. The case study is a 70-Pax regional jet capable of covering a 500 nautical mile mission. The complete hybrid electric propulsion chain is designed by optimization, integrating models resulting from technological developments of the major electrical components. The reference point of the design methodology is a conventional aircraft with thermal propulsion (propeller, gearbox, gas turbines). Snowball effects caused by weight gain are taken into account through an internal loop on the aircraft thrust. The initial investment cost of building the aircraft is not taken into account in this study. Only the environmental costs (fuel mass) will be evaluated during the overall optimization of the propulsion system.

The first chapter focuses on the state of the art of electric (hybrid) propulsion configurations. Several design axes for new aircraft architectures are being studied: Optimal turboshaft designs, improvement of aerodynamics and new energy management of the different mission profiles. Subsequently, the HASTECS project is described with all the assumptions and associated input data. The study areas of the work packages are also presented, as well as their objective within the framework of the project. Finally, the coupling between this work and the previous work packages will be specified by explaining the integrated design approach; the internal loop taking the snowball effect into account will also be detailed.

The second chapter will present a series of "scale models" that can be integrated into an optimization process for the global powertrain (with a reasonable calculation time): these models come from previous studies or from an adaptation (reduction) of technological models from the HASTECS work packages. These models have been modified in order to obtain reasonable calculation times and are presented in the rest of the chapter.

An initial study is carried out in Chapter III to explore the design space for a regional aircraft with series hybrid-electric propulsion. The energy missions of each source (electric and thermal) will be modified in order to evaluate the impact of these variations on the aircraft's weight and fuel consumption. Subsequently, a global sensitivity analysis (GSA) is implemented in order to highlight the parameters which have the greatest impact on the previous output variables (aircraft mass/ fuel consumption). This sensitivity analysis is based on the study of

Sobol indices which express the sensitivity of each input variable on the output. First, fixed configurations of hybrid electric aircraft will be studied by varying power densities and efficiency. Then the global sensitivity analysis will be applied to the masses and efficiencies of the components themselves by directly varying the sizing variables. The propeller-gearbox-electric motor assembly will be studied in more detail because it is the most crucial part of the propulsion system to be sized.

Finally, the last part and the final objective of this project concerns the optimal design of the complete powertrain integrating an energy management to the hybrid electric architecture. The same path as the sensitivity analysis will be studied for optimization. A first optimization on the component itself (electric machine) will be performed taking all interactions into account (electromagnetic, thermal and partial discharges) for its sizing. Then the complete propulsion system will be optimized in several ways in order to highlight the difference in "approach level" (local approach / systemic approach). Finally, the hybridization ratios will be added to the optimization variables to obtain the most optimal regional hybrid-electric aircraft from a fuel consumption point of view.

This entire study has highlighted the interest of a multidisciplinary approach to the design of a hybrid electric propulsion aircraft. In reality, the process is even more complex because all the surfaces of the plane must be resized at the same time as the propulsion and the mass. However, one essential thing has been underlined in this study, the hybrid electric propulsion brings even more complexity and this is not free, an additional investment cost for the construction of this aircraft should not be overlooked. Is hybridization of the propulsion system really the solution for this type of single-aisle aircraft? Is a true complete technological breakthrough more interesting?

CHAPTER I. The electric revolution impacts aviation.

CONTENTS

<i>I.1 Why are (hybrid-)electric aircrafts headed for a takeoff?</i>	6
I.1.1 An air traffic growth that was not ready to stabilize before COVID-19.	6
I.1.2 Flygskam or flight shame.....	8
I.1.3 Towards a new revolution in the aviation industry?.....	8
I.1.4 Enemy number one in aeronautics: weight!	10
<i>I.2 Potential hybridization gains of the hybrid-electric aircraft propulsive system.</i>	13
I.2.1 A complicated hybridization of the propulsive system.....	13
I.2.2 Turboshaft design gains (performance and fuel burn).....	17
I.2.2.1 Optimal design of gas turbines.	17
I.2.2.2 Intelligent use of gas turbines.	17
I.2.3 Aerodynamic gains.	18
I.2.3.1 The distributed propulsion (blown wing).	18
I.2.3.2 The Boundary Layer Ingestion propulsion (BLI).	20
I.2.4 Energy gains: how to operate high electric efficiency in a hybrid-electric propulsion?.....	22
I.2.4.1 Parallel hybrid electric propulsive system (PH).	23
I.2.4.2 Propulsion Series/Parallel Partial Hybrid (SPPH).	25
I.2.4.3 Partial Turbo electric propulsive system (PT).	26
I.2.4.4 Turbo Electric propulsive system (TE).....	27
I.2.4.5 Series Hybrid propulsive system (SH).	27
I.2.4.6 All-electric propulsion (AE).	30
I.2.5 Towards greener aircrafts: hydrogen power, a huge challenge that seems reachable	32
<i>I.3 Presentation of the HASTECS Project and thesis objectives.</i>	41
I.3.1 Input data.....	42
I.3.2 Project description	45
I.3.3 A major “snowball effect” involving an integrated looped process.....	47
I.3.4 About sensitivity of technologies on both max take off weight and fuel burn.	48
I.3.5 Thesis objectives.	52

I.1 Why are (hybrid-)electric aircrafts headed for a takeoff?

I.1.1 An air traffic growth that was not ready to stabilize before COVID-19.

Global air traffic grew by 6.5 percent in 2018, according to the International Air Transport Association (IATA [1]). Before the COVID-19, passenger air travel was expected to maintain positive growth rates up to 2030, despite a number of industrial challenges to be faced: airlines around the world are struggling with high jet fuel prices and slow economic growth. After COVID, this growth has been brutally blocked probably for some years: according to IATA assessments, the air traffic will be decreased by 88% for 2020 (see [2]-[3]). Some economic analysis is currently ongoing that will assess the time to recover the 2019 air traffic and the new growth perspectives but it seems that major trends (assessed before COVID) would be slowed down but maintained (after COVID). In that context the lines below were written before the new pandemic situation but remain relevant at the whole, at least for long term situation.

Through the previous different crises air traffic has proven its robustness by doubling every fifteen years. Moreover, with low-cost airlines such as Ryanair or Easyjet entering the race, airline tickets are increasingly accessible to the world's population and do not make things better for the air sector. In order to avoid doubling carbon emissions at the same time as the growth of air transport, major research and development effort required today must be continuous and synchronized. Innovations and technological breakthroughs in the field of propulsion, materials, aerodynamics, on-board systems, must be coordinated in order to design a new generation of innovating devices. In French aircraft industry this is the whole purpose of the CORAC (Council of Civil Aeronautical Research): a state-industry think tank which acts for the set up of the French research program. This is also the object of ACARE (Advisory Council for Aeronautical Research in Europe), CleanSky [4] and SESAR technological research programs, bringing together thousands of researchers and European engineers mobilized to change the future of aviation.

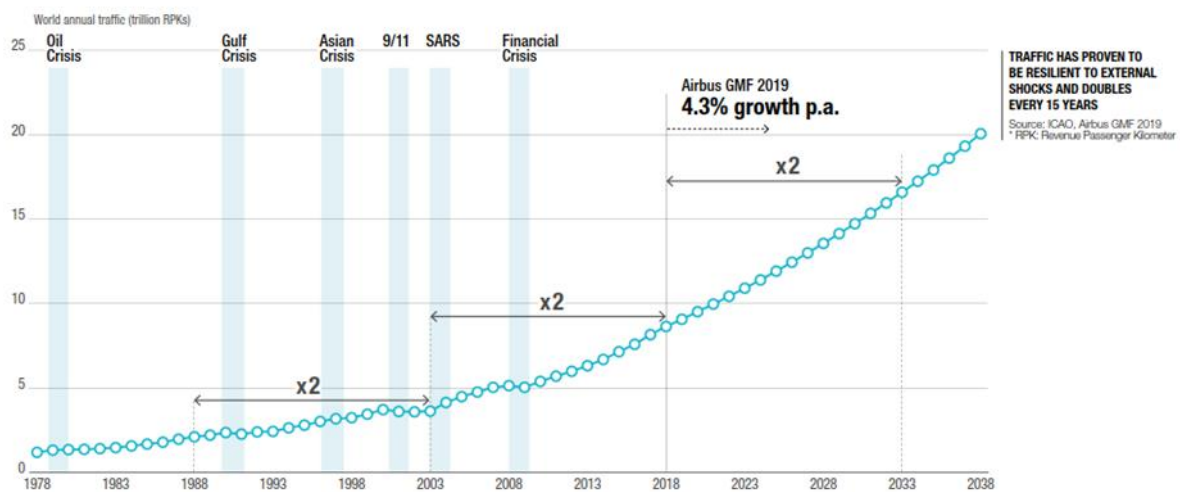


Fig. I-1: Air traffic evolution since 1977 and estimate to 2037 (Source AIRBUS GMF 2019 [5]).

In 2000, the ACARE has launched two programs: one for 2020 named VISION 2020 [6] and the second is the FLIGHTPATH 2050 [7]. For the environment, the 2020 target predicted a 50% reduction in CO₂ emissions per passenger kilometer and an 80% NOx emission reduction. In 2050 available technologies and procedures would allow a 75% reduction in CO₂ emissions per passenger kilometer and a 90% reduction in NOx emissions to support the ACARE target. The perceived noise emission of flying aircrafts has to be reduced by 40% for the first target 2020 and 60% for the second one. These are relative to the capabilities of typical new aircraft in 2000 ([7]).

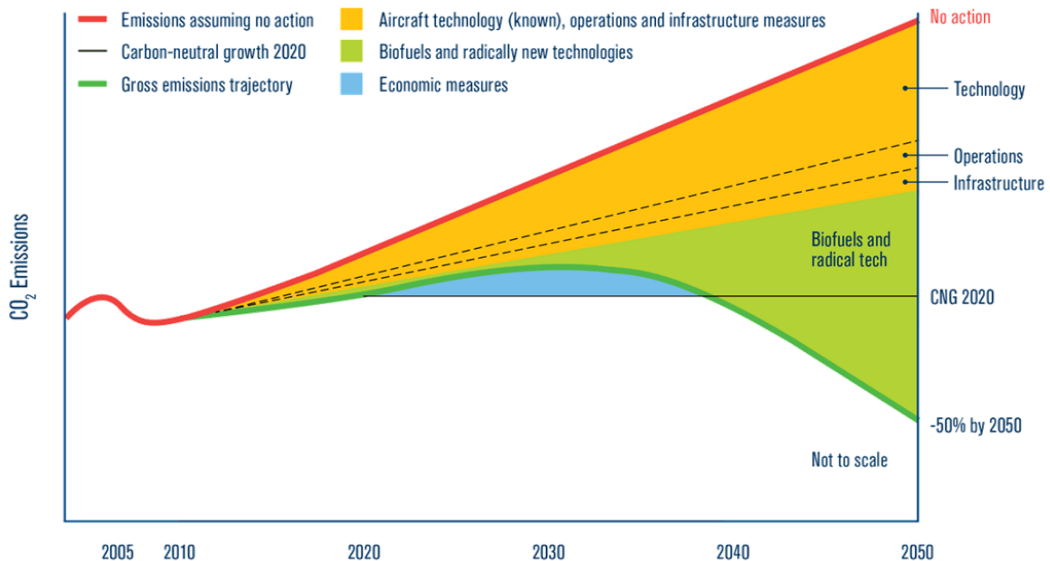


Fig. I-2: Schematic CO₂ emissions reduction roadmap (Source IATA [8]).

The International Air Transport Association (IATA) announced three huge level goals for the greenhouse gas emissions roadmap (green line) [8]:

- An average improvement in fuel efficiency of 1.5% per year from 2009 to 2020.
- A cap net emission from 2020 through carbon neutral growth between 2020 and 2040.
- By 2050, net aviation carbon emissions will be half what they were in 2005.

Although aircrafts appear to be a polluting means of transport the aviation's contribution to global man-made CO₂ emissions currently reaches between 2% and 4% depending on various studies.

Furthermore, a new global movement called "Flygskam" meaning flight shame wants to raise people's awareness about airplane pollution.

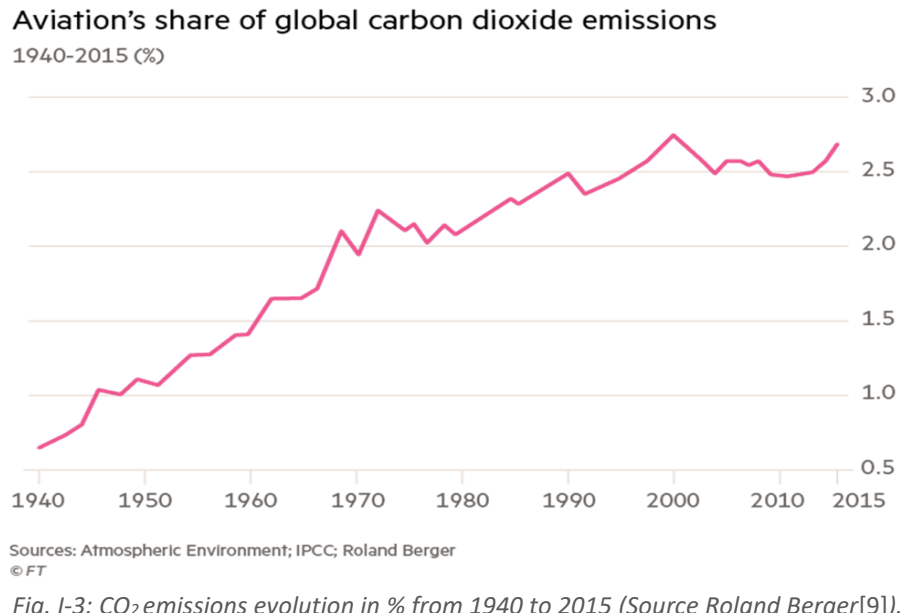


Fig. I-3: CO₂ emissions evolution in % from 1940 to 2015 (Source Roland Berger[9]).

I.1.2 Flygskam or flight shame.

“We stay on the ground” said Maja Rosén in 2018 [10] recruiting people in her group of the same name, to pledge to give up flying for one year. So far, more than 8000 people around the world have made the pledge. The length of Sweden, 1570-km-long, explains why its inhabitants use the plane more than the global average (5 times more). The use of regional aircraft releases 14 to 40 times more CO₂ gas emissions. Another Swedish, a 16-year-old climate change activist named Greta Thunberg campaigns against air travel. She went on strike from school the same year protesting against the country government’s inaction on climate change. She attended the United Nations Climate Change Conference (COP 24) and addressed the summit, explaining the severity of global warming. In other countries, AVINOR (the Norwegian Civil Aviation Administration) works to ensure that Norway takes a leading role at an international level on a development and innovation project for electric aircrafts. According to this administration, by 2040, all short haul and regional aircrafts should be electrically-powered. A good example is that of the consortium Airbus and SAS Scandinavian Airlines which are collaborating to explore the hybrid-electric and electric potential.

More generally, that whole context push aviation sector to innovate towards greener aircraft solutions.

I.1.3 Towards a new revolution in the aviation industry?

Since Frank Whittle (the jet engine inventor) in 1937, aircrafts have been fuel powered. After decades, improvements have been made in the field of materials, battery technology and electric systems. This revolution does not prevent established leaders to maintain their pole position. That is why major aerospace companies are competing to put electrically powered devices on market so as to avoid competition from a new generation of aircraft manufacturers. Since 2009, more than 150 electric aviation projects have been launched worldwide. A third of these come from them (Airbus, Boeing, Roll Royce...), others come from start up or new born companies in aviation industry.



Fig. I-4: Electric propulsion is finally on the map (or hybrid-electric aviation) (Source Roland Berger [11]): number of electric or hybrid electric aviation projects.

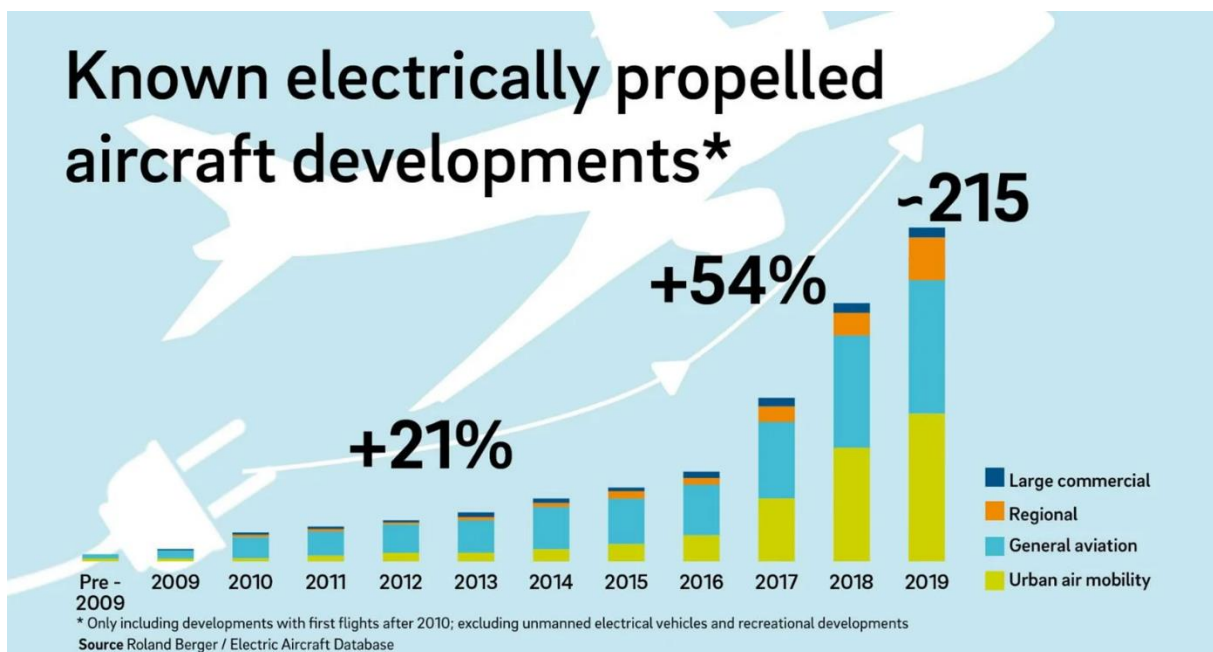


Fig. I-5: Evolution of the number of projects aimed at taking off electric planes according to the type of aircraft (Source Roland Berger[11]).

The growing trend of electric propulsion is emerging: all over the world, a convergence of factors contributing to electric propulsion is becoming a reality. From technological development to investments by new entrants, including the activity of the main aerospace players, the sector seems ready to undergo a radical change.

I.1.4 Enemy number one in aeronautics: weight!

To make the dream of electric propulsion a reality, aeronautical companies must bridge the technological gap due to the power required for flight: for a 70 Pax regional aircraft the power required for the takeoff is around 4MW. The challenges to be met are mainly technological challenges for the system components of hybrid electric propulsion system. But adding electric components to transform mechanical power into electricity in the propulsive system, adds weight to the hybrid-electric aircraft. A heavier aircraft needs more wing surface and all the more power to fly therefore a more powerful propulsive system this consequently entails overconsumption: this is the snowball effect. In the following study [12], a conventional reference aircraft was taken to show the snowball effects of mass additions on fuel consumption. The Fig. I-6 is a comparison between three conventional aircrafts (thermal propulsion system) with three different payloads (6500/8500/10500 kg).

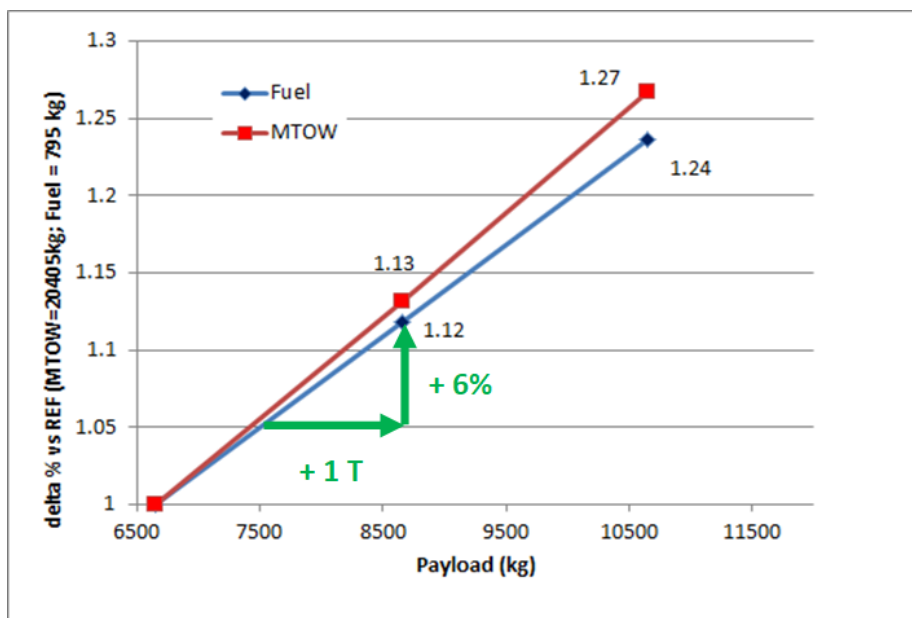


Fig. I-6: "Snowball effect" on conventional architecture fixed aircraft mass additions and fuel consumption effects.

The conclusion is clear: each ton added to the aircraft cause a 6% over consumption of fuel. In this study, the thermal propulsive system has been adapted and resized in order to succeed with a 400 nm flight mission. The red line shows the snowball effect on the Max Take Off Weight (MTOW) caused by the new propulsion system. A prediction can be made concerning the hybrid-electric aircraft: it will be heavier than conventional ones. Heavy electric components like e-motors and e-generators will increase the weight of the propulsive system also involving snowball effects. That is why their design and efficiency are essential to improve hybrid-electric aircraft performance.

An electric aviation roadmap has been made by a French aeronautical equipment manufacturer SAFRAN, it predicts increasing both voltage and power for electric devices. For huge powers increasing the voltage reduces the current and tends consequently to reduce the mass. For example, a cable is sized by its thermal limit directly conditioned by the Joule losses related to the current rating. The same applies to electric motors and generators which may require high voltages for high conversion powers.

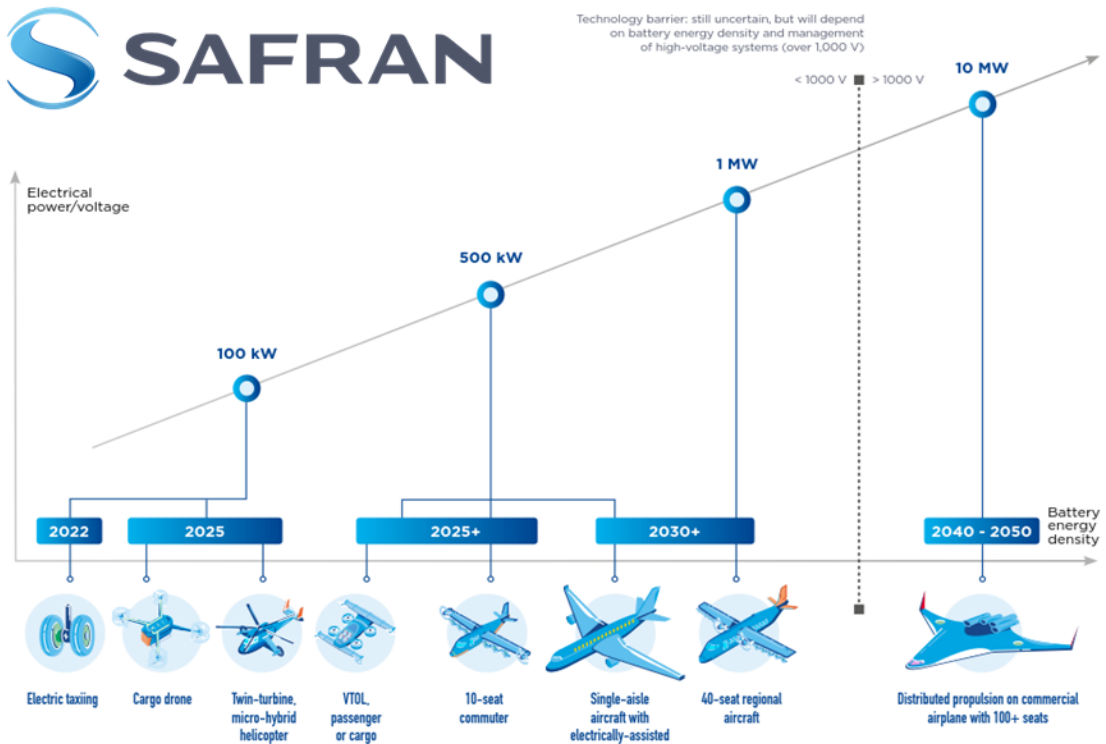


Fig. I-7: Safran aircraft electrification roadmap [13].

Unfortunately, beyond voltage values of ~1000V new phenomena appear: the partial discharges. They are created by a large potential difference between two conductors which could damage their insulation. In electric motors, partial discharges in windings may appear that can affect the lifetime of actuators. This is all more critical than electric machines are supplied by high frequency power electronics with high voltage derivatives.

Success of the electric aircraft does depend on both the power efficiencies and specific powers. These two factors must be enhanced not only on electric powertrain devices but also on electrical sources whatever if hybrid or full electric architectures are considered.

Stephane Cueille (Safran Chief Technical Officer at Safran) has estimated the weight of a full electric Airbus A320: it should carry a 170 tonnes battery-pack while its whole mass is about 60 tonnes today...

In the PhD thesis of Jerome Thauvin [12] in cooperation with airbus, a full electric aircraft prospective study has been made in order to determine the maximum aircraft range with respect to the battery specific energy assessment. Two different entry in service (EIS) were assessed for a 2025 and a 2030+ EIS. The overall aircraft structure are optimized for each value of both design range and specific energy. For both EIS, the assumptions taken into account for the main powertrain devices are the following:

Table I-1: Electrical component assumptions according to EIS (Source: J. Th PhD Thesis).

		EIS2025	EIS2030+
Electric machine	Specific power Efficiency	7 kW/kg 96 %	11 kW/kg 98.5 %
Power electronics	Specific power \bar{P}_{pe} Efficiency η_{pe}	15 kW/kg 99 %	20 kW/kg 99.5 %
Battery	Specific energy \bar{E}_b Max. ch./disch. C Efficiency η_b	280 Wh/kg 2/5 90%	380 Wh/kg 2/5 95 %
Cable	Voltage V_c	540 V	1500 V

In that table, reference figures for the specific energy of batteries are assessed. In the figure below, three different aircraft with MTOW of 25, 30 and 35 tons are compared. By varying the reachable range in nm, the target on battery specific energy is calculated. For the reference values related to EIS prediction, the acceptable is still very limited:

- for EIS2025 with 280 Wh/kg, the aircraft with a MTOW@25 tons is unable to take off while the MTOW@30 tons is limited to a range of 100nm.
- for EIS2030+ with 380 Wh/kg, the three aircraft ranges are limited below 200nm.

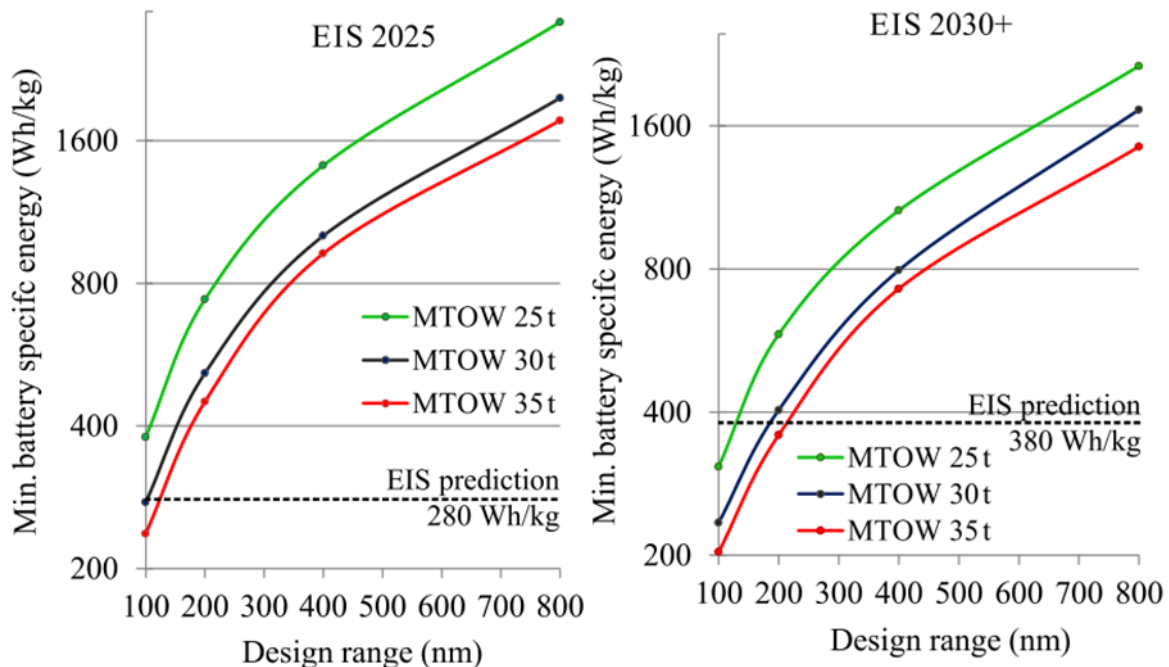


Fig. I-8: Determination of a minimal value of battery specific energy function of the design range according to EIS of three different MTOW aircrafts (Source: J. Th PhD Thesis[12]).

The dream of the electric aircraft may become a reality whereas electric source performance strongly progresses in terms of specific energy and/or specific power. In addition, the aircraft structure has to be resized and optimized to reduce weight. As example three studied aircrafts are the results of the previous study for a 400 nm design range and a 2030+ EIS:

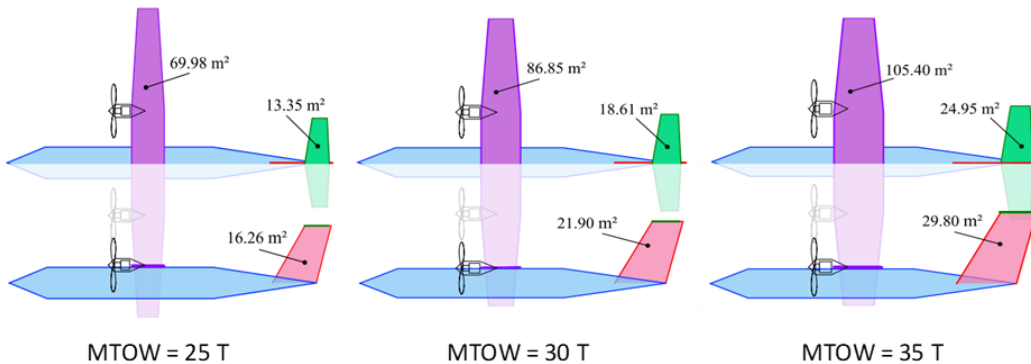


Fig. I-9: Aircraft geometry comparison for a 400nm design range and a 2030+ EIS (Source: J. Th PhD Thesis [12]).

A structural compensation has been found caused by the lack of battery specific energy. These aircrafts need more lift to make the flight mission successful, so the area of wing, horizontal tail and fin are larger. In these cases, the specific energy values will be difficult to reach, that is why the commercial electric flight is not ready to take off. The electric air revolution must learn from hybrid-electric aircraft propulsion to find disruptive technologies in order to create the full electric flight opportunity.

I.2 Potential hybridization gains of the hybrid-electric aircraft propulsive system.

I.2.1 A complicated hybridization of the propulsive system...

If in automotive application, or even in railway traction field, hybrid electric propulsion systems exist and are becoming more and more spread hybridization is still a long way off in the aeronautical field. An automotive profile mission is much more intermittent with numerous braking phases with energy recory opportunities contrarily to the aeronautic case. It is interesting to build hybridization indicators to copare these application sectors. In the thesis of Akli [14], two kinds of indicators have been set up:

- The Power Hybridization Potential (PHP) assesses the potential degree of primary energy source undersizing.

$$PHP = 1 - \frac{\text{mean}(P_{\text{primary source}})}{\text{max}(P_{\text{primary source}})} \quad (\text{I-1})$$

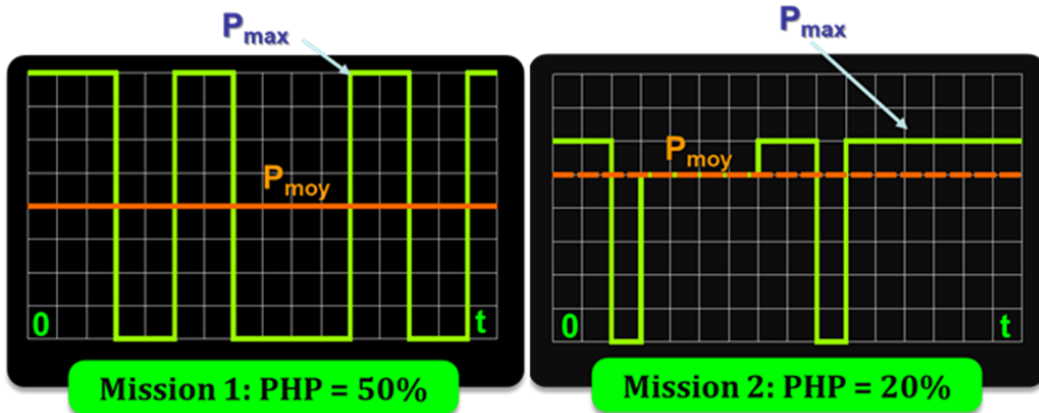


Fig. I-10: Example of different PHP missions.

In this example, P_{mean} and P_{max} are respectively the mean and the maximal power values of the profile missions. In the first case, the PHP value is higher than for the second mission. In deed, the maximal power represents the double of the mean power whereas the maximal power in mission 2 is just slightly higher than the mean one (20% higher): this difference causes the distinct PHP values. The higher the PHP the easier to undersize the primary source power to optimize its integration.

- The Energy Hybridization Potential (EHP) assesses the frequency and the regularity of mission intermittence.

$$EHP = 1 - \frac{\max(P_{primary\ source})}{E_u} \quad (I-2)$$

In the following figure Fig. I-11, the E_u represents the required (useful) energy for each profile mission. The two missions have both the same mean and maximal power. Consequently, they have the same PHP values but with distinct EHP. The required energy for the first mission is more important than the second one, so the energy design (for example in a storage device) will be bigger for the first mission than for the second one. If the source to be designed is a fuel cell, that could be matched by a more important dihydrogen mass (H_2).

The higher the EHP the easier to face the mission in terms of energy.

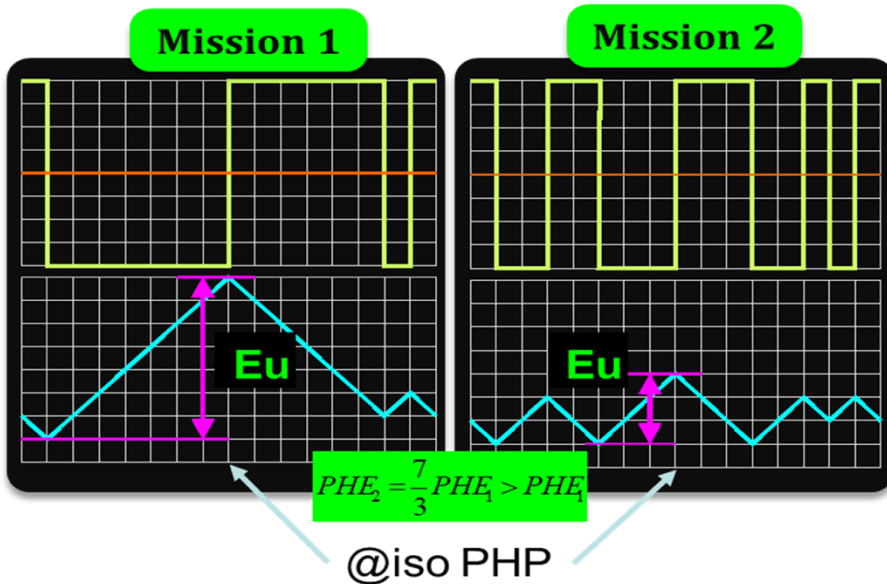


Fig. I-11: Example of two same-PHP value missions with different EHP values.

These indicators permit to evaluate the difficulty of power (PHP) energy (EHP) design. The following figure shows a comparison of different energy storage in the Ragone plan:

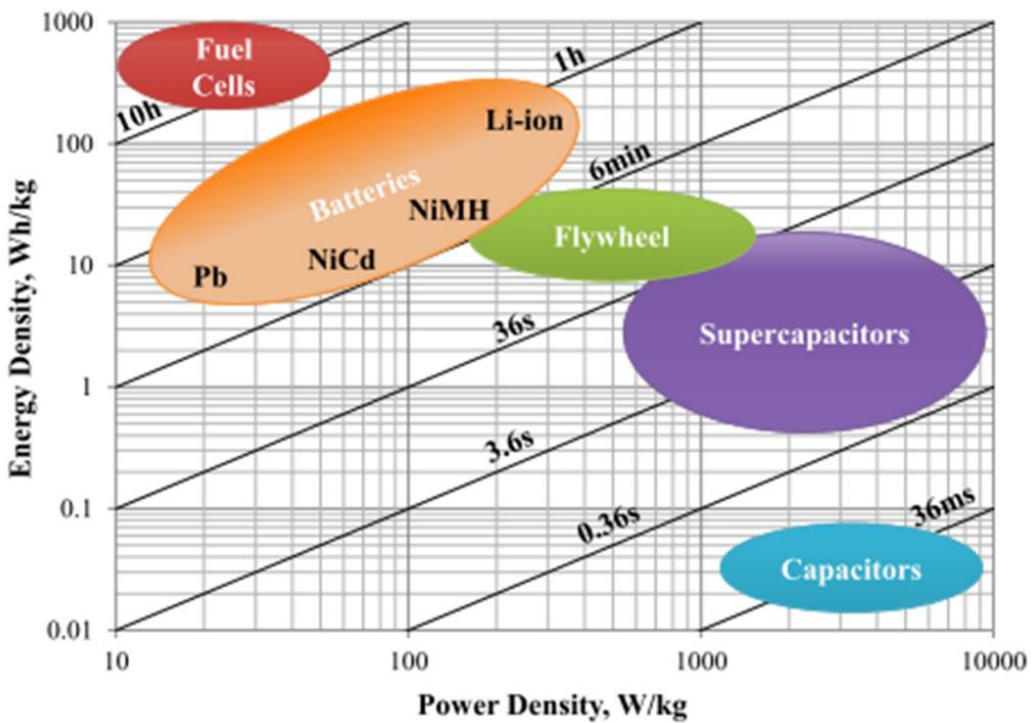


Fig. I-12: Ragone Plan – electric energy storage comparison (specific energy and specific power).

Black lines represent the required discharge/charge time of the different energy storages: low times (high frequencies) are at the bottom right while the low frequencies are on the left top corner. In the aeronautic case, typical profile missions are few intermittent high energy and rather simple, composed of steps of power for the flight phases. It explains that very low PHP and EHP values are assessed compared to other means of transportation (automotive, train, maritime...).

Table I-2: Profile mission comparison (Source: J. Th PhD Thesis[12]).

	Car			Train			Ship		Aircraft
	Urban	Rural road	Motorway 150km/h	Local service	Switching	Urban transport	Container	Ro/Ro ferry	Regional 200nm
PHP (%)	94	85	74	65	83	91	43	63	33
EHP (mHz)	66	30	12	3	29	20	n/a	n/a	0.22

The aircraft complexity is partly located in the multitude of interactions between different fields: lift, drag, wing, propulsive system, thrust... as illustrated on the following schematic diagram:

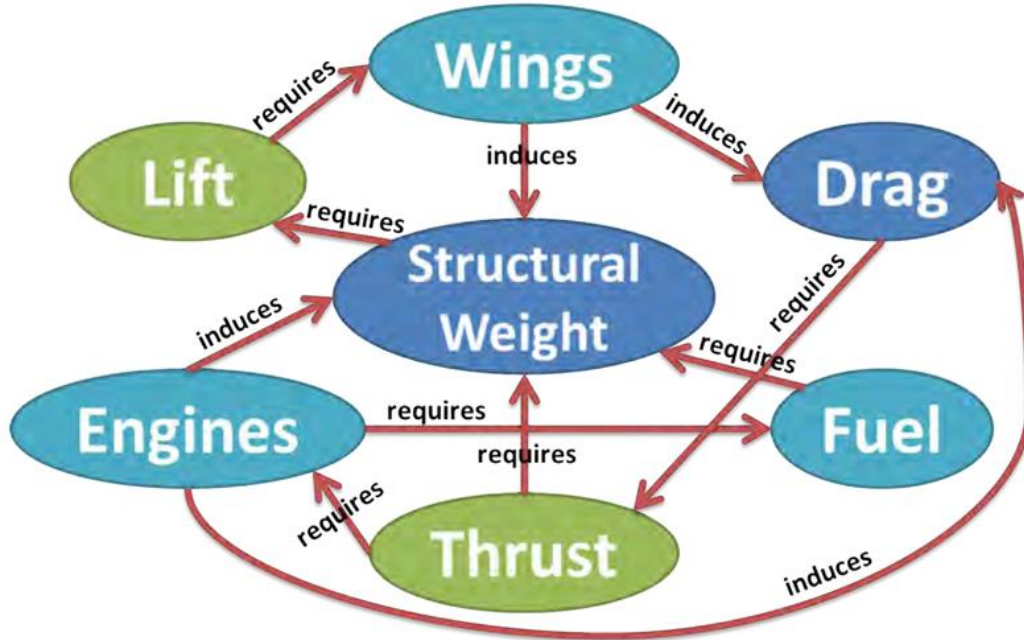


Fig. I-13: Interactions during a complete aircraft design (Source: J. Th PhD Thesis [12]).

A complete aircraft design is thus complex because of its high number of decision variables and its high discipline interactions. A systemic study takes into account all (whenever possible) disciplines, and not just components alone. The discrete sum of local optimal solutions rarely leads to the optimal solution of the whole system. It is within this framework that MultiDisciplinary Optimization (MDO) is working because it allows to gather different fields around a single mathematical problem. The complete design of future aircrafts is based on a triptych:

- Optimal turboshaft designs considering good performance and fuel burn.
- Performant aircraft aerodynamics.
- Energy management of different mission profiles.

Using the MultiDisciplinary Optimization (MDO) can determine indicators in order to find optimal solutions for the future (hybrid-) electric aircrafts.

I.2.2 Turboshaft design gains (performance and fuel burn).

I.2.2.1 Optimal design of gas turbines.

Above all engine manufacturers look at the turbomachine design optimization level from a consumption point of view but aiming also at view of changing fuels (biofuels, hydrogen, etc...). This is the work of a small company called TURBOTECH [15] which develops engines using several types of fuel or with relatively low specific fuel consumption.

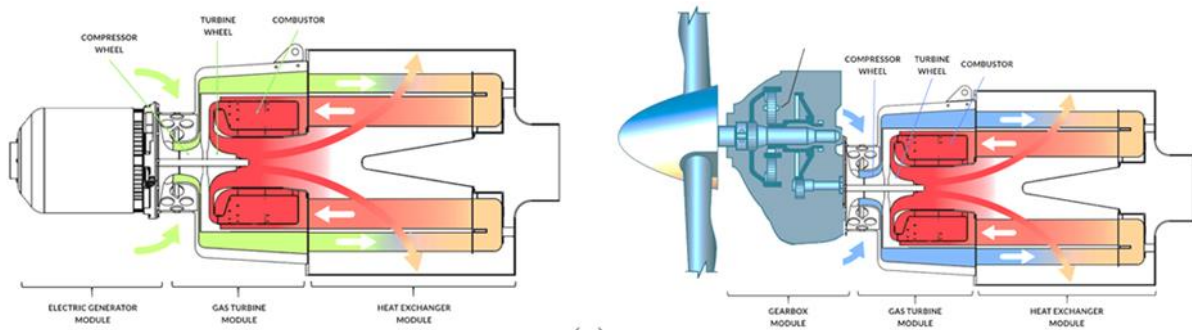


Fig. I-14: Start-up TURBOTECH products: Turbogen and Turboprop.

These products are designed for general aviation and allow important fuel burn gains. Turboprop reduces the noise from the gas turbine, and Turbogen is a module composed of an electric generator and a gas turbine. This product is dedicated to hybrid-electric aircrafts in order to increase their range and their flight time. The principle of the latter is quite simple: the hot exhaust gas is recycled through a heat exchanger and reinjected in the gas turbine. This process is named "regenerative cycle turbine". This system induces a better efficiency.

I.2.2.2 Intelligent use of gas turbines.

In the Clean Sky 2 European project framework a project named RACER [16] deals with hybridization with the aim of optimizing the more electric twin-engine helicopter power. The concept is to develop an economic cruise mode using only one engine at high power to reduce the second engine power (idle mode) for a more efficient mode and consequently save more fuel. An electric motor is used to fast-reactivate the standby turboshaft to meet the needs of high power if required, in the same way as in the automotive sector with the "start and stop" function available in most models.



Fig. I-15: Racer European project concept and its ecomode presentation.

This project suggests potential fuel consumption gains by hybridizing the propulsive system with an electric motor. Generally, engines are more efficient at a 100% rating power having lower specific fuel consumption (SFC) (Fig. I-16).

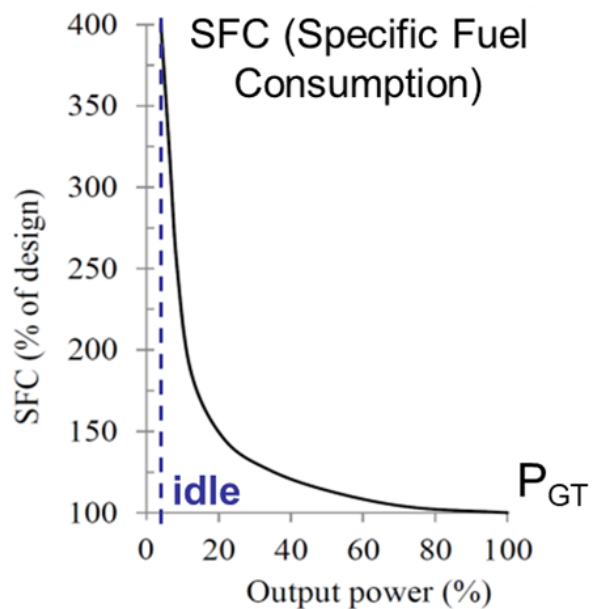


Fig. I-16: Specific fuel consumption of a gas turbine versus the output power rating.

During low power demand flight phases (as for taxiing or descent), the turboshaft fuel consumption strongly increases in a hyperbolic way. That is why hybridization with an electric source can be a solution to save fuel for reduced power ratings. Once the engine is optimally designed, the aircraft structure has to be studied in order to obtain a better aerodynamic performance.

I.2.3 Aerodynamic gains.

I.2.3.1 *The distributed propulsion (blown wing).*

This configuration has several advantages. The National Aeronautics and Space Administration (NASA) worked on the X-57 concept [17]–[21] since 2014 through the LEAPTECH project (*Leading Edge Asynchronous Propeller TECHnology*). The aim of this study is to improve the aerodynamic performance and the aircraft flight quality with a distributed

propulsion thanks to electric motors. The reference aircraft for this study is the TECNAM P2006T, where the wingspan has been changed to incorporate the blown wing concept.

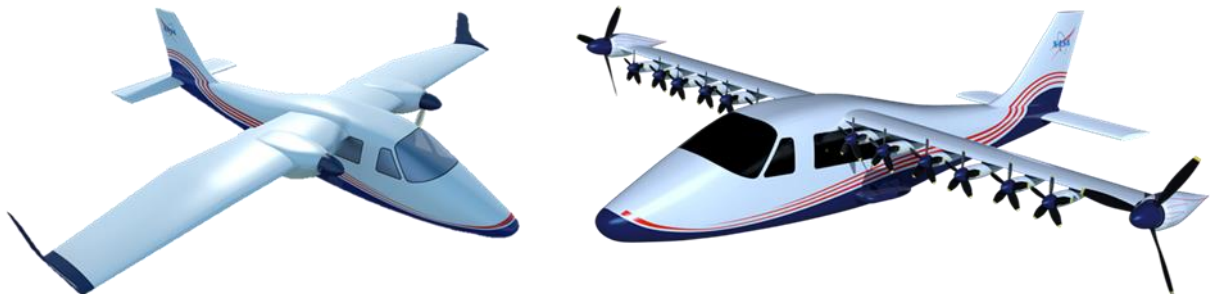


Fig. I-17: Tecnam P2006T (conventional wing) – NASA X-57 Maxwell (distributed powered wing).

- The first benefit of this propulsive system is the blown wing. The aircraft wingspans are sized for an approach speed (low speed performance), so they are oversized for cruise. Dividing the power by using small electric motors at the leading edge of the wing permit to “blow” the latter and consequently to reduce its size. With a reduced wing surface, the wingspan can be designed for cruise improving aerodynamic performance: a benefit of 2.5% in fuel consumption is assessed with only 10% more lift [22].
- In addition to electric motors at the leading edge, electric propellers called “wingtip propellers” are placed at wingtips. These propellers rotate in opposite direction of the vortices created by the wingtips and permit to reduce the drag induced, improving the fuel consumption. The NASA announced a benefit of +18% propulsive efficiency [23] which induces a 13% energy saving [24] thanks to these wingtip propellers. In addition, in this very specific case, distributed propellers along the wing can be retracted in order to let the wingtip propellers propel the plane and to reduce the drag during cruise.
- Another benefit of the distributed propulsion is the differential thrust in failure case: if one electric motor breaks down (among the others), the thrust could be divided on each side to avoid the use of rudder. This is another potential mass gain for future aircrafts.

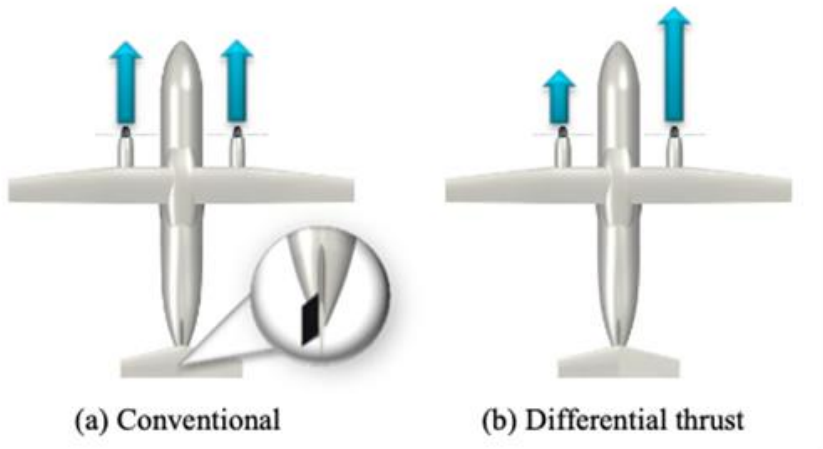


Fig. I-18: Illustration of a yaw control (Source : J. Th PhD Thesis [12]).

In the same way, the ONERA (Office National d'Etudes et de Recherche Aérospatiale) works on distributed propulsion with its European project: AMPERE [25], [26]. It is a regional full electric jet able to bring 4 to 6 Pax. This concept plane allows to study the performance of distributed propulsion on aircraft aerodynamics.

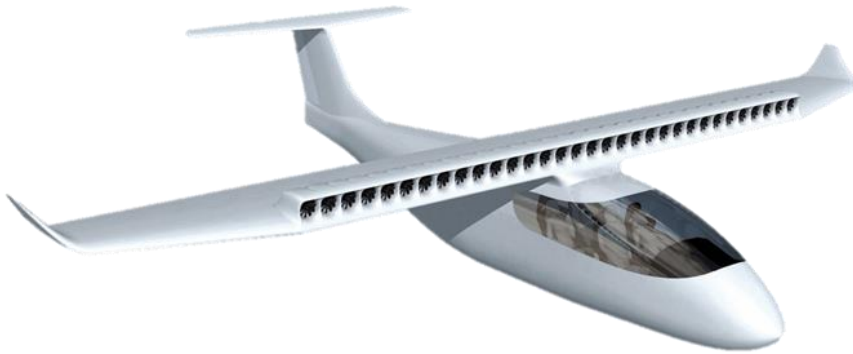


Fig. I-19: AMPERE european project studied by ONERA.

I.2.3.2 The Boundary Layer Ingestion propulsion (BLI).

In the boundary layer the air speed is lower than the aircraft speed. The BLI technique consists in injecting a reduced air flow to correct the output air flow and improve aircraft thrust. This air flow can be injected by a turbofan located at the rear of the fuselage. This principle is used in ship propulsive system. The exact principle is to place the engine downstream of the fuselage to absorb its wake and "reform" it. In Fig. I-20 a lack of air flow is created by the shape of the fuselage marked in blue, while the surplus marked in green is created by the push of the motor. In the case of BLI, the aim is to compensate for the lack of flow by repositioning the motor. The thrust is improved to obtain the same power at the level of the turbofan.

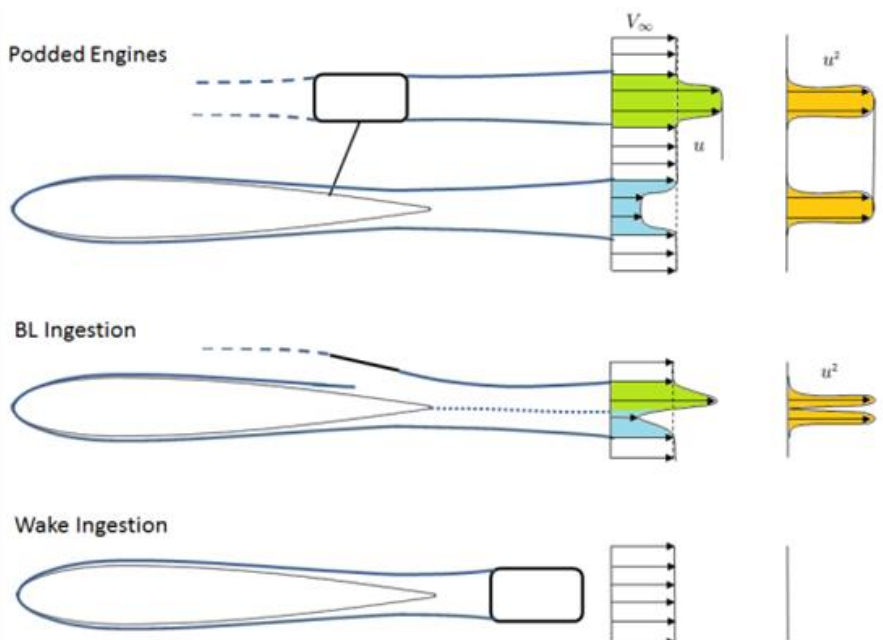


Fig. I-20: Boundary Layer Ingestion Principle (BLI) - Source ONERA [27].

NASA is working on several BLI projects:

- The first one is named Starc-ABL [28]–[32] (Single-aisle Turbo-electric AiRCraft with an Aft Boundary Layer propulsor). The aircraft integrates the BLI concept from a conventional one adding a turbofan at the end of the fuselage. The airplane is a Single aisle with a cruise speed at 0.72 Mach number at 37 000 altitude feet. The propulsion is carried out by a partially turboelectric propulsive system. Conventional turbofans are classically used under wings which are coupled through an electric generator which feeds the BLI electric propulsor at the fuselage rear.
- In the same way, the N3X concept [33]–[36] is another NASA study. The aircraft uses the BLI concept with an optimal fuselage in the wing shape (wing body). This geometric shape helps to reduce the wing length. The difference with the previous one (Starc-ABL) is to anticipate an entry in service of a turbo electric aircraft with optimistic targets in fuel consumption and noise reduction by 2035. There is also another difference in the propulsive system: The N3X concept would use electric supraconductors components to obtain a better and a maximal efficiency.

The fuel saving is between 5% and 12%, it depends of the BLI configuration.



Fig. I-21: Starc-ABL and N3X NASA projects.

On the French side, the ONERA works on the same concept through one European project called DRAGON [37], [38]. This is a partial turboelectric aircraft able to carry 150 Pax with an aircraft speed around 0.8 Mach. The BLI concept is used through gas turbines which supply the distributed electric propulsion under the wings thanks to electric generators. The twin-engines located at the rear of the fuselage help the blown wing generating thrust like turbofans.



Fig. I-22: DRAGON European project studied in ONERA.

I.2.4 Energy gains: how to operate high electric efficiency in a hybrid-electric propulsion?

The electric propulsion holds several benefits:

- Low or null emissions potential during flight.
- Reduced aircraft noise potential.
- New profile mission available for the aircraft.
- Improvement of aerodynamic performance by possible distributed propulsion.

There exist 3 levels of advancement from the more electric aircraft to the full electric one:

1. The turbo electric propulsion (propulsion made by electric motors but with a unique thermal source involving turboshafts which switch on electric generators to produce the whole electrical power).
2. The hybrid-electric propulsion (the system is supplied by two different sources: an electric one involving batteries or fuel cells and a thermal one through gas turbines).
3. The full electric propulsion (aircraft propelled by batteries or fuel cells).

Hybridization ratio in energy and power can be used and permit to locate the propulsive system at these technological advancement levels.

$$H_p = \frac{P_{ELEC}}{P_{TOT}} \text{ and } H_E = \frac{E_{ELEC}}{E_{TOT}} \quad (I-3)$$

In a hybrid electric solution P_{ELEC} represents the maximal value of power during which the propulsive system is supplied by the electric source, while P_{TOT} is the maximal power designed by the total propulsive system. In terms of energy, E_{ELEC} is the energy profile mission covered by the electric source while E_{TOT} is the total energy mission. It is possible to list the following propulsive systems with these previous indicators.

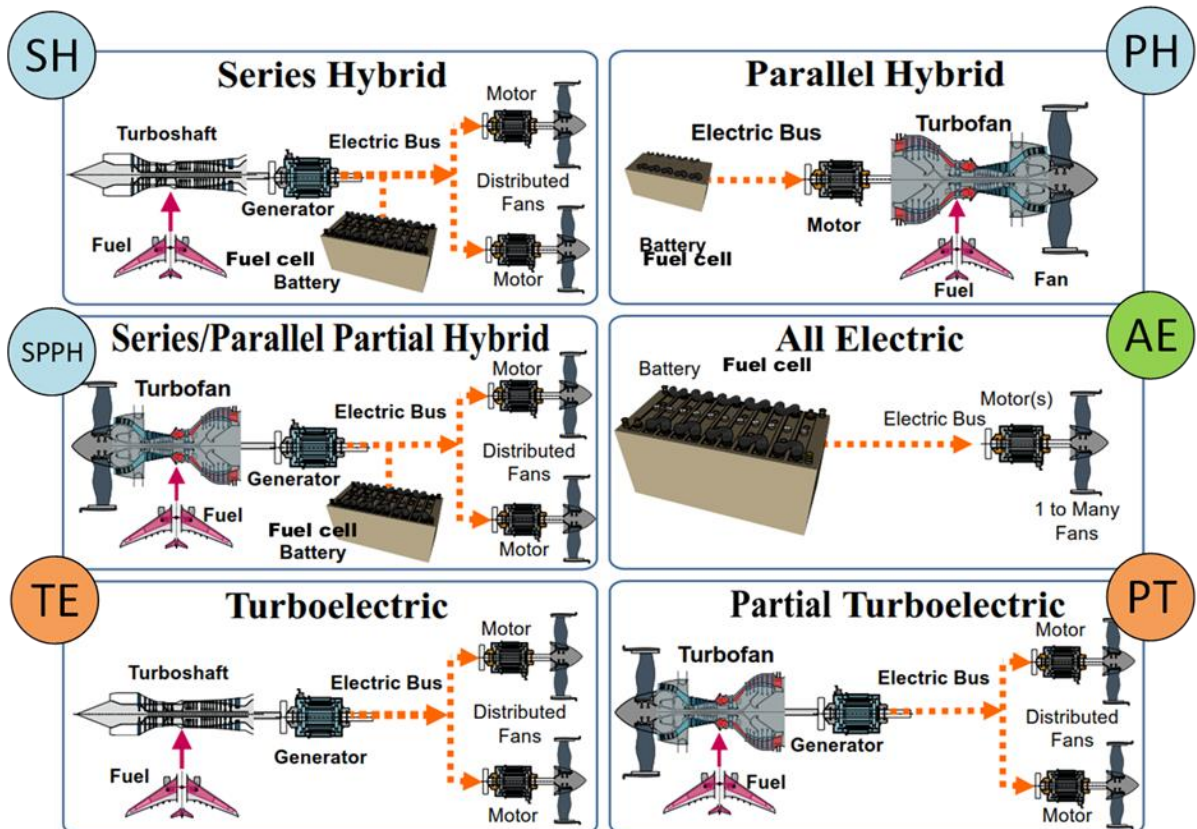


Fig. I-23: Hybrid-electric propulsive system state of the art (NASA [29]).

Table I-3: Listing of hybrid-electric propulsive system thanks to energy and power ratio.

Propulsive system	H_P	H_E
Parallel hybrid (PH)	< 1	< 1
Series/Parallel Partial Hybrid (SPPH)	< 1	< 1
Partial Turboelectric (PT)	< 1	0
Turboelectric (TE)	1	0
Series Hybrid (SH)	1	< 1
All electric (AE)	1	1

I.2.4.1 Parallel hybrid electric propulsive system (PH).

With a parallel hybrid electric propulsion design, the thermal conventional motor is relieved by the electric motor which takes over in high fuel consumption demand phases. This is exactly the same system as in automotive, especially in parallel hybrid electric buses: the electric motor is configured to operate at low speed and high torque. Given these frequency phases and the low power required, the electric motor and its power supply system (battery / power electronics) is light and not very bulky: it is not restrictive. In aeronautics, weights and volumes are problematic with snowball effects: since a more powerful propulsion system is heavier the aircraft's MTOW is impacted.

I.2.4.1.1 UTC Bombardier Dash 8-100 (hybrid-electric).

United Technologies Advanced Projects (UTAP), a subsidiary of the American leader in aeronautical equipment in 2017 (UTC Aerospace), has embarked on the electrification of aircraft by redeveloping the propulsion system of a 78 Pax aircraft [39]: Bombardier Dash 8-100. The power range of the current propulsive system is about 2 megawatts, the project consists in undersizing the gas turbine by about 1 MW (optimal cruise power) with an additional 1MW-electric propulsion (e-motor and batteries) to complement the 2MW take off power. In this case, the electric source assists the thermal engine during the phases of high-power demand (take-off and climb). According to the Original Equipment Manufacturer (OEM), the fuel economy on a one-hour mission should be around 30%. Both motors (thermal and electric) are mechanically connected by a reduction gearbox (cf Fig. I-24) which is designed to adapt the rotational speed between propellers, eMotors and engines. The advantage of this topology is its simplicity: The electric motor is easy to install in a conventional propulsion system, mechanically coupled to the gas turbine. This is a short-term solution; indeed, the design power of the electric devices is reduced.

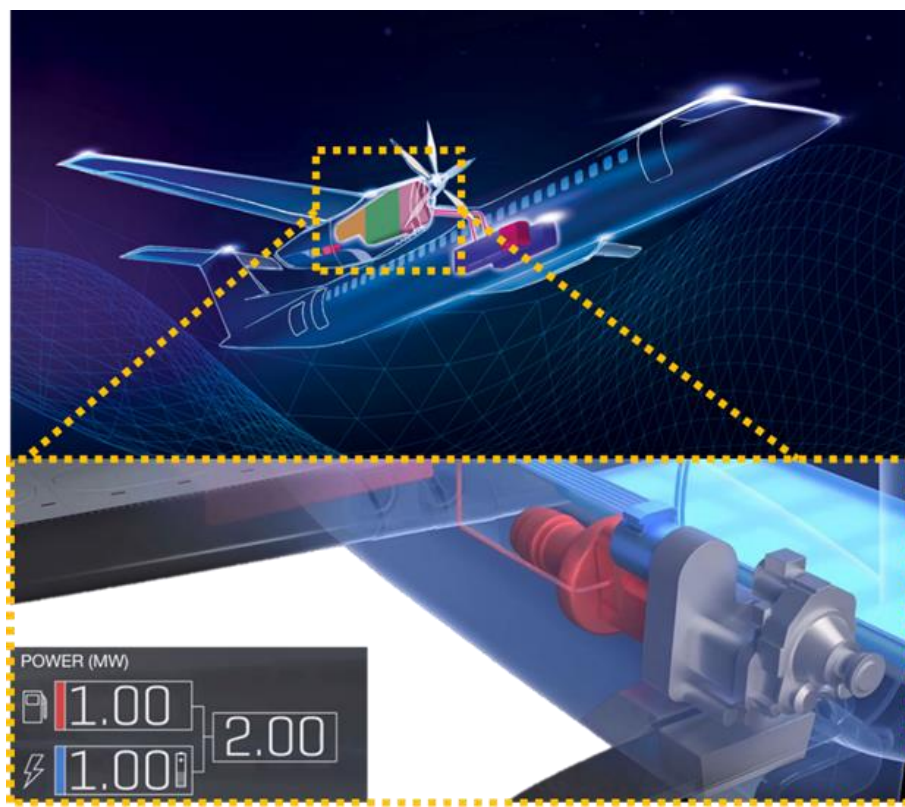


Fig. I-24: 804 Project - UTAP parallel hybrid-electric propulsion system.

I.2.4.1.2 Ampaire Electric EEL.

Still in the USA, a start-up called AMPAIRE has already flown a prototype hybrid-electric parallel aircraft, in June 2019 at the Camarillo airport in California. This was the first flight of a hybrid-electric powered aircraft. The prototype comes from a conventional aircraft (the Cessna 337 Skymaster) [40], whose propulsive system is hybridized with an electric motor and battery system that optimizes fuel consumption in parallel with the conventional combustion engine.



Fig. I-25: Ampaire Electric EEL.

I.2.4.2 Propulsion Series/Parallel Partial Hybrid (SPPH).

Compared to the parallel hybrid system, this partial serial/parallel hybrid electric propulsion system consists of a turboshaft engine that partly drives an electric generator powering electric motors distributed along the wing of the aircraft and coupled to batteries. The thrust of the aircraft is generated by electric and thermal engines.

I.2.4.2.1 Eco-Pulse Project

A collaborative project with SAFRAN, AIRBUS and DAHER named Eco-Pulse project [41] aims to develop an aircraft with this specific propulsive system.



Fig. I-26: Eco-Pulse project (Series/Parallel Partial Hybrid).

Propulsion is divided between the turboprop (single engine in the middle) and the electric motor on the wings. The aircraft can carry 6 Pax with a total power of 600 kW. The

main idea of this architecture is to provide take-off and landing in fully electric mode and to use the thermal part for the low fuel consumption phase: cruising. The first flight of this aircraft is planned for 2022.

I.2.4.2.2 Voltaéro – Cassio

A French start-up named VOLTAERO [42] is also in the race for hybrid-electric propulsion and has chosen a partial series/parallel hybrid-electric propulsion system. This small company is the continuity of the AIRBUS E-fan as its founders are the main protagonists responsible for the all-electric two-seater program in 2011. The available power of the aircraft is about 440 kW and the airplane should carry 4 to 9 Pax. As before, the objective of this study is to combine the advantages of electric propulsion with those of conventional propulsion. Two 60-kW electric motors are placed at the front of the plane and will be used during take off and climb, powered by batteries. The 170-kW combustion engine will drive 3 electric generators to recharge the batteries and propel the aircraft during the cruise phase. The original plane is the same as for the start-up AMPAIRE: Cessna 337 Skymaster.



Fig. I-27: VOLTAERO Cassion hybrid-electric aircraft.

I.2.4.3 Partial Turbo electric propulsive system (PT).

The only benefit of this propulsion system is the improved aerodynamics of the aircraft. The partial turbo-electric propulsion combines conventional and electric propulsion: the aim is to use the compactness and additional degrees of freedom offered by electric devices to improve the air flow around the airplane. The Starc-ABL (Fig. I-21) and the DRAGON project (cf Fig. I-22) are good examples of this propulsive system. It is a first step towards the turboelectric aircraft.

1.2.4.4 Turbo Electric propulsive system (TE).

This time, the complete propulsion is electric (not to mention sources). The goal is once again to use electric motors to improve the aircraft aerodynamics. Another example is the Aurora Lightning Strike which is a Vertical Take Off and Landing aircraft (VTOL). This is a new and growing market where hybrid-electric and fully electric propulsion will be used.



Fig. I-28: VTOL Aurora Lightning Strike.

The path to the all- electric aircraft is not easy and a series hybrid-electric architecture will be more interesting to study in order to anticipate the future technologies.

1.2.4.5 Series Hybrid propulsive system (SH).

A series hybrid electric propulsion system (see Fig. I-23) is composed of gas turbines as main energy sources that drive electric generators. This architecture is also powered by auxiliary electric sources consisting of batteries or fuel cells.

In such powertrain, generators may be directly coupled to electric propulsion with an AC architecture. Another option consists in coupling generators to a DC distribution through voltage rectifiers. Depending on the power range, a ultra-high voltage (uHVDC – beyond the conventional voltage of $\pm 270V$) standard can be involved in the Electric Power Distribution Unit (EPDU): this option is studied in our thesis involved in the HASTECs project presented latter in this chapter. This power distribution unit supplies electric motors by inverters that drive propellers through a gearbox. Several ambitious projects are being studied all over the world:

1.2.4.5.1 E-Fan X collaborative project

This European project brings together major companies such as AIRBUS, ROLLS-ROYCE and SIEMENS to design a hybrid propulsion system in a regional aircraft the BAE 146. This aircraft is equipped with 4 turbofan engines and the consortium's project foresees the replacement of one gas turbine by an electric motor. The replaced gas turbine is located in the fuselage and is coupled to a 2 MW electric generator to build a series hybrid propulsion system. A 2 MW battery pack is also installed at the rear of the fuselage to study the hybrid mode.

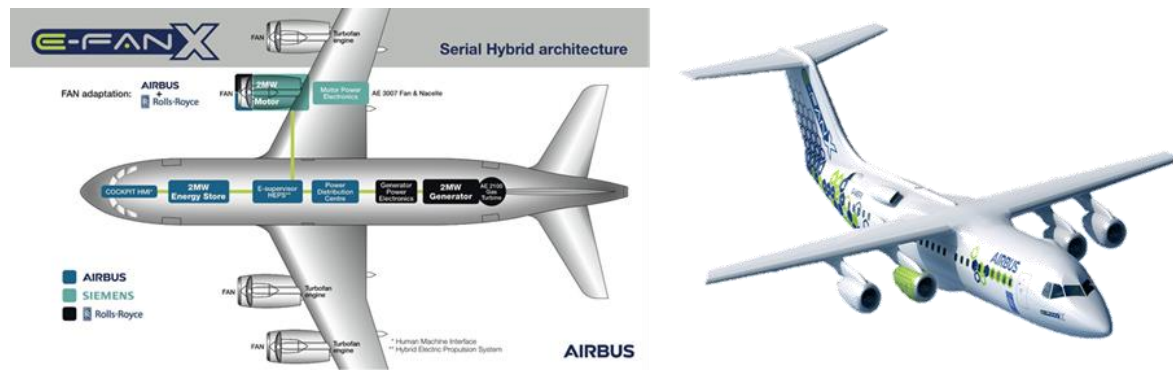


Fig. I-29: E-fan X description and its propulsive system [43].

The objective is to anticipate the arrival of the all-electric aircraft. This “flying laboratory” aims at exploring the challenges of high-power propulsion systems to enable a less polluting commercial flight (thermal effects, electric thrust management, altitude and dynamic effects on electrical systems...).

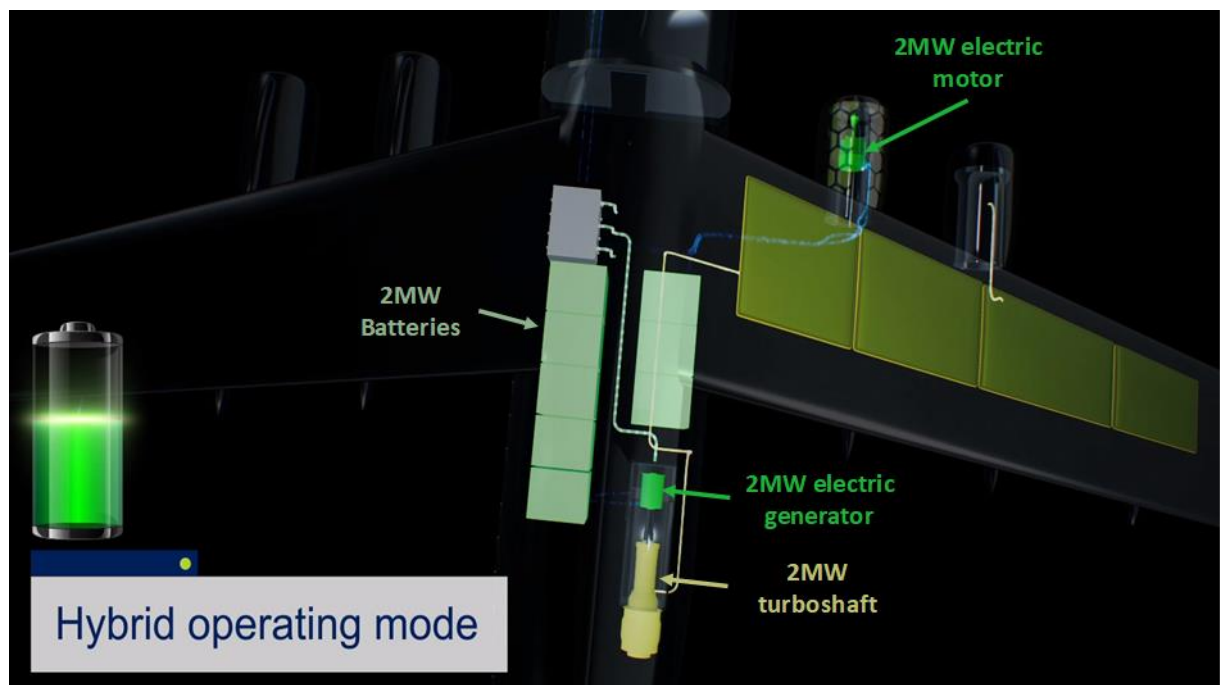


Fig. I-30: E-fan X architecture description.

Despite the great compactness of electric motors (green) compared to turboshafts (yellow), the main challenge of the more electric aircraft remains the electric source and the powertrain. In this case (See Fig. I-30Fig. I-22) the batteries (light green “cabinets”) are sized at 2 MW. The biggest challenge of electric propulsion is the compactness and the weight of the electric devices, especially the energy sources.

I.2.4.5.2 Zunum Aero.

For this American start-up, the aircraft sizing is more reduced. The company supported by Boeing is considering a family of hybrid-electric regional aircrafts. The first element of this family is the ZA10 able to carry 10 Pax operating over a distance of 600 nm range. The concept of the aircraft is based on the use of an either all-electric or hybrid-electric mode to extend the flight mission. In this case the gas turbine will be used in the cruise phase.

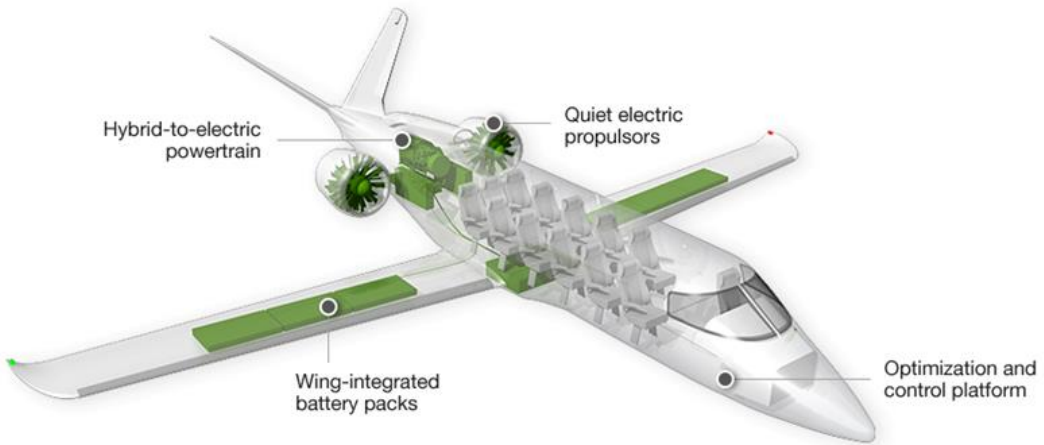


Fig. I-31: ZA10 description concept [44].

In this aircraft a partnership with SAFRAN has been signed and a 500-kW helicopter gas turbine will be the thermal source for hybrid-electric ZA 10.

I.2.4.5.3 Bell NEXUS.

Once again, the hybrid electric propulsion concept can be applied to VTOL and STOL (Vertical & Short Take-Off and Landing aircraft). The Bell NEXUS concept is a hybrid-electric air taxi using a series hybrid-electric propulsion. A thermal source will power a distribution core through electric generators, in the same way as a battery pack. Hybridization is necessary to extend the range of these aircrafts.

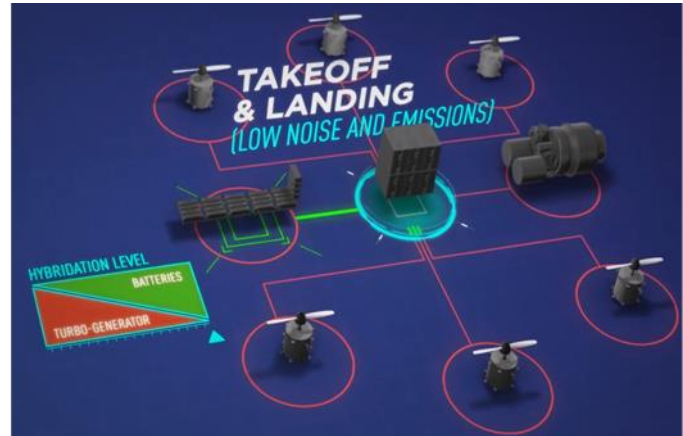


Fig. I-32: VTOL Bell NEXUS propulsive system description from SAFRAN [45].

1.2.4.6 All-electric propulsion (AE).

There is still a long way to go before flying an all-electric drive. The major problem with electrification is energy storage, but the study of small aircrafts is still ongoing. Since 2010, (with the Cricri [46]) commercial aviation has been eager to see electric flights in order to obtain more efficient and lighter propulsion systems to integrate them in heavy / powerful aircraft.



Fig. I-33: Airbus E-fan [46], [47] and Siemens Extra 330LE all electric aircraft.

In 2017, the Siemens has propelled the aerobatic plane Extra 330 flying at more than 340 km/h [48], thanks to an electric motor. The specific power of this electric motor exceeds 5 kW/kg. This is a world record for a plane weighing more than one ton. Beyond these exceptional exploits, a newborn Israeli aviation company, Eviation, is working on another all-electric aircraft. The start-up presented its e-aircraft Alice at the Paris Air Show in 2019. The airplane plans to carry 9 Pax thanks to an all-electric propulsive system of 800 kW. The electric source is composed of Lithium-Ion batteries (Li-Ion) and 95% of the fuselage is made of composite.



Fig. I-34: Eviation Alice (Paris Air Show 2019).

Two electric motors have been chosen by the company: the SP-260D Siemens e-motor [48] and the Magni250 magniX e-motor with a power of about 250 kW each. The first one is a radial electric motor while the other is an axial flux electric motor. The choice of the electric motor is essential in an all-electric drive; it is the most important electrical component to design. A new record has been set by the all-electric hydroplane company powered by the

magniX company: HARBOUR AIR which made its first commercial electric flight the 10 December 2019.



Fig. I-35: Successful Flight of World's First Commercial Electric Airplane (Harbour Air – magniX [49]–[51]).

Another axial flux electric motor was chosen by Rolls-Royce with its all-electric aerobatic plane project. The name of the project is: ACCEL [52], [53], the propulsive system is composed of three Yasa 750R e-motors [54] in order to approach the 750-kW maximum required power.



Fig. I-36: ACCEL project (Rolls-Royce).

The aim of the study is clear as Rolls-Royce industry wants to reach a speed of 480 km/h. Owing to this speed the airplane will be the fastest all-electric plane in history. Rolls-Royce is joining the electric race by working on the all-electric propulsion system thanks to electric motor specialists such as Yasa motors.



Fig. I-37: CityAirbus [55].

Alongside these new generations of aircrafts, the VTOL and STOL aircraft are also in the all-electric race. The European aircraft manufacturer is working on the CityAirbus, a four-seater multi-copter vehicle. The prototype is currently undergoing a flight test period. The power of the aircraft is about 800 kW powered by Lithium-Ion batteries. The VTOL and STOL market is growing rapidly: the aircraft manufacturer wants to relieve road traffic congestion and make it more fluid.

I.2.5 Towards greener aircrafts: hydrogen power, a huge challenge that seems reachable

So far, most hybrid electric aircraft are battery-powered, but hydrogen with ICE or fuel cells should not be overlooked. The subsidiary H3 Dynamics (HES Energy systems) announced in 2018 the first regional aircraft powered a 100% by hydrogen: Element One. The evolution is logical: The Singaporean company has been working for 10 years on a hydrogen drone. The aircraft could carry four Pax over distances between 500 and 5,000 km depending on storage (liquid or compressed).



Fig. I-38: Element One (Hydrogen powered aircraft).

A promising American start-up, ZeroAvia, has the same objective: to get a hydrogen-powered plane off the ground. The ambition is greater than the previous one as the plane will carry 6 to 20 passengers on journeys of up to 500 miles. The goal of the Californian company is to change the conventional propulsion system to use a hydrogen-powered plane. Several flight tests are underway on regional aircrafts.



Fig. I-39: Hydrogen aviation vision by ZeroAvia.

Hydrogen seems to be the most promising energy vector in aeronautics thanks to its specific energy. Compared to batteries, the specific energy, recharging time and recycling are better arguments in favour of the fuel cell and its hydrogen storage. But the technological maturity of fuel cells and hydrogen storage is not as developed as that of batteries. This is why batteries are still more used in electrical applications. The American aerospace agency NASA is interested in carbon-free power sources: a project has been launched with the idea of a plane powered by liquid hydrogen. [56].

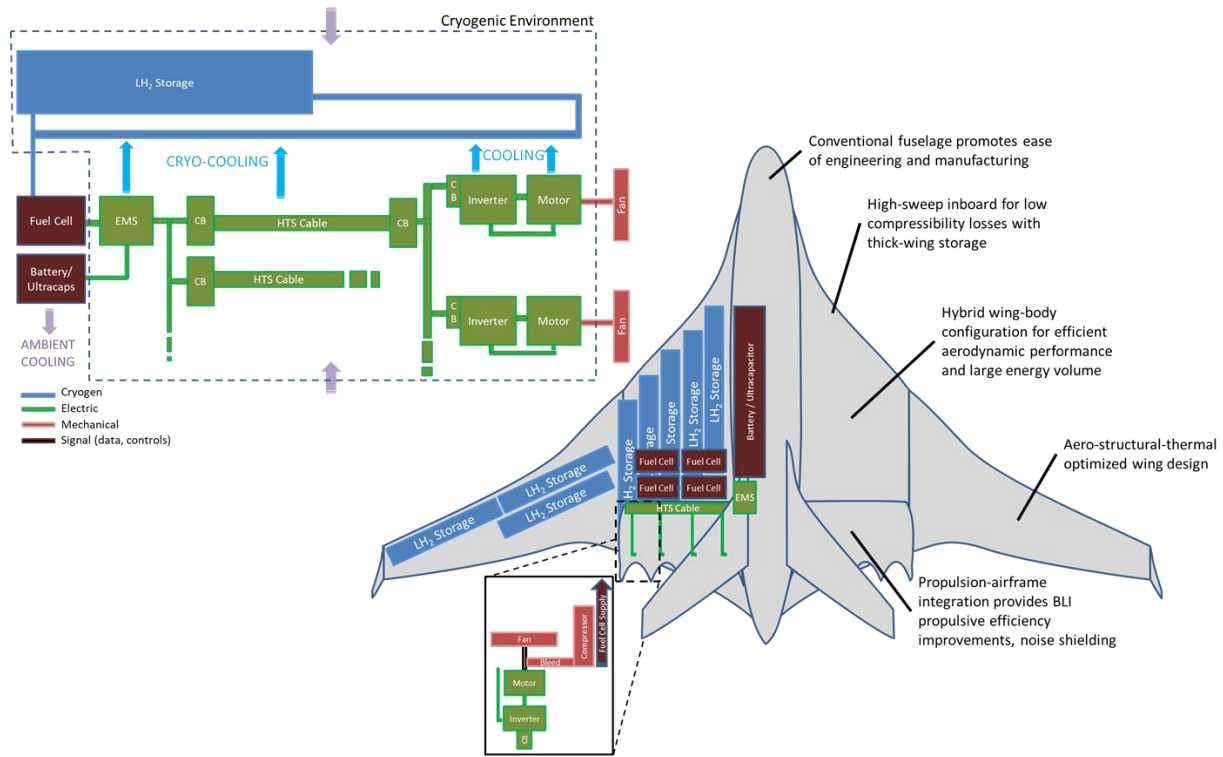


Fig. I-40: Cryogenic hydrogen powered aircraft NASA project.

The liquid hydrogen storage is more efficient than pressured one. The only disadvantage is the very low operating temperature (20 K degrees). The storage of liquid hydrogen is more efficient (15% compacity) than storing hydrogen under pressure (5% compacity). The objective of this study is to use the cryogenic cooling of hydrogen to cool the other electrical components. The cooling of superconducting electrical components allows better performance (low losses) on the electrical conversion chain.

An initial awareness of the climate emergency that has been growing since the end of 2019. With the advent of the Covid19 pandemic, the entire trajectory of global aviation has been called into question. The lockdown measures taken by various governments around the world have caused air traffic drop in particular in Europe the air traffic fell by 88% [2], [3] (see Fig. I-41).

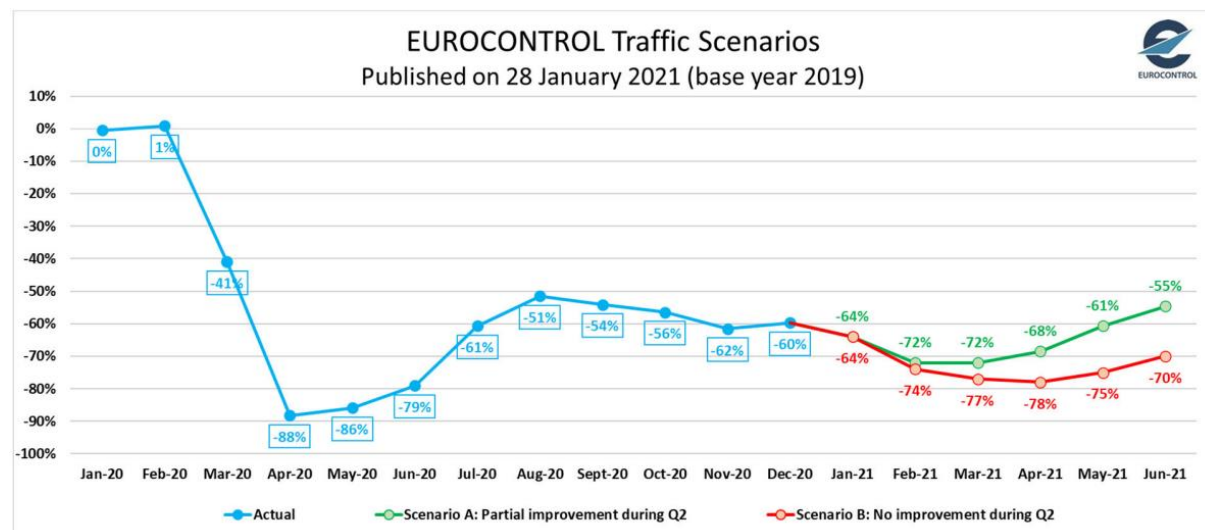


Fig. I-41: EUROCONTROL draft Traffic scenarios (European aviation).

The entire aviation industry is concerned about these numbers. The lack of coordination between states and the lack of confidence on the part of passengers do not help the scenario. The decline in air activity may be a sign of economic crisis, but it is a positive for the planet. This could be an opportunity for the aviation industry to adapt its most polluting practices in order to maintain the reduction in CO₂ emissions that is essential to achieve the objectives of the Paris Agreements.

In 2020, the European Union (EU) announced its Clean Hydrogen Plan [57], European Member States put hydrogen at the top of their investment priorities as part of the post-Covid-19 economic recovery. In particular, France and Germany have planned to devote 7 and 9 billion euros respectively of public funds in the hydrogen industry. The systemic approach is the one that has been favoured and which directs consciences towards hydrogen. Electricity networks are not capable of supporting the battery-powered electricity revolution; it is necessary to be able to store the excess energy at sometimes of the year so that it can be reused later on at times when the energy demand is greater than the production.

About aviation, hydrogen feasibility study, made by Clean Sky 2 and Fuel Cells & Hydrogen 2 Joint Undertakings has been realized and presented in June 2020 [58]. “*Hydrogen as an energy source will play a key role in transforming aviation into a zero-carbon / climate-neutral system over the next few decades.*” According to the study if several scenarios are studied, hydrogen seems to be the main actor (burned in turbines, or used through fuel cells). It would be feasible to propel airplanes for regional distances using fuel cells (see Fig. I-42 and Fig. I-43).

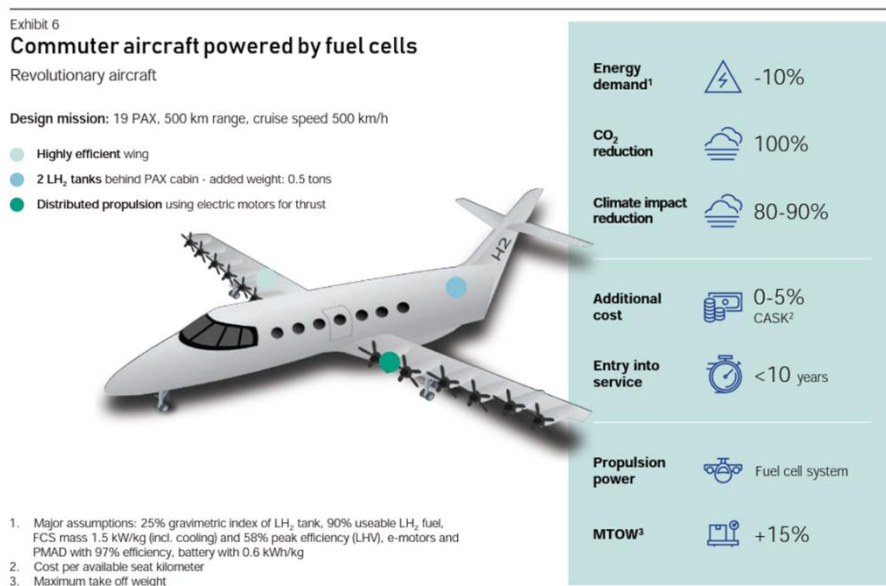


Fig. I-42: Commuter aircraft powered by fuel cells.

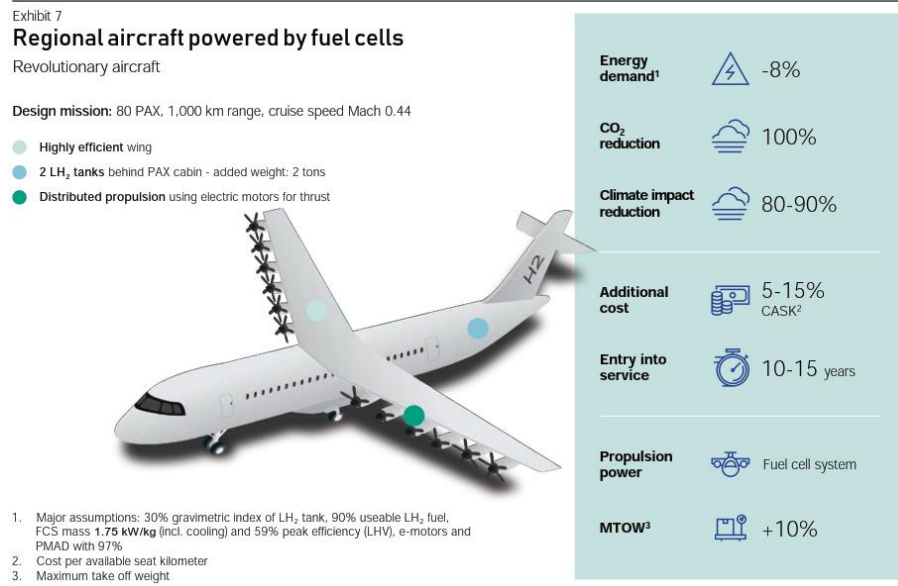


Fig. I-43: Regional aircraft powered by fuel cells.

In the regional aircraft case, for a reasonable weight gain (+10%), the gains on the environment are considerable (-100% CO₂). The high specific energy of the hydrogen molecule combined with the efficiency of the all-electric propulsion chain saves the energy required to fly the aircraft (-8%). With the assumptions taken by the McKinsey company, hydrogen seems to be a viable solution to propel small aircraft using fuel cells.

European entities are not alone in believing in the hydrogen revolution in aeronautics, several private industries are also betting on. A general aviation project (see Fig. I-44) in Belfort was also unveiled, promising to carry 6 passengers, have a range of 1,500 km and reach a cruising speed of 370 km/hour.



Fig. I-44: Avion Mauboussin fuel cell powered aircraft concept (AlcyonM3c)[59].

Concerning single-aisle aircrafts, three hydrogen-powered aircraft projects (see Fig. I-45) were recently unveiled by the European aircraft manufacturer Airbus.



Fig. I-45: Airbus ZEROe aircraft concepts[60].

- A turboprop aircraft able to carry about 100 Pax with a maximum range of 1000 nm.
- A turbofan aircraft able to carry about 100 Pax with a maximum range of 2000 nm.
- Finally, the most technologically advanced aircraft a blended-wing body which has the same characteristics as the turbofan.

They all use liquid hydrogen storage as an energy source.

In addition to airplanes, the world of VTOL is also looking for a way into hydrogen. The American company Skai, supported by NASA, imagines to bring five passengers in a new electric vertical take-off landing (VTOL) air taxi using a hydrogen fuel cell powertrain.



Fig. I-46: Alaka'i Skai Hydrogen powered VTOL air taxi[61].

The effervescence around hydrogen is palpable, and with aeronautics, all mobility seems to be turning towards this energy vector.

Let's start with the automobile, only a few companies at the moment, such as Toyota has been developing the hydrogen-powered car model since 2015: The Toyota Mirai. A second edition, released very recently[62], significantly improves the vehicle's performance.



Fig. I-47: Toyota Mirai 1 & 2 (hydrogen powered car).

Hopium, the first 100% hydrogen car manufacturer founded by French driver Olivier Lombard, plans to present the first prototype of its "Hopium Māchina" model in 2021. This innovative vehicle [63] with a neutral carbon footprint will offer an exceptional range of 1000km.



Fig. I-48: Hydrogen Motive Company: the Hopium Machina.

Let's continue in the maritime field, with yachts. In October 2020, Hynova Yachts presented the world's first hydrogen-powered yacht [64].

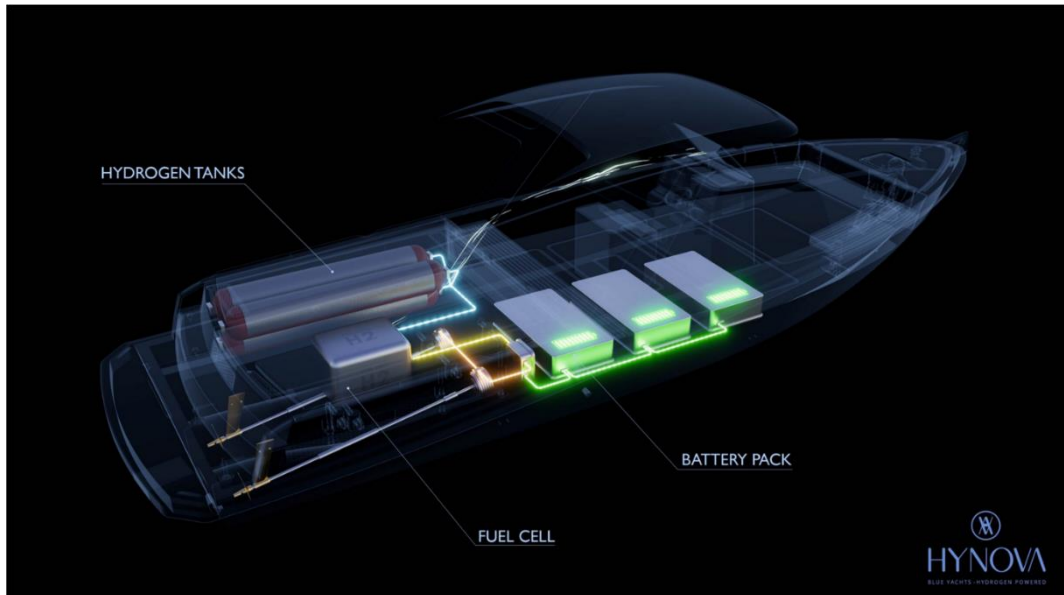


Fig. I-49: Hynova yachts: hydrogen propulsion system

Approximately 12 meters long, the yacht can accommodate up to 12 people and is propelled by an electric motor powered by a fuel cell. There are many other companies that have decided to use hydrogen in their activities.

The difference between these mobilities that require less energy (car, boat, etc...) and aeronautics is the sensitivity to weight, and against this problem fuel cells equipped with a hydrogen tank are much more promising than battery-powered system.

Hybrid-electric aircraft propulsion was beginning to promise us advances on more electric aircraft, but hydrogen brings us the real solution by integrating a real breakthrough technology in our aircraft.

Hydrogen is well on its way to launch the third industrial revolution!

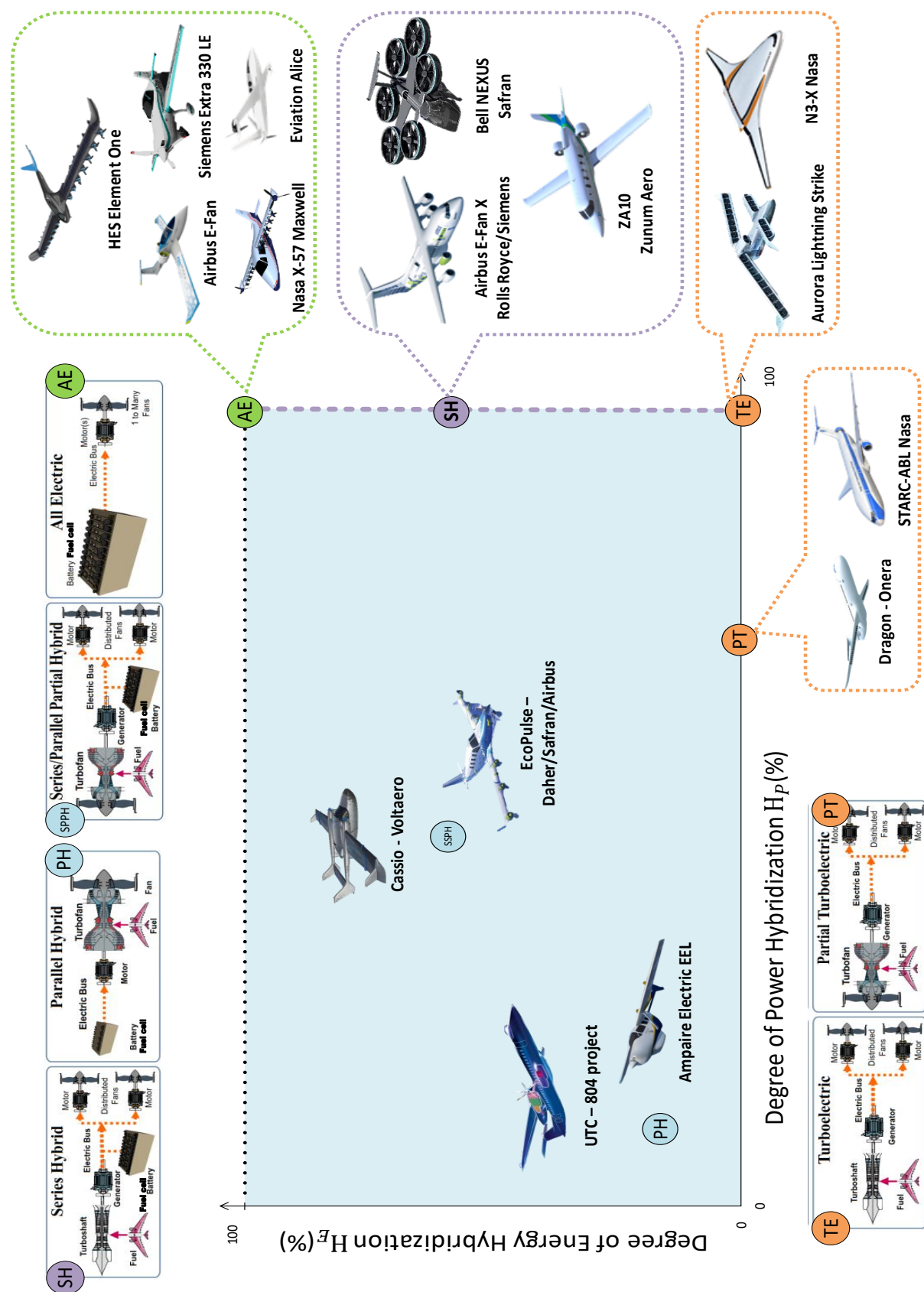


Fig. I-50: Hybrid electric aircraft representation considering hybridization power degree and hybridization energy degree.

I.3 Presentation of the HASTECS Project and thesis objectives.

Some further research is contained in HASTECS, a European project in the framework of CleanSky II. HASTECS means: Academic Research on Hybrid Aircraft Thermal and Electrical Components and Systems. The objective of the project is to identify disruptive technologies to significantly improve the specific power and efficiency of electrical components used in hybrid electric aircraft. The stakes are high because, unlike in the automotive, rail or even maritime sectors, the weight of the propulsion system is not the main concern of designers. In aeronautics, weight is the first enemy, which is why objectives have been set within the framework of the project in order to lead the studies with a first level of entry into service in 2025 and a second level of entry into service for 2035. The objectives are as follows:

Table I-4: HASTECS electric component targets.

	2025 target	2035 target
Electric motor + cooling system		
Specific power	5 kW/kg	10 kW/kg
Cruise efficiency	96%	98.5%
Maximal design point efficiency	94.5%	97%
Power electronics + cooling system		
Specific power	15 kW/kg	25 kW/kg
Cruise efficiency	98%	99.5%
Maximal design point efficiency	96.5%	99%

The basic design of the aircraft is a series hybrid-electric architecture, consisting of turboshaft engines as the main source, and batteries and/or fuel cells as auxiliary sources. Each propeller is connected to a gearbox that adjusts the rotation speed between the propeller itself and the electric machine. The electric motors are powered by power inverters, which are themselves electrically connected to an electrical power distribution centre generally known as ultra-high voltage direct current (uHVDC), ultra meaning that the selected bus voltage is beyond the standard voltage network which is ± 270 V.

I.3.1 Input data.

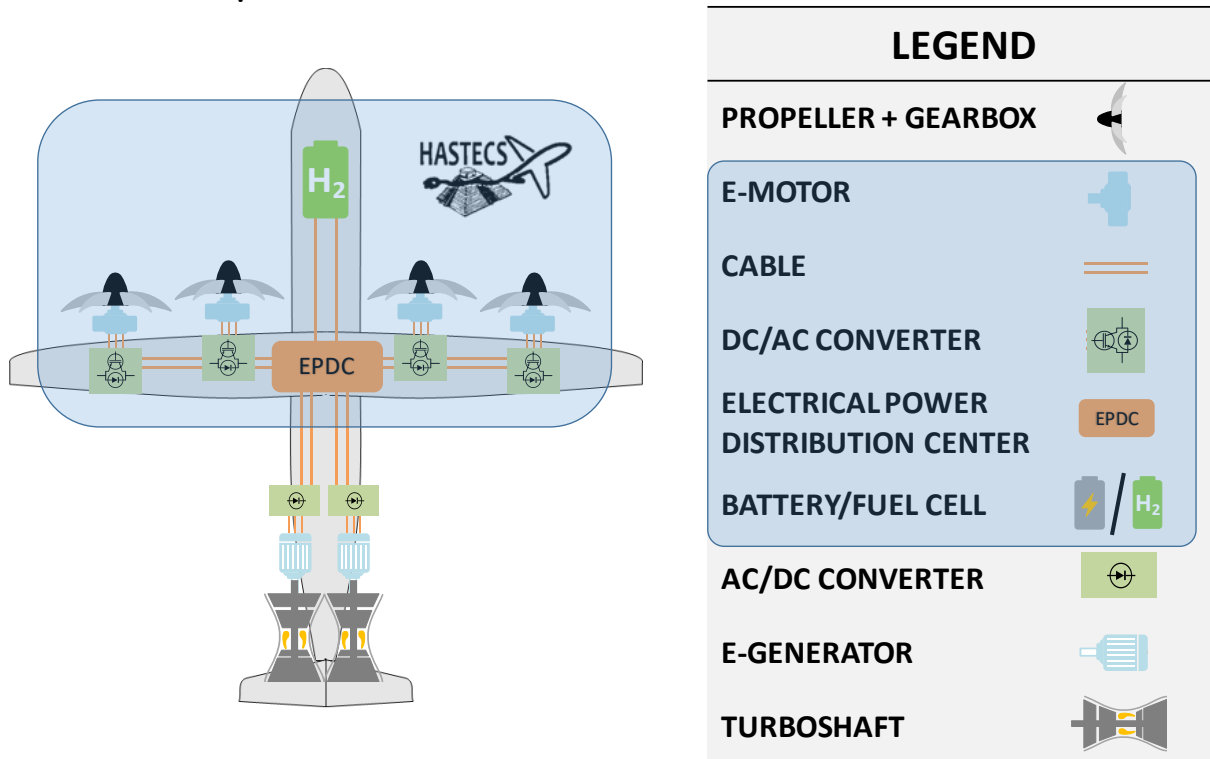


Fig. I-51: HASTECs project reference aircraft.

The aircraft under consideration is based on an ATR-72 which can carry 70 passengers with a reference maximum take-off weight ($MTOW_{ref}$) (without electric propulsion cf [65]). The different mission profiles are given in requirements (see Fig I-42). This reference aircraft has been defined with Airbus, the HASTECs project leader, setting power, thrust and speed requirements:

- Flies to 25000 feet in a cruise altitude.
- Flies at 0.5 Ma at cruise altitude.
- Takes off with an 80 kN- thrust.
- Takes off with a 4 MW power ($P_{aircraft} = Thrust_{aircraft} \times V_{aircraft}$).

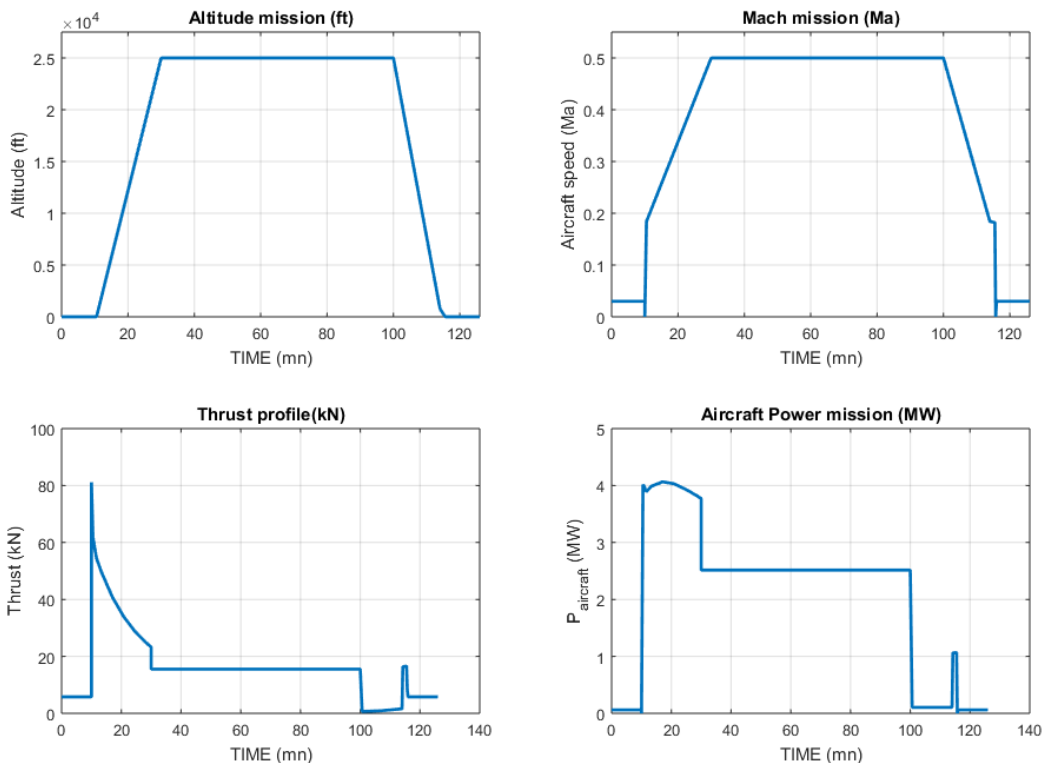


Fig. I-52: Altitude, Mach, Thrust, Aircraft power profile missions.

Table I-5: Flight phase duration.

Flight phase	Taxi (in & out)	Take off & Climb	Cruise	Descent	Approach and landing
Time (min)	5	20	70	14	2

The variation of the speed of sound is taken into account in an environment model. The flight domain of the studied regional aircraft corresponds to the following figure:

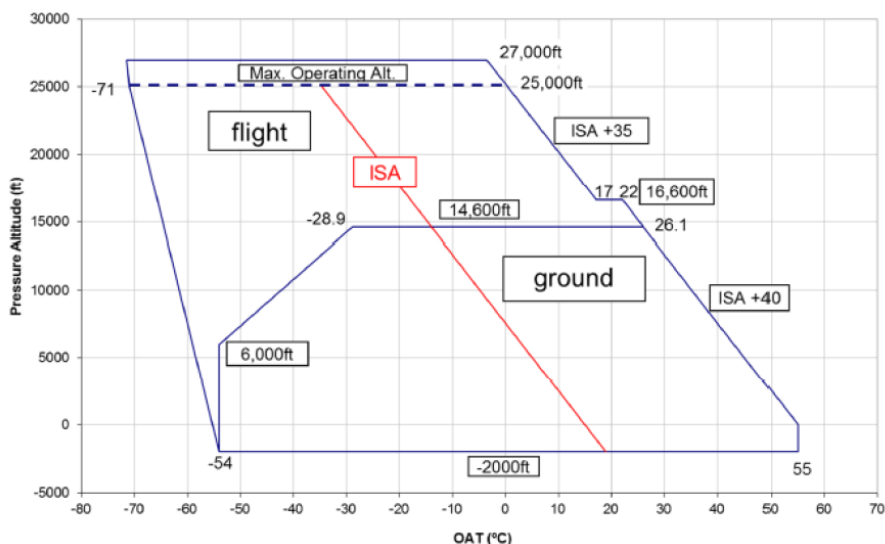


Fig. I-53: Environmental aircraft flight domain conditions (OAT: Outside Air Temperature).

In addition to these design areas, the propeller design must face certain constraints. The main constraint to be checked is the blade tip speed (this latter speed V_b is defined in the scheme below). The maximum blade tip speed must be less than 80% of the speed of sound, as the performance of the propeller is strongly degraded beyond this value. The use of a speed triangle makes it possible to define the blade tip speed versus both the aircraft speed and the tangential rotation speed of the propeller:

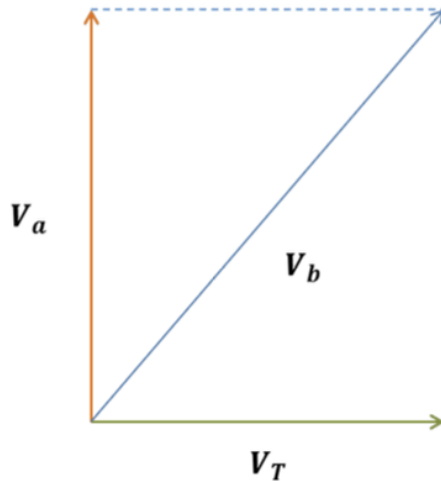


Fig. I-54: Speed triangle (Aircraft speed = V_a ; tangential rotation speed = V_T ; blade tip speed = V_b).

The diameter of the reference propeller (a four-propelled-drive aircraft) and the dimensions of the nacelle are given in the requirements:

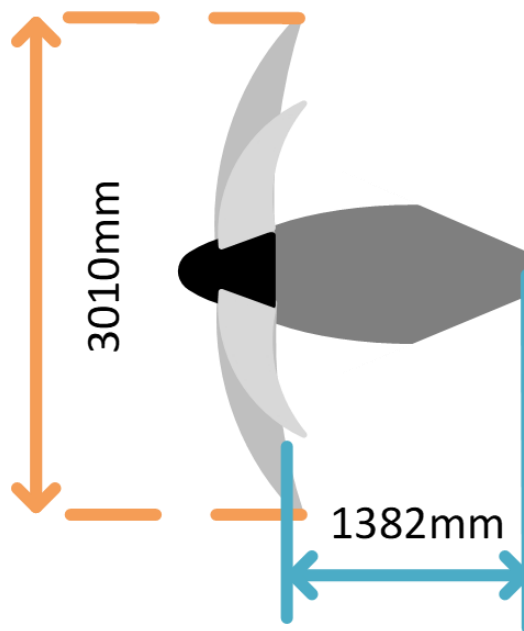


Fig. I-55: Nacelle and propeller sizes.

1.3.2 Project description

From a technical point of view, the project is divided into several work packages (WP), which involve 6 PhD theses and 2 post doc:

1. The WP1 aimed at developing an analytical tool for the design of electric motors. The objective of this work package was to find electric machines with high performance in terms of specific power and efficiencies. This work has been done by the “GREM3” research group in the LAPLACE lab in Toulouse.
2. WP2 done by the LAPLACE “CS” (Static Converter Group) research team was in charge of developing high performance power electronics and design tool. They had to find breakthrough technologies for power converters (inverters and DC DC choppers) in order to highlight the best topology with the best integration performance.
3. WP3 was in charge of developing a tool for the design of high-performance cooling device for electric motors. The objective of the study was to imagine the best technologies and concepts for cooling electric motors. This research has been done in the PPRIME institute in Poitiers.
4. The WP4 mission was quite similar the one dedicated to the WP3 but for power electronic cooling. The aim was to find efficient cooling concepts and technologies to optimize the specific power of the overall power electronic system. This research group is located in the PPRIME institute in Poitiers.
5. The fifth working group has studied partial discharges and their impact on high power electrical devices (power electronics, bus bars and electric motors) by taking account of the aircraft environmental conditions (altitude, pressure, temperature). The partial discharge phenomenon can create temporary short circuits if the insulation is damaged. This LAPLACE “MDCE” research group was in charge of that study.
6. Finally, our thesis is situated in the WP6 which has to integrate all devices in the powertrain and every subsequent fields. A design-oriented model has to be developed based on both state of the art, Airbus data and other work packages in order to optimize the overall hybrid-electric traction chain. A post doctoral study also achieved a review of auxiliary electric sources (batteries and fuel cells) in the typical framework of HASTECS (related to a serie hybrid electric powertrain). These studies have been done by the LAPLACE “GENESYS” research group in Toulouse.

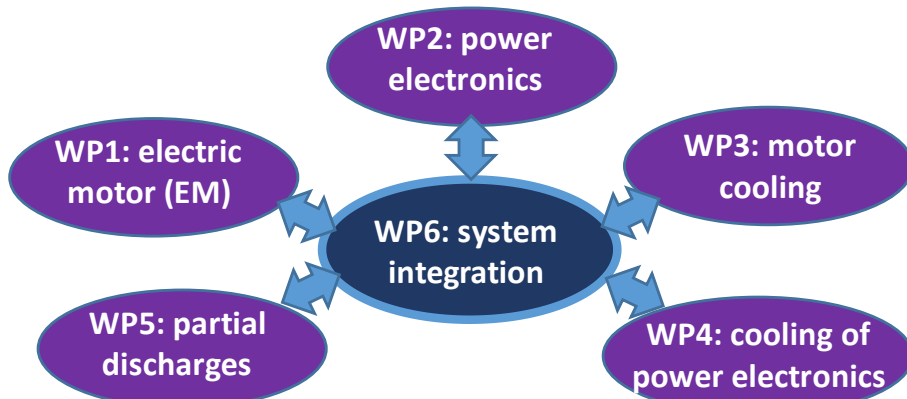


Fig. I-56: Interactions between the system integration work package and the others.

The project leaded by Airbus has been coordinated by the “Toulouse INP” University and includes the following entities:

- Université Toulouse III Paul Sabatier, Toulouse (UPS).
- Institut Supérieur de l'Aéronautique et de l'Espace - Ecole Nationale Supérieure de Mécanique et d'Aérotechnique de Poitiers (ISAE-ENSMA).
- Centre National de la Recherche Scientifique (CNRS).

Three research labs were also involved:

- CIRIMAT Carnot Institute (WP6).
- Laboratoire Plasma et Conversion d'Energie (LAPLACE) (WP1/WP2/WP5/WP6).
- P PRIME Institute (WP3/WP4).

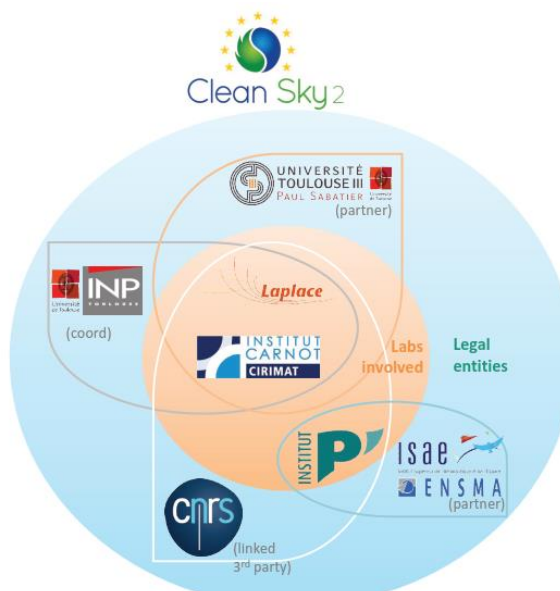


Fig. I-57: Academic HASTECS project perimeter (universities and laboratories).

I.3.3 A major “snowball effect” involving an integrated looped process

The hybridization of a regional aircraft is a complex challenge considering that electrical components are added in the hybrid powertrain compared with a full-thermal airplane. Despite the “hopefully” high efficiency power chain, both the powertrain mass and the power to be supplied are significantly increased. This double effect due to the additional mass and the increase of the supplied power leads to an additional fuel mass itself potentially increasing the aircraft structure (wing surface). This successive increase of the embedded mass is wellknown in aircrafts as a “snowball effect” which constitutes a major effect of hybrid aircrafts to be included in the design process. In our case, with regard to the reference value of the MTOW (see the reference aircraft definition in the section III.1), this snowball effect has to be integrated. In order to do that, a looped process has been implemented considering both a reference MTOW ($MTOW_{ref}$) and a reference thrust $Thrust_{ref}$ which correspond to the figure linked with the reference aircraft (defined in III.1). Following the added weights from all designed devices, a “new MTOW” ($MTOW_{new}$) is estimated from which a “new Thrust” is derived. This derivation is based on the linear approximation in Equation (I-4):

$$Thrust_{new} = Thrust_{ref} * \frac{MTOW_{new}}{MTOW_{ref}} \quad (I-4)$$

Both efficiency and weight are assessed from each component model at the end of each iteration of the looped process. After one iteration, based on the new (after redesign) MTOW ($MTOW_{new}$) and its ratio versus the weight reference value ($MTOW_{ref}$) at the initial point of the process, a new thrust must be derived as illustrated in the next figure Fig. I-58:

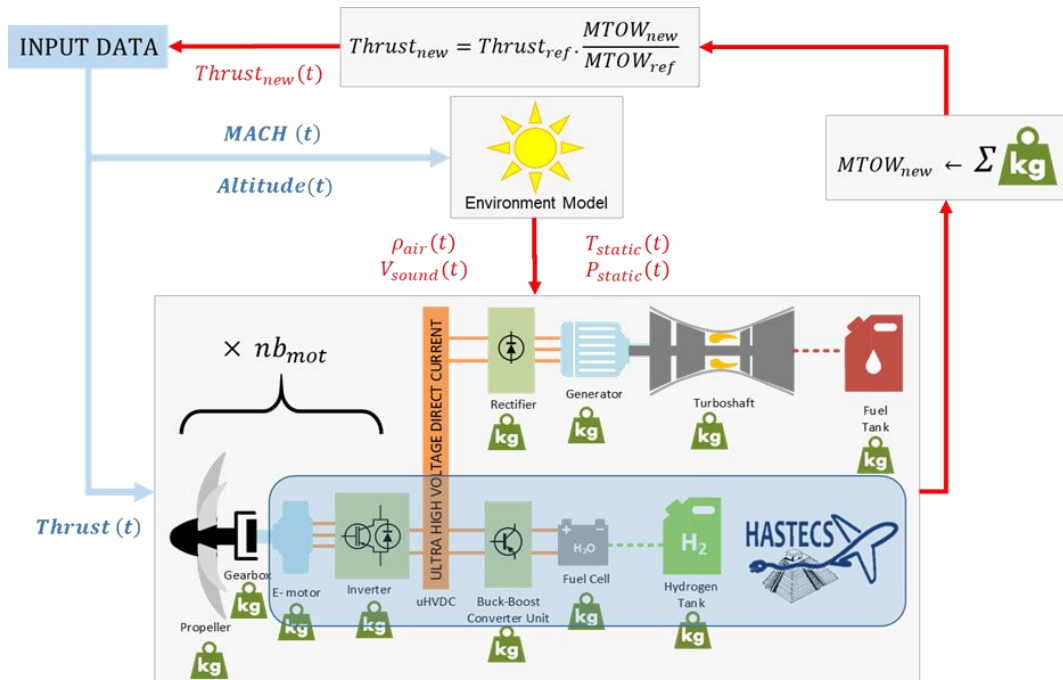


Fig. I-58: Implicit looped integrated process

Thus, by considering the evolution of "new" design variables displayed in equation (I-4) at each iteration, an implicit looped process is achieved which is stopped when the MTOW error between two successive iterations is lower than 50 kg. The process is initialized with a full thermal reference aircraft with a $MTOW_{ref}$. Then, adding the embedded weights corresponding with the electric devices (power electronics, electric motors, auxiliary source, cables), new MTOW and consequently new thrust values are derived. As emphasized on the next figure Fig. I-59, our looped simplified model has been validated with reference to a complete aerodynamic model described in Jerome THAUVIN's PhD thesis [12]. During the flight mission, this comparison shows that thrust shape is quite the same by comparing aerodynamic models with a final MTOW and the previous linear derivation.

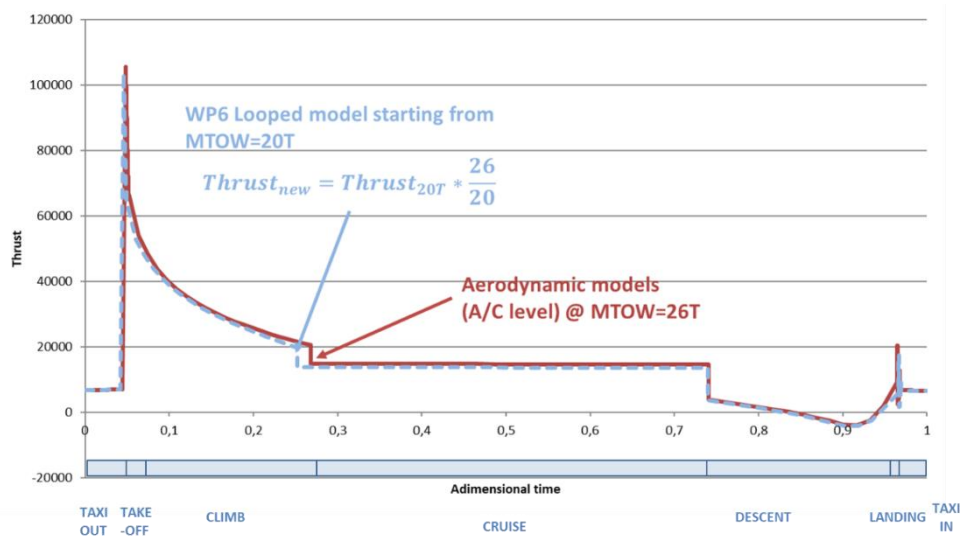


Fig. I-59: Validation of the looped process by comparison of aerodynamic and looped models

The study was carried out on a 20 T aircraft and a 26 T aircraft. Based on the reference aircraft of 20 T weight, the linear extrapolation was used to determine the thrust for a 26 T aircraft: the model used in our case will be the following $MTOW_{end} \leq MTOW_{ref} + 6T$. Note that this implicit loop converges within 10 iterations which corresponds to an acceptable CPU cost in view of an integrated design by optimization. Aircraft weight and performance can be deduced using the model loop.

I.3.4 About sensitivity of technologies on both max take off weight and fuel burn.

The main target of the European project HASTECS (Hybrid Aircraft Academic reSearch on Thermal and Electrical Components and Systems) is to couple thermal and electrical studies for a regional aircraft. The series hybrid electric architecture has been studied in this project as it leads to huge power constraints on the electric power train, the thrust being fully provided by electric devices. From an input data set and given environment conditions (temperature, pressure, aircraft speed, etc) we will present in this thesis different "surrogate" models to simplify assessments of efficiencies and masses from each device of the whole powertrain. A fixed aircraft structure is considered and only the propulsive system is refined through a looped process linking weight variations and thrust consequences as described in

chapter II: this integrated design approach allows assessing energy efficiency and mass benefits.

Technological models with corresponding design have been achieved in every work packages of the HASTECS project and will be discussed latter in that thesis. However, in order to complete this thesis introduction, it is interesting to propose a preliminary analysis at system level in order to emphasize: “how much technologies are sensitive on the integration level (weights, fuel burn)”? This preliminary analysis is simply based on assessments on both efficiencies and specific power/energy defining three successive targets as detailed in [66]. In the HASTECS project, two targets have been challenged for 2025 and for 2035 as displayed in the first (left) column of Table I-6. In the right column of this table, more “aggressive” assessments for a future “20xx target” has been added. In our case, specific powers of both electric motors, (respectively electric generators) and power electronics (rectifiers and inverters) include the cooling devices. Figures corresponding with a liquid hydrogen storage with fuel cell stack are considered with corresponding assessments in Table I-6.

Table I-6: Electric component assessments.

	2025 target	2035 target	20xx target
Emotor/ Egenerator			
SP +cooling	5 kW/kg	10 kW/kg	15 kW/kg
Efficiency	96%	98.5%	99%
Power Electronics			
SP +cooling	15 kW/kg	25 kW/kg	35 kW/kg
Efficiency	98%	99.5%	99.8%
Fuel Cell - Liquid H2			
H ₂ + tank SE		3.3 kWh/kg	
Auxiliary SP		1.3 kW/kg	
Stack SP		4 kW/kg	
DC Bus			
Ultra HVDC		2000V	

SP = Specific Power - SE = Specific Energy

Aggressive targets have been chosen, but certain targets are already achieved in other studies. In particular Siemens, with the electric motor SP260D has announced 5.2 kW/kg. The University of Illinois is designing and building a permanent magnet synchronous motor to exceed a specific power of 13 kW/kg and efficiency of 96% showing that these targets may be reached [67]. Concerning inverters, General Electric [68], [69], [70], has reached a specific power greater than 10kW/kg for its product. Other simple models have been developed to assess cable weights and losses, following the transferred power, the voltage level and the cable type (AC or DC). Based on this model set, the mass distribution of the hybrid power train is displayed in Fig. I-60 with the particular assessments dealing with the “2035 Target”.

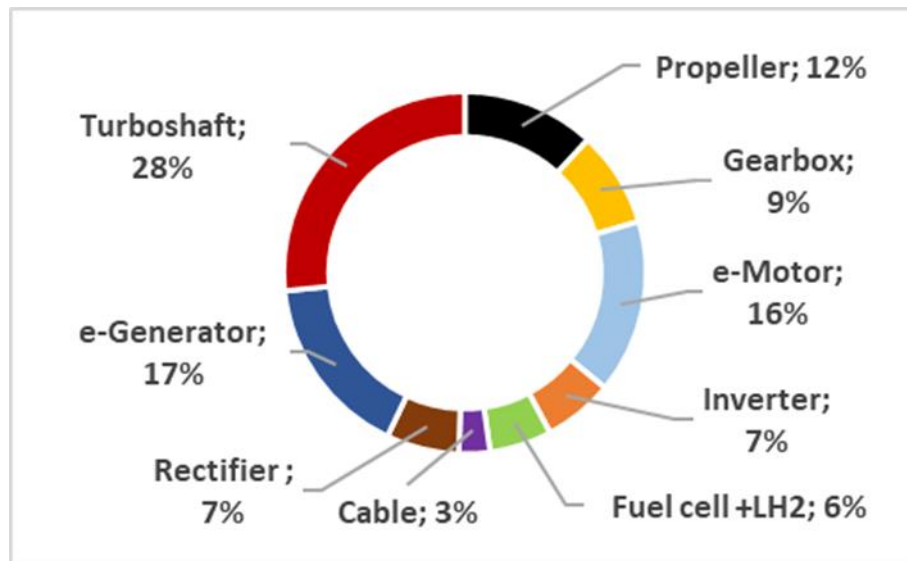


Fig. I-60: Hybrid power train mass sharing.

In this analysis a hybrid-electric aircraft is considered with two similarly sized turboshaft engines which turn generators to supply the electric powertrain. The power distribution over the flight sequences is displayed on Fig. I-61: in this simple but realistic management strategy, electric sources (fuel cells) are used during “full electric” taxi and descent phases which may correspond to a “light hybridization scenario”. For the other sequences, the power is equally shared between both turboshafts.

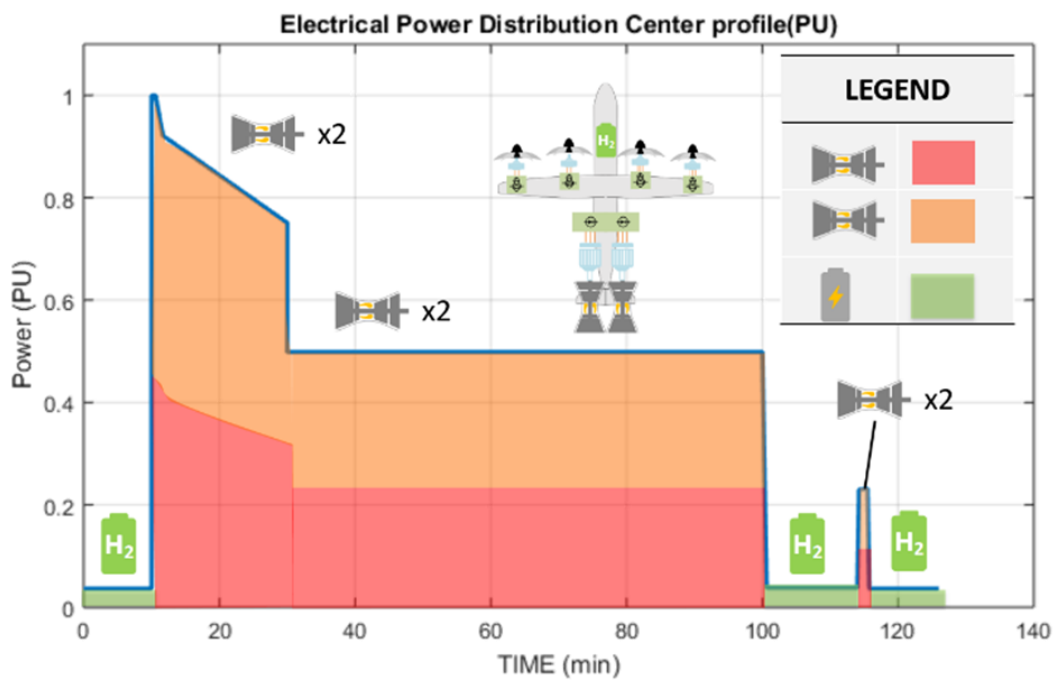


Fig. I-61: Power distribution between sources.

The sensitivity analysis consists in varying two input factors (i.e. the efficiencies and specific powers) on two device classes: the power electronics and electric machines. Taking the 2025 target as the reference and crossing successively towards 2035 (orange bars) and 20XX (grey bars) targets the figure below shows the improvements in terms of fuel burn if the

successive steps on the input factors are achieved. The four first set of bars (left of the figure) are related to progress on motors and power electronics considered one by one. The fifth and sixth set of bars gather the influence of these two devices for specific powers and efficiencies. Finally, the set of bars at the right of the figure shows that the overall gain on the fuel burn.

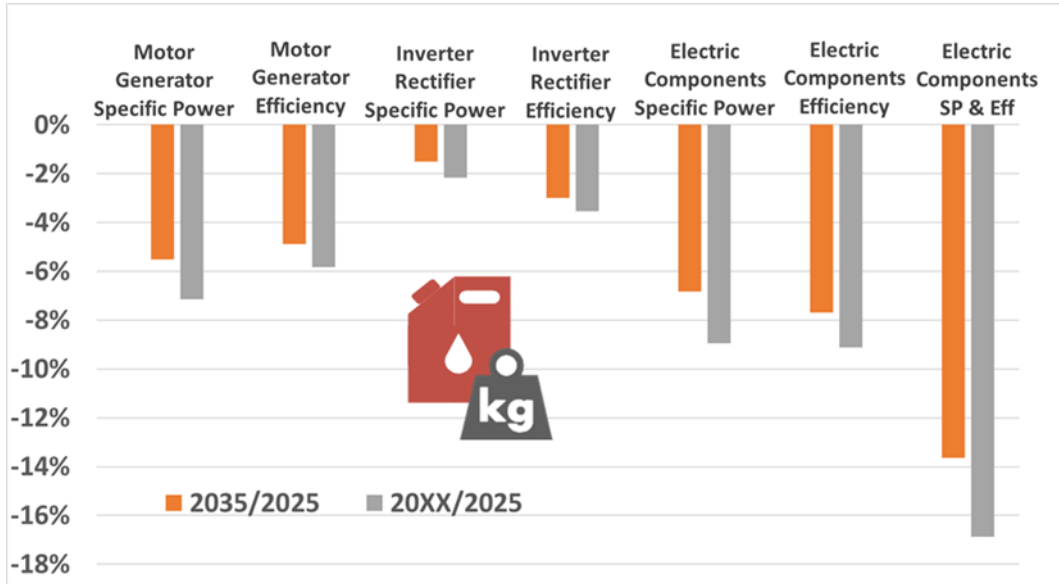


Fig. I-62: Fuel burn variation versus technological improvement of the electric propulsion system from the 2025 target.

It can be noticed that the impact of technological progress both in terms of specific powers and efficiency is significant on the fuel burn even if this impact is slightly lower for power electronics than for electromechanical converters. The figure below shows the results of the same kind of analysis but considering the sensitivity on the overall weight (MTOW) at the aircraft level. The same trends as previously can be observed.

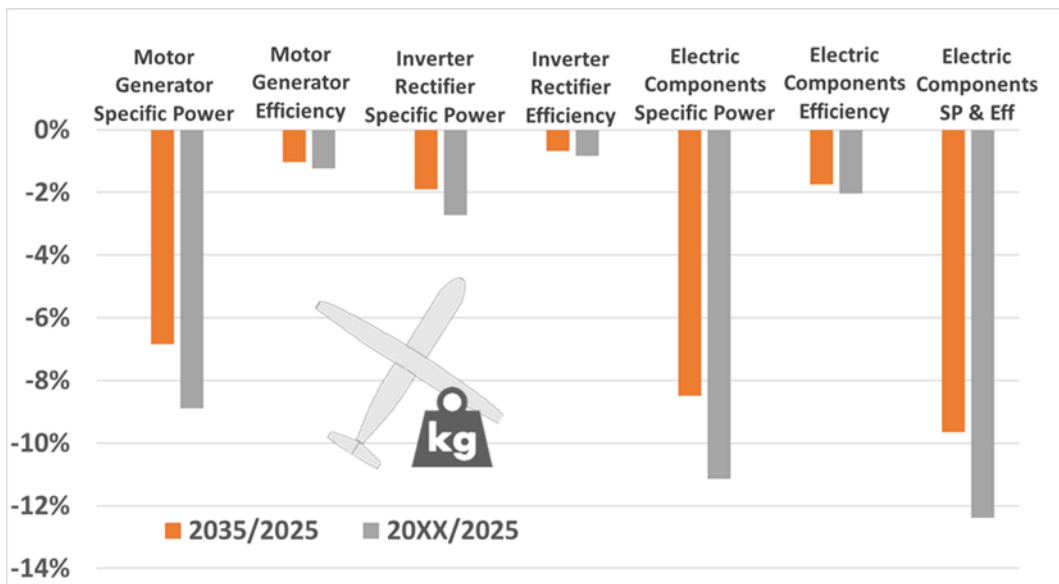


Fig. I-63: MTOW variation versus technological improvement of the electric conversion chain from the 2025 target.

It can also be seen that both progress axis (efficiency and specific power) are really influent on optimization objectives of this study (i.e the fuel burn and weight reduction). With reference to the less aggressive assumptions (target 2025) and regarding the targets 2035 then 20XX assessments, the whole weight (MTOW) would be reduced by more than 12% (Fig. I-63) when the fuel burn would be reduced by 17% (Fig. I-62). Let also notice that specific power is more sensitive to lower the MTOW, but the efficiency effect is not negligible: a trade-off between both specific powers and efficiencies has to be find.

I.3.5 Thesis objectives.

This PhD thesis aims to integrate the technological devices (electrical machines, power electronics, storage components, cooling systems) of the hybrid electric powertrain from new concepts proposed by other work packages (WP1 to 5) and taking into account external information from Airbus data and from the state of the art. In the future context of all-electric aircraft propulsion, this integrated design is a major challenge. The complexity of the optimal design process of the whole powertrain is huge but really relevant.

The first sensitivity study on mass variations of both fuel burn and MTOW in the light of technological advances shows that series hybrid electric propulsion system is sensitive to technology. The specific powers and efficiencies must be optimized to lower the mass impact due to the addition of electrical components in the powertrain. The HASTECS project makes it possible to take all the phenomena into account between electrical and thermal components of the hybrid-electric propulsion of the regional aircraft. Meta-models representing different fields of the system integration have to be built but these models need to be simplified (with “acceptable computational time”) in order to be able to optimize the complete system in a system integration loop. The second chapter will then focus on the presentation of surrogate models used in the global optimization. These models are based on reference models out of the HASTECS scope, and also on expert models considered in the HASTECS work packages.

Before going towards the overall design optimization and in order to understand couplings between devices, a Global Sensitivity Analysis (GSA) will be proposed highlighting most influent decision variables. Less impacting input variables will be removed from the overall optimization. The Sobol approach has been used for that GSA and will be presented in chapter III. Finally, a Multidisciplinary Design Optimization (MDO) at hybrid aircraft level will be the focus of the last chapter IV. The interest of the MDO will be highlighted. The electric machine and its cooling will be especially focused, being one of the most important (and complex) component to be designed in the powertrain.

CHAPTER II. Modeling for multidisciplinary design optimization of the overall propulsion system

CONTENTS

<i>II.1 Reference models out of the HASTECS scope.....</i>	57
II.1.1 Propeller model.....	57
II.1.2 Gearbox model.....	59
II.1.3 Turboshaft model.....	60
II.1.4 Cable model.	60
<i>II.2 "HASTECS" MODELS.....</i>	61
II.2.1 Electric motor design model.	61
II.2.1.1 Presentation of the electromechanical analytic model, modeling process and results.	61
II.2.1.2 Adaptation of the PMSM analytical model for system optimization.....	63
II.2.2 Electric machine cooling system.	71
II.2.2.1 Presentation of the e-motor cooling research team model.	71
II.2.3 Modeling of partial discharges.....	73
II.2.3.1 Presentation of the partial discharges model.....	73
II.2.3.2 Adaptation for system optimization.....	75
II.2.4 Power Electronics design model.	76
II.2.4.1 Presentation of the power electronics model and results.	76
II.2.4.2 Adaptation for system optimization.....	77
II.2.5 Power converter cooling system.	81
II.2.5.1 Presentation of the power electronics cooling model.....	81
II.2.5.2 Adaptation for system optimization.....	82
II.2.6 Fuel cell and battery model.....	83

The main objectives of this thesis, especially the requirements for the modelling process have been introduced in the previous chapter. In order to integrate design models, the system integrator should simplify them and identify trends and trade-offs between the different application fields of the problem. This task can be performed using Multidisciplinary Design Optimization (MDO) which allows a number of phenomena to be taken into account while integrating correlations between the different disciplines. Multidisciplinary integrated design was born from aeronautics; several theses cover the subject [71], [72]. It can be used for the global design of aircraft, for questions of aeroelasticity or industrial problems as in [73]. The success of the MDO has been reflected in other disciplines, notably in the design of electromechanical actuators [74], [75]; in order to minimize the production, maintenance and resistance of a ship [76] or in the design of submarine cables [77].

Beyond the complexity related to the multidisciplinarity of our class of systems, several levels of optimization classically exist in engineering systems. As typical example, 5 levels of expertise can be listed in an aircraft design (Fig. II-1). In the HASTECS project the “component” approach is studied to feed the “system” point of view. Several disciplines are coupled in our models: fluid mechanics (environment and propeller models), electromagnetism and electrical engineering (electric machine and power converter models) and thermics (associated cooling and gas turbine). Furthermore, the effects of the aircraft environment must be involved: the partial discharges effects will be studied especially within the electromechanical actuator. Real disruptive technologies will not be found not only in the specialized application areas but also at the interface of the different fields.

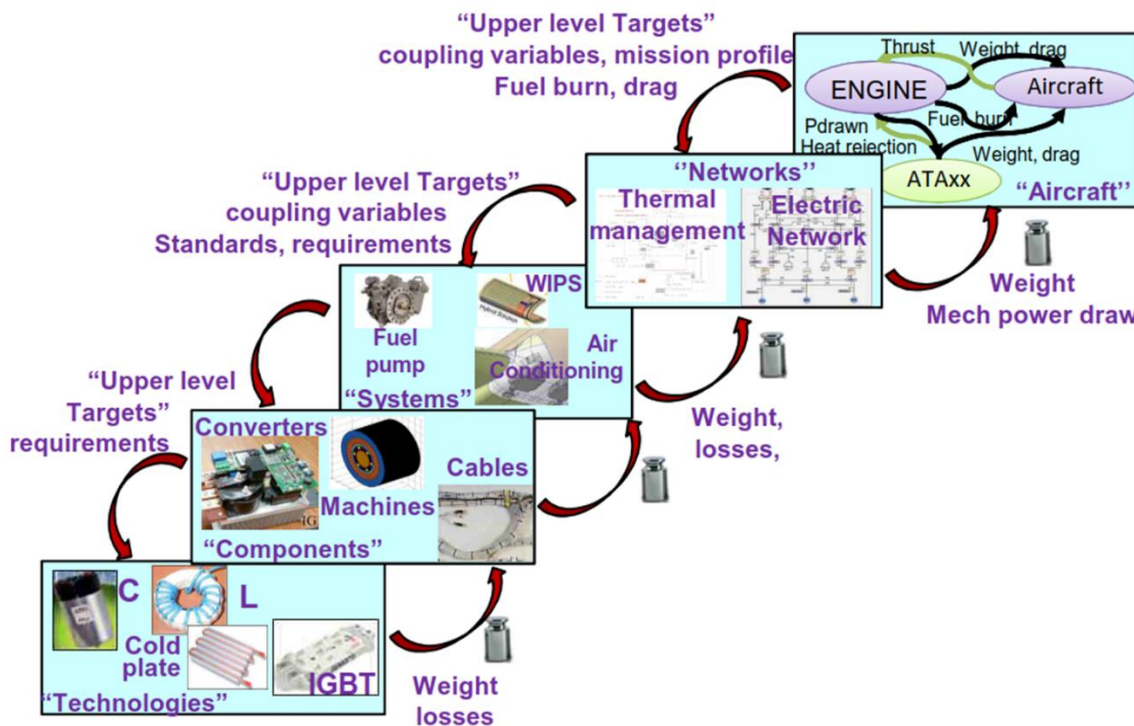


Fig. II-1: Five levels of optimization from "technologies" to "aircraft".

In aeronautics, MDO is popular because of the complexity resulting from the number of components and disciplines which have to be included in the design process. It should also be noted that the aircraft should be optimized at the lowest technology and component level

itself as well as the higher aircraft level which represents an additional difficulty, especially in the case of this 5-level architecture.

The hybrid-electric propulsion system is illustrated in the Fig. II-2. In this study the following components have been studied:

- Propeller
- Gearbox
- Electric motor (with a cooling system model and a partial discharge model)
- AC/DC converter (and its cooling system)
- DC/AC converter
- Electric Generator
- Turboshaft
- Electric source:
 - Fuel cell (stack+ auxiliaries + storage)
 - Battery (Battery Management System and its packaging/cooling)

The components written in orange are part of the HASTECS study framework, for the other models come from previous studies.

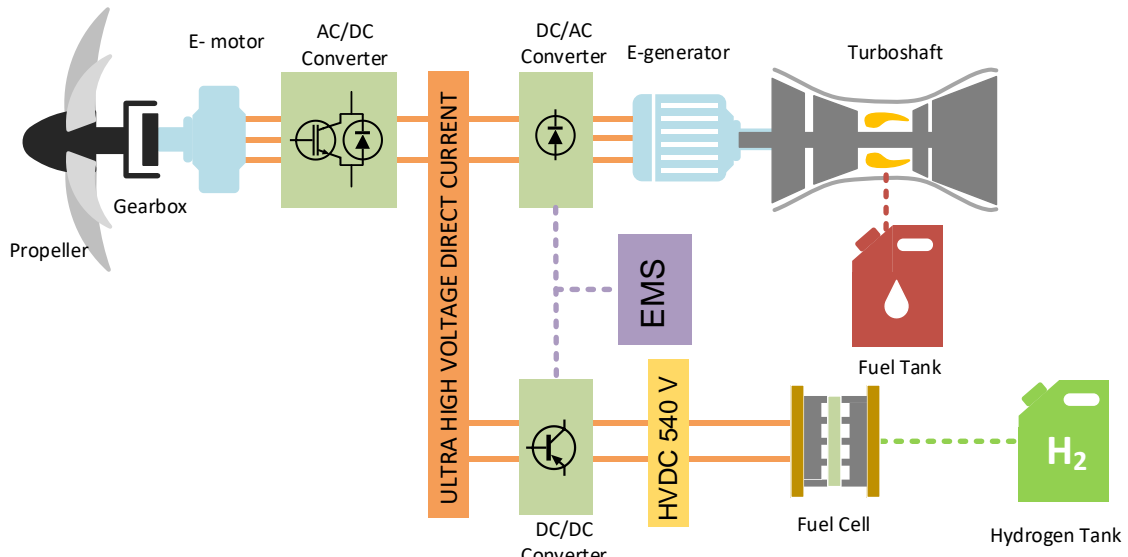


Fig. II-2: Description of the total hybrid-electric powertrain.

II.1 Reference models out of the HASTECS scope.

II.1.1 Propeller model.

The blown wing effect sometimes exploited with distributed electric propulsion (multi propeller) has not been considered in this study.

The propeller model is based on the disk actuator theory [78]. The air flow is steady and it behaves as an incompressible fluid. The schematic model of the disk actuator is illustrated in Fig. II-3 where:

- u_0 is the aircraft velocity,
- u_e is the air flow velocity behind the propeller,
- P_0, P_1, P_2 are respectively the ambient, before and behind the disk (propeller) pressure values. The pressure difference due to the propeller motion is then $P_1 - P_2$ which creates the thrust:

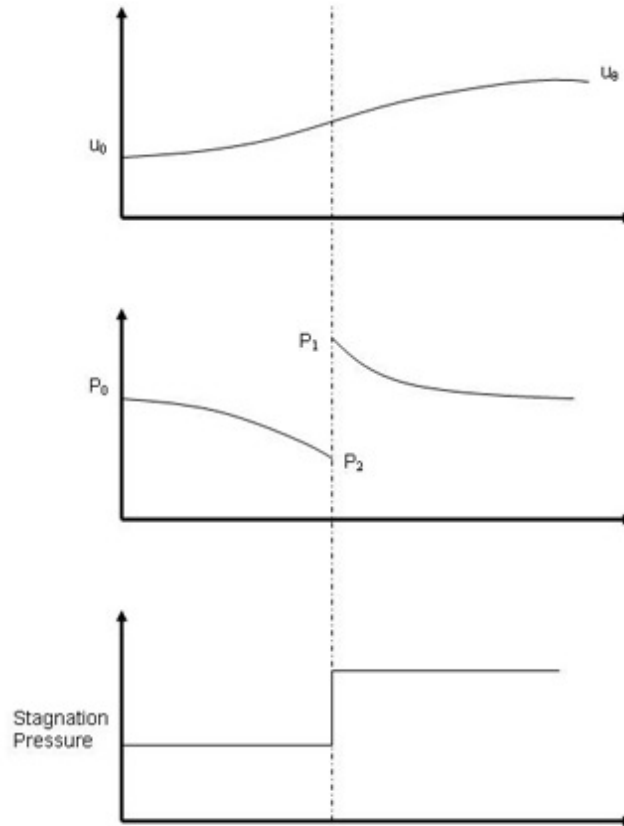


Fig. II-3: Schematic model of disk actuator (dotted line = location of the propeller).

The process consists in determining the propeller shaft power based on flow equations. The thrust $T_{A/C}$ of the disk is:

$$T_{A/C} = \pi \cdot \frac{D_{prop}^2}{4} \times (P_2 - P_1) = A_{disk} \times (P_2 - P_1) \quad (\text{II-1})$$

Where D_{prop} is the propeller diameter, A_{disk} is the disk area. Applying the Bernoulli equation in the regions of the fluid where the pressure and velocity are varying continuously leads to:

$$(P_2 - P_1) = \frac{1}{2} \rho \cdot (u_e^2 - u_0^2) \quad (\text{II-2})$$

The thrust T can be rewritten as:

$$T_{A/C} = A_{disk} \times \frac{1}{2} \rho \cdot (u_e^2 - u_0^2) = A_{disk} \times \frac{\rho}{2} \times u_0^2 \left(\frac{u_e^2}{u_0^2} - 1 \right) \quad (\text{II-3})$$

Then, the following relation can be established:

$$\frac{u_e}{u_0} = \left(\frac{T_{A/C}}{A_{disk} \times \frac{\rho}{2} \times u_0^2} + 1 \right)^{1/2} \quad (\text{II-4})$$

Using the diagram in the Fig. II-3, the disk (medium) velocity u_{disk} is expressed as:

$$u_{disk} = \frac{(u_e + u_0)}{2} \Leftrightarrow u_e = 2 \cdot u_{disk} - u_0 \quad (\text{II-5})$$

Combining (4) and (5) leads to;

$$2 \cdot u_{disk} - u_0 = u_0 \times \left(\frac{T_{A/C}}{A_{disk} \times \frac{\rho}{2} \times u_0^2} + 1 \right)^{1/2} \quad (\text{II-6})$$

We can finally express the power P required from the propeller shaft as a function of the thrust $T_{A/C}$.

$$P = T_{A/C} \times u_{disk} = T_{A/C} \times \frac{u_0}{2} \times \left(\left(\frac{T_{A/C}}{A_{disk} \times \frac{\rho}{2} \times u_0^2} + 1 \right)^{\frac{1}{2}} + 1 \right) \quad (\text{II-7})$$

This model comes from [12] and is referred in APPENDIX B.

II.1.2 Gearbox model.

The gearbox model is based on a surrogate model used by the National Aeronautics and Space Administration in [79]. The maximum torque value and the gearbox ratio are input data for the model.

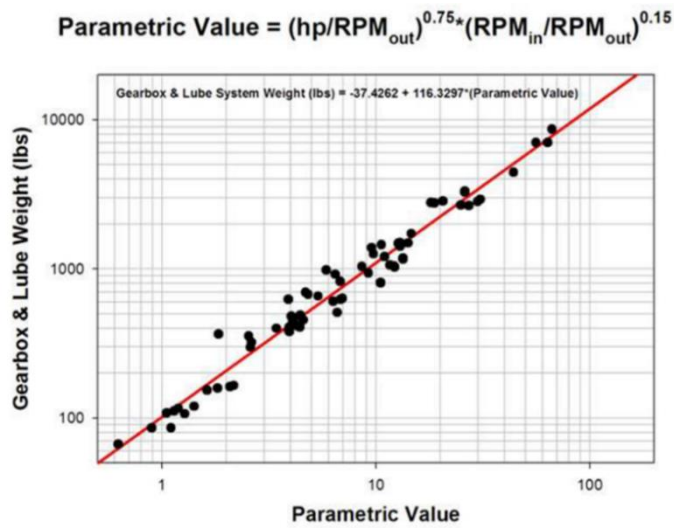


Fig. II-4: Transmission and lubrication system weight correlation [79].

Where:

- hp represents the propeller shaft power in [hp],
- RPM_{out}/RPM_{in} represents the rotation speed ratio with rotation speeds in Round Per Minute (out = propeller side/ in = e-motor side).

A fixed gearbox efficiency is considered in this model ($\eta_{gbox} = 98,5\%$) which is detailed in APPENDIX C.

II.1.3 Turboshaft model.

The same kind of study has been carried out in the thesis of J. THAUVIN [12] to build a model based on data regression for the gas turbine system. The collected data come from turboprop and helicopter engines which have high specific powers. The model is detailed in APPENDIX D.

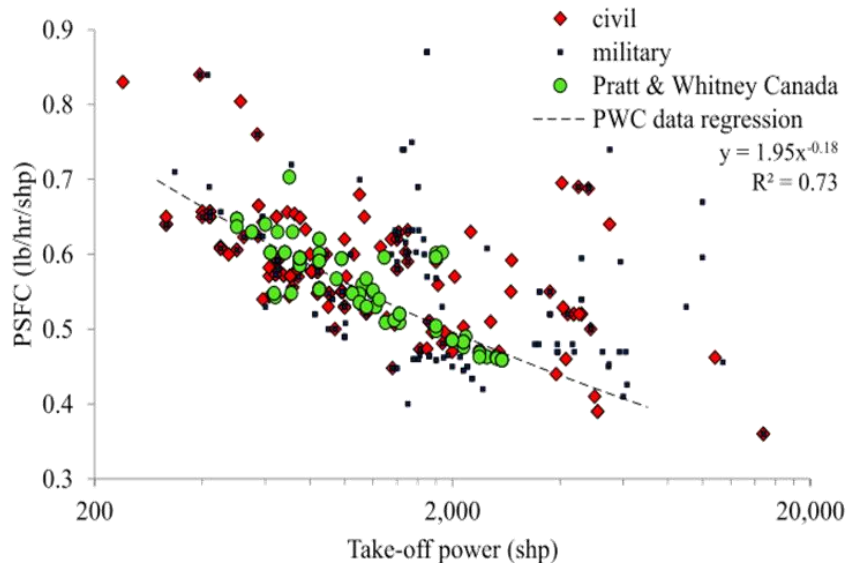


Fig. II-5: Turboshaft data regression.

II.1.4 Cable model.

The cable sizing model is based on an Airbus internal report [80]. Both thermal (based on Joule effect) and voltage drop constraints allows designing cables according to the voltage and the power factor, the cable length and type (AC or DC), the number of phases and wires per phase. Two materials are available in the cable sizing model: Aluminium and copper. The model is explained in details in APPENDIX E.

II.2 “HASTECS” MODELS.

II.2.1 Electric motor design model.

II.2.1.1 *Presentation of the electromechanical analytic model, modeling process and results.*

II.2.1.1.1 The electric machine topology choice.

The electric motor choice has been driven by efficiency and specific power targets: (cf Table I-6). Indeed, a study of different topologies has been carried out in the automotive field for hybrid (and/or electric) applications [81], [82].

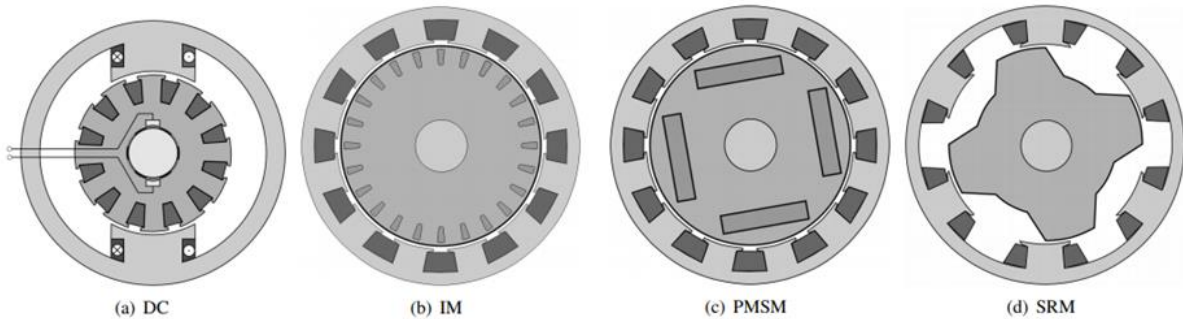


Fig. II-6: Four popular motors in Hybrid Electric Vehicle: direct current machines (DC), Induction machines (IM), permanent magnet synchronous machines (PMSM) and switched reluctance machines (SRM) [82].

Considering both efficiency and specific power the permanent magnet synchronous machine has the best performance. The efficiency is as important as the specific power in aeronautics because the thermal power for cooling adds drag to the aircraft level. Increasing the power density of the actuator is equivalent to improve each term in the following equation (II-8):

$$\frac{P_{electromagnetic}}{V_{rotor}} = 2 k_w A_{rms} B_{gap_{rms}} \Omega \quad (\text{II-8})$$

With:

- k_w is the winding coefficient depending on the winding configuration,
- A_{rms} is the root mean square lineic density in A/m depending on the current density,
- $B_{gap_{rms}}$ is the root mean square of the flux density in the airgap,
- Ω is the mechanical rotational speed of the electric actuator,
- V_{rotor} is the rotor volume.

Increasing rotational speed allows decreasing rotor volume and thus its weight. Simultaneously, it leads to increase Iron and mechanical losses. The evacuation of the heat generated due to losses through winding insulation is the main limitation for increasing specific power of electric motors.

II.2.1.1.2 First part of the electromechanical analytic model: Target Setting Tool (TST).

In the following, an analytical model and its evolutions to be in accordance with a MDO process is described. This electromagnetic and electromechanical conversion model has been developed in LAPLACE by the GREM3 team, especially in the PHD thesis of Sarah Touhami [83], [84]. This modelling approach was based on two complementary design tools (TST and SM-PMSM) also developed by this research team.

The following schematic shows the power balance in the PMSM and the associated powers.

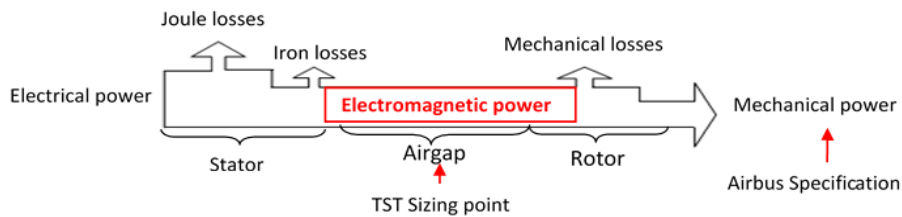


Fig. II-7: Power balance of the permanent magnet synchronous motor (PMSM).

From an input set data, main stator sizes and losses are determined thanks to the TST pre-design model. In a second step a more accurate model is used: The Surface Mounted Permanent Magnet Synchronous Machine model (SM-PMSM). The process is described in the Fig. II-8:

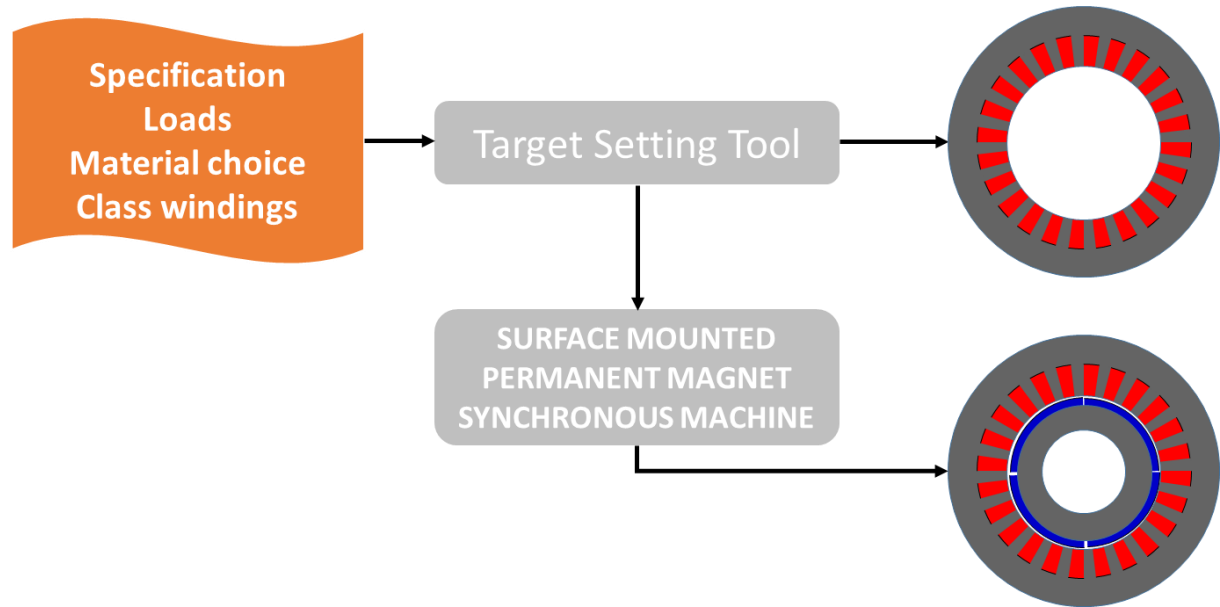


Fig. II-8: Electromagnetic model design process

The second design model SM-PMSM allows determining all sizes of the structure (rotor and stator). The losses are given at the design point. All values have been checked through a Finite Element Analysis (FEA). Fig. II-9 presents the comparison between all models for the air gap flux density.

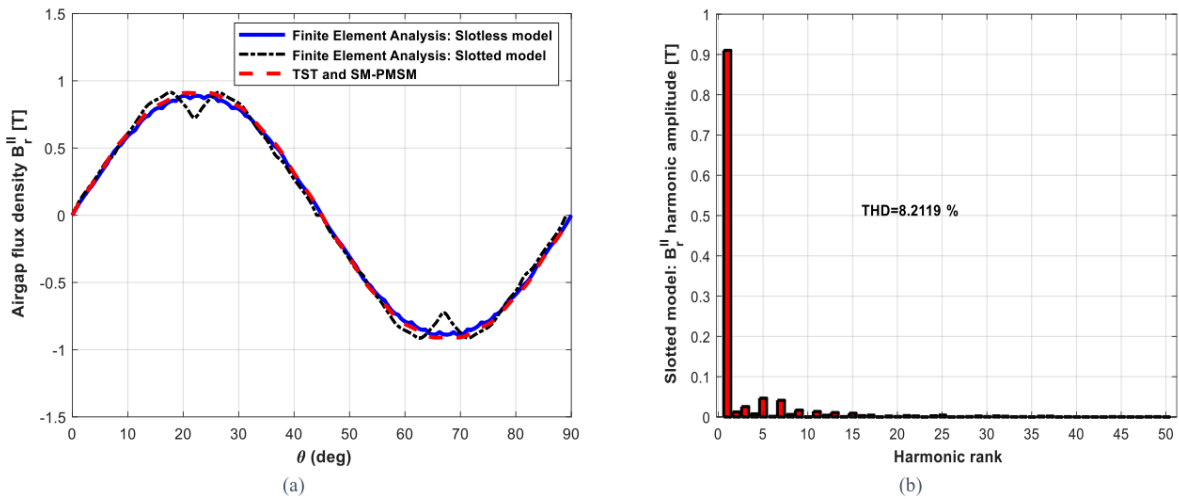


Fig. II-9: Air gap flux density at no load (a) slotless and slotted models, (b) harmonic analysis [83][83]

In order to optimize the CPU time in the context of a global system optimization, several changes and adaptations have been performed.

II.2.1.2 Adaptation of the PMSM analytical model for system optimization.

II.2.1.2.1 First observation at global system level.

A first overall powertrain optimization was carried out in order to prepare the integration of all models. First results were surprising: the optimizer converged towards several “spread” solutions in the parametric space depending on the initialization conditions. This preliminary analysis forced us to go back to a local study especially at the eMotor level and to review its design model and the choice of the decision variables at the input of the optimization algorithm [85]. While the objective function of the overall system optimization will be the fuel burn, we have reduced in this report the optimization at the local level of the eMotor, the objective function in that case being only the electric machine weight (local objective). The first set of decision variables (input data set) was the following:

- The torque design point $T_{emot_{siz}}$ in Nm,
- The mechanical rotational speed design point $N_{emot_{siz}}$ in RPM,
- The tangential pressure σ_T in Pa,
- The current density design point $J_{rms_{siz}}$ in A/mm²,
- The maximal value of flux density in the airgap $B_{gap_{max}}$ in T,
- The flux density value in the stator yoke B_{yoke} in T,
- The flux density value in the stator teeth B_{teeth} in T,
- The ratio between the inner stator diameter and the active length $R_{Drot_{Lm}}$,
- The number of conductor per slot N_{ce} ,
- The number of pole pair p ,
- The number of slot per pole and per phase n_{epp} .

Regarding the torque speed characteristic, the following preliminary optimization results were obtained using a parameter free version of the CMAES algorithm [86] (100 iterations with 20 same objective function results) :

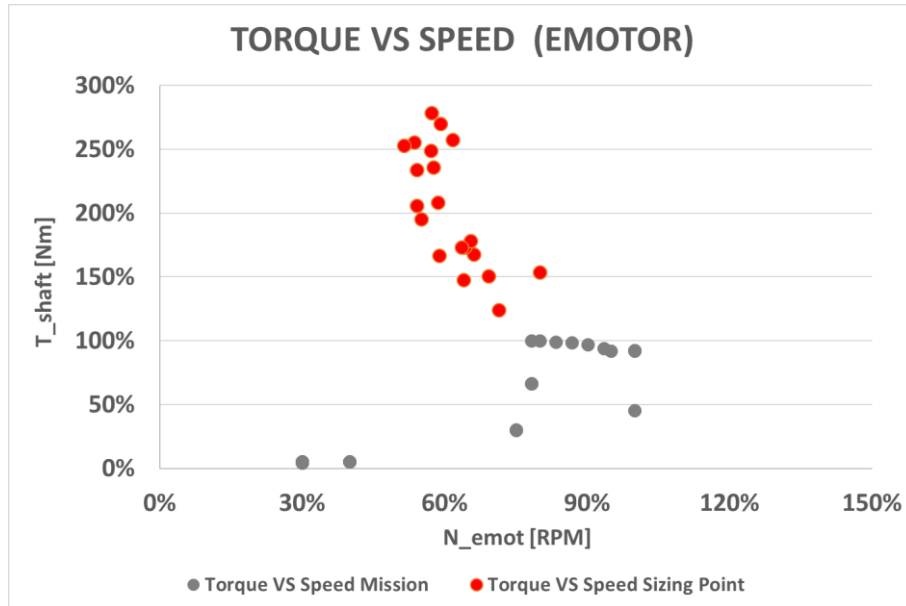


Fig. II-10: First results considering the overall powertrain.

In red color, the results of twenty independent optimization runs are compared with the torque VS speed mission in grey. Several power variables did not seem to converge:

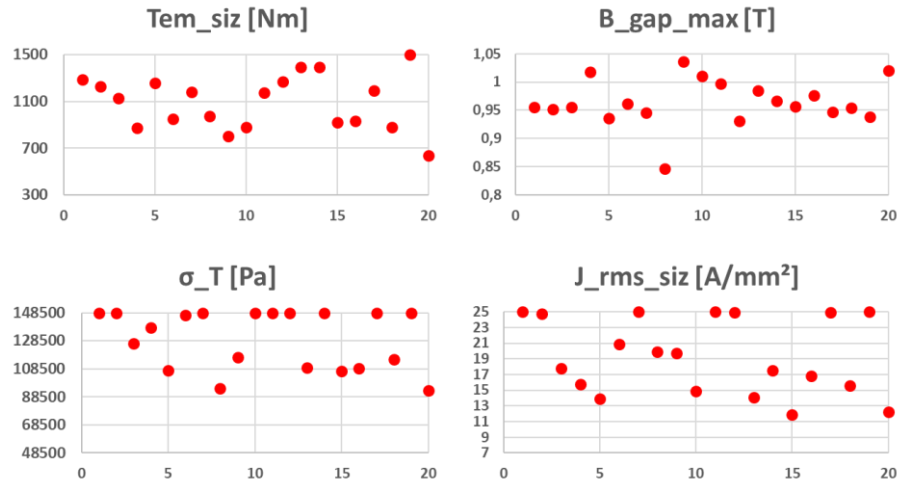


Fig. II-11: 20 independent run solutions.

The optimization seems to find several solutions and to spread decision variables in a wide parameter space. In order to avoid such results, several modifications have been made on the eMotor model.

II.2.1.2.2 A first model modification ($B_{gap_{max}} = \text{air gap flux density}$).

The flux density in the air gap was initially an input data. But in order to have the correct causality of calculation another decision variable has been chosen to replace the induction value in the air gap. Firstly, to determine the ratio between the magnet thickness

and the inner stator radius (R_{pm_ral}), it is necessary to know the value of the ratio between the air gap and the inner stator radius (R_{g_ral}). The process of the original model is described in the left part of the Fig. II-12:

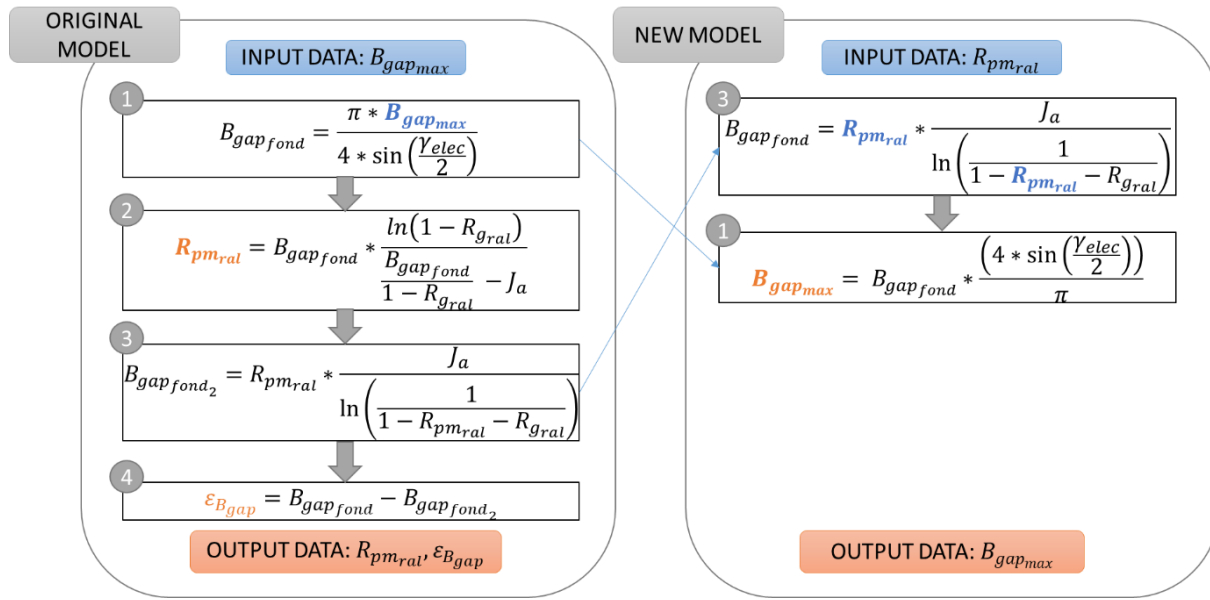


Fig. II-12: Process to determine the real value of flux density in the air gap and magnet thickness (Original model and the new one).

Where:

- J_a is the magnet polarization in T,
- γ_{elec} is the electric pole angle in rad,
- R_{pm_ral} the ratio between the magnet thickness and the inner stator radius in %,
- R_{g_ral} the ratio between the air gap thickness and the inner stator radius in %,

The original model uses the air gap flux density as an input data. After that, a first equation computes the fundamental value of the flux density in the air gap. From this calculation, an approximation is made for finding the ratio R_{pm_ral} (Equation 2 in the Fig. II-12). The direct model of the flux density (Equation 3 in the Fig. II-12) permits to check the real value but an error remains between the approximation and the direct model (Equation 2 and Equation 3 in the Fig. II-12). The new model avoids the approximation by calculating directly the value of flux density in the air gap.

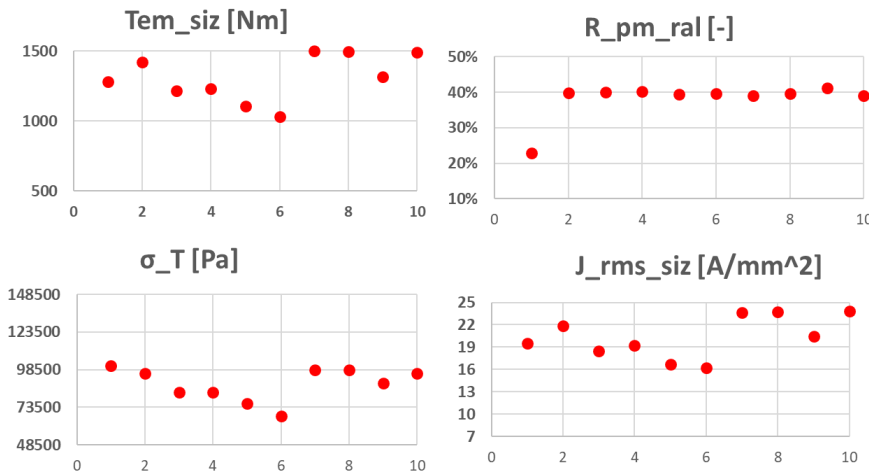


Fig. II-13: 15 independent run solutions after the first model modification.

After this first model adaptation, an apparent coupling is highlighted between three sizing variables ($T_{em,siz}$, σ_T , $J_{rms,siz}$) even for best results at iso weight. The analysis of the code shows that the torque design point ($T_{em,siz}$) appears in two equations:

- The equation associated with the rotor volume (Eq. (II-9)).
- The equation associated with slot height (Eq. (II-10)).

$$V_{rotor} = 2 \cdot \pi \cdot R_{alesage}^2 \cdot L_{motor} = \frac{T_{em,siz}}{2\sigma_T} \quad (\text{II-9})$$

$$h_{slot} = \frac{T_{em,siz}}{R_{alesage} \cdot L_{motor} \cdot B_{gap,rms} \cdot J_{rms,siz} \cdot k_{remp} \cdot n_{enc}} \quad (\text{II-10})$$

In order to avoid this effect (spread variables), a second change to the model has been proposed.

II.2.1.2.3 A second model modification (σ_T tangential pressure).

Both variables (design point torque and tangential pressure ($T_{em,siz}$, σ_T)) permit us to determine the stator inner radius through Eq.(9). In order to avoid the problems seen in the previous paragraph, the tangential pressure σ_T has been replaced by the value of the stator inner radius $R_{alesage}$ as a new decision variable. Now the tangential pressure becomes an output of the pre-design model and the torque design point is used for the estimation of the slot height. At this stage, new electric motor optimizations have been carried out and “spread variable” effects are still present when several optimizations are run from various initial situations for the decision variables:

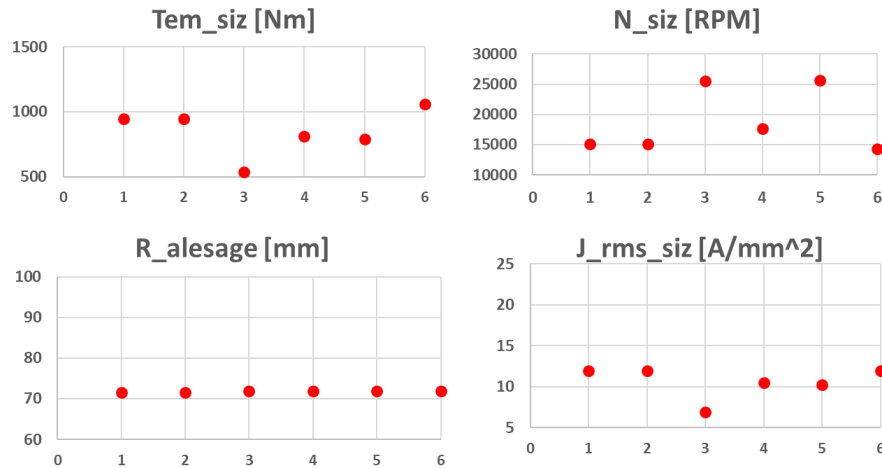


Fig. II-14: 6 independent run solutions after the second model modification.

The corresponding torque/speed characteristic is the following:

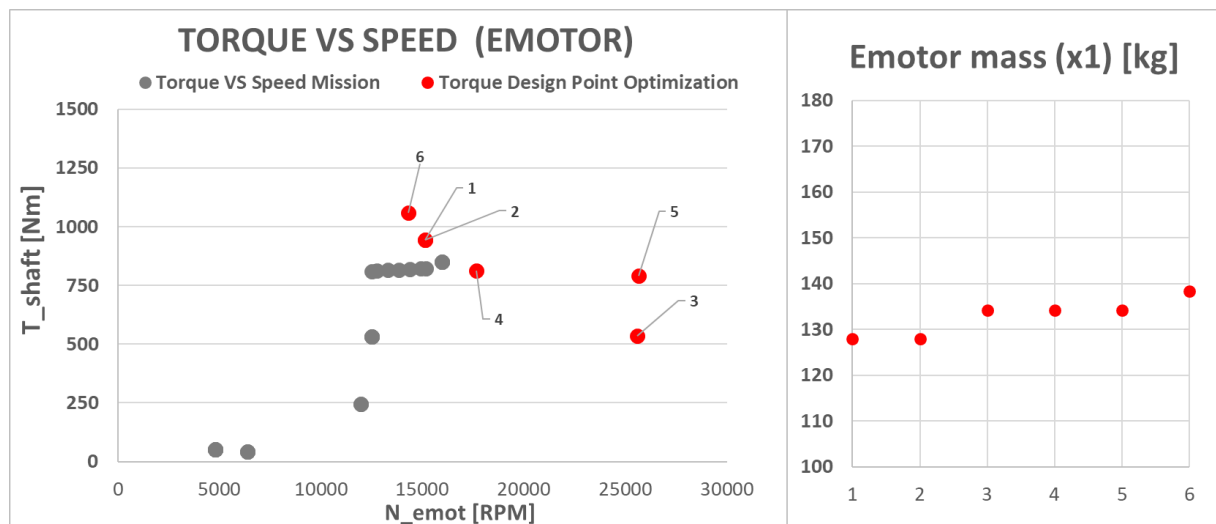


Fig. II-15: Torque/speed characteristic(left) - Emotor mass (objective function)(right).

Once again the obtained results are spread on the parameter space. From an objective function point of view, "optimal results" have the same weight order but the corresponding torque/speed characteristics are totally different. For example, between the sixth and the third solutions, the torque design point is divided by two, while the rotational speed is doubled. Considering both current density and torque design point, their obtained ratio is constant. The Eq. (10) shows the dependency between the slot height and these two latter parameters: if the ratio is constant, the slot height is also fixed. As seen previously with the tangential pressure and the rotor volume, a modification of the decision variable set has to be done.

II.2.1.2.4 A third and final model change (J_{rms} current density and others).

Usually for electric motor design, a base point is used in order to determine the corresponding performances. The current density at design point gives a current at design point, and the supplied voltage is determined through a Behn-Eschenburg diagram without field weakening ($I_d = 0$) (cf Fig. II-16).

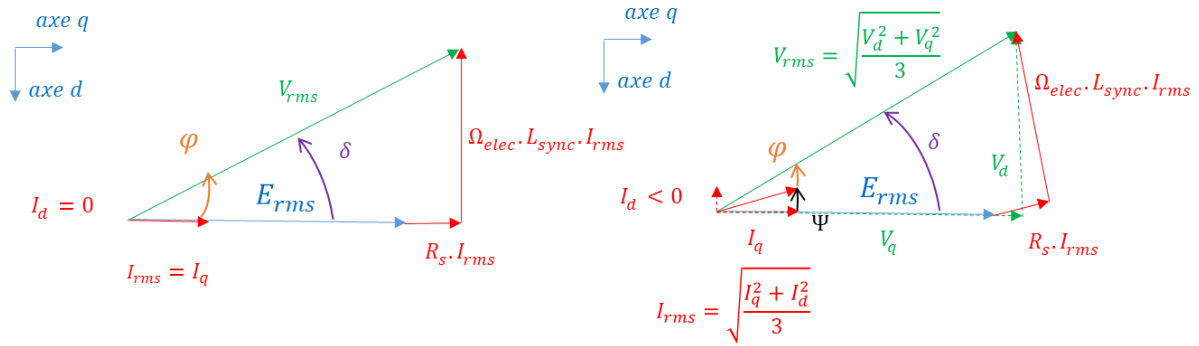


Fig. II-16: Behn-Eschenburg diagrams (without and with field weakening).

- E_{rms} is the root mean square electromotive force in V,
- I_{rms} is the root mean square value of the current in A,
- V_{rms} is the root mean square value of the voltage in V,
- I_d, I_q, V_d, V_q are respectively current and voltage in Park model,
- R_s is the resistor in Ω ,
- L_{sync} is the inductor in H,
- Ω_{elec} is the synchronous rotation speed in rad/s,
- φ, δ, ψ are respectively power factor angle, internal angle and the field weakening angle in rad.

The current density appears in the following equation (equation used with a design point):

$$V_{rms_{siz}} = \sqrt{(E_{rms_{siz}} + R_s \cdot J_{rms_{siz}} \cdot S_{cu_{total}})^2 + (L_{sync} \cdot \Omega_{elec_{siz}} \cdot J_{rms_{siz}} \cdot S_{cu_{total}})^2} \quad (\text{II-11})$$

Indeed:

$$I_{rms_{siz}} = J_{rms_{siz}} \cdot S_{cu_{total}} \quad (\text{II-12})$$

- $J_{rms_{siz}}$ is the root mean square value of current density in A/mm^2 ,
- $S_{cu_{total}}$ is the required copper area to perform the mission in mm^2 ,

But based on this equation and given a fixed motor geometry, a set of solutions exist in the torque speed plan for a same V_{rms} : in the next figure, the blue dots represent the set of solutions of the Eq. (5) for a same supplied voltage V_{rms} given an example of electric machine characteristic. The DC bus voltage becomes a sizing parameter, design points in torque and speed are no longer necessary for electric actuator design.

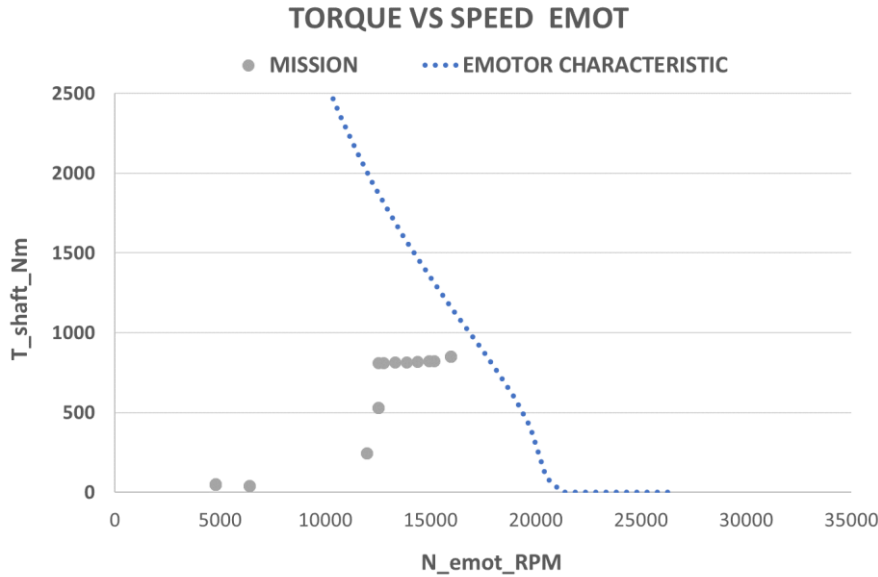


Fig. II-17: Set of solutions of Eq (10) in the torque speed plan for an example of electric motor characteristic and given a sizing voltage

In order to define the voltage value, the following equation is added:

$$V_{emot_{rmsmax}} = \frac{V_{uHVDC}}{2\sqrt{2}} \cdot m_{a_{max}} \quad (\text{II-13})$$

With:

- $m_{a_{max}}$ is the maximal value of depth modulation in [%],

Thanks to this modification the following design point input parameters are removed for the optimization:

- The torque design point $T_{emot_{siz}}$ in Nm,
- The mechanical rotational speed design point $N_{emot_{siz}}$ in RPM,
- The root mean square value of current density at design point $J_{rms_{siz}}$ in A/mm²,

Finally, based on this analysis, a review of the electric machine design model is proposed where the initial decision variable ($T_{emot_{siz}}$, $N_{emot_{siz}}$) are suppressed. In the same time, the current density at design point $J_{rms_{siz}}$ has been replaced with the ratio between slot height and stator inner radius ($R_{hs_{ral}}$). Now, the ultra-high direct current voltage V_{uHVDC} is used in order to set the maximal value of e-motor voltage by applying the equation (10).

II.2.1.2.5 Summary of changes and final model checking.

Table II-1 : Summary of changes between the initial sizing model and the integrated model used in optimization.

Initial set of input parameters	1 st modification	2 nd modification	3 rd modification	Final set of input parameters
$T_{em,siz}$	-	-	×	×
N_{siz}	-	-	×	×
σ_T	-	$R_{alesage}$	$R_{alesage}$	$R_{alesage}$
$J_{rms,siz}$	-	-	$R_{hs,ral}$	$R_{hs,ral}$
$R_{Drot,ral}$	-	-	-	$R_{Drot,ral}$
$R_{g,ral}$	-	-	-	$R_{g,ral}$
$B_{gap, rms}$	$R_{pm,ral}$	$R_{pm,ral}$	$R_{pm,ral}$	$R_{pm,ral}$
B_{yoke}	-	-	-	B_{yoke}
B_{teeth}	-	-	-	B_{teeth}
N_{ce}	-	-	-	N_{ce}
p	-	-	-	p
n_{epp}	-	-	-	n_{epp}

The original model needed 12 input parameters to design the electric machine. Now thanks to the previous changes resulting from the causality analysis, only 10 decision variables are required. Several optimizations have been performed for different values of V_{uHVDC} showing the consistency of this choice. All results are consistent now.

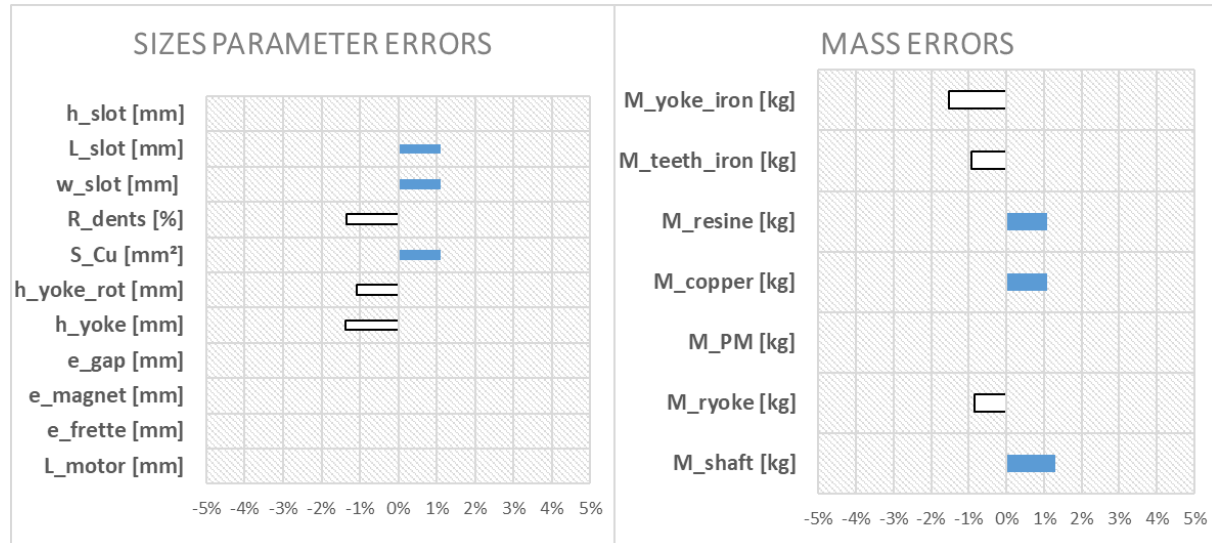


Fig. II-18: Differences between the new model and the original model.

A final checking has been done in order to ensure representativeness between the original model and the integrated. The Fig. II-18 highlights the fact that the new model is well representative, most errors are below 2%, it can be implemented in the optimization process. The new model equations are described in the Appendix F.

II.2.2 Electric machine cooling system.

II.2.2.1 *Presentation of the e-motor cooling research team model.*

The cooling system integrated in our MDO integrated process has been developed in the HASTECS framework (Work Package 3) by the Pprime institute, especially by Amal Zeaiter [87].

In general, a cooling system is used to maintain the temperature controlled on the device to be cooled by evacuating the required thermal load. To accomplish this function, two different methods can be used:

- Cool the device by directly using external air (air cooling also qualified as open loop circuit cooling).
- Cool the device by using an intermediate circuit (liquid cooling also qualified as closed loop circuit cooling).

In order to have smarter and more efficient solutions, only closed loop circuits will be considered here.

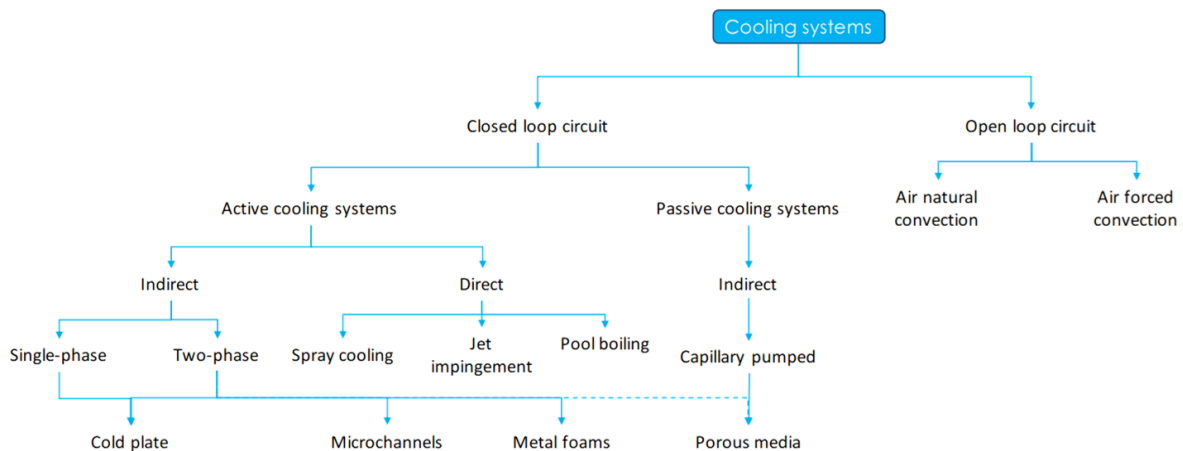


Fig. II-19: Cooling systems classification [88].

According to [88], closed loop circuits cooling systems can be divided into two categories: active and passive cooling. Active cooling systems are characterised by the presence of a pump or a compressor, following the technology, to move the fluid into the circuit. For the electric motor cooling an active cooling system has been considered:

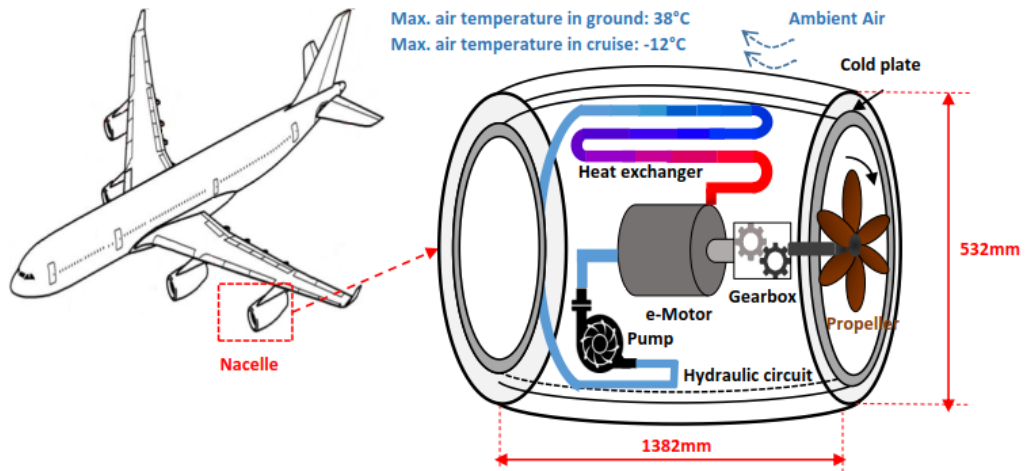


Fig. II-20: Nacelle architecture (electric machine and its cooling system) [83], [87].

The heat exchanger is completely part of the nacelle skin. The cooling primary circuit is composed of a heat exchanger placed near to the cold source, a hydraulic circuit and a pump [87]. Heat exchanger allows the evacuation of heat generated by electric motor to the outside air through plate embedded around the nacelle. It is composed of pipes and a cold plate. Inside the e-motor there is a shaft cooling channel to cool down the rotor part and a water jacket in order to cool the stator part.

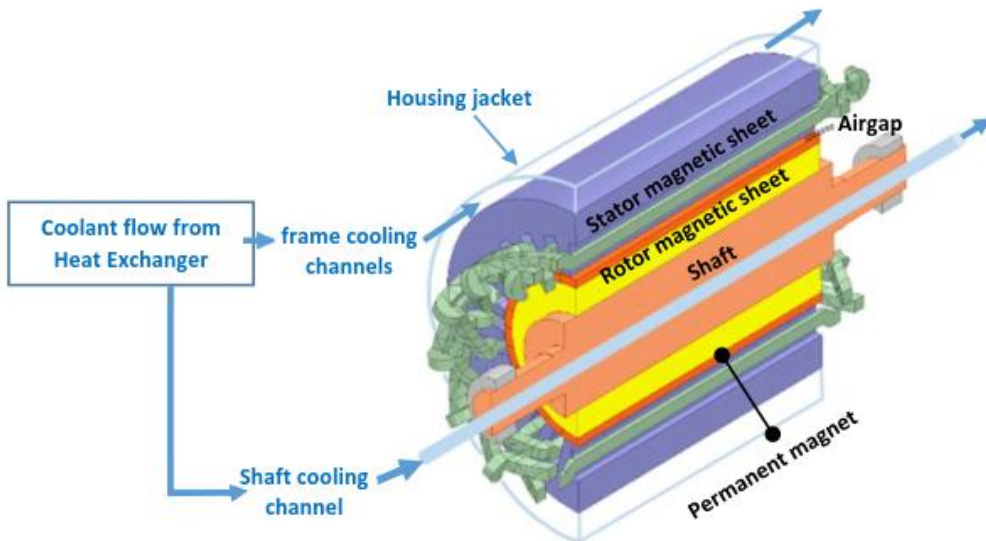


Fig. II-21: Cross section of the electric motor schematic (with its cooling system) [83], [87].

The model will be presented in Appendix G.

II.2.3 Modeling of partial discharges.

II.2.3.1 Presentation of the partial discharges model.

The environment constraint due to high voltage issues and partial discharges phenomenon influencing the insulation system was studied in HASTECS by the LAPLACE/MDCE research team, especially in the PHD thesis of Philippe Collin [89]. The aim of this work package (WP5) is to provide one tool to help designers in order to avoid or to reduce Partial Discharges (PD) that may occur in the Electrical Insulation System (EIS) of motors. If the electric motor voltage is higher than 700 V (2025 target for the WP5 [90]) (i.e.: high voltage value), this tool will reduce both level and amount of PD occurring in the EIS that has been specifically designed to resist to PD. In the literature, the Paschen's criterion [91] is widely used for determining if there partial discharges may occur or not. However, this criterion has been established for metallic plane electrodes.

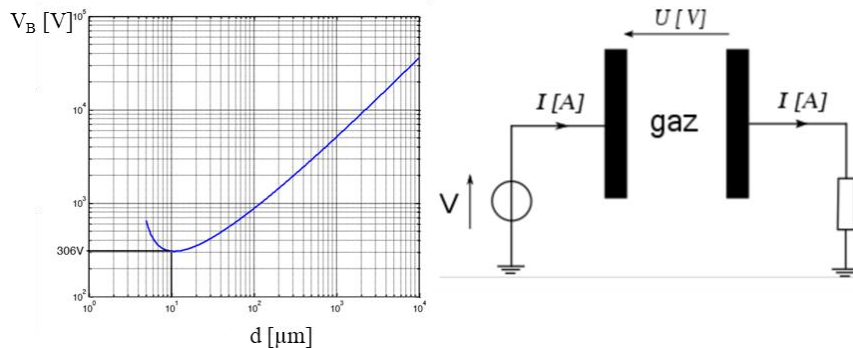


Fig. II-22: Paschen curve in air gap between plane electrodes at normal conditions and at $p = 760$ Torr.

The previous study has been carried out at ambient temperature (20°C) and ambient pressure (1 bar). To be more accurate with the reality, a finite element software is used in order to compute the voltage distribution in the stator slot for the electric motor. Matlab Software is used to process the data. The tools are presented in the following figure:

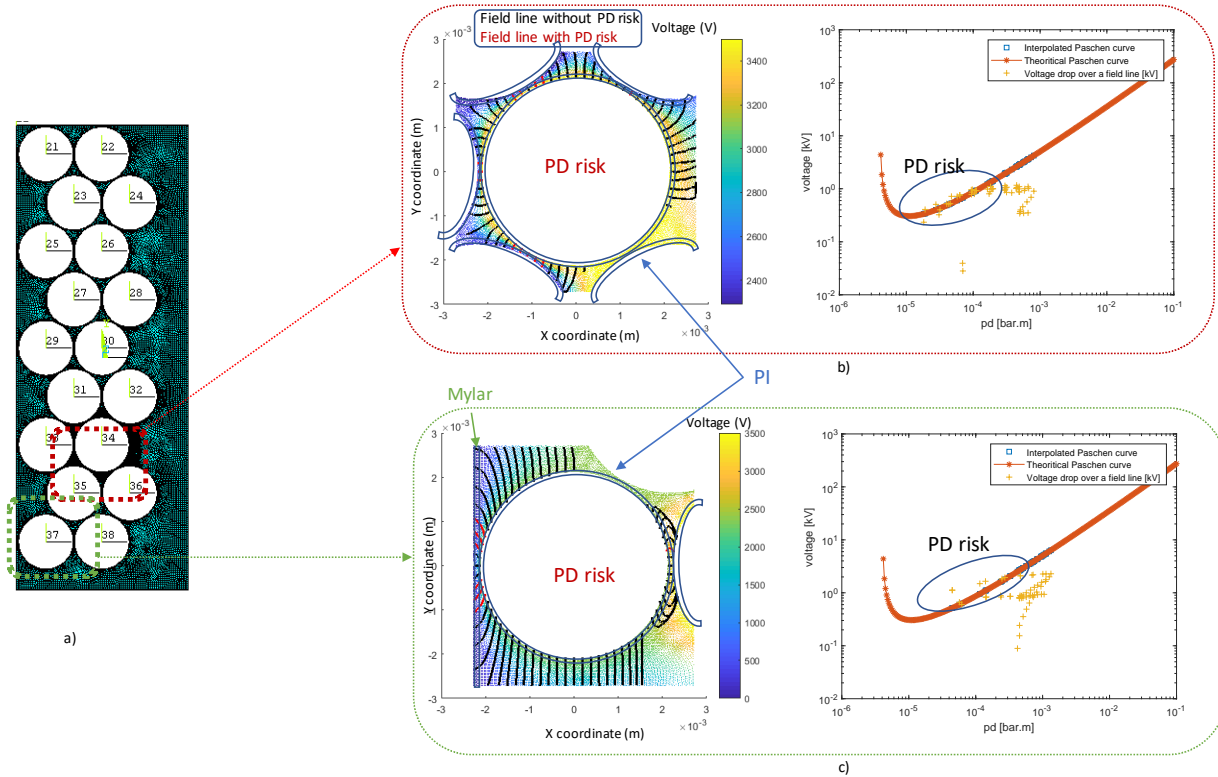


Fig. II-23: WP5 tool outputs: (a) FEA software mesh; (b) & (c) electric field and voltage drops along fields lines ($p=1\text{bar}$).

The figure represents two high-risk areas:

- Between conductors
- Between the stator yoke and the conductor.

Two strategies are developed in order to avoid discharges in these areas: the first is to increase the enamel thickness and the second consists in the integration of a liner in the stator slot. The process is explained in the [92] and [89]:

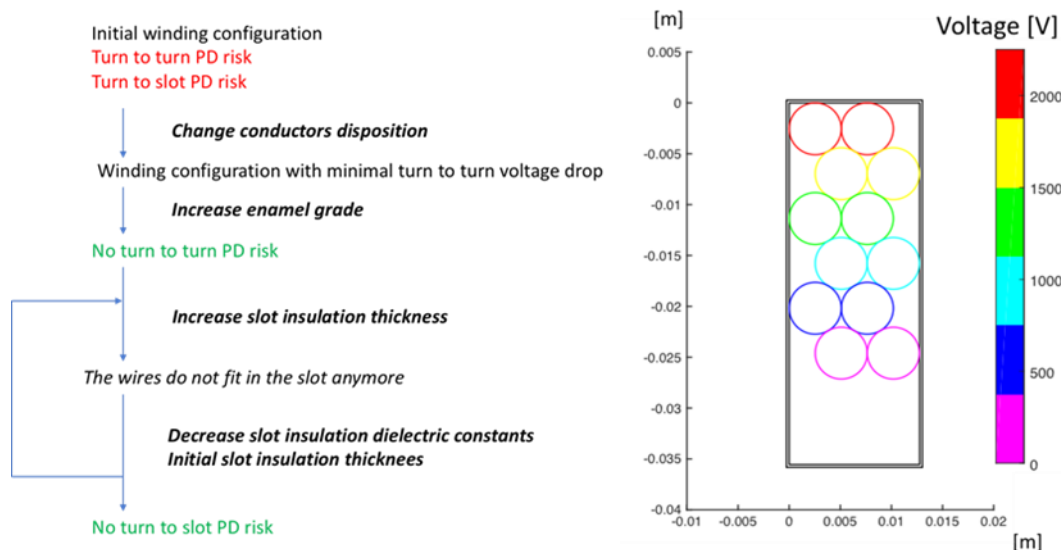


Fig. II-24: WP5 tool process (left), example of a PD free solution with 6 conductors (right).

The loop between the ANSYS finite element software and Matlab allows determining the high-risk locations for the partial discharges. Considering the computational cost, it was impossible to integrate the whole process in an overall optimization. The next part of the chapter deals with the model adaption.

II.2.3.2 Adaptation for system optimization.

The Paschen curve has been established for normal conditions, but in stator slots, winding temperature can reach 200°C. An abacus taking temperature and pressure conditions into account is integrated into the design process.

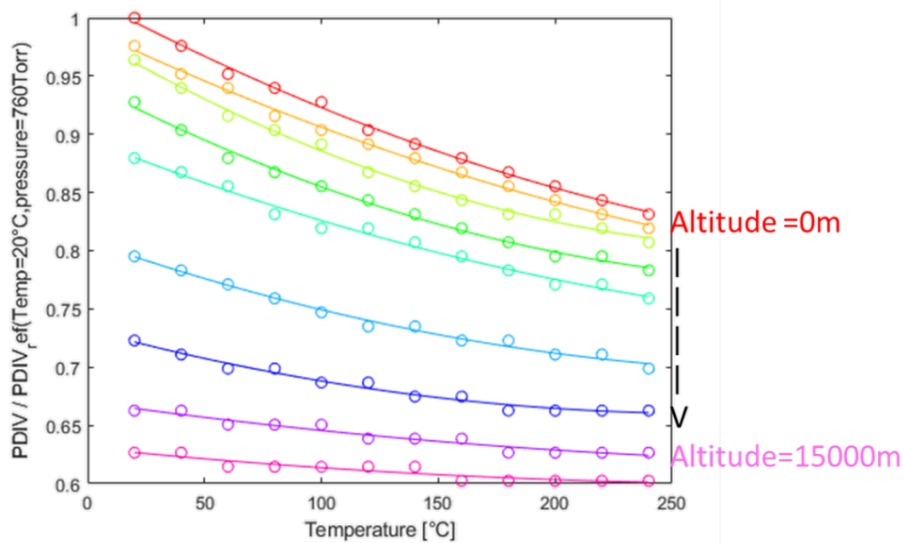


Fig. II-25: Decrease of PDIV for a combined variation of pressure and temperature.

Regarding this figure, a high sensitivity with regard to environmental conditions is highlighted. The PDIV is the maximum withstand voltage value, and it is decreasing with the altitude and the temperature. In order to avoid voltage overshoot another abacus is considered.

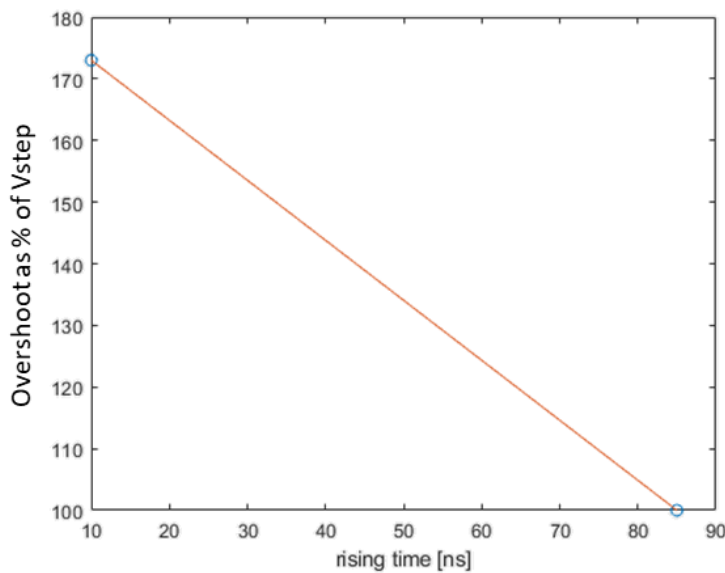


Fig. II-26: Voltage phase overshoot evaluation as a function of the switch rise time.

In the HASTECS case the 7th generation of Mitsubishi IGBT has been considered, with a switch rise time of 200 ns, so there is no overshoot case. Finally, the process presentend Fig. II-24 is used in order to find the right winding configuration. For the complete model, polynomials are created from the FE software in order to reduce the CPU time.

II.2.4 Power Electronics design model.

II.2.4.1 Presentation of the power electronics model and results.

For the power electronics (PE) the work objective is to design a highly integrated inverter with a specific power of 15 kW/kg for 2025 target and 25 kW/kg for 2035 target including its cooling system. The main factor to increase the specific power is finding a trade-off between cooling and electric device masses, the bigger the losses, the heavier the cooling. A study has been realized by the WP2 in the HASTECS project demonstrating that the 2-level power module design was not feasible to achieve the targets. As a consequence, multilevel converters were selected. The Fig. II-27 illustrates the multilevel converter classification. The chosen converter topologies resulting from the WP2 study are underlined in red circles [93].

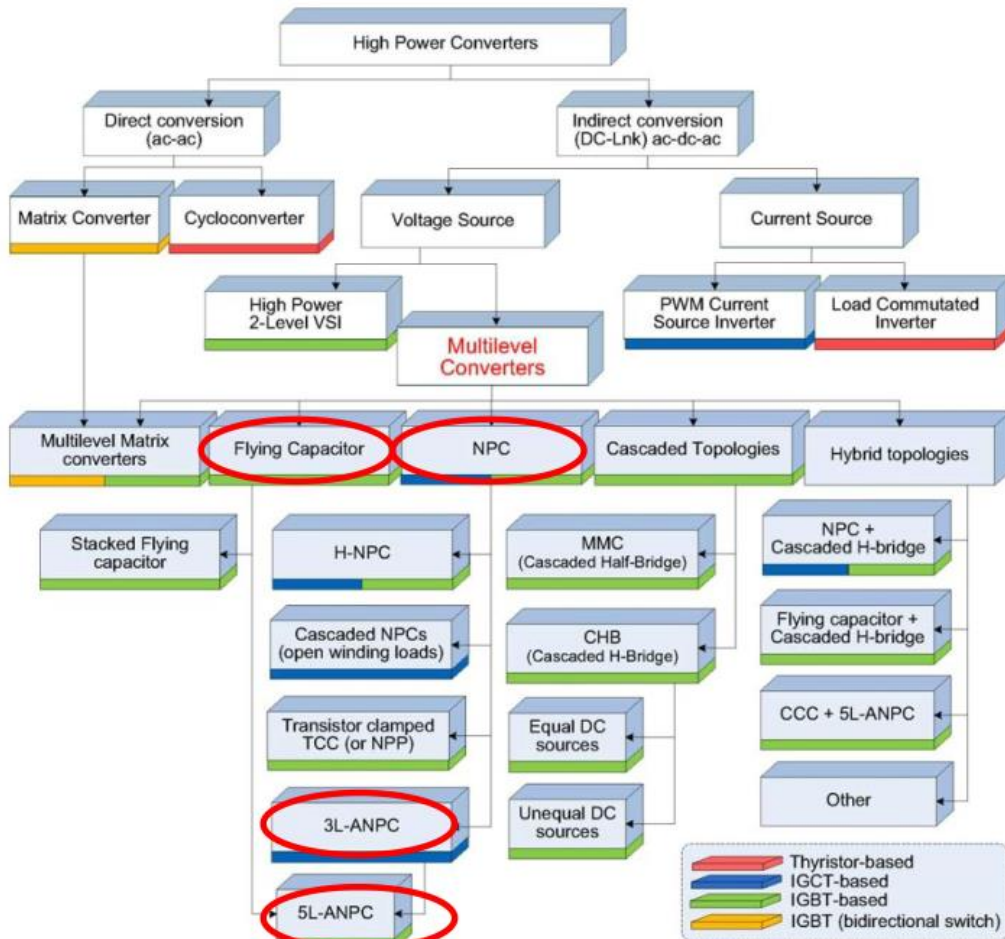


Fig. II-27: Multilevel converter classification.

Where:

- NPC is the Neutral Point Clamped,
- FC is the Flying Capacitor,
- SMC is the Stacked Multicellular Converter.
- ANPC is the Active NPC topology.
- xL denotes the number of levels.

The simulation tool used by WP2 permits us to design these converters with different control strategies. The software organization is described in the following figure [93]:

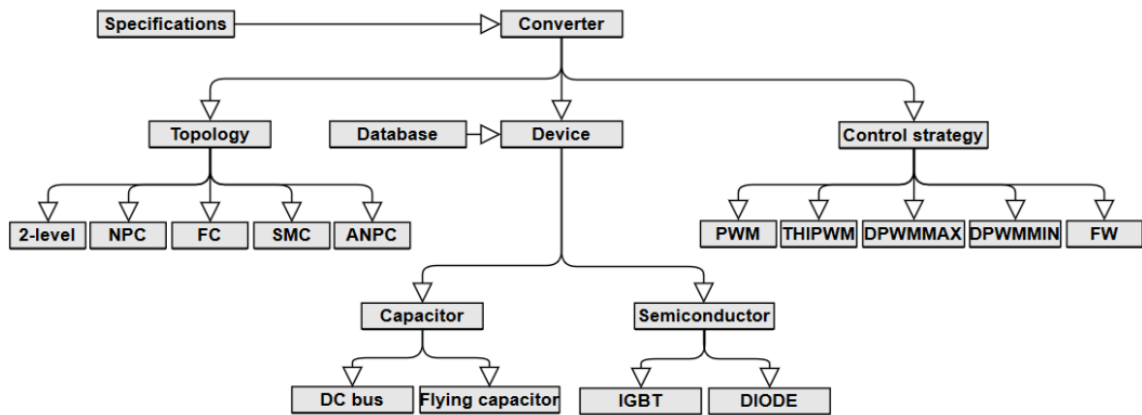
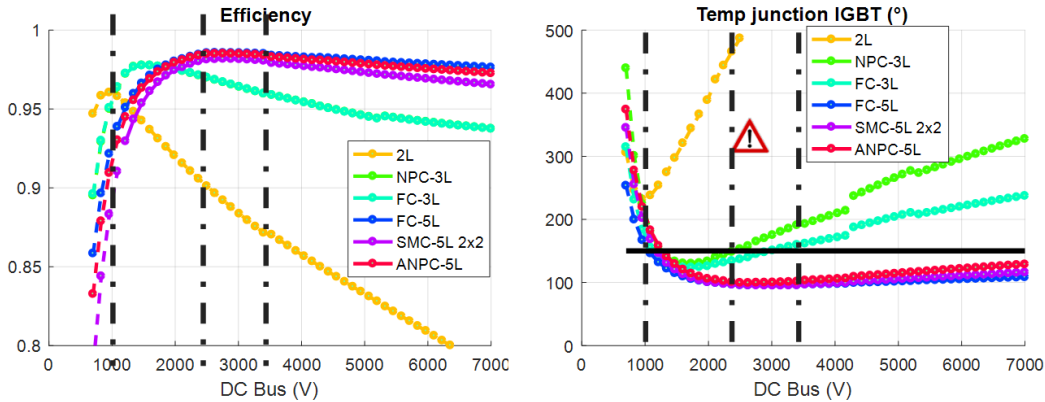


Fig. II-28: Simulation tool organisation.

In order to adapt this simulation tool for system optimization, a performance study has been performed by the power electronics research team to select best topologies.

II.2.4.2 Adaptation for system optimization.

A lot of topologies have been studied and best converters have been selected to adapt this model for system optimization [94]. In fact, DC bus voltage was not established, so the power converter team made a trade-off between best efficiency and maximal specific power at DC bus values.



Switching frequency (Hz)	Topology	Maximal specific power (kW/kg)	Corresponding DC bus voltage (V)	Efficiency (%)
5855	2-level	6.73	957	96.04
	3-level NPC	11.39	1600	97.76
	3-level FC	10.42	1730	97.77
	5-level FC	8.43	3143	98.53
	5-level SMC	12.24	3143	98.12
	5-level ANPC	14.05	3143	98.47
879	2-level	14.98	1986	98.19

- 5-level ANPC close to the 15 kW/kg target
 - Low frequency switching with the 2-level topology
- ⇒ Used losses model accuracy

Fig. II-29: Comparison of possible solutions sized [94].

Considering specific power and efficiencies, the best multilevel configurations are:

- 3-Level NPC (Fig. II-30).
- 5-Level ANPC (Fig. II-31).
-

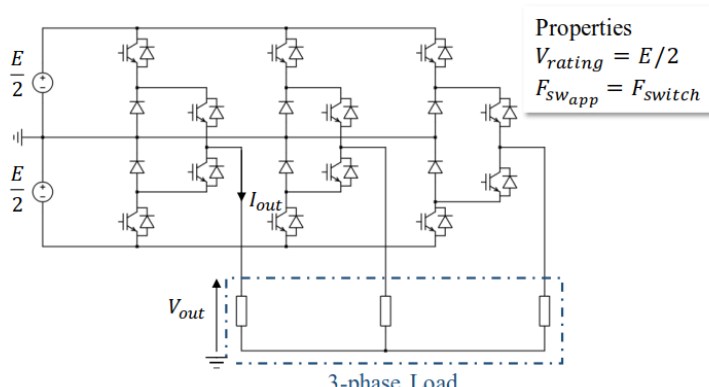


Fig. II-30: 3-level NPC inverter.

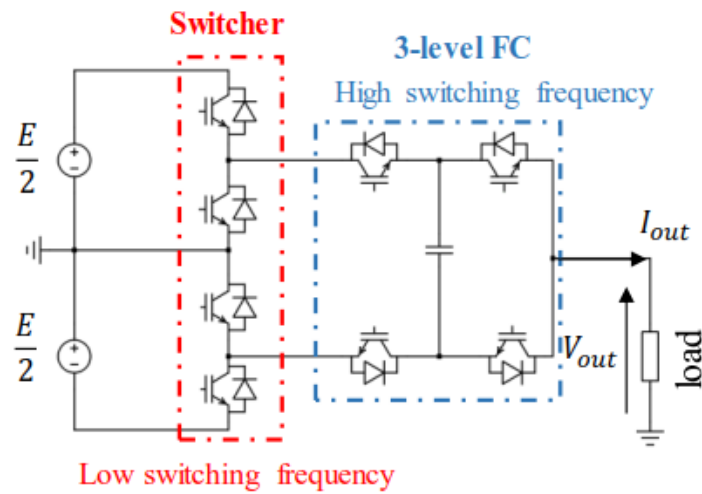


Fig. II-31: 5-level ANPC single phase inverter.

To simplify the use of the simulation tool only two control strategies and two IGBTs have been selected. At the end of the adaptation for system optimization, the following rule related to the bus voltage level has been established.

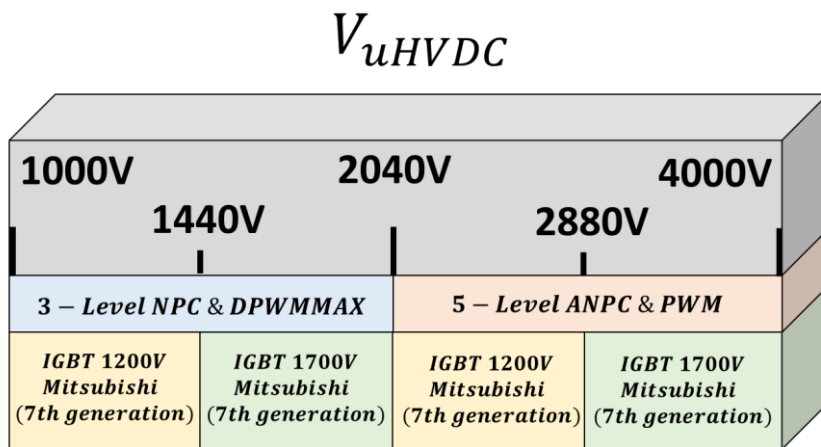


Fig. II-32: Voltage rule for determining the topology and the component to be used.

The first constraint equation permits us to choose the power electronics topology. The summary of topology properties is described in the following table:

Table II-2: Summary of converter topology properties.

Topology	Number of Levels	Voltage rating	Output switching frequency	Passive components
2-levels	2	V_{uHVDC}	f_{sw}	-
FC N cells ($N \geq 2$)	$N + 1$	$\frac{V_{uHVDC}}{N}$	$f_{sw} \times N$	($N-1$) Capacitors
3-levels NPC	3	$\frac{V_{uHVDC}}{2}$	f_{sw}	-
(1×2)-levels SMC	3	$\frac{V_{uHVDC}}{2}$	f_{sw}	-
($n \times p$)-levels SMC	$n \times p + 1$	$\frac{V_{uHVDC}}{n \times p}$	$f_{sw} \times n$	N Capacitors
5-levels ANPC (FC 2cells)	5	$\frac{V_{uHVDC}}{4}$	FC cells = $f_{sw} \times 2$ Switcher: $f_{flow_{frequency}}$	1 Capacitor

The maximal DC bus voltage value for the 3-level NPC topology is determined by the maximal value of the voltage rating. In this case, two IGBTs are used, the first voltage rating is 1200V and the second is 1700V. The DC bus voltage range covered by the 3L – NPC is determined by Eq (II-14)[93]:

$$V_{uHVDC} \leq K_{v_{max}} \times V_{IGBT_{rating_{max}}} \times (N_{level} - 1) = V_{limit_{NLevelPE}} = 2040 \text{ V} \quad (\text{II-14})$$

Where:

- $K_{v_{max}}$ is the maximum voltage utilization rate of the component in [%],
- $V_{IGBT_{rating_{max}}}$ the maximum voltage rating given by IGBTs datasheet in [V],
- N_{level} the number of level of the converter topology [-],
- $V_{limit_{NLevelPE}}$ is the voltage limit for the N-Level power electronics topology in [V],

$K_{v_{max}}$ has the value of 60%, and $V_{IGBT_{rating_{max}}}$ has the value of 1700 V:

- The voltage limit value is 2040 V for a 3-level NPC power converter.
- The voltage limit value is 4080 V for a 5-level ANPC power converter.

After choosing the converter topology, The IGBT choice (1200V or 1700V) is determined by the Eq (II-15).

$$V_{IGBT_{rating}} \geq \frac{V_{uHVDC}}{K_{v_{max}} \times (N_{level} - 1)} \quad (\text{II-15})$$

II.2.5 Power converter cooling system.

II.2.5.1 Presentation of the power electronics cooling model.

This aspect has been studied into details by the Pprime institute which was in charge of a dedicated Work Package (WP4) in the HASTECS project, especially in the framework of Flavio Accorinti's PHD thesis [88], [95], [96].

In contrast to active cooling systems, passive cooling systems do not require any external source of energy to move the coolant. Neglecting systems using natural convection because of its low heat transfer coefficient, here we will only refer to two-phase passive technologies. Passive cooling systems use gravity or capillary forces to make the fluid flow into the loop. For the power electronic cooling system, the passive method has been studied, in particular the Capillary Pumped Loop for Integrated power (CPLIP). This is a two-phase passive loop which design has been enhanced from classical CPLs. Thanks to gravity and a higher thermo-hydraulic coupling between the compensation chamber and the evaporator, linked by a vertical tube, problems affecting CPLs were solved in CPLIP. Mass exchanges are so possible: the liquid contained in the reservoir is forced by gravity to come down to the evaporator, and if vapour bubbles are formed in the latter, they can return to the tank.

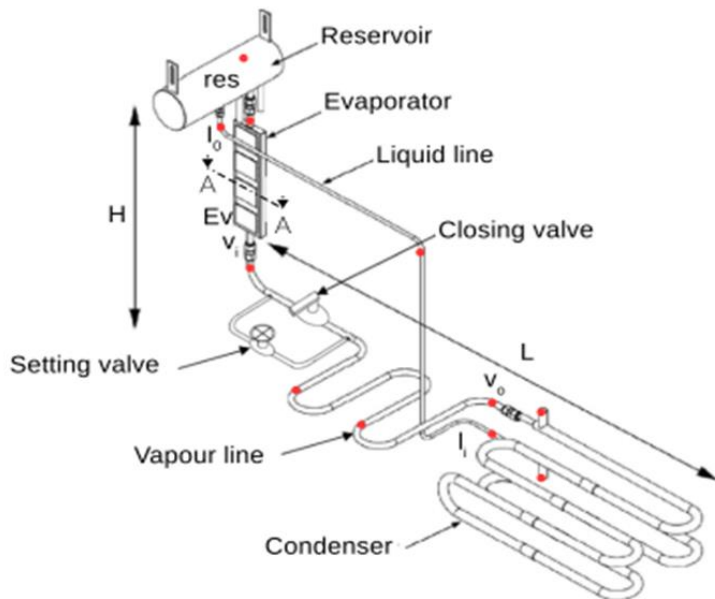


Fig. II-33: CPLIP schematic [88].

The semiconductor modules are placed on both evaporator sides as shown in Fig. II-34. This was recommended by WP4 to take advantage of both the evaporator side in order to evacuate the thermal losses and balance the constraints on both sides. This solution will also help to reduce the volume and weight of the inverter since it creates a more compact inverter and divides by 2 the number evaporators compared to the use of one side of the evaporator. In this case, we end up with 3 evaporators in parallel for the three phases instead of six.

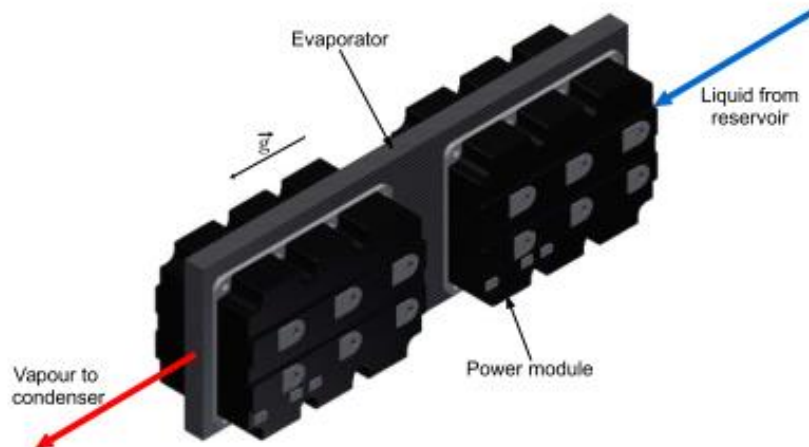


Fig. II-34: Module/evaporator assembly [93].

II.2.5.2 Adaptation for system optimization.

A meta-model totally decoupling the thermal from the other physical fields has been created for the power electronic module. The calculation of the cooling mass is obtained through a simple surrogate model (see APPENDIX I). Converter losses are directly translated into kilograms of cooling system for both targets (2025 and 2035) [88].

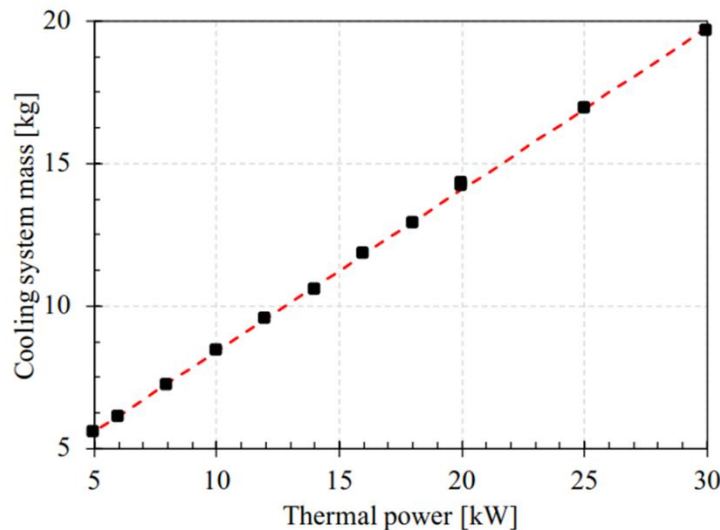


Fig. II-35: CPLIP mass variation as function of the heat power (2025 Target).

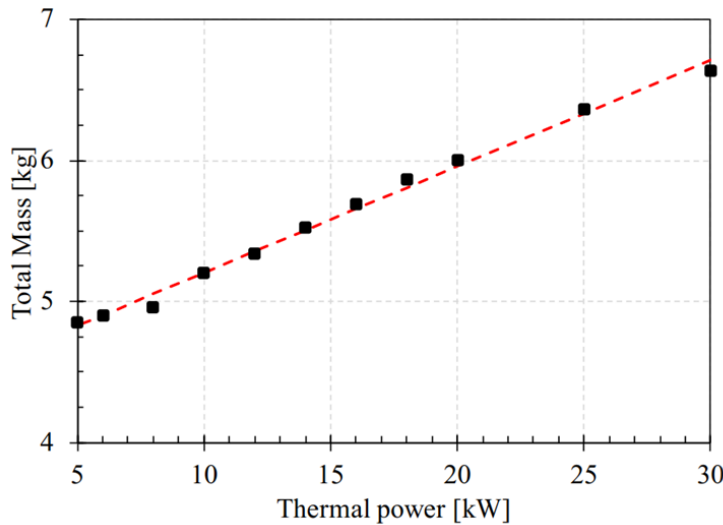


Fig. II-36: CPLIP mass variation as function of the heat power (2035 Target).

II.2.6 Fuel cell and battery model.

This part deals with the auxiliary electric sources hybridizing the main thermal engines, i.e. batteries and/or Fuel Cells (FC) with their associated H₂ storage. A review of the state of the art and a prospective study has been detailed in Laplace by M. Tognan in [97]. In order to limit the study inside reasonable borders, three Lithium-ion battery “families” are pre-considered:

- High Power type: Lithium Titanate Oxide (LTO) anode based Li-ion battery, or their more modern version replacing LTO for a mixed valency Ti-Nb oxide (TiNb₂O₇).
- High Energy type: Nickel Manganese Cobalt (NMC) cathode based Li-ion battery (coupled with a graphite anode – cells using Si at the anode are also included here).
- Very High Energy type: Lithium Sulfur (LiS) cathode based battery.

Based on that study, the following assessments in terms of energy density have been proposed at cell level.

Table II-3: Electrochemical source assumptions.

Specific energy e_m (Wh/kg @ cell scale)	Today	2025	2035
High Power: LTO / TNO	~ 140 Wh/kg _{cell}	~ 180 Wh/kg _{cell}	~ 200 Wh/kg _{cell}
High Energy: NMC	~ 250 Wh/kg _{cell}	~ 350 Wh/kg _{cell}	~ 500 Wh/kg _{cell}
Very-high Energy: LiS	~ 500 Wh/kg _{cell}	~ 600 Wh/kg _{cell}	~ 650 Wh/kg _{cell}

In order to jump from the cell to the system (integrating packaging, cooling and BMS), constant integrating factor parameters (f_m and f_v) are considered ($kg_{system} = kg_{cell} * f_m$; $Vol_{system} = Vol_{cell} * f_v$). These values are estimated to be respectively: $f_m = 2$ and $f_v = 2.5$.

Based on these assessments battery energy densities are strongly limitated at system level knowing that most powerful technologies in kWh/kg are often limitated in terms of cycling performance and life duration.

For that reasons, hydrogen fuel cells seem more appropriate for our case study.

On Fuel Cell side, three technologies are examined:

- Low Temperature (~ 70 °C) Proton Exchange Membrane Fuel Cell (LT PEMFC).
- High-Temperature (~ 170 °C) Proton Exchange Membrane Fuel Cell (HT PEMFC).
- Solid Oxide Fuel Cell (SOFC) working at very high temperatures (~ 800 °C).

Table II-4: Fuel cell specific power assessments.

<u>FC stack and system</u>			
specific powers & volumes p_m / p_v (kW/kg and kW/L)	Today	2025	2035
LT PEMFC	~ 2 kW/kg _{stack}	~ 4 kW/kg _{stack}	> 5 kW/kg _{stack}
	~ 0.6 kW/kg _{system}	~ 1 kW/kg _{system}	> 1.1 kW/kg _{system}
	~ 3 kW/L _{stack}	~ 5 kW/L _{stack}	> 6 kW/L _{stack}
	~ 0.3 kW/L _{system}	~ 0.8 kW/L _{system}	> 0.9 kW/L _{system}
HT PEMFC	~ 0.4 kW/kg _{stack}	~ 1 kW/kg _{stack}	-
SOFC	~ 0.33 kW/kg _{stack}	-	-

Three H₂ storage possibilities are also considered: compressed H₂ (350 bara or 700 bara) in composite tanks (CH₂), liquid H₂ (T ~ 20 K) in cryogenic tanks (LH₂), and H₂ storages through metal hydrides.

Table II-5: H₂ storage specific energy assessments.

<u>H₂ storage gravimetric efficiencies (-) and specific energy (Wh/kg based on H₂ LHV)</u>			
	Today	2025	2035
Gazeous (700 bar)	$\sim 5 - 7.5$ wt. %	~ 10 wt. %	> 10 wt. %
	$\sim 1.67 - 2.5$ kWh/kg	~ 3.3 kWh/kg	> 3.3 kWh/kg
Liquid (20 K)	~ 15 wt. %	~ 20 wt. %	> 20 wt. %
	~ 5 kWh/kg	~ 6.6 kWh/kg	> 6.6 kWh/kg
Solid (metal hydrides)	$\sim 2 - 3$ wt. %	~ 7 wt. %	> 7 wt. %
	$\sim 0.67 - 1$ kWh/kg	~ 2.3 kWh/kg	> 2.3 kWh/kg

Due to readiness level and performance, the selected technology for our study will be the Low Temperature Proton Exchange Membrane Fuel Cell. Contrarily to batteries for which power and energy figures are coupled, the fuel stack is sized from power requirements while stored gas volume (i.e energy) is driven by the mission profile. Thus, to compare battery with

fuel cell solutions in terms of specific energy (this factor being the most constraining in our requirements), the overall H2 system mass including fuel cell stack, auxiliaries and H2 storage with the gas volume to fulfill the whole flight mission must be estimated. From that estimation, the table below clearly shows that battery technologies are outclassed by fuel cells:

		Power oriented	Energy oriented	
Specific energy e_m		LTO / TNO ^{1, 4}	NMC Solid State ³	FC System (LH ₂)
Perspectives (5 – 10 years)	Cell level	~ 180 – 200 Wh/kg	~ 650 Wh/kg	~ 1 kW/kg
	System level	~ 100 Wh/kg	~ 325 Wh/kg	~ 560 Wh/kg

x 1.8

Fig. II-37: Technological comparison in terms of specific energy given the mission profile.

Looking at all these numbers the fuel cell coupled with liquid hydrogen storage seems to be the best trade-off from a specific power and specific energy point of view. Both models are detailed in Appendix K.

CHAPTER III. Sensitivity analysis on the hybrid-electric aircraft.

CONTENTS

<i>III.1</i>	<i>New technologies that broaden the scope of possibilities.</i>	88
III.1.1	Reference aircraft.....	88
III.1.2	Preliminary target results (2025 – 2035).....	88
III.1.2.1	TEA (TurboElectric aircraft).....	89
III.1.2.2	HEA (Hybrid-electric aircraft).....	89
III.1.2.3	Global sensitivity analysis of target assessments on global weight and fuel burn.	92
<i>III.2</i>	<i>Sobol indices-based sensitivity analysis.</i>	93
III.2.1	An overview of Sobol indices.	94
III.2.2	Calculation process of the Sobol indices.	95
III.2.3	Whole sensitivity analysis based on specific power assessments.....	96
<i>III.3</i>	<i>Sobol Indices based sensitivity analysis at component level.</i>	98
III.3.1	Analysis of 1st order Sobol indices on the design-oriented electric motor model.	100
III.3.2	Revisited sensitivity analysis with total indices and refined bounds (e-motor level).	101
III.3.3	Sensitivity analysis of the electromechanical powertrain (propeller, gearbox, electric-motor).	103
<i>III.4</i>	<i>Conclusion</i>	111

In this chapter, we will focus on the sensitivity analysis of the powertrain, from a global vision at aircraft level to a local one at device level. First, a list of the different aircraft architectures with their associated energy management is presented in order to show the impact of our technological improvements on aircraft performance. A first study taking into account the snowball effects with the target hypotheses will be detailed thereafter. Finally, a global sensitivity analysis of the components will help us to remove the less sensitive variables of the propulsion system and set the decision variables of the optimization process developed in the next chapter.

III.1 New technologies that broaden the scope of possibilities.

III.1.1 Reference aircraft.

Our case study is a regional aircraft which means around 70 pax. For this kind of aircraft, the first reference MTOW is assumed around 23 tons with classical thermal engines without electrical propulsion. The propulsion system is composed of two propellers, two gearboxes directly driven by two turboshafts leading to an embedded mass ("propulsion mass") of 2880 kg. The fuel mass consumed by this reference aircraft during its reference mission is 1160 kg,

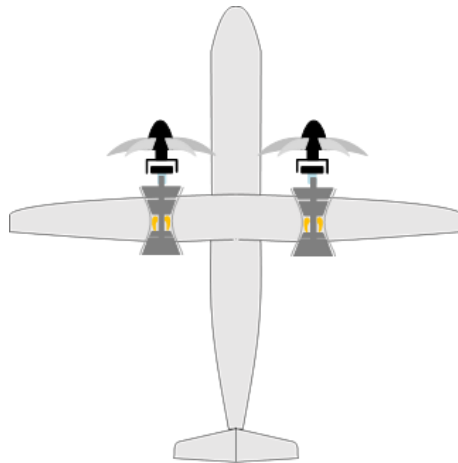


Fig. III-1: Reference aircraft architecture (REF).

III.1.2 Preliminary target results (2025 – 2035).

Several hybrid-electric architectures exist and are reported in the Fig. I-23. The aircraft studied in the next section are all fully powered by electric motors (no direct propulsion generated by gas turbines or turbojets).

III.1.2.1 TEA (TurboElectric aircraft).

In TEA architecture, two turboshafts sized at top of climb are the only power sources and the whole thermal power is converted in electrical power through electric generators (cf Fig. III-2). This architecture is studied with reference to a full thermal aircraft in order to compare the fuel burn saving with electrically driven propellers. This architecture is studied by the NASA with the N3X concept [33]. In this concept the distributed propulsive system permits the improvement of aircraft aerodynamic. But in the HASTECS project, only energy gains are focused and aerodynamic effects are not taken into account.

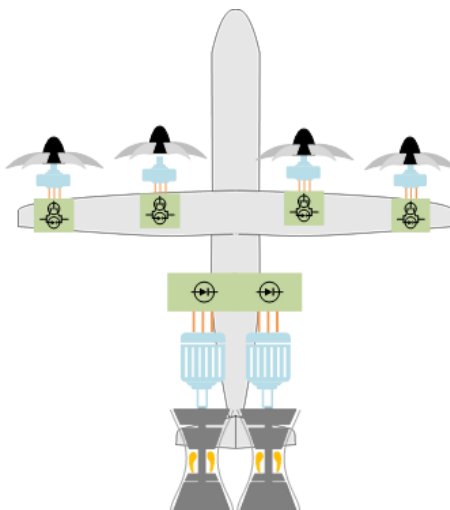


Fig. III-2: Turbo-Electric aircraft architecture (TEA).

III.1.2.2 HEA (Hybrid-electric aircraft).

Unlike the TEA architecture an auxiliary electrical power source is set up in HEA in addition to the main thermal sources. In the following, based on the study proposed in the previous subsection, the considered auxiliary source will be a fuel cell with a liquid hydrogen storage because it seems to be the most adequate candidate (see Fig. II-37) in terms of embedded weight [71]. Thanks to the source hybridization some degrees of freedom are useful to size the main turboshafts by optimizing the energy management. Thus, it results in several candidate architectures linked with several power management strategies.

III.1.2.2.1 Symmetrical HEA (HEASYM)

The first architecture is the “symmetrical hybrid electric aircraft” for which both turboshafts are equally sized: the electric power source (H₂ fuel cell) is used for both full electric taxi phases and descent, which corresponds to a “light hybridization scenario” (no hybridization during take off, climb and cruise). These sequences require a low power demand where the turboshafts could be replaced by electric power sources which are really more efficient at low powers. In our case the specific fuel consumption variation of the turboshaft model is taken into account. At low rating the SFC evolution may be referred to a hyperbolic function (Fig. II-5). In that way, using auxiliary energy source in taxi/descent phases and switching off the main thermal source is energy efficient for a hybrid electric aircraft. However,

a reliable and fast stop and go system is mandatory in order to be able to restart main engines in case of huge power demand or failures. The architecture schematic is the following:

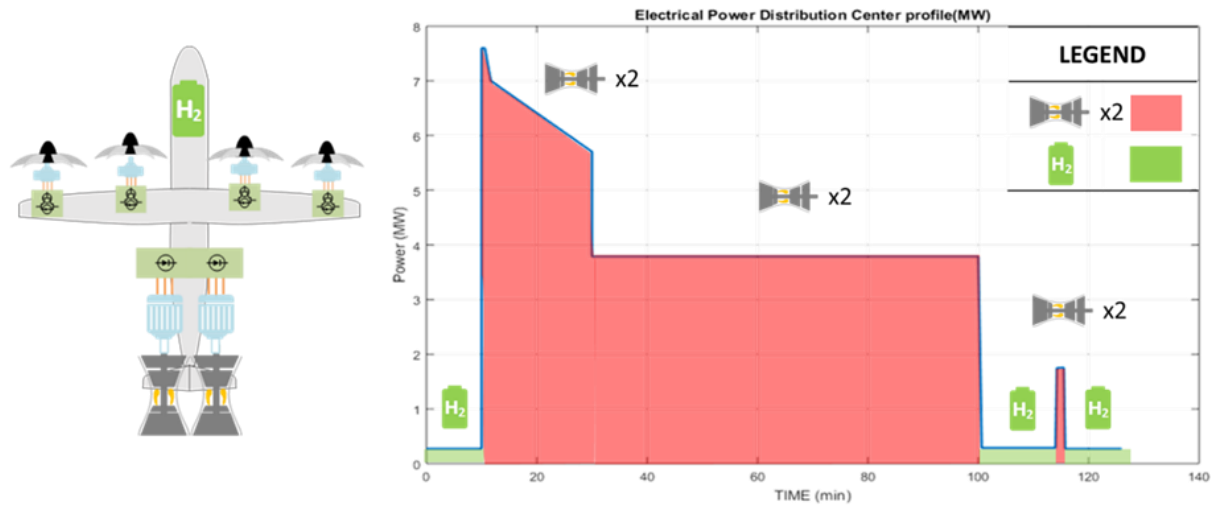


Fig. III-3: Symmetrical Hybrid Electric Aircraft (HEASYM) with the Energy management.

III.1.2.2.2 Asymmetrical architectures

The two next architectures are close to the previous one, except that both turboshaft sizing are not identical in the “Asymmetrical HEA structure” and that only one engine as the main source is considered in the “One engine HEA”. Thus, for these two architectures, particular safety criterion (related to major failure cases) has to be fulfilled: the take-off with one component failure has especially to be carefully studied, especially the One Engine Inoperative (OEI) case. In the OEI case, when the aircraft exceeds the “decision maximum speed” V_1 , the take-off is mandatory during the acceleration phase whatever the failure occurrence beyond this speed limit. We have taken this failure case into account based on assessments related to the ATR datasheet (cf Fig. III-4):

ENGINES	
Take-off power	2,475 SHP
Take-off power - One engine	2,750 SHP
Max continuous	2,500 SHP
Max climb	2,192 SHP
Max cruise	2,132 SHP

Fig. III-4: ATR 72-600 datasheet [65].

In our case, we consider the same ratio between the “take-off power” versus “take-off power One engine” as in the case of the ATR. The value of this power ratio is then 1.11 (2.75/2.475). Finally, the main engine or/and the auxiliary electric source has to be sized according to this power requirement: in other words, the remaining power, whatever the one device failure case must be enhanced at least by 111% of the normal take-off power.

Asymmetrical HEA (HEA ASYM).

For this architecture, we asymmetrically design both turboshafts: the “main turboshaft” is sized for optimizing the efficiency during cruise while the “auxiliary turboshaft” is switched

off. Both turboshafts are used for climb and during take-off at 100% of their rating powers. The auxiliary turboshaft is sized for the take-off phase in the event of an engine failure case; the electric source is required too during this failure case. Subsequently a boost for the top of climb is required, which is ensured by the fuel cell (green part in Fig. III-5).

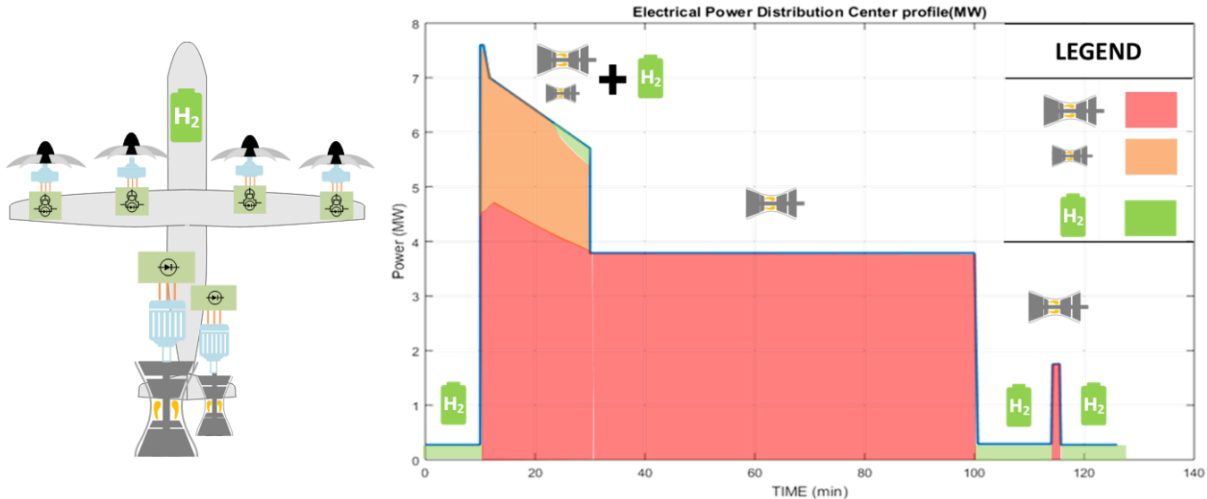


Fig. III-5: Asymmetrical architecture (HEA ASYM) with an energy management.

III.1.2.2.3 One Engine – HEA (HEA -1GT).

Following the same idea and in order to reduce the source rating, one architecture with only one gas turbine may be studied with a “huge hybridization”. The remaining power is then supplied by a high power fuel cell: only two power sources are then considered. In such a case, both sources must be sized in order to face alone the take-off while the other source is failed (OEI case) beyond the V_1 limit of speed. Then, the propulsion system weight is reduced with only one turboshaft - electric generator – rectifier association. For this architecture, the MTOW is strongly reduced. This concept is used by Zunum Aero [44], a hybrid electric aircraft manufacturer startup.

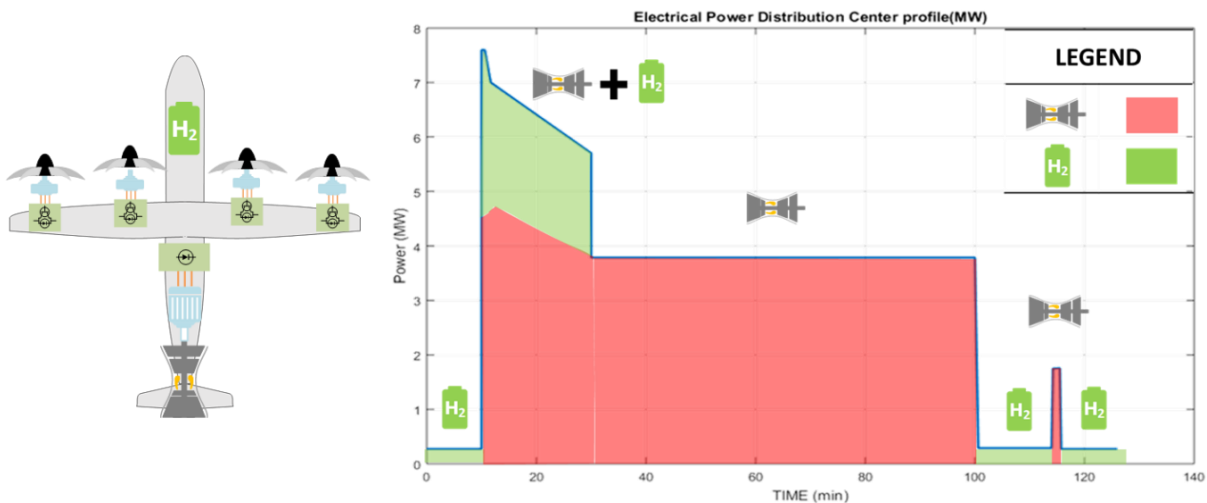


Fig. III-6: One Engine architecture (HEA-1GT) with one energy management.

This sub section has summarized a review of several series hybrid electric architectures. Different energy management scenarios can be guessed as emphasized in the previous examples which consist in an introduction on this topic.

For the rest of the work, the aircraft studied will be based on symmetrical architecture (HEA SYM) because of industrial choices.

III.1.2.3 Global sensitivity analysis of target assessments on global weight and fuel burn.

In this section, a preliminary sensitivity analysis based on target assessments can be done. Both targets (2025, 2035) with respect to the reference aircraft (see Fig. III-1) with full thermal optimized sizing are assessed in order to analyze the sensitivity of technological improvements with regard to the architectures previously presented in this chapter. For the asymmetrical architectures two aircrafts were designed:

- without the failure case of One Engine Inoperative (OEI).
- with the failure case of One Engine Inoperative (OEI).

Let us note that, while variable masses (variable specific powers) are assessed in the sensitivity analysis, snowball effects exist to assess the MTOW as emphasized in the chapter I: the looped process validated in the section I.3.3 is used to adapt the thrust during the flight mission with respect to the MTOW variations.

This global sensitivity analysis shows the effect of technological improvements assuming that 2025 or 2035 targets are reached as defined in the following table. Another “more aggressive” target (named “20xx target”) has been guessed for analysis proposed in the next section of this chapter.

Table III-1: Electric component assessments.

	2025 target	2035 target	20xx target
Emotor/ Egenerator			
Specific power	5 kW/kg	10 kW/kg	15 kW/kg
Efficiency	96%	98.5%	99%
Power Electronics			
Efficiency	15 kW/kg 98%	25 kW/kg 99.5%	35 kW/kg 99.8%
FC stack + Liquid H2 storage			
H₂ + tank specific energy	3.3 kWh/kg		
Auxiliary specific power	1.3 kW/kg		
Stack specific power	4 kW/kg		
DC Bus Voltage			
Ultra HVDC	2000V		

Based on these assessments, the following analysis results show the positioning of each architecture in the MTOW vs fuel burn plan with reference to the full thermal optimized aircraft (“reference aircraft”).

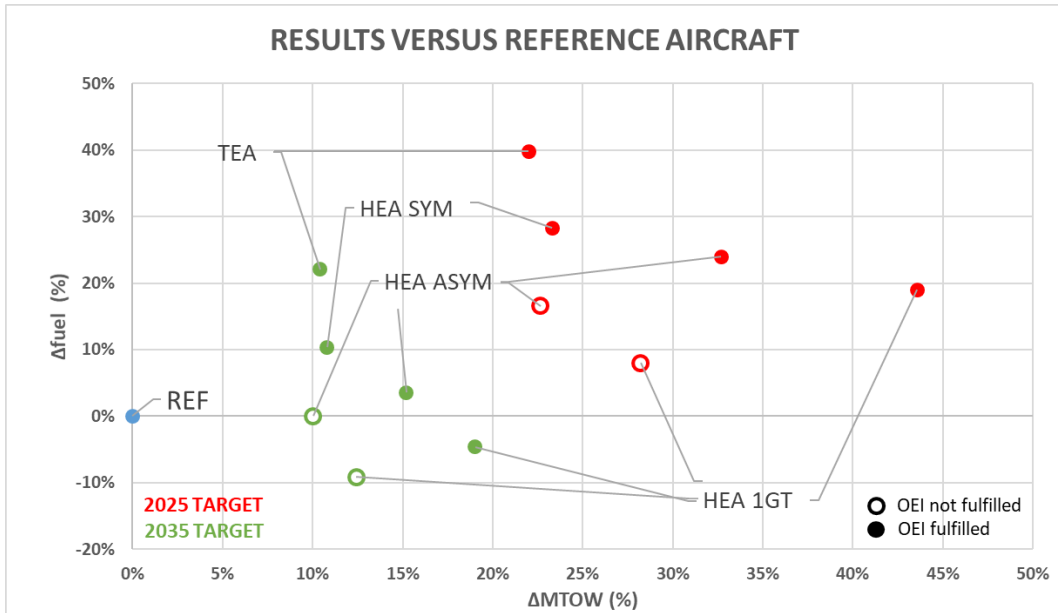


Fig. III-7: Summary of results versus reference aircraft with both targets.

The aircraft performance is really improved crossing from the 2025 to the 2035 target assessments whose specific powers and efficiencies are enhanced. The improvement of electric components is then really sensitive on the design performance of future hybrid-electric aircrafts. The snowball effects due to the weight added to the propulsion system strongly impacts the fuel consumption. Moreover, failure cases, especially the OEI (One Engine Inoperative) must not be neglected. In every case, the MTOW of electrically powered aircrafts are higher than the full thermal reference which seems normal as several devices (power converters, electric generators and motor, etc) are added in the electric powertrain.

In the next section, a further sensitive analysis has been realized using an analysis method based on the Sobol indices. Firstly, studies were carried out at aircraft level in order to retrieve the results previously presented in the chapter I (see Fig. I-62 & Fig. I-63). Then, a local analysis at component level is highlighted. The impact of each design variable on both weight and efficiency of the corresponding device is analyzed.

III.2 Sobol indices-based sensitivity analysis.

In order to prepare the global optimization of the overall hybrid-electric powertrain, a study of each design model of devices has to be assessed with the aim of limiting the number of decision variables. The issue is the selection of the most sensitive variables at the powertrain level.

Among the sensitivity analysis methods, the Sobol indices appeared as one of the most promising. G. Chastaing's work [98] deals with Sobol indices for global sensitivity analysis.

Such indices were used for dependent variable values in the case study related to an energy efficient building design. Another reference uses these indices to study the most impacting variables of a problem such as the optimization of a cooling system of an electromechanical actuator [99]. In our case, variables are assumed to be independent.

III.2.1 An overview of Sobol indices.

Sobol indices allow identifying particularly sensitive input variables, X_i , with regard to certain output mean values, Y . Such indices are obtained by decomposition of the variance in the case of independent inputs. Model output may be written as follows:

$$f : \mathbb{R}^n \rightarrow \mathbb{R}$$

$$[X_1, X_2, X_3, \dots, X_{nb_{var}}] \rightarrow Y$$

Following the Hoeffding decomposition [100], the output variable is:

$$Y = f_0 + \sum_{i=1}^{nb_{var}} f_i(X_i) + \sum_{1 \leq i \leq j \leq nb_{var}} f_{i,j}(X_i) + \dots + f_{1,2,\dots,nb_{var}}(X_1, X_2, \dots, X_{nb_{var}}) \quad (\text{III-1})$$

Where f_0 is constant and calculated by the mean of Y , f_i is a function of X_i , nb_{var} is the number of variables, i and j are the indices. To obtain variance decomposition expression, f function is assumed to be square-integral, while the decomposition may be squared and integrated. Dividing Eq.(III-1) by the output variance $Var(Y)$ the following equation is obtained:

$$1 = \sum_{i=1}^{nb_{var}} \frac{V_i}{Var(Y)} + \sum_{1 \leq i \leq j \leq nb_{var}} \frac{V_{ij}}{Var(Y)} + \dots + \frac{V_{1,2,\dots,nb_{var}}}{Var(Y)} \quad (\text{III-2})$$

Where

$$V_i = Var(\mathbb{E}[Y|X_i]) \quad (\text{III-3})$$

$$V_{i,j} = Var(\mathbb{E}[Y|X_i, X_j]) - V_i - V_j \quad (\text{III-4})$$

Sobol indices, $S_i, S_{i,j}, \dots$ are defined as follows. They may be of different orders: first order indices express the effects of each variable, X_i with respect to the output Y , but not considering correlation effects between inputs which are considered in the terms $S_{i,j}$:

$$0 \leq S_i = \frac{Var(\mathbb{E}[Y|X_i])}{Var(Y)} \leq 1 \quad (\text{III-5})$$

$$0 \leq S_{i,j} = \frac{Var(\mathbb{E}[Y|X_i, X_j])}{Var(Y)} - S_i - S_j \leq 1 \quad (\text{III-6})$$

Second order indices express correlations between two input variables X_i, X_j .

Finally, total order indices: consider the effects of the X_i variable alone and the correlation effects of all other X_j with $j \neq i$.

III.2.2 Calculation process of the Sobol indices.

Multidisciplinary system studies require the variation of a large number of variables. Most computers are limited by their storage, that is why it is necessary to adopt new calculation methods. In this part two methods have been compared. A choice has been made in order to approximate the indices by limiting the calculation time:

- The ANOVA (Analyze Of VAriance) method based on a regular disposition of the inputs (with nb_{pts} the number of level). In the example of an electric motor model the number of calculated points is: $(nb_{pts})^{nb_{var}} = 4^{13} = 67 \times 10^6 \text{ pts}$.
- The Pick and Freeze method [101], [102], [103], based on two random samplings of the inputs. In the example of the electric motor model the number of calculated points is:
 $2 \times nb_{pts} \times nb_{var} = 13 \times 10^5 \text{ pts}$.

The difference in the number of evaluations between the two methods is equivalent to the ratio expressed by Eq. (III-7):

$$\frac{ANOVA_{eval}}{Pick\&Freeze_{eval}} = \frac{((nb_{pts})^{nb_{var}})}{2 \times nb_{pts} \times nb_{var}} \sim 26 \quad (\text{III-7})$$

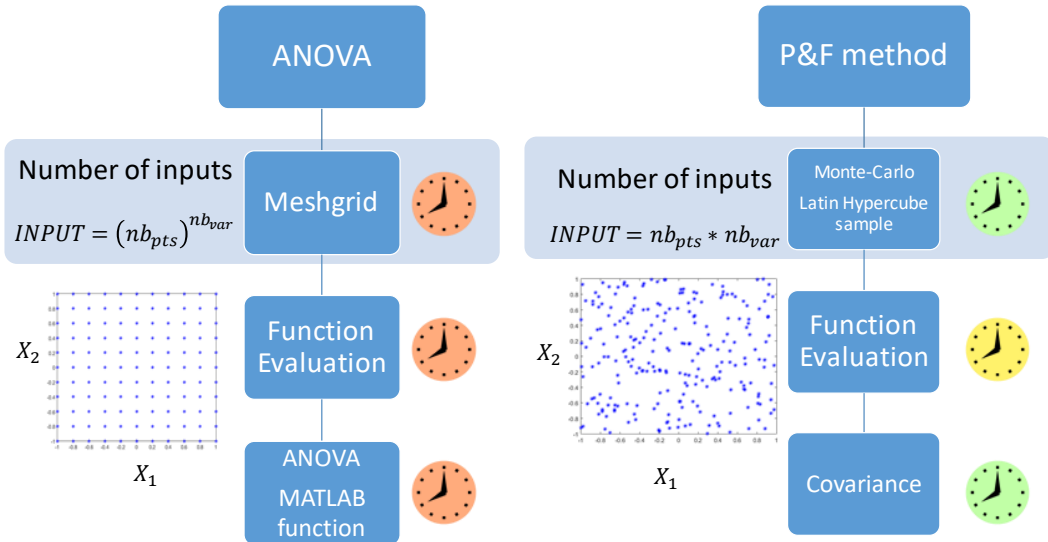


Fig. III-8: Comparison of two Sobol indices estimation methods.

The CPU time cost of ANOVA method is huge due to its input combinatorial explosion when the number of decision variables is also important, the function evaluation being directly amplified by the number of inputs. On the contrary, the Pick&Freeze method complexity mainly depends on the number of points used for sensitivity analysis. The random draw for the

Pick&Freeze method has a small CPU cost. In the study case related to the electrical motor model, the comparison in terms of CPU cost gives explicit differences:

1. for ANOVA method, 1.5 days (four levels (nb_{pts}) and $nb_{var} = 13$ input variables)
2. for Pick&Freeze method: 20 minutes for 100000 points (this number of points being sufficient for obtaining the same results as with ANOVA).

III.2.3 Whole sensitivity analysis based on specific power assessments.

In this section, a sensitivity analysis based on the Sobol indices is carried out at a global level for each hybrid electrical architecture previously presented in that chapter. Two outputs are considered: MTOW and fuel burn mass. These outputs are evaluated using the looped process presented in section I-3.3. For each iteration of this looped process, all components of the powertrain are sized by following the flow chart of Fig. III-9 and it is detailed in APPENDIX L.

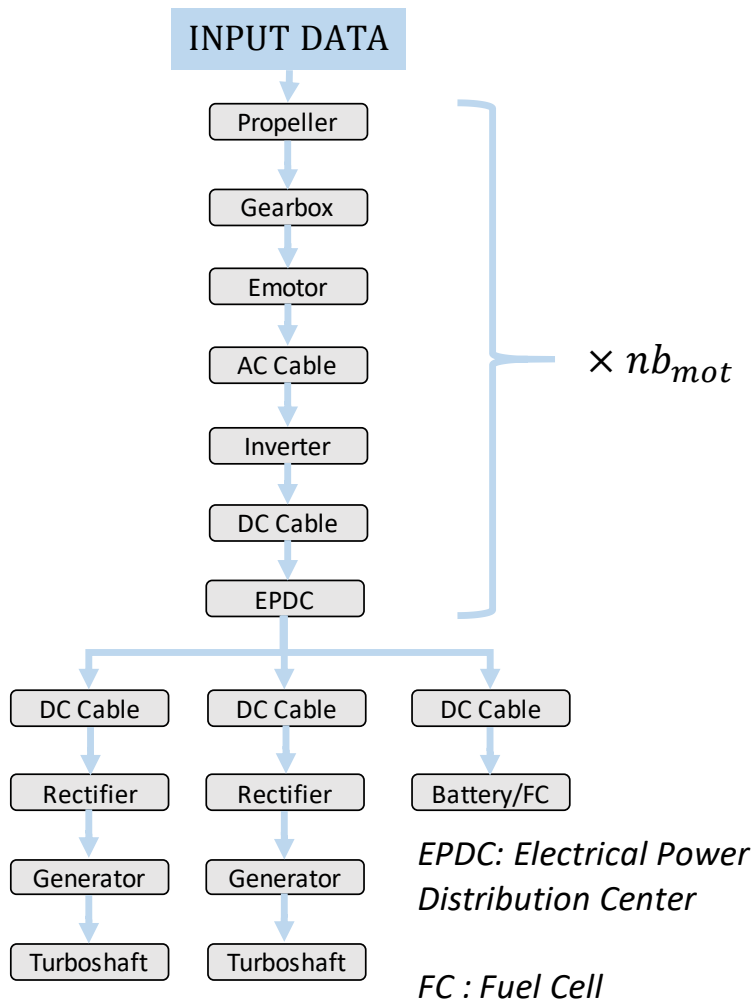


Fig. III-9: Integrated design process flow chart.

The current section aims at confirming the results obtained in the section I.3.4 and presented in [66]. The input variables of sensitivity analysis are related to the assessments of the Table III-1 which correspond to both specific powers and efficiencies for electric motors and power inverters. These assessments are considered to set the upper and lower bounds of the input variables.

Three hybrid-electric architectures are compared: the Turbo electric architecture (TEA), the symmetrical Hybrid-electric architecture (HEASYM called hereafter HEA) and the hybrid-electric architecture with one turboshaft (HEA1GT) corresponding to the previous section (III.1.2.2).

Regarding fuel burn and then the MTOW as the outputs, analysis results are detailed in Fig. III-10 and Fig. III-11 respectively. These analysis confirms the trends previously presented in section I.3.4 (Fig. I.49, I.50) in the particular case of the HEA architecture: based on a simple analysis case with a reduced number of input variables, this comparison allows to prove the ability of Sobol Indices to correctly set the sentitivity effects. In particular, as previously, the electric motor is the most sensitive electrical component so the most important to be optimized with regard to the MTOW. The efficiency (η) also affects the fuel mass. Observing Fig. III-10, efficiencies (η_{emotor} and $\eta_{inverter}$) are sensitive as they directly impact the source sizing so the fuel burn demand. On the other side, the fuel mass is also highly sensitive to the specific power variations confirming the results obtained in section I.3.4 and presented in [66].

Concerning the impact analysis on the MTOW (see Fig. III-11), the specific power ($P_{SPE_{emotor}}$) of the electric motor clearly appears to be the most sensitive variable compared with the effect of efficiencies.

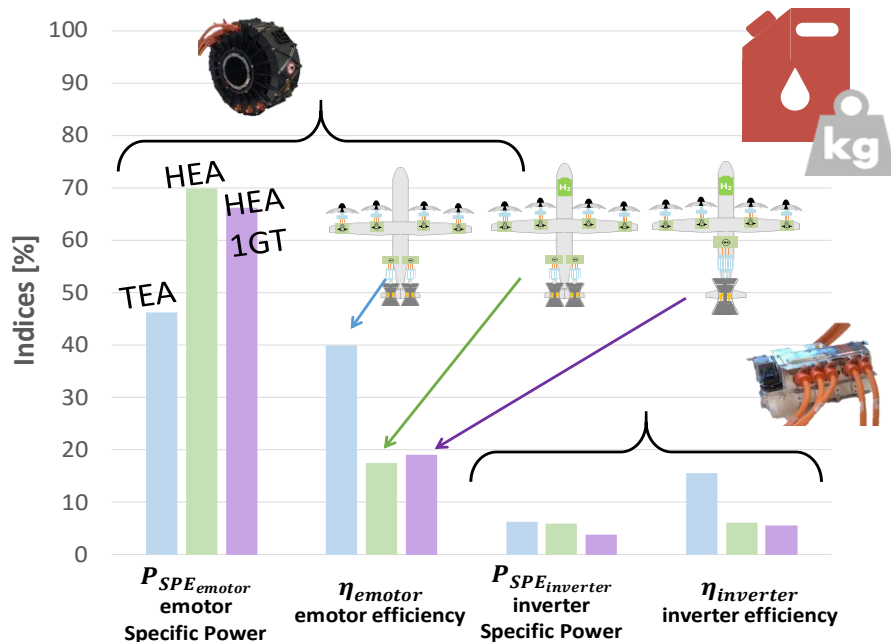


Fig. III-10: First order Sobol indices for three hybrid-electric architectures regarding the fuel mass; bar colors are related to the 3 compared architectures.

In these analyses only the first-order Sobol index is represented (sum of all the first-order indices = 1 therefore no correlation between the variables) because the variables are totally dissociated and have a direct impact on the aircraft's weight or fuel. As stated above, the first-order index represents the sensitivity specific to the parameter (see section III.2.1).

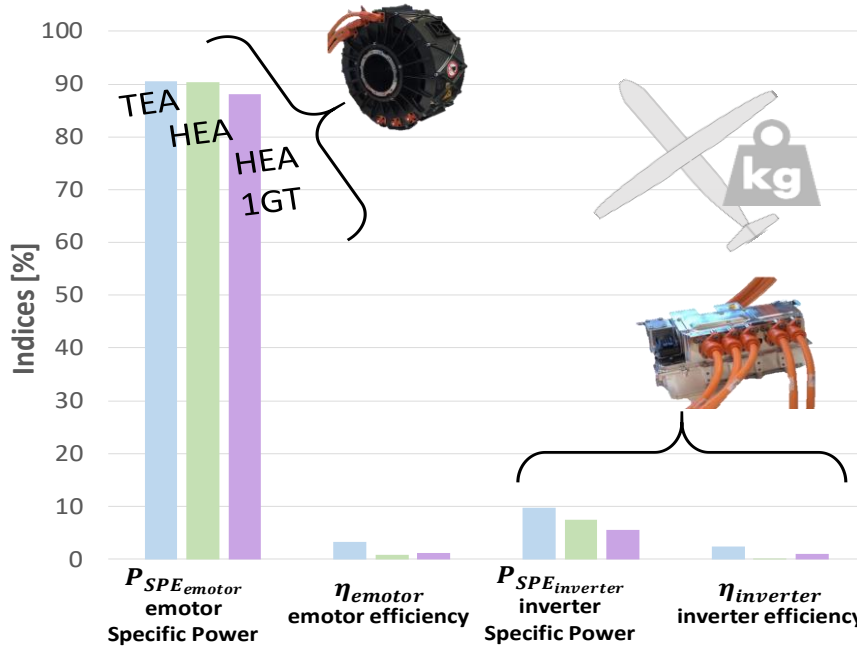


Fig. III-11: First order Sobol indices for three hybrid-electric architectures regarding the MTOW; bar colors are related to the 3 compared architectures.

This analysis was based on very simple models for electronic powers and electric motors which allows validating the sensitivity analysis based on Sobol indices using the Pick&Freeze calculation method which the trends have confirmed previous sensitivity analysis presented in chapter I. The same approach may be used for more complex design models as in the case of the electromechanical actuator models reported in [104]. In order to select the most sensitive design variables in actuators which have been seen to be the most sensitive devices on weight and fuel burn, a local sensitivity analysis based on Sobol indices is investigated in the next section by means of technological design models.

III.3 Sobol indices based sensitivity analysis at component level.

In this section, the attention is focused on the electric motor which has been seen as very sensitive at aircraft level for HEA architectures. The original sizing model developed in [84] for the electric motor design has been considered in order to illustrate the interest of this approach; this model is nearly the same as the one presented in the Chapter II (some adaptations of the original model have been presented in that previous chapter) and used in our thesis for the overall optimal design.

After the choice of the index calculation method, input variables (and subsequent bounds) have to be determined. In our case an input vector including thirteen variables has been chosen for the motor model inputs. A first set of input variables with corresponding lower and upper bounds is presented n the following table:

Table III-2: 1rst sensitivity analysis input variables and their bounds

Input Variables	Name of the variable	Lower bound	Upper bound
$P_{em,siz} [\%]$	% of Power sizing point from the maximum value	80	130
$N_{siz} [\%]$	% of rotational speed sizing point from the maximum value	80	150
$f_T [Pa]$	Tangential stress in the airgap	40000	148500
$J_{rms} [A/mm^2]$	Current density at sizing point	6	25
$B_{gap,max} [T]$	Maximum air gap flux density	0.8	1.05
$B_{teeth,max} [T]$	Maximum teeth flux density	1	1.53
$B_{yoke,max} [T]$	Maximum stator yoke flux density	1	1.53
$B_{yoke-rotor,max} [T]$	Maximum rotor yoke flux density	1	1.5
$R_{drot,lm} [\%]$	Ratio between the rotor diameter and the rotor active length	0.5	1.25
$V_{uHVDC} [V]$	Ultra-high direct current Voltage	1000	3000
$n_{epp} [-]$	Number of slots per poles and per phases	1	4
$N_{ce} [-]$	Number of conductors per slot	1	4
$p [-]$	Number of pole pairs	2	10

As in the previous section, mass and efficiency have been chosen as the outputs for the model. The process to determine Sobol indices is illustrated in Fig. III-12:

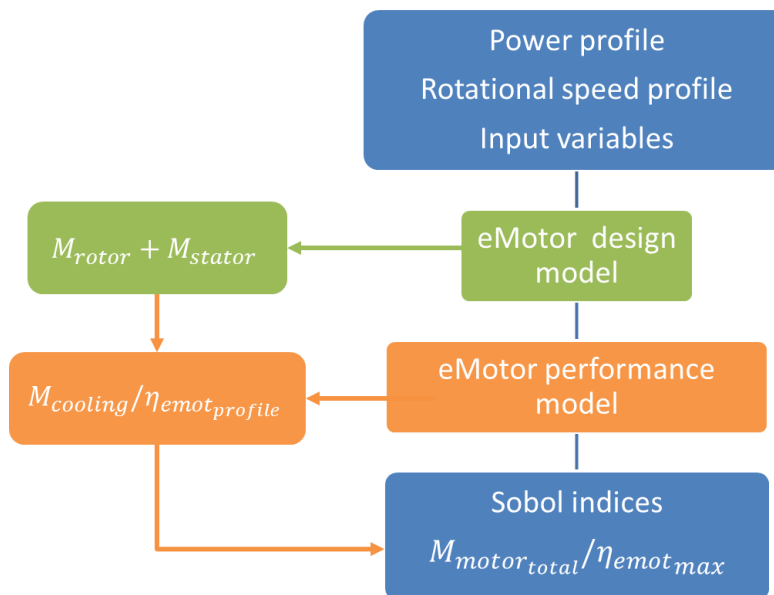


Fig. III-12: Process to determine Sobol Indices for the electric motor sensitivity analysis.

In order to estimate the cooling mass, a specific power of cooling equal to 1 kW (of losses)/kg is assessed. In that way, losses are simply converted into a roughly estimated cooling mass.

III.3.1 Analysis of 1st order Sobol indices on the design-oriented electric motor model.

In the first analysis, both methods (Anova vs Pick&Freeze) for estimating Sobol Indices have been compared. First order Sobol indices comparison is described in Fig. III-13 and Fig. III-14:

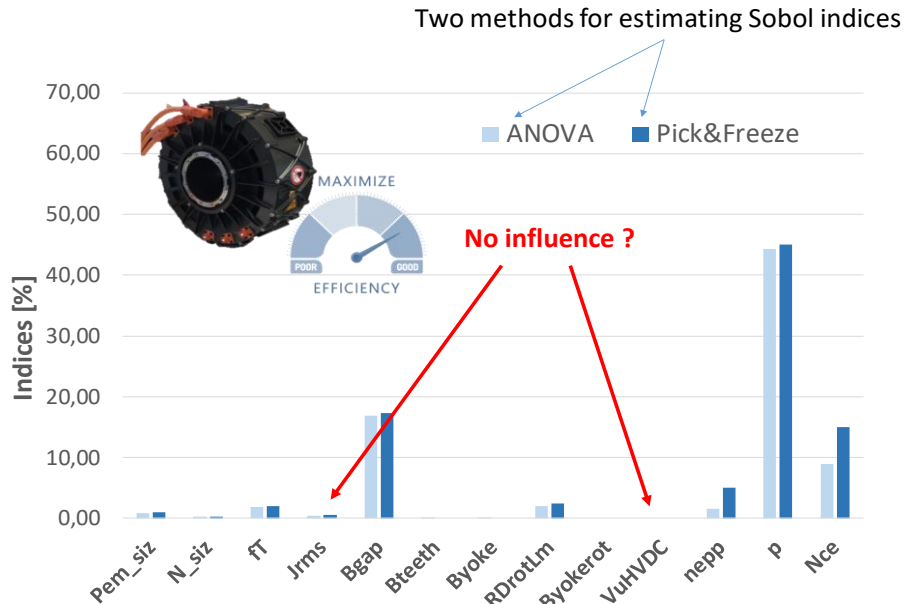


Fig. III-13: First order Sobol indices calculated by the two estimation methods.
Output variable: efficiency. Input variables: motor parameters

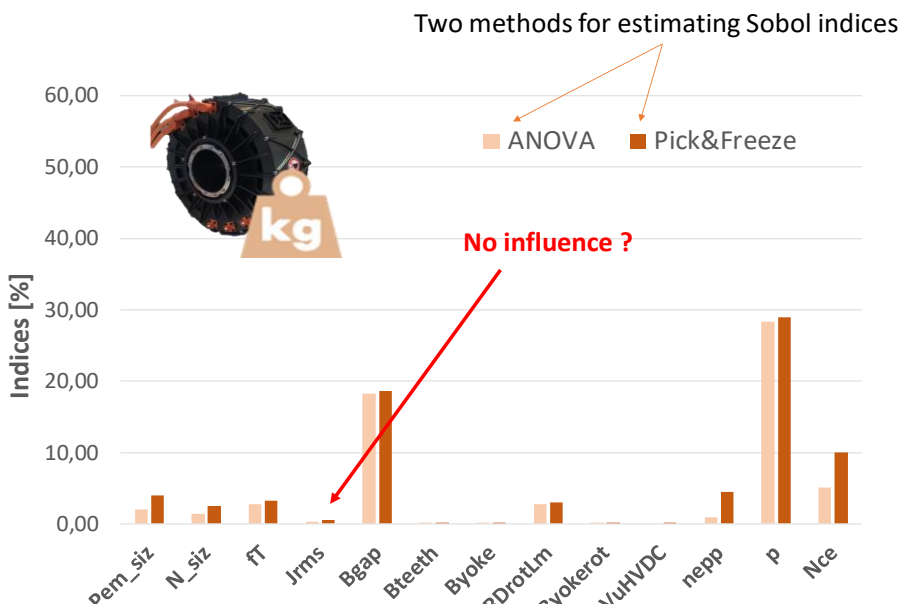


Fig. III-14: First order Sobol indices calculated by the two estimation methods.
Output variable: mass. Input variables: motor parameters

At first, this analysis shows that results provided by both estimation methods (Anova vs Pick&Freeze) are quite similar, validating such approaches. In the following the Pick & Freeze method (less consuming in CPU time) is used.

- Regarding the obtained values from this sensitivity analysis, the results are quite surprising. Indeed, some variables which are usually (physically) impacting the electric motor mass for experts as the current density (J_{rms}) are not highlighted by the 1st order Sobol indices. This effect can be explained as follows: the bounds of the corresponding input variable have a clear influence on the Sobol indices; thus, with the help of the electric motor experts, all input variable bounds have been revisited (see the Table III-3).
- The “low influence” of certain input variables is also due to the dependences between input variables: it should be reminded that Sobol’s method assumes the independence of input variables. However, it can be observed from Eq. III-6 that the number of conductors per slot (N_{ce}), is directly linked to other variables of the input data set. :

$$N_{ce} = \text{floor} \left(\frac{ma * V_{uHVDC}}{2 * \sqrt{2} * V_{1spire}} \right) \quad \text{with} \quad (\text{III-8})$$

$$V_{1spire} = f(p, n_{epp}, R_{DrotLm}, \dots) \quad (\text{III-9})$$

- V_{1spire} : voltage in one spire [V].
- ma : the modulation depth [-].

Finally, the “dependent variable” (such as N_{ce}) have been suppressed to the input data set keeping only independent inputs. Furthermore, it has to be underlined that 1st order indices do not take account correlation effects which are rich in information. The total Sobol indices have to be considered for that purpose. Based on those remarks, a second sensitivity analysis study has been carried out by changing the bounds of input variables, suppressing dependent variables and also analyzing the total indices with correlation effects.

III.3.2 Revisited sensitivity analysis with total indices and refined bounds (e-motor level).

As previously mentioned, the total order Sobol index are useful to be exploited (effect of the X_i parameter alone plus correlation effects of all other X_j with $j \neq i$). The new (12) input variables are the following:

Table III-3: 2nd sensitivity analysis input variables and their bounds

Input Variables	Name of the variable	Lower bound	Upper bound
$P_{em,siz}$ [%]	Power sizing point from the maximum value	80	130
N_{siz} [%]	Rotational speed sizing point from the maximum value	80	150
f_T [Pa]	Tangential stress in the airgap	40000	148500
J_{rms} [A/mm ²]	Current density at the sizing point	6	25
$B_{gap,max}$ [T]	Maximum air gap flux density	0.8	1.05
$B_{teeth,max}$ [T]	Maximum teeth flux density	1	1.53
$B_{yoke,max}$ [T]	Maximum stator yoke flux density	1	1.53
$B_{yoke-rotor,max}$ [T]	Maximum rotor yoke flux density	1	1.5
R_{drotLm} [%]	Ratio between the rotor diameter and the rotor active length	0.5	1.25
V_{uHVDC} [V]	Ultra-high voltage direct current	1000	3000
n_{epp} [-]	Number of slots per poles and per phases	1	4
p [-]	Number of pole pairs	2	10

Main results of such analysis are reported comparing first order and total Sobol indices with respect of the 12 input variables [105]:

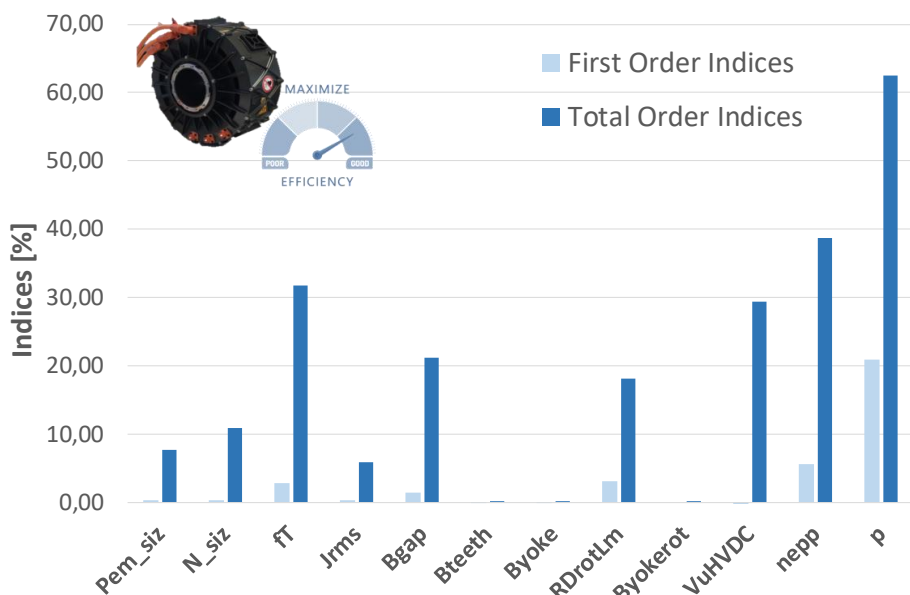


Fig. III-15: First order (pale color) and total order (dark color) Sobol indices and its effects on the e-motor efficiency.

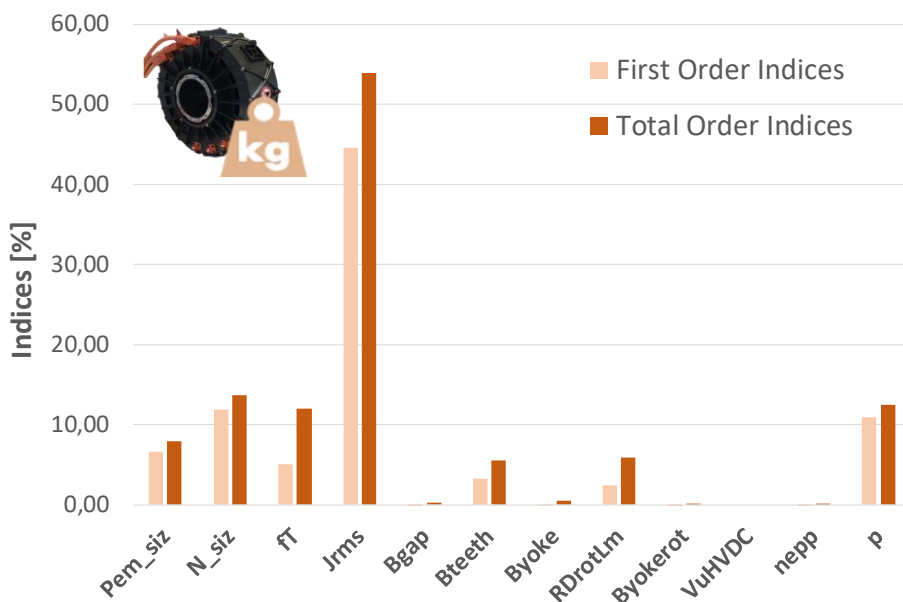


Fig. III-16: First order (pale color) and total order (dark color) Sobol indices and its effects on the e-motor mass.

Analyzing Sobol indices and their effects on electric motor mass, four total order Sobol indices are close to zero. But these variables are impacting the eMotor efficiency (see Fig. III-15). It shows that both outputs (mass and efficiency) need to be considered in order to obtain relevant and complete sensitivity analysis. Finally, only two motor input parameters can be considered as insensitive with regard to both output criteria and whatever if 1st order or total Sobol indices are observed:

- $B_{yoke_{rot}}$ the rotor yoke flux density.
- B_{yoke} the stator yoke flux density.

Thus, in the following, these two variables will be set at a fixed rating value which tends to reduce the number of decision variables for optimization also reducing the computation time and facilitating the convergence of algorithm. For the next sensitivity analysis proposed at electromechanical powertrain level, the number of input variables for the motor is then reduced to 10.

III.3.3 Sensitivity analysis of the electromechanical powertrain (propeller, gearbox, electric-motor).

This section aims to analyze the sensitivity of the electromechanical powertrain coupling gearbox and propeller devices with eMotor.

Previous studies have been performed without considering feasibility constraints: it means that numerous tests in the peak&freeze method do not fulfill feasibility constraints which will be considered in the optimization approach. In the following, two feasibility constraints have been added:

- A thermal constraint (used by research teams in charge of the electric motor design and its cooling) is related to an estimation of the necessary cooling effort and is emphasized by the $A \times J_{eq}$ product. The constraint is: $A \times J_{eq} \leq 2.10^{12}$ with the following parameters:

$$A \times J_{eq} = \frac{(P_{Joule} + P_{Iron} + P_{windage} + P_{friction})}{k_{tb} * S_{alesage} * \rho_{CU}(T_{win})} \quad (\text{III-10})$$

- P_{Joule} : the Joule losses [W].
- P_{Iron} : the iron losses [W].
- $P_{windage}$: the windage losses [W].
- $P_{friction}$: the friction losses in bearings [W].
- $S_{alesage}$: the bore area of the e-motor [m^2].
- $\rho_{CU}(T_{win})$: the copper resistivity [$\Omega.m$] function of winding temperature T_{win}
- k_{tb} : the end-winding coefficient [-].

This thermal constraint (see Eq (III-10)) allows designing the electromechanical actuator by considering the cooling system. Exceeding this thermal limit prevents the cooling system from cooling the electric motor.

- The 2nd constraint is related to the maximum peripheral speed: $V_{peripheral} \leq 150m/s$. This is the maximum value reachable without inducing mechanical deformation that can damage the actuator.

Moreover, the variables involved in the propeller and gearbox models have been added in order to complete the sensitivity analysis. The input data are the requirement data (Thrust, Mach, Altitude) and the analysis process is illustrated in Fig. III-17.

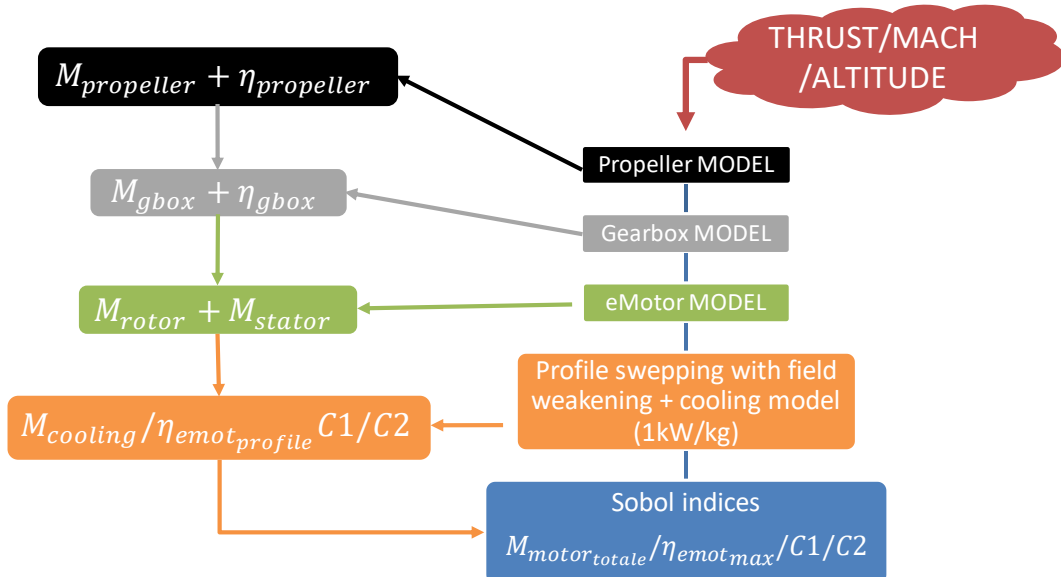


Fig. III-17: Electromechanical powertrain sensitivity analysis process.

The following set of input variables is chosen with their corresponding bounds:

Tab. III-1: 3rd sensitivity analysis input variables and their bounds.

Input Variables	Lower bound	Upper bound
$D_{prop_{siz}} [\%]$	100	150
$R_{gbox} [-]$	1	15
$P_{em_{siz}} [\%]$	80	130
$N_{siz} [\%]$	80	150
$f_T [Pa]$	40000	148500
$J_{rms} [A/mm^2]$	6	25
$B_{gap_{max}} [T]$	0.8	1.05
$B_{teeth_{max}} [T]$	1	1.53
$R_{drot_{lm}} [\%]$	0.5	1.25
$V_{uHVDC} [V]$	1000	3000
$n_{epp} [-]$	1	4
$p [-]$	2	10

Two inputs parameters have been added in addition to the ten remaining variables for eMotor in order to highlight the interactions between elements.

- $D_{prop_{siz}}$: oversizing of the propeller in %.
- R_{gbox} : gearbox ratio.

III.3.3.1 Sensitivity analysis without feasibility constraint fulfilment.

In this section, the sensitivity of the electromechanical powertrain is analyzed during cruise [106]: the efficiency, the mass, and the feasibility constraints are successively displayed as outputs in order to determine the Sobol indices. In addition to the previous outputs (masses and efficiency), the constraint levels are calculated and displayed to emphasize their influence following the values of the input variables. The results are quite similar to those observed in the previous study (see Fig. III-15) except for the tangential pressure and the flux density in the air gap (+10% on the total order Sobol index). This difference arises due to the introduction of the gearbox ratio. Adding this variable allows adapting the rotational speed of the electric motor. Thus, the rotation speed range is higher than in the previous study. Consequently, the tangential stress and the flux density in the air gap are more sensitive on the rotor volume and so on the motor mass. If the constraint fulfilment is not mandatory in the analysis, propeller and gearbox inputs are not too sensitive on outputs.

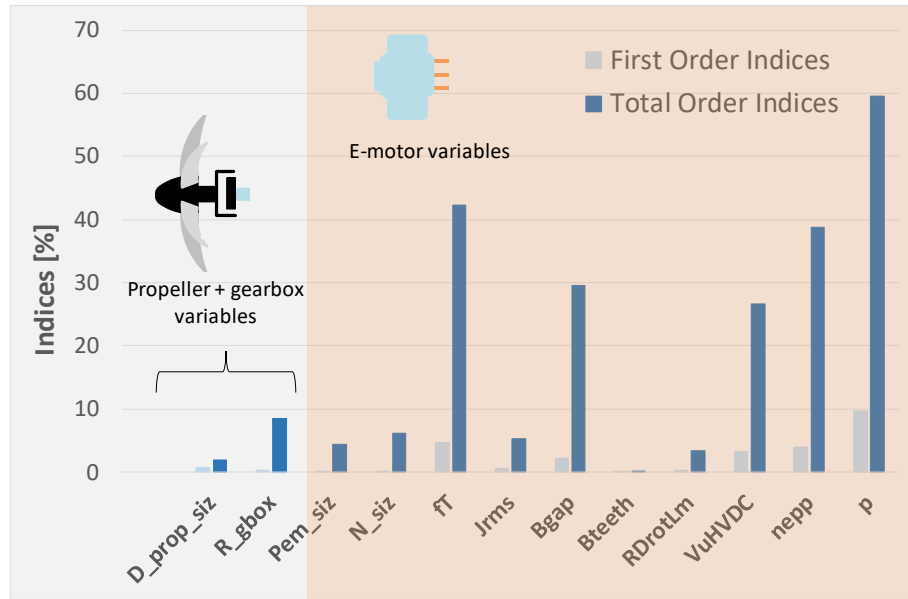


Fig. III-18: First order (pale color) and total order (dark color) Sobol indices with e-motor efficiency as output without considering constraint fulfillment.

Losses of the electrical machine depend on the volume of copper and the volume of magnetic yoke in the stator. The higher the copper and magnetic yoke volume, the larger the amount of losses. Thus, while the stator volume depends on rotor volume, stator yoke and copper volumes are impacted as well, and so the losses. The gearbox ratio directly impacts e-motor rotor volume (consequently the e-motor mass); thus, it becomes the most impacting variable on the overall system mass. This gearbox ratio index highlights an interaction between the electromechanical and propeller devices: this is a key parameter considering the mass of the propulsion system.

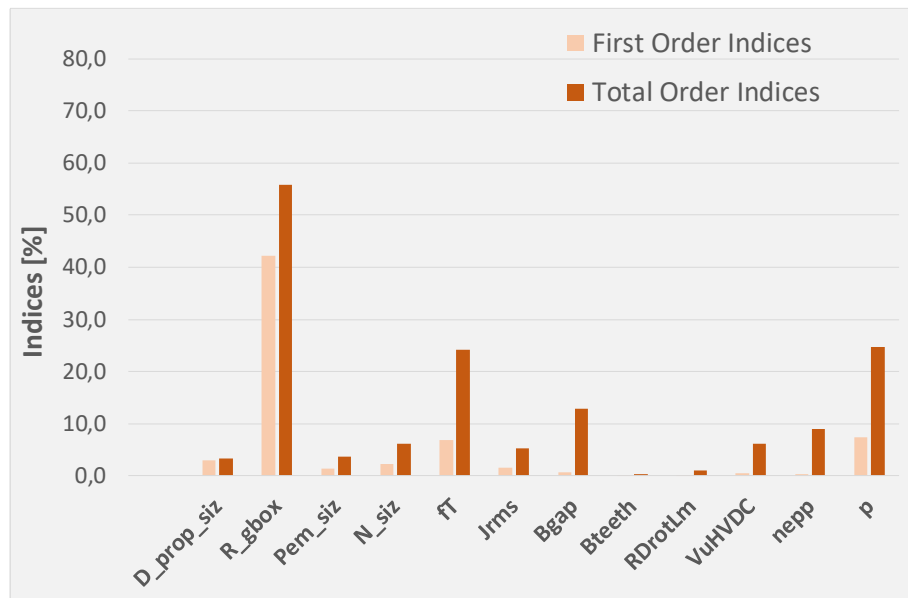


Fig. III-19: First order (pale color) and total order (dark color) Sobol indices with e-motor mass as output without considering constraint fulfillment

The first constraint to be analyzed is the peripheral speed constraint.

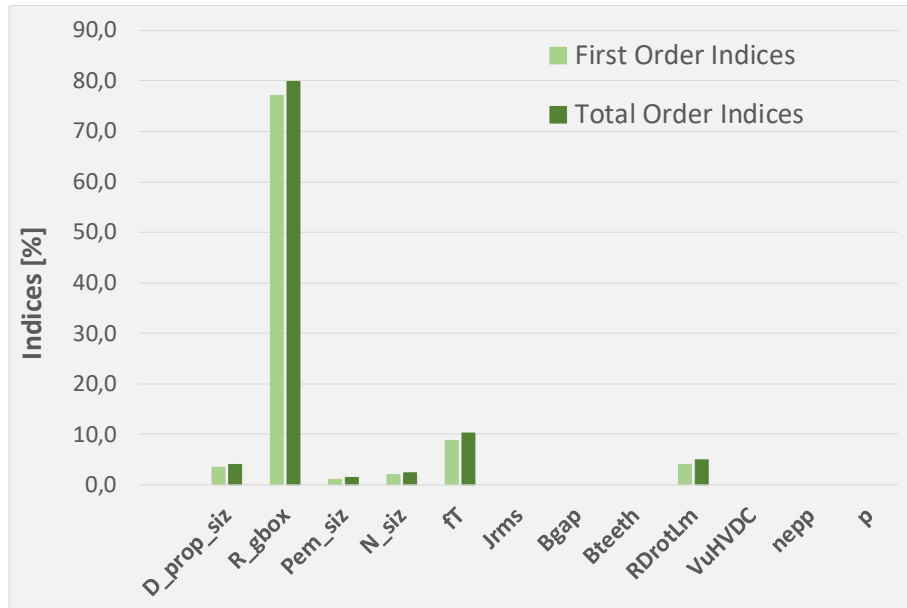


Fig. III-20: First order (pale color) and total order (dark color) Sobol indices with the e-motor peripheral speed as output without considering constraint fulfillment

Several input parameters are directly involved in the maximal peripheral speed equation:

$$V_{\text{peripheral}} = \left(\frac{P_{\text{em}}}{N_{\text{siz}}} * \max \left(\frac{P_{\text{prop}} * \eta_{\text{gbox}}}{N_{\text{prop}} * R_{\text{gbox}}} \right) * \frac{30\pi}{4f_T} * R_{\text{Drot/Lm}} \right)^{\frac{1}{3}} \frac{R_{\text{gbox}} * N_{\text{prop}} * N_{\text{siz}}}{30} \quad (\text{III-11})$$

Where

- η_{gbox} : gearbox efficiency [%]
- N_{prop} : propeller rotation speed [RPM]
- P_{prop} : propeller shaft power [W]

The propeller diameter is indirectly involved through the propeller shaft power, P_{prop} . So, all the sensitive parameters in Eq (III-11) appear in the previous equation. Some sobol indices are null, this can be explained by the absence of the studied parameters in the peripheral velocity equation (for instance, B_{gap} is not necessary to calculate the peripheral speed and therefore its Sobol indices are null).

The second analysis is related to the thermal limit as reported in Fig. III-21.

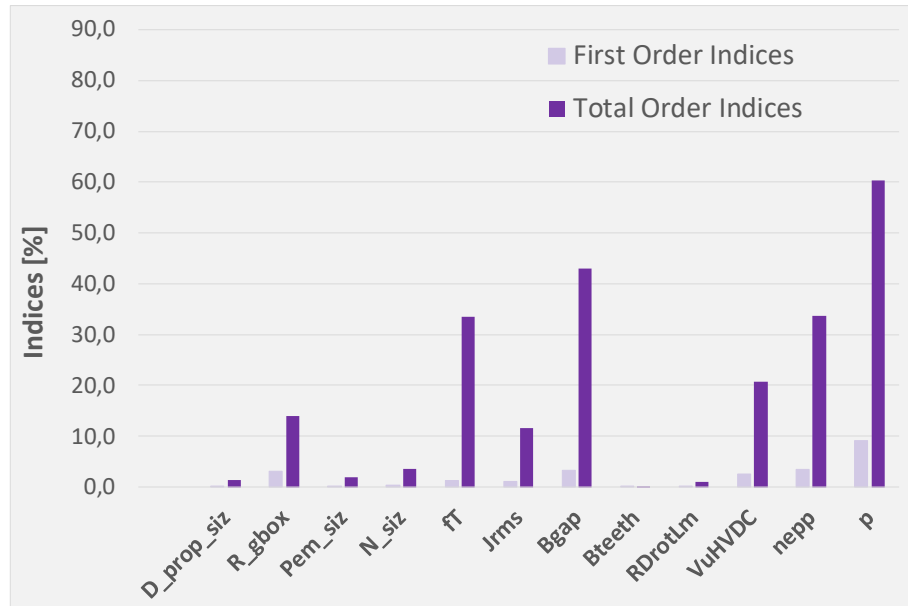


Fig. III-21: First order (pale color) and total order (dark color) Sobol indices on the thermal constraint as output without considering constraint fulfillment

The results are quite similar to those of Fig. III-18 (output: efficiency). Indeed, losses are directly linked to the $A \times J_{eq}$ product which qualitatively represents the thermal constraint. The efficiency is then directly represented in the thermal constraint.

III.3.3.2 Sensitivity analysis with feasibility constraint fulfilment

It is interesting to compare results related to the design of the propulsion system following if constraints are fulfilled or not [106]. In that subsection, only tested solutions fulfilling both constraints (peripheral speed and thermal constraints) are considered in the sensitivity analysis (i.e. for the calculation of Sobol indices).

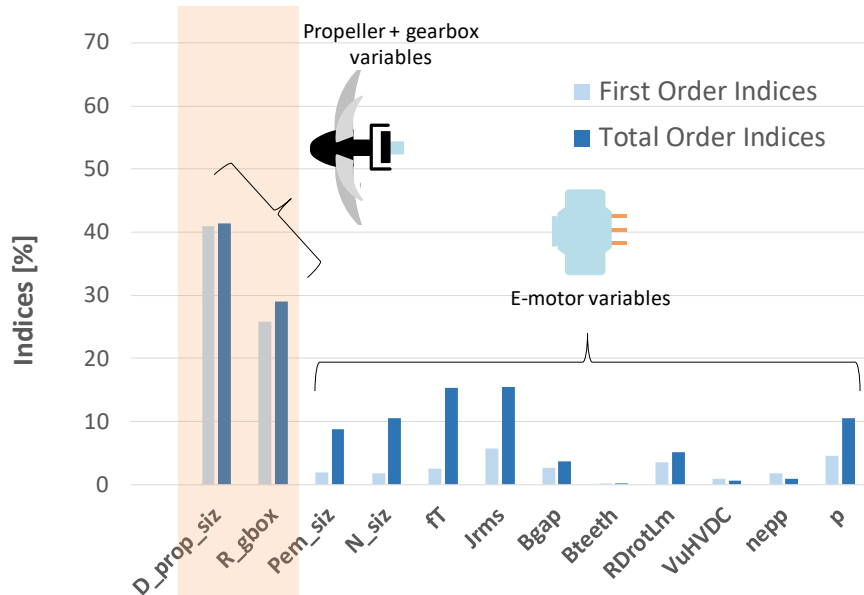


Fig. III-22: First order (pale color) and total order (dark color) Sobol indices with e-motor efficiency as output by considering constraint fulfillment.

If constraint fulfilment is not considered (cf Fig. III-18), electric motor variables are the most sensitive with regard to the efficiency. On the contrary, when constraints are fulfilled, the propeller and gearbox variables become particularly sensitive. This observation shows that constraint fulfilment is essential for a sensitivity analysis process in a technological framework. The propeller is the element of the propulsive system characterized by the broadest efficiency variation range.

The gearbox efficiency is fixed at 98.5%, while the electric motor has an average efficiency of 97%. Considering that the propeller has a maximum efficiency value of 85%, its diameter oversizing significantly impacts the efficiency of the whole electromechanical propulsive system. In the next chapter related to system optimization, this issue will be seen as a major trend of the integrated overall design leading to oversize the propeller diameter to enhance the global efficiency of the powertrain although the mass increase on this device!

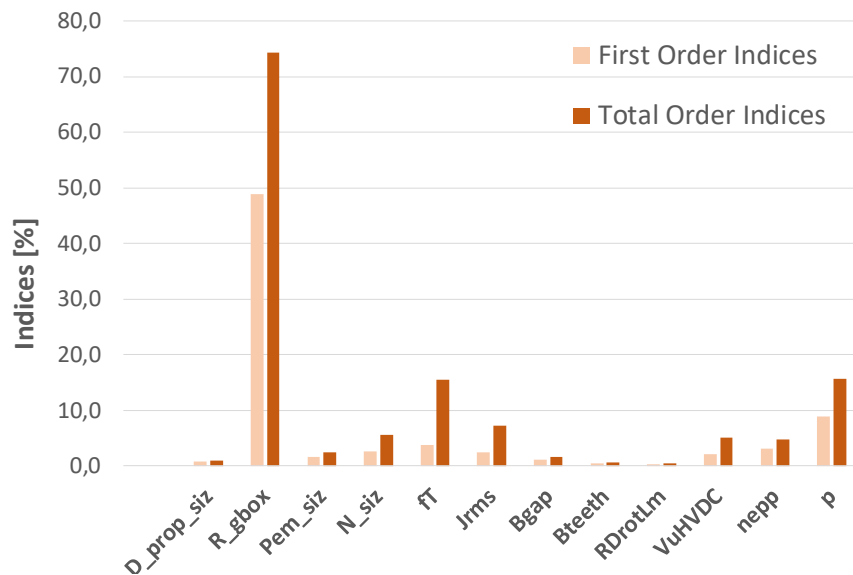


Fig. III-23: First order (pale color) and total order (dark color) Sobol indices with e-motor mass as output by considering constraint fulfillment

Comparing Fig. III-19 and Fig. III-23 for the analysis of motor mass following if constraints are checked or not leads to quite similar trends in both cases even if the gearbox ratio is more sensitive when constraints are fulfilled. In fact, this variable drives the rotor volume and the torque which is directly linked with the thermal constraint. Similarly, the gearbox ratio determines the motor rotational speed and consequently the peripheral speed.

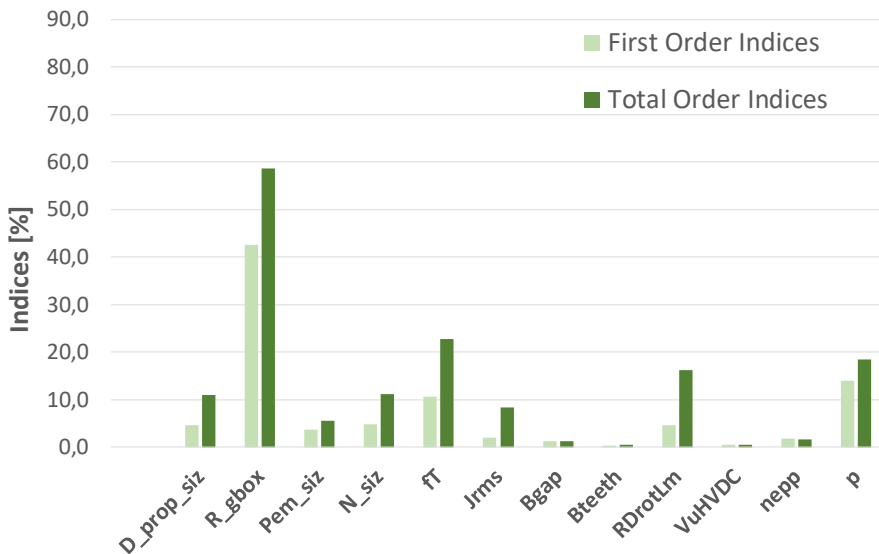


Fig. III-24: First order (pale color) and total order (dark color) Sobol indices with the e-motor peripheral speed as output by considering constraint fulfillment.

By comparing the Fig. III-20 with Fig. III-24 which set influence the peripheral speed seen as output, other input variables are sensitive when both constraints are checked. In other words, in Fig. III-20, the current density J_{rms} , the flux density in the air gap B_{gap} , the flux density in the teeth B_{teeth} , the HVDC bus V_{uHVDC} and the number of slot per poles and per phases n_{epp} were few sensitive (Sobol indices tends to zero while, in Fig. III-24, these indices have a small (but not null) impact on the output.

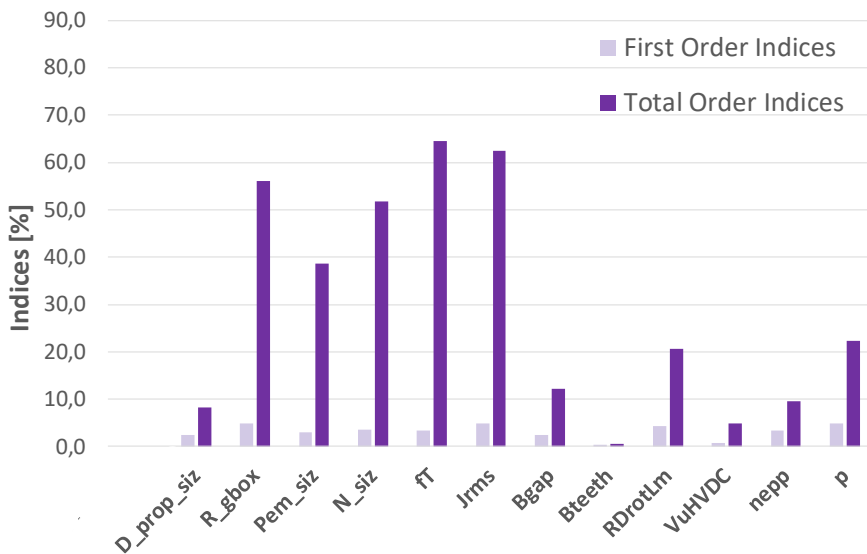


Fig. III-25 : First order (pale color) and total order (dark color) Sobol indices with the e-motor thermal constraint as output by considering constraint fulfillment.

Considering the thermal limit as the analyzed output when both constraints are fulfilled, huge correlation effects appear (see Fig. III-21 and Fig. III-25) and the total Sobol indices are pretty high for most of input variables. It is not surprising that the most impacting variables are the gearbox ratio –which determines the torque–, the power and rotational speed sizing, the tangential stress and the current density which constitutes a direct image of the copper losses.

III.4 Conclusion

These sensitivity analyses based on Sobol indices is useful to drive a convenient sizing the electrical components of the powertrain before to think of optimizing it.

At aircraft level, power densities have a huge impact on the global weight (MTOW). Compared with efficiency sensitivity, embedded masses have a greater impact on the fuel burn.

When the sensitivity analysis is locally carried out on the devices the study allows setting the sensitivity of each sizing variable, providing more accurate results. In particular, three sizing variables on the eMotor device have been suppressed, simplifying the optimization complexity.

At first glance, certain variables were only slightly sensitive with regard to the mass of the system or its performance when the eMotor is analyzed alone. By adding new electromechanical devices (gearbox and propeller) to the system under study (electromechanical powertrain), system couplings were emphasised which led to the emergence of new sensitive parameters.

In the framework of technological design, adding the constraint fulfilment in the analysis process (in particular the thermal constraint) is also essential because they the feasibility constraints radically drive the impact of certain variables on mass or efficiency. Parameters that had a small impact at first glance can (through the addition of stresses) be more than essential to the design of the total propulsion chain. Cooling constraints have huge effect in the sizing of electrical components as it will be shown in the next chapter. It is clearly necessary to couple these domains in the sensitivity analysis.

In our case study the propeller is an essential element of the propulsion system, which the efficiency at low speed (during take-off) is a key point for the weight and performance of the aircraft: the sensitivity of its diameter has also been emphasized in this chapter. This point and many others will be clearly confirmed and detailed in the next chapter which deals with the optimization of the overall system.

CHAPTER IV. Multi-disciplinary design optimization of the hybrid-aircraft powertrain.

CONTENTS

<i>IV.1</i>	<i>Optimal design of the electric motor weight</i>	114
IV.1.1	the cooling system: the main challenge.....	114
IV.1.2	Electric motor optimization results.....	115
IV.1.2.1	Electric motor optimization with the steady state thermal model.	117
IV.1.2.2	Electric motor optimization with the transient state thermal model.	119
IV.1.2.3	Comparison of motor optimization between steady state and transient state thermal models with reference to the electric motor sized by the WP1.....	121
<i>IV.2</i>	<i>Hybrid-electric aircraft design with a “light hybridization scenario”</i>	128
IV.2.1	Optimization of aircraft fuel burn with a “light hybridization scenario”.....	130
IV.2.2	Adaptation of sizing models to formulate a system optimization problem.....	131
IV.2.3	Optimization results and analysis.....	133
<i>IV.3</i>	<i>Integrated design of a hybrid-electric aircraft coupled with its energy management system</i>	138
<i>IV.4</i>	<i>Exploration of the performance of a hybrid-electric aircraft taking account of technological advances in electrical components (target 2035)</i>	147
IV.4.1	Optimization of the eMotor weight (2025 vs 2035 assessments).....	147
IV.4.2	System optimization including energy management strategies	150
<i>IV.5</i>	<i>Conclusion</i>	158

From chapter III, we have seen that the heaviest elements of the power chain are the electric motors. It is then necessary to focus on their local optimization before to go further towards the overall optimization of the hybrid powertrain.

Starting with the motor optimization, the prime criterion to be optimized is the weight: it is the unique optimization objective in the next section. At the motor optimization level, only the assessments related to the 2025 targets will be considered to simplify the analysis. A comparison with the 2035 targets is proposed in the second part of that chapter which present the overall optimization at the powertrain level. Several analysis and several formulation of the optimization problem are proposed.

IV.1 Optimal design of the electric motor weight.

In this part, the optimization process of the electric motor is presented taking account of cooling device and partial discharges based on the sizing models presented in chapter 2 and detailed in APPENDIX F (electric motor model) and APPENDIX G (motor cooling model). A relatively large amount of heat may be generated by these motors over operating cycles. To efficiently remove this heat and to maintain the motor temperature within the prescribed range while minimizing energy consumption is the cooling system challenge, certainly the main challenge for this device as we will see in this section. Thus, a smart motor thermal management system with substantial heat transfer capability, compact structure, and low energy consumption is essential for aircrafts. This electro-thermal optimization is all the more important when the specific power of the electromechanical assembly needs to be improved.

IV.1.1 The cooling system: the main challenge.

The model of the motor cooling is described in APPENDIX G. A thermal nodal network is defined in order to calculate main temperatures in the electric motor. In the thermal model equations solving, the transient (capacitive) effects are taken into account: we will see in that section that using thermal capacitance effects during the high power phases (takeoff - climb) is essential for the design.

The qualitative thermal limit defined in the section III.3.3 ($A \times J_{eq} \leq 2.10^{12}$) has been used in [84] to size the electrothermal group. The thermal constraints fulfilment based on a thermal model is verified *a posteriori*. In such process, both electric and thermal model were not coupled inside the motor optimization.

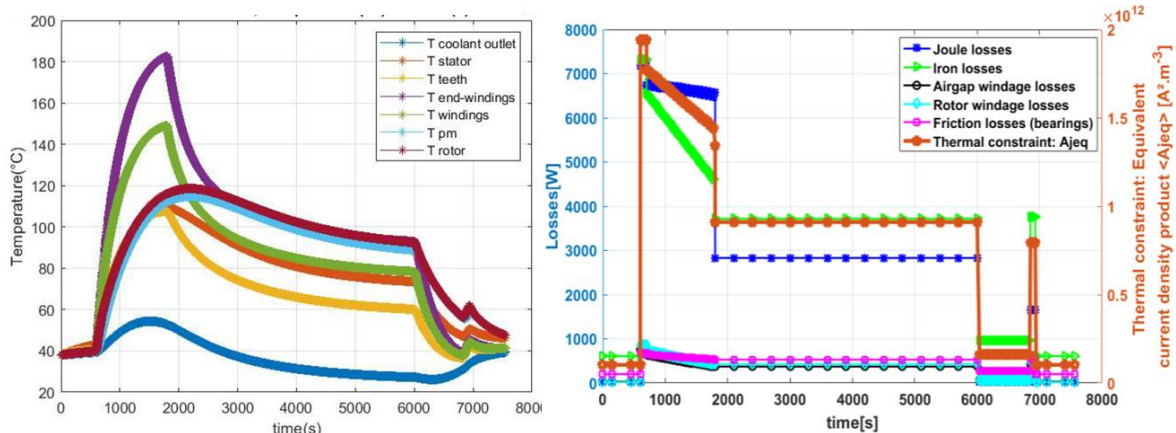


Fig. IV-1: Temperature evolution(left) and losse profile (right) during flight mission [84].

Regarding the example of the Fig. IV-1, the capacitive effect is more than representative, all maximum temperature values appear at the top of climb: as it can be observed, the temperature transient at that point is far from being completed. The thermal system has been designed in order to reach the limit temperature for the end-windings. The other temperatures are below their limits showing that certain electromagnetic components may be oversized. For example, the stator yoke temperature reaches the value of 120°C which proves that the stator yoke volume can be reduced. In order to face that issue, a multidisciplinary optimization problem can be solved by integrating the cooling model with the electromagnetic design model of the electric motor. The previously used qualitative thermal limit ($A \times J_{eq}$) is then replaced by temperature limits at the most critical points: end-windings, stator yoke and magnets.

For both targets, common limit temperature of 180°C is used for coils and yoke. 150° is the limit for magnets.

IV.1.2 Electric motor optimization results.

In this section, only the electric motor mass is optimized. The main issue is to analyze the performance differences comparing the cooling model at steady state and transient conditions.

The thrust mission (so the aerodynamic power mission) is here fixed and this is the same for both model cases. Thus, the propeller diameter and the gearbox ratio are fixed according to that thrust requirement. The electromechanical MDO process is illustrated in Fig. IV-2. Based on a reference power profile, and after defining the geometry of the machine, the magnetic model allows calculating most of its dimensions. Then, the electrical model specifies the different electrical circuit parameters of the machine which are required for coupling the motor with its power supply. At this stage, the structure of the machine is fully defined, and its mass and volume are determined. The losses in the different parts of the machine are computed for each operating point of the flight mission, enabling the electro-thermal coupling. Finally, the machine design must satisfy specific requirements in terms of thermal resistance of its various parts and the magnetic state of the magnets. Thus, a thermal model has been integrated taking into account the cooling systems.

A more detailed optimization process is illustrated in APPENDIX L in Fig. L-1.

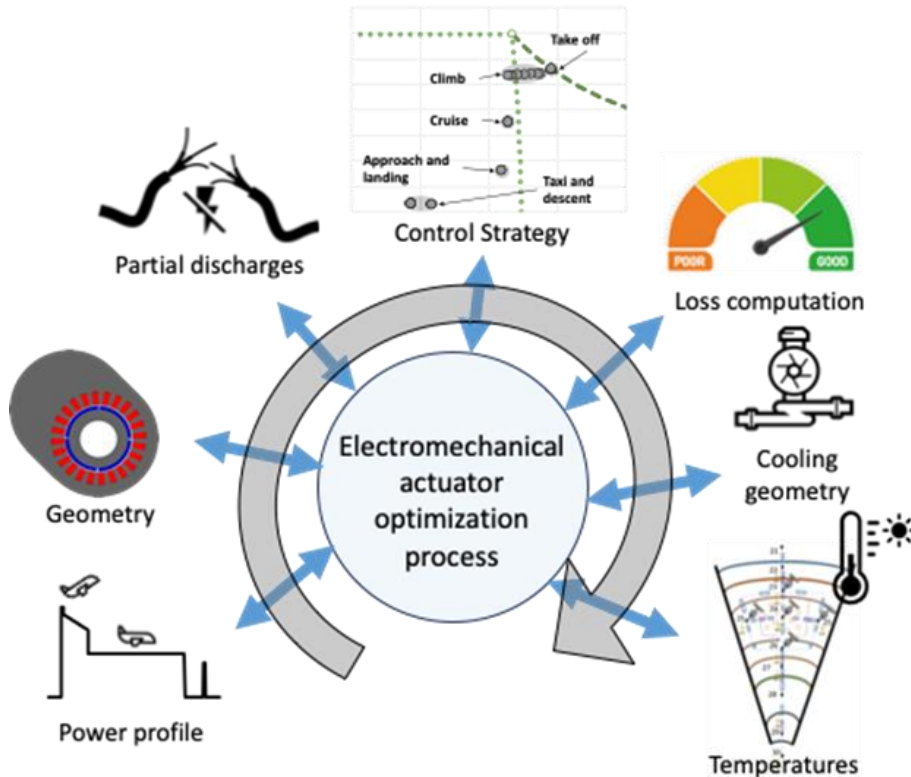


Fig. IV-2: MDO formulation process.

Some electric motor sizing limits are set (detailed in the APPENDIX F section F.2):

1. A minimum shaft radius (given by SKF datasheet linear regression [83]);
2. A minimum airgap thickness;
3. A maximum pressure on the sleeve;
4. A maximum rotor peripheral speed.

The partial discharge model (cf APPENDIX H) is implemented in this optimization which involves supplementary constraints:

5. To make sure that the final value of the fill factor (after partial discharge constraint fulfilment) is close to the initial value considered *a priori* in the electric motor sizing (see APPENDIX H, section H4);
6. A flag to check the correct integration of windings in the slot.

Performance constraint: another indicator checks that the mission has been completed (cf APPENDIX F section F.4).

The machine class H is considered in this (target 2025) case, for which the winding temperature must not exceed 220°C. In order to be conservative in the case of the transient model, this limit value is decreased to 180°C for windings and inside the yoke. The temperature of 150°C will be the limit temperature for magnets. For the steady state model, the used values are 220°C and 200°C for coils and magnets respectively (the considered maximum temperature of the yoke is the same as that of the coils).

Three supplementary constraints derive from the thermal model (cf APPENDIX G section G.4):

7. The limit temperature of the end-windings (180°C in transient and 220°C in steady).
8. The limit temperature of the yoke (180°C in transient and 220°C in steady).
9. The limit temperature of the magnet (150°C in transient and 200°C in steady).

The optimization variables and their ranges are summarized in the following table:

Table IV-1: Decision variables (11) for optimization with their respective bounds.

Decision Variables	Name of the variable	Lower bound	Upper bound
V_{uHVDC} [V]	Ultra-high direct current voltage	540	2040
$R_{alesage}$ [m]	Inner radius of the stator	0.05	0.25
R_{drotm} [%]	Ratio between rotor diameter and active length	50	125
R_{hsral} [%]	Ratio between stator slot and inner radius	10	150
R_{gral} [%]	Ratio between the air gap thickness and the inner radius of the stator	1	10
R_{pmral} [%]	Ratio between the magnet thickness and the inner radius of the stator	5	50
B_{yoke_max} [T]	Maximum yoke flux density	1	1.53
B_{teeth_max} [T]	Maximum teeth flux density	1	1.53
N_{ce} [-]	Number of conductors per slot	1	4
n_{epp} [-]	Number of slots per poles and per phases	1	3
p [-]	Number of pole pairs	1	7

Let us note that the bus voltage (V_{uHVDC}) has been limited here to 2040V which corresponds to the crossing limit between the 3 level NPC and the 5 level ANPC power converter structures (see Fig. II-32 in section II.2.4.2). This choice was made to simplify this local optimization. In the second part of that chapter (section IV.2) this limit will be extended to higher voltage values in order to analyze the system tradeoff in terms of bus voltage regarding its influence on motor, power electronics and cables and including partial discharge constraints.

IV.1.2.1 Electric motor optimization with the steady state thermal model.

All the optimizations were carried out using a niching genetic algorithm (“clearing”) [85]. The clearing procedure was used for optimizing the PMSM mass with regard to the design constraints. Clearing is a niching elitist genetic algorithm which usually out performs standard genetic algorithms on difficult problems with multiple non linear constraints and multimodal features. All constraints were scaled and integrated into the objective function with penalty coefficients. The population size and the number of generations were respectively set to 100 and 200. Classical values for crossover and mutation rates were used (i.e., $pc = 1$ and $pm =$

1%). For each optimization case, multiple runs were carried out in order to take the stochastic nature of the algorithm into account and to ensure the reproducibility of results.

In the steady state thermal model case only thermal resistances and density of the material are not taken into account. Therefore, the temperatures only depend on the geometrical dimensions. After optimization, the sizes of the electric motor are enlarged and the power density regarding the 2025 target is not reached: $P_{SPE_{steady}} = 2.60 \text{ kW/kg}$ (including the cooling device).

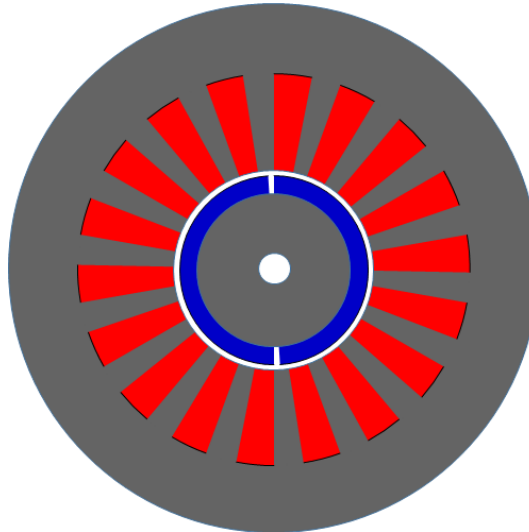


Fig. IV-3: Cross section of the electric motor (optimization with steady thermal model)

$$P_{SPE_{steady}} = 2.60 \text{ kW/kg}.$$

The major constraints that drive the so called "optimal" electric motor are clearly the thermal constraints mainly due to end-windings and magnet temperature limits.

A cross section of the obtained machine is presented in the Fig. IV-3 showing the distribution of the different elements (copper, magnet, etc..). This shape clearly illustrates that stator and rotor yokes are prominent. This is mainly due to the stator losses level which involves sufficiently large surface in order to evacuate corresponding heat loads, the outer surface of the motor being the exchange surface with the cooling system.

The number of pole pairs is minimized (1 pole pair) because of the iron losses strong influence: reducing the number of pole pairs also reduces the electrical frequency of the machine and thus the iron losses.

Several constraints (3/9) have been reached:

1. End-windings temperature is maximum at 220°C;
2. Magnet temperature is maximum at 200°C;
3. Shaft radius is minimum (that is why the shaft radius is so small on the figure).

The end-winding temperature has reached its limit because most of the machine losses (70%) are concentrated between the air gap and the stator yoke. The addition of iron losses (in stator teeth) to the Joule losses accelerates the temperature rise in windings and particularly that of the end-windings. The stator yoke temperature has not reached its limit because of its proximity with the cooling system and a reasonable level of losses in relation to the exchange area. The heat dissipation in magnets is all the more complicated because these latter are

“blocked” between stator windings and rotor bearings. Moreover, magnets are also heated by aerodynamic losses in the air gap.

Since the diameter of the cooling tube at the rotor depends on the radius of the shaft (10%), it becomes strongly difficult to evacuate losses if the shaft radius is small.

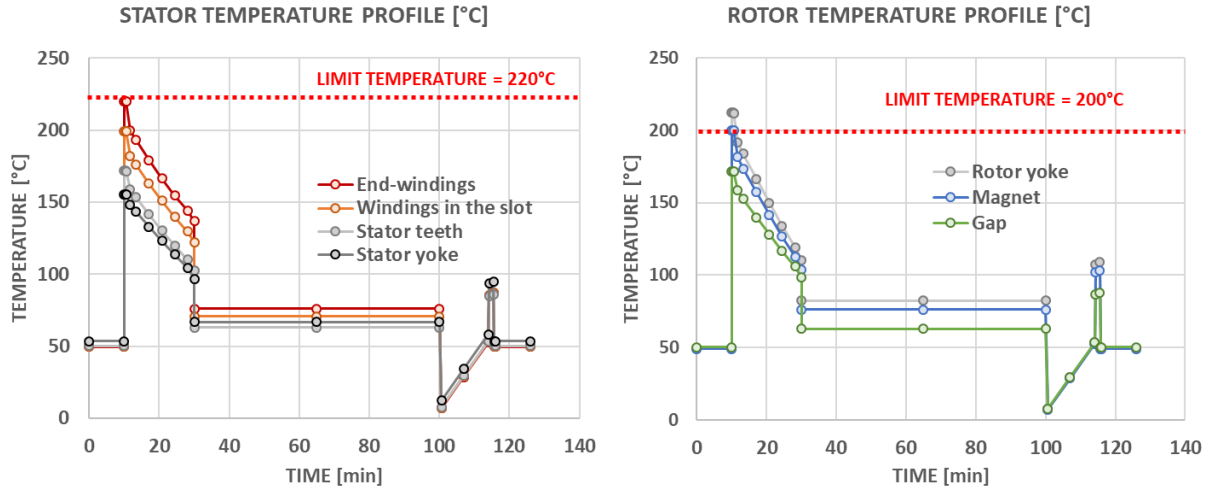


Fig. IV-4: e-Motor temperatures (optimization with steady state thermal) during the flight mission.

Regarding the temperatures of each element on Fig. IV-4 over the flight mission, the sizing (critical) point in the case of the steady state thermal model is during take-off. With that steady state thermal model the maximum of losses is reached at takeoff since this is the phase that consumes the most power even is this flight sequence duration is very short (some seconds). Using thermal capacitance is clearly favourable in order to cross takeoff and climb by reducing thermal constraints which would increase motor power density as it is shown in the next subsection.

IV.1.2.2 Electric motor optimization with the transient state thermal model.

With the transient model, limit temperatures are lower than for the previous study in order to be conservative in sizing. In this optimization two constraints (2/9) have been reached: End-windings temperature and stator yoke temperature are maximum at 180°C. Including the cooling device, the specific power of the electric motor obtained is much better thanks to the use of thermal capacitance, reaching: $P_{SPE} = 7.45 \text{ kW/kg}$.

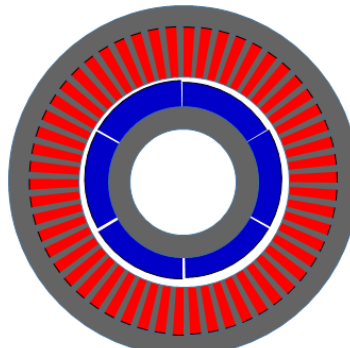


Fig. IV-5: Cross section of the electric motor (optimization with transient state thermal model)
 $P_{SPE} = 7.45 \text{ kW/kg}$.

Numerous slots along the stator yoke "distribute" the losses. The stator yoke is clearly thinner than before. The thermal capacitance depends here on the density of each material; the stator/rotor yokes have a high capacitive effect due to their high volume density. The magnets are larger than previously involving the air gap induction increase. The rotor yoke is directly linked to the stator one: both yokes become thinner due to the induction increase in teeth and yokes.

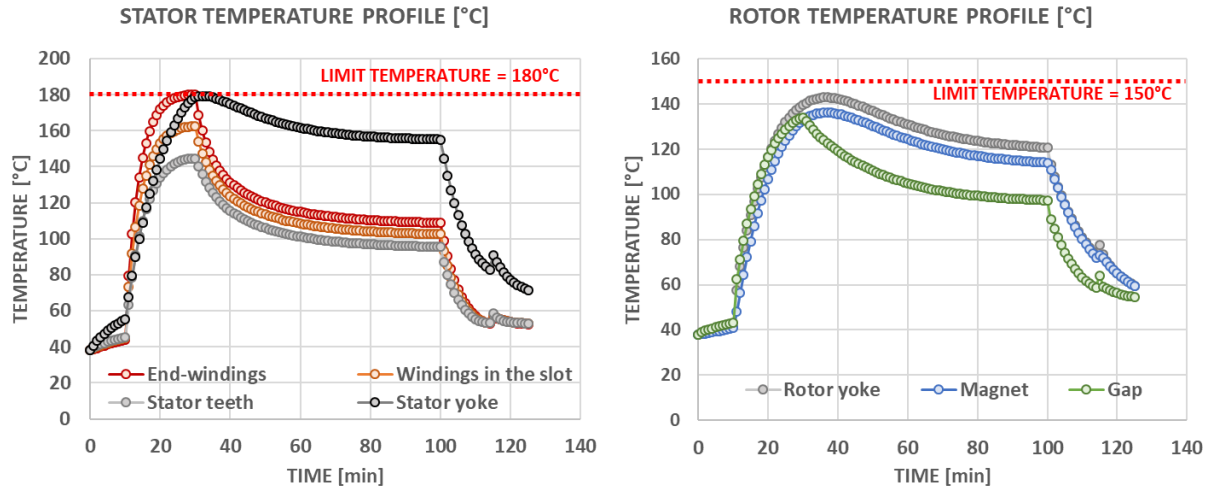


Fig. IV-6: e-Motor temperatures (optimization with transient state thermal model) during the flight mission.

The new temperature profile in Fig. IV-6 highlights the use of thermal capacitances. The temperatures of each part of the electric machine use the capacitive effect of their material. The temperature profile in each figure follows the beginning of the exponential function corresponding to the (R, C) equivalent circuit couplings. It is the same for magnets whose capacitive effect is as important as for the yokes because of their similar densities. The stator teeth are less sensitive to this thermal capacitance because of their small sizes (thin teeth). The thermal capacitance allows us to significantly push back thermal limits which clearly drives the motor sizing. Thus, optimizing with the transient model allows decreasing the electric machine mass, thus increasing its specific power.

In order to illustrate the influence of these capacitive effects, a simulation of the thermal model at steady state was carried out from the sizing obtained with the previous optimization (based on the transient thermal model): in that case, the maximum temperatures are reached by the machine during take off as for the previous optimization based on the steady state thermal model. The end winding temperature is beyond 320°C compared to the maximum obtained with the transient model (see Fig. IV-7) which stays below the limit of 180°C: a gap of 78% is obtained between both thermal models with the same motor sizing.

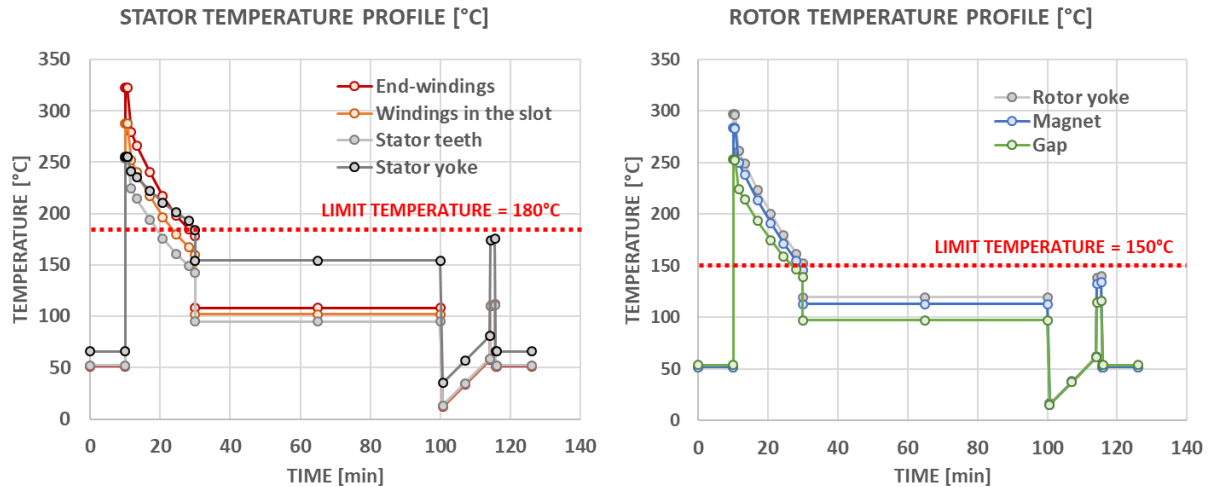


Fig. IV-7: e-Motor temperatures (optimization with transient state thermal model – steady state display) during the flight mission.

In Fig. IV-7, the waveforms are identical to those obtained through optimization in steady state Fig. IV-4:

- The limit temperature of the end-windings and the windings reach respectively 320°C and 288°C.
- The limit temperature of the stator and rotor yoke reach respectively 255°C and 300°C.
- The limit temperature of the magnet reaches 285°C.

The next part focuses on the differences in motor size and in performance (electric actuator torque-speed characteristic).

IV.1.2.3 Comparison of motor optimization between steady state and transient state thermal models with reference to the electric motor sized by the WP1.

In this section, the input variables proposed by the motor design team (in WP1) [83] have been used to optimize the performance of the actuator with the adapted model defined in chapter II. In order to compare sizes, the cross sections of the machines are shown side by side in Fig. IV-8, obviously displaying the main differences.

As presented before, only the thermal model was changed between both optimizations.

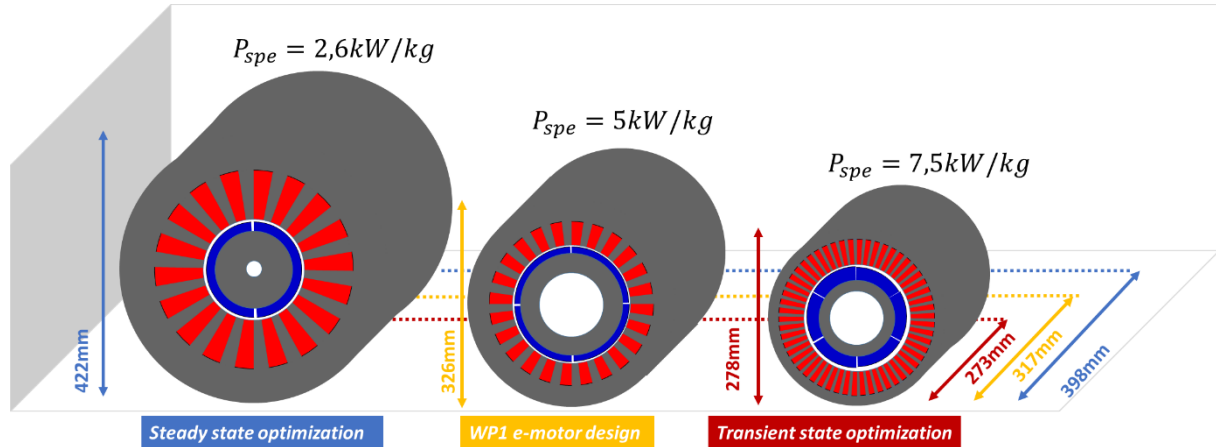


Fig. IV-8: Cross sections of three electric motors (left: steady state optimization, middle: WP1 e-motor design , right: transient state optimization).

In order to be able to make a performance comparison, the torque-speed characteristics of each motor are displayed. The characteristic of the optimized e-motor with a steady state (SS) thermal model is shown in blue; the characteristic of the optimized e-motor with a transient state (TS) thermal model is shown in red and the electric motor designed (without optimization) by the experts of the WP1 is in yellow. An actuator characteristic is limited by a maximum current (maximum torque) while its speed limit is given by a limit voltage which must not be exceeded. When this voltage is reached, the user has 2 possibilities:

- reduce the I_q current of the actuator to allow its to go into a higher speed phase without shifting the current ($I_d = 0$).
- add current in the d-axis of the actuator ($I_d < 0$) to reduce the flux density in the air gap and thus keep a constant power by increasing speed.

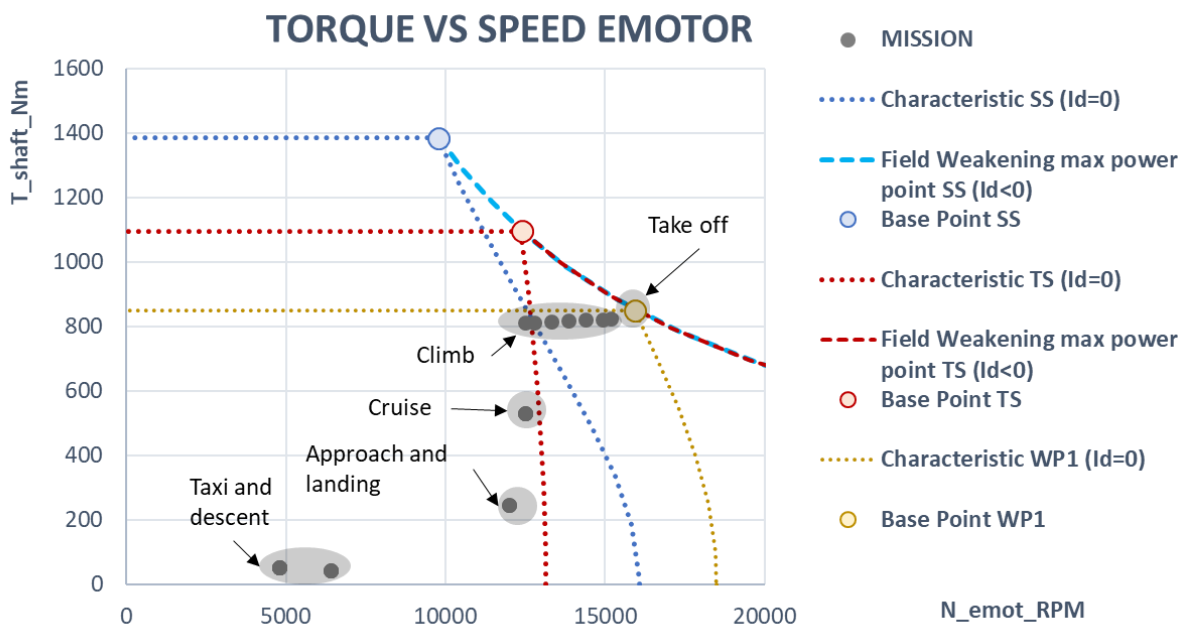


Fig. IV-9: Torque - Speed characteristic (blue steady state (SS) optimization, red transient state (TS) optimization and yellow WP1 electric motor).

Contrarily to the yellow characteristic (WP1 design), both optimized machines (with both thermal models) use field weakening, oversizing the sizing torque compared to maximum torque of the mission profile. Field weakening strategy reduces iron losses when the joule losses are at their maximum. This choice allows shifting the maximum of iron losses with respect to the Joule losses maximum in order to spread out thermal constraints. Field weakening is used by both machines (SS and TS) exactly at the same time during take off and almost during the whole duration of the climb.

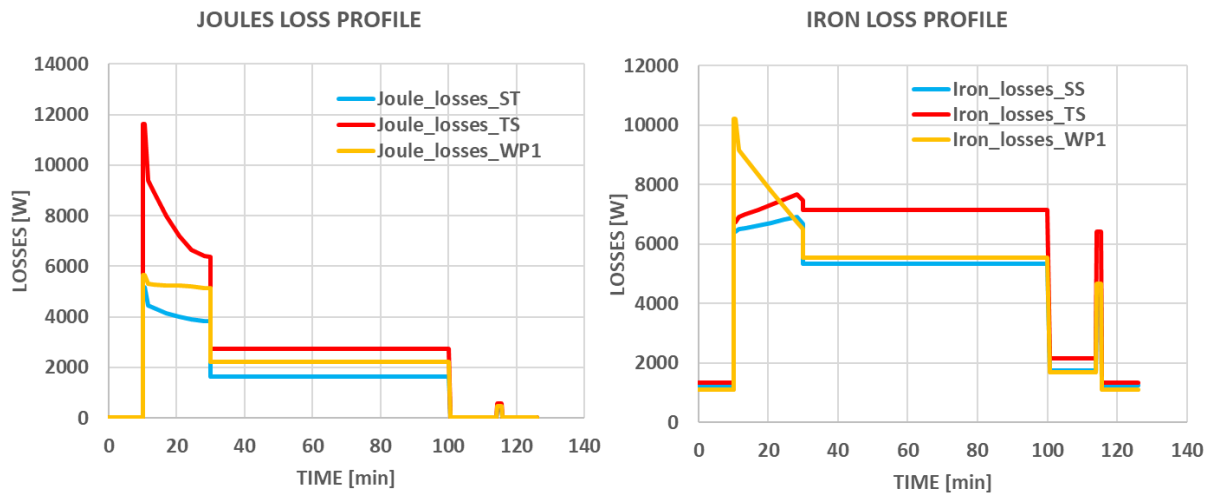


Fig. IV-10: Joules and Iron loss profiles.

Looking at loss side, the most preponderant heat sources are Joule losses and iron losses. The use of field weakening is well illustrated by the comparison of the Fig. IV-10. For the machine designed by the WP1 (yellow curve), iron losses rise up to a value of 10 kW during takeoff. Let us note that this design was made only considering a unique (the maximum power during take off) sizing point instead of the complete mission profile. Contrarily, the maximum of iron losses is shifted at top of climb for both field weakened machines (blue and red curves) optimized on the whole mission profile. Beyond the loss distribution, another difference between each design is related to the amount of losses that can be dissipated by cooling devices depending if a steady-state thermal model or a transient-state model is coupled with the optimization:

- for the steady state thermal model based optimization, the maximum total level of losses is around 13 kW
- the maximum of total losses is around 20 kW for optimization using thermal capacitance effects.
- Regarding the electric motor designed by WP1, the amount of total losses reaches the value of 19kW, showing that the actuator has not been optimized.

It also means that there are trade-offs between specific power and efficiency because increasing the specific power also means increasing losses thus being less efficient. These results show the importance of system couplings (here electro thermal couplings) in multidisciplinary studies. This will be all the more important on the plane because the added kilos on the powerplant bring snowball effects on the final sizing. Losses are directly linked to the current and voltage levels in the machine.

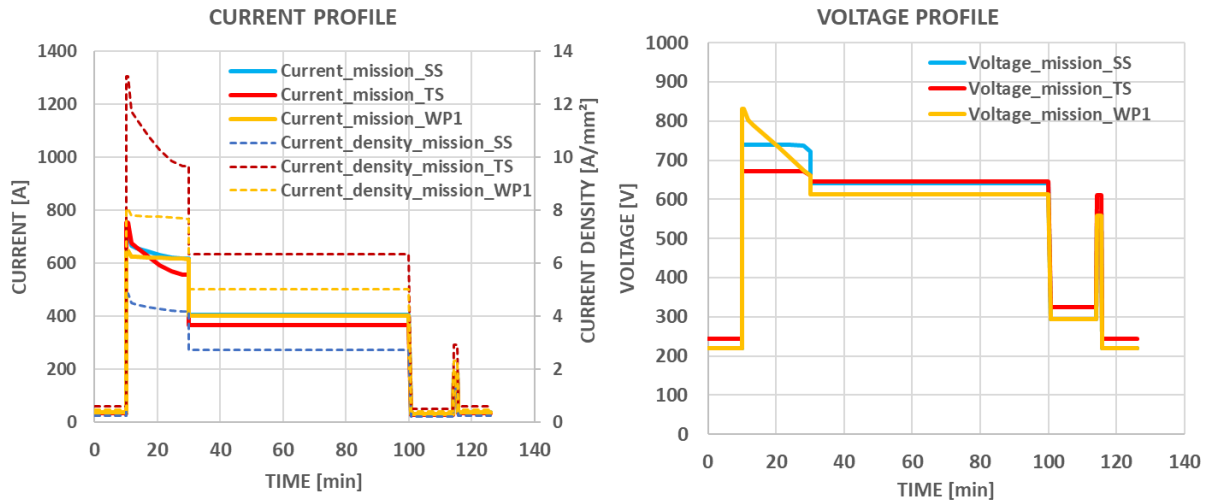


Fig. IV-11: Current, current density and voltage in the three electric motors.

The current shape seems to be similar in steady state thermal model-based optimization (blue curve) and with the transient state thermal model based optimization (red curve). However, looking at the current density, it is clear that there is a huge difference between both optimized machines. The difference in Joule losses is mainly due to the resistance of winding: the copper surface is smaller in the optimal motor in transient thermal regime. This explains the difference in current density between both machines. The voltage profile provides is typical of the use of field weakening during take-off and climb phases (constant voltage operation) for the optimized electric actuators. Contrarily, the field weakening has not been used for the WP1 design based on a unique (maximum) mission point.

The next comparative analysis is related to motor sizes.

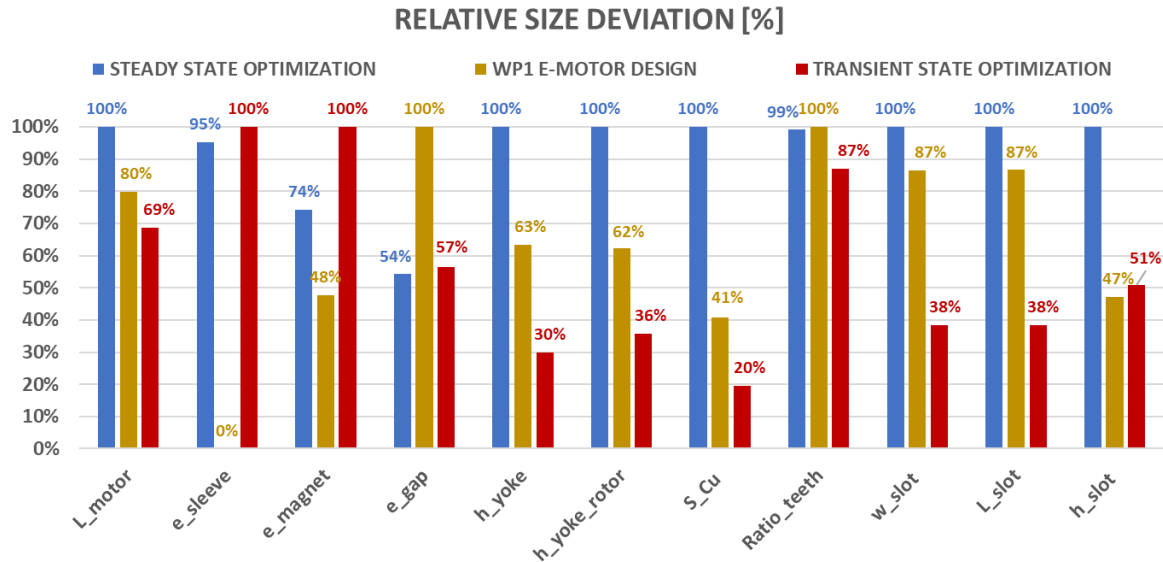


Fig. IV-12: Relative size deviations versus the maximum values.

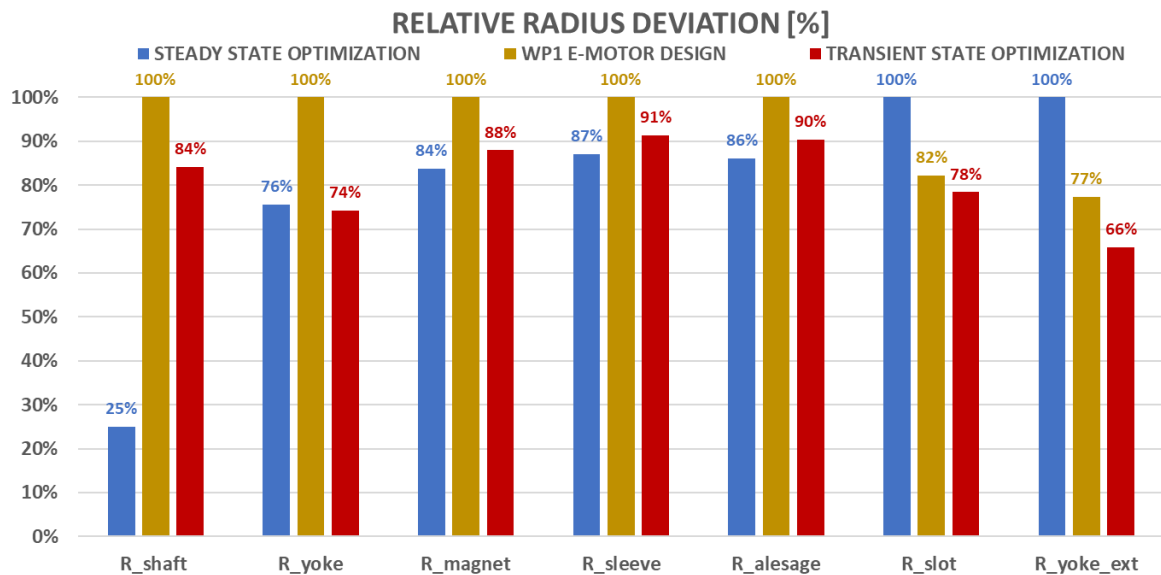


Fig. IV-13: Relative radius deviations versus the maximum values.

In the diagrams of Fig. IV-12 and Fig. IV-13, relative deviations are displayed to better compare the three design: each absolute value has been divided by the maximum value between the three electric machines. This representation shows directly the relative differences between the size of each optimization. For example, the copper surface is at 20% of the maximum in the transient optimization, which means that there is a ratio of 5 between the copper surface of the steady-state optimization and the transient one, moreover there is a ratio of 2 between the WP1 machine and the transient optimization.

In the Fig. IV-12 sleeve thickness has not been considered but the air gap is too small in order to install a sleeve. This is why the air gap thickness is maximum for the WP1 machine. Apart from the absence of sleeve in the WP1 design, the optimized machine coupled with the steady state thermal model has the largest dimension in absolute value, which seems consistent. The copper surface area has been divided by 5 between both optimizations based on both thermal models (the motor height has been divided by 2 and the length by 2,5) leading to the specific power increase as previously mentioned. The yokes have followed the same reduction way (with a ratio of 3 between both optimizations). All these size reductions obviously have an impact on the masses of each component (see Fig. IV-14).

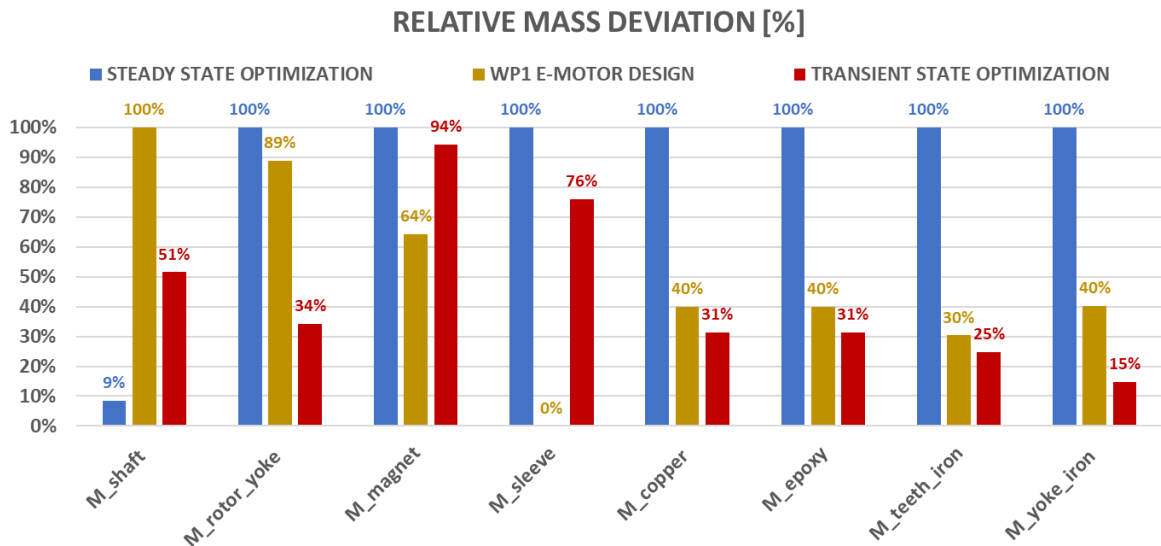


Fig. IV-14: Relative mass deviations to the maximum values.

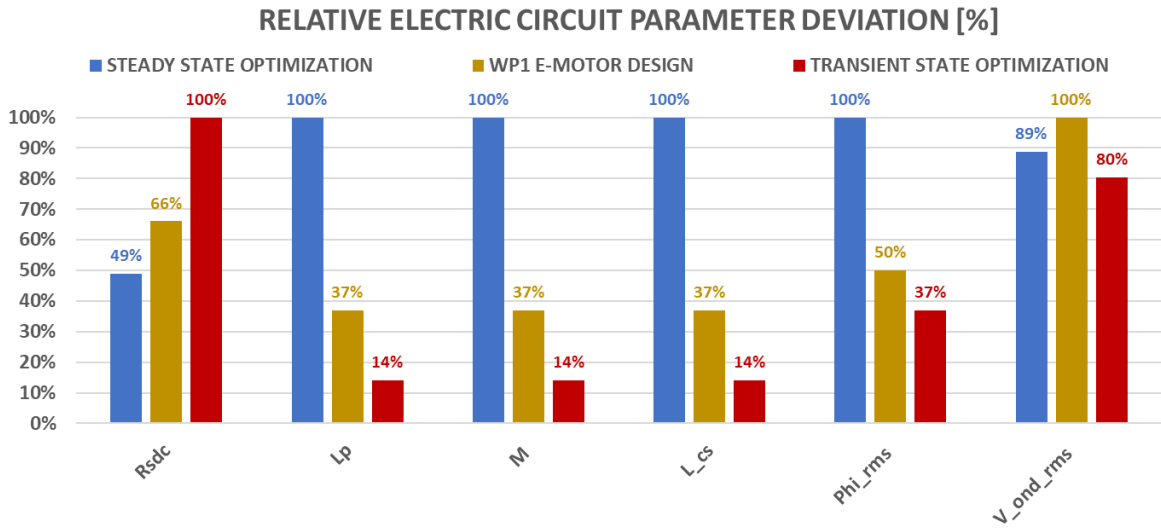


Fig. IV-15: Electric circuit parameter deviations to the maximum values.

Differences on circuit parameters result from different motor sizes. The resistance of the stator windings increases for with the transient thermal model. This comes directly from the equation (see APPENDIX F.1.5 the Eq F-36) because the copper surface area decrease provokes the resistance increase. It can be noticed that the electrical time constant (L/R) of the three machines is strongly different, with a fast-electrical mode for the optimization based on the transient thermal model.

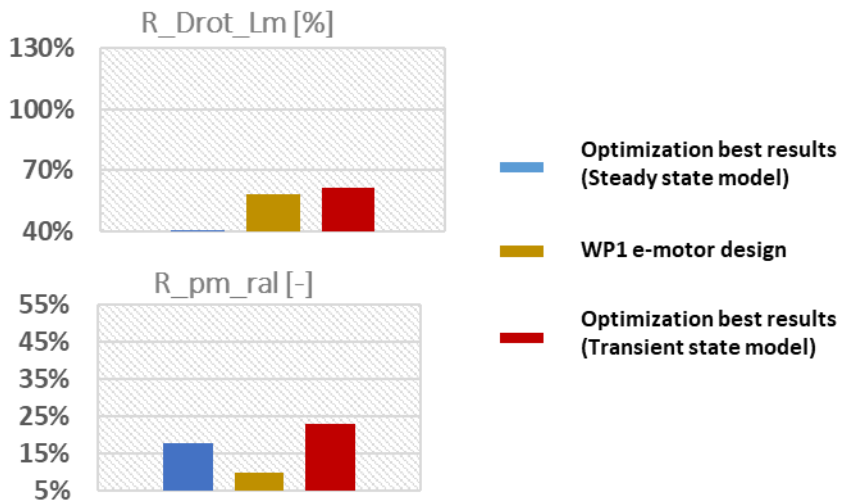


Fig. IV-16: Both values giving the best objective function for both optimizations (blue and red), compared to with the e-motor designed made by the team in charge of WP1.

The model difference on the magnetic flux density of the air gap pushes the optimization to magnify the magnets, during both optimizations (steady state and transient) the value is much larger see Fig. IV-16. The final results of the two optimizations compared with the WP1 design have been summarized in the Fig. IV-17.

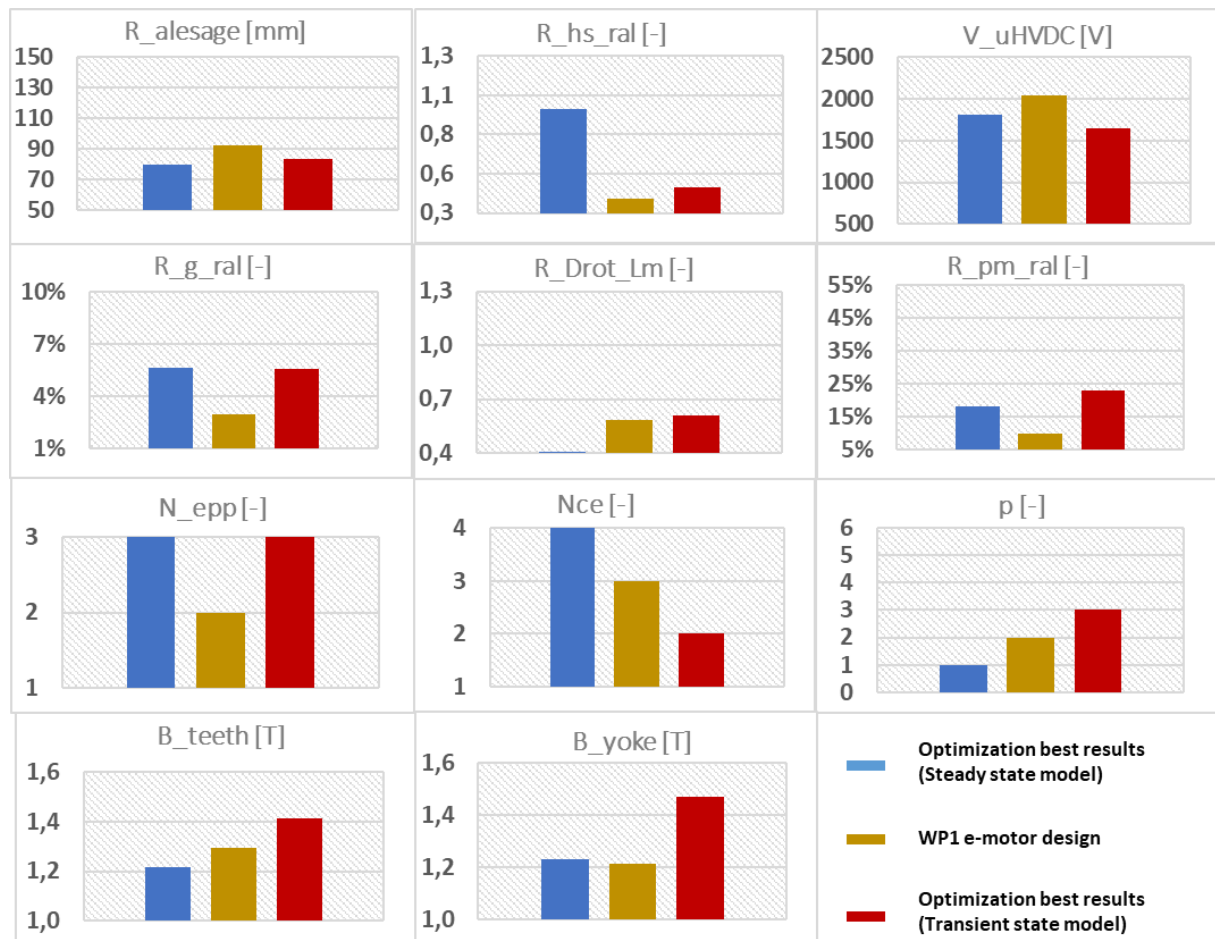


Fig. IV-17: Decision variables giving the best objective function for both optimizations (blue and red), compared with the e-motor designed by the team in charge of WP1.

With lower thermal constraints (as in the case of the transient thermal model), the number of pole pairs can be increased and the actuator sizes are directly reduced. However, the increase in the number of pole pairs increases iron losses in the stator yoke, especially if the flux densities (yoke and teeth) follow the same trend. The field weakening strategy allows counterbalancing this significant increase in iron losses by decreasing them when they are at highest operation during the mission. The electric machine with the best specific power still has to pay for its weight loss by a lower efficiency (even if it remains significantly high 97%>: remember that the motor weight is the unique optimization objective, losses being only limited by thermal constraints.

In the case of a regional aircraft with hybrid electric propulsion, weight plays a first determining role compared with an all-thermal aircraft. However, once the weight is on board the aircraft, efficiency will play an even more essential role in the sizing of the sources as well as consumption. By coming back to the aircraft level, the best trade-off between weight and losses will be found by optimizing the “less consuming aircraft” at system level.

The electric machine optimization has shown the importance of interactions between fields (electric, electromagnetic, thermal, partial discharges constraints, etc). In particular, cooling aspect plays a key role in the sizing of electromechanical components. In the following of that chapter, the overall propulsion system has been integrated with the corresponding set of model. In that case, the fuel burn mass becomes a key objective but this global optimization will also be compared with a mass based optimization by considering the whole powertrain. These two latter optimization problem can also be compared with a local vision based on the optimization of the motor mass alone. Another issue is relative to the energy management strategy of the hybrid electric architecture. Two cases will be successively considered:

- A “light hybridization scenario” (see section IV.2) for which the hybrid ratio (power ratio between electric vs thermal sources) are *a priori* fixed (with a 100% electric taxi and descent);
- A “variable hybridization scenario” for which the optimization is in charge of setting the hybrid ratio along the flight mission (see section IV.3).

IV.2 Hybrid-electric aircraft design with a “light hybridization scenario”.

Several studies focus on the aerodynamic gains possible with electric motor propulsion (distributed electric propulsion) [107], [108]. The scalability of the electrical components makes it possible to intelligently position the various actuators at strategic locations on the aircraft. This thesis focuses on the energy aspects and in particular on the system variables of electric propulsion. The use of electrical component sizing models allows the study of several problems:

- the increase of the power density thanks to an optimal electro-thermal coupling.
- the increase of the DC bus voltage of components to reduce their volume without causing partial discharge problems.
- the impact of ideal component sizing on the propulsion system of a hybrid electric aircraft.

In that subsection, the energy management of the hybrid electric structure is *a priori* fixed as displayed on Fig. IV-18: a full electric taxi and descent (HR¹=1) is considered while a full thermal operation has been set for climb and cruise flight sequences (HR=0).

The looped process presented in chapter I section I.3.3 was previously conceived to take account of the snowball effects between embedded masses and consequences of the whole mass (MTOW) including the fuel burn. In the context of the integrated optimal design, this looped process has been revised. Indeed, in order to obtain a stable result in terms of MTOW, the process needed to be looped 5 times given one system sizing. Thus, in the optimal design context, two imbricated loops would have to be considered:

- an outer loop dedicated to sizing optimization;
- an inner loop to take account of snowball effects (Equation (I-4)).

In order to avoid multiple loops but keeping snowball effects into consideration, the equation linking thrust and MTOW is conserved but only by adding a new optimization constraint (Eq.(IV-2)). A new optimization variable also appears: the thrust ratio $RThrust$ (Eq.(IV-1)). This new optimization parameter makes possible to anticipate (and to face) the new max take-off weight $MTOW_{new}$ of the hybrid-electric aircraft obtained after the sizing choice set by the optimizer. It should be reminded that the starting point (ref point) of the optimization is a conventional thermally propelled aircraft with a reference max takeoff weight: $MTOW_{ref} = 23\text{ T}$.

$$RThrust = \frac{Thrust_{new}}{Thrust_{ref}} \quad (\text{IV-1})$$

Thus the following constraint is implemented in the optimization model in order to find the thrust needed to take off the hybrid-electric aircraft:

$$RThrust \cdot MTOW_{ref} \geq MTOW_{new} \quad (\text{IV-2})$$

The new optimization problem has then a new constraint to satisfy but it has been necessary to make this change to drastically improve the computational time and to break the multiple loops approach.

Taking the fuel burn weight as the objective function, this constraint will behave nearly as an equality because an oversized thrust would lead to increase the power demand consequently rising consumption at the aircraft level. In other words, the fuel burn based optimization will set the “just necessary thrust” to fly the optimized aircraft.

A mass limit has also been introduced in the optimization problem. Indeed, the powertrain sizing process is based on a reference aircraft with a given wingspan, this latter being considered as conserved during the optimization convergence: only the propulsion system is reconsidered in this process. Consequently, a gap limit of 6T has been introduced in terms of MTOW: $MTOW_{max} = MTOW_{ref} + 6T$.

$$MTOW_{new} \leq MTOW_{max} \quad (\text{IV-3})$$

¹ HR is the Hybrid Ratio between powers from both thermal (Gas turbine) and electric (fuel cell) sources: HR=0 means that only the gas turbine is powered; contrarily, HR=1 means that a full electric operation is considered.

It is already possible to anticipate the maximum value of the new optimization variable R_{Thrust} . By respecting these two new constraints, the thrust ratio will not be able to exceed a maximum value.

IV.2.1 Optimization of aircraft fuel burn with a “light hybridization scenario”.

In this section, the topic is focused on the symmetrical hybrid electric aircraft (HEASYM) shown in Fig. III-3 reminded in the figure Fig. IV-18.

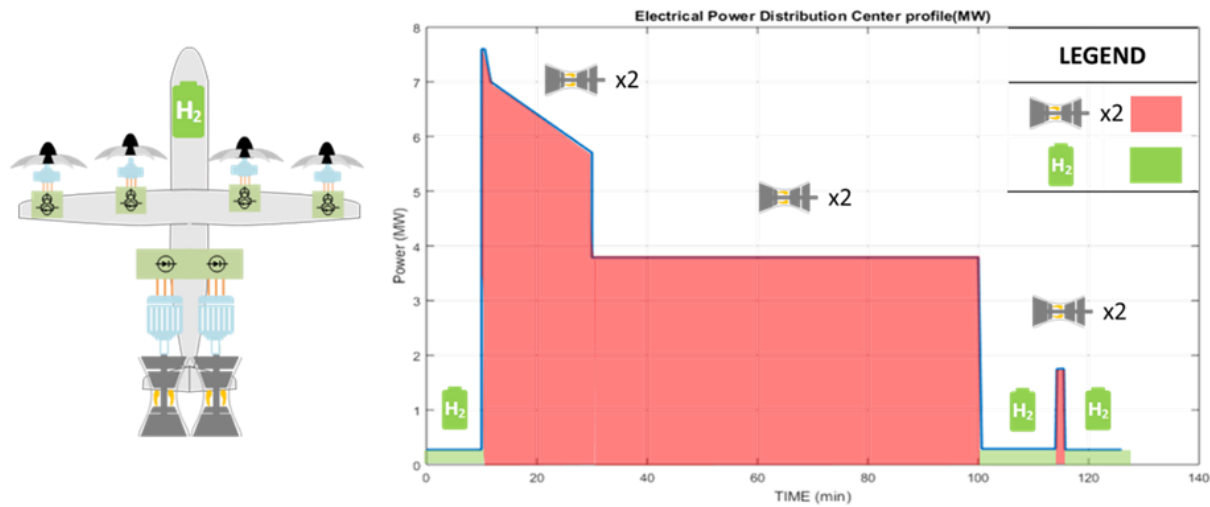


Fig. IV-18: Symmetrical Hybrid Electric Aircraft (HEASYM) with the Energy management..

The hybridization scenario is considered as “light”, while the fuel cell is only sized to power the aircraft alone during the taxi and descent phases. All the rest of the mission is supported by the 2 gas turbines: thus the hybrid ratio (HR) are a priori fixed for the whole flight. Three different optimizations have been carried out in order to highlight the systemic approach compared with other, “more local”, approaches:

- “Fuel mass optimization”: the first optimization has the fuel mass as objective function;
- “propulsion system mass optimization”: the second one has the mass of the complete propulsion system as objective function without counting the mass of the fuel burn in the gas turbines;
- “Emotor mass optimization”: the last optimization consists in optimizing the electric machine mass alone (as for the previous subsection) with a propeller and a gearbox with fixed performance. This is equivalent to a local approach for the sizing of an electric machine. In that local approach, the machine and its performance will be simulated together with other devices at the aircraft level in order to compute the fuel burn of the gas turbines.

IV.2.2 Adaptation of sizing models to formulate a system optimization problem

In this case study, the level of precision and uncertainty of the models will not allow to draw quantitative conclusions on the absolute values obtained after optimization, but rather to observe trends and correlations.

With these system oriented formulation, 2 propeller and gear box sizing variables are added to the previous decision variables considered for the motor optimization alone.

Except the bus voltage, no additional decision variables are necessary to formulate the optimization problem, neither for the power electronics nor for the hybrid sources (remember in that case that hybrid ratio are *a priori* set).

Let us also note that the bus variable V_{uHVDC} becomes a system coupling variable having influence on cables, power electronics and machine.

Based on the cable sizing model, the gauge, number and material (Cu, Al) of cables are automatically derived knowing the maximum cable voltage (directly linked with V_{uHVDC}), the maximum transferred power and the power factor for AC cables between inverters and Emotors. Thus, no additional decision variables are added for cable optimization.

A frequency ratio (between switching and electric motor frequency) of 7 has been fixed here as proposed in [109] and this is justified in this reference [110]. This ratio is set to limit harmonics due to the inverter – motor coupling. With that ratio choice, the inverter switching losses are strongly limited. Furthermore, in order to simplify the inverter system design, the bar bus mass is assessed by considering a simple percentage of the inverter mass (see APPENDIX I).

The adaptation of power electronics model for system optimization was previously explained in the section II.2.4.2. We remind that:

- two particular structures are selected depending on bus voltage level: 3 level NPC converter is selected if $V_{uHVDC} < 2040V$ else a 5 level ANPC is preferred. For each of these structures, both voltage and current ratings are fixed according to input data from the power electronic experts [93].
- The switching frequency is directly derived from the maximum electrical frequency of the eMotor [110] : $f_{switch} = 7 \times \max(f_{elec_emot})$.

Then the IGBT ratings are deducted without additional decision variables. The conducting and switching are then derived with a PWM strategy.

Based on these adaptations, 14 decision variables are sufficient to drive the optimization which are described in the Table IV-1 with their bounds.

Finally, this multidisciplinary design optimization includes (see Fig. IV-19):

- a specification (flight mission data: velocity, altitude, thrust requirement)
- an environment model to take pressure and temperature variations into account over the flight mission
- an integrated powertrain design identifying masses and efficiencies of each component (from the propeller to the power sources)
- the snowball effect at aircraft level into account: the reference mission is adjusted from the reference aircraft

Tab. IV-1: optimization input variables and their bounds.

Decision Variables	Lower bound	Upper bound
R_{Thrust}	1	1.26
$D_{prop siz}$ [m]	2	5
R_{gbox} [-]	1	20
$R_{alesage}$ [m]	0.05	0.20
R_{DrotLm} [%]	40	125
R_{hsral} [%]	10	130
R_{gral} [%]	1	10
R_{pmral} [%]	5	50
Nce [-]	2	4
n_{epp} [-]	1	3
p [-]	1	7
V_{uHVDC} [V]	540	5000
$B_{teethmax}$ [T]	0.7	1.53
$B_{yokemax}$ [T]	0.7	1.53

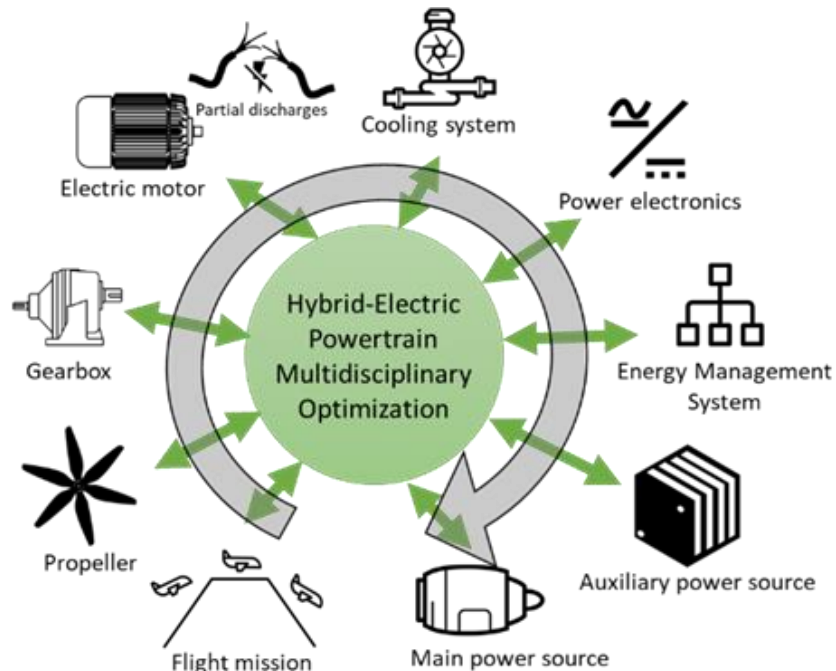


Fig. IV-19: Presentation of the multifields loop approached by the MDO of the hybrid-electric powertrain.

At the end of the process a hybrid-electric aircraft with its own powertrain is designed , the optimization process is illustrated in APPENDIX L - Fig. L-2.

IV.2.3 Optimization results and analysis

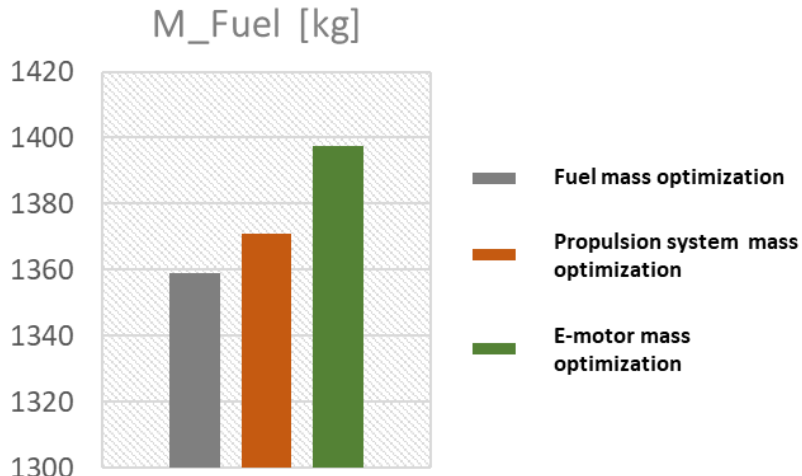


Fig. IV-20: Three optimization results on the fuel burn.

The first optimization (fuel mass) shows the advantages of taking all system couplings into account on the sizing of the propulsion system. The previous figure shows the consequences on the fuel consumption. Compared with others, the second optimization shows that a lightweight propulsion system does not necessarily mean an efficient system with a decreased fuel consumption. The last optimization is based on a local approach as an electric motor designer could have done: “the sum of the local optimum of each element is not the global optimum” from a system of view. This last point is also seen through the results on the specific power of the electric motor.

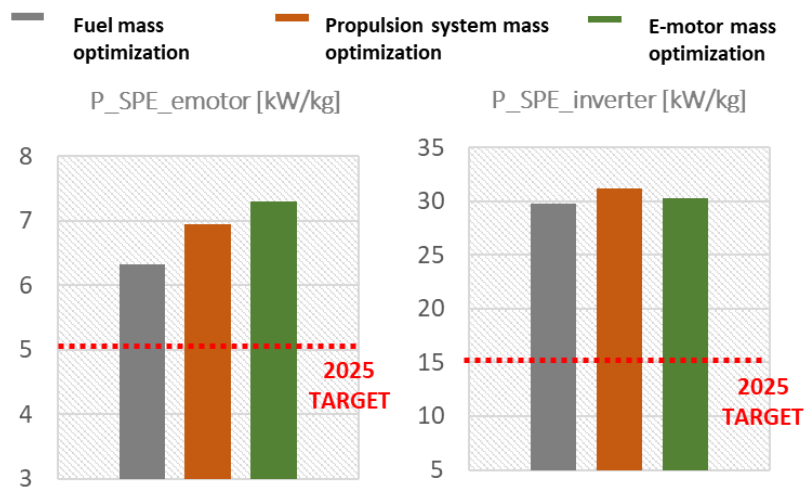


Fig. IV-21: Three optimization results on the specific power of the electric motor and the inverter (including cooling.)

The specific power increase of one component does not guarantee the reduction of fuel consumption, best fuel consumption results being obtained in that study with the lowest electric motor power density.

In the previous figures it can be observed that both specific powers (for inverter as for e-motor) are beyond the 2025 targets for the 3 different optimizations. In particular, the specific power of voltage source inverters is close to 30kW/kg for the three optimizations. This

very good ratio is firstly due to the strong limitation of switching losses with a ratio of 7 between switching and electrical frequencies [110]. Secondly, the 3 level NPC structure offers a good tradeoff in terms of losses and structure mass. Finally, with that case study at low switching losses, the 7th generation IGBT power switches combined with the high performance of the cooling system are really convenient for optimization.

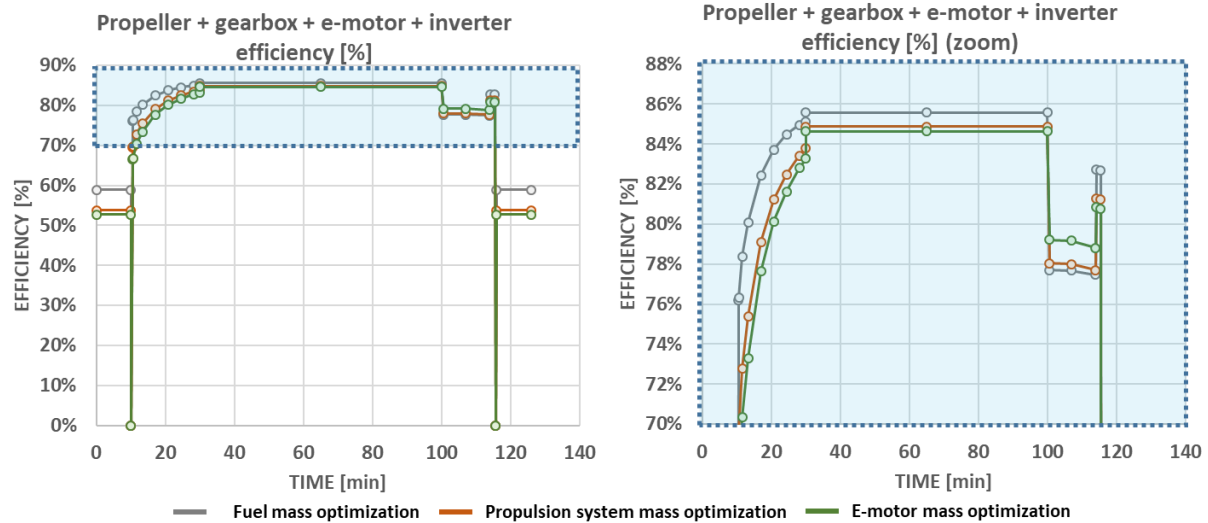


Fig. IV-22: Efficiency of the electro-propulsion chain during the flight mission (propeller -> inverter).

The powertrain efficiencies during the flight mission are displayed in the previous Fig. IV-22. It is important to note that the power density evolves in the opposite direction of the efficiency improvement: the best powertrain efficiency is obtained for the optimization of the fuel mass which drives the lowest specific powers at component (power electronics and Emotors) level. The optimization of the fuel mass highlights the importance of the propulsion system efficiency with regard to the final fuel consumption (see Fig. IV-20 & Fig. IV-22): these efficiency gains finally save 40 kg of fuel burn with respect to a local optimization. Several parameters are at the origin of the improvement in the whole chain performance especially the propeller sizing.

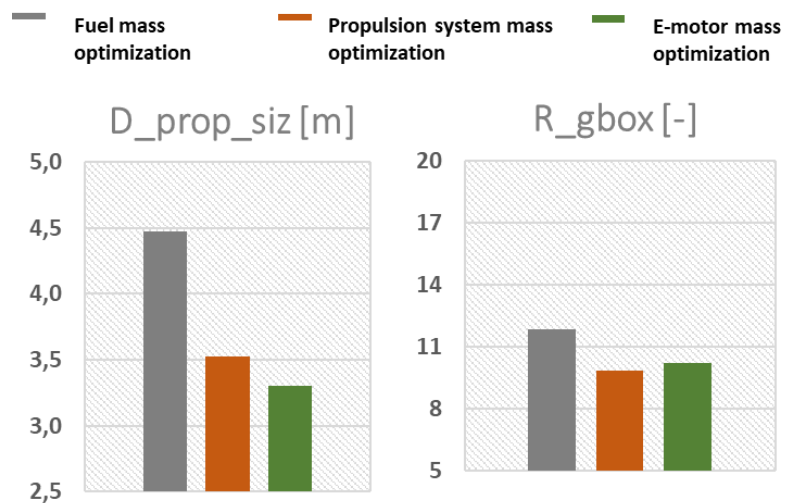


Fig. IV-23: Optimization result on propeller and gearbox input variables.

Indeed, the global sensitivity analysis studied in the previous chapter has shown the importance of the propeller design on the power chain efficiency (Fig. III-22). One point (1%) of efficiency was gained during cruise by oversizing the propeller, between both optimizations on the fuel mass and on the e-motor mass. The efficiency gain is also observed during takeoff and climb involving snowball effects: less power required to get the aircraft off the ground. The ratio of the gearbox is also important for the optimisation of the electromechanical actuator as it adapts the right sizing of the motor rotational speed given a propeller diameter. The gearbox model involving a constant efficiency, the mechanical efficiency improvement comes only from the propeller oversizing.

Differences on system efficiency are directly visible on the masses of both electric generators and rectifiers. Indeed, constant specific powers and efficiencies have been assumed for these devices. So the generator and rectifier masses are a “direct image” of the maximum power to be supplied for each optimization. The same trend can be observed for the Gas Turbine (GT) given a fixed (a priori) energy management. The figure below highlights the mass distribution for all powertrain devices and power sources.

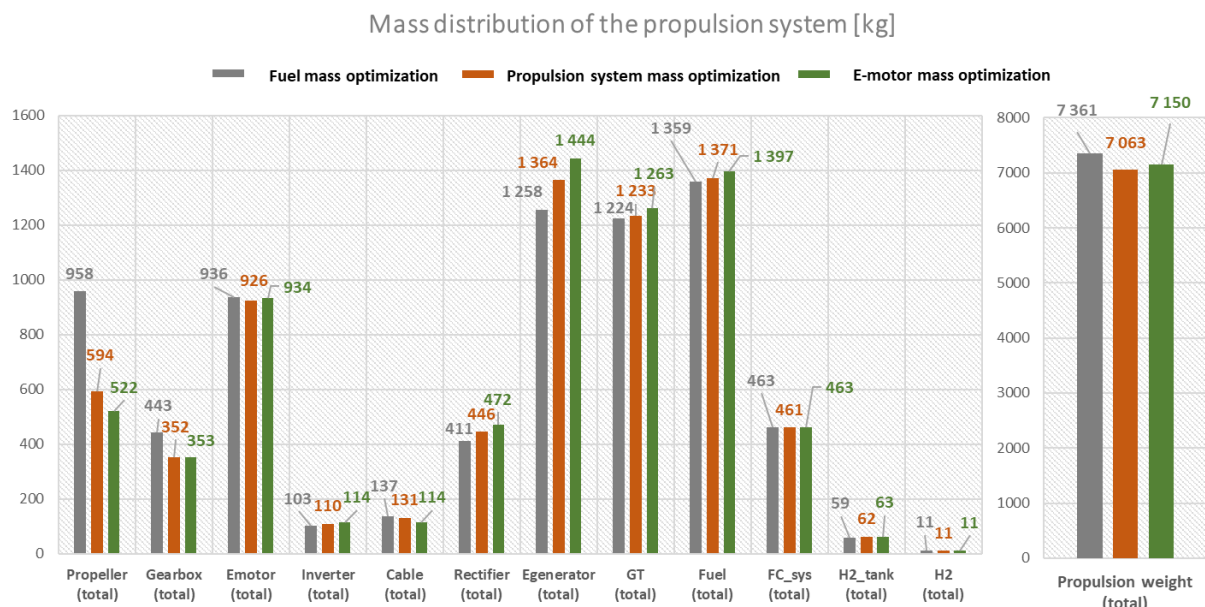


Fig. IV-24: Propulsion system mass distribution

Regarding the mass distribution:

- on propulsion side the motor-gearbox-propeller assembly is the most significant component;
- on source side, the electric generators and gas turbines involve highest masses;
- with a high DC bus voltage around 2 kV, the cable masses are negligible compared with the other components. The cables are thermally designed based on the current they conduct, which explains their low masses at high voltage;
- with this “light” hybridization strategy, the fuel mass saved by hybridization is quite reduced, being mainly due to the whole chain efficiency increase.

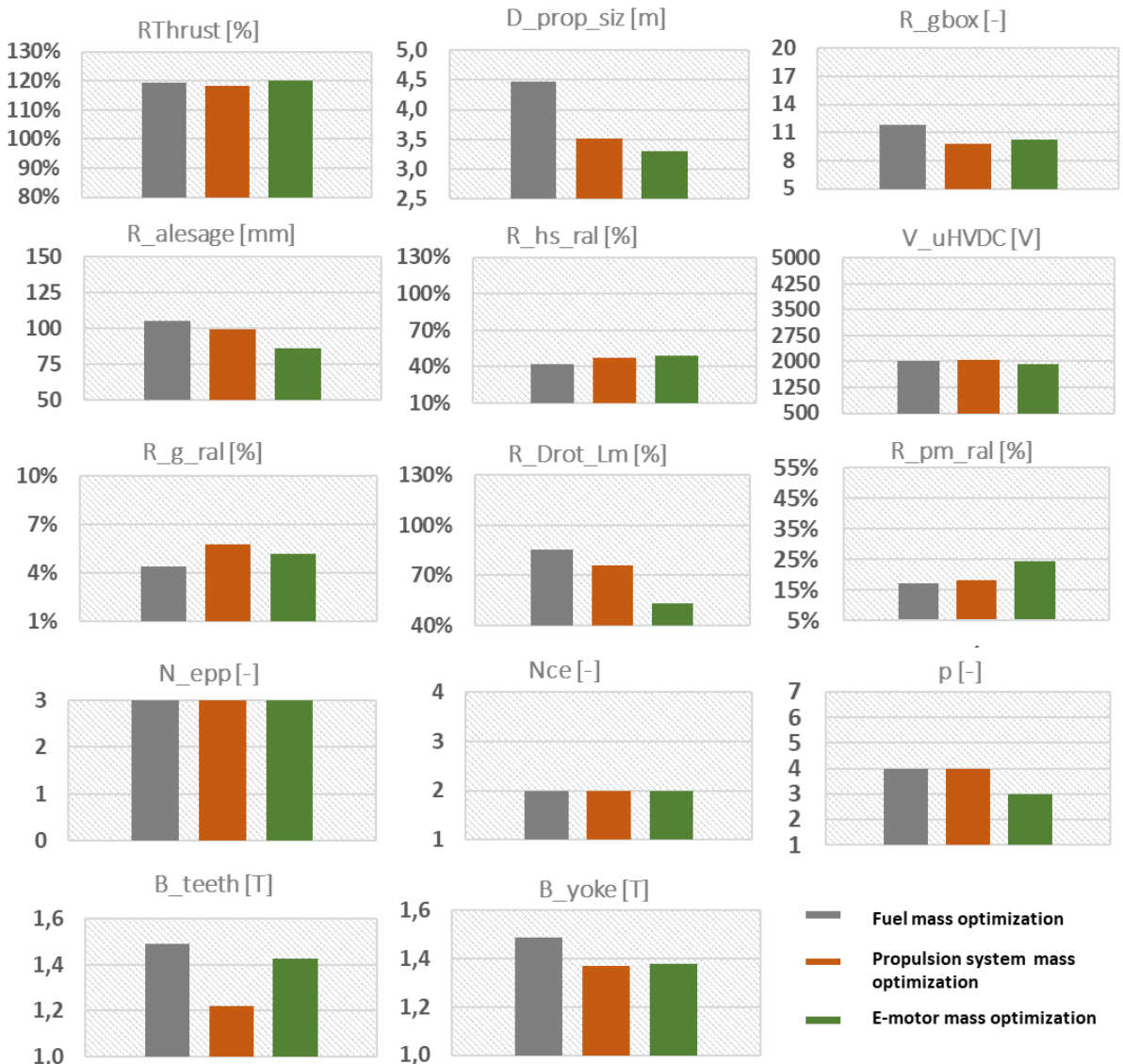


Fig. IV-25: Final decision variables giving the best objective function for the three optimizations.

The previous figure (see Fig. IV-25) shows the decision variables obtained for the best results of the three optimizations.

First of all, the V_{uHVDC} converges towards a value close to 2000 V. Remember that bus voltages lower than 2040 V involve the choice of a NPC 3L topology whereas the ANPC 5L converter structure is used for higher bus values. The 5L topology is more complex, heavier (presence of a flying capacitor). Thus, the bus voltage is close to the maximum permissible voltage provided by the 3L-topology. Based on the simplified model of winding insulation, the partial discharge issue is processed preserving the motor lifetime.

Regarding the electric motor, the improvement of its efficiency is mainly based on the aspect ratio R_{DrotLm} between diameter and length, and on the increase of the inner stator radius $R_{alesage}$. All parameters related to iron losses (number of pole pairs p and inductions in the teeth and the yoke B_{teeth}/B_{yoke}) have been increased by the system optimization with respect to the local one.

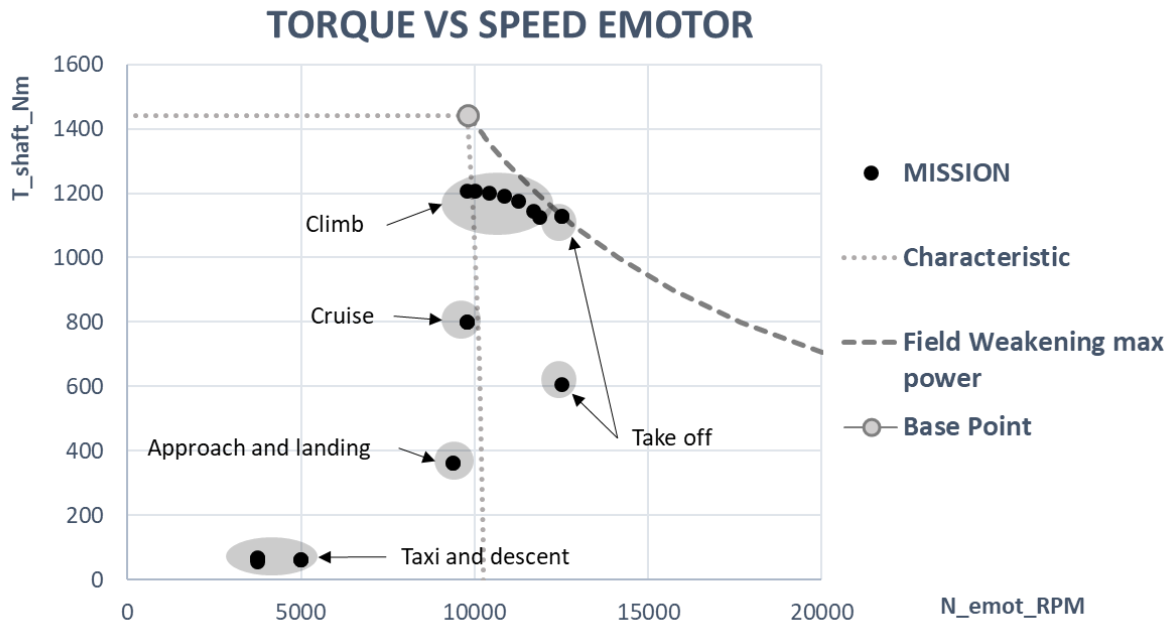


Fig. IV-26: Electric motor torque-speed characteristic for the fuel mass optimization.

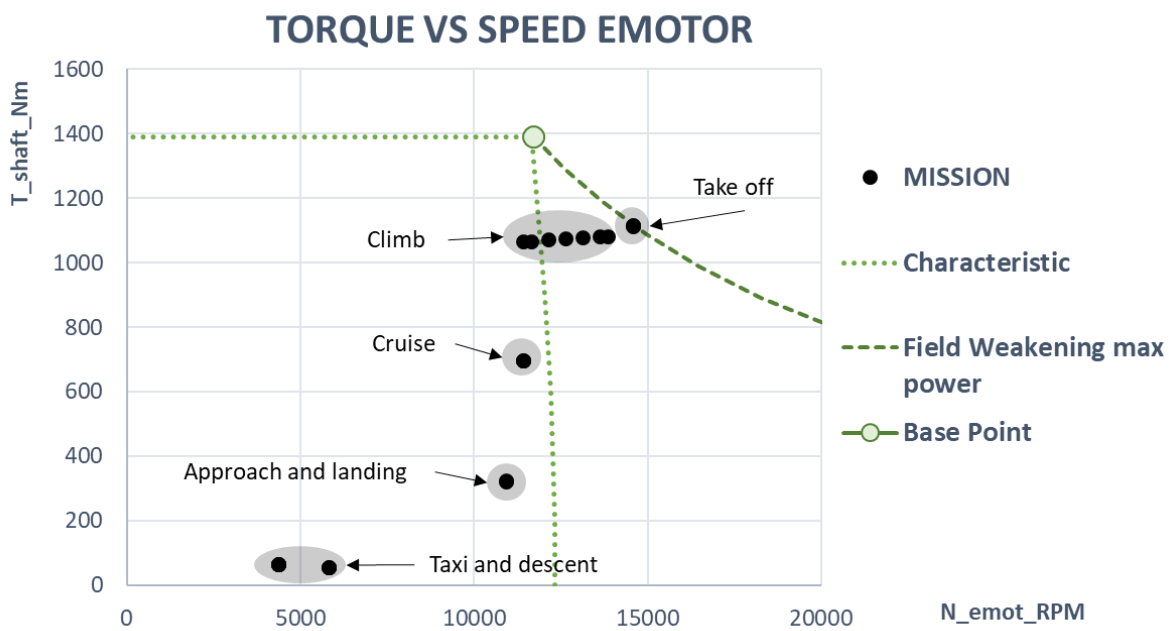


Fig. IV-27: Electric motor torque-speed characteristic for the e-motor mass optimization.

The two previous figures highlight the coupling between sizing choices and the flight mission by displaying the torque-speed plan of the electromechanical actuators for:

- optimization on the fuel mass (Fig. IV-26),
- optimization on the electric machine mass alone (local approach see Fig. IV-27).

In the system optimization, the oversizing of the propeller (involving system efficiency improvement) leads to a reduced the power required during takeoff and climb with respect to the operation of the system based on the local optimization. In the case where the propeller has not been oversized (local optimization), the maximum torque is requested during takeoff, contrarily to the system optimization case where the whole efficiency is improved and for which the maximum torque is reached at top of climb. The fuel burn optimization case is the most favorable for a field weakening strategy: compared to the local optimization case, the maximum power is reached with a lower value of rotational speed. The torque base point is not as oversized as in the case where the maximum torque is reached at maximum speed.

At the end of these two optimizations, the MTOWs are quite the same, which means that the masses gained by the improved efficiency compensate the increase on propeller mass oversized for system optimization to obtain an efficiency gain (see Fig. IV-24 propeller mass). The propeller is an essential parameter in the propulsion of an aircraft, especially when coupled to an electric motor. The analysis made in the chapter III had predicted this sensitivity to propeller and gearbox design parameters. Last results (see Fig. IV-24) strongly highlight that issue.

While the energy management strategy was *a priori* established for each flight sequence, the next section will be devoted to couple the optimization of the same propulsion system with management strategy. This can be achieved by implementing variable hybridization ratios during the mission, these latter being included as new decision variables of the optimization.

IV.3 Integrated design of a hybrid-electric aircraft coupled with its energy management system.

The objective of this new optimization integrating system sizing and energy management aims at reducing fuel consumption beyond the results obtained in the previous section with the *a priori* fixed management strategy.

The Fig. III-3, Fig. III-5 and the Fig. III-6 in chapter III summarized different ideas of possible EMS for a hybrid-electric aircraft, following if the source power demand is the same for both gas turbines (HEA SYM) or not (HEA ASYM) or also if only 1 GT is embedded (HEA 1GT). In this section the EMS strategy will be determined via hybridization ratios (HR) variable during the mission. When these ratio equals 1, the electrical source provides all the mission power whereas only the gas turbine ensures the propulsion when the HR equals 0.

By adding hybridization ratios in the decision variable set, the optimization problem complexity is increased: 12 variables (HR values spread during the flight mission) are added into the previous set of parameters. Obviously, moving from 14 to 26 decision variables is not without consequence in terms of convergence with such optimization solved under huge

constraints. In particular, the calculation time has been strongly increased. The optimization results “after 14 days of computation” are as follows:

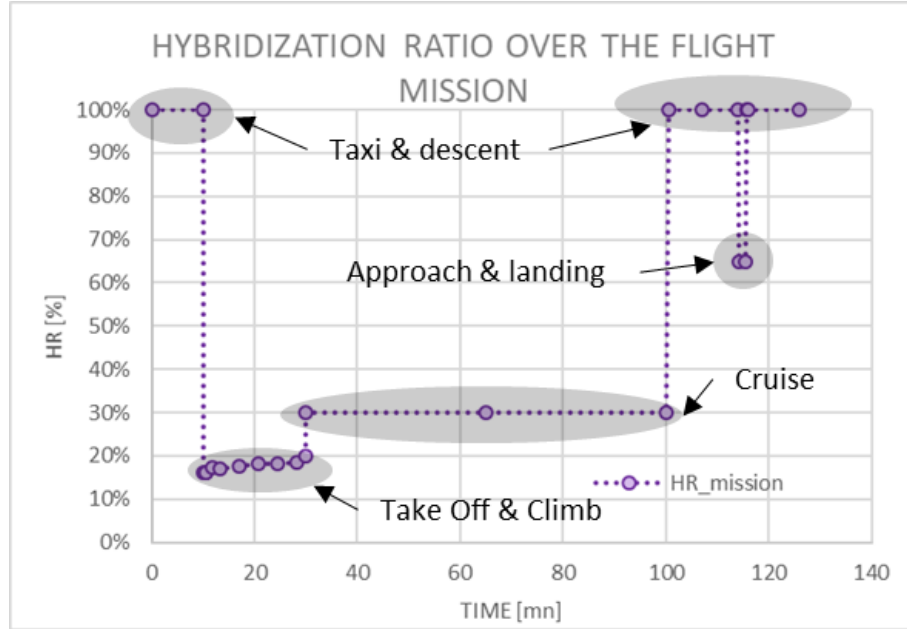


Fig. IV-28: Hybridization ratio over the flight mission.

First, the hybridization ratios (see Fig. IV-28) seems to be quite constant for each flight phases, except for the take-off/climb phases where the HR increases as the airplane climbs (15% -> 20%).

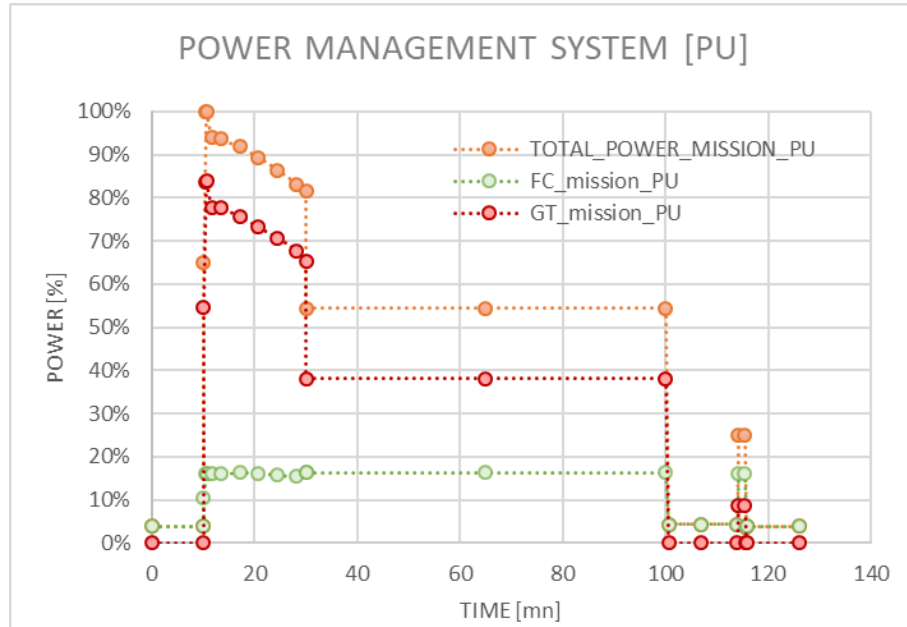


Fig. IV-29: Power management system over the flight mission per unit.

But regarding the total power drawn during the mission (see Fig. IV-29), the power drawn from the fuel cell stack seems to be constant (especially during climb and cruise) when the total requested power is higher than its sizing power. When a fuel cell is integrated to the hybrid propulsion system, the optimizer choices to use it at its design point (optimizing its efficiency) over the flight mission. The main benefit of the fuel cells (with respect to battery

technologies) is the dissociation of energy and power. The fuel cell stack is designed according to the power to be supplied, while the storage volume is sized according to the energy needs. This last result will allow us to reduce the number of decision variables to be optimized in the following. Indeed, by using only the fuel cell design power as an optimization parameter, the hybridization ratio profile is simply derived from a division of the sizing fuel cell power with the power profile. This new rule Eq.(IV-4) is now implemented in the optimization problem reducing the number of decision variables from 26 to 15 !

$$HR = \begin{cases} \frac{P_{siz_fuelcell}}{P_{mission}} & \text{if } \frac{P_{siz_fuelcell}}{P_{mission}} \leq 1 \\ 1 & \text{otherwise} \end{cases} \quad (\text{IV-4})$$

We also point out that the aircraft weight has reached the sizing limit $MTOW_{ref} + 6T$ by releasing the fuel cell sizing. Indeed, the additional cost in terms of Hydrogen consumption is not counted in the optimization of the fuel burn only focused on kerosen consumption. The propulsion system is then heavier, especially increasing the fuel cell stack and the hydrogen volume of storage but snowball effects in terms of mass are not compensated by the fuel saving induced by an increased use of the auxiliary electric source. Thus, it should be noted that a heavier propulsion system does not necessarily lead to an increase of the fuel consumption.

NB: it is important to point out that one limit among our model assumptions is certainly reached in that case, due to the linearization of the MTOW variations versus the thrust ones. Indeed, this assumption is considered as valid only if the reached values of MTOW are not too far (here less than 6T) from the “reference aircraft sizing”. Here, the MTOW limit is reached with this optimization showing that this (more electric) hybrid aircraft is not completely optimized. In order to explore design solutions with higher MTOW figures, it would become necessary to couple our powertrain sizing model with more complete and accurate aerodynamic design involving flight mechanic equations as it was done in the thesis of Jerome Thauvin [12]. This research direction seems clearly to be a major prospect of our work “on the road of more electric and of course zero emission future aircrafts”.

A new optimization has been performed with the new energy management rule Eq. (IV-4) only considering the fuel cell sizing as supplementary decision variable. The hybridization ratio obtained during climb and cruise is close to 20% (close to values observed for the Fig. IV-29). The fuel (kerosen) mass saved is around 200 kg (-15%) with respect to the “light hybridization scenario” but the objective function of this optimization still consider the kerosen burn only, without taking account of hydrogen burn during climb and cruise (remember that fuel cell is off in the previous “light hybridization strategy” during these high power flying sequences).

Fuel economy has an impact on the allowable take-off weight: as in the latest optimization result, the weight of the aircraft has reached (as anticipated) the allowable take-off weight limit $MTOW_{ref} + 6T$. Compared to the light hybridization scenario optimization, the snowball effect variable $Thrust_{siz}$ has reached its maximum value allowed during the optimization.

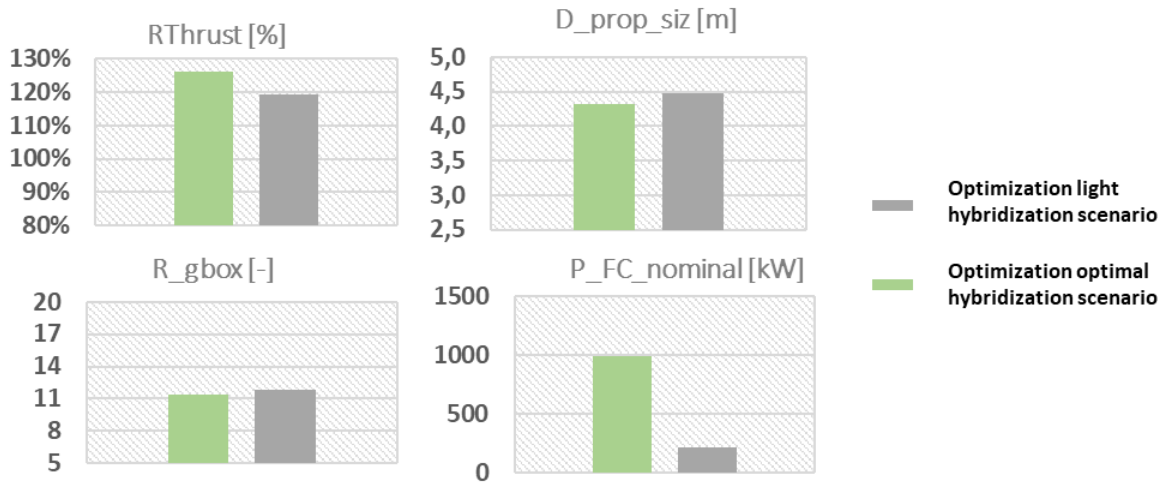


Fig. IV-30: Design variables for the snowball effect, the propeller, the gearbox and the fuel cell stack nominal power for both scenario (green: optimization including fuel cell stak power in the decision variable set – grey: “light hybridization”).

The propeller diameter is slightly smaller than for the previous optimization with a light hybridization scenario because the take-off weight value has reached its limit. Therefore, a trade-off was found between improving performance (oversizing the propeller and its weight) and fuel economy by adding a more powerful auxiliary source (more powerful fuel cell and its associated storage). Same conclusions apply for the gearbox ratio between the propeller and the electric actuator which is slightly decreased, consequently reducing its mass in order to allow supplementary mass for the electrochemical source. The hybridization ratios cannot be compared because the light hybridization scenario does not use the fuel cell during the whole mission (HR = 0 during the cruise) see Fig. IV-30.

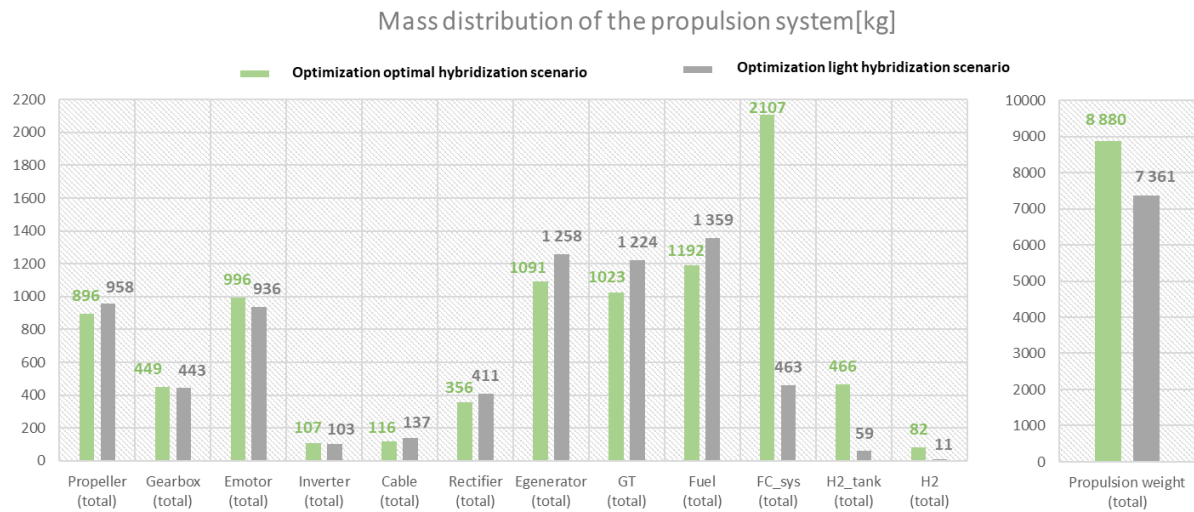


Fig. IV-31: Propulsion system mass distribution for the 2025 HASTECs target.

The fuel cell nominal power was multiplied by five between the light hybridization scenario and the optimal energy management scenario. This difference in sizing has a direct effect on the masses of the electrochemical source. Thanks to the sizing point (~20%), the fuel cell allows to save a large part of the aircraft fuel (around 150kg saved see Fig. IV-31).

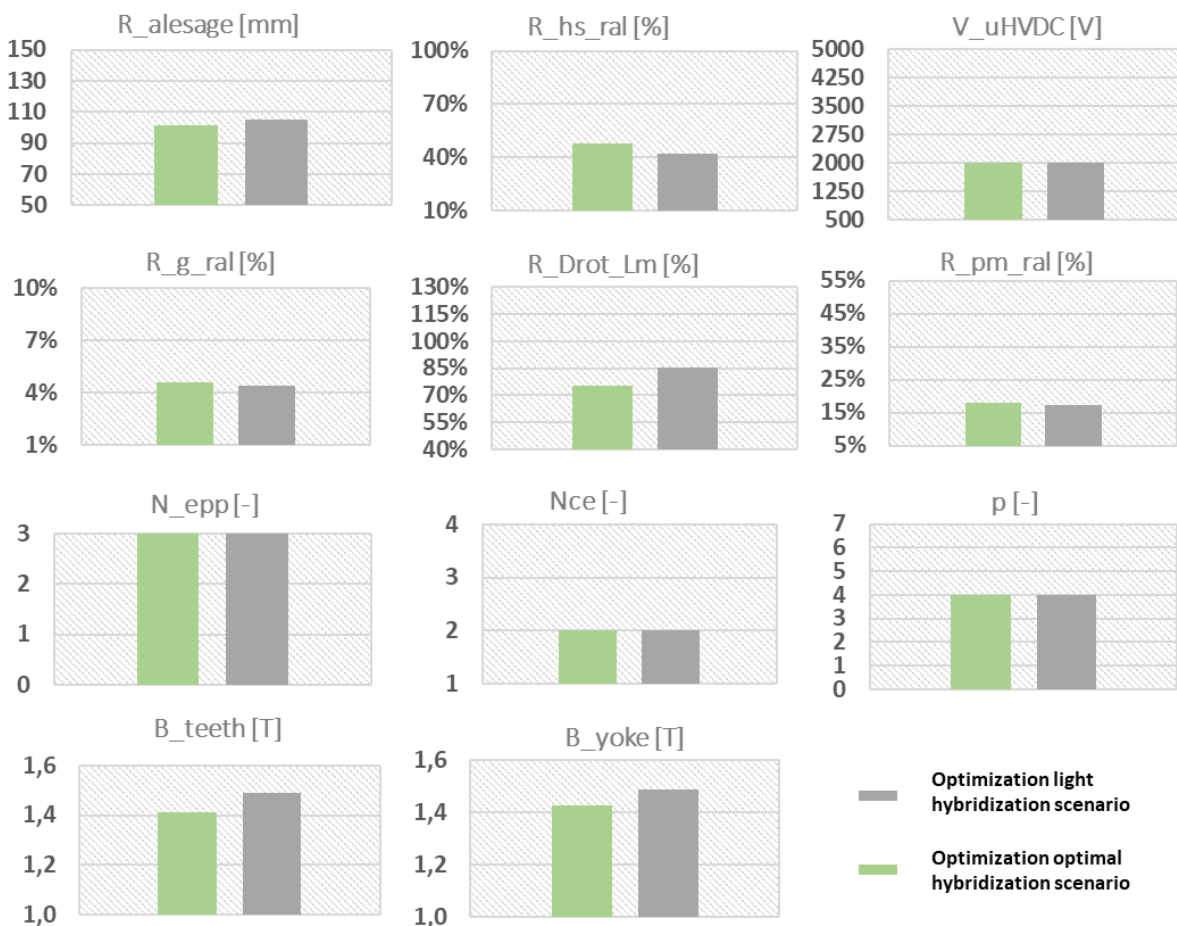


Fig. IV-32: Optimisation comparison (green: optimal hybridization ratio – grey: light hybridization scenario).

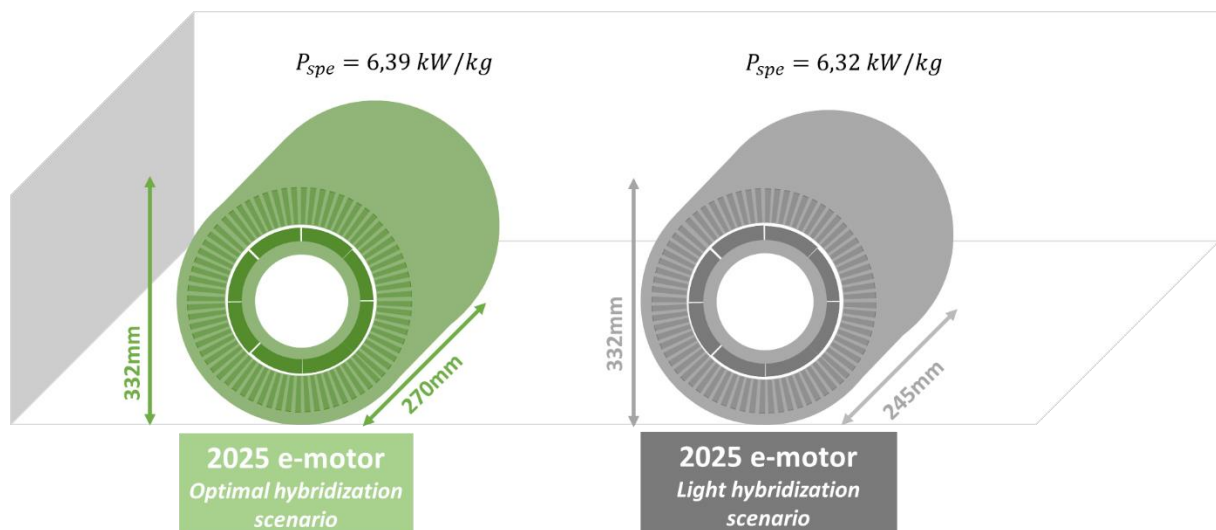


Fig. IV-33: Geometrical comparison (green: optimal hybridization ratio – grey: light hybridization scenario).

In spite of a different hybridization strategy, electric machines have almost the same decision variables and are therefore geometrically very similar. But the use of these machines differs during the mission.

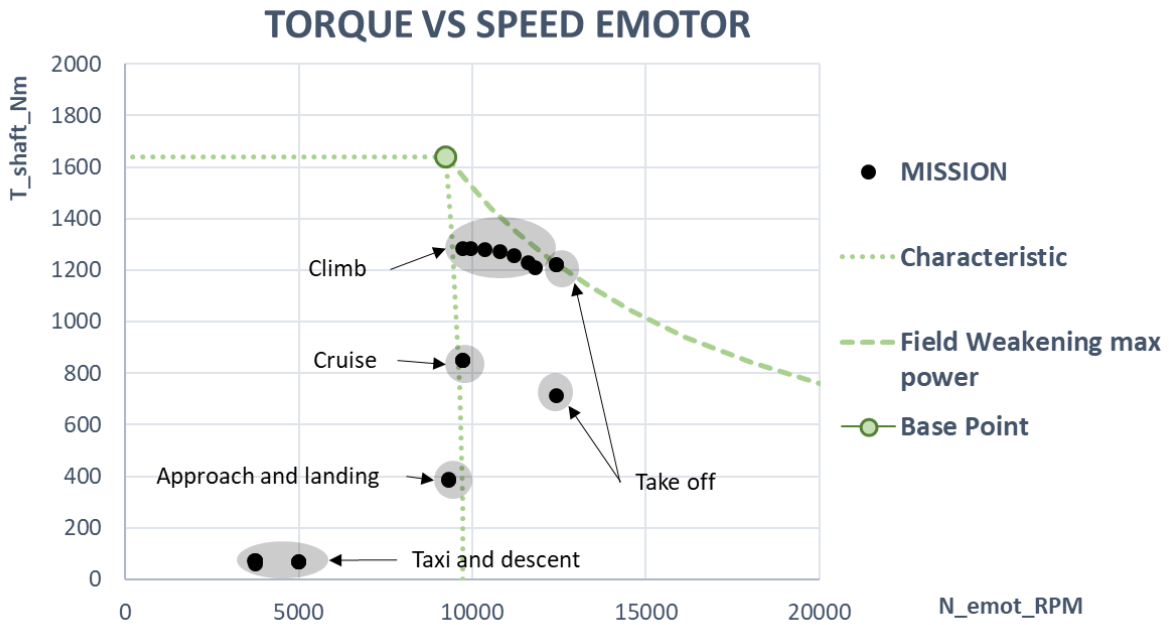


Fig. IV-34: Torque-Speed characteristic for the 2025 optimum results (including FC stack sizing).

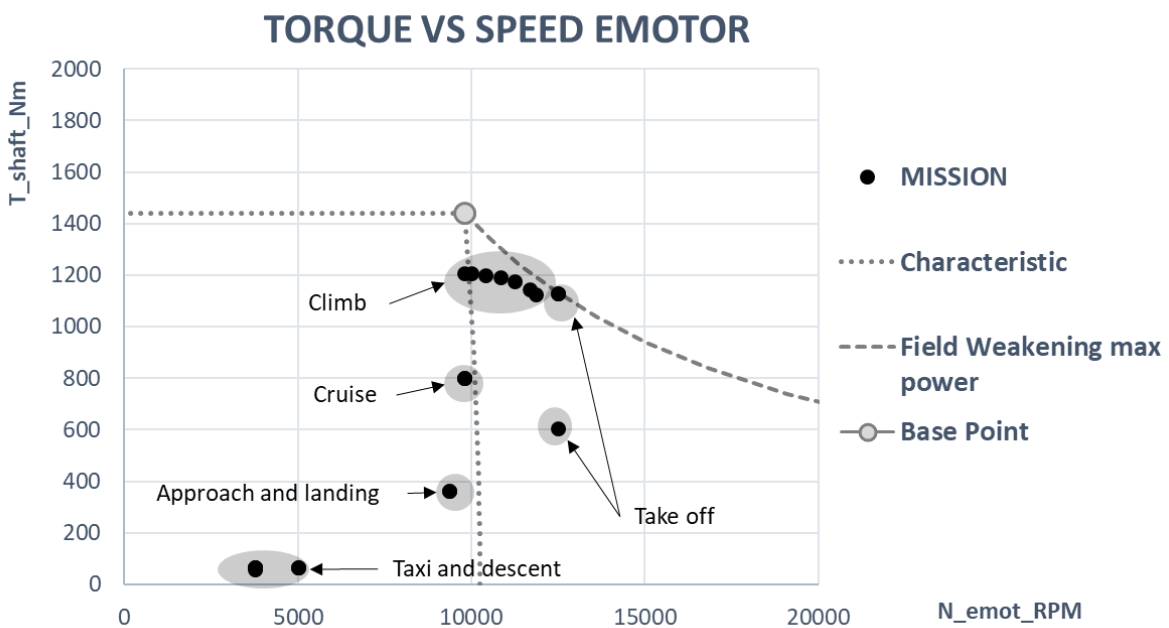


Fig. IV-35: Torque-Speed characteristic for the 2025 light hybridization scenario results.

Both actuators slightly differ in performance during the flight mission (see Fig. IV-34 & Fig. IV-35):

- the base point in the torque-speed plane changes during the mission, with a torque sizing point increased for this new optimization;
- the actuator device exploits the magnetic field weakening operation during cruise (the green dotted characteristic is on the left of the cruise mission point), contrarily to the previous optimization case (the grey dotted characteristic is on the right of the cruise mission point). This field reduction also reduces iron losses improving therefore the actuator efficiency during the cruise phase (the longest in time during the flight

mission). By improving the performance during the cruise, the electromechanical actuator improves the efficiency of the chain, especially when the fuel cell is in operation.

The power densities of the electrical components studied has reached the same values as before (see Fig. IV-21).

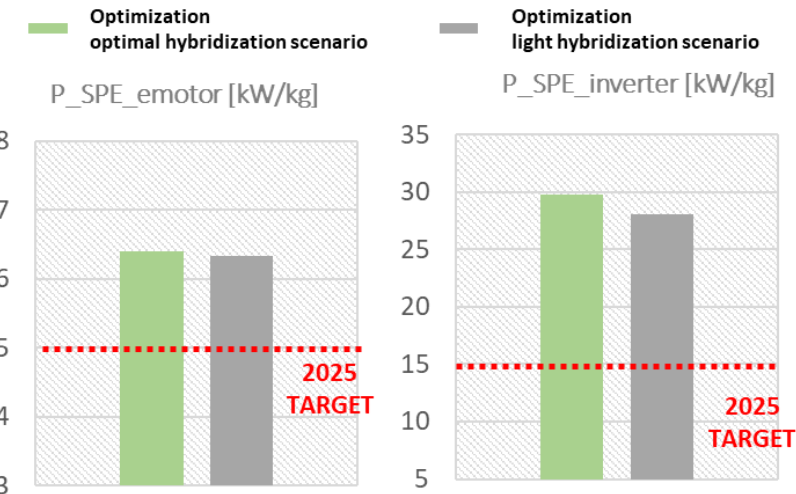


Fig. IV-36: Specific power of the electrical components.

The power densities for both optimizations, the difference in fuel consumption is mainly due to the missions of both sources: with 20% of the power supplied by the fuel cell, the fuel economy is remarkable, at around 150 kg (see Fig. IV-37).

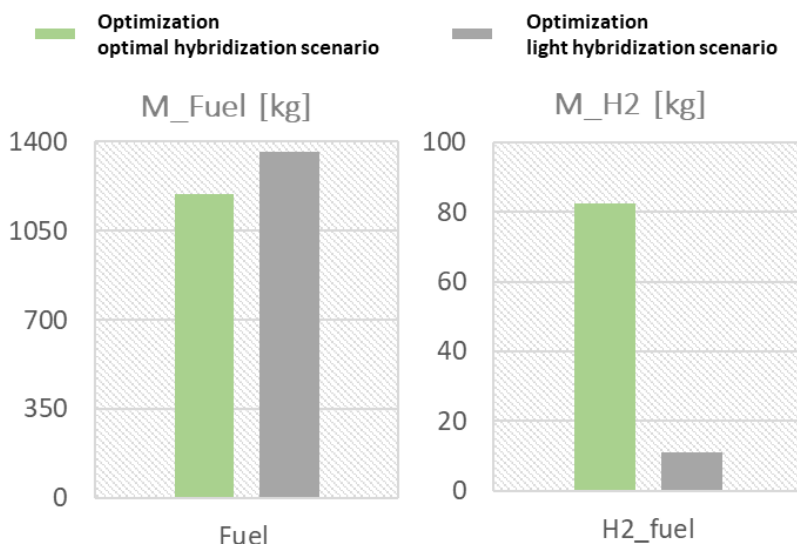


Fig. IV-37: Comparison of the fuels required for the mission.

Looking at the power distribution, the fuel cell element provides up to 20% of the total power required during high power phases (Fig. IV-38). As mentioned before, a MTOW limit has been incorporated into the optimization to avoid reaching too large masses. Without this limit, and with an objective function only dealing with kerosen burn, the optimization would have probably converged towards an all-hydrogen aircraft.

The 150 kg of fossil fuel have been replaced with 80 kg of hydrogen. This difference highlights the difference in energy density between the 2 molecules as well as the difference in efficiency: the efficiency of the gas turbine is lower than the efficiency of the fuel cell.

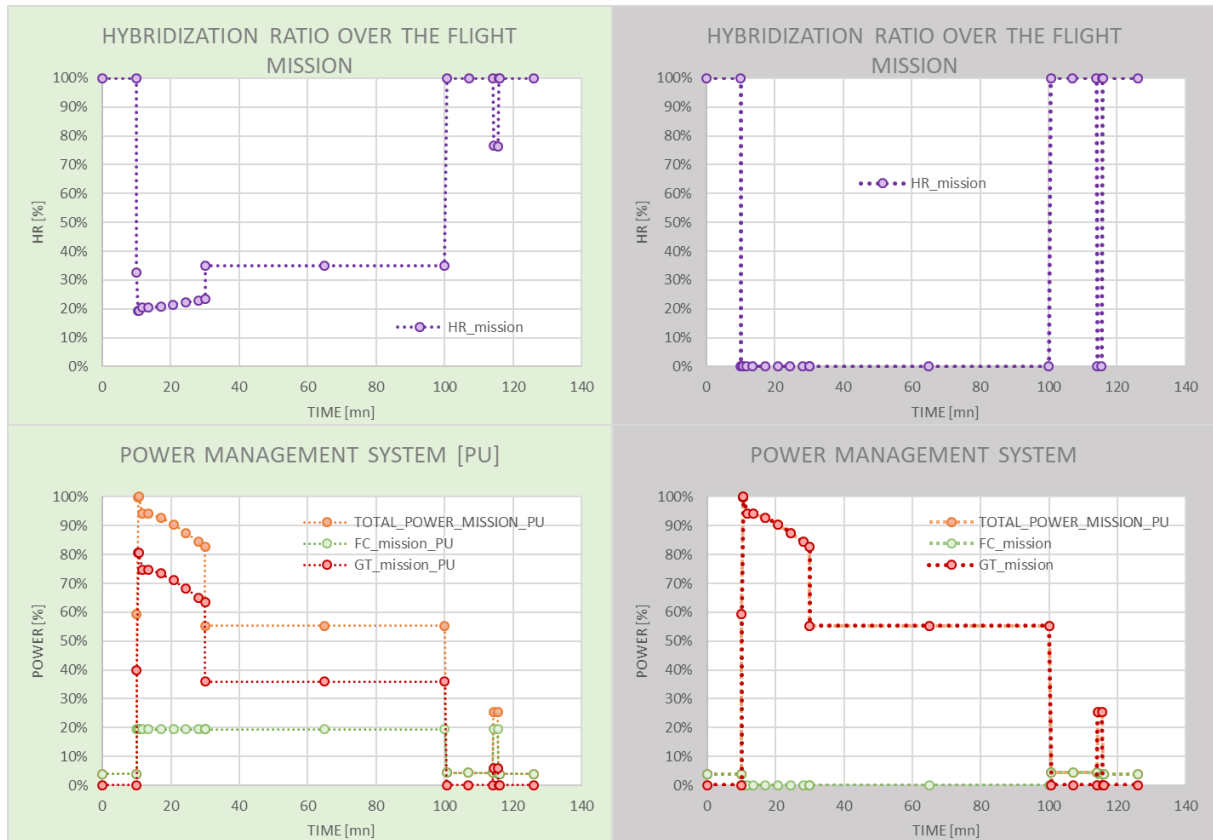


Fig. IV-38: Hybridization ratio and consequence on the power management of the propulsion system (green background: optimal hybridization scenario – grey background: light hybridization scenario).

Regarding the reference (optimized full thermal) aircraft, the optimized “HASTECS 2025 hybrid-electric aircraft” is much heavier (+26%). From a fuel consumption point of view, the “HASTECS aircraft” consumes only 3% more fuel meaning that efficiency improvements do not compensate the aircraft weight increase with the assessments set in the “HASTECS 2025 requirements”.

To conclude to this section:

- Taking partial discharges into account and looping back to the sum of all the component masses during the optimization, a system trade-off has been highlighted on the DC bus voltage of the electrical network. This was confirmed during both optimizations. Without taking account of partial discharges in the Emotor insulation, the DC bus voltage would go to its maximum limit in order to relieve the sizing of the electrical components (cables). Considering the insulation issues, the value of 2000 V seems to be the correct system tradeoff, noting that it was also the local optimum obtained by the power electronics research team for the 2025 requirements applied on the inverter itself.
- The coupling of thermal and electromagnetic issues has highlighted the importance of the field weakening strategy for the actuator sizing. The energy-optimized aircraft uses

this strategy during cruise in order to always reduce losses during the most significant phases in terms of energy demand.

- Finally, the change of energy mission allows the saving of kerosene over the whole mission. Once the sizing power is installed in the propulsion system, the fuel cell is used at its rated power in order to save the maximum amount of fossil fuel drawn from gas turbines. The last optimization has shown that the fuel cell was used throughout the mission. Compared to the conventional all-thermal aircraft, the results obtained are more promising than those obtained using constant power density and efficiency (called “target aircraft”) as it was previously presented in the chapter III. The Fig. IV-39 illustrates the relative deviations in MTOW and weight of on-board fuel with respect to the reference aircraft.

RESULTS VERSUS REFERENCE AIRCRAFT

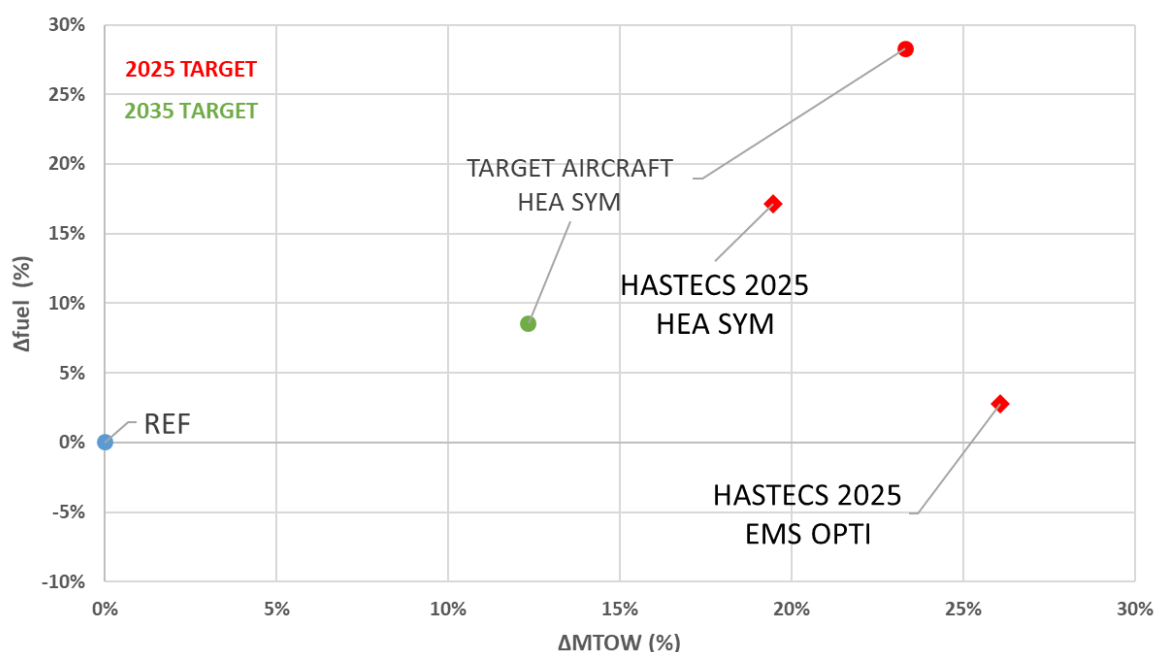


Fig. IV-39: Relative deviations in MTOW and fuel mass with respect to the reference aircraft

Compared to the 2025 “target aircraft” results, “HASTECS optimization” provides better solutions. When hybridization is used during flight (“HASTECS 2025 EMS OPTI”), the aircraft takes off a lot of weight in order to save fuel thanks to an increased fuel cell and hydrogen sizing. These results show here the interest of a multidisciplinary system approach for designing the propulsion chain.

The HASTECS study has focused on two targets: one entry into service for 2025 and another for 2035, these two targets dealing with different technological assessments. Crossing from 2025 to 2035 assessments, the next section will examine the influence of technological improvements on the performance of future aircrafts.

IV.4 Exploration of the performance of a hybrid-electric aircraft taking account of technological advances in electrical components (target 2035).

The major changes between both 2025 and 2035 targets concern the cooling systems, especially for the electric machine, where spaces in stator slots are reserved for adding an internal cooling channel [87]. For the voltage source inverter, a new condenser technology has been studied in order to improve the power density of the converter [88]. All the details are explained in APPENDIX G (Electric motor cooling model), APPENDIX I (Power electronics and its cooling system).

IV.4.1 Optimization of the eMotor weight (2025 vs 2035 assessments)

In the first part of the chapter IV section IV.1, several optimizations have been carried out in order to observe the sizing differences between steady state and transient models. The power profile was identical for all these optimizations considered for the machine alone. Strongly better specific power has been obtained by the optimization with a transient thermal model allowing the machine to perform the mission with lower temperature rise during the phases of very high power demands (takeoff, climb). The following part is related to the same “exercice” with the new internal cooling model (‘target 2035’) (APPENDIX G). The power mission is still identical to the study carried out previously (chapter IV section IV.1), only the cooling model was changed.

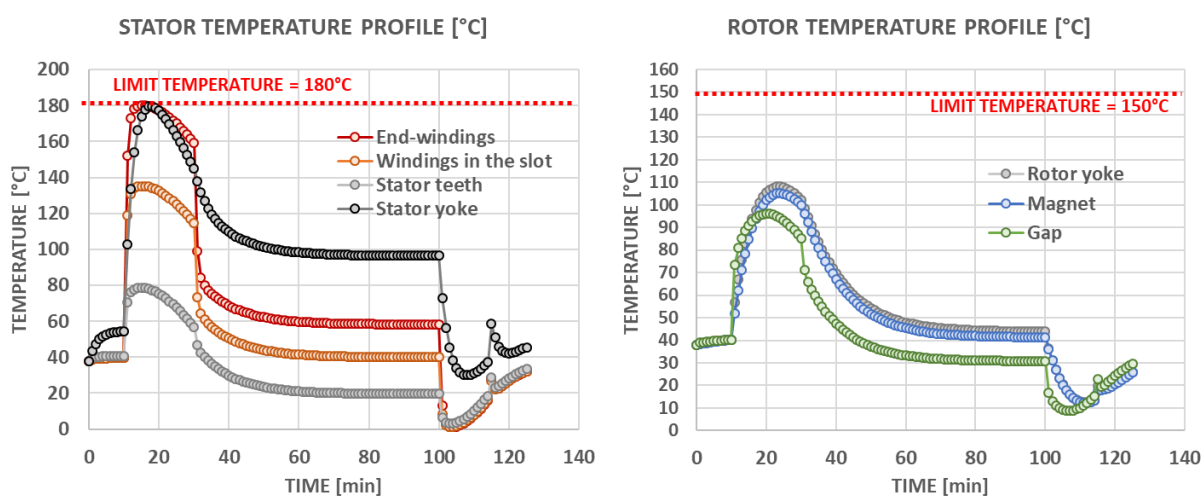


Fig. IV-40: e-Motor temperature (2035 target) over time.

The new 2035 optimization in Fig. IV-40 shows a different dynamic of the thermal behaviour. Indeed, the machine has become so small that the transient is no longer marked to avoid overheating the electric motor during very high power demand phases. The sizing constraints remain once again the temperatures in the stator (yoke and end-windings). The magnet temperature is well reduced. In fact the rotational speed of the actuator is not too

high and the stator losses are sufficiently evacuated that they do not disturb the rotor temperatures.

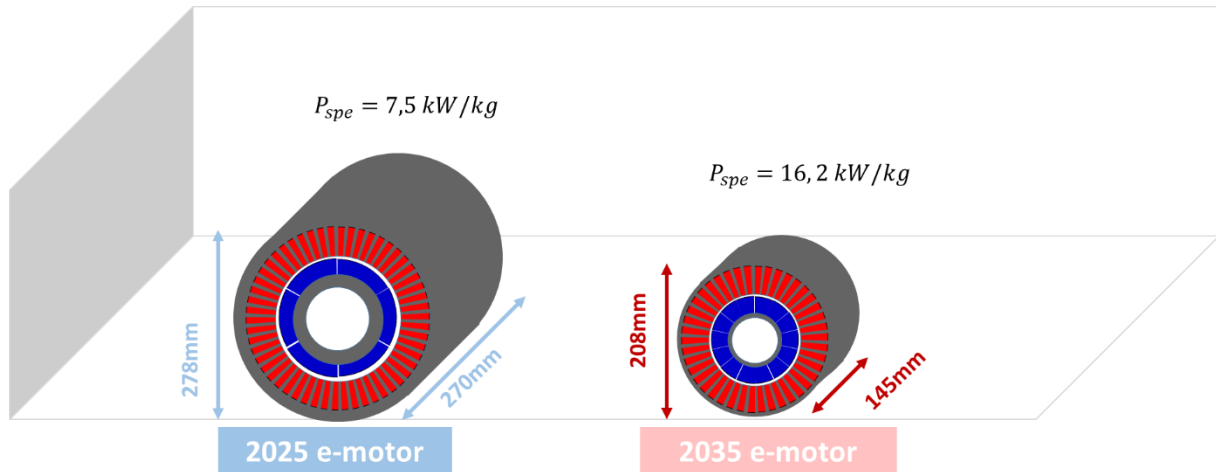


Fig. IV-41: Geometrical comparison (blue: optimal 2025 emotor – red: optimal 2035 emotor).

The difference between the volumes of both actuators illustrated in Fig. IV-41 makes it possible to double the specific power between 2025 and 2035.

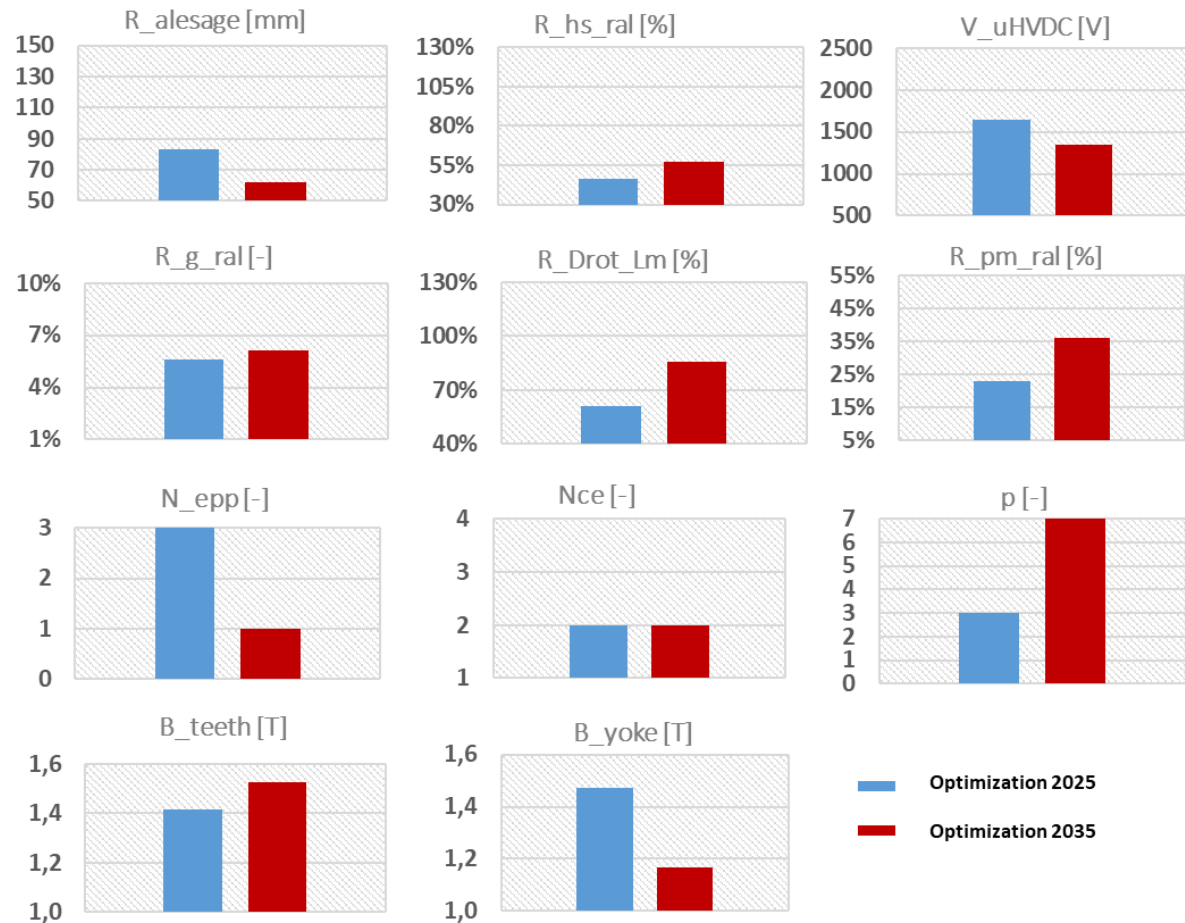


Fig. IV-42: Optimisation comparison (blue: optimal 2025 emotor – red: optimal 2035 emotor).

- The DC bus voltage is reduced for ‘optimization 2035’ according to the insulation constraint: the slot is here smaller than for 2025 target because cooling channels are integrated inside the slot. The insulation is directly linked with the DC bus voltage. The lower the DC bus voltage the thinner the wire insulation inside the slots. To continue on the same idea, the number of slots per pole and phase is reduced to 1 to best integrate the cooling channels.
- The ratio between the inner stator radius and the magnet thickness is higher for the 2035 target, the volume of the electric motor being reduced, the air gap flux density needs bigger magnets.
- The cooling system is so efficient that it is possible to increase the number of poles pairs till 7. Increasing the number of pole pairs considerably reduces the thickness of yokes and other sizes of the actuator, however greater iron losses are to be expected which is managed by the highly performant cooling. The same explanation can be used for the flux densities in the teeth and in the yoke. The cooling channels are in touch with the windings and the stator teeth, so the flux density in the teeth can be maximized.

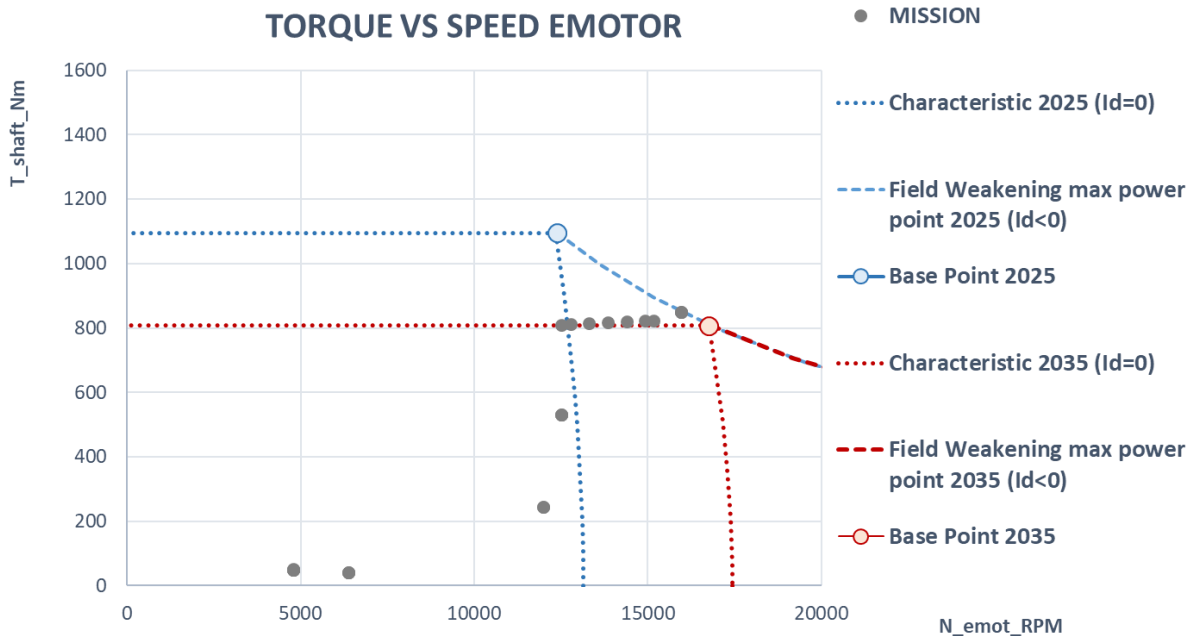


Fig. IV-43: Torque-Speed characteristic for the 2025/ 2035 optimum results.

Compared to the 2025 target (see Fig. IV-43), the mass-optimized 2035 actuator does not use field weakening strategy. The characteristic 2035 is below the maximum torque point: this cooling system is so efficient that it is possible for the actuator to explore an over-torque zone. This is possible because the actuator has become really small and the torque design point has gone down along the iso power curve (maximum power).

This new technological performance of the cooling system for the 2035 target will strongly reduce the mass of the actuator thus increasing its power density. As the machine is one of the heaviest elements in the propulsion system, this will allow the aircraft to lighten the mass of the propulsion system and thus consume less fuel.

IV.4.2 System optimization including energy management strategies

Compared with the previous study (target 2025), the same ecological objective function is considered (reduction of fuel mass) and the same hybridization strategies are used:

- A “light hybridization scenario” for which taxi and descent phases are full electric, the other sequences being full thermal
- An “optimal energy sharing scenario” for which the fuel cell tank can provide 20% of the maximum power demanded over the duration of the mission (see the previous sub section).

An improvement in aircraft performance in terms of weight and fuel consumption is expected with new assessments (“Target 2035”), as a lighter aircraft would consume less fuel because of higher specific powers installed on board.

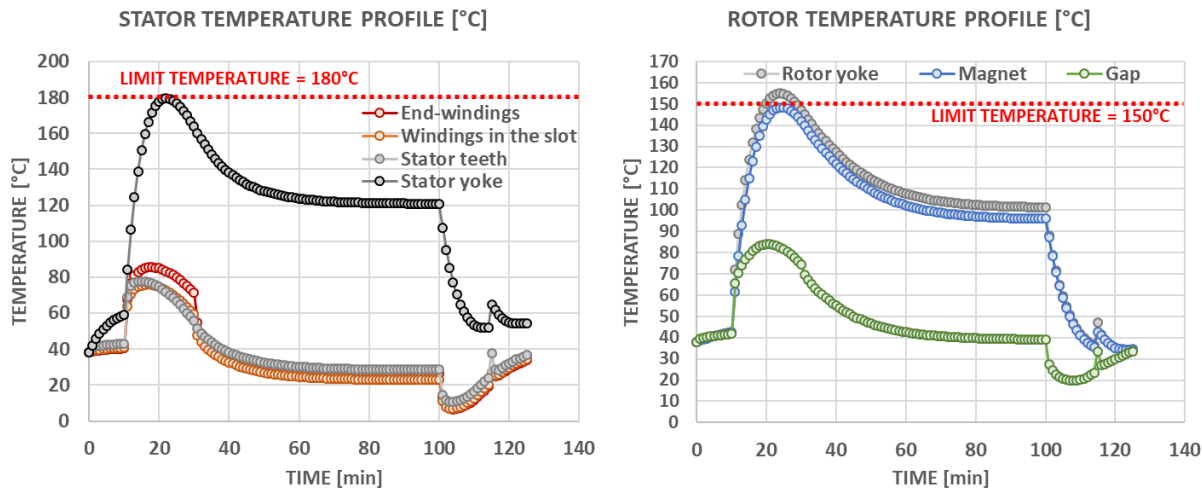


Fig. IV-44: e-Motor temperature (2035 target for both optimisations) over time.

Targets 2035 bring new perspectives from an electromechanical actuator sizing point of view as Joule losses are no longer a thermal limit contrarily to the previous case study (“target 2025”). Indeed, the stator internal cooling channel in the slots allows a direct cooling at the core of the winding. As previously announced the temperatures in the slots of the electric machine (see Fig. IV-44) are lower due to the direct cooling in the windings. Consequently, a new constraint appears on the actuator stator yoke. The current density increases due to the internal cooling of the slots leading to the increase of the magnetic flux density in the stator yoke. Critical constraints are now located at the stator yoke level compared with the “target 2025” case where they were situated at the windings level. These constraints are all the more important considering the reduced volume of the actuator. In addition to the thermal design limits, a new constraint reaches its limit: the centrifugal pressure on the carbon sleeve. The rotational speed of the actuator has been increased, making more difficult to hold the magnets. This constraint also becomes a dimensioning constraint for the 2035 target optimizations.

During the previous optimization of the HASTECS 2025 propulsion system, two energy strategies were presented (“light hybridization scenario” – grey color and the “optimal” one-green color). Furthermore, in order to present the improvements between 2025 and 2035, the same strategies were represented with fuel consumption as the optimization objective function.

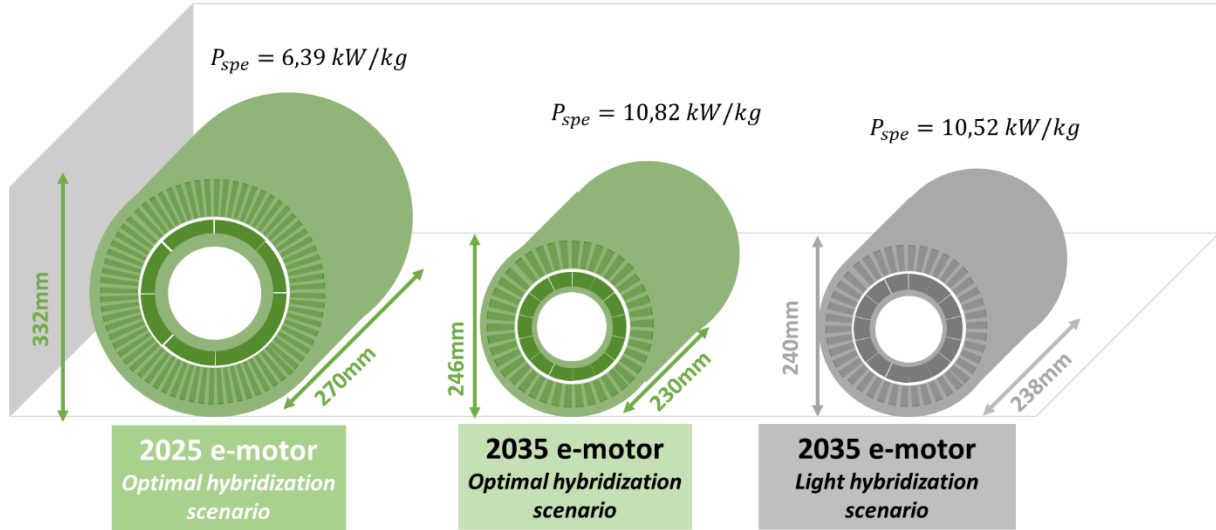


Fig. IV-45: Geometrical comparisons of three electric motors.

From a geometrical point of view (see Fig. IV-45), both machines optimized with “2035 target” are much smaller than their predecessors obtained with “2025 target”. The first machine (“2025 e-motor”) on the left in this figure is the optimal actuator for the 2025 target with an “optimal hybridization scenario”: it reaches 6.39 kW/kg of power density. Both “2035 machines” are the optimal sizing trade-off with the addition of the stator internal cooling system:

- the second actuator obtained with the “optimal hybridization scenario” is much smaller than the previous one. Indeed, its power density reaches 10.8 kW/kg based on the “target 2035” assessments.
- The third actuator obtained with the “light hybridization scenario” involves a specific power of 10.52 kW/kg.

As for the 2025 target, the results between the two hybridization strategies are quite similar (iso geometry for the energy optimal scenario - machine 2 and the light hybridization scenario - machine 3). In order to simplify the comparison, only the energy optimal scenario will be compared between the targets 2025 - machine 1 and 2035 - machine 2.

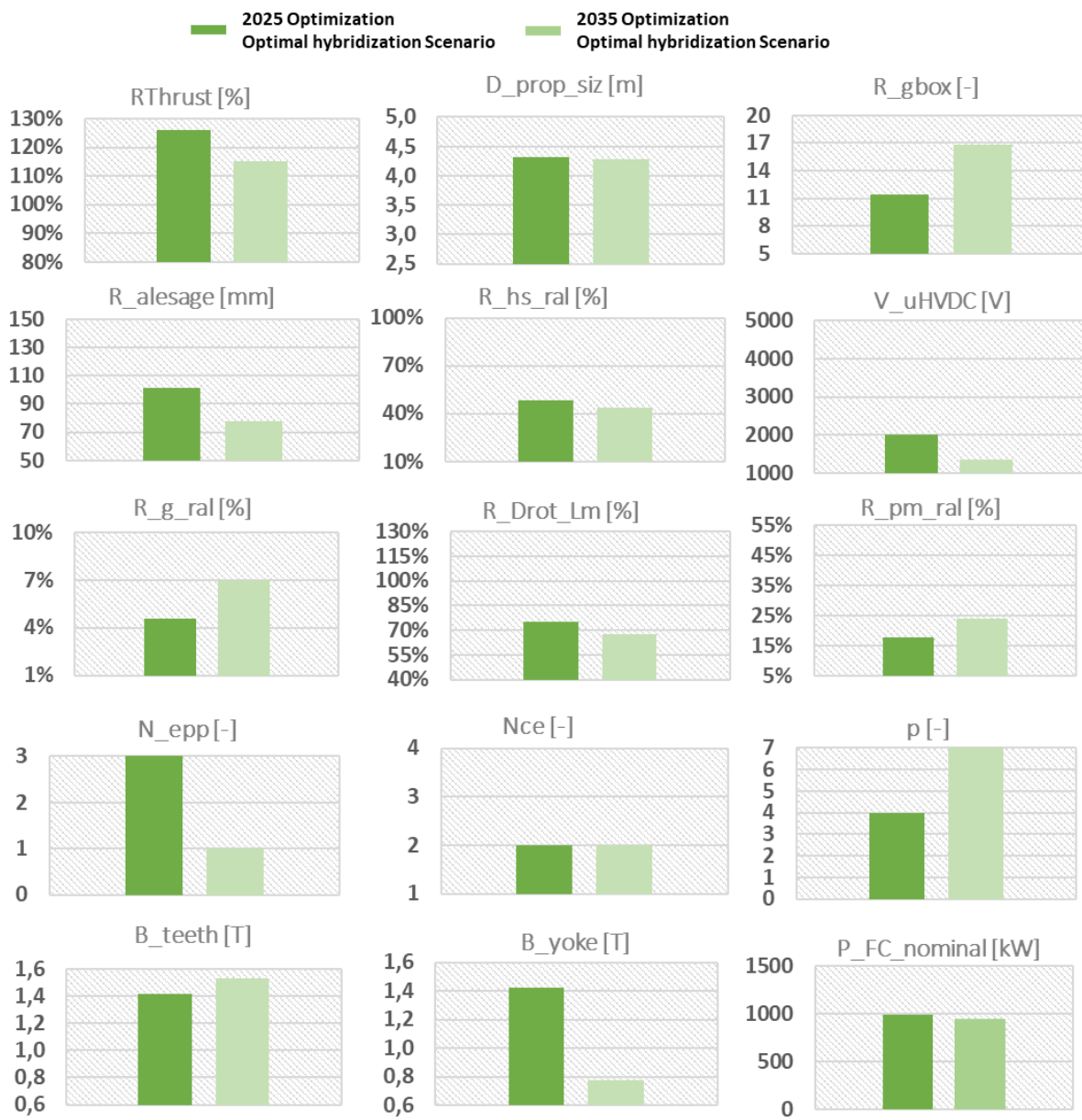


Fig. IV-46: Comparison between 2025 target and 2035 target.

Comparing results obtained with both “2035 motors” with respect to the “2025 Motor”, several changes can also be noted on the decision variables after the three optimizations (see Fig. IV-46):

- The gain in power density avoids a significant oversizing of the aircraft thrust which can be explained by the variation of the *RThrust* variable, this latter being decreased with both .
- This thrust variation also involves evolutions of several devices: the propeller diameter is slightly smaller, but with oversizing values which remains high compared to the necessary diameter ($D_{prop} > 4$ m).
- A drastic change has appeared for the gearbox ratio: by increasing the transmission ratio between the propeller and the actuator, this decreases the torque mission while it increases the speed of the actuator. This evolution is not without consequences since the increase in the actuator speed combined with the increase of the number of pole

pairs will considerably increase the electrical frequency and consequently the iron losses of the electric motor.

- As previously announced, the reduction of the torque mission reduces the inner stator radius of the actuator. The ratio between the inner stator radius and the slot height seems to be constant but by comparing these values with the inner stator radius itself, the slot height varies in the same way.
- The DC bus voltage has been indirectly reduced after the evolution of the stator cooling system: the current density through the 2035 machines is higher than that of the 2025 machines. Indeed, the integration of the cooling channels inside the slots leads to additional constraints on the actuator windings. The DC voltage value to be held determines the required insulation thickness, the thickness of the slot layer as well as the copper radius and its reduction makes it easier to integrate the windings into the slot. The “2035 motor” optimization converge towards a DC voltage of 1300 V compared to the 2000 V obtained for the “2025 motor”, given the same energy management scenario. This voltage reduction is directly related to the thickness of the insulation. The presence of the cooling channels in the slot of the actuator causes the optimizer to optimize the available space in the slot. In addition to the thickness of the insulation, the voltage also affects the thickness of the slot insulation paper. The voltage reduction is also due to the reduction of required power, the 2035 aircraft is lighter than the previous one and consequently the amount of power is reduced for the mission profile, thus the required voltage can be reduced. This argument is also supported by the number of slots per pole and per phase which is reduced to 1. The slots are therefore wider than for the 2025 targets.
- The radius-to-length ratio R_{drotLm} decreases and the actuator operates at higher speeds than before.
- Stator inner radius and magnet thickness ratio are set to compensate the change in inner stator radius to have the same magnet height (~18mm).
- The number of pole pairs increases from 4 to 7 to reduce the main dimensions of the electromechanical actuator especially the yokes. However, as mentioned before, this increase contributes to increase the iron losses: there seems to be a tradeoff between size reduction and losses which moves regarding the cooling efficiency.
- The results of the magnetic flux densities in teeth and in the stator yoke are directly related to the cooling mode of the actuator: the flux density in the tooth is higher due to the fact that the cooling is closer to the teeth than to the yoke itself. This means that more iron losses can be evacuate through the stator teeth than through the stator yoke.
- Regarding the Fuel cell nominal power, the same difference is highlighted between light hybridization scenario (grey figure) and optimal scenario (green figures). The improvement from 2025 to 2035 is illustrated by the difference of nominal power between green figures.

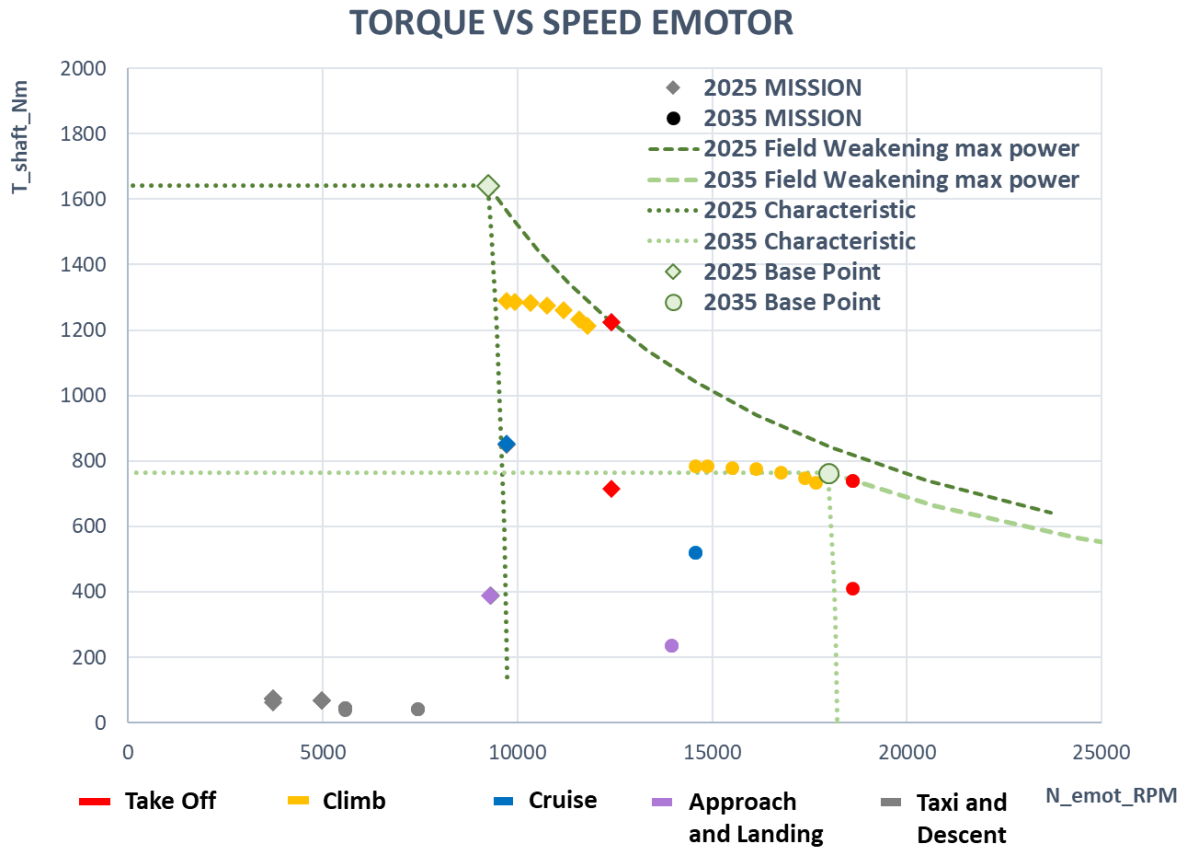


Fig. IV-47 : Torque-speed plan of the electromechanical actuators obtained by optimization of 2025 and 2035 (optimal hybridization scenario).

The previous figure Fig. IV-47 illustrates the characteristics of the 2 electric machines for 2025 and 2035 targets including the field weakening strategies proposed by each optimization. This display corresponds to the less fuel consuming hybridization scenarios (“optimal hybridization scenario”) for both motor targets. The actuator mission is completely changed with differences in terms of field weakening strategy: in the “2035 case”, the field weakening strategy is not necessary.

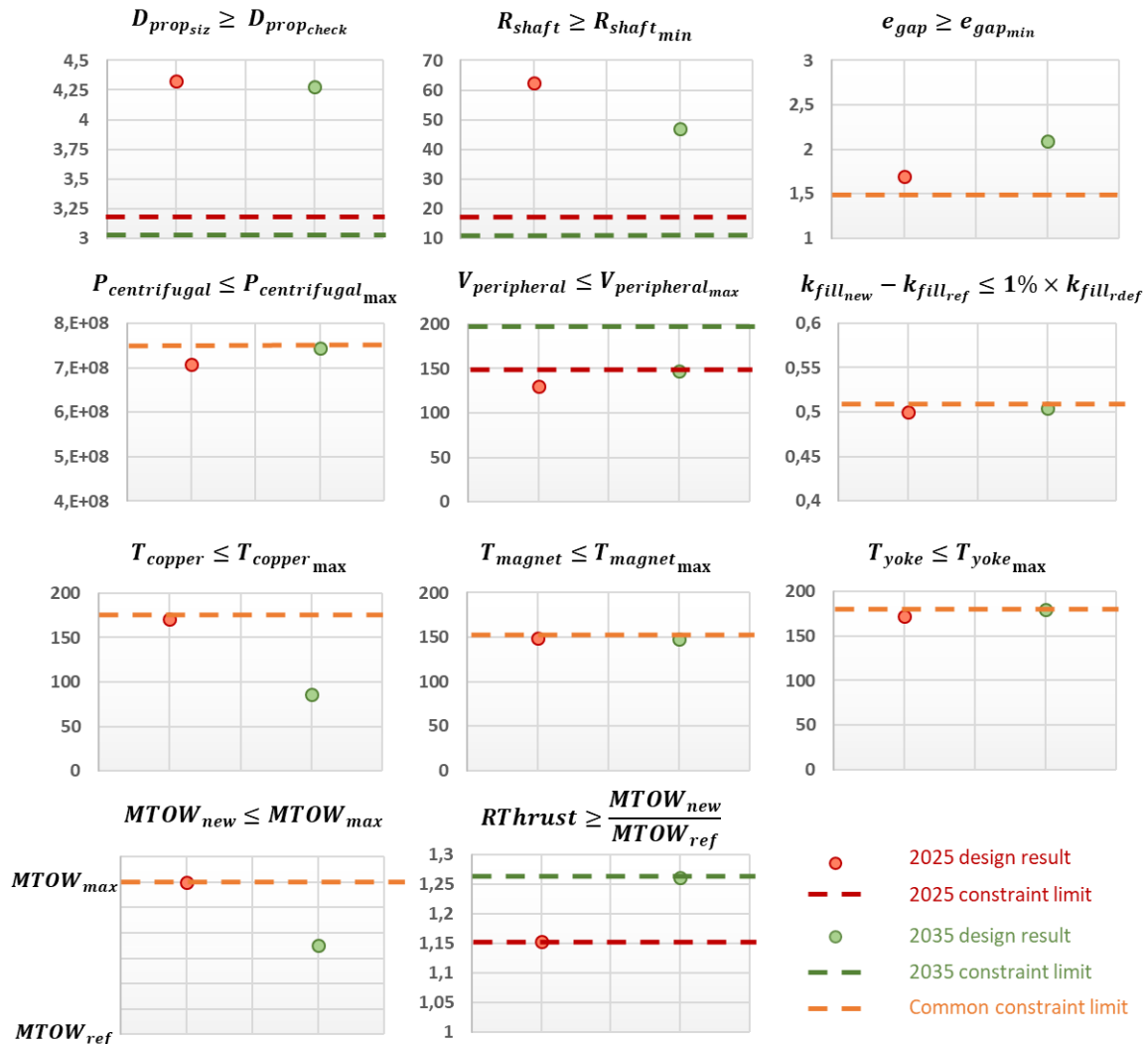


Fig. IV-48 : 2025 and 2035 dashboard of optimization constraints (optimal hybridization scenario).

Regarding the constraints (see Fig. IV-48):

- The oversize of the propeller is once again seen, the required values for the propulsion are around 3m while the design values are above 4m.
- The shaft radius is not a main constraint; the design value is higher than the limit (the minimum value is given by the bearing datasheets).
- The mechanical air gap thickness limit has been reached during the 2025 optimal integrated design in order to maintain an interesting specific power at aircraft level. With the winding cooling system, the mechanical air gap thickness is less restrictive.
- Two constraints have been set for the limitation of rotationnal speed of the actuator, a centrifugal pressure constraint and a peripheral speed limit. The most important constraint is the centrifugal pressure because the peripheral speed limit has not been reached for both optimizations. The design of the electric motor is so compact for the 2035 target that the centrifugal pressure on the carbon sleeve has reached the limit.
- The fill factor has remained close to the reference design value (0,5) in order to avoid undersizing at the actuator level.

- The Joule and Iron losses in the teeth are no longer constraining for the sizing of the actuator with a more efficient cooling system (2035 design results) in contact with copper windings and close to the stator teeth ($T_{copper} \leq T_{copper_max}$).
- Furthermore, the temperature in the stator yoke has reached the thermal limit, caused by the increased iron losses in the yoke ($T_{yoke} \leq T_{yoke_max}$). This is again a strong sizing constraint because of its connection with the stator yoke thickness and consequently the specific power of the electric actuator.
- The magnet temperature is a strong limitation too, this temperature is directly linked to the magnet thickness, thus the performance of the electric machine.
- At aircraft level, the limit MTOW has been reached for the 2025 optimization, this constraint allows the optimizer to lead the design to a hybrid-electric aircraft, without this constraint the optimizer would converge to full-electric one: the design has reached the limit of the validity domain. The 2035 optimization has lead to a lighter aircraft taking the same EMS strategy as 2025 into account.
- Finally, the snowball effect constraint ($R_{thrust} \geq \frac{MTOW_{new}}{MTOW_{max}}$) is the limit of convergence for our MDO process. The process of designing the hybrid-electric aircraft from a conventional aircraft stops when the required thrust of the aircraft corresponds to the weight ratios (assumption of constant glide in cruise). It is thus normal to see the 2 optimizations converging towards these 2 own limits.

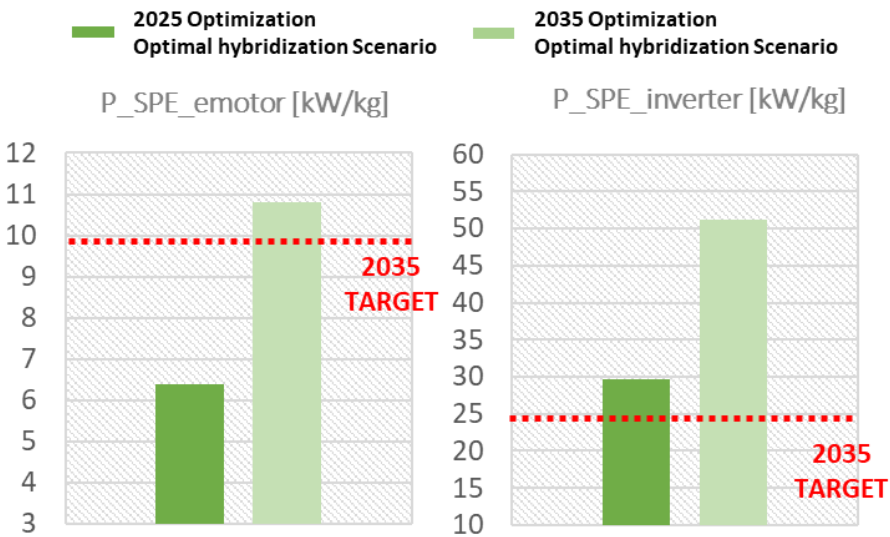


Fig. IV-49: Specific power of the electrical components found by optimization of 2025 and 2035 (optimal hybridization scenario).

The previous figure displays the strong increase in terms of specific powers for both power electronic and eMotors. The results obtained for 2035 assessments are beyond the 2035 targets (i.e. 25kW/kg for power electronics and 10kW/kg for eMotors). This result shows, one more time, the prime importance of the electro thermal coupling.

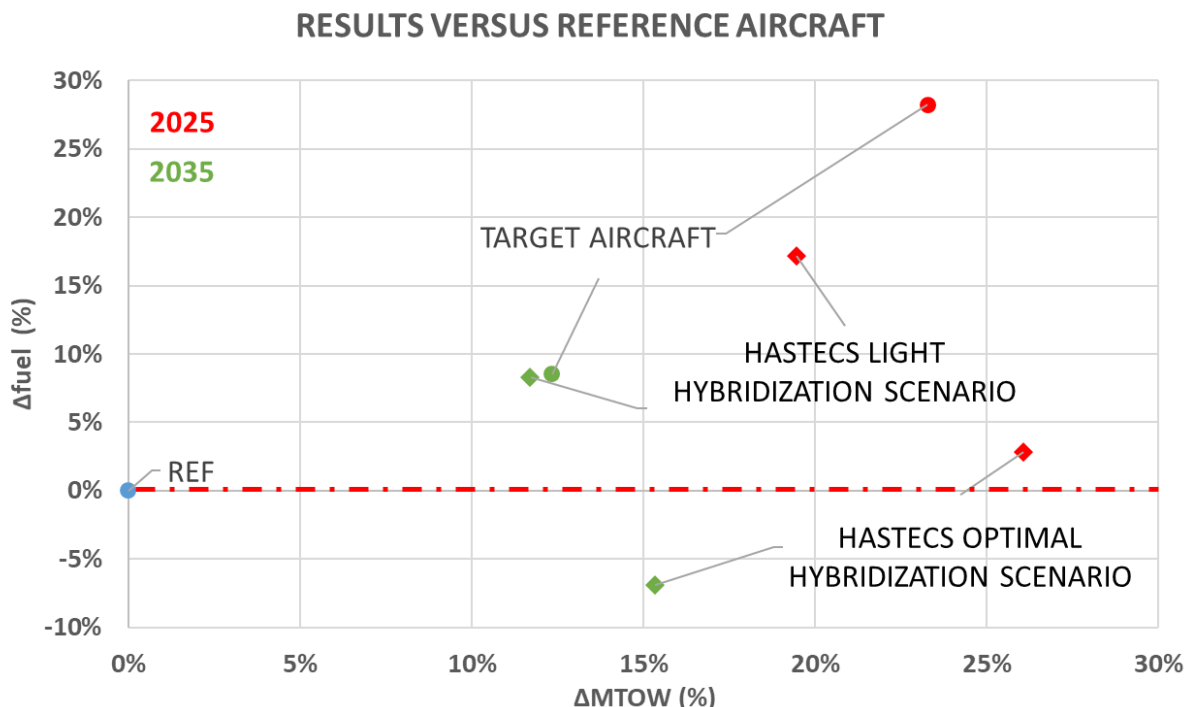


Fig. IV-50: Relative deviations in MTOW and fuel mass with respect to the reference thermal aircraft

"Target Aircraft" means that devices are simply modelled through specific power coefficients

"HASTECS XXX" means that sizing models (see chapter II) are used in optimization

Finally, by completing the relative deviations in the fuel vs MTOW plan with reference to a conventional full thermal-propulsion aircraft, the green diamonds display a less fuel-consuming solution for "target 2035".

The "HASTECS 2035" results coincide with the "target" results of the 2035 aircraft with a light hybridization scenario (8% ΔM_{fuel} and 12% $\Delta MTOW$). This particular case shows the coherence between rough assumptions on power densities and the results obtained with a multi-disciplinary design optimization approach based on sizing models.

A more fuel-efficient solution has emerged for the "2035 target" (-7% ΔM_{fuel}), resulting from the optimized overall performance of the chain as well as the fuel savings made by the use of a fuel cell. Note the weight of the aircraft is still 15% higher due to the addition of the electrical components of the powertrain.

IV.5 Conclusion.

Through the trends emphasized after several optimizations conducted at component (Emotor) and system level, this chapter has allowed us to reinforced the understanding of main couplings in that complex and multidisciplinary powertrain. The multiple analysis completes the trends shown off from the sensitivity analysis proposed in chapter 3. Among these trends, it is clear that sizing of electromechanical components is strongly constrained by the electro thermal coupling: the integration performance of actuators is directly driven by the thermal cooling performance. It is then important to include thermal sizing models which allow the estimation of temperature profiles over the whole flight mission. In our case study where the high power demand phases correspond to relatively short duration sequences (take off, climb), the involvement of thermal capacitances and transient thermal phenomena has been proved to be essential in terms of sizing. With reference to actuator model sized with quasi static (“R only”) thermal models, transient thermal model based optimization has allowed to multiply the power density by 3!

The multidisciplinary optimization of the electro-propulsion unit (propeller + gearbox + electric motor + inverter), taking thermal and partial discharges studies into account, has highlighted the importance of certain system parameters:

- the DC bus voltage remains an important parameter strongly coupling these devices (cable, inverter and motor).
- Geometrical parameters of actuators are of course also important as they constrain the winding sizing of the electric motor, this latter being coupled with insulation (partial discharges) constraints and also with the field weakening strategy which is applied along the flight mission: many results have shown that the field weakening is clearly adapted according to the geometry of the actuator.
- The propeller size (diameter) has been strongly oversized in system oriented optimization. Even if such oversizing increases the device (propeller) weight, it also increases significantly its efficiency lowering the power demand of all devices situated upstream in the powertrain. This latter aspect is a clear example of “property emergence” that only occur at system level: a typical systemic issue”.

The complete looped process at aircraft level makes possible to integrate interactions between fields. A complete MDO process has then allowed find the best trade-offs between weight and efficiency of electrical, thermal and mechanical components in order to obtain the optimum solution in terms of fuel mass consumption. However, the complexity of this MDO process pushes designers towards limits in terms of computation cost: indeed, optimizations solved with an “up to date” personal computer have lasted between 8 and 15 days for the whole powertrain optimization involving the management strategy while optimization of motor weight lasted only 1 day of computation!

Two successive management strategy have been proposed: a first (“light hybridization scenario”) setting a priori the hybrid ratio to use the electric source (fuel cell) only during taxi and descent. These hybrid ratios have been released in the second “optimal hybridization scenario” for which the fuel cell sizing is adapted by optimization to minimize the kerosene consumption along the whole mission. In that case, hydrogen is burnt during the whole mission at taxi and descent phases but also during climb and cruise: the corresponding optimization results show that heavier but less CO₂ emitting aircrafts would be possible.

The last analysis (see Fig. IV-49 & Fig. IV-50) has synthesized the importance of technology improvements especially involving two axis related to specific power and efficiency variations:

- The power density is firstly essential because it will induce sizing variations amplified by the through snowball effects on the whole propulsion chain, thus varying fuel consumption.
- Once a new maximum take-off weight has been estimated by the looped process, the efficiency in turn influences the gas turbine fuel consumption. An increased efficiency downstream of the powertrain will lead to lower power constraints on upstream devices reducing all the more the power demand on both sources (thermal and/or electrical), consequently lowering aircraft fuel burn.

Based on that results, the HASTECs framework is now in an intermediate stage between conventional all-thermal aircrafts and future electrically-powered aircrafts; these studies are still necessary in order to more fully anticipate the possibilities and challenges of a zero-emission aircraft potential.

CONCLUSION

Integrating a hybrid-electric propulsion system into an aircraft brings additional complexity compared to the conventional full thermal powertrains. Many interactions are present in the design of an aircraft. Its structure is designed by the propulsion thrust vs drag balance and is also directly influenced by the embedded mass to take off the aircraft: this latter aspect involves snowball effects which are specific in aeronautics as supplementary transported kilos involves an increase of the structure surface consequently with additional penalties on fuel burn and transported kerosene. In order to integrate all phenomena, reduced and specific design models must be implemented in a problem to design the whole aircraft in an optimal way: "this process is called Multidisciplinary Design Optimization (MDO)". The MDO approach makes easier to understand couplings between components.

Even if the efficiency and specific power of the electrical components are excellent, the hybrid propulsion system (due to its more complex architecture) will inevitably be penalized in terms of embedded weight with respect to a full thermal reference aircraft.

However, it can be noticed that only the energy point of view has been focused in our work. Supplementary potential gains offered by electric powertrains are shortly reminded in the first chapter but are not assessed in the study. Indeed, the electrification of the propulsion system is leading to rethink new aircraft architectures, in particular distributed propulsion. The scalability and dynamic of electrical component is better than thermal components: distributing propulsion permits to blow the entire wing for example, bringing a lift gain which improves stall performance, thus allowing reduced sizing of the wings. Distributed propulsion may also provide a certain degree of safety against engine failure, as the propulsion is much more robust with several actuators. While thermal engine efficiency decreases with altitude contrarily to electric motors, which constitutes another advantage of the electric propulsion. These numerous advances have also led to the introduction of new aircraft concepts: Urban Air Mobility (UAM). These VTOLs are mostly electrically powered and have static flight performance allowing them to land on platforms such as helicopters. The aircraft electrification promises to be increasingly present in the aerial landscape.

The HASTECS project is definitely in line with this innovative dynamic, the goal being to couple several technological studies with the integrated process proposed in that thesis in order to optimize the sizing of the hybrid-electric propulsion system. The studies resulting from the technological developments of the various work packages make it possible to provide models for an integrated design by optimization. The problem is clearly multidisciplinary because of the number of involved themes: thermal, electromagnetic, power electronics, electrical networks, partial discharges, electric machines.

All the models are presented in chapter II and completed by the appendices at the end of this thesis in order to illustrate the level of precision and complexity of the models integrated in the optimization.

The global sensitivity analysis presented in the chapter III was the first study to emphasize these interactions between components. The sensitivity analysis was based on Sobol indices. An initial global study was carried out, highlighting the first-order impact of power densities and efficiency on aircraft performance. Specific power has a major impact on aircraft performance (weight and fuel consumption), indeed the snowball effect leads to the aircraft resizing. Efficiency also has a huge impact on aircraft fuel consumption, all devices downstream in the powertrain impacting on the sizing of the gas turbine and therefore on its consumption. The sensitivity analysis at component level has highlighted the importance of the sizing constraints, some parameters that would be sensitive from a mathematical point of view are no longer sensitive by taking the actual constraints into account. The study of a set of electromechanical components (propeller + gearbox + electric motor) with and without constraints has highlighted the sensitivities of each parameter with their interactions. Without taking account of the actuator constraints, the propeller and its gearbox were not so sensitive to the sub system efficiency, but, taking the thermal and peripheral speed constraints into account, the propeller diameter and the gearbox ratio has become among the most sensitive variables of the electro-propulsion unit. These results have been confirmed by the overall optimization of the propulsion system.

In the chapter IV, several levels of optimizations have been studied. The first level of optimization is at “component level” dealing with the electromechanical actuator which is probably the most sensitive of the integrated design. In the HASTECs project, three complementary technological developments have been performed around the electromechanical actuator: the actuator design, its cooling and the partial discharges constraints in windings. The first optimization study has highlighted the multidisciplinary context of the design of an electromechanical actuator and its sensitivity to cooling performance. The sizing of an electrical component is directly related to its cooling system which is definitely the most sensitive factor. This part of the study has shown that using the thermal capacitances of the actuator greatly helps to relieve thermal constraints which reduces the volume of the actuator.

The optimization of the complete propulsion system makes it possible to take into account all the interaction phenomena between components, in particular between propeller, gearbox and electric motor. The sensitivity analysis performed in the previous chapter has predicted the results obtained by the optimization. The improvement in the power density of the electromechanical actuator is directly linked to the performance of the propeller and its gearbox; a lighter engine will lead to an oversizing of the aero-propulsion components (propeller-gearbox). Fuel economy is possible by improving efficiency in the very high power phases: this improvement is made possible thanks to the oversizing of the propeller diameter. This latter issue is a typical example of “emergence property”, rather usual in systemic studies: indeed, the propeller oversizing emerges only through the integrated design coupling all devices in a whole system!

But an aircraft would really save fuel burn when the power sharing between both sources in the hybrid architecture is released. The rest of the study has focused on a complete optimization of the propulsion system sizing, also taking the hybridization ratios as decision

variables during the flight mission: an adaptation of the optimization problem formulation has been proposed to reduce its complexity; finally, only the fuel cell stack power has been added as supplementary decision variable. By changing hybridization ratio during the mission, the auxiliary electrical source is more or less used to save fuel used by the turboshafts. The mass of the hydrogen storage becomes more cumbersome in our case and a new constraint is reached related to the maximum weight allowed by the aircraft without changing its wingspan (initial assumption).

The optimal integrated design of a hybrid-electric aircraft has emphasized and partly solved several key locks on the design of the powertrain components. Thermal issue plays a major role in the design since the temperature limits are reached at the critical points of the components (coil head, stator yoke and magnets). This issue is also fundamental for power electronics, but high performance two-phase cooling system (CPLIP) has tackled the problem to offer highly integrated power electronic systems. The study of partial discharges allows to find the optimal compromise on the DC bus value. The higher the voltage value, the more insulation thickness will have to be added. On the other hand, increasing this voltage value also reduces the cable mass and more generally the current flowing through the electrical components, thus their mass. In addition to the mass issue, the powertrain efficiency can be improved thanks mainly to the oversizing of the downstream elements of the chain (propeller, gearbox). At the global aircraft level, the nominal power rating of fuel cells has a clear impact on the reduction of kerosene consumption.

Finally, the optimal hybrid-electric aircraft will tend to be heavier than its predecessors but will consume less fuel. However, such a propulsion system brings with it a complexity of control, design and integration issues. Despite the fact that the aircraft will consume slightly less fuel, the cost at purchase is far from derisory compared to a conventional aircraft. The addition of electrical components, combined with an oversize of the mechanical devices (gearbox, propeller) will also increase the price of the aircraft. These elements make the concept of hybrid electric propulsion less attractive.

Several issues may be of interest for future studies:

- The linear approximation between thrust and mass (MTOW) ratio has allowed us to tackle the snowball effect and the interaction between the powertrain design and the aerodynamic structure. However, the simplification assumption has strong limits in terms of MTOW range. Coupling the electric powertrain design with aerodynamic simplified design seems necessary to explore new concepts of aircraft, typically for hydrogen based aircrafts.
- This latter issue would lead to an increase of the design complexity which was even really high with our optimization problem (remember that several days ~10-15) of computation was necessary for solving the more complex problem in our thesis (with up to date personal computer without parallel computing). A general methodological thinking on the “MDO approach”, splitting the optimization process with several hierarchical levels with imbricated loops (multi level optimization) is clearly necessary beyond our application to hybrid electric design.

- In terms of architecture, the project leader of HASTECS (i.e. Airbus) has proposed to focus on series hybrid chain, being the most critical in terms of technological constraints (with the highest electric power). As shown in J. Thauvin's thesis, other structures as parallel architectures may be more appropriate in terms of MTOW and should be studied coupled with technological model and optimization.
- However, the main technological breakthrough, certainly of major interest, is the zero emission aircraft powered entirely by fuel cells: it is clearly the main prospect of this thesis.

REFERENCES

- [1] “IATA - Healthy Passenger Demand Continues in 2018 with Another Record Load Factor.” [Online]. Available: <https://www.iata.org/en/pressroom/pr/2019-02-07-01/>. [Accessed: 18-Mar-2020].
- [2] EUROCONTROL, “Press release Press release.”
- [3] “Eurocontrol Predicts A Bleak Winter Ahead For European Aviation - Simple Flying.” [Online]. Available: <https://simpleflying.com/eurocontrol-european-winter-predictions/>. [Accessed: 28-Dec-2020].
- [4] “Welcome to Clean Sky | Clean Sky.” [Online]. Available: <https://www.cleansky.eu/>. [Accessed: 25-Feb-2021].
- [5] AIRBUS, “GMF 2019-2038 Airbus Commercial Aircraft book,” 2019. [Online]. Available: <http://gmf.airbus.com/>. [Accessed: 18-Mar-2020].
- [6] European Commission, “European aeronautics: a vision for 2020.”
- [7] European Commission, “Flightpath 2050 Europe’s vision for aviation: Report of the high level group on aviation research,” p. 28, 2011, doi: 10.2777/50266.
- [8] IATA, “Technology Roadmap to 2050,” *International Air Transport Association*, 2013. [Online]. Available: <https://www.iata.org/contentassets/8d19e716636a47c184e7221c77563c93/technology20roadmap20to20205020no20foreword.pdf>.
- [9] R. Thomson *et al.*, “Aircraft Electrical Propulsion – Onwards and Upwards,” *Roland Berger*, 2018. [Online]. Available: www.rolandberger.com.
- [10] “Would you pledge not to fly for a year? - BBC News.” [Online]. Available: <https://www.bbc.com/news/av/world-europe-46362159/the-two-swedish-mums-who-want-people-to-give-up-flying-for-a-year>. [Accessed: 18-Mar-2020].
- [11] “Electric propulsion is finally on the map — Roland Berger.” [Online]. Available: <https://www.rolandberger.com/fr/Point-of-View/Electric-propulsion-is-finally-on-the-map.html>. [Accessed: 18-Mar-2020].
- [12] J. Thauvin, “Exploration de l'espace de conception d'un avion régional hybride par optimisation multidisciplinaire.,” PhD Thesis, Institut National Polytechnique de Toulouse (Toulouse INP), 2018.
- [13] SAFRAN, “SAFRAN AND AVIATION-S ELECTRIC FUTURE - Press Kit Paris Air Show 2019,” 2019.
- [14] R. C. AKLI, “Conception systémique d'une locomotive hybride autonome. Application à la locomotive hybride de démonstration et d'investigations en énergétique LHyDIE développée par la SNCF,” PhD Thesis, Institut National Polytechnique de Toulouse (Toulouse INP), 2008.

-
- [15] TURBOTECH, “Innovative turbines, Turboprops, Turbogenerators & Range-Extenders.” [Online]. Available: <https://www.turbotech-aero.com/>. [Accessed: 18-Mar-2020].
 - [16] AIRBUS, “Clean Sky 2 - Helicopters - Airbus.” [Online]. Available: <https://www.airbus.com/newsroom/news/en/2016/06/clean-sky-2.html>. [Accessed: 18-Mar-2020].
 - [17] J. R. Welstead, D. Caldwell, R. Condotta, and N. Monroe, “An overview of the layered and extensible aircraft performance system (Leaps) development,” *AIAA Aerosp. Sci. Meet. 2018*, no. 210059, 2018, doi: 10.2514/6.2018-1754.
 - [18] K. V. Papathakis, P. A. Burkhardt, D. W. Ehmann, and A. M. Sessions, “Safety Considerations for Electric, Hybrid-Electric, and Turbo-Electric Distributed Propulsion Aircraft Testbeds,” 2017, doi: 10.2514/6.2017-5032.
 - [19] S. Clarke, M. Redifer, K. Papathakis, A. Samuel, and T. Foster, “X-57 Power and Command System Design,” in *IEEE Transportation Electrification Conference and Expo (ITEC)*, 2017, doi: 10.1109/ITEC.2017.7993303.
 - [20] K. A. Deere *et al.*, “Computational Component Build-up for the X-57 Distributed Electric Propulsion Aircraft,” in *2018 AIAA Aerospace Sciences Meeting*, 2018, doi: <https://doi.org/10.2514/6.2018-1275>.
 - [21] J. Murray and J. Lechniak, “The LEAPTech Experiment Approach Results Recommendations,” 2016. .
 - [22] J. Thauvin, G. Barraud, X. Roboam, B. Sareni, M. Budinger, and D. Leray, “Hybrid propulsion for regional aircraft: A comparative analysis based on energy efficiency,” *2016 Int. Conf. Electr. Syst. Aircraft, Railw. Sh. Propuls. Road Veh. Int. Transp. Electrif. Conf. ESARS-ITEC 2016*, 2016, doi: 10.1109/ESARS-ITEC.2016.7841392.
 - [23] K. R. Antcliff and F. M. Capristan, “Conceptual design of the parallel electric-gas architecture with synergistic utilization scheme (PEGASUS) concept,” *18th AIAA/ISSMO Multidiscip. Anal. Optim. Conf. 2017*, no. June, pp. 1–15, 2017, doi: 10.2514/6.2017-4001.
 - [24] N. K. Borer *et al.*, “Design and performance of the NASA SCEPTOR distributed electric propulsion flight demonstrator,” in *16th AIAA Aviation Technology, Integration, and Operations Conference*, 2016, pp. 1–20, doi: 10.2514/6.2016-3920.
 - [25] J. Hermetz, M. Ridel, and C. Doll, “Distributed electric propulsion for small business aircraft a concept-plane for key-technologies investigations,” in *ICAS 2016*, 2016, p. 11.
 - [26] E. Dillinger *et al.*, “Handling qualities of ONERA’s small business concept plane with distributed propulsion,” in *ICAS 2018*, 2018, p. 10.
 - [27] A. Arntz, O. Atinault, D. Destarac, and A. Merlen, “Exergy-based aircraft aeropropulsive performance assessment: CFD application to boundary layer ingestion,” *32nd AIAA Appl. Aerodyn. Conf.*, 2014, doi: 10.2514/6.2014-2573.
 - [28] J. S. Gray, “Design Optimization of a Boundary Layer Ingestion Propulsor Using a Coupled Aeropropulsive Model,” PhD Thesis, University of Michigan, 2018.

-
- [29] R. H. Jansen, C. Bowman, A. Jankovsky, R. Dyson, and J. Felder, "Overview of NASA electrified aircraft propulsion research for large subsonic transports," *53rd AIAA/SAE/ASEE Jt. Propuls. Conf.* 2017, pp. 1–20, 2017, doi: 10.2514/6.2017-4701.
- [30] D. J. Sadey, J. T. Csank, P. A. Hanlon, and R. H. Jansen, "A generalized power system architecture sizing and analysis framework," *2018 Jt. Propuls. Conf.*, pp. 1–11, 2018, doi: 10.2514/6.2018-4616.
- [31] A. Yildirim, J. S. Gray, C. A. Mader, and J. Martins, "Aeropropulsive Design Optimization of a Boundary Layer Ingestion System," pp. 1–23, 2019, doi: 10.2514/6.2019-3455.
- [32] J. Welstead *et al.*, "Overview of the NASA STARC-ABL (Rev . B) Advanced Concept," Washington, DC, 2017.
- [33] J. L. Felder, H. D. Kim, and G. V. Brown, "Turboelectric distributed propulsion engine cycle analysis for hybrid-wing-body aircraft," *47th AIAA Aerosp. Sci. Meet. Incl. New Horizons Forum Aerosp. Expo.*, no. January, pp. 1–25, 2009, doi: 10.2514/6.2009-1132.
- [34] L. Bruno, "Turboelectric Distributed Propulsion in a Hybrid Wing Body Aircraft," in *20th International Society for Airbreathing Engines (ISABE 2011)*, 2011, vol. 53, no. 9, pp. 1689–1699, doi: 10.1017/CBO9781107415324.004.
- [35] K. P. Duffy and R. H. Jansen, "Turboelectric and Hybrid Electric Aircraft Drive Key," *2018 AIAA/IEEE Electr. Aircr. Technol. Symp.*, pp. 1–9, 2018.
- [36] J. L. Felder, "NASA N3-X with Turboelectric Distributed Propulsion," *IMechE Disruptive Green Propuls. Technol. Conf.*, p. 18, 2014, doi: 2060/20150002081.
- [37] P. Schmollgruber *et al.*, "Multidisciplinary exploration of dragon: An onera hybrid electric distributed propulsion concept," *AIAA Scitech 2019 Forum*, 2019, doi: 10.2514/6.2019-1585.
- [38] P. Schmollgruber *et al.*, "Multidisciplinary Design and performance of the ONERA Hybrid Electric Distributed Propulsion concept (DRAGON)," in *American Institute of Aeronautics and Astronautics (AIAA)*, 2020, doi: 10.2514/6.2020-0501.
- [39] "Project 804: The Opportunity - YouTube." [Online]. Available: <https://www.youtube.com/watch?v=mTWLebimFOk>. [Accessed: 18-Mar-2020].
- [40] "Ampaire Electric EEL™ - YouTube." [Online]. Available: <https://www.youtube.com/watch?v=KIM50ILeK9Q>. [Accessed: 18-Mar-2020].
- [41] "Daher, Airbus et Safran s'associent pour développer EcoPulse™, un démonstrateur d'avion à propulsion hybride distribuée - Daher." [Online]. Available: <https://www.daher.com/daher-airbus-et-safran-sassocient-pour-developper-ecopulse-un-demonstrateur-davion-a-propulsion-hybride-distribuee/>. [Accessed: 18-Mar-2020].
- [42] "VoltAero hybrid-electric flight testing with the Cassio 1 testbed aircraft - YouTube." [Online]. Available: <https://www.youtube.com/watch?v=X5mUGg6DFw4>. [Accessed: 18-Mar-2020].

-
- [43] “E-Fan X - Electric flight - Airbus.” [Online]. Available: <https://www.airbus.com/innovation/future-technology/electric-flight/e-fan-x.html>. [Accessed: 18-Mar-2020].
 - [44] “Zunum Aero.” [Online]. Available: <https://zunum.aero/>. [Accessed: 18-Mar-2020].
 - [45] “Découvrez le nouveau système de propulsion hybride électrique ‘by Safran’ - YouTube.” [Online]. Available: <https://www.youtube.com/watch?v=7wfZyZU4Io8>. [Accessed: 18-Mar-2020].
 - [46] E. Joubert, D. Chapuis, D. Esteyne, J.-C. Lambert, O. Siri, and D. Müller-Wiesner, “The E-FAN all electrical aircraft demonstrator and its industrialization.,” in *ICAS 2016*, 2016.
 - [47] L. Juvé, J. Fosse, E. Joubert, and N. Fouquet, “Airbus group electrical aircraft program, the E-FAN project,” in *52nd AIAA/SAE/ASEE Joint Propulsion Conference, 2016*, 2016, doi: 10.2514/6.2016-4613.
 - [48] F. Anton, “eAircraft: Hybrid-elektrische Antriebe für Luftfahrzeuge,” 2019. [Online]. Available: https://www.bbaa.de/fileadmin/user_upload/02-preis/02-02-preistraeger/newsletter-2019/02-2019-09/02_Siemens_Anton.pdf. [Accessed: 16-Jan-2021].
 - [49] “Our Products | magniX.” [Online]. Available: <https://magnix.aero/products/#>. [Accessed: 19-Mar-2020].
 - [50] “Magni 500 Specification - Google Drive.” [Online]. Available: https://drive.google.com/file/d/1Lxbs4wx_0a_HOSaR0l0nLdMbOroXPJvu/view. [Accessed: 19-Mar-2020].
 - [51] “Harbour Air and magniX Announce Successful Flight of World’s First Commercial Electric Airplane – Harbour Air Seaplanes: World’s Largest Seaplane Airline – Since 1982 – Harbour Air.” [Online]. Available: <https://www.harbourair.com/harbour-air-and-magnix-announce-successful-flight-of-worlds-first-commercial-electric-airplane/>. [Accessed: 19-Mar-2020].
 - [52] M. Westlake, “Electrifying flight,” *Aerosp. Am.*, vol. 49, no. 9, pp. 8–10, 2011.
 - [53] “Our stories - Introducing ACCEL –Rolls-Royce.” [Online]. Available: <https://www.rolls-royce.com/media/our-stories/innovation/2018/introducing-accel.aspx>. [Accessed: 19-Mar-2020].
 - [54] K. Memmott and E. Jacobson, “YASA 750 Product Sheet,” *Internal Auditor*. [Online]. Available: <https://www.yasa.com/wp-content/uploads/2018/01/YASA-750-Product-Sheet.pdf>.
 - [55] “CityAirbus - Vehicle demonstrators - Airbus.” [Online]. Available: <https://www.airbus.com/innovation/urban-air-mobility/vehicle-demonstrators/cityairbus.html>. [Accessed: 19-Mar-2020].
 - [56] NASA, “NASA to Develop a Novel Approach for All-Electric Aircraft Using Cryogenic Liquid Hydrogen as Energy Storage - FuelCellsWorks.” [Online]. Available: <https://fuelcellsworks.com/news/nasa-to-develop-a-novel-approach-for-all-electric->

aircraft-using-cryogenic-liquid-hydrogen-as-an-energy-storage/. [Accessed: 19-Mar-2020].

- [57] “Clean Hydrogen for Europe | Hydrogen.” [Online]. Available: <https://hydrogèneurope.eu/clean-hydrogen-europe>. [Accessed: 28-Dec-2020].
- [58] McKinsey & Company, *Hydrogen-powered aviation*, no. May. 2020.
- [59] “Avions Mauboussin obtient une subvention de 800 000 €.” [Online]. Available: <https://www.air-cosmos.com/article/avions-mauboussin-obtient-une-subvention-de-800-000-24290>. [Accessed: 26-Feb-2021].
- [60] “Airbus reveals new zero-emission concept aircraft - Innovation - Airbus.” [Online]. Available: <https://www.airbus.com/newsroom/press-releases/en/2020/09/airbus-reveals-new-zeroemission-concept-aircraft.html>. [Accessed: 26-Feb-2021].
- [61] “Skai revises targets for its liquid-hydrogen, long-range eVTOL.” [Online]. Available: <https://newatlas.com/aircraft/alakai-skai-liquid-hydrogen-evtol-update/>. [Accessed: 26-Feb-2021].
- [62] “Essai nouvelle Toyota Mirai hydrogène : les taxis vont-ils l’adorer ?” [Online]. Available: <https://www.automobile-propre.com/essai-nouvelle-toyota-mirai-hydrogene-les-taxis-vont-ils-ladorer/>. [Accessed: 26-Feb-2021].
- [63] “Hopium Machina : une berline hydrogène française hors normes.” [Online]. Available: <https://www.h2-mobile.fr/actus/hopium-machina-berline-hydrogene-francaise-hors-normes/>. [Accessed: 26-Feb-2021].
- [64] “Le premier yacht à hydrogène dévoilé à Monaco.” [Online]. Available: <https://www.h2-mobile.fr/actus/premier-yacht-hydrogène-devoile-monaco/>. [Accessed: 26-Feb-2021].
- [65] ATR, “ATR 72-600 Datasheet,” 2020. [Online]. Available: http://www.atr-aircraft.com/wp-content/uploads/2020/07/Factsheets_-_ATR_72-600.pdf.
- [66] M. Pettes-Duler, X. Roboam, and B. Sareni, “Integrated design process of a hybrid electric propulsion system for future aircraft,” *Electrimacs 2019*, no. May, pp. 1–6, 2019, doi: https://doi.org/10.1007/978-3-030-37161-6_6.
- [67] X. Yi, A. Yoon, and K. S. Haran, “Multi-physics optimization for high-frequency air-core permanent-magnet motor of aircraft application,” *2017 IEEE Int. Electr. Mach. Drives Conf. IEMDC 2017*, 2017, doi: [10.1109/IEMDC.2017.8002293](https://doi.org/10.1109/IEMDC.2017.8002293).
- [68] L. Cheng, F. Zhang, S. Liu, and Z. Zhang, “Configuration method of hybrid energy storage system for high power density in More Electric Aircraft,” *J. Power Sources*, 2020, doi: [10.1016/j.jpowsour.2019.227322](https://doi.org/10.1016/j.jpowsour.2019.227322).
- [69] D. Zhang, J. He, and D. Pan, “A Megawatt-Scale Medium-Voltage High-Efficiency High Power Density ‘SiC+Si’ Hybrid Three-Level ANPC Inverter for Aircraft Hybrid-Electric Propulsion Systems,” *IEEE Trans. Ind. Appl.*, vol. 55, no. 6, pp. 5971–5980, 2019, doi: [10.1109/TIA.2019.2933513](https://doi.org/10.1109/TIA.2019.2933513).
- [70] D. Zhang, J. He, D. Pan, M. Dame, and M. Schutten, “Development of Megawatt-Scale

Medium-Voltage High Efficiency High Power Density Power Converters for Aircraft Hybrid-Electric Propulsion Systems," *2018 AIAA/IEEE Electr. Aircr. Technol. Symp. EATS 2018*, 2018, doi: 10.2514/6.2018-5007.

- [71] A. Iwaniuk, W. Wisniowski, and J. Zóltak, "Multi-disciplinary optimisation approach for a light turboprop aircraft-engine integration and improvement," *Aircr. Eng. Aerosp. Technol.*, vol. 88, no. 2, pp. 348–355, Mar. 2016, doi: 10.1108/AEAT-02-2015-0070.
- [72] A. Sgueglia and T. M. Young, "Wing-Body with distributed electric ducted fans," PhD Thesis, Institut Supérieur de l'Aéronautique et de l'Espace, 2020.
- [73] A. Gazaix *et al.*, "Industrial application of an advanced bi-level mdo formulation to an aircraft engine pylon optimization," in *AIAA Aviation 2019 Forum*, 2019, pp. 1–28, doi: 10.2514/6.2019-3109.
- [74] S. Kreuawan, F. Gillon, and P. Brochet, "Optimal design of permanent magnet motor using multidisciplinary design optimization," *Proc. 2008 Int. Conf. Electr. Mach. ICEM'08*, pp. 1–6, 2008, doi: 10.1109/ICELMACH.2008.4800108.
- [75] N. Bracikowski *et al.*, "Multi-physics design rules using lumped models for a permanent magnet synchronous machine," *Int. J. Appl. Electromagn. Mech.*, 2018.
- [76] D. Temple and M. Collette, "Understanding lifecycle cost trade-offs for naval vessels: minimising production, maintenance, and resistance," *Ships Offshore Struct.*, vol. 12, no. 6, pp. 756–766, Aug. 2017, doi: 10.1080/17445302.2016.1230039.
- [77] A. Matine *et al.*, "Optimal sizing of submarine cables from an electro-thermal perspective," *Eur. Wave Tidal Conf.*, 2017.
- [78] MIT, "Production of Thrust with a Propeller." [Online]. Available: <https://web.mit.edu/16.unified/www/FALL/thermodynamics/notes/node86.html>. [Accessed: 18-Mar-2019].
- [79] K. R. Antcliff, M. D. Guynn, T. V. Marien, D. P. Wells, S. J. Schneider, and M. T. Tong, "Mission analysis and aircraft sizing of a hybrid-electric regional aircraft," *54th AIAA Aerosp. Sci. Meet.*, no. January, pp. 1–18, 2016, doi: 10.2514/6.2016-1028.
- [80] A. J. Eyne3, "Airbus HASTECS deliverable."
- [81] M. Cheng, L. Sun, G. Buja, and L. Song, "Advanced electrical machines and machine-based systems for electric and hybrid vehicles," *Energies*, vol. 8, no. 9, pp. 9541–9564, 2015, doi: 10.3390/en8099541.
- [82] T. Finken, M. Felden, and K. Hameyer, "Comparison and design of different electrical machine types regarding their applicability in hybrid electrical vehicles," *Proc. 2008 Int. Conf. Electr. Mach. ICEM'08*, pp. 1–5, 2008, doi: 10.1109/ICELMACH.2008.4800044.
- [83] S. Touhami, "Analytical Sizing Models to Assess the Performances of High Specific Power Electric Motors for Hybrid Aircraft," PhD Thesis, Institut National Polytechnique de Toulouse (Toulouse INP), 2020.
- [84] S. Touhami, A. Zeaiter, M. Fénot, Y. Lefevre, and J. Llibre, "Electro-thermal Models and

Design Approach for High Specific Power Electric Motor for Hybrid Aircraft,” in *Aerospace Europe Conference*, 2020.

- [85] A. Petrowski, “Clearing procedure as a niching method for genetic algorithms,” *Proc. IEEE Conf. Evol. Comput.*, pp. 798–803, 1996, doi: 10.1109/icec.1996.542703.
- [86] C. Igel, N. Hansen, and S. Roth, “Covariance Matrix Adaptation for Multi-objective Optimization.”
- [87] A. Zeaiter, “Thermal modeling and cooling of electric motors application to the propulsion of hybrid aircraft,” PhD Thesis, Ecole Nationale Supérieure de Mécanique et d’Aérotechnique (ENSMA), 2020.
- [88] F. Accorinti, “Two-phase power electronics cooling solution design in air context answer to the objectives of the hybrid aircraft 2035.,” PhD Thesis, Ecole Nationale Supérieure de Mécanique et d’Aérotechnique (ENSMA), 2020.
- [89] P. Collin, “Design, taking into account the partial discharges phenomena, of the electrical insulation system (eis) of high power electrical motors for hybrid electric propulsion of future regional aircrafts,” PhD Thesis, Institut National Polytechnique de Toulouse (Toulouse INP), 2020.
- [90] Eyne3 and J. Allias, “Specification dossier for HASTECS,” 2018.
- [91] F. Paschen, “Ueber die zum Funkenübergang in Luft, Wasserstoff und Kohlensäure bei verschiedenen Drucken erforderliche Potentialdifferenz,” *Ann. Phys.*, vol. 273, no. 5, pp. 69–96, 1889, doi: 10.1002/andp.18892730505.
- [92] P. Collin, D. Malec, and Y. Lefevre, “Tool to predict and avoid Partial Discharges in stator slot of rotating motors fed by inverter,” in *Aerospace Europe Conference*, 2020.
- [93] N. Erroui, “Chaine de conversion forte puissance pour la propulsion aéronautique hybride,” PhD Thesis, Insititut National Polytechnique de Toulouse (Toulouse INP), 2019.
- [94] N. Erroui, N. Roux, and G. Gateau, “Pré-dimensionnement de Convertisseur de Très Forte Puissance pour une Application à la Propulsion Aéronautique Hybride,” in *JCGE 2017*, 2017.
- [95] F. Accorinti, V. Ayel, and Y. Bertin, “Steady-state analysis of a Capillary Pumped Loop for Terrestrial Application with methanol and ethanol as working fluids,” *Int. J. Therm. Sci.*, vol. 137, no. October 2018, pp. 571–583, 2019, doi: 10.1016/j.ijthermalsci.2018.10.036.
- [96] F. Accorinti *et al.*, “High-efficiency cooling system for highly integrated power electronics for hybrid propulsion aircraft,” *IEEE Int. Symp. Ind. Electron.*, vol. 2019-June, pp. 870–877, 2019, doi: 10.1109/ISIE.2019.8781086.
- [97] M. Tognan, “Preliminary delivery Battery & Fuel Cell metamodels; ‘HASTECS M6.1’ Technical report.”
- [98] G. Chastaing, “Indices de Sobol généralisés pour variables dépendantes,” PhD Thesis, Institut National Polytechnique de Grenoble (Grenoble INP), 2013.

-
- [99] M. Le Guyadec, L. Gerbaud, E. Vinot, and B. Delinchant, "Sensitivity analysis using Sobol indices for the thermal modelling of an electrical machine for sizing by optimization," *COMPEL - Int. J. Comput. Math. Electr. Electron. Eng.*, vol. 38, no. 3, pp. 965–976, 2019, doi: 10.1108/COMPEL-09-2018-0360.
 - [100] I. M. SOBOL, "Sensitivity Estimates for Nonlinear Mathematical Models," *Math. Mod. Comput. Exp.*, vol. 1, no. 4, pp. 407–414, 1993.
 - [101] F. Gamboa *et al.*, "Statistical inference for Sobol pick freeze Monte Carlo method," in *Statistics, Taylor & Francis: STM, Behavioural Science and Public Health Titles*, 2016, p. pp.881-902, doi: 10.1080/02331888.2015.1105803.
 - [102] M. Grandjacques, B. Delinchant, and O. Adrot, "Pick and Freeze estimation of sensitivity index for static and dynamic models with dependent inputs," *J. la Société Française Stat.*, vol. 157, no. 2, pp. 65-89–89, 2016.
 - [103] F. Gamboa, A. Janon, T. Klein, and A. Lagnoux, "Sensitivity analysis for multidimensional and functional outputs," *Electron. J. Stat.*, vol. 8, no. 1, pp. 575–603, 2014, doi: 10.1214/14-EJS895.
 - [104] Y. Lefevre, S. El-Aabid, J. F. Llibre, C. Henaux, and S. Touhami, "Performance assessment tool based on loadability concepts," *Int. J. Appl. Electromagn. Mech.*, vol. 59, no. 2, pp. 687–694, 2019, doi: 10.3233/JAE-171059.
 - [105] M. Pettes-Duler, B. Sareni, and X. Roboam, "Analyse de sensibilité d'un système de propulsion hybride électrique pour des futurs aéronefs," in *JCGE*, 2019.
 - [106] M. Pettes-Duler *et al.*, "Sensitivity analysis of a hybrid-electric aircraft powertrain based on Sobol indices," in *Aerospace Europe Conference*, 2020.
 - [107] S. Biser *et al.*, "Design space exploration study and optimization of a distributed turbo-electric propulsion system for a regional passenger aircraft," *AIAA Propuls. Energy 2020 Forum*, pp. 1–27, 2020, doi: 10.2514/6.2020-3592.
 - [108] M. Hepperle, "Aspects of Distributed Payload," *Present. Symp. Elektrisches Flieg. - Stuttgart 2016*, pp. 1–26, 2016.
 - [109] H. Ounis, B. Sareni, X. Roboam, and A. De Andrade, "Multi-level integrated optimal design for power systems of more electric aircraft," *Math. Comput. Simul.*, vol. 130, pp. 223–235, 2016, doi: 10.1016/j.matcom.2015.08.016.
 - [110] "Pulse Width Modulation for Power Converters: Principles and Practice - D. Grahame Holmes, Thomas A. Lipo." [Online]. Available: https://books.google.fr/books?hl=fr&lr=&id=ckETEAAQBAJ&oi=fnd&pg=PR13&dq=pulse+width+modulation+for+power+converters+principles+and+practice&ots=-_e-OJhnCV&sig=22tj0ocnVNPyU_086qZFqgFNG28#v=onepage&q=pulse width modulation for power converters principles. [Accessed: 19-Feb-2021].

APPENDIX

CONTENTS

APPENDIX A. ENVIRONMENT MODEL.....	179
APPENDIX B. PROPELLER MODEL.....	181
APPENDIX C. GEARBOX MODEL.....	185
APPENDIX D. TURBOSHAFT MODEL	189
APPENDIX E. CABLE MODEL	193
APPENDIX F. ELECTRIC MOTOR MODEL	195
APPENDIX G. ELECTRIC MOTOR COOLING MODEL	205
APPENDIX H. PARTIAL DISCHARGES IN THE SLOT.....	215
APPENDIX I. POWER ELECTRONICS AND ITS COOLING	223
APPENDIX J. FUEL CELL SYSTEM AND BATTERY MODEL.....	231
APPENDIX K. RECTIFIER AND GENERATOR EFFICIENCY AND WEIGHT ASSESSMENTS	235
APPENDIX L. MULTIDISCIPLINARY DESIGN OPTIMIZATION PROCESS OF A HYBRID ELECTRIC AIRCRAFT PROPULSION SYSTEM	237

APPENDIX A. ENVIRONMENT MODEL

The input and output of the environment model are summarized in the Table A.1:

Table A-1: Input/output variable used in the model:

INPUT VARIABLES		
$Altitude(t)$	[m]	Flight Altitude
$MACH(t)$	[−]	MACH speed
OUTPUT VARIABLES		
$P_{static}(t)$	[Pa]	Static Pressure
$P_{dynamic}(t)$	[Pa]	Dynamic Pressure
$\rho_{air}(t)$	[kg/m ³]	Air density
$T_{static}(t)$	[K]	Static Temperature
$T_{dynamic}(t)$	[K]	Dynamic Temperature
$V_{sound}(t)$	[m/s]	Sound speed

The process is illustrated in the Fig. A-1:



Fig. A-1: Process chart of the model.

From AIRBUS side, input data are related to [90]:

- Environmental aircraft data: $Altitude(t)$
- Mach speed along the mission profile: $MACH(t)$

It should be noted that both input data, i.e. flight altitude $Altitude(t)$ and Mach speed over the mission profile were provided by the Airbus company at the beginning of the HASTECS project.

Given these inputs, some examples of surrogate models are proposed to design the hybrid-electric power train of the studied aircraft. Readers will find more detailed models in [12]. An environment model is required to design different devices of the power train (turboshaft, propeller, thermal cooling, etc) over the flight mission. Main environment variables are derived:

Table A-1: Environmental model

$P_{static} = 101325 \times \left(1 - \frac{Altitude}{44331}\right)^{5,256}$	Static pressure [Pa]	(A-1)
$T_{static} = 288,15 - 0,0065 \times Altitude + DISA$	Static temperature [K]	(A-2)
$\rho_{air} = 0,0034837 \times \frac{P_{static}}{T_{static}}$	Air density [kg/m^3]	(A-3)
$P_{dynamic} = P_{static} \times (1 + 0,2 \times MACH^2)^{3,5}$	Dynamic pressure [Pa]	(A-4)
$T_{dynamic} = T_{static} \times (1 + 0,2 \times MACH^2)$	Dynamic temperature [K]	(A-5)
$V_{sound} = \sqrt{401,8 \times T_{static}}$	Sound speed [m/s]	(A-6)

Where $Altitude$ is related to the input flight mission is in meter, $DISA$ is the temperature difference from the International Standard Atmosphere (ISA). ρ_{air} is the air density in kg/m^3 . These variables will be used in particular in turboshaft and propeller models. Let us remind that other input requirements related to Altitude, MACH, Thrust and A/C speed (thus Aircraft power) mission profiles have been defined in section I.3.

APPENDIX B. PROPELLER MODEL

This appendix describes the design model for a variable-pitch propeller. The disk actuator theory permits to predict performance according to the propeller geometry. The propeller geometry is defined by the diameter and the rotation speed. The following input/output variables are used:

Table B-1: Input/output variables used in the propeller model.

INPUT VARIABLES (in bold blue, the decision variable for optimization)		
$\rho_{air}(t)$	[kg. m ⁻³]	Air density
$V_{A/C}(t)$	[m. s ⁻¹]	A/C Velocity
$T_{A/C}(t)$	[N]	A/C Thrust
D_{prop}	[m]	Propeller diameter
OUTPUT VARIABLES		
$P_{shaft}(t)$	[W]	Propeller Shaft Power
$\eta_{prop}(t)$	[%]	Propeller Efficiency
M_{prop}	[kg]	Propeller Mass
$N_{prop\max}$	[RPM]	Maximum propeller rotation speed
$D_{prop\check{}}$	[m]	Propeller diameter checking law

The propeller model is illustrated in Fig. B-1.

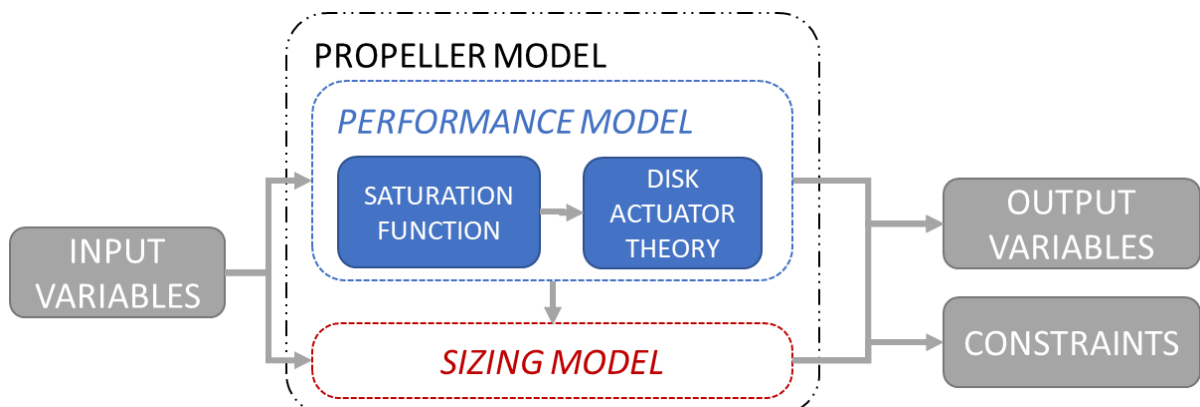


Fig. B-1: Process chart of the propeller model

B.1 Sizing model:

The ATR 72 based sizing point has been considered as a reference:

$D^{ref}_{prop} = 3,93 \text{ m}$	Propeller Diameter (m)
$M^{ref}_{prop} = 185 \text{ kg}$	Propeller mass (kg)
$N^{ref}_{prop} = 1200 \text{ RPM}$	Propeller rotational speed (RPM).
$P^{ref}_{max_{shaft}} = 2,4 \text{ MW}$	Maximum Propeller shaft power (MW)

A 6-blades variable-pitch propeller is considered. The propeller geometry is sized from two equations. The same tip speed limit is considered as for the ATR 72 propeller [65] used in [12]. The following relationships are based on the similitude principle which sets relationships between ratio of variables (X/X^{ref}) divided by reference variables: in our case, reference values are related to the ATR72 case:

Table B-1: Propeller design model

$D_{prop_{check}} = D^{ref}_{prop} \times \sqrt{\frac{P_{max_{shaft}}}{P^{ref}_{max_{shaft}}}}$	Checking rule for the propeller [m]	(B-1)
$N_{prop_{max}} = N^{ref}_{prop} \times \frac{D^{ref}_{prop}}{D_{prop}}$	Rotational speed of the propeller [RPM]	(B-2)
$M_{prop} = M^{ref}_{prop} \times \left(\frac{D_{prop}}{D^{ref}_{prop}} \right)^3$	Propeller mass estimation [kg]	(B-3)

B.2 Disk Actuator Theory:

The performance model used during simulations (over the mission profile) is based on the Disk Actuator Theory Eq (B-4) which defines shaft power versus thrust and aircraft speed ($V_{A/C}$).

$$P_{shaft} = \frac{1}{2k_{eff}} \left(V_{A/C} \cdot T_{vir} + \sqrt{\left(V_{A/C} \cdot T_{vir} \right)^2 + \frac{2T_{vir}^3}{\rho_{air} A_{prop}}} \right) \quad (B-4)$$

The thrust value (T_{vir}) is refined from the real input thrust ($T_{A/C}$) with a saturation function at low speed which is implemented in Eq (B-9).

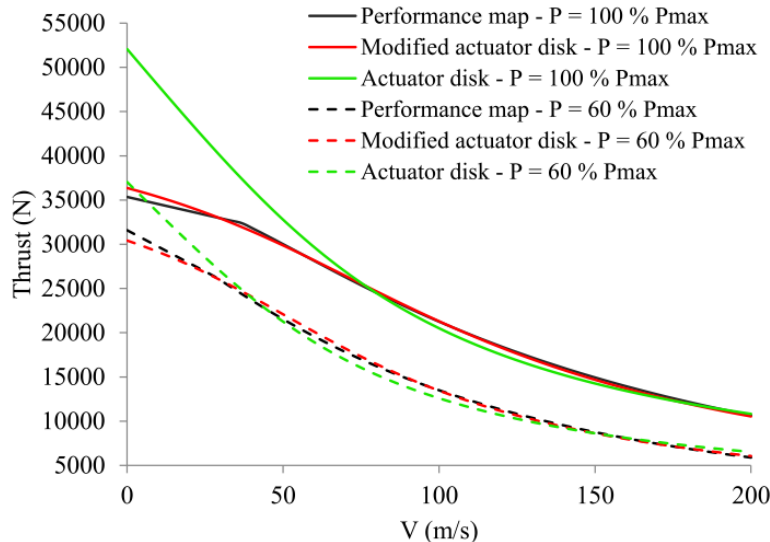


Fig. B-2: Comparison of propeller performance models for a 6-bladed propeller of 3.93 m diameter rotating at maximum tip speed at sea level [12].

In Eq (B-7), the maximum thrust T_{max} has been estimated versus the maximum shaft power. The use of the actuator disk theory during low speed phases tends to over-evaluate the propeller thrust (green lines in Fig. B-2). That is why a “virtual” thrust T_{vir} (red lines in Fig. B-2) is redefined in a saturation function Eq (B-9) from the real thrust $T_{A/C}$. $T_{A/C}$ comes from the aerodynamic input data set in section I.3.

B.3 Saturation function:

Table B-2: Detailed saturation function.

$kP = \frac{1}{\rho_{air}}$	$0,1 \leq kP \leq 1,5$	Saturation factor [-]	(B-5)
$k = 1.6 + \frac{V_{A/C}}{\frac{D_{ref_prop} \times N_{ref_prop}}{60}}$		Equivalent advance ratio [-]	(B-6)
$T_{max} = 10^{f(kP)} \cdot P_{max_shaft}$		Maximum thrust deliverable by the thrust [N]	(B-7)
$f(kP) = \alpha_{prop} + \beta_{prop} \times \log(kP)^{\gamma}$		Linear regression function of the saturation factor [-]	(B-8)
$T_{vir} = \left(\frac{2.k.T_{max}}{\pi} \right) \times \tan \left(\frac{\pi.T_{A/C}}{2.k.T_{max}} \right)$		Virtual thrust used in the disk actuator theory [N].	(B-9)

Where kP is the input value of the linear regression model set in Eq(B-8); ρ_{air} is the air density in kg/m^3 varying during the flight mission. $V_{A/C}$ is the aircraft speed in m/s also defined by the mission profile defined in section I.3. An equivalent advance ratio k for the saturation function has been imposed. $f(kP)$ is the linear regression function used by the model where α_{prop} , β_{prop} and γ are constant values. The modified disk actuator theory formula is modelled with a constant value $k_{eff} = 0.9$ and with the propeller disk area: $A_{prop} = \frac{\pi.D_{prop}^2}{4}$.

At the end of the process the efficiency of the propeller is determined by the equation (B-10):

$$\eta_{prop} = \frac{T_{A/C} \times V_{A/C}}{P_{shaft}} \quad (B-10)$$

B.4 Constraint:

A constraint on the shaft power has been added in the model in order to ensure that the propeller fulfill the mission Eq(B-11).

$$D_{prop} \geq D_{prop_{check}} \quad (B-11)$$

$D_{prop_{check}}$ is the propeller diameter allowing to face $P_{max_{shaft}}$.

The actual D_{prop} can be set (and possibly oversized) by the optimizer (see Chapter IV) fulfilling the previous equation.

APPENDIX C. GEARBOX MODEL

The required parameters for the gearbox model are the following:

Table C-1: Input/output variables used in the gearbox model.

INPUT VARIABLES (in bold blue, the 1 decision variable for optimization)		
R_{gbox}	[–]	Gearbox ratio
$P_{prop_{HP}}(t)$	[HP]	Maximum propeller shaft power
$RPM\% (t)$	[%]	Propeller rotation speed in per unit
$N_{prop_{max}}$	[RPM]	Maximum propeller rotation speed
OUTPUT VARIABLES		
M_{gbox}	[kg]	Gearbox mass
$P_{shaft_{emot}}(t)$	[W]	E-motor mechanical power
$T_{shaft_{emot}}(t)$	[Nm]	E-motor torque
$\Omega_{emot}(t)$	[rad/s]	E-motor rotation speed

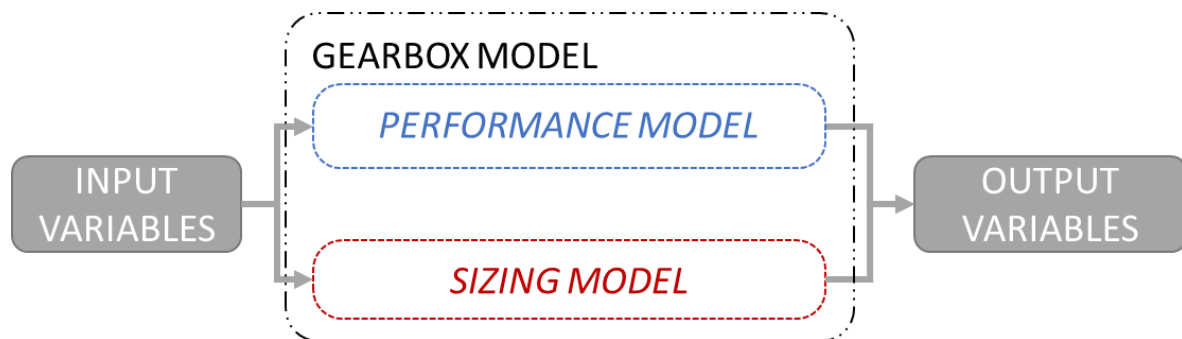


Fig. C-1: Process chart for the gearbox model.

C.1 Sizing model:

To determine the performance of the gearbox and its mass, a rotational speed profile is required. Several studies have been done with the aim of providing the maximum rotational speed during the mission respecting speed limits (cf Chapter I.3.1). The final rotational speed profile is given in Fig. C-2.

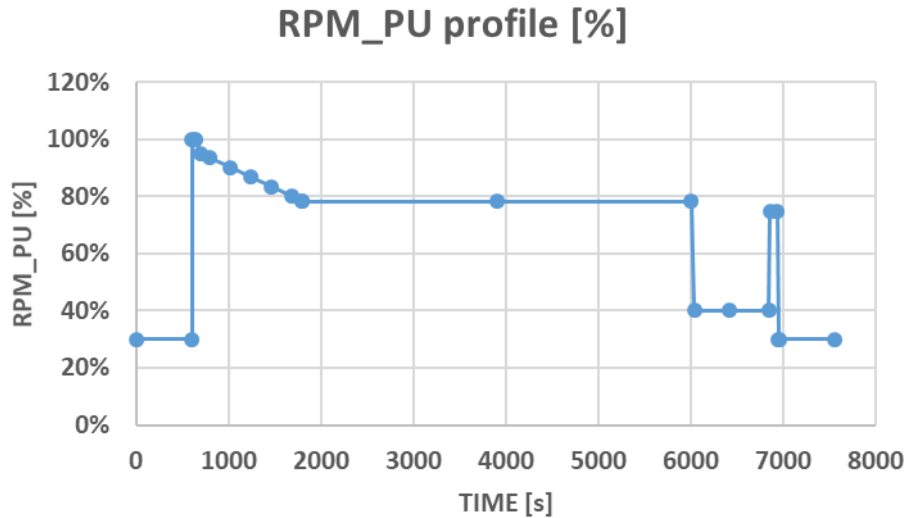


Fig. C-2: Propeller rotation speed profile.

A linear regression model proposed by NASA in [79] is considered for estimating the gearbox mass:

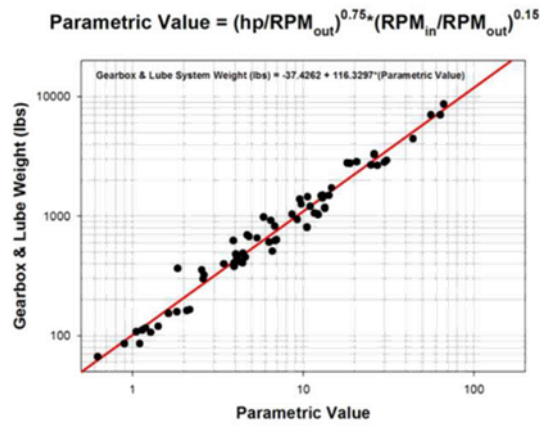


Fig. C-3: Transmission and lubrication system weight correlation from Nasa.

The “parametric value set in the Fig. C-3 is defined by the following equations:

Table C-2: Gearbox mass estimation.

$RPM_{prop}(t) = RPM_{PU}(t) \times RPM_{prop_{max}}$	Propeller rotational speed mission [RPM]	(C-1)
$Gbox = \left(\max \left(\frac{P_{prop_{HP}}(t)}{RPM_{prop}(t)} \right) \right)^{0.75} \times R_{gbox}^{0.15}$	Gearbox parameter (abscissa of the Fig C-3) [-]	(C-2)
$M_{Gbox} = 0.45 \times (-37.4 + 116.3 \times Gbox)$	Gearbox mass estimation [kg]	(C-3)

Where $P_{prop_{HP}}$ is the maximum propeller shaft power in horsepower [HP], RPM_{prop} the propeller rotational speed in [rpm] and R_{gbox} is the gearbox ratio. A linear function allows estimating the gearbox weight Eq(C-3).

C.2 Performance model:

A constant efficiency value is finally assessed in Eq(C-4).

$$\eta_{gbox} = 0.985 \quad (C-4)$$

Thanks to the rotational speed profile, the mechanical power mission (torque $T_{shaft_{emot}}$ and rotational speed Ω_{emot}) can be established:

$$P_{shaft_{emot}}(t) = \frac{P_{prop_{HP}}(t)}{\eta_{gbox}} \times \frac{1000}{1.34} \quad (C-5)$$

$$\Omega_{emot}(t) = N_{prop}(t) \times R_{gbox} \times \frac{\pi}{30} \quad (C-6)$$

$$T_{shaft_{emot}}(t) = \frac{P_{shaft_{emot}}(t)}{\Omega_{emot}(t)} \quad (C-7)$$

APPENDIX D. TURBOSHAFT MODEL

To move an airplane through the air, some kind of propulsion system are used to generate thrust. This figure shows drawings of four different variations of a gas turbine or jet engine. In this study only the turboshaft has been considered.

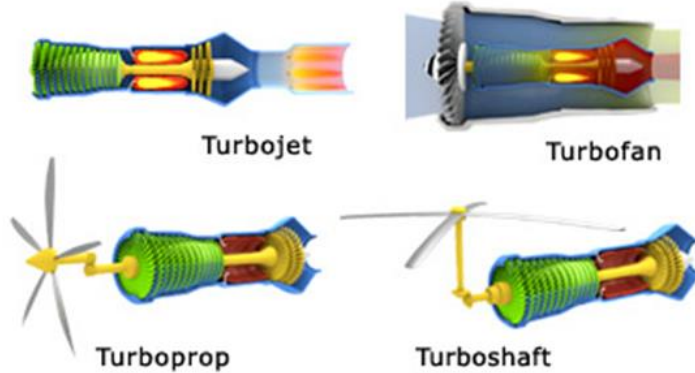


Fig. D-1: Example of gas turbine.

Table D-1: Input/output variables for the turboshaft model.

INPUT VARIABLES		
$P_{dynamic}(t)$	[Pa]	Dynamic Pressure
$T_{dynamic}(t)$	[K]	Dynamic Temperature
P_{SLS}	[W]	Sea Level Thermal Power
$P_{mech_{GTmission}}(t)$	[W]	Turboshaft power mission
OUTPUT VARIABLES		
M_{fuel}	[kg]	Fuel mass
$M_{turboshaft}$	[kg]	Turboshaft mass

The model is illustrated in Fig. D-2.

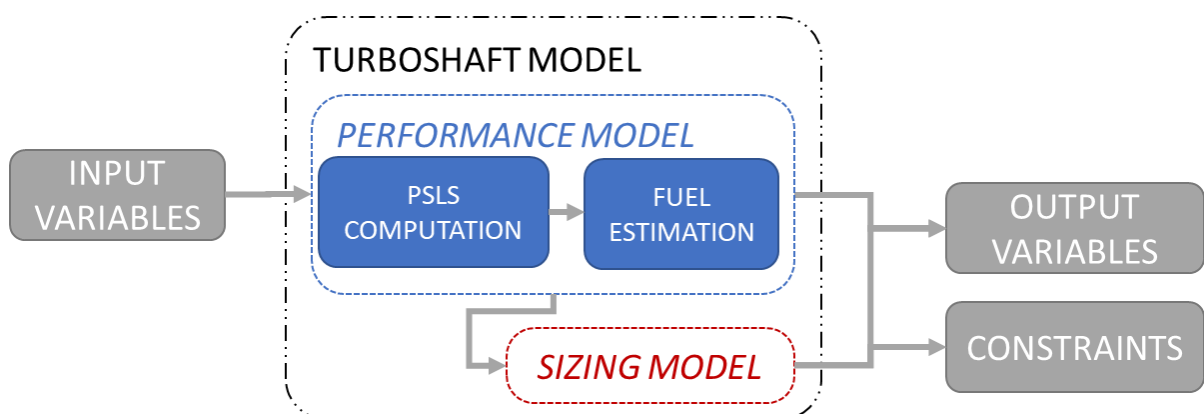


Fig. D-2: Process chart of the turboshaft model.

The turboshaft model is based on response surfaces as mentioned on the data regression of Fig. II-5. Three inputs have been considered: the static power at sea level P_{SLS} , the ratio δ [Pa] between total and static pressures at sea level and the ratio θ [K] between total and static temperatures at sea level previously calculated in Eqs (A-4) and (A-5). From these inputs, a one column-vector is derived in Eq(D-3) in order to assess the maximum mechanical turboshaft power $P_{max_{shaft_{GT}}}$. α_1 and β_1 are two constant values related to the linear regression.

Table D-2: Turboshaft mechanical power functions.

$$\delta = \frac{P_{dynamic}}{101325} \quad \text{Pressure ratio [-]} \quad (D-1)$$

$$\theta = \frac{T_{dynamic}}{288.15} \quad \text{Temperature ratio [-]} \quad (D-2)$$

$$x_c = \begin{bmatrix} \log(P_{SLS}) \\ \log(\delta) \\ \log(\theta) \\ \log(P_{SLS})^2 \\ \log(\delta)^2 \\ \log(\theta)^2 \\ \log(P_{SLS}) \times \log(\delta) \\ \log(P_{SLS}) \times \log(\theta) \\ \log(\delta) \times \log(\theta) \end{bmatrix} \quad \text{Regression vector [-]} \quad (D-3)$$

$$P_{max_{shaft_{GT}}} = 10^{\alpha_1 + \beta_1 \cdot x_c} \quad \text{Maximum mechanical power of the gas turbine [kW]} \quad (D-4)$$

The input parameter P_{SLS} is a constant value and it will determine the maximum mechanical turboshaft power during the mission considering altitude and Mach speed. That is why, a convenient P_{SLS} value must be designed (P_{SLS} Computation function) in order to suitably supply the hybrid electric propulsion during the whole flight mission, the $P_{max_{shaft_{GT}}}$ has to be higher than the $P_{mission}(t)$. But this process needs an internal loop that is why, another function " P_{SLS} Computation" is added in this model for determining the right value.

D.1 P_{SLS} computation:

From the Eq(D-4), the process was reversed:

$$\log(P_{max_{shaft_{GT}}}) = \alpha_1 + \beta_1 \cdot x_c \quad (D-5)$$

Using the Eq(D-5), a second order polynomial function of P_{SLS} has been found:

$$\alpha_{P_{SLS}} \times \log(P_{SLS}^2) + \beta_{P_{SLS}} \times \log(P_{SLS}) + \gamma_{P_{SLS}} = 0 \quad (D-6)$$

Which the roots are:

$$\log(P_{SLS}) = \min \left(\frac{(-\beta_{P_{SLS}} \pm \sqrt{\beta_{P_{SLS}}^2 - 4 \times \alpha_{P_{SLS}} \times \gamma_{P_{SLS}}})}{2 \times \alpha_{P_{SLS}}} \right) \quad (D-7)$$

In the equation (D-6), $\alpha_{P_{SLS}}$, $\beta_{P_{SLS}}$, $\gamma_{P_{SLS}}$ represent constant values of the 2nd order polynomial function of P_{SLS} . These constant values are determined by three input variables δ , θ , $P_{mission}$. For each mission point, a P_{SLS} value is determined and finally the maximum value of this set is chosen.

D.2 Fuel estimation:

Given the vector (x_C) with the right value of P_{SLS} , the maximum Power Specific Fuel Consumption $PSFC_{max}$ is assessed (in [kg/s/kW] as defined in: it corresponds to the turboshaft PSFC when this engine provides its maximum power leading to a minimum consumption. For the real turboshaft fuel consumption, a ratio ($Part_{load}$) is set in Eq(D-9) between the required power function (of the environmental data δ and θ° and the maximum mechanical power). Another linear regression is used to estimate the actual PSFC Eq(D-11) from which the fuel flow rate is defined given a required power $P_{mission}$ and used in Eq (D-3).

Table D-3: Fuel estimation model

$PSFC_{max} = 10^{\alpha_2 + \beta_2 \cdot x_C}$	Maximum Specific fuel consumption [kg/s/kW]	(D-8)
$Part_{load} = \frac{P_{mech GT mission}}{P_{max shaft GT}} \times \delta \times \sqrt{\theta}$	Power ratio [-]	(D-9)
$y = \begin{bmatrix} \log(Part_{load}) \\ \log(Part_{load})^2 \\ \dots \\ \log(Part_{load})^{10} \end{bmatrix}$	Regression vector [-]	(D-10)
$PSFC = 10^{\alpha_3 + \beta_3 \cdot y} \times \frac{PSFC_{max}}{\theta}$	Specific fuel consumption [kg/s/kW]	(D-11)
$D_{m_{fuel}} [\text{kg/s}] = PSFC \times \frac{P_{mech GT mission}}{1000}$	Mass flow rate [kg/s]	(D-12)

In this model, the specific fuel consumption variation is taken into account. The fuel burn can be calculated over the aircraft mission by integrating the $D_{m_{fuel}}$ variable. As displayed in Fig. I-16, the turboshaft consumption is minimum at 100% of the rating power. Contrarily, at low rating, the SFC evolution may be referred to a hyperbolic function. In that way, using secondary energy source in taxi and descent phases and switching off the main thermal source could be interesting in a hybrid electric aircraft. However, an efficient, reliable and fast starting system is mandatory as in modern ground vehicles.

D.3 Sizing model:

Estimating the turboshaft mass is difficult. For that purpose, a typical specific power $P_{SPE} = 9.86 \text{ kW/kg}$ is assessed from experimental data set [12]. Finally, the fuel mass is obtained by the time integral of the mass flow rate.

$$M_{fuel} = \int Dm_{fuel}(t)dt \quad (D-13)$$

$$M_{turboshaft} = P_{SLS} \times P_{SPE} \quad (D-14)$$

D.4 Power constraint:

A constraint associated with the shaft power is set in this model in order to ensure that the turboshaft will provide enough power to the propulsion system.

$$P_{max shaft GT} \geq P_{mech GT mission} \quad (D-15)$$

APPENDIX E. CABLE MODEL

Table E-1: Input/output variables for the cable model.

INPUT VARIABLES		
$P_{elec,cable}(t)$	[W]	Cable electric power
$PF(t)$	[–]	Power Factor
m	[–]	Number of phases
V	[V]	AC/DC voltage (depending on the cable)
OUTPUT VARIABLES		
$\eta_{cable}(t)$	[%]	Cable efficiency
$T_{cable}(t)$	[°C]	Cable warming
ΔV	[V]	Voltage drop
M_{cable}	[kg]	Cable mass

The model is illustrated in Fig. E-1.

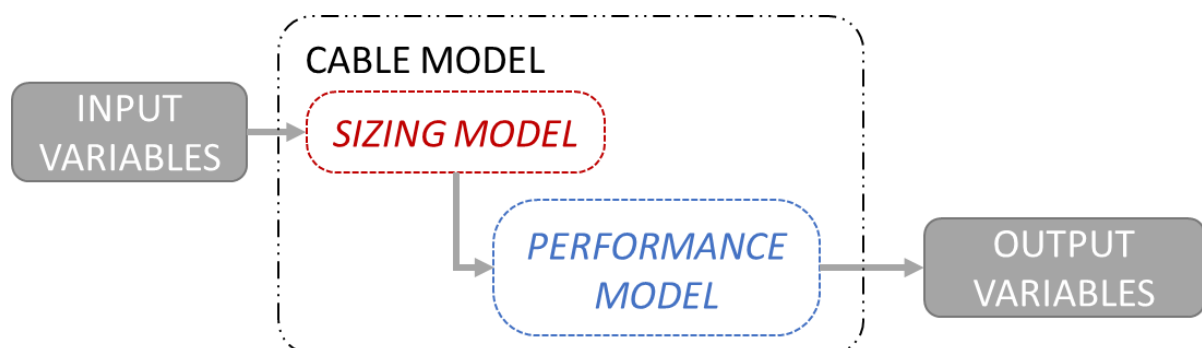


Fig. E-1: Process chart for the cable model.

Several locations have been selected with different ambient temperature assessments. They are listed in the following table:

Table 1: Ambient temperature in each part of the aircraft.

PLACE	T_{amb}
Nacelle	80
Pylon	80
Wing	80
Fuselage	60

Two materials are considered: copper and aluminum.

Table 2: Copper data table

GAUGE	1	0	00	000	0000
K_c [-]	11e-4	8,4e-4	6,0e-4	4,3e-4	3,1e-4
M_{lin} [g/m]	470	600	750	950	1200
R_{lin} [Ω /m]	0,5e-3	0,4e-3	0,31e-3	0,25e-3	0,2e-3
$T_{cable_{max}}$ [$^{\circ}$ C]	220	220	220	220	220

Table 3: Aluminum data table.

GAUGE	1	0	00	000
K_c [-]	20e-4	15e-4	11e-4	8,4e-4
M_{lin} [g/m]	143	181	230	276
R_{lin} [Ω /m]	0,75e-3	0,60e-3	0,43e-3	0,36e-3
$T_{cable_{max}}$ [$^{\circ}$ C]	160	160	160	160

The idea is to estimate the cable weight per meter of length for different voltages and locations inside the structure (nacelle, fuselage). The details for this model cannot be provided for confidentiality reasons.

APPENDIX F. ELECTRIC MOTOR MODEL

Table F-1: Input/output variables for the electric motor sizing model.

INPUT VARIABLES (in bold blue, the 10 decision variables for optimization)		
$R_{alesage}$	[m]	Bore radius of the electric motor
R_{Drotlm}	[%]	Rotor diameter/rotor length ratio
R_{gral}	[%]	Air gap thickness/ bore radius ratio
R_{hsral}	[%]	Slot height/ bore radius ratio
$R_{pm_{ral}}$	[%]	Magnet thickness/ bore radius ratio
τ_{magnet}	[%]	Pole pitch (=100%)
τ_{slot}	[%]	Slot pitch (=100% full pitch winding)
k_{carbon}	[–]	Carbon fiber constant for sleeve equation
p	[–]	Number of pole pairs
q	[–]	Number of phases
$nepp$	[–]	Number of slots per pole and per phase
N_{ce}	[–]	Number of conductors per slot
k_{fill}	[–]	Fill factor in the slot
J_a	[T]	Permanent magnet flux density
B_{yoke}	[T]	Stator yoke flux density
B_{teeth}	[T]	Stator teeth flux density
$B_{yoke_{rotor}}$	[T]	Rotor yoke flux density
V_{uHVDC}	[V]	Ultra high voltage direct current
OUTPUT VARIABLES		
M_{motor}	[kg]	Electric motor mass
$PF(t)$	[–]	Power factor mission
$m_a(t)$	[–]	Modulation depth mission
$P_{JDC}(t)$	[W]	DC Joule losses
$P_{Iron}(t)$	[W]	Iron losses
$P_R(t)$	[W]	Friction losses
$P_{Aero}(t)$	[W]	Aerodynamic losses
$h_{XX}, e_{XX}, L_{XX}, R_{XX}, w_{XX}$	[m]	Sizes of the e-motor

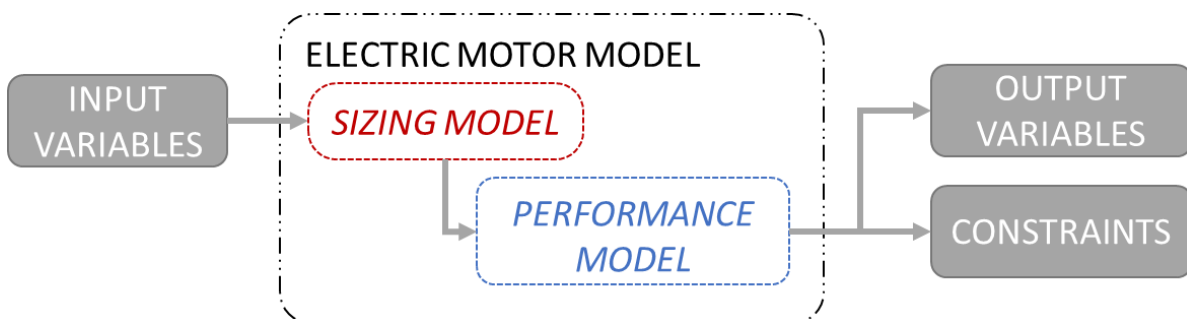


Fig. F-1: Process chart of the electric motor.

More details related to the assumptions of this model can be found in [A5].

F.1 Sizing model.

F.1.1 1rst harmonic air gap flux density

The computation of the air gap flux density is the first step of this model. Most of variables use this parameter. In equation (F-2), the direct calculation is used for determining the air gap flux density [A5].

Table F-2: First harmonic flux density computation process.

$$\gamma_{elec} = \pi \times \frac{\tau_{magnet}}{2} \quad (F-1)$$

$$Bfond_{gaprms} = \frac{R_{pm_{ral}} \times J_a}{\log(-(1-R_{pm_{ral}}-R_{gral}))} \quad (F-2)$$

$$B_{gaprms} = Bfond_{gaprms} \times 2\sqrt{2} \times \frac{\sin(\gamma_{elec})}{\pi} \quad (F-3)$$

F.1.2 Electric motor geometry.

All sizes of the electric motor are determined from the input variables. The Fig. F-2 represents each variable name on the cross section of an electric machine.

Table F-3: Geometry of the electric permanent magnet synchronous machine.

$L_{motor} = \frac{2 \times R_{alesage}}{R_{DrotLm}}$	E-motor length [m]	(F-4)
$e_{gmag} = R_{alesage} \times R_{gral}$	Magnetic air gap thickness [m]	(F-5)
$e_{magnet} = R_{alesage} \times R_{PM_{ral}}$	Permanent magnet thickness [m]	(F-6)
$h_{slot} = R_{hs_{ral}} \times R_{alesage}$	Slot height [m]	(F-7)
$N_{enc} = 2p \times q \times nepp$	Number of slot [m]	(F-8)
$h_{yoke} = \frac{B_{gaprms}\sqrt{2}}{B_{yoke}} \times \frac{R_{alesage}}{p}$	Stator yoke height [m]	(F-9)
$h_{yokerotor} = \frac{B_{yoke}}{B_{yokerotor}} \times h_{yoke}$	Rotor yoke height [m]	(F-10)
$Ratio_{teeth} = \frac{2}{\pi} \times \frac{B_{gaprms}\sqrt{2}}{B_{yoke}}$	Teeth Ratio [%]	(F-11)
$e_{sleeve} = \frac{(R_{alesage}-e_{gmag})}{\left(\frac{1}{k_{carbon} \times \max(\Omega_{emot}(t))} \right) - 1}$	Sleeve thickness [m]	(F-12)
$e_{gap} = e_{gmag} - e_{sleeve}$	Mechanical air gap thickness [m]	(F-13)
$\tau_{teeth+slot} = \frac{2\pi \times R_{alesage}}{N_{enc}}$	Slot + teeth arc [m]	(F-14)
$w_{slot} = (1 - Ratio_{teeth}) \times \tau_{teeth+slot}$	Slot arc [m]	(F-15)
$w_{teeth} = (Ratio_{teeth}) \times \tau_{teeth+slot}$	Teeth arc [m]	(F-16)

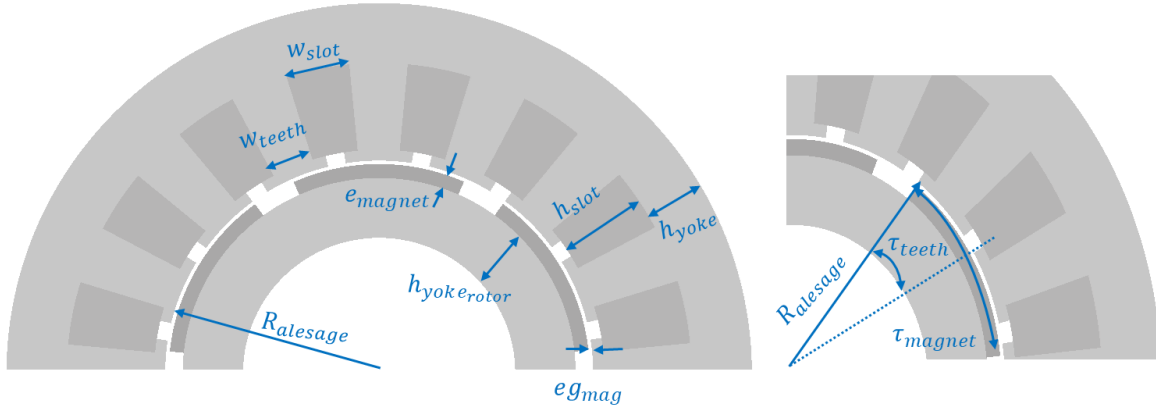


Fig. F-2: Cross section of an electric motor with each variable name.

The slot arc w_{slot} is not sufficient for determining the exact sizes of the slot. That is why the Fig. F-3 describes the geometry of the slot and the process related to the calculation of the slot length in order to find the right value of the slot section.

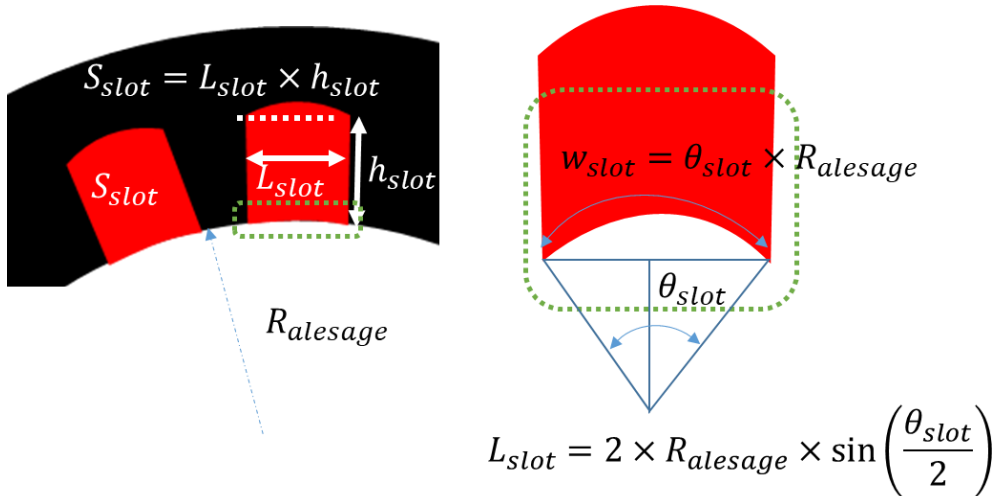


Fig. F-3: Description of the slot length calculation

Table F-4: Slot sizes details.

$\theta_{slot} = \frac{w_{slot}}{R_{alesage}}$	Slot angle [rad]	(F-17)
$L_{slot} = 2 \times R_{alesage} \times \sin\left(\frac{\theta_{slot}}{2}\right)$	Slot length [m]	(F-18)
$S_{slot} = L_{slot} \times h_{slot}$	Slot area [m^2]	(F-19)
$S_{CU\ total} = S_{slot} \times k_{fill}$	Useful copper area [m^2]	(F-20)

F.1.3 Centrifugal pressure and peripheral speed.

The centrifugal pressure and the peripheral speed will be used for the mechanical constraint computations.

Table F-5: Mechanical constraints calculation.

$$R_{yoke_{rotorOUT}} = R_{shaft} + h_{yoke_{rotor}} \quad (F-21)$$

$$R_{magOUT} = R_{yoke_{rotorOUT}} + e_{magnet} \quad (F-22)$$

$$R_{sleeveOUT} = R_{magOUT} + e_{sleeve} \quad (F-23)$$

$$P_{centrifugal} = \frac{1}{3} \frac{\Omega_{mechmax}^2}{e_{sleeve}} \left(\rho_{carbon} \cdot (R_{sleeveOUT}^3 - R_{magOUT}^3) + \rho_{PM} \cdot (R_{magOUT}^3 - R_{yoke_{rotorOUT}}^3) \right) \quad (F-24)$$

$$V_{peripheral} = R_{sleeveOUT} \times \Omega_{mechmax} \quad (F-25)$$

The centrifugal pressure $P_{centrifugal}$ and peripheral speed $V_{peripheral}$ constraints are set in order to design the right carbon sleeve thickness.

F.1.4 Electric motor winding configuration.

The head winding coefficient k_{tb} is determined by the geometry of the electric motor. For the winding layout, several winding factors are taken into account, the global winding factor $k_{windings}$ is the product of these factors for the 1rst harmonic.

Table F-6: Winding factors description.

$$k_{tb} = \frac{(L_{motor} + \tau_{slot} \times \frac{\pi}{p} \times R_{alesage} + \pi \times \tau_{teeth+slot})}{L_{motor}} \quad \text{head winding coefficient [-]} \quad (F-26)$$

$$kd1 = \frac{\sin\left(\frac{1}{2} \times nepp \times p \times \frac{\tau_{teeth+slot}}{R_{alesage}}\right)}{nepp \times \sin\left(\frac{1}{2} \times p \times \frac{\tau_{teeth+slot}}{R_{alesage}}\right)} \quad \text{twist factor [-]} \quad (F-27)$$

$$kr1 = \sin\left(\tau_{slot} \times \frac{\pi}{2}\right) \quad \text{shortening factor [-]} \quad (F-28)$$

$$ki1 = 1 \quad \text{distribution factor [-]} \quad (F-29)$$

$$k_{windings} = kd1 \times kr1 \times ki1 \quad \text{global winding factor [-]} \quad (F-30)$$

$$k_{lc} = 1 \quad (1,15 \text{ if 2035 target}) \quad \text{AC coefficient losses (2035 target)} \quad (F-31)$$

F.1.5 Electric parameters.

The single-phase equivalent circuit of a permanent magnet synchronous machine is presented in the Fig. F-4.

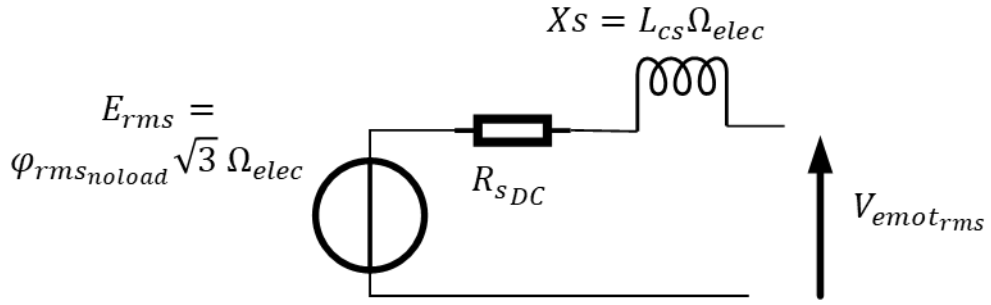


Fig. F-4: Circuit parameters of the PMSM and its electric equivalent circuit.

Table F-7: Circuit parameter equations.

$$\varphi_{rms\,no\,load} = \frac{N_{ce} \times N_{enc}}{2.q.p} \times 2.k_{windings} \times L_{motor} \times R_{alesage} \times \sqrt{2}.B_{gap\,rms} \quad (F-32)$$

$$L_p = \frac{4}{\pi} \times \mu_0 \times k_{windings}^2 \left(\frac{N_{ce} \times N_{enc}}{2.q.p} \right)^2 \times \frac{L_{motor} \times R_{alesage}}{e_{magnet} + e_{mag}} \quad (F-33)$$

$$M = -\frac{1}{2}L_p \quad (F-34)$$

$$L_{cs} = L_p - M \quad (F-35)$$

$$R_{s\,DC} = \frac{\rho_{CU} \times 2 \times \frac{N_{ce} \times N_{enc}}{2.q} \times k_{tb} \times L_{motor} \times k_{lc}}{S_{CU\,total}} \quad (F-36)$$

The circuit parameters are the following:

- $\varphi_{rms\,no\,load}$ is the RMS value of no load flux in [Wb].
- L_p is the self-inductance of one phase [H].
- M is the mutual inductance of one phase in [H].
- L_{cs} is the cyclic inductance of one phase [H].
- $R_{s\,DC}$ is the DC resistance of one phase [Ω].

Once these parameters have been determined, the performance model can be run over the flight mission.

F.2 Sizing constraints.

The maximum peripheral speed is 200 m/s and the maximum centrifugal pressure is $7,5 \times 10^8 Pa$.

Table F-8: Sizing constraints.

$R_{shaft} \geq R_{shaft\,min}$	Shaft radius constraint	(F-37)
$e_{gap} \geq e_{g\,min}$	Air gap thickness constraint	(F-38)
$V_{peripheral} \leq V_{peripheral\,max}$	Peripheral speed constraint	(F-39)
$P_{centrifugal} \leq P_{centrifugal\,max}$	Centrifugal pressure constraint	(F-40)

F.3 Performance model.

F.3.1 Field weakening control

The Maximum Torque Per Ampere strategy has been implemented with capability of field weakening during the flight mission. This strategy is based on the Behn-Eschenburg model presented in Fig. F-4.

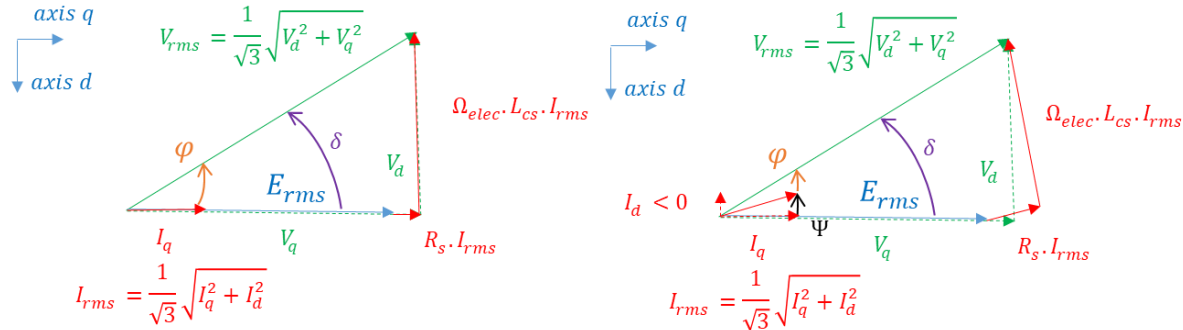


Fig. F-5: Behn-Eschenburg model (left: without field weakening $\Psi = 0^\circ$)(right: with field weakening $\Psi > 0^\circ$).

The principle of the maximum torque per ampere control is implemented with the angle Ψ equals to 0. Indeed, the choice of " $\Psi = 0^\circ$ " represents the optimal angle which allows having the maximum torque with minimal Joule losses. Maintaining a constant torque (" I_q " constant) at a higher speed than the base speed induces a negative current " I_d ": this "counter-field current" reduces the air gap flux " Φ_g ". This operation in field weakening mode ensures the same power value for a higher speed while remaining at the induced stop-voltage (maximum voltage allowed by the DC bus).

Table F-9: Initialization of the field weakening control.

$Iq_{mission} = \frac{T_{emot}}{p \times \varphi_{rms,noload} \times \sqrt{3}}$	Required torque => Iq current	(F-41)
$Id_{centre} = \frac{\varphi_{rms,noload} \times \sqrt{3}}{L_{cs}}$	Center of the actuator circle	(F-42)
$V_{dqmax} = V_{ondmax} \times \sqrt{\frac{3}{2}} = \Omega_{elec} \times \Phi_g$	Stop-voltage (max inverter voltage)	(F-43)
$R_{mission} = \frac{V_{dqmax}}{L_{cs} \times \Omega_{elec,mission}}$	Radius of the actuator circle	(F-44)

From a geometrical point of view, the radius of the actuator circle is defined by the maximum available voltage, V_{dqmax} , and the actuator rotational speed over the flight mission, $\Omega_{elec,mission}$ (see Table F-9). The intersection between the actuator circle and the current vector defines the operation point (OP1,2 see Fig. F-6a).

When the voltage is not limited (without field-weakening), the circle must contain the operating point (blue circle in Fig. F-6b) and the equivalent condition is the following:

$$R_{mission}^2 \geq Iq_{mission}^2 + Id_{centre}^2$$

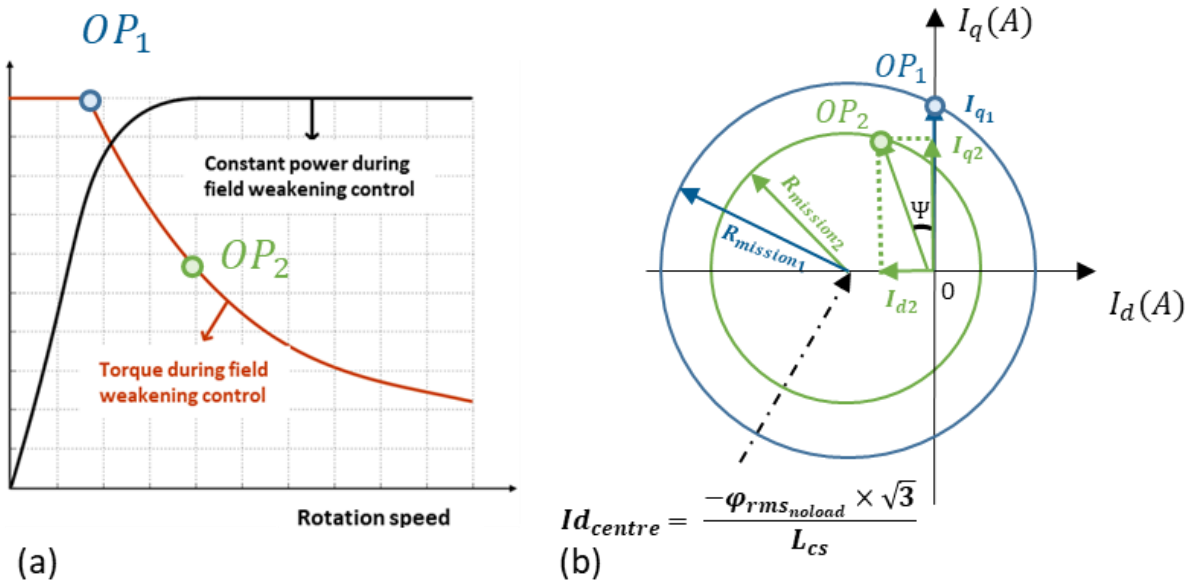


Fig. F-6: Field-weakening operation. (a) Power/torque versus rotational speed plane. (b) Analysis in the d - q plane. Two representations of actuator circles (blue circle: maximum torque per ampere strategy, with $I_d = 0$, green circle: field-weakening strategy, with increased speed and constant limited voltage).

The inequation becomes an equation when the voltage of the electric actuator reaches the maximum available voltage, V_{dqmax} . In this case, the field-weakening strategy occurs. The operating is then defined by the green circle. During that overspeed operation, the actuator usually operates at constant power, as illustrated in Fig. F-6a. The blue circle shrinks to the green circle (increasing speed) and the current is shifted in phase to reach the operating point (see Fig. F-6b). Both operating points (OP_1 and OP_2) are represented in the torque-speed plan (see Fig. F-6a). The circle characteristic is defined by:

$$R_{mission}^2 = I_{q_{mission}}^2 + (I_{d_{mission}} - I_{d_{centre}})^2$$

This second order is derived in Figure 8 to set the current $I_{d_{mission}}$ in the case of the field-weakening operation:

$$I_{d_{mission}}^2 - 2 \times \frac{-\varphi_{rms,noload} \times \sqrt{3}}{L_{cs}} \times I_{d_{mission}} + I_{q_{mission}}^2 + \left(\frac{-\varphi_{rms,noload} \times \sqrt{3}}{L_{cs}} \right)^2 - \left(\frac{V_{dqmax}}{L_{cs} \times \Omega_{elec,mission}} \right)^2 = 0$$

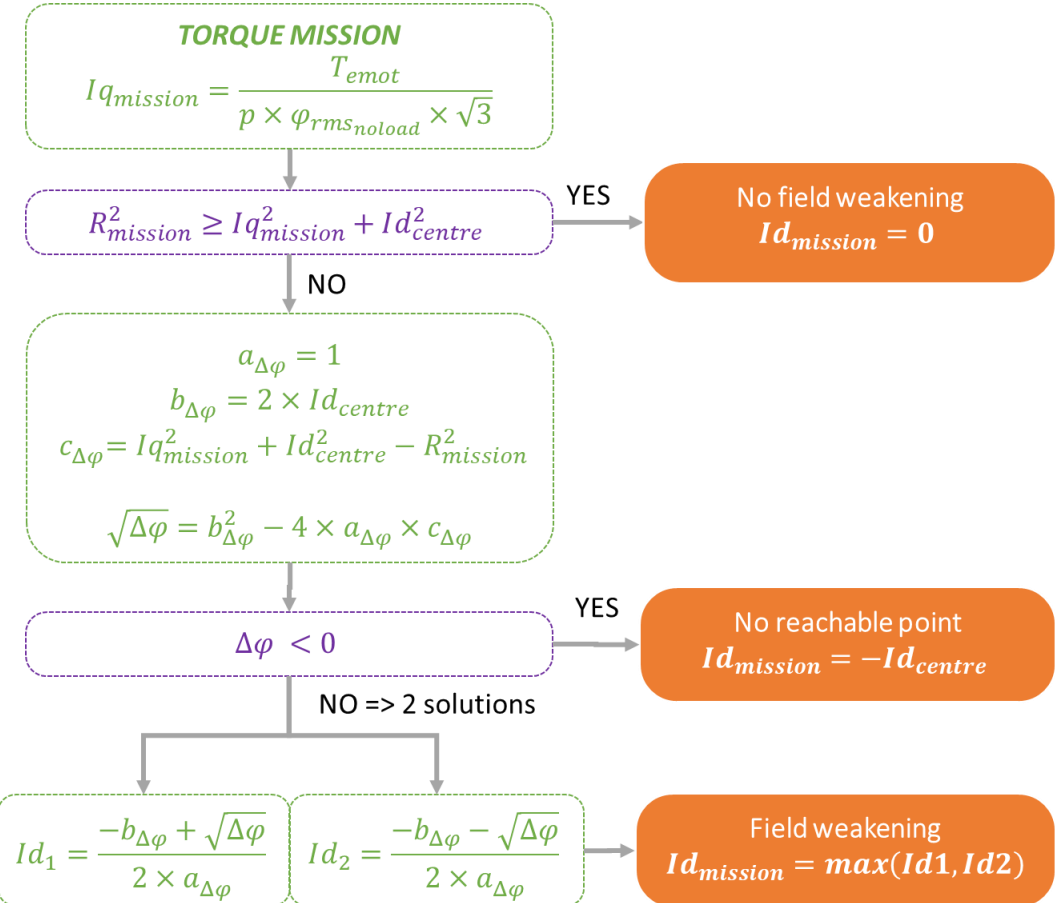


Fig. F-7: Field weakening control description.

Fig. F-7 shows the resolution process of the control strategy. The discriminant is computed to check if there are solutions. Finally, if solutions exist, the least restrictive I_d value is kept. After this calculation process, the electromechanical actuator characteristics can be computed. The currents and voltages are derived from the d, q axis values (see Table F-10).

Table F-10: PMSM electric parameters and flux densities.

$$E_{rms,mission} = \varphi \sqrt{3} \Omega_{elec,mission} \quad (F-45)$$

$$Vd_{mission} = RS_{DC} \times Id_{mission} - L_{cs} \times \Omega_{elec,mission} \times Iq_{mission} \quad (F-46)$$

$$Vq_{mission} = RS_{DC} \times Iq_{mission} + L_{cs} \times \Omega_{elec,mission} \times Id_{mission} + E_{rms,mission} \quad (F-47)$$

$$Is_{rms,mission} = \frac{1}{\sqrt{3}} \sqrt{Id_{mission}^2 + Iq_{mission}^2} \quad (F-48)$$

$$Vs_{rms,mission} = \frac{1}{\sqrt{3}} \sqrt{Vd_{mission}^2 + Vq_{mission}^2} \quad (F-49)$$

$$\Phi_{g,noload} = \varphi_{rms,noload} \times \sqrt{3} \quad (F-50)$$

$$\Phi_{g,field-weakening} = \sqrt{(Iq_{mission} \times L_{cs})^2 + (\Phi_{g,noload} + Id_{mission} \times L_{cs})^2} \quad (F-51)$$

$$B_{yoke,mission} = B_{yoke,noload} \times \frac{\Phi_{g,field-weakening}}{\Phi_{g,noload}} \quad (F-52)$$

$$B_{teeth,mission} = B_{teeth,noload} \times \frac{\Phi_{g,field-weakening}}{\Phi_{g,noload}} \quad (F-53)$$

The electric parameters are the following:

- $E_{rms\ noload}$ is the RMS value of no load voltage in [V].
- $V_{d\ mission}$ and $V_{q\ mission}$ are the “d” and “q” axis mission voltages [V].
- $V_{S\ rms\ mission}$ and $I_{S\ rms\ mission}$ are the voltage and the current in one phase [V/A].
- $\Phi_{g\ noload}$ and $\Phi_{g\ field-weakening}$ are the air gap flux density (no load and in load [Wb]).
- $B_{yoke\ mission}$ and $B_{teeth\ mission}$ are teeth and yoke flux densities during the mission [T].

All inverter parameters can be computed from the Behn-Eschenburg diagram in the Fig. F-5:

Table F-11: Inverter parameters

$ma_{mission} = \frac{V_{S\ rms\ mission}}{\frac{V_{u\ HVDC}}{2\sqrt{2}}}$	modulation depth [-]	(F-54)
$\delta(t) = -\text{atan}\left(\frac{V_d(t)}{V_q(t)}\right)$	internal angle [rad]	(F-55)
$\Psi(t) = \text{atan}\left(\frac{I_d(t)}{I_q(t)}\right)$	field weakening angle [rad]	(F-56)
$\varphi(t) = \delta(t) - \Psi(t)$	power factor angle [rad]	(F-57)
$PF_{mission} = \cos(\varphi(t))$	power factor [-]	(F-58)

F.3.2 Losses model

In this study the following losses have been taken into account:

- $P_{JDC\ mission}$ is the DC Joule losses in the stator windings [W].
- $P_{Iron\ mission}$ is the Iron losses in the stator yoke [W].
- $P_{R\ mission}$ is the friction losses in the bearings [W].
- $P_{Agap\ mission}$ is the windage losses in the air gap [W].
- $P_{Arotor\ mission}$ is the windage losses in the two rotor surfaces [W].

Table F-12: Electric engine losses description.

$$P_{JDC\ mission} = q \times R_{S\ DC} \times I_{S\ rms\ mission}^2 \quad (F-59)$$

$$P_{Iron\ mission} = 2 \times \left(\sum f^\alpha B_{yoke}^\beta M_{stator\ yoke} + \sum f^\alpha B_{teeth}^\beta M_{stator\ teeth} \right) \quad (F-60)$$

$$P_{R\ mission} = 2 \cdot C_{froul} \times \Omega_{elec\ mission} \quad (F-61)$$

$$P_{Agap\ mission} = k_1 \times C_{f\ air} \cdot \pi \cdot \rho_{air} \times \Omega_{elec\ mission}^3 \times R_{alesage}^4 \times k_{tb} \times L_{motor} \quad (F-62)$$

$$P_{Arotor\ mission} = C_{f_r} \cdot \pi \cdot \rho_{air} \times \Omega_{elec\ mission}^3 \times R_{alesage}^5 \quad (F-63)$$

F.4 Performance constraints.

Table F-13: Performance constraints.

$\Delta\varphi \geq 0$	Mission fulfillment (cf Fig. F-7)	(F-64)
$Demag \leq 0$ <i>(Demagnetization ok ?</i> <i>Yes = 0 , No = 1)</i>	Demagnetization constraint [-]	(F-65)

The (F-65) constraint equation concerns the problem of irreversible demagnetization of the magnet generally caused by its heating and/or by the operation in overspeed (field weakening).

APPENDIX G. ELECTRIC MOTOR COOLING MODEL

Table G-1: Input/output variables for the electric motor cooling model.

INPUT VARIABLES		
$R_{alesage}$	[m]	Bore radius of the e-motor
$h_{XX}, e_{XX}, L_{XX}, R_{XX}, w_{XX}$	[m]	Sizes of the e-motor
p	[–]	Number of pole pairs
N_{enc}	[–]	Number of slots
k_{fill}	[–]	Fill factor in the slot
ρ_{fluid}, ρ_{air}	[kg/m ³]	Fluid and air density
C_{Pfluid}, C_{Pair}	[J/(kg.K)]	Fluid and air thermal capacity
$\nu_{isd_{fluid}}, \nu_{isd_{air}}$	[Pa.s]	Fluid and air dynamic viscosity
ν_{air}	[m ² /s]	Air kinematic viscosity
$\lambda_{fluid}, \lambda_{air}, \lambda_{epoxy}, \lambda_{winding_{channel}}$	[W/(m.K)]	Fluid, air, epoxy and winding channels thermal conductivity
$D_{tube_{total}}$	[m]	Output diameter of the e-motor cooling system
$e_{winding_{channel}}$	[m]	Winding channel thickness
$h_{waterjacket_{housing}}$	[m]	Water jacket housing thickness
$R_{windchannel_{Lslot}}$	[%]	Ratio between winding channels and slot length
$\dot{q}_{stator}, \dot{q}_{rotor}, \dot{q}_{windings}$	[m ³ /s]	Stator, rotor winding channel flow rate
N_{nodes}	[–]	Number of nodes
$P_{JDC_{mission}}, P_{Iron_{mission}}, P_{A_{mission}}, P_{R_{mission}}$	[W]	DC Joule, Iron, Aerodynamic, Friction losses.
OUTPUT VARIABLES		
$M_{motor+cooling}$	[kg]	E- motor + cooling mass
$P_{SPE_{emotor+cooling}}$	[kW/kg]	E-motor + cooling specific power
$T_{yoke_{stator}}(t)$	[°C]	Stator yoke temperature
$T_{windings}(t)$	[°C]	Winding temperature
$T_{magnet}(t)$	[°C]	Magnet temperature

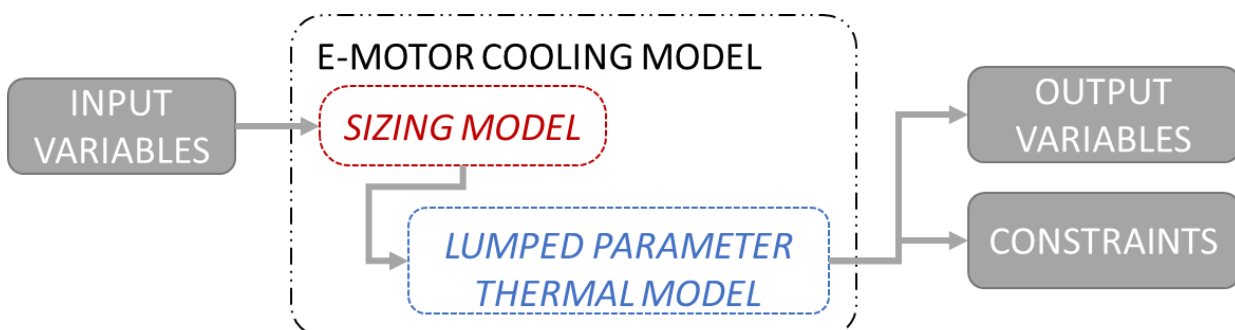


Fig. G-1: Process chart of the electric motor cooling model.

G.1 Sizing model.

Three direct cooling systems studied in [87] have been implemented in the optimization process:

- internal cooling inside the slots of the electric motor (2035 target),
- External cooling outside of the stator through a water jacket,
- and inside the rotor through a shaft cooling system.

G.1.1 Winding channel model for internal cooling (2035 target).

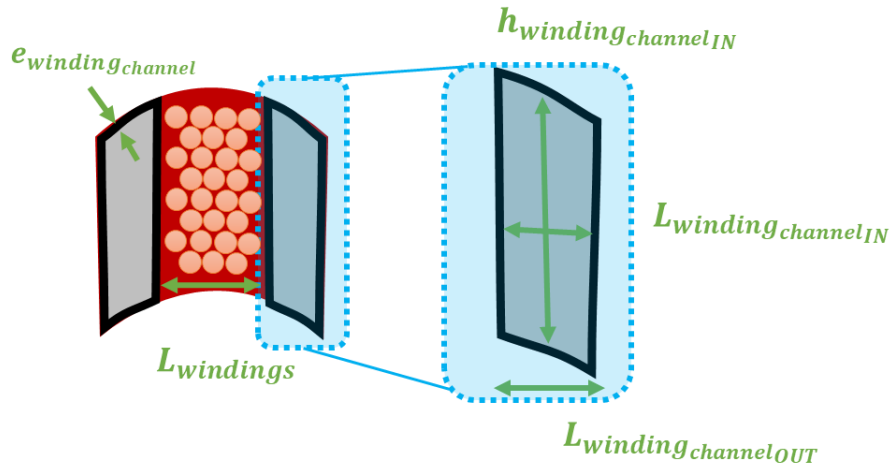


Fig. G-2: Winding channel layout details in the cross section of the slot.

Table G-2: Winding channel sizes.

$$h_{winding\text{channel}IN} = h_{slot} - 2 \cdot e_{winding\text{channel}} \quad (G-1)$$

$$L_{winding\text{channel}OUT} = \frac{R_{wind\text{channel}Lslot}}{2} \cdot L_{slot} \quad (G-2)$$

$$L_{winding\text{channel}IN} = L_{winding\text{channel}OUT} - 2 \cdot e_{winding\text{channel}} \quad (G-3)$$

$$k_{fill\text{winding\text{channel}}} = \frac{k_{fill}}{1 - R_{wind\text{channel}Lslot}} \quad (G-4)$$

$$A_{hydro\text{winding}} = L_{winding\text{channel}IN} \times h_{winding\text{channel}IN} \quad (G-5)$$

$$Perim_{hydro\text{winding}} = 2 \times (L_{winding\text{channel}IN} + h_{winding\text{channel}IN}) \quad (G-6)$$

$$D_{hydro\text{winding}} = 4 \times \frac{A_{hydro\text{winding}}}{Perim_{hydro\text{winding}}} \quad (G-7)$$

$$u_{fluid\text{winding}} = \frac{\dot{q}_{winding}}{A_{hydro\text{winding}}} \quad (G-8)$$

The channel height $h_{winding\text{channel}IN}$ and external/internal length $L_{winding\text{channel}OUT}$ & $L_{winding\text{channel}IN}$ are determined by the slot height h_{slot} , the slot length L_{slot} , the thickness of the channel $e_{winding\text{channel}}$ and the ratio $R_{wind\text{channel}Lslot}$. A new fill factor $k_{fill\text{winding\text{channel}}}$ is computed from the new useful slot area. Hydraulic parameters are computed from the new configuration.

Table G-3: Differences between 2025 and 2035 targets

TARGET	2025	2035
$R_{windchannelLslot}$	0	25%
$e_{windingchannel}$	0	0.1 mm
$\dot{q}_{winding}$	0	5.5e-4 m^3/s

G.1.2 Water Jacket and shaft cooling design (2025 and 2035).

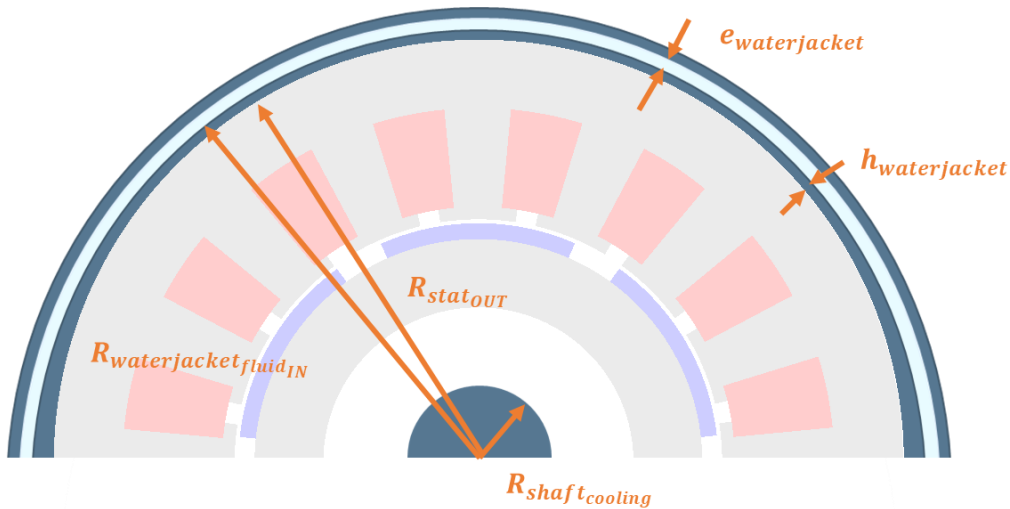


Fig. G-3: Cross section of the electric motor with water jacket and shaft cooling representation.

Table G-4: Water-jacket design equations.

$$R_{waterjacketfluid_IN} = R_{statOUT} + h_{waterjacket_housing} \quad (G-10)$$

$$e_{waterjacket_fluid} = 2\% \times R_{waterjacketfluid_IN} \quad (G-11)$$

$$R_{waterjacketfluid_OUT} = R_{waterjacketfluid_IN} + e_{waterjacket_fluid} \quad (G-12)$$

$$A_{hydrostator} = \pi \left(R_{waterjacketfluid_OUT}^2 - R_{waterjacketfluid_IN}^2 \right) \quad (G-13)$$

$$Perim_{hydrostator} = 2 \times \pi \left(R_{waterjacketfluid_OUT} + R_{waterjacketfluid_IN} \right) \quad (G-14)$$

$$D_{hydrostator} = 4 \times \frac{A_{hydrostator}}{Perim_{hydrostator}} \quad (G-15)$$

$$u_{fluid_stator} = \frac{\dot{q}_{stator}}{A_{hydrostator}} \quad (G-16)$$

Table G-5: Shaft cooling design equations.

$$D_{tubero_rotor} = 10\% \times R_{shaft_IN} \quad (G-17)$$

$$A_{hydro_rotor} = \frac{\pi D_{tubero_rotor}^2}{4} \quad (G-18)$$

$$Perim_{hydro_rotor} = \pi (D_{tubero_rotor}) \quad (G-19)$$

$$D_{hydro_rotor} = 4 \times \frac{A_{hydro_rotor}}{Perim_{hydro_rotor}} = D_{tubero_rotor} \quad (G-20)$$

$$u_{fluid,rotor} = \frac{\dot{q}_{rotor}}{A_{hydro,rotor}} \quad (G-21)$$

Table G-6: Heat exchanger tube design equations.

$$A_{hydro,total} = \frac{\pi D_{tube,total}^2}{4} \quad (G-22)$$

$$u_{fluid,total} = \frac{\dot{q}_{rotor} + \dot{q}_{stator} + \dot{q}_{winding}}{A_{hydro,total}} \quad (G-23)$$

G.1.3 Fluid convection coefficients computation.

Once these systems are designed, Reynolds and Prandtl numbers are computed in order to determine fluid convection coefficients in the cooling system:

Table G-7: Reynolds and Prandtl number used in the fluid convection coefficients computation.

$$Re_{XX} = \frac{\rho_{fluid} \times u_{fluid,XX} \times D_{tube,XX}}{\lambda_{fluid}} \quad (G-24)$$

$$Pr = \frac{c_p_{fluid} \times \nu_{fluid} \times \lambda_{fluid}}{\lambda_{fluid}} \quad (G-25)$$

The following process is used for determining each H_{XX} fluid convection coefficients. In the case where the Reynolds number is lower than the critical Reynolds number, the flow is laminar and the Nusselt number is constant. In the other case, a Nusselt equation is computed with a particular one for the heat exchanger.

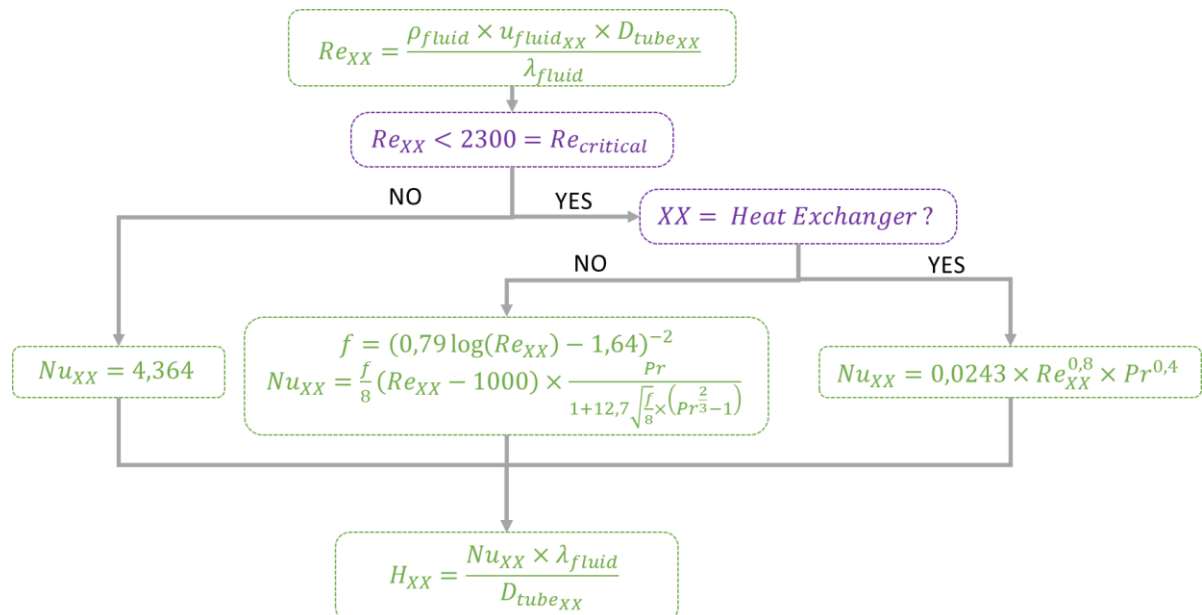


Fig. G-4: Fluid convection coefficient calculation process.

G.1.4 Computation of air convection coefficients.

G.1.4.1 Air gap.

Other processes are used for the air convection coefficients inside the electric motor housing:

Table G-8 : Prandtl and Taylor number in the air gap.

$$Pr_{air} = \frac{Cp_{air} \times \nu_{air}}{\lambda_{air}} \quad (G-26)$$

$$Ta = \Omega_{emot}^2 \times \left(\frac{L_{total_{emot}}}{2} \right)^3 \times \frac{R_{sleeveout}}{\nu_{air}^2} \quad (G-27)$$

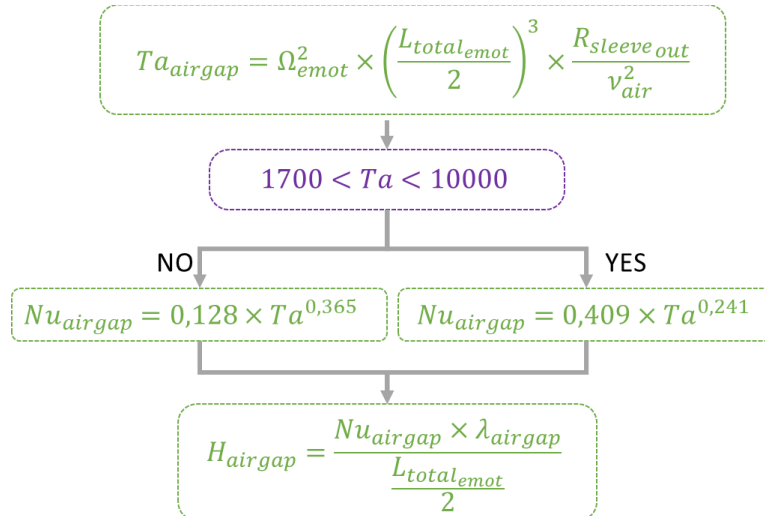


Fig. G-5: Air gap convection coefficient calculation process.

G.1.4.2 End-space frame.

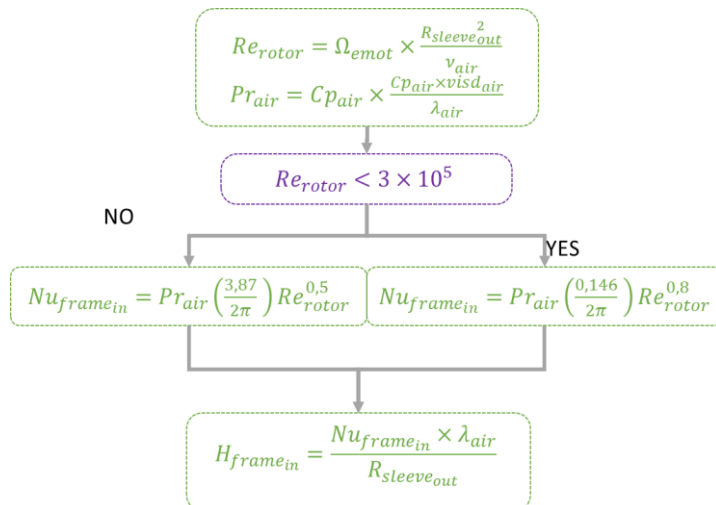


Fig. G-6: End-space frame convection coefficient calculation process

G.1.4.3 End-space rotor.

Table G-9: Prandtl and Nusselt number in the end-space rotor.

$$Re_{rotor} = \Omega_{emot} \times \frac{R_{sleeveOUT}^2}{\nu_{air}} \quad (G-28)$$

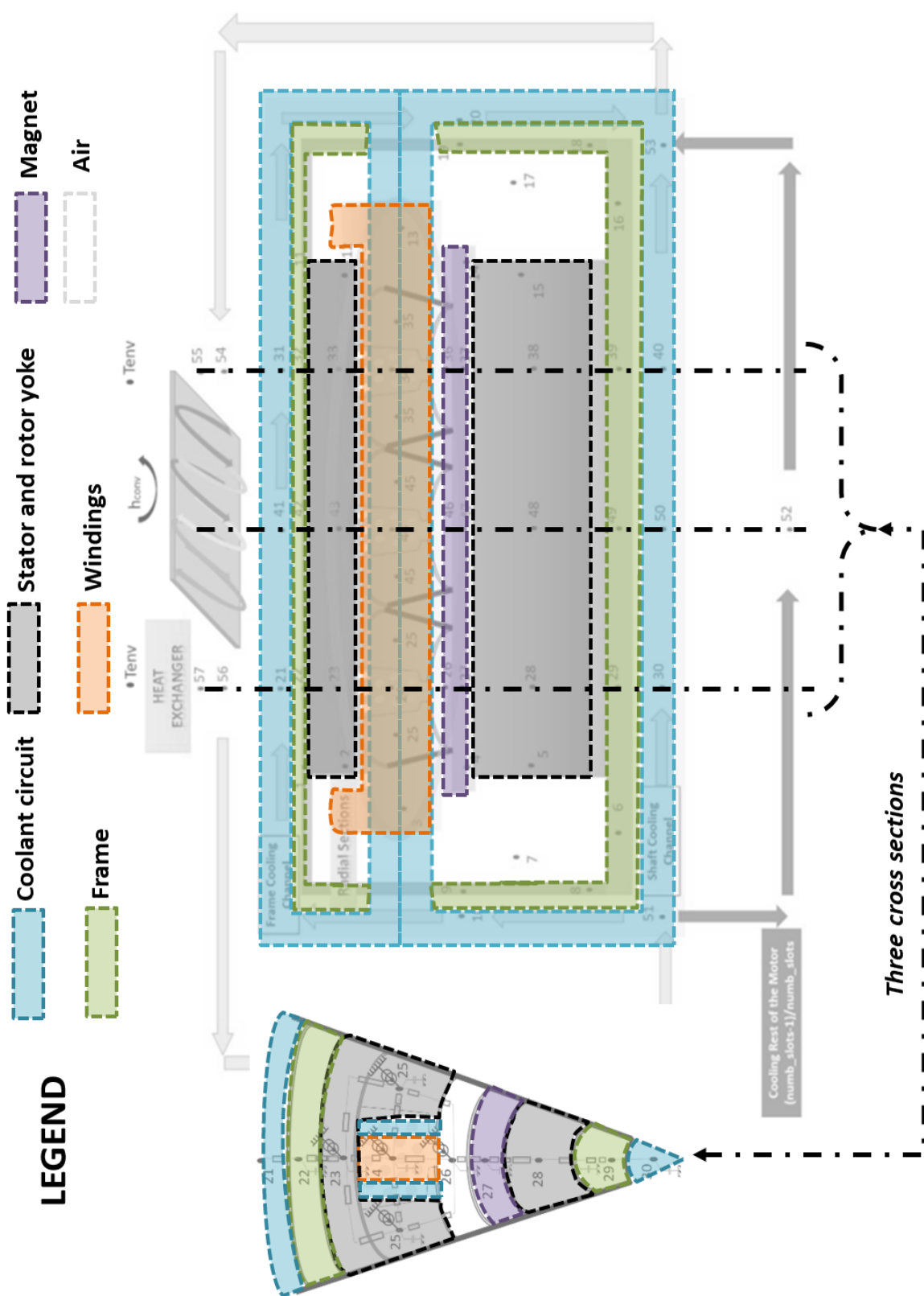
$$Nu_{rotor} = 0.00823 \times (L_{endspace})^{-1/6} \times Re_{rotor}^{0.75} \quad (G-29)$$

$$H_{end-space_{rotor}} = \frac{Nu_{rotor} \times \lambda_{air}}{R_{sleeveOUT}} \quad (G-30)$$

G.1.4.4 End-space windings.

Table G-10: Convection coefficient in the end-space windings.

$$H_{end-space_{windings}} = 110 \text{ W/(m}^2\text{.K)} \quad (G-31)$$



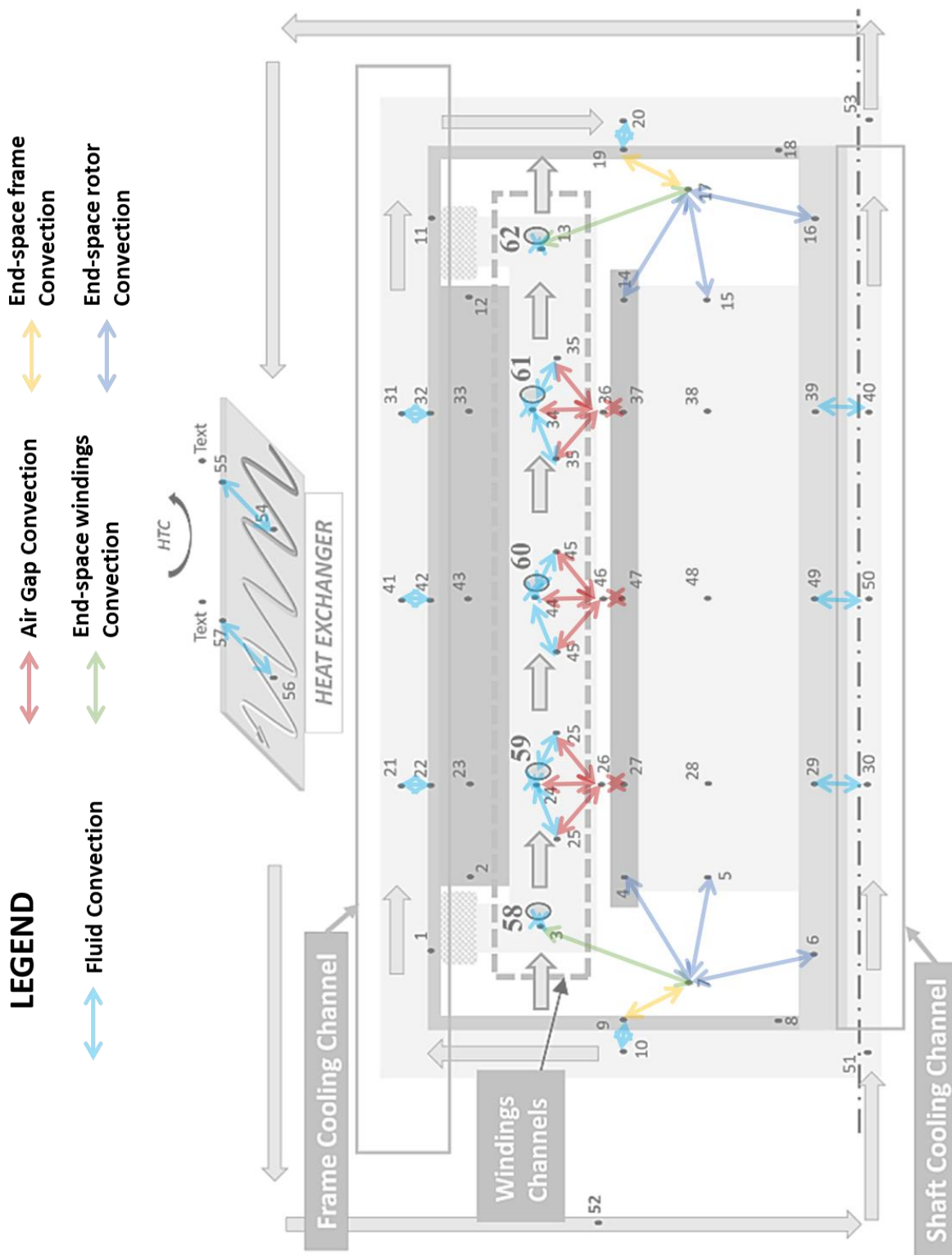


Fig. G-8: Lumped parameter thermal network detailed.

G.2 Lumped parameter thermal model.

The transient model is based on a lumped parameter thermal model Fig. G-7 and Fig. G-8. Solving the system equation in transient regime provides the temperature evolution during the flight mission considering the thermal capacity matrix G of the motor system, with respect to and any variation in input data such as the external temperature and to heat flow profile (motor losses profiles). The thermal balance equation is the following:

$$C \cdot \frac{dT}{dt} = GT + \Psi \quad (G-32)$$

Where C and G are $[n \times n]$ respectively the matrices representing capacity and conductance effects, and T and Ψ are the vectors $[n \times 1]$ representing temperatures and heat generation in a system. An implicit Euler method is used to solve Eq.(G-32).

Thermal conductance matrix G .

The Table G-11 gives the expressions of the thermal conductances for each heat transfer mode.

Table G-11: Flux and conductance expressions for each heat transfer mode.

Heat transfer mode	Conductance	Heat flow expression
Conduction (axial and ortho-radial)	$G_{\text{axial}}^{\text{cond}}(i,j) = \lambda \cdot \frac{S_{ij}}{L_{ij}}$	$G_{\text{axial}}^{\text{cond}}(i,j)(T_j - T_i)$
Conduction (radial)	$G_{\text{radial}}^{\text{cond}}(i,j) = \frac{2\pi\lambda h}{\ln\left(\frac{r_j}{r_i}\right)}$	$G_{\text{radial}}^{\text{cond}}(i,j)(T_j - T_i)$
Convection	$G_S^{\text{conv}}(i) = HS_i$	$G_S^{\text{conv}}(i)(T_f - T_i)$
Fluidic flow	$G^{\text{fluid}}(i,j) = \dot{m}C_p$	$G^{\text{fluid}}(i,j)(T_j - T_i)$

- S_{ij} is the surface of heat transfer between volumes represented by nodes i and j [m^2]
- S_i is the surface exposed to convection heat transfer [m^2]
- T_f is the average temperature of the fluid surrounding surface S_i [$^\circ C$]
- r_i, r_j are the radius of nodes i and j (with $r_j \geq r_i$) [m]
- L_{ij} is the distance between nodes i and j [m]
- h is the height of the cylindrical object [m]
- H is the heat transfer coefficient $\left[\frac{W}{m^2 \cdot K}\right]$
- \dot{m} is the mass flow rate [kg/s]
- λ is the thermal conductivity $\left[\frac{W}{m \cdot K}\right]$
- C_p is the thermal capacitance $\left[\frac{J}{kg \cdot K}\right]$

Once all coefficient calculations are made, the equation (G-32) can be calculated in order to find the temperature in each part of the electric motor.

G.3 Constraints.

The thermal constraints are usually the most sensitive with regard to the electrical machine sizing. Three were selected in the optimization process.

Table G-12: Performance constraints.

$T_{statoryoke} \leq T_{statoryokemax}$	Stator yoke temperature constraint [°C]	(G-35)
$T_{windings} \leq T_{windingsmax}$	Winding temperature constraint [°C]	(G-36)
$T_{magnet} \leq T_{magnetmax}$	Permanent magnet temperature constraint [°C]	(G-37)

Different values are chosen for the two (2025 and 2035) targets of the HASTECS project.

Table G-13: Differences between 2025 and 2035 targets.

TARGET	2025	2035
$T_{statoryokemax}$ [°C]	180	180
$T_{windingsmax}$ [°C]	180	180
$T_{magnetmax}$ [°C]	150	150

APPENDIX H. PARTIAL DISCHARGES IN THE SLOT

Table H-1: Input/output variables for the partial discharges model in the slot.

INPUT VARIABLES		
h_{slot}	[m]	Slot height
L_{slot}	[m]	Slot length
k_{fill}	[–]	Fill factor in the slot
N_{ce}	[–]	Number of conductors per slot
T_{wind}	[°C]	Maximum winding temperature
ALT_{CRS}	[m]	Cruise altitude
V_{uHVDC}	[V]	Ultra-high voltage direct current
$V_{emot_{rms}}$	[V]	RMS value of the e-motor voltage
t_{rise}	[s]	Switch rising time of the IGBT
OUTPUT VARIABLES		
e_{liner}	[m]	Liner thickness
$e_{insulation}$	[m]	Insulation thickness
R_{cu}	[m]	Copper radius of one wire
$n_{bturn_{cond}}$	[–]	Number of turns per conductor
$k_{remp_{real}}$	[–]	Real fill factor in the slot
$Flag_{pos_{windings}}$	[–]	Flag for the integration of the windings in the slot (1 = No, 0=Yes)

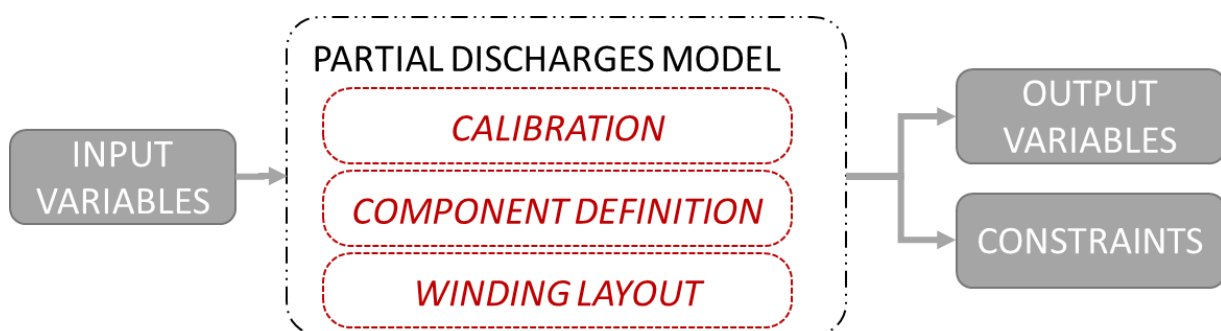


Fig. H-1: Process chart of the partial discharge model in the slot.

H.1 Calibration model.

The partial discharge model are studied in detail in [A8] and simplified (as presented in this Appendix) to face constraints of an optimization base system integration. Basics of partial discharges are based on the physic law of F. Paschen. In 1889, Friedrich Paschen investigated the breakdown of air located between two metallic plane electrodes. In order to take account of environment conditions in this model a calibration considering the temperature and the altitude has been implemented. An abacus permits us to anticipate the reduction of the Partial Discharge Inception Voltage (PDIV) with respect to the ground environmental conditions.

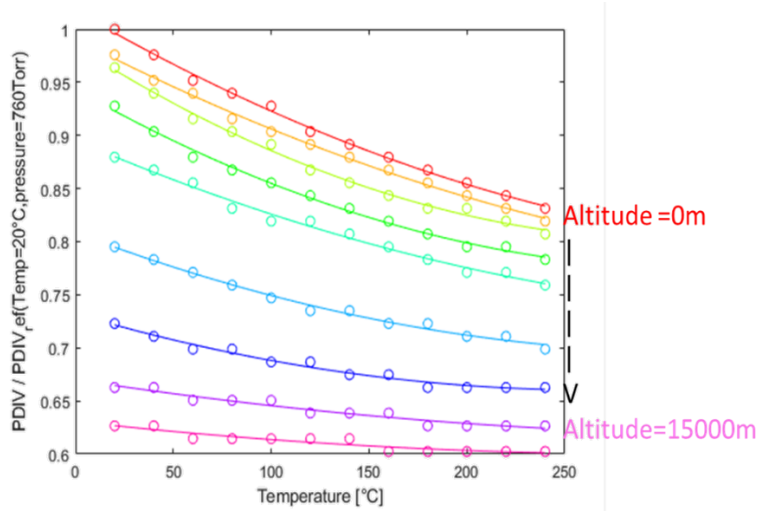


Fig. H-2: PASCHEN abacus: PDIV decrease for a combined variation of temperature and pressure.

The PDIV is maximum at normal temperature and pressure conditions (i.e.: 20 °C, 760 Torr), this maximum value is designated as $PDIV_{ref}$. Using the graph in Fig. H-2, the PDIV level between two enameled round wires in close contact for any point of the mission profile can be evaluated with respect to the actual environment. It is directly derived from $PDIV_{ref}$ obtained with a numerical model. It was assumed that the decrease of the PDIV level with temperature and pressure is the same, considering the turn/slot close contact. A limit winding temperature of $T_{wind_limit} = 180^\circ\text{C}$ and $ALT_{CRS} = 25\,000\text{ ft}$ - (cruise) altitude are used for the $PASCHEN_{abacus}$.

Table H-2: Calibration factor determined by the PASCHEN abacus.

$$\text{Factor} = PASCHEN_{abacus}(T_{wind_limit}, ALT_{CRS}) \quad \text{Calibration factor [-]} \quad (H-1)$$

H.2 Slot component definition model.

H.2.1 Wire definition model.

The maximum voltage seen by the turns is the one given by power electronics through the equation (H-2). An example of 5-level power electronics voltage waveforms is illustrated in the figure Fig. H-3:

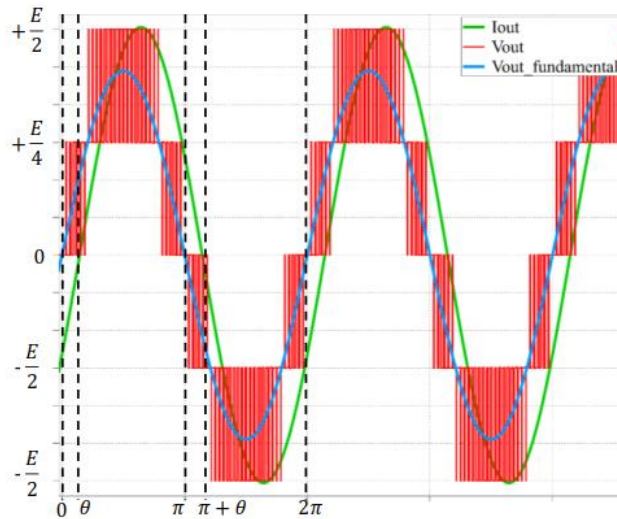


Fig. H-3: 5-level PE voltage and current curves.

The blue line represents the fundamental of the voltage, while the red one is the peak voltage values over two periods. The maximum voltage step (between two successive pulses) value has been taken into consideration for the PDIV value. For a 5-level the voltage step is $\frac{E}{4}$. For a 3-level converter, this step is doubled ($\frac{E}{2}$), E being here equivalent with the bus voltage (V_{uHVDC}).

Table H-3: Detailed wire definition model.

$V_{maxtransient} = \frac{V_{uHVDC}}{nb_{level}-1}$	Max transient voltage seen by the turns [V]	(H-2)
$PDIV_{windings_ref} = \frac{V_{maxtransient}}{\text{Factor}}$	Related PDIV value for enamel thickness estimation [V]	(H-3)

A simple analytical model has been implemented for determining the minimal enamel thickness avoiding partial discharges from the $PDIV_{ref}$ value find previously.

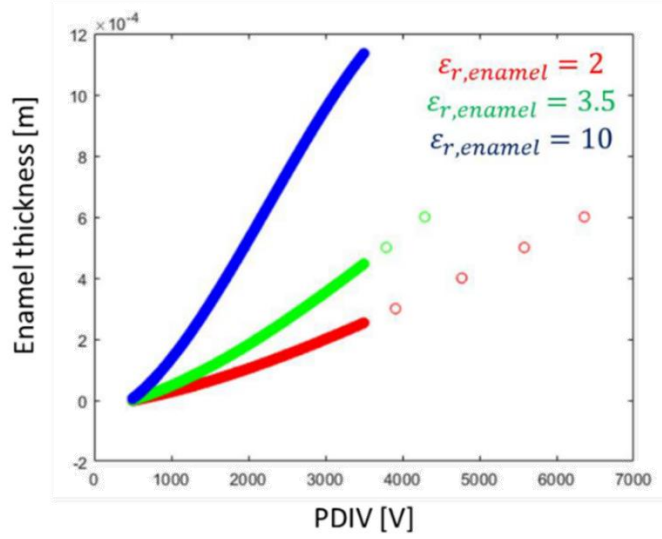


Fig. H-4: Enamel thickness as a function $PDIV_{windings_{ref}}$ ($T=20^\circ\text{C}$, $P = 760 \text{ Torr}$).

The required enamel thickness e was interpolated versus the PDIV domain using a 3rd order polynomial. The polynomial coefficients depend on the material dielectric constant ($\epsilon_{r,enamel}$). Thanks to a data sheet, correlations have been highlighted between the copper radius and its enamel thickness, they are illustrated in the next figure Fig. H-5:

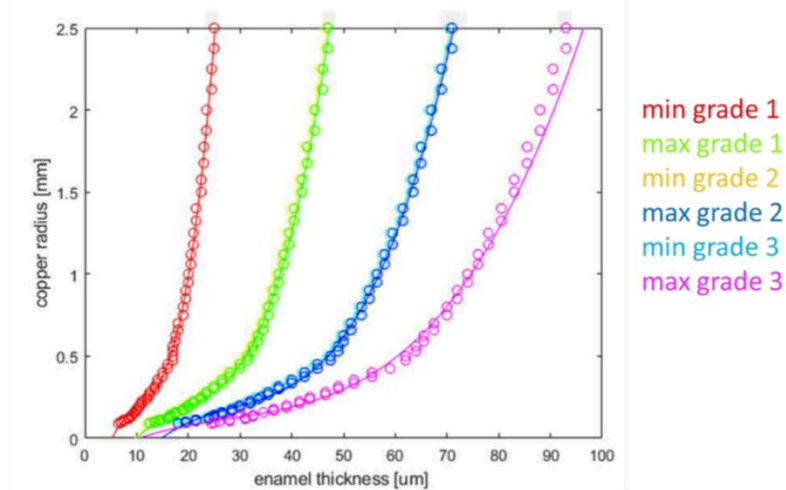


Fig. H-5: Copper radius versus enamel thickness for all grade tolerances ($T=20^\circ\text{C}$, $P = 760 \text{ Torr}$).

The Fig. H-5 displays the copper radius as a function of the enamel thickness given by the grade tolerance (min/max), 6 grade tolerances are available. Another 3rd order polynomial has been implemented for each grade tolerance.

H.2.2 Liner definition model.

The maximum voltage seen between the slot and the turn is the maximum voltage of the power electronic supplied electric motor.

Table H-4: Detailed liner definition model.

$V_{max,steady} = ma_{max} \times \frac{V_{u,HVDC}}{2}$	Max steady voltage seen by the yoke (for a classical PWM without over-modulation) [V]	(H-4)
$PDIV_{liner,ref} = \frac{V_{max,steady}}{\text{Factor}}$	Related PDIV value for liner thickness estimation [V]	(H-5)

The figure Fig. H-6 gives the slot liner thickness according to the enamel thickness of the windings and the material permittivity.

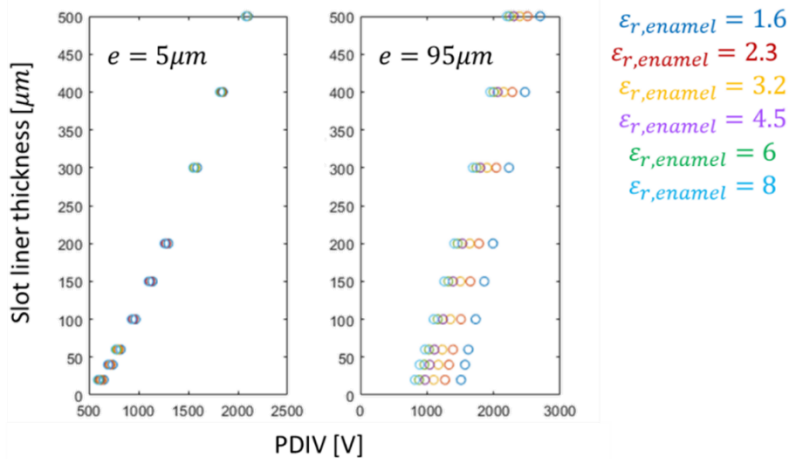


Fig. H-6: Slot liner thickness as a function of $PDIV_{liner,ref}$ and enamel thickness ($T=20^\circ C$, $P = 760$ Torr).

In that case a 2nd order polynomial has been set considering the enamel thickness and the permittivity of enamel and liner.

H.3 Winding layout model.

Once calculations are done, the slot can be filled by turns and the liner until reaching the right value of k_{fill} .

Table H-5: Detailed winding layout model.

$nb_{turn,cond} = \frac{\text{floor}\left(\frac{L_{slot} \times h_{slot} \times k_{fill}}{\pi \times R_{cu}^2}\right)}{Nce} + 1$	Number of turns per conductor [-]	(H-7)
$nb_{wires} = nb_{turn,cond} \times Nce$	Number of wires [-]	(H-8)
$k_{fill,real} = \frac{nb_{wires} \times \pi \times R_{cu}^2}{L_{slot} \times h_{slot}}$	Real value of fill factor [-]	(H-9)

Two colors are used here symbolizing two different conductors. In this example, three wires per conductor are considered.

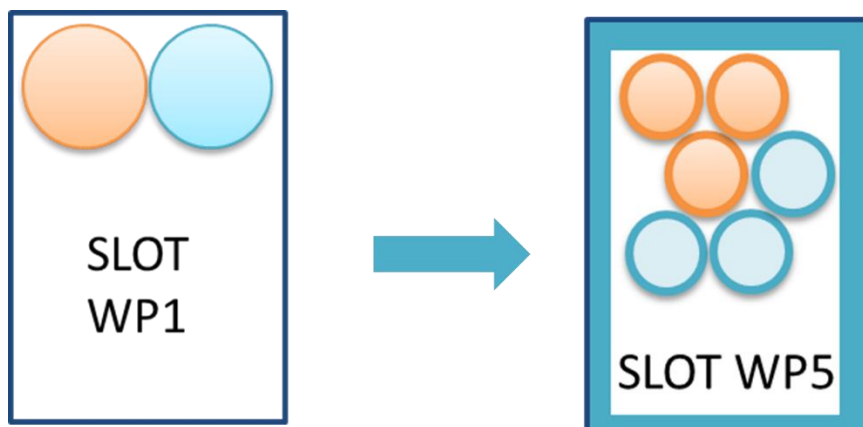


Fig. H-7: Example of winding layout.

The final process is displayed in
Fig. H-8:

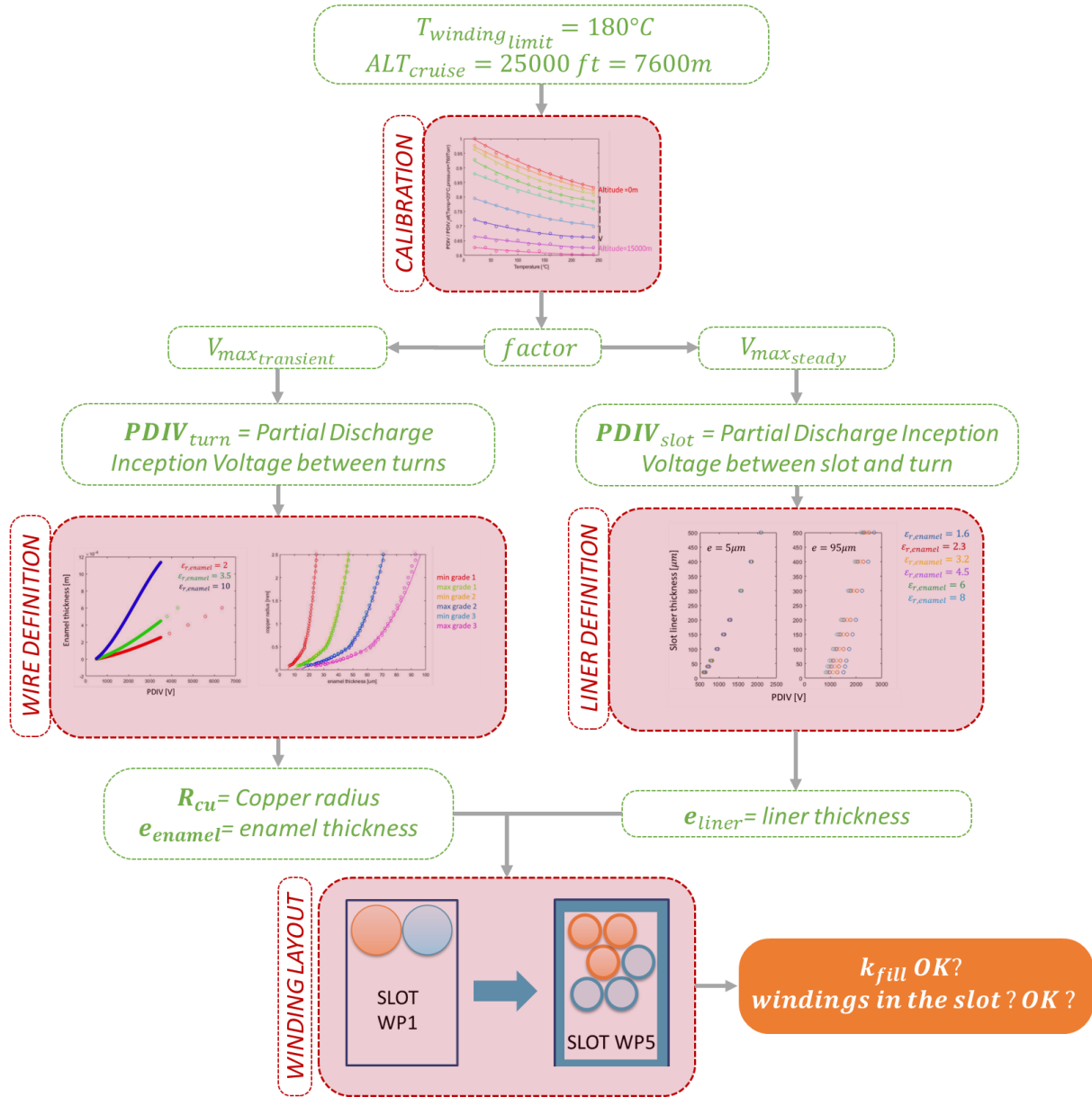


Fig. H-8: WP5 detailed process.

H.4 Constraints.

Two constraints are used in the optimization process:

Table H-6: Constraints.

$$k_{fill_{new}} - k_{fill_{ref}} \leq 1\% \times k_{fill_{ref}} \quad \text{Fill factor constraint [-]} \quad (H-10)$$

$$\text{Flag}_{pos_{windings}} \leq 0 \quad \text{Winding layout constraint [-]} \quad (H-11)$$

(Windings in the slot ? Yes = 0 , No = 1)

The first constraint ensures the proximity with the initial value of fill factor. And the second constraint certifies the integration of the winding in the slot.

APPENDIX I. POWER ELECTRONICS AND ITS COOLING

Table I-1: Input/output variables for the power electronics model.

INPUT VARIABLES		
$ma_{mission}(t)$	[–]	Modulation depth over mission
$FP_{mission}(t)$	[–]	Power factor over mission
$f_{elec_emot}(t)$	[Hz]	Electric frequency
nb_{phase}	[–]	Number of phases
COM	[–]	CONTROL of the Power Electronics (PE)
$TOPO$	[–]	Topology of the PE
I_{rating}	[A]	Current rating of IGBTs
V_{uHVDC}	[V]	Ultra-high direct current voltage
$P_{elec_{mission}}(t)$	[W]	Electric power over mission
OUTPUT VARIABLES		
$M_{cooling}$	[kg]	Cooling mass
$M_{inverter}$	[kg]	Inverter mass
$\eta_{inverter}(t)$	[%]	Inverter efficiency over mission
$P_{DC_{cable}mission}(t)$	[W]	Electric power required at the PE input

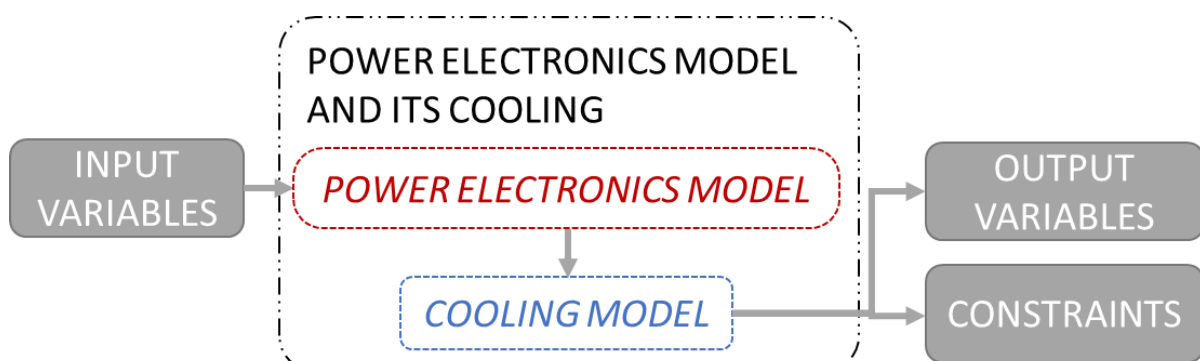


Fig. I-1: Process chart of the models.

I.1 Power Electronics model.

I.1.1 Semiconductor sizing model.

The design of power electronics for the HASTECS project was studied in [A9]. A simplification of this design is proposed here to face the constraints of optimization based system integration. In that context, a voltage based law has been implemented in this model in order to choose the right converter topology with respect to the bus voltage. The process defined in Fig. I-2 is related to the Fig. II-32 in CHAPTER II.

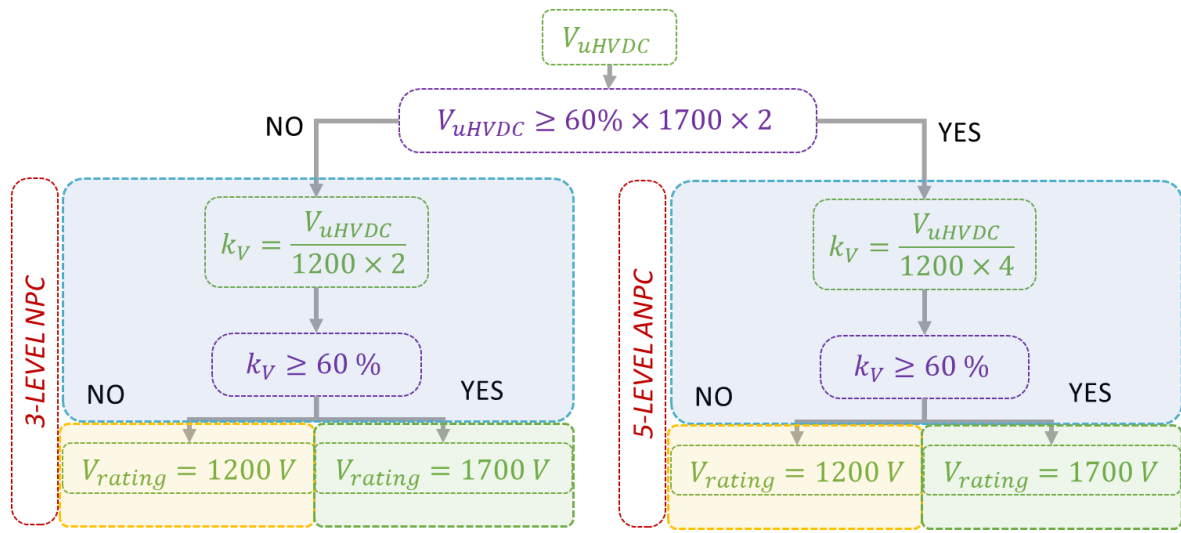


Fig. I-2: Topology and IGBT choice process.

k_V is the IGBT rate of use in voltage; the fixed value of 60% has been assessed by AIRBUS in order to avoid the cosmic radiations. In the previous process, the ultra-high DC voltage V_{uHVDC} firstly determines the topology of the converter: based on the [A9] study, only 3 and 5 multilevel structures have been selected for this system integration. The maximum permissible voltage in this case is given by the higher voltage rating (1700V) and the lower level topology (times 2 because of the 3-level topology).

Once the topology is determined, another rule allows choosing the right IGBT device. Both IGBTs (1200 and 1700V) have the same current rating $I_{rating} = 600 A$. A certain number of IGBTs are parallelized to fulfill motor current constraints depending on both the voltage and the converter structure. The inverter current and the electric frequency can be determined over the mission profile:

Table I-2: Current and electric frequency computation.

$I_{rmsmission} = \frac{(P_{elecmission} \times 2\sqrt{2})}{nb_{phases} \times V_{uHVDC} \times ma_{mission} \times FP_{mission}}$	RMS value of the current in the PE [A]	(I-1)
$f_{switch} = 7 \times f_{elecemot}$	Switching electric frequency [Hz]	(I-2)
$nb_{IGBTpar} = \text{floor} \left(\frac{\max(I_{rmsmission})}{I_{rating}} \right) + 1$	Number of semiconductor in parallel [-]	(I-3)

To avoid subharmonics and AC joule losses in the electric motor, a minimum ratio of 7 has been set between the switching frequency and the maximum electric motor frequency. According to the topology, this frequency is redefined.

Table I-3: Switching frequency seen by IGBT and definition of the number of semiconductors per phase.

TOPOLOGY	3-LEVEL NPC	5-LEVEL ANPC
Control name	DPWM/MAX	PWM
Number of semiconductors per phase.	$nb_{SC_{pp}} = 6$	$nb_{SC_{pp}} = 12$
Switching frequency seen by IGBTs	$f_{switch_{IGBT}} = f_{switch}$	$f_{switch_{IGBT}} = f_{switch} \times 2$

In the ANPC-topology there is two part: a switcher part and the 3-Level FC part, for the switcher part, 2 IGBT in series are considered. The Fig. II-31 shows the 5L-ANPC single phase inverter where there are 4 switches for the switcher part and 4 switches for the other part. Finally, 8 switches for the switcher (4×2) and 4 switches for the 3-level FC equals to 12.

I.1.2 Capacitor sizing model.

The capacitor values can be calculated from the stored energy as shown in the following equations. In both (3 and 5 level) structures, a DC bus capacitor has to be sized. In the 5 level (ANPC) case, an additional flying capacitor must also be sized. In order to choose the most appropriate component from the datasheet, the capacitor current is required:

Table I-4: Capacitor sizing model.

$$I_{capa_{rms}} = \sqrt{I_{rms}^2 - I_{avg}^2} \quad \text{RMS value of the capacitor current [A]} \quad (I-4)$$

$$C_{capa_{DC}} = \frac{I_{capa_{rms}}}{f_{switch_{IGBT}} \times \Delta V_{DC}} \quad \text{DC bus capacitor capacity [F]} \quad (I-5)$$

$$V_C = \frac{V_{uHVDC}}{2} \quad \text{Voltage value for the 5L-ANPC converter topology} \quad (I-6)$$

$$C_{capa_{FY}} = \frac{I_{out_{max}}}{\Delta V_{C_{FY}} \times V_C \times f_{emot}} \quad \text{Flying capacitor capacity for 5L ANPC converter [F]} \quad (I-7)$$

In this case, we have set certain quality constraints for voltages: $\Delta V_{DC} = 5\%$ and the $\Delta V_{C_{FY}} = 10\%$. The current and the capacity of the capacitor allow choosing a component in the database; its mass is directly extracted from the catalogue.

I.1.3 Loss model.

In order to estimate the efficiency of the power converter, several assumptions have been made:

- The output current is sine
- Steady state is considered

Two kinds of losses are integrated in the model: the conduction and the switching losses.

Table I-5: Conduction and switching losses description.

$P_{cond_{IGBT}} = \frac{1}{T_{mod}} \int V_{ce}(t) \times I_c(t) dt$	IGBT conduction losses [W]	(I-8)
$P_{cond_{Diode}} = \frac{1}{T_{mod}} \int V_d(t) \times I_d(t) dt$	Diode conduction losses [W]	(I-9)
$E_X(I) = A_X + B_X \times I + C_X \times I^2$	Energy losses for the X component (X: IGBT/Diode) [J]	(I-10)
$P_{sw} = \frac{f_{sw}}{T_{mod}} \int \frac{V_{sw}}{V_{def}} E_X(I) dt$	Switching losses [W]	(I-11)

A_X, B_X, C_X are the 2nd order polynomial coefficients which approximate the curve in the datasheet. $E_{v_{def}}$ is the energy losses of the component, V_{def} and V_{sw} are respectively the half component voltage and the switched voltage of the semiconductor. f_{sw} is the switching frequency and T_{mod} is the modulation period.

I.1.4 Mass and efficiency.

Table I-6: Mass table.

$M_{SC} = nb_{phase} \times nb_{SC_{pp}} \times m_{1device} \times \left(\text{floor} \left(\frac{nb_{IGBTpar}}{2} \right) + 1 \right)$	SC mass [kg]	(I-12)
$M_{PE} = M_{SC} + M_{capa_{DC}} + M_{capa_{FY}}$	PE mass [kg]	(I-13)

Where $m_{1device}$ is the mass of one electronic component and nb_{phase} is the number of phases. The DC capacitor mass $M_{capa_{DC}}$ and the flying capacitor mass $M_{capa_{FY}}$ are taken from the database.

Table I-7: Efficiency table.

$\eta_{invertermission} = \frac{P_{mission}}{P_{sw} + P_{cond} + P_{mission}}$	Efficiency [%]	(I-14)
--	----------------	--------

I.2 Cooling model.

The thermal analysis integrates a heat source (losses) as inputs and temperature at different nodes as outputs and is based on thermal resistors depending on the thermal conductivity and chip sizes.

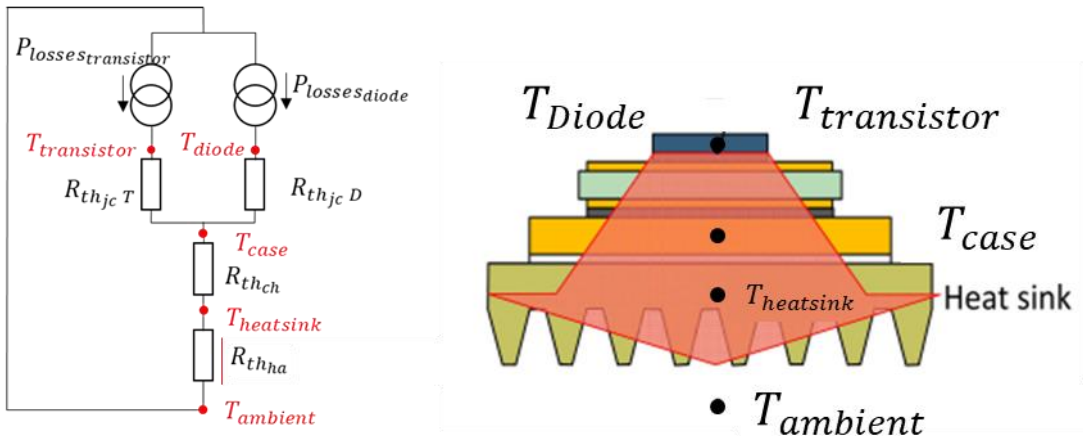


Fig. I-3: Representation the equivalent thermal model of a single module.

Table I-8: Thermal equations related to the Fig. I-3.

$$T_{transistor} = P_{losses_{transistor}} \times R_{th_{jc_T}} + T_{case} \quad \text{Transistor temperature } [{}^\circ\text{C}] \quad (\text{I-15})$$

$$T_{diode} = P_{losses_{diode}} \times R_{th_{jc_D}} + T_{case} \quad \text{Diode temperature } [{}^\circ\text{C}] \quad (\text{I-16})$$

$$T_{case} = (P_{losses_{diode}} + P_{losses_{transistor}}) \times R_{th_{ch}} + T_{heatsink} \quad \text{Case temperature } [{}^\circ\text{C}] \quad (\text{I-17})$$

Where $R_{th_{jc_T}}$, $R_{th_{jc_D}}$ are the junction to case thermal resistance (T = Transistor, D = Diode), and $R_{th_{ch}}$ is the case to heatsink thermal resistance. The equation for the heat sink temperature has not been considered because the work package in charge of the cooling system imposes the thermal resistance $R_{th_{ha}}$ in order to set the heat sink temperature to 70°C [A10]. The new equivalent thermal model is detailed in the Fig. I-4:

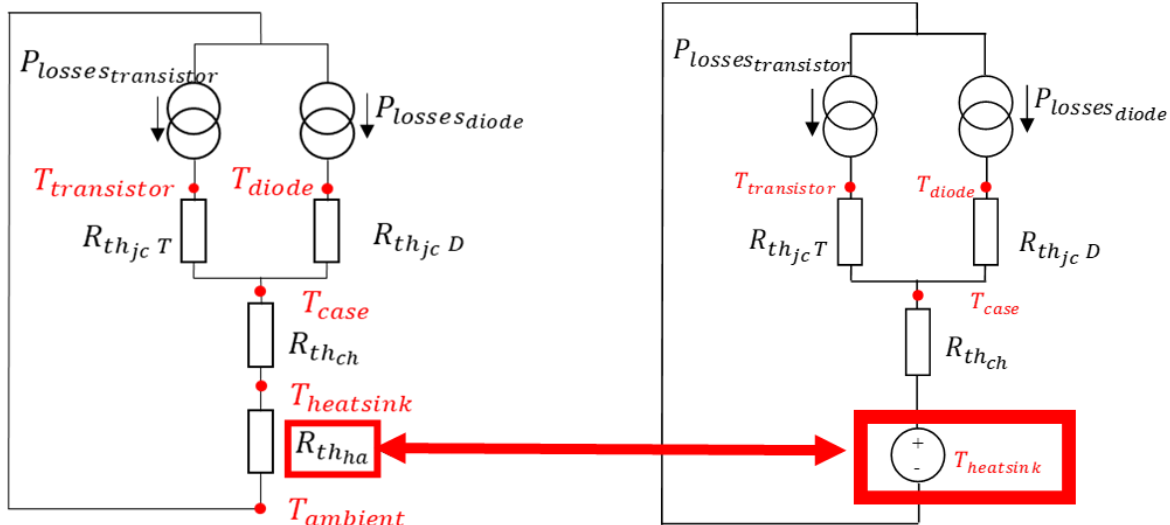


Fig. I-4: New equivalent thermal model for the power electronics.

Based on the detailed study of [A10], the cooling mass estimation has been totally simplified and integrated in the power electronics model. A surrogate model has been built by the work package in charge of the PE cooling system. Two linear curves function of the total losses over the mission $P_{tot_mission}$ estimate the cooling system mass.

Table I-9: Cooling system mass linear function.

$$P_{tot_max} = \max(P_{sw_mission} + P_{cond_mission}) \quad \text{Total losses [W]} \quad (I-18)$$

$$M_{cooling} = a_{cool} \times P_{tot_max} + b_{cool} \quad \text{Cooling system mass estimation [kg]} \quad (I-19)$$

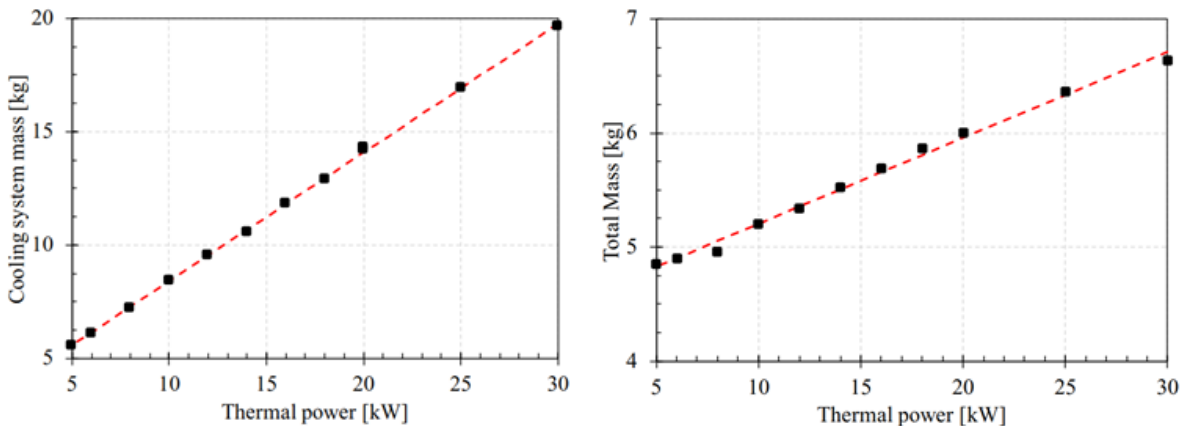


Fig. I-5: Cooling system mass estimation (LEFT: 2025 TARGET and RIGHT: 2035 TARGET).

All parameters are summarized in the Table I-10 below:

Table I-10: Differences between 2025 and 2035 targets

TARGET	2025	2035
a_{cool} [-]	0.5681	0.0692
b_{cool} [-]	2.7323	2.674

In order to integrate the bus bar mass into the total mass for power converter and its cooling, an integration factor $\left(\frac{1}{3}\right)$ has been assessed. Finally, the whole mass can be estimated:

Table I-11: Total inverter mass.

$$M_{busbar} = \frac{1}{3} \times (M_{PE} + M_{cooling}) \quad \text{DC bus bar mass estimation [kg]} \quad (I-20)$$

$$M_{total_{inverter}} = M_{PE} + M_{cooling} + M_{busbar} \quad \text{Total PE mass [kg]} \quad (I-21)$$

APPENDIX J. FUEL CELL SYSTEM AND BATTERY MODEL

Table J-1: Input/output variables for the fuel cell and the battery.

INPUT VARIABLES		
MISSION		
$P_{elec_{mission}}$	[W]	Electric source power over mission
$P_{elec_{sizing}}$	[W]	Electric source power sizing point
FUEL CELL		
$P_{SPE_{stack}}$	[kW/kg]	Stack specific power
$P_{SPE_{aux}}$	[kW/kg]	Auxiliary specific power
$\eta_{FC_{stack}}$	[%]	Stack efficiency
$\eta_{FC_{system}}$	[%]	System efficiency
$comp_{H2_{gaz}}$	[%]	Compression ratio ¹ @700 bar compressed H2
$comp_{H2_{liquid}}$	[%]	Compression ratio ¹ @20K liquid H2
BATTERY		
E_{XX}	[kWh/kg]	Cell specific energy of the cell
$C_{rate_{XX}}$	[h ⁻¹]	Cell C-rate of the cell
f_{sys}	[−]	Integration factor (cell -> system)
OUTPUT VARIABLES		
$M_{fuel\ cell}$	[kg]	Fuel cell mass
$M_{H2_{storage}}$	[kg]	H2 storage mass
$M_{battery}$	[kg]	Battery mass
$M_{electric\ soruce}$	[kg]	Electric source mass

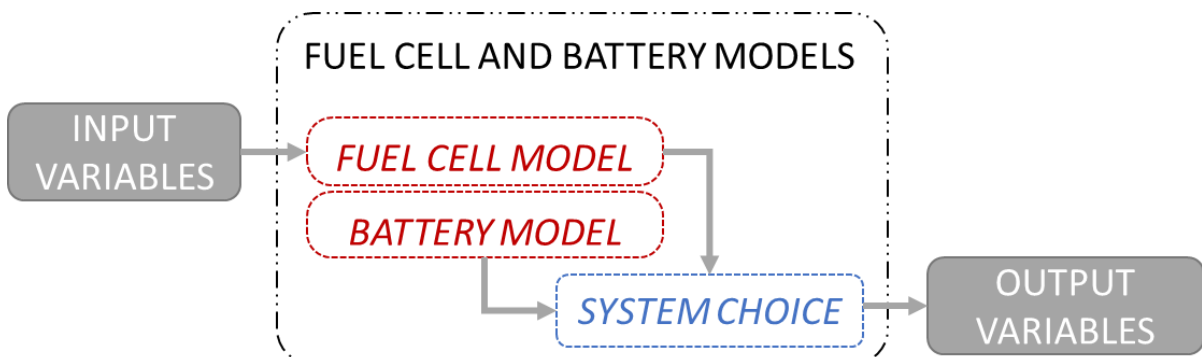


Fig. J-1: Process chart of the electric source model.

¹ Set the mass percentage of H2 versus the whole storage

A strongly simplified assessment model is proposed here based on the detailed study of [A11]. The assumptions in terms of specific power, specific energy and c-rate have been presented in chapter II in the Table II-1 and the Table II-2. Once these coefficients are known, the masses of the fuel cell system and of the battery pack system can be evaluated from [A11].

J.1 Fuel cell model.

Table J-2: Fuel cell system mass estimation.

$M_{FC\ stack} = \frac{\max(P_{elec\ sizing})}{P_{spe\ FC\ stack}} \times \frac{\eta_{FC\ stack}}{\eta_{FC\ system}}$	Fuel cell stack mass [kg]	(J-1)
$M_{FC\ aux} = \frac{\max(P_{elec\ sizing})}{P_{spe\ FC\ aux}} \times \frac{\eta_{FC\ stack}}{\eta_{FC\ system}}$	Auxiliary mass [kg]	(J-2)
$E_{FC\ mission} = \int^t \frac{P_{elec\ mission}(t)}{\eta_{FC\ system}(t)} dt$	Hydrogen energy required [kWh]	(J-3)
$m_{H2\ gaz} = \frac{\max(E_{FC\ mission})}{E_{SPE\ H2} \times comp_{H2\ gaz}}$	Mass of storage with gaseous hydrogen [kg]	(J-4)
$m_{H2\ liquid} = \frac{\max(E_{FC\ mission})}{E_{SPE\ H2} \times comp_{H2\ liquid}}$	Mass of storage with liquid hydrogen [kg]	(J-5)

An oversizing of the fuel cell is mandatory in order to take account of the power to be supplied to auxiliaries. This oversizing is modeled by the ratio between these two efficiencies in the fuel cell system mass estimation. The following figure (Fig. J-2) represents both efficiency according the net power per unit.

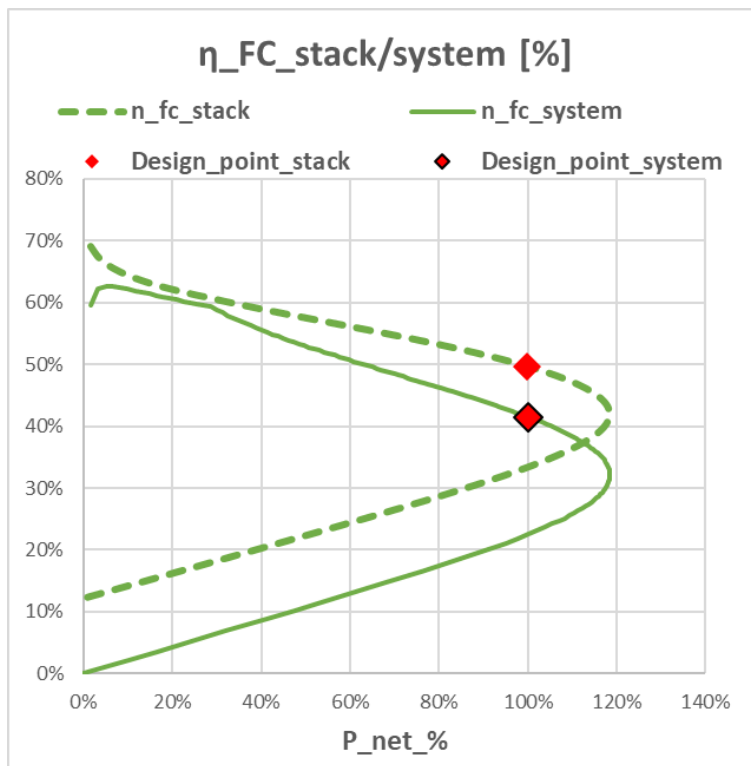


Fig. J-2: Stack/system efficiencies versus the net power to supply per unit.

A linear regression has been implemented for the efficiency estimation during the fuel cell mission. Green points here represent the linear function Fig. J-3.

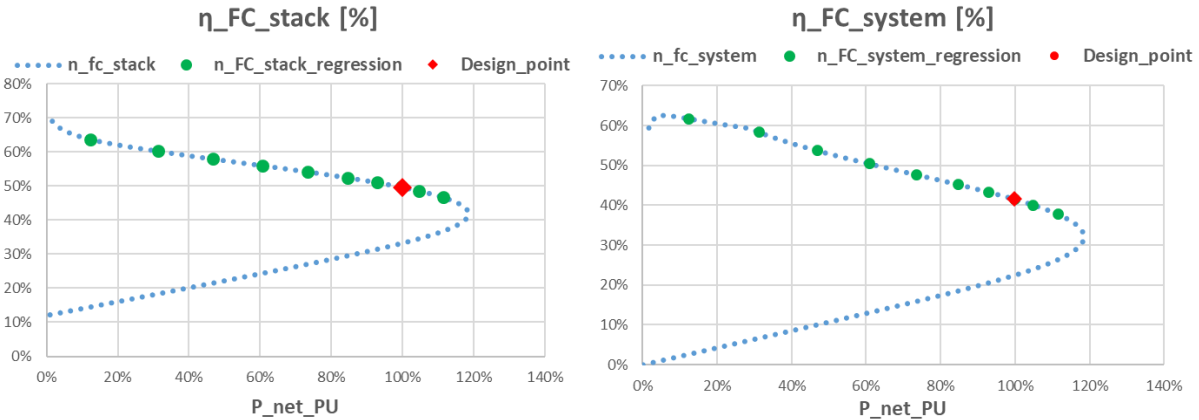


Fig. J-3: Stack and system efficiencies.

Table J-3: Linear function of the fuel cell efficiencies.

$$\eta_{FC_{stack}}(t) = \alpha_{FC_{stack}} \times P_{FC_{PU}}(t) + \beta_{FC_{stack}} \quad \text{Fuel cell stack efficiency [%]} \quad (J-6)$$

$$\eta_{FC_{system}}(t) = \alpha_{FC_{system}} \times P_{FC_{PU}}(t) + \beta_{FC_{system}} \quad \text{Fuel cell system efficiency [%]} \quad (J-7)$$

J.2 Battery model.

The mass estimation model for the battery is depending on the technology considered. In this study, three cells have been considered : *LTO – NTO/NMC/LiS*, all parameters are displayed in the Table II-2. Two equations are implemented in this surrogate model: an energy and a power sizing equation:

Table J-4: Mass estimation considering the discharge energy and the C-rate (Power).

$$E_{BATT_{mission}} = \int^t P_{elec_{mission}}(t) dt \quad \text{Energy required [kWh]} \quad (J-8)$$

$$m_{batt_E} = \frac{\max(E_{BATT_{mission}})}{E_{SPE}} \quad \text{Cell mass estimation considering the energy [kg]} \quad (J-9)$$

$$m_{batt_P} = \frac{\max(P_{elec_{mission}})}{E_{SPE} \times C_{rate}} \quad \text{Cell mass estimation considering the power and the C-rate [kg]} \quad (J-10)$$

$$m_{batt} = \max(m_{batt_E}; m_{batt_P}) \times f_m \quad \text{System mass estimation [kg]} \quad (J-11)$$

J.3 Auxiliary electrical power source choice.

To simplify the study, the lightest system between battery and fuel cell will be taken into account in the calculation of the powertrain mass.

APPENDIX K. RECTIFIER AND GENERATOR EFFICIENCY AND WEIGHT ASSESSMENTS

Table K-1: Input/output variables for the rectifier and the e-generator.

INPUT VARIABLES		
$P_{elecGTmission}$	[W]	Electric power mission for the turboshaft
$P_{SPErectifier}$	[kW/kg]	Rectifier specific power
$P_{SPEgenerator}$	[kW/kg]	E-generator specific power
$\eta_{rectifier}$	[%]	Rectifier efficiency
$\eta_{generator}$	[%]	E-generator efficiency
OUTPUT VARIABLES		
$P_{mechGTmission}$	[W]	Mechanical Power of the turboshaft
$M_{rectifier}$	[kg]	Rectifier mass
$M_{e-generator}$	[kg]	E-generator mass

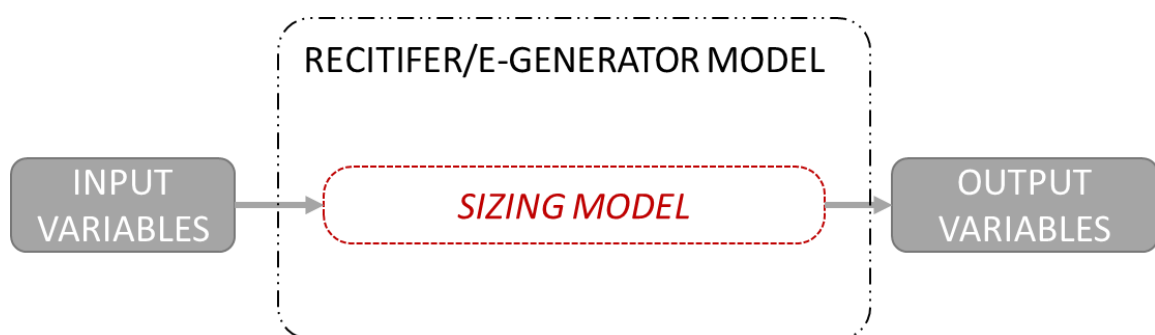


Fig. K-1: Process chart for the rectifier/e-generator model.

K.1 Sizing model.

For these components, simple assessment models have been set simply based on specific power and fixed efficiency. The HASTECS targets are used for assessing the rectifier and electric generator masses.

Table K-2: Assumptions for the electric device fed by the turboshaft.

	2025 TARGET	2035 TARGET
Electric generator specific power	5 kW/kg	10 kW/kg
Electric generator efficiency	96%	98.5%
Rectifier specific power	15 kW/kg	25 kW/kg
Rectifier efficiency	98%	99.5%

With these assumptions the mass estimation is simply:

Table K-3: Mass and power estimation for the rectifier and the e-generator.

$m_{rectifier} = P_{elecRectifier} \times P_{SPE_{rectifier}}$	Rectifier mass [kg]	(K-1)
$m_{e-generator} = P_{elecGT} \times \frac{P_{SPE_{e-generator}}}{\eta_{rectifier}}$	E-generator mass [kg]	(K-2)
$P_{mech_{GT_mission}} = \frac{P_{elecRectifier}}{\eta_{rectifier} \times \eta_{e-generator}}$	Mechanical power of the turboshaft	(K-3)

APPENDIX L. MULTIDISCIPLINARY DESIGN OPTIMIZATION PROCESS OF A HYBRID ELECTRIC AIRCRAFT PROPULSION SYSTEM

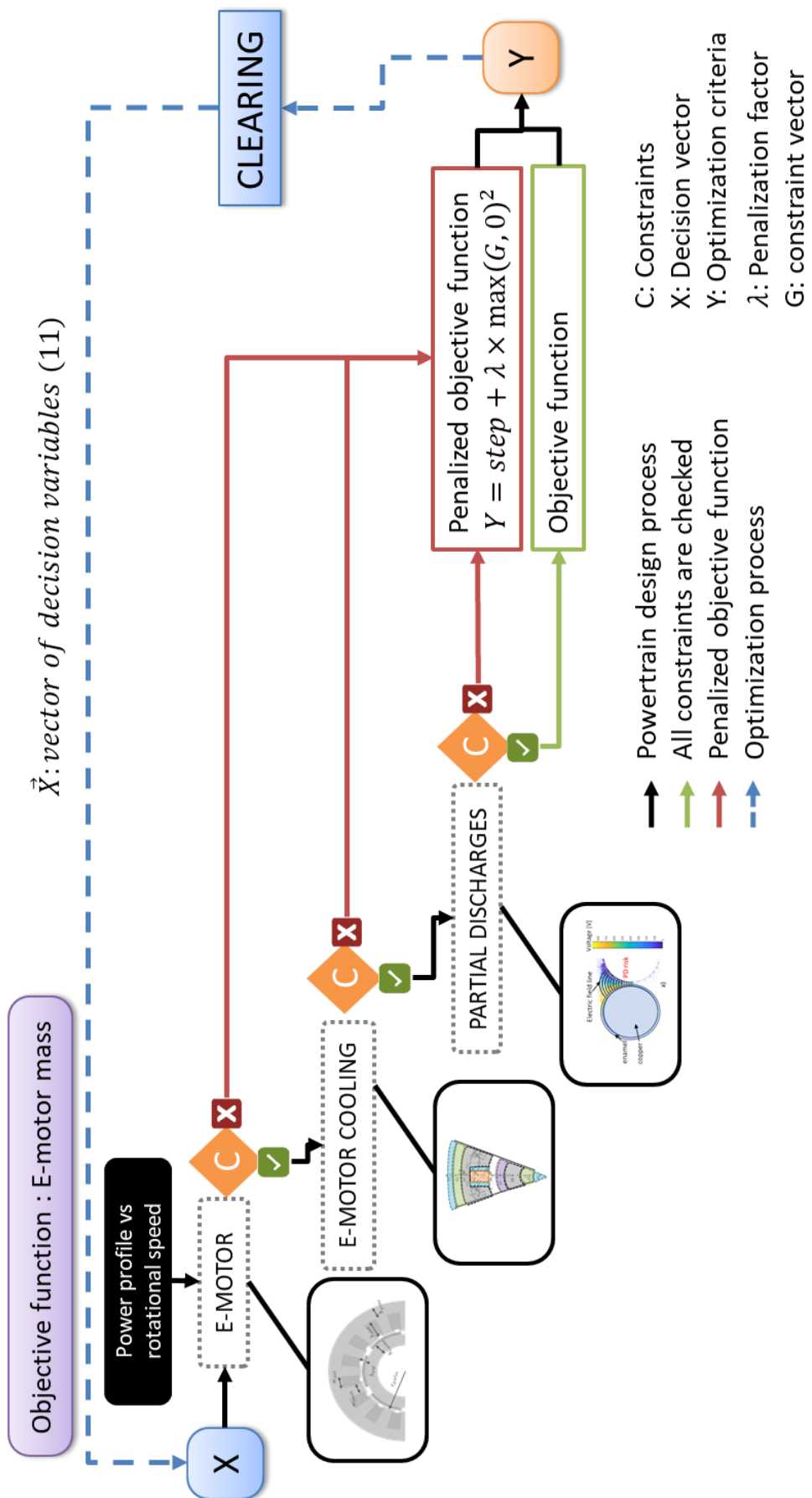


Fig. L-1: Weight optimization process for electric motor.

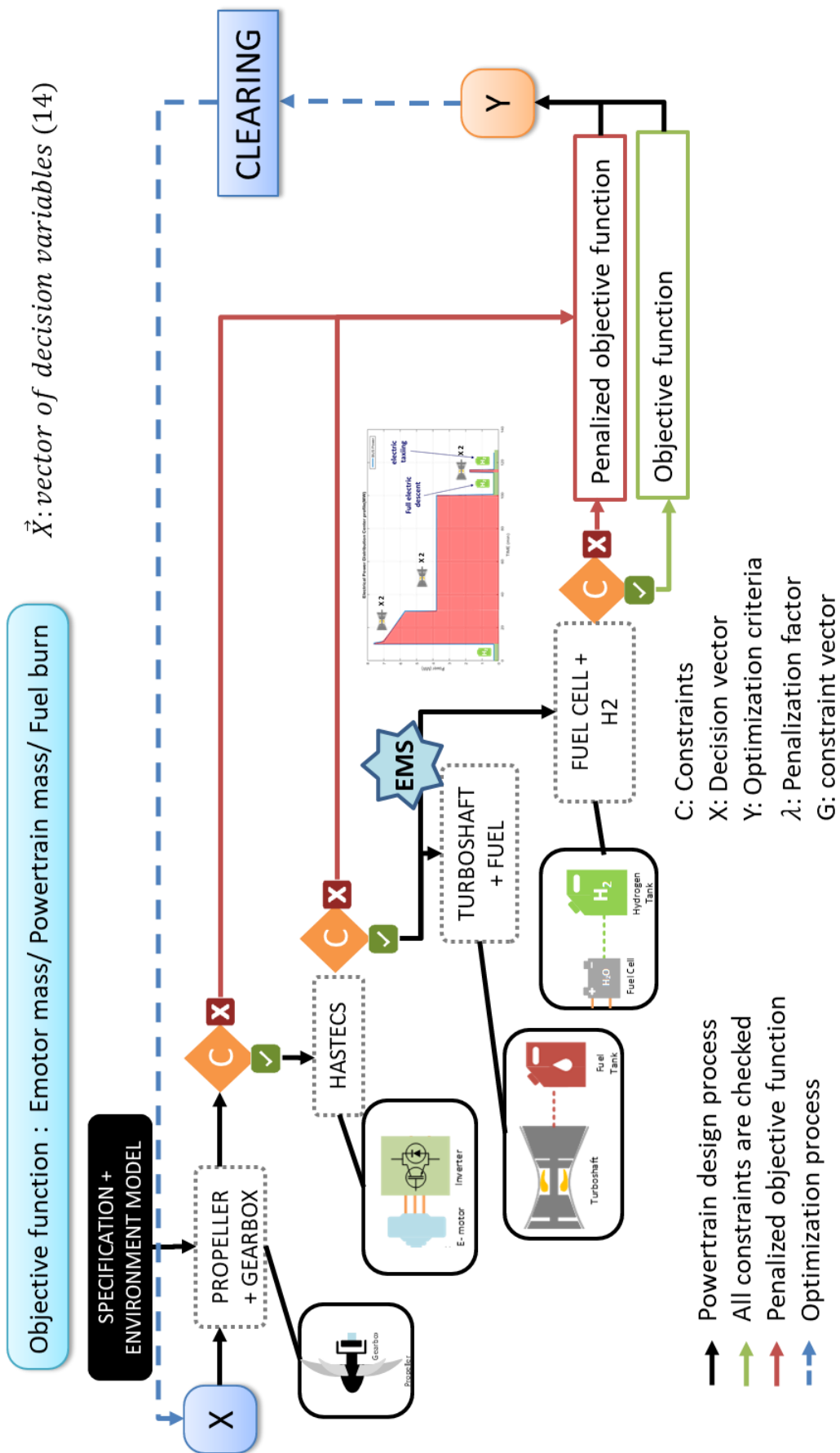


Fig. L-2: Integrated optimal design process of a hybrid electric powertrain.

